CODEN: JASMAN

The Journal of the Acoustical Society of America

ISSN: 0001-4966

Vol. 124, No. 6 December 2008

ACOUSTICAL NEWS-USA 3351

USA Meeting Calendar 3355

ACOUSTICAL NEWS-INTERNATIONAL 3357

International Meeting Calendar 3357

ADVANCED-DEGREE DISSERTATION ABSTRACTS 3359

REVIEWS OF ACOUSTICAL PATENTS 3361

LETTERS TO THE EDITOR

Shear elasticity estimation from surface wave: The time reversal approach (L) — J. Brum, S. Catheline, N. Benech, C. Negreira — 3377

Comment on "Linear and nonlinear frequency shifts in acoustical resonators with varying cross sections" [J. Acoust. Soc. Am. 110, 109–119 (2001)] (L) — Michael P. Mortell, Brian R. Seymour — 3381

Reply to "Comment on 'Linear and nonlinear frequency shifts in acoustical resonators with varying cross sections' [J. Acoust. Soc. Am. 110, 109–119 (2001)]" (L) — Mark F. Hamilton, Yurii A. Ilinskii, Evgenia A. Zabolotskaya — 3386

GENERAL LINEAR ACOUSTICS [20]

A new method to generate an almost-diagonal matrix in the boundary integral equation formulation — B. Chandrasekhar, Sadasiva M. Rao — 3390

NONLINEAR ACOUSTICS [25]

Nonlinear modulation of Lamb modes by clapping delamination — G. Shkerdin, C. Glorieux — 3397

Infrasound induced instability by modulation of condensation process in the atmosphere — Konstantin Naugolnykh, Samuil Rybak — 3410

AEROACOUSTICS, ATMOSPHERIC SOUND [28]

Source localization from an elevated acoustic sensor array in a refractive atmosphere — Vladimir E. Ostashev, Michael V. Scanlon, D. Keith Wilson, Sergey N. Vecherin — 3413

Correction techniques for the truncation of the source field in acoustic analogies — Paula Martínez-Lera, Christophe Schram — 3421

UNDERWATER SOUND [30]

The structure of raylike arrivals in a shallow-water waveguide — Philippe Roux, Bruce D. Cornuelle, W. A. Kuperman, W. S. Hodgkiss — 3430

Measuring the target strength spectra of fish using dolphin-like short broadband sonar signals — Tomohito Imaizumi, Masahiko Furusawa, Tomonari Akamatsu, Yasushi Nishimori — 3440

The acoustic excitation of air bubbles fragmenting in sheared flow — Grant B. Deane, M. Dale Stokes — 3450

Effects of shear waves on boundary-coupled vector sensors — Kevin B. Smith — 3464

(Continued)

CONTENTS—*Continued from preceding page*

ULTRASONICS, QUANTUM ACOUSTICS, AND PHYSICAL EFFECTS OF SOUND [35]

Simulations of photoacoustic wave propagation using a finite-difference time-domain method with Berenger's perfectly matched layers — Yae-Lin Sheu, Pai-Chi Li — 3471

High-resolution ultrasonic thermometer for radiation dosimetry — Eugene V. Malyarenko, Joseph S. Heyman, H. Heather Chen-Mayer, Ronald E. Tosh — 3481

Finite element modeling of the temperature rise due to the propagation of ultrasonic waves in viscoelastic materials and experimental validation — B. Hosten, C. Bacon, C. Biateau — 3491

TRANSDUCTION [38]

Personal audio with multiple dark zones — Matthew Jones, Stephen J. Elliott — 3497

STRUCTURAL ACOUSTICS AND VIBRATION [40]

Diffusion regime for high-frequency vibrations of randomly heterogeneous structures — Éric Savin — 3507

Modeling a surface-mounted Lamb wave emission-reception system: Applications to structural health monitoring — Emmanuel Moulin, Sébastien Grondel, Jamal Assaad, Laurent Duquenne — 3521

Anderson localization of ultrasound in plates: Further experimental results — Oleg I. Lobkis, Richard L. Weaver — 3528

NOISE: ITS EFFECTS AND CONTROL [50]

Effect of internal resistance of a Helmholtz resonator on acoustic energy reduction in enclosures — Ganghua Yu, Deyu Li, Li Cheng — 3534

A logistic prediction model for individual allowable noise levels — Kenji Furihata — 3544

Evaluating roadside noise barriers using an annoyance-reduction criterion — Mats E. Nilsson, Mikael Andéhn, Paulina Leśna — 3561

Variations of road traffic noise in residential areas — Rufin Makarewicz, Maciej Żółtowski — 3568

ARCHITECTURAL ACOUSTICS [55]

Estimates and bounds of dynamic permeability of granular media — Claude Boutin, Christian Geindreau — 3576

Sound transmission through a microperforated-panel structure with subdivided air cavities — Masahiro Toyoda, Daiji Takahashi — 3594

Vibroacoustic behavior of clamp mounted double-panel partition with enclosure air cavity — F. X. Xin, T. J. Lu, C. Q. Chen — 3604

ACOUSTICAL MEASUREMENTS AND INSTRUMENTATION [58]

Speed of sound in bubble-free ice — Christian Vogt, Karim Laihem, Christopher Wiebusch — 3613

ACOUSTIC SIGNAL PROCESSING [60]

Sonar signal processing using probabilistic signal and ocean environmental models — R. Lee Culver, H. John Camin — 3619

Low probability of detection underwater acoustic communications using direct-sequence spread spectrum — T. C. Yang, Wen-Bin Yang — 3632

Moving microphone arrays to reduce spatial aliasing in the beamforming technique: Theoretical background and numerical investigation — Alfredo Cigada, Massimiliano Lurati, Francesco Ripamonti, Marcello Vanali — 3648

The time-reversal operator with virtual transducers: Application to far-field aberration correction — Jean-Luc Robert, Mathias Fink — 3659

Speech enhancement in discontinuous transmission systems using the constrained-stability least-mean-squares algorithm — J. M. Górriz, J. Ramírez, S. Cruces-Álvarez, D. Erdogmus, C. G. Puntonet, E. W. Lang — 3669

Fast volumetric integral-equation solver for high-contrast acoustics — E. Bleszynski, M. Bleszynski, T. Jaroszewicz — 3684

(Continued)

CONTENTS—*Continued from preceding page*

PHYSIOLOGICAL ACOUSTICS [64]

Source of level dependent minima in rabbit distortion product otoacoustic emissions — P. F. Fahey, B. B. Stagner, G. K. Martin — 3694

Wideband absorbance tympanometry using pressure sweeps: System development and results on adults with normal hearing — Yi-Wen Liu, Chris A. Sanford, John C. Ellison, Denis F. Fitzpatrick, Michael P. Gorga, Douglas H. Keefe — 3708

Synchronized spontaneous otoacoustic emissions analyzed in a time-frequency domain — W. Wiktor Jedrzejczak, Katarzyna J. Blinowska, Krzysztof Kochanek, Henryk Skarzynski — 3720

Dissociation between distortion-product and click-evoked otoacoustic emissions in sheep (*Ovis aries*) — Dennis McFadden, Edward G. Pasanen, Michelle D. Valero, Eila K. Roberts, Theresa M. Lee — 3730

Comparing the optimal signal conditions for recording cubic and quadratic distortion product otoacoustic emissions — Lin Bian, Shixiong Chen — 3739

PSYCHOLOGICAL ACOUSTICS [66]

A cocktail party with a cortical twist: How cortical mechanisms contribute to sound segregation — Mounya Elhilali, Shihab A. Shamma — 3751

The role of temporal-masking patterns in the determination of subjective duration and loudness for ramped and damped sounds — Dennis T. Ries, Robert S. Schlauch, Jeffrey J. DiGiovanni — 3772

Level dominance in sound source identification — Robert A. Lutfi, Ching-Ju Liu, Christophe Stoelinga — 3784

Listening to every other word: Examining the strength of linkage variables in forming streams of speech — Gerald Kidd, Jr., Virginia Best, Christine R. Mason — 3793

Time-series analysis for online recognition and localization of sick pig (*Sus scrofa*) cough sounds — Vasileios Exadaktylos, Mitchell Silva, Sara Ferrari, Marcella Guarino, C. James Taylor, Jean-Marie Aerts, Daniel Berckmans — 3803

Mapping unpleasantness of sounds to their auditory representation — Sukhbinder Kumar, Helen M. Forster, Peter Bailey, Timothy D. Griffiths — 3810

Role of masker predictability in the cocktail party problem — Gary L. Jones, Ruth Y. Litovsky — 3818

Estimates of internal templates for the detection of sequential tonal patterns — Rong Huang, Virginia M. Richards — 3831

Age-related differences in the temporal modulation transfer function with pure-tone carriers — Ning-ji He, John H. Mills, Jayne B. Ahlstrom, Judy R. Dubno — 3841

Binaural signal detection, overall masking level, and masker interaural correlation: Revisiting the internal noise hypothesis — Leslie R. Bernstein, Constantine Trahiotis — 3850

Observer weighting of level and timing cues in bilateral cochlear implant users — Richard J. M. van Hoesel — 3861

Lateralization of Huggins pitch — Peter Xinya Zhang, William M. Hartmann — 3873

SPEECH PRODUCTION [70]

Reducing the number of vocal fold mechanical tissue properties: Evaluation of the incompressibility and planar displacement assumptions — Douglas D. Cook, Eric Nauman, Luc Mongeau — 3888

Frequency distributions of uniphones, diphones, and triphones in spontaneous speech — Victor Kuperman, Mirjam Ernestus, Harald Baayen — 3897

Clear speech production of Korean stops: Changing phonetic targets and enhancement strategies — Kyoung-Ho Kang, Susan G. Guion — 3909

SPEECH PERCEPTION [71]

Speaker normalization using cortical strip maps: A neural model for steady-state vowel categorization — Heather Ames, Stephen Grossberg — 3918

The concept of signal-to-noise ratio in the modulation domain and speech intelligibility — Finn Dubbelboer, Tammo Houtgast — 3937

(Continued)

CONTENTS—*Continued from preceding page*

The contribution of obstruent consonants and acoustic landmarks to speech recognition in noise	Ning Li, Philipos C. Loizou	3947
The relationship between native allophonic experience with vowel duration and perception of the English tense/lax vowel contrast by Spanish and Russian listeners	Maria V. Kondaurova, Alexander L. Francis	3959
Recognition of spectrally degraded phonemes by younger, middle-aged, and older normal-hearing listeners	Kara C. Schvartz, Monita Chatterjee, Sandra Gordon-Salant	3972

SPEECH PROCESSING AND COMMUNICATION SYSTEMS [72]

Analysis and prediction of acoustic speech features from mel-frequency cepstral coefficients in distributed speech recognition architectures	Jonathan Darch, Ben Milner, Saeed Vaseghi	3989
Frequency response of the skin on the head and neck during production of selected speech sounds	Jacob B. Munger, Scott L. Thomson	4001

MUSIC AND MUSICAL INSTRUMENTS [75]

Structural acoustics model of the violin radiativity profile	George Bissinger	4013
Beyond the beat: Modeling metric structure in music and performance	Stefan T. Tomic, Petr Janata	4024

BIOACOUSTICS [80]

Ultrasonic attenuation in parallel-nylon-wire cancellous-bone-mimicking phantoms	Keith A. Wear	4042
Velocity dispersion in trabecular bone: Influence of multiple scattering and of absorption	G. Haïat, A. Lhémery, F. Renaud, F. Padilla, P. Laugier, S. Naili	4047
Low-frequency components in harbor porpoise (*Phocoena phocoena*) clicks: Communication signal, by-products, or artifacts?	M. Hansen, M. Wahlberg, P. T. Madsen	4059
Modified variance ratio for objective detection of transient evoked potentials in bottlenose dolphins (*Tursiops truncatus*)	James J. Finneran	4069
Analysis of frequency dependence of ultrasonic backscatter coefficient in cancellous bone	Dean Ta, Weiqi Wang, Kai Huang, Yuanyuan Wang, Lawrence H. Le	4083
Acoustic characterization of single ultrasound contrast agent microbubbles	Jeroen Sijl, Emmanuel Gaud, Peter J. A. Frinking, Marcel Arditi, Nico de Jong, Detlef Lohse, Michel Versluis	4091

JASA EXPRESS LETTERS

On the use of a loudspeaker for measuring the viscoelastic properties of sound absorbing materials	Olivier Doutres, Nicolas Dauchez, Jean-Michel Génevaux, Guy Lemarquand	EL335
Numerical investigation of out-of-plane sound propagation in a shallow water experiment	Frédéric Sturm, Sven Ivansson, Yong-Min Jiang, N. Ross Chapman	EL341
Angle-dependent ultrasonic detection and imaging of two types of brachytherapy seeds using singular spectrum analysis	Jonathan Mamou, Sarayu Ramachandran, Ernest J. Feleppa	EL347
Noise reduction in binaural hearing aids: Analyzing the benefit over monaural systems	Sriram Srinivasan	EL353
Visualizations of sound energy across coupled rooms using a diffusion equation model	Yun Jing, Ning Xiang	EL360

INDEX TO VOLUME 124

How to Use This Index	4015
Classification of Subjects	4015
Subject Index to Volume 124	4109
Author Index to Volume 124	4159

On the use of a loudspeaker for measuring the viscoelastic properties of sound absorbing materials

Olivier Doutres, Nicolas Dauchez, Jean-Michel Génevaux, and Guy Lemarquand
LAUM, CNRS, Université du Maine, Av. O. Messiaen, 72095 Le Mans, France
olivier.doutres@univ-lemans.fr, nicolas.dauchez@univ-lemans.fr,
jean-michel.genevaux@univ-lemans.fr, guy.lemarquand@univ-lemans.fr

Abstract: This paper investigates the feasibility to use an electrodynamic loudspeaker to determine viscoelastic properties of sound-absorbing materials in the audible frequency range. The loudspeaker compresses the porous sample in a cavity, and a measurement of its electrical impedance allows one to determine the mechanical impedance of the sample: no additional sensors are required. Viscoelastic properties of the material are then estimated by inverting a 1D Biot model. The method is applied to two sound-absorbing materials (glass wool and polymer foam). Results are in good agreement with the classical compression quasistatic method.

© 2008 Acoustical Society of America
PACS numbers: 43.20.Ye, 43.20.Jr, 43.38.Dv [MS]
Date Received: August 1, 2008 **Date Accepted:** September 20, 2008

1. Introduction

Characterization of sound-absorbing materials, like mineral wool or polymer foam, in the context of building or transport applications, requires the determination of viscoelastic properties of the skeleton.[1] Classical methods to measure viscoelastic properties of porous materials can be sorted in two groups: the quasistatic methods neglect the inertial effects of the frame and give relevant information in the low-frequency range before the first resonance of the system[2,3] (usually for $f < 100$ Hz); the dynamic methods are based on the vibration of a porous sample,[4] or of a structure which includes a porous layer,[5] and give information at the resonance frequencies of the structure. More recently, methods based on the propagation on surface waves at the free surface of a porous layer have been investigated.[6,7] These methods require the use of an actuator, usually a shaker, and specific sensors: accelerometer, force sensor, or laser vibrometer [Fig. 1(a)].

This paper investigates an alternative method of the classical compression quasistatic setup to measure the viscoelastic properties of porous material. The method is based on the use of an electrodynamic loudspeaker as actuator and sensor.[8] Since no specific sensors are required, the experimental setup is simplified. Moreover, designed to radiate in the audible frequency range, a loudspeaker has the ability to excite the porous sample in the relevant frequency range for noise control applications. The proposed method is described in Fig. 1(b): the porous sample is set in a cavity and compressed by an electrodynamic loudspeaker. Measurement of the electrical impedance of the loudspeaker allows one to determine the mechanical impedance of the sample by inverting an electroacoustic model. The viscoelastic properties of the porous frame are then estimated using the classical Biot model.[9,10].

The first part of the paper presents the experimental setup. The principle of measurement and the poroelastic model used for the determination of the viscoelastic properties are then described. Results for two porous materials are finally compared with the classical compression quasistatic method of Fig. 1(a).

2. Measurement setup

The experimental setup to validate the proposed electrodynamic technique is presented in Fig. 1(b). A loudspeaker of 71 mm diameter is mounted between two cavities and applies static and

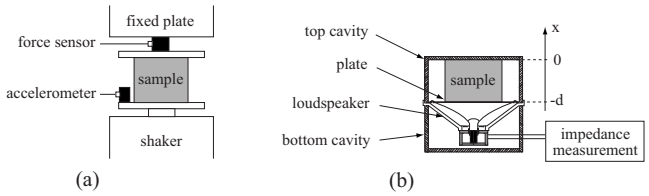


Fig. 1. Measurement setup: (a) classical compression quasistatic method; (b) new method using an electrodynamic loudspeaker.

dynamic strains to a porous sample set in the top cavity. The sample diameter is smaller than the one of the cavity to avoid any lateral strain. The depth of the cavity can be adjusted to the size of the porous sample to impose a static compression (see Table 2). The cavity is used to simplify the inversion procedure and to limit the effect of air pumping.[3]

A circular aluminum plate of 1 mm thickness is bonded on the loudspeaker cone to ensure a planar and unidirectional compression of the porous sample. The association of the plate and the cone is called the diaphragm. It has its first resonance frequency around 2 kHz and is considered to behave as a rigid body far below this frequency.

Measurement of the electrical impedance is performed with a precision magnetic analyzer (Wayne Kerr PMA 3260A) using a sine step signal from 25 to 200 Hz.

3. Principal of measurement

3.1 Determination of the sample mechanical impedance

The equivalent electroacoustic circuit given by Thiele and Small[11] is used to model the loudspeaker. This low-frequency model is valid below the first structure resonance frequency of the loudspeaker diaphragm. Figure 2 is the analogous circuit for the setup of Fig. 1(b), with U the output voltage of the source, r_e the dc resistance of the voice coil, L_e the inductance of the voice coil, r_f a shunting parallel resistance which accounts for eddy current loss in the pole piece, B the magnetic flux density in the air gap, l the length of the voice coil in the magnetic field, R_{ms} the mechanical resistance of the driver suspension losses, M_{ms} the mass of the diaphragm including voice coil, C_{ms} the compliance of the loudspeaker suspensions, Z_{2a} the mechanical impedance of the bottom air cavity, Z_{1a} the mechanical impedance of the top air cavity surrounding the porous sample, and Z_{1p} the mechanical impedance of the porous sample.

Mechanical impedance is defined by the ratio of the force F applied to the diaphragm on its velocity v. In the considered frequency range, the two air cavities can be considered as simple compliances and the corresponding mechanical impedances are given by

$$Z_{1a} = \frac{S'^2}{j\omega(V_{1a}/\rho_0 c^2)}, \quad Z_{2a} = \frac{S^2}{j\omega(V_{2a}/\rho_0 c^2)}, \tag{1}$$

where j is the square root of -1, ω the circular frequency of the excitation, ρ_0 the air density and c the velocity of sound in air, V_{1a} and V_{2a} the volume of air in the top and bottom cavity respec-

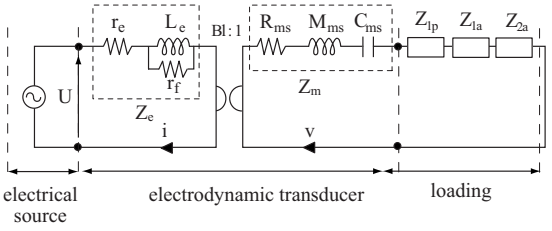


Fig. 2. Electrical equivalent circuit of the measurement setup.

tively, S the equivalent surface area of the diaphragm in contact with the bottom cavity, and S' the equivalent surface area of the upper face of the diaphragm in contact with the air layer in the top cavity.

The electrical impedance of the circuit (Fig. 2) is written

$$Z_{vc} = \frac{U}{i} = Z_e + \frac{(Bl)^2}{Z_m + [Z_{1p} + Z_{1a} + Z_{2a}]} \tag{2}$$

with

$$Z_e = r_e + \frac{j\omega L_e r_f}{j\omega L_e + r_f} \tag{3}$$

and

$$Z_m = R_{ms} + j\omega M_{ms} + \frac{1}{j\omega C_{ms}}. \tag{4}$$

Hence, the mechanical impedance of the sample can be derived from the measurement of Z_{vc}, the properties of the loudspeaker and of the two air cavities, as

$$Z_{1p} = \frac{(Bl)^2}{Z_{vc} - Z_e} - (Z_m + Z_{1a} + Z_{2a}). \tag{5}$$

3.2 Determination of the loudspeaker properties

The properties of the loudspeaker are determined from the measurement of the electrical impedance without porous sample in the top cavity. In that case, the equivalent electrical circuit model gives

$$Z_{vc} = Z_e + \frac{(Bl)^2}{Z_m + [Z_{1a} + Z_{2a}]}, \tag{6}$$

with $Z_{1a}=S^2\rho_0 c^2/j\omega V_{1a}$ and V_{1a} the volume of the top cavity. The model is fitted on the measurement using a nonlinear least-squares method to get re, Le, r_f, Bl, R_{ms}, C_{ms}, and M_{ms}.

3.3 Calculation of the material viscoelastic properties

The viscoelastic properties of the porous frame are estimated from the impedance Z_{1p} by the inverse method using the Biot model. In the considered model, the material is isotropic and the displacements of the frame and air are one-dimensional along the sample thickness [x direction in Fig. 1(b)]. The porous material is considered as infinite in the lateral directions and the effects of the boundary conditions are neglected. This assumption is valid for porous materials such as glass wool with a Poisson's ratio equal to 0, but it can induce an evaluation discrepancy for foam materials which can bulge sideways when compressed between two rigid plates.[12]

The mechanical impedance can be derived analytically from the calculation of the total stress (σ_{xx}^t) applied by the porous sample to the vibrating diaphragm,

$$Z_{1p}^{th}(\omega) = \frac{F}{v} = \frac{S_p'' \sigma_{xx}^t}{j\omega u_w}, \tag{7}$$

with S_p the surface area of the porous sample in contact with the vibrating diaphragm ($S_p=S-S'$) and u_w the amplitude of the displacement imposed by the diaphragm. According to Biot theory,[9,10] two compressional waves propagate in a porous media having a one-dimensional behavior. These waves are characterized by a complex wave number δ_i ($i=1,2$) and a displacement ratio μ_i. The total stress exerted by the sample to the diaphragm is thus the sum of the stress exerted by the fluid and solid phases characterized by these two waves as

Table 1. Properties of the loudspeaker.

M_{ms} (g)	C_{ms} (μm N^{-1})	R_{ms} (N s m^{-1})	Bl (N A^{-1})	r_e (Ω)	L_e at 100 Hz (μH)	r_f at 100 Hz (Ω)
9.37	484	1.05	4.93	12.03	878	2.93

$$\sigma_{xx}^{t} = \sigma_{xx}^{s} + \sigma_{xx}^{f}$$
$$= [(\tilde{P} + \tilde{Q}) + \mu_1(\tilde{R} + \tilde{Q})]\delta_1 \cos(\delta_1 d)D_1 + [(\tilde{P} + \tilde{Q}) + \mu_2(\tilde{R} + \tilde{Q})]\delta_2 \cos(\delta_2 d)D_2. \quad (8)$$

In these equations, d is the sample thickness, $\tilde{P}$ and $\tilde{R}$ are the bulk modulus of the solid and fluid phases, respectively, and $\tilde{Q}$ quantifies the potential coupling between the two phases. The expression for these two last coefficients can be found in Ref. 10. Note that viscoelastic properties of the frame, Young's modulus E, and loss factor η, are present in the expression of $\tilde{P}$,

$$\tilde{P} = \frac{E(1 + j\eta)(1 - \nu)}{(1 + \nu)(1 - 2\nu)} + \frac{\tilde{Q}^2}{\tilde{R}}. \quad (9)$$

D_1 and D_2 are the amplitude coefficients of the two compressional waves and can be determined from the boundary conditions applied to the sample. Here, the displacement is zero at $x=0$ and is equal to the one of the diaphragm at $x=-d$, which gives

$$D_1 = \frac{u_w(\mu_2 - 1)}{\sin(\delta_1 d)(\mu_1 - \mu_2)}, \quad D_2 = \frac{u_w(1 - \mu_1)}{\sin(\delta_2 d)(\mu_1 - \mu_2)}. \quad (10)$$

4. Results

The properties of the loudspeaker determined from the measurement of the electrical impedance when the top cavity is empty [see Eq. (6)] are given in Table 1. Note that the inductance L_e decreases and the shunt resistance r_f increases with frequency because of the eddy currents flowing in the iron pole structure.[13] These properties have thus been determined according to the frequency and only the values at 100 Hz are given in Table 1.

Measurements of the electrical impedance Z_{vc} are then carried out with a light glass wool and a stiff polymer foam placed in the top cavity. The properties of the materials given in Table 2 have been measured in our laboratory.

The mechanical impedance determined from Eq. (5) and the simulations derived from Eq. (7) are shown in Fig. 3. The Young's moduli used in the model have been measured at 5 Hz using the compression quasistatic method[2] (see the measurements Fig. 4). Note that the Young's

Table 2. Properties of materials A and B.

Porous	Glass wool A	Foam B
Nominal thickness: d (mm)	63	40.7
Static compression rate (%)	37	0.95
Sample diameter (mm)	57	44.5
Airflow resistivity: σ (kN s/m^4)	105	3.3
Porosity: ϕ	0.95	0.98
Tortuosity: α_∞	1	1.03
Viscous length: Λ (μm)	35.1	78.8
Thermal length Λ' (μm)	105.3	236.4
Frame density: ρ_1 (kg/m^3)	17	29

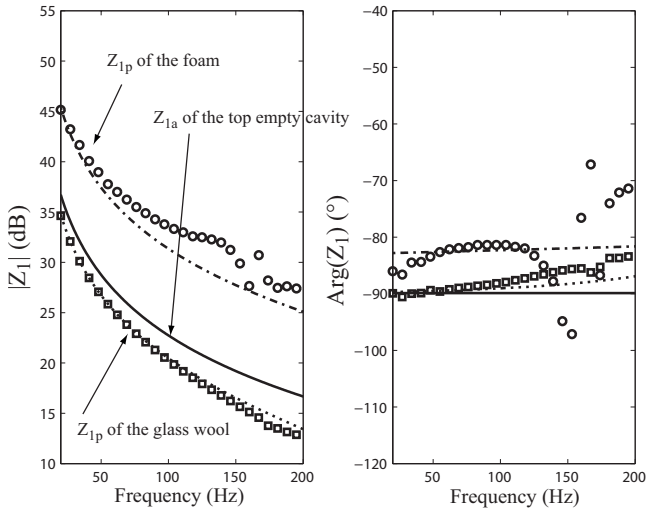


Fig. 3. Measurements (discontinuous plots) and simulations (continuous plots) of the mechanical impedance of the top empty cavity and of two porous samples: (left) magnitude, (right) phase.

moduli are considered constant in the model, which explains the discrepancy of $|Z_{1p}|$ at low frequencies ($f < 140$ Hz) in the case of the foam B: the difference increases with frequency because the Young modulus increases.[2] Above 140 Hz, measurements of the mechanical impedance Z_{1p} are not valid because of several well-known drawbacks of the loudspeaker which are not taken into account in the model:[13] the stiffness of the viscoelastic suspension is nonlinear, the effect of which is paramount at the resonance frequency of the loudspeaker (around 160 Hz), the inductance of the voice coil L_e is nonconstant, and eddy currents are present in the iron-pole structure, the effects of which are predominant especially at high frequencies.

Viscoelastic properties according to frequency are finally determined by fitting the poroelastic model on the measurements. Figure 4 gives the Young's modulus and the loss factor evaluated with the classical compression quasistatic method of Fig. 1(a) and the proposed electrodynamic method for the two materials. Results determined with the electrodynamic technique are given in the linear frequency range of the loudspeaker, i.e., below 130 Hz. Good agreements are found in the evaluation of the Young's modulus: the one of the foam is around 400 kPa and increases with frequency; in the case of the glass wool, it is evaluated around 2.5 kPa and is barely constant. The loss factor of the foam is also given around 0.17 by the two

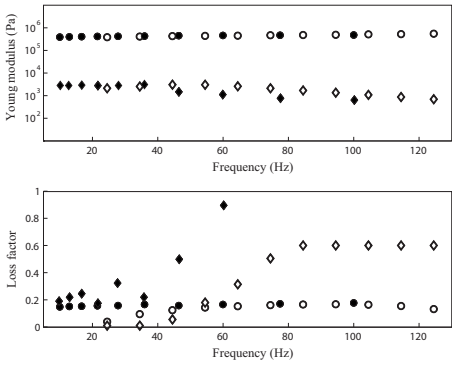


Fig. 4. Measured Young's modulus (top) and loss factor (bottom) of the glass wool (diamond) and of the polymer foam (circle): (black) classical compression quasistatic method; (white) electrodynamic method.

methods. However, the one given by the electrodynamic method is underestimated at low frequencies. The loss factor of the glass wool estimated by the two methods does not seem realistic:[3] the quasistatic method overestimates the value because of the lateral airflow, and the electrodynamic method is greatly disturbed by the electrical drawbacks of the loudspeaker, which are not accounted for in the loudspeaker modeling.

5. Conclusion

The feasibility to measure the viscoelastic properties of sound-absorbing materials using an electrodynamic loudspeaker has been demonstrated. The mechanical impedance of the porous sample is determined from the measurement of the electrical impedance of the loudspeaker by inverting an electroacoustic model: no additional sensors are required. Viscoelastic properties of the material are then estimated by inverting a 1D Biot model. The method has been applied using a traditional loudspeaker for frequencies below the mass-spring resonance of the system ($f < 130$ Hz). Results obtained with this method are validated by comparison to the classical compression quasistatic method. The accuracy on the loss factor and the high-frequency limit could be extended with a loudspeaker free of major nonlinearities.

Acknowledgments

The authors thank the CNRS, Région Pays de la Loire and the European Commission (CREDO project) for their financial support.

References and links

[1]O. Doutres, N. Dauchez, and J. M. Génevaux, "Validity of the limp model for porous materials: A criterion based on the Biot theory," J. Acoust. Soc. Am. **122**, 2038–2048 (2007).
[2]M. Etchessahar, S. Sahraoui, L. Benyahia, and J. F. Tassin, "Frequency dependence of elastic properties of acoustic foams," J. Acoust. Soc. Am. **117**, 1114–1121 (2005).
[3]V. Tarnow, "Dynamic measurements of the elastic constants of glass wool," J. Acoust. Soc. Am. **118**, 3672–3678 (2005).
[4]T. Pritz, "Dynamic Youngs modulus and loss factor of plastic foams for impact sound isolation," J. Sound Vib. **178**, 315–322 (1994).
[5]L. Jaouen, A. Renault, and M. Deverge, "Elastic and damping characterizations of acoustical porous materials: Available experimental methods and applications to a melamine foam," Appl. Acoust. **69**, 1129–1140 (2008).
[6]L. Boeckx, P. Leclaire, P. Khurana, C. Glorieux, W. Lauriks, and J. F. Allard, "Investigations of the phase velocities of guided acoustic waves in soft porous layers," J. Acoust. Soc. Am. **117**, 545–554 (2005).
[7]J.-F. Allard, B. Brouard, N. Atalla, and S. Ghinet, "Excitation of soft porous frame resonances and evaluation of rigidity coefficients," J. Acoust. Soc. Am. **121**, 78–84 (2007).
[8]H. O. Taylor, "Tube method of measuring sound absorption," J. Acoust. Soc. Am. **24**, 701–7014 (1952).
[9]M. A. Biot, "The theory of propagation of elastic waves in a fluid-saturated porous solid. I. Low frequency range. II. Higher frequency range," J. Acoust. Soc. Am. **28**, 168–191 (1956).
[10]J. F. Allard, *Propagation of Sound in Porous Media: Modelling Sound Absorbing Materials* (Elsevier, New York, 1993).
[11]R. H. Small, "Closed-box loudspeakers systems, part 1: Analysis," J. Audio Eng. Soc. **20**, 798–808 (1972).
[12]C. Langlois, R. Panneton, and N. Atalla, "Polynomial relations for quasi-static mechanical characterization of isotropic poroelastic materials," J. Acoust. Soc. Am. **110**, 3032–3040 (2001).
[13]G. Lemarquand, "Ironless Loudspeakers," IEEE Trans. Magn. **43**(8), 3371–3374 (2007).

 [DOI: 10.1121/1.3008068] Published Online 11 November 2008

Numerical investigation of out-of-plane sound propagation in a shallow water experiment

Frédéric Sturm
LMFA UMR CNRS 5509, Ecole Centrale de Lyon, 36, avenue Guy de Collongue, 69134 Ecully Cedex, France
frederic.sturm@ec-lyon.fr

Sven Ivansson
Swedish Defence Research Agency, SE-16490 Stockholm, Sweden
sveni@foi.se

Yong-Min Jiang and N. Ross Chapman
School of Earth and Ocean Sciences, University of Victoria, Victoria, BC, Canada, V8W 3P6
minj@uvic.ca, chapman@uvic.ca

Abstract: In an experiment in the Florida Straits, broadband pulses were transmitted over a range of 10 km and received by a vertical hydrophone array. For pulses with center frequency below 400 Hz, the received signal consisted of a dominant arrival followed by a secondary one delayed by about 0.4 s. A hypothesis that the secondary arrival was caused by 3D out-of-plane propagation is investigated here numerically with a 3D parabolic equation model (3DWAPE) and a 3D ray model (MOC3D). Both models clearly predict a secondary arrival caused by 3D horizontal refraction from the sloping bottom in the shoreward direction.

© 2008 Acoustical Society of America
PACS numbers: 43.30.Bp, 43.30.Dr, 43.30.Cq [GD]
Date Received: July 30, 2008 **Date Accepted:** September 30, 2008

1. Introduction

Results from an inversion to estimate geoacoustic bottom parameters using broadband data from an experiment in the Florida Straits have recently been reported by Jiang *et al.*[1] M-sequence sound pulses were transmitted over a range of 10 km and received by a vertical hydrophone array. For the sound pulses whose center frequency was lower than 400 Hz, the received signal consisted of a dominant first arrival followed by a secondary component delayed by about 0.4 s in arrival time. Initial inversions using conventional matched-field inversion methods that assumed the second arrival was due to the sub-bottom structure were not successful. Although many different geoacoustic models were tested, from simple half-spaces to multiple layers, with and without shear parameters, none of the models was able to account for the secondary arrival. Examination using a beamforming algorithm showed that the secondary arrival was received at higher angles compared to the first one. This result suggested that the secondary arrival could be explained by horizontal refraction due to the interaction with a steeply sloping ocean bottom closer to the shore, a well known 3D propagation effect.[2] Successful inversions were then obtained by spatially filtering out the secondary arrival and modeling the first arrival in the 2D plane.

After some experimental and environmental information in Sec. 2, this Letter presents a numerical investigation of the 3D propagation hypothesis. A 3D parabolic equation (PE)-based model (3DWAPE) is applied in Sec. 3, and a 3D ray model (MOC3D) in Sec. 4. Both models clearly predict a secondary arrival caused by 3D horizontal refraction from the sloping bottom that steepens in the shoreward direction. Efforts to further improve the fit between modeled and measured signals are discussed in Sec. 5.

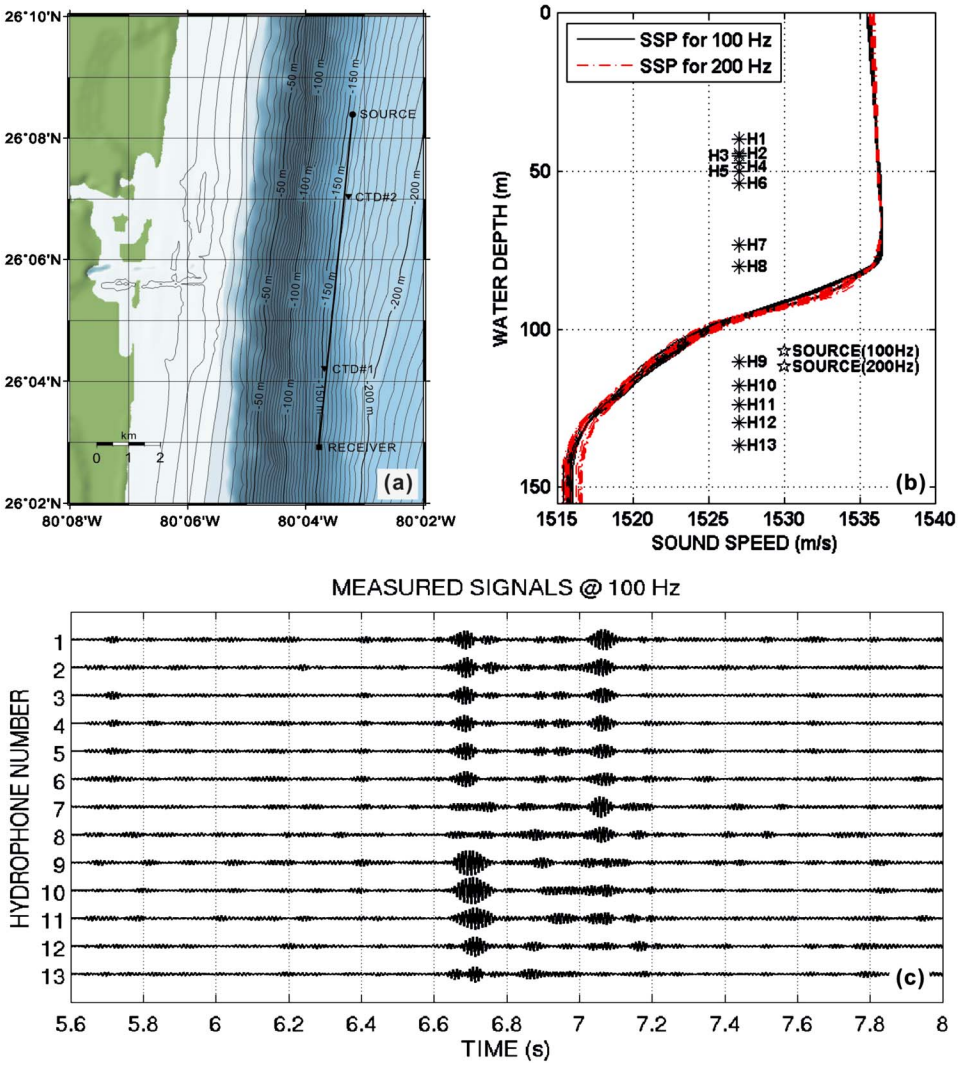


Fig. 1. (Color online) (a) experimental site and geometric setup, showing the steep portion of the bottom slope about 1.4 km west of the experimental site. The depth contours are 5 m apart; (b) sound-speed profiles of two consecutive hours. The profiles consist of an isospeed layer in the upper 80 m of the water column, followed by a strong negative gradient profile; (c) measured 100-Hz bandlimited impulse response signals at the 13 different hydrophones.

2. Description of the experiment

The data were collected at the South Florida Ocean Measurement Center during an acoustic propagation experiment at 10-km range in December, 1999.[3] Figure 1(a) is a sketch of the experimental site and the geometric setup of the measurement system. The source and vertical line array were deployed on the elevation contours of 155 and 150 m, respectively. Two environmental arrays (black triangles) were placed between the source and the array. The experimental setup was designed to study sound propagation along the shore.

The vertical line array (VLA) used in this analysis consists of 13 of the array hydrophones, unevenly spaced on the array with the shallowest at a depth of 39.8 m and the deepest at 136.7 m [see Fig. 1(b)]. The sources were at 107 m (100 Hz) and 112 m (all other frequencies). The hydrophones and low-frequency sources had broad directivities, horizontally as well as

vertically. Typical sound-speed profiles (SSPs) during the collection of the acoustic data analyzed in this paper are shown in Fig. 1(b). They were derived from the conductivity, temperature, and depth data collected by the two environmental arrays. The high correlation between these array data, and the stability in time of the SSP, support an assumption of range-independent SSP in the source-receiver plane. M-sequence coded pulses at center frequencies of 100, 200, 400, 800, 1600, and 3200 Hz were transmitted sequentially for 1 h at each frequency. The received signals were ensemble averaged over 1 min, and then compressed to get bandlimited impulse responses.

The data shown in Fig. 1(c) are the measured 100-Hz bandlimited impulse responses at the receiver depths. Notable features are (1) a second distinct group of arrivals appears at some of the hydrophones approximately 0.4 s later than the first group of arrivals; and (2) for the shallowest hydrophones, the amplitude of the second arrival is stronger than the first one. The second group of arrivals was observed experimentally in the 200- and 400-Hz data as well. However, the strength of the later arrivals decreased when frequency increased, and was negligible at frequencies greater than 800 Hz. The later arrivals at 100 Hz are the focus of attention in this Letter.

3. Comparisons with 3DWAPE

The numerical model 3DWAPE (Ref. 4) is an acoustic parabolic equation-based model which solves the problem of acoustic waves emanating from an isotropic (omnidirectional) point source and propagating in general 3D oceanic environments. The time dependence of the source can be either transient (broadband) or harmonic (cw). Computations with 3DWAPE were performed assuming the 100-Hz SSP in Fig. 1(b) throughout the waveguide. Bottom depths for the computation domain were obtained by bilinear interpolation on a rectangular grid of the bathymetry data.[5] The grid size of the bathymetry is equal to 3′, i.e., approximately 83.2 m in longitude and 92.66 m in latitude in this region. In the vertical plane containing the source and the VLA, the water depth varies between 150 and 160 m. The time dependence of the source is modeled by a Gaussian-weighted cosine pulse with bandwidth 50 Hz, covering the band 75–125 Hz, and pulse length approximately 0.12 s. The omnidirectional point source was positioned at a depth of 107 m as suggested by the experiment. In the 2D (i.e., azimuthally uncoupled) and fully 3D computations, a lossy half-space fluid sediment bottom was considered with a (compressional) wave speed of 1676 m/s, a density of 1.779 g/cm^3, and an attenuation of 0.05 dB per wavelength, leading to 8–9 proper modes in an approximately 155-m-deep water column.

The computed received signals on the 13 unevenly spaced hydrophones are displayed in the top two panels of Fig. 2. For comparison, the envelopes of the experimentally measured signals displayed in Fig. 1(c) are plotted as gray traces in both panels. In addition, to help understand the depth variation of the signal, the two bottom panels of Fig. 2 display the simulated time series versus depth with a very fine resolution (every 2 m in depth), thus giving evidence of modal structures of the received signals. Several observations can be made by comparing the 2D and 3D numerical predictions. The onset (around 6.7 s) of the received signals is weakly affected by 3D effects. These first arrivals correspond to time arrivals of mode 1 up to mode 4. It can be verified that both mode 5 and mode 8 are weakly excited at the source. As a result, they are absent or strongly attenuated at the vertical receiver array. The 2D and 3D late arrivals are clearly different. These arrivals correspond to time arrivals of modes 6 and 7. The 3D modal arrivals are shifted in time. This shift can explain the second group of strong arrivals around 0.45 s after the first group of strong arrivals, which is consistent with the observation from the experimental data. However, these second arrivals are strong for all depths, even below the thermocline where they are weaker in the experimental data.

4. Comparisons with MOC3D

Albeit less reliable, ray modeling is useful as a complement to the computer intensive 3D PE modeling. Methods which avoid the demanding 3D eigenray problem are particularly attractive. In an approach by Piskarev,[6] the emitted energy from the source is viewed as confined to the thin

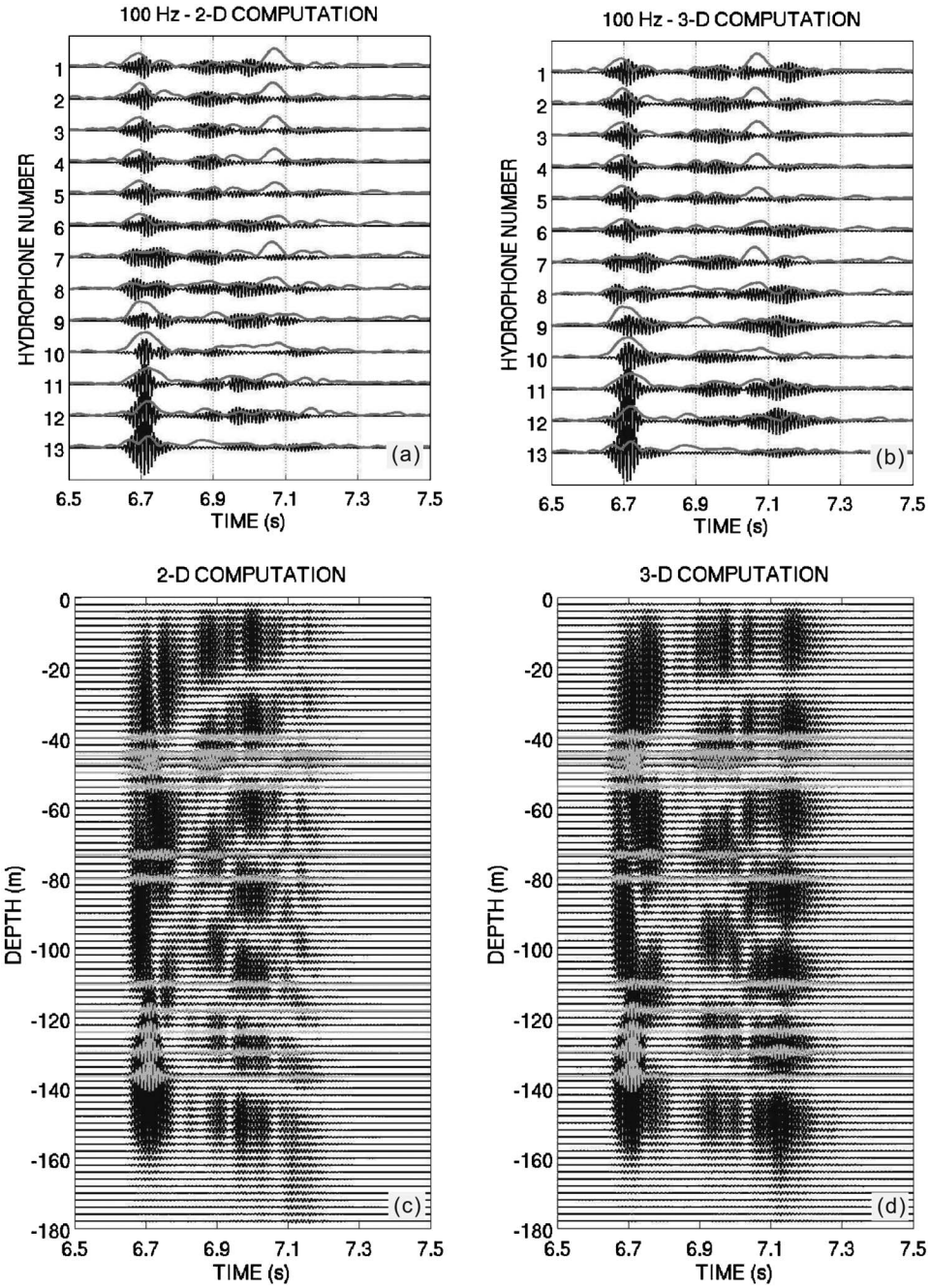


Fig. 2. Simulated time series versus hydrophone number obtained using 2D (a) and 3D (b) PE computations with 3DWAPE. The gray traces show the envelopes of the corresponding experimental data. Simulated time series versus depth obtained using 2D (c) and 3D (d) PE computations with 3DWAPE. The gray traces correspond to the simulated signals received on the 13 hydrophones.

rays, and intensities are determined as probe volume averages using the ray density. Schneider's model MOCASSIN (Ref. 7) is a 2D ray model for transmission loss and reverberation based on similar ideas. It has been taken as a starting point for developing the 3D model MOC3D,[8] including simulation of time series envelopes by positioning ray intensities along a time axis. The

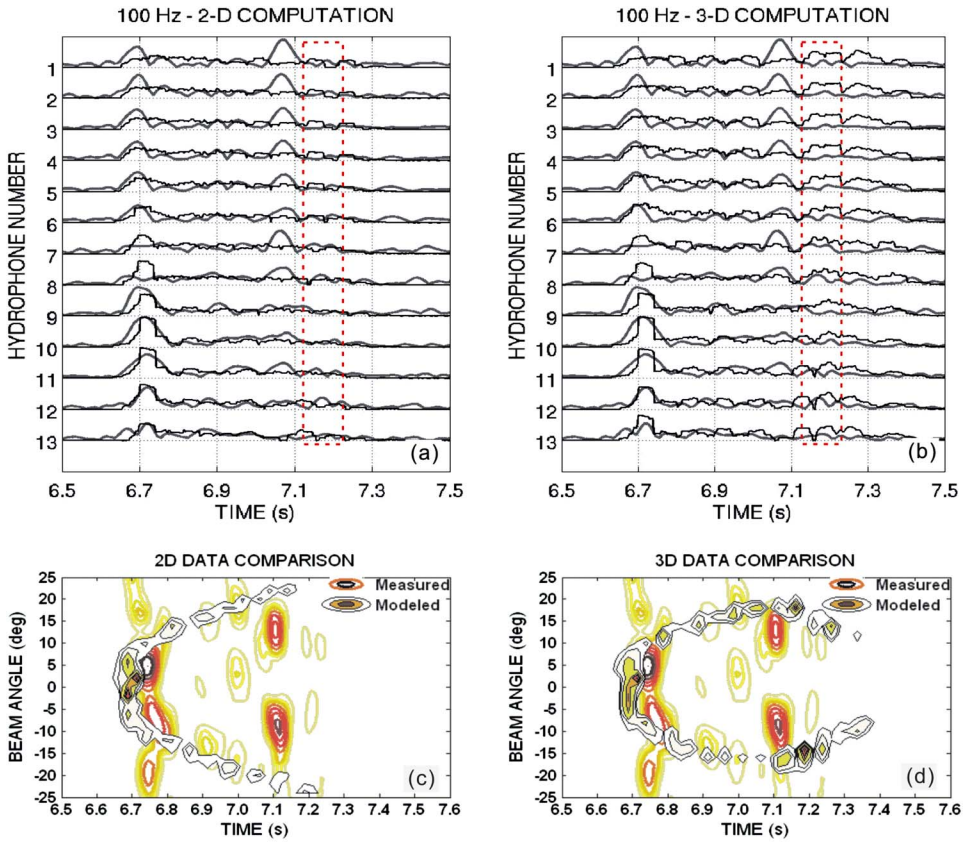


Fig. 3. (Color online) Simulated time series envelopes versus hydrophone number obtained using 2D (a) and 3D (b) computations with MOC3D. The gray traces show the corresponding experimental data. Measured vertical directionality at the array, 100-Hz case, together with ray arrival energy contours for the 2D (c) and 3D (d) MOC3D results.

ray models may be applicable down to frequencies corresponding to wavelengths of about one-tenth of the water depth. For the Florida Straits case, with the coastal slope from depths of about 155 m in the source-receiver section, results for 400 and perhaps 200 Hz may be justified. However, the applicability to low frequencies is improved by a frequency-dependent smoothing of the sound-speed profiles.[7]

Figures 3(a) and 3(b) show numerical results obtained with MOC3D for the 100-Hz frequency and the 13 unevenly spaced hydrophones. Following the initial arrival at about 6.7 s, and some intermediate arrivals, clear 3D effects appear at about 7.15 s in the model traces. As verified by ray path plots and travel-time/back-azimuth diagrams, the corresponding arrivals are caused by horizontal refraction from the sloping bottom. Indeed, as the ray travel times increase from 7.1 to 7.3 s in the 3D computation, the ray back-azimuths at the array decrease from about −10° to about −20°. The source is at about +5° from north at 0° [see Fig. 1(a)] and 3D propagation out of the vertical source-receiver plane has clearly taken place. As in the 3DWAPE solutions in Fig. 2, the time delay (about 0.45 s) is somewhat larger than in the measured data (about 0.4 s), and the 3D effects are clearly seen also below the thermocline.

The vertical arrival structure of the measured data obtained by beamforming[1] is shown in Figs. 3(c) and 3(d), together with energy contours for the MOC3D ray arrivals as positioned in time and vertical angle. The 3D modeling produces highlights in the travel-time/beam-angle plane with an improved fit to the measured data, as compared to the 2D modeling.

5. Discussion and Conclusion

The results from this investigation provide support for the 3D propagation hypothesis used by Jiang *et al.* in their inversion of the Florida Straits data. Both numerical propagation models predict a secondary arrival caused by 3D horizontal refraction from the sloping bottom that steepens closer to the shore. The modeled and measured delay times and the vertical directionality of the signal agree reasonably well, given the lack of information about the sound-speed variation in the water column over the 3D grid. Other ray simulations (not shown here) showed that the amplitude reduction of the secondary arrival at higher frequencies can be modeled by introducing a 1-m-thick sediment layer (wavespeed 1500 m/s, density 1.2 g/cm^3, attenuation 0.4 dB per wavelength) on top of the bottom half-space. The effect of this additional thin sediment layer on the secondary arrival is very small in the 100-Hz case. It is worth mentioning that further adaptations of the environmental parameters can improve the fit to the 100-Hz measurement data, for example, by increasing the sound speed in the water column and making the bottom half-space (below the 1-m-thick sediment layer) harder as the bottom depth decreases in the shoreward direction. Overall, the investigation shows that 3D propagation should not be ignored in interpretation of data from shallow-water environments, particularly in long-range, along shelf propagation geometries.

Acknowledgments

Support from Office of Naval Research Ocean Acoustics Team is acknowledged by Y-M.J. and N.R.C.

References and links

[1]Y. Jiang, N. R. Chapman, and H. A. DeFerrari, "Geoacoustic inversion of broadband data by matched beam processing," J. Acoust. Soc. Am. **119**, 3707–3716 (2006).
[2]A. Tolstoy, "3-D propagation issues and models," J. Comput. Acoust. **4**, 243–271 (1996).
[3]H. B. Nguyen, H. A. DeFerrari, and N. J. Williams, "Ocean acoustic sensor installation at the South Florida ocean Measurement Center," IEEE J. Ocean. Eng. **27**, 235–244 (2002).
[4]F. Sturm, "Numerical study of broadband sound pulse propagation in three-dimensional oceanic waveguides," J. Acoust. Soc. Am. **117**, 1058–1079 (2005).
[5]GEODAS Search and Data Retrieval Systems, National Geophysical Data Center (NGDC) (http://www.ngdc.noaa.gov/mgg/gdas/gd_designagrid.html) Last viewed 11/2006.
[6]A. L. Piskarev, "Calculation of the average intensity distributions of sound fields in the ocean," Sov. Phys. Acoust. **35**, 418–422 (1989).
[7]H. G. Schneider, "MOCASSIN sound propagation and sonar range prediction model for shallow water environments," User's guide, Technical Report 1990-9, FWG, Kiel, Germany (1990).
[8]S. Ivansson, "Stochastic ray-trace computations of transmission loss and reverberation in 3-D range-dependent environments," in Proceedings of the 8th ECUA, Portugal, 2006, pp. 131–136.

Angle-dependent ultrasonic detection and imaging of two types of brachytherapy seeds using singular spectrum analysis

Jonathan Mamou, Sarayu Ramachandran, and Ernest J. Feleppa
Frederic L. Lizzi Center for Biomedical Engineering, Riverside Research Institute, 156 William Street, 9th floor, New York, NY 10038
mamou@rrinyc.org, sarayu@rrinyc.org, feleppa@rrinyc.org

Abstract: Brachytherapy to treat prostate cancer uses transrectal ultrasound to guide implantation of titanium-shelled radioactive seeds. Transperitoneal implantation allows errors in placement that cause suboptimal dosimetry. Conventional ultrasound cannot reliably image implanted seeds; therefore, seed misplacements cannot be corrected in the operating room. Previously, an algorithm based on singular spectrum analysis was shown to image palladium seeds better than B-mode ultrasound could. The algorithm is now applied to imaging an iodine seed in gel and in beef tissue as a function of seed angle relative to the incident ultrasound. Results indicate that both seed types are imaged reliably by the algorithm.

© 2008 Acoustical Society of America
PACS numbers: 43.60.Lq, 43.80.Vj, 43.35.Yb [CC]
Date Received: June 20, 2008 **Date Accepted:** September 8, 2008

1. Introduction

This letter discusses a candidate method of imaging brachytherapy seeds in real-time using transrectal ultrasound (TRUS). Brachytherapy is a procedure used to treat gland-confined prostate cancer by permanent implantation of radioactive seeds within the prostate gland; currently, the most-commonly used seeds contain radioactive iodine or palladium.[1,2] These seeds have a thin, rigid, cylindrical, ultrasonically specular, titanium shell that is 4.5 mm long by 0.8 mm in diameter and TRUS is the standard imaging modality for treatment-planning dosimetry, guiding, and monitoring seed implantation.[3,4] Seeds are inserted transperitoneally through a needle attached to the TRUS probe. After insertion, the seeds ideally would be oriented normally to the ultrasonic beam and parallel to the implanting needle axis. However, suboptimal seed insertion typically causes seeds to rotate slightly so they are not normal to the transducer beam. Because the seeds are small and highly specular, they cannot be reliably imaged with TRUS if they are not normal to the ultrasound beam axis.

In two previous publications, we described development and evaluation of a seed-imaging algorithm based on a signal-processing framework called singular spectrum analysis (SSA).[5,6] The algorithm uses only echo-signal envelopes to generate color-coded images termed *P*-mode images. The *P*-mode images are indicative of the likelihood of seed presence as quantified by the algorithm. Evaluations of *P*-mode images showed them to be quantitatively superior to conventional ultrasound B-mode images to detect seeds. In the previous studies, all experiments were conducted on a popular type of palladium-based seed. This letter describes the performance of the SSA algorithm for imaging a different, popular type of iodine-based seed. SSA algorithm performance was evaluated as the iodine seed orientation was varied with respect to the transducer. Ultrasound experiments were conducted with seeds embedded in an ideal, clutter-free acoustical environment (i.e., acoustically transparent gel pad) and in a tissue-like, clutter-containing environment (i.e., degassed *ex vivo* beef). Iodine-seed experiments were performed in a manner identical to the previously reported experiments conducted with the palladium seeds. We also performed iodine-seed simulations based on empirical data acquired

from the ideal-environment experiments. Score metrics previously developed to evaluate palladium-seed imaging performance were used to quantify iodine-seed imaging performance.[6]

2. Material and methods

The two types of seeds used in this study were devoid of radioactive content. The first type of seed was a commonly used version of radioactive palladium (Pd^{103}) seeds.[7,5,6] The second type of seed was a commonly used version of radioactive iodine (I^{125}) seeds. The palladium and iodine seeds are termed Pd-103 and I-125 seeds, respectively. New data were acquired with I-125 seeds and compared to data previously published and obtained with Pd-103 seeds.[5,6] Both types of seeds consist of cylindrical thin titanium shells having the standard outer dimensions of brachytherapy seeds: 4.5 mm in length and 0.8 mm in diameter. However, the I-125 seed has convex rounded ends[8] and the Pd-103 seed has concave cupped ends. The I-125 seed has radioactive material coated on a 3-mm-long silver rod centered within its titanium shell and the Pd-103 seed has radioactive material coated on two graphite cylinders separated by a lead cylinder.[5]

Experimental data were collected using exactly the previously published protocol.[6] Briefly, data were acquired with a 5-MHz single-element transducer (Panametrics Inc., Waltham, MA). The transducer had a focal length of 51 mm and a diameter of 14 mm and was excited with a Panametrics 5900 pulser/receiver unit. The radio-frequency (rf) echo signals were digitized at a sampling rate of 50 MS/s, and the spacing between adjacent A-lines was 100 μm. Gel-pad and *ex vivo* beef experiments were conducted using I-125 seeds in the same manner as the Pd-103 experiments were previously conducted,[6] with scanning performed in transverse and longitudinal planes and with angles between the beam axis and the normal to the seed axis varying from 0 to 22 deg. (Longitudinal-scan data were acquired by scanning in a plane parallel to the long axis of the seed and transverse-scan data were acquired by scanning in a plane perpendicular to the plane in which the seed was tilted.)

The simulation methods previously used for Pd-103 seeds were used to simulate rf echo-signal data from an I-125 seed.[6] I-125 echo data was simulated for tilt angles ranging from 0 to 10 deg in both longitudinal and transverse seed orientations. The I-125 simulations were based on empirical data obtained from the gel-pad experiments and designed so that a complete B-mode image could be formed. Simulation parameters for I-125 seeds were different for Pd-103 results. These differences are presented and discussed in Sec. 3.

Two types of scoring metrics were developed to evaluate the performance of the SSA algorithm to detect and image Pd-103 seeds at various angles.[6] The same metrics were used to quantitatively compare the ability of the SSA algorithm to detect I-125 and Pd-103 seeds. The first type of scoring metric, termed Score, was developed specifically for gel-pad experiments because no false-positives were present. The second type of scoring metric was developed to evaluate performance in beef experiments and to account for possible false-positives as well as false-negatives. The two measures second type were termed seed score (SS) and worst false positive (WFP); SS quantified how well the seed was detected and imaged while WFP quantified possible false-positives. The scores (i.e., WFP and SS) were computed from the *P*-mode images formed by the SSA algorithm and also from the conventional B-mode images. The subscripts *P* or B indicated scores based on *P*-mode and B-mode images, respectively. Computing scores for *P*-mode and B-mode images allowed quantitatively comparing the performance of the SSA algorithm with respect to the performance of conventional B-mode images.

3. Results

The longitudinal and transverse scans of a single I-125 seed in a gel pad were analyzed with the SSA algorithm. The simulations of rf echo signals from I-125 seeds were derived from experimental data and then used to generate *P*-mode images. To evaluate simulation performance, each angle (i.e., 0 to 10 deg) in each direction was simulated ten times with different realizations of white Gaussian noise. The white Gaussian noise amplitude was chosen to match the

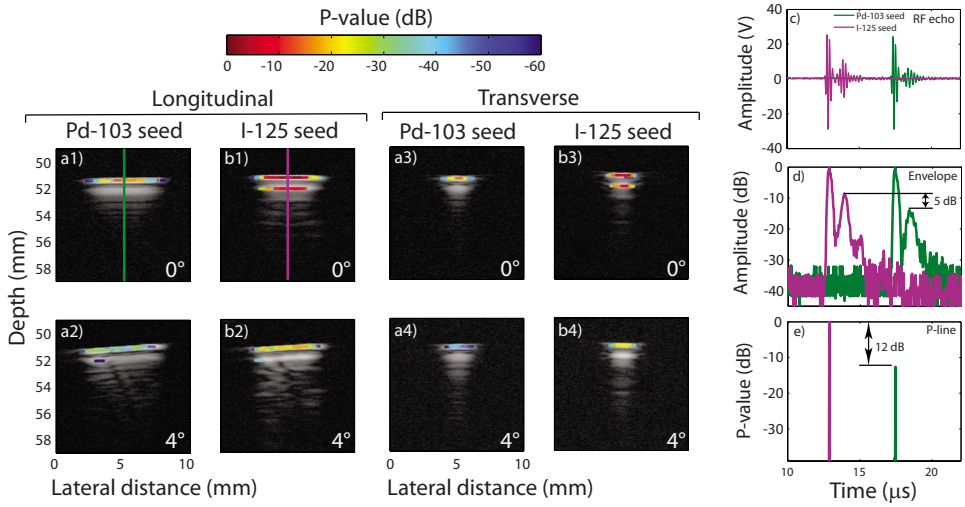


Fig. 1. (Color online) (a1)–(a4): *P*-mode images of Pd-103 seed in a gel pad at transverse and longitudinal orientations of 0 and 4 deg. (b1)–(b4): *P*-mode images of I-125 seed in gel pad at transverse and longitudinal orientations of 0 and 4 deg. (c) and (d) rf and envelope of central A-lines. (e) *P*-line obtained by processing the central A-lines with the SSA algorithm.

experimental signal-to-noise ratio (SNR) for the same angle and orientation. Experimentally, the SNR varied from 46 to 27 dB. The largest SNR was found for the longitudinal orientation at 0 deg and the smallest SNR for the transverse orientation at 10 deg.

Figure 1 presents the results obtained from gel-pad experiments. All the *P*-mode images (Figs. 1a1–a4 and 1b1–b4) are displayed with the same color scale to facilitate visual comparison. These *P*-mode images indicate that for both orientations and both angles, the I-125 and Pd-103 are perfectly detected and imaged by the SSA algorithm. The most striking difference between the *P*-mode images of I-125 and Pd-103 occur in the actual *P*-values. The *P*-values always are higher for the I-125 seed as shown by the dark red compared to the orange present on the *P*-mode images at 0 deg (i.e., Fig. 1a1 compared Fig. 1b1 and Fig. 1a3 compared Fig. 1b3) and the orange compared to the blue on the *P*-mode images at 4 deg (i.e,. Fig. 1a2 compared Fig. 1b2 and Fig. 1a4 compared Fig. 1b4). (The tilt angle of 4 deg was chosen to illustrate the differences between the two types of seeds because for this modest angle, both seed types should be reliably imaged. Therefore, performance differences should be apparent at this angle.)

To investigate why the I-125 seed yields larger *P*-values (i.e., is better detected by the SSA algorithm), the central A-lines of Figs. 1a1 and 1b1 are displayed in Figs. 1(c) (time-delayed for visualization). Both A-lines contain a main signal followed by a repetition signal about 0.8 μs later. The main-signal amplitudes are nearly identical for both seeds ($<$3.3% relative difference), but the repetition-signal amplitude of the I-125 seed is approximately 44% greater than that of the Pd-103 seed. This difference is clear in the envelope of the two A-lines shown in Fig. 1(d). The envelope of the repetition signal from the I-125 seed is 5 dB greater than that from the Pd-103 seed. Figure 1(e) displays the resulting *P*-line obtained by processing the central A-lines of Fig. 1(c) with the SSA algorithm. It reveals that the peak *P*-value for the I-125 seed is 12 dB greater than that for the Pd-103 seed. The SSA algorithm uses envelope signals to quantify the signal repetition.[5] Therefore, the SSA algorithm is expected to yield greater *P*-values for the I-125 seeds than for the Pd-103 seeds because of the greater repetition-signal amplitude of the I-125 seed. This greater repetition-signal amplitude was incorporated in the I-125 seed simulations. These simulations were performed in the same manner as for the

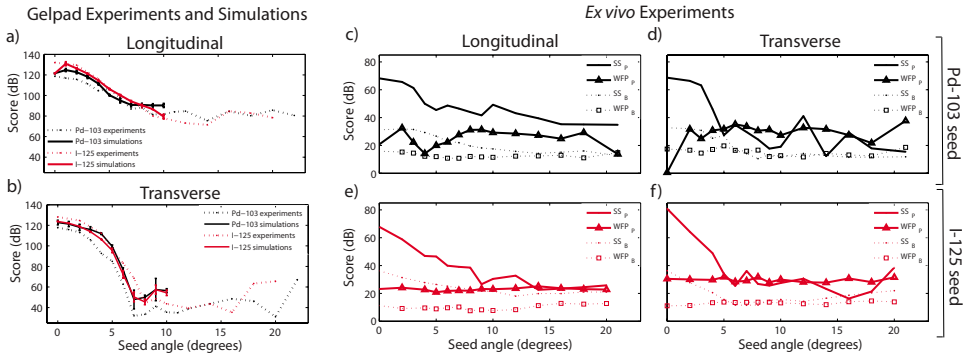


Fig. 2. (Color online) SSA-algorithm performance on simulations and experimental data. Scores for I-125 and Pd-103 seeds in a gel pad (a) from longitudinal-orientation scans and simulations and (b) from transverse-orientation scans and simulations. Seed scores and worst false positive scores from *P*-mode and B-mode images of a Pd-103 seed in *ex vivo* beef for (c) longitudinal- and (d) transverse-orientation scans and of an I-125 seed in *ex vivo* beef for (e) longitudinal- and (f) transverse-orientation scans.

Pd-103 seed as described in detail previously.[6] The empirical values from the I-125 seed gel-pad experiments were used to determine the amplitudes of the pulses used to simulate I-125 seed RF echo signals.

Figures 2(a) and 2(b) display the scores obtained for I-125 and Pd-103 for simulations and gel-pad experiments. For the simulations, each data point was the average of 10 realizations, displayed with error bars representing the standard deviations. From 0 to 4 degrees, the experimental longitudinal scores for the I-125 seed were between 8 and 12 dB greater than those for the Pd-103 seed. At angles greater than 5 degrees, the I-125 and Pd-103 experimental scores become nearly identical and reached a plateau near 85 dB. The simulated scores for I-125 seeds in the longitudinal orientation had similar values to the corresponding experimental scores except for the low value at 0 degrees. At angles smaller than 5 degrees, the simulated Pd-103 scores for the longitudinal orientation were about 8 dB higher than the experimental value, but again the trends were equivalent and the scores were nearly equal at angles greater than 5 deg. The experimental scores for the I-125 seed in the transverse orientation were 10 dB higher than those for Pd-103 seed from 0 to 8 degrees. At angles larger than 8 deg, the experimental transverse scores reached a plateau at about 45 dB. The scores from the simulated data in the transverse orientation are approximately the same for both types of seeds and follow the trend of the experimental data. The simulated I-125 scores are about 5 dB lower than the experimental values, and the simulated Pd-125 scores are about 5 dB higher than the experimental values.

As expected, visual inspection of the beef *P*-mode images (Fig. 3) reveals that algorithm performance worsens as the angle increases. For both orientations, imaging of the I-125 seed is satisfactory only at angles <9 degrees. When the angle of the I-125 seed increases

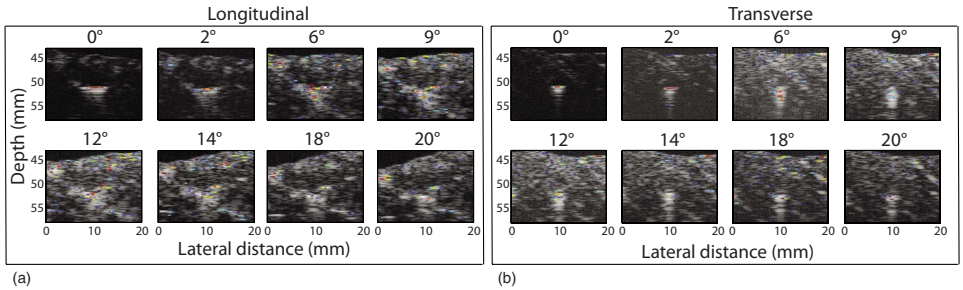


Fig. 3. (Color online) *Ex vivo* experiments: *P*-mode images (40-dB dynamic range) of an I-125 seed inserted into beef. (a) and (b) Longitudinal- and transverse-orientation scans of the seed at various angles, respectively.

beyond 10 deg, more false-positive *P*-values are visible in the surrounding tissue, and the *P*-values at the actual seed location decrease. Visual comparison of the *P*-mode images from both seed types reveals the same trends, but the *P*-mode images alone do not clearly reveal whether the SSA algorithm detects I-125 seeds better or worse than it detects Pd-103 seeds.

To quantify detection performance, Figs. 2(c)–2(f) display SS and WFP from experimental *ex vivo* beef results. At 0 deg, the longitudinal SS_P for both seed types is approximately 68 dB. As the angle increases, SS_P gradually decreases to 27 and 40 dB for the I-125 and Pd-103 seeds, respectively. Nevertheless, for both seed types and at every angle, SS_P is greater than SS_B. In other words, the contrast provided by the *P*-mode image is greater than that provided by the B-mode image, i.e., seeds can be visualized better on *P*-mode than B-mode. However, at angles greater than 9 degrees, the SS_P value for Pd-103 is higher than the SS_P value for I-125. This result means that the algorithm would detect the Pd-103 seed better than the I-125 seed at these angles. The values for WFP_P and WFP_B are nearly equal for both seed types with values between 25 and 30 dB for WFP_P and between 10 and 13 dB for WFP_B. For the I-125 seed and at angles smaller than 14 deg, SS_P is greater than WFP_P. This result means that at angles smaller than 14 deg, the *P*-mode image of the SSA algorithm would detect a seed before any false positives. However, beyond 14 deg, approximately equal values of WFP_P and SS_P imply that the algorithm could produce false-positive seed detections. By comparison, at every angle SS_B is greater than WFP_B which means that no false-positives would occur by visually inspecting the B-mode images.

The transverse I-125 scores for the transverse orientation are similar to the corresponding Pd-103 scores. As shown in Fig. 2(f), SS_P decreases quickly from 80 dB at 0 deg and remains constant at approximately 30 dB for angles beyond 5 deg. Furthermore, beyond 5 deg, WFP_P approximately equals SS_P. Similar to the longitudinal-orientation scores, for every angle (except the odd value at 16 deg), SS_P exceeds SS_B. These results indicate that the P-mode image has higher contrast than the B-mode image. Finally, at low angles (i.e., angles <3 deg), the SS_P value for the I-125 seed is about 10 dB higher than the SS_P value for the Pd-103 seed. Therefore, for near optimal insertion (i.e., at seed-tilt angles smaller than 3 deg), the SSA algorithm detects I-125 seeds better than Pd-103 seeds.

4. Discussion and conclusions

In this letter, we discuss the extension of a previously developed algorithm to image and detect brachytherapy seeds. The algorithm successfully imaged a popular type of palladium seed as described in prior publications.[5,6] This letter describes how the algorithm was applied to imaging a popular type of iodine seeds. Overall, results indicate that the algorithm successfully imaged the iodine seeds. The algorithm reliably imaged iodine seeds in *ex vivo* beef specimens at tilt angles smaller than 13 and 5 deg for longitudinal and transverse orientations, respectively.

Gel-pad experiments revealed that the repetition-signal amplitude of the I-125 seeds was greater than that of the Pd-103 seeds. The SSA algorithm exploits that repetition signals to make images; therefore, the algorithm detected I-125 seeds better than Pd-103 seeds in the gel pad. Although we remain unable to identify the mechanism that creates the repetition signal, the fact that a similar repetition signal was observed with two different types of seeds having a similar geometry (at least at 5 MHz) suggests that the repetition mechanism might be associated with the cylindrical shape of the seed. Furthermore, because the repetition-signal amplitude is greater for the I-125 seeds than for the Pd-103 seeds, signal differences may be attributable to differences in internal structure or details of shell shape. An encouraging conclusion of this study is that because both brachytherapy seeds produced a repetition signal, we were able to image these two different types of seeds with the same algorithm. This indicates that the algorithm may be robust to the type of seeds that are used, and this robustness could be very valuable clinically where many types of seeds can be encountered, even though the overall geometry (i.e., the diameter and length) of all seeds is well standardized.

Another valuable question that the results may answer is what type of seeds should be used clinically if the highest-priority criterion for seed selection is provision of the best possible

feedback about seed location. Gel-pad experiments indicate that I-125 would constitute a better choice based on this criterion because I-125 consistently produced larger *P*-values. However, the *ex-vivo* beef experiments did not yield a conclusive answer. SS_P values were found to be greater for the I-125 seeds in the more-clinically transverse direction, but in the longitudinal direction, SS_P values were approximately the same for both seed types. Also, WFP_P values led to the conclusion that the SSA algorithm might produce slightly more false-positives when imaging I-125 seeds *ex vivo* than when imaging Pd-103 seeds for identical SS_P. Some of these findings can be explained by the experimental conditions. Although we carefully tried to acquire data for both seed types under identical experimental conditions, some minor differences existed. For example, the beef tissue was purchased from the same supplier and was of the same general type (i.e., cut) of beef, but the specimens for the Pd-103 and I-125 seeds were not identical.

The next step of this study will be evaluation of the SSA algorithm using clinical data. Because the SSA algorithm uses only signal envelopes, its translation to the clinic should be straightforward. We plan to evaluate its performance on a significant number of patients and to present performance in terms of receiver operator curves (ROCs).

Acknowledgments

This research is supported in part by NIH Grant No. CA098465.

References and links

[1]H. H. Holm, N. Juul, J. F. Pedersen, H. Hansen, and I. Stroyer, "Transperineal ^{125}iodine seed implantation in prostatic cancer guided by transrectal ultrasonography," J. Urol. (Baltimore) **130**, 283–286 (1983).

[2]J. C. Blasko, H. Ragde, and D. Schumacher, "Transperineal percutaneous iodine-125 implantation for prostatic carcinoma using transrectal ultrasound and template guidance," Endocurie. Hypertherm. Oncol. **3**, 131–139 (1987).

[3]J. Crook, M. McLean, C. Catton, I. Yeung, J. Tsihlias, and M. Pintilie, "Factors influencing risk of acute urinary retention after trus-guided permanent prostate seed implantation," Int. J. Radiat. Oncol., Biol., Phys. **52**, 453–460 (2002).

[4]Z. Wei, M. Ding, D. Downey, and A. Fenster, "3D TRUS guided robot assisted prostate brachytherapy," Medical Image Computing and Computer-Assisted Intervention (2005), Vol. **8**, pp. 17–24.

[5]J. Mamou and E. J. Feleppa, "Singular spectrum analysis applied to ultrasonic detection and imaging of brachytherapy seeds," J. Acoust. Soc. Am. **121**, 1790–1801 (2007).

[6]J. Mamou, S. Ramachandran, and E. J. Feleppa, "Angle-dependent ultrasonic detection and imaging of brachytherapy seeds using singular spectrum analysis," J. Acoust. Soc. Am. **123**, 2148–2159 (2008).

[7]J. F. Williamson, B. M. Coursey, L. A. DeWerd, W. F. Hanson, R. Nath, M. J. Rivard, and G. Ibbott, "Recommendations of the American Association of Physicists in Medicine on 103Pd interstitial source calibration and dosimetry: Implications for dose specification and prescription," Med. Phys. **27**, 634–642 (2000).

[8]http://www.isoaid.com/I125.html.

Noise reduction in binaural hearing aids: Analyzing the benefit over monaural systems

Sriram Srinivasan
Philips Research, High Tech Campus 36, 5656AE Eindhoven, The Netherlands
sriram.srinivasan@philips.com

Abstract: Binaural beamforming using signals from both left and right hearing aids offers greater potential for noise reduction than using signals from a single aid. However, wireless transmission of data imposes power constraints. Since most modern hearing aids have multiple microphones and are capable of spatial filtering, it is of interest to study the conditions when a binaural system offers significant improvements over a multi-microphone monaural system, and the situations when the noise reduction benefits are only marginal. An intelligent transmission scheme could then be designed such that signals are exchanged between the hearing aids only when the benefits are significant.

© 2008 Acoustical Society of America
PACS numbers: 43.60.Fg [DOS]
Date Received: June 20, 2008 **Date Accepted:** August 29, 2008

1. Introduction

A monaural hearing aid solution consists of a single hearing aid fit onto one ear of the user and provides functions such as compression, amplification, and feedback cancellation. A binaural system comprises two such devices, one on each ear, and they collaborate with one another over a wireless link. Previous studies (Welker *et al.*, 1997) have demonstrated the benefit of binaural noise reduction using two single-microphone hearing aids, where the binaural system enabled spatial filtering. A binaural multi-channel Wiener filter employing multiple microphones at each hearing aid was introduced in Klasen *et al.* (2005), but no comparisons to the monaural multi-channel filter were provided. Most modern hearing aids have two or more microphones mounted on them, and thus a monaural hearing aid is itself capable of directional processing through spatial filtering techniques. In this paper, the conditions under which a binaural system offers significant improvements over a multi-microphone monaural noise reduction system, and the situations when the benefits are only marginal, are studied. As wireless communication of audio signals is power intensive, it is advantageous to transmit the signals only in situations when the resulting benefits are high.

Viewing the the binaural beamforming problem as a remote Wyner-Ziv problem, an elegant relation between the communication bit-rate and the resulting beamforming gain was derived in Roy and Vetterli (2006). However, determining the optimal rate allocation is computationally complex and the associated overhead is high, especially for conditions where the resulting benefit over a monaural system is only marginal. In this paper, by analyzing the performance gain across different parameters (e.g., frequency, location of the interferer, signal-to-interference ratio, etc.), broad criteria for determining whether or not signals need to be transmitted are defined. For those conditions where a binaural scheme offers significant gains, the rate allocation can then be performed optimally according to the scheme of Roy and Vetterli (2006).

2. Monaural and binaural speech enhancement

Section 2.1 introduces the signal model. Section 2.2 describes the model employed to incorporate the effect of head shadow. This is followed in Sec. 2.3 by a brief description of the multi-channel Wiener filter (MWF) that forms the basis of the monaural and binaural speech enhancement systems considered in this paper.

2.1 Signal model

Consider a desired source $S(\omega)$ with power spectral density (PSD) $\mathrm{E}\{S(\omega)S^{\dagger}(\omega)\}=\Phi_s(\omega)$, and an interfering source $I(\omega)$ with PSD $\mathrm{E}\{I(\omega)I^{\dagger}(\omega)\}=\Phi_i(\omega)$, where $\dagger$ indicates complex conjugate transpose. The signal observed at the kth microphone on the left hearing aid can be written as

$$X_L^k(\omega) = H_L^k(\omega)S(\omega) + G_L^k(\omega)I(\omega) + U_L^k(\omega) + V_L^k(\omega), \quad k = 1, \ldots, N, \tag{1}$$

where $H_L^k(\omega)$ and $G_L^k(\omega)$ are the transfer functions between the kth microphone on the left hearing aid and the desired and interfering sources, respectively, $U_L^k(\omega)$ and $V_L^k(\omega)$ correspond to uncorrelated (e.g., sensor) noise and ambient diffuse noise, respectively, at the kth microphone on the left hearing aid; and N is the number of microphones on the left hearing aid. The PSD of the uncorrelated noise is given by $\mathrm{E}\{U_L^k(\omega)U_L^{l\dagger}(\omega)\}=\delta(k-l)\Phi_u(\omega)\ \forall k,l$. The PSD of the ambient noise, which is assumed to be diffuse, is given by $\mathrm{E}\{V_L^k(\omega)V_L^{l\dagger}(\omega)\}=\Phi_v(\omega)\mathrm{sinc}(\omega d|k-l|/c)\ \forall k,l$, where $\mathrm{sinc}(x)=\sin(x)/x$, d is the distance between two adjacent microphones, and c is the speed of sound in air. Further, we assume that $S(\omega)$, $I(\omega)$, $U(\omega)$, and $V(\omega)$ are pairwise independent. A similar right ear model follows:

$$X_R^k(\omega) = H_R^k(\omega)S(\omega) + G_R^k(\omega)I(\omega) + U_R^k(\omega) + V_R^k(\omega), \quad k = 1, \ldots, N, \tag{2}$$

where the relevant terms are defined analogously to the left ear. Define $\mathbf{H}_L(\omega)=[H_L^1(\omega), H_L^2(\omega), \ldots, H_L^N(\omega)]^T$. The vectors $\mathbf{G}_L(\omega)$, $\mathbf{X}_L(\omega)$, $\mathbf{U}_L(\omega)$, and $\mathbf{V}_L(\omega)$ are constructed analogously. Define the right ear quantities $\mathbf{H}_R(\omega)$, $\mathbf{G}_R(\omega)$, $\mathbf{X}_R(\omega)$, $\mathbf{U}_R(\omega)$, and $\mathbf{V}_R(\omega)$ similarly. Finally, define the binaural quantities $\mathbf{H}(\omega)=[\mathbf{H}_L^T(\omega), \mathbf{H}_R^T(\omega)]^T$, $\mathbf{G}(\omega)=[\mathbf{G}_L^T(\omega), \mathbf{G}_R^T(\omega)]^T$, $\mathbf{X}(\omega)=[\mathbf{X}_L^T(\omega), \mathbf{X}_R^T(\omega)]^T$, $\mathbf{U}(\omega)=[\mathbf{U}_L^T(\omega), \mathbf{U}_R^T(\omega)]^T$, and $\mathbf{V}(\omega)=[\mathbf{V}_L^T(\omega), \mathbf{V}_R^T(\omega)]^T$. The left ear, right ear, and binaural signal models can be written in vector notation as

$$\mathbf{X}_L(\omega) = \mathbf{H}_L(\omega)S(\omega) + \mathbf{G}_L(\omega)I(\omega) + \mathbf{U}_L(\omega) + \mathbf{V}_L(\omega),$$

$$\mathbf{X}_R(\omega) = \mathbf{H}_R(\omega)S(\omega) + \mathbf{G}_R(\omega)I(\omega) + \mathbf{U}_R(\omega) + \mathbf{V}_R(\omega),$$

$$\mathbf{X}(\omega) = \mathbf{H}(\omega)S(\omega) + \mathbf{G}(\omega)I(\omega) + \mathbf{U}(\omega) + \mathbf{V}(\omega). \tag{3}$$

2.2 Head shadow model

The spherical head shadow model described in Duda and Martens (1998) is used to obtain the transfer functions $\mathbf{H}(\omega)$ and $\mathbf{G}(\omega)$. Let the origin be the center of the sphere. Let a be the radius of the sphere and r be the distance between the origin and the sound source, and define $\rho=r/a$. Let θ denote the angle between a ray from the origin to the sound source and a ray from the origin to the point of observation on the surface of the sphere as in Fig. 1. The head related transfer function (HRTF) corresponding to the angle of incidence θ is then given by

$$H(\rho, \omega, \theta) = -\frac{\rho c}{\omega a} e^{-j\omega a/c}\Psi, \tag{4}$$

with

$$\Psi(\rho, \omega, \theta) = \sum_{m=0}^{\infty} (2m+1)P_m(\cos\theta)\frac{h_m(\omega\rho a/c)}{h_m'(\omega a/c)}, \tag{5}$$

where P_m is the Legendre polynomial of degree m, h_m is the spherical Hankel function of order m, and h_m' is the derivative of h_m w.r.t. its argument.

Let θ_s denote the angle between the vertical y axis and a ray from the origin to the desired source. Let θ_i be defined similarly for the interfering source. The first microphone on the left and right ears is assumed to be located at $5\pi/9$ and $-5\pi/9$, respectively. The microphones

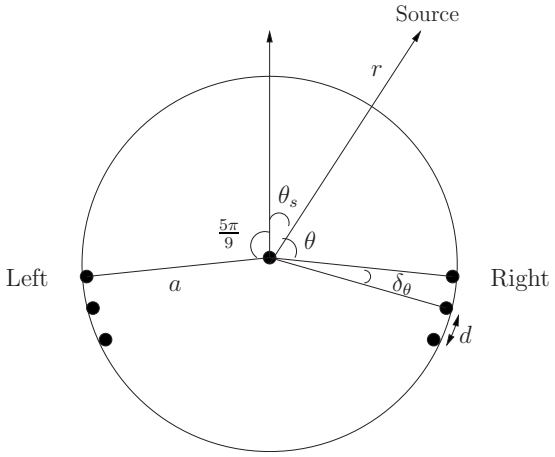


Fig. 1. A binaural hearing aid setup with three microphones on each ear. In this example, the source is located at $\theta_s = -20°$.

are assumed to be located on the surface of the sphere. Let d denote the length of the arc between two adjacent microphones on a single hearing aid. The HRTFs are given by

$$H_L^k(\omega) = H(\rho, \omega, -\theta_s + 5\pi/9 - (k-1)\delta_\theta), \tag{6}$$

$$H_R^k(\omega) = H(\rho, \omega, -\theta_s - 5\pi/9 + (k-1)\delta_\theta), \quad k = 1, \ldots, N, \tag{7}$$

where $\delta_\theta = d/a$ is the angle subtended by the arc between two adjacent microphones. Similarly, the transfer functions corresponding to the interferer are given by

$$G_L^k(\omega) = H(\rho, \omega, -\theta_i + 5\pi/9 - (k-1)\delta_\theta), \tag{8}$$

$$G_R^k(\omega) = H(\rho, \omega, -\theta_i - 5\pi/9 + (k-1)\delta_\theta), \quad k = 1, \ldots, N. \tag{9}$$

2.3 Multi-channel Wiener filter

The problem is viewed from the perspective of the left hearing aid. Similar results hold at the right ear due to symmetry. For both the monaural and binaural systems, the MWF is used to obtain a minimum mean squared error (MMSE) estimate of the desired signal observed at the first microphone of the left ear device, $H_L^1(\omega)S(\omega)$. The monaural MWF is given by

$$\mathbf{W}_M(\omega) = \mathrm{E}\{H_L^1(\omega)S(\omega)\mathbf{X}_L^\dagger(\omega)\}\mathrm{E}\{\mathbf{X}_L(\omega)\mathbf{X}_L^\dagger(\omega)\}^{-1} = \Phi_s(\omega)H_L^1(\omega)\mathbf{H}_L^\dagger(\omega)\Phi_{x,L}^{-1}(\omega), \tag{10}$$

where $\Phi_{x,L}(\omega) = \mathrm{E}\{X_L(\omega)X_L^\dagger(\omega)\} = \Phi_s(\omega)\mathbf{H}_L(\omega)\mathbf{H}_L^\dagger(\omega) + \Phi_i(\omega)\mathbf{G}_L(\omega)\mathbf{G}_L^\dagger(\omega) + \Phi_u\mathbf{I}_N + \Phi_v(\omega)\mathbf{\Gamma}_M(\omega)$, $\mathbf{I}_N$ is the identity matrix of dimension N, and the (i,j)th entry of the diffuse noise coherence matrix $\mathbf{\Gamma}_M(\omega) = \mathrm{E}\{\mathbf{V}_L(\omega)\mathbf{V}_L^\dagger(\omega)\}$ is given by

$$\mathbf{\Gamma}_M^{ij}(\omega) = \mathrm{sinc}(\omega d|i-j|/c), \quad 1 \le i,j \le N. \tag{11}$$

The binaural MWF is given by

$$\mathbf{W}_B(\omega) = \mathrm{E}\{H_L^1(\omega)S(\omega)\mathbf{X}^\dagger(\omega)\}\mathrm{E}\{\mathbf{X}(\omega)\mathbf{X}^\dagger(\omega)\}^{-1} = \Phi_s(\omega)H_L^1(\omega)\mathbf{H}^\dagger(\omega)\Phi_x^{-1}(\omega), \tag{12}$$

where $\Phi_x = \mathrm{E}\{X(\omega)X^\dagger(\omega)\} = \Phi_s(\omega)\mathbf{H}(\omega)\mathbf{H}^\dagger(\omega) + \Phi_i(\omega)\mathbf{G}(\omega)\mathbf{G}^\dagger(\omega) + \Phi_u\mathbf{I}_{2N} + \Phi_v(\omega)\mathbf{\Gamma}_B(\omega)$, $\mathbf{I}_{2N}$ is the identity matrix of dimension $2N$, and the (i,j)th entry of $\mathbf{\Gamma}_B(\omega) = \mathrm{E}\{\mathbf{V}(\omega)\mathbf{V}^\dagger(\omega)\}$ is given by

$$\mathbf{\Gamma}_B^{ij}(\omega) = \begin{cases} \text{sinc}(\omega d|i-j|/c), & 1 \le i,j \le N \quad \text{or} \quad N \le i,j \le 2N, \\ \text{sinc}(\omega(2a)|i-j|/c) & \text{otherwise}. \end{cases} \tag{13}$$

Equation (13) assumes $d \ll 2a$ so that the distance between any pair of microphones on the left and right hearing aids can be assumed to be $2a$. The corresponding mean squared error (MSE) can be written as

$$\xi_M(\omega) = \text{E}\{|H_L^1(\omega)S(\omega) - \mathbf{W}_M(\omega)\mathbf{X}_L(\omega)|^2\} = |H_L^1(\omega)|^2\Phi_s(\omega)[1 - \Phi_s(\omega)\mathbf{H}_L^\dagger(\omega)\Phi_{x,L}^{-1}(\omega)\mathbf{H}_L(\omega)],$$

$$\xi_B(\omega) = \text{E}\{|H_L^1(\omega)S(\omega) - \mathbf{W}_B(\omega)\mathbf{X}(\omega)|^2\} = |H_L^1(\omega)|^2\Phi_s(\omega)[1 - \Phi_s(\omega)\mathbf{H}^\dagger(\omega)\Phi_x^{-1}(\omega)\mathbf{H}(\omega)]. \tag{14}$$

Using the expression for the MSE given in Eq. (14), the improvement in the signal-to-interference-plus-noise ratio (SINR) in the monaural and binaural cases is given by

$$\Delta_M = 10\log_{10}\left(\frac{|H_L^1(\omega)|^2\Phi_s(\omega)}{\xi_M(\omega)}\right) - 10\log_{10}\left(\frac{|H_L^1(\omega)|^2\Phi_s(\omega)}{|G_L^1(\omega)|^2\Phi_i(\omega) + \Phi_u + \Phi_v(\omega)}\right),$$

$$\Delta_B = 10\log_{10}\left(\frac{|H_L^1(\omega)|^2\Phi_s(\omega)}{\xi_B(\omega)}\right) - 10\log_{10}\left(\frac{|H_L^1(\omega)|^2\Phi_s(\omega)}{|G_L^1(\omega)|^2\Phi_i(\omega) + \Phi_u + \Phi_v(\omega)}\right), \tag{15}$$

where $10\log_{10}(|H_L^1(\omega)|^2\Phi_s(\omega)/|G_L^1(\omega)|^2\Phi_i(\omega)+\Phi_u+\Phi_v(\omega))$ is the input SINR (before processing) at the first microphone on the left hearing aid.

3. Performance analysis

Using Eq. (15), this section studies the benefit at the left ear due to monaural and binaural processing as a function of the azimuthal location of the interferer, the number of interferers, the signal-to-interference ratio (SIR), and the signal-to-noise ratio (SNR). The SIR and SNR at a certain ω are defined as $10\log_{10}(\Phi_s(\omega)/\Phi_i(\omega))$ and $10\log_{10}(\Phi_s(\omega)/\Phi_v(\omega))$, respectively. The level of the uncorrelated sensor noise is fixed at -40 dB (i.e., $\Phi_u = 1^{-4}$). The desired and interfering sources are assumed to be white Gaussian. The other relevant parameters are $a = 0.0875$ m, $d = 0.008$ m, $N = 2$ (two microphones on each hearing aid), and $c = 343$ m/s.

3.1 Effect of interferer location

Section 3.1.1 discusses the case when only one interferer is present. In a binaural system, as there are more than two microphones, it is possible to cancel more than one interferer. Section 3.1.2 discusses the case with two interferers. The case of more than two interferers is not considered in this paper.

3.1.1 Single interferer

For a desired source located at 0 deg and for different locations of the interferer, Fig. 2 plots Δ_M and Δ_B for four different frequencies 2, 4, 6, and 8 kHz corresponding to an input SIR of 0 dB and input SNR of 30 dB. Both the desired and interfering sources are located at a distance of $r = 1.5$ m from the head. It can be seen from Fig. 2 that across all frequencies, the differences between the monaural and binaural systems are most pronounced for interferers located approx. in $[-60°, 60°]$. This is because of the broad main lobe for the small microphone array in the monaural case. The larger microphone spacing in the binaural setup enables better separation of closely located desired and interfering sources. At low frequencies, e.g., in Fig. 2(a), the monaural array is not able to perform well and the benefit due to the binaural system is larger.

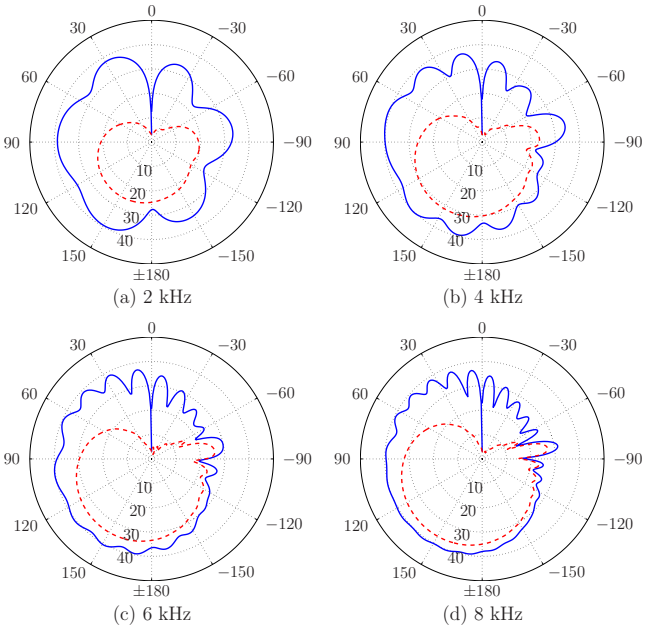


Fig. 2. (Color online) Improvement in SINR (dB) after monaural (dotted) and binaural (solid) processing for SIR =0 dB and SNR=30 dB.

3.1.2 Two interferers

When two interferers are simultaneously active, the four-microphone binaural system has a clear advantage over the two-microphone monaural system. This can be seen from Fig. 3(b), which plots the additional improvement $\Delta_B - \Delta_M$ provided by the binaural system. The binaural system provides good performance in most of the regions where the monaural system fails to perform.

The binaural system offers only marginal additional benefits in three situations. First is the case when both interferers are co-located, as indicated by the dark diagonal line in Fig. 3(b). This situation is equivalent to the case of one interferer, where the monaural system performs well, and thus the additional benefit from the binaural system is only marginal. The second situation is when both interferers are located close to the desired source, as indicated by the dark regions in all four corners of Fig. 3(b). The binaural array is unable to place two spatial nulls in the vicinity of the desired source. Finally, when one of the interferers is located around 180°, the

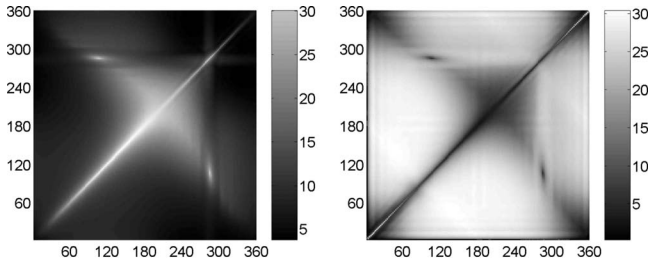


Fig. 3. Two simultaneous interferers, each at SIR 0 dB. Results are in dB and averaged over all frequencies for SNR 30 dB and are shown for different locations of the two interferers on the horizontal and vertical axes. (a) Improvement due to monaural processing (Δ_M). (b) Additional improvement due to binaural processing ($\Delta_B - \Delta_M$).

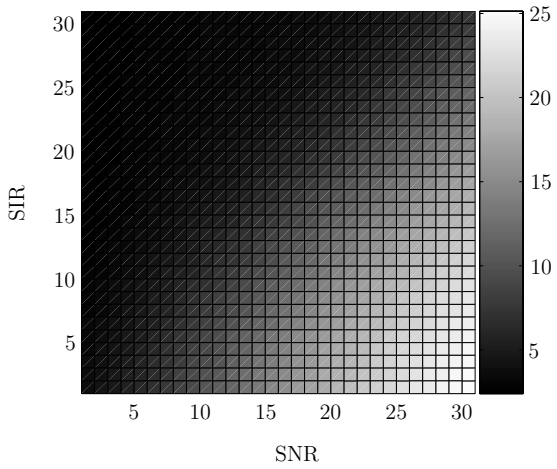


Fig. 4. Additional improvement (dB) due to binaural processing ($\Delta_B - \Delta_M$). Interferer located at 30°, results averaged over all frequencies for different values of SIR and SNR.

monaural system performs well, as seen in Fig. 3(a). Due to the front-back ambiguity in a broadside array, when a desired source is active at 0°, the binaural system is unable to provide additional suppression for interferers located around 180°, as indicated by the dark region in the center of Fig. 3(b).

3.2 Effect of SIR and SNR

The additional benefit due to binaural processing decreases as the SIR increases and the SNR decreases as shown in Fig. 4, which plots $\Delta_B - \Delta_M$ averaged over all frequencies for different SIR and SNR values for an interferer located at 30°. At high SIR values, the additional benefit reduces to the 3 dB gain resulting from the reduction of uncorrelated noise due to the doubling of microphones.

4. Discussion

A wireless binaural noise reduction system requires an exchange of the observed microphone signals between the left and right hearing aids. It is evident from the analysis so far that the benefit due to binaural beamforming varies depending on interferer location and frequency. It is important to incorporate this dependency in the transmission scheme to conserve power. First, a hard decision may be made on whether or not to transmit, and in cases when transmission is necessary, an appropriate bit-rate may be calculated based on Roy and Vetterli (2006). We provide a sample hard decision scheme below based on the observations in the previous section.

(1) **SINR dependency**: At low SIRs (e.g., below 15 dB) and high SNRs (e.g., above 15 dB), signals may be exchanged between the left and right hearing aids. The gain in performance resulting from a binaural system is only marginal at high SIRs and low SNRs. By restricting transmission to this range, power consumption can be minimized.
(2) **Single interferer:** If only one localized interferer is present, transmission is beneficial when the interferer is located within $[-60°, 60°]$. Outside this range, the low frequency content (e.g., up to 2 kHz) may be transmitted. At higher frequencies, the monaural system provides good performance for interferers located outside $[-60°, 60°]$, thus eliminating the need for a binaural system.
(3) **Two interferers:** If two localized interferers are present, transmission is beneficial when at least one interferer is located within [60°, 300°]. If both interferers are located within a 60° neighborhood of 0° or 180°, the benefit is only marginal.

This paper has considered a simple model for head shadow and reverberation. It may be that the set of conditions where wireless transmission is beneficial is further narrowed in more realistic room environments, and this is a topic for further study.

References and links

Duda, R. O., and Martens, W. L. (**1998**). "Range dependence of the response of a spherical head model," J. Acoust. Soc. Am. **104**, 3048–3058.

Klasen, T. J., Moonen, M., van den Bogaert, T., and Wouters, J. (**2005**). "Preservation of interaural time delay for binaural hearing aids through multi-channel Wiener filtering based noise reduction," in *Proc. IEEE Int. Conf. Acoustics, Speech, Signal Processing*, pp. 29–32.

Roy, O., and Vetterli, M. (**2006**). "Rate-constrained beamforming for collaborating hearing aids," in *International Symposium on Information Theory (ISIT)*, pp. 2809–2813.

Welker, D. P., Greenberg, J. E., Desloge, J. G., and Zurek, P. M. (**1997**). "Microphone-array hearing aids with binaural output-part II: a two-microphone adaptive system," IEEE Trans. Speech Audio Process. **5**, 543–551.

Visualizations of sound energy across coupled rooms using a diffusion equation model

Yun Jing and Ning Xiang
Graduate Program in Architectural Acoustics, School of Architecture, Rensselaer Polytechnic Institute, Troy, New York 12180
xiangn@rpi.edu; jingy@rpi.edu

Abstract: Visualizations, based on a diffusion equation model, are presented for both steady-state and transient sound energy. For steady-state sound-pressure level distributions, animations created by scanning from the primary room to the secondary room reveal discontinuous transitions of sound energy caused by a location change from the wall area to the aperture area. Animations of time-dependent energy flow directions visualize the energy flows across coupled spaces. This study also reveals a "reversal" characteristic of energy flow directions which seems to be dependent on the size and location of the aperture.

© 2008 Acoustical Society of America
PACS numbers: 43.55.Br, 43.55.Ka [DKW]
Date Received: April 6, 2008 **Date Accepted:** September 5, 2008

1. Introduction

Acoustics in coupled spaces has been gaining a wide interest due to its ability to create nonexponential energy decay resulting from energy exchange at an aperture coupling multiple spaces. Coupled chambers have already been built in some concert halls to attach to the main hall, in order to produce a double-sloped energy decay, which has a fast decay at the beginning and a slow decay at the tail. This specific decay profile has been considered to be beneficial for both perceived clarity and reverberance.

The objective of this paper is to visualize sound-pressure distributions and sound energy flows. Most recently, a diffusion equation model has been applied to acoustically coupled spaces. Its validity has been experimentally substantiated.[1] The diffusion equation model for room-acoustic predictions was first validated by Picaut *et al.*[2] and has been recently extended in room-acoustics applications, mainly to various types of single-volume spaces.[2–6]

The previous work on the diffusion equation model in acoustically coupled rooms[1] has not considered sound-energy flows in coupled spaces. Energy flow is of significant importance since a double-sloped energy decay is caused by energy flow feedback: when sound energy in the primary room decays to a certain level, the slower decreasing, but higher energy in the secondary room flows back to the primary room and dominates the decay. While in previous literature steady-state figures are of the majority, the aim of this work is to visualize sound-pressure distributions and the sound-energy flows across the coupling aperture of two coupled rooms.

2. Diffusion equation model for room-acoustic prediction

Given the slow rates of energy change with time, according to Fick's law, the gradient of the sound-energy density $w(\mathbf{r},t)$ at position $\mathbf{r}$ and time t in the room under investigation causes the sound-energy flow vector $\mathbf{J}$,[2,3]

$$\mathbf{J} = -D\,\mathbf{grad}\,w(\mathbf{r},t), \tag{1}$$

where $D=\lambda c/3$ is defined as the diffusion coefficient, with λ being the mean-free path. The expression in Eq. (1) follows a physical analogy with the diffusion of particles in a scattering medium.[2] It implicitly assumes sound particles traveling along straight lines at sound speed c in the room under investigation with diffusely reflecting walls. In a region without sound sources,

 © 2008 Acoustical Society of America

a change of the sound energy density per unit time is associated with changes in the sound-energy flow vector,

$$\frac{\partial w(\mathbf{r},t)}{\partial t} = -\operatorname{div}\mathbf{J} = D\nabla^2 w(\mathbf{r},t). \tag{2}$$

The sound-energy density is then governed by the diffusion equation

$$\frac{\partial w(\mathbf{r},t)}{\partial t} - D\nabla^2 w(\mathbf{r},t) + cmw(\mathbf{r},t) = q(\mathbf{r},t) \quad \in V, \tag{3}$$

where the subroom, denoted by domain V with a source term $q(\mathbf{r},t)$, is zero for any subdomain where no source is present. The term $cmw(\mathbf{r},t)$ accounts for air dissipation in the room(s),[7] and can be extended to account for absorption due to scattering objects inside the room(s).[4] Equation (3) is the interior equation in domain V, being subject to the boundary condition on the interior surface S,

$$D\frac{\partial w(\mathbf{r},t)}{\partial n} + \frac{c\alpha}{2(2-\alpha)}w(\mathbf{r},t) = 0. \tag{4}$$

Jing and Xiang[6] have demonstrated that the diffusion equation with this boundary condition can model surfaces with absorption coefficients ranging from 0 to 1.0.

In modeling coupled rooms, the domain V comprises an arbitrary number of subdomains, which are the subrooms of the coupled-room system. Diffusion coefficients for each subroom are assigned based on the mean-free path of each subroom under the assumption that coupling these subrooms does not significantly change their free-path distributions.[1] Coupling configurations with weak coupling (small coupling apertures) approximately meet this assumption.

3. Sound pressure and energy flow distributions

An inherent advantage of the diffusion equation model is its ability to model sound-energy density at all locations within the space with a computational load on the order of minutes on a current personal computer. The gradient of the sound-energy density expressed in Eq. (1) then can be obtained. Therefore, the diffusion equation model is intrinsically suitable for modeling the sound-pressure level distribution as well as the energy flows. This section presents the animations of both steady sound-pressure level distributions and time-dependent energy flows.

3.1 Coupled-room description

Figure 1(a) illustrates the geometry of the coupled-room system as defined within a Cartesian coordinate system. The aperture is a square with a width of 3 m, and spans from $y=0.32$ m to $y=3.32$ m. The smaller room is the primary room with an acoustic source located at $(-5, 2.4, 1.3)$ m. Three different sets of absorption coefficients are assigned to the primary room and the secondary room, to obtain three configurations of the natural reverberation times (RTs) of both rooms, which cover the cases where the natural reverberation time T_1 of the primary room is smaller, the same as, and larger than the natural reverberation time T_2 of the secondary room, respectively. Table 1 lists relevant parameters. The purpose of using these configurations is to explore the relationship between the energy flow and each room's natural reverberation times.

3.2 Sound-pressure level distributions

In a previous study,[1] the sound-pressure level distributions along a line drawn perpendicularly across the aperture have been studied both experimentally and numerically. In this study, we provide more insight into the sound-pressure level distribution parallel to the aperture and the

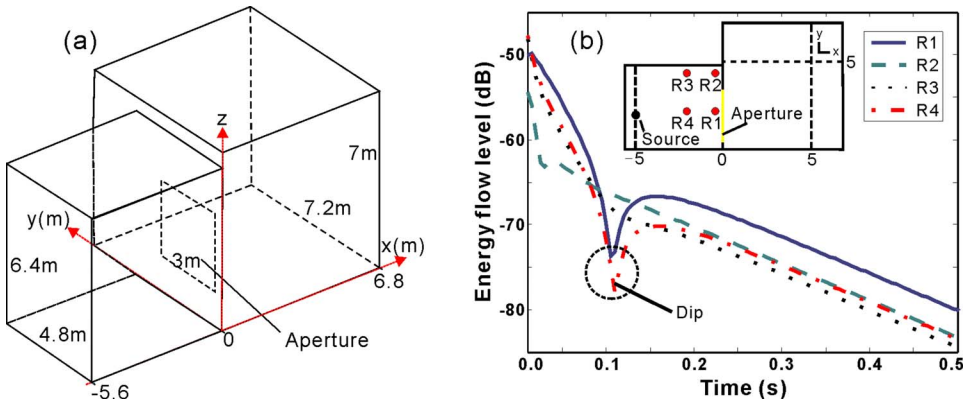


Fig. 1. (Color online) (a) Dimensions and coordinate definition of the two coupled rooms. (b) Energy-flow decays in the primary room for case 1 ($T_1 < T_2$).

wall containing the aperture, starting from a location near the aperture to a location far away from the aperture. The transition of the sound-pressure level caused by the location changing from the aperture opening to the wall is of particular interest.

All three room configurations are included in the investigation of the sound-pressure level distributions. The sound source has a power of 0.01 W. The diffusion equation is solved by a commercial finite element solver with approximately 8000 meshes which fulfills the mesh condition determined by the mean-free path length.[3] The direct sound field is excluded,[3] leaving only the reverberant sound field. The animations show the sound-pressure level distributions scanning from $x=-2$ m to $x=2$ m (i.e., from the primary room to the secondary room), at a height of 3 m. Multimedia 1 represents case 1 as listed in Table 1. To highlight the continuity of the sound-pressure level distributions across the aperture, the sound-pressure level distribution at $x=-0.05$ m holds on in the animations while the scanning goes further into the secondary room.

Mm. 1. Sound-pressure level distribution from the primary room (4.8 m wide) to the secondary room (7.2 m wide) for case 1 ($T_1 < T_2$). The last sound-pressure level distribution in the primary room (at $x=-0.05$) holds on while the scanning goes further into the secondary room to highlight the continuity of the distribution at the aperture. This is a file of type "avi" (304 Kb).

To save space, the animations for cases 2 and 3 are not included in this paper. However, all three animations show the sound-pressure continuity from the primary room to the secondary room across the aperture and the noncontinuous transition in each room from the wall to the opening area when the receivers get close to the aperture. Experimental verifications have been undertaken and will be reported in a follow-up paper.

Table 1. Values of absorption coefficients and natural reverberation times in two rooms

	Case 1	Case 2	Case 3
α_1[a]	0.2	0.2	0.2
α_2	0.1	0.25	0.60
T_1/s[b]	0.66	0.66	0.66
T_2/s	1.78	0.66	0.20

[a]1 represents the main room, 2 represents the secondary room.
[b]The RTs are estimated by the Eyring equation.

3.3 Energy flows

To calculate the time-dependent energy flow, an impulsive sound energy is generated by the acoustic source to excite the room. The time step is set to 5 ms, and the modeling time is from 10 to 150 ms for the three cases listed in Table 1. The diffusion equation model is not valid within the "mean-free time,"[3] which is around 0 to 10 ms in this configuration. After 150 ms, the energy flows do not change significantly for all three cases. The time-dependent energy flows are determined using Eq. (1). Multimedia 2 provides three-dimensional (3D) energy flow distributions for case 1. The 3D arrows show the direction of the energy flow. For the purpose of clarity, Mm. 3 and 4 illustrate case 1 and case 2 in a two-dimensional representation where energy flows are presented on the xy-plane at a height of $z=3$ m.

Mm. 2. Three-dimensional time-dependent sound-energy flow for case 1 ($T_1 < T_2$). This is a file of type "avi" (2.4 Mb).

Mm. 3. Two-dimensional time-dependent sound-energy flow for case 1 ($T_1 < T_2$). This is a file of type "avi" (2.2 Mb).

Mm. 4. Two-dimensional time-dependent sound energy flow for Case 2 ($T_1 = T_2$). This is a file of type "avi" (1.8 Mb).

For case 1, where the natural RT in the primary room is smaller than that in the secondary room, Mm. 2 shows a clear energy feedback near the aperture beginning at around 110 ms in terms of the energy flow directions, i.e., the sound-energy flows from the secondary room into the primary room via the aperture. In addition, the start of the energy feedback appears earlier around the aperture than it does at a location further inside the secondary room. This delay in energy feedback inside the secondary room is probably due to the fact that the primary room draws the sound energy from the secondary room faster at the position near the aperture (i.e., near the primary room). For the other two cases, no apparent energy feedback from the secondary room can be found, especially in case 3, where the RT of the secondary room is much smaller than the primary room. However, the animation for case 3 also has not been included in order to minimize the number of animations. For case 2, in the proximity of the source, reversal of flow directions occurs. Additional simulations show that this phenomenon also occurs in single rooms. In a single room, initially when the energy decays from an impulse, the energy is strongest around the source and the energy flows point away from the source. As time progresses, the region with the strongest energy moves from the source to the other place (usually not far away from the source) in the room and stays steady, indicating that the energy flow now points outwards from a different spot, which is the reason why the energy flow directions reverse. Therefore, the reversal in flow direction near the source probably has little relevance to the energy feedback through the aperture from the coupled room. Although it seems plausible that the energy flow in case 2, when $T_1 = T_2$, shows a trend going back to the primary room at the aperture area, a longer time simulation shows negligible energy feedback around the aperture.

3.4 Energy-flow decays

While the aforementioned animations create visualization of the direction of energy flows, this section elaborates on sound-energy flow decays. Since distinct energy feedback can be demonstrated only in case 1, energy-flow decays are discussed only under this circumstance. The time-dependent decaying function at location $\mathbf{r}$ of energy-flow levels is defined as

$$J_L(\mathbf{r},t) = 10\log\left[\left(\frac{\partial w(\mathbf{r},t)}{\partial x}\right)^2 + \left(\frac{\partial w(\mathbf{r},t)}{\partial y}\right)^2 + \left(\frac{\partial w(\mathbf{r},t)}{\partial z}\right)^2\right]^{1/2}, \quad (5)$$

with the diffusion coefficient D being neglected, because the relative levels of the energy flow in each room are of major concern.

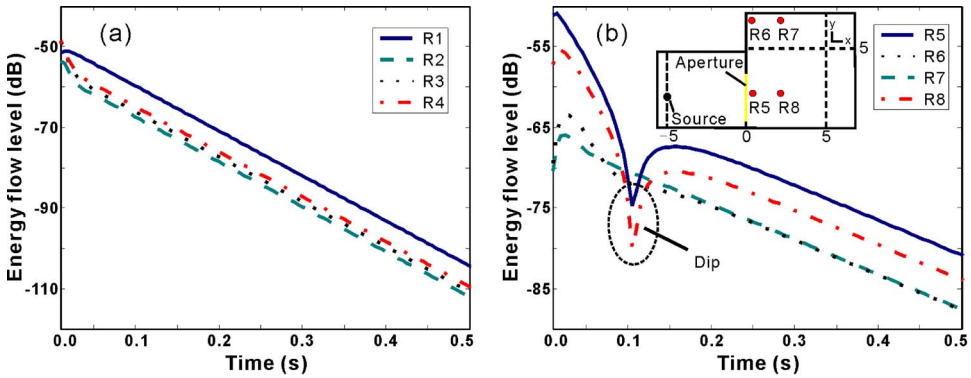


Fig. 2. (Color online) (a) Energy-flow decays in a single room; in the primary room the aperture is replaced by a wall material with an absorption coefficient 1.0. (b) Energy-flow decays in the secondary room for case 1 ($T_1 < T_2$).

Figure 1(b) illustrates the energy-flow decays in the primary room for case 1. Four positions at R1 $(-0.05, 2.5, 3)$ m, R2 $(-0.05, 4.5, 3)$ m, R3 $(-2, 4.5, 3)$ m, and R4 $(-2, 2.5, 3)$ m are chosen. Distinct "dips" of the energy flows are found for R1 and R4, both being along the line $y=2.5$ m. The energy-flow dips occurs at around 105 and 110 ms, the time at which the energy feedback from the secondary room is about to happen. The dip of the energy-flow level strongly suggests that, in a certain area, the magnitude of the energy flow abruptly drops and rises along a reversal of direction, when the energy feedback happens or is about to happen. Thus, a sharp dip in the energy-flow decay function is formed. For R2 and R3, both along the line at $y=4.5$ m, the energy flows decay monotonously, showing no abrupt transition. Additional simulations show that the dip is more likely to take place between $y=0.1$ m and $y=4$ m, provided that the receiver position is not too close to the source. Notice that the aperture ranges from $y=0.3$ m to $y=3$ m, implying that the energy-flow dip area (refers to the area where the flow dips occur) is dependent on the aperture size and location. Moreover, the flow direction reversal is most intense along the line $y=2$ m, which is approximately the center line of the aperture. The energy flow at R1 decays rapidly before the dip, and has the largest energy-flow amplitude after the reversal, which has occurred because R1 is in the vicinity of the aperture.

To demonstrate that the reversal characteristic of the energy-flows around the opening region is uniquely associated with coupled spaces, the energy-flow decays are also presented here for a single room where the aperture on the primary-room side is replaced by a wall surface with an absorption coefficient of 1.0 without the secondary room. To enable the comparison, the four receivers remain at the same positions as they were in the coupled space scenario. Figure 2(a) illustrates all the energy-flow decays following a similar exponential decay. Therefore, reversal of the energy-flow direction around the opening region does not occur in this single-room case.

Figure 2(b) illustrates the energy-flow decays in the secondary room for the coupled configuration of case 1. Four receiver positions are at R5 $(0.05, 2.5, 3)$ m, R6 $(0.05, 7, 3)$ m, R7 $(2, 7, 3)$ m, and R8 $(2, 2.5, 3)$ m. Among them, R5 and R8 show the reversal characteristic while the other two receiver positions do not. Further simulations show that the energy-flow dip area is larger in the secondary room than it is in the primary room, probably because the secondary room has a larger size than the primary room.

So far, the discussion has focused on the impulse response of the energy-flow decay, to serve the purpose of visualizing the energy feedback. Additional simulations show that the steady-state impulse response of the energy flow decay has slightly different curve in that the dip occurs at different times. Moreover, the steady-state energy flow decay allows the comparison between itself and the steady-state energy decay (Schroeder decay function), which will reveal the relationship between the energy-flow reversal and the energy decay curve transition

from the first decay curve to the second decay curve.

4. Conclusion

In this paper, the diffusion equation model is used to visualize both steady state-sound-pressure level distribution and time-dependent energy flow in two coupled rooms via multimedia animations. The diffusion equation model is briefly reviewed. Because of its high efficiency in calculating the sound-energy density everywhere in the rooms, it can be used to obtain both sound-energy flows and sound-pressure level distributions with a computational load on the order of minutes. Three different absorption configurations are assigned to a coupled-volume system consisting of two rooms connected by a square opening aperture. Three configurations are investigated: the natural reverberation time in the primary room is shorter, the same, and longer than in the secondary room, respectively.

Animations discussed in Sec. 2.2 illustrate sound-pressure level distributions parallel to the wall containing the aperture by scanning from the primary room to the secondary room. Along the lines parallel to the wall containing the aperture, a distinct pressure level discontinuity is found at the edge of the aperture for all three cases. The time-dependent sound-energy flow directions were presented in two- and three-dimensions. When the natural reverberation time of the primary room is shorter than that of the secondary room, the animation clearly shows the energy feedback, especially in regions around the aperture.

This work also studies time-dependent sound-energy flow levels. Simulations discussed in Sec. 3.3 using the diffusion equation model reveal a distinct characteristic of the energy-flow level decay: a dip in the energy-flow decay function associated with reversal of the energy-flow directions. Around the aperture region, the dip of the energy-flow decay occurs at the time when the energy feedback from the secondary room starts to compensate for the energy outflow. Furthermore, the dip characteristic does not happen everywhere, but is rather in some way restricted by the aperture size and location.

Experimental verifications of sound-pressure level distributions for the two coupled rooms will be discussed in detail in a follow-up paper. Future work should include the experimental verification of sound-energy flow distributions, and the relationship between the time when the dip occurs and the time point where the sound-energy decay turns over from the first decay slope to the second decay.

Acknowledgments

The authors would like to thank Dr. Jason Summers for helpful discussions, and Mr. Clemeth Abercrombie for polishing the language.

References and links

[1]A. Billon, V. Valeau, A. Sakout, and J. Picaut, "On the use of a diffusion model for acoustically coupled rooms," J. Acoust. Soc. Am. **120**, 2043–2054 (2006).
[2]J. Picaut, L. Simon, and J. D. Polack, "A mathematical model of diffuse sound field based on a diffusion equation," Acta Acust. (Beijing) **83**, 614–621 (1997).
[3]V. Valeau, J. Picaut, and M. Hodgson, "On the use of a diffusion equation for room-acoustic prediction," J. Acoust. Soc. Am. **119**, 1504–1513 (2006).
[4]V. Valeau, M. Hodgson, and J. Picaut, "A diffusion-based analogy for the prediction of sound fields in fitted rooms," Acta Acust. (Beijing), **93**, 94–105 (2007).
[5]Y. Jing, and N. Xiang, "A modified diffusion equation for room-acoustic predication (L)," J. Acoust. Soc. Am. **121**, 3284–3287 (2007).
[6]Y. Jing, and N. Xiang, "On boundary conditions for the diffusion equation in room-acoustic prediction: Theory, simulations, and experiments," J. Acoust. Soc. Am. **123**, 145–153 (2008).
[7]A. Billon, J. Picaut, C. Foy, V. Valeau, and A. Sakout, "Introducing atmospheric attenuation within a diffusion model for room-acoustic predictions," J. Acoust. Soc. Am. **123**, 4040–4043 (2008).

ACOUSTICAL NEWS—USA

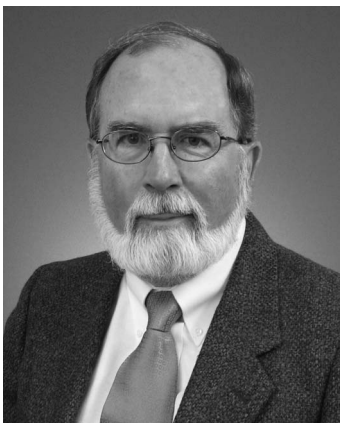
Elaine Moran
Acoustical Society of America, Suite 1NO1, 2 Huntington Quadrangle, Melville, NY 11747-4502

Editor's Note: *Readers of this journal are encouraged to submit news items on awards, appointments, and other activities about themselves or their colleagues. Deadline dates for news and notices are 2 months prior to publication.*

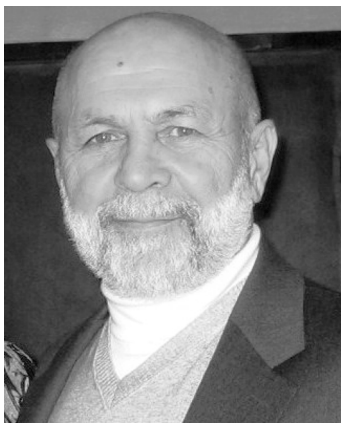
New Fellows of the Acoustical Society of America



Yiu W. Lam—For contributions to building acoustics



Bryan E. Pfingst—For contributions to cochlear implants



Arman Sarvazyan—For contributions to radiation force imaging



Ann K. Syrdal—For contributions to female speech synthesis

President's report on the 155th meeting of the Acoustical Society of America held as part of Acoustics'08 Paris, France

The 155th meeting of the Acoustical Society of America was held 29 June–4 July 2008 in Paris, France as part of *Acoustics'08 Paris* (See Fig. 1). Acoustics'08 Paris was the title given to the 2nd joint meeting of the Acoustical Society of America (ASA) and the European Acoustics Association which was organized by the French Acoustical Society (SFA). This is the second time that the Society has met in Europe and the first time it has met in Paris.

The meeting drew a total of 5018 registrants, including 980 students, from 75 countries including 2644 from Europe, 1092 from North America (992 from US), 337 from the Far East, 162 from Asia and the Middle East, and 42 from Africa, 58 from Oceania, and 44 from South America.

A total of 3547 papers, organized into 419 sessions, covered the areas of interest to the technical committees of ASA, EAA and SFA (See Figs. 2 and 3).

Acoustics'08 Paris began with an Opening Ceremony on Monday morning, 30 June which included welcoming remarks from the Presidents of ASA, EAA and SFA and the presentation of two plenary lectures: "How sound from human activities affects marine mammals" by Peter Tyack of the Woods Hole Oceanographic Institution, MA, USA and "New trends in aeroacoustics: From acoustic analogies to direct numerical simulations" by Daniel Juvé of the Ecole Centrale de Lyon, France.

 0001-4966/2008/124(6)/3351/5/$23.00 © 2008 Acoustical Society of America



FIG. 1. (Color online) Acoustics'08 Paris logo.



FIG. 2. (Color online) Sessions were well attended.

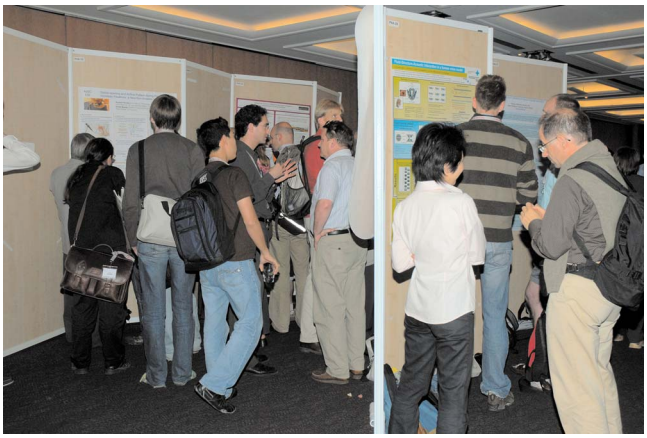


FIG. 3. (Color online) Poster sessions were set-up in corridors for maximum attendance.

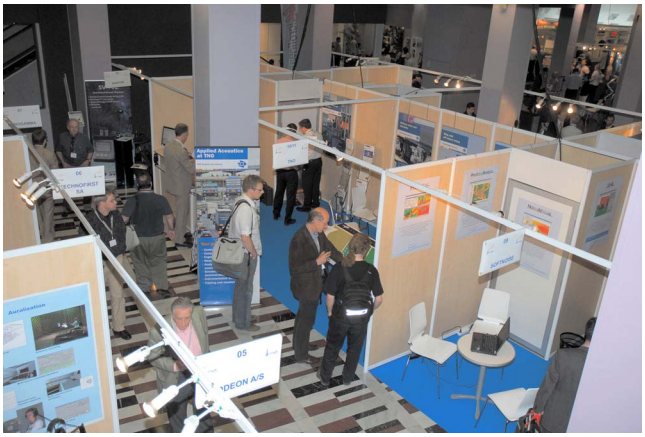


FIG. 4. (Color online) Aerial view of the exhibit booths.

The Society's thirteen Technical Committees held open meetings during Acoustics'08 Paris—some cosponsored by Technical Committees of the European Acoustics Association where they made plans for special sessions at upcoming ASA meetings, discussed topics of interest to the attendees and held informal socials after the end of the official business. These are working, collegial meetings and all people attending Society meetings are encouraged to attend and to participate in the discussions. More information about Technical Committees, including minutes of meetings, can be found on the ASA Website ⟨http://asa.aip.org/committees.html⟩ and in the Acoustical News USA section of JASA in the October and November issues.

An exhibit was held in conjunction with the meeting and included displays with materials and services for the acoustics and vibration community. Exhibitors from 52 companies and 6 associations participated. It included exhibits of computer-based instrumentation, sound level meters, devices for noise control and sound prediction, and acoustics books among others. The exhibit began with an opening reception on Monday afternoon and was open through Friday. (See Fig. 4)

A Student Reception was held drawing participation from students from around the word. Technical Committees awarded Best Student Paper Awards to students who presented papers at the meeting. The list of award recipients, as well as other information for students, can be found online at the ASA Student Zone website ⟨http://www.acosoc.org/student/⟩

A wide array of technical tours was organized and included visists to IRCAM (Institut de Recherche et Coordination Acoustique/Musique), Musée des Arts et Métiers (museum of science and technology), UGC theatre in Paris La Défense, ONERA/CEPR (the French Aerospace Laboratory, CSTB (French Center for Building Technologies), LAM (Musical Acoustics Laboratory), IAT Aerotechnical Institute (Wind tunnels for car testing), and a guided tour of the "Pipe organs of Paris."

Social events included a social hour at the Palais des Congrès on Tuesday and a banquet at the Maison de la Chimie on Wednesday, which drew over 1000 particpants. The Women in Acoustics Luncheon was held on Thursday afternoon.

The *Acoustics'08 Paris* organizing committee also arranged for a program for Accompanying Persons which included a French cooking course, a tour of the Museum of Textiles and Fashion and a tour that included the former royal palace and royal gardens.

The medals and awards ceremonies included acknowledgment of the members and other volunteers who organized the meeting and the presentation of awards and certificates to newly-elected Fellows. The plenary session followed and included two plenary lectures: "Binaural hearing and systems for sound reproduction," by Philip Nelson of the University of Southampton, UK and "Light and sound: Ultrasonic imaging in molecular medicine" by Matthew O'Donnell of the University of Washington, USA.

ASA President Gilles Daigle presided over the ASA portion of the ceremony which was followed by the EAA and SFA ceremonies.



FIG. 5. (Color online) ASA President Gilles Daigle (l) presents the Medwin Prize in Acoustical Oceanography to Mark V. Trevorrow (r).



FIG. 6. (Color online) ASA President Gilles Daigle (r) presents the Distinguished Service Citation to Charles Schmid (l).

Mary K. Fagan was announced as recipient of the 2007 Research Grant in Speech Science of the American Speech-Language-Hearing Foundation.

The 2008 Medwin Prize in Acoustical Oceanography was presented to Mark Trevorrow, _Defence R&D Canada Atlantic, who presented the Acoustical Oceanography Prize Lecture titled "The use of moored inverted echosounders for monitoring near-surface processes" in a session following the awards ceremony (See Fig. 5).

The Distinguished Service Citation was presented to Charles E. Schmid "for contributions as Executive Director of the Acoustical Society of America" (See Fig. 6). The R. Bruce Lindsay Award was presented to Tyrone M. Porter "for contributions to ultrasound-guided drug delivery" (See Fig. 7). The Helmholtz-Rayleigh Interdisciplinary Silver Medal was presented to James V. Candy "for contributions to signal processing and underwater acoustics." (See Fig. 8). The Gold Medal was presented to Patricia K. Kuhl "for contributions to understanding how children acquire spoken language and for leadership in the Society." (See Fig. 9).

Election of fourteen members to Fellow grade was announced and fellowship certificates were presented. New fellows are: Michael A. Aker-



FIG. 7. (Color online) ASA President Gilles Daigle (r) presents the R. Bruce Lindsay Award to Tyrone Porter (l).



FIG. 8. (Color online) ASA President Gilles Daigle (r) presents the Helmholtz-Rayleigh Interdisciplinary Silver Medal to James V. Candy (l).



FIG. 9. (Color online) ASA President Gilles Daigle (r) presents the Gold Medal to Patricia K. Kuhl (l).



FIG. 10. (Color online) New Fellows of the ASA (l to r): Gilles Daigle (ASA President), John C. Osler, Anthony P. Nash, Vera A. Khokhlova, Larry E. Humes, Subramaniam D. Rajan, Richard M. Stern, Lily M. Wang



FIG. 11. (Color online) New Fellows of the ASA: (l to r): Dani M. Byrd, Dick B. Botteldooren, Susanna B. Blackwell, Michael A. Akeroyd.

oyd, Susanna B. Blackwell, Dick B. Botteldooren, Dani M. Byrd, Brian R. Glasberg, Larry E. Humes, Vera A. Khokhlova, Christophe D. Micheyl, Anthony P. Nash, John C. Osler, Subramaniam D. Rajan, Richard M. Stern, Brad H. Story, and Lily M. Wang (see Figs. 10 and 11).

ASA President Gilles Daigle expressed the Society's thanks to the Organizing Committees for the excellent execution of the meeting, which clearly evidenced meticulous planning. Member of the Organizing Committee are: Co-chairs: Bertrand Dubus, SFA, Michael Vorländer, EAA, William Yost, ASA, Manell Zakharia, SFA; Didier Cassereau, SFA, Information System Manager; Bertrand Dubus, SFA, Exhibition; Bastian Epp, EAA Student Representative; Guillaume Pellerin, Webmaster; Catherine Lavandier, SFA, Secretary; Francine Luppé, SFA, Publications; Manuel Melon, SFA, Webmaster, Vice-treasurer; Brian Monson, Michael Canney, ASA Student Representatives; Jean Dominique Polack, Archives and Publications; Franck Teston, SFA, Treasurer; ASA: Elaine Moran (ASA Office Manager), Charles Schmid (ASA Executive Director); SFA: Evelyne Dewayse (SFA Secretary); Armelle Guilloux: Conference Secretary. Members of the Technical Committee: Co-chairs: Philippe Blanc-Benon, SFA, Dick Botteldooren, EAA, William Hartmann, ASA, Pascal Laugier, SFA; Architectural Acoustics: Lily



FIG. 12. (Color online) ASA Vice President George Frisk (r) receives the Vice President's gavel from ASA Vice President-Elect Victor Sparrow (l)



FIG. 13. (Color online) ASA President Gilles Daigle (r) receives the President's Tuning Fork from ASA President-Elect Mark F. Hamilton (l).

Wang, Brandon Tinianov, ASA, Jens Holger Rindel, EAA; Animal Bioacoustics: Richard Fay, ASA, Michel André, EAA; Biomedical Ultrasound / Bioresponse to Vibration: Michael Bailey, ASA, Oleg Sapozhnikov, EAA; Engineering Acoustics: Daniel Warren, ASA, Gerhard Sessler, EAA; Musical Acoustics: James Beauchamp, ASA, Murray Campbell, EAA; Noise: Brigitte Schulte-Fortkamp, ASA, Pierre-Etienne Gautier, Euronoise; Physical Acoustics: Murray Korman, ASA, Walter Lauriks, EAA; Psychological/Physiological Acoustics: Elizabeth Strickland, ASA, Armin Kohlrausch, EAA; Signal Processing in Acoustics: David Chambers, ASA, Stephen Elliott, EAA; Speech Communication: Maureen Stone, ASA, Carol Espy-Wilson, ASA, Pierre Badin, EAA, Xavier Pelorson, AFCP (Association Française de Communication Parlée); Structural Acoustics and Vibration: Sean Wu, ASA, Wolfgang Kropp, EAA; Underwater Acoustics & AO: Acoustical Oceanography: James Miller, ASA/AO, Kevin LePage, ASA/UW, Yann Stéphan, ECUA, David Bradley, ECUA.

Victor W. Sparrow, ASA Vice President-Elect, presented the Vice President's gavel to George V. Frisk whose term as Vice President ended at the close of the meeting (see Fig. 12) followed by the presentation of the President's tuning fork to ASA President Gilles A. Daigle by ASA President-Elect Mark Hamilton (see Fig. 13).

The full technical program and award encomiums can be found in the printed meeting program or online at http://scitation.aip.org/jasa and select Volume 123, Issue 5, from the list of available volumes.

We hope that you will consider attending a future meeting of the Society to participate in the many interesting technical events and to meet with colleagues in both technical and social settings. Information about future meetings can be found in the *Journal* and on the ASA Home Page at ⟨http://asa.aip.org⟩.

GILLES A. DAIGLE

President 2007–2008

USA Meetings Calendar

Listed below is a summary of meetings related to acoustics to be held in the U.S. in the near future. The month/year notation refers to the issue in which a complete meeting announcement appeared.

2009

18–22 May	157th Meeting of the Acoustical Society of America, Portland, OR [Acoustical Society of America, Suite 1NO1, 2 Huntington Quadrangle, Melville, NY 11747-4502; Tel.: 516-576-2360; Fax: 516-576-2377; Email: asa@aip.org; WWW: http://asa.aip.org].
26–30 Oct	158th Meeting of the Acoustical Society of America, San Antonio, TX [Acoustical Society of America, Suite 1NO1, 2 Huntington Quadrangle, Melville, NY 11747-4502; Tel.: 516-576-2360; Fax: 516-576-2377; Email: asa@aip.org; WWW: http://asa.aip.org].

2010

19–23 April	158th Meeting of the Acoustical Society of America, Baltimore, MD [Acoustical Society of America, Suite 1NO1, 2 Huntington Quadrangle, Melville, NY 11747-4502; Tel.: 516-576-2360; Fax: 516-576-2377; Email: asa@aip.org; WWW: http://asa.aip.org].
15–19 Nov	2nd Iberoamerican Conference on Acoustics (Joint Meeting of the Acoustical Society of America, Mexican Institute of Acoustics, and Iberoamerican Federation on Acoustics), Cancun, Mexico [Acoustical Society of America, Suite 1NO1, 2 Huntington Quadrangle, Melville, NY 11747-4502; Tel.: 516-576-2360; Fax: 516-576-2377; Email: asa@aip.org; WWW: http://asa.aip.org].

Cumulative Indexes to the Journal of the Acoustical Society of America

Ordering information: Orders must be paid by check or money order in U.S. funds drawn on a U.S. bank or by Mastercard, Visa, or American Express credit cards. Send orders to Circulation and Fulfillment Division, American Institute of Physics, Suite 1NO1, 2 Huntington Quadrangle, Melville, NY 11747-4502; Tel.: 516-576-2270. Non-U.S. orders add $11 per index. Some indexes are out of print as noted below.

Volumes 1-10, 1929-1938: JASA, and Contemporary Literature, 1937-1939. Classified by subject and indexed by author. Pp. 131. Price: ASA members $5; Nonmembers $10

Volumes 11-20, 1939-1948: JASA, Contemporary Literature and Patents. Classified by subject and indexed by author and inventor. Pp. 395. Out of Print

Volumes 21-30, 1949-1958: JASA, Contemporary Literature and Patents. Classified by subject and indexed by author and inventor. Pp. 952. Price: ASA members $20; Nonmembers $75

Volumes 31-35, 1959-1963: JASA, Contemporary Literature and Patents. Classified by subject and indexed by author and inventor. Pp. 1140. Price: ASA members $20; Nonmembers $90

Volumes 36-44, 1964-1968: JASA and Patents. Classified by subject and indexed by author and inventor. Pp. 485. Out of Print.

Volumes 36-44, 1964-1968: Contemporary Literature. Classified by subject and indexed by author. Pp. 1060. Out of Print

Volumes 45-54, 1969-1973: JASA and Patents. Classified by subject and indexed by author and inventor. Pp. 540. Price: $20 (paperbound); ASA members $25 (clothbound); Nonmembers $60 (clothbound)

Volumes 55-64, 1974-1978: JASA and Patents. Classified by subject and indexed by author and inventor. Pp. 816. Price: $20 (paperbound); ASA members $25 (clothbound); Nonmembers $60 (clothbound)

Volumes 65-74, 1979-1983: JASA and Patents. Classified by subject and indexed by author and inventor. Pp. 624. Price: ASA members $25 (paperbound); Nonmembers $75 (clothbound)

Volumes 75-84, 1984-1988: JASA and Patents. Classified by subject and indexed by author and inventor. Pp. 625. Price: ASA members $30 (paperbound); Nonmembers $80 (clothbound)

Volumes 85-94, 1989-1993: JASA and Patents. Classified by subject and indexed by author and inventor. Pp. 736. Price: ASA members $30 (paperbound); Nonmembers $80 (clothbound)

Volumes 95-104, 1994-1998: JASA and Patents. Classified by subject and indexed by author and inventor. Pp. 632, Price: ASA members $40 (paperbound); Nonmembers $90 (clothbound)

Volumes 105-114, 1999-2003: JASA and Patents. Classified by subject and indexed by author and inventor. Pp.616, Price: ASA members $50; Nonmembers $90 (paperbound)

ACOUSTICAL NEWS—INTERNATIONAL

Walter G. Mayer
Physics Department, Georgetown University, Washington, DC 20057

International Meetings Calender

Below are announcements of meetings and conferences to be held abroad. Entries preceded by an * are new or updated listings.

December 2008

9-12 **19th International Acoustic Emission Symposium**, Kyoto, Japan (www.19iaes-kyoto.com/index.html).

17-19 **Symposium on the Acoustics of Poro-Elastic Materials (sapem 2008)**, Bradford, UK (sapem2008.matelys.com).

January 2009

11-17 ***International Congress on Ultrasonics,** Santiago, Chile (icu2009.usach.cl).

March 2009

17-19 ***Spring Meeting of the Acoustical Society of Japan,** Tokyo. Japan (www.asj.gr.jp/index-en.html)

23-26 **International Conference on Acoustics (NAG/DAGA 2009),** Rotterdam, The Netherlands (www.nag-daga.nl).

31-2 ***5th International Conference on Bio-Acoustics,** Loughborough, UK (bioacoustics2009.lboro.ac.uk).

April 2009

5-9 **Noise and Vibration: Emerging Methods (NOVEM 2009),** Oxford, UK (www.isvr.soton.ac.uk/**NOVEM**2009).

13-17 **2nd International Conference on Shallow Water Acoustics,** Shanghai, China: (www.apl.washington:edu/projects/SWAC09/index.html).

9-24 **International Conference on Acoustics, Speech, and Signal Processing,** Taipei. R.O.C. (icassp09.com).

May 2009

19-22 **XXI Session of the Russian Acoustical Society,** Moscow, Russia (www.akin.ru/main.html).

June 2009

17-19 **3rd International Conference on Wind Turbine Noise,** Aalborg, Denmark (www.windturbinenoise2009.org).

22-26 ***3rd International Conference on Underwater Acoustic Measurements: Technologies and Results,** Nafplion, Peleponnese, Greece (www.uam2009.gr).

July 2009

5-9 **16th International Congress on Sound and Vibration,** Krakow, Poland (www.icsv16.org).

August 2009

23-28 **Inter-noise 2009,** Ottawa, Ont., Canada (www.internoise2009.com).

September 2009

6-10 **InterSpeech 2009,** Brighton, UK (www.interspeech2009.org).

9-11 ***9th International Conference on Theoretical and Computational Acoustics, Dresden, Germany** (ictca2009.com.).

14-18 **5th Animal Sonar Symposium**, Kyoto, Japan (cse.fra.affrc.go.jp/akamatsu/AnimalSonar.html).

15-17 **Autumn Meeting of the Acoustical Society of Japan,** Koriyama, Japan (www.asj.gr.jp/index-en.html).

19-23 **IEEE 2009 Ultrasonics Symposium, Rome, Italy** (e-mail: pappalar@uniroma3.it).

21-23 ***10th Western Pacific Acoustics Conference (WESPAC),** Beijing, China (www.weapacx.org).

23-25 ***Pacific Rim Underwater Acoustics Conference 9pruac**), Xi' an, China (e-mail: lfh@mail.ioa.ac.cn).

23-25 **TECNIACUSTICA2010,**Cádiz, Spain (www.sea-acustica.es).

October 2009

26-28 **Euronoise 2009,** Edinburgh, UK (www.euronoise2009.org.uk).

June 2010

13-16 **INTERNOISE2010**, Lisbon, Portugal, (www.internoise2010.org).

August 2010

23-27 **20th International Congress on Acoustics (ICA2010),** Sydney, Australia (www.ica2010sydney:org).

September 2010

26-30 **Interspeech 2010,** Makuhari, Japan (www.interspeech2010.org).

August 2011

27-31 **Interspeech 2011**, Florence, Italy (www.interspeech2011.org).

September 2011

4-7 **International Congress on Ultrasonics**, Gdansk, Poland.

June 2013

2-7 ***21st International Congress on Acoustics (ICA2013)**, Montréal, Canada.

 0001-4966/2008/124(6)/3357/1/$23.00 © 2008 Acoustical Society of America

ADVANCED-DEGREE DISSERTATIONS IN ACOUSTICS

***Editor's Note**: Abstracts of Doctoral and Master's theses will be welcomed at all times. Please note that they must be limited to 200 words, must include the appropriate PACS classification numbers, and formatted as shown below. If sent by postal mail, note that they must be double spaced. The address for obtaining a copy of the thesis is helpful. Submit abstracts to: Acoustical Society of America, Thesis Abstracts, Suite 1NO1, 2 Huntington Quadrangle, Melville, NY 11747-4502, e-mail: asa@aip.org*

Home office worker performance and perception as affected by residential audible distractions through various wall constructions [43.55.Rg, 43.50.Qp, 43.55.Hy] —Alicia J. Wagner, *Department of Architectural Engineering, University of Nebraska, Lincoln, Nebraska 68588, July 2008 (M.S.).* This research examines the effects that residential audible distractions have on task performance and subjective perception of home office workers when transmitted across various residential wall constructions. Subjects performed math, verbal, and typing tasks while exposed to 16-h-long sound signals. These signals were generated using four audio filters simulating residential wall constructions providing varying degrees of acoustic attenuation ranging from field sound transmission classes of 36–58. The audio filters were applied to four types of audible distractions: (1) pop music, (2) television, (3) conversation, and (4) a potpourri of kitchen, pet, and children's noises. A questionnaire was also administered to determine participants' perception of loudness, variation in time, distraction, and annoyance. Statistical analyses indicate that none of the wall constructions or audible distractions significantly affected task performance. However, subjective perception does appear to be related to both factors. The relationship between task performance and subjective perception was also examined, yielding significant results between typing and subjective perception.

Advisor: Lily M. Wang

Modeling the dynamic interactions of rolling bearings [43.20.Ye, 43.40.At, 43.38.Fx] —João Henrique Diniz Guimarães, *Institute of Technical Acoustics (ITA), RWTH Aachen University, Neustrasse 50, 52056 Aachen, Germany; ique@akustik.rwth-aachen.de, October 2007 (Ph.D.).* This work deals with the generation and propagation of structure-borne sound by the rolling contact in bearings. Rolling bearings are widely used in machines and, in early stages of operation, the interaction of the rough surfaces of races and rolling bodies produces an excitation that will propagate to the surrounding structure. The dissertation presents a model for the determination of the structure-borne excitation due to rolling, using the condition of the surfaces and the dynamics of the rolling movement as input. The model is able to simulate the time evolution of the excitation generated by the bearing that is imposed to the machine. Additionally, this work describes the experimental evaluation of the influence of the path between the point where the excitation is generated (in the bearing) to the point where it is usually measured (on the machine's housing) using special actuators made of one rolling element. Measurements under running conditions are made for comparisons with cylindrical and spherical rolling bearings. This approach shows that a deeper insight in the understanding of machine vibration can be gained when one tries to model sources and treats the system as a filter that has to be described in order to evaluate the influence of the transfer path. Publisher: Logos Verlag Berlin, 2008; ISBN: 978-3-8325-2010-6.

Advisor: Michael Vorländer

From children to adults: How binaural cues and ear canal impedances grow [43.66.Pn, 43.64.Ha, 43.66.Yw] —Janina Fels, *Institute of Technical Acoustics (ITA), RWTH Aachen University, Neustrasse 50, 52056 Aachen, Germany; janina.fels@akustik.rwth-aachen.de, January 2008 (Ph.D.).* In this thesis the growth dependency of head-related transfer functions and their resulting parameters (interaural time and level differences) are analyzed as well as ear canal impedances. Differences in the anatomy of children and adults thus result in different binaural cues. The individual anthropometric parameters, however, affect the binaural cues to a varying extent. In this thesis the most important anthropometric parameter with regard to their influence on binaural cues, is determined. Ear canal impedances are undergoing certain changes as well while children are growing up and finally reach adulthood. This thesis presents, for the first time, the age-related development of data that is most decisive for the impedances. These new findings open up new possibilities to develop artificial child heads and couplers for hearing aids that are suitable for children. Thus, improvements in certain fields of applications, such as the development and fitting of hearing aids for children, are now possible, and measurement techniques that are used for classroom acoustics can now be optimized significantly as well. Moreover, these new findings are vital when it comes to re-evaluating standardized artificial heads. Publisher: Logos Verlag Berlin, 2008; ISBN: 978-3-8325-1855-4.

Advisor: Michael Vorländer

Binaural technology for virtual reality [43.66.Pn, 43.66.Qp, 43.55.Ka, 43.60.Dh] —Tobias Lentz, *Institute of Technical Acoustics (ITA), RWTH Aachen University, Neustrasse 50, 52056 Aachen, Germany; tle@akustik.rwth-aachen.de, November 2007 (Ph.D.).* The use of nonintrusive virtual environments is gaining more and more importance but was focused mainly on addressing the visual sense. However, the human perception consists not only of visual input and thus it would be worthwhile to create multimodal and interactive virtual environments. This thesis describes the techniques required to include the acoustic component into virtual environments and the implementation of a software system, which creates complex artificial acoustical scenes in real time. The system is based on the binaural technology. It features spatially distributed sound sources, which are utilized to create an environment that is as authentic as possible. This comprises a description of the source, including its relevant angle-, distance-, and time-dependent radiation, the sound distribution in the virtual scene, the perception-related consideration of all sound field components, and the exact reproduction at the ears of the user. In this context, an approach for dynamic crosstalk cancellation is presented, which enables a loudspeaker-based reproduction. The required filters are processed in real time on the basis of the position data and measured transfer functions of the outer ear. Furthermore the integration of this spatial audio system into a five-sided Virtual Reality display system is described and evaluated.

Advisor: Michael Vorländer

Contributions to discrete-time methods for room acoustic simulation [43.55.Ka, 43.58.Ta, 43.28.Js] —José Escolano-Carrasco, *Communications Department, Technical University of Valencia, Camino de Vera S/N, Valencia 46022, Spain; escolano@ujaen.es, July 2008 (Ph.D.).* The sound field distribution in a room is the consequence of the acoustic properties of radiating sources and the geometry and absorbing characteristics of the surrounding boundaries. Despite there existing a consolidated acoustic wave theory, it is very difficult, nearly impossible, to find an analytical expression of the sound variable distribution in a real room, as a function of time and position. This scenario represents as an inhomogeneous boundary value problem, where the complexity of source properties and boundary conditions make that problem extremely hard to solve. The use of discrete-time methods arises as a suitable solution for solving those partial differential equations, particularized by some specific constrains. Together with the constant growth of computer power, those methods are increasing their suitability for room acoustic simulation. However, there exists an important lack of accuracy in the definition of some of these conditions so far: Current frequency-dependent boundary conditions do not comply with any physical model, and directive sources in discrete-time methods have been hardly treated. This thesis discusses the current state-of-the-art boundary conditions and source modeling in discrete-time methods for room acoustic simulation, and it contributes some algorithms to enhance them.

Advisor: Dr. José J. López

REVIEWS OF ACOUSTICAL PATENTS

Sean A. Fulop
Dept. of Linguistics, PB92
California State University Fresno
5245 N. Backer Ave., Fresno, California 93740

Lloyd Rice
11222 Flatiron Drive, Lafayette, Colorado 80026

The purpose of these acoustical patent reviews is to provide enough information for a Journal reader to decide whether to seek more information from the patent itself. Any opinions expressed here are those of reviewers as individuals and are not legal opinions. Printed copies of United States Patents may be ordered at $3.00 each from the Commissioner of Patents and Trademarks, Washington, DC 20231. Patents are available via the internet at http://www.uspto.gov.

Reviewers for this issue:

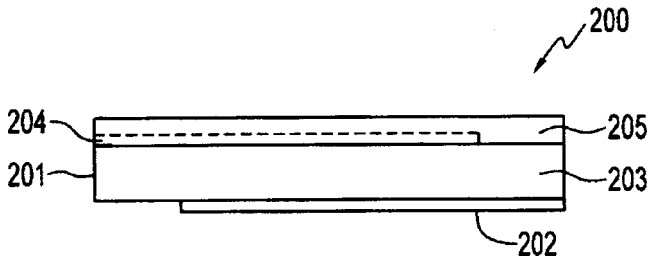
GEORGE L. AUGSPURGER, *Perception, Incorporated, Box 39536, Los Angeles, California 90039*
ANGELO CAMPANELLA, *3201 Ridgewood Drive, Hilliard, Ohio 43026-2453*
SEAN A. FULOP, *California State University, Fresno, 5245 N. Backer Avenue M/S PB92, Fresno, California 93740-8001*
JEROME A. HELFFRICH, *Southwest Research Institute, San Antonio, Texas 78228*
DAVID PREVES, *Starkey Laboratories, 6600 Washington Ave. S., Eden Prairie, Minnesota 55344*
NEIL A. SHAW, *Menlo Scientific Acoustics, Inc., Post Office Box 1610, Topanga, California 90290*
ERIC E. UNGAR, *Acentech, Incorporated, 33 Moulton Street, Cambridge, Massachusetts 02138*
ROBERT C. WAAG, *Department of Electrical and Computer Engineering, University of Rochester, Rochester, New York 14627*

7,322,243

43.35.Yb ACOUSTIC WAVE ETCH RATE SENSOR SYSTEM

James Z. T. Liu *et al.*, assignor to Honeywell International Incorporated
29 January 2008 (Class 73/579); filed 16 June 2005

Several internal combustion engine lubricating oil etch rate sensors are claimed, where the mechanical properties of an acoustic resonator are altered by the etchant, typically acids that may develop in that oil over time. One such sensor **200** comprises a quartz **203** resonator vibrating in a thickness shear mode and an etchable material **205** (e.g., iron) on electrode **204**



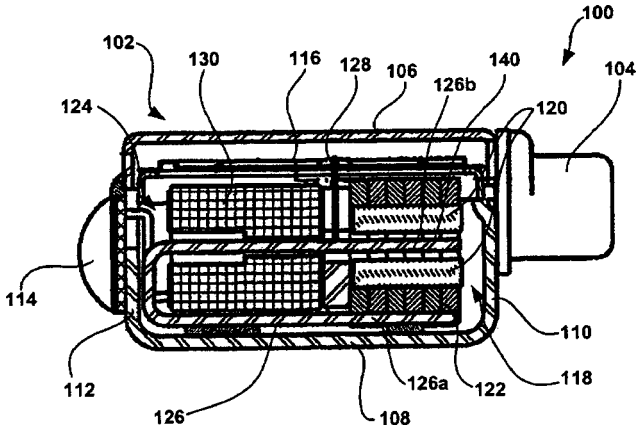
(of any conducting material). The mass of material **205** helps determine the resonator resonance frequency. The second electrode **202** is of nonetching material such as gold or silver.—AJC

7,362,878

43.38.Dv MAGNETIC ASSEMBLY FOR A TRANSDUCER

Thomas E. Miller and Evan Llamas-Young, assignor to Knowles Electronics, LLC.
22 April 2008 (Class 381/418); filed 14 June 2004

A balanced armature transducer is described that can be used as either a microphone or receiver in which it appears that the high magnetic flux density of the magnet structure **118**, which consists primarily of magnets **120** (high energy and high coercivity) and the yoke **122** material (high



saturation inductance, high permeability, and low coercivity), are the basis for the claims made. The text is a clear example of the dialect known as patentese.—NAS

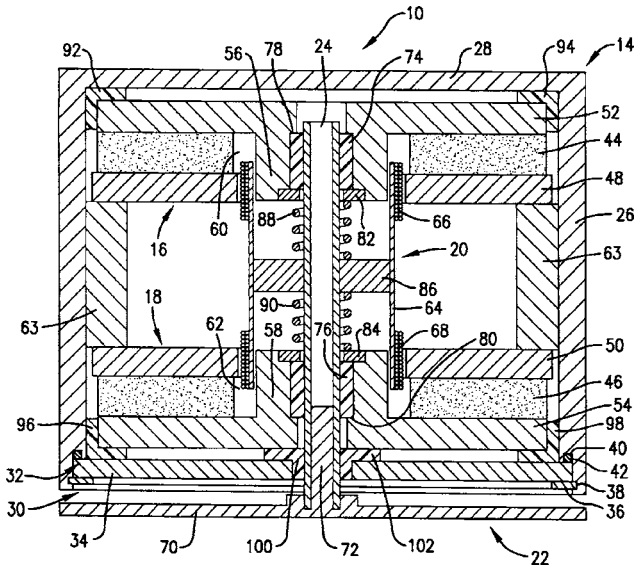
7,386,137

43.38.Dv SOUND TRANSDUCER FOR SOLID SURFACES

Christopher Combest, assignor to Multi Service Corporation
10 June 2008 (Class 381/182); filed 1 March 2005

An inertial transducer operates like a tuning fork to excite audio frequency vibrations in existing walls, tables, and other surfaces. Most commercial versions are b'guess and b'gosh designs that do not attempt to do more than deliver recognizable audio. This patent has a loftier goal: "…the present invention provides a sound transducer for imparting acoustical energy directly to a solid surface while achieving the sound quality and frequency response found only in conventional diaphragm speakers." A dual magnetic assembly houses a pair of voice coils **66**, **68** in a push-pull

 0001-4966/2008/124(6)/3361/15/$23.00 © 2008 Acoustical Society of America



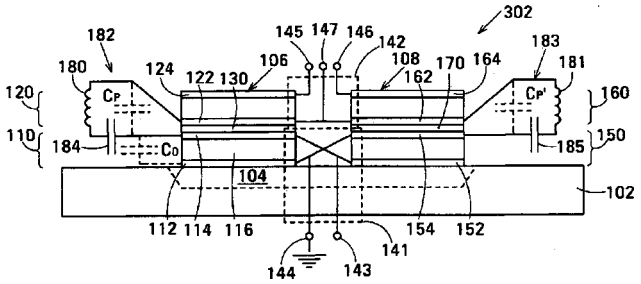
configuration, not to reduce distortion but because it is "more powerful." Central armature **24** is guided by sliding or ball bearings **74**, **78** and centered by coil springs **88**, **90**. Actuator foot **22** is made as large as practical, but its shape and size can vary depending on the size and strength of the magnetic assembly. Well, in comparison with most prior art, it is certainly more expensive to manufacture, and that must count for something.—GLA

7,388,455

43.38.Fx FILM ACOUSTICALLY-COUPLED TRANSFORMER WITH INCREASED COMMON MODE REJECTION

John D. Larson III *et al.*, assignor to Avago Technologies Wireless IP Pte Limited
17 June 2008 (Class 333/189); filed 13 October 2004

This patent is a continuation of an exposition on the idea of a piezoelectrically coupled transformer for UHF frequencies. The general idea is expressed in the figure, which indicates how a single-ended source connected to terminals **143**, **144** may be coupled to a floating or differential-connected load connected across **145**, **146**, **147** via twin stacks of AlN piezoelectric material **116**. The connections shown allows obtaining either a 2:1 voltage ratio up or down, depending on the connection of the output



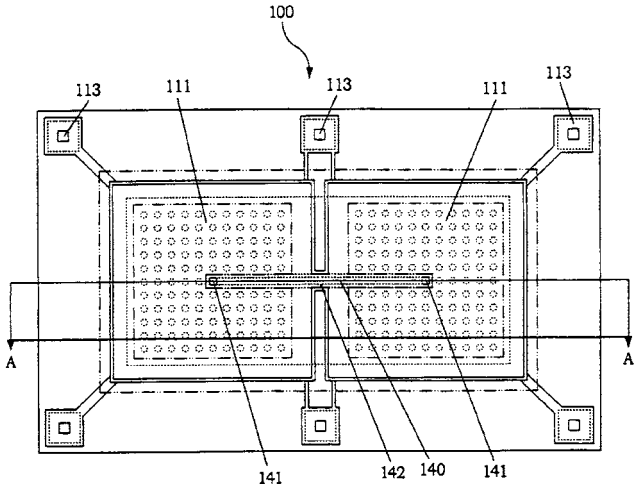
terminals. The plan view of the whole device is very complex, having various construction features designed to either reduce the effects of parasitic capacitance or reduce the effects of transverse resonances in the piezo structures and electrodes. The patent discusses the design parameters for a transformer with a center frequency of 1.9 GHz but does not discuss the bandwidth or insertion loss of these structures. The fabrication plans do appear to be quite advanced, indicating production of these devices is occurring or imminent.—JAH

7,362,873

43.38.Gy MINIATURE CONDENSER MICROPHONE AND FABRICATION METHOD THEREFOR

Michael Pedersen, assignor to Corporation for National Research Initiatives
22 April 2008 (Class 381/175); filed 12 September 2006

A directional microphone **100** comprised of conductive diaphragms **111** supported by attachment springs **113** and mechanical coupling beam **140** sit over fixed electrodes that have air gaps. Since the spacing between the diaphragms and fixed electrodes is small, the polarizing voltage can be small. Detection circuitry as well as signal processing can be fabricated on



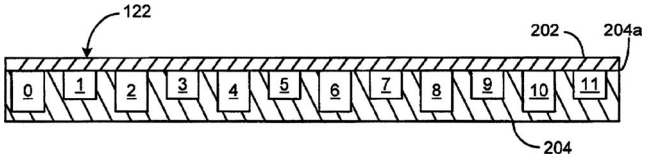
the semiconductor substrate. The patent is informative and clear and contains specific manufacturing steps. Anyone interested in this type of transducer, as well as the parameters that affect microphone performance (sensitivity, frequency response, etc.), will find the patent informative.—NAS

7,391,872

43.38.Hz PARAMETRIC AUDIO SYSTEM

Frank Joseph Pompei, Wayland, Massachusetts
24 June 2008 (Class 381/111); filed 11 January 2001

This patent describes a complete parametric loudspeaker system including an array of ultrasonic transducers, modulator, signal conditioner, and driving amplifier. Most of these seem to be variants of familiar prior art, however, the history of the patent goes back to 1999, making the chronology a little hazy. One novel feature is the design of the array, which may be made up of individual transducers or a conductive membrane **202** stretched



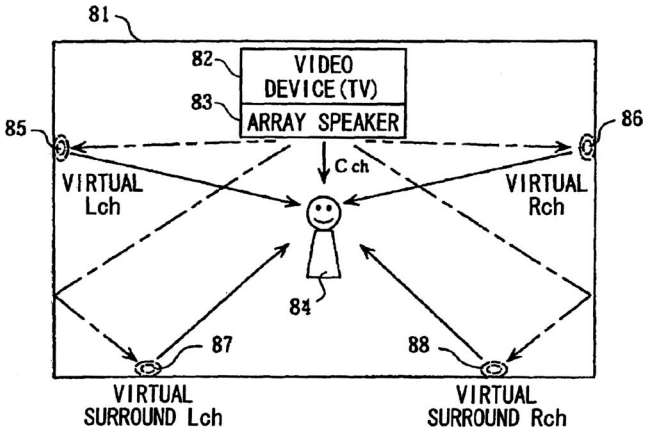
over a grooved backplate **204**. In either case, the backcavities of alternating rows have different depths, establishing two different resonance frequencies. The useful bandwidth of the array is thus widened to about 10 kHz. The patent also goes into considerable detail regarding the use of delay for beam steering and beam splitting, but this definitely is prior art familiar to most sound system designers.—GLA

7,397,923

43.38.Hz ARRAY SPEAKER SYSTEM

Yusuke Konagai, assignor to Yamaha Corporation
8 July 2008 (Class 381/17); filed in Japan 2 June 2003

A commercial version of this array is used in some current Yamaha television receivers. To create a consistent surround sound experience throughout a large listening area, a single array of small loudspeakers generates several directional beams of sound, each reproducing a separate audio channel. In theory, such beam forming is easy—all that is required is a multitapped delay line. To achieve a high degree of accuracy, however, the



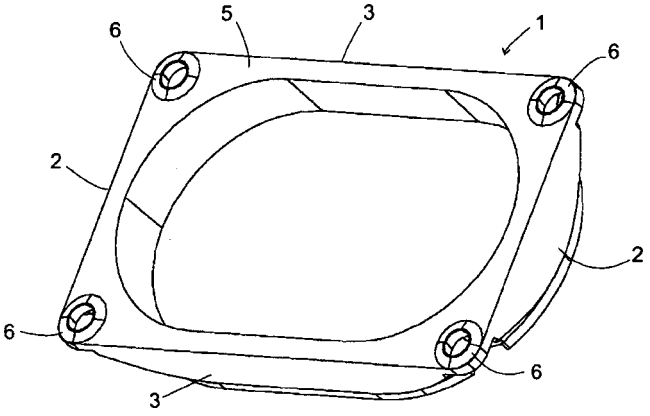
difference between adjacent taps must be only a few microsecends, requiring a very high sampling frequency and a very large number of taps. Other steered array designs have already run into this problem. Yamaha's solution is to interpolate between two or more relatively coarse taps. The patent points out that a by-product of linear interpolation is some degree of high frequency rolloff, and if this is appreciable then interpolation processing can make use of a low-order finite impulse response lowpass filter instead.—GLA

7,364,009

43.38.Ja LOUDSPEAKER MOUNTING FRAME, LOUDSPEAKER AND CABINET COMPRISING A LOUDSPEAKER

Cornelius Sperle *et al.*, assignors to Thomson Licensing
29 April 2008 (Class 181/150); filed 30 April 2004

A mounting device into which a loudspeaker is affixed that in turn can be "easily and reproducibly" mounted to the cabinet of a television set,



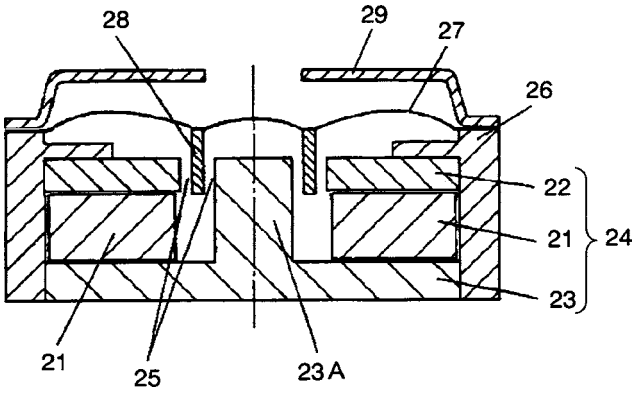
radio, or "other type of audio/video appliance" is described.—NAS

7,388,964

43.38.Ja LOUDSPEAKER, AND MODULE AND ELECTRONIC APPARATUS USING THE LOUDSPEAKER

Shigeru Tomoeda *et al.*, assignors to Matsushita Electric Industrial Company, Limited
17 June 2008 (Class 381/412); filed in Japan 31 January 2003

By using two bar magnets—each labeled **21**—instead of one, this miniature rectangular loudspeaker achieves higher flux density without adding



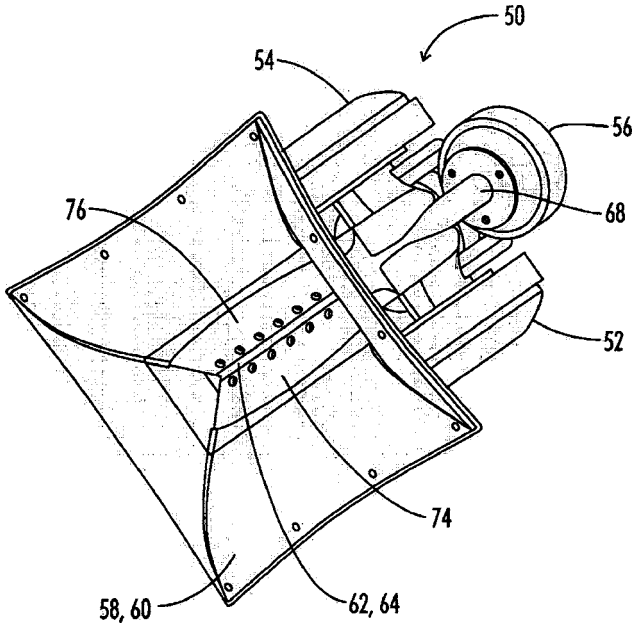
depth. The information conveyed in the preceding sentence has been fluffed out to fill 26 patent claims.—GLA

7,392,880

43.38.Ja DUAL RANGE HORN WITH ACOUSTIC CROSSOVER

Marshall D. Buck, assignor to Gibson Guitar Corporation
1 July 2008 (Class 181/152); filed 31 March 2003

This is not the first time the inventor has used perforated plates as acoustic filters in loudspeaker designs. In this dual range horn, sound from high frequency driver **56** travels through a straight coupler section to diffraction slot **62**, **64** in the throat of horn **58, 60**. Sound from midfrequency



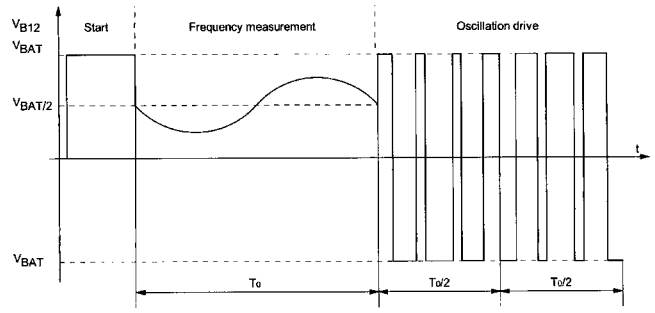
drivers **52** and **54** enters the sides of the diffraction slot section through perforated plates **74** and **76**. Measured response and transmission loss plots are included to demonstrate that the design meets its performance goals.—GLA

7,385,362

43.38.Lc METHOD FOR DRIVING A VIBRATING DEVICE FOR A PORTABLE OBJECT THAT COMPRISES A COIL AND A MOVING MASS

Daho Taghezout, assignor to ETA SA Manufacture Horlogere Suisse
10 June 2008 (Class 318/114); filed in the European Patent Office 9 December 2004

Using known prior art, a cellular phone vibrator can be driven by alternating positive and negative pulses timed to match the resonance frequency of the device. This patent argues that such a drive circuit is inefficient and can generate dangerous overvoltage spikes. An alternative scheme



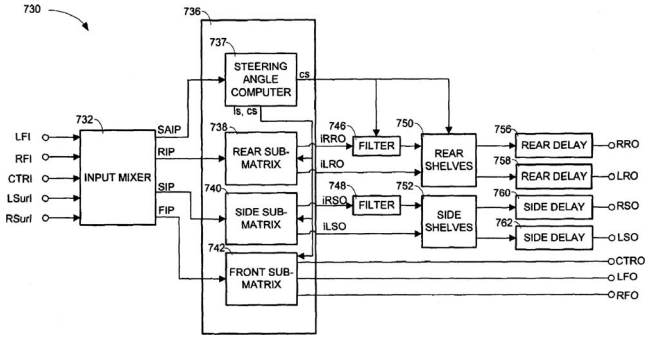
is proposed that utilizes pulse-width modulation to synthesize a sine wave tuned to the resonance frequency. Tuning is accomplished during a preliminary phase that starts by exciting the vibrator with a single pulse.—GLA

7,391,869

43.38.Lc BASE MANAGEMENT SYSTEMS

Bradley F. Eid and Hans-Juergen Nitzpon, assignors to Harman International Industries, Incorporated
24 June 2008 (Class 381/22); filed 25 June 2003

Most surround sound systems in houses and automobiles employ some kind of bass management, using one or more subwoofers to handle the combined low frequency content of all channels. So far, so good. But in a tricky acoustic environment like an auto, it might be better to use different



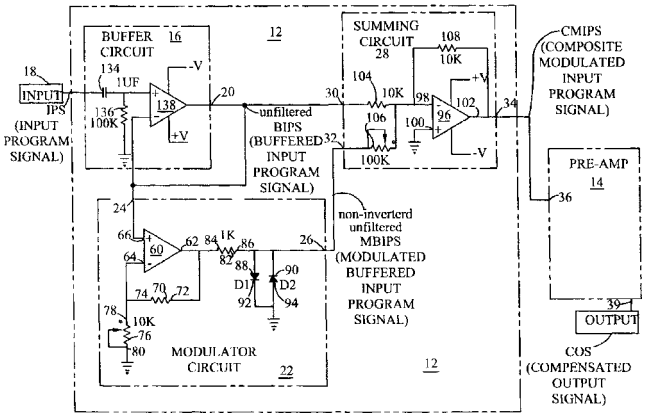
processing for different subwoofers or bass management on some channels but not others, or steer some subwoofer signals as part of matrix decoding. These and all other conceivable permutations and combinations are included in this patent.—GLA

7,388,959

43.38.Lc HARMONIC GENERATOR AND PRE-AMP

Paul R. Gagon, assignor to BBE Sound, Incorporated
17 June 2008 (Class 381/98); filed 20 August 2004

The assignee of this patent manufactures various kinds of audio processing gear. The circuit shown is highly specific; to be covered by the patent claims, it must be used in conjunction with preamp **14**, which is a previously patented state-variable filter circuit. This latest refinement adds a harmonic generator. "A determination has been made that some applications



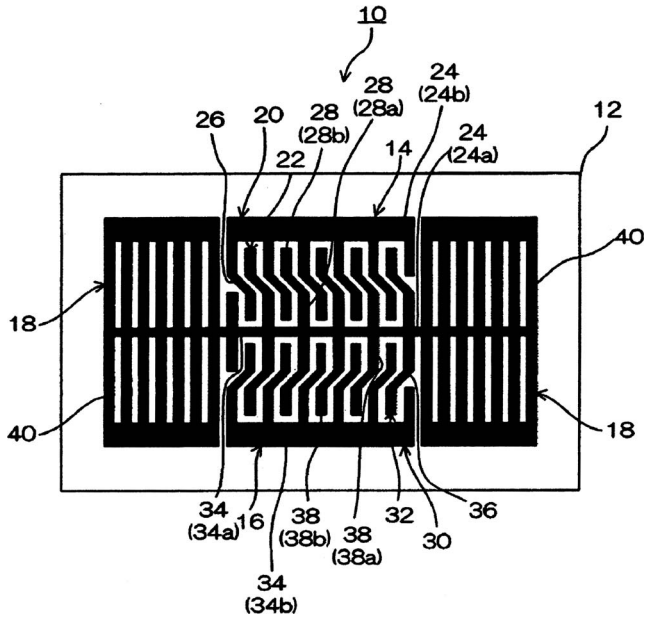
benefit from the introduction of a predetermined amount of harmonic distortion…." Modulator circuit **22** generates harmonics in relation to signal level, and its output is combined with the unprocessed signal in summing amplifier **28**.—GLA

7,321,279

43.38.Rh SURFACE ACOUSTIC WAVE ELEMENT

Katsuro Yoneya, assignor to Seiko Epson Corporation
22 January 2008 (Class 333/195); filed in Japan 22 July 2004

A surface acoustic wave (SAW) radio frequency filter **10** having reduced insertion loss and greater bandwidth is claimed using SAW propagation parallel to interdigital transducer (IDT) conductors **22**, **32**, reducing the



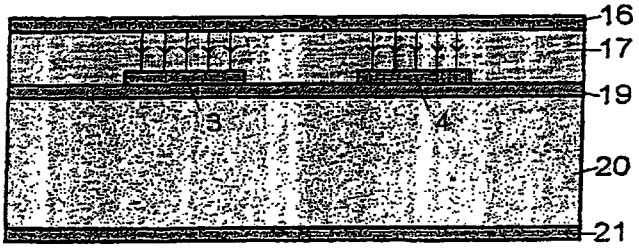
length of power supply conductors **20**, **16**. Useful SAW waves are launched via half wave sidewise shifts **28**, **28a**, **38**, and **38a** of IDT conductors.—AJC

7,323,802

43.38.Rh SURFACE ACOUSTIC WAVE DEVICE

Chan Hin Kam *et al.*, assignor to Acoustical Technologies Singapore Pte., Limited
29 January 2008 (Class 310/313 B); filed in United Kingdom 31 May 2000

A two-frequency surface acoustic wave (SAW) device for RF applications is claimed where interdigital transducer conducting fingers **3**, **4** on piezo layer **17** are driven in phase using overlay conductor **16** as the second terminal. Fingers **3**, **4** are spaced a wavelength apart for the higher frequency mode. Fingers **3** and **4** can also be driven by opposite phases at half



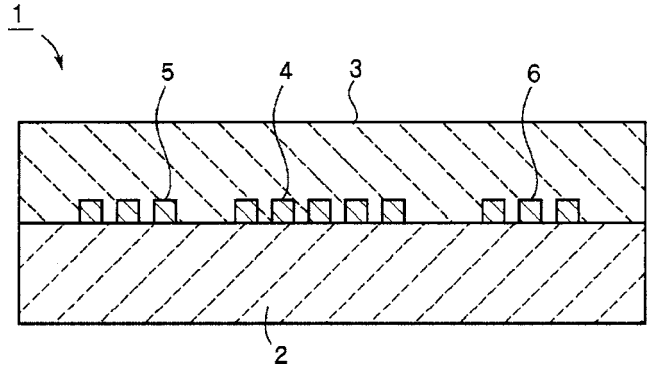
that frequency, where the spacing becomes a half wavelength. Layer **19** is a silicon oxide buffer while substrate **20** is the elastic medium (sapphire, etc.) in which internal SAW waves travel. Layer **21** is a backing electrode.—AJC

7,323,803

43.38.Rh BOUNDARY ACOUSTIC WAVE DEVICE

Hajime Kando, assignor to Murata Manufacturing Company, Limited
29 January 2008 (Class 310/313 A); filed in Japan 5 March 2004

To reduce the size at any frequency of a surface acoustic wave device **1**, a slow horizontal shear wave mode is utilized that propagates along the



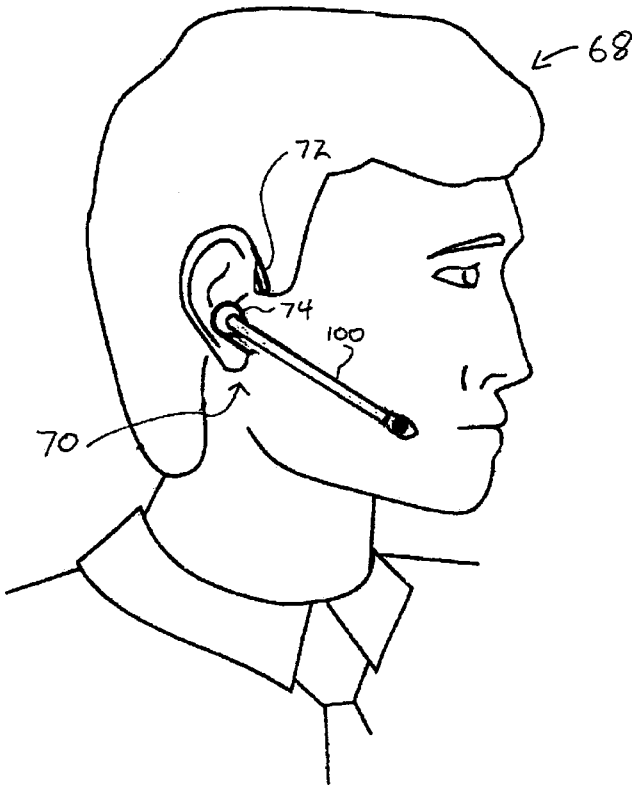
internal boundary between piezoelectric material **3** and substrate **2**. Interdigital transducer conductors ("fingers") **4**, **5**, **6** are placed between materials **2** and **3**. Accordingly, no clearance space is required around package **1**.—AJC

7,359,525

43.38.Si MULTI-FUNCTION MICROPHONE BOOM WITH ON-LINE INDICATOR

James F. Bobisuthi, assignor to Plantronics, Incorporated
15 April 2008 (Class 381/375); filed 13 December 2005

A light emitting device is mounted in ear piece **74** of boom headset **74**. The light travels down boom **100** which illuminates translucent/transparentring at the tip of the microphone end of boom **100**. This feature



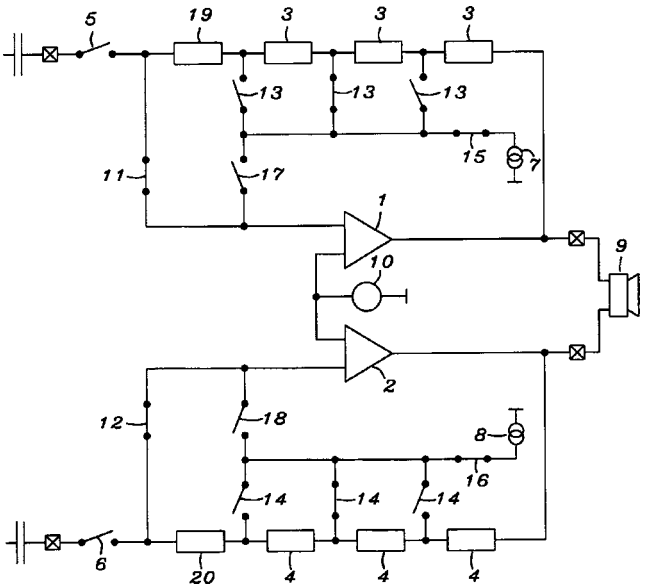
can let passers-by know that user **68** is actually on a call and not just talking to him or herself.—NAS

7,388,955

43.38.Si COMBINE AUDIO AND RINGING MODE

Klaus Graef and Edgar Sexauer, assignors to Dialog Semiconductor GmbH
17 June 2008 (Class 379/387.01); filed 1 February 2005

In a cellular telephone the loudspeaker must reproduce ring signals as well as audio signals, however, the two types of signals are generated by different circuits. This patent explains that the signal level of a pulse-width



modulated ring tone generator is difficult to control and may overload the loudspeaker. A logical solution would be to use the same level control circuitry for both functions, and that is what has been patented here.—GLA

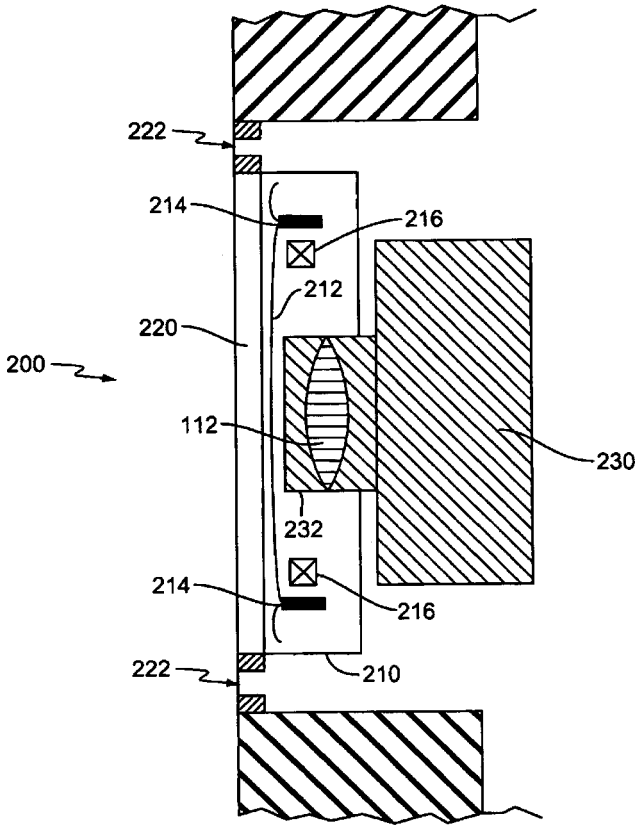
7,388,619

43.38.Si MOBILE DEVICE WITH A COMBINATION CAMERA AND LOUDSPEAKER

Chris Eaton and Matt Murray, assignors to Sony Ericsson Mobile Communications AB

17 June 2008 (Class 348/552); filed 11 December 2003

In this scramble to provide more and more features in smaller and smaller cellular phones the loudspeaker is sometimes combined with another function—making the video display panel also serve as the loudspeaker



diaphragm for example. In this patent, loudspeaker diaphragm **212** is transparent so that camera lens **112** can look through it. The patent sets forth the peculiar notion that varying the curvature of the transparent film, or changing the distance between the film and the lens, will somehow set the focal length of the camera.—GLA

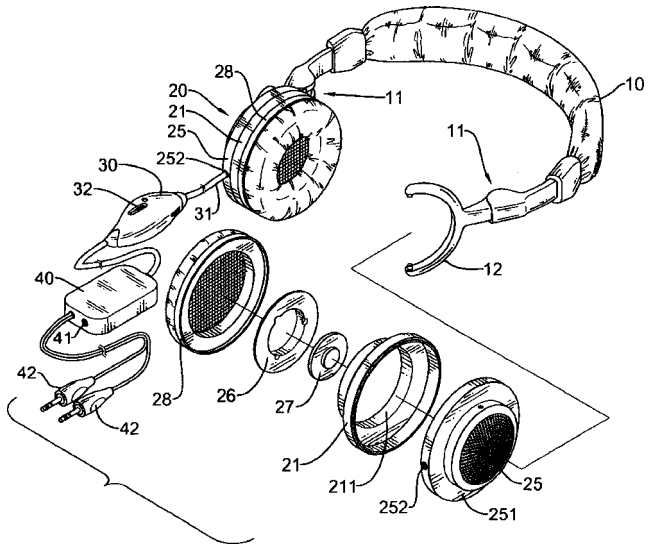
7,388,960

43.38.Si MULTIMEDIA SPEAKER HEADPHONE

Ching-Chang Kuo and Chang-Ning Hung, both of Kaohsiung, Taiwan

17 June 2008 (Class 381/186); filed 19 January 2005

Each earcup of this dual-purpose headset contains a conventional inward-facing "earphone speaker" **27** and an outward-facing "audio speaker" **25**. A switch **32** allows the user to, "…listen to music with or without wearing of the multimedia speaker headphone." Presumably, the



headset is simply draped over the neck when listening to the audio speakers.—GLA

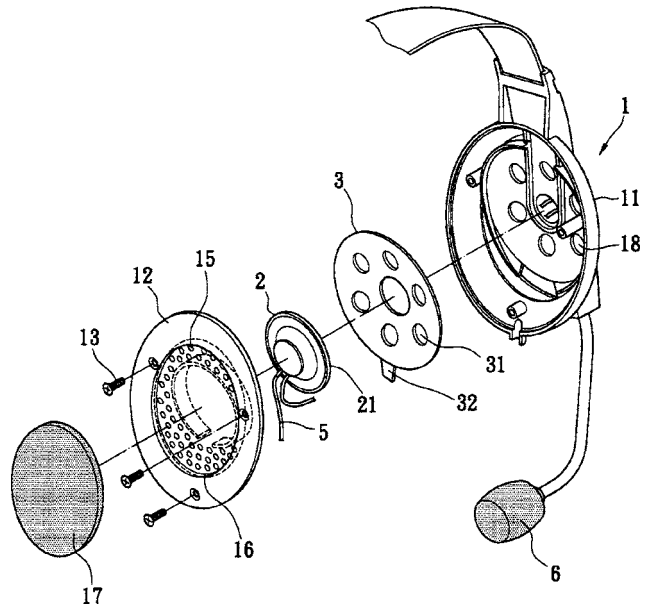
7,391,878

43.38.Si EARPHONE DEVICE HAVING COMPOSITE FUNCTIONS

Sheng-Hsin Liao, Shulin City, Taipei Hsien, Taiwan

24 June 2008 (Class 381/370); filed 12 January 2005

According to the patent abstract, "The earphone device is comfortable for use and can reduce pathological changes in ear and hearing decay to



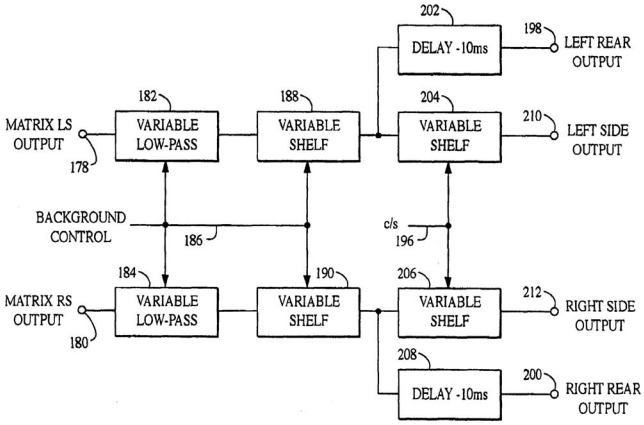
keep the human body healthy. Moreover, the earphone device has the functions of earphone, sound amplifier, and sound box." The novel feature appears to be rotatable shutter **3** which opens or closes vents **18** between the loudspeaker back chamber and the outside air.—GLA

7,386,132

43.38.Vk 5-2-5 MATRIX ENCODER AND DECODER SYSTEM

David H. Griesinger, assignor to Harman International Industries, Incorporated
10 June 2008 (Class 381/18); filed 7 August 2006

This patent must set some kind of record for sheer persistence. It is a continuation of a continuation of a continuation-in-part of U.S. Patent No. 5,796,844 which was filed in 1996. Each of the subsequent three patents discloses improvements in a method for converting a two-channel signal



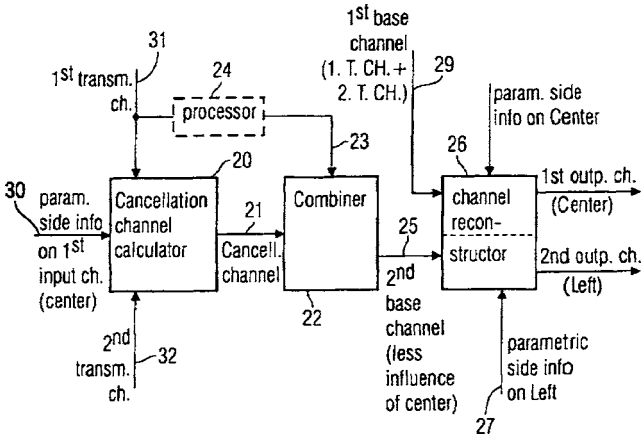
into multichannel surround sound. This latest version includes sophisticated mapping techniques to enhance the correlated components of the input signals in a desired direction and reduce the strength of channels not contributing to the desired direction.—GLA

7,391,870

43.38.Vk APPARATUS AND METHOD FOR GENERATING A MULTI-CHANNEL OUTPUT SIGNAL

Jürgen Herre *et al.*, assignors to Fraunhofer-Gesellschaft zur Foerderung der Angewandten Forschung E V
24 June 2008 (Class 381/23); filed 7 September 2004

"Parametric" stereo encoding creates two transmission channels plus a separate channel for parametric side information. The relatively coarse parametric data include scale factors, weighting by multiplication, frequency shifting, and so on. These are used in the reconstruction process to recover all five channels for surround sound playback. As might be expected, such a



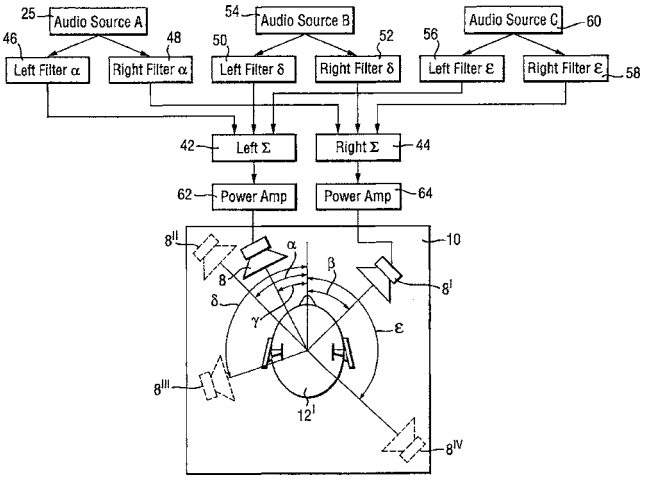
compression and reconstruction scheme can introduce unwanted artifacts. To make such artifacts less audible, this patent sets forth an improved reconstruction concept that inserts a cancellation channel calculator into each of the two main channels, permitting more robust multichannel reconstruction. At least, that is my limited understanding of this highly technical patent.—GLA

7,391,876

43.38.Vk METHOD AND SYSTEM FOR SIMULATING A 3D SOUND ENVIRONMENT

Yuval Cohen *et al.*, assignors to BE4 Limited
24 June 2008 (Class 381/309); filed in Israel 5 March 2001

During the past 20 years or so, considerable engineering effort has been devoted to the goal of achieving realistic surround sound from a pair of loudspeakers. Most methods utilize simplified head related transfer functions as basic elements of the circuitry. Such "universal" HRTFs can be derived from tests made with a dummy head for example. This patent points out that such nonspecific HRTFs introduce a number of problems, including front-back confusion and a severely restricted sweet spot for the listener. An



interesting method is disclosed for generating improved pseudo-HRTFs. A dummy head is involved, but measurements are taken with loudspeakers and headphones. A series of transfer functions is obtained, these are subjected to mathematical operations, and the results are used to design left and right channel filters. The restrictions used in solving the math equations can be adjusted to change the behavior of the playback system. Those interested in surround sound reproduction will want to study this patent.—GLA

7,389,999

43.40.Tm WHEEL ASSEMBLY

Yoshiaki Kimura and Tadashi Imamura, assignors to Topy Kogyo Kabushiki Kaisha
24 June 2008 (Class 280/93.512); filed in Japan 5 June 2003

Shock absorbers are incorporated in this relatively complicated automotive wheel assembly, making reduced width of vehicles possible.—EEU

7,393,575

43.40.Tm SHEET MOLDING COMPOUND DAMPER COMPONENT, AND METHODS FOR MAKING AND USING THE SAME

Daniel Boss, assignor to Material Sciences Corporation
1 July 2008 (Class 428/68); filed 26 December 2006

This patent, in essence, deals with sandwich arrangements consisting of a viscoelastic energy dissipation layer enclosed by relatively stiff constraining layers made of materials with comparatively high elastic moduli. The constraining layers are of a sheet molding compound that is substantially immiscible with the viscoelastic material so that a discrete interface is maintained between each constraining layer and the viscoelastic layer in the manufacturing process; however, continuity of the viscoelastic layer need

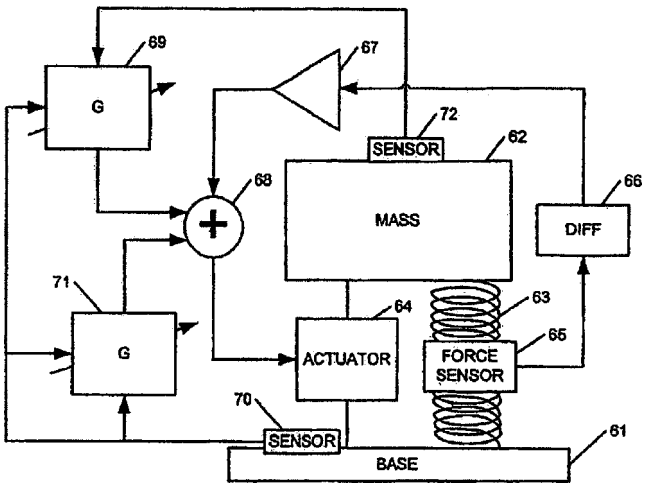
not be maintained. Data indicate rather good damping performance. Components made of these damping arrangements may replace conventional components in some applications.—EEU

7,398,143

43.40.Vn ACTIVE VIBRATION ABSORBER AND METHOD

Ian Stothers *et al.*, assignors to Ultra Electronics, Limited
8 July 2008 (Class 701/37); filed in United Kingdom 24 September 2003

This absorber, like conventional passive absorbers, consists of a mass that is supported via an elastic element (e.g., a spring) from a base whose vibrations are to be suppressed. Signals indicative of the motion of the base and of the motion of the mass are fed to a controller, which causes an actuator to exert a force between the base and the mass so as to reduce the vibration of the base. In the embodiment illustrated by the attached figure, which is one of several embodiments discussed in the patent, a force sensor **65** measures the force between the mass **62** and the base **61**. The output of



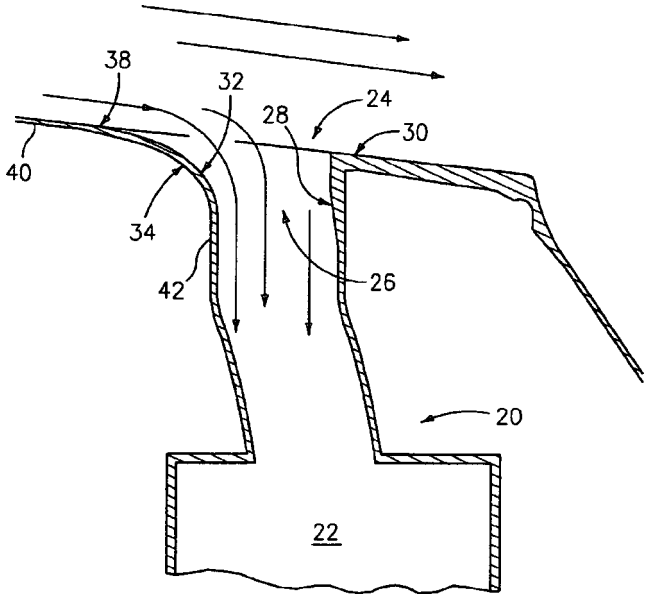
the force sensor is fed to a differentiator **66**, which provides a signal indicative of the relative velocity between the base and the mass. This signal is amplified with negative gain by amplifier **67** and then fed to a summer **68**. A sensor **70** mounted on the base provides a signal proportional to a suitable vibration parameter, which signal is fed to controller **71** to perform adaptive feedback control. The output of a sensor **72** that measures a suitable vibration parameter of mass **62** is fed to controller **69**, which also uses a signal from sensor **70** to perform adaptive feedforward control, generating a signal that is input to summer **68**. The output of this summer controls actuator **64**, which exerts a force between the base and the mass.—EEU

7,322,195

43.50.Gf ACOUSTIC DAMPERS

Mark Edward Borja and Gavin Julian Hendricks, assignors to United Technologies Corporation
29 January 2008 (Class 60/725); filed 19 April 2005

An improved Helmholtz resonator **20** and inlet **24** for turbine and rocket engine gas flow resonance noise absorption is claimed. Gas flow



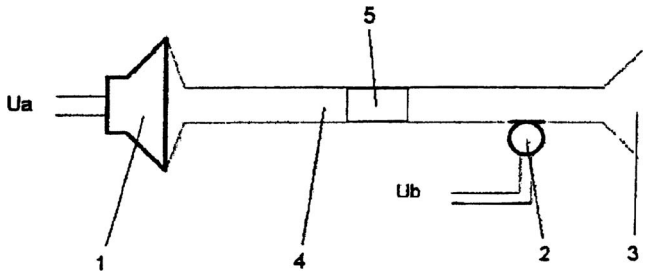
separation at the resonator opening **24** leading edge **32** reduces sound absorption. Flow resonance sound reduction is doubled by the leading edge rounding **38**, **34**, **32**, **42** of opening **24**.—AJC

7,398,166

43.58.Bh METHOD AND APPARATUS FOR THE MEASUREMENT OF THE ACOUSTIC IMPEDANCE

Alfred Stirneman, assignor to Phonak AG
8 July 2008 (Class 702/54); filed in the European Patent Office 6 March 2003

The system disclosed in this patent can be used to measure the acoustic impedance of a human ear or for more general purposes. Adaptor flange **3** is attached to a probe tube or other acoustic coupler. Microphone **2** can be located at some noncritical distance between the flange and driving transducer **1**. For improved accuracy, an acoustic resistance **5** is located between the microphone and the driver. In use, the assembly is calibrated using a



wide-range signal and several known acoustic impedances. For each known impedance the complex transfer function (driver input versus microphone output) is measured and stored. The transfer function obtained from an unknown acoustic impedance is then "merged" (compared?) with the reference functions using a chain matrix model. All of which can be accomplished with a relatively straightforward computer program.—GLA

7,386,141

43.66.Ts HEARING DEVICE AND METHOD OF OPERATING A HEARING DEVICE

Bernd Beimel and Kristin Rohrseitz, assignors to Siemens Audiologische Technik GmbH
10 June 2008 (Class 381/313); filed in Germany 1 December 2003

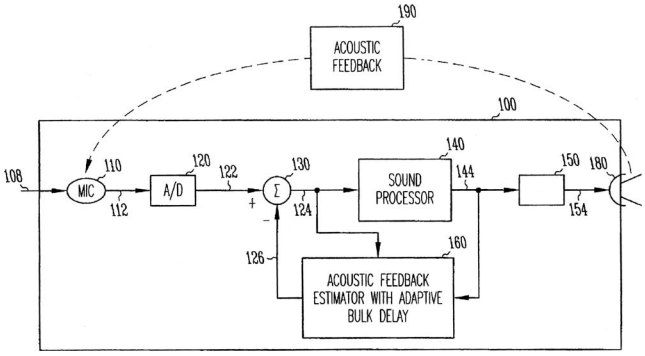
This patent addresses when a noise that should be perceived by the wearer, e.g., for safety reasons, is attenuated via directionality in a hearing device. The direction of the incoming audio noise is detected by the directional microphone system, and the signal is fed to a signal classifier which compares it to recordings including car/bus/truck horns, baby cries, train whistles, etc. If the signal is deemed potentially dangerous, the directional characteristic is adjusted such that the signal is not maximally attenuated, and the wearer is notified of the signal class and direction by an audio or tactile signal.—DAP

7,386,142

43.66.Ts METHOD AND APPARATUS FOR A HEARING ASSISTANCE SYSTEM WITH ADAPTIVE BULK DELAY

Jon S. Kindred, assignor to Starkey Laboratories, Incorporated
10 June 2008 (Class 381/318); filed 27 May 2004

To help prevent acoustic feedback oscillation, the bulk delay in an acoustic feedback estimator in a hearing assistance device is made adjustable to account for changes in the acoustic feedback path. An error signal,



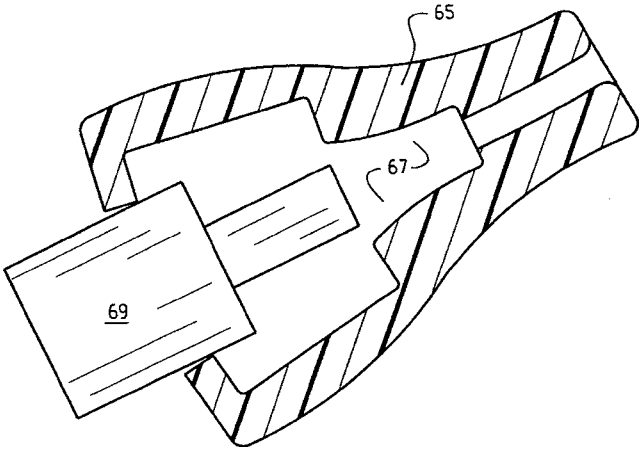
created by subtracting the estimated feedback path from the digitized incoming signal, is minimized by varying bulk delay. Higher power filter coefficients, for example, are adaptively changed by positioning them in different filter tap locations.—DAP

7,387,187

43.66.Ts CUSTOM-MOLDED EAR-PLUG, AND PROCESS FOR PRODUCING A CUSTOM-MOLDED EAR-PLUG DEVICE

Christoph Widmer *et al.*, assignors to Phonak AG
17 June 2008 (Class 181/130); filed 15 October 2002

To accommodate children with custom hearing aids as their ears grow, a replaceable, flexible outer shell has an opening to insert and remove the electronic components that are packaged in a reusable module. The elastic



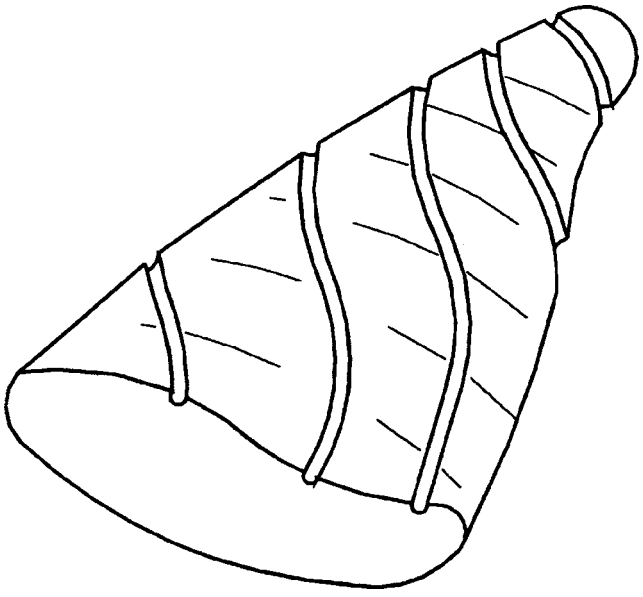
outer shell conforms to the shape of the standard-shaped module/components inside.—DAP

7,394,909

43.66.Ts HEARING DEVICE WITH EMBEDDED CHANNNEL

Christoph Widmer *et al.*, assignors to Phonak AG
1 July 2008 (Class 381/322); filed 25 September 2000

To open up more space and provide more flexibility in positioning the microphone and receiver in a custom-molded hearing device, channels molded throughout the shell via rapid prototyping are utilized for venting



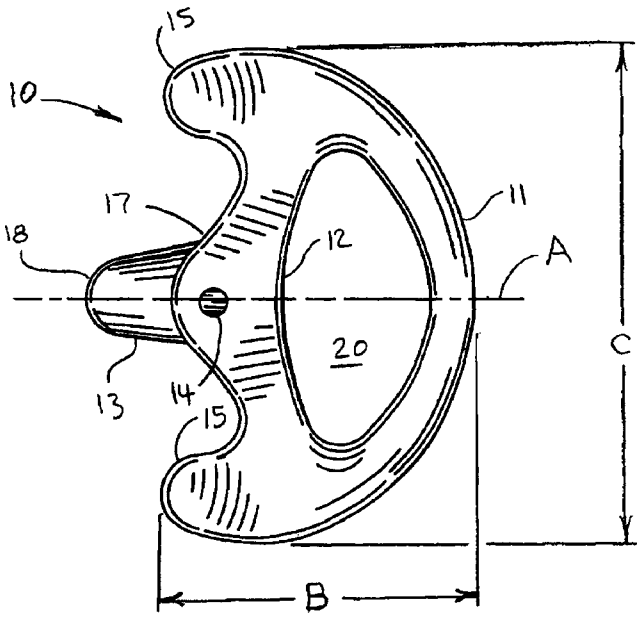
and acoustical input and output rather than traditional channels and tubings located inside in their usual positions. Several channels may be combined to tune acoustical parameters and their acoustical impedances adjusted via varying cross-sectional area or shape.—DAP

7,394,910

43.66.Ts AMBIDEXTROUS EARPIECE

Richard C. Smith and Diann Y. Smith, assignors to Surefire, LLC
1 July 2008 (Class 381/322); filed 29 January 2004

A resilient, one-size-fits-most earpiece that is intended, for example, for two-way radio listening, is configured symmetrically for use in either



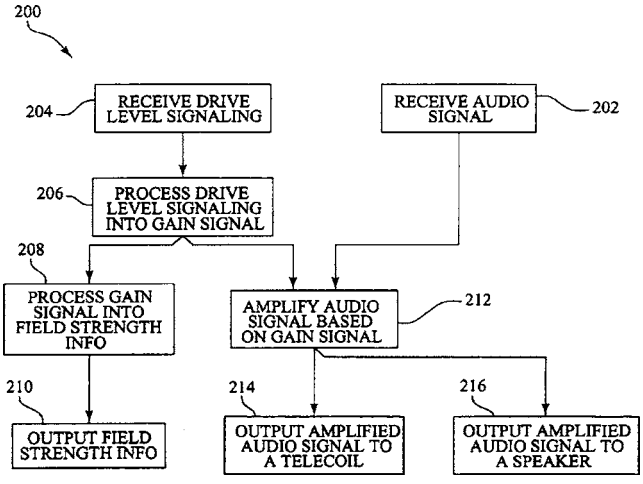
ear. The earpiece is held in place by the antihelix and protrusions of the concha interfacing with detents in the earpiece.—DAP

7,397,926

43.66.Ts SYSTEM AND METHOD FOR OPTIMIZING THE STRENGTH AND ORIENTATION OF THE INDUCTIVE FIELD OF A HEARING AID COMPATIBLE DEVICE

Melvin Duane Frerking, assignor to AT&T Mobility II LLC
8 July 2008 (Class 381/315) ; filed 2 September 2004

To improve telephone use by hearing aid wearers, desired signals are frequently coupled from telephones to hearing aids via induction to eliminate ambient noise and prevent acoustical feedback oscillation. In this



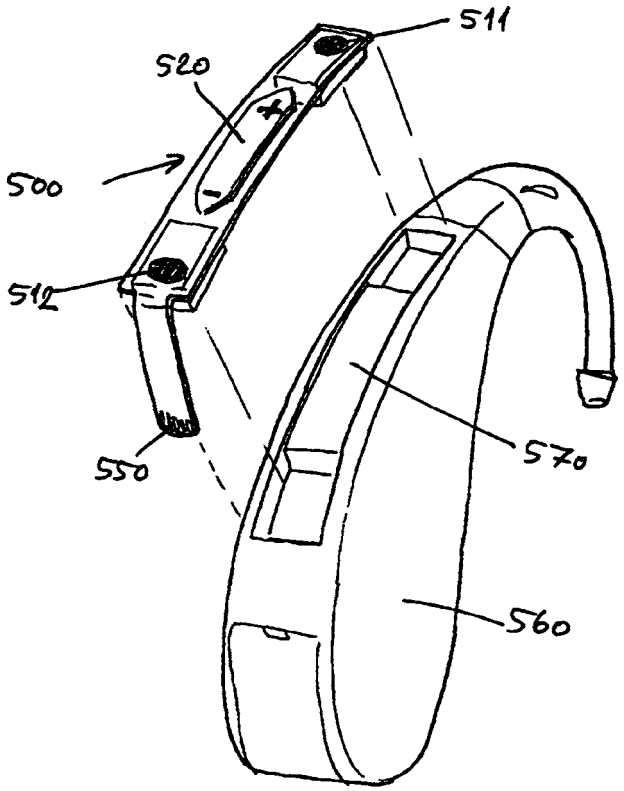
patent, the inductive field provided by a device such as a mobile telephone handset is improved to provide optimum coupling by allowing the user to select, e.g., via a keypad on a wireless device, the best drive level for a transmitting coil.—DAP

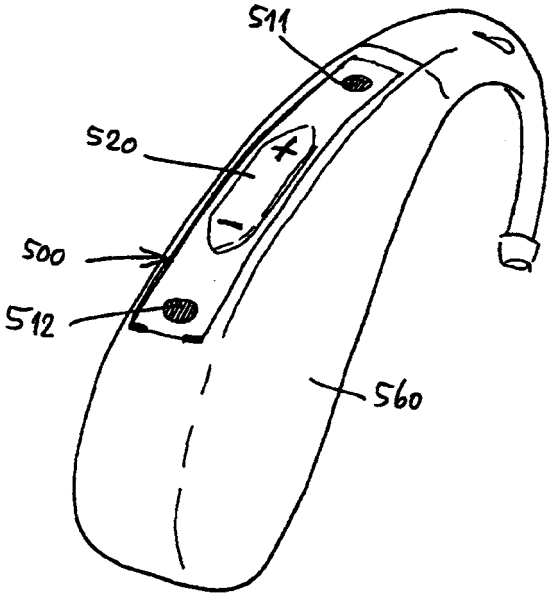
7,394,911

43.66.Ts CONTROL PANEL WITH ACTIVATION ZONE

Martin Bondo Joergensen and Joergen Ahm Petersen, assignors to Sonian Roskilde A/S
1 July 2008 (Class 381/322); filed 7 July 2004

An interchangeable, connectorized control panel for a behind-the-ear or in-the-ear hearing aid, which can be selectively placed in an actuated mode, has at least one user activation zone that interfaces at a distance to a compressible layered structure. Located below the activation zone are aconducting surface, like a foil, and a conducting path mounted on an electrically nonconducting substrate. In the actuated state, when the user touches





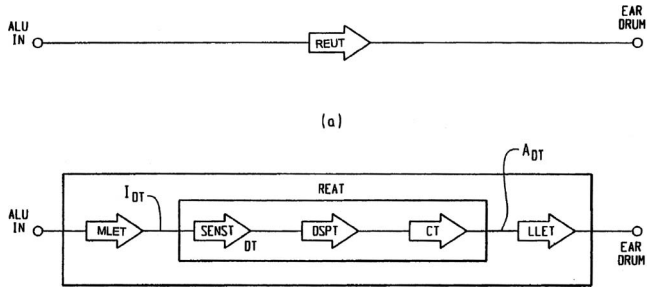
the control panel, the foil is connected to the conducting path. The control panel may be exchanged to provide different functions. The connector provides activation information to the hearing aid and may contain a communication unit that performs wireless transmission.—DAP

7,397,925

43.66.Ts HEARING DEVICE SYSTEM AND METHOD FOR MANUFACTURING SUCH DEVICE

Alfred Stirnemann and Hilmar Meier, assignors to Phonak AG
8 July 2008 (Class 381/312); filed 10 February 2004

A hearing device works in at least two acoustic operating modes: (1) a transparent mode with the device in situ that produces an acoustically transparent response re the unaided ear whose associated independent reference parameters are stored; and (2) independent operating mode(s) whose parameters are determined during an interactive fitting process and are weighted



variants of the transparent mode. The transparent mode parameters are obtained by subtracting from the unaided transfer function the measured effects of hearing device microphone position and individual ear canal impedance on receiver output and the modeled device transfer function itself.—DAP

7,398,204

43.72.Gy BIT RATE REDUCTION IN AUDIO ENCODERS BY EXPLOITING INHARMONICITY EFFECTS AND AUDITORY TEMPORAL MASKING

Hossein Najaf-Zadeh *et al.*, assignors to Her Majesty in Right of Canada as Represented by the Minister of Industry
8 July 2008 (Class 704/207); filed 26 August 2003

The audio signal is encoded in several frequency bands using a masking threshold determined from the pitch variance of the band output signal envelopes (inharmonicity index) and a psychoacoustic model such as that for MPEG.—DAP

7,206,390

43.72.Ja SIMULATED VOICE MESSAGE BY CONCATENATING VOICE FILES

Scott R. Smith *et al.*, assignors to Extended Data Solutions, Incorporated
17 April 2007 (Class 379/88.04); filed 13 May 2004

Here we have a patent on a method for concatenating (splicing together) simple voice recordings of someone who wants to make automated "personalized" phone calls. The method includes having the caller prerecord a database of themselves speaking every name in the phone book that they want to call. This is sort of like patenting a "cleaning method" that involves bending over and picking up grains of dirt one by one.—SAF

7,219,060

43.72.Ja SPEECH SYNTHESIS USING CONCATENATION OF SPEECH WAVEFORMS

Geert Coorman *et al.*, assignors to Nuance Communications, Incorporated
15 May 2007 (Class 704/258); filed 1 December 2003

A few methods are presented for selecting speech synthesis units from a large database of recordings. A "waveform selector" is considered, which will determine which candidate speech units can be concatenated incurring the least acoustic degradation. Candidate-to-candidate matching uses information from the signal frames (energy, pitch, and spectrum) to compute a cost function, thereby determining how well two candidates fit together. The best overall sequence of unit candidates is selected using dynamic programming. Surely all of this has been done before in one way or another, resulting in highly specific claims which describe some very particular ways envisioned here.—SAF

7,219,061

43.72.Ja METHOD FOR DETECTING THE TIME SEQUENCES OF A FUNDAMENTAL FREQUENCY OF AN AUDIO RESPONSE UNIT TO BE SYNTHESIZED

Caglayan Erdem and Martin Holzapfel, assignors to Siemens Aktiengesellschaft
15 May 2007 (Class 704/268); filed in Germany 28 October 1999

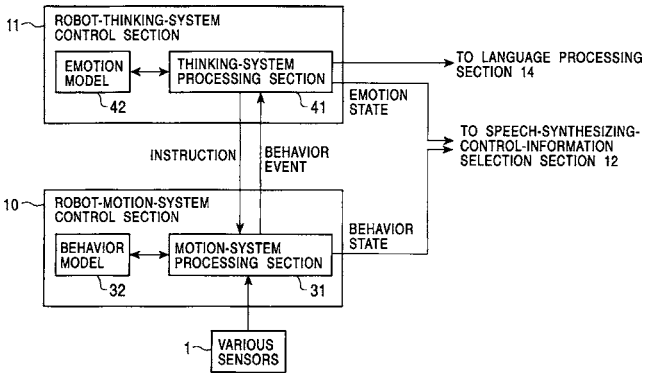
This patent presents a portion of a complete method for speech synthesis. What is focused on here is a method for synthesizing speech with a natural "fundamental frequency." The latter term seems to be used in the sense of "frequency of a speech sound" (the "microstructure" of the fundamental frequency), and simultaneously in the more familiar sense referring to the prosody of an utterance (the "macrostructure"). Natural voice synthesis is said to be achieved using neural networks to compute the macrostructure, and a Viterbi search to compute the microstructure. It is not said just exactly how one would do this, so it is not entirely clear what has been patented. Using neural networks, perhaps?—SAF

7,379,871

43.72.Ja SPEECH SYNTHESIZING APPARATUS, SPEECH SYNTHESIZING METHOD, AND RECORDING MEDIUM USING A PLURALITY OF SUBSTITUTE DICTIONARIES CORRESPONDING TO PRE-PROGRAMMED PERSONALITY INFORMATION

Masato Shimakawa *et al.*, assignors to Sony Corporation
27 May 2008 (Class 704/260); filed in Japan 28 December 1999

One of the common complaints about talking robots and talking computers in general is that they are not responsive to human conditions. Although this situation is not likely to change for a few years yet, this patent offers a small step in the direction of making machines that are able to interact in a little more humanlike manner. The patented system would include specific computational elements to manage a dialog state, a behavioral



state, an "emotional" state, and elements to control movements of the device. The synthesis software includes lists of alternatives for both vocabulary and syntax so as to avoid excessive repetition of speech elements.—DLR

7,206,741

43.72.Ne METHOD OF SPEECH RECOGNITION USING TIME-DEPENDENT INTERPOLATION AND HIDDEN DYNAMIC VALUE CLASSES

Li Deng *et al.*, assignors to Microsoft Corporation
17 April 2007 (Class 704/254); filed 6 December 2005

As usual from Microsoft, we have a detailed description of a method of considerable novelty and value. Moving on from the usual recursive Hidden Markov Models of speech sounds, the patented method improves upon previous literature proposing to directly model a "production-related parameter" of speech. The proposed "Hidden Trajectory Model" comprises a trajectory component that describes hidden production-related parameters such as resonances, and also a mapping component that connects the production-related parameters into acoustic features such as Mel-frequency cepstral coefficients. A separate set of trajectory parameters are trained for each phone in the language at hand. "The trajectory within a phone is determined based on the value of the trajectory at the beginning of the phone and the amount of time that has passed since the beginning of the phone." Ultimately, six different model parameters must be trained using expectation-maximization.—SAF

7,209,883

43.72.Ne FACTORIAL HIDDEN MARKOV MODEL FOR AUDIOVISUAL SPEECH RECOGNITION

Ara V. Nefian, assignor to Intel Corporation
24 April 2007 (Class 704/256); filed 9 May 2002

A method for audiovisual speech recognition is described, employing a "factorial Hidden Markov Model" (HMM). This is "a distributed state representation that can be seen as a collection of HMMs, one for each data stream, where the discrete nodes at time t for each HMM are conditioned by the discrete nodes at time t_1 of all the related HMMs." The method described employs two coupled data streams, one for the speech sound and one for analyzed video of the mouth. The usual algorithms for HMMs such as Viterbi search and maximum likelihood training are adapted to the present description, all of which derives heavily from the prior art. It seems that only very minor adjustments to the prior art are novel here.—SAF

7,216,076

43.72.Ne SYSTEM AND METHOD OF PATTERN RECOGNITION IN VERY HIGH-DIMENSIONAL SPACE

Bishnu Saroop Atal, assignor to AT&T Corporation
8 May 2007 (Class 704/238); filed 19 December 2005

This is one of the rare ones, a patent that is valuable as a piece of literature, and more interesting than most journal papers. An approach to speech recognition is described which is considerably different from most. The method involves first creating a database of recorded and catalogued phonemes. The phonemes are then transformed into n-dimensional hyperspherical space for comparison in that space with received audio speech, which is also segmented into phonemes and transformed into the same n-dimensional space. It is claimed that "by transforming the database signal and the received voice signal to high-dimensional space, a sharp boundary will exist." Then this boundary between phonemes can be used to improve speech recognition.—SAF

7,219,056

43.72.Ne DETERMINING AND USING ACOUSTIC CONFUSABILITY, ACOUSTIC PERPLEXITY AND SYNTHETIC ACOUSTIC WORD ERROR RATE

Scott Elliot Axelrod *et al.*, assignors to International Business Machines Corporation
15 May 2007 (Class 704/235); filed 19 April 2001

The effectiveness of a language model in speech recognition is often measured by computing the "lexical perplexity." It is known that this is not a good metric. The patent introduces two better statistics for determining the quality of language models, namely the *acoustic perplexity* and the *synthetic acoustic word error rate*. Computation of these latter requires computing the acoustic confusability of words, for which some methods are introduced which substitute modeled acoustic data in place of real acoustic data. It is impossible to briefly summarize the richly detailed presentation of these notions in a couple of sentences; it could simply be said, to serve the purpose of a review, that this patent seems definitely worth studying.—SAF

7,219,057

43.72.Ne SPEECH RECOGNITION METHOD

Yin-Pin Yang, assignor to Koninklijke Philips Electronics
15 May 2007 (Class 704/236); filed 8 June 2005

This patent concerns a method for minimizing the network capacity used by a distributed speech recognition process (i.e., a process in which sound features are extracted and encoded at a front end, and transmitted via network to a back end where speech recognition as such is performed). Initially extracted feature vectors are often compressed using a codebook, so that each vector is replaced by a codebook index. The codebook has a size suitable for encoding every possible vector in a quantized vector space, and each index then requires a certain number of bits to be transmitted over the network. The patented method seeks to minimize the codebook size for each dialogue as a function of a tradeoff between signal bitrate and an expected recognition rate that is calculated.—SAF

7,219,062

43.72.Ne SPEECH ACTIVITY DETECTION USING ACOUSTIC AND FACIAL CHARACTERISTICS IN AN AUTOMATIC SPEECH RECOGNITION SYSTEM

Antonio Colmenarez and Andreas Kellner, assignor to Koninklijke Philips Electronics N.V.
15 May 2007 (Class 704/270); filed 30 January 2002

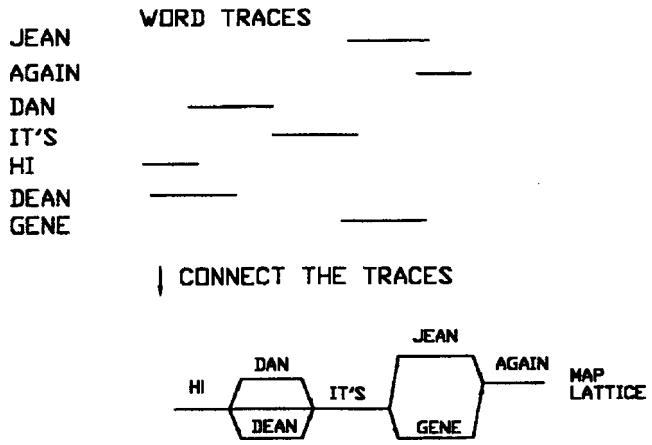
An audio-visual method is described (using the term charitably) by which a speech recognition system will activate only in the presence of both "acoustic energy having a spectrum associated with speech utterances" and "at least one facial characteristic associated with speech utterances." The detailed description is not very detailed, however. Some vague remarks are made concerning overall acoustic energy and the detection of lip motion.—SAF

7,216,077

43.72.Ne LATTICE-BASED UNSUPERVISED MAXIMUM LIKELIHOOD LINEAR REGRESSION FOR SPEAKER ADAPTATION

Mukund Padmanabhan *et al.*, assignors to International Business Machines Corporation
8 May 2007 (Class 704/240); filed 26 September 2000

A method is described which uses information from a word graph provided by a speech recognizer to adapt the recognition to a speaker. The word graph or lattice (e.g., Fig. 2) is a representation of all word sequences that are assigned any significant probability. Either the speaker data or the speech recognition model can then be adapted "in a manner to maximize the



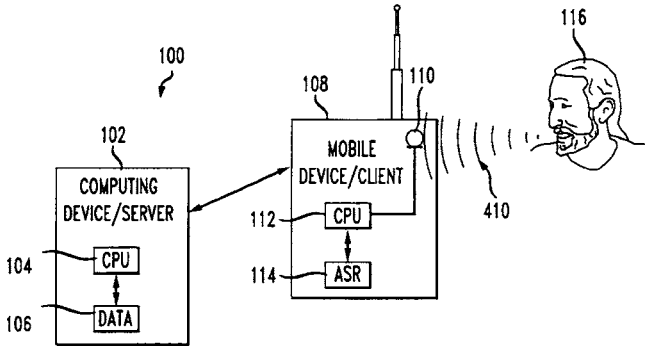
likelihood of the speaker data with respect to the generated word lattice." The contemplated word lattice is a maximum *a-posteriori* probability lattice, and methods for its construction are provided. Adaptation is suggested using maximum likelihood linear regression to transform the means of a Gaussian mixture model in accordance with the word lattice.—SAF

7,386,443

43.72.Ne SYSTEM AND METHOD FOR MOBILE AUTOMATIC SPEECH RECOGNITION

Sarangarajan Parthasarathy and Richard Cameron Rose, assignor to AT&T Corporation
10 June 2008 (Class 704/201); filed 9 January 2004

Mobile devices with embedded automatic speech recognition (ASR) capability have intermittent network connectivity and are resource-limited for battery life, computational power, and memory space, thus limiting ASR



performance. In this patent, user-specific adaptation data are transmitted from a wireless device to a computing device/server when a communication channel is available. New ASR adaptation parameters are then generated from speech utterances and ASR results and are transmitted back to the mobile device to enable the embedded ASR system to perform more accurately.—DAP

7,386,452

43.72.Ne AUTOMATED DETECTION OF SPOKEN NUMBERS IN VOICE MESSAGES

Cary Lee Bates *et al.*, assignors to International Business Machines Corporation
10 June 2008 (Class 704/270); filed 27 January 2000

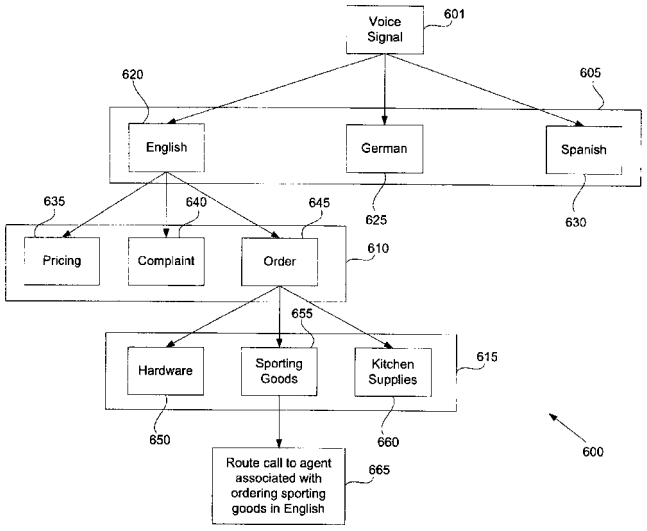
The goal is to assist persons in retrieving numbers, such as telephone numbers, in voice messages. Rather than requiring the entire message to be replayed for hearing the number again, recognition is performed automatically on the portion of a voice message containing numbers to determine a start position for message playback. Alternatively, the desired telephone number may be dialed automatically and viewed in text form.—DAP

7,389,230

43.72.Ne SYSTEM AND METHOD FOR CLASSIFICATION OF VOICE SIGNALS

Israel Nelken, assignor to International Business Machines Corporation
17 June 2008 (Class 704/255); filed 22 April 2003

Voice signals are classified in one category of a set of predefined categories using a statistical analysis of extracted features recovered



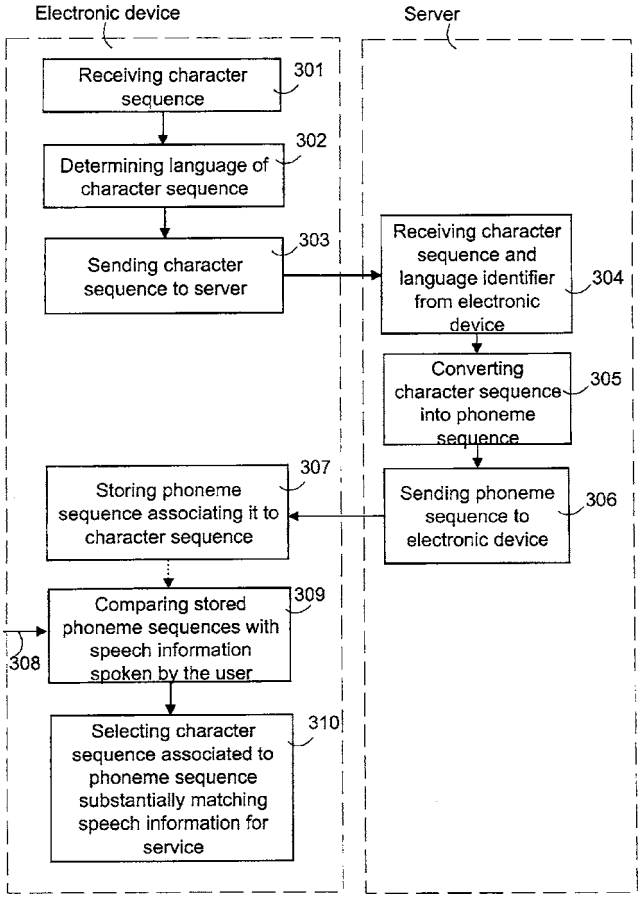
from feature vectors and/or integer labels output from an acoustic processor.—DAP

7,392,184

43.72.Ne ARRANGEMENT OF SPEAKER-INDEPENDENT SPEECH RECOGNITION

Olli Viikki and Kari Laurila, assignors to Nokia Corporation
24 June 2008 (Class 704/236); filed in Finland 17 April 2001

Speaker-independent speech recognition is preferred for such applications as calling a person by saying his/her name because it eliminates training. In this patent, accuracy is improved and multiple languages are supported by performing pronunciation modeling in a separate server that has more memory capacity than a portable device. The character sequence intended for speech recognition is sent from the portable device to the server,



which determines the language, and formulates and sends back a phoneme sequence in text format. The portable device compares this sequence to the speech received for a match, selects the matched character sequence, and forms an appropriate audio output.—DAP

7,392,189

43.72.Ne SYSTEM FOR SPEECH RECOGNITION WITH MULTI-PART RECOGNITION

Marcus Hennecke *et al.*, assignors to Harman Becker Automotive Systems GmbH
24 June 2008 (Class 704/254); filed in Germany 23 February 2002

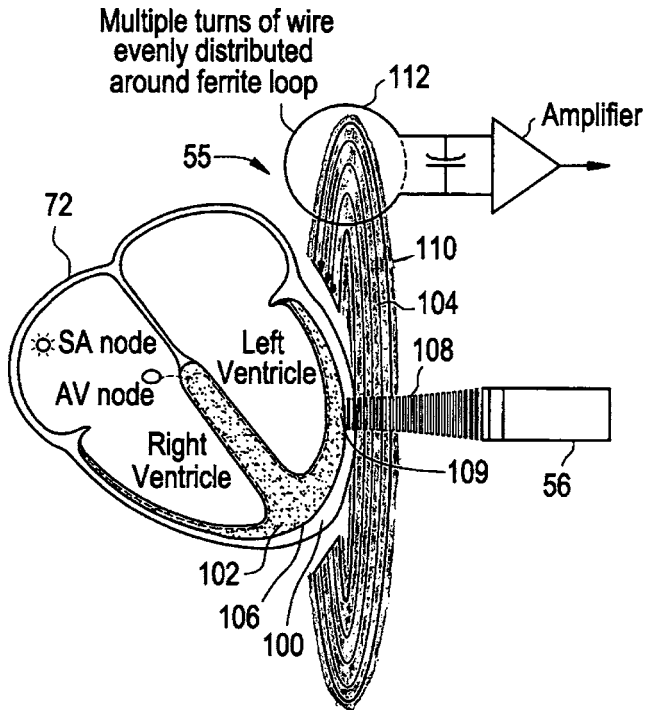
In situations where voice inputs are provided to a speech recognizer to select an element from a list, e.g., in vehicular navigation devices, recognition difficulties can occur when there are a large number of list elements or similar sounding list elements. To prevent this, the user speaks the entire desired list element, which is then separated with a first recognition procedure into at least one sequence of speech subunits (e.g., phonemes). The subunits are used to create a sublist that, with matching, forms a vocabulary for a second recognition procedure which compares the voice input of the whole word to the vocabulary of list elements in order to select one.—DAP

7,367,943

43.80.Vj SYSTEMS AND METHODS FOR DETERMINING THE ELECTRICAL ACTIVITY OF A MATERIAL

Paul S. Schluter, assignor to General Electric Company
6 May 2008 (Class 600/438); filed 6 January 2004

This very general patent discloses a means of detecting the magnetic field from "insonated" portion **109** of heart **72**, to solve the "inverse problem" of the EKG, i.e., determining "the electrical source distribution within the heart that produces the set of signals observed on the surface of the



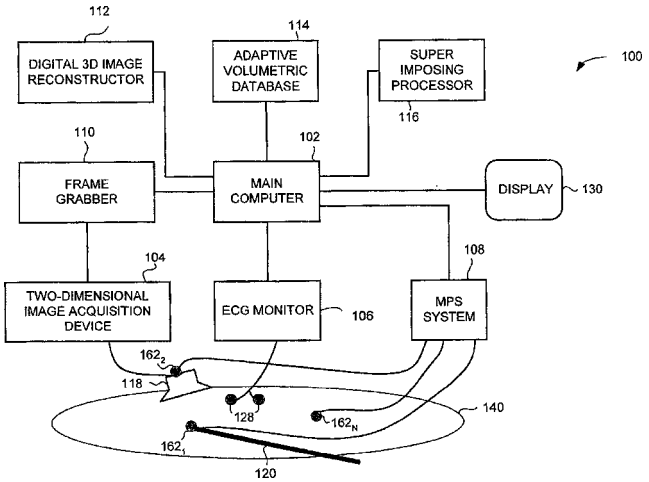
body." The patent notes that the power density of the ultrasonic stimulus **108** from transducer **55**, which may be limited by regulation, needs to be at least 250 W/cm^3 or more. The patent is clearly written and is a quick study in the physics of tissue acoustics.—NAS

7,386,339

43.80.Vj MEDICAL IMAGING AND NAVIGATION SYSTEM

Gera M. Strommer and Uzi Eicher, assignors to Mediguide, Limited
10 June 2008 (Class 600/424); filed 13 February 2001

This system senses the position of an ultrasonic imaging transducer, the position of a surgical tool, and a timing signal such as an ECG. The system shows the location and orientation of the surgical tool within the



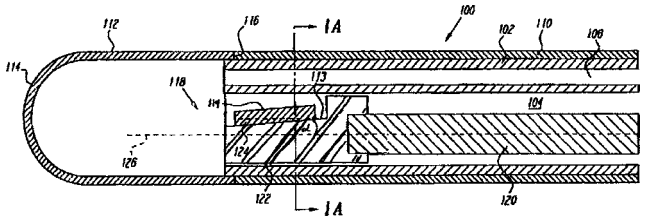
same coordinate system as the images. An image sequence of a moving organ is displayed along with the location and orientation of the surgical tool.—RCW

7,396,332

43.80.Vj TRANSDUCER WITH MULTIPLE RESONANT FREQUENCIES FOR AN IMAGING CATHETER

Miriam H. Taimisto and Richard Lardner, assignors to SciMed Life Systems, Incorporated
8 July 2008 (Class 600/467); filed 10 June 2002

This catheter-mounted transducer element is capable of oscillation at different resonant frequencies so that a user can switch from one frequency



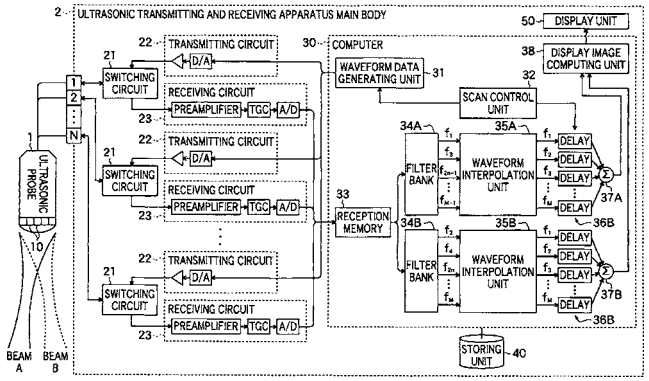
to another for improved resolution or depth of field without the need to switch the catheter or transducer.—RCW

7,393,324

43.80.Vj ULTRASONIC TRANSMITTING AND RECEIVING APPARATUS

Tomoo Satoh, assignor to FUJIFILM Corporation
1 July 2008 (Class 600/437); filed in Japan 13 July 2004

Ultrasonic beams are simultaneously transmitted in different directions. Each beam has a different center frequency. Echos received at the



different center frequencies are processed to form multiple focal points along each of the transmitted beams.—RCW

7,393,326

43.80.Vj APPARATUS FOR SCREENING AND DIAGNOSING BY DUAL STETHOSCOPIC AND DOPPLER DETECTION

Herve Bindefeld, Paris, France
1 July 2008 (Class 600/453); filed in France 27 March 2002

An ultrasound Doppler probe and a stethoscope sensor membrane are mounted together in a housing. The Doppler echos are processed to obtain an audio signal and a video signal. This information is presented simultaneously with stethoscopic sounds for diagnosis.—RCW

LETTERS TO THE EDITOR

This Letters section is for publishing (a) brief acoustical research or applied acoustical reports, (b) comments on articles or letters previously published in this Journal, and (c) a reply by the article author to criticism by the Letter author in (b). Extensive reports should be submitted as articles, not in a letter series. Letters are peer-reviewed on the same basis as articles, but usually require less review time before acceptance. Letters cannot exceed four printed pages (approximately 3000–4000 words) including figures, tables, references, and a required abstract of about 100 words.

Shear elasticity estimation from surface wave: The time reversal approach (L)

J. Brum
Laboratorio de Acústica Ultrasonora, Instituto de Física, Facultad de Ciencias, Universidad de la Republica, Montevideo, Uruguay

S. Catheline
Laboratoire Ondes et Acoustique, ESPCI, Université Paris VII, U.R.A. C.N.R.S. 1503, 10 Rue Vauquelin, 75231 Paris cedex 05, France

N. Benech and C. Negreira
Laboratorio de Acústica Ultrasonora, Instituto de Física, Facultad de Ciencias, Universidad de la Republica, Montevideo, 11400 Uruguay

(Received 23 April 2008; revised 16 July 2008; accepted 12 September 2008)

In this work the shear elasticity of soft solids is measured from the surface wave speed estimation. An external source creates mechanical waves which are detected using acoustic sensors. The surface wave speed estimation is extracted from the complex reverberated elastic field through a time-reversal analysis. Measurements in a hard and a soft gelatin-based phantom are validated by independent transient elastography estimations. In contrast with other elasticity assessment methods, one advantage of the present approach is its low sound technology cost. Experiments performed in cheese and soft phantoms allows one to envision applications in the food industry and medicine. © *2008 Acoustical Society of America.* [DOI: 10.1121/1.2998769]

PACS number(s): 43.60.Tj, 43.20.Jr, 43.80.Pe, 43.20.Ye [SFW] Pages: 3377–3380

Draeger[1] experimented the time-reversal (TR) invariance of acoustic waves inside chaotic cavities. In this experiment an ultrasonic pulse is sent from a transducer (source) and propagates inside a silicon plate. The acoustic trapped energy reverberated for a very long time is measured on a second transducer (receiver). The recorded signal lasts hundreds of times the initial pulse duration. A portion of this long and complex field is then time reversed and re-emitted from the receiver. The acoustic field is shown to propagate back to the source, recreating the short initial pulse. These experiments applied in the audible frequency range have shown to be an efficient localizing technique in the field of interactivity[2] and sound perception.[3] Indeed, the impact location coincides with the maximum energy position of its TR field. However, in addition to the source location, other information is conveyed by the TR field: measuring the focal size of a TR refocusing field is a way to estimate the wavelength and thus to deduce the wave speed and finally the elasticity. Applied to shear waves within soft solids, this concept of TR elastography allows estimation of the shear elasticity.[4,5] In the present paper, we have adapted the TR elastography to surface wave measurements. In contrast with TR bulk experiment in solid,[5] the surface wave field can be considered in a first approximation as a scalar wave field[6] so the TR focal size Δ of surface waves is simply related to the wavelength λ through the classic Rayleigh criterion: $\Delta=\lambda/2$. Moreover, the whole technique uses surface acoustic sensors and audible sound technology. This ultrasonic-free elastography is low cost compared to optical[7] or ultrasonic[8] methods.

A TR experiment is composed of two steps: the first step consists of observing a forward acoustic scene. As shown in Fig. 1, a circular piston 1 cm in diameter mounted on a shaker is applied at the surface of an agar-gelatin based phantom (1% agar, 3% gelatin for soft phantoms, and 2% agar for hard phantoms diluted in water). The shaker (Bruel&Kjaer type 4810) is connected to an arbitrary waveform generator (HP 33120A) and delivers a two-cycle sinusoid burst of 60 Hz for the soft phantom and 100 Hz for the hard one. The resulting field is measured by a passive sensor (Murata PKS1-4A type) with a working bandwidth ranging from 0.1 to 5 kHz. This kind of sensor can be placed anywhere on the medium surface. The acoustic signal is digitized at a sampling rate of 500 Hz by a HP 54520A type oscilloscope and finally sent to a personal computer for TR processing. This acoustic signal can be written mathematically as a convolution product between the emitted signal

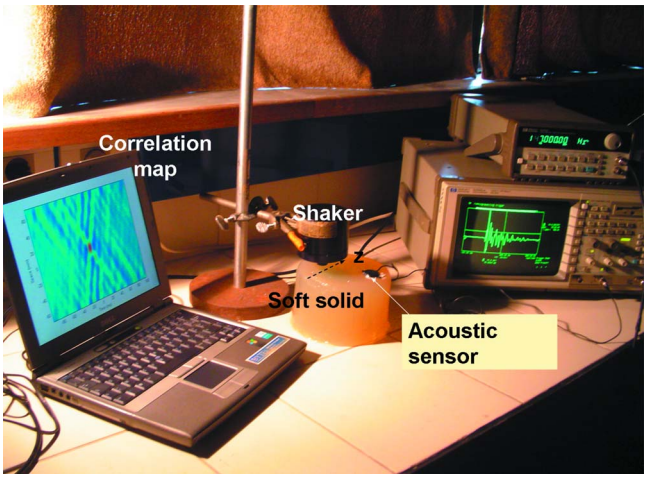


FIG. 1. (Color online) A shaker delivers an acoustic pulse detected by a surface sensor. The shaker is then moved along the z-axis at the surface of the gelatin-based phantom and another signal is stored in the computer via the oscilloscope.

$e(t)$ from the piston point P, and the impulse response to the sensor S, $h_{PS}(t)$,

$$\Psi(t) = e(t) \underset{t}{\otimes} h_{PS}(t). \tag{1}$$

The signal shown in Fig. 2(a) was acquired at a 12-cm distance from the emission point. Vibration observed on the surface near the surface-based point source is dominated by surface (Rayleigh) waves. It is conjectured that, despite the presence of bulk waves, Rayleigh waves dominate the reverberated surface wave field $\Psi(t)$. Indeed, according to diffraction laws, the amplitude of surface-guided waves has a typical $1/\sqrt{r}$ decreasing law, whereas bulk waves vanishes as $1/r$. Other surface modes (leaky[9] or capillary[10,11] waves) of lower amplitude are thought to have a negligible impact. The total time duration of about 100 ms is long compared to the initial pulse duration of about 10 ms. Reverberations are observed within the sample despite the viscous effects. Viscosity is responsible for the low-frequency shift of reverberations, well visible in Fig. 2(a) at late time. The quality factor was estimated from the spectrum as the mean −6-dB width of resonances divided by their frequency ($Q \sim 10$). This rather low Q-factor does not prevent a good TR experiment as demonstrated in Ref. 5.

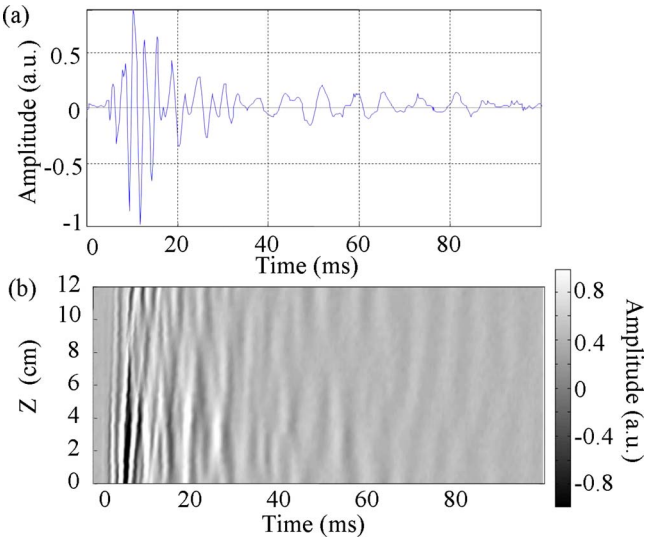


FIG. 2. (Color online) Acoustic signal as measured by surface sensors. (a) The visible reverberations are dominated by Rayleigh waves. (b) Gray scale representation of 24 signals corresponding to source positions aligned along the z-axis.

Given that the emitted pulse is brief enough and that the piston's diameter (1 cm) is smaller than a shear wavelength ($\lambda \sim 2-3$ cm), the emitted signal can be approximated to a delta function $\delta_P(t)$ in time and space. Thus, Eq. (1) becomes

$$\Psi(t) \cong h_{PS}(t). \tag{2}$$

It means that the signal measured by the sensor is simply the impulse response between points P and S.

The second step of a TR experiment consists of replaying the acoustic scene backward in time. In reverberating cavities, the time-reversed signal of duration T is sent from the observing point, $e(t)=h_{PS}(T-t)$. According to Eq. (1), the TR field at any observing point Π around the piston point P is

$$\Psi^{\mathrm{TR}}(t) = h_{PS}(T-t) \underset{t}{\otimes} h_{S\Pi}(t). \tag{3}$$

The maximum is found at time $t=T$ when P and Π coincides: on the source. However, in the present experiments, the Murata sensors are only passive so the TR experiment is conducted through correlation algorithms as described in Ref. 2. After the acquisition of a first impulse response $h_{P_1S}(t)$, the shaker is moved by 3 mm and a second signal $h_{P_2S}(t)$ is kept in memory and so on. Finally, a whole data set corresponding to 24 acoustic impulse responses $h_{P_iS}(t)$ of points aligned along the z-axis and on a total distance of 12 cm is acquired. They are represented in the gray scale image of Fig. 2(b). Then, the TR field is achieved by choosing a pseudopoint source P_j, and by computing the following spatio-temporal TR field:

$$\Psi_{ij}^{\mathrm{TR}}(t) = h_{P_jS}(T-t) \underset{t}{\otimes} h_{P_iS}(t). \tag{4}$$

The spatial reciprocity applied to the discrete observing points P_i stipulates that $h_{P_iS}(t)=h_{SP_i}(t)$, which shows the equivalence of Eqs. (3) and (4). In this latter equation, the TR field thus simply appears as cross correlation of the acoustic signals represented in Fig. 2(b).

The time-reversal approach can be slightly improved by pointing out that all the information contained in the spectrum is not optimally used; as a result of correlation properties, the most energetic components dominate the computation of Eq. (4). In order to give the same weight to each frequency, a whitening processing is applied; if $H_{P_jS}(f)$ is the Fourier transform of $h_{P_jS}(t)$, the normalized spectrum is

$$\tilde{H}_{P_iS}(f) = H_{P_iS}(f)/|H_{P_iS}(f)|. \tag{5}$$

A modified impulse response of equal frequency components is given by the inverse Fourier transform,

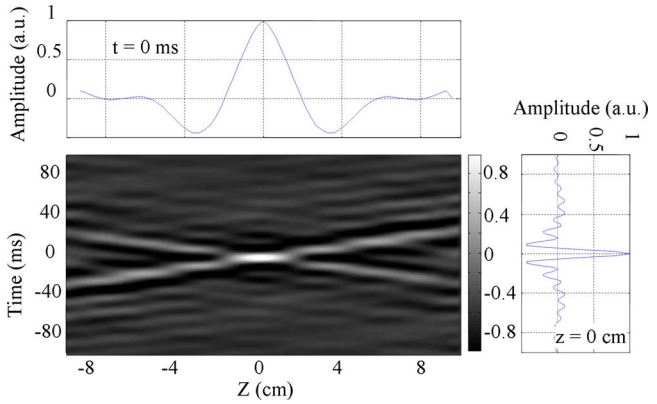


FIG. 3. (Color online) Gray scale image of the spatio-temporal TR field $\Psi_i^{\mathrm{TR}}(t)$ and its projection at $t=0$ and $z=0$ in the hard phantom.

$$\tilde{h}_{P_jS}(t) = FT^{-1}[\tilde{H}_{P_jS} W_{\Delta f}(f - f_0)]. \tag{6}$$

The gate function $W_{\Delta f}(f-f_0)$ is defined as 1 if the frequency $f \in [f_0 - (\Delta f/2), f_0 + (\Delta f/2)]$ and 0 elsewhere. This gate function and a threshold at −30 dB are used to avoid nondesired effects due to noisy components. Best results were observed in the experiments for frequency ranging from 60 to 120 Hz. The same computation is then applied to the whole set of signals as in Eq. (4),

$$\Psi_{ij}^{\mathrm{TR}}(t) = \tilde{h}_{P_jS}(T - t) \otimes \tilde{h}_{P_iS}(t). \tag{7}$$

Since the amplitude of the frequency components has been set equal to 1, Eq. (7) is referred to as the phase correlation or inverse filter approach.[12] From a physical point of view, it describes a time-reversal scene in an ideal medium where all the frequency components of waves conserve constant amplitude. One last manipulation is needed. An average on each pseudosource position is executed in order to improve the final TR field,

$$\Psi_i^{\mathrm{TR}}(t) = \langle \Psi_{ij}^{\mathrm{TR}}(t) \rangle \tag{8}$$

In Fig. 3, the source position is set at the origin and the refocusing time is defined as $t=0$ s. As predicted by TR theory, the maximum amplitude is observed on the source $(z=0)$ at the refocusing time $(t=0)$. The crosslike shape is a one dimensional manifestation of a TR converging $(t<0)$, collapsing $(t=0)$, and diverging $(t>0)$ wave observed along a diameter.

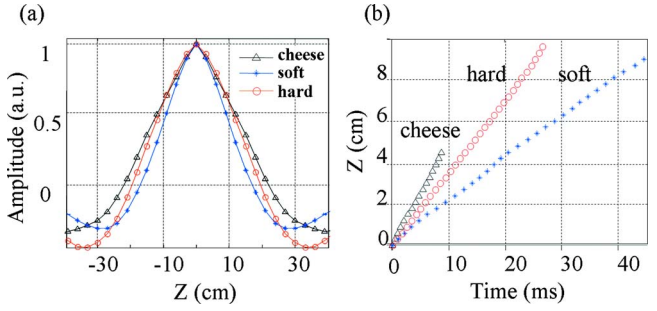


FIG. 4. (Color online) (a) Spatial refocusing of a TR field in media showing different stiffness. (b) Distance versus time delay of the TR diverging wave of Fig. 3. These measurements are extracted from a branch of the cross.

TABLE I. Shear elasticity estimation μ obtained in a hard and a soft gelatin-based phantom and a cheese.

μ (kPa)	Transient elastography	TR (focus size)	TR (delay)
Soft	4.9	6.1	4.7
Hard	15.7	14.9	14.0
Cheese	∅	25.5	28.7

Measurements on solids presenting different elasticity were performed. In order to validate the TR method, the elasticity estimations were performed using the technique of transient elastography.[13] In the hard phantom a shear wave speed of 3.96 ± 0.05 m s^{-1} was obtained. The soft phantom gave a shear wave speed of 2.21 ± 0.04 m s^{-1}. Using a simple elastic model of solid with a constant density $\rho = 1000$ kg m^{-3}, the shear elasticity was deduced: 15.7 and 4.9 kPa, respectively. Besides, the TR method was tested in a cheese where the absence of ultrasonic speckle did not allow the use of transient elastography.[14] Two approaches were tested in order to estimate the shear elasticity μ from the TR field of Fig. 3. The first one consists of extracting the central frequency of the wave $(f \sim 80$ Hz) from the time refocusing on the source point $(z=0)$, right-hand side of Fig. 3. The associated central wavelength is estimated from the spatial refocusing at $t=0$ ms, according to the Rayleigh criteria:[6,15] the half wavelength is equal to the −6-dB width, $\lambda/2 = 2.3$ cm. Consequently, the Rayleigh wave speed is found to be $v_R = \lambda . f = 3.68$ m s^{-1}. In incompressible media, the relationship between shear wave speed and Rayleigh wave speed is, in a first approximation, $v_R = 0.95 v_S$. Thus, the final shear elasticity estimation is $\mu = \rho v_s^2 = 14.9$ kPa. The same computation conducted for the soft phantom gives the following shear elasticity: $\mu = 6.1$ kPa. In a cheese, the central frequency, the wavelength, the Rayleigh wave speed, and the elasticity were found to be 100 Hz, 4.8 cm, 4.8 m s^{-1}, and 25.5 kPa, respectively. The spatial refocusing are represented in Fig. 4(a) for the three media. The comparison shows a classical result: the harder the medium, the larger the wavelength and the broader the TR focus.

The second approach consists of measuring the speed of the wave when it converges to the focal spot or, equally, when it diverges from it. The phase is thus measured on one branch of the cross that appears in the TR field of Fig. 3. This phase shift is translated in time delay and represented as function of distance, Fig. 4(b). The slope gives the speed of the wave. The speed information is thus extracted in the vicinity of the focus point. Consequently, the focus size approach is totally independent of the time delay approach. With the latter method, the Rayleigh wave speed results are 3.56 m s^{-1} for the hard phantom, 2.07 m s^{-1} for the soft one, and 5.09 m s^{-1} for the cheese. All the experimental measurements are summarized in Table I. A general agreement within 10% in average was found between the different measurements of shear elasticity. One may point out the time delay approach probably gives a more accurate estimation of elasticity. An agreement of 4% on speed estimation was found.

The strengths of the TR method are

(1) Its low cost: this technique only uses acoustic surface sensors which rely on cheap sound technology.
(2) Its robustness with regard to the experimental configuration; conversions from Rayleigh to bulk waves allow one to set the surface sensor on any face of the medium.[16] Besides, in contrast with a classical time-of-flight technique, the focus size approach does not need any synchronization between emission and reception. Thus, in its light version, the TR technique only uses one acoustic sensor and a personal computer, low-frequency shear waves being generated by finger impacts. When natural shear wave sources exist within the medium, as recently reported for skeletal muscle,[17] the TR approach is also a good candidate as a passive *in vivo* method for tissue elasticity assessment. The future investigations will concern its potential as a surface imaging modality.

[1]C. Draeger and M. Fink, "One-channel time reversal of elastic waves in a chaotic 2D-silicon cavity," Phys. Rev. Lett. **79**(3), 407–410 (1997).
[2]R. Ing, N. Quieffin, S. Catheline, and M. Fink, "In solid localization of finger impacts using acoustic time-reversal process," Appl. Phys. Lett. **87**(1–3), 204104 (2005).
[3]S. Catheline, N. Quieffin, R. Ing, and M. Fink, "Acoustic source localization model using in-skull reverberation and time reversal," Appl. Phys. Lett. **90**, 063902 (2007).
[4]N. Benech, S. Catheline, J. Brum, T. Gallot, and C. Negreira, "Elasticity estimation by time reversal of shear waves," Proc.-IEEE Ultrason. Symp. **2007**, 2263–2266).
[5]S. Catheline, N. Benech, J. Brum, and C. Negreira, "Time reversal of elastic waves in soft solids," Phys. Rev. Lett. **100**, 064301 (2008).
[6]R. K. Ing, M. Fink, and O. Casula, "Self-focusing Rayleigh wave using a time reversal mirror," Appl. Phys. Lett. **68**(2), 161–163 (1996).
[7]T. J. Royston, H. A. Mansy, and R. H. Sandler, "Excitation and propagation of surface waves on a viscoelastic half-space with application to medical diagnosis," J. Acoust. Soc. Am. **106**, 3678–3686 (1999).
[8]X. Zhang, and J. F. Greenleaf, "Estimation of tissue's elasticity with surface wave speed," J. Acoust. Soc. Am. **122**(5), 2522–2525 (2007).
[9]C. T. Schröder and W. R. Scott, "On the complex conjugate roots of the Rayleigh equation: The leaky surface wave," J. Acoust. Soc. Am. **110**(6), 2867–2877 (2001).
[10]F. Monroy, and D. Langevin, "Direct experimental observation of the crossover from capillary to elastic surface waves on soft gels," Phys. Rev. Lett. **81**(15), 3167–3170 (1998).
[11]Y. A. Kosevich, K. Ahn, and M. W. Kim, "Reevaluation of the crossover from elastic to capillary surface waves on soft gels," Phys. Rev. Lett. **90**(5), 059601 (2003).
[12]M. Tanter, J.-F. Aubry, J. Gerber, J.-L. Thomas, and M. Fink, "Optimal focusing by spatio-temporal inverse filter. I. Basic principles," J. Acoust. Soc. Am. **110**(1), 37 (2001).
[13]S. Catheline, F. Wu, and M. Fink, "A solution to diffraction biases in sonoelasticity: The acoustic impulse technique," J. Acoust. Soc. Am. **105**(5), 2941–2950 (1999).
[14]T. Klinkosz, C. J. Lewe, and J. Paczkowski, "Propagation velocity and attenuation of a shear wave pulse measured by ultrasound detection in Agarose and Polyacrylamide gels," Ultrasound Med. Biol. **34**(2), 265–275 (2008).
[15]J. de Rosny and M. Fink, "Overcoming the diffraction limit in wave physics using a time-reversal mirror and a novel acoustic sink," Phys. Rev. Lett. **89**, 124301 (2002).
[16]V. V. Kazakov and B. N. Klochkov, "Low frequency mechanical properties of the soft tissue of human arm," Biophysics (Engl. Transl.) **34**(4), 742–747 (1989).
[17]K. Sabra, S. Conti, P. Roux, and W. Kuperman, "Passive in vivo elastography from skeletal muscle noise," Appl. Phys. Lett. **90**(1–3), 194101 (2007).

Comment on "Linear and nonlinear frequency shifts in acoustical resonators with varying cross sections" [J. Acoust. Soc. Am. 110, 109–119 (2001)] (L)

Michael P. Mortell
Department of Applied Mathematics, University College Cork, Cork, Ireland

Brian R. Seymour
Department of Applied Mathematics, University of British Columbia, Vancouver V6T 1Z2, Canada

(Received 15 August 2008; revised 19 September 2008; accepted 30 September 2008)

The effects of the shape of the container on nonlinear resonant oscillations have been of interest for the past decade. Resonant oscillations in a closed straight tube can contain shocks, but for some tube shapes shock formation can be prevented. How the magnitude of the variation of the shape from a straight tube affects the prevention of shocks is discussed. Criteria to determine whether tuning curves bend right or left are addressed, including that proposed by Hamilton *et al.* ["Linear and nonlinear frequency shifts in acoustical resonators with varying cross sections," J. Acoust. Soc. Am. **110**, 109–119 (2001)]. © *2008 Acoustical Society of America.* [DOI: 10.1121/1.3003932]

PACS number(s): 43.25.Gf, 43.25.Cb, 43.20.Ks [OAS] Pages: 3381–3385

I. INTRODUCTION

Resonant oscillations in a closed cylindrical tube have been studied experimentally and analytically for over 70 years; see, for example, the review of Ilgamov *et al.*[1] Shock formation, normally a characteristic of the motion, is now well understood. An understanding of the effect of the geometry of the container is of a much more recent vintage.

Mortell and Seymour[2] studied the effect of a varying cross-sectional area on pulse propagation in a nonlinear viscoelastic rod, and found that, under a "high frequency" or "geometrical acoustics" approximation, the area variation could not of itself prevent the formation of a shock. The consequence of this for resonant oscillations of a gas in a closed tube with slowly varying area was immediate—shocks were still a feature of the motion. Keller[3] derived a nonlinear differential-integral equation describing the motion of a gas in a slowly varying cylindrical tube, where again shocks appeared in the flow. As far as we are aware, the first paper to show that the geometry could prevent shock formation in resonant oscillations was Chester,[4] where radially symmetric oscillations in a sphere were studied. This was followed by Ellermeier,[5] who showed that resonant motions of cylindrically symmetric waves could be shockless. Ockendon *et al.*[6] investigated how the increase of geometric imperfection from a uniform cylinder could affect the resonant flow, and, in particular, whether a shock is obviated by such imperfections. Various geometrical effects, all "small" in some sense, were investigated, and their conclusion was that "the detuning range in which shocks are possible decreases as the geometrical imperfection increases." Keller,[3] Ockendon *et al.*,[6] and Chester[7] each predicted that a single mode shockless solution can occur only when the imperfection exceeded a threshold value.

The experiments of Lawrenson *et al.*[8] changed the landscape. They showed that by appropriately designing the shape of a closed container the resonant oscillations of a gas in the container could reach macrosonic pressures while remaining shockless. They called this resonant macrosonic synthesis (RMS). Ilinskii *et al.*[9] produced numerical solutions of the governing partial differential equations that corresponded to the experimental results in Ref. 8 for cone, horn, and bulb shaped resonators. In particular, the bending of the tuning curves to right or left was correctly predicted. Hamilton *et al.*[10] examined analytically the case of a tube with slowly varying cross section. Their analysis was confined to small perturbations from a cylindrical tube and thus did not encompass either the experimental or numerical results for cones, horns, and bulbs. They gave a criterion to predict the bending of the tuning curves in the restricted setting of their analysis. Mortell and Seymour[11] considered analytically the resonant motions in closed containers such as cones, horns, and bulbs with no restriction on the size of the shape perturbation. Their results agreed well with the experiments in Ref. 8. This was the first analytical work that encompassed the experimental and numerical findings.

The experiments described in Ref. 8 confirmed that for a closed cylindrical tube there are shocks in the flow and no hysteresis. In these circumstances "the resonance curve is not skewed"[9] or "In experiments performed by MacroSonix, no significant hardening or softening is observed."[9] Shocks and hysteresis are antithetical. Additionally, according to Ref. 9, damping has a lower order effect on hysteresis. Further, damping is not necessary to ensure a finite response, see Refs. 4 and 11.

The key to solving the small amplitude nonlinear problem is an understanding of the equivalent linear problem with varying coefficients. There have been various attempts to find approximate analytical expressions for eigenvalues and eigenfunctions, usually for small perturbations, going back to Rayleigh.[12] However, for several tube shapes, including a cone, horn, and bulb, exact values can be found.[11] Then the key to finding analytical solutions of the nonlinear problem lies in an appropriate perturbation method. Here we ex-

amine exact and approximate solutions to the linear problem and compare two perturbation methods for the nonlinear problem. In the process, we give a careful analysis of the results presented in Ref. 10. We are particularly concerned with the assumptions underlying their analysis, their failure to predict a minimum value of the shape perturbation below which shocks occur, and the criterion given for determining whether the tuning curves bend left or right.

II. LINEAR THEORY

All theories of weakly nonlinear oscillations rely on some kind of expansion about the relevant linear equations. For tubes with varying cross sections, $S(x)$, $0 \leqslant x \leqslant 1$, this means solving a linear wave equation with variable coefficients, typically of the form

$$\omega^2 S(x)\frac{\partial^2 P}{\partial \theta^2} - \frac{\partial}{\partial x}\left(S(x)\frac{\partial P}{\partial x}\right) = 0, \quad P'(0,\theta) = P'(1,\theta) = 0, \tag{1}$$

where $\theta = \omega t$, ω is the frequency of the input, and the tube length and ambient sound speed have both been normalized to unity. For periodic oscillations, it is assumed the pressure has the form $P(x,\theta) = c^{i\omega\theta}p(x,\omega)$.

A. Exact eigenvalues

There are many container shapes $S(x)$ for which exact solutions of Eq. (1) can be constructed, see Ref. 13. These include a cone, horn, and bulb where the perturbation from a uniform cylinder is not small.[11] A simple case is the cone where, for any $k > 0$,

$$\frac{S(x)}{S_0} = (1+kx)^2, \quad 0 < x < 1, \tag{2}$$

where $S_0 = S(0) = \text{const}$. This is one of the shapes, with $k=7$, used in the experiments.[8] The exact solution to Eq. (1) with $S(x)$ given by Eq. (2) is[11]

$$p(x,\omega) = \left(\frac{1}{1+kx}\right)\left(\cos(\omega x) + \frac{k}{\omega}\sin(\omega x)\right), \tag{3}$$

where the eigenvalues are solutions of

$$\tan\omega = \frac{\omega k^2}{\omega^2 + k\omega^2 + k^2}. \tag{4}$$

For the experimental cone with $k=7$, the first three eigenvalues are 1.27π, 2.21π, and 3.17π. We note that these eigenvalues are incommensurate and the motion is continuous, see Refs. 8, 9, and 11.

For comparison with the perturbation approach in Sec. II B, we expand $p(x,\omega)$ and $\omega(k)$ for k small, i.e., for a slender cone. Then Eqs. (3) and (4) become

$$p(x,\omega) = \cos(\pi x) + k\left(\frac{1}{\pi}\sin\pi x - x\cos\pi x\right) + O(k^2), \tag{5}$$

$$\omega_1(k) = \delta_0 + \delta_1 k + \delta_2 k^2 + O(k^3) = \pi + \frac{k^2}{\pi} + O(k^3). \tag{6}$$

B. Approximate eigenvalues

For arbitrary small changes in $S(x)$, approximate values of the pressure and eigenvalues can be calculated from a perturbation expansion for small k; $S(x)$ is not restricted to the cone (2). Let $S(x) = S_0(1 + kS_1(x) + k^2 S_2(x) + \ldots)$, where S_0 is a constant reference area, and assume that the pressure, which has the form $P(x,\theta) = e^{i\omega\theta}p(x)$, and frequency ω have similar expansions. Then $p_0(x) = \cos(\pi x)$ and the orthogonality condition for a solution at $O(k)$ requires that

$$\delta_1 = -\int_0^1 \frac{1}{\delta_0} S_1' p_0' p_0' dx = -\delta_0 \int_0^1 S_1(x)\cos(2\omega_1 x)dx. \tag{7}$$

This result was obtained by Rayleigh.[12] The second correction, at $O(k^2)$, is

$$\delta_2 = \frac{1}{\delta_0}\int_0^1 \left[S_1(p_0 p_1') - \frac{1}{2}\left(\frac{1}{2}S_1^2 - S_2\right)\frac{d^2}{dx^2}(p_0^2)\right]dx. \tag{8}$$

For a cone given by Eq. (2), $\delta_1 = 0$, $\delta_2 = \frac{1}{\pi}$, and

$$S_1(x) = 2x,\ S_2(x) = x^2,\ p_1(x) = \frac{1}{\pi}\sin\pi x - x\cos\pi x. \tag{9}$$

These agree with the expansion of the exact solution given by Eqs. (3) and (4).

We contrast the above with the perturbation results in Ref. 10. It is assumed there that

$$S(x) = S_0 + \delta S(x), \tag{10}$$

but the precise meaning of $\delta S(x)$ is not given. This results in an incorrect linear perturbation analysis. The result (28) in Ref. 10, the equivalent of Eq. (7) here, is incorrect. The function $\ln(S/S_0)$ should be replaced by $S_1(x)$ and all subsequent expressions containing ln or exp are incorrect. At the level of approximation in Ref. 10 odd spatial modulations in $S(x)$ have no effect on the natural frequencies. However, the cone example given above, where $\delta_1 = 0$ but $\delta_2 \neq 0$, shows that this result is not correct to second order. Any cone lies outside the scope of the theory in Ref. 10.

III. NONLINEAR THEORY

All analytical studies of the nonlinear tuning curves rely on perturbation expansions. Here we compare the consequences of a general expansion in terms of general time periodic functions,[11] and harmonic balance, in terms of linear spatial eigenfunctions.[10] Other differences to note between the methods are the order at which the forcing amplitude, $A = O(\varepsilon^n)$, enters the expansion, and also the order at which the detuning enters.

Following Refs. 9 and 11, we use Eulerian coordinates moving with the resonator. If $S(x)$ is the cross-sectional area and $a(t)$ is the imposed acceleration of the resonator, $0 \leqslant x \leqslant 1$, the equations of conservation of mass and momentum in dimensionless variables are

$$\frac{\partial(S\rho)}{\partial t}+\frac{\partial}{\partial x}(Su\rho)=0, \quad \frac{\partial u}{\partial t}+u\frac{\partial u}{\partial x}+\rho^{\gamma-2}\frac{\partial \rho}{\partial x}=-a(t). \tag{11}$$

For a closed resonator, the boundary conditions are $u(0,t)=0=u(1,t)$.

A. General periodic expansion

Here we introduce a general perturbation expansion that is valid for continuous periodic motions. It should be noted that as the motion becomes discontinuous the expansion breaks down. We first introduce the new variables $f(x,t)=S(x)u(x,t)$ and assume that the applied acceleration is given by $a(t)=A\varepsilon^3\cos\theta$, with $\theta=\omega t$ and $0<\varepsilon\ll 1$.

We let $f(x,t)=\varepsilon f_1(x,\theta)+\varepsilon^2 f_2(x,\theta)+\varepsilon^3 f_3(x,\theta)+\ldots$, where $f_i(x,\theta)$ are periodic in θ with period 2π, and define the detuning by

$$\omega=\omega_1(1+\varepsilon^2\delta+\ldots). \tag{12}$$

The form of f_i at the first two orders is,[11]

$$f_1(x,\theta)=D\phi(x)\sin\theta, \quad f_2(x,\theta)=D^2B(x)\sin 2\theta, \tag{13}$$

where D is an arbitrary response amplitude at this order. $\phi(x)$ is the eigenfunction corresponding to the fundamental eigenvalue ω_1.

At $O(\varepsilon^3)$, using an orthogonality condition, the amplitude D satisfies the tuning curve equation relating D to δ,

$$\bar{A}-\delta D=ND^3, \quad N=\int_0^1 C(x)\phi(x)dx, \quad \bar{A}=\frac{A}{2}\int_0^1 \phi dx. \tag{14}$$

Here $C(x)$ is a cubic function in $\phi(x)$ and $\phi'(x)$ with coefficients depending on $S(x)$; see equations Eqs. (29), (31), and (38) in Ref. 11.

The tuning curves for a cone, horn, and bulb derived from Eq. (14) agree with the experimental results in Ref. 8 and numerical results in Ref. 9. Whether these bend right or left depends on the sign of N. However, we note that N is a complicated integral function of the eigenfunction and the tube shape function and cannot be given a simple interpretation.

For the perturbation scheme to be valid, and thus for a tuning curve to exist, it is required that $|\varepsilon DB|\ll 1$. Typically as the size of the shape perturbation decreases, then $|\varepsilon DB|\to O(1)$ and all terms in the expansion become of equal order and this signals the occurrence of shocks. This observation is in agreement with the results of Refs. 3, 6, and 7. As an example, for the cone with slope k and typical output amplitude 0.04, for $k=1$, $|\varepsilon DB|=0.36$, while for $k=0.5$, $|\varepsilon DB|=4.4$. Clearly the perturbation scheme breaks down for some value of k between 1 and 0.5. The breakdown of the perturbation expansion given in Ref. 11 predicts the onset of a threshold value for the shape perturbation below which the motion is no longer single mode and continuous. This is confirmed by a direct numerical simulation of the exact equations used in Ref. 8, including the damping effect, for the case of the cone given in Eq. (2) with $k=0.5$. It is found that there is shock in the flow, see Fig. 1.

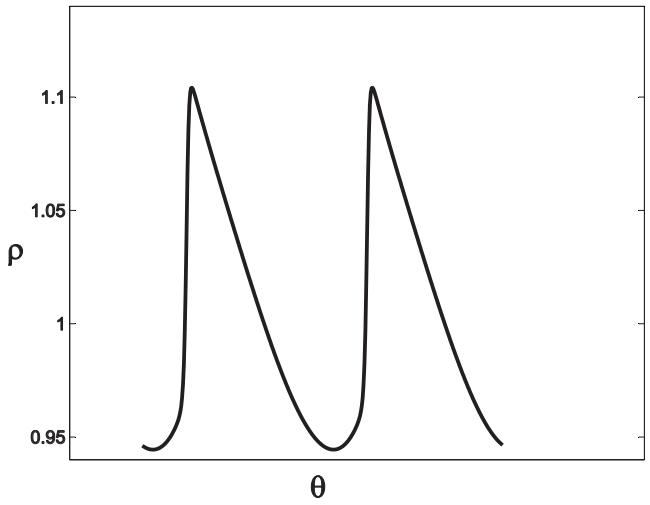


FIG. 1. Shocked density profile at $x=0$ for $S(x)=(1+kx)^2$, $k=0.5$, $\varepsilon^3=0.0025$, $\omega=\omega_1=1.016\pi$.

B. Eigenfunction expansion by harmonic balance

An alternative approach to the resonant problem, used in Ref. 10, is to expand the variables in the spatial eigenfunctions associated with the linear problem, $\xi_n(x)$:

$$\xi(x,t)=\sum_{n=1}\xi_n(x)q_n(t). \tag{15}$$

When the *ad hoc* loss factors δ_n are neglected, the coefficient functions q_n satisfy the nonlinear equations

$$q_1''+\omega_1^2 q_1+\frac{A}{4\pi}e_1\cos\omega t=K(q_1q_2-M(q_1^3+2q_1^2q_2)) \simeq K(q_1q_2-Mq_1^3), \tag{16}$$

$$q_2''+\omega_2^2 q_2=\frac{K}{2}(q_1^2-4Mq_1^2q_2)\simeq\frac{K}{2}q_1^2, \tag{17}$$

where A is the amplitude of the forcing term, and e_1 is an $O(1)$ coefficient. The order of magnitude of the detuning is not specified, and the amplitude of the applied velocity A is $O(1)$.

We note first that the ansatz given in Eqs. (93) and (94) of Ref. 10 for the form of the solution to Eqs. (16) and (17) is

$$q_1(t)=d_1\cos\omega t, \quad q_2(t)=d_0+d_2\cos 2\omega t. \tag{18}$$

It is assumed there that q_2 is $O(d_1^2)$, an order lower than q_1, where $|d_1|\ll 1$. When the *ad hoc* loss factors δ_n are neglected, the resulting tuning curve is

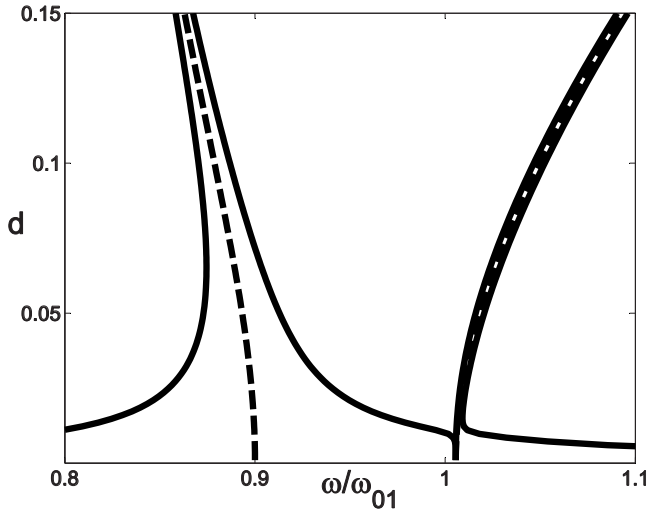


FIG. 2. Tuning curves calculated from Eqs. (24) and (25) with $\bar{A}=0.001$; $a_1=0.2$; dashed lines show $\delta+\bar{G}(\delta)D^2=0$.

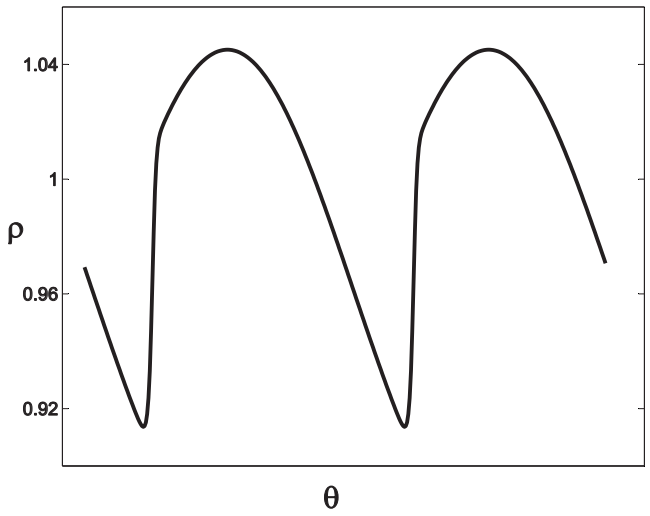


FIG. 3. Shocked density profile for $S(x)=1+a_1\cos(2\pi x)$, $a_1=0.05$, $\varepsilon^3=0.0025$, $\omega=\omega_1=0.975\pi$.

$$\omega_1^2-\omega^2+\frac{4A}{\pi d_1}=K\left(d_0-\frac{1}{2}Md_1^2\right)+Kd_1^2\cos(2\omega t)\times\left(\frac{K}{4(\omega_2^2-4\omega^2)}-\frac{1}{2}M\right). \tag{19}$$

This is not the result

$$\omega_1^2-\omega^2+\frac{4A}{\pi d_1}=d_1^2\left[K\left(\frac{2}{\omega_2^2}-\frac{1}{4\omega^2-\omega_2^2}\right)-6M\right]\frac{K}{8}, \tag{20}$$

given as Eq. (95) of Ref. 10. The result (19), containing the term $\cos(2\omega t)$, is clearly incorrect. However, it emerges that Eq. (20) results from the alternative ansatz (not specified in Ref. 10)

$$q_1(t)=d_1\cos\omega t+D_3\cos 3\omega t,\quad q_2(t)=d_0+d_2\cos 2\omega t, \tag{21}$$

$$D_3(\omega)=\left(M+\frac{1}{2}\frac{K}{4\omega^2-\omega_2^2}\right)\frac{K}{4(9\omega^2-\omega_1^2)}d_1^3, \tag{22}$$

$$d_0=\frac{K}{4\omega_2^2}d_1^2,\quad d_2(\omega)=\frac{K}{4(\omega_2^2-4\omega^2)}d_1^2. \tag{23}$$

We note that d_2 and D_3 depend on ω.

For a resonant oscillation with $\omega(\delta)=\omega_1(1+\delta)$ and δ ($\ll 1$), a small dimensionless detuning parameter, Eq. (20) becomes

$$\bar{A}-\delta D=\bar{G}(\delta)D^3, \tag{24}$$

where $\bar{A}=(2/\pi l\omega_1^2)A$ is a dimensionless measure of the applied acceleration, and the dimensionless function $\bar{G}(\delta)$ is

$$\bar{G}(\delta)=\left[K\left(\frac{2}{\omega_2^2}-\frac{1}{4\omega^2-\omega_2^2}\right)-6M\right]\frac{Kl^2}{8\omega_1^2}. \tag{25}$$

The coefficient $\bar{G}(\delta)$ has a zero and a singularity (when $4\omega^2-\omega_2^2=0$), giving a tuning curve that bends both left and right, see Fig. 2. Note that both $D_3(\omega)$ and $d_2(\omega)$ have similar singularities. The problem here is that the coefficients are not constant but depend on the frequency. The consequence is that as $2\omega-\omega_2\to 0$, the expansion is no longer valid.

It would appear that the tuning curves exhibited in Figs. 4 and 5 of Ref. 10 are the result of arbitrarily setting $\omega=\omega_1$ ($\delta=0$) in $\bar{G}(\delta)$, thus avoiding the singularity. However, no justification is given for this adjustment.

Based on the arbitrarily adjusted equation (20), a criterion is then given in Ref. 10 for predicting whether tuning curves bend right or left, depending on the sign of $2\omega_1-\omega_2$. This criterion is not a consequence of the analysis of Eq. (20). It is also not valid for finite shape perturbations.[11]

If we consider the case when the resonator shape is given by $S(x)=1+a_1\cos(2\pi x)$, $0\leqslant x\leqslant 1$, a direct numerical simulation shows that the solution is continuous for $a_1=0.2$ (in agreement with Ref. 10), but there are shocks in the flow for $a_1=0.05$, when $\omega_1=3.0635$ and $\omega_2=6.2865$, see Fig. 3. Then the criterion in Ref. 10 implies that there is hysteresis with a softening of the tuning curve. However, as there is a shock, there is no hysteresis.

C. Model equation for large variations in tube shape

We consider the model problem

$$\frac{\partial^2 e}{\partial t^2}=\frac{1}{S(x)}\frac{\partial}{\partial x}\left(S(x)\frac{\partial P(e)}{\partial x}\right)-h(t), \tag{26}$$

when the variation in $S(x)$ is not small, P,e correspond to the excess pressure ratio and condensation, and $h(t)$ is the applied periodic forcing. For small amplitude motions, $P(e)=e+\frac{1}{2}ae^2+\frac{1}{6}be^3+\ldots$, where a and b are the material constants.

On expanding $e(x,t)$ and $h(t)$ in terms of the normalized spatial eigenfunctions, $\phi_i(x)$, with coefficients $e_i(t)$, h_i we obtain, on truncating at the second term,

$$e_1''+\omega_1^2e_1+h_1\cos\omega t=a[Ke_1^2+Le_1e_2]+\tfrac{1}{2}bMe_1^3, \tag{27}$$

$$e_2'' + \omega_2^2 e_2 + h_2 \cos \omega t = a[Ne_1^2 + Pe_1 e_2] + \tfrac{1}{2} bQe_1^3, \qquad (28)$$

where the coefficients K, L, M, N, P, Q are definite integrals involving products of $S(x)$, $\phi_n(x)$, and $\phi_n'(x)$. The basic assumption is that $|e_1| \ll 1$, and $|e_{n+1}| \ll |e_n|$.

The cylinder approximation used in Ref. 10 leads to $K = P = Q = h_2 = 0$, while the other constants are nonzero; this agrees with Ref. 10. For the cone example given by Eq. (2) with $S_0 = 1$, the exact eigenfunctions and eigenvalues are given by Eqs. (3) and (4). Then the asymptotic forms of these coefficients when $k \ll 1$, where the cylinder is the case $k = 0$, are $K \sim -16/9k$, $P \sim -1094/225k$, and $Q \sim -448/225k$. Hence, if $k = O(|e_1|)$, then Eq. (27) should include the term aKe_1^2, while the terms involving P and Q in Eq. (28) may still be neglected. It is now clear that using the "cylinder" approximation when considering small tube perturbations requires care, as the extra term will directly affect the shape of the tuning curve. In particular, the presence of a quadratic term, like aKe_1^2, changes the criterion for bending left or right, see Ref. 14.

IV. CONCLUSIONS

For particular shape functions, there are exact solutions for the eigenfunctions and eigenvalues of the linear problem. Thus we can find the result for a small perturbation in the tube shape and compare with the classical approximation due to Rayleigh.[12] A general perturbation scheme for continuous periodic motions with no restriction on the perturbation of the tube shape is given, and the resulting tuning curve is calculated.[11] The relevant coefficient that determines whether bending is left or right is a complicated integral of the eigenfunction, its derivative, and the shape function, and the results of this analysis compare well with experimental results. However, no simple criterion for determining whether the tuning curve bends right or left seems possible from this. Using a parameter, it is possible to limit to the case of a cylindrical tube, and in this process the perturbation scheme for continuous motions breaks down indicating the advent of shocks in the flow. Thus there is a critical minimum level of the perturbation below which shocks occur. This is consistent with the analyses given in Refs. 3, 6, and 7 that lie within the scope of Ref. 10. Such a minimum is not present in Ref. 10. Consequently, the criterion for hardening or softening of the tuning curves can be misleading. Direct numerical simulation shows that for the shape $S(x) = 1 + a_1 \cos(2\pi x)$ the criterion for determining hardening or softening does not apply, for example when $a_1 = 0.05$, see Fig. 3, in contrast to the case $a_1 = 0.2$.

In the context of a spatial eigenfunction expansion that results in Eqs. (89) and (90) of Ref. 10 it is found that a harmonic balance does not give a satisfactory tuning curve. Further, the application of these equations is confined to small perturbations about a cylinder. They cannot be used to make predictions about the experiments of Ref. 8.

We consider a model nonlinear partial differential equation where there is no restriction on the shape perturbation and produce the equivalent of Eqs. (89) and (90) of Ref. 10 for finite shape perturbations. In the limit as the shape tends to a cylinder, we recover the equations used in Ref. 10 and the first correction to them, showing that an extra term should be present in Eq. (89). The basic conclusion is that, for this nonlinear problem, simple expansions in spatial eigenfunctions typically produce results that are inconsistent.

ACKNOWLEDGMENTS

The research reported in this paper was supported in part by the Natural Sciences and Engineering Research Council of Canada under Grant No. A9117. The authors wish to thank Professor D. Amundsen for his numerical solutions of the nonlinear partial differential equations, leading to Figs. 1 and 3.

[1] M. A. Ilgamov, R. G. Zaripov, R. G. Galiullin, and V. R. Repin, "Nonlinear acoustic oscillations of a column of gas in a tube," Appl. Mech. Rev. **49**, 137–154 (1996).
[2] M. P. Mortell and B. R. Seymour, "Pulse propagation in a nonlinear viscoelastic rod of finite length," SIAM J. Appl. Math. **22**, 209–224 (1972).
[3] J. J. Keller, "Nonlinear acoustic resonances in shock tubes with varying cross-sectional area," ZAMP **28**, 107–122 (1977).
[4] W. Chester, "Acoustic resonance in spherically symmetric waves," Proc. R. Soc. London, Ser. A **434**, 459–463 (1991).
[5] W. Ellermeier, "Acoustic resonance of cylindrically symmetric waves," Proc. R. Soc. London, Ser. A **445**, 181–191 (1994).
[6] H. Ockendon, J. R. Ockendon, M. R. Peake, and W. Chester, "Geometrical effects in resonant gas oscillations," J. Fluid Mech. **257**, 201–217 (1993).
[7] W. Chester, "Nonlinear resonant oscillations of a gas in a tube of varying cross-section," Proc. R. Soc. London, Ser. A **444**, 591–604 (1994).
[8] C. C. Lawrenson, B. Lipkens, T. S. Lucas, D. K. Perkins, and T. W. Van Doren, "Measurements of macrosonic standing waves in oscillating closed cavities," J. Acoust. Soc. Am. **104**, 623–636 (1998).
[9] Y. A. Ilinskii, B. Lipkens, T. S. Lucas, and T. W. Van Doren, "Nonlinear standing waves in an acoustic resonator," J. Acoust. Soc. Am. **104**, 2664–2674 (1998).
[10] M. F. Hamilton, Y. A. Ilinskii, and E. A. Zabolotskaya, "Linear and nonlinear frequency shifts in acoustical resonators with varying cross sections," J. Acoust. Soc. Am. **110**, 109–119 (2001).
[11] M. P. Mortell and B. R. Seymour, "Nonlinear resonant oscillations in closed tubes of variable cross-section," J. Fluid Mech. **519**, 183–199 (2004).
[12] Lord Rayleigh (J. W. Strutt), *The Theory of Sound*, 2nd ed. (Dover, New York, 1945).
[13] E. Varley and B. R. Seymour, "A method for obtaining exact solutions to partial differential equations with variable coefficients," Stud. Appl. Math. **78**, 183–225 (1988).
[14] A. H. Nayfeh and D. T. Mook, *Nonlinear Oscillations* (Wiley, New York, 1979).

Reply to "Comment on 'Linear and nonlinear frequency shifts in acoustical resonators with varying cross sections' [J. Acoust. Soc. Am. 110, 109–119 (2001)]" (L)

Mark F. Hamilton, Yurii A. Ilinskii, and Evgenia A. Zabolotskaya
Applied Research Laboratories, The University of Texas at Austin, Austin, Texas 78713-8029

(Received 23 September 2008; revised 30 September 2008; accepted 30 September 2008)

M. P. Mortell and B. R. Seymour [M. P. Mortell and B. R. Seymour [J. Acoust. Soc. Am. **124**, 3381–3385 (2008)] offer commentary on the analysis and the conclusions reached in a paper by Hamilton *et al.* [M. F. Hamilton, Yu. A. Ilinskii, and E. A. Zabolotskaya, J. Acoust. Soc. Am. **110**, 109–119 (2001)] on linear and nonlinear frequency shifts in acoustical resonators that are close to cylindrical in shape. The present reply demonstrates that the criticisms made in the Comment are unwarranted when placed in context of the stated restrictions on the theory and the applications for which the theory is intended. It is also shown that the strongest criticisms made in the Comment stem from a mathematical error they introduced when attempting to reproduce the results of Hamilton *et al.*
© *2008 Acoustical Society of America.* [DOI: 10.1121/1.3003934]

PACS number(s): 43.25.Gf, 43.20.Ks, 43.25.Cb [OAS] Pages: 3386–3389

The paper by Hamilton *et al.*[1] that is the focus of Mortell and Seymour's Comment[2] was written with the aim of providing physical insight into why frequency-response curves for acoustical resonators that are driven at finite amplitudes lean right (increasing resonance frequency) or left (decreasing resonance frequency), behavior that in nonlinear dynamics is referred to as hardening or softening nonlinearity, respectively. The paper by Hamilton *et al.* is hereafter referred to as the 2001 paper. When the 2001 paper was written there were already numerical models available, developed at MacroSonix Corporation,[3] that accurately predicted the observed resonance frequency shifts for resonators having a wide variety of shapes.[4] However, at that time there was no available explanation for the direction of the resonance frequency shift.

The analysis in the 2001 paper employed Lagrangian dynamics to describe the amplitudes of the normal modes of the resonator.[1] This method of analysis can be used for resonators of any shape for which the Webster horn equation is a valid model in the linear approximation (this more general theory is presented elsewhere[5]), but a decision was made to limit the analysis to resonators that are close to cylindrical in shape in order that perturbation methods could be used to obtain simple analytical solutions that clearly reveal the underlying physics. The cross-sectional area of the resonator as a function of the axial coordinate was expressed as $S(x) = S_0 + \delta S(x)$, where $\delta S(x)$ is a small shape perturbation, with $|\delta S(x)|/S_0 \ll 1$. Within this framework, the normal modes, natural frequencies, and resonance frequencies are restricted to small perturbations about their values for a cylinder with constant cross-sectional area S_0.

There is also a second restriction, one not stated explicitly in the 2001 paper but which is discussed by Mortell and Seymour.[2] While the perturbations of the natural frequencies must be small, they must not be so small as to allow shock formation. Since the theory was developed with applications such as thermoacoustic engines and acoustical compressors in mind, for which a design goal is to tailor the natural frequency distribution specifically with the aim of preventing shock formation, the second restriction was thought to be self-evident. Moreover, shock formation in acoustical resonators is a special subject that cannot be described by any perturbation theory, including those developed by Mortell and Seymour themselves[2,6] for describing nonlinear resonance frequency shifts.

Within this context—shape perturbations of a cylindrical resonator that are small, but not so small as to allow shock formation—the analysis in the 2001 paper is correct, and it has been verified by comparison with numerical solutions that are not restricted to small shape perturbations. Nevertheless, the existence of the Comment by Mortell and Seymour requires us to respond to their concerns.

We start with Eq. (10) in the Comment, $S(x) = S_0 + \delta S(x)$, in reference to which Mortell and Seymour write that "This results in an incorrect linear perturbation analysis. The result (28) in [the 2001 paper], the equivalent of Eq. (7) here, is incorrect. The function $\ln(S/S_0)$ should be replaced by $S_1(x)$ and all subsequent expressions containing ln or exp are incorrect." None of these statements is warranted.

Two specific resonator shapes were considered in the 2001 paper,

$$\ln(S/S_0) = a_1 \cos(2\pi x/l) \tag{1}$$

and

$$S/S_0 = 1 + a_1 \cos(2\pi x/l), \tag{2}$$

each with small parameter a_1, and where l is the length of the resonator with $0 \leqslant x \leqslant l$. Equation (1), which may be rewritten $S/S_0 = \exp[a_1 \cos(2\pi x/l)]$, is associated with the

 © 2008 Acoustical Society of America

following perturbation operator that is defined by Eq. (17) in the 2001 paper:

$$\delta L = \frac{S'}{S}\frac{d}{dx} = -\frac{2\pi}{l}a_1 \sin(2\pi x/l)\frac{d}{dx}, \tag{3}$$

where $S' = dS/dx$. Similarly, for Eq. (2)

$$\delta L = -\frac{(2\pi/l)a_1 \sin(2\pi x/l)}{1 + a_1 \cos(2\pi x/l)}\frac{d}{dx} = \left[-\frac{2\pi}{l}a_1 \sin(2\pi x/l) + \frac{\pi}{l}a_1^2 \sin(4\pi x/l) + \cdots\right]\frac{d}{dx}. \tag{4}$$

As discussed in the 2001 paper, all results based on these two perturbations are equivalent at first order. For a theory at first order in the perturbation δS, it is therefore only a matter of preference as to whether one bases it on the operator given by Eq. (3) or Eq. (4). It is meaningless to assert that one is correct whereas the other is not. Specifically, there is nothing wrong with the results in the 2001 paper containing the term $\ln(S/S_0)$ associated with Eqs. (1) and (3) above.

The motivation for using Eq. (1) above in the 2001 paper was connected with an interest in identifying a simple shape perturbation that shifts the natural frequency of the fundamental mode but not the natural frequency of any higher order mode. This was considered merely as a convenient way to keep harmonics of the drive frequency away from the natural frequencies of the resonator as a means of preventing shock formation. With this in mind, consider the natural frequency shifts produced by Eqs. (1) and (2). At first order the results are the same. The relative shifts in the natural frequencies are $\delta\omega_1/\omega_{01} = -\frac{1}{2}a_1$ for mode 1 (the fundamental mode) and $\delta\omega_2/\omega_{02} = 0$ for mode 2, where $\omega_{0n} = n\pi c_0/l$ is the natural frequency of the nth mode of a cylindrical resonator. In fact, any function of $a_1 \cos(2\pi x/l)$ produces the same relative frequency shift $-\frac{1}{2}a_1$ for the fundamental mode at first order. For mode 2, the relative shift at second order is $\delta\omega_2/\omega_{02} = \frac{1}{6}a_1^2$ for Eq. (1) and $\delta\omega_2/\omega_{02} = \frac{4}{6}a_1^2$ for Eq. (2). These results suggest that of the two resonator shapes, Eq. (1) is the better choice because $\delta\omega_2/\omega_{02}$ is smaller, i.e., if $\delta\omega_n/\omega_{0n} = 0$ is desired for $n = 1$. However, one cannot know for sure which choice is better in this context without comparison with a numerical calculation that is not restricted to small shape perturbations. Figures 1–3 in the 2001 paper provide such comparisons and support the choice of Eq. (1).

Mortell and Seymour then continue to write after Eq. (10) in the Comment that "At the level of approximation in [the 2001 paper] odd spatial modulations in $S(x)$ have no effect on the natural frequencies. However, the cone example given above, where $\delta_1 = 0$ but $\delta_2 \neq 0$, shows that this result is not correct to second order. Any cone lies outside the scope of the theory in [the 2001 paper]." It is stating the obvious to point out that a theory based on a first-order perturbation in the shape variation cannot be used to describe second-order effects. The first-order theory in the 2001 paper indeed predicts no shift in the natural frequencies of a conical resonator, which is to say that it predicts the frequency shifts to be negligible (second order). This is borne out by the parameters in the caption of Fig. 1 in the Comment, which show that, even for a cone with a cross-sectional area that increases by a factor of 2.25 from one end to the other, which is far from being a small perturbation of a cylinder, the shift in the fundamental natural frequency is still only 1.6%. But, if natural frequency shifts for resonators with spatial modulations that are odd at first order would happen to be of particular interest, and if one wishes to adhere to a perturbation scheme, it is straightforward to extend the theory in the 2001 paper to second order and account for these frequency shifts at their leading order. This is precisely what was done to calculate analytically the second-order frequency shifts $\delta\omega_2/\omega_{02} = \frac{1}{6}a_1^2$ and $\delta\omega_2/\omega_{02} = \frac{4}{6}a_1^2$ presented above for the resonator shapes given by Eqs. (1) and (2), respectively. However, a far preferable approach in this case is to remove the restriction to small shape perturbations and solve the eigenvalue problem for the normal modes and their natural frequencies numerically, as has been done elsewhere.[5]

In Sec. III B of the Comment, Mortell and Seymour purport to correct the solution obtained in the 2001 paper for the amplitude of the fundamental mode. They obtain a different result, and then following Eq. (20) they conclude that "The result (19), containing the term $\cos(2\omega t)$, is clearly incorrect." On the basis of this conclusion they allege that the "criterion…given in [the 2001 paper] for predicting whether tuning curves bend right or left, depending on the sign of $2\omega_1 - \omega_2$", is "based on the arbitrarily adjusted equation (20)," that "the tuning curves exhibited in Figs. 4 and 5 of [the 2001 paper] are the result of arbitrarily setting $\omega = \omega_1$", and more generally that the analysis in the 2001 paper is "not valid for finite shape perturbations." The quantity ω_n is the natural frequency of the nth mode, equal to ω_{0n} for a cylinder.

The term $\cos 2\omega t$ is indeed incorrect, and Mortell and Seymour obtained it because they introduced a mathematical error in their derivation by failing to distinguish between secular and nonsecular terms. Substitution of their Eqs. (18) into (16) and (17) yields $(\omega_1^2 - \omega^2)d_1 \cos \omega t$ on the left-hand side of Eq. (16), and on the right-hand side there appear terms proportional to $\cos \omega t \cos 2\omega t$. Mortell and Seymour then mistakenly cancel out $\cos \omega t$ from both sides of the equation and are left with their $\cos 2\omega t$. In doing so they discarded secular terms in favor of nonsecular terms, but the secular terms are the ones that provide the dominant contribution. Instead, one should write $2 \cos \omega t \cos 2\omega t = \cos \omega t + \cos 3\omega t$ and retain only the secular term proportional to $\cos \omega t$, doing which produces the correct result in the 2001 paper. The allegations in the previous paragraph are therefore groundless.

Figure 2 in the Comment is a perfect illustration of why it is so important to include losses, which are ignored by Mortell and Seymour.[2,6] Suppose for the lossless case described by Fig. 2 that a dimensionless loss coefficient of order $\delta_1 \sim 10^{-2}$ (quality factor $Q_1 \sim 10^2$) is introduced for the fundamental mode and one of order $\delta_2 \sim 10^{-3}$ for the second mode. The latter is in fact too small because, in practice, losses for the second mode are always higher than for the fundamental mode, but even this small value is sufficient to make the point. The tuning curve in Fig. 2 can be recalcu-

lated with losses taken into account by using either the analytical result given by Eq. (100) in the 2001 paper or with a numerical algorithm that is not restricted to small shape perturbations.[3] First, the branch on the left will have a finite peak amplitude and a finite resonance frequency shift associated with this peak. In contrast, Fig. 2 shows an infinite peak amplitude and an infinite resonance frequency shift associated with this peak. Second, and more important, the branch on the right will disappear completely. However, it is the branch on the right that led Mortell and Seymour to conclude that, in reference to the normal mode expansion, "as $2\omega-\omega_2\rightarrow 0$, the expansion is no longer valid." Since the branch on the right is entirely suppressed for any real resonator with actual losses, the normal mode expansion in the 2001 paper does indeed remain valid in this limit. Moreover, as a practical matter for a resonator designed to provide amplification at the drive frequency and suppression of the second harmonic, it makes no sense to drive the system so far off resonance, and at the same time choose the drive frequency that most efficiently generates a second harmonic through resonance with the second mode.

Mortell and Seymour's concerns about the 2001 paper date back to a paper they published in 2004,[6] where below Fig. 3 they wrote that "Hamilton *et al.* (2001) found analytically for a slowly varying 'cylindrical' tube that if $2\lambda_1>\lambda_2$ there was a hardening response curve, while if $2\lambda_1<\lambda_2$ the response was softening. This is clearly not the case for the bulb resonator in figure 3 where $\lambda_1=1.41\pi$ and $\lambda_2=2.22\pi$." In their notation λ_n is a normalized natural frequency that is proportional to ω_n in our notation. Their calculation is for excitation near the natural frequency of the fundamental mode, $\lambda\simeq\lambda_1$, and the second harmonic at frequency $2\lambda\simeq 2\lambda_1=2.82\pi$ lies midway between $\lambda_2=2.22\pi$ and $\lambda_3\simeq 3.1\pi$, which are the natural frequencies of modes 2 and 3, respectively. Since $2\lambda-\lambda_2\simeq 0.6\pi$ and $\lambda_3-2\lambda\simeq 0.3\pi$ the second harmonic lies closer to the natural frequency of mode 3, and therefore one may expect it to couple more strongly with mode 3 than mode 2. This situation is well beyond the stated limitations of the theory in the 2001 paper, which takes into account only modes 1 and 2 because it is assumed that the shape perturbations are sufficiently small that the second harmonic lies in close proximity to the natural frequency of mode 2.

As noted above, the restriction on the theory in the 2001 paper to resonator shapes that are close to cylindrical has since been removed, and all modes are now taken into account.[5] If the second harmonic happens to lie in close proximity to any particular mode n, such that $2\omega\simeq 2\omega_1\simeq\omega_n$ where ω is the drive frequency, a hardening response curve is obtained for $2\omega_1>\omega_n$ and a softening response curve is obtained for $2\omega_1<\omega_n$. The results for the resonator modeled by Mortell and Seymour in Fig. 3(c) of their 2004 paper suggest that the second harmonic lies sufficiently close to the natural frequency of mode 3 that coupling with this mode, rather than with mode 2, provides the dominant contribution to the nonlinearity. Since the relation $2\omega_1<\omega_3$ applies to their example, the downward shift of the resonance frequency (softening response) exhibited in Fig. 3(c) of that paper is indeed consistent with the normal mode theory.

In general, when the second harmonic is not very close to any natural frequency, whether the resonance curve will bend right or left cannot be predicted knowing only the natural frequency distribution. In the 2001 paper the condition $2\omega\simeq 2\omega_1\simeq\omega_2$ is satisfied automatically because of the restriction to small shape perturbations. As a result, only the first two modes were required to model the frequency response, and a simple criterion for determining the direction of the resonance frequency shift was obtained.

We now return to Mortell and Seymour's concerns about shocks. Figure 3 in the Comment is presented to demonstrate that shocks form in a cylindrical resonator with a shape perturbation defined by $a_1=0.05$ in Eq. (2) above. Although it is not stated, we assume that the drive amplitude is the same as was used for their Fig. 2, which corresponds to the drive amplitudes used for Figs. 4 and 5 in the 2001 paper. In the discussion of their Fig. 3 they write that "the criterion in [the 2001 paper] implies there is hysteresis with a softening of the tuning curve. However, as there is a shock, there is no hysteresis." As discussed above, the theory in the 2001 paper is not intended to cover shock formation. It is then reasonable to ask whether, in order to avoid shocks, the value of the parameter a_1 must be so large that it violates the restriction on the theory in the 2001 paper to small shape perturbations. The values $a_1=\pm 0.2$ were chosen for the calculations presented in Figs. 4 and 5 of the 2001 paper specifically because their magnitudes are sufficiently large to prevent shock formation at the stated drive amplitudes, for which peak acoustic Mach numbers surpassing 0.1 are obtained inside the resonator. Mortell and Seymour themselves confirm that there are no shocks for $a_1=0.2$. The comparisons with numerical solutions[3] in Figs. 4 and 5 of the 2001 paper, which are not restricted to small shape perturbations and which account for shocks when they do exist, show that the perturbation solution remains reasonably accurate for $a_1=\pm 0.2$.

More generally, consider a cylindrical resonator with losses. Even without any shape perturbation, there are no shocks for sufficiently low drive amplitudes. As the drive amplitude is increased, shocks eventually form, and a finite value of a_1 is required to suppress these shocks. The theory in the 2001 paper then predicts the direction of the corresponding resonance frequency shift. With further increase in the drive amplitude, in order to prevent shock formation a_1 ultimately must be so large that the perturbation theory is no longer valid. There is thus a finite range of drive amplitudes, such that a_1 is neither too small nor too large, for which the perturbation theory is applicable.

In conclusion, no claim is made in the 2001 paper that the theory applies to arbitrary natural frequency distributions. There is also no suggestion that the theory can be applied when there are shocks, as it is intended only for resonators designed specifically to prevent shock formation. The primary goal of the 2001 paper was to provide a physical explanation for the resonance frequency shift, and for resonators that are close to cylindrical in shape this goal was accomplished. This limited objective may be contrasted with the claim made in Sec. I of the Comment that "Mortell and Seymour[6] considered analytically the resonant motions in closed containers such as cones, horns, and bulbs with no

restriction on the size of the shape perturbation." However, this is not true because their theory[6] is restricted to containers for which the Webster horn equation, which is a 1D model, provides an accurate description of the sound field in the linear approximation.

Of greater significance is that Mortell and Seymour fail to mention that their theory[6] can be used only for specific resonator shapes that admit closed-form solutions of their eigenvalue problem. This class of functions is so restricted that in the comparison of their theory with a MacroSonix experiment on a bulb resonator (Fig. 3 in their 2004 paper,[6] discussed above), the ratio of the maximum to the minimum cross-sectional area of the bulb used in their calculations differs by an order of magnitude from that for the bulb used in the experiment. As a result, the natural frequency distribution calculated for the resonator shape used in their theory is substantially different from that for the bulb used in the experiment. It is therefore not surprising that the percentage change in the resonance frequency they predicted is an order of magnitude different from what was reported in the experiment that the calculations were intended to model.

[1]M. F. Hamilton, Yu. A. Ilinskii, and E. A. Zabolotskaya, "Linear and nonlinear frequency shifts in acoustical resonators with varying cross sections," J. Acoust. Soc. Am. **110**, 109–119 (2001).

[2]M. P. Mortell and B. R. Seymour, "Comment on 'Linear and nonlinear frequency shifts in acoustical resonators with varying cross sections' [J. Acoust. Soc. Am. **110**, 109–119 (2001)]," J. Acoust. Soc. Am. **124**, 3381–3385 (2008).

[3]Yu. A. Ilinskii, B. Lipkens, T. S. Lucas, T. W. Van Doren, and E. A. Zabolotskaya, "Nonlinear standing waves in an acoustical resonator," J. Acoust. Soc. Am. **104**, 2664–2674 (1998).

[4]C. C. Lawrenson, B. Lipkens, T. S. Lucas, D. K. Perkins, and T. W. Van Doren, "Measurments of macrosonic standing waves in oscillating closed cavities," J. Acoust. Soc. Am. **104**, 623–636 (1998).

[5]Yu. A. Ilinskii, M. F. Hamilton, and E. A. Zabolotskaya, "Nonlinear resonance frequency shifts in acoustical resonators with varying cross sections," J. Acoust. Soc. Am. **124**, 2491–2492(A) (2008).

[6]M. P. Mortell and B. R. Seymour, "Nonlinear resonant oscillations in closed tubes of variable cross-section," J. Fluid Mech. **519**, 183–199 (2004).

A new method to generate an almost-diagonal matrix in the boundary integral equation formulation

B. Chandrasekhar[a)]
Supercomputer Education and Research Center, Indian Institute of Science, Bangalore 560012, India

Sadasiva M. Rao[b)]
Department of Electrical and Computer Engineering, Auburn University, Aburn, Alabama 36849

(Received 6 June 2008; revised 10 September 2008; accepted 13 September 2008)

In this work, a new numerical procedure is developed to generate an almost-diagonal matrix for the solution of boundary integral equation formulation dealing with acoustic scattering problems. The major drawback of the traditional boundary integral equation procedure resulting in a dense system matrix is eliminated in this new procedure by grouping the basis functions into a cluster. The geometry of the structure is modeled by planar triangles and the basis functions are defined on the nodes. By doing so, one can get a benefit of a smaller size matrix to begin with. Furthermore, by grouping these node-based basis functions into a cluster, an almost-diagonal matrix is generated. Thus, the solution procedure developed in this work may be utilized for very large scattering problems since the required computer resources are very low. The solution procedure developed in this work is validated for the scattering cross section of the simple shapes with the closed form solutions wherever available and with the other numerical solution procedures.
© *2008 Acoustical Society of America.* [DOI: 10.1121/1.2998774]

PACS number(s): 43.20.Fn [DSB] Pages: 3390–3396

I. INTRODUCTION

There has been quite a good amount of research work happening in the area involving acoustic scattering studies using boundary integral equation (BIE) formulation. The obvious advantage of this method is that the solution space confines only to the surface of the structure thus requiring fewer unknowns as compared to differential equation-based solution methods. Another important advantage is the exact application of the radiation condition by using suitable Green's function.

All the various formulations involving BIE methods, combined Helmholtz integral equation formulation [Schenck (1968)], combined outward normal derivative overlap relation [Burton and Miller (1971)], and method of moments based combined layer formulation (MoMCLF) [Chandrasekhar and Rao (2004b)], are based on the integral equation formulations and results in a linear system of equations $\boldsymbol{ZX}=\boldsymbol{Y}$, which need to be solved for the unknowns $\boldsymbol{X}$ either by inverting the $\boldsymbol{Z}$-matrix or by solving the $\boldsymbol{ZX}=\boldsymbol{Y}$ iteratively. The $\boldsymbol{Z}$-matrix generated in these methods is a full matrix and computationally very expensive for large structures. Hence attention must be focused to reduce the matrix size and develop alternate procedures to make the solution procedure more efficient.

The generation of a sparse matrix in the BIE procedure may be achieved in two ways, viz., (a) by handling the influence of the kernel function in a novel way such as fast multipole method (FMM) [Coifman *et al.* (1993)] and (b) by defining a special set of basis functions to represent the unknown quantity. In the FMM scheme, the matrix-vector product is carried out in a novel way and seems to work well for many complex problems. Unfortunately, the FMM is a complicated scheme and any reasonable summary of the method is beyond the scope of the present article.

Recently, a new set of basis functions was used in the single layer formulation (SLF) and double layer formulation (DLF) which in turn can be used in MoMCLF solution, by defining the basis functions on the nodes [Chandrasekhar (2005)] in contrast to defining on the edges. Thus, the order of the resulting matrix is reduced to almost one-third to that of defining the basis functions on edges.

To make the method even more efficient, in this work, we develop a new solution procedure utilizing the node-based basis functions and generate an almost-diagonal moment matrix. This is done by grouping the node-based basis functions into a cluster to form an array of acoustic sources. The weights of the array are adjusted such that the combined acoustic field generated is zero everywhere except at the center of the array. The numerical procedure essentially develops a new set of basis functions depending on geometrical features of the structure; hence, the procedure is named as node-based adaptive basis functions (NABFs). Since the new set of basis functions is defined in such a way that the final matrices generated by the method of moment's solution procedure are diagonal, the matrix inversion algorithms to solve the linear system of equations can be entirely eliminated. The new functions, popularly known as adaptive basis functions in the electromagnetic scattering/radiation areas [Waller and Rao (2002)], are used as basis functions in this work while the pulse functions are used as testing functions.

In this paper, Sec. II briefly describes the method of moment's solution procedure [Harrington (1968)]. In Sec. III

a)Electronic mail: drchandrasekhar.b@gmail.com
b)Electronic mail: raosada@auburn.edu

the combined layer formulation (CLF) along with the numerical solution procedure is described for the sake of completeness. In Sec. IV, we describe the adaptive basis function method. Numerical results, based on the development of new basis functions, are given in Sec. V. Lastly we present some important conclusions drawn from the present work.

II. OUTLINE OF METHOD OF MOMENTS

Consider the deterministic equation

$$\boldsymbol{Lf} = \boldsymbol{g}, \tag{1}$$

where $\boldsymbol{L}$ is a linear operator, $\boldsymbol{g}$ is a known function, and $\boldsymbol{f}$ is an unknown function to be determined. Let $\boldsymbol{f}$ be represented by a set of known functions $\boldsymbol{f}_j$, $j=1,2,\ldots,N$, termed as basis functions in the domain of $\boldsymbol{L}$ as a linear combination given by

$$\boldsymbol{f} = \sum_{n=1}^{N} \beta_j \boldsymbol{f}_j, \tag{2}$$

where β_j are scalar coefficients to be determined. Substituting Eq. (2) into Eq. (1), and using the linearity of $\boldsymbol{L}$, we have

$$\sum_{n=1}^{N} \beta_j \boldsymbol{L}\boldsymbol{f}_j \approx \boldsymbol{g}, \tag{3}$$

where the equality is usually approximate. Let $(w_1, w_2, w_3, \ldots)$ define a set of testing functions in the range of $\boldsymbol{L}$. Now, taking the inner product of Eq. (3) with each w_i and using the linearity of inner product defined as $\langle \boldsymbol{f}, \boldsymbol{g} \rangle = \int_s \boldsymbol{f} \cdot \boldsymbol{g} ds$, we obtain a set of linear equations given by

$$\sum_{n=1}^{N} \beta_j \langle w_i, \boldsymbol{L}\boldsymbol{f}_j \rangle = \langle w_i, \boldsymbol{g} \rangle, \quad i = 1,2,\ldots,N. \tag{4}$$

The set of equations in Eq. (4) may be written in the matrix form as

$$\boldsymbol{ZX} = \boldsymbol{Y}, \tag{5}$$

which can be solved using any standard linear equation solution methodologies. In a broad sense, the MoM is similar to Ritz procedure [Mikhiln (1964)] and Bubnov–Galerkin procedure [Purczynski *et al.* (1975)].

III. NODE-BASED COMBINED LAYER FORMULATION

Consider an acoustic wave, with pressure and velocity $(p^i, \boldsymbol{u}^i)$, incident on a three-dimensional arbitrarily shaped rigid body placed in a source free homogeneous medium of density ρ and speed of sound c through the medium. When the incident wave interacts with the body, the acoustic wave gets scattered with a pressure and velocity $(p^s, \boldsymbol{u}^s)$. Here, we note that incident fields are defined in the absence of the scattering body. Φ is the scalar velocity potential satisfying the Helmholtz differential equation $\nabla^2\Phi + k^2\Phi = 0$ for the time harmonic waves present in the region exterior to the surface S of the body. One more condition on velocity potential is that it should satisfy the appropriate boundary conditions on the surface S of the body along with the Sommerfeld radiation condition. The pressure and velocity fields of acoustic wave are related to the scalar velocity potential Φ as $\boldsymbol{u} = -\nabla\Phi$ and $p = j\omega\rho\Phi$. In this paper, integral equation formulations are based on potential theory and free space Green's function. The scattered velocity potential may be defined using three different formulations based on monopole and/or dipole distribution. Formulations based on monopole distribution and dipole distributions are called as SLF and DLF, respectively. Third formulation, namely, combined layer formulation (CLF) is a linear combination of SLF and DLF [Chandrasekhar and Rao (2004b)].

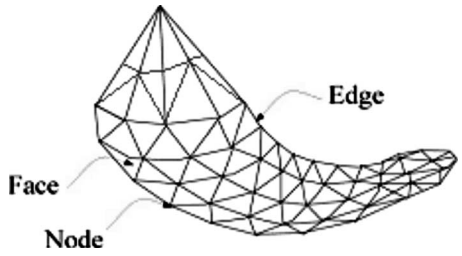


FIG. 1. Triangular patch modeling of an arbitrarily shaped three-dimensional body.

Referring to the earlier work [Chandrasekhar and Rao (2004b)], the necessary integral equation for the CLF may be written as

$$\frac{\sigma(\boldsymbol{r}')}{2} - \int_s \sigma(\boldsymbol{r}') \frac{\partial G(\boldsymbol{r},\boldsymbol{r}')}{\partial n} ds' + \eta \int_s \boldsymbol{n} \cdot \boldsymbol{n}' k^2 \sigma(\boldsymbol{r}') G(\boldsymbol{r},\boldsymbol{r}') ds' + \eta \int_s (\boldsymbol{n}' X \nabla' \sigma) \cdot (\boldsymbol{n} X \nabla G) ds' = \frac{\partial \Phi'}{\partial n}. \tag{6}$$

In Eq. (6), σ is the source density function, $\boldsymbol{r}$ and $\boldsymbol{r}'$ are the position vectors of observation and source points, respectively, with respect to a global coordinate system O, and $\partial G/\partial n$ is the normal derivative of Green's function at observation point. Coefficient η is a complex coupling parameter to be chosen based on the guidelines given by Burton and Miller (1971).

$$k \text{ real or imaginary} \Rightarrow \mathrm{Im}(\eta) \neq 0, \tag{7}$$

$$k \text{ complex} \Rightarrow \mathrm{Im}(\eta) = 0, \tag{8}$$

where k is the wave number in the medium.

Also, in Eq. (6), $G(\boldsymbol{r},\boldsymbol{r}')$ is the free space Green's function given by

$$G(\boldsymbol{r},\boldsymbol{r}') = \frac{e^{-jk|\boldsymbol{r}-\boldsymbol{r}'|}}{4\pi|\boldsymbol{r}-\boldsymbol{r}'|}. \tag{9}$$

$\boldsymbol{n}$ and $\boldsymbol{n}'$ are the unit normal vectors at $\boldsymbol{r}$ and $\boldsymbol{r}'$, respectively. In the following, we briefly discuss the numerical solution method of Eq. (6). Figure 1 shows the triangular patch modeling of the surface of an arbitrarily shaped three-dimensional body. The triangular patch modeling is an approximation of the surfaces. The accuracy of approximation can be increased by modeling the surface with large number of triangular patches of smaller size. The three geometric

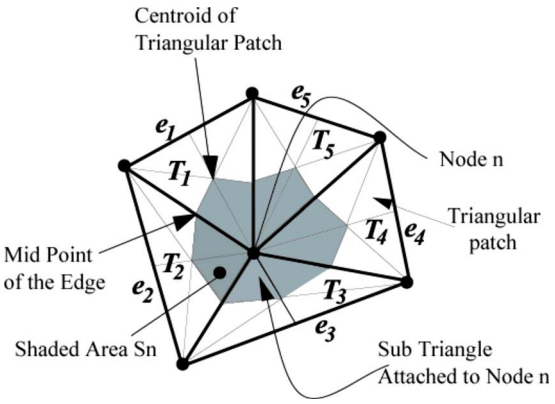


FIG. 2. (Color online) Node-based basis function and geometric parameters associated with the node.

entities that are present in the triangular patch modeling are triangular patches, edges, and nodes. Let N_f, N_e, and N_n represent the number of triangular patches, number of edges, and number of nodes, respectively, on the surface of triangulated body. For a closed body, every edge is common to two adjacent triangular patches, and every node is common to at least three triangular patches as well as at least three edges.

Consider a node n about which the basis function is defined. For illustration purposes, consider one such node as shown in Fig. 2 [Chandrasekhar (2005)], where there are five triangular patches attached to it. Let $T_1, T_2, \ldots, T_5$ be the triangular patches and $e_1, e_2, \ldots, e_5$ be the edges surrounding the node. The shaded region, shown in Fig. 2 as S_n, is formed by joining the midpoints of the edges that are connected to the node n, the centroids of adjacent triangular patches thus forming a closed boundary around the node.

Since the method of moments solution calls for the definition of expansion/basis as well as testing/weighting functions, expansion/basis functions are defined on the source node n and the testing/weighting functions are defined on the field node m. Let there be p number of triangular patches attached to field node m and q number of triangular patches attached to the source node n. By joining the node on which the basis function or weighting function is defined, to the centroid of the attached triangular patches, the shaded area on each triangular patch is divided into two subtriangles, resulting in u number of subtriangles around field node m and v number of subtriangles around the source node n. In this paper, index x is used to represent the subtriangle attached to the field node and index y is used to represent the subtriangle attached to the source node.

The node-based basis function is defined over the shaded area as follows:

$$f_n(\boldsymbol{r}') = \begin{cases} 1, & \boldsymbol{r}' \in S_n \\ 0, & \text{otherwise}. \end{cases} \tag{10}$$

Note that the basis functions defined in Eq. (10) are, in fact, piecewise constant functions over the specially defined area S_n. Although such functions represent a low-order approximation, BIE formulation is robust enough to provide accurate numerical results unlike the differential equation-based finite element methods.

The source density function σ over the surface of the scattering object is approximated by

$$\sigma(\boldsymbol{r}') = \sum_{n=1}^{N_n} \beta_n f_n, \tag{11}$$

where β_n represent the unknown coefficients to be determined and the equal sign is usually approximate. The basis functions defined over the node have all advantages as edge based basis functions [see Chandrasekhar and Rao (2004a)].

In the derivation of matrix equations for the CLF, Galerkin's approach is used by defining the testing function in the same manner as it is defined for the basis function.

$$w_m = \begin{cases} 1, & \boldsymbol{r} \in S_m \\ 0, & \text{otherwise}. \end{cases} \tag{12}$$

The next three subsections describe the numerical solution procedure for the CLF. In order to derive the matrix equations for the CLF, which is a linear combination of SLF and DLF, the matrix equations for the SLF and DLF are derived first. Matrix equations for the CLF are derived by linearly combining the matrix equations of the SLF and DLF.

A. Single layer formulation

The matrix equation for the SLF may be written as [Chandrasekhar (2005)]

$$\boldsymbol{Z}_{\mathrm{SLF}}\boldsymbol{X} = \boldsymbol{Y}, \tag{13}$$

where $\boldsymbol{Z}_{\mathrm{SLF}}$ is the moment matrix of size $N_n \times N_n$ and $\boldsymbol{X}$ and $\boldsymbol{Y}$ are the column vectors of size N_n. The elements of $\boldsymbol{Z}_{\mathrm{SLF}}$, $\boldsymbol{X}$, and $\boldsymbol{Y}$ are given as

$$\boldsymbol{Z}_{\mathrm{SLF}}^{mn} = \begin{cases} \dfrac{1}{2}\displaystyle\sum_{x=1}^{u} A_m^x & \text{for } m = n \text{ and } x = y \\ -\displaystyle\sum_{x=1}^{u}\sum_{y=1}^{v} A_m^x \int_s \frac{\partial G(\boldsymbol{r}_m^{cx}, \boldsymbol{r}_n^{cy})}{\partial n_m^x} ds' & \text{otherwise} \end{cases} \tag{14}$$

and

$$\boldsymbol{Y}^m = \sum_{x=1}^{u} A_m^x \frac{\partial \Phi^i(\boldsymbol{r}_m^{cx})}{\partial n_m^x}, \tag{15}$$

where $\boldsymbol{r}_m^{cx}$ is the position vector to the centroid of the xth subtriangle attached to the field node, $\boldsymbol{r}_n^{cy}$ is the position vector to the centroid of the yth subtriangle attached to the source node, and $\partial G / \partial n_m^x$ is the normal derivative of Green's function at the centroid of the xth subtriangle attached to the field node. In Eqs. (14) and (15), A_m^x is the area of the subtriangle attached to the field node.

B. Double layer formulation

Similarly, the matrix equations for the DLF [Chandrasekhar (2005)] is given by

$$\boldsymbol{Z}_{\mathrm{DLF}}\boldsymbol{X} = \boldsymbol{Y}, \tag{16}$$

where $\boldsymbol{Z}_{\mathrm{DLF}}$ is the moment matrix for DLF of size $N_n \times N_n$ and $\boldsymbol{X}$ and $\boldsymbol{Y}$ are column vectors of size N_n.

$$Z_{\mathrm{DLF}}^{mn} = \sum_{x=1}^{u}\sum_{y=1}^{v} k^2 A_m^x \boldsymbol{n}_m^x \cdot \boldsymbol{n}_n^y \int_s G(\boldsymbol{r}_m^{cx}, \boldsymbol{r}_n^{cy}) ds' + \frac{l_m}{2} \cdot \frac{l_n}{2A_{fn}} \left(\sum_{x=1}^{p}\sum_{y=1}^{q} \int_{sf} G(\boldsymbol{r}_m^{cfp}, \boldsymbol{r}_n^{cfq}) ds' \right). \quad (17)$$

Note that the integration on the first term of right-hand side of the above equation is on the subtriangle attached to the source node and the integration on the second term is on the triangular patch attached to the source node.

$$Y^m = \sum_{x=1}^{u} A_m^x \frac{\partial \Phi^i(\boldsymbol{r}_m^{cx})}{\partial n_m^x}, \quad (18)$$

where A_m^x is the area of the subtriangle attached to the field node, A_{fn} is the area of the triangular patch attached to the source node, $\boldsymbol{r}_m^{cx}$ is the position vector to the centroid of the xth subtriangle attached to the field node, $\boldsymbol{r}_n^{cy}$ is the position vector to the centroid of the yth subtriangle attached to the source node, r_m^{cfp} is the position vector to the centroid of the pth triangular patch attached to the field node, and r_n^{cfq} is the position vector to the centroid of the qth triangular patch attached to the source node.

C. Combined layer formulation

The matrix equations of the CLF, which is a linear combination of the matrix equations of SLF and DLF, can be expressed as

$$\boldsymbol{Z}_{\mathrm{CLF}}^{mn} \boldsymbol{X} = \boldsymbol{Y}^m, \quad (19)$$

where

$$\boldsymbol{Z}_{\mathrm{CLF}}^{mn} = \boldsymbol{Z}_{\mathrm{SLF}}^{mn} + \eta \boldsymbol{Z}_{\mathrm{DLF}}^{mn}. \quad (20)$$

The moment matrix of CLF is free from ill-conditioning [Chandrasekhar and Rao (2004b)] at all frequencies and ensures a unique solution. Integrals appearing in Eqs. (14) and (17) may be evaluated using the techniques mentioned in Wilton *et al.* (1984) and Hammer *et al.* (1956) for an accurate solution, as the former contains singular kernels.

For a plane wave incidence, we set

$$\Phi^i = e^{jk\hat{\boldsymbol{k}}\cdot\boldsymbol{r}}, \quad (21)$$

where the propagation vector $\hat{\boldsymbol{k}}$ is given by

$$\hat{\boldsymbol{k}} = \sin\theta_0 \cos\phi_0 \boldsymbol{a}_x + \sin\theta_0 \sin\phi_0 \boldsymbol{a}_y + \cos\theta_0 \boldsymbol{a}_z. \quad (22)$$

(θ_0, ϕ_0) define the angles of arrival of the plane wave in the conventional spherical coordinate system and $\boldsymbol{a}_x$, $\boldsymbol{a}_y$, and $\boldsymbol{a}_z$ are the unit vectors along the x, y, and z axes, respectively.

The normal derivative of the incident field may be written as

$$\frac{\partial \Phi'}{\partial n} = n \cdot \nabla \Phi^i = jk\boldsymbol{n} \cdot \hat{\boldsymbol{k}} e^{jk\hat{\boldsymbol{k}}\cdot\boldsymbol{r}}. \quad (23)$$

Once the elements of the moment matrix $\boldsymbol{Z}$ and the forcing vector $\boldsymbol{Y}$ are determined, one may solve the linear system of equations, Eq. (19), for the unknown vector $\boldsymbol{X}$ using any standard matrix inversion techniques.

IV. NODE-BASED ADAPTIVE BASIS FUNCTIONS

In method of moments solution procedure, the basis functions can be defined either on the patch [Raju *et al.* (1991), Rao and Sridhara (1991), Rao *et al.* (1992), Rao and Raju (1989)], on the edges [Chandrasekhar and Rao (2004a)], or on the nodes [Chandrasekhar (2005)]. That means the basis function can be defined on any type of geometric entity created by the triangular patch modeling. In all the cases, if one uses an isolated basis function on any type of geometric entity and calculates the effect of this basis function somewhere else on the same type of geometric entity of the structure, the value would be a nonzero which means the effect of the unit source located at one point will be experienced by every other point on the structure. Imagine a case where there is a group of sources located at different points and by assigning different weights to each of these sources or basis functions a weight in such a way that the total effect of the entire group of sources at a given point can be made zero or produce a null field. Keeping this idea in mind the basis functions, namely, adaptive basis functions, may be developed as follows.

First of all, a cluster of basis functions is formed and the weights are assigned to each basis function. Let there be K basis functions in the cluster and the complex weights attached to these basis functions are $\alpha_k, k=1,2,\ldots,K$. Now let us assume that there are N nodes on the surface of the structure and the number of basis functions K in the set is very less compared to N, i.e., $K \ll N$. The entire cluster of basis functions when tested at any point outside the cluster results in a null field when the weights α_k are attached to each basis function. Here, one may note that the points that are chosen for testing the basis functions need not completely lie outside the cluster, which is made clear in the following paragraphs. In order to evaluate the weights α_k, the cluster of basis functions needs to be tested at number points equal to or greater than the number of basis functions in the cluster. This results in a linear system of equations equal to or greater than the number of weights to be determined depending on the case where the number of testing points chosen is equal to or greater than the number of basis functions in the cluster, respectively. In either case, the weights can be solved for. In the next paragraph, an example of the cluster of basis functions and the procedure to calculate the weights α_k is illustrated.

Let us consider a node i and a set of nodes around it in the triangular patch modeling which has a total of N nodes, as shown in Fig. 3. Let there be K number of nodes around the node i. There are totally $K+1$ number of nodes in the cluster. Let us assign a weight of unity or 1 to the node i and the rest of the weights α_k, $k=1,2,\ldots,K$ are unknowns which need to be determined. Since there are K number of unknowns, the basis functions need to be tested at the number of points equal to at least K or greater than K. For the sake of clarity let us assume $K=10$. Then for notational purposes the indices of the nodes range from $i-5, i-4, \ldots, i, \ldots, i+4, i+5$, which is arbitrary. When the testing is carried out, it results in a system of linear equations given by

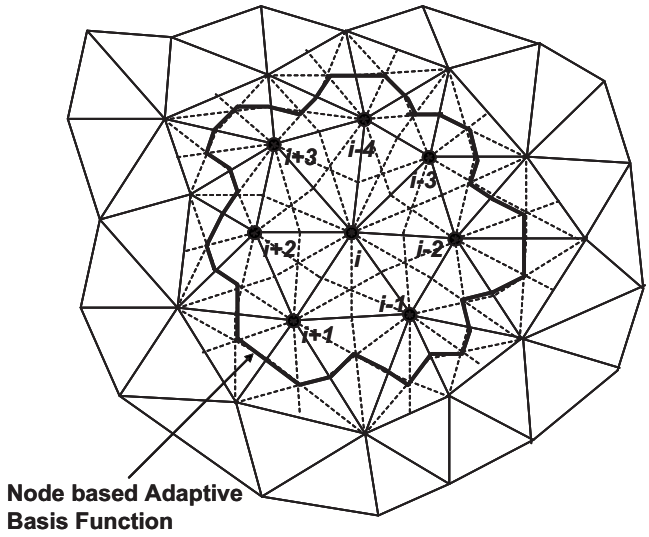


FIG. 3. NABF.

$$Z_{1,i-5}\alpha_{i,i-5} + Z_{1,i-4}\alpha_{i,i-4} + \cdots + Z_{1,i} + \cdots + Z_{1,i+4}\alpha_{i,i+4} + Z_{1,i+5}\alpha_{i,i+5} = 0,$$

$$Z_{2,i-5}\alpha_{i,i-5} + Z_{2,i-4}\alpha_{i,i-4} + \cdots + Z_{2,i} + \cdots + Z_{2,i+4}\alpha_{i,i+4} + Z_{2,i+5}\alpha_{i,i+5} = 0$$

$$\cdots$$

$$Z_{N,i-5}\alpha_{i,i-5} + Z_{N,i-4}\alpha_{i,i-4} + \cdots + Z_{N,i} + \cdots + Z_{N,i+4}\alpha_{i,i+4} + Z_{N,i+5}\alpha_{i,i+5} = 0. \quad (24)$$

This can be represented in matrix form as

$$\begin{bmatrix} Z_{1,i-5} & Z_{1,i-4} & \cdots & Z_{1,i+5} \\ Z_{2,i-5} & Z_{2,i-4} & \cdots & Z_{2,i+5} \\ \cdots & \cdots & \cdots & \cdots \\ Z_{N,i-5} & Z_{N,i-5} & \cdots & Z_{N,i-5} \end{bmatrix} \begin{Bmatrix} \alpha_{i,i-5} \\ \alpha_{i,i-4} \\ \cdots \\ \alpha_{i,i+5} \end{Bmatrix} = \begin{Bmatrix} -Z_{1,i} \\ -Z_{2,i} \\ \cdots \\ -Z_{N,i} \end{Bmatrix}. \quad (25)$$

In the above matrix, the first suffix of Z, ranging from 1 to N, represents the index of the node on which the testing is carried out while the second index represents the source node. The $Z_{j,i}$ are computed in the same procedure as described in Sec. III. By solving Eq. (24) in the least squares sense, the $\alpha_{i,k}$ can be evaluated. Once the $\alpha_{i,k}$ are obtained, one can construct the ith adaptive basis function given by

$$h_i = f_i + \sum_{k=1}^{K} \alpha_{i,k} f_k. \quad (26)$$

By using h_i as the basis function, it produces a null field at every point other than at the ith node. Thus it results in the whole ith column of the $[Z]$-matrix as zero or below a certain threshold value, barring the diagonal term.

By repeating the above mentioned procedure for all the nodes and constructing N adaptive basis functions h_i, $i = 1, \ldots, N$, the MoM procedure produces a diagonal $[Z]$-matrix which can be easily solved for the source distribution without using any matrix inversion algorithms or linear equation solvers. The off-diagonal elements of the $[Z]$-matrix are not zero but below a certain threshold value which can be set to zero.

The question that arises is how many basis functions should be included in the cluster to obtain satisfactory results. The cluster may be formed by choosing the basis functions nearest to the ith basis functions; however, this is not a necessary condition. The basis functions chosen into the cluster need not necessarily be adjacent to each other. In order to address the issue of the minimum number of basis functions in the cluster, an example is given in Waller and Rao (2002) which proves that when the number of basis functions in the cluster is about 10% of the total number of unknowns in the triangulated model, the solution gives satisfactory results for the simple and acoustically small problems. The higher the number of basis functions in the cluster, the higher the accuracy of the solution with respect to the MoM solution based on the independent basis functions.

Next, let us consider a case when the number of basis functions chosen is less than the minimum number of basis functions required to get the satisfactory results. The results obtained will not be accurate since the off-diagonal elements will be of higher values and may not be close to zero as defined by the threshold value. This is because one may have to gather a certain number of basis functions into the cluster to get the given threshold limit. In case this is not possible, then one may choose the solution obtained as an initial guess to solve Eq. (24) iteratively. This is an effective method of solving Eq. (24) and it will take only a fewer number of iterations as proved in the next section.

It is also possible to use the adaptive basis functions as testing functions as well. Furthermore for the Galerkin procedure, one can use these functions both as basis and testing functions. But it is more computationally expensive to use these functions in the Galerkin procedure.

The salient features of the proposed method are as follows.

(1) The computer storage requirement for the proposed method is considerably less than the traditional MoM solution. It contains two parts. The first one being the storage required to create the adaptive basis functions which is $K \times N$, where $K \ll N$. The second one being the storage of the diagonal matrix as the off-diagonal elements of the $[Z]$-matrix are assumed to be below the threshold value or zero. In fact, only K columns of the storage space are required for the weights of basis functions for each column. In case one uses an iterative solution based on the initial guess as explained above, then an additional storage space for the $[Z]$-matrix may be needed, which is worth as the computational time required for the solution of the linear system of equations is eliminated. However, this step may be carried out as a completely independent module.

(2) The computational time required for solving the scattering problem is also very less as the matrix inversion is eliminated, which usually is the more time consuming step in the scattering or radiation problems when the number of unknowns is large. In the case of the number

of unknowns of 100 000 the time required for the generation of the $[Z]$-matrix is an order less compared to the time required to invert it. We note that matrix filling is N^2 operation and inversion is N^3. Since this step of inversion is completely eliminated in the proposed method, it is more efficient than the traditional MoM. However, one may have to solve the linear system of equations given by Eq. (24), N times. This is not computationally expensive as $K \ll N$ when N is very large. The operation count to solve the linear system of equations given in Eq. (24) is of the order $(K^2N+KN+cK^3)$, where c is the constant. As long as $K \ll N^{1/2}$, the operation count is similar to the MoM solution. However, for acoustically large problems, with $N \approx 100\,000$, we envisage $K \approx N^{1/3}$ and the proposed method gives a more efficient solution than the traditional MoM. Furthermore, the number of equations in Eq. (24) can be reduced to K [Rius *et al.* (1997)] which implies a very large reduction in the computational operations. Thus when the computer storage and solution time are factors in solving the large problems, the efficiency of the proposed method is more pronounced.

Finally, note that the new adaptive basis functions are linear combinations of nodal-constant basis functions chosen to null out everywhere but at a single node resulting in a diagonal moment matrix.

V. NUMERICAL RESULTS

In this section, the numerical solutions developed for the CLF using NABF are validated against the exact solution for the case of a sphere and against the node-based traditional MoM solution for the cases of a cylinder and a cube. Note that for the cases of a cube and a cylinder, closed form solution does not exist and hence, the traditional MoM solution is used as a baseline for these cases. For all the three cases, the three-dimensional body is placed at the center of the coordinate system and a plane wave, traveling along the $-Z$ axis, is incident on the body. Here, it may be noted that no convergence study is carried out to ascertain the optimum number of basis functions required in the cluster to obtain a certain degree of accuracy. The scattering cross section is defined by

$$S = 4\pi \left| \frac{\Phi^s}{\Phi^i} \right|^2 \approx \frac{1}{4\pi} \left| \sum_{n=1}^{N_n} \alpha_n A_n \boldsymbol{n}_n \cdot \boldsymbol{r}_n e^{jk\boldsymbol{n}_n \cdot \boldsymbol{r}_n} \right|^2. \quad (27)$$

As a first case, a sphere of radius 1 m is considered and the geometries with sharp corners and sharp edges such as cube and cylinder are also considered in order to demonstrate the capability of the NABF using method of moments solution.

The sphere considered here is modeled with 178 nodes, 352 patches, and 528 edges. Figure 4 shows the scattering cross section versus polar angle for an acoustically rigid sphere of radius 1 m, subjected to an axially incident plane wave of $k=1$ rad/m, based on CLF. Triangular patch modeling is carried out by dividing the surface of the sphere in θ and ϕ directions in equal segments and the complete modeling procedure is described in Chandrasekhar and Rao (2004a). The traditional MoM solution for this case of sphere is compared with the closed form solution [Bowman *et al.* (1969)]. Again, the same problem is solved using NABF with a cluster of five basis functions, and three iterations are used to refine the solution which is in well agreement with the exact solution as well as the traditional MoM solution. In the case of the traditional MoM solution, the size of the matrix would be 178×178 for the node-based basis functions, 352×352 for the patch based basis functions, and 528×528 for the edge based basis functions. However, if the NABFs are used, the size of the matrix will be 178×178 which is diagonal. In other words, it results in a vector of size 178 to store the diagonal elements of the moment matrix. Hence the matrix inversion is eliminated and the storage space is also greatly reduced.

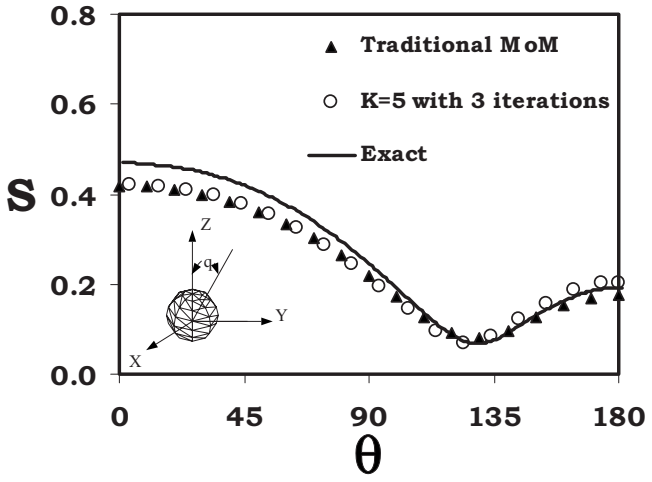


FIG. 4. Scattering cross section vs polar angle for an acoustically rigid sphere of radius 1 m, subjected to an axially incident plane wave of $k=1$ rad/m, based on CLF.

Figure 5 shows the scattering cross section versus polar angle for an acoustically rigid cylinder of radius 1 m and height 1 m, subjected to an axially incident plane wave of $k=1$ rad/m, based on CLF. Cylinder is modeled using trian-

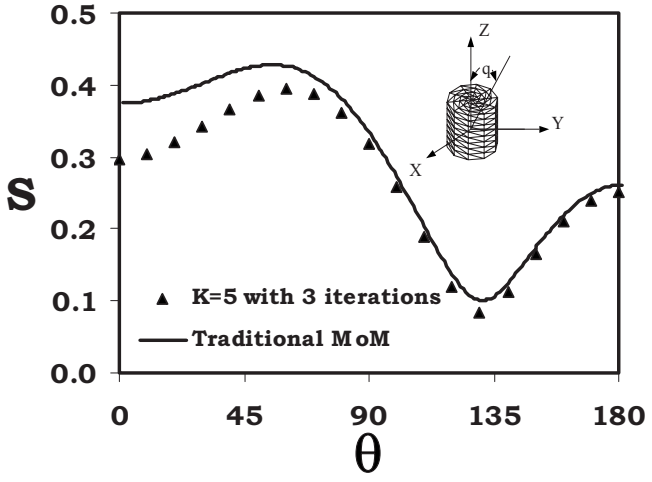


FIG. 5. Scattering cross section vs polar angle for an acoustically rigid cylinder of radius 1 m and height 1 m, subjected to an axially incident plane wave of $k=1$ rad/m, based on CLF.

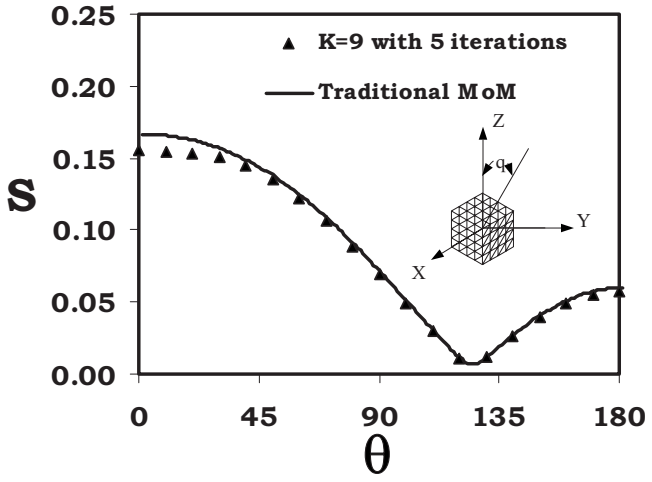


FIG. 6. Scattering cross section vs polar angle for an acoustically rigid cube of length 1 m, subjected to an axially incident plane wave of $k=1$ rad/m, based on CLF.

gular patch modeling with 152 nodes, 300 patches, and 450 edges. The number basis functions chosen in the cluster are 5, and three iterations were carried out to refine the solution further. The solution based on the NABF is in well agreement with the solution based on the traditional MoM solution in which the independent pulse functions are used as basis functions on each node. Again in this case, the size of the vector required to store the nonzero elements of the resulting diagonal matrix is 152, which otherwise would be 450×450 had the edge based basis functions are used.

As a next example to show the capability of the NABF which can handle a large number of nodes in the triangulated model, a cube is modeled with 866 nodes, 1728 patches, and 2592 edges using triangular patch modeling. Here, in the case of the traditional MoM, one has to invert/solve a matrix of size 866×866 for the case of node based basis functions, which is completely eliminated by using the NABF, where only nine basis functions are considered in the cluster. The solution obtained by the cluster of basis functions is further refined five times to get more accurate solution. Figure 6 shows the scattering cross section versus polar angle for an acoustically rigid cube of length 1 m, subjected to an axially incident plane wave of $k=1$ rad/m, based on CLF.

VI. CONCLUSIONS

In this work, a faster solution procedure based on MoM is developed for the solution of acoustic scattering problems, and the method is based on grouping the node-based basis functions into a cluster to generate a diagonal moment matrix. The major drawback of the MoM solution procedure, which generally results in a full moment matrix, is eliminated by grouping the basis functions into a cluster, namely, NABFs. Although the basis functions may be defined either on a node, edge, or a patch for a triangulated model, the node-based basis functions are most efficient. By doing this, one can get the combined benefit of smaller size of the moment matrix and a smaller diagonal moment matrix by grouping these node-based basis functions into a cluster. The solution procedure developed in this work is validated for the scattering cross section of the simple shapes with the closed form solutions wherever available. The numerical results prove that the solutions which are based on the NABF are accurate enough and can provide the solutions faster than the traditional MoM solutions.

Bowman, J. J., Senior, T. B. A., and Uslenghi, P. L. E. (**1969**). *Electromagnetic and Acoustic Scattering by Simple Shapes*, North-Holland, Amsterdam.

Burton, A. J., and Miller, G. F. (**1971**). "The application of integral equation methods to the numerical solution of some exterior boundary value problems," Proc. R. Soc. London, Ser. A **323**, 601–618.

Chandrasekhar, B. (**2005**). "Acoustic scattering from arbitrarily shaped three dimensional rigid bodies using method of moments solution with node based basis functions," Comput. Model. Eng. Sci. **9**, 243–254.

Chandrasekhar, B., and Rao, S. M. (**2004a**). "Acoustic scattering from rigid bodies of arbitrary shape: Double layer formulation," J. Acoust. Soc. Am. **115**, 1926–1933.

Chandrasekhar, B., and Rao, S. M. (**2004b**). "Elimination of internal resonance problem associated with acoustic scattering by three-dimensional rigid body," J. Acoust. Soc. Am. **115**, 2731–2737.

Coifman, R., Rokhlin, V., and Wandzura, S. (**1993**). "The fast multipole method for the wave equation: A pedestrian prescription," IEEE Antennas Propag. Mag. **35**, 7–12.

Hammer, P. C., Marlowe, O. P., and Stroud, A. H., (**1956**). "Numerical integration over simplexes and cones," Math. Tables Aids Comput. **10**, 130–138.

Harrington, R. F. (**1968**). *Field Computation by Method of Moments*, Macmillan, New York.

Mikhiln, S. G. (**1964**). *Variational Methods in Mathematical Physics*, Macmillan, New York, pp. 74–78.

Purczynski, J., Rolicz, P., and Sikora, R. (**1975**). Arch. Elektrotech. (Berlin) **57**, 119–126.

Raju, P. K., Rao, S. M., and Sun, S. P. (**1991**). "Application of the method of moments to acoustic scattering from multiple infinitely long fluid filled cylinders," Comput. Struct. **39**, 129–134.

Rao, S. M., and Raju, P. K. (**1989**). "Application of method of moments to acoustic scattering from multiple bodies of arbitrary shape," J. Acoust. Soc. Am. **86**, 1143–1148.

Rao, S. M., Raju, P. K., and Sun, S. P. (**1992**). "Application of the method of moments to acoustic scattering from fluid-filled bodies of arbitrary shape," Commun. Appl. Numer. Methods **8**, 117–128.

Rao, S. M., and Sridhara, B. S. (**1991**). "Application of the method of moments to acoustic scattering from arbitrary shaped rigid bodies coated with lossless, shearless materials of arbitrary thickness," J. Acoust. Soc. Am. **90**, pp. 1601–1607.

Rius, J. M., Parron, J., Ubeda, E., and Mosig, J. R. (**1997**). "Integral equation MEI applied to three-dimensional arbitrary surfaces," Electron. Lett. **20**, 2029–2031.

Schenck, H. A. (**1968**). "Improved integral formulation for acoustic radiation problems," J. Acoust. Soc. Am. **44**, 41–58.

Waller, M. L., and Rao, S. M. (**2002**). "Application of adaptive basis functions for a diagonal moment matrix solution of arbitrarily shaped three-dimensional conducting body problems," IEEE Trans. Antennas Propag. **50**, 1445–1452.

Wilton, D. R., Rao, S. M., Glisson, A. W., Schaubert, D. H., Al-Bundak, O. M., and Bulter, C. M. (**1984**). "Potential integrals for uniform and linear source distributions on polygons and polyhedra domains," IEEE Trans. Antennas Propag. **AP-32**, 276–281.

Nonlinear modulation of Lamb modes by clapping delamination

G. Shkerdin[a] and C. Glorieux[b]
Laboratorium voor Akoestiek en Thermische Fysica, Departement Natuurkunde, K. U. Leuven, Celestijnenlaan 200 D, B-3001 Leuven, Belgium

(Received 2 November 2007; revised 30 August 2008; accepted 2 September 2008)

The nonlinear interaction between a high frequency probing Lamb wave and a bilayer containing a tangential delamination at the interlayer interface, whose contact conditions are dynamically changing due to a high amplitude Lamb wave with a long wavelength, is modeled in a quasistationary approach. The impact of the evolution of the contact condition on the mode conversion coefficients that describe the interaction of the probing wave with the delamination region leads to spectral enrichment due to cross-modulation spectral components between the probing wave and the modulating wave. The dynamical behavior of the normal displacement at the externally accessible surfaces is investigated for two different types of incident probing wave, both for an absorbing and a nonabsorbing bilayer structure, for variations in the contact quality modulation and as a function of defect size. The results can serve as a parametric guide for experimentalists considering the use of nonlinear harmonic generation of Lamb waves as a tool for nondestructive testing of bilayers, such as rubber-steel composites, in storage tanks and pipelines.
© *2008 Acoustical Society of America.* [DOI: 10.1121/1.2996301]

PACS number(s): 43.25.Fe [OAS] Pages: 3397–3409

I. INTRODUCTION

Delaminations form an important class of defects in materials and devices. Delaminations are likely to grow in mechanically strained or chemically hostile structures and finally lead to global malfunctioning or even failure. Therefore, understanding their nature and being able to detect their occurrence in a nondestructive way are of great interest in the field of quality control and safety preservation. Ultrasonic testing is an excellent nondestructive technique (NDT) for delamination detection and investigation. Indeed ultrasonic waves can probe both surface and bulk regions in a material, and they are sensitive to any kind of usually significant defect-induced acoustic impedance mismatch. Their interaction with a defect thus leads to reflection, diffraction, scattering, or mode conversion effects that can be easily monitored, often in a noncontact and remote way, e.g., using air-coupled excitation and laser displacement wave detection.

In particular, the interaction of Lamb modes in platelike samples with different kinds of defects, including delaminations, has already been extensively studied.[1–8] Also the study and exploitation of the interaction of Rayleigh waves with defects in semi-infinite substrates represent an important technological challenge. However, the theoretical treatment is much more difficult than for Lamb waves since for semi-infinite substrates decomposition in a discrete number of modes is impossible, and only approximate *ad hoc* approaches are possible.[9–11] Auld and Tan[1,2] predicted the reflection of Lamb modes from vertical delaminations normal to plate surfaces, and this effect was revisited by many authors (see, e.g., Refs. 6–8). Rokhlin studied Lamb mode diffraction on horizontal delaminations situated exactly in the middle of the plate.[3–5]

Horizontal delaminations typically appear in composite layered plates where the existence of stresses leads to a deterioration of the coupling between layers and thus to the development of delaminations. Also the effect of mode conversion by a horizontal delamination in absorbing bilayers was theoretically studied, and it was shown that depending on the delamination length a considerable part of an incident Lamb mode energy is converted into transmitted Lamb modes.[12] The spatial evolution of the normal displacement amplitude of a Lamb wave at the plate interfaces, a quantity which can typically be easily assessed in practical situations,[13–15] was theoretically analyzed for plates coated with highly absorptive materials. Both stress-free and slip delaminations (mechanical contact between slip delamination surfaces is only lost for tangential displacement components) were taken into consideration, and it was shown that both types of delaminations could be detected for different types of incident modes.[13] In practice, such measurements could provide information about the presence of delaminations and could allow us to characterize their nature, which is important for nondestructive testing of composite materials. Although the accurate determination of, e.g., the shear wave velocity and attenuation in highly absorbing materials is a complicated problem (see, e.g., Refs. 16–20), using the approach proposed in Ref. 15, information about the velocity and attenuation of waves in the absorbing layer could also be retrieved.

An important limitation of the classical linear ultrasonic approach described above is that delaminations act as if they are closed. In spite of the absence of adhesion, the two delaminated surfaces are touching; they typically do not represent an impedance mismatch for incident acoustic waves,

[a]Permanent address: Institute of Radio Engineering and Electronics, Russian Academy of Sciences, Vedensky Square 1, Fryazino, Moscow, Russia.
[b]Electronic mail: christ.glorieux@fys.kuleuven.be

thus remaining "unnoticed." However, it is known that acoustic waves of a moderate to high power can considerably modulate the delamination thickness, such that the mechanical contact between parts of the delamination interfaces is temporarily restored during strongly compressive motions. This leads to the appearance of a "clapping" effect. The accompanying time dependent wave induced response of the material via the dynamically changing boundary conditions leads to nonlinear acoustic effects[21] and higher harmonic generation. Since the nonlinear effect is locally induced by the defect, this effect offers an interesting possibility for the detection of defects with high spatial resolution and contrast, whose feasibility has been demonstrated.[22–28]

The spatial and temporal behaviors of the acoustic field of a Lamb mode propagating through a clapping delamination region are very complicated, especially if the clapping effect is created by the mode itself and "self-modulation" occurs. Although clapping has been studied for longitudinal waves,[29–32] to the best of our knowledge, this nonlinear and nonstationary problem has not yet been theoretically analyzed.

In this article, we simplify the problem of a probing periodic Lamb wave in a bilayer that is interacting with a clapping delamination by assuming that the clapping is independently induced either by a slowly varying periodical external force, uniformly exerted on the whole delamination region, or by another Lamb mode of much smaller frequency that is itself not affected by the clapping. In these two cases, an approximate quasistationary approach can be used as follows. For every state, i.e., for every temporal phase of the clapping cycle, the boundary condition at every position in the delamination region is determined by a "closing criterion" that is based on the normal displacement induced by the slow force or wave. Using a standard modal decomposition approach[13] for waves in a bilayer, this boundary condition (described in detail in Sec. II) is used to calculate the coefficients of the modes and thus the overall dynamic displacement dependence in and around the delamination region for that state. In this approach, the solution is obtained for the imposed delamination geometry as a combination of known Lamb waveforms with coefficients chosen in order to satisfy boundary conditions at the outer sides of the biplate and the inner interface. Combining the solutions for all states, or equivalently temporal phases, of the modulation cycle, the time dependence of the expansion coefficients is found, and so is the time dependence of the dynamic displacement pattern, which includes the fundamental probing frequency as well as cross-modulation induced sum and difference combinations between the probing and modulating frequencies and their harmonics.

The generalization of the linear modal decomposition model for the interaction of a probing Lamb mode with a uniform delamination region[13] to a more complicated region sectioned in locally uniform subregions, i.e., a configuration as evoked by the chosen contact closing criterion, is given in Sec. II. In Sec. III, using the above model in a quasistationary approach assuming slowly varying boundary conditions, the cases of a spatially uniform modulation of the boundary condition by an external force varying according to a square wave with a 50% duty cycle are elaborated for an absorbing bilayer. In Sec. IV this is done for a spatially nonuniform modulation induced by an incident low frequency Lamb wave. In Secs. IV B and IV C, this approach is followed, respectively, for an absorbing and nonabsorbing bilayer. In the Conclusion, the possibilities and limitations of the proposed model for a nonlinear interaction of Lamb waves with delaminations are summarized, and perspectives are drawn for the development of more refined and realistic models.

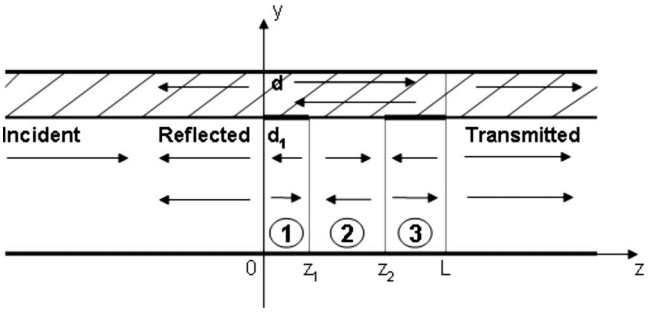


FIG. 1. Schematic view of the Lamb wave incident on a sectioned delamination in a bilayer structure.

II. MODAL DECOMPOSITION METHOD IN A BILAYER WITH THREEFOLD SUBSECTIONED DELAMINATION

A. Definition of "open" and "closed" contacts

In view of calculating the interaction of an incident probing Lamb wave with a tangentially oriented (parallel with plate surfaces) clapping delamination in the quasistationary approach in the following sections, we start to describe the model for a stationary periodic Lamb mode incident on a delamination region that is tangentially subsectioned in open and closed parts. The terms "open" and "closed" refer to the nature of the contact between the delaminated layers. In a simplified approach, we consider the open boundary condition as stress-free and associate the closed condition with stress and displacement continuity. Also the intermediate case of partial continuity or "slip" is handled as a special case of the open state. More sophisticated intermediate boundary conditions, e.g., described by a nonlinear or hysteretic stress-strain relation,[29,30] are not treated here since it can be expected that those cases can be addressed by qualitatively interpolating between the extreme open/closed cases.

B. Threefold delamination geometry

The detailed two-dimensional geometry under consideration is shown in Fig. 1. The incident Lamb wave propagates along the z-direction in an isotropic bilayer of thickness d. The outer bilayer surfaces at $y=0$ and $y=d$ are stress-free overall. The plate consists of two parallel layers with y-coordinates $0 \leqslant y \leqslant d_1$ and $d_1 \leqslant y \leqslant d$, respectively. The layers are in perfect mechanical contact; i.e., all displacement components and all normal and shear stress are continuous everywhere at the interface $y=d_1$, except in the delamination region between $z=0$ and $z=L$. The delamination consists of three parts: a left and right exterior open part

for, respectively, $0 \leqslant z \leqslant z_1$ and $z_2 \leqslant z \leqslant L$ (indicated by bold lines in Fig. 1) and an interior closed part for $z_1 < z < z_2$.

The choice for this geometry is inspired by the quasistationary model assumptions used in Secs. III and IV, where a probing Lamb wave encounters a delamination structure, which slowly changes as a result of the modulating force or wave. In the absence of external forces or a modulating wave, the delamination is considered to be open overall, and partial waves can travel uncoupled in the upper and lower layers. We are aware of the fact that this assumption is not representative of many real life cases. Extensions of this model to normally closed delaminations that are opened due to external forces or modulating wave induced interface stresses will be presented in future work.

C. Closing criterion and implication to the threefold delamination structure

In the case of an external force (Sec. III), it is assumed that the whole delamination region $(0 < z < L)$ is uniformly modulated between open and closed conditions, so the closing criterion purely depends on the temporal phase of the on-off periodical force. In the used model for a modulating wave (Sec. IV), the contact at any position z within the delamination is in a normally (not excited rest situation) open state and becomes closed if the following closing criterion is fulfilled:

$$\Delta u_y(z) = u_y(y \to d_1^-, z) - u_y(y \to d_1^+, z) > d_{\text{crit}}. \tag{1}$$

Equation (1) expresses that the mechanical contact is closed because of the bridging of the delamination gap that results from the overlap between the assumed independent modulating wave induced normal displacements of the two adjacent interfaces. For the simulations, we have chosen *ad hoc*, but somehow realistically, the value $d_{\text{crit}} = 1\ \mu\text{m}$ for the gap width between the two delaminated surfaces. We also assume that the acoustic wave amplitude is much smaller than the acoustic wavelength, and we neglect the curvature of the modulated delamination.

Because of the continuity in the tangential z-direction of displacements and stresses within the individual layers, the interface displacement discontinuity Δu_y in the exterior zones, close to the ends of the delaminations (where the mismatch is zero because of the perfect mechanical contact for $z \leqslant 0$ and $z \geqslant L$), remains too small to close the contact. The displacement difference can only develop away from the edges, and only in the interior zone of the delamination region does it become sufficiently large to switch on the closing criterion. In this way, provided that the acoustic wavelength is long enough compared with the delamination length, a threefold open $(0 < z < z_1)$-closed $(z_1 \leqslant z \leqslant z_2)$-open $(z_2 < z < L)$ partition is established, with the position parameters z_1 and z_2 dynamically changing according to the displacement difference profile induced by the modulating partial waves in the upper and lower layers. For the sake of simplicity here, we do not treat the case of a modulating wave with a wavelength shorter than the delamination length, which would lead to a far more complicated clapping geometry.

D. Classification of "perfect" and "slip" closed contacts

The nature of the boundary condition depends on the quality of the delaminated surfaces. For rough surfaces, it can be expected that by closing the mechanical contact between the previously fully stress-free open delamination surfaces is fully restored for both longitudinal and shear displacements and stresses so that boundary conditions for a perfectly bonded interface between two solids can be used for the closed state. On the other hand, for smooth surfaces in the closed state, the mechanical contact could be only partially present in the form of a slip contact; i.e., there is limited continuity for the normal displacement (u_y) and stress (σ_{yy}), while the tangential displacement (u_z) and shear stress (σ_{yz}) of the adjacent surfaces still remain uncoupled.[31] In this case the contact in the closed state of the interior part is represented by a slip condition.

The problem of boundary conditions across interfaces between two solids has already been extensively studied (see, e.g., Ref. 32 and references therein). Slip boundary conditions idealize the real physical contact between two solids and describe the delamination with transverse slip without friction between delamination surfaces but give a satisfactory approximation for many real cases.[32] A slip delamination can be considered as an intermediate case between a perfectly bonded interface and a stress-free delamination, where the physical contact between two adjacent layers is completely lost.

E. Modal expansion and determination of expansion coefficients for mode conversion of Lamb wave interacting with a threefold delamination

In our quasistationary approach, it is necessary to calculate the interaction of the sinusoidal probing Lamb wave with the partitioned delamination, with z_1 and z_2 as parameters. The method to calculate the acoustic field is based on an expansion of this field in a truncated discrete series of Lamb eigenmodes in the different parts of this composite plate structure and on the use of boundary conditions at the normal planes $z=0$, $z=z_{1,2}$, and $z=L$ to determine the expansion coefficients. Since this method has already been described in detail in Refs. 12 and 13 for the case of a uniform $(z_1=z_2)$ stress-free and slip delamination. Here we just give the concise description of its generalization for the threefold structured delamination in Fig. 1.

The components of the stress tensor S_{ik}^n and the mechanical displacement vector U_i^n $(i=y,z$ and $k=y,z)$ of the nth Lamb mode can be written down as follows:

$$(S_{ik}^n, U_i^n) = (\sigma_{ik}^n, u_i^n)\exp(iq_n z - i\omega t) + (\sigma_{ik}^n, u_i^n)^* \times \exp(i\omega t - iq_n^* z), \tag{2}$$

where q_n and ω are, respectively, the wave number and angular frequency and the asterisk symbol refers to complex conjugation. S_{ik}^n, U_i^n, σ_{ik}^n, and u_i^n are y-dependent and satisfy the wave equation, the stress-strain relations, the continuity conditions at the interface $y=d_1$, and the stress-free conditions at $y=0$ and at $y=d$. The functional forms of U_i^n and S_{ik}^n for Lamb modes of homogeneous plates are given by well-

known expressions for symmetric and antisymmetric Lamb modes (see, for example, Ref. 33). The same functions for a bilayer with perfect and slip mechanical contacts at $y=d_1$ are given in the Appendices of Refs. 12 and 13. All Lamb modes satisfy orthogonality conditions (see, for example, Eq. (2) in Ref. 12).

The expansion of the mechanical displacement vector for the transmitted acoustic waves $\vec{u}^{\mathrm{tr}}$ $(z>L)$ is given by

$$\vec{U}^{\mathrm{tr}} = \sum_n C_n^{\mathrm{tr}} \vec{u}_{\mathrm{tr}}^n \exp(i(q_n(z-L)-\omega t)), \tag{3}$$

with C_n^{tr} expansion coefficients for transmitted acoustic waves, which are to be determined. The expression is analogous for the reflected acoustic waves $(z<0)$,

$$\vec{U}^{\mathrm{ref}} = \sum_n C_n^{\mathrm{ref}} \vec{u}_{\mathrm{ref}}^n \exp(-i(q_n z+\omega t)). \tag{4}$$

The expansion of the mechanical displacement vector for right- and left-going (respectively, index dir=tr/ref) acoustic waves in the three subsections, labeled by indices $\alpha=1,2,3$, of the delamination, $\vec{U}_{\pm}^{\mathrm{dir},\alpha}$, is equivalent with Eqs. (3) and (4), provided the substitutions in the prefactors: $C_n^{\mathrm{dir}} \rightarrow C_{n,\pm}^{\mathrm{dir},\alpha}$, $\vec{u}_{\mathrm{dir}}^n \rightarrow \vec{u}_{\mathrm{dir}}^{n,\pm}$, $q_n \rightarrow q_{n,\pm}$. The $\pm$ signs indicate, respectively, transmission in the upper $(d_1<y<d)$ and lower $(0<y<d_1)$ parts of the delamination region. Also the exponential functions in the solutions in the subsections of the delamination are similar to Eqs. (3) and (4) and of the form $\exp(i(\beta q_{n,\pm}(z-z_\beta)-\omega t))$, with $\beta=\pm 1$ for, respectively, right-and left-going waves, and z_β the position of the interface from where the concerned wave is transmitted/reflected. In the case of a perfectly bonded interface $y=d_1$ in the interior delamination part $(\alpha=2)$, the functions $\vec{u}_{\mathrm{dir}}^n$ are the same as the ones outside the delamination region. For a slip delamination, they are referred to as $\vec{u}_{\mathrm{tr,ref}}^{n,\mathrm{sd}}$.

Similar to Refs. 12 and 13, applying boundary conditions at the interface plane $z=0$, $z=z_{1,2}$, and $z=L$ and using the orthogonality conditions, an infinite system of linear equations [Eqs. (5)–(12)] in the unknown mode coefficients C_n^{dir} and $C_n^{\mathrm{dir},\alpha}$ (dir=ref,tr and $\alpha=1,2,3$) can be derived,

$$A(n)C_n^{\mathrm{tr},2} = \sum_{m,\pm} (C_{m,\pm}^{\mathrm{tr},1} e^{iq_{m,\pm}z_1}(K_{n,m}^{\pm}+I_{n,m}^{\pm}) + C_{m,\pm}^{\mathrm{ref},1}(I_{n,m}^{\pm}-K_{n,m}^{\pm})), \tag{5}$$

$$A(n)C_n^{\mathrm{ref}} = \sum_{m,\pm} (C_{m,\pm}^{\mathrm{ref},1} e^{iq_{m,\pm}z_1}(K_{n,m}^{\pm}+I_{n,m}^{\pm}) + C_{m,\pm}^{\mathrm{tr},1}(I_{n,m}^{\pm}-K_{n,m}^{\pm})), \tag{6}$$

$$A^{\pm}(m)C_{m,\pm}^{\mathrm{tr},1} = \sum_n (C_n^{\mathrm{in}}(K_{n,m}^{\pm}+I_{n,m}^{\pm}) + C_n^{\mathrm{ref}}(K_{n,m}^{\pm}-I_{n,m}^{\pm})), \tag{7}$$

$$A^{\pm}(m)C_{m,\pm}^{\mathrm{ref},1} = \sum_n (C_n^{\mathrm{tr},2}(K_{n,m}^{\pm}-I_{n,m}^{\pm})) + C_n^{\mathrm{ref},2} e^{iq_n(z_2-z_1)} \times (K_{n,m}^{\pm}+I_{n,m}^{\pm})), \tag{8}$$

$$A(n)C_n^{\mathrm{tr}} = \sum_{m,\pm} (C_{m,\pm}^{\mathrm{tr},3} e^{iq_{m,\pm}(L-z_2)}(K_{n,m}^{\pm}+I_{n,m}^{\pm}) + C_{m,\pm}^{\mathrm{ref},3}(I_{n,m}^{\pm}-K_{n,m}^{\pm})), \tag{9}$$

$$A(n)C_n^{\mathrm{ref},2} = \sum_{m,\pm} (C_{m,\pm}^{\mathrm{ref},3} e^{iq_{m,\pm}(L-z_2)}(K_{n,m}^{\pm}+I_{n,m}^{\pm}) + C_{m,\pm}^{\mathrm{tr},3}(I_{n,m}^{\pm}-K_{n,m}^{\pm})), \tag{10}$$

$$A^{\pm}(m)C_{m,\pm}^{\mathrm{tr},3} = \sum_n (C_n^{\mathrm{tr},2} e^{iq_n(z_2-z_1)}(K_{n,m}^{\pm}+I_{n,m}^{\pm}) + C_n^{\mathrm{ref},2}(K_{n,m}^{\pm}-I_{n,m}^{\pm})), \tag{11}$$

$$A^{\pm}(m)C_{m,\pm}^{\mathrm{ref},3} = \sum_n C_n^{\mathrm{tr}}(K_{n,m}^{\pm}-I_{n,m}^{\pm}), \tag{12}$$

where $I_{n,m}^{\pm}=\int_{a_\pm}^{b_\pm} dy(\sigma_{yz,\mathrm{tr}}^n u_{y,\mathrm{tr}}^{m,\pm} - u_{z,\mathrm{tr}}^n \sigma_{zz,\mathrm{tr}}^{m,\pm})$, $K_{n,m}^{\pm}=\int_{a_\pm}^{b_\pm} dy \times(\sigma_{yz,\mathrm{tr}}^{m,\pm} u_{y,\mathrm{tr}}^n - u_{z,\mathrm{tr}}^{m,\pm} \sigma_{zz,\mathrm{tr}}^n)$, $a_-=0$, $a_+=b_-=d_1$, $b_+=d$, and $A(n)$ and $A^{\pm}(m)$ are the normalization factors in the orthogonality conditions. Equations (5)–(12) were written down for the case of a perfectly bonded interface in the interior delamination subsection $(z_1<z<z_2)$. The case of a slip boundary condition is described by an analogous system of equations with the following substitutions in Eqs. (5), (8), (10), and (11): $I_{n,m}^{\pm} \rightarrow I_{\mathrm{sl},n,m}^{\pm}$, $K_{n,m}^{\pm} \rightarrow K_{\mathrm{sl},n,m}^{\pm}$; $I_{\mathrm{sl},n,m}^{\pm}=\int_{a_\pm}^{b_\pm} dy(\sigma_{yz,\mathrm{tr}}^{n,\mathrm{sl}} u_{y,\mathrm{tr}}^{m,\pm} - u_{z,\mathrm{tr}}^{n,\mathrm{sl}} \sigma_{zz,\mathrm{tr}}^{m,\pm})$, $K_{\mathrm{sl},n,m}^{\pm}=\int_{a_\pm}^{b_\pm} dy(\sigma_{yz,\mathrm{tr}}^{m,\pm} u_{y,\mathrm{tr}}^{n,\mathrm{sl}} - u_{z,\mathrm{tr}}^{m,\pm} \sigma_{zz,\mathrm{tr}}^{n,\mathrm{sl}})$, where the components of the stress tensor $\sigma_{yz,\mathrm{tr}}^{n,\mathrm{sl}}$ and the mechanical displacement vector $u_{z,\mathrm{tr}}^{n,\mathrm{sl}}$ in the second delamination part are calculated using slip boundary conditions at the interface $y=d_1$. The system of equations [Eqs. (5)–(12)] contains twice as many equations as in the case of an ordinary delamination, assuming the same number of considered modes in each part of the structure (see Refs. 12 and 13).

F. Simulation parameters

For the numerical implementation of the acoustic field calculations in a bilayer with a delamination, we consider two cases: (1) the case of an absorptive bilayer consisting of two materials with a large discrepancy of acoustic properties and (2) the case of a nonabsorptive bilayer with similar acoustic properties of both materials.

In both cases, one layer $(0 \leqslant y<d_1)$ consists of steel. The second layer $(d_1<y \leqslant d)$ is taken to be either rubber (absorbing bilayer) or aluminium (nonabsorbing bilayer). The material properties and wave parameters at the probing wave frequency $f=0.6$ MHz are summarized in Table I. Absorption of acoustic waves propagating in steel and aluminium is neglected. Rubber, on the other hand, is highly absorptive, with a frequency dependent velocity and high attenuation, particularly for shear waves. For the chosen frequency, the wavelength for this frequency is larger than the bilayer thickness but significantly smaller than the length of the delamination. Steel and aluminum have quite different densities, but their shear and longitudinal velocities are quite similar so that, contrary to the steel-rubber case, the case of a steel-aluminium bilayer represents situations, in general, with a nonabsorptive bilayer with a small mismatch in material parameters. Resulting from the closing criterion [Eq.

TABLE I. Material properties and relevant wave parameters.

	ρ (kg m^{-3})	v_1 (m s^{-1})	v_s (m s^{-1})	α_1 (cm^{-1})	α_s (cm^{-1})	λ (cm)	v (m s^{-1})	q (cm^{-1})	λ (cm)	v (m s^{-1})	q (cm^{-1})
Frequency		All				f=0.6 MHz				Ω=20 kHz	
Steel	7800	5720	3600	0	0	⋯		⋯	⋯	⋯	⋯
Aluminium	2700	6370	3110	0	0	⋯		⋯	⋯	⋯	⋯
Rubber	1100	1800	200	2.3	30	⋯		⋯	⋯	⋯	⋯
LM1	⋯	⋯	⋯	⋯	⋯	0.25	1488.1	25.33+0.08i	1.5	298.6	4.209+0.003i
LM2	⋯	⋯	⋯	⋯	⋯	0.88	5255.9	7.17+0.05i			

(1)], the difference between the displacements of the waves in the individual layers, which is obviously related to the mismatch between the material parameters, turns out to be a crucial aspect concerning nonlinear effects, as discussed in Secs. III and IV.

In the following simulations, we take $d_1=d_2=0.5$ mm ($d_2=d-d_1$) and $d_1=d_2=1$ mm for the first and second bilayer cases, respectively, with an incident probing Lamb wave mode of 0.6 MHz frequency. For this choice of geometrical and material parameters and frequency, besides modes that are highly localized at the interfaces between the different sections at $z=0,z_1,z_2,L$, there are only two possible propagating Lamb modes, which simplifies the analysis. In order to illustrate the behavior of a Lamb wave in bilayers, in general, and the effect of nonlinear modulation, in particular, we start from the case of an absorbing steel-rubber bilayer. Next, results for a nonabsorbing steel-aluminium are shortly summarized, with special attention to the differences with respect to the steel-rubber case.

G. Dispersion and spatial profile of Lamb modes in absorptive bilayer

Figure 2 shows the frequency dependence of the phase velocity and attenuation coefficient of weakly attenuated propagating Lamb modes for an absorptive steel/rubber bilayer with a perfectly bonded interface $y=d_1$. For comparison also the fundamental modes A0 and S0 of the free steel plate are shown. The longitudinal and shear attenuation coefficients in rubber are taken to be proportional to the acoustic frequency: $\alpha_{s,r}=f/\nu_{s,r}$ and $\alpha_{l,r}=0.69f/\nu_{l,r}$ ($\alpha_{l,r}=230$ m^{-1} for $f=0.6$ MHz).

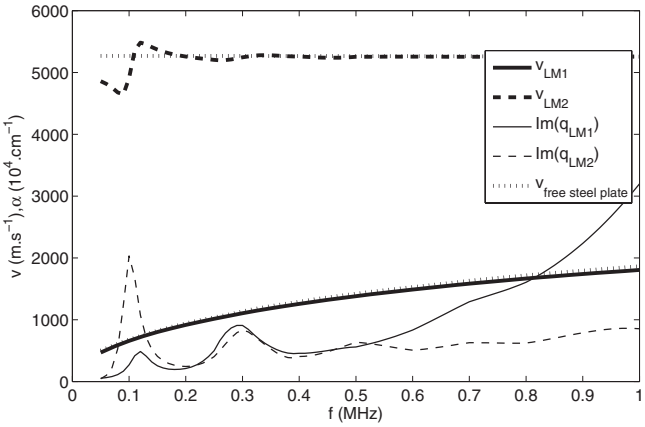


FIG. 2. Dispersion curves (full and dashed lines) of Lamb modes in a steel-rubber bilayer ($d_1=d_2=0.5$ mm). The dotted curves correspond with the A0 and S0 modes in a free 0.5 mm steel plate. The bold curves correspond with the real part of the propagation velocity of the LM1 (dashed lines) and LM2 (full lines) modes, while the thin curves correspond with the imaginary part of their wave numbers.

The relative difference between the real parts of the phase velocities of these bilayer Lamb modes, from here on referred to as "LM1" and "LM2" modes, and the respective fundamental modes A0 and S0 of a free steel plate of the same thickness is less than 5%. Also the rubber-induced absorption is quite weak. This is due to the fact that the energy flow of these modes is mainly concentrated in the steel layer (about 97.6%) for the LM1 mode and very close to 100% for the LM2 mode for $f=0.6$ MHz. The LM1 and LM2 mode wave numbers $q_{\mathrm{LM1,2}}$ are, respectively, $q_{\mathrm{LM1},z}\approx(25.334+0.083i)$ cm^{-1} and $q_{\mathrm{LM2},z}\approx(7.173+0.051i)$ cm^{-1} for $f=0.6$ MHz. The damping of the LM1 and LM2 modes moderately increases with increasing frequency, showing a maximum around the rubber layer cutoff frequencies. In this frequency interval, there exist also rubber-layer-like modes with high attenuation coefficients.

When a propagating Lamb mode enters the delamination region, the possible propagating modes and an infinity of (almost) nonpropagating local Lamb modes can be excited at the delamination end points $z=0,L$ (L is the delamination length), creating a total mechanical displacement given by expansions over these eigenmodes [see, for example, Eqs. (3) and (4)]. To calculate the normal displacement amplitude u_y at the bilayer surfaces for this case, it is in principle necessary to solve an infinite system of linear equations [Eq. (5)–(8) for the case of ordinary delamination] with the coefficients of the eigenmodes as unknowns. In practice, this system is solved numerically by truncating the expansions, taking into account only a finite number of local modes and using orthogonality relations between eigenmodes, resulting in a finite set of equations with as many equations as unknowns.

H. Calculation accuracy

As a validation of the calculation method, we have assessed the energy conservation law errors δ_0 and δ_L at the delamination end planes $z=0,L$ as follows:[13]

$$\delta_{0,L}=(P^{+}(z=0,L)-P^{-}(z=0,L))/P_{\mathrm{in},0}, \tag{13}$$

with $P_{\mathrm{in},0}$ as the incident acoustic energy flow brought by the incident mode. $P^{+,-}$ are the energy flows at the respective sides of the end planes $z=0,L$. Note that the $\delta_{0,L}$ values are mainly related to the calculation error for the propagating modes and do not reflect much on the calculation error of the

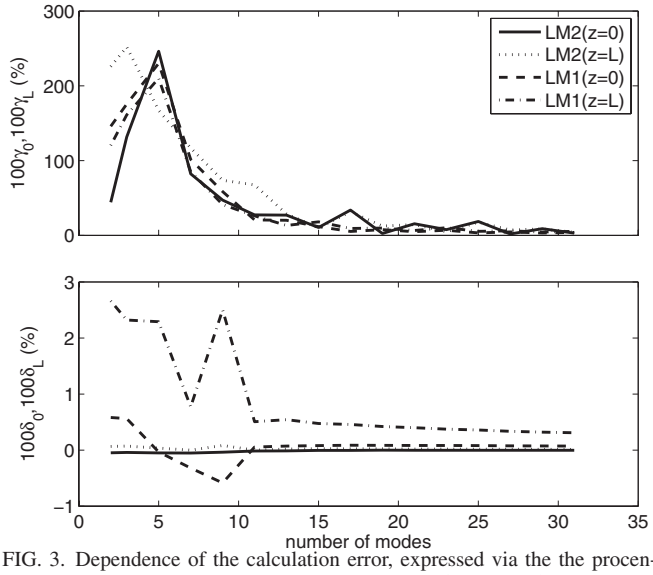


FIG. 3. Dependence of the calculation error, expressed via the the procentual normal displacement mismatch parameter γ (upper plot) and via the energy nonconservation parameter δ (lower plot) evaluated at the $z=0$ and $z=L$ interface on the number of Lamb modes taken into account in the modal decomposition. Results are shown for a rubber-steel bilayer with incident LM1 ($z=0$ interface: dashed line; $z=L$ interface: dash-dot line) and LM2 ($z=0$ interface: full line; $z=L$ interface: dotted line) modes.

nonpropagating modes since their contribution to the total energy flow is usually very small or zero. Therefore it is more useful to estimate the calculation error on the basis of the fulfillment of the boundary condition at the delamination end planes since the mechanical displacement amplitude must be all over continuous along the z-coordinate. In view of this, the relative calculation error can, e.g., be estimated by the dimensionless relative normal displacement discontinuity parameter $\gamma_{\zeta,\varepsilon}=|\Delta u_y(y=\varepsilon,z=\zeta)/u_{y,\mathrm{in}}(y=\varepsilon,z=\zeta)|$, with $\varepsilon=0$ or d and $\zeta=0$ or L.

A typical dependence of the relative energy conservation and displacement mismatch values at the free rubber surface on the number of modes taken into account is shown in the upper plot of Fig. 3 for LM1 and LM2 incident modes and a stress-free delamination length $L=1$ cm. The discontinuity values at the free steel surface $y=0$ are much smaller and therefore not shown. In the selection procedure of local modes taken into account in the truncated expansion, priority was given to modes with the lowest wave number modulus. It is important to mention that in order to reach satisfactory convergence while incrementing the expansion, local modes with both positive and negative real parts of the wave number should be taken into account. At least about 30 modes had to be included to reach a satisfactory level of calculation errors $[\gamma_{0,L}\sim(3-5)\%$ on the rubber surface $y=d$ and $\delta_{0,L}<0.5\%$ for $N_m\approx 30]$.

In the numerical mode conversion calculations for dynamically varying states of the delamination structure in Secs. III and IV, 31 right-going waves (and 31 left-going, where applicable) were taken into account in every subregion. This came down to solve, for every modulation state, 186 equations for an ordinary delamination and twice as many (372) for the threefold delamination structure shown in Fig. 1.

III. UNIFORM DELAMINATION CLAPPING

In this section, we calculate the simplest case of the modulation of the reflection, transmission, and mode conversion of an incident probing Lamb wave by a delamination that is uniformly clapped over its whole length L. In this case, one can consider $z_1=z_2$ in Fig. 1. We presume a periodical on-off type artificial external modulation force with period T. The mechanical contact between the steel and rubber layer is assumed to be either stress-free ('open' state during time interval with duration τ) and either 'perfect' or 'slip' otherwise ('closed' state during the remaining time interval with duration $T-\tau$). $T\gg 1/f$ is chosen so that a quasistationary approach can be used; i.e., the normal mechanical displacement around the delamination region is calculated separately for the two extreme stationary states, $U_{\mathrm{open}}(y,z)$ and $U_{\mathrm{closed}}(y,z)$, using the model described in Sec. I. The switching time between the "stress-free" and the perfect (or slip) mechanical contacts between the steel and rubber layers is assumed to be negligible. Under these assumptions, the full (real part of the) dynamical normal mechanical displacement $U_y(y,z,t)$ can be written as follows:

$$U_y(y,z,t)=u_y(y,z,t)e^{-i\omega t}+(u_y(y,z,t))^*e^{i\omega t}, \tag{14}$$

where for every cycle $[0,T]$ of the modulation $u_y(y,z,t)$ corresponds with $u_{y,\mathrm{closed}}(y,z)$ for $0\leqslant t_{\mathrm{cycle}}<\tau$ and with $u_{y,\mathrm{open}}(y,z)$ for $\tau\leqslant t_{\mathrm{cycle}}<T$, with t_{cycle} as the elapsed time counted from the beginning of the cycle.

The Fourier transform of the time periodic function $u_y(y,z,t)$ is given by

$$u_y(y,z,t)=\sum_{n=-\infty}^{n=+\infty}u_{y,n}(y,z)e^{in\Omega t}, \tag{15}$$

where $\Omega=2\pi/T$ and

$$u_{y,n}(y,z)=T^{-1}\int_0^T u_y(y,z,t)e^{-in\Omega t}dt. \tag{16}$$

In the case of a square wave type modulation with duty cycle τ/T, the expressions for the Fourier harmonics are given by

$$u_{y,n=0}(y,z)=(u_{\mathrm{open}}(y,z)-u_{\mathrm{closed}}(y,z))\tau/T+u_{\mathrm{closed}}(y,z), \tag{17a}$$

$$u_{y,n\neq 0}(y,z)=(u_{\mathrm{open}}(y,z)-u_{\mathrm{closed}}(y,z))\times\exp(-in\pi\tau/T)\sin(n\pi\tau/T)/\pi n. \tag{17b}$$

The numerical evaluation of Eqs. (17a) and (17b) requires the calculation of $u_{\mathrm{open,closed}}(y,z)$ by solving the system of Eqs. (5)–(12) for the configuration of interest. $u_{\mathrm{open}}(y,z)$ is calculated for static stress-free conditions, while depending on the chosen configuration $u_{\mathrm{closed}}(y,z)$ is calculated for a slip or for a perfect mechanical contact between rubber and steel.

Since in our model the nonlinear effects for the case of uniform modulation are simply related to the difference between u_{open} and u_{closed}, in the following, we will first focus

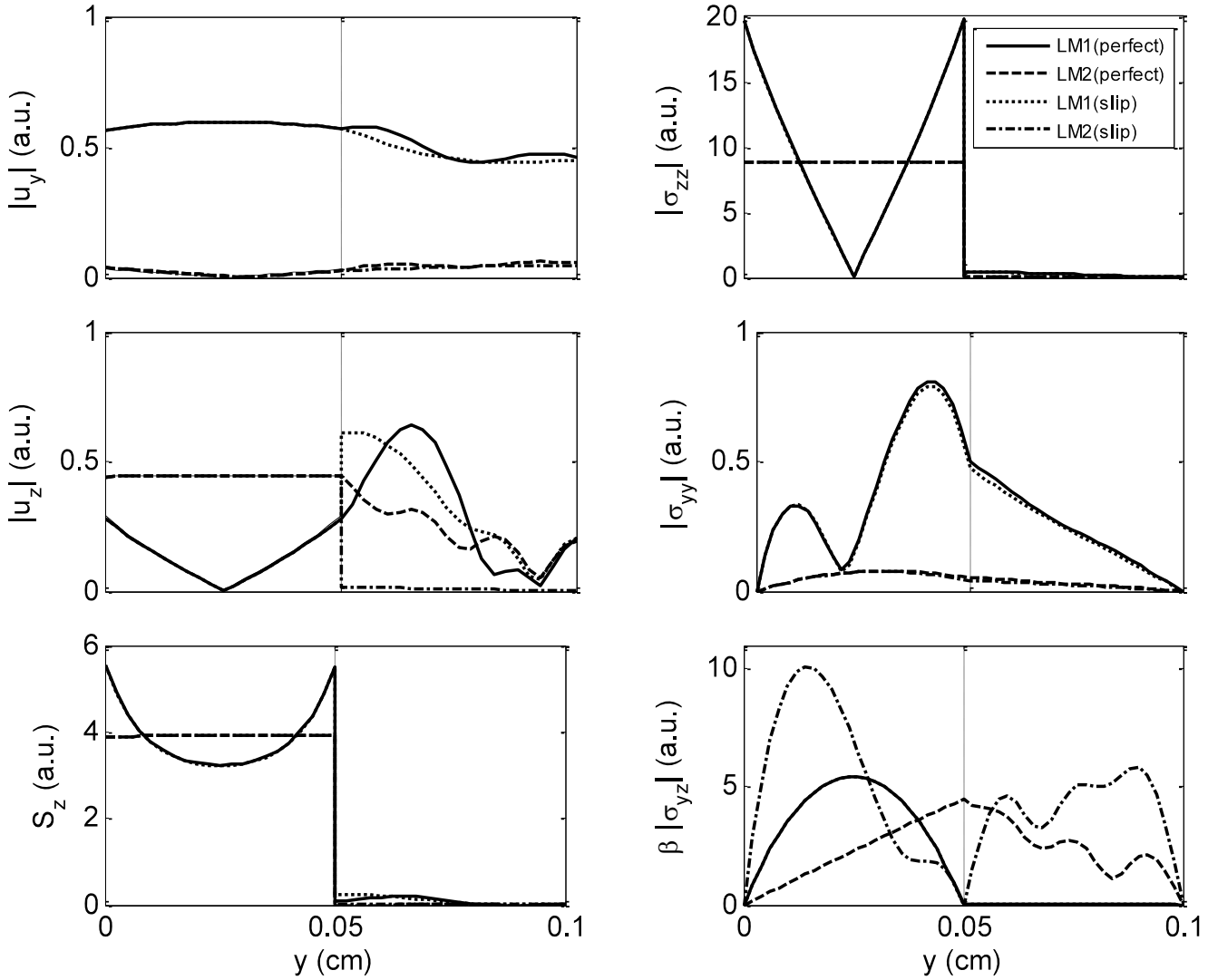


FIG. 4. Position dependence in the direction normal to the bilayer of the magnitude of the mechanical displacement components u_y (top left) and u_z (middle left), the stress components σ_{zz} (top right), σ_{yy} (middle right), and $\beta\sigma_{yz}$ (bottom right), and the energy flow S_z (bottom left) of the LM1 and LM2 modes for perfect (LM1: full line; LM2: dashed line) and slip (LM1:dotted line; LM2: dash-dot line) contacts at the interface of a steel-rubber bilayer. The σ_{yz} scaling factor $\beta=1$ for the LM1 mode (perfect and slip contacts), $\beta=100$ for the LM2 mode with a perfect contact, and $\beta=10^4$ for the LM2 mode with a slip contact. The used probing frequency is $f=0.6$ MHz.

thereon (Figs. 4 and 5) and then to its effect for harmonic generation (Figs. 6–8) when the state of the contact is periodically switched.

In spite of the wave energy of the LM1 and LM2 modes being dominantly localized in the steel layer, we will mainly focus on the free rubber surface component ($y=d$). This choice is supported by the depicted displacement cross-sections for different contact conditions in Fig. 4 ($d=0.1$ cm, $d_1=0.05$ cm). In spite of the strong localization of the acoustic energy (Fig. 4, bottom left) and tangential stress (Fig. 4, top right) in the steel layer due to the low density of rubber and the wave penetration depth being of the order of the rubber layer thickness, in the case of a closed contact, the normal (Fig. 4, top left) and tangential (Fig. 4, middle left) mechanical displacement components for these modes are fairly spread over the whole cross-section of the bilayer. Therefore, the displacement behavior at both free bilayer surfaces carries information about the inner plate structure and the nature of the delamination. In particular, if nonzero rubber displacement is observed in the delamination zone, then this is a reliable indicator for the contact being closed.

The middle left plot in Fig. 4 also illustrates that in the case of slip contact, quite a large discontinuity in the tangential displacement u_z can occur between rubber and steel. However, this discontinuity is not taken into account in our closing criterion [Eq. (1)] since the mechanical behavior of the interface boundary is most crucially determined by the normal displacement mismatch in open conditions. Also the stresses (Fig. 4, right plots), which would be very relevant for the opening/closing response of a delamination in normally closed delaminations, are high at the interface.

Note that as a more sophisticated closing criterion, one could also involve the tangential displacement discontinuity (as depicted in the middle left plot of Fig. 4) or, when assuming continuous contact conditions at rest, the magnitude of the normal strain at the interface.

In view of illustrating the effect of open and closed contact conditions on experimentally accessible quantities, the

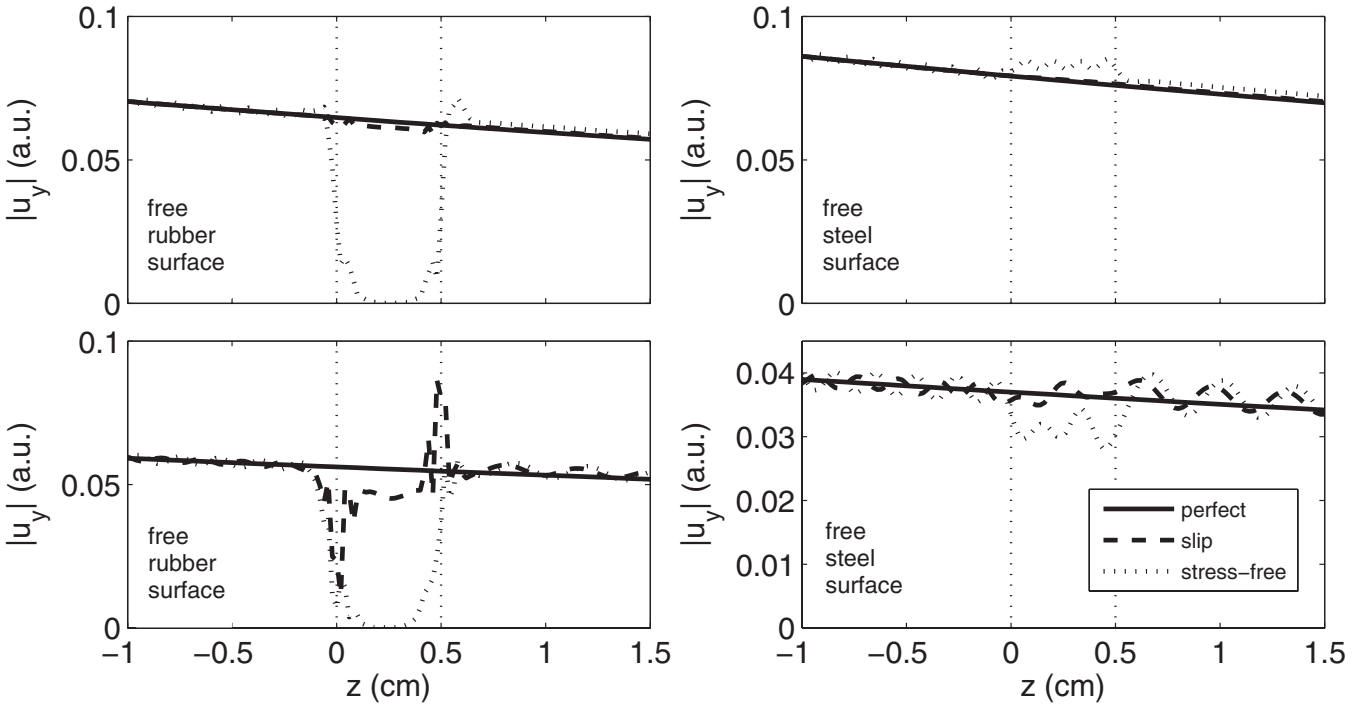


FIG. 5. Tangential evolution of the normal displacement magnitude at the free rubber (left plots) and steel (right plots) surface of LM1 (upper plots) and LM2 (lower plots) probing waves in the neighborhood of an $L=0.5$ cm delamination for perfect (full line), slip (dashed line), and stress-free (dotted line) mechanical contact conditions at the steel-rubber interface. The probing frequency $f=0.6$ MHz.

tangential dependence of the normal displacement at the free rubber surface, calculated for stress-free and slip delaminations of length $L=0.5$ cm, is shown in the plots on the left in Fig. 5. With the delamination open, the normal rubber surface is almost motionless because waves cannot be carried by the strongly absorbing rubber alone. In this case the steel-born waves travel unattenuated and independent of the rubber. On the other hand, where and when the perfect/slip mechanical contact is completely/partially restored (delamination closed) by the modulating wave, then in the normal direction the rubber layer moves more or less together with the energy carrying steel layer (see the top left plot of Fig. 4); in this case the steel-born wave is more attenuated than that for an open delamination. Also in the case of slip contact, the restoration of the contact in the normal direction, induced by a satisfied closing criterion due to the modulating wave, is quite good, such that the normal displacement is to a great extent transmitted to the rubber. In summary, the nonlinear closing of a delamination that is open at rest would easily be observed, but it is quasi-impossible to extract from the displacement characteristics whether the closed state is in a perfect or in a slip contact.

A comparison between the upper and lower left plots in Fig. 5 learns that for normal displacement detection on the rubber side, the delamination contact condition affects differently the transmission of the LM1 (slight increase) than the one of the LM2 (oscillations) mode due to the higher attenuating effect of the rubber for LM1. On the other hand, for a situation where a delamination is in perfect contact in the rest conditions, then in the delamination region the transmitted LM2 is more sensitive (oscillations) to modulation induced slip. The motion and stresses of the S0-like LM2 mode are mainly tangential along the steel-rubber interface (see Fig. 4), and thus the coupling between the rubber and steel motion is strongly affected by slip.

On the steel side (right plots in Fig. 5), which is usually the accessible one in nondestructive testing conditions for an inspection of rubber-protected steel containers of chemicals or pipelines,[34,35] the effect of the delamination on the tangential dependence of the normal displacement is limited to the occurrence of rather weak oscillations. In particular the difference between perfect and slip conditions is very small, both for LM1 and LM2. The oscillatory effect of the open delamination on the LM2 wave can be explained by the complex interference conditions between different wave modes in the transmission region, which travel at different velocities.

Figure 6 shows the tangential dependence of the fundamental wave and of the lowest ($n=1$) and second lowest ($n=3$) modulation induced harmonics of the normal displacement at the free rubber (left plots) and steel (right plots) surfaces. In practice this signal could, e.g., be collected as the amplitude of the spectral mixing frequencies $\omega+\Omega$ and $\omega-\Omega$ of an experimentally detected normal displacement signal or, via a lock-in amplifier, monitoring at frequency Ω, the demodulated amplitude of the displacement signal at frequency ω. In Eqs. (17a) and (17b), the Fourier harmonic index n appears only in the factor behind the displacement discontinuity factor. Therefore, in the case of uniform modulation, the spatial dependences of all harmonics are isomorphic; i.e., they only differ in the overall amplitude. This is clearly illustrated both in Fig. 6, which depicts nonlinear modulation of the LM1 and LM2 mode conversion due to clapping between stress-free and perfect contact conditions,

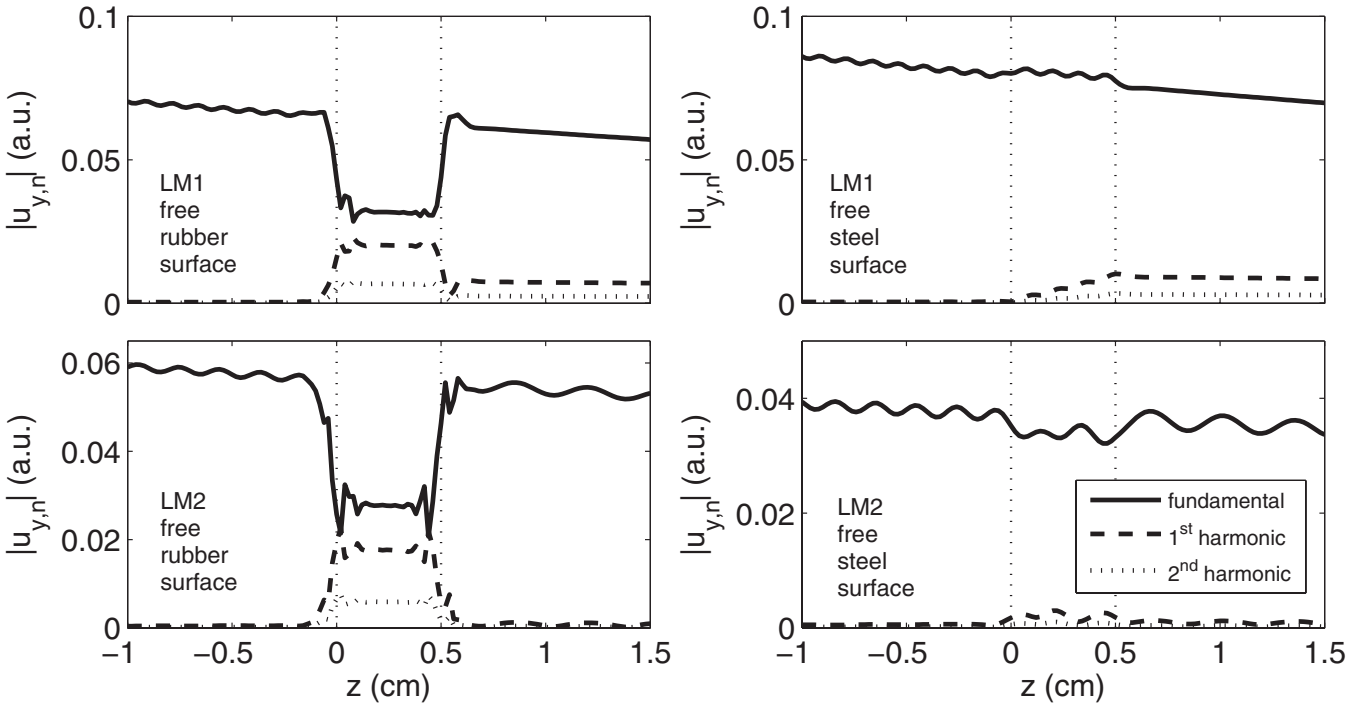


FIG. 6. Tangential evolution of the magnitude of the fundamental (full line) component and the cross-modulation frequency components with the first (dashed line) and third (dotted line) harmonics of the normal displacement of an $f=0.6$ MHz probing wave for a modulation of the contact state with 50% duty cycle ($\tau/T=0.5$). The displacement is evaluated at the free rubber (left plots) and steel (right plots) surfaces for LM1 (upper plots) and LM2 (lower plots) probing waves in the neighborhood of an $L=0.5$ cm delamination. Nonlinearly induced clapping is assumed to happen uniformly in the delamination region between stress-free and perfect contact conditions. The curves for the cross-modulation were obtained by calculating the pairwise difference between normal displacement patterns in Fig. 5.

and in Fig. 7, where stress-free–slip (upper plot) and slip-perfect (lower plot) clapping are compared. The tangential dependence of the fundamental frequency displacement, as well as of the displacement nonlinearly induced by the lowest (first) and second lowest (third) harmonics of the modulation, is shown. For the shown situation calculated for a modulation with 50% duty cycle ($\tau/T=0.5$) square wave time evolution, only odd harmonics of the modulating force mix into the converted probe wave spectrum, and the harmonic amplitudes have a simple $1/n$-dependence. The spatial dependence of the third harmonic amplitude is thus systematically equal to $1/3$ of the pattern of the first harmonic amplitude.

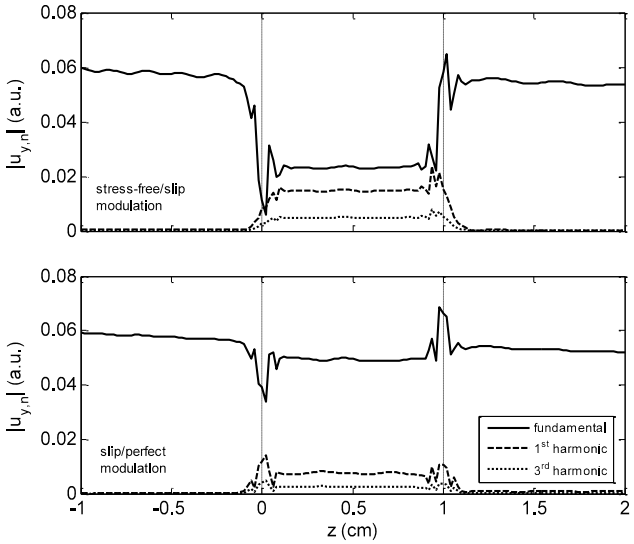


FIG. 7. Tangential evolution of the magnitude of the fundamental (full line) and the cross-modulation components with the first (dashed line) and third (dotted line) harmonics of the modulating wave of the normal displacement of an LM2 probing wave (0.6 MHz) at the free rubber surface in the neighborhood of an $L=1$ cm delamination. Clapping modulation with 50% duty cycle is considered between stress-free and slip (upper plot) and between slip and perfect (lower plot) mechanical contact conditions at the steel-rubber interface.

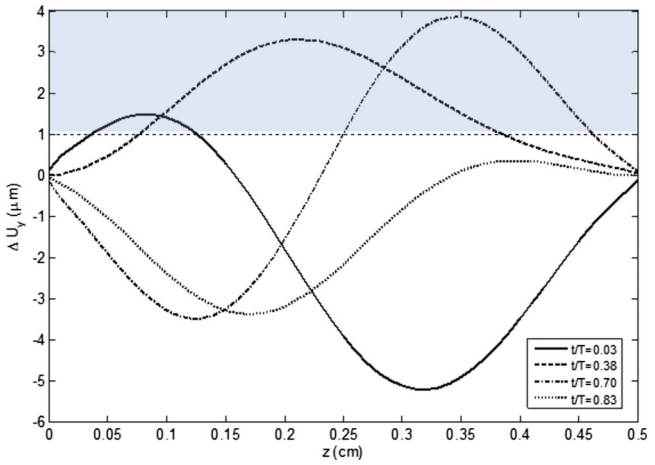


FIG. 8. (Color online) Tangential profile of rubber-steel displacement difference ΔU_y for different instants in the vibration cycle ($t/T=0.03$: full line, $t/T=0.38$: dashed line, $t/T=0.70$: dash-dot, and $t/T=0.83$: dotted line) of an LM1 mode ($\Omega=20$ kHz) of 1.47 W cm^{-1} power density incident on an $L=0.5$ cm delamination. According to our choice of closing criterion with $d_{crit}=1$ μm, the implication of the large modulating wave displacement is that the delamination becomes closed for all z-values for which the mismatch curve lies in the darkened zone above the horizontal dotted line, giving rise to a threefold clapping structure with two open outer parts and a closed inner part, except for $t/T=0.83$ where there is no clapping.

Since in Eqs. (17a) and (17b) the nonlinear signals are proportional to the difference between the stationary solutions for the two delamination states, all clapping-induced signals in Figs. 6 and 7 can be easily deduced from the difference between pairs of curves in Fig. 5. As can be expected in Fig. 5, the motion polarization of LM1 and LM2 explained earlier, the state of the delamination affects the displacement dynamics only locally for an incident LM2 mode (Fig. 7), while also in transmission of an incident LM1 mode, particularly for a long delamination length L. Comparing Fig. 7 to Fig. 6 confirms that for a delamination which is stress-free at rest, the induced modulation effects to, respectively, slip and perfect contact conditions are very similar. On the other hand, as explained earlier, slip/perfect modulation (lower plot in Fig. 7) results in smaller but still quite significant harmonic generation for the slip-sensitive LM2 mode. This is much less the case for LM1, whose motion is mainly polarized normal to the rubber-steel interface.

As mentioned before, in practical circumstances, mainly the steel surface is technically accessible for displacement evaluation. The right plots in Fig. 6 show that the fundamental probing frequency displacement characteristics are only weakly affected by the presence of a delamination. However, the clapping of the delamination evokes clearly cross-modulation frequencies above the delamination and, in the case of LM1, also in the transmitted zone. Without clapping, there would be no spectral cross-modulation components. As a consequence, detecting spectral conversion yields a high-contrast technique for delamination detection with high spatial resolution, especially when using the LM2 mode.

We have also studied the dependence of harmonic generation on the length L of the delamination. Roughly speaking, for small L, the degree of harmonic generation increases with L and saturates for $L \cong 0.02$ cm. The influence of defect size on nonlinear scattering is thus similar to the case of linear scattering.

IV. MODULATION BY LOW FREQUENCY MODULATING WAVE

A. Essentials of the followed approach

The previous case of the interaction of a probing Lamb wave with a delamination whose contact situation is uniformly switched over its whole length was very instructive but not fully representative for practical situations. In this section we treat the more realistic situation of a periodical, high amplitude, long wavelength incident Lamb wave that enters the metastable delamination region and therefore changes the quality of the boundary between the two layers. As a result, the reflection, transmission, and mode conversion coefficients for a low amplitude, high frequency mode probing the same region are time modulated, resulting in cross-modulation and frequency mixing.

Before illustrating the approach by concrete case studies, we summarize the made assumptions and their consequences of our approach. (1) The high amplitude modulating wave locally (cross-) modulates the boundary conditions for the probing wave, but not for itself. Self-modulation is thus neglected. (2) The frequency of the modulating wave is chosen much lower than the one of the probing wave, so that a quasistationary approach can be used; i.e., the time dependence of the nonlinear modulation of the probing wave is assessed by calculating, using the previously described modal expansion method, its mode conversion for stationary "frozen" delamination contact conditions. (3) Those are calculated for every temporal phase of the modulating wave according to the earlier described closing criterion [Eq. (1)] that is based on the nonsynchronicity between the normal displacements of the partial waves in the upper and lower layers in unbound conditions. As explained in the previous section, at every temporal phase of the modulation cycle, due to the long wavelength of the modulating wave and due to the nature of the closing criterion, the delamination has a slowly varying three-fold sectioned structure. (4) As a result of the followed approach, the dynamical displacement pattern of the incident probing wave interfering with the respective reflected and transmitted waves is amplitude and phase modulated according to the slow periodically changing rhythm that contains the fundamental frequency of the modulating wave and its harmonics. Since the total displacement contains products of sinusoidally varying functions at frequency ω (probe wave and mode converted waves) and mode conversion coefficients varying at multiples of Ω, the frequency of the modulating incident wave, this results in a very rich frequency content in the global spectrum of the experimentally accessible dynamical normal surface displacement. Besides the fundamental frequency of the probing wave at frequency ω, its sums and differences with the modulating wave frequency Ω and its multiples $2\Omega, 3\Omega, \ldots$ are present in the spectrum. (5) Since the closing criterion is nonlinear and since the relation between the mode conversion coefficients and the contact conditions is nonlinear, the spectral content of the modulated probe wave depends strongly and nonlinearly on the amplitude of the modulating wave, on the mismatch between the modulating wave components of the upper and lower layers, and on the parameter d_{crit} in the closing criterion. (6) The probing wave has a small amplitude and therefore does not modulate the boundary conditions. This approximation is easy to achieve.

B. Simulation conditions for rubber-steel bilayers

We start to illustrate the followed approach and its consequences by the simulation of the case of a high amplitude, low frequency ($\Omega = 20$ kHz) LM1 mode entering a delamination region in the earlier described rubber-steel bilayer. At this frequency (see Table I), the wave number of the wavelength $\lambda_{\mathrm{LM1}} \approx 1.5$ cm is somewhat larger than the delamination lengths L under consideration and much larger than the wavelength of the probing wave. The acoustical linear power density P_z (in W/cm) for the modulating wave is given by (see Refs. 12 and 33)

$$P_z = 4\pi f |C_{\mathrm{in}}|^2 F_0, \tag{18}$$

with C_{in} the expansion coefficient of the incident LM1 mode [see, e.g., Eq. (2)] and

$$F_0 = \mathrm{Im}\left(\int_0^d dy (\sigma_{zz,\mathrm{in}}^{\mathrm{LM1}} (u_{z,\mathrm{in}}^{\mathrm{LM1}})^* - (\sigma_{yz,\mathrm{in}}^{\mathrm{LM1}})^* u_{y,\mathrm{in}}^{\mathrm{LM1}}) \right) \quad (18a)$$

is calculated for the stress tensor and mechanical displacement vector components integrated over a cross-section of the bilayer. The average acoustic intensity over a cross-section of the bilayer can be evaluated as P_z/d. Introducing all material and geometrical parameters in the LM1 modal profiles for stress and displacement calculated in Ref. 12 into Eq. (18) gives the following approximate relation between the (closed) delamination interface displacement $|u_y(y=d_1)|$ (in micron) and the linear power density P_z:

$$|u_y(y=d_1)| \approx 1.09\sqrt{P_z}. \quad (19a)$$

In practice, we have chosen *ad hoc* $P_z = 1.47$ W cm^{-1}, corresponding to $|u_y(y=d_1)| \approx 1.32$ μm, a value that is of the order of $d_{\mathrm{crit}} = 1$ μm, so that, given the closing criterion Eq. (1), the incident wave can be expected *a priori* to locally open and close the delamination with a rhythm depending (in a complex way) on the temporal phase of the modulating wave. The displacement discontinuity used in the closing criterion can be explicitized as

$$\Delta U_y(z) = U_y(z, y=d_1^-) - U_y(z, y=d_1^+) = 2|u_y(z, y=d_1^-) - u_y(z, y=d_1^+)|\cos(\phi(z) - 2\pi t/T), \quad (19b)$$

with $\phi(z) = \arg(u_y(z, y=d_1^-) - u_y(z, y=d_1^+))$. Its tangential dependence is shown for different temporal phases of the modulation cycle in Fig. 8 for delamination length $L = 0.5$ cm. The displacements were calculated using 43 modes in all parts of the structure under consideration, and the relative error for the amplitude of delamination thickness modulation at the end points $z = 0, L$ was about 5%. A comparison of the displacement discontinuity pattern with the closing threshold level at $\Delta U_y = d_{\mathrm{crit}}$ learns that for a range $t_a < t < t_b$ of temporal phases in the cycle $[0, T]$ the closing criterion is fulfilled in an interior region between $z = z_1$ and $z = z_2$, while due to continuity the exterior regions around the two end points $z = 0$ and $z = L$ are never closing. This results, as announced in Sec. II, in a dynamically changing threefold delamination structure. The temporal phase dependence of z_1 and z_2, and of the width $z_2 - z_1$ of the closed section, is shown in the upper ($L = 0.3$ cm) and lower ($L = 0.5$ cm) plots of Fig. 9, respectively. For $L = 0.3$ cm, the closing criterion is locally fulfilled for $0 \leqslant t/T \leqslant 0.46$. For the longer delamination $L = 0.5$ cm, the closing criterion has more probability to be fulfilled because the partial waves in the individual layers have more distance (far from the edges $z = 0, L$) to develop normal displacement differences, resulting in a longer duration of the modulation induced closed state, i.e., for $0 \leqslant t/T \leqslant 0.81$. Note that the higher the nonlinearity of the temporal phase dependence of z_1 and z_2 is, the more complex and rich is the spectrum of a probing Lamb wave interacting with the dynamically changing sectioned delamination.

Figure 10 illustrates the cross-modulation effect of the clapping delamination described in the lower plot of Fig. 9 ($L = 0.5$ cm) and for clapping between stress-free and perfect mechanical interface contacts by showing the z-dependence of the magnitude of some nonlinearly induced cross-

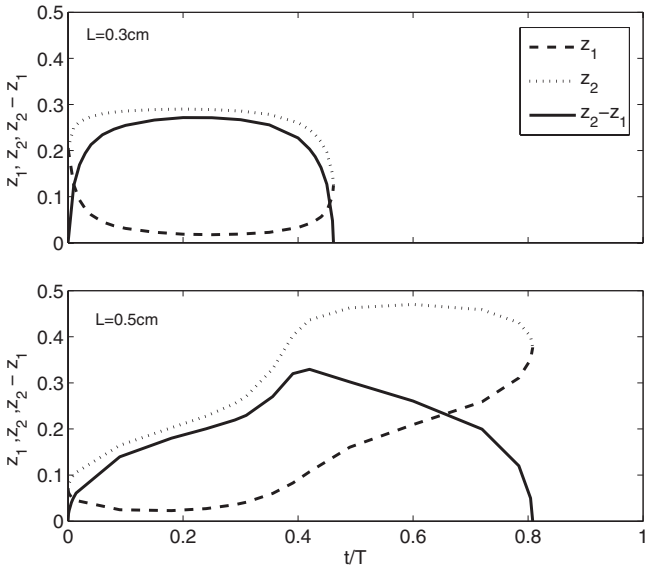


FIG. 9. Temporal evolution of the length of the three delamination sections for $L = 0.3$ cm (upper plot) and $L = 0.5$ cm (lower plot): z_1 (dashed line) and z_2 (dotted line) correspond with the open outer parts, and $z_2 - z_1$ (full line) to the clapping part where the closing criterion is fulfilled.

modulation frequencies at the free rubber (left plots) and steel (right plots) surfaces for incident probing LM1 and LM2 waves. Because of our choice for the delamination being stress-free in nonmodulated conditions, the presence of the delamination is also very clear in the fundamental frequency of the probing wave when the normal displacement is detected on the rubber side. However, at the steel side, the fundamental frequency is only weakly affected by the presence of the delamination, but here the existence and pattern of the cross-modulation frequencies are clearly linked with the delamination. The higher the mixing frequency, the stronger the exclusive localization of the harmonic in the delamination area. The same is typically true for modulation between stress-free and slip contacts. As mentioned earlier, comparing Fig. 7 to Fig. 6 confirms that for a delamination, which is stress-free at rest, the induced modulation effects to respectively slip and perfect contact conditions are very similar. Thus, detecting frequency mixing can be of great help to detect and localize delaminations with high contrast in practical NDT situations where typically only the steel side is experimentally accessible.

Note that contrary to the more artificial case of uniform clapping, in the case of modulation by a high amplitude, low frequency incident Lamb wave, the different frequency components have different patterns due to the nonlinear dependence of the delamination geometry (described by the parameters z_1 and z_2) on the temporal phase of the modulation cycle.

C. Aluminium-steel bilayers

For completeness, and using the same model, we also give a brief overview of the situation for nonabsorbing (aluminium-steel) bilayers, focusing on the differences with the previous situation for absorbing bilayers. In the case of an aluminium-steel bilayer, the nonsynchronism between the phase velocities of the partial (low frequency) modulating

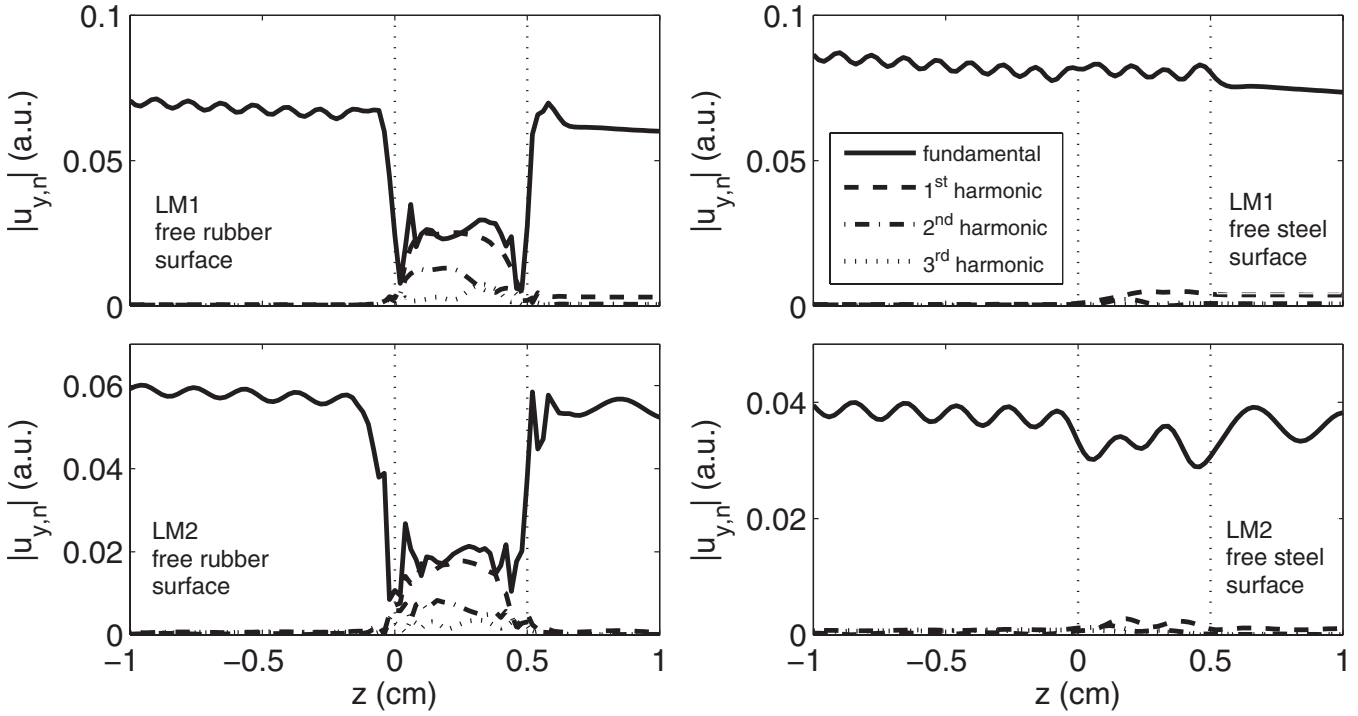


FIG. 10. Tangential evolution of the magnitude of the fundamental frequency component of the normal displacement of a 0.6 MHz probing wave (full line) and cross-modulation components with the first (dashed line), second (dash-dot line), and third (dotted line) harmonics of a modulating wave (Ω=20 kHz). The normal displacement component is considered at the free rubber (left plots) and steel (right plots) surfaces of LM1 (upper plots) and LM2 (lower plots) probing waves (f=0.6 MHz) in the neighborhood of an L=0.5 cm delamination for modulation induced nonuniform and time dependent clapping between stress-free and perfect contact conditions.

waves in the upper and lower layers in stress-free delamination conditions is much smaller than in the case of rubber-steel. As a result, the normal displacement mismatch between them is also smaller, such that a much higher acoustic power is needed (in our simulation we increased P_z more than 50 times) to switch on the closing criterion and to induce nonlinear effects on a probing wave.

For the partial waves in both the aluminium and steel layers, the state of the contact is important for the displacement amplitude: it is easier to move an aluminium or steel layer alone than a composite aluminium-steel layer. Therefore, the nonlinear effect of the closing delamination on the displacement pattern of a probing wave is quite significant and rather localized around the clapping site, with one exception. Namely, for long delamination lengths and for stress-free/slip clapping, the partial probing waves have available a long distance to develop a motional phase difference induced by their different phase velocity. As a result, the transmitted and reflected waves at the fundamental frequency in open delamination conditions are strongly affected by interference effects between the two partial waves recombining and mode converting with a significant phase mismatch at z=0 and z=L. This displacement phase mismatch strongly depends on their velocity mismatch and on the delamination length, and its effect on the recombination remains very strong outside of the delamination due to the slow beating between the LM1 and LM2 modes (one of which corresponds to, respectively, the incident and converted modes). For the same reason, also all higher harmonics are weakly localized in this case.

V. CONCLUSION

The nonlinear interaction between a high frequency probing Lamb wave and a locally delaminated bilayer, whose geometrical parameters were periodically changing due to an artificial uniform source and due to a low frequency modulating Lamb wave, was modeled using a quasistationary approach. For every temporal phase of the modulating wave, when implementing a closing criterion that was based on the normal displacement jump between the partial waves in the upper and lower layers, a threefold sectioned contact geometry of the delamination was found. Based on the derived delamination structure, the reflection, transmission, and mode conversion coefficients for the incident probing wave were calculated using a modal decomposition method. In this approach, for a given incoming Lamb wave, a basis set of Lamb waveforms for the reflected and transmitted waves is considered with coefficients calculated in order to satisfy boundary conditions at the outer sides of the bilayer and the inner interface. As a result of the dynamically changing interaction, cross-modulation occurred, leading to a frequency mixing process and an enrichment of the frequency spectrum of the normal displacement signal evaluated at the free surfaces of the bilayer. Both nonattenuating and attenuating bilayers were investigated, generally showing a significant localization of the generated frequencies around the delamination and an improved delamination detection contrast of the harmonics with respect to the fundamental probing frequency. A closed delamination with slip contact behaves very similar to one with perfect contact and quite different from one with stress-free contacts. In the case of a

rubber-steel bilayer, the impact of nonlinear frequency mixing is quite localized at the delamination site, indicating that for this kind of material the detection of sum and difference frequency components can be an efficient tool to detect hidden delaminations with higher contrast and spatial resolution than detecting mode conversion effects at the probing frequency, as is done in linear acoustics. For the aluminium-steel bilayer, the localization of nonlinear effects was less pronounced.

The advantage of the followed semianalytical approach, with different frequencies of the modulating and probing waves, is that different effects remain clearly separated, improving our insight in the complex phenomenon of nonlinear interaction. In a future step, it will be necessary to also include self-modulation, i.e., the phenomenon where the modulating wave itself is influenced by the interfacial contact changes that it has created. This could be done in an iterative approach by sequentially calculating the modulating wave pattern for a given delamination structure, modifying the delamination state according to a closing criterion, recalculating the modulating wave pattern for the modified geometry, etc.

In the followed approach, the contact criterion was based on a delamination interface whose state was stress-free at rest and only closed (to a mechanical slip or perfect contact state) if the above described normal displacement mismatch exceeded a threshold value. Although many aspects of the phenomenology of the nonlinear wave-defect interaction are qualitatively nicely predicted by this model. In the future, we will address the more realistic model, where the delamination is closed at rest—and thus invisible for Lamb waves linearly interacting with it—and opened according to an alternative criterion, e.g., based on the normal or shear stress gradient across the delamination exceeding some threshold value. Also, we envisage a nonlinearity inducing dynamic contact condition, which depends in a continuous way on the normal interface strain.

ACKNOWLEDGMENTS

The authors would like to thank the Research Council of the K. U. Leuven for the fellowship awarded to Professor G. N. Shkerdin and for financial support provided by Project No. OT/07/035, which enabled us to perform this research.

[1]B. A. Auld and M. Tan, "Symmetrical Lamb wave scattering at a symmetrical pair of thin slots," Ultrason. Symp. Proc. **1977**, 61–66.
[2]M. Tan and B. A. Auld, "Normal mode variational method for two and three dimensional acoustic scattering in an isotropic plate," Ultrason. Symp. Proc. **1980**, 857–861.
[3]S. Rokhlin, "Interaction of Lamb waves with elongated delaminations in thin sheets," Int. Adv. Nondestr. Test. **6**, 263–285 (1979).
[4]S. Rokhlin, "Diffraction of Lamb waves by a finite crack in an elastic layer," J. Acoust. Soc. Am. **67**, 1157–1165 (1980).
[5]S. Rokhlin, "Resonant phenomena of Lamb waves scattering by a finite crack in a solid layer," J. Acoust. Soc. Am. **69**, 922–928 (1981).
[6]L. Wang and J. Shen, "Scattering of elastic waves by a crack in an isotropic plate," Ultrasonics **35**, 451–457 (1997).
[7]M. Castaings, E. Le Clezio, and B. Hosten, "Modal decomposition method for modeling the interaction of Lamb waves with cracks," J. Acoust. Soc. Am. **112**, 2567–2582 (2002).
[8]M. J. Love, P. Cawley, J.-Y. Kao, and O. Diligent, "The low frequency reflection characteristics of the fundamental antisymmetric Lamb wave A0 from a rectangular notch in a plate," J. Acoust. Soc. Am. **112**, 2612–2622 (2002).
[9]P. Malischewsky, *Surface Waves and Discontinuities* (Elsevier, Amsterdam, 1987).
[10]P. Malischewsky, "Surface waves in media having lateral inhomogeneities," Pure Appl. Geophys. **114**, 833–843 (1976).
[11]T. Meier, P. G. Malischewsky, and H. Neunhöfer, "Reflection and transmission of surface waves at a vertical discontinuity and imaging of lateral heterogeneity using reflected fundamental rayleigh waves," Bull. Seismol. Soc. Am. **87**, 1648–1661 (1997).
[12]G. Shkerdin and C. Glorieux, "Lamb mode conversion in an absorptive bilayer with a delamination," J. Acoust. Soc. Am. **118**, 2253–2264 (2005).
[13]G. Shkerdin and C. Glorieux, "Interaction of Lamb modes with delaminations in plates coated by highly absorbing materials," IEEE Trans. Ultrason. Ferroelectr. Freq. Control **54**, 368–377 (2007).
[14]C. Glorieux, K. Van de Rostyne, K. A. Nelson, W. Gao, W. Lauriks, and J. Thoen, "On the character of acoustic waves at the interface between hard and soft solids and liquids," J. Acoust. Soc. Am. **110**, 1299–1306 (2001).
[15]K. Van de Rostyne, C. Glorieux, W. Gao, W. Lauriks, and J. Thoen, "Experimental investigation of leaky Lamb modes by an optically induced grating," IEEE Trans. Ultrason. Ferroelectr. Freq. Control **49**, 1245–1253 (2002).
[16]J. D. Ferry, *Viscoelastic Properties of Polymers* (Wiley, New York, 1980).
[17]F. Simonetti, "Lamb wave propagation in elastic plates coated with viscoelastic materials," J. Acoust. Soc. Am. **115**, 2041–2053 (2004).
[18]J. Wu, "Determination of velocity and attenuation of shear waves using ultrasonic spectroscopy," J. Acoust. Soc. Am. **99**, 2871–2875 (1996).
[19]C. W. Chan and P. Cawley, "Lamb modes in highly attenuative plastic plates," J. Acoust. Soc. Am. **104**, 874–881 (1998).
[20]P. H. Mott, C. M. Roland, and R. D. Corsaro, "Acoustic and dynamic mechanical properties of polyurethane rubber," J. Acoust. Soc. Am. **111**, 1782–1790 (2002).
[21]M. F. Hamilton, *Nonlinear Wave Propagation in Mechanics* (The American Mechanical Engineers, New York, 1986), Vol. **AMD-77**.
[22]N. Krohn, R. Stoessel, and G. Busse, "Acoustic non-linearity for defect selective imaging," Ultrasonics **40**, 633–637 (2002).
[23]K. Pfleiderer, N. Krohn, R. Stoessel, and G. Busse, "Defect-selective imaging by nonlinear scanning vibrometry and by nonlinear air-coupled ultrasound inspection," Proceedings of the Eighth ECNDT, Barcelona (2002).
[24]T. Stratoudaki, M. Clark, and M. G. Somekh, "Novel optical transducers for non-linear ultrasonic applications," Proceedings of ECNDT (2006), Paper No. Tu.4.7.3, http://www.ndt.net/article/ecndt2006/topic~37.htm (last viewed May 2, 2008).
[25]I. Y. Solodov, "Ultrasonics of non-linear contacts: Propagation, reflection and NDE-applications," Ultrasonics **36**, 383–390 (1998).
[26]I. Y. Solodov, N. Krohn, and G. Busse, "CAN: An example of nonclassical nonlinearity in solids," Ultrasonics **40**, 621–625 (2002).
[27]M. Meo and G. Zumpano, "Nonlinear elastic wave spectroscopy identification of impact damage on a sandwich plate," Compos. Struct. **71**, 469–474 (2005).
[28]K. Van Den Abeele, P. A. Johnson, and A. Sutin, "Nonlinear elastic wave spectroscopy (NEWS) techniques to discern material damage. Part I: Nonlinear wave modulation spectroscopy (NWMS)," Res. Nondestruct. Eval. **12**, 17–30 (2000).
[29]M. Scalerandi, V. Agostini, P. P. Delsanto, K. Van Den Abeele, and P. A. Johnson, "Local interaction simulation approach to modeling nonclassical, nonlinear elastic behavior in solids," J. Acoust. Soc. Am. **113**, 3049–3059 (2003).
[30]S. Hirsekorn, "Nonlinear transfer of ultrasound by adhesive joints: A theoretical description," Ultrasonics **39**, 57–68 (2001).
[31]G. J. Kuhn and A. Lutsch, "Elastic wave mode conversion at a solid-solid boundary with transverse slip," J. Acoust. Soc. Am. **33**, 949–954 (1961).
[32]S. I. Rokhlin and Y. J. Wang, "Analysis of boundary conditions for elastic wave interaction with an interface between two solids," J. Acoust. Soc. Am. **89**, 503–515 (1991).
[33]B. A. Auld, *Acoustic Fields and Waves in Solids* (Wiley, New York, 1973).
[34]D. N. Alleyne and P. Cawley, "The interaction of Lamb waves and defects," IEEE Trans. Ultrason. Ferroelectr. Freq. Control **39**, 381–397 (1992).
[35]P. Cawley, M. J. S. Lowe, D. N. Alleyne, B. Pavlakovic, and P. Wilcox, "Practical long range guided wave testing: Applications to pipes and rail," Mater. Eval. **61**, 66–74 (2003).

Infrasound induced instability by modulation of condensation process in the atmosphere

Konstantin Naugolnykh[a)]
NOAA, Earth System Research Laboratory and Zel Technologies, LLC, and CIRES, University of Colorado, Boulder, Colorado 80303-0000

Samuil Rybak[b)]
N. N. Andreev Acoustics Institute, 4 Shvernik Street, Moscow, 117036 Russia

(Received 2 June 2008; revised 1 October 2008; accepted 2 October 2008)

A sound wave in supersaturated water vapor can modulate both the process of heat release caused by condensation, and subsequently, as a result, the resonance interaction of sound with the modulated heat release provides sound amplification. High-intensity atmospheric perturbations such as cyclones and thunderstorms generate infrasound, which is detectable at large distances from the source. The wave-condensation instability can lead to variation in the level of infrasound radiation by a developing cyclone, and this can be as a precursor of these intense atmospheric events.
© *2008 Acoustical Society of America.* [DOI: 10.1121/1.3006377]

PACS number(s): 43.25.Lj, 43.28.Dm [OAS] Pages: 3410–3412

I. INTRODUCTION

High-intensity atmospheric events such as cyclones and thunderstorms produce strong atmospheric perturbations, where the ascending flow of warm, dense water vapor reaching a cold area transforms into supersaturated vapor with water droplets. Stormy atmospheric areas generate infrasound,[1] detectable at a large distance from the source, and this can be a precursor to intense atmospheric events.[2]

There are a variety of ways in which sound can interact with the atmosphere, including air parcels, clouds, and fog. Situations include acoustic "illumination" of a saturated air parcel, of clouds containing supercooled liquid water droplets, of clouds passing through ice crystals, and of supersaturated air parcels containing water droplets.

Atmospheric condensation processes can generate Lamb waves.[3] In addition, infrasound in the atmosphere containing a layer of supersaturated vapor and water droplets experiences attenuation.[4] Also, infrasound amplification can take place.

A thermodynamic model of infrasound amplification in a mixture of water vapor containing homogeneously distributed droplets of equal radii is suggested by Nemtsov.[5] The spontaneous increase in mixture density ρ_{eff} releases heat. The fact that during an adiabatic process the temperature increase T is accompanied by further density growth due to the adiabatic equation $T \sim \rho_{\text{eff}}^{\gamma-1}$, where γ is the specific heat ratio, leads to instability. The effects of droplet size fluctuation and droplet electrical charge were taken into account.[6]

Infrasound amplification in the atmosphere can also be connected to the process of induced instability, which we consider herein. This model is based on the theory of vapor condensation,[7] which is applied to a supersaturated vapor in the atmosphere. A sound wave in supersaturated vapor modulates the process of heat release due to condensation and then the resonance interaction of sound with the modulated process of heat input provides sound amplification. This wave-condensation instability is analogous to the wave-turbulence amplification, described by Chimonas[8] and considered comprehensively by Moiseev *et al.*,[9] who have entitled it induced nonlinear instability or a wave-turbulence dynamo. The wave-condensation instability that leads to variation in the level of infrasound radiation by a developing cyclone can provide an infrasound precursor of an intense atmospheric event.

II. MODULATION OF CONDENSATION

Consider propagation of sound in air containing water vapor and water droplets. In supersaturated vapor, containing water droplets, the process of condensation of vapor on water drop nuclei takes place. There exists a critical droplet radius a_{cr}, such that droplets become larger when $a > a_{\text{cr}}$ and evaporate when $a < a_{\text{cr}}$. In a system of droplets of different sizes small droplets evaporate while large droplets grow up at given vapor temperature.

The process of droplet variation[7] is governed by the equation

$$\frac{da}{dt} = \frac{D\Delta}{a^2}(a - a_{\text{cr}}), \tag{1}$$

where a is the liquid droplet radius, t is the time, and a_{cr} is the critical radius at the point when condensation begins,

$$a_{\text{cr}} = \frac{\sigma}{\Delta(t)}, \quad \sigma = 2\alpha v' c_{0\infty}/kT, \quad \Delta(t) = c - c_{0\infty}, \tag{2}$$

where D is the diffusion coefficient of water vapor, k is the Boltzmann constant, T is the temperature, c is the mean water vapor concentration, $c_{0\infty}$ is the concentration of saturated water vapor above a plane water surface, α is the water surface tension, and v' is the molecular volume of water, which

a)Electronic mail: konstantin.naugolnylh@noaa.gov
b)Electronic mail: samuil-rybak@rambler.ru

 © 2008 Acoustical Society of America

appears as a result of condensation. The concentration is defined in terms of the volume of water dissolved in a unit volume of gas, and $a_{cr}(0)$ is the initial value of the critical radius. $\Delta(t)$ is the dimensionless concentration difference. If droplet radius $a > a_{cr}$, it becomes larger according to Eq. (1), if $a < a_{cr}$ it diminishes and the droplet evaporates. The density of the droplet distribution as a function of its radius a in the range 10^{-1}–10 μm is, for atmospheric condition,[10]

$$\frac{dN}{da} = \frac{A}{a^3}, \quad A = 10^{-6}\ 1/\mathrm{cm}, \tag{3}$$

which is normalized in such a way that

$$N(t) = \int_{a_{\min}}^{\infty} \frac{A}{a^3} da = \frac{A}{a_{\min}^2} \tag{4}$$

is the number of droplets per unit volume, $a_{\min}$ is the minimum of droplet radius, and A is a constant. The droplet volume is $(4\pi/3)a^3$ and the volume of water content per unit volume of the atmosphere variation that appears as a result of the condensation of droplets of size is between a and $a+da$ is

$$\frac{A}{a^3} 4\pi a^2 \frac{da}{dt} = \frac{4\pi A}{a} \frac{da}{dt}. \tag{5}$$

The total water volume variation obtained as a result of integration of this equation with respect to droplet size is

$$V' = \int_{a_{\min}}^{\infty} \frac{4\pi A}{a} \frac{D\Delta}{a} (a - a_{cr}) da$$
$$= 4\pi AD\Delta \left(\frac{1}{a_{\min}} - \frac{a_{cr}}{2a_{\min}^2} \right), \tag{6}$$

where Eq. (1) is used for the velocity of droplet radius variation.

Condensation of vapor produces heat release per unit volume per unit time

$$H = \rho_w l_w V' = \rho_w l_w 4\pi AD\Delta \left(\frac{1}{a_{\min}} - \frac{a_{cr}}{2a_{\min}^2} \right) (\mathrm{erg/sl^3}), \tag{7}$$

where ρ_w is the water density and l_w is the specific evaporation of heat per water unit of mass.

Consider the modulation of the amount of heat release with respect to time induced by a sound wave. The changes of the critical radius of the droplet produce heat release variation

$$\frac{\partial H}{\partial t} = -\frac{4\pi AD\Delta}{2a_{\min}^2} \rho_w l_w \frac{\partial a_{cr}}{\partial t}. \tag{8}$$

The value of the critical radius is in reciprocal proportion to temperature according to Eq. (2). The sound wave produces variations in the vapor temperature T, and correspondingly, variation in $a_{cr}(T)$, which in the case of small supersaturation is

$$\frac{\partial a_{cr}}{\partial t} = \frac{\partial a_{cr}}{\partial T} \frac{\partial T}{\partial t} = -\frac{2\alpha v' c_{0\infty}}{kT^2\Delta} \frac{\partial T}{\partial t} = -\frac{a_{cr}}{\beta_p T} \frac{\partial p_a}{\partial t},$$

where p_a is the sound wave pressure amplitude and $\beta_p = (\partial p/\partial T)_S$ is the pressure thermal coefficient.

Correspondingly, the rate of the amount of heat release is

$$\frac{\partial H}{\partial t} = \frac{2\pi AD\Delta a_{cr}}{a_{\min}^2 T} \frac{\rho_w l_w}{\beta_p} \frac{\partial p_a}{\partial t}. \tag{9}$$

III. INFRASOUND AMPLIFICATION

Consider perturbations produced by a harmonic sound wave of the form

$$p = p_a \cos\varphi, \quad \varphi = \kappa x - \omega t. \tag{10}$$

Then the heat release is modulated with the frequency of the sound wave

$$\frac{\partial H}{\partial t} = \frac{2\pi AD\Delta a_{cr}}{a_{\min}^2} \frac{\rho_w l_w}{\beta_p} p_a \omega \sin\varphi. \tag{11}$$

The sound generation by heat discharge in a fluid is determined by[11]

$$\nabla^2 p - \frac{1}{c_0^2} \frac{\partial^2 p}{\partial t^2} = -\frac{\beta}{c_{pa}} \frac{\partial H}{\partial t}, \tag{12}$$

where β is the thermal expansion coefficient and c_{pa} is the saturated vapor specific heat at a constant pressure. In the slowly varying amplitude approximation for the harmonic wave

$$\frac{\partial^2 p}{\partial t^2} \simeq 2\omega \frac{\partial p_a}{\partial t} \sin\varphi - \omega^2 p_a \cos\varphi, \tag{13}$$

and Eq. (12) transforms into

$$-\frac{2\omega}{c_0^2} \frac{\partial p_a}{\partial t} \sin\varphi = -\frac{\beta}{c_{pa}} \frac{\partial H}{\partial t}. \tag{14}$$

Substitute the heat release modulated by sound into the right-hand side of this equation and one obtains the equation for the sound wave amplitude in the form

$$\frac{\partial p_a}{\partial t} = \frac{\beta}{c_{pa}} \frac{\rho_w l_w}{\beta_p} \frac{2\pi AD\Delta a_{cr}}{a_{\min}^2 T} c_0^2 p_a, \tag{15}$$

or

$$\frac{\partial p_a}{\partial t} = K_t p_a, \tag{16}$$

where K is the increment of the sound wave

$$K_t = \frac{\beta}{c_{pa}} \frac{\rho_w l_w}{\beta_p} \frac{2\pi AD\Delta a_{cr}}{a_{\min}^2 T} c_0^2, \tag{17}$$

which can be presented as, using Eq. (4) for N,

$$K_t = 2\pi \rho_w l_w \frac{\beta}{c_{pa}} \frac{c_0^2 D}{\beta_p} \frac{N\Delta a_{cr}}{T}. \tag{18}$$

The space increment K is determined as

$$K = \frac{K_t}{c_0}.$$

Substituting the thermodynamic coefficients one obtains

$$K = 2\pi\rho_w l_w \frac{\beta}{c_{pa}} \frac{c_0 D}{\beta_p} \frac{N\Delta a_{\mathrm{cr}}}{T} \ 1/\mathrm{cm}, \tag{19}$$

where according to Eqs. (2) and (4)

$$a_{\mathrm{cr}} = \frac{2av' c_{0\infty}}{kT\Delta(t)}, \quad N = \frac{A}{a_{\mathrm{min}}^2}.$$

It is seen that there are four parameters that determine the sound amplification rate

$$N, \quad T, \quad \Delta, \quad a_{\mathrm{cr}}, \tag{20}$$

where N is the water droplets per unit volume amount, a_{cr} is the critical radius of droplet, T is the temperature of vapor, and Δ is the excess of vapor concentration above the saturated level.

IV. CONCLUSION

The dynamic stability of a supersaturated vapor is modulated by the presence of a finite amplitude wave. This can cause condensation in the region of reduced stability. The interaction of the modulated heat release with infrasound wave is a resonance process and can lead to wave amplification.

Let us evaluate the efficiency of the process of wave-condensation instability, using the characteristics for supersaturated atmospheric layer data, given in Refs. 12 and 13.

If the number of droplets of radius $a = 10^{-3}$ cm/cm^3 is $N = 10^2$ 1/cm^3, then the obtained infrasound amplification increment is

$$K = 10^{-4} \ 1/\mathrm{cm} = 10^{-2} \ 1/\mathrm{m},$$

which exceeds 100 times the increment of thermodynamic instability.[5]

Notice that for infrasound frequency of 10^{-1} Hz this increment exceeds ten times the coefficient of attenuation of sound in fog,[4] at lower frequencies the excess of amplification becomes more pronounced.

ACKNOWLEDGMENTS

We are grateful to L. Pitaevskii, A. Bedard, and O. Godin for many helpful discussions. This work was supported in part by NATO Grant No. ESP.NR.NRCLG 982524.

[1] E. E. Gossard and W. H. Hooke, *Waves in the Atmosphere* (Elsevier, New York, 1975), Chap. 12.
[2] S. N. Netreba and A. N. Svirkunov, "On a possibility of cyclone intensity prediction based on the variability of an amplitude of infrasonic pressure pulsations," Met. Gidrol. **3**, 28–36 (1955).
[3] R. A. Pielke, M. E. Nicholls, and A. J. Bedard, "Using thermal compression waves to assess latent heating from clouds," EOS (Wash. D.C.) **74**, 493 (1993).
[4] R. Wei, Y. Tian, and Q. Lu, "Absorption of sound water fog composed of submicron droplets," J. Acoust. Soc. Am. **81**, 1350–1354(1987).
[5] B. E. Nemtsov, "A coherent mechanism of sound amplification during vapor condensation," Dokl. Akad. Nauk SSSR **314**, 355–358 (1990).
[6] S. N. Netreba, "Infrasound amplification during atmospheric condensation," Izv. Akad. Nauk, Fiz. Atmos. Okeana **34**, 734–742 (1998).
[7] E. M. Lihshitz and L. P. Pitaevskii, *Physical Kinetics* (Nauka, Moscow, 1979), Chap. 12.
[8] G. Chimonas, "The stability of a coupled wave-turbulence system in a parallel shear flow," Boundary-Layer Meteorol. **2**, 444–452 (1972).
[9] S. S. Moiseev, V. G. Pungin, and V. N. Oracvsky, *Nonlinear Instabilities in Plasmas and Hydrodynamics* (IOP, Bristol, 2000), Chaps. 4 and 5.
[10] R. G. Fleagle and J. A. Businger, *Atmospheric Physics* (Academic, New York, 1963).
[11] P. J. Westervelt and R. S. Larson, "Laser-excited broadside array," J. Acoust. Soc. Am. **54**, 121–122 (1973).
[12] E. L. Andreas, *Handbook of Physical Constants and Functions for Use in Atmospheric Boundary Layer Studies* (U.S. Army Engineer Research and Development Center, Hanover, 2005).
[13] E. Linacre and B. Geerts, "Cloud liquid water content, drop sizes, and number of droplets," http//:www-das.uwyo.edu/~geerts/cwx/notes/chap08/moist_cloud.html (Last viewed May, 2008).

Source localization from an elevated acoustic sensor array in a refractive atmosphere

Vladimir E. Ostashev
NOAA/Earth System Research Laboratory, Boulder, Colorado 80303 and Physics Department, New Mexico State University, Las Cruces, New Mexico 88003

Michael V. Scanlon
U.S. Army Research Laboratory, AMSRD-ARL-SE-SP, Adelphi, Maryland 20783

D. Keith Wilson
U.S. Army Engineer Research and Development Center, Hanover, New Hampshire 03755

Sergey N. Vecherin
Physics Department, New Mexico State University, Las Cruces, New Mexico 88003

(Received 21 February 2008; revised 27 September 2008; accepted 29 September 2008)

Localization of sound sources on the ground from an acoustic sensor array elevated on a tethered aerostat is considered. To improve estimation of the source coordinates, one should take into account refraction of sound rays due to atmospheric stratification. Using a geometrical acoustics approximation for a stratified moving medium, formulas for the source coordinates are derived that account for sound refraction. The source coordinates are expressed in terms of the direction of sound propagation as measured by the sensor array, its coordinates, and the vertical profiles of temperature and wind velocity. Employing these formulas and typical temperature and wind velocity profiles in the atmosphere, it is shown numerically that sound refraction is important for accurate predictions of the source coordinates. Furthermore, it is shown that the effective sound speed approximation, which is widely used in atmospheric acoustics, fails to correctly predict the source coordinates if the grazing angle of sound propagation is relatively large.
© *2008 Acoustical Society of America.* [DOI: 10.1121/1.3003085]

PACS number(s): 43.28.Fp, 43.20.Dk [RMW] Pages: 3413–3420

I. INTRODUCTION

Ground-based acoustic sensor arrays are used for detection and ranging of sound sources located close to the earth's surface.[1] However, performance of such arrays is limited by several factors, including absorption of sound waves in the ground, sound reflections by obstacles (e.g., houses and trees), irregular terrain, multipath sound propagation, and formation of an acoustic shadow zone in the upwind direction. These limitations can be overcome in part by elevating sensors above the ground. Several experiments in source localization using acoustic sensor arrays suspended below tethered aerostats (stationary balloons) have been carried out.[2] The aerostats can be elevated from several hundreds meters up to 1–2 km above the ground. The experiments showed that the acoustic sensor arrays can reliably measure sound signals from sources on the ground and allow determination of the direction of sound propagation at the height of the array. Using this direction and assuming straight-line sound propagation, it is straightforward to find the coordinates of a source on the ground. However, this approach to source localization (which is currently being used) ignores refraction of sound signals due to temperature and wind velocity stratification in the atmosphere. Refraction results in bending of ray paths of sound signals emitted by a source and changes its apparent bearing.

The goal of the present paper is to develop a theory enabling accurate determination of the source coordinates by taking into account refraction of sound signals in a stratified moving atmosphere. Using geometrical acoustics in a moving medium,[3] exact and approximate formulas for the source coordinates are derived as a function of the direction of sound signal propagation at the sensor array, its coordinates, and vertical profiles of temperature and wind velocity. The approximate formula actually contains only integrated vertical profiles rather than the values of temperature and wind velocity at every height.

In practical applications, temperature and wind velocity profiles might not be known. Three methods are suggested to overcome this issue. The first one employs the Monin–Obukhov similarity theory[4] (MOST), which allows one to express these profiles in terms of some parameters measured near the ground. The other two methods enable one to find the integrated vertical profiles.

Furthermore, we study the effects of atmospheric stratification on source localization numerically. This is done for typical meteorological regimes of an unstable atmospheric boundary layer (ABL): mostly sunny or cloudy with light wind, mostly sunny or cloudy with moderate wind, and mostly sunny or cloudy with strong wind. A stable ABL, which usually occurs at night, is also considered.

Besides sound refraction, other factors interfere with accurate determination of the source coordinates. Among these are sound scattering by atmospheric turbulence, errors in determining the direction of signal propagation at the sensor

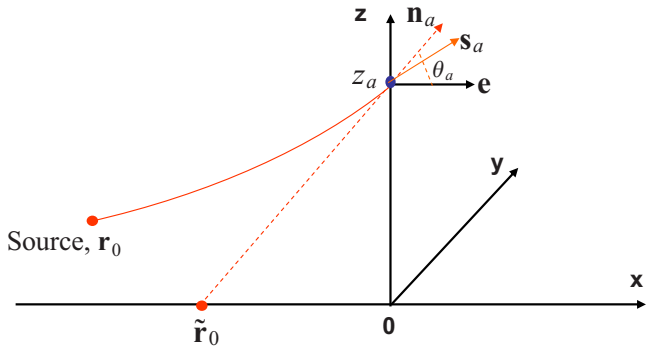


FIG. 1. (Color online) The geometry of the problem. The acoustic sensor array is located at the height z_a, the coordinates of the source on the ground are $\mathbf{r}_0$, and the coordinates obtained in the straight-line approximation are $\tilde{\mathbf{r}}_0$. The solid curve is the sound ray path from the source to the sensor array.

array, and the uncertainties in the array coordinates and the vertical profiles of temperature and wind velocity. However, these factors are mostly independent of each other and can be studied separately. Some of these factors are briefly discussed in Conclusions.

The paper is organized as follows. In Sec. II, the geometry of the problem is described and formulas for the source coordinates are derived. The MOST vertical profiles of temperature and wind velocity are presented in Sec. III. In Sec. IV, numerical results are discussed. Last, in Sec. V, the results obtained in the paper are summarized.

II. THEORY

A. Formulation of the problem

The geometry of the problem is shown in Fig. 1. An acoustic source is situated on the ground, which coincides with the horizontal plane $z=0$ of the Cartesian coordinate system x,y,z. The horizontal coordinates of the source are $\mathbf{r}_0=(x_0,y_0)$. An acoustic sensor array is located at the height z_a. Its horizontal coordinates are $\mathbf{r}_a=(x_a,y_a)$. (Figure 1 shows the case when $\mathbf{r}_a=\mathbf{0}$.) The light solid curve in Fig. 1 is the path of a sound wave emitted by the source, which reaches the sensor array. The unit vector $\mathbf{s}_a$ indicates the direction of propagation of this sound wave at the array location. Hereinafter, the subscript a indicates that a function of z is evaluated at the height of the sensor array, e.g., $\mathbf{s}_a=\mathbf{s}(z_a)$. In a moving atmosphere, the unit vector $\mathbf{s}_a$ does not coincide with the unit vector $\mathbf{n}_a$ normal to the wave front of this wave and can be expressed in the following form [e.g., see Eq. (3.33) from Ref. 3]:

$$\mathbf{s}_a = \frac{\mathbf{n}_a + \mathbf{u}_a/c_a}{|\mathbf{n}_a + \mathbf{u}_a/c_a|}. \tag{1}$$

Here, c_a and $\mathbf{u}_a$ are the values of the adiabatic sound speed $c(z)$ and the wind velocity vector $\mathbf{u}(z)$ at the height of the sensor array. In the atmosphere, the vertical component of the wind velocity is usually small and can be ignored for present purposes. Therefore, we will assume that the vector $\mathbf{u}$ lies in a horizontal plane.

It is worthwhile to express the vector $\mathbf{n}_a$ in the following form: $\mathbf{n}_a=(\mathbf{e}\cos\theta_a,\sin\theta_a)$, where $\mathbf{e}\cos\theta_a$ and $\sin\theta_a$ are the horizontal and vertical components of $\mathbf{n}_a$. Here, $\mathbf{e}$ is the unit vector in the direction of projection of $\mathbf{n}_a$ on a horizontal plane and θ_a is the grazing angle between $\mathbf{n}_a$ and this plane, as shown in Fig. 1. (The figure depicts the case when $\mathbf{e}$ coincides with the positive direction of the x-axis.) Note that the vector $\mathbf{e}$ remains constant along the sound propagation path.[3]

The direction of sound propagation at a sensor array is usually determined by cross correlation of the signals recorded by different sensors. This signal processing allows one to determine the unit vector $\mathbf{n}_a$ normal to the wave front of a sound wave. Therefore, we assume that the vector $\mathbf{n}_a$ and, hence, the values of θ_a and $\mathbf{e}$ are known. Note that, if the vector $\mathbf{s}_a$ is determined by especially designed signal processing, the vector $\mathbf{n}_a$ can be calculated with the use of Eq. (3.34) from Ref. 3:

$$\mathbf{n}_a = \mathbf{s}_a\left[\sqrt{1+(\mathbf{s}_a\cdot\mathbf{u}_a/c_a)^2 - u_a^2/c_a^2} + \mathbf{s}_a\cdot\mathbf{u}_a/c_a\right] - \mathbf{u}_a/c_a. \tag{2}$$

[This formula is a solution of Eq. (1) for n_a.] We also assume that the coordinates of the sensor array $(\mathbf{r}_a,z_a)$ and the vertical profiles of the sound speed $c(z)$ and horizontal wind velocity $\mathbf{u}(z)$ are known. The problem that is solved in this paper is to find the horizontal coordinates $\mathbf{r}_0=(x_0,y_0)$ of the source on the ground in terms of θ_a, $\mathbf{e}$, $(\mathbf{r}_a,z_a)$, $c(z)$, and $\mathbf{u}(z)$.

B. Source coordinates

In a stratified moving medium, the sound ray path $\mathbf{r}=\mathbf{r}(z)$ can be determined by different equivalent approaches, e.g., see Refs. 5 and 6. However, for the problem considered here, it is worthwhile to determine this path by using Eq. (3.57) from Ref. 3:

$$\mathbf{r}(z) = \mathbf{r}_0 + \int_{z_0}^{z} \frac{\boldsymbol{\kappa}c(z') + [\omega - \boldsymbol{\kappa}\cdot\mathbf{u}(z')]\mathbf{u}(z')/c(z')}{\sqrt{[\omega-\boldsymbol{\kappa}\cdot\mathbf{u}(z')]^2 - \kappa^2 c^2(z')}}\,dz'. \tag{3}$$

(This equation is written for the considered case when the vertical component of the wind velocity is zero.) In Eq. (3), $(\mathbf{r}_0,z_0)$ are the initial coordinates of the sound ray $\mathbf{r}(z)$, ω is the sound frequency of a plane sound wave, which corresponds to this ray, and $\boldsymbol{\kappa}$ is the horizontal component of the wave vector $\mathbf{k}(z)=(\boldsymbol{\kappa},q(z))$ of the plane wave. Here, $q(z)$ is the vertical wave number. Note that the vector $\boldsymbol{\kappa}$ remains constant (does not depend on z) along a sound ray path (e.g., see Ref. 3). Equation (3) can be used for both geometrical and wave descriptions of sound propagation.

Setting in Eq. (3), $\mathbf{r}=\mathbf{r}_a$, $z=z_a$, and $z_0=0$, the horizontal coordinates $\mathbf{r}_a$ of the sensor array are expressed in terms of other parameters of the problem

$$\mathbf{r}_a = \mathbf{r}_0 + \int_{0}^{z_a} \frac{\boldsymbol{\kappa}c(z) + [\omega - \boldsymbol{\kappa}\cdot\mathbf{u}(z)]\mathbf{u}(z)/c(z)}{\sqrt{[\omega-\boldsymbol{\kappa}\cdot\mathbf{u}(z)]^2 - \kappa^2 c^2(z)}}\,dz. \tag{4}$$

In this equation, the ratio $\boldsymbol{\kappa}/\omega$ plays the role of ray parameters which determine a particular ray. Usually, the ray parameters are chosen as the grazing angle and the azimuthal direction of a sound ray at the source. However, this choice of ray parameters is not convenient for the problem considered. Equation (4) is a convenient starting point for our analysis since it allows expression of the ray parameters in

terms of θ_a and $\mathbf{e}$, which can be measured by the sensor array.

To do this, let us consider the dispersion equation $\omega = k(z')c(z') + \mathbf{k}(z')\cdot\mathbf{u}(z')$ in a moving medium. Here, z' is an arbitrary height. In the dispersion equation, we set $z' = z_a$ and take into account that $\mathbf{k}_a\cdot\mathbf{u}_a = \boldsymbol{\kappa}\cdot\mathbf{u}_a$. (Recall that $\mathbf{u}$ is a horizontal vector.) As a result, we obtain $\omega = k_a c_a + \boldsymbol{\kappa}\cdot\mathbf{u}_a$. The value of ω given by this expression is substituted into Eq. (4). In the integrand of the resulting formula, the numerator and denominator are divided by k_a. Then, the integrand will contain the ratio $\boldsymbol{\kappa}/k_a$, which is the horizontal component of the unit vector $\mathbf{k}_a/k_a = \mathbf{n}_a$. Now recall that $\mathbf{n}_a = (\mathbf{e}\cos\theta_a, \sin\theta_a)$. Therefore, $\boldsymbol{\kappa}/k_a = \mathbf{e}\cos\theta_a$. As a result of these manipulations, Eq. (4) takes the form

$$\mathbf{r}_0 = \mathbf{r}_a - \int_0^{z_a} \frac{\mathbf{e}\cos\theta_a + \{c_a + \mathbf{e}\cdot[\mathbf{u}_a - \mathbf{u}(z)]\cos\theta_a\}\mathbf{u}(z)/c^2(z)}{\sqrt{\{c_a + \mathbf{e}\cdot[\mathbf{u}_a - \mathbf{u}(z)]\cos\theta_a\}^2/c^2(z) - \cos^2\theta_a}}\,dz. \tag{5}$$

This formula allows us to determine the source coordinates $\mathbf{r}_0$ on the ground given the values of θ_a, $\mathbf{e}$, $(\mathbf{r}_a, z_a)$, $c(z)$, and $\mathbf{u}(z)$. In the geometrical acoustics approximation, and provided that the atmosphere is stratified, Eq. (5) gives an exact formula for the coordinates. Note that this equation is valid if there is no turning point along the sound propagation path connecting the source and the sensor array. In practice, this can always be achieved by elevating the sensor array relatively high above the ground.

In the atmosphere, a small parameter $\varepsilon = \max(|c - c_0|/c_0, u/c_0) \ll 1$ can be introduced, where c_0 is a reference value of the sound speed. Neglecting terms of order ε^2, Eq. (5) simplifies to

$$\mathbf{r}_0 = \tilde{\mathbf{r}}_0 + \frac{\mathbf{e}\cos\theta_a}{\sin^3\theta_a} \times \int_0^{z_a} \left\{ \frac{c_a - c(z)}{c_0} + \frac{\mathbf{e}\cdot[\mathbf{u}_a - \mathbf{u}(z)]\cos\theta_a}{c_0} \right\} dz - \frac{1}{\sin\theta_a}\int_0^{z_a} \frac{\mathbf{u}(z)}{c_0}\,dz + O(\varepsilon^2). \tag{6}$$

On the right-hand side of this formula, the first term $\tilde{\mathbf{r}}_0 = \mathbf{r}_a - z_a\mathbf{e}\cot\theta_a$ determines the source coordinates in the straight-line approximation, i.e., when sound refraction is ignored. The vector $\tilde{\mathbf{r}}_0$ is shown in Fig. 1. The second and third terms on the right-hand side of Eq. (6) give corrections (to order ε) to the source coordinates due to sound refraction. The correction due to the second term is always in the direction of the vector $\mathbf{e}$. However, the correction due to the third term is, generally, in a different direction. For the geometry shown in Fig. 1, the correction to the source coordinates due to the second term is in the direction of the x-axis, while that due to the third term can have components along the x-and y-axes.

Note that, at a first sight, the source coordinates $\mathbf{r}_0$ could be obtained by other simpler approaches than that resulting in Eqs. (5) and (6). For example, one could employ the effective sound speed approximation, which is widely used in atmospheric acoustics. In this approximation, a moving atmosphere is replaced by a motionless medium with the effective sound speed given by $c_{\text{eff}}(z) = c(z) + \mathbf{s}(z)\cdot\mathbf{u}(z)$. Here, the dot product is equal to the component of wind velocity in the direction of sound propagation. To obtain a formula for the source coordinates $\mathbf{r}_{0,\text{eff}}$ in the effective sound speed approximation, in Eq. (6) we set $\mathbf{u} = 0$ and replace $c(z)$ with $c_{\text{eff}}(z)$. In the resulting formula to order ε (to which this approximation is usually considered and believed to be valid), the dot product can be written as $\mathbf{s}\cdot\mathbf{u} = \mathbf{n}\cdot\mathbf{u} + O(\varepsilon^2) = \mathbf{e}\cdot\mathbf{u}\cos\theta_a + O(\varepsilon^2)$. As a result, we have

$$\mathbf{r}_{0,\text{eff}} = \tilde{\mathbf{r}}_0 + \frac{\mathbf{e}\cos\theta_a}{\sin^3\theta_a} \times \int_0^{z_a} \left\{ \frac{c_a - c(z)}{c_0} + \frac{\mathbf{e}\cdot[\mathbf{u}_a - \mathbf{u}(z)]\cos\theta_a}{c_0} \right\} dz. \tag{7}$$

Comparing this formula with Eq. (6), we conclude that the effective sound speed approximation correctly gives the first two terms on the right-hand side of Eq. (6). However, it fails to produce the third term. Note that the third term is much less than the second one if the angle θ_a is small. This is usually the case for near-ground sound propagation. On the other hand, for an elevated array, the angle θ_a may not be small, so that the third term on the right-hand side of Eq. (6) cannot be ignored and the effective sound speed approximation fails to predict correctly the source coordinates. Numerical examples demonstrating this conclusion will be presented in Sec. IV.

C. Analysis

Equations (5) and (6) determine the exact coordinates $\mathbf{r}_0$ of a source on the ground and those calculated to order ε. Both equations are easy to implement numerically provided that the vertical profiles of the sound speed $c(z)$ and wind velocity $\mathbf{u}(z)$ are known.

In practical applications, however, these profiles might not be known. Here, we suggest three methods that can be used to overcome this issue. In the first method, $c(z)$ and $\mathbf{u}(z)$ are estimated by measuring some meteorological parameters near the ground and then using MOST. This is explained in more details in Sec. IV.

To understand the second proposed method, Eq. (6) is written in the following form:

$$\mathbf{r}_0 = \tilde{\mathbf{r}}_0 + \frac{\mathbf{e}z_a\cos\theta_a}{\sin^3\theta_a}\left(\frac{c_a}{c_0} + \frac{\mathbf{e}\cdot\mathbf{u}_a\cos\theta_a}{c_0}\right) - \frac{\mathbf{e}\cos\theta_a}{\sin^3\theta_a} I_c - (\mathbf{j}_x + \mathbf{e}\cot^2\theta_a\cos\beta)\frac{I_x}{\sin\theta_a} - (\mathbf{j}_y + \mathbf{e}\cot^2\theta_a\sin\beta)\frac{I_y}{\sin\theta_a}. \tag{8}$$

Here, β is the angle between the unit vector $\mathbf{e}$ and the x-axis so that $\mathbf{e} = (\cos\beta, \sin\beta)$, $\mathbf{j}_x$ and $\mathbf{j}_y$ are the unit vectors in the directions of the x- and y-axes, and I_c, I_x, and I_y are the integrated vertical profiles of the sound speed $c(z)$ and two components of the wind velocity vector $\mathbf{u}(z) = (u_x(z), u_y(z))$:

$$I_c = \int_0^{z_a} \frac{c(z)}{c_0} dz, \quad I_x = \int_0^{z_a} \frac{u_x(z)}{c_0} dz, \quad I_y = \int_0^{z_a} \frac{u_y(z)}{c_0} dz. \tag{9}$$

The values of c_a and $\mathbf{u}_a$ appearing in Eq. (8) can be measured by meteorological equipment mounted with the sensor array. Therefore, according to this equation, the integrated profiles I_c, I_x, and I_y need to be known to calculate the source coordinates $\mathbf{r}_0$. On the other hand, the values of $c(z)$ and $\mathbf{u}(z)$ at every height z should be known to find $\mathbf{r}_0$ using Eq. (5). Generally speaking, the integrated profiles I_c, I_x, and I_y can be determined more easily than the values of $c(z)$ and $\mathbf{u}(z)$ at every height. Therefore, in some cases, Eq. (8) and its equivalent Eq. (6) might have an advantage in comparison with Eq. (5).

This feature of Eqs. (8) and (6) is employed in the second proposed method. In some practical applications, it would be feasible to put two sound sources on the ground whose coordinates $\mathbf{r}_i$ are known. Here, $i=1,2$. Using the sensor array suspended below the aerostat, the propagation directions of sound signals emitted by these two sources can also be measured. These directions are characterized by the grazing angles θ_i and the unit vectors $\mathbf{e}_i$, which are similar to θ_a and $\mathbf{e}$ considered above. Equations for the coordinates $\mathbf{r}_i$ are still given by Eq. (8) if θ_a and $\mathbf{e}$ are replaced with θ_i and $\mathbf{e}_i$, respectively. The two vector equations for $\mathbf{r}_1$ and $\mathbf{r}_2$ are sufficient to determine three integrated profiles I_c, I_x, and I_y in terms of $\mathbf{r}_i$, θ_i, $\mathbf{e}_i$, and $(\mathbf{r}_a, z_a)$, which are known or can be measured. Formulas for I_c, I_x, and I_y are derived in the Appendix [see Eqs. (A6) and (A7)]. After I_c, I_x, and I_y are found, Eq. (8) allows us to calculate the source coordinates $\mathbf{r}_0$. Note that the proposed method for determining the integrated profiles I_c, I_x, and I_y might be important for other applications, e.g., for artillery aiming.

The third suggested method is somewhat similar to the second one. The source coordinates $\mathbf{r}_0$ can be determined by acoustic sensor arrays suspended below three tethered aerostats. For each of the three sensor arrays, Eq. (8) is still valid if θ_a and $\mathbf{e}$ are replaced with θ_j and $\mathbf{e}_j$, respectively. Here, the index $j=1,2,3$ characterizes a particular sensor array. Three vector equations, i.e., Eq. (8) for three values of j, are sufficient to determine the integrated profiles I_c, I_x, and I_y, and the source coordinates $\mathbf{r}_0$. The corresponding formulas can be derived similarly to those in Appendix and are not presented here for brevity.

Finally, note that some combinations of the three proposed methods can be used to determine the source coordinates. For example, two aerostats and one source with known coordinates would allow one to find the integrated profiles I_c, I_x, and I_y, and the coordinates $\mathbf{r}_0$.

III. VERTICAL PROFILES OF TEMPERATURE AND WIND VELOCITY

In the atmosphere, the adiabatic sound speed c is related to the temperature T by the following formula:[3] $c = \sqrt{\gamma R(1+0.511q)T}$. Here, $\gamma=1.40$ is the ratio of specific heats, $R=287.05\ \mathrm{m^2/s^2\ K}$ is the gas constant for dry air, and q is the concentration of water vapor in the atmosphere (which, to good accuracy, is equal to specific humidity). For simplicity, we assume that $q=0$. In this case, the sound speed c can be calculated if the temperature profile is known.

This profile can be determined from MOST as (e.g., Refs. 7 and 8)

$$T(z) = T_r - (z - z_r)\Gamma_d + \frac{P_t T_*}{\kappa_v}[\ln(z/z_r) - \Psi_h(z/L_o) + \Psi_h(z_r/L_o)]. \tag{10}$$

Here, z_r is a reference height, $T_r = T(z_r)$ is the value of temperature at this height, $\Gamma_d = 0.0098\ \mathrm{K/m^2}$ is the dry adiabatic lapse rate, $P_t=0.95$ is the turbulent Prandtl number, T_* is a temperature scale, $\kappa_v=0.40$ is the von Kármán constant, L_o is the Obukhov length, and $\Psi_h(\xi)$ is the universal profile function defined below.

MOST also provides with the wind velocity profile:

$$u(z) = \frac{u_*}{\kappa_v}[\ln(z/z_0) - \Psi_m(z/L_o) + \Psi_m(z_0/L_o)]. \tag{11}$$

Here, u_* is the friction velocity, z_0 is the surface roughness length, and $\Psi_m(\xi)$ is another universal profile function. Slightly different expressions for the universal profiles $\Psi_{h,m}(\xi)$ are known in the literature. Here, we use those suggested in Ref. 9:

$$\Psi_{h,m}(\xi) = \begin{cases} 2\ln\dfrac{1+\sqrt{1+a_{h,m}|\xi|^{2/3}}}{2}, & \xi < 0 \\ -b_{h,m}\xi, & \xi \geqslant 0, \end{cases} \tag{12}$$

where $a_h=7.9$, $a_m=3.6$, $b_h=8.4$, and $b_m=5.3$ are numerical constants.

Equations (10)–(12) allow determination of $T(z)$ and $u(z)$ if the values of the parameters T_r, u_*, z_0, L_o, and T_* are known. The first three of these parameters can be measured near the ground. The last two parameters can be calculated using the formulas $L_o = -u_*^3 T_r \rho_0/(\kappa_v \Gamma_d Q_s)$ and $T_* = u_*^2 T_r/(\kappa_v g L_0)$, provided that the surface sensible heat flux Q_s is measured. Here, ρ_0 is the air density and g is the gravitational acceleration. Examples of vertical profiles of temperature and wind velocity for different values of these parameters are presented in the next section.

Equations (10) and (11) are valid for $z \gg z_0$. Furthermore, they are usually applied to determine the vertical profiles of temperature and wind velocity within the atmospheric surface layer, which is roughly 100–200 m for unstable stratification. (For the stable stratification, the top of the surface layer is typically of order L_o.) However, since $T(z)$ and $u(z)$ often vary slowly above the surface layer, it is reasonable to use Eqs. (10) and (11) for larger heights in illustrative calculations, which will be done in the next section. Note that, as mentioned above, the values of T_a and u_a can be measured by meteorological sensors mounted on the aerostat. In this case, $T(z)$ and $u(z)$ can be obtained by interpolation of temperature and wind velocity from the top of the atmospheric surface layer up to the aerostat height z_a.

IV. SOURCE LOCALIZATION RESULTS

In this section, the effects of atmospheric stratification on source localization are studied numerically. Furthermore, the accuracy of different approximate formulas for the source coordinates are considered.

In the numerical examples to follow, we assume that $z_a=500$ m and $\theta_a=45°$, which are typical values of the height of a sensor array and the grazing angle. To determine the vertical profiles of temperature and wind velocity, we set $z_r=1$ m, $T_r=288.15$ K, and $z_0=0.01$ m (this value of z_0 is a representative of a flat ground with a short grass). Furthermore, we assume that $T(z)=T_r$ if $z<z_r$ and $u(z)=0$ if $z<z_0$. [Since z_r and z_0 are small, the exact values of $T(z)$ and $u(z)$ very close to the ground are not important for the considered problem.] Finally, we assume that the direction of the wind velocity vector $\mathbf{u}$ is independent of height.

With these parameters, the surface heat flux Q_s and the friction velocity u_* need to be specified to determine the vertical profiles of temperature and wind velocity. The values of Q_s and u_* span wide ranges. For example, for summer weather at midlatitudes, $-50\ \mathrm{W/m^2} \lesssim Q_s \lesssim 600\ \mathrm{W/m^2}$ and $0.05\ \mathrm{m/s} \lesssim u_* \lesssim 0.7\ \mathrm{m/s}$. To roughly cover different meteorological regimes of an unstable ABL (where Q_s is positive), Ostashev and Wilson[10] suggested six benchmark regimes: mostly sunny or cloudy with light wind, mostly sunny or cloudy with moderate wind, and mostly sunny or cloudy with strong wind. For mostly sunny or cloudy conditions, we set $Q_s=200\ \mathrm{W/m^2}$ or $Q_s=40\ \mathrm{W/m^2}$, respectively. To characterize light, moderate, or strong wind, the friction velocity u_* is chosen as 0.15, 0.3, or 0.7 m/s, respectively.

For mostly sunny and light wind conditions ($Q_s=200\ \mathrm{W/m^2}$ and $u_*=0.15$ m/s), Fig. 2(a) shows the vertical profiles of temperature and wind velocity obtained with Eqs. (10)–(12). It follows from the figure that the temperature decreases with height, while the wind velocity increases. Figure 2(b) depicts the source coordinates calculated with the different approaches considered in Sec. III and for eight values of the angle α between the wind velocity vector $\mathbf{u}$ and the x-axis: $\alpha=-180°$, $-135°$, $-90°$, $45°$, $0°$, $45°$, $90°$, and $135°$. In the figure, "exact" stands for the source coordinates $\mathbf{r}_0$ obtained with Eq. (5), which is an exact solution of the problem; "to order ε" for the coordinates $\mathbf{r}_0$ calculated to order ε and given by Eq. (6); "c_{eff} approx." for the coordinates $\mathbf{r}_{0,\mathrm{eff}}$ obtained in the effective sound speed approximation, Eq. (7); and "straight line" for the coordinates $\tilde{\mathbf{r}}_0$ calculated in the straight-line approximation. It follows from Fig. 2(b) that the source coordinates calculated with Eqs. (5) and (6) are almost identical (the maximum difference is 0.3 m), while those obtained with the straight-line and effective sound speed approximations significantly differ from them. Note that the coordinates $\tilde{\mathbf{r}}_0$ in the straight-line approximation do not depend on the angle α, while the coordinates $\mathbf{r}_{0,\mathrm{eff}}$ in the effective sound speed approximation do not depend on the sign of this angle. The difference between the exact coordinates $\mathbf{r}_0$ and the straight-line approximation $\tilde{\mathbf{r}}_0$ can be as large as 11.2 m.

Figure 3(a) depicts the vertical profiles of temperature and wind velocity obtained for mostly sunny and moderate wind conditions ($Q_s=200\ \mathrm{W/m^2}$ and $u_*=0.3$ m/s). The temperature profile is similar to that in Fig. 2(a), while the wind velocity at 500 m is greater than that in Fig. 2(a) by a factor of about 3. Figure 3(b) shows the source coordinates obtained with the various approaches for the same eight values of the angle α. As in Fig. 2(b), the source coordinates calculated to order ε are very close to those calculated exactly, with the maximum difference between them being 0.3 m. The source coordinates found with the straight-line and effective sound speed approximations differ significantly from the exact coordinates. The maximum deviation between $\mathbf{r}_0$ and $\tilde{\mathbf{r}}_0$ is 16.8 m.

The vertical profiles of temperature and wind velocity for mostly sunny conditions with strong wind ($Q_s=200\ \mathrm{W/m^2}$ and $u_*=0.7$ m/s) are presented in Fig. 4(a). The temperature profile is similar to that in Fig. 3(a), while the wind velocity is significantly greater at the height of the array than those in Figs. 2(a) and 3(a). The source coordinates calculated with the various approaches are shown in Fig. 4(b). Note that the scales of the x- and y-axes are twice

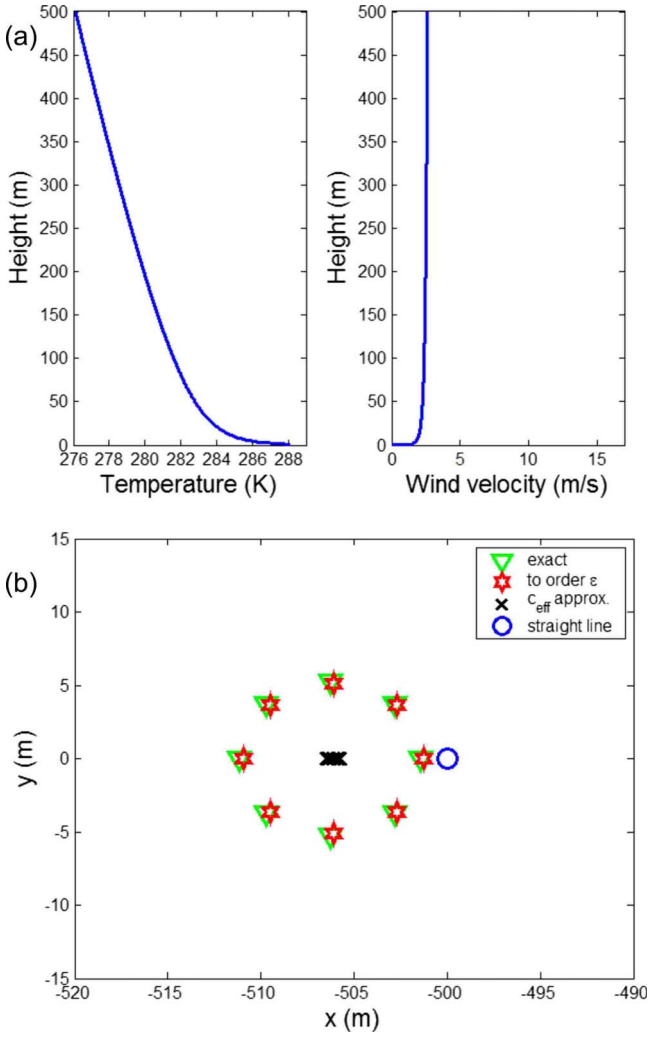


FIG. 2. (Color online) (a) Vertical profiles of temperature and wind velocity for mostly sunny and light wind conditions when $Q_s=200\ \mathrm{W/m^2}$ and $u_*=0.15$ m/s. (b) The source coordinates on the ground obtained with the use of different approaches and for eight values of the angle α between the wind velocity and the x-axis.

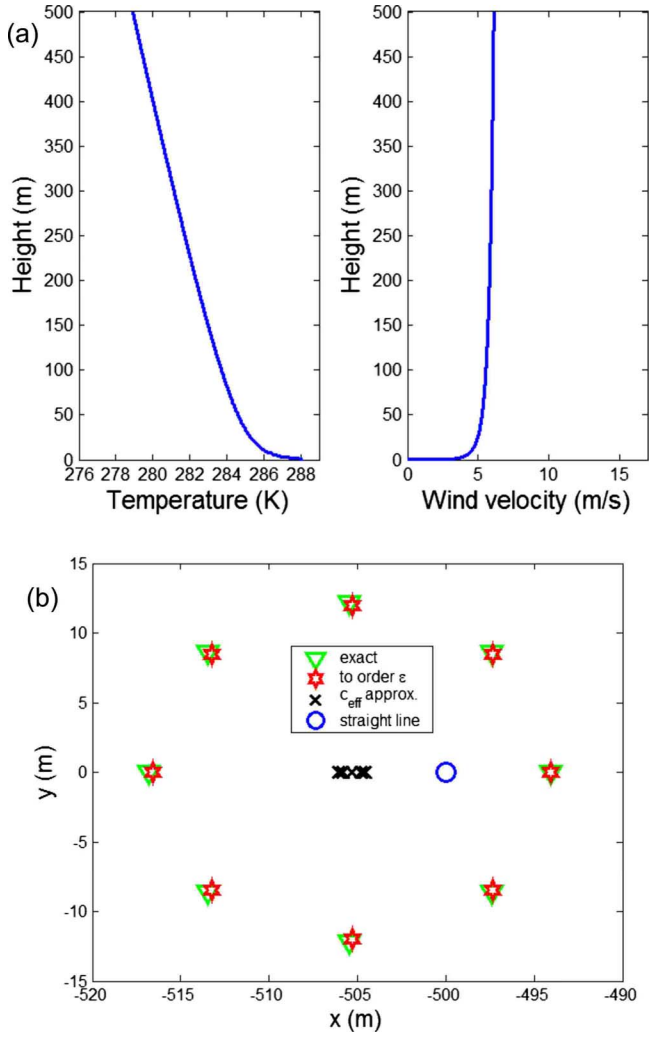


FIG. 3. (Color online) The same as in Figs. 2(a) and 2(b) but for mostly sunny and moderate wind conditions when $Q_s=200\ \mathrm{W/m^2}$ and $u_*=0.3\ \mathrm{m/s}$.

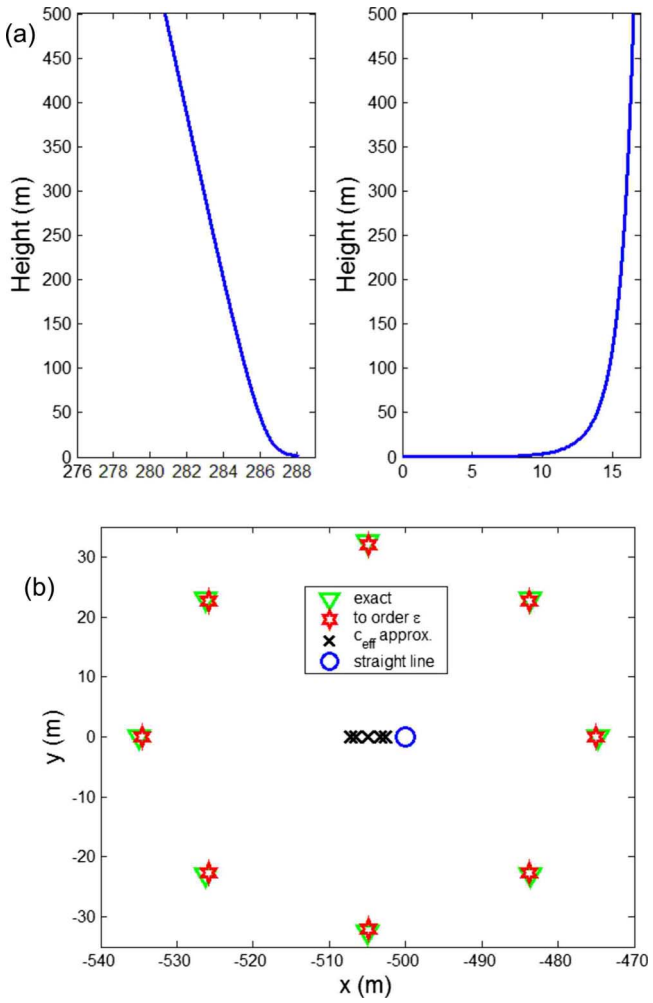


FIG. 4. (Color online) The same as in Figs. 2(a) and 2(b) but for mostly sunny and strong wind conditions when $Q_s=200\ \mathrm{W/m^2}$ and $u_*=0.7\ \mathrm{m/s}$.

as much as those in Figs. 2(b) and 3(b). The source coordinates calculated to $O(\varepsilon)$ are again close to those calculated exactly; the maximum difference is 0.4 m. The straight-line and effective sound speed approximations significantly differ from the exact coordinates, with the maximum deviation between $\mathbf{r}_0$ and $\tilde{\mathbf{r}}_0$ being 35.0 m.

Note that, in the numerical examples above, both the temperature and wind velocity profiles contribute significantly to sound refraction. Therefore, it is infeasible to simplify the problem by assuming that one of the profiles $T(z)$ or $u(z)$ can be assumed constant.

Calculations were also done for mostly cloudy conditions ($Q_s=40\ \mathrm{W/m^2}$) with light, moderate, or strong wind ($u_*=0.15$, 0.3, or 0.7 m/s). Though not presented here for brevity, the results obtained are similar to those presented above. For light, moderate, and strong wind conditions, the velocity profiles are very close to those in Figs. 2(a)–4(a), respectively; the temperature also decreases with height, though the difference in T between the ground and $z=500$ m is less than those for sunny conditions. Furthermore for cloudy conditions, the source coordinates calculated with the considered approaches slightly differ from those for sunny conditions. However, the main conclusions about these approaches remain the same: The source coordinates calculated to order ε are almost identical to the exact coordinates; the straight-line and effective sound speed approximations significantly differ from $\mathbf{r}_0$.

Let us now consider an example of a stable stratification (when Q_s is negative), which usually occurs during night. Figure 5(a) shows the vertical profiles of temperature and wind velocity for the case when $Q_s=-3\ \mathrm{W/m^2}$ and $u_*=0.1\ \mathrm{m/s}$. The temperature increases nearly linearly with height, while those in Figs. 2(a)–4(a) decrease. The wind velocity is greater than that in Fig. 4(a) and also has a nearly linear height dependence. (Note that, for the considered case, $L_o=30.0$ m. Therefore, the profiles depicted in Fig. 5(a) correspond to MOST only upto a few tens of meters above the ground and play an illustrative role at higher altitudes, as discussed in the last paragraph of Sec. III.)

The source coordinates obtained with the considered approaches are plotted in Fig. 5(b). The differences between the exact and $O(\varepsilon)$ solutions are larger than those in Figs. 2(b)–4(b): However, they are still small (with the maximum difference equal to 1.6 m). The source coordinates obtained with the straight-line and effective sound speed approximations differ significantly from the exact coordinates; the

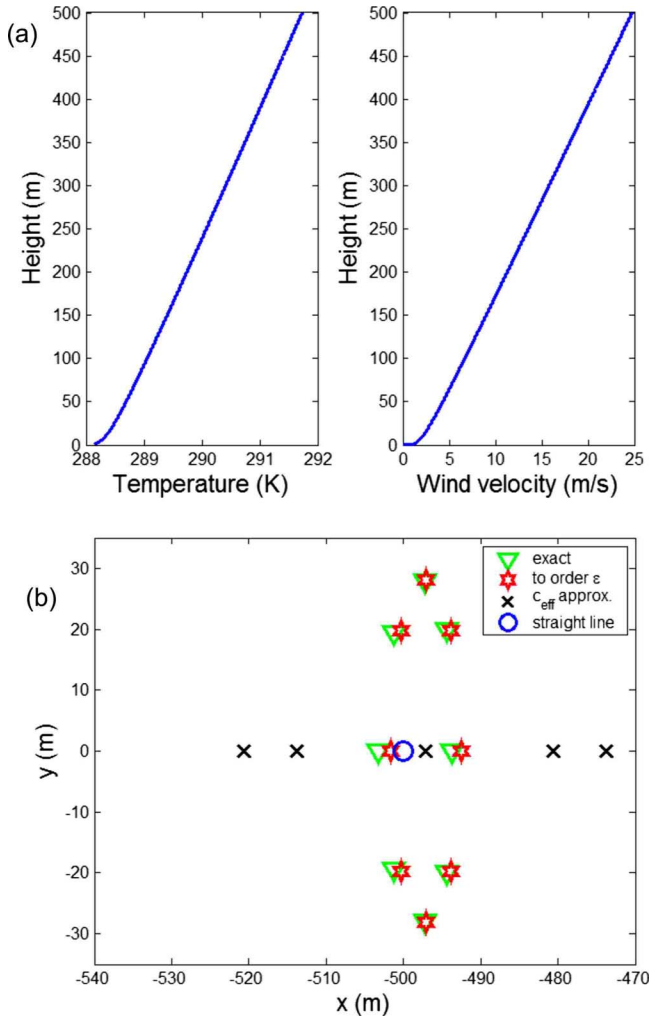


FIG. 5. (Color online) The same as in Figs. 2(a) and 2(b) but for a stable stratification with $Q_s=-3$ W/m^2 and $u_*=0.1$ m/s.

maximum deviation between $\mathbf{r}_0$ and $\tilde{\mathbf{r}}_0$ is 28.0 m. In Fig. 5(b), the source locations calculated with the effective sound speed approximation do not cluster as they do in the previous examples. The leftmost cross in Fig. 5(b) corresponds to $\alpha=-180°$. As the angle α increases, the corresponding crosses move to the right, reaching the rightmost cross at $\alpha=0°$; then, they move back to the left. The correspondence between α and the exact source coordinates is as follows. The case $\alpha=-180°$ corresponds to the source location just right of the straight-line approximation. When α increases, the source location moves in the anticlockwise direction along an imaginary ellipse passing through the exact source coordinates.

In all examples considered above, the height of the sensor array is $z_a=500$ m and the grazing angle of sound propagation at the height of the array $\theta_a=45°$. It follows from Eqs. (5) and (6) that the increase in z_a and decrease in θ_a generally result in increasing difference between the exact source coordinates and those calculated with the straight-line approximation. For example, for $\theta_a=25°$ and the vertical profiles shown in Figs. 2(a)–4(a), the maximum difference between the exact source coordinates and those in the straight-line approximation increases to 67.9 m.

V. CONCLUSIONS

In this paper, a theory was developed that enables one to account for sound refraction in the localization of a source on the ground using an acoustic sensor array suspended below a tethered aerostat. Using geometrical acoustics in a stratified moving atmosphere, an exact formula, Eq. (5), for the source coordinates $\mathbf{r}_0$ was derived. This formula determines $\mathbf{r}_0$ in terms of the direction of sound propagation at the height of the sensor array, the array coordinates, and the vertical profiles of sound speed $c(z)$ and horizontal wind velocity vector $\mathbf{u}(z)$. Then, Eq. (5) was simplified by omitting terms of order ε^2, where $\varepsilon=\max(|c-c_0|/c_0, u/c_0)$ is a small parameter. The resulting equation (6) determines the source coordinates $\mathbf{r}_0$ to order ε and has a significant advantage in comparison with Eq. (5): only the integrated vertical profiles of the sound speed and wind velocity are needed to find $\mathbf{r}_0$, rather than the values of c and $\mathbf{u}$ at every height.

In practical applications, vertical profiles of the sound speed and wind velocity might not be known. To overcome this issue, three methods were suggested. In the first method, these profiles can be determined using MOST. The other two suggested methods allow one to find integrated vertical profiles of the sound speed and wind velocity. Then, the source coordinates $\mathbf{r}_0$ are calculated with Eq. (8), which is equivalent to Eq. (6). Note that the proposed methods for determining the integrated vertical profiles might be useful in other applications, e.g., in artillery aiming.

The effects of atmospheric stratification on source localization were studied numerically. It was assumed for concreteness that the height of the sensor array is $z_a=500$ m and that the grazing angle of sound propagation at the array $\theta_a=45°$. The vertical profiles of the sound speed and wind velocity needed in such studies were modeled using MOST. Typical conditions of an unstable ABL were considered: mostly sunny or cloudy with light wind, mostly sunny or cloudy with moderate wind, and mostly sunny or cloudy with strong wind. A stable stratification, which is typical at night, was also considered. The results showed that the source coordinates determined to order ε [Eq. (6)] are very close (with a maximum deviation of 1.6 m) to the exact source coordinates given by Eq. (5). Therefore, Eq. (6), which is simpler than Eq. (5), can be used for source localization. Furthermore, it was revealed that, if refraction is ignored in determining the source coordinates, the resulting errors can be as large as 35 m. Note that these errors generally increase with increasing z_a and decreasing θ_a. Thus, it is important to account for sound refraction in source localization. Last, it was shown that the effective sound speed approximation, which is widely employed in atmospheric acoustics, fails to predict correctly the source coordinates if the grazing angle of sound propagation is relatively large.

Finally, note that the results obtained can be used in studies of the effects of other factors mentioned in the Introduction on accuracy in determining the source coordinates. First, the coordinates $(\mathbf{r}_a, z_a)$ of the sensor array and the direction of signal propagation at the height of the array, which is characterized by the grazing angle θ_a and the unit vector $\mathbf{e}$, are known with some errors. Equations (5) and (6) contain

the values of $(\mathbf{r}_a, z_a)$, θ_a, and $\mathbf{e}$, and can be employed in studies of the effects of these errors on accuracy in finding the source coordinates. Second, the vertical profiles of the sound speed and wind velocity are known only with some uncertainties. Again, Eqs. (5) and (6) contain $c(z)$ and $\mathbf{u}(z)$, and can be used to investigate the effects of these uncertainties. (If the vertical profiles can be determined with MOST, this investigation simplifies since the uncertainties can be modeled as uncertainties in the parameters z_0, Q_s, and u_*.) Third, due to sound scattering by atmospheric turbulence, the direction of sound propagation fluctuates so that θ_a and $\mathbf{e}$ become random quantities. The effect of this randomness on determining of the source coordinates can also be studied with the use of Eqs. (5) and (6).

ACKNOWLEDGMENTS

This research was supported by the Army Research Laboratory via a subagreement with the DoD Center for Geosciences/Atmospheric Research at Colorado State University under Cooperative Agreement W911NF-06-2-0015.

APPENDIX: INTEGRATED PROFILES OF THE SOUND SPEED AND WIND VELOCITY

In this Appendix, the integrated profiles of the sound speed and two components of the wind velocity vector are expressed in terms of $\mathbf{r}_i$, θ_i, $\mathbf{e}_i$, and $(\mathbf{r}_a, z_a)$.

Consider two sound sources on the ground, whose coordinates $\mathbf{r}_i=(x_i, y_i)$ are known. Here, $i=1,2$. For these sources, Eq. (8) takes the form

$$\mathbf{r}_i = \tilde{\mathbf{r}}_i + \frac{\mathbf{e}_i z_a \cos\theta_i}{\sin^3\theta_i}\left(\frac{c_a}{c_0} + \frac{\mathbf{e}_i\cdot\mathbf{u}_a\cos\theta_i}{c_0}\right) - \frac{\mathbf{e}_i\cos\theta_i}{\sin^3\theta_i} I_c - (\mathbf{j}_x + \mathbf{e}_i\cot^2\theta_i\cos\beta_i)\frac{I_x}{\sin\theta_i} - (\mathbf{j}_y + \mathbf{e}_i\cot^2\theta_i\sin\beta_i)\frac{I_y}{\sin\theta_i}. \quad \text{(A1)}$$

In this equation, $\tilde{\mathbf{r}}_i=\mathbf{r}_a-\mathbf{e}_i z_a\cot\theta_i$ and β_i is the angle between the unit vector $\mathbf{e}_i$ and the x-axis so that $\mathbf{e}_i=(\cos\beta_i, \sin\beta_i)$. Other notations are introduced in Sec. II C.

Let $\boldsymbol{\tau}_i=(-\sin\beta_i, \cos\beta_i)$ be the unit vector perpendicular to the vector $\mathbf{e}_i$. Then, both sides of Eq. (A1) are multiplied by the vector $\boldsymbol{\tau}_i$. The resulting equation can be written as a set of two equations, with the first corresponding to $i=1$ and the second to $i=2$:

$$\sin\beta_1 I_x - \cos\beta_1 I_y = b_1, \quad \text{(A2)}$$

$$\sin\beta_2 I_x - \cos\beta_2 I_y = b_2. \quad \text{(A3)}$$

Here, b_i is given by

$$b_i = \boldsymbol{\tau}_i\cdot(\mathbf{r}_i-\mathbf{r}_a)\sin\theta_i. \quad \text{(A4)}$$

We now assume that

$$\beta_1 \neq \beta_2. \quad \text{(A5)}$$

In this case, a set of Eqs. (A2) and (A3) can be solved for I_x and I_y:

$$I_x = \frac{b_1\cos\beta_2 - b_2\cos\beta_1}{\sin(\beta_1-\beta_2)}, \quad I_y = \frac{b_1\sin\beta_2 - b_2\sin\beta_1}{\sin(\beta_1-\beta_2)}. \quad \text{(A6)}$$

Next, both sides of Eq. (A1) are multiplied by the unit vector $\mathbf{e}_i$. In the resulting formula, I_x and I_y are replaced with their values given by Eq. (A6). After some algebra, the following formula for I_c is obtained:

$$I_c = \frac{\mathbf{e}_i\cdot(\mathbf{r}_a-\mathbf{r}_i)\sin^3\theta_i}{\cos\theta_i} + z_a\left(\frac{c_a}{c_0} + \frac{\mathbf{e}_i\cdot\mathbf{u}_a\cos\theta_i}{c_0} - \sin^2\theta_i\right) - \frac{b_1\cos(\beta_2-\beta_i) - b_2\cos(\beta_1-\beta_i)}{\cos\theta_i\sin(\beta_1-\beta_2)}. \quad \text{(A7)}$$

To calculate I_c, either $i=1$ or $i=2$ can be used in this formula. Equations (A7) and (A6) are the desired formulas for the integrated profiles I_c, I_x, and I_y.

Note that, if errors in the measurements of $\mathbf{r}_i$, θ_i, $\mathbf{e}_i$, and $(\mathbf{r}_a, z_a)$ are relatively large, another method can be used to find the integrated profiles I_c, I_x, and I_y. Equation (A1) with $i=1,2$ represents a set of four scalar equations for these three integrated profiles. This set can be solved for I_c, I_x, and I_y by the least squares solution (or similar inverse algorithms) to minimize the errors in estimation of the integrated profiles.

[1]S. L. Collier, V. E. Ostashev, and D. K. Wilson, "Angle-of-arrival estimation for acoustic waves propagating in atmospheric turbulence," Forum Acusticum, Budapest, Hungary, 2005.
[2]M. Scanlon, C. Reiff, and J. Noble, "Acoustic transient source localization from an aerostat," Proceedings of the 12th International Symposium on Long Range Sound Propagation, New Orleans, 2006.
[3]V. E. Ostashev, *Acoustics in Moving Inhomogeneous Media* (E & FN SPON, London, 1997).
[4]A. S. Monin and A. M. Obukhov, "Basic laws of turbulent mixing in the ground layer of the atmosphere," Trans. Geophys. Inst. Akad. Nauk USSR **151**, 163–187 (1954).
[5]P. Ugincius, "Ray acoustics and Fermat's principle in a moving inhomogeneous medium," J. Acoust. Soc. Am. **55**, 1759–1763 (1972).
[6]C. I. Chessel, "Three-dimensional acoustic-ray tracing in an inhomogeneous anisotropic atmosphere using Hamilton's equations," J. Acoust. Soc. Am. **53**, 83–87 (1973).
[7]R. B. Stull, *An Introduction to Boundary Layer Meteorology* (Kluwer, Dordrecht, 1988).
[8]J. R. Garratt, *The Atmospheric Boundary Layer* (Cambridge University Press, Cambridge, 1992).
[9]D. K. Wilson, "An alternative function for the wind and temperature gradients in unstable surface layer," Boundary-Layer Meteorol. **99**, 151–158 (2001).
[10]V. E. Ostashev and D. K. Wilson, "Relative contributions from temperature and wind velocity fluctuations to the statistical moments of a sound field in a turbulent atmosphere," Acust. Acta Acust. **86**, 60–268 (2000).

Correction techniques for the truncation of the source field in acoustic analogies

Paula Martínez-Lera and Christophe Schram
LMS International, Researchpark Z1, Interleuvenlaan 68, 3001 Leuven, Belgium

(Received 3 March 2008; revised 20 September 2008; accepted 23 September 2008)

The truncation of the source field may induce large overpredictions in the acoustic field computed through acoustic analogies. A comparative study of different correction approaches proposed in the literature is carried out, considering three different techniques: correction terms based on a convection assumption, use of model extensions, and windowing techniques. It is shown that convection-based correction terms need to take into account noncompactness effects of the source field in order to yield accurate results. A modified correction term that includes these effects is derived, and its equivalence to the method of model extensions in the case of purely convected flows is highlighted. Moreover, the performance of different windowing techniques is investigated.
© *2008 Acoustical Society of America.* [DOI: 10.1121/1.2999555]

PACS number(s): 43.28.Py, 43.20.Wd, 43.28.Ra [AH] Pages: 3421–3429

I. INTRODUCTION

The use of acoustic analogies, pioneered by Lighthill,[1] is a widely extended approach to predict flow generated sound. A matter of concern in the application of Lighthill's based analogies is where to truncate the source region.[2,3] This problem is frequently, but not only, faced in cases with extensive wakes, where Lighthill's stresses still have a significant value at the outlet of the computational domain. Such truncation of the source field may alter the balance of sources inside the domain, yielding large overpredictions of the acoustic field.

Wang *et al.*[4] showed that the error produced by truncating a wake is proportional to the time derivative of Lighthill's stresses at the truncation surface for a far-field approximation. They proposed a correction term based on a frozen eddy assumption and consisting of a surface integral over the truncating surface. This correction term has been adapted to other formulations.[5] Cheung and Lele[6] derived an alternative correction term for Lighthill's analogy from Ffowcs Williams and Hawkings equation that in certain limits is equivalent to the correction term proposed by Wang *et al.*

The correction term proposed by Wang *et al.* is applied with the sources being defined in a framework that moves with the characteristic convection velocity of the flow; this allows eliminating linear terms from Lighthill's tensor and improves numerical robustness. In general circumstances, however, the determination of a moving framework that is representative of the whole source domain can be ambiguous. Moreover, defining the sources in a moving framework involves solving a convected wave equation, for which Lighthill's solution is only valid in the low Mach number limit. A derivation of a modified correction term that is applicable to a general formulation of Lighthill's analogy, where sources are defined in a fixed framework, is proposed in the present work.

Other authors have addressed the problem of truncation of the sources with different techniques. Mitchell *et al.*[7] proposed to model extensions of the computational domain. Oberai *et al.*[8] used ramp windowing functions to force the sources to decay slowly toward the outlet; other authors have used Gaussian functions for the same purpose.[9,10] Obrist *et al.*,[11] in the framework of a spectral formulation of the analogy, interpreted the effect of the domain finiteness as a problem of spatial spectral leakage and also suggested appropriate windowing as a remedy.

The present work provides a comparison between different correction techniques for Lighthill's based analogies. We show that if the correction term by Wang *et al.*[4] is modified in order to include noncompactness effects, it can become equivalent to the method of model extensions proposed by Mitchell *et al.*[7] Furthermore, some guidelines are provided to apply the otherwise *ad hoc* windowing approach.

The outline of this paper is as follows. In Sec. II, some theoretical fundamentals are presented. In Sec. III, the problem of source truncation is illustrated, and a new correcting approach is presented and compared to other techniques available in the literature. In Sec. IV, results are presented for the test case of the sound generated by a flow past a cylinder. Finally, some conclusions are given in Sec. V.

II. BACKGROUND THEORY

Lighthill[1] derived the first acoustic analogy through a rearrangement of the Navier–Stokes equations. The so-called Lighthill equation, in the absence of external forces, can be expressed as

$$\frac{\partial^2 \rho'}{\partial t^2} - c_0^2 \frac{\partial^2 \rho'}{\partial x_i^2} = \frac{\partial^2 T_{ij}}{\partial x_i \partial x_j}, \tag{1}$$

where T_{ij} is Lighthill's tensor:

$$T_{ij} = \rho u_i u_j + (p' - c_0^2 \rho') \delta_{ij} - \tau_{ij}. \tag{2}$$

For isentropic flows, the acoustic pressure p' and density ρ' are related through $p' = c_0^2 \rho'$. Furthermore, the viscous stresses τ_{ij} are considered negligible compared to the inertial term $\rho u_i u_j$ at large Reynolds numbers, yielding $T_{ij} \simeq \rho u_i u_j$.

It is assumed that the listener is embedded in a medium at rest where sound propagates with speed c_0; moreover, it is

considered that there is no flow-acoustic coupling for the low Mach numbers considered here. The right-hand side of Eq. (1) can therefore be interpreted as the acoustic source of a nonhomogeneous acoustic propagation equation. In the presence of fixed rigid surfaces S bounding the volume V in the source region and neglecting viscous effects on the walls, a solution to Lighthill's equation is given by

$$\rho'(\mathbf{x},t) = \int_{-\infty}^{t}\int_{V} T_{ij}(\mathbf{y},\tau)\frac{\partial^2 G(\mathbf{x},t|\mathbf{y},\tau)}{\partial y_i \partial y_j} d^3\mathbf{y} d\tau - \int_{-\infty}^{t}\int_{S} P(\mathbf{y},\tau)\frac{\partial G(\mathbf{x},t|\mathbf{y},\tau)}{\partial y_i} n_i d^2\mathbf{y} d\tau, \tag{3}$$

where G is a Green's function, P is the pressure on the surface, and $\mathbf{n}$ is the normal vector directed toward the interior of the solid body defined by surface S.

If the free field Green's function $G=G_0$ is used, Curle's solution[12] can be obtained. For a listener located in the acoustical far field, it yields

$$\rho'(\mathbf{x},t) \simeq \frac{x_i x_j}{4\pi|\mathbf{x}|^2 c_0^4}\frac{\partial^2}{\partial t^2}\int_V \frac{T_{ij}^e}{r} d^3\mathbf{y} - \frac{x_i}{4\pi|\mathbf{x}|c_0^3}\frac{\partial}{\partial t}\int_S \frac{P^e n_i}{r} d^2\mathbf{y}, \tag{4}$$

where $r=|\mathbf{x}-\mathbf{y}|$ is the distance from the listener to the sources and the superscript e indicates that the variable is evaluated at the retarded time $t^e=t-r/c_0$.

The quadrupolar contribution ρ_q' to the sound, according to Eq. (4), may be expressed as

$$\rho_q'(\mathbf{x},t) = \frac{x_i x_j}{4\pi|\mathbf{x}|^2 c_0^4}\frac{\partial \dot{Q}_{ij}}{\partial t}, \tag{5}$$

where $\dot{Q}_{ij}$ is defined as

$$\dot{Q}_{ij} \equiv \frac{\partial}{\partial t}\int_V \frac{T_{ij}^e}{r} d^3\mathbf{y}. \tag{6}$$

III. CORRECTION TECHNIQUES FOR THE TRUNCATION OF THE DOMAIN

A. Correction term for the truncation on a wake

In Eq. (4), the volume integral formally extends over the whole domain of sources, which comprises all the regions with flow unsteadiness. However, the necessary finiteness of the computational fluid dynamics (CFD) domain often implies that a part of the unsteady field is not contained in it. The flow beyond the computational domain might not contribute significantly to the source field compared to the most active region captured in the volume V; this is the case, for example, of the wake behind a bluff body for low convection Mach numbers. Nevertheless, the abrupt truncation of the source region will break the balance between sources, leading to errors in the predicted acoustic field.

The quantity $\dot{Q}_{ij}$ in Eq. (5) is the sum of two contributions, those corresponding to volume V_c, included in the computational domain, and $\bar{V}_c$, which is left out of the computational domain, as illustrated in Fig. 1.

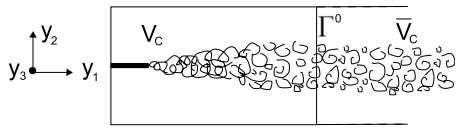


FIG. 1. Truncation of a wake.

$$\dot{Q}_{ij} = (\dot{Q}_{ij})_{V_C} + (\dot{Q}_{ij})_{\bar{V}_C} = \frac{\partial}{\partial t}\int_{V_C}\frac{T_{ij}^e}{r} d^3\mathbf{y} + \frac{\partial}{\partial t}\int_{\bar{V}_C}\frac{T_{ij}^e}{r} d^3\mathbf{y}. \tag{7}$$

Wang *et al.*[4] proposed a correction term to take into account in the computation the missing part $(\dot{Q}_{ij})_{\bar{V}_C}$. An important aspect of their approach is the elimination of the terms that are linear in the fluctuating velocities from Lighthill's tensor in order to reduce the magnitude of the truncation error. To this end, they define the sources with respect to a framework that moves with a characteristic velocity of the flow U. Considering that the direction of convection corresponds to coordinate y_1, modified Lighthill's tensor is defined as

$$\tilde{T}_{ij} = \rho\tilde{u}_i\tilde{u}_j = \rho(u_i - U\delta_{1i})(u_j - U\delta_{1j}). \tag{8}$$

In their work, U is the freestream velocity U_∞, but it may also be defined as the flow convection velocity U_c. This definition leads to a convected wave equation that replaces the original equation (1):

$$\frac{D^2\rho'}{Dt^2} - c_0^2\frac{\partial^2\rho'}{\partial x_i^2} = \frac{\partial^2\tilde{T}_{ij}}{\partial x_i \partial x_j}, \tag{9}$$

where D/Dt is defined as

$$\frac{D}{Dt} \equiv \frac{\partial}{\partial t} + U\frac{\partial}{\partial y_1}. \tag{10}$$

For low Mach numbers, Eq. (9) can be approximated as

$$\frac{\partial^2\rho'}{\partial t^2} - c_0^2\frac{\partial^2\rho'}{\partial x_i^2} = \frac{\partial^2\tilde{T}_{ij}}{\partial x_i \partial x_j}, \tag{11}$$

so that Curle's solution may still be applied. It must be noted that for finite Mach numbers, this approximation may fail to give accurate results.

In the framework of this formulation, Wang *et al.* proposed a correction term based on the idea that turbulence is frozen at the outlet of the computational domain. With this, and for a compact source region so that differences in the retarded times over it may be neglected, the correction term results in an integral over the truncation surface Γ^0:

$$(\dot{Q}_{ij})_{\bar{V}_C} = \int_{\Gamma^0} U_c\frac{\tilde{T}_{ij}}{r} d^2\mathbf{y}, \tag{12}$$

where U_c is the convection velocity at the outlet.

For the case of a noncompact source field, they proposed a straightforward generalization of Eq. (12) considering the retarded time t^e:

$$(\dot{Q}_{ij})_{\bar{V}_C} = \int_{\Gamma^0} U_c \frac{\tilde{T}^e_{ij}}{r} d^2\mathbf{y}. \tag{13}$$

The convection Mach number M_c gives a measure of the compactness of the sources ($M_c = U_c/c_0 \propto L_f/\lambda$, L_f being a typical length of the convected flow structures and λ the acoustic wavelength). In Sec. IV, our results will illustrate how the correction term given by Eq. (13), which has been obtained through generalization of the compact case, can become inaccurate for finite Mach numbers. In the following section, a correction term that improves this behavior is derived.

B. Derivation of a correction term considering noncompactness effects

The problem described by Fig. 1 is considered. Beyond the computational domain, Lighthill's stresses are negligible, except in region $\bar{V}_C$, where the flow is convected along the coordinate y_1 with the uniform convection velocity U_c.

The aim of this section is to derive a correction term for a general formulation of the analogy, without defining the sources with respect to a moving framework. Reynolds transport theorem is applied in volume $\bar{V}_C$ to obtain $(\dot{Q}_{ij})_{\bar{V}_C}$:

$$(\dot{Q}_{ij})_{\bar{V}_C} = \frac{\partial}{\partial t}\int_{\bar{V}_C} \frac{T^e_{ij}}{r} d^3\mathbf{y} = \frac{D}{Dt}\int_{\bar{V}'_C(t)} \frac{T^e_{ij}}{r} d^3\mathbf{y} + \int_{\Gamma^0} U_c \frac{T^e_{ij}}{r} d^2\mathbf{y}, \tag{14}$$

where it is considered that volume $\bar{V}_C$ extends downstream far enough as to make T^e_{ij}/r vanish. The volume related to the integral inside the derivative D/Dt [defined as in Eq. (10) with $U \equiv U_c$] has been denoted as $\bar{V}'_C(t)$; this is a volume that moves with the convection velocity U_c, but that coincides with $\bar{V}_C$ at the time t.

It must be noted that if in Eq. (14) the source region is assumed to be compact and the listener in the far field, and the flow to be driven strictly by convection, the term with the derivative D/Dt vanishes, and the correction term proposed by Wang *et al.* is obtained. However, if the sources are not compact or, equivalently, if the Mach number is not low enough, this term may have a non-negligible value and should be taken into account in the correction term. This can be interpreted as a consequence of the relative motion between volume $\bar{V}'_C(t)$ and the listener. In order to derive a correction term that acknowledges this effect, tensor T_{ij} for a purely convected flow is defined as

$$T_{ij}(y_1, y_2, y_3, t) = T^0_{ij}\left(y_2, y_3, t - \frac{y_1 - y^0_1}{U_c}\right), \tag{15}$$

where y^0_1 is the y_1-coordinate of surface $\Gamma^0(y_2, y_3)$. Furthermore, tensor T^e_{ij} evaluated at the retarded time becomes

$$T^e_{ij} = T^0_{ij}(y_2, y_3, t'),$$

where

$$t' \equiv t - (y_1 - y^0_1)/U_c - r/c_0.$$

With this definition, it can be proved that

$$\frac{D}{Dt}\left(\frac{T^e_{ij}}{r}\right) \simeq M_c \cos\theta \frac{\partial}{\partial t}\left(\frac{T^e_{ij}}{r}\right), \tag{16}$$

where M_c is the Mach number $M_c = U_c/c_0$, $\theta = \arccos((x_1 - y_1)/r)$ is the angle between the convective direction and the listener direction, and where near-field terms $\propto (1/r^2)$ have been neglected, as the listener is considered to be in the acoustic far field.

In the (geometrical) far field, $\cos\theta$ can be considered independent of the source spatial coordinates $\mathbf{y}$. Using Eq. (16), the term with the derivative D/Dt in Eq. (14) can be expressed as

$$\frac{D}{Dt}\int_{\bar{V}'_C(t)} \frac{T^e_{ij}}{r} d^3\mathbf{y} = \int_{\bar{V}_C} \frac{D}{Dt}\left(\frac{T^e_{ij}}{r}\right) d^3\mathbf{y} = M_c \cos\theta \int_{\bar{V}_C} \frac{\partial}{\partial t}\left(\frac{T^e_{ij}}{r}\right) d^3\mathbf{y}. \tag{17}$$

The combination of Eqs. (14) and (17) yields

$$(1 - M_c \cos\theta)\frac{\partial}{\partial t}\int_{\bar{V}_C} \left(\frac{T^e_{ij}}{r}\right) d^3\mathbf{y} = \int_{\Gamma^0} U_c \frac{T^e_{ij}}{r} d^2\mathbf{y} \tag{18}$$

and, finally, variable $(\dot{Q}_{ij})_{\bar{V}_C}$ is obtained:

$$(\dot{Q}_{ij})_{\bar{V}_C} = \int_{\Gamma^0} \frac{U_c}{1 - M_c \cos\theta} \frac{T^e_{ij}}{r} d^2\mathbf{y}. \tag{19}$$

Substituting in Eq. (5), the total quadrupolar field yields

$$\rho'_q(\mathbf{x}, t) = \frac{x_i x_j}{4\pi|\mathbf{x}|^2 c_0^4}\frac{\partial^2}{\partial t^2}\int_{V_C} \frac{T^e_{ij}}{r} d^3\mathbf{y} + \frac{x_i x_j}{4\pi|\mathbf{x}|^2 c_0^4}\frac{\partial}{\partial t}\int_{\Gamma^0} \frac{U_c}{1 - M_c \cos\theta} \frac{T^e_{ij}}{r} d^2\mathbf{y}. \tag{20}$$

It may be observed that for low Mach numbers, the proposed correction term reduces to Eq. (13). However, Eq. (19) may yield considerable improvements for finite Mach numbers, as suggested by previous numerical results.[13] Some physical insight can be gained if we interpret the factor $(1 - M_c \cos\theta)$, which is a Doppler factor,[14] as an effect of convective amplification of the sources in $\bar{V}_C$. The partial time derivative of the integral over this volume is substituted by a surface integral over Γ^0; however, the latter must be interpreted as a moving source for it to be representative of a volume where the flow has a non-negligible mean convection velocity.

Finally, we want to point out that, although in the derivation U_c has been assumed to be uniform, its dependence on coordinates y_2 and y_3 would not prevent obtaining the same result. Although in many cases one single convection velocity U_c will be representative enough to give an accurate correction term, in other situations the use of a locally varying convection velocity might be preferred.

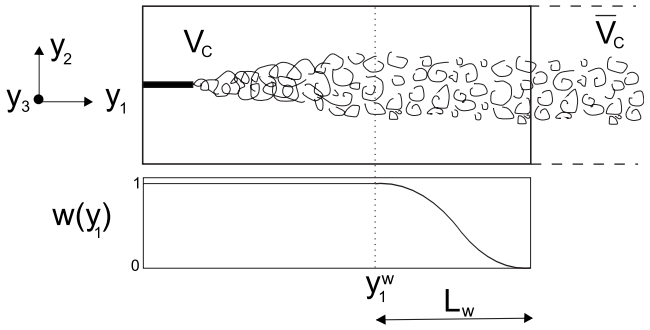


FIG. 2. Windowing in the source domain.

C. Method of model extensions

Mitchell *et al.*[7] proposed an alternative correction approach, consisting in modeling Lighthill's tensor in the zones outside the computational domain (what they called the passive domain) using information from the computed source field:

$$\hat{T}_{ij}(y_1,y_2,y_3,\omega) = \hat{T}^0_{ij}(y_2,y_3,\omega)e^{ik_0(y_1-y_1^0)}, \tag{21}$$

where the hatted variables are expressed in Fourier domain and where k_0 is a constant parameter to be determined from the flow data inside the computational domain using

$$k_0 = -i\frac{1}{\hat{T}_{11}}\frac{\partial \hat{T}_{11}}{\partial y_1}. \tag{22}$$

With this model for the sources beyond the computational domain, the quadrupolar field is integrated along coordinate y_1 after doing a Taylor expansion and neglecting terms that vanish in the far field. An expression in frequency domain is obtained, which presents similarities with Eq. (20). Indeed, both correction methods are equivalent provided that the parameter k_0, which is in principle a complex number, becomes a real number related to the convection velocity U_c through

$$k_0 = \omega/U_c. \tag{23}$$

This relationship is only verified in the case of a flow purely driven by convection, which was a hypothesis assumed to derive Eq. (19).

While the real part of k_0 is associated with convection in the model, its imaginary part relates to an exponential decay of the source amplitude. Therefore, in the case where sources experience a decay as the flow is convected, the method of model extensions may have the advantage of being able to model it. However, an exponential law may, in general, not be an adequate model for this decay, as suggested by the results obtained by Mitchell *et al.*,[7] who reported for the case of a jet large uncertainties in the calculation of the imaginary part of k_0.

D. Windowing techniques

The principle of the windowing technique is described in Fig. 2. The sources at the downstream region of the computational domain are weighted by a windowing function that makes the source amplitude decay slowly toward the limits of the domain, so that no error is produced due to an abrupt source truncation.

The windowing functions must be smooth enough to prevent a large deformation of the sources and, as a result, the alteration of the acoustic results. They are defined in the interval $y_1^w < y_1 < y_1^w + L_w$. Oberai *et al.*[8] used ramp functions

$$w(y_1) = 1 - \frac{y_1 - y_1^w}{L_w}, \tag{24}$$

where y_1^w corresponds to the beginning of the windowing and L_w is the windowing length, as described by Fig. 2. Other authors[9,10] applied Gaussian functions

$$w(y_1) = \exp\left[\frac{(y_1 - y_1^w)^2}{2\sigma^2}\right], \tag{25}$$

where σ^2 is the variance. Hann windows have been used, too.[11]

$$w(y_1) = \frac{1}{2}\left[1 + \cos\left(\frac{\pi}{L_w}(y_1 - y_1^w)\right)\right]. \tag{26}$$

IV. TEST CASE: SOUND GENERATED BY THE FLOW PAST A CYLINDER

A two-dimensional (2D) laminar flow past a cylinder,[15,16] is considered in order to illustrate the nature of the error introduced by the truncation of a wake, as well as the performance of the correction approaches. This case is characterized by a clean vortex shedding with negligible broadband content, and therefore allows highlighting the effects of convection and of the large coherent structures of a flow. As argued in Sec. III, the linear components of the source term that are related to the mean convection velocity of the flow can have a large impact on the correction. In this work, the correction techniques are studied under this perspective, without considering possible effects of three dimensionality or of the smallest scales of turbulence.

A. Flow computation

The relevant dimensional parameters of the problem are the cylinder diameter D, the free field velocity U_∞, and the density ρ_∞, which are used to normalize the other quantities. The Reynolds number $\mathrm{Re} = U_\infty D/\nu$ is $\mathrm{Re} = 100$. The Strouhal was defined as $\mathrm{St} = Df_0/U_\infty$, with the main frequency f_0 of the lift coefficient of the cylinder. Other dimensionless measured quantities were the lift and drag coefficients, and the base-pressure coefficient defined as the pressure coefficient at the rear stagnation point of the cylinder $C_{\mathrm{pb}} = (P - P_\infty)/(\rho_\infty U_\infty^2/2)$, with P_∞ measured at the inlet.

For the considered Reynolds number, the flow is in the laminar unsteady regime and practically 2D. The CFD simulation was run with an incompressible 2D solver that uses an implicit second-order unsteady formulation. No turbulence modeling was applied, and the mesh contained 52,000 quadrilateral cells. The origin of coordinates of the computational domain was placed at the center of the cylinder. The distances from the center of the cylinder to the inlet and outlet

TABLE I. Comparison of Strouhal number, peak-to-peak lift coefficient, time-averaged drag coefficient, and time-averaged base-pressure coefficient. Reference values: empirical functions (Ref. 20); 2D numerical simulations (Ref. 17) for $L_{b|i}/D=10$ and in the asymptotic limit $L_{b|i}/D\to\infty$.

	St	ΔC_L	$\bar{C}_D$	$-\bar{C}_{\mathrm{pb}}$
Ref. 20	0.164	0.643	—	—
Ref. 17 (asymptotic)	0.163	0.632	1.312	0.690
Ref. 17 ($L_{b\|i}/D=10$)	0.170	0.685	1.381	0.790
Present ($L_{b\|i}/D=10$)	0.170	0.686	1.393	0.787

were $L_i=10D$ and $L_o=30D$, respectively, while the distance to the lateral boundaries was $L_b=10D$. A sponge zone was added at the end of the domain (from the downstream limit $30D$ up to $50D$), where the mesh size gradually increases in order to damp the vortical structures before they reach the outlet and avoid the pressure disturbances that would otherwise contaminate the source region. It should be noted that the source region considered in the acoustic computations did not include this sponge zone. The following boundary conditions were imposed: no-slip conditions at the cylinder walls, a uniform velocity profile at the inlet, symmetry conditions at the lateral boundaries, and a constant pressure at the end of the sponge zone.

The distance from the cylinder to the boundaries plays an important role in the computation. Posdziech and Grundmann[17] quantified the dependence on L_i and L_b of typical results such as Strouhal number and drag and lift coefficients. Table I compares several results to reference values available in the literature. A very good agreement is observed with the reference values that use the same value for $L_{b|i}=L_b=L_i$. A detail of the instantaneous vorticity field is shown in Fig. 3, where the vortex shedding behind the cylinder can be observed.

The velocities around the cylinder and the pressure on the cylinder surface were exported during four periods of the lift coefficient, with 50 samples per period, in order to compute the source terms involved in Curle's analogy.

B. Acoustic computation

2D acoustic computations were carried out in Fourier domain. According to Eq. (4), the acoustic pressure given by Curle's analogy can be expressed as a sum of a dipolar and a quadrupolar contribution:

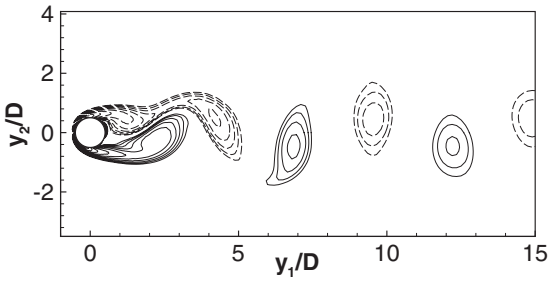


FIG. 3. Detail of the vorticity field. Twelve levels for positive (solid) and negative (dashed) vorticities from $\pm 0.5U_\infty/D$ to $\pm 20U_\infty/D$ with an exponential increase.

$$\hat{P}(\mathbf{x},\omega)=\hat{P}_d+\hat{P}_q \tag{27}$$

with

$$\hat{P}_d(\mathbf{x},\omega)=-\int_S \hat{P}n_i\frac{\partial\hat{G}_0}{\partial y_i}d^2\mathbf{y} \tag{28}$$

and

$$\hat{P}_q(\mathbf{x},\omega)=-\int_V \hat{T}_{ij}\frac{\partial^2\hat{G}_0}{\partial y_i\partial y_j}d^3\mathbf{y} \tag{29}$$

becoming, respectively, a line and a surface integral in two dimensions. The hatted variables are in Fourier domain. Note that the results obtained in this section are applicable in three dimensions as well.

The source field was integrated with a trapezoidal rule. The results that are shown in this section correspond to the frequency f_0 of the lift on the cylinder, which is the dominant contribution to the acoustical field. In order to study effects of noncompactness of the source field, several Mach numbers $M_\infty=U_\infty/c_0$ were simulated by varying the speed of sound. The relationship between this reference Mach number M_∞ and the convection Mach number M_c defined in Sec. III was found to be for this flow

$$\frac{M_c}{M_\infty}=\frac{U_c}{U_\infty}=0.91. \tag{30}$$

As indicated in Sec. III A, the Mach number gives a measure of the compactness of the flow structures, as

$$M_c=\frac{U_c}{c_0}=\frac{\lambda_f}{\lambda}, \tag{31}$$

where $\lambda_f\simeq 5.35D$ is the flow characteristic wavelength related to the considered frequency through $\lambda_f=U_c/f_0$.

Following a similar approach as the one developed by Gloerfelt *et al.*,[18] we consider in addition the use of a tailored Green's function $\hat{G}_t$ for validation purposes. This Green's function implicitly accounts for the acoustic scattering so that the wall-normal derivative vanishes exactly over the cylinder surface, and the acoustic field can be computed using only the quadrupoles distributed in the volume (surface in two dimensions):

$$\hat{P}(\mathbf{x},\omega)=-\int_V \hat{T}_{ij}\frac{\partial^2\hat{G}_t}{\partial y_i\partial y_j}d^3\mathbf{y}. \tag{32}$$

As a corollary, the dipolar contribution in Curle's analogy verifies the relationship

$$\hat{P}_d(\mathbf{x},\omega)=-\int_V \hat{T}_{ij}\frac{\partial^2\hat{G}_s}{\partial y_i\partial y_j}d^3\mathbf{y}, \tag{33}$$

where $\hat{G}_s$ is the part of the tailored Green's function corresponding to the acoustic scattering on the cylinder walls

$$\hat{G}_s\equiv\hat{G}_t-\hat{G}_0. \tag{34}$$

The tailored Green's function for a 2D cylinder can be found in the literature (e.g., Ref. 18). Figure 4 shows the directivity

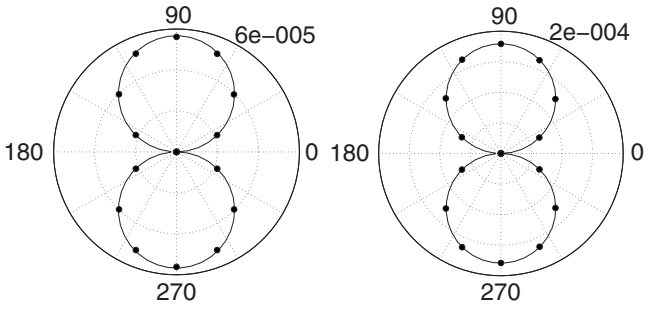


FIG. 4. Directivity plots for the dipole pressure amplitude $|\hat{P}_d/\rho_\infty U_\infty^2|$, measured at $|\mathbf{x}|/D=6000$ for the lift frequency. $M_\infty=0.02$ (left) and $M_\infty=0.2$ (right). Results obtained with Curle's surface integral (solid lines) and with scattering Green's function (symbols).

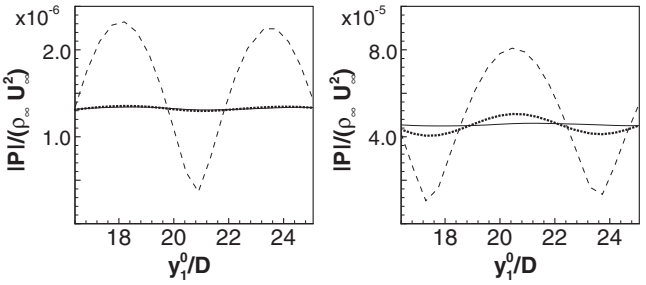


FIG. 5. Moving framework: Quadrupole pressure amplitude at $[|\mathbf{x}|/D=6000,\ \phi=\pi/4]$ vs truncation position y_1^0. Lift frequency, $M_\infty=0.02$ (left) and $M_\infty=0.2$ (right). Uncorrected (dashed), with correction (dotted), and with modified correction (solid).

plots for the dipolar contribution at two different Mach numbers, $M_\infty=0.02$ and 0.2. In each plot, the results obtained with the surface integral in Eq. (28) are compared to the scattered part of the field obtained with the tailored Green's function, according to Eq. (33). The agreement between both predictions demonstrates that the wall pressure and the flow velocities have been calculated accurately and are consistent with each other. It also illustrates that for a compact body as the cylinder in the present case $[\lambda/D=1/(\mathrm{St}M_\infty)\simeq 5.88/M_\infty]$, the error induced by obtaining the pressure on the cylinder through incompressible CFD is negligible, as also shown by Gloerfelt *et al.*[18]

Furthermore, these results suggest that the effect of the truncation of the quadrupoles is negligible in the integral in Eq. (33). This is due to the fact that the scattering Green's function G_s is a fast-decaying function of the distance between the sources and the cylinder, such that the quadrupole components close to the cylinder dominate compared to the quadrupoles in the truncation region, which are weighted with negligible coefficients. However, the behavior is different when integrating using the free field Green's function as in Curle's analogy; it is shown in this section that the truncation effect poses serious issues in that case.

The quadrupolar sound is computed as

$$\hat{P}_q=(\hat{P}_q)_{V_C}+(\hat{P}_q)_{\bar{V}_C}, \tag{35}$$

where $(\hat{P}_q)_{\bar{V}_C}$ is a correction term. The numerical robustness of the prediction is evaluated by considering different longitudinal positions of the truncation surface Γ^0. Following the argument that the turbulent structures in the truncation region are mainly convected with little distortion and that the convection Mach number is low, that region should be essentially silent and the sound prediction independent of the truncation surface coordinate y_1^0. We present results for three cases.

- Uncorrected quadrupolar field,

$$(\hat{P}_q)_{\bar{V}_C}=0. \tag{36}$$

- Correction proposed by Wang *et al.*,

$$(\hat{P}_q)_{\bar{V}_C}=-\int_{\Gamma^0}\frac{U_c}{i\omega}\hat{T}_{ij}\frac{\partial^2\hat{G}_0}{\partial y_i\partial y_j}d^2\mathbf{y}. \tag{37}$$

- Modified correction term,

$$(\hat{P}_q)_{\bar{V}_C}=-\int_{\Gamma^0}\frac{U_c}{i\omega(1-M_c\cos\theta)}\hat{T}_{ij}\frac{\partial^2\hat{G}_0}{\partial y_i\partial y_j}d^2\mathbf{y}, \tag{38}$$

where i is the imaginary unit.

In the case of using a moving framework of reference, tensor $\hat{\tilde{T}}_{ij}$ replaces $\hat{T}_{ij}$ in Eqs. (29), (37), and (38).

1. Moving framework (tensor $\hat{\tilde{T}}_{ij}$)

The speed of the reference framework used in this section is $U\equiv U_\infty$, as the one used by Wang *et al.* Figure 5 shows the computed acoustic pressure at a point as a function of the position y_1^0/D of the truncation surface for the two considered Mach numbers. It can be observed that the uncorrected field presents a strong dependence on the position of the truncation surface Γ^0 for both Mach numbers $M_\infty=0.02$ and 0.2. This dependence makes the results fluctuate with the variation of y_1^0 with the same wavenumber that characterizes the flow structures. By contrast, the corrected results with either Eq. (37) or (38) show improved behavior. For the case with $M_\infty=0.02$, the results are practically independent from the size of the domain for both correction terms. In the case with $M_\infty=0.2$, some dependence on the truncation surface is observed in the results obtained with the original correction term; by contrast, this variability is suppressed if the modified correction term is used instead. Directivity plots of the corrected quadrupolar field at both Mach numbers are shown in Fig. 6.

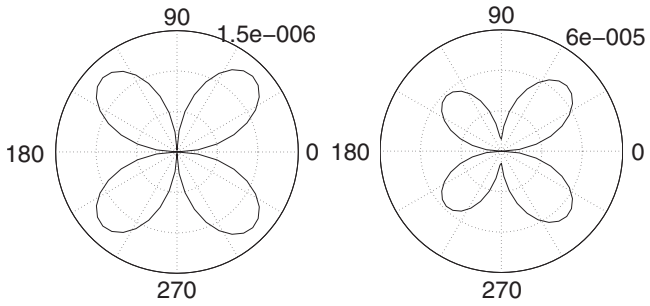


FIG. 6. Moving framework: Directivity plots for the quadrupole pressure amplitude $|\hat{P}_q/\rho_\infty U_\infty^2|$, measured at $|\mathbf{x}|/D=6000$ for the lift frequency. $M_\infty=0.02$ (left) and $M_\infty=0.2$ (right).

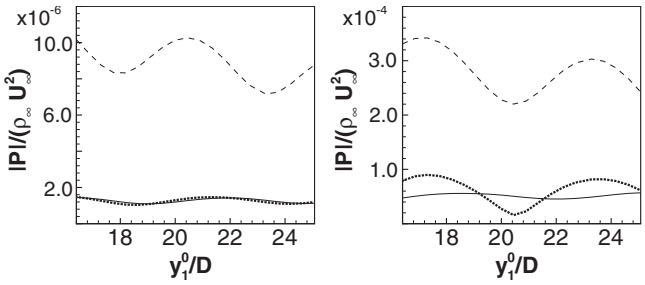


FIG. 7. Fixed framework: Quadrupole pressure amplitude at $[|\mathbf{x}|/D=6000, \phi=\pi/4]$ vs truncation position y_1^0. Lift frequency, $M_\infty=0.02$ (left) and $M_\infty=0.2$ (right). Uncorrected (dashed), with correction (dotted), and with modified correction (solid).

2. Fixed framework (tensor $\hat{T}_{ij}$)

Figure 7 shows the acoustic pressure at a point as a function of the position of the truncation surface. Remarkably, the uncorrected quadrupolar field shows an overprediction for both considered Mach numbers that is considerably larger than the one shown in Fig. 5. This is due to the linear terms that make the tensor defined in a fixed framework larger in magnitude.

The magnitude of the truncation error is illustrated in Fig. 8. Consistently with Curle's theory in 2D, dipolar and quadrupolar contributions scale, respectively, with $U_\infty^{5/2}$ and $U_\infty^{7/2}$, and the ratio between them is $\propto M_\infty^{-1}$. However, the uncorrected quadrupolar sound presents an overprediction of one order of magnitude. This involves that also the correction term is one order of magnitude larger than the corrected field, making the latter very sensitive to the accuracy of the correction.

Due to this sensitivity, some remaining variability can be observed in the corrected field for $M_\infty=0.02$ in Fig. 7. This can be better appreciated in Fig. 9, where the corrected results are compared with the corrected results of the previous section, where a moving framework was used to define the sources. Another consequence of this sensitivity that is shown in Fig. 7 is that the unimproved correction simply fails to yield acceptable results for $M_\infty=0.2$. By contrast, the more accurate modified correction term succeeds to give

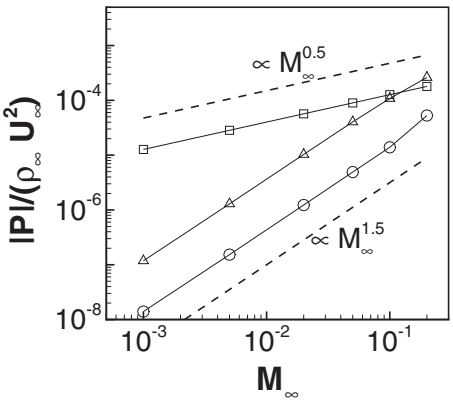


FIG. 8. Maximum pressure amplitude at $|\mathbf{x}|/D=6000$ for the lift frequency: dipolar noise (squares), uncorrected quadrupolar noise (triangles), corrected quadrupolar noise (circles). Dipolar noise measured at an angle $\phi=\pi/2$; quadrupolar at $\phi=\pi/4$.

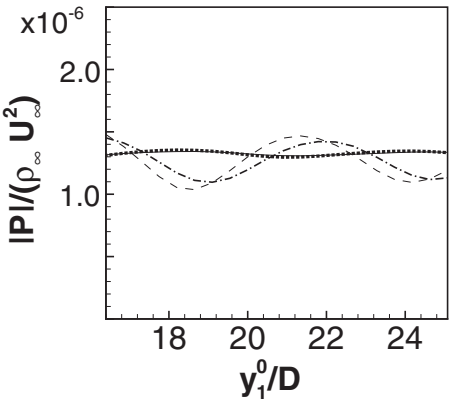


FIG. 9. Quadrupole pressure amplitude at $[|\mathbf{x}|/D=6000, \phi=\pi/4]$ vs truncation position y_1^0. Lift frequency, $M_\infty=0.02$. Computed with: fixed framework and correction (dashed), fixed framework and modified correction (dash-dotted), moving framework and correction (dotted), and moving framework and modified correction (solid).

consistent results, only remaining a small residual variability, equivalent to the one obtained for the case with $M=0.02$.

Figure 10 shows the directivity plots of the quadrupolar field (corrected with the modified term) for both Mach numbers, along with the variation interval of the acoustic prediction as the truncation position varies. It can be observed that for $M_\infty=0.2$ there is a significant asymmetry with respect to the vertical axis $\phi=\pi/2-3\pi/2$. This is due to the phenomenon of convective amplification, which becomes more relevant as the Mach number increases. By contrast, the directivity pattern in Fig. 6 showed a less strong influence of convection effects, due to the approximation involved in the definition of the sources with respect to a moving framework. As expected, Eq. (11) becomes inaccurate for finite Mach numbers and fails to reproduce the real directivity pattern.

Alternatively to the correction terms, the method of model extensions may be applied. However, the results do not vary significantly in this case with respect to the use of the correction term. The imaginary part of k_0 in Eq. (22) presented a large variability in space, indicating that the decay of the sources is not well approximated by the exponential law in the model extension. Similar observations were reported by Mitchell *et al.*[7] for the case of a jet. Moreover, its value was small in comparison to the real part of k_0. The

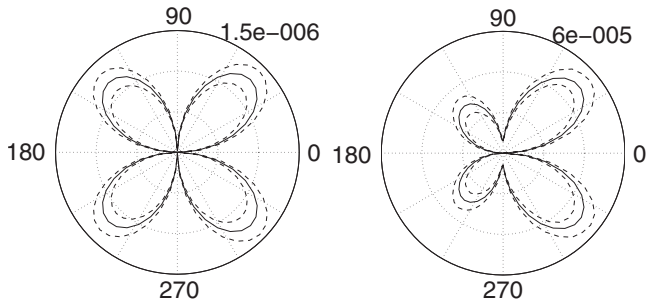


FIG. 10. Fixed framework: Directivity plots for the quadrupole pressure amplitude $|\hat{P}_q/\rho_\infty U_\infty^2|$, measured at $|\mathbf{x}|/D=6000$ for the lift frequency. $M_\infty=0.02$ (left) and $M_\infty=0.2$ (right). The average directivity (solid line) is plotted together with the limits of the uncertainty interval (dashed lines) for varying y_1^0.

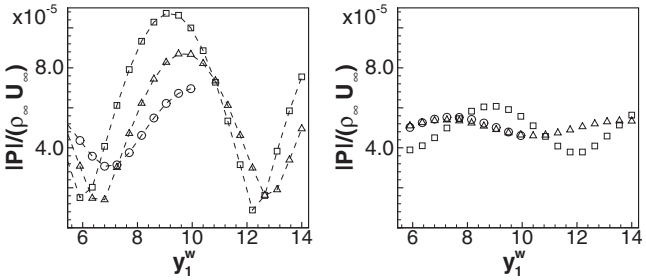


FIG. 11. Windowing technique: Quadrupole pressure amplitude at $[|\mathbf{x}|/D=6000, \phi=\pi/4]$ vs windowing starting coordinate y_1^w. Lift frequency, $M_\infty=0.2$. Computed with ramp functions (left) and Hann functions (right). Windowing length $L_w=10$ (squares), 15 (triangles), and 20 (circles).

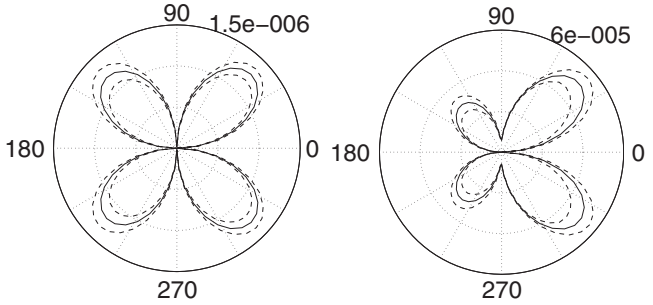


FIG. 12. Hann windowing with $L_w=20$: Directivity plots for the quadrupole pressure amplitude $|\hat{P}_q/\rho_\infty U_\infty^2|$, measured at $|\mathbf{x}|/D=6000$ for the lift frequency. $M_\infty=0.02$ (left) and $M_\infty=0.2$ (right). The average directivity (solid line) is plotted together with the limits of the uncertainty interval (dashed lines) for varying y_1^w. Sources defined in a fixed framework.

relationship given by Eq. (23) is a good approximation in this case, making both correction approaches equivalent.

Finally, we present results where instead of a correction term, windowing techniques have been applied to correct the source truncation. Figure 11 shows the results for the pressure amplitude obtained with ramp windowing functions [Eq. (24)] and Hann windows [Eq. (26)] with different parameters. The ramp functions fail to give consistent results, presenting a great dependence on the windowing parameters even for large windowing lengths. By contrast, the results obtained with the Hann windows demonstrate a higher independence from the windowing parameters, provided that a minimum windowing length L_w is available. Our observations suggest that the failure of the ramp functions to give consistent results is due to the discontinuous derivative they present at y_1^w and at $y_1^w+L_w$, which makes them deform the sources too abruptly. Hann windows present zero derivatives at those points, providing a smoother decay of the sources. Results of a recent study[19] also suggest that the optimal windowing function is the one that combines small derivatives near both ends y_1^w and $y_1^w+L_w$.

It must be noted that a set of windowing parameters (y_1^w, L_w) may introduce an error that is more marked in some region of the directivity. Figure 11 shows similar error levels for windowing lengths $L_w=15$ and 20 at $\phi=\pi/4$; nevertheless, in the directivity region $\pi/2<\phi<3\pi/2$, the observed error was significantly larger for $L_w=15$. The variability in the results obtained with the Hann window with the largest value of the windowing length $L_w=20$ is comparable with the variability observed using the improved correction term. This is confirmed in Fig. 12, which displays the directivity of the quadrupolar noise computed with Hann windows for the two considered Mach numbers. Gaussian functions, for which results are not shown, gave results of approximately similar quality when an appropriate value of the variance was chosen. An optimal value for the variance in Eq. (25) was found around $\sigma^2=0.09L_w^2$.

For all correction approaches, the results that have been shown correspond to positions of the truncation surface that are relatively far from the cylinder. As discussed, this is necessary in the case of the windowing approach, because the windowing length determines the accuracy of the correction. However, in the case of the correction term (or, equivalently, the model extensions technique), the truncation surface may be closer to the cylinder, provided that it is placed in the region where convection is dominant, and that all the most active source regions are contained inside the domain. This convection region begins for the discussed case at around $y_1^0=5D$.

V. CONCLUSIONS

The truncation of the source field may produce a large error in the acoustic far field computed through Lighthill's based analogies such as Curle's. This is confirmed by the presented results for the sound produced by the flow past a cylinder, which show a truncation error that is one order of magnitude larger than the real quadrupolar sound. The correction techniques for the truncation must therefore be very accurate in order to obtain consistent results.

The correction term proposed by Wang *et al.*[4] provides a straightforward and efficient method. However, its success strongly relies on the definition of the sources with respect to a translating framework in order to eliminate linear terms. The definition of a suitable moving framework may become an issue for problems in which convection cannot be characterized by a uniform velocity and therefore involves a loss of generality in the approach. Moreover, Curle's solution yields inaccurate results for finite Mach numbers if the sources are defined in a moving framework, and a convected wave equation must be solved instead in order to obtain a more realistic directivity pattern.

In the present work, a correction term that overcomes these limitations has been derived, being applicable to a general formulation of Lighthill's analogy. The modified correction term accounts for convective effects at the outflow region; acknowledging these effects is necessary to accurately determine the correction term for finite Mach numbers. This becomes especially crucial when the sources are defined with respect to a fixed framework, in which case the truncation error can be very large.

The relationship between the modified correction term and the method of model extensions proposed by Mitchell *et al.*[7] has been highlighted: both methods yield similar results and, in the case of a purely convected flow, are formally equivalent.

Finally, the technique of windowing has been investigated. This approach is *ad hoc* and less efficient than the others, as it requires a minimum windowing length to be

successful, leading to unnecessarily large CFD computational domains. On the other hand, it has the advantage of being applicable in regions where a convection velocity cannot be easily defined. The application of this technique in the wake of the cylinder flow has demonstrated that the success of the method depends critically on the windowing length and on the shape of the windowing function. Smooth functions with zero or small derivative at the limits of the window, such as Hann or Gaussian functions, provide the best performance.

The test case used to analyze the correction techniques is 2D and laminar. The study has focused on the effects of the mean convection velocity and the largest structures of the flow, which have a large impact on the error due to source truncation. A study of possible additional effects due to three dimensionality and turbulence is beyond the scope of this work and is therefore left for future investigation.

ACKNOWLEDGMENTS

The authors gratefully acknowledge the EC support for the present work, performed within the Marie Curie RTN project AETHER (Contract No. MRTN-CT-2006-035713).

[1]M. J. Lighthill, "On sound generated aerodynamically. Part I. General theory," Proc. R. Soc. London, Ser. A **211**, 564–587 (1952).
[2]C. Bailly, C. Bogey, and X. Gloerfelt, "Some useful hybrid approaches for predicting aerodynamic noise," C. R. Mec. **333**, 666–675 (2005).
[3]M. Wang, J. B. Freund, and S. K. Lele, "Computational prediction of flow-generated sound," Annu. Rev. Fluid Mech. **38**, 483–512 (2006).
[4]M. Wang, S. K. Lele, and P. Moin, "Computation of quadrupole noise using acoustic analogy," AIAA J. **34**, 2241–2254 (1996).
[5]E. J. Avital, N. D. Sandham, and K. H. Luo, "Calculation of basic sound radiation of axisymmetric jets by direct numerical simulations," AIAA J. **37**, 161–168 (1999).
[6]L. C. Cheung and S. K. Lele, "Evaluation of far-field sound with open surface corrections to Lighthill's equation," *AIAA Paper No. 2006–2488*, (2006).
[7]B. E. Mitchell, S. K. Lele, and P. Moin, "Direct computation of the sound generated by vortex pairing in an axisymmetric jet," J. Fluid Mech. **383**, 113–142 (1999).
[8]A. A. Oberai, F. Roknaldin, and T. J. R. Hughes, "Computational procedures for determining structural-acoustic response due to hydrodynamic sources," Comput. Methods Appl. Mech. Eng. **190**, 345–361 (2000).
[9]C. Bogey, C. Bailly, and D. Juvé, "Numerical simulation of the sound generated by vortex pairing in a mixing layer," J. Sound Vib. **287**, 129–151 (2000).
[10]F. Bastin, P. Lafon, and S. Candel, "Computation of jet mixing noise due to coherent structures: the plane jet case," J. Fluid Mech. **335**, 261–304 (1997).
[11]D. Obrist and L. Kleiser, "The influence of spatial domain truncation on the prediction of acoustic far-fields," *AIAA Paper No. 2007–3725*, 2007.
[12]N. Curle, "The influence of solid boundaries upon aerodynamic sound," Proc. R. Soc. London, Ser. A **231**, 505–514 (1955).
[13]P. Martínez-Lera, A. Pradera, and C. Schram, "Efficient implementation of equivalent sources from CFD data in Curle's analogy," *AIAA Paper 2007–3569*, (2007).
[14]M. Roger, "Aeroacoustics: Some theoretical background—The acoustic analogy," in *Computational Aeroacoustics*, edited by J. Anthoine and T. Colonius (Von Karman Institute, Rhode-St-Genese, 2006), Vol. **LS** 2006–05.
[15]M. M. Zdravkovich, "Flow around circular cylinders," *Fundamentals* (Oxford University Press, New York, 1997), Vol. **1**.
[16]O. Inoue and N. Hatakeyama, "Sound generation by a two-dimensional circular cylinder in a uniform flow," J. Fluid Mech. **471**, 285–314 (2002).
[17]O. Posdziech and R. Grundmann, "A systematic approach to the numerical calculation of fundamental quantities of the two-dimensional flow over a circular cylinder," J. Fluids Struct. **23**, 479–499 (2007).
[18]X. Gloerfelt, F. Pérot, C. Bailly, and D. Juvé, "Flow-induced cylinder noise formulated as a diffraction problem for low Mach numbers," J. Sound Vib. **287**, 129–151 (2005).
[19]M. Piellard and C. Bailly, "Validation of a hybrid CAA method. Application to the case of a ducted diaphragm at low Mach number," *AIAA Paper No. 2008–2873*, (2008).
[20]C. Norberg, "Fluctuating lift on a circular cylinder: Review and new measurements," J. Fluids Struct. **17**, 57–96 (2003).

The structure of raylike arrivals in a shallow-water waveguide

Philippe Roux[a)]
LGIT, Université Joseph Fourier, CNRS UMR 5559, Grenoble 38041, France

Bruce D. Cornuelle, W. A. Kuperman, and W. S. Hodgkiss
Scripps Institution of Oceanography, University of California at San Diego, 9500 Gilman Drive, La Jolla, California 92093-0230

(Received 7 February 2008; revised 30 July 2008; accepted 4 September 2008)

Acoustic remote sensing of the oceans requires a detailed understanding of the acoustic forward problem. The results of a shallow-water transmission experiment between a vertical array of sources and a vertical array of receivers are reported. The source array is used to provide additional degrees of freedom to isolate and track raylike arrivals by beamforming over both source and receiver arrays. The coordinated source-receiver array processing procedure is presented and its effectiveness in an example of tracking raylike arrivals in a fluctuating ocean environment is shown. Many of these arrivals can be tracked over an hour or more and show slowly varying amplitude and phase. The use of a double-beamforming algorithm lays the foundation for shallow-water acoustic remote sensing using travel time and source and receive angles of selected eigenrays.
© *2008 Acoustical Society of America.* [DOI: 10.1121/1.2996330]

PACS number(s): 43.30.Cq, 43.60.Fg [WLS] Pages: 3430–3439

I. INTRODUCTION

Ocean acoustic tomography was introduced by Munk and Wunsch[1] as a remote-sensing technique for large-scale monitoring of the ocean interior using low-frequency sound. This method depends on identification and tracking of stable ray arrivals and uses the arrival time changes to estimate ocean variability. It is typically performed between a few widely separated sources and receive arrays and can provide rapid surveys[2] in deep or shallow water.[3,4]

Acoustic propagation at smaller scale and higher frequency can be similar to deep water based on wavelength scaling. Deep water refracted rays do not resemble shallow-water bottom-reflected rays, but in both cases (deep water or shallow water), there are multiple eigenrays between a source and a receiver. These eigenrays provide more information than a single direct path, but also create difficulties in terms of identification and separation. The advantages of the smaller scale are easier measurement of the environment parameters such as bathymetry and the sound-speed fluctuations. Array deployments are also simpler in shallow water since array lengths can be shorter.

For an arrival to be useful, it must also be stable enough to track over time and be identifiable unambiguously with a ray path (or ray sampling kernel[5]) so that the sampling of the ocean sound-speed field is known. With a single source and receiver it can be difficult to identify each multipath with calculated arrivals from an ocean model. This problem may be eased with an array of receivers using time-delay beamforming.[2] In this case two wave fronts arriving on the receive array at the same time but different angles can be identified and used as observations. However, depending on the complexity of the sound-speed structure, distinct wave front arrivals may seem to share the same arrival angle and time on the receive array due to the resolution limits imposed by the pulse bandwidth and the array size. In this work, we present experimental results obtained between two source/receive arrays. Time-delay beamforming is performed simultaneously on both the source and receive arrays, allowing us to identify each acoustic ray by its launch angle, receive angle, and arrival time. This is related to the problem of underwater communications in shallow water with receiver arrays,[6,7] and where source arrays can be used to achieve enhanced channel capacity.[8]

In the past few years, a series of broadband shallow-water acoustic experiments has been performed, employing both source and receive arrays and focusing on time reversal.[9–15] Typical geometries for these experiments range from 1 to 8 km of acoustic propagation in a 50–120 m deep waveguide with a set of transducers and hydrophones on two vertical arrays spanning most of the water column. The broadband signals were designed to estimate the impulse response of the ocean acoustic waveguide in the kilohertz frequency range. The observed impulse responses were first used for time-reversal focusing of the arrivals, studying time evolution of time-reversal focusing in a fluctuating environment.[16]

Time reversal implies a forth and back propagation through the waveguide. When a time-reversed signal is sent repeatedly over time, the degradation of the time-reversal focus with time results from the growing phase and amplitude differences of the acoustic field between the initial and actual propagation. Experimental results confirmed the stability of time-reversal focusing despite sound-speed fluctuations that were strongly affecting the acoustic forward propagation. On the other hand, the degradation of the time-reversal focus did not provide straightforward information on the location and amplitude of the sound-speed fluctuations in the waveguide.[17]

[a)]Electronic mail: philippe.roux@obs.ujf-grenoble.fr

 © 2008 Acoustical Society of America

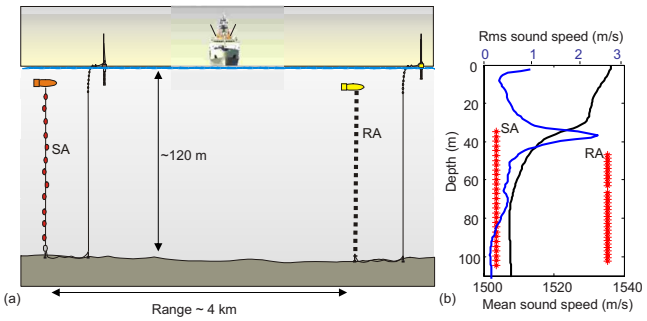


FIG. 1. (Color online) (a) Cartoon of experimental layout, showing source and receiver arrays. (b) Mean (black) and rms (gray) sound-speed profiles for the region. The rms sound-speed axis is shown on the top and the mean sound-speed axis is presented on the bottom. Source and receiver depths are indicated by the plus signs to the left and right of the figure, respectively.

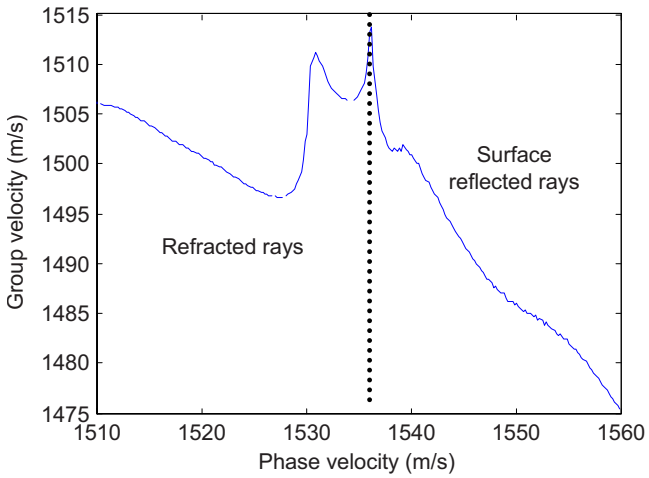


FIG. 2. (Color online) Group velocity vs phase velocity for the mean sound-speed profile shown in Fig. 1. The dotted line indicates the dividing line between surface-reflected rays to the right and refracted rays to the left.

The repeated acquisition of the acoustic transfer matrix between the two arrays was also performed during the experiment for estimation of the waveguide itself, using the evolution of the transfer matrix to estimate the evolving sound-speed field. Having both source and receive arrays enables array processing at both source and receive locations, enhancing the arrival identification process that is the starting point for time-of-arrival based estimates of ocean structure.

In the following, we describe observations of stable identifiable arrivals and show that the rapid sampling and high signal-to-noise ratio of the observations provide for high precision measurements of arrival time changes. The goal of this paper is to study forward propagation between the two arrays using a double-beamforming algorithm that allows us to separate and identify each ray path between the source and receive arrays. Travel-time measurements on these ray paths could be used for shallow-water ocean remote sensing in a fluctuating environment.

II. EXPERIMENT

We have performed an experiment in July 2005 north of Elba Island, Italy with the same equipment, location, and basic setup as discussed in previous work.[16] As shown in Fig. 1(a), there was a vertical line array of $N_s=29$ equally spaced transducers (SA) spanning 78 m in 120 m water depth and $N_r=32$ equally spaced receiving hydrophones (RA) covering 62 m [Fig. 1(b)]. We record the time domain pressure field $p(t,z_r,z_s)$ transmitted from a point source at depth z_s on a vertical line array to a receiver at depth z_r. The arrays were linked to the ship via two-way radio telemetry, so the data were recorded on the ship in real time. The range between the two arrays was 4.071 km. The transducers had a central frequency of 3.2 kHz with a 1 kHz bandwidth. The pulses transmitted during the experiment were 200 ms linear frequency modulated chirps that were compressed after reception to their pulse equivalent by matched filtering. This produced broadband receptions with signal-to-noise ratio greater than 40 dB with power-limited transmissions. The coded pulse signal is transmitted sequentially by each element of the SA with a separation between transmissions of 250 ms to allow for maximum channel dispersion of 200 ms (Fig. 3). The acquisition of the transfer function between each source of the SA and each receiver of the RA thus requires about 7 s to complete. The transfer function is recorded every 20 s to monitor fluctuations of the oceanic waveguide.

During the 7 days of the experiment, 26 conductivity-temperature-depth (CTD) casts and 32 expendable bathythermograph (XBT) casts were taken at multiple locations (and times of day) in the area. The average depth-dependent sound-speed profile measured by CTD is shown in Fig. 1(b). The water column is stratified in both temperature and salinity, with warm, fresher water on top of colder saltier water. Salinity was supplied for the XBT casts from the observed *T-S* relation from the CTD data, but the salinity variation had a relatively small effect on sound speed. The sound-speed profile is downward refracting, with high gradients in the thermocline between 30 and 60 m. The buoyancy frequency (not shown) of the mean profile has a maximum of 20 cycles/h near 38 m depth, allowing for a rich spectrum of internal wave variability. The sound-speed profile was qualitatively similar throughout the transmission experiments reported below, but showed significant variability in the region of strong gradients, as shown by the root-mean-square (rms) sound speed plotted in the same figure. Peak rms variability is 2.3 m/s at about 35 m, reducing to less than 1 m/s below 41 m and less than 0.1 m/s below 90 m. The analysis of the sources of the sound-speed variability is outside the scope of this paper, but the main contributors are adiabatic internal wave (and tide) displacement of the isopycnals, diabatic processes (heating, cooling, and wind mixing) in the upper 20 m, and horizontal advection.

The acoustic propagation predicted from the reference sound-speed profile must be matched to the observed impulse responses to confirm that the arrivals are understood. The vertical arrays provide critical information for identification of the observed arrival peaks with theoretical arrivals.

Group velocity versus phase velocity is shown in Fig. 2 from a ray-tracing numerical simulation based on the average sound speed. For comparison with a ray representation, group velocity can be matched to range divided by travel time, while phase velocity is related to local sound speed

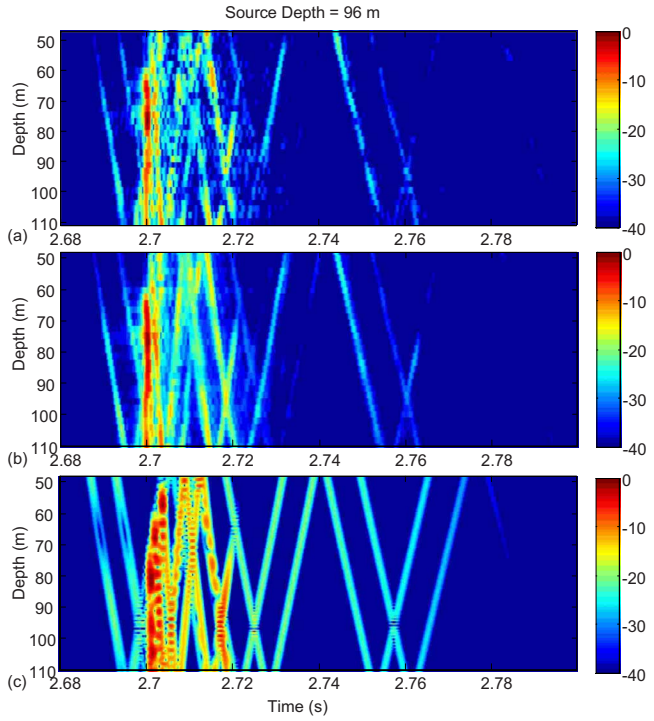


FIG. 3. (Color online) The logarithm of the intensity of the pressure field received on the RA for a source on the SA at 96 m depth plotted as a color image for depth and arrival time. (a) Field received from a single transmission. (b) Incoherent average of 60 transmissions over 1 h (averaging one transmission per minute). (c) Numerical simulation of the field using a high-angle broadband PE code. Computation has been performed for a 1 kHz bandwidth Gaussian pulse centered at 3 kHz using the sound-speed profile shown in Fig. 1(b). Bottom sound speed is uniform and equal to 1600 m/s.

divided by the cosine of the angle the ray makes with the horizontal axis. Path length increases with increasing phase velocity, so group speed can only increase if the mean sound speed along the ray path increases faster than the path length. The arrivals to the left of the vertical dashed line at a phase velocity of 1536 m/s are refracted in the upper ocean, while those to the right are surface reflected. The group velocity increases sharply near the point of surface reflection because of the strong increase in sound speed near the surface and decreases after surface reflection due to increased path length. The figure shows that several different phase velocities (rays) can have the same group velocity (arrival time) for group velocities above about 1496 m/s (arrival times earlier than about 2.72 s).

The logarithm of the intensity of the pressure field received on the RA for a source on the SA at 96 m depth is shown in Fig. 3(a) for depth and arrival time. The acoustic field is a mixture of clear wave fronts spanning the RA and speckle due to interference between acoustic paths. The maximum signal-to-noise ratio is around 40 dB. The field received from a single transmission is shown in Fig. 3(a) while Fig. 3(b) is an incoherent average of 60 transmissions over 1 h.

The average filters out some of the speckle observed in single transmissions, emphasizing the strong wave front arrivals.

A numerical simulation of the field using a high-angle broadband PE code[18] is shown in Fig. 3(c) using the sound-speed profile seen in Fig. 1(b). There is visual agreement between the numerical simulation and the incoherently averaged field at least in the arrival structure of the multiply reflected/refracted paths.

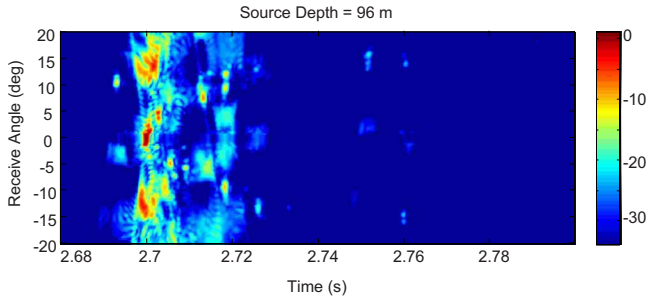


FIG. 4. (Color online) Angle-travel time output from incoherently averaged time-delay beamforming for a 96 m source depth performed on all receptions over a $d_{RA}=16$ m aperture subarray of the RA centered at 96 m depth.

This agreement is due in part to the monotonicity of the observed sound-speed profiles. In other experiments, surface cooling created a sound-speed minimum near the surface, leading to complicated arrival patterns with strong sensitivity of the arrival pattern to small changes in the sound-speed profile. In these cases, identification of the superposed timefronts was much more difficult because small differences between the estimated and actual sound-speed field resulted in significant mismatches between observed and calculated arrival patterns.

Because of the structure of the sound-speed profile, the earliest arrivals correspond to ray paths which nearly touch the surface, as seen in Fig. 2. These have the least travel time because the sound energy propagates in the high-speed region of the waveguide enough to more than compensate for the increased path length. The direct path can be seen to arrive at about 2.7 s (group velocity of 1507.8 m/s), overlapping with surface-reflected energy, so that there is considerable difficulty in unscrambling the superposed arrivals.

The incoherently averaged beamformer output for the 96 m source using a $d_{RA}=16$ m aperture subarray of the RA centered at 96 m depth is shown in Fig. 4. There are three clear arrival spots at about 2.719 s travel time, which is in the region of no multivalued group velocities. The later arrivals are also clearly separated and show the array side lobes. We also see the early arrivals from the ray(s) that turn near the surface, as seen in Fig. 3 around 2.69 s, the direct path at near-zero angle and travel time of 2.7 s, and some well-separated arrivals for times after about 2.706 s. However, the array side lobes (the large patches between $\pm 10°-15°$ on each side of the zero-angle intensity maximum at 2.7 s) and the superposition of high- and low-angle arrivals at similar times complicate the beamformed output in the region of overlap. The group velocity versus phase velocity plot (Fig. 2) is easier to interpret.

The observed data set is four dimensional, consisting of acoustic pressure as a function of source, receiver, travel time, and transmission time, but only two-dimensional slices can be displayed on paper. The arrival pattern for a single source-receiver pair is more difficult to decipher without the array information. The matched-filtered (but not demodu-

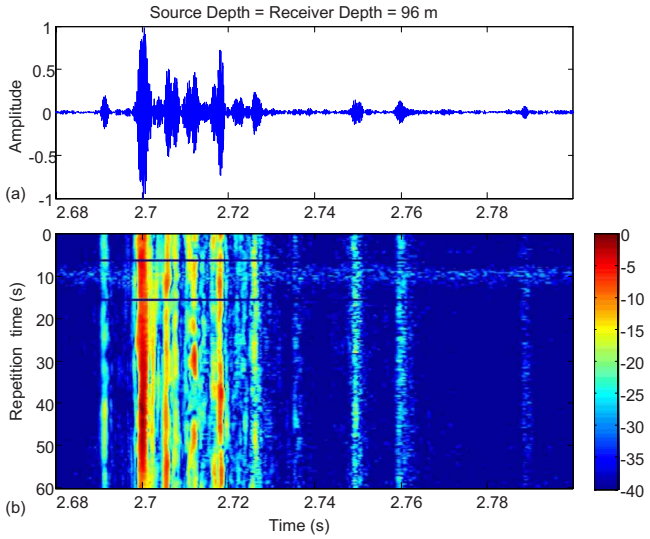


FIG. 5. (Color online) (a) Matched-filtered (but not demodulated) time record for a single reception for source and receiver depths of 96 m. (b) Logarithm of intensity of the envelope of the impulse response for this source-receiver pair for 1 h at a rate of one acquisition every 20 s. Acquisitions are missing at 8 and 16 min.

lated) time record for a single reception for source and receiver depths of 96 m is shown in Fig. 5. The carrier frequency is retained in the analysis below to clearly show phase shifts. This is an estimate of the instantaneous impulse response between the source and receiver. This depth is below most of the sound-speed variability observed over the course of the experiment which was concentrated at the depth of the thermocline and near the surface.

The sound-speed variability produced significant changes to the measured impulse responses for all source-receiver pairs over time. The logarithm of intensity of the envelope of the impulse response for this source-receiver pair for 1 h at a rate of one acquisition every 20 s is shown in Fig. 5(b). Acquisitions are missing at 8 and 16 min. Strong acoustic interference is seen between refracted/reflected signals in the waveguide in the region of overlapping arrivals. The amplitude of the largest peak never fades out, but the width of the peak fluctuates due to interference between multiple ray paths as well. The time evolution of this impulse response due to the changing sound-speed field should be useful for estimating those sound-speed changes, but the complexity of the arrival makes it hard to interpret these changes as changes in arrival time for separated rays. Skarsoulis[19] suggested using the peak arrivals as observations without needing to separate them, using the sensitivity kernel for the combined peak, but this requires a very good estimate of the background sound-speed field, which is not available in this case because of the strong thermocline variability. For this reason, we explore methods for separating the rays.

III. RAY IDENTIFICATION THROUGH DOUBLE BEAMFORMING

In order to identify the arrivals by their reception angle on the array, we perform time-delay beamforming on the received field to transform depth into reception angle:

$$p(t,\theta_r,z_s) = \frac{1}{N_r}\sum_{i=1}^{N_r} p(t+\tau(\theta_r,z_i),z_i\,.\,z_s), \tag{1}$$

where N_r is the number of receivers on the array and $\tau(\theta_r,z_i)$ is the delay calculated at each receiver depth in a depth-dependent sound-speed profile $c(z)$. The source depth, z_s, is a constant. Plane-wave beamforming is not optimal when the sound speed changes significantly over the array, so we adjust the time delays in accordance with mode group velocities:[20]

$$\tau(\theta_r,z_i) = \int_{z_0}^{z_i} \sqrt{\frac{1}{c^2(z)} - \frac{\cos^2(\theta_r)}{c_0^2}}\,dz, \tag{2}$$

where z_0 is the depth of the sound channel axis (or sound-speed minimum) chosen as a reference and c_0 is the sound speed at the reference depth.

The time delay $\tau(\theta_r,z_r)$ at the center of the vertical array is set to zero so that the arrival times are referenced to that center. Performing time-delay beamforming (1) for a range of θ_r transforms the data from the (t,z_r,z_s) domain to the (t,θ_r,z_s) domain. In the (t,θ_r,z_s) domain, each acoustic ray arrival from a particular source which spans the receive array in the (t,z_r,z_s) domain (Fig. 3) is localized around its reception time and angle. When ray theory is applicable to the data, time-delay beamforming allows an efficient ray identification that is limited by the array size.

Distinct rays can arrive at the same time with similar receive angles, so that time-delay beamforming at the receiver is not always sufficient to separate arrivals. Taking advantage of the experimental configuration where both transmit and receive arrays are used, we perform a time-delay beamforming on both arrays. Time-delay beamforming over both arrays transforms the data from the (t,z_r,z_s) physical domain to the (t,θ_r,θ_s) domain where θ_s is the angle of the wave front at the source array.

$$p(t,\theta_r,\theta_s) = \frac{1}{N}\sum_{i=1}^{N_r}\frac{1}{N_s}\sum_{j=1}^{N_s} p(t+\tau(\theta_r,z_i)+\tau(\theta_s,z_j),z_i,z_j). \tag{3}$$

In the (t,θ_r,θ_s) domain, the acoustic wave fronts are identified by propagation time, receive, and transmit angle.

This double beamforming was applied to the observations taken during a 2 h period. For each set of transmissions, the received waveforms as a function of arrival time and source and receiver depth were transformed to time and source and receiver angle space.

The three-dimensional output fields must be shown in slices for two-dimensional representation. To show the angular structure of the arrivals, we sum the intensity over a 1 ms range of travel arrival times centered on ray arrivals. An example of double-beamforming output for a single set of transmissions between a $d_{SA}=16.7$ m aperture subarray of the SA and a $d_{RA}=16$ m aperture subarray of the RA both centered at 96 m depth is shown in Fig. 6. The subarray apertures were chosen to maximize the array gain provided by the time-delay beamforming algorithm.[21] The fact that the

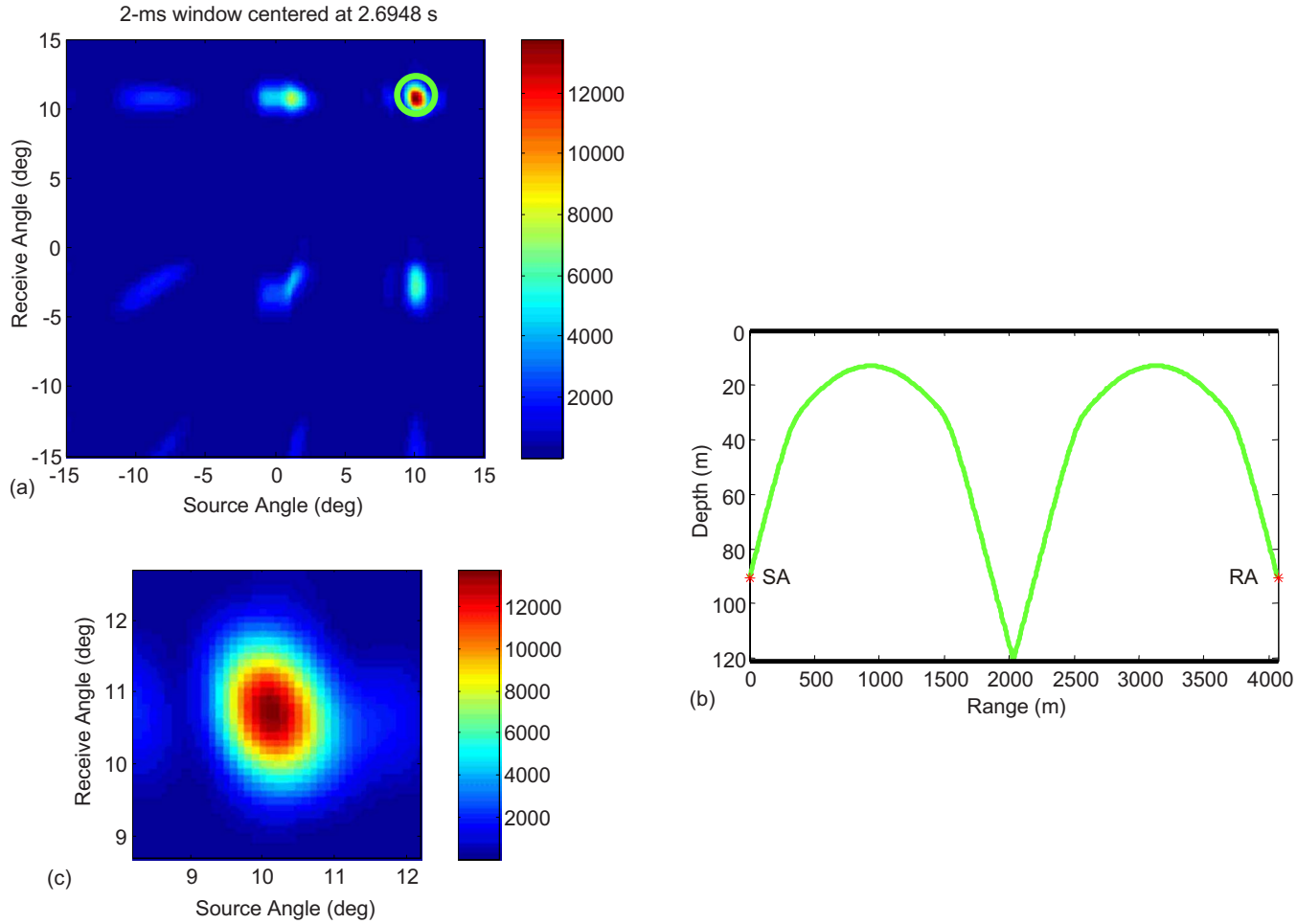


FIG. 6. (Color online) Example of double-beamforming output on a linear scale for a single set of transmissions between a $d_{SA}=16.7$ m aperture subarray of the SA and a $d_{RA}=16$ m aperture subarray of the RA both centered at 96 m depth. (a) Average intensity in the (θ_r,θ_s) domain for a time window of 1 ms centered around the observed ray arrival time at 2.6948 s. The circle is centered at the launch and receive angles for a numerically calculated ray that propagates between the centers of the two subarrays. (b) Associated ray path as depth vs range. (c) Same as Fig. 6(a) but for a subset of the angle domain centered on the observed peak.

array gain saturates for subarrays larger than $D\approx 16$ m means that the acoustic field coherence vanishes for interelement distances larger than D.

The average intensity in the (θ_r,θ_s) domain for a time window of 1 ms centered around the observed ray arrival time at 2.6948 s is shown in Fig. 6(a). This arrival corresponds to one of the two early arrivals seen in Figs. 3 and 5 and is a ray that nearly reaches the ocean surface. The green circle is centered at the launch and receive angles for a numerically calculated ray that propagates between the centers of the two subarrays [Fig. 6(b)]. This ray path has been obtained with a ray trace code using the depth-dependent sound-speed profile of Fig. 1(b). Note in Fig. 6(a) the presence of angular side lobes due to the element spacing on the SA and RA. Calling $\delta\theta_{SA}$ and $\delta\theta_{RA}$ the angular separation between main lobe and side lobe for the SA and RA, respectively, we have $\delta\theta_{SA}=\sin^{-1}(\lambda/a_{SA})=9.8°$ and $\delta\theta_{RA}=\sin^{-1}(\lambda/a_{RA})=13.7°$, where $\lambda=0.475$ m is the wavelength of the center frequency and $a_{SA}=2.786$ m and $a_{RA}=2$ m are the interelement separation for the SA and RA. Finally, Fig. 6(c) shows a magnified image of the average intensity in a subset of the angle domain centered on the observed peak. The diffraction-limited angular width of the peak is determined by the SA and RA subapertures as $\sin^{-1}(\lambda/d_{SA})\approx\sin^{-1}(\lambda/d_{RA})\approx 1.7°$. Given the estimated signal-to-noise ratio and peak width, we estimate the precision of source and receive angles at 0.25°.

The ray selected in Fig. 6—with arrival time=2.6948 s for a 96 m source and receiver depth—is well separated from other ray paths, as can be seen in Figs. 3(a), 3(b), and 5(b). As such, double beamforming was not necessary to isolate it from interference by other ray paths. Working with this ray path allows us then to compare the time-domain waveform obtained from the double-beamforming algorithm [Fig. 7(a)] to the time-domain signal obtained directly from the point-to-point source-receiver pair at 96 m [Fig. 7(b)].

The amplitude of the matched-filtered arrival as a function of arrival (travel) time and transmission time is shown as color in Fig. 7. A vertical slice of the plot at a single transmission time corresponds to an expanded plot of the region around $t=2.6948$ s from the time-domain signal represented in Fig. 5(a). The evolution of this waveform over a 1 h set of transmissions shows the phase and amplitude effects of the ocean fluctuations since no multipath interference is expected for this isolated path. In the case of the double-beamforming algorithm [Fig. 7(a)], the waveform has

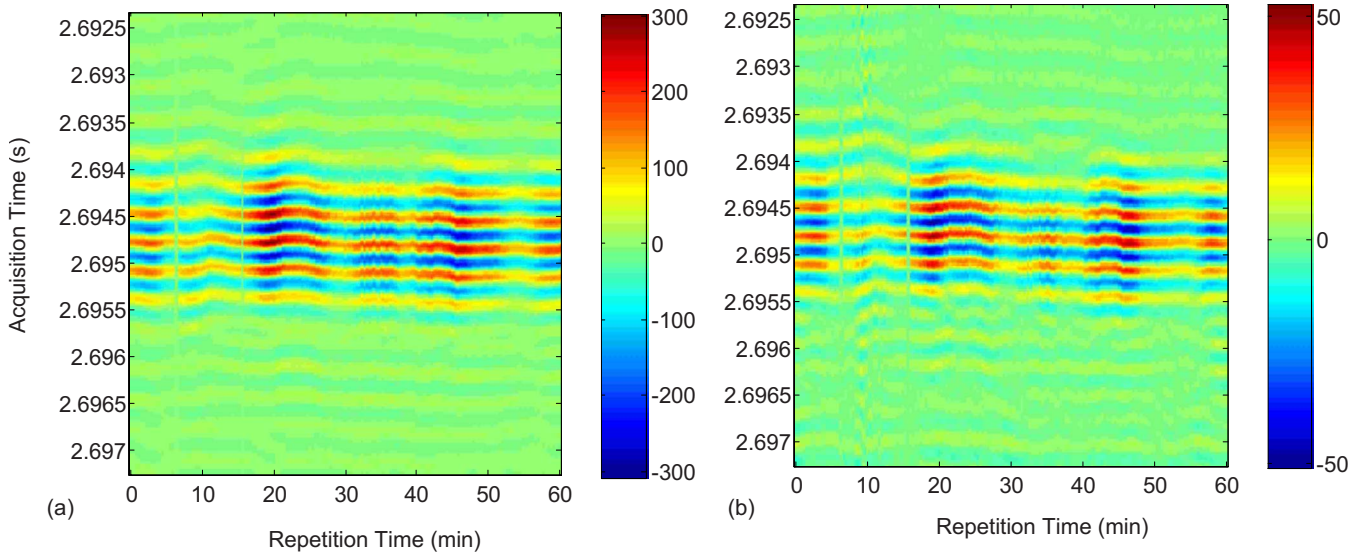


FIG. 7. (Color online) Amplitude of the matched-filtered arrival as a function of arrival (travel) time and transmission time for 1 h of transmissions. Color scale gives positive and negative pressures. (a) Double-beamformed waveform for the source and receiver angles ($\theta_s = 10.2°$ and $\theta_r = 10.7°$). (b) Same as (a), but for only 96 m source and receiver depths.

been extracted for the source and receiver angles ($\theta_s = 10.2°$ and $\theta_r = 10.7°$). Figures 7(a) and 7(b) are very similar except for the improved signal-to-noise ratio for the double-beamforming output due to the array gain associated with the processing. As a consequence, the time-domain waveform for each ray path can be tracked as a function of transmission time.

In addition to variations in amplitude and phase of the arrival, the source and receiver angles vary in time. The evolution of the source and receive angles (θ_s and θ_r) for 1 h of transmissions for the ray arrival shown in Fig. 7 is shown in Fig. 8. For each transmission, the double beamforming has been performed on the two subarrays and the intensity in a limited angle range is plotted. This is the time behavior of a slice through the maximum intensity spots, as shown in Fig. 6(c). Figures 8(a) and 8(b) only show intensity values for the source and receive angle ranges that were above 80% of the maximum intensity (at the time of the peak arrival) for this particular ray at each time.

Figure 8 shows that both source and receive angles of the maximum intensity vary by less than 1° peak to peak over 1 h. Part of this variability is due to the motion of the SA and RA in response to ocean currents. However, we expect that some of the variability of source and receive angles is due to variability of the sound-speed profile, so angle information could be used to estimate ocean structure in combination with waveform travel time.

Assuming that the sound-speed fluctuations only occur at the turning point (depth z_t, grazing angle $\theta_t = 0$) for a given eigenray with sound speed $c(z_0)$ and angle θ_0 at the source (or receiver), Snell's law gives

$$\Delta c(z) = \Delta\theta_0 c(z_0)\sin(\theta_0)/\cos^2(\theta_0). \tag{4}$$

In the observations, $c(z_0)$ does not vary for z_0 deeper than 90 m. We measure $\approx 1°$ in source/receive angle maximum variation over time, as seen in Fig. 8. Taking $\theta_0 = 10°$, Eq. (4) gives $\Delta c(z) \approx 4.5$ m/s which is consistent with a 2.3 m/s rms fluctuation at a depth of 30 m.

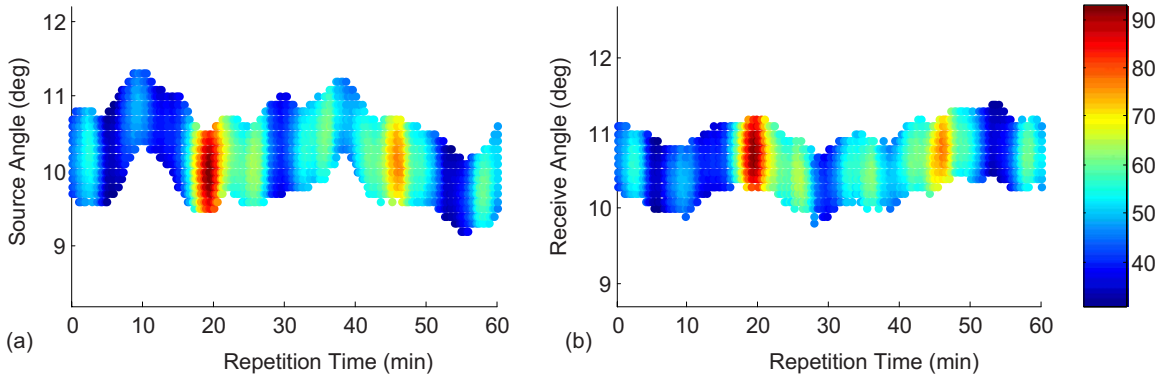


FIG. 8. (Color online) Evolution of the source, (a), (left), and receive, (b), (right) angles (θ_s and θ_r) for 1 h of transmissions for the ray arrival shown in Fig. 7. For each transmission, the double-beamforming process has been performed on the two subarrays and only the intensity above 80% of the maximum intensity (at the time of the peak arrival) for this particular ray at each time is shown.

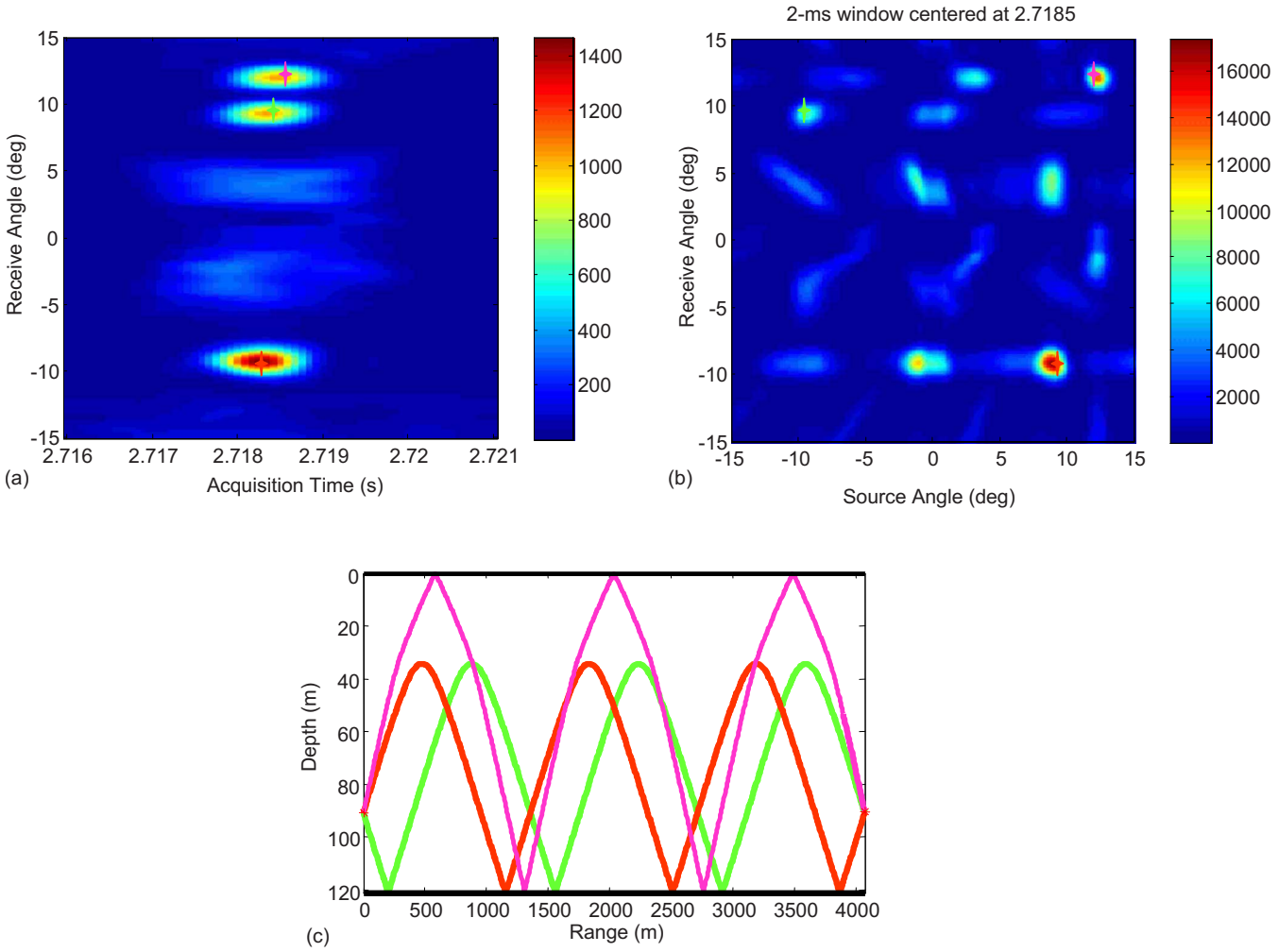


FIG. 9. (Color online) (a) Average result of a single (receiver array only) time-delay beamforming for a 96 m source depth performed on the aforementioned $d_{RA}=16$ m aperture subarray of the RA centered at 96 m depth. The plot has been limited to the region in arrival time containing three rays that arrive near 2.7185 s. The intensity has been incoherently averaged over a 1 h set of transmissions. (b) Intensity in the (θ_r, θ_s) domain after double beamforming. (c) Ray paths between the source and receive subarray centers for the three rays.

In some cases double beamforming is necessary to isolate multiple paths that arrive at nearly the same time. An example is shown in Fig. 9. Figure 9(c) displays three ray paths between the source and receive subarray centers that each arrive near 2.7185 s. The source is on the left and the receiver is on the right. Figure 9(a) shows the average result of a single (receiver array only) time-delay beamforming performed on the RA for a 96 m source depth. For clarity, the beamformed result has been limited to the region in arrival time containing only these peaks. The intensity has been incoherently averaged over a 1 h set of transmissions. Figure 9(a) shows that two of the rays have receive angles in the interval of 9°–12°. The angle separation between the centers of the rays is close to the 1.7° width of the peak in angle space. Knowing that source and receive angles vary with time (Fig. 8), these two rays are likely to interfere over time, preventing the use of single time-delay beamforming for travel-time estimation. On the other hand, Fig. 9(b) shows that these two rays are well separated after beamforming on both the SA and RA. The intensity plot in the (θ_r, θ_s) domain matches the ray calculation for source and receive angles. The rays are now clearly identified and isolated, so that an unambiguous waveform extraction as shown in Fig. 7 is feasible.

Figures 10(b)–10(d) show expanded views of the incoherently averaged intensity spots in source angle-receiver angle space associated with each ray in Fig. 9. As expected, Fig. 10(a) exhibits array side lobes for each spot as in Fig. 6(a) and the spot widths in Figs. 10(b)–10(d) are consistent with the diffraction limits.

Figure 11(a) shows the pulse-compressed received waveform as a function of transmission time for the surface-reflected ray shown in Fig. 9(c). The time evolution of the waveform has been constructed by choosing angles of maximum intensity near $\theta_s=12.3°$ and $\theta_r=11.8°$ for each transmission during a 1 h period. The ray shown in Fig. 11(a) has a path that is distinct in space from the ray shown in Fig. 7(a), so the two rays are expected to experience different oceanic environments. The time evolution of the arrival amplitude and phase is very different from that shown in Fig. 7. The time variability of the ray source and receive angles is plotted in Figs. 11(b) and 11(c) as in Fig. 8. The source and

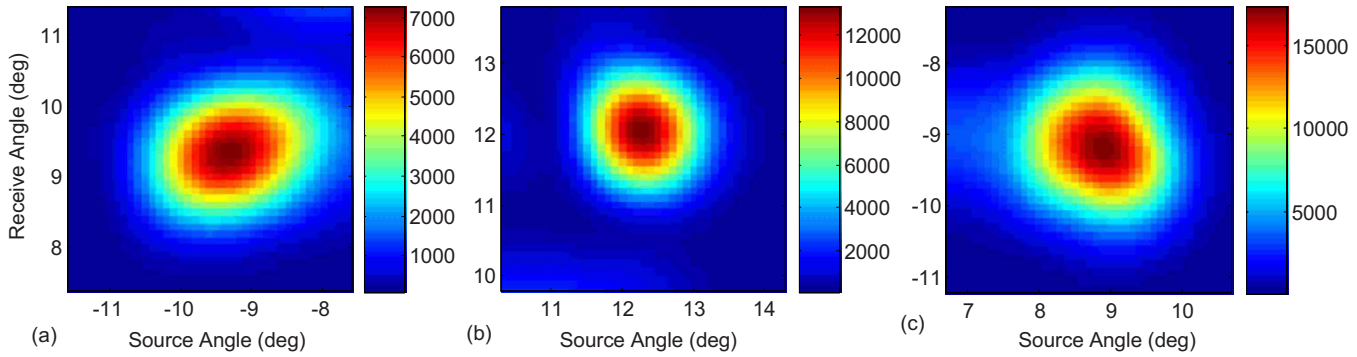


FIG. 10. (Color online) [(a)–(c)] Expanded views of the incoherently averaged intensity spots as a function of (θ_r, θ_s) associated with each ray that arrives in a 2 ms window centered at 2.7185 s [Fig. 9(b)]. The three spots are associated with the three rays in Fig. 9(b). Note again that the widths of the intensity spots in the (θ_r, θ_s) domain are in agreement with diffraction laws as already observed in Fig. 6(c).

receive angle variability as a function of transmission time differs from Fig. 8, confirming that the time-evolving ocean sound-speed structure is important along with SA and RA motion. The intensity fluctuations vary more sharply from transmission to transmission in Figs. 11(b) and 11(c) than in Figs. 8(a) and 8(b) as could be expected because of surface scattering for this surface-reflected ray.

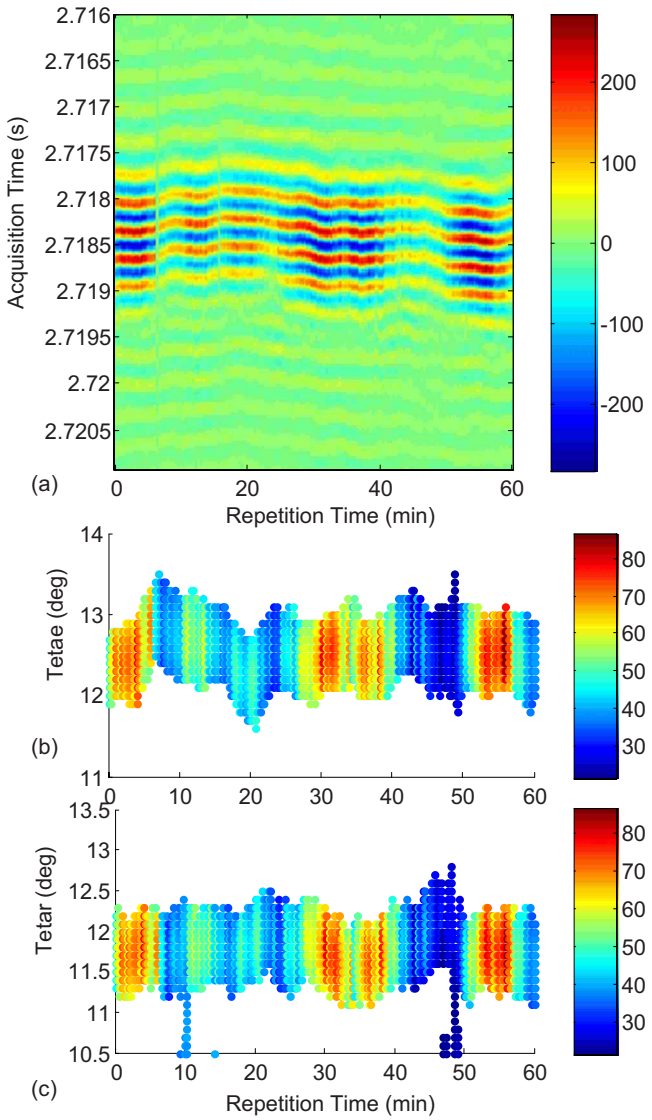


FIG. 11. (Color online) (a) Pulse-compressed received waveform on a linear scale as a function of transmission time for the surface-reflected ray shown in Fig. 9(c). [(b) and (c)] Time variability of the ray source and receive angles, respectively, as in Fig. 8.

The variability of angle for the refracted ray shown in green in Fig. 9(c) is shown in Fig. 12. In Fig. 12(a), the waveform has been extracted for the arrival angles with peak intensity near $\theta_s = 8.8°$ and $\theta_r = -9.1°$ for each transmission during a 1 h set of transmissions. This ray has a turning point near the depth of maximum sound-speed variability. Figure 12(a) shows very large intensity fluctuations during the 1 h interval. Figures 12(b) and 12(c) show the time evolution of the intensity in angle ranges near the peak intensity, as in Figs. 11(b) and 11(c). The evolution of the receiver angle shows two angle peaks at some times, with the peak at more negative receiver angle showing significant intermittency. An incoherent average of the power in a 1 ms time interval centered on the arrival time is shown in Figs. 12(d) and 12(e) for transmissions at 15 and 33 min, respectively. Figure 12(d) shows two peaks in angle-angle space as confirmed by the receive angle evolution in Fig. 12(c). The double peak is probably a signature of interfering micromultipaths for this particular ray resulting in a destructive interference between two out-of-phase waveforms. At a time when the arrival is not doubled [Fig. 12(e)], the intensity spot is similar in intensity to those obtained in Figs. 6 and 10 which shows that the double spot observed in Fig. 12(c) is not a consequence of the double-beamforming algorithm.

IV. CONCLUSIONS

In this shallow-water propagation experiment, ray paths can be isolated, identified, and tracked over time, yielding time series of arrival time, amplitude, and even carrier phase for use in characterizing the channel. Double beamforming can isolate some arrivals not resolvable with single beamforming and increases signal-to-noise ratio. Peaks can be tracked for several hours and show phase stability for accurate travel-time measurements. Source and receive angles of a selected eigenray are also time-evolving observable that can be tracked with the double-beamforming algorithm. Internal wave displacements are expected to be the dominant source of sound-speed variability on hourly timescales, producing the largest changes in the thermocline. There is a

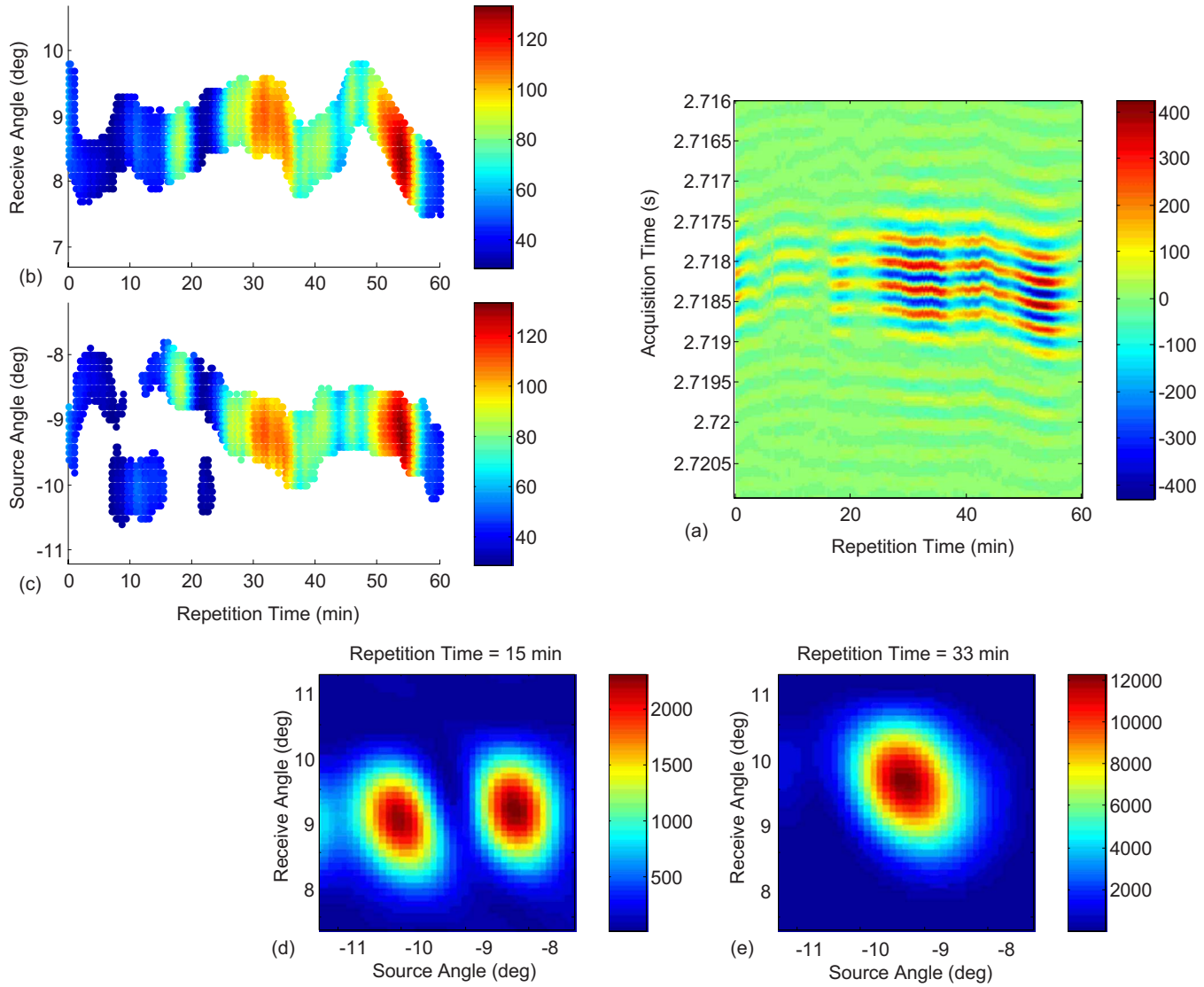


FIG. 12. (Color online) [(a)–(c)] Same as Figs. 11(a)–11(c) for one refracted ray shown in Fig. 9(c). [(d) and (e)] Average power in a 1 ms time interval centered on the arrival time for transmissions at 15 and 33 min, respectively.

significant difference in the time stability of ray paths that remain below the thermocline (most stable), refract in the thermocline, refract above the thermocline, and interact with the surface. Through the use of the double-beamforming algorithm, shallow-water acoustic remote sensing may be then revisited between densely sampled source and receive arrays from which travel time, source, and receive angles of a large number of eigenrays are monitored.

ACKNOWLEDGMENTS

This work was performed in collaborative experiments with the NATO Underwater Research Center (NURC), La Spezia, Italy, with Mark Stevenson as Chief Scientist. Scientists contributing to these experiments include Tuncay Akal, Pierrot Boni, Pierrot Guerreni, other NURC staff, and the officers and crew of the RV Alliance. The work was funded by the Office of Naval Research.

[1]W. Munk and C. Wunsch, "Ocean acoustic tomography: A scheme for large scale monitoring," Deep-Sea Res., Part A **26**, 123–161 (1979).
[2]W. H. Munk, P. F. Worcester, and C. Wunsch, *Ocean Acoustic Tomography* (Cambridge University Press, Cambridge, 1995).
[3]J. F. Lynch, G. Jin, R. Pawlowicz, D. Ray, C.-S. Chiu, J. H. Miller, R. H. Bourke, A. R. Parsons, A. J. Plueddemann, and R. Muench, "Acoustic travel time perturbations due to shallow water internal waves and internal tides in the Barents Sea Polar Front: Theory and experiment," J. Acoust. Soc. Am. **99**, 803–821 (1996).
[4]J. Apel, M. Badiey, C.-S. Chiu, S. Finette, R. Headrick, J. Kemp, J. Lynch, A. Newhall, M. Orr, B. Pasewark, D. Tielbuerger, A. Turgut, K. V. D. Heydt, and S. Wolf, "An overview of the 1995 SWARM shallow-water internal wave acoustic scattering experiment," IEEE J. Ocean. Eng. **22**, 465–500 (1997).
[5]E. Skarsoulis and B. Cornuelle, "Travel-time sensitivity kernels in ocean acoustic tomography," J. Acoust. Soc. Am. **116**, 227 (2004).
[6]M. Stojanovic and Z. Zvonar, "Multichannel processing of broad-band multiuser communication signals in shallow water acoustic channels," IEEE J. Ocean. Eng. **21**, 156–166 (1996).
[7]D. Kilfoyle and A. B. Baggeroer, "The state of the art in underwater acoustic telemetry," IEEE J. Ocean. Eng. **25**, 4–27 (2000).
[8]D. B. Kilfoyle, J. C. Preisig, and A. B. Baggeroer, "Spatial modulation experiments in the underwater acoustic channel," IEEE J. Ocean. Eng. **30**, 406–415 (2005).
[9]D. Rouseff, W. L. J. F. D. R. Jackson, C. D. Jones, J. A. Ritcey, and D. R. Dowling, "Underwater acoustic communication by passive phase conjugation: Theory and experimental results," IEEE J. Ocean. Eng. **26**, 821–831 (2001).
[10]H. C. Song, W. A. Kuperman, W. S. Hodgkiss, T. Akal, and C. Ferla,

"Iterative time reversal in the ocean," J. Acoust. Soc. Am. **105**, 3176–3184 (1999).
[11]S. Kim, G. F. Edelmann, W. A. Kuperman, W. S. Hodgkiss, H. C. Song, and T. Akal, "Spatial resolution of time-reversal arrays in shallow water," J. Acoust. Soc. Am. **110**, 820–829 (2001).
[12]S. Kim, W. A. Kuperman, W. S. Hodgkiss, H. C. Song, and G. F. Edelmann, "Robust time-reversal focusing in the ocean," J. Acoust. Soc. Am. **114**, 145–157 (2001).
[13]G. F. Edelmann, T. Akal, W. S. Hodgkiss, S. Kim, W. A. Kuperman, and H. C. Song, "An initial demonstration of underwater acoustic communication using time-reversal," IEEE J. Ocean. Eng. **27**, 602–608 (2002).
[14]W. S. Hodgkiss, H. C. Song, W. A. Kuperman, T. Akal, C. Ferla, and D. R. Jackson, "A long-range and variable focus phase-conjugation experiment in shallow water," J. Acoust. Soc. Am. **105**, 1597–1604 (1999).
[15]W. A. Kuperman, W. S. Hodgkiss, H. C. Song, T. Akal, C. Ferla, and D. R. Jackson, "Phase conjugation in the ocean: Experimental demonstration of an acoustic time-reversal mirror," J. Acoust. Soc. Am. **103**, 25–40 (1998).
[16]P. Roux, W. A. Kuperman, W. S. Hodgkiss, H. C. Song, T. Akal, and M. Stevenson, "A nonreciprocal implementation of time reversal in the ocean," J. Acoust. Soc. Am. **116**, 1009–1015 (2004).
[17]K. Raghukumar, B. D. Cornuelle, W. S. Hodgkiss, and W. A. Kuperman, "Pressure sensitivity kernels applied to time-reversal acoustics," J. Acoust. Soc. Am. **124**, 98–112 (2008).
[18]M. D. Collins and E. K. Westwood, "A higher-order energy-conserving parabolic equation for range-dependent ocean depth, sound speed, and density," J. Acoust. Soc. Am. **89**, 1068–1075 (1991).
[19]E. Skarsoulis, "A matched-peak inversion approach for ocean acoustic travel-time tomography," J. Acoust. Soc. Am. **107**, 1324–1332 (2000).
[20]M. A. Dzieciuch, P. F. Worcester, and W. H. Munk, "Turning point filters: Analysis of sound propagation on a gyre-scale," J. Acoust. Soc. Am. **110**, 135–149 (2001).
[21]H. Cox, R. M. Zeskind, and M. Myers, "A subarray approach to matched-field processing," J. Acoust. Soc. Am. **87**, 168–178 (1990).

Measuring the target strength spectra of fish using dolphin-like short broadband sonar signals

Tomohito Imaizumi[a] and Masahiko Furusawa
Tokyo University of Marine Science and Technology, Kounan, Minato, Tokyo 108-8477, Japan

Tomonari Akamatsu
National Research Institute of Fisheries Engineering, Fisheries Research Agency, Hasaki, Kamisu, Ibaraki 314-0408, Japan

Yasushi Nishimori
Furuno Electric Co., Ltd., Nishinomiya, Hyougo 662-8580, Japan

(Received 15 May 2007; accepted 26 August 2008)

Dolphins identify their prey using broadband sonar signals. The broadband spectrum of the target strength (TS) of fish is believed to be a key factor in target discrimination. In this study, the TS spectrum was measured using sonar signals generated by two different dolphin species: finless porpoise and bottlenose dolphin. First, the broadband form functions of a tungsten carbide sphere and a copper sphere were measured in a water tank, and a close agreement between measurements and theoretical values was confirmed. Second, the TS spectra of anesthetized fish from three species were measured in a water tank. Although the results showed characteristics similar to previous measurements, they varied among species, individuals, and tilt angles. Third, the TS spectra of live fish suspended and tethered by nylon monofilament lines were measured at sea. The dolphin-like sonar signals were effective in obtaining the broadband TS spectra of the fish. Cross-correlation processing of the echo from a tungsten carbide sphere showed a further advantage of using the dolphin-like sonar signals: the signal-to-noise ratio increased by more than 10 dB. The variation of TS spectra with fish behavior provides useful information for target identification.
© *2008 Acoustical Society of America.* [DOI: 10.1121/1.2990703]

PACS number(s): 43.30.Gv, 43.30.Vh, 43.80.Ka [KGF] Pages: 3440–3449

I. INTRODUCTION

Acoustic surveys of fishery resources using scientific echo sounders are used worldwide.[1] To obtain the fish distribution density from the volume backscattering strength (SV) measured by the sounder, it is necessary to know the target strength (TS) of the fish. Thus, numerous studies of fish TS have been conducted.[2–4]

However, the acoustic survey method has several problems, two important examples of which are given below. Although there have been many studies of the classification of fish species via echo data, e.g., the study described in the ICES Cooperative Research Report No. 238,[5] there is no definitive method for classification. Thus, difficulties sometimes arise in assigning a suitable TS to the SV. *In situ* TS measurement methods such as the split beam method are practical and trustworthy, but they can only be applied to resolvable fish at a short range or in a sparse fish school.[6] These problems must be solved to improve the reliability of acoustic fishery surveys.

Dolphins detect, pursue, and prey on fish using their excellent sonar capability.[7,8] Au[7] extensively studied the sonar ability of dolphins and reported that dolphins can recognize not only the target size but also the material and shape. Harley *et al.*[9] showed that dolphins extract object characteristics directly from echoes. Because the main target of dolphins is fish, dolphin sonar capability is applicable to the improvement of the artificial sounders that are used in acoustic surveys and selective fishing. This is the motivation for a detailed investigation of the dolphin sonar capability.

This study focused on the broadband characteristics of the dolphin sonar sound and the measurement of TS spectra of fish using that sound. To confirm the accuracy of the measurement method, which was based on broadband scattering characteristics, dolphin-like sonar sounds were transmitted artificially to metal spheres for which scattering characteristics could be accurately calculated. The frequency characteristics of fish TS (TS spectra) in a tank and in the sea were then measured. The aim was to examine the applicability of the dolphin-like sonar signals in improving sounder performance, especially in fish species identification.

Previous studies have examined the scattering from fish using broadband signals or dolphin sonar signals. Zakharia *et al.*[10] attempted to determine the fish species of sardine (*Sardina pilchardus*), anchovy (*Engraulis encrasicdus*), and horse mackerel (*Trachurus trachurus*) at sea using a 40–60 kHz broadband chirp signal with a duration of 1 or 5 ms. To classify the species, they used neural networks for which the inputs were the autoregressive and/or cepstral coefficients of the echo spectrum signature. They succeeded in species identification with a maximum correct classification of 74%. Simmonds *et al.*[11] attempted to identify fish species for caged aggregations using neural network and discriminant

[a]Electronic mail: i-tommy@f5.dion.ne.jp

 © 2008 Acoustical Society of America

analyses using the mean spectra of target echoes. Their species recognition rate was approximately 95%. These studies used the spectra of the echoes from fish schools but did not obtain the spectra of the individual fish TS as in the present study.

The TS spectra of individual zooplanktons have been measured using broadband signals. Traykovski *et al.*[12] measured the TS spectra of Antarctic krill (*Euphausia superba*) using a chirp signal at high frequencies (350–750 kHz) and demonstrated the variable nature of the TS with respect to animal orientation. Stanton *et al.*[13] examined the spectral and temporal scattering characteristics of three typical zooplankton groups and confirmed that the spectral features and temporal highlights correspond to the body or material structure of the animals.

There have been several observational studies of echoes from fish using dolphin-like signals. Benoit-Bird *et al.*[14] used such a signal to study the depth dependence of the TS for physoclistous fish such as snappers. They found that the TS and echo waveforms were similar for both deep observations by the manned submersible and surface control measurements and concluded that the TS of snappers did not have prominent depth dependence. Benoit-Bird *et al.*[15] also studied the TS characteristics of snappers using a FM sweep signal and dolphin-like click. They demonstrated the relationship between the TS pattern and the TS value, body length, and the weight of the target. Au and Benoit-Bird[16] observed the temporal and spectral structures of echoes from Hawaiian lutjanid snappers using linear FM signals and dolphin-like sonar signals. They discovered that the structure was complicated and dependent on the fish aspect and species, but the species were distinguishable from the structure. Au *et al.*[17] measured the TS as a function of aspect angle for four species of fish using dolphin-like signals to estimate the detection ranges of bottlenose dolphin and harbor porpoise. Benoit-Bird *et al.*[18] transmitted three kinds of dolphin sonar signals with source levels of approximately 200 dB with respect to 1 μPa peak-to-peak at 1 m to three species of fish: Atlantic herring (*Clupea harengus*), sea bass (*Dicentrarchus labrax*), and Atlantic cod (*Gadus morhua*). They examined whether the targets were paralyzed or killed by the sounds and reported that no such effect occurred. These studies observed fish echoes using dolphin-like signals but did not measure the absolute TS spectra as in the present study.

The aim of this study was to measure the TS spectra of individual fish using a broadband sonar with pulse durations of a few tens of microseconds, similar to what dolphins have. Imaizumi *et al.*[19] measured the frequency characteristics of the scattering amplitude of metal spheres and an anesthetized goldfish (*Carassius auratus*). They validated the broadband scattering amplitude or TS measurement method under a high signal-to-noise ratio (SNR) using a simple system. This study is a more realistic extension of the work of Imaizumi *et al.*[19] The TS spectra of some commercially important fish species were measured in a tank from various aspects using a more sophisticated system. The TSs of tethered live fish and wild fish swimming freely in the sea were also measured. The application of dolphin-like sonar signals to fish detection and quantification is also discussed.

II. MATERIALS AND METHODS

A. Broadband transmitting and receiving systems and sonar sounds

Broadband transmitting and receiving systems were constructed. All of the equipments used were commercially available, except for the two broadband transducers for transmitting and receiving and a preamplifier. In the transmitting system, the signal from a signal generator (NF Co., WF1946) was amplified by a power amplifier (Accuphase, PRO-100; maximum gain of 40 dB) and was sent to the transmit transducer. In the receiving system, the reflected wave was sensed by the receive transducer, and the signal was amplified by the preamplifier. The output signals were observed, measured, and transformed into digital data by an oscilloscope (Tektronix, TDS3000), and the data were transferred to a personal computer via a GPIB interface, where they were recorded.

The transmit and receive transducers were similar but were separated. This enabled an easy measurement of the overall characteristics of the transmitting and receiving systems; the transducers were simply placed face to face. The transmitting sensitivity had a peak at 110 kHz, fell off rapidly below 60 kHz, and varied as much as 5 dB in the flat area between 65 and 140 kHz [Fig. 1(a)]. The product of the transmitting and receiving sensitivities had a broadband characteristic of 58–140 kHz at a level of −10 dB [Fig. 1(c)]. The beam width of the transmit transducer was 19.2° at 50 kHz and 7.9° at 130 kHz. The combined beam widths for the transmit and receive transducers was 19.5° and 7.1° for the same frequencies, respectively.

Dolphin sonar sounds are composed of trains of clicks for which the time interval (click interval) is generally dependent on the target range.[7] The waveform is similar among the pulses.[7,20] The characteristics of the sonar sound vary among the dolphin species, but they can be roughly divided into two types. The bottlenose dolphin type has a broad frequency bandwidth and is composed of a small number of cycles, whereas the finless porpoise type has a narrower bandwidth and is composed of a larger number of cycles. The term "dolphin" is used for both dolphins and porpoises in this paper.

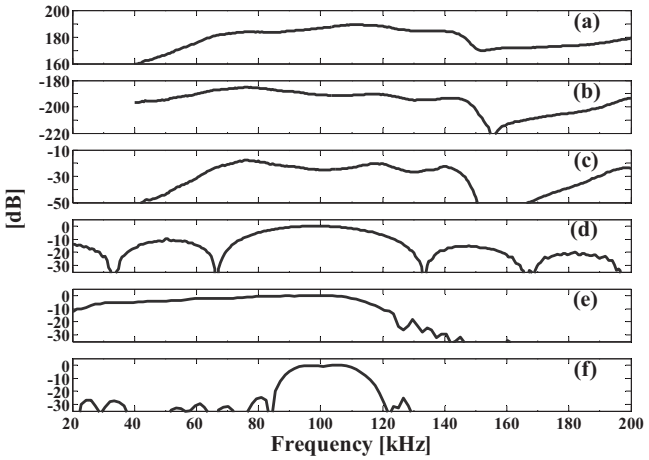


FIG. 1. Frequency characteristics of (a) transmit and (b) receive transducers and (c) the product of both sensitivities. (d) Amplitude spectra of tone burst, (e) bottlenose dolphin sound, and (f) finless porpoise sound.

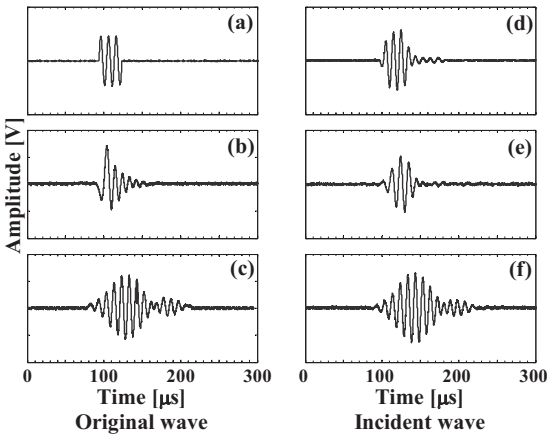


FIG. 2. Original waveforms of the sonar sounds used: (a) tone burst wave, (b) bottlenose dolphin, and (c) finless porpoise. Incident waveforms obtained by setting the transducers face to face: (d) tone burst wave, (e) bottlenose dolphin, and (f) finless porpoise.

Dolphins transmit highly focused sonar sounds forward from the head.[7] Nakamura and Akamatsu[21] measured the sonar signals of nine different dolphin species from five breeding families using a broadband hydrophone. It is well known that both the waveform and the frequency characteristics of the sounds measured off-axis are different from those measured on-axis. Therefore, Nakamura and Akamatsu[21] recorded the sounds of dolphins underwater and simultaneously captured their behavior using a video camera. Only sonar signals that were recorded when the dolphins were facing the direction of the hydrophone were selected. The present study used the typical sonar signals of the bottlenose dolphin and finless porpoise recorded by Nakamura and Akamatsu[21] [Figs. 2(b) and 2(c)]. For comparison, a short-pulsed sinusoidal waveform (tone burst), which was three cycles of 100 kHz with 30 μs duration, was also used [Fig. 2(a)].

The amplitude spectra of the tone burst and dolphin sonar sounds used are shown in Figs. 1(d)–1(f), along with the sensitivity characteristics. The −3 dB bandwidth of the tone burst is 30 kHz, from 84 to 114 kHz. The sonar sound spectrum of the bottlenose dolphin has a peak near 100 kHz, and its −3 dB bandwidth is 60 kHz wide, from 55 to 115 kHz. The spectrum of the finless porpoise sound has a peak near 110 kHz, and its −3 dB bandwidth is 20 kHz, from 92 to 112 kHz. This bandwidth is one-third of that of the bottlenose dolphin, yet it is wider than that of a normal echo sounder. Comparing these spectra with the sensitivity product in Fig. 1(c), it is clear that the transducer system can transmit and receive the majority of the spectral content of these broadband signals. These two types of signal were originally generated by using the dolphin's signals. However, some degradation occurred in the process of transmission and reception. Therefore, the signals are termed "dolphin-like" in this paper. Figures 2(d)–2(f) show the incident waveforms obtained by setting the transducers face to face with a 2 m separation range. The far-field distance was computed as 1.3 m at the highest frequency of 140 kHz, which was much shorter than the separation range. Because of the transducer frequency characteristics, the incident waveforms are distorted versions of the transmitting signals.

B. Scattering amplitude measurement method

In the system described above, the Fourier transform of the incident wave as a function of direction angle θ, $P_i(\omega,\theta)$, is given by

$$P_i(\omega,\theta) = E_0(\omega)G_s(\omega)S(\omega)D_s(\omega,\theta)\frac{e^{j\omega r/c}}{r}\frac{1}{e^{r\alpha(\omega)}}, \tag{1}$$

where ω is the angular frequency, $E_0(\omega)$ is the Fourier transform of the signal from the signal generator, $G_s(\omega)$ is the transfer function or gain of the power amplifier, $S(\omega)$ is the transmitting sensitivity, $D_s(\omega,\theta)$ is the directivity of the transmit transducer, r is the range between the transmit and receive transducers, α is the absorption coefficient, j is the imaginary unit, and c is the speed of sound in water. The Fourier transform of a reflected wave measured by the receive transducer at the same location as the transmitter is

$$P_r(\omega,\theta) = P_i(\omega,\theta)\Gamma(\omega)\frac{e^{j\omega r/c}}{r}\frac{1}{e^{r\alpha(\omega)}}D_r(\omega,\theta), \tag{2}$$

where $\Gamma(\omega)$ is the scattering amplitude of the target and $D_r(\omega,\theta)$ is the directivity of the receive transducer. The Fourier transform of the reflected wave received at the oscilloscope is then

$$E_r(\omega,\theta) = P_r(\omega,\theta)M(\omega)G_r(\omega), \tag{3}$$

where $M(\omega)$ is the receiving sensitivity of the hydrophone and $G_r(\omega)$ is the gain of the preamplifier.

In the case of the tank experiment, $\theta=0$ because the experiments were conducted on the directivity axes and the absorption loss was ignored. The Fourier transform of the incident wave $E_i(\omega,0)$, which was measured by the receive transducer when set face to face with the transmit transducer, is

$$E_i(\omega,0) = P_i(\omega,0)D_r(\omega,0)M(\omega)G_r(\omega). \tag{4}$$

Taking the ratio of Eq. (3) to Eq. (4) cancels out the frequency characteristics of the transmitting and receiving systems and gives a spectrum ratio,

$$R_t(\omega) \equiv \frac{E_r(\omega,0)}{E_i(\omega,0)} = \frac{e^{j\omega r/c}}{r}\Gamma(\omega). \tag{5}$$

Therefore, the frequency characteristics of the scattering amplitude can be measured in the frequency range independent of the system characteristics.

A similar method was used by Dragonette *et al.*[22] in experiments to measure the scattering amplitudes of several metal spheres, and the method has been applied to other broadband scattering measurements.[12,13,15,16] This "spectrum ratio method" using two separate transducers was used throughout this study, even for the experiments at sea.

The TS value is related to the backscattering cross section δ_{bs}, the scattering amplitude, and the spectrum ratio as

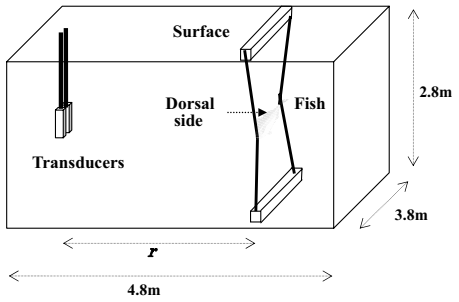


FIG. 3. System for the measurement of the fish target strength (TS) spectra in a tank.

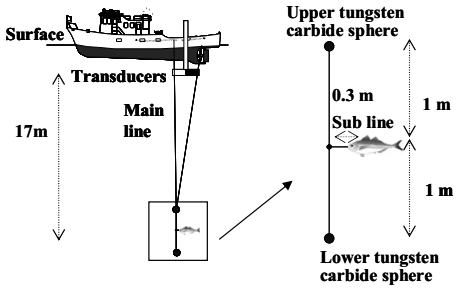


FIG. 4. Setup for the measurement of the TS spectra of tethered fish swimming in the sea.

$$TS(\omega) = 10 \log \sigma_{bs}(\omega) = 20 \log|\Gamma(\omega)| = 20 \log|rR_t(\omega)|. \tag{6}$$

C. Measurement of TS spectra in a tank

The measurement method and the overall system were first validated using metal spheres. The TS spectra of metal spheres could be calculated accurately using a theoretical model, and their backscattering was unidirectional. A 38.1 mm φ tungsten carbide (TC) sphere and a 32.1 mm φ copper sphere were used. These are standard devices for the calibration of scientific echo sounders.[23] Reflected waves were collected for 100 pings (50 s in time because of the 0.5 s pulse repetition period) at a 10 MHz sampling frequency and were then averaged.

The TS spectra of three species of anesthetized fish were then measured in a tank. All of the fish had swim bladders. The fish consisted of ten horse mackerel (*Trachurus japonicus*; average fork length of 207.6 mm, standard deviation of 3.0 mm), five sea bream (*Pagrus major*; 296.2 mm, 4.7 mm), and five chub mackerel (*Scomber japonicas*; 256.0 mm, 5.1 mm). The standard deviations of fork length were small because all of the fish in each species were of similar size.

To measure the fish TS spectra, the experimental fish were anesthetized and suspended by nylon monofilaments in the freshwater tank, which was 4.8 m long, 3.8 m wide, and 2.8 m deep. The orientations of the fish were adjusted until the transmitted wave was incident to their dorsal regions. One hundred pings (50 s in time) of reflected waves were measured for each sonar signal (Fig. 3).

The variation in TS spectra with respect to the tilt angle θ_t of the fish was measured for one sea bream. The tilt angle was defined as 0° when the sound wave was perpendicular to the body axis of the fish, with $\theta_t = +90°$ for the fish head-on and $\theta_t = -90°$ for the fish tail-on. The fish tilt angle was changed from +90° to −90° in 10° steps.

D. Measurement of TS spectra of tethered live fish at sea

The TS spectra of tethered live fish were measured at sea from the training vessel *Hiyodori* of Tokyo University of Marine Science and Technology, which was anchored at a depth of 30 m. Each fish was suspended with two TC spheres such that the sound was incident to the fish's dorsal region (Fig. 4). Before the experiment, the fish were kept alive in a small tank on the deck. The fish were tethered to a nylon monofilament and placed in the sea as soon as possible. At an upper sphere depth of 17.3 m, the beam spreads were 4.7 m at 50 kHz and 1.9 m at 130 kHz. The sphere and the fish were near the center of the beam because they were suspended approximately vertically beneath the transducers. The angles from the transducers to the TC spheres and the fish were similar because the distance from the main suspension line to the center of the fish body was approximately 0.4 m.

For the experiments in the tank, no compensation for directivity was required. For the experiment at sea, however, the suspended fish moved in the beam. Therefore, the directivities were compensated using echoes from the upper or lower TC sphere. Substituting the distance to the fish r_f and the fish scattering amplitude $\Gamma_f(\omega, \theta_t)$ into Eqs. (2) and (3) with a tilt angle variable θ_t yields the Fourier transform of the wave reflected from the fish, $E_{rf}(\omega, \theta_t)$. In the same way, substitution of r_s and $\Gamma_s(\omega)$ yields $E_{rs}(\omega, \theta)$ for the TC spheres. Taking the ratio R_{fs} of the two reflected signals cancels out the transmitting and receiving directivity functions,

$$R_{fs} = \frac{E_{rf}(\omega, \theta)}{E_{rs}(\omega, \theta)} = \frac{\Gamma_f(\omega, \theta_t) r_f^{-2} \exp[-2r_f\alpha(\omega) + j\omega r_f/c]}{\Gamma_s(\omega) r_s^{-2} \exp[-2r_s\alpha(\omega) + j\omega r_s/c]}$$
$$\cong \frac{\Gamma(\omega, \theta_t)}{\Gamma_s(\omega)} \exp[j\omega/c(r_f - r_s)]. \tag{7}$$

The scattering amplitude of the fish was calculated using this ratio with the theoretical scattering amplitude of the TC sphere. Taking the absolute value of Eq. (7) causes the last exponential term to disappear.

Three fish were used for the sea experiment: one horse mackerel (*Trachurus japonicus*) and two chicken grunt (*Parapristipoma trilineatum*, Table I). The bottlenose dolphin-like and finless porpoise-like sounds (see Fig. 2) were transmitted with a pulse repetition period of 0.1 s. Because the measurements were conducted for live swimming fish and the transducer directivity was compensated to give TS values, the conditions were almost similar to those for *in situ* TS measurement.

E. Experiment to detect fish

Echoes from wild fish were collected using a method similar to normal echo sounding to test how effective the dolphin-like sonar sound was at detection. The Hiyodori

TABLE I. Maximum, average, and normalized target strengths (TSs) for three fish at 70 and 100 kHz.

Sample	Horse mackerel	Chicken grunt 1	Chicken grunt 2
Fork length (mm)	175	145	152
70 kHz maximum TS (dB)	−35.40	−34.32	−30.90
Average TS (dB)	−50.93	−45.92	−52.77
TS_{cm} (dB)	−75.79	−69.15	−76.41
100 kHz maximum TS (dB)	−36.42	−35.18	−35.49
Average TS (dB)	−52.29	−46.93	−52.10
TS_{cm} (dB)	−77.15	−70.16	−75.74

sailed at a speed of 1–2 kt with the transducers pointed vertically from the side of the ship, transmitting the sound with a period of 0.5 s.

The dolphin-like sonar sound was very short, providing a very high-range resolution. Therefore, it could separate single fish echoes much more easily than ordinary echo sounders. The product of the directivity functions and the scattering amplitude, $D_s(\omega,\theta)\Gamma_s(\omega,\theta_t)D_r(\omega,\theta)$, called the single echo amplitude, was derived from a single echo. The results obtained using the finless porpoise-like sonar sound, which had better SNRs than those that used the bottlenose dolphin-like sound, are also presented. The results obtained using this system were compared with those of the normal echo sounder installed onboard the vessel.

III. RESULTS

A. Evaluation of the method using metal spheres

For the amplitude spectrum of the incident wave and the reflected wave from the TC and the copper spheres, as well as the measured form functions using the three sonar signals, the measured form functions were in good agreement with the theoretical curves in the −3 dB band of the incident wave and also in the −6 dB band (Fig. 5). However, the agreement deteriorated significantly outside of the −6 dB band because of the low SNR.

The rms errors between the theoretical and measured values were examined. The rms error ε is defined by

$$\varepsilon = \sqrt{\frac{1}{\beta-\alpha}\int_{\alpha}^{\beta}\{|f_m(ka)|-|f_t(ka)|\}^2 d(ka)}, \tag{8}$$

where $|f_m(ka)|$ and $|f_t(ka)|$ are the absolute values of the measurement and theory form functions, respectively, and α and β are the lower and upper ka bounds of the −3 dB bandwidth for each sonar signal. The averages of the rms errors for 100 pings are shown in the lower panels of Fig. 5 for each signal. The errors were approximately 0.1, independent of the sonar signals and the metal materials. They were much smaller than unity, which is the approximate average value of the form function. Therefore, the accuracy of the measurement method and system was high.

B. Measurement of fish TS spectra in a tank

The TS spectra of three species of fish using the bottlenose dolphin-like sonar sound (Fig. 6) were similar to the TS spectra obtained for the respective −3 dB bands of the other sonar signals (data not shown). No changes were observed in the spectrum shapes for 100 pings (50 s in time), except for one horse mackerel (H-10) and one sea bream (S-5) that woke up from anesthetization; the spectra shown for these individuals were obtained before they regained consciousness.

Figure 7 shows the normalized TS (TS_{cm}) at 70 and 100 kHz for comparison with previous results. The normalized TS is defined by[24]

$$TS_{cm} = TS - 20\log L \tag{9}$$

where L is the fork length in centimeters, defined as the length between the snout and the fork of the caudal fin. The TS_{cm} for the averaged TS was generally approximately −66 dB for fish with swim bladders (Fig. 7, dotted line).[25,26] The results were similar to those of previous studies. One point for the chub mackerel was extraordinarily low (−83 dB). This occurred because the value was right at the 75 kHz dip, as seen in C-4 of Fig. 6.

Figure 8 shows the variation in the waveforms and the TS spectra of a sea bream due to the changes in tilt angle. Both the waveform and the TS spectra varied considerably with changes in tilt angle from −30° to +30° in 10° increments (Fig. 8). The results for a 28.5 cm sea bream observed using the bottlenose dolphin-like signal and previous data for a similar-sized sea bream at 100 kHz (Ref. 4) (Fig. 9) show similar trends, but the variation in TS as a function of tilt angle was large among individual fish.

C. Measurement of TS spectra of fish at sea

The violent motion of the fish can be seen in the echogram of a chicken grunt and two TC spheres obtained using the bottlenose dolphin-like signal (Fig. 10). There were depth changes of approximately 40 cm within 5 s. This distance is nearly the same as the subline length (Fig. 4).

The directivity functions of transmitting and receiving were removed by the echoes from the TC sphere using Eq. (7), and the TS spectra of the chicken grunt were calculated [Fig. 11(a)]. There were rapid changes in the TS near 92 kHz. This phenomenon was due to the resonance in the scattering amplitude of the 38.1 mm φ TC sphere, as seen in Fig. 5. Compensation using Eq. (7) was difficult here. Figure 11(b) shows the TS spectra for 10 pings (1 s in time), with nearly the same echo level. These data are highlighted by the dotted lines in Fig. 10. The TS spectra are similar and nearly flat for pings 101 and 102. However, they gradually diminish at higher frequencies by as much as 20 dB from pings 103 to 107. The spectra then decay greatly at ping 108, retrieving approximately the original TS spectrum shape at ping 110. It is likely that the change in the tilt angle of the chicken grunt affected the TS spectra.

Table I shows the fork length and the maximum, average, and normalized TSs for each fish at 70 and 100 kHz. The normalized TS ranged from −76 to −68 dB, which are lower than the abovementioned general value of −66 dB.

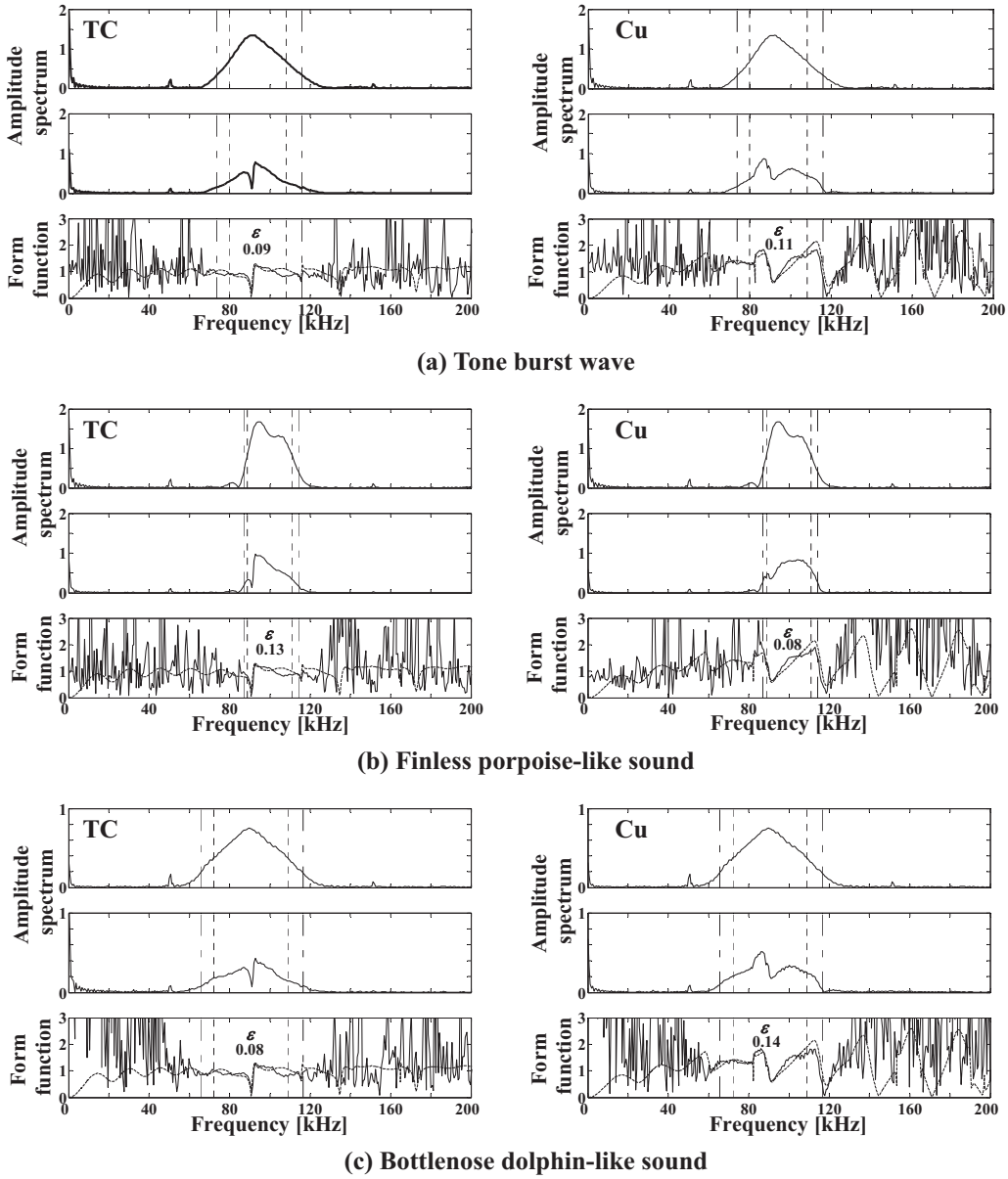


FIG. 5. The form function of tungsten carbide (TC) (left) and copper (right) spheres measured using (a) a tone burst wave, (b) a finless porpoise-like sound, and (c) a bottlenose dolphin-like sound. Also shown is the amplitude spectrum of the incident wave (upper), the reflected wave (middle), and the measured (lower, thin line) and theoretical (lower, bold line) form functions. The dotted and dot-dashed lines show the −3 and −6 dB bandwidths of the incident waves, respectively. The rms errors, ε, between the measurements and the theory are shown in the form function panel.

This was attributable to the violent motion of the suspended fish, which was large enough to cause a large change in the tilt angle.

D. Fish detection experiment

Figure 12(a) shows an example of a school of fish echogram that was taken using echo signals that contained all frequency components. The echogram was obtained using the finless porpoise signal. Figure 12(b) shows the spectra of the single echo amplitude at nearly the same depths as in Fig. 12(a). Because the pulse repetition period was 0.5 s, Fig. 12(b) shows the changes in the echo spectra of four fish for approximately 3 s. The pulse duration of the finless porpoise sound was approximately 100 μs [see Fig. 2(c)]. Therefore, it could resolve single echoes, unlike a conventional echo sounder.

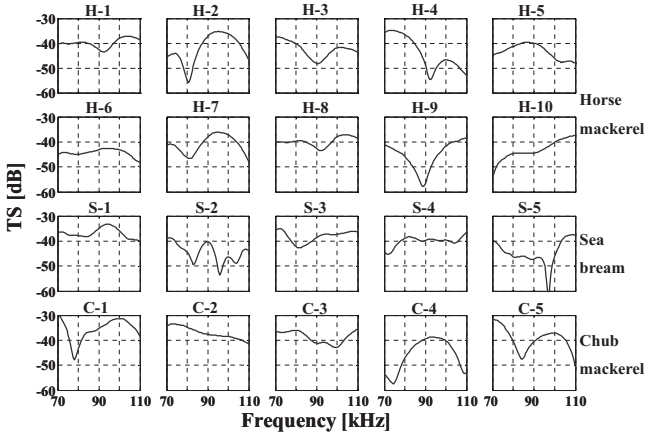


FIG. 6. Measured TS spectra of horse mackerel (H-1 to H-10), sea bream (S-1 to S-5), and chub mackerel (C-1 to C-5).

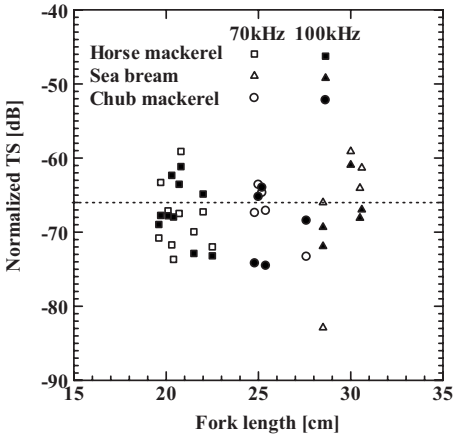


FIG. 7. Normalized TS at 70 and 100 kHz for three species of fish. The dotted line at −66 dB shows the normalized average TS.

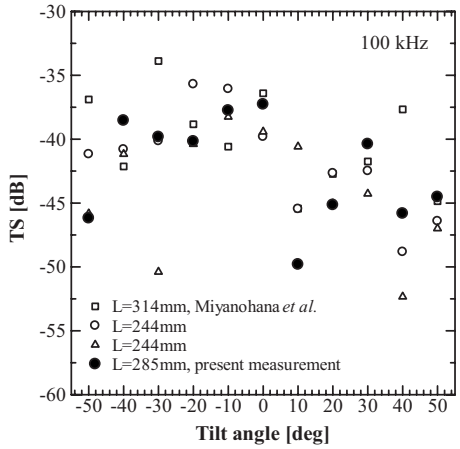


FIG. 9. Comparison of the dependence of TS on the tilt angle for sea bream of similar sizes at 100 kHz. The white markers are data obtained from Miyanohana *et al.*;[4] black circles denote the TS for a 28.5 cm sea bream from Fig. 8.

IV. DISCUSSION

A. Measurement of the TS spectra using broadband sonar sound

The form functions of the metal spheres were measured using the broadband sonar sounds with the spectrum ratio method and were found to agree closely with theory. Therefore, this method was capable of accurately measuring the frequency characteristics of backscattering in the −3 dB band, independent of the sonar sound used. The subsequent measurements for fish were also very accurate.

It was possible to measure the broadband TS spectrum by applying the spectrum ratio method to a short and broadband pulse similar to that produced by a dolphin. If it is assumed that dolphins use a method similar to the spectrum ratio method, it is possible that they could use reflected waves from the water surface, instead of incident waves. The spectrum ratio method is an excellent calibration method for broadband transmitting and receiving systems. It can compensate for the frequency characteristics of the transmitting and receiving systems without measuring the frequency characteristics of each component. It can measure TS spectra such as those of zooplankton easily and directly.[12,13] The TS spectrum is different from the echo spectrum, which includes the characteristics of the transmitting and receiving systems and conveys fewer target characteristics than the TS spectrum. Thus, TS spectra allow the estimation of the size, behavior, and species of fish.

The equipment and methods were first validated using measurements involving metal spheres. The metal spheres were also used for directivity compensation, as described in Sec. III C. The use of these spheres has several advantages: their exact scattering characteristics are known, the effect of environmental characteristics such as temperature on scattering can be minimized, and they have no directivity of backscattering. For these reasons, they are extensively used for the calibration of scientific echo sounders.[27] This study demonstrated additional useful applications of metal sphere calibration.

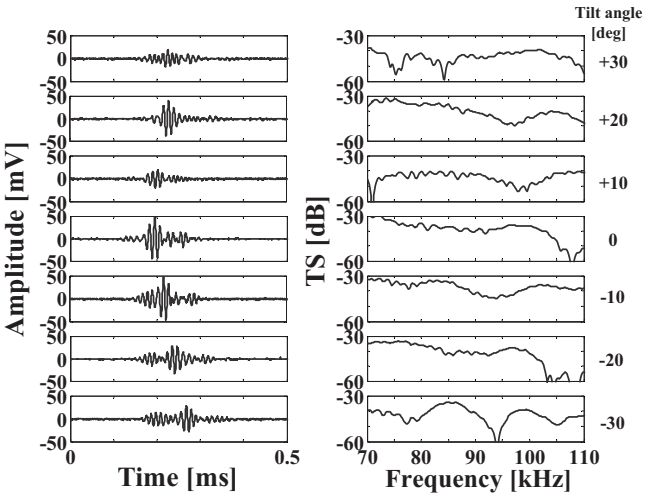


FIG. 8. Variations in echo waveforms (left) and TS spectra (right) of a sea bream obtained by changing the tilt angle from +30° (top) to −30° (bottom). For comparison, −40 dB grid lines are shown. The TS values at 100 kHz shown by solid lines were sampled for Fig. 9.

B. Variation in TS spectra with individual, tilt angle, and species

The TS spectra of fish varied greatly with species and among individuals of the same species with similar sizes

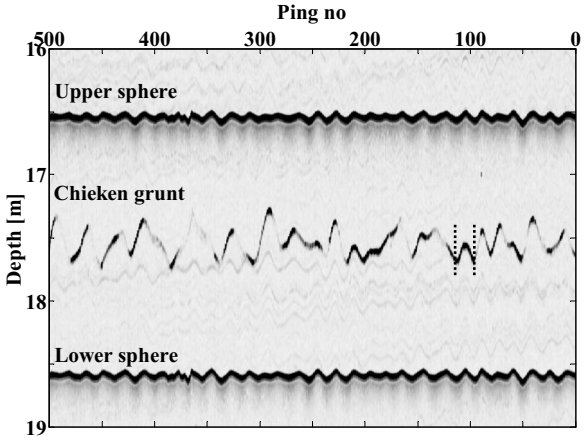


FIG. 10. Echogram showing two TC spheres and a chicken grunt fish with fork length of 14.5 cm. The dotted lines at pings 100 and 110 (1 s in time) indicate the detailed analysis region shown in Fig. 11(b).

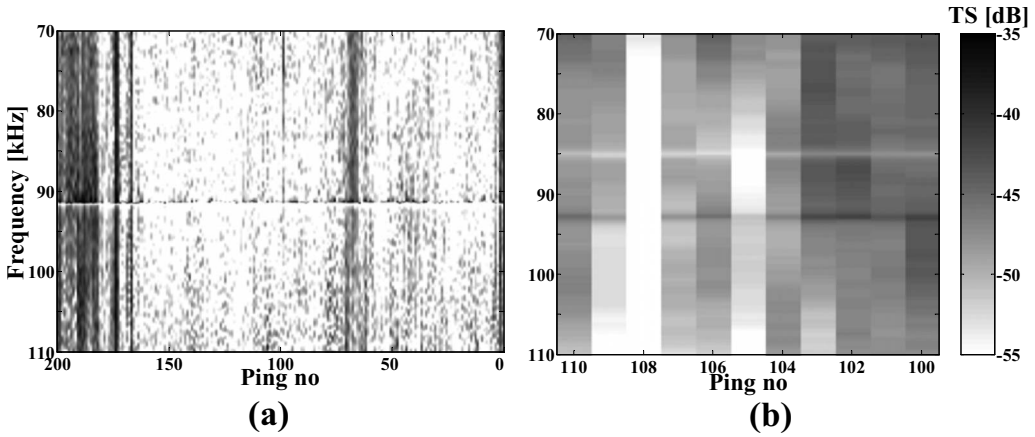


FIG. 11. The TS spectra of a chicken grunt fish. The directivities of the transducers were compensated for by TC sphere echoes. The *x*-axis shows the ping number, the *y*-axis shows the frequency, and the gray scale indicates the TS value. The variations in TS spectra at pings 101–110 indicated by the dotted lines in Fig. 10 are expanded and shown in (b).

(Fig. 6). The experimental fish were suspended such that the sound was incident to their dorsal area. However, the method of suspension introduced some variation in the tilt angle around the dorsal perspective. This could have caused the variation in TS spectra. However, a more reasonable explanation is that the variation is intrinsic to sonar scattering by fish. The echo from any fish is a composite of many partial echoes from many parts of the fish body such as the specular reflection from the frontal surface of the swim bladder and from many acoustic paths. Internal reflections, for example, can propagate along different paths. In general, when increasing from a 0° tilt, the waveform became lengthened with more highlights, the amplitude became smaller, and the spectrum tended to gain notches or troughs (Fig. 8). A similar correspondence of the spectral variation in the TS with fish tilt angle and the temporal waveform variation was apparently observed in the experiments using dolphin-like signals.[17]

Here, the factors involved in the variation of the TS spectra are evaluated. For this purpose, a standard deviation SD in dB is defined as

$$\mathrm{SD} = \sqrt{\frac{1}{n}\sum_{i=1}^{n}\{\mathrm{TS}_i(\omega) - \overline{\mathrm{TS}(\omega)}\}^2}, \tag{10}$$

where $\mathrm{TS}_i(\omega)$ is the TS spectrum of each experimental fish or tilt angle and $\overline{\mathrm{TS}(\omega)}$ is the average for the same species or for the tilt angles. The standard deviations were compared to determine the effects of the individual for three different species (Fig. 6) and the effects of the tilt angle (Fig. 8). In Eq. (10), n is the number of fish in each species (ten horse mackerel, five sea bream, and five chub mackerel). For the tilt angle effects, only the cases of a nearly dorsal perspective were used, i.e., data from −30° to +30°. In this case, $n=7$. Body length effects were neglected because the deviation of the body length was not large. The standard deviation of the TS spectra of the sea bream was large at 97 kHz (Fig. 13); this was caused mainly by a deep dip of the TS spectrum for S-5 at this frequency (Fig. 6). Standard deviations for the tilt angle were large at 71, 75.5, 84.5, 94, and 108 kHz (Fig. 13). They were caused by the dips in the TS spectra observed at these frequencies for tilt angles between +30° and −30° (Fig.

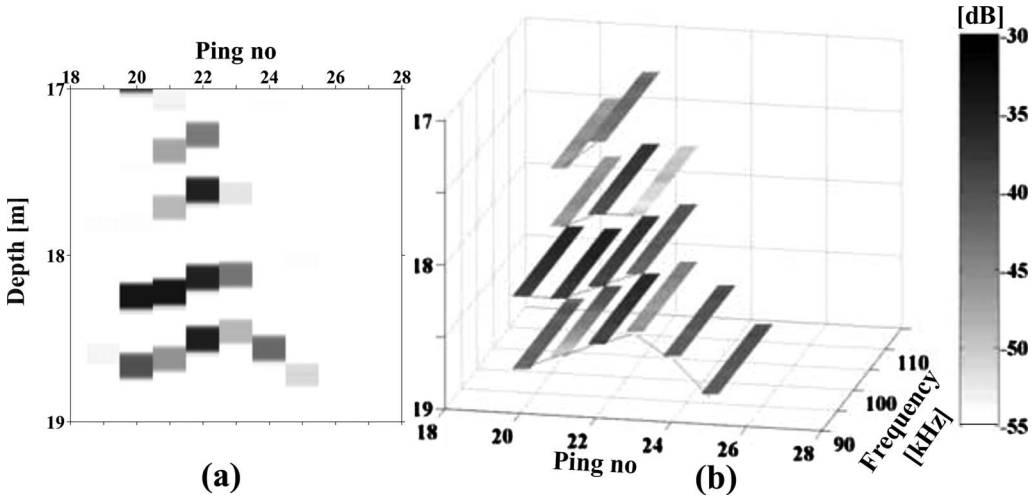


FIG. 12. (a) Echogram of a school of fish obtained at sea using the finless porpoise-like sound and (b) the spectra of a single echo amplitude.

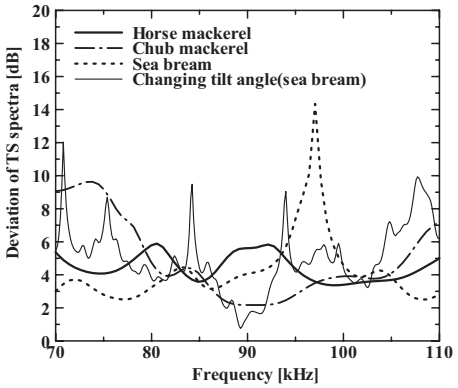


FIG. 13. Standard deviation of the TS spectra for different individuals and tilt angles. The standard deviation for the tilt angle was calculated in 10° steps from +30° to −30°.

8). However, the standard deviation was extremely small at 89 kHz because the TS values were nearly −40 dB for this tilt angle range. The large standard deviation of the chub mackerel at low frequencies was an anomaly. Excluding these extreme points, the average standard deviation was approximately 4 dB, with no significant difference between species or tilt angles.

The differences in the TS spectra can be extremely useful for fish species identification. The spectra of TS obtained at sea depend on several parameters, including species, body length, tilt angle, and individual differences. In their natural habitat, fish move, and their changing tilt angles cause continuous changes in the TS spectra. Such changes can be used for effective target identification.

Despite the variable nature of the TS, our observations generally agree with previous results (see Figs. 7 and 9). This suggests that the average TS could be used to convert SV to distribution density. It is also likely to be extremely useful for estimating the average size of fish.

C. The TS spectra of live fish measured at sea

The variations in the TS spectra of the tethered swimming fish were observed continuously, with the transducer directivities compensated for by the scattering amplitude of the TC sphere (Fig. 11). A large variation was observed in the echo level (Fig. 10) and TS spectra [Fig. 11(b)]. Probably because of the violent motion of the fish, the measured normalized TS values were small compared to previous data (Table I). It is clear that the echo levels were high when the fish were directed downward (Fig. 10), in agreement with previous studies of TS. Combining the echogram and the TS spectra would likely provide information on fish behavior. Different species will have different behaviors. Thus, behavior information should be helpful in target identification.

The variation in the spectra of single echo amplitudes for four fish in a school [Fig. 12(b)] was thought to have been caused by both the directivity changes of the transducers and the viewing direction of the target fish from the sailing ship. It was not thought to have been caused by any changes in behavior during the short 3 s period. Certainly, the spectrum change was within a 10 dB range. If a broadband system incorporated the split beam method to compensate directivities, it could measure the variation in *in situ* TS spectra. This would supply additional information for fish species identification.

D. The merits of using dolphin sonar signals

The echogram of the fish school [Fig. 12(a)] showed that because of the very short pulse of the dolphin-like sonar sound, it was possible to obtain well-separated single echoes that would otherwise be multiple echoes for ordinary echo sounders. The mean distance between the fish was estimated as approximately 40 cm on this echogram. If a high-range resolution using a short pulse could be used, it would allow the classification of fish species through an analysis of the school structure. This would reduce the limitations of TS measurements, which have long been a serious problem for measurements of fish *in situ*.

If it were easy to obtain single echoes using a high-range resolution, it would also become possible to derive the TS spectrum. In this study, it was not possible to use the TS spectrum to directly identify fish species. However, if the variations in the TS spectra were categorized by behavior or other factors, this would provide useful information for fish species identification. Therefore, if a broadband split beam method were developed, which would allow the measurement of TS spectra of dense schools of fish *in situ*, great improvements in fishery acoustics would be possible.

No significant differences were observed between the TS spectra measurements for the sonar sounds of dolphins and the artificial tone burst wave used in this study (Fig. 2). Although the comparison of the sounds was not a main aim of this work, a trial was conducted to find other uses for the sonar sounds of dolphins. An attempt was made to improve the SNR through cross-correlation processing. In an experiment at sea, echoes from a TC sphere were measured using three sonar signals. The echo data from the TC sphere obtained by the three different signals were cross correlated with each incident waveform as a reference or a replica. The SNRs of the results were then compared with those of the original data. The SNRs were improved by more than 10 dB for all sonar signals and by more than 20 dB for the finless porpoise signal. When the SNRs were compared after the cross-correlation, the bottlenose dolphin and finless porpoise sonar signals improved the SNRs by 3 and 9 dB, respectively, over the tone burst wave. Further study of the SNR is left for future work. However, the possibility that dolphin sonar signals have greater potential than others to observe TS spectra of objects is noted. The double chirp structure recently revealed by Capus *et al.*[28] suggests such a possibility.

Despite the advantages described above, dolphin sonar could be limited for biological reasons, and a theoretically derived waveform (e.g., an amplitude-weighted FM signal) combined with a matched filter might be superior. It is easy to construct such a broadband system that would work with several waveforms such as different dolphin signals and chirp signals with several combinations of pulse and sweep widths. Using such a system, one could compare the performance of various objects and conditions. Such a study would be an interesting topic for future research.

V. CONCLUSIONS AND FUTURE WORK

The following conclusions are made:

(1) The frequency characteristics of the form function of metal spheres, measured using the spectrum ratio method using the dolphin-like sonar signals, agreed closely with the theoretical calculations. Therefore, this method is capable of measuring TS spectra accurately.
(2) The TS spectra of fish varied considerably among species, individuals, and tilt angles.
(3) The TS spectra of tethered live fish and swimming fish were successfully measured using the metal sphere echoes to compensate for the transducer directivities. The TS spectra varied considerably due to fish behavior.
(4) Natural fish echoes were detected with a very high-range resolution using the dolphin-like sonar signals. It was also possible to measure the spectra of the single echo amplitudes of fish.
(5) A continuous measurement of the fish TS spectra should be useful for estimating the behavior of and classifying fish species.
(6) Using a high-range resolution sonar signal such as a dolphin sound relaxes the requirement for single echo measurement *in situ*.
(7) It may be possible to use the dolphin sound for other purposes such as the improvement of the SNR through cross-correlation processing.

The following topics are suggested for future work:

(1) a study aimed at improving the SNR of a short broadband pulse to gain quantitative information
(2) a study of TS spectra variations to allow fish species identification and behavior estimation
(3) the development of a broadband split beam method that can compensate for the directivity of the transducers to measure broadband TS spectra *in situ*
(4) a comparative study of broadband signals from dolphins and artificial sounds such as chirp signals

ACKNOWLEDGMENTS

This study was supported by the Bio-Oriented Technology Research Advancement Institution (BRAIN) Promotion of Basic Research Activities for Innovative Biosciences, the Research and Development Program for New Bio-Industry Initiatives, and Grants-in-Aid for Scientific Research from the Ministry of Education, Culture, Sports, Science and Technology, Japan. We are grateful to Dr. Kenneth G. Foote and three anonymous referees for their useful comments and advice. We also thank Yapp Min Lee, who refined the English.

[1]E. J. Simmonds, N. J. Williamson, F. Gerlotto, and A. Aglen, "Acoustic survey design and analysis procedure: A comprehensive review of current practice," ICES Cooperative Research Report No. 187 (International Council for the Exploration of the Sea, Denmark, 1992).
[2]O. Nakken and K. Olsen, "Target strength measurements of fish," Rapp. P.-V. Reun.-Cons. Int. Explor. Mer **170**, 52–69 (1977).
[3]K. G. Foote, "Fish target strengths for use in echo integrator surveys," J. Acoust. Soc. Am. **82**, 981–987 (1987).
[4]Y. Miyanohana, K. Ishii, and M. Furusawa, "Measurements and analyses of dorsal-aspect target strength of six species of fish at four frequencies," Rapp. P.-V. Reun.-Cons. Int. Explor. Mer **189**, 317–324 (1990).
[5]D. G. Reid, "Report on echo trace classification," ICES Cooperative Research Report No. 238 (International Council for the Exploration of the Sea, Denmark, 2000).
[6]E. Ona, "Methodology for target strength measurements (with special reference to *in situ* techniques for fish and mikro-nekton)," ICES Cooperative Research Report No. 235 (International Council for the Exploration of the Sea, Denmark, 1999).
[7]W. W. L. Au, *The Sonar of Dolphins* (Springer-Verlag, New York, 1993).
[8]T. Akamatsu, D. Wang, and K. Wang, "Off-axis sonar beam pattern of free-ranging finless porpoises measured by a stereo pulse event data logger," J. Acoust. Soc. Am. **117**, 3325–3330 (2005).
[9]H. E. Harley, E. A. Putman, and H. L. Roltblat, "Bottlenose dolphins perceive object features through echolocation," Nature (London) **424**, 667–669 (2003).
[10]M. E. Zakharia, F. Magand, F. Hetroit, and N. Diner, "Wideband sounder for fish species identification at sea," ICES J. Mar. Sci. **53**, 203–208 (1996).
[11]E. J. Simmonds, F. Armstrong, and P. J. Copland, "Species identification using wideband backscatter with neural network and discriminant analysis," ICES J. Mar. Sci. **53**, 189–195 (1996).
[12]M. Traykovski, R. L. O'Driscoll, and D. E. McGehee, "Effect of orientation on broadband acoustic scattering of Antarctic krill *Euphausia superba*: Implications for inverting zooplankton spectral acoustic signatures for angle of orientation," J. Acoust. Soc. Am. **104**, 2121–2135 (1998).
[13]T. K. Stanton, D. Chu, P. H. Wiebe, L. V. Martin, and R. L. Eastwood, "Sound scattering by several zooplankton groups. I: Experimental determination of dominant scattering mechanisms," J. Acoust. Soc. Am. **103**, 225–235 (1998).
[14]K. J. Benoit-Bird, W. W. L. Au, C. D. Kelley, and C. Taylor, "Acoustic backscattering by deepwater fish measured in situ from a manned submersible," Deep-Sea Res., Part I **50**, 221–229 (2003).
[15]K. J. Benoit-Bird, W. W. L. Au, and C. D. Kelley, "Acoustic backscattering by Hawaiian lutjanid snappers: I. Target strength and swimbladder characteristics," J. Acoust. Soc. Am. **114**, 2757–2766 (2003).
[16]W. W. L. Au and K. J. Benoit-Bird, "Acoustic backscattering by Hawaiian lutjanid snappers: II. Broadband temporal and spectral structure," J. Acoust. Soc. Am. **114**, 2767–2774 (2003).
[17]W. W. L. Au, K. J. Benoit-Bird, and R. A. Kastelein, "Modeling the detection range of fish by echolocating bottlenose dolphins and harbor porpoises," J. Acoust. Soc. Am. **121**, 3954–3962 (2007).
[18]K. J. Benoit-Bird, W. W. L. Au, and R. Kastelein, "Testing the odontocete acoustic prey debilitation hypothesis: No stunning results," J. Acoust. Soc. Am. **120**, 1118–1123 (2006).
[19]T. Imaizumi, M. Furusawa, and T. Akamatsu, "Measurement of the frequency characteristics of the scattering amplitude using the dolphin's sonar signal," Journal of Marine Acoustics Society of Japan **33**, 9–16 (2006) (in Japanese).
[20]C. Kamminga, A. C. Stuart, and G. K. Silber, "Investigations on cetacean sonar XI: Intrinsic comparison of the wave shapes of some members of the *Phocoenidae* family," Aquat. Mamm. **22**, 45–55 (1996).
[21]K. Nakamura and T. Akamatsu, "Comparison of echolocation signal among dolphins and porpoises," Transactions of Technical Committee on Physiological Acoustics **H-98**, 106 (1998) (in Japanese).
[22]L. R. Dragonette, R. H. Vogt, L. Flax, and W. G. Neubauer, "Acoustic reflection from elastic spheres and rigid spheres and spheroids: II. Transient analysis," J. Acoust. Soc. Am. **55**, 1130–1137 (1974).
[23]K. G. Foote, "Spheres for calibrating an eleven-frequency acoustic measurement system," J. Cons., Cons. Int. Explor. Mer **46**, 284–286 (1990).
[24]M. Furusawa, "Prolate spheroidal models for predicting general trends of fish target strength," J. Acoust. Soc. Jpn. (E) **9**, 13–24 (1988).
[25]K. G. Foote, "Fish target strength for use in echo integrator surveys," J. Acoust. Soc. Am. **82**, 981–987 (1987).
[26]J. J. Traynor, "Target-strength measurements of walleye pollock (*Theragra chalcogramma*) and Pacific whiting (*Merluccius productus*)," ICES J. Mar. Sci. **53**, 253–258 (1996).
[27]K. G. Foote, H. P. Knudsen, and G. Vestnes, "Calibration of acoustic instruments for fish density estimation: A practical guide," ICES Cooperative Research Report No. 144, 1987.
[28]C. Capus, Y. Paihas, K. Brown, D. M. Lana, P. W. Moore, and D. Houser, "Bio-inspired wideband sonar signals based on observations of the bottlenose dolphin (*Tursiops truncates*)," J. Acoust. Soc. Am. **121**, 594–604 (2007).

The acoustic excitation of air bubbles fragmenting in sheared flow

Grant B. Deane and M. Dale Stokes
Marine Physical Laboratory, Scripps Institution of Oceanography, UCSD, La Jolla, California 92093-0238

(Received 18 September 2007; revised 16 September 2008; accepted 27 September 2008)

An analysis of the acoustic emissions of air bubbles fragmenting in sheared fluid flow is presented. The fragmentation of bubbles into two products only is considered. While the measured pressure amplitude is highly variable, the partition of energy between fragmentation products is highly correlated. The partition of energy between products is, on average, approximately equal irrespective of the relative sizes of the bubble products. This observation suggests that the acoustic excitation mechanism is common to both bubbles immediately prior to fragmentation. A model for the excitation mechanism based on symmetric collapse of the neck of air joining fragmentation products is proposed and found to be sufficient to explain the range of observed bubble pulse amplitudes and the equal partition of energy.
© *2008 Acoustical Society of America.* [DOI: 10.1121/1.3003076]

PACS number(s): 43.30.Lz, 43.30.Nb [KGF] Pages: 3450–3463

I. INTRODUCTION

There is a significant body of theoretical and experimental works relating to linear and nonlinear bubble behaviors.[1–3] It has been long known that the sounds of running water (fountains, waterfalls, and brooks) are associated with the breathing mode oscillations of air bubbles,[4] but the excitation mechanism is not yet adequately measured or modeled. The dynamics of bubble pinchoff from the impact cavity of rain drops and nozzles has been treated both experimentally and theoretically,[5,6] and is relatively well understood. In contrast, a quantitative analytical model that explains the fluid mechanics driving the acoustic emissions of gas bubbles fragmenting in fluid shear has not been presented.

A number of mechanisms that could provide the initial excitation energy of bubble breathing mode oscillations have been proposed. These include the sudden increase in the internal pressure of the bubble associated with surface tension and wall curvature (the Laplace pressure), hydrostatic pressure effects, shape mode coupling, and a fluid jet associated with the initial bubble distortion.[1,7,8] Pumphrey and Ffowcs Williams made order-of-magnitude estimates of the Laplace and hydrostatic pressure effects on a bubble with natural frequency of 2 kHz at a depth of 0.01 m and drew the conclusion that these two processes, although they must exist for every bubble, are not the most important processes.[9] A second-order nonlinear theory describing the shape mode and volume mode couplings has been presented by Longuet-Higgins.[10–12] His second-order perturbation analysis that begins with the nonlinear dynamical boundary condition at the bubble wall shows that energy can transfer efficiently between shape and breathing mode oscillations if the shape mode frequency is equal to or near half the breathing mode frequency.

The case of a bubble released by a nozzle represents a simple and experimentally reproducible system for examining the acoustic excitation mechanism. Longuet-Higgins suggested that in this case sound production is driven by the jet of water associated with the collapse of the neck of air formed immediately after bubble pinchoff.[6] This idea has been examined by Manasseh *et al.*[13,14] through the use of high-speed photographs and acoustic recordings for rapidly air-sparged bubble columns. An analytical model for the collapse of the neck of air has been presented by Deane and Czerski[15] who showed that acoustic excitation can be explained by the decrease in bubble volume that accompanies neck collapse, and is driven by surface tension forces.

Some experimental and numerical modeling work has been done on the acoustics of fragmenting bubbles. Pumphrey and Ffowcs Williams[9] studied bubble excitation through air entrainment by spilling flow over an obstacle and bubbles injected into a turbulent jet from a hypodermic needle. Air entrainment and bubble fragmentation were examined with a high-speed camera system and acoustic recordings, although pressure amplitude and decay rates were not reported. They concluded that the most likely times for bubbles to become excited are when they are formed at the surface and when they are sheared into smaller fragments. In terms of excitation mechanism, their conclusion was that the main source of energy is the radial flow around the protobubble at the moment it breaks away to form an actual free bubble. The evidence presented here indicates a different mechanism, which is the surface tension driven collapse of the neck of air joining the protobubble to its daughter product. The acoustic emissions of fragmenting vapor bubbles have been studied by Choi *et al.*[16,17] While these studies are obviously related to the present work, fragmenting vapor bubbles do not exhibit the same oscillatory response of excited gas bubbles of interest here. Here we further develop the acoustics of air bubbles fragmenting in fluid shear, observed in a laboratory experiment reported by Deane and Stokes.[18]

 © 2008 Acoustical Society of America

A. Bubble fragmentation in breaking waves

This work is motivated by a desire to understand the origin of breaking wave noise. Wave-induced bubbles in the upper ocean boundary layer play an important role in aerosol production, bubble-mediated, air-sea gas transport, and the production of underwater ambient noise. The transient medium to large bubbles within a few centimeters of the ocean surface that persist for only a few seconds during and immediately after wave breaking are thought to be important for the enhanced transport of highly soluble gases such as CO_2.[19,20] These larger bubbles are particularly difficult to measure in the field and the hope is that, with a suitable understanding of the mechanisms involved, their creation rates can be inferred from measurements of wave noise.

It has been widely accepted since the seminal works of Banner and Cato[21] and Medwin and Daniel[22] that breaking wave noise, at least above a few hundred Hertz, is due to the sound radiated by bubbles at the moment of their formation. This raises the questions, as follows: what are the bubble formation mechanisms within whitecaps? and how do those mechanisms result in breathing mode oscillations?

Although there are a number studies reporting the noise generated by individual whitecaps[23–25] and individual waves in the surf zone,[26,27] there are only a few measurements of emissions from individual bubbles in reverberation-free environments. The sound of bubbles entrained in gently spilling laboratory breakers have been reported by Medwin and Beaky[28] and Banner and Cato.[21] Updegraff[23] reported the measurements of the sound produced beneath spilling breakers in the open ocean. Kolaini *et al.*[29] reported the measurements of the acoustic emissions of individual bubbles entrained by wind-generated breaking capillary waves in a reverberant laboratory flume. Leighton *et al.*[30] reported on the acoustic emissions of bubbles entrained by a waterfall and a plunging jet. Hahn *et al.*[31] described the acoustic resonances in the bubble plume formed by a plunging water jet.

Recent progress has been made in understanding the role of bubble fragmentation during the first few seconds of wave breaking. From a series of laboratory wave flume experiments and bubble size distribution measurements in the surf zone and open ocean, Deane and Stokes[32] found experimental evidence that bubbles larger than the Hinze scale in breaking wave crests undergo a cascade of fragmentation events induced by turbulent pressure fluctuations. The Hinze scale is the bubble radius at which the distorting force due to turbulent pressure fluctuations is balanced by the stabilizing force of surface tension and is given by $a_H = 2^{-8/5}\varepsilon^{-2/5}(\sigma \mathrm{We}_c/\rho)^{3/5}$, where ε is the turbulent energy dissipation rate, σ is the surface tension, We_c is the critical Weber number (see Sec. V B), and ρ is the fluid density. One of the key observations was that the scaling of bubbles larger than the Hinze scale follows a $a^{-10/3}$ power law, where a is the bubble radius. This scaling law was anticipated by Garret *et al.*,[33] who derived it based on theoretical arguments. Both experiment and theory point to an important connection between turbulent fluid motions and bubble creation processes within breaking waves.

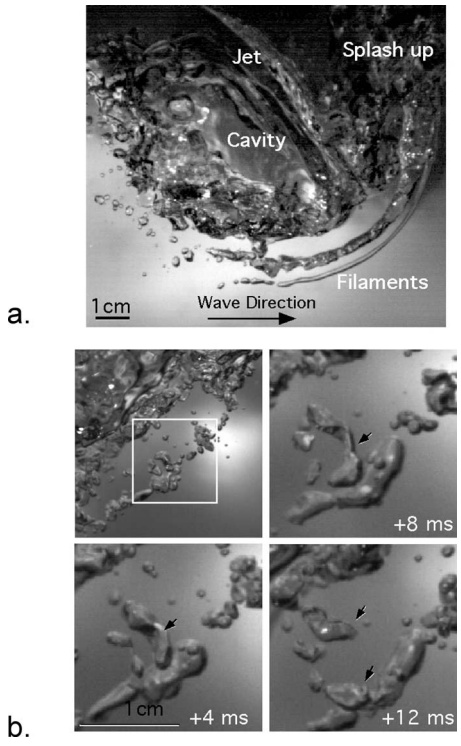


FIG. 1. Images of air entrainment in a laboratory breaker. (a) The main features of the wave seen through the sidewall of the SIO hydraulics laboratory glass-walled flume. The wave is moving toward the right. The plunging jet, splash-up region, and cavity of air trapped between the jet and wave face can be seen. Fragmenting filaments of air caught between the jet and wave face are shedding bubbles. (b) The upper left frame shows remnants of a filament of air trapped between the overturning jet and the wave face. The white box in the first of these images provides a context for the next three, which illustrate the progressive elongation and fragmentation of the bubble identified by the black arrow.

Figure 1 illustrates bubble fragmentation regions within a laboratory plunging breaker. The wave was created with a focused wave packet[34] approximately 10 cm in height in the 33 m long glass-walled flume at the Scripps Institution of Oceanography Hydraulics facility. The wave-packet center frequency, wavelength, relative bandwidth, and slope were, respectively, 0.73 Hz, 2.3 m, 1, and 0.4. The wave was viewed from the side using a high-speed video camera. Figure 1(a) shows the main features of the wave, which are the overturning wave crest (jet), the tube of air enclosed by the jet and the wave face (cavity), and the reactionary splash-up at the leading edge of the wave crest (splash-up). The four frames in Fig. 1(b) show a bubble fragmenting within the highly sheared region where the overturning jet interacts with the leading edge of the wave crest. The white box in the first of these images provides a context for the next three, which illustrate the progressive elongation and fragmentation of the bubble identified by the black arrow.

B. Sound from a newly formed bubble

Newly formed gas bubbles, whether they are pinched off from nozzle, a free surface, or another bubble, radiate a pulse of sound. The radiated pressure pulse has the overall form of a damped sinusoid with frequency proportional to the square

root of pressure within the bubble and inversely proportional to the bubble radius.[1,4] The ideal form for the radiated pulse is

$$p(t,a) = p_0 \cos(\omega_0(t-t_0)+\phi)\exp(-\omega_0\delta(t-t_0)/2), \quad t \geqslant t_0, \tag{1}$$

where $p(t,a)$ is the sound pressure at 1 m from the bubble center as a function of time t and bubble equilibrium radius a, p_0 is the pulse amplitude at 1 m, ω_0 is the natural angular frequency of oscillation, t_0 is the bubble formation time, ϕ is the pulse phase, and δ is the total dimensionless damping constant. Assuming that the thermal behavior of the gas within the bubble follows a polytropic law, the natural frequency of the bubble is given by

$$\omega_0(a) = \left(3\kappa\frac{p_{\text{amb}}}{\rho a^2} - \frac{2\sigma}{\rho a^3}\right)^{1/2}, \tag{2}$$

where $\kappa \approx 1.2-1.4$ is the polytropic index for the bubble gas, p_{amb} is the hydrostatic pressure outside the bubble, $\rho = 1022\ \text{kg/m}^3$ is the fluid density, and $\sigma = 0.072\ \text{N/m}$ is the water surface tension.[35] The final term on the right-hand side of Eq. (2) accounts for the Laplace pressure associated with surface tension and represents a small correction (less than 2%) to the natural frequency of bubbles greater than 10 μm radius. A 1 mm radius bubble close to the sea surface resonates at a frequency of approximately 3.3 kHz. The bubble oscillations are damped by thermal losses and acoustic radiation (viscous losses can be neglected for the larger bubbles of interest here), and the radiated pressure pulse has the form of a decaying sinusoid with a quality factor Q of about 5–20 depending on bubble size. The thermal and radiation losses are characterized by their respective dimensionless damping constants δ_r and δ_t. The theory for thermal damping is involved,[35] but an approximate expression for the sum of thermal and acoustic losses accurate enough for our needs is given by $\delta \approx \delta_t + \delta_r \propto 0.0025 f^{1/3}$ (Ref. 36, p. 302). The dimensionless damping constant for radiation loss is given by $\delta_r = \omega_0 a/c$, where c is the speed of sound in water.

The energy in the pulse of sound can be obtained by integrating the acoustic intensity around a sphere of radius $R=1$ m enclosing the bubble:

$$\Psi_s = 4\pi R^2 \int_0^\infty \frac{p^2(t)}{\rho c} dt, \tag{3}$$

where p is the pressure at 1 m and is assumed to be of the form given by Eq. (1) and c is the speed of sound in water, taken to be 1500 m/s. Setting $\phi = t_0 = 0$ in Eq. (1) and substitution into Eq. (3) yield

$$\Psi_s = \frac{4\pi R^2 p_0^2}{\rho c}\int_0^\infty (e^{-\delta\omega_0 t/2}\cos(\omega_0 t))^2 dt = \frac{4\pi R^2 p_0^2}{\omega_0 \rho c}\frac{2(1+\delta^2/2)}{\delta(\delta^2+4)}, \tag{4}$$

where R is taken to be 1 m. The amplitude of the bubble's volume mode oscillation can be determined from the initial peak pressure at 1 m from the bubble:

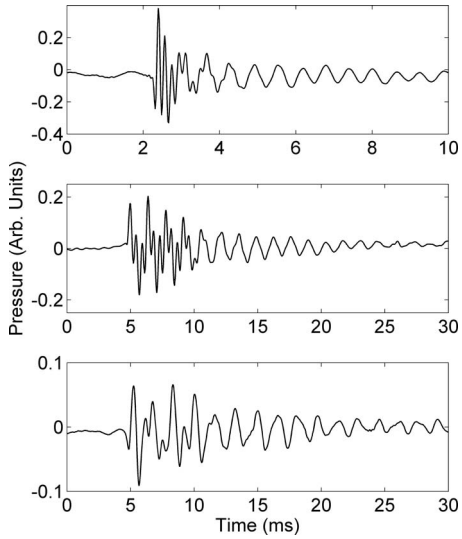


FIG. 2. Examples of the pressure pulses radiated by bubbles fragmenting at a depth of a few centimeters of water in the swash zone of La Jolla Shores beach.

$$a_\varepsilon = \frac{R}{3\kappa p_{\text{amb}}} p_0, \tag{5}$$

where R is taken to be 1 m and p_0 is the pressure at 1 m. Using the estimate of the breathing mode amplitude, the maximum potential energy at the onset of oscillation of a ringing bubble can be calculated (Ref. 1, p. 138):

$$\Phi_{p,\max} = 6\pi\kappa p_{\text{amb}} a a_\varepsilon^2. \tag{6}$$

Neglecting bubble–bubble interactions (these are discussed in Sec. VI) and shape mode to volume mode coupling, the sound radiated by the two products of a binary fragmentation event consists of the superposition of two exponentially decaying sinusoids, each one of which is associated with an acoustically excited bubble. Examples of the pulse of sound radiated by bubbles fragmenting in the surf zone are shown in Fig. 2. These data were taken in a few centimeters of water in the swash zone off the La Jolla Shores beach. In this region, the remnants of shoaling waves cross the beach as air-entraining bores. The superposition of pulses from two bubble products can be seen in the first few milliseconds of data in each of the events. The higher frequency pulse associated with the smaller of the bubble products decays more rapidly than the lower frequency pulse from the larger bubble, which persist later into the record. The waveforms are distorted from their ideal forms, which is not entirely surprising given that they were collected in a real world environment with the close proximity of other bubbles, and atmospheric and sedimentary boundaries.

II. RESULTS FROM AN EXPERIMENT

An experiment was conducted to study the acoustic signatures of bubbles fragmenting in fluid shear in a 15 m deep pool.[18] Two opposing fluid jets were positioned 20 cm above a bubble injection device and a nearby hydrophone was used to record the sound of fragmentation events. The jets were fan shaped and slightly offset in the vertical to create a re-

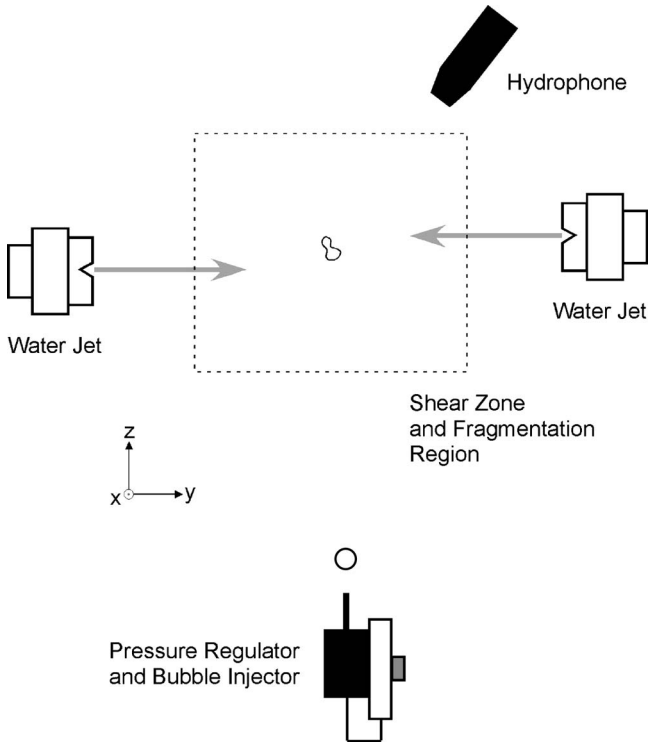


FIG. 3. Schematic of the geometry used for the bubble fragmentation experiment. Two opposing water jets create a region of turbulence and shear that fragment 1/3 of all bubbles injected from below. A hydrophone, positioned 25 cm from the fragmentation region and synchronized with an imaging camera, recorded the fragmentation noise.

gion of high fluid shear (see Fig. 3). A high-speed video camera positioned with its imaging plane aligned with the y, z axes was used to record bubble fragmentation at 250 frames/s.

The bubble injector consisted of a differential pressure regulator that provided a constant 60 kPa above ambient pressure and fed a bubble injection needle via a constant gas flow valve. Bubbles of radius approximately 1.8 mm were injected at a rate of about 1 every 2 s, permitting the study of individual fragmentation events. Approximately one in three bubbles fragmented into two (binary) or three (ternary) bubble products as they passed through the high shear region. The other two in three bubbles did not break. Experiments were conducted in both fresh and salt water, and are reported in Ref. 18.

The 2 m distant surface was the nearest reflecting boundary to the bubble fragmentation region. The hydrophone was placed approximately 0.25 m above the fragmentation region, leading to the expectation that the surface return amplitude be roughly 1/14 times the amplitude of the direct pulse at the hydrophone location. The actual reverberation level can be investigated by analyzing the pulse radiated by bubbles released from the nozzle. Figure 4 shows one such pulse (black dashed line) superimposed on the best-fit exponentially decaying sinusoid described by Eq. (1) (gray, solid line). The solid black line shows the difference between the observed and ideal waveforms. The greatest deviation occurs at the beginning of the pulse when the bubble is forced into excitation by the nonequilibrium conditions prevailing during initial bubble formation. Within a single

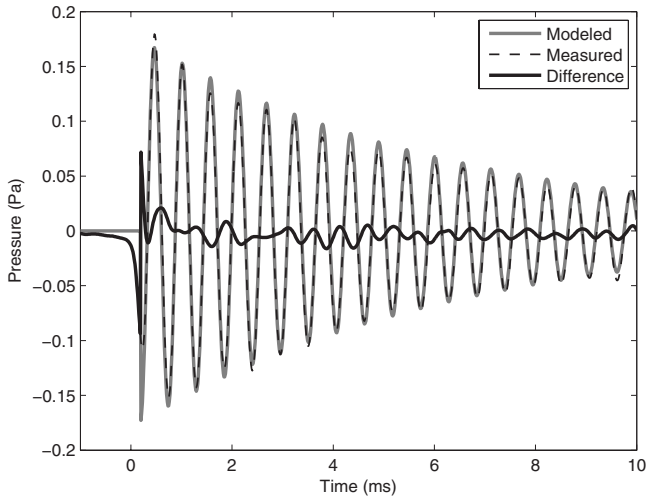


FIG. 4. The pressure pulse radiated by a bubble released from a nozzle 2 m below the water surface (broken black line), The least mean squares fit to an exponentially decaying sinusoidal pulse (solid gray line) and the difference between the observed and fitted pulses (solid black line).

bubble oscillation period, the observed pulse lies within 10% or so of the idealized waveform. The residue is a superposition of all effects driving the bubble from an idealized oscillator response, including reverberation, non-spherical shape and buoyancy-driven volume changes.

Figure 5 shows the superposed acoustic emission from two oscillating bubble products along with images of the fragmentation process taken with the high-speed video camera for a typical binary event. The center of the bubble images is positioned on the time axis with an error corresponding to roughly half the interimage interval (4 ms). The beginning of the acoustic emissions coincides with the short length and time-scale processes occurring immediately following fragmentation. As with the binary fragmentation events observed in the swash zone, the acoustic pulse consists of an interference pattern resulting from the addition of

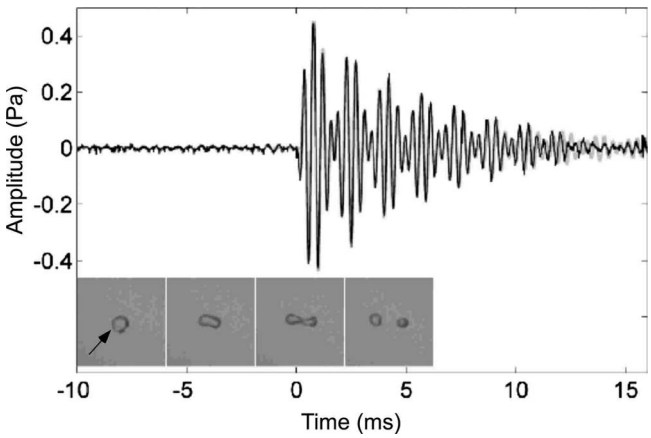


FIG. 5. The solid black line traces the acoustic emissions from the products of a binary fragmentation event. The vertical scale is the acoustic pressure at 1 m from the bubble products. The beating pattern is a result of interference between the two acoustic signatures. The gray line (see right-hand side of the trace) is a ten parameter fit of the emissions based on Eq. (1). The images below the acoustic trace show the fragmenting bubble and bubble products at 4 ms time increments. For scale, the diameter of the bubble indicated by the arrow in the left-hand image is 3.4 mm.

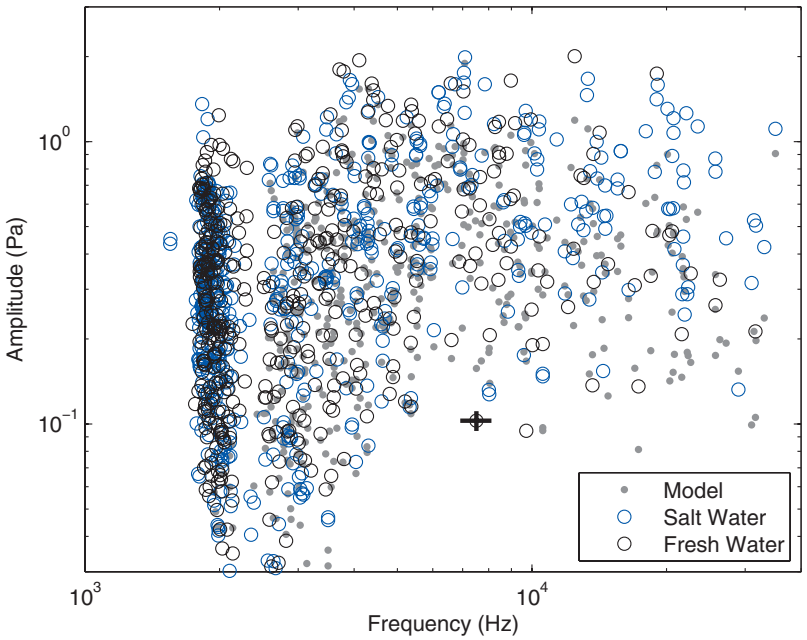


FIG. 6. (Color) The peak pressure for 505 binary fragmentation events (blue open circles are salt water; black open circles are fresh water) plotted as a function of bubble natural frequency. The gray dots are model predictions based on calculations described in Sec. V. The horizontal and vertical black lines indicate the estimated magnitude of systematic errors for one of the data points. The upper limit of the frequency band for the measurements was limited to 37.4 kHz by the recording equipment.

individual bubble pulses. The amplitude and decay rate of the individual pulses can be estimated by assuming that each has the form of Eq. (1). As each bubble signature contains five variables (frequency, amplitude, decay rate, start time, and phase), there are ten unknown parameters to be estimated. This was done using an unconstrained nonlinear optimization for the best fit between the sum of two bubble pulses and the measured emission signature, implemented with the SIMPLEX search method.[18,37] The optimal parameter fit yielded the gray line plotted in Fig. 5. The agreement is within a linewidth over most of the pulse and it is difficult to distinguish the two curves except for the final few milliseconds on the right-hand side of the figure. The major disagreement at the onset of the oscillation is due to the nonequilibrium initial conditions driving the bubble into oscillation.

Figure 6 shows the initial amplitude in pascals of 505 binary fragmentation events in fresh and salt water. Although the pressure pulse amplitude shows significant scatter, spanning more than an order of magnitude for a fixed frequency, casual observation shows surprisingly little frequency dependence in the mean bubble pressure response. There are systematic errors in the amplitude and frequency measurements which we can estimate. The deviations of the ideal and observed pressure pulses in Fig. 4 show an order 10% error in the amplitude fit. The error in the natural frequency of the bubble can be estimated to be 8% from the calculations of Strasberg[38] assuming the major-to-minor axis ratio of the distorted fragmenting bubble to be 4.

The peak volume mode oscillation amplitude can be calculated from Eq. (5) and the measured peak pressure values of the acoustic pulses. Values of a_ε/a have been calculated for $\gamma=1.4$ and bubbles at a depth of 2.0 m ($p_{\text{amb}}\approx 1.22\times 10^5$ Pa) and are plotted as a function bubble radius in Fig. 7. It is clear from Fig. 7 that the excitation mechanism drives smaller bubbles with a greater fractional amplitude (a_ε/a) than larger ones. The oscillation amplitude as a fraction of bubble radius for the smallest bubbles measured (order 60 μm) was around 0.02, decreasing to 0.0002 for the largest bubbles (order 2 mm). The peak amplitude values (approximately 2 μm) are consistent with the results of Pumphrey and Crum[39] who obtained an amplitude of 3.3 μm for oscillating bubbles entrained through the impact of liquid drops on a body of water. The lower limit of our measurements (order 0.1 μm) is consistent with the value discussed by Leighton (Ref. 1 p. 195).

There is a clue to the nature of the bubble excitation mechanism in the division of breathing mode energy in pairs of bubble products, calculated using Eq. (6). The data from this calculation are shown by the open circles in Fig. 8 as a scatter plot of initial oscillation energy of the smaller of the two bubble products in Joules (Φ_1) versus the initial oscillation energy in the larger bubble product (Φ_0). The energy in the bubble product pairs spans more than four orders of magnitude and is remarkably correlated over this range. These data can be used to calculate an energy partition ratio, which is the fraction of energy in a single bubble product divided

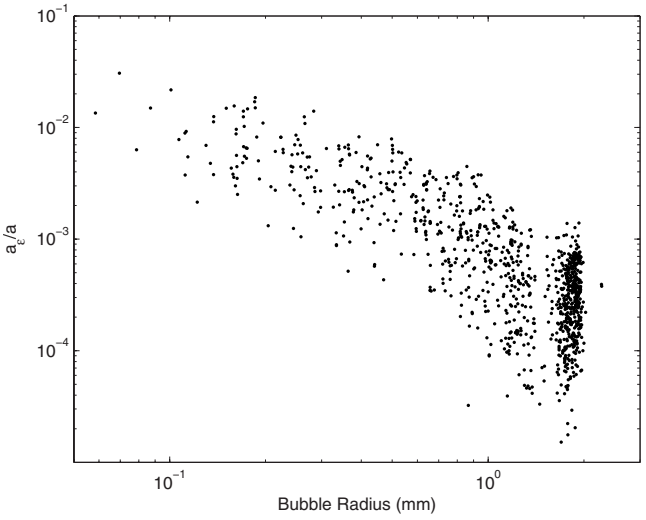


FIG. 7. Breathing mode radial oscillation amplitude normalized by bubble radius, plotted as a function of bubble radius.

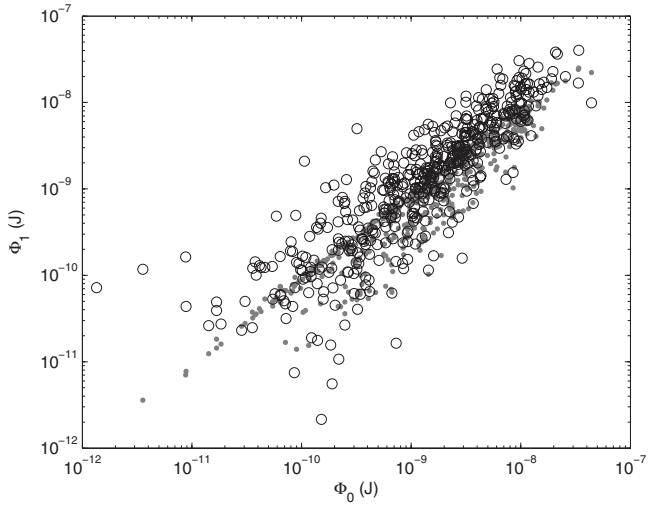


FIG. 8. A scatter plot of energy in the breathing mode of the smaller bubble (Φ_1) vs the energy of the larger bubble (Φ_0) for 505 binary fragmentation events. The scatter plot shows the strong correlation between breathing mode energies, suggesting an excitation mechanism common to both bubbles before fragmentation. The gray dots are model predictions based on calculations described in Sec. V.

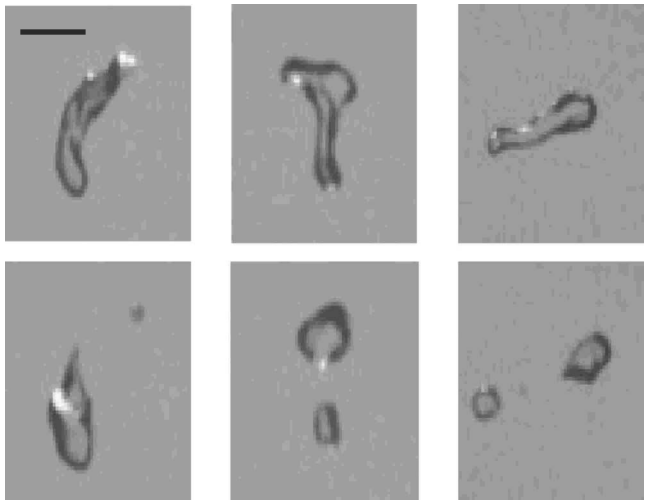


FIG. 10. Images of bubbles immediately before (top row) and after (bottom row) fragmentation. The time interval between the frames is 4 ms. The leftmost and middle image pairs show binary fragmentation events. A small tertiary bubble can be seen in the bottom image of the right-hand pair. These pictures illustrate the high degree of distortion the occurs immediately before bubble fragmentation.

by the total energy in the bubble pair. The energy partition ratio can then be compiled into a probability density function, and this is done in Fig. 9. The mean (0.43) and standard deviation (± 0.10) of the distribution are, respectively, annotated with the short vertical and horizontal black lines.

The approximately equal partition of energy between bubble fragmentation products, irrespective of bubble size, is quite remarkable and holds over four orders of magnitude of energy level. The implication is that the mechanism driving bubble oscillation is common to both bubbles prior to fragmentation and provides equal amounts of energy to each bubble irrespective of its size.

III. SHAPE DISTORTIONS AND ENERGY CONSTRAINTS

A bubble in fluid turbulence is likely to break up if the differential pressure forces across the bubble exceed the surface tension force. The ratio of these forces is the Weber number, given by $\mathrm{We}=(\rho/\gamma)u^2 d$, where u is the turbulent velocity on the scale of the bubble and d is the bubble diameter. Bubble fragmentation[40,41] occurs when the critical Weber number We_c exceeds 3–4.7. An additional constraint is that the bubble undergoes shape oscillations[42] so that the bubble eccentricity exceeds approximately 3. Figure 10 shows the shape of three randomly selected bubbles a few milliseconds prior to fragmentation (top images) illustrating the significant degree of bubble asymmetry associated with fragmentation. A full account of the energetics of bubbles fragmenting in fully developed fluid turbulence can be found in Ref. 41.

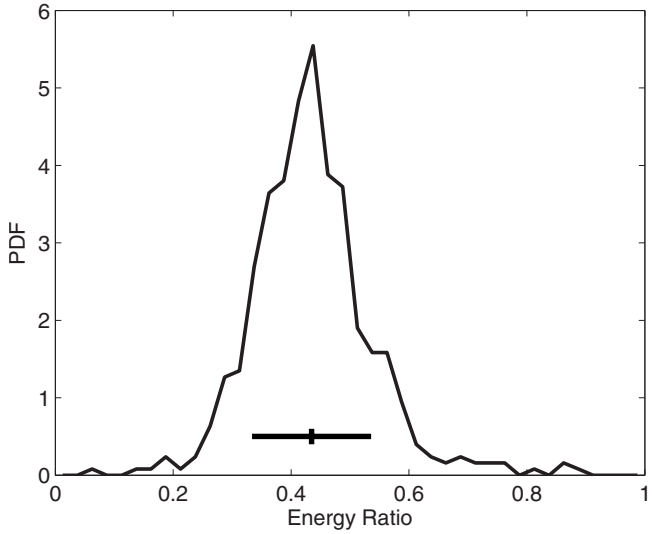


FIG. 9. Probability density function of energy distribution between fragmentation products. The horizontal and vertical black lines indicate the mean (0.43) and standard deviation (± 0.10) of the distribution.

The time line for bubble fragmentation can be broken down into three phases, illustrated in Fig. 11. During the first phase, the bubble is assumed to be nearly spherical in shape, corresponding to its lowest state of surface tension energy. During the second phase, fluid forces acting on the bubble boundary give rise to a distorted shape and an elevated state of surface tension energy. At some time during the distortion phase, immediately prior to fragmentation, the bubble wall pinches to form a neck, as illustrated in Fig. 11(c). There are a number of mechanisms that could potentially fragment the bubble during this phase. There is a critical radius at which the Laplace pressure in the neck is comparable to the gas pressure within the bubble. Once this critical radius is achieved, surface tension will rapidly close the neck. Rayleigh–Taylor instabilities on the neck may also play a role in neck closure resulting in the formation of a third small bubble occasionally observed between the two primary fragmentation products. The third phase consists of the collapse of the neck remnants and the concomitant acoustic radiation.

It is a worthwhile exercise to compute the surface tension energy constraints associated with volume-conserving shape distortions through the three phases. A rough estimate

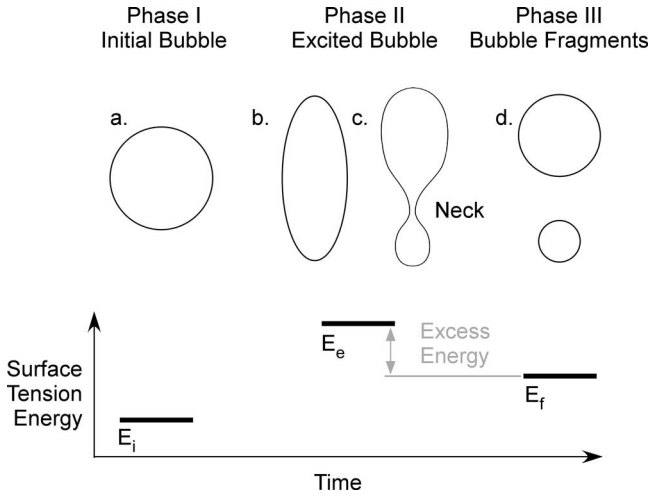


FIG. 11. A conceptual overview of the idealized fragmentation process showing the evolution of the bubble and fragmentation products over time. (a). The initially spherical bubble. (b) Flow forces distort the bubble into a prolate spheroid. (c) The distorted bubble assumes a form topologically similar to a dumbbell. (d) The neck pinches off resulting in two or three fragmentation products. The neck remnants collapse, initiating breathing mode oscillations and capillary waves on the bubble wall. The surface tension energies corresponding to the bubble state are shown below.

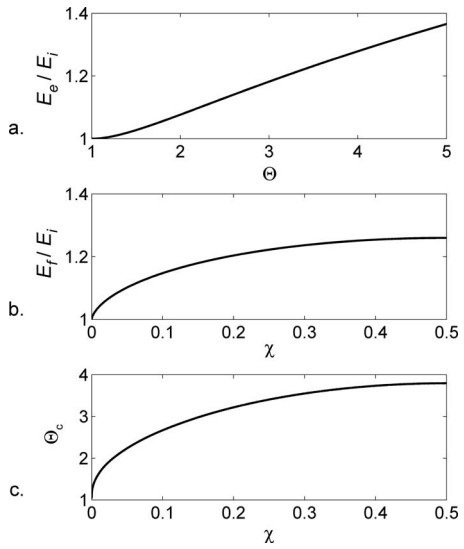


FIG. 12. (a) Surface tension energies normalized by energy in the initial spherical bubble as a function of major to minor radius ratio Θ for the prolate spheroid. (b) Bubble product volume ratio χ for the fragmentation products. (c) The minimum ratio of radii required for an excited bubble undergoing a volume-conserving distortion to contain the same surface tension energy as the fragmentation products with a volume ratio χ.

of the excess surface tension energy released between fragmentation phases II and III can be made as follows. Suppose a bubble with initial radius a_i undergoes a volume-conserving shape distortion into a prolate spheroid with major radius b_e and minor radius a_e (the excited bubble), which then fragments into two daughter products with radii a_0, a_1. It will prove convenient to characterize the process through the ratio of major to minor axes of the prolate spheroid $\Theta = b_e/a_e$, where $\Theta > 1$, and the ratio of initial bubble radius to bubble product radius, cubed: $\chi = (a_0/a_i)^3$, where $0 < \chi < 1$. Since the process is assumed to be volume conserving, and noting that the volume of the prolate spheroid is $4\pi b_e^2 a_e/3$ yields equations for the excited bubble radius, $a_e = \Theta^{-1/3} a_i$, and product bubble radii $a_0 = \chi^{1/3} a_i$ and $a_1 = (1-\chi)^{1/3} a_i$.

The surface tension energy associated with each phase is the product of surface tension and bubble surface area, which leads to

$$E_i = 4\pi a_i^2 \sigma, \tag{7a}$$

$$E_e = \frac{1}{2}\left(\Theta^{-2/3} + \Theta^{1/3}\frac{\sin^{-1}(e)}{e}\right)E_i, \tag{7b}$$

$$E_f = (\chi^{2/3} + (1-\chi)^{2/3})E_i, \tag{7c}$$

where E_i, E_e, and E_f, respectively, correspond to the surface tension energy in the initial and excited bubbles, and sum of surface tension energy in the product bubbles. To derive Eq. (7b), we have used the fact that surface area of a prolate spheroid is $2\pi a_e^2 + 2\pi a_e b_e \sin^{-1}(e)/e$, where the ellipticity $e \equiv (b_e^2 - a_e^2)^{1/2}/b_e = (\Theta^2 - 1)/\Theta$. Figures 12(a) and 12(b), respectively, show the excited and final energies normalized by the initial energy. The excited bubble energy increases monotonically with increasing bubble distortion Θ. The summed energy of the bubble products is a minimum in the limit $\chi \to 0$, corresponding to the pinchoff of a small bubble, and reaches a maximum value $2^{1/3} \approx 1.26$ for bubbles of equal size, $\chi = 0.5$. Because the surface tension of the excited bubble must be at least equal to the energy in the final bubble products, there is a minimum bubble distortion Θ_c required for fragmentation. This has been plotted in Fig. 12(c) as a function of product pair asymmetry, χ. Experimental observation places the minimum Θ required for fragmentation[32] in the range of 3–4.7. For values for χ greater than approximately 0.2, the calculated value of Θ_c lies within this observed range.

IV. NECK COLLAPSE AND FORCING FUNCTION MODEL

Here we explore the idea that the acoustic excitation of bubble fragmentation products is driven by the collapse of the neck remnants joining the distorted bubble immediately prior to rupture. This mechanism is implicated by the observed equal partition of energy between fragmentation products, which suggests a common symmetrical mechanism in existence prior to rupture. Furthermore, recent studies have demonstrated the role of neck collapse in stimulating the acoustic emission of bubbles released from a nozzle.

The model we propose here is based on the assumption that the neck of air joining the two bubble products immediately prior to fragmentation is symmetrical about a plane containing the rupture point and perpendicular to the parent bubble long axis (the rupture plane). The length scale over which this symmetry is required can be estimated for a 2.2 mm radius bubble from the duration of the initial forcing period, approximately 400 μs, and the neck collapse distance over this time scale, which is approximately 400 μm.[15] We can expect that smaller bubbles will require symmetry over even shorter length scales. This symmetry is certainly observed in the case of a bubble released from a nozzle, where the upper terminus of the neck is a bubble and the lower

terminus is the nozzle. In this special case, the tangent plane to the neck wall at the point of rupture is vertical and has rotational symmetry about the long axis, and the symmetry about the rupture plane can be expected on sufficiently short length scales. What constitutes a "sufficiently short" length scale will depend on the particular boundary conditions and physical properties of the liquid and gas defining the problem. Although we have no observation evidence to suggest neck symmetry in the case of fragmenting bubbles, comparison with the nozzle-released bubbles suggests that it is a reasonable starting assumption.

The forcing function model for bubbles fragmenting in fluid shear developed here is based on the neck collapse model for nozzle released single bubbles presented in Ref. 15. The model consists of two parts: (1) a description of the rapid retraction of the neck fragment formed immediately after neck rupture and (2) incorporating the change in volume associated with the neck collapse into the linearized Rayleigh–Plesset equation. The model of neck collapse is based on an energy balance argument whereby the surface tension energy in a frustum of the retracting neck is converted into kinetic energy of the fluid within it. The result of the neck collapse and acoustic excitation analysis is a driving term on the right-hand side of the linearized Rayleigh–Plesset equation. The linearized Rayleigh–Plesset is expressed in terms of the fractional increase in bubble radius $\varepsilon(t)=R(t)/a-1$, where $R(t)$ is the time-dependent bubble radius. Modifying the analysis presented by Prosperetti[35] to include the effects of neck collapse, the equation can be expressed as

$$\frac{\partial^2\varepsilon}{\partial t^2}+\left[\frac{4(\mu+\mu_{th})}{\rho a^2}+\frac{ka}{1+k^2a^2}\omega\right]\frac{\partial\varepsilon}{\partial t}+\left[\frac{3\kappa p_{\mathrm{in},0}}{\rho a^2}-\frac{2\sigma}{\rho a^3}+\frac{k^2a^2}{1+k^2a^2}\omega^2\right]\varepsilon=F(t), \tag{8}$$

where μ is the fluid viscosity, μ_{th} is an effective viscosity accounting for thermal losses, $p_{\mathrm{in},0}$ is the internal equilibrium pressure within the bubble, k and ω, respectively, are the wave number and angular frequency of sound at the bubble's natural frequency, and the forcing function is given by

$$F_t(t)=-\frac{9\kappa\sigma\eta p_{\mathrm{in},0}(1+\eta^2)^{1/2}}{4\rho^2a^5}t^2,\quad t>0, \tag{9}$$

where η is the slope of the neck fragment, which was observed to be approximately constant during the neck collapse. This theory does not account for any loss mechanisms associated with the neck collapse, such as fluid viscosity, the generation of capillary waves, or increasing pressure within the bubble. Loss mechanisms will tend to dissipate the kinetic energy of the neck collapse and reduce the value of the forcing function compared with the lossless result. Over time scale such that $t\ll 1$, this suggests that loss mechanisms will have the effect of increasing the exponent of t in Eq. (9).

Equation (9) can be compared with an estimate of the actual forcing function driving a bubble released from a nozzle by analyzing the bubble's acoustic signature. During the bubble fragmentation experiment described in Ref. 18, recordings were made of the sound generated by both bubbles fragmenting in fluid turbulence and bubbles released from the nozzle below the fluid jet. Fifty signatures from nozzle-generated bubbles have been analyzed for peak amplitude, frequency, and damping, providing the distribution of these parameters. From these 50 events, an "average" bubble was chosen that had amplitude, frequency, and damping within half a standard deviation of the respective parameter mean.

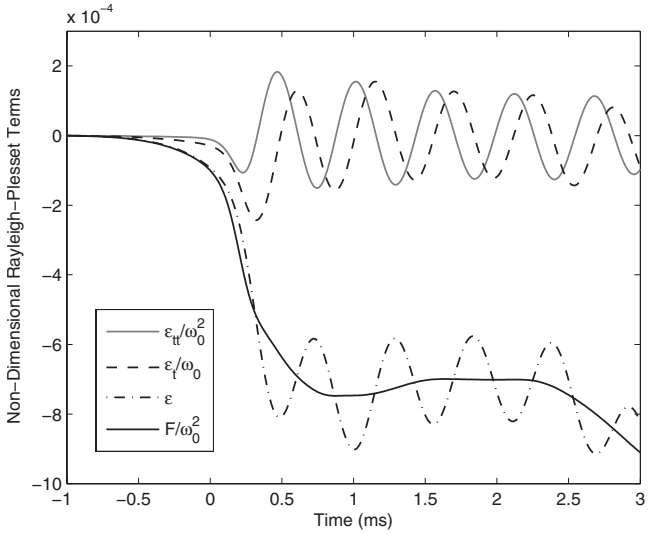


FIG. 13. An analysis of the acoustic pressure pulse radiated by a bubble released from a nozzle. The bubble wall accelerations normalized by the bubble natural radian frequency squared, the bubble wall velocity normalized by the bubble natural radian frequency, and the bubble wall acceleration are, respectively, plotted vs time as the gray solid line, broken black line, and the dash-dot black line. The solid black line shows the forcing function normalized by the bubble natural radian frequency squared. In the figure legend, a single subscript "t" denotes differentiation with respect to time and a repeated subscript "tt" denotes double differentiation with respect to time.

The forcing function analysis is based on estimates of the three terms on the left-hand side of Eq. (8). The acceleration of the bubble wall can be calculated from the bubble sound pulse using

$$\frac{\partial^2\varepsilon}{\partial t^2}=\frac{p_a(t)}{\rho a^3}, \tag{10}$$

where $p_a(t)$ is the observed pressure pulse radiated by the bubble at 1 m from the bubble. The acceleration is integrated to obtain the velocity, $\partial\varepsilon/\partial t$, and integrated again to obtain the displacement, ε. The first three terms in ε on the left-hand side of Eq. (8) are then summed to obtain $F(t)$. The result of this procedure is plotted in Fig. 13. The gray solid curve shows bubble wall acceleration normalized by the natural frequency of the bubble squared, ω_0^2. The initial rarefaction in the acoustic field corresponds to an inward acceleration of the bubble wall followed by the onset of breathing mode oscillations. The wall velocity, normalized by ω_0, and the wall displacement are, respectively, plotted with the dash-dot black line and broken black line. The solid black line shows the sum of the three terms on the left-hand side of Eq. (8), which is the forcing function normalized by ω_0^2.

Both the velocity and displacement terms are obtained by integrating the bubble sound pulse and are therefore sensitive to low frequency noise. Systematic errors introduced

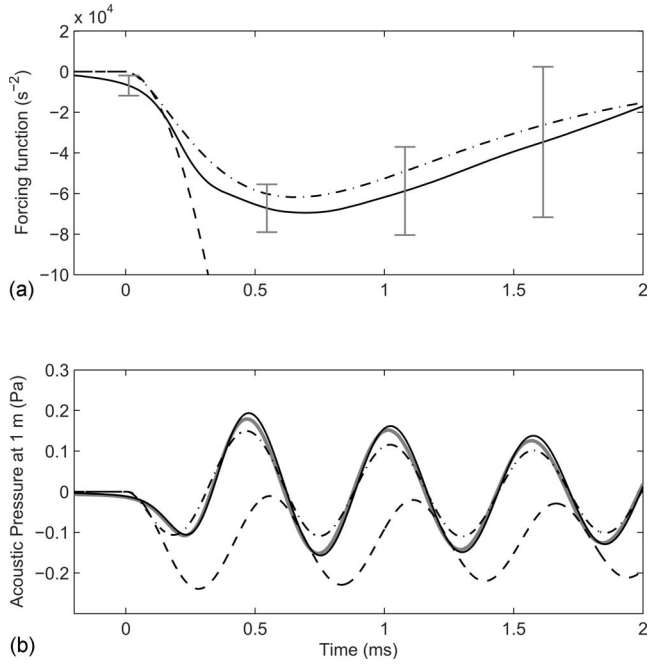


FIG. 14. (a) Observed and modeled forcing functions plotted as a function of time. The solid black line is the average of 50 forcing functions obtained from the analysis of the acoustic pulses radiated by bubbles released from a nozzle. The four vertical gray lines show the standard deviation in the estimate of the forcing function. The broken black line shows the theoretical forcing function based on an analytical model for neck collapse. The dash-dot black line shows a theoretical forcing function that includes an *ad hoc* modification for the effects of dissipation. (b) Observed and modeled pressure pulses. The solid black line shows the pressure pulse for a selected average bubble. The solid gray, broken black, and dash-dot black lines, respectively, show calculated pulses for the observed, theoretical, and modified theoretical forcing functions.

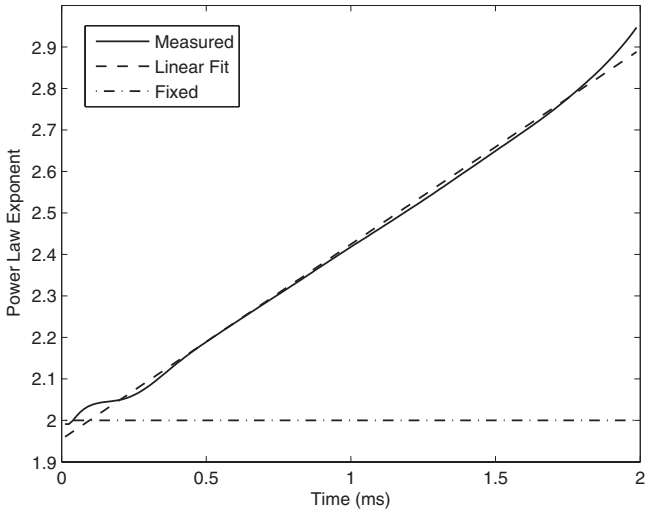


FIG. 15. An analysis of the time-varying power law exponent of the observed forcing function. The black line shows the measured power law exponent vs time calculated from the mean forcing function plotted in Fig. 14(a), using Eq. (12). The broken black line shows a least mean squares linear fit to the observed exponent. The dash-dot black line shows the ideal theoretical exponent.

by reverberation and distortions in bubble shape cannot be removed by averaging, but low frequency acoustic noise present in the pool, which is phase incoherent from one fragmentation event to another, can be reduced by averaging the forcing functions estimated from an ensemble of bubble release events. The average of the 50 events described above, F_m, is plotted with the solid line in the top plot in Fig. 14. The vertical lines with short horizontal bars show the standard error of the ensemble average, which increases with time as the integration errors grow. The dashed line in the same plot, F_t, shows the forcing function calculated according to Eq. (9) with the values $\kappa=1.4$, $\sigma=0.072$ N/m, $\eta=0.84$, $p_{\text{in},0}=120\,300$ Pa, $\rho=1022$ kg/m^3, and $a=1.96$ mm.

The accuracy of the forcing function can be determined by using it to drive the linearized Rayleigh–Plesset equation, which is solved using a numerical Runge–Kutta integration scheme. The bubble radius and damping for this calculation are taken to be the mean values determined from the 50 event ensemble average. The bubble wall acceleration calculated in this way is then used to compute the radiated pressure pulse, which can be compared with the observed pulse. This has been done for both F_m and F_t, and the results are plotted with the black solid and dashed lines in the bottom plot of Fig. 14. For comparison, the gray solid line shows the acoustic signature of the average bubble selected as described above. Since F_m was estimated using the acoustic pulse and the linearized Rayleigh–Plesset equation, it is inevitable that it yield a good fit to the observed pulse. The fit is not exact because the forcing function is an average over 50 events, whereas the bubble signature is from a single bubble selected as being a representative average. Although the theoretical forcing function F_t does an adequate job of reproducing the correct bubble signature amplitude, it does not capture the bubble dynamics at the start of the pulse and also leads to an overall decrease in pressure, which is unphysical. Both of these effects arise because the deceleration of the collapsing neck fragment is not accounted for in the neck collapse model.

To allow for the neck deceleration, we introduce a time-varying power law exponent into Eq. (9):

$$F_v(t) = -\phi t^{n(t)}, \quad t > 0 \tag{11}$$

where ϕ is the multiplicative constant of t^2 in Eq. (9). In the ideal case $n=2$, but the presence of loss mechanisms changes the index over time. As $t \ll 1$ over the forcing interval, an increase in n results in a decrease in the forcing function, accounting for a decelerating neck. An estimate of the exponent can be made from the measured forcing function by noting that

$$n = \frac{\log(-F_m/\phi)}{\log(t)}, \quad t > 0, \quad F_m > 0. \tag{12}$$

An estimate of n was made using Eq. (12) and is plotted with the solid black line in Fig. 15. The exponent maintains a value close to 2 for the first 200 μs or so after neck rupture, and then increases linearly with time up to 2 ms. The exponent analysis is limited to positive values of F_m and we have not extended it further than the first few milliseconds. This does not represent much of a limitation as most of the forcing occurs within the first 400 μs.

A linear least mean squares fit to the measured exponent results in the equation

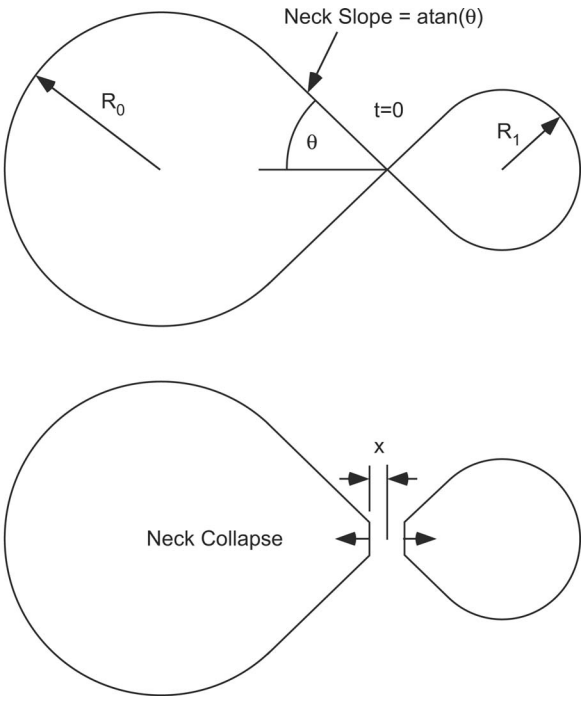


FIG. 16. A schematic of the neck collapse geometry for a binary fragmentation event.

$$n = 469.5t + 1.955, \quad t > 0 \tag{13}$$

which is plotted with the broken line in Fig. 15. The dash-dot black line indicates the ideal theoretical exponent. The forcing function specified by Eqs. (11) and (13) is plotted as the dash-dot line in upper plot of Fig. 14. This function is still not entirely accurate as it does not account for the small amount of forcing driven by the inward acceleration of the neck walls that occurs immediately prior to neck rupture. The long-term trend, however, provides a reasonably accurate representation for F_m. The bubble pulse generated by the forcing function with a time-varying exponent, F_v, is plotted with the dash-dot line in the lower part of Fig. 14. The function underpredicts the amplitude by about 20% but otherwise reproduces the details of the pulse reasonably well.

The modified forcing function for the nozzle release bubble, which incorporates in a heuristic way the effects of dissipation on the neck retraction, can be extended to the case of a fragmenting bubble by assuming that the neck is axially symmetric around its long axis and bilaterally symmetric across the rupture point (see Fig. 16). In the calculations that follow, we have made the simplifying assumptions that the nearby neck remnants collapse as though they are isolated, and the nearby, radiating fragmentation products act as decoupled oscillators. The first assumption is somewhat justified by the fact that the neck collapse model for the nozzle release bubble also assumes an isolated neck retraction, and has proven to give an adequate description of the neck dynamics in this case despite the symmetrical neck remnant retracting into the nozzle. The second assumption is more problematic, and unlikely to be justifiable in the case of equal or nearly equal-sized fragmentation products (see Sec. VI B).

V. MODEL CALCULATIONS

The forcing function model described in Sec. IV can be used to analyze the partition of acoustic energy between the bubble fragment products. In order to perform these calculations, we require estimates of the fragmenting bubble neck slope and bubble product radii, in addition to the water density, surface tension, gas polytropic index, and gas equilibrium pressure. All of these parameters are known or can be estimated to a reasonable degree of accuracy except for the neck slope. Ideally, observations of the neck slope would be used to predict the peak pressure of both bubble products, but the required observations are not available. Instead we will employ an indirect method and use the neck slope inferred from the larger bubble product to predict the amplitude of the smaller product. Even without measurement of the slope, this is an exacting test of the model because of the a^{-5} scaling of the forcing function. As the difference in bubble product radii differs by as much as an order of magnitude, the forcing function amplitude varies over five orders of magnitude, providing a sensitive test of the model predictions.

The first model calculations were a study of the efficiency of the forcing function in stimulating the acoustic radiation of bubbles as a function of radius with a fixed neck slope. The chosen neck slope, $\eta_0 = 0.84$, corresponds to the neck slope of a 2 mm radius bubble slowly released from a nozzle. The bubble damping was taken to be that given by the theoretical calculation of acoustic and thermal losses (see Sec. III B). The calculations were performed by solving the linearized Rayleigh–Plesset equation driven by the collapsing neck forcing function described in Sec. IV using a Runge–Kutta numerical integration scheme—see Eqs. (8) and (9). The resulting synthetic pressure pulses were then analyzed for peak pressure amplitude using the same least mean squares estimation method used to analyze the observed bubble pulses, although with a single bubble analysis only five parameters need to be fitted. This procedure yielded a peak pressure amplitude calculated for the fixed neck slope, $p_{\eta 0}$, versus radius plotted in Fig. 17 over the range 0.3–4 mm. Over this radius range, the peak radiated pressure decreases from approximately 0.2 to 0.09 Pa. The slight kink in the curve around 2 mm is an artifact of the parameter fitting algorithm. Given the roughly five orders of magnitude variation in forcing function amplitude over this radius range, there is remarkably little variation in the peak pressure of the radiated pulse. There is a balance between the fixed time scale of the forcing function, which is determined by neck angle and surface tension, the response time of the bubble, which is determined by bubble radius, and the forcing function amplitude.

The neck slope calculations for a given fragmentation event were done as follows. For the larger product of a bubble product pair, the peak pressure of the acoustic pulse was estimated using the least mean squares method described in Sec. II. The equivalent spherical radius of the bubble was estimated from the pulse frequency. As we are assuming a linear response to forcing, Eqs. (8) and (9) show

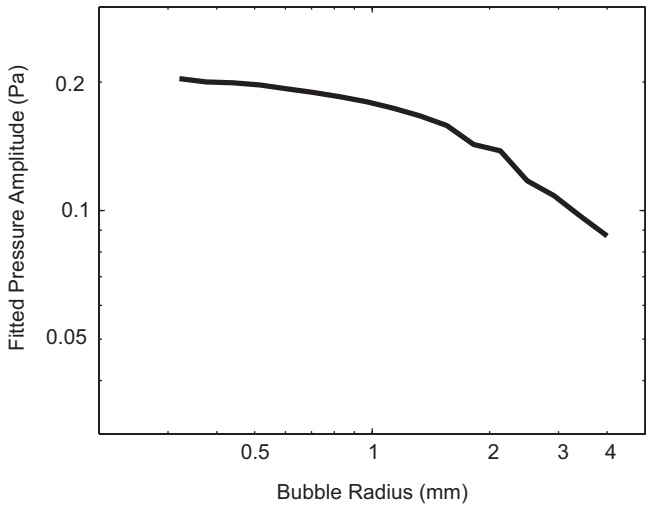


FIG. 17. The fitted pressure amplitude vs bubble radius obtained from the analysis of synthetic pulses excited by the modified theoretical forcing function. Synthetic pulses were obtained from numerical integration of the Rayleigh–Plesset equation based on a Runge–Kutta integration scheme. The fitted pressure amplitude was determined using the same parameter fitting routine used to analyze the bubble fragmentation pulses.

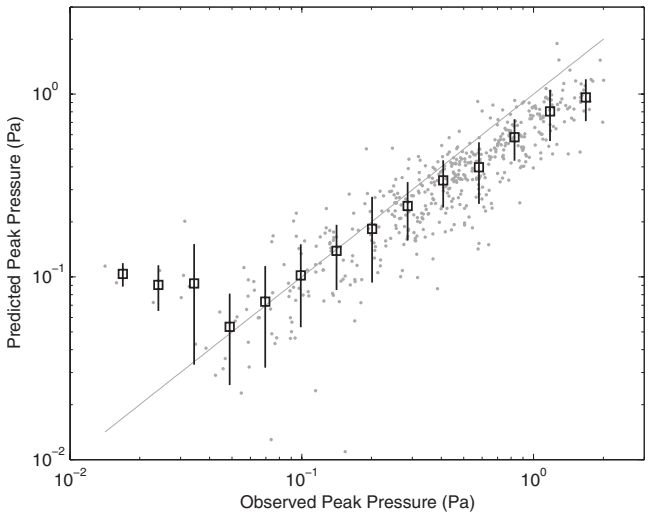


FIG. 18. The predicted peak pressure vs observed peak pressure of the smaller bubble in a fragmentation product pair. The gray dots show a scatter plot of predicted vs observed pressure. The 14 black squares show the mean of the predicted peak pressure for all data points lying within an observed pressure bin centered on the square. The vertical black lines running through the center of the squares show the standard deviation of the data points. The solid gray line shows the a 1:1 correspondence between the predicted and observed pressures.

that the ratio of observed peak pressure, p_0, to peak pressure calculated for the fixed neck angle, $p_{\eta 0}$, must obey

$$\frac{p_0}{p_{\eta 0}} = \frac{\eta\sqrt{1+\eta^2}}{\eta_0\sqrt{1+\eta_0^2}}, \tag{14}$$

where $\eta_0 = 0.84$ and $p_{\eta 0}$ is plotted as a function of radius in Fig. 17. Equation (14) is used to solve for the event neck angle η using the observed p_0 and the calculated $p_{\eta 0}$. For the range of pressure amplitudes observed, this resulted in a distribution of slopes varying from 0.1 to 3 with a mean of 1.2 and a standard deviation of 0.57.

The peak pressure for the smaller of the two bubbles was determined by assuming it has the same slope as the larger bubble, and performing the same numerical integration and parameter estimation procedure described above. The results of this procedure are shown in Fig. 18, which plots predicted peak pressure versus observed peak pressure as gray dots. The black squares show the mean predicted peak pressure for 14 amplitude bins. The vertical lines running through the squares indicate the variance of the data within an amplitude bin. The solid gray line shows a 1:1 correspondence between the observed and predicted pressures, representing a perfect model fit. Although there is significant scatter in the data, the mean predicted peak pressure follows the observed pressure well between 0.05 and 0.3 Pa. There is a systematic underprediction of approximately 20% beginning at about 0.3 Pa and increasing to 100% at 2 Pa. The few data points at amplitudes less than 0.05 Pa do not show a good agreement between the predicted and observed pressures. The small bubble amplitude calculations are also plotted as gray dots in Fig. 6, which shows amplitude versus bubble natural frequency, and in Fig. 8, which shows volume-mode oscillation energy in the small bubble product versus the large bubble product. The overall agreement in Fig. 18, which spans almost two orders of magnitude in amplitude and an order of magnitude in bubble radius, is encouraging.

VI. SOURCES OF SYSTEMATIC ERROR

There are sources of systematic error in our estimates for the bubble acoustic parameters, and some of these are discussed here. However, we note that the observed amplitudes, frequencies, and energies of the bubble fragmentation products span from one to two orders of magnitude, and minor (order 20%) adjustments to individual values of these parameters will not alter the substance of our conclusions. The question of bubble-bubble interaction effects is somewhat more complicated, as discussed below.

A. Bubble shape

An estimate of effect of sphericity on bubble natural frequency has been made by Strasberg.[38] Although we do not have direct measurements of the bubble deformation immediately following fragmentation, it is known that the parent bubble must be distorted for fragmentation to occur and we can reasonably expect distorted fragmentation products (see Fig. 10). The surface tension energy calculations presented here indicate that a bubble eccentricity of 4 is sufficient to fragment a bubble into two equal-sized products (see Fig. 12). Fragmentation into unequal-sized products requires a smaller eccentricity, so we will take 4 as a representative value for parent bubble and bubble product distortion. Strasbergs' calculations show that a bubble with a ratio of major to minor axis of 4 has an increase in natural frequency of approximately 8%. We have used the observed natural frequency to calculate the bubble radius, which is then used to compute volume mode oscillation energy—see Eq. (6)—and we can thus expect order 10% systematic errors in these estimates, which scale linearly with radius. As we anticipate at least order 20% error in our hydrophone calibrations (cor-

responding to 1.5 dB), we do not anticipate bubble distortions to bias our results beyond existing instrumentation uncertainties.

B. Bubble-bubble interactions

A full discussion of bubble-bubble interaction effects is beyond the scope of this manuscript. Some order-of-magnitude calculations of the effects of bubble coupling can, however, be made. The coupling will be greatest when the bubble products are of equal size, so that the radiation of one bubble occurs at the natural frequency of the other, and this worst case is considered as an example. We will assume that the close proximity of the two bubbles does not affect the collapse of the bubble necks. This assumption is supported by the adequate agreement obtained between the neck collapse model and the observed neck collapse for a bubble released from a nozzle,[15] which also has two necks of air in close proximity collapsing simultaneously. A rough estimate of radiation forcing can be made by considering the decoupled problem. That is, we will compute the magnitude of the radiation forcing due to a bubble on its neighbor, neglecting the fact that the driving bubble is also forced. A representative value for the distance between the bubbles can be taken to be the parent bubble diameter. From Prosperetti,[35] the forcing term that appears on the right-hand side in the Rayleigh–Plesset equation when there is a driving acoustic field can be expressed as

$$\frac{\partial^2 \varepsilon}{\partial t^2} + \left[\frac{4(\mu+\mu_{th})}{\rho a^2} + \frac{ka}{1+k^2a^2}\omega\right]\frac{\partial \varepsilon}{\partial t} + \left[\frac{3\kappa p_{\mathrm{in},0}}{\rho a^2} - \frac{2\sigma}{\rho a^3} + \frac{k^2a^2}{1+k^2a^2}\omega^2\right]\varepsilon = F(t) - \varphi\alpha, \tag{15}$$

where $\alpha = p_{\mathrm{amb}}/\rho a^2$, and φ is the ratio of driving pressure at the bubble wall to the external equilibrium pressure:

$$\varphi = \frac{p(t,a)}{p_{\mathrm{amb}}}\frac{R}{d}, \tag{16}$$

where R is taken to be 1 m and d is the distance from the center of the driving bubble to the wall of the driven bubble. An order-of-magnitude estimate for the radiation driving term is thus $p_0 R/2\rho a^3 \sim 10\,000\ \mathrm{s}^{-2}$ where we have taken $R=1$ m, $d=2a$, $p_0=0.2$ Pa as a representative peak fitted pressure, and $a=2.2$ mm. This term represents a forcing that is order 20% of the neck forcing, but at the natural frequency of the bubble and over a period of time commensurate with the bubble pulse. At the upper limit of our observed pressure values (2 Pa, see. Fig. 6), the radiation forcing is roughly 200% of the neck forcing. Based on this estimates, it is reasonable to assume that bubble-bubble coupling effects will be important, especially for fragmentation events resulting in bubble products of approximately equal size. When the bubbles are of dissimilar size, the narrowband nature of the radiation driving term will rapidly decrease the magnitude of the coupling effect.

VII. DISCUSSION

A re-examination of the fragmenting bubble data presented by Deane and Stokes[18] shows that the peak pressure amplitude of sound radiated by fragmenting bubble products is highly variable, but the partition of acoustic energy between fragmentation products is highly correlated and (on average) approximately equal irrespective of relative bubble product size. Observed breathing mode energies show a similar partition of energy between bubble fragmentation products which is also largely independent of relative bubble size. One possible explanation of this result is the symmetrical collapse of the neck of air joining the bubble products immediately prior to fragmentation. Numerical calculations based on an analytical model for neck collapse, developed in the context of bubbles released from a nozzle and extended here to fragmenting bubbles, have reproduced the partition of energy and the correlation of bubble product oscillation amplitudes.

Despite its success in reproducing the gross features of the observations, there are some inconsistencies in the model that require additional discussion. The first of these is that the neck collapse calculations suggest that the initial radiation from an excited bubble product should always appear as a rarefaction, but the superposed radiation from the bubble products sometimes show an initial compression. It is possible that events showing an initial compression do so because of bubble dynamics occurring immediately prior to neck rupture. In the case of a bubble released from a nozzle, for example, simultaneous photographs and acoustic recordings have shown that the first few hundred microseconds of the acoustic signal, accounting for about 30% of the first peak, occur prior to neck rupture. However, it is also possible that there is some major aspect of the acoustic excitation process that is not adequately captured by the neck collapse model explored here. For example, the model assumes symmetry about two spatial axes, which is probably inaccurate. In addition, the neck collapse model does not account for the fact that the neck is attached to a bubble reservoir and at some point in the collapse process there must be an interaction between the collapsing neck and the bubble to which it is connected through an increase in the gas pressure and changes in the neck shape. The time at which this interaction becomes important is presumably a function of bubble size and will occur earlier in the neck collapse for smaller bubbles. A rough calculation of the bubble scale, based on an initial excitation period of 0.4 ms and equating it to the neck width at this time, places it around 0.3 mm in radius for a neck slope of 0.84. In addition to neck symmetry and neck-bubble interactions, there is also the question of the jet of water formed within the bubble when the neck collapses. Measurements of this jet for 2 mm bubbles slowly released from a nozzle show that the jet does not account for much more than 30% of the total volume change associated with the neck collapse. However, jets formed during the much more energetic events that can occur when bubbles fragment may play a more important role in stimulating acoustic emissions. Energetic jets have been observed as part of the detachment process for bubbles entrained by falling drops.[43]

A final reservation about the model is the evidence for frequency-dependent structure in the amplitude versus frequency scatter plot shown in Fig. 6. There is some indication in the data that there are preferred frequencies for maximum excitation (2, 4, and perhaps 7 kHz), but there is no mechanism in the present model to account for this. It may be that further study will show this to be an artifact of our experimental measurements. If further study substantiates the presence of preferred frequencies, they may be due to nonlinear, resonant, bubble-bubble interactions via their radiated fields or shape to volume-mode coupling via the second-order nonlinear interactions described by Longuet-Higgins.[10–12]

Assuming that the neck collapse model is correct, then the large scatter in the pressure amplitude observed in the data set is due to the scatter in the slope of the neck of air joining bubbles prior to breakup. The range of slopes implied by the data is presumably related to the details of the turbulent fluid motions responsible for bubble fragmentation. If this is indeed the case, then it will be necessary to obtain a deeper understanding of the nature of turbulence in spilling and plunging breakers before a quantitative model of wave noise can be formulated.

ACKNOWLEDGMENTS

The authors gratefully acknowledge helpful discussions with Professor David Farmer and the assistance of Cary Humphries who constructed the bubble smasher. We are grateful to Beswick Engineering who provided the pressure regulator for the bubble injector. This work has been supported by a grant from the Office of Naval Research, Ocean Acoustics Division, ONR Grant No. N00014-04-1-0728 and the National Science Foundation, Grant No. OCE 07-27140.

[1]T. Leighton, *The Acoustic Bubble* (Academic, London, 1994).
[2]M. S. Plesset and A. Prosperetti, "Bubble Dynamics and Cavitation," Annu. Rev. Fluid Mech. **9**, 145–185 (1977).
[3]Z. C. Feng and L. G. Leal, "Nonlinear bubble dynamics," Annu. Rev. Fluid Mech. **29**, 201–243 (1997).
[4]M. Minnaert, "On musical air bubbles and the sounds of running water," Philos. Mag. **16**, 235–248 (1933).
[5]A. Prosperetti and H. N. Oguz, "The impact of drops on liquid surfaces and the underwater noise of rain," Annu. Rev. Fluid Mech. **25**, 577–602 (1993).
[6]M. S. Longuet-Higgins, B. R. Kerman, and K. Lunde, "The release of air bubbles from an underwater nozzle," J. Fluid Mech. **230**, 365–390 (1991).
[7]M. S. Longuet-Higgins, "Bubble noise," IMA J. Appl. Math. **46**, 67–70 (1991).
[8]M. S. Longuet-Higgins, "Bubble noise mechanisms-a review," in *Natural Physical Sources of Underwater Sound*, edited by B. R. Kerman (Kluwer Academic, Netherlands, 1993) Vol. **2**, pp 419–452.
[9]H. C. Pumphrey and J. E. Ffowcs Williams, "Bubbles as sources of ambient noise," IEEE J. Ocean. Eng. **15**, 268–274 (1990).
[10]M. S. Longuet-Higgins, "Monopole emission of sound by asymmetric bubble oscillations. Part 1. Normal modes," J. Fluid Mech. **201**, 525–541 (1989).
[11]M. S. Longuet-Higgins, "Monopole emission of sound by asymmetric bubble oscillations. Part 2. An initial-value problem," J. Fluid Mech. **201**, 543–565 (1989).
[12]M. S. Longuet-Higgins, "Resonance in nonlinear bubble oscillations," J. Fluid Mech. **224**, 531–549 (1991).
[13]R. Manasseh, A. Bui, J. Sandercock, and A. Ooi, "Sound emission processes in bubble detachment," Proceedings of the 14th Australasian Fluid Mechanics Conference, Adelaide, South Australia, 9–14 December 2001, edited by Dally, Vol. **1**, pp. 857–860.
[14]R. Manasseh, S. Yoshida, and M. Rudman, "Bubble formation processes and bubble acoustic signals," Proceedings of the third International Conference on Multiphase Flow (ICMF'98), Lyon, France, June 8–12 1998, Paper No. 202.
[15]G. B. Deane and H. Czerski, "A mechanism stimulating sound production from air bubbles released from a nozzle," J. Acoust. Soc. Am. **123**, EL126–EL132 (2008).
[16]J. K. Choi and S. L. Ceccio, "Dynamics and noise emission of vortex cavitation bubbles," J. Fluid Mech. **575**, 1–25 (2007).
[17]J. K. Choi and G. L. Chahine, "Noise due to extreme bubble deformation near inception of tip vortex cavitation," Phys. Fluids **16**, 2411–2418 (2004).
[18]G. B. Deane and M. D. Stokes, "The acoustic signature of bubbles fragmenting in sheared flow," J. Acoust. Soc. Am. **120**, EL84–EL89 (2006).
[19]D. M. Farmer, C. L. McNeil, and B. D. Johnson, "Evidence for the importance of bubbles in increasing air-sea gas flux," Nature (London) **361**, 620–623 (1991).
[20]R. F. Keeling, "On the role of large bubbles in air-sea gas exchange and supersaturation in the ocean," J. Mar. Res. **51**, 237–271 (1993).
[21]M. Banner and D. H. Cato, "Physical mechanisms of noise generation by breaking waves: a laboratory study," NATO ASI Ser., Ser. C **238**, 429–436 (1988).
[22]H. Medwin and J. A. C. Daniel, "Acoustical measurements of bubble production by spilling breakers," J. Acoust. Soc. Am. **88**, 408–412 (1990).
[23]G. E. Updegraff, *In situ investigation of sea surface noise from a depth of* 1 m (Ph.D. dissertation, University of California at San Diego, La Jolla, CA, 1989).
[24]L. Ding and D. M. Farmer, "On the dipole acoustic source level of breaking waves," J. Acoust. Soc. Am. **96**, 3036–3044 (1994).
[25]R. Manasseh, A. V. Babanin, C. Forbes, K. Rickards, I. Bobevski, and A. Ooi, "Passive acoustic determination of wave-breaking events and their severity across the spectrum," J. Atmos. Ocean. Technol. **23**, 599–618 (2006).
[26]G. B. Deane, "Sound generation and air entrainment by breaking waves in the surf zone," J. Acoust. Soc. Am. **102**, 2671–2689 (1997).
[27]S. L. Means and R. M. Heitmeyer, "Surf-generated noise signatures: a comparison of plunging and spilling breakers," J. Acoust. Soc. Am. **112**, 481–488 (2002).
[28]H. Medwin and M. M. Beaky, "Bubble sources of the Knudsen sea noise spectra," J. Acoust. Soc. Am. **86**, 1124–1130 (1989).
[29]A. Kolaini, L. A. Crum, and R. Roy, "Bubble production by capillary-gravity waves," J. Acoust. Soc. Am. **95**, 1913–1921 (1994).
[30]T. G. Leighton, P. R. White, and M. F. Schneider, "The detection and dimension of bubble entrainment and comminution," J. Acoust. Soc. Am. **103**, 1825–1835 (1998).
[31]T. R. Hahn, T. K. Berger, and M. J. Buckingham, "Acoustic resonances in the bubble plume formed by a plunging water jet," Proc. R. Soc. London, Ser. A **459**, 1751–1782 (2003).
[32]G. B. Deane and M. D. Stokes, "Scale dependence of bubble creation mechanisms in breaking waves," Nature (London) **418**, 839–844 (2002).
[33]C. Garrett, M. Li, and D. Farmer, "The connection between bubble size spectra and energy dissipation rates in the upper ocean," J. Phys. Oceanogr. **30**, 2163–2171 (2000).
[34]M. S. Longuet-Higgins, in *Breaking Waves: In Deep or Shallow Water*, Tenth Symposium on Naval Hydrodynamics, Cambridge, Mass., edited by R. D. Cooper and S. W. Doroff (ONR, Cambridge, MA, 1974) pp. 597–605.
[35]A. Prosperetti, "Thermal effects and damping mechanisms in the forced radial oscillations of gas bubbles in liquids," J. Acoust. Soc. Am. **61**, 17–27 (1977).
[36]H. Medwin and C. S. Clay, *Fundamentals of Acoustical Oceanography* (Academic, San Diego, 1998).
[37]J. C. Lagarias, J. A. Reeds, M. H. Wright, and P. E. Wright, "Convergence properties of the Nelder-Mead simplex method in low dimensions," SIAM J. Optim. **9**, 112–147 (1998).
[38]M. Strasberg, "The pulsation frequency of nonspherical gas bubbles in liquids," J. Acoust. Soc. Am. **25**, 536–537 (1953).
[39]H. C. Pumphrey and L. A. Crum, "Free oscillations of near-surface bubbles as a source of the underwater noise of rain," J. Acoust. Soc. Am. **87**, 142–148 (1990).
[40]D. A. Lewis and J. F. Davidson, "Bubble Splitting in Shear Flow," Trans. Inst. Chem. Eng. **60**, 283–291 (1982).

[41]C. Martinez-Bazan, J. L. Montanes, and J. C. Lasheras, "On the breakup of an air bubble injected into a fully developed turbulent flow. Part 2. Size PDF of the resulting daughter bubbles," J. Fluid Mech. **401**, 183–207 (1999).
[42]L.-S. Fan and K. Tsuchiya, *Bubble Wake Dynamics in Liquids and Liquid-Solid Suspensions* (Butterworth-Heinemann, Boston, 1990).
[43]D. E. Cole and J. L. Liow, "Bubble entrapment during water drop impacts," *Proceedings of the 15th Australasian Fluid Mechanics Conference*, edited by M. Behnia, W. Lin, and G. D. McBain (The University of Sydney, Sydney, 2004).

Effects of shear waves on boundary-coupled vector sensors

Kevin B. Smith[a)]
Department of Physics, Naval Postgraduate School, Monterey, California 93943

(Received 7 November 2007; revised 1 September 2008; accepted 3 September 2008)

The impact of the acoustic properties of a solid medium on the response of an acoustic vector sensor placed at the boundary between water and the solid is examined. In particular, the components of the vector field both normal and tangential to the boundary are studied. It is shown that the component of the velocity tangential to the boundary is affected by the introduction of shear in the solid medium, which leads to amplitude and phase discontinuities across the boundary. Such discontinuities can lead to mismatches between the vector sensor components that interfere with common, coherent processing techniques. Implications for ocean bottom- and hull-mounted examples are provided. © *2008 Acoustical Society of America.* [DOI: 10.1121/1.2996324]

PACS number(s): 43.30.Xm, 43.30.Ma, 43.20.Tb [RAS] Pages: 3464–3470

I. INTRODUCTION

Previous work examining the acoustic vector field measured in the presence of a reflecting boundary focused on the impact of the boundary on the field in the water medium. Most notably, Hawkes and Nehorai[1–3] examined the influence of boundary reflections on vector sensors and array processing of such sensors. However, their work assumed that the sensors responded solely to the field within the fluid adjacent to the boundary, and did not consider any coupling between the boundary and the vector sensor itself. Complete decoupling of the mounting from the solid medium across the boundary can be difficult in practice.

A significant amount of work has been presented in the geophysics literature that investigates the coupling between sensors (most notably accelerometers or seismometers) and the seafloor.[4–6] The focus there was on the mechanical coupling of the sensor housing and the motion of the medium to which it responds, including the combined effects at the water/bottom interface of the seafloor. Some of the seminal work was presented by Sutton *et al.* (1981),[4] and later expanded upon by Duennebier and Sutton (1995).[5] Subsequently, Osler and Chapman (1998) (Ref. 6) used this theoretical framework to characterize the experimental results obtained from an ocean bottom seismometer (OBS). [As the work of Osler and Chapman (1998) is cited frequently in this paper, it shall henceforth be referred to as OC.] Readers are referred to those papers for more extensive discussions on the coupling between the mechanical sensor and the motion of the medium at the boundary.

In all of the geophysics papers cited, it is noted repeatedly that the coupling between the motion normal to the boundary and the sensor is relatively well behaved and can be calibrated. However, the coupling between the motion tangential to the boundary and the sensor is quite difficult and often cannot be appropriately calibrated. In OC, they state, "… one could possibly relate horizontal motion of the OBS motion to the true horizontal motion of the seabed if the ratio [of tangential fluid velocity to tangential seabed velocity] were known…" But, they also point out that this ratio is a complicated function of frequency, type of wave, and other propagation parameters.

The goal of this paper is to explore some of the features of this ratio created by the discontinuity of the field across a boundary separating an inviscid fluid and a shear-supporting solid. The dependence on frequency and shear wave speed will be examined closely, and the general impact of attenuation within the solid will be considered. The impact of these results on the potential for sensor calibrations will then be discussed.

II. THEORETICAL ANALYSIS

We begin by presenting a brief overview of some of the theory developed in OC. Their work was specifically intended to describe the response of an ocean bottom seismometer (OBS) to deployment on the seafloor, but we can generalize this to a vector sensor's response at the planar boundary between a fluid and a solid. It was generally assumed that the sensor in question was "resting" on the seafloor. This is followed by a detailed examination of the fields interacting at such a planar boundary. The impact of hard mounting a sensor to a structure (e.g., ship hull, structural truss, etc.) is then discussed.

A. Coupling ratios and transfer functions

In the work of OC, they define two key parameters: the coupling ratio and the transfer function. The coupling ratio was defined as the ratio between the bottomed velocity of the sensor to the suspended velocity of the sensor subject to an identical driving force. OC showed that this coupling ratio could be written[6]

$$r = \frac{v_{\mathrm{bot}}}{v_{\mathrm{sus}}} = \frac{i\omega(m + m_{\mathrm{sus}})}{i\omega(m + m_{\mathrm{bot}}) + Z}, \tag{1}$$

where m_{sus} (m_{bot}) is the added mass of the water (sediment) needed to account for the reaction force of the medium to the sensor's motion, and Z is a frequency-dependent, generally complex interaction impedance that accounts for the sedi-

[a)]Work completed while serving as Visiting Professor at the Naval Undersea Warfare Center, Newport, RI

 © 2008 Acoustical Society of America

ment stiffness and damping. For high frequencies (much greater than the associated resonant frequency), the coupling ratio takes the simplified form[6]

$$r_\infty = \frac{m + m_{\text{sus}}}{m + m_{\text{bot}}}. \tag{2}$$

It should be noted that the quantities m_{sus}, m_{bot}, Z, and r are, in general, different for tangential and normal motion.

The transfer function was defined as the ratio of the sensor velocity to the velocity of the medium (seabed, water, or both). Since this defines the physically significant measure of the sensor input in terms of motion induced by a passing acoustic wave, it is this quantity that is of primary concern here. Naturally, there is also expected to be a local sensor transfer function between the sensor motion and the actual data recorded, but we shall assume the sensor being used is capable of providing an exact representation of its own motion.

For tangential motion of the seabed only (water at rest), the transfer function was shown to be[6]

$$T_h = \frac{Z}{i\omega(m + m_{\text{bot}}) + Z} = 1 - \frac{r}{r_\infty}. \tag{3}$$

Note that for very low frequencies, $r \ll r_\infty$. Then $T_h \to 1$, and the motion of the seafloor is accurately registered by the motion of the sensor. For very high frequencies, however, $r \to r_\infty$ and $T_h \to 0$, indicating a complete lack of response of the sensor to the seabed. For example, this could be the result of having a very light sensor (e.g., neutrally buoyant in water) that does not couple well with seafloor motion, or one that is very heavy, producing a large damping term.

For tangential motion of the water only, the transfer function takes the form[6]

$$T_w = \frac{i\omega(m_w + m_{\text{bot}})}{i\omega(m + m_{\text{bot}}) + Z} = \frac{r}{r_\infty}\left(\frac{m_w + m_{\text{bot}}}{m + m_{\text{bot}}}\right), \tag{4}$$

where m_w is the mass of the water displaced by the motion of the sensor. If the sensor is made to be neutrally buoyant, $m = m_w$, then the transfer function reduces to the coupling ratio, $T_w = r/r_\infty$. In this case, the high-frequency limit of the transfer function is $T_w \to 1$, indicating that the sensor motion accurately represents the fluid flow. For very low frequencies, in contrast, $T_w \to 0$, and the sensor does not provide a good measure of the fluid flow.

For combined tangential motion of the water and sediment, the ratio of sensor tangential velocity to the seabed tangential velocity was shown to be[6]

$$T_{h+w} = T_h + \frac{v_w}{v_0} T_w, \tag{5}$$

where v_w is the tangential water velocity and v_0 is the tangential velocity of the seabed. Based on the limiting behavior described above, in the presence of a low-frequency forcing function,

$$T_{h+w}(\omega \to 0) \approx T_h(\omega \to 0) \to 1. \tag{6}$$

Thus, the sensor provides a good, direct measure of the motion of the seabed at the interface. Alternatively, in the presence of a high-frequency forcing function,

$$T_{h+w}(\omega \to \infty) \approx \frac{v_w}{v_0} T_w(\omega \to \infty) \to \frac{v_w}{v_0}, \tag{7}$$

where the final limit applies if the sensor is nearly neutrally buoyant. In this case, we find that the sensor's response to the motion of the seabed is scaled by the ratio of tangential components of water velocity to seabed velocity.

Although no rigorous treatment will be performed here in an attempt to extend this type of analysis to systems of sensors mounted to hard structures (e.g., sensors on steel supports or ship hulls), one may expect that a reasonable extrapolation of the above approach could be made by letting m_{bot} become very large. Then $T_w \to r/r_\infty \to 1$, $T_h \to 0$, and $T_{h+w} \to v_w/v_0$. Regardless of the validity of this extrapolation, the discontinuity across the interface will still have a direct impact on the response of a mounted vector sensor, and so the analysis to follow will be generalized to substances harder than typical seafloor sediments.

It is also worth pointing out that all of the analysis presented here assumes pointlike sensor responses. More specifically, the impact of rotational sensor motion is neglected. For extended sensors weakly coupled to an interface, such rotational motion could certainly occur, making accurate measurements significantly more complicated than presented here. Experimental results have been presented by Duennebier and Sutton which show the response of sensor package tilt to horizontal motion of the ocean floor.[7]

B. Analysis of displacement fields at a planar boundary

Let us first address the issue of a manifestation of the shear wave energy in the field within the fluid medium. It is well known[8] that oscillatory motion of a solid boundary next to a viscous fluid will transmit energy into the fluid. The amplitude of this motion decays exponentially away from the boundary, scaled by the *depth of penetration*, δ, given by

$$\delta = \sqrt{\frac{2\nu}{\omega}}, \tag{8}$$

where ν is the kinematic viscosity of the fluid. Note that this penetration depth increases with the viscosity and with decreasing frequency of oscillation.

For seawater, the kinematic viscosity is approximately 0.01 cm^2/s. Thus, the depth of penetration at 1 Hz is only 0.6 mm. At 100 Hz, this drops to 60 μm. Therefore, for most frequencies of interest, the scale of this effect is vanishingly small and may be neglected. This allows us to treat the fluid as an ideal, nonviscous fluid. In other words, there is no *direct* manifestation of the shear in the acoustic field of the fluid adjacent to a solid. This same type of assumption is consistent with the previous work of vector sensor responses next to a general reflecting boundary.[1–3]

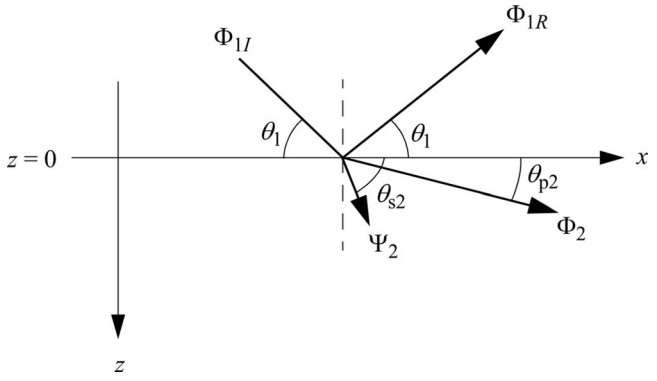


FIG. 1. Representation of incident, reflected, and transmitted displacement potential fields at a plane interface separating a fluid and a solid.

Although we may neglect the impact on the field within the fluid beyond the typical response defined from the reflection coefficient, the previous analysis showed that the coupling between the sensor and seafloor motion must characterize the ratio of velocity components just above and just below the interface. Motion of the solid that is not directly coupled into the overlying fluid will, therefore, still affect the motion of the sensor housing.

Consider the geometry depicted in Fig. 1 of a plane wave incident on an interface separating two semi-infinite, homogeneous half-spaces. The upper (fluid) medium has density ρ_1 and compressional sound speed c_{p1}, while the lower (solid) medium has density ρ_2, compressional speed c_{p2}, and shear speed c_{s2}. Such problems have been formally examined in numerous texts, e.g., Ref. 9 and 10. For a plane wave incident in the x-z plane, the corresponding particle displacement in the shear-supporting medium will, in general, be defined in terms of a scalar potential, Φ, and a vector potential, $\boldsymbol{\Psi}$, i.e.,

$$\mathbf{d} = \nabla\Phi + \nabla \times \boldsymbol{\Psi}. \tag{9}$$

Since $\boldsymbol{\Psi} = \Psi\hat{y}$ here, then

$$\mathbf{d} = \left(\frac{\partial\Phi}{\partial x} + \frac{\partial\Psi}{\partial z}\right)\hat{x} + \left(\frac{\partial\Phi}{\partial z} - \frac{\partial\Psi}{\partial x}\right)\hat{z}. \tag{10}$$

We assume a unit amplitude displacement potential wave is incident on the interface defined by

$$\Phi_{1I} = e^{i(\beta x + \gamma_1 z - \omega t)}, \tag{11}$$

generating a reflected wave back into the upper half-space,

$$\Phi_{1R} = \Re e^{i(\beta x - \gamma_1 z - \omega t)}. \tag{12}$$

The parameter $\Re$ is the displacement potential reflection coefficient, and the total solution in the upper space is then $\Phi_1 = \Phi_{1I} + \Phi_{1R}$. The wavenumber components in the fluid medium are $\beta = (\omega/c_{p1})\cos\theta_1$ and $\gamma_1 = (\omega/c_{p1})\sin\theta_1$, where θ_1 is the grazing angle relative to the interface. Energy is transmitted into the lower, solid half-space as both compressional,

$$\Phi_2 = \mathfrak{I}_p e^{i(\beta x + \gamma_2 z - \omega t)}, \tag{13}$$

and shear wave energy,

$$\Psi_2 = \mathfrak{I}_s e^{i(\beta x + \delta_2 z - \omega t)}, \tag{14}$$

where $\mathfrak{I}_p$ and $\mathfrak{I}_s$ represent the compressional and shear transmission coefficients, respectively, of the displacement potentials. The compressional wavenumber components in the solid medium are $\beta = (\omega/c_{p2})\cos\theta_{p2}$ and $\gamma_2 = (\omega/c_{p2})\sin\theta_{p2}$, while the shear wavenumber components are $\beta = (\omega/c_{s2})\cos\theta_{s2}$ and $\delta_2 = (\omega/c_{s2})\sin\theta_{s2}$. Note that $\mathfrak{I}_s$ provides a measure of the transition from compressional to shear. This transition can only occur at the boundary.

The boundary conditions at the water/bottom interface then include continuity of normal (vertical) displacement,

$$d_{z1} = d_{z2} \Rightarrow \frac{\partial\Phi_1}{\partial z} = \frac{\partial\Phi_2}{\partial z} - \frac{\partial\Psi_2}{\partial x}, \tag{15}$$

continuity of normal stress,

$$p_1 = -\sigma_{2,zz} \Rightarrow \rho_1 c_{p1}^2\left(\frac{\partial^2\Phi_1}{\partial x^2} + \frac{\partial^2\Phi_1}{\partial z^2}\right) = \rho_2 c_{p_2}^2\left(\frac{\partial^2\Phi_2}{\partial x^2} + \frac{\partial^2\Phi_2}{\partial z^2}\right) + 2\rho_2 c_{s_2}^2\left(\frac{\partial^2\Psi_2}{\partial z\partial x} - \frac{\partial^2\Phi_2}{\partial x^2}\right), \tag{16}$$

and (for ideal fluid) a vanishing of tangential stress,

$$0 = -\sigma_{2,zx} \Rightarrow \left(2\frac{\partial^2\Phi_2}{\partial z\partial x} + \frac{\partial^2\Psi_2}{\partial x^2} - \frac{\partial^2\Psi_2}{\partial z^2}\right) = 0. \tag{17}$$

Equations (15)–(17) may be combined to define the reflection coefficient[9]

$$\Re = \frac{4\gamma_2\delta_2\beta^2 + (\delta_2^2 - \beta^2)^2 - (\rho_1/\rho_2)(\gamma_2/\gamma_1)(\omega^4/c_{s2}^4)}{4\gamma_2\delta_2\beta^2 + (\delta_2^2 - \beta^2)^2 + (\rho_1/\rho_2)(\gamma_2/\gamma_1)(\omega^4/c_{s2}^4)}. \tag{18}$$

Note that attenuation in the solid may be incorporated by replacing either compressional or shear speed by $c_2 \rightarrow c_2(1 - i(c_2/\omega)\alpha_2)$, where α_2 represents the corresponding exponential attenuation rate. Furthermore, because the relationship between acoustic pressure and displacement potential in a fluid is simply $p = \rho\omega^2\Phi$, then $(\Phi_{1R}/\Phi_{1I}) = (p_{1R}/p_{1I}) = \Re$, and the reflection coefficient in Eq. (18) also corresponds to the pressure reflection coefficient.

One can also show that the displacement potential transmission coefficients are given by

$$\mathfrak{I}_p = \frac{\gamma_1(\delta_2^2 - \beta^2)}{\gamma_2(\delta_2^2 + \beta^2)}(1 - \Re) \tag{19}$$

and

$$\mathfrak{I}_s = \frac{2\beta\gamma_1}{(\delta_2^2 + \beta^2)}(1 - \Re) = \frac{2\beta\gamma_1 c_{s2}^2}{\omega^2}(1 - \Re). \tag{20}$$

Note that in the limit of $c_{s2} \rightarrow 0$, then $\theta_{s2} \rightarrow 90^\circ$ and $\delta_2 \rightarrow \infty$. This leads to $\mathfrak{I}_s \rightarrow 0$ and $\mathfrak{I}_p \rightarrow (\gamma_1/\gamma_2)(1 - \Re)$, which is equivalent to the fluid-fluid transmission coefficients for the particle displacement potential.

The first boundary condition stated, Eq. (15), also requires continuity of the normal component of particle velocity, i.e.,

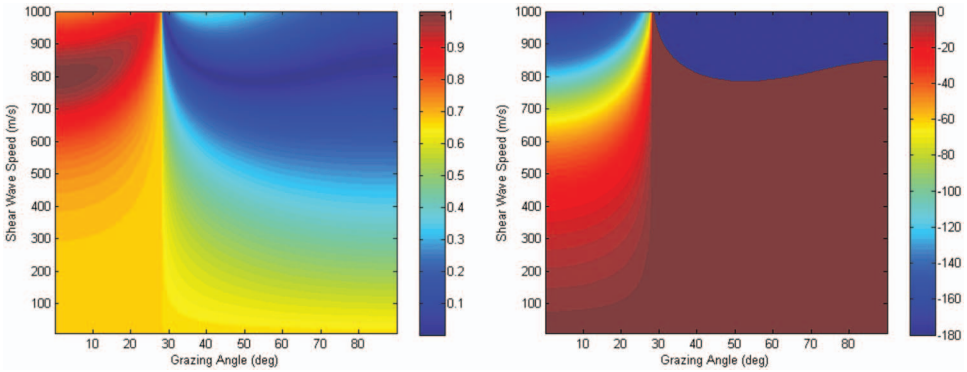


FIG. 2. (Color online) Ratio of sediment horizontal velocity component to water horizontal velocity component, as defined in Eq. (27). Left plot shows magnitude, while right plot displays phase (in deg) for water/sediment boundary.

$$v_{z1} = \frac{\partial d_{z1}}{\partial t} = -i\omega d_{z1} = -i\omega d_{z2} = \frac{\partial d_{z2}}{\partial t} = v_{z2}. \tag{21}$$

Thus, the measurement of normal velocity should be the same in the water above the interface or within the solid below the interface. Thus, the complete characterization of the sensor response to normal seafloor motion may be described in terms of the transfer functions defined in the previous section.

In contrast, however, the tangential component of particle velocity is not, in general, continuous, i.e.,

$$v_{x1} = \frac{\partial d_{x1}}{\partial t} = -i\omega d_{x1} \neq -i\omega d_{x2} = \frac{\partial d_{x2}}{\partial t} = v_{x2}. \tag{22}$$

From Eq. (10), we find that

$$d_{x2} = \frac{\partial \Phi_2}{\partial x} + \frac{\partial \Psi_2}{\partial z} = i\beta\Phi_2 + i\delta_2\Psi_2, \tag{23}$$

and so

$$v_{x2} = \frac{\partial d_{x2}}{\partial t} = \beta\omega\Phi_2 + \delta_2\omega\Psi_2. \tag{24}$$

Evaluating this at the interface and at the reference position $x=0$, we obtain

$$v_{x2} = (\beta\omega\mathfrak{I}_p + \delta_2\omega\mathfrak{I}_s)e^{-i\omega t}. \tag{25}$$

If the lower medium does support shear, Eq. (25) provides us with a correction term for the amplitude of the tangential component observed by the sensor.

If we compare this response with what would be observed in the overlying fluid,

$$v_{x1} = \beta\omega(1+\Re)e^{-i\omega t}, \tag{26}$$

we find the response of the sensor coupled to the solid changes by the factor

$$\frac{v_{x2}}{v_{x1}} = \frac{\beta\mathfrak{I}_p + \delta_2\mathfrak{I}_s}{\beta(1+\Re)}. \tag{27}$$

III. NUMERICAL RESULTS

All quantities used in Eq. (27) were defined generally as complex values. The ratio of tangential velocity components is then also complex. A simple MATLAB® code was then developed that computes the amplitude and phase of this complex ratio. Figure 2 displays the magnitude and phase of this tangential velocity component ratio for a range of grazing angles and shear wave speeds of potential interest in ocean bottom-deployed vector sensors. For these calculations, we have assumed $\rho_1 = 1.0\ \mathrm{g/cm^3}$, $c_{p1} = 1500\ \mathrm{m/s}$, $\rho_2 = 1.5\ \mathrm{g/cm^3}$, and $c_{p2} = 1700\ \mathrm{m/s}$. The bottom sediment material is assumed to be lossless, so there is no frequency dependence in Eq. (27).

Note that if the bottom does not support shear, then $\mathfrak{I}_s = 0$, and

$$\left(\frac{v_{x2}}{v_{x1}}\right)_{c_{s2}=0} = \frac{\mathfrak{I}_p}{(1+\Re)} = \frac{\rho_1}{\rho_2}. \tag{28}$$

In general, this ratio does not lead to an equivalent response observed in the field above the bottom, but rather is scaled simply by the ratio of the densities (approximately 0.67 here). This limit is observed in Figs. 2 and 3. Thus, the response of the tangential component of the vector sensor

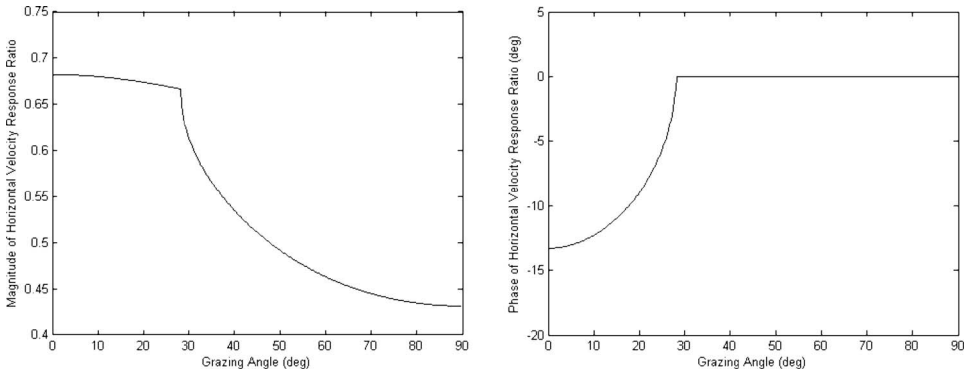


FIG. 3. Results extracted from Fig. 2 for a shear speed of 400 m/s. Left plot shows magnitude of ratio, while right plot displays phase (in deg) of ratio for water/sediment boundary.

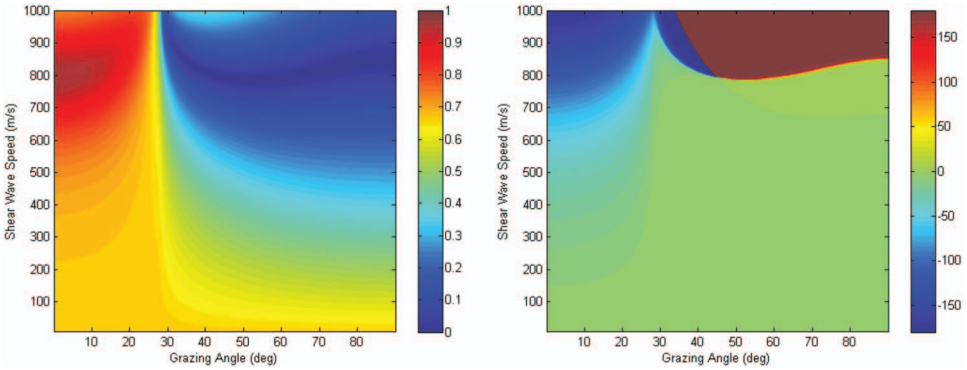


FIG. 4. (Color online) Ratio of sediment horizontal velocity component to water horizontal velocity component, as defined in Eq. (27), with compressional and shear attenuation in the sediment. Left plot shows magnitude, while right plot displays phase (in deg) for water/sediment boundary.

resting on the bottom will typically be reduced from that in the field above the interface.

The results in Fig. 2 indicate that, for most typical shear wave speeds ($\leqslant$200 m/s), the amplitude difference between results with and without shear is negligible and the phase difference is typically less than 5° for grazing angles less than critical. The simple, asymptotic limit in Eq. (28) may then be assumed to hold. At steeper angles, the phase is insensitive to the shear wave speed, but the amplitude can vary by 30% or more even for low values of bottom shear. This could make sensor calibrations challenging, and exposes a difference in the way the sensor would respond to distant signals versus near-field, surface generated signals such as noise.

For larger shear speeds (~400 m/s), the amplitude difference approaches 50% (at steep angles) when shear is included, and the phase difference can be as much as 15° (near grazing). The rapid change in the phase mismatch near the critical angle could be significant in signal processing applications, and should be treated with caution. Knowledge of the bottom shear properties then becomes increasingly important when values exceed a few hundred meters per second.

The introduction of typical sediment attenuation factors (α_p=0.2 dB/m/kHz and α_s=0.5 dB/m/kHz) has little impact on these results, as observed in Figs. 4 and 5.

Similar calculations were performed for a sensor mounted on a steel hull. In this case, the water properties were the same as before, but now ρ_2=8.0 g/cm^3 and c_{p2} =5500 m/s, and we allow the shear speed to range from less than to greater than the water sound speed. The results are displayed in Figs. 6–8. Note the asymptotic limit (0.125 here) is obtained at very low shear speeds. However, for steel-like materials, such low shear speeds are unrealistic.

Here we find the results much more complicated than before. If the shear speed of the solid is less than the water (not typical for something like steel), then the relative response of the tangential component is similar to that seen before. The relative amplitude is on the order of the density contrast, but can vary by 50% or more. The phase difference,

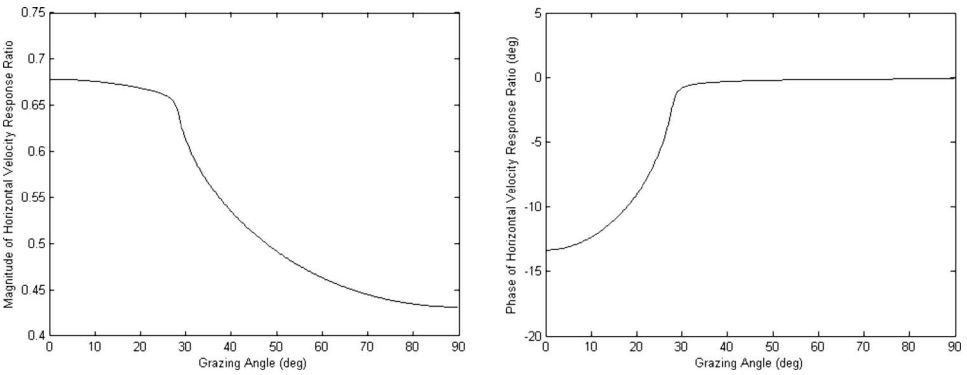


FIG. 5. Results extracted from Fig. 4 for a shear speed of 400 m/s. Left plot shows magnitude of ratio, while right plot displays phase (in deg) of ratio for water/sediment boundary.

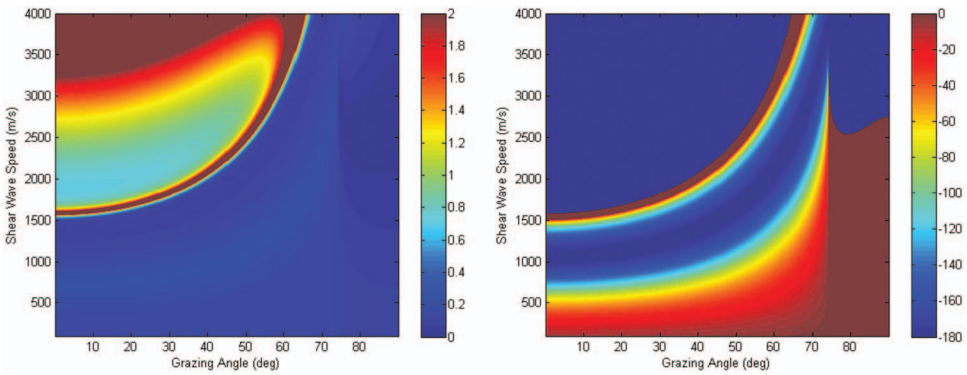


FIG. 6. (Color online) Ratio of solid horizontal velocity component to water horizontal velocity component, as defined in Eq. (27). Left plot shows magnitude, while right plot displays phase (in deg) for water/steel boundary.

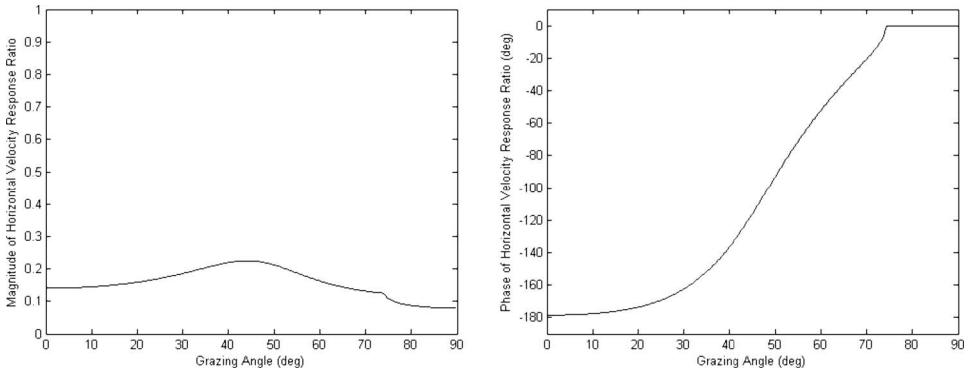


FIG. 7. Results extracted from Fig. 6 for a shear speed of 1000 m/s. Left plot shows magnitude of ratio, while right plot displays phase (in deg) of ratio for water/steel boundary.

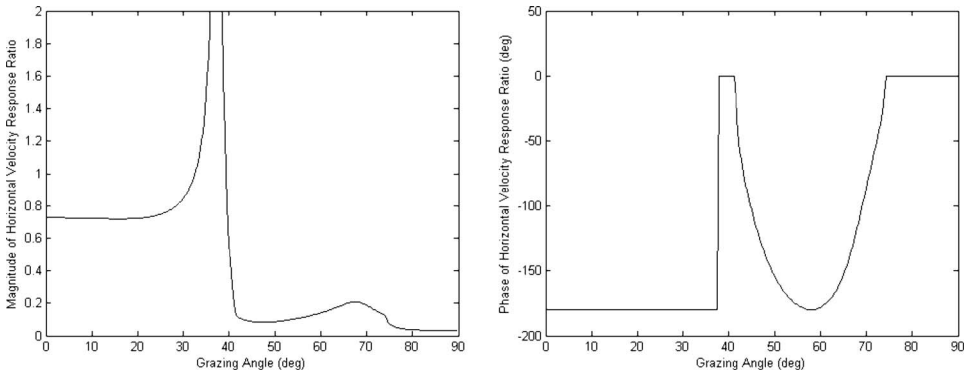


FIG. 8. Results extracted from Fig. 6 for a shear speed of 2000 m/s. Left plot shows magnitude of ratio, while right plot displays phase (in deg) of ratio for water/steel boundary.

however, varies over a full 180°, and changes rapidly as the compressional critical angle is approached. If the shear speed exceeds that of the surrounding water, the amplitude and phase of the ratio are found to be generally constant well below critical. However, a singularity in the ratio occurs near the critical angle as the reflection coefficient goes through a point where it becomes −1, corresponding to the generation of a Rayleigh wave at the boundary between the water and solid.[9,10] Beyond critical, the amplitude of the ratio drops significantly, and the phase varies almost continuously over a 180° range.

Figures 9–11 present the results when attenuation in the solid material is considered (α_p=1.0 dB/m/kHz and α_s =5.0 dB/m/kHz). This produces a fairly dramatic change in

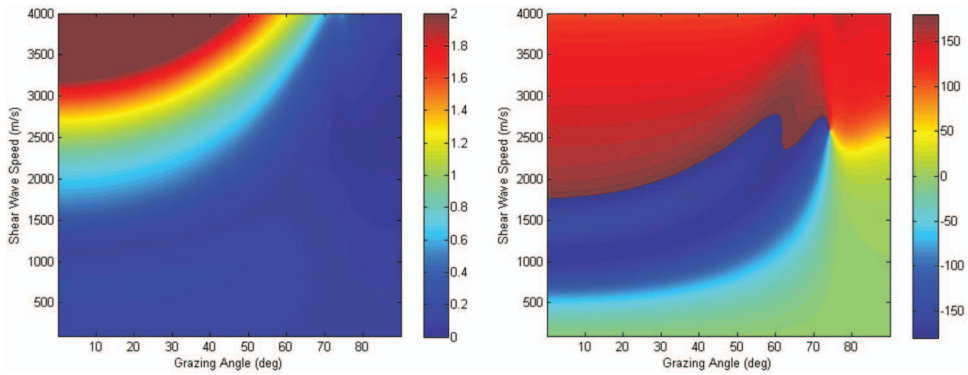


FIG. 9. (Color online) Ratio of solid horizontal velocity component to water horizontal velocity component, as defined in Eq. (27), with compressional and shear attenuation in the solid. Left plot shows magnitude, while right plot displays phase (in deg) for water/steel boundary.

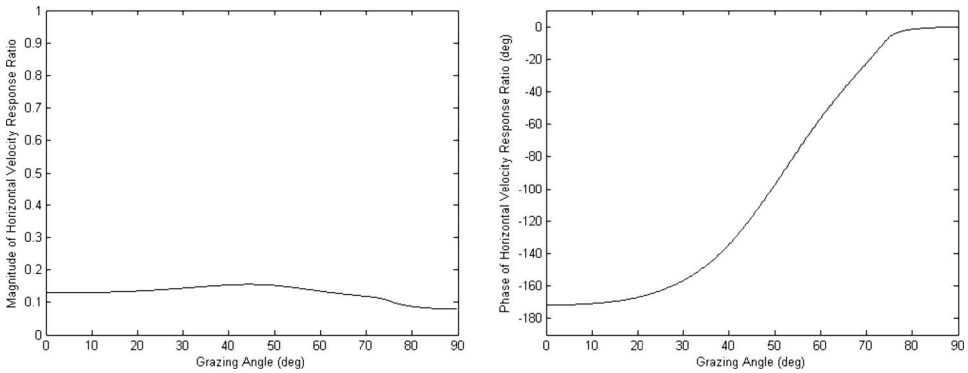


FIG. 10. Results extracted from Fig. 9 for a shear speed of 1000 m/s. Left plot shows magnitude of ratio, while right plot displays phase (in deg) of ratio for water/steel boundary.

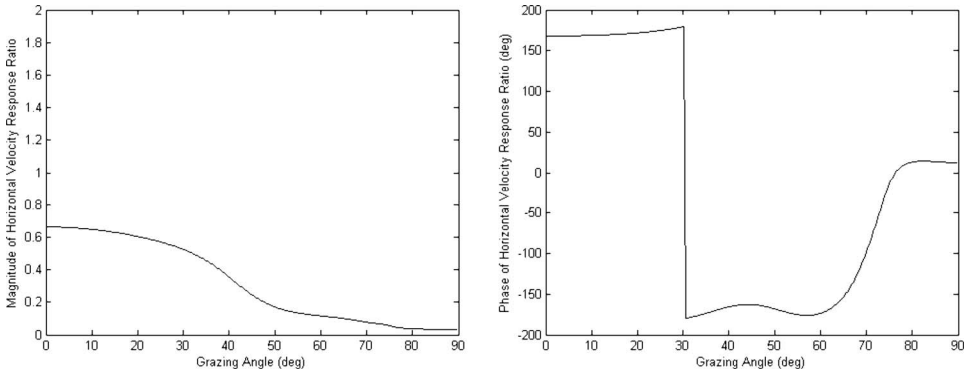


FIG. 11. Results extracted from Fig. 9 for a shear speed of 2000 m/s. Left plot shows magnitude of ratio, while right plot displays phase (in deg) of ratio for water/steel boundary.

the influence of the near-critical singularity observed above, as the impact of the Rayleigh wave is significantly diminished. The amplitude of the ratio for shear speeds both below and above the water sound speed show fairly smooth changes. While the low shear case shows an amplitude nearly constant and approximately equal to the density ratio, the high shear case shows relatively large variations (nearly an order of magnitude) in the amplitude of the tangential velocity component ratio. In both cases, the phase is relatively constant for grazing angles well below critical, but changes significantly beyond critical.

IV. SUMMARY

In this paper, the discontinuity in the tangential velocity components across a boundary between water and a shear-supporting solid was examined. The impact this has on the sensor's response to a passing acoustic wave was discussed. Understanding this coupling is important for vector sensors deployed on the ocean floor or hard-mounted on a solid structure.

For solid materials with very low shear (which behave nearly fluidlike), the tangential component response was simply rescaled by the density ratio across the boundary. For sedimentlike materials (faster than water), increasing the shear speed above a few hundred meters per second began to introduce both relative amplitude and phase variations as a function of grazing angle. These results were rather insensitive to attenuation levels appropriate for marine sediments. Although much of this could presumably be accounted for in calibration studies, some of the differences were observed to vary rapidly with angle, and could prove difficult to properly characterize for an entire system of sensors.

When a very hard material such as steel was considered, the results became quite complex in the absence of any attenuation. A singularity in the relative amplitude scaling and a discontinuous change in relative phase were observed at grazing angles just below critical due to the generation of the Rayleigh wave. These were significantly tempered by the introduction of attenuation in the solid properties. As before, though, the results indicated fairly rapid changes in relative amplitude and phase as a function of grazing angle.

This work suggests that decoupling an acoustic vector sensor from an interface may not be necessary in all cases, even when the goal is to provide an accurate measurement of the overlying fluid motion. When the shear speed is very low, the expected response of the sensor is predictable, and can be calibrated through the wave-sensor transfer functions. As shear speeds become significant, even just a few hundred meters per second, the field discontinuity becomes complicated and accurate prediction of the full sensor response becomes difficult. Thus, for vector sensors deployed on high-shear seafloors or hard structures, it becomes increasingly necessary to properly de-couple the sensor from the response of the interface in order to accurately record the field within the fluid.

ACKNOWLEDGMENTS

This work was supported by the U.S. Office of Naval Research (Code 321OA), PEO-IWS5a, and the Naval Undersea Warfare Center Division, Newport (Code 152).

[1]M. Hawkes and A. Nehorai, "Hull-Mounted Acoustic Vector-Sensor Processing," IEEE, Asilomar Conference Proceedings, Vol. **29**, pp. 1046–1050 (1996).
[2]M. Hawkes and A. Nehorai, "Surface-Mounted Acoustic Vector-Sensor Array Processing," IEEE, ICASSP Proc., Vol. **6**, pp. 3169–3172 (1996).
[3]M. Hawkes and A. Nehorai, "Acoustic vector-sensor processing in the presence of a reflecting boundary," IEEE Trans. Signal Process. **48**, 2981–2993 (2000).
[4]G. H. Sutton, F. K. Duennebier, and B. Iwatake, "Coupling of ocean bottom seismometers to soft bottom," Mar. Geophys. Res. **5**, 35–51 (1981).
[5]F. K. Duennebier and G. H. Sutton, "Fidelity of ocean bottom seismic observations," Mar. Geophys. Res. **17**, 535–555 (1995).
[6]J. C. Osler and D. M. F. Chapman, "Quantifying the interaction of an ocean bottom seismometer with the seabed," J. Geophys. Res. **103**, 9879–9894 (1998).
[7]F. K. Duennebier and G. H. Sutton, "Why bury ocean bottom seismometers?," Geochem., Geophys., Geosyst. **8**, Q02010 (2007).
[8]L. D. Landau and E. M. Lifshitz, *Fluid Mechanics* (Pergamon Press, New York, 1987), Chap. II, Sec. 24.
[9]I. Tolstoy and C. S. Clay, *Ocean Acoustics* (AIP, New York, 1987), Ch. 2, Sec. 2.4.
[10]L. M. Brekhovskikh, *Waves in Layered Media* (Academic, San Diego, 1980), Ch. 7, Sec. 7.1–7.2.

Simulations of photoacoustic wave propagation using a finite-difference time-domain method with Berenger's perfectly matched layers

Yae-Lin Sheu
Department of Electrical Engineering, National Taiwan University, No. 1, Section 4, Roosevelt Road, Taipei, Taiwan 106, Taiwan

Pai-Chi Li
Department of Electrical Engineering, National Taiwan University, No. 1, Section 4, Roosevelt Road, Taipei, Taiwan 106, Taiwan and Institute of Biomedical Electronics and Bioinformatics, National Taiwan University, No. 1, Section 4, Roosevelt Road, Taipei, Taiwan 106, Taiwan

(Received 10 December 2007; revised 3 June 2008; accepted 29 September 2008)

This study developed a numerical solution of the general photoacoustic generation equations involving the heat conduction theory and the state, continuity, and Navier–Stokes equations in 2.5*D* axisymmetric cylindrical coordinates using a finite-difference time-domain scheme. The numerical techniques included staggered grids and Berenger's perfectly matched layers (PMLs), and linear-perturbation analytical solutions were used to validate the simulation results. The numerical results at different detection angles and durations of laser pulses agreed with the theoretical estimates to within an error of 2% in the absolute differences. It was also demonstrated that the simulator can be used to develop advanced photoacoustic imaging methods. The performance of Berenger's PMLs was also assessed by comparisons with the traditional first-order Mur's boundary condition. At the edges of the simulation domain, a ten-layer PML medium with polynomial attenuation coefficient grading from 0 to 5×10^{6} $m^3/kg\ s$ was designed to reduce the reflection to as low as −60 and −32 dB in the axial and radial directions, respectively. The reflections at the axial and radial boundaries were 32 and 7 dB lower, respectively, for the ten-layer PML absorbing layer than for the first-order Mur's boundary condition.
© *2008 Acoustical Society of America.* [DOI: 10.1121/1.3003087]

PACS number(s): 43.35.Ud, 43.58.Ta [RR] Pages: 3471–3480

I. INTRODUCTION

Emerging photoacoustic (PA) techniques in biomedical fields utilize parameters involved in the conversion of optical energy into acoustic energy, such as the thermal expansion coefficient, the specific heat capacity at a constant pressure, the acoustic velocity, and especially the absorption coefficient. Because the acoustic waves are generated by optical energy absorption, detection of such signals is less susceptible to optical scattering because acoustic scattering in biological tissues is much weaker than optical scattering. In addition, the PA image is free of the speckle noise that fundamentally limits contrast resolution of ultrasonic imaging.[1] Thermal expansion dominates the generation of PA signals in biomedical imaging applications.

The several mechanisms that can be utilized exhibit varying efficiencies, including absorption processes such as ablation and dielectric breakdown, or nonabsorption processes such as electrostriction and the impact of the optical radiative pressure. In the thermal expansion process, the temperature changes are due to local heating controlled by energy absorption and deposition in the medium. The stress field that subsequently propagates through the sample results from the inhomogeneous temperature distribution. The intensity and waveform of the generated pressure wave depend on the temporal profile of the laser irradiation and the energy distribution in the medium. In liquids, the conversion efficiency from optical to acoustic energy is typically below 0.01%.[2] The ablation or vaporization mechanism also gives rise to a PA wave if the irradiation energy density reaches the threshold at which the sample medium changes phase. This process is usually accompanied by plasma formation. The conversion efficiency may reach 1% for liquids. The most efficient energy conversion of the PA wave is via dielectric breakdown, reaching up to 30% in liquids.[2] At laser intensities above 10^{10} W/cm^2, the excited PA signals consist of a shock wave front and plasma. A property of dielectrics is that the electrostriction mechanism varies the volume of the sample through realigning the electrical domains within the material during electromagnetic irradiation. Fast modulation of electromagnetic waves changes the density gradient so as to induce an acoustic wave. In a weakly absorbing medium (absorption coefficient smaller than $10^{-5}/cm$), the electrostriction process predominates the generation of the PA wave.[3] The excitation of an acoustic wave by the laser irradiance pressure is negligible compared with the above-mentioned sound-generating processes. Other generation mechanisms occur under specific circumstances, such as the photochemical effect and cavitation. The photochemical process involves molecules combining and dissociating via photosynthesis and photochemical chain reactions. During cavitation, shock waves are produced when bubbles generated at high laser intensities collapse.[4]

For nondestructiveness and noninvasiveness, most biomedical applications utilize PA waves generated by the thermal expansion process. For biological tissues constituting up to 70% water, the characteristics of a PA wave are considered to be similar to those in an aqueous medium. Theories of PA waves generated by thermal expansion in aqueous media have been explored previously.[2,4,5] Sigrist[2] and some other pioneers considered several cases of optical excitation in a homogeneous medium, characterized by different temporal and spatial energy distributions in the samples. Described by three types of geometries, namely, planar, spherical, and cylindrical, the initially generated acoustic field is classified according to the optical absorption coefficient and laser irradiation radius. If the absorption coefficient of the sample is sufficiently large so that the optical penetration depth is significantly smaller than the diameter of the pulsed light beam, the shape of the PA source resembles a plane, and thenceforth a plane acoustic wave propagates outward.[6,7] When the optical penetration depth in an absorbing liquid is similar to the beam radius of a laser pulse, the PA source resembles a hemisphere and emits a spherical sound wave.[4,8–10] For low optical absorption in a liquid, the optical source penetrates deep into the medium and gives rise to a cylindrical sound wave that propagates radially.[6,7] When the particle velocity approaches zero at the interface, the boundary is regarded as rigid and the initial PA source continues to the other side of the surface as an even function from an analytic point of view. On the other hand, the condition of zero pressure along the incident boundary is referred as a free interface, which the acoustic source travels across as an odd analytic function. Furthermore, the dependence of the maximum PA wave amplitude on the duration of the laser pulses is considered for the cases of long and short pulses, which are discriminated by the time taken for the generated acoustic wave to travel the depth of optical penetration. The case of short pulse generation is also regarded as stress confinement. By neglecting the influence of heat conduction and attenuation of sound, the propagating pressure wave, p, is described by

$$\nabla^2 p - \frac{1}{c_0^2}\frac{\partial^2 p}{\partial t^2} = -\frac{\beta}{C_P}\frac{\partial H}{\partial t}, \tag{1}$$

where β represents the thermal expansion coefficient, C_P is the specific heat at constant pressure, and $H(x,y,z,t)$ is the density of the electromagnetic energy absorbed and converted into heat per unit time, which is commonly described by the Beer–Lambert law. The maximum generated amplitudes for all cases mentioned above were listed by Zhao *et al.*[11] Equation (1) is commonly quoted in applications such as PA imaging and parameter imaging. Nonetheless, it is worth noting that nonlinearities are neglected in such a formulation.

Hoelen and de Mul[4] proposed an alternative perspective on PA signal generation. The PA pulse induced by a spherical acoustic source with a homogeneous energy deposition is considered first. Conservation of energy means that the magnitude of the outgoing wave is inversely proportional to the distance between the center of the sphere and the point of observation, while that of the wave propagating toward the center of the source increases analogously. When the inward-propagating wave front has reached the center, the wavelength of the PA wave remains constant, equal to the diameter of the sphere. The transient waveform thenceforth moves outward as an antisymmetric bipolar waveform. Taking the limit of a vanishing spherical source radius yields the PA signal generated by a point source, regarded as the delta function. The expression for the PA wave generated by the planar and cylindrical energy distributions can be determined by integrating the delta function over the respective geometry.

The heuristic approach to the generation of a PA wave in an inhomogeneous medium proposed by Karabutov *et al.*[5] first determines the temperature variation in the medium. Under stress confinement, the stress developed will be proportional to the temperature rise. If the light penetration depth is larger than the average distance among light-absorbing particles, the sample is considered as microhomogeneous when the light-absorbing particles are sufficiently small and present at a sufficiently high concentration. The particles need to be small to ensure uniform heating by the laser pulse; that is, the radius of the particle, r_p, must be lower than the diffusion length therein, $r_p \ll \sqrt{\chi_p \tau_L}$, where χ_p is the thermal diffusivity of the particle and τ_L is the duration of the laser pulses. The particle concentration, n_p, is high if $n_p \gg (4\chi\tau_L)^{-3/2}$, where χ is the thermal diffusivity of the surrounding medium; otherwise, the sample is microinhomogeneous. The stress profiles are similar in microhomogeneous and homogeneous media, consisting of sections of an exponential curve whose exponents depend on the light absorption coefficient for excitation by a short pulse. A PA signal in a microinhomogeneous structure is generally represented as a superposition of that in a microhomogeneous medium with a certain average light absorption coefficient and acoustic pulses from individual light-absorbing particles. The waves generated by individual particles are derived by first establishing the thermal field and then finding the pressure profile.

The above-mentioned theories of the generation and propagation of a PA wave are derived from intuitive concepts of the processes related to this effect. A rigorous analysis of the phenomenon, which involves solving a nonstationary thermoelasticity problem, was performed by Gusev and Karabutov.[3] Deriving the answer from the governing equations for the general case is tedious, especially for a complicated energy distribution geometry. To this end, we employed a numerical finite-difference time-domain (FDTD) method to directly solve the governing equations of the PA wave. The similar work by Huang *et al.*[12] used the first-order Mur's boundary condition, with the numerical results being compared only with the proposed backward-mode signal.[13] However, in practice the first-order Mur's boundary condition is poor in eliminating reflected waves from truncated edges. We overcame this shortcoming by using perfectly matched layers (PMLs) to minimize the interference. Also in this study, the numerical results were validated according to the analytical solution derived by solving the linear-perturbation equations with the Laplace transform for several detection angles and different laser-source parameters.[3]

The use of numerical methods falls between rigorous theoretical mathematical derivations, which are usually lim-

ited to simple geometries of energy deposition due to the assumptions necessary to make the task feasible, and experiments, in which the PA signals are generally small and suffer from unavoidable noise interference, such that considerable effort using advanced devices is required to ensure the accuracy of results when the data cannot be estimated theoretically. The continuing rapid increases in computer processing power and memory means that numerical methods can now be applied to energy deposition and source conditions with arbitrary geometries, such as the design of the temporal profile of the laser irradiation, linear scanning of the laser source, and tomography, providing results that are more consistent with the governing equations.

Section II presents that formulation of the 2.5*D* FDTD scheme. Section III shows the numerical validation and a demonstration on how the simulation can be applied for reconstruction of initial optical energy distribution. Section IV evaluates the performance at the boundary.

II. FORMULATION

The following heat conduction, continuity, Navier–Stokes, and state equations proposed by Gusev and Karabutov[3] describe a thermally generated PA wave:

$$\rho_0 T_0 \frac{\partial s'}{\partial t} = \Delta \cdot \kappa \nabla T' - \nabla \cdot \langle \vec{S} \rangle, \tag{2a}$$

$$T' = \frac{T_0 \beta}{C_P \rho_0} p' + \frac{T_0}{C_V} s', \tag{2b}$$

$$p' = c_0^2 \rho' + \frac{c_0^2}{\rho_0} \frac{B}{2A} \rho'^2 + \rho_0 c_0^2 \frac{\beta T_0}{C_P} s', \tag{2c}$$

$$\frac{\partial \rho'}{\partial t} + \nabla \cdot (\vec{u}(\rho_0 + \rho')) = 0, \tag{2d}$$

$$(\rho_0 + \rho') \frac{\partial \vec{u}}{\partial t} + \nabla p' = -(\rho_0 + \rho')(\vec{u} \cdot \nabla)\vec{u} + \eta \nabla^2 \vec{u} + \left(\xi + \frac{\eta}{3}\right) \nabla (\nabla \cdot \vec{u}). \tag{2e}$$

The heat conduction theory in Eq. (2a) describes the temporal diffusion of energy in the sample, stating that the net energy flowing in equals the applied energy, which is the Umov–Poynting vector $\langle \vec{S} \rangle$ of the incident laser source averaged over the electromagnetic oscillation. The divergence of the radiation intensity in the medium (i.e., the energy distribution) is commonly described by the Beer–Lambert law when the sample is assumed to be homogeneous. The states, namely, the pressure deviation per unit mass (p') and the temperature deviation (T'), are associated with other states (density deviation ρ' and entropy deviation per unit mass s') by Maxwell relations [i.e., Eqs. (2b) and (2c)]. Constants ρ_0, c_0, and T_0 correspond to the ambient density, velocity, and temperature, respectively, while κ, β, C_P, C_V, and B/A are the coefficients of thermal conductivity, thermal expansion, specific heat at constant pressure, specific heat at constant volume, and nonlinear acoustic parameter of the medium, respectively. Equations (2a)–(2c) describe the generation of an optical signal. According to the conservation of mass and momentum [Eqs. (2d) and (2e), respectively], the generated PA wave will propagate outward and be subject to diffraction, nonlinear distortion, and dissipation. Here $\vec{u}$ is the vibration velocity of the particles in the medium, while ξ and η are the bulk and shear viscosities of the medium, respectively.

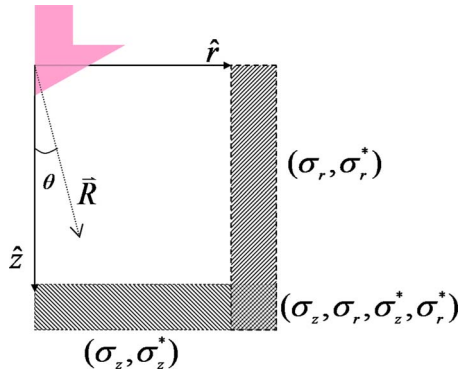


FIG. 1. (Color online) Simulation configuration. The direction of light irradiation was along the symmetric axis $\check{z}$, and the interface at $z=0$ was rigid. The simulation domain was enclosed by the PMLs (region denoted by dashed lines) for free-space boundaries.

A staggered mesh is adopted in the FDTD discretization. The spatial grid size is commonly chosen to be smaller than one-tenth of the minimum wavelength of the PA wave (i.e., $\frac{1}{10}\min\{\alpha^{-1}, c_0\tau_L\}$). The temporal grid size is then determined by Courant's criterion for ensuring stability. The midpoint method is adopted in time-domain integration. A 2.5*D* axisymmetric cylindrical-coordinate system (with the z-axis parallel to the direction of irradiation) is employed so as to reduce the memory required for computation. The simulation configuration is depicted in Fig. 1. The boundary condition at the surface of the incident irradiation ($z=0$) is set to be rigid, which indicates that $\vec{u}=0$.

For the free-space simulation, Berenger's PMLs were designed to eliminate artificial reflections of incoming waves induced at the truncated edges.[14] A PML medium is a perfect simulation of free space in that a plane wave does not change its direction of propagation or its speed when it propagates from free space into a PML medium. The idea behind a PML boundary condition is to define a nonphysical set of equations in the PML region that exhibit large attenuation while simultaneously producing no reflections for a wave propagating into the PML region from an adjoining lossless acoustic region. Berenger's method requires splitting the nonvector variables such as ρ' manually into two additive components: $\rho' = \rho'_r + \rho'_z$. Mathematical manipulation of Eqs. (2a)–(2e) yields the following set of PA equations comprising the PMLs:

$$\rho_0 T_0 \frac{\partial s'}{\partial t} = \nabla \cdot \kappa \nabla T' - \nabla \cdot \langle \vec{S} \rangle, \tag{3a}$$

$$\frac{1}{\rho_0} \frac{\partial \rho'_r}{\partial t} + \sigma_r \rho'_r = -\frac{1}{r} \frac{\partial}{\partial r} r u_r + N_{r1}, \tag{3b}$$

$$\frac{1}{\rho_0}\frac{\partial \rho_z'}{\partial t} + \sigma_z \rho_z' = -\frac{\partial u_z}{\partial z} + N_{z1}, \tag{3c}$$

$$\frac{(\rho_0+\rho')}{c_0^2}\frac{\partial u_r}{\partial t} + \sigma_r^* u_r = -\frac{\partial \rho'}{\partial r} - \rho_0 \frac{\beta T_0}{C_P}\frac{\partial s'}{\partial r} + N_{r2} + D_{r1}, \tag{3d}$$

$$\frac{(\rho_0+\rho')}{c_0^2}\frac{\partial u_z}{\partial t} + \sigma_z^* u_z = -\frac{\partial \rho'}{\partial z} - \rho_0 \frac{\beta T_0}{C_P}\frac{\partial s'}{\partial z} + N_{z2} + D_{z1}, \tag{3e}$$

$$p' = c_0^2 \rho' + \frac{c_0^2}{\rho_0}\frac{B}{2A}\rho'^2 + \rho_0 c_0^2 \frac{\beta T_0}{C_P} s', \tag{3f}$$

$$T' = \frac{T_0 \beta}{C_P \rho_0} p' + \frac{T_0}{C_V} s', \tag{3g}$$

where

$$N_{r1} = -\frac{1}{r}\frac{\partial}{\partial r}(r u_r \rho'/\rho), \tag{3h}$$

$$N_{z1} = -\frac{\partial}{\partial z}(r u_z \rho'/\rho), \tag{3i}$$

$$N_{r2} = -\frac{\partial}{\partial r}\left(\frac{1}{\rho_0}\frac{B}{2A}\rho'^2\right) - \frac{(\rho_0+\rho')}{c_0^2}\left\{u_r\frac{\partial u_r}{\partial r} + u_z\frac{\partial u_r}{\partial z}\right\}, \tag{3j}$$

$$D_{r1} = \frac{4\eta/3+\xi}{c_0^2}\left\{-\frac{1}{r^2}\frac{\partial}{\partial r} r u_r + \frac{1}{r}\frac{\partial^2}{\partial r^2} r u_r + \frac{\partial}{\partial r}\frac{\partial u_z}{\partial z}\right\} - \frac{\eta}{c_0^2}\left\{\frac{\partial}{\partial z}\frac{\partial u_z}{\partial r} - \frac{\partial}{\partial z}\frac{\partial u_r}{\partial z}\right\}, \tag{3k}$$

$$N_{z2} = -\frac{\partial}{\partial z}\left(\rho' + \frac{1}{\rho_0}\frac{B}{2A}\rho'^2 + \rho_0\frac{\beta T_0}{C_P}s'\right) - \frac{(\rho_0+\rho')}{c_0^2}\left\{u_r\frac{\partial u_z}{\partial r} + u_z\frac{\partial u_z}{\partial z}\right\}, \tag{3l}$$

$$D_{z1} = \frac{4\eta/3+\xi}{c_0^2}\left\{\frac{1}{r}\frac{\partial}{\partial z}\frac{\partial}{\partial r} r u_r + \frac{\partial^2 u_z}{\partial z^2}\right\} + \frac{\eta}{c_0^2}\left\{\frac{1}{r}\frac{\partial u_z}{\partial r} - \frac{1}{r}\frac{\partial u_r}{\partial z} + \frac{\partial^2 u_r}{\partial r^2} - \frac{\partial}{\partial r}\frac{\partial u_r}{\partial z}\right\}. \tag{3m}$$

Parameters σ_r and σ_z are the artificial attenuation coefficients in the PMLs for ρ_r' and ρ_z', respectively, while σ_r^* and σ_z^* are those for u_r and u_z. Perfect matching at the interface between the simulation medium and PMLs is achieved by ensuring that

$$\sigma_r^* = (\rho_0^2/c_0^2)\sigma_r, \tag{4a}$$

$$\sigma_z^* = (\rho_0^2/c_0^2)\sigma_z. \tag{4b}$$

However, numerical reflections arise due to finite spatial sampling when implementing the PML as a single step discontinuity of $\sigma_{r,z}$ and $\sigma_{r,z}^*$ in the FDTD lattice. To overcome this problem, Berenger proposed that the PML losses along the direction normal to the interface should gradually increase from zero.[14] The polynomial grading adopted is simply

$$\sigma_r(r) = (r/(L\Delta_r))^m \sigma_{r,\max}, \tag{5a}$$

$$\sigma_z(z) = (z/(L\Delta_z))^m \sigma_{z,\max}, \tag{5b}$$

where m is the polynomial order, L is the number of the PMLs, and Δ_r and Δ_z are the spatial grid sizes in the r and z directions, respectively. The PML parameters can be readily determined for a given reflection factor of the boundary $R(\phi)$ (where ϕ is the incident angle of the wave at the truncated boundary):

$$\sigma_{r,\max}, \sigma_{z,\max} = -\frac{(m+1)\ln R(0)}{2(\rho_0/c_0)\Delta_{r,z} L}. \tag{6}$$

In aqueous media such as water, where the relaxation of the thermal field is generally slower than that of the PA wave transiting the heated region, Eq. (2a) does not cause significant reflection along the truncated edges, especially at boundaries far from where the wave is generated. Therefore it is set to be zero.[15]

III. RESULTS

Two test cases were analyzed to justify the numerical results from the FDTD code. The accuracy of the simulation was evaluated in the first case, while the flexibility of the simulation approach was demonstrated via a homogeneously irradiated sphere in the second case. We further demonstrated the use of simulation by generating PA signals in a cluster of cylinders for imaging applications. In this study, the synthetic aperture focusing technique (SAFT) and coherence weighting[16] are employed to improve the degraded lateral resolution of the backward-mode images of objects with arbitrary geometry.

The first case considered the analytical solution of Eqs. (2a)–(2e) while only retaining linear-perturbation terms (and hence neglecting acoustic dissipation). The problem could then be easily solved by the spectral method by introducing the scalar potential of the velocity field. According to Gusev and Karabutov,[3] the analytical solution in spectral form is

$$\tilde{\vec{u}}(\omega,\vec{R}) = \frac{1}{2\pi|\vec{R}|} i(\omega/c_0)\exp[i(\omega/c_0) \times|\vec{R}|]\cdot I_0 \tilde{f}(\omega)\cdot \tilde{H}((\omega/c_0)\hat{r})\cdot K_{\|}((\omega/c_0)\cos\theta), \tag{7a}$$

where $\tilde{\vec{u}}(\omega,\vec{R})$ is the transfer function for the vibrational velocity $\vec{u}(t,\vec{R})$, $\tilde{f}(\omega)$ is that of the temporal profile of the laser irradiation $(f(t))$, and I_0 is the laser intensity. The distance vector from the origin to detection location $\vec{R}=\vec{r}+\vec{z}$ is indi-

cated in Fig. 1, where θ is the angle between the symmetric axis and $\vec{R}$. Transfer functions $\tilde{H}((\omega/c_0)\hat{r})$ and $K_{\|}((\omega/c_0)\cos\theta)$ in Eq. (7a) apply to a light distribution in beam cross-sectional direction $H(r')$ and depthwise direction $\bar{g}(z')$, respectively:

$$\tilde{H}((\omega/c_0)\hat{n}_r) = \int_{-\infty}^{\infty} H(r')\exp[-i(\omega/c_0)\hat{n}_r\vec{r'}]d\vec{r'}, \tag{7b}$$

$$K_{\|}((\omega/c_0)\cos\theta) = \frac{\beta}{2\rho_0 C_P}\int_{-\infty}^{\infty} \bar{g}(z') \times \exp[-i(\omega/c_0)z'\cos\theta]d\vec{z'}. \tag{7c}$$

The boundary condition for the interface at $z=0$ is already included by considering the source as a continuous function to the domain $z<0$, either evenly for a rigid boundary or oddly for a free boundary.

However, Eq. (7a) does not have a closed form for the inverse transform, and hence further simplification is required to obtain a time-domain analytical solution. Two assumptions by Gusev and Karabutov[3] were made to obtain a closed-form equation. For both assumptions, a homogeneous medium with a rigid interface at $z=0$ was considered, where light decayed exponentially with increasing depth with an attenuation coefficient α. The light distribution in the beam cross section was considered to be Gaussian with a length of R_D. By locating the detector place far from the source with $\theta=0°$, Eq. (7b) can be reduced to a constant and the inverse transform of Eq. (7a) becomes

$$\begin{aligned} u(\tau,|\vec{R}|) = \frac{\beta W_0}{16\pi\rho_0 C_P}\{&\alpha c_0 \exp(\alpha c_0\tau)[1-\operatorname{erf}(\tau/\tau_L \\ &+ \alpha c_0\tau_L/2)] - (1/\tau_L)\exp(\alpha c_0\tau)G(\tau/\tau_L \\ &+ \alpha c_0\tau_L/2) - \alpha c_0\exp(-\alpha c_0\tau)[1-\operatorname{erf}(\tau/\tau_L \\ &- \alpha c_0\tau_L/2)] + (1/\tau_L)\exp(-\alpha c_0\tau)G(\tau/\tau_L \\ &- \alpha c_0\tau_L/2)\}, \end{aligned} \tag{8}$$

where $\tau=t-|\vec{R}|/c_0$ is the retarded time, $W_0=\alpha\pi R_D^2 I_0\int_{-\infty}^{\infty} f(t)dt$ is the total absorbed energy, and $G(t)$ is the Gaussian function. Note that the profile of $|u|=\sqrt{|u_r|^2+|u_z|^2}$ is similar to that of the pressure.

Equation (7a) was further simplified by only considering a short pulse, such that $1/\tau_L > 2c_0/(R_D\sin\theta) > \alpha c_0/\cos\theta$. This criterion is easily satisfied when using a laser that generates nanosecond pulses. Hence, spectrum $\tilde{H}((\omega/c_0)\hat{r})$ can be viewed as an effective Gaussian light pulse of duration

$$\tau_L^* = R_D\sin\theta/c_0. \tag{9}$$

Substituting Eq. (9) into Eq. (8) and assuming a large detection distance yields the temporal analytical solution for this assumption.

In order to be consistent to the assumptions made in the analytical solutions, the nonlinear and dissipation parts of the governing equations [i.e., Eqs. (3h)–(3m)] and ρ' in the first terms of Eqs. (3c) and (3d) were omitted from the FDTD code. The parameters of the test case for the PA wave simulation in a homogeneous medium were as follows: $c_0=1500$ m/s, $\rho_0=1000$ kg/m^3, $T_0=27+273$ K, $\alpha=1$/cm, $R_D=0.1$ mm, $\Delta_r=\Delta_z=\Delta=\frac{1}{15}\min\{\alpha^{-1}, c_0\tau_L\}=1$ μm, and $\Delta_t=6.67\times10^{-11}$ s. Other constants used in Eqs. (3a)–(3m), such as κ, β, C_P, C_V, and B/A, were chosen as the corresponding values for water at T_0. The FDTD grid used in the simulation comprised 800×800 sample points, corresponding to a real size of 0.8×0.8 mm^2. For a reflection of -100 dB from the PML boundaries, the PML parameters in Eqs. (5a) and (5b) were set as follows: $m=5$, $L=10$, and $\sigma_{r,\max},\sigma_{z,\max}=5\times10^6$ m^3/kg s.

For the source for the governing equations (i.e., $-\nabla\cdot\langle\vec{S}\rangle$), the Umov–Poynting vector $\langle\vec{S}\rangle$ had an exponential decay in the z direction and a Gaussian temporal profile. The light distribution then became $\alpha I_0\exp(\alpha z)\cdot G(t/\tau_L)$, where $G(t)$ is the Gaussian function and $I_0=10/(\sqrt{\pi}\tau_L)$ mJ/cm^2. For a laser beam with a Gaussian profile in the lateral direction, the source could be formulated as

$$-\nabla\cdot\langle\vec{S}\rangle = \alpha I_0\exp(\alpha z)\cdot G(t/\tau_L)\cdot G(r/R_D). \tag{10}$$

The FDTD results and the analytical solution obtained by Eq. (8) are compared in Fig. 2. In each graph, the solid and dashed lines indicate the numerical and theoretical results, respectively. The error (indicated by each dashed-dotted line) was calculated as the absolute difference between the simulation result and analytical solution. For both graphs, the detection distance was $|\vec{R}|=0.8$ mm, which is greater than the characteristic attenuation depth (α^{-1}). The laser pulse durations for Figs. 2(a) and 2(b) were $\tau_L=10$ ns and $\tau_L=120$ ns, respectively. It is evident that $\tau_L=120$ ns does not fulfill stress confinement as is usually assumed in heuristic approximations. Figures 2(a) and 2(b) indicate that the results from the numerical simulation agreed with Eq. (8) within average errors of 1.3% and 2%, respectively. The maximum error occurred at the rarefaction peak of the PA wave and was 11% and 15% for the short- and long-pulse cases, respectively.

The simulation results for an off-axis PA wave are shown in Figs. 3(a) and 3(b) for $\theta=7.34°$ and $\theta=14.46°$, respectively. The average errors between the simulations and analytical solution using Eqs. (8) and (9) were about 1%, and the maximum error, of around 11%, was located at the most negative part of each wave. One possible reason for this is that the far-distance assumption when deriving the temporal form analytical solution from its spectrum [i.e., Eq. (7a)] oversimplified the diffraction phenomenon. However, the closed-form equation could not be defined without making this assumption. The deviation in the exponentially rising part of the wave is due to the accumulated errors when using finite differences to estimate a fast-rising function. The numerical experiments for the first case demonstrated that FDTD method was capable of solving a system of partial differential equations and that the results were consistent with those derived theoretically.

The second test case did not involve solving the governing equations, but utilized the theoretical PA wave for a ho-

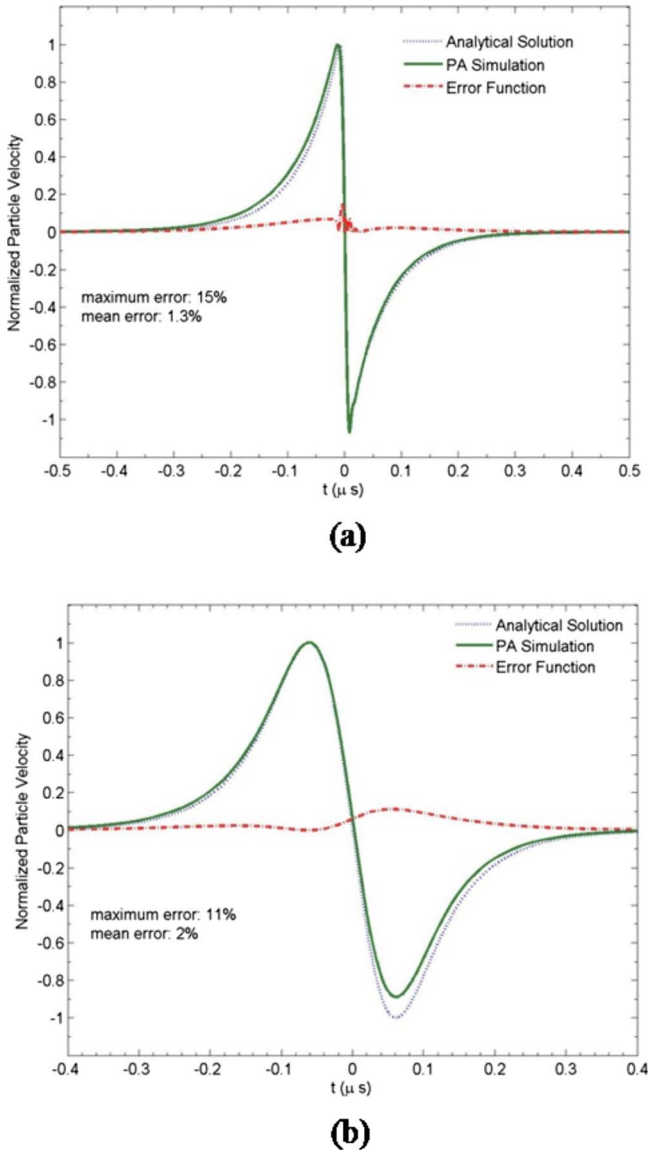


FIG. 2. (Color online) Forward PA wave computed by the FDTD method (solid lines) and using Eq. (8) (dashed lines) for $\tau_L = 10$ ns (a) and $\tau_L = 120$ ns (b). The absolute error is indicated by the dashed-dotted lines.

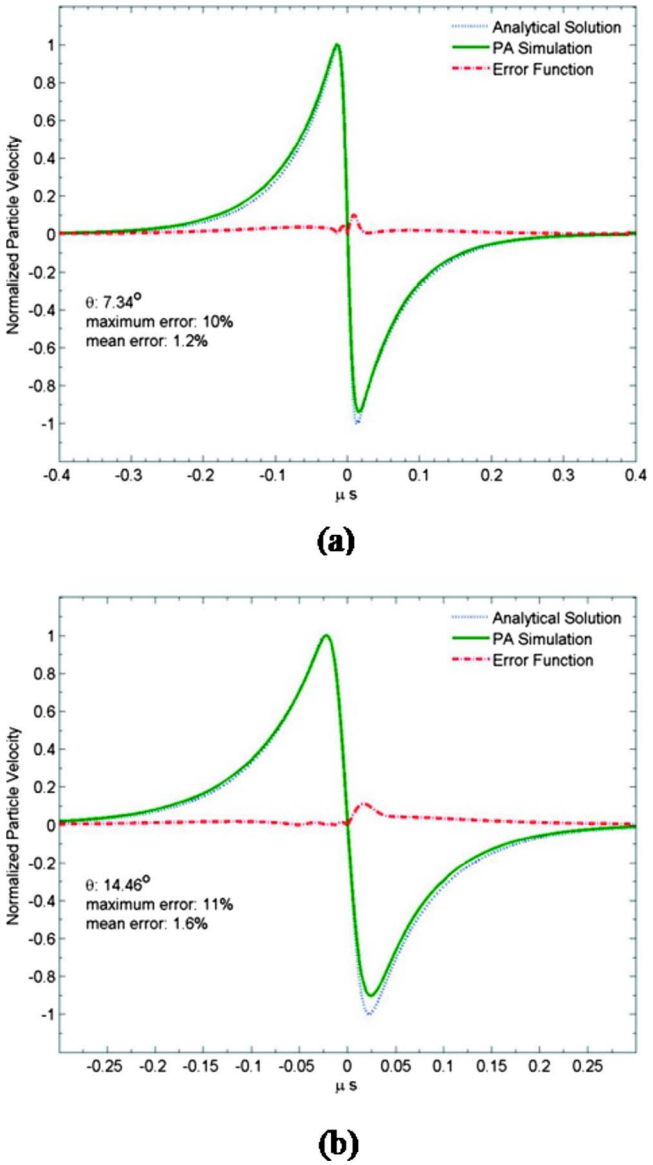


FIG. 3. (Color online) Off-axis PA wave computed by the FDTD method (solid line) and using Eqs. (8) and (9) (dashed line) for $\theta = 7.34°$ (a) and $\theta = 14.46°$ (b). The absolute error is indicated by the dashed-dotted lines.

mogeneously irradiated sphere proposed by Hoelen and de Mul.[4] The expression for the spherical wave outside the absorption sphere is given as

$$P_{\mathrm{HS}}(R,t) = \beta c_0^2 \alpha I_0 / C_P \left\{ U(R_S - c_0 t - R) + \frac{R - c_0 t}{2R} \cdot U(R - |R_S - c_0 t|) \cdot U(R_S + c_0 t - R) \right\} U(t) \times G(t/\tau_L), \quad (11)$$

where R is the detection distance, R_S is the radius of the homogeneous sphere, $U(t)$ is the step function, and $G(t)$ is the Gaussian function for the temporal profile of the laser irradiation. The simulation parameters were similar to that in the first case, except that the absorption coefficient and the laser beam radius were modified to $\alpha = 1/\mathrm{cm}$ and $R_D = 10$ cm, respectively. With the sphere radius set to $R_S = 0.1$ mm, the PA wave detected at 0.6 mm along the z-axis is shown in Fig. 4. This figure includes the line plotted by Eq. (11) and the error between the theoretical and numerical solutions. The average error was 2.37%, and the maximum error was 11.54% at the wave minimum. In addition to accuracy, this demonstrates the flexibility of the FDTD approach for different light distribution geometries.

As a demonstration, the numerical tool was used to generate PA data from two cylindrical objects (one is embedded in the other). This demonstration is used to test a reconstruction algorithm for initial optical energy distribution that we previously developed.[16,17] Simulations can be extensively and efficiently performed when evaluating such algorithms before costly measurements are performed. In this algorithm, the initial optical energy distribution is reconstructed from the PA signals detected in the backward mode. Two critical steps are involved: the integration along the z-direction[16] following a SAFT in combination with coherence factor weighting.[17]

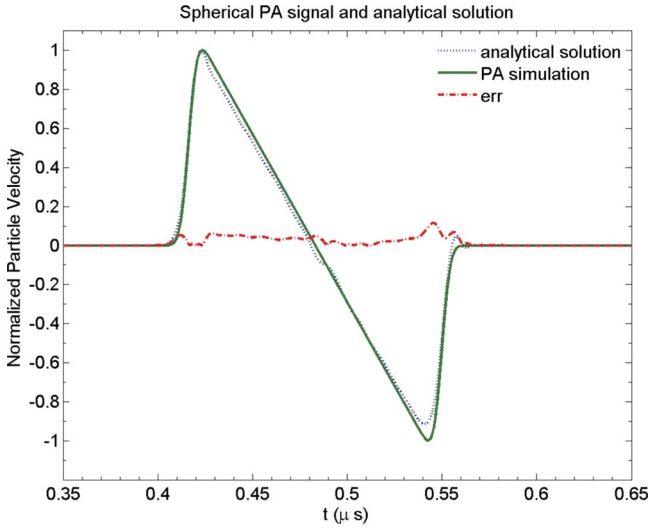


FIG. 4. (Color online) PA wave from a homogeneously irradiated sphere computed by the FDTD method (solid line) and using Eq. (11) (dashed line). The absolute error is indicated by the dashed-dotted line.

Specifically, the optical energy distribution shown in Fig. 5 was used in backward-mode imaging (i.e., laser irradiation and acoustic detection are from the same side of the object). It is calculated based on the Beer–Lambert law. The signals received in the backward direction were used to form a conventional PA image, as shown in Fig. 6(a). Note that the gray region near the top surface was caused by weak absorption of the ambient medium. On the other hand, the long tails were due to lack of focusing. The SAFT (i.e., synthesizing a larger aperture by summing properly delayed signals received at different positions from a smaller aperture) is applied to achieve dynamic focusing along the z-direction (i.e., uniform lateral resolution), as shown in Fig. 6(b). As described in Ref. 17 the sidelobes can be further suppressed by weighting the image shown in Fig. 6(b) by its corresponding coherence factor map. The weighted image is demonstrated

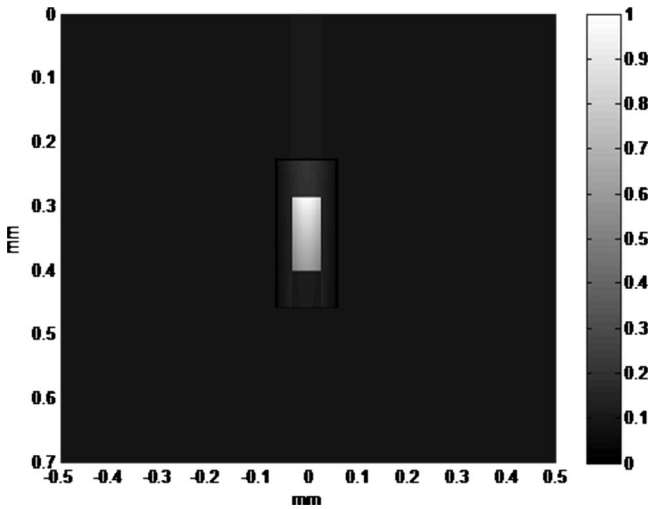


FIG. 5. The initial optical energy distribution.

in Fig. 6(c). In the figure, the upper and lower fringes of the two cylinders are distinguishable. Adopting the reconstruction method in Ref. 16 the initial optical energy distribution can be reconstructed by integration along the depth direction, as shown in Fig. 6(d). Note that although the reconstructed image shown in Fig. 6(d) is not perfect, the purpose of this example is to demonstrate that this numerical tool can be used to generate data such that different imaging algorithms can be tested. Nonetheless, performance of a particular reconstruction method is beyond the scope of this study.

IV. DISCUSSION

Reflection errors from truncated boundaries must be carefully considered so as to avoid the generation of noise that interferes with the PA signal. The normalized boundary reflection error function was defined by[14]

$$\text{error}(r,z) = 10\log_{10}\frac{\int_0^T |p_{\text{true}}(r,z,t) - p(r,z,t)|^2 dt}{\int_0^T |p_{\text{true}}(r_B,z_B,t)|^2 dt}, \quad (12)$$

where T is the total simulation interval. Interval T was chosen to be 130 times the duration of laser irradiation, where waves reflected from edges r and z have not yet arrived at the symmetrical axis and the rigid interface, respectively. The uncontaminated field, p_{true}, was computed by executing the FDTD code on a larger area; that is, 1600×1600 sample points with a ten-layer PML boundary condition. The power was normalized relative to the time-integrated power at (r_B,z_B), which are the coordinates of the maximum wave incident at the z boundary. The error functions for different types of boundary conditions are displayed in Fig. 7. The average, maximum, and minimum errors for the r and z boundaries corresponding to the boundary conditions are listed in Table I. In Fig. 7(a), where there is no absorbing boundary but instead total reflection at the r and z boundaries, the maximum errors were 2.35 and 0.04 dB at the r and z boundaries, respectively. Both z boundaries in Figs. 7(b) and 7(c) have the first-order Mur's condition, and the maximum error was about –24 dB. The r boundary in Fig. 7(c) was improved by about 4 dB by applying the first-order Bayliss–Turkel condition rather than the first-order Mur's condition in Fig. 7(b). The boundary condition for Fig. 7(d) is the ten-layer PML condition. At the r boundary, the reflection error from the PML was similar to that from the first-order Bayliss–Turkel condition, while in the z direction the maximum error in the PML was 25 dB lower than that of the first-order Mur's boundary. Moreover, the performance in the z direction was consistent for different incident angles of the wave, where the maximum reflection in Figs. 7(b) and 7(c) occurred near a grid index of 400 pixels. The average reflection error of the PML was about −60 dB, and although this was 32 dB lower than that of the first-order Mur's boundary, it did not meet the design value of −100 dB. This was due to the discretization error dominating when $\sigma_{z,\max}$ was too large, and the actual reflection error was potentially orders of magnitude higher than that predicted by Eq. (6). The optimal

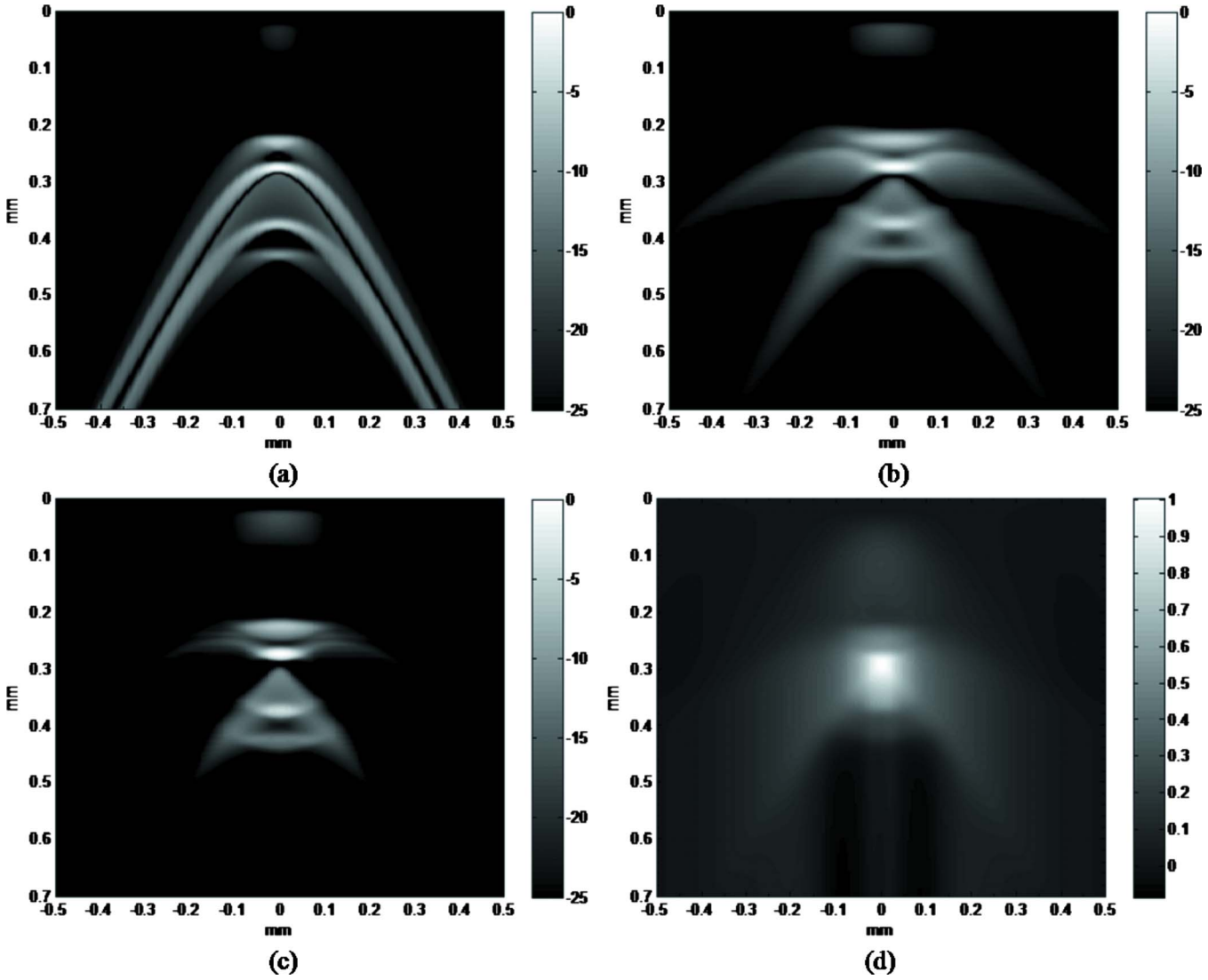


FIG. 6. (Color online) Reconstruction of optical energy distribution. The original PA image is shown in (a), and the resultant image after applying SAFT is shown in (b). The image shown in (c) is after coherence factor weighting, and (d) shows the final reconstruction results after integration along the depth direction is applied.

choice for $\sigma_{z,\max}$ that balances reflection from the outer boundary of the PML and the discretization error is usually determined using numerical experiments. The result in Fig. 7(d) demonstrates that the PML boundary is an excellent absorbing boundary condition in the z direction for wave with diverse incident angles. However, the performance was degraded in the r direction of the cylindrical coordinates. This reflection usually accumulates and causes a false signal that can interfere with the PA signal if it is not avoided.

Solving the PA equations with a FDTD method provides the benefits of including the nonlinear terms and the flexibility of incorporating a generation source of arbitrary geometry. However, the main drawback of using a FDTD method for PA simulation is the high cost of the large amount of computation memory required. Since the minimum wavelength for PA wave including the generation process is $c_0\tau_L$, which is small if the laser pulses are very short, the grid size must be much smaller than the detection distance (of several

TABLE I. Errors for several types of boundaries.

	Boundary error: r (dB)			Boundary error: z (dB)		
Type of boundary ($T=130\sigma$)	Max.	Min.	Average	Max.	Min.	Average
Rigid	2.35	−15.85	−2.39	0.04	−15.85	−4.19
First-order Mur (r and z)	−22.02	−30.43	−24.86	−24.03	−35.71	−27.57
First-order Bayliss–Turkel (r) and first-order Mur (z)	−26.23	−57.51	−32.54	−24.03	−35.71	−27.81
Ten-layer PML	−28.09	−48.91	−31.88	−48.91	−61.88	−60.05

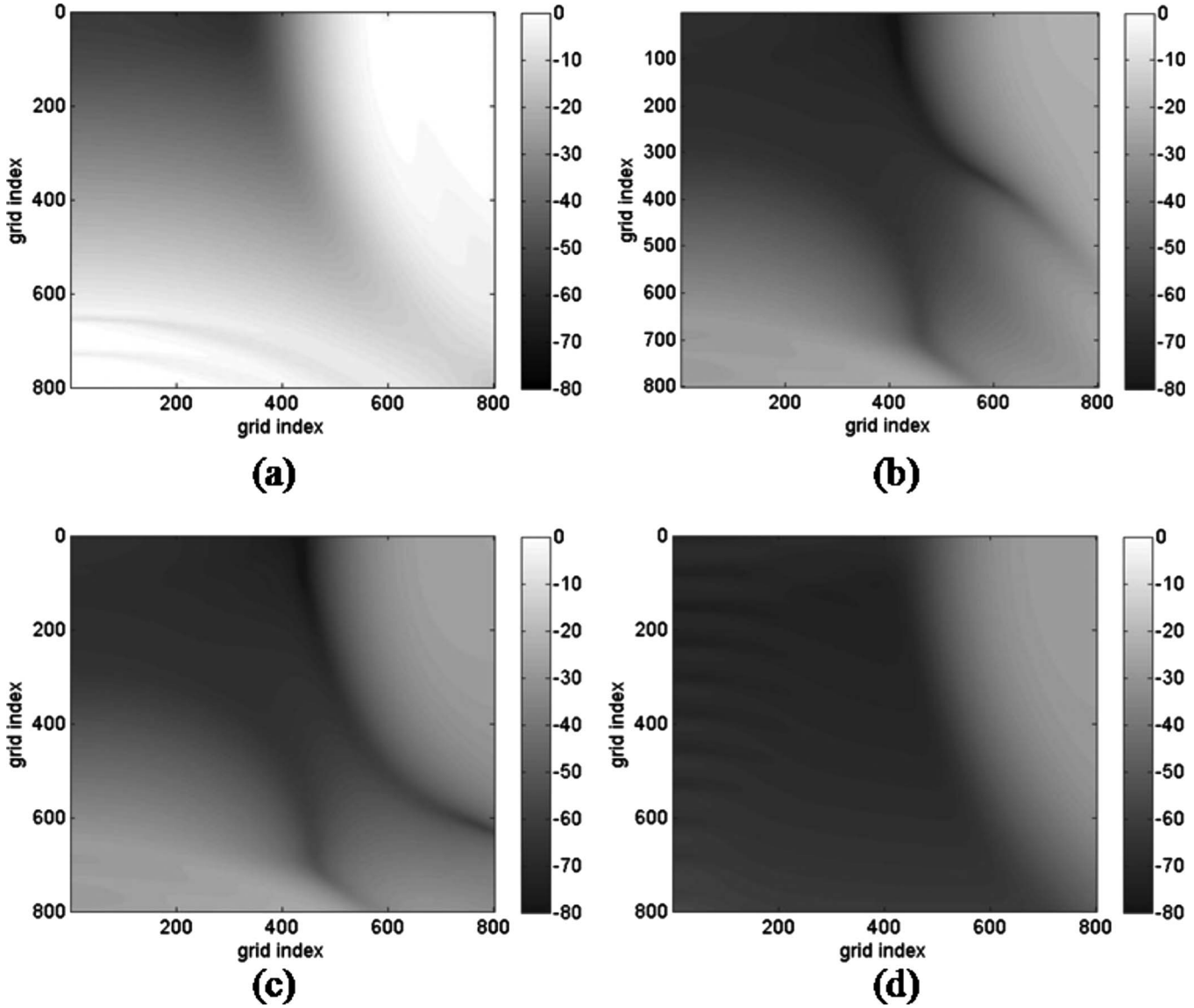


FIG. 7. Error functions for different boundaries: rigid (a), first-order Mur (b), first-order Bayliss–Turkel at the r boundary and first-order Mur at the z boundary (c), and ten-layer PML boundary (d). The reflected r wave has not reached the symmetric axis. The unit for the gray scale is decibel.

centimeters). The average simulation time for a computation region of 800×800 pixels with 13 000 time steps on a personal computer was about 1.8 h, with about 18 Mbytes of memory required.

V. CONCLUSIONS

In this paper, the general thermally induced PA wave equations were solved using a FDTD scheme in a 2.5D axisymmetric cylindrical-coordinate domain. The results from the simulations corresponded well to those from analytical equations derived from the original equations with several assumptions. PA waves with various geometries of energy distribution were successfully simulated by the FDTD method. The spherical PA wave was validated by heuristic theory. As a free-space boundary, the ten-layer PML produced the lowest reflection error for commonly used boundary conditions.

ACKNOWLEDGMENTS

Financial support from National Science Council (Grant No. NSC 96-2221-E-002-030), National Health Research Institutes, NTU Center for Genomic Medicine, and NTU Nano Center for Science and Technology is gratefully acknowledged.

[1]L. Wang, "High-resolution functional photoacoustic tomography," IEEE International Symposium on Biomedical Imaging: Nano to Macro (2004), Vol. **2**, pp. 1479–1481.
[2]M. Sigrist, "Laser generation of acoustic waves in liquids and gases," J. Appl. Phys. **60**, 83–121 (1986).
[3]V. Gusev and A. Karabutov, *Laser Optoacoustics* (American Institute of Physics, New York, 1993), Chap. 2, pp. 45–48.
[4]C. Hoelen and F. de Mul, "A new theoretical approach to photoacoustic signal generation," J. Acoust. Soc. Am. **106**, 695–706 (1999).
[5]A. Karabutov, N. Pldymova, and V. Letokhov, "Time-resolved laser optoacoustic tomography of inhomogeneous media," Appl. Phys. B: Lasers Opt. **63**, 545–563 (1996).
[6]H. Lai and K. Young, "Theory of the pulsed optoacoustic technique," J. Acoust. Soc. Am. **72**, 2000–2007 (1982).
[7]L. Gournay, "Conversion of electromagnetic to acoustic energy by surface

heating," J. Acoust. Soc. Am. **40**, 1322–1330 (1966).
[8]G. Diebold and P. Westervelt, "The photoacoustic effect generated by a spherical droplet in fluid," J. Acoust. Soc. Am. **84**, 2245–2251 (1988).
[9]M. Sigrist and F. Kneubuhl, "Laser-generated stress waves in liquids," J. Acoust. Soc. Am. **64**, 1652–1662 (1978).
[10]G. Diebold, A. Beveridge, and T. Hamilton, "The photoacoustic effect generated by an incompressible sphere," J. Acoust. Soc. Am. **112**, 1780–1786 (2002).
[11]Z. Zhao, S. Nissilä, O. Ahola, and R. Myllylä, "Production and detection theory of pulsed photoacoustic wave with maximum amplitude and minimum distortion in absorbing liquid," IEEE Trans. Instrum. Meas. **47**, 578–583 (1998).
[12]D. Huang, C. Liao, C. Wei, and P. Li, "Simulations of optoacoustic wave propagation in light-absorbing media using a finite-difference time-domain method," J. Acoust. Soc. Am. **117**, 2795–2801 (2005).
[13]A. Karabutov, E. Savateeva, and N. Podymova, "Backward mode detection of laser-induced wide-band ultrasonic transients with optoacoustic transducer," J. Appl. Phys. **87**, 2003–2014 (2000).
[14]X. Yuan, D. Borup, J. Wiskin, M. Berggren, R. Eidens, and S. Johnson, "Formulation and validation of Berenger's PML absorbing boundary for the FDTD simulation of acoustic scattering," IEEE Trans. Ultrason. Ferroelectr. Freq. Control **44**, 816–822 (1997).
[15]J. Berenger, "A perfectly matched layer for the absorption of electromagnetic waves," J. Comput. Phys. **114**, 185–200 (1994).
[16]C.-K. Liao and P.-C. Li, "Reconstruction of optical energy deposition for backward optoacoustic imaging," Opt. Quantum Electron. **39**, 1339–1351 (2005).
[17]C. Liao, "Optoacoustic imaging with synthetic aperture focusing and coherence weighting," Opt. Lett. **29**, 2506–2508 (2004).

High-resolution ultrasonic thermometer for radiation dosimetry

Eugene V. Malyarenko[a] and Joseph S. Heyman
Luna Innovations Incorporated, 130 Research Drive, Suite 300, Hampton, Virginia 23666

H. Heather Chen-Mayer and Ronald E. Tosh
Ionizing Radiation Division, NIST, 100 Bureau Drive, Stop 8460, Gaithersburg, Maryland 20899-8460

(Received 12 June 2007; revised 5 September 2008; accepted 8 September 2008)

This paper describes recent developments in the area of high-precision ultrasonic thermometry with the potential to provide on-site direct determination of radiation doses administered for cancer treatment. Conventional calorimeters used for this purpose measure radiation-induced heating in a water phantom at one point in space by means of immersed thermistors and are subject to various thermal disturbances due to Ohmic heating and interactions of the radiation with the sensor probes. By contrast, the method described here is based on a high-resolution ultrasonic system that determines the change of the speed of sound due to small temperature changes in an acoustic propagation path in the radiation-heated water, thereby avoiding such undesired thermal effects. The thermometer is able to measure tens of microkelvin changes in the water temperature averaged over the acoustic path of about 60 cm at room temperature, with root-mean-squared noise of about 5 μK. Both incandescent and ionizing radiation heating data are presented for analog and digital implementations of a laboratory prototype. This application of the ultrasonic technique opens up possibilities for a new approach to performing therapy-level radiation dosimetry for medical clinics and standards laboratories. © *2008 Acoustical Society of America.* [DOI: 10.1121/1.2997431]

PACS number(s): 43.35.Yb, 43.35.Bf, 43.30.Es, 43.20.Hq [TDM] Pages: 3481–3490

I. INTRODUCTION

A. Background

Radiation treatment plans, by which clinicians determine a course of optimized radiation dose for patients, are designed from knowledge of the beam absorption and scattering and precise time-controlled position and orientation of the moving radiation source. A radiation dose standard is an essential calibration element for assuring correspondence of the expected absorbed dose to its actual value in the tissue. The dose standard is based on the energy imparted to a water phantom from a radiation source. Ionizing radiation dose in radiotherapeutic applications typically is determined by measuring either the ionization charge in an air cavity or the temperature increase in a calorimeter. In the latter, the kinetic energy of the charged particles is converted to thermal energy that results in an increase in the temperature of the water. A precise measurement of the change in temperature within the calorimeter is required to estimate the absorbed radiation dose. Conventional water calorimeters for radiotherapy applications, based on the original design of Domen,[1] detect very small (tens of microkelvin) temperature changes in irradiated water with thermistors that are sealed inside thin sheaths of glass. Recovering absorbed dose to water from these measurements requires the application of several correction factors to compensate for self-heating of the thermistors, excess heat induced in nonwater materials by the radiation, effects of heat transfer due to dose gradients within the phantom, and heat conduction in the wires. This work presents recent developments in an alternative temperature measurement technique based on an ultrasonic method[2,3] that can compete in sensitivity with the existing thermistor-based technology. This noninvasive approach reduces the complexity of the heat exchange problem by eliminating nonwater materials inside the water phantom.

B. Overview of acoustic thermometry

Acoustic thermometers operate by measuring the effect of changing temperature on the propagation of sound waves through the medium. In gases, the speed of sound is related to the gas temperature by a fundamental thermodynamic equation. Various acoustic techniques have been used to measure remotely the temperature of hot dust-laden gases where traditional sample-drawing approaches prove slow and inaccurate. One method[4] uses inversion of several acoustic arrival time measurements across a gas chamber. Another method[5] simultaneously measures the frequencies of microwave and acoustic resonances in a spherical cavity to deduce the speed of sound and has reportedly been used to evaluate the temperature of the triple point of gallium to the precision of 0.5 mK. Interaction between acoustic and radio waves can also be utilized to measure gas temperature.[6] Solids support both compressional and shear waves, as well as numerous types of guided modes, depending on the elastic properties and geometry of the sample. Each of these waves is sensitive to temperature variations and could be employed in a solid-state acoustic thermometer. In water, the speed of sound under constant atmospheric pressure and concentration of impurities depends only on the temperature and can be approximated by the empirical formula[7,8]

$$V(T) = c + bT + aT^2, \quad (1)$$

[a]Present address: Tessonics Corp., 2019 Hazel St., Birmingham, MI 48009. Electronic mail: evmaly@yahoo.com

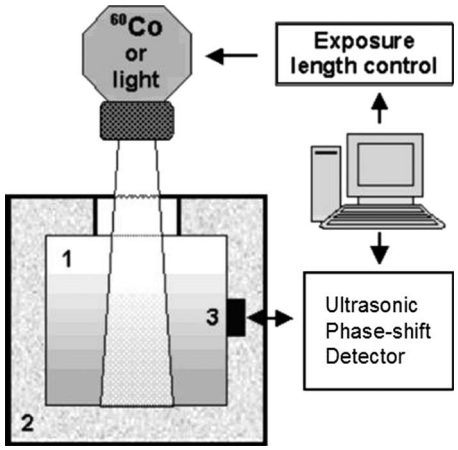


FIG. 1. Experimental setup of the high-resolution single-channel ultrasonic thermometer to measure thermal effect of ionizing or light radiation in water: (1) water phantom, (2) Styrofoam enclosure for thermal insulation, and (3) ultrasonic transducer.

where $V(T)$ is the speed of sound (m/s) at temperature T (°C), $c=1405.03$ m/s is the speed of sound at 0 °C, $b=4.624$ (m/s °C), and $a=-0.038$ (m/s °C^2). Exposure to radiation changes the temperature distribution in the water and, hence, affects the speed of sound. From a single ultrasonic time-of-flight or phase measurement one can derive only information about the average sound speed value $\bar{V}$ along the acoustic path,[9] and solving Eq. (1) therefore yields information about spatial averages of the temperature distribution along this path. For very small temperature gradients in otherwise undisturbed water, the acoustic path can be accurately approximated as a straight line between the tank walls. Multiple ultrasonic techniques,[10] including Doppler velocimetry, particle-image velocimetry, and others, are available to measure signal phase or time of flight with various degrees of precision. One common limitation to all of these techniques is their resolution, which is insufficient for the present application. In this work, we describe two ultrasonic technologies—one, based on an ultrasonic pulsed phase-locked loop[11–14] (PPLL) and another that employs dual-reference heterodyning phase detection[18,19]—that can resolve microkelvin temperature changes in water.

II. PRINCIPLE OF OPERATION AND EXPERIMENTAL SETUP

A. Temperature dependence of signal phase

For the water calorimetry experiments described in this paper, high-precision ultrasonic phase detectors were used for monitoring subtle changes of the signal phase in water caused by radiation heating. The signal in this case is an ultrasonic tone burst that traverses a volume of water being heated by ionizing radiation (Fig. 1). Its echo from the far wall of the water phantom is detected and compared to a reference signal that is derived from the same oscillatory waveform used to generate the tone burst. The time of flight, τ, of a (conveniently chosen) point on the tone-burst pulse is thus associated with a distinct phase, φ, as follows:

$$\varphi = 2\pi f \tau = 2\pi f \frac{2L}{\bar{V}}, \tag{2}$$

where f is the centroid frequency (of both tone burst and reference signal), $2L$ is the acoustic path length in the water, and $\bar{V}$ is the average speed of sound along the acoustic path. In general for such measurements, the radiation exposure occurs over a period of 1 or 2 min, and the temperature increase is obtained as a function of time by measuring phase changes for a succession of tone-burst pulses. Since the latter require less than 1 ms to traverse the phantom, such measurements provide essentially instantaneous information about the time dependence of phase shifts due to temperature changes.

As shown in Fig. 1, the radiation beam intersects both top and bottom surfaces of the phantom and passes through part of the enclosed volume of water. Radiation-induced heating produces changes in L via thermal expansion of the phantom walls, and $\bar{V}$, in accordance with Eq. (1). The relative change in phase φ due to these effects may then be expressed as follows:

$$\frac{\Delta\varphi}{\varphi} = \frac{\Delta L}{L} - \frac{\Delta\bar{V}}{\bar{V}}. \tag{3}$$

For the extremely small temperature changes considered here (<0.25 mK per 1 min exposure, typically), a linear dependence on temperature change ΔT may be expected for both terms on the right of Eq. (3). An estimate of the relative contribution of each term is readily obtained from Ref. 15 and Eq. (1), respectively, which show that, at $T=20$ °C, the L term is proportional to ΔT with a coefficient of 7.6×10^{-5} °C^{-1} and that the corresponding coefficient for the $\bar{V}$ term is 2.09×10^{-3} °C^{-1}. Given the nonuniformity of exposure and the different material properties of the phantom walls and the water, we allow for the possibility of different temperature increases in the two components; thus, in the vicinity of $T=20$ °C,

$$\frac{\Delta L/L}{\Delta\bar{V}/\bar{V}} \approx 0.036\frac{\Delta T_{\text{wall}}}{\Delta T_{\text{water}}}. \tag{4}$$

If the radiation-induced temperature increase for both components were the same, Eq. (4) indicates that changes in acoustic path length would contribute no more than a few percent to the total phase change specified by Eq. (3). Closer inspection of the relative doses and material properties of the phantom walls and water in the large phantom suggests that $\Delta T_{\text{wall}}/\Delta T_{\text{water}}\leq 0.95$ so that the effect of path length is slightly smaller, about 3% of the fractional phase change (about 7% for the small phantom). Thus, neglecting the L term in Eq. (3) introduces a systematic error that leads to underestimates in temperature changes deduced from changes in the tone-burst phase or time of flight alone. Its probable effects are taken into account in the discussion of results, but are neglected in the discussion of measurements done with incandescent sources because the relatively stronger attenuation of infrared radiation by water would suggest

that such corrections would be one or two orders of magnitude smaller.

The central issue of this paper is to determine temperature-induced changes of the average speed of sound by tracking the associated phase changes of a tone burst using ultrasonic phase measurement techniques. Two instruments were developed for this purpose: a variable-frequency analog PPLL and a constant-frequency digital phase monitor (DPM). The PPLL tracks signal phase by continuously adjusting the frequency (of tone burst and reference) to cancel phase shifts induced by changing temperature, i.e., such that $\Delta f/f = -\Delta\varphi/\varphi \cong \Delta\bar{V}/\bar{V}$. Integrating this relationship we obtain $\bar{V} = \bar{V}_o(f/f_o)$ where f_o is the initial lock-point frequency of the PPLL and $\bar{V}_o$ is the initial average sound speed. By contrast, the DPM works at constant frequency, but uses a dual-reference heterodyning technique to detect temperature-induced phase changes directly and converts them into estimates of the time of flight τ, which is then used to calculate $\bar{V}$. From $\bar{V}$, average temperature $\bar{T}$ may be obtained by inverting Eq. (1):

$$\bar{T}(\bar{V}) = \frac{-b + \sqrt{b^2 - 4a(c - \bar{V})}}{2a}, \tag{5}$$

if it is permissible to replace the spatial average of T^2 by $\bar{T}^2$ (in the experiments with radiation, temperature variations along the acoustic path likely varied by no more than 0.1 °C, a small fraction of the 20 °C ambient temperature, so this approximation would be justified). Equation (5) yields expressions for $\bar{T}(f)$, appropriate for the PPLL, and $\bar{T}(\tau)$, for the DPM, by substituting $\bar{V} = \bar{V}_o(f/f_o)$ or $\bar{V} = L/\tau$, respectively.

B. Experimental setup

The experimental setup of a laboratory single-channel ultrasonic thermometer is shown in Fig. 1. A contact 5 MHz ultrasonic transducer is acoustically coupled to the side wall of a thermally isolated water phantom. The ultrasonic system includes a tone-burst pulser, a receiver, and a precision phase detector (variable-frequency PPLL or DPM) that locks on a chosen segment of the signal and tracks its phase changes in time. The output data in the form of signal frequency for the PPLL or signal delay for the DPM are read by the computer and converted into temperature changes. Initial tests of the first (PPLL) prototype responding to injections of cool and warm water were simultaneously monitored by an array of solid-state sensors laid out parallel to the acoustic path in order to provide a rudimentary calibration check on the instrument. Subsequent testing of both instruments was done with a 500 W heat lamp, a 40 W light bulb, and a 60 W spotlight (see Table I) to verify temperature resolution and assess baseline noise. For ionizing radiation, we used a ^{60}Co source with square-collimator openings of 50 and 100 mm and a computer controlled shutter to regulate exposure time. Two water phantoms were built of cast acrylic sheet with thicknesses of 9 and 11 mm, respectively (dimensions are listed in Table I). The wall thicknesses were large enough to avoid overlapping of successive ultrasonic echoes (originating from wall interfaces with water or air), which distorts the original phase of the signal and leads to measurement errors. The duration of a 24 cycle, 5 MHz tone burst is 4.8 μs, and the 6.74 μs acoustic delay provided by a 9 mm acrylic wall is enough to resolve individual echoes. Both phantoms had acrylic lids to minimize heat losses on evaporation and to damp free surface vibrations that can affect the phase of acoustic signals and are equipped with 100 mm thick styrofoam enclosures and covered from the outside with aluminized bubble wrap to reduce energy exchange with the environment through IR radiation/absorption and to protect the foam from mechanical damage.

TABLE I. Summary of measurement conditions and results of incandescent and gamma radiation tests on the two water phantoms using the PPLL thermometer.

Phantom volume	Small (0.39 l)	Large (28.4 l)
Dimensions (mm)	76×67×76	305×305×305
Incandescent test		
Light source	Heat lamp	Light bulb
Power (W)	500	40
Exposure time (s)	2	60 on/off
Sampling interval (s)	4	4
Thermal drift (μK/s)	28.9	1.6
Temperature increase (μK)	200	120
rms noise (μK)	9.6	5
^{60}Co test		
Estimated beam width (at 90% intensity) at measurement depth (mm)	60	90
Distance from source (mm)	840	900
Beam path depth from surface (mm)	32	100
Nominal dose rate at measurement depth (Gy/min)	1.28	0.573
Expected averaged temperature increase per 60 s irradiation (μK)	217±10	57.5±3
Derived temperature increase from measurement (μK)	225±5.2	56.1±4.1

C. Analog PPLL and digital phase monitor

As noted above, the analog, variable-frequency PPLL tracks signal phase by continuously adjusting the output frequency to compensate for phase shifts due to changing temperature. The instrument uses a feedback loop in which the output frequency of a voltage-controlled oscillator (VCO) is adjusted to maintain a constant 90° phase difference between the transmitted ultrasonic tone burst and the reference waveform. The phase detector in the analog instrument is a homodyne detection system involving a mixer followed by a low-pass filter. The mixer forms the product between the output reference signal $V_1 = A_1 \sin(\omega t + \phi_1)$ and the return echo $V_2 = A_2(t)\sin(\omega t + \phi_2)$, with $A_2(t)$ specifying the (attenuated and delayed) envelope of the reflected tone-burst pulse. The output of the mixer is fed to a low-pass filter, which removes the sum-frequency component and determines the overall PLL time constant (0.1–1.1 s) and equivalent noise bandwidth (ENBW). The output of the filter is the error voltage $V_P = \frac{1}{2}A_1A_2(t)\cos(\phi_2 - \phi_1)$, which is passed to a sample-and-hold

circuit that is synchronized with the tone-burst generator. Successive values of V_P are accumulated by an integrator whose output is fed back as a correction voltage to the VCO so that its output adjusts to zero out V_P and thereby achieve the desired quadrature condition $\Delta\phi=\phi_2-\phi_1=90°$ (within the precision permitted by the instrument resolution). The VCO frequency f is subsequently measured with a counter and digitized for further analysis. The accuracy and precision of this approach are limited by the frequency dependence of hardware components and by resolution of the frequency counter, respectively. Frequency-dependent phases from electronic components, principally, but also cables, the transducer and the various physical interfaces encountered by the tone burst, have been invoked[11] to explain large errors (of order 20%) in measuring phase shifts by means of this variable-frequency PPLL technique. Subsequent workers[16,17] identified the primary source of these errors to be ripple in the frequency response of the low-pass filter used in the phase detector, and suggested filter-design criteria for mitigating the problem and an alternative synchronous detection scheme that dispenses with the filter altogether. The design of the present instrument, while based on that used in these earlier studies, incorporates numerous improvements intended to alleviate this problem. Additional systematic errors due to frequency-dependent phases in components external to the PPLL are not expected to be large given the narrow ranges of frequency adjustment (typically less than 100 Hz, or 1 part in 5×10^4) employed here in a typical experiment with radiation. The primary contributor in this regard is believed to be the 15.25 m coaxial cable between the PPLL and the phantom that adds a delay of approximately $\theta\approx150$ ns to the echo signal. This would introduce a correction factor of $1+(\theta/\tau)$ to Eq. (2) (and other consequences for equations derived from it); however, for the path length of 610 mm in the large phantom, the time of flight $\tau=412$ μs, so that $\theta/\tau=4\times10^{-4}$ (additional phase errors induced by changes in the ambient room temperature would be orders of magnitude smaller than this). The correction associated with the small phantom is only four times larger; thus, the effect may be safely neglected.

The precision of the analog ultrasonic thermometer also depends on the resolution of the frequency measurements. The detection sensitivity, obtained by differentiating $\bar{T}(f)$ [from Eq. (5)], approaches 1×10^{-4} °C/Hz for the conditions of temperature and ultrasonic frequency employed here (≈20 °C, 5 MHz). Thus, to reach the desired temperature resolution of 10 μK, frequency measurements would require a precision of 0.1 Hz, which is easily achieved with commercially available frequency counters employing gating times of order 1 s or less. By contrast, the DPM is capable of measuring the desired quantity without the need for other external instruments and works at constant frequency, thereby avoiding the problem of frequency-dependent phases. The DPM algorithm directly assesses the time of flight τ of a user-selected signal feature (target) through mixing of the digitized echo waveform with two time-shifted reference waves and subsequent heterodyne phase detection via digital low-pass filtering. This simpler design does not require the feedback loop architecture to maintain a quadrature condition (as is done in the PPLL). The output of the DPM is a stream of target-delay data acquired at a high repetition rate (500–5000 Hz) and sent to the computer via Universal Serial Bus (USB).

The precision of the digital system is limited by the precision of measuring changes in the signal phase, which for this instrument is affected mostly by jitter in system synchronization and quantization or rounding errors in the phase-extraction algorithms implemented within the DPM. Differentiating $\bar{T}(\tau)$ [from Eq. (5)] yields sensitivity of the order of 10^6 °C/s for our typical experimental setting; thus, 10 μK resolution in temperature would require an ability to resolve 10 ps changes in time of flight. The temporal jitter of the trigger pulse in the signal generator is as small as a few picoseconds and is not the main source of error. Conventional delay estimation algorithms that track position of a zero crossing or the maximum of a cross-correlation function are limited by the sample rate and resolution of the analog-to-digital converter and are able to resolve changes no smaller than the sampling interval. In the present system, this limit would be 20 ns (50 MHz sample rate)—more than 1000× coarser time resolution than is required to achieve the desired temperature resolution. The dual-reference heterodyne detection method described above is less sensitive to the sampling rate and resolution of the analog-to-digital converter. The algorithm works with finite portions of the signal in the neighborhood of the monitored point and therefore produces smoother output than conventional point-by-point methods. The effective time constant for this instrument, like that for the PPLL instrument, is determined by the low-pass filter. Here the filter is implemented in firmware and can be configured with time constants as small as 2×10^{-4} s. The relatively higher repetition rates attainable with this instrument allow for additional temporal averaging that further improves temperature resolution. The algorithm implemented in the DPM in combination with averaging has been shown to be able to resolve 2 ps in hardware emulation tests[18] and an equivalent of 20 ps from measurements in tissue displacement.[19]

III. MEASUREMENTS

A. Calibration of the PPLL

Whereas the DPM requires only a measurement of the path length to process the transducer signal directly into an estimate of temperature, Eq. (5) indicates that a measurement of the initial average sound speed or, by Eq. (1), the initial average temperature along the acoustic path is needed for the PPLL. Early calibration testing of the PPLL prototype was done using the latter approach. To measure average temperature changes, several (three to five) single-point temperature sensors (Analog Devices AD22100) were placed parallel to and immediately above the acoustic path, and their outputs were connected through separate 1 kΩ resistors to a single point. The resistors were used to limit currents so that large temperature differences (several °C) between devices could be sustained without inducing saturation, and then precautions were taken to distribute warm or cold water across the acoustic path (with a syringe) so that such temperature dif-

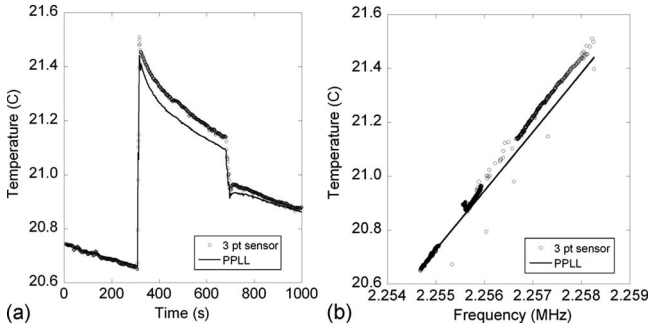


FIG. 2. Comparison of temperature measurements obtained from the PPLL and the three-point array of temperature sensors: (a) on the left, time dependence of both signals and (b) on the right, temperature vs frequency.

ferences likely did not exceed 1 °C. Thus, it is believed that the sensors were able to function well within their design specification as voltage sources, and the summing point of the circuit, monitored with an HP 3478A multimeter, provided a good estimate of the average voltage, hence average temperature, among the sensors.

Figure 2(a) shows the results of such an experiment in which both the PPLL frequency, in the range of 2.25 MHz, and the average temperature, via the three-point probe, were monitored. The PPLL output was converted to temperature using Eq. (5), with the initial value being supplied by the three-point probe. At two different moments of time, small quantities of warm and then cold water were added to the phantom, and very close similarity between the frequency and sensor temperature outputs was observed over the course of the run. A deviation, however, is clearly visible between the two traces, likely caused by one or more of the following factors: offset errors or nonlinearity in the AD22100 sensors comprising the three-point probe, differences between the average water temperature along the acoustic path and that experienced by the sensors, and frequency-dependent phases in the PPLL.

Using Eq. (5), we investigated the effect of an offset error in the temperature reading from the sensors and found that the deviation could be nearly eliminated if the average temperature reported by the sensors were raised by about 4 °C. However, since the maximum offset error is only 2 °C for these sensors, such offset errors would not appear to be the likely cause of the deviation. Similarly, the device specification of the AD22100 indicates a maximum deviation of 0.5% due to nonlinearity, which is about 10% of what is indicated in Fig. 2(a). The somewhat crude method by which temperature perturbations were applied to the phantom would certainly allow for the possibility of ≈50 mK differences in the average temperature of the water sampled by the two different probes. Because of the relative buoyancy of warmer water, higher temperatures would be expected from the sensors than from the PPLL, which is evident in Fig. 2(a). Moreover, such temperature differences would tend to persist in time when warmer water is introduced rather than cooler water, whose higher density would likely cause it to sink toward the bottom of the phantom and accelerate the temperature equilibration process by convective mixing. This is in accord with the data in Fig. 2(a), where the difference between traces persists after addition of the warm water, but diminishes after addition of the cool water.

Thus, certain features of the data in Fig. 2(a) suggest that the discrepancy is explained in part by temperature stratification in the phantom; however, this does not explain the difference in the traces that occurs in the drift segment preceding the addition of warm water. The difference looks negligible in the figure because the PPLL trace was scaled using the initial temperature from sensors, but closer inspection shows a difference in slope of about 20%. This becomes evident in Fig. 2(b), where the temperature from the sensors and the PPLL is plotted versus PPLL output frequency. Ignoring the five outlier points in the plot (due to a small temporal lag in the arrival of heat from the top of the phantom to the sensor depth versus the depth of the ultrasonic path, just after the warm water was injected), a correlation is evident in the deviation between plots that is suggestive of the phase errors reported by earlier workers[11,16,17] (discussed above). The magnitude of the relative error in Fig. 2 for measuring changes in temperature is about 10% over the 3 kHz range in output frequency, comparable to what had been reported by Yost *et al.*,[11] although its variation with frequency is much smoother over that range (comparison here is made with respect to Figs. 6 and 7 in Ref. 11). At the time of writing, the cause of this deviation in our data is unknown and is being investigated. If the effect proves to be partly a consequence of frequency-dependent phases in the PPLL, then a careful calibration study over the frequency range of interest would be done to characterize its magnitude for purposes of correcting subsequent measurements. For the radiation results presented in this initial study, upper limits to its magnitude deduced from comparisons with theoretical expectation and with comparable measurements taken with the DPM (which is immune to this problem because of its fixed-frequency design) suggest that it is negligible compared to system noise.

Finally, while this method was able to provide initial validation of the PPLL instrument, it was not feasible for *in situ* measurement of initial values because of the need for placing sensors in the acoustic path. Accordingly, we developed a separate procedure to determine the initial average sound speed and temperature by first manually tuning the PPLL to achieve quadrature condition between the echo and reference signals (and identify a suitable lock point for subsequent measurements), then obtaining a time-of-flight estimate using oscilloscope markers, and finally restoring automatic control of the PPLL.

B. Noise estimation and tests with incandescent radiation

The detection of submillikelvin changes of temperature in water encountered in quantifying radiotherapeutic absorbed dose poses several challenges experimentally. In addition to the design criteria outlined above regarding instrument resolution, special precautions must be taken to eliminate sources of noise, and appropriate test conditions must be devised that are able to verify that one really measures such small changes of temperature.

The principal sources of noise associated with these instruments were expected to be of acoustic or electronic origin. Fluctuating convection currents, a consequence of thermal inversions caused by dose nonuniformity, were observed, but their characteristic time constants were generally quite large (e.g., see Fig. 8, where time constants approach several hundred seconds), so they are not believed to have contributed significantly to noise observed at the shorter time scales (tens of seconds or less) defining the signal features of interest. More rapid statistical fluctuations of temperature, estimated from equilibrium thermodynamics as $\langle \delta T^2 \rangle = kT^2/C$ (where k is Boltzmann's constant and C denotes heat capacity of water), yield a root-mean-squared (rms) temperature fluctuation of 10^{-10} K for our system, which would not be resolvable with our instruments. Most measurements were conducted with the phantom surrounded by 10 cm of foam insulation and positioned on a platform that was mechanically isolated from certain large disturbances, such as the mechanical shutter used to chop the ^{60}Co beam. Smaller mechanical disturbances, such as vibrations from cooling fans in electronic equipment or from vehicular traffic, were not believed to be significant because the electronics were kept at several meters distance, and no changes were observed in noise levels that correlated with times of increased vehicular traffic on adjacent roads or with changes of venue to relatively isolated laboratory settings, such as the subbasement facility at National Institute of Standards and Technology.

Likely causes of electronic noise would be imperfections in phase stability and frequency purity of the VCO of the PPLL instrument, related imperfections in the analog/digital converters and phase-extraction algorithm in the DPM, and, for both, irreproducibility or jitter in the gating circuitry of the tone burst and/or triggering point of the sample/hold amplifiers. In the PPLL instrument, such causes would contribute to an overall noise spectral density whose impact on the measured output would be limited by the ENBW of the circuit, which is estimated to be 0.14 Hz (obtained by multiplying the upper limit of the time constant in the analog PPLL of 1.1 s by 2π and taking the reciprocal). Because the signal is coupled to the PPLL through a preamplifier with an estimated output rms noise spectral density of at least 27 $\mathrm{nV}/\sqrt{\mathrm{Hz}}$, the minimum rms noise voltage present at the output of the filter would be 10 nV. The 5 $\mathrm{Hz}/\mu\mathrm{V}$ sensitivity of the VCO would then convert this noise voltage to an output-frequency noise of about 50 mHz rms, which, given the 10^{-4} °C/Hz sensitivity figure derived from Eq. (5), would constitute a minimum rms noise in the measured temperature waveform of about 5 μK. Actual noise in excess of this would be expected due to contributions from other PPLL circuit elements.

In the DPM, the smaller time constant of 2×10^{-4} s corresponds to a much higher ENBW of about 800 Hz, but the associated estimate of filtered Johnson noise of 800 nV (rms) is far below the minimum 6.1 μV detectable with the 14 bit analog/digital converter at a full scale of 0.1 V. Instability of the least significant bit in the analog/digital converters could introduce fractional errors in voltage, hence phase, of 1 part in 2^{14}, which amounts to a maximum 2 ps variability in a 5 MHz waveform. This, however, is negligible compared to the 50–150 ps rms noise we deduce from observed temperature waveforms using the estimated conversion sensitivity of 1.2×10^6 °C/s obtained from Eq. (5). The deduced rms noise is not likely to be an artifact of discrete sampling by the analog/digital converters since the former is less than 1% of the 20 ns sampling interval of the ultrasonic data and several orders of magnitude larger than the jitter in the sample clocks. Other imperfections in system components might play a role in the observed noise, but the primary contributor is believed to be the phase-extraction algorithm because noise levels were found to vary significantly when different algorithms were tested. The best noise performance, cited above, was obtained with the current implementation of the heterodyne mixing—low-pass filtering algorithm. While we are unable to specify a minimum theoretical estimate of the noise generated by the algorithm, signal averaging over a 1 s window produced noise levels approaching 2 μK (see Table II).

TABLE II. Settings and results from the comparison gamma radiation test of PPLL and DPM prototypes.

	PPLL thermometer	DPM thermometer
Pulse repetition rate (Hz)	500	500
Time constant (s)	*RC* filter related, 0.1–1.1	Software related, less than 2×10^{-4}
Raw measurement interval (s)	1.14	0.002
Effective measurement interval after averaging	1.14	1.14
rms noise at 1.14 s measurement interval (μK)	5.8	2.5
Average temperature increase per cycle (μK)	43.5 ± 2.6	48.9 ± 4.2

Thus, both instruments should be capable of measuring temperature changes as small as a few microkelvins with an update rate of 1 Hz, and higher precision than that could be realized with additional signal averaging. In order to verify that such small changes in temperature could be observed, initial tests were devised with incandescent sources that were adequately collimated and attenuated to produce small temperature changes in water. Test conditions are listed in Table I. In all cases, the illuminated solid angle could be controlled to produce an approximate temperature slew rate of 10–100 μK/s. Since certain details about the spectral composition of the incandescent sources were unknown, only crude estimates of the expected temperature responses could be made. They were, nevertheless, believed to be sufficient for purposes of proof-of-principle testing of temperature sensitivity. Consider the 500 W lamp, which was located about 20 cm above a 3.5×75 mm^2 slit oriented parallel to the ultrasonic path. The rated power is reduced by a factor of about 5.2×10^{-4} due to the subtended solid angle and by an additional factor of about 0.05 for luminous efficiency, which leads to an estimate of the incident power of about 13 mW. With the ultrasonic path located at a few centimeters depth in the water, the temperature increase in the volume traversed by the tone burst would then depend on how the incident radiation is absorbed by the water. Assuming that the spec-

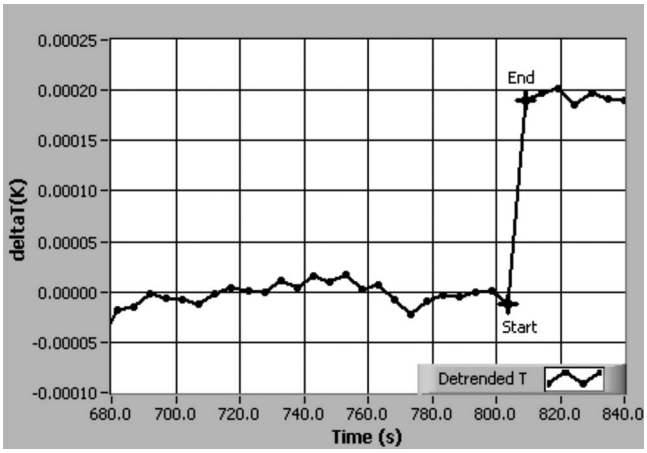


FIG. 3. PPLL-based thermometer: Temperature increase in the small water phantom due to a 2 s pulse of a 500 W lamp.

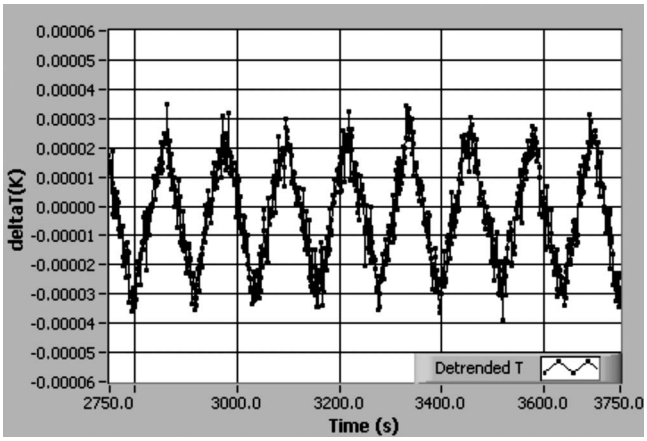


FIG. 4. PPLL-based thermometer: Detrended water temperature history in the large phantom under periodic exposure to incandescent radiation with 60 s on/off cycle.

trum conforms to that of a blackbody with a temperature of about 3000 K, the peak wavelength would be nearly 1 μm, at which the Lambert absorption coefficient for water[20] is about 0.36 cm^{-1}. Thus, the net power absorbed within the depth of about 1 cm traversed by the tone burst would be of order 1 mW, corresponding to a rate of temperature increase within the 0.03 l exposed sample volume of order 100 μK/s. For the tests done with lower-power sources, adjustments in source collimation and sampling depth were made to produce temperature signals in the desired range of magnitudes.

In the initial test performed with the PPLL instrument, involving the smaller phantom and the 500 W source, the water temperature was first monitored for several minutes to estimate the existing thermal gradient (28.9 μK/s) and the noise level (9.6 μK, obtained by subtracting the trend from the data and calculating the rms deviation). Then the heat lamp was flashed for 2 s and the data were recorded at 4 s intervals. Figure 3 shows the detrended temperature history with designated start and end moments of the exposure event. The heat deposited in the system during this exposure created a 200 μK step in the temperature curve, as detected by the ultrasonic thermometer. Figure 4 presents the results of another experiment for which the larger water phantom was periodically illuminated with a 40 W light bulb. The detrended temperature curve, originally with a slope of 1.6 μK/s, shows oscillations with a 120 s period, consisting of alternating heating and drift segments of 60 s duration each. Determining the radiation-induced temperature increase in each heating segment requires subtracting the underlying temperature drift that characterizes the segments immediately before and after it when necessary, as in the case shown in Fig. 4. The midpoint extrapolation procedure (extrapolate the pre- and postirradiation drift segments to the midpoint of the heating segment and take the difference) was used to produce the estimate of temperature increase for the larger phantom given in Table I. Tests with the DPM were conducted using the smaller phantom with a 60 W spotlight, a 5 MHz transducer in pulse-echo mode, and a 500 Hz pulse repetition rate. Figure 5 shows the two events when the spotlight was twice turned on for 8–10 s. The temperature increased by approximately 4 mK for each event, whose determination is complicated by large swings in the background drift due to heat transport. The shaded curve in Fig. 5 represents raw temperature data captured, with noise level of approximately 400 μK p.-p. The solid curve in Fig. 5 shows the same data filtered with a 200 point moving average and effective sampling interval of 0.4 s. This reduced the noise amplitude to approximately 30 μK p.-p. while preserving features of the plot important for the interpretation of the temperature data.

C. Gamma radiation tests: PPLL-based thermometer

The PPLL instrument was the first to be tested in the ^{60}Co radiation beam. The measurements were conducted on two occasions, the first of which involved only the smaller phantom and the second involved only the larger phantom at a nominal dose rate of 1 Gy/min (1 Gy, or 1 J/kg, of absorbed dose to water causes the temperature to increase by about 0.24 mK at room temperature). The details of the measurement conditions are listed in Table I. Dose rates at depths other than 5 cm were deduced from known depth-dose profiles,[21] which characterize the relative energy deposition of ^{60}Co beams in water. The phantoms were filled with once-filtered water which was allowed to reach thermal equilibrium with the room air, and measurements were carried out with different geometries for each. The expected averaged temperature increase at the measurement depth is estimated using the illuminated fraction of the ultrasound path in the phantom based on the beam lateral image obtained with a photostimulated luminescent imaging plate (Fuji plate), carrying an uncertainty of about 5%.

In the test with the small phantom, the radiation beam was chopped at 60 s intervals, and the ultrasonically measured raw temperature data were recorded and are shown in Fig. 6. The drift segments before and after the radiation show a slow decline in the temperature of −3.3 mK/s and rms noise level of 4.4 μK (averaged over 60 s). The start and end of radiation cycles are marked on the temperature curve, and the effects of 30 cycles of periodic temperature modulation are clearly visible. To illustrate the resolution of the

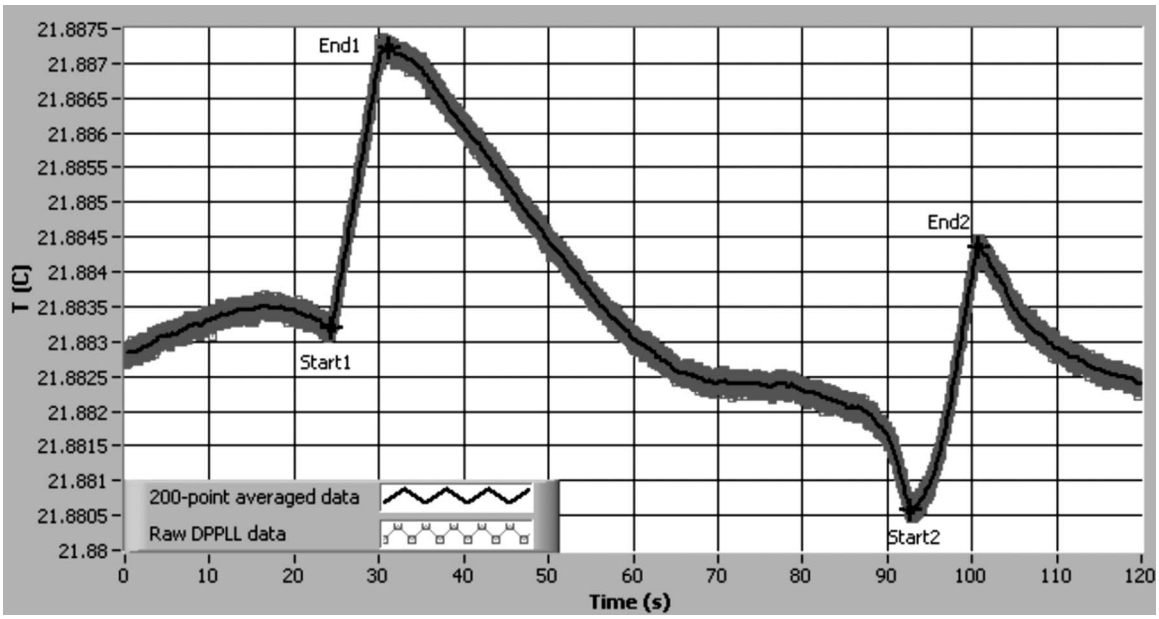


FIG. 5. DPM thermometer: Temperature history in the small water phantom exposed to two events of 8–10 s flashing of a 60 W light bulb demarcated by $start_{1,2}$ and $end_{1,2}$. The gray curve represents raw data recorded at 500 Hz. The black curve represents the same data after averaging with 200-point period.

ultrasonic thermometer, Fig. 7 represents a magnified view of a 1600 s subsection of the plot in Fig. 6. This detrended section contains 12 complete 60 s on/off cycles with an average temperature increase of 210 ± 5.2 μK, obtained by midpoint extrapolation. Correcting for the estimated reduction in sensitivity associated with heating of the phantom walls, we arrive at an estimate of 225 ± 5.2 μK. This is consistent with the expected value for this set of experimental conditions, 217 ± 10 μK, for which an uncertainty of about 5% is associated with estimating the lateral dose profile. Figure 7 also shows the detrended temperature history recorded using the large phantom in the 60 s on/off radiation cycles. The temperature increase is expected to be about 1/4 of that in the small phantom, due to the smaller illuminated portion of the beam path and the lower dose rate at this measurement geometry (greater depth of acoustic path in water). The average temperature increase over the 12 cycles shown, including a 3% correction for heating of the walls, 56.1 ± 4.1 μK, is in good agreement with the expected value. When the exposure time was extended to 120 s, the upward step in temperature (that corresponds to radiation heating) was followed by a sequence of decaying oscillations. Figure 8 shows a succession of such events separated by 1 h intervals. Such oscillations were not observed with the small phantom in ^{60}Co, but only with the large phantom at extended exposure times. The phenomenon is very likely to be a consequence of incipient convection driven by radiation-induced thermal inversions, which were much more pronounced in the larger phantom because the larger lateral dose gradients near the edges of the beam were fully contained within the

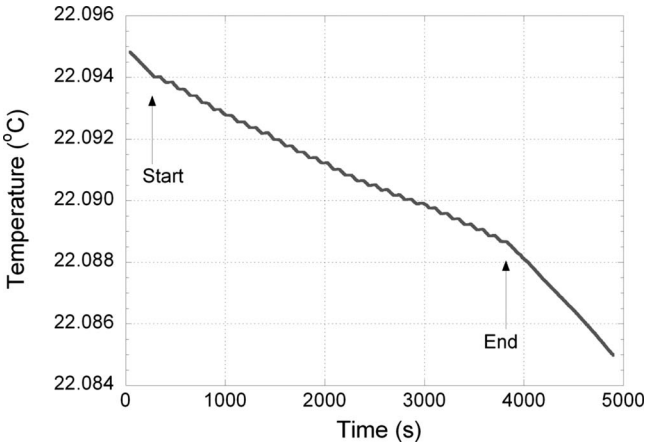


FIG. 6. Water temperature history in the small tank. "Start" and "end" are the beginning and the end of periodic exposure to ionizing radiation with 60 s on/off cycle.

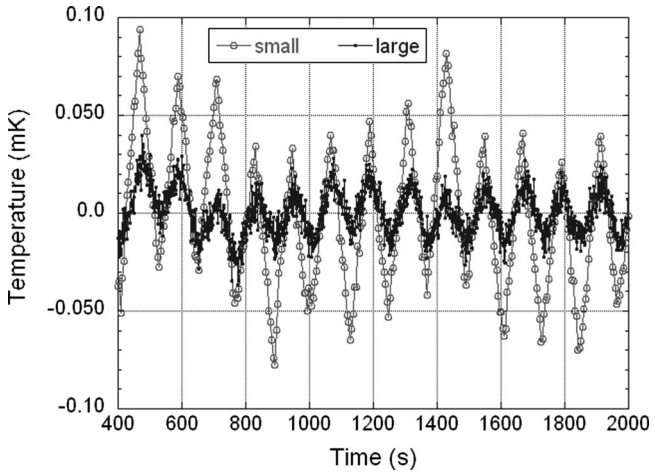


FIG. 7. Detrended temperature response of the system to periodic excitations of 60 s on/off cycles in the ^{60}Co radiation field obtained from the two phantoms. Circles: Data from the small phantom—a larger scale view of the 13 cycles between 400 and 2000 s shown in Fig. 6. The noise level in this measurement was 4.4 μK rms (averaged over 60 s). The average temperature increase over the 12 complete cycles shown is 227 ± 5.2 μK. Dots: Data from the large phantom with a rms noise level of 5.5 μK averaged over 60 s. The average temperature increase over the 12 cycles is 56.1 ± 4.1 μK.

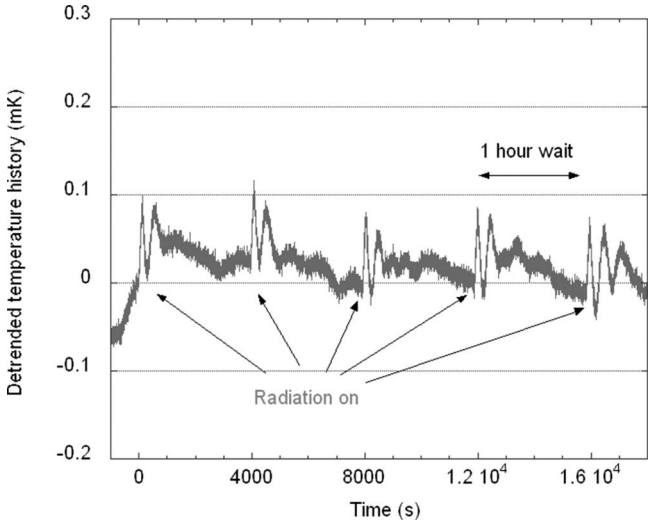


FIG. 8. Individual 120 s radiation exposures separated by 1 h of wait time showing the after-shot oscillations caused by convection in the large water phantom.

water. Because of the depth-dose profile, vertical motion of the water due to such buoyant forces would bring differently heated water layers into the flight path of the probe pulse and influence the measurement. Thus, the phenomenon of ringing observed in the temperature waveform is indicative of small oscillations of the water that are driven by radiation heating and damped out by a combination of viscous forces and thermal conduction. Further analysis of radiation-induced convective oscillations is beyond the scope of this paper but is discussed in Ref. 22.

D. Gamma radiation tests: PPLL and DPM

The test described in this section was constructed to facilitate a more direct side-by-side comparison of the PPLL and DPM systems. First, the PPLL instrument was connected to the ultrasonic transducer attached to the large water phantom, and the temperature history was monitored during 30 exposure cycles (60 s on/off time) of ^{60}Co radiation. Then, the DPM was connected to the same transducer and the periodic exposure test repeated. This setup ensured very similar measurement conditions suitable for a sensitivity comparison. The PPLL thermometer data were collected at 1.14 s intervals while the DPM thermometer data were collected at 2 ms intervals. To enable comparison we averaged DPM thermometer data with a period of 570 points, thus bringing both data sets to the same sampling interval of 1.14 s. The detrended results of two such tests, plotted in Fig. 9, indicate very similar responses to temperature variations of about 45 μK per irradiation cycle (see Table II), an agreement achieved through two totally different detection principles. Also evident in the figure (and quantified in Table II) are differences in the types of noise arising from each instrument: within a given radiation heating cycle, rms noise is relatively higher in the PPLL trace, but the DPM trace shows a relatively higher variation in amplitude from cycle to cycle. Such observations suggest that the relative contributions of white noise and inverse-frequency noise are different for the two instruments, although this has not yet been studied in detail.

IV. CONCLUSIONS

High-precision ultrasonic pulse processing technology has been used to conduct high-resolution thermometry in water. Developed for purposes of medical radiation dosimetry and tested with incandescent and ^{60}Co radiation sources, the two prototypes described here use no hardware in the water phantom, eliminating thermal disturbances from wires and radiation absorption by the temperature sensor body used in conventional calorimeters. The first prototype monitors (and compensates) phase changes of an ultrasonic tone burst using an analog variable-frequency PPLL, and simultaneous tests conducted with independent electronic temperature sensors under incandescent radiation verified its capabilities to resolve submillikelvin temperature changes with noise levels approaching a few times the estimated theoretical lower limit. Similar tests performed with a newer digital prototype

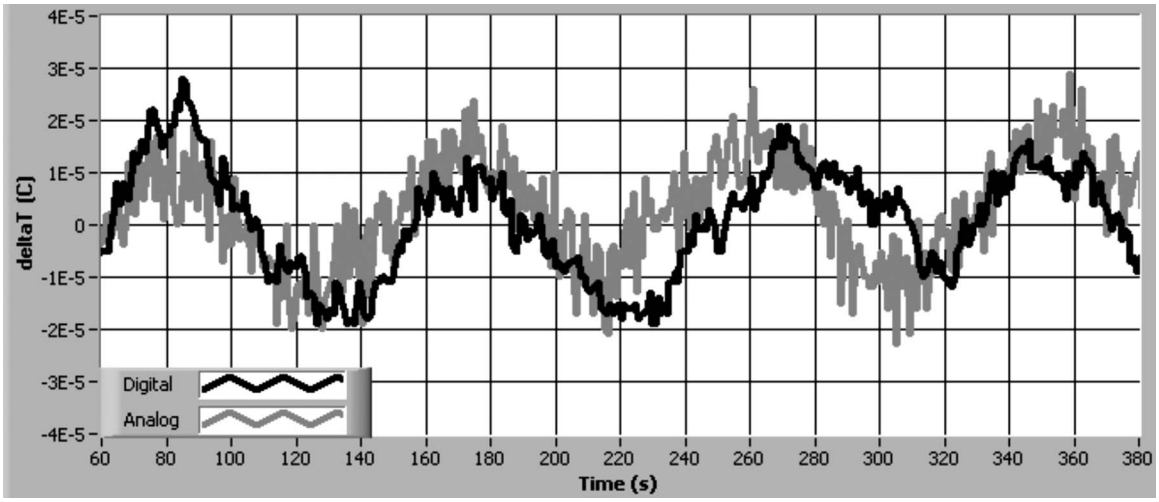


FIG. 9. Sensitivity comparison of the PPLL and DPM ultrasonic thermometers in the large water phantom under periodic exposure to ionizing radiation with a 60 s on/off cycle. The average temperature increases per cycle over the 15 cycles obtained by midpoint extrapolation are 43.5 ± 2.6 and 48.9 ± 4.2 μK, respectively.

that resolves very small changes in time of flight of an ultrasonic tone burst demonstrated similar capabilities under incandescent sources. More definitive tests with radiotherapy-level ^{60}Co gamma rays involving both prototypes yielded results that were in good agreement with each other and with expected values.

Achievable temperature resolutions of both prototypes approach a few microkelvins at update rates of 1 Hz, which exceeds the resolution of other acoustic thermometers described in literature by orders of magnitude [3.8 mK rms,[23] 1–2 K,[4] and 0.05 K rms (Ref. 9)]. This level of resolution is desirable for measuring temperature changes due to clinical doses of ionizing radiation in water; thus, the ultrasonic techniques described here show particular promise for development of noninvasive alternatives to existing reference standards in medical radiation dosimetry. Since the current reference standards quantify absorbed dose to water at a single point in space with precision and accuracy approaching a few tenths of 1%, such developments would require re-examining the approximations made in formulas derived above for analyzing the instrument response. In this regard, the DPM is less susceptible than the variable-frequency PPLL to certain types of systematic error, such as frequency-dependent phase error and uncertainties associated with the determination of a frequency-to-temperature conversion factor. In addition, for ultrasonic thermometry to be viable as a reference standard for medical radiation dosimetry, it would need to be capable of assessing dose at a given point in space (volumes smaller than 1 mm^3). To this end, either prototype could be adapted to accommodate multiple channels for purposes of tomographic reconstruction of spatially resolved dose profiles. However, here again, the digital approach offers distinct advantages for development since it is better suited to leverage advances in phase-extraction algorithms and specialized hardware, such as digital signal processors and gate arrays. Such an effort is underway at present, and initial results using the PPLL prototype have been obtained that demonstrate tomographic reconstruction of the heating profile of an incandescent beam in water.[24] Thus, the technology described here offers the potential for surpassing the capabilities of existing reference dosimetry standards by assessing three-dimensional absorbed radiation dose profiles in real time.

ACKNOWLEDGMENTS

This research was supported by NIST Contract Nos. SB1341-04-W-1127 and SB1341-05-C-0025.

[1]S. R. Domen, "A sealed water calorimeter for measuring absorbed dose," J. Res. Natl. Inst. Stand. Technol. **99**, 121–141 (1994).
[2]E. Malyarenko, J. Heyman, S. Guy, H. Chen-Mayer, and R. Tosh, "Absorbed radiation dose measurement with a μK-resolution ultrasonic thermometer," Med. Phys. **33**, 2292 (2006).
[3]E. Malyarenko, J. Heyman, S. Guy, R. Tosh, and H. Chen-Mayer, "An ultrasonic high-resolution thermometer for radiation dosimetry," Biomedical Imaging Research Opportunities Workshop 3, Hyatt Regency, Bethesda, MD, 11–12 March (2005).
[4]S. F. Green, "An acoustic technique for rapid temperature distribution measurement," J. Acoust. Soc. Am. **77**, 759–763 (1985).
[5]M. R. Moldover, S. J. Boyes, C. W. Meyer, and A. R. H. Goodwin, "Thermodynamic temperatures of the triple points of mercury and gallium and in the interval 217 K to 303 K," J. Res. Natl. Inst. Stand. Technol. **104**, 11–46 (1999).
[6]M. Weiss and R. Knöchel, "A monostatic radio-acoustic sounding system used as an indoor remote temperature profiler," IEEE Trans. Instrum. Meas. **50**, 1043–1047 (2001).
[7]J. Lubbers and R. Graaff, "A simple and accurate formula for the sound velocity in water," Ultrasound Med. Biol. **24**, 1065–1068 (1998).
[8]V. A. Del Grosso, "New equation for the speed of sound in natural waters (with comparisons to other equations)," J. Acoust. Soc. Am. **56**, 1084–1091 (1974).
[9]*Ultrasonic Instruments and Devices: Reference for Modern Instrumentation, Techniques, and Technology*, edited by E. P. Papadakis (Academic Press, New York, 1999), p. 809.
[10]S. Fife, C. D. Andereck, and S. Rahal, "Ultrasound thermometry in transparent and opaque fluids," Exp. Fluids **35**, 152–158 (2003).
[11]W. T. Yost, J. H. Cantrell, and P. W. Kushnick, "Fundamental aspects of pulse phase-locked loop technology-based methods for measurement of ultrasonic velocity," J. Acoust. Soc. Am. **91**, 1456–1469 (1992).
[12]J. S. Heyman, "Pulsed phase-locked loop strain monitor," U.S. Patent No. 4,363,242 (1982).
[13]E. J. Chern, J. S. Heyman, and J. H. Cantrell, Jr., "Determination of material stress from the temperature dependence of the acoustic natural velocity," Proceedings of the IEEE Ultrasonics Symposium, New York (1981).
[14]W. T. Yost, B. R. Macias, P. Cao, A. R. Hargens, and T. Ueno, "System for determination of ultrasonic wave speeds and their temperature dependence in liquids and *in vitro* tissues," J. Acoust. Soc. Am. **117**, 656–652 (2005).
[15]H. H. Chandler, R. L. Bowen, and G. C. Paffenbarger, "Physical properties of a radiopaque denture base material," J. Biomed. Mater. Res. **5**, 335–357 (1971).
[16]M. E. Froggatt and S. G. Allison, "Pulsed phase-locked loop technology improvements for greater accuracy and expanded capabilities," IEEE Trans. Instrum. Meas. **45**, 117–122 (1996).
[17]M. E. Froggatt, S. G. Allison, and J. P. Moore, "Pulsed phase-locked loop calibration over frequency," IEEE Trans. Instrum. Meas. **45**, 123–126 (1996).
[18]T. Lynch, J. Heyman, D. Blaker, and E. Malyarenko, "High resolution time of flight measurements with the pulsed phase locked loop," Proceedings of the Fourth International Conference on the Ultrasonic Measurement and Imaging of Tissue Elasticity, Lake Travis, Austin, TX, 16–19 October (2005).
[19]T. Lynch, B. Hefner, C. Domack, and D. Coombs, "High resolution time of flight measurements with the pulsed phase locked loop: Experimental validation," Proceedings of the Fifth International Conference on the Ultrasonic Measurement and Imaging of Tissue Elasticity, Snowbird, UT, 8–11 October (2006).
[20]G. M. Hale and M. R. Querry, "Optical constants of water in the 200-nm to 200-micrometer wavelength region," Appl. Opt. **12**, 555–563 (1973).
[21]American Association of Physicists in Medicine, Task Group 51, "AAPM's TG-51 protocol for clinical reference dosimetry of high-energy photon and electron beams," Med. Phys. **26**, 1847–1870 (1999).
[22]R. E. Tosh and H. H. Chen-Mayer, "A transfer-function approach to characterizing heat transport in water calorimeters used in radiation dosimetry," Proceedings of the International Thermal Conductivity Conference (ITCC29), University of Alabama, 24–27 June (DEStech, Lancaster, PA, 2007).
[23]E. K. Skarsoulis, U. Send, G. Piperakis, and P. Testor, "Acoustic thermometry of the western Mediterranean basin," J. Acoust. Soc. Am. **116**, 790–798 (2004).
[24]E. Malyarenko, J. Heyman, H. Chen-Mayer, and R. Tosh, "High-resolution digital ultrasonic thermometers," Proceedings of the 49th Annual Meeting of the American Association of Physicists in Medicine (AAPM), Minneapolis, MN, 22 July (2007).

Finite element modeling of the temperature rise due to the propagation of ultrasonic waves in viscoelastic materials and experimental validation

B. Hosten,[a] C. Bacon, and C. Biateau
Laboratoire de Mécanique Physique, Université de Bordeaux, UMR CNRS 5469 351, Cours de la Libération, 33405 Talence Cedex, France

(Received 4 June 2008; revised 10 September 2008; accepted 11 September 2008)

The ultrasound stimulated thermography method is usually used to detect the temperature rise at a defect position. The temperature rise can be due to the friction between the edges of the defect and/or the plastic deformation around the defect. This paper presents another aspect of the method when the ultrasounds are propagating in a viscoelastic anisotropic material, such as polymers or fiber-reinforced polymers. The attenuation of the waves produces a distributed temperature field. Therefore, even a defect that does not produce some heat can be detected, the ultrasonic field is modified. A finite element model is used for computing the temperature field and for predicting the possibility for an infrared camera of detecting the temperature rise and its modification due to a defect. The model computes the stress and displacement fields associated with the propagation and the loss of energy. Then the heat equation is solved with this loss as a source of heating. An experiment is done with a sonotrode that excites a PVC plate. The ultrasonic displacement at the top of the plate is measured with a laser velocimeter and introduced in the model. Finally, the model result is compared to the image produced by the camera.
© *2008 Acoustical Society of America.* [DOI: 10.1121/1.2998392]

PACS number(s): 43.35.Zc, 43.35.Cg, 43.20.El [YHB] Pages: 3491–3496

I. INTRODUCTION

In the field of nondestructive evaluation and testing (NDE/NDT) of materials and structures, there is no unique and satisfactory method for revealing any kind of defect. Then it is imperative to search for new NDE/NDT methods, knowing that the industry needs some fast, noncontact, nonexpensive, single sided methods.

One of these methods, the thermography inspection, using flash lamp heating, has the advantage of being noncontact and is able to detect the defects that have an effect on the diffusion of heat into the structure.[1] This method has the capability to detect only entities resulting in a measurable change of thermal properties and to inspect a limited thickness of material under the surface.[1]

The use of the ultrasound propagation is probably one of the more useful methods since it involves stress and displacement fields that are strongly dependent on the state of the structures and their mechanical properties.

The thermography inspection can be associated with the heat field generated by the interaction between ultrasounds and defect.[2–6] This ultrasound stimulated thermography (UST) method is based on the temperature rise due to the friction between the edges of the defect and/or the plastic deformations around the defect.

This paper presents another aspect of the UST method applied to viscoelastic materials such as polymers or fiber-reinforced polymers. These materials submitted to vibrations or ultrasonic wave propagation absorb the mechanical energy that is transformed into heat. If the level of energy is sufficient, the temperature field can be acquired with an infrared camera; and if the influence of a defect is greater than the thermal resolution of the camera, this method can bring some information about the state of a structure.

Before applying the method, it is very important to predict the level of the temperature rise for a specified situation. If the geometry and the mechanical and the thermal properties are known, one of the methods able to predict the temperature effect of a mechanical loading is the finite element (FE) method. With this method, there is no limitation on the complexity of the structure and the shape of the defect. Moreover the ability to predict the temperature rise will be very useful for the study of a NDE/NDT method based on this heat generation effect.

The first step of the paper is to establish the theory that permits to compute the temperature field generated by a mechanical loading in a viscoelastic material. Then the FE model is adapted to the propagation of the ultrasonic waves in viscoelastic anisotropic solids for computing the energy losses and to the heat generation and propagation. To validate the model, an experiment is presented and used as a preliminary simple test for a sample made of PVC.

II. THEORY

A. General case

The aim of this section is to calculate the mechanical dissipation for a dynamic problem where the structural components are made of linearly viscoelastic materials. Then this dissipation will be used to determine the corresponding temperature rise by means of the heat equation.

[a]Author to whom correspondence should be addressed. Electronic mail: b.hosten@lmp.u-bordeaux1.fr

If it is considered that the viscoelastic strain tensor can be separated in an elastic part ε^e and a viscous one ε^ν, the heat equation can be written as[7]

$$\rho c_p \partial_t T = \boldsymbol{\sigma}:\partial_t \boldsymbol{\varepsilon}^\nu + r + \nabla(\mathbf{k}\,\nabla\, T) + T\partial_T \boldsymbol{\sigma}:\partial_t \boldsymbol{\varepsilon}^e, \tag{1}$$

where the symbol ∂_t denotes the time derivative, the symbol ":" denotes the double-contracted tensor product, ρ denotes the density, c_p denotes the specific heat (heat capacity at constant pressure), T denotes the temperature rise from the room temperature T_r, $\boldsymbol{\sigma}$ denotes the stress tensor, r denotes the heat production rate due to external sources, and $\mathbf{k}$ denotes the thermal conductivity tensor. The Nabla vector, $\nabla = \{\partial_1, \partial_2, \partial_3\}$, is represented by the space derivatives in an x, y, z (or 1,2,3) coordinate system. The term $\boldsymbol{\sigma}:\partial_t \boldsymbol{\varepsilon}^\nu$ represents the mechanical dissipation rate caused by the energy loss of the waves propagating in the viscoelastic medium.

It can be assumed that there is no external source and that the stress tensor does not depend on the temperature rise since this rise is low in this situation. Moreover, one can consider two time scales to solve this problem: a "mechanical time scale" characterized by the period T_0 of the monochromatic mechanical loading, and a "thermal time scale" characterized by the duration of the temperature rise. For a frequency υ_0 of several kilohertz, the period T_0 is smaller than 1 ms while the observed temperature rise will be more than several seconds or minutes. Thus these two time scales are very different. This fact justifies that the mean value of the mechanical dissipation rate for a monochromatic loading at frequency υ_0 will only be used for the resolution of the heat equation

$$\langle \boldsymbol{\sigma}:\partial \boldsymbol{\varepsilon}^\nu \rangle_{\upsilon_0} = \frac{1}{T_0}\int_0^{T_0} \boldsymbol{\sigma}\partial_t \boldsymbol{\varepsilon}^\nu dt. \tag{2}$$

The linearly viscoelastic materials are anisotropic *a priori*. As already demonstrated[8] and due to Boltzmann's principle of superposition,[9,10] an efficient way to treat this kind of problem is to solve the equations in the frequency domain, by using the Fourier transform of the variables, instead of the time domain. In this paper, the Fourier transform is defined by[11]

$$F(f(t)) = \int_{-\infty}^{+\infty} f(t)\exp(i\,\omega\, t)dt, \tag{3}$$

where ω is the angular frequency related to the frequency ν by $\omega = 2\pi\nu$.

In a viscoelastic anisotropic material, Hooke's law, applied to small displacements and small strains, is represented by

$$\tilde{\sigma}_{ij} = C_{ijkl}\partial_l \tilde{u}_k, \tag{4}$$

where $1 \leqslant i, j \leqslant 3$ and there is an implicit summation over the k and l indices with $1 \leqslant k, l \leqslant 3$. The terms $\tilde{\sigma}_{ij}$ are the Fourier transforms of the components of the stress tensor, $\tilde{u}_k$ are the Fourier transforms of the components of the displacement, and C_{ijkl} are the components of the complex stiffness tensor. The thermal dilatation due to the small temperature rise is neglected in this equation. The local equilibrium equation in the considered domain gives

$$\partial_j \tilde{\sigma}_{ij} = -\rho\omega^2 \tilde{u}_i. \tag{5}$$

Then, from Eq. (4), with the hypothesis of small deformations, Eq. (5) becomes

$$C_{ijkl}\partial_j\partial_i \tilde{u}_k = -\rho\omega^2 \tilde{u}_i. \tag{6}$$

Associated with the mechanical boundary conditions, this equation can be solved numerically in the frequency domain, by a FE method. Afterwards, the stresses can be calculated by Eq. (4) and the Fourier transforms of strains are determined by

$$\tilde{\varepsilon}_{ij} = \tfrac{1}{2}(\partial_j \tilde{u}_i + \partial_i \tilde{u}_j). \tag{7}$$

All results are given in the frequency domain. In order to calculate the viscous part of the strain, it can be written that

$$\tilde{\varepsilon}_{ij} = \tilde{\varepsilon}^e_{ij} + \tilde{\varepsilon}^\nu_{ij} = S_{ijkl}\tilde{\sigma}_{kl} = (S'_{ijkl} + iS''_{ijkl})\tilde{\sigma}_{kl} \tag{8}$$

where S_{ijkl} are the components of the complex compliance tensor and the inverse tensor of the stiffness tensor. The viscous part is related to the imaginary part of tensor

$$\tilde{\varepsilon}^\nu_{ij} = iS''_{ijkl}\tilde{\sigma}_{kl}. \tag{9}$$

In the Fourier domain, the mechanical dissipation rate involves a convolution product

$$F[\boldsymbol{\sigma}:\partial_t \boldsymbol{\varepsilon}^\nu] = [\tilde{\sigma}_{ij}] * [i\omega\tilde{\varepsilon}^\nu_{ij}] = [\tilde{\sigma}_{ij}] * [-\omega S''_{ijkl}\tilde{\sigma}_{kl}], \tag{10}$$

with an implicit summation over the i, j, k, and l indices.

Since, a monochromatic loading is supposed at the frequency υ_0 with $\omega_0 = 2\pi\upsilon_0$, the stress can be written in the following form:

$$\tilde{\sigma}_{ij}(\omega) = \tilde{\sigma}_{ij}(\omega_0)\delta(\omega - \omega_0) + \tilde{\sigma}_{ij}(-\omega_0)\delta(\omega + \omega_0), \tag{11}$$

with $\delta(\omega)$ the Dirac distribution. Then it can be demonstrated that the mean value of the convolution product (10), which is the mean value of the mechanical dissipation, is given by

$$\langle \boldsymbol{\sigma}:\partial_t \boldsymbol{\varepsilon}^\nu \rangle_{\upsilon_0} = -\omega_0 S''_{ijkl}(\omega_0)\mathrm{Re}\{\tilde{\sigma}_{ij}(\omega_0)\overline{\tilde{\sigma}_{kl}(\omega_0)}\}, \tag{12}$$

where $\overline{\tilde{\sigma}_{kl}(\omega_0)}$ is the conjugate of $\tilde{\sigma}_{kl}(\omega_0)$ and $\mathrm{Re}\{\cdot\}$ denotes the real part. In a similar way, we could demonstrate the following relationships:

$$\boldsymbol{\sigma}:\partial_t \boldsymbol{\varepsilon}^\nu_{\upsilon_0} = \omega_0 C_{ijkl}(\omega_0)\mathrm{Re}\{\tilde{\varepsilon}_{ij}(\omega_0)\overline{\tilde{\varepsilon}_{kl}(\omega_0)}\}, \tag{13}$$

and we can notice that these equations are equivalent to

$$\langle \boldsymbol{\sigma}:\partial_t \boldsymbol{\varepsilon}^\nu \rangle_{\upsilon_0} = \omega_0\, \mathrm{Im}\{\tilde{\sigma}_{ij}(\omega_0)\overline{\tilde{\varepsilon}_{ij}(\omega_0)}\}. \tag{14}$$

For a short duration where the mean value cannot be considered, the mechanical dissipation rate could be calculated by means of the inverse Fourier transform of Eq. (10) with stress given by Eq. (11) as follows:

$$\boldsymbol{\sigma}:\partial_t \boldsymbol{\varepsilon}^\nu = -\frac{\omega_0 S''_{ijkl}(\omega_0)}{2}[\tilde{\sigma}_{ij}(\omega_0)\tilde{\sigma}_{kl}(\omega_0)e^{i2\omega_0 t} + \overline{\tilde{\sigma}_{ij}(\omega_0)\tilde{\sigma}_{kl}(\omega_0)}e^{-i2\omega_0 t} + 2\,\mathrm{Re}\{\tilde{\sigma}_{ij}(\omega_0)\overline{\tilde{\sigma}_{kl}(\omega_0)}\}]. \tag{15}$$

This expression could be useful for modeling the dissipation along very short distances.

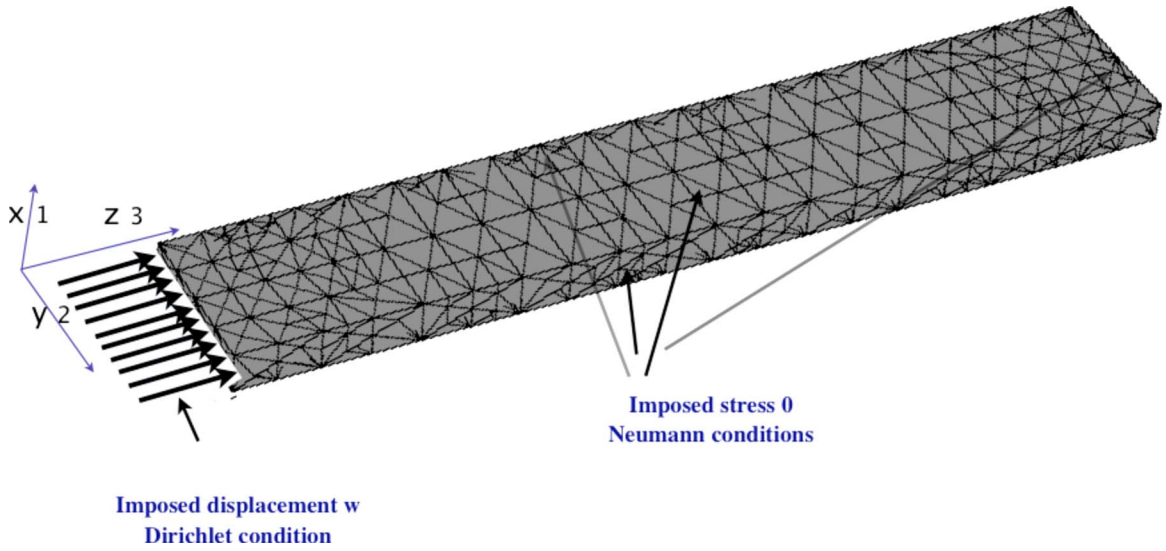


FIG. 1. (Color online) Schematic of the FE model to simulate the generation of the incident bulk wave propagating in air and converted to guided wave propagating inside the plate.

B. Wave propagation

The previous general case is now applied to a propagating monochromatic wave. The energy velocity of an ultrasonic wave is considered very fast in comparison with the propagating velocity of the heat due to the conduction of the solid. Then it is possible to consider the mean value during a period of the energy going through an element of surface, represented by the complex Poynting vector **P** integrated over a temporal cycle.[12] Therefore the energy flux carried by a monochromatic wave is computed from

$$\mathbf{P} = -\frac{1}{2}\,\mathrm{Re}(\boldsymbol{\sigma}\bar{\boldsymbol{V}}) = \begin{bmatrix} p_1 = \dfrac{\omega}{2}\,\mathrm{Im}(\sigma_1\bar{\mathrm{u}}_1 + \sigma_6\bar{\mathrm{u}}_2 + \sigma_5\bar{\mathrm{u}}_3) \\ p_2 = \dfrac{\omega}{2}\,\mathrm{Im}(\sigma_6\bar{\mathrm{u}}_1 + \sigma_2\bar{\mathrm{u}}_2 + \sigma_4\bar{\mathrm{u}}_3) \\ p_3 = \dfrac{\omega}{2}\,\mathrm{Im}(\sigma_5\bar{\mathrm{u}}_1 + \sigma_4\bar{\mathrm{u}}_2 + \sigma_3\bar{\mathrm{u}}_3) \end{bmatrix}, \tag{16}$$

where $\bar{\boldsymbol{V}} = \partial_t\bar{\boldsymbol{U}} = i\omega\bar{\boldsymbol{U}}$ is the particulate velocity field and the strain and stress tensor are given here in simplified notation of index.[12] The loss of energy in an element of volume is given by

$$\nabla\cdot\mathbf{P} = \mathrm{div}(\mathbf{P}). \tag{17}$$

By mixing the relations (5), (16), and (17) and suppressing the real terms, this expression

$$\mathrm{div}(\mathbf{P}) = \frac{\omega}{2}\,\mathrm{Im}(\sigma_I\bar{\varepsilon}_I) \quad \text{for } I \in (1\cdots 6) \tag{18}$$

is equivalent to the previous result (14) obtained for the more general case. This expression avoids the computations of the second derivatives of the field when using the derivatives of the Poynting vector. Then it is much more efficient for performing the numerical computations.

III. FE MODEL FOR SOLID PROPAGATION IN AN ANISOTROPIC VISCOELASTIC SOLID

A. Equations of dynamic equilibrium

Although the model is tested for an isotropic material in this paper, the model is built for the NDE/NDT of composite materials. Then its introduction in the FE model is presented for the viscoelastic and orthotropic materials.

In a recent reference,[13] it was described how to model with a 2.5 dimensional FE model, the propagation of wave in viscoelastic and orthotropic medium with application to composite materials. In a similar way, the equations of dynamic equilibrium (6) are solved in the frequency domain for a three dimensional problem. They are implemented in a software[14] that is a numerical tool for solving the partial differential equations by a FE method. These equations must be written in the following FE-code form:[14]

$$\nabla\cdot(\mathbf{C}_s\,\nabla\,\mathbf{U}) - a\mathbf{U} = 0, \tag{19}$$

where C_s is a 3×3 matrix composed of nine submatrices. These submatrices and a are given by

$$\mathbf{C}_s = \begin{bmatrix} \begin{pmatrix} C'_{11} & 0 & 0 \\ 0 & C'_{66} & C'_{56} \\ 0 & C'_{56} & C'_{55} \end{pmatrix} & \begin{pmatrix} 0 & C'_{12} & C'_{14} \\ C'_{66} & 0 & 0 \\ C'_{56} & 0 & 0 \end{pmatrix} & \begin{pmatrix} 0 & C'_{14} & C'_{13} \\ C'_{56} & 0 & 0 \\ C'_{55} & 0 & 0 \end{pmatrix} \\ \begin{pmatrix} 0 & C'_{66} & C'_{56} \\ C'_{12} & 0 & 0 \\ C'_{14} & 0 & 0 \end{pmatrix} & \begin{pmatrix} C'_{66} & 0 & 0 \\ 0 & C'_{22} & C'_{24} \\ 0 & C'_{24} & C'_{44} \end{pmatrix} & \begin{pmatrix} C'_{56} & 0 & 0 \\ 0 & C'_{24} & C'_{23} \\ 0 & C'_{44} & C'_{34} \end{pmatrix} \\ \begin{pmatrix} 0 & C'_{56} & C'_{55} \\ C'_{14} & 0 & 0 \\ C'_{13} & 0 & 0 \end{pmatrix} & \begin{pmatrix} C'_{56} & 0 & 0 \\ 0 & C'_{24} & C'_{44} \\ 0 & C'_{23} & C'_{34} \end{pmatrix} & \begin{pmatrix} C'_{55} & 0 & 0 \\ 0 & C'_{44} & C'_{34} \\ 0 & C'_{34} & C'_{33} \end{pmatrix} \end{bmatrix},$$

$$a = \begin{pmatrix} -\rho\omega^2 & 0 & 0 \\ 0 & -\rho\omega^2 & 0 \\ 0 & 0 & -\rho\omega^2 \end{pmatrix}. \tag{20}$$

These matrices are given in an axis system defined in Fig. 1, for which axis 1 is the normal to the plate. This axis is

TABLE I. Complex viscoelasiticity moduli (in GPa) and thermal properties for the PVC plate.

Dimensions: $5\times20\times120$ mm^3
C_{11}: $7.9(1+I0.03)$ GPa
C_{22}: C_{11}
K: 0.1 W/(m/K)
Density ρ: 1.17 g/cm^3
C_{66}: $1.6(1+I0.03)$ GPa
C_{12}: $C_{11}-2C_{66}$
c_p: 1000 J/(kg K)

usually an axis of symmetry in a plate made of a composite material. However, the direction of propagation of the waves is not always the same as an axis of symmetry. Then it is mandatory to define these matrices in a system of coordinates rotated around axis 1. The azimuthal angle φ defined this rotation. The C'_{IJ} are obtained by rotation of the azimuthal angle from the nine complex moduli, C_{11}, C_{22}, C_{12}, C_{66}, C_{33}, C_{13}, C_{55}, C_{23}, and C_{44} defined in the axes of symmetry[12] and computed with the following relations:

$$C'_{11} = C_{11},$$

$$C'_{22} = c^4C_{22} + s^4C_{33} + 2c^2s^2C_{23} + 4c^2s^2C_{44},$$

$$C'_{33} = s^4C_{22} + c^4C_{33} + 2c^2s^2C_{23} + 4c^2s^2C_{44},$$

$$C'_{44} = (c^2 - s^2)^2C_{44} + c^2s^2(C_{33} + C_{22} - 2C_{23}),$$

$$C'_{13} = s^2C_{12} + c^2C_{13},$$

$$C'_{55} = c^2C_{55} + s^2C_{66}, \quad C'_{66} = s^2C_{55} + c^2C_{66},$$

$$C'_{12} = c^2C_{12} + s^2C_{13},$$

$$C'_{14} = cs(C_{13} - C_{12}), \quad C'_{56} = cs(C_{55} - C_{66}),$$

$$C'_{24} = cs(C_{23}(c^2 - s^2) - C_{22}c^2 + C_{33}s^2 + 2(c^2 - s^2)C_{44}),$$

$$C'_{34} = cs(C_{23}(s^2 - c^2) - C_{22}s^2 + C_{33}c^2 + 2(c^2 - s^2)C_{44}),$$

$$C'_{23} = s^2c^2(C_{22} + C_{33}) + (c^4 + s^4)C_{23} - 4c^2s^2C_{44} \quad \text{with}$$

$$c = \cos(\varphi) \text{ and } s = \sin(\varphi). \tag{21}$$

B. Boundary conditions

The solid that is submitted to ultrasounds is a small plate that is connected to a sonotrode. The effect of the sonotrode is simulated by an imposed displacement (Dirichlet condition) at the edge that is in contact with the sonotrode. The other surfaces are free of stress. The Neumann condition, $\mathbf{n}\cdot(\mathbf{C}_s\nabla\mathbf{U})=0$, is applied at each of these surfaces for which the normal vector is noted by $\mathbf{n}$. Figure 1 shows the geometry of the plate, the mesh, and the axis system.

IV. FE MODEL FOR HEAT GENERATION AND PROPAGATION

A. Heat equation

When the acoustic solution is known, the loss of energy $\text{div}(\mathbf{P})$ can be computed anywhere in the solid and corresponds to the heating source in the heat equation. Then Eq. (1), taking into account the hypothesis of Sec. II A, can be simplified and becomes

$$\rho c_p \partial_t T - \nabla\cdot(\mathbf{k}\,\nabla\,T) = \text{div}(\mathbf{P}). \tag{22}$$

This equation corresponds exactly to the partial derivative equation used in the FE software to solve the heat transfer by conduction.[14] For orthotropic materials, the thermal conductivity $\mathbf{k}$ is a second rank tensor that is diagonal in the axes of symmetry. Its components are given by the following relations when the axes are rotated of the angle φ:

$$k'_{11} = k_{11}, \quad k'_{23} = k'_{32} = cs(k_{33} - k_{22}), \quad k'_{12} = k'_{113} = 0,$$

$$k'_{22} = c^2k_{22} + s^2k_{33}, \quad k'_{33} = s^2k_{22} + c^2k_{33}. \tag{23}$$

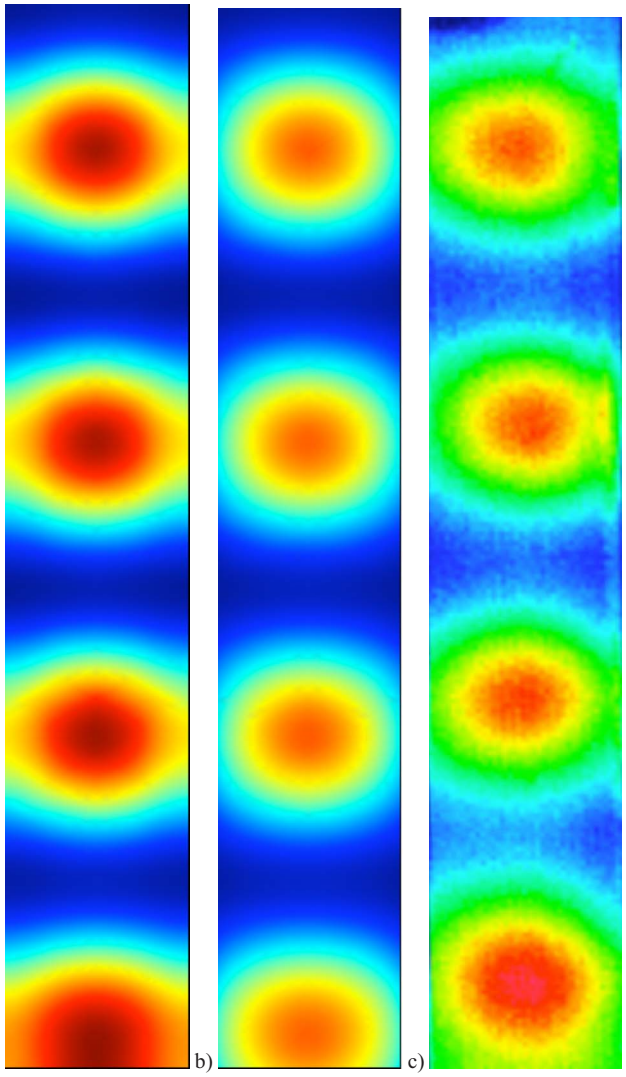


FIG. 2. (Color online) Temperature field after 2 min of excitation: (a) FE model result with $h=0$ W/(m^2 K), (b) FE model result with $h=5$ W/(m^2 K), and (c) infrared camera result.

B. Boundary conditions

In the FE code,[14] the thermal boundary conditions are introduced by the equation

$$-\mathbf{n}\cdot\mathbf{k}\,\nabla\,T = h(T - T_r). \tag{24}$$

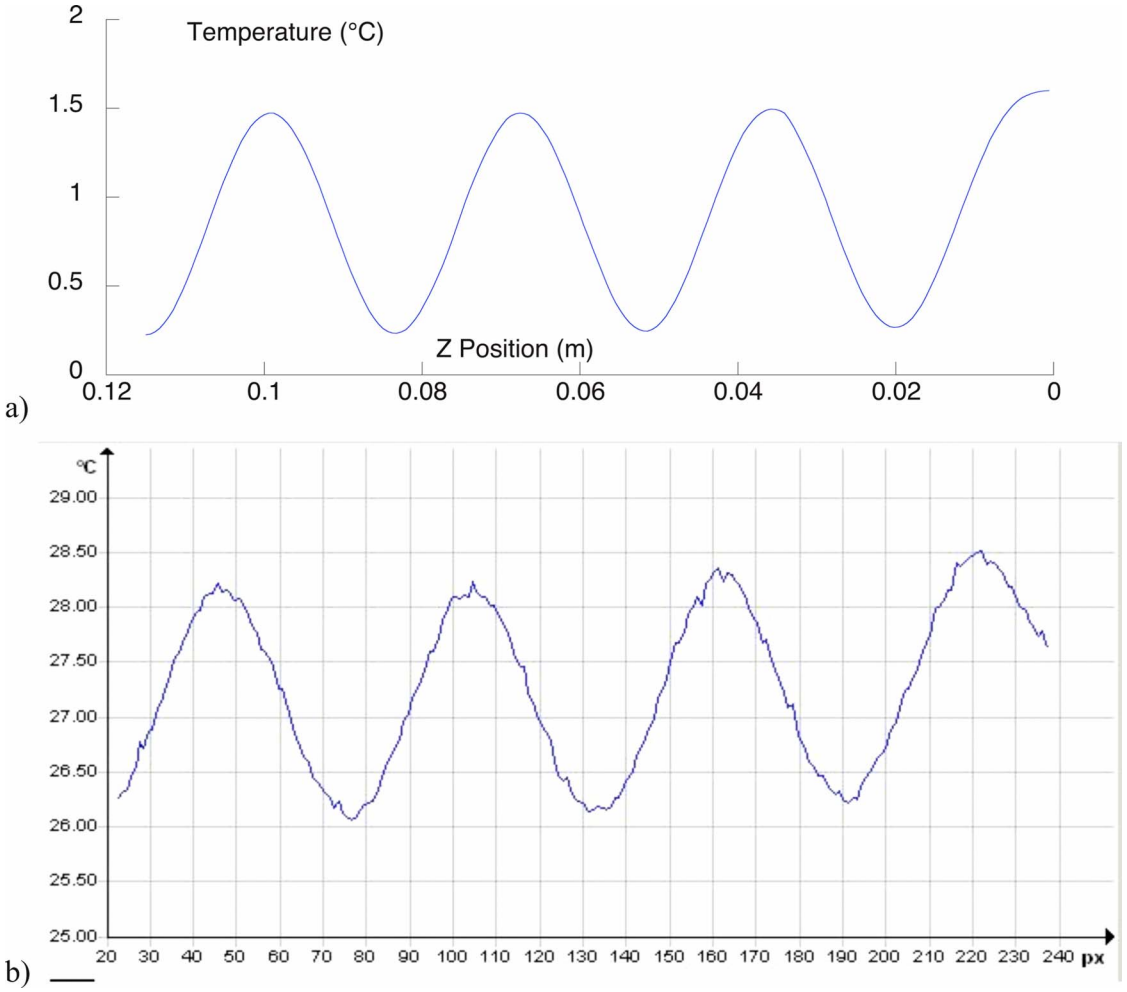


FIG. 3. (Color online) Temperature field at the center of the surface of the plate. (a) FE model result and (b) infrared camera result. (The 240 pixel position corresponds to the position $z=0$.)

The left hand side term represents the temperature flux through the surface with a normal **n**. h is a heat transfer term that represents the exchange with the ambient temperature T_r and is difficult to estimate. In a first approach, it is taken to be zero and the thermal boundary condition corresponds to a thermal isolation. This hypothesis is justified at the beginning of the excitation, since the heating phenomenon induced by ultrasonic wave is fast and limited to a small temperature rise. It will be shown in the following that this hypothesis becomes wrong after a longer time.

V. EQUIPMENT FOR HIGH LEVEL ULTRASONIC EXCITATION AND FOR IMAGING THE TEMPERATURE FIELD

The purpose of this equipment is to realize a preliminary test of the model and to verify the feasibility to measure the temperature field induced by the ultrasonic field with an infrared camera. If the viscoelastic and the thermal properties of the sample are known, the model should be able to predict the temperature rise in function of the time. Then one can verify if an infrared camera has a thermal resolution low enough to follow the temperature rise. The sample is a PVC plate for which the viscoelastic and thermal properties are given in Table I. This material is used as a reference since its properties can be found in literature. The width (20 mm) and the thickness (5 mm) of the plate were chosen to correspond to the size of the sonotrode used to excite the plate. The length (115 mm) was chosen to obtain some standing waves at the excitation frequency (27 kHz) and a temperature field with a lot of features. The laboratory made sonotrode is based on a Cedrat actuator (PPA10M) (Ref. 15) that excites a stainless steel block. Since it is difficult to measure the imposed displacement at the interface plate/sonotrode, the displacement is measured at the end of the plate with a laser Doppler velocimeter. Typically, the value of this displacement is in the order of 400 nm. Then the imposed displacement (Fig. 1) is adjusted to obtain the same displacement at this extremity in the model as in the experiment. The tem-

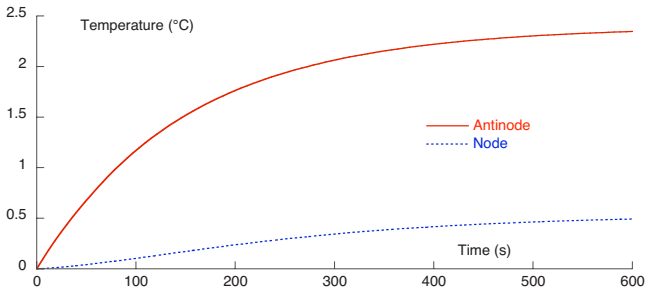


FIG. 4. (Color online) Temperature rise as a function of time at the position of a node and an antinode.

perature field is measured with an infrared camera (Cedip Jade III) with a thermal resolution of 20 mK.

VI. COMPARISON BETWEEN MODEL AND EXPERIMENT

Figure 2(a) presents the temperature field computed at the time of 120 s. The high and low temperature zones correspond to the antinodes and nodes of the standing wave, respectively. The temperature wavelength is the half of the acoustic wavelength. The noncontact measurement of this wavelength could be seen as a NDE method to follow the acoustic properties. Figure 2(c) presents the temperature field measured by the infrared camera after 2 min of excitation by the sonotrode. It is clear that the computed and experimental temperature fields have similarities: the same numbers of nodes, the same wavelength, and roughly the same shape around the antinodes. However, this shape is closer to a circle in the measured field. To change this aspect, the heat transfer term h in Eq. (24) was equal to 5 $W/(m^2\,K)$ instead of zero in order to simulate an exchange with the ambient air. Figure 2(b) gives the result of the computed temperature field with these new thermal boundary conditions. This has an effect on the shape of the temperature field around the antinodes. The value of h was varied arbitrarily to get the better likeness.

Another important unknown is the boundary condition that must be applied at the interface between the sonotrode and the plate. The imposed displacement at this interface is probably the main reason of the difference between the computed and experimental results, which is the shift in the position of the antinodes and the nodes and the phase difference in Fig. 3.

Figure 3(a) presents the computed temperature variations along a line situated in the center of the surface of the plate and Fig. 3(b) presents the results extracted with the software of the infrared camera. It is noticeable that the order of the temperature rise is the same although the precisions of the thermal properties are not well known.

If the conductivity is neglected Eq. (22) gives a linear evolution for the temperature as follows:

$$T = \frac{\mathrm{div}(\mathbf{P})}{\rho c_P} t. \tag{25}$$

Figure 4 permits to compare the temperature rise as a function of time at two positions of an antinode and a node. The temperature rise is almost linear at the beginning of the excitation at the antinode position and is almost zero at the node position. However, after around 1 min, the conductivity changes the shape of the temperature rise and the temperature increases slightly at the node. Then this proves that the conductivity must not be neglected in that situation. The conductivity limits the difference between hot and cold zones and the exchange with the ambient medium limits the temperature rise that tends to reach an asymptote.

VII. CONCLUSIONS

The theory that determines the temperature rise due to the loss of mechanical energy in an anisotropic viscoelastic material has been applied in a FE model. The computed loss of energy permits to predict the temperature rise and the resolution of the heat equation gives the repartition of this rise in time and in space.

As a preliminary test of the model, it has been applied to the propagation of an ultrasonic wave in a sample made of PVC. The comparison of the temperature rise computed and measured by an infrared camera was satisfactory enough to validate the model.

This method could be used as a NDE method since the temperature field is directly linked to the mechanical and thermal properties. By sending the waves in various directions, the anisotropic properties could be assessed locally by using high frequencies or homogenized on a large area by using low frequencies.

If the acoustic and thermal properties of the tested structure are known, the model can predict the potentialities of the NDT method to detect a defect. It is a guide to define the frequency, the nature of the acoustic mode, and the characteristics of the infrared camera for detecting a specified defect. In the near future, the method will be tested with anisotropic and viscoelastic materials such as composite materials.

[1] X. Maldague, *Nondestructive Evaluation of Materials by Infrared Thermography* (Springer-Verlag, London, 1993), p. 224; *ibid.*, rev. ed. (Wiley, New York, 2001).
[2] J. Rantala, D. Wu, and G. Busse, "NDT of polymer materials using lock-in thermography with water-coupled ultrasonic excitation," NDT & E Int. **31**, 43–49 (1998).
[3] L. D. Favro, X. Han, Z. Ouyang, G. Sun, H. Sui, and R. L. Thomas, "Infrared imaging of defects heated by a sonic pulse," Rev. Sci. Instrum. **71**, 2418–2421 (2000).
[4] L. D. Favro, R. L. Thomas, X. Han, Z. Ouyang, G. Newaz, and D. Gentile, "Sonic infrared imaging of fatigue cracks," Int. J. Fatigue **23**, 471–476 (2001).
[5] W. Hassan, C. Homma, Z. Wen, F. Vensel, and B. Hogan, "Detection of tight fatigue cracks at the root of dampers in fan blades using sonic IR inspection: A feasibility demonstration," AIP Conf. Proc. **894**, 3–13 (2002).
[6] M. Morbidini, P. Cawley, T. Barden, D. Almond, and P. Duffour, "Prediction of the thermosonic signal from fatigue cracks in metals using vibration damping measurements," J. Appl. Phys. **100**, 104905 (2006).
[7] J. Lemaître and J. L. Chaboche, *Mechanics of Solid Materials* (Cambridge University Press, New York, 1990).
[8] M. Castaings, C. Bacon, B. Hosten, and M. V. Predoi, "Finite element predictions for the dynamic response of thermo-viscoelastic material structures," J. Acoust. Soc. Am. **115**, 1125–1133 (2004).
[9] J. D. Ferry, *Viscoelastic Properties of Polymers* (Wiley, New York, 1980).
[10] R. M. Christensen, *Theory of Viscoelasticity: An Introduction* (Academic, New York, 1971).
[11] R. N. Bracewell, *The Fourier Transform and Its Applications* (McGraw-Hill, New York, 1965).
[12] B. A. Auld, *Acoustic Fields and Waves in Solids* (Wiley-Interscience, New York, 1973), Vol. **2**.
[13] B. Hosten and C. Biateau, "Finite element simulation of the generation and detection by air-coupled transducers of guided waves in viscoelastic and anisotropic materials," J. Acoust. Soc. Am. **123**, 1963–1971 (2008).
[14] COMSOL Multiphysics User's Guide, Version 3.3, http://www.comsol.com (Last viewed May, 2008).
[15] http://www.cedrat-groupe.com/fr/produits-mecatroniques/actuators/ppa.html (Last viewed May, 2008).

Personal audio with multiple dark zones

Matthew Jones[a] and Stephen J. Elliott[b]
Institute of Sound and Vibration Research, University of Southampton, University Road, Highfield, Southampton S017 1BJ, United Kingdom

(Received 10 January 2008; revised 29 August 2008; accepted 3 September 2008)

This work considers providing personal audio for a listener by use of a local array of acoustic sources driven in such a way as to maintain the reproduced levels in one seat, in the so-called "bright zone," while minimizing the levels experienced by others sitting close by, in the so-called "dark zones." Multiple dark zones are considered both adjacent to and in front of the listener, initially using monopole simulations to investigate three different control strategies, and it is shown that a particular orientation of two sources is able to provide good control over the dark zones in these directions. It is shown that minimizing the sound power radiated by the local array while constraining the reproduced level in the bright zone is an effective method of achieving isolation when the dark zones are numerous. The findings of the investigations are used to design an optimal source arrangement, for which the isolation performance is improved by about 20 dB up to 1 kHz, which is verified with Boundary Element Method (BEM) models and predictions based on measured responses. © *2008 Acoustical Society of America.* [DOI: 10.1121/1.2996325]

PACS number(s): 43.38.Hz, 43.38.Md, 43.50.Ki, 43.38.Ja [AJZ] Pages: 3497–3506

I. INTRODUCTION

In certain environments such as aircraft and cars, it may be unsafe for individuals to listen to audio using headsets since this may prevent the wearer from hearing important announcements and may also be uncomfortable over long periods of time. Therefore it is desirable to use loudspeakers mounted in the headrest of the seat for the reproduction of sound, although this approach suffers from problems with leakage of sound to those around.

This work looks at using a local array of sources in the headrest to attempt to faithfully reproduce the audio in one seat while minimizing the leakage of sound to seats nearby so that each seat provides personal, isolated audio. Such scenarios can occur when there is more than one row of seats positioned close together, as is often the case in aircraft. Previous work[1] has looked at the problem when there are just two adjacent seats, where audio is reproduced in one of the seats, termed the "bright zone," while the levels are reduced in the adjacent seat, termed the "dark zone." Here the work is extended to consider the problem when there is more than one dark zone, so that the leakage of sound to multiple seats is minimized.

The performance of three different control approaches for increasing the isolation is evaluated in this work using simulations in which multiple dark zones are defined around a single bright zone, and the improvement in isolation for each approach is predicted. The performance of each approach is evaluated in terms of the achieved *acoustic contrast*, which is the ratio of the mean square pressures in the bright zone to the mean square pressures in the dark zones, such that a large acoustic contrast indicates good isolation performance. Two of these control approaches were previously investigated by Choi and Kim,[2] but a third, involving minimization of the sound power radiated by the source array, is introduced here and appears to have significant advantages in designing such systems.

The particular problem of concern in this work is shown by the plan view in Fig. 1, where the geometrical arrangement used is depicted, including the locations of the sources and sensors employed in the simulations and experiments undertaken here. The dimensions are measured from a pair of adjacent airline-style seats, for which loudspeakers have been attached to the headrests. Three seats are shown in the diagram, where one of the seats corresponds to the bright zone and the others are the two dark zones, with one of these dark zones located to the side of the bright zone (Dark Zone A) and one located in front (Dark Zone B), separated from the bright zone by a typical seat pitch of 0.79 m (Ref. 3). In each zone there are four microphones, where two microphones are clamped to the sides of the headrest and two are located at the positions of the ears of those sitting in the seats. Although in some control approaches the microphones are not used in the calculation of the optimal filters, these microphones are used for the calculation of performance in terms of the acoustic contrast between these seats and the bright zone, and by spreading microphones around each seat, predictions of the average levels experienced in that seat can be made. In this work only the single-sided problem will be considered, where we assume that the audio reproduced with the loudspeakers on one side of the headrest in the bright zone is uncorrelated with that reproduced on the opposite side, so that only one side is required to be simulated due to the fact that the problem is symmetrical. The full stereo problem can be split into two parts: one where the signals are perfectly correlated and one where they are perfectly uncorrelated. The latter problem is considered here, but the former problem, requiring two primary and two secondary sources, is discussed in Ref. 4.

[a]Electronic mail: mj@isvr.soton.ac.uk
[b]Electronic mail: sje@isvr.soton.ac.uk

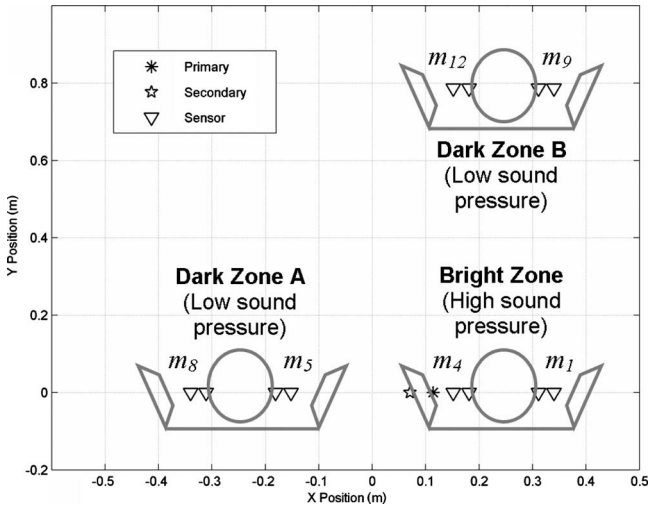


FIG. 1. Plan view of the geometrical arrangement with two dark zones used in the monopole simulations, in which the ellipses denote the notional head positions and the quadrilateral shapes denote the position of the wings of the headrest, neither of which are modeled here.

To begin with, free-field monopole simulations are used to identify the source arrangement that gives the greatest average acoustic contrast for both dark zones. Although modeling the sources as monopoles ignores several effects that will be important in determining the detailed behavior of a practical system, a monopole model gives a useful indication of the average behavior, which is independent of the physical details of headrest geometry. Similarly the anechoic conditions assumed for these simulations ignore the acoustic effects of the enclosure, but provided that the enclosure is reasonably large, it is expected that the near-field responses near the headrest, reproduced by the monopole simulations, will dominate the reverberant field. Three different control approaches are investigated for each arrangement to determine the best strategy when there are multiple dark zones present. The results are then used to model a pair of adjacent seats with the source positions corresponding to this optimal arrangement found from the monopole simulations, which is then used in a more sophisticated Boundary Element Method (BEM) simulation. This allows predictions of the performance when there are reflective and absorptive surfaces present, which are more representative of the real system.

II. CONTROL APPROACHES

The three different control approaches evaluated in this work are discussed here, with some comparisons between the behaviors of each. In each case the relative strength of the array of sources is adjusted to maximize various measures of performance.

A. Contrast maximization

With this approach, the difference in the mean square pressure in the bright and dark zones, or the acoustic contrast, is directly maximized. For a single frequency, this can be defined as the ratio:

$$R_C = \frac{\boldsymbol{p}_b^H \boldsymbol{p}_b}{\boldsymbol{p}_d^H \boldsymbol{p}_d}. \tag{1}$$

Here $\boldsymbol{p}_b$ is a vector of complex pressures in the bright zone, i.e., m_1 to m_4 in Fig. 1, and $\boldsymbol{p}_d$ is a vector of complex pressures in both of the dark zones, i.e., m_5 to m_{12} in Fig. 1. Since the pressure arriving at a sensor due to a single source is related to the complex source volume velocity by the complex impedance associated with the path from the source to the sensor, the vectors $\boldsymbol{p}_b$ and $\boldsymbol{p}_d$ due to multiple sources can be written as $\boldsymbol{p}_b = \boldsymbol{Z}_b \boldsymbol{q}_c$ and $\boldsymbol{p}_d = \boldsymbol{Z}_d \boldsymbol{q}_c$, respectively. The quantity $\boldsymbol{q}_c$ is the [N-by-1] vector of complex source strengths, which are to be optimized, and $\boldsymbol{Z}_b$ and $\boldsymbol{Z}_d$ are [M-by-N] matrices of complex impedances to the bright and dark zone sensors, where M is the number of sensors and N is the number of sources. By combining these expressions with Eq. (1), the acoustic contrast can now be expressed as

$$R_C = \frac{\boldsymbol{q}_c^H \boldsymbol{Z}_b^H \boldsymbol{Z}_b \boldsymbol{q}_c}{\boldsymbol{q}_c^H \boldsymbol{Z}_d^H \boldsymbol{Z}_d \boldsymbol{q}_c}. \tag{2}$$

As Choi and Kim show,[2] this ratio is maximized if the vector of complex source strengths is equal to the eigenvector of the matrix $[\boldsymbol{Z}_d^H \boldsymbol{Z}_d]^{-1} \boldsymbol{Z}_b^H \boldsymbol{Z}_b$ associated with the largest eigenvalue.

B. Control effort minimization

An alternative cost function also developed by Choi and Kim is what the authors term the brightness constraint, where the control effort is explicitly minimized while a constraint exists to maintain the reproduced levels in the bright zone. The control effort can be described as the mean square source strengths, which may be written as $\boldsymbol{q}_c^H \boldsymbol{q}_c$. The ratio to be maximized in this case becomes

$$R_E = \frac{\boldsymbol{q}_c^H \boldsymbol{Z}_b^H \boldsymbol{Z}_b \boldsymbol{q}_c}{\boldsymbol{q}_c^H \boldsymbol{q}_c}. \tag{3}$$

The vector of source strengths that maximizes this ratio is the eigenvector of the matrix $\boldsymbol{Z}_b^h \boldsymbol{Z}_b$ corresponding to the largest eigenvalue.

C. Sound power minimization

Another control strategy is to minimize the sound power output of the array directly while constrained to maintain the reproduced levels in the bright zone. The cost function is obtained from the definition of the sound power W for multiple monopole sources, which can be written as $W = \frac{1}{2} \boldsymbol{q}_c^H \mathrm{Re}\{\boldsymbol{Z}_q\} \boldsymbol{q}_c$. Here $\boldsymbol{Z}_q$ is the N-by-N matrix of transfer impedances from each source to the pressure at every other source position, in other words, the contribution of the pressure at each of the source positions due to each source divided, in turn, by the volume velocity of that source, as described, for example, in Ref. 5.

As the number of dark zone microphones is increased to include a shell all around the bright zone, the contrast maximization results naturally converge to the power minimization results in an anechoic environment.

The denominator used in Eq. (2) is replaced by this expression for the sound power, and so the ratio to be maximized becomes

$$R_p = \frac{2\boldsymbol{q}_c{}^H \mathbf{Z}_b{}^H \mathbf{Z}_b \boldsymbol{q}_c}{\boldsymbol{q}_c{}^H \mathrm{Re}\{\mathbf{Z}_q\}\boldsymbol{q}_c}. \quad (4)$$

The solution to this expression in which the ratio R_p is maximized will be equal to the eigenvector associated with the largest eigenvalue of the matrix $2[\mathrm{Re}\{\mathbf{Z}_q\}]^{-1}\mathbf{Z}_b$. For simplicity, the factor of 2 can be ignored since the eigenvalues themselves are not employed.

D. Comparison of different control approaches

When analyzing the performance of the different approaches in terms of the acoustic contrast achieved, the contrast maximization approach will always yield the maximum performance. However, the problem with the contrast maximization approach is that since the approach has no knowledge of the pressure outside the dark zones, the solution may result in regions of high pressure levels away from the defined dark zones. To avoid this problem, a more straightforward approach would be to attempt to minimize the sound power output of the array while maintaining the reproduced levels in the bright zone. In this way, high sound pressure levels for all regions outside the bright zone are minimized, and the acoustic contrast is maximized when considering the whole region of space surrounding the source array; therefore the solution will be more appropriate when there are a large number of dark zones located close to the bright zone.

The control effort minimization seeks solutions that give the largest reproduced pressure in the bright zone using the weakest possible individual source strengths. When the distance between the primary and secondary sources becomes large compared with the wavelength, their power outputs become almost independent. The sound power minimization solution then approaches that of control effort minimization since the matrix $\mathbf{Z}_q$ becomes proportional to the identity matrix in this high frequency case. It is, however, the lower frequency case where greatest improvement in contrast can be obtained.

III. MONOPOLE SIMULATIONS

In the simulations presented here, it is assumed that all sources act as monopoles in an anechoic environment so that free-field radiation conditions apply. This provides an estimate of the limits of performance with each arrangement, so that the results are not applicable for just one particular headrest design but can be used to gain insight into the generalized problem.

Several simulations are carried out, where the source positions are adjusted and the resulting sound field and the acoustic contrast achieved are evaluated for the different control approaches outlined above. Initially, a single "primary" source and a single "secondary" source are employed, as illustrated for the simulations in Fig. 2, and the best relative position of these sources is investigated. Afterward, the performance using an additional secondary source is predicted through the simulations, and while the original secondary source is kept in the optimal location, the location of this extra source is investigated and adjusted to yield the maximum performance. Because of the analogy with active control, the behavior in the absence of the secondary source is termed the *passive* performance and with the optimized secondary source is termed the *active* performance.

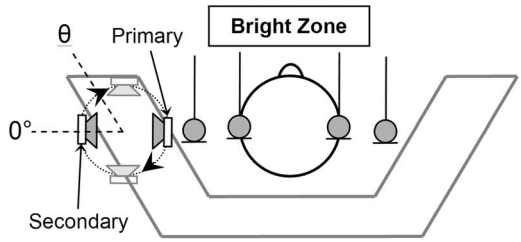


FIG. 2. Details of the primary and secondary source arrangements near the bright zone, showing the rotation of the primary and secondary source pair from the original position (dark) to a 90° rotation (faint).

A. Single secondary source

In defining the arrangement used in the simulations, there are a finite number of possible locations for the primary source. In this work, it is assumed that the primary source is mounted on one of the wings of the headrest attached to the bright zone seat. In this arrangement the mounting is straightforward, and due to the proximity of the loudspeakers to the ears of those sitting in the seat, the perceived levels in the seat can be high without needing to drive the loudspeakers hard.

Typically it is desirable to locate the secondary source as close as possible to the primary source to achieve most acoustic control,[5] and therefore the distance separating the primary and secondary sources in the first set of simulations is maintained at a minimum of 4 cm, which is the separation distance of a pair of small 3 in. full-range Fostex drivers used in earlier experiments when mounted face to face.[6] The first set of simulations considers the effect of rotating the primary and secondary source pair around the central pivot of this pair, as shown in the diagram in Fig. 2, in which the primary and secondary sources are shown in both their original positions, in dark, and rotated positions, in feint. For a number of discrete values of the orientation angle θ, shown in Fig. 2, the sound field surrounding the bright zone is computed before and after optimization, where the three different cost functions are employed to find the optimal complex source strengths. Figure 3 shows the results for these simulations in terms of the acoustic contrast averaged for both dark zones shown in Fig. 1 and averaged over frequencies up to 2 kHz as a function of the source orientation angle. Also shown in Fig. 3 is the sound power output of the array averaged over the frequency as a function of the source orientation angle. The frequency average is taken from 0 Hz to 2 kHz in small enough steps that the result is independent of step size.

It can be seen in Fig. 3 that for a maximum contrast with the arrangement in Fig. 1, the optimal source orientation angles are around 50°–60°, where a good isolation performance is achieved without the high sound power output levels that occur at around 90°. The orientation angles of

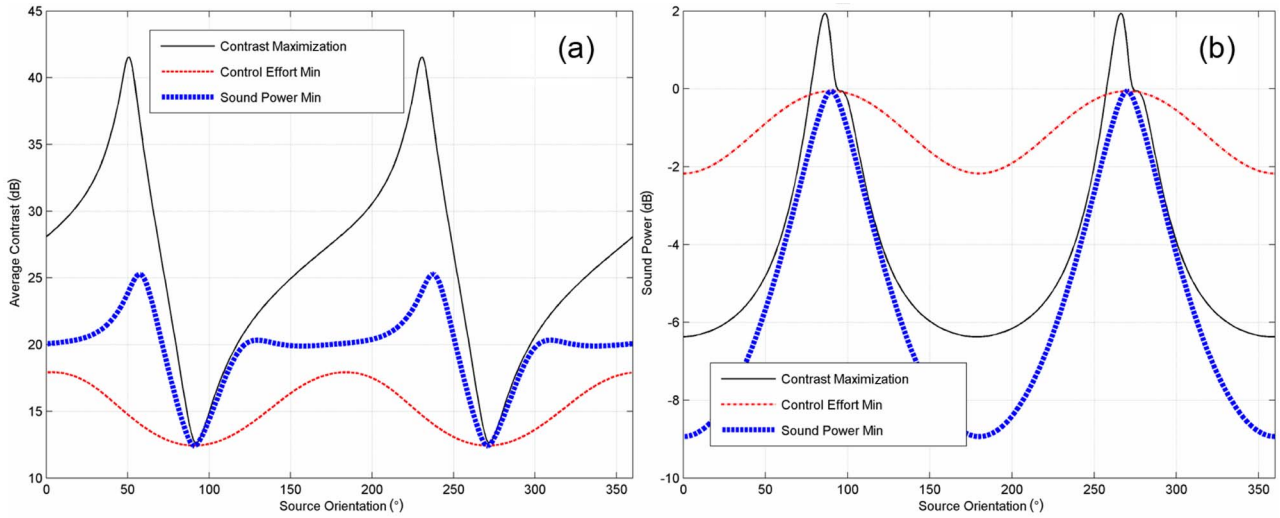


FIG. 3. (Color online) Monopole simulation results of (a) average acoustic contrast achieved with the different control approaches as a function of source orientation angle and (b) average sound power output of the array with constant mean square pressure in the bright zone for the different control approaches as a function of source orientation angle.

50° – 60° correspond to the case where the nulls in the directivity pattern of the array, which are generated by the relative source strengths determined by the result of the optimization processes described in Sec. II, line up with the locations of the two dark zones, as shown in Fig. 4. As expected, the results from 180° to 360° are the same as the results from 0° to 180° when both sources are active since the arrangement of the array is identical when rotated by 180°. The high sound power output at 90° is due to the null in the directivity, which this approach gives, being directed toward the bright zone so that the array must increase the output level in order to maintain the reproduced levels. The minimum sound power output of −9dB is obtained at 0° since in this case the bright zone microphones are in line with the main beam, while the increase in sound power between 50° and 60° is roughly 3 to 4 dB. Contour plots of the sound field at 500 Hz are provided in Fig. 4 for sources placed at the orientation angle of 50°, where the contrast maximization and the sound power minimization approaches are used. The angle of 50° has been chosen here since it corresponds to the maximum contrast using the contrast maximization method and is significantly superior to the performance achieved with the sound power minimization approach. Figure 5 shows the acoustic contrast and sound power output for these two approaches as functions of frequency when the source orientation angle is fixed at 50°.

From these results, it can be concluded that with just two dark zones, the sound power minimization approach achieves an average of 17 dB less acoustic contrast than that achieved by directly maximizing the acoustic contrast while obtaining only a small decrease in the sound power output, especially at high frequencies. The control effort minimization approach is shown to achieve poor performance in terms

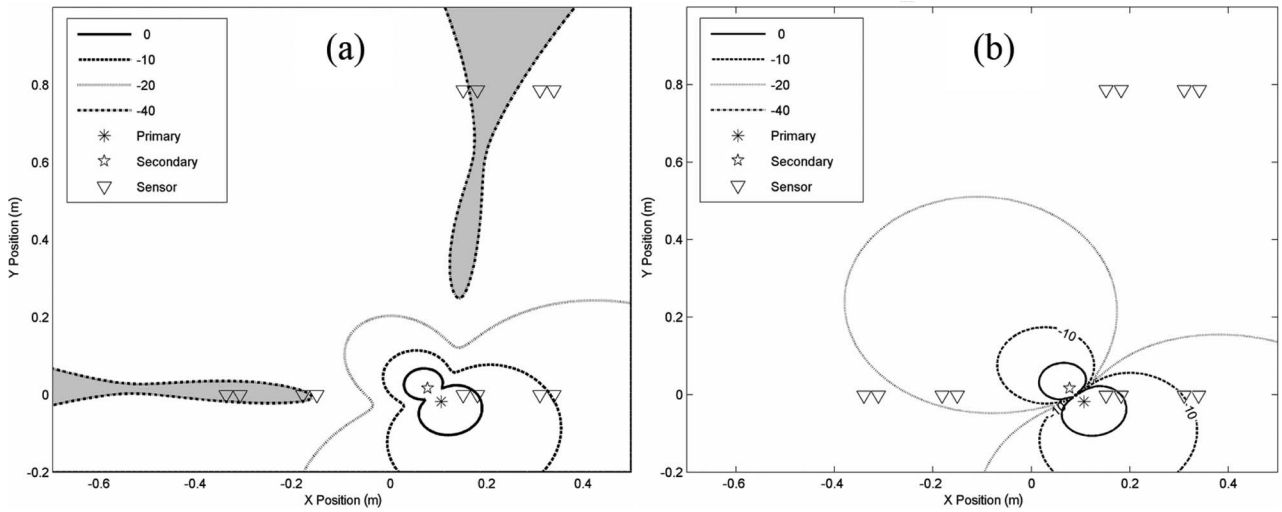


FIG. 4. Monopole simulation results of the (a) contour plot of the sound pressure level, in decibels, at a frequency of 500 Hz for a source orientation angle of 50° using the contrast maximization approach and (b) using the sound power minimization approach.

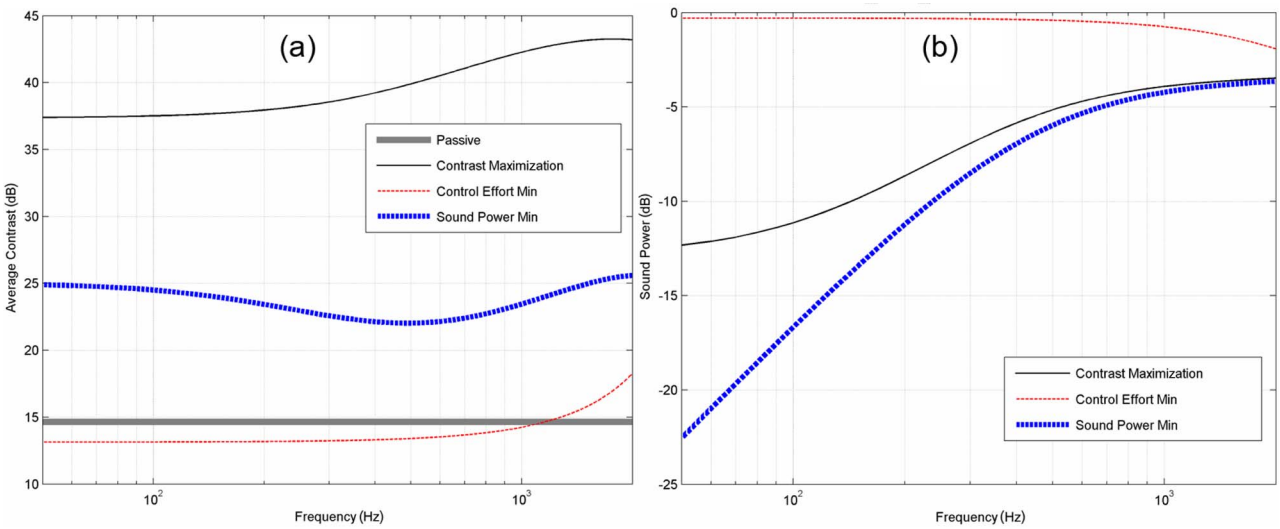


FIG. 5. (Color online) (a) Passive contrast (no secondary source) and active contrast (with optimized secondary source) predicted from monopole simulations of two dark zones, as a function of frequency, using all three control approaches and a source orientation of 50°. (b) Sound power output of the two-source array as a function of frequency using all three control approaches.

of both the acoustic contrast and the sound power output and is therefore not considered any further in this work.

Using the contrast maximization method, there is an unexpected increase in contrast at higher frequencies. Usually the control performance would be expected to drop due to the smaller zones of silence,[5] but in this case the orientation of the source array has been optimized, and the zones of silence continue to enclose the dark zones while the reproduced level in the bright zone increases due to local interference.

B. Two secondary sources

In this next set of simulations, the orientation of the primary and secondary source pair is maintained at an angle of 50°, and an additional secondary source is employed. In the final sound field plot, only the contrast maximization approach is employed since it provides solutions that achieve significantly greater reductions of levels at the two dark zones compared to the sound power minimization method, despite the fact that sound power minimization achieves more attenuation in the average far-field levels.

Initially, to locate the optimal position for this third source, the source is moved across a grid of locations surrounding the seats, and the average contrast at the dark zones to the front and side is calculated for each position. A plot of the active acoustic contrast as a function of the third source position, as predicted from the simulation, is provided in Fig. 6, along with a plot of the sound power for each of the source positions.

From these results, it appears that the optimal position for the third source is in a line that joins the primary and secondary sources. The maximum acoustic contrast is achieved when the third source is positioned close to either the secondary or the primary source, which is to be expected

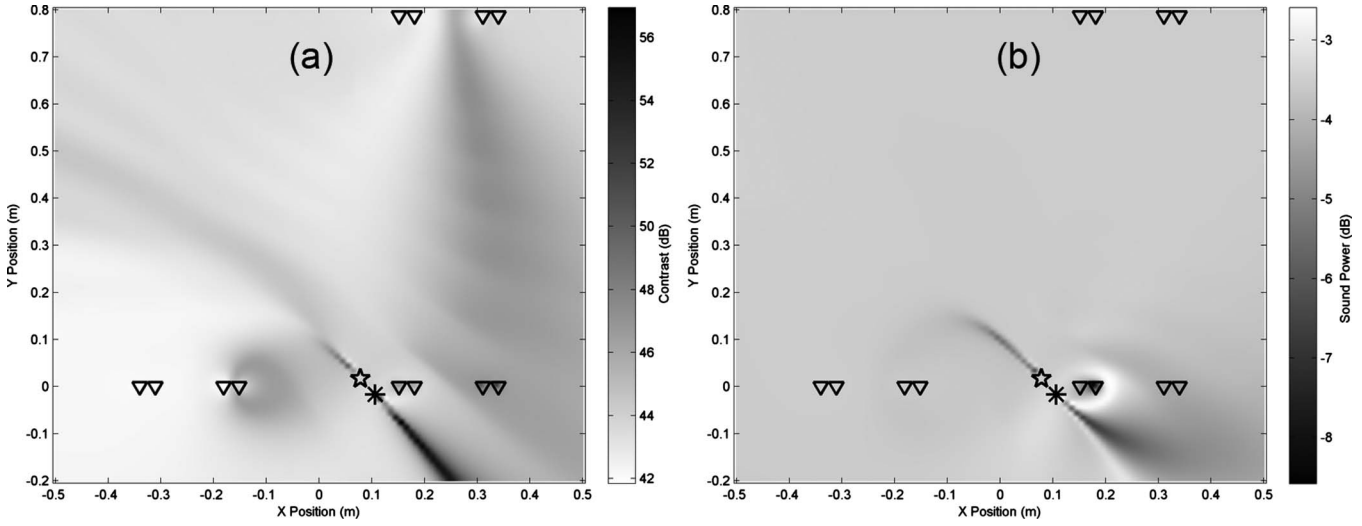


FIG. 6. Monopole simulation results of (a) averaged acoustic contrast achieved as a function of the third source position and (b) sound power output of the array as a function of the third source position using the contrast maximization approach.

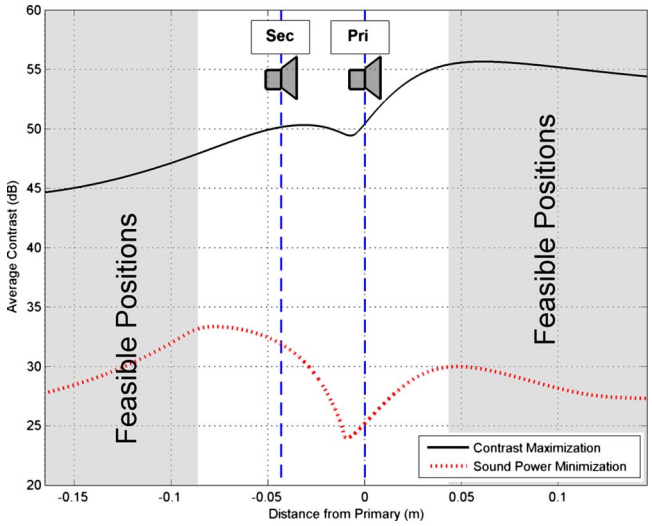


FIG. 7. (Color online) Monopole simulation results of the active contrast averaged for both dark zones and averaged over frequency as a function of the distance of the third source from the primary, in a line joining the secondary and primary sources, using both the contrast maximization and the sound power minimization approaches.

since by colocating a source it is easier to control the sound field over the whole region since the sound fields due to the two sources match. However, it is not possible to mount the sources any closer than 4 cm since this is the minimum separation distance when the two drivers chosen for this work are mounted face to face.

By moving the third source along the line joining the primary and secondary sources, a plot can be produced that shows the average acoustic contrast achieved and also the sound power output as a function of distance from the primary source position. These plots are shown in Figs. 7 and 8, respectively, where the grayed areas show the locations for the third source that are as close as possible to either the

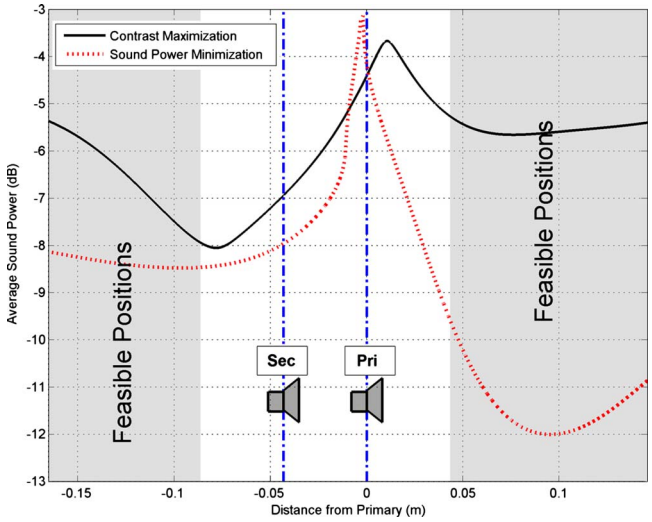


FIG. 8. (Color online) Monopole simulation results of the frequency averaged sound power output of the array as a function of the distance of the third source from the primary, in a line joining the secondary and primary sources, using both the contrast maximization and the sound power minimization approaches.

primary or the secondary source given the minimum separation distance of 4 cm. These plots show the results using both the contrast maximization and the sound power minimization approaches.

For the purposes of generating a large zone of silence, it is clearly a wise choice to attempt to locate the third source close to one of the existing sources. However, this particular geometry shows optimal performance with contrast maximization for a separation distance slightly larger than 4 cm when placed next to the primary source and exhibits decreasing performance for smaller separations. This is due to a null being directed toward the bright zone for small separation distances, and so the contrast suffers.

By locating the third source close to the primary source, the average acoustic contrast achieved is around 8 dB more than that achieved by locating the source next to the secondary, although placing the source next to the primary incurs an increase in the sound power output of approximately 2.5 dB. The increased contrast is due to the dark zone to the side being located in line with the null when the additional source is clamped to the primary source. The fact that the sound power output is very similar for both source arrangements indicates that although the solutions for both cases give similar sound fields, the bright zone sensors are located at a similar angle from the null in the directivity of the source array for both cases. Therefore the output of the array does not need to be amplified to generate the same level at the bright zone microphone m_3. Plots of the acoustic contrast and the sound power output for the two possible locations of the third source are also shown in Fig. 9, which are compared to the results using contrast maximization with just a single secondary source.

These results demonstrate that the contrast maximization approach is able to achieve large localized increases in the contrast with little increase in the sound power output. The use of a third source clamped to the primary source allows increases of around 15–20 dB in the acoustic contrast and decreases in the average sound power output of around 1 dB, with increasing performance at low frequencies. There is a drop in the predicted contrast for the three-source cases, where at a few hundred hertz the source separation becomes comparable to one-tenth of a wavelength, and therefore the performance becomes localized as the zones of silence become smaller. By placing the third source close to the primary source, the sizes of the zones of silence directed toward the two dark zones are much larger than when the third source is placed next to the secondary source. This is likely to be a consequence of the contrast maximization approach attempting to steer the null away from the bright zone, which is easier when the third source is placed next to the primary. Therefore the benefits of using a third source are evident, although the nature of the optimal arrangement suggested may present difficulties in the manufacture of such a loudspeaker, with a requirement for three closely spaced drivers.

IV. BEM SIMULATIONS AND EXPERIMENTS

Two BEM simulations of the source arrangements of interest were developed to verify that the suggested solution

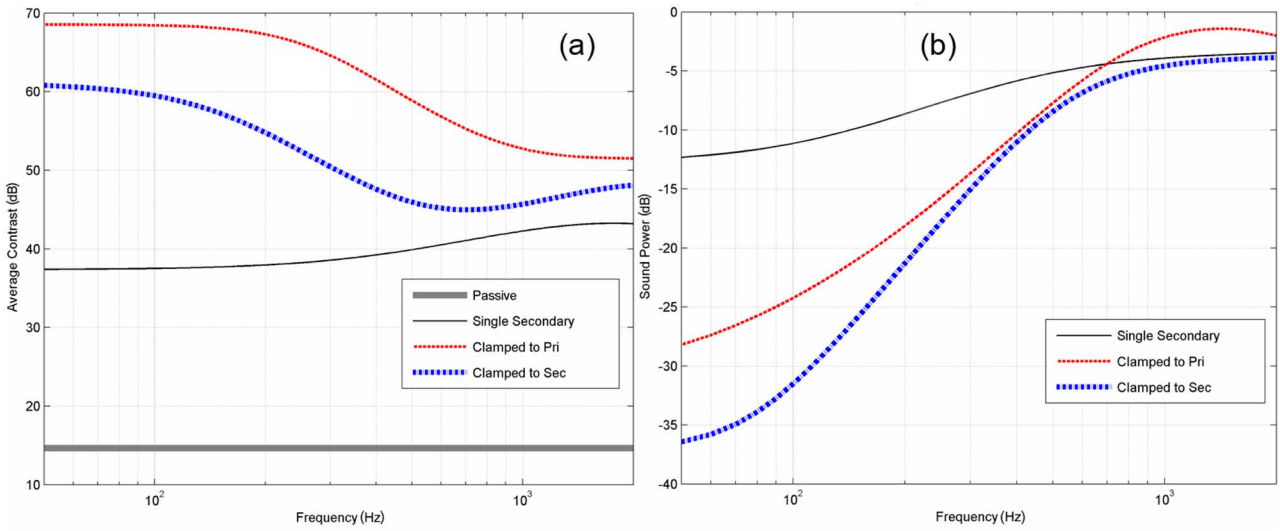


FIG. 9. (Color online) (a) Passive and active contrasts averaged for both dark zones as a function of frequency for the two-source arrangements. (b) Sound power output of the array as a function of frequency for the two-source arrangements.

applies to a real seat when there are multiple reflecting and absorbing surfaces present. An acoustic mesh consisting of 28 164 elements is constructed with two torsos in a pair of airline seats that were obtained for this work (Fig. 10) using ANSYS with an average element size of about 0.019 m, giving an upper frequency limit of around 3 kHz. The arrangement is assumed to be housed in an anechoic environment. The sources are represented by a nonzero velocity boundary condition being defined on certain elements of this mesh. In this case the source array consists of a cylinder in which the disks at either end act as separate sources. The cylinder is oriented such that the top and bottom faces represent the sources with an orientation of 50°, which is the angle found to achieve optimal performance using the contrast maximization approach. The variational BEM is employed for this work since this method was found to be more robust with such thin-walled structures present compared to the direct BEM (e.g., see Ref. 7), even when using overdetermination points.

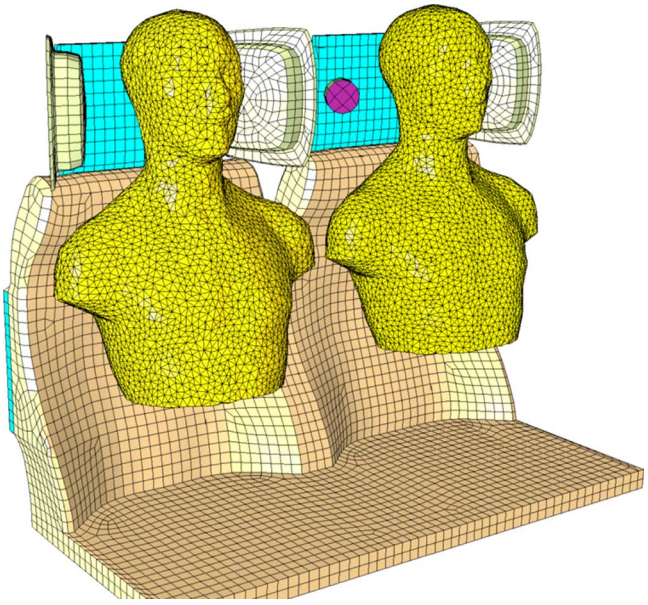


FIG. 10. (Color online) Image of the acoustic mesh used in the BEM simulations, including dummy head meshes (laser scanned meshes provided courtesy of Y. Kahana).

In order to plot the sound field after control, a high density planar array of field points is defined around the locations of the three seats, and the numerical problem is solved for each source individually to define the impedance matrices in Sec. II using LMS VIRTUALLAB, which takes around 60 h on a PC. Using the complex pressures at the field point locations that are obtained from these solutions, the optimal source strengths are calculated, from which the performance can be predicted.

The first set of results shows the sound field and the acoustic contrast performance when a single secondary source is employed, placed at an orientation of 50°. Figure 11 shows the sound field after contrast maximization at frequencies of 500 and 1550 Hz calculated with the primary and secondary source pair at an optimal orientation of 50°. The average acoustic contrasts before and after control for the two dark zones are shown in Fig. 12(a), where results have been obtained using two separate high and low resolution acoustic meshes to allow accurate results for both frequency regions.

Figure 12(b) shows the predicted passive and active contrast results using frequency responses measured with a real seat in an anechoic chamber, as described in more detail in Ref. 1. Due to the nature of the way the drivers are mounted, the secondary source radiates sound even when only the primary source is driven, and so the back radiation from this source is compensated for in the passive contrast results so that they can be directly compared to the BEM results, which assume that only one surface radiates.

The numerical simulations using the BEM show reasonable agreement with the predictions from the monopole simulations at low frequencies, shown in Fig. 5. The increase in performance with increasing frequency predicted by the monopole simulations is not seen here for the real seat, but

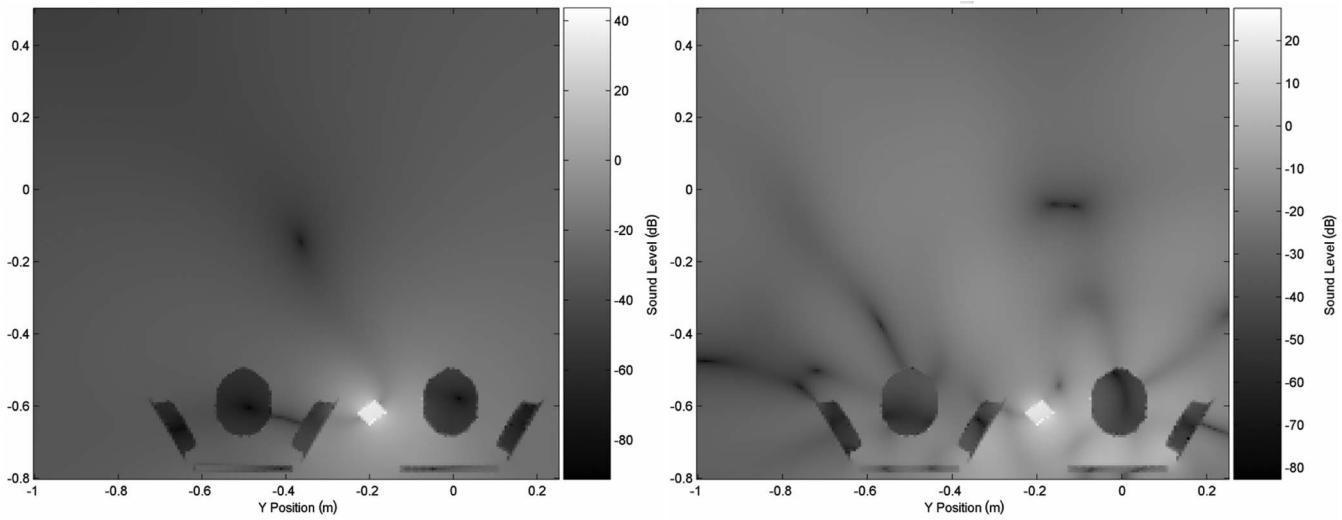


FIG. 11. Sound field plot at 500 Hz (left) and 1550 Hz (right) using results from the BEM simulation where a single secondary source is used at an angle of 50°.

rather a falloff is predicted. The frequency region of this falloff agrees with the theory that the active control performance becomes significantly worse when the sources are spaced greater than $\lambda/10$ apart,[5] which equates to approximately 800 Hz in this case. This is compounded by the fact that the sound field becomes increasingly complex at higher frequencies when there are reflecting/absorbing objects present, so that the regions of destructive interference become small. The BEM simulation results, shown in Fig. 12(a), are supported by the reasonable agreement with the results using measured frequency responses shown in Fig. 12(b), where even some of the higher frequency effects are seen. The ripples at lower frequencies in the passive results in Fig. 12(b) (below 400 Hz) are due to the nonperfect compensation of back radiation from the secondary source. The peaks in the experimental results at higher frequencies (about 800 Hz, 1.2, 1.5, and 2 kHz) are thought to be caused by the detailed features of the experimental headrest that were not reproduced in the BEM model, shown in Fig. 10.

Next the three-source arrangement is modeled, where the optimal arrangement suggested from the monopole simulations is used so that the third source is mounted close to the primary source. The loudspeaker cabinet design can have a large effect on the results, and for these simulations a cylindrical design shown in Fig. 13 was chosen with a vibrating surface at each end, which is similar to the design used in the two-source model but a little more than twice as long and with an additional vibrating surface consisting of a disk in the middle of the cylinder. The surface area of this disk is chosen to be identical to the surface area of the ends of the cylinder used as the vibrating surfaces for the other two sources.

Comparing Figs. 15 and 12, the three-source arrangement shows little increase in the predicted performance com-

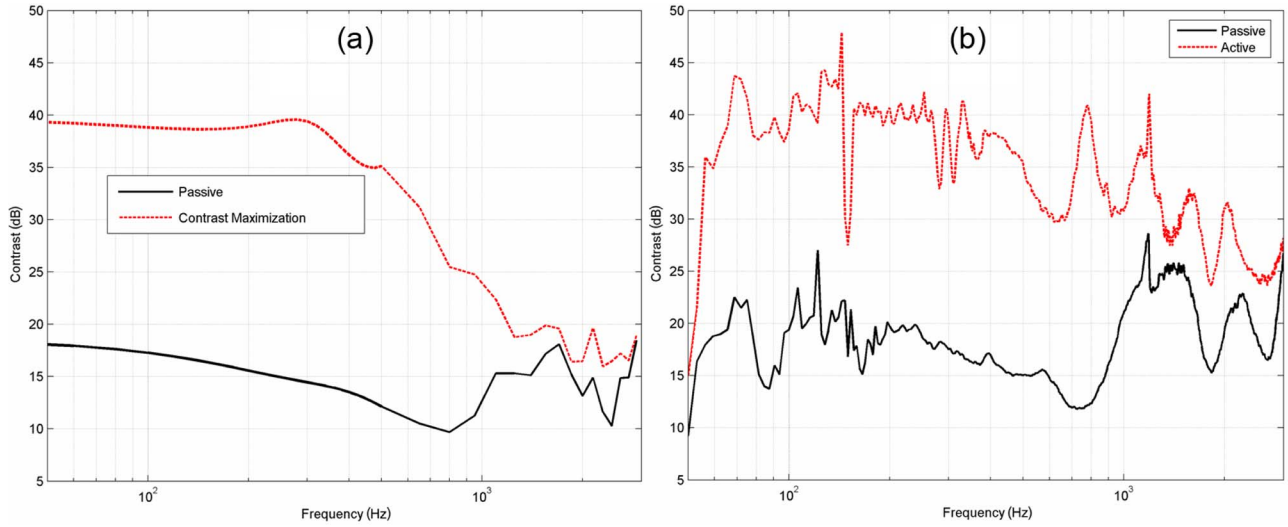


FIG. 12. (Color online) (a) Predicted passive and active contrasts from BEM results averaged over both dark zones as a function of frequency, using a single secondary source. (b) Predicted passive and active contrasts using measured frequency responses under anechoic conditions, averaged over both dark zones and using a single secondary source.

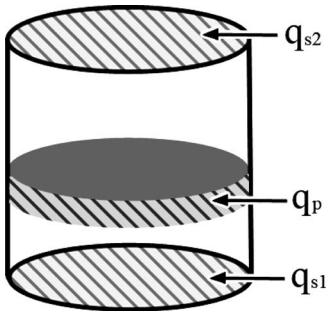


FIG. 13. Diagram of the loudspeaker design used in the three-source model, showing the two secondary sources as the disks on the end of a closed cylinder and the primary source as the outer surface of the central disk.

pared with using two sources, with an increase in contrast of only about 3 dB over the entire frequency range considered. The reason for the differences between the results of the BEM simulation and the monopole simulations seen in Fig. 5 is the presence of the reflecting/absorbing objects, which significantly complicate the sound field around the sensor locations, thereby resulting in large differences in the pressure throughout each bright and dark zone. An additional complication is that the sources will not interfere with each other in the same way that monopole sources would since they consist of vibrating surfaces with some degree of directivity, and the resulting sound fields are more complex. This is illustrated in Fig. 11, where the sound field becomes rather complicated and is even more evident in simulations at higher frequencies, and this effect is even more prominent with three sources, shown in Fig. 14. The sizes of the zones of silence will thus not be as large as those predicted in the monopole simulations. The small differences in the passive contrast using three sources compared to two sources [Figs. 12(a) and 15] are due to the fact that the active source is the middle face (Fig. 13), corresponding to the primary source, which is of a different shape than the flat face when two sources are used. The predictions from the BEM model are more representative of the physical system since they include

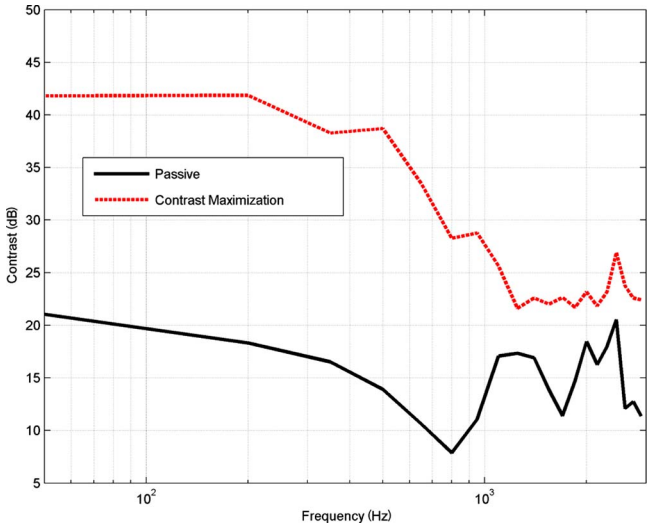


FIG. 15. (Color online) Predicted passive and active contrasts from BEM results, averaged over both dark zones as a function of frequency and using two secondary sources in the optimized arrangement.

many effects not considered in the monopole simulations. Therefore predictions from monopole simulations may be misleading when a larger number of sources are employed.

V. CONCLUSIONS

The sound power minimization approach has been shown to provide good performance when multiple dark zones are present, although the contrast maximization approach is able to provide significant increases in the acoustic contrast for any particular geometry by directing localized zones of silence around the dark zones, with little increase in the sound power output. As the number of dark zones increases, the problem becomes more like the problem of minimizing the levels for *all* regions outside the bright zone, and so the contrast maximization solution will approach that of the sound power minimization solution. The solutions that result from minimizing the sound power output are those in

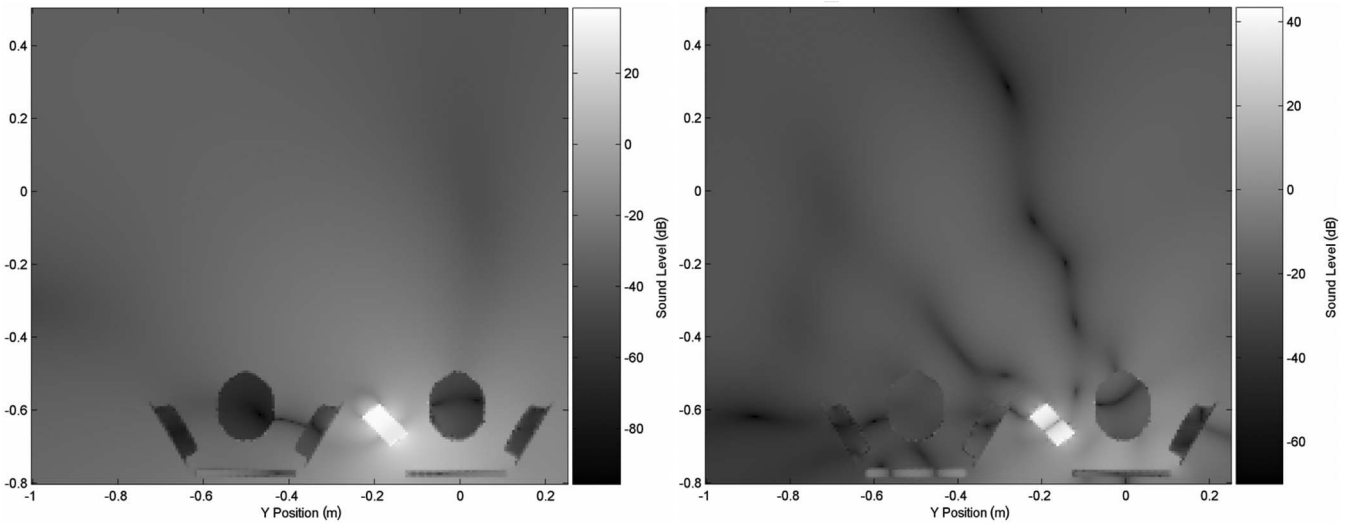


FIG. 14. Sound field plot at 500 Hz (left) and 1550 Hz (right) using results from the BEM simulation where two secondary sources are used.

which the sources are driven such that the array is as self-canceling as possible, provided that the sources are closely spaced. Control effort minimization does not appear to be a suitable approach for this application since this will penalize self-canceling solutions, which is not always desirable since self-canceling source arrays may give a lower sound power output.

Use of a third source, although shown to improve performance in the monopole simulations, shows little improvement in the more realistic BEM simulations when the reflecting and absorbing surfaces are considered due to the increased complexity of the sound field. Therefore the main improvement in contrast is achieved by the addition of a single secondary source placed as close to the primary source as possible. Choice of the source arrangement and the control strategy will depend on the location and number of the dark zones present, but multiple sources should be placed close together in a linear arrangement to give the minimum sound power output.[4] By steering nulls in the directivity of the array toward the dark zones, isolation can be enhanced in certain regions, and optimization for different geometries can be achieved by a simple rotation of the array. Much of the isolation performance achieved here is due to the near-field cancellation with localized zones of silence, which performs significantly better than simply adjusting the far-field directivity response.

[1]S. J. Elliott and M. Jones, "An active headrest for personal audio," J. Acoust. Soc. Am. **119**, 2702–2709 (2006).

[2]J.-W. Choi and Y.-H. Kim, "Generation of an acoustically bright zone with an illuminated region using multiple sources," J. Acoust. Soc. Am. **111**, 1695–1700 (2002).

[3]British Airways' published statistics for Euro Traveller seats, www.britishairways.com (Last viewed August, 2008).

[4]M. Jones, "Personal audio in a headrest," Ph.D. thesis, University of Southampton, 2008.

[5]S. J. Elliott and P. A. Nelson, *Active Control of Sound* (Academic, New York, 1992).

[6]Fostex, professional audio equipment manufacturer, www.fostex.com (Last viewed August, 2008).

[7]R. Martinez, "The thin-shape breakdown (TSB) of the Helmholtz integral equation," J. Acoust. Soc. Am. **90**, 2728–2738 (1991).

Diffusion regime for high-frequency vibrations of randomly heterogeneous structures

Éric Savin
Aeroelasticity and Structural Dynamics Department, ONERA, 29 avenue de la Division Leclerc, 92322 Châtillon cedex, France

(Received 5 March 2008; revised 23 July 2008; accepted 29 September 2008)

The evolution of the high-frequency vibrational energy density of slender heterogeneous structures such as Timoshenko beams or thick shells is depicted by transport equations or radiative transfer equations (RTEs) in the presence of random heterogeneities. A diffusive regime arises when their correlation lengths are comparable to the wavelength, among other possible situations, and waves are multiply scattered. The purpose of this paper is to expound how diffusion approximations of the RTEs for elastic structures can be derived and to discuss the relevance of the vibrational conductivity analogy invoked in the structural acoustics literature. Its main contribution is the consideration of a heterogeneous background medium with varying parameters and the effects of polarization of elastic waves. The paper also outlines some of the remarkable features of the diffusive regime: depolarization of waves, energy equipartition, and asymptotic Fick's law.
© *2008 Acoustical Society of America.* [DOI: 10.1121/1.3003088]

PACS number(s): 43.40.At, 43.40.Ey, 43.35.Cg, 43.20.Bi [RLW] Pages: 3507–3520

I. INTRODUCTION

The analysis of high-frequency vibrations of elastic structures has been the subject of intense research for the past decades either in the applied mathematics or the engineering mechanics literature. This issue has a great engineering relevance in the automotive or aerospace industries, for example, for the prediction of the vibroacoustic behavior of complex systems under broadband mechanical or acoustical excitations. The best known and oldest technique is the method of geometrical optics, or WKB ansatz, for which an extensive literature exists: see Refs. 1–3 for some classical references in structural dynamics. This theory shows that the high-frequency energy density of a wave field is the solution of a transport equation. Similar results are obtained by an alternative approach accounting for the cumulative effects of multiple scattering in random media, as done by Stott,[4] Weaver,[5] or Margerin,[6] among others, for electromagnetic, acoustic, or elastic waves. They are also obtained in the frame of the (rigorous) mathematical theory of microlocal analysis developed in the late 1980s and early 1990s by several researchers[7–10] and extended to random media in Refs. 11–15.

In the limit of small transport mean free paths, transport equations can be approached by diffusion equations.[16,17] This is the sense of the diffusion approximation originally used by Rybak[18] for elastic waves in a randomly heterogeneous plate. The author derived a diffusion equation for the associated energy density, and this result was used later on by some Russian researchers whose papers were cited by Nefske and Sung in their formulation of the vibrational conductivity analogy (VCA) of structural dynamics.[19] But in this latter publication, it appears that the conditions which have led to the diffusion approximation are no longer stated. Again, it was obtained in a random medium for multiply scattered waves or can be obtained in a *bounded* homogeneous medium for multiply reflected waves: this is the diffuse field approximation used in room acoustics or in the statistical energy analysis (SEA) of engineering structures[20] (see also Ref. 21, for example, for an analysis of finite plates with this assumption). For a homogeneous medium, the transport mean free path is infinite and a diffusive regime can theoretically never be reached. Despite its lack of theoretical ground, VCA has been the subject of several investigations in the structural acoustics literature, but the latter were always limited to simple homogeneous structures, typically rods, beams, and more rarely plates; see, for example, Refs. 22–24. More recently, attempts have been made to fit the band-limited smoothed late-time mean square response of large undamped structures to the solution of a diffusion equation of which parameters depend on the early-time response, with a constraint of energy equipartition between modes at late times.[25] In the proposed analysis, disorder is taken into account through random generalized forces and observabilities—the projections of the spatial source and receiver filters on the eigenmodes, respectively. The purpose of this paper is to establish, from the (formal) theory of transport of high-frequency waves in randomly heterogeneous media,[11,12] the correct derivation of diffusion approximations in order to clarify the range of validity, if any, of the VCA and to a lesser extent SEA. The need of such a clarification is also strongly motivated by observations of the diffuse behavior of elastic waves in seismology,[11] nondestructive evaluation,[26] or structural dynamics.[27]

The analysis presented here considers random heterogeneities at the same length scale as the wavelength. However, diffusive regimes also arise for random heterogeneities at an intermediate scale between the scale of oscillations and the size of the medium, or for strongly forward-peaked scattering, for example. The more general theory of transport applies to heterogeneous media, does not neglect the possible interferences between energetic propagation modes, and does

not rely on the artificial use of time and/or spatial averages, contrary to what is done in the VCA literature. The derivation of diffusion approximations for linear or nonlinear Boltzmann equations has been considered for several decades and the related literature is too vast to be listed exhaustively here. Some popular approaches are the Hilbert expansion method, e.g., Refs. 28–30, or stochastic averaging, e.g., Ref. 31. In Sec. II, some basic results pertaining to high-frequency wave propagation in a heterogeneous elastic slender structure are summarized. The linear Boltzmann equations or radiative transfer equations (RTEs) which characterize its energy density evolution are introduced. The presentation focuses on the case of thick shells and then beams, but all results apply to plates as well. RTEs for slender structures form a system of multigroup transport equations which is discussed in Sec. III. The collision operators on its right-hand side are projected on the unit sphere with respect to the direction variable. This step identifies the collision process, which mixes wave directions until the memory of initial wave fronts is lost. Such a situation, together with wave depolarization, characterizes a diffusive behavior. The main contribution of the paper is Sec. IV, where the derivation of diffusion equations from multigroup transport equations in the limit of small scattering mean free paths is outlined. The analysis is based on a formal Hilbert expansion, which can be made rigourous as in Refs. 28–30, for example, and uses some crucial algebraic properties of the collision operators. It extends the previous conclusions of Refs. 32–34 for a homogeneous elastic medium to a heterogeneous background medium with varying wave speeds. Apart from losing the memory of their initial directions of propagation, transported waves in the diffusive regime also become approximately depolarized and their energy densities equally partitioned; the proposed analysis clearly exhibits this property. These results are summarized and briefly commented in Sec. V.

II. HIGH-FREQUENCY ENERGY EVOLUTION IN SLENDER STRUCTURES

This section summarizes the high-frequency energy evolution properties of slender structures as derived in Ref. 33 on the basis of the kinetic models developed in Refs. 10–12. The setting presented here for polarized elastic waves is in many respects similar to the setting of Ref. 35 for electromagnetic waves.

A. Shells

Let us consider a thick curved shell occupying the domain $\Sigma\times(-h/2,h/2)$ of $\mathbb{R}^3$, where the (regular) mean surface Σ is parametrized by its curvilinear coordinates $\mathbf{x}=(x,y)\in\mathbb{R}^2$ and $h>0$ is its thickness. The associated natural tangent basis is denoted by $(\mathbf{e}_1,\mathbf{e}_2)$ such that $\mathbf{e}_1=\partial_x\mathbf{x}$ and $\mathbf{e}_2=\partial_y\mathbf{x}$. Tangent motions of the mean surface are denoted by $\mathbf{u}^\epsilon$, w^ϵ is the radial displacement (deflection), and $\boldsymbol{\theta}^\epsilon$ is the vector of changes of slope of the unit normal $\hat{\mathbf{n}}=\mathbf{e}_1\times\mathbf{e}_2/|\mathbf{e}_1\times\mathbf{e}_2|$ to Σ (see Fig. 1) in the local tangent basis. The overall displacement field of the shell in the local basis $(\mathbf{e}_1,\mathbf{e}_2,\hat{\mathbf{n}})$ thus writes

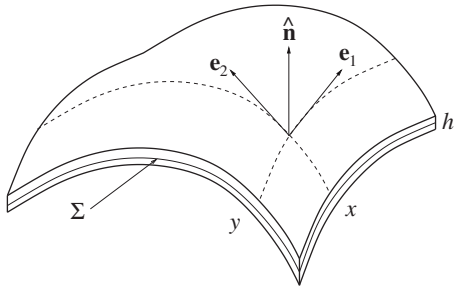


FIG. 1. An elastic shell structure occupying the domain $\Sigma\times(-h/2,h/2)$ of $\mathbb{R}^3$. Σ is the mean surface of the shell, h is its thickness, and $(\mathbf{e}_1,\mathbf{e}_2)$ is its natural tangent basis at the point $\mathbf{x}=(x,y)$. $\hat{\mathbf{n}}$ is the unit normal outward to the mean surface.

$$\mathbf{U}^\epsilon(\mathbf{x})=\mathbf{u}^\epsilon(\mathbf{x})-z\boldsymbol{\theta}^\epsilon(\mathbf{x})+w^\epsilon(\mathbf{x})\hat{\mathbf{n}}(\mathbf{x}),\tag{1}$$

where $-h/2<z<h/2$ is the radial coordinate along $\hat{\mathbf{n}}$. The above expression corresponds to the first-order approximation of the displacement field of an elastic three-dimensional medium with respect to its thickness, and is nothing but the kinematic assumption which *defines* a shell. Its second-ordered normal curvature tensor $\mathbb{B}$ is

$$\mathbb{B}=\sum_{\alpha,\beta=1}^{2}B_{\alpha\beta}\mathbf{e}_\alpha\otimes\mathbf{e}_\beta,\quad B_{\alpha\beta}=-\mathbf{e}_\alpha\cdot\partial_\beta\hat{\mathbf{n}}=\hat{\mathbf{n}}\cdot\partial_\beta\mathbf{e}_\alpha$$

and it is symmetric. The mean radius of the shell $R(\mathbf{x})=(\mathrm{Tr}\,\mathbb{B})^{-1}$ at each point $\mathbf{x}$ of Σ, where $\mathrm{Tr}\,\mathbb{B}$ is the sum of the principal curvatures, is assumed to be much larger than the thickness h. The latter is in turn significantly lower than the typical wavelength ϵ of the excitations, which means that functions $\mathbf{u}^\epsilon$, w^ϵ and $\boldsymbol{\theta}^\epsilon$ oscillate at frequencies of order ϵ^{-1} (see below).

The elastic material constituting this shell is characterized by its density $\rho^\epsilon(\mathbf{x})$ and its elasticity tensor $\mathbf{C}^\epsilon(\mathbf{x})$, depending on two parameters if it is isotropic. Let $E^\epsilon(\mathbf{x})$ be its Young's modulus and $\nu^\epsilon(\mathbf{x})$ be its Poisson's coefficient, then Lamé's parameters are $\mu^\epsilon=E^\epsilon/2(1+\nu^\epsilon)$ (the shear modulus) and $\lambda^\epsilon=2\nu^\epsilon\mu^\epsilon/1-2\nu^\epsilon$, and the constitutive equation is written as

$$\mathbf{C}^\epsilon:\boldsymbol{\epsilon}=\lambda^\epsilon(\mathrm{Tr}\,\boldsymbol{\epsilon})\mathbf{I}+2\mu^\epsilon\boldsymbol{\epsilon}$$

for the second order linearized strain tensor $\boldsymbol{\epsilon}$. Using, for example, the model of Naghdi and Cooper,[36] the membrane forces tensor $\mathbb{N}^\epsilon$, shear forces $\mathbf{T}^\epsilon$, and bending moments tensor $\mathbb{M}^\epsilon$ are given by

$$\mathbb{N}^\epsilon=h\mathbf{C}^\epsilon:(\boldsymbol{\epsilon}(\mathbf{u}^\epsilon)-w^\epsilon\mathbb{B}),\quad \mathbf{T}^\epsilon=\mu_r^\epsilon h(\boldsymbol{\nabla}_\Sigma w^\epsilon-\boldsymbol{\theta}^\epsilon-\mathbb{B}\mathbf{u}^\epsilon),$$
$$\mathbb{M}^\epsilon=\frac{h^3}{12}\mathbf{C}^\epsilon:\boldsymbol{\epsilon}(\boldsymbol{\theta}^\epsilon),\tag{2}$$

where $\boldsymbol{\epsilon}(\mathbf{u})=\boldsymbol{\nabla}_\Sigma\otimes_s\mathbf{u}$, $\otimes_s$ is the symmetrized tensor product, and $\boldsymbol{\nabla}_\Sigma=(\partial_x,\partial_y)$ is the gradient on the mean surface. $\mu_r^\epsilon=\kappa^\epsilon\mu^\epsilon$ is the reduced shear modulus, where $\kappa^\epsilon<1$ is the reduced shear coefficient which depends on Poisson's ratio. The equations of motion are

$$\rho^\epsilon \partial_t^2 \mathbf{u}^\epsilon = \mathrm{div}_\Sigma \mathbb{N}^\epsilon + \mathbb{B}\mathbf{T}^\epsilon, \quad \rho^\epsilon \partial_t^2 w^\epsilon = \mathrm{div}_\Sigma \mathbf{T}^\epsilon + \mathbb{B}:\mathbb{N}^\epsilon,$$
$$\frac{\rho^\epsilon h^2}{12} \partial_t^2 \boldsymbol{\theta}^\epsilon = \mathrm{div}_\Sigma \mathbb{M}^\epsilon + \mathbf{T}^\epsilon. \tag{3}$$

These evolution equations are completed by initial conditions $(\mathbf{u}^\epsilon, w^\epsilon, \boldsymbol{\theta}^\epsilon, \partial_t \mathbf{u}^\epsilon, \partial_t w^\epsilon, \partial_t \boldsymbol{\theta}^\epsilon)(\mathbf{x},0) = (\mathbf{u}_0^\epsilon, w_0^\epsilon, \boldsymbol{\theta}_0^\epsilon, \mathbf{u}_1^\epsilon, w_1^\epsilon, \boldsymbol{\theta}_1^\epsilon)(\mathbf{x})$ which oscillate at frequencies of order ϵ^{-1}, and conservation of the elastic energy if materials are nondissipative writes

$$\mathcal{E}^\epsilon(t) = \frac{1}{2}\int_\Sigma [\mathbb{N}^\epsilon:(\boldsymbol{\epsilon}(\mathbf{u}^\epsilon) - w^\epsilon \mathbb{B}) + \mathbb{M}^\epsilon:\boldsymbol{\epsilon}(\boldsymbol{\theta}^\epsilon) + \mathbf{T}^\epsilon \cdot (\boldsymbol{\nabla}_\Sigma w^\epsilon - \boldsymbol{\theta}^\epsilon - \mathbb{B}\mathbf{u}^\epsilon)] d\mathbf{x} = \mathcal{E}^\epsilon(0). \tag{4}$$

Kinetic models such as transport or radiative transfer are aimed at describing the evolution of the elastic energy *density*:

$$\mathcal{E}^\epsilon(\mathbf{x},t) = \frac{1}{2}[\mathbb{N}^\epsilon:(\boldsymbol{\epsilon}(\mathbf{u}^\epsilon) - w^\epsilon \mathbb{B}) + \mathbb{M}^\epsilon:\boldsymbol{\epsilon}(\boldsymbol{\theta}^\epsilon) + \mathbf{T}^\epsilon \cdot (\boldsymbol{\nabla}_\Sigma w^\epsilon - \boldsymbol{\theta}^\epsilon - \mathbb{B}\mathbf{u}^\epsilon)] \tag{5}$$

and power flow *density*:

$$\Pi^\epsilon(\mathbf{x},t) = -(\mathbb{N}^\epsilon \partial_t \mathbf{u}^\epsilon + \mathbb{M}^\epsilon \partial_t \boldsymbol{\theta}^\epsilon + \mathbf{T}^\epsilon \partial_t w^\epsilon) \tag{6}$$

in the high-frequency limit $\epsilon \to 0$, when material parameters $\rho^\epsilon(\mathbf{x})$, $\lambda^\epsilon(\mathbf{x})$, and $\mu^\epsilon(\mathbf{x})$ are randomly varying at a length scale comparable with the typical wavelength ϵ. More precisely, it is assumed that

$$\rho^\epsilon(\mathbf{x}) = \underline{\rho}(\mathbf{x})\left[1 + \sqrt{\epsilon} X_1\left(\frac{\mathbf{x}}{\epsilon}\right)\right],$$
$$\frac{1}{\lambda^\epsilon(\mathbf{x})} = \frac{1}{\underline{\lambda}(\mathbf{x})}\left[1 + \sqrt{\epsilon} X_2\left(\frac{\mathbf{x}}{\epsilon}\right)\right],$$
$$\frac{1}{\mu^\epsilon(\mathbf{x})} = \frac{1}{\underline{\mu}(\mathbf{x})}\left[1 + \sqrt{\epsilon} X_3\left(\frac{\mathbf{x}}{\epsilon}\right)\right],$$
$$\frac{1}{\mu_r^\epsilon(\mathbf{x})} = \frac{1}{\underline{\mu}_r(\mathbf{x})}\left[1 + \sqrt{\epsilon} X_4\left(\frac{\mathbf{x}}{\epsilon}\right)\right], \tag{7}$$

where $(X_j(\mathbf{x}), \mathbf{x} \in \mathbb{R}^2)$, $j=1,\ldots,4$, are four real-valued statistically homogeneous and centered second-ordered stochastic processes with correlation lengths comparable to the wavelength in the medium. $\underline{\rho}(\mathbf{x}) = \mathbb{E}\{\rho^\epsilon(\mathbf{x})\}$, $\underline{\lambda}(\mathbf{x}) = \mathbb{E}\{\lambda^\epsilon(\mathbf{x})^{-1}\}^{-1}$, $\underline{\mu}(\mathbf{x}) = \mathbb{E}\{\mu^\epsilon(\mathbf{x})^{-1}\}^{-1}$, and $\underline{\mu}_r(\mathbf{x}) = \mathbb{E}\{\mu_r^\epsilon(\mathbf{x})^{-1}\}^{-1}$ are averaged macroscopic density and Lamé's modulii, respectively, $\mathbb{E}\{X\}$ standing for the mathematical expectation of a random variable X. The perturbation amplitudes in the above model are chosen as the square root of the normalized small wavelength ϵ in order to avoid localization if they were too large, while this scaling still allows the energy within the medium to be significantly modified by material fluctuations.[11,12,14] In this setting, the effect of scattering on heterogeneities is comparable to the effect of the slowly varying background medium, evading localization at this scale. Equation (7) is general enough to embed the occurrence of discrete scatterers, in which case random processes $(X_j(\mathbf{x}), \mathbf{x} \in \mathbb{R}^2)$ are simply random characteristic functions, as in, e.g., Ref. 37. Note that Lamé's and reduced shear modulii depend nonlinearly on Young's modulus and Poisson's ratio, thus random variables X_2, X_3, and X_4 are *a priori* strongly correlated but the above model does not enforce any quantification of these correlations.

Then it is shown in Ref. 33, based on the works of Refs. 11 and 12, that there exist a positive scalar w_T and Hermitian, positive two-by-two matrices $\mathbf{W}_P$ and $\mathbf{W}_S$ such that

$$\lim_{\epsilon \to 0} \mathcal{E}^\epsilon(\mathbf{x},t) = \int_{\mathbb{R}^2} w_T(\mathbf{x},\mathbf{k},t) d\mathbf{k} + \sum_{\alpha=P,S} \int_{\mathbb{R}^2} \mathrm{Tr}\, \mathbf{W}_\alpha(\mathbf{x},\mathbf{k},t) d\mathbf{k}, \tag{8}$$

whence w_T, $\mathrm{Tr}\,\mathbf{W}_P$, and $\mathrm{Tr}\,\mathbf{W}_S$ correspond to phase-space energy densities in $T^*\mathbb{R}^2 \equiv \mathbb{R}^2_\mathbf{x} \times \mathbb{R}^2_\mathbf{k}$. They are associated with pure transverse waves propagating at an average speed $c_T = \sqrt{\underline{\mu}_r h/\underline{\rho}}$ and polarized normally to the mean surface Σ, and to compressional and shear waves propagating at the average speeds $c_P = \sqrt{(\underline{\lambda}+2\underline{\mu})h/\underline{\rho}}$ and $c_S = \sqrt{\underline{\mu} h/\underline{\rho}}$, respectively, and polarized in Σ. Equation (8) states that these energy densities must be added up for all possible directions of propagation $\hat{\mathbf{k}} := \mathbf{k}/|\mathbf{k}|$ and all wavenumbers $|\mathbf{k}| > 0$. Compressional waves in shells are generated by either in-plane motions or pure bending motions polarized along the propagation direction $\hat{\mathbf{k}}$, as seen from the kinematic definition (1): $\mathbf{u}^\epsilon \cdot \hat{\mathbf{k}}$ is the in-plane contribution, and $-z\boldsymbol{\theta}^\epsilon \cdot \hat{\mathbf{k}}$ is the pure bending contribution. This induces a two-by-two matrix structure of the compressional energy coherence matrix $\mathbf{W}_P$. Its diagonal entries are the energy densities themselves and its off-diagonal entries characterize all interactions between both types of motion just like the Stokes parameters used for the description of light polarization. Likewise, shear waves are generated by in-plane and pure bending motions polarized perpendicularly to the propagation direction $\hat{\mathbf{k}}$, hence the two-by-two matrix structure of the shear energy coherence matrix $\mathbf{W}_S$ as well. The interpretation of its diagonal and off-diagonal entries is the same as for $\mathbf{W}_P$. Furthermore, w_T, $\mathbf{W}_P$, and $\mathbf{W}_S$ satisfy a system of coupled RTEs written as

$$\partial_t w_T + \{\lambda_T, w_T\} = \int_{\mathbb{R}^2} \sigma_{TT}(\mathbf{x},\mathbf{k},\mathbf{k}') w_T(\mathbf{x},\mathbf{k}',t) \delta(\lambda_T(\mathbf{x},\mathbf{k}) - \lambda_T(\mathbf{x},\mathbf{k}')) d\mathbf{k}' - \Sigma_T(\mathbf{x},\mathbf{k}) w_T(\mathbf{x},\mathbf{k},t), \tag{9}$$

and

$$\partial_t \mathbf{W}_P + \{\lambda_P, \mathbf{W}_P\} = \int_{\mathbb{R}^2} \sigma_{PP}(\mathbf{x},\mathbf{k},\mathbf{k}') \mathbf{W}_P(\mathbf{x},\mathbf{k}',t) \delta(\lambda_P(\mathbf{x},\mathbf{k}) - \lambda_P(\mathbf{x},\mathbf{k}')) d\mathbf{k}' + \int_{\mathbb{R}^2} \sigma_{PS}(\mathbf{x},\mathbf{k},\mathbf{k}') \mathbf{W}_S(\mathbf{x},\mathbf{k}',t) \delta(\lambda_P(\mathbf{x},\mathbf{k}) - \lambda_S(\mathbf{x},\mathbf{k}')) d\mathbf{k}' - \Sigma_P(\mathbf{x},\mathbf{k}) \mathbf{W}_P(\mathbf{x},\mathbf{k},t), \tag{10}$$

$$\partial_t \mathbf{W}_S + \{\lambda_S, \mathbf{W}_S\}$$
$$= \int_{\mathbb{R}^2} \sigma_{SS}(\mathbf{x},\mathbf{k},\mathbf{k}')\mathbf{W}_S(\mathbf{x},\mathbf{k}',t)\,\delta(\lambda_S(\mathbf{x},\mathbf{k}) - \lambda_S(\mathbf{x},\mathbf{k}'))d\mathbf{k}'$$
$$+ \int_{\mathbb{R}^2} \sigma_{SP}(\mathbf{x},\mathbf{k},\mathbf{k}')\mathbf{W}_P(\mathbf{x},\mathbf{k}',t)\,\delta(\lambda_S(\mathbf{x},\mathbf{k}) - \lambda_P(\mathbf{x},\mathbf{k}'))d\mathbf{k}'$$
$$- \Sigma_S(\mathbf{x},\mathbf{k})\mathbf{W}_S(\mathbf{x},\mathbf{k},t), \tag{11}$$

where

$$\lambda_\alpha(\mathbf{x},\mathbf{k}) = c_\alpha(\mathbf{x})|\mathbf{k}|, \quad \alpha = T,P,S, \tag{12}$$

$\{f,g\} = \nabla_{\mathbf{k}} f \cdot \nabla_{\mathbf{x}} g - \nabla_{\mathbf{x}} f \cdot \nabla_{\mathbf{k}} g$ stands for the usual Poisson bracket, and $\mathbf{u}_1 \cdot \mathbf{u}_2$ stands for the Euclidean scalar product of two vectors $\mathbf{u}_1$ and $\mathbf{u}_2$. The so-called differential scattering cross sections $\sigma_{\alpha\beta}$, $\alpha,\beta = T,P,S$, are positive functions which are known explicitly as functions of the power spectral density functions $\mathbf{k} \mapsto S_{jj}(\mathbf{k})$, $j = 1,\ldots,4$, and cross-spectral density functions $\mathbf{k} \mapsto S_{jk}(\mathbf{k})$, $j \neq k = 1,\ldots 4$, of the processes $(X_j(\mathbf{x}), \mathbf{x} \in \mathbb{R}^2)$. For thick shells, they are given by

$$\sigma_{TT}(\mathbf{x},\mathbf{k},\mathbf{k}') = \frac{\pi}{2}\lambda_T^2(\mathbf{x},\mathbf{k})[S_{11}(\mathbf{k}-\mathbf{k}') + (\hat{\mathbf{k}}\cdot\hat{\mathbf{k}}')^2 \times S_{44}(\mathbf{k}-\mathbf{k}') + 2(\hat{\mathbf{k}}\cdot\hat{\mathbf{k}}')\mathrm{Re}\, S_{14}(\mathbf{k}-\mathbf{k}')], \tag{13}$$

and

$$\sigma_{PP}(\mathbf{x},\mathbf{k},\mathbf{k}') = \frac{\pi}{2}\lambda_P^2(\mathbf{x},\mathbf{k})\Bigg[(\hat{\mathbf{k}}\cdot\hat{\mathbf{k}}')^2 S_{11}(\mathbf{k}-\mathbf{k}') + \left(1 - 2\frac{c_S^2}{c_P^2}\right)^2 S_{22}(\mathbf{k}-\mathbf{k}') + 4\frac{c_S^4}{c_P^4}(\hat{\mathbf{k}}\cdot\hat{\mathbf{k}}')^4 \times S_{33}(\mathbf{k}-\mathbf{k}') + 2\left(1 - 2\frac{c_S^2}{c_P^2}\right)(\hat{\mathbf{k}}\cdot\hat{\mathbf{k}}') \times \mathrm{Re}\, S_{12}(\mathbf{k}-\mathbf{k}') + 4\frac{c_S^2}{c_P^2}(\hat{\mathbf{k}}\cdot\hat{\mathbf{k}}')^3 \times \mathrm{Re}\, S_{13}(\mathbf{k}-\mathbf{k}') + 4\frac{c_S^2}{c_P^2}\left(1 - 2\frac{c_S^2}{c_P^2}\right) \times (\hat{\mathbf{k}}\cdot\hat{\mathbf{k}}')^2\, \mathrm{Re}\, S_{23}(\mathbf{k}-\mathbf{k}')\Bigg], \tag{14}$$

$$\sigma_{SS}(\mathbf{x},\mathbf{k},\mathbf{k}') = \frac{\pi}{2}\lambda_S^2(\mathbf{x},\mathbf{k})\Big[(\hat{\mathbf{k}}\cdot\hat{\mathbf{k}}')^2 S_{11}(\mathbf{k}-\mathbf{k}') + (2(\hat{\mathbf{k}}\cdot\hat{\mathbf{k}}')^2 - 1)^2 S_{33}(\mathbf{k}-\mathbf{k}') + 2(\hat{\mathbf{k}}\cdot\hat{\mathbf{k}}') \times (2(\hat{\mathbf{k}}\cdot\hat{\mathbf{k}}')^2 - 1)\mathrm{Re}\, S_{13}(\mathbf{k}-\mathbf{k}')\Big], \tag{15}$$

$$\sigma_{PS}(\mathbf{x},\mathbf{k},\mathbf{k}') = \frac{\pi}{2}(1 - (\hat{\mathbf{k}}\cdot\hat{\mathbf{k}}')^2)[\lambda_P^2(\mathbf{x},\mathbf{k})S_{11}(\mathbf{k}-\mathbf{k}') + 4\lambda_S^2(\mathbf{x},\mathbf{k})(\hat{\mathbf{k}}\cdot\hat{\mathbf{k}}')^2 S_{33}(\mathbf{k}-\mathbf{k}') + 4\lambda_P(\mathbf{x},\mathbf{k})\lambda_S(\mathbf{x},\mathbf{k})(\hat{\mathbf{k}}\cdot\hat{\mathbf{k}}')\mathrm{Re}\, S_{13}(\mathbf{k}-\mathbf{k}')], \tag{16}$$

and $\sigma_{SP}(\mathbf{x},\mathbf{k},\mathbf{k}') = \sigma_{PS}(\mathbf{x},\mathbf{k}',\mathbf{k})$. At last, the total extinction coefficients $\Sigma_\alpha(\mathbf{x},\mathbf{k})$ are given by

$$\Sigma_\alpha(\mathbf{x},\mathbf{k}) = \sum_{\beta=P,S} \Sigma_{\alpha\beta}(\mathbf{x},\mathbf{k}) + \eta_\alpha(\mathbf{x}), \quad \alpha = P,S,$$
$$\Sigma_T(\mathbf{x},\mathbf{k}) = \Sigma_{TT}(\mathbf{x},\mathbf{k}) + \eta_T(\mathbf{x}), \tag{17}$$

where $0 < \eta_\alpha < +\infty$ are intrinsic attenuation coefficients, and the total scattering cross sections $\Sigma_{\alpha\beta}$, $\alpha,\beta = T,P,S$, are computed by

$$\Sigma_{\alpha\beta}(\mathbf{x},\mathbf{k}) = \int_{\mathbb{R}^2} \sigma_{\alpha\beta}(\mathbf{x},\mathbf{k},\mathbf{k}')\,\delta(\lambda_\alpha(\mathbf{x},\mathbf{k}) - \lambda_\beta(\mathbf{x},\mathbf{k}'))d\mathbf{k}'. \tag{18}$$

The above expressions of scattering cross sections are derived from a model of random media where fluctuations are seen as potentially continuous; however, their particularization to discrete scatterers is straightforward, using the expression of the scattering cross section of a single scatterer multiplied by the density of scatterers, as in, e.g., Refs. 38–40. Inclusions in the form of random localized boundary impedances may also be considered.[41,42] Clearly, it is first seen from these results that the high-frequency energy density evolution is independent of the shell curvature tensor $\mathbb{B}$. Therefore, all equations above apply to plates as well. Second, the pure transverse shear energy decouples from the compressional and shear energies because Eq. (9) and Eqs. (10) and (11) are uncoupled. In addition, the compressional and shear energies are coupled entrywise only, that is, their different entries do not mix. Thus only the diagonals of Eqs. (10) and (11) need be retained for the computation of the overall energy density (8). Third, Eqs. (9)–(11) with the definition of the Poisson bracket indicate that the energy densities are transported at speeds equal to the group velocities:

$$\mathbf{c}_{g,\alpha}(\mathbf{x},\mathbf{k}) := \nabla_{\mathbf{k}}\lambda_\alpha(\mathbf{x},\mathbf{k}) = c_\alpha(\mathbf{x})\hat{\mathbf{k}}. \tag{19}$$

Their amplitudes $|\mathbf{c}_{g,\alpha}|$ are equal to the corresponding phase velocities because plate/shell waves are nondispersive in the high-frequency setting expounded above (the c_α's are independent of the frequency in the limit $k_E/k_P \to 0$, where k_E is the bending wavenumber for Kirchhoff–Love thin plate kinematics, and k_P is the bending wavenumber for Mindlin–Reissner–Uflyand thick plate kinematics considered here). This model differs from a Lamb model, where a plate is defined as a three-dimensional elastic medium bounded by two traction-free surfaces at $z = \pm h/2$. Lamb waves are dispersive, and the group velocities of the associated energy densities are clearly different from the phase velocities. This situation has been considered in, e.g., Ref. 38, and would apply to short wavelengths Λ with respect to the plate thickness h. However, in the very limit $\Lambda/h \to 0$, Lamb modes also become nondispersive.

B. Beams

The constitutive equations and equations of motion for a thick curved beam in the plane $\mathbb{R}^2$ are easily deduced from the previous expressions (2) and (3) for shells. The beam

centerline $\mathcal{L}$ is parametrized by its curvilinear absissa $x \in \mathbb{R}$, and its tangent motion, deflection, and bending rotation are denoted by $u^\epsilon(x)$, $w^\epsilon(x)$, and $\theta^\epsilon(x)$, respectively. The local tangent and normal vectors to $\mathcal{L}$ are denoted by $\mathbf{e}$ and $\hat{\mathbf{n}}$, respectively. The overall displacement field of the beam in the local basis $(\mathbf{e},\hat{\mathbf{n}})$ thus writes

$$\mathbf{U}^\epsilon(x) = (u^\epsilon(x) - z\theta^\epsilon(x))\mathbf{e}(x) + w^\epsilon(x)\hat{\mathbf{n}}(x),$$

which is nothing but the (Timoshenko) kinematic assumption *defining* a beam in a plane, up to the first order in the radial coordinate z. Note that torsional motions are not considered here, but the following analysis can be generalized to beams in $\mathbb{R}^3$ to account for them, as well as for the coupled bending waves along both principal normal directions. Integrating the constitutive equation over the beam cross section yields

$$N^\epsilon = E^\epsilon S\left(\partial_x u^\epsilon + \frac{w^\epsilon}{R}\right), \quad T^\epsilon = \mu_r^\epsilon S\left(\partial_x w^\epsilon - \theta^\epsilon + \frac{u^\epsilon}{R}\right), \tag{20}$$

$$M^\epsilon = E^\epsilon I \partial_x \theta^\epsilon,$$

for the compressional force N^ϵ, shear force T^ϵ, and bending moment M^ϵ; S and I are the beam cross-section area and inertia, respectively, and $R(x)$ is its radius of curvature. The equations of motion are

$$\rho^\epsilon \partial_t^2 u^\epsilon = \partial_x N^\epsilon - \frac{T^\epsilon}{R}, \quad \rho^\epsilon \partial_t^2 w^\epsilon = \partial_x T^\epsilon - \frac{N^\epsilon}{R}, \tag{21}$$

$$\frac{\rho^\epsilon I}{S}\partial_t^2 \theta^\epsilon = \partial_x M^\epsilon + T^\epsilon.$$

Now assume as for shells that the elastic parameters are

$$\rho^\epsilon(x) = \underline{\rho}(x)\left[1 + \sqrt{\epsilon} X_1\left(\frac{x}{\epsilon}\right)\right],$$

$$\frac{1}{E^\epsilon(x)} = \frac{1}{\underline{E}(x)}\left[1 + \sqrt{\epsilon} X_2\left(\frac{x}{\epsilon}\right)\right], \tag{22}$$

$$\frac{1}{\mu_r^\epsilon(x)} = \frac{1}{\underline{\mu}_r(x)}\left[1 + \sqrt{\epsilon} X_3\left(\frac{x}{\epsilon}\right)\right],$$

where $(X_j(x), x \in \mathbb{R})$, $j=1,2,3$, are three real-valued statistically homogeneous and centered second-ordered stochastic processes with correlation lengths comparable to the wavelength in the medium, and $\underline{\rho}(x)=\mathbb{E}\{\rho^\epsilon(x)\}$, $\underline{E}(x) = \mathbb{E}\{E^\epsilon(x)^{-1}\}^{-1}$, and $\underline{\mu}_r(x)=\mathbb{E}\{\mu_r^\epsilon(x)^{-1}\}^{-1}$ are the averaged macroscopic density, Young's modulus, and reduced shear modulus, respectively. As for shells, the perturbation amplitude scaling above is chosen in order to evade localization while the energy propagation pattern is still significantly perturbed by the heterogeneities. Of course localization in such a one-dimensional disordered medium is unavoidable in the end; however, the localization length is expected to be much larger than the observation distances imposed by this setting; for example, its *minimum* value is of order ϵ^{-1} in the framework of Ref. 43. Then there exist positive scalars w_T and w_P such that the elastic energy density of the beam in the high-frequency limit $\epsilon \to 0$ is

$$\lim_{\epsilon \to 0} \mathcal{E}^\epsilon(x,t) = \sum_{\alpha=T,P} \int_{\mathbb{R}} w_\alpha(x,k,t)dk. \tag{23}$$

They satisfy the RTEs:

$$\partial_t w_\alpha + \{\lambda_\alpha, w_\alpha\} = \int_{\mathbb{R}} \sigma_{\alpha\alpha}(x,k,k')w_\alpha(x,k',t)\,\delta(\lambda_\alpha(x,k) - \lambda_\alpha(x,k'))dk' - \Sigma_\alpha(x,k)w_\alpha(x,k,t), \tag{24}$$

where $\lambda_\alpha(x,k)=c_\alpha(x)|k|$ for either $\alpha=T$ or $\alpha=P$ with

$$c_T = \sqrt{\frac{\underline{\mu}_r S}{\underline{\rho}}}, \quad c_P = \sqrt{\frac{\underline{E}S}{\underline{\rho}}}.$$

Again, w_T and w_P are interpreted as phase-space energy densities in $T^*\mathbb{R}=\mathbb{R}_x \times \mathbb{R}_k$ associated with pure transverse waves polarized in the normal direction, and coupled bending-compressional waves polarized in the propagation direction $\hat{k}=\text{sign}(k)=\pm 1$. The differential scattering cross sections $\sigma_{\alpha\alpha}$ in Eq. (24) are given by

$$\sigma_{TT}(x,k,k') = \frac{\pi}{2}\lambda_T^2(x,k)[S_{11}(k-k') + S_{33}(k-k') + 2\,\text{sign}(k)\text{sign}(k')\text{Re}\,S_{13}(k-k')],$$

$$\sigma_{PP}(x,k,k') = \frac{\pi}{2}\lambda_P^2(x,k)[S_{11}(k-k') + S_{22}(k-k') + 2\,\text{sign}(k)\text{sign}(k')\text{Re}\,S_{12}(k-k')],$$

and the extinction coefficients Σ_α are as for shells:

$$\Sigma_\alpha(x,k) = \eta_\alpha(x) + \int_{\mathbb{R}} \sigma_{\alpha\alpha}(x,k,k')\,\delta(\lambda_\alpha(x,k) - \lambda_\alpha(x,k'))dk', \quad \alpha = T,P,$$

where $0 < \eta_\alpha < +\infty$. Note that all transport characteristics above are independent of the radius of curvature of the beam. The group velocities $\pm c_T$ and $\pm c_P$ are equal to the phase velocities because waves in thick beams are nondispersive in the high-frequency limit $k_E/k_P \to 0$, the ratio of bending wavenumbers for Euler–Bernoulli thin beam and Timoshenko thick beam kinematics, respectively.

III. MULTIGROUP RADIATIVE TRANSFER EQUATIONS

In this section, the characteristic features of the coupled RTEs satisfied by the phase-space energy densities are discussed. The crucial role played by scattering on random heterogeneities as described by the integral operators in Eqs. (9)–(11) or Eq. (24) is emphasized. The directional part of these scattering processes is analyzed more in detail in Sec. III B below.

A. Transport versus diffusion

Let d be the physical space dimension, typically $d=2$ for a plate or a shell and $d=1$ for a beam. The streaming operator in phase space $T^*\mathbb{R}^d$ corresponding to the Poisson bracket on the left-hand-side in Eqs. (9)–(11) for plates and shells or

Eq. (24) for beams describes the propagation of the phase-space energy density associated with a given mode α at a velocity $|\mathbf{c}_{g,\alpha}|$ along rays which are the bicharacteristics of the Hamiltonian $\lambda_\alpha(\mathbf{x},\mathbf{k})$. The latter are defined as the functions $t \mapsto \mathbf{x}_\alpha(t)$ and $t \mapsto \mathbf{k}_\alpha(t)$ solving the ordinary differential equations:

$$\dot{\mathbf{x}}_\alpha(t) = \nabla_{\mathbf{k}} \lambda_\alpha(\mathbf{x}_\alpha(t),\mathbf{k}_\alpha(t)),$$

$$\mathbf{k}_\alpha(t) = -\nabla_{\mathbf{x}} \lambda_\alpha(\mathbf{x}_\alpha(t),\mathbf{k}_\alpha(t)),$$

in $T^*\mathbb{R}^d \backslash \{(\mathbf{x},\mathbf{k});\mathbf{k}=0\}$, such that

$$\partial_t w + \{\lambda_\alpha, w\} \equiv \frac{dw}{dt}.$$

Then the Hamiltonian λ_α is constant along its bicharacteristics.

The scattering or linear Boltzmann's operators corresponding to the right-hand sides in Eqs. (9)–(11) or Eq. (24) describe the various interaction processes undergone by a ray $[\mathbf{x}(t),\mathbf{k}(t)]$ in phase space $T^*\mathbb{R}^d$ transporting the energy density w_α: (a) collisions on random heterogeneities which convert all incident rays in the directions $\hat{\mathbf{k}}'$ and modes β into $\hat{\mathbf{k}}$ and α, respectively, at the rate $\sigma_{\alpha\beta}(\mathbf{x},\mathbf{k},\mathbf{k}')$ at the position $\mathbf{x}$, balanced by the reciprocal conversion of the actual direction $\hat{\mathbf{k}}$ and mode α to all other directions and modes at the rate $\Sigma_\beta \Sigma_{\alpha\beta}(\mathbf{x},\mathbf{k})$; (b) attenuation at the rate $\eta_\alpha(\mathbf{x})$. The scattering process (a) is conservative and characterized by a so-called scattering mean free path ℓ which is defined for a particular energy mode α by

$$\ell_\alpha(\mathbf{x},\mathbf{k}) = \frac{|\mathbf{c}_{g,\alpha}(\mathbf{x},\mathbf{k})|}{\Sigma_\alpha(\mathbf{x},\mathbf{k})}. \tag{25}$$

ℓ_α corresponds to the mean distance traveled by an energy ray in the mode α before its direction $\hat{\mathbf{k}}$ is significantly altered by scattering on the heterogeneities. Derivation of the RTEs (9)–(11) or (24) is carried out in the limit $\epsilon \equiv \Lambda/L \to 0$, where Λ is a typical wavelength and $L \equiv c_\alpha t$ is the distance at which propagation of the mode α is observed. This transport regime remains applicable as long as $\Lambda \ll \ell_\alpha$, while it does not require short wavelength compared with the size of heterogeneities. A diffusion regime sets up when (i) attenuations in the medium are small, (ii) scattering is important, and (iii) one considers propagation distances/times much larger than the scattering mean free paths/times, or equivalently multiply scattered energy rays: $c_\alpha t \gg \ell_\alpha$. Scattering operators play a crucial role in the emergence of this regime in that they mix all directions of all existing energy modes. Therefore, the analysis of the diffusion limit relies on an explicit identification of their directional part; this is done in the next section. For that purpose, both Eq. (9) or Eq. (24) and the diagonals of Eqs. (10) and (11) [in view of estimating the energy density by Eq. (8)] are recast into the following system of multigroup transport equations:

$$\partial_t w_\alpha + \{\lambda_\alpha, w_\alpha\} = \sum_{\beta=1}^{M} \int_{\mathbb{R}^d} \sigma_{\alpha\beta}(\mathbf{x},\mathbf{k},\mathbf{k}') w_\beta(\mathbf{x},\mathbf{k}',t) \delta(\lambda_\alpha(\mathbf{x},\mathbf{k}) - \lambda_\beta(\mathbf{x},\mathbf{k}')) d\mathbf{k}' - \Sigma_\alpha(\mathbf{x},\mathbf{k}) w_\alpha(\mathbf{x},\mathbf{k},t),$$
$$\alpha = 1,2,\ldots,M. \tag{26}$$

The remaining of the paper considers this generic form for an arbitrary *finite* number m of different energy modes, each having an order of multiplicity R_α such that $\Sigma_{\alpha=1}^m R_\alpha = M$. The particular case of shells is recovered from this model provided that one defines $m=M=R_T=1$ for Eq. (9) or $m=2$ and $R_P=R_S=2$ such that $M=4$ for Eqs. (10) and (11); for curved beams, $m=M=R_\alpha=1$ for either $\alpha=T$ or P (of course the interesting case is $m>1$). Once the solutions $\{w_\alpha\}_{\alpha=1,\ldots,M}$ of Eq. (26) with known initial conditions have been recovered, the high-frequency energy in the medium is obtained as

$$\lim_{\epsilon \to 0} \mathcal{E}^\epsilon(t) := \mathcal{E}(t) = \sum_{\alpha=1}^{M} \int_{T^*\mathbb{R}^d} w_\alpha(\mathbf{x},\mathbf{k},t) d\mathbf{k} d\mathbf{x},$$

while the associated high-frequency power flow vector is

$$\lim_{\epsilon \to 0} \mathbf{\Pi}^\epsilon(t) := \mathbf{\Pi}(t) = \sum_{\alpha=1}^{M} \int_{T^*\mathbb{R}^d} \mathbf{c}_{g,\alpha}(\mathbf{x},\mathbf{k}) w_\alpha(\mathbf{x},\mathbf{k},t) d\mathbf{k} d\mathbf{x},$$

recalling the definition (19) of the group velocities $\mathbf{c}_{g,\alpha}$.

To conclude on this section, we note that if all scattering cross sections are zero, that is, if parameters ρ^ϵ, E^ϵ, and ν^ϵ in Sec. II vary at the macroscopic scale $O(1)$ only and not at the microscopic scale $O(\epsilon)$, then the scattering mean free paths (25) are infinite and no diffusion limit arises. This is the regime of pure transport of high-frequency waves, where by Eqs. (9)–(11) for shells or Eq. (24) for plates, energy rays for distinct modes evolve without ever mixing, even if the background medium is heterogeneous at the macroscopic scale. However, a strong mixing of directions and polarizations (modes) may be obtained by the reflections and transmissions of the energy rays at boundaries, interfaces, or junctions between different substructures. One may also define finite scattering mean paths in this situation, which is considered in room acoustics or in the SEA of engineering structures (see Ref. 20). Boundary conditions will *not* be considered in this paper. In Ref. 31, for example, the authors have derived diffusion equations relevant to either smooth or rough boundaries corresponding to specularlike or diffusivelike reflections, respectively, in a general framework.

B. Renormalization of the scattering operators

Let us introduce the spectral density matrix $\mathbf{S}(\mathbf{k})$ of parameters random fluctuations, defined by $[\mathbf{S}(\mathbf{k})]_{jk} = S_{jk}(\mathbf{k})$, the power $(j=k)$ or cross- $(j \neq k)$ spectral density function of random fluctuations $(X_j(\mathbf{x}), \mathbf{x} \in \mathbb{R}^d)$ and $(X_k(\mathbf{x}), \mathbf{x} \in \mathbb{R}^d)$; it is a four-by-four complex matrix for shells and plates or a three-by-three complex matrix for beams. A spectral density matrix is always positive, Hermitian, and satisfies $\mathbf{S}(-\mathbf{k}) = \overline{\mathbf{S}(\mathbf{k})} = \mathbf{S}(\mathbf{k})^T$, where $\mathbf{A}^T$ stands for the matrix transpose and $\bar{z}$ stands for the complex conjugate. Thus $\mathbf{k} \mapsto \mathrm{Re}\, S_{jk}(\mathbf{k})$ are even functions and $\mathbf{k} \mapsto S_{jj}(\mathbf{k})$ are in addition real. Differential scattering cross sections $\sigma_{\alpha\beta}(\mathbf{x},\mathbf{k},\mathbf{k}')$

in Eq. (26) are completely determined by $\mathbf{S}(\mathbf{k}-\mathbf{k}')$, thus they are always non-negative[11] owing to the positivity of $\mathbf{S}$. Its symmetries imply that they also satisfy the reciprocity relation:

$$\sigma_{\alpha\beta}(\mathbf{x},\mathbf{k},\mathbf{k}')\delta(\lambda_\alpha(\mathbf{x},\mathbf{k})-\lambda_\beta(\mathbf{x},\mathbf{k}'))=\sigma_{\beta\alpha}(\mathbf{x},\mathbf{k}',\mathbf{k})\delta(\lambda_\beta(\mathbf{x},\mathbf{k}')-\lambda_\alpha(\mathbf{x},\mathbf{k}))=\sigma_{\beta\alpha}(\mathbf{x},-\mathbf{k}',-\mathbf{k})\delta(\lambda_\beta(\mathbf{x},\mathbf{k}')-\lambda_\alpha(\mathbf{x},\mathbf{k})).$$

as long as there is scattering between modes α and β. If the fluctuations $(X_j(\mathbf{x}), \mathbf{x}\in\mathbb{R}^d)$ are statistically isotropic, then S_{jj} and $\mathrm{Re}\,S_{jk}$ depend on $|\mathbf{k}|$ solely, and the differential scattering cross sections depend on $|\mathbf{k}|$ and $\hat{\mathbf{k}}\cdot\hat{\mathbf{k}}'$ solely because $|\mathbf{k}-\mathbf{k}'|=|\mathbf{k}|(1+(c_\alpha^2/c_\beta^2)-2(c_\alpha/c_\beta)\hat{\mathbf{k}}\cdot\hat{\mathbf{k}}')^{1/2}$ whenever $\lambda_\alpha(\mathbf{x},\mathbf{k})=\lambda_\beta(\mathbf{x},\mathbf{k}')$. They are now written as

$$\sigma_{\alpha\beta}(\mathbf{x},\mathbf{k},\mathbf{k}')\delta(\lambda_\alpha(\mathbf{x},\mathbf{k})-\lambda_\beta(\mathbf{x},\mathbf{k}'))=\frac{c_\beta}{|\mathbf{k}'|^{d-1}}\tilde{\sigma}_{\alpha\beta}(\mathbf{x},|\mathbf{k}|,|\mathbf{k}'|,\hat{\mathbf{k}}\cdot\hat{\mathbf{k}}')\delta(\lambda_\alpha(\mathbf{x},\mathbf{k})-\lambda_\beta(\mathbf{x},\mathbf{k}'))$$

such that

$$\tilde{\sigma}_{\alpha\beta}\left(\mathbf{x},|\mathbf{k}|,\frac{c_\alpha}{c_\beta}|\mathbf{k}|,\hat{\mathbf{k}}\cdot\hat{\mathbf{k}}'\right)=\left(\frac{c_\alpha}{c_\beta}\right)^d\tilde{\sigma}_{\beta\alpha}\left(\mathbf{x},\frac{c_\alpha}{c_\beta}|\mathbf{k}|,|\mathbf{k}|,\hat{\mathbf{k}}\cdot\hat{\mathbf{k}}'\right) \tag{27}$$

in order to satisfy the reciprocity property of the $\sigma_{\alpha\beta}$'s. This last relation is known as the detailed balance principle in the neutron transport literature. Then,

$$\begin{aligned}\Sigma_{\alpha\beta}(\mathbf{x},\mathbf{k})&=\tilde{\Sigma}_{\alpha\beta}(\mathbf{x},|\mathbf{k}|)\\&=\int_{S^{d-1}}\tilde{\sigma}_{\alpha\beta}\left(\mathbf{x},|\mathbf{k}|,\frac{c_\alpha}{c_\beta}|\mathbf{k}|,\hat{\mathbf{k}}\cdot\hat{\mathbf{k}}'\right)d\Omega(\hat{\mathbf{k}}')\\&=\left(\frac{c_\alpha}{c_\beta}\right)^d\tilde{\Sigma}_{\beta\alpha}\left(\mathbf{x},\frac{c_\alpha}{c_\beta}|\mathbf{k}|\right),\end{aligned} \tag{28}$$

where S^{d-1} is the unit sphere of $\mathbb{R}^d$ and $d\Omega$ is its Euclidean measure. As $d\mathbf{k}=r^{d-1}drd\Omega(\hat{\mathbf{k}})$ with $r=|\mathbf{k}|$, Eq. (26) yields

$$\begin{aligned}\partial_t w_\alpha+\{\lambda_\alpha,w_\alpha\}&=\sum_{\beta=1}^M\int_{S^{d-1}}\tilde{\sigma}_{\alpha\beta}\left(\mathbf{x},|\mathbf{k}|,\frac{c_\alpha}{c_\beta}|\mathbf{k}|,\hat{\mathbf{k}}\cdot\hat{\mathbf{k}}'\right)\\&\quad\times w_\beta\left(\mathbf{x},\frac{c_\alpha}{c_\beta}|\mathbf{k}|\hat{\mathbf{k}}',t\right)d\Omega(\hat{\mathbf{k}}')\\&\quad-\tilde{\Sigma}_\alpha(\mathbf{x},|\mathbf{k}|)w_\alpha(\mathbf{x},|\mathbf{k}|\hat{\mathbf{k}},t),\quad\alpha=1,2,\ldots,M,\end{aligned} \tag{29}$$

where $\tilde{\Sigma}_\alpha=\Sigma_{\beta=1}^M\tilde{\Sigma}_{\alpha\beta}+\eta_\alpha$. The last step of this analysis is to project the streaming operators onto the unit phase space $S^*\mathbb{R}^d\equiv\mathbb{R}^d_{\mathbf{x}}\times S^{d-1}_{\hat{\mathbf{k}}}$ (the unit cosphere bundle of $\mathbb{R}^d$). The multigroup transport equations for the phase-space energy densities $w_\alpha(\mathbf{x},\mathbf{k},t)$ are conveniently written in the form of a coupled system for the so-called specific intensities $a_\alpha(\mathbf{x},\omega,\hat{\mathbf{k}},t)$, or radiances in the optical literature,[35] defined here by

$$a_\alpha(\mathbf{x},\omega,\hat{\mathbf{k}},t)=w_\alpha\left(\mathbf{x},\frac{\omega}{c_\alpha(\mathbf{x})}\hat{\mathbf{k}},t\right). \tag{30}$$

In Eq. (29), or in Eq. (26) above, $\omega=\lambda_\alpha(\mathbf{x},\mathbf{k})=c_\alpha(\mathbf{x})|\mathbf{k}|$ is a fixed parameter along the rays, and the projection of the usual gradient $\nabla_{\mathbf{k}}$ in $\mathbb{R}^d$ onto S^{d-1} is $(\mathbf{I}_d-\hat{\mathbf{k}}\otimes\hat{\mathbf{k}})\nabla_{\hat{\mathbf{k}}}$, where $\mathbf{I}_d$ is the $d\times d$ identity matrix. Specific intensities $\{a_\alpha\}_{\alpha=1,\ldots,M}$ are then solutions of the multigroup transport equations:

$$\begin{aligned}&\partial_t a_\alpha+c_\alpha(\mathbf{x})\hat{\mathbf{k}}\cdot\nabla_{\mathbf{x}}a_\alpha-\nabla_{\mathbf{x}}c_\alpha(\mathbf{x})\cdot(\mathbf{I}_d-\hat{\mathbf{k}}\otimes\hat{\mathbf{k}})\nabla_{\hat{\mathbf{k}}}a_\alpha\\&\quad+\eta_\alpha(\mathbf{x})a_\alpha=\sum_{\beta=1}^M\int_{S^{d-1}}\tilde{\sigma}_{\alpha\beta}\left(\mathbf{x},\frac{\omega}{c_\alpha},\frac{\omega}{c_\beta},\hat{\mathbf{k}}\cdot\hat{\mathbf{k}}'\right)\\&\quad\times(a_\beta(\mathbf{x},\omega,\hat{\mathbf{k}}',t)-a_\alpha(\mathbf{x},\omega,\hat{\mathbf{k}},t))d\Omega(\hat{\mathbf{k}}').\end{aligned} \tag{31}$$

The high-frequency energy of the medium is now given by

$$\mathcal{E}(t)=\sum_{\alpha=1}^M\int_{S^*\mathbb{R}^d}c_\alpha^{-d}(\mathbf{x})\times\left(\int_0^{+\infty}\omega^{d-1}a_\alpha(\mathbf{x},\omega,\hat{\mathbf{k}},t)d\omega\right)d\Omega(\hat{\mathbf{k}})d\mathbf{x}, \tag{32}$$

and the power flow vector by

$$\mathbf{\Pi}(t)=\sum_{\alpha=1}^M\int_{S^*\mathbb{R}^d}c_\alpha^{-d}(\mathbf{x})\mathbf{c}_{g,\alpha}(\mathbf{x},\mathbf{k})\times\left(\int_0^{+\infty}\omega^{d-1}a_\alpha(\mathbf{x},\omega,\hat{\mathbf{k}},t)d\omega\right)d\Omega(\hat{\mathbf{k}})d\mathbf{x}. \tag{33}$$

It should be noted that the a_α's, as well as the w_α's, all have their values in $\mathbb{R}_+$. Also the group velocities $\mathbf{c}_{g,\alpha}(\mathbf{x},\mathbf{k})=c_\alpha(\mathbf{x})\hat{\mathbf{k}}$ in the model equation (31) have amplitudes independent of the wavenumber and equal to the phase velocities c_α, as in Sec. II A or II B. The assumption of statistical isotropy invoked above is technically essential for the derivation which follows. Diffusion approximations can also be constructed for statistically anisotropic media (called anisomeric random media) by a rather identical approach, see, e.g., Ref. 6, invoking, however, different technical arguments. This issue will not be pursued in the subsequent analysis.

IV. DIFFUSION REGIME IN THE LIMIT OF SMALL SCATTERING MEAN FREE PATHS

In this section, one introduces the small parameter $\delta=\ell_\alpha/L$ and let $\delta\to0$ to obtain the diffusion limit by an asymptotic expansion method, the so-called Hilbert expansion method. The derivation is based on the algebraic properties of the conservative part of the scattering operators recalled below. Some important features of the diffusive regime that can be obtained from the analysis are also outlined: depolarization of the waves, equipartition of their energy densities, and asymptotic Fick's law.

A. Properties of the collision operators

We first give the main properties of the linear collision operators on the right-hand side of Eq. (31). They correspond to the conservative part of the scattering operators on the unit sphere S^{d-1}. Define the average over S^{d-1} by

$$\langle f\rangle = \frac{1}{\Omega_d}\int_{S^{d-1}} f(\hat{\mathbf{k}})d\Omega(\hat{\mathbf{k}}), \quad \Omega_d = \int_{S^{d-1}} d\Omega(\hat{\mathbf{k}}).$$

For $\mathbf{x}\in\mathcal{O}\subseteq\mathbb{R}^d$ and $\omega>0$, let

$$\mathcal{K}_\omega f(\hat{\mathbf{k}}) = \frac{1}{\Omega_d}\int_{S^{d-1}} \boldsymbol{\sigma}(\mathbf{x},\omega,\hat{\mathbf{k}}\cdot\hat{\mathbf{k}}')f(\hat{\mathbf{k}}')d\Omega(\hat{\mathbf{k}}'),$$

$$\mathcal{Q}_\omega f(\hat{\mathbf{k}}) = \Sigma_\omega f(\hat{\mathbf{k}}) - \mathcal{K}_\omega f(\hat{\mathbf{k}}),$$

where

$$\boldsymbol{\Sigma}_\omega = \frac{1}{\Omega_d}\tilde{\boldsymbol{\Sigma}}\mathbf{C}^d, \quad \boldsymbol{\sigma} = \tilde{\boldsymbol{\sigma}}\mathbf{C}^d, \quad \mathbf{C} = \mathrm{diag}(c_\alpha)_{\alpha=1,\ldots,M},$$

$$\tilde{\boldsymbol{\Sigma}} = \mathrm{diag}\left(\sum_{\beta=1}^{M}\tilde{\Sigma}_{\alpha\beta}\right)_{\alpha=1,\ldots,M},$$

and $\tilde{\boldsymbol{\sigma}}$ is the $M\times M$ matrix of which elements are the scattering cross sections $\tilde{\sigma}_{\alpha\beta}$ such that Eq. (27) holds

$$[\tilde{\boldsymbol{\sigma}}(\mathbf{x},\omega,\hat{\mathbf{k}}\cdot\hat{\mathbf{k}}')]_{\alpha\beta} = \tilde{\sigma}_{\alpha\beta}\left(\mathbf{x},\frac{\omega}{c_\alpha},\frac{\omega}{c_\beta},\hat{\mathbf{k}}\cdot\hat{\mathbf{k}}'\right).$$

Then $\mathcal{Q}_\omega$ is self-adjoint on $H=(L^2(S^{d-1},d\Omega))^M$; if we assume that $\boldsymbol{\sigma}$ is such that

$$\sup_{\mathbf{x}\in\mathcal{O},\omega>0}\int\int_{S^{d-1}\times S^{d-1}}\|\boldsymbol{\sigma}(\mathbf{x},\omega,\hat{\mathbf{k}}\cdot\hat{\mathbf{k}}')\|_2^2 d\Omega(\hat{\mathbf{k}})d\Omega(\hat{\mathbf{k}}') < +\infty,$$

with the entrywise matrix norm $\|\mathbf{A}\|_p=(\Sigma_{\alpha,\beta=1}^M|A_{\alpha\beta}|^p)^{1/p}$, then $\mathcal{K}_\omega$ is a Hilbert–Schmidt operator on H. Owing to the fact that the scattering cross sections are non-negative functions, such that $\exists\alpha$, $\tilde{\sigma}_{\alpha\beta}>0$ for each $\beta=1,2,\ldots,M$ [otherwise the RTEs are split in subgroups, and diffusion limits are reached for each group separately, as for the two groups of Eqs. (10) and (11) and Eq. (9) above, respectively], one can show in addition that the null space of $\mathcal{Q}_\omega$ is

$$N(\mathcal{Q}_\omega) = \{\phi\mathbf{d};\ \phi=\langle\phi\rangle\}, \tag{34}$$

with $\mathbf{d}=\mathbf{C}^{-d}\mathbf{u}$, $\mathbf{u}=(1,1,\ldots,1)^T$ in $\mathbb{R}^M$, and ϕ scalar functions independent of $\hat{\mathbf{k}}$. Indeed, $\mathcal{K}_\omega$ is compact and strongly positive on the cone $K=\{f\in H; f_\alpha\geqslant 0,\alpha=1,2,\ldots,M\}$, and one observes that $\mathbf{d}$ is a positive eigenvector of $\mathcal{K}_\omega$. Thus by the Krein–Rutman theorem,[44] it is the sole positive eigenvector associated with the simple eigenvalue $\rho(\mathcal{K}_\omega)$, its spectral radius, that is, $N(\mathcal{Q}_\omega)$ is the one-dimensional subspace of H spanned by $\mathbf{d}$. Now by Fredholm alternative, the equation $\mathcal{Q}_\omega f=g$ in $N(\mathcal{Q}_\omega)^\perp=R(\mathcal{Q}_\omega)$ has a unique solution f^*, which satisfies $(f^*,\phi\mathbf{d})_H=\phi\mathbf{d}\cdot\langle f^*\rangle=0$ for any constant function ϕ.

B. Asymptotic analysis

Recalling conditions (i)–(iii) of Sec. III A for the emergence of a diffusive regime, the system of Eq. (31) is rescaled as

$$\delta\partial_t a_\alpha^\delta + c_\alpha\hat{\mathbf{k}}\cdot\nabla_{\mathbf{x}}a_\alpha^\delta - \nabla_{\mathbf{x}}c_\alpha\cdot(\mathbf{I}_d-\hat{\mathbf{k}}\otimes\hat{\mathbf{k}})\nabla_{\hat{\mathbf{k}}}a_\alpha^\delta + \delta\eta_\alpha a_\alpha^\delta = \sum_{\beta=1}^{M}\int_{S^{d-1}}\delta^{-1}\tilde{\sigma}_{\alpha\beta}\left(\mathbf{x},\frac{\omega}{c_\alpha},\frac{\omega}{c_\beta},\hat{\mathbf{k}}\cdot\hat{\mathbf{k}}'\right)(a_\beta^\delta(\mathbf{x},\omega,\hat{\mathbf{k}}',t) - a_\alpha^\delta(\mathbf{x},\omega,\hat{\mathbf{k}},t))d\Omega(\hat{\mathbf{k}}'), \tag{35}$$

for $\alpha=1,2,\ldots,M$. This setting corresponds to the near critical case of Ref. 17; however, different scalings may be considered, for example, splitting the collision operator into its elastic (jumps in directions only) and inelastic (jumps in energy modes only) parts and adopt a different scaling for both, as in Ref. 29. It also allows the specific intensities to be effectively observed at large times or distances with respect to mean free times/distances after multiple scattering on small perturbations, diverting potential localization effects. The fact that the latter always prevail at late times in dimension $d=1$ or 2 does not invalidate the following developments; however, the existence of a localization length ξ_d for $d\leqslant 2$ implies that the diffusive regime holds in an intermediate range between ℓ_α and ξ_d with $\delta^{-1}\ell_\alpha\ll\xi_d$ in accordance with the scaling of Eq. (35). Let $\mathbf{a}^\delta=(a_1^\delta,a_2^\delta,\ldots,a_M^\delta)^T$, then it is expanded in power series of δ as

$$\mathbf{a}^\delta(\mathbf{x},\omega,\hat{\mathbf{k}},t) = \mathbf{a}^{(0)}(\mathbf{x},\omega,\hat{\mathbf{k}},t) + \delta\mathbf{a}^{(1)}(\mathbf{x},\omega,\hat{\mathbf{k}},t) + \delta^2\mathbf{a}^{(2)}(\mathbf{x},\omega,\hat{\mathbf{k}},t) + o(\delta^2)$$

and plugged into Eq. (35). Balancing order by order, one has to the leading order $O(\delta^0)$:

$$\mathcal{Q}_\omega\mathbf{C}^{-d}\mathbf{a}^{(0)} = \mathbf{0}, \tag{36}$$

which shows that $\mathbf{a}^{(0)}$ does not depend on $\hat{\mathbf{k}}$, because $\mathbf{C}^{-d}\mathbf{a}^{(0)}$ lies in the null space (34) of $\mathcal{Q}_\omega$. Therefore, $\mathbf{C}^{-d}\mathbf{a}^{(0)}=\phi\mathbf{d}$, where $\phi=\langle\phi\rangle$, that is, $\mathbf{a}^{(0)}=\phi\mathbf{u}$: this is depolarization of initially coupled modes, stating that

$$a_\alpha^{(0)}(\mathbf{x},\omega,t) = a_\beta^{(0)}(\mathbf{x},\omega,t) := \phi(\mathbf{x},\omega,t), \quad \forall\,\alpha,\beta=1,2\ldots,M, \tag{37}$$

independent of the direction $\hat{\mathbf{k}}$.

To the first order $O(\delta)$, one has

$$-\Omega_d\mathcal{Q}_\omega\mathbf{C}^{-d}\mathbf{a}^{(1)} = (\mathbf{C}\otimes\hat{\mathbf{k}})\nabla_{\mathbf{x}}\otimes\mathbf{a}^{(0)}. \tag{38}$$

Its general solution is

$$\mathbf{a}^{(1)}(\mathbf{x},\omega,\hat{\mathbf{k}},t) = \mathbf{a}^{(11)}(\mathbf{x},\omega,t) - (\boldsymbol{\Lambda}^*\otimes\hat{\mathbf{k}})\nabla_{\mathbf{x}}\otimes\mathbf{a}^{(0)}(\mathbf{x},\omega,t), \tag{39}$$

where $\boldsymbol{\Lambda}^*(\mathbf{x},\omega)$ is the solution of $\mathbf{C}\otimes\hat{\mathbf{k}}=\Omega_d\mathcal{Q}_\omega(\mathbf{C}^{-d}\boldsymbol{\Lambda}^*\otimes\hat{\mathbf{k}})$, which is uniquely invertible since $\langle\mathbf{C}\otimes\hat{\mathbf{k}}\rangle=\mathbf{0}$. Representation (39) above holds because $\hat{\mathbf{k}}\cdot\mathbf{e}$ is an eigenfunction of the operator $\mathbf{K}_0 f(\hat{\mathbf{k}}) := \int_{S^{d-1}}\sigma(\hat{\mathbf{k}}\cdot\hat{\mathbf{k}}')f(\hat{\mathbf{k}}')d\Omega(\hat{\mathbf{k}}')$ whenever $\langle\mathbf{e}\rangle=\mathbf{e}$.[17,28] Indeed, for any linear transform R of the orthogo-

nal group $O(S^{d-1})$ leaving invariant the unit sphere S^{d-1} and its measure $d\Omega$, i.e., rotations and symmetries, one has

$$\mathcal{K}_0(\hat{\mathbf{k}}\cdot\mathbf{e}) = \int_{S^{d-1}} \sigma(R\hat{\mathbf{k}}\cdot R\hat{\mathbf{k}}')\hat{\mathbf{k}}'\cdot\mathbf{e}d\Omega(\hat{\mathbf{k}}') = \int_{S^{d-1}} \sigma(R\hat{\mathbf{k}}\cdot\hat{\mathbf{k}}')\hat{\mathbf{k}}'\cdot R\mathbf{e}d\Omega(\hat{\mathbf{k}}'),$$

using the change of variable $R\hat{\mathbf{k}}'\to\hat{\mathbf{k}}'$ and $R^{-1}=R^{\mathrm{T}}$. Introducing $\mathbf{e}^{\perp}$ such that and $\mathbf{e}=(\hat{\mathbf{k}}\cdot\mathbf{e})\hat{\mathbf{k}}+\mathbf{e}^{\perp}$ yields $\hat{\mathbf{k}}'\cdot R\mathbf{e}=(\hat{\mathbf{k}}\cdot\mathbf{e})R\mathbf{k}\cdot\hat{\mathbf{k}}'+R\mathbf{e}^{\perp}\cdot\hat{\mathbf{k}}'$ with $\int_{S^{d-1}}\sigma(R\hat{\mathbf{k}}\cdot\hat{\mathbf{k}}')R\mathbf{e}^{\perp}\cdot\hat{\mathbf{k}}'\mathrm{d}\Omega(\hat{\mathbf{k}}')=0$ by symmetry (this can be seen by expressing this last integral in polar coordinates). Therefore,

$$\mathcal{K}_0(\hat{\mathbf{k}}\cdot\mathbf{e}) = \int_{S^{d-1}} \sigma(R\hat{\mathbf{k}}\cdot\hat{\mathbf{k}}')(\hat{\mathbf{k}}\cdot\mathbf{e})R\hat{\mathbf{k}}\cdot\hat{\mathbf{k}}'d\Omega(\hat{\mathbf{k}}') = \left(\int_{S^{d-1}} \sigma(\hat{\mathbf{k}}\cdot\hat{\mathbf{k}}')\hat{\mathbf{k}}\cdot\hat{\mathbf{k}}'d\Omega(\hat{\mathbf{k}}')\right)(\hat{\mathbf{k}}\cdot\mathbf{e}).$$

Plugging Eq. (39) into Eq. (38) with $\mathbf{e}\equiv\boldsymbol{\nabla}_{\mathbf{x}}\phi$ from the above analysis, Eq. (37), it is deduced that $\boldsymbol{\Lambda}^*$ satisfies

$$(\tilde{\boldsymbol{\Sigma}}-\tilde{\boldsymbol{\Sigma}}^*)\boldsymbol{\Lambda}^*\mathbf{u}=\mathbf{C}\mathbf{u}, \tag{40}$$

with

$$\tilde{\boldsymbol{\Sigma}}^*(\mathbf{x},\omega)=\int_{S^{d-1}}\tilde{\boldsymbol{\sigma}}(\mathbf{x},\omega,\hat{\mathbf{k}}\cdot\hat{\mathbf{k}}')\hat{\mathbf{k}}\cdot\hat{\mathbf{k}}'d\Omega(\hat{\mathbf{k}}').$$

To the second order $O(\delta^2)$, we have

$$-\Omega_d\mathcal{Q}_\omega\mathbf{C}^{-d}\mathbf{a}^{(2)}=\partial_t\mathbf{a}^{(0)}+\boldsymbol{\eta}\mathbf{a}^{(0)}+(\mathbf{C}\otimes\hat{\mathbf{k}})\boldsymbol{\nabla}_{\mathbf{x}}\otimes\mathbf{a}^{(1)}-(\mathbf{C}\otimes\boldsymbol{\nabla}_{\mathbf{x}})(\mathbf{I}_d-\hat{\mathbf{k}}\otimes\hat{\mathbf{k}})\boldsymbol{\nabla}_{\hat{\mathbf{k}}}\otimes\mathbf{a}^{(1)},$$

with $\boldsymbol{\eta}(\mathbf{x})=\mathrm{diag}(\eta_\alpha(\mathbf{x}))_{\alpha=1,\ldots,M}$. The compatibility condition for $\mathbf{C}^{-d}\mathbf{a}^{(2)}$ to exist is that the right hand side in the above equation should belong to $N(\mathcal{Q}_\omega)^{\perp}$, that is, its averaged scalar product with any constant function $\phi\mathbf{d}$ should vanish. Therefore,

$$\mathbf{d}\cdot\langle\partial_t\mathbf{a}^{(0)}+(\mathbf{C}\otimes\hat{\mathbf{k}})\boldsymbol{\nabla}_{\mathbf{x}}\otimes\mathbf{a}^{(1)}-(\mathbf{C}\otimes\boldsymbol{\nabla}_{\mathbf{x}})(\mathbf{I}_d-\hat{\mathbf{k}}\otimes\hat{\mathbf{k}})\times\boldsymbol{\nabla}_{\hat{\mathbf{k}}}\otimes\mathbf{a}^{(1)}+\boldsymbol{\eta}\mathbf{a}^{(0)}\rangle=0,$$

or, upon using Eq. (39) and reminding that neither $\mathbf{a}^{(0)}$ nor $\mathbf{a}^{(11)}$ depend on $\hat{\mathbf{k}}$:

$$\mathbf{d}\cdot\partial_t\mathbf{a}^{(0)}+\mathbf{d}\cdot\langle(\mathbf{C}\otimes\hat{\mathbf{k}})\boldsymbol{\nabla}_{\mathbf{x}}\otimes\mathbf{a}^{(11)}\rangle-\mathbf{d}\cdot\langle(\mathbf{C}\otimes\hat{\mathbf{k}})\times\boldsymbol{\nabla}_{\mathbf{x}}\otimes(\boldsymbol{\Lambda}^*\otimes\hat{\mathbf{k}})\boldsymbol{\nabla}_{\mathbf{x}}\otimes\mathbf{a}^{(0)}\rangle+\mathbf{d}\cdot\langle(\mathbf{C}\otimes\boldsymbol{\nabla}_{\mathbf{x}})\times(\mathbf{I}_d-\hat{\mathbf{k}}\otimes\hat{\mathbf{k}})\boldsymbol{\nabla}_{\hat{\mathbf{k}}}\otimes(\boldsymbol{\Lambda}^*\otimes\hat{\mathbf{k}})\boldsymbol{\nabla}_{\mathbf{x}}\otimes\mathbf{a}^{(0)}\rangle+\mathbf{d}\cdot\langle\boldsymbol{\eta}\rangle\mathbf{a}^{(0)}=0.$$

Here it is assumed that $\langle\boldsymbol{\eta}\rangle\neq\boldsymbol{\eta}$ for generality purposes, as $\boldsymbol{\eta}$ may also depend on $\mathbf{k}$. But by definition of the product of a third order tensor and a second order tensor $(\mathbf{A}\otimes\mathbf{e})\mathbf{f}\otimes\mathbf{g}=(\mathbf{e}\cdot\mathbf{f})\mathbf{A}\mathbf{g}$, one first has

$$\mathbf{d}\cdot\langle(\mathbf{C}\otimes\hat{\mathbf{k}})\boldsymbol{\nabla}_{\mathbf{x}}\otimes\mathbf{a}^{(11)}\rangle=\mathbf{d}\cdot\mathbf{C}\langle\hat{\mathbf{k}}\cdot\boldsymbol{\nabla}_{\mathbf{x}}\rangle\mathbf{a}^{(11)}=0$$

because $\langle\hat{\mathbf{k}}\cdot\boldsymbol{\nabla}_{\mathbf{x}}\rangle=0$. Second,

$$\langle(\mathbf{C}\otimes\hat{\mathbf{k}})\boldsymbol{\nabla}_{\mathbf{x}}\otimes(\boldsymbol{\Lambda}^*\otimes\hat{\mathbf{k}})\boldsymbol{\nabla}_{\mathbf{x}}\otimes a^{(0)}\rangle=\mathbf{C}\langle(\hat{\mathbf{k}}\cdot\boldsymbol{\nabla}_{\mathbf{x}})\boldsymbol{\Lambda}^*(\hat{\mathbf{k}}\cdot\boldsymbol{\nabla}_{\mathbf{x}})\rangle\mathbf{a}^{(0)}=\frac{1}{d}\mathbf{C}\boldsymbol{\nabla}_{\mathbf{x}}\cdot\boldsymbol{\Lambda}^*(\mathbf{a}^{(0)}\otimes\boldsymbol{\nabla}_{\mathbf{x}})$$

because $\langle(\hat{\mathbf{k}}\cdot\boldsymbol{\nabla}_{\mathbf{x}})f(\hat{\mathbf{k}}\cdot\boldsymbol{\nabla}_{\mathbf{x}})\rangle=(1/d)\boldsymbol{\nabla}_{\mathbf{x}}\cdot f\boldsymbol{\nabla}_{\mathbf{x}}$. Finally,

$$\begin{aligned}\langle(\mathbf{C}\otimes\boldsymbol{\nabla}_{\mathbf{x}})(\mathbf{I}_d-\hat{\mathbf{k}}\otimes\hat{\mathbf{k}})\boldsymbol{\nabla}_{\hat{\mathbf{k}}}\otimes(\boldsymbol{\Lambda}^*\otimes\hat{\mathbf{k}})\boldsymbol{\nabla}_{\mathbf{x}}\otimes\mathbf{a}^{(0)}\rangle&=(\mathbf{C}\otimes\boldsymbol{\nabla}_{\mathbf{x}})\langle(\mathbf{I}_d-\hat{\mathbf{k}}\otimes\hat{\mathbf{k}})\boldsymbol{\nabla}_{\hat{\mathbf{k}}}\otimes\boldsymbol{\Lambda}^*(\hat{\mathbf{k}}\cdot\boldsymbol{\nabla}_{\mathbf{x}})\rangle\mathbf{a}^{(0)}\\&=(\mathbf{C}\otimes\boldsymbol{\nabla}_{\mathbf{x}})\langle\mathbf{I}_d-\hat{\mathbf{k}}\otimes\hat{\mathbf{k}}\rangle\boldsymbol{\Lambda}^*(\mathbf{a}^{(0)}\otimes\boldsymbol{\nabla}_{\mathbf{x}})\\&=\frac{d-1}{d}(\mathbf{C}\otimes\boldsymbol{\nabla}_{\mathbf{x}})\cdot\boldsymbol{\Lambda}^*(\mathbf{a}^{(0)}\otimes\boldsymbol{\nabla}_{\mathbf{x}}),\end{aligned}$$

since $\boldsymbol{\nabla}_{\hat{\mathbf{k}}}\otimes\hat{\mathbf{k}}=\mathbf{I}_d$ and $\langle\mathbf{I}_d-\hat{\mathbf{k}}\otimes\hat{\mathbf{k}}\rangle=(1-(1/d))\mathbf{I}_d$. Therefore $\mathbf{a}^{(0)}$ satisfies the diffusion equation:

$$\mathbf{d}\cdot(\partial_t\mathbf{a}^{(0)}-\boldsymbol{\nabla}_{\mathbf{x}}\cdot\mathbf{D}(\mathbf{a}^{(0)}\otimes\boldsymbol{\nabla}_{\mathbf{x}})+(\mathbf{C}\otimes\boldsymbol{\nabla}_{\mathbf{x}})\cdot\boldsymbol{\Lambda}^*\times(\mathbf{a}^{(0)}\otimes\boldsymbol{\nabla}_{\mathbf{x}})+\langle\boldsymbol{\eta}\rangle\mathbf{a}^{(0)})=0, \tag{41}$$

where the diffusion matrix $\mathbf{D}$ is

$$\mathbf{D}(\mathbf{x},\omega)=\frac{1}{d}\mathbf{C}(\mathbf{x})\boldsymbol{\Lambda}^*(\mathbf{x},\omega).$$

This result extends the conclusions of Refs. 32–34 to the case of heterogeneous background media with multimode diffusion. The main advantage of the diffusion equation is that its solution is independent of the direction $\hat{\mathbf{k}}$. Its numerical solution is therefore much faster to construct than that of the full multigroup transport equations (31). Alternatively, Eq. (41) may be written in a conservative form for the constant function ϕ of Eq. (37) as:[35]

$$\frac{1}{\tilde{c}^d(\mathbf{x})}\partial_t\phi-\boldsymbol{\nabla}_{\mathbf{x}}\cdot\tilde{D}(\mathbf{x},\omega)\boldsymbol{\nabla}_{\mathbf{x}}\phi+\tilde{\eta}(\mathbf{x},\omega)\phi=0, \tag{42}$$

where $\tilde{c}=\|\mathbf{C}\|_{-d}$, $\tilde{D}=\|\mathbf{C}^{-d}\mathbf{D}\|_1$ and $\tilde{\eta}=\|\mathbf{C}^{-d}\langle\boldsymbol{\eta}\rangle\|_1$:

$$\tilde{c}(\mathbf{x})=\left(\sum_{\alpha=1}^{M}c_\alpha^{-d}(\mathbf{x})\right)^{-1/d},\quad \tilde{D}(\mathbf{x},\omega)=\frac{1}{d}\sum_{\alpha=1}^{M}\frac{\ell_\alpha^*(\mathbf{x},\omega)}{c_\alpha^{d-1}(\mathbf{x})},$$

$$\tilde{\eta}(\mathbf{x},\omega)=\sum_{\alpha=1}^{M}\frac{\langle\eta_\alpha\rangle(\mathbf{x},\omega)}{c_\alpha^{d}(\mathbf{x})}.$$

The so-called transport mean free paths $(\ell_1^*,\ell_2^*,\ldots,\ell_M^*)^T=\boldsymbol{\Lambda}^*\mathbf{u}$ are computed by Eq. (40). They characterize the distance waves must propagate until their direction $\hat{\mathbf{k}}$ is randomized. Generally $\ell_\alpha^*>\ell_\alpha$ for a tendency of forward scattering such that the matrix $\tilde{\boldsymbol{\Sigma}}^*$ is positive definite. If scattering is uniform, then $\tilde{\boldsymbol{\Sigma}}^*=\mathbf{0}$ and $\ell_\alpha^*=\ell_\alpha$ for $\alpha=1,2,\ldots,M$.

C. Energy density equipartition

Using the equipartition rule (37), the space-time energy density of Eq. (32) in the limit $\delta\to0$ is

$$\mathcal{E}^{(0)}(\mathbf{x},t) = \frac{1}{\tilde{c}_\alpha^d(\mathbf{x})}\int_0^{+\infty} e^{(0)}(\mathbf{x},\omega,t)\omega^{d-1}d\omega,$$

$$e^{(0)}(\mathbf{x},\omega,t) = \Omega_d \phi(\mathbf{x},\omega,t). \tag{43}$$

Introducing the energy density $\mathcal{E}_\alpha^{(0)}$ of a particular mode α among the m existing ones, such that $\mathcal{E}^{(0)}=\Sigma_{\alpha=1}^m R_\alpha \mathcal{E}_\alpha^{(0)}$, where the αth mode has an order of multiplicity R_α, one typically has for $t>\ell_\alpha^*/c_\alpha$:

$$\frac{\mathcal{E}_\alpha^{(0)}(\mathbf{x},t)}{\mathcal{E}_\beta^{(0)}(\mathbf{x},t)} = \frac{R_\alpha}{R_\beta}\left(\frac{c_\beta(\mathbf{x})}{c_\alpha(\mathbf{x})}\right)^d, \quad \forall\, \alpha,\beta = 1,2,\ldots,m,$$

$$\forall \mathbf{x} \in \mathcal{O}, \tag{44}$$

whatever the underlying random heterogeneity of the medium or the loads may be.

D. Fick's law

The "transmission relationship" or "energetic behavior law" which links the power flow with the gradient of the energy density, as invoked in the VCA literature, is derived from the previous results as follows. Taking the scalar product of Eq. (39) with $\mathbf{C}^{1-d}\mathbf{u}$, then premultiplying it with $\hat{\mathbf{k}}$ and integrating over S^{d-1} [see Eq. (33)], yields the space-time power flow density vector as

$$\mathbf{\Pi}^\delta(\mathbf{x},t) = \sum_{\alpha=1}^M \frac{1}{c_\alpha^d(\mathbf{x})}\int_0^{+\infty} \boldsymbol{\pi}_\alpha^\delta(\mathbf{x},\omega,t)\omega^{d-1}d\omega,$$

$$\boldsymbol{\pi}_\alpha^\delta(\mathbf{x},\omega,t) = -\delta D_\alpha(\mathbf{x},\omega)\nabla_{\mathbf{x}} e^{(0)} + o(\delta), \tag{45}$$

where $D_\alpha(\mathbf{x},\omega)=(1/d)c_\alpha(\mathbf{x})\ell_\alpha^*(\mathbf{x},\omega)$ is a partial diffusion coefficient. Thus $\mathbf{\Pi}^\delta(\mathbf{x},t)=\mathbf{0}$ in the limit $\delta\to 0$, as expected for a diffusive regime. Recalling Eq. (36) and (39), one has the expansion:

$$a_\alpha^\delta(\mathbf{x},\omega,\hat{\mathbf{k}},t) = \frac{1}{\Omega_d}\left[e^{(0)}(\mathbf{x},\omega,t) + \frac{d}{c_\alpha^2(\mathbf{x})}\mathbf{c}_{g,\alpha}(\mathbf{x},\mathbf{k})\cdot\boldsymbol{\pi}_\alpha^\delta(\mathbf{x},\omega,t)\right] + O(\delta^2), \tag{46}$$

which is, ignoring the $O(\delta^2)$ terms, the usual P_1-approximation invoked in neutron transport theory[16,28] in order to derive diffusion approximations from the lowest-order moment equations induced by Eq. (31).

E. Examples

The scalar case $m=M=1$ has been considered in Ref. 35. The diffusion equation (41) reduces to

$$\partial_t a^{(0)} - \nabla_{\mathbf{x}}\cdot D(\mathbf{x},\omega)\nabla_{\mathbf{x}} a^{(0)} + \ell^*(\mathbf{x},\omega)\nabla_{\mathbf{x}} c\cdot\nabla_{\mathbf{x}} a^{(0)} + \langle\eta\rangle(\mathbf{x},\omega)a^{(0)} = 0, \tag{47}$$

where the diffusion coefficient D and the transport mean free path ℓ^* are

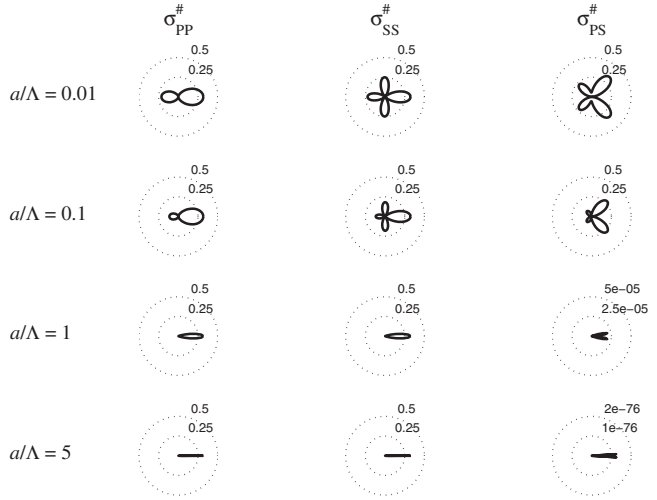


FIG. 2. Normalized differential scattering cross-sections $\sigma_{\alpha\beta}^\# = (\Lambda/ac_\alpha)^2\sigma_{\alpha\beta}$ for a thick shell as functions of $\Theta=\arccos(\hat{\mathbf{k}}\cdot\hat{\mathbf{k}}')$ for various ratio a/Λ and Gaussian correlation model; $\nu=0.2$, $r_{11}=r_{12}=r_{13}=0.1$, $r_{22}=r_{33}=1.0$, and $r_{23}=0.9$.

$$D(\mathbf{x},\omega) = \frac{1}{d}c(\mathbf{x})\ell^*(\mathbf{x},\omega),$$

$$\ell^*(\mathbf{x},\omega) = c(\mathbf{x})\left(\int_{S^{d-1}} \tilde{\sigma}(\mathbf{x},\omega,\hat{\mathbf{k}}\cdot\hat{\mathbf{k}}') \times(1-\hat{\mathbf{k}}\cdot\hat{\mathbf{k}}')d\Omega(\hat{\mathbf{k}}')\right)^{-1},$$

respectively. In a conservative form, the diffusion equation is

$$\frac{1}{c^d(\mathbf{x})}\partial_t a^{(0)} - \nabla_{\mathbf{x}}\cdot\left(\frac{D(\mathbf{x},\omega)}{c^d(\mathbf{x})}\nabla_{\mathbf{x}} a^{(0)}\right) + \frac{\langle\eta\rangle(\mathbf{x},\omega)}{c^d(\mathbf{x})}a^{(0)} = 0.$$

Note that it is also applicable to the phase-space energy density $w^{(0)}$ or to the space-time energy density $\mathcal{E}^{(0)}$ (in the limit $\delta\to 0$) of Eq. (43):[30]

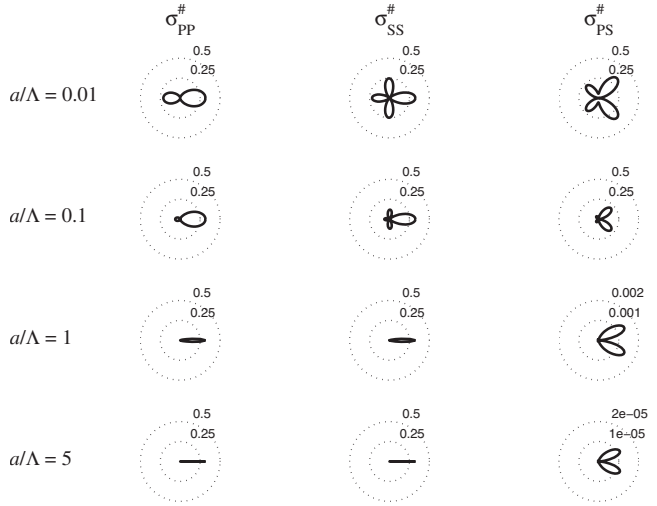


FIG. 3. Normalized differential scattering cross sections $\sigma_{\alpha\beta}^\# = (\Lambda/ac_\alpha)^2\sigma_{\alpha\beta}$ for a thick shell as functions of $\Theta=\arccos(\hat{\mathbf{k}}\cdot\hat{\mathbf{k}}')$ for various ratio a/Λ and exponential (Markov) correlation model; same parameters as for Fig. 2.

$$\mathcal{E}^{(0)}(\mathbf{x},t) = \frac{\Omega_d}{c^d(\mathbf{x})}\int_0^{+\infty} a^{(0)}(\mathbf{x},\omega,t)\omega^{d-1}d\omega.$$

This example covers the diffusive regime for shear and bending energy densities in Timoshenko beams with $d=1$ (Sec. II B) and for the transverse energy density in thick shells with $d=2$ (Sec. II A).

For the in-plane and bending energy densities of a thick shell, $m=2$ and $M=4$ since each mode $m=P$ or $m=S$ has multiplicity 2 (see Sec. II A). The diffusion constant $\tilde{D}_{PS}$ in Eq. (42) for this group of coupled energy modes is

$$\tilde{D}_{PS}(\mathbf{x},\omega) = \frac{1}{2}\left(\frac{\ell_P^*(\mathbf{x},\omega)}{c_P(\mathbf{x})} + \frac{\ell_S^*(\mathbf{x},\omega)}{c_S(\mathbf{x})}\right),$$

where the transport mean free paths ℓ_P^* and ℓ_S^* are given by Eq. (40):

$$\begin{pmatrix}\ell_P^*\\ \ell_S^*\end{pmatrix} = \begin{bmatrix}\tilde{\Sigma}_{PP}\left(\mathbf{x},\frac{\omega}{c_P}\right)+\tilde{\Sigma}_{PS}\left(\mathbf{x},\frac{\omega}{c_P}\right)-\tilde{\Sigma}^*_{PP}\left(\mathbf{x},\frac{\omega}{c_P}\right) & -\tilde{\Sigma}^*_{PS}\left(\mathbf{x},\frac{\omega}{c_P}\right)\\ -\tilde{\Sigma}^*_{SP}\left(\mathbf{x},\frac{\omega}{c_S}\right) & \tilde{\Sigma}_{SS}\left(\mathbf{x},\frac{\omega}{c_S}\right)+\tilde{\Sigma}_{SP}\left(\mathbf{x},\frac{\omega}{c_S}\right)-\tilde{\Sigma}^*_{SS}\left(\mathbf{x},\frac{\omega}{c_S}\right)\end{bmatrix}^{-1}\begin{pmatrix}c_P(\mathbf{x})\\ c_S(\mathbf{x})\end{pmatrix},$$

with

$$\tilde{\Sigma}^*_{\alpha\beta}\left(\mathbf{x},\frac{\omega}{c_\alpha}\right) = \left(\frac{c_\alpha}{c_\beta}\right)^2\tilde{\Sigma}^*_{\beta\alpha}\left(\mathbf{x},\frac{\omega}{c_\beta}\right) = \int_{S^1}\tilde{\sigma}_{\alpha\beta}\left(\mathbf{x},\frac{\omega}{c_\alpha},\frac{\omega}{c_\beta},\hat{\mathbf{k}}\cdot\hat{\mathbf{k}}'\right)\hat{\mathbf{k}}\cdot\hat{\mathbf{k}}'d\Omega(\hat{\mathbf{k}}'),\quad \alpha,\beta=P,S.$$

If the background medium is homogeneous, such that the wave speeds c_α are independent of $\mathbf{x}$ for $\alpha=1,2,\ldots,M$, the diffusion equation reduces to

$$\mathbf{d}\cdot(\partial_t\mathbf{a}^{(0)} - \boldsymbol{\nabla}_\mathbf{x}\cdot\mathbf{D}(\mathbf{a}^{(0)}\otimes\boldsymbol{\nabla}_\mathbf{x}) + \langle\boldsymbol{\eta}\rangle\mathbf{a}^{(0)}) = 0.$$

Its solution also satisfies the equipartition rule (37), that is, $\mathbf{a}^{(0)}=\phi\mathbf{u}$ where ϕ is a constant function of $\hat{\mathbf{k}}$ ($\langle\phi\rangle=\phi$) which solves

$$\partial_t\phi - \tilde{\tilde{D}}\Delta_\mathbf{x}\phi + \tilde{\tilde{\eta}}\phi = 0, \tag{48}$$

where

$$\tilde{\tilde{D}}(\omega) = \frac{\Sigma_{\alpha=1}^M c_\alpha^{1-d}\ell_\alpha^*(\omega)}{d\Sigma_{\alpha=1}^M c_\alpha^{-d}},\quad \tilde{\tilde{\eta}}(\omega) = \frac{\Sigma_{\alpha=1}^M c_\alpha^{-d}\langle\eta_\alpha\rangle(\omega)}{\Sigma_{\alpha=1}^M c_\alpha^{-d}},$$

as in Refs. 32 and 33 for slender structures or Ref. 34 for three-dimensional media. For a thick shell the diffusion constant of the PS group is

$$\tilde{\tilde{D}}_{PS}(\omega) = \frac{c_P c_S}{2(c_P^2+c_S^2)}(c_S\ell_P^*(\omega) + c_P\ell_S^*(\omega)),$$

and Fick's law writes

$$\boldsymbol{\pi}_{PS}^\delta(\mathbf{x},\omega,t) = -\delta\tilde{\tilde{D}}_{PS}(\omega)\boldsymbol{\nabla}_\mathbf{x}e_{PS}^{(0)}(\mathbf{x},\omega,t) + o(\delta). \tag{49}$$

Figures 2–5 display the normalized differential scattering

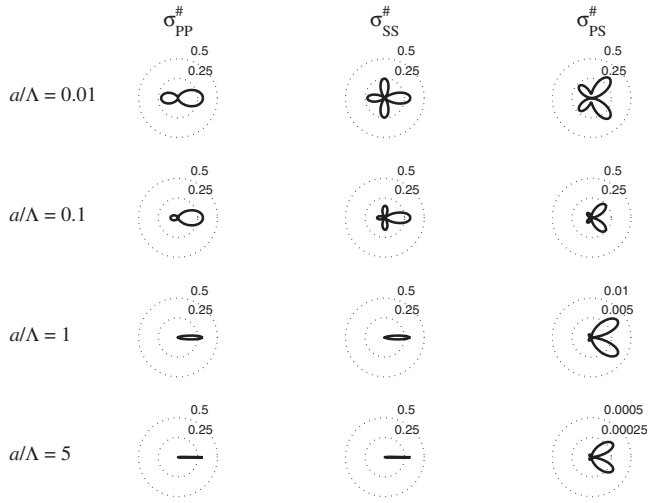


FIG. 4. Normalized differential scattering cross-sections $\sigma^\#_{\alpha\beta}=(\Lambda/ac_\alpha)^2\sigma_{\alpha\beta}$ for a thick shell as functions of $\Theta=\arccos(\hat{\mathbf{k}}\cdot\hat{\mathbf{k}}')$ for various ratio a/Λ and Von Karman correlation model; same parameters as for Fig. 2.

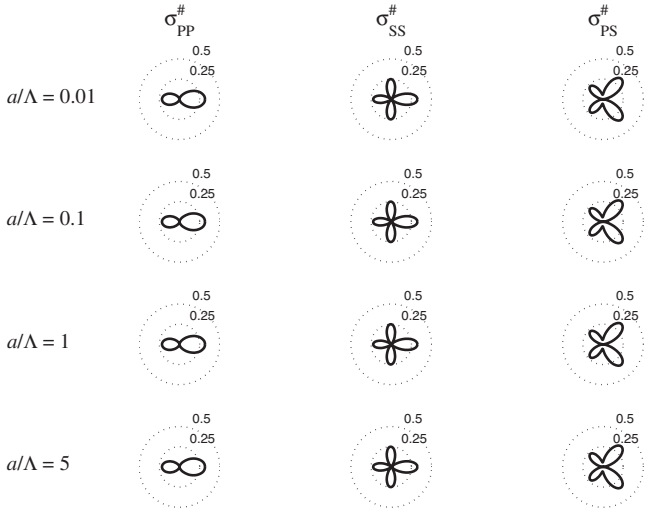


FIG. 5. Normalized differential scattering cross-sections $\sigma^\#_{\alpha\beta}=(\Lambda/ac_\alpha)^2\sigma_{\alpha\beta}$ for a thick shell as functions of $\Theta=\arccos(\hat{\mathbf{k}}\cdot\hat{\mathbf{k}}')$ for various ratio a/Λ and delta (Rayleigh) correlation model; same parameters as for Fig. 2.

TABLE I. Correlation models; K_0 is the zeroth order modified Bessel function.

Correlation function	$N(\mathbf{x})$	$\hat{N}(\mathbf{k})$
Gaussian	$\exp\left(-\frac{\lvert\mathbf{x}\rvert^2}{2a^2}\right)$	$\frac{a^2}{2\pi}\exp\left(-\frac{1}{2}a^2\lvert\mathbf{k}\rvert^2\right)$
Markov	$\exp\left(-\frac{\lvert\mathbf{x}\rvert}{a}\right)$	$\frac{a^2}{2\pi}(1+a^2\lvert\mathbf{k}\rvert^2)^{-3/2}$
von Karman	$K_0\left(\frac{\lvert\mathbf{x}\rvert}{a}\right)$	$\frac{a^2}{2\pi}(1+a^2\lvert\mathbf{k}\rvert^2)^{-1}$
Rayleigh	$\delta\left(\frac{\lvert\mathbf{x}\rvert}{a}\right)$	$\frac{a^2}{2\pi^2}$

cross sections $\sigma^{\#}_{\alpha\beta}=(\Lambda/ac_\alpha)^2\sigma_{\alpha\beta}$ of a shell as functions of $\Theta=\arccos(\hat{\mathbf{k}}\cdot\hat{\mathbf{k}}')$ for four different models of correlation functions parametrized by a characteristic length a of random heterogeneities, and for different values of the ratio a/Λ with $\Lambda=2\pi c_P/\omega$. The correlation functions are defined by $R_{jk}(\mathbf{x}-\mathbf{y})=\int_{\mathbb{R}^2}e^{-i\mathbf{k}\cdot(\mathbf{x}-\mathbf{y})}S_{jk}(\mathbf{k})d\mathbf{k}$ and the four models are gathered in Table I below. They have the form $R_{jk}(\mathbf{x})=r_{jk}N(\mathbf{x})$, where r_{jk} is a correlation coefficient and $N(\mathbf{x})$ is the normalized correlation function, such that $S_{jk}(\mathbf{k})=r_{jk}\hat{N}(\mathbf{k})$ and $\hat{N}(\mathbf{k})$ stands for the two-dimensional Fourier transform of $N(\mathbf{x})$. The parameters chosen for all computations are $\underline{\nu}=1-2(c_S^2/c_P^2)=0.2$ (mean Poisson's ratio), $r_{11}=0.1$ and $r_{22}=r_{33}=1$ (small fluctuations of the density versus Lamé's modulii), and $r_{12}=r_{13}=0.1$ and $r_{23}=0.9$ (weak correlation of the density with Lamé's modulii). It is observed that for the first three models the scattering cross sections get strongly forward peaked as the ratio a/Λ increases, and scattering is mostly elastic. Indeed, the inelastic scattering process corresponding to mode conversions $P\leftrightarrow S$ as quantified by σ_{PS} or σ_{SP} becomes negligible. A noteworthy exception is the delta (Rayleigh) correlation model for which neither elastic or inelastic scattering dominates, and backscattering as well as S-transverse scattering subsist even at the higher ratios a/Λ; delta-correlated scatterers may therefore be more amenable to localize than others. As a global trend, the amounts of inelastic scattering and backscattering increase with the roughness of the correlation function. Next, the normalized scattering and transport mean free paths ℓ_α/Λ and ℓ^*_α/Λ are plotted in Figs. 6 and 7 below for modes $\alpha=P$ and $\alpha=S$, respectively, as functions of a/Λ. Figure 8 displays the normalized diffusion constant $\tilde{D}_{PS}/c_P\Lambda$ for the same models of correlation functions and parameters. Note that the normalization chosen here for the figures is different from Refs. 33 and 34. These results agree remarkably well with the ones reported in Ref. 45 for diffuse light propagation in porous glasses in the range $0<a/\Lambda<1$, both qualitatively and quantitatively for the exponential (Markov) model. It may also be observed that they are only slightly affected by variations in the correlation parameters r_{jk} (plots not displayed here). The scattering mean free paths are almost equal for the first three models; however, the transport mean free paths differ significantly from one model to another. One may observe from these results that smooth perturbations (Gaussian model) tend to delay the onset of the diffusion regime compared to sharper perturbations (other models). Also, the sharper the perturbations are, the smaller the diffusion constant is, indicating a possible prominence of weak localization at the higher frequencies. For example, the diffusion constant with a delta correlation function apparently scales inversely with the correlation length a, in accordance with Thouless' assertion.

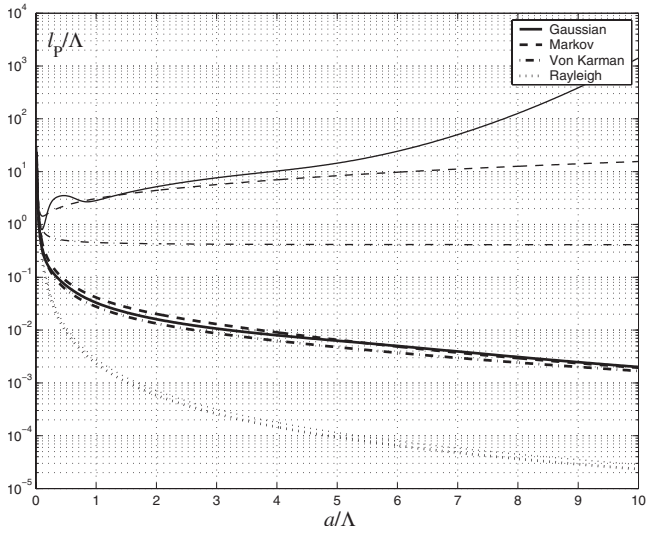


FIG. 6. Normalized scattering (thick lines) and transport (thin lines) P-mode mean free paths ℓ_P/Λ for a thick shell as functions of a/Λ for various models of correlation; same parameters as for Fig. 2.

V. SUMMARY

The elastic energy and power flow densities $\mathcal{E}^\epsilon(\mathbf{x},t)$ and $\mathbf{\Pi}^\epsilon(\mathbf{x},t)$, respectively, e.g., Eqs. (5) and (6) for shells, satisfy the continuity equation:

$$\partial_t\boldsymbol{\mathcal{E}}^\epsilon+\boldsymbol{\nabla}_\mathbf{x}\cdot\mathbf{\Pi}^\epsilon=0,$$

for any fixed $\epsilon>0$, up to a possible dissipative term. However, the passage to the limit $\epsilon\to0$ is difficult because it requires the estimation of the limit of the *square* of highly oscillating functions, together with the passage to the limit in

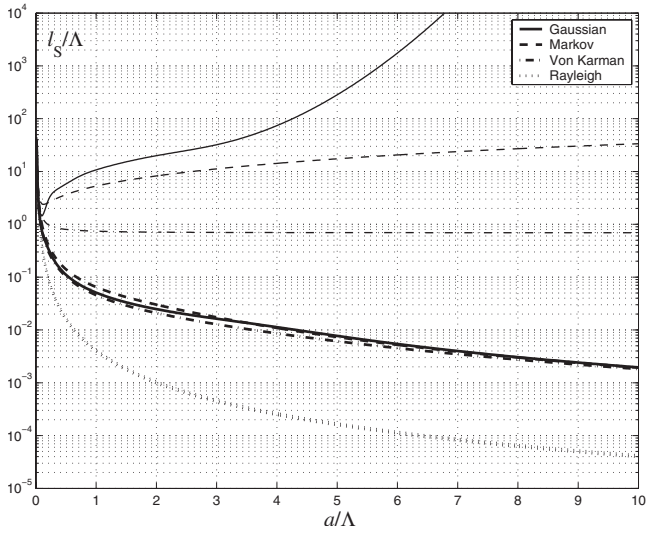


FIG. 7. Normalized scattering (thick lines) and transport (thin lines) S-mode mean free paths ℓ_S/Λ for a thick shell as functions of a/Λ for various models of correlation; same parameters as for Fig. 2.

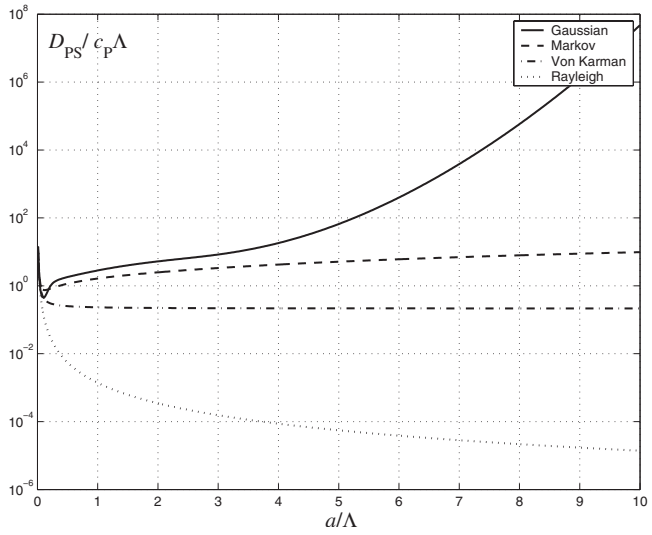


FIG. 8. Normalized diffusion constant $\tilde{\tilde{D}}_{PS}/c_P\Lambda$ for a thick shell as function of a/Λ for various models of correlation; same parameters as for Fig. 2.

the above partial differential equation. Microlocal analysis and kinetic models describe how this should be done, as expounded in Sec. II for slender structures. In turn, the multigroup transport equations (35) in the near critical diffusion scaling correspond to a continuity equation:

$$\partial_t e^\delta + \frac{1}{\delta}\nabla_{\mathbf{x}} \cdot \boldsymbol{\pi}^\delta + P^\delta = 0,$$

for any fixed $\delta > 0$, where

$$e^\delta(\mathbf{x},\omega,t) = \sum_{\alpha=1}^{M} c_\alpha^{-d}(\mathbf{x}) \int_{S^{d-1}} a_\alpha^\delta(\mathbf{x},\omega,\hat{\mathbf{k}},t) d\Omega(\hat{\mathbf{k}}),$$

$$\boldsymbol{\pi}^\delta(\mathbf{x},\omega,t) = \sum_{\alpha=1}^{M} c_\alpha^{-d}(\mathbf{x}) \int_{S^{d-1}} \mathbf{c}_{g,\alpha}(\mathbf{x},\mathbf{k}) a_\alpha^\delta(\mathbf{x},\omega,\hat{\mathbf{k}},t) d\Omega(\hat{\mathbf{k}}),$$

and

$$P^\delta(\mathbf{x},\omega,t) = \sum_{\alpha=1}^{M} c_\alpha^{-d}(\mathbf{x}) \int_{S^{d-1}} \eta_\alpha(\mathbf{x},\mathbf{k}) a_\alpha^\delta(\mathbf{x},\omega,\hat{\mathbf{k}},t) d\Omega(\hat{\mathbf{k}}),$$

for the dissipated power density. Its limit $\delta \to 0$ is the diffusion equation (42), which may be recovered formally from the continuity equation above and Fick's law (45). This is what is done in the VCA literature,[19] ignoring, however, the essential phase dependence of the energy and power flow densities before diffusion sets up, and all possible interactions between different modes. As already noted in Sec. IV D, a crude derivation of the diffusion equation may also be carried on resorting to the so-called P_1-approximation, which corresponds to the lowest-order spherical harmonics expansion of the specific intensities. This approach is used in Ref. 38 to formally derive "generalized" diffusion equations (of the form obtained in Ref. 29) using several additional assumptions, including a Fick-like law. The present analysis allows to estimate the error induced by this assumption and a P_1-approximation, i.e., Eqs. (45) and (46).

The universal equipartition rule of Eq. (44) can be used as an indicator of the relevance of the diffusive approximation, the latter being acceptable as soon as this relation is satisfied by the energy densities up to an acceptable accuracy level. It should be noted incidentally that this relation is fully compatible with the assumption of *modal* energy equipartition in SEA since modal densities of bounded media are proportional to the inverse wave speed to the power of dimension d to the leading order versus frequency. Another indicator of a diffusive behavior is the fact that power flows vanish in the limit of small scattering mean free paths, see Eq. (45), as a consequence of the strong mixing of wave directions induced by multiple scattering. Having in mind that energy fluxes are roughly proportional to the gradient of the wave phases, high-frequency vibrations should exhibit smooth, indeed constant, phase variations for different receivers. This trend has been clearly observed on the complex structure studied in Ref. 27, among others. For this system, one must invoke the many reflections of the waves on stiffeners, bulkheads, and other structural components (the scatterers) to justify a diffuse vibrational energy field after some time. Then it should always be possible to estimate a diffusion constant for such a structure, as done for complex enclosures in room acoustics. That possibility shall be investigated in future works.

[1] C. R. Steele, "Asymptotic analysis of stress waves in inhomogeneous elastic solids," AIAA J. **7**, 896–902 (1969).
[2] A. D. Pierce, "Physical interpretation of the WKB or eikonal approximation for waves and vibrations in inhomogeneous beams and plates," J. Acoust. Soc. Am. **48**, 275–284 (1970).
[3] O. A. Germogenova, "Geometrical theory for flexural waves in shells," J. Acoust. Soc. Am. **53**, 535–540 (1973).
[4] P. E. Stott, "A transport equation for the multiple scattering of electromagnetic waves by a turbulent plasma," J. Phys. A **1**, 675–689 (1968).
[5] R. L. Weaver, "Diffusivity of ultrasound in polycrystals," J. Mech. Phys. Solids **38**, 55–86 (1990).
[6] L. Margerin, "Attenuation, transport and diffusion of scalar waves in textured random media," Tectonophysics **416**, 229–244 (2006).
[7] L. Tartar, "H-measures, a new approach for studying homogenisation, oscillations and concentration effects in partial differential equations," Proc. - R. Soc. Edinburgh, Sect. A: Math. **115A**, 193–230 (1990).
[8] P. Gérard, "Microlocal defect measures," Commun. Partial Differ. Equ. **17**, 1785–1865 (1991).
[9] P.-L. Lions and T. Paul, "Sur les mesures de Wigner ("On Wigner measures")," Rev. Mat. Iberoam. **9**, 553–618 (1993).
[10] P. Gérard, P. A. Markowich, N. J. Mauser, and F. Poupaud, "Homogenization limits and Wigner transforms," Commun. Pure Appl. Math. **L**, 323–379 (1997).
[11] G. C. Papanicolaou and L. V. Ryzhik, "Waves and Transport," in *Hyperbolic Equations and Frequency Interactions*, IAS/Park City Mathematics Series Vol. **5**, edited by L. Caffarelli and W. E (American Mathematical Society, Providence, RI, 1999), pp. 305–382.
[12] M. Guo and X.-P. Wang, "Transport equations for a general class of evolution equations with random perturbations," J. Math. Phys. **40**, 4828–4858 (1999).
[13] L. Erdös and H.-T. Yau, "Linear Boltzmann equation as the weak coupling limit of a random Schrödinger equation," Commun. Pure Appl. Math. **LIII**, 667–735 (2000).
[14] G. Bal, "Kinetics of scalar wave fields in random media," Wave Motion **43**, 132–157 (2005).
[15] J. Lukkarinen and H. Spohn, "Kinetic limit for wave propagation in a random medium," Arch. Ration. Mech. Anal. **183**, 93–162 (2007).
[16] K. M. Case and P. F. Zweifel, *Linear Transport Theory* (Addison-Wesley, Reading MA, 1967), Chap. 8.
[17] E. W. Larsen and J. B. Keller, "Asymptotic solution of neutron transport problems for small mean free paths," J. Math. Phys. **15**, 75–81 (1974).
[18] S. A. Rybak, "Waves in a plate containing random inhomogeneities," Sov. Phys. Acoust. **17**, 345–349 (1972).
[19] D. J. Nefske and S. H. Sung, "Power flow finite element analysis of

dynamic systems: basic theory and application to beams," ASME J. Vib., Acoust., Stress, Reliab. Des. **111**, 94–100 (1989).
[20]P. W. Smith and R. H. Lyon, "Sound and Structural Vibration," NASA CR-160, Washington, DC, 1965.
[21]R. L. Weaver, "Diffuse waves in finite plates," J. Sound Vib. **94**, 319–335 (1984).
[22]O. M. Bouthier and R. J. Bernhard, "Models of space-averaged energetics of plates," AIAA J. **30**, 616–623 (1992).
[23]R. S. Langley, "On the vibrational conductivity approach to high frequency dynamics for two-dimensional structural components," J. Sound Vib. **182**, 637–657 (1995).
[24]A. Le Bot, M. N. Ichchou, and L. Jézéquel, "Energy flow analysis for curved beams," J. Acoust. Soc. Am. **102**, 943–954 (1997).
[25]N. L. Wolff and R. L. Weaver, "Toward a theory of wave energy transport in large irregular structures," J. Acoust. Soc. Am. **118**, 222–231 (2005).
[26]P. Anugonda, J. S. Wiehn, and J. A. Turner, "Diffusion of ultrasound in concrete," Ultrasonics **39**, 429–435 (2001).
[27]E. Savin, "Midfrequency vibrations of a complex structure: experiments and comparison with numerical simulations," AIAA J. **40**, 1876–1884 (2002).
[28]R. Dautray and J.-L. Lions, *Mathematical Analysis and Numerical Methods for Science and Technology* (Springer-Verlag, Berlin, 1993), Vol. **6**, Chap. XXI.
[29]T. Goudon and A. Mellet, "Discrete version of the SHE asymptotics: multigroup neutron transport equations," J. Math. Phys. **43**, 3232–3260 (2002).
[30]M. Portilheiro and A. E. Tzavaras, "Hydrodynamic limits for kinetic equations and the diffusive approximation of radiative transport for acoustic waves," Trans. Am. Math. Soc. **359**, 529–565 (2007).
[31]C. Costantini and T. G. Kurtz, "Diffusion approximation for transport processes with general reflection boundary conditions," Math. Models Meth. Appl. Sci. **16**, 717–762 (2006).
[32]É. Savin, "Diffusive regime for the high-frequency dynamics of randomly heterogeneous plates," in *Mathematical and Numerical Aspects of Wave Propagation*, edited by G. C. Cohen, E. Heikkola, P. Joly, and P. Neittaanmäki (Springer, Berlin, 2003), pp. 357–362.
[33]É. Savin, "Transient transport equations for high-frequency power flow in heterogeneous cylindrical shells," Waves Random Media **14**, 303–325 (2004).
[34]É. Savin, "Radiative transfer theory for high-frequency power flows in fluid-saturated, porovisco-elastic media," J. Acoust. Soc. Am. **117**, 1020–1031 (2005).
[35]G. Bal, "Radiative transfer equations with varying refractive index: a mathematical perspective," J. Opt. Soc. Am. A **23**, 1639–1644 (2006).
[36]P. M. Naghdi and R. M. Cooper, "Propagation of elastic waves in cylindrical shells, including the effects of transverse shear and rotatory inertia," J. Acoust. Soc. Am. **28**, 56–63 (1956).
[37]D. Liu and J. A. Turner, "Influence of spatial correlation function and attenuation of ultrasonic waves in two-phase materials," J. Acoust. Soc. Am. **123**, 2570–2576 (2008).
[38]N. P. Trégourès and B. A. van Tiggelen, "Quasi-two-dimensional transfer of elastic waves," Phys. Rev. E **66**, 036601 (2002).
[39]R.-S. Wu, "Multiple scattering and energy transfer of seismic waves—separation of scattering effect from intrinsic attenuation—I. Theoretical modelling," Geophys. J. R. Astron. Soc. **82**, 57–80 (1985).
[40]J. A. Turner and R. L. Weaver, "Radiative transfer of ultrasound," J. Acoust. Soc. Am. **96**, 3654–3674 (1994).
[41]C. Soize, "Probabilistic structural modeling in linear dynamic analysis of complex mechanical systems. I—Theoretical elements," Rech. Aerosp. (English edition), **5**, 23–48 (1986).
[42]J. A. Turner and R. L. Weaver, "Diffuse energy propagation on heterogeneous plates: Structural acoustics radiative transfer theory," J. Acoust. Soc. Am. **100**, 3686–3695 (1996).
[43]P. Sheng, B. White, Z.-Q. Zhang, and G. C. Papanicolaou, "Minimum wave-localization length in a one-dimensional random medium," Phys. Rev. B **34**, 4757–4761 (1986).
[44]M. G. Krein and M. A. Rutman, "Linear operators leaving invariant a cone in a Banach space," Usp. Mat. Nauk **3**, 3–95 (1948) [AMS Translations **26**, 199–325 (1950)].
[45]S. Kawato, T. Hattori, T. Takemori, and H. Nakatsuka, "Short-range interference effect in the diffusion of light in random media," Phys. Rev. B **58**, 6180–6193 (1998).

Modeling a surface-mounted Lamb wave emission-reception system: Applications to structural health monitoring

Emmanuel Moulin,[a] Sébastien Grondel, Jamal Assaad, and Laurent Duquenne
IEMN, UMR CNRS 8520, OAE Department, Université de Valenciennes et du Hainaut Cambrésis, Le Mont Houy, 59313 Valenciennes Cedex 9, France

(Received 11 January 2008; revised 10 July 2008; accepted 7 September 2008)

The work described in this paper is intended to present a simple and efficient way of modeling a full Lamb wave emission and reception system. The emitter behavior and the Lamb wave generation are predicted using a two-dimensional (2D) hybrid finite element–normal mode expansion model. Then the receiver electrical response is obtained from a finite element computation with prescribed displacements. A numerical correction is applied to the 2D results in order to account for the in-plane radiation divergence caused by the finite length of the emitter. The advantage of this modular approach is that realistic configurations can be simulated without performing cumbersome modeling and time-consuming computations. It also provides insight into the physical interpretation of the results. A good agreement is obtained between predicted and measured signals. The range of application of the method is discussed.
© *2008 Acoustical Society of America.* [DOI: 10.1121/1.2996337]

PACS number(s): 43.40.Le, 43.20.Ks, 43.60.Qv, 43.38.Ar [YHB] Pages: 3521–3527

I. INTRODUCTION

Over the past decade, the concept of structural or integrated health monitoring has taken a growing importance. The application field spreads from civil engineering to transportation systems, and both increased security and reduced maintenance costs are expected. Among the variety of potential techniques, acoustic wave propagation has been considered a serious candidate. In particular, in plate-shaped structures, Lamb waves propagate over relatively long distances, and their damage detection capabilities have been known for a long time.[1,2] By implanting small piezoelectric transducers (PZTs) into the structures, Lamb waves can be emitted and received, and it is theoretically possible to monitor a whole given area.[3,4]

However, the integrated nature and the requirement for an in-service use of such systems, along with the complexity of the physical phenomena involved, make the design and optimization particularly difficult. Therefore, a pertinent and efficient modeling of the global behavior of the system, both from the acoustical and the electrical point of views, is necessary. In previous works,[5–7] the problem of harmonic or transient Lamb wave emission in lossless or moderately viscoelastic plates has been treated. It has been shown that a partial uncoupling of the physical effects was possible. Then the use of a hybrid numerical-analytical formulation based on this uncoupling principle has allowed a very efficient and versatile modeling. The work presented in this paper consists in an extension of the previous modeling technique in order to incorporate the reception problem. The typical configuration considered is described in Fig. 1. The receiver will be modeled using the finite element method with prescribed displacements at the plate-transducer interface (Dirichlet-type boundary conditions). The model then makes it possible to predict the electrical response of the receiver after the emitter has been subject to a time-dependent electrical excitation. The finite lengths (along the *y*-direction) of both transducers can be taken into account by using the "pseudo-three-dimensional (3D)" formulation described in previous works.[8,9]

Recently, a number of authors have treated the question of Lamb wave emission and/or reception using thin surface-bonded PZT transducers. Giurgiutiu[10] used a "pin-force" model to account for the mechanical excitation provided by the emitter. Then, the response of the plate in terms of Lamb wave excitation has been derived analytically in a two-dimensional (2D) plane strain situation. Nieuwenhuis *et al.*[11] obtained more accurate results by using 2D finite element modeling, which allows a better representation of the transducer behavior. The reception process is modeled as well, and the transfer function of the overall system is obtained. However, the method still has the drawbacks of a purely numerical modeling (no explicit mode separation, time consumption etc.), and no solution for finite-dimensional transducers is proposed. di Scalea *et al.*[12] focused on the reception of unidirectionally propagating straight-crested Lamb or Rayleigh waves by a rectangular transducer. Since a simplifying plane stress assumption is made, the analytical model developed is essentially valid for a very thin transducer. Although the successful treatment of general oblique incidence on a finite-dimensional sensor makes this work of really great interest, the plane wave hypothesis and the fact that no emitter is included in the model constitute clear limitations. Raghavan and Cesnik,[13] on the other hand, considered the emission and reception by rectangular- and circular-shaped transducers. Full 3D analytical solutions are proposed through a generalization of the pin-force assumption for the emitter. The receiver response is derived analytically once again using a thin-layer approximation.

[a]Electronic mail: emmanuel.moulin@univ-valenciennes.fr

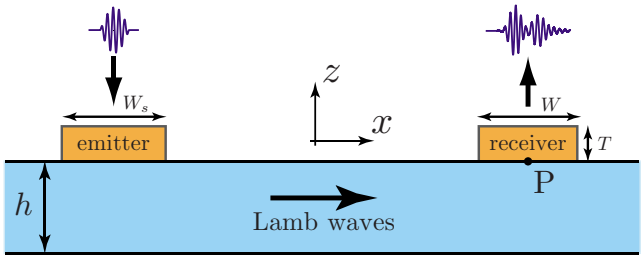


FIG. 1. (Color online) Description of the Lamb wave emission and reception configuration

In the case of finite-sized rectangular-shaped transducers, however, it will be shown that the hybrid model presented in this paper provides very satisfying results in a much simpler way. Unlike in the pin-force related models, quantitative predictions that can be directly compared to measurements are obtained. Besides, although the assumptions in the model still require small dimensions for the receiver, no particular limitation on the emitter thickness is imposed.

As for the wave-damage interaction problem, it has been the subject of an impressive amount of work already[14–17] and is still currently into intensive investigation. Since it is an entire study in itself, it will not be treated here. If required, the corresponding interaction models could be interfaced to the emission-reception model developed here.

In Sec. II, the 2D plane strain modeling principle will be explained. Since it has been the subject of previous works, the treatment of the emission process will be only very briefly discussed. The essential point will concern the reception. Then, in Sec. III, it will be shown how the effect of the third spatial dimension (actual transducer lengths) can be introduced in the receiver response as an approximate after-correction. In each case the required assumptions are given and commented on. Finally, in Sec. IV, predictions will be compared to experimental results.

II. BASIC MODEL

A. Emission

When the piezoelectric emitter is subject to a time-dependent electrical field, a part of the subsequent electrical power is converted into acoustical power propagating inside the plate through some electromechanical process due to the converse piezoelectric effect. Previous works by the authors[5,7] have shown how this transduction phenomenon can be predicted by using a 2D hybrid (numerical-analytical) modeling technique. The piezoelectricity problem is treated through a finite element computation, which allows us to take into account the actual geometry and material properties (mechanical as well as piezoelectric and dielectric coefficients) of the emitter. Then, the wave generation and propagation processes are described using an analytical normal mode expansion. It results in a prediction of the generated velocity and stress tensors $(\mathbf{v},\boldsymbol{\sigma})$ of the following form:[18,19]

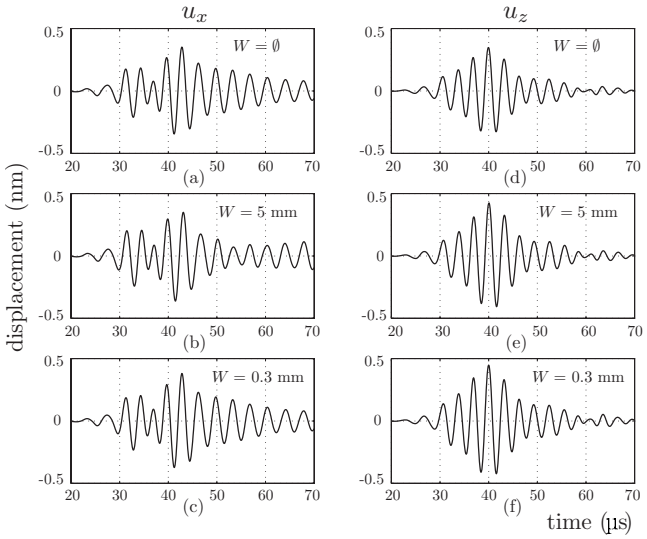


FIG. 2. Displacement at the middle point (P) of the receiver area. (a) Tangential displacement, no receiver. (b) Tangential displacement, receiver 1. (c) Tangential displacement, receiver 2. (d) Normal displacement, no receiver. (e) Normal displacement, receiver 1. (f) Normal displacement, receiver 2.

$$\mathbf{v}(x,z,f) = \sum_m A_m(f)\mathbf{v}_m(z,f)e^{jk_m x},$$
$$\boldsymbol{\sigma}(x,z,f) = \sum_m A_m(f)\boldsymbol{\sigma}_m(z,f)e^{jk_m x}, \quad (1)$$

where $\mathbf{v}_m$ and $\boldsymbol{\sigma}_m$ are the normalized velocity and stress fields associated with the mth Lamb mode, respectively, A_m is the amplitude at which the mode is excited, and k_m is the wavenumber. $\mathbf{v}_m$ and $\boldsymbol{\sigma}_m$ can be computed once and for all using classical eigenmode algorithms[20,21] for virtually any kind of materials.

Since the hybrid method has already been extensively described, it will not be further developed here. It allows the prediction of the values of A_m in either harmonic or transient excitation cases and in either lossless or moderately viscoelastic materials.

B. Reception

It will be assumed here that the bonded piezoelectric receiver has a small influence on the wave propagation. This point has been discussed in a previous work,[22] and some validity conditions have been given. As a consequence, the displacement imposed at the plate-receiver interface will be simply considered to be the surface displacement field associated with the incident Lamb waves.

Intuitively, the validity of this assumption seems reasonable if either the transducer is very thin compared to the plate thickness $(T/h \ll 1)$ or very small compared to the shortest wavelength $(W/\lambda \ll 1)$. This idea is confirmed by the results shown in Fig. 2, representing the tangential and normal displacements at the middle point (denoted by P in Fig. 1) of the interface between the plate and the receiver.

Indeed, in these test configurations, two different receivers have been considered. The first one [Figs. 2(b) and 2(e)] is 5 mm wide and 300 μm thick $(T/h=0.05 \ll 1)$. The sec-

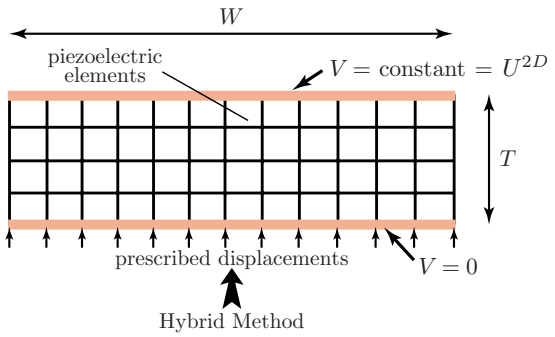


FIG. 3. (Color online) Finite element model of the receiver

ond one [Figs. 2(c) and 2(f)] is 300 μm wide and 1 mm thick ($W/\lambda \leqslant 0.034 \ll 1$). Both of them are located 10 cm away from the source, which is 3 mm wide and 500 μm thick. All these transducers are bonded onto a 6-mm-thick aluminum plate. The excitation is a 5 cycle, 10 V amplitude, Hanning-windowed sinusoid voltage at 300 kHz applied to the emitter electrodes. The wavelengths of the propagated Lamb modes are then 9 mm for A_0 and 17 mm for S_0.

All these results have been computed through a full 2D finite element modeling including the emitter, the plate, and the receiver [except for Figs. 2(a) and 2(d) which correspond to the displacement at the receiver-free surface]. This electromechanical problem is treated using a very classical finite element formulation, including the piezoelectric effect,[23] by the code ATILA. The material properties introduced in the code for the transducers are those of a standard "C6" material from Fuji Ceramics and can be found on their website.

The rather good comparison observed shows that the assumption made is not a severe one, provided that the receiver thickness and width are small compared, respectively, to the plate thickness and the shortest propagating wavelength.

Then, the reception problem can be reduced to a very simple plane strain (2D) finite element model (Fig. 3). Indeed, the piezoelectric receiver alone can be meshed with the following boundary conditions imposed: known displacements (Dirichlet condition) and zero electrical potential at the plate-receiver interface nodes; stress-free condition and uniform potential at the receiver upper surface (electrodes).

In order to validate this modeling principle, comparisons to the results provided by a complete finite element model (emitter+plate+receiver) have been performed. The same conditions as above are considered. The results for receivers 1 (5×0.3 mm^2) and 2 (0.3×1 mm^2) are presented in Figs. 4 and 5, respectively.

Since receiver 1 is very thin compared to the plate thickness, it is essentially subject to lateral extension and compression. Thus, the electrical potential at its electrodes should be related mainly to the shear strain or displacement u_x at the plate surface. Accordingly, the fact that the curves of Figs. 2(a) and 2(b) are similar is consistent with the very good match of both potential curves in Fig. 4. The noticeable amplitude difference in Figs. 2(d) and 2(e) has obviously no significant influence, and the simplified model is perfectly validated.

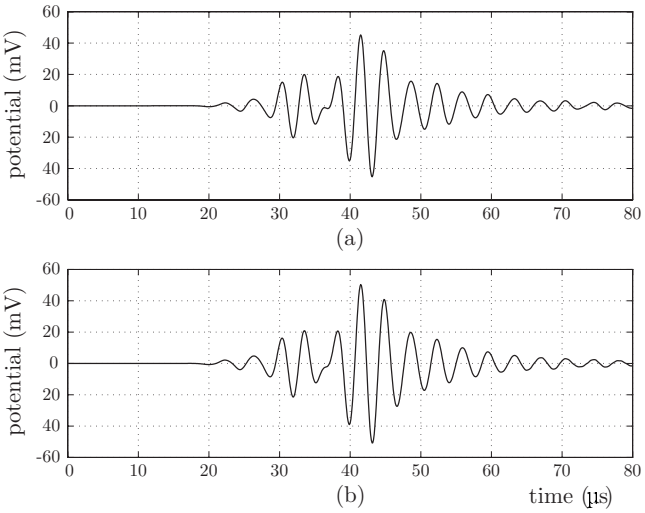


FIG. 4. Electrical potential at the 5-mm wide, 0.3-mm thick receiver (1), for a 300-kHz excitation. (a) Complete finite element modeling. (b) Hybrid model

On the contrary, the vibrations of the relatively thick receiver 2 should be strongly coupled to the normal displacement u_z as well as the shear displacement. Logically, then, the amplitude mismatch between Figs. 2(d) and 2(f) has apparent repercussions on the potential [Figs. 5(a) and 5(b)]. However, even in this less favorable case, the simplifying assumption is still reasonably applicable since the subsequent error is only marginal.

A significant advantage of such a hybrid model is that variations of geometrical dimensions, such as the emitter-receiver distance or the receiver width, do not necessitate a complete new computation to be run again. Indeed, contrary to a purely numerical modeling, the predictions relative to some invariant parts of the physical process can be kept and used at will.

III. THREE-DIMENSIONAL CORRECTION

The modeling method presented in the previous section allows us to take into account actual widths and thicknesses

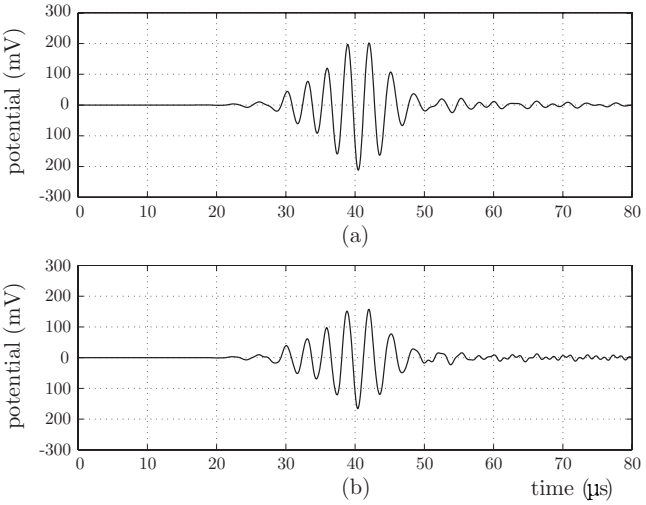


FIG. 5. Electrical potential at 0.3-mm wide, 1-mm thick receiver (2), for a 300-kHz excitation. (a) Complete finite element modeling. (b) Hybrid model

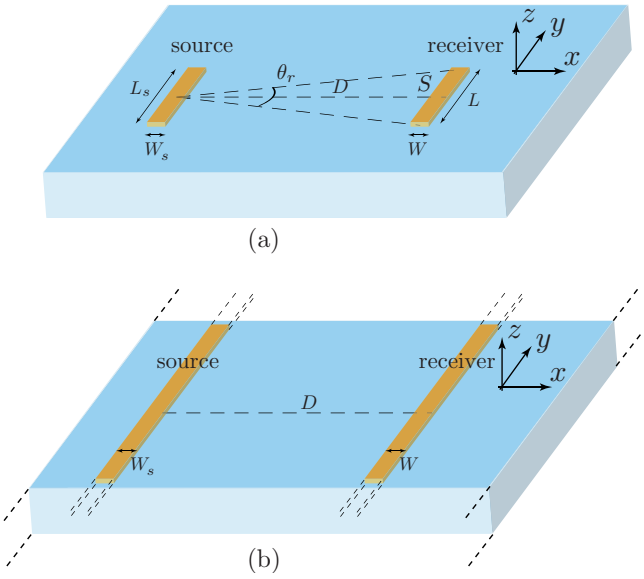


FIG. 6. (Color online) Source–receiver configuration. (a) Three-dimensional, realistic situation. (b) Related infinite-length situation.

for both the emitting and receiving transducers. However, since a plane strain assumption is made, the model is only valid for transducers that are very long (ideally infinite) in the y-direction.

When the source and receiver both have limited lengths L_s and L, respectively [Fig. 6(a)], the received energy is only a part of the total incident energy. In fact, the source finite length makes the wave radiation strongly dependent on the angular direction (beam divergence), whereas the receiver finite length makes the effective reception surface limited. A complete rigorous treatment of this aspect is a full 3D problem. This section aims at establishing how the results given by the presented 2D hybrid model can be merely corrected in order to take this divergence effect into account.

First, in the case of a finite-sized rectangular-shaped emitter such as that in Fig. 6(a), it has been shown in a previous work[9] that the emitted 3D field could be directly related to the 2D, plane wave, normal Lamb modes, which would be obtained in the plane strain infinite-length case of Fig. 6(b). The velocity field $\mathbf{v}$ at the plate surface can then be formally written as

$$\mathbf{v}(x,y) = g(x,y)A_m\mathbf{v}_m, \tag{2}$$

where $\mathbf{v}_m$ is the modal velocity field of the considered Lamb mode and A_m is the modal amplitude. The function $g(x,y)$ represents the distribution of the field over the surface. Its exact expression is unsignificant at this stage, and this point will be addressed later.

The acoustic power flow P_a across the receiver lower surface S (plate-receiver interface) is derived from Poynting's vector along the z-direction,[24]

$$P_a = -\frac{1}{2}\int\int_S (v_x^*\sigma_{xz} + v_y^*\sigma_{yz} + v_z^*\sigma_{zz})dS. \tag{3}$$

The presence of the receiver, which constitutes an additionnal layer at the plate surface, can be modelized, in an approximate way, by introducing an acoustic impedance matrix $\mathbf{Z}_a$. Then the velocity and stress components on the surface S are related to each other by the following relation:

$$\begin{pmatrix}\sigma_{xz}\\ \sigma_{yz}\\ \sigma_{zz}\end{pmatrix}_S = \mathbf{Z}_a\mathbf{v}, \tag{4}$$

where $\mathbf{Z}_a$ is a 3×3 matrix depending on the receiver thickness T and material properties.[24]

If the transducer length L is significantly bigger than its width W, then $\mathbf{Z}_a$ can be considered uniform along L (negligible lateral edge effects) and thus only dependent on x. In addition, if W is small compared to the emitter-receiver distance D, then the variations of g along W are very limited, and considering $x \simeq D$ in the expression of $g(x,y)$ is a correct approximation. Thus Eqs. (2)–(4) yield (in condensed notations)

$$P_a = -\frac{1}{2}|A_m|^2\int_W (\mathbf{v}_m^{*t}\mathbf{Z}_a\mathbf{v}_m)dx\int_L |g(D,y)|^2dy, \tag{5}$$

where ^{*t} indicates the complex transpose.

A fraction of P_a is converted by the piezoelectric material into electric power P_e. This can be written in the following form:

$$P_e = k^2P_a, \tag{6}$$

where k is an unknown constant homogeneous to an electromechanical coupling coefficient. It will be supposed in the following that k depends on W and T, but not on L. For the same reason as indicated above for $\mathbf{Z}_a$, this assumption is justifiable provided that $L \gg W,T$.

From another point of view, P_e corresponds to the power dissipated in the electrical impedance Z of the receiver. Then P_e can be expressed as

$$P_e = \frac{1}{2}\frac{U^2}{Z^*}, \tag{7}$$

where U is the electric potential at the electrodes.

By introducing Eqs. (5) and (7) into Eq. (6), the potential U at the receiver electrodes can be expressed as a function of L,

$$U(L) = \mathcal{K}\sqrt{\frac{1}{L}\int_L |g(D,y)|^2dy}, \tag{8}$$

with

$$\mathcal{K} = |A_m|\sqrt{-k^2LZ^*\int_W (\mathbf{v}_m^{*t}\mathbf{Z}_a\mathbf{v}_m)dx}. \tag{9}$$

Since it contains a number of unknown and not-easily-determined terms (k, $\mathbf{Z}_a$, Z), $\mathcal{K}$ would be rather difficult to compute directly from Eq. (9). However, since it is related to the piezoelectric conversion, which occurs in the receiver, its value should be contained somewhere in the results provided by a finite element model of the receiver (as seen in Sec. II B). This is what will be shown now.

For that, we will consider for a moment the corresponding infinite-length problem [Fig. 6(b)]. Its solution can be expressed in a 2D plane strain formalism, as treated in Sec.

II. In that case, the velocity field $\mathbf{v}$ is uniform along y, and its value is merely the modal field $\mathbf{v}_m$ multiplied by the modal amplitude A_m and the phase-delay term $e^{jk_m x}$ corresponding to the one-directional propagation along x, as given by Eq. (1).

In that context, applying Eqs. (3) and (4) then allows us to express a normalized acoustic power flow per unit length in the following way:

$$p_a^{2D} = -\frac{1}{2}|A_m|^2 \int_W (\mathbf{v}_m^{*t} \mathbf{Z}_a \mathbf{v}_m) dx. \tag{10}$$

Considering an arbitrary length L_0 and using Eqs. (6), (7), and (10), the electric potential at the receiver can then be expressed as

$$U^{2D} = |A_m| \sqrt{-k^2 L_0 Z_0^* \int_W (\mathbf{v}_m^{*t} \mathbf{Z}_a \mathbf{v}_m) dx}. \tag{11}$$

Since the planes of the electrodes contain the O_y axis, the electrical impedance is inversely proportional to the transducer length. Consequently, $ZL = Z_0 L_0$, and thus it appears that $U^{2D} = \mathcal{K}$, where $\mathcal{K}$ is as defined in Eq. (9).

Then, coming back to the finite-length case, Eq. (8) can be rewritten as

$$U(L) = U^{2D} \sqrt{\frac{1}{L} \int_L |g(D,y)|^2 dy}. \tag{12}$$

Additionally if L is small compared to the distance D between the source and the receiver, then, at the first order, the polar coordinates can be approximated by $r \simeq D$ and $\theta \simeq y/D$. Then, by performing the corresponding change in variable, the integral over y in Eq. (12) can be more conveniently expressed as an integral over θ. This yields

$$U(L) = U^{2D} \sqrt{\frac{1}{\theta_r} \int_{-\theta_r/2}^{\theta_r/2} |\alpha(D,\theta)|^2 d\theta}, \tag{13}$$

where θ_r is the angle with which the receiver length L is seen from the source location [see Fig. 6(a)] and $\alpha(r,\theta)$ is the polar representation of $g(x,y)$,

$$\alpha(r,\theta) = g(r\cos\theta, r\sin\theta) \simeq g(D, D\theta). \tag{14}$$

The function $\alpha(r,\theta)$ is identified as the directivity of the finite source. Its expression has been derived in a previous work[9] for the case of a source with moderate width to length ratio,

$$\alpha(r,\theta) = \frac{1-j}{\sqrt{\pi}} \sqrt{\frac{k_m}{r}} \frac{\sin\left(\frac{1}{2} k_m L_s \sin\theta\right)}{k_m \sin\theta}, \tag{15}$$

where k_m is the wavenumber of the considered mode.

Since α is dimensionless, the square-rooted term in Eq. (13) is also a dimensionless coefficient. It can be interpreted as a correction coefficient, applied to the received electric potential U^{2D} predicted by a 2D computation, in order to account for the 3D radiation effects related to the transducers' finite lengths. Since the finite element model is exploited to process all the electromechanical conversion aspects (direct and converse piezoelectric effects) in the 2D hybrid model, as seen in Sec. II, U^{2D} is directly a time-dependent voltage, whose value depends on the model parameters (transducers' widths and thicknesses, plate thickness, all material properties, and emitter-receiver distance) and the input electrical signal at the receiver.

Hence, if all the assumptions made in the derivation presented in this section are valid, then the electric potential $U(L)$ resulting from the application of Eq. (13), conjointly with Eq. (15), should be a fair approximation of the true potential measured at the actual finite-length receiver's electrodes. The experimental results presented in the next section are intended to verify prediction capability.

IV. EXPERIMENTAL VALIDATION

A. Experimental setup and modeling details

Two experimental configurations have been tested. In each case, two parallelepiped-shaped PZTs have been glued on the upper surface of a 6-mm-thick aluminum plate. One of them is 3 mm wide, 500 μm thick, and 2 cm long and is used as the emitter. In the case that will be referred to as setup 1, the receiver is 3 mm wide, 200 μm thick, and 2 cm long and has been placed 20 cm away from the emitter. In setup 2, the emitter-receiver distance is 15 cm, and the receiver is 0.5 mm wide, 1 mm thick, and 2 cm long. This choice for the dimensions of the receivers has been guided by the assumption discussed in Sec. II B. Indeed, the first receiver is thin compared to the plate thickness, whereas the second one has a small width compared to the wavelengths. All the transducers used are made of PZT material C6 from Fuji Ceramics.

The electric excitation signal is provided by a standard waveform generator with output impedance of 50 Ω. The signal received at the second transducer is directly measured, without any amplification or filtering, using a digital oscilloscope with a sampling rate of 25 Msamples/s and input impedance of 1 MΩ.

The lateral dimensions of the plate have been chosen to be large enough to avoid parasitic reflections mixed with the useful parts of the received signals. The frequency range considered for the study spreads from 100 to 500 kHz. In this scope, several representative examples will be shown and commented on in the next section.

First of all, the emission process is modeled using the finite element–normal mode technique briefly discussed in Sec. II A, thus allowing us to predict the modal amplitudes A_m [see Eq. (1)]. Then each Lamb mode is treated separately as a displacement input on the lower surface of the receiving transducer, as described in Sec. II B. Finally, the divergence correction [Eq. (13), Sec. III] is computed for each mode and applied before the summation of all modal contributions. In summary, the input of the model is the electrical signal (in volts) applied to the emitter, and the output is the electrical signal (in volts) received at the receiver. Therefore, the theoretical and measured results can be directly compared to each other without any adjustment parameters.

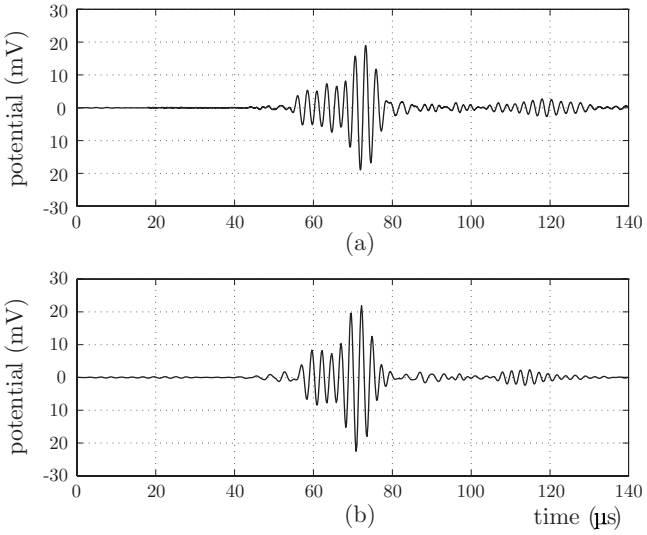


FIG. 7. Electrical potential at the 3-mm wide, 0.2-mm thick receiver (setup 1), for a 350 kHz excitation ($T/h=0.033$). (a) Experimental. (b) Predicted.

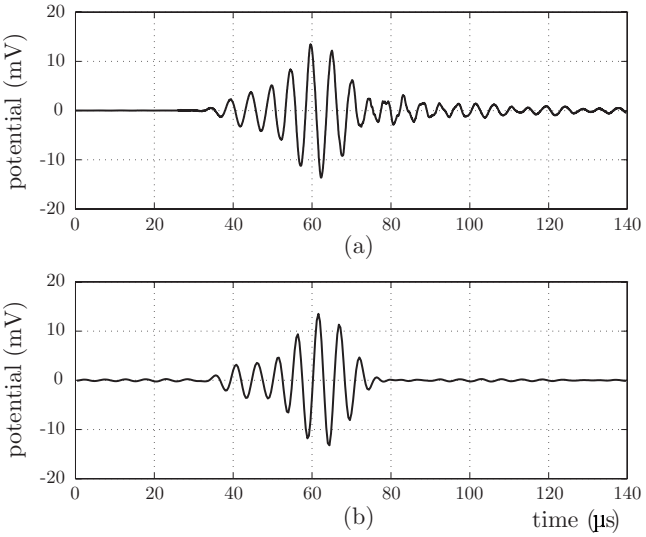


FIG. 9. Electrical potential at the 0.5-mm wide, 1-mm thick receiver (setup 2), for a 175 kHz excitation ($W/\lambda \leqslant 0.037$). (a) Experimental. (b) Predicted.

B. Results and comments

The first example, presented in Fig. 7, corresponds to setup 1, where the emitter is excited by a 5 cycle, 10 V amplitude, Hanning-windowed sinusoid signal with a central frequency of 350 kHz. In this case, the first three Lamb modes, A_0, S_0, and A_1, are expected.

The measured and predicted waveforms [Figs. 7(a) and 7(b), respectively] appear to be in very good agreement. Only some very small phase shift is visible. This can probably be explained by uncertainties on experimental data such as mechanical and piezoelectric constants, propagation distance, and so on.

In the second test case, the same experimental setup has been considered, except that the central excitation frequency has been set to 450 kHz. The corresponding measured and predicted results are shown in Figs. 8(a) and 8(b).

Although the comparison is perhaps less convincing than in the previous example, the theoretical result still represents a satisfying prediction of the received signal. The three main wavepackets, corresponding to the three generated Lamb modes, are clearly visible in both waveforms. Since the S_0 and A_1 modes are highly dispersive in the frequency range considered, the results are logically more affected by any uncertainty on the experimental data.

The two last examples presented below correspond, respectively, to the results obtained for setup 2, with excitation frequencies of 175 kHz (Fig. 9) and 450 kHz (Fig. 10). Comments very similar to those above can be made. However, in the first case, some particularities can be noted. Only the two fundamental modes are generated. Here, again, both the absolute amplitudes as well as the global waveforms are correctly predicted, but some remaining oscillations after 80 μs are observed in the experimental waveform [Fig. 9(a)]. This can be probably attributed to some sort of coupling between the receiver and the plate. Indeed, from the point of view of Lamb wave propagation, the presence of the

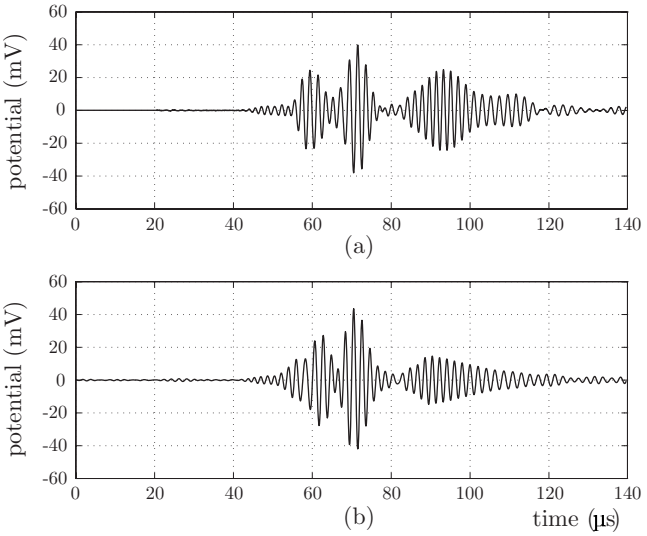


FIG. 8. Electrical potential at the 3-mm wide, 0.2-mm thick receiver (setup 1), for a 450 kHz excitation ($T/h=0.033$). (a) Experimental. (b) Predicted.

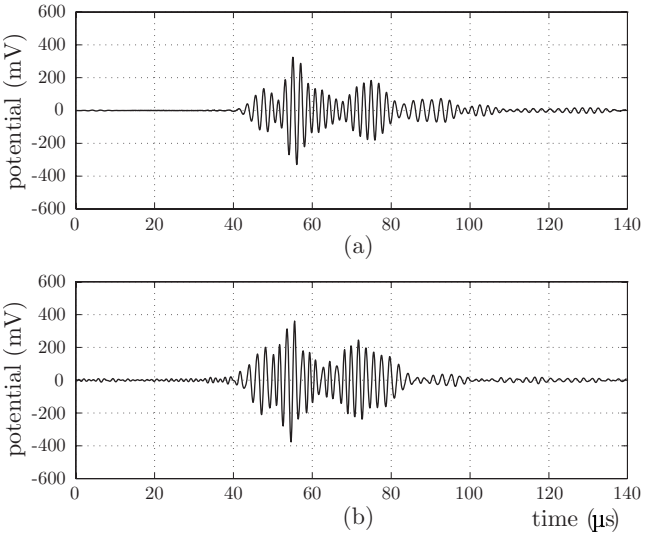


FIG. 10. Electrical potential at the 0.5-mm wide, 1-mm thick receiver (setup 2), for a 450 kHz excitation ($W/\lambda \leqslant 0.08$). (a) Experimental. (b) Predicted.

receiver on the plate surface constitutes a local heterogeneity. Then, multiple reflection inside the receiver, which would result in some sort of "tail" or "coda" in the received signal, is a possible consequence. Since the receiver response is computed independently of the plate (see Sec. II B), such effects are not present in the predicted results.

V. CONCLUSION

In this paper, an original modeling technique of an integrated Lamb wave emission and reception system has been presented. It has been shown how the different physical processes (emission, propagation, reception, and beam divergence) could be partially uncoupled from each other. This consideration results in a very efficient and versatile modeling principle. Compared to a purely numerical 3D modeling, time consumption is considerably decreased at every step of the computation (2D degrees of freedom instead of 3D, mesh preparation, processing, postprocessing, and data exploitation). Besides, since the numerical part is reduced to a minimum, parametric studies (e.g., influence of dimensional changes) are made considerably easier. Also, the physical mechanisms can be more clearly interpreted. In particular, it is possible to distinguish in the modal amplitudes in the received signal the contributions related to the transducer width and thickness from the length-related contributions.

Comparisons between theoretical and experimental results have demonstrated the very good prediction capabilities of the model. The very slight time and amplitude shifts of the modal wavepackets are barely significant and are compensated for by the simplicity and versatility of the modeling technique.

Furthermore, by interfacing a wave-damage interaction description to the present model, it should be possible to get a rather complete simulation tool of a Lamb wave based integrated health monitoring system.

[1]D. C. Worlton, "Ultrasonics testing with Lamb waves," Nondestr. Test. (Chicago) **15**, 218–222 (1957).

[2]D. N. Alleyne and P. Cawley, "The interaction of Lamb waves with defects," IEEE Trans. Ultrason. Ferroelectr. Freq. Control **39**, 381–397 (1992).

[3]R. S. C. Monkhouse, P. D. Wilcox, and P. Cawley, "Flexible interdigital pvdf Lamb wave transducers for the development of smart structures," Rev. Prog. Quant. Nondestr. Eval. **16A**, 877–884 (1997).

[4]J.-B. Ihn and F.-K. Chang, "Detection and monitoring of hidden fatigue crack growth using a built-in piezoelectric sensor/actuator network: I. diagnostics," Smart Mater. Struct. **13**, 609–620 (2004).

[5]E. Moulin, J. Assaad, C. Delebarre, and D. Osmont, "Modeling of Lamb waves generated by integrated transducers in composite plates using a coupled finite element—normal modes expansion method," J. Acoust. Soc. Am. **107**, 87–94 (2000).

[6]S. Grondel, C. Paget, C. Delebarre, J. Assaad, and K. Levin, "Design of optimal configuration for generating a_0 Lamb mode in a composite plate using piezoceramic transducers," J. Acoust. Soc. Am. **112**, 84–90 (2002).

[7]L. Duquenne, E. Moulin, J. Assaad, and S. Grondel, "Transient modeling of Lamb waves generated in viscoelastic materials by surface bonded piezoelectric transducers," J. Acoust. Soc. Am. **116**, 133–141 (2004).

[8]E. Moulin, N. Bourasseau, J. Assaad, and C. Delebarre, "Directivity of integrated piezoelectric Lamb wave sources," Proc.-IEEE Ultrason. Symp. **2**, 1081–1084 (2001).

[9]E. Moulin, S. Grondel, M. Baouahi, and J. Assaad, "Pseudo-3d modeling of a surface-bonded Lamb wave source," J. Acoust. Soc. Am. **119**, 2575–2578 (2006).

[10]V. Giurgiutiu, "Tuned Lamb wave excitation and detection with piezoelectric wafer active sensors for structural health monitoring," J. Intell. Mater. Syst. Struct. **16**, 291–305 (2005).

[11]J. H. Nieuwenhuis, J. J. Neumann, D. W. Greve, and I. J. Oppenheim, "Generation and detection of guided waves using pzt wafer transducers," IEEE Trans. Ultrason. Ferroelectr. Freq. Control **52**, 2103–2111 (2005).

[12]F. L. di Scalea, H. Matt, and I. Bartoli, "The response of rectangular piezoelectric sensors to Raleigh and Lamb ultrasonic waves," J. Acoust. Soc. Am. **121**, 175–187 (2007).

[13]A. Raghavan and C. E. S. Cesnik, "Finite-dimensional piezoelectric transducer modeling for guided wave based structural health monitoring," Smart Mater. Struct. **14**, 1448–1461 (2005).

[14]M. Castaings, E. L. Clézio, and B. Hosten, "Modal decomposition method for modeling the interaction of Lamb waves with cracks," J. Acoust. Soc. Am. **112**, 2567–2582 (2002).

[15]T. Hayashi and K. Kawashima, "Multiple reflections of Lamb waves at a delamination," Ultrasonics **40**, 193–197 (2002).

[16]T. Grahn, "Lamb wave scattering from a circular partly through-thickness hole in a plate," Wave Motion **37**, 63–80 (2003).

[17]F. Benmeddour, S. Grondel, J. Assaad, and E. Moulin, "Study of the fundamental Lamb modes interaction with symmetrical notches," NDT & E Int. **41**, 1–9 (2008).

[18]B. A. Auld, *Acoustic Fields and Waves in Solids*, 2nd ed. (Krieger, Malabar, FL, 1990), Vol. 2.

[19]X. Jia, "Modal analysis of Lamb waves generation in elastic plates by liquid wedge transducers," J. Acoust. Soc. Am. **101**, 834–842 (1997).

[20]I. A. Viktorov, *Rayleigh and Lamb Waves* (Plenum, New York, 1967).

[21]A. H. Nayfeh, "The general problem of elastic wave propagation in multilayered anisotropic media," J. Acoust. Soc. Am. **89**, 1521–1531 (1991).

[22]L. Duquenne, F. Elyoubi, E. Moulin, S. Grondel, J. Assaad, and C. Delebarre, "The use of permanently-mounted surface transducers to characterize Lamb wave propagation," in Proceedings of the World Congress on Ultrasonics, Paris, France (2003), pp. 601–604.

[23]E. Moulin, J. Assaad, C. Delebarre, H. Kaczmarek, and D. Balageas, "Piezoelectric transducer embedded in a composite plate: Application to Lamb wave generation," J. Appl. Phys. **82**, 2049–2055 (1997).

[24]B. A. Auld, *Acoustic Fields and Waves in Solids*, 2nd ed. (Krieger, Malabar, FL, 1990), Vol. 1.

Anderson localization of ultrasound in plates: Further experimental results

Oleg I. Lobkis and Richard L. Weaver[a)]
Department of Physics, University of Illinois at Urbana-Champaign, 1110 West Green, Urbana, Illinois 61801

(Received 22 May 2008; accepted 22 September 2008)

Diffuse wave transport is studied in a thick plate with densely machined-in multiple scatterers. As anticipated by theory, energy at short wavelengths diffuses across the structure. Energy localizes at longer wavelengths for which $\lambda/2\pi$ is comparable to the mean free path.
© *2008 Acoustical Society of America.* [DOI: 10.1121/1.2999345]

PACS number(s): 43.40.Qi, 43.20.Fn, 43.40.Hb [JGM] Pages: 3528–3533

I. INTRODUCTION/BACKGROUND

Localization of classical waves in disordered media has been studied for many years,[1–8] but numerous questions remain. Except for one-dimensional and quasi-one-dimensional systems,[9,10] there are no unequivocal laboratory demonstrations of the phenomenon.[8] Questions about the dynamics of localized wave energy transport remain also: How shall we generalize the diffusion equation? How does the picture change in statistically nonhomogeneous systems, particularly those with boundaries? Most theories for localization are predicated on the phenomenon of weak Anderson localization (also called enhanced or coherent backscatter). Yet weak localization arguments do not apply in time-reversal noninvariant systems, so such theories cannot be correct. How does quantum fidelity (Lochshmidt echo) behave in diffusing and localizing media?[11,12] Can the time dependence of fidelity be used as a signature of localization? Is enhanced backscatter[13–15] stronger in such media? These questions lead us to revisit an old experimental system. In this report we confine ourselves to repeating and improving the older measurements, thereby generating conclusions that are more quantitatively precise and less equivocal than previously obtained. We save the more modern questions for another occasion after we have better understood the behavior of the structure we have.

It is useful to distinguish several parameter regimes in the study of waves in random media. If the mean free path is comparable to or longer than the length scale L of an experiment, we anticipate a ballistic propagation at a speed c, albeit attenuated and dispersed. This regime is described by theories for mean responses or mean Green's functions.[16] If L is much greater than the mean free path or if times of interest are greater than the time of arrival of the ballistic pulse, the field is diffuse. A signal from such a field is seemingly incoherent noise, under a slowly varying envelope. The envelope is described by theories for mean square Green's function or energy. At modest distances, it is natural to describe the energy by radiative transport theories.[17] At greater distance or greater time, it is simpler to do so with a diffusion equation: $D\nabla^2 E - \sigma E = \partial E/\partial t$. The diffuse field suffers more from absorption σ than does the ballistic field and in some cases is difficult to observe.

The above is what may be termed the classical view of waves in random media. Classical diffuse field theories such as radiative transfer and diffusion[17] are derived by neglecting coherence in the field. There are, however, behaviors of a multiply scattered field that do not follow from such an ansatz. Enhanced backscatter,[13–15] field-field correlations,[18] and Anderson localization are amongst these. Anderson localization is expected to obtain in all disordered one-dimensional systems, in all disordered two-dimensional (2D) systems (although the localization length in 2D can be enormous if the disorder is weak), and in three-dimensional (3D) systems with sufficiently strong disorder. The standard criterion for disorder sufficient for significant Anderson localization is that $k\ell$, or the mean free path ℓ times wavenumber $k = 2\pi/\lambda$, should be small. In 3D the Ioffe–Regel criterion[19] for localization is $k\ell \leqslant 1$. The corresponding formula for 2D is that the localization length is exponential in $k\ell$. The localization length in 2D can also be estimated in terms of bare diffusivity and the modal density.[1]

At moderate distances r from a transient source in an unbounded localizing medium, with r comparable to but larger than a localization length ξ, localization theory predicts a response governed by diffusion at short times and predicts slower transport at later times. At very late times, the transport will have ceased and the mean square amplitude ("energy") will have reached a steady state profile $\sim\exp(-r/\xi)$ concentrated in the vicinity of the source. This exponential dependence is the prime signature of localization. Transport is effectively zero at a great distance from a source. Hence the conclusion, valid in the thermodynamic limit, that conductance across a localizing system is zero.

The laboratory observation of this behavior has proved to be challenging. One difficulty is due to absorption. The observation of an exponential steady state response $\exp(-x/\Lambda)$ due to a steady source does not permit the identification $\Lambda = \xi$. Λ could be classical and related to a balance between absorption and transport $\Lambda = \sqrt{D/\sigma}$. Even when studying a transient signal for which the effects of absorption and localization are separable, absorption may reduce it below noise before signs of localization are evident. Many

a)Author to whom correspondence should be addressed. Electronic mail: r-weaver@uiuc.edu

 © 2008 Acoustical Society of America

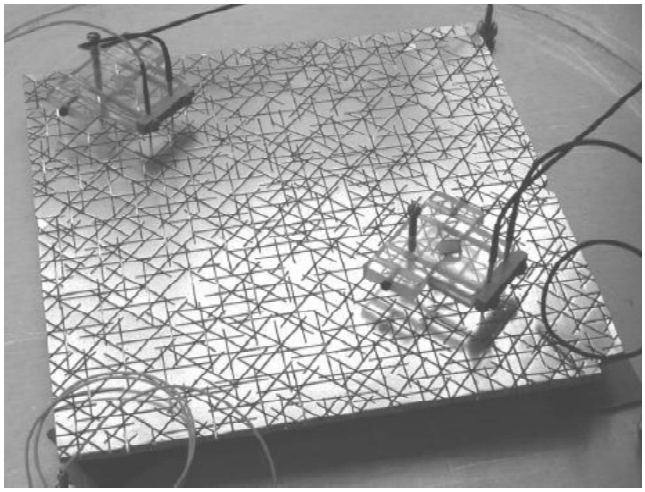


FIG. 1. The structure is an aluminum plate of dimensions $30.5 \times 30.5 \times 0.6$ cm^3 cut with hundreds of scalloped slits. The four pin transducers are attached to co-axial cables.

measurements[5,9] are in systems for which only the boundary is accessible; dependence on x is not ascertainable. Boundaries further complicate interpretations of measurements, as radiative losses there are not negligible; a full treatment of these requires a dynamic theory for localized transport[20–26] in statistically inhomogeneous media.

The system studied here has been designed to permit transient measurements in the interior of a localizing structure, to have minimal absorption, and to have no radiative losses from its boundaries. These features, as will be seen, permit unequivocal conclusions.

II. A HETEROGENEOUS PLATE

We consider diffuse wave transport in the structure introduced earlier[1] and pictured in Fig. 1. A $30.5 \times 30.5 \times 0.6$ cm^3 aluminum plate has been machined with hundreds of scalloped cuts. The cuts, illustrated in Fig. 2, provide the random scattering; they also break the plate's up/down symmetry. The plate is chemically polished after machining in order to reduce its internal friction. Ultrasound with frequencies up to 900 kHz is introduced by broadband transient piezoelectric excitation and detected piezoelectrically at various other points as a function of time. Nominal shear wavelengths for these frequencies range from 25 mm at 80 kHz to 3 mm at 1 MHz. If the plate were homogeneous, without scatterers, it would be well described in terms of the Lamb and SH modes of guided wave propagation.[27] Below 250 kHz, there are only three such modes. Below about 100 kHz, one of these three is simple Kirchoff bending, and two are Poisson-plate longitudinal and shear waves with in-plane material displacements. A homogeneous plate at higher frequencies is a thick waveguide, with many Lamb and SH modes of propagation. It is not particularly helpful to think in terms of these waves for the cut plate, however, as strong scattering complicates notions of independent modes of propagation or definite wavelengths.

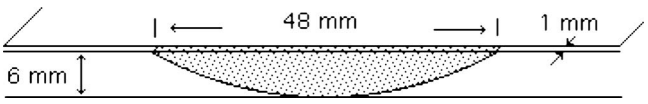


FIG. 2. The scalloped slits are cut with a circular saw of diameter of 10 cm and thickness of 1 mm. The slits just pierce the opposite side of the plate.

It is difficult to estimate mean free paths in the plate of Fig. 1. At a very high frequency, a picture based on ray trajectories suggests that ℓ is approximately a few millimeters. Thus the Ioffe–Regel parameter $k\ell$ is larger than 1, and localization is unlikely to be observed in a sample of only 30 cm. At a moderate frequency, e.g., 500 kHz, nominal wavelengths are 6 mm and are comparable to mean free paths. If this estimate of the mean free path is valid at 200 kHz, where nominal k is 0.25 mm^{-1}, the Ioffe–Regel parameter is about unity, and localization is plausible.

At very low frequency where wavelengths are long compared to the microscale, the plate should appear as effectively homogeneous. Here the parameter ℓ becomes larger than λ. At a low enough frequency, the Ioffe–Regel parameter must therefore be large, and localization effects must disappear. Localization should be confined to a finite frequency band.

The earlier work studied diffuse transport in this plate in the regime from 150 to 800 kHz and over time periods from 0 to 16 ms (and in one case to 50 ms) as limited by absorption and by the finite record length of the digitizer. As predicted by the above arguments, we saw diffusive transport at the higher frequencies and anomalously weak transport at lower frequencies. The behavior was equivocal. It was not clear if the transport had ceased within the times studied or if the plate required more time to reach its asymptotic localized state. We now revisit this system with various improvements designed to permit an unambiguous conclusion that the structure is Anderson localized.

III. SIGNAL PROCESSING

The signal received and amplified at a point x after an impulse is applied to a source transducer at position x_s is given by

$$V(t) = T_1(t) \otimes G(\vec{x},\vec{x}_s,t) \otimes T_2(t), \tag{1}$$

where $\otimes$ represents a temporal convolution and the functions T describe transduction from voltage to force (T_2) of the transducer at x_s and from displacement to voltage (T_1) of the transducer at x. T varies between transducers but is the same if the transducer is used as a source or a receiver. That transduction T is independent of the structure and position follows from weak coupling. G is the elastodynamic Green's function relating dynamic force at one point to material displacement response at another. We recognize that spectral power density in V (essentially the square of its short-time Fourier transform) is a surrogate for energy density in the structure near x, and we construct a quantity we call $E(x,x_s,t,f)$ defined by

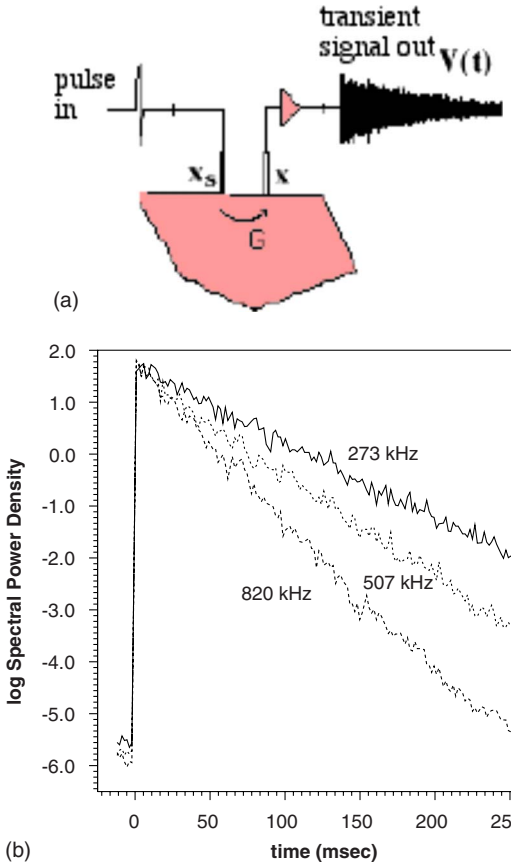


FIG. 3. A measurement in a monolithic block of aluminum. log E is plotted vs time for various frequencies; energy decays exponentially at frequency-dependent rates.

$$E(x,x_s,t,f) = \int \left| \int V(\tau) W_t(\tau) \exp(-i\omega\tau) d\tau \right|^2 B_f(\omega) d\omega. \tag{2}$$

It is formed by taking the square of the Fourier transform of a signal windowed by a function W centered on times t. This is then summed into frequency bins with tapered weightings B centered on various frequencies f. As the transducer functions T have time scales less than 20 μs that are much less than the window width (1.6 ms), they may be taken out of the above integral,

$$E(x,x_s,t,f) = |T_1(2\pi f)|^2 |T_2(2\pi f)|^2 \times \int \left| \int G(\tau) W_t(\tau) \exp(-i\omega\tau) d\tau \right|^2 B_f(\omega) d\omega. \tag{3}$$

The dependence on the transducers and their coupling is now explicit and simple. If the factors T were known, we would have a direct measurement of the time-dependent spectral energy density in G.

The factors $|T|$ are not known. They furthermore lack reproducibility as a transducer is removed and reapplied, and they vary between transducers. This is not an issue for measurements of the time dependence of energy density. The factors T are constant in time and thus unimportant. Figure 3(b) illustrates various $E(t,f)$ for responses in a reverberant

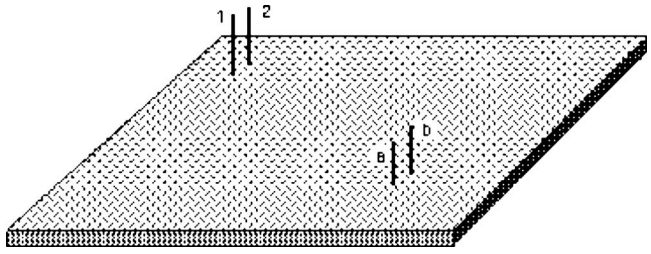


FIG. 4. In order to remove the effect of the unknown transducer functions T, we make several measurements for each position pair of interest x, x_s. Two transducers (labeled 1 and 2) are placed, with a small drop of oil to aid coupling, near position x_s; two others (labeled a, b) are placed near position x. Pairs are separated by 2 cm, short compared to localization lengths but long compared to a quarter wavelength.

block of aluminum with ballistic internal propagation and no random scatterers, hence no significant spatial dependence to energy density. For such systems, the energy evolution is well described by a simple decaying exponential.

The unknown T's can be problematic if the desire is for measurements of the spatial dependence of energy density. It is not possible to reliably compare signals from two different transducers or signals from one transducer at two different positions. For this reason, we design a self-calibrating set of signals, as illustrated in Fig. 4. By constructing the six energies E_{12}, E_{ab}, E_{1a}, E_{1b}, E_{2a}, and E_{2b} and taking the ratio

$$R = [E_{1b},E_{2a}E_{2b}E_{1a}]^{1/4}/[E_{12}E_{ab}]^{1/2}, \tag{4}$$

we construct something that is independent of the transducer functions. The ratio R is a function of distance r between the transducer pairs (we treat the distances 1a, 2a, 1b, and 2b as equivalent), time, and frequency; it represents a ratio of the energy densities in G itself. It is unity if the two pairs are close to each other. The construction has the further advantage that it removes dependence on internal friction. Like the quantities E plotted in Fig. 3(b), all factors in the ratio are expected to decay exponentially at the same rate; so the ratio R will not decay. The construction has the further virtue of normalizing the energy density at x by the energy density at x_s. Thus if the source happens to be at a point with particularly high admittance (local density of states), it will deposit extra energy. Similarly the receiver may happen to be at a point with a particularly enthusiastic displacement response for a given local energy density.[28] Fluctuations in E due to rapidly varying local densities of states (at either or both receiver and source) were seen in the earlier work;[1] they diminished the quality of its statistics. These fluctuations are called C_0 by some.[29] They drop out of the construction R.

It might have been simpler had we constructed a ratio

$$[E_{1a}E_{a1}/E_{11}E_{aa}]^{1/2} \tag{5}$$

that requires only two transducers. Like Eq. (4), this construction removes the effect of internal friction and the effect of the unknown transducer functions. It is interesting in its own right, but it demands a more complicated analysis and understanding because it includes the effects of enhanced backscatter[13–15] and has a nonunit value even if the source and receiver are within a quarter wavelength.

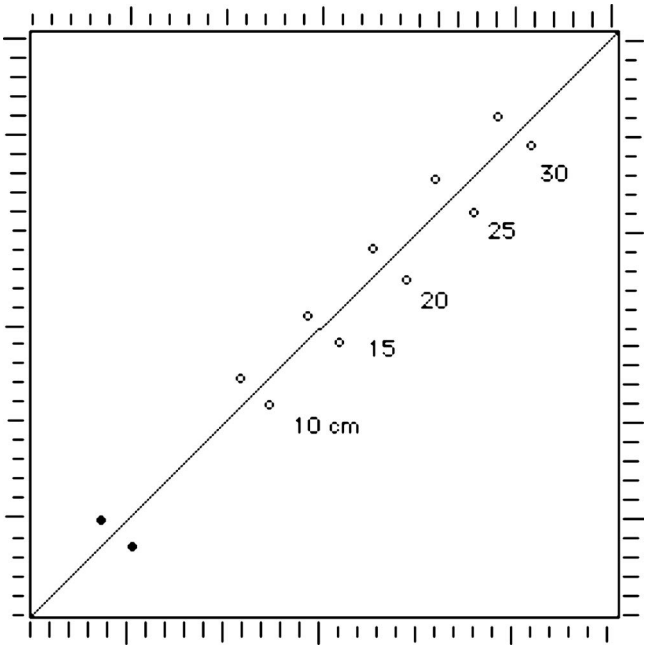


FIG. 5. One pair of transducers (1,2) is positioned near a corner; the other pair (a, b) is placed at various distances along the diagonal.

Backscatter quantities like E_{ii} are more challenging to measure piezoelectrically than transmissions E_{ij} $i \neq j$, as it is necessary to isolate the receiving circuit from the pulser. Otherwise electronic noise leaks from the pulser to the detector and swamps the signal. Elsewhere,[19] we have accomplished this by inserting a mechanical relay that quickly switches the transducer from the pulser to the receiver circuit after the excitation pulse is emitted. A quantity like that of Eq. (5) was measured in bodies like that of Fig. 3(a) that lack scatterers and was shown in such systems to take a value between 2 and 3.[14]

In a highly heterogeneous medium such as our plate, a ratio like $[E_{11}E_{22}]^{1/2}/E_{12}$ is not a very meaningful quantity. At late times it corresponds to the ratio of the mean fourth power of an eigenmode to the square of a mean square, and thus to the distribution of modal amplitudes. But this ratio is affected by material features unrelated to localization. Consider, for example, a medium with inclusions of infinite stiffness and density into which eigenmodes cannot penetrate. If the inclusions are large compared to wavelength, then they do not cause localization, yet they do affect the above ratio.

IV. TRANSPORT MEASUREMENTS

For each pair of positions x, x_s of interest, six waveforms were captured and digitized at 2.5 MSa/s; each waveform had 2^{19} samples and a duration of 210 ms. The presented data corresponds to a fixed position for one pair, at coordinates relative to the plate corner of (3.93, 5.35 cm) and (5.35, 3.93 cm), and a set of positions for the other pair arranged along the diagonal, as in Fig. 5.

A four-pole low pass filter was inserted with a 3 dB point at 900 kHz to avoid aliasing. The measurements were conducted in an evacuated chamber in order to avoid the losses into the air.[30] Each waveform was divided into 128 distinct 1.638 ms windows. Each of the windows for each of the six source receiver combinations was then Fourier transformed, squared, and summed into distinct bands centered on each of 21 frequencies from 40 to 920 kHz, each with a width of 80 kHz.

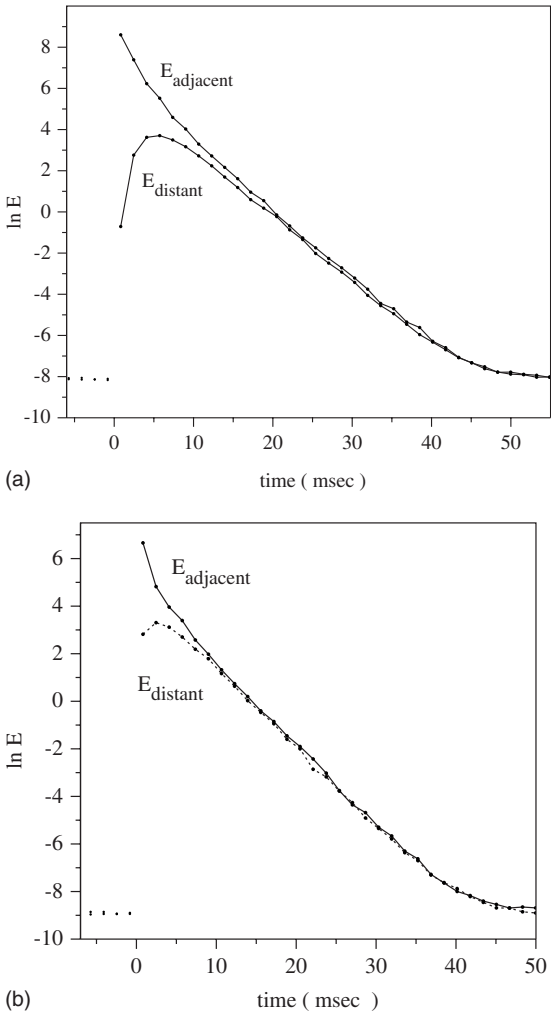


FIG. 6. (a) The adjacent and distant energy densities in a bin at a frequency of 664 kHz (and width of 80 kHz) and a distance of 30 cm vs time. These data are well described by a diffusivity $D=20$ cm^2/ms. (b) Classical diffusion at 664 kHz is also observed at $r=15$ cm. These data are well described by a diffusivity $D=25$ cm^2/ms.

This produces, for each distance r, frequency f, and time t, two quantities: the energy adjacent to the source $E_{\text{adj}}(r,f,t)=[E_{12}E_{\text{ab}}]^{1/2}$ and the energy distant from the source $E_{\text{distant}}(r,f,t)=[E_{1\text{a}}(t,f)E_{1\text{b}}(t,f)E_{2\text{a}}(t,f)E_{2\text{b}}(t,f)]^{1/4}$. The ratio of these quantities is the chief quantity of interest and is independent of the transducer functions T. They are plotted in Figs. 6 and 7.

At higher frequencies, e.g., those in Fig. 6, we see classical transport. Most noteworthily, we observe that at late times the adjacent and distant E's, while both diminishing exponentially due to internal friction, approach each other in accord with an equipartition principle that energy density becomes uniformly distributed over the entire plate at late times. The two energy densities start at very different levels and then approach each other, in accord with a recognition that it takes a finite amount of time for wave energy to diffuse a distance r. The time scales to diffuse across the plate

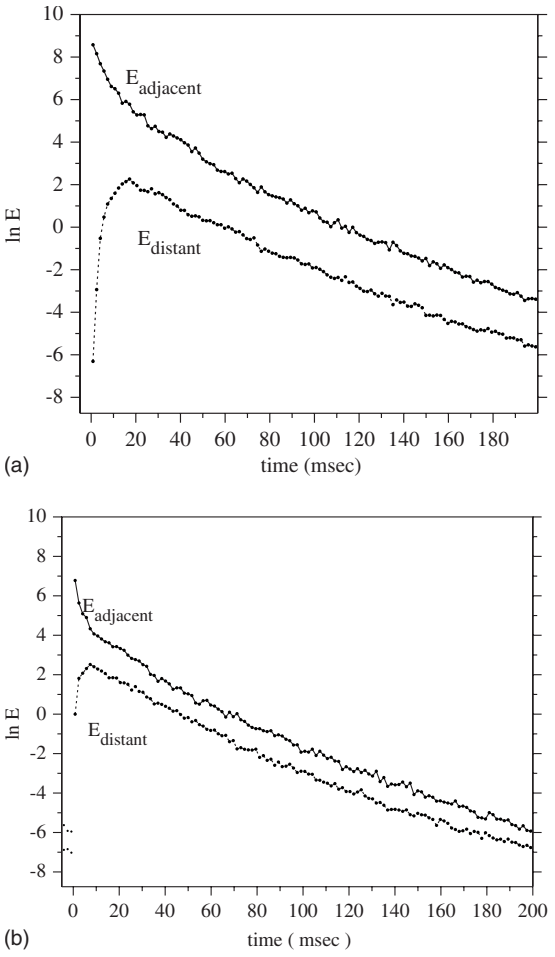


FIG. 7. (a) Energy transport is very different in a frequency bin centered on 195 kHz (full width of 80 kHz). Here it is plotted for a distance $r=30$ cm. Early time diffusive behavior ceases at about 30 ms, leaving an energy density that is about 12 times greater adjacent to the source than at distance. (b) Energy densities at 195 kHz and a distance $r=15$ cm show, as in (a), early time diffusion followed by an absence of transport at late times.

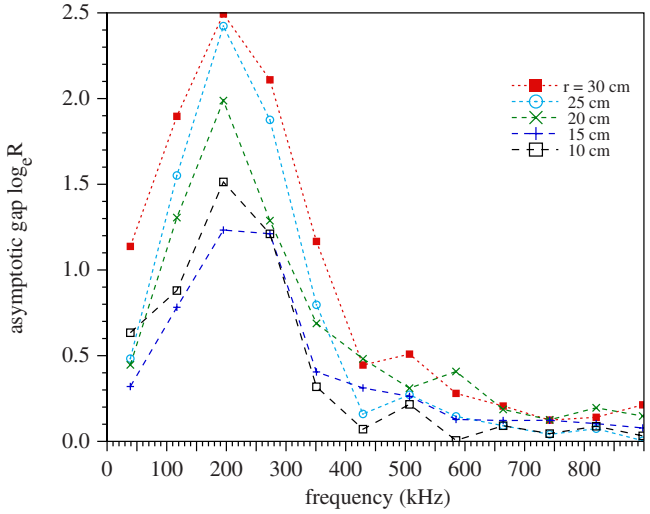


FIG. 8. The asymptotic gap, $\ln R$ averaged over late times, is plotted vs frequency for several source receiver separations r.

are several microseconds, a length of time that waves in a homogeneous plate would propagate tens of meters. It is clear that the multiple scattering has significantly slowed the transport relative to the ballistic case. Fits to classical diffusion (not shown) suggest diffusivity $D=20$ cm^2/ms for the data of Fig. 6(a) and $D=25$ cm^2/ms for the data of Fig. 6(b).

At lower frequencies, the behavior is qualitatively different (Fig. 7). Early times show a behavior similar to that seen at early times in Fig. 6. But at late times the transport has ceased; equipartition is not achieved. The ratio R approaches a constant. In the most severe case (195 kHz, $r=30$ cm), the asymptotic ratio is 12, showing that a steady state is achieved with 12 times more energy density near the source than at distance. In spite of an energy density gradient, there is no further transport. This late time regime was not accessible in the previous experiments.[1] Putting the plate in a vacuum chamber to reduce the losses and using digitizers with deeper memory have permitted access to times as late as 200 ms. This may be compared with the 16–50 ms range achieved in the previous work. The difficulties in the earlier analyses can now be attributed to simply having had insufficient time to resolve the asymptote.

The late time behavior at low frequencies, as in Fig. 7, is not a simple exponential. This curvature is familiar from other experiments[31] where it was shown to be caused by different modes, even at essentially the same frequency, having different absorption rates. This was in turn caused by the presence of a small number of distinct decay channels, as opposed to a continuous distribution thereof.[32] It may be that the loss channels in the plate tend to be concentrated at a finite number of sites, perhaps sites with particularly large plastic damage from the machining. Another possibility is that the concentrated loss mechanisms are the transducers themselves. The matter is intriguing but not critical for the present purposes. The decay rates and curvatures of the distant and adjacent energies are virtually identical, thus permitting unambiguous determination of relative asymptotic energy densities.

The asymptotic ratio may be considered a measure of localization. Figure 8 shows the difference of late time logarithms as a function of frequency f and distance r. The ratio of the distance r to this logarithm is an estimate of localization length. This implies a localization length of 12 cm at 195 kHz. As anticipated from the arguments above regarding k times mean free path, the gap peaks at a frequency of about 200 kHz and diminishes both below and above this. Localization is observed over the expected finite band.

V. CONCLUSIONS

Ultrasound in the highly heterogeneous plate pictured in Fig. 1 has been shown to Anderson localize over a finite frequency band. In accord with theoretical expectations, classical diffusion is seen at high frequencies; localization is seen at others. Structures like this will permit studies of localization near boundaries, transport dynamics in the presence of localization, and fidelity in localizing systems.

ACKNOWLEDGMENTS

This work was supported by the NSF Grant Nos.CMS 05-28096 and CMS 02-01346.

[1]R. Weaver, "Anderson Localization of Ultrasound," Wave Motion **12**, 129–142 (1990).
[2]P. W. Anderson, "The question of classical localization: A theory of white paint?," Philos. Mag. B **52**, 505–509 (1985).
[3]S. John, "Electromagnetic absorption in a disordered medium near a photon mobility edge," Phys. Rev. Lett. **53**, 2169–2172 (1984).
[4]C. A. Condat, "Acoustic localization and resonant scattering," J. Acoust. Soc. Am. **83**, 441–452 (1988).
[5]D. S. Wiersma, P. Bartolini, A. Lagendijk, and R. Righini, "Localization of light in a disordered medium," Nature (London) **390**, 671–673 (1997).
[6]F. Scheffold, R. Lenke, R. Tweer, and G. Maret, Nature (London) **398**, 206–207 (1999).
[7]*Scattering and Localization of Classical Waves in Random Media*, edited by P. Sheng (World Scientific, Singapore, 1990).
[8]For a recent report of localization phenomena in three dimensions see J. H. Page, H. Hu, S. Skipetrov, and B. A. van Tiggelen, "Localization of sound in an open three-dimensional system," *Photonic Metamaterials: From Random to Periodic*, OSA Technical Digest (CD) (Optical Society of America, Washington, D.C., 2007).
[9]A. Genack and N. Garcia, "Observation of photon localization in a 3d disordered system," Phys. Rev. Lett. **66**, 2064–2067 (1991).
[10]C. Pierre and E. H. Dowell, "Localization of vibrations by structural irregularity," J. Sound Vib. **114**, 549–564 (1987); C. Pierre, "Weak and strong localization in disordered structures: A statistical investigation," *ibid.* **139**, 111–132 (1990); D. Li and H. Benaroya, "Dynamics of periodic and near periodic structures," Appl. Mech. Rev. **45**, 447–460 (1992).
[11]Y. Adamov, I. V. Gornyi, and A. D. Mirlin, "Loschmidt echo and Lyapunov exponent in a quantum disordered system," Phys. Rev. E **67**, 056217 (2003).
[12]G. S. Ng, J. Bodyfelt, and T. Kottos, "Critical fidelity at the metal-insulator transition," Phys. Rev. Lett. **97**, 256404 (2006).
[13]J. de Rosny, A. Tourin, and M. Fink, "Coherent backscattering of an elastic wave in a chaotic cavity," Phys. Rev. Lett. **84**, 1693–1696 (2000).
[14]R. L. Weaver and O. I. Lobkis, "Enhanced backscattering and modal echo of reverberant elastic waves," Phys. Rev. Lett. **84**, 4942–4945 (2000).
[15]E. Larose, L. Margerin, B. A. van Tiggelen, and M. Campillo, "Weak localization of seismic waves," Phys. Rev. Lett. **93**, 048501 (2004).
[16]U. Frisch, "Wave propagation in random media," in *Probabalistic Methods in Applied Mathematics*, edited by Bharucha-Reid (Academic, New York, 1968), Vol. **1**, pp. 75–197; F. Stanke and G. Kino, "A unified theory for elastic wave propagation in polycrystalline materials," J. Acoust. Soc. Am. **75**, 665–681 (1984).
[17]J. A. Turner and R. L. Weaver, "Radiative transfer of ultrasound," J. Acoust. Soc. Am. **96**, 3654–3674 (1994); L. V. Ryzhik, G. Papanicolaou, and J. B. Keller, "Transport equations for elastic and other waves in random media," **24**, 327–370 (1996); R. Weaver, "Diffusivity of ultrasound in polycrystals," J. Mech. Phys. Solids **38**, 55–86 (1990).
[18]R. L. Weaver and O. I. Lobkis, "On the emergence of the Green's function in the correlations of a diffuse field," J. Acoust. Soc. Am. **110**, 3011–3017 (2001).
[19]A. F. Ioffe and A. R. Regel, "Non-crystalline, amorphous, and liquid electronic semiconductors," Prog. Semicond. **4**, 237 (1960).
[20]B. White, P. Sheng, Z. Q. Zhang, and G. Papanicolau, "Wave localization characteristics in the time domain," Phys. Rev. Lett. **59**, 1918–1921 (1987).
[21]R. L. Weaver, "Anderson localization in the time domain: Numerical studies of waves in two-dimensional disordered media," Phys. Rev. B **49**, 5881–5895 (1994).
[22]R. L. Weaver, "On anomalous diffusivity and localization of classical waves in disordered media: The effect of dissipation," Phys. Rev. B **47**, 1077–1080 (1993).
[23]B. A. van Tiggelen, A. Lagendijk, and D. S. Wiersma, "Reflection and transmission of waves near the localization threshold," Phys. Rev. Lett. **84**, 4333–4336 (2000).
[24]N. Cherroret and S. E. Skipetrov, "Microscopic derivation of self-consistent equations of Anderson localization in a disordered medium of finite size," Phys. Rev. E **77**, 046608 (2008).
[25]S. E. Skipetrov and B. A. van Tiggelen, "Dynamics of weakly localized waves," Phys. Rev. Lett. **92**, 113901 (2004).
[26]O. I. Lobkis and R. L. Weaver, "Self-consistent transport dynamics for localized waves," Phys. Rev. E **71**, 011112 (2005).
[27]K. F. Graff, *Wave Motion in Elastic Solids* (Dover, New York, 1975); J. Miklowitz, *Elastic Waves and Waveguides* (North-Holland, Amsterdam, 1978).
[28]For example, sources acting on an infinitely dense stiff inclusion will not work, and detectors there will be insensitive to local average energy density.
[29]B. Shapiro, "New type of intensity correlation in random media," Phys. Rev. Lett. **83**, 4733–4735 (1999).
[30]Losses into air may be roughly estimated by $\sigma=(Ac_{\mathrm{air}}/V)\ (\rho_{\mathrm{air}}/\rho_{\mathrm{solid}})$, where A and V are the surface area and volume of the solid. Neglecting the extra surface area in the slits, this number is 0.048/ms for our plate, or nine powers of e in 200 msec. . In spite of the enormous impedance mismatch between air and aluminum, losses into the air are not unimportant.
[31]O. Lobkis, I. Rozhkov, and R. Weaver, "Non-exponential dissipation in a lossy elastodynamic billiard, comparison with Porter-Thomas and random matrix predictions," Phys. Rev. Lett. **91**, 194101 (2003).
[32]One might hypothesize that this curvature is due to a distribution of absorption rates across the frequency bin. Absorption in these samples is linear in frequency up to about 1 MHz. Thus a frequency bin of width of 80 kHz at 200 kHz has a range of absorption rates that varies by 40%. It is not difficult to show that after a time corresponding to decay by 12 factors of e at the initial decay rate [e.g., Fig. 7(b) at 200 ms], the energy density in such a bin would be one factor of e greater than it would be if it had sustained its initial rate of decay. This is too small to explain the curvatures seen in Fig. 7.

Effect of internal resistance of a Helmholtz resonator on acoustic energy reduction in enclosures

Ganghua Yu, Deyu Li, and Li Cheng[a)]
Department of Mechanical Engineering, The Hong Kong Polytechnic University, Hung Hom, Kowloon, Hong Kong, SAR of China

(Received 1 April 2008; revised 21 August 2008; accepted 4 September 2008)

The effect of internal resistance of a Helmholtz resonator on acoustic energy reduction in an enclosure and the multimodal coupling-based Helmholtz resonator design are investigated. Using the analytical solution of a resonator-enclosure interaction model, an energy reduction index is defined in a frequency band to optimize the resonator resistance. The dual process of energy dissipation and radiation of the resonator is quantified. Optimal resistance of the resonator and its physical effect on the resonator-enclosure interaction are numerically evaluated and categorized in terms of frequency bandwidths. Predictions on the resonator performance are confirmed by experiments. Comparisons with existing models based on different optimization criteria are also performed. It is shown that the proposed model serves as an effective design tool to determine the internal resistance of the resonator in order to achieve sound reduction in the frequency band enclosing acoustic resonances. © *2008 Acoustical Society of America.* [DOI: 10.1121/1.2996328]

PACS number(s): 43.50.Gf, 43.50.Jh, 43.20.Ks [KA] Pages: 3534–3543

I. INTRODUCTION

Studies on Helmholtz resonators (HRs) have been arousing persistent interest for many decades as evidenced by a large body of existing literature. On one hand, HRs have been extensively used to control noise transmissions in various systems such as ducts, cylindrical shells,[1] ducts,[2] and double panels.[3] On the other hand, they have also been used as sound amplifying devices to perform energy conversion of different types as shown by some very recent work.[4–6] Irrespective of applications, the design of HRs with suitable characteristics has always been a key issue. Effort has been made not only on the development of prediction models[7,8] but also on the design and realization of HRs.[9]

Early work concerning HR coupled to an enclosure can be traced back to Van Leeuwen who proposed a design chart based on electrical circuit analogy.[10] Due to the simplicity of the HR, its use was found in controlling the interior noise inside an enclosure. It was also observed, however, that the proposed design chart in Ref. 10 might lead to an apparent discrepancy with experiments at enclosure resonances.[11] Subsequently, Fahy and Schofield proposed another model to improve the work in Ref. 10 by taking into account the coupling between a single resonator and a single enclosure mode of interest.[11] By maximizing the energy dissipation of the resonator at the targeted frequency, a formula was proposed to determine the Q-factor of the resonator. They cautioned, however, that the resonator designed using their formula might not lead to the maximum reduction in sound pressure level (SPL) inside the enclosure around the targeted frequency. To cover the small frequency range around the targeted frequency, which can be loosely called "broad band," they equalized the dominant peaks inside the band and provided an equation to determine the Q-factor of the resonator. Also in that work, three different types of damping materials were used in the resonator to improve the dissipation and to broaden the working bandwidth. Experimental results showed that the performance of the resonator was reduced by either excessive or insufficient damping of the resonator. Proper damping materials were experimentally determined to achieve an optimal reduction in SPL around the targeted resonance inside the enclosure. Recently, similar observations were made by Slaton and Zeegers in their experimental work on a flow-duct system with a damped HR.[12] The existence of an optimal value of the resonator resistance has been clearly shown in their experiments. Fahy and Schofield's work is important in that it provides insightful information to guide the resonator design. It also sets an important milestone in the HR design that, even nowadays, is still being used.[1,13] Meanwhile, their work also shows the need for a general model to count for the acoustic interaction among resonators and multiple acoustic modes of the enclosure. With a view to further increase the control performance, Cummings[14] extended Fahy and Schofield's model to multiple resonators, along with the consideration of multiple modes of the enclosure. By considering resonators as pseudo pulsating sphere sources, characterized by the averaged sound pressure over the surface of the sphere, the singularity problem in the equation set was avoided. However, this treatment of the equivalent sphere induced a large discrepancy between the predicted coupled frequencies and the measured ones.[15] Recently, a new model was proposed by Li and Cheng[15] to analyze the interaction between an acoustic resonator array and an enclosure with multiple modes. Different from Ref. 14, they solved the interaction equation inside the enclosure to obtain the modal responses and employed these modal responses to find the sound pressures at the resonator apertures. This avoided the singularity problem encountered in Ref. 14 when calculating the sound pressure at the center of a point source radiated by its own. Comparisons between

a)Electronic mail: mmlcheng@polyu.edu.hk

 © 2008 Acoustical Society of America

theoretical and experimental results showed that the model provides a good approximation to real multimode setup.

Despite the persistent effort made in the past, researchers still need ways and tools to achieve optimal design of HRs, which right now still involves extensive experimental measurements on a trial-and-error basis. It is known that resonators interact with the enclosure through dissipating energy on one hand and radiating energy back to the enclosure on the other hand. A clear demarcation and quantification of these two effects may be one of the key elements to explain the way in which an optimally designed resonator works. On the other hand, insertions of acoustic resonators create new peaks around the original targeted peak, which are referred to as coupled or newly emerged peaks hereafter.[11,13] An ideal resonator design should target a frequency band including both targeted and coupled resonance peaks. Upon enlarging the frequency band of interest, the possible multimodal coupling effect on the resonator design needs to be qualified and somehow be taken into account in the design process. Unfortunately, these issues have not been fully investigated even up to now, mainly due to the lack of reliable, yet simple enough model.

The model proposed by Li and Cheng[15] admits analytical solutions when only one HR is involved, such providing an opportunity for the aforementioned issues to be addressed. This paper attempts to explore this unique feature of the model and makes contributions in the following aspects: (1) a systematic demarcation and quantification of the energy radiation and dissipation effect of the resonator when coupled to a multimodal enclosure; (2) determination of the internal resistance of the resonator to ensure the maximum sound energy reduction (ER) inside the enclosure within a frequency band around a targeted resonance frequency, along with experimental validations; (3) qualification of the impact of the frequency band and the modal coupling on resonator design; and (4) reassessment of the existing models through comparisons with the present one. These analyses are believed to shed light on the underlying physics of the HRs coupled to an acoustic enclosure and bring significant improvement on the existing knowledge on HR design for acoustic ER in enclosures.

II. THEORY

The system under investigation comprises a rigid-walled acoustic enclosure with a classical HR. The resonator consists of a cavity of volume V^R with a neck of area S^R and effective length L^R, as shown in Fig. 1. Throughout the paper, the superscripts and subscripts E, R, and S indicate variables associated with "enclosure," "resonator," and "source," respectively. In this section, an ER index is established based on the analytical solutions. Formulas for calculating dissipation energy and radiation energy from an HR are derived, which depend on the internal resistance of the resonator.

A. Energy radiation and dissipation of HR

When installing a resonator in an enclosure having a primary sound source, the vibration of the lumped mass in the resonator neck radiates sound back to the enclosure, resulting in an acoustic interaction with the enclosure. Meanwhile, energy dissipation also takes place inside the resonator neck. This dual process occurs simultaneously and depends on the property of the resonator, particularly the particle velocity strength in the resonator neck and the internal resistance of the resonator. The lumped mass inside the resonator neck follows Newton's second law and the sound pressure inside the enclosure is governed by the wave equation. Assuming that all time dependent variables are harmonic, after expending the sound pressure p inside the enclosure over a basis of enclosure eigenfunctions $\varphi_j(\mathbf{r})$ as $p=\sum_{j=1}^{J}P_j\varphi_j(\mathbf{r})$ (J is the maximum number of the truncated mode series) and applying orthogonality properties, analytical solutions of the volume velocity source strength $\tilde{Q}^R$ directed outward of the resonator into the enclosure and the jth modal pressure response P_j of the enclosure are, respectively, obtained as[15]

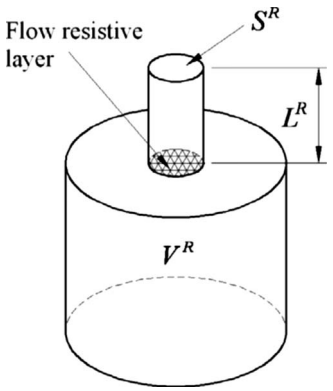


FIG. 1. A damped classical Helmholtz resonator.

$$\tilde{Q}^R=\frac{A^R\frac{V^R}{V^E}\sum_{h=1}^{J}\left[\frac{\omega^2}{\omega^2-(\gamma_h^E)^2}\frac{\varphi_h(\mathbf{r}^R)}{\Lambda_h}\tilde{\varphi}_h(\mathbf{r}^S)\tilde{Q}^S\right]}{1-A^R\frac{V^R}{V^E}\sum_{h=1}^{J}\left[\frac{\omega^2}{\omega^2-(\gamma_h^E)^2}\frac{\varphi_h^2(\mathbf{r}^R)}{\Lambda_h}\right]}, \tag{1}$$

$$P_j=\underbrace{-\frac{i\omega\rho_0}{k^2V^E}\frac{\omega^2}{\omega^2-(\gamma_i^E)^2}\frac{\tilde{\varphi}_j(\mathbf{r}^S)}{\Lambda_j}\tilde{Q}^S}_{\text{contribution from primary source}}$$

$$\underbrace{-\frac{i\omega\rho_0}{k^2V^E}\frac{\omega^2}{\omega^2-(\gamma_j^E)^2}\frac{\varphi_j(\mathbf{r}^R)}{\Lambda_j}\tilde{Q}^R}_{\text{contribution from resonator}}, \tag{2}$$

where

$$A^R=\frac{(\omega^R)^2}{\omega^2-icR\omega-(\omega^R)^2},$$

$\tilde{Q}^S$ is the volume velocity source strength of the primary source located at $\mathbf{r}^S$; $\mathbf{r}^R$ is the location of the resonator; V^E is the volume of the enclosure; γ_j^E is the jth eigenvalue of the enclosure expressed as $\gamma_j^E=\omega_j^E+iC_j^E$, in which the real part is the angular frequency and the imaginary part is an equivalent

ad hoc damping coefficient; $\Lambda_j=\int_{V^E}[\varphi_j(\mathbf{r})]^2 dV/V^E$; $\tilde{\varphi}_j(\mathbf{r}^S)$ is the averaged $\varphi_j(\mathbf{r}^S)$ over the volume of the primary source;[14] z_0 is the characteristic impedance of the air $(\rho_0 c)$; $R=R_i/z_0 L^R$, with R_i being the specific acoustic resistance of the resonator; and $\omega^R=c(S^R/L^R V^R)^{1/2}$, which is the uncoupled resonance frequency of the HR.

Equation (2) provides an analytical solution in terms of modal pressure response inside the enclosure under the effect of the resonator. It also provides insightful information about the interaction between the resonator and the enclosure. The first term on the right hand side of Eq. (2) represents the effect of the primary sound source and the second term characterizes the effect of inserting an acoustic resonator. As expected, the resonator is coupled with all acoustic modes of the enclosure. If a targeted enclosure mode is well separated from other enclosure modes, the interaction among these modes and the resonator can be neglected.[11] On the contrary, high modal density or a larger frequency band of interest may necessitate the consideration of the interaction among the resonator and multiple modes of the enclosure. Same applies if the control performance of the resonator should be evaluated in a broad band. Equation (2) also shows that, when the resonator location is fixed, the internal resistance of the resonator, through A^R, plays an important role in determining the effect of the resonator. An excessively high internal resistance renders A^R approach to zero, such annulling the effect of the resonator. On the contrary, if the internal resistance is too low, A^R tends toward infinity at the resonance frequency, which causes unacceptable high amplitude P_j at the two newly emerged frequencies (coupled peaks) after the resonator is installed.[13] None of the two above scenarios is desirable. Therefore, the internal resistance of the resonator needs to be investigated and properly chosen.

1. Energy radiation from resonator aperture

The sound energy radiated from the resonator is determined by shutting down the primary source in the enclosure. In this circumstance, only the vibration of the mass inside the resonator neck acts as the sound source, which has been previously determined under the presence of the primary source. Setting $\tilde{Q}^S$ to zero in Eq. (2), the modal response P_j^R caused by the resonator radiation alone is calculated as

$$P_j^R=\frac{\omega^2}{\omega^2-(\gamma_j^E)^2}A^R\frac{V^R}{V^E}\frac{\varphi_j(\mathbf{r}^R)}{\Lambda_j}\sum_{h=1}^{J}\varphi_h(\mathbf{r}^R)P_h, \tag{3}$$

where P_h is computed from Eq. (2) when keeping $\tilde{Q}^S$, which is used to calculate the initial displacement and velocity of the lumped mass inside the resonator neck. The acoustic pressure purely created by the resonator radiation is expressed as

$$\hat{p}(\mathbf{r})=\sum_{j=1}^{J}P_j^R\varphi_j(\mathbf{r}). \tag{4}$$

In a typical sound field, the fluctuation of the entropy is usually small compared with that of the pressure. Therefore, the influence of entropy deviation can be neglected, and the energy radiated from the resonator in a period T can be calculated as[16]

$$E_{\text{radi}}^R=w+w_d, \tag{5a}$$

where w is the time-averaged acoustic energy inside the enclosure, including kinetic and potential energy, and w_d is the time-averaged energy dissipation inside the enclosure, which can be determined using the measured Q-factor of the enclosure Q^E as[16]

$$w_d=\frac{\pi S^E}{4Q^E}\frac{w}{V^E}, \tag{5b}$$

where S^E is the surface area of the enclosure. Alternatively, w_d can also be evaluated by adding the energy loss at the boundaries of the enclosure and inside the enclosure caused by thermal conduction and viscosity:

$$w_d=\int_0^T\int_{S^E}\left[\underbrace{\left(\frac{\omega\rho_0\mu}{8}\right)^{1/2}\hat{\mathbf{v}}_T(\mathbf{r}^S)\cdot\hat{\mathbf{v}}_T^*(\mathbf{r}^S)+(\gamma-1)\left(\frac{\omega\rho_0\kappa}{8c_p}\right)^{1/2}}_{\text{Energy loss at boundaries}}\frac{|\hat{p}(\mathbf{r}^S)|^2}{(\rho_0 c)^2}\right]dSdt$$
$$+\int_0^T\int_{V^E}\left[\underbrace{\frac{\kappa}{T_0}(\nabla T')^2}_{\text{thermal conduction loss}}+\underbrace{\mu_B(\nabla\cdot\mathbf{v})^2+\frac{1}{2}\mu\sum_{ij}\alpha_{ij}^2}_{\text{viscosity loss}}\right]dVdt, \tag{5c}$$

where μ is the shear viscosity, $\mathbf{v}$ is the particle velocity, $\hat{\mathbf{v}}_T$ is the tangential component of the amplitude of velocity $\mathbf{v}$ on the enclosure boundary, γ is the specific heat ratio, κ is the coefficient of thermal conductivity, c_p is the specific heat coefficient at constant pressure, T_0 is the ambient temperature, T' is the temperature perturbation given by $p\sqrt{T_0(\gamma-1)/c_p/\rho_0 c}$, μ_B is the bulk viscosity, and α_{ij} is the rate of shear tensor, which is computed from the particle velocity $\mathbf{v}$ as[16]

$$\alpha_{ij}=\frac{\partial v_i}{\partial x_j}+\frac{\partial v_j}{\partial x_i}-\frac{2}{3}\nabla\cdot\mathbf{v}\delta_{ij}\quad(i,j=1,2,3),$$

where x_i apply to x, y, and z and v_i to the component of $\mathbf{v}$ in x, y, and z directions when i equals to 1, 2, 3, respectively.

The time-averaged acoustic energy w over a volume V is calculated by

$$w=\int_V\frac{1}{4\rho_0 c^2}\left[\left(\frac{c}{\omega}\right)^2\nabla\hat{p}\cdot\nabla\hat{p}^*+|\hat{p}|^2\right]dV. \tag{6}$$

The first item in Eq. (6) is the time-averaged kinetic energy and the second item is the time-averaged potential energy. When the volume is the volume of the whole enclosure V^E, Eq. (6) yields

$$w=\frac{V^E}{4\rho_0 c^2}\left[\frac{1}{\omega^2}\sum_{j=1}^{J}(\omega_j^E)^2(P_j^R)^2\Lambda_j+\sum_{j=1}^{J}(P_j^R)^2\Lambda_j\right]. \tag{7}$$

2. Energy dissipation by resonator

The energy dissipated by the resonator in a period T is computed by

$$E_d^R = -\frac{1}{2}\int_0^T \int_{S^R} \mathrm{Re}[p(\mathbf{r}^R)v^*(\mathbf{r}^R)]dSdt, \tag{8}$$

where v is the amplitude of particle speed.

Substituting $p(\mathbf{r}^R)=ZS^R v(\mathbf{r}^R)$ into Eq. (8) yields

$$E_d^R = -\frac{1}{2}S^R \int_{S^R} T|v(\mathbf{r}^R)|^2 \mathrm{Re}(Z)dS, \tag{9}$$

where Z is the acoustic impedance of the HR (Ref. 14)

$$Z = -\frac{R_i}{S^R} - i\left(\frac{L^R\rho_0\omega}{S^R} - \frac{\rho_0 c^2}{V^R\omega}\right). \tag{10}$$

Under the lumped mass assumption, the dissipated energy is calculated from

$$E_d^R = \tfrac{1}{2}S^R R_i T|v(\mathbf{r}^R)|^2, \tag{11}$$

where $|v(\mathbf{r}^R)|^2$ is computed as

$$|v(\mathbf{r}^R)|^2 = \frac{1}{(\rho_0 L^R)^2}\frac{\omega^2|\Sigma_{h=1}^J \varphi_h(\mathbf{r}^R)P_h|^2}{[(\omega^R)^2-\omega^2]^2+(cR\omega)^2}. \tag{12}$$

Substituting Eq. (12) into Eq. (11) and replacing T by $2\pi/\omega$ yield

$$E_d^R = \frac{\pi S^R}{\rho_0 L^R}\frac{cR\omega}{[(\omega^R)^2-\omega^2]^2+(cR\omega)^2}\left|\sum_{h=1}^J \varphi_h(\mathbf{r}^R)P_h\right|^2. \tag{13}$$

If only jth mode of the enclosure is considered, the dissipated power by the resonator at the targeted resonance frequency ($\omega=\omega_j=\omega^R$) is simplified from Eq. (13) as

$$PW_d^R = \frac{E_d^R}{T} = \frac{S^R}{2\rho_0 L^R}\frac{1}{cR}|\varphi_i(\mathbf{r}^R)P_j(\omega^R)|^2. \tag{14}$$

From Eq. (2), the modal response at this natural frequency can be expressed as

$$\frac{P_j}{\tilde{\varphi}_j(\mathbf{r}^S)\tilde{Q}^S} = \frac{cz_0 Q_j^E}{\omega^R V^E \Lambda_j^E}\frac{1}{1+Q^R Q_j^E \varepsilon^2}, \tag{15}$$

where ε^2 is the coupling parameter which equals to $\varphi_j^2(\mathbf{r}^R)V^R/\Lambda_j V^E$, Q^R is the Q-factor of the resonator without its radiation resistance, which is calculated by $Q^R=\omega^R/cR$, and Q_j^E is the Q-factor of the jth enclosure mode given by $Q_j^E=\omega^R/2C_j^E$, in which C_j^E is the jth equivalent *ad hoc* damping coefficient of the enclosure. Without resonator, the modal response of the enclosure at the resonator location is

$$\frac{P_j^0}{\tilde{\varphi}_j(\mathbf{r}^S)\tilde{Q}^S} = \frac{cz_0 Q_j^E}{\omega^R V^E \Lambda_j^E}. \tag{16}$$

Substituting Eqs. (15) and (16) into Eq. (14), the power dissipated by the resonator at the resonance frequency of the jth enclosure mode is determined as

$$PW_d^R = \frac{S^R}{2\rho_0 L^R}\frac{Q^R}{\omega^R}\left|\frac{1}{1+Q^R Q^E \varepsilon^2}\right|^2 |P_j^0\varphi(\mathbf{r}^R)|^2$$
$$= \frac{S^R}{2\rho_0 c k_j L^R}\left|\frac{Q^R}{1+Q^R Q^E \varepsilon^2}\right|^2 |p^{R_0}|^2, \tag{17}$$

where k_j is the wave number at the natural frequency of the jth mode and p^{R_0} is the pressure at the resonator location. When only one targeted mode is considered, the above equation leads to the same expression given in Ref. 11.

B. Quantification of band-averaged performance of HR

In order to achieve a good control performance in the vicinity of the targeted frequency, an "energy reduction index" was defined in a frequency band around the targeted frequency, which was used as the object parameter to optimally determine the internal resistance of the resonator. Upon obtaining the modal response from Eq. (2), the acoustic energy inside the enclosure can be directly computed from Eq. (6). The averaged energy within a frequency band $[\omega_1,\omega_2]$ is defined as

$$E^R = \frac{1}{\omega_2-\omega_1}\int_{\omega_1}^{\omega_2} w d\omega. \tag{18}$$

The frequency band $[\omega_1,\omega_2]$ is chosen to include major frequency components in the vicinity of the targeted original resonance peak (such as the coupled resonance frequencies due to the insertion of the resonator). When computing w using Eq. (6), volume V can either be the local volume or the whole enclosure, depending on whether a local or global sound attenuation is expected. The ER index is defined as

$$\mathrm{ER} = -10\log_{10}\frac{E^R}{E^0}, \tag{19}$$

where E^R and E^0 are energy terms with and without a resonator, respectively.

III. SIMULATIONS AND EXPERIMENTAL VALIDATION

A right parallelepiped enclosure (Fig. 2) with dimensions $l_x=0.976$ m, $l_y=0.695$ m, and $l_z=1.188$ m was used in both numerical simulations and experiments. The enclosure was composed of six plywood boards, 2 in. thick each. Five of them were bolted together to form a cavity and one of them was made removable as a cover. To prevent any possible leakage, sound-proof strips were used in the connecting surfaces between the bolted boards and the removable board, and silicon gel was also used at the connection corners of bolted boards. A square hole of 100×100 mm^2 was cut at (100,59) mm in the cover through which a loudspeaker was installed to create a primary sound field in the enclosure. The Q-factors of the enclosure modes were obtained from measured frequency response function before installing the resonator (see Table I). For each mode, its Q-factor is defined as the resonance frequency divided by the bandwidth between its half-power points. Because of the increasing modal density at higher frequencies, the Q-factors for higher-order modes were assumed to be 45, which is the same as the

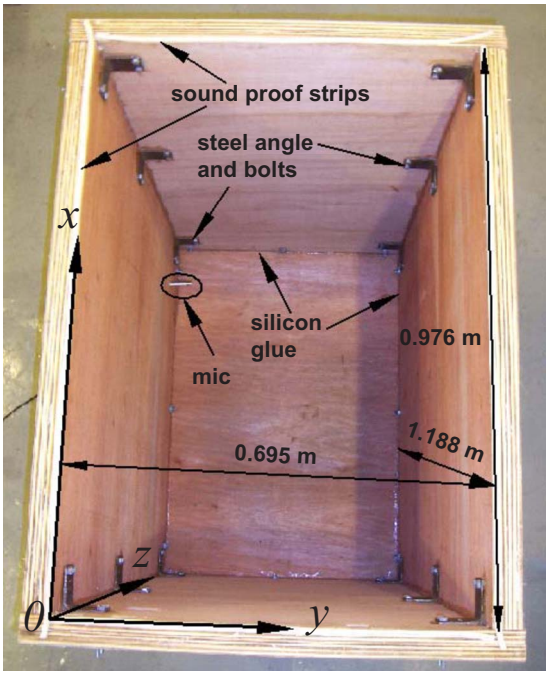


FIG. 2. (Color online) Enclosure used in simulations and experiments.

measured Q-factor for mode (2, 0, 1). Given an ambient temperature of 20 °C and the humidity of 90%, the sound speed was determined as 344.5 m/s. The air density ρ_0 was 1.205 kg/m^3.

The enclosure mode (1, 0, 1) at the predicted natural frequency of 228.4 Hz was chosen as the targeted mode in simulations. A HR having the same frequency of 228.4 Hz was designed. The internal neck diameter of the resonator is 21 mm and the physical neck length is 52 mm. The body of the resonator is a circular tube having a 73.5 mm internal diameter and a 74.1 mm depth. The resonator was installed at (100,300,0) mm.

In simulations, 216 enclosure modes were used, as determined by a convergence study. The eigenfunctions $\varphi_j(\mathbf{r}^R)$ of the enclosure, having thermalviscous boundary conditions, were given in Ref. 14. The calculated natural frequencies of the first 13 modes are tabulated in Table I. The SPL inside the enclosure was evaluated at one arbitrary point (816,70,1028) mm. The predicted baseline SPL at the same location without the resonator is shown in Fig. 3, in which four major peaks correspond to the first four enclosure modes.

TABLE I. Computed natural frequencies and measured Q-factors of the enclosure.

Index	Mode number (lmn)	Natural frequency (Hz)	Q-factor
1	000	0	⋯
2	001	145	32
3	100	176.5	42
4	101	228.4	44
5	010	247.8	46
6	011	287.1	84
7	002	290	42
8	110	304.3	51
9	111	337	79
10	102	339.5	60
11	200	353	80
12	012	381.5	60
13	201	381.6	45
⋯	⋯	>400.0	45

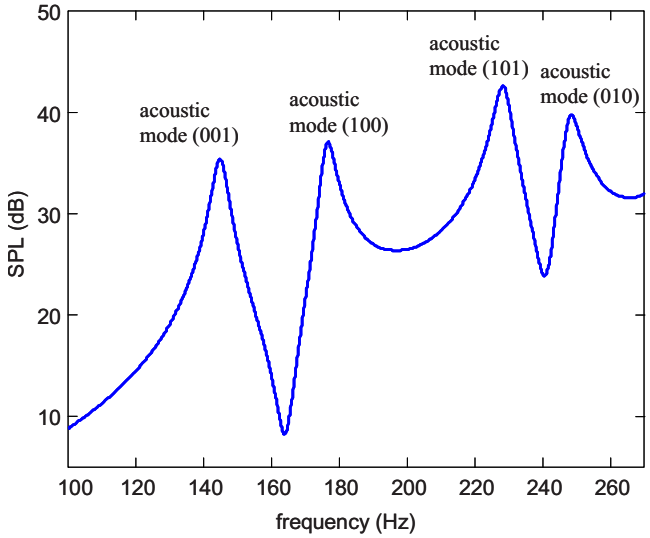


FIG. 3. (Color online) Predicted baseline SPL at (816,70,1028) mm.

A. Experimental validation

The effect of the internal resistance of the resonator is first demonstrated and experimentally validated for a chosen frequency bandwidth of 20 Hz centered at 228.4 Hz. By choosing three typical R_i values (2.25, 3.82, and 9.62 mks Rayls), the SPL variations are shown and compared to the case without resonator in Fig. 4. Note that the case corresponding to R_i=3.82 mks Rayls was obtained as a result of optimization, which will be detailed later in Sec. III B. Figure 4 shows that a 5.8 dB reduction in SPL is achieved when the resonator takes the optimal resistance value of 3.82 mks

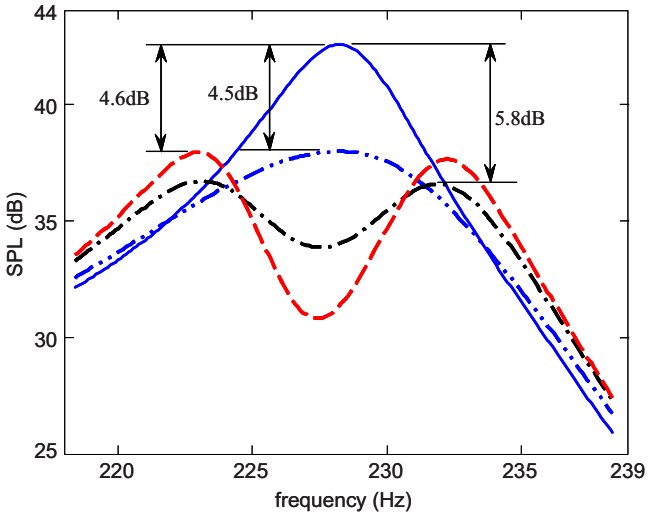


FIG. 4. (Color online) Predicted SPL curves at (0.816,0.07,1.028) m:—without resonator;—·—with a damped resonator, R_i=3.82 mks Rayls; – – with an empty-neck resonator, R_i=2.25 mks Rayls; and —··— with a damped resonator, R_i=9.62 mks Rayls.

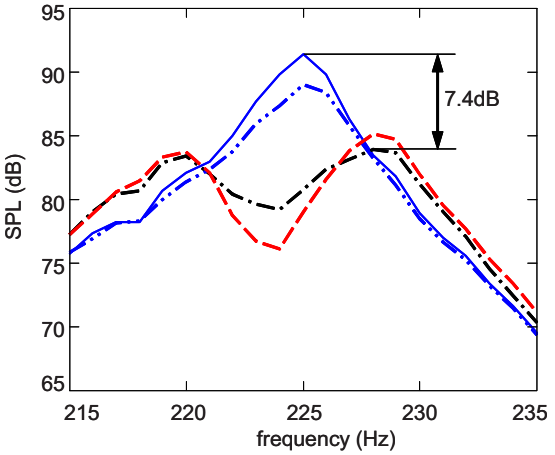


FIG. 5. (Color online) Measured SPL curves at (0.816, 0.07, 1.028) m:—without resonator; —·— with a damped resonator, R_i=3.59 mks Rayls; – – with an empty-neck resonator, R_i=2.25 mks Rayls; and —··— with a damped resonator, R_i=9.62 mks Rayls.

Rayls. When R_i is increased to 9.62 mks Rayls, the performance of the resonator deteriorates, resulting in a 4.5 dB reduction in SPL. With a lightly damped resonator (R_i =2.25 mks Rayls), two sharp peaks appear. This is not acceptable since usually an overall reduction in the frequency band of interest is required.

Experimental measurements were conducted to validate the above predicted results. Similar to the simulation, the enclosure mode (1, 0, 1) was chosen as the targeted mode at the measured natural frequency of 225 Hz. Three resonators, all having a resonance frequency of 225 Hz but different internal resistances, were designed, fabricated, tuned, and installed at (100, 300, 0) mm, respectively. Thin layers of damping material (loudspeaker grill) were inserted in the resonator's neck to produce different internal resistances. For each case, the Q-factor of the resonator was first determined from its measured frequency response curves, which were then used to compute the internal resistance of the resonator.[11] Since it was difficult to fabricate a resonator having exactly the same optimal internal-resistance value as that used in the simulation, the optimal configuration being tested slightly differs from the one used in the simulation. The first resonator has an empty neck, with R_i=2.25 mks Rayls, lower than the theoretically determined optimal value R_{opt} =3.82 mks Rayls. For the second resonator, R_i=3.59 mks Rayls, close to R_{opt}. The third resonator has a R_i=9.62 mks Rayls, which is higher than R_{opt}.

A Brüel & Kjær type 4189 $\frac{1}{2}$ in. microphone was installed at (816, 70, 1028) mm to collect the SPL inside the enclosure. Figure 5 shows the measured SPL curves. Similar to prediction, the resonator with R_i close to the optimal resistance outperforms the other two resonators, resulting in a 7.4 dB reduction in SPL. The other two resonators with either lower or higher R_i than R_{opt} produce changes in the SPL in a very similar manner as numerically predicted. Comparing the predicted SPL curves shown in Fig. 4 with the measured results shown in Fig. 5, the same tendency is found. When the resistance of the resonator is the optimal value or approximates the optimal value, the noise reduction is maximum and the peaks at the coupled frequencies are relatively flat, such resulting in an overall sound reduction within the frequency band. When the internal resistance of the resonator is much lower than the optimal value, the insertion of the resonator produces two pronounced peaks, such affecting the sound attenuation ability of the resonator within the chosen band. In this case, most of energy is radiated back to the enclosure with little amount of energy dissipated by the resonator. Excessive R_i also jeopardizes the effect of the resonator. This attributes to the low mobility of the resonator aperture so that the resonator and the enclosure cannot be effectively coupled. Generally speaking, numerical predictions agree well with measured data. Therefore, the model shows its reliability to guide the resonator design.

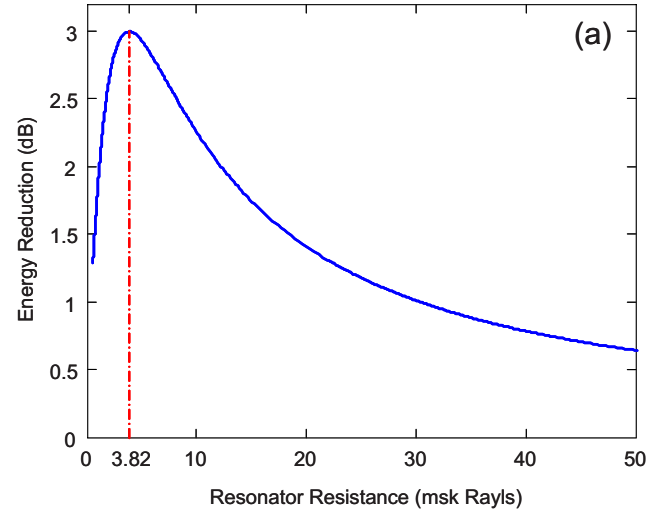
B. Analyses

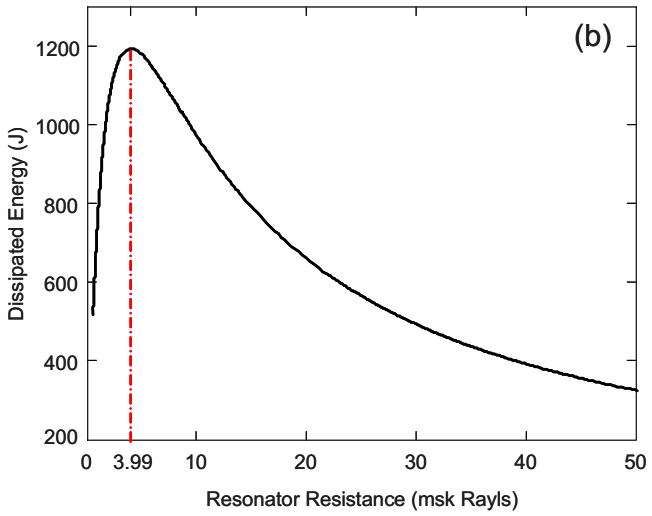
1. Effect of the internal resistance on ER

A 20 Hz bandwidth centered at 228.4 Hz is first chosen as the frequency band of interest for optimization. The internal resistance of the resonator was varied from 0.55 to 50 mks Rayls in the simulation. With the variation in the resonator resistance, the ER was calculated by Eq. (19) and the radiated energy and dissipated energy were also calculated using Eqs. (5a)–(5c) and (13) based on the measured Q-factors of the enclosure, respectively. Notice that the acoustic energy w was computed using Eq. (7). Figures 6(a)–6(c) show the ER inside the enclosure, band-averaged dissipated energy by the resonator, and band-averaged energy radiated from the resonator versus the internal resistance R_i respectively. A maximum reduction of 3.0 dB in ER is observed from Fig. 6(a) when R_i=3.82 mks Rayls, which can be referred to as the optimal value. A similar variation trend as that in Fig. 6(a) is observed in Fig. 6(b), except that the maximum energy dissipation occurs at R_i=3.99 mks Rayls, which is 4% higher than the optimal value determined in Fig. 6(a). This confirms that the effect of the resonator on the ER in the enclosure is mainly dominated by the dissipation ability of the resonator for the frequency band considered here. Figures 6(b) and 6(c) also show that a strong coupling between the resonator and the enclosure takes place with lower R_i value, as evidenced by the efficient sound radiation from the resonator aperture. It means that more energy is returned back to the enclosure from the resonator aperture. As R_i increases, however, more energy was dissipated by the resonator and the radiated energy drastically decreases. Excessive R_i significantly reduces the vibration of the aperture and consequently energy transmission to the resonator so that both energy dissipation inside the resonator and energy radiation from resonator are compromised.

2. Effect of bandwidth

The 20 Hz bandwidth which was previously used covers both the original resonance peak and the newly emerged peaks due to the insertion of the resonator. Should a narrower frequency band be used, it was observed that it has significant impact on the physical effect of the HR as well as the optimal values of its internal resistance. This issue is systematically investigated in this section.





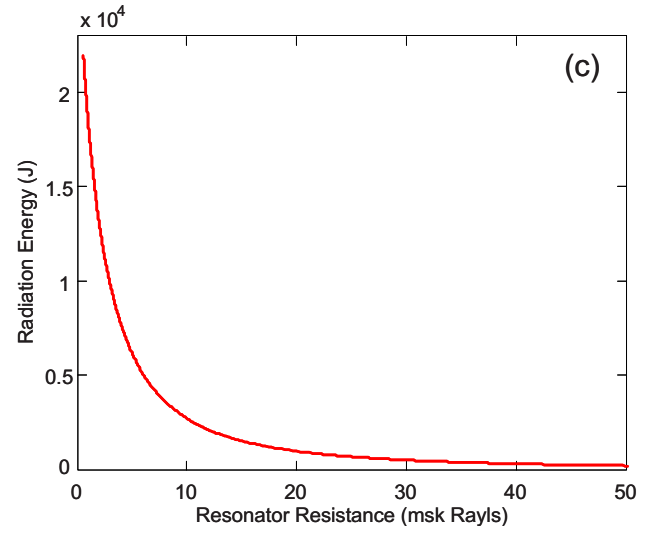


FIG. 6. (Color online) Energy computed in the frequency band of 20 Hz: (a) ER in the enclosure, (b) dissipated energy by the resonator, and (c) radiated energy from the resonator.

The frequency bandwidth was varied from 0.2 to 30 Hz and centered at the targeted resonance of 228.4 Hz. For each frequency band, the internal resistance of the resonator was obtained in two different ways. First, it was determined by

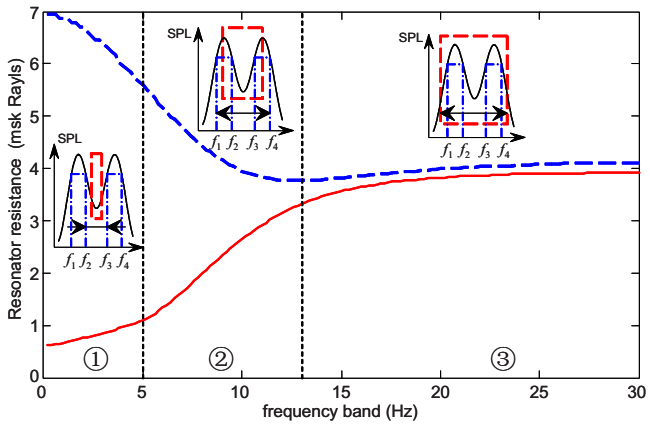


FIG. 7. (Color online) Effect of the chosen frequency band on the resonator resistance: — optimal internal resistance from maximum ER and – – the internal resistance having maximum energy dissipation.

maximizing ER within each frequency band, resulting in the so-called optimal resistance R_{opt}. Second, it was determined by maximizing the energy dissipation by the resonator, giving a resistance value denoted by R_{dis}. R_{opt} and R_{dis} are compared in Fig. 7 with respect to the bandwidth. In order to better quantify the effect of the bandwidth on R_{opt}, Fig. 7 is divided into three different zones, with reference to the half-power frequency bandwidths (denoted by f_2-f_1 and f_4-f_3 in the figure) of the two newly emerged peaks. Zone 3 is featured by a relatively large frequency band completely covering the two new peaks, such as the 20 Hz case which was investigated previously. Within this zone, R_{opt} undergoes slight changes and is relatively close to R_{dis}. This observation is consistent with the analyses carried out in Sec. III B 1, which suggests a dominance of the energy dissipation effect of the resonator. It should be cautioned, however, that even in this case, an accurate determination of R_{opt} cannot be simplified as a problem of maximizing energy dissipation of the resonator, as demonstrated previously in Fig. 6. As opposed to zone 3, zone 1 corresponds to a very narrow band, which only covers the original resonance peak and its very close vicinity. It can be seen that R_{opt} is relatively low, corresponding to lightly damped resonator, and differs significantly from R_{dis}. The low R_{opt} and the apparent difference with R_{dis} indicate that the dissipation of the resonator becomes weak, while the radiation of the resonator becomes strong, resulting in a strong interaction between the resonator and the enclosure. In this case, the targeted resonance peak is sharply split into two new and closely spaced peaks, as illustrated previously in Fig. 4. Meanwhile, the response level inside the enclosure at the targeted resonance is significantly reduced at the expense of creating two high level peaks. Zone 2, which confines the frequency region between the two coupled peaks generated by the insertion of the resonator, is a transition region from narrow band to broad band. Within this zone, R_{opt} undergoes drastic changes, rapidly approaching R_{dis} as the frequency bandwidth increases, suggesting the increasing importance of the energy dissipation.

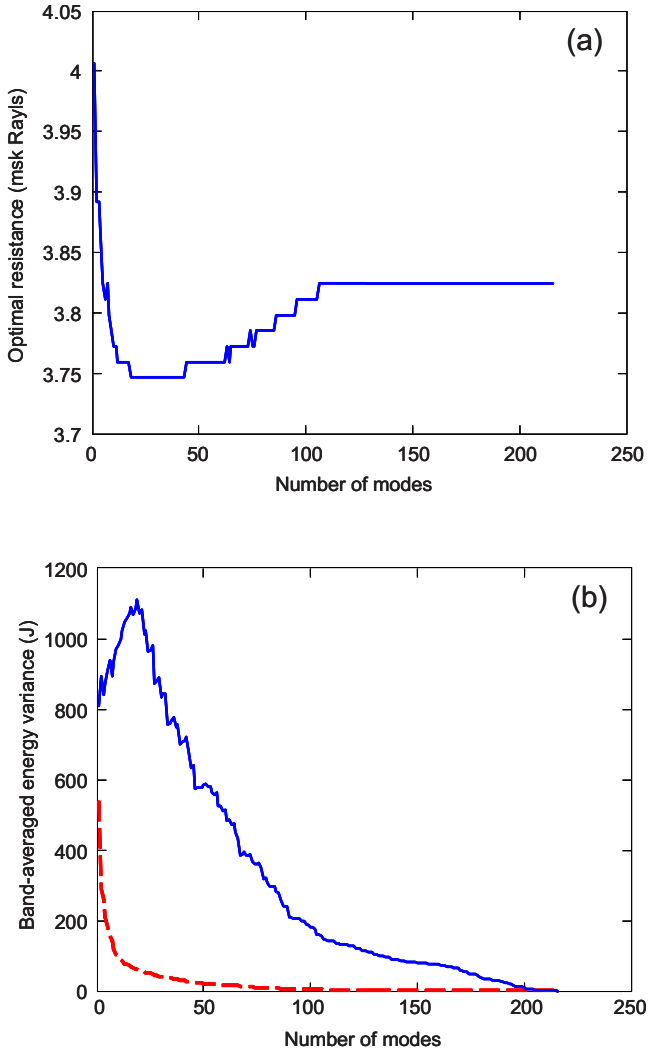


FIG. 8. (Color online) Effect of the modal coupling on (a) optimal resistance of the resonator and (b) band-averaged EV: – – without resonator and — with a resonator, R_i=3.82 mks Rayls.

3. Effect of the modal coupling

As mentioned before, the current model takes into account the multiple modes of the enclosure for HR design. To show this necessity, the effect of modal coupling is investigated.

Figure 8(a) shows the variation in the R_{opt} for 20 Hz bandwidth centered at 228.4 Hz, with the number of the enclosure modes used in the calculation. Enclosure modes used for the sound pressure decomposition are determined according to their closeness to the targeted central frequency to truncate the decomposition series. It can be seen that R_{opt} converges only when a sufficient number of enclosure modes are considered. This suggests that reliable R_{opt} cannot be obtained by only considering the targeted mode or a very limited number of enclosure modes. This phenomenon is apparently due to the choice of a frequency band as performance optimization target instead of one particular frequency, which inevitably enhances the effect of more distant modes. Another plausible explanation may lie in the fact that modal coupling is enhanced due to the insertion of the resonator. This surmise can be ascertained by examining the acoustic energy variation (EV) within the enclosure before and after the resonator is deployed. To this end, a band-averaged EV term is defined as

$$\text{EV} = \frac{1}{\omega_2 - \omega_1}\int_{\omega_1}^{\omega_2} |w - w_0| d\omega, \tag{20}$$

where w and w_0 are the acoustic energies inside the enclosure when a certain number of enclosure modes and 216 enclosure modes are used, respectively. The EV reflects the deviation of the predicted pressure field to the converged state both in frequency and the spatial domains because of the integration in the frequency band and the enclosure volume. The EV was calculated before and after the resonator was used, with comparison given in Fig. 8(b) with respect to the number of enclosure modes. It is seen that when the resonator is absent, the EV inside the enclosure converges rapidly, suggesting that only a small number of enclosure modes actively contribute to system response. Upon insertion of the resonator, however, more modes are activated. This indicates that the insertion of the resonator enhances the modal coupling strength among the enclosure modes through effective interactions with the resonator, as reflected by the second item of Eq. (2).

It is therefore concluded that the consideration of multimodal coupling is necessary in the resonator design when a band performance is expected. One can surmise that this coupling effect will be less apparent if the frequency band of interest becomes narrower.

C. Comparison with Fahy and Schofield's model

It is relevant to compare the present model proposed in this paper and the ones suggested by Fahy and Schofield.[11] Under the assumption of modal separation, Fahy and Schofield proposed two methods to determine the internal resistance of the resonator. (A) For resonance control, the dissipated power at the targeted resonance frequency by the resonator was maximized, leading to

$$Q^R Q^E \varepsilon^2 = 1 \tag{21}$$

and a design chart to choose Q^R. (B) For band control, modal responses at the new coupled frequencies and the original resonance frequency were equalized, leading to an equation

$$\varepsilon Q^E = \frac{2(\varepsilon Q^R)^3}{1 - (\varepsilon Q^R)^2 - (\varepsilon Q^R)^4}. \tag{22}$$

The present work differs from Fahy and Schofield's ones mainly in two aspects: one is the consideration of multiple modal coupling and the other one is the use of a different optimization objective function. It is therefore important to assess and compare the band-control ability of these models.

To this end, the optimal internal resistances of resonators were determined using the current model and Fahy and Schofield's methods, respectively. The ER levels were then computed and compared for four resonant frequencies of the enclosure. Each enclosure mode was targeted by one resonator. By varying the neck length, the body volume of the resonator was kept constant of 0.0009 m^3. Parameters used in the calculation are listed in Table II. R_i values determined

TABLE II. Frequency bands and resonator parameters for the first four nonzero modes of the enclosure.

Natural frequency (Hz)	Frequency band (Hz)		Resonator parameters					
	Lower limit	Upper limit	Diameter of neck (mm)	Diameter of body (mm)	Body volume (m^3)	Location (m)		
						x	y	z
145	135	155	36	100	0.0009	0.964	0.013	1.188
176.5	166.5	186.5				0	0.013	0.1
224.8	214.8	234.8				0.1	0.3	0
247.8	237.8	257.8				0.1	0	0.1

by above three models and the corresponding ER values are listed in Table III. Figure 9 shows the ER levels at each targeted mode. It can be seen that the present model leads to the best sound reduction performance among three cases.

The SPL curves corresponding to the frequency band around 228.4 Hz were chosen for deeper analyses in Fig. 10. It can be seen that Fahy and Schofield's resonance-control method maximizes the dissipated power at the targeted frequency and results in a large resistance and a 5.9 dB peak reduction in SPL. On the contrary, Fahy and Schofield's band-control approach results in a low resistance and consequently produces two pronounced peaks with similar amplitudes. The optimal resistance from the current model provides a 7.9 dB reduction in the frequency band of interest, and a broad band behavior is also observed.

It is also observed that the resistances predicted by Fahy and Schofield's resonance-control model and band-control model give, respectively, the upper and lower bounds for the optimal resistance. In the former case, the resistance is independent of the resonator volume since $Q^R Q^E \varepsilon^2 = 1$, $\varepsilon^2 = \varphi_j^2(\mathbf{r}^R) V^R / \Lambda_j V^E$ and $R_i = \rho_0 c^2 Q^E S^R \varphi_j^2(\mathbf{r}^R) / \Lambda_j V^E \omega^R$. Other models, including the present one, are volume dependent. Figure 11 shows the variation in the optimal resistances, determined using the current model and Fahy and Schofield's models, versus the body volume of the resonator for the targeted enclosure mode (1, 0, 1) at 228.4 Hz. The optimal resistance generally decreases when the volume of the resonator increases, as suggested by the present model. Fahy and Schofield's resonance-control model seems to better apply to the cases where very small resonators are used. With large resonators, Fahy and Schofield's band-control model seems to better approach the true optimal resistance value.

IV. CONCLUSIONS

Based on the analytical solution of a resonator-enclosure interaction model, the effects of internal resistance of a HR on acoustic ER within an enclosure and on the resonator design are investigated. Main conclusions are summarized as follows:

(1) The model and design methodology proposed in this paper allow maximization of the acoustic ER inside an enclosure within a frequency band around a resonance frequency. It provides a good cutoff between the peak reduction and the resonator working bandwidth. Numerical predictions are in fair agreement with experiments.
(2) When the frequency band of interest is wide enough (zone 3), which covers both the original resonance peak and the newly emerged peaks caused by the insertion of the resonator, the dissipation ability of the resonator dominates its control performance, which greatly depends on both the internal resistance of the resonator neck and the vibrating velocity of the lumped mass in the neck. While acknowledging the importance of energy dissipation, the determination of the optimal internal resistance of the resonator cannot simply be trimmed down to the maximization of energy dissipation. A narrow band of interest (zone 1), however, requires a lightly damped resonator, which promotes more energetic interaction with the enclosure.
(3) The insertion of the resonator in an acoustic enclosure enhances the modal coupling strength among the acoustic modes of the cavity. It is therefore necessary to consider a sufficient number of acoustic modes to achieve an

TABLE III. Optimal R_i and ER of three different models for the first four nonzero modes of the enclosure.

Natural frequency (Hz)	Current model		Fahy and Schofield's model			
			Resonance control		Band control	
	Optimal R_i (mks Rayls)	ER (dB)	Optimal R_i (mks Rayls)	ER (dB)	Optimal R_i (mks Rayls)	ER (dB)
145	10	2	12.7	2	1.25	0.9
176.5	6.4	3.9	13.7	3.2	0.95	1.3
224.8	5.93	5.4	19.94	3.4	1.1	2.9
247.8	3.52	5.5	11.39	3.7	0.65	3.6

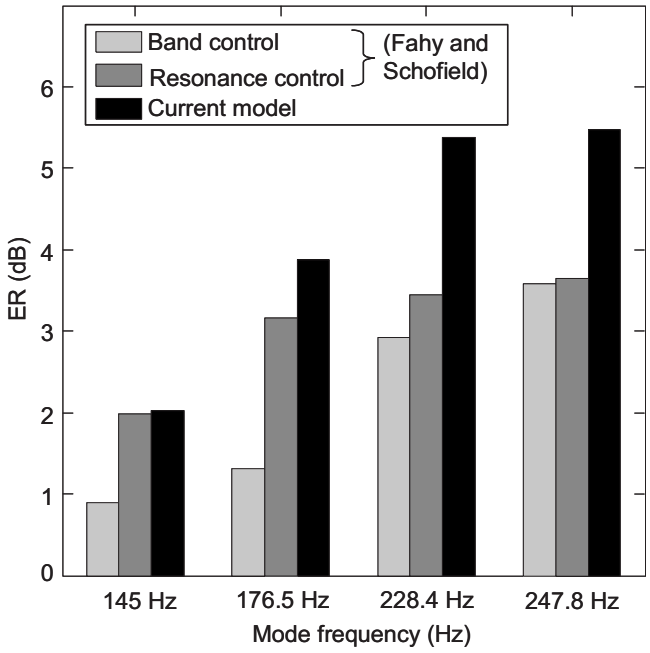


FIG. 9. Comparison of different models in terms of ER.

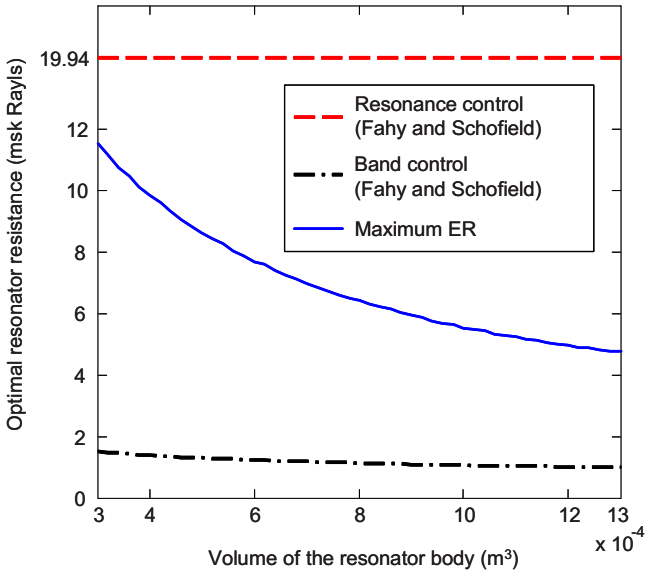


FIG. 11. (Color online) Variation in optimal resonator resistance with respect to the body volume of the resonator for the targeted enclosure mode (1, 0, 1) at 228.4 Hz.

optimal design of the resonator. This becomes increasingly important when the frequency band of interest is large.

(4) Compared with the model proposed in this paper, the two models provided by Fahy and Schofield are found to provide the upper and lower bounds of the optimal resistance. The applicability of the two models depends on the volume of the resonators.

ACKNOWLEDGMENTS

The authors wish to acknowledge a grant from Research Grants Council of Hong Kong Special Administrative Region, China (Project No.PolyU 5137/06E) and support by the Central Research Grant of The Hong Kong Polytechnic University through Grant No.G-YG19.

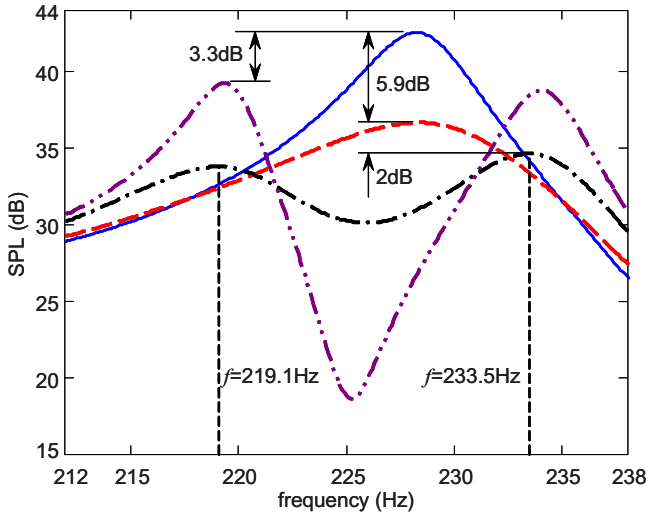


FIG. 10. (Color online) Predicted SPLs at (0.816, 0.07, 1.028) m: — without resonator; – – with resonator, R_i=19.94 mks Rayls from Fahy and Schofield's resonance-control model; —··— with resonator, R_i=1.1 mks Rayls from Fahy and Schofield' band-control model; and —·— with resonator, R_i=5.93 mks Rayls from current model.

[1]S. J. Estève and M. E. Johnson, "Reduction of sound transmission into a circular cylindrical shell using distributed vibration absorbers and Helmholtz resonators," J. Acoust. Soc. Am. **112**, 2840–2848 (2002).
[2]S. H. Seo and Y. H. Kim, "Silencer design by using array resonators for low-frequency band noise reduction," J. Acoust. Soc. Am. **118**, 2332–2338 (2005).
[3]S. R. Kim, Y. H. Kim, and J. H. Jang, "A theoretical model to predict the low-frequency sound absorption of a Helmholtz resonator array (L)," J. Acoust. Soc. Am. **119**, 1933–1936 (2006).
[4]N. Sugimoto, M. Masuda, and T. Hashiguchi, "Frequency response of nonlinear oscillations of air column in a tube with an array of Helmholtz resonators," J. Acoust. Soc. Am. **114**, 1772–1784 (2003).
[5]T. Starecki, "Loss-improved electroacoustical modeling of small Helmholtz resonators," J. Acoust. Soc. Am. **122**, 2118–2123 (2007).
[6]F. Liu, A. Phipps, S. Horowitz, K. Ngo, L. Cattafesta, T. Nishida, and M. Sheplak, "Acoustic energy harvesting using an electromechanical Helmholtz resonator," J. Acoust. Soc. Am. **123**, 1983–1990 (2008).
[7]A. Selamet and I. Lee, "Helmholtz resonator with extended neck," J. Acoust. Soc. Am. **113**, 1975–1985 (2003).
[8]A. Selamet, M. B. Xu, I. J. Lee, and N. T. Huff, "Helmholtz resonator lined with absorbing material," J. Acoust. Soc. Am. **117**, 725–733 (2005).
[9]F. Liu, S. Horowitz, T. Nishida, L. Cattafesta, and M. Sheplak, "A multiple degree of freedom electromechanical Helmholtz resonator," J. Acoust. Soc. Am. **122**, 291–301 (2007).
[10]F. J. Van Leeuwen, "The damping of eigen-tones in small rooms by Helmholtz resonators," European Broadcasting Union Review, A-Technical **62**, 155–161 (1960).
[11]F. J. Fahy and C. Schofield, "A note on the interaction between a Helmholtz resonator and an acoustic mode of an enclosure," J. Sound Vib. **72**, 365–378 (1980).
[12]W. V. Slaton and J. C. H. Zeegers, "Acoustic power measurements of a damped aeroacoustically driven resonator," J. Acoust. Soc. Am. **118**, 83–91 (2005).
[13]S. Griffin, S. A. Lane, and S. Huybrechts, "Coupled Helmholtz resonators for acoustic attenuation," J. Vibr. Acoust. **123**, 11–17 (2001).
[14]A. Cummings, "The effects of a resonator array on the sound field in a cavity," J. Sound Vib. **154**, 25–44 (1992).
[15]D. Li and L. Cheng, "Acoustically coupled model of an enclosure and a Helmholtz resonator array," J. Sound Vib. **305**, 272–288 (2007).
[16]A. D. Pierce, *Acoustics: An Introduction to Its Physical Principles and Applications* (Acoustical Society of America, New York, 1989).

A logistic prediction model for individual allowable noise levels

Kenji Furihata[a)]
Department of Electrical and Electronic Engineering, Faculty of Engineering, Shinshu University, 4-17-1 Wakasato, Nagano 380-8553, Japan

(Received 31 October 2007; revised 9 August 2008; accepted 28 September 2008)

Annoyance to noise is probably a good measure of the potential for complaint and community action. Each individual's degree of annoyance to noise cannot be accurately predicted from conventional laboratory studies and social surveys. Therefore, a logistic prediction model for individual allowable noise levels has been developed. In a previous paper [K. Furihata *et al.*, Acta Acust. Acust. **93**, 73–83 (2007)], an annoyance scale using the most frequently used annoyance ratings related to noise for community noise assessment in Japan was constructed. The dose-response relationships were obtained by actually listening to sounds in a field situation (1474 subjects) carried out at 14 metropolitan cities in Japan. The logistic prediction model was developed using the logistic regression parameters estimated from each cumulative percentage curve of seven annoyance scale scores based on all data ($n=2940$). To verify the hypothesis, individual relationships between annoyance and $L_{Aeq,\ (5\ min)}$ for 24 normal-hearing subjects were constructed using a laboratory experiment. The main conclusion drawn from the results is that if at least one dose-response relation is obtained from each subject, the model can predict whether a sound is annoying or not from its $L_{Aeq,(5\ min)}$ value. Moreover, validation of the model is needed in a field situation. © *2008 Acoustical Society of America.* [DOI: 10.1121/1.3003080]

PACS number(s): 43.50.Qp, 43.50.Ba [BSF] Pages: 3544–3560

I. INTRODUCTION

The effects of noise on people can be categorized as follows:

(a) subjective effects of annoyance, nuisance, and dissatisfaction;
(b) interference with activities such as speech, sleep, and learning; and
(c) psychological and physiological effects such as fear and startle responses, stress, and hearing loss.

The levels associated with environmental noise, in almost every case, produce effects only in the first two categories. Workers in industrial plants can experience noise in the last category. Based on attitude surveys used for measuring the annoyance felt in a community for noises intruding into homes or affecting outdoor activity areas, the main causes for annoyance are interference with speech, radio and television, house vibrations, and interference with sleep and rest.

The noise limits and environmental guidelines specify physical energy-equivalent sound pressure levels: the average energy-equivalent level of the *A*-weighted sound over a period $T(L_{Aeq,T}[\mathrm{dB}])$, and the noise exposure metrics day-night level (DNL) and day-evening-night level. Currently sound measurement is usually done using sound pressure level meters. Miedema and Vos[1] presented synthesis curves for the relationship between DNL and percentage highly annoyed for three transportation noise sources. They were derived from 45 surveys with a total of 58 065 respondents. A difference between sources was found for aircraft, road traffic, and railway noise. The recommended limit values (WHO guidelines for community noise) typically correspond to a noise level at which about 10%–15% (those most sensitive to noise) state that they are seriously annoyed by the noise. What do the recommended limit values mean? The limit values provide the basis for the authorities' assessment of noise pollution. The limit values are only a guide and can be relaxed or tightened in specific cases if there are special circumstances to justify this. Generally speaking, the concepts of noise levels are only understood by key people such as noise control officers, acoustical consultants, and regulatory officers. However, to judge "acceptable" noise levels, anyone interested in housing (residents, buyers, builders, and researchers) will need to understand the significance of such noise levels to make housing more comfortable and individually suitable.

A handful of researchers have begun to use true annoyance modeling by introducing computer assisted models such as neural networks or Bayesian networks. In previous work, Botteldooren and Lercher[2] focused on fuzzy rule based models to account for both the vagueness in concepts involved and uncertainty in relations between them. Although the models mentioned above try to model noise annoyance for a small group, there is still none of predicting the reaction of an individual to noise exposure. Muer *et al.*[3] proposed a model for noise annoyance based on notice events that follow a completely different approach. The model is based on the difference between the intruding sound and the sum of the background noise level and the noise produced by the individual, and compares this to the threshold for noticing a sound. This threshold depends on the sensitivity, alertness, and habituation of the individual. Factors related to the noise event are also taken into account. This mathematical model

a)Electronic-mail: kennfur@shinshu-u.ac.jp

 © 2008 Acoustical Society of America

is useful to understand the great variability in annoyance reported in annoyance studies from persons who are equally exposed to noise. Results from the model were compared with a field experiment. The correlation between experimental results and predictions by a model purely based on L_{Aeq} was 70.1%. The correlation with the proposed model was 73.8%. General correlation improves only slightly.

$L_{Aeq,T}$ [dB] supplemented with additional acoustical indicators is strongly felt; a model for such a new composite noise exposure indicator should be built, and then utilize the combination as one explanatory single variable for a new sample. Therefore, the present paper focuses on the development of a logistic prediction model for individual allowable noise levels.

This paper is organized as follows. Section II describes the collection of data and the analysis results for annoyance to noise obtained by a field-listening survey carried out at 14 metropolitan cities in Japan.[4–7] Section III develops a logistic prediction model fitted to the noise annoyance data. To verify the hypothesis, Sec. IV describes a laboratory experiment that is performed to assess noise annoyance in a realistic setting, because in a field situation it is difficult to construct individual relationships between annoyance scale scores and $L_{Aeq,\ (5\ min)}$ values from 25 to 80 dB. One laboratory procedure uses an adjustable playback level and annoyance matching. Subjects adjust the playback level until the annoyance level presented matches individual subjective impressions. After presentation of both a visual stimulus and an annoyance level, their main task is to respond to the following request: Please adjust the volume to match your image of the present annoyance level. In the other laboratory procedure for annoyance scaling, their main task is to respond after each stimulus presentation to the following question: How annoying would you find the noise you just listened to for 5 min if you were exposed to it at home regularly? The results are given in Sec. V, with a discussion and concluding remarks in Secs. VI and VII, respectively.

II. DATA COLLECTION AND ANALYSIS RESULTS FOR ANNOYANCE TO NOISE

A. Development of a seven-point annoyance scale

First, an annoyance scale[4–7] with the aid of words to represent an individual's annoyance level caused by various kinds of noise sources evaluated by residents in and around Nagano city was developed. These annoyance ratings were elicited from a listening experiment where the subjects listened to various kinds of noise sources for 5 min in or near their houses. As the equivalent continuous *A*-weighted sound pressure level ($L_{Aeq,(5\ min)}$[dB]) was measured for each of the sounds, it became possible to link the noise level to the annoyance ratings. Therefore, the categories of the annoyance scale are determined by actually listening to sounds, and not by asking without presenting any noise stimuli at all, as is usually done.[8–10]

What types of annoyance ratings are used in and around Nagano city in Japan to represent an individual's annoyance level caused by noise exposure? First, this is the question that was central to my study. The most frequently used annoyance ratings related to noise in everyday life are effective and useful, because an easy to understand psychological scale can be provided for people of all ages. The procedure to collect the noise annoyance data used the following four tasks to evaluate various kinds of noise sources.

Task 1. Residents living in an area with a special noise source were selected.

Task 2. Each subject listened to the noise for 5 min in or near one's house, and the noise at the same place for the same time was measured.

Task 3. Immediately after listening, the experimenter asked the following: Please write your own words to describe your subjective impression to the noise you listened to for the past 5 min.

Task 4. To collect various kinds of annoyance ratings, the subjects listened to the noise (the total listening time was 15 min) indoors (windows opened and closed) and outdoors near their houses.

From the percentage of 941 rating words used by 572 residents in Nagano city for representing annoyance ratings caused by each noise source in daily life, the following were found.

(a) For noise annoyance, the most frequently used noise-rating word was "Urusai" (annoying), which was used by 73.2% of annoyance ratings (485) to describe road traffic noise sources, 63.8% of annoyance ratings (47) to describe steady noise sources (ventilating fans for air-conditioning use, air compressors and ventilators, power-driven motors, crushers and rubbing crushers of quarries for concrete use, circular saw machines, and planers for sawmill use), 52.6% of annoyance ratings (57) to describe train noise sources, and 66.7% of annoyance ratings (30) to describe other noise sources (ironworks, press machine shops, buildings under construction, and road repairing).

(b) For no annoyance, the most frequently used noise-rating word was "Kininaranai" (not annoying) [road traffic noise sources: 40.1% of no annoyance ratings (182), steady noise sources: 38.0% of no annoyance ratings (50), train noise sources: 27.4% of no annoyance ratings (62), and other noise sources: 32.1% of no annoyance ratings (28)].

As seen, the response words Urusai (annoying) and Kininaranai (not annoying) are common for the noise sources in and around Nagano city.

From the frequency of rating words representing annoyance level for each noise source, the annoyance ratings and no annoyance ratings are clustered into seven levels by frequency of use.

(c) The seven descriptors are ″Hizyôni Urusai″ (extremely annoying; 6.2% of annoyance ratings), ″Kanari Urusai″ (very annoying; 14.7% of annoyance ratings), "Urusai" (annoying; 48.0% of annoyance ratings), "Sukoshi Urusai" (somewhat annoying; 8.7% of annoyance ratings), "Amari Kininaranai" (a little annoying; 22.9% of no annoyance ratings), "Kininaranai" (not annoying; 38.1% of no annoyance ratings), and "Mattaku Kininaranai" (not

TABLE I. Cities selected, noise sources, gender, and the mean and standard deviation of age.

Cities		Noise sources	Gender		Age	
			Male	Female	Mean	S.D.
Nagano	(1982/1983/1984/1994/1995/2001/2002)	Road traffic	195	244	34.0	16.3
	(1987/1988/1994/1995)	Railway traffic	27	73	44.9	18.9
	(1987/1988/2001/2002)	Steady	24	76	33.3	18.8
	(1987/1988/2001/2002)	Other	25	75	40.9	16.0
Tokyo	(1994)	Road traffic (Yokohane highway)	18	15	24.2	17.3
	(1994)	Railway traffic (Shinkannsen)	23	10	33.5	17.9
	(1994)	Construction	20	13	39.4	15.9
	(1994)	Jet aircraft (Haneda airport)	20	16	42.5	19.5
Sapporo	(1995)	Road traffic	51	49	30.5	18.4
Aomori	(1995)	Road traffic	24	26	28.8	17.9
Morioka	(1995)	Road traffic	25	25	31.4	18.0
Fukushima	(1995)	Road traffic	25	25	36.0	19.7
Utsunomiya	(1995)	Road traffic	21	29	29.8	16.6
Kanazawa	(1997)	Road traffic	18	32	26.8	16.5
Takamatsu	(1997)	Road traffic	27	33	34.7	20.2
Hiroshima	(1997)	Road traffic	16	14	25.0	15.0
Yamaguchi	(1996)	Road traffic	11	15	38.1	19.0
Shimonoseki	(1996)	Road traffic	15	19	30.9	15.6
Fukuoka	(1996)	Road traffic	22	38	24.2	13.8
Saga	(1996)	Road traffic	19	21	27.0	17.9

annoying at all; 14.4% of no annoyance ratings). Therefore, the above seven annoyance levels were selected.

A weakness with the methodology employed by the ICBEN team[10] is the implicit assumption that it is possible to place annoyance categories on a 0–100 annoyance scale irrespective of the sound stimulus. An alternative is to employ a sound stimulus to elicit verbal descriptors, and afterwards select the descriptors that divide the annoyance scale evenly. Therefore, it should be discussed how an annoyance scale where respondents perceive truly equal-sized gradations between the points on a physical scale ($L_{Aeq,7}$[dB]) can be constructed.

B. Procedure of a field-listening survey

The data used were collected in a field-listening survey (residents gave their subjective impressions after 5 min of listening) on the effects of noise sources.[6,7] The field tests were carried out at 14 metropolitan cities in Japan as shown in Table I. These data were collected between 1982 and 2002. The total subjects were 1474 residents (626 males, and 848 females), and the total number of data was 2940. Table I shows the 14 cities selected, noise sources, gender, and the mean and standard deviation of age.

1. Cities selected

An investigation was conducted for residents in the Hokkaidô, Tôhoku, Kanto, Hokuriku, Chûgoku, Shikoku, and Kyûshû districts. Those cities with some serious noise problems were selected from the seats of the metropolitan and prefectural governments as follows: Nagano, Tokyo, Sapporo, Aomori, Morioka, Fukushima, Utsunomiya, Kanazawa, Hiroshima, Shimonoseki, Yamaguchi, Takamatsu, Fukuoka, and Saga cities.

2. Noise sources selected

The common noise sources selected in all cities were road traffic noise sources as shown in Table I. Those selected in Nagano were railway traffic, steady noise sources (industry, crushers and rubbing crushers of quarries for concrete use, circular saw machines, and planers for sawmill use), and other noise sources (press machine shops, ironwork, buildings under construction, and road repairing). Those selected in Tokyo were railway trains on the Tokaido Shinkansen line, jet aircraft taking off from and landing at Haneda airport, and construction equipment of a nearby building under construction at JR Ebisu station.

3. Actual audio-visual test

The field-listening condition over a period of 5 min for noise was controlled. In and around Nagano city, to exclude subjective variables from the field conditions as much as possible, $L_{Aeq,(5\ min)}$ (RION NL-11 or NL-14) was measured while the subjects listened to noise (the total listening time was 15 min) indoors (windows opened and closed) and outdoors near their houses.

At other 13 cities in Japan, a test was carried out at each conspicuous place selected outdoors out of the sun. Each of the subjects listened to the specific noise for a measurement time of 5 min.

4. Questionnaire

Questions used in the analyses of the present study were the following.

(1) Environmental noise was investigated using the following question: For how many years have you noticed environmental noise in your home during your lifetime?
(2) Noise sources were investigated using the following question: Which were the sources of environmental noise you have noticed in your home during your lifetime?
(3) Noise sensitivity was investigated using the following question: People experience environmental noise in different ways. Do you experience environmental noise generally as very disturbing, disturbing, not especially disturbing, not at all disturbing, or cannot say?
Noise sensitivity was determined from the answers in the following way: "Very disturbing" answers were ranked as "very sensitive," "disturbing" answers were ranked as "sensitive," "not especially disturbing" answers were ranked as "neutral," and "not disturbing at all" answers were ranked as "insensitive."
(4) Annoyance was determined by using the following scale: (I) Mattaku Kininaranai (not annoying at all), (II) Kininaranai (not annoying), (III) Amari Kininaranai (a little annoying), (IV) Sukoshi Urusai (somewhat annoying), (V) Urusai (annoying), (VI) Kanari Urusai (very annoying) category, or (VII) Hizyôni Urusai (extremely annoying).

C. Degrees of annoyance as a function of $L_{Aeq,(5\ min)}$

The contingency table between an annoyance scale using seven typical terms selected from the most frequently used terms in everyday speech and $L_{Aeq,(5\ min)}$ [dB], (1) 81.1–78.1, (2) 78.0–73.1, (3) 73.0–68.1, (4) 68.0–63.1, (5) 63.0–57.1, (6) 57.0–52.1, (7) 52.0–47.1, (8) 47.0–43.1, (9) 43.0–38.1, (10) 38.0–34.1, (11) 34.0–24.2 dB as shown in Table II, is necessary to verify whether it is an optimal contingency table.[4–7] Here "optimal" means that the combination demonstrates the most significant dependence between the variable predicted and the predictors. To solve these problems, the discrepancy of a model fitted to a set of observed data by the maximum likelihood method is evaluated by the statistic Akaike information criterion (AIC).[11,12]

Three models are examined. Model A, with the smallest AIC, to be the best contingency table having the optimal categorization of explanatory variable $L_{Aeq,(5\ min)}$ was calculated based on Eq. (1) and all the data from Table II as

$$\begin{aligned}\mathrm{AIC} &= (-2)\sum_{i}^{r}\sum_{j}^{q} n_{ij}\log(nn_{ij}/n_{i\bullet}n_{\bullet j}) + 2(r-1)(q-1)\\ &= (-2)\sum_{i}^{7}\sum_{j}^{11} n_{ij}\log(nn_{ij}/n_{i\bullet}n_{\bullet j}) + 2(7-1)(11-1)\\ &= -3017.7, \end{aligned} \tag{1}$$

where $n=\Sigma_i^7\Sigma_j^{11}n_{ij}=2940$, $n_{i\bullet}=\Sigma_j^{11}n_{ij}$, and $n_{\bullet j}=\Sigma_i^7 n_{ij}$.

In addition to reporting the results of measurements of existing environmental noise and the results of calculations of noise from projected activities, a presentation in terms of noise zones may be useful. ISO 1996-2: 1987(E) (Ref. 13) is recommended that contours indicating boundaries between zones in multiples of 5 dB be used. Reference to zones should be made by quoting the upper and lower noise limits, in decibels. For model B, with a categorization of $L_{Aeq,(5\ min)}$ (81.1–75.1, 75.0–70.1, 70.0–65.1, 65.0–60.1, 60.0–55.1, 55.0–50.1, 50.0–45.1, 45.0–40.1, 40.0–35.1, and 35.0 dB below) zoned in 5 dB steps ($q=10$), the AIC value is −3003.8.

In some cases, it may be sufficient to use a zone width of 10 dB; for model C, with a categorization of $L_{Aeq,(5\ min)}$ (81.1–75.1, 75.0–65.1, 65.0–55.1, 55.0–45.1, and 45.0 dB below) zoned in 10 dB steps ($q=5$), the AIC value is −2686.5.

Therefore, apparently, the minimum AIC estimate procedure suggests that model A as the most effective predictor should be adopted.

The interval distances between categories of each scale were estimated using the method of successive categories.[14] The data obtained by the method of successive categories may be exhibited in a frequency table $n_{i,j}$ of the form of Table II. By Pearson's formula,[14] normal deviates, $z_{i,j}$, for the centroidal points of the intervals spanned by the categories (seven annoyance ratings) in each distribution in the rows ($n_{i,j}$) of Table II may be determined. Normal deviates to the interval marks were estimated by the formula

$$z_{i,j} = (y_{(i-1),j} - y_{i,j})/(n_{i,j}/n_{\bullet,j}), \tag{2}$$

where $y_{i,j}$ and $y_{(i-1),j}$ are ordinates of the normal curve for the cumulative frequencies of the ith and $(i-1)$st categories, and for the jth $L_{Aeq,(5\ min)}$ [dB]; the extreme ordinates are taken to be zero.

First, the deviates $z_{i,j}$ were calculated from the $n_{i,j}$ in Table II based on Eq. (2) and shown in the middle of Table II. Second, for each column j in the $z_{i,j}$ array, the column mean value on the scale was computed as follows:

$$\left(\sum_j z_{i,j} - \sum_j z_{i-1,j}\right) \Big/ \sum_j . \tag{3}$$

Therefore, from the lower part of Table II, the intervals from each other column mean of the seven categories on the scale were obtained.

The Mattaku Kininaranai (not annoying at all) category was set at the mean score of 1.00. Then, the mean score of the Kininaranai (not annoying) category is 2.12. In addition, the mean score of the Amari Kininaranai (a little annoying) category is 3.18, the score of the Sukoshi Urusai (somewhat annoying) category is 4.17, the score of the Urusai (annoying) category is 5.33, the score of the Kanari Urusai (very annoying) category is 6.53, and the score of the Hizyôni Urusai (extremely annoying) category is 7.80.

Therefore, using the standardized seven-annoyance scores S_i obtained, each mean score (Annoy_j) can be computed as

TABLE II. The $n_{i,j}$ show a two-way contingency table between an annoyance scale using seven typical terms selected from the most frequently used terms in everyday speech: (I) Mattaku Kininaranai (not annoying at all), (II) Kininaranai (not annoying), (III) Amari Kininaranai (a little annoying), (IV) Sukoshi Urusai (somewhat annoying), (V) Urusai (annoying), (VI) Kanari Urusai (very annoying), and (VII) Hizyôni Urusai (extremely annoying), related to various kinds of noise sources and $L_{Aeq,(5\ min)}$: (1) 81.1–78.1, (2) 78.0–73.1, (3) 73.0–68.1, (4) 68.0–63.1, 63.0–57.1, (6) 57.0–52.1, (7) 52.0–47.1, (8) 47.0–43.1, (9) 43.0–38.1, (10) 38.0–34.1, and (11) 34.0–24.2 dB. The $z_{i,j}$ are the normal deviates to the interval marks for the centroidal points of the intervals spanned by the categories (seven annoyance ratings) based on Eq. (2). The lower part of table shows the calculation process for each category width based on Eq. (3).

		I	II	III	IV	V	VI	VII	$n_{\cdot,j}$
$n_{i,j}$	1	0	0	0	0	0	5	13	18
	2	0	0	0	4	51	90	86	231
	3	0	0	1	7	46	178	27	259
	4	0	0	7	45	244	90	13	399
	5	0	3	36	136	373	65	14	627
	6	1	13	83	212	120	24	1	454
	7	2	15	127	166	67	4	0	381
	8	6	54	104	69	16	1	0	250
	9	8	55	92	36	2	0	0	193
	10	11	25	16	6	0	0	0	58
	11	33	30	6	1	0	0	0	70
	$n_{i,\cdot}$	61	195	472	682	919	457	154	2940
$z_{i,j}$	1	0	0	0	0	0	−1.207	0.464	
	2	0	0	0	−2.473	−1.208	−0.177	1.016	
	3	0	0	−2.973	−2.154	−1.223	0.154	1.735	
	4	0	0	−2.469	−1.495	−0.182	1.110	2.236	
	5	0	−2.906	−1.892	−0.985	0.217	1.484	2.380	
	6	−3.142	−2.194	−1.214	−0.142	0.933	1.980	3.149	
	7	−2.877	−2.002	−0.856	0.256	1.363	2.642	0	
	8	−2.353	−1.178	−0.137	0.858	1.866	2.962	0	
	9	−2.140	−0.954	0.175	1.339	2.653	0	0	
	10	−1.429	−0.254	0.727	1.739	0	0	0	
	11	−0.844	0.519	1.624	2.542	0	0	0	
$\sum_j z_{i-1,j}$		$j=6-11$ −12.785	$j=5-11$ −8.969	$j=3-11$ −7.015	$j=2-9$ −4.796	$j=2-8$ 1.766	$j=1-6$ 3.344		
$\sum z_{i,j}$			$j=6-11$ −6.063	$j=5-11$ −1.573	$j=3-11$ 1.958	$j=2-9$ 4.419	$j=2-8$ 10.155	$j=1-6$ 10.981	
$\left(\sum_j z_{i,j} - \sum_j z_{i-1,j}\right) \Big/ \sum_j$			6.721/6	7.395/7	8.972/9	9.215/8	8.390/7	7.633/7	
Estimate of each category width			1.120	1.056	0.997	1.152	1.199	1.272	
Annoyance scale scores		1.00	2.12	3.18	4.17	5.33	6.53	7.80	

$$\text{Annoy}_j = \sum_{i=1}^{7} n_{i,j} S_i / n_{\bullet,j} \tag{4}$$

on the standardized annoyance scale from the $n_{i,j}$ in Table II for each column j of mean values $L_{Aeq,(5\ min)}$ [(1) 78.7, (2) 75.2,(3) 70.1, (4) 65.3, (5) 60.1, (6) 54.4, (7) 49.7, (8) 45.0, (9) 41.1, (10) 36.7, and (11) 31.5 dB]. Last, a simple regression analysis to obtain the relationship between annoyance reaction and $L_{Aeq,(5\ min)}$ is used. The statistical analyses were employed using a statistical data management software, SPSS® version 13.0J.

Figure 1 shows the relationship between the standardized annoyance scale score (Annoy) and $L_{Aeq,(5\ min)}$. It can be seen that the seven descriptors mark roughly equal-sized intervals. The regression line is also shown in Fig. 1. The equation of the regression line is

$$\text{Annoy} = 0.112 L_{Aeq\ (5\ min)} - 1.654. \tag{5}$$

The coefficient of determination is $R^2 = 0.651$. Therefore, it can be found that "extremely annoying" corresponds to 84.4 dB, "very annoying" corresponds to 73.1 dB, "annoying" corresponds to 62.4 dB, "somewhat annoying" corre-

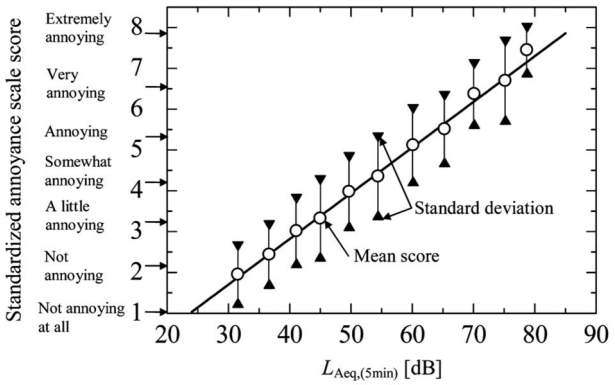


FIG. 1. Relationship between the standardized annoyance scale scores and $L_{Aeq,(5\ min)}$ for various noise sources.

sponds to 52.0 dB, "a little annoying" corresponds to 43.2 dB, "not annoying" corresponds to 33.7 dB, and "not annoying at all" corresponds to 23.7 dB.

D. Model for predicting annoyance from $L_{Aeq,(5\ min)}$ and noise sensitivity

Table III shows a two-way contingency table between self-reported noise sensitivity ratings and annoyance responses. Therefore, the data obtained by the method of successive categories may be exhibited in a frequency table of the form of Table III. From this table, the intervals from each other column mean of four categories are obtained.

The mean score of the insensitive category is set as 1.00. The mean score of the neutral category is 2.34. In addition, the mean score of the sensitive category is 3.45, and the score of the very sensitive category is 4.54. Therefore, the four descriptors are spaced at roughly equal-sized intervals.

The purpose of multiple regression analysis is to learn more about the relationship between several independent or predictor variables ($L_{Aeq,(5\ min)}$ [dB] and noise sensitivity Y_{NS}) and a dependent or criterion variable (annoyance Y_{Annoy} as shown in the last row of Table II: not annoying at all, 1.00; not annoying, 2.12; a little annoying, 3.18; somewhat annoying, 4.17; annoying, 5.33; very annoying, 6.53; and extremely annoying, 7.80).

The equation of the regression line for a multiple regression model is

$$\text{Annoy} = 0.108L_{Aeq\ (5\ min)} + 0.408Y_{NS} - 2.499, \tag{6}$$

where Y_{NS} are the noise sensitivity scores above. The coefficient of determination is $R^2=0.723$.

Figure 2 shows the relationships between the standardized annoyance scale scores obtained and $L_{Aeq,(5\ min)}$ for noise sensitivity calculated using Eq. (6) of all outdoor noise sources (see Table I). The regression lines show the standardized annoyance scale score as a function of $L_{Aeq,(5\ min)}$ for insensitive (dashed line), neutral (solid line), sensitive (dash-dotted line), and very sensitive (dotted line) people. From this figure, it can be found that noise sensitivity does not appear to increase annoyance levels only at high levels of noise exposure. Rather, it seems that noise sensitivity influences noise annoyance irrespective of the noise level. At all levels of noise sensitivity, noise-sensitive people are likely to be more annoyed than the general population, i.e., the increase in $L_{Aeq,(5\ min)}$ that gives a difference in annoyance that is the same as the difference found between slightly and highly noise-sensitive persons.

E. Development of a noise annoyance meter based on these results

An experimental noise annoyance meter, which can evaluate psychological effects on humans simultaneously, $L_{Aeq,(5\ min)}$ was developed.[6,7] After having constructed the annoyance meter, it was validated using a separate sample of residents from other typical cities in Japan. They were presented to similar noise stimuli and both the measured noise levels and associated annoyance ratings associated with the sounds were recorded. Through this process, the annoyance meter was shown to have face validity. Therefore, the noise annoyance meter could be used for combined noise exposure and noise impact rating in Japan.

For example, after 5 min, subjects responded to the following question: Can you determine whether the noise is over or under the allowable threshold (or translate decibel limits into annoyance limits)? Please answer numerically an index value of L_{Aeq} to maintain your lifestyle and the condition of your health. From the results, it can be found that the cumulative percentage of the allowable noise levels caused by road traffic noise sources at $L_{Aeq}=40$ dB corresponds to 10%, at 49 dB to 50%, and at 58 dB to 90%.

From these results, the experimental noise annoyance meter proposed here can use a common noise-rating scale for the degree of psychological effects on different subjects due to noise sources at seven districts investigated in Japan. It gives insight into improving building construction and design of more comfortable buildings for residents.

III. A LOGISTIC PREDICTION MODEL FOR NOISE ANNOYANCE

A. Psychometric function

For outdoor environmental noise, the decibel levels are typically normally distributed, and the underlying sound pressures have a log-normal distribution. In psychophysical studies, the psychometric function is used to model the relation between physical stimulus intensity and the observer's ability to detect or discriminate between stimuli of different intensities.[15] A common way of characterizing the sensitivity of a subject is the (inverse) slope of the psychometric function at the threshold location. As pointed out by Hall,[16] the underlying distributions of signal and noise for many psychometric tasks can be assumed to be Gaussian with mean μ and variance σ^2, so that the psychometric function is cumulatively normal in form.[17] Such a cumulative normal curve can be approximated by a logistic function such as[18,19]

$$P(L) = \alpha + (1-\alpha)\frac{1}{1+e^{-(L-M)/S}}, \tag{7}$$

where $P(L)$ is the probability of a positive response at stimulus level $L=L_{Aeq,(5\ min)}$ [dB], α is the false alarm probability

TABLE III. The $n_{i,j}$ show a two-way contingency table between self-reported noise sensitivity ratings: (I) insensitive, (II) neutral, (III) sensitive, and (IV) very sensitive; and the annoyance scale: (1) Mattaku Kininaranai (not annoying at all), (2) Kininaranai (not annoying), (3) Amari Kininaranai (a little annoying), (4) Sukoshi Urusai (somewhat annoying), (5) Urusai (annoying), (6) Kanari Urusai (very annoying), and (7) Hizyôni Urusai (extremely annoying). Each deviate z_{ij} obtained by Eq. (2), the interval distances between categories of noise sensitivity ratings, and the noise sensitivity scale scores estimated in the method of successive categories.

		I	II	III	IV	$n_{\cdot j}$
$n_{i,j}$	1	3	46	50	55	154
	2	21	215	165	56	457
	3	113	464	263	79	919
	4	120	334	196	32	682
	5	149	238	68	17	472
	6	62	104	27	2	195
	7	32	20	9	0	61
	$n_{i,\cdot}$	500	1421	778	241	2940
	Percentage (%)	17.0	48.3	26.5	8.2	100.0
$z_{i,j}$	1	−2.431	−1.036	−0.050	1.045	
	2	−2.098	−0.642	0.542	1.657	
	3	−1.655	−0.346	0.773	1.826	
	4	−1.470	−0.215	0.926	2.089	
	5	−1.126	0.185	1.273	2.196	
	6	−1.122	0.234	1.478	2.657	
	7	−0.759	0.511	1.563	0.000	
	$\sum_j z_{i-1,j}$	$j=1-7$	$j=1-7$	$j=1-6$		
		−10.660	−1.310	4.941		
	$\sum_j z_{i,j}$		$j=1-7$	$j=1-7$	$j=1-6$	
			−1.310	6.504	11.469	
	$\left(\sum_j z_{i,j} - \sum_j z_{i-1,j}\right) \Big/ \sum_j$		$\frac{9.351}{7}$	$\frac{7.813}{7}$	$\frac{6.528}{6}$	
Estimate of each category width			1.336	1.116	1.088	
Noise sensitivity scale scores		1.00	2.34	3.45	4.54	

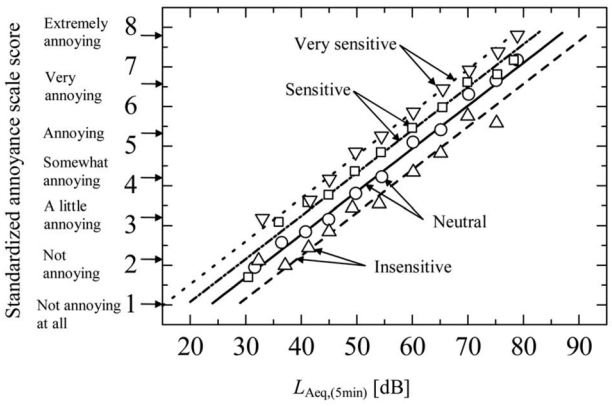


FIG. 2. Comparison of regression lines giving the standardized annoyance scale scores as a function of $L_{\mathrm{Aeq,(5\ min)}}$ for insensitive (△), neutral (○), sensitive (□), and very sensitive (▽) noise sensitivity groups.

(of a positive response at a very low stimulus level),[20] M is the midpoint of the psychometric function, and S is the spread parameter that affects the slope of the function. The four sampling points for estimating parameters in the form of Eq. (7) are[21]

$$L_{12} = M - 2S, \quad L_{27} = M - S, \quad L_{73} = M + S, \quad L_{88} = M + 2S, \tag{8}$$

where L_p is a stimulus level with the cumulative $p\%$ of annoyance responses. The responses from these four sets of stimuli are then used in nonlinear regression to estimate the parameters of the psychometric function of Eq. (7).[22]

B. Logistic functions based on the data of on-the-spot investigations

First, Table IVa shows the percentages of $(n_{i,j}/n_{\bullet,j})$ as shown in Table II. However, because there are some small data sets $(n_{\bullet,j} < 100)$, $j=1$ and 2, and 10 and 11 were

TABLE IV. The cumulative percentage of annoyance responses using results to those previously obtained (see Table II). (a) Percentages of $(n_{i,j}/n_{\cdot,j})$ as shown in Table II. However, because there are some small data sets $(n_{\cdot,j}<100)$, $j=1$ and 2, and 10 and 11 were summed. (b) Relationships between cumulative percentages from $i=7$ to 1 of $\Sigma_i(n_{i,j}/n_{\cdot,j})$ and the upper $L_{Aeq,(5\ min)}$ levels of each range.

	Annoyance scale							
	Japanese English	Mattaku Kininaranai Not annoying at all	Kininaranai Not annoying	Amari Kininaranai A little annoying	Sukoshi Urusai Somewhat annoying	Urusai Annoying	Kanari Urusai Very annoying	Hizyôni Urusai Extremely annoying
Upper $L_{Aeq,(5\ min)}$ [dB] of each range	81.1	0.00	0.00	0.00	1.61	20.48	38.15	39.76
	73.0	0.00	0.00	0.39	2.70	17.76	68.73	10.42
	68.0	0.00	0.00	1.75	11.28	61.15	22.56	3.26
	63.0	0.00	0.48	5.74	21.69	59.49	10.37	2.23
	57.0	0.22	2.86	18.28	46.70	26.43	5.29	0.22
	52.0	0.52	3.94	33.33	43.57	17.59	1.05	0.00
	47.0	2.40	21.60	41.60	27.60	6.40	0.40	0.00
	43.0	4.14	28.50	47.67	18.65	1.04	0.00	0.00
	38.0	34.37	42.97	17.19	5.47	0.00	0.00	0.00
Upper $L_{Aeq,(5\ min)}$ [dB] of each range	81.1	100.00	100.00	100.00	100.00	98.39	77.91	39.76
	73.0	100.00	100.00	100.00	99.61	96.91	79.15	10.42
	68.0	100.00	100.00	100.00	98.25	86.97	25.81	3.26
	63.0	100.00	100.00	99.52	93.78	72.09	12.60	2.23
	57.0	100.00	99.78	96.92	78.63	31.94	5.51	0.22
	52.0	100.00	99.48	95.54	62.20	18.64	1.05	0.00
	47.0	100.00	97.60	76.00	34.40	6.80	0.40	0.00
	43.0	100.00	95.85	67.36	19.69	1.04	0.00	0.00
	38.0	100.00	65.63	22.66	5.47	0.00	0.00	0.00

summed. Table IVb shows the relationships between the cumulative percentages from $i=7$ to 1 of $\Sigma_i(n_{i,j}/n_{\cdot,j})$ and the upper $L_{Aeq,(5\ min)}$ levels of each range. The cumulative percentages determine placement among a group of subjects. For example, (a) if each subject responded to extremely annoying, very annoying, and annoying at $L_{Aeq,(5\ min)}=81.1$ dB, each cumulative percentage is 39.76%, 77.91%, and 98.39%, respectively. (b) If each subject responded to extremely annoying, very annoying, and annoying at $L_{Aeq,(5\ min)}=73.0$ dB, each cumulative percentage is 10.42%, 79.15%, and 96.91%, respectively. (c) If each subject responded to extremely annoying, very annoying, and annoying at $L_{Aeq,(5\ min)}=68.0$ dB, each cumulative percentage is 3.26%, 25.81%, and 86.97%, respectively. Therefore, converting raw data into cumulative percentages allows for meaningful comparisons. The logistic distribution has a cumulative distribution function. The logistic model is a useful alternative to the normal model. Logistic regression and discrimination are based on converting predictions to probabilities through the logistic function. The data of each cumulative function are formed to simulate each calculated cumulative percentage of the annoyance responses using Eq. (7) and are shown in Fig. 3. As seen from Fig. 3, (a) the different percent between a double dot-dashed curve with symbol + (called the not annoying curve) and 100% means the percentage of not annoying at all responses at the $L_{Aeq,(5\ min)}$ level. (b) The different percent between the double dot-dashed curve and a dot-dashed curve with symbol ◇ (called the a little annoying curve) represents the percentage of not annoying responses. (c) The different percent between the dot-dashed curve and a dotted curve with symbol ∇ (called the somewhat annoying curve) represents the percentage of a little annoying responses. (d) The different percent between the dotted curve and a solid curve with symbol ○ (called the annoying curve) represents the percentage of somewhat annoying responses. (e) The different percent between the solid curve and a dashed curve with symbol △ (called the very annoying curve) represents the percentage of annoying responses. (f) The different percent between the dashed curve and a boundary curve by hatching with symbol □ (called the extremely annoying curve) represents the per-

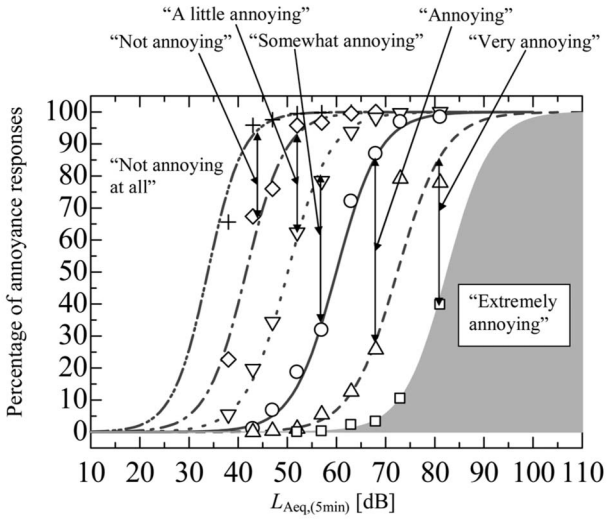


FIG. 3. Relationships between each cumulative percentage of annoyance responses and $L_{Aeq,(5\ min)}$ for various noise sources. The curves are the calculated cumulative percentage of annoyance responses using Eq. (7).

TABLE V. The logistic regression parameters estimated from each cumulative percentage curve shown in Table IVb based on the psychometric function of Eq. (7).

	False alarm probability a	Midpoint M	Spread parameter S	Explained variance Pseudo-R^2
Not annoying curve	0	33.83	3.60	0.9575
A little annoying curve	0	41.63	4.02	0.9711
Somewhat annoying curve	0	50.11	4.37	0.9946
Annoying curve	0	59.96	4.43	0.9763
Very annoying curve	0	72.41	4.77	0.9716
Extrmely annoying curve	0	82.56	4.46	0.9695

centage of very annoying responses. (g) The different percent between the boundary curve by hatching and 0% represents the percentage of extremely annoying responses. Table V shows the logistic regression parameters estimated from each cumulative percentage curve shown in Table IVb based on the psychometric function of Eq. (7). A relevant measurement of explained variance using nonparametric statistics is Nagelkerke pseudo $-R^2$.[23]

The results are summarized in Fig. 3. (a) The cumulative percentage of not annoying (double dot-dashed) curve increases monotonically. For logistic regression parameters estimated the midpoint M to be 33.8 dB and the spread S to be 3.6 dB. It can be seen that the midpoint 33.8 dB is very similar to the noise rating scale using Eq. (5) where not annoying corresponds to 33.7 dB. (b) From the a little annoying (dot-dashed) curve, the midpoint M is 41.6 dB and the spread S is 4.0 dB. It can be seen that the midpoint 41.6 dB is similar to the noise-rating scale using Eq. (5) where a little annoying corresponds to 43.2 dB. (c) From the somewhat annoying (dotted) curve, the midpoint M is 50.1 dB and the spread S is 4.4 dB. It can be seen that the midpoint 50.1 dB is similar to the noise-rating scale using Eq. (5) where somewhat annoying corresponds to 52.0 dB. (d) From the annoying (solid) curve, the midpoint M is 60.0 dB and the spread S is 4.4 dB. It can be seen that the midpoint 60.0 dB is similar to the noise-rating scale using Eq. (5) where annoying corresponds to 62.4 dB. (e) From the very annoying (dashed) curve, the midpoint M is 72.4 dB and the spread S is 4.8 dB. It can be seen that the midpoint 72.4 dB is similar to the noise-rating scale using Eq. (5) where very annoying corresponds to 73.1 dB. (f) From the extremely (boundary curve by hatching) curve, the midpoint

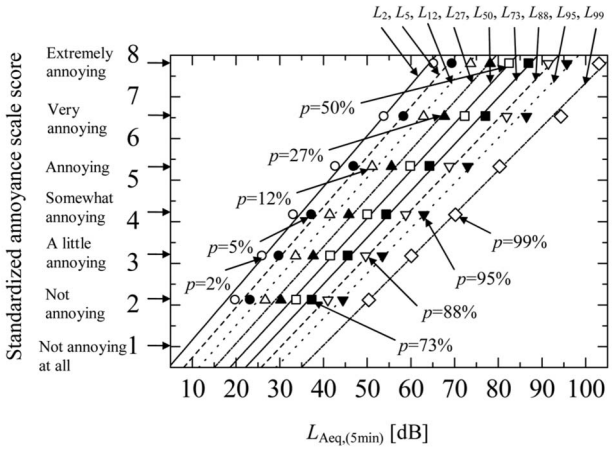


FIG. 4. Relationships between the standardized annoyance scale scores and $L_{Aeq,(5\ min)}$ for each stimulus level L_p with the cumulative p% (from 2% to 99%) of annoyance responses obtained by Eq. (7).

M is 82.6 dB and the spread S is 4.5 dB. It can be seen that the midpoint 82.6 dB is similar to the noise-rating scale using Eq. (5) where extremely annoying corresponds to 84.4 dB.

Second, Table VI shows the relationships between the annoyance scale scores and each stimulus level L_p with the cumulative p% from 2% to 99% including Eq. (8) of annoyance responses. The regression lines are also shown in Fig. 4. The equations of these regression lines are as follows:

$$L_2\text{: Annoy} = 0.1226L_{Aeq\ (5\ min)} - 0.0635 \quad (R^2 = 0.9940),$$

$$L_5\text{: Annoy} = 0.1205L_{Aeq\ (5\ min)} - 0.4668 \quad (R^2 = 0.9955),$$

$$L_{12}\text{: Annoy} = 0.1184L_{Aeq\ (5\ min)} - 0.8565 \quad (R^2 = 0.9966),$$

$$L_{27}\text{: Annoy} = 0.1163L_{Aeq\ (5\ min)} - 1.2489 \quad (R^2 = 0.9974),$$

$$L_{50}\text{: Annoy} = 0.1141L_{Aeq\ (5\ min)} - 1.6242 \quad (R^2 = 0.9979),$$

$$L_{73}\text{: Annoy} = 0.1121L_{Aeq\ (5\ min)} - 1.9843 \quad (R^2 = 0.9981),$$

TABLE VI. Relationships between the annoyance scale scores and $L_{Aeq,(5\ min)}$ for each stimulus level L_p with the cumulative p% from 2% to 99% including Eq. (8) of annoyance responses obtained by Eq. (7).

	$L_{Aeq,(5\ min)}$ (dB)								
	p=2%	p=5%	p=12%	p=27%	p=50%	p=73%	p=88%	p=95%	p=99%
Extremely annoying	65.2	69.4	73.7	78.1	82.6	87.0	91.4	95.7	103.0
Very annoying	53.9	58.4	62.9	67.7	72.4	77.2	81.9	86.4	94.3
Annoying	42.7	46.9	51.1	55.6	60.0	64.4	68.8	73.0	80.3
somewhat annoying	33.1	37.3	41.4	45.8	50.1	54.5	58.8	63.0	70.2
A little annoying	26.0	29.8	33.6	37.6	41.6	45.6	49.6	53.5	60.1
Not annoying	19.8	23.2	26.7	30.2	33.8	37.4	41.0	44.4	50.4

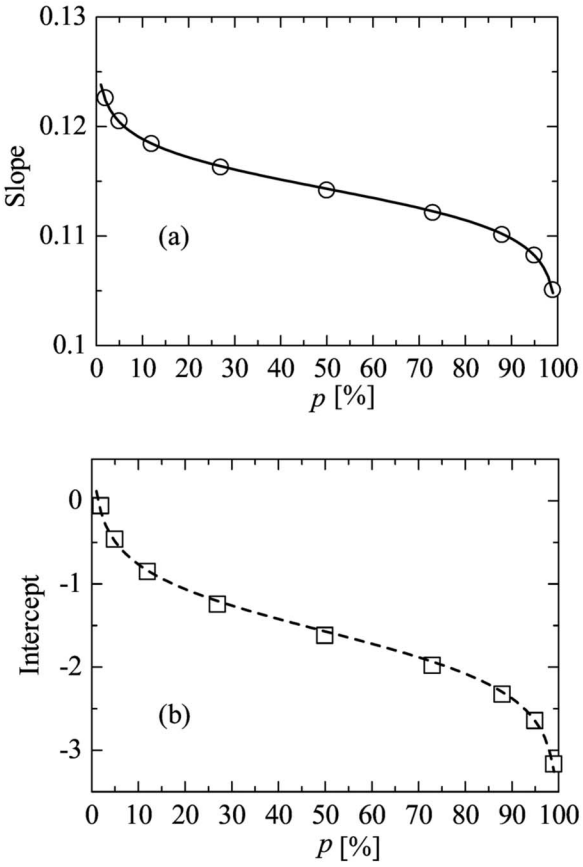


FIG. 5. (a) The relationship between the slopes and the cumulative $p\%$ of annoyance responses, and (b) the relationship between the intercepts and the cumulative $p\%$.

$$L_{88}\text{: Annoy} = 0.1101L_{A\text{eq (5 min)}} - 2.3309 \quad (R^2 = 0.9981),$$

$$L_{95}\text{: Annoy} = 0.1082L_{A\text{eq (5 min)}} - 2.6485 \quad (R^2 = 0.9978),$$

$$L_{99}\text{: Annoy} = 0.1051L_{A\text{eq (5 min)}} - 3.1703 \quad (R^2 = 0.9968), \tag{9}$$

where R^2 is the coefficient of determination.

It can be seen that that L_p does not appear to increase annoyance levels only at high levels of noise exposure. Rather, it seems that L_p influences noise annoyance irrespective of noise level. However, the slopes appear to decrease from 0.1226 to 0.1051. The relationship between the slopes and the cumulative $p\%$ of annoyance responses is

$$\text{Slope} = -0.002\,07 \ln\{p\,\%/(100 - p\,\%)\} + 0.1143 \quad (R^2 = 0.9993). \tag{10}$$

The relationship between the intercepts and the cumulative $p\%$ of annoyance responses is

$$\text{Intercept} = -0.366\,96 \ln\{p\,\%/(100 - p\,\%)\} - 1.5706 \quad (R^2 = 0.9974). \tag{11}$$

Figure 5(a) shows the relation between the slope and the cumulative $p\%$ of annoyance responses using Eq. (10), and (b) the relation between the intercept and $p\%$ using Eq. (11).

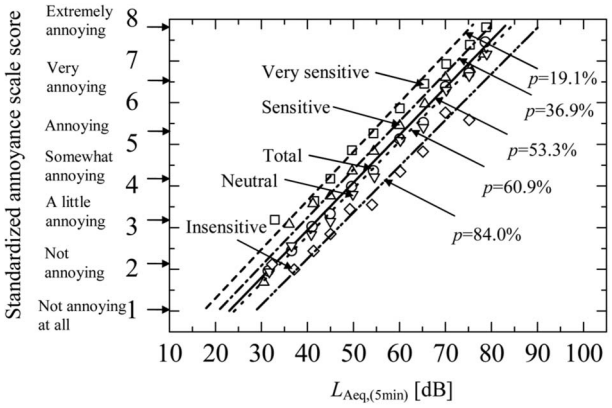


FIG. 6. Comparison of the $L_{A\text{eq},(5\text{ min})}$ annoyance relationships for noise sensitivity as shown in Fig. 2 and the regression lines for L_p as shown in Fig. 4.

Figure 6 shows the comparison of the $L_{A\text{eq, (5 min)}}$ annoyance relationships for noise sensitivity as shown in Fig. 2 and the regression lines for L_p as shown in Fig. 4. From Fig. 6, it can be found that (a) the $L_{A\text{eq, (5 min)}}$ annoyance relationship with symbol □ for very sensitive corresponds to the regression line of $p=19.1\%$, (b) the $L_{A\text{eq, (5 min)}}$ annoyance relationship with symbol △ for sensitive corresponds to the regression line of $p=36.9\%$, (c) the $L_{A\text{eq, (5 min)}}$ annoyance relationship with symbol ○ for the total corresponds to the regression line of $p=53.3\%$, (d) the $L_{A\text{eq, (5 min)}}$ annoyance relationship with symbol ▽ for neutral corresponds to the regression line of $p=60.9\%$, and (e) the $L_{A\text{eq, (5 min)}}$ annoyance relationship with symbol ◇ for insensitive corresponds to the regression line of $p=84.0\%$.

Therefore, the best way to predict one's noise sensitivity may be thought to measure one's cumulative $p\%$ of annoyance response.

C. Prediction method for individual noise annoyance

The step by step procedure for obtaining individual noise annoyance scale values is given as follows.

(1) The subject listens to the noise for 5 min in or near his house, and the experimenter measures the noise at the same place for the same time.
(2) Immediately after listening, the experimenter asks the following: From this seven-point annoyance scale [(1) not annoying at all, (2) not annoying, (3) a little annoying, (4) somewhat annoying, (5) annoying, (6) very annoying, and (7) extremely annoying], please choose the annoyance level you felt due to the noise you listened to for the past 5 min.
(3) From the relationship between the annoyance level obtained and the value of $L_{A\text{eq, (5 min)}}$ measured, one's cumulative $p\%$ of annoyance responses can be calculated from Eq. (7) using the parameter values of M and S as shown in Table V. For example, if subject J (see Table VIII) chose somewhat annoying on the seven-point annoyance scale when the measured value of $L_{A\text{eq, (5 min)}}$

was 49.7 dB, the $p\%$ can be calculated from Eq. (7) using the parameter values of $M=50.11$ and $S=4.37$ (the somewhat annoying curve shown in Table V) as follows:

$$p\,\% = \frac{100}{1+\exp\{-(49.7-50.11)/4.37\}} = 47.6\,\%\,. \quad (12)$$

(4) Therefore, the regression line between the annoyance scale score (Annoy) and $L_{Aeq,\,(5\ min)}$ can be determined from the slope given by Eq. (10) and the intercept given by Eq. (11) using the $p=47.6\%$, i.e., the slope is 0.1145 using Eq. (10), and the intercept is −1.535 using Eq. (11).

(5) The relationship between Annoy and $L_{Aeq,\,(5\ min)}$ of subject J can be obtained as follows:

$$L_{47.6}\text{:Annoy} = 0.1145 L_{Aeq\ (5\ min)} - 1.535. \quad (13)$$

(6) Consequently, the $\overline{L_{Aeq,\,(5\ min)}}$ [dB] predicted from each annoyance scale score as follows:

$$\overline{L_{Aeq\ (5\ min)}} = (\text{Annoy} + 1.535)/0.1145. \quad (14)$$

(7) Concretely, it can be shown that the relationship between each score of the standardized annoyance scale (Annoy $=7.80, 6.53, 5.33, 4.17, 3.18, 2.12, 1$) and each corresponding predicted value of $L_{Aeq,\,(5\ min)}$ is (81.5, 70.4, 60.0, 49.8, 41.2, 31.9, and 22.1 dB).

(8) It can be determined whether a noise is over or under the allowable threshold, which is the middle point score (Annoy=3.68) between a little annoying (3.18) and somewhat annoying (4.17), as follows

$$\overline{L_{Aeq\ (5\ min)}} = (3.68 + 1.535)/0.1145 = 45.5\ \text{dB}. \quad (15)$$

Validation of the semantic scale is needed in a field situation. However, because a subject can only listen to noise indoors (windows opened and closed) and outdoors near one's house for undesired outdoor sounds, it is difficult to construct individual relationships between annoyance ratings and $L_{Aeq,\,(5\ min)}$ from 25 to 80 dB using a field experiment.

IV. TESTING THE MODEL USING A LABORATORY EXPERIMENT

Because a laboratory study does not take into account the different context levels, a laboratory experiment was designed to better understand the visual information of the spatial presentation of cognitive processes in laboratory conditions.

A. Stimuli and apparatus

To create a realistic setting for environmental noise, noise from undesired outdoor sounds caused by human activities was recorded by using a digital video recorder (Sony DCR-VX2000 NTSC: digital video recording with over 530 lines of horizontal resolution, 640×480 still image resolution, and pulse code modulation (PCM) stereo digital audio 16 bits, 48 kHz) and a digital audio tape (DAT) recorder (Technics SV-MD11: at a sampling rate of 48 kHz and an amplitude resolution of 16 bits) with two cardioid condenser

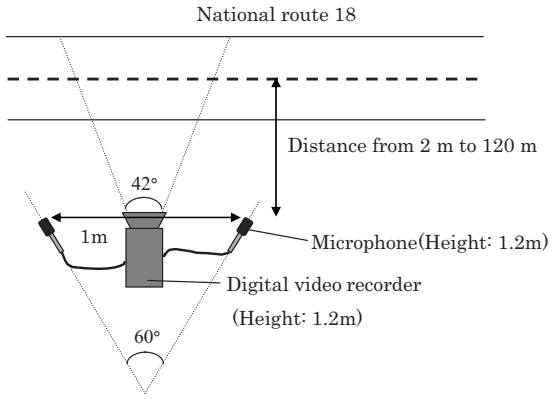


FIG. 7. Configuration of the recording apparatus.

microphones (National Ramsa WM-8150) separated by 1 m. When microphones are exposed to wind, noise is generated. For the effective reduction of wind noise, a gray foam windscreen (RION WS-02) for microphones was used. The recording level $L_{Aeq,(5\ min)}$ [dB] was measured with an integration-type sound level meter (RION NL-11). The digital video camera can be connected to a PC very easily by using a digital interface (Sony i.LINK). The recorded images and sounds were stored as 40 files on the hard disk of a personal computer. With a signal processing card, sampled sounds could be filtered and converted into analog signals.

Figure 7 shows the configuration of the above recording apparatus for noise emitted by road vehicles. The digital video recorder and microphones were located at 2, 30, 60, and 120 m from the center of a two-lane road, along a line perpendicular to the road, at approximately 1.2 m above the ground level. Information about the five kinds of noise and types of noise sources is given in the first two columns of Table VII. These noise sources can be classified as noise emitted by road vehicles, train noise, aircraft noise, steady noise, and other noise. The recording locations were Nagano, Numazu, and Tokyo. In train noise and aircraft noise for which the specific noise was single-shot type, automobile noise, sound of waves, and the sounds of birds and dogs were included in the background noise level shown in the fifth column of Table VII.

The experiment was entirely computer controlled.[24] The playback location was an anechoic room ($4\times5\times3$ m^3) at Shinshu University. Figure 8 shows the configuration of the playback apparatus in the anechoic room. Each noise was played back randomly for 5 min in stereo from two loudspeakers (ONKYO D-77 FX) placed on one side (3 m) of an equilateral triangle containing the subject being tested. At the subject's listening position the response was flat within 2.5 dB over a frequency range from 50 Hz to 7 kHz. For aircraft noise, two loudspeakers (PIONEER S-55 TSD) suspended from the ceiling were used for playback.

Guastavino and Katz[25] observed that the traditional two-channel stereo configuration is characterized as providing precise localization in a frontal image, stable with regard to head shifting, but distant from the listener and spatially poorly defined. We perceive our environment by integrating multimodal information.[26] In this experiment, therefore, to include visual impression effects based on our experience of

TABLE VII. Selected noise sources and playback levels.

Class	Sources		Distance (m)	Recording level (dB) $L_{Aeq,(5\ min)}$	Background noise level	Playback level (dB) $L_{Aeq,(5\ min)}$
Vehicles	(a) National route 18 with average flow; 128/5 min (Nagano City)					
	Large vehicles mixed at	16%	2	72.9		72.9
		24%	30	62.2		62.2
		11%	60	50.8		50.8
		13%	120	45.5		45.5, 35.5
	(b) Tomei Express with average flow; 240/5 min (Numazu City)					
	Large vehicles mixed at	32%	5	68.7		68.7
		39%	50	60.2		60.2
		32%	50	59.2		49.2
		39%	71	58.1		38.1, 28.1
Trains	(c) JR conventional	3	3	69.3	35	69.3
	limited express	2	10	65.2	34	65.2
	Local:	3	20	54.6	37	54.6
	(Nagano City)	1	50	51.1	39	41.1, 31.1
	(d) Tokaido Shinkansen:	3	5	69.8	44	59.8
	(Numazu City)	3	5	71.9	42	71.9
		3	6	70.9	41	50.9
		2	50	59.5	39	39.5, 29.5
Airplanes	(e) Haneda Airport (various jets)					
	Overhead:	3	Keihin	76.3	39	71.3
		2	Jima	62.3	38	62.3
		3	(Tokyo)	77.4	42	77.4
		3		80.1	38	80.1
	Landing in the opposite direction:					
		2		56.5	44	41.5, 31.5
		3		65.1	45	55.1
		3		62.5	44	52.5
		3		59.3	47	39.5, 29.3
Steady noise	(f) (Nagano City)					
	Air-conditioner fan (factory)		25	54.2		54.2, 34.2
	Air-compressor and fan		12	65.8		65.8, 45.8
	Stone crusher and concrete		10	74.6		74.6
	Stone crusher and polisher		34	63.9		63.9, 43.9
	Table saw		5	68.2		68.2
	Plane		8	61.5		51.5, 31.5
Other Noise	(g) (Nagano City)					
	Scrap metal crusher/collector		13	65.4		45.4
	Press machine		23	56.8		26.8
	Press machine		2	75.6		75.6
	Crane, frame assembly		16	65.2		55.2
	Concrete breaker		23	62.4		62.4
	(h) (Haneda Steel Works area) (Tokyo)					
	Metal works		3	67.3		52.3
	Grinder		5	62.0		32.0
	Press machine		5	70.8		60.8
	Press and air compressor		2	79.0		74.0
	Press and fan		5	64.9		44.9

environmental noise, a liquid crystal projector (ELMO EDP-2000: 60 in. in screen size)[27] was used. The background noise of the projector's fan was continuously present throughout the experiment at an *A*-weighted average level as low as 30 dB. For one playback condition, only one subject was tested, whose head was located at a vertex of an equilateral triangle, and the subject sat on a chair.

B. Procedure

1. Annoyance matching

Test stimuli with different noise sources accompanied by images were matched subjectively to a degree of annoyance. One of the stimuli shown in Table VII and a degree of seven-point annoyance were selected from the relationship between

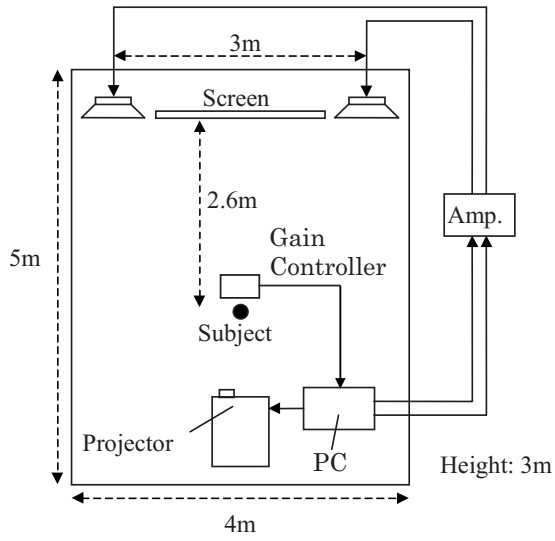


FIG. 8. Configuration of the playback apparatus in an anechoic room.

the annoyance scale score and $L_{Aeq,(5\ min)}$ shown in Fig. 1. Each subject was asked to read the instructions. Their main task was to respond to the following question: Please adjust the volume to match your image of the present degree of annoyance.

To match the playback level to the given annoyance rating, subjects adjusted the noise volume. In each trial, a stimulus and a degree of annoyance were presented in random order for 5 min. Matching was performed for 5 min based on the method of adjustment. Each subject performed this task ten times for each degree of annoyance for a total of 70 trials.

2. Annoyance scaling

To match the original noise level at the time of recording for each noise source, the playback level was adjusted to be in the range 25–80 dB at the subject's ear (without the test subject). The right-hand column of Table VII indicates the playback level $L_{Aeq,(5\ min)}$ set in this way. Because the overall noise environment from 25 to 80 dB is selected with equal probability, the playback level is different from the recording level for some sources.

Each subject was asked to read the instructions. After each stimulus presentation their main task was to respond to the following question: How annoying would you find the noise you just listened to for 5 min if you were exposed to it at home regularly? They responded by pressing one of the following buttons: (1) (not annoying at all), (2) (not annoying), (3) (a little annoying), (4) (somewhat annoying), (5) (annoying), (6) (very annoying), or (7) (extremely annoying).

Subjects performed 50 experimental trials, twice each for a total of one 100 trials.

C. Subjects

The subjects were 25 male students between 21 and 26 years of age. None of these subjects had a hearing loss larger than 15 dB (over 125–8000 Hz) in their best ear. A group of nine subjects was asked to participate in annoyance matching. The group of the remaining 15 subjects was asked to participate in annoyance scaling.

V. RESULTS

If at least one dose-response relationship is obtained from each subject, it is examined whether the logistic model can predict the individual relationships between annoyance scale scores (Annoy) and $L_{Aeq,(5\ min)}$.

Table VIII shows the relationships between annoyance scale scores and individual average energy levels (L_{Aeq} [dB]), each cumulative $p\%$ calculated from the parameters of the psychometric function of Eq. (7) shown in Table V for 24 normal-hearing subjects, and the mean $p\%$ for each subject at the far right column. For the annoyance matching method, the average energy level (L_{Aeq} [dB]) is the quantity calculated by taking ten times the common logarithm of the arithmetic average of the antilogs of one-tenth of each of the $L_{Aeq,(5\ min)}$ levels being averaged. For the annoyance scaling method, the average energy level (L_{Aeq} [dB]) of each $L_{Aeq,(5\ min)}$ that was reported by pressing one of the buttons from (2) not annoying to (6) very annoying is described. For extremely annoying and not annoying at all, the data are left out in this table because the number of responses was very small.

From Table VIII, it can be seen that extremely annoying corresponds to the L_{Aeq} range from 78.7 to 83.7 dB (the annoyance matching method only), very annoying corresponds to the range from 68.7 to 80.7 dB, annoying corresponds to the range from 58.2 to 71.0 dB, somewhat annoying corresponds to the range from 44.3 to 67.2 dB, a little annoying corresponds to the range from 34.0 to 56.9 dB, and not annoying corresponds to the range from 28.7 to 44.0 dB.

From the relationships between each annoyance level and L_{Aeq}, Table VIII shows the cumulative $p\%$ of annoyance response predicted below.

For example, subject A matched a little annoying to 35.2 dB. It can be determined that the cumulative $p\%$ can be calculated from Eq. (7) using the parameter values of $M=41.63$ and $S=4.02$ (the a little annoying curve shown in Table V) as follows:

$$p\,\% = \frac{100}{1+\exp\{-(35.2-41.63)/4.02\}} = 16.8\,\%\,. \qquad (16)$$

Therefore, the regression line between annoyance scale score (Annoy) and $L_{Aeq,(5\ min)}$ can be determined from the slope given by Eq. (10) and the intercept given by Eq. (11) using the $p=47.6\%$, i.e., the slope is 0.1176 using Eq. (10), and the intercept is −0.9836 using Eq. (11). The relationship between Annoy and L_{Aeq} of the subject can be obtained as follows:

$$L_{16.8}\text{:Annoy} = 0.1176L_{Aeq} - 0.9836,$$

$$\overline{L_{Aeq}} = (\text{Annoy} + 0.9836)/0.1176. \qquad (17)$$

Concretely, each score of the standardized annoyance scale: (Annoy=7.80, 6.53, 5.33, 4.17, 3.18, 2.12, 1)

TABLE VIII. Relationships between annoyance scale scores and individual average energy levels (L_{Aeq}[dB]), each cumulative p% calculated from the parameters of the psychometric function of Eq. (7) shown in Table V for 24 normal-hearing subjects, and mean p% for each subject at the far right column.

		Annoyance						
Subjects		Extremely annoying	Very annoying	Annoying	Somewhat annoying	A little annoying	Not annoying	Mean p%
A	L_{Aeq}[dB]	79.3	68.8	58.2	44.7	35.2	31.0	
	p	32.5%	31.9%	40.2%	22.5%	16.8%	31.3%	27.9%
B	L_{Aeq}[dB]	78.7	68.7	58.3	47.8	37.1	32.6	
	p	29.6%	31.5%	40.7%	37.1%	24.5%	41.6%	33.5%
C	L_{Aeq}[dB]	82.3	72.7	61.7	51.8	41.0	33.4	
	p	48.6%	51.5%	59.7%	59.6%	46.1%	47.0%	54.2%
D	L_{Aeq}[dB]	80.1	71.5	62.5	52.5	44.6	38.4	
	p	36.6%	45.3%	64.0%	63.3%	67.7%	78.1%	60.1%
E	L_{Aeq}[dB]	83.7	74.3	62.2	44.3	34.0	28.7	
	p	56.4%	59.8%	62.4%	20.9%	13.0%	19.4%	39.0%
F	L_{Aeq}[dB]	82.0	71.8	63.9	56.3	41.6	35.9	
	p	46.9%	46.8%	70.9%	80.5%	49.8%	64.0%	62.0%
G	L_{Aeq}[dB]	83.3	75.3	64.0	53.4	40.9	30.5	
	p	54.2%	64.7%	71.4%	68.0%	45.5%	28.4%	62.4%
H	L_{Aeq}[dB]	80.6	73.3	63.6	55.3	46.0	38.6	
	p	39.2%	54.7%	69.5%	76.6%	74.8%	79.0%	68.9%
I	L_{Aeq}[dB]	81.5	73.2	65.5	53.2	45.0	38.2	
	p	44.1%	54.1%	77.8%	67.0%	69.8%	77.1%	67.2%
J	L_{Aeq}[dB]		70.3	58.7	49.7	40.7	32.1	
	p		39.1%	42.9%	47.6%	44.2%	38.2%	42.4%
K	L_{Aeq}[dB]		71.5	63.7	49.6	42.1	36.1	
	p		45.3%	70.0%	47.1%	52.9%	65.3%	56.1%
L	L_{Aeq}[dB]		70.8	64.5	55.7	44.4	38.4	
	p		41.6%	73.6%	78.2%	66.6%	78.1%	67.6%
M	L_{Aeq}[dB]		71.7	65.4	57.8	45.6	38.6	
	p		46.3%	77.4%	85.3%	72.8%	79.0%	72.2%
N	L_{Aeq}[dB]		70.6	62.4	57.8	46.9	37.4	
	p		40.6%	63.4%	85.3%	78.8%	73.0%	68.2%
O	L_{Aeq}[dB]		80.7	71.0	59.8	47.4	38.4	
	p		85.1%	92.4%	90.2%	80.8%	78.1%	85.3%
P	L_{Aeq}[dB]		70.1	59.9	50.8	41.4	37.6	
	p		38.1%	49.7%	53.9%	48.5%	43.6%	46.8%
Q	L_{Aeq}[dB]		71.3	61.6	49.1	40.0	43.6	
	p		44.2%	59.2%	44.2%	40.0%	42.2%	46.0%
R	L_{Aeq}[dB]		72.2	62.5	52.2	42.3	32.7	
	p		48.9%	64.0%	61.7%	54.1%	42.2%	54.2%
S	L_{Aeq}[dB]		80.3	70.3	61.3	56.9	44.0	
	p		84.0%	91.2%	92.8%	97.8%	94.4%	92.0%
T	L_{Aeq}[dB]		73.8	62.0	54.9	47.1	37.7	
	p		57.2%	61.3%	75.0%	79.6%	74.6%	69.5%
U	L_{Aeq}[dB]		78.2	69.5	67.2	56.0	40.9	
	p		77.1%	89.6%	98.0%	97.3%	87.7%	89.9%
V	L_{Aeq}[dB]		76.6	64.9	57.7	48.1	38.2	
	p		70.7%	75.3%	85.0%	83.3%	77.1%	78.3%
W	L_{Aeq}[dB]		75.3	68.8	54.6	46.1	36.4	
	p		64.7%	88.1%	73.7%	75.2%	67.1%	73.8%
X	L_{Aeq}[dB]		72.1	69.1	57.3	46.2	37.3	
	p		48.4%	88.7%	83.8%	75.7%	72.4%	73.8%

corresponds to the following predicted values of L_{Aeq} (74.7, 63.9, 53.7, 43.8, 35.4, 26.4, and 16.9 dB). Therefore, the relationship between each predicted value of L_{Aeq} (74.7, 63.9, 53.7, 43.8, 35.4, and 26.4 dB) and each measured value of L_{Aeq} (79.3, 68.8, 58.2, 44.7, 35.2, and 31.0 dB) for subject A can be obtained.

Subject P evaluated that very annoying corresponds to 70.1 dB. It can be determined that the cumulative p% can be calculated from Eq. (7) using the parameter values of M =72.41 and S=4.77 (the very annoying curve shown in Table V) as follows:

TABLE IX. Correlation coefficients between measured and predicted L_{Aeq} from not annoying only to very annoying only.

Individual noise rating scales predicted from	Correlation coefficient
Not annoying only	0.9803
A little annoying only	0.9799
Somewhat annoying only	0.9825
Annoying only	0.9849
Very annoying only	0.9811

$$p\,\% = \frac{100}{1+\exp\{-(70.1-72.41)/4.77\}} = 38.1\,\%\,. \qquad (18)$$

Therefore, the slope is 0.1153 using Eq. (10), and the intercept is −1.393 using Eq. (11). The noise-rating scale of subject P can be obtained as follows:

$$L_{38.1}\text{:Annoy} = 0.1153L_{Aeq} - 1.393,$$

$$\overline{L_{Aeq}} = (\text{Annoy} + 1.393)/0.1153. \qquad (19)$$

Concretely, each score of the standardized annoyance scale: (Annoy=7.80,6.53,5.33,4.17,3.18,2.12,1) corresponds to the following predicted value of L_{Aeq} (79.7, 68.7, 58.3, 48.2, 39.7, 30.5, and 20.8 dB). Therefore, the relationship between each predicted value of L_{Aeq} (68.7, 58.3, 48.2, 39.7, and 30.5 dB) and each evaluated value of L_{Aeq} (70.1, 61.6, 50.8, 41.4, and 37.6 dB) for subject P can be obtained. The same procedure was repeated.

Table IX shows the correlation coefficients between measured and predicted L_{Aeq} [dB] from not annoying only to very annoying only. It can be seen that the correlation coefficients, which are independent of each annoyance level from not annoying only to very annoying only, are about 0.98.

Figure 9 shows the relationships between individual average energy levels of $L_{Aeq,(5\ min)}$ measured by 24 normal-hearing subjects and L_{Aeq} predicted with the noise-rating scale given in Eqs. (10) and (11) from each cumulative $p\%$ of all data. The correlation coefficient between experimental results for individual noise annoyance and predictions by the proposed model is 0.9797.

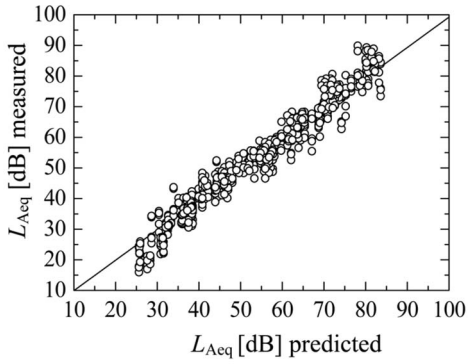


FIG. 9. Relationships between individual average energy levels of $L_{Aeq,(5\ min)}$ measured by 24 normal-hearing subjects and L_{Aeq} predicted with the noise-rating scale given in Eqs. (10) and (11) from each cumulative $p\%$ of all data.

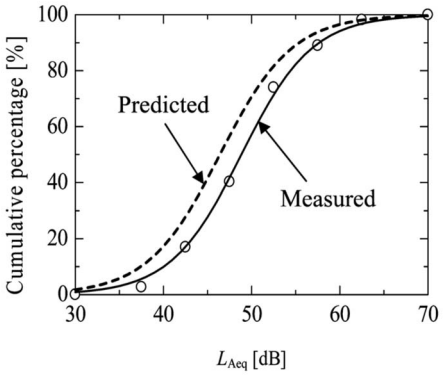


FIG. 10. Comparison between the cumulative percentages of the allowable noise levels obtained by the noise annoyance meter (solid curve) and the logistic prediction model (dashed curve).

VI. DISCUSSION

Using the logistic prediction model proposed, from step (8) of Sec. III C, it can be determined based on Eq. (9) whether a noise is over or under the allowable threshold, which is the middle point score (Annoy=3.68) between a little annoying (3.18) and somewhat annoying (4.17): The allowable threshold of the stimulus level L_2 with the cumulative $p=2\%$ of annoyance response is $L_{Aeq,(5\ min)}$ =30.5 dB, $p=5\%$ is 34.4 dB, $p=12\%$ is 38.3 dB, $p=27\%$ is 42.3 dB, $p=50\%$ is 46.4 dB, $p=73\%$ is 50.5 dB, $p=88\%$ is 54.5 dB, $p=95\%$ is 58.4 dB, and $p=99\%$ is 65.1 dB. Figure 10 shows the cumulative percentage of the allowable noise levels (dashed curve) obtained by the logistic prediction model, and the cumulative percentage of the allowable noise levels (solid curve with symbol ○) caused by road traffic noise sources estimated by residents using the experimental noise annoyance meter mentioned in Sec. II E. As seen from this figure, the level difference between these solid and dashed curves is about 2.6 dB at the 50% of cumulative percentage of the allowable noise levels.

In these conditions, it can be thought that the cause is the difference between the two listening conditions: (a) To collect various kinds of annoyance ratings,[4,5] the subjects listened to the noise (the total listening time was 15 min) indoors (windows opened and closed) and outdoors near their houses. (b) An actual audio-visual test using the noise annoyance meter[7] was carried out at each conspicuous place selected outdoors out of the sun.

The noise annoyance meter proposed would not solve the problem of describing the difference between average population responses and those of individuals. Subsequent research must determine whether one should provide calibration buttons for noise-sensitive persons, hospital, or other sensitive areas. Moreover, validation of the model is needed in a field situation.

VII. CONCLUSIONS

In this paper, a logistic prediction model for individual allowable noise levels has been developed. The aim is to quantify the degree to which subjective noise sensitivity can

be accounted for by annoyance responses. The best way proposed to predict one's noise sensitivity is to measure one's percentage $p\%$ of annoyance responses.

From the results, the following can be found.

(a) The cumulative $p\%$ of the not annoying curve increases at higher levels monotonically as a psychometric logistic function of $L_{Aeq,(5\ min)}$; the midpoint M is 33.8 dB and the spread S is 3.6 dB.
(b) From the cumulative $p\%$ of the little annoying curve, a midpoint M is 41.6 dB and the spread S is 4.0 dB.
(c) From the cumulative $p\%$ of the somewhat annoying curve, a midpoint M of 50.1 dB and a spread S of 4.4 dB were estimated.
(d) From the cumulative $p\%$ of the annoying curve, a midpoint M of 60.0 dB and a spread S of 4.4 dB were estimated.
(e) From the cumulative $p\%$ of the very annoying curve, a midpoint M of 72.4 dB and a spread S of 4.8 dB were estimated.
(f) From the cumulative $p\%$ of the extremely annoying curve, a midpoint M of 82.6 dB and a spread S of 4.5 dB were estimated.
(g) From the relationship between the annoyance level responded by a subject and the value of $L_{Aeq,(5\ min)}$ measured, one's cumulative $p\%$ of annoyance responses can be calculated from the logistic function using the parameter values of M and S estimated from (a) to (f) above.
(h) The relationship between the slopes and the cumulative $p\%$ is

$$\text{Slope} = -0.002\,07 \ln\{p\,\%/(100 - p\,\%)\} + 0.1143.$$

(i) The relationship between the intercepts and the cumulative $p\%$ is

$$\text{Intercept} = -0.366\,96 \ln\{p\,\%/(100 - p\,\%)\} - 1.5706.$$

(j) The relationship between annoyance scale score (Annoy) and $L_{Aeq,(5\ min)}$ of the cumulative $p\%$ can be obtained from the slope calculated with (h) and the intercept calculated with (i).
(k) Therefore, one's allowable noise level can be determined from whether a noise is over or under the allowable threshold, which is the middle point score (Annoy =3.68) between a little annoying (3.18) and somewhat annoying (4.17).

To verify the model, individual relationships between annoyance ratings and $L_{Aeq,(5\ min)}$ for 24 normal-hearing subjects were constructed using a laboratory experiment. From the results, the following can be found.

(l) If at least one relationship between the annoyance scale score and $L_{Aeq,(5\ min)}$ [dB] is obtained from each subject, the logistic prediction model can give individual relationships between annoyance scale scores and $L_{Aeq,(5\ min)}$. The correlation coefficient between measured and predicted L_{Aeq} [dB] for all data is about 0.98.

To judge acceptable noise levels, anyone interested in housing (residents, buyers, builders, and researchers) will need to understand the significance of such noise levels to make housing more comfortable and individually suitable. The logistic prediction model presented here can be used to estimate individual relationships between annoyance scale scores and $L_{Aeq,(5\ min)}$. Therefore, the logistic prediction model can predict individual acceptable noise levels.

ACKNOWLEDGMENTS

The author would like to thank Professor Emeritus Takesaburo Yanagisawa (Shinshu University) for his encouragement during the early days of the study, Professor David Asano (Faculty of Engineering, Shinshu University) for helpful discussions, and Professor Brigitte Schulte-Fortkamp and two anonymous reviewers for valuable feedback on this manuscript.

[1] H. M. E. Miedema and H. Vos, "Exposure-response relationships for transportation noise," J. Acoust. Soc. Am. **104**, 3432–3445 (1998).
[2] D. Botteldooren and P. Lercher, "Soft-computing base analyses of the relationship between annoyance and coping with noise and odor," J. Acoust. Soc. Am. **115**, 2974–2985 (2004).
[3] T. D. Muer, D. Botteldooren, B. D. Coensel, B. Berglund, M. Nilsson, and P. Lercher, "A model for noise annoyance based on notice-events," in Proceedings of Inter-Noise 2005, The 2005 Congress and Exposition on Noise Control Engineering, Rio de Janeiro, Brazil, 7–10 August 2005.
[4] K. Furihata and T. Yanagisawa, "Reconstruction of vehicle noise-rating scale based on judgment of residents in and around Nagano city and its effectiveness (in Japanese)," J. Acoust. Soc. Jpn. **44**, 108–115 (1988).
[5] K. Furihata and T. Yanagisawa, "Investigation on composition of a rating scale possible common to evaluate psychological effects on various kinds of noise sources (in Japanese)," J. Acoust. Soc. Jpn. **45**, 577–582 (1989).
[6] K. Furihata and T. Yanagisawa, "Comparison between some results measured with Urusasa and conventional sound level meters (in Japanese)," J. Acoust. Soc. Jpn. **52**, 19–23 (1996).
[7] K. Furihata, T. Yanagisawa, D. K. Asano, and K. Yamamoto, "Development of an experimental noise annoyance meter," Acta. Acust. Acust. **93**, 73–83 (2007).
[8] N. Levine, "The development of an annoyance scale for community noise assessment," J. Sound Vib. **74**, 265–279 (1981).
[9] S. Fidell, "Comments on The development of an annoyance scale for community noise assessment," J. Sound Vib. **78**, 299–305 (1981).
[10] J. M. Fields, R. G. De Jong, T. Gjestland, I. H. Flindell, R. F. S. Job, S. Kurra, P. Lercher, M. Vallet, T. Yano, R. Guski, U. Felscher-Suhr, and R. Schuemer, "Standardized general-purpose noise reaction questions for community noise surveys: Research and a recommendation," J. Sound Vib. **242**, 641–679 (2001).
[11] H. Akaike, "A new look at the statistical model identification," IEEE Trans. Autom. Control **AC-19**, 716–723 (1974).
[12] Y. Sakamoto and H. Akaike, "Analysis of cross classified data by AIC," Ann. Inst. Stat. Math. **30**, 185–197 (1978).
[13] ISO, "Acoustics—Description and measurement of environmental noise. Part 2: Acquisition of data pertinent to land use," ISO 1996–2 (ISO, New York, 1987).
[14] J. P. Guilford, *Psychometric Methods* (McGraw-Hill, New York, 1954).
[15] M. Kuss, F. Jäkel, and F. A. Wichmann, "Bayesian inference for psychometric functions," J. Vision **5**, 478–492 (2005).
[16] J. L. Hall, "Hybrid adaptive procedure for estimation of psychometric functions," J. Acoust. Soc. Am. **89**, 1763–1769 (1981).
[17] D. M. Green and J. A. Swets, *Signal detection theory and psychophysics* (Wiley, New York, 1966), pp. 219–222.
[18] M. M. Taylor and C. D. Creelman, "PEST: Efficient estimates on probability functions," J. Acoust. Soc. Am. **41**, 782–787 (1967).
[19] L. A. Jeffress, "The logistic distribution as an approximation to the normal curve," J. Acoust. Soc. Am. **53**, 1296 (1973).
[20] D. M. Green, "A maximum-likelihood method for estimating thresholds in a yes-no task," J. Acoust. Soc. Am. **93**, 2096–2105 (1993).
[21] C. F. Lam, J. H. Mills, and J. R. Dubno, "A change of subscripts of the stimulus placements for a four-point sampling method," J. Acoust. Soc. Am. **101**, 1742 (1997).

[22]C. F. Lam, J. R. Dubno, J. B. Ahlstrom, N. J. He, and J. H. Mills, "Estimating parameters for psychometric functions using the four-point sampling method," J. Acoust. Soc. Am. **102**, 3697–3703 (1997).
[23]N. J. D. Nagelkerle, "A note on the general definition of the coefficient of determination," Biometrika **78**, 691–692 (1991).
[24]K. Kobayashi, Y. Yasuda, K. Furihata, and T. Yanagisawa, "A new questionnaire using WWW system for road traffic noise," in Proceedings of Inter-Noise 2002, Dearborn, MI, Paper No. N603.
[25]C. Guastavino and B. F. G. Katz, "Perceptual evaluation on multi-dimensional spatial audio reproduction," J. Acoust. Soc. Am. **116**, 1105–1115 (2004).
[26]K. Abe, K. Ozawa, Y. Suzuki, and T. Sone, "Comparison of the effects of verbal versus visual information about sound sources on the perception of environmental sounds," Acta. Acust. Acust. **92**, 51–60 (2006).
[27]S. Okamoto, K. Furihata, and T. Yanagisawa, "Vehicle noise simulator based on the sensory characteristics of sight and hearing," in Proceedings of Inter-Noise 1999, Fort Lauderdale, FL, Vol. **3**, pp. 1777–1782.

Evaluating roadside noise barriers using an annoyance-reduction criterion[a)]

Mats E. Nilsson[b)]
Institute of Environmental Medicine, Karolinska Institutet, Stockholm SE-17177, Sweden and Department of Psychology, Stockholm University, Stockholm SE-106 91, Sweden

Mikael Andéhn
Department of Psychology, Stockholm University, Stockholm SE-106 91, Sweden

Paulina Leśna
Institute of Acoustics, Adam Mickiewicz University, Poznan 61–614, Poland

(Received 9 January 2008; revised 7 August 2008; accepted 10 September 2008)

A common indicator of effectiveness for roadside noise barriers is the reduction in *A*-weighted sound pressure level (L_A). The present experimental study considered alternative indicators using an annoyance-reduction criterion. A large number of 8 s experimental sounds were created from binaural recordings conducted at various distances from a highway at a location with a 4.6 m high roadside barrier (barrier sounds) and at a location along the same road with no barrier (nonbarrier sounds). Eighteen listeners scaled the annoyance of the experimental sounds with the method of magnitude estimation. The barrier sounds recorded 10–45 m from the road and nonbarrier sounds recorded 50–200 m from the road were of similar L_A. Despite this, the barrier sounds were found to be more annoying than the nonbarrier sounds. The annoyance difference corresponded to approximately a 3 dB increase in L_A and was mainly related to the barrier sounds' higher relative level of low-frequency sound. This suggests that L_A reduction may not be a valid indicator of the annoyance reduction caused by a noise barrier. The loudness level (ISO 532B) and a low-frequency corrected sound pressure level (L_A^*) were found to be better than L_A as indicators of the barrier's annoyance-reduction efficiency. © *2008 Acoustical Society of America.* [DOI: 10.1121/1.2997433]

PACS number(s): 43.50.Qp, 43.50.Gf, 43.66.Lj, 43.50.Ba [BSF] Pages: 3561–3567

I. INTRODUCTION

Roadside noise barriers are evaluated in terms of the accomplished reduction in *A*-weighted sound pressure level (ISO, 1997; ANSI, 1998). However, more important than sound-level reduction is the extent to which barriers reduce adverse effects of noise, such as perceived annoyance (e.g., Nilsson and Berglund, 2006). A roadside noise barrier reduces the overall sound pressure level of the noise at the shielded side of the barrier. The corresponding changes in perceived loudness may not be well predicted by *A*-weighted sound pressure level, which has been criticized for overcompensating for the hearing system's reduced sensitivity at low frequencies (Kjellberg *et al.*, 1984; Schomer, 2004). In addition, a barrier modifies the spectral composition (Kragh *et al.*, 2002) and time variability (Forssén and Hornikx, 2006) of road-traffic noise, and thereby its perceived character (Nilsson *et al.*, 2004). Perceived annoyance is related to the loudness as well as to the perceived character of noise (Berglund *et al.*, 1990). Thus, road-traffic sounds of *similar* *A*-weighted sound pressure level may differ in annoyance depending on whether or not they were influenced by a noise barrier. The present listening experiment tested this hypothesis. The issue is of great importance because it concerns the cost effectiveness of noise barriers as methods for reducing noise annoyance.

Several studies have shown that *A*-weighting is not suitable as an indicator of perceived annoyance of low-frequency sound (Bengtsson *et al.*, 2004), impulse noise (Vos, 2001), and noise with strong tonal components (Landström *et al.*, 1995). The picture is less clear for road-traffic noise. In several experimental studies on road-traffic noise, *A*-weighting has performed as well or better than alternative indicators of perceived annoyance, noisiness, or loudness (Cermak and Cornillon, 1976; Cermak, 1979; Yaniv *et al.*, 1982; Namba and Kuwano, 1984; Kuwano *et al.*, 1988; Watts and Nelson, 1993). However, Watts (1995) and Nilsson (2007) showed that *A*-weighting is not a valid indicator of perceived annoyance of road-traffic noise with wide variability in relative level of low-frequency sound. Noise barriers increase the relative level of low-frequency sound of road-traffic noise at the shielded side of the barrier. Thus, the reduction in *A*-weighted sound pressure level caused by a noise barrier may overestimate the estimated reduction in perceived annoyance due to the increase in relative level of low-frequency sound.

The purpose of the present listening experiment was to evaluate the annoyance-reduction efficiency of a roadside noise barrier. The experiment included excerpt sounds re-

[a)]Portions of this work were presented in "Perceptual efficiency of road-traffic noise barriers," Proceedings of Inter-Noise 2007, Istanbul, August 2008.

[b)]Present address: Department of Psychology, Stockholm University, SE-106 91 Stockholm, Sweden. Electronic mail: mats.nilsson@psychology.su.se



FIG. 1. Noise barrier and binaural recording equipment.

corded at various distances to a highway at one location without a noise barrier and at one location with a 4.6 m high noise barrier. Importantly, the sound-level range of nonbarrier sounds recorded at 50–200 m distance from the road was comparable to the sound-level range of barrier sounds recorded at 10–45 m distance. Thus, perceived annoyance of road-traffic noise affected by a barrier could be compared to the annoyance of road-traffic noise of comparable A-weighted sound pressure levels (L_A) but without the influence of a barrier. If L_A was a valid indicator of perceived annoyance, then equal levels of L_A would mean approximately equal levels of perceived annoyance.

II. METHOD

A. Binaural recordings

Binaural recordings were conducted outdoors along a Swedish four-lane highway (speed limit of 90 km/h, approximately 65 000 vehicles per 24 h). Recordings were conducted during afternoon peak hours at two locations along the road, one with and one without protection from a 4.6 m high conventional reflective roadside noise barrier of wood. The barrier location was a residential area with detached houses. The nonbarrier location was an open field approximately 4 km from the barrier location. Recordings with the barrier were conducted at 10, 20, 30, and 45 m distance from the roadside. Recordings without barrier were conducted at 5, 10, 20, 50, and 200 m distance from the roadside. Two binaural recording systems were used simultaneously at two distances from the road. Microphone heights were 1.6 m. Recordings with and without barrier were conducted on two different days in the same week and on the same time of the day. Figure 1 shows a photograph of the barrier and of the binaural recording equipment.

The traffic flow was registered using a video camera. The traffic composition was similar for recordings with and without barrier, approximately 4000 vehicles per hour passed the recording locations of which 8% were heavy vehicles.

In order to assure that all recordings were completely dominated by road-traffic noise, periods with major wind disturbances, unusual traffic sounds such as sounds from car horns, motorcycles without silencer, or emergency-vehicle sirens, and sounds from people talking were carefully removed from the recordings. After this editing, the recordings had a total duration of 3 h and 29 min. Table I gives a description of the edited recordings including acoustic measures of overall level, spectral content, and variability. The levels were calculated as the average of the antilog of decibel values from each channel of the binaural recordings (Nilsson, 2007). The logarithm of this average was used in all analyses reported below.

As expected, sound pressure levels (L_{Aeq}) at recordings with a barrier were considerably lower than recordings at the same distance without barrier. The differences in sound pressure level were 15 and 11 dB at 10 and 20 m distances from the road, respectively. The relative level of low-frequency sound ($L_{Ceq}-L_{Aeq}$) was higher, and the sound-level variability ($L_{A10}-L_{A90}$) was lower for recordings with than without barrier.

B. Selection of experimental sounds from a stimulus population

The edited recordings were divided into 8 s excerpts using a program written in MATLAB. In order to obtain a very

TABLE I. Description of the sound recordings from which experimental sounds were selected.

Duration edited recording, T (s)	Distance to roadside (m)	Barrier[a]	L_A[b]	L_C-L_A[c]	$L_{A10}-L_{A90}$[d]	L_N[e]
1814	5	0	74	1	14	90
2169	10	0	71	2	9	87
1300	20	0	64	4	7	82
896	50	0	62	4	7	79
736	200	0	54	6	7	70
989	10	1	56	8	4	75
1602	20	1	53	9	4	72
1143	30	1	53	10	4	71
1338	45	1	51	9	3	70

[a]0=recording at location without noise barrier; 1=recording at location with noise barrier.
[b]A-weighted equivalent continuous sound pressure level, $L_{Aeq,T}$ (in decibels).
[c]Relative level of low-frequency sound (Nilsson, 2007), $L_{Ceq,T}-L_{Aeq,T}$ (in decibels).
[d]Variability (Nilsson, 2007), difference between levels exceeded 10% and 90% of the time (in decibels).
[e]Loudness level (phon) (ISO 532B, ISO, 1975).

TABLE II. Description of selected experimental sounds.

Distance to roadside (m)	Barrier[a]	No. of sounds	Mean of acoustic variables (parenthetical numbers signify the ranges of measured data)			
			L_A[b]	L_C-L_A[c]	$L_{A10}-L_{A90}$[d]	L_N[e]
5	0	11	73 (67–78)	1 (0–2)	10 (5–15)	89 (84–93)
10	0	10	70 (65–75)	1 (0–3)	7 (4–16)	86 (82–91)
20	0	10	64 (59–69)	3 (1–5)	4 (1–9)	81 (77–85)
50	0	10	61 (57–65)	4 (1–7)	3 (2–5)	78 (74–82)
200	0	10	53 (48–58)	5 (2–9)	2 (1–4)	69 (64–73)
10	1	6	55 (53–57)	7 (5–11)	2 (1–5)	73 (71–76)
20	1	7	53 (50–56)	8 (6–11)	2 (1–5)	71 (68–75)
30	1	6	52 (50–54)	10 (7–12)	2 (1–4)	71 (69–73)
45	1	7	51 (48–53)	7 (5–11)	2 (1–7)	69 (65–72)

[a]0=recording at location without noise barrier; 1=recording at location with noise barrier.
[b]*A*-weighted equivalent continuous sound pressure level, $L_{Aeq,T}$ (in decibels).
[c]Relative level of low-frequency sound (Nilsson, 2007), $L_{Ceq,T}-L_{Aeq,T}$ (in decibels).
[d]Variability (Nilsson, 2007), difference between levels exceeded 10% and 90% of the time (in decibels).
[e]Loudness level (phon) (ISO 532B, ISO, 1975).

large set of excerpts, the 8 s excerpts were sampled each second of the recording (i.e., there was a 7 s overlap between adjacent excerpts). This procedure generated a "stimulus population" of more than 11 000 excerpts, from which experimental sounds were chosen (cf. Nilsson, 2005).

The selection of experimental sounds from the stimulus population was conducted in the following way. First, all excerpts from a given distance and recording location (with or without barrier) were grouped in 1 dB categories (± 0.5 dB $L_{Aeq,8s}$). Second, one excerpt was randomly selected from each 1 dB category containing more than ten excerpts. This generated totally 77 experimental sounds, between 6 and 11 from each distance and recording location. The selected sounds were all from different time periods in the recordings; thus, there was no overlap in time between any of the selected sounds. In the following, sounds recorded with barrier and without barrier will be referred to as "barrier sounds" and "nonbarrier sounds," respectively.

Table II gives mean and range of a selected set of acoustic variables for barrier and nonbarrier sounds at various distances to the road. These variables are related to the overall level ($L_{Aeq,8s}$ denoted L_A and loudness level denoted L_N calculated from 8 s average 1/3-octave-band sound pressure levels), the spectral content ($L_{Ceq,8s}-L_{Aeq,8s}$ denoted L_{C-A}), and the time variability of the sounds ($L_{A10}-L_{A90}$). Levels of the experimental sounds were comparable to the levels of the original recordings (compare Tables I and II), the exception being sound-level variability ($L_{A10}-L_{A90}$) which was greater when referring to the entire recordings (736–2169 s) compared to when calculated for the 8 s experimental sounds. In order to further illustrate the range of the experimental sounds, Fig. 2 plots their *A*-weighted sound pressure level against the distance between roadside and microphone.

Several other acoustic variables than those listed in Table II were analyzed, including the psychoacoustic indicator sharpness, roughness, and fluctuation strength (Zwicker and Fastl, 1990). However, the variation across experimental sounds in these indicators was limited, and they did not substantially contribute to the prediction of perceived annoyance over and above the indicators listed in Table II. Therefore, these indicators were not included in the following analysis.

C. Procedure

The listener was seated in a soundproof room in front of a computer screen connected to a computer in another room. The experimental sounds were binaurally presented using ear phones. The experiment consisted of four listening sessions. In each of these sessions, the 77 experimental sounds were presented once. The experimental sounds were presented in random orders, which were different for each session and participant. Listening session duration was approximately 7 min. The sessions were separated from one another with 1 min pauses, except for the pause between sessions 2 and 3, which was 10 min. A training session with six sounds was conducted prior to the first session. Perceived annoyance was assessed with the method of free number magnitude estimation (e.g., Gescheider, 1997). The participants entered their magnitude estimates on a computer keyboard.

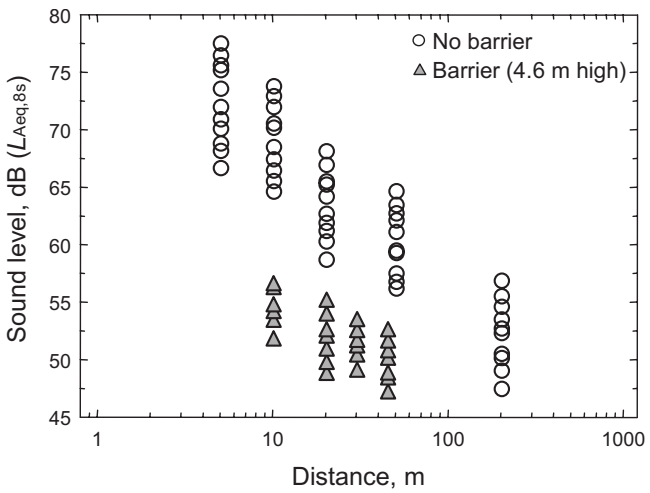


FIG. 2. *A*-weighted sound pressure levels ($L_{Aeq,8s}$) of selected experimental sounds vs distance from the roadside.

D. Listeners

Eighteen university students participated in the experiment (12 women and 6 men; mean age=28 years). All participants' hearing threshold levels were below 25 dB in their best ear in all tested frequencies (0.5, 1, 2, 3, 4, 6, and 8 kHz, Interacoustics Diagnostic Audiometer, model AD226). The listeners received course credit for their participation.

E. Equipment

The binaural recording system consisted of two head and torso simulators (Brüel & Kjær type 4100, with two microphones type 4190 and two preamplifiers type 2669), two conditioning amplifiers (NEXUS Brüel & Kjær type 2690 A 0S4), and a calibrator (Brüel & Kjær type 4231 plus adapter model 0887). Sounds were recorded on a portable computer (Dolch NPAC-Plus P111) with a six-channel sound card (LynxTwo) using a software for sound recordings with 24 bit resolution and 48 kHz sampling frequency (SOUND FORGE 7.0). The recordings were edited on a personal computer (Dell Precision 220) using the SOUND FORGE 7.0 software. A large number of 8 s excerpt sounds were created using a script written in MATLAB. Experimental sounds were analyzed using the ARTEMIS software.

Experimental sounds were stored on a personal computer (Dell Precision 220 with a LynxTwo sound card). The digital signal was fed into a digital filter and digital/analog converter (Rane RPM 26z) and were then presented through ear phones (Sennheiser HD 600). The whole listening system was calibrated using a pink-noise signal, which was measured at the point of the listener's ear. The frequency response of the whole listening system was flat within 2 dB (1/3-octave-band levels, 25–16 000 Hz).

III. RESULTS

Each listener assessed each experimental sound four times. A magnitude estimate that was more than three times greater than the next largest estimate or less than a third of the next smallest estimate of the same sound was defined as an outlier and therefore excluded (cf. Eisler, 1975). In total, 65 estimates (1%) were excluded.

The consistency of individual data was found to be good, as determined by Pearson's coefficients of correlation between magnitude estimates of sounds in the first two and last two sessions. Coefficients ranged between 0.48 and 0.94 (median=0.86). Three listeners had coefficients below 0.7. However, the general trend of the data of these participants was not different from the other participants. Overall, the interindividual agreement was found to be high. Pearson's coefficient of correlation between individual scales of annoyance ranged from 0.63 to 0.96 (median=0.86). It was therefore justified to include data from all participants in the group analyses.

The magnitude estimates assigned to each experimental sound were brought to a common modulus for all listeners and were then averaged geometrically (Lane *et al.*, 1961; Algom *et al.*, 1988). Figure 3 shows the resulting group scale of perceived annoyance on a log scale (log[R]) as a function of A-weighted sound pressure level (L_A). The relationship is approximately linear in log-log coordinates, as typically found with magnitude estimation data (Gescheider, 1997). Importantly, sounds recorded behind the barrier (triangles) were more annoying than sounds of similar level recorded without noise barrier (circles) at equal levels of L_A. That is, the road-traffic noise of 10–45 m behind the barrier was more annoying than the road-traffic noise of the same level at farther distance from the road (50–200 m). The difference corresponds to approximately 3 dB, as seen by the horizontal distance between circles and triangles in Fig. 3 (and confirmed by dummy-variable regression analyses described below).

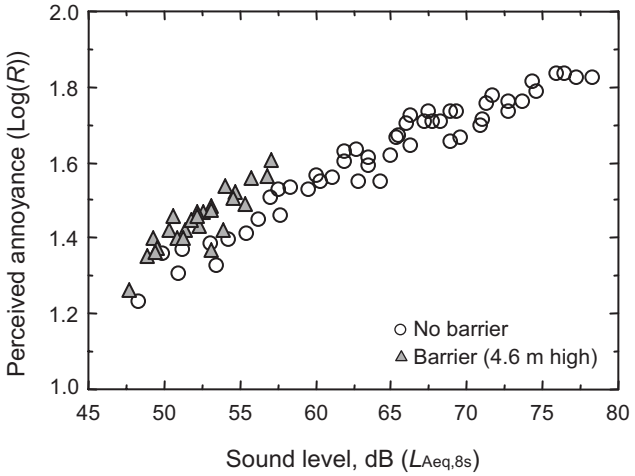


FIG. 3. Perceived annoyance (log scale) as a function of A-weighted sound pressure level ($L_{Aeq,8s}$).

Four linear regression models were fitted to the annoyance data in order to (i) statistically evaluate the effect of the noise barrier (model 2) and (ii) evaluate L_A (model 1) as an indicator of perceived annoyance in comparison to a model including both L_A and L_{C-A} (model 3) and in comparison to loudness level (model 4). The empirical equations and model fits, r^2, are given in Table III.

Model 1, the reference model, included L_A as the only independent variable. The fit, r^2, of this model was 0.922. Model 2 included L_A and a dummy-coded variable, B, representing noise-barrier presence/absence (1=barrier, 0=no barrier). The addition of B in the model increased r^2 to 0.939 (F-increase$_{1,74}$=19.4, $p<0.001$) A positive regression coefficient was obtained for B (0.055, $p<0.001$). The ratio of the coefficients for B and L_A was 2.8 (0.055/0.020). Thus, for equal levels of L_A, sounds recorded behind the barrier

TABLE III. Linear relationship between perceived annoyance (log scale) and acoustic variables determined using linear regression analysis.

Model	Empirical relationship[a]	Goodness of fit, r^2
1	$\log(R)=0.497+0.018L_A$	0.922
2	$\log(R)=0.346+0.020L_A+0.055B$	0.939
3	$\log(R)=0.202+0.022L_A+0.012L_{C-A}$	0.942
4	$\log(R)=0.036+0.020L_N$	0.955

[a]$\log(R)$=perceived annoyance (log scale); $L_A=L_{Aeq,8s}$; B=barrier, dummy coded (1=barrier, 0=no barrier); $L_{C-A}=L_{Ceq,8s}-L_{Aeq,8s}$; and L_N=loudness level (ISO 532B).

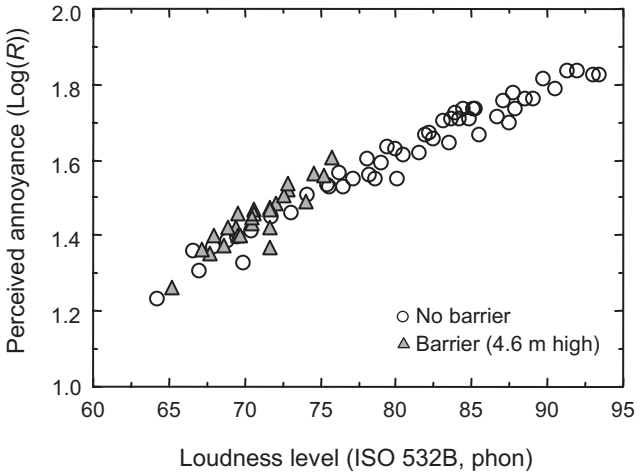


FIG. 4. Perceived annoyance (log scale) as a function of loudness level (ISO 532B).

were more annoying than the sound recorded without barrier, a difference corresponding to an increase in L_A of 2.8 dB.[1]

Model 3 included sound pressure level (L_A) and relative level of low-frequency sound (L_{C-A}) as independent variables. The addition of L_{C-A} increased r^2 from 0.922 (model 1) to 0.943 (model 3). This increase was statistically significant (F-increase$_{1,74}$=26.8, $p<0.001$) and the coefficient for L_{C-A} was significantly greater than zero ($p<0.001$). Thus, L_{C-A} explained a significant part of the variance in perceived annoyance not accounted for by L_A. The ratio of the coefficients for L_{C-A} to L_A was 0.55 (0.012/0.022), suggesting that a 1 dB change in L_{C-A} has the same effect on annoyance as a change in L_A of approximately 0.55 dB (cf. Nilsson, 2007).

Model 4 included loudness level, L_N, (ISO 532B) as the only independent variable. This model fitted the data better than any of the other tested models, in spite of having one free parameter less than models 2 and 3. Figure 4 shows perceived annoyance on a log scale as a function of L_N.

Adding the dummy-coded barrier variable, B, to L_N marginally increased the model fit (r^2-increase=0.002; $F_{1,74}$ =3.2, p=0.076). The ratio of the coefficients for B and L_N was 0.9 (0.017/0.020). Thus, for equal levels of L_N, sounds recorded behind the barrier were slightly more annoying than the sound recorded without barrier, a difference corresponding to an increase in L_N of 0.9 dB. This is equivalent to the small horizontal distance between barrier sounds (triangles) and nonbarrier sounds (circles) in Fig. 4.

We also tested a model with sound-level variability ($L_{A10}-L_{A90}$) as predictor variable. However, this variable did hardly explain any of the variance in perceived annoyance over and above the variance related to L_A. In a model with L_A and $L_{A10}-L_{A90}$ predictor variables, the coefficient for $L_{A10}-L_{A90}$ was close to zero (−0.001) and the model fit did not increase compared to the model with L_A as the only independent variable (model 1).

IV. DISCUSSION

The results showed that barrier sounds recorded 10–50 m from the road were more annoying than nonbarrier sounds of similar A-weighted sound pressure level (L_A) recorded at farther distance from the road (50–200 m). This suggests that, for the same L_A-reduction, increasing the distance to the source would reduce perceived annoyance more than erecting a noise barrier. In the present case, the annoyance difference corresponded to an increase in L_A of approximately 3 dB. Thus, an evaluation of the present barrier in terms of L_A would overestimate its annoyance-reduction efficiency by 3 dB compared to the annoyance reduction due to increased distance. In contrast, barrier and nonbarrier sounds of equal loudness level, L_N, [ISO 532B, (ISO, 1975)] were approximately equally annoying. This suggests that L_N is better than L_A as an indicator of the annoyance-reduction efficiency of noise barriers.

Compared to the nonbarrier sounds, the barrier sounds had a higher relative level of low-frequency sound (L_{C-A}), whereas the sound-level variability ($L_{A10}-L_{A90}$) did not differ much between barrier and nonbarrier sounds of comparable L_A. The results of multiple regression analyses suggested that L_{C-A} was the main acoustical factor behind the annoyance difference between barrier and nonbarrier sounds of equal L_A. This agrees with previous research which has shown that L_A is not a valid indicator of perceived annoyance of road-traffic noise with wide variation in L_{C-A} (Watts, 1995; Nilsson, 2007). It should be observed that the levels of L_{C-A} of nonbarrier sounds increased with distance to the source due to air absorption. Despite this, levels of L_{C-A} were substantially higher for barrier sounds than for nonbarrier sounds.

The barrier was relatively high (4.6 m) and therefore had a considerable influence on the spectral composition of the road-traffic noise behind the barrier. A lower barrier would typically increase the relative level of low-frequency sound to a lesser extent, and the annoyance-prediction error associated with barrier evaluation in terms of L_A reduction would be smaller than the 3 dB estimated in the present experiment.

A common critique of L_A is that it overcompensates for the hearing system's reduced sensitivity at low frequencies (Kjellberg *et al.*, 1984; Schomer, 2004). Barrier sounds would then be perceived as louder and thereby as more annoying than nonbarrier sounds, which contain less energy in the low-frequency part of the spectrum. This agrees with the finding that L_{C-A} explained a substantial part of the variance in perceived annoyance and that L_N was better than L_A as predictor of perceived annoyance of barrier and nonbarrier sounds. L_N predicts perceived loudness and is based on a detailed model of the auditory periphery (Zwicker and Fastl, 1990), whereas L_A only is based on a rough approximation of the auditory system's frequency sensitivity. It should be pointed out that the present results refer to perceived annoyance in a listening situation. Therefore, the results cannot be directly generalized to residential annoyance, as measured in socioacoustic questionnaires, which refers to feelings of annoyance and activity disturbances evoked by noise at home. Questionnaire studies would be needed in order to evaluate acoustic indictors of barriers in relation to residential annoyance. It seems, however, plausible that an improved acoustic indicator of perceived annoyance would also be an improved indicator of annoyance and activity disturbance in residential settings.

Although better than L_A, L_N was not a perfect indicator of perceived annoyance. Barrier sounds were slightly more annoying than nonbarrier sounds of equal L_N, a difference equivalent to a L_N-increase of 0.9 dB. It is possible that this deviation was related to perceptual variables, other than loudness, affecting perceived annoyance. Distance to source has been found to explain a part of the variance in perceived noise annoyance not accounted for by sound level (De Coensel *et al.*, 2007). Carefully listening through barrier and nonbarrier sounds of equal L_A suggested that nonbarrier sounds (200 m distance) were perceived as more distant and backgroundlike than barrier sounds (10–50 m distance), in which single vehicle passages often could be distinguished. It is possible that distant sources are perceived as less threatening and thereby less annoying than sources perceived to be at a closer distance (cf. Neuhoff, 2004). This may partly explain the annoyance difference between barrier and nonbarrier sounds of equal L_A. Another perceptual explanation would be in terms of figure-ground perception. It is possible that annoyance estimates were largely based on the part of the sound clearly identified as traffic noise (figure), ignoring the part of the sound perceived as background (ground). This could partly explain why the more backgroundlike nonbarrier sounds at 200 m distance were less annoying than barrier sounds at 10–50 m distance in which road-traffic events were clearly audible.

The present results suggest that the loudness level reduction in road-traffic noise would be a better indicator of the barrier's annoyance-reduction efficiency than the reduction in *A*-weighted sound pressure level. Unfortunately, the loudness level is hardly known outside the psychoacoustic research community, although Zwicker introduced it more than 40 years ago (Zwicker and Scharf, 1965). Most handheld sound-level meters measure both *A*- and *C*-weighted sound pressure levels, but not loudness level, and it is typically not implemented in standard noise prediction software. For these practical reasons, an indicator based on *A*- and *C*-weighted sound pressure levels may be more applicable.

Nilsson (2007) suggested a corrected sound pressure level as an indicator of road-traffic noise annoyance: $L_A^* = L_A + 0.4L_{C-A}$. This correction adds a low-frequency related "penalty" to L_A. The factor of 0.4 was derived from the experimental results. In the present experiment, the derived factor was slightly higher, 0.55 dB. Further studies would be needed in order to determine the appropriate magnitude of the penalty and how it relates to factors such as distance to the road, number of vehicles, and presence and type of shielding structures. Nevertheless, the present results give further support to the use of both *C*- and *A*-weighted levels for evaluating annoyance of road-traffic noise, as previously suggested for impulse (Vos, 2001) and occupational noise (Kjellberg *et al.*, 1997). Such a method may be particularly useful for evaluating effects of noise mitigation methods, which typically affect L_{C-A}. The predicted L_A-reduction accomplished by a specific noise mitigation method could thus be corrected using a penalty for the increase in L_{C-A}. Different noise mitigation methods, for example, barriers or speed limitations, may have different effects on L_{C-A}. Consequently, decisions between different mitigation methods may come out differently if they take into consideration the predicted change in relative level of low-frequency sound and not only, as today, considers the predicted reduction in *A*-weighted sound pressure level.

V. CONCLUSIONS

(1) Road-traffic noise behind barriers may be somewhat more annoying than expected from their *A*-weighted sound pressure level mainly due to the increase in relative level of low-frequency sound. This suggests that evaluation of the annoyance-reduction efficiency of noise barriers should not only rely on the expected reduction in *A*-weighted sound pressure level but also take into account the associated increase in relative level of low-frequency sound.

(2) Loudness level (ISO 532B) was found to be better than *A*-weighted sound pressure level as an indicator of perceived annoyance of road-traffic noise.

(3) As an alternative to loudness level, a corrected sound pressure level may be useful for evaluating noise-barrier efficiency. The correction adds a "penalty" to the sound pressure level depending on its relative level of low-frequency sound (L_{C-A}). The present results suggest that a 1 dB increase in L_{C-A} would correspond to a 0.55 dB increase in *A*-weighted sound pressure level, whereas previous research has suggested a correction of 0.4 dB per L_{C-A} (Nilsson, 2007).

(4) The method of systematic selection of experimental sounds from a "stimulus population" (Nilsson, 2005) was found to be useful for obtaining a representative set of environmental sounds at various distances to the road at locations with or without a noise barrier.

ACKNOWLEDGMENTS

This research was conducted in the research program "Soundscape Support to Health," sponsored by the Swedish Foundation for Strategic Environmental Research (MISTRA), the Swedish Agency for Innovation Systems (Vinnova), and the Swedish Road Administration. The research was also supported by grants to M.E.N. from the Institute of Environmental Medicine, Karolinska Institutet and by grants to Professor Birgitta Berglund from the European Community (Calm Tracks and Routes Project No. COOP-CT-2005-017609). The authors would like to thank Mr. Owe Gustafsson for recording assistance and Dr. Tomasz Kaczmarek and Dr. Piotr Pekala for help with computer programming.

[1]We also conducted a regression analysis restricted to sound pressure levels <58 dB L_A in order only to include nonbarrier sounds of similar levels as the barrier sounds. The ratio of the coefficients for *B* and L_A was 2.9 (0.076/0.026), that is, sounds recorded behind the barrier were more annoying than the sound recorded without barrier, a difference corresponding to an increase in L_A of 2.9 dB. This is close to the 2.8 dB derived from the analysis including all sounds.

Algom, D., Adam, R., and Cohen-Raz, L. (**1988**). "Binaural summation and lateralization of transients: A combined approach," J. Acoust. Soc. Am. **84**, 1302–1315.

ANSI (**1998**). *ANSI S12.8: Methods for Determination of Insertion Loss of Outdoor Noise Barriers* (Acoustical Society of America, New York).

Bengtsson, J., Persson Waye, K., and Kjellberg, A. (**2004**). "Sound characteristics in low frequency noise and their relevance for the perception of

pleasantness," Acta. Acust. Acust. **90**, 171–180.
Berglund, B., Preis, A., and Rankin, K. (**1990**). "Relationship between loudness and annoyance for ten community sounds," Environ. Int. **16**, 523–531.
Cermak, G. W. (**1979**). "Exploratory studies of the relative aversiveness of traffic sounds," J. Acoust. Soc. Am. **65**, 112–123.
Cermak, G. W., and Cornillon, P. C. (**1976**). "Multidimensional analyses of judgments about traffic noise," J. Acoust. Soc. Am. **59**, 1412–1420.
De Coensel, B., Botteldooren, D., Berglund, B., Nilsson, M. E., De Muer, T., and Lercher, P. (**2007**). "Experimental investigation of noise annoyance caused by high-speed trains," Acta. Acust. Acust. **93**, 589–601.
Eisler, H. (**1975**). "Subjective duration and psychophysics," Psychol. Rev. **82**, 429–450.
Forssén, J., and Hornikx, M. (**2006**). "Statistics of A-weighted road traffic noise levels in shielded urban areas," Acta. Acust. Acust. **92**, 998–1008.
Gescheider, G. A. (**1997**). *Psychophysics: The Fundamentals* (Lawrence Erlbaum, London).
ISO (**1975**). *ISO 532(E): Acoustics: Method for Calculating Loudness Level* (ISO, Geneva, Switzerland).
ISO (**1997**). *ISO 10847: Acoustics-In Situ Determination of Insertion Loss of Outdoor Noise Barriers of All Types* (ISO, Geneva, Switzerland).
Kjellberg, A., Goldstein, M., and Gamberale, F. (**1984**). "An assessment of dB(A) for predicting loudness and annoyance of noise containing low frequency noise," Low Freq. Noise, Vib., Act. Control **3**, 10–16.
Kjellberg, A., Tesarz, M., Holmberg, K., and Landström, U. (**1997**). "Evaluation of frequency-weighted sound level measurements for prediction of low-frequency noise annoyance," Environ. Int. **23**, 519–527.
Kragh, J., Plovsing, B., Storeheier, S. Å., Taraldsen, G., and Jonasson, H. G. (**2002**). "Nordic environmental noise prediction methods, NORD2000," *Summary Report: General Nordic Sound Propagation Model and Applications in Source-Related Prediction Methods* (DELTA Acoustics and Vibration, Lyngby, Denmark).
Kuwano, S., Namba, S., and Fastl, H. (**1988**). "On the judgment of loudness, noisiness and annoyance with actual and artificial noises," J. Sound Vib. **127**, 457–465.
Landström, U., Åkerlund, E., Kjellberg, A., and Tesarz, M. (**1995**). "Exposure levels, tonal components, and noise annoyance in working environments," Environ. Int. **21**, 265–275.
Lane, H. L., Catania, A. C., and Stevens, S. S. (**1961**). "Voice level: Autophonic scale, perceived loudness and effects of sidetone," J. Acoust. Soc. Am. **33**, 160–167.
Namba, S., and Kuwano, S. (**1984**). "Psychological study on Leq as a measure of loudness of various kinds of noises," J. Acoust. Soc. Jpn. (E) **5**, 135–148.
Neuhoff, J. G. (**2004**) "Auditory motion and localization," in *Ecological Psychoacoustics*, edited by J. G. Neuhoff (Elsevier, London), pp. 89–113.
Nilsson, M. E. (**2005**). "A method for stimulus sampling in environmental psychoacoustics," Arch. Acoust. **30**, 169–172.
Nilsson, M. E. (**2007**). "A-weighted sound pressure level as an indicator of perceived loudness and annoyance of road-traffic sound," J. Sound Vib. **302**, 197–207.
Nilsson, M. E., and Berglund, B. (**2006**). "Noise annoyance and activity disturbance before and after the erection of a roadside noise barrier," J. Acoust. Soc. Am. **119**, 2178–2188.
Nilsson, M. E., Kaczmarek, T., and Berglund, B. (**2004**). "Perceived soundscape evaluation of noise mitigation methods," Inter-Noise 2004 (International Institute of Noise Control Engineering, Prague), Paper No. 514.
Schomer, P. D. (**2004**). "The importance of proper integration of and emphasis on the low-frequency sound energies for environmental noise assessment," Noise Control Eng. J. **52**, 26–39.
Watts, G. (**1995**). "A comparison of noise measures for assessing vehicle noisiness," J. Sound Vib. **180**, 493–512.
Watts, G., and Nelson, P. M. (**1993**). "The relationship between vehicle noise measures and perceived noisiness," J. Sound Vib. **164**, 425–444.
Vos, J. (**2001**). "On the annoyance caused by impulse sounds produced by small, medium-large, and large firearms," J. Acoust. Soc. Am. **109**, 244–253.
Yaniv, S. L., Danner, W. F., and Bauer, J. W. (**1982**). "Measurement and prediction of annoyance caused by time-varying highway noise," J. Acoust. Soc. Am. **72**, 200–207.
Zwicker, E., and Fastl, H. (**1990**). *Psychoacoustics: Facts and Models* (Springer-Verlag, Berlin).
Zwicker, E., and Scharf, B. (**1965**). "A model for loudness summation," Psychol. Rev. **72**, 3–26.

Variations of road traffic noise in residential areas

Rufin Makarewicz and Maciej Żółtowski
Institute of Acoustics, A. Mickiewicz University, 61-614 Poznan, Umultowska 14, Poland

(Received 7 March 2008; revised 7 December 2008; accepted 7 December 2008)

The ability to predict road noise in urban area is important. The community noise equivalent level (L_{den}) varies from day to day (weekdays, weekends, holidays, etc.). There is a need to compromise between the accuracy in the determination of L_{den} and limited resources of input data, the measuring equipment, and time. The problem can be managed using the method proposed in this study. It requires only one short-term measurement of the time-average sound level, $L_{Aeq,T}$.
© *2008 Acoustical Society of America.* [DOI: 10.1121/1.3008003]

PACS number(s): 43.50.Rq, 43.50.Lj [KA] Pages: 3568–3575

INTRODUCTION

The community noise equivalent level, L_{den} (Section I), is based on the day, evening, and night average sound levels ($L_{Aeq,T}=L_d$, L_e, and L_n) with the time intervals, $T=12$, 3, and 9 h, respectively.[1] The objective of this study has been to find a method for estimating L_d, L_e, L_n, and L_{den} in residential areas (Fig. 1). The influence of multiple reflections and diffraction by buildings, as well the ground effect and topography (Sec. III), can be estimated by only one measurement of $L_{Aeq,\tilde{T}}$, with $\tilde{T} \ll T$. The most important element of weather attenuation, in terms of the wind adjustment ΔL_α (Appendix), is taken into account. The method requires the means and standard deviations of the traffic flow $[\langle q\rangle, \sigma_q]$ and the traffic velocity $[\langle V\rangle, \sigma_V]$. All of them for the day, evening, and night time periods. Similar but not equivalent results are presented elsewhere.[2–22]

I. TIME AVERAGE SOUND EXPOSURE—*e*

The day-average sound level L_d is the time-average sound level between 07:00 and 19:00 h,[1]

$$L_d = 10\log\{e_d\}, \tag{1}$$

where

$$e_d = \frac{1}{T_d}\int_{t-T_d}^{t} \frac{p_A^2(t)}{p_o^2}dt \tag{2}$$

denotes the *day-average sound exposure*. In the above integral p_A^2 is the A-weighted squared sound pressure (Fig. 2), $T_d=12\cdot 3600t_o$, with $t_o=1$ s and $p_o=20$ μPa. The evening average sound level, for the time period from 19:00 to 22:00 h, can be calculated from

$$L_e = 10\log\{e_e\}, \tag{3}$$

with the corresponding *evening average sound exposure* e_e [Eq. (2) with T_d replaced by $T_e=3\cdot 3600t_o$]. Finally, the night average sound level between 22:00 to 07:00 h is defined by

$$L_n = 10\log\{e_n\}, \tag{4}$$

with the *night average sound exposure* e_n [Eq. (2) with T_d replaced by $T_n=9\cdot 3600t_o$].

Making use of L_d, L_e, and L_n, one can find the community noise equivalent level,[1]

$$L_{\text{den}} = 10\log\left\{\frac{12}{24}10^{0.1L_d} + \frac{3}{24}10^{0.1(L_e+5)} + \frac{9}{24}10^{0.1(L_n+10)}\right\}, \tag{5}$$

which can be rewritten as

$$L_{\text{den}} = 10\log\{e_{\text{den}}\}, \tag{6}$$

where

$$e_{\text{den}} = \frac{12}{24}e_d + \frac{3\sqrt{10}}{24}e_e + \frac{9\cdot 10}{24}e_n \tag{7}$$

is the *day-evening-night average sound exposure*.

Definitions of the noise descriptors, L_d, L_e, L_n, and L_{den} [Eqs. (1), (3), (4), and (6)] are similar to each other, namely,

$$L = 10\log\{e\}, \tag{8}$$

where the sound exposures, $e=e_d$, e_e, e_n, and e_{den} [Eqs. (2) and (7)], are positive, $e \geqslant 0$.

Varying number of vehicles and speed of their motion, as well as varying wind, are the major reasons of the variations in time-average sound exposure, $e_1, e_2, \ldots$, and e_N, for $N=365$ days, evenings, and nights of a year.

To prove that it is quite reasonable to assume normal distribution of e, we start with the results of noise measurements of $L_{Aeq}(06-22)$.[23] Figure 3 shows the typical histogram of road traffic noise, which can be approximated by the probability density function,

$$G(L) = \frac{0.1\ln(10)}{\sqrt{2\pi}}\frac{e}{\sigma}\exp\left\{-\frac{1}{2}\left[\frac{e^2}{\sigma^2} - \frac{\langle e\rangle^2}{\sigma^2}\right]\right\}, \tag{9}$$

where $e=10^{0.1L}$. The above function peaks at

$$L_{\max} = 10\log\{\langle e\rangle + \sqrt{\langle e\rangle^2 + 4\sigma^2}\} - 3 \text{ dB}. \tag{10}$$

Additional features of $G(L)$,

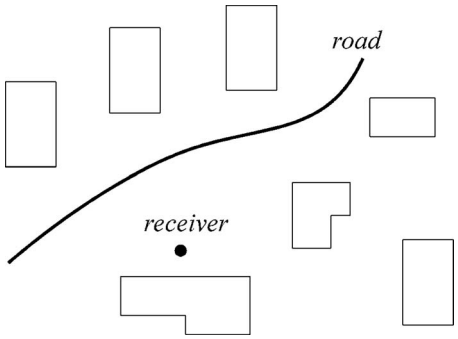


FIG. 1. Example of a road and receiver within an urban area.

$$\lim_{L\to 0} G(L) = 0, \quad \lim_{L\to 0} \frac{dG}{dL} = 0,$$
$$G(L_{\max} - \Delta L) > G(L_{\max} + \Delta L), \tag{11}$$

with $\langle e\rangle \approx 10^8$ and $\sigma \approx 10^7$ [Eq. (9)], are in accordance with the histogram shape of $L=L_{Aeq16}$ (Fig. 3). Conditions defined by Eq. (11) are met when the sound exposure distribution is normal,

$$F(e) = \frac{1}{\sigma\sqrt{2\pi}} \exp\left[-\frac{(e-\langle e\rangle)^2}{2\sigma^2}\right], \quad \sigma^2 = \langle e^2\rangle - \langle e\rangle^2, \tag{12}$$

with (Fig. 4)

$$\sigma \ll \langle e\rangle. \tag{13}$$

Under such circumstances, one can write

$$\int_{-\infty}^{+\infty} F(e)de \approx \int_{0}^{+\infty} F(e)de \approx 1, \tag{14}$$

and neglect the negative values of e (see definition 8). The probabilities that the sound exposure e falls within the intervals,

$$\langle e\rangle - 2\sigma < e < \langle e\rangle, \quad \langle e\rangle < e < \langle e\rangle + 2\sigma, \tag{15}$$

are equal to the half of 95%,[24]

$$\int_{\langle e\rangle-2\sigma}^{\langle e\rangle} F(e)de = \int_{\langle e\rangle}^{\langle e\rangle+2\sigma} F(e)de = \frac{1}{2}\cdot 0.95. \tag{16}$$

We describe the distribution of $L_1, L_2, \ldots$, and L_{365} with the measure of central tendency $\bar{L}$ and the measure of variation

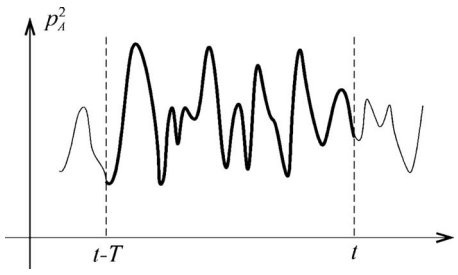


FIG. 2. Time pattern of the continuous A-weighted squared sound pressure, $p_A^2(t)$, of road traffic noise.

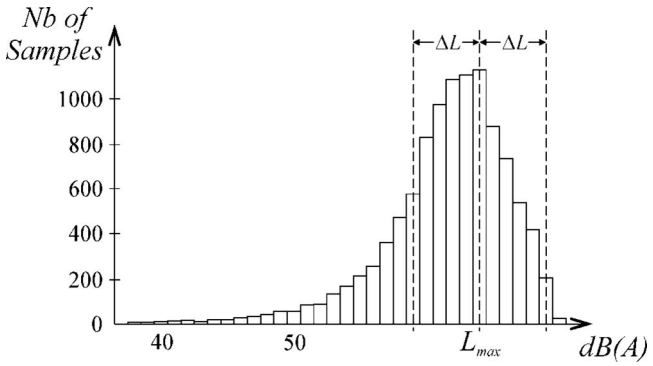


FIG. 3. Histogram of the time-average sound level, $L=L_{Aeq16}$.[23]

U_{95}. The former is related to the mean value of the average sound exposure $\langle e\rangle$ [Eq. (12)],

$$\bar{L} = 10\log\langle e\rangle, \tag{17}$$

and the latter to the boundaries of the confidence level,

$$L^{(1)} = 10\log\{\langle e\rangle - 2\sigma\}, \quad L^{(2)} = 10\log\{\langle e\rangle + 2\sigma\}. \tag{18}$$

The *width of the confidence interval* is defined by

$$U_{95} = L^{(2)} - L^{(1)} = 10\log\left\{1 + 2\frac{\sigma}{\langle e\rangle}\right\} - 10\log\left\{1 - 2\frac{\sigma}{\langle e\rangle}\right\}. \tag{19}$$

Thus, with the confidence level 0.95, any value of level L lies in the confidence interval [Eq. (18)],

$$L^{(1)} < L < L^{(2)}. \tag{20}$$

Now we translate Eq. (16) into

$$\int_{L^{(1)}}^{\bar{L}} G(L)dL = \int_{\bar{L}}^{L^{(2)}} G(L)dL = \frac{1}{2}\cdot 0.95, \tag{21}$$

where the probability density function $G(L)$ is defined by Eq. (9).

II. TIME AVERAGE SOUND LEVEL—*L*

Variations in the day-average sound level L_d are characterized by [Eqs. (17) and (19)]

$$\bar{L}_d = 10\log\langle e_d\rangle. \tag{22}$$

and

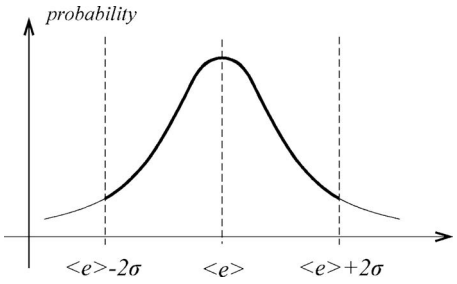


FIG. 4. Probability distribution function $F(e)$ of the sound exposure e [Eq. (12)] with the confidence level of 0.95. Statistical distribution $F(L)$ of the time-average sound level L [Eq. (22)] with the confidence level of 0.95.

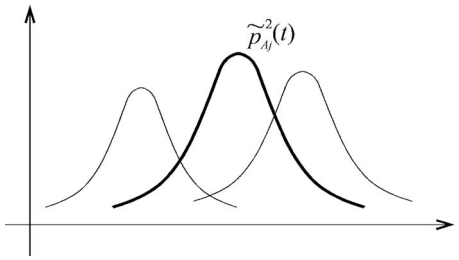


FIG. 5. Time pattern of the A-weighted squared sound pressure, $\tilde{p}^2_{Aj}(t)$, of noise produced by the jth vehicle.

$$U_{95}^{(d)} = 10\log\left\{1 + 2\frac{\sigma_d}{\langle e_d\rangle}\right\} - 10\log\left\{1 - 2\frac{\sigma_d}{\langle e_d\rangle}\right\}. \tag{23}$$

Similarly, for the evening average sound level L_e and the night average sound level L_n, one gets,

$$\bar{L}_e = 10\log\langle e_e\rangle, \tag{24}$$

$$U_{95}^{(e)} = 10\log\left\{1 + 2\frac{\sigma_e}{\langle e_e\rangle}\right\} - 10\log\left\{1 - 2\frac{\sigma_e}{\langle e_e\rangle}\right\}, \tag{25}$$

and

$$\bar{L}_n = 10\log\langle e_n\rangle, \tag{26}$$

$$U_{95}^{(n)} = 10\log\left\{1 + 2\frac{\sigma_n}{\langle e_n\rangle}\right\} - 10\log\left\{1 - 2\frac{\sigma_n}{\langle e_n\rangle}\right\}, \tag{27}$$

respectively. Ultimately, mindful of Eqs. (6) and (7) the measures of central tendency and variation of the day-evening-night average sound level are as follows:

$$\bar{L}_{\text{den}} = 10\log\left\{\frac{12}{24}\langle e_d\rangle + \frac{3\sqrt{10}}{24}\langle e_e\rangle + \frac{90}{24}\langle e_n\rangle\right\} \tag{28}$$

and

$$U_{95}^{(\text{den})} = 10\log\left\{1 + 2\frac{\sigma_{\text{den}}}{\langle e_{\text{den}}\rangle}\right\} - 10\log\left\{1 - 2\frac{\sigma_{\text{den}}}{\langle e_{\text{den}}\rangle}\right\}, \tag{29}$$

where

$$\frac{\sigma_{\text{den}}}{\langle e_{\text{den}}\rangle} = \frac{\sqrt{16\sigma_d^2 + 10\sigma_e^2 + 900\sigma_n^2}}{4\langle e_d\rangle + \sqrt{10}\langle e_e\rangle + 30\langle e_n\rangle}. \tag{30}$$

III. VEHICLE SOUND EXPOSURE

In order to determine the community noise equivalent level, $\bar{L}_{\text{den}}$, and the width of the confidence interval $U_{95}^{(\text{den})}$ [Eqs. (28) and (30)], the values of $\langle e_d\rangle$, $\langle e_e\rangle$, $\langle e_n\rangle$, and σ_d, σ_e, σ_n are required. If q vehicles pass the receiver within the time interval $T = 12\cdot 3600$, $3\cdot 3600$, or $9\cdot 3600$ s, then the road traffic noise is a combination of q_i noise events (Figs. 2 and 5),

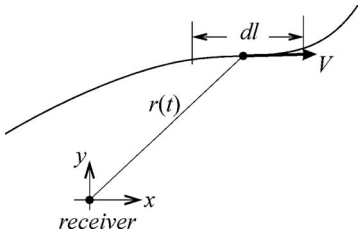


FIG. 6. A vehicle moving along its path at a steady speed V.

$$p_A^2(t) = \sum_{j=1}^{q} \tilde{p}^2_{Aj}(t), \tag{31}$$

where $\tilde{p}^2_{Aj}(t)$ is the time pattern of the A-weighted squared sound pressure due to the jth vehicle. Inserting Eq. (31) into Eq. (2) gives the sound exposure for the ith day, evening, or night,

$$e_i = \frac{t_o}{T}\sum_{j=1}^{q_i} \varepsilon_{ij}. \tag{32}$$

Here, the noise coming from the jth vehicle is characterized by the *vehicle sound exposure*,

$$\varepsilon_j = \frac{1}{p_o^2 t_o}\int_l \tilde{p}^2_{Aj}\frac{dl}{V}, \tag{33}$$

where V is the vehicle speed and the above integration runs over the vehicle trajectory (Figs. 1 and 6). For 365 days of a year, Eq. (32) yields the mean sound exposure,

$$\langle e\rangle = \frac{t_o}{365T}\sum_{i=1}^{365}\sum_{j=1}^{q_i} \varepsilon_{ij}. \tag{34}$$

For the total number of vehicles passing the receiver during a year, i.e., within the time interval $365T$,

$$Q = \sum_{i=1}^{365} q_i, \tag{35}$$

Eq. (34) can be modified to the form

$$\langle e\rangle = \frac{t_o}{T}\langle q\rangle\langle\varepsilon\rangle, \tag{36}$$

with the means

$$\langle q\rangle = \frac{1}{365}\sum_{i=1}^{365} q_i, \quad \langle\varepsilon\rangle = \frac{1}{Q}\sum_{j=1}^{Q} \varepsilon_j. \tag{37}$$

Definition of the second moment of the sound exposure for 365 days and formula (32) imply,

$$\langle e^2\rangle = \left(\frac{t_o}{T}\right)^2\left\{\frac{1}{365}\sum_{i=1}^{365}\sum_{j=1}^{q_i}\varepsilon_{ij}^2 + \frac{1}{365}\sum_{i=1}^{365}\sum_{j\neq k=1}^{q_i^2-q_i}\varepsilon_{ij}\varepsilon_{ik}\right\}. \tag{38}$$

With

$$\langle\varepsilon^2\rangle = \frac{1}{Q}\sum_{j=1}^{Q}\varepsilon_j^2, \quad \langle q^2\rangle = \frac{1}{365}\sum_{i=1}^{365} q_i^2, \tag{39}$$

Eq. (38) simplifies to the form[18]

$$\langle e^2\rangle = \left(\frac{t_o}{T}\right)^2 \{\langle q\rangle\langle \varepsilon^2\rangle + [\langle q^2\rangle - \langle q\rangle]\langle \varepsilon\rangle^2\}. \tag{40}$$

Finally, Eqs. (12), (26), and (40) combine into the variance of the sound exposure

$$\sigma^2 = \left(\frac{t_o}{T}\right)^2 [\langle q\rangle\sigma_\varepsilon^2 + \langle \varepsilon\rangle^2\sigma_q^2], \tag{41}$$

where the variances of the traffic flow q and the variance of the vehicle sound exposure ε are

$$\sigma_q^2 = \langle q^2\rangle - \langle q\rangle^2, \quad \sigma_\varepsilon^2 = \langle \varepsilon^2\rangle - \langle \varepsilon\rangle^2. \tag{42}$$

The Technical Committee of the Acoustical Society of Japan has accumulated thousands of data about four categories of road vehicles: passenger, small, medium, and large sized. Then, for simplicity, two subdivisions have been adopted with light (l) and heavy vehicles.[25] For the vehicle percentage, $0 \leqslant \alpha \leqslant 1$, one can write,

$$q_{li} = \alpha \cdot q_i, \quad q_{hi} = (1-\alpha)\cdot q_i. \tag{43}$$

Thus, Eqs. (36), (40), and (41) yield

$$\langle e\rangle = \frac{t_o}{T}\langle q\rangle[\alpha\cdot\langle \varepsilon_l\rangle + (1-\alpha)\cdot\langle \varepsilon_h\rangle] \tag{44}$$

and

$$\sigma^2 = \left(\frac{t_o}{T}\right)^2 \{\langle q\rangle[\alpha\sigma_{\varepsilon l}^2 + (1-\alpha)\sigma_{\varepsilon h}^2] + [\alpha^2\langle \varepsilon_l\rangle^2 + (1-\alpha)^2\langle \varepsilon_h\rangle^2]\}. \tag{45}$$

Here the sound exposures for light and heavy vehicles are characterized by [Eq. (37), (39), and (43)],

$$\langle \varepsilon_l\rangle = \frac{1}{\alpha Q}\sum_{j=1}^{\alpha Q}\varepsilon_{lj}, \quad \langle \varepsilon_l^2\rangle = \frac{1}{\alpha Q}\sum_{j=1}^{\alpha Q}\varepsilon_{lj}^2, \quad \sigma_{\varepsilon l}^2 = \langle \varepsilon_l^2\rangle - \langle \varepsilon_l\rangle^2, \tag{46}$$

and

$$\langle \varepsilon_h\rangle = \frac{1}{(1-\alpha)Q}\sum_{j=1}^{(1-\alpha)Q}\varepsilon_{hj},$$

$$\langle \varepsilon_h^2\rangle = \frac{1}{(1-\alpha)Q}\sum_{j=1}^{(1-\alpha)Q}\varepsilon_{hj}^2, \quad \sigma_{\varepsilon h}^2 = \langle \varepsilon_h^2\rangle - \langle \varepsilon_h\rangle^2, \tag{47}$$

where αQ and $(1-\alpha)Q$ denote the total number of light and heavy vehicles [Eq. (35)]. Now we show how to determine $\langle \varepsilon\rangle$ and σ_ε.

We start with the A-weighted squared sound pressure of noise generated by a single vehicle,[26]

$$\tilde{p}_A^2 = \frac{W_A(V)\rho c}{4\pi r^2}Q(\bar{r}_o, \ldots)\cdot G(r, \ldots), \tag{48}$$

where r is the vehicle-receiver distance (Fig. 6), ρc denotes the characteristics impedance of air, and $W_A(V)$ expresses the speed dependent A-weighted sound power. With the unit vector $\bar{r}_o$, the function $Q(\bar{r}_o, \ldots)$ represents the radiation pattern of the source and the function $G(r, \ldots)$ quantifies the attenuation in excess of geometrical spreading. The latter includes ground effect, multiple reflections and diffraction by buildings (Fig. 1), and last but not least, influence of wind (see Appendix). The explicit forms of both $Q(\ldots)$ and $G(r, \ldots)$ are not needed, because the method presented here is based on a noise measurement at the site of interest. Inserting expression (48) into the integral (33) brings about the vehicle sound exposure,[18]

$$\varepsilon_j = s_j \cdot K. \tag{49}$$

Here the *generation parameter* s and *propagation parameter* k are as follows:

$$s_j = \frac{W_A(V_j)}{W_o}\frac{V_o}{V_j}, \quad K = \frac{l_o}{4\pi}\int_l Q(\bar{r}_o, \ldots)\frac{G(r, \ldots)}{r^2}dl, \tag{50}$$

where $l_o = 1$ m. Taking into account Eqs. (37), (42), and (49), the mean and the standard deviation of the vehicle sound exposure are

$$\langle \varepsilon\rangle = K\cdot\langle s\rangle, \quad \langle \varepsilon^2\rangle = K^2\cdot\langle s^2\rangle, \quad \sigma_\varepsilon = K\cdot\sigma_s, \tag{51}$$

where

$$\langle s\rangle = \frac{1}{Q}\sum_{j=1}^{Q}s_j, \quad \langle s^2\rangle = \frac{1}{Q}\sum_{j=1}^{Q}s_j^2, \quad \sigma_s^2 = \langle s^2\rangle - \langle s\rangle^2. \tag{52}$$

By applying Eqs. (36), (41), and (51), we find,

$$\langle e\rangle = \frac{t_o}{T}K\cdot\langle q\rangle\langle s\rangle, \quad \sigma^2 = \left(\frac{t_o}{T}\right)^2 K^2\cdot[\langle q\rangle\sigma_s^2 + \langle s\rangle^2\sigma_q^2], \tag{53}$$

and

$$\frac{\sigma^2}{\langle e\rangle^2} = \frac{1}{\langle q\rangle}\frac{\sigma_s^2}{\langle s\rangle^2} + \frac{\sigma_q^2}{\langle q\rangle^2}. \tag{54}$$

The case of noise produced by two categories of vehicles is described by [Eqs. (44), (45), and (51)],

$$\langle e\rangle = \frac{t_o}{T}K\cdot\langle q\rangle[\alpha\cdot\langle s_l\rangle + (1-\alpha)\cdot\langle s_h\rangle], \tag{55}$$

$$\sigma^2 = \left(\frac{t_o}{T}\right)^2 K^2\cdot\{\langle q\rangle[\alpha\sigma_{sl}^2 + (1-\alpha)\sigma_{sh}^2] + [\alpha\langle s_l\rangle + (1-\alpha)\langle s_h\rangle]^2\sigma_q^2\}, \tag{56}$$

and

$$\frac{\sigma^2}{\langle e\rangle^2} = \frac{1}{\langle q\rangle}\frac{\alpha\sigma_{sl}^2 + (1-\alpha)\sigma_{sh}^2}{[\alpha\langle s_l\rangle + (1-\alpha)\langle s_h\rangle]^2} + \frac{\sigma_q^2}{\langle q\rangle^2}. \tag{57}$$

Note that either $\alpha = 1$ or $\alpha = 0$ simplifies the above relation into Eq. (54).

A. Calculation of the generation parameter—*s*

Measurements of road traffic noise in Japan[25] have shown that the A-weighted sound power of a single vehicle, which moves at a steady speed, is given by

$$L_{Wl} = L_l + 30\log(V/V_o), \quad L_{Wh} = L_h + 30\log(V/V_o), \quad (58)$$

where $V_o = 1$ km/h. The constants $L_l = 46.7$ and $L_h = 53.2$ describe the noise emission by a light and a heavy vehicle, respectively. Both values include the effects of tires and pavements. From definition of the A-weighted sound power level it follows the A-weighted sound power,

$$W_{Al} = W_l \cdot (V/V_o)^3, \quad W_{Ah} = W_h \cdot (V/V_o)^3, \quad (59)$$

where

$$W_l = W_o \cdot 10^{0.1L_l}, \quad W_h = W_o \cdot 10^{0.1L_h}, \quad (60)$$

and the reference sound power, $W_o = 10^{-12}$ W. Here we see that the generation parameter s becomes proportional to the second power of the vehicle speed [Eqs. (50), (59), and (60)],

$$s_j = \frac{10^{0.1L_{(\ldots)}}}{V_o^2} V_j^2, \quad (61)$$

where $L_{(\ldots)}$ equals either L_l or L_h. Definitions (52) imply the mean and the variance of the generation parameter,

$$\langle s\rangle = \frac{10^{0.1L_{(\ldots)}}}{V_o^2} \cdot \langle V^2\rangle, \quad \sigma_s^2 = \frac{10^{0.2L_{(\ldots)}}}{V_o^4}[\langle V^4\rangle - \langle V^2\rangle^2], \quad (62)$$

where the second and the fourth moments of the vehicle speed are

$$\langle V^2\rangle = \frac{1}{Q}\sum_{j=1}^{Q} V_j^2, \quad \langle V^4\rangle = \frac{1}{Q}\sum_{j=1}^{Q} V_j^4. \quad (63)$$

At off-peak hours the vehicle speed variation is likely to approach the normal distribution,[27]

$$F(V) = \frac{1}{\sigma_V\sqrt{2\pi}} \exp\left[-\frac{(V-\langle V\rangle)^2}{2\sigma_V^2}\right], \quad (64)$$

where

$$\langle V\rangle = \frac{1}{Q}\sum_{j=1}^{Q} V_j, \quad \sigma_V^2 = \langle V^2\rangle - \langle V\rangle^2. \quad (65)$$

For a normal distribution, the fourth moment $\langle V^4\rangle$ depends on the mean $\langle V\rangle$ and the variance σ_V^2,[28]

$$\langle V^4\rangle = 3\sigma_V^4 + 6\sigma_V^2 \cdot \langle V\rangle^2 + \langle V\rangle^4. \quad (66)$$

Equations (62), (65), and (66) combine into the mean and variance of the generation parameter, for light (l) and heavy (h) vehicles,

$$\langle s_l\rangle = 10^{0.1L_l}\frac{\langle V_l\rangle^2}{V_o^2}\left[1 + \frac{\sigma_{Vl}^2}{\langle V_l\rangle^2}\right],$$
$$\sigma_{sl}^2 = 2 \cdot 10^{0.2L_l}\frac{\langle V_l\rangle^4}{V_o^4} \cdot \frac{\sigma_{Vl}^2}{\langle V_l\rangle^2}\left[2 + \frac{\sigma_{Vl}^2}{\langle V_l\rangle^2}\right], \quad (67)$$

and

$$\langle s_h\rangle = 10^{0.1L_h}\frac{\langle V_h\rangle^2}{V_o^2}\left[1 + \frac{\sigma_{Vh}^2}{\langle V_h\rangle^2}\right],$$
$$\sigma_{sh}^2 = 2 \cdot 10^{0.2L_h}\frac{\langle V_h\rangle^4}{V_o^4} \cdot \frac{\sigma_{Vh}^2}{\langle V_h\rangle^2}\left[2 + \frac{\sigma_{Vh}^2}{\langle V_h\rangle^2}\right]. \quad (68)$$

For both categories of vehicles, the relative measure of variance in the process of noise generation is

$$\frac{\sigma_s^2}{\langle s\rangle^2} = 2\frac{\sigma_V^2}{\langle V\rangle^2}\left[2 + \frac{\sigma_V^2}{\langle V\rangle^2}\right] \cdot \left[1 + \frac{\sigma_V^2}{\langle V\rangle^2}\right]^{-2}. \quad (69)$$

In Ref. 29, one can find $\sigma_V/\langle V\rangle = 0.308$, 0.195, 0.163, 0.163, and 0.185 for motorcycles, cars, light goods, buses-coaches, and two axle trucks, respectively. Consequently, Eq. (69) yields rather small values of $\sigma_s/\langle s\rangle = 0.33$, 0.14, 0.10, 0.15, and 0.13. Thus, the following approximations seems to be admissible [Eqs. (67)–(69)],

$$\langle s_l\rangle \approx 10^{0.1L_l}\frac{\langle V_l\rangle^2}{V_o^2}, \quad \sigma_{sl}^2 \approx 4 \cdot 10^{0.2L_l}\frac{\langle V_l\rangle^4}{V_o^4} \cdot \frac{\sigma_{Vl}^2}{\langle V_l\rangle^2}, \quad (70)$$

and

$$\langle s_h\rangle \approx 10^{0.1L_h}\frac{\langle V_h\rangle^2}{V_o^2}, \quad \sigma_{sh}^2 \approx 4 \cdot 10^{0.2L_h}\frac{\langle V_h\rangle^4}{V_o^4} \cdot \frac{\sigma_{Vh}^2}{\langle V_h\rangle^2}. \quad (71)$$

B. Measurement of the propagation parameter—*K*

To determine the propagation parameter K, one measurement (within the interval time $\tilde{T} \ll T$) of the time averages sound level, $\tilde{L} = L_{\mathrm{Aeq},\tilde{T}}$, is needed. The result of measurement is related to the average sound exposure $\tilde{e}$ [Eq. (8)],

$$\tilde{L} = 10\log\{\tilde{e}\}, \quad (72)$$

where [Eq. (32)]

$$\tilde{e} = \frac{t_o}{\tilde{T}}\left[\sum_{j=1}^{\tilde{q}_l}\tilde{\varepsilon}_{lj} + \sum_{j=1}^{\tilde{q}_h}\tilde{\varepsilon}_{hj}\right], \quad (73)$$

with the vehicle sound exposures [Eqs. (49) and (61)],

$$\tilde{\varepsilon}_{lj} = K\frac{10^{0.1L_l}}{V_o^2}\tilde{V}_{lj}^2, \quad \tilde{\varepsilon}_{hj} = K\frac{10^{0.1L_h}}{V_o^2}\tilde{V}_{hj}^2. \quad (74)$$

Taking into regard Eqs. (73) and (74), one arrives at

$$\tilde{e} = K\frac{t_o}{\tilde{T}}\left[\tilde{q}_l \cdot 10^{0.1L_l}\frac{\langle\tilde{V}_l^2\rangle}{V_o^2} + \tilde{q}_h \cdot 10^{0.1L_h}\frac{\langle\tilde{V}_h^2\rangle}{V_o^2}\right], \quad (75)$$

where

$$\langle\tilde{V}_l^2\rangle = \frac{1}{\tilde{q}_l}\sum_{j=1}^{\tilde{q}_l}\tilde{V}_{lj}^2, \quad \langle\tilde{V}_h^2\rangle = \frac{1}{\tilde{q}_h}\sum_{j=1}^{\tilde{q}_h}\tilde{V}_{hj}^2. \quad (76)$$

Replacing $\tilde{e}$ in Eq. (72) by formulas (75) yields the propagation parameter,

$$K = \frac{\tilde{T}}{t_o}\left[\tilde{q}_l 10^{0.1(L_l-\tilde{L})}\frac{\langle \tilde{V}_l^2\rangle}{V_o^2} + \tilde{q}_h 10^{0.1(L_h-\tilde{L})}\frac{\langle \tilde{V}_h^2\rangle}{V_o^2}\right]^{-1}, \quad (77)$$

where $L_l=46.7$, $L_h=53.2$, and $\tilde{L}$ is the result of noise measurement. It is assumed that the values of $\tilde{q}_l$, $\tilde{q}_h$, and $\langle \tilde{V}_l^2\rangle$, $\langle \tilde{V}_h^2\rangle$ [Eq. (76)] are known.

IV. EXAMPLE

The receiver was located at the distance 75 m from the center line of the four lane road. In 1 h time period, $\tilde{T}=1$ h $=3600t_o$, velocities of light and heavy vehicles, V_l and V_h [km/h], were measured. Their second moments are [Eq. (76)]: $\langle \tilde{V}_l^2\rangle=18.225\times10^3$ and $\langle \tilde{V}_h^2\rangle=8.281\times10^3$. The result of measurement, $\tilde{L}=L_{Aeq,1h}=57.4$ dB, encompasses the noise from $\tilde{q}_l=243$ light and $\tilde{q}_h=316$ heavy vehicles. Substitution all of these values into Eq. (77) yields the parameter of propagation, $K\approx2.62\times10^{-3}$, which characterizes, among others, geometrical spreading, ground effect, and reflection from nearby buildings.

Now we will show how to estimate the night average sound level L_n [Eqs. (26) and (27)]. Making use of the data from Ref. 29 for the speed of light and heavy vehicles, $\sigma_{Vl}/\langle V_l\rangle=0.195$, $\sigma_{Vh}/\langle V_h\rangle=0.185$, expressions (70) and (71) take the form

$$\langle s_l\rangle \approx 4.67\times10^4\frac{\langle V_l\rangle^2}{V_o^2}, \quad \sigma_{sl}^2 \approx 3.33\times10^8\frac{\langle V_l\rangle^4}{V_o^4}, \quad (78)$$

and

$$\langle s_h\rangle \approx 2.10\times10^5\frac{\langle V_h\rangle^2}{V_o^2}, \quad \sigma_{sh}^2 \approx 5.97\times10^9\frac{\langle V_h\rangle^4}{V_o^4}. \quad (79)$$

For the night time interval $T_n=9\cdot3600t_o$, combination of Eqs. (17), (55), (78), and (79), with the propagation parameter, $K\approx2.62\times10^{-3}$ (see above), gives the central tendency of the night average sound level,

$$\bar{L}_n \approx 10\log\left\{\langle q_n\rangle\left[4.67\alpha_n\frac{\langle V_l\rangle^2}{V_o^2} + 21.0\cdot(1-\alpha_n)\frac{\langle V_h\rangle^2}{V_o^2}\right]\right\} - 1 \text{ dB}, \quad (80)$$

where $10\log\{(9\cdot3600)/26.2\}\approx31$ dB and $\langle q_n\rangle$ denotes the mean number of vehicles (both categories), which pass the receiver between 22:00–7:00 h.

For mean speeds of light and heavy vehicles: $\langle V_l\rangle=120$ and $\langle V_h\rangle=80$ km/h, Eq. (65) enables to transform the expression (80) into the relationship between, $\bar{L}_n$—measure of central tendency, α_n—vehicle percentage, and $\langle q_n\rangle$—mean number of vehicle passing the receiver during nine night hours (Fig. 7),

$$\bar{L}_n \approx 10\log\{\langle q_n\rangle[6.72\alpha_n + 13.4(1-\alpha_n)]\} + 9 \text{ dB}. \quad (81)$$

For example, with $\alpha_n=0.5$, one obtains

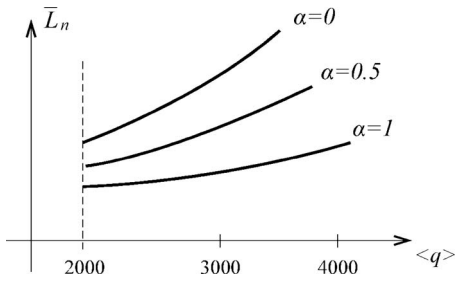


FIG. 7. Plot of Eq. (81) for vehicle percentages: $\alpha_n=0$ (only heavy vehicles), $\alpha_n=0.5$, and $\alpha_n=1$ (only light vehicles).

$$\bar{L}_n = 10\log\{\langle q_n\rangle\} + 19 \text{ dB}. \quad (82)$$

Then, taking $\sigma_q/\langle q\rangle=0.143$ (result of measurements), Eqs. (57), (78), and (79), with $\langle V_l\rangle=120$ and $\langle V_h\rangle=80$ km/h, give

$$\frac{\sigma_n^2}{\langle e_n\rangle^2} = \frac{1}{\langle q_n\rangle}\frac{6.91\alpha_n + 24.2(1-\alpha_n)}{[6.72\alpha_n + 13.4(1-\alpha_n)]^2} + 0.02. \quad (83)$$

Ultimately, combination of Eqs. (27) and (83) yields the width of the confidence interval, $U_{95}^{(n)}(\alpha_n,\langle q_n\rangle)$ (Fig. 8). For special case of $\alpha_n=0.5$,

$$U_{95}^{(n)} = 10\log\left\{1+2\sqrt{\frac{0.154}{\langle q_n\rangle}+0.02}\right\} - 10\log\left\{1-2\sqrt{\frac{0.154}{\langle q_n\rangle}+0.02}\right\}. \quad (84)$$

Setting the mean number of vehicles for night hours $\langle q_n\rangle=3000$ (veh), the above expression the width of the confidence interval, $U_{95}^{(n)}=2.5$ dB.

V. CONCLUSIONS

The purpose of this study is to estimate the time average sound levels, such as day evening- and night-average sound levels, L_d, L_e, L_n, (Eqs. (1), (3), and (4)), and community noise equivalent level, L_{den} (Eq. (5)). The estimation encompasses the measure of the central tendency $\bar{L}$ [Eqs. (17), (22), (24), (26), and (28)] and the width of the confidence interval U_{95} [Eqs. (19), (23), (25), (27), and (29)]. To determine all these characteristics, only one measurement of the time-average sound level, $\tilde{L}=L_{Aeq,\tilde{T}}$, has to be performed. Additionally the means and standard deviations of the traffic flow, $\langle q\rangle$; σ_q, and traffic speed, $\langle V\rangle$; σ_V, are needed.

The limitations of the method come from the basic as-

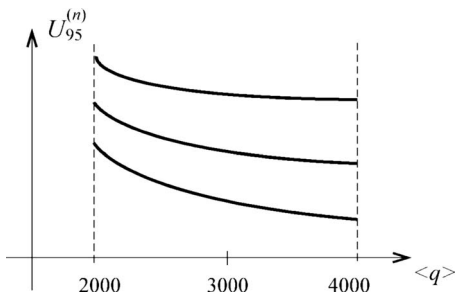


FIG. 8. Dependence of the confidence interval width, $U_{95}^{(n)}$, on the mean number of vehicles, $\langle q_n\rangle$, for $\alpha_n=0$, $\alpha_n=0.5$, and $\alpha_n=1$ [Eqs. (27) and (83)].

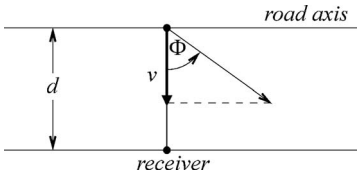


FIG. 9. Component of the wind speed perpendicular to the road axis, v.

sumptions are as follows:

- normal distribution of day-evening-night average sound exposure, e;
- there are two categories of vehicles: light and heavy;
- the vehicles speed is constant;
- the distance between the receiver and the road axis does not exceed 100 m, so the variations in air attenuation can be neglected.

Despite its limitations, the method does not fall entirely outside the sphere of reality. It would become more precise by refining the above assumptions. For example, by rejecting the assumption of normal distribution [Eq. (12)], by including a few categories of vehicles and assuming varying traffic speed.[30] The wind effect is discussed in the Appendix.

ACKNOWLEDGMENT

The authors are grateful to the reviewers for their valuable comments.

APPENDIX

Most predictions method of road traffic noise, such as FHWA TNM (Ref. 31) and ASJ RTA,[32] compute the noise descriptors through the series of adjustments. To account the influence of wind, we write the propagation parameter as a product,

$$K = \alpha \cdot K_o, \tag{A1}$$

where α represents the wind effect and K_o characterizes the remaining propagation phenomena. In order to find the time-average sound level, $L_{Aeq,T}$, we combine Eqs. (11), (23), (49), and (A1),

$$L_{Aeq,T} = 10 \log\left\{\frac{t_o}{T} s K_o\right\} + \Delta L_\alpha, \tag{A2}$$

where

$$\Delta L_\alpha = 10 \log \alpha, \tag{A3}$$

represents the adjustment for wind. In Ref. 32, one finds

$$\Delta L_\alpha = 0.88 \cdot v \log\left\{\frac{d}{d_o}\right\}, \tag{A4}$$

where $d_o = 15$ m and v [m/s] is the wind speed component perpendicular to the road axis (Fig. 9). Comparing Eqs. (A3) and (A4), one arrives at the *wind parameter* for jth vehicle,

$$\alpha_j = \left(\frac{d}{d_o}\right)^{0.088 v_j}. \tag{A5}$$

Variations in wind direction makes the wind speed component v_j, either positive $(-\pi/2 < \Phi < +\pi/2)$ or negative $(+\pi/2 < \Phi < +3\pi/2)$. In the former and the latter cases, one gets $\alpha_j > 1$ (noise level increase—$\Delta L_\alpha > 0$) and $\alpha_j < 1$ (noise level decrease—$\Delta L_\alpha < 0$), respectively. Now, for the mean, second moment, and variance of the wind parameter,

$$\langle \alpha \rangle = \frac{1}{Q} \sum_{j=1}^{Q} \left(\frac{d}{d_o}\right)^{0.088 v_j}, \quad \langle \alpha^2 \rangle = \frac{1}{Q} \sum_{j=1}^{Q} \left(\frac{d}{d_o}\right)^{0.176 v_j}, \quad \sigma_\alpha^2 = \langle \alpha^2 \rangle - \langle \alpha \rangle^2, \tag{A6}$$

expressions (53) and (54) take the forms,

$$\langle e \rangle = \frac{t_o}{T} K_o \cdot \langle q \rangle \langle s \rangle \langle \alpha \rangle, \tag{A7}$$

$$\sigma^2 = \left(\frac{t_o}{T}\right)^2 K^2 \cdot [\langle q \rangle (\langle s \rangle^2 \sigma_\alpha^2 + \langle \alpha \rangle^2 \sigma_s^2) + \langle s \rangle^2 \langle \alpha \rangle^2 \sigma_q^2], \tag{A8}$$

and

$$\frac{\sigma^2}{\langle e \rangle^2} = \frac{1}{\langle q \rangle} \left[\frac{\sigma_s^2}{\langle s \rangle^2} + \frac{\sigma_\alpha^2}{\langle \alpha \rangle^2}\right] + \frac{\sigma_q^2}{\langle q \rangle^2}. \tag{A9}$$

[1] ANSI S1.1, "Acoustical Terminology," (1994).
[2] P. D. Schomer, R. E. De Vor, and W. A. Kline, "Sampling strategies for monitoring noise in the vicinity of airports," J. Acoust. Soc. Am. **73**, 2041–2050 (1983).
[3] M. Ohta and Y. Mitani, "A practical prediction method for road traffic noise at a T-type road intersections based on the image method," Acustica **67**, 152–156 (1988).
[4] R. Makarewicz, "Moments of probability distribution of equivalent continuous A-weighted sound pressure level," J. Acoust. Soc. Jpn. (E) **14**, 25–28 (1993).
[5] M. Yoshida, "Estimation of equivalent sound pressure levels of community noise and road traffic noise," J. Acoust. Soc. Jpn. (E) **15**, 53–57 (1995).
[6] M. Maurin, "Stochastic processes in environmental acoustics," Tenth International Symposium on Applied Stochastic Models and Data Analysis, Compiegne, 2001.
[7] ANSI S12.9-1992, Part 2, "Quantities and procedures for description and measurement of environmental sound," Part 2 (2003).
[8] E. Gaja, A. Gimenez, S. Sancho, and A. Reig, "Sampling techniques for the estimation of the annual equivalent noise level under urban traffic conditions," Appl. Acoust. **64**, 43–53 (2003).
[9] J. Alberola, I. H. Flindell, and A. J. Bullmore, "Variability in road traffic noise levels," Appl. Acoust. **66**, 1180–1195 (2005).
[10] J. Defrance, F. Aballea, and M. Baulac, "Accuracy of outdoor sound propagation prediction in a complex environment using some reference numerical model," International INCE Symposium, Le Mans, 2005.
[11] R. Diehl and U. Kurze, "Uncertainty in prediction of railroad noise emission," International INCE Symposium, Le Mans, 2005.
[12] A. Heiss, "The natural uncertainty descriptors for continuously fluctuating sound levels and its measurement," International INCE Symposium, Le Mans, 2005.
[13] W. Probst, "Uncertainties in acoustic and vibration simulation," International INCE Symposium, Le Mans, 2005.
[14] G. Thomann and W. Krebs, "Uncertainty of measured and calculated aircraft noise," International INCE Symposium, Le Mans, 2005.
[15] G. Zambon, S. Radaelli, and A. Bisceglie, "Error's evaluation in the estimate of the noise from the road traffic," International INCE Symposium, Le Mans, 2005.
[16] J. Ejsmont and G. Ronowski, "Estimation of the A-weighted long term

average sound level," Inter-Noise 2006, Honolulu, 2006.
[17]R. Makarewicz and R. Gołebiewski, "Estimation of the A-weighted long term average sound level," Acta. Acust. Acust. **92**, 574–577 (2006).
[18]R. Makarewicz and R. Golebiewski, "Uncertainty of traffic noise prediction," Acta. Acust. Acust. **92**, 578–582 (2006).
[19]G. Brambilla, F. Castro, A. Cerniglia, and P. Verardi, "Accuracy of temporal sampling of environmental noise," Inter-Noise 2007, Instanbul, 2007.
[20]H. Jonasson, "Determination of L_{den} and L_{night} using measurements," IMA32-040510-SP10, 2007.
[21]S. Kephalopoulus, M. Paviotti, D. Knauss, and M. Berengier, "Uncertainties in long-term road noise monitoring including meteorological variations," Noise Control Eng. J. **55**, 133–141 (2007).
[22]R. Makarewicz, "Day-evening-night level calculation from road traffic noise measurements in residential areas," Acta. Acust. Acust. **93**, 324–326 (2007).
[23]D. Ecotiere, B. Gauvreau, and M. Berengier, "Long-term sound levels: experimental observation and theoretical estimation," Inter-Noise 2006, Honolulu, 2006.
[24]W. T. Eadie, D. Drijard, F. E. James, M. Roos, and B. Sadoulet, *Statistical Methods in Experimental Physics* (North-Holland, Amsterdam, 1982).
[25]S. Kono, Y. Oshino, T. Iwase, T. Sone, and H. Tachibana, "Road traffic noise prediction model ASJ RTN-Model 2003 proposed by the Acoustical Society of Japan, Part 2," ICA 2004, Kyoto.
[26]A. D. Pierce, *Acoustics: An Introduction to Its Physical Principles and Applications* (Acoustical Society of America, New York, 1989).
[27]G. Watts, D. van Maercke, H. van Leeuwen, R. Barelds, M. Beuving, J. Defrance, H. Jonasson, R. Nota, G. Taraldsen, and J. Witte, "Effects of speed distribution on the Harmonoise model predictions," Inter-Noise 2004, Prague 2004.
[28]R. Feynman, *Statistical Mechanics* (W. A. Benjamin, Reading, 1972).
[29]R. Nota, J. J. A. van Leeuwen, R. Barelds, M. Beuving, C. Cremezi, J. Drefrance, H. G. Jonasson, D. van Maecke, G. Taraldsen, G. Watts, and J. Witte, "Harmonoise: simplification of comprehensive source and propagation models," Inter Noise 2004, Prague, 2004.
[30]R. Makarewicz and P. Kokowski, "Prediction of noise changes due to traffic speed control," J. Acoust. Soc. Am. **122**, 2074–2081 (2007).
[31]FHWA Traffic Noise Model, U.S. Department of Transportation, FHWA-PD-96–010, Washington, DC, 1998.
[32]S. Yamamoto, K. Yoshishisa, T. Miyake, T. Tajika, and H. Tachibana, "Road traffic noise prediction model ASJ RTN-Model 2003 proposed by the Acoustical Society of Japan, Part 3," ICA 2004, Kyoto.

Estimates and bounds of dynamic permeability of granular media

Claude Boutin[a)]
Laboratoire Geomateriaux, DGCB-URA CNRS 1652, Ecole Nationale des Travaux Publics de l'Etat, Universite de Lyon, 69518 Vaulx-en-Velin Cedex, France

Christian Geindreau[b)]
Laboratoire Sols-Solides-Structures-Risques, UMR 5521 CNRS-UJF-INPG, 38041 Grenoble Cedex 9, France

(Received 20 December 2007; revised 28 June 2008; accepted 19 September 2008)

This paper presents a study of dynamic permeability of porous media combining homogenization of periodic media (HPM) and the self-consistent method (SCM). By taking advantage of the physical principles identified with HPM, the application of SCM leads to the determination of two physically admissible dynamic permeability assessments, both different from that given by the cell model. A comparison with numerical modeling demonstrates the fairly good reliability of the three estimates for granular media consisting of a periodic array of spherical grains. Furthermore, the self-consistent values enable exact bounds for the dynamic permeability of a wide class of porous media to be derived with a clear identification of their microstructure (grain and fluid size distribution).
© *2008 Acoustical Society of America.* [DOI: 10.1121/1.2999050]

PACS number(s): 43.55.Ev, 43.20.Bi, 43.35.Bf [KA] Pages: 3576–3593

I. INTRODUCTION

Among the effective transfer coefficients of heat, mass, solute, etc., through porous media, the dynamic permeability is a physical parameter that is used in various domains of the mechanics, such as soil mechanics, petroleum engineering, geophysics, and acoustics of noise absorbing materials. The prediction of the permeability from the basic morphological information of a given medium is thus of interest both in scientific and industrial fields. It is worth noting that the dynamic permeability is a highly variable parameter (over several decades) according to pore size, solid volume fraction, and frequency. This makes its prediction even more important than other parameters and explains why its identification and characterization receive particular attention.

Two theoretical methods have made major contributions to the clarification of the nature of the dynamic permeability, namely, the pioneering phenomenological approach based on the thermodynamics—developed by Biot,[1] continued, for instance, by Attenborough,[2] Johnson *et al.*[3] and Allard[4]—and the micro-macro approach using the homogenization of periodic media (HPM).[5–7] However, if the physics is well known, the question of reliable assessments and bounds of the dynamic permeability is still an open problem. As for *static* permeability, parametric studies were performed from numerical simulations[8] or using the self-consistent method (SCM) as proposed by Berdichevsky and Cai[9] for fibrous materials and by Boutin[10] for granular media. Fibrous materials were also investigated by a cell model close to the SCM by Tarnow.[11] In the dynamic range, exact expressions are available for plane slits or circular cylinders. As for more realistic morphologies, Auriault *et al.*[12] treated two dimensional channels, and Zhou and Sheng[13] and Chapman and Higdon[14] estimated, numerically, the dynamic permeability of packing of monodisperse spheres, for which Umnova *et al.*[15] proposed an analytical calculation based on a cell model.

By combining the advantages of the HPM and SCM approaches, the aim of this paper is to go further in this modeling by establishing *estimates* and *bounds* of the dynamic permeability valid for porous media made of packing of polydisperse spheres. The HPM enables us (i) to derive rigorously the macroscopic law from the equations at the pore scale and (ii) to give the theoretical expression of the macroscopic coefficients—such as the dynamic permeability—whatever the periodic microstructure is. However the quantification of these coefficients requires numerical computations. This involves numerous simulations for identifying correlations between coefficients and microstructure. Complementary to HPM, the interest of SCM is to propose plausible values. They are based on analytical solutions in simplified configurations assumed to capture the salient morphologic features, i.e., in the present case, the connection of the fluid, the pore size, and the porosity. If the basic analytical solution is exact, the application of the result to real porous media is generally conjectured[16] since, conversely to HPM, the microstructure is not treated explicitly. As for permeability, an additional difficulty arises because the governing equations are of different nature at the microscale (Navier–Stokes equation) and at the pore scale (Darcy law). Thus different estimates may be derived according to the assumptions taken for the basic solutions.

This paper is organized as follows. In Sec. II the derivation of the dynamic permeability using the HPM method is reviewed. Section III is devoted to the same problem using

a)Electronic mail: claude.boutin@entpe.fr
b)Electronic mail: christian.geindreau@hmg.inpg.fr

 © 2008 Acoustical Society of America

SCM and the principles identified by HPM. It is shown that two values of dynamic permeability can be conjectured, both being different from that given by the cell model. The interpretation of these results is covered in Sec. IV. First, a comparison with numerical modeling demonstrates the reliability of the estimates for granular media made of periodic arrays of identical spheres. Then, bounds of dynamic permeability are established for packing of polydisperse spheres.

II. DERIVATION OF DYNAMIC PERMEABILITY BY PERIODIC HOMOGENIZATION

A. Basic principles of periodic homogenization

The macroscopic representation of heterogeneous media makes sense only if there is a scale separation. This implies that[17]

- the material is regular enough to be described by a representative volume (this is mathematically expressed by assuming a periodic material made of identical cells Ω of size) and
- the physical variables driving the phenomenon—for flow in porous media, the pressure at the leading order—varies according to a size L larger than l.

To describe the variations at the well distinct lengths L and l, two spatial variables are introduced, $\mathbf{x}$ for the macroscopic variations and $\mathbf{y}$ for the microscopic variations, $\mathbf{x}$ and $\mathbf{y}$ being related by the scale ratio,

$$\varepsilon = l/L \ll 1, \quad \mathbf{y} = \varepsilon^{-1}\mathbf{x}.$$

The small parameter ε suggests seeking for any unknown u (scalar, vector, etc.) in the form of asymptotic expansions in powers of ε. As the material periodicity and the scale separation induce the same periodicity for the physical quantities, all the terms are Ω-periodic according to the variable $\mathbf{y}$,

$$u(\mathbf{x},\mathbf{y}) = \sum_{0}^{\infty} \varepsilon^i u^i(\mathbf{x},\mathbf{y}) \quad \text{with} \quad u^i(\mathbf{x},\mathbf{y}) \quad \Omega\text{-periodic in } \mathbf{y}. \tag{1}$$

The process of periodic homogenization consists in introducing the expansions in the two-variable rescaled equations that govern the physics at the local scale (i.e., equations where powers of ε are used for expressing the order of magnitude of the dimensionless numbers and where the common spatial derivative is transformed into $\varepsilon^{-1}\partial_y + \partial_x$), then identifying the terms of the same power in ε, and finally solving the boundary value problems obtained in series.

B. Dynamic permeability

The derivation of the dynamic Darcy law from HPM was established by Levy[18] and Auriault.[5] The main results that will be used in the following are now recalled. For briefness, they are presented in the case of a rigid porous media saturated by an incompressible fluid. It is known that the same derivations apply in the case of elastic skeleton and compressible fluid.[5] Consider a porous media (Fig. 1) of porosity ϕ, saturated by a fluid of viscosity μ and density ρ,

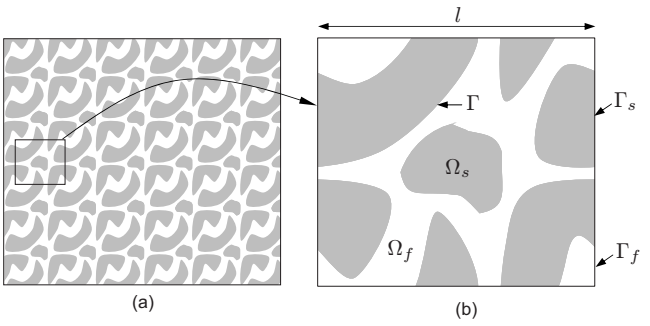


FIG. 1. (a) Macroscopic porous medium. (b) Periodic cell Ω of porous media. Ω_f and Ω_s are, respectively, the volume of the fluid and solid. Γ is the fluid-solid interface inside Ω. Γ_f and Γ_s are the fluid and solid interfaces at the boundary of Ω. $\phi = \Omega_f/\Omega$ is the porosity.

submitted to small harmonic perturbations of frequency $f = \omega/2\pi$. In the pores, the pressure variations p, fluid velocity $\mathbf{v}$ [$\mathbf{D}(\mathbf{v})$ is the strain rate tensor] is driven by the following linearized equations, in which the term $e^{+i\omega t}$ is omitted.

- In the pores Ω_f, the incompressibility [Eq. (2)], the viscous behavior [Eq. (3)], and the Navier–Stokes equation (momentum balance) [Eq. (4)] are written,

$$\nabla \cdot \mathbf{v} = 0, \tag{2}$$

$$\boldsymbol{\sigma} = -p\mathbf{I} + 2\mu\mathbf{D}(\mathbf{v}), \tag{3}$$

$$\nabla \cdot \boldsymbol{\sigma} = -\nabla p + \nabla \cdot [2\mu\mathbf{D}(\mathbf{v})] = i\omega\rho\mathbf{v}. \tag{4}$$

- On the fluid-solid interface Γ, the adherence condition is written as

$$\mathbf{v}_{/\Gamma} = \mathbf{0}. \tag{5}$$

In these equations ∇, $\nabla\cdot$, and Δ stand for the gradient, the divergence, and the Laplacian operators, respectively, and $\mathbf{I}$ is the unit tensor.

1. Dimensional analysis and rescaling

The physics of the flow has to be precisely stated. The dynamic Darcy regime is reached when the pressure gradient, viscous forces, and inertial forces are all of the same order of magnitude, i.e., when

$$O(\nabla p) = O(\nabla \cdot [2\mu\mathbf{D}(\mathbf{v})]) = O(i\omega\rho\mathbf{v}). \tag{6}$$

The pores' geometry and the adherence condition enforce the velocity to vary at the pore scale. Therefore a macroscopic description is only possible if the pressure varies at a larger scale. This suggests expressing the pressure and the velocity as the products of reference pressure and velocity (subscript ^{r}), with dimensionless pressure and velocity (subscript *). These latter depend on both dimensionless variables $\mathbf{x}/\mathbf{L} = \mathbf{x}^*$ and $\mathbf{x}/l = \mathbf{y}^*$, with $\mathbf{y} = \varepsilon^{-1}\mathbf{x}$,

$$p(\mathbf{x}) = p^r p^*(\mathbf{x}^*), \quad \mathbf{v}(\mathbf{x}) = v^r \mathbf{v}^*(\mathbf{y}^*)$$
$$\text{with} \quad p^* = O(1); \quad \mathbf{v}^* = O(1). \tag{7}$$

Thus, we have

$$O(\nabla p) = p^r/L, \quad O(\nabla \cdot [2\mu \mathbf{D}(\mathbf{v})]) = \mu v^r/l^2,$$

$$O(i\omega\rho\mathbf{v}) = \omega\rho v^r,$$

so that with Eq. (6), the viscous layer and the pore size are of the same order, i.e., $|\delta_v| = |\sqrt{\mu/(i\rho\omega)}| = O(l)$. Therefore, in a dimensionless form where *all the terms are of the same order*, the Navier–Stokes equation that properly accounts for the physics of the flow reads

$$-\frac{p^r}{L}\nabla_{x^*}[p^*(\mathbf{x}^*)] + \frac{2\mu v^r}{l^2}\nabla_{y^*} \cdot [\mathbf{D}_{y^*}(\mathbf{v}^*(\mathbf{y}^*))] = i\omega\rho v^r \mathbf{v}^*(\mathbf{y}^*),$$

which may be rewritten, in terms of physical variables and derivatives, as follows:

$$-\nabla_x[p(\mathbf{x})] + \nabla_y \cdot [2\mu \mathbf{D}_y(\mathbf{v}(\mathbf{x}))] = i\omega\rho\mathbf{v}(\mathbf{x}),$$

and changed into x-derivatives $\nabla_y \cdot [2\mu \mathbf{D}_y] = \varepsilon^2 \nabla_x \cdot [2\mu \mathbf{D}_x]$, so that the viscous term in the Navier–Stokes equation (and thus in the stress) is rescaled by the factor ε^2. This leads Eqs. (3) and (4) to be modified to

$$-\nabla p + \varepsilon^2 \nabla \cdot [2\mu \mathbf{D}(\mathbf{v})] = i\omega\rho\mathbf{v}, \tag{8}$$

$$\boldsymbol{\sigma} = -p\mathbf{I} + \varepsilon^2 2\mu \mathbf{D}(\mathbf{v}). \tag{9}$$

2. Treatment by homogenization

Homogenization is applied to Eqs. (2), (5), (8), and (9). First, momentum balance [Eq. (8)] at the order ε^{-1} reduces to $-\nabla_y p^0 = 0$, giving, as expected, a constant pressure in the pores,

$$p^0(\mathbf{x},\mathbf{y}) = P(\mathbf{x}).$$

Then, the velocity $\mathbf{v}^0$ and pressure p^1 are derived from equations $(8-\epsilon^0, 2-\epsilon^{-1}, 5-\varepsilon^0)$,

$$S_v^0 \begin{cases} -\nabla_y p^1 - \nabla_x P - i\omega\rho\mathbf{v}^0 + \nabla_y \cdot [2\mu \mathbf{D}_y(\mathbf{v}^0)] = 0, \\ \nabla_y \cdot \mathbf{v}^0 = 0, \\ \mathbf{v}^0_{/\Gamma} = 0, \\ \mathbf{v}^0 \text{ and } p^1 \text{ are } \Omega - \text{periodic}. \end{cases}$$

This set of equations defines the linear dynamic permeability problem where $\nabla_x P$ acts as a forcing term. Consequently the solution has the form (Auriault[5])

$$\mu\mathbf{v}^0(\mathbf{x},\mathbf{y}) = -\mathbf{k}^i \nabla_{xi} P, \quad p^1(\mathbf{x},\mathbf{y}) = \zeta^i \cdot \nabla_{xi} P + \widehat{p^1}(\mathbf{x}), \tag{10}$$

where $(-\mathbf{k}^i/\mu, \zeta^i)$ are the three velocities and pressure distributions corresponding to the unit pressure gradient in the three directions, $\nabla_x P = \mathbf{e}_i$. They are complex and depend on the local spatial variables and frequency through the dimensionless variable $\mathbf{y}/\delta$. Finally macroscopic mass balance is derived from the compatibility condition, which must be satisfied by the local mass balance. By integrating $(2-\varepsilon^0)$ over the pore volume, we get

$$\int_{\Omega_f} (\nabla_y \cdot \mathbf{v}^1 + \nabla_x \cdot \mathbf{v}^0) d\Omega = 0.$$

From the divergence theorem, the periodicity, and the adherence condition $(5-\varepsilon^1)$ on Γ, the first term vanishes. Then, inverting $\mathbf{y}$-integration and $\mathbf{x}$-differentiation, we have

$$\nabla_x \cdot \left(\frac{1}{\Omega} \int_{\Omega_f} \mathbf{v}^0 d\Omega \right) = \nabla_x \cdot \mathbf{V} = 0,$$

where $\mathbf{V}$ is the Darcy velocity. The macroscopic description reads

$$\nabla_x \cdot \mathbf{V} = 0, \quad \mathbf{V} = -\frac{1}{\mu}\mathbf{K}\nabla_x P,$$

$$\mathbf{K} = \frac{1}{\Omega}\int_{\Omega_f} \mathbf{e}^i \otimes \mathbf{k}^i d\Omega = \mathbf{K}^R + i\mathbf{K}^I, \tag{11}$$

where $\mathbf{K}^R$ and $\mathbf{K}^I$ are the real and imaginary parts of the complex dynamic permeability tensor $\mathbf{K}$. The inverse form of the macroscopic description is written as

$$\mu\mathbf{H} \cdot \mathbf{V} = -\nabla_x P, \quad \mathbf{H} = \mathbf{K}^{-1} = \mathbf{H}^R + i\mathbf{H}^I.$$

The features of the tensor $\mathbf{H}$ derived by HPM[12] are written below in the isotropic case, i.e., when $\mathbf{H} = H\mathbf{I}$ (and $K = H^{-1}$).

- In the quasistatic regime (low frequency), i.e., when $l/\delta \to 0$, viscous effects dominate the inertia. Consequently, we have

$$H(\omega) \simeq \frac{1}{\mathcal{K}} + \frac{i\omega\rho}{\mu}\frac{\alpha_0}{\phi}, \tag{12}$$

  where $\mathcal{K}$ is the intrinsic permeability and α_0 is the low frequency tortuosity.
- At high frequencies, i.e., when $l/\delta \to \infty$, inertial effects dominate, and viscous effects are confined to a viscous layer, giving

$$\frac{\mu}{i\omega\rho}H(\omega)\phi \simeq \alpha_\infty\left(1 + \sqrt{\frac{M}{2}\frac{\omega_c}{i\omega}}\right), \tag{13}$$

  where α_∞ is the tortuosity, M is a shape factor, and ω_c is the critical frequency delimiting the low and high frequency domains. This latter, which is obtained by equalizing viscous and inertial effects of the macroscopic flow, is written as

$$\omega_c = \frac{\phi\mu}{\mathcal{K}\rho\alpha_\infty}.$$

  Following Johnson *et al.*,[3] $\sqrt{(M/2)(\omega_c/i\omega)}$ may also be expressed as $2\delta/\Lambda$, where Λ is the characteristic viscous length.

The dimensionless terms $K/\mathcal{K}$ and $H\phi\mu/(i\omega\rho\alpha_\infty) = H\mathcal{K}\omega_c/\omega$ depend only on the dimensionless frequency ω/ω_c. Note that the complex dynamic density defined by

$$\rho_d(\omega) i\omega\mathbf{V} = -\nabla_x P \tag{14}$$

is related to $H(\omega)$ by $\rho_d(\omega) = \phi(\mu H/i\omega)$.

3. Variational formulation and energy consistency

The variational formulation equivalent to the set S_v^0 is derived[5] by taking the scalar product of the momentum balance with any field $\mathbf{w}$ belonging to the vector space $\mathcal{W}$ defined as

$$\mathcal{W}=\{\mathbf{w}/\quad \mathbf{w}\quad \Omega\text{-periodic},\quad \mathbf{w}_{/\Gamma}=0,\quad \nabla\cdot\mathbf{w}=0\}.$$

After integrating over the pore and denoting the average over the representative volume $|\Omega|^{-1}\int_{\Omega_f}-d\Omega$ by $\langle-\rangle$, one obtains

$$-\langle\nabla_y p^1\cdot\mathbf{w}\rangle+\langle\nabla_y\cdot[2\mu\mathbf{D}_y(\mathbf{v}^0)]\cdot\mathbf{w}\rangle-i\omega\rho\langle\mathbf{v}^0\cdot\mathbf{w}\rangle = \nabla_x P\cdot(\mathbf{w}).$$

From the divergence theorem, the first term may be transformed as

$$-\langle\nabla_y p^1\cdot\mathbf{w}\rangle=\langle p^1\nabla_y\cdot\mathbf{w}\rangle-\frac{1}{\Omega}\int_{\partial\Omega_f}p^1\mathbf{w}\cdot\mathbf{n}ds=0$$

because of the zero divergence, the adherence, and the periodicity of $\mathbf{w}$. Similarly, from the divergence theorem, we get

$$\langle\nabla_y\cdot[2\mu\mathbf{D}_y(\mathbf{v}^0)]\cdot\mathbf{w}\rangle=-2\mu\langle\mathbf{D}_y(\mathbf{v}^0):\mathbf{D}_y(\mathbf{w})\rangle+\frac{1}{\Omega}\int_{\partial\Omega_f}[2\mu\mathbf{D}_y(\mathbf{v}^0)\mathbf{n}]\cdot\mathbf{w}ds.$$

The surface integral vanishes because of the adherence and periodicity. Thus, this results in

$$\forall\mathbf{w}\in\mathcal{W},$$

$$2\mu\langle\mathbf{D}_y(\mathbf{v}^0):\mathbf{D}_y(\mathbf{w})\rangle+i\omega\rho\langle\mathbf{v}^0\cdot\mathbf{w}\rangle=-\nabla_x P\cdot\langle\mathbf{w}\rangle. \tag{15}$$

Taking $\mathbf{w}=\overline{\mathbf{v}^0}$ as a field test (the overbar stands for conjugate) gives the following identity:

$$2\mu\langle\mathbf{D}_y(\mathbf{v}^0):\mathbf{D}_y(\overline{\mathbf{v}^0})\rangle+i\omega\rho\langle\mathbf{v}^0\cdot\overline{\mathbf{v}^0}\rangle=-\nabla_x P\cdot\langle\overline{\mathbf{v}^0}\rangle = \frac{1}{\mu}\nabla_x P\cdot\bar{\mathbf{K}}\cdot\overline{\nabla_x P}=\mu\mathbf{V}\cdot\mathbf{H}\cdot\bar{\mathbf{V}}. \tag{16}$$

The above relation demonstrates consistency of viscous and kinetic energies between the microscopic (right hand side) and macroscopic (left hand side) descriptions. Applied to fields $\mathbf{k}^i$ and $\mathbf{k}^j$, relation (15) enables proof of the symmetry and positiveness of $\mathbf{H}$ and $\mathbf{K}$, which read in the isotropic case[5] as

$$K^R>0,\quad K^I<0\quad\text{and}\quad H^R>0,\quad H^I>0.$$

The real and imaginary parts of K/μ (or μH) correspond to the viscous dissipation and the effective kinetic power produced by a cycle under a unit macroscopic pressure gradient in the direction $\mathbf{e}_i$ (or a unit macroscopic flow in the same direction). Concerning the variation of H versus frequency, it may also be demonstrated (see Appendix A) that with a time dependence $e^{+i\omega t}$,

$$\frac{dH^R}{d\omega}>0\quad\text{and}\quad\frac{d(H^I/\omega)}{d\omega}<0. \tag{17}$$

Reformulated in terms of dynamic density [Eq. (14)], these inequalities become

$$\frac{d\rho_d^R}{d\omega}<0\quad\text{and}\quad\frac{d(\omega\rho_d^I)}{d\omega}<0. \tag{18}$$

C. Links between the microscopic to macroscopic descriptions

The quantities appearing in the macroscopic description are related to the following local quantities:

- The macroscopic velocity, $\mathbf{V}$, is the average of the local velocity.
- The Darcy pressure P is the stress of zero order in the pores. Because of the periodicity, the stresses of higher order are self-equilibrated on the boundary of the cell, i.e.,

$$\int_{\Gamma_f}\boldsymbol{\sigma}^1\mathbf{n}ds=0.$$

- The permeability tensor $\mathbf{K}$ expresses the energy consistency: the viscous dissipation and the kinetic powers developed within the representative cell and in the same volume of the equivalent Darcy media are identical.

In the next section, the information gathered from HPM is introduced in a self-consistent approach.

III. SELF-CONSISTENT ASSESSMENT OF DYNAMIC PERMEABILITY

The self-consistent approach enables a conjecture of the effective coefficients of heterogeneous media.[19] The method consists in

- assuming the nature of the macroscopic behavior and considering a generic inclusion representative of the local physics in the medium,
- solving the basic problem in the inclusion submitted to a homogeneous macroscopic forcing term and expressing the energy equivalence between the inclusion and the equivalent medium, and
- deducing from this relation the macroscopic coefficients.

The SCM was applied to the static intrinsic permeability of fibrous[9] and granular materials[10]. Tarnow[11] and Umnova *et al.*[15] used a similar philosophy but introduced a condition of vanishing vorticity at the cell boundary as an alternative to energy consistency.

A. Problem definition

Following the HPM results, the behavior of the equivalent macroscopic medium complies with the dynamic Darcy law described by Eq. (52). For convenience, the analysis is presented for isotropic media (the same reasoning also applies for the principal values of a macroscopic anisotropic media). The idea is to fit the inclusion with the same volume of equivalent media—whose K is to be determined—when both are subjected to a uniform forcing pressure gradient $\mathbf{G}$ of amplitude G and direction $\mathbf{E}$ (capital letters are used for the Darcy medium variables),

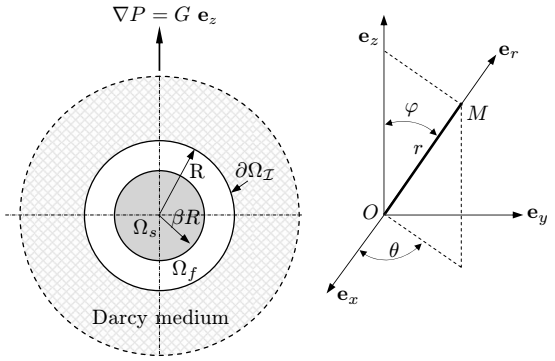


FIG. 2. The generic fluid-solid spherical inclusion I of volume Ω_i, boundary $\partial\Omega_{\mathcal{I}}$, and the associated spherical system of coordinates. Solid sphere: radius $R_i=\beta R$ and volume Ω_s. Concentric spherical shell filled by the viscous Newtonian fluid: external radius R and volume $\Omega_f=\Omega_{\mathcal{I}}-\Omega_s$. $\phi=\Omega_f/\Omega_{\mathcal{I}}=1-\beta^3$ is the porosity.

$$\nabla P = \mathbf{G} = G\mathbf{E} \quad \text{so that} \quad \mathbf{V} = -\frac{K}{\mu}G\mathbf{E}.$$

As for the generic inclusion $\mathcal{I}$ (of volume $\Omega_{\mathcal{I}}$ and surface $\partial\Omega_{\mathcal{I}}$), the simplest way to account for the connection of the fluid, the pore size, and the porosity is to consider a solid rigid sphere of radius $R_i=\beta R$ $(0<\beta<1)$ and volume Ω_s, surrounded by a concentric spherical shell filled by the fluid whose external radius is R and whose volume is $\Omega_f=\Omega_{\mathcal{I}}-\Omega_s$, so that the porosity $\phi=1-\beta^3$ (Fig. 2). Because of the spherical symmetry and the privileged direction introduced by the pressure gradient, the spherical coordinates (r,θ,φ) oriented as described in Fig. 2 will be used ($\theta=0$ corresponds to $\mathbf{e_r}=\mathbf{e_z}=\mathbf{E}$).

The Navier–Stokes equation in the fluid shell, $\beta R<r<R$, expressed with a single spatial variable, reads (lowercase letters are used for the variables of the fluid in the inclusion) as

$$-\nabla p - \frac{1}{\delta^2}\mu\mathbf{v} + \Delta(\mu\mathbf{v}) = \mathbf{0}, \tag{19}$$

$$\nabla\cdot\mathbf{v} = 0, \tag{20}$$

$$p = \pi + \mathbf{r}\cdot\mathbf{G}, \tag{21}$$

where δ is the complex number $\delta=\sqrt{\mu/i\rho\omega}$ and $\mathbf{r}=r\mathbf{e}_r$. Note that the total pressure p is decomposed into the pressure induced by the macroscopic uniform gradient, $\mathbf{r}\cdot\mathbf{G}$, and an additional pressure π. When adding the adherence condition on the solid, i.e., $\mathbf{v}(\beta R)=0$, the equations governing the fluid within the inclusion are identical to those derived by HPM, except for the periodicity (see II B 2).

1. General expression of the fields p and v

To satisfy spatial isotropy, the fields in the inclusion must be isotropic functions of *both* position vector and forcing vector, namely, $\{\mathbf{r},\mathbf{G}\}$. According the tensor theory,[20] the pressure p and the velocity $\mathbf{v}$ are written as

$$p = \mathcal{F}_p(\mathbf{r}\cdot\mathbf{r},\mathbf{G}\cdot\mathbf{G},\mathbf{r}\cdot\mathbf{G}),$$

$$\mu\mathbf{v} = \mathbf{r}\mathcal{F}_r(\mathbf{r}\cdot\mathbf{r},\mathbf{G}\cdot\mathbf{G},\mathbf{r}\cdot\mathbf{G}) + \mathbf{G}\mathcal{F}_G(\mathbf{r}\cdot\mathbf{r},\mathbf{G}\cdot\mathbf{G},\mathbf{r}\cdot\mathbf{G}),$$

where $\mathcal{F}_p$, $\mathcal{F}_r$, and $\mathcal{F}_G$ are any functions of the three scalar $\mathbf{r}\cdot\mathbf{r}$, $\mathbf{G}\cdot\mathbf{G}$, and $\mathbf{r}\cdot\mathbf{G}$. In the present case, the solution depends *linearly* on $\mathbf{G}$. Consequently, the general form of the solution can be specified more precisely through three independent functions of r,

$$p = (\mathbf{r}\cdot\mathbf{G})h_1(r), \quad \mu\mathbf{v} = \mathbf{r}(\mathbf{r}\cdot\mathbf{G})f_1(r) + \mathbf{G}g_1(r).$$

Following Howells,[21] these equations may be transformed conveniently into

$$p = \mathbf{G}\cdot\nabla h(r), \quad \mu\mathbf{v} = \mathbf{G}\cdot[\nabla\otimes\nabla f(r) + g(r)\mathbf{I}]. \tag{22}$$

The functions f, g, and h have to be determined now to satisfy the Navier–Stokes equation and the incompressibility. Taking the divergence of Eq. (19) and using the incompressibility condition, we get $\Delta p=0$. Using Eq. (22), this relation yields (here and in the following, the derivative d/dr is denoted by a prime $'$)

$$\Delta(\mathbf{G}\cdot\nabla h) = \mathbf{G}\cdot\mathbf{e_r}(\Delta h)' = 0.$$

Thus, introducing the constants c_0, c_1, and c_2, we have

$$\Delta h = c_0 \quad \text{and} \quad h(r) = c_0\frac{r^2}{6} - c_1\frac{1}{r} + c_2. \tag{23}$$

Later on, the constant c_2 of no physical meaning is set to zero. Using Eq. (22), the incompressibility reads

$$\nabla\cdot(\mathbf{G}\cdot[\nabla\otimes\nabla f + g\mathbf{I}]) = \mathbf{G}\cdot\nabla[\Delta f + g] = \mathbf{G}\cdot\mathbf{e_r}(\Delta f + g)' = 0.$$

Consequently, we have

$$g = -\Delta f + a_0 \quad \text{and}$$

$$\nabla\otimes\nabla f + g\mathbf{I} = \nabla\otimes\nabla f - \Delta f\mathbf{I} + a_0\mathbf{I}.$$

Noting that $\nabla\nabla(r^2)-\Delta(r^2)\mathbf{I}=-4\mathbf{I}$, the constant a_0 can be set to zero by including a term $-(a_0/4)r^2$ into f. Consequently, $\mathbf{v}$ is expressed from a single potential function f,

$$\mu\mathbf{v} = \mathbf{G}\cdot[\nabla\otimes\nabla f - \mathbf{I}\Delta f]. \tag{24}$$

Now, inserting expression (24) of $\mathbf{v}$ in the Navier–Stokes equation leads to

$$\mathbf{0} = -\nabla\cdot(\mathbf{G}\cdot\nabla h) - \frac{1}{\delta^2}\mathbf{G}\cdot[\nabla\otimes\nabla\mathbf{f} - \mathbf{I}\Delta\mathbf{f}] + \Delta(\mathbf{G}\cdot[\nabla\otimes\nabla f - \mathbf{I}\Delta f]) = \mathbf{G}\cdot\left[-\mathbf{I}\Delta h + [\nabla\otimes\nabla - \mathbf{I}\Delta]\left[-h + \left(\Delta - \frac{1}{\delta^2}\right)f\right]\right]. \tag{25}$$

Therefore, using Eq. (23) and denoting $A=-h+(\Delta-1/\delta^2)f$, we obtain

$$\mathbf{G}\cdot[-c_0\mathbf{I} + (\nabla\otimes\nabla - \mathbf{I}\Delta)A] = \mathbf{G}\cdot\left[-\mathbf{I}\left(c_0 + \frac{(rA')'}{r}\right) + \mathbf{r}\otimes\mathbf{r}\frac{(A'/r)'}{r}\right] = 0.$$

This last equation implies that

$$\frac{(A'/r)'}{r}=0 \quad \text{and} \quad \frac{(rA')'}{r}=-c_0,$$

whose integration gives (since any constant may be incorporated into h without any other change)

$$A=-h+\left(\Delta-\frac{1}{\delta^2}\right)f=-c_0\frac{r^2}{4}.$$

Finally, from the expression for h given by Eq. (23), f satisfies the Helmohltz equation (associated with viscous waves) with the following forcing terms:

$$\left(\Delta-\frac{1}{\delta^2}\right)f=-c_0\frac{r^2}{12}-c_1\frac{1}{r}.$$

The solution is the sum of particular solutions and spherical wave functions that introduce two additional constants c and c',

$$f=\delta^2\left[c_0\left(\frac{r^2}{12}+\frac{\delta^2}{2}\right)+c_1\frac{1}{r}+\delta^2\left(c\frac{e^{r/\delta}}{r/\delta}+c'\frac{e^{-r/\delta}}{-r/\delta}\right)\right]. \quad (26)$$

To summarize, the general expressions of the pressure p and the velocity $\mathbf{v}$ are given by the set of Eqs. (22)–(24) and (26) that involve four constants. The next step is to define appropriate boundary conditions for the identification of the constants and the dynamic permeability.

2. Boundary conditions

The following expressions for the velocity and the shear stress in the direction normal to the surface are useful for writing the boundary conditions:

$$\mu\mathbf{v}=\mathbf{G}[\nabla\nabla f-\mathbf{I}\Delta f]=\mathbf{G}\cdot[f'/r-\Delta f]+\mathbf{e_r}(\mathbf{G}\cdot\mathbf{r})(f'/r)', \quad (27)$$

$$\mu v_r=(\mathbf{G}\cdot\mathbf{e_r})[f'/r-\Delta f+r(f'/r)']=-2(f'/r)(\mathbf{G}\cdot\mathbf{e_r}), \quad (28)$$

$$\mu v_\theta=(\mathbf{G}\cdot\mathbf{e}_\theta)[f'/r-\Delta f]=-[f'/r+f'']\mathbf{(G}\cdot\mathbf{e}_\theta), \quad (29)$$

$$2\mu\mathbf{D(v)}\cdot\mathbf{e_r}=-\mathbf{G}\cdot f'''+\mathbf{e_r}(\mathbf{G}\cdot\mathbf{e_r})[f'''+4(f'/r)'], \quad (30)$$

$$2\mu D_{rr}=-4(f'/r)'(\mathbf{G}\cdot\mathbf{e_r}), \quad (31)$$

$$2\mu D_{r\theta}=-f'''(\mathbf{G}\cdot\mathbf{e}_\theta), \quad (32)$$

$$\mu\ \text{curl}\ (\mathbf{v})=-[\mathbf{G}\times\mathbf{r}]\frac{(\Delta f)'}{r}. \quad (33)$$

a. Conditions for the velocity. At the fluid-solid interface ($r=\beta R$), the adherence condition $\mathbf{v}(\beta R)=0$ gives, by combining Eqs. (28) and (29),

$$-2\frac{f'(\beta R)}{\beta R}=0, \quad (34)$$

$$-\frac{2}{3}\Delta f(\beta R)=0. \quad (35)$$

Moreover, the average velocity within the inclusion $\mathcal{I}$ is equal to the velocity in the equivalent Darcy medium. Thus we have

$$\mathbf{V}=\frac{1}{\Omega_\mathcal{I}}\int_{\Omega_f}\mathbf{v}d\Omega=\frac{1}{\Omega}\int_{\partial\Omega_\mathcal{I}}\mathbf{r}(\mathbf{v}\cdot\mathbf{e}_r)ds+0$$
$$=-2\frac{f'(R)}{R}\frac{\mathbf{G}}{\mu}=-\frac{K}{\mu}\mathbf{G}.$$

Therefore, we get

$$-2\frac{f'(R)}{R}+K=0. \quad (36)$$

From Eq. (28), this equation also means that the normal velocities in the fluid and in the equivalent Darcy medium are identical at any point on the inclusion boundary, i.e., $v_r(R)=V_r(R)$.

b. Condition for the stress at the inclusion boundary. The momentum balance in the fluid is not expressed by the Darcy law, and since the viscous stresses are transferred to the skeleton of the porous media it is not possible to impose *a priori* the pressure nor the stress at the boundary. However, it is physically justified to transpose the result proven by HPM to the present situation: on the boundary of the inclusion the drag force exerted by the corrective stresses $\boldsymbol{\sigma}_c$—i.e., the difference between the stress in the fluid inclusion and the pressure in the equivalent Darcy medium—equals zero. This means that the inclusion equilibrium is satisfied on average by the stress of zero order. This leads to

$$\int_{\partial\Omega_\mathcal{I}}\boldsymbol{\sigma}_c\mathbf{n}ds=0 \quad \text{with} \quad \boldsymbol{\sigma}_c=-(p-P)\mathbf{I}+2\mu\mathbf{D(v)}. \quad (37)$$

Introducing the pressure expressions and the shear stress components, then integrating, gives

$$0=\int_{\partial\Omega_\mathcal{I}}(\mathbf{G}\cdot\mathbf{r})(-h'+1)\mathbf{e_r}$$
$$+(-\mathbf{G}\cdot f'''+\mathbf{e_r}(\mathbf{G}\cdot\mathbf{e_r})[f'''-4(f'/r)'])\cdot\mathbf{e_r}ds$$
$$=\frac{4\pi R^2}{3}\mathbf{G}[-h'+R+f'''-4(f'/r)'-3f'''],$$
$$=\frac{4\pi R^2}{3}\mathbf{G}[-h'+R-2(\Delta f)'].$$

Thus the equation expressing the overall equilibrium reads

$$-h'(R)+R-2(\Delta f)'(R)=0. \quad (38)$$

c. Micro-macro energy consistency. It remains to express the energy equivalence between the inclusion and the same volume of the equivalent Darcy medium. According to Eq. (16) derived by HPM, the conservation of energy throughout upscaling is written as

$$\int_{\Omega_f} [2\mu \mathbf{D}_y(\mathbf{v}):\mathbf{D}_y(\bar{\mathbf{v}}) + i\omega\rho \mathbf{v}\cdot\bar{\mathbf{v}}]d\Omega = -\nabla P \cdot \int_{\Omega_f} \bar{\mathbf{v}} d\Omega. \tag{39}$$

Now, following the same reasoning as in Sec. II B 3, taking the scalar product of the momentum balance equation [Eq. (19)] with the field $\bar{\mathbf{v}}$, and integrating over the pores' volume, we obtain

$$\int_{\Omega_f} [2\mu \mathbf{D}(\mathbf{v}):\mathbf{D}(\bar{\mathbf{v}}) + i\omega\rho \mathbf{v}\cdot\bar{\mathbf{v}}]d\Omega = \int_{\partial\Omega_{\mathcal{I}}} [-p\mathbf{e_r} + 2\mu \mathbf{D}(\mathbf{v})\mathbf{e_r}]\cdot\bar{\mathbf{v}} ds.$$

By comparison with the previous equality, the following relation must be fulfilled:

$$\int_{\partial\Omega_{\mathcal{I}}} [-p\mathbf{e_r} + 2\mu \mathbf{D}(\mathbf{v})\mathbf{e_r}]\cdot\bar{\mathbf{v}} ds = -\nabla P \cdot \int_{\Omega_f} \bar{\mathbf{v}} d\Omega.$$

Note that the right hand side term may be changed into

$$-\nabla P \cdot \int_{\Omega_f} \bar{\mathbf{v}} d\Omega = -\nabla P \cdot \int_{\partial\Omega_{\mathcal{I}}} \mathbf{r}(\bar{\mathbf{v}}\cdot\mathbf{e_r}) ds = -\int_{\partial\Omega_{\mathcal{I}}} P(\bar{\mathbf{v}}\cdot\mathbf{e_r}) ds,$$

so that combined with the overall equilibrium condition [Eq. (37)] and multiplied by the conjugate of the mean velocity $\bar{\mathbf{V}}$, the energy equivalence takes the form

$$\int_{\partial\Omega_{\mathcal{I}}} [(P-p)\mathbf{e_r} + 2\mu \mathbf{D}(\mathbf{v})\cdot\mathbf{e_r}]\cdot[\bar{\mathbf{v}} - \bar{\mathbf{V}}] ds = 0.$$

And since the normal velocities are identical on $\partial\Omega_{\mathcal{I}}$, see Eq. (36), one obtains

$$\int_{\partial\Omega_{\mathcal{I}}} 2\mu D_{r\theta}[\bar{v}_\theta - \bar{V}_\theta] ds = 0.$$

According to the field expressions, one gets two possibilities on the boundary $(r=R)$:

- The shear stress $D_{r\theta}$ vanishes uniformly, and therefore,

$$f'''(R) = 0. \tag{40}$$

In that case, on the inclusion boundary, the stress in the normal direction in the fluid equals the pressure in the equivalent Darcy medium, i.e., $\sigma(R)\cdot\mathbf{e_r} = P(R)\mathbf{e_r}$.

- The tangential velocities are equal, i.e., $v_\theta = V_\theta$, giving,

$$-\tfrac{2}{3}\Delta f(R) + K = 0. \tag{41}$$

In that case the velocities in the fluid and in the equivalent Darcy medium are identical on the inclusion boundary, i.e., $\mathbf{v}(R) = \mathbf{V}(R)$. It can also be derived that $D_{rr}(R) = 0$.

To summarize, two alternative sets of five conditions are obtained [Eqs. (34)–(36), (38), and (40) or Eqs. (34)–(36), (38), and (41)]. Four of them are common to both sets, i.e., the two conditions related to the adherence condition, the condition expressing the identity between the normal microvelocity and the Darcy flow, and the averaged or overall equilibrium condition. The remaining equation is derived from the energy equivalence. Thus two possibilities are consistent:

- The shear stress vanishes, and the stress vector at the boundary of the fluid inclusion matches the pressure in the Darcy medium, which corresponds to the assumption made by Berdichevsky and Cai.[9] This will be called the *pressure approach* (denoted as P-) in the following. The tangential microvelocity is not continuous with the tangential Darcy flow.
- The microvelocity matches the Darcy flow, and neither the pressure nor the stress vector at the boundary of the fluid inclusion matches the pressure in the equivalent media. This will be called the *flow approach* (denoted as V-).

d. Remark about the "zero vorticity assumption." The assumption used by Tarnow[11] and Umnova *et al.*[15] of vanishing vorticity at the boundary of the cell (denoted hereafter as C-estimate) does not arise from the SCM and thus transgresses the energy consistency. Despite this drawback, considerations on the kinematics of the flow at the boundary of identical cells argue in favor of the zero vorticity assumption. Indeed, the level of vorticity is the highest in the narrow gaps between particles but vanishes when the velocity reaches its maximum at the middle of the gap, i.e., at the boundary of the cell. According to Eq. (33), this assumption leads to

$$(\Delta f)'(R) = 0. \tag{42}$$

Moreover, combined with overall equilibrium [Eq. (38)], one obtains

$$-h'(R) + R = 0,$$

meaning that (i) the pressure (not the stress) at the boundary of the fluid equals the pressure in the Darcy medium and (ii) the dissipated energy due to $\mathbf{v}-\mathbf{V}$ on the surface is neglected. The P- and C-assumptions may be expected to give more reliable results because, referring to the HPM approach, the P- and C-boundary conditions are correct up to the first order, which is not the case for the V-boundary conditions. In the following, the three approaches are investigated.

B. Resolution and estimates

Expressions (23)–(26) for functions h and f are introduced in the two possible sets of five conditions. This leads to two linear systems whose resolution allows the determination in both cases of the five parameters (c_0, c_1, c, c', and K).

1. Pressure approach: Fields $\mathbf{v}_p = \boldsymbol{\varpi}_p$ and p_p

Writing the complex number $x = R/\delta$, with $\delta = \sqrt{\mu/i\rho\omega}$, the linear system [Eqs. (34), (35), (40), (36), and (38)] reads

$$c\frac{e^{\beta x}}{\beta x} + c'\frac{e^{-\beta x}}{-\beta x} + 0 + \frac{c_0}{2} + 0 = 0,$$

$$c\frac{1}{\beta x}\left(1-\frac{1}{\beta x}\right)\frac{e^{\beta x}}{\beta x}-c'\frac{1}{\beta x}\left(1+\frac{1}{\beta x}\right)\frac{e^{-\beta x}}{-\beta x}-\frac{c_1}{(\beta R)^3}+\frac{c_0}{6}+0=0,$$

$$c\left[\left(1+\frac{6}{x^2}\right)(x-1)-2\right]\frac{e^x}{x}-c'\left[\left(1+\frac{6}{x^2}\right)(x+1)+2\right]\frac{e^{-x}}{-x}-\frac{6c_1}{R^3}+0+0=0,$$

$$-c\frac{1}{x}\left(1-\frac{1}{x}\right)\frac{e^x}{x}+c'\frac{1}{x}\left(1+\frac{1}{x}\right)\frac{e^{-x}}{-x}-\frac{c_1}{2R^3}-\frac{c_0}{6}+0=\frac{1}{2},$$

$$\frac{3c_1}{R^3}+0-\frac{K_p}{\delta^2}=0.$$

The analytical solution leads to the following permeability P-estimate, denoted as K_p:

$$K_p=\frac{\delta^2}{1-3/x^2C_p},\quad C_p=\frac{A_p+B_p\tanh[x(\beta-1)]/x}{a_p+b_p\tanh[x(\beta-1)]/x},\quad (43)$$

where

$$A_p=[3+(\beta x)^2][1+x^2/6]-3\beta[1+x^2/2],$$

$$B_p=[3+(\beta x)^2][1+x^2/2]-3\beta x^2[1+x^2/6],$$

$$a_p=[3+(\beta x)^2]/3-3\beta-[1+x^2/6]2/\beta+\frac{4}{\cosh[x(\beta-1)]},$$

$$b_p=[3+(\beta x)^2]-\beta x^2-[1+x^2/2]2/\beta.$$

The reciprocal of K_p, H_p, takes the form

$$H_p=\frac{1}{\delta^2}\left[1-\frac{3}{x^2}C_p\right].$$

In addition, from the coefficients c, c', c_0, and c_1 (not detailed here), which are solutions of the system of equations [Eqs. (34), (35), (40), (36), and (38)], one builds the velocity field $\mathbf{v}_p=\boldsymbol{\varpi}_p$. This field is the exact solution for the flow through the fluid shell under the imposed pressure conditions at the external boundary ($r=R$): $\boldsymbol{\sigma}\mathbf{n}=-P\mathbf{n}$, with $\nabla P=\mathbf{e_z}$.

2. Flow approach: Fields $\mathbf{v}_v=\boldsymbol{\varpi}_v$ and p_v

For this approach, the set of equations [Eqs. (34), (35), (41), (36), and (38)] to be solved is

$$c\frac{e^{\beta x}}{\beta x}+c'\frac{e^{-\beta x}}{-\beta x}+0+\frac{c_0}{2}+0=0,$$

$$c\frac{1}{\beta x}\left(1-\frac{1}{\beta x}\right)\frac{e^{\beta x}}{\beta x}-c'\frac{1}{\beta x}\left(1+\frac{1}{\beta x}\right)\frac{e^{-\beta x}}{-\beta x}-\frac{c_1}{(\beta R)^3}+\frac{c_0}{6}+0=0,$$

$$c\frac{e^x}{x}+c'\frac{e^{-x}}{-x}+0+\frac{c_0}{2}+\frac{3K_v}{2\delta^2}=0,$$

$$-c\frac{1}{x}\left(1-\frac{1}{x}\right)\frac{e^x}{x}+c'\frac{1}{x}\left(1+\frac{1}{x}\right)\frac{e^{-x}}{-x}-\frac{c_1}{2R^3}-\frac{c_0}{6}+0=\frac{1}{2},$$

$$\frac{3c_1}{R^3}+0-\frac{K_v}{\delta^2}=0.$$

The analytical solution reads

$$K_v=\frac{\delta^2}{1-3/x^2C_v},\quad C_v=\frac{A_v+B_v\tanh[x(\beta-1)]/x}{a_v+b_v\tanh[x(\beta-1)]/x},\quad (44)$$

where

$$A_v=[3+(\beta x)^2]-3\beta[1+x^2/3],$$

$$B_v=[3+(\beta x)^2][1+x^2/3]-3\beta x^2,$$

$$a_v=-2[\beta+1/\beta]+\frac{4}{\cosh[x(\beta-1)]},$$

$$b_v=[3+(\beta x)^2]2/3-[1+x^2/3]2/\beta.$$

The reciprocal of K_v, H_v, takes the form

$$H_v=\frac{1}{\delta^2}\left[1-\frac{3}{x^2}C_v\right].$$

The coefficients c, c', c_0, and c_1 (not detailed here), which are solutions of the system of Eqs. (34), (35), (41), (36), and (38), defines the velocity field $\mathbf{v}_v=\boldsymbol{\varpi}_v$. The field $\boldsymbol{\varpi}_v\mu H_v$ is the exact solution for the flow through the fluid shell under the imposed unit flow condition at the external boundary ($r=R$): $\boldsymbol{\varpi}_v\mu H_v=-\mathbf{e_z}$.

It is worth noting that embedded in a medium of permeability K_p (or K_v), the inclusion $\mathcal{I}\{\beta,R\}$ is *almost* neutral in the sense that its presence modifies neither the average density of dissipated and kinetic powers nor the field in the Darcy medium and that the condition of stress (or the flow) continuity is satisfied.

3. Zero vorticity approach: C-estimate

Similarly, the resolution of the set of Eqs. (34), (35), (42), (36), and (38) leads to the following K_c-estimate:

$$K_c=2\delta^2\left(1-\frac{1}{1-A_c}\right),\quad A_c=\frac{(1-\beta^3)}{3}+\frac{\beta^2}{x^2}\frac{1-1/\beta+(x^2-1/\beta)\tanh((\beta-1)x)/x}{1+\tanh((\beta-1)x)/x}.\quad (45)$$

This expression differs from that given by Umnova *et al.*[15] [in this latter case, it seems that the porosity ϕ is missing in the right hand of expression (12) of D].

4. Comments

a. Low frequency. Expanding the dynamic permeability at low frequency gives a behavior in conformity to Eq. (12) whose coefficients correspond to the intrinsic permeability and the added mass effect α_0 of the Darcy medium P- or V-consistent with the inclusion $\mathcal{I}\{\beta,R\}$. The intrinsic permeabilities are

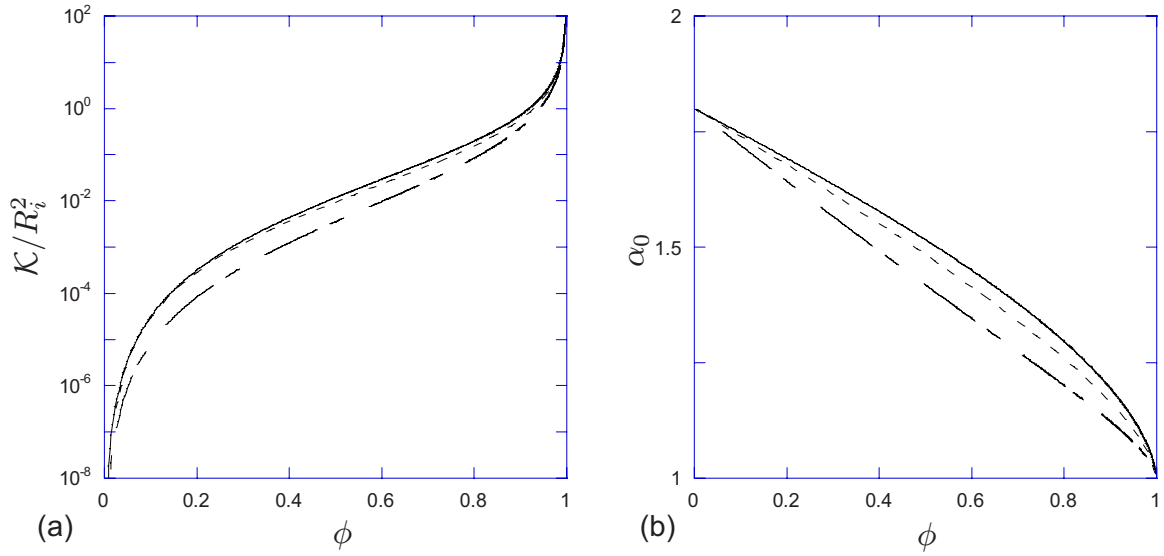


FIG. 3. (Color online) Low frequency parameters. (a) Dependence of dimensionless estimates $\mathcal{K}_p/R_i^2$ (P-estimate, continuous line), $\mathcal{K}_v/R_i^2$ (V-estimate, mixed line), and $\mathcal{K}_c/R_i^2$ (C-estimate, dashed line) on the porosity. (b) Dependence of the low frequency tortuosities α_{0p}, α_{0v}, and α_{0c} on the porosity.

$$\mathcal{K}_p = \frac{1}{3}\left[-1+\frac{2+3\beta^5}{\beta(3+\beta^5)}\right]R^2, \tag{46}$$

$$\mathcal{K}_v = \frac{1}{18}\left[4\frac{1-\beta}{\beta}-5\frac{(1-\beta^2)^2}{1-\beta^5}\right]R^2, \tag{47}$$

where $R=\beta^{-1}R_i$. These values coincide with those established for permanent flow in Boutin.[10] Concerning the C-estimate, the static permeability is written as

$$\mathcal{K}_c = \frac{2}{45}\left[\frac{5-9\beta+5\beta^3-\beta^6}{\beta}\right]R^2. \tag{48}$$

Figure 3(a) shows the dependence of the three dimensionless estimates on the porosity $\phi=1-\beta^3$. This figure underlines the tremendous effect of the porosity on the intrinsic permeability, while the ratio $\mathcal{K}_p/\mathcal{K}_v$ varies from 1 (dilute solid concentration, i.e., large porosity) to 4 (dense solid concentration, i.e., small porosity). We note that the ratio $\mathcal{K}_p/\mathcal{K}_c$ reaches a maximum of about 1.3 when $\phi\approx 3/4$.

The analytical expressions for the low frequency tortuosity, which depends on β only, are rather complicated and not presented here. Figure 3(b) shows the dependence of the three tortuosities, α_{0_p}, α_{0_v}, and α_{0_c}, on the porosity ϕ. The values lie in a narrow range $[1;9/5]$; moreover $\alpha_{0_p}/\alpha_{0_v}>1$ and $\alpha_{0_p}/\alpha_{0_c}>1$.

b. High frequency. The high frequency behavior derived by expanding the dynamic permeabilities complies with Eq. (13). It provides the added mass effect α_∞ (or tortuosity) and the form factor M. For the tortuosity, the P-, V- and C-estimates lead to the same value,

$$\alpha_{\infty p,v,c} = 1+\beta^3/2 = \frac{3-\phi}{2} < \alpha_{0v} < \alpha_{0c} < \alpha_{0p}.$$

The reason for this coincidence lies in the fact that at high frequencies, the viscous effects are much smaller than the inertia. Thus, the tortuosity α_∞ may be derived from a perfect fluid flow, where the interface conditions involve only the radial component $\mathbf{v}\cdot\mathbf{n}$, so that the three approaches give the same results.

This latter is identical to a thermal problem[19] where the inverse of $i\omega\rho$ plays the role of thermal conductivity (the solid can be considered of infinite density, i.e., of zero thermal conductivity). Transposing Hashin's results in terms of tortuosity leads to the above result. Figure 4(a) shows the dependence of the high frequency tortuosity $\alpha_{\infty p,v,c}$ on the porosity.

Using the low and high frequency limits, the P-, V-, and C-equivalent media present different critical frequencies.

$$\omega_{ci} = \frac{\mu\phi}{\mathcal{K}_i\rho\alpha_\infty}, \quad i=p,v,c.$$

Finally, the form factors are written as

$$M_p = 2\left[\frac{9\beta^2}{2\phi^2}\right]^2\frac{\phi\mathcal{K}_p}{\alpha_\infty R^2}, \quad M_v = 2\left[\frac{9(\beta^2+\beta^6)}{2\phi^2}\right]^2\frac{\phi\mathcal{K}_v}{\alpha_\infty R^2},$$

$$M_c = 2\left[\frac{9\beta^3}{2\phi^2}\right]^2\frac{\phi\mathcal{K}_c}{\alpha_\infty R^2}. \tag{49}$$

In terms of characteristic viscous length, one obtains

$$\frac{\Lambda_p}{R_i} = \frac{\Lambda_c}{R_i} = \frac{4\phi}{9(1-\phi)}\alpha_\infty = \frac{2\phi(3-\phi)}{9(1-\phi)}, \quad \Lambda_v = \frac{\Lambda_p}{1+\beta^4},$$

Figure 4(b) shows the dependence of form factors M_p, M_v, and M_c on the porosity. These coefficients vary from 0 at high porosity to 2/3 at low porosity, and $1<M_p/M_v<2$.

c. Whole frequency range. The dependencies of K_p, K_v, and K_c and H_p, H_v, and H_c on the dimensionless frequency (ω/ω_{cp}) are presented in Figs. 5 and 6, respectively, for a porosity $\phi=1/3$. Figure 5 shows that three estimates comply with properties (12) and (13) of the dynamic permeability. Figure 6 shows the dependence of the real and imaginary parts of the dimensionless estimates on ω/ω_c. Figure 6 highlights the following inequalities:

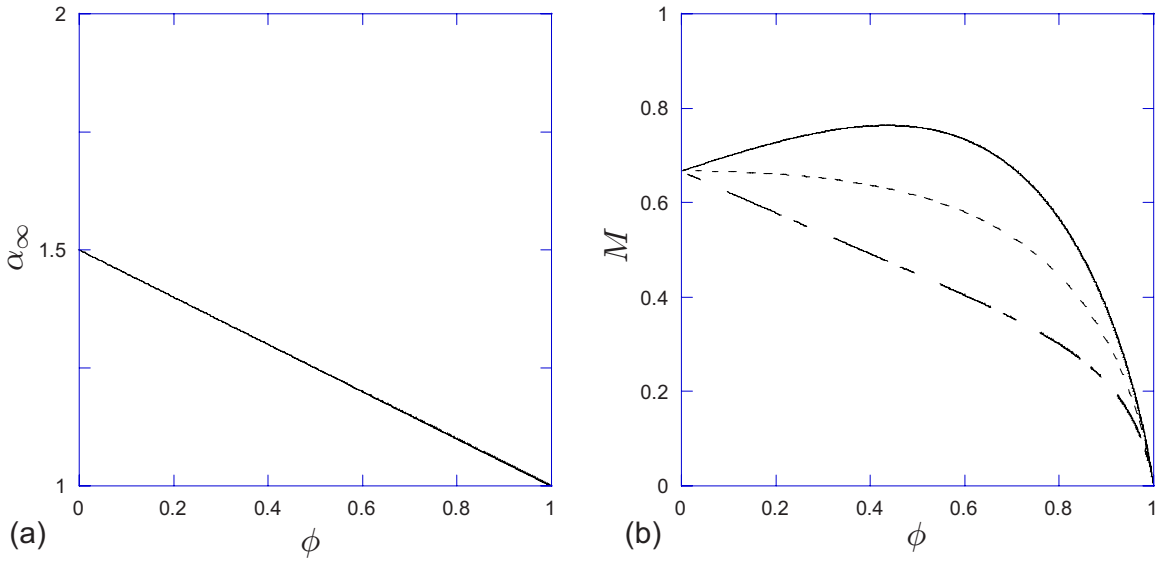


FIG. 4. (Color online) High frequency parameters. (a) Dependence of high frequency tortuosities $\alpha_{\infty p,v,c}$ on the porosity. (b) Dependence of form factors M_p (continuous line), M_v (mixed line), and M_c (dashed line) on the porosity.

$$\mathcal{K}_p H_p^R(\omega/\omega_{cp}) \geqslant \mathcal{K}_v H_v^R(\omega/\omega_{cv}),$$

$$\frac{\phi\mu}{\omega\rho} H_p^I(\omega/\omega_{cp}) \geqslant \frac{\phi\mu}{\omega\rho} H_v^I(\omega/\omega_{cv}).$$

The dimensionless curves present the same main qualitative features and, according to the theoretical result [Eq. (17)], H^R increases monotonically versus frequency and H^I/ω decreases.

Differences (related to the P-, V-, and C-approaches and to the porosity) are noticeable, quantitatively, for the viscous effect at high frequencies and the added mass at low frequencies. The difference in the critical frequencies of both approaches makes the discrepancy magnified for the dimensional coefficients.

To conclude, the three estimates present the same qualitative features. The C-estimate lie between the P-estimate and the V-estimate in the whole porosity range and predict a similar behavior as the P-estimate.

d. Comparison with the models of Johnson et al. and Pride et al.. The formula giving the frequency dependencies of the dynamic permeability, proposed by Johnson *et al.*[3] and Pride *et al.*,[22] require to be applied the knowledge of $\mathcal{K}$, M, and α_∞ (and α_0 with the correction of Pride *et al.*). This limitation is overcome in our approach since the microstructure knowledge is sufficient to assess analytically the dynamic permeability in the whole frequency range. Thus $\mathcal{K}$, M, α_∞, and α_0 are also analytically derived. As mentioned above, K_p, K_v, and K_c follow the general features of any parameter $K(\omega)$ at low and high frequencies. The formula of Johnson *et al.* is elaborated to match three aspects of the two asymptotic behaviors (i.e., low and high frequency dissipation and high frequency inertia). Thus, provided that the values of $(\mathcal{K}, M, \alpha_\infty)$ obtained in the present paper are used, the formula of Johnson *et al.* would naturally give correct approximations of K_p, K_v, and K_c if one only focuses on three aspects of the low and high frequency asymptotic behaviors. This will be also the case for the four aspects of the asymptotic behavior when using the formula of Pride *et al.* Note also that the expressions of K_p, K_v, and K_c are issued the solution of physical problems, and therefore they are causal functions by construction. If this is also the case for the formula of Johnson *et al.*, it remains an open question for the formula of Pride *et al.*

IV. FROM SOLID-FLUID INCLUSION TO POROUS MEDIA

The determination of the equivalent parameter usually constitutes the ultimate step of a self-consistent approach. The obtained value is assumed to be the effective coefficient of heterogeneous media characterized by inclusions $\mathcal{I}$. The present case requires a more detailed attention since

- different values that seem physically acceptable have been obtained,
- conversely to other physical problems (elasticity, conductivity, etc.), the real part of K depends on the size of the inclusion (in addition to the usual dependence on the concentration of the constituents), and
- the local physics that mixes dissipative process and kinetic energy involves an internal intrinsic length (the viscous layer thickness).

Below is discussed how these results apply by examining first the reliability of the estimates for the periodic array of solid spheres and, second, by establishing bounds for polydisperse sphere packing.

A. Dynamic permeability of periodic arrays of solid overlapping and nonoverlapping spheres

A usual exploitation of the SCM estimates is to consider that they provide a reasonable assessment of the macroscopic properties of sphere packing presenting the same fluid-solid concentration as the generic inclusion. This assumption results from a geometrical approximation that leads to compare

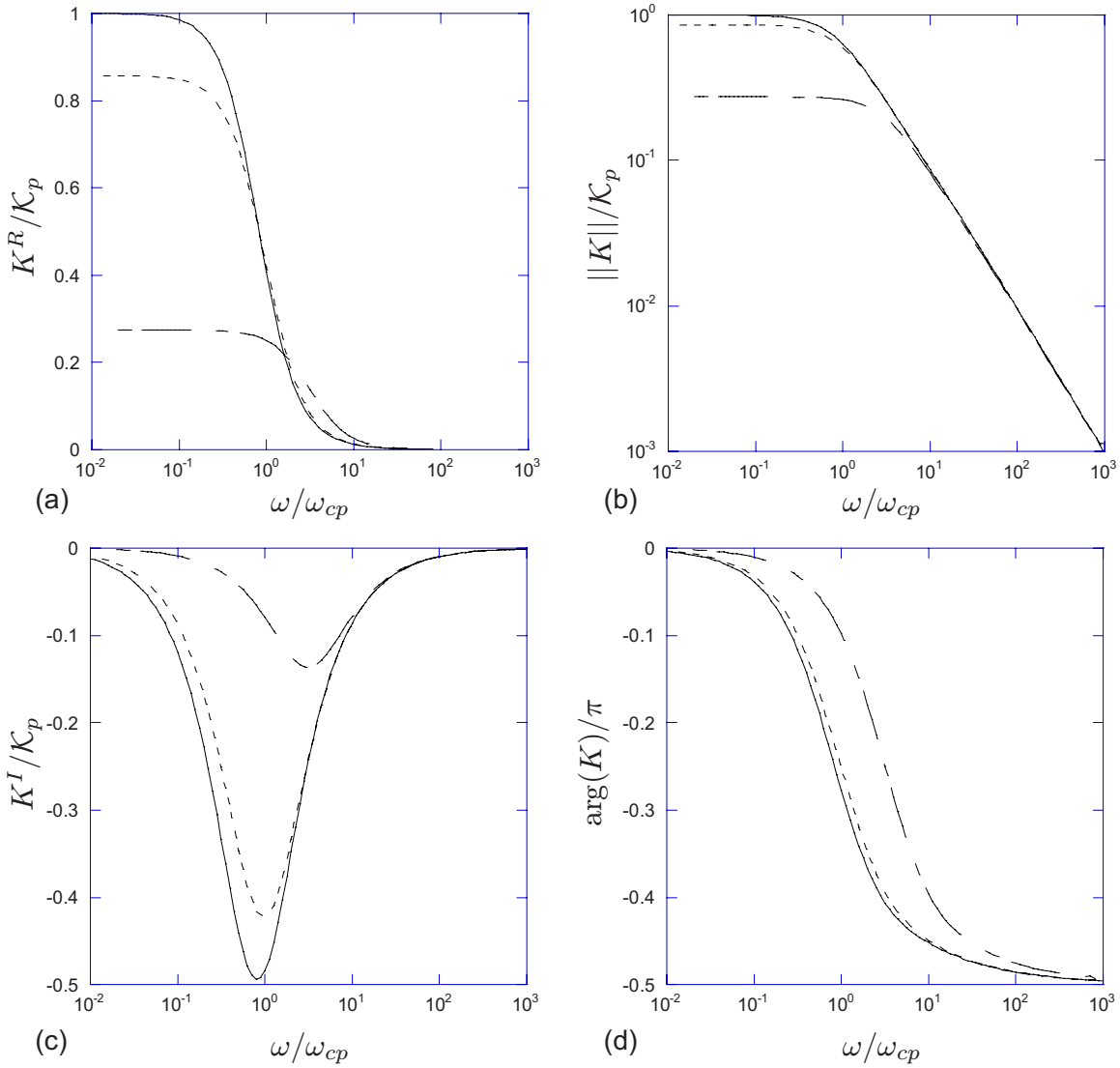


FIG. 5. (Color online) Dynamic permeability estimates K_p, K_v, and K_c vs ω/ω_{cp} when the porosity $\phi=1/3$. (a) Real part normalized by the intrinsic permeability $\mathcal{K}_p$, (b) modulus normalized by $\mathcal{K}_p$, (c) imaginary part normalized by $\mathcal{K}_p$, and (d) phase normalized by π. Note that the difference in intrinsic permeability induces a shift between the P-, V-, and C-curves corresponding to the shift in critical frequencies.

the periodic cell to the spherical inclusion. The objective of this section is to check how far the analytical estimates agree with finite element numerical results obtained by solving boundary value problems arising from the homogenization process on the representative elementary volume (REV) of simple cubic (sc), body-centered cubic (bcc), and face-centered cubic (fcc) arrays of nonoverlapping and overlapping spheres with the same radius R_i. These periodic lattices of spheres are ranging from dilute systems with isolated spheres and highly concentrated consolidated media. Let us remark that the transition between nonoverlapping and overlapping spheres occurs when the porosity values are equal to 0.47, 0.32, and 0.26 for the sc, bcc, and fcc microstructures, respectively. Due to the symmetry properties of each microstructure, finite simulations have been performed on 1/16 of the total REV. Figure 7 shows typical meshes used to perform finite element simulations.[23] Figure 8 underlines the influence of the ratio ω/ω_c on the microscopic velocity field deduced from numerical simulations in a sc array of nonoverlapping spheres ($\phi=0.3$). We can observe that by increasing ω/ω_c, inertial effects dominate and viscous effects are confined to a thin viscous layer around the spheres.

a. Low frequency. At low frequencies, the static permeability and the low frequency tortuosity are obtained by solving the boundary value S_v^0 (Sec. II B 2) when $\omega=0$ for a given macroscopic pressure gradient $\nabla_x P$. The microscopic velocity field $\mathbf{v}^0$, solution of S_v^0, is in the form

$$\mathbf{v}^0(\mathbf{x},\mathbf{y}) = -\frac{1}{\mu}\mathbf{k}\cdot\nabla_x P, \tag{50}$$

where $\mathbf{k}$ is a second order tensor. The static permeability tensor is defined as

$$\mathbf{K}(\omega=0) = \frac{1}{\Omega}\int_{\Omega_f}\mathbf{k}d\Omega = \phi\langle\mathbf{k}\rangle. \tag{51}$$

From relations (12), (16), and (50), it can be shown that the low frequency tortuosity tensor $\boldsymbol{\alpha}_0$ is written as

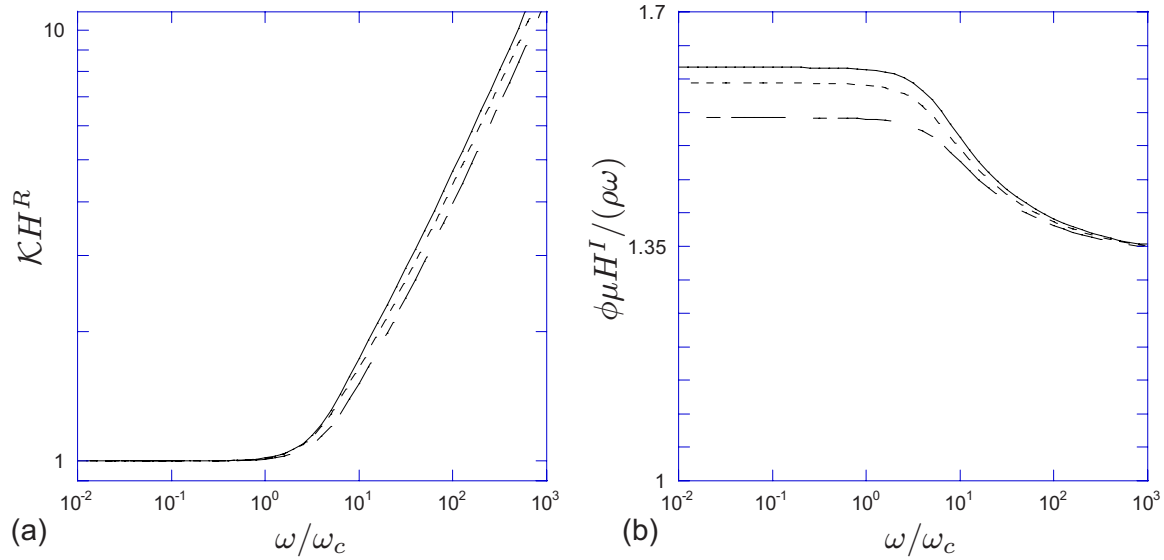


FIG. 6. (Color online) Dynamic estimates H_p (continuous line), H_v (mixed line), and H_c (dashed line) vs ω/ω_c for a porosity $\phi=1/3$: (a) Dependence of $\mathcal{K}_p H_p^R/\mu$, $\mathcal{K}_v H_v^R/\mu$, and $\mathcal{K}_c H_c^R/\mu$ on the dimensionless frequency ω/ω_c, where ω_c equals ω_{cp}, ω_{cv}, and ω_{cc}, respectively. (b) Dependence of $\phi\mu H_p^I/(\rho\omega)$, $\phi\mu H_v^I/(\rho\omega)$, and $\phi\mu H_c^I(\rho\omega)$ on ω/ω_c.

$$\boldsymbol{\alpha}_0 = \langle \mathbf{k}\cdot\mathbf{k}\rangle(\langle\mathbf{k}\rangle\cdot\langle\mathbf{k}\rangle)^{-1}. \tag{52}$$

The symmetry properties of the microstructures under consideration imply that the tensors in such porous media are isotropic. Thus $\mathbf{K}(\omega=0)=\mathcal{K}\mathbf{I}$ and $\boldsymbol{\alpha}_0=\alpha_0\mathbf{I}$. Figures 9(a) and 9(b) present the dependence with the porosity of the static dimensionless permeability $\mathcal{K}/R_i^2$ and the low frequency tortuosity α_0 for sc, bcc, and fcc microstructures.

On both figures, self-consistent estimates (P-estimate, V-estimate, and C-estimate) are also reported. Figure 9(a) shows that the computed dimensionless static permeabilities mainly depend on the porosity. They slightly depend on the arrangement of spheres when the porosity is smaller than 0.4. As expected, the permeability of the periodic arrays is closer to P- and C-estimates than to the V-estimate. P- and C-estimates appear as accurate analytical approximations up to the maximum packing concentration. Because of the weak dependence on the sphere arrangement (conversely to the case of fibrous media, Berdichevsky and Cai[9]), these estimates should also be relevant for media with uniform grain distribution. Beyond, as explained by Chapman and Higdon,[14] the geometry of the flow path changes significantly, so that the discrepancies increase. Figure 9(b) shows that the low frequency tortuosity α_0 for the sc, bcc, and fcc microstructures mainly track the P- and C-estimates when the porosity is larger than 0.6. When the porosity is lower than 0.6, P-, V-, and C-approximations underestimate numerical values.

b. High frequency. Figure 10 depicts the dependence of the high frequency tortuosity α_∞ and the form factor M on the porosity. In this figure, numerical results for the sc, bcc, and fcc microstructures are compared with the different estimates. Once again, a good agreement of P- and C-estimates with numerical results is observed when the porosity is larger than 0.6. When the porosity is lower than 0.6, P-, V-, and C-approximations underestimate numerical values, specially

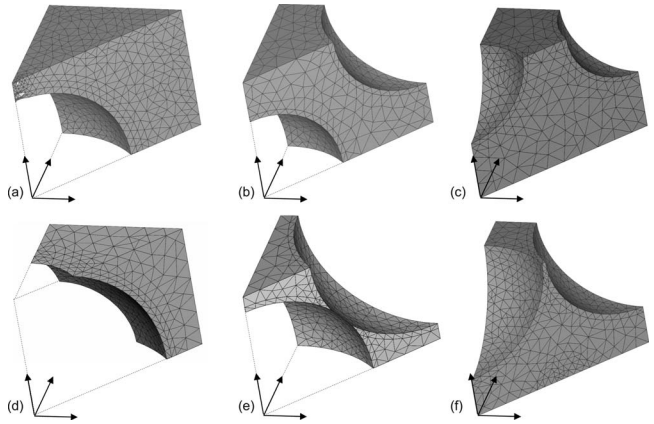


FIG. 7. Typical meshes of [(a) and (d)] sc, [(b) and (e)] bcc, and [(c) and (f)] fcc arrays (1/16 of the total REV) used to perform finite element simulations. (a)–(c) $\phi=0.7$. (b)–(d) $\phi=0.3$.

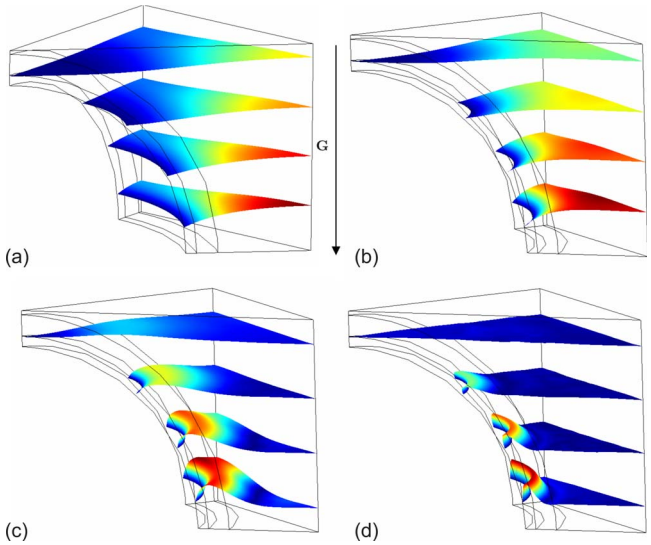


FIG. 8. (Color online) Influence of the ratio ω/ω_c on the microscopic velocity field in a sc array of nonoverlapping spheres ($\phi=0.3$): (a) $\omega/\omega_c=0$, (b) $\omega/\omega_c=1$, (c) $\omega/\omega_c=10$, and (d) $\omega/\omega_c=100$.

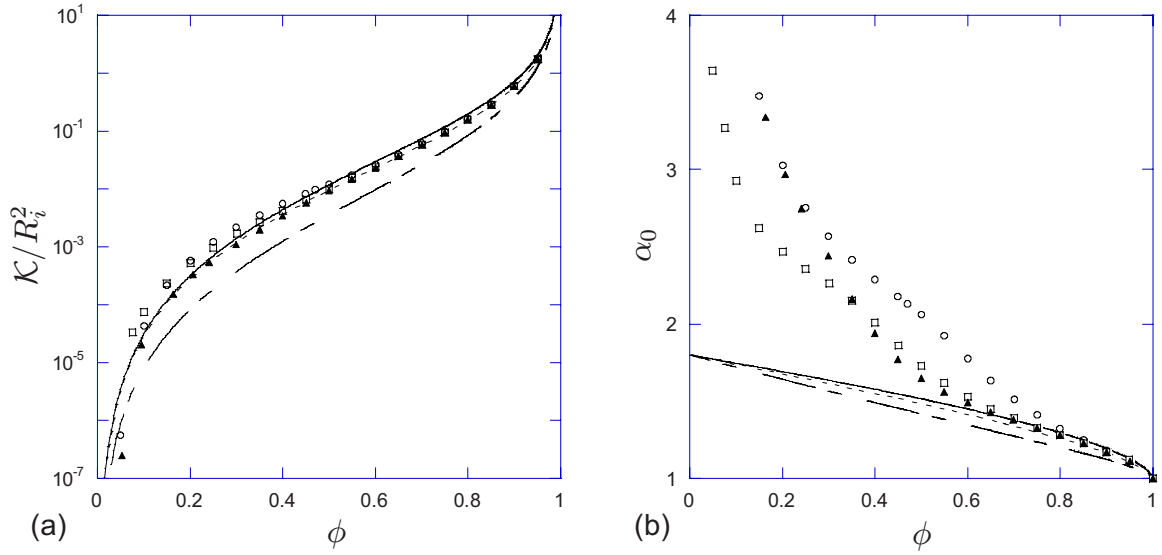


FIG. 9. (Color online) Dependence of the dimensionless permeability and the low frequency tortuosity on the porosity. Comparison between numerical results and self-consistent estimates: P-estimate (continuous line), V-estimate (mixed line), and C-estimate (dashed line). (○), (□), and (▲) correspond to numerical results of sc, bcc, and fcc microstructures, respectively.

when the porosity is very small. The form factor M of the three periodic microstructures presents a maximum for porosity corresponding to the maximum packing.

c. Whole frequency range. Figures 11 and 12 present the dependence of the dimensionless real and imaginary parts of $\mathbf{H}$ with the dimensionless frequency ω/ω_c on porosities equal to 0.7 and 0.3, respectively. Once again, when the porosity is large, Fig. 11 shows that P- and C-estimates mainly track numerical results of the bcc and fcc microstructures in the whole dimensionless frequency range. When the porosity is small, the discrepancy with estimates are more significant in the whole frequency range.

In conclusion, considering a periodic array of overlapping and nonoverlapping spheres, the three estimates are quite good qualitatively. Quantitatively, the C- and P-estimates are more accurate in the whole frequency range. This accuracy is fairly good for the four parameters (K, α_0, α_∞, and M) when the porosity is larger than 0.5. For a lower porosity, discrepancy up to a factor of around 2 may be observed.

B. Bounds of dynamic permeability for polydisperse sphere packing

Consider granular media constituted by spherical fixed inclusions $\mathcal{I}\{\beta_J, R_J\}$ of volume Ω_J filling all the space, whose REV (Fig. 13) is denoted as $\hat{\Omega} = \cup \mathcal{I}\{\beta_J, R_J\}$ (index $_J$ relates to inclusion J and exponent * relates to the media),

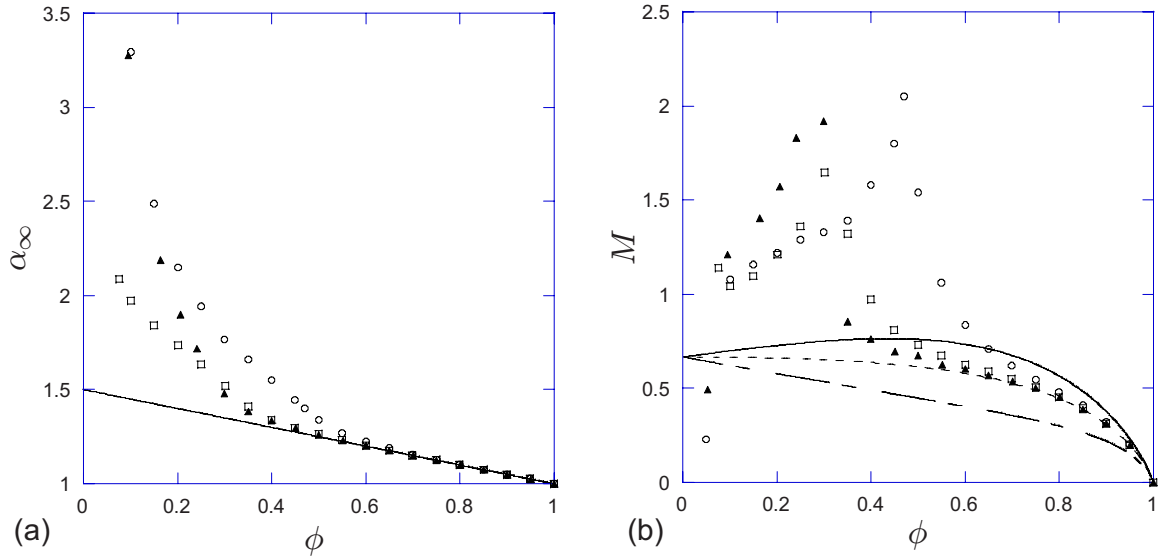


FIG. 10. (Color online) Dependence of the high frequency tortuosity and the coefficient M on the porosity. Comparison between numerical results and self-consistent estimates: P-estimate (continuous line), V-estimate (mixed line), and C-estimate (dashed line). (○), (□), and (▲) correspond to numerical results of sc, bcc, and fcc microstructures, respectively.

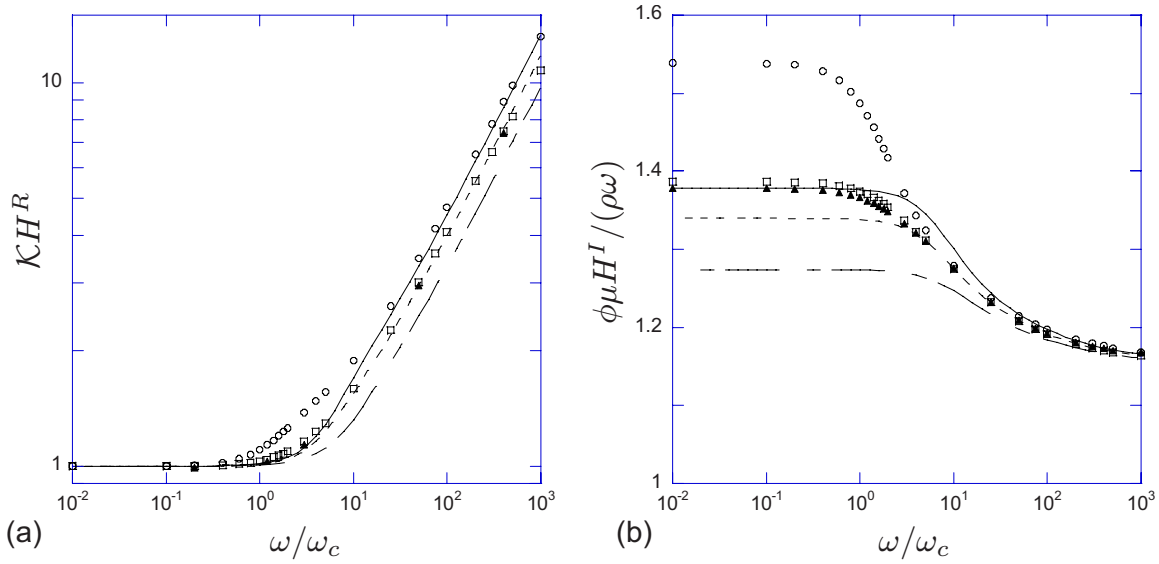


FIG. 11. (Color online) Comparison between numerical results and dimensionless estimates H_p, H_v, and H_c vs ω/ω_c when the porosity ϕ=0.7: P-estimate (continuous line), V-estimate (mixed line), and C-estimate (dashed line). (○), (□), and (▲) correspond to numerical results of sc, bcc, and fcc microstructures, respectively.

$$\hat{\Omega} = \cup \mathcal{I}_J\{\beta_J, R_J\}, \quad |\hat{\Omega}| = \sum_J \Omega_J.$$

In statics, the P- and V-solutions enable us to set bounds to the intrinsic permeability $\mathcal{K}^*$[24]. For the effective conduction, i.e., the tortuosity α_∞^*, Hashin and Shtrikman[10] proved that the SCM estimates are exact values for any arrangement of inclusions of the same solid concentration $\mathcal{I}\{\beta, R_J\}$, filling the whole space. Using an energetic approach, these results are extended to the real and imaginary parts of the dynamic permeability in the whole frequency range.

a. Complex power function. Assume that the medium undergoes a unit macroscopic pressure gradient $\nabla P = \mathbf{e_z}$ corresponding to a macroscopic homogeneous flux $\mathbf{V} = -(K^*/\mu)\mathbf{e_z}$. Among the local fields in the fluid that fulfill the Navier–Stokes equation, the incompressibility, and the adherence condition, let us distinguish ([ ] stands here for the jump through the inclusion boundary) the following.

- "stress-continuous" velocity field $\mathbf{v}_p$ such that on any inclusion boundary, $[\boldsymbol{\sigma}_p \mathbf{n}] = 0$,
- velocity-continuous fields $\mathbf{v}_v$ such that on any inclusion boundary, $[\mathbf{v}_v] = 0$, and
- the exact solution, $\mathbf{v}^*$, which is the only field whose stress and velocity are continuous.

Introduce for any stress- and velocity-continuous fields defined on the whole inclusions of the REV the following complex power function E:

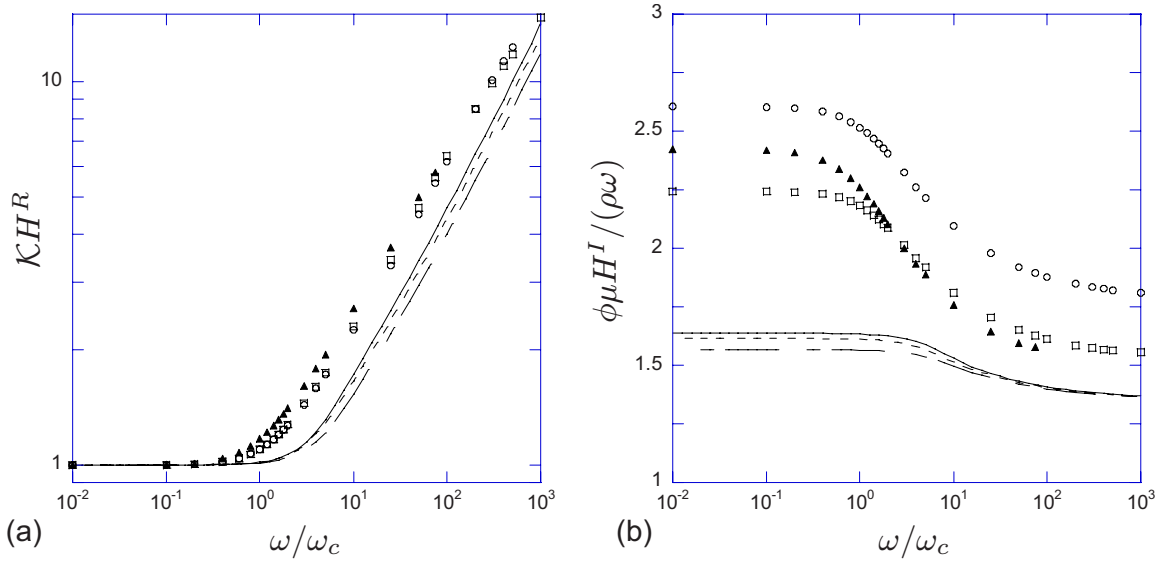


FIG. 12. (Color online) Comparison between numerical results and dimensionless estimates H_p, H_v, and H_c vs ω/ω_c when the porosity ϕ=0.3: P-estimate (continuous line), V-estimate (mixed line), and C-estimate (dashed line). (○), (□), and (▲) correspond to numerical results of sc, bcc, and fcc microstructures, respectively.

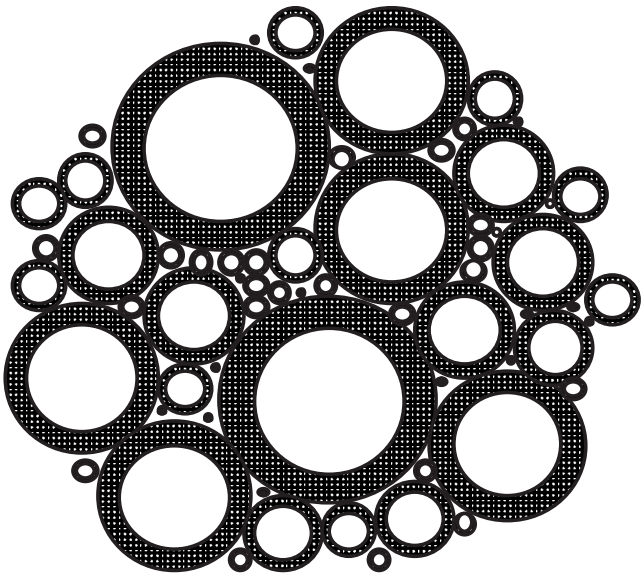


FIG. 13. REV of granular media constituted by spherical fixed inclusions $\mathcal{I}\{\beta_J, R_J\}$ of volume Ω_J filling all the space.

$$2E(\mathbf{v}_p,\mathbf{v}_v)=\sum_J\left\{2\mu\int_{\Omega_{fJ}}\mathbf{D}(\mathbf{v}_p-\mathbf{v}_v):\overline{\mathbf{D}(\mathbf{v}_p-\mathbf{v}_v)}d\Omega+i\omega\rho\int_{\Omega_{fJ}}(\mathbf{v}_p-\mathbf{v}_v)\cdot\overline{(\mathbf{v}_p-\mathbf{v}_v)}d\Omega\right\}. \tag{53}$$

By construction, the *real and imaginary parts of E are positive*, and their minima (zero) are reached when $\mathbf{v}_p=\mathbf{v}_v=\mathbf{v}^*$. Developing E gives

$$\begin{aligned}2E(\mathbf{v}_p,\mathbf{v}_v)=\sum_J\Bigg\{&\int_{\Omega_{fJ}}[2\mu\mathbf{D}(\mathbf{v}_p):\overline{\mathbf{D}(\mathbf{v}_p)}+i\omega\rho\mathbf{v}_p\cdot\overline{\mathbf{v}_p}]d\Omega\\&+\int_{\Omega_{fJ}}[2\mu\mathbf{D}(\mathbf{v}_v):\overline{\mathbf{D}(\mathbf{v}_v)}+i\omega\rho\mathbf{v}_v\cdot\overline{\mathbf{v}_v}]d\Omega\\&-\int_{\Omega_{fJ}}[2\mu\mathbf{D}(\mathbf{v}_p):\overline{\mathbf{D}(\mathbf{v}_v)}+i\omega\rho\mathbf{v}_p\cdot\overline{\mathbf{v}_v}]d\Omega\\&-\int_{\Omega_{fJ}}[2\mu\overline{\mathbf{D}(\mathbf{v}_p)}:\mathbf{D}(\mathbf{v}_v)+i\omega\rho\overline{\mathbf{v}_p}\cdot\mathbf{v}_v]d\Omega\Bigg\}.\end{aligned}$$

Integrating by part and using the properties of the fields ($\nabla\cdot\mathbf{v}_v=0$; $\nabla\cdot\boldsymbol{\sigma}_p=0$), the two last integrals may be transformed into surface integrals, so that

$$2E(\mathbf{v}_p,\mathbf{v}_v)=2E(\mathbf{v}_p,\mathbf{0})+2E(\mathbf{0},\mathbf{v}_v)-\sum_J\int_{\partial\Omega_J}[(\sigma_p\cdot\mathbf{n})\cdot\bar{\mathbf{v}}_v+(\bar{\sigma}_p\cdot\mathbf{n})\cdot\mathbf{v}_v]ds. \tag{54}$$

b. Bound of the real part of K.* A stress-continuous field $\tilde{\mathbf{v}}_p$ can be built by partitioning the media inclusion by inclusion, and setting in each $\mathcal{I}_J$, $\tilde{\mathbf{v}}_p=\boldsymbol{\varpi}_{pJ}$, where $\boldsymbol{\varpi}_p$ was defined in Sec. III B 1. Consequently, the condition $\tilde{\sigma}_p\cdot\mathbf{n}=P\cdot\mathbf{n}$ is satisfied on the boundary of each inclusion. Now, choose for velocity-continuous field $\mathbf{v}_v$ the solution $\mathbf{v}^*$. Then it comes successively:

(i) By construction of the fields $\boldsymbol{\varpi}_{pJ}$ [see Eq. (39)],

$$\int_{\Omega_{fJ}}[2\mu\mathbf{D}_y(\overline{\boldsymbol{\varpi}_{pJ}}):\mathbf{D}_y(\overline{\boldsymbol{\varpi}_{pJ}})+i\omega\rho\boldsymbol{\varpi}_{pJ}\cdot\overline{\boldsymbol{\varpi}_{pJ}}]d\Omega=-\nabla P\cdot\int_{\Omega_{fJ}}\overline{\boldsymbol{\varpi}_{pJ}}d\Omega=\Omega_J\frac{\overline{K_{pJ}}}{\mu},$$

so that

$$2E(\tilde{\mathbf{v}}_p,\mathbf{0})=\sum_J\Omega_J\frac{\overline{K_{pJ}}}{\mu}. \tag{55}$$

(ii) Because of the energy consistency of the dynamic permeability K^* [see Eq. (16)],

$$2E(\mathbf{0},\mathbf{v}^*)=\sum_J\int_{\partial\Omega_J}[2\mu\mathbf{D}_y(\mathbf{v}^*):\mathbf{D}_y(\overline{\mathbf{v}^*})+i\omega\rho\mathbf{v}^*\cdot\overline{\mathbf{v}^*}]=-\hat{\Omega}\nabla_x P\cdot\overline{\mathbf{v}^*}=\hat{\Omega}\frac{\overline{K^*}}{\mu}. \tag{56}$$

(iii) Finally, using the continuity of the stress induced by $\boldsymbol{\varpi}_{pJ}$ on $\partial\Omega_J$ with the macroscopic pressure,

$$\begin{aligned}-\sum_J\int_{\partial\Omega_J}&[(\tilde{\sigma}_p\cdot\mathbf{n})\cdot\bar{\mathbf{v}}^*+(\bar{\tilde{\sigma}}_p\cdot\mathbf{n})\cdot\mathbf{v}^*]ds\\&=\sum_J\int_{\partial\Omega_J}[P\mathbf{n}\cdot\bar{\mathbf{v}}^*+\bar{P}\mathbf{n}\cdot\mathbf{v}^*]ds\\&=\sum_J\int_{\Omega_{fJ}}[\nabla P\bar{\mathbf{v}}^*+\nabla\bar{P}\cdot\mathbf{v}^*]ds\\&=\hat{\Omega}[\nabla P\cdot\bar{\mathbf{V}}+\nabla\bar{P}\cdot\mathbf{V}]=-2\hat{\Omega}\frac{K^{*R}}{\mu}.\end{aligned} \tag{57}$$

Reporting Eqs. (55)–(57) into Eq. (54) yields

$$2E(\tilde{\mathbf{v}}_p,\mathbf{v}^*)=\sum_J\left\{\Omega_J\frac{\overline{K_{pJ}}}{\mu}+\Omega_J\frac{\overline{K^*}}{\mu}\right\}-2\hat{\Omega}\frac{K^{*R}}{m}=\hat{\Omega}\left\{\sum_J\frac{\Omega_J}{\hat{\Omega}}\frac{\overline{K_{pJ}}}{\mu}-\frac{K^*}{\mu}\right\},$$

and from the positiveness of the real part of $E(\tilde{\mathbf{v}}_p,\mathbf{v}^*)$ one deduces the inequality, giving an upper bound of K^{*R},

$$\left\{\sum_J\frac{\Omega_J}{\hat{\Omega}}K^R_{p,J}-K^{*R}\right\}\geqslant 0.$$

c. Bound of the imaginary part of K.* Similarly, choosing $\mathbf{v}_v=i\mathbf{v}^*$ leads us to consider $2E(\tilde{\mathbf{v}}_p,i\mathbf{v}^*)$. Observing that $E(\mathbf{0},i\mathbf{v}^*)=E(\mathbf{0},\mathbf{v}^*)$ and that

$$-\sum_J\int_{\partial\Omega_J}[(\tilde{\sigma}_p\cdot\mathbf{n})\cdot i\overline{\mathbf{v}^*}+(\bar{\tilde{\sigma}}_p\cdot\mathbf{n})\cdot i\mathbf{v}^*]ds=\hat{\Omega}[\nabla P\cdot i\bar{\mathbf{V}}+\nabla\bar{\mathbf{P}}\cdot i\mathbf{V}]=+2i\hat{\Omega}\frac{K^{*I}}{\mu},$$

we obtain

$$2E(\tilde{\mathbf{v}}_p, i\mathbf{v}^*) = \sum_J \left\{ \Omega_J \overline{\frac{K_{pJ}}{\mu}} + \Omega_J \overline{\frac{K^*}{\mu}} \right\} + 2i\hat{\Omega}K^{*I}$$
$$= \hat{\Omega}\left\{ \sum_J \frac{\Omega_J}{\hat{\Omega}} \overline{\frac{K_{pJ}}{\mu}} + \frac{K^*}{\mu} \right\}. \quad (58)$$

Expressing the positiveness of the imaginary part of $E(\tilde{\mathbf{v}}_p, i\mathbf{v}^*)$ (recall that $K^{*I} < 0$),

$$\left\{ \sum_J \frac{\Omega_J}{\hat{\Omega}} |K^I_{pJ}| - |K^{*I}| \right\} \geqslant 0,$$

which yields to upper bounds of $|K^{*I}|$.

d. Bound of the imaginary parts of K^* and H^*. A similar approach based on field $\boldsymbol{\varpi}_{vJ}$ leads to upper bounds of H^{*R} and H^{*I} (see Appendix B). Finally, the bounds valid in the whole frequency range read

$$K^{R*} \leqslant \sum_J \frac{\Omega_J}{\hat{\Omega}} K^R_{pJ}, \quad |K^{I*}| \leqslant \sum_J \frac{\Omega_J}{\hat{\Omega}} |K^I_{pJ}|,$$

$$H^{R*} \leqslant \sum_J \frac{\Omega_J}{\hat{\Omega}} H^R_{vJ}, \quad H^{I*} \leqslant \sum_J \frac{\Omega_J}{\hat{\Omega}} H^I_{vJ}.$$

These bounds are valid for any random or periodic spatial distribution of inclusions. In the low and high frequency limits, these general bounds give

$$\left[\sum_J \frac{\Omega_J}{\hat{\Omega}} \frac{1}{\mathcal{K}_{vJ}} \right]^{-1} \leqslant \mathcal{K}^* \leqslant \sum_J \frac{\Omega_J}{\hat{\Omega}} \mathcal{K}_{pJ},$$

$$\frac{\alpha_0^*}{\phi^*} \leqslant \sum_J \frac{\Omega_J}{\hat{\Omega}} \frac{\alpha_{0vJ}}{\phi_J},$$

$$\left[\sum_J \frac{\Omega_J}{\hat{\Omega}} \frac{\phi_J}{a_{\infty J}} \right]^{-1} \leqslant \frac{\alpha_\infty^*}{\phi^*} \leqslant \sum_J \frac{\Omega_J}{\hat{\Omega}} \frac{\alpha_{\infty J}}{\phi_J}.$$

Note that if all the inclusions present the same porosity ($\phi_J = \phi^*$), the upper and lower bounds are identical for the tortuosity at high frequency, so that the estimates provide the exact value ($\alpha_\infty^* = \alpha_{\infty J}$), in agreement with Hashin's result.

V. CONCLUSION

This study provides three analytical expressions of the dynamic permeability of granular media and emphasizes the physical assumption sustaining these results. Theses estimates follow the physical requirements in the whole frequency range and the whole porosity range. Among the two estimates energetically consistent, the P-estimate gives a good qualitative approximation of numerical results computed by the finite element method for periodic arrays (sc, bcc, and fcc) of overlapping and nonoverlapping spheres. Quantitatively, when $\phi > 0.5$, the agreement is excellent and is still reasonable otherwise. Although the zero vorticity assumption is not energetically consistent, the associated estimate leads to a value very close to the consistent P-estimate (and even more accurate as for periodic arrays of spheres). The P- and V-estimate enable us to bound the dynamic permeability of polydisperse sphere packing.

Meanwhile the spherical fluid-solid inclusion is an extremely simple and regular 3D pore geometry, these results underline the great sensitivity of the macroscopic parameters to the morphology of the medium. Nevertheless such a geometry is not sufficient to capture all the complexities of the flow in actual geometry, such as that of overlapping spheres. For this reason, the present estimates may apply to porous media whose pores are sufficiently regular (for instance, granular media made of polyhedron packing instead of sphere packing) but should be used cautiously otherwise.

It is worth mentioning that the rigorous physical analysis performed with the HPM plays a determining role in establishing these estimates. In the problem under scrutiny, other results would have been obtained if, instead of the dynamic Darcy law, a macroscopic Brinkman law was assumed—which actually occurs for a very dilute array of particles[25]—or a macroscopic viscoelastic behavior, which actually occurs for fluid of very high viscosity.[26] Note finally that the obtained results may easily be extended to linear viscoelastic saturating fluids.

APPENDIX A: VARIATION OF REAL AND IMAGINARY PARTS OF *H* VERSUS FREQUENCY

The leading idea to establish the variations of H (assumed to be isotropic, or in a given principal direction) is to calculate the virtual crossed energies of a particular velocity field—solution at a given frequency—under a particular velocity field—solution at another frequency—and reciprocally. For this purpose, let us introduce the field solutions $\mathbf{u}$ and $\mathbf{u}'$ corresponding to unit real mean velocity at the frequency ω (respectively ω'), i.e.,

$$\langle \mathbf{u} \rangle = \langle \mathbf{u}' \rangle = \mathbf{e}, \quad |\mathbf{e}| = 1, \quad \arg \mathbf{e} = 0.$$

The associated forcing pressure gradients are $-\mu H\mathbf{e}$ and $-\mu H'\mathbf{e}$, and the corresponding variational formulation [Eq. (15)] reads, for $\mathbf{u}$ [and similarly for $\mathbf{u}'$, ω', $H' = H(\omega')$],

$$\forall \mathbf{w} \in \mathcal{W},$$

$$2\mu \langle \mathbf{D}_y(\mathbf{u}) : \mathbf{D}_y(\mathbf{w}) \rangle + i\omega\rho \langle \mathbf{u} \cdot \mathbf{w} \rangle = + \mu H \mathbf{e} \langle \mathbf{w} \rangle. \quad (A1)$$

Choose now in the ω-variational formulation (or ω'), the field test $\mathbf{w} = H'\mathbf{u}'$ (or $\mathbf{w} = H\mathbf{u}$). One obtains

$$2\mu \langle \mathbf{D}_y(\mathbf{u}) : \mathbf{D}_y(\mathbf{u}') \rangle H' + i\omega\rho \langle \mathbf{u} \cdot \mathbf{u}' \rangle H' = \mu H H',$$

$$2\mu \langle \mathbf{D}_y(\mathbf{u}') : \mathbf{D}_y(\mathbf{u}) \rangle H + i\omega'\rho \langle \mathbf{u}' \cdot \mathbf{u} \rangle H = \mu H H'.$$

Subtracting these two expressions yields to the following identity, valid for any frequency ω and ω':

$$2\mu \langle \mathbf{D}_y(\mathbf{u}) : \mathbf{D}_y(\mathbf{u}') \rangle (H' - H) + i\rho \langle \mathbf{u} \cdot \mathbf{u}' \rangle (\omega H' - \omega' H) = 0.$$

Taking ω close to ω', one deduces

$$2\mu\langle \mathbf{D}_y(\mathbf{u}):\mathbf{D}_y(\mathbf{u})\rangle \frac{dH}{d\omega} + i\rho\langle \mathbf{u}\cdot\mathbf{u}\rangle \omega^2 \frac{d(H/\omega)}{d\omega} = 0. \quad \text{(A2)}$$

However, choosing $\mathbf{w}=\mathbf{u}$ in the ω-variational formulation gives

$$2\mu\langle \mathbf{D}_y(\mathbf{u}):\mathbf{D}_y(\mathbf{u})\rangle + i\rho\langle \mathbf{u}\cdot\mathbf{u}\rangle \omega = \mu H. \quad \text{(A3)}$$

Then from Eqs. (60) and (61), we get

$$\frac{dH}{d\omega} = \frac{i\rho}{\mu}\langle \mathbf{u}\cdot\mathbf{u}\rangle, \quad \omega^2 \frac{d(H/\omega)}{d\omega} = -2\langle \mathbf{D}_y(\mathbf{u}):\mathbf{D}_y(\mathbf{u})\rangle,$$

and coming back to the real and imaginary parts,

$$2\frac{dH^R}{d\omega} = \frac{i\rho}{\mu}\langle (\mathbf{u}+\bar{\mathbf{u}})\cdot(\mathbf{u}-\bar{\mathbf{u}})\rangle,$$

$$2i\omega^2 \frac{d(H^I/\omega)}{d\omega} = -2\langle [\mathbf{D}_y(\mathbf{u})+\mathbf{D}_y(\bar{\mathbf{u}})]:[\mathbf{D}_y(\mathbf{u})-\mathbf{D}_y(\bar{\mathbf{u}})]\rangle.$$

In order to establish the sign of these derivatives, we use $\mathbf{w}=\mathbf{u}-\bar{\mathbf{u}}$ as a field test in the natural and conjugate ω-variational formulations. One obtains

$$2\mu\langle \mathbf{D}_y(\mathbf{u}):[\mathbf{D}_y(\mathbf{u})-\mathbf{D}_y(\bar{\mathbf{u}})]\rangle + i\omega\rho\langle \mathbf{u}\cdot(\mathbf{u}-\bar{\mathbf{u}})\rangle = 0,$$

$$2\mu\langle \mathbf{D}_y(\bar{\mathbf{u}}):[\mathbf{D}_y(\mathbf{u})-\mathbf{D}_y(\bar{\mathbf{u}})]\rangle - i\omega\rho\langle \bar{\mathbf{u}}\cdot(\mathbf{u}-\bar{\mathbf{u}})\rangle = 0,$$

which yields the following by summing and subtracting:

$$i\omega\rho\langle (\mathbf{u}+\bar{\mathbf{u}})\cdot(\mathbf{u}-\bar{\mathbf{u}})\rangle = 8\mu\langle [\mathbf{D}_y(\mathbf{u})]^I:[\mathbf{D}_y(\mathbf{u})]^I\rangle,$$

$$\mu\langle [\mathbf{D}_y(\mathbf{u})+\mathbf{D}_y(\bar{\mathbf{u}})]:[\mathbf{D}_y(\mathbf{u})-\mathbf{D}_y(\bar{\mathbf{u}})]\rangle = 8i\omega\rho\langle (\mathbf{u}^I)^2\rangle.$$

In the left hand side terms, the squares of the imaginary parts are positive, and therefore,

$$\frac{dH^R}{d\omega} \geqslant 0, \quad \frac{d(H^I/\omega)}{d\omega} \leqslant 0,$$

which proves the monotonic increases in the viscous part with the frequency and, conversely, the monotonic decrease in tortuosity (or added mass) in the whole frequency range.

APPENDIX B: BOUNDS OF REAL AND IMAGINARY PARTS OF H^*

We assume now in $\hat{\Omega}$ a macroscopic flux $\mathbf{V}=-\mathbf{e_z}$, which corresponds to the macroscopic pressure gradient $\nabla P = \mu H^* \mathbf{e_z}$ and the exact flow $\mathbf{v}^* H^*$. A velocity-continuous field $\tilde{\mathbf{v}}_v$ is built by setting in each $\mathcal{I}_J$, $\tilde{\mathbf{v}}_v = \varpi_{vJ} H_{vJ}$, where ϖ_v is defined in Sec. III B 2.

Let us calculate $2E(\mathbf{v}^* H^*, \tilde{\mathbf{v}}_v)$. On the boundary of each inclusion, $\tilde{\mathbf{v}}_v \cdot \mathbf{n} = \mathbf{v}$, and $\mathbf{v}^* H^*$ is chosen as the stress-continuous field,

$$-\sum_J \int_{\partial\Omega_J} [(H^*\sigma^*\cdot\mathbf{n})\cdot\overline{\tilde{\mathbf{v}}_v} + (\overline{H^*\sigma^*}\cdot\mathbf{n})\cdot\tilde{\mathbf{v}}_v]ds$$

$$= -\sum_J \int_{\partial\Omega_f} [(H^*\sigma^*\cdot\mathbf{n})\cdot\bar{\mathbf{V}} + (\overline{H^*\sigma^*}\cdot\mathbf{n})\cdot\mathbf{V}]ds$$

$$= \sum_J \int_{\partial\Omega_f} (P\mathbf{n}\cdot\bar{\mathbf{V}} + \bar{P}\mathbf{n}\cdot\mathbf{V})ds$$

$$= \hat{\Omega}[\nabla P\cdot\bar{\mathbf{V}} + \nabla\bar{P}\cdot\mathbf{V}] = -2\hat{\Omega}H^{*R}.$$

Then, from (i) the above equality, (ii) Eq. (16) applied to $\mathbf{v}^* H^*$, and (iii) Eq. (39) applied to $\varpi_{vJ} H_{vJ}$, we get,

$$2E(\mathbf{v}^* H^*, \tilde{\mathbf{v}_v}) = \sum_J \{\Omega_J H^* + \Omega_J (H_{vJ}\overline{H_{vJ}})\overline{K_{vJ}}\} - 2\hat{\Omega}H^{*R}$$

$$= \hat{\Omega}\left\{\sum_J \frac{\Omega_J}{\hat{\Omega}} H_{vJ} - \overline{H^*}\right\}.$$

Furthermore, one may also establish

$$2E(-i\mathbf{v}^* H^*, \tilde{\mathbf{v}}_v) = \sum_J \{\Omega_J H^* + \Omega_J (H_{vJ}\overline{H_{vJ}})\overline{K_{vJ}}\}$$

$$-2\hat{\Omega}iH^{*I} = \hat{\Omega}\left\{\sum_J \frac{\Omega_J}{\hat{\Omega}} H_{vJ} + \overline{H^*}\right\}.$$

The positiveness of the real part of $E(\mathbf{v}^*\overline{H^*}, \tilde{\mathbf{v}_v})$ and of the imaginary part of $E(-i\mathbf{v}^*\overline{H^*}, \tilde{\mathbf{v}_v})$ gives

$$H^{*R} < \sum_J \frac{\Omega_J}{\hat{\Omega}} H^R_{vJ}, \quad H^{*I} < \sum_J \frac{\Omega_J}{\hat{\Omega}} H^I_{vJ}.$$

[1] M. A. Biot, "Theory of propagation of elastic waves in a fluid saturated porous solid. I. low frequency range. II. Higher frequency range," J. Acoust. Soc. Am. **28**, 168–191 (1956).
[2] K. Attenborough, "Acoustical characteristics of rigid fibrous absorbents and granular Media," J. Acoust. Soc. Am. **73**, 785–799 (1983).
[3] D. L. Johnson, J. Koplik, and R. Dashen, "Theory of dynamic permeability and tortuosity in fluid saturated porous media," J. Fluid Mech. **176**, 379–402 (1987).
[4] J.-F. Allard, *Propagation of Sound in Porous Media* (Elsevier Applied Science, England, 1993).
[5] J.-L. Auriault, "Dynamic behaviour of a porous medium saturated by a Newtonian fluid," Int. J. Eng. Sci. **18**, 775–795 (1980).
[6] J.-L. Auriault and E. Sanchez-Palencia, "Etude du comportement macroscopique d'un milieu poreux saturé déformable (Study of the macroscopic behaviour of saturated deformable porous media)," Journal de Mécanique **16**, 576–603 (1977).
[7] E. Sanchez-Palencia, "Non-homogeneous media and vibration theory," *Lecture Notes in Physics* (Springer-Verlag, Berlin, 1980), Vol. **127**.
[8] A. S. Sangani and A. Acrivos, "Slow flow past periodic periodic arrays of cylinders with application to heat transfer," Int. J. Multiphase Flow **8**, 193–206 (1982).
[9] A. L. Berdichevsky and Z. Cai, "Perform permeability predictions by self consistent method and finite element simulation," Polym. Compos. **14**, 132–143 (1993).
[10] C. Boutin, "Study of permeability by periodic and self consistent homogenisation," Eur. J. Mech. A/Solids **19**, 603–632 (2000).
[11] V. Tarnow, "Air flow resistivity of models of fibrous acoustic materials," J. Acoust. Soc. Am. **100**, 3706–3713 (1996).
[12] J.-L. Auriault, L. Borne, and R. Chambon, "Dynamics of porous saturated media, checking of the generalized law of Darcy," J. Acoust. Soc. Am. **77**, 1641–1650 (1985).
[13] M.-Y. Zhou and P. Sheng, "First principle calculations of dynamic permeability in porous media," Phys. Rev. B **39**, 12027–12039 (1989).
[14] A. M. Chapman and J. J. L. Higdon, "Oscillatory stokes flow a in periodic porous media," Phys. Fluids A **4**, 2099–2116 (1992).
[15] O. Umnova, K. Attenborough, and K. Ming Li, "Cell model calculations of dynamic drag parameters in packings of spheres," J. Acoust. Soc. Am. **107**, 3113–3118 (2000).
[16] R. M. Christensen and K. H. Lo, "Solutions for effective shear properties in three phase sphere and cylinder model," J. Mech. Phys. Solids **27**, 315–330 (1979).
[17] J.-L. Auriault, "Heterogeneous medium: Is an equivalent description possible?," Int. J. Eng. Sci. **29**, 785–795 (1991).
[18] T. Levy, "Propagation of waves in fluid saturated porous elastic solid," Int. J. Eng. Sci. **17**, 1005–1014 (1979).

[19]Z. Hashin, "Assessment of self consistent scheme approximation: Conductivity of particulate composites," J. Compos. Mater. **2**, 284–304 (1968).
[20]J.-P. Boelher, *Applications of Tensor Functions in Solid Mechanics*, CISM Courses and Lectures (Springer, Wien, 1987).
[21]I. D. Howells, "Drag due to the motion of a Newtonian fluid through a sparse random array of small fixed rigid objects," J. Fluid Mech. **64**, 449–485 (1974).
[22]S. R. Pride, F. D. Morgan, and A. F. Gangi, "Drag force of porous medium acoustics," Phys. Rev. B **47**, 4964–4978 (1993).
[23]COMSOL MULTIPHYSICS, Version 3.4, Reference Manual, http://www.comsol.com (Last viewed December 1, 2007).
[24]Z. Hashin and S. Shtrikman, "A variational approach to the theory of elastic behavior of multiphase materials," J. Mech. Phys. Solids **11**, 127–140 (1963).
[25]T. Levy, "Fluid flow through an array of fixed particles," Int. J. Eng. Sci. **21**, 11–23 (1983).
[26]C. Boutin and J.-L. Auriault, "Dynamic behaviour of porous media saturated by a viscoelastic fluid: Application to bituminous concretes," Int. J. Eng. Sci. **28**, 1157–1181 (1990).

Sound transmission through a microperforated-panel structure with subdivided air cavities

Masahiro Toyoda[a)]
Kyoto University Pioneering Research Unit, B104, Kyoto University Katsura, Nishikyo-ku, Kyoto, 615-8530, Japan

Daiji Takahashi
Department of Urban and Environmental Engineering, Graduate School of Engineering, Kyoto University, C1-4-352, Kyoto University Katsura, Nishikyo-ku, Kyoto, 615-8540, Japan

(Received 13 March 2008; revised 23 September 2008; accepted 25 September 2008)

The absorption characteristics of a microperforated-panel (MPP) absorber have been widely investigated, and MPPs are recognized as a next-generation absorbing material due to their fiber-free nature and attractive appearance. Herein, further possibilities of MPPs are investigated theoretically from a sound transmission viewpoint. Employing an analytical model composed of a typical MPP and a back wall with an infinite extent, transmission loss through the structure is obtained. Although MPP structures generally have great potential for sound absorption, an improvement in the transmission loss at midfrequencies, which is important for architectural sound insulation, is not sufficient when using a backing cavity alone. Hence, to improve transmission loss at midfrequencies, an air-cavity-subdivision technique is applied to MPP structures. By subdividing the air cavity with partitions, each cell can create a local one-dimensional sound field as well as lead to a normal incidence into the apertures, which is the most effective condition for Helmholtz-type resonance absorption. Moreover, by providing the same motion as the back wall to the MPP, the sound-insulation performance can be further improved at midfrequencies.
© *2008 Acoustical Society of America.* [DOI: 10.1121/1.3001711]

PACS number(s): 43.55.Ti, 43.55.Ev, 43.55.Rg [KA] Pages: 3594–3603

I. INTRODUCTION

Microperforated panels (MPP) have been used for decades. They were initially proposed by Maa[1] as sound-absorbing material, and since then their theoretical basis and potential have been demonstrated. MPPs can be made of any material from plastic, plywood, acryl glass, to sheet metal. Furthermore, MPPs can provide wideband absorption without fibrous and porous materials, which have undesirable characteristics in severe environments. Therefore, MPPs are recognized as next-generation absorbing materials.

The absorbing mechanism of an MPP absorber is Helmholtz-type resonance absorption, which is typically backed by an air cavity and a rigid wall. In order to improve the absorption characteristics, Maa[2] has developed double resonators with two MPPs because double resonators can broaden the absorption band. Moreover, from the viewpoint of architectural acoustics, MPP absorbers are attractive because they can be made of transparent materials like acryl grass. Fuchs *et al.*[3] have proposed transparent MPP applications for indoor use, while Asdrubali *et al.*[4] have shown the feasibility of transparent MPP absorbers as outdoor noise barriers. To create an absorbing structure without a rigid back wall, Sakagami *et al.*[5] have proposed a double-leaf MPP (DLMPP) absorber, which consists solely of two MPPs. It has been shown that the DLMPP structure can provide additional absorption at low frequencies.

Although numerous theoretical analyses have assumed an immobile MPP, previous experimental results have indicated unexpected absorption peaks around low frequencies.[6] Therefore, some studies have focused on panel vibration. Sakagami *et al.*[7] have theoretically investigated the effect of vibration, which often deteriorates the efficiency of the absorbing structure. Lee *et al.*[8] have theoretically and experimentally studied the coupling effect between an MPP and a back cavity, and proposed a prediction model.

As described above, MPP structures have been investigated in detail as sound absorbers. However, to further develop applications of MPPs, herein the sound insulation characteristics of MPP structures are theoretically studied. The analytical model used in this study consists of a typical MPP and a nonrigid back wall with an infinite extent. Using this model, the transmission loss of an MPP structure is calculated analytically. Moreover, to improve the transmission loss at midfrequencies, the air-cavity-subdivision technique proposed by the authors[9,10] is applied to the MPP structure, and the improvement is estimated theoretically. Additionally, the effects of this technique are validated by an experiment using an acryl MPP structure and a paper honeycomb. Parametric studies are also performed to provide further information about the effects.

[a)]Electronic mail: masahiro.toyoda@kupru.iae.kyoto-u.ac.jp

 © 2008 Acoustical Society of America

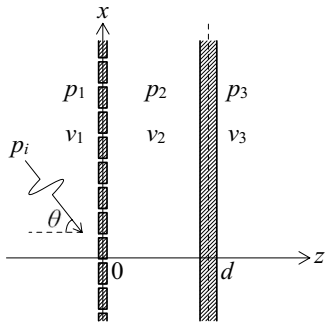


FIG. 1. Analytical model of a typical MPP structure consisting of an MPP located at $z=0$ and a back wall located at $z=d$. Incident wave $p_i(x,z)$ is assumed to be a plane wave with an incident angle θ. Subscripts 1, 2, and 3 denote the incident side, cavity between panels, and transmission side, respectively.

II. ANALYTICAL MODEL

To investigate the sound insulation performance of the MPP structure, an analytical model to calculate the transmission loss through the structure, which consists of a typical MPP and a back wall with an infinite extent, is introduced in this section. The calculation method for the absorption coefficient of the structure is also described.

A. Formulation

Figure 1 shows the analytical model considered in this paper. The MPP is located at $z=0$, while the back wall is located at $z=d$. An incident wave $p_i(x,z)$ is assumed to be a plane wave, given by

$$p_i(x,z) = e^{ik_0(\sin\theta\cdot x+\cos\theta\cdot z)}, \tag{1}$$

where i is the imaginary unit, k_0 is the wavenumber of air, and θ is the incident angle. The time factor $e^{-i\omega t}$ is suppressed throughout, and ω is the angular frequency.

In the following discussion, subscripts 1, 2, and 3 denote the incident side, the cavity between the panels, and the transmission side, respectively. With the aid of the Helmholtz integral formula for a two-dimensional problem, the sound pressures $p_1(x)$ at $z=0$ and $p_3(x)$ at $z=d$ can be expressed[11] as

$$p_1(x) = 2p_i(x,0) - \frac{\rho_0\omega}{2}\int_{-\infty}^{\infty} \mathbf{H}_0^{(1)}(k_0|x-x_0|)v_1(x_0)dx_0, \tag{2}$$

$$p_3(x) = \frac{\rho_0\omega}{2}\int_{-\infty}^{\infty} \mathbf{H}_0^{(1)}(k_0|x-x_0|)v_3(x_0)dx_0, \tag{3}$$

where ρ_0 is the density of air, $\mathbf{H}_0^{(1)}$ is the Hankel function of the first kind of order zero, $v_1(x)$ and $v_3(x)$ are the particle velocities of air at $z=0$ and $z=d$, respectively. In the case of a cavity filled with air, the sound pressure $p_2(x,z)$ and the particle velocity $v_2(x,z)$ can be expressed in terms of unknown quantities $P^{\pm}$ as

$$p_2(x,z) = (P^+e^{ik_0\cos\theta\cdot z} + P^-e^{-ik_0\cos\theta\cdot z})e^{ik_0\sin\theta\cdot x}, \tag{4}$$

$$v_2(x,z) = \frac{\cos\theta}{\rho_0 c_0}(P^+e^{ik_0\cos\theta\cdot z} - P^-e^{-ik_0\cos\theta\cdot z})e^{ik_0\sin\theta\cdot x}, \tag{5}$$

where c_0 is the speed of sound.

The force per unit area that excites the MPP and the back wall are given as the pressure differences $p_1(x) - p_2(x,0)$ and $p_2(x,d) - p_3(x)$, respectively. Let the displacements of the MPP and the back wall excited by a unit force $\delta(x)$, which is the Dirac delta function, be denoted as $u_p(x)$ and $u_b(x)$, respectively; then, the equations of motion of the panels are written as

$$\frac{\partial^4 u_{p,b}(x)}{\partial x^4} - k_{p,b}^4 u_{p,b}(x) = \frac{\delta(x)}{D_{fp,b}}, \tag{6}$$

where $k_{p,b}^4 = \rho_{p,b}h_{p,b}\omega^2/D_{fp,b}$, ρ is the density, h is the thickness, D_f is the flexural rigidity, and the subscripts p and b denote the MPP and the back wall, respectively. From the convolution theorem, the displacements $w_p(x)$ and $w_b(x)$ of the MPP and the back wall can be expressed as

$$w_p(x) = \int_{-\infty}^{\infty} \{p_1(\xi) - p_2(\xi,0)\}u_p(x-\xi)d\xi, \tag{7}$$

$$w_b(x) = \int_{-\infty}^{\infty} \{p_2(\xi,d) - p_3(\xi)\}u_b(x-\xi)d\xi. \tag{8}$$

Let z_0 be the acoustic impedance of the apertures of the MPP, which can be represented with its resistance term z_{resist} and reactance term z_{react} as $z_0 = z_{\text{resist}} + z_{\text{react}}$. According to the acoustic coupling theory for perforated plates, which has been studied theoretically in detail[12] and validated by experiments,[9,10] the boundary conditions at each surface in Fig. 1 are given by

$$v_1(x) = v_2(x,0) = -i\omega\zeta w_p(x) + \frac{\sigma}{z_0}\{p_1(x) - p_2(x,0)\}, \tag{9}$$

$$v_2(x,d) = v_2(x) = -i\omega w_b(x), \tag{10}$$

where σ is the perforation ratio of the MPP and $\zeta = 1 - (z_{\text{react}}/z_0)\sigma$.

B. Solution

By substituting Eqs. (4) and (5) into Eqs. (9) and (10), $P^{\pm}$ can be expressed with $p_1(x)$, $w_p(x)$, and $w_b(x)$ as

$$P^{\pm} = \left\{ CE^{\mp}p_1(x) - D\zeta E^{\mp}w_p(x) + D\left(1 - \frac{\rho_0 c_0\sigma}{z_0\cos\theta}\right)w_b(x)\right\}e^{-ik_0\sin\theta\cdot x}, \tag{11}$$

where $A^{\pm} = E^+ \pm E^-$, $B^{\pm} = \sigma A^{\pm}/z_0 - A^{\mp}\cos\theta/(\rho_0 c_0)$, $C = \sigma/(z_0 B^+)$, $D = i\omega/B^+$, and $E^{\pm} = e^{\pm ik_0\cos\theta\cdot d}$. Combining Eqs. (4) and (11) with Eqs. (7) and (8) yields

$$w_p(x) = \int_{-\infty}^{\infty} \{(1 - CA^+)p_1(\xi) + D\zeta A^+ w_p(\xi) - 2Dw_b(\xi)\}u_p(x-\xi)d\xi, \tag{12}$$

$$w_b(x) = \int_{-\infty}^{\infty} \left\{ 2Cp_1(\xi) - p_3(\xi) - 2D\zeta w_p(\xi) - \frac{\rho_0 c_0 DB^- w_b(\xi)}{\cos\theta} \right\} u_b(x-\xi)d\xi. \quad (13)$$

The solutions can be obtained analytically in wavenumber space using Fourier transform techniques. The transform pairs with respect to x and the wavenumber space k are defined as

$$w_{p,b}(x) = \int_{-\infty}^{\infty} W_{p,b}(k)e^{ikx}dk, \quad (14)$$

$$W_{p,b}(k) = \frac{1}{2\pi}\int_{-\infty}^{\infty} w_{p,b}(x)e^{-ikx}dx. \quad (15)$$

Taking the transform of Eqs. (6), (12), and (13) gives

$$U_{p,b}(k) = \frac{1}{2\pi D_{fp,b}(k^4 - k_{p,b}^4)}, \quad (16)$$

$$W_p(k) = 2\pi\{\alpha_1 P_1(k) + \alpha_p W_p(k) + \alpha_b W_b(k)\}U_p(k), \quad (17)$$

$$W_b(k) = 2\pi\{\beta_1 P_1(k) + \beta_3 P_3(k) + \beta_p W_p(k) + \beta_b W_b(k)\}U_b(k), \quad (18)$$

where $U_{p,b}(k)$, $P_1(k)$, and $P_3(k)$ are the transformed expressions of $u_{p,b}(x)$, $p_1(x)$, and $p_3(x)$, respectively, and $\alpha_1 = 1 - CA^+$, $\alpha_p = D\zeta A^+$, $\alpha_b = -2D$, $\beta_1 = 2C$, $\beta_3 = -1$, $\beta_p = -2D\zeta$, $\beta_b = -\rho_0 c_0 DB^-$.

Using the integral representation of the Hankel function, which is given by

$$\mathbf{H}_0^{(1)}(k_0|x-x_0|) = \int_{-\infty}^{\infty} \frac{e^{ik(x-x_0)}}{\pi\sqrt{k_0^2 - k^2}}dk, \quad (19)$$

the following expressions can be obtained from Eqs. (2), (3), (9), and (10):

$$P_1(k) = \gamma_i(k)\delta(k - k_0\sin\theta) + \gamma_p(k)W_p(k) + \gamma_b(k)W_b(k), \quad (20)$$

$$P_3(k) = \epsilon_b(k)W_b(k), \quad (21)$$

where

$$\gamma_i(k) = \frac{2\sqrt{k_0^2 - k^2}}{\sqrt{k_0^2 - k^2} - k_0 CA^-\cos\theta}, \quad (22)$$

$$\gamma_p(k) = -\frac{k_0 D\zeta A^-\cos\theta}{\sqrt{k_0^2 - k^2} - k_0 CA^-\cos\theta}, \quad (23)$$

$$\gamma_b(k) = \frac{2\rho_0\omega D\sigma}{z_0(\sqrt{k_0^2 - k^2} - k_0 CA^-\cos\theta)}, \quad (24)$$

$$\epsilon_b(k) = -\frac{i\rho_0\omega^2}{\sqrt{k_0^2 - k^2}}. \quad (25)$$

Solving Eqs. (17), (18), (20), and (21) simultaneously yields

$$W_{p,b} = F_{p,b}(k)\delta(k - k_0\sin\theta), \quad (26)$$

$$P_1(k) = \{\gamma_i(k) + \gamma_p(k)F_p(k) + \gamma_b(k)F_b(k)\}\delta(k - k_0\sin\theta), \quad (27)$$

$$P_3(k) = \epsilon_b(k)F_b(k)\delta(k - k_0\sin\theta), \quad (28)$$

where

$$F_p(k) = \{\alpha_1\kappa_b(k) - \beta_1\lambda_b(k)\}\gamma_i(k)/G(k), \quad (29)$$

$$F_b(k) = \{\beta_1\lambda_p(k) - \alpha_1\kappa_p(k)\}\gamma_i(k)/G(k), \quad (30)$$

$$G(k) = \kappa_b(k)\lambda_p(k) - \lambda_b(k)\kappa_p(k), \quad (31)$$

$$\lambda_p(k) = 1/\{2\pi U_p(k)\} - \alpha_1\gamma_p(k) - \alpha_p, \quad (32)$$

$$\lambda_b(k) = -\alpha_1\gamma_b(k) - \alpha_b, \quad (33)$$

$$\kappa_p(k) = -\beta_1\gamma_p(k) - \beta_p, \quad (34)$$

$$\kappa_b(k) = 1/\{2\pi U_b(k)\} - \beta_1\gamma_b(k) - \beta_b - \beta_3\epsilon_b(k). \quad (35)$$

From Eqs. (26)–(28), $w_{p,b}(x)$ and $p_{1,3}(x)$ can be written by

$$w_{p,b}(x) = F_{p,b}(k_0\sin\theta)e^{ik_0\sin\theta\cdot x}, \quad (36)$$

$$p_1(x) = Q_p(k_0\sin\theta)e^{ik_0\sin\theta\cdot x}, \quad (37)$$

$$p_3(x) = \epsilon_b(k_0\sin\theta)F_b(k_0\sin\theta)e^{ik_0\sin\theta\cdot x}, \quad (38)$$

where

$$Q_p(k) = \gamma_i(k) + \gamma_p(k)F_p(k) + \gamma_b(k)F_b(k). \quad (39)$$

Substituting Eqs. (36)–(38) into Eqs. (9) and (10), $v_1(x)$ and $v_3(x)$ can be given by

$$v_1(x) = Q_v(k_0\sin\theta)\cos\theta\cdot e^{ik_0\sin\theta\cdot x}/(\rho_0 c_0), \quad (40)$$

$$v_3(x) = -i\omega F_b(k_0\sin\theta)e^{ik_0\sin\theta\cdot x}, \quad (41)$$

where

$$Q_v(k) = -CA^-\gamma_i(i) - \{C\gamma_p(k) - D\zeta\}A^- F_p(k) - CA^-\gamma_b(k)F_b(k). \quad (42)$$

C. Transmission loss

The transmitted sound intensity $I_t(\theta)$ can be expressed as

$$I_t(\theta) = \frac{1}{2}\mathbf{Re}\{p_3(x)\cdot v_3^*(x)\} = \frac{\rho_0 c_0\omega^2}{2\cos\theta}|F_b(k_0\sin\theta)|^2, \quad (43)$$

where the asterisk denotes the complex conjugate. The incident sound intensity $I_i(\theta)$ can be written as $I_i(\theta) = \cos\theta/(2\rho_0 c_0)$. Then, the transmission loss of the structure $\tau(\theta)$ can be expressed as $\tau(\theta) = I_t(\theta)/I_i(\theta)$, and the mean transmission loss $\overline{\mathrm{TL}}$ can be given by

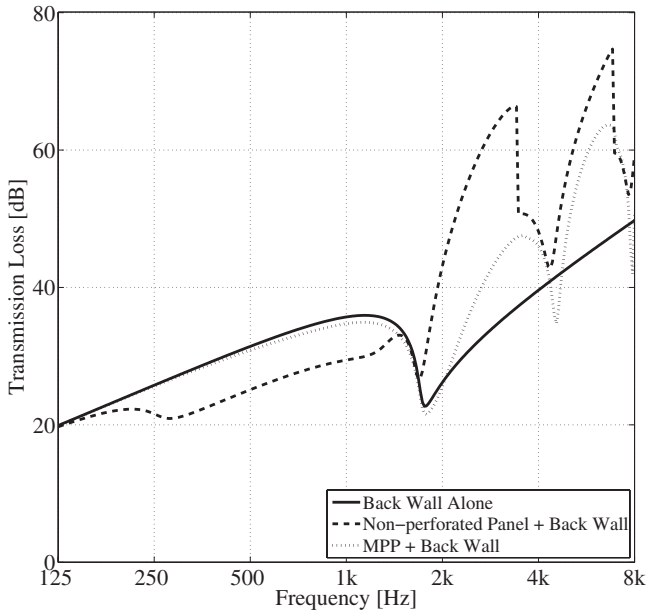


FIG. 2. Calculated transmission loss through a typical MPP structure under a field incidence of plane waves. MPP, 0.4 mm thick, is assumed to be made of aluminum, and the back wall, 0.25 mm thick, is assumed to be made of plaster. Cases of the back wall alone and a standard double-leaf panel are also shown as references.

$$\overline{\mathrm{TL}} = 10\log_{10}\frac{\pi\int_0^{\theta_{\lim}}\sin 2\theta d\theta}{2\int_0^{\pi/2}\int_0^{\theta_{\lim}}\tau(\theta)\sin 2\theta d\theta d\phi}, \tag{44}$$

where $\theta_{\lim}$ is 78° for the field incidence or 90° for random incidence.

D. Absorption coefficient

The reflected sound intensity $I_r(\theta)$ can be expressed as

$$I_r(\theta) = \frac{1}{2}\,\mathbf{Re}[\{p_1(x) - p_i(x,0)\}\cdot\{-v_1(x) + v_i(x,0)\}^*]$$
$$= \frac{\cos\theta}{2\rho_0 c_0}\,\mathbf{Re}[\{Q_p(k_0\sin\theta) - 1\}\cdot\{-Q_v(k_0\sin\theta) + 1\}^*], \tag{45}$$

where $v_i(x,z) = \cos\theta\cdot e^{ik_0(\sin\theta\cdot x + \cos\theta\cdot z)}/(\rho_0 c_0)$ is the z-directional particle velocity of the incident wave. Then, the absorption coefficient of the structure $\alpha(\theta)$ can be expressed as $\alpha(\theta) = 1 - I_r(\theta)/I_i(\theta)$, and the mean absorption coefficient $\bar{\alpha}$ can be given by

$$\bar{\alpha} = 10\log_{10}\frac{2\int_0^{\pi/2}\int_0^{\theta_{\lim}}\alpha(\theta)\sin 2\theta d\theta d\phi}{\pi\int_0^{\theta_{\lim}}\sin 2\theta d\theta}. \tag{46}$$

III. NUMERICAL EXAMPLES

In this section, numerical examples of the calculated results are shown in order to discuss the sound insulation performance of a typical MPP structure.

Figure 2 shows the calculated results of the transmission loss under field incidence of plane waves and a cavity depth of 50 mm. The parameters of an aluminum MPP are an aperture diameter of 0.4 mm, 3.5 mm distance between the apertures, a 1.0% perforation ratio, 0.4 mm thickness, 2700 kg/m^3 density, Young's modulus of 2.7×10^{10} N/m^2, Poisson's ratio of 0.3, and a loss factor of 0.001. The parameters of the plaster back wall are 25 mm thickness, 750 kg/m^3 density, Young's modulus of 1.8×10^9 N/m^2, Poisson's ratio of 0.2, and a loss factor of 0.03. The acoustic impedance of the aperture is calculated by Maa's approximation formulas,[2]

$$z_{\mathrm{resist}} = \frac{8\eta_0 h_p}{(d_p/2)^2}\left(\sqrt{1 + \frac{X^2}{32}} + \frac{\sqrt{2}d_p X}{8h_p}\right), \tag{47}$$

$$z_{\mathrm{react}} = -i\rho_0\omega h_p\left(1 + \frac{1}{\sqrt{9 + (X^2/2)}} + \frac{0.85d_p}{h_p}\right), \tag{48}$$

where

$$X = \frac{d_p}{2}\sqrt{\frac{\rho_0\omega}{\eta_0}}. \tag{49}$$

In these equations, d_p is the aperture diameter and η_0 is the viscosity coefficient of air. Figure 2 depicts the reference cases of a back wall alone and a standard double-leaf panel. In the case of the back wall alone, with the exception of the dip around the critical frequency of coincidence at 1645 Hz, the results follow the mass law. The double-leaf panel contains a back wall and a nonperforated panel, which has identical parameters as the MPP, except for the aperture parameters. Although the double-leaf panel can improve the transmission loss above the coincidence, adverse effects are observed at low frequencies. These adverse effects are caused by the mass-air-mass resonance of the double-leaf panel.

In the case of the MPP structure, the improvement in the transmission loss at high frequencies is less than the case of the double-leaf panel. However, adverse effects at low frequencies are not observed because the mass-air-mass resonance does not occur due to the ventilation through the MPP apertures. Although MPP structures generally have great potential for sound absorption, the improvement in the transmission loss is insignificant at midfrequencies, which is important for sound insulation of human voices and so on.

IV. IMPROVEMENT FOR SOUND INSULATION

To improve the transmission loss of the MPP structure at midfrequencies, the air-cavity-subdivision technique[9,10] is applied to the model. The technique can be achieved by inserting partitions, like a honeycomb structure, into the air cavity and gluing partitions tightly to the MPP and the back wall so that the back wall and MPP have the same motion. If the cell size of the partitions is sufficiently smaller than the wavelength at the maximum target frequency, then the particle motion in the cavity is constrained to move in a direction normal to the panel (z-direction). In this case, Eqs. (4) and (5) can be replaced by

$$p_2(x,z) = (P^+e^{ik_0 z} + P^-e^{-ik_0 z})e^{ik_0\sin\theta\cdot x}, \tag{50}$$

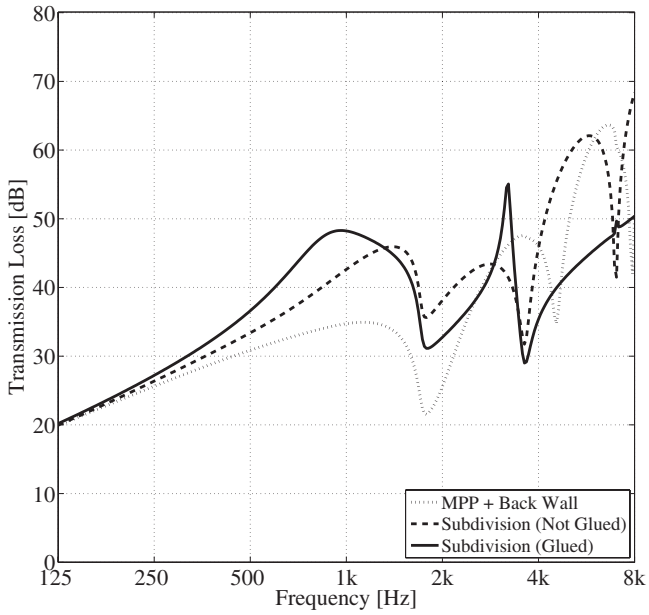


FIG. 3. Calculated transmission loss of the proposed MPP structures in which the air-cavity-subdivision technique is applied. Parameters of the MPP and the back wall are same as those in Fig. 2. Case where the panels and the partitions are not glued is also shown as a reference.

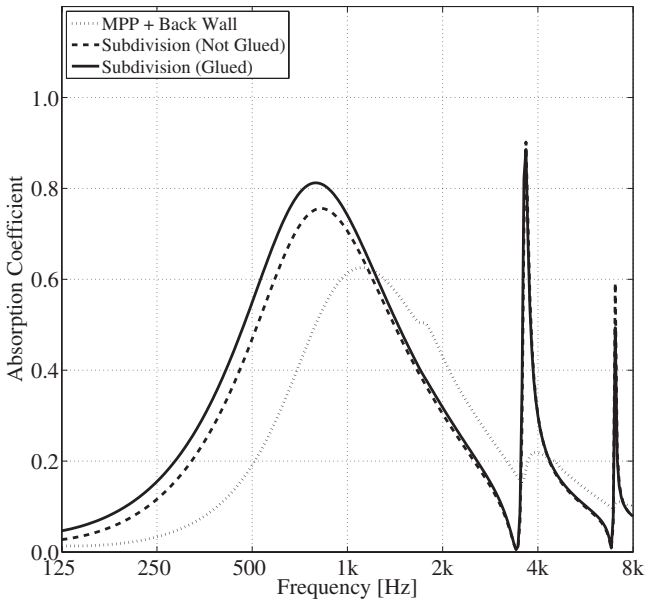


FIG. 4. Calculated absorption coefficient of the proposed MPP structures in which the air-cavity-subdivision technique is applied. The parameters of the MPP and the back wall are same as those in Fig. 2. Case where the panels and the partitions are not glued is shown as a reference.

$$v_2(x,z) = \frac{1}{\rho_0 c_0}(P^+ e^{ik_0 z} - P^- e^{-ik_0 z}) e^{ik_0 \sin\theta \cdot x}. \tag{51}$$

In the case of gluing the panels and inserting partitions, Eqs. (7) and (8) can be replaced by

$$w_p(x) = w_b(x), \tag{52}$$

$$w_b(x) = \int_{-\infty}^{\infty} \{p_1(\xi) - p_2(\xi,0) + p_2(\xi,d) - p_3(\xi)\} \times u_b(x-\xi)d\xi. \tag{53}$$

In these equations, interaction effects resulting from differences between displacements of the MPP and the back wall are neglected because the thickness and the flexural rigidity of the back wall are much greater than those of the MPP. Although partitions should have an appropriate rigidity and cell size to achieve these conditions, it has been experimentally demonstrated that the assumptions regarding Eqs. (50)–(53) can be satisfied with paper honeycomb structures.[9,10,13]

Figures 3 and 4 show the calculated results of the transmission loss and the absorption coefficient under field incidence of plane waves, respectively. Additionally, the case where the panels and the partitions are not glued is shown as a reference. Both figures indicate a dramatic improvement at midfrequencies. These effects are because each of the subdivided cells creates a local one-dimensional sound field and leads to a normal incidence into the apertures, which is the most effective condition for Helmholtz-type resonance absorption. Therefore, energy loss in the air cavity is increased, improving both the transmission loss and the absorption coefficient. Furthermore, the same motion of the MPP and the back wall should cancel the undesirable effect of the vibration of the MPP.[7] Therefore, the glued case provides a slightly greater absorption coefficient than that without gluing. As for the transmission loss, the improvement above the coincidence, which is due to the effect of double-leaf structure, is canceled. However, the transmission loss at midfrequency is greater than the case without gluing. Hence, the preferred structure for a particular situation depends on the desired characteristics.

V. EXPERIMENTAL STUDY

Due to certain assumptions and simplifications, the model proposed in the preceding section should be validated. Therefore, to confirm the assumptions and simplifications and to investigate the tendency of the practical effects obtained by employing MPP and the air-cavity-subdivision technique, experiments were performed using a reverberation box constructed of plywood boards and glass wool. Figure 5 shows a schematic of the apparatus. Although the dimensions of the test structure are limited, the small wavefront curvature at 2.5-m radius suggests that the plane-wave assumption is reasonable even at 125 Hz.

The reverberation box had an opening with dimensions 0.35×0.45 m and a volume of about 0.35 m^3. Although the setup is too small to measure transmission loss at low frequencies, the tendency toward the predicted improvement can be tested by this experiment. As depicted in Fig. 6, the samples were installed at the opening. As a reference, sample (a) was composed of a 1.0-mm-thick nonperforated panel made of acryl. Sample (b) consisted of an acryl MPP and a 1.0-mm acryl nonperforated panel with a cavity of depth 60 mm. The MPP had a 0.5-mm thickness, 0.5-mm aperture diameter, a 5.0-mm distance between the apertures, and a 0.78% perforation ratio. Sample (c) had the same configuration as sample (b), except a paper honeycomb with a depth of 60 mm was inserted into the air cavity. Thus, sample (c)

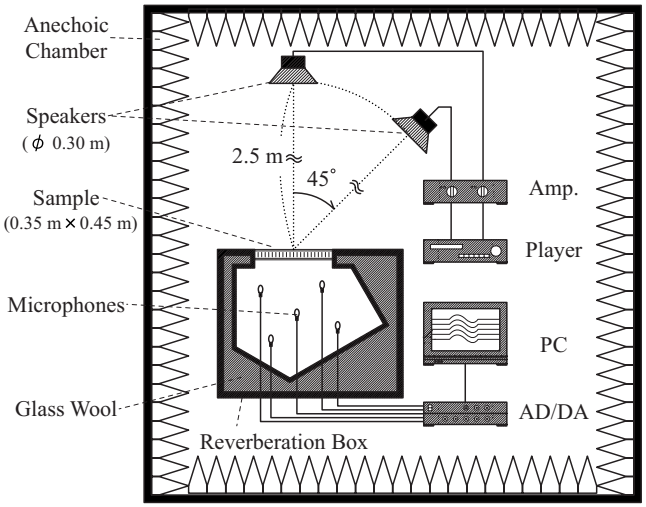


FIG. 5. Experimental setup to measure transmission loss using a reverberation box. Five microphones are located in the reverberation box, and a loud speaker is the sound source. Pink noise is used for the source signal.

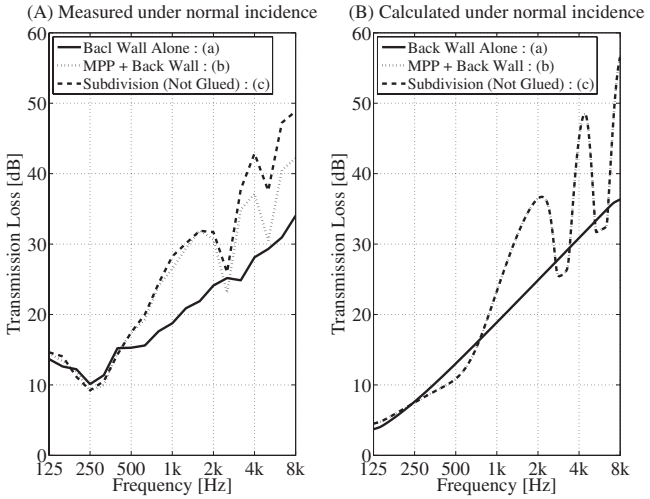


FIG. 7. (A) Measured transmission loss of the samples (a), (b), and (c) under normal incidence. (B) Calculated transmission loss of the infinite analytical model given the corresponding parameters with the samples (a), (b), and (c) under normal incidence.

represents the subdivision technique without gluing. The honeycomb structure was located with slight spaces between the honeycomb and both of the panels in order to avoid stiffening the panels as well as to avoid the mechanical propagation of vibration. The cell size of the honeycomb was 10 mm, which is sufficiently smaller than one-half wavelength at 8 kHz. Sample (d) represents the subdivision technique with gluing. An MPP, a paper honeycomb, and a nonperforated panel, which had the same properties as sample (c), were tightly glued with caution in order to avoid covering the apertures with an adhesion bond. In this case, the mass and the rigidity differ from those of samples (a), (b), and (c). Therefore, as discussed above, to extract the effects of the subdivision technique, sample (e) was prepared as a reference to evaluate sample (d). Sample (e) was composed of a paper honeycomb and two acryl nonperforated panels with thicknesses of 0.5 and 1.0 mm. They were glued tightly

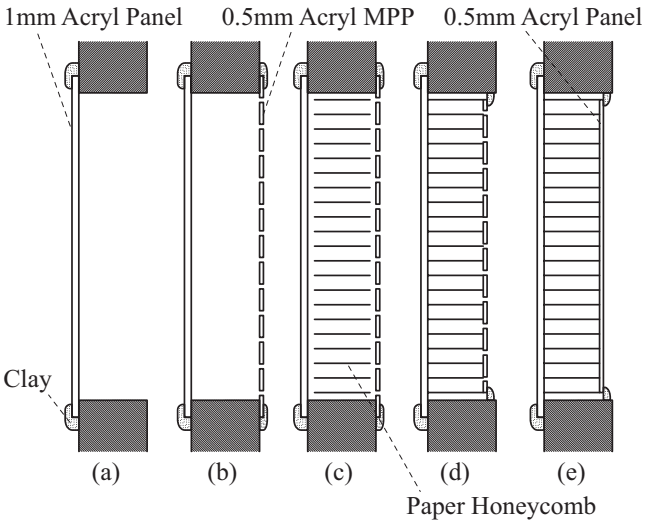


FIG. 6. Experimental samples. (a) Back wall alone; (b) MPP+back wall; (c) subdivision (not glued); (d) subdivision (glued); (e) reference for sample (d). Samples (d) and (e) have the same mass and rigidity. Sample (e) is expected to behave as a single panel.

so that the sample had nearly the same mass and rigidity as sample (d). Thus, sample (e) was expected to behave like a single panel. To cut off the sound transmission through the spaces in all the above cases, undesirable spaces between panel edges and the opening were filled with clay.

Five microphones were placed in the reverberation box, and a loudspeaker, which was used as the sound source and had a speaker unit with a 0.3-m diameter, was located 2.5 m away from the opening. The incident angles considered here were the normal and 45° directions. Pink noise was used for the source signal, and spatially averaged sound-pressure levels over each 1/3-octave band were measured by the five microphones. To obtain transmission loss, the incident sound pressures at the points, where the samples were supposed to be located, were also measured without the reverberation box and the samples. Thus, the transmission loss from the sound pressures was corrected for the reverberation time for each 1/3-octave band. In advance of the experiment, the signal-to-noise (S/N) ratios and the dynamic ranges of the measuring instruments were checked, and it was confirmed that transmission loss over 50 dB can be measured below 8 kHz.

Figures 7 and 8, respectively, show the experimental and theoretical results of transmission loss for samples (a), (b), and (c) under normal incidence and 45° incidence. The theoretical results were calculated under the same conditions as the experiments except for the panel dimensions. In the case of sample (a), similar to theoretical predictions, the experimental transmission loss results basically follow the mass law, but all the experimental results for transmission loss below 250 Hz are larger than the theoretical ones due to the differences between finite and infinite conditions. With regard to sample (b), improvement is obtained under both normal and 45° incidences. However, the improvement for the 45° incidence is inferior to the case under normal incidence. Comparing samples (b) and (c) shows that the characteristics under 45° incidence become closer to those for the case of normal incidence by the subdivision technique. Because of these effects, improvement of the transmission loss can be

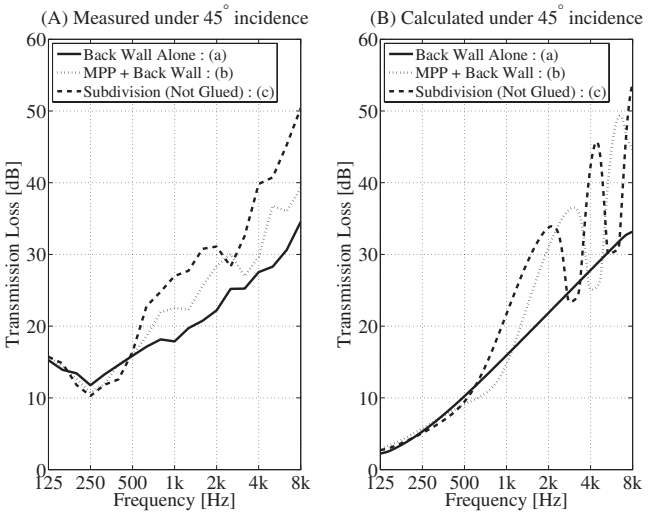


FIG. 8. (A) Measured transmission loss of the samples (a), (b), and (c) under 45° incidence. (B) Calculated transmission loss of the infinite analytical model given the corresponding parameters with the samples (a), (b), and (c) under 45° incidence.

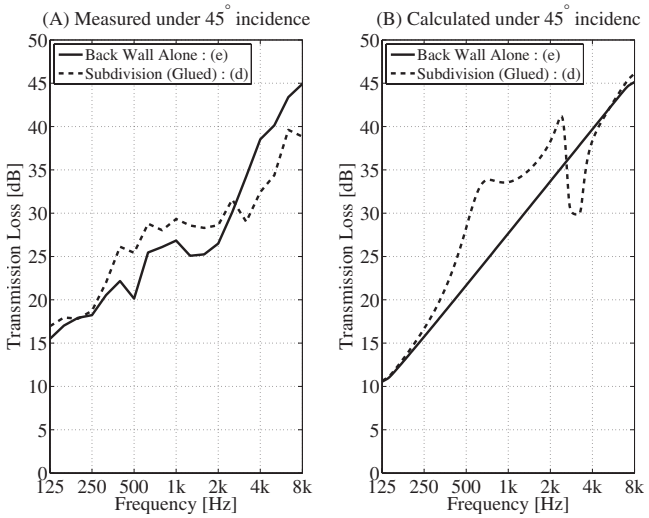


FIG. 10. (A) Measured transmission loss of the samples (d) and (e) under 45° incidence. (B) Calculated transmission loss of the infinite analytical model given the corresponding parameters with the samples (d) and (e) under 45° incidence, where the parameter of mass is determined by the data measured for the samples.

obtained as discussed in the preceding section. Moreover, it is interesting that improvement can be seen above 3 kHz in the experimental results shown in Fig. 7 because the theoretical results predict that the subdivision technique does not have an effect under normal incidence. However, these experimental results are caused by friction between air particles and the paper wall inside each cell, which the theory does not consider.

Figures 9 and 10 show the experimental and theoretical results for samples (d) and (e) under normal incidence and 45° incidence, respectively. In calculating the theoretical results, the parameter of mass was replaced by the measured data from samples (d) and (e). As seen by comparing samples (d) and (e), adverse effects above 3 kHz are observed in both the theoretical and experimental results. These adverse effects are due to z-directional resonance in each cell. However, under both normal incidence and 45° incidence, transmission loss from 300 Hz to 3 kHz can be improved by the subdivision technique with gluing, but the frequency range where improvement is achieved is lower than that using the subdivision technique without gluing.

On the whole, the characteristics of the experimental results are in good agreement with the theoretical ones. Hence, it is concluded that the subdivision technique can practically improve the transmission loss at midfrequencies and that the MPP characteristics can be changed by gluing.

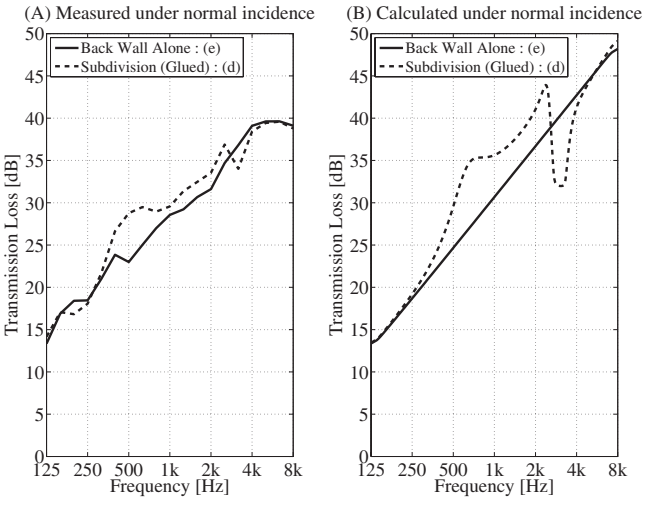


FIG. 9. (A) Measured transmission loss of the samples (d) and (e) under normal incidence. (B) Calculated transmission loss of the infinite analytical model given the corresponding parameters with the samples (d) and (e) under normal incidence, where the parameter of mass is determined by the data measured for the samples.

VI. PARAMETRIC STUDY

To provide further information on the subdivision technique, parametric studies were performed from the viewpoint of the effect on the transmission loss due to inserting partitions into a typical MPP structure. To easily determine the tendencies of the effect, ΔTL is defined as

$$\Delta \mathrm{TL} = \overline{\mathrm{TL}}_p - \overline{\mathrm{TL}}_t, \tag{54}$$

where $\overline{\mathrm{TL}}_p$ is the transmission loss for the cases of the proposed MPP structures with subdivided air cavities, and $\overline{\mathrm{TL}}_t$ is the transmission loss for the case of a typical MPP structure without a subdivision technique ("MPP+back wall"' as shown in Fig. 3). In the following discussion, the basic values of the parameters of a back wall and a MPP are the same as those given in the previous section; only the target parameter is changed. The target parameters considered here are material and thickness of the back wall, perforation ratio, thickness of an MPP, and air cavity depth.

Figures 11 and 12 show the calculated results of ΔTL for the cases with and without gluing the plates, respectively. In these figures, three types of back walls are considered: 5-mm-thick plywood, 25-mm-thick plaster, and 50-mm-thick concrete. As discussed in the previous section, the glued case provides improvement at midfrequencies, while adverse effects are observed at high frequencies because the effect of

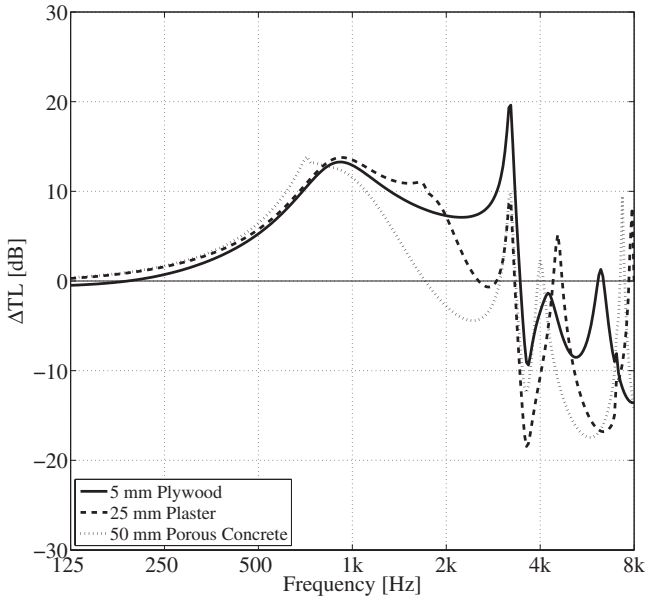


FIG. 11. Effects of the back wall material on ΔTL when the plates are glued. MPP, 0.4 mm thick, is assumed to be made of aluminum, and the perforation ratio is 1.0%. Cavity depth is 50 mm.

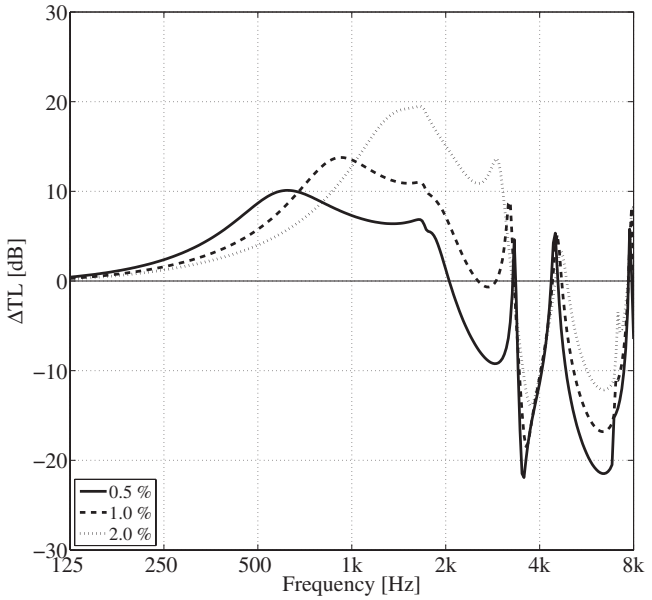


FIG. 13. Effects of the perforation ratio of MPP on ΔTL when the plates are glued. MPP, 0.4 mm thick, is assumed to be made of aluminum, and a back wall, 25 mm thick, is assumed to be made of plaster. Cavity depth is 50 mm.

the double-leaf structure is canceled upon gluing the plates. It can be also seen that both the maximum value of ΔTL and the target frequency are negligibly affected by the back wall material. For the case without gluing, the transmission loss at midfrequencies increases. Moreover, peaks and dips, which are caused by shifts in the dip frequencies observed in Fig. 3, occur at high frequencies. The improvement at midfrequencies for the case of porous concrete is smaller than the other cases, implying that it is difficult to obtain improvement using a back wall with a low critical frequency of coincidence.

Figures 13 and 14 show the effects of the perforation ratio for the cases with and without gluing, respectively. The values of the perforation ratio considered here are 0.5%, 1.0%, and 2.0%. For the glued case, as the perforation ratio increases, the maximum value of ΔTL tends to increase, and the effect shifts to higher frequencies. In contrast, for the case without gluing, ΔTL tends to decrease as the perforation ratio increases, and the effect does not shift the frequency.

Figures 15 and 16 show the effects of MPP thickness for the cases with and without gluing, respectively. The results show the opposite tendency to that of the effect of the perforation ratio; ΔTL for the glued case tends to decrease, while that for the case without gluing tends to increase as the

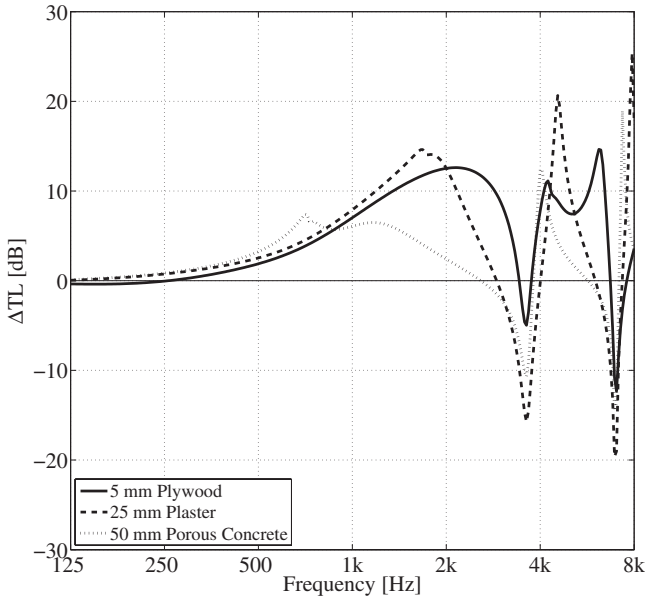


FIG. 12. Effects of the back wall material on ΔTL when the plates are not glued. MPP, 0.4 mm thick, is assumed to be made of aluminum, and the perforation ratio is 1.0%. Cavity depth is 50 mm.

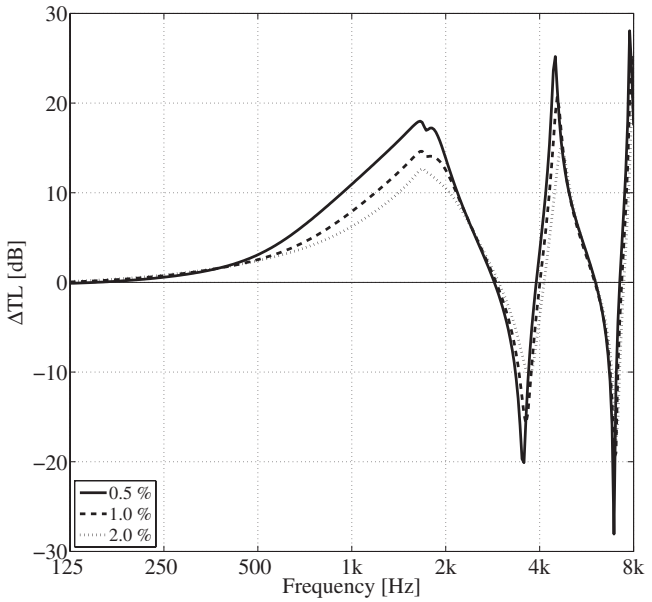


FIG. 14. Effects of the perforation ratio of MPP on ΔTL when the plates are not glued. MPP, 0.4 mm thick, is assumed to be made of aluminum, and a back wall, 25 mm thick, is assumed to be made of plaster. Cavity depth is 50 mm.

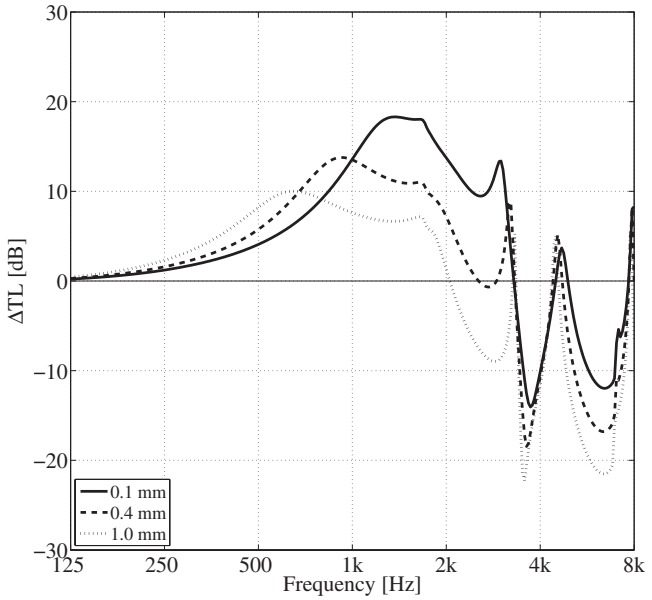


FIG. 15. Effects of MPP thickness on ΔTL when the plates are glued. MPP with a perforation ratio of 1.0% is assumed to be made of aluminum and a back wall, 25 mm thick, is assumed to be made of plaster. Cavity depth is 50 mm.

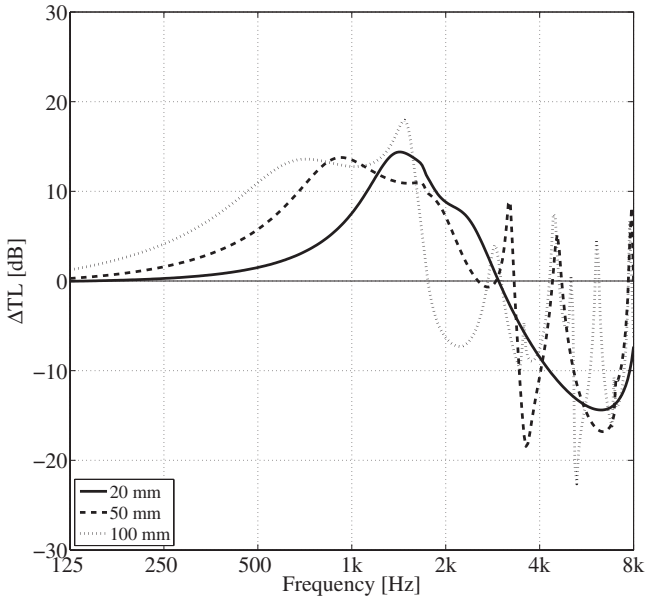


FIG. 17. Effects of cavity depth on ΔTL when the plates are glued. MPP, 0.4 mm thick, is assumed to be made of aluminum, and a back wall, 25 mm thick, is assumed to be made of plaster. Perforation ratio is 1.0%.

thickness increases. Moreover, only the case with gluing shifts the effect to lower frequencies as the thickness increases.

Figures 17 and 18 show the effects of the air-cavity depth. These figures illustrate that both the improvement and the resonance shift to lower frequencies as the depth increases. These tendencies are seen for both cases with and without gluing.

From the discussion above, it can be concluded that a robust improvement at midfrequencies can be obtained with the glued structure because ΔTL does not significantly change due to the back wall parameters. In addition, by tuning the parameters of a MPP, the improvement can be obtained at an arbitrary frequency. For example, although adverse effects are observed at high frequencies for the glued case, these are not observed in the case without gluing. Therefore, it is possible to easily improve the transmission loss by only inserting partitions into the cavity. However, a back wall with a low critical frequency of coincidence might decrease the improvement.

The material of an MPP has a negligible effect on the subdivision technique itself. Therefore, ΔTL is not affected by changes in the flexural rigidity and density of an MPP.

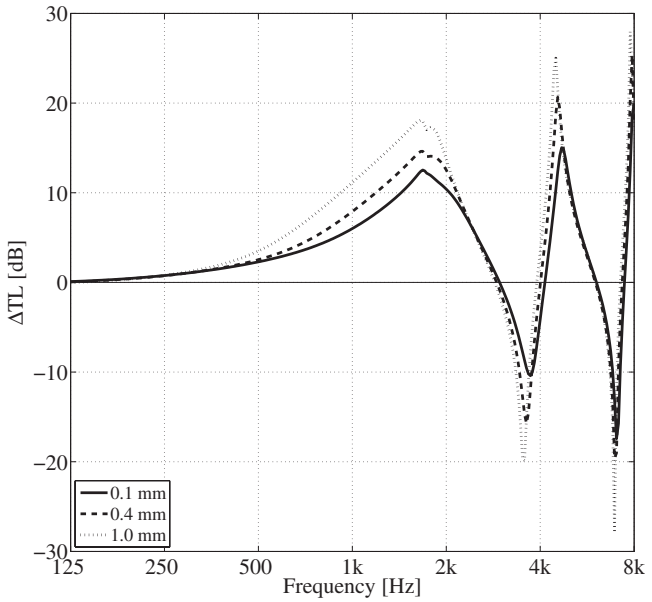


FIG. 16. Effects of MPP thickness on ΔTL when the plates are not glued. MPP with a perforation ratio 1.0% is assumed to be made of aluminum, and a back wall, 25 mm thick, is assumed to be made of plaster. Cavity depth is 50 mm.

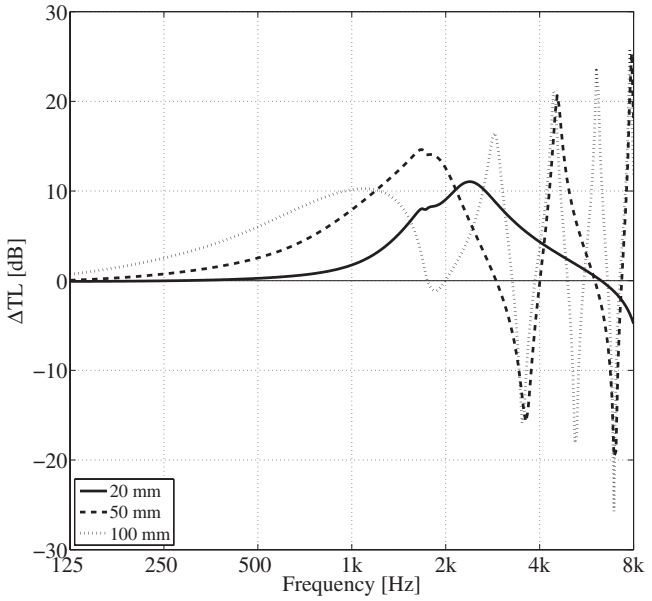


FIG. 18. Effects of cavity depth on ΔTL when the plates are not glued. MPP, 0.4 mm thick, is assumed to be made of aluminum, and a back wall, 25 mm thick, is assumed to be made of plaster. Perforation ratio is 1.0%.

VII. CONCLUSION

In this study, the possibility of an MPP is theoretically investigated from a sound transmission viewpoint. An analytical model composed of an MPP and a back wall with an infinite extent can predict the transmission loss of a typical MPP. The improvement in the transmission loss at midfrequencies, which is important for architectural sound insulation, is not significant compared to the back wall alone. Hence, applying the air-cavity-subdivision technique[9,10] to the structure improves the performance. Each of the subdivided cells can create a local one-dimensional sound field, leading to a normal incidence into the apertures, which is the most effective condition for Helmholtz-type resonance absorption. Furthermore, the same motion of the MPP and the back wall should cancel the undesirable effect of the vibration of the MPP.[7] Therefore, energy loss in the air cavity is increased, improving both of the transmission loss and the absorption coefficient. Practical effects of this technique are experimentally demonstrated, and further information for tuning the parameters is provided from parametric studies. Our findings suggest that the wide use of these structures for both sound insulation and sound absorption is imminent.

ACKNOWLEDGMENTS

This study was supported by the Program for Improvement of Research Environment for Young Researchers from Special Coordination Funds for Promoting Science and Technology (SCF) commissioned by the Ministry of Education, Culture, Sports, Science and Technology (MEXT) of Japan.

[1] D. Y. Maa, "Theory and design of microperforated panel sound-absorbing constructions," Sci. Sin. English Edition **18**, 55–71 (1975).
[2] D. Y. Maa, "Microperforated panel wide-band absorber," Noise Control Eng. J. **29**, 77–84 (1987).
[3] H. V. Fuchs and X. Zha, "Acrylic-glass sound absorbers in the plenum of the Deutscher Bundestag," Appl. Acoust. **51**, 211–217 (1997).
[4] F. Asdrubali and G. Pispola, "Properties of transparent sound-absorbing panels for use in noise barriers," J. Acoust. Soc. Am. **121**, 214–221 (2007).
[5] K. Sakagami, M. Morimoto, and W. Koike, "A numerical study of double-leaf microperforated panel absorbers," Appl. Acoust. **67**, 609–619 (2006).
[6] J. Lee and G. W. Swenson, "Compact sound absorbers for low frequencies," Noise Control Eng. J. **38**, 109–117 (1992).
[7] K. Sakagami, M. Morimoto, and M. Yairi, "A note on the effect of vibration of a microperforated panel on its sound absorption characteristics," Acoust. Sci. & Tech. **26**, 204–207 (2005).
[8] Y. Y. Lee, E. W. M. Lee, and C. F. Ng, "Sound absorption of a finite flexible microperforated panel backed by an air cavity," J. Sound Vib. **287**, 227–243 (2005).
[9] M. Toyoda and D. Takahashi, "Reduction of acoustic radiation by impedance control with a perforated absorber system," J. Sound Vib. **286**, 601–614 (2005).
[10] M. Toyoda, M. Tanaka, and D. Takahashi, "Reduction of acoustic radiation by perforated board and honeycomb layer systems," Appl. Acoust. **68**, 71–85 (2006).
[11] D. Takahashi, "Sound transmission through single plates with absorptive facings: Improved theory and experiment," J. Acoust. Soc. Am. **88**, 879–882 (1990).
[12] D. Takahashi, "Flexural vibration of perforated plates and porous elastic materials under acoustic loading," J. Acoust. Soc. Am. **112**, 1456–1464 (2002).
[13] M. Toyoda, M. Tanaka, and D. Takahashi, "Effects of air-layer subdivision: A new method of improving sound insulation," Build. Acoust. **13**, 49–59 (2006).

Vibroacoustic behavior of clamp mounted double-panel partition with enclosure air cavity

F. X. Xin, T. J. Lu,[a] and C. Q. Chen[b]
MOE Key Laboratory for Strength and Vibration, School of Aerospace, Xi'an Jiaotong University, Xi'an 710049, People's Republic of China

(Received 19 July 2008; accepted 6 October 2008)

A theoretical study on the vibroacoustic performance of a rectangular double-panel partition clamp mounted in an infinite acoustic rigid baffle is presented. With the clamped boundary condition taken into account by the method of modal function, a double Fourier series solution to the dynamic response of the structure is obtained by employing the weighted residual method (i.e., the Galerkin method). The double series solution can be considered as the exact solution of the problem, as the structural and acoustic-structural coupling effects are fully accounted for and the solution converges numerically. The accuracy of the theoretical predictions is checked against existing experimental data, with good agreement achieved. The influence of several key parameters on the sound isolation capability of the double-panel configuration is then systematically studied, including panel dimensions, thickness of air cavity, elevation angle, and azimuth angle of incidence sound. The present method is suitable for double-panel systems of finite or infinite extent and is applicable for both low- and high-frequency ranges. With these merits, the proposed method compares favorably with a number of other approaches, e.g., finite element method, boundary element method, and statistical energy analysis method.
© *2008 Acoustical Society of America.* [DOI: 10.1121/1.3006956]

PACS number(s): 43.55.Ti, 43.55.Rg, 43.20.Tb [DF] Pages: 3604–3612

I. INTRODUCTION

Vibroacoustic problems involving the interaction of structural vibration and acoustic-structural coupling effects are of particular significance in engineering applications.[1–37] A typical such problem addresses a configuration comprising two parallel rectangular panels with an airproof cavity sealed in between, mounted in acoustic rigid baffle, with the whole system immersed in a fluid (e.g., air). These double-panel partitions have found increasingly wide applications in modern buildings, vehicles, aerospace and aeronautical structures, etc., due to their superior sound insulation properties over single-panel configurations as a result of structural discontinuity and sound impedance mismatch.

Numerous analytical,[1–28] experimental,[19,21,29–31] statistical,[32–35] and numerical[36,37] studies on the transmission of sound across a double-panel partition have been conducted, aiming to provide fundamental insight into the physical understanding of the acoustic-structural coupled system, so that an effective guidance for structural design and system control can be derived. Early work can be traced back to Beranek and Work[15] who developed a simple theory of sound transmission for normal wave incident on an infinite double-layer structure. Almost at the same time, London[16] proposed a different but also simple model to discuss the reverberant sound transmission through infinite double-leaf constructions made of two identical panels. Although both models offer certain advantages, such as low computational cost and relatively good agreement with experiments, they contain a few parameters, which are difficult to determine. Moreover, the former is too simple to gain a fundamental and physical understanding of the problem while the latter can only be applied to structures consisted of two identical panels.

With the assumption of infinite periodicity, Lin and Garrelick[13] proposed a theoretical model to investigate the sound-transmission properties of periodically frame-stiffened, double-panel structures. The transmission of sound across the same infinite periodically stiffened double-panel structure was addressed by Wang *et al.*[12] using the space-harmonic method, with detailed physical interpretation of the transmission mechanism presented. Takahashi[11] studied the problem of sound radiation from periodically connected infinite double-panel structures excited by a harmonic point force and calculated the sound radiated power of two different structures (i.e., point connected and point connected with rib stiffening). Yairi *et al.*[10] studied theoretically sound radiation from a double-leaf partition subjected to point force excitation and found that it is difficult to reduce the radiated sound power by an interior panel alone, even if its mass is increased. Kropp and Rebillard[25] investigated the possibilities to optimize the sound insulation property of double wall constructions at low frequencies. A comprehensive review of existing analytical methods relying largely on the wave approach to compute the loss of sound transmission across double-panel partitions was given by Pellicier and Trompette.[38]

The aforementioned investigations are mainly focused on infinitely large partitions. For finitely bounded constructions, the influence of boundary conditions and additional factors in relation to the finiteness of the structure on sound

[a]Electronic mail: tjlu@mail.xjtu.edu.cn
[b]Electronic mail: cchen@mail.xjtu.edu.cn

 © 2008 Acoustical Society of America

transmission is no longer negligible, promoting the search of effective and accurate modeling means. The transmission[23,24] or radiation[22] of sound through finite single-leaf panels have been discussed from different viewpoints. Sgard *et al.*[36] and Panneton and Atalla[37] employed finite element method (FEM) models to predict sound-transmission loss (STL) across finite-sized, double-panel sound barrier with poroelastic linings. In order to take account of the finite size of a plane structure in sound radiation and transmission calculations, Villot *et al.*[20] proposed a new technique based on spatial widowing of plane waves. Additionally, on the basis of simply supported boundary condition, a variety of theoretical models[7,18,19,21] were formulated to analyze the sound transmission through double-panel partitions of finite extent. However, to the authors' best knowledge, as far as sound transmission across finite-sized, double-panel partitions is concerned, the influence of one important type of boundary condition, namely, the clamped boundary condition, has yet to be addressed theoretically.

For airborne sound incident on one side of a single-leaf panel, it is well known that the physical phenomenon of coincidence occurs when the flexural bending wavelength of panel vibration matches with the trace wavelength of the incident sound.[4,12] For double-panel partitions composed of two single-leaf panels, similar coincidence effect occurs for each panel but with a complicated influence by the other. Apart from this coincidence effect, dips appear in the plot of STL versus frequency where the mass-air-mass effect and the standing-wave effect occur. In the present article, an analytical approach capable of handling accurately such effects and the clamped boundary condition is developed to study the acoustic-structural performance of rectangular double-panel partitions of finite extent. The validity of the theoretical predictions is checked against existing test data. The effects of air cavity thickness, panel dimensions, and sound incidence angles on the sound isolation capability of the structure are quantified.

II. VIBROACOUSTIC COUPLED SYSTEM MODELING

A. Geometry and assumption of the vibroacoustic structure

With reference to Fig. 1, the finite-sized, double-panel partition with airproof cavity is assumed to be rectangular, baffled, and clamp supported along its boundaries, occupying the spatial region $(0<x<a,\ 0<y<b,\ 0<z<H)$ in Cartesian coordinates. The two single-leaf panels are homogeneous and isotropic, but may have different physical properties. Each panel is modeled as a classical thin plate, implying that transverse shear deformation of the panel is neglected. The bottom and upper panels (Fig. 1) have thicknesses h_1 and h_2, respectively, and are separated by an airproof cavity of thickness H. The infinitely large acoustic rigid baffle hosting the double-panel partition divides the spatial space into two fields, i.e., sound incidence field $(z<0)$ and sound radiating field $(z>H)$.

Let a uniform plane sound wave varying harmonically in time impinge on the bottom panel with elevation angle φ and azimuth angle θ. Vibration of the bottom panel due to harmonic sound excitation alters dynamically the pressure field within the hermetical air cavity. This dynamically altering pressure causes vibration of the upper panel, which then radiates sound waves into the upper domain. For convenience, the bottom panel adjacent to the incidence field is defined as the incidence panel, while the upper panel is named the radiating panel. The incidence field contains three components, i.e., the incidence pressure, the reflection pressure, and the radiation pressure.[7] In general, the radiation pressure is negligible with regard to the other two components. It is readily understandable that only radiation pressure exists in the radiating field.

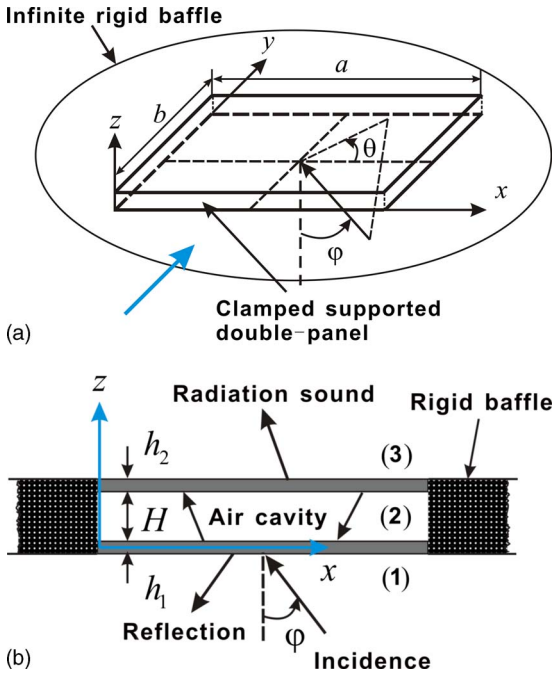


FIG. 1. (Color online) Schematic of sound transmission through a baffled and clamp supported double-panel partition: (a) Global view and (b) side view along the arrow direction in (a).

B. Outline of theoretical formulation

The acoustic velocity potential of a uniform plane incident sound wave varying harmonically in time can be expressed as

$$\phi = Ie^{-j(k_x x + k_y y + k_z z - \omega t)}, \tag{1}$$

where I is the sound amplitude, $j=\sqrt{-1}$, ω is the angular frequency, and k_x, k_y, and k_z are the wavenumber components along the positive directions of x-, y-, and z-axes, respectively:

$$k_x = k_0 \sin\varphi\cos\theta, \quad k_y = k_0 \sin\varphi\sin\theta, \quad k_z = k_0\cos\varphi. \tag{2}$$

Here, $k_0=\omega/c_0$ is the acoustic wavenumber in air, and c_0 denotes the acoustic speed in air.

The vibroacoustic response of a double-panel partition with air cavity (Fig. 1) is induced by sound pressure fluctuations and differences between two adjacent fields (above and below each panel) and is governed by

$$\left\{D_1\left(\frac{\partial^2}{\partial x^2}+\frac{\partial^2}{\partial y^2}\right)^2-m_1\omega^2\right\}w_1=p_1|_{z=0^-}-p_2|_{z=0^+}, \quad (3)$$

$$\left\{D_2\left(\frac{\partial^2}{\partial x^2}+\frac{\partial^2}{\partial y^2}\right)^2-m_2\omega^2\right\}w_2=p_2|_{z=H^-}-p_3|_{z=H^+}, \quad (4)$$

where ρ_0 is the density of air, w_1 and w_2 are the transverse displacements, and (m_1,m_2) and (D_1,D_2) are the surface densities and flexural rigidities of the bottom and upper panels, respectively.

The acoustic field is separated by the two single-leaf panels into three regions, namely, half-space $z<0$ (sound incident region), airproof cavity, and half-space $z>H$ (sound radiating region), which are referred to as regions 1, 2, and 3, respectively [see Fig. 1(b)]. Correspondingly, three velocity potentials Φ_i $(i=1,2,3)$ are introduced to characterize the distribution of sound pressure and velocity in each region. These velocity potentials satisfy the Helmholtz equation:

$$\left[\frac{\partial^2}{\partial x^2}+\frac{\partial^2}{\partial y^2}+\frac{\partial^2}{\partial z^2}+k_0^2\right]\Phi_i=0 \quad (i=1,2,3). \quad (5)$$

In terms of the velocity potentials, the velocity and pressure fields in the three acoustic regions can be expressed as

$$\hat{\mathbf{u}}_i=-\nabla\Phi_i, \quad p_i=\rho_0\frac{\partial\Phi_i}{\partial t}=j\omega\rho_0\Phi_i \quad (i=1,2,3). \quad (6)$$

The flexural motions of the bottom and upper panels induced by a time-harmonic incident plane sound wave can be expressed in the form of double series as

$$w_1(x,y;t)=\sum_{m,n}\phi_{mn}(x,y)q_{1,mn}(t), \quad (7)$$

$$w_2(x,y;t)=\sum_{m,n}\phi_{mn}(x,y)q_{2,mn}(t), \quad (8)$$

where the modal functions ϕ_{mn} and modal coefficients $q_{i,mn}$ $(i=1,2)$ are given by

$$\phi_{mn}(x,y)=\left(1-\cos\frac{2m\pi x}{a}\right)\left(1-\cos\frac{2n\pi y}{b}\right), \quad (9)$$

$$q_{1,mn}(t)=\alpha_{1,mn}e^{j\omega t}, \quad q_{2,mn}(t)=\alpha_{2,mn}e^{j\omega t}. \quad (10)$$

Clearly, the assumed deflections of the bottom and upper panels [i.e., Eqs. (7) and (8) with Eq. (9)] satisfy the clamped boundary condition.

Accordingly, the velocity potentials for the sound incident region, airproof cavity, and sound radiating region may be expressed as

$$\Phi_1(x,y,z;t)=Ie^{-j(k_x x+k_y y+k_z z-\omega t)}+\sum_{m,n}\beta_{mn}\phi_{mn}e^{-j(-k_{z,mn}z-\omega t)}, \quad (11)$$

$$\Phi_2(x,y,z;t)=\sum_{m,n}\varepsilon_{mn}\phi_{mn}e^{-j(k_{z,mn}z-\omega t)}+\sum_{m,n}\zeta_{mn}\phi_{mn}e^{-j(-k_{z,mn}z-\omega t)}, \quad (12)$$

$$\Phi_3(x,y,z;t)=\sum_{m,n}\xi_{mn}\phi_{mn}e^{-j(k_{z,mn}z-\omega t)}, \quad (13)$$

where ε_{mn} and ξ_{mn} are the amplitudes of acoustic velocity potentials for positive going waves, β_{mn} and ζ_{mn} are associated with negative going waves, and $k_{z,mn}$ are the wavenumbers in the z-direction.

By taking the clamped boundary condition into account and substituting Eqs. (7), (8), and (11)–(13) into the governing equations (3) and (4), the lateral deflections of the two panels can be obtained. With the condition of continuity of velocity at the air-panel interface, the velocity potentials in the sound incident region and the sound radiating region can be expressed as

$$\Phi_1=2Ie^{-j(k_x x+k_y y)}-\sum_{m,n}\frac{\omega}{k_z}\alpha_{1,mn}\left(1-\cos\frac{2m\pi x}{a}\right)\times\left(1-\cos\frac{2n\pi y}{b}\right), \quad (14)$$

$$\Phi_3=\frac{\omega}{k_z}\sum_{m,n}\alpha_{2,mn}\left(1-\cos\frac{2m\pi x}{a}\right)\left(1-\cos\frac{2n\pi y}{b}\right). \quad (15)$$

C. Definition of sound-transmission loss

The power of incident sound is defined as[19,37]

$$\Pi_{in}=\frac{1}{2}\,\mathrm{Re}\int\int_A p_{in}\cdot v_{in}^* dA, \quad (16)$$

where the symbol * denotes complex conjugate, $v_{in}=p_{in}/(\rho_0 c_0)$ is the local acoustic velocity, and

$$p_{in}=j\omega\rho_0\Phi_1=j\omega\rho_0\left[2Ie^{-j(k_x x+k_y y)}-\sum_{m,n}\frac{\omega}{k_z}\alpha_{1,mn}\times\left(1-\cos\frac{2m\pi x}{a}\right)\left(1-\cos\frac{2n\pi y}{b}\right)\right] \quad (17)$$

is the incident sound pressure. Substituting p_{in} and v_{in} into Eq. (16) yields

$$\begin{aligned}\Pi_{in}&=\frac{\rho_0\omega^2}{2c_0}\int\int_A|\Phi_1|^2dA=\frac{\rho_0\omega^2}{2c_0}\int\int_A\left|2Ie^{-j(k_x x+k_y y)}-\sum_{m,n}\frac{\omega}{k_z}\alpha_{1,mn}\left(1-\cos\frac{2m\pi x}{a}\right)\left(1-\cos\frac{2n\pi y}{b}\right)\right|^2dA\\&=\frac{\rho_0\omega^2}{2c_0}\left|4I^2\int\int_A e^{-2j(k_x x+k_y y)}dA-4I\frac{\omega}{k_z}\sum_{m,n}\alpha_{1,mn}\int\int_A e^{-j(k_x x+k_y y)}\left(1-\cos\frac{2m\pi x}{a}\right)\times\left(1-\cos\frac{2n\pi y}{b}\right)dA+\left(\frac{\omega}{k_z}\right)^2\sum_{mn,kl}\alpha_{1,mn}\alpha_{1,kl}\int\int_A\times\left(1-\cos\frac{2m\pi x}{a}\right)\left(1-\cos\frac{2n\pi y}{b}\right)\left(1-\cos\frac{2k\pi x}{a}\right)\times\left(1-\cos\frac{2l\pi y}{b}\right)dA\right|.\end{aligned} \quad (18)$$

In a similar manner, the radiated sound power can be defined as

$$\Pi_r = \frac{1}{2}\,\mathrm{Re}\int\int_A p_r \cdot v_r^* dA, \tag{19}$$

where $v_r = p_r/(\rho_0 c_0)$ is the acoustic velocity in the radiation field and

$$p_r = j\omega\rho_0\Phi_3 = j\omega\rho_0\frac{\omega}{k_z}\sum_{m,n}\alpha_{2,mn}\left(1-\cos\frac{2m\pi x}{a}\right)\times\left(1-\cos\frac{2n\pi y}{b}\right) \tag{20}$$

is the radiation sound pressure. Combination of Eqs. (19) and (20) and the expression of v_r results in

$$\Pi_r = \frac{\rho_0\omega^2}{2c_0}\int\int_A |\Phi_3|^2 dA = \frac{\rho_0\omega^2}{2c_0}\int\int_A \left|\sum_{m,n}\frac{\omega}{k_z}\alpha_{2,mn}\times\left(1-\cos\frac{2m\pi x}{a}\right)\left(1-\cos\frac{2n\pi y}{b}\right)\right|^2 dA$$
$$= \frac{\rho_0\omega^2}{2c_0}\left|\left(\frac{\omega}{k_z}\right)^2\sum_{mn,kl}\alpha_{2,mn}\alpha_{2,kl}\int\int_A\left(1-\cos\frac{2m\pi x}{a}\right)\times\left(1-\cos\frac{2n\pi y}{b}\right)\left(1-\cos\frac{2k\pi x}{a}\right)\times\left(1-\cos\frac{2l\pi y}{b}\right)dA\right|. \tag{21}$$

The three integrations in Eqs. (18) and (21) can be calculated as

$$\int\int_A e^{-2j(k_x x+k_y y)}dA = \begin{cases} ab & \text{for } k_x=0 \text{ and } k_y=0 \\ \dfrac{ja(-1+e^{-2jk_y b})}{2k_y} & \text{for } k_x=0 \text{ and } k_y\neq 0 \\ \dfrac{jb(-1+e^{-2jk_x a})}{2k_x} & \text{for } k_x\neq 0 \text{ and } k_y=0 \\ -\dfrac{1}{4}\dfrac{(1-e^{-2jk_x a}-e^{-2jk_y b}+e^{-2j(k_x a+k_y b)})}{k_x k_y} & \text{for } k_x\neq 0 \text{ and } k_y\neq 0, \end{cases} \tag{22}$$

$$\int\int_A e^{-j(k_x x+k_y y)}\left(1-\cos\frac{2m\pi x}{a}\right)\left(1-\cos\frac{2n\pi y}{b}\right)dA = \begin{cases} ab & \text{for } k_x=0 \text{ and } k_y=0 \\ \dfrac{4jn^2\pi^2 a(1-e^{-jk_y b})}{k_y(k_y^2 b^2-4n^2\pi^2)} & \text{for } k_x=0 \text{ and } k_y\neq 0 \\ \dfrac{4jm^2\pi^2 b(1-e^{-jk_x a})}{k_x(k_x^2 a^2-4m^2\pi^2)} & \text{for } k_x\neq 0 \text{ and } k_y=0 \\ -\dfrac{16m^2n^2\pi^4(1-e^{-jk_x a})(1-e^{-jk_y b})}{k_x k_y(k_x^2 a^2-4m^2\pi^2)(k_y^2 b^2-4n^2\pi^2)} & \text{for } k_x\neq 0 \text{ and } k_y\neq 0, \end{cases} \tag{23}$$

$$\int\int_A\left(1-\cos\frac{2m\pi x}{a}\right)\left(1-\cos\frac{2n\pi y}{b}\right)\left(1-\cos\frac{2k\pi x}{a}\right)\left(1-\cos\frac{2l\pi y}{b}\right)dA = \begin{cases} \dfrac{9}{4}ab & \text{for } m=k \text{ and } n=l \\ \dfrac{3}{2}ab & \text{for } m=k \text{ and } n\neq l \\ \dfrac{3}{2}ab & \text{for } m\neq k \text{ and } n=l \\ ab & \text{for } m\neq k \text{ and } n\neq l. \end{cases} \tag{24}$$

The power transmission coefficient can be obtained as

$$\tau(\varphi,\theta) = \frac{\Pi_r}{\Pi_{in}}, \tag{25}$$

which is dependent on the sound incident angles (φ and θ). Finally, the STL across the double-panel partition, defined as the inverse of the power transmission coefficient in decibel scale, is given by

$$\mathrm{STL} = 10\log_{10}\left(\frac{1}{\tau}\right). \tag{26}$$

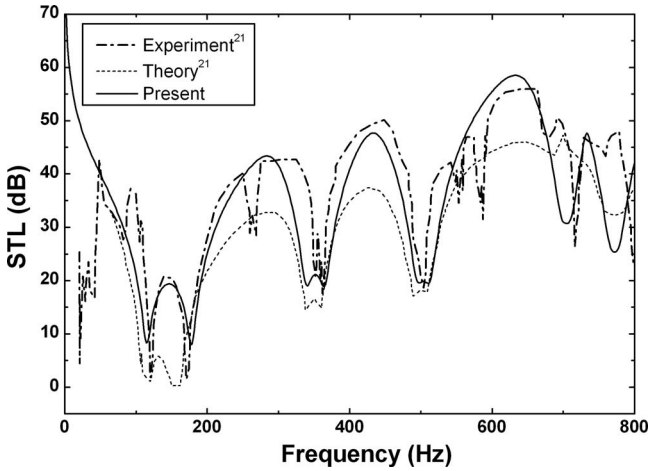


FIG. 2. STL of clamped aluminum double-panel partition under normal sound excitation: Comparison of the present analytical predictions with the theoretical results and experimental measurements of Carneal and Fuller (Ref. 21).

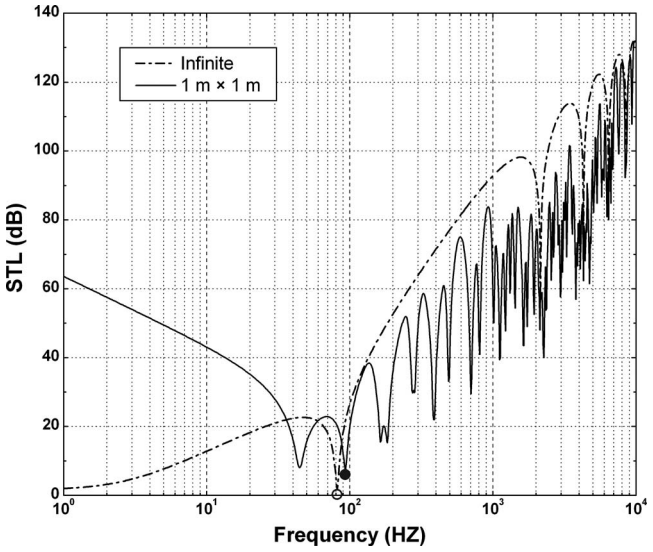


FIG. 3. STL plotted as a function of frequency for clamped double-panel partition with airproof cavity under normal sound excitation: Dashed line—infinite system (H=0.08 m and h_1=h_2=0.005 m); solid line—finite system with 1 m (length)×1 m (width), H=0.08 m, and h_1=h_2=0.005 m. (○): mass-air-mass resonance for infinite system; (●): panel-cavity-panel resonance for finite system.

III. NUMERICAL RESULTS AND DISCUSSION

With the theoretical model described in previous sections, numerical calculations are carried out to quantify the effects of several key system parameters on the sound insulation property of clamped double-panel partitions of finite extent. First, the accuracy of model predictions is checked against existing test data, with structural dimensions and material properties taken in accordance with the experiment measurements of Carneal and Fuller.[21]

A. Model validation

The present analytical approach is validated by comparing the predicted STL with the theoretical and experimental results of Carneal and Fuller,[21] as shown in Fig. 2. The double-panel partition considered consists of two identical clamp-supported aluminum plates (0.38×0.30 m^2, 1.6 mm thickness), separated by a 0.048 m air cavity. Other physical parameters used are listed in Table I. The STL measurements were obtained by Carneal and Fuller under a normal incident sound excitation, who also provided theoretical results derived by modifying a theory developed originally for simply supported boundary condition. The results of Fig. 2 demonstrate clearly that the present analytical predictions are in closer agreement with the experimental measurements than the theoretical predictions of Carneal and Fuller. Notice first that the experimental results are not reliable for frequencies below 50 Hz where the flanking paths of the test facility play a prominent role in measurements. Second, the extra dips in the experiment curve (compared with the theoretical curves) associated with (1, 2) (~260–280 Hz) and (4, 1) (~520–560 Hz) modes are attributed to the imperfect normal acoustic plane wave, unevenly damped plate, and/or the structural flanking path, as emphasized by Carneal and Fuller.[21]

TABLE I. Structural dimensions and material properties for model validation.

	Panels
Length	a=1 m
Width	b=1 m
Thickness	h_1=h_2=2 (or 5,10) mm
Young's modulus	E=70 GPa
Density	ρ=2700 kg/m^3
Poisson ratio	ν=0.33
Loss factor	η=0.01
	Acoustic field
Air cavity depth	H=0.08 (or 0.04,0.06) m
Density	ρ_0=1.21 kg/m^3
Sound speed	c_0=343 m/s
Initial amplitude	I_0=1 m^2/s

It should be pointed out that the present method is not only applicable to double-panel systems of finite extent but also applicable to those of infinite extent. Furthermore, the method can be applied in both low- and high-frequency ranges, which is hardly achievable by other approaches, e.g., FEM, (parallel construction) boundary element method (BEM), and statistical energy analysis (SEA) method.

B. Finite versus infinite double-panel partition

Numerical calculations are performed in this section to quantify the effects of panel dimensions (length, width, and thickness) on STL of clamped double-panel structures.

Figure 3 compares the predicted structural STL of a double-panel system of finite extent (dashed line) with that of an infinite double-panel system (solid line), both subjected to normal sound excitation, with H=0.08 m and h_1=h_2=0.005 m for both systems and 1 m (length)×1 m (width) for the finite system. The two panels are identical, made of aluminum (Table I).

The results of Fig. 3 exhibit analogous trend, with dips caused by the modal behavior of the double-panel system. For the finite double-panel system, the original modal behav-

ior of the two panels (the radiating panel, in particular) interacts strongly with the system behavior (including panel-cavity-panel resonance and standing-wave resonance), and hence plays a major role in the vibroacoustic performances of the whole system. For the infinite double-panel system, however, the original modal behavior of the panels has no influence on the overall system behavior. As a result, only dips related to system resonances show up in Fig. 3, with the first dip representing the mass-air-mass resonance and the remaining dips caused by the standing-wave resonance.

The intense peaks and dips in the STL versus frequency curve of the finite double-panel system occur because the finite system possesses a higher modal density than the infinite system over a wide range of frequency (approximately above 100 Hz, Fig. 3). Consequently, the infinite system provides an asymptotic maximum of STL for the finite system in this frequency range. Conversely, in the low-frequency range (less than about 100 Hz), there is no mode existing for the finite system. In other words, the infinite system is incapable of providing the right STL values at low frequencies for practical finite systems.

The dip denoted by a full black circle in Fig. 3 is associated with the so-called panel-cavity-panel resonance[37] for finite double-panel systems, while that represented by an open circle corresponds to the mass-air-mass resonance of infinite double-panel systems. The location of the former deviates slightly from the latter (the deviation increases with panel thickness, see Fig. 4 later) due to modal interactions of the finite system.

C. Effects of panel thickness on STL

To quantify the effects of panel thickness, the STL versus frequency curve is presented in Fig. 4(a) for an infinite system and in Fig. 4(b) for a finite system; the geometrical and material parameters are identical to those used to calculate Fig. 3, and normal sound excitation is imposed. Three values of panel thickness are selected: 2, 5, and 10 mm.

As expected and consistent with the well-known mass law, for both infinite and finite double-panel systems, it is seen from Fig. 4 that the STL values drastically increase as the panel thickness is increased. The influence of panel thickness on STL is particularly strong for finite systems at low frequencies [Fig. 4(b)], the significance of which should not be overlooked when designing clamped sound-proof double-panel partitions of finite extent in practice.

For the infinite system, as the panel thickness is increased, the location of mass-air-mass resonance shifts to a lower frequency whereas the locations of standing-wave resonances remain unchanged [Fig. 4(a)] because they are only dependent on air cavity thickness and wavelength but independent of panel thickness.

Note that the STL predictions for the finite system [Fig. 4(b)] are only exhibited in the frequency range of 1–1000 Hz as intense peaks and dips are present in this regime, much more complicated than those of the infinite system [Fig. 4(a)]. This is attributed to the strong interaction of individual panel behavior with the overall system performance for the finite system, which is absent for the infinite

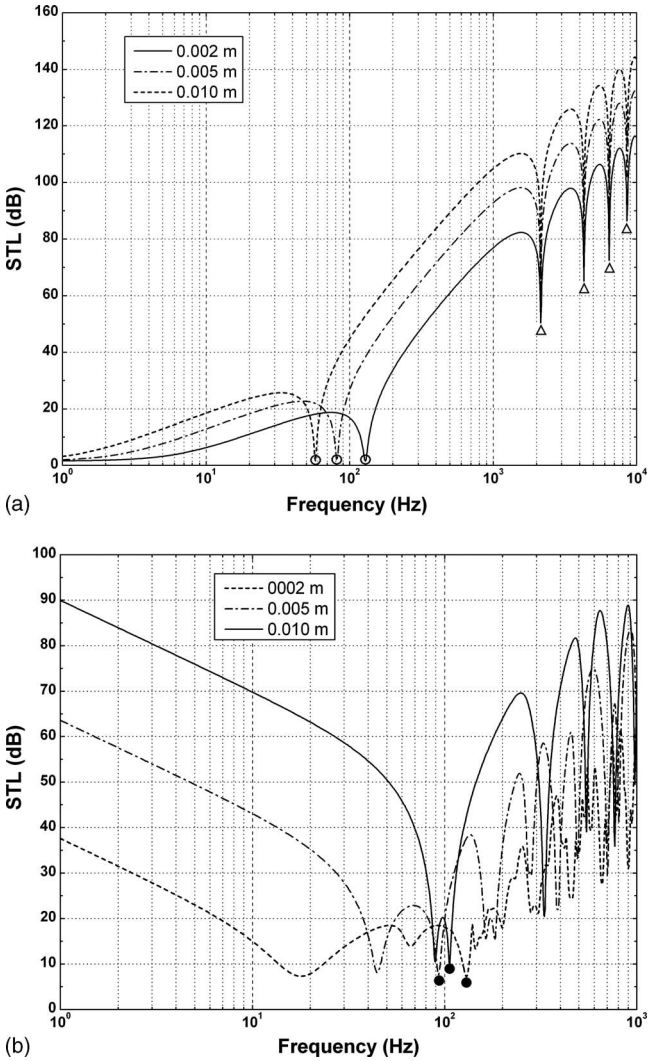


FIG. 4. Effects of panel thickness on STL of clamped double-panel partition under normal sound excitation: (a) infinite system (H=0.08 m), (○): mass-air-mass resonance; (△): standing-wave resonance and (b) finite system (1 × 1 m^2, H=0.08 m), (●): panel-cavity-panel resonance. Three different panel thicknesses (i.e., 2, 5, and 10 mm) were considered.

system. For the same reason, the positions of panel-cavity-panel resonances in Fig. 4(b) move to higher frequencies as the panel thickness is increased, in contrast to what is observed for the infinite system [Fig. 4(a)].

D. Effects of air cavity thickness on STL

In order to explore the effects of air cavity thickness on STL and identify which mode (including panel mode and system coupling mode) is primarily responsible for each dip in the STL versus frequency curve of a clamped double-panel partition, the STLs are calculated for both infinite and finite systems with selected values of air cavity thickness (H=0.04, 0.06, and 0.08 m), as shown in Fig. 5. Again, normal sound excitation is imposed, with 1 m (length) × 1 m (width) and $h_1=h_2$=0.01 m for the finite system and $h_1=h_2$ =0.002 m for the infinite system. Both panels are made of aluminum (Table I).

For the infinite system, as previously mentioned, the behavior of individual panels can be neglected, and only the

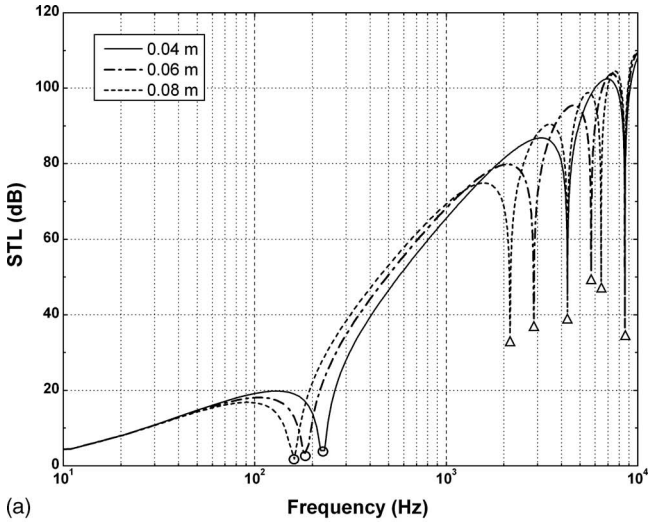


FIG. 5. Effects of air cavity thickness (H=0.04, 0.06, and 0.08 m) on STL of clamped double-panel partition under normal sound excitation: (a) infinite system (h_1=h_2=0.002 m), (○): mass-air-mass resonance; (△): standing-wave resonance and (b) finite system (1×1 m^2, h_1=h_2=0.010 m), (●): panel-cavity-panel resonance.

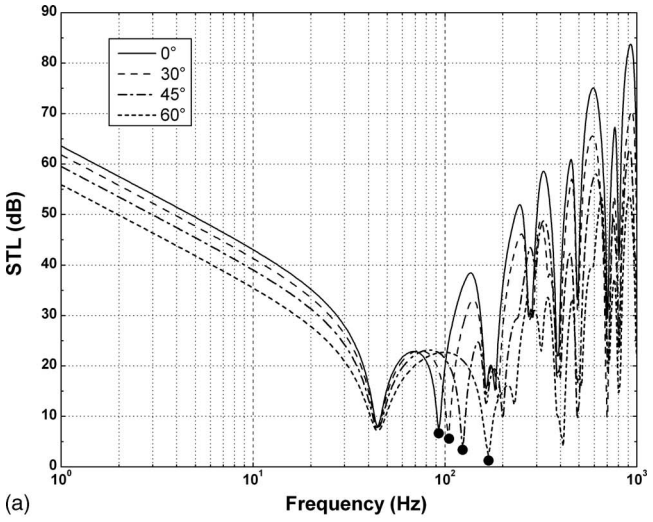


FIG. 6. STL plotted as a function of frequency for clamped double-panel partition of finite extent (1×1 m^2, H=0.08 m, and h_1=h_2=0.005 m) under sound excitation with (a) varying elevation angle φ (azimuth angle fixed at θ=0° and (b) varying azimuth angle θ (elevation angle fixed at φ=45°). (●): panel-cavity-panel resonance.

system coupling effects (mass-air-mass resonance and standing-wave resonance) are of primary concern; see Fig. 5(a). The positions of both mass-air-mass (or panel-cavity-panel) resonance and standing-wave resonances shift to lower frequencies with increasing air cavity thickness [Fig. 5(a)]. Conversely, for the finite system, as can be seen from Fig. 5(b), the position of the first dip is independent of air cavity thickness since it is completely addressed by the panel mode. However, the position of the second dip alters drastically as the air gap thickness is increased [in fact, moves to a lower frequency; Fig. 5(b)], owing to the fact that the system coupling effect (i.e., panel-cavity-panel resonance) plays a dominant role in this case. For the remaining dips exhibited in Fig. 5(b), their locations remain largely unchanged, implying that the panel mode and the system coupling effect are active in synchronization. Therefore, by tailoring the thickness of air cavity, it is possible to design finite double-panel partitions with better sound insulation properties over a wide frequency range [Fig. 5(b)]. In comparison, the influence of air cavity on infinite systems is relatively small [Fig. 5(a)].

E. Effects of incident angles on STL

The influence of sound incident angles (elevation angle and azimuth angle) on the sound insulation property of a clamped double-panel partition of finite extent (1×1 m^2, H=0.08 m, and h_1=h_2=0.005 m; both panels made of aluminum) is shown in Fig. 6.

The results of Fig. 6(a) demonstrate considerable influence of the incident elevation angle φ (with azimuth angle fixed at θ=0°) on the structural STL of the clamped finite system: the double-panel partition has marked selectivity for incident sound waves with different incident elevation angles. Generally speaking, incident sound waves with large elevation angles are easier to transmit through the double-panel structure than those with smaller elevation angles. For the case studied, the STL values decrease with increasing elevation angle for frequencies below about 43 Hz, while for frequencies above this value the overall trend is similar apart from the complicated system modal behavior. In addition, it is worthwhile to note that the panel-cavity-panel resonance

frequency increases with the elevation angle, which can be approximately described by a simple formula[10]

$$f_\alpha = \frac{1}{2\pi \cos\varphi}\sqrt{\frac{\rho_0 c_0^2}{H}\frac{(m_1+m_2)}{m_1 m_2}}. \quad (27)$$

The sound insulation properties of the clamped finite double-panel partition for selected incident azimuth angles ($\theta=0°,15°,30°,45°$) are compared in Fig. 6(b), with the elevation angle fixed at $\varphi=45°$. For frequencies below about 210 Hz, the STL curves for the four cases studied fall into one master curve. Beyond this frequency, small variations with varying azimuth angle are observed, caused by more complex structural modal behavior of the system at relatively high frequencies. Therefore, it may be concluded that the incident azimuth angle has negligible influence on the structural STL behavior of clamped finite systems. In other words, the selectivity of clamped double-panel partitions of finite extent for sound waves to different incident azimuth angles is limited.

IV. CONCLUSIONS

An analytical model has been developed for studying the vibroacoustic behavior of a finite double-panel partition clamp mounted in an infinite acoustic rigid baffle. The method of modal function is used to simulate the clamped boundary condition, and a double Fourier series solution of the dynamic structural response is obtained with the weighted residual (Galerkin) method. The validity of model predictions is checked against existing experimental data, with good agreement achieved. The influence of several key system parameters on the sound insulation capability of clamped double-panel partitions is then systematically explored, including panel dimensions, thickness of air cavity, elevation angle, and azimuth angle of incidence sound.

For relatively high frequencies (above 100 Hz for the cases considered here), an infinite double-panel system sets an upper bound on the STL of clamped finite systems. For a finite double-panel system, the original modal behavior of individual panels (radiating panel, in particular) interacts strongly with the system behavior (including panel-cavity-panel resonance and standing-wave resonance), and hence plays a major role in dictating the vibroacoustic performance of the whole system. For an infinite double-panel system, however, the original modal behavior of the panels has no influence on the overall system behavior. In the low-frequency range, there is no mode existing for the finite system and hence the infinite system is incapable of providing the right STL values for practical finite systems.

Analogous to the mass law for single-leaf partitions, the increase in panel thickness (equivalent to increasing surface mass) considerably enhances the sound insulation property of clamped double-panel partitions. The influence of panel thickness on STL is particularly strong for finite systems at low frequencies, which is useful when designing clamped sound-proof double-panel partitions.

As the thickness of air cavity is increased, the frequencies corresponding to the mass-air-mass (or panel-cavity-panel) resonance and standing-wave resonance change significantly. Moreover, by increasing the air cavity thickness, it is possible for the finite system to achieve better sound insulation capability in a wide frequency range. In comparison, air cavity thickness only has minimal influence on the infinite system.

Incident sound waves with bigger elevation angles are easier to transmit through a clamped double-panel structure than those with smaller elevation angles. The incident azimuth angle on the other hand has negligible effect on the structural STL of the system.

The proposed model is suitable for double-panel systems of finite or infinite extent and is applicable for both low- and high-frequency ranges. With these merits, it compares favorably with a number of other approaches, e.g., FEM, BEM, and SEA methods.

ACKNOWLEDGMENTS

This work is supported by the National Basic Research Program of China (2006CB601202), the National 111 Project of China (B06024), the National Natural Science Foundation of China (10572111, 10632060, and 10832002), and the National High Technology Research and Development Program of China (2006AA03Z519).

[1] J. H. Lee and J. Kim, "Analysis of sound transmission through periodically stiffened panels by space-harmonic expansion method," J. Sound Vib. **251**, 349–366 (2002).
[2] S. Narayanan and R. L. Shanbhag, "Sound transmission through elastically supported sandwich panels into a rectangular enclosure," J. Sound Vib. **77**, 251–270 (1981).
[3] B. Liu, L. Feng, and A. Nilsson, "Sound transmission through curved aircraft panels with stringer and ring frame attachments," J. Sound Vib. **300**, 949–973 (2007).
[4] S. Narayanan and R. L. Shanbhag, "Sound transmission through a damped sandwich panel," J. Sound Vib. **80**, 315–327 (1982).
[5] O. Foin, J. Nicolas, and N. Atalla, "An efficient tool for predicting the structural acoustic and vibration response of sandwich plates in light or heavy fluid," Appl. Acoust. **57**, 213–242 (1999).
[6] A. C. Nilsson, "Wave propagation in and sound transmission through sandwich plates," J. Sound Vib. **138**, 73–94 (1990).
[7] L. Cheng, Y. Y. Li, and J. X. Gao, "Energy transmission in a mechanically-linked double-wall structure coupled to an acoustic enclosure," J. Acoust. Soc. Am. **117**, 2742–2751 (2005).
[8] K. Sakagami, S. Nakanishi, M. Daido, M. Morimoto, and D. Takahashi, "Reflection of a spherical sound wave by an infinite elastic plate with an air-back cavity," Acust. Acta Acust. **83**, 963–971 (1997).
[9] J. Brunskog, "The influence of finite cavities on the sound insulation of double-plate structures," Acta Astronaut. **117**, 3727–3739 (2005).
[10] M. Yairi, K. Sakagami, E. Sakagami, M. Morimoto, A. Minemura, and K. Andow, "Sound radiation from a double-leaf elastic plate with a point force excitation: Effect of an interior panel on the structure-borne sound radiation," Appl. Acoust. **63**, 737–757 (2002).
[11] D. Takahashi, "Sound radiation from periodically connected double-plate structures," J. Sound Vib. **90**, 541–557 (1983).
[12] J. Wang, T. J. Lu, J. Woodhouse, R. S. Langley, and J. Evans, "Sound transmission through lightweight double-leaf partitions: Theoretical modeling," J. Sound Vib. **286**, 817–847 (2005).
[13] G.-F. Lin and J. M. Garrelick, "Sound transmission through periodically framed parallel plates," J. Acoust. Soc. Am. **61**, 1014–1018 (1977).
[14] R. J. M. Craik and R. S. Smith, "Sound transmission through double leaf lightweight partitions part I: Airborne sound," Appl. Acoust. **61**, 223–245 (2000).
[15] L. L. Beranek and G. A. Work, "Sound transmission through multiple structures containing flexible blankets," J. Acoust. Soc. Am. **21**, 419–428 (1949).
[16] A. London, "Transmission of reverberant sound through double walls," J. Acoust. Soc. Am. **22**, 270–279 (1950).
[17] Y. Y. Li and L. Cheng, "Energy transmission through a double-wall struc-

ture with an acoustic enclosure: Rotational effect of mechanical links," Appl. Acoust. **67**, 185–200 (2006).
[18]F. G. Leppington, E. G. Broadbent, and G. F. Butler, "Transmission of sound through a pair of rectangular elastic plates," IMA J. Appl. Math. **71**, 940–955 (2006).
[19]J. D. Chazot and J. L. Guyader, "Prediction of transmission loss of double panels with a patch-mobility method," J. Acoust. Soc. Am. **121**, 267–278 (2007).
[20]M. Villot, C. Guigou, and L. Gagliardini, "Predicting the acoustical radiation of finite size multi-layered structures by applying spatial windowing on infinite structures," J. Sound Vib. **245**, 433–455 (2001).
[21]J. P. Carneal and C. R. Fuller, "An analytical and experimental investigation of active structural acoustic control of noise transmission through double panel systems," J. Sound Vib. **272**, 749–771 (2004).
[22]A. Berry, J.-L. Guyader, and J. Nicolas, "A general formulation for the sound radiation from rectangular, baffled plates with arbitrary boundary conditions," J. Acoust. Soc. Am. **88**, 2792–2802 (1990).
[23]D. Takahashi, "Effects of panel boundedness on sound transmission problems," J. Acoust. Soc. Am. **98**, 2598–2606 (1995).
[24]B. K. Kim, H. J. Kang, J. S. Kim, H. S. Kim, and S. R. Kim, "Tunneling effect in sound transmission loss determination: Theoretical approach," J. Acoust. Soc. Am. **115**, 2100–2109 (2004).
[25]W. Kropp and E. Rebillard, "On the air-borne sound insulation of double wall constructions," Acust. Acta Acust. **85**, 707–720 (1999).
[26]J. M. P. Antonio, A. Tadeu, and L. Godinho, "Analytical evaluation of the acoustic insulation provided by double infinite walls," J. Sound Vib. **263**, 113–129 (2003).
[27]M. Ruzzene, "Vibration and sound radiation of sandwich beams with honeycomb truss core," J. Sound Vib. **277**, 741–763 (2004).
[28]K. S. Sum and J. Pan, "An analytical model for bandlimited response of acoustic-structural coupled systems. I. Direct sound field excitation," J. Acoust. Soc. Am. **103**, 911–923 (1998).
[29]J. D. Quirt, "Sound transmission through windows I. Single and double glazing," J. Acoust. Soc. Am. **72**, 834–844 (1982).
[30]J. D. Quirt, "Sound transmission through windows II. Double and triple glazing," J. Acoust. Soc. Am. **74**, 534–542 (1983).
[31]C. Bao and J. Pan, "Experimental study of different approaches for active control of sound transmission through double walls," J. Acoust. Soc. Am. **102**, 1664–1670 (1997).
[32]M. Gideon, "Response of ribbed panels to reverberant acoustic fields," J. Acoust. Soc. Am. **34**, 809–826 (1962).
[33]A. J. Price and M. J. Crocker, "Sound transmission through double panels using statistical energy analysis," J. Acoust. Soc. Am. **47**, 683–693 (1970).
[34]M. J. Crocker and A. J. Price, "Sound transmission using statistical energy analysis," J. Sound Vib. **9**, 469–486 (1969).
[35]R. S. Langley, J. R. D. Smith, and F. J. Fahy, "Statistical energy analysis of periodically stiffened damped plate structures," J. Sound Vib. **208**, 407–426 (1997).
[36]F. C. Sgard, N. Atalla, and J. Nicolas, "A numerical model for the low frequency diffuse field sound transmission loss of double-wall sound barriers with elastic porous linings," J. Acoust. Soc. Am. **108**, 2865–2872 (2000).
[37]R. Panneton and N. Atalla, "Numerical prediction of sound transmission through finite multilayer systems with poroelastic materials," J. Acoust. Soc. Am. **100**, 346–354 (1996).
[38]A. Pellicier and N. Trompette, "A review of analytical methods, based on the wave approach, to compute partitions transmission loss," Appl. Acoust. **68**, 1192–1212 (2007).

Speed of sound in bubble-free ice

Christian Vogt,[a] Karim Laihem,[b] and Christopher Wiebusch[c]
III. Physikalisches Institut, RWTH Aachen University, Aachen NRW 52056, Germany

(Received 21 May 2008; revised 2 September 2008; accepted 2 September 2008)

The speed of sound in a large volume of bubble-free ice was measured with high accuracy using a linear array of six piezoceramic lead zirconium titanate (PZT) receivers. This array was deployed in an ~3 m^3 water tank, which was cooled down to −20 °C. The freezing process was performed inside a cooling container. Bubble-free ice was obtained using a freeze control unit, which filters and degases the water during the freezing process. A dedicated geometry was used to position PZT receivers and an emitter such that systematic errors were minimized. With this setup the longitudinal and the transverse components of the speed of sound were measured at temperatures between 17 and 0 °C in water and between 0 and −20 °C in ice with an uncertainty of ~0.3%. © *2008 Acoustical Society of America.* [DOI: 10.1121/1.2996304]

PACS number(s): 43.58.Dj, 43.20.Hq, 43.30.Ma, 43.38.Fx [RR] Pages: 3613–3618

I. INTRODUCTION

Within the R&D program of the acoustic detection of ultrahigh energy neutrino interactions in the deep glacial ice at the South Pole,[1,2] a good understanding of the acoustic properties of ice is essential. For this aim the Aachen Acoustic Laboratory (AAL) has been installed and commissioned[3] in 2007. It provides an infrastructure and a test facility for the development and tests of new methods for the acoustic neutrino detection, in particular, detector development and ice properties. The first result, the speed of sound in bubble-free ice measured with high precision, is reported here.

II. EXPERIMENTAL SETUP

A linear array of six receivers and one transmitter was built and deployed inside a large water tank (1.85 m diameter and 1 m depth). Due to this large size, the speed of sound can be measured with a time-of-flight setup without being affected by distortions from reflections at the surfaces. The water tank has been developed for the IceTop airshower detector[4] at the South Pole. Its frozen ice is used as an optical Cherenkov detector. Perfectly clear ice without air bubbles and cracks throughout the whole volume is produced by a freeze control unit (FCU), which was developed at the University of Delaware.

A. The acoustic array

One transmitter and six identical acoustical receivers labeled S1–S6 (2 mm thick and 5 mm radius) were accurately (~1 mm) positioned to form a linear array. The setup is illustrated in Fig. 1. The relative position of the transducers (receivers and transmitter) provides an equal propagation path length (d_0=20 cm) between each two adjacent receivers of the array. The faces of the receivers are placed perpendicular to the expected direction of the acoustic wave. No preamplification was used. For the precise positioning of the transducers weights of 5 kg were attached to them. Above each receiver a temperature sensor of type DS28B20 (Dallas Semiconductors) was placed to monitor the local temperature. The absolute calibration of the sensor has an uncertainty of 0.5 °C and corresponds to a constant offset in the temperature dependent measurement of the speed of sound.

Piezoceramic Lead Zirconium Titanate (PZT) disks of type PRYY+0372 (PI Ceramics) were used as acoustical receivers. They were sealed in a resin of epoxy to make them waterproof. The epoxy layer was cut to a thickness of 3.5 mm to permit a high transmission rate of the sound wave. A PZT tube (2 cm high, 7 mm inner diameter, and 1 cm outer diameter) labeled E1 was used as a transmitter.

B. Cooling and ice production

The central element of the setup is an IceTop tank with a FCU embedded in a cooling container. The tank and the FCU were developed within the IceCube project[5] for the surface detector IceTop with the purpose to detect air showers induced by cosmic rays. The inside of the container is supplied with cold air (down to a minimum of −25 °C) via a cooling plant provided with a regulation of the temperature. In this setup the freezing is mainly caused by the heat transfer of air convection. The sides of the tank are isolated and the ice layer inside the tank starts to grow progressively from the top (water surface) to the bottom. During the cooling process, the FCU runs permanently to degas the water via a circulation pump with a semipermeable membrane and a vacuum system. In addition to the degassing, the FCU removes the excess water resulting from density difference between water and ice to avoid cracks caused by overpressure. By using this method the produced ice is completely crack/bubble-free. Visual inspections of the ice confirm the high quality of the frozen ice. No imperfections such as bubbles or cracks are visible within the entire volume. Three sets of temperature sensors monitored the temperature at different locations. The first set measured the air temperature inside the container, the second set measured the water/ice tempera-

[a]Electronic mail: c.vogt@geophysik.rwth-aachen.de
[b]Electronic mail: karim.laihem@physik.rwth-aachen.de
[c]Electronic mail: christopher.wiebusch@physik.rwth-aachen.de

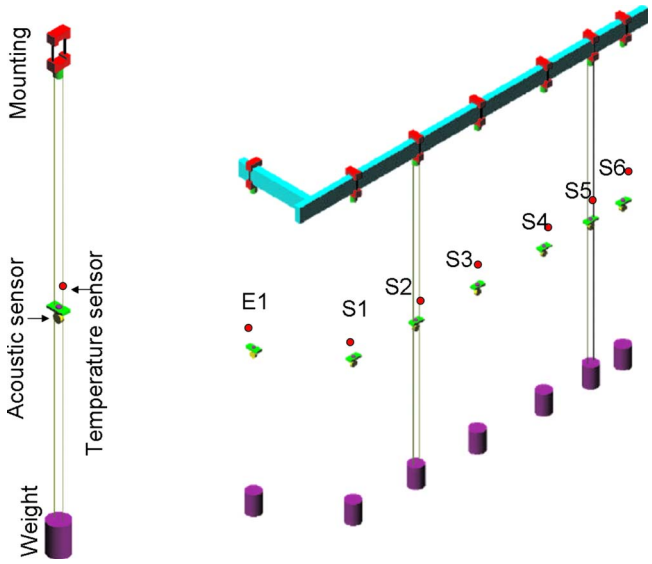


FIG. 1. (Color online) L-shaped setup inside the ice tank. (E1) Emitter. (S1–S6) Receivers.

ture at different depths close to the walls of the tank, and the third set measured the temperatures close to the acoustic transducers.

In vertical direction the temperature of the ice has a strong gradient corresponding to the freezing from top to bottom while in horizontal direction the temperature is homogenous throughout the tank. Differences in the measured temperatures close to the receiver sensors are used to estimate the temperature errors.

III. MEASUREMENT METHOD

The acoustic signal was generated with the transmitter E1, which was pulsed with a 20 V peak to peak square signal with a duration of 50 μs. The response of the six receivers was recorded simultaneously and averaged over 128 transmitter pulses. Figure 2(b) shows the square pulse fed to the transmitter and the response from the six receivers S1–S6. Figure 2(b) demonstrates the requirement of a large volume in order to separate a directly propagated signal from reflections off the walls.

The measurement of the speed of sound is based on the determination of the arrival time difference (time delay) Δt_{ij} between two adjacent receivers i and j. As mentioned in Sec. II A, the relative position of the transmitter and the six receivers was set such that the propagation path length $\Delta t_{ij} v_{\text{sound}}$ corresponds to $d_0 = 20$ cm (v_{sound} stands for the speed of sound in the medium). A schematic of the setup is illustrated in Fig. 2(a).

The determination of the time delay and hence of the speed of sound is independent of the starting time of the transmitter pulse. From the recorded signal at the receivers, six arrival times t_i $(i=1,2,3,4,5,6)$ are extracted and five time delays Δt_{ij} with $\Delta t_{12} \approx \Delta t_{23} \approx \Delta t_{34} \approx \Delta t_{45} \approx \Delta t_{56}$ are calculated. Note that with this method, the error related to the definition of the leading edge cancels. The speed of sound v_{sound} can be calculated as

$$v_{\text{sound}} = \frac{d_0}{\langle \Delta t_{ij} \rangle}, \tag{1}$$

where d_0 is the propagation path length and $\langle \Delta t_{ij} \rangle$ is the mean value of the time delay between two adjacent receivers.

IV. RESULTS

A. Measurements in water

As a proof of principle the speed of sound was determined at different temperatures in water. Figure 3 shows the agreement between the measured values (points) and the dashed curve (fifth order polynomial) describing the literature values.[6] The good agreement proves the validity of the method. Systematic errors, given by the position of the transducers and their size, are included in the plot. The agreement of the measured values with literature is better than the assumed systematic errors indicate.

B. Measurements in ice

1. Longitudinal component

Using a similar approach as in water, the speed of sound was determined in ice at different temperatures in the range between 0 and −20 °C. Figure 4 shows a linear behavior of the measured longitudinal speed of sound $v^l_{\text{sound}}(T)$ versus temperature T. From a linear fit the slope, which expresses the temperature coefficient, is extracted. It is compared to literature values in Sec. V. The slope is

$$\frac{dv^l_{\text{sound}}(T)}{dT} = -2{,}812(\pm 0{,}012)\ \text{m/(s °C)} \tag{2}$$

and the offset at 0 °C is

$$v^l_{\text{sound}}(T = 0\ ^\circ\text{C}) = 3837{,}9(\pm 5{,}3)\ \text{m/s}. \tag{3}$$

The slope has been determined with statistical errors only as systematic errors are suspected to affect the temperature dependence insignificantly. The error in the offset includes statistical and systematic errors.

Since the horizontal temperature field is homogeneous, the uncertainty in the path length due to diffraction is much smaller than the uncertainty related to the positions of the sensors.

2. Transverse component

Ice, as a solid medium, allows in addition to pressure waves the propagation of shear waves. The corresponding transverse component of the speed of sound is expected to be smaller than the longitudinal component. In our setup, the challenging part was to separate the signal of the shear wave from different reflections of the pressure wave off the walls. The arrival time of all possible reflections was calculated and identified in the recorded signal. These calculations were possible by taking into account the geometry of the ice block, the position of the PZT transducers, and the longitudinal speed of sound. For receivers S3–S6 the reflections arrived earlier than the shear wave [see Fig. 2(b)]. For receiver S1, the separation between the decaying signal from the pressure wave front and the signal from the shear wave

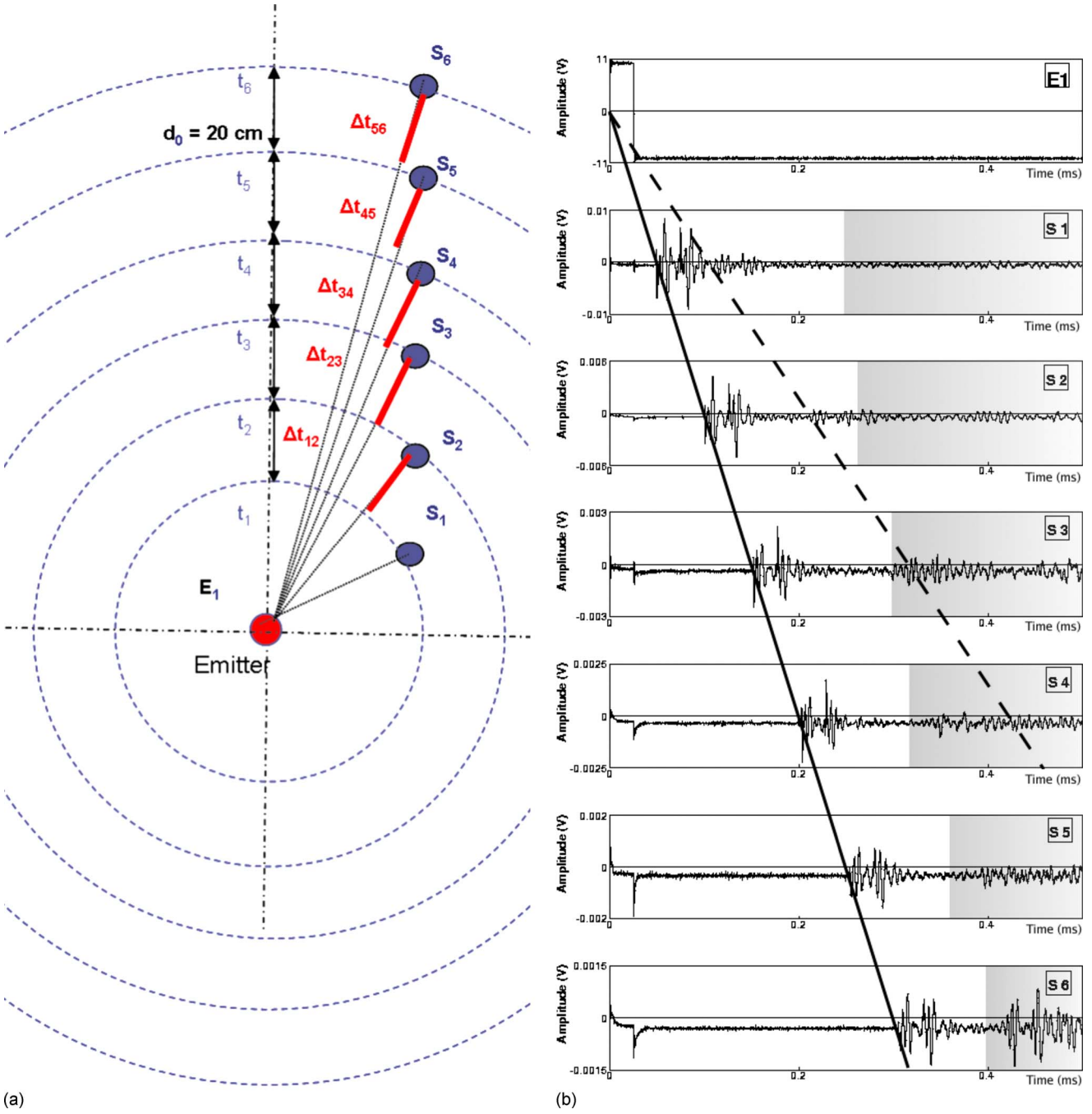


FIG. 2. (Color online) (a) Propagation of the sound wave. The positioning provides equal time steps between each received signal in adjacent receivers. (b) Emitted trigger signal at transmitter E1 and received signals at receivers S1–S6. Reflections may appear inside the shaded region. The two lines indicate the expected arrival time of pressure and shear waves, respectively.

was not possible. Thus, the signal of the shear wave was identified by receiver S2 in a temperature range between −20 and −13 °C. Here the border between ice and water is sufficiently deep below the receivers. The position of this border changes during the cooling process.

Figure 5 shows the transverse speed of sound versus temperature. From a linear fit the slope is extracted. Because only one receiver was able to identify the signal, the measurement here depends on the starting time of the emitted and received signals. Thus, the uncertainties are larger than before. The resulting slope is

$$\frac{dv^t_{\text{sound}}(T)}{dT} = -1{,}435(\pm 0{,}028)\ \text{m/(s °C)}. \quad (4)$$

The offset at 0° is

$$v^t_{\text{sound}}(T = 0\ ^\circ\text{C}) = 1826(\pm 47)\ \text{m/s}. \quad (5)$$

V. COMPARISON WITH LITERATURE

A. Longitudinal component

Table I shows the measured temperature coefficients of the longitudinal component of the speed of sound. These

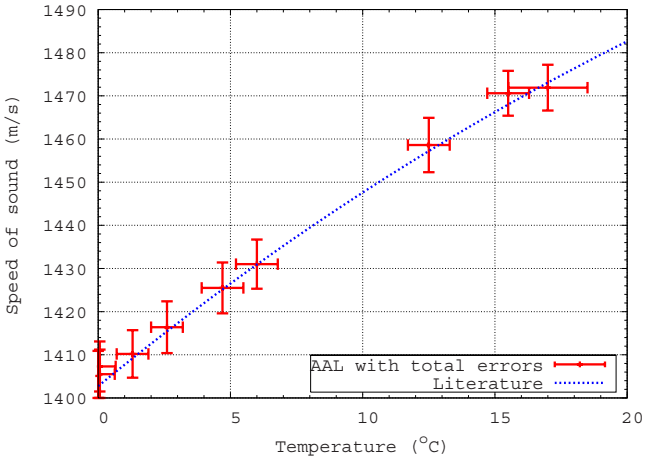


FIG. 3. (Color online) Speed of sound in water. The error bars are the sum of statistical and systematic errors (see text).

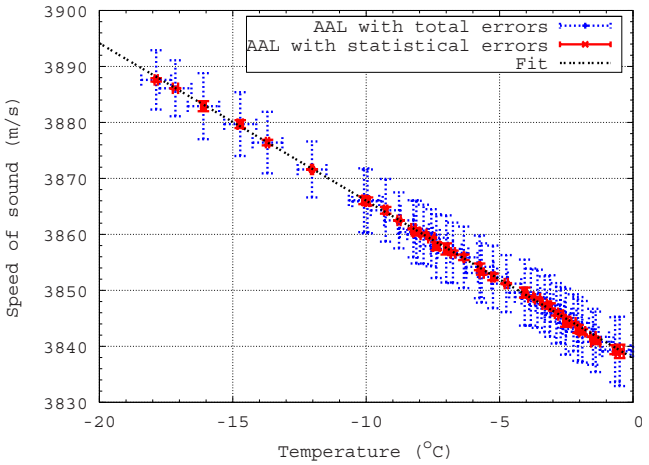


FIG. 4. (Color online) Speed of sound for pressure waves in bubble-free ice. The error bars are the sum of statistical and systematic errors. The line fit to the values is done using statistical errors only.

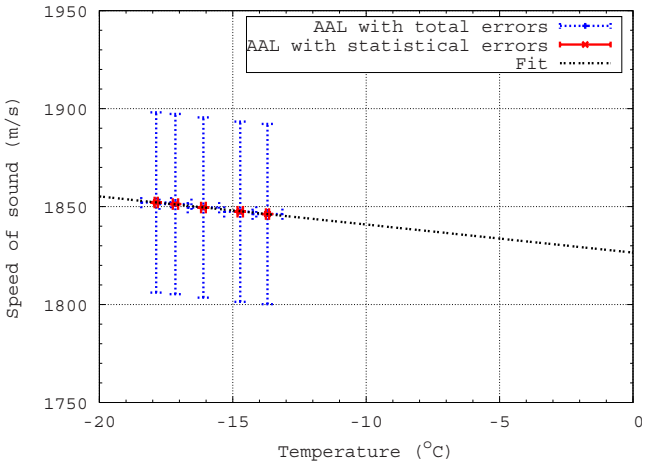


FIG. 5. (Color online) Speed of sound for shear waves in bubble-free ice. The error bars are the sum of statistical and systematic errors. The line fit to the values is done using statistical errors only.

TABLE I. Comparison between temperature coefficients of the speed of sound of pressure waves for laboratory measurements and *in situ* measurements in Antarctica and Greenland.

$dv^{l}_{\mathrm{sound}}(T)/dT$ m/(s °C)	Author
In situ	
−18	Joset and Holtzscherer[a]
−7.4	Thiel and Ostenso[b]
−5.5	Brockamp and Kohnen[c]
−4.5	Thyssen[d]
-2.30 ± 0.17	Kohnen[e]
Laboratory	
−2.3	Robin[f]
−3.4	Bass *et al.*[g]
−2.2	Brockamp and Querfurth[h]
-2.81 ± 0.01	AAL

[a] Reference 24.
[b] Reference 20.
[c] Reference 25.
[d] Reference 26.
[e] Reference 7.
[f] Reference 27.
[g] Reference 21.
[h] Reference 22.

values are separated into laboratory and *in situ* experiments in Greenland and Antarctica. The listed temperature coefficients differ strongly. The temperature coefficient determined in this paper using the AAL setup is consistent with the range of previous measurements listed in the table.

Figure 6 shows *in situ* measurements in a temperature range of −16 to −58 °C as unfilled dots and a fit to all of these data done by Kohnen.[7] In this figure a clear difference compared to the values obtained by the AAL setup is visible. We suspect these differences to be related to differences in the elastic properties of the considered ice. The ice of the

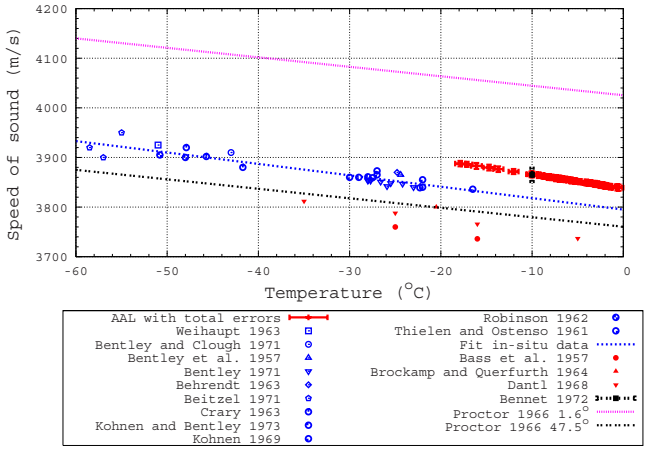


FIG. 6. (Color online) *In situ* and laboratory data for the speed of sound of pressure waves in comparison with the AAL results (errors extrapolated to low temperatures). Authors (*in situ*): Weihaupt (Ref. 10), Bentley and Clough (Ref. 11), Bentley *et al.* (Ref. 12), Bentley (Ref. 13), Behrendt (Ref. 14), Beitzel (Ref. 15), Crary (Ref. 16), Kohnen and Bentley (Ref. 17), Kohnen (Ref. 18), Robinson (Ref. 19), and Thiel and Ostenso (Ref. 20). Laboratory data for the speed of sound of pressure waves in comparison with the AAL results (errors extrapolated to low temperatures). Authors (laboratory): Bass *et al.* (Ref. 21), Bennet (Ref. 8), Brockamp and Querfurth (Ref. 22), Dantl (Ref. 23), and Proctor (Ref. 9).

TABLE II. Comparison between temperature coefficients of the speed of sound of shear waves for laboratory measurements and *in situ* measurements in Antarctica and Greenland.

$dv^t_{\text{sound}}(T)/dT$ m/(s °C)	Author
In situ	
−3,4	Thiel and Ostenso[a]
−3,6	Brockamp and Kohnen[b]
−1,20 ± 0,58	Kohnen[c]
Laboratory	
−1,4	Bass *et al.*[d]
−1,1	Brockamp and Querfurth[e]
−1.43 ± 0.03	AAL

[a]Reference 20.
[b]Reference 25.
[c]Reference 7.
[d]Reference 21.
[e]Reference 22.

AAL setup is perfectly clear and the residual gas has been extracted before freezing. The *in situ* measurements in ice in Greenland and Antarctica were done with seismic waves (seismic shooting) over large distances (4–20 km)[7] mostly in not bubble-free firn ice.

The comparison of the AAL results with other laboratory data is shown in Fig. 6 as filled dots. All but one values were calculated from the elastic properties of ice and are below the AAL results. The value of Bennet[8] was measured directly with a 24 cm long core of polar deep ice. This measurement, done with PZTs in the same temperature range with deep ice of high quality, agrees with the error band of the AAL measurement. Also values for the speed of sound in single crystal ice for different angles (1.6° and 47.5°) between propagation path and crystal axis are shown as lines (measurements done by Proctor[9]). The AAL result, obtained in polycrystalline ice, agrees with the range set by these lines.

B. Transverse component

Table II shows the result of the AAL setup for the temperature coefficient of shear waves, which agrees in this range with laboratory and *in situ* data in literature. The result shown in Eqs. (4) and (5) agrees with the value calculated from the elastic properties, which is 23 $v^t_{\text{sound}}(T=-16\ ^\circ\text{C})=1900$ m/s.

VI. SUMMARY

The measurement of the speed of sound in bubble-free ice was performed by building a setup using very accurate positioned PZT disks and calculating time differences between two received signals. The ice was degassed during freezing and clear bubble-free ice was obtained. The measurement was tested in water and compared with literature yielding a good agreement. The speed of sound for pressure waves at different temperatures was determined with an accuracy of ~0.3%. For shear waves a value could be measured by separating the signal from that of pressure waves and the corresponding reflections. Differences to previous measurements obtained *in situ* in Greenland and Antarctica appear and are assumed to be related to the quality of the considered ice. Our result is consistent with the result of Bennet.[8]

ACKNOWLEDGMENTS

We acknowledge the support of the following institutes and persons: The IceCube project and the U.W., Madison graduate school for providing the IceTop-Tank 81A, the University of Delaware for training with the FCU, and the University of Wuppertal for providing emitter E1. We thank the IceCube acoustic neutrino detection working group and, in particular, R. Nahnhauer and J. Vandenbroucke for support and discussions, as well J. Roth and J.-P. Hülß.

[1]S. Böser, C. Bohm, F. Descamps, J. Fischer, A. Hallgren, R. Heller, S. Hunertmark, K. Krieger, R. Nahnhauer, M. Pohl, P. Price, K.-H. Sulanke, D. Tosi, and J. Vandenbroucke, "Feasibility of acoustic neutrino detection in ice: Design and performance of the South Pole Acoustic Test Setup (SPATS)," in Proceedings of the 30th International Cosmic Ray Conference (ICRC07), Merida, Mexico (2007).
[2]D. Besson, S. Boeser, R. Nahnhauer, P. Price, and J. Vandenbroucke, "Simulation of a hybrid optical/radio/acoustic extension to IceCube for EeV neutrino detection," Int. J. Mod. Phys. A **21S1**, 259–264 (2006).
[3]C. Vogt, "Aufbau eines messplatzes zum test akustischer sensoren für den nachweis ultra-hochenergetischer neutrinowechselwirkungen (A test setup for acoustic detection of ultra-high energy neutrino interactions)," Diploma thesis, RWTH Aachen University, Germany, 2007.
[4]T. K. Gaisser (for the IceCube Collaboration), "Performance of the IceTop array," in Proceedings of the 30th International Cosmic Ray Conference (ICRC07), Merida, Mexico (2007).
[5]J. Ahrens, J. Bahcall, X. Bai, (the IceCube Collaboration), "Sensitivity of the IceCube detector to astrophysical sources of high energy muon neutrinos," Astropart. Phys. **20**, 507–264 (2004).
[6]W. Schaafs, "The sound velocity in water, H2O and D2O," *Molecular acoustics*, Landolt-Börnstein, New Series, Group II Molecules and Radicals V (Springer-Verlag, Berlin, 2006), pp. 69–72.
[7]H. Kohnen, "The temperature dependence of seismic waves in ice," J. Glaciol. **13**, 144–147 (1974).
[8]H. Bennet, "Measurement of ultrasonic wave velocities in ice cores from Greenland and Antarctica," CRREL Research Report No. 237, Hanover, NH, 1972.
[9]T. Proctor, "Low-temperature speed of sound in single-crystal ice," J. Acoust. Soc. Am. **39**, 972–977 (1966).
[10]J. Weihaupt, "Seismic and gravity studies at the South Pole," Geophysics **28**, 582–592 (1963).
[11]C. Bentley and J. Clough, "Seismic refraction shooting in Ellsworth and Dronning Maud Land," in Symposium on Antarctic Geology and Solid Earth Geophysics, Oslo (1971), pp. 169–172.
[12]C. Bentley, P. Pommeroy, and H. Dormanothers, "Seismic measurements on the Greenland ice cap," Ann. Geophys. **13**, 253–285 (1957).
[13]C. Bentley, "Seismic anisotropy in the West Antarctic ice sheet," Antarct. Res. Ser. **16**, 131–177 (1971).
[14]J. Behrendt, "Seismic measurements on the ice sheet of the Antarctic Peninsula," J. Geophys. Res. **68**, 5973–5990 (1963).
[15]J. Beitzel, "Geophysical exploration in Queen Maud Land, Antarctica," Antarct. Res. Ser. **16**, 131–177 (1971).
[16]A. Crary, "Results of United States traverses in East Antarctica, 1958–1961," IGY Glaciological Report No. 7, New York, 1963.
[17]H. Kohnen and C. Bentley, "Seismic refraction and reflection measurements at "Byrd" station, Antarctica," J. Glaciol. **12**, 101–111 (1973).
[18]H. Kohnen, "Über den Aufbau des grönlandischen inlandeises nach refraktionsseismischen messungen (About the composition of the Greenland inland ice from refraction seismics)," Ph.D. thesis, Westfälische Wilhelms-Universität Münster, Münster (1969).
[19]E. Robinson, "Results of geophysical studies of the McMurdo to South Pole traverse," University of Wisconsin, Geophysical and Polar Research Center, Research Report Series 62–66, 1962.
[20]E. Thiel and N. Ostenso, "Seismic studies on Antarctic ice shelves," Geophysics **26**, 706–715 (1961).
[21]R. Bass, D. Rossrerg, and A. Ziegler, "Die elastischen konstanten des eises

(The elastic constants of ice)," Z. Phys. **149**, 199–203 (1957).
[22]B. Brockamp and H. Querfurth, "Untersuchungen über die elastizitätskonstanten von see- und kunsteis (Measurements of the elastic constants of lake and artificial ice)," Polarforschung **5**, 253–262 (1964).
[23]G. Dantl, "Elastic moduli of ice," *Physics of Ice* (Plenum, New York, 1968), pp. 223–230.
[24]A. Joset and J.-J. Holtzscherer, "Sondages séismiques au Greenland. Première partie: Étude des vitesses de propagation des ondes séismiques sur l'inlandsis du Groenland (Seismics in Greenland. Part one: Study of the propagation velocity of seismic waves in the inland of Greenland)," Ann. Geophys. **9**, 329–344 (1953).
[25]B. Brockamp and H. Kohnen, "Ein beitrag zu den seismischen untersuchungen auf dem grönländischen inlandeis (A contribution to seismics in Greenland inland ice)," Polarforschung **6**, 2–12 (1967).
[26]F. Thyssen, "Die temperaturabhängigkeit der P-wellengeschwindigkeit in gletschern und inlandeisen (The temperature dependance of the P-wave velocity in glaciers and inland ice)," Z. Geophys. **33**, 65–79 (1966).
[27]G. Robin, "Glaciology III, seismic shooting, and related investigations," Norwegian-British-Swedish Antarctic Expedition 1949–1952, Scientific Results 5, 1958.

Sonar signal processing using probabilistic signal and ocean environmental models

R. Lee Culver and H. John Camin
Applied Research Laboratory and Graduate Program in Acoustics, The Pennsylvania State University, State College, Pennsylvania 16804

(Received 12 November 2007; revised 2 October 2008; accepted 4 October 2008)

Acoustic signals propagating through the ocean are refracted, scattered, and attenuated by the ocean volume and boundaries. Many aspects of how the ocean affects acoustic propagation are understood, such that the characteristics of a received signal can often be predicted with some degree of certainty. However, acoustic ocean parameters vary with time and location in a manner that is not, and cannot be, precisely known; some uncertainty will always remain. For this reason, the characteristics of the received signal can never be precisely predicted and must be described in probabilistic terms. A signal processing structure recently developed relies on knowledge of the ocean environment to predict the statistical characteristics of the received signal, and incorporates this description into the processor in order to detect and classify targets. Acoustic measurements at 250 Hz from the 1996 Strait of Gibraltar Acoustic Monitoring Experiment are used to illustrate how the processor utilizes environmental data to classify source depth and to underscore the importance of environmental model fidelity and completeness.
© *2008 Acoustical Society of America.* [DOI: 10.1121/1.3006379]

PACS number(s): 43.60.Cg, 43.30.Re [EJS] Pages: 3619–3631

I. INTRODUCTION

Sonar signal processors are designed to detect and/or classify signals against a background of noise and interference. Obviously the signal processor requires information about the signals to be detected and the noise or interference to be rejected, and conceptually we would like better knowledge to result in improved performance. This article describes and demonstrates the performance of a signal processing structure that incorporates available knowledge of the ocean environment into the processor in order to improve detection and classification performance. The processor works by combining environmental knowledge with an acoustic propagation model to predict received signal parameter statistics, which are in turn used to detect or classify the signals. Received signals are affected by the characteristics of both the signal source and the propagation channel, but only the latter are discussed here.

The processor utilizes signal parameter statistics calculated from environmental knowledge in the form of models and data, so it is not surprising that processor performance depends on the accuracy and resolution of the environmental models. This paper addresses the probabilistic descriptions of the ocean environment that are required to construct useful probabilistic descriptions of the received signal that can, in turn, be used to detect or classify underwater targets. The objective is to link the following two areas of current research.

- *Understanding and reducing environmental uncertainty*. Generally speaking, United States Navy-sponsored ocean acoustic research is directed toward gaining a better understanding of how the ocean environment affects acoustic propagation. The gap between belief and truth is termed *uncertainty*. There is currently an ocean acoustic program entitled "Quantifying, Predicting, and Exploiting Uncertainty."
- *The estimated ocean detector (EOD)*. Sibul (2006), Ballard *et al.* (2006), and Ballard (2007) presented a new signal processing structure that utilizes a probabilistic description of received signal parameters and provides improved sonar performance. The processor is described further below.

We start by defining terms. The *spatial dependence* and *temporal dependence* refer to how ocean acoustic parameters (e.g., sound speed) vary with or depend on location and time, respectively. All ocean acoustic parameters of practical interest vary with location and over time; of course the scales of variability can be considerably different from one parameter to the next. Perfect understanding of relevant oceanographic processes could enable perfect knowledge of acoustic parameter's spatial and temporal dependences. However, the available knowledge of acoustic parameter characteristics is always incomplete to some degree. The term *uncertainty* is used to refer to how well parameter behavior is (or is not) understood, independent of spatial and temporal dependences, and is given as follows.

- Uncertainty is high regarding parameters whose spatial and temporal dependence is poorly understood, regardless of the rate at which they change over time.
- Uncertainly is low regarding parameters whose spatial and temporal dependences are well understood, independent of the spatial and temporal scales of variation.

The results of this paper show why it is important to treat incomplete knowledge of ocean acoustic parameters in probabilistic terms that incorporate the variability that cannot be predicted in terms of either temporal or spatial variation. The advantage of using a probabilistic model is that it allows

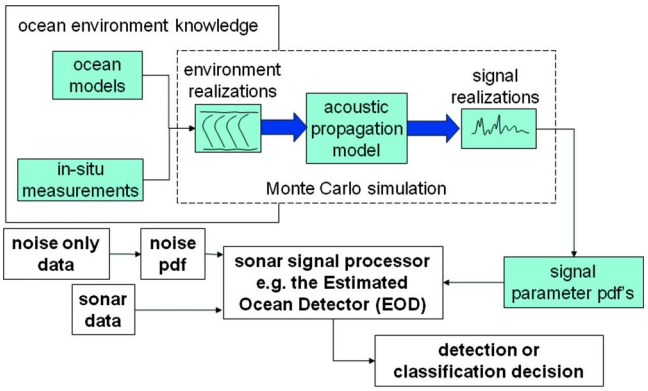


FIG. 1. (Color online) Overall processing scheme by which knowledge of the environment is used to generate statistical signal parameter descriptions, which are then incorporated into the signal processor such as the EOD.

all available ocean acoustic knowledge (i.e., models, measurements, and uncertainty), however incomplete, to be incorporated into the signal processor and provides improved performance relative to using only the mean values of the parameters. Regardless of the quantity or quality of ocean environmental information that is available, one can always construct probabilistic descriptions of acoustic parameters. Knowledge and uncertainty are both reflected in the probability density function (pdf) of the parameter. A pdf can be constructed from theory or data or both, using an expected value and some number of higher order moments. The pdf can reflect what is known about the space-time dependence of the parameter. Better knowledge or less uncertainty is indicated by pdf's that are more tightly grouped about the (possibly time- and space-varying) expected value. A good probabilistic parameter model should reflect all available knowledge but should not make assumptions that are not supported by understanding or data.

Figure 1 shows our overall processing scheme. Knowledge of the ocean environment in the form of space- and time-dependent environmental parameter models and (when available) *in situ* measurements are used to construct a statistically valid realization of the ocean surface, volume, and bottom acoustic properties. An acoustic propagation model is then used to generate a statistically valid realization of the received signal. The propagation model is run for multiple realizations of the environment to produce multiple realizations of the received signal. Desired parameters, e.g., amplitude, frequency, and temporal correlation, are calculated from the ensemble of received signals. Signal parameter pdf's are estimated from the parameter ensemble and provided to the signal processor, where they are used to process sonar data and produce detection or classification decisions.

It is important that the spatial and temporal scales represented in the environmental parameter description match the spatial and temporal scales present in the sonar data. In other words, if the received signals span a particular ocean region (space) and a particular time interval, then the environment parameter pdf's must be valid over the same space and time. Acoustic measurements from the 1996 Strait of Gibraltar Acoustic Monitoring Experiment (SGAME) are used to demonstrate how probabilistic environment and signal parameter models can be employed by a signal processor to decide whether received signals originate from a shallow or deep source. The effects of environmental parameter model fidelity and completeness on processor performance are quantified using receiver operating characteristic (ROC) curves.

Incorporation of a propagation model into the signal processor has been investigated by Candy (2005). In this case, model-based signal processing (MBSP) generally consists of Kalman filtering utilizing second-order probabilistic process and measurement models.[1] For MBSP applied to passive sonar, an acoustic propagation model is incorporated into the measurement model (Candy, 2005, Sec. 9.5). For nonlinear and non-Gaussian problems in which a second-order characterization is not sufficient but a parameter pdf is available, particle filtering techniques can be applied (Arulampalam *et al.*, 2002). Matched-field processing (MFP) is MBSP in which a measured acoustic field is correlated with acoustic fields predicted using an acoustic model in order to estimate source location (e.g., Candy, 2005).

Richardson and Nolte (1991) presented an optimum uncertain field processor (OUFP) for source localization utilizing source position, transmitted signal, and environmental parameter knowledge and uncertainty. The OUFP provides a capability similar to the EOD but is restricted to Gaussian-distributed noise and Rayleigh-distributed signal amplitude statistics. Song and Ritcey (1996) presented a solution to the angle of arrival estimation problem for a random medium that causes signal correlation loss across the array. Wave propagation in random media theory is applied and a Gaussian-distributed index of refraction is assumed. Sha and Nolte (2005a, 2005b, 2006) presented an approach to improving sonar performance prediction that incorporates ocean environmental uncertainty. They derived analytical expressions for the ROC curves that predict detection performance for Gaussian signals in Gaussian noise (Sha and Nolte, 2005a, 2005b) and MFP processing with vertical aperture (Sha and Nolte, 2006).

Finette (2006) investigated a method of relating acoustic variability to environmental variability using polynomial chaos basis functionals as stochastic representations of the environment and the acoustic field. The method promises to be up to 100 times faster than Monte Carlo simulation, but at the present time is limited to relatively simple boundary conditions and sound speed fields. James and Dowling (2005) applied the fine-grained pdf method (successfully used in hydrodynamics) to propagate an acoustic parameter pdf through the environment; their method is likewise limited to simple environments.

Other researchers discussed the relationship between environmental uncertainty and sonar system performance. Robinson *et al.* (2002) stated the requirement for an "end-to-end system" analysis of how uncertainty propagates from the environment through the acoustics and the sonar system in order to obtain a probabilistic performance prediction. Wang *et al.* (2006) presented a method for reducing environmental uncertainty using ocean and acoustic models to design the environmental sampling scheme. Finally, many tactical decision aids (TDAs) have been developed, which use environmental knowledge to improve sonar performance (e.g., Ur-

ban, 1990). For example, some TDAs utilize an acoustic propagation program to predict optimal values for sonar setup parameters such as array depth or transmit vertical angle.

The processor described here is a MBSP in which the propagation model is used to predict signal statistics, which are used by the processor. In this way, it is unlike MFP, which compares the measured acoustic field to mean fields predicted for different source locations. The present work is distinct from the previous environmental uncertainty work referenced above due to the following reasons.

(1) It uses environmental knowledge to improve sonar *performance* as opposed to improving performance *prediction*.
(2) It uses environmental and signal parameter *statistics* rather than the *mean field* to detect and/or classify.
(3) It does not require the signal parameter distribution to be in any particular form.
(4) It requires the noise pdf to belong to an extremely broad class of pdf's, one that can be fitted from measurements using the well known maximum entropy method (discussed below).
(5) It shows that processor performance depends critically on using environmental parameter descriptions that contain the same time and spatial dependences, as well as uncertainty, that are present in the sonar data.

The paper is organized as follows. A brief overview of the EOD processor is given in Sec. I. Characteristics of probabilistic environmental and signal parameter models are discussed in Secs. II and III, respectively. The 1996 SGAME is described in Sec. IV, and in Sec. V the signal processing method described in this paper is applied to the SGAME data.

II. THE ESTIMATED OCEAN DETECTOR (EOD)

The EOD sonar signal processor was conceived by the late Leon Sibul and developed by his student Ballard (Ballard *et al.*, 2006; Ballard, 2007). This section provides an overview of the processor and describes how it incorporates knowledge of environmental parameter statistics into the signal processing.

The signal processor is based on a derivation by Schwartz (1977), and has been implemented as a binary hypothesis test in which the processor must decide between two options (or hypotheses), indicated by H_1 and H_2. Generalization to multiple hypotheses is straightforward, as is redefining the problem as one of classification rather than detection. The column vector of observations (the received signal) is denoted $\mathbf{x}$. Bold lowercase variables denote vectors and superscript T indicating transpose, such that $\mathbf{x}^T = \{x_1, x_2, x_3, \ldots, x_k\}$, where x_k indicates the kth observation. The pdf of $\mathbf{x}$ under hypothesis H_1 or H_2 is denoted $f(\mathbf{x}|H_1)$ or $f(\mathbf{x}|H_2)$. This *conditional pdf* notation indicates the distribution of $\mathbf{x}$ given that hypothesis H_i is true, $i=1,2$. The EOD is a maximum likelihood ratio detector (Van Trees, 2001) that decides between H_1 and H_2 based on the value of the log-likelihood ratio (LLR)

$$L(\mathbf{x}) = \ln\frac{f(\mathbf{x}|H_1)}{f(\mathbf{x}|H_2)} = \ln\frac{\int_{\Theta} f(\mathbf{x}|\boldsymbol{\theta},H_1) f(\boldsymbol{\theta}|H_1) d\boldsymbol{\theta}}{\int_{\Theta} f(\mathbf{x}|\boldsymbol{\theta},H_2) f(\boldsymbol{\theta}|H_2) d\boldsymbol{\theta}}. \quad (1)$$

Here $\boldsymbol{\theta}$ is a vector of signal parameters, $f(\mathbf{x}|\boldsymbol{\theta},H_i)$ is the composite likelihood function (a distribution of $\mathbf{x}$ given that $\boldsymbol{\theta}$ and hypothesis H_i are known), and $f(\boldsymbol{\theta}|H_i)$ is the pdf of $\boldsymbol{\theta}$ under hypothesis H_i. The integration is over the domain of all elements of the vector $\boldsymbol{\theta}$. The conditional pdf's $f(\mathbf{x}|\boldsymbol{\theta},H_i)$ represent our understanding of how the observation depends on the signal parameters. The method by which the signal parameter pdf's $f(\boldsymbol{\theta}|H_i)$ are calculated is shown in Fig. 1.

It has been noted that Eq. (1) can be hard to implement. The EOD processor offers an alternative when the conditional pdf's belong to the exponential class and thus have the form

$$f(\mathbf{x}|H_i,\boldsymbol{\theta}) = K(\boldsymbol{\theta})\exp[g_i(\boldsymbol{\theta},\mathbf{x}) + B_i(\mathbf{x})], \quad (2)$$

where $g_i(\boldsymbol{\theta},\mathbf{x})$ and $B_i(\mathbf{x})$ are scalar functions of the vectors $(\boldsymbol{\theta},\mathbf{x})$ and $\mathbf{x}$, respectively. As stated above, an important point is that pdf's of this form can be obtained from samples of $\mathbf{x}$ using the maximum entropy method (Kapur and Kesavan, 1992). Putting Eq. (2) into either the numerator or denominator of Eq. (1), differentiating with respect to $\mathbf{x}$, and applying Bayes rule

$$f(\boldsymbol{\theta}|\mathbf{x})f(\mathbf{x}) = f(\mathbf{x}|\boldsymbol{\theta})f(\boldsymbol{\theta}) \quad (3)$$

results in a partial differential equation with solution

$$f(\mathbf{x}|H_i) = c_i \exp[G_i(\mathbf{x}) + B_i(\mathbf{x})]. \quad (4)$$

Here c_i is a normalizing constant, $B_i(\mathbf{x})$ was identified in Eq. (2), $G_i(\mathbf{x})$ is a scalar function defined by

$$G_i(\mathbf{x}) = \int \mathbf{h}_i(\mathbf{x}) \cdot \mathbf{dx}, \quad (5)$$

and $\mathbf{h}_i(\mathbf{x})$ is a vector function identified as the *conditional moment*

$$\mathbf{h}_i(\mathbf{x}) = \int_{\Theta} \left[\frac{\partial}{\partial \mathbf{x}} g_i(\boldsymbol{\theta},\mathbf{x})\right] f(\boldsymbol{\theta}|\mathbf{x},H_i) d\boldsymbol{\theta}. \quad (6)$$

Equation (4) allows the LLR to be expressed in the following simple form:

$$\ln\frac{f(\mathbf{x}|H_1)}{f(\mathbf{x}|H_2)} = G_1(\mathbf{x}) + B_1(\mathbf{x}) - G_2(\mathbf{x}) - B_2(\mathbf{x}) + \ln\left(\frac{c_1}{c_2}\right). \quad (7)$$

Ballard (2007) evaluated EOD performance for the case in which H_1 and H_2 correspond to received sinusoidal signals having the same mean level but with different variations about the mean. This is a useful case for passive sonar because the mean received level is affected by both source level (SL) and transmission loss (TL) and thus cannot be used to classify signal sources. The noise was taken to be additive and Gaussian distributed [the Gaussian distribution belongs to the exponential class, Eq. (2)]. The conditional density function for this case is the pdf of the additive noise.

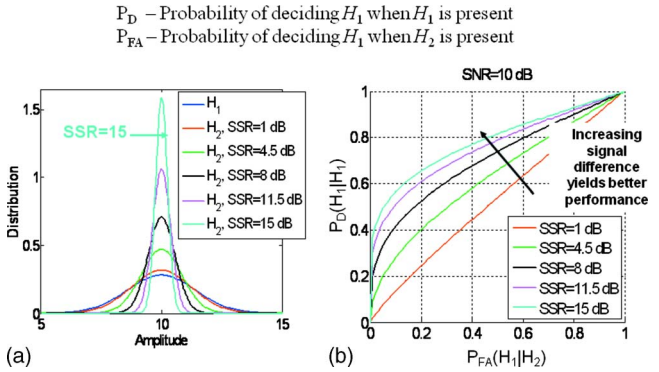


FIG. 2. (Color online) Performance of the EOD signal processor for Gaussian signal amplitudes with the same mean but difference variances. (a) Signal amplitude pdf's. (b) ROC curves for different signal amplitude pdfs. (from Ballard, 2007).

The signal processor performance is shown in Fig. 2 as a function of the signal-to-signal ratio (SSR)

$$\mathrm{SSR} = 10 \log \frac{\sigma_1^2}{\sigma_2^2}, \tag{8}$$

where σ_1^2 and σ_2^2 are the signal variances. The ability of the processor to identify the correct signal source improves with increasing difference between the signal variances. It also depends fundamentally on being able to correctly predict the signal variance. This latter requirement will be explored further using ocean measurements.

III. PROBABILISTIC ENVIRONMENTAL PARAMETER MODELS

The term *probabilistic environmental model* refers to statistical descriptions of ocean environmental parameters, e.g., sound speed or bottom reflection loss. The model mean describes the expected dependence of the parameter on location and time, and perhaps on measurable parameters such as wind speed or water temperature. The probabilistic model incorporates the model mean but adds information to reflect the uncertainty associated with the model mean.

Historically, environmental models have described only the mean or expected value of parameters; they have not generally included pdf's or higher order moments that characterize the expected variability about the mean. For example, databases of ocean sediment type (or grain size) provide only the expected value versus location and no information about what variation about the mean should be expected. Perhaps the primary reasons for this are that (1) there are often very little data with which to estimate higher order moments, (2) historically there has been no real use for parameter pdf's or higher order moments, and (3), in general, it is difficult to relate changes in environmental parameters to signal parameter changes in a simple linear way (Dosso *et al.*, 2007); the relationship is usually complex and nonlinear. Ocean acoustic research to reduce environmental uncertainty is addressing the first point, the EOD signal processing structure provides an answer to the second point, and the simulation method used in this paper to transform environmental parameter pdf's into signal parameter pdf's is one method of addressing the third point.

Some environmental parameters are better understood than others. For example, the height and phase of the ocean tide can be predicted very accurately, whereas the height of individual internal waves, solitons, and surface waves can be predicted with considerably less accuracy. The mean value and higher order moments can be predicted relatively well for some parameters, but instantaneous values are totally unpredictable. For example, a probabilistic model for ocean surface wave height might provide the mean (space- and time-dependent) wave height spectrum, together with higher order moments of wave height, but the phase of individual waves must be treated as a random variable, perhaps uniformly distributed between $(-\pi, \pi)$.

From an operational perspective, the amount of environmental information available depends on the location. Typically a chart or database provides ocean depth versus position (bathymetry) with some resolution but unknown certainty, and a database provides monthly averages for the sound speed profile (SSP) (the sound speed versus depth) computed by averaging past measurements. More recently devices such as the glider (cf. Rudnick *et al.*, 2004) have been developed to provide real-time measurements of sound speed over large areas. Also, the modular ocean data assimilation system (MODAS) program provides an update to the average SSP obtained using sea surface temperature and satellite-derived sea surface elevation (Washington, 2004). Also, MODAS can apply optimal interpolation to incorporate SSP measurements if available.

It is always possible to construct a probabilistic model from a mean (possibly space- and time-dependent) model. If there is absolutely no information about the uncertainty associated with the mean model, one can take the parameter to be uniformly distributed over the range of reasonable values possibly centered at the mean. If an estimate of the parameter variance is available, the maximum entropy principle shows that the Gaussian distribution makes full use of available information but makes no further unwarranted assumptions (Kapur and Kesavan, 1992). Put another way, the Gaussian pdf is maximally uncertain about the true parameter value consistent with the available knowledge. The probabilistic model specifies the parameter to be Gaussian distributed with known mean and variance. If higher order moments (e.g., skew or kurtosis) are known, they can be incorporated into a pdf belonging to the exponential class identified in Eq. (2) above.

It is important to ensure that the probabilistic environmental model encompasses the time and spatial scales over which the signal processor will be operating. Spatially this means that environmental models for location A should not be used to predict signal parameter statistics for use by a signal processor at location B many miles away. Temporally, this means that if the processing interval is on the order of hours, then the environmental model must include the temporal variability and uncertainty associated with those phenomena that are important over hourly intervals. The mean will be affected by longer term processes, e.g., regional circulation, fronts and eddies, and the tidal current, while the variation about the mean will be affected by shorter term processes, e.g., internal waves, solitons, and surface waves.

This point will be illustrated using the Strait of Gibraltar acoustic data, in which a time- and space-dependent and uncertain SSP model was required in order for the signal model to reflect the variability observed in hourly measurements over several days and for processor performance to be acceptable.

IV. PROBABILISTIC SIGNAL PARAMETER MODELS

The term *probabilistic signal model* refers to statistical descriptions of the temporal and spatial dependences of signal parameters such as amplitude, phase, frequency, and spatial correlation. As with environmental parameters, signal models have historically encompassed only predicted mean values, e.g., mean received level and mean Doppler frequency. TDAs typically use an acoustic propagation model and a single environmental realization (the "mean" environment) to predict mean TL. Using the sonar equation (Burdic, 1990), the mean received signal level (RL) can be found by subtracting mean TL from the SL. Probabilistic environmental parameter models are usually not considered in TL computations, and probabilistic expressions for TL and RL are uncommon. However, use of the EOD signal processor requires probabilistic signal parameter predictions that include time and spatial dependences together with uncertainty in these expressions.

Analysis is required to identify the probabilistic signal parameter models that are important to the processor in a particular case. For example, if the receiver aperture is large or if the source or receiver (or both) are in motion, it is important to know how well the received signal remains correlated over time and/or space. These parameters are referred to as *temporal* and *spatial coherences* (some authors prefer the term correlation), respectively. In this case the signal model might need to include the pdf of coherence versus lag or separation. As another example, variation in RL referred to as *scintillation* (cf. Cotte *et al.*, 2007) can be induced by forward scattering from a moving surface. In some cases a second-order measure of RL variation, the *scintillation index*, may provide a sufficient characterization. Other signal parameters that may be important are frequency shift or spread, which can be affected by motion of the source and/or receiver as well as the medium, and signal phase, which can be affected by sound speed variability along the propagation path.

V. THE 1996 STRAIT OF GIBRALTAR ACOUSTIC MONITORING EXPERIMENT (SGAME)

Acoustic and environmental measurements from the 1996 SGAME will be used in Sec. VI to investigate the use of probabilistic environment and signal parameter models in a signal processor to decide whether a received signal originated from a shallow or deep source. An overview of the measurement is presented in this section. The SGAME experiment was conducted by Scripps Institution of Oceanography, San Diego, CA and the Institut für Meereskunde, Kiel, Germany. Many details of the measurement have already been reported by Tiemann *et al.* (2001a, 2001b), and only information necessary to understand the present paper is provided here. From an oceanographic perspective, the temperature and salinity of water in the upper 150 m of the Strait are dominated by westerly flow of relatively dense Mediterranean water underlying an easterly flowing layer of less dense (warmer and fresher) Atlantic water. Substantial variation in the depth of the interface between these two layers is introduced by the internal tide (Farmer and Armi, 1988). In addition, large tidal bores are generated periodically at the Camarinal Sill on the Atlantic side and propagate eastward along the interface between the two layers, adding to the complexity of the sound speed field. The tidal bores can be seen in sea surface radar images (Tiemann *et al.*, 2001a).

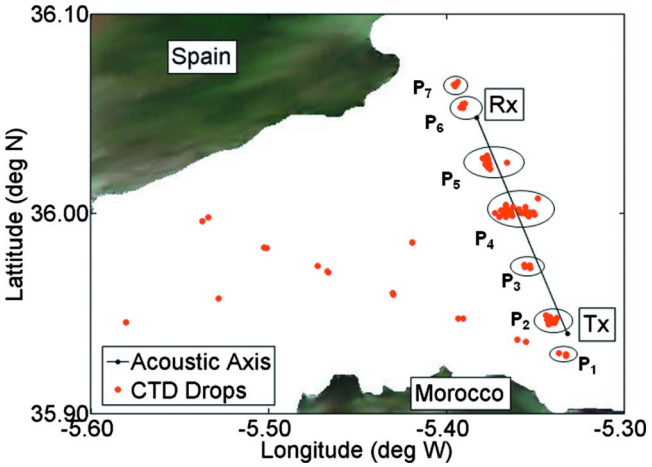


FIG. 3. (Color online) Location of the 1996 SGAME. Tx=transmitter location; Rx=receive hydrophone location. P_n indicates groupings of conductivity and temperature vs depth (CTD) measurements.

The acoustic data analyzed and reported by Tiemann *et al.* (2001a, 2001b) consisted of ~2 kHz acoustic transmissions across the Strait from a source at 200 m depth to a receive hydrophone at the same depth. The acoustic data are supported by a comprehensive set of conductivity and temperature versus depth (CTD) drops spanning the full tidal cycle at several locations along the propagation path. Tiemann *et al.* (2001a, 2001b) developed a mean range- and time-dependent SSP model[2] from the CTD measurements (from which sound speed may be calculated), satellite data, and knowledge of the internal wave structure and seafloor topology. The goal of the 2 kHz measurements was to examine the feasibility of acoustically detecting tidally driven internal waves and bores. The authors demonstrated that temporal variability in the arrival time structure for the ~2 kHz transmissions is well predicted using range-dependent ray tracing and the range- and time-varying SSP model constructed for the region.

A. 250 Hz acoustic measurements

The present analysis utilizes acoustic data from the SGAME experiment which have not been reported prior to now. The data consist of 8 s M sequence pulses centered at 250 Hz, transmitted hourly across the Strait over a 3.5 day (84 h) period containing just over 7 cycles of the internal tide. The measurement utilized a 100 m deep bottom-moored source and 10 bottom-moored hydrophones evenly spaced at 81–387 m depth. Figure 3 shows the locations of the acoustic

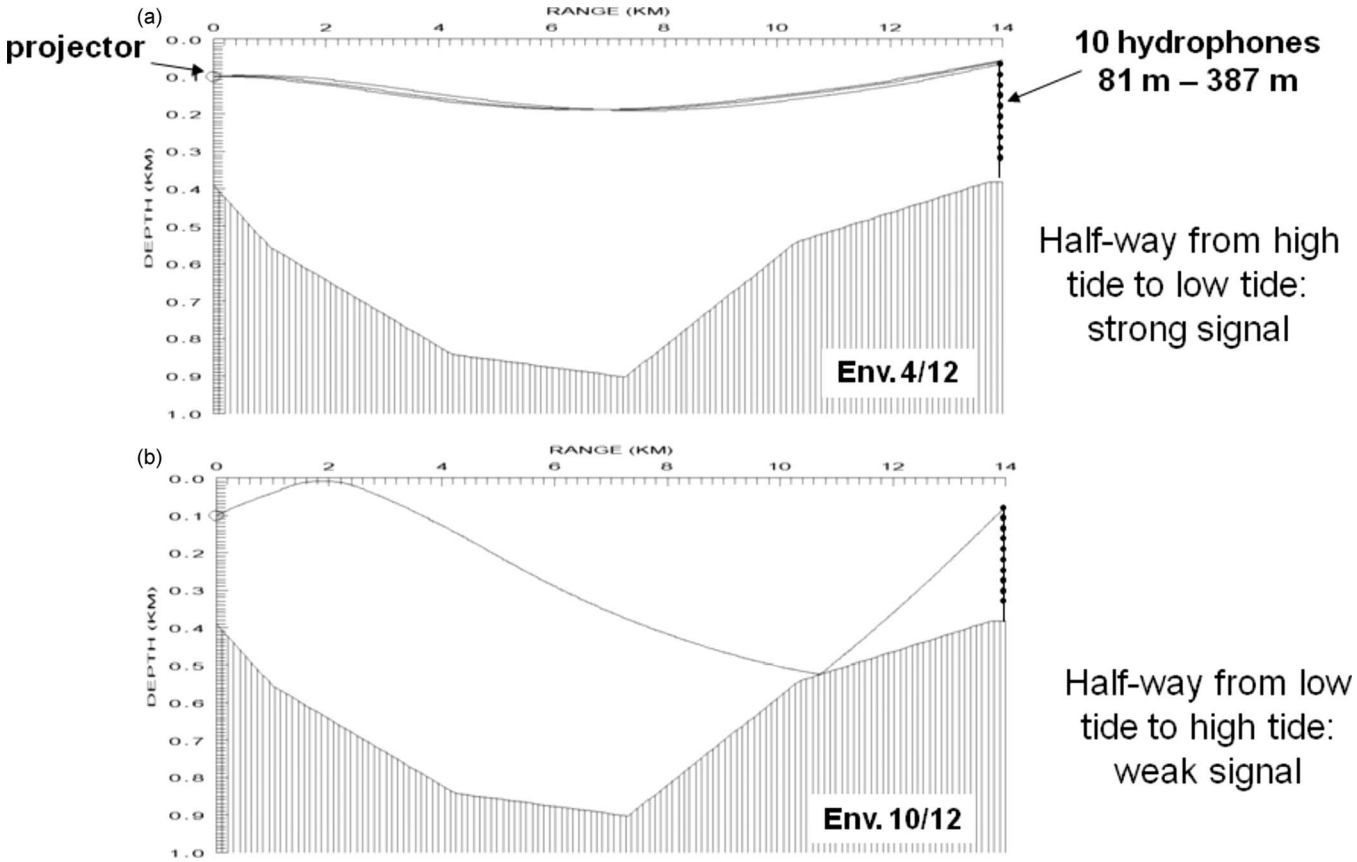


FIG. 4. Trace of earliest rays connecting the 100 m deep source and the 81 m deep hydrophone for the 1996 SGAME site at two times in tidal cycle. (a) sound speed profile (SSP) half-way from high tide to low tide. (b) SSP half-way from low tide to high tide.

source (T_x) and receive hydrophones (R_x) along with the locations of the more than 100 CTD measurements made in conjunction with the acoustic measurements. The CTD measurements have been grouped into locations P_1, P_2, etc. Figure 4 shows the experiment geometry and the bathymetry of the Strait, along with the earliest arrivals connecting the source and shallow hydrophone at two times in the tidal cycle. The RL was high when sound propagated as shown in the upper panel and low when it propagated via a bottom bounce as shown in the bottom panel. Note that the vertical axis scale ($1''=180$ m) is significantly expanded relative to the horizontal axis scale ($1''=1600$ m). The bathymetry is complicated but essentially bathtub shaped.

The 250 Hz signals were transmitted hourly during an 84 h period spanning Julian day (JD) 111–115. Each transmission consisted of two identical, consecutive 8 s long pseudorandom, phase coded pulses centered at 250 Hz with approximately 75 Hz bandwidth. The acoustic signals have been match filtered (MF) using a replica of the transmitted signal and frequency domain correlation (e.g., Burdic, 1990)

$$X(t) = i\mathrm{FFT}\{P(f)S^*(f)B\}. \tag{9}$$

Here $P(f)$ and $S(f)$ are the Fourier transforms of the received signal and the signal replica, respectively, iFFT is the inverse fast Fourier transform, and B is a constant that ensures unity gain in the MF. MF processing provides $10\log_{10}(8\times 75)=27.8$ dB gain against shipping noise present in the Strait. Figure 5 shows the MF output, in decibels, with each column of pixels representing the MF output for a single transmission. The approximate source-to-receiver travel time determined by dividing the path length by the average sound speed is 8.55 s. Each panel shows the MF output of 84 transmissions received by a single hydrophone whose depth is labeled beside the y axis.

The MF output in Fig. 5 shows considerable semidiurnal (twice daily) variation that is associated with the internal tide. The first arrival [usually a direct path (DP)] is generally the strongest at all hydrophones; however, its time of arrival

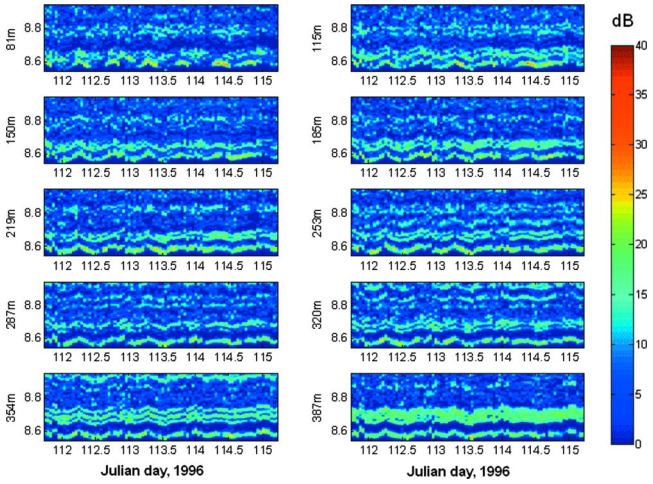


FIG. 5. (Color online) MF output (dB). Transmitted signal: 8 s coded pulse centered at 250 Hz, transmitted hourly. Each panel represents MF output for a single hydrophone whose depth is noted (81 m to 387 m). Horizontal axis of each panel indicates transmit time; vertical axes are propagation time.

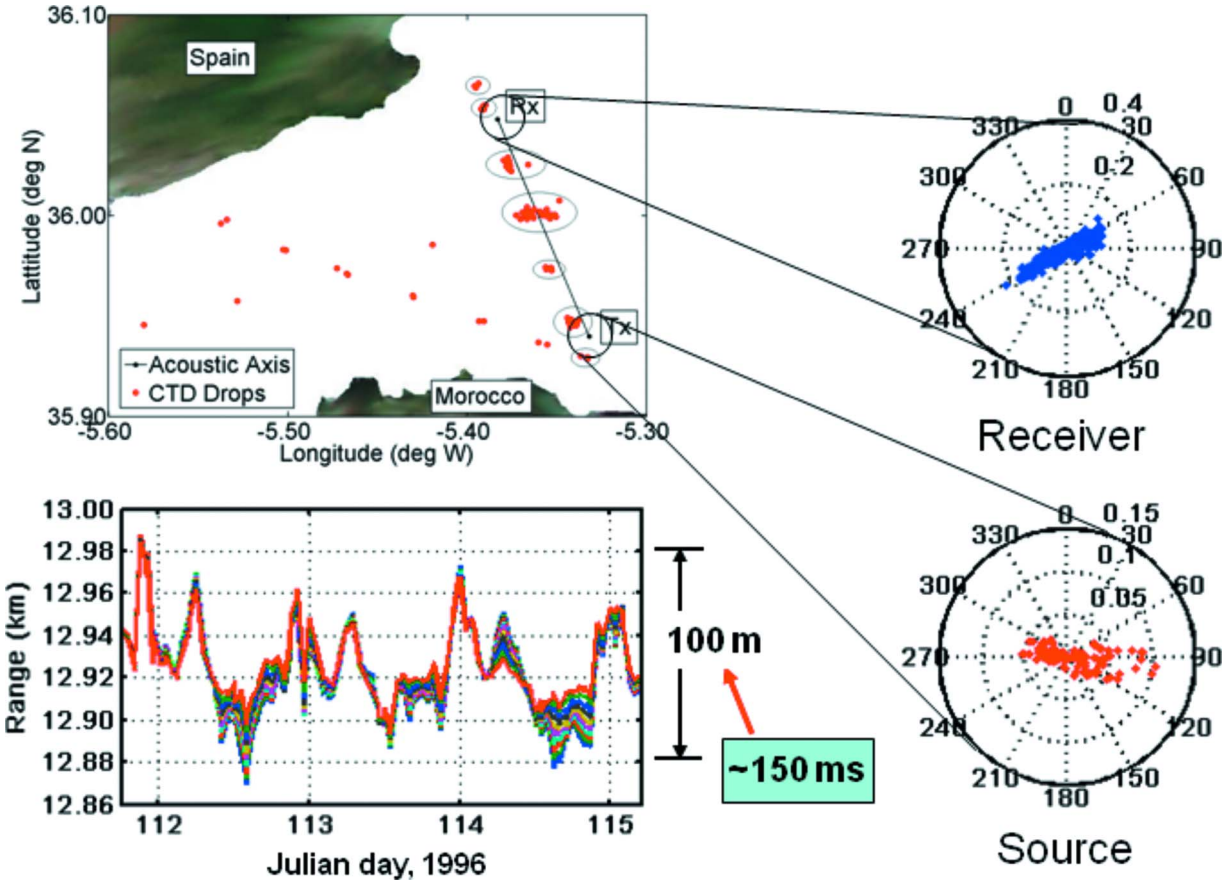


FIG. 6. (Color online) Array motion during SGAME (right two panels) and the instantaneous source-receiver ranges (lower left).

varies by up to 75 ms (peak to peak) with approximately a semidiurnal period. There are a number of later arrivals present at all hydrophones throughout the measurement. A notable feature of the data is variation in the level of the DP and multipath (later arriving) signals. Arrivals sometimes disappear completely for 1 hour or several hours, a behavior also observed by Tiemann *et al.* (2001a, 2001b) in the higher frequency acoustic data. This variability is not unique to the SGAME data and is quite similar to that commonly observed in MF oceanic signals (e.g., Yang, 2006). From the standpoint of a sonar signal processor, variability in the travel time and signal level are important characteristics of the received signal model.

B. Travel time variation

During the SGAME measurement, the positions of the source and the hydrophones were tracked using four seafloor mounted acoustic transponders operating at 9–12 kHz and located approximately 350 m from the base of each mooring. The positions of the bottom-mounted transponders were determined using the ship borne global positioning system. As shown in Fig. 6, the receiver mooring motion is approximately east-northeast to west-southwest, and the projector motion is approximately east-west. The projector and receive hydrophone motion were combined to estimate the instantaneous separation, which is shown in the lower left panel of Fig. 6. Notice that there are range minima at about JD 112, 112.5, 113, and 113.5, which correspond to DP travel time drops at the same times in Fig. 5. Also, there are range maxima at JD 114 and 115 in Fig. 6, which correspond to DP travel time peaks in Fig. 5.

To correct for the travel time variation shown in Fig. 6, the instantaneous source-hydrophone range was used to shift the start time of the MF output. The result is shown in Fig. 7, and it is evident that most of the arrival time variability seen in Fig. 5 has been removed and that the DP arrivals now line up. We now focus on received signal amplitude variation and its relationship to the SSP.

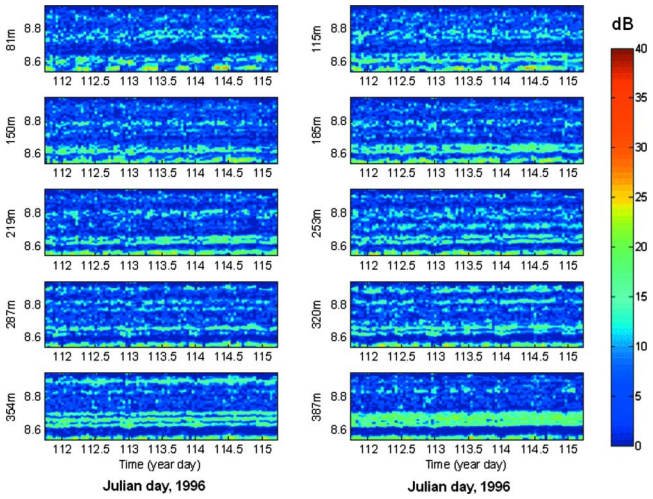


FIG. 7. (Color online) MF output (dB) as in Fig. 5 but adjusted for projector and receiver motion.

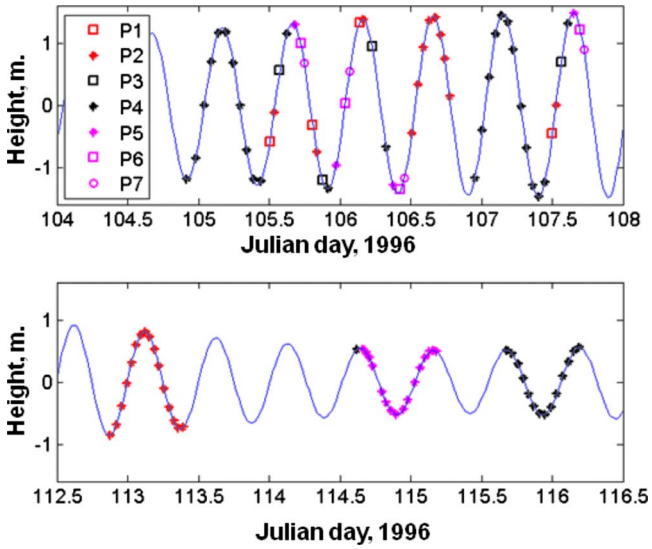


FIG. 8. (Color online) Times of CTD drops relative to the tidal cycle during SGAME. Pn refers to the location of CTD drop as shown in Fig. 3.

C. CTD measurements and the mean sound speed model

The CTD measurement scheme carried out during the SGAME experiment was designed to measure how the SSP varied temporally during a single tidal cycle and spatially along the acoustic propagation path. The time and location of temperature and salinity measurements are shown in Fig. 8. The times of measurements are shown as dots on the plot of tidal height at a nearby station to show that the measurements spanned complete tidal cycles at each position. As in Fig. 3, P_1, P_2, etc., indicate the measurement location.

Tiemann *et al.* (2001a, 2001b) used the CTD measurements to construct a model for the time- and space-varying SSP using a 1 m spacing in depth, a 1 km spacing in range along the propagation path, and 5 min spacing in time. Underlying the model is a single profile shifted up and down by 75 m during the course of each tidal cycle. The effects of tidal bores propagating through the Strait at particular times during the tidal cycle were added. As an example, the left panel of Fig. 9 shows the SSP model for all times at one location. The model shows two ducts, with sound speed minima at approximately 75 and 150 m in depth, which are manifestations of the two water layers. The center panel of Fig. 9 shows all of the SSP measurements made at this location, and the right panel shows the difference between each measurement and the corresponding model SSP for that time in the tidal cycle. Although there are some differences between the model and measurements, Tiemann *et al.* (2001a) showed that the model resolved the sound speed field sufficiently well such that ray tracing very accurately predicted the acoustic arrival structure for source and receiver at 200 m depth throughout several tidal cycles.

VI. APPLYING THE SIGNAL PROCESSOR TO THE SGAME DATA

A portion of the 250 Hz SGAME data are now used in the signal processor discussed earlier to demonstrate how environment and signal parameter models are used and to

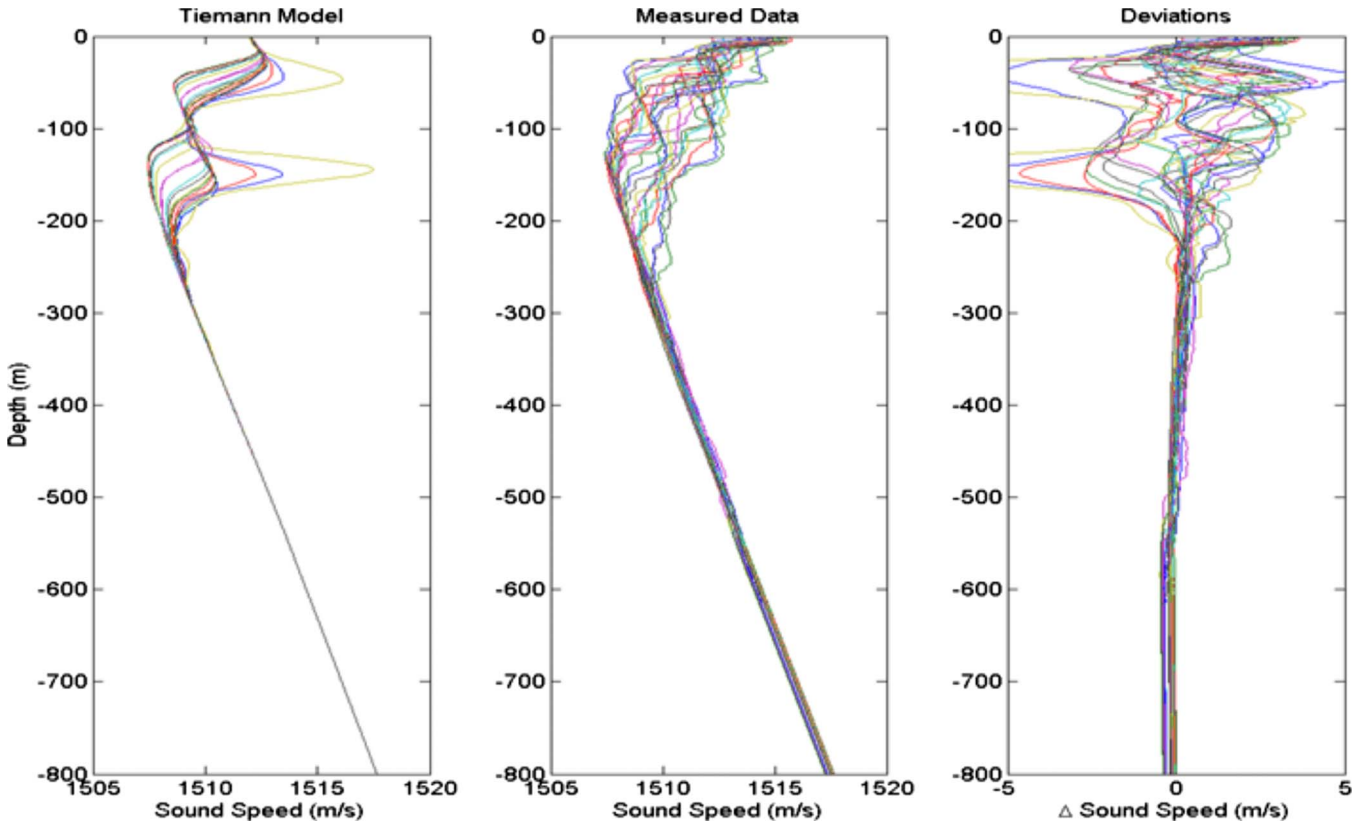


FIG. 9. (Color online) SSPs for all tidal cycle times at one location of SGAME. Left: Tiemann model; center: all measurements from this location; right: measurement minus the Tiemann model for the particular time.

illustrate dependence of processor performance on model fidelity. The signals received hourly at the shallowest hydrophone (81 m depth) and those received at the deepest hydrophone (387 m depth) are employed. Due to reciprocity, these signals are identical to those that would be received at the source location if transmitted from the two hydrophone locations. The signal processor must utilize the received signal to decide between two hypotheses as follows.

- H_1: The source is 81 m deep.
- H_2: The source is 387 m deep.

The observations are the highest values (peaks) in the first 60 ms of the output of the MF $\mathbf{X}=[X_1,X_2,\ldots,X_N]$. The signal parameter vector consists of signal amplitude alone, i.e., $\mathbf{A}=[A_1,A_2,\ldots,A_N]$. A LLR processor is employed as in Eq. (1),

$$L(\mathbf{X}) = \ln \frac{\int_{\Theta} f(\mathbf{X}|\mathbf{A},H_1) f(\mathbf{A}|H_1) d\mathbf{A}}{\int_{\Theta} f(\mathbf{X}|\mathbf{A},H_2) f(\mathbf{A}|H_2) d\mathbf{A}}. \tag{10}$$

The signal-to-noise ratio is high in these data and the conditional likelihood function is taken to be a delta function

$$f(\mathbf{X}|\mathbf{A},H_i) = f(\mathbf{X}-\mathbf{A}|\mathbf{A},H_i) = \delta(\mathbf{X}-\mathbf{A}). \tag{11}$$

The LLR then becomes the ratio of the received signal amplitude pdf's predicted for H_1 (source depth is 81 m) and H_2 (source depth is 387 m) as follows:

$$L(\mathbf{X}) = \ln \frac{\int_{\Theta} \delta(\mathbf{X}-\mathbf{A}) f(\mathbf{A}|H_1) d\mathbf{A}}{\int_{\Theta} \delta(\mathbf{X}-\mathbf{A}) f(\mathbf{A}|H_2) d\mathbf{A}} = \ln \frac{f(\mathbf{X}|H_1)}{f(\mathbf{X}|H_2)}. \tag{12}$$

The received signal amplitude pdf's are calculated as outlined in Fig. 1. The environment realizations consist of range-dependent sound speed fields and the boundary parameter values. Acoustic signals are propagated through the environments using the range-dependent acoustic model (RAM) propagation model (Collins, 1993) at the frequencies contained in the acoustic pulse (frequencies between 212 and 288 Hz with a 0.122 Hz separation). The individual (single frequency) RAM outputs are weighted according to the transmit signal spectrum and Fourier transformed (across frequency) to produce time-domain signals. The time-domain signals are MF using the transmitted signal in the same manner as for the in-water data, and the peak amplitudes in the first 60 ms are extracted and used to calculate pdf's using the kernel density estimator.

Figure 10 shows the MF output calculated using time- and range-dependent sound speed fields constructed using SSP profiles from the Tiemann SSP model. Comparing Fig. 10 with Fig. 7 shows some similarities and differences. The simulated received signals show temporal variability that is similar to that seen in the in-water measurements, but the most striking difference is that the later arrivals are predicted to be much stronger than they are in the acoustic measurements. The DP and later arriving signals are present at roughly the same times, but the later arrivals are predicted to be 5–15 dB higher than they appear in the in-water data. Possible reasons for this discrepancy are as follows.

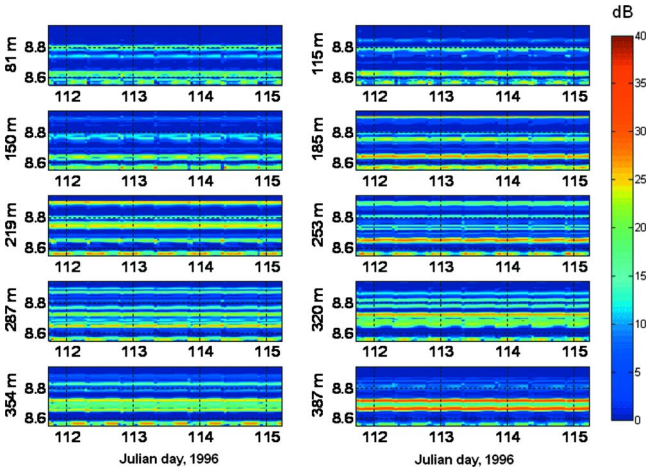


FIG. 10. (Color online) Matched filter output (dB) for simulated signals produced using the Tiemann model sound speed field.

- The bottom reflection loss used in the propagation model could be too low.
- There may be errors in the bathymetry model.
- Time and frequency spread induced by surface and bottom interaction may be causing correlation loss which is not accounted for in the propagation model.

The first two factors are discussed briefly here; the third is discussed in Sec. VII. The bottom parameters used in the propagation model are based on core samples taken farther out in the Atlantic (Habgood *et al.*, 2003). Depth-independent values of 1.8 g/cc for the density, 1725 m/s for the sound speed, and 0.75 dB/wavelength attenuation lead to a fluid-fluid reflection loss of ~1 dB per bounce loss in the subcritical region. (The critical angle is about 30° and the ray grazing angles are no greater than 20° including slope.) Analysis indicates that the TL for the multipath is weakly dependent on the sound speed, density, and attenuation in the bottom, so that bottom loss error does not appear to be the cause of the 5–15 dB difference. Regarding bathymetry, the two-dimensional slice used in the propagation model was spline interpolated from a 200 m contour map (Tiemann *et al.*, 2001b). Although more accurate bathymetry could be obtained, the fact that the arrivals seems to come at about the right time indicates that bathymetry error is not a significant factor.

Returning our attention to the first arrivals, Fig. 11 shows pdf's of the amplitude of the first arrival in the MF output for several cases. The MATLAB kernel density function routine was used to calculate the pdf's from 84 data points. In all cases the amplitudes have been normalized by their mean value so that all pdf's have a mean of 1. As stated earlier, this is appropriate for sonar data because received signal amplitude is affected by SL and TL, neither of which are generally known, with the result that mean received level cannot be used to classify signals. Figure 11(a) shows the amplitude pdf's of the first arrival in the MF output for the

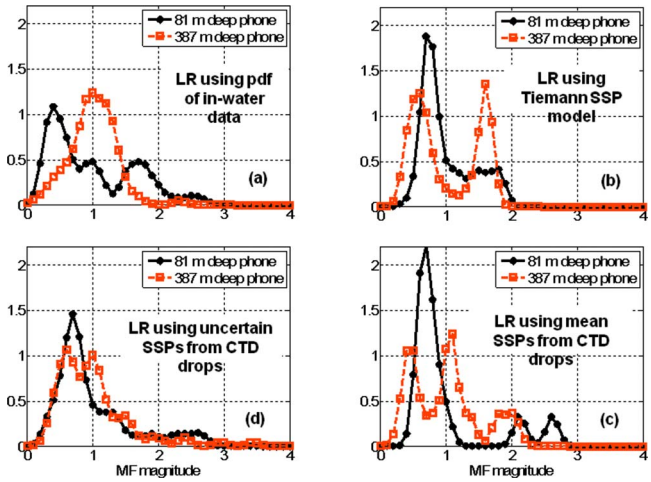


FIG. 11. (Color online) Probability density function of peak level of first arrivals in matched filter output. Data are (a) in-water measurements, (b) predicted using the Tiemann sound speed model, (c) predicted using the mean (but time and space-varying) sound speed profiles from CTD drops, and (d) predicted using mean sound speed with uncertainty included as described by Eqs. (18) and (19) in the text.

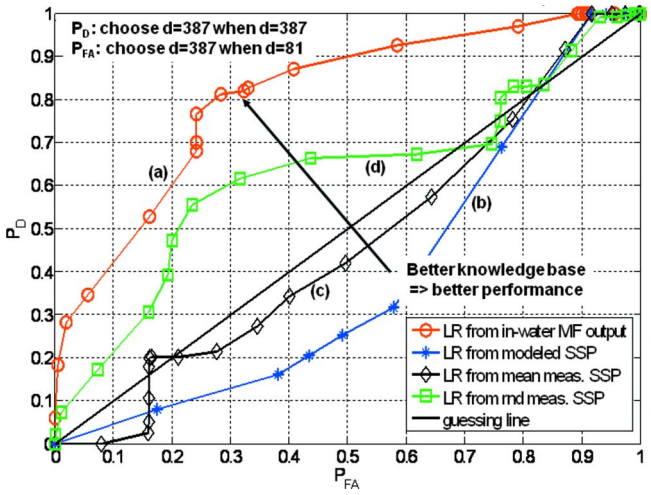


FIG. 12. (Color online) ROC curves constructed using in-water data MF output and likelihood ratios from in-water data (a) and predictions using the Tiemann SSP model (b), mean SSP from CTD drops (c), and random SSP from CTD drops (d). The solid line is the coin flip or guessing line.

in-water data (Fig. 7) for the shallowest and deepest hydrophones. The two pdf's are considerably different from each other in that the pdf of the shallow phone shows considerably more spread than that of the deep phone. Figure 11(b) shows the amplitude pdf's predicted using RAM and the Tiemann SSP model, i.e., the peak values in the first 60 ms of the data shown in Fig. 10. The pdf's in Fig. 11(b) do not closely resemble those in Fig. 11(a). The lower two panels are discussed below.

ROC curves provide a means of quantifying signal processor performance by comparing the probability of detection (P_D) versus the probability of false alarm (P_{FA}). They are defined here as follows.

- P_D=probability of detection$\triangleq$probability of choosing H_2 when H_2 is true.
- P_{FA}=probability of false alarm$\triangleq$probability of choosing H_2 when H_1 is true.

Figure 12 shows ROC curves for several cases in which the LLR $L(\mathbf{X})$ was constructed according to Eq. (12) but with $f(\mathbf{X}|H_1)$ and $f(\mathbf{X}|H_2)$ obtained in different ways. In all cases, the peak values of the first arrivals in the MF in-water data were fed to the processor. Figure 12(a) indicates processor performance when $f(\mathbf{X}|H_1)$, $f(\mathbf{X}|H_2)$, and $L(\mathbf{X})$ were computed from the in-water data. In other words, the pdf's $f(\mathbf{X}|H_1)$ and $f(\mathbf{X}|H_2)$ were estimated from the in-water data and the quotient formed to obtain the likelihood ratio. Although this would not be possible in an operational situation, it provides an upper bound on processor performance. The curve labeled (a) in Fig. 12 indicates two things regarding the amplitudes of the first arrivals for these two cases, i.e., source at 81 m depth versus source at 387 m depth.

(1) The amplitude pdf's are sufficiently different to allow good classification performance.
(2) If amplitude pdf's predicted using environmental realizations and the acoustic propagation model match the true underlying pdf's sufficiently well, they can be expected to provide good classification performance.

The curve labeled (b) in Fig. 12 indicates the performance of a LLR receiver constructed using the pdf's in Fig. 11(b), which were obtained using RAM and the mean SSP model used quite successfully by Tiemann *et al.* (2001a, 2001b) to match the arrival structure in the 2 kHz data. However, it indicates worse performance than a coin flip ($P_D = P_{\mathrm{FA}}$); the predicted pdf's do not enable good processor performance, consistent with the dissimilar appearance of the pdf's shown in Figs. 11(a) and 11(b).

The reason for the disagreement may be that the SSP model was constructed to match travel times recorded for a 200 m deep, 2 kHz source and receiver, whereas the 250 Hz source depth is 100 m closer to the surface. The background profile used for the SSP model was a single profile shifted vertically over time. However, it was "recognized that in doing so, agreement between the modeled and measured SSPs would be less at the very top and bottom of the tidal cycles" (Tiemann *et al.*, 2001a). In addition, the model fidelity was lower near the ocean surface where it was necessary to truncate or extend the single representative profile.

Referring back to Fig. 8, note that the CTD drops covered full tidal cycles at different locations along the source-receiver path, but the measurements were not synoptic (i.e., did not provide simultaneous measurements at all locations during a single tidal cycle). Rather, measurements over a full tidal cycle were obtained at one location, after which the ship moved to another location and took CTD drops over a full tidal cycle there, and then moved again, and so on. To construct a synoptic sound speed model it is necessary to assume that the SSPs do not change significantly from one cycle to the next. Tiemann *et al.* (2001a, 2001b) made this assumption, and it was made in the present work as well in order to obtain mean, time- and location-dependent SSP fields, and a measure of SSP uncertainty.

The approach taken in the present work was to group CTD measurements made in close proximity to each other

and at close to the same time in the tidal cycle. It is straightforward to simply average those profiles in order to obtain a mean SSP for different times during the tidal cycle along the source-receiver path. Estimating uncertainty was a bit more involved. Denote the kth profile of a group of K SSPs measured in a small region over a short time interval as

$$\mathbf{C}(k) \triangleq [c_1(k), c_2(k), \ldots, c_N(k)]^T, \tag{13}$$

where there are N values in the SSP and the superscript T indicates transpose. The mean SSP for this location and time relative to high tide is $\overline{\mathbf{C}}(k) = E\{\mathbf{C}(k)\}$. If the process is stationary and ergodic, the mean can be estimated by averaging values at each depth

$$\overline{\mathbf{C}} = [\overline{c}_1, \overline{c}_2, \ldots, \overline{c}_N]^T = \frac{1}{K}\left[\sum_{k=1}^{K} c_1(k), \ldots, \sum_{k=1}^{K} c_N(k)\right]^T. \tag{14}$$

The covariance matrix of the SSPs is $\mathbf{R}_x = E\{[\mathbf{C}(k) - \overline{\mathbf{C}}(k)] \times [\mathbf{C}(k) - \overline{\mathbf{C}}(k)]^T\}$. If the process is stationary over the observation interval and ergodic, then we can estimate the covariance by averaging over the measurements as follows:

$$\hat{\mathbf{R}}_x = \frac{1}{K}\sum_{k=1}^{K} [\mathbf{C}(k) - \overline{\mathbf{C}}][\mathbf{C}(k) - \overline{\mathbf{C}}]^T \tag{15}$$

Following Van Trees (2002, Appendix A.5), the covariance estimate can also be written as (redefining $\mathbf{C}(k) \triangleq [\mathbf{C}(k) - \overline{\mathbf{C}}]$ to simplify the notation)

$$\hat{\mathbf{R}}_x = \frac{1}{K}[\mathbf{C}(1)\mathbf{C}(2)\ldots\mathbf{C}(K)]\begin{bmatrix} \mathbf{C}^T(1) \\ \mathbf{C}^T(2) \\ \vdots \\ \mathbf{C}^T(K) \end{bmatrix} \tag{16}$$

and defining a data matrix

$$\tilde{\mathbf{C}} \triangleq \frac{1}{\sqrt{K}}\begin{bmatrix} c_1(1) & c_1(2) & \cdots & c_1(K) \\ c_2(1) & c_2(2) & \cdots & c_2(K) \\ \vdots & \vdots & \vdots & \vdots \\ c_N(1) & c_N(2) & \cdots & c_N(K) \end{bmatrix}, \tag{17}$$

we can write $\hat{\mathbf{R}}_x = \tilde{\mathbf{C}}\tilde{\mathbf{C}}^T$. Note that $\tilde{\mathbf{C}}$ is $(N \times K)$ and $\tilde{\mathbf{C}}^T$ is $(K \times N)$ so that $\hat{\mathbf{R}}_x$ is $(N \times N)$ as required. We can generate random vectors having covariance $\hat{\mathbf{R}}_x$ by multiplying a random zero mean white sequence $\mathbf{W}$ of dimension $(K \times 1)$ by $\tilde{\mathbf{C}}$, as may be seen from the following:

$$\mathbf{Y} \triangleq \tilde{\mathbf{C}}\mathbf{W}, \quad E[\mathbf{W}\mathbf{W}^T] = \mathbf{I}, \tag{18}$$

where $\mathbf{I}$ is a $(K \times K)$ identity matrix, and

$$E\{\mathbf{Y}\mathbf{Y}^T\} = E\{\tilde{\mathbf{C}}\mathbf{W}\mathbf{W}^T\tilde{\mathbf{C}}^T\} = \tilde{\mathbf{C}}E\{\mathbf{W}\mathbf{W}^T\}\tilde{\mathbf{C}}^T = \hat{\mathbf{R}}_x. \tag{19}$$

The vector $(\overline{\mathbf{C}} + \tilde{\mathbf{C}}\mathbf{W})$ will be a statistically valid random realization of a SSP at a particular location and particular time in the tidal cycle. Correlations in range and time were introduced by making the random vector $\mathbf{W}$ correlated in range and time.

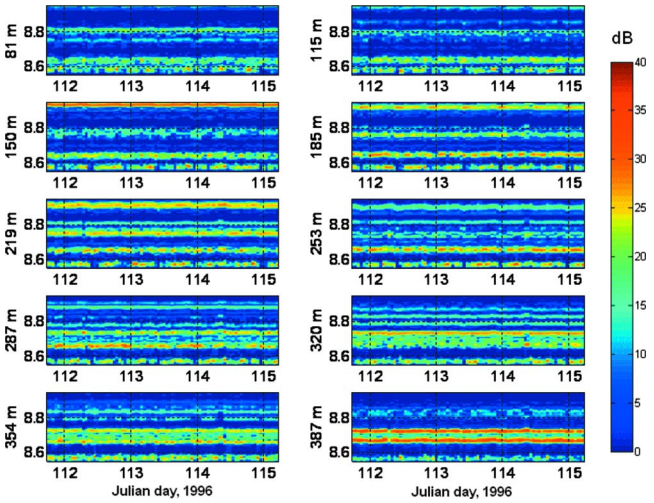


FIG. 13. (Color online) Matched filter output (dB) for simulated signals produced using the mean (but time and space-varying) sound speed profiles from CTD drops, with uncertainty included as described by Eqs. (18) and (19) in the text.

A mean range- and time-dependent SSP field was calculated using Eq. (14) and the CTD data. The MF output is almost identical to that obtained using the SSP model (Fig. 10) and is not shown here. The first arrival amplitude pdf was calculated and is shown in Fig. 11(c), and the corresponding ROC curve is shown in the curve labeled (c) in Fig. 12. There is a little difference between the pdf's calculated using the SSP model and the mean CTD data. The ROC curves labeled (b) and (c) in Fig. 12 are likewise similar, although the data-derived SSP field does produce slightly better performance, though still no better than a coin flip.

The final effort was to produce a set of time- and space-dependent SSP fields whose mean values were calculated from the CTD drops, and including uncertainty in the manner described by Eqs. (18) and (19). The resulting MF output is shown in Fig. 13, and the pdf and ROC curves are shown in Figs. 11(d) and the labeled (d) curve in Fig. 12, respectively. The effect of adding uncertainty has been to improve the match between the predicted and in-water pdf's, and to improve the ROC curve such that the processor performance approaches that obtained when the in-water measurements are used to form the LLR processor. The prediction is not perfect and the processor performance is not outstanding; however, we suspect that marginally better performance could be obtained with different CTD groupings or reference to oceanographic models.

VII. CORRELATION LOSS OF LATER ARRIVALS

Returning to the anomalously high late arrivals evident in the predicted MF output (Fig. 10), errors in bathymetry or bottom loss do not seem to be likely causes for the 5–15 dB discrepancy. Another possibility is that time and frequency spread induced by motion of the medium, and surface and bottom interaction, may be causing correlation loss in the received signals which is not accounted for in the propagation model. Weston (1965) described how signals that are forward-scattered by a rough surface are subject to *time spread*, which causes loss of correlation relative to the trans-

mitted signal. Time spreading of signals forward-scattered by the ocean surface has been measured and modeled for high frequency signals by Dahl (2004). Reeves (1974), and Culver and Bradley (2005) published measurements showing that correlation loss of broadband high frequency acoustic signals forward-scattered by the ocean surface increased with signal bandwidth. Similarly, signals that are forward-scattered by moving surfaces are subject to *frequency spread*, which causes correlation loss that increases with signal length.

Decorrelation of signals due to boundary interaction is very different from the temporal correlation[3] investigated by other authors (e.g., Yang, 2006), which measures the degree to which *a received signal remains correlated with itself* as a function of delay between the time that two signals are transmitted. Usually temporal correlation is calculated by integrating over an interval that includes the DP and a few boundary-interacting paths or modes, causing it to be dominated by the ping-to-ping correlation of the earliest arrival, which is usually the strongest. The *correlation time* is a scalar measure of how fast temporal correlation decreases, and is commonly defined as the time required for the correlation to drop by a factor of e^{-1}. Correlation times of tens of minutes have been reported for frequencies below 500 Hz, propagation ranges of 10–40 km, and water depths of 50–100 m (Yang, 2006). In contrast, the correlation loss considered here is due to loss of correlation *between the transmitted and received signals*. Perhaps more similar to this boundary-interaction driven correlation loss are measurements of temporal correlation for higher order modes alone, which show considerably lower correlation times. For example, Rouseff (2002) reported 1–2 min correlation times for modes 2 and 3 measured in SWARM 95 in 50 m deep water. He attributed the decorrelation in this case to internal waves propagating through the medium, which cause mode coupling (transfer of energy from one mode to another).

Therefore it seems reasonable that the later arrivals in Fig. 7 are lower due to correlation loss caused by time and frequency spread induced by scattering at the surface and bottom. Although correlation loss has been shown to increase with bandwidth and signal duration, the authors are not aware of a predictive model for the bandwidth and pulse length-dependent correlation loss of low frequency signals forward-scattered by the ocean surface or bottom.

VIII. DISCUSSION

The results shown here indicate how an accurate statistical model for received signal amplitude can be used to distinguish between (or classify) signals originating from different depths on the opposite side of Strait of Gibraltar. Accurate signal amplitude statistics can be calculated from SSP statistics provided the latter accurately reflect the time and spatial dependences of sound speed in the areas of the water column through which sound travels from source to receiver, as well as the uncertainty associated with the sound speed values. However, the SSPs used in the analysis are based on more than 100 CTD drops and required many days of ship time to acquire, and it is unrealistic to expect this quantity of resources to be available to measure sound speed at all areas of the ocean that are of interest to the United States Navy. So is this work of any value? The answer is that it can become useful to the operational United States Navy if probabilistic SSP description can be developed from many fewer CTD drops combined with knowledge of the oceanography and oceanographic processes. In addition, there are much faster methods of measuring sound over a large area. Gliders are now being used to measure sound speed field over long distances, albeit somewhat sparsely in range (Rudnick *et al.*, 2004), and a string of towed CTD sensors can be used to measure sound speed field with high resolution in range and depth (Lyons, 2004). Both instruments provide information about the sound speed field with higher spatial and temporal resolutions than was heretofore available, but there remains a need for physics-based oceanographic models that predict time- and space-varying SSPs from knowledge of regional circulation, local currents, tides, bathymetry, and sea surface measurements of temperature and elevation. Such models cannot be completely deterministic, and must include estimates of the uncertainty associated with predicted values.

Operational passive sonar tracking events typically evolve on a scale of tens of minutes to an hour or more and extend over distances (in a frequency-dependent manner) out to as much as hundreds of kilometers. Sonar signal processors such as the EOD will require signal parameter statistical models that predict variation over the same space and time intervals. Statistical models that describe environmental parameter variability over time intervals down to fractions of an hour will be needed. The 1–2 h CTD sampling interval used in the SGAME was sufficient to capture the variability seen in hourly acoustic transmissions, but insufficient to capture acoustic variability that might be observed over a period of minutes. Thus physics-based models for environmental variability over order of 5 min intervals are needed to predict variability affecting passive sonar tracking over periods of about 1 h.

Correlation loss between transmitted and received signals appears to be responsible for the predicted levels of the later arrivals being much higher than the measured values. Correlation loss may be important in situations where the multipath is strong relative to the DP, for example, downward refracting environments and shallow sources and receivers. Studies at higher frequencies have shown that correlation loss increases with signal bandwidth because scattering from rough boundaries varies across frequency (e.g., Culver and Bradley, 2005). By hypothesis, correlation loss will also increase with pulse duration because scattering from moving boundaries changes with time. The authors know of no low frequency (<1 kHz) boundary reflection correlation loss model that parametrizes loss with bandwidth, pulse duration, and boundary conditions. This seems to be an area where further research is needed.

IX. SUMMARY

A new signal processing architecture has been developed that can provide improved detection and classification per-

formance by utilizing *a priori* statistical information about the received signal. We have shown how statistical signal models that resolve variability over a specified temporal and/or spatial interval can be obtained using statistical environmental models with the same temporal and spatial resolutions. For passive sonar operation, the order 1 km and 5 min space/time resolution required in the signal model must be represented in the environmental model. Despite new methods that allow larger areas of the ocean to be sampled more rapidly than ever before, it is still impractical to obtain empirical high resolution environmental models by comprehensive measurements at all times and locations of interest; oceanographic knowledge and models must be employed to predict how the environment varies over space and time.

Additionally, we have shown the importance of understanding the loss of correlation between a transmitted signal and signals that have been forward-reflected by rough and/or time-varying surfaces. A low frequency (<1 kHz) model for correlation loss dependence on surface condition and pulse bandwidth and duration is indicated as a research need.

ACKNOWLEDGMENTS

This work was sponsored by the Office of Naval Research Undersea Signal Processing under Grant No. N00014-07-1-0047. The authors are grateful to Leon Sibul for his vision of the EOD, and wish to thank Colin Jemmott, Jeffrey Ballard, and Dr. Nirmal Bose for many helpful discussions. The authors are indebted to Dr. Chris Tiemann of ARL:UT and Dr. Peter Worcester of SIO for providing the 1996 Strait of Gibraltar Acoustic Monitoring Experiment (SGAME) data and helping with its interpretation.

[1]The *process* model describes the temporal evolution of state variables such as source position, heading, and speed, while the *measurement* model relates the state variables to measured quantities such as bearing and range.

[2]The term profile indicates that the model describes how sound speed varies with depth.

[3]Some authors prefer the term "coherence" over correlation.

Arulampalam, M. S., Maskell, S., Gordon, N., and Clapp, T. (**2002**). "A tutorial on particle filters for online nonlinear/non-Gaussian Bayesian tracking," IEEE Trans. Signal Process. **50**, 174–188.

Ballard, J. A., Jemmott, C. W., Sibul, L. H., Culver, R. L., and Camin, H. J. (**2006**). "The estimated ocean detector: Derivation and predicted performance under gaussian assumptions," Proceedings of the MTS/IEEE OCEANS 2006 Conference, Boston, MA, 18–26 September.

Ballard, J. A. (**2007**). "The estimated signal parameter detector: Incorporating acoustic variability into the signal processing to detect stochastic signals based on the received statistics," M.S. thesis, The Pennsylvania State University, State College, PA.

Burdic, W. (**1990**). *Underwater Acoustic System Analysis*, 2nd ed. (Prentice-Hall, Englewood Cliffs, NJ), pp. 134–136.

Candy, J. V. (**2005**). *Model-Based Signal Processing* (Wiley, New York).

Collins, M. (**1993**). "A split-step Padá solution for the parabolic equation method," J. Acoust. Soc. Am. **93**, 1736–1742.

Cotte, B., Culver, R. L., and Bradley, D. L. (**2007**). "Scintillation index of high frequency acoustic signals forward scattered by the ocean surface," J. Acoust. Soc. Am. **121**, 120–131.

Culver, R. L., and Bradley, D. L. (**2005**). "On the relationship between signal bandwidth and frequency correlation for ocean surface forward scattered signals," J. Acoust. Soc. Am. **118**, 129–138.

Dahl, P. H. (**2004**). "Forward scattering from the sea surface and the van Cittert-Zernike theorem," J. Acoust. Soc. Am. **115**, 589–599.

Dosso, S. E., Giles, P. M., Brooke, G. H., McCammon, D. F., Pecknold, S., and Hines, P. C. (**2007**). "Linear and nonlinear measures of ocean acoustic environmental sensitivity," J. Acoust. Soc. Am. **121**, 42–45.

Farmer, D. M., and Armi, L. (**1988**). "The flow of Atlantic water through the Strait of Gibraltar," Prog. Oceanogr. **21**, 1–105.

Finette, S. (**2006**). "A stochastic representation of environmental uncertainty and its coupling to acoustic wave propagation in ocean waveguides," J. Acoust. Soc. Am. **120**, 2567–2579.

Habgood, E. L., Kenyon, N. H., Masson, D. G., Akhmetzhanov, A., Weaver, P. P. E., Gardner, J., and Mulder, T. (**2003**). "Deep-water sediment wave fields, bottom current sand channels and gravity flow channel-lobe systems: Gulf of Cadiz, NE Atlantic," Sedimentology **50**, 483–510.

James, K. R., and Dowling, D. R. (**2005**). "A probability density function method for acoustic field uncertainty analysis," J. Acoust. Soc. Am. **118**, 2802–2810.

Kapur, J., and Kesavan, H. (**1992**). *Entropy Optimization, Principles With Applications* (Academic, Boston, MA), pp. 133–142.

Lyons, J. E. (**2004**). "The effect of ocean variability on acoustic variability: Tilt and spice," M.S. thesis, The Pennsylvania State University, State College, PA.

Reeves, J. C. (**1974**). "Distortion of acoustic pulses reflected from the sea surface," Ph.D. thesis, University of California, Los Angeles, CA.

Richardson, A. M., and Nolte, L. W. (**1991**). "A posteriori probability source localization in an uncertain sound speed, deep ocean environment," J. Acoust. Soc. Am. **89**, 2280–2284.

Robinson, A., Abbot, P., Lermusiaux, P., and Dillman, L. (**2002**). "Transfer of uncertainties through physical-acoustical-sonar end-to-end systems: A conceptual basis," in *Impact of Littoral Environmental Variability on Acoustic Predictions and Sonar Performance*, edited by N. G. Pace and F. B. Jensen (Kluwer, Dordrecht), pp. 603–610.

Rudnick, D. L., Davis, R. E., Eriksen, C. C., Fratantoni, D. M., and Perry, M. J. (**2004**). "Underwater gliders for ocean research," Mar. Technol. Soc. J. **38**, 73–84.

Rouseff, D. (**2002**). "Coherence of acoustic modes propagating through shallow water internal waves," J. Acoust. Soc. Am. **111**, 1655–1666.

Schwartz, S. C. (**1977**). "The estimator-correlator for discrete-time problems," IEEE Trans. Inf. Theory **IT-23**, 93–100.

Sha, L., and Nolte, L. W. (**2005a**). "Effects of environmental uncertainties on sonar detection performance prediction," J. Acoust. Soc. Am. **117**, 1942–1953.

Sha, L., and Nolte, L. W. (**2005b**). "Bayesian sonar detection performance prediction in the presence of interference in uncertain environments," J. Acoust. Soc. Am. **117**, 1954–1964.

Sha, L., and Nolte, L. W. (**2006**). "Bayesian sonar detection performance prediction sixth source position uncertainty using SWellEX-96 vertical array data," IEEE J. Ocean. Eng. **31**, 345–355.

Sibul, L. H. (**2006**). "Overview of signal processing in uncertain and random environments," J. Acoust. Soc. Am. **119**, 3342.

Song, B. G., and Ritcey, J. A. (**1996**). "Angle of arrival estimation of plane waves propagating in random media," J. Acoust. Soc. Am. **99**, 1370–1379.

Tiemann, C., Worcester, P., and Cornuelle, B. (**2001a**). "Acoustic scattering by internal solitary waves in the Strait of Gibraltar," J. Acoust. Soc. Am. **109**, 143–154.

Tiemann, C., Worcester, P., and Cornuelle, B. (**2001b**). "Acoustic remote sensing of internal solitary waves and internal tides in the Strait of Gibraltar," J. Acoust. Soc. Am. **110**, 798–811.

Urban, C. D. (**1990**). "Design and evaluation of a tactical decision aid," Proceedings of the IEEE International Conference on Systems, Man and Cybernetics, 4–7 November.

Van Trees, H. (**2001**). *Detection, Estimation, and Modulation Theory: Part I* (Wiley, New York).

Van Trees, H. L. (**2002**). *Optimum Array Processing* (Wiley, New York).

Wang, D., Lermusiaux, P. F. J., Haley, P. J., Leslie, W. G., and Schmidt, H. (**2006**). "Adaptive acoustical-environmental assessment for the focused acoustic field-05 at-sea exercise," Proceedings of the MTS/IEEE OCEANS 2006 Conference, Boston, MA, 18–26 September.

Washington, P. J. (**2004**). "MODAS: The warfighters' view of the undersea environment," *The Navigator* (NAVO MSRC, Stennis Space Center, MS).

Weston, D. E. (**1965**). "Correlation loss in echo ranging," J. Acoust. Soc. Am. **37**, 119–124.

Yang, T. C. (**2006**). "Measurements of temporal coherence of sound transmissions through shallow water," J. Acoust. Soc. Am. **120**, 2595–2614.

Low probability of detection underwater acoustic communications using direct-sequence spread spectrum

T. C. Yang[a)]
Naval Research Laboratory, Washington, DC 20375

Wen-Bin Yang
National Institute of Standards and Technology, Gaithersburg, Maryland 20899

(Received 23 May 2008; revised 3 September 2008; accepted 4 September 2008)

Direct-sequence spread spectrum is used for underwater acoustic communications between nodes, at least one of which is moving. At-sea data show that the phase change due to source motion is significant: The differential phase between two adjacent symbols is often larger than the phase difference between symbols. This poses a challenge to phase-detection based receiver algorithms when the source or receiver is moving. A pair of energy detectors that are insensitive to the phase fluctuations is proposed, whose outputs are used to determine the relationship between adjacent symbols. Good performance is achieved for a signal-to-noise ratio (SNR) as low as −10 dB based on at-sea data. While the method can be applied to signaling using short code sequences, the focus in this paper is on long code sequences for the purpose of achieving a high processing gain (at the expense of a low data rate), so that communications can be carried out at a low input SNR to minimize the probability of detection (P_D) by an interceptor. P_D is calculated for a typical shallow water environment as a function of range for several source levels assuming a broadband energy detector with a known signal bandwidth. [DOI: 10.1121/1.2996329]

PACS number(s): 43.60.Dh [EJS] Pages: 3632–3647

I. INTRODUCTION

Direct-sequence spread-spectrum (DSSS) signaling uses phase coherent signals where the information symbols are multiplied with a code sequence, commonly known as chips.[1] The signals are processed at the receiver using the code sequence as a matched filter to extract the information symbols.[1–3] Taking advantage of the processing gain derived from the matched filter, communications can be carried out at low signal levels (e.g., below the noise level) to avoid detection and interception by an unfriendly party. This paper examines the probability of detection and counterdetection range for DSSS signaling in an underwater acoustic environment for acoustic communications involving mobile platforms. As is expected, the probability of detection, as well as the probability of interception, is very much dependent on the input signal-to-noise ratio (SNR) at the interceptor[4,5] and the recognition differential of the signal waveform. The fact that a low level source can be used for DSSS communications and that the signal is noiselike presents certain advantages from the point of view of low probability of detection (LPD). This topic will be analyzed later in this paper.

The problem for DSSS communications in an underwater acoustic channel is the multipath arrivals, which create severe interchip and intersymbol interferences. Decision feedback equalizer (DFE) and Rake receiver have been adapted for DSSS communications.[6,7] To achieve precise symbol synchronization and channel equalization, high SNR signals are required.[8] Recently, Yang and Yang[9,10] have demonstrated two new approaches for low input-SNR DSSS communications in a dynamic ocean environment between fixed nodes. Minimal (<1%) bit error rate (BER) can be achieved for in-band SNR as low as −11 to −14 dB. Signal phase distortion due to signal propagation in a random medium, achievable matched-filter gain (the ratio of output signal level to input signal level), and achievable processing gain (the ratio of output SNR to input SNR) were measured from data. Performance degradation of the receiver algorithm due to coarse synchronization at low input SNRs, signal fading, and imprecise knowledge of the channel were modeled and compared with data.

The DSSS signaling method uses code "orthogonality" to minimize interference between symbols. The code orthogonality requires that the code sequence is almost orthogonal to any of the cyclically shifted code sequences. With orthogonality, the matched-filter output yields a low sidelobe level and thus ensures minimum interference in a simple environment (dominated by a single path). It assures accurate symbol synchronization. The phase of the matched-filter output can then be used to determine the symbol sequence. In an underwater acoustic channel containing many multipath arrivals, the code orthogonality is severely degraded resulting in interchip interference. The phase is often path dependent and changing rapidly with time. At-sea data showed that the symbol phase error estimated from the matched-filter output is often larger than the phase difference between the symbols, resulting in unacceptable bit errors even with a high input SNR.[9,10] The challenge is to develop a receiver algorithm, patterned after the simple DSSS signal processing mentioned above, without employing a DFE to equalize the multipath arrivals, and a phase-locked loop (PLL) to remove/compensate the phase fluctuations in a dy-

[a)]Electronic mail: yang@wave.nrl.navy.mil

namic ocean. Toward this goal, a second layer of correlator, which cross-correlates the matched-filter outputs of two adjacent symbols, was implemented by Yang and Yang,[9,10] to estimate their differential phase. This method requires only "coarse" synchronization at the symbol level and is applicable to low input-SNR communications between fixed nodes.

In practice, underwater acoustic communications often involve mobile platforms. For DSSS signaling, Doppler shift, if not corrected for, destroys the orthogonality of the code sequences between the replica signal and data, and between code sequences of different users. In addition, the signal coherence time is significantly reduced due to the source/receiver motion.[11] The reason is traced to the rapidly fluctuating (relative) phases of the multipaths. As a symbol phase is determined by interference between the multipaths, medium fluctuation causes a symbol phase to change with time. For a moving source, the individual paths encounter, in addition, a different phase change (ray path-length change) due to source changing range. A higher rate of phase fluctuation is thus expected, resulting in a shorter coherence time for a moving source than for a fixed source. One finds[9,10] for a fixed source/receiver pair that while the phase of individual symbols changes rapidly with time, the differential phase between the symbols is relatively small. In contrast, the analysis below will show that, for the moving-source data, after proper Doppler compensation, the differential phase between symbols changes rapidly with time, and is often larger than the phase difference between true symbols even with a high input SNR. Hence, while differential phase shift keying (DPSK) can be used to decode the signal for the fixed-source data, this method (based on the differential phase) is expected to encounter high bit errors when applied to the moving-source data.

For DSSS signaling involving a mobile platform, a new method, which is insensitive to the phase fluctuation, is developed in this paper and applied to at-sea data. This method can also be applied to fixed-source data. It will be shown below that the method, applied to the fixed-source data reported previously, yields a slightly degraded, but still satisfactory, performance compared with the method mentioned above.

Like the cross-correlation method, the new method can be applied to DSSS signals with short or long code sequences so long as the code length is longer than the multipath spread. Similar to the previous work,[9,10] the focus of this paper is on communications with a long code sequence for the purpose of LPD. A long sequence yields a high processing gain, which allows communications using a low source level (SL), thus minimizing the probability of detection by a hostile party.[9,10] For a given bandwidth, longer sequences imply lower data rates. One can increase the data rate through other means, such as spreading the data over multiple orthogonal codes at the price of a slightly higher SL. That topic is beyond the scope of this paper.

This paper is organized as follows: In Sec. II the characteristics of a signal emitted from a moving source are analyzed, including the fluctuation of the Doppler shift found in the data. In Sec. III, the phase insensitive method is presented, tested against the fixed-source data, and then applied to the moving-source data. In Sec. IV, the probability of detection and the probability of false alarm are analyzed for an energy detector assuming the interceptor has no knowledge of the signal waveform and signal parameter. The ability to communicate with a lower SL using the DSSS signaling is shown to significantly reduce the probability of detection by an interceptor.

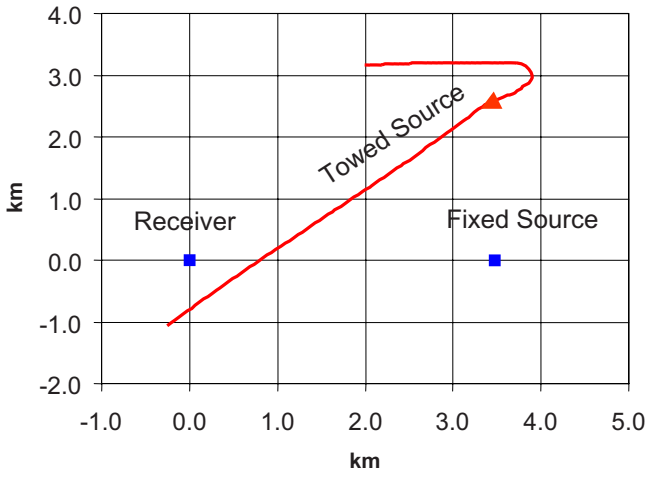


FIG. 1. (Color online) Source-receiver geometry including the towed source run.

Regarding LPD underwater acoustic communications, a simple system concept may be helpful to motivate and guide the analysis below. A potential scenario for LPD communications will be cooperative operation between autonomous underwater vehicles (AUVs), which stay together within a certain range from each other and use LPD acoustic communications to avoid detection by a nearby interceptor. From the system point of view, the SL needs to be high enough to assure reliable communications with neighboring AUVs, and yet low enough so not to alert the interceptor of their presence. The question is at what range will the detection (by the interceptor) become unavoidable, i.e., the counterdetection range. Counterdetection range is calculated in Sec. IV for a typical shallow water environment assuming certain system parameters.

II. SIGNAL CHARACTERISTICS

The data were taken during the TREX04 (time reversal experiment) conducted by the Naval Research Laboratory in April 2004, off the coast of New Jersey, southwest of the Hudson Canyon. The sound speed profile presented a minimum in the middle of the water column (see Fig. 1, Ref. 10). Acoustic communication data were transmitted from a fixed source to a fixed-receiver array at the range of 3.4 km, and from a towed source to the fixed receiver as shown in Fig. 1. The water depth in the experimental area is about 70 m. The fixed source and receivers were located at about 35 m depth. The towed source was at a depth of approximately 20 m. The vertical array has an aperture of approximately 2 m and contains eight hydrophones with nonuniform spacing. Only one receiver is used for communications from the fixed and towed sources.

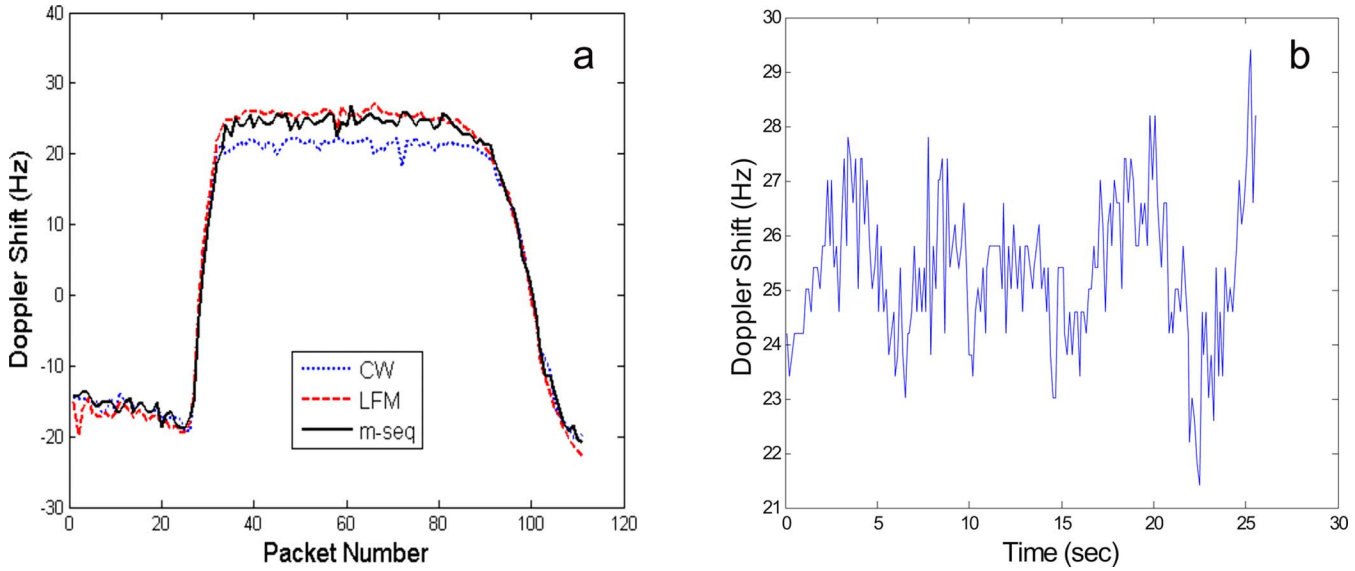


FIG. 2. (Color online) Estimation of the mean Doppler shift over a packet as a function of packet number using different signals (a). Instantaneous Doppler shift within a packet based on *m*-sequence ambiguity function (b).

The DSSS signals were centered at 17 kHz and had a bandwidth of 4 kHz. The transmitted symbols were spread with (multiplied by) an *m*-sequence containing 511 chips yielding a theoretical processing gain of 27 dB at the receiver. The sequence of chips coded with the message data was then transmitted using binary phase-shift-keying modulation. Each symbol has a duration of 127.8 ms, yielding a data rate of ~8 bits/s. So long as the symbol duration is longer than the multipath spread, the interference between adjacent symbols is minimal. [For example, see Fig. 1(b) of Ref. 10.] Each packet contains 200 symbols lasting approximately 25.55 s. A total of 111 packets were transmitted over approximately an hour. The signal properties are discussed in this section. BERs are reported in the next section.

In this experiment, some auxiliary signals, such as pilot tones and linear frequency modulation (LFM) signals, were added to each packet for independent probing of the channel properties. Pilot tones signals shall not be used for DSSS communications at a low SNR. Data acquisition and symbol synchronization can be done by matched filtering the data with the LFM or *m*-sequence replicas.[9,10]

A. Doppler shift

A key feature of the moving-source data is the Doppler shift/spread. The Doppler shift is path dependent as multipaths arrive with different depression/elevation (D/E) angles. At long ranges, the multipaths are confined to shallow ($<10°$) D/E angles as deep D/E angle paths are attenuated by the bottom. Under these conditions, one can assume the same Doppler shift for all the paths. At short ranges, both shallow and deep rays exist. As a result, the path-dependent Doppler shifts create a (large) Doppler spread. Note that an individual path may also have a Doppler spread due to scattering with ocean medium and/or surface. The path-dependent Doppler spread, most notable at short ranges, can be (much) larger than the medium/boundary induced Doppler spread.

The first task in the data analysis is Doppler estimation as the data have to be corrected for the Doppler shift.[12] The temporal variation of the Doppler shift on the scale of the order of a minute can be obtained by measuring the average Doppler shift for each packet. Three methods are used to estimate the average Doppler shift. The first method determines the average Doppler shift from the pilot tones, which were placed above and below the DSSS signal band. The result is shown as the dotted line in Fig. 2(a). The second method determines the average Doppler shift from the time separation between the two LFM signals placed before and after the data packet measured against that of the transmitted signal. The measured Doppler shift is shown as the dashed line in Fig. 2(a). The third method measures the Doppler shift from each *m*-sequence. The input data are bandpass filtered and shifted to the base band. The base band data are synchronized and partitioned into (overlaying) blocks, each containing one *m*-sequence. A wideband ambiguity function is created for each block of data by correlating the data with a Doppler-shifted transmitted *m*-sequence signal. The output is an impulse response as a function of Doppler shift and delay time, referred to as the ambiguity function. The peak of the ambiguity surface determines the Doppler shift for the data block. The measured Doppler shift as a function of the block (or sequence) number is shown in Fig. 2(b) using one packet of data as an example. The Doppler shift is averaged for each packet, and the result is shown in Fig. 2(a) by the solid line as a function of packet number.

Based on the source track in Fig. 1, the source moved out initially by an opening range. It turned around at a range about 5 km and moved toward the receiver; it reached a closest point of approach near the end of the run. [The source-receiver range is shown in Fig. 3(a) as a function of the packet number.] One thus expects initially a negative Doppler shift, which should change into a positive Doppler shift and then crosses over into a negative Doppler shift again. This is in accord with the measured Doppler shift. One finds

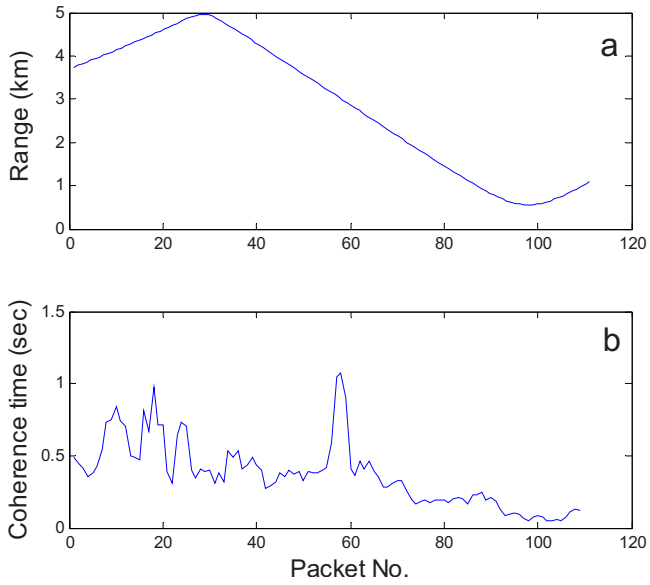


FIG. 3. (Color online) Source-receiver range as a function of time (packet number) (a). Signal coherence time as a function of time (packet number) (b).

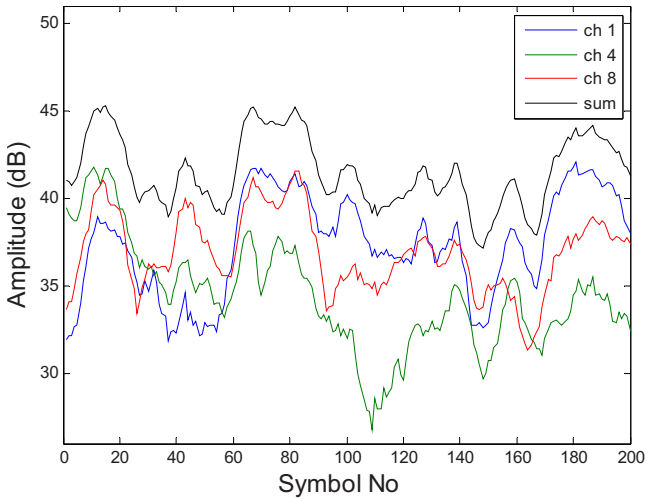


FIG. 4. (Color online) Signal amplitude as a function of time within a packet for three selected receivers.

that the Doppler shift measured from the LFM and *m*-sequence signals agree relatively well with each other. The measurement using the pilot tones is somewhat (a few hertz) lower than using LFM and *m*-sequence. The reason is the ambiguity in the spectral determination of the Doppler shift. Using the spectral analysis, an integration time of 2 s is required, for example, to achieve a Doppler resolution of 0.5 Hz. However, during the 2 s period, the Doppler shift changes with time as shown next.

Figure 2(b) shows the Doppler shift within a packet. One may expect the Doppler shift to vary slowly with time [based on Fig. 2(a)], and be surprised that the Doppler shift varies by 3–5 Hz with a period of 4–7 s. This variation is attributed to the heave motion of the ship, which was observed during the experiment, and expected to cause the tow body to speed up and down with the ship motion. For data processing, what is significant is that the Doppler shift varies from symbol to symbol [Fig. 2(b)]; each symbol is ~128 ms long. This requires the Doppler shift to be estimated for every symbol, which increases significantly the data processing load.

B. Temporal coherence: Signal coherence time

The Doppler corrected impulse responses are used to estimate the temporal coherence of the *m*-sequence signals as defined by

$$\rho(\tau) = \frac{[p^*(t)p(t+\tau)]}{\sqrt{[p^*(t)p(t)][p^*(t+\tau)p(t+\tau)]}}, \quad (1)$$

where $p(t)$ and $p(t+\tau)$ are the impulse responses of the two consecutive *m*-sequences separated by a lag time τ; t is the sample time of the impulse response. The square bracket $[ab]$ denotes the maximum absolute value of the correlation between $a(t)$ and $b(t)$. (For the measurement of the impulse response and temporal coherence using *m*-sequences, the reader is referred to Ref. 13.) The signal coherence time $\tau_{0.8}$ is defined as the lag time when the coherence value drops from 1 to 0.8. Temporal coherence of the *m*-sequence signal is measured for each packet and the measured signal coherence time is shown as a function of packet number in Fig. 3(b).

One finds in Fig. 3(b) that the signal coherence time at close ranges (<1 km) is ~0.1 s compared with the signal coherence time at 3 km, which is of the order of 0.5 s. Note that the signal coherence time is inversely proportional to the signal Doppler spread. At close ranges, the multipaths have different Doppler shifts, resulting in a decreased coherence time. Later in Sec. III, it will be shown that the "large" Doppler spread presents a problem for Doppler compensation and is responsible for degraded BER performance at close ranges.

C. Signal-fading statistics

Figure 4 shows an example of the time variation of the symbol amplitude using one packet of data. The amplitude variation is shown for three receivers spaced by approximately 0.3 m, as well as the amplitude of the linear sum of the pressure fields on all eight receivers. Fading by as much as 10–20 dB is seen in the data. Since detection performance is affected by signal fading, one needs to examine the signal-fading statistics for a moving source (on a single receiver). For amplitude statistics, the amplitude is estimated from the square root of the symbol energy, conventionally denoted as E_b. Figure 5(a) shows the symbol amplitude distribution at a fixed range of 3.4 km (Fig. 10 of Ref. 10). It was found consistent with a log-normal distribution

$$p(s) = \frac{1}{\sqrt{2\pi}\sigma_s} s^{-1} \exp\left(-\frac{(\ln s - \mu_s)^2}{2\sigma_s^2}\right), \quad (2)$$

where s is the signal amplitude; $s>0$. The mean and variance of the signal amplitude are expressed in terms of two parameters, μ_s and σ_s, as follows:

$$m_s = \exp(\mu_s + \sigma_s^2/2),$$

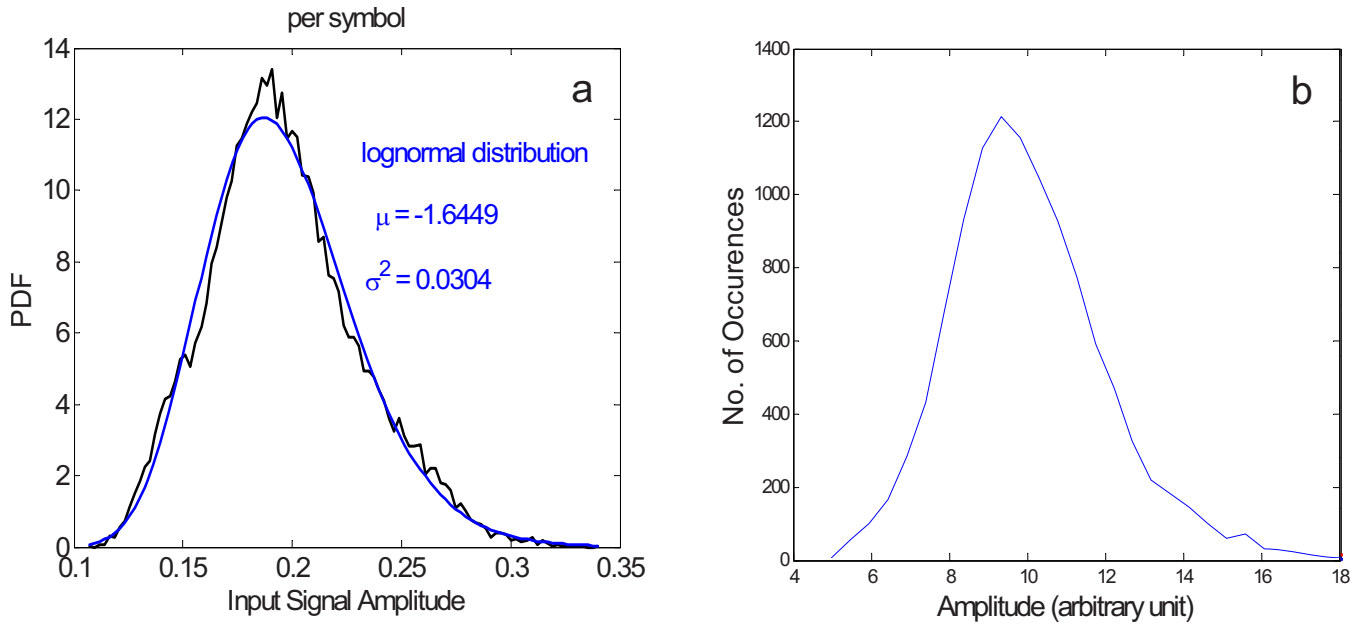


FIG. 5. (Color online) Probability distribution of signal amplitude for fixed-source data compared with the log-normal distribution (a) and histogram distribution of signal amplitude from the moving-source data (b).

$$v_s^2 = \exp(2\mu_s + \sigma_s^2)[\exp(\sigma_s^2) - 1].$$

The data were fitted in Fig. 5(a) using $\mu_s = -1.6449$ and $\sigma_s^2 = 0.0304$; the corresponding mean signal level and its variance are $m_s = 0.196$ and $v_s^2 = 1.186 \times 10^{-3}$.

One can generalize Eq. (2) to model the data from a moving source, such as communication data from an autonomous underwater vehicle. As the range changes from r_1 to r_2, the amplitude-fading statistics will be a weighted average as

$$p(s) = \int_{m_1}^{m_2} p(m_s) p_S(s|m_s) dm_s, \tag{3}$$

where m_1 and m_2 are the mean signal level at ranges r_1 and r_2, respectively, $p(m_s)$ is the probability function for the mean signal level over the range track, and $p_s(s|m_s)$ is the amplitude-fading distribution given in Eq. (2). The resulting amplitude-fading statistics is not expected to be log-normal unless m is nearly constant.

Figure 5(b) shows the histogram distribution of the symbol amplitude determined from the packets transmitted when the source moves from 5 to 0.5 km. Compared with Fig. 5(a), one finds that the two distributions are similar. One observes that the mean signal energy of the packets fluctuates by ± 3 dB over the track. This small variation (limited range change) is the reason for the qualitatively similar distributions between Figs. 5(a) and 5(b).

III. PHASE ERROR, TRANSITION DETECTOR, AND BER ANALYSIS

A. Symbol phase error

Figure 6(a) shows the differential-phase error between symbols (the error of the differential phase of symbols between data and transmitted signal) determined from the fixed source/receiver data [repeated from Fig. 6(b) of Ref. 10]. As discussed above, the differential phase is determined from the peak of the cross correlation of the matched-filter outputs of two adjacent symbols. The cross correlation of the matched-filter outputs yields $(h_i^* h_{i+1}) S_i^* S_{i+1}$ plus terms containing noise,[10] which will be ignored for the moment, where h_i is the channel impulse response for the ith symbol, denoted by S_i. Assuming that the channel has not changed much within the time period of two symbols, i.e., $h_i^* h_{i+1} \sim I$, one can estimate the differential phase between the two symbols from the cross-correlation result. This is a simple way to estimate the symbol differential phase without requiring a channel equalizer. The differential-phase error [shown in Fig. 6(a)] is obtained by subtracting the true differential phase (between the two symbols) from the measured differential phase. The small differential-phase error (smaller than the phase difference between symbols, i.e., $\pm 90°$) suggests that for the fixed-source data, the symbol phase error can be corrected using a PLL. For practical applications where processing power is limited, it is much simpler to use DPSK signaling without requiring the PLL. For the data shown in Fig. 6(a), there is no bit error since the phase error is $< \pm 90°$.

When either of the source and receiver is moving, one needs to estimate the Doppler shift for each symbol (as discussed above) and apply Doppler correction (including both carrier phase offset and symbol dilatation) to the data. A block diagram for the processing is shown in Fig. 7. For details see Sec. III C. Applying this method to the moving-source data, one can deduce the differential-phase error of symbols as shown in Fig. 6(b). It shows that a high percentage of the symbols are in error for the moving-source data. As explained above, the symbol phase is rapidly changing for a moving source since the phase of each individual path is varying with time. The interference among the time-varying multipath arrivals results in a fast changing differential phase between symbols. To mitigate the fast changing symbol phase, an energy detector that is insensitive to the symbol phase fluctuations is proposed below.

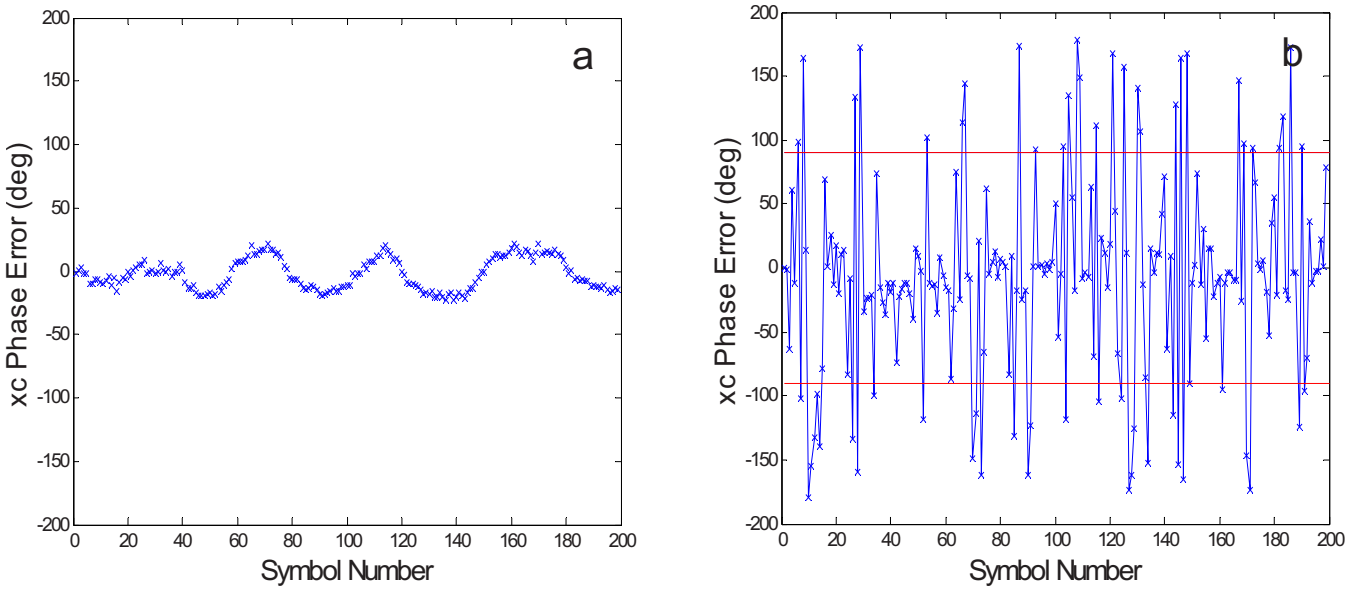


FIG. 6. (Color online) Differential symbol phase error as function of symbol number: fixed-source data (a) and moving-source data (b). Fixed-source data are reproduced from Ref. 10. Moving-source data points (×) are connected by lines to show the magnitude of the phase variation.

B. Transition detectors

In a time-invariant environment without multipaths, one could determine the next symbol from the current symbol using a pair of code sequences proposed previously,[14]

$$T_+ = [C, C] \quad \text{and} \quad T_- = [C, -C], \tag{4}$$

where C is the code sequence expressed as a row vector. The data, after proper synchronization and Doppler correction, are divided into blocks. The data blocks containing two symbols can be expressed as

$$d = [s_n C e^{i\theta_n}, s_{n+1} C e^{i\theta_{n+1}}] + N, \tag{5}$$

where s_n is the nth symbol, $s_n = \pm 1$, θ_n is the random symbol phase, and N denotes the noise; in Eq. (5) the signal amplitude is normalized to 1. The matched-filter output between Eqs. (4) and (5) yields

$$T_+ \cdot d = (s_n e^{i\theta_n} + s_{n+1} e^{i\theta_{n+1}})\rho + \rho_N,$$

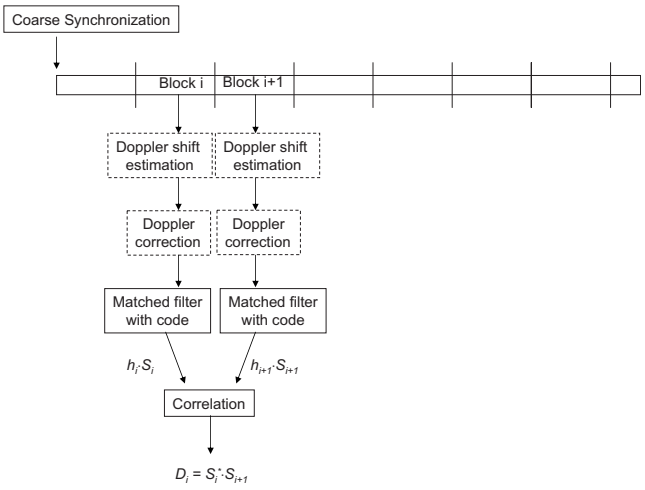


FIG. 7. Block diagram of the cross-correlation method for DPSK signals.

$$T_- \cdot d = (s_n e^{i\theta_n} - s_{n+1} e^{i\theta_{n+1}})\rho + \rho_N, \tag{6}$$

where ρ is the autocorrelation function of the code sequence, $\rho = C \cdot C$, and ρ_N denotes the correlation of the code sequence with the noise, $\rho_N = C \cdot N$. Since $\rho > \rho_N$ assuming a high processing gain, the noise contribution is negligible except at very low SNRs. For simplicity we shall drop the noise in the discussions throughout this paper.

In a channel without or with minimal differential-phase error, i.e., $\theta_n = \theta_{n+1}$, one finds $\max|T_+ \cdot d|^2 > \max|T_- \cdot d|^2$, if $s_n s_{n+1} = 1$ (adjacent symbols remain the same, no transition), and $\max|T_- \cdot d|^2 > \max|T_+ \cdot d|^2$, if $s_n s_{n+1} = -1$ (adjacent symbol not the same). Thus by comparing the outputs of the matched filters, Eq. (6), one can determine the next symbol based on the current symbol. However, one finds that this method may not work in a channel that contains a significant differential-phase error since the output squared of the matched filter [Eq. (6)] is a function of the symbol differential phase, which, when in error, can cause incorrect symbol decisions.

To process the moving-source data, which contain a significant differential-phase error, a new pair of transition detector is proposed, which is insensitive to the differential-phase error and therefore robust for symbol estimation/decision. Let C_1 be the first half of the code sequence, and C_2 be the second half of the code sequence, i.e., $C \equiv [C_1, C_2]$. The new transition detectors are given by

$$C_P = [C_2, C_1] \quad \text{and} \quad C_N = [C_2, -C_1]. \tag{7}$$

To see how the new transition detector works, one compares with the (conventional) matched-filter operation. In a multipath time-varying environment, the data of Eq. (5) can be expressed in four half-blocks as

$$d = [s_n h_n C_1, s_n h_{n+1/2} C_2, s_{n+1} h_{n+1} C_1, s_{n+1} h_{n+1+1/2} C_2], \tag{8}$$

where h_n is the impulse response at t_n, and $h_{n+1/2}$ is the impulse response at $t_n + \tau/2$; τ is the symbol duration. The matched filter (using the code sequence C) yields

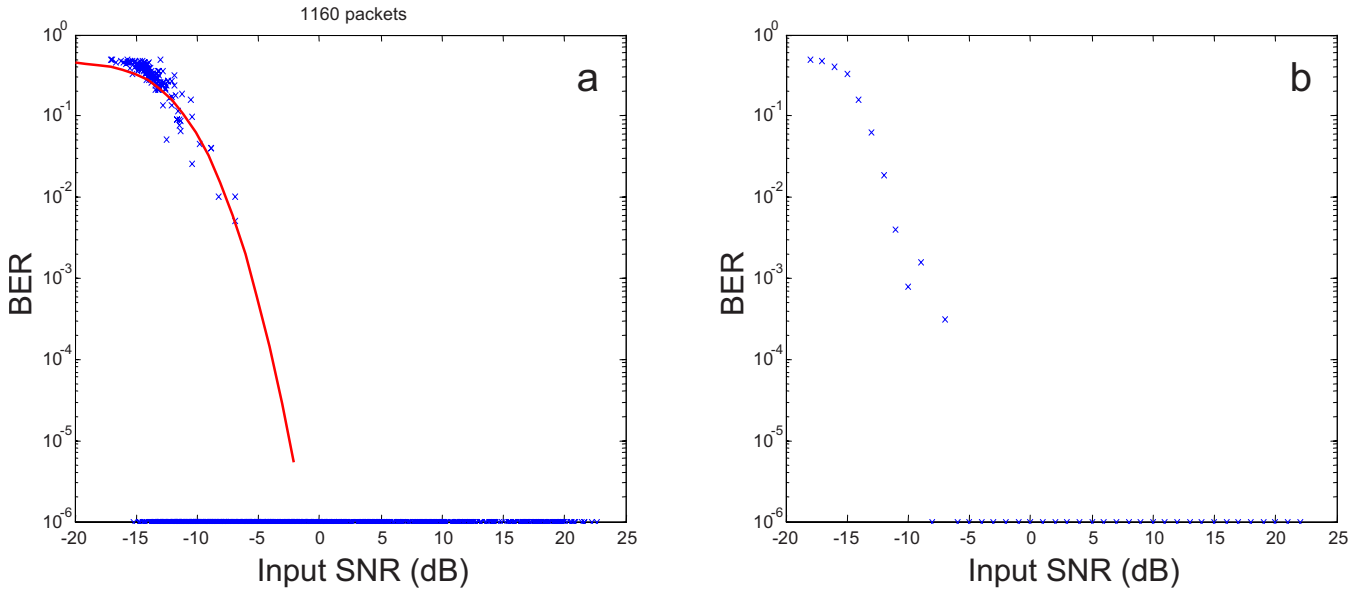


FIG. 8. (Color online) BER (a) and average BER (b) as a function of input SNR using the cross-correlation method for fixed-source data. The solid line is a model prediction. See Ref. 10. Zero BER is represented by 10^{-6} on the logarithmic scale.

$$C \cdot d \simeq [s_n \bar{h}_n \rho, s_{n+1} \bar{h}_{n+1} \rho], \tag{9}$$

where one approximates h_n, $h_{n+1/2}$ by $\bar{h}_n$; the conventional matched filter assumes that the channel is time invariant during a symbol period. The correlation of the matched-filter outputs between the two symbols yields

$$(s_n^* s_{n+1})(\bar{h}_n^* \cdot \bar{h}_{n+1})(\rho \,.\, \rho) = (s_n^* s_{n+1}) |\bar{h}_n^* \bar{h}_{n+1}| e^{i\phi_{n+1}} (\rho \cdot \rho), \tag{10}$$

where ϕ is the differential phase between the symbol due to the random medium, which causes the differential-phase error.

The new transition filter works by the same principle as the (conventional) matched filter, Eq. (9). One finds

$$C_\pm \cdot \bar{d} = \bar{h}_{n+1/2} C_\pm \cdot [s_n C_2, s_{n+1} C_1], \tag{11}$$

where $\bar{d}$ contains two half-blocks of data, i.e., $\bar{d} = [s_n h_{n+1/2} C_2, s_{n+1} h_{n+1} C_1]$, again assuming that the channel is invariant during one symbol block $\bar{d}$. One can determine whether the next symbol is the same as (or opposite to) the current symbol by comparing the energy of the above transition detector. For example, if $s_{n+1} = s_n$, one has

$$\max |C_\pm \cdot \bar{d}|^2 = |s_n \bar{h}_{n+1/2}|^2 (\max |C_\pm \cdot C_+|)^2 = |\bar{h}_{n+1/2}|^2 \begin{bmatrix} M^2 \\ \beta^2 \end{bmatrix}, \tag{12}$$

where the autocorrelation function of C_+ is the same as the autocorrelation function of C itself; it has a peak value equal to the length of the code sequence, M, and a sidelobe level equal to 1, and the correlation of C_- against C_+ has a peak value β much less than M; the actual value depends on the sequence used. Thus the C_+ matched filter will yield a higher peak energy than the C_- matched filter. Conversely, if the peak energy of the C_+ matched-filter output is higher than that of the C_- matched filter, it would suggest that $s_{n+1} = s_n$.

Likewise, if $s_{n+1} = -s_n$, one has

$$\max |C_\pm \cdot \bar{d}|^2 = |s_n \bar{h}_{n+1/2}|^2 (\max |C_\pm \cdot C_-|)^2 = |\bar{h}_{n+1/2}|^2 \begin{bmatrix} \beta^2 \\ M^2 \end{bmatrix}, \tag{13}$$

where the correlation of C_- against itself has a peak value equal to the length of the code sequence and a sidelobe level that varies depending on the sequence; normally close to 1. The correlation of C_+ against C_- has a peak value β much less than M as mentioned above. Since $M \gg \beta$, the C_- matched filter will yield a higher peak energy than the C_+ matched filter. Conversely, if the peak energy of the C_- matched-filter output is higher than that of the C_+ matched filter, it would suggest that $s_{n+1} = -s_n$.

Note that the outputs of Eqs. (12) and (13) are real numbers. The proposed transition $C_\pm$ detector is thus not affected by the problem of rapid phase variations and can be applied to the moving-source data. The results will be shown in Secs. III C and III D. The transition detector can also be applied to the fixed-source data. We will first analyze the fixed-source data using the transition detector to compare its performance and with the cross-correlation method of Ref. 10.

The fixed-source data contained 1160 packets with an input SNR varying from −15 to 23 dB. The BER result by cross-correlating the matched-filter outputs of two adjacent symbols is shown in Fig. 8 (Fig. 8 of Ref. 10) assuming DPSK signaling. Figure 8(a) shows the BER as a function of the packet input SNR (the input SNR averaged over each packet) and Fig. 8(b) shows the BER averaged over packets with approximately the same input SNR, plotted as a function of the input SNR. Also shown in Fig. 8(a) is the modeled BER for the DPSK signal. Using the transition filter, the BER result is shown in Fig. 9(a) as a function of the packet input SNR, and the average BER is shown in Fig. 9(b) as a

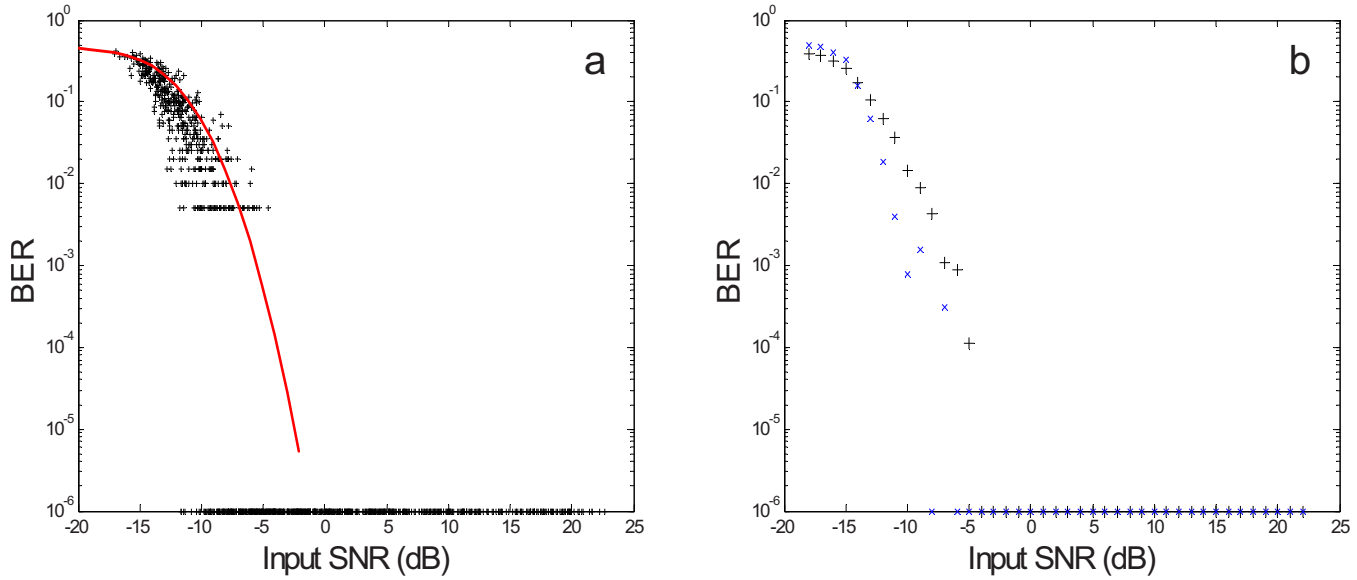


FIG. 9. (Color online) BER (a) and average BER (b) as a function of input SNR using the transition detector method applied to the fixed-source data. × denotes the data of Fig. 8(b) using the cross-correlation method. The solid line is a model prediction. Zero BER is represented by 10^{-6} on the logarithmic scale.

function of the input SNR; both denoted by "+." Also shown in Fig. 9(b) is the average BER repeated from Fig. 8(b), shown by "x." One finds that the BER results using the transition detector are slightly higher than that using the cross correlation of the matched-filter outputs. For the latter method, as pointed out in Ref. 10, the phase estimation can be improved under certain channel conditions by synchronizing the cross-correlation output based on symbols with higher SNRs. The BER in the actual data can be better than expected (modeled) whenever the symbols happen to be properly synchronized. This feature is not available to the transition detector (an energy detector) for LPD applications.

C. Moving-source data results: High SNR

The moving-source data require initial data processing involving Doppler estimation and correction. The block diagram of data processing is shown in Fig. 10. Doppler estimation is done in the base band with two samples with fractional sampling (two samples per chip). After coarse synchronization, the data are divided into overlapping blocks with a length larger than the code length to include the synchronization error. Doppler shift is estimated for each block (symbol) using the wideband ambiguity functions as described above. The signal phase shift (due to Doppler shift) is corrected for each block of data based on the estimated Doppler shift. The data are resampled based on the estimated Doppler shift to correct for time dilation or compression and resynchronized. The symbols are detected by applying the transition filter $C_{\pm}$ to the data to determine if the two adjacent symbols are the same or not. In actual implementations, one finds other ways to simplify the processing. For example, it is simpler to Doppler-shift the transition filter $C_{\pm}$ and apply the filter to the data according to Eqs. (12) and (13).

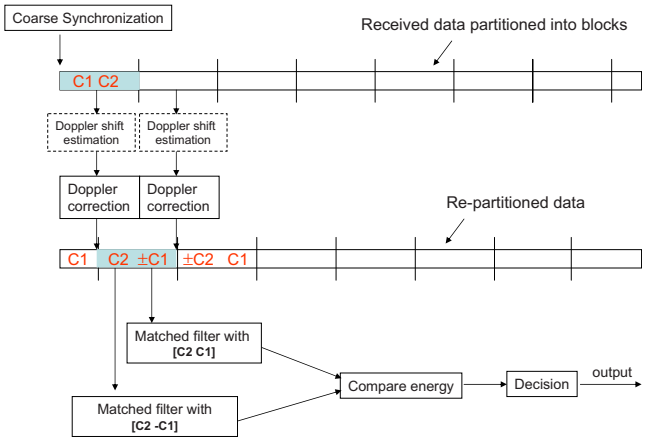


FIG. 10. (Color online) Block diagram of the transition detector method. $C1$ and $C2$ are the first and second halves of the code sequence as described in Sec. III B.

The moving-source data along the track shown in Fig. 1 are processed using the above method, and the result is shown in Fig. 11(b). One finds zero BER except near the end of the run when the source-receiver range is ⩽1 km. The reason is attributed to the fact that at close ranges, the various multipaths arrive with significantly different D/E angles and different Doppler shifts; the spread of the Doppler shifts creates an effective Doppler spread. This finding was supported by Fig. 3(b), which indicates a decreased channel coherence time or a higher Doppler spread at close ranges. To improve the BER at close (⩽1 km) ranges, one needs to estimate the Doppler shift for each path, which is significantly more difficult.

D. BER as a function of decreasing input SNR

To assess the performance of the transition filter at a low input SNR, ambient noise data collected during the same experiment are added to the signal data (see Ref. 10). 2 h of noise data were also collected producing 278 packets of noise. Multiple packets of noise data, randomly chosen, were added to the signal data to generate packets of data with different input SNRs ranging from −13 to +30 dB. The

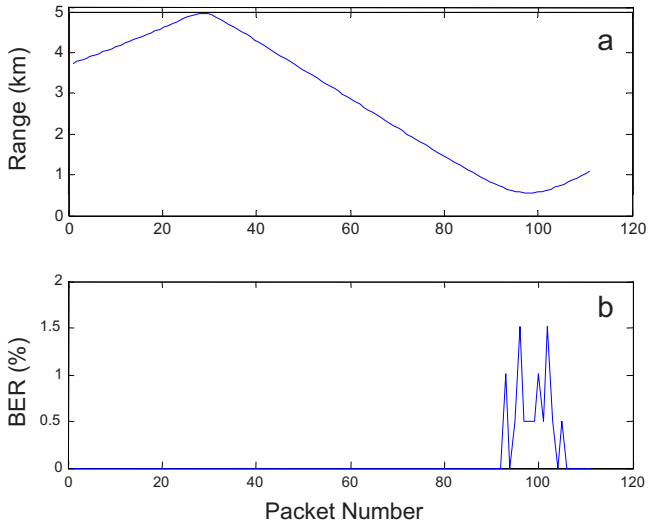


FIG. 11. (Color online) Source-receiver range as a function of time (packet number) repeated from Fig. 3(a) (upper figure). BER as a function of packet number (lower figure).

close range ($\leqslant$1 km) data are excluded from this analysis as remarked above. BER is then deduced as a function of input SNR. The result is shown in Fig. 12(a) as a function of the packet input SNR. The average BER is shown in Fig. 12(b) as a function of input SNR. Compared with the average BER determined from the fixed-source data [repeated from Fig. 9(b), shown by +], one finds a performance degradation of 1–2 dB. Note that while the cross-correlation method failed for the moving-source data, the transition filter method works pretty well for both fixed- and moving-source data.

IV. PROBABILITY OF DETECTION AND COUNTERDETECTION RANGE

The probability of detection (P_D) depends on the construction of the detector; the more the detector knows about the signal, the more features the detector can use to improve the detection. If the signal waveform is known, one can employ a coherent detector, e.g., a matched filter, which often yields a high P_D given the processing gain derivable from the signal. Noiselike signals are difficult to detect using a coherent detector as the signal is random and difficult to replicate compared with, for example, an impulselike signal. This also favors the DSSS signaling as compared with, for example, frequency-hopping frequency-shift-keying signaling. For the latter, while the average SNR is low, the SNR for information carrying frequency bins is high. As a result, the repeated (or time-varying) frequency hopping pattern may alert the operator to the presence of a man-made signal. Once the operator is alerted, more sophisticated signal processing can be used to search for the signal parameters and construct an improved detector.

If the signal waveform is not known, one is left with an energy detector. A commonly used energy detector is the spectrogram, which detects a sudden increase in the SNR as a function of frequency and time. This normally requires a fairly good SNR (say 5 dB) over the signal frequency band and is most effectively done by a human being who can interactively adjust the Fourier transform window to match the signal. A computer-aided detector needs to know the signal bandwidth and signal duration, as mismatch in bandwidth and duration between the signal and detector can significantly decrease the detection performance. The mismatch in bandwidth is self-evident, as incorrect bandwidth results in a loss of part of the signal energy and addition of more noise energy. Likewise, the signal duration also influences the detector performance (see Sec. IV C). If the integration time is much longer than the signal duration, it effectively reduces the SNR as more noise is included in the detector output. Without knowing the signal duration, a narrowband detector is often used to detect narrowband energy and a broadband pulse detector (i.e., short integration time) is commonly used to detector a burst energy. The detectors will alert the opera-

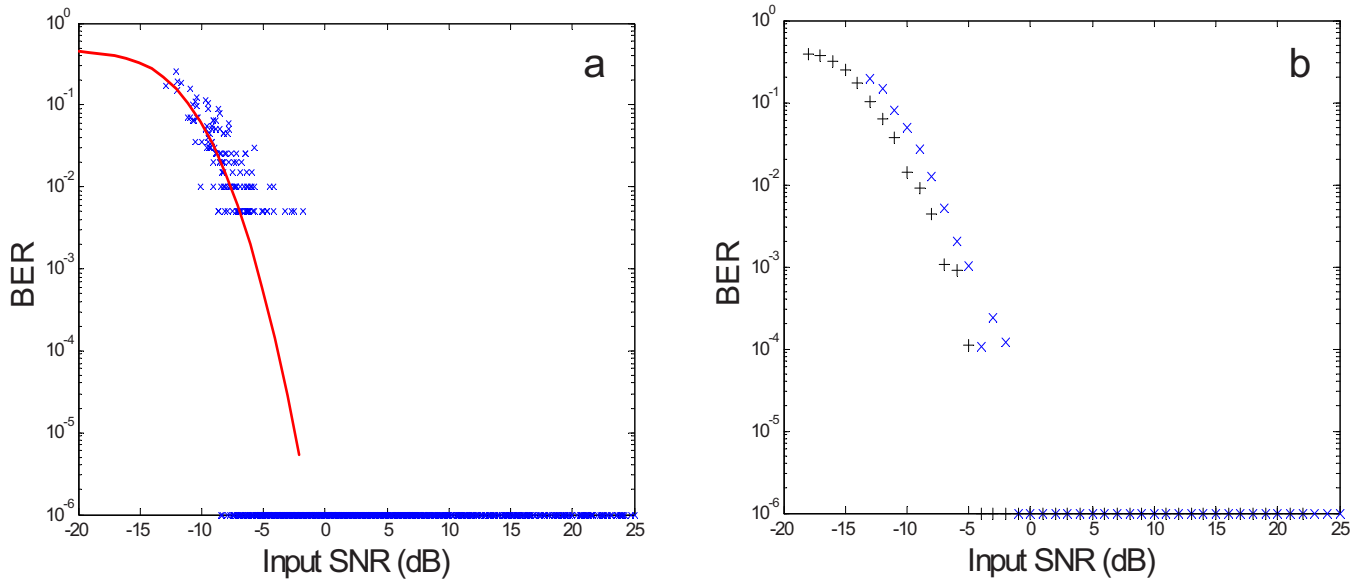


FIG. 12. (Color online) BER (a) and average BER (b) as a function of input SNR using the transition detector method applied to the moving-source data. + denotes the fixed-source data of Fig. 9(b). The solid line is a model prediction shown in Fig. 8(a). Zero BER is represented by 10^{-6} on the logarithmic scale.

tor for a potential signal of interest, when P_D exceeds the recognition differential for the signal of interest.

The P_D for an energy detector depends very much on the input SNR. Pseudorandom noiselike DSSS signals with an input level lower than the ambient noise (e.g., SNR $\sim$−8 dB within the signal band) are difficult to detect by a narrowband or broadband energy detector assuming an unalerted listener. As input SNR increases (as when source-receiver ranges decrease), the probability that the signal will be detected increases. From a system point of view, the question is as follows: At what range will the signal be detected or what is the counterdetection range? The answer is channel dependent. It requires a determination of the P_D and the probability of false alarm (P_{FA}) as a function of input SNR, for a given signal-fading distribution. This topic is addressed in Sec. IV A. To determine the input SNR, one needs to calculate the signal transmission loss (TL) as a function of source-receiver range for a given source power and noise level. This calculation is done for a typical shallow water environment in Sec. IV B. This section also shows the P_D as a function of source-receiver range for a given P_{FA}. The analysis involves two receivers. One is the intended (friendly) receiver and the other is the unfriendly receiver, the interceptor. The objective is to minimize P_D of the signal by the interceptor for a given P_{FA}, which means the lower the SL, the better the result. On the other hand, the SL of the transmitting node should be high enough so that the message is received at the intended receiver with a high enough SNR for decoding the message. The SL is a system parameter that needs to be determined first. See Sec. IV B.

A. P_D and P_{FA} of an energy detector

The P_D and P_{FA} for a broadband pulse energy detector are well known for a nonfading channel[15,16] and a Rayleigh-fading channel,[1] but not for a log-normal-fading channel. The data as discussed above indicate that the fading statistics for the DSSS signal in an underwater acoustic channel follows the log-normal distribution.[10] A derivation of the P_D and the P_{FA} is reviewed below, which can be generalized to include the log-normal distribution.

1. Nonfading channel

For a nonfading channel, the signal (each symbol) has a constant amplitude a. Assuming additive white Gaussian noise, with a Rayleigh amplitude distribution, the probability of detection is given by the following two statistics:

$$p_r(x) = \begin{cases} \dfrac{x}{\sigma_N^2} \exp(-(x^2+a^2)/2\sigma_N^2) I_0(ax/\sigma_N^2) & \text{with signal present} \\ \dfrac{x}{\sigma_N^2} \exp(-x^2/2\sigma_N^2) & \text{with signal absent,} \end{cases} \tag{14}$$

where σ_N is the noise variance and I_0 is the modified Bessel function of zeroth order. Let $Y=X^2$ be the square-law output of an energy detector. It can be shown that the probability density function of Y becomes

$$p_r(y) = \begin{cases} \dfrac{1}{2\sigma_N^2} \exp(-(y/2\sigma_N^2+\gamma)) I_0(2\sqrt{\gamma y/2\sigma_N^2}) & \text{with signal present} \\ \dfrac{1}{2\sigma_N^2} \exp(-y/2\sigma_N^2) & \text{with signal absent,} \end{cases} \tag{15}$$

where $\gamma=a^2/2\sigma_N^2$ is the mean SNR at the input of an energy detector (mean input SNR). Given a threshold η, let the P_{FA} be the probability that the noise energy is higher than η. Using the lower equation of Eq. (15), one has

$$P_{\mathrm{FA}} = \int_\eta^\infty \frac{1}{2\sigma_N^2} \exp\left[-\frac{y}{2\sigma_N^2}\right] dy = \exp\left[-\frac{\eta}{2\sigma_N^2}\right]. \tag{16}$$

The probability of detection, P_D, is the probability that the signal plus noise energy is higher than η. Using the upper equation of Eq. (15), it can be expressed as a function of the P_{FA} as follows:

$$P_D = \int_\eta^\infty \frac{1}{2\sigma_N^2} \exp(-(y/2\sigma_N^2+\gamma)) I_0(2\sqrt{\gamma y/2\sigma_N^2}) dy$$
$$= \int_{-\ln(P_{\mathrm{FA}})}^\infty \exp(-(u+\gamma)) I_0(2\sqrt{\gamma u}) du, \tag{17}$$

where $u=y/2\sigma_N^2$ is the integration variable and γ is the mean input SNR.

2. Fading channel

The P_{FA} in a fading channel is the same as that in a nonfading channel [Eq. (16)] for a given threshold η. The P_D can be expressed as

$$P_D = \int_0^\infty p_{D|S} p_S(s) ds$$
$$= \int_0^\infty p_S(s) \int_\eta^\infty \frac{1}{2\sigma_N^2} \exp[-(y+s^2)/2\sigma_N^2] I_0(s\sqrt{y}/\sigma_N^2) dy ds$$
$$= \int_\eta^\infty \frac{1}{2\sigma_N^2} \exp(-y/2\sigma_N^2) A(y) dy, \quad (18)$$

where $P_{D|S}$ is the conditional probability of detection for a signal with an instantaneous signal amplitude s as given in Eq. (17), p_s is the amplitude distribution of the signal, and

$$A(y) = \int_0^\infty \exp(-s^2/2\sigma_N^2) I_0(s\sqrt{y}/\sigma_N^2) p_s(s) ds. \quad (19)$$

For a Rayleigh-fading channel,

$$p_S(s) = \begin{cases} \frac{s}{\sigma_s^2} \exp\left(-\frac{s^2}{2\sigma_s^2}\right) & \text{if } s > 0 \\ 0 \quad \text{if } s \leq 0. \end{cases} \quad (20)$$

One finds

$$A(y) = \int_0^\infty \exp(-s^2/2\sigma_N^2) I_0(s\sqrt{y}/\sigma_N^2) \frac{s}{\sigma_s^2} \exp(-s^2/2\sigma_s^2) ds$$
$$= \frac{\sigma_N^2}{\sigma_s^2 + \sigma_N^2} \exp\left[\frac{\sigma_s^2 y}{2\sigma_N^2(\sigma_s^2 + \sigma_N^2)}\right] \quad (21)$$

and

$$P_D = \int_\eta^\infty \frac{1}{2\sigma_N^2} \exp(-y/2\sigma_N^2) \frac{\sigma_N^2}{\sigma_s^2 + \sigma_N^2} \times \exp\left[\frac{\sigma_s^2 y}{2\sigma_N^2(\sigma_s^2 + \sigma_N^2)}\right] dy$$
$$= \exp\left[\frac{-\eta}{2(\sigma_s^2 + \sigma_N^2)}\right], \quad (22)$$

where η is the threshold set by P_{FA}. The relationship between P_D and P_{FA} can be expressed as follows:

$$P_{\mathrm{FA}} = (P_D)^{1+\gamma}, \quad (23)$$

where $\gamma = 2\sigma_s^2/2\sigma_N^2 = \sigma_s^2/\sigma_N^2$ is the mean input SNR.

For a log-normal-fading channel, the amplitude-fading statistics are given by Eq. (2) for the signal present case. Substituting the log-normal distribution into the $A(y)$, Eq. (19), one finds

$$P_D = \int_\eta^\infty \frac{1}{2\sigma_N^2} \exp(-y/2\sigma_N^2) A(y) dy$$
$$= \int_\eta^\infty \frac{1}{2\sigma_N^2} \exp(-y/2\sigma_N^2) \int_0^\infty \exp(-s^2/2\sigma_N^2) \times I_0(s\sqrt{y}/\sigma_N^2) \frac{1}{\sqrt{2\pi}\sigma_s} s^{-1} \exp\left(-\frac{(\ln s - \mu_s)^2}{2\sigma_s^2}\right) ds dy. \quad (24)$$

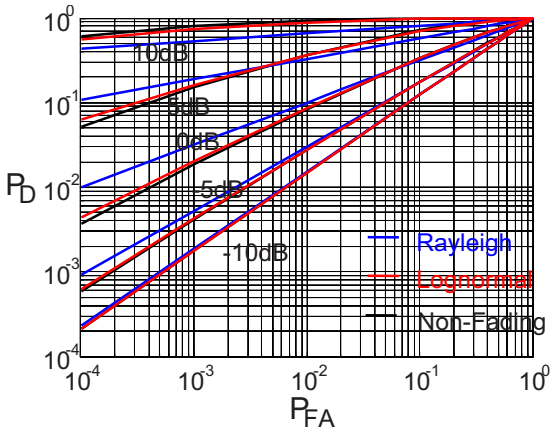


FIG. 13. (Color online) Receiver operation characteristic curves showing P_D as a function of P_{FA} for various SNRs and signal-fading distributions.

The relationship between the detection probability and the false alarm probability is

$$P_D = \int_{-\ln(P_{\mathrm{FA}})}^\infty e^{-u} \int_0^\infty e^{-\gamma\alpha^2 s^2} I_0(2s\alpha\sqrt{\gamma u}) \frac{1}{\sqrt{2\pi}\sigma_s} s^{-1} \times \exp\left(-\frac{(\ln s - \mu_s)^2}{2\sigma_s^2}\right) ds du, \quad (25)$$

where $\gamma = E(S^2)/2\sigma_N^2 = e^{2\mu_s + 2\sigma_s^2}/2\sigma_N^2 = \xi^{-2}/2\sigma_N^2$ is the mean input SNR and $\xi = e^{-\mu_s - \sigma_s^2}$.

Using Eqs. (17), (23), and (25), one can calculate P_D as a function of P_{FA} for a given input SNR, the so called receiver operation characteristic (ROC) curve, for nonfading, Rayleigh-fading, and log-normal-fading cases. The results are shown in Fig. 13. For the log-normal fading, we have used $\mu_s = -1.6449$ and $\sigma_s^2 = 0.0304$ obtained from the distribution of input signal amplitude.

The ROC curve (Fig. 13) is commonly used for detection analysis. It shows the dependence of P_D as a function of P_{FA} for a given SNR. The same results can also be displayed in a different manner, for example, showing the P_D as a function of SNR for a given P_{FA} as will be done in the next section to calculate the counterdetection. One notes from Fig. 13 that the P_D versus P_{FA} relation based on the log-normal statistics is much closer to the nonfading case than to the Rayleigh-fading case. There are differences between the log-normal- and nonfading cases, which are not clearly seen in a log-log plot.

B. Counterdetection range

As P_D is a function of the (mean) input SNR and the input SNR is a function of source-receiver range for a given SL, one can calculate the P_D as a function of source-receiver range for a given P_{FA}. Counterdetection range will be defined as the range below which $P_D > 0.5$. To model the SNR at the receiver, we calculate the TL in the TREX04 environment using the range-dependent acoustic model parabolic equation (RAM PE) model.[17] The result is shown in Fig. 14 for a 17 kHz signal. Superimposed is a sonar-equation-based calculation, which assumes spherical spreading to a range of

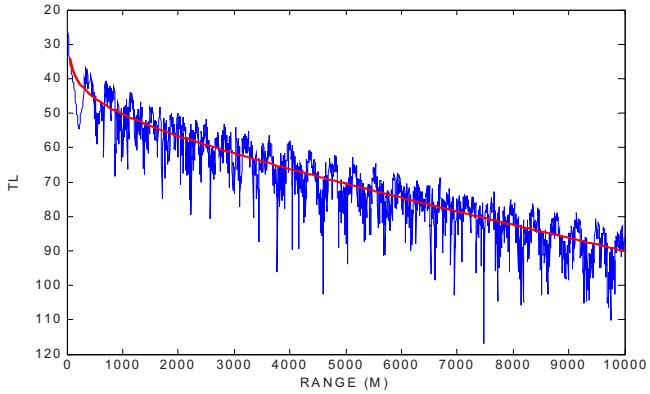


FIG. 14. (Color online) TL as a function of range using the RAM PE model. The smooth line is the empirical model calculation based on sound attenuation by sea water.

50 m and cylindrical spreading beyond 50 m. For absorption by the water medium we use the following expression due to Thorp:[18]

$$\alpha = \left(\frac{0.1f^2}{1+f^2} + \frac{40f^2}{4100+f^2} + 2.75 \times 10^{-4} f^2 + 0.003 \right) \times 0.875, \tag{26}$$

where α is the absorption loss in dB/km, f is the acoustic frequency in kHz, and 0.875 is a depth correction factor determined by fitting the RAM calculation; the original formula is for a depth of 1000 m. To determine the SNR at the receiver, we note that at 17 kHz, the noise is dominated by wind generated noise, with a spectral level given by[19]

$$10 \log N(f) = 50 + 7.5w^{1/2} + 20 \log f - 40 \log(f + 0.4), \tag{27}$$

where w is the wind speed in m/s. Assuming $w = 10$ m/s, one finds NL=49 dB. Given the TL and noise level, one can calculate the SNR as a function of range for a given SL. Given the SNR one can then calculate the P_D as a function of range for a given P_{FA} using the equation in Sec. IV A. The following are the numerical results shown in Fig. 15 for P_D as a function of range assuming three SLs: 143, 155, and 164 dB and $P_{\mathrm{FA}}=0.01$. These SLs are needed for communications to an intended (friendly) receiver at a range of ~2, 4, and 7 km. Based on Fig. 12(b), a minimum input SNR of −10 dB is required at the intended receivers to achieve a minimum (<1%) BER. The minimum input SNR is used with TL to determine the minimum SLs.

Figures 15(a) and 15(b) show the P_D as a function of the source-to-interceptor range for Rayleigh signal-fading and log-normal signal-fading statistics, respectively. One finds that the counterdetection range (for $P_D \geqslant 0.5$) is approximately 1.3, 3.6, and 5.8 km for the three SLs assuming Rayleigh-fading statistics and approximately 1.4, 3.8, and 6.1 km for the three SLs assuming log-normal-fading statistics. Naturally, the higher the SL, the greater the counterdetection range. As expected, the counterdetection range for an energy detector is shorter than the communication range to a friendly receiver using a matched filter. Hence, the communication signal will not likely be detected by an interceptor located outside the communication range (or the operation area). But as the interceptor approaches one of the transmitting nodes, detection by the interceptor is unavoidable. The hope is that the interceptor remains unalerted, such as when the signal is noiselike.

Note that at $P_D=0.5$ the differences in the counterdetection ranges are relatively small between the two signal-fading scenarios. However, if the detection ranges were defined at a higher P_D, e.g., $P_D=0.9$, the differences between the two cases would be significant. The difference is that the P_D increases faster with a decreasing range for the log-normal than for the Rayleigh distribution.

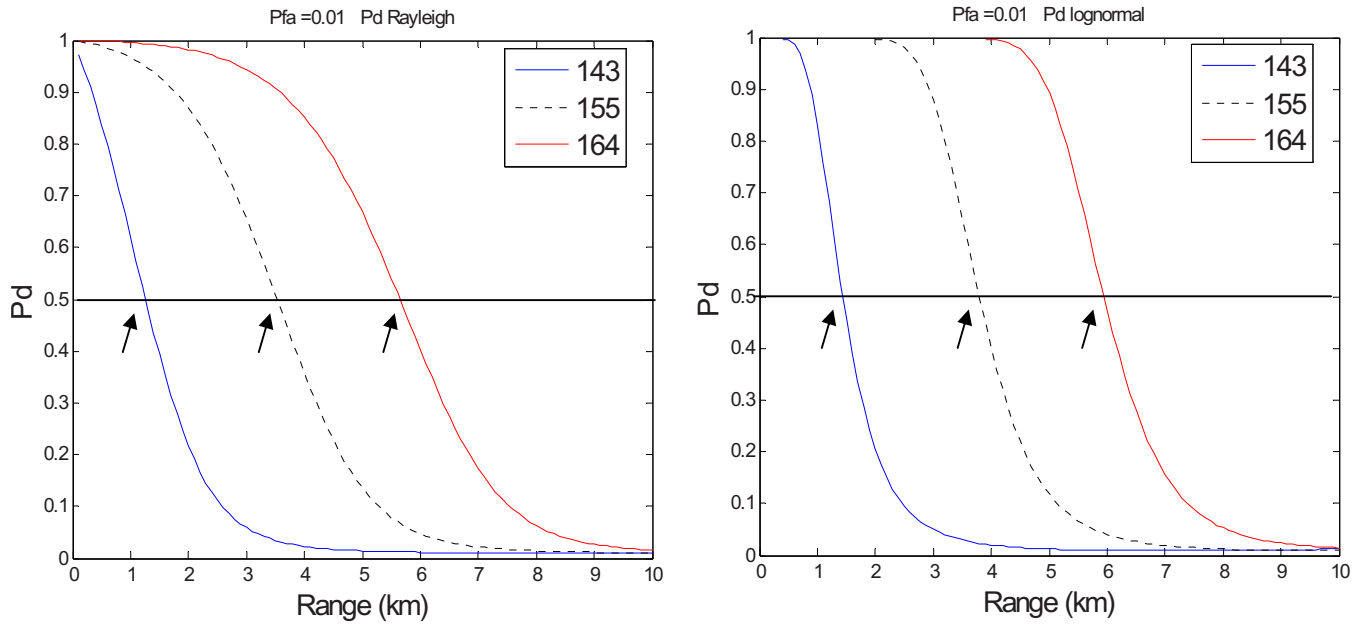


FIG. 15. (Color online) P_D as a function of source-receiver range for $P_{\mathrm{FA}}=0.01$ for three assumed SLs. The left figure assumes Rayleigh signal fading and the right figure assumes log-normal signal fading.

C. Integrating over multiple observations

If the signal is present for a long period of time, the interceptor, if alerted, can improve its detection by integrating the signal energy over multiple observations (normally in postprocessing after the operator has been alerted.) Let T be the sample interval and $y(t)$ be the *energy* at time t. Assuming that all samples are independent, then the integrated energy over a dwell time τ_d can be approximated as follows:

$$z = \frac{1}{T}\int_0^{\tau_d} y(t)dt \approx \sum_{k=0}^{N_s-1} y(kT), \tag{28}$$

where $N_s = \tau_d / T$ is the number of samples.

For large N_s, Z is approximately Gaussian distributed. In contrast with Eq. (16), the P_{FA} for a given threshold η_z is given by

$$P_{\mathrm{FA}} = \int_{\eta_z}^{\infty} \frac{1}{\sqrt{2\pi}\sigma_2} \exp\left[-\frac{(z_z-\mu_2)^2}{2\sigma_2^2}\right] dz \equiv Q\left(\frac{\eta_z-\mu_2}{\sigma_2}\right)$$

$$= Q\left(\frac{\eta_z - 2_s\sigma_N^2}{2\sigma_N^2\sqrt{N_s}}\right), \tag{29}$$

where $\mu_2 = 2N_s\sigma_N^2$ and $\sigma_2^2 = 4N_s\sigma_N^4$ are the mean and variance of the noise only case.

Assuming that the signal, y, follows a log-normal distribution (Sec. IV A), then the probability distribution function of z is given by (details given in the Appendix)

$$P(z) = \frac{1}{\sqrt{2\pi}\sigma_1} \exp\left[-\frac{(z-\mu_z)^2}{2\sigma_z^2}\right], \tag{30}$$

where

$$\mu_z = 2N_s\sigma_N^2(1+\gamma),$$

$$\sigma_z^2 = 4N_s\sigma_N^4(1+2\gamma) + N_s \exp(4\mu_s + 4\sigma_s^2)[\exp(4\sigma_s^2) - 1], \tag{31}$$

where $\gamma = E_s(s^2)/2\sigma_N^2 = \exp(2\mu_s + 2\sigma_s^2)/2\sigma_N^2$ is the mean input SNR, and μ_s and σ_s^2 are the parameters of the log-normal distribution [Eq. (2)]. In contrast with Eq. (25), the P_D is now given by [see Eq. (A11)]

$$P_D = Q\left(\frac{\eta_z - 2N_s\sigma_N^2(1+\gamma)}{\sqrt{4N_s\sigma_N^4[1+2\gamma+\gamma^2(\exp(4\sigma_s^2)-1)]}}\right). \tag{32}$$

Using Eqs. (29) and (32), one plots the P_D as a function of input SNR for a $P_{\mathrm{FA}}=0.01$ as shown in Fig. 16 for various values of N_s. Comparing $N_s=25$ with $N_s=1$, one finds $\sim$10 dB improvement in SNR at $P_D=0.5$. Thus, knowing that the signal bandwidth and hence T and that the signal is at least N_sT long, the signal could be detected by long integration time. As an example, an input SNR of −8 dB, which has a low probability being detected by a broadband pulse detector, could now be detected because the integration yields an effective +2 dB SNR. This assumes that the operator has been alerted that there is a man-made signal and turns on the search for the signal parameters and long integration detector.

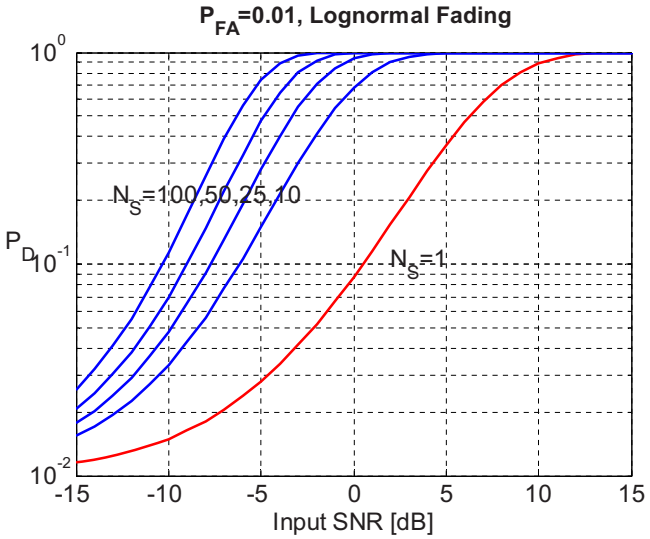


FIG. 16. (Color online) P_D as a function of input SNR for $P_{\mathrm{FA}}=0.01$ for different values of N_s.

Figure 17 shows the probability density distributions of the noise only (upper figure) and signal plus noise (lower figure) for the $N_s=1$ and $N_s=25$ cases. For the $N_s=1$ case, $z=y$, one finds that the noise density distribution decreases exponentially with energy. With the signal present, while the signal (amplitude) has a log-normal distribution, the probability density distribution of the signal plus noise decreases with the signal+noise energy. For $N_s=25$, the probability density is approximately normally distributed. While y and z/N_s have the same mean and same SNR in Fig. 17, they have different probability distributions. The fact that z has the same probability distribution for the signal-plus-noise and noise only cases is the reason that P_D for $N_s=25$ is large for $P_{\mathrm{FA}}=0.01$ (higher than that for $N_s=1$, for the same P_{FA}). One may argue that a smaller P_{FA} (e.g., $P_{\mathrm{FA}}=0.01/25$ or 4×10^{-4}) should be used for the $N_s=25$ case, since there are

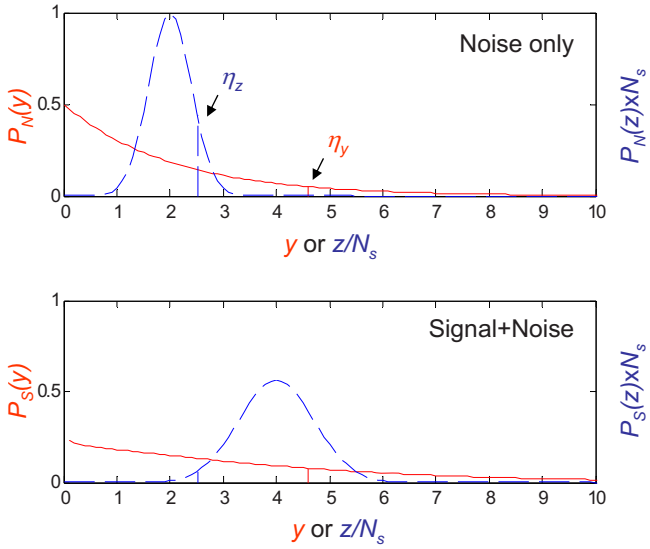


FIG. 17. (Color online) Probability distribution of noise only (upper figure) and signal plus noise (lower figure). The solid line is for $N_s=1$, showing the probability as a function of y. The dashed line is for $N_s=25$, showing the probability $p(z)\times N_s$ as a function of z/N_s.

more counts of false alarms for $N_s=25$ than for $N_s=1$. Note that for the $N_s=25$ case, the detector does not require the signal to be detectable for each sample interval T but only for the entire time period of $25T$. What values of P_{FA} to use are system dependent and likely also environment dependent; it is beyond the scope of this paper. This section presents only an example. One can calculate P_D versus P_{FA} based on the equations in the Appendix.

V. SUMMARY AND DISCUSSION

The rapid symbol phase change as a function of time for PSK signals has been well noted in underwater acoustic communications. For DSSS signaling, each symbol covers many chips and the symbol phase change, accumulating over the chips, can be large. The symbol phase change can be caused by a random medium, which produces different phases for different multipath arrivals. The TREX04 data showed that the differential phase between adjacent symbols for fixed-source and fixed-receiver transmissions was smaller than $\pm 90°$, suggesting that the phase imposed by the random medium changes gradually between symbols.[10] In that case, DPSK signals can be decoded by cross-correlating the matched-filter outputs of two adjacent symbols. For a moving source or receiver, the fact that the range is changing with time also contributes to the symbol phase change. The additional phase change contains both a deterministic as well as a random component; the latter is a result of multipaths traveling through different parts of the random medium at different times. The TREX04 data showed that the differential phase between adjacent symbols for a moving-source and a fixed-receiver transmission is often larger than $\pm 90°$. In this case, the cross-correlation method does not work for the moving-source data.

A pair of transition detectors, based on the same principle as the matched filter, are proposed in this paper for moving, as well as for fixed source data. Whether adjacent symbols are of the same kind or opposite kind is determined by the energy of the transition detectors. The transient (pulse) detector, being an energy detector, is insensitive to the symbol phase fluctuations. The method is applied to the TREX04 data. At-sea noise was added to the signal data to generate data of low input SNR. BER was measured for an input SNR from +25 to −15 dB. The moving-source data yielded a comparable, slightly degraded BER compared with the fixed-source data using the same method. For the fixed-source data, the performance is slightly degraded compared with that using the cross-correlation method. Whether the performance degradation is data dependent remains to be investigated.

The purpose of low SNR DSSS communications is to minimize the probability of detection and interception by a hostile interceptor. Since the probability of detection and interception is detector specific, assuming that the detector does not have infinite resources to employ different kinds of detectors simultaneously, the first line of defense is to minimize the probability of detection by the two most popular detectors, i.e., a narrowband energy detector and a broadband pulse detector, under the assumption that the detector has no a priori knowledge of the signal parameters or the signal parameters are constantly changing with time. Obviously, one does not have to worry about narrowband energy detector for DSSS communications. Anticipating the use of a broadband pulse detector, the question is at what range will the signal be detected, the counterdetection range. The answer is case dependent. As an illustration, we assume a typical shallow water environment and analyze the probability of detection as a function of range. Three SLs are used for three intended (friendly) receivers. Counterdetection range is calculated based on $P_D>0.5$ and $P_{\mathrm{FA}}=0.01$. The analysis assumes a single receiver, and can be extended to an array of receivers using the directivity index. As expected, the lower the SL, the shorter the counterdetection range.

If the interceptor is aware of a man-made signal in the water, and that it has many snapshots of data to investigate, the interceptor could improve its detection probability by integrating the signal energy over the snapshots of data. The probability of detection using a long integration time is also analyzed in this paper.

Generally, one expects the lower the input SNR, the lower the probability of detection, as illustrated by the numerical examples given above. But communications at a lower input SNR comes with the price of a lower data rate for DSSS signaling. It requires a longer transmission time to get the same throughput compared with a higher data rate, higher SNR communications scheme. One expects that all signals could eventually be detected if the detector knows about the existence of the signal and has infinite resources to investigate the signal properties. By way of illustration, it is pointed out that low SNR DSSS signal could be detected by long integration even using an incoherent detector, if such signals are known to be present. In practice, one does not have infinite resources. The advantage of low SNR DSSS communications is, from the practical point of view, that it has a low input SNR and it is noiselike. It has a LPD by a broadband pulse energy detector. In doing so, as long as the operator remains unalerted of the existence of the signal, the signaling can be considered covert.

ACKNOWLEDGMENT

This work is supported by the Office of Naval Research. We are grateful to the NRL Acoustic Division personnel who supported and conducted the TREX04 experiment.

APPENDIX: PROBABILITY OF DETECTION AND PROBABILITY OF FALSE ALARM WITH MULTIPLE OBSERVATIONS

Let T be the sample interval and $y(t)$ be the energy at time t. Assuming that all samples are independent, then the integrated energy over a dwell time τ_d can be approximated as follows:

$$z=\frac{1}{T}\int_0^{\tau_d} y(t)dt \approx \sum_{k=0}^{N_s-1} y(kT), \tag{A1}$$

where $N_s=\tau_d/T$ is the number of samples. For large N_s, Z may be approximately Gaussian distributed.

Assuming Gaussian distribution for z, one has

$$P_D = \int_{\eta_z}^{\infty} \frac{1}{\sqrt{2\pi}\sigma_1} \exp\left[-\frac{(z-\mu_1)^2}{2\sigma_1^2}\right] dz \equiv Q\left(\frac{\eta_z - \mu_1}{\sigma_1}\right), \tag{A2}$$

where Q is defined in Eq. (29). Thus to calculate P_D, one needs only to evaluate the mean and variance of the signal plus noise.

With the signal present, the mean and the variance of $y_k = y(kT)$ for a given instantaneous signal energy s in the presence of AWGN are given by

$$\mu_a = 2\sigma_N^2 + s^2 \quad \text{and} \quad \sigma_a^2 = 4\sigma_N^2(\sigma_N^2 + s^2). \tag{A3}$$

Letting the distribution of Y_k for a given s be $p_{y_k|s}(y_k|s)$, the distribution of Y_k becomes

$$p_{\gamma_k}(y_k) = \int p_{\gamma_k|S}(y_k|s) p_s(s) ds. \tag{A4}$$

Thus, the mean and the variance of Y_k are obtained as follows:

$$\begin{aligned}
\mu_k &= \int y_k p_{\gamma_k}(y_k) dy_k = \int \int y_k p_{\gamma_k|S}(y_k|s) p_S(s) ds dy_k \\
&= \int \int y_k p_{\gamma_k|S}(y_k|s) dy_k \cdot p_S(s) ds \\
&= \int (2\sigma_N^2 + s^2) p_S(s) ds = 2\sigma_N^2 + E_s(s^2) = 2\sigma_N^2(1+\gamma)
\end{aligned} \tag{A5}$$

and

$$\begin{aligned}
\sigma_k^2 &= E(y_k^2) - [E(y_k)]^2 = \int y_k^2 p_{\gamma_k}(y_k) dy_k - \mu_k^2 \\
&= \int \int y_k^2 p_{\gamma_s|s}(y_k|s) p_S(s) ds dy_k - \mu_k^2 \\
&= \int (\sigma_a^2 + \mu_a^2) p_s(s) ds - \mu_k^2 \\
&= \int (8\sigma_N^4 + 8\sigma_N^2 s^2 + s^4) p_s(s) ds - \mu_k^2 \\
&= 8\sigma_N^4 + 8\sigma_N^2 E_s(s^2) + E_s(s^4) - \mu_k^2 \\
&= 4\sigma_N^4(1+2\gamma) + E_s(s^4) - [E_s(s^2)]^2 \\
&= 4\sigma_N^4(1+2\gamma) + \mathrm{var}(s^2)
\end{aligned} \tag{A6}$$

where $E_s(s^2)$ and $\mathrm{var}(s^2)$ are the mean and variance of the signal intensity, and $\gamma = E_s(s^2)/2\sigma_N^2$ is the mean input SNR. For large N_s, assuming a Gaussian distribution for z, the mean and variance of z are as follows:

$$\mu_1 = 2N_s\sigma_N^2(1+\gamma), \quad \sigma_1^2 = 4N_s\sigma_N^4(1+2\gamma) + N_s\,\mathrm{var}(s^2). \tag{A7}$$

The corresponding detection probability is

$$\begin{aligned}
P_D &= \int_{\eta}^{\infty} \frac{1}{\sqrt{2\pi}\sigma_1} \exp\left[-\frac{(z-\mu_1)^2}{2\sigma_1^2}\right] dz = Q\left(\frac{\eta - \mu_1}{\sigma_1}\right) \\
&= Q\left(\frac{\eta - 2N_s\sigma_N^2(1+\gamma)}{\sqrt{4N_s\sigma_N^4(1+2\gamma) + N_s\,\mathrm{var}(s^2)}}\right).
\end{aligned} \tag{A8}$$

For a Rayleigh-fading channel, using Eq. (20), one finds $\mathrm{var}(s^2) = 4\sigma_s^4$ and

$$P_D = Q\left(\frac{\eta - 2N_s\sigma_N^2(1+\gamma)}{\sqrt{4N_s\sigma_N^4(1+2\gamma) + 4N_s\sigma_s^4}}\right), \tag{A9}$$

where $\gamma = E_s(s^2)/2\sigma_N^2 = \sigma_s^2/\sigma_N^2$ is the mean input SNR. The relationship between the detection probability and the false alarm probability is given by

$$P_D = Q\left(\frac{Q^{-1}(P_{\mathrm{FA}}) - \gamma\sqrt{N_s}}{\sqrt{1+2\gamma+4\sigma_s^4/4\sigma_N^4}}\right) = Q\left(\frac{Q^{-1}(P_{\mathrm{FA}}) - \gamma\sqrt{N_s}}{1+\gamma}\right). \tag{A10}$$

For a log-normal-fading channel, using Eq. (2), one finds $E_s(s^2) = \exp(2\mu_s + 2\sigma_s^2)$ and $\mathrm{var}(s^2) = \exp(4\mu_s + 4\sigma_s^2) \times [\exp(4\sigma_s^2) - 1]$. Equation. (A8) then yields

$$P_D = Q\left(\frac{\eta - 2N_s\sigma_N^2(1+\gamma)}{\sqrt{4N_s\sigma_N^4[1+2\gamma+\gamma^2(\exp(4\sigma_s^2)-1)]}}\right), \tag{A11}$$

where $\gamma = E_s(s^2)/2\sigma_N^2 = \exp(2\mu_s + 2\sigma_s^2)/2\sigma_N^2$ is the mean input SNR. The relationship between the detection probability and the false alarm probability is given by

$$p_D = Q\left(\frac{Q^{-1}(P_{\mathrm{FA}}) - \gamma\sqrt{N_s}}{\sqrt{[1+2\gamma+\gamma^2(\exp(4\sigma_s^2)-1)]}}\right). \tag{A12}$$

[1] J. G. Proakis, *Digital Communications* (McGraw-Hill, New York, 2001).
[2] M. Stojanovic, J. G. Proakis, J. A. Rice, and M. D. Green, "Spread spectrum underwater acoustic telemetry," Proceedings of MTS/IEEE OCEANS '98, 1998, Vol. **2**, pp. 650–654.
[3] E. M. Sozer, J. G. Proakis, M. Stojanovic, J. A. Rice, A. Benson, and M. Hatch, "Direct sequence spread spectrum based modem for under water acoustic communication and channel measurements," Proceedings of MTS/IEEE OCEANS '99, 1999, Vol. **1**, pp. 228–233.
[4] G. D. Weeks, J. K. Townsend, and J. A. Freebersyser, "A method and metric for quantitatively defining low probability of detection," IEEE Military Communication Conference Proceedings, 1998, Vol. **3**, pp. 821–826.
[5] H. Urkowitz, "Energy detection of unknown deterministic signals," Proc. IEEE **55**, 523–531 (1967).
[6] M. Stojanovic and L. Freitag, "Hypothesis-feedback equalization for direct-sequence spread-spectrum underwater communications," Proceedings of MTS/IEEE OCEANS '00, 2000, Vol. **1**, pp. 123–129.
[7] F. Blackmon, E. M. Sozer, M. Stojanovic, and J. Proakis, "Performance comparison of RAKE and hypothesis feedback direct sequence spread spectrum techniques for underwater communication applications," Proceedings of MTS/IEEE OCEANS '02, 2002, Vol. **1**, pp. 594–603.
[8] M. Stojanovic and L. Freitag, "MMSE acquisition of DSSS acoustic communications signals," Proceedings of MTS/IEEE Oceans '04, 2004, Vol. **1**, pp. 14–19.
[9] T. C. Yang and W.-B. Yang, "Low signal-to-noise-ratio underwater acoustic communications using direct-sequence spread-spectrum signals," Proceedings of OCEANS 2007, Aberdeen, UK, 2007.
[10] T. C. Yang and W.-B. Yang, "Performance analysis of direct-sequence spread-spectrum underwater acoustic communications with low signal-to-noise-ratio input signals," J. Acoust. Soc. Am. **123**, 842–855 (2008). The cross-correlation method was introduced in this paper using the concept of time-updated passive-phase conjugation. Channel estimation is not required in actual implementation.

[11]T. C. Yang, "Temporal fluctuations of broadband channel impulse functions and underwater acoustic communications at 2–5 kHz," Proceedings of IEEE/MTS OCEANS 2002, Biloxi, Oct. 2002, Vol. **4**, pp. 2395–2400.
[12]R. A. Iltis and A. W. Fuxjaeger, "A digital DS spread-spectrum receiver with joint channel and Doppler shift estimation," IEEE Trans. Commun. **39**, 1255–1267 (1991).
[13]T. C. Yang, "Measurements of temporal coherence of sound transmissions through shallow water," J. Acoust. Soc. Am. **120**, 2595–2614 (2006).
[14]B. Sklar, *Digital Communications: Fundamentals and Applications* (Prentice-Hall, Englewood Cliffs, NJ, 1988), Chap. 3, Sec. 7.
[15]J. H. Park, Jr., "LPI techniques in the underwater acoustic channel," Proceedings of IEEE Military Communication Conference, 1986, Vol. **1**, pp. 10.5.1–10.5.5.
[16]D. G. Woodring, "Performance of optimum and suboptimum detectors for spread spectrum waveforms," Naval Research Laboratory Report No. 8432, Washington, DC (1980).
[17]M. D. Collins, "A higher-order parabolic equation for wave propagation in an ocean overlying an elastic bottom," J. Acoust. Soc. Am. **86**, 1459–1464 (1989).
[18]R. J. Urick, *Principles of Underwater Sound* (McGraw-Hill, New York, 1983).
[19]R. Coates, *Underwater Acoustic Systems* (Wiley, New York, 1989).

Moving microphone arrays to reduce spatial aliasing in the beamforming technique: Theoretical background and numerical investigation

Alfredo Cigada, Massimiliano Lurati, Francesco Ripamonti,[a] and Marcello Vanali
Mechanical Engineering Department, Politecnico di Milano, Via La Masa 1, 20156 Milano, Italy

(Received 23 April 2008; revised 10 September 2008; accepted 14 September 2008)

This paper introduces a measurement technique aimed at reducing or possibly eliminating the spatial aliasing problem in the beamforming technique. Beamforming main disadvantages are a poor spatial resolution, at low frequency, and the spatial aliasing problem, at higher frequency, leading to the identification of false sources. The idea is to move the microphone array during the measurement operation. In this paper, the proposed approach is theoretically and numerically investigated by means of simple sound propagation models, proving its efficiency in reducing the spatial aliasing. A number of different array configurations are numerically investigated together with the most important parameters governing this measurement technique. A set of numerical results concerning the case of a planar rotating array is shown, together with a first experimental validation of the method. © *2008 Acoustical Society of America.* [DOI: 10.1121/1.2998778]

PACS number(s): 43.60.Fg, 43.60.Jn, 43.60.Lq, 43.60.Qv [EJS] Pages: 3648–3658

INTRODUCTION

In the design of a new component, a complete machine, or a new plant, particular care must be paid to avoid annoyance related to high noise levels. When, referring to laws and standards (e.g. ISO 362-1 and ISO 3095), noise levels exceeding the limits are encountered, the project engineer is interested in identifying the sources of the perceived noise in order to develop and implement solutions to reduce it. Therefore, techniques that able not only to measure the overall emission level but also to localize the single sound sources are useful to solve the problem.

Literature offers different techniques dealing with noise source localization. Among these, the most relevant are the sound intensity techniques,[1] the beamforming,[2,3] the near field acoustic holography (NAH),[5,6] and the Helmholtz equation least square (HELS) method.[7,8] The sound intensity method measures the intensity from different directions using a specific probe with two closely spaced microphones. All the other methods (beamforming, NAH, and HELS) instead use microphone arrays in order to measure the acoustic pressure field in a great number of points at the same time, involving advantages in the identification capability and the achievable performances. Each method then processes the measured data in order to reconstruct the pressure field on the source surface, allowing the localization of the most emitting regions.

Among these techniques, the beamforming[2,3] is a powerful analysis tool in a wide range of practical situations. In particular, it requires a lower number of measurement points with respect to NAH (Refs. 5 and 6) and HELS,[7,8] involving therefore fewer microphones and lower costs; measurements can be performed in the far field, while NAH and HELS need to place the transducers in the near field, very close to the source surface, and sometimes this is not feasible; the beamforming algorithm can be applied to both static and moving sources, while the static case is a NAH and HELS prerequisite.

On the other hand, beamforming presents two main disadvantages:

- a worse spatial resolution if compared to NAH and HELS, i.e., a worse capability to distinguish two close sound sources;
- the appearance of false sources in the reconstructed field at higher frequencies, as a consequence of spatial aliasing errors.

The actual method performances depend on the specific array characteristics: number of transducers, array dimension (aperture), microphone distribution, source-to-array distance,[2,3] but the frequency range is limited by the above mentioned problems. A typical frequency range is between 500 Hz and 2 kHz. These limits strongly reduce the beamforming applications, raising, at the same time, the interest of the scientific community toward possible improvements.

The present work is focused on the spatial aliasing issue. A new approach is suggested and developed in order to reduce errors due to this phenomenon. This new approach is based on the use of moving microphone arrays in the measurement operation.

In this paper, the proposed approach is theoretically studied and numerically investigated. In Sec. I, a theoretical analysis is given, describing the beamforming algorithms. In Sec. II, the real performances of the proposed method are analyzed by means of numerical simulations. At the end, the first example of experimental result is given, while the extensive series of tests performed to validate the method and some examples of practical applications will be published in the following paper.

[a]Author to whom correspondence should be addressed. Electronic mail: francesco.ripamonti@polimi.it

 © 2008 Acoustical Society of America

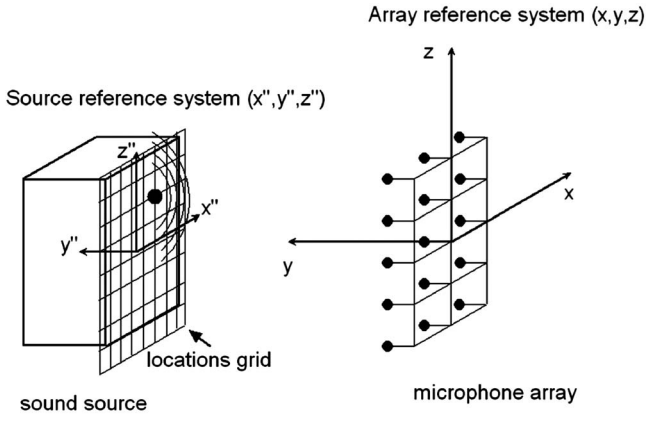


FIG. 1. Microphone array measurements for beamforming technique.

I. THEORETICAL BACKGROUND

Different beamforming algorithms can be applied to the microphone array measurements. In this paper, the DELAY&SUM algorithm[2] is considered, summarizing its formulation and focusing on the spatial aliasing phenomenon.

The beamforming method assumes all the possible sound sources as point ones, therefore radiating spherical waves in the space.[3] It means that a sound wave emitted at time t_e from a source will be received by an observer (e.g., a generic microphone) after a time delay $\Delta t = R/c$, where R is the source-to-observer distance and c is the sound speed in the considered medium. The same wave undergoes an amplitude reduction, which can be considered linear with the distance in the adopted spherical propagation model.[4]

The method starts from a number of acoustic measurements, collected with a microphone array and combines them (*Sum*) taking into account the different acoustic paths (*Delay*) between the suspected source locations and the measurement points. Besides the measured pressures, the method requires as inputs the position of the microphones and the coordinates of the reconstruction grid, i.e., the output locations (Fig. 1). The time delays, or phase shifts in the frequency domain, are calculated knowing the distances between the measurement points and the reconstruction locations. For each location, the beamforming output is calculated averaging the properly shifted microphone signals. By changing the different locations, a full scan of the area, to which the sources are presumed to belong, is performed and an acoustic map of the generated sound field is obtained. The key points, allowing the source identification, are as follows.

- If the focused location corresponds to an actual sound source, the DELAY&SUM algorithm performs a constructive sum (all the corrected signals will have the same phase), and the algorithm output is equal to the actual source sound pressure level[4] (SPL).
- If, conversely, the location does not correspond to a source, the sum is destructive and the output is attenuated.

The beamforming equation is

$$b(t,x,z) = \frac{1}{N}\sum_{i=1}^{N} R_i \cdot p_i(t + R_i/c), \tag{1}$$

where $b(t,x,z)$ is the algorithm output (function of the location coordinates x,z and the time t), N is the number of microphones, p_i is the pressure measured by the ith microphone, R_i is the distance between the source and the ith microphone, and c is the speed of the sound in the medium.

When the acoustic emission is stationary, Eq. (1), written in the time domain, can be replaced by its transformation in the frequency domain. This change of domain is useful as the computational effort is reduced by means of fast Fourier transform algorithms and the beamforming process becomes faster. In the frequency domain, the time delays are replaced by the phase shift terms, and the algorithm output is a function of the circular frequency ω instead of time t. Expression (1) becomes

$$\tilde{B}(\omega,x,z) = \frac{1}{N}\sum_{i=1}^{N} R_i \cdot \tilde{P}_i(\omega) \cdot e^{j\omega(t+R_i/c)}, \tag{2}$$

where $\tilde{B}$ and $\tilde{P}_i$ are the Fourier transform of the beamforming output (b) and the measured pressures (p_i), respectively. Since this formulation requires the phenomenon to be stationary, it cannot be used with moving sound sources (e.g., in pass-by tests [9–11]).

The beamforming output is usually graphically represented by the beampattern, a three dimensional plot that shows the SPL as a function of the considered location coordinates. Figure 2 gives an example of the beampattern typical shape. Its most important features are a main lobe, in correspondence of the source position, and other lower amplitude side lobes. The side lobe height decreases moving away from the main lobe. The side lobe level and their amplitude attenuation rate are representatives of the actual array capability to correctly separate the different source contributions similar to classical time domain window performances.

The method, as previously stated, has two main limits that reduce its performances and possibility of practical applications.

- Under conditions that will be discussed in the following (Sec. I A), the side lobes can grow to a level close to the main lobe or even higher, causing the appearance of the so called "ghost sources;" this phenomenon, called spatial aliasing, becomes critical at high frequencies and introduces mistakes in the identification process.
- The spatial resolution capability, defined as the lowest distance at which two adjacent sources can be separated in the array output, becomes worse for low frequency values; the first estimation of the theoretical spatial resolution (RES) can be calculated with the Rayleigh formula:[2,3]

$$\mathrm{RES} = a\frac{h \cdot \lambda}{L\cos^3 \vartheta}, \tag{3}$$

where a is a coefficient ($a=1$ for linear arrays and $a=1.2$ for circular arrays), h is the distance between the array plane and the source plane, λ is the source wavelength, L

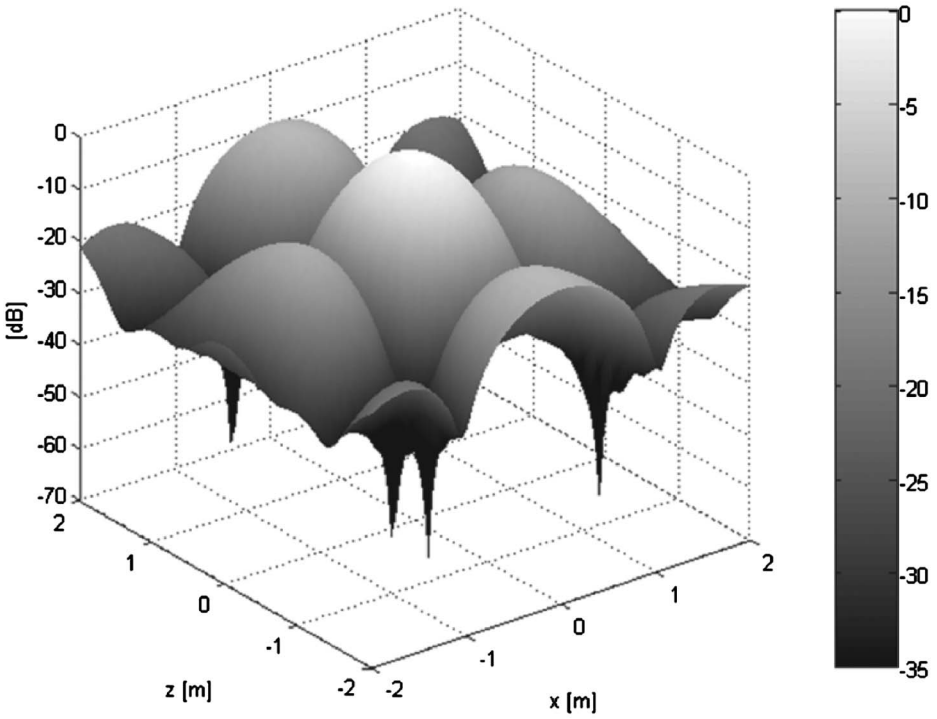


FIG. 2. Numerical beampattern for a sound source placed in $x=0$ m, $y=0$ m.

is the array dimension, and ϑ is the angular source position as seen from the array center (Fig. 3).

It is remembered that the paper aim is the investigation of the first aspect, spatial aliasing, and developing an innovative methodology in order to reduce or possibly suppress its effects. Anyway, because of the link between the two topics, the benefits due to the aliasing suppression allow a better resolution capability as well. The next section deeply investigates the spatial aliasing phenomenon, justifies the appearance of ghost sources, and explores the existing solutions.

A. Spatial aliasing

From a theoretical point of view, aliasing occurs when the reconstruction process, applied to a generic location, leads to the same phase lags in the microphone signals as those calculated for the source location. Under these conditions, the DELAY&SUM algorithm finds local maxima in the output, not necessarily corresponding to real sources, therefore failing the identification. As the well known frequency/time aliasing problem, the error introduced in this reconstruction cannot be corrected *a posteriori*. The phenomenon is linked to the phase shift between different measurement points, whose position is fixed in space; therefore, it depends on the wavelength of the considered signal and then on its frequency. In order to better understand the origin of the spatial aliasing, some evaluations on general cases are given. Let us consider a linear and equally spaced array placed in the far field, in front of a generic source, for two different positions with respect to the array (Fig. 4). Under these hypotheses, the wave fronts become almost planar, and a simpler propagation model can be adopted.[2,3] From geometrical evaluations, it is possible to estimate the maximum allowable frequency as that at which the wave front impacts all microphones with the same phase in both the considered situations (source 1 and source 2, Fig. 4):

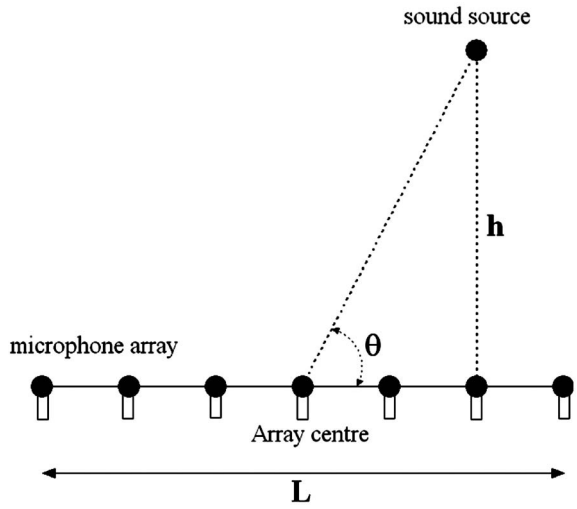


FIG. 3. Parameters influencing spatial resolution.

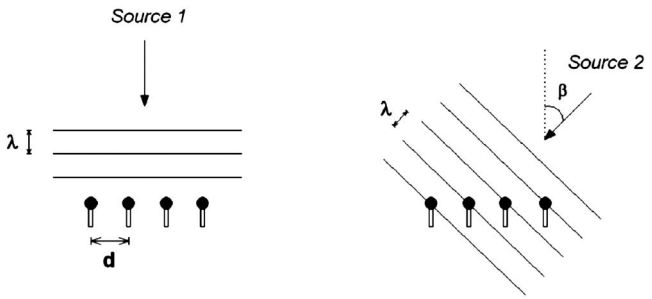


FIG. 4. The spatial aliasing phenomenon under planar wave assumption.

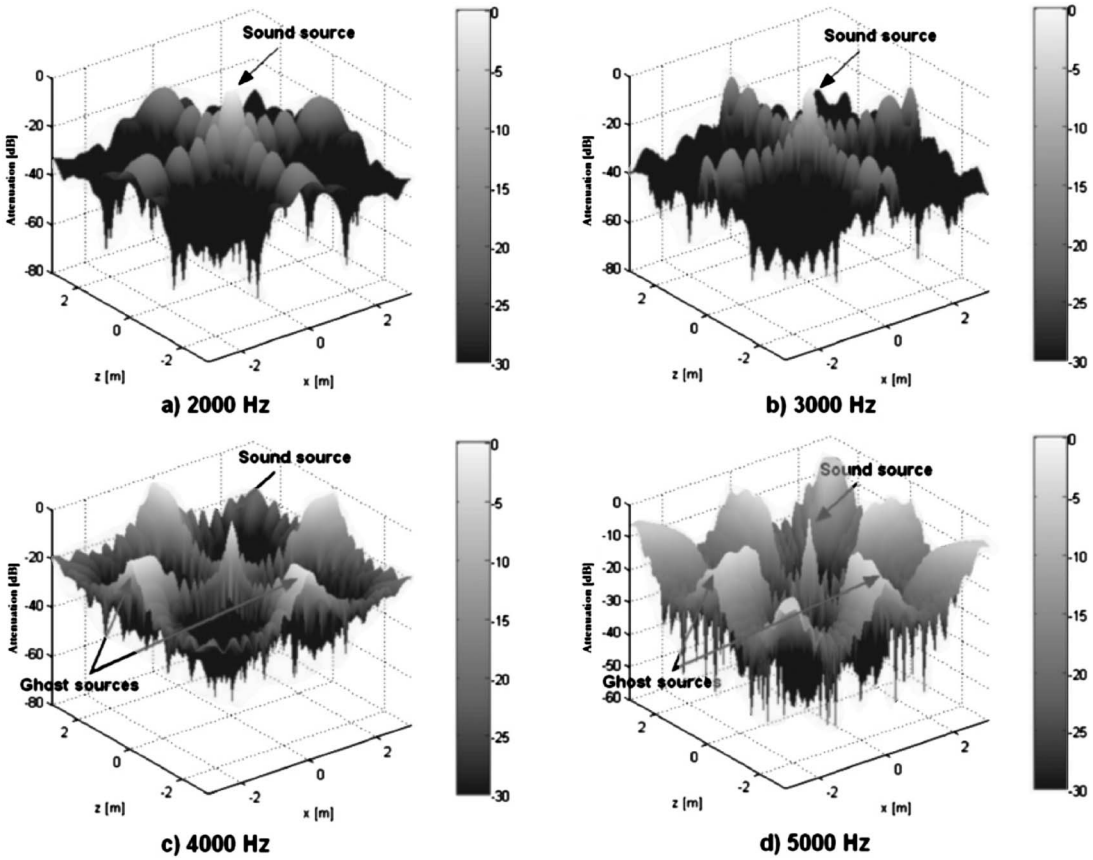


FIG. 5. Numerical beampattern for a 2000–5000 Hz sound source placed in $x=0$ m, $y=0$ m; spatial aliasing effects and ghost sources appearance.

$$f_{\max} = \frac{c}{d \sin \beta}, \tag{4}$$

where d is the microphone spacing, β is the source angular position as seen from the array center and normal to the array line, while c is the sound speed in the considered medium. As an example, a linear array with $d=10$ cm has a maximum measurable frequency of about 3400 Hz, considering that the most critical condition is $\beta=90°$.

In the case of planar (grid) arrays, the aliasing effects can be observed in Fig. 5. A pure tone source placed in front of the array center ($x=0$ m, $z=0$ m), increasing its frequency from 2 to 5 kHz is considered, for the same array configuration ($d=10$ cm). Ghost sources appear in the beampattern when the source frequency exceeds the calculated limit, revealing the presence of sources which actually do not exist. It can be noted, in fact, that, when the frequency value is equal to 2 kHz [Fig. 5(a)] and 3 kHz [Fig. 5(b)], the source is correctly identified in $x=0$ m, $z=0$ m, but when the value is equal to 4 kHz [Fig. 5(c)] and 5 kHz [Fig. 5(d)], the side lobe growth is well visible, and ghost sources appear near the real one.

From this theoretical analysis, it can be drawn that the only way to avoid aliasing errors is to reduce the microphone spacing d. Anyway, this involves an increase in the transducers number in order not to reduce the geometrical aperture L^3 and, as a consequence, not to worsen the resolution [as previously introduced in Eq. (3)]. In most cases, this important need in the microphone number is not practically achievable due to the high involved costs.

A partial practical solution can be the multistep acquisition technique. The single step acquisition with a high number of microphones is replaced by the use of a subarray composed by a smaller number of transducers, sharing the acquisition process in subsequent sessions and changing the

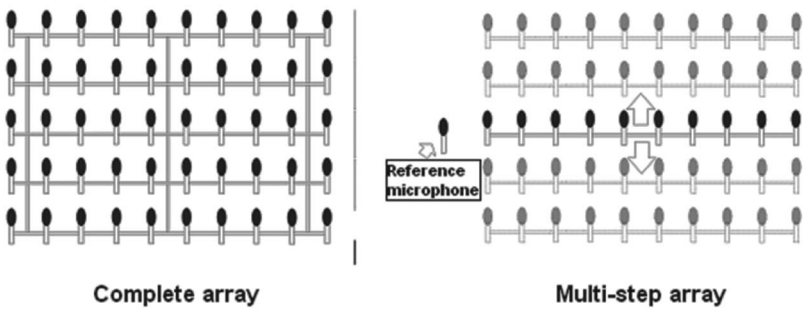


FIG. 6. The complete array and the multistep array configuration.

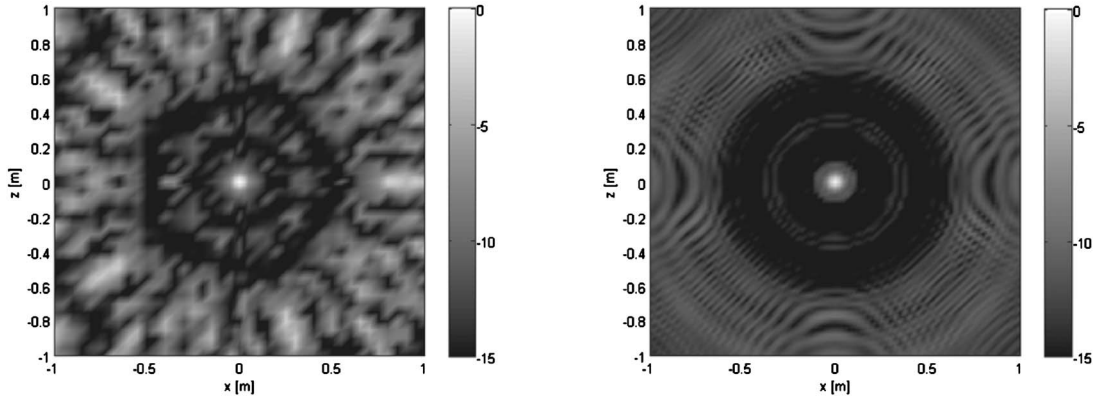


FIG. 7. Numerical beampattern for a 8000 Hz sound source placed in $x=0$ m, $y=0$ m; comparison between static (a) and moving arrays (b).

position step by step (Fig. 6). An extra microphone, whose position is fixed, is needed as "phase reference" for the postprocessing. This approach allows to preserve the microphone number and so the measurement setup costs, but an important increase in the measurement time is generated, thus requiring the sources to be active and stationary for a long time period (not always possible). Another technique adopted for side lobe reduction is the use of sparse or irregular arrays,[12] e.g., geometrical configurations in which the microphone positions are nonredundant. It means that the relative distances between transducers are not repeated between different pairs, thus decreasing the probability that different source positions would give the same algorithm outputs. Anyway these solutions, even if widely used in practice, do not completely cancel the aliasing phenomenon, enforcing the idea that something better could be done in terms of aliasing suppression and measurement efficiency, as will be shown in the following section.

B. Aliasing suppression using moving arrays

In this paper, a different approach is proposed in order to reduce and even suppress the spatial aliasing errors. The new idea is to increase the number of measurement points by actuating, with a never stopping motion, the frame supporting the array during the acquisition process. The number of measurement points is therefore increased in a fictitious way, without actually increasing the transducer number and only slightly increasing the measurement time, since the data acquisition is still performed in a single session. Due to the array movement, each pressure value is sampled at a different position along the trajectory described by each microphone, allowing to virtually increase the number of microphones.

In the case of moving arrays, the DELAY&SUM algorithm in the frequency domain (2) cannot be applied, being the phenomenon, as seen by the microphones, nonstationary. On the other hand, the time domain formulation (1) is still valid. The more general expression considers that the source-to-array distance R can be a function of time t:

$$b(t,x,z) = \frac{1}{N}\sum_{i=1}^{N} R_i(t) \cdot p_i(t + R_i(t)/c). \tag{5}$$

As a consequence of the time domain formulation, a greater computational effort is needed in order to postprocess the data, even if this drawback is partially overcome by the modern computer performances.

The method capabilities in suppressing the aliasing errors are illustrated with a simulated example. A comparison between the beampattern in the case of static (a) and moving (b) array processing has been performed and shown in Fig. 7. The test case conditions are listed below:

- a 8 kHz sound source placed in $x=0$ m, $z=0$ m;
- a 20 microphone pentagonal array (Fig. 8), placed in front of the source at 1 m distance.

Figure 7 shows that the beampattern (two dimensional representation), obtained using the traditional beamforming,

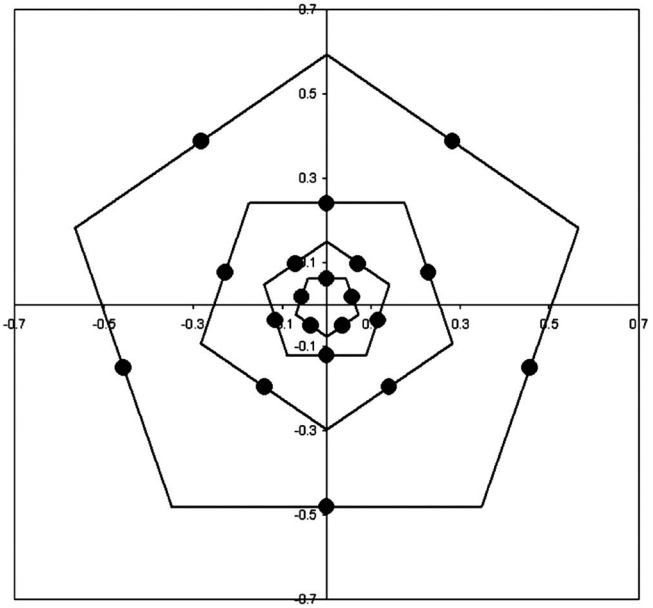


FIG. 8. 20 microphone pentagonal array.

is strongly influenced by the aliasing errors (the presence of at least five ghost sources in the surrounding of the main lobe). The ghost sources disappear using the moving array, therefore showing the possible improvements and demonstrating the method capability.

The type of movement and the microphones trajectories represent a key point in this method employment. Different motions can be used in different kinds of applications, both for the static and dynamic sources. The proposed method is valid for all possible motion laws and this specific paper deals with the case of static sources and rotating arrays, leaving the study of other more complicated solutions to future works. Microphones follow circular trajectories and uniformly cover the measurement plane in front of the fixed source. The use of rotating microphone arrays was previously proposed by Bryden *et al.*[13,14] in order to maximize the spatial resolution in the case of underwater acoustic measurements with hydropohone arrays.

As previously explained, the array motion allows to measure the sound pressure in a higher number of points with respect to the static case. In the following, the term "measurement grid" will be replaced by "measurement curves", since the microphone trajectories, from a theoretical point of view, are continuously covered.

II. NUMERICAL SIMULATIONS

In order to show the possible improvement that this solution is able to achieve, a set of tests has been planned and carried out. Results are presented and commented in this section. As the closed formula, giving the method output for the moving array approach, is not available, the performances have been investigated through numerical simulations.

In the classical beamforming, as stated by Eq. (3), the most important influencing parameters are as follows:

(i) the array aperture L;
(ii) the source-to-array distance h;
(iii) the microphone spacing d;
(iv) the angular position of the source ϑ.

All these parameters will not be directly investigated in the present paper, as their effects on the resulting beampatterns are the same as in the static case.[3]

In this paper, instead, attention is focused on the new variables introduced by the moving array technique to state their influence on the method performances.

Due to the kind of the considered motion (rotating array), the influence of the following parameters has been investigated: angular velocity, angle covered by the rotation, and array geometry.

Simulations have been performed relying on numerical models reproducing the sound propagation from the source toward the moving microphones. Two equal sources (113 dB SPL placed at 2 m from the microphone plane) have been modeled as monopoles, therefore involving a spherical wave propagation model, while the microphones have been considered as ideal transducers, i.e., not introducing amplitude or phase distortions.

The array rotation has been simulated moving the measurement points on circular trajectories with different velocities. The general time domain DELAY&SUM algorithm[2] has been applied to process the data and to obtain the output beampattern. The most important results are summarized in the next sections.

A. Angular velocity

The angular velocity range is practically limited by the aerodynamic noise generated by the array motion, producing a relative speed. High rotation speed will produce a nonnegligible air flow around the microphones, leading to an important background noise. Specific windscreens applied to the microphones allow to accept air speed up to about 6 m/s, although this is a limit not to be reached in practical applications.

This means that considering a common array with an outer diameter of about 2 m, acceptable values for the angular velocity should be lower than 6 rad/s. The effects of different speed values, 1.57, 6.28, and 12.56 rad/s, have been investigated. It has to be noted that the third case trespasses the above mentioned threshold: all the same, this situation has been numerically simulated, not accounting for the windscreen problems, in order to investigate the effects of higher speeds. The simulations refer to a single sound source (1 kHz), placed in $x=0$ m, $z=0$ m, analyzed with a 20 microphone linear array rotating around its centre (Fig. 9, type A). Because the velocity influences the number of virtual microphones, it could be expected that different speed values would lead to different performances, worsening for higher values.

On the other hand, the results shown in Fig. 10 clearly demonstrate that the frame angular velocity does not influence the method output.

B. Angle covered by the rotation

Two different situations can be identified for the rotation: partial and complete revolutions. The effects on the beampattern have been investigated performing simulations with a 20 microphone linear array, rotating around its center, in four different conditions: 1/3 of turn, 1 full turn, 5 full turns, and 1+1/3 turn. The reasons leading to these choices will be clear discussing the obtained results (Fig. 11).

Figure 11(a) shows the incomplete revolution case; only 120° are covered by the rotation. In this case, the scanned surface is not uniformly cover. The resulting beampattern shows a stretched main lobe and a strongly asymmetric shape with two different side lobe attenuation levels: a −5 dB zone corresponding to the space covered during the microphones motion and a −15 dB zone elsewhere. This asymmetry in the side lobe levels disappears performing a complete rotation [Fig. 11(b)]. In this case, due to the uniformly covered scanned surface, the beampattern has a symmetrical shape and the side lobe suppression level is about −7 dB. Even if this value is not much higher than the −5 dB obtained in the previous case, it is a great asset in the case of multiple emitting sound sources (analyzed in detail in the following), when the final beampattern comes from the sum

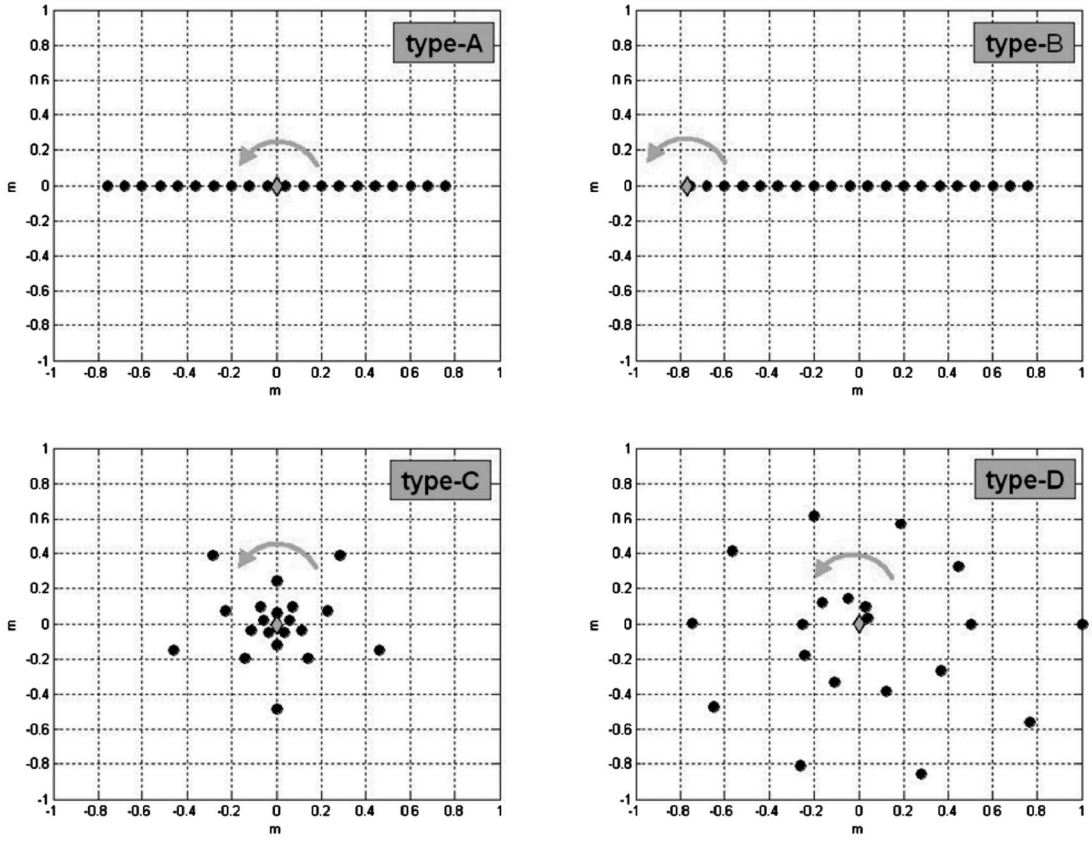


FIG. 9. Microphone array configurations.

of different contributions. Figure 11(c) shows that there are no differences performing five complete turns instead of only one turn: no improvements are obtained covering the same measurement points several times. Finally, considering a complete rotation with a noninteger number of turns [1 +1/3 turns, Fig. 11(d)], it is possible to observe a behavior similar to the partial revolution case [Fig. 11(a)], even if the asymmetry is not as marked as in the case of the 120° rotation.

Going back to the case of multiple emitting sources, a further simulation is given with two sources (a 1 kHz source in $x=0$ m, $z=0$ m, and a 2 kHz source in $x=-1$ m, $z=0$ m). The negative effects due to an incomplete rotation can be better highlighted in this case [Fig. 12(a)]: a growing side lobe on the left region of the plot causes a false identification, and a worse spatial resolution is clearly visible in the two main lobes. The complete rotation with an integer number of turns corrects both these problems [Fig. 12(b)].

C. Array geometry

The investigation of this aspect is highly complicated due to the great number of possible array geometries (almost infinite). Even if the correct design of the array (which should be specific for each application) is very important for the static case too, in the moving approach it becomes a key

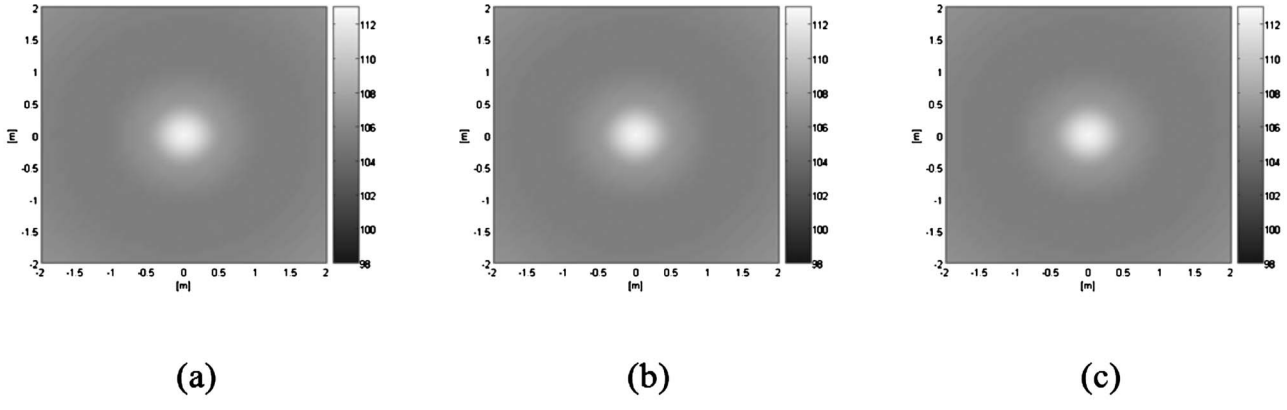


FIG. 10. Numerical beampattern for a 1000 Hz sound source placed in $x=0$ m, $y=0$ m; comparison between 1.57 rad/s (a), 6.28 rad/s (b), and 12.56 rad/s (c) angular velocities.

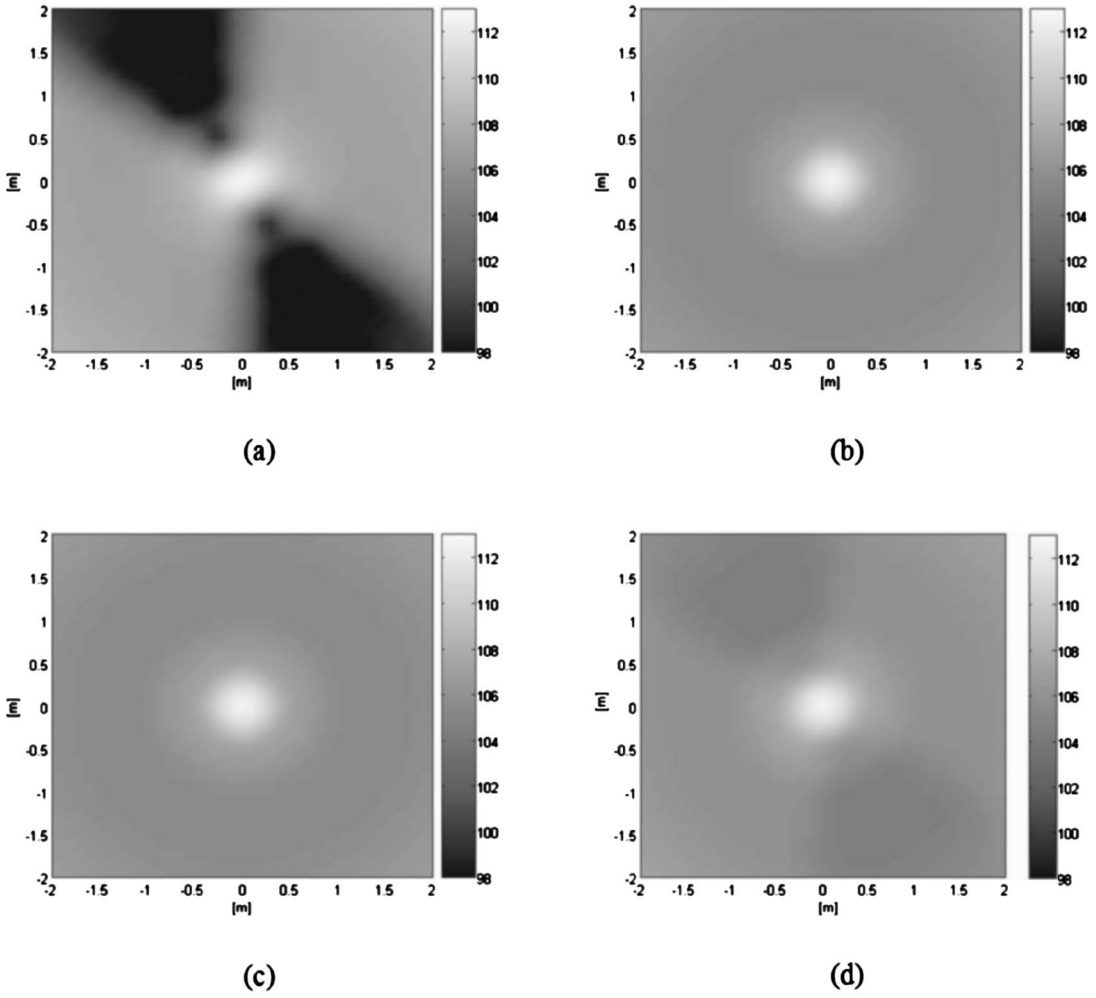


FIG. 11. Numerical beampattern for a 1000 Hz sound source placed in $x=0$ m, $y=0$ m; comparison between 1/3 of turn (a), 1 full turn (b), 5 full turns (c), and 1+1/3 of turn (d) revolution angle.

point. In general, the idea, suggesting to uniformly cover the measurement space, is considered valid also in the case of moving arrays.

In this paper, five different array configurations, taken as an example to represent different geometry concepts and named in the following type A-B-C-D (Fig. 9), have been proposed and tested. In order to perform a direct comparison of the performances in terms of side lobe suppression, all the configurations are composed by the same number of transducers, equal to 20, and used in the same test conditions, i.e., with two emitting sound sources (a 1 kHz source in $x=0$ m, $z=0$ m, and a 2 kHz source in $x=-1$ m, $z=0$ m). The array

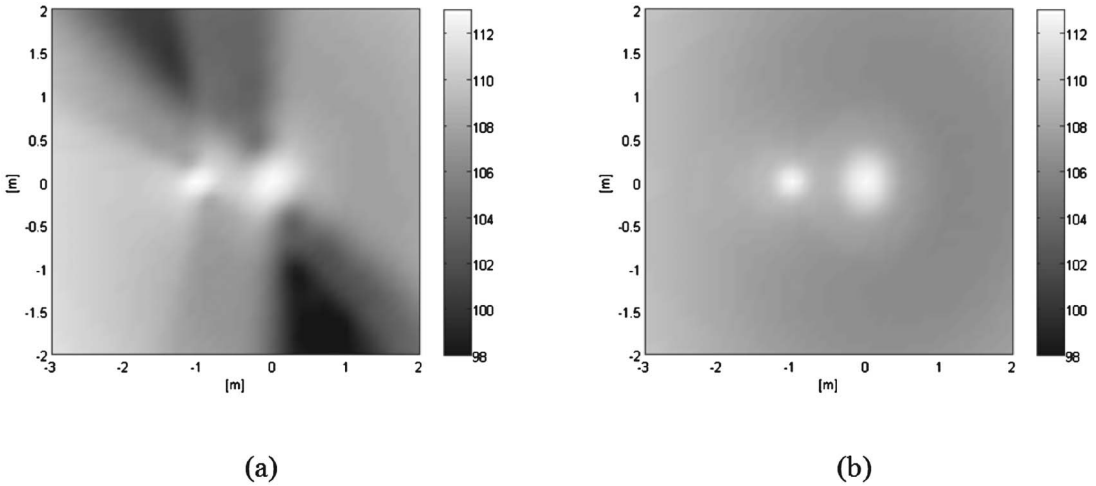


FIG. 12. Numerical beampattern for two close sound sources; comparison between partial (a) and complete (b) rotations.

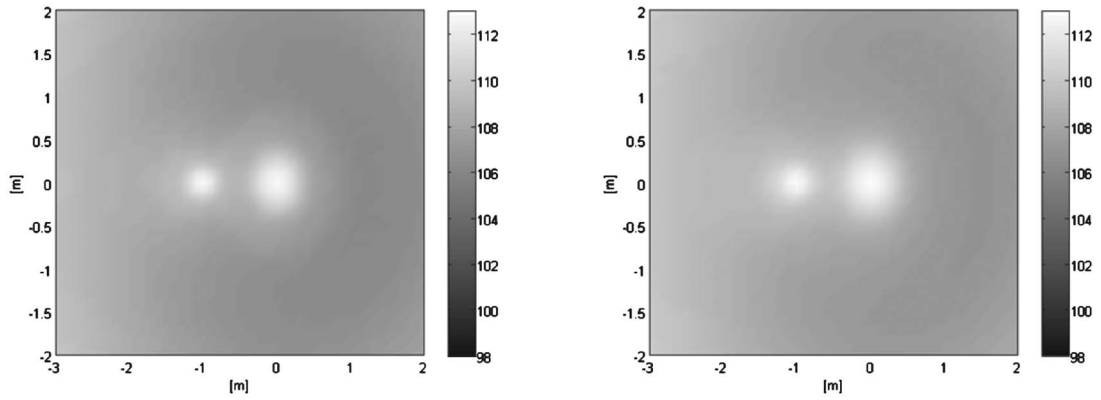


FIG. 13. Numerical beampattern for two close sound sources for the type A (a) and type B (b) arrays.

configurations are as follows:

- linear array, 8 cm spacing, rotating around its center (Fig. 9, type A);
- linear array, 8 cm spacing, rotating around its extreme point (Fig. 9, type B);
- pentagonal array,[3] rotating around its center (Fig. 9, type C);
- geometric spiral array, rotating around its center (Fig. 9, type D).

The obtained results are shown in Figs. 13 and 14. Type A array [Fig. 13(a)] shows a generally good behavior, evidencing a good side lobe suppression besides a good resolution capability. Type B array [Fig. 13(b)], based on the same static geometry but with a shifted rotation center, shows worse results. Even if a better spatial resolution could be expected because of the greater array aperture generated by the rotation,[3] actually the effect is the opposite: both side lobe attenuation and spatial resolution are worse than expected. This is due to the source position that is always not centered with respect to the array during the motion, causing a strong decrease in the resolution capability [as stated by the Rayleigh formula (3)]. Type C array [Fig. 14(a)] has better performances in terms of side lobe suppression, due to its well balanced planar configuration. On the other hand, it has a worse spatial resolution due to the narrow aperture. Better performances can be achieved placing microphones along a spiral distribution, thus optimizing the static configuration. The geometric step spiral [Fig. 14(b)] achieves better results in terms of both resolution and side lobe suppression.

In order to better understand the improvements related to use of the proposed rotating array, a comparison between the static and the moving case is reported in Fig. 15, for the pentagonal geometry (type C), and in Fig. 16, for the spiral geometry (type D).

It is to be highlighted that both these configurations, if used in the traditional static way, are already influenced by aliasing errors at 2 kHz. The array rotation allows to reduce and even avoid the problem, eliminating the ghost images and providing the correct sound source identification.

III. EXPERIMENTAL VALIDATION

The first experimental validation of the proposed method has been achieved creating a rotating array and comparing

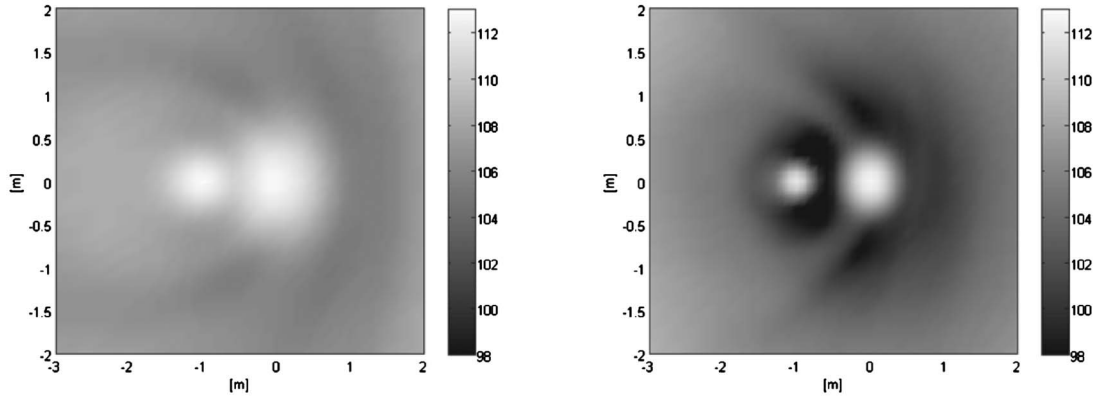


FIG. 14. Numerical beampattern for two close sound sources for the type C (a) and type D (b) arrays.

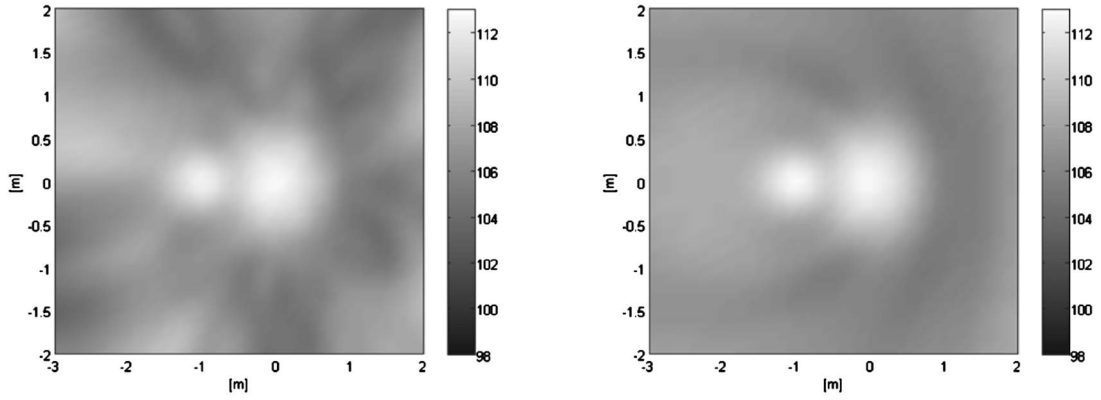


FIG. 15. Numerical beampattern for two close sound sources; comparison between static (a) and rotating (b) applications for the type C array.

the experimental to the numerical results. To this aim, a 20 microphone pentagonal array has been designed and assembled. An experimental campaign has been carried out in an external environment. The experimental setup (Fig. 17) uses a loudspeaker, placed in front of the array, to reproduce the emitting sound source. Several tests have been performed in order to investigate the system performances in different conditions, varying the frequency in the range between 1000 and 8000 Hz. Figure 18 reports the comparison between the simulation (a) and the experimental (b) test in the case of rotating approach, showing a very good agreement, for a 4000 Hz emitting sound source. Figure 18(c) shows the experimental beampattern in the traditional static case, influenced by some ghost sources, demonstrating the improvements of the proposed approach.

CONCLUSIONS

This paper presented an improvement to the beamforming sound source localization technique. In the first part, a general introduction to this widely employed measurement technique has been presented, pointing out its main advan-

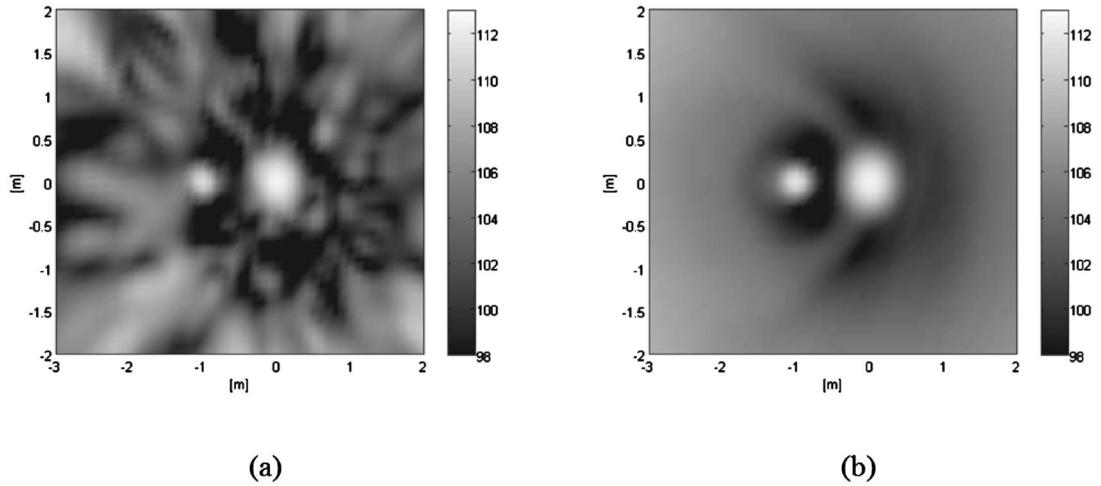


FIG. 16. Numerical beampattern for two close sound sources; comparison between the static (a) and rotating (b) applications for the type D array.

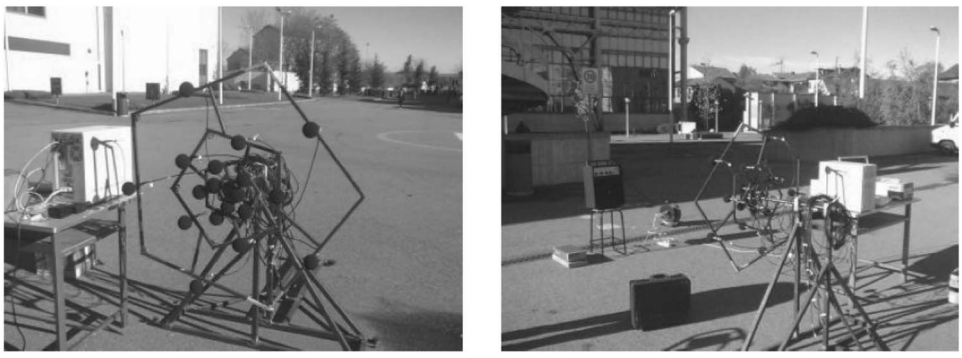


FIG. 17. The experimental setup.

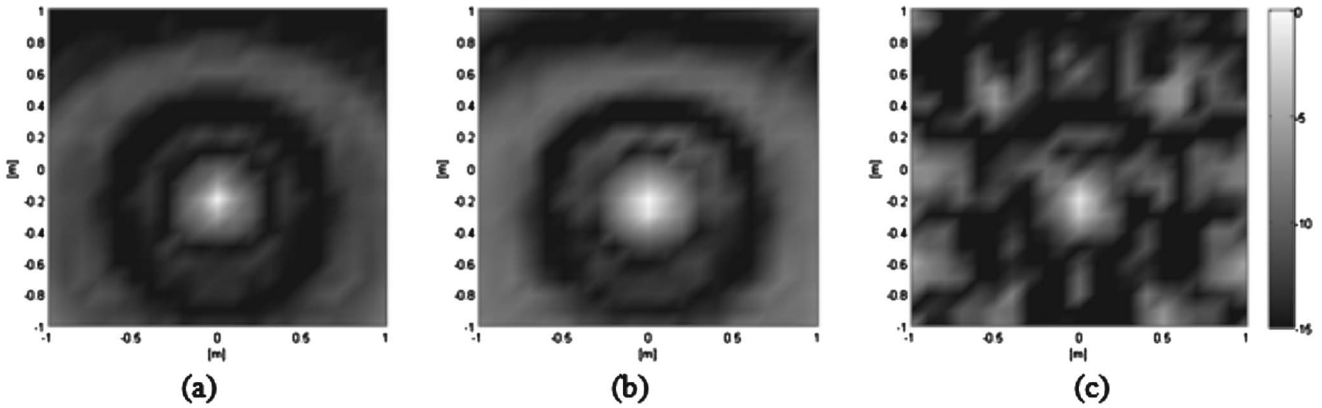


FIG. 18. Beampattern for a 4000 Hz sound source placed in $x=0$ m, $y=-0.2$ m; comparison between the numerical rotating (a), the experimental rotating (b), and the experimental static (c) beampattern for the type C array.

tages and drawbacks. Among the latter, spatial aliasing is an important one, putting strict limits on the beamforming employment at high frequencies. A solution to this problem, based on the use of moving arrays, has been proposed and its efficiency numerically investigated. The performed numerical simulations showed that this improvement is able to reduce and possibly suppress spatial aliasing at frequencies usually impossible for the commonly used arrays. The main parameters influencing the measurement quality have been investigated and their effects on the final results have been numerically proven in comparison with the commonly adopted beamforming algorithm. An extensive experimental campaign will be carried out to prove all the numerical simulation results and to show the performances in a practical application.

[1]S. Baker, "An acoustic intensity meter," J. Acoust. Soc. Am. **27**(2), 269–273 (1955).
[2]D. H. Johnson and D. E. Dudgeon, *Array Signal Processing: Concepts and Techniques* (PTR Prentice-Hall, Englewood Cliffs, NJ, 1992).
[3]A. Cigada, F. Ripamonti, and M. Vanali, "The delay & sum algorithm applied to microphone array measurements: numerical analysis and experimental validation," Mech. Syst. Signal Process. **21**(6), 2645–2664 (2007).
[4]P. M. Morse and U. Ingard, *Theoretical Acoustics* (Princeton University Press, Princeton, NJ, 1968).
[5]J. D. Maynard, E. G. Williams, and Y. Lee, "Nearfield acoustic holography: I. Theory of generalized holography and the development of NAH," J. Acoust. Soc. Am. **78**(4), 1395–1413 (1985).
[6]W. A. Veronesi and J. D. Maynard, "Nearfield acoustic holography: II. Holographic reconstruction algorithms and computer implementation," J. Acoust. Soc. Am. **81**(5), 1307–1322 (1987).
[7]Z. Wang and S. F. Wu, "Helmholtz equation least square method for reconstructing the acoustic pressure field," J. Acoust. Soc. Am. **102**(4), 2020–2032 (1997).
[8]N. Rayess and S. F. Wu, "Experimental validations of the HELS method for reconstructing acoustic radiation from a complex vibrating structure," J. Acoust. Soc. Am. **107**(6), 2955–2964 (2000).
[9]H. Kook, G. B. Moebs, P. Davies, and J. S. Bolton, "An efficient procedure for visualizing the sound field radiated by vehicles during standardized pass-by tests," J. Sound Vib. **233**(1), 137–156 (2000).
[10]F. G. De Beer and J. W. Verhej, "Experimental determination of pass-by noise contribution from the bogies and superstructure of a freight wagon," J. Sound Vib. **231**(3), 639–652 (2000).
[11]B. Barsikow, W. F. King III, and E. Pfizenmaier, "Wheel/rail noise generated by a high-speed train investigated with a line array of microphones," J. Sound Vib. **118**(1), 99–122 (1987).
[12]R. P. Dougherty and R. W. Stoker, "Sidelobe suppression for phased array aeroacoustic measurements," 19th AIAA Aeroacoustics Conference, 1998, Paper No. AIAA-1998–2242.
[13]I. G. Bryden, "Three-Dimensional acoustic mapping using small rotating arrays," J. Offshore Mech. Arct. Eng., **3**, 318–322 (1989).
[14]A. K. Lee and I. G. Bryden, "Acoustic beamforming using a novel correlation technique," Meas. Sci. Technol. **2**, 229–237 (1991).

The time-reversal operator with virtual transducers: Application to far-field aberration correction

Jean-Luc Robert
Philips Research North America, 345 Scarborough Road, Briarcliff Manor, New York 10510

Mathias Fink
Laboratoire Ondes et Acoustique, ESPCI, Université Paris 7, 10 rue Vauquelin, 75005 Paris, France

(Received 14 May 2008; revised 1 October 2008; accepted 1 October 2008)

The decomposition of the time-reversal operator (DORT) is a detection and focusing technique using an array of transmit receive transducers. It can extract Green's functions of scatterers in a medium. A variant consists in transmitting focused beams (FDORT). It is shown here that the FDORT method can be interpreted as the decomposition of a time-reversal operator between an array of virtual transducers located at the transmit beams' foci and the physical array. The receive singular vectors correspond to scatterers' Green's functions expressed in the physical array while the transmit singular vectors correspond to Green's functions expressed in the virtual array. The position of the virtual array can be changed by varying the position of the foci, thus offering different points of view. Parameters and performance of some transmit schemes are discussed. Appropriately positioning the virtual transducers can simplify some problems. One application is measuring and correcting aberration in the case of a far-field phase screen model. Placing the virtual transducers near the phase screen transforms the problem in a simpler near-field phase screen problem.
© *2008 Acoustical Society of America.* [DOI: 10.1121/1.3005560]

PACS number(s): 43.60.Fg, 43.80.Qf, 43.20.Fn [TDM] Pages: 3659–3668

I. INTRODUCTION

The DORT method[1] (French acronym for decomposition of the time-reversal operator) is a time-reversal based method that can detect point scatterers in a medium and extract their Green's functions. Green's functions can then be used to focus on the scatterers without knowledge of the medium. Applications of the method include autofocusing in inhomogeneous media and detection of scatterers.[1] It has been applied to the detection of flaw in nondestructive testing,[2] target detection and identification in underwater acoustics,[3] electromagnetism,[4] and medical imaging.[5] It has also been used with music[6] or other nonlinear methods[7] to provide localization of scatterer with super-resolution.

The original DORT method is based on the acquisition of *full data sets.* This means that the signals are transmitted with one element at a time. Drawbacks of full data sets include poor signal to noise ratio (SNR) and poor robustness to motion compared to acquisition with focused transmits typically used in ultrasonic imaging.[8] This limits the use of the method particularly in medical ultrasound.

Therefore, a method using focused transmits, termed FDORT, has been introduced in Ref. 5. An additional advantage of the method is the ability to resolve scatterers axially and to better detect point scatterers in the presence of speckle noise.[5] A modified FDORT method has also been successfully used to autofocus when only speckle signal was present.[9] It is applied to aberration correction in medical ultrasound.

The FDORT method is illustrated in Fig. 1. A beam is transmitted, and the received signals are recorded for each element. The Fourier transform of the signals is then taken. The Fourier coefficient at frequency ω for the signal received by element j when the beam i is transmitted gives the element $K_{ij}(\omega)$ of the transfer matrix $K(\omega)$.

The FDORT theory was described in Ref. 5 using a mathematical formalism. It was derived that, mathematically, the FDORT method was equivalent to the decomposition of a time-reversal operator between the physical array (corresponding to the receive process) and a virtual array (corresponding to the transmit process). The virtual array was only introduced mathematically and no physical meaning was given to it. In the present paper, it is shown that the virtual array can be interpreted physically and that the virtual transducers are located at the foci of the transmits. A more intuitive description of FDORT is proposed.

Different transmit sequences using groups of elements (like HADAMARD codes) have previously been proposed with the DORT method to improve the SNR. More recently, acquisitions using orthogonal codes have been proposed to improve the SNR and the motion robustness in a waveguide.[10] These schemes were interpreted as alternative bases where the time-reversal operator could be expressed. It is shown here that, under certain conditions, the transmit beams form an orthogonal basis.

First, we develop the concept of virtual transducers and virtual arrays. It is shown that a focused beam can be conceptually replaced by a virtual transducer located at the focus. This description is used to propose an intuitive description of the FDORT method and to give a physical meaning to the singular vectors. The main transmit beam sequences are reviewed, along with their performance. Simulation results are presented.

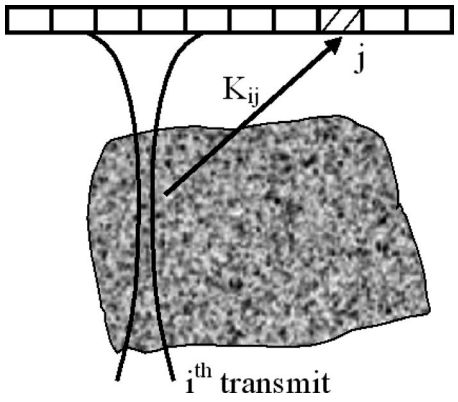


FIG. 1. Acquisition of the transfer matrix with the FDORT method. It differs from the conventional DORT method by the use of focused transmit. The element K_{ij} of the matrix is the signal received by element j after the ith focused beam has been transmitted.

Then, an application to the problem of focusing through a far-field phase screen (an aberrator located at a certain distance from the array) is presented. It is shown that the problem is simplified with the concept of virtual array, and that FDORT can provide a characterization of the phase screen. This application is particularly interesting in medical ultrasound for focusing through inhomogeneous media. An overview of the problem is also given at the beginning of Sec. III.

Further developments and figures can be found in the second chapter (in English) of the author's Ph.D. thesis.[11]

II. FOCUSED BEAMS AND VIRTUAL TRANSDUCERS

A. Virtual transducer model

In this section, it is shown that a focused beam can be conceptually replaced by a virtual transducer located at the focus.

When a transmit is focused on a point P, at depth Z, the evolution of the wave front can be separated in two different steps, as seen in Fig. 2. First, one observes a wave that converges to the focal point P [Fig. 2(a)]. As the wave gets closer from P, the lateral size of the wave front reduces. When the wave front is at P, most of the energy is concentrated in an area of lateral width $\lambda Z/D$, where D is the aperture size and λ is the wave length. The wave front is at P at time $t_0=Z/c$, where c is the speed of sound.

The wave front does not stop at P, and one observes then a wave that diverges from the point P, propagating outward [Fig. 2(a)].

1. Virtual transducer for $t>t_0$

For an observer located at a depth greater than Z, it looks like the wave is originating from a *virtual transducer* located at P. This analogy has been verified in simulation by Passman and Ermert.[12] The equivalent virtual transducer is not isotropic but has a directivity pattern with an angle θ, as shown in Fig. 2(b), so that it generates the same cone of sound as the focused transmit.

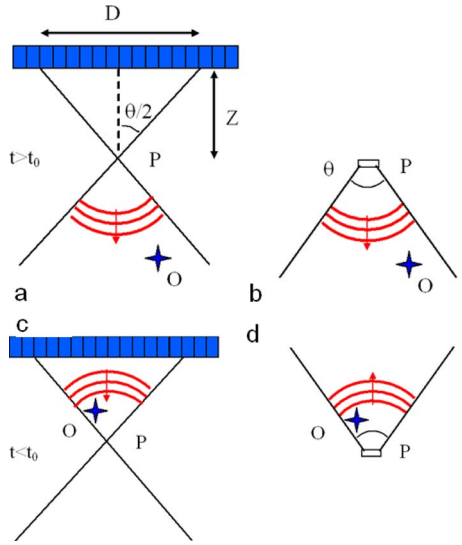


FIG. 2. (Color online) [(a) and (c)] Wave front resulting from a focused transmit, before (c) and after (a) it reaches the focal point P. For $t<t_0$, the wave is propagating inward, converging toward P. For $t>t_0$, the wave is propagating outward, diverging from P. An observer O located in the sound cone hears the wave front as if it were coming from a virtual transducer located at P. (b) Wave front for an equivalent virtual transducer (right) located at P, with a directivity angle θ, transmitting a pulse at t_0. For the observer O, fields in (a) and (b) are very similar. (d) Wave front for an equivalent virtual transducer (right) located at P and facing the array. For the observer O, the field in (c) appears similar to the time-reversed version of the field in (d).

The angle θ of the cone is defined by the geometrical relationship

$$\tan\left(\frac{\theta}{2}\right)=\frac{D/2}{Z}, \tag{1}$$

as seen in Fig. 2(b). Most of the time, the angles are small, and

$$\theta=\frac{D}{Z} \tag{2}$$

is a good approximation.

From the directivity angle of the virtual transducer, it is possible to find the size and shape of the tranducer. The directivity and size of a transducer are linked. The Fresnel relationship in polar coordinates teaches that the field pattern is given by the Fourier transform of the transducer, scaled by a factor λ. Therefore, the field produced by a virtual square element of width $\lambda Z/D$ would be a good approximation for the actual field. In fact, a more accurate equivalent virtual transducer would be a sinc function whose main lobe width is $\lambda Z/D$. The apodization of such a transducer would be described by

$$A(x)=\mathrm{sinc}\left(\frac{\pi X}{\frac{\lambda Z}{D}}\right), \tag{3}$$

where X is the azimuth in the focal plan. One can notice that the apodization function of the virtual transducer is equal to the amplitude of the transmit field in the focal plane.

The shape of the virtual transducer does not really matter. What is important for the following is that for an observer O, deeper than Z, the wave front of a focused transmit generated at $t=0$ is (almost) the same as the wave front generated at $t=t_0$ from a virtual transducer located at P, with a directivity angle $\theta=D/Z$.

By spatial reciprocity, the same concept applies in reception, if a static focused receive on P is used. Let us imagine that the observer generates a pulse at $t=0$, and then the signal recorded by the array focused in reception on P would be the same as the signal recorded by the virtual transducer t_0 seconds earlier.

In this work, the focused beams will be used mainly in transmission. But all the results could be generalized to apply in reception as well.

2. Virtual transducer for $t<t_0$

For $t<t_0$, the wave front is converging toward the focal point. It is like observing the wave front emitted by a transducer at the focal spot, but in a movie played backward. For an observer located shallower than Z, the wave front appears as a time-reversed version of the wave front emitted at $t=-t_0$ by a virtual transducer facing the array, as shown in Fig. 2(d). The virtual transducer has the same directivity $\theta=D/Z$ as the one discussed in the previous part.

In reception, the analogy is the same: by spatial reciprocity, the signal recorded by the array focused on P would be a time-reversed version of the signal recorded by a virtual transducer located at P.

The strong analogy between a focused beam and a transducer in a homogeneous medium can be understood by considering them both as Green's functions. When a single real element is fired, the signal propagating in the medium is Green's function of the element (if we consider the transducer as an ideal point). On the other hand, when one focuses on a point P using time reversal, one actually transmits Green's function of the point P (most commonly, focusing is obtained by time delays and apodization that only approximates Green's function). The real transducer has only a forward (propagating outward) component because it acts as a source. The virtual transducer has both backward and forward components because there are no sources or sinks.

A similar concept of virtual sources can be found in the literature, for example, Refs. 8 and 13.

B. The DORT method between a real array and a virtual array

It has been shown that the focused transmits were equivalent to virtual transducers. The FDORT method uses focused transmits and per element receives; therefore, it is equivalent to a DORT method between a *virtual array* whose elements are the foci for each transmit and the real physical array.

1. The focused transfer matrix and its singular vectors

The notation K now refers to the transfer matrix for the FDORT method. In this case, K_{ij} is the signal received by element j when the ith focused beam is transmitted. Using the virtual transducer model, it can be seen as the interelement response between the virtual transducer i and the real transducer j. Therefore, the matrix K describes a time-reversal operator between the virtual array and the real array. The results derived in Refs. 14 and 5 for the time reversal between two different arrays can be used.

The singular value decomposition (SVD) of the K matrix gives $\boldsymbol{K}=\boldsymbol{USV}^{\boldsymbol{H}}$, where U would contain the invariants of the time-reversal operator in the physical array (also termed *canonical array*) and V would contain the invariants expressed in the virtual array. In the case of resolved point scatterers, U contains Green's function of each scatterer in the physical array, while V contains Green's function of the same scatterers in the virtual array. For scatterers located shallower than the focal depth ($t<t_0$), V contains actually the conjugate of Green's function, because the wave fronts for the focused transmits are the time reversed of the virtual transducers wave fronts, as explained in Sec. II A 2.

The condition for scatterers' Green's functions to be separated is that the scatterers are resolved by both the real and virtual arrays. The resolution of the virtual array actually depends on the focused beams sequence. This is discussed in Sec. II B 2.

2. Example of virtual arrays and properties

There are several possibilities of choosing a scheme of focused beams. Here are the most popular ones. The consequences of each scheme on the FDORT properties are discussed.

a. Linear scan. In a linear scan, only a subaperture of the total array is usually used for a transmit. The consecutive transmits are obtained by translation of the subaperture. As a result, the virtual array is linear. This scan sequence is typically used when the region to image is a rectangle whose lateral extent is equal or less than the array width. The directivity of the elements depends on the size of the subaperture and on the focal depth, as stated in Eqs. (1) and (2).

Resolution. An important parameter is the resolution of the virtual array, as it determines if scatterers' Green's functions can be separated. The resolution is proportional to the ratio z/d, where z is the distance to the virtual array, and d is the width of the virtual array. As can be seen from Fig. 3 (right), the resolution is in this case the same for every depth and is limited by the directivity of the virtual transducers. Indeed, if z increases, the number of virtual transducers that the point can hear increases also, because of the directivity. To a good approximation, the resolution for any point is given by the formula $\lambda Z/D$, where Z is the focal depth (and not the depth of the scatterers) and D is the size of the transmit aperture. The resolution at any depth is then given by the resolution chosen for the focal depth. In general, the resolution is less good than the resolution obtained with the conventional DORT method where the full aperture is used at every depth [shown in dash line in Fig. 3 (right)].

Transducers spacing. A key parameter is the separation between two consecutive virtual transducers. A way of determining this is to use similar design rules as for an array of real transducers[15] (Sec. 6B1). Another approach, involving

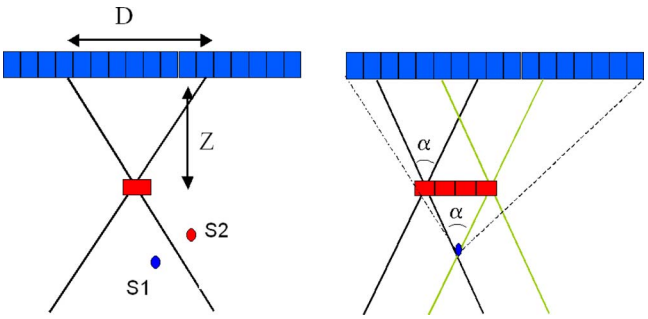


FIG. 3. (Color online) Left: each virtual transducer has a directivity function corresponding to the sound cone of the beam. Therefore, only the scatterer inside the cone (scatterer S1) will hear and be heard by the virtual transducer. The scatterer S2 does not hear the virtual transducer. Right: because of this directivity effect, a scatterer hears only a limited number of virtual transducer. The virtual array that insonifies a given point has then a limited size, which limits the resolution of the FDORT method with linear scan. It can be seen geometrically that the angle α between the scatterer and the virtual array is the same as the angle of the beams. Therefore, the resolution for any point in the medium, independent of its depth, is the same and is equal to the resolution of the focus, $a=\lambda Z/D$. The angle that would be obtained with the full aperture is shown in dash line.

the orthogonality between Green's functions, is discussed in the Sec. II C.

When the element spacing in an array is too large, grating lobes appear. Indeed, the Fresnel approximation in polar coordinates states that the field at the focal radius is given by the Fourier transform of the aperture, with scaling by λ. For a continuous aperture, this gives the well-known sinc shape of the beam pattern. However, an array is not continuous but made of a few discrete elements. To a first approximation, each element can be considered as a point. In this case, it is like the continuous array has been sampled or multiplied by a Dirac comb. Let a be the distance between the two elements. In the Fourier domain, this results in a periodic repetition of the sinc at a period $\Delta \sin\theta=\lambda/a$.[15] The repetitions of the sinc form the so-called grating lobes. The first grating lobes are then at an angle $\Delta \sin\theta=\lambda/a$ from the main lobe. As the transducer spacing increases, the grating lobes get closer to the main lobe. In fact, each element is not a point, but has a finite extent, which gives its directivity. For example, an element equivalent to a virtual transducer has a shape of $\mathrm{sinc}(\pi X/(\lambda Z/D))$ [Eq. (3)]. Therefore, the array is better modeled by the Dirac comb convolved by the sinc. In the Fourier domain, the field of the pointlike array is multiplied by the directivity function (here the Fourier transform of the sinc function). The directivity should be narrow enough so that the grating lobes are suppressed. In our case, the directivity is approximately given by $\Delta \sin\theta=D/Z$ [Eq. (2)]. The worst case happens when the main lobe is steered on the edge of the directivity function, and therefore the appropriate spacing between transducers is $a\leqslant\lambda Z/D$. If the spacing between elements is larger than this, the method may not be able to separate two scatterers when a scatterer is in the main lobe while the other one is in a grating lobe.

To summarize, with a linear scan, both the resolution and the maximum spacing are equal to $\lambda Z/D$, which is the inverse of the spatial bandwidth.

b. Sector scan (or phased scan). In a sector scan, the full aperture is usually used on transmit. Consecutive transmits

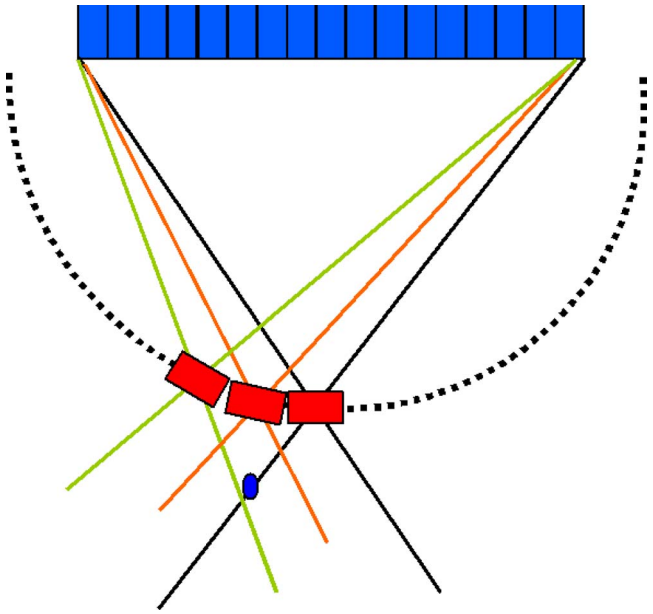


FIG. 4. (Color online) Example of sector scan. The foci are located on a circle, and the beams are steered. The array of the three virtual transducers insonifiing the scatterer is shown. In this geometry, the virtual array sees the scatterer with the same angle as the full physical array. The resolution depends then only on the size of the physical array.

are obtained by steering (rotating) the beam. Thus, the foci are located on a circle at a constant radius from the array center. This is shown in Fig. 4. Therefore, the virtual array is a curved array. The sector scan is especially interesting when a wide field of view is required.

Resolution. A geometrical derivation similar to the one in Fig. 3 shows that with this scheme the resolution of the virtual array is the same as the real array. As shown in Fig. 4, the angle between the scatterer and the virtual array is the same as the angle between the scatterer and the real array. Thus with such a transmit sequence, the performance of FDORT in terms of scatterers separation is identical to DORT and is equal to the array resolution $\Delta \sin\theta=\lambda/D$.

Transducers spacing. The maximum transducers spacing is derived in Sec. II C, using orthogonality condition between the transmits. It is found that the maximum spacing between two consecutive virtual transducers is $\Delta \sin\theta=\lambda/D$.

c. Hybrid scan. A possible hybrid combines the advantages of linear and sector scan. The whole aperture is used for each transmit, which results in a resolution identical to the DORT method. However, the foci are located on a line at constant depth, and thus the virtual array is linear, which makes the method more intuitive.

3. Simulations

Two point scatterers located at depth 30 mm have been simulated using FIELD II.[16] One of the points was twice as bright as the other. An array with 128 elements and 7.3 MHz center frequency was used. Three sets of acquisitions were performed, using the hybrid scheme of Section II.B.2.c, with a beam spacing equal to 0.2 mm. The focal depths were, respectively, 10 mm, 30 mm (the scatterers' depth), and 60 mm. For each case, the transfer matrix K was built for

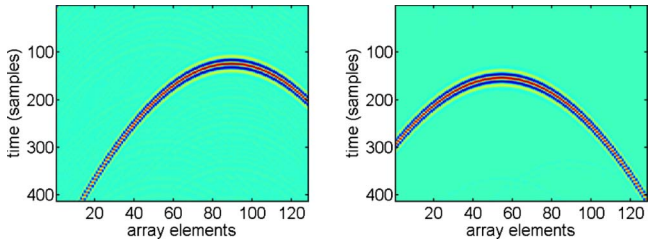


FIG. 5. (Color online) Temporal singular vectors expressed in the real array. They correspond to each scatterer's wave front.

several frequencies ranging from 0 to 12 Mhz, using a fast Fourier transform of the received signal. The SVD of each matrix was performed. According to Sec. II B 1, the singular vector U gives Green's function in the physical array, whereas the singular vector V gives Green's functions in the virtual array.

The temporal singular vectors for each scatterer were then reconstructed by taking the Fourier transform of the monochromatic singular vectors.

The distribution of singular values and the singular vectors U are similar for all three focal depths. There are two nonzero singular values, indicating the presence of two scatterers in the medium. The temporal singular vectors associated with the two nonzero singular values in the physical array (U) are shown in Fig. 5. Each singular vector is temporal Green's function or wave front of one of the scatterer. These results are identical to what one would obtain with the classical DORT method.

However, with FDORT, additional information can be obtained from the other singular vector V. It gives Green's function in the virtual array. The position of the virtual array can be adjusted by changing the focal depth. Three cases can be distinguished: the scatterers can be, respectively, deeper than [Figs. 6(a) and 6(b)], at the same depth as [Figs. 6(c) and 6(d)], or shallower [Figs. 6(e) and 6(f)] than the virtual array. In the case where the scatterer is shallower than the virtual array, time-reversed Green's function is observed, as explained in Sec. II A 2, which is why the curvature is inversed compared to the other wave front. When the virtual array is at the scatterer depths, only a few virtual transducers insonify the scatterers and therefore Green's function is narrow. The amplitude of Green's function actually corresponds to the amplitude of the transmit beam at the focal depth.

For all focal depths, the ability to separate the scatterers is the same, according to the chosen transmit scheme and Sec. II B 2. Changing the focal depth is simply a way of changing the point of view. Examples of applications will be developed in Sec. III.

C. The focused transmits as an orthogonal basis

The DORT method has been implemented in the past with transmit sequences other than single element transmits.[10] In these cases, orthogonal combinations of array elements were used. These kinds of transmits are interesting because the SNR is increased compared to single element transmits.

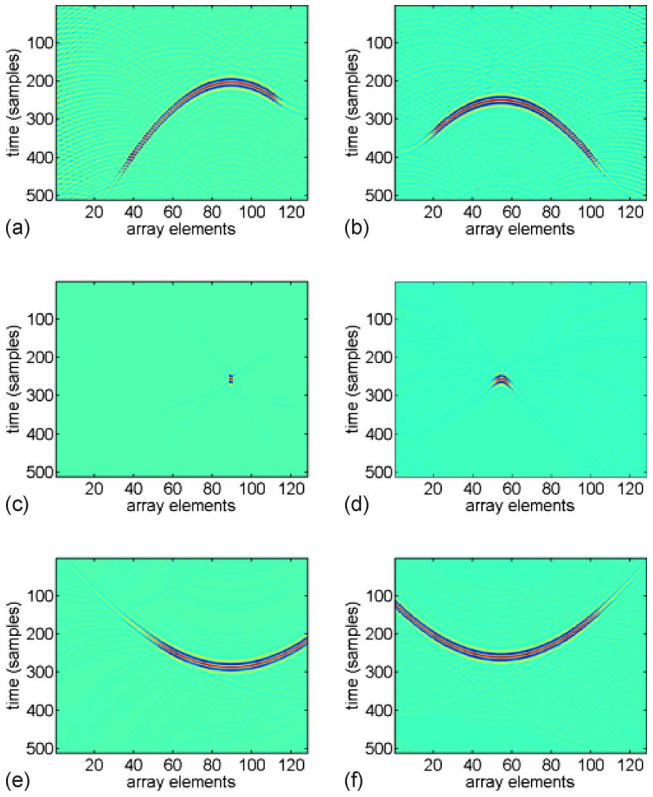


FIG. 6. (Color online) Temporal singular vectors expressed in the virtual array at depth 10 mm [(a) and (b)], 30 mm [(c) and (d)], and 60 mm [(e) and (f)]. The scatterers were located at 30 mm. The temporal singular vectors are obtained by the Fourier transform of the frequency domain vectors V. [(a) and (b)] The wave fronts are truncated on the edges compared to figure because of the directivity of the virtual transducers. The scatterers do not hear the virtual transducers on the edges. [(c) and (d)] The virtual array is in the scatterer plane. In this plane, the virtual transducers, or transmit beams, are sinc functions, with a narrow main lobe, and only a few insonify significantly the scatterer. [(e) and (f)] The curvature of the wave front and of the phase are inversed compared to (a) and (b), because the scatterer is now shallower than the focal depth, and as explained in Sec. III A 2, the signals are time reversed in this case.

The focused beams can themselves be considered as an orthogonal basis. Each focused beam is mathematically represented by Green's function of the corresponding focal point. For one frequency, it is given by $H_i = e^{jkr_i(P)}/r_i(P)$. The condition of orthogonality of Green's functions is given in Ref. 5 (Sec. II A 2 c): Green's functions of two points P and Q are orthogonal if it is possible to focus with the array on P without sending energy on Q. This is derived by interpreting the Rayleigh–Sommerfeld formula as a projection on Green's function.

For the linear scan, in the focal plane and in the Fresnel approximation, the monochromatic field is given by $\mathrm{sinc}(\pi X/(\lambda Z/D))$. The main lobe of the sinc is centered on the focus, here the point P. The points that are not insonified, and therefore whose Green's functions are orthogonal to P's Green's function, are the points located at the zeros of the sinc function. The distance between these points is $a = \lambda Z/D$. Therefore, by choosing foci that are separated by

$$a = \frac{\lambda Z}{D} \tag{4}$$

in the focal plane, each beam will be orthogonal to every other, and one is able to build an orthogonal family of beams. This correspond to the Nyquist sampling requirement.

For the phase scan, one needs to reason on a line at constant radius from the center of the array, in polar coordinates. The Fresnel approximation states that, in the focal radius, the field is the Fourier transform of the aperture, for the spatial frequency $\sin(\theta/\lambda)$. The field for a beam focusing on $\theta=0$ is then given by $\mathrm{sinc}(\pi D \sin(\theta/\lambda))$. The other beams will then be orthogonal if their foci are located at angles such that

$$\sin\left(\frac{\theta}{\lambda}\right) = \frac{n}{D}, \tag{5}$$

where n is an integer. In other words, $\Delta \sin\theta = \lambda/D$.

In the case where the array elements have a width equal to $\lambda/2$, which is the condition to have a directivity angle equal to π (half-plane), the array images the half-plane. To span the whole field of view, one needs foci ranging from $\sin\theta=-1$ to $\sin\theta=+1$. Combined with Eq. (5), this yields $D/(\lambda/2)$ beams, which is also equal to the number of element in the array. In this case, the canonical basis and the beam basis are two equivalent orthogonal bases of the same space.

It is easy to see the beams as an orthogonal basis in the case where the foci are in the very far field. In this case, the Fraunhoffer approximation is valid, and the signal applied in the array to generate a beam is $e^{j2\pi \sin(\theta/\lambda)x}$. Together with Eq. (5), this yields $e^{j2\pi(n/D)x}$. This forms a family of Fourier harmonic functions, which is the well-known orthogonal basis for Fourier series.[17]

Note that only the sector scan can form an orthogonal basis of the same space as the canonical basis. With the linear scan, it has been seen in Sec. II.B.2.a that some resolution was lost compared to the canonical basis. The space spanned by a linear scan is then a subspace of the canonical space.

The condition of orthogonality for the beams, stated in Eqs. (4) and (5), is equivalent to the grating lobe condition given in Sec. II B 2. This gives an upper bound on the distance between beams that yields optimal results. If the spacing is greater than the upper bound, the performance of the method is reduced. It is possible to use a spacing smaller than the bound. However, in this case the beams are no longer orthogonal and more beams are required to span the whole space. There will be some redundancy, but this is not a problem for FDORT, as the SVD will make sense of the information.

D. Link to backpropagation

Let Q be the position of a scatterer. Its Green's function is $H(Q)$. Let P_m be the focus of a focused beam. Focusing on P_m is equivalent to delaying the signals in the physical array by $r_i(P_m)/c$ and summing. In a monochromatic formalism, it is equivalent (at least approximately, depending on the apodization) to projecting signals on Green's function of P_m. Therefore, the echo from Q heard by P_m is expressed as $S_m=\langle H(Q)|H(P_m)\rangle$, the scalar product between Green's functions of Q and P_m. By reciprocity, S_m is also the field at position P_m when the echo from the scatterer Q is backpropagated from the array. Again, this shows that the focused beams act like virtual transducers that *probe* the value of the field at the focal distance. The difference with the previous virtual transducer interpretation is that here the virtual transducers do not have a directivity: they are isotropic. However, the field is now the backpropagated field, which means that the signal is nonzero only in a cone.

To summarize, there are two ways to interpret the virtual transducers: (a) either as transducers with a directivity probing the free space field from the scatterer (b) or as isotropic transducer probing the back-propagated field of the transducer.

The interest of the last interpretation is to give a physical interpretation of the change of basis between the canonical basis (physical array) and the focused basis (virtual array). The change of basis is obtained by a backpropagation, or time reversal, of the signals from the array plane to the focal plane.

III. APPLICATION TO FOCUSING THROUGH A FAR-FIELD PHASE SCREEN

A. Changing a far-field phase screen problem into a near-field phase screen problem using a virtual array

1. Aberration and far-field phase screen model

The quality of an ultrasound image is degraded when the beam propagates through inhomogeneous media. This effect is known as aberration.[18,19] Several methods have been proposed to deal with this problem, but most of them assume that the aberration can be modeled by a near-field phase screen.[20–23] This model lumps the inhomogeneous medium into a thin layer of varying propagation delay placed immediately in front of the aperture. It assumes that the effect of aberration is only a time shift of the wave front. Because of that additional time shift, the signals from the different transducers are no longer in phase at the desired focal point, and the focusing quality is degraded. To be able to restore the quality of the image, one only needs the knowledge of the Green's function of one point in the medium. By backpropagating that Green's function, one is able to focus on the point, and by adding a steering term (which corresponds to the difference in geometrical delays between the reference point and the new point) one can focus to any other point in the medium, since the aberration in the near-field model does not depend on the point position. Green's function can, for example, be obtained using the DORT method.[1] Other methods exist that estimate the time shift due to the phase screen.[20–23] The near-field model is attractive due to its simplicity. However, measurements of propagation through an abdominal wall show not only time shifts but also amplitude and wave-front distortion.[18,24]

A more general model for the aberration is a far-field phase screen, where the phase screen is no longer necessarily in front of the aperture but at an appropriate distance away from the transducer.[24,25] The wave front is only delayed when it goes through the phase screen, but as the wave front

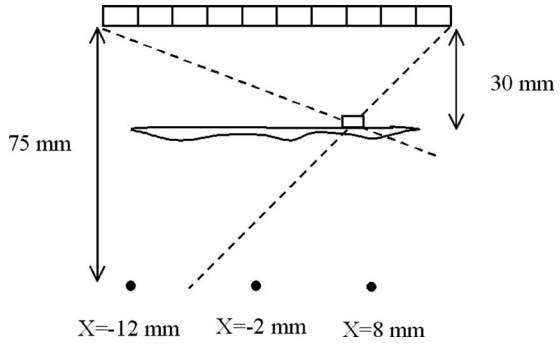


FIG. 7. Simulation setup. A virtual transducer is shown, with its directivity pattern in dashed line.

continues to propagate through the medium, different components of the wave front, which are no longer in phase, interfere, distorting the amplitude and phase of the received wave front.

However, the far-field model is more complicated to deal with than the near-field phase screen model. First, time delays are no longer enough to correct the aberration, and a matched filter (time reversal) is necessary. Second, with a near-field phase screen, if one knows Green's function of a single point in the medium, one is able to focus anywhere in the medium as the aberration (as seen by the physical array) does not depend on the target's position. With the far-field phase screen, the aberration seen by the physical array does depend on the target's position. Thus knowledge of a point's Green's function only enables focusing in the neighborhood of that point. A proposed method[24] to deal with the far-field phase screen is backpropagating the wave fronts to the plane of the phase and then steering. This approach was used successfully to focus at neighbors points of a scatterer through a far-field phase screen.[25]

The virtual transducer formalism helps simplifying the problem. Indeed, in the case where the aberrator is in the far field, it is possible to use an array of virtual transducers close to the phase screen. This can be done by choosing a focal depth for the focused transmit that is slightly shallower than the phase screen. In this case, the aberrator is still in the far-field for the physical array, but it is in the near field for the array of virtual transducers (the virtual elements are immediately in front of the aberrator). Thus, with the virtual array, we benefit from the practicality of the near-field phase screen model. Using FDORT with the appropriate focal depth allows a simple characterization of the far-field phase screen in terms of mere delays.

In the following section, we illustrate what we have just said on an example. In Sec. III B, we show how using the virtual transducer array simplify the problem. Finally, in Sec. III C, we show how this method can be practically implemented, without direct access to the virtual transducers.

2. Example

We illustrate this with a simulated example. The simulation setup is illustrated in Fig. 7.

A phase screen, which applies a differential delay of 100 ns rms, with a spatial correlation of 4.5 mm (full width at half maximum), was located at 30 mm from an array (128 elements of 0.2 mm). The center frequency was 7.5 MHz. Three point scatterers were located at a depth of 75 mm, and at azimuths of −12, −2, and +8 mm. FDORT was performed using the hybrid scheme, with foci at $z=30$ mm, corresponding to the phase screen depth. The spacing between the virtual transducers (foci) was 0.2 mm, which is slightly below the orthogonal condition (0.23 mm). The monochromatic singular vectors were computed both in the physical array and the virtual array. The temporal singular vectors are obtained by the Fourier transform of the frequency domain vectors. Temporal Green's functions for the physical array are shown in Fig. 8 (top), while temporal Green's functions in the virtual array are shown in Fig. 8 (bottom).

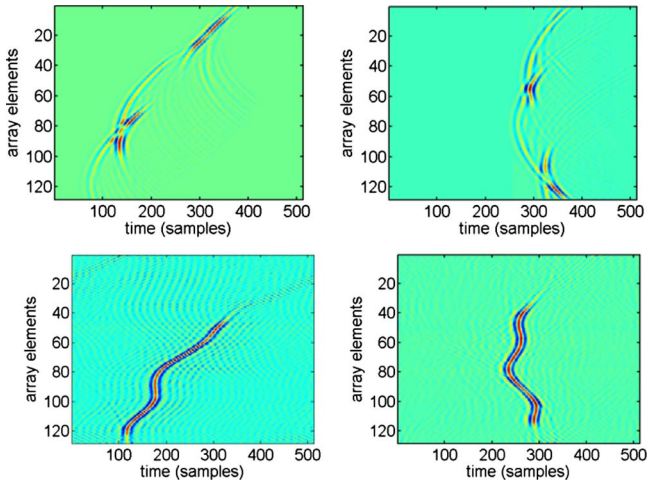


FIG. 8. (Color online) Top: Temporal Green's function of two scatterers (respectvely −12 and −2 mm) in the physical array. Because of the far-field phase screen, the signals are distorted in time, and there are important variations of amplitude across the array. Moreover, the effect of the aberration depends on the position of the scatterer. For example, the amplitude peaks are at different position for each scatterer. Bottom: Same in virtual array, located just behind the phase screen. The wave fronts are merely delayed by the aberration. There is no distortion of the pulse or variation of amplitude. For each scatterer, the signal is received only by about 80 virtual elements, because of the directivity of the virtual transducers.

It is obvious in this example that from the virtual array point of view, the aberration acts as a near-field phase screen. The wave fronts are merely delayed, and the aberration delays are the same for all scatterers. The only difference with a true phase screen is due to the directivity of the virtual transducers. This phenomenon is fully predicted by our model, as described in Sec. III A. For example, one can see that the virtual transducer depicted in Fig. 7 cannot *hear* the leftmost ($x=-12$ mm) scatterer.

B. Steering from the virtual array

With the far-field phase screen, the knowledge of Green's functions of the three scatterers enables focusing only in the immediate neighborhood (isoplanatic patch)[26] of each point. The size of the isoplanatic patch, which is the area where the aberration effect is constant, depends on the strength of the phase screen and the distance to the array. With the phase screen chosen in the simulations, the isoplanatic patch is very narrow, as seen in Fig. 9: Green's

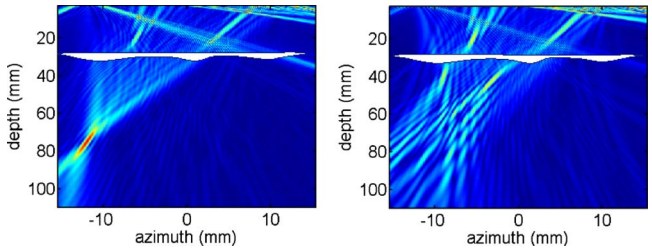


FIG. 9. (Color online) Focusing from the physical array, respectively, from left to right: −12 and −10 mm. Green's function for the scatterer at −12 mm was used to correct the aberration. Therefore, the focusing is perfect at −12 mm. However, it degrades very rapidly, as the aberration varies with the position.

function of a scatterer located at −12 mm was used to focus at this point and 2 mm away. To focus at neighboring points, a steering term was added to the phase of Green's function, which corresponds to the difference in geometrical delays between the reference point and the new point. This is equivalent to assuming that the aberration is the same for all points. Both the amplitude and phase of Green's function are used.

The focusing degrades very rapidly. This indicates that the isoplanatic patch size is small.

The same steering process was then performed from the virtual array, to focus at the same neighboring point. In this case, the focusing on a neighboring point was very good, even if the point was far away from the reference. The focusing on a point at $x=-10$ mm (2 mm away from the initial point) is shown in Fig. 10, and is much better than the focusing on the same point from the physical array.

From the virtual array, we can in theory focus anywhere in the medium using the knowledge of single Green's function, because the phase screen is near field. However, because of the directivity of the virtual transducers, one Green's function gives only information about a part of the phase screen. For example, Green's function of the scatterers at $x=-12$ mm gives a nonzero signal only on the 80 leftmost virtual transducers. Therefore, only the delay experienced by these 80 transducers can be deduced. To characterize completely the phase screen delay, it is necessary to use another scatterer that is *heard* by the remaining virtual transducers. The scatterer at $x=8$ mm is suitable. From the knowledge of these two Green's functions, one can completely characterize the phase screen, and then focus on any point in the medium using the proper geometrical delay.

Using the unwrapped phase of Green's functions for the

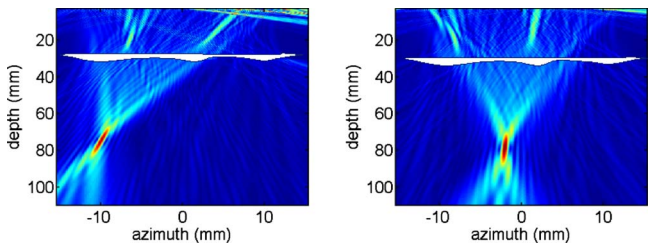


FIG. 10. (Color online) Focusing from the virtual array at, respectively, from left to right, −10 and −2 mm. Reference Green's function was at −12 mm in the first case, and −12 and +8 mm in the second case.

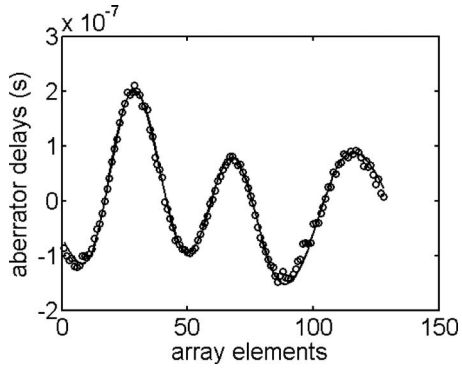


FIG. 11. Estimated delay profile of the phase screen (circles) compared to the true delay profile (solid line).

two scatterers at −12 and 8 mm, we were able to deduce the phase screen delay profile shown in Fig. 11. The estimated profile was very close to the true profile. Then, using this profile we were able to focus anywhere in the medium by adding the proper geometrical delay, $r_i(P)/c$, where $r_i(P)$ is the distance between a point and the virtual tranducer i. The focusing on a point at $x=-2$ mm is shown in Fig. 10. The focusing was not obtained from measured Green's function of the scatterer located at this point, but by steering using the knowledge of only the two other Green's function ($x=-12$ and $x=8$ mm).

Using the virtual transducers, it was then possible to achieve a very good focusing on a point that was 1 cm away from closest estimated Green's function, through a far-field phase screen. This is remarkable, as the size of the isoplanatic patch (seen from the physical array) was hardly 0.5 mm.

C. Practical implementation

1. Determination of the phase screen position

In a practical setting, the depth of the phase screen is not necessarily known. A way to find it would be to perform FDORT several times, each time with a different focal depth. For each focal depth, the temporal singular vectors are computed in the virtual array. The position of the phase screen corresponds to the depth where the singular vectors are the less distorted and mostly time delayed, as in Fig. 8 (bottom).

Instead of performing several experiments with different focal depths, it is more convenient to backpropagate the singular vectors computed in the physical array. Indeed, backpropagating the singular vectors to different depths is equivalent to computing them for different focal depths, as explained in Sec. II D. Computation of an objective criterion for the wavefront distortion may be preferred to visual inspection.

Criterion based on the distortion. An approach proposed by Liu and Waag[24] and Dorme and Fink[25] is to use a wavefront similarity factor. Indeed, the propagation after the phase screen does not lead only to amplitude variation but also to pulse distortion. The criterion is based on the correlation between pulses at two separate locations of the wave front. By numerical back propagation in a homogeneous medium, the wave front is computed at any depth. For each

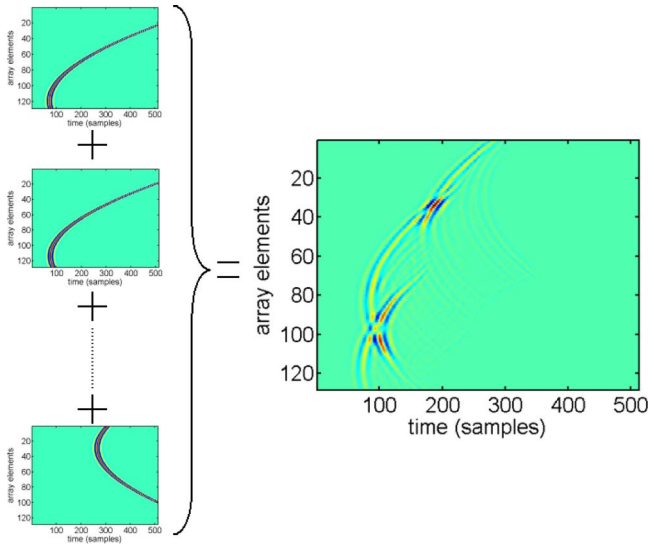


FIG. 12. (Color online) To compute Green's function of any point in the medium in the physical array, one merely has to add the wave front corresponding to each virtual transducer that insonify the point with the proper time delays. The virtual transducers that do not insonify the point (because of the directivity) are not summed.

depth, a similarity factor is computed by correlating the pulses. The phase screen is at a depth where the similarity factor is a maximum. Other criterions are proposed in Ref. 11. One of them is based on the amplitude: If the phase screen only delays the wave front, and does not introduce any attenuation, the amplitude of the wave front immediately after going through the phase screen is approximately constant. During the propagation after the phase screen, interferences lead to amplitude variation. Monochromatic Green's function is numerically backpropagated in a homogeneous medium and the depth where the amplitude is the most constant is chosen as the aberrator depth. Another criterion is based on spatial invariance: at the phase screen depth, the main difference between the wave fronts for two different scatterers is a tilt. That is no longer the case when the wave fronts keep propagating.

2. Focusing in real experiments

In Sec. III.B, it was shown how to focus from the virtual array of transducers in a numerical experiment. We now describe how this can be done in a real experiment, where we want to be able to focus on any point through a far-field phase screen, using a time-reversal approach (time-reversed Green's function is transmitted). In a real experiment, we do not have access directly to the virtual transducers but to the physical transducers. In order to focus on a point, we need to know the signal to apply to each physical transducer. Therefore, we need to express Green's function in the real array.

We already know how to generate each focused beam (virtual transducer) from the physical array. The signals applied in the real array to form a few focused beams are shown in Fig. 12. We also know how to focus from the array of virtual transducer on any point in the medium. We just have to apply the appropriate delay to each virtual transducer. This means that some focused beams are transmitted later than others. Therefore, if we delay the wave fronts corresponding to each focused beam by the appropriate amount, and add the signals together, we obtain the signal to transmit in order to focus on any point in the medium. This is illustrated in Fig. 12.

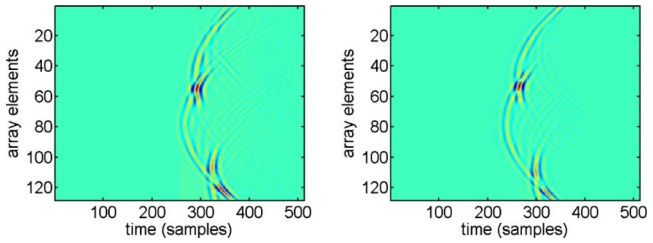


FIG. 13. (Color online) Temporal Green's function of the point at $x=-2$ mm, measured (left) and synthesized using the method described in this paper (right).

Note that this operation is equivalent to backpropagating the signal from the virtual array to the canonical array, as proposed in Ref. 25. In the case where the virtual transducers forms an orthogonal basis, it is also equivalent to change bases (from the basis of focused beams to the canonical basis; Green's function of each focal point is then the coordinate of each focused beam in the canonical basis)

The method was used to synthesize Green's function of the point at $x=-2$ mm. Green's function obtained is very close to Green's function measured when a scatterer is present at this point (Fig. 13).

This method is particularly interesting as it shows how a complicated wave front, where the pulse is distorted and the amplitude varies, can be synthesized by a mere sum of simpler wave fronts.

3. Focusing for imaging

To obtain a high quality image, focusing in transmit and in receive at every point is required. However, in imaging, physical transmit focusing as explained in the previous section is not needed. Indeed, the FDORT data set can be interpreted as a *full data set* between the virtual transmit array and the physical receive array. Transmit focusing can then be achieved using a synthetic aperture algorithm: signals corresponding to each transmit are delayed by the proper amount and added together. The delays are the same as in Sec. III C 2 and Fig. 12. A similar synthetic transmit aperture imaging method is described in Ref. 8. Notice that to focus shallower than the virtual array, the delay introduced by the phase screen is not taken into account since the phase screen is just slightly deeper than the virtual array. Also delays have to be "inversed," as explained in Sec. II A 2. The virtual transducers can also be used in reception to achieve receive focusing through the far-field phase screen. An image of the setup in Fig. 7 obtained with the synthetic aperture method is shown in Fig. 14. The aberrator delay profile estimated in Fig. 11 was used to correct the aberration in the virtual plan.

IV. CONCLUSION

It has been demonstrated how the FDORT method can be intuitively described by a time reversal process between the physical array and an array of virtual transducers located

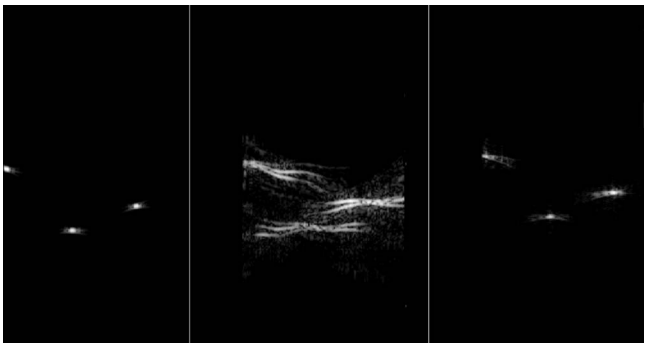


FIG. 14. From left to right: image of an unaberrated point-scatterer phantom, image of the same phantom with a 100 ns rms phase screen located at 30 mm; image of the aberrated phantom corrected using the FDORT method. The corrected image is not perfect but much better than the aberrated image.

at the transmit beams' foci. With appropriate beams (sector or hybrid scan), the performance, in terms of scatterers' resolution, is the same as the conventional DORT method. A condition in terms of beam spacing for the beams to form an orthogonal basis has been derived.

In the presence of point scatterers, the number of singular values of FDORT is equal to the number of scatterers in the medium, like DORT, and the singular vectors correspond to Green's functions of these scatterers. However, unlike DORT, FDORT yields two different singular vectors: the receive singular vectors are Green's functions expressed in the physical array, whereas the transmit singular vectors are Green's functions expressed in the virtual array. The position of the virtual array can be changed by varying the position of the foci, thus offering different points of view.

Appropriately selecting the position of the virtual array can greatly simplify some problems. An application of the virtual array is the problem of the far-field phase screen. By choosing appropriately the location of the virtual transducers, one is able to transform the problem into the simpler near-field phase screen problem that has been widely treated in the literature. Focusing through the far-field phase screen on any point of the medium is now possible by steering from the virtual array. It requires a knowledge of only one or two Green's functions. It is shown that using the virtual array, a very good focusing can be achieved on points far away from reference scatterers, whereas using the physical array, the quality of the focusing drops very quickly a few millimeters away from the reference point scatterers. Methods to optimize the position of the virtual array are presented, along with a method to generate the distorted wave fronts required to focus through the far-field phase screen from a mere delay and sum of simple focused wave fronts.

[1]C. Prada and M. Fink, "Eigenmodes of the time reversal operator: A solution to selective focusing in multiple-target media," Wave Motion **20**, 151–163 (1994).

[2]E. Kerbrat, C. Prada, D. Cassereau, and M. Fink, "Imaging in the presence of grain noise using the decomposition of the time reversal operator," J. Acoust. Soc. Am. **113**, 1230–1240 (2003).

[3]J. F. Lingevitch, H. C. Song, and W. A. Kuperman, "Time reversed reverberation focusing in a waveguide," J. Acoust. Soc. Am. **111**, 2609–2614 (2002).

[4]H. Tortel, G. Micolau, and M. Saillard, "Decomposition of the time reversal operator for electromagnetic scattering," J. Electromagn. Waves Appl. **13**, 687–719 (1999).

[5]J.-L. Robert, M. Burcher, C. Cohen-Bacrie, and M. Fink, "Time reversal operator decomposition with focused transmission and robustness to speckle noise: Application to microcalcification detection," J. Acoust. Soc. Am. **119**, 3848–3859 (2006).

[6]F. K. Gruber, E. A. Marengo, and A. J. Devaney, "Time-reversal imaging with multiple signal classification considering multiple scattering between the targets," J. Acoust. Soc. Am. **115**, 3042–3047 (2004).

[7]C. Prada and J. L. Thomas, "Experimental subwavelength localization of scatterers by decomposition of the time reversal operator interpreted as a covariance matrix," J. Acoust. Soc. Am. **114**, 235–243 (2003).

[8]K. L. Gammelmark and J. A. Jensen, "Multielement synthetic transmit aperture imaging using temporal encoding," IEEE Trans. Med. Imaging **22**, 552–563 (2003).

[9]J.-L. Robert and M. Fink, "Green's function estimation in speckle using the decomposition of the time reversal operator: Application to aberration correction in medical imaging," J. Acoust. Soc. Am. **123**, 866–877 (2008).

[10]T. Folegot, J. de Rosny, C. Prada, and M. Fink, "Adaptive instant record signals applied to detection with time reversal operator decomposition," J. Acoust. Soc. Am. **117**, 3757–3765 (2005).

[11]J.-l. Robert, "Evaluation of Green's functions in complex media by decomposition of the Time Reversal Operator: Application to Medical Imaging and aberration correction," http://tel.archives-ouvertes.fr/docs/00/32/43/95/PDF/total.pdf (Last viewed September 2008).

[12]C. Passman and H. Ermert, "A 100 MHz ultrasound imaging system for dermatologic and ophthalmologic diagnostics," IEEE Trans. Ultrason. Ferroelectr. Freq. Control **43**, 545–552 (1996).

[13]C. H. Frazier and W. D. O'Brien, Jr., "Synthetic aperture techniques with a virtual source element," IEEE Trans. Ultrason. Ferroelectr. Freq. Control **45**, 196–207 (1998).

[14]C. Prada, M. Tanter, and M. Fink, "Flaw detection in solid with the D.O.R.T. method," presented at the IEEE Ultrasonic Symposium Proceedings 1997.

[15]B. A. Angelsen, *Ultrasound Imaging*, Vol. **I**, www.ultrasoundbook.com (Last Viewed September 2008).

[16]J. A. Jensen, "Field: A program for simulating ultrasound systems," Med. Biol. Eng. Comput. **34**, 351–353 (1996).

[17]M. Unser, "Sampling-50 years after shannon," Proc. IEEE **88**, 569–587 (2000).

[18]L. M. Hinkelman, T. D. Mast, L. A. Metlay, and R. C. Waag, "The effect of abdominal wall morphology on ultrasonic pulse distortion. Part I. Measurements," J. Acoust. Soc. Am. **104**, 3635–3649 (1998).

[19]T. D. Mast, L. M. Hinkelman, M. J. Orr, and R. C. Waag, "The effect of abdominal wall morphology on ultrasonic pulse distortion. Part II. Simulations," J. Acoust. Soc. Am. **104**, 3651–3664 (1998).

[20]S. W. Flax and M. O'Donnell, "Phase-aberration correction using signals from point reflectors and diffuse scatterers: basic principles," IEEE Trans. Ultrason. Ferroelectr. Freq. Control **35**, 758–767 (1988).

[21]M. O'Donnell and S. W. Flax, "Phase-aberration correction using signals from point reflectors and diffuse scatterers: measurements," IEEE Trans. Ultrason. Ferroelectr. Freq. Control **35**, 768–774 (1988).

[22]R. C. Gauss, G. Trahey, and M. S. Soo, "Wavefront estimation in the human breast," Proc. SPIE **4325**, 172–181 (2001).

[23]N. Levin, E. T. Gregg, and W. S. Stephen, "Phase aberration correction in medical ultrasound using speckle brightness as a quality factor," J. Acoust. Soc. Am. **85**, 1819–1833 (1989).

[24]D.-L. Liu and R. C. Waag, "Correction of ultrasonic wavefront distortion using backpropagation and a reference waveform method for time-shift compensation," J. Acoust. Soc. Am. **96**, 649–660 (1994).

[25]C. Dorme and M. A. Fink, "Ultrasonic beam steering through inhomogeneous layers with a time reversal mirror," IEEE Trans. Ultrason. Ferroelectr. Freq. Control **43**, 167–175 (1996).

[26]J. J. Dahl, M. S. Soo, and G. E. Trahey, "Spatial and temporal aberrator stability for real-time adaptive imaging," IEEE Trans. Ultrason. Ferroelectr. Freq. Control **52**, 1504–1517 (2005).

Speech enhancement in discontinuous transmission systems using the constrained-stability least-mean-squares algorithm

J. M. Górriz[a] and J. Ramírez
Department of Signal Theory, University of Granada, Andalucia 18071, Spain

S. Cruces-Álvarez
Department of Signal Theory, University of Seville, Seville 41004, Spain

D. Erdogmus
Dana Research Center, Northeastern University, Boston, Massachusetts 02115

C. G. Puntonet
Department of Computer Architecture and Technology, University of Granada, Andalucia 18071, Spain

E. W. Lang
Institut für Biophysik und Physikalische Biochemie, University of Regensburg, D-93040 Regensburg, Germany

(Received 16 May 2008; revised 30 September 2008; accepted 30 September 2008)

In this paper a novel constrained-stability least-mean-squares (LMS) algorithm for filtering speech sounds is proposed in the adaptive noise cancellation (ANC) problem. It is based on the minimization of the squared Euclidean norm of the weight vector change under a stability constraint over the *a posteriori* estimation errors. To this purpose, the Lagrangian methodology has been used in order to propose a nonlinear adaptation in terms of the product of differential input and error. Convergence analysis is also studied in terms of the evolution of the natural modes to the optimal Wiener–Hopf solution so that the stability performance depends *exclusively* on the adaptation parameter μ and the eigenvalues of the difference matrix $\Delta\mathbf{R}(1)$. The algorithm shows superior performance over the referenced algorithms in the ANC problem of speech discontinuous transmission systems, which are characterized by rapid transitions of the desired signal. The experimental analysis carried out on the AURORA 3 speech databases provides an extensive performance evaluation together with an exhaustive comparison to the standard LMS algorithms, i.e., the normalized LMS (NLMS), and other recently reported LMS algorithms such as the modified NLMS, the error nonlinearity LMS, or the normalized data nonlinearity LMS adaptation.
© *2008 Acoustical Society of America.* [DOI: 10.1121/1.3003933]

PACS number(s): 43.60.Mn, 43.72.Lc, 43.72.Dv [EJS] Pages: 3669–3683

I. INTRODUCTION

The widely used least-mean-squares (LMS) algorithm has been successfully applied to many filtering applications including modeling,[1] equalization, control,[2,3] echo cancellation biomedicine, or beamforming.[4] One of these important applications is found in voice communication systems such as dialogue systems in airplane or helicopter cockpits where the extraction of noise from the desired speech is required. Another major application concerns filtering biosignals in adverse noise conditions that usually are present in medical instruments. These applications include the cancellation of several kinds of interference in electrocardiograms (ECGs) such as canceling the power line interference, the donor ECG in heart-transplant electrocardiography, or the maternal ECG in fetal electrocardiography;[5] and adaptive noise canceling (ANC) in modern techniques such as positron emission tomography or single positron emission computed tomography images.[6]

The typical noise cancellation scheme of a voice communication system is shown in Fig. 1. Two distant microphones are needed for such application capturing the nature of the noise and the speech sound simultaneously. The correlation between the additive noise that corrupts the clean speech (primary signal) and the random noise in the reference input (adaptive filter input) is necessary to adaptively *cancel* the noise of the primary signal. Note that the primary signal $d(n)$ consists of the clean speech $s(n)$ and the additive noise $v_1(n)$ recorded by the primary microphone. The reference noise signal $v_2(n)$ is the input of the FIR filter defined by the $L\times 1$ weight vector $\mathbf{w}(n)$. Its output $y(n)$ is the "best" estimation of the additive noise in the primary signal. The criterion for the best estimation is the minimization of the expected value of the squared sequence $e(n)$, which tends to equal the original signal $s(n)$. The weights are typically adjusted using the LMS algorithm[5] because of its simplicity, ease of implementation, and low computational complexity. The weight update equation for ANC is

[a]URL: http://www.ugr.es/~gorriz. Electronic mail: gorriz@ugr.es

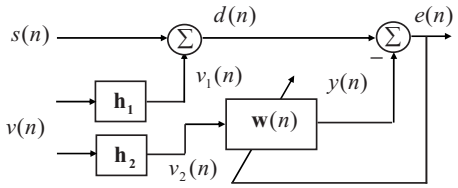


FIG. 1. Adaptive noise canceler.

$$\mathbf{w}(n+1) = \mathbf{w}(n) + \mu e^*(n)\mathbf{x}(n), \tag{1}$$

where μ is a step-size parameter with units of inverse power, $e(n)=d(n)-y(n)=s(n)+v_1(n)-\mathbf{w}^H(n)\mathbf{x}(n)$ is the system output, where ^{H} stands for conjugate transpose, * denotes complex conjugate, and $\mathbf{x}(n)=(x(n),\ldots,x(n-L-1))^T$ is the data vector containing L samples of the reference signal, $v_2(n)$, that are present in the adaptive filter's tapped delay line at time n. Many ANCs (Refs. 5 and 7–10) have been proposed in the past years using modified LMS (MLMS) algorithms in order to simultaneously improve the tracking ability and speed of convergence. In this way, many efforts have been directed to reduce computational load and power consumption in adaptive filter implementations.[11,12]

On the other hand, the emerging applications of speech technologies (particularly in mobile communications, robust speech recognition, or digital hearing aid devices) often require a noise reduction scheme working in combination with a precise voice activity detector (VAD).[13,14] During the past decade numerous researchers have studied different strategies for detecting speech in noise and the influence of the VAD decision on speech processing systems.[15–21] The nonspeech detection algorithm is an important and sensitive part of most of the existing single-microphone noise reduction schemes.[22,23] The VAD is even more critical for nonstationary noise environments since it is needed to update the constantly varying noise statistics. A VAD achieves silence compression in modern mobile telecommunication systems reducing the average bit rate by using the discontinuous transmission (DTX) mode.[16] VADs have been used extensively in the open literature as a reference for assessing the performance of new algorithms.

This paper shows a novel adaptation in combination with a VAD to enhance speech signals in DTX systems, which are characterized by a sudden change in channel signal statistics. The algorithm is derived assuming stability in the sequence of *a posteriori* errors instead of the more restrictive hypothesis used in previous approaches,[24] that is, enforcing it to vanish. The result of the Lagrange minimization is the application of the normalized LMS (NLMS) algorithm to a new set that consists of difference signals that are more suitable for ANC of speech signals in DTX systems. In this way, the sudden transitions in the channel are counteracted by the use of the concurrent change of the processing variables. The deterministic version of the proposed adaptation is also shown to be equivalent to the gradient descent method, from which the NLMS algorithm derives, in the sense that they have the same optimal solution.

The paper is organized as follows. In Sec. I A the background on LMS algorithms applied to the ANC problem is summarized. Then a novel constrained-stability (CS) LMS algorithm for filtering speech signals in additive noise is proposed in Sec. II. This is achieved by minimizing the norm of the difference weight vector and imposing a stability constraint in the sequence of errors in order to reach the *equilibrium condition*. In Sec. III A a connection to the previous LMS algorithm is shown, which allows to analyze: the conditions for convergence. This novel methodology for weight adaptation provides both higher filtering performance as well as enhanced tracking ability over the traditional LMS methods in context of ANC applications. In addition, an improvement in filtering results by means of a VAD is also achieved in Sec. IV. The VAD scheme combines the operation of the proposed CS-LMS with a suitable MLMS algorithm, the lag CS-LMS, which is intended for filtering nonstationary noise segments, exclusively. Thus, we select the best adaptation on each kind of frame (speech or noise) achieving an additional improvement in filtering performance and a clear reduction of background noise, on the filtering algorithms operating separately. The experimental analysis conducted in Sec. V provides the information on how the proposed and referenced algorithms operate on discontinuous speech segments in the ANC application. Finally, we state some conclusions in Sec. VI.

A. Background on modified LMS algorithms

Many researchers have proposed modifications to the LMS algorithm, which are motivated by two factors: (i) reducing the computational burden, and (ii) improving the trade-off between convergence time and steady-state performance. One approach for improving LMS algorithms is to modify the time-varying step size, i.e., applying nonlinearities to the quantities used to update the weights (the data vector and/or the output signal). For instance, Bershad studied the performance of the NLMS with an adaptive step size $(\mu_{\text{adap}})=\mu/\|\mathbf{x}(n)\|^2$ in Ref. 25, showing advantages in convergence time and steady state. Later, Douglas and Meng[9] proposed the optimum nonlinearity for any input probability density of the independent input data samples, obtaining the normalized data nonlinearity LMS (NDN-LMS) adaptation

$$\mathbf{w}(n+1) = \mathbf{w}(n) + \frac{\mu}{1+\mu\|\mathbf{x}(n)\|^2} e^*(n)\mathbf{x}(n). \tag{2}$$

Although this algorithm is designed to improve steady-state performance, its derivation did not consider the ANC with a strong target signal in the primary input.[7] Greenberg's MLMS extended the latter approach to the case of the ANC with the nonlinearity applied to the data vector and the *target signal itself*, obtaining substantial improvements in the performance of the canceler. The disadvantage of this method is that it requires unknown *a priori* information of the processes

$$\mathbf{w}(n+1) = \mathbf{w}(n) + \frac{\mu_L}{(e_{\min}^2(n)+\mu_L\|\mathbf{x}(n)\|^2)} e^*(n)\mathbf{x}(n), \tag{3}$$

where $\mu_L=\mu_{\text{opt}}/L$ and μ_{opt} is a dimensionless step-size parameter. Further $e_{\min}$ is the Wiener–Hopf solution in stationary environment. Recently, an interesting approach has been proposed based on a nonlinearity applied to the data vector

exclusively.[10] The error nonlinearity LMS (EN-LMS) algorithm is described in terms of the following LMS adaptation:

$$\mathbf{w}(n+1) = \mathbf{w}(n) + \frac{\alpha_{\text{opt}}}{e + \|\mathbf{e}(n)\|^2} e^*(n)\mathbf{x}(n), \tag{4}$$

where $\|\mathbf{e}(n)\|^2 = \Sigma_{i=0}^{n-1} |e(n-i)|^2$ is the squared norm of the error vector, which is estimated over its entire history. As in the NLMS algorithm, ϵ is usually added to prevent instability in the variable step size of the algorithm if $\|\cdot\|^2$ is too small. For both stationary and nonstationary noise environments, the EN-LMS algorithm has shown a good trade-off between speed of convergence and misadjustment (M) (Ref. 26) improving the performance over Douglas' NDN-LMS.[10]

II. CONSTRAINED-STABILITY (CS)-LMS ALGORITHM

In this section, a novel adaptation that applies nonlinearities to the error sequence and the input signal in terms of difference values is presented. The main motivation of the CS-LMS algorithm is to obtain a suitable adaptation for DTX systems, in which the sudden transitions in the channel, due to the presence of intermittent signals, affect the performance of the standard filtering algorithms because of their limited tracking ability. The adaptation is derived as a solution to a constrained optimization problem,[27] by using the Lagrangian formulation that minimizes the norm of the difference weight vector under the *stability constraint*, which makes the error sequence as constant as possible. Our approach belongs to the class of MLMS algorithms based on applying nonlinearities to one or both of the quantities used to update the adaptive weights (the data vector and/or the output signal),[9,24,28,29] rather than optimizing the step-size function.[7,30] The derivation of the nonlinearity applied to the *target signal and the data vector* is reached as a generalization of the NLMS algorithm, which may be also obtained using this formulation indeed.[27] In this case the constraint of the standard LMS algorithm (the error sequence must be canceled) is relaxed to be as smooth as possible. In this way, consider the following constrained optimization problem:

$$\text{minimize} \|\delta\mathbf{w}(n+1)\|^2$$
$$\text{subject to the constraint } e^{[n+1]} = e^{[n+1]}(n-1), \tag{5}$$

where $\delta\mathbf{w}(n+1) = \mathbf{w}(n+1) - \mathbf{w}(n)$, and $e^{[k]}(n) = d(n) - \mathbf{w}^H(k)\mathbf{x}(n)$ is the error at time n using the weight vector at time k. The method of Lagrange multipliers converts the problem of constrained minimization into one unconstrained minimization by introducing Lagrange multipliers

$$\mathcal{L}(\mathbf{w}(n+1)) = \|\delta\mathbf{w}(n+1)\|^2 + \text{Re}[\lambda^*(e^{[n+1]}(n+1) - e^{[n+1]}(n))]. \tag{6}$$

The solution to this optimization problem $\mathbf{w}^{\text{opt}}(n+1)$ minimizes the norm of the difference between two consecutive weight vectors and satisfies the equilibrium constraint or condition $e^{[n+1]}(n) = e^{[n+1]}(n-1)$. This equilibrium constraint imposes *stability* on the sequence of *a posteriori errors*, i.e., the optimal solution $\mathbf{w}^{\text{opt}}(n+1)$ that is obtained from the minimization of Eq. (5) under the constraint is the one that renders the sequence of errors as smooth as possible. Taking partial derivative in Eq. (6) with respect to $\mathbf{w}^H(n+1)$ and setting it equal to zero, the Lagrange multiplier is found to be (the complete derivation can be seen for clarity in Appendix A)

$$\lambda = \frac{2\delta e^{[n]}(n)}{\|\delta\mathbf{w}(n)\|^2}, \tag{7}$$

where $\delta e^{[n]}(n) = e^{[n]}(n) - e^{[n]}(n-1)$ is the difference of the *a priori* error sequence and $\|\delta\mathbf{x}(n)\|^2 = \|\mathbf{x}(n) - \mathbf{x}(n-1)\|^2$ is the squared norm of the difference of consecutive input vectors. Thus, the minimum of the Lagrangian function satisfies the following adaptation equation:

$$\mathbf{w}(n+1) = \mathbf{w}(n) + \frac{\mu}{\|\delta\mathbf{w}(n)\|^2 + \varepsilon} \delta\mathbf{x}(n)(\delta e^{[n]}(n))^*. \tag{8}$$

This algorithm for adapting the weight vector is based on difference quantities and the concept of the equilibrium condition given by the constraint. It is interesting to notice that the equilibrium condition enforces the convergence of the algorithm if $\|\delta\mathbf{x}(n)\|^2 \neq 0$. The adaptation has been completed by introducing ϵ to prevent instability for small $\|\delta\mathbf{x}(n)\|^2$ and the constant step μ to control the speed of the adaptation. It can be seen readily that the computational load of the proposed adaptation is of the same order as with the standard LMS algorithm. The CS-LMS algorithm requires only $2L+1$ complex multiplications and $3L+1$ complex additions per iteration, where L is the number of tap weights used in the adaptive filter. Thus, the computational complexity of the algorithm is $\mathcal{O}(L)$. In addition, like the NLMS algorithm, the CS-LMS adaptation requires computation of the normalization term $\|\delta\mathbf{x}(n)\|^2$, which involves only two squaring operations, one addition and one substraction if it is evaluated recursively.

As shown in following sections, the convergence of the algorithm, the excess minimum squared error (EMSE) and the misadjustment (M) could be readily analyzed in a fashion similar to the NLMS algorithm for the proposed nonlinearities[26] since the adaptation rule is *equivalent* except for the difference data. Then, we will show that the EMSE of the proposed adaptation algorithm is lower than the one obtained with the standard NLMS algorithm in DTX systems, i.e., an intermittent, strongly correlated desired signal under an adverse noisy environment. In addition, under certain conditions imposed onto the difference data and the step size μ of the adaptation rule, the deterministic CS-LMS algorithm converges to the Wiener solution $\mathbf{w}_0$.

III. THE OPTIMAL SOLUTION OF THE CS-LMS ADAPTATION

As shown in the previous section, the CS-LMS adaptation rule is equivalent to the NLMS algorithm but over a different set of data. It is interesting to consider the conditions needed for both algorithms to have the same Wiener solution in the following.

Theorem 1 (convergence equivalence): *Consider a transversal filter with tap input in vector* $\mathbf{x}(n)$ *and a corresponding set of tap weights in vector* $\mathbf{w}(n)$. *By comparing the estimate given by the filter* $y(n)$ *with the desired response*

$d(n)$ we produce the estimation error denoted by $e(n)=d(n)-y(n)$. If the desired signal $d(n)$ is generated by the multiple linear regression model, i.e., $d(n)=\mathbf{w}_0^H\mathbf{x}(n)+e_0(n)$, where $e_0(n)$ is an uncorrelated white-noise process that is statistically independent of the input vector $\mathbf{x}(n)$, then the optimal solution of the deterministic CS-LMS algorithm is the Wiener solution $\mathbf{w}_0$.

Proof: See Appendix B.

Thus, the Wiener solution is the same for both LMS and CS-LMS algorithms and then the deterministic CS-LMS algorithm is justified. As a consequence, the stochastic CS-LMS adaptation using an estimated gradient, or equivalently the NLMS algorithm over the difference data set, will converge in the mean to the Wiener solution. In this case, instead of minimizing the power of the difference error in Eq. (B1) we try to make the error sequence as smooth as possible as shown in Eq. (6).

A. A connection between CS-LMS and LMS adaptations

From Eq. (8) we can derive an interesting connection between our adaptation and the classical LMS algorithm. The classical LMS adaptation is obtained using the simplest way to estimate the deterministic gradient vector $\nabla J(n)$ in the steepest descent (SD) algorithm. In this way, we use instantaneous values $\hat{\nabla} J(n)=-e(n)\mathbf{x}(n)$, where $J(n)=E[|e(n)|^2]$ is the mean squared error (MSE) function. Expressing Eq. (8) in terms of the differences of the error sequence $e(n)$ and the input vector $\mathbf{x}(n)$ and redefining the variable step size as $\hat{\mu}$, we find that

$$\begin{aligned}\mathbf{w}(n+1)=\mathbf{w}(n)+\hat{\mu}[&(e^{[n]}(n))^*\mathbf{x}(n)\\&+(e^{[n]}(n-1))^*\mathbf{x}(n-1)-(e^{[n]}(n))^*\mathbf{x}(n-1)\\&-(e^{[n]}(n-1))^*\mathbf{x}(n)].\end{aligned}\tag{9}$$

The first two elements in the adaptation correspond to the instantaneous estimation of the gradient vector $\nabla J^{[n]}(k)=\nabla E[|e^{[n]}(k)|^2]$ at times $k=n$ and $n-1$, in the direction of minimization. The second two terms correspond to the instantaneous estimation of the gradient vectors $\nabla \hat{J}^{[n]}(n)=\nabla E[e^{[n]}(n)(e^{[n]}(n-1))^*]=\nabla r_e(1)$ and $\nabla \hat{J}^{[n]}(n-1)=\nabla E[e^{[n]}\times(n-1)(e^{[n]}(n))^*]=\nabla r_e(-1)$, where $r_e(k)$ denotes the correlation function of the error sequence and $\tilde{J}^{[n]}(n-1)=(\hat{J}^{[n]}\times(n))^*$, in the direction of maximization [we assume $e(n)$ is wide sense stationary then the correlation function is symmetric for real variables: $r_e(k)=r_e(-k)$]. Thus, our algorithm can be viewed as a pair of LMS or SD adaptations at times $n,n-1$ and a pair of adaptations that try to *maximize* the correlation function at lag 1. The maximum value of the correlation function is achieved for lag $k=0$; thus, the second pair of adaptations tries to equalize $e^{[n]}(n)=e^{[n]}(n-1)$ in order to render $r_e(1)$ as close as possible to $r_e(0)$. This is equivalent to the above mentioned *equilibrium condition* that we imposed in the Lagrange formulation in order to solve the filtering problem.

B. Relationship between stochastic information gradients and CS-LMS

Several learning algorithms, where the learning relies on the concurrent change of processing variables, have been proposed in the past for decorrelation, blind source separation, or deconvolution applications.[31,32] Classical approaches propose a cost function estimator and a gradient descent learning algorithm based adaptation to find the optimal solution. The stochastic information gradient (SIG) algorithms[32] maximize (or minimize) Shannon's entropy of the sequence of error terms using an instantaneous value based estimator of the probability density function (pdf) and Parzen windowing. Given a random variable Y with pdf $f_Y(y)$ Shannon's entropy and its stochastic entropy estimator are expressed as

$$\begin{aligned}H_S(Y)&=-\int_{-\infty}^{\infty}f_Y(y)\log(f_Y(y))dy=E_Y[-\log(f_Y(y))]\\&\approx\hat{H}_S(Y)=-\log(f_Y(y(k))),\end{aligned}\tag{10}$$

where $y(k)$ denotes the most recent sample at time k. Since in practice the pdf of Y is unknown a biased Parzen window estimate is utilized as follows:

$$\hat{f}_Y(y(k))=1/N\sum_{i=k-N}^{k-1}\kappa_\sigma(y(k)-y(i)),\tag{11}$$

where N is the window length and $\kappa_\sigma(x)$ is the kernel function with size σ.[32] The result for the maximization (or minimization) of Eq. (10) using Eq. (11) with respect to a set of parameters $\mathbf{w}$, which generates $Y=g(\mathbf{w})$, is an adaptation depending on fixed-width σ kernel functions.[32] If we select $N=1$ and Gaussian kernels the adaptation reduces to

$$\delta\mathbf{w}(n+1)=\frac{\mu}{\sigma^2}(y(k)-y(k-1))\left(\frac{\partial y(k)}{\partial\mathbf{w}}-\frac{\partial y(k-1)}{\partial\mathbf{w}}\right).\tag{12}$$

The latter adaptation is essentially the CS-LMS algorithm except for the constant factor given the fixed kernel size (the maximization of Shannon's entropy is related, in some sense, to the description made in the above section in terms of correlation functions). Our approach can be described as the maximization of Shannon's entropy estimator but using a variable-size σ kernel, which experimentally provides a better estimator for the unknown pdf. The benefits of using variable kernel density estimators are clear from works such as Refs. 33–35. We refer the interested reader to them for a treatment of the problem of kernel size estimation, which is beyond the scope of this paper.

The CS-LMS and SIG methodologies can be further understood in the greater context of errors-in-variables techniques; specifically in the field of adaptive system identification also referred to as instrumental variable approach. The connection between CS-LMS presented in Eqs. (8), (B1), and (B2) and the error whitening criterion proposed by Rao *et al.*[36] should be noted at this point. Utilizing difference input and error data effectively corresponds to exploiting autocorrelation statistics at lags other than zero. The benefits of

such departures from classical error-energy (zero-lag error autocorrelation) measures of performance enables the filters to become more robust to noise present in the signals.

IV. CONVERGENCE ANALYSIS OF THE CS-LMS ALGORITHM

Let us first consider the convergence of the deterministic CS-LMS algorithm, which is described as the SD algorithm on the novel data set. Taking the connection expressed in Eq. (9) into consideration we can formulate the following deterministic adaptation for the CS-LMS:

$$\mathbf{w}(n+1) = \mathbf{w}(n) + \hat{\mu}[-\nabla\{J^{[n]}(n) + J^{[n]}(n-1)\} + 2\,\mathrm{Re}\{\nabla\hat{J}^{[n]}(n)\}]. \tag{13}$$

In terms of the novel data model $\{\mathbf{x}_1(n), d_1(n), e_1(n)\}$ introduced in Appendix B the adaptation could be expressed as

$$\mathbf{w}(n+1) = \mathbf{w}(n) + \hat{\mu}[-\nabla\{J_1^{[n]}(n)\}], \tag{14}$$

where $J_1^{[n]}(n) = E[|e_1(n)|^2]$. Since $e_1(n) = d_1(n) - \mathbf{w}^H\mathbf{x}_1(n)$ then

$$J_1^{[n]}(n)\sigma_{d_1}^2 - \mathbf{w}^H\mathbf{r}_{\mathbf{d}_1\mathbf{x}_1}\mathbf{r}_{\mathbf{d}_1\mathbf{x}_1}{}^H\mathbf{w} - \mathbf{w}^H\mathbf{R}_{\mathbf{x}_1}\mathbf{w}. \tag{15}$$

As shown in Appendix C, a necessary and sufficient condition for the convergence can be expressed, in terms of the step-size parameter $\hat{\mu}$ and the largest eigenvalue $\lambda_{\max}$ of the difference matrix $\Delta\mathbf{R}(1) = \mathbf{R}(0) - \mathbf{R}(1)$ where $\mathbf{R}(k) = E[\mathbf{x}(n+k)\mathbf{x}^H(n)]$, as

$$0 < \hat{\mu} < \frac{1}{\lambda_{\max}}. \tag{16}$$

A. Convergence analysis of the stochastic CS-LMS algorithm

From Eq. (8) it can be seen readily that the stochastic CS-LMS algorithm is equivalent to the NLMS adaptation over the novel difference data set, which was defined in the previous section. Thus, once we have proven in Sec. III that (i) they have the same Wiener solution and (ii) the stochastic CS-LMS is equivalent to the NLMS on the novel data set, we can assume the same properties of the standard NLMS algorithm[26] to our approach using the difference data set. As a consequence, the stochastic CS-LMS adaptation using an estimated gradient is convergent in the MSE sense if Eq. (16) is satisfied. In this case, instead of minimizing the power of the difference error in Eq. (B1) the error sequence is made as smooth as possible as shown in Eq. (6). Further the evolution of the expected value of the stochastic weight vector $\mathbf{w}(n)$ also satisfies Eq. (C3) as in the deterministic CS-LMS algorithm.

1. Learning curves in the ANC application

It is common in practice to use ensemble-average learning curves to study the statistical performance of adaptive filters. In the ANC application the derivation of these curves is slightly different due to the presence of the desired clean signal $s(n)$. The estimation error produced by the filter in the ANC application is expressed as

$$e(n) = s(n) + e_0(n) + \varepsilon_0^H(n)\mathbf{x}(n) \quad \text{for } \mu \text{ small}, \tag{17}$$

where e_0 is the estimation error produced by the Wiener filter and ε_0 is the zero-order weight-error vector, which satisfies the stochastic difference equation described in Ref. 37, i.e., we invoke the direct-averaging method. Hence, assuming that e_0 is statistically independent of $\mathbf{x}(n)$ and $s(n)$, the MSE produced by the filter on the novel data is given by

$$J(n) = J_0 + E[|s(n)|^2] + E[\varepsilon_0^H(n)\mathbf{x}(n)\mathbf{x}(n)^H\varepsilon_0(n)], \tag{18}$$

where $J_0 = E[|e_0(n)|^2]$ and $J_{\min} = J_0 + E[|s(n)|^2]$. It can be seen readily that a reduction in MSE $J(n)$ is obtained by the CS-LMS algorithm if the desired signal $s(n)$ and the input signal $\mathbf{x}(n)$ are either strongly and weakly correlated, respectively (see Appendix D). Since the evolution of the weight-error vector is

$$\varepsilon_0(n+1) = (I - \mu\mathbf{R}_{\mathbf{x}_1})\varepsilon_0(n) - \mu\mathbf{x}_1(n)\delta\tilde{e}_0^*(n), \tag{19}$$

where $\delta\tilde{e}_0(n) = \delta e_0(n) + s_1(n)$ and the excess error in the steady state is expressed and bounded as

$$\begin{aligned} J_{\mathrm{ex}}(\infty) &= \lim_{n\to\infty} E[\varepsilon_0^H(n)\mathbf{x}(n)\mathbf{x}(n)^H\varepsilon_0(n)] \\ &= \lim_{n\to\infty} \mathrm{tr}[\mathbf{R}_{\mathbf{x}}E[\varepsilon_0(n)\varepsilon_0(n)^H]] \\ &\le \mu J \sum_{k=1}^{L} \frac{\lambda_k}{2-\mu\lambda_k} < J_{\mathrm{ex}}^{\mathrm{LMS}}(\infty), \end{aligned} \tag{20}$$

where $\tilde{J} = 2(J_{\min} - \mathrm{Re}\{r_s(1)\})$ and $r_s(1)$ is the correlation function of the desired signal at lag 1. If the input signal $\mathbf{x}(n)$ is weakly correlated [first inequality: if $\mathbf{R}(1) \sim \mathbf{0}$] and the desired signal is strongly correlated $s(n)$ (second inequality: if $\mathrm{Re}\{r_s(1)\} > 3/4J_{\min}$, we achieve a clear reduction in excess MSE.

In addition, if the power of the desired signal is neglected [or disappears in time, i.e., when $s(n)$ is intermittent] the misadjustment (M) satisfies the following approximate equality:

$$\begin{aligned} M &= \frac{J_{\mathrm{ex}}(\infty)}{J_{\min}} \simeq \mu\,\mathrm{tr}(\mathbf{R}_{\mathbf{x}_1}) = \mu[2(\mathrm{tr}(\mathbf{R}) - \mathrm{tr}(\mathrm{Re}\{\mathbf{R}(1)\}))] \\ &= \tfrac{1}{2}\mu_D\,\mathrm{tr}(\mathbf{R}), \end{aligned}$$

$$J(n) \simeq J_0 + \mu J_0\,\mathrm{tr}(\mathbf{R}_{\mathbf{x}_1}), \tag{21}$$

where $J_{\mathrm{ex}}(\infty)$ denotes the steady-state EMSE, $J_{\min} = J_0$, tr stands for the trace of a matrix, and $\mu_D = 4\mu\,(1 - \mathrm{tr}(\mathrm{Re}\{\mathbf{R}(1)\})/\mathrm{tr}(\mathbf{R}))$.

In DTX systems, the adaptive filter is required to have a high step size μ to cope with changing statistics in the channel. This affects the misadjustment (M) of the algorithm, which is increased substantially. Beforehand, a clear reduction of $J_{\mathrm{ex}}(\infty)$ of the CS-LMS algorithm is achieved by reducing $J_{\min}$ to $\tilde{J}$ [see Eq. (20)] and/or the trace of the input correlation matrix since $M \simeq \mu\,\mathrm{tr}(\mathbf{R}_{\mathbf{x}_1})$ [see Eqs. (20) and (21)]. The condition for the reduction of M, which depends on the input sequence, is the following:

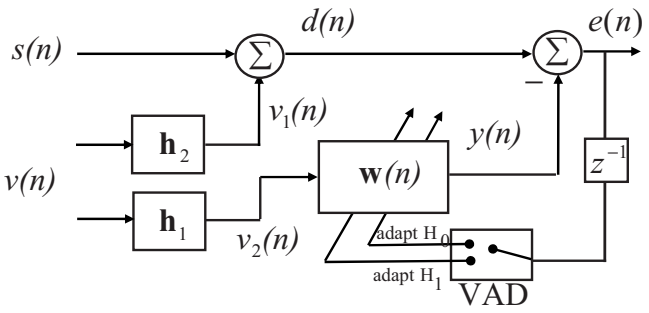


FIG. 2. Improving adaptive noise canceler using VAD.

$$\mathrm{tr}(\mathrm{Re}\{\mathbf{R}(1)\}) > \tfrac{3}{4}\mathrm{tr}(\mathbf{R}) \quad \text{or } \mu_D < \mu. \tag{22}$$

Note that this condition is incompatible with the one assumed to obtain the upper bound for $J_{\mathrm{ex}}(\infty)$ ($\mathbf{R}(1)\sim\mathbf{0}$) (see Appendix D for further details). Thus, the reduction of M by using *the trace of the input correlation matrix* is unfeasible.

It also follows from the NLMS analysis[26] that the high value of μ balances the trade-off between M and the average time constant. Indeed the average time constant for the stochastic CS-LMS algorithm can be expressed as

$$\tau \simeq \frac{L}{\mu\,\mathrm{tr}(\mathbf{R}_{\mathbf{x1}})}, \tag{23}$$

where L is the filter length. On the basis of this formula, we may make the same observations as in Ref. 26 about the connection between M and τ. This constant is higher than the standard LMS algorithm for the same μ but fits with the ANC application for DXT systems (a high value of step size is needed). In the following section we show a customized version of the CS-LMS algorithm, the lag-CS-LMS algorithm, that allows to select a suitable trade-off between convergence and average time constant over noise segments.

V. IMPROVING SPEECH FILTERING IN ANC USING VAD

Based on the properties and production of the speech signal, different assumptions can be derived to allow distinction between speech periods and noise-only periods. The equilibrium condition in Eq. (5) is hardly met in distinctly nonstationary segments [of course the condition imposed by the NLMS algorithm is even more unfeasible, $e^{[n+1]}(n)=0$, see Ref. 26], i.e., in DTX systems, these segments correspond to the presence of noisy speech ($t\sim 0.2$ s). However, background noise is usually assumed stationary for much longer periods, e.g., $t>1$ s, than speech. Thus, a better performance of the algorithm is expected in noise segments in which the equilibrium condition could be even more *relaxed*. In the past, the use of a VAD has been critical in attaining a high level of performance in speech processing systems, even more, for nonstationary noise environments since it is needed to update the constantly varying noise statistics.[38] In this section we propose the use of a standard energy-based VAD in order to exchange the application of different filtering algorithms providing a better tracking of the variability of statistics in noise/speech transitions as shown in Fig. 2. One solution is to apply CS-LMS to noise segments (H_0), where the equilibrium condition can be easily achieved, and a MLMS algorithm,[7] using the initial weight vector provided by the CS-LMS, on speech segments (H_1) (see Fig. 3). As shown in Sec. VI, the combination of both methods provides synergy that would be expected to enhance the filter effectiveness over the referenced algorithms. Based on the same philosophy, we propose the lag-CS-LMS algorithm that relaxes the equilibrium constraint over noise segments, and combined with the CS-LMS over speech segments, obtains a better performance in terms of EMSE and M than all the referenced filtering algorithms.

A. A filtered energy-based VAD

In order to avoid the inconvenience of high noise level conditions in VAD,[15] we use the filtered sequence of *a priori* errors $e^{[n]}(n)$ of the ANC to detect the presence of speech segments. The use of the reference signal $d(n)$ for this task would cause a poor hit rate of speech/nonspeech segments at high noise conditions. Then the application of VAD to this speech processing system would be completely unnecessary, i.e., it would show a low level of performance.

Short time average energy is the most evident way to classify signal to speech and nonspeech periods, since the signal is assumed to have higher energy, when speech is present in the filtered sequence. The short time average energy-based decision at time $n+1$ can be described as

$$E(n+1) = \frac{1}{N}\sum_{k=0}^{N-1} (e^{[n]}(n-k))^2 \underset{H_0}{\overset{H_1}{\gtrless}} \eta(n), \tag{24}$$

where N denotes the amount of contextual information included in the VAD decision and $\eta(n)$ is an empirical threshold that models the background noise. In particular, we compute the average energy of a set of initial noise segments and update it according to the VAD decision (during nonspeech periods), that is, in order to adapt the operation to nonstationary and noisy environment we compute

$$n(n+1) = \alpha\eta(n) + (1-\alpha)E(n), \tag{25}$$

where $\alpha=0.9$ for a soft decision function. To overcome the difficulties in the low signal-to-noise ratio (SNR) regime subband energies have been employed.[18–20] Subband energies will describe the energy distribution of the signal in frequency domain with some predefined resolution. Energy-based VAD algorithms can provide a good performance, when the energies of the speech periods are significantly higher than the energies of the background noise-only periods. Most of the features used in VAD algorithms are related to energy[15–20] indeed. However, when the energy of the background noise is comparable, the signal energy alone will result in a poor performance. Moreover, the unvoiced parts of the speech will have low energy constantly, which makes the classification of the unvoiced phonemes more difficult than the ones with voice present. Nevertheless, this situation can be avoided using the filtered sequence provided by the ANC that is characterized by a high SNR in the steady state of the filter. On one hand, this allows the use of effective classical VADs, i.e., based on energy to exchange the operation of the ANC; on the other hand, it provides a small delay

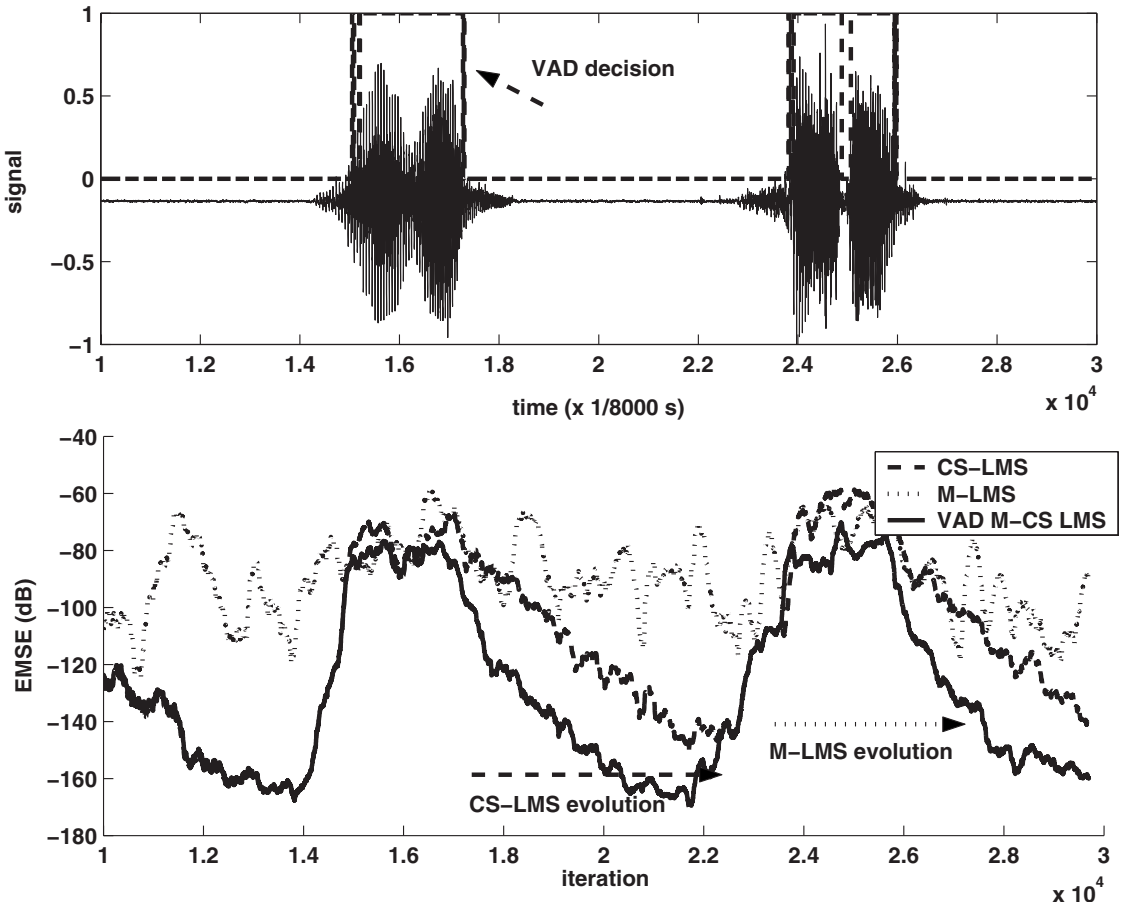


FIG. 3. ANC application: The effect of combining MLMS and CS-LMS over an utterance of AURORA 3 database using VAD in terms of EMSE [EMSE in dB=20 $\log_e(.)$; Gaussian noise with variance $\sigma_v^2=0.01$, $L=12$, $\mu=0.1$, and $\mathbf{h}_1$, $\mathbf{h}_2$ as defined in Sec. VI].

to the VAD that detects the presence of speech at a later stage. Regardless, that is not a serious implementation obstacle since the ANC works sample by sample unlike most VADs that works over contextual information windows.[18]

B. The lag-CS-LMS algorithm

We can exploit the advantages of the CS-LMS algorithm in noise segments just relaxing the equilibrium condition. In many cases, constraining the least squares filter to minimize Eq. (B1) is overly restrictive (see page 171 in Ref. 39). For example, if a delay may be tolerated, then we may consider minimizing the expected value of the difference as follows:

$$\min_{\mathbf{w}} E[|e_k(n)|^2], \tag{26}$$

where $e_k(n)=e(n)-e(n-k)$. In most cases, a nonzero delay k will produce a better approximate filter and, in many cases, the improvement will be substantial. Following the same methodology as in Sec. II and imposing the condition

$$e^{[n+1]}(n) = e^{[n+1]}(n-k), \tag{27}$$

we obtain an additional improvement in the filtering of noise segments unlike the speech segments where the high nonstationary noise affects the solution provided by the algorithm. The explanation of this behavior is that using the novel data set $e_k(n)=e(n)-e(n-k)$, which is increasing the lag k, we decrease the average time constant τ in Eq. (C10) by increasing the trace of the input autocorrelation matrix $\mathbf{R}_{\mathbf{x}_k}$ (and consequently increasing M). This is really effective over noise segments as shown in Fig. 4, given that a small average time constant provides a smaller averaged M over nonspeech frames. Thus, the combination of both operation modes using an effective VAD, i.e., based on energy and contextural information,[20] is expected to supply better filtering performance. The evaluation of the proposed strategy over an utterance of the Speech-Dat-Car (SDC) AURORA 3 is shown in Fig. 4. As clearly stated in the latter figure and in Sec. VI, the use of VAD in ANC provides the best results obtained by the CS-LMS algorithms separately. The selection of lag k is motivated by the trade-off between the M and the average time constant (see Fig. 5). In this case, given a large step size $\mu=0.25$, a higher convergence speed does not reduce the averaged EMSE in noise segments as clearly stated in Fig. 5(a). However, when the specifications of the problem require a good filtering performance (i.e., a reduced M), a smaller step size $\mu=0.1$ should be selected. Then the averaged EMSE in noise segments may be reduced by incorporating a lag into the algorithm, which speeds up the algorithm convergence (see also the experimental analysis in Sec. VI). In Fig. 5 the robustness of the CS-LMS algorithm against the noise power is also highlighted.

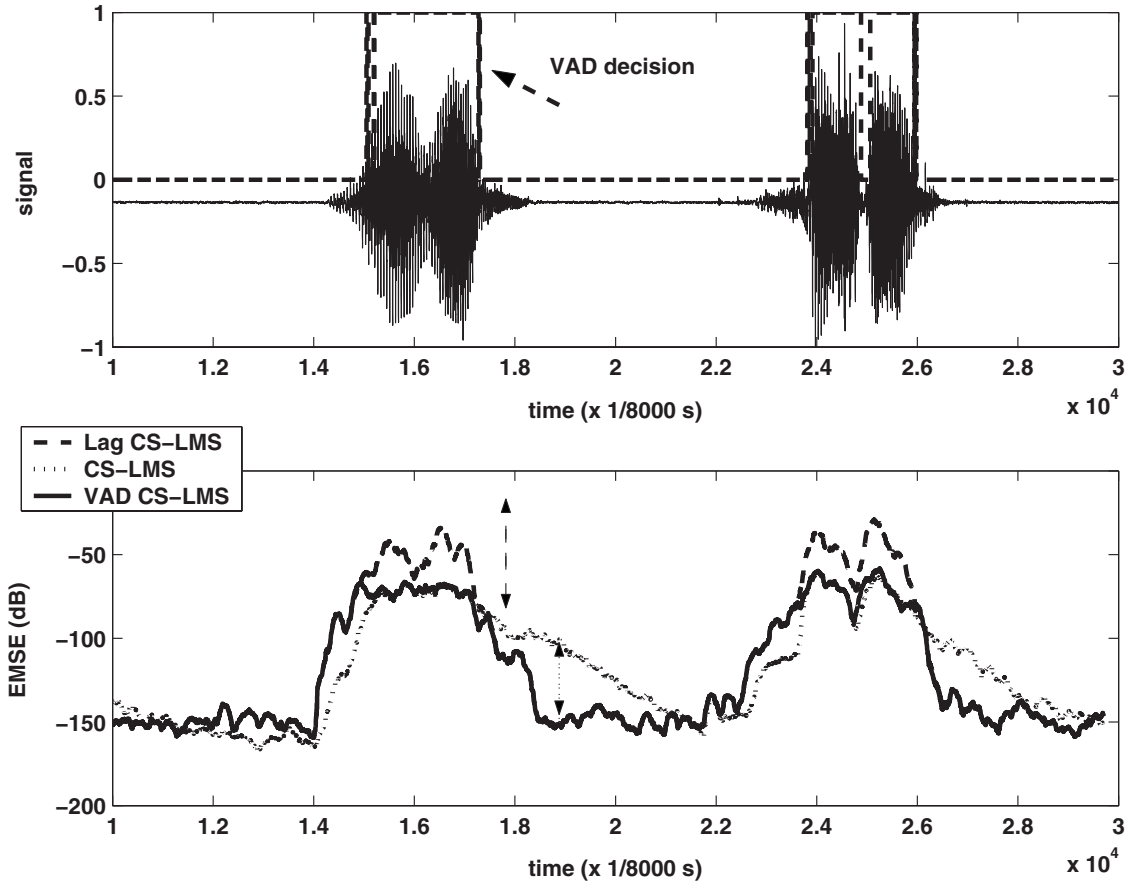


FIG. 4. ANC application: The effect of combining the lag CS-LMS ($k=5$) and CS-LMS using VAD in terms of EMSE. [EMSE in dB$=20\log_e(.)$; Gaussian noise with variance $\sigma_v^2=0.01$, $L=12$, $\mu=0.1$, and $\mathbf{h}_1$, $\mathbf{h}_2$ as defined in Sec. VI].

VI. EXPERIMENTS

Several experiments are commonly conducted in order to evaluate the performance of the CS-LMS algorithm. The experimental analysis is mainly focused on the determination of the EMSE and misadjustment (M) (Ref. 26) at different SNR levels, step sizes, and environments. This section describes the experimental framework and the objective performance measures conducted to evaluate the proposed algorithm. For this purpose, the AURORA subset of the original Spanish SDC database[40] was used. This database contains 4914 recordings using close-talking (CH0) and distant hands-free microphone (CH1) from more than 160 speakers. The files are categorized into three noisy conditions: quiet, low, and high noise conditions, which represent different driving conditions with average SNR values between 25 and 5 dB. The EMSE and M were determined for each recording using the close-talking microphone high noise condition for the CS-LMS, NDN-LMS,[9] NLMS,[25] EN-LMS,[10] and MLMS (Ref. 7) algorithms. The *experimental* EMSE at the kth iteration is defined by

$$\mathrm{EMSE}(k)=\frac{1}{J}\sum_{j=1}^{J}|e(k-j)-s(k-j)|^2, \tag{28}$$

where J is the number of samples used in the estimation of the EMSE. On the other hand, M is defined as a normalized MSE, i.e., the ratio of the steady-state EMSE ($J_{\mathrm{ex}}(\infty)$) to the minimum MSE (J_{min}). The MSE is obtained removing $s(n)$ in Eq. (28) [estimation of the power of $s(n)$].

A. Numerical experiment

The initial set of simulations used a simple ANC configuration to test the analytical results derived in Sec. IV. In this case, the desired signal $s(n)$ is a sum of an intermittent zero-mean AR(1) process with variance 1 and its pole at $a_s(1)=0.99$ and a zero-mean additive white noise with variance 0.001. The AR(1) process turns on and off every 3000 samples. The noise source $v(n)$ is a zero-mean Gaussian process with variance 1, and it is assumed to be independent of $s(n)$. The impulse response of the filters $\mathbf{h}_1$ and $\mathbf{h}_2$ were modeled as low pass IIR filters according to

$$H_1^{-1}(z)=1-0.3z^{-1}-0.1z^{-2},\quad H_2^{-1}(z)=1-0.2z^{-1}. \tag{29}$$

Both CS-LMS and NLMS algorithms use an eight tap weight vector initialized to zero and different step sizes (0.001, 0.01, and 0.1). The experimental setting described above models the conditions of the ANC in DXT systems except if only stationary signals are present. In order to show the performance of the filtering algorithms we use the MSE in the steady-state averaging over $J=200$ samples. The Monte Carlo simulation results (over 100 trials) of running the two algorithms are shown for different values of μ in Fig. 6. As shown in the figures the MSE of the CS-LMS algorithm is larger than the MSE of the NLMS over noise

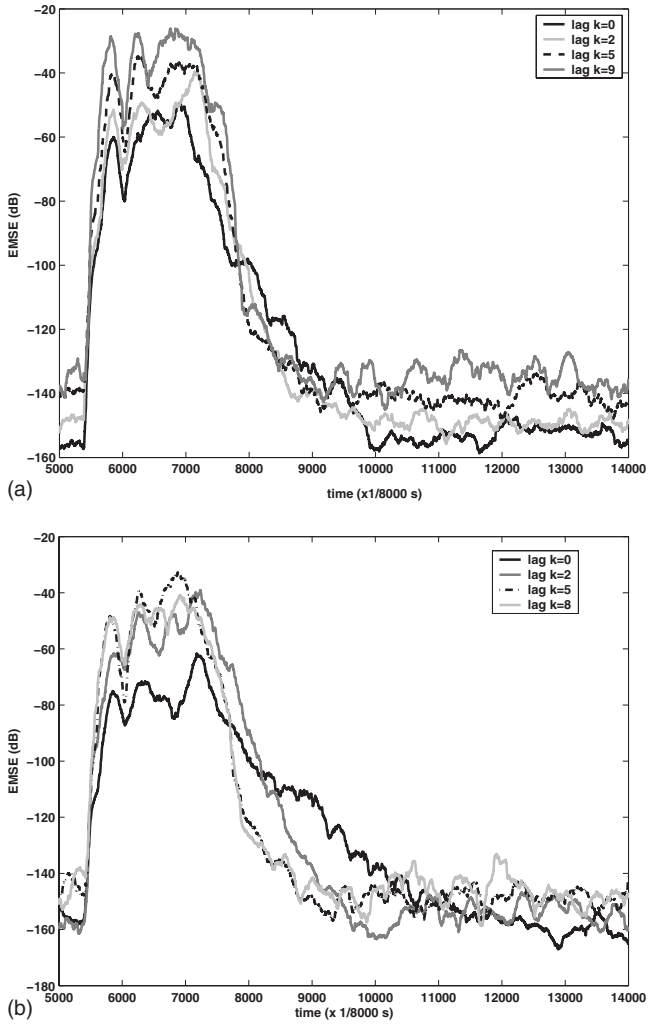


FIG. 5. ANC application: The trade-off between M and τ of the CS-LMS algorithm with increasing k over an utterance of the Spanish AURORA 3 database. (a) Evolution of EMSE [in dB$=20\log_e(.)$] for ($\mu=0.25$, $\sigma_v^2=0.3$ $L=12$). (b) Evolution of EMSE [in dB$=20\log_e(.)$] for ($\mu=0.1$, $\sigma_v^2=0.5$ $L=12$).

segments as expected [using Eq. (21) $\mathrm{MSE}_{\mathrm{LMS}} \simeq -29.8227$ dB; $\mathrm{MSE}_{\mathrm{CS\text{-}LMS}} \simeq -29.7170$ dB for $\mu=0.01$ and $\mathrm{MSE}_{\mathrm{LMS}} \simeq -28.4873$ dB; $\mathrm{MSE}_{\mathrm{CS\text{-}LMS}} \simeq -27.7641$ dB for $\mu=0.1$] [$\sigma_x^2=\sigma_v^2/(1-a^2(1)) < 4(\sigma_x^2-a(1))$, where $a(1)=0.2$ and $\sigma_x^2=1.0417$]. Note that $J_{\min}=-30$ dB on noise segments. Somehow when $s(n)$ turns on (to model correlated speech segments) there is a clear reduction in EMSE if μ is sufficiently high (to cope with high nonstationary environment). As also shown in theoretical section, on speech segments: $\mathrm{MSE}_{\mathrm{LMS}} \simeq 0.1932$ dB; $\mathrm{MSE}_{\mathrm{CS\text{-}LMS}} \simeq 0.0113$ dB for $\mu=0.01$ and $\mathrm{MSE}_{\mathrm{LMS}} \simeq 1.6012$ dB; $\mathrm{MSE}_{\mathrm{CS\text{-}LMS}} \simeq 0.074$ dB for $\mu=0.1$. Observe how when μ is increased the *small-step-size statistical theory* gives a rough result in the value of MSE comparing with the experimental one, although the relation between the performance of both algorithms is preserved. Note that the τ in CS-LMS is also larger than NLMS as expected.

B. ANC application: Stationary noise environment

Finally, to check the tracking ability of the set of algorithms we study the ANC problem using the previously defined AURORA 3 database. It is expected to obtain a better performance on the previous approaches since voice signals are nonstationary in nature. The simulations were carried out using recordings sampled at 8 kHz and processing 20 000 samples/recording ($\sim$2.5 s of real time). In the stationary case, the noise v was assumed to be zero mean white Gaussian with three different variances ($\sigma_v^2=0.01, 0.1, 0.5$) under severe noise condition as shown in Table I. The incoming clean signal was normalized using its entire span for convenience. In the simulations the filter length was varied in the set $L=\{8, 12, 24\}$, $\epsilon=0.0001$ and the constant step size was varied in the range $\mu=\{0.01, 0.5\}$. The impulse response of the filters $\mathbf{h}_1$ and $\mathbf{h}_2$ were modeled as low pass IIR filters according to Eq. (29). Observe the effect of the equilibrium condition in the evaluation of the CS-LMS over an utterance of the Spanish AURORA 3 database in Fig. 7(a). The equilibrium condition can be easily achieved over the noise stationary segments; over the speech segments the equilibrium constraint is hardly satisfied because of the nonstationary nature of speech [regardless there is still an improvement in EMSE reduction—computed as $20\log_e(.)$ to highly decompress the EMSE—over classical LMS methods]. In the bottom of Fig. 7(a) we show the spectrogram of the estimated clean signal $e(n)$ by using the CS-LMS adaptation.

Table I shows the filtering results using the proposed and referenced algorithms over the complete Spanish AURORA 3 databases. As clearly demonstrated, the proposed method provides the minimum EMSE and M averaged over a set of filter lengths L for a wide range of noise variances (delimited by "\) except for the case $\sigma_v^2=0.01$, i.e., the EMSE of the NLMS is not affected by the step size μ since it is also proportional to the input power. In the case of nonstationary speech segments, this reduction of EMSE and M means better trade-off between convergence speed and misadjustment and then better filtering performance. The combination of the MLMS with the proposed CS-LMS using a VAD (as described in Sec. V) provides an improvement over the classical method MLMS operating separately at noise adverse conditions. Of course, the proposed CS-LMS still improves the combination of both using the VAD, since its more effective filtering on speech segments over MLMS. This behavior can be observed also in nonstationary experiments as shown in the following section. It is interesting to notice that for both environments, stationary and nonstationary, and for a wide range of parameters (L, μ, σ_v^2, etc.) we found a better performance over the referenced filtering algorithms.

Moreover, an additional improvement can be achieved by relaxing the equilibrium condition of the CS-LMS algorithm over noise segments and by employing the filtered energy-based VAD described in Sec. V B. The results using the SNR of 10 dB, which is the most probable application scenario for telecommunication terminals, are shown in Table II. The right combination of the lag-CS-LMS algorithm ($k=5$) and the standard CS-LMS outperforms all the references ANCs including the proposed CS-LMS working separately. Even if the combination of both ANCs is inversely used, that is the lag-LMS is applied to speech segments and the standard CS-LMS to noise periods, the results are still fair enough as shown in Table II.

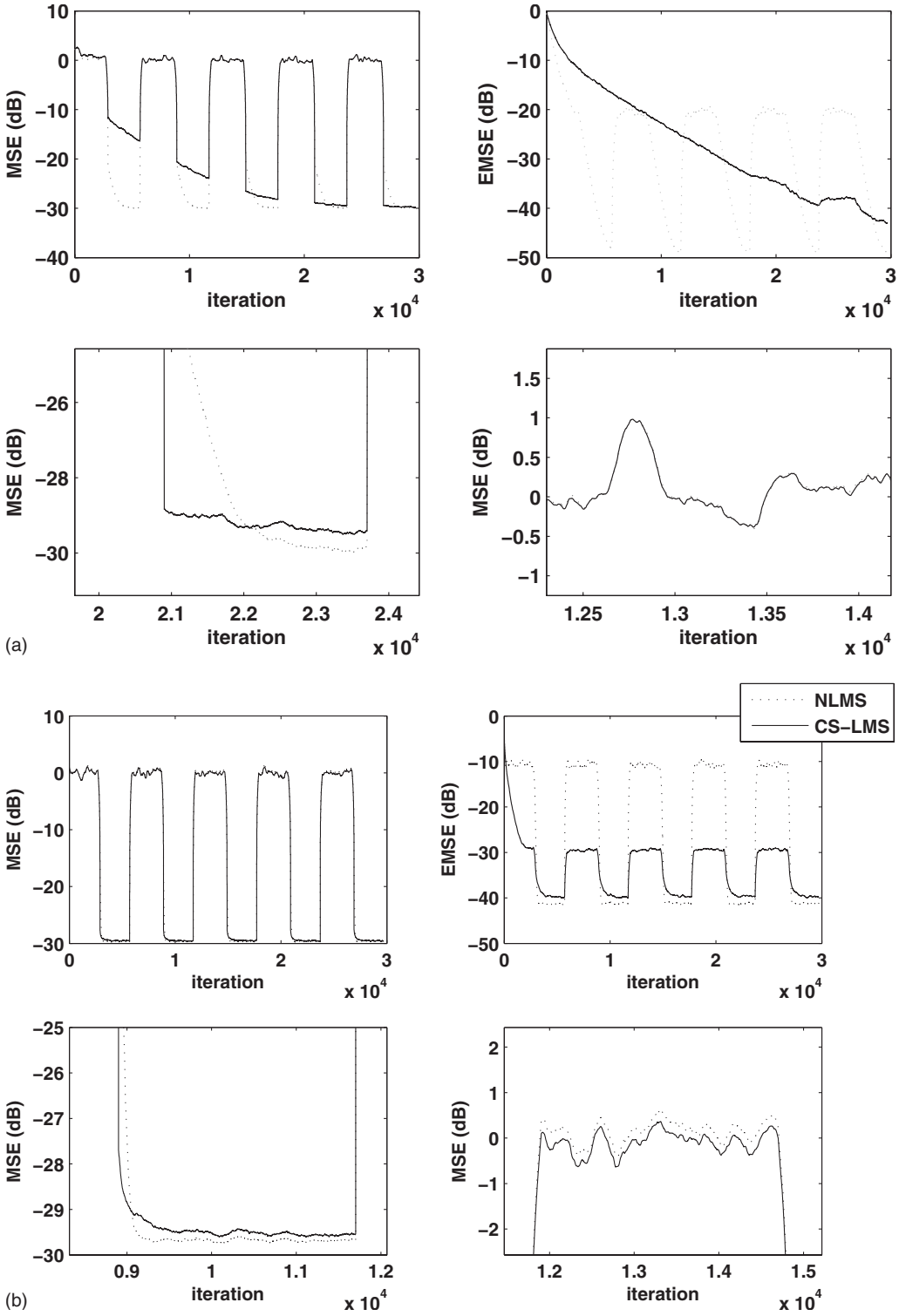


FIG. 6. Numerical experiment in the ANC problem. Top: MSE [in dB=10 $\log_{10}(.)$] and EMSE [in dB=20 $\log_e(.)$] comparison between the CS-LMS (line) and NLMS (dotted) algorithms. Bottom: zoom on MSE evolution over noise and speech segments. (a) Stationary environment (μ=0.01, σ_v^2=1 L=8). (b) Stationary environment (μ=0.1, σ_v^2=1 L=8).

C. ANC application: Nonstationary noise environment

For the nonstationary case the noise is also assumed to be zero mean Gaussian but with a variance linearly increasing from $\sigma_{v,\min}^2$=0.1 to $\sigma_{v,\max}^2$=0.5. The effect of increasing the noise variance is illustrated in Fig. 7(b). We also show the filtering result (spectrogram) of the CS-LMS algorithm. Table III shows the results obtained (EMSE and M) by the complete set of algorithms for different values of μ and L. Again, the proposed algorithm obtains the better trade-off between convergence speed and misadjustment although the computational burden is slightly increased by the novel adaptation. Obviously, the filtering performance is also affected by the nonstationarity of noise segments, unlike the stationary experiment described above, since a larger tracking abil-

TABLE I. Performance of referenced and proposed LMS algorithms in stationary environment.

Stationary white noise $E[v(n)]=0$ $\sigma_v^2=0.01/0.1/0.5$	NLMS		NDN-LMS		MLMS	
	$\overline{\text{EMSE}}$ (dB) $L=8;12;24$	$\bar{M}$ $L=8;12;24$	$\overline{\text{EMSE}}$ (dB) $L=8;12;24$	$\bar{M}$ $L=8;12;24$	$\overline{\text{EMSE}}$ (dB) $L=8;12;24$	$\bar{M}$ $L=8;12;24$
$\mu=0.1$	−42.23/−35.17/−23.42	0.22/0.43/1.61	−27.04/−26.15/−25.64	1.00/1.07/1.06	−47.26/−33.77/−22.88	0.11/0.56/1.82
$\mu=0.25$	−42.66/−31.80/−20.86	0.21/0.62/2.15	−22.75/−21.99/−21.94	1.57/1.67/1.67	−46.97/−30.31/−20.64	0.12/0.82/2.30
$\mu=0.5$	−42.91/−29.80/−19.31	0.20/0.85/2.56	−19.18/−18.85/−18.92	2.24/2.38/2.38	−45.47/−27.84/−19.25	0.14/1.07/2.65
Stationary white noise $E[v(n)]=0$ $\sigma_v^2=0.01/0.1/0.5$	EN-LMS		CS-LMS		VAD CS+MLMS	
	$\overline{\text{EMSE}}$ (dB) $L=8;12;24$	$\bar{M}$ $L=8;12;24$	$\overline{\text{ESME}}$ (dB) $L=8;12;24$	$\bar{M}$ $L=8;12;24$	$\overline{\text{EMSE}}$ (dB) $L=8;12;24$	$\bar{M}$ $L=8;12;24$
$\mu=0.1$	−41.90/−23.19/−6.95	0.23/1.85/13.25	−40.06/−39.36/−38.02	0.26/0.28/0.34	−45.29/−41.55/−38.02	0.11/0.22/0.34
$\mu=0.25$	−41.98/−21.02/−0.85	0.23/2.68/28.93	−36.50/−35.97/−35.71	0.39/0.41/0.43	−41.42/−38.09/−35.71	0.19/0.31/0.43
$\mu=0.5$	−41.70/−16.75/6.40	0.24/4.79/63.98	−33.49/−33.00/−32.91	0.56/0.59/0.59	−38.21/−35.21/−32.91	0.27/0.44/0.59

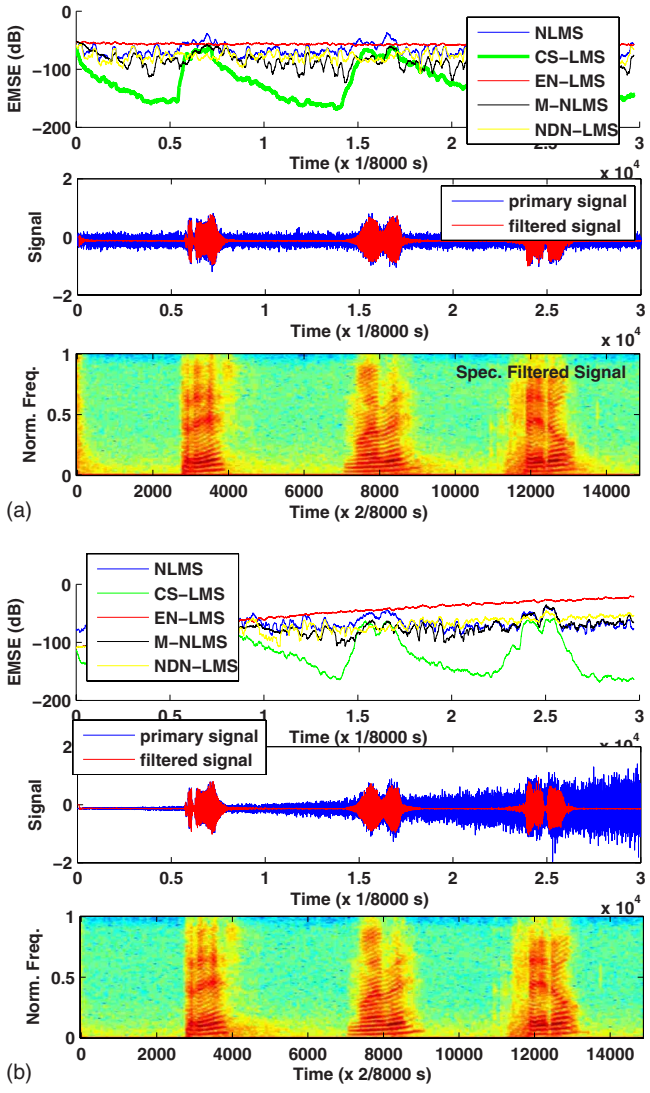


FIG. 7. (Color online) ANC application using the CS-LMS algorithm over an utterance of the Spanish AURORA 3 databases. Top: EMSE evolution [in dB=20 $\log_e(.)$]; middle: corrupted and error (clean) signal; bottom: spectrogram of the error signal. (a) Stationary environment ($\mu=0.1$, $\sigma_v^2=0.1$ $L=12$). (b) Nonstationary environment ($\mu=0.1$, $\sigma_{v,\min}^2=0.1$, $\sigma_{v,\max}^2=0.7$, $L=12$).

ity is required during the whole utterance. The robustness of the proposed method under severe noise condition can be seen in Fig. 7(b). The above mentioned properties of our algorithm on the stationary scenario are still visible. Substantial improvements of the proposed ANC are also evident on this new scenario, particularly under conditions of strong noise. In addition, the combination of the selected ANC adaptations with a VAD again improves the filtering performance over the one obtainable with the referenced algorithms.

VII. CONCLUSION

In this paper we showed an ANC using the novel CS-LMS algorithm that is based on the minimization of the squared Euclidean norm of the change $\delta\mathbf{w}(n+1)$ subject to the constraint of equilibrium condition in the sequence of *a posteriori estimation errors*. To solve this constrained optimization problem, we used the well-known method of Lagrange multipliers for the general case of complex-valued data. We obtained a novel adaptation algorithm, which is a combination of a deterministic gradient function in order to minimize the MSE, with a gradient function maximizing the correlation function at lag 1 that was assumed to be real valued. Convergence analysis was studied in terms of the evolution natural modes toward the optimal Wiener–Hopf solution and convergence conditions were given: The stability performance depends *exclusively* on μ and the eigenvalues of $\Delta\mathbf{R}(1)$. In addition, we checked the benefits of a VAD scheme for improving the performance of the proposed algorithm. We combined the tracking ability and the higher performance on nonstationary speech segments of the latter algorithm for different lags under nonsevere noise conditions. For both stationary and nonstationary adverse noise environments, the proposed ANC based on the CS-LMS algorithm showed superior performance in decreasing excess MSE compared with referenced algorithms,[7,9,10] etc., using the AURORA 3 Spanish SDC database.[40]

ACKNOWLEDGMENTS

This work was partly supported by the Spanish Government under the PETRI DENCLASES (PET2006-0253),

TABLE II. Performance of referenced and proposed LMS algorithms in stationary environment.

Stationary white noise $E[v(n)]=0$ $\sigma_v^2=0.3$	NLMS		NDN-LMS		MLMS	
	EMSE (dB) $L=8$	M $L=8$	EMSE (dB) $L=8$	M $L=8$	EMSE (dB) $L=8$	M $L=8$
$\mu=0.01$	−36.60	0.38	−34.56	0.40	−34.29	0.55
Stationary white noise $E[v(n)]=0$ $\sigma_v^2=0.3$	Inv. VAD lag CS-LMS		CS-LMS		VAD lag CS-LMS	
	EMSE (dB) $L=8$	M $L=8$	EMSE (dB) $L=8$	M $L=8$	EMSE (dB) $L=8$	M $L=8$
$\mu=0.01$	−39.09	0.32	−40.18	0.28	−40.82	0.25

TEC2008-02113, NAPOLEON (TEC2007-68030-C02-01) projects, and the Consejería de Innovación, Ciencia y Empresa (Junta de Andalucía, spain) under the Excellence Project (TIC-02566). The authors would like to thank Mrs. M. E. Cobo-Lara for help in writing this paper in English. J.M.G. would like to thank Mr. Monson Hayes for introducing him to the field of statistical signal processing.

APPENDIX A: PROOF OF THE CONSTRAINED-STABILITY LMS ADAPTATION

Once the Lagrangian function has been established in Eq. (6), we need to derive the minimum weight vector under the equilibrium constraint. Taking partial derivative of Eq. (6) with respect to the vector $\mathbf{w}^H(n+1)$ and set it equal to zero, we obtain

$$\frac{\partial \mathcal{L}(\mathbf{w}(n+1))}{\partial \mathbf{w}^H(n+1)} = \frac{\partial \delta\mathbf{w}^H(n+1)\delta\mathbf{w}(n+1)}{\partial \mathbf{w}^H(n+1)} + \lambda^*\left(\frac{\partial e^{[n+1]}(n)}{\partial \mathbf{w}^H(n+1)} - \frac{\partial e^{[n+1]}(n-1)}{\partial \mathbf{w}^H(n+1)}\right) = 0. \tag{A1}$$

Since $\delta\mathbf{w}(n+1)=\mathbf{w}(n+1)-\mathbf{w}(n)$ and $e^{[n+1]}(k)=d(k)-\mathbf{w}^H(n+1)\mathbf{x}(k)$ for $k=n$, $n-1$ then

$$\frac{\partial \mathcal{L}(\mathbf{w}(n+1))}{\partial \mathbf{w}^H(n+1)} = 2\delta\mathbf{w}(n+1) - \lambda^*\delta\mathbf{x}(n) = 0. \tag{A2}$$

thus, the step of the algorithm is

$$\delta\mathbf{w}(n+1) = \tfrac{1}{2}\lambda^*\delta\mathbf{x}(n) \Rightarrow \mathbf{w}(n+1) = \mathbf{w}(n) + \tfrac{1}{2}\lambda^*\delta\mathbf{x}(n). \tag{A3}$$

To complete the minimization procedure we must determine the Lagrange multiplier by applying the equilibrium constraint. Multiplying both sides of Eq. (A2) by $\delta\mathbf{x}^H(n+1)$ we have

$$2\delta\mathbf{x}^H(n)\delta\mathbf{w}(n+1) - \lambda^*\delta\mathbf{x}^H(n)\delta\mathbf{x}(n) = 0. \tag{A4}$$

Thus, we find that the Lagrange multiplier can be expressed as

$$\lambda^* = \frac{2\delta\mathbf{x}^H(n)\delta\mathbf{w}(n+1)}{\|\delta\mathbf{x}(n)\|^2} = \frac{2(\delta e^{[n+1]}(n) - \delta e^{[n]}(n))^*}{\|\delta\mathbf{x}(n)\|^2} \tag{A5}$$

since $e^{[k]}(n)=d(n)-\mathbf{x}^H(n)\mathbf{w}(k)$ and the numerator on the left side of Eq. (A5) is equal to $\mathbf{x}^H(n)\mathbf{w}(n+1)-\mathbf{x}^H(n-1)\mathbf{w}(n+1)-\mathbf{x}^H(n)\mathbf{w}(n)+\mathbf{x}^H(n-1)\mathbf{w}(n)$. Therefore applying the equilibrium constraint on the right hand side of Eq. (A5) ($\delta e^{[n+1]}(n)=0$), we have that λ is given by Eq. (7).

TABLE III. Performance of referenced and proposed LMS algorithms in nonstationary environment.

Nonstationary white noise $E[v(n)]=0$ $\sigma^2_{v,\text{min-max}}=0.1-0.5$	NLMS		NDN-LMS		MLMS	
	EMSE (dB) $L=8/12/24$	M $L=8/12/24$	EMSE (dB) $L=8/12/24$	M $L=8/12/24$	EMSE (dB) $L=8/12/24$	M $L=8/12/24$
$\mu=0.1$	−27.92/−26.27/−23.80	0.95/1.14/1.53	−24.72/−25.78/−27.01	1.09/1.07/1.05	−25.27/−25.16/−25.11	1.41/1.43/1.44
$\mu=0.25$	−24.70/−23.26/−21.13	1.37/1.62/2.07	−21.22/−22.01/−22.17	1.71/1.67/1.64	−22.65/−22.58/−22.49	1.86/1.88/1.89
$\mu=0.5$	−22.57/−21.32/−19.53	1.75/2.02/2.49	−18.70/−18.82/−19.07	2.43/2.38/2.34	−20.95/−20.91/−20.84	2.23/2.38/2.25
Nonstationary white noise $E[v(n)]=0$ $\sigma^2_{v,\text{min-max}}=0.1-0.5$	EN-LMS		CS-LMS		VAD CS+MLMS	
	EMSE (dB) $L=8/12/24$	M $L=8/12/24$	EMSE (dB) $L=8/12/24$	M $L=8/12/24$	EMSE (dB) $L=8/12/24$	M $L=8/12/24$
$\mu=0.1$	−16.49/−16.43/−16.44	3.30/3.35/3.35	−39.41/−38.79/−37.02	0.28/0.30/0.37	−26.97/−26.67/−26.98	1.26/1.29/1.33
$\mu=0.25$	−20.94/−20.80/−20.63	1.73/1.80/1.89	−35.97/−35.80/−35.14	0.42/0.42/0.42	−24.62/−24.32/−23.87	1.64/1.67/1.72
$\mu=0.5$	−23.61/−24.08/−24.18	1.31/1.28/1.23	−32.80/−32.92/−32.77	0.60/0.59/0.60	−23.10/−22.85/−22.41	1.92/1.96/2.02

APPENDIX B: PROOF OF THEOREM 1

One way to see this equivalence is to redefine the problem as follows. Let $\mathbf{x}_1(n)=\delta\mathbf{x}(n)$ be the difference incoming signal, $d_1(n)=\delta d(n)=d(n)-d(n-1)$ the difference desired signal, and $e_1(n)=\delta e(n)=d_1(n)-\mathbf{w}^H\mathbf{x}_1(n)$ the difference error signal (any other system variable will be denoted this way for short). Using this new set of transformed data and applying the Wiener–Hopf methodology, the classical filtering problem is to minimize the cost function

$$\mathbf{w}_{0,1}=\arg\min_{\mathbf{w}} E[|e_1(n)|^2]. \tag{B1}$$

Note that the gradient of the latter cost function defines the deterministic CS-LMS algorithm, that is, in terms of expected values. The optimum Wiener solution for the novel data set is then achieved at

$$\mathbf{w}_{0,1}=\mathbf{R}_{\mathbf{x}_1}^{-1}\mathbf{r}_{\mathbf{d}_1\mathbf{x}_1}, \tag{B2}$$

where the autocorrelation matrix $\mathbf{R}_{\mathbf{x}_1}=E[\mathbf{x}_1\mathbf{x}_1^H]$ is assumed to be positive definite and $\mathbf{r}_{\mathbf{d}_1\mathbf{x}_1}=E[\mathbf{x}_1 d_1^*]$ is the cross-correlation vector. The optimal solution $\mathbf{w}_{0,1}$ is indeed related, under some conditions, to the original optimal solution $\mathbf{w}_0$ given the generic data set. Generally, $\mathbf{w}_0\neq\mathbf{w}_{0,1}$, that is,

$$\mathbf{R}_{\mathbf{x}_1}^{-1}\mathbf{r}_{\mathbf{d}_1\mathbf{x}_1}\neq\mathbf{R}_{\mathbf{x}}^{-1}\mathbf{r}_{\mathbf{dx}}. \tag{B3}$$

but if we assume that the desired signal is generated by the multiple linear regression model then

$$\mathbf{r}_{\mathbf{d}_1\mathbf{x}_1}=\mathbf{R}_{\mathbf{x}_1}\mathbf{w}_0\Rightarrow\mathbf{w}_0=\mathbf{w}_{0,1}. \tag{B4}$$

This can be also demonstrated in terms of the expected value of the difference error sequence in Eq. (B1) since

$$E[|e_1(n)|^2]=E[|(\mathbf{w}_0-\mathbf{w})^H\mathbf{x}_1(n)|^2]+E[|\delta e_0(n)|^2] \tag{B5}$$

is minimal only when $\mathbf{w}_{0,1}=\mathbf{w}_0$. In addition, once the optimal solution is achieved, the estimated desired signal $y_0(n)=\mathbf{w}_{0,1}^H\mathbf{x}(n)$ provides the minimum error sequence $e_{\min}=d(n)-y_0=e_0(n)$.

APPENDIX C: PROOF OF THE CONVERGENCE OF THE CS-LMS ALGORITHM

If the original tap-input vector $\mathbf{x}(n)$ and the desired response $d(n)$ are assumed to be jointly stationary, the correlation matrix and the cross-correlation vector of the difference input signal $\mathbf{x}_1(n)$ and the desired signal $d_1(n)$ can be expressed in terms of the original correlation matrix and cross-correlation vector

$$\mathbf{R}_{\mathbf{x}_1}=2\mathbf{R}-2\,\mathrm{Re}\{\mathbf{R}(1)\},$$

$$\mathbf{r}_{\mathbf{d}_1\mathbf{x}_1}=2\mathbf{r}_{\mathbf{dx}}(0)-2\,\mathrm{Re}\{\mathbf{r}_{\mathbf{dx}}(1)\}, \tag{C1}$$

where $\mathbf{R}(k)=E[\mathbf{x}(n+k)\mathbf{x}^H(n)]$ and $\mathbf{r}_{\mathbf{dx}}(k)=E[\mathbf{x}(n+k)d^*(n)]$, then the gradient vector in Eq. (14) is given by

$$\mathbf{w}(n+1)=\mathbf{w}(n)+\hat{\mu}[2[\mathbf{r}_{\mathbf{dx}}(\mathbf{0})-\mathbf{R}(0)\mathbf{w}(n)]+2\,\mathrm{Re}\{\mathbf{R}(1)\mathbf{w}(n)-\mathbf{r}_{\mathbf{dx}}(1)\}]. \tag{C2}$$

If real processes are also assumed, Eq. (C2) transforms into

$$\mathbf{w}(n+1)=\mathbf{w}(n)+2\hat{\mu}[\Delta\mathbf{r}_{\mathbf{dx}}(1)-\Delta\mathbf{R}(1)], \tag{C3}$$

where $\Delta\mathbf{r}_{\mathbf{dx}}(1)=\mathbf{r}_{\mathbf{dx}}(0)-\mathbf{r}_{\mathbf{dx}}(1)$ and $\Delta\mathbf{R}(1)=\mathbf{R}(0)-\mathbf{R}(1)$ is a Hermitian positive definite matrix. As in the SD algorithm the weight-error vector at time n can be defined as $\mathbf{c}(n)=\mathbf{w}_0-\mathbf{w}(n)$, where $\mathbf{w}_0$ is the optimal value of the tap-weight vector given by the Wiener–Hopf equations.[26] Then, eliminating the cross-correlation vector $\mathbf{r}_{\mathbf{dx}}(k)$ and rewriting the result in terms of the weight vector $\mathbf{c}(n)$, we get

$$\mathbf{c}(n+1)=(I-2\hat{\mu}\Delta\mathbf{R}(1))\mathbf{c}(n). \tag{C4}$$

In the latter expression we assume that $\mathbf{r}_{\mathbf{dx}}(1)=\mathbf{R}(1)\mathbf{w}_0$, that is, the desired signal is generated by a linear multiple regression model. Using eigendecomposition, we may express the difference correlation matrix as

$$\Delta\mathbf{R}(1)=\mathbf{Q}\mathbf{\Lambda}\mathbf{Q}^H, \tag{C5}$$

where $\mathbf{Q}$ is the eigenvector matrix in columns and $\mathbf{\Lambda}$ is a diagonal matrix containing the real and non-negative eigenvalues $\{\lambda_1,\ldots,\lambda_n\}$. Thus, we can study the convergence analysis in terms of the evolution of each natural mode of the transformed form of Eq. (C4) as follows:

$$\mathbf{v}(n+1)=(I-2\hat{\mu}\mathbf{\Lambda})\mathbf{v}(n), \tag{C6}$$

where $\mathbf{v}(n+1)=\mathbf{Q}^H\mathbf{c}(n)$. For stability or convergence of the deterministic CS-LMS algorithm the following inequality must be satisfied:

$$-1<1-2\hat{\mu}\lambda_k<1\quad\text{for all } k, \tag{C7}$$

where λ_k is the kth eigenvalue of the difference correlation matrix $\Delta\mathbf{R}(1)$. Since the eigenvalues are real and positive, it follows that a necessary and sufficient condition for convergence of the algorithm is that the step-size parameter $\hat{\mu}$ must satisfy the double inequality

$$0<\hat{\mu}<\frac{1}{\lambda_{\max}}, \tag{C8}$$

where $\lambda_{\max}$ is the largest eigenvalue of the difference correlation matrix $\Delta\mathbf{R}(1)$. If the convergence condition is compared with the one obtained using the SD algorithm, it can be seen that the latter is less restrictive by a factor of 2 than our algorithm (assuming that we have the same set of eigenvalues). It is also readily seen that an exponential envelope of the time constant τ_k can be fitted to the evolution of the natural modes, and its value, for the special case of slow adaptation (for small $\hat{\mu}$), is given by

$$\tau_k\simeq\frac{1}{2\hat{\mu}\lambda_k},\quad\hat{\mu}\ll 1. \tag{C9}$$

In this case, the convergence time of each mode, using the same set of eigenvalues, is smaller than the natural modes of the SD algorithm by a factor of 2. As shown, the stability performance of the deterministic SC-LMS algorithm depends exclusively on μ and the eigenvalues of $\Delta\mathbf{R}(1)$. Note that a connection in terms of τ can be shown if we establish the following upper bound in the stability condition of the CS-LMS algorithm.

1. Stability condition for the stochastic CS-LMS algorithm

In the previous section we derived the stability condition for the deterministic CS-LMS algorithm, that is, the one that produces the adaptation in Eq. (8), when gradients are replaced with instantaneous estimates. It also follows from the NLMS analysis[26] that the high value of μ balances the trade-off between the M and the average time constant τ, which is larger than the one obtained with the standard LMS algorithm if $\mathrm{tr}(\mathbf{R}_{\mathbf{x}_1}) < \mathrm{tr}(\mathbf{R})$ since

$$\tau \simeq \frac{L}{\mu\,\mathrm{tr}(\mathbf{R}_{\mathbf{x}1})}, \tag{C10}$$

where L is the filter length. On the basis of this formula, we may make the same observations as in Ref. 26 about the connection between M and τ.

APPENDIX D: ON THE LEARNING CURVES OF THE STOCHASTIC CS-LMS ALGORITHM IN THE ANC APPLICATION

Using the definition of the weight-error vector $\varepsilon(n) = \mathbf{w}_0 - \mathbf{w}(n)$ and Eq. (8) with the step size defined as μ we may express the evolution of $\varepsilon(n)$ as

$$\varepsilon(n+1) = \varepsilon(n) - \mu\mathbf{x}_1(n)(s_1(n) + v_1(n) - (\mathbf{w}_0 - \varepsilon(n))^H\mathbf{X}_1(n))^*, \tag{D1}$$

where $v_1(n) = v(n) - v(n-1)$ and $v(n)$ denotes the noise in the primary signal $d(n)$. If we assume that $v(n)$ is generated by the multiple regression model: $v(n) = \mathbf{w}_0^H\mathbf{x}(n) + e_0(n)$ we find that the weight-error vector may be expressed as

$$\varepsilon(\nu+1) = (I - \mu\mathbf{x}_1(n)\mathbf{x}_1(n)^H)\varepsilon(n) - \mu\mathbf{x}_1(n)(\delta e_0(n) + s_1(n))^*, \tag{D2}$$

where $\delta\mathbf{x}(n)$ is denoted by $\mathbf{x}_1(n)$ for short. Invoking the direct-averaging method[26,37] we finally obtain Eq. (19). The stochastic evolution on the natural modes can be also studied transforming Eq. (19) into

$$\mathbf{v}(n+1) = (I - \mu\mathbf{\Lambda})\mathbf{v}(n) - \phi(n) \tag{D3}$$

by applying the unitary similarity transformation to the correlation matrix $\mathbf{R}_{\mathbf{x}_1}$, where $\mathbf{\Lambda} = \mathbf{Q}^H\mathbf{R}_{\mathbf{x}_1}\mathbf{Q}$ and the stochastic force vector is defined as $\phi(n) = \mu\mathbf{Q}^H\mathbf{x}_1\delta\tilde{e}_0^*(n)$. It is seen readily that the latter vector has the following properties.

*P*1. The mean of the stochastic force vector $\phi(n)$ is zero: $E[\phi(n)] = \mathbf{0}$.

Proof: $E[\phi(n)] = \mathbf{Q}^H E[\mathbf{x}_1(n)\delta\tilde{e}_0^*(n)] = \mathbf{Q}^H E[\mathbf{x}_1(n)(\delta e_0(n) + s_1(n))^*] = 0$ by virtue of the principle of orthogonality[26] and statistical independence between input variables ($\mathbf{x}(n)$ and $s(n)$).

*P*2. The correlation matrix of the stochastic force vector is a diagonal matrix: $E[\phi(n)\phi^H(n)] = \mu^2\tilde{J}\mathbf{\Lambda}$, where $\tilde{J} = 2(E[|e_0(n)^2|] + E[|s(n)^2|] - \mathrm{Re}\{E[s^*(n+1)s(n)]\})$.

Proof: Assuming $e_0(n)$ is a stationary and uncorrelated sequence and $s(n)$ is stationary,

$$E[\phi(n)\phi^H(n)] - \mu^2\mathbf{Q}^H E[\mathbf{x}_1(n)\delta\tilde{e}_0^*(n)\delta\tilde{e}_0(n)\mathbf{x}_1^H(n)]\mathbf{Q} = \mu^2\mathbf{Q}^H(E[\delta e_0^*(n)\delta e_0(n)] + E[s_1^*(n)s_1(n)])\mathbf{R}_{\mathbf{x}_1}\mathbf{Q}, \tag{D4}$$

which, by virtue of the principle of orthogonality and statistical independence, reduces to P2.

Using the properties P1 and P2 we obtain the same formulas for the first two moments of the natural modes $\mathbf{v}(n)$ as in Ref. 26, which allows to obtain the evolution of $J(n)$ with time step n. The second term of Eq. (18) in light of the direct-averaging method is equal to

$$\begin{aligned} E[\varepsilon_0^H(n)\mathbf{x}(n)\mathbf{x}(n)^H\varepsilon_0(n)] &\simeq E[\varepsilon_0^H(n)\mathbf{R}\varepsilon_0(n)] = \mathrm{tr}\{\mathbf{R}E[\varepsilon_0^H(n)\varepsilon_0(n)]\} \\ &= E\left[\mathrm{tr}\left\{\mathbf{v}^H\mathbf{Q}^H\left(\tfrac{1}{2}\mathbf{R}_{\mathbf{x}_1} + \mathrm{Re}\{\mathbf{R}(1)\}\right)\mathbf{Q}\mathbf{v}\right\}\right] \\ &= \tfrac{1}{2}\sum_{k=1}^{L}\lambda_k E[|v_k(n)|^2] + E[\mathrm{tr}\{\mathbf{v}^H\mathbf{Q}^H\,\mathrm{Re}\{\mathbf{R}(1)\}\mathbf{Q}\mathbf{v}\}]. \end{aligned} \tag{D5}$$

Assuming that the input signal is weakly correlated ($\mathbf{R}(1) \sim \mathbf{0}$) we may bound the second term in the last equality of Eq. (D5) with the first term (natural evolution), i.e., $E[\mathrm{tr}\{\mathbf{v}^H\mathbf{Q}^H\,\mathrm{Re}\{\mathbf{R}(1)\}\mathbf{Q}\mathbf{v}\}] \leq \frac{1}{2}\sum_{k=1}^{L}\lambda_k E[|v_k(n)|^2]$ then

$$J_{\mathrm{ex}}(n) \leq \sum_{k=1}^{L}\lambda_k E[|v_k(n)|^2] = \sum_{k=1}^{L}\lambda_k\left(\frac{\mu\tilde{J}}{2-\mu\lambda_k} + (1-\mu\lambda_k)^{2n}\left(|v_k(0)|^2 - \frac{\mu\tilde{J}}{2-\mu\lambda_k}\right)\right), \tag{D6}$$

where $v_k(n)$ denotes the component of natural mode $\mathbf{v}(n)$.[26] If the exponential factor is neglected with increasing n,

$$J_{\mathrm{ex}}(\infty) \leq \sum_{k=1}^{L}\lambda_k\left(\frac{\mu\tilde{J}}{2-\mu\lambda_k}\right) \simeq \frac{1}{2}\mu\tilde{J}\,\mathrm{tr}\{\mathbf{R}_{\mathbf{x}_1}\}. \tag{D7}$$

The reduction in $J_{\mathrm{ex}}(\infty)$ is achieved whenever

$$J_{\mathrm{ex}}(\infty) = \tfrac{1}{2}\mu J\,\mathrm{tr}(\mathbf{R}_{\mathbf{x}_1}) \simeq \mu J\,\mathrm{tr}(\mathbf{R}) \leq J_{\mathrm{ex}}^{\mathrm{LMS}}(\infty) = \tfrac{1}{2}\mu J_{\min}\,\mathrm{tr}(\mathbf{R}) \Leftrightarrow \mathrm{Re}\{r_s(1)\} \geq \tfrac{3}{4}J_{\min}, \tag{D8}$$

where $r_s(1) = E[s^*(n+1)s(n)]$.

[1] J. Burg, "Application of the wiener filter theory to the design of seismic arrays," J. Acoust. Soc. Am. **33**, 1651–1684 (1961).
[2] D.-L. Liu and R. C. Waag, "Time-shift compensation of ultrasonic pulse focus degradation using least-mean-square error estimates of time delay," J. Acoust. Soc. Am. **92**, 2377–2378 (1992).
[3] D.-L. Liu and R. C. Waag, "Time-shift compensation of ultrasonic pulse focus degradation using least-mean-square error estimates of arrival time," J. Acoust. Soc. Am. **95**, 542–555 (1994).
[4] B. Widrow and S. D. Stearns, *Adaptive Signal Processing* (Prentice-Hall, Englewood Cliffs, NJ, 1985).
[5] B. Widrow, J. Glover, J. Mccool, J. Kaunitz, C. Williams, R. Hean, J. Zeidler, E. Dong, and R. Goodlin, "Adaptive noise cancelling: Principles and applications," Proc. IEEE **63**, 1696–1716 (1975).
[6] P. D. D. of neurodegenerative diseases using preprocessing techniques and classification algorithms, Reference No. PET2006-0253.
[7] J. Greenberg, "Modified lms algorithms for speech processing with an adaptive noise canceller," IEEE Trans. Speech Audio Process. **6**, 338–351 (1998).

[8]W. Harrison, J. S. Lim, and E. Singer, "A new application of adaptive noise cancellation," IEEE Trans. Acoust., Speech, Signal Process. **34**, 21–27 (1986).
[9]S. Douglas and T. H.-Y. Meng, "Stochastic gradient adaptation under general error criteria," IEEE Trans. Signal Process. **42**, 1335–1351 (1994).
[10]Z. Ramadan and A. Poularikas, "An adaptive noise canceller using error nonlinearities in the lms adaptation," in IEEE Proceedings of SoutheastCon (1979), Vol. **1**, pp. 359–364.
[11]M. Godavarti and I. A. O. Hero, "Partial update lms algorithms," IEEE Trans. Signal Process. **53**, 2382–2399 (2006).
[12]A. Osama and V. DeBrunner, "Hirschman optimal transform block lms adaptive filter," in IEEE International Conference on Acoustics, Speech and Signal Processing (2007), Vol. **3**, pp. 1305–1308.
[13]R. Bouquin-Jeannes and G. Faucon, "Study of a voice activity detector and its influence on a noise reduction system," Speech Commun. **16**, 245–254 (1995).
[14]J. M. Górriz, J. Ramírez, J. Segura, and C. Puntonet, "An effective cluster-based model for robust speech detection and speech recognition in noisy environments," J. Acoust. Soc. Am. **120**, 470–481 (2006).
[15]J. M. Górriz, J. Ramírez, J. Segura, and C. Puntonet, "Improved mo-lrt vad based on bispectra gaussian model," Electron. Lett. **41**, 877–879 (2005).
[16]ITU, "A silence compression scheme for G.729 optimized for terminals conforming to recommendation V.70," ITU-T Recommendation G.729-Annex B 1996.
[17]ETSI, "Voice activity detector (VAD) for adaptive multi-rate (AMR) speech traffic channels," ETSI EN 301 708 Recommendation, 1999.
[18]J. M. Górriz, J. Ramírez, E. Lang, and C. Puntonet, "Hard c-means clustering for voice activity detection," Speech Commun. **48**, 1638–1649 (2006).
[19]J. M. Górriz, J. Ramírez, C. Puntonet, and J. Segura, "Generalized lrt-based voice activity detector," IEEE Signal Process. Lett. **13**, 636–639 (2006).
[20]J. M. Górriz, J. Ramírez, and C. Puntonet, "An effective jointly pdf-based voice activity detector for real time applications," Electron. Lett. **3**, 251–253 (2007).
[21]J. Ramírez, J. M. Górriz, J. Segura, C. Puntonet, and A. Rubio, "Speech/non-speech discrimination based on contextual information integrated bispectrum lrt," IEEE Signal Process. Lett. **13**, 497–500 (2006).
[22]M. Berouti, R. Schwartz, and J. Makhoul, "Enhancement of speech corrupted by acoustic noise," in Proceedings of the International Conference on Acoustics, Speech and Signal Processing (1979), Vol. **1**, pp. 208–211.
[23]S. Boll, "Suppression of acoustic noise in speech using spectral subtraction," IEEE Trans. Acoust., Speech, Signal Process. **27**, 113–120 (1979).
[24]S. Douglas, "A family of normalized lms algorithms," IEEE Signal Process. Lett. **1**, 49–51 (1994).
[25]N. J. Bershad, "Analysis of the normalized lms algorithm with gaussian inputs," IEEE Trans. Acoust., Speech, Signal Process. **34**, 793–806 (1986).
[26]S. Haykin, *Adaptive Filter Theory* (Prentice-Hall, Englewood Cliffs, NJ, 1986).
[27]G. Goodwin and K. Sin, *Adaptive Filtering, Prediction and Control* (Prentice-Hall, Englewood Cliffs, NJ, 1984).
[28]N. J. Bershad, "On the optimum data nonlinearity in lms adaptation," IEEE Trans. Acoust., Speech, Signal Process. **34**, 69–76 (1986).
[29]O. Tobias and R. Seara, "On the lms algorithm with constant and variable leakage factor in a nonlinear environment," IEEE Trans. Signal Process. **54**, 3448–3458 (2006).
[30]D. T. M. Slock, "On the convergence behavior of the lms and the normalized lms algorithms," IEEE Trans. Signal Process. **41**, 2811–2825 (1993).
[31]S. Choi, "Differential learning algorithms for decorrelation and independent component analysis," Neural Networks **19**, 1558–1567 (2006).
[32]D. Erdogmus, K. E. Hild, and J. C. Principe, "Online entropy manipulation: Stochastic information gradient," IEEE Signal Process. Lett. **10**, 242–245 (2003).
[33]D. Loftsgaarden and C. Queseberry, "A nonparametric estimate of a multivariate density function," Ann. Math. Stat. **36**, 1049–1051 (1965).
[34]G. Terrel and D. Scott, "Variable kernel density estimation," Ann. Math. Stat. **20**, 1236–1265 (1992).
[35]L. Breiman, W. Meisel, and E. Purcell, "Variable kernel estimates of probability densities," Technometrics **19**, 135–144 (1982).
[36]Y. Rao, D. Erdogmus, and J. Principe, "Error whitening criterion for adaptive filtering: Theory and algorithms," IEEE Trans. Signal Process. **53**, 1057–1069 (2005).
[37]H. Kushner, *Approximation and Weak Convergence Methods for Random Processes With Applications to Stochastic System Theory* (MIT, Cambridge, MA, 1984).
[38]J. Ramírez, J. M. Górriz, and J. Segura, "Statistical voice activity detection based on integrated bispectrum likelihood ratio tests for robust speech recognition," J. Acoust. Soc. Am. **121**, 2946–2958 (2007).
[39]M. Hayes, *Statistical Digital Signal Processing and Modeling* (Wiley, New York, 1996).
[40]A. Moreno, L. Borge, D. Christoph, R. Gael, C. Khalid, E. Stephan, and A. Jeffrey, "Speechdat-car: A large speech database for automotive environments," in Proceedings of the II LREC Conference (2000).

Fast volumetric integral-equation solver for high-contrast acoustics

E. Bleszynski,[a] M. Bleszynski,[b] and T. Jaroszewicz[c]
Monopole Research, 739 Calle Sequoia, Thousand Oaks, California 91360

(Received 17 April 2008; revised 11 September 2008; accepted 16 September 2008)

An approach for solving volumetric integral equations in acoustics, applicable to problems involving large density contrasts, is described. While the conventional Lippmann–Schwinger integral equations become under such circumstances ill conditioned, the proposed approach reformulates them and casts them into an equivalent system of well-conditioned surface and volume integral equations. The corresponding fast solver [utilizing stiffness matrix compression based on fast Fourier transforms and characterized by $\mathcal{O}(N \log N)$ solution complexity and storage requirements, where N is the number of unknowns] was enhanced to incorporate the proposed formulation. Features of the solution method and of the solver are illustrated on representative examples of numerically large problems.
© *2008 Acoustical Society of America.* [DOI: 10.1121/1.2998787]

PACS number(s): 43.60.Pt, 43.20.Bi [TDM] Pages: 3684–3693

I. INTRODUCTION

Recently an algorithm applicable to fast and accurate large-scale numerical simulations of acoustic fields in complex inhomogeneous media by means of an integral-equation formulation has been constructed.[1,2] The approach utilizes the fast Fourier transform (FFT) based adaptive integral method (AIM)[3–5] to compress the originally dense stiffness matrix and thus to overcome prohibitive memory and execution time requirements of conventional integral-equation formulations. An important feature of the method is its nonlossy character, i.e., the compression of the stiffness matrix does not compromise the solution accuracy. The FFT-based AIM method was initially developed in the context of electromagnetics[3–5] and was extended to acoustics[1,2] to solve acoustic wave propagation through inhomogeneous materials characterized by variable compressibility and density.

An important type of acoustic wave propagation problems through inhomogeneous materials are large-contrast problems, i.e., problems involving acoustically dense objects immersed in a low-density medium (e.g., a biological tissue surrounded by air). In the previous paper difficulties arising in situations involving high-contrast materials were noted. The present paper addresses the high-contrast problem in more detail and describes a solution method which resolves the encountered difficulties.

A prominent feature of high-contrast problems is the fact that most of the incident wave energy is reflected from interfaces between the low- and the high-density media due to a large impedance mismatch between the materials. This circumstance does not cause computational problems in solving purely scattering problems when these are formulated in terms of the boundary-element method, i.e., as surface integral equations involving boundary conditions on the surface of the scatterer. Difficulties, however, arise if one attempts to determine pressure distribution *within* an inhomogeneous body by means of the volumetric integral equations [the Lippmann–Schwinger (LS) equations]. In this case, the fact that only a small fraction of the incident energy penetrates inside the scatterer causes the solution inside the object to be poorly determined. Mathematically, the integral equations describing the system become ill conditioned: the solution is then strongly dependent on small changes in the incident field and may become completely unreliable.

The approach proposed here for solving ill-conditioned high-contrast problems consists of two stages: (1) solving an integral equation for the surface problem and (2) solving the volume problem with a modified incident field, defined in terms of the original field and the solution of the surface problem. Both the surface and the modified volume problems are well conditioned. The procedure is rigorous, it does not involve expansions in the ratios of the material parameters, and it does not require alternating solving the surface and the volume equations (although each of the two problems may be and usually is—for large systems—solved iteratively).

II. INTEGRAL EQUATIONS IN ACOUSTICS

The approach used in this paper is based on the volumetric LS integral equation for the acoustic wave propagating through an inhomogeneous object characterized by compressibility $\kappa(\mathbf{r})$ and density $\rho(\mathbf{r})$, and occupying a region (domain) $\Omega \subset \mathbb{R}^3$ in an infinite "background medium" $\mathbb{R}^3$ of constant compressibility κ_0 and density ρ_0. The LS equation in this case has the form given in Ref. 6, Eq. (8.1.13),

[a]Electronic mail: elizabeth@monopoleresearch.com
[b]Electronic mail: marek@monopoleresearch.com
[c]Electronic mail: tomek@monopoleresearch.com

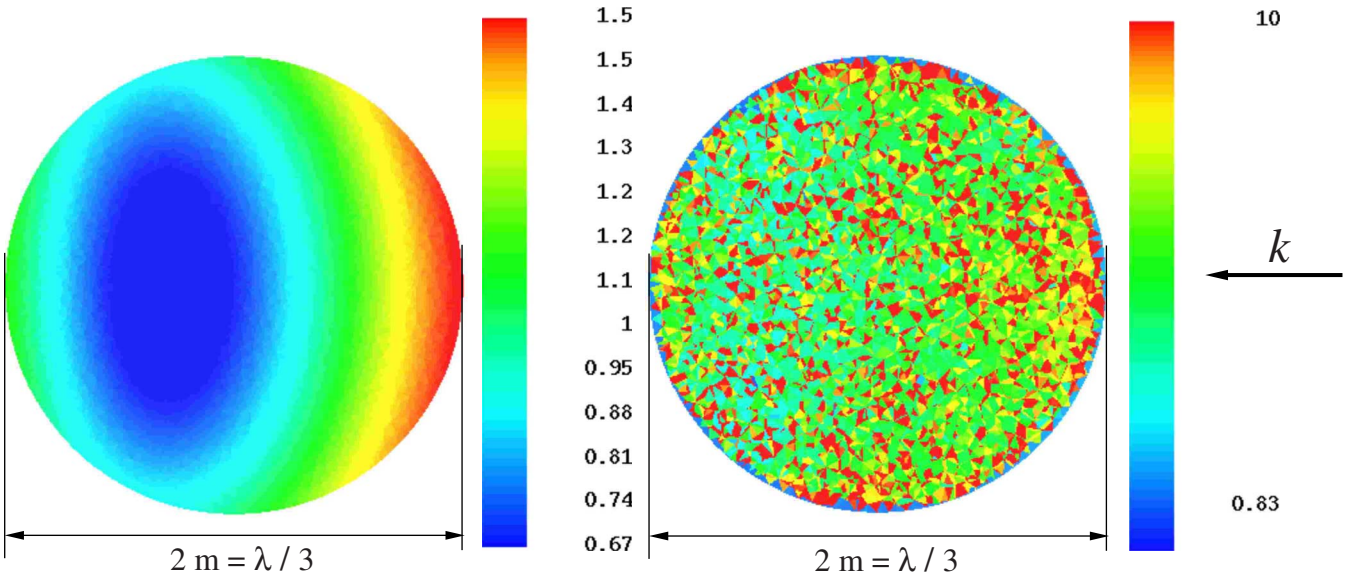


FIG. 1. (Color online) Distribution of the absolute value of the pressure, $|p(\mathbf{r})|$, on a plane parallel to the incident wave vector and passing through the sphere center. Analytic solution is compared with the conventional solution of the LS integral equations for $\rho/\rho_0=10^3$ and $\kappa/\kappa_0=10^{-4}$ and for a discretization with $N=200\,000$ tetrahedra. Note different pressure scales for the two distributions.

$$p(\mathbf{r})+\int_{\bar{\Omega}} d^3r'\left\{k^2 g(\mathbf{r}-\mathbf{r}')\left(1-\frac{\kappa(\mathbf{r}')}{\kappa_0}\right)p(\mathbf{r}')-[\nabla_{\mathbf{r}'}g(\mathbf{r}-\mathbf{r}')]\cdot\left(1-\frac{\rho_0}{\rho(\mathbf{r}')}\right)\nabla_{\mathbf{r}'}p(\mathbf{r}')\right\}=p^{(\mathrm{inc})}(\mathbf{r}) \quad \text{for} \quad \mathbf{r}\in\Omega, \tag{1}$$

where $k=\sqrt{\kappa_0\rho_0}\omega$ is the wave number in the background medium, $g(\mathbf{r})=\exp(ik|\mathbf{r}|)/(4\pi|\mathbf{r}|)$ is the Green's function of the Helmholtz equation, and $p^{(\mathrm{inc})}$ is the incident wave satisfying the Helmholtz equation in the absence of the scatterer [i.e., with $\kappa(\mathbf{r})=\kappa_0$, $\rho(\mathbf{r})=\rho_0$]; $\bar{\Omega}$ denotes the domain Ω with its boundary. The frequency-domain equations used in the present paper assume the $\exp(-i\omega t)$ time dependence of the fields.

Validity of Eq. (1) is discussed in Ref. 7. It is assumed there that the boundary $\partial\Omega$ is smooth (C^2) and the material parameters are continuous [$\rho\in C^2(\bar{\Omega})$, $\kappa\in C^1(\bar{\Omega})$], but only piecewise so; in particular, the density may have a jump across the boundary. Under these assumptions, Eq. (1) is uniquely solvable.

As in Ref. 1, the integral equation (1) is discretized by means of the Galerkin method, i.e., by expanding the solution in terms of (volumetric) basis functions ϕ_α as

$$p(\mathbf{r})=\sum_{\alpha=1}^{N} x_\alpha\phi_\alpha(\mathbf{r}), \tag{2}$$

and by using the same set of basis functions as test functions. The resulting matrix equation becomes

$$Ax=b, \tag{3}$$

where b is the projection of the incident wave on the basis functions,

$$b_\alpha=\int_\Omega d^3r\,\phi_\alpha(\mathbf{r})p^{(\mathrm{inc})}(\mathbf{r}), \tag{4}$$

and the elements of the stiffness matrix are given by

$$A_{\alpha\beta}=\int d^3r\,\phi_\alpha(\mathbf{r})\frac{\rho_0}{\rho(\mathbf{r})}\phi_\beta(\mathbf{r}) \tag{5a}$$

$$+k^2\int d^3r_1 d^3r_2\,\phi_\alpha(\mathbf{r}_1)g(\mathbf{r}_1-\mathbf{r}_2)\cdot\left(\frac{\rho_0}{\rho(\mathbf{r}_2)}-\frac{\kappa(\mathbf{r}_2)}{\kappa_0}\right)\phi_\beta(\mathbf{r}_2) \tag{5b}$$

$$-\int d^3r_1 d^3r_2[\nabla_{\mathbf{r}_1}\phi_\alpha(\mathbf{r}_1)]g(\mathbf{r}_1-\mathbf{r}_2)\cdot\left(\nabla_{\mathbf{r}_2}\frac{\rho_0}{\rho(\mathbf{r}_2)}\right)\phi_\beta(\mathbf{r}_2) \tag{5c}$$

$$\equiv A^R_{\alpha\beta}+A^M_{\alpha\beta}+A^D_{\alpha\beta}. \tag{5d}$$

In the following, the terms A^R, A^M, and A^D [given by Eqs. (5a)–(5c)] are referred to as the *material*, *monopole*, and *dipole* contributions.

III. IMPLICATIONS FOR LARGE-CONTRAST PROBLEMS

In applications to acoustic wave scattering and propagation through biological objects the mass/stiffness matrix of Eq. (5) exhibits a particular feature: the component $A^D_{\alpha\beta}$ of Eq. (5c) becomes the dominant contribution due to the discontinuity of the ratio $\rho_0/\rho(\mathbf{r})$ at the interface of the object and the surrounding air [$\rho_0/\rho(\mathbf{r})=1$ outside of the object and $\rho_0/\rho(\mathbf{r})\sim 10^{-3}$ inside]. The remaining terms, $A^R_{\alpha\beta}$ and $A^M_{\alpha\beta}$, are small because both ρ_0/ρ and κ/κ_0 are small. Since the surface contributions to the dipole term $A^D_{\alpha\beta}$ dominate, the system of Eq. (3) is much more sensitive to the values of the solution (the pressure p) on the surface than to its values in

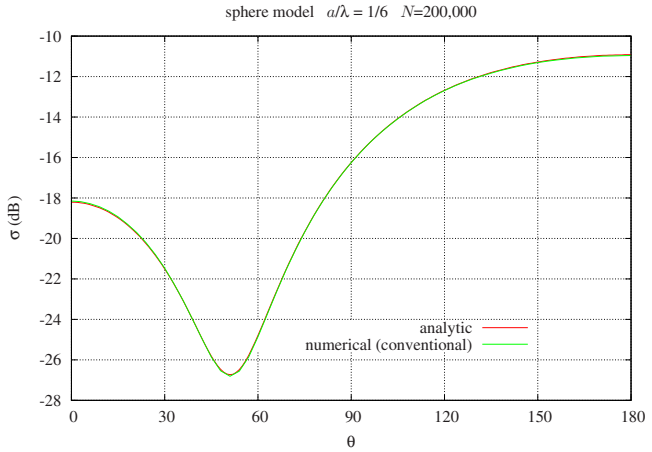


FIG. 2. (Color online) Scattering cross section as a function of the scattering angle θ for the sphere of Fig. 1 compared to the analytic solution.

the interior of the object. In other words, the system is ill conditioned, and the solution inside the object is poorly defined.

This fact is illustrated in Fig. 1 by an example of the scattering on a homogeneous sphere of radius $a=1$ m, with $\rho/\rho_0=10^3$ and $\kappa/\kappa_0=10^{-4}$, discretized with $N=200\,000$ tetrahedra, and subject to an incident plane pressure wave of unit amplitude and wavelength $\lambda=6$ m. Figure 1 clearly shows that the conventional numerical solution for the pressure inside the sphere may become completely unreliable. (It should be noted that the pressure distributions in Fig. 1 are plotted in two different scales: up to 1.5 for the analytic solution and up to 10 for the numerical solution; in fact, in the latter case the pressure exceeds at some points the value of 600.) At the same time, the scattering cross section (which is, practically, sensitive only to the pressure at the object surface) is reproduced with a very good accuracy (Fig. 2). Both these facts are consistent with the ill conditioning of the discretized LS integral equations, which leads to a poorly determined solution in the interior of the object.

IV. A TWO-STAGE SOLUTION SCHEME OF INTEGRAL EQUATIONS IN ACOUSTICS

A. Reformulation of the integral equations

In order to separate the surface and volume contributions to the solutions, the original LS integral equation (1) can be recast in an equivalent form

$$\frac{\rho_0}{\rho(\mathbf{r})}p(\mathbf{r})+\int_{\bar{\Omega}} d^3r'\left\{k^2 g(\mathbf{r}-\mathbf{r}')\left(\frac{\rho_0}{\rho(\mathbf{r}')}-\frac{\kappa(\mathbf{r}')}{\kappa_0}\right)p(\mathbf{r}')-[\nabla_{\mathbf{r}'}g(\mathbf{r}-\mathbf{r}')]\cdot\left(\nabla_{\mathbf{r}'}\frac{\rho_0}{\rho(\mathbf{r}')}\right)p(\mathbf{r}')\right\}=p^{(\mathrm{inc})}(\mathbf{r})\quad\text{for}\quad\mathbf{r}\in\Omega; \tag{6}$$

the matrix elements (5) follow directly from the expression above.

The following discussion is based on the assumption that there is a large density jump at the boundary $\partial\Omega$ of the object. Consequently, the gradient in the last term of Eq. (6) behaves near $\partial\Omega$ as

$$\nabla_{\mathbf{r}}\frac{\rho_0}{\rho(\mathbf{r})}=\hat{\mathbf{n}}(\mathbf{r})\Lambda(\mathbf{r})\delta_{\partial\Omega}(\mathbf{r})+\text{regular terms}, \tag{7}$$

where $\delta_{\partial\Omega}$ is the delta function concentrated on the surface $\partial\Omega$, $\hat{\mathbf{n}}$ is the exterior normal to that surface, and where

$$\Lambda(\mathbf{r})=\lim_{\varepsilon\to 0+}\left(\frac{\rho_0}{\rho(\mathbf{r}+\varepsilon\hat{\mathbf{n}}(\mathbf{r}))}-\frac{\rho_0}{\rho(\mathbf{r}-\varepsilon\hat{\mathbf{n}}(\mathbf{r}))}\right)\equiv\lim_{\varepsilon\to 0+}\left(1-\frac{\rho_0}{\rho(\mathbf{r}-\varepsilon\hat{\mathbf{n}}(\mathbf{r}))}\right)\quad\text{for}\quad\mathbf{r}\in\partial\Omega; \tag{8}$$

the last equality follows from the fact that $\rho(\mathbf{r})=\rho_0$ outside the domain Ω.

The operator of Eq. (6) can now be separated into two terms,

$$Kp\equiv K_s p+K_v p=p^{(\mathrm{inc})}, \tag{9}$$

where the surface and volume operators, K_s and K_v, are defined by

$$(K_s p)(\mathbf{r})=-\int_{\partial\Omega} d^2r'[\hat{\mathbf{n}}(\mathbf{r}')\cdot\nabla_{\mathbf{r}'}g(\mathbf{r}-\mathbf{r}')]\Lambda(\mathbf{r}')p(\mathbf{r}')\equiv-\int_{\partial\Omega} d^2r'\frac{\partial g(\mathbf{r}-\mathbf{r}')}{\partial n(\mathbf{r}')}\Lambda(\mathbf{r}')p(\mathbf{r}') \tag{10a}$$

and

$$(K_v p)(\mathbf{r})=\frac{\rho_0}{\rho(\mathbf{r})}p(\mathbf{r})+k^2\int_{\bar{\Omega}} d^3r' g(\mathbf{r}-\mathbf{r}')\times[1-n^2(\mathbf{r}')]\frac{\rho_0}{\rho(\mathbf{r}')}p(\mathbf{r}')-\int_{\bar{\Omega}\setminus\partial\Omega} d^3r'\times[\nabla_{\mathbf{r}'}g(\mathbf{r}-\mathbf{r}')]\cdot\left(\nabla_{\mathbf{r}'}\frac{\rho_0}{\rho(\mathbf{r}')}\right)p(\mathbf{r}'), \tag{10b}$$

and where the compressibility κ is expressed in terms of the refractive index squared $n^2=\kappa\rho/(\kappa_0\rho_0)$. The surface operator K_s of Eq. (10a) is, by definition, due to the discontinuity of the density on the object boundary $\partial\Omega$, which is large for a large density contrast; the volume operator K_v includes contributions due to variations in the density in the interior of the object. The last integral in Eq. (10b) (over the interior $\bar{\Omega}\setminus\partial\Omega$ of the object) includes the regular terms of Eq. (7).

In the following, a derivation of a set of integral equations, equivalent to Eq. (9), but characterized by better conditioning in the limit of high object density, $\rho/\rho_0\gg 1$, and a fixed value of the refractive index n, is presented. The derivation utilizes the standard representation theorem for exterior scattering problems in acoustics,

$$p^{(\mathrm{inc})}(\mathbf{r})+\int_{\partial\Omega} d^2r'\left[\frac{\partial g(\mathbf{r}-\mathbf{r}')}{\partial n(\mathbf{r}')}p(\mathbf{r}')-g(\mathbf{r}-\mathbf{r}')\frac{\partial p(\mathbf{r}')}{\partial n(\mathbf{r}')}\right]=\begin{cases}p(\mathbf{r}) & \text{for}\quad\mathbf{r}\in\mathbb{R}^3\setminus\bar{\Omega}\\ \frac{1}{2}p(\mathbf{r}) & \text{for}\quad\mathbf{r}\in\partial\Omega\\ 0 & \text{for}\quad\mathbf{r}\in\Omega,\end{cases} \tag{11}$$

where p (here interpreted as the total pressure field) satisfies

the Helmholtz equation in $\mathbb{R}^3\backslash\bar{\Omega}$, and approaches $p^{(\mathrm{inc})}$ at infinity, in the sense that the scattered field $p^{(\mathrm{sc})} \equiv p - p^{(\mathrm{inc})}$ satisfies the Sommerfeld boundary condition. The representation theorem (11) is valid under the assumption of a smooth boundary;[8] its generalization to nonsmooth (e.g., Lipschitz) boundaries is presented in Ref. 9.

The first step in reformulating the integral equation (9) consists of defining an operator $K^{(0)}$ as the $\rho(\mathbf{r})/\rho_0 \to \infty$ [i.e., $\Lambda(\mathbf{r}) \to 1$] limit of the surface operator K_s,

$$(K^{(0)}p)(\mathbf{r}) = -\int_{\partial\Omega} d^2r' \frac{\partial g(\mathbf{r}-\mathbf{r}')}{\partial n(\mathbf{r}')} p(\mathbf{r}') \quad \text{for} \quad \mathbf{r} \in \Omega; \tag{12}$$

the operator $K^{(0)}$ maps functions p supported on $\partial\Omega$ onto functions defined on Ω.

Subsequently, on the boundary $\partial\Omega$, a function $p_s^{(0)}(\mathbf{r})$ is defined, in terms of the operator $K^{(0)}$, as the solution of an auxiliary surface integral equation,

$$(K^{(0)}p_s^{(0)})(\mathbf{r}) = p^{(\mathrm{inc})}(\mathbf{r}) \quad \text{for} \quad \mathbf{r} \in \partial\Omega_-, \tag{13}$$

or

$$-\int_{\partial\Omega} d^2r' \frac{\partial g(\mathbf{r}-\mathbf{r}')}{\partial n(\mathbf{r}')} p_s^{(0)}(\mathbf{r}') = p^{(\mathrm{inc})}(\mathbf{r}) \quad \text{for} \quad \mathbf{r} \in \partial\Omega_-, \tag{14}$$

where $\partial\Omega_- \subset \Omega$ is a surface infinitesimally close to the boundary $\partial\Omega$ and located inside the domain Ω [such surfaces can be defined, as in Ref. 8, Eq. (2.7), for a smooth (C^2) boundary $\partial\Omega$)].

The behavior of the double-layer potential on the boundary $\partial\Omega$ [as indicated in Eq. (11)] now implies that Eq. (14) is equivalent to the conventional double-layer potential integral equation,

$$\frac{1}{2}p_s^{(0)}(\mathbf{r}) - \int_{\partial\Omega} d^2r' \frac{\partial g(\mathbf{r}-\mathbf{r}')}{\partial n(\mathbf{r}')} p_s^{(0)}(\mathbf{r}') = p^{(\mathrm{inc})}(\mathbf{r}) \quad \text{for} \quad \mathbf{r} \in \partial\Omega, \tag{15}$$

for the associated exterior Neumann (hard-surface) problem.[8] In other words, $p_s^{(0)}$ is the boundary value of a field $p^{(0)}(\mathbf{r})$, satisfying the Helmholtz equation in $\mathbb{R}^3\backslash\bar{\Omega}$ with the incident field $p^{(\mathrm{inc})}(\mathbf{r})$ and the boundary condition

$$\frac{\partial p^{(0)}(\mathbf{r})}{\partial n(\mathbf{r})} = 0 \quad \text{for} \quad \mathbf{r} \in \partial\Omega. \tag{16}$$

By applying the representation theorem (11) to this field we find

$$-\int_{\partial\Omega} d^2r' \frac{\partial g(\mathbf{r}-\mathbf{r}')}{\partial n(\mathbf{r}')} p_s^{(0)}(\mathbf{r}') = p^{(\mathrm{inc})}(\mathbf{r}) \quad \text{for} \quad \mathbf{r} \in \Omega, \tag{17}$$

or

$$(K^{(0)}p_s^{(0)})(\mathbf{r}) = p^{(\mathrm{inc})}(\mathbf{r}) \quad \text{for} \quad \mathbf{r} \in \Omega; \tag{18}$$

i.e., if Eq. (13) holds on the surface $\partial\Omega_-$, it also holds everywhere in the domain Ω.

The second step in the solution procedure is to represent the operator K as

$$K = K^{(0)} + \xi K^{(1)}, \tag{19}$$

with

$$K^{(1)} = \xi^{-1}(K - K^{(0)}), \tag{20}$$

and with a rescaling parameter ξ, depending on the function $\rho(\mathbf{r})$, chosen such that the operator $K^{(1)}$ remains finite when $|\rho(\mathbf{r})| \to \infty$.

It should be noted that, while $K^{(0)}$ is a purely surface operator (it depends only on the boundary values of its operand p), $K^{(1)}$ includes both surface and volume terms. In analogy to Eq. (9), $K^{(1)}$ can now be written as

$$K^{(1)} = K_s^{(1)} + K_v^{(1)}, \tag{21}$$

where, after combining Eqs. (9), (10), (14), and (20), the operators $K_s^{(1)}$ and $K_v^{(1)}$ become

$$(K_s^{(1)}p)(\mathbf{r}) = \int_{\partial\Omega} d^2r' \frac{\partial g(\mathbf{r}-\mathbf{r}')}{\partial n(\mathbf{r}')} \frac{\rho_0}{\xi\rho(\mathbf{r}')} p(\mathbf{r}'), \tag{22a}$$

$$(K_v^{(1)}p)(\mathbf{r}) = \frac{\rho_0}{\xi\rho(\mathbf{r})} p(\mathbf{r}) + k^2 \int_{\bar{\Omega}} d^3r' g(\mathbf{r}-\mathbf{r}')[1 - n^2(\mathbf{r}')] \times \frac{\rho_0}{\xi\rho(\mathbf{r}')} p(\mathbf{r}') - \int_{\bar{\Omega}\backslash\partial\Omega} d^3r' [\nabla_{\mathbf{r}'} g(\mathbf{r}-\mathbf{r}')] \cdot \left(\nabla_{\mathbf{r}'} \frac{\rho_0}{\xi\rho(\mathbf{r}')}\right) p(\mathbf{r}'), \tag{22b}$$

and where ξ may be specified, e.g., as the average value of $\rho_0/\rho(\mathbf{r})$ over the domain Ω,

$$\xi \sim \left\langle \frac{\rho_0}{\rho} \right\rangle_\Omega. \tag{23}$$

With the operators $K^{(0)}$ and $K^{(1)}$ specified, and with $p_s^{(0)}$ defined as the solution of the associated surface Neumann problem, the full solution can be represented as

$$p(\mathbf{r}) = \begin{cases} p_s^{(0)}(\mathbf{r}) + \xi p_s^{(1)}(\mathbf{r}) & \text{for} \quad \mathbf{r} \in \partial\Omega \\ p_v(\mathbf{r}) & \text{for} \quad \mathbf{r} \in \Omega, \end{cases} \tag{24}$$

where $p_s^{(1)}$ is the correction to the surface solution $p_s^{(0)}$ and p_v is the volume part of the solution; by continuity, $p_v(\mathbf{r}) \to p_s^{(0)}(\mathbf{r}) + \xi p_s^{(1)}(\mathbf{r})$ as $\Omega \ni \mathbf{r} \to \partial\Omega$. In view of Eq. (21),

$$K^{(0)}p = K^{(0)}(p_s^{(0)} + \xi p_s^{(1)}), \tag{25a}$$

$$K^{(1)}p = K_s^{(1)}(p_s^{(0)} + \xi p_s^{(1)}) + K_v^{(1)}p_v. \tag{25b}$$

By substituting Eqs. (19) and (24) into Eq. (9) and making use of Eqs. (18) and (24), one obtains the *volumetric equation*

$$([K^{(0)} + \xi K_s^{(1)}]p_s^{(1)})(\mathbf{r}) + (K_v^{(1)}p_v)(\mathbf{r}) = -(K_s^{(1)}p_s^{(0)})(\mathbf{r}) \quad \text{for} \quad \mathbf{r} \in \Omega \tag{26}$$

for the unknown fields $p_s^{(1)}$ and p_v, with the right hand side (rhs) expressed in terms of the previously determined surface problem solution $p_s^{(0)}$.

The solution procedure amounts then to

(1) solving the surface equation (13),
(2) using the solution $p_s^{(0)}$ to compute the rhs of Eq. (26),
(3) solving the volumetric Eq. (26), and
(4) forming the final solution according to Eq. (24).

It should be emphasized that Eq. (18) [i.e., extension of Eq. (13) to the interior of the domain Ω] is critical in the derivation of Eq. (26). Equation (18) is necessary for cancellation of large terms $\sim\xi^{-1}$, which would be otherwise present in Eq. (26).

B. Solution of the discretized problem

In the following a discretized representation of the surface and volume integral equations, Eqs. (13) and (26), is constructed in order to obtain the numerical solution.

A rigorous approach would require to show that the *discretized* original LS equation (6) is equivalent to the system of discretized surface and volume integral equations (13) and (26). In particular, if one shows that the solution of the (volume-) discretized equation (14) converges to that of the conventional surface-discretized equation (15), then Eq. (18) can be applied to the discretized equations as well, and the discretized counterpart of the crucial equation (26) follows.

A rigorous formulation of the above statement (including conditions of its validity) is beyond the scope of this paper. Here the equivalence of the two solution schemes is demonstrated, both numerically and analytically for a spherically symmetric problem (Appendix). Furthermore, Eq. (35) is followed by a briefly sketched reasoning supporting the conjecture that solutions obtained by the respective volume and surface discretizations of Eqs. (14) and (15) converge to the same limit. The primary focus of this paper is, however, to demonstrate numerically the validity of the proposed discretization approach.

The problem of constructing a discretized representation of the integral equation can be stated as follows: In analogy to the integral operator decomposition (19), the stiffness matrix of Eq. (5) can be represented as

$$A \equiv A^R + A^M + A^D = A^{(0)} + \xi A^{(1)}, \tag{27}$$

where the elements of the matrices $A^{(0)}$ and $A^{(1)}$ are given, explicitly, by

$$A^{(0)}_{\alpha\beta} = -\int_{\bar{\Omega}} d^3r_1 \int_{\partial\Omega} d^2r_2 [\nabla_{\mathbf{r}_1}\phi_\alpha(\mathbf{r}_1)] g(\mathbf{r}_1-\mathbf{r}_2)\cdot\hat{\mathbf{n}}(\mathbf{r}_2)\phi_\beta(\mathbf{r}_2), \tag{28a}$$

and

$$A^{(1)}_{\alpha\beta} = \int_{\bar{\Omega}} d^3r_1 \int_{\partial\Omega} d^2r_2 [\nabla_{\mathbf{r}_1}\phi_\alpha(\mathbf{r}_1)] g(\mathbf{r}_1-\mathbf{r}_2) \cdot\hat{\mathbf{n}}(\mathbf{r}_2)\frac{\rho_0}{\xi\rho(\mathbf{r}_2)}\phi_\beta(\mathbf{r}_2) + \int_\Omega d^3r \phi_\alpha(\mathbf{r})\frac{\rho_0}{\xi\rho(\mathbf{r})}\phi_\beta(\mathbf{r}) + k^2\int_\Omega d^3r_1 d^3r_2 \phi_\alpha(\mathbf{r}_1) g(\mathbf{r}_1-\mathbf{r}_2)[1-n^2(\mathbf{r}_2)] \times\frac{\rho_0}{\xi\rho(\mathbf{r}_2)}\phi_\beta(\mathbf{r}_2) - \int_{\bar{\Omega}} d^3r_1 \int_{\bar{\Omega}\setminus\partial\Omega} d^3r_2 [\nabla_{\mathbf{r}_1}\phi_\alpha(\mathbf{r}_1)] \times g(\mathbf{r}_1-\mathbf{r}_2)\cdot\left(\nabla_{\mathbf{r}_2}\frac{\rho_0}{\xi\rho(\mathbf{r}_2)}\right)\phi_\beta(\mathbf{r}_2). \tag{28b}$$

It should be noted that, when $\rho(\mathbf{r})/\rho_0 \to \infty$ uniformly in the volume Ω and ξ is defined by Eq. (23), the matrices $A^{(0)}$ and $A^{(1)}$ remain finite.

It is clear from Eq. (28a) that the matrix elements $A^{(0)}_{\alpha\beta}$ may be nonzero only for basis functions ϕ_β overlapping the boundary $\partial\Omega$ of the object. These basis functions will be termed as the "surface" basis functions, and the remaining ones will be referred to as "volume" basis functions. Accordingly, the matrix (27) will be decomposed into blocks as

$$A = A^{(0)} + \xi A^{(1)} = \begin{bmatrix} A^{(0)}_{ss} + \xi A^{(1)}_{ss} & \xi A^{(1)}_{sv} \\ A^{(0)}_{vs} + \xi A^{(1)}_{vs} & \xi A^{(1)}_{vv} \end{bmatrix}, \tag{29}$$

where use was made of the fact that, by construction, the elements $A^{(0)}_{\alpha\beta}$ are nonzero only for surface column indices β [cf. Eq. (25)].

Similarly, the solution vector x [Eq. (2)] can be decomposed into surface and volume blocks as

$$x = \begin{bmatrix} x_s \\ x_v \end{bmatrix} = \begin{bmatrix} x^{(0)}_s + \xi x^{(1)}_s \\ x_v \end{bmatrix}, \tag{30}$$

where $x^{(0)}_s$ is defined as the solution of the equation

$$A^{(0)}_{ss} x^{(0)}_s = b_s; \tag{31}$$

here b_s is the surface block of the rhs vector b,

$$b = \begin{bmatrix} b_s \\ b_v \end{bmatrix}. \tag{32}$$

By substituting Eqs. (29), (30), and (32) into the original equation

$$Ax = b \tag{33}$$

and by using Eq. (31), the following system of equations is obtained:

$$(A^{(0)}_{ss} + \xi A^{(1)}_{ss}) x^{(1)}_s + A^{(1)}_{sv} x_v = -A^{(1)}_{ss} x^{(0)}_s, \tag{34a}$$

$$(A^{(0)}_{vs} + \xi A^{(1)}_{vs}) x^{(1)}_s + A^{(1)}_{vv} x_v = -A^{(1)}_{vs} x^{(0)}_s + \xi^{-1}(b_v - A^{(0)}_{vs} x^{(0)}_s), \tag{34b}$$

where the rhss are expressed in terms of the solution of Eq. (31).

In order to proceed, it needs to be shown that Eq. (31) implies, as the discretization is being refined, that

$$A^{(0)}_{vs} x^{(0)}_s = b_v, \tag{35}$$

i.e., that the discretized form (31) of the integral equation (13), after being solved *on the surface*, holds also inside the domain Ω. If this is the case, the second term on the rhs of Eq. (34b) can be dropped.

The implication Eq. (31)$\Rightarrow$Eq. (35) is the discrete counterpart of Eq. (13)$\Rightarrow$Eq. (18), and the latter relies only on the representation theorem (11). Therefore, to prove Eq. (35), it is sufficient to show that (i) the solution of Eq. (31)

converges to the solution of the exterior Neumann problem, i.e., to Eq. (13) [or, equivalently, to Eq. (15)] and that (ii) the discretized field in Ω given by the left hand side of Eq. (35) converges to the integral appearing in the representation theorem (11).

The second part of the proof amounts, essentially, to proving convergence of the (volumetrically) discretized LS equation (since the LS equation follows directly from the representation theorem).

The first part of the proof is nontrivial, particularly because the integral-equation system has been discretized with volumetric basis functions, while the Neumann problem equation (15) is a surface equation. A possible convergence proof could be based on showing that volumetric and surface discretizations of Eqs. (14) and (15) converge to the same limit as the discretization scale h tends to zero. The idea of the proof relies on the observation that both equations, Eqs. (14) and (15), involve only trial basis functions restricted to the boundary $\partial\Omega$, i.e., the expansion (2) of the solution in volumetric basis functions is equivalent to the expansion in surface basis functions. The only difference is in the choice of test functions: volume basis functions in the first case and surface basis functions in the second. The use of volumetric basis functions in the first equation compensates for the absence of the identity term $(\frac{1}{2}p)$ in that case and is related to the behavior of the double-layer potential. However, it is also necessary to show that the matrix elements evaluated with surface basis functions infinitesimally close to the boundary $\partial\Omega$ are sufficiently well approximated by matrix elements obtained with volumetric basis functions (i.e., at the distance $\sim h$ from the boundary). This element of the proof has to rely on regularity properties of the solution since it is not true in general that the difference of the stiffness matrices obtained with the two discretizations converges to zero in the norm.

In the following it is conjectured that the discretization procedure outlined above leads to a convergent formulation; the numerical results shown below may be considered an empirical justification of this statement.

It follows then from Eq. (35) that Eq. (34) reduces to

$$\begin{bmatrix} A_{ss} & A_{sv}^{(1)} \\ A_{vs} & A_{vv}^{(1)} \end{bmatrix} \begin{bmatrix} x_s^{(1)} \\ x_v \end{bmatrix} = - \begin{bmatrix} A_{ss}^{(1)} x_s^{(0)} \\ A_{vs}^{(1)} x_s^{(0)} \end{bmatrix} \equiv \hat{b}. \tag{36}$$

It should be noted that the solution depends on the original rh. b only through its surface block b_s appearing in Eq. (31).

Thus, finally, the solution procedure for the discretized equations is the exact counterpart of the procedure described in Sec. IV A. It amounts to

(1) solving the *surface* problem (31),
(2) using the solution $x_s^{(0)}$ to compute the rhs of Eq. (36),
(3) solving the *volumetric* problem (36) for $x_s^{(1)}$ and x_v, and
(4) constructing the full solution according to Eq. (30).

The fast solver based on the FFT compression of the stiffness matrix (see Ref. 1) was generalized to include a two-stage solution approach presented above. This solver extension made possible large-scale simulations of problems involving density contrasts $\rho/\rho_0 \simeq 10^3$ which, due to instabilities caused by ill conditioning, were not feasible before by using the conventional one-stage formulation. Some representative results are presented in Sec. V.

Before concluding this section, a remark should be made on an apparent possibility of overcoming the ill-conditioning difficulty by means of a simple rescaling of the unknowns. Such a rescaling is, in fact, routinely used when solving large density contrast problems in the finite-element method (FEM): since the elements of the stiffness matrix in the FEM are inversely proportional to the local density value, their magnitudes can be equalized (and the matrix conditioning improved) by simply introducing a rescaled pressure variable $\tilde{p}(\mathbf{r}) = p(\mathbf{r})/\rho(\mathbf{r})$, which is equivalent to multiplying the elements of the stiffness matrix by the density $\rho(\mathbf{r})$.

In the context of integral equations (6), an analogous rescaling would amount to multiplying the "volume columns" of the stiffness matrix [i.e., the second column of blocks in Eq. (29)] by the factor $1/\xi$. This procedure does balance the magnitudes of the columns of the stiffness matrix and improves convergence; however, it does not solve another difficulty associated with the loss of accuracy due to summing large and small contributions to the matrix elements in the first column of blocks in Eq. (29). An analysis similar to that used in deriving the two-stage solution scheme shows that the small contributions $\xi A_{\mu s}^{(1)}$, $\mu = s, v$, are equally important as the large ones in the sense that the relative error in the solution is controlled by the relative error, say. ε, in $\xi A_{\mu s}^{(1)}$. But, since only the sum of the two contributions is evaluated, a relative error ε in the small component requires a very small relative error $\sim \xi\varepsilon$ of the computed matrix elements. Such an accuracy, e.g., $10^{-3} \times 10^{-2} = 10^{-5}$ for $\xi = 10^{-3}$ and $\varepsilon = 10^{-2}$, is difficult to achieve in practice. In the proposed two-stage solution scheme, on the other hand, the contributions $A_{\mu s}^{(0)}$ and $\xi A_{\mu s}^{(1)}$ are computed *separately*; in this situation the elements of all the matrix blocks appearing in Eqs. (31) and (36) need to be evaluated only to the relative accuracy ε.

V. EXAMPLES

Any problem involving scattering on acoustic objects immersed in air must necessarily involve large ratios of densities. In particular, the ratio of density of a biological tissue (or water) to that of air is about 1000. Accordingly, the validation tests presented here consider such densities and refractive indices in the range $0 < n < 1$, also typical of biological media (at least for pressure waves).

In order to verify the accuracy of the proposed high-contrast acoustic integral-equation solver, a number of computations have been carried out for homogeneous, as well as layered spheres composed of large-contrast materials. The results were compared with the exact analytical solutions expressed as series involving Bessel functions and Legendre polynomials.

Further examples of computations for high-contrast problems can be found in our previous paper.[1] That reference contains also a detailed discussion of the algorithm complexity and its performance for large problems.

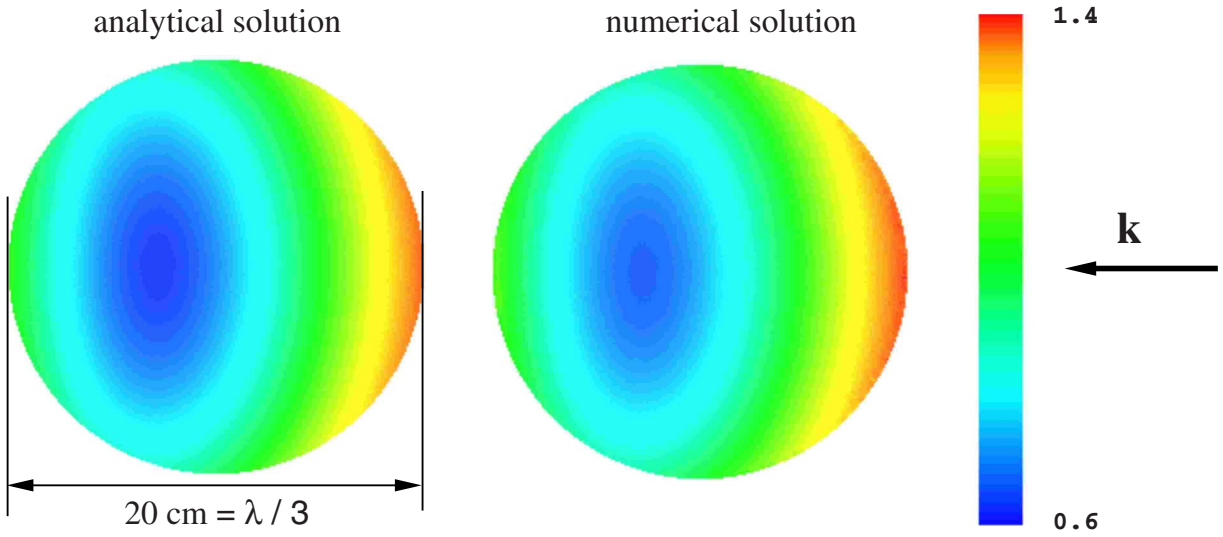


FIG. 3. (Color online) Distribution of the absolute value of the pressure, $|p(\mathbf{r})|$, on a plane parallel passing through the homogeneous sphere center, computed analytically and by means of the developed acoustic solver, for a discretization with $N=970\,000$ tetrahedra.

It should be stressed again that the use of the developed two-stage solution scheme was crucial in obtaining the results; otherwise the numerical problems would become ill conditioned and the solutions unstable.

A. Homogeneous spheres

Figures 3 and 4 show results for a sphere of radius $a=10$ cm, immersed in air, and filled with an acoustic material of the relative density $\rho/\rho_0=10^3$ and relative compressibility $\kappa/\kappa_0=10^{-4}$, corresponding to $n^2=0.1$ or $n\simeq 0.316$. The numerical solution employed a sphere discretized with about $N=970\,000$ tetrahedra. The sphere was excited by a plane wave of the wavelength of $\lambda=60$ cm (i.e., of the frequency of $f\simeq 573$ Hz).

Figure 3 shows the distribution of the absolute value of the pressure on a plane parallel to the incident wave vector and passing through the center of the sphere, computed analytically and numerically, by using the two-stage solution scheme. In Fig. 4 comparison is made between the stage-1 and stage-2 convergence of the two-stage iterative solution scheme, and the convergence of the conventional scheme. The slow convergence of the conventional procedure [and the resulting large fluctuations in the pressure distributions (not shown here)] are typical symptoms of poor conditioning. These difficulties do not appear in the two-stage solution approach.

The current version of the solver, partly parallelized for shared-memory platforms, was run on an SGI Origin 3900 system. The total computation time on eight processors was about 130 min. The maximum required memory was about 6.4 Gbytes.

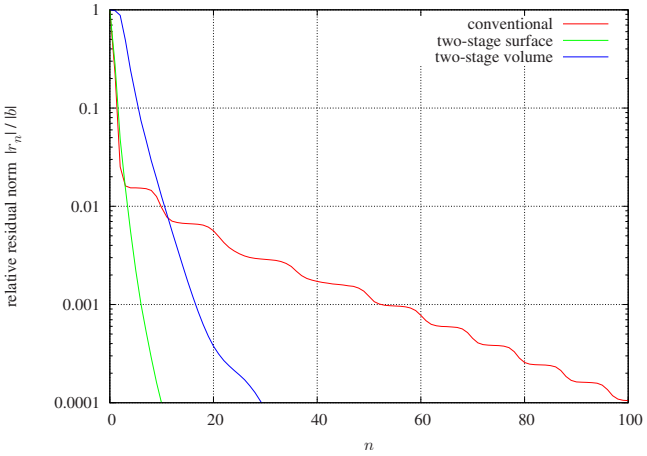


FIG. 4. (Color online) Convergence of the stage-1 (surface) and stage-2 (volume) iterative solutions in the two-stage scheme compared to the convergence of the conventional solution. The figure shows the relative residual $|r_n|=|b-Ax_n|/|b|$ as the function of the number of iterations n.

B. Multilayered spheres

Figures 5 and 6 show results for the pressure distribution in a layered sphere, with the outer shell chosen to represent the bone, and the interior of the sphere described by mechanical parameters of water. The parameters of the inner region approximate the behavior of pressure waves in the brain tissue. As shown in Fig. 5, the outer radius of the sphere is 10 cm, and the inner radius is 9 cm. The calculations employed a tetrahedral mesh with the tetrahedron sizes of about 4 mm; hence the thickness of the shell was about

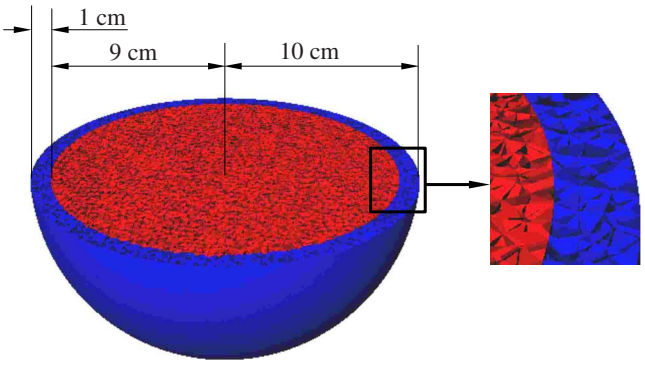


FIG. 5. (Color online) Discretization of the layered sphere with $N=755\,000$ tetrahedra.

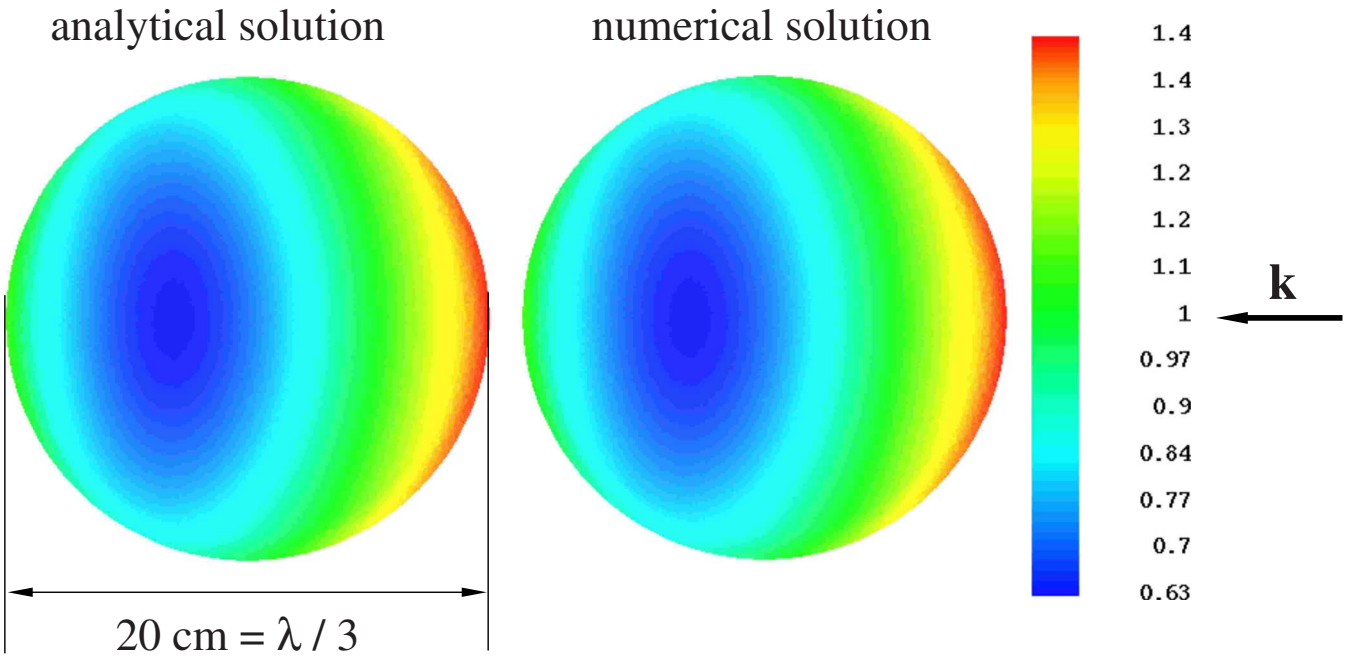


FIG. 6. (Color online) Distribution of the absolute value of the pressure, $|p(\mathbf{r})|$, on a plane parallel passing through the layered sphere center, computed analytically and by means of the described acoustic solver, for a discretization with $N=755\,000$ tetrahedra.

three times the tetrahedron size. The total number of tetrahedra is about $N=755\,000$. Figure 6 shows distribution of the absolute value of the pressure, $|p(\mathbf{r})|$, for the incident wave with $\lambda=60$ cm (frequency $f\simeq 573$ Hz). The histogram of the relative pressure errors on that plane, plotted in Fig. 7, shows that the error of the numerical solution is on the order of 1% [the relative solution error is defined as $|p(\mathbf{r})-p_{\text{exact}}(\mathbf{r})|/|p_{\text{exact}}|_{\max}$, and the numbers of "events" in the histogram are the numbers of discretization points within the indicated error bins].

VI. SUMMARY

The present paper describes a reformulation of the LS volumetric integral equations for acoustics, applicable to problems characterized by large density contrasts and moderate values of the refractive index. In such problems (which arise, e.g., in acoustic wave scattering on biological tissues immersed in air), only a small fraction of incident wave energy penetrates through large-contrast interfaces and, as the result, the solution is poorly determined in the regions where the power level is small; in other words, the problem is ill conditioned. The conditioning difficulties are avoided by first solving an appropriately specified surface problem, and then a modified volumetric problem, in which the incident wave involves the solution of the surface problem. Both the surface and volumetric problems are well conditioned.

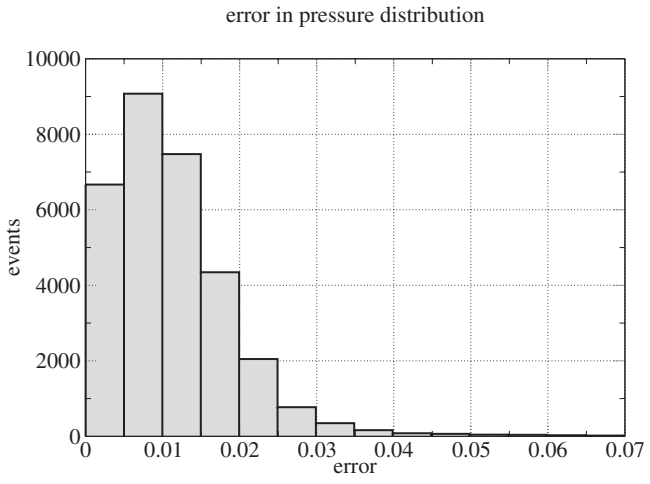


FIG. 7. Histogram of the relative error in the pressure for the section shown in Fig. 6.

The described method has been implemented in our fast solver (utilizing an FFT-based stiffness matrix compression), and verification of the results of computation for representative large high-contrast problems has been made.

Similar conditioning difficulties are expected to arise in elasticity problems with large contrast of material parameters. A future publication will describe a generalization of the approach proposed here to that case.

ACKNOWLEDGMENTS

The support of Air Force Office for Scientific Research under Contract No. FA9550-06-C-0034 is gratefully acknowledged.

APPENDIX: SOLUTION OF INTEGRAL EQUATIONS FOR SCATTERING ON A HOMOGENEOUS SPHERE

In this section an explicit analytic example is presented of an acoustic wave scattering from a homogeneous sphere of radius a, constant relative density ρ/ρ_0, and constant refractive index n. It shows that

(1) the known analytic solution of the original differential equation solves the conventional LS equation and the two-stage system of equations proposed here;

(2) solutions of discretized forms of both the conventional and two-stage systems converge to the analytic solution; and
(3) for large density ratio, the condition number of the discretized conventional LS equation is proportional to ρ/ρ_0, while the condition number of the two-stage system remains constant.

In this example a simplifying assumption was made that the sphere is homogeneous and the incident wave is spherically symmetric,

$$p^{(\mathrm{inc})}(r) = \frac{\sin(kr)}{kr}, \tag{A1}$$

and thus, so is the solution. This problem can be generalized to a stratified sphere and to all partial waves; however, the considered example illustrates all the main features of the proposed approach and yet it is easy to analyze.

Analytic solution. The acoustic wave equation

$$n^2k^2p(\mathbf{r}) + \frac{\rho(\mathbf{r})}{\rho_0}\nabla\cdot\left(\frac{\rho_0}{\rho(\mathbf{r})}\nabla p(\mathbf{r})\right) = 0 \tag{A2}$$

[equivalent to Eq. (1)] reduces in the present case to the system

$$\frac{1}{r}\frac{d^2(rp(r))}{dr^2} + n^2k^2p(r) = 0 \quad \text{for} \quad 0 \le r \le a, \tag{A3a}$$

$$\frac{1}{r}\frac{d^2(rp(r))}{dr^2} + k^2p(r) = 0 \quad \text{for} \quad a \le r \le \infty, \tag{A3b}$$

with the boundary conditions at $r=a$,

$$p(a-) = p(a+), \quad \frac{p'(a-)}{\rho} = \frac{p'(a+)}{\rho_0}, \tag{A4}$$

and with the requirement that the solution approaches the incident wave (A1) for $r\to\infty$. The solution to the problem is given, for $r\le a$, by

$$p(r) = C\frac{\sin(nkr)}{kr}, \tag{A5}$$

with

$$C = \frac{kae^{-ika}}{(1-ika)\sin(nka) - \frac{\rho_0}{\rho}[\sin(nka) - nka\cos(nka)]}. \tag{A6}$$

Integral operators. The integral operator K in the LS equation (6) becomes, in the considered problem,

$$(Kp)(r) \equiv \frac{\rho_0}{\rho}p(r) + k(1-n^2)\frac{\rho_0}{\rho}\frac{1}{r} \times\left\{\int_0^r dr'r'e^{ikr}\sin(kr')p(r') + \int_r^a dr'r'e^{ikr'}\sin(kr)p(r')\right\} + \left(1-\frac{\rho_0}{\rho}\right) \times(1-ika)e^{ika}\frac{\sin(kr)}{kr}p(a) \quad \text{for} \quad r<a. \tag{A7}$$

This expression follows from the representations of the angular averages of the Green's function and its normal derivative,

$$\langle g(\mathbf{r}-\mathbf{r}')\rangle = \frac{k}{4\pi}\frac{e^{ikr_>}}{kr_>}\frac{\sin(kr_<)}{kr_<} \tag{A8}$$

and

$$\left\langle\frac{\partial g(\mathbf{r}-\mathbf{r}')}{\partial n(\mathbf{r}')}\right\rangle = -\frac{k^2}{4\pi}(1-ikr_>)\frac{e^{ikr_>}}{k^2r_>^2}\frac{\sin(kr_<)}{kr_<}, \tag{A9}$$

with $r_>=\max\{r,r'\}$ and $r_<=\min\{r,r'\}$. Equations (A8) and (A9) can be obtained from the addition theorem for the Bessel functions.

Analogous explicit expressions for the operators $K^{(0)}$ and $K^{(1)}$ of Eqs. (12) and (20) are

$$(K^{(0)}p)(r) = (1-ika)e^{ika}\frac{\sin(kr)}{kr}p(a) \tag{A10}$$

and

$$(K^{(1)}p)(r) = \frac{\rho_0}{\xi\rho}p(r) + k(1-n^2)\frac{\rho_0}{\xi\rho}\frac{1}{r} \times\left\{\int_0^r dr'r'e^{ikr}\sin(kr')p(r') + \int_r^a dr'r'e^{ikr'}\sin(kr)p(r')\right\} - \frac{\rho_0}{\xi\rho}(1-ika) \times e^{ika}\frac{\sin(kr)}{kr}p(a) \quad \text{for} \quad r<a. \tag{A11}$$

Conventional, one-stage scheme for solving LS equation. A straightforward calculation shows that the function (A5) solves the conventional LS equation,

$$(Kp)(r) = p^{(\mathrm{inc})}(r) \quad \text{for} \quad r<a. \tag{A12}$$

Two-stage system scheme for solving LS equation. The surface equation (13),

$$(K^{(0)}p_s^{(0)})(r) = p^{(\mathrm{inc})}(r) \quad \text{for} \quad r=a-, \tag{A13}$$

is now solved by

$$p_s^{(0)}(a) = \frac{1}{1-ika}e^{-ika}. \tag{A14}$$

It can be checked that Eq. (17) holds, and the rhs, $-K^{(1)}p_s^{(0)}$, of Eq. (26) can be evaluated explicitly. Finally, it can be verified, by direct calculation, that Eq. (26) is solved by

$$p_s^{(1)}(a) = \xi^{-1}[p(a) - p_s^{(0)}(a)] \quad \text{and} \quad p_v(r) = p(r) \tag{A15}$$

[cf. Eq. (24)], with p and $p_s^{(0)}$ given by Eqs. (A5) and (A14).

Discretized integral equations. Since the main goal of the present analysis is to establish dependence of the equations' conditioning as function of the material parameters, the simplest possible discretization (expected to yield first-

order convergence) is assumed. The radius interval $[0,a]$ is partitioned into N segments of length $h=a/N$ each, and the solution $p(r)$ is expanded, as in Eq. (2), with piecewise constant basis functions $\phi_\alpha(r)$ of value 1, supported on intervals of widths h, centered at points $r_\alpha=(N-\alpha+\frac{1}{2})h$, $\alpha=1,2,\ldots,N$. Furthermore, the collocation method is used, and the r'-integrals are approximated by the rectangle quadrature. With these assumptions, the matrices A, $A^{(0)}$, and $A^{(1)}$ (corresponding to the operators K, $K^{(0)}$, and $K^{(1)}$) are given by

$$A_{\alpha\beta}=\frac{\rho_0}{\rho}\delta_{\alpha\beta}+kh(1-n^2)\frac{\rho_0}{\rho}\frac{r_\beta}{r_\alpha}e^{ik\max\{r_\alpha,r_\beta\}}\sin(k\min\{r_\alpha,r_\beta\})+\left(1-\frac{\rho_0}{\rho}\right)(1-ika)e^{ika}\frac{\sin(kr_\alpha)}{kr_\alpha}\delta_{\beta 1}, \tag{A16a}$$

$$A^{(0)}_{\alpha\beta}=(1-ika)e^{ika}\frac{\sin(kr_\alpha)}{kr_\alpha}\delta_{\beta 1}, \tag{A16b}$$

and

$$A^{(1)}_{\alpha\beta}=\frac{\rho_0}{\xi\rho}\delta_{\alpha\beta}+kh(1-n^2)\frac{\rho_0}{\xi\rho}\frac{r_\beta}{r_\alpha}e^{ik\max\{r_\alpha,r_\beta\}}\sin(k\min\{r_\alpha,r_\beta\})-\frac{\rho_0}{\xi\rho}(1-ika)e^{ika}\frac{\sin(kr_\alpha)}{kr_\alpha}\delta_{\beta 1}, \tag{A16c}$$

with $\xi=\rho_0/\rho$. The rhs vectors b and $\hat{b}$ now become

$$b_\alpha=\frac{\sin(kr_\alpha)}{kr_\alpha} \tag{A17a}$$

and

$$\hat{b}_\alpha=-A^{(1)}_{\alpha 1}x^{(0)}_1. \tag{A17b}$$

It should be noted that, in this problem, the "surface blocks" consist only of one element, $\alpha=1$, while in the "volume blocks" $\alpha=2,\ldots,N$.

The explicit expressions for the matrices and rhs [Eqs. (A16a) and (A17a) above] allow now to solve the spherically symmetric problem in the conventional one-stage [Eq. (3)] as well as in the two-stage [Eqs. (31), (36), and (30)] formulations.

Such computations have been carried out, with the result that both the conventional and the two-stage solutions converge to the analytic solution (A5). As expected, the first-order convergence (i.e., the l_2 relative error proportional to $1/N$) was observed. It was also found that the condition number of the linear system in the conventional formulation grows linearly with ρ/ρ_0, while in the two-step solution scheme it remains constant for the increasing density ρ; the ratio of the condition numbers is, almost exactly, equal to ρ/ρ_0.

[1]E. Bleszynski, M. Bleszynski, and T. Jaroszewicz, "Fast volumetric integral solver for acoustic wave propagation through inhomogeneous media," J. Acoust. Soc. Am. **124**, 396–408 (2008).

[2]E. Bleszynski, M. Bleszynski, and T. Jaroszewicz, "A fast integral equation algorithm for large scale simulation of acoustics field propagation in biological tissues," Proceedings of the 19th International Congress on Acoustics, Madrid, Spain (2007), pp. 156.

[3]E. Bleszynski, M. Bleszynski, and T. Jaroszewicz, "A fast integral equation solver for electromagnetic scattering problems," Proceedings of the 1994 IEEE AP-S International Symposium, Seattle, WA, 20–24 June (1994), pp. 416–419.

[4]E. Bleszynski, M. Bleszynski, and T. Jaroszewicz, "AIM: Adaptive integral method for solving large-scale electromagnetic scattering and radiation problems," Radio Sci. **31**, 1225–1251 (1996).

[5]E. Bleszynski, M. Bleszynski, and T. Jaroszewicz, "Least-squares based far-field expansion in the adaptive integral method (AIM)," Proceedings of the 13th Annual Review of Progress in Applied Computational Electromagnetics, Monterey, CA, 17–21 March (1997), pp. 944–950.

[6]P. M. Morse and K. U. Ingard, *Theoretical Acoustics* (McGraw-Hill, New York, 1968).

[7]P. A. Martin, "Acoustic scattering by inhomogeneous obstacles," SIAM J. Appl. Math. **64**, 297–308 (2003).

[8]D. Colton and R. Kress, *Integral Equation Methods in Scattering Theory* (Wiley, New York, 1983).

[9]C. E. Kenig, *Harmonic Analysis Techniques for Second Order Elliptic Boundary Value Problems*, CBMS Regional Conference Series in Mathematics (American Mathematical Society, Providence, RI, 1994).

Source of level dependent minima in rabbit distortion product otoacoustic emissions

P. F. Fahey[a)]
Department of Physics/EE, University of Scranton, Scranton, Pennsylvania 18510

B. B. Stagner
VA Loma Linda Healthcare System, Loma Linda University Medical Center, Loma Linda, California 92357

G. K. Martin
VA Loma Linda Healthcare System, Loma Linda University Medical Center, Loma Linda, California 92357 and Department of Otolaryngology, Loma Linda University Medical Center, Loma Linda, California 92357

(Received 30 May 2008; revised 19 September 2008; accepted 27 September 2008)

Sharp level dependent minima (commonly called nulls or notches) in the distortion product otoacoustic emissions (DPOAEs) have been postulated to be due to two different mechanisms. It is shown here that the level dependent nulls in rabbit $2f_1-f_2$ DPOAEs carry the signature of the mixing of a third order nonlinear term with a fifth order nonlinear term. This suggests that the minima are not due to the mixing of signals from two different physical sites of origin, but rather are due to the nature of the nonlinearity itself. Model simulations show that null production is indifferent to several properties of nonlinear input/output functions.
© *2008 Acoustical Society of America.* [DOI: 10.1121/1.3003078]

PACS number(s): 43.64.Bt, 43.64.Jb [WPS] Pages: 3694–3707

I. INTRODUCTION

Direct and indirect measurements of the mechanical response of the inner ear show evidence of a compressive nonlinearity. This mechanical compressive nonlinearity is one source of the large dynamic range of hearing. The mechanical nonlinearity is manifested by the generation of harmonics and intermodulation distortion products (DPs) when the inner ear is driven by pure tones. The compressiveness is manifest by the saturation of the DPs and that the phase differs by π between adjacent odd order DPs. Because the DPs generated by the mechanical response of the cochlea propagate out of the inner ear via the middle and outer ears, the properties of the inner ear mechanical nonlinearity can be noninvasively studied. Signals generated within and then propagating out of the inner ear have been named otoacoustic emissions (OAEs), and when they are DPs they are labeled DPOAEs. The most easily observable, hence the most studied DPOAE, is the one whose frequency is $f_{DP}=2f_1-f_2$.

It has been observed that $2f_1-f_2$ DPOAE levels can have abrupt decreases and then equally abrupt increases when either (a) the input frequencies are scanned or, alternatively, (b) when the levels of the input tones are scanned. Commonly associated with these abrupt changes in level (or "nulls") is an equally abrupt change in phase of close to π radians. Hence, these sharp nulls in DPOAE level resemble wave interference patterns due to two or more sources.

When the primary frequencies are swept (by varying either f_2 alone or f_1 alone or varying both at constant f_2/f_1) the DPOAEs often show patterns that resemble classical wave interferometry. Experiments have shown that there is evidence of two sources of some DPOAEs. For example, in humans, there are many measurements of "fine structure." The fine structure consists of nulls closely spaced in frequency that modulate the overall level versus frequency pattern. This fine structure has been extensively studied and its source is thought to be understood. For example, Stover *et al.* (1996), Brown *et al.* (1996), Knight and Kemp (2000), and Kalluri and Shera (2001), among many others, made convincing arguments for two separate wave sources. Kalluri and Shera (2001) demonstrated the concordance of results using different techniques.

In experimental animals nulls similar to the human fine structure have also been observed. In experimental animals the signal time delays are much shorter than in humans (Whitehead *et al.*, 1996); hence, the null frequency spacing is much larger and the appellation, "fine structure," is not as appropriate. Using the technique of Stover *et al.* (1996), Fahey and Allen (1997) made the case for two separate wave sources in cats. Bergevin (2007) made the argument that chicken DPOAEs also show evidence of two sources. In all of the aforementioned swept frequency studies the data are consistent with the first source being the site of generation at the f_2 place and the second source being re-emission from the DP place. The rabbit preparation used in this study does not show swept frequency nulls like the animal preparations mentioned above.

In experimental animals (such as cats, gerbils, guinea pigs, and rabbits) the observation of sharp nulls in the

[a)]Author to whom correspondence should be addressed. Electronic mail: faheyp1@scranton.edu

 © 2008 Acoustical Society of America

DPOAE level when varying the input levels of the primaries also looks like two wave mixing. One possible mechanism would be that there are two separate sources (from a generation site and also from a physically distinct re-emission site) and that the one source grows relative to the other source as level is changed. A second possibility would be within the generation mechanics of nonlinearity itself. Lukashkin and Russell (1999) modeled how a compressive nonlinearity itself can produce sharp nulls with a changing level. Lukashkin *et al.* (2002) observed this π phase change associated with a level dependent null in guinea pigs, and Whitehead *et al.* (1992a) earlier observed a π phase change associated with a level dependent nulls in rabbits.

Since both the two-site explanation, where the DP signal from the generation site grows relative to the DP signal from the re-emission site, and the single-site explanation (only a generation site) of the nulling would exhibit a π phase change at the same parameters for which the null occurs, we look here for other elements in the signature of the single-site nonlinearity induced null. Using simulations akin to Frank and Kossl (1996), Lukashkin and Russell (1999), and Fahey *et al.* (2000), it is found that one signature of the single-site mechanism, when modeled, is that the level of the $3f_1-2f_2$ DP has a local maximum at parameters where the $2f_1-f_2$ null occurs and that this maximum is comparable to the level of $2f_1-f_2$ just before or just after the null. In the rabbit data shown below this signature is observed. Another signature in simulations is that there is a line of nulling for a particular constant value of either L_1 or L_2 (where L_1 and L_2 are the levels of the input tones at f_1 and f_2) accompanied by an abrupt phase shift. In the rabbit data presented here this signature is observed. Therefore, it seems likely that rabbits present level dependent sharp nulls that are due to properties of the basilar membrane nonlinearity alone and not due to any re-emission site. It will be shown below how to toggle the properties of nonlinearities to create nulls and, thereby, it will be shown which properties of the nonlinearity are indifferent to null production.

II. METHODS

The data presented here were measured as per previously published protocols (Fahey *et al.*, 2006). Some lower level resolution data that motivated this study were presented by Stagner *et al.* (2005). The data shown here were acquired with the high level resolution of 1 dB difference between adjacent levels of both L_1 and L_2. This high level density is useful for bringing out some features of the data shown below.

A. Subjects

Young female albino rabbits ($n=4$) were tested in a sound-treated booth while awake, confined in a standard plastic rabbit holder. The human data are from one young adult and were corroborated in another young adult. The animal studies were approved by the Animal Care and Use Committee and the humans studies by the Human Subjects Institutional Review Board of the VA Loma Linda Healthcare System.

B. DPOAE measurement

The f_1 and f_2 primary tones for eliciting DPOAEs were generated by a digital signal processor (DSP) board mounted in a Macintosh personal computer and presented over ER-2 speakers. Ear canal sound pressure was measured with an ER-10 microphone, sampled at 44100 Hz, and synchronously averaged by the DSP board. 2048 point spectra over a frequency range from 0 to $\approx$22 kHz were collected at the input sound pressure levels (SPLs) shown in the figures (each of L_1 and L_2 ranging from 25 to 80 dB SPL in 1 dB steps). For measurements made at $f_2/f_1=1.0125$, a 4096 point spectrum was used. The DPOAE levels and phase were extracted from the spectra. A control run in a 1.5 cc hard-walled cavity produced no consistent artifacts at any of the emission frequencies measured.

III. MODEL RESULTS

The goal of the modeling study is twofold. First, signature features of null creation that are due to the form of nonlinear input/output (I/O) functions will be numerically demonstrated. The following will be shown.

(1) There are null lines that are parallel to each of the two input level axes. (The intersection of these lines when the DP is plotted as a function of L_1 and L_2 is called a null spot in the text that follows.)
(2) There are phase discontinuities of π radians at levels that produce the nulls.
(3) The level of the fifth order DP at $3f_1-2f_2$ is comparable to the level of the $2f_1-f_2$ DP just before the occurrence of a null. At the levels at which a $2f_1-f_2$ null spot occurs $3f_1-2f_2$ is near a local maximum. Likewise a null in the $3f_1-2f_2$ DP is associated with a local maximum in the $4f_1-3f_2$ DP, etc. Obviously, the same correlations also apply to the upper sidebands ($2f_2-f_1$, $3f_2-2f_1$, etc.).
(4) There are nonlinear I/O functions that can generate multiple null spots.

Second, the effect of various attributes of I/O functions on null production will be explored. For example, the modeling shows the following.

(1) Contrary to implications in literature, some purely odd symmetry saturating I/O functions produce nulls.
(2) Not all saturating nonlinearities with even symmetry produce nulls.
(3) Abruptness of the onset of clipping is not a determinant of null production.
(4) Nulls can be produced by I/O functions that are linear for one polarity of the signal and saturating for the other polarity. That is, both polarities of the signal need not be clipped.
(5) The nulls in the DP of order n do not occur at the same values as the zeros in the nth derivatives of the I/O functions.

A. Saturating nonlinearities

Hyperbolic tangent type functions, $y=A\tanh(f(x-a))+B$ where a, A, and B are constants and f is a polynomial,

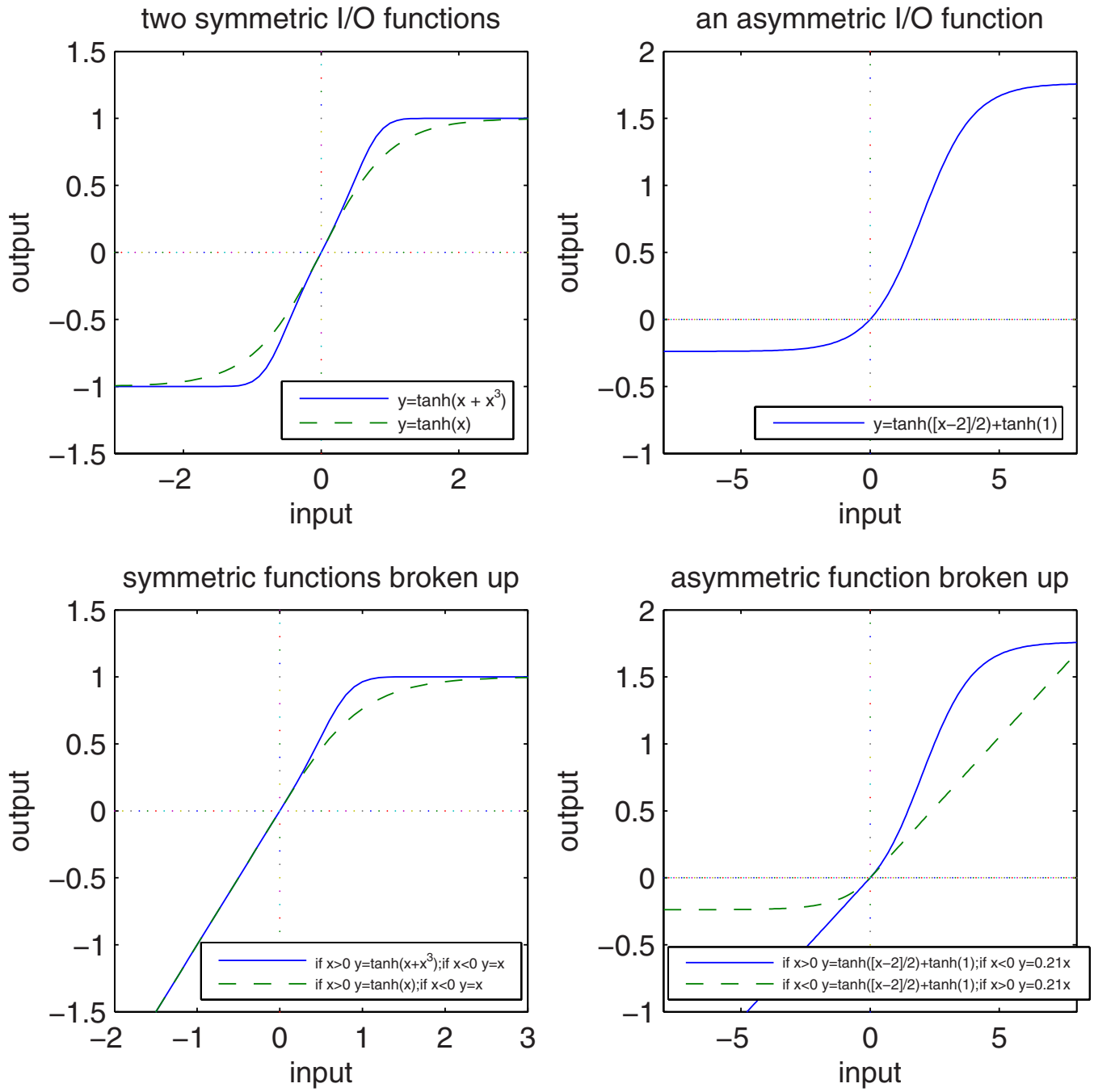


FIG. 1. (Color online) The nonlinearities $y=\tanh(x)$ and $y=\tanh(x+x^3)$ are plotted in the top lefthand side, and the same nonlinearites, except with linear output for negative signal polarities, are shown in the bottom lefthand side. On the righthand side are the nonlinearity $y=\tanh([x-2]/2)+\tanh(1)$ in the top and that same function except that now it has been broken up so that only one polarity of the signal is clipped. For all of these I/O functions both the function and its first derivative are continuous.

constitute a fairly general class of saturating nonlinear I/O functions that have often been used to model inner ear nonlinear responses (Weiss and Leong, 1985; Frank and Kossl, 1996; Lukashkin and Russell, 1999; Fahey *et al.*, 2000). [Kossl and Coro (2006) also used these functions, and these functions blended with an expansive cubic term.] This class of functions [with $f(x-a)=(x-a)/2$] was successfully used by Weiss and Leong (1985) to model hair cell receptor potentials as a function of stereocilia deflection angle. Functions of this type are common in the description of the physics of systems having two equilibrium states that are separated in energy, e.g., the thermodynamic description of the magnetic moment of paramagnetic materials often studied in introductory thermal physics courses (e.g., Feynman *et al.*, 1964). In the context of the mammalian inner ear, the two states would be assumed to be the open and closed states of stereociliary motion activated outer hair cell ion channels. Therefore there is a natural saturation when all channels are (a) open or (b) closed. The specifics of the transition from outer hair electrical properties to basilar membrane mechanical properties is not known. However, this mechanical nonlinearity would show saturation as long as it is the outer hair cell electrical response that is somehow controlling the nonlinearity. If the energy states associated with the channels are

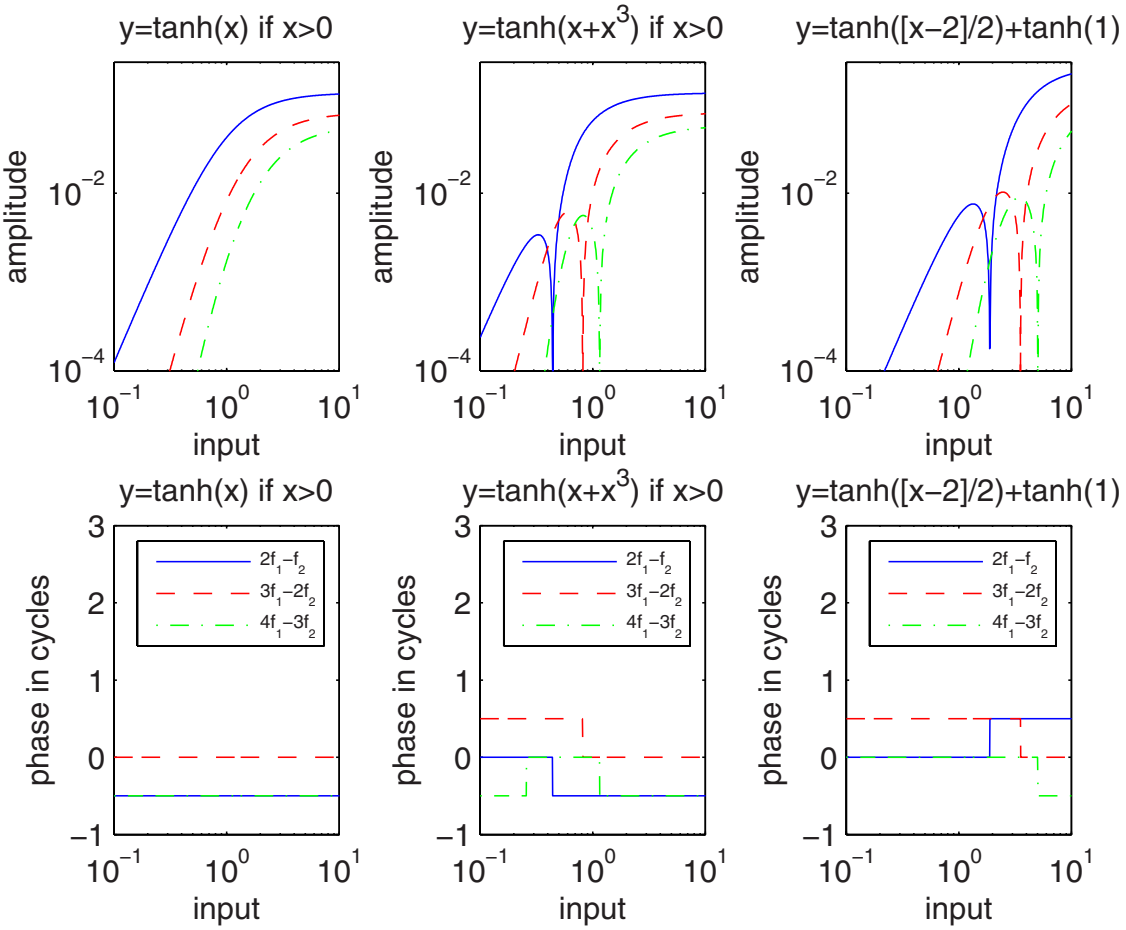


FIG. 2. (Color online) Graphs of the output of three DPs as a function of the amplitude of the two input tones. The input is $x=A_1\cos(\omega_1 t)+A_2\cos(\omega_2 t)$, where the A's are the tone amplitudes and the ω's are the angular frequencies. Here $A_1=A_2$. On the lefthand side are DPs for the single-polarity I/O function, $y=\tanh(x)$ if $x\geqslant 0$ and linear otherwise, and in the middle for the single-polarity I/O function, $y=\tanh(x+x^3)$ if $x\geqslant 0$ and linear otherwise; and on the righthand side the two-polarity clipper $y=\tanh([x-2]/2)+\tanh(1)$. The middle and the righthand sides show nulls in the three DPs plotted. The null in the $2f_1-f_2$ DP is near the local maximum of the $3f_1-2f_2$ DP and the null in the $3f_1-2f_2$ DP is associated with a maximum in the $4f_1-3f_2$ DP.

mechanically nonlinear, then arguments of the tanh would be nonlinear, containing one or more terms of the form x^n where n is an integer.

Weiss and Leong (1985) showed that functions of this class can exhibit level dependent nulls in harmonics, and Lukashkin and Russell (1999) and Fahey *et al.* (2000) showed level dependent nulls in intermodulation DPs. Since the A above is just a scale factor (twice the difference between the asymptotic limits as $x\to\infty$ and $\to-\infty$), it is no loss of generality to set $A=1$. In order to guarantee that the output is zero at zero input $B=\tanh(a/2)$. Adjusting the a parameter about zero gives the nonlinearity some even symmetry. It will be shown here that I/O functions with purely odd symmetry can also exhibit level dependent nulling. However, these purely odd symmetry functions producing nulling are hyperbolic tangents with nonlinear arguments.

The forms of some model nonlinear I/O functions are shown in Fig. 1. On the top lefthand side are the odd symmetry nonlinearities $y=\tanh(x)$ and $y=\tanh(x+x^3)$. These I/O functions clip both the positive and the negative polarity of an input signal. On the bottom lefthand side are two single-polarity nonlinearities $y=\tanh(x)$ if $x\geqslant 0$ but $y=x$ otherwise and $y=\tanh(x+x^3)$ if $x\geqslant 0$ but $y=x$ otherwise. The nonlinearities on the bottom clip only the positive polarity of the signal. On the top righthand side is the nonlinearity $y=\tanh([x-a]/2)+b$ where $a=2$ and $b=\tanh(a/2)$. This nonlinearity [in the form $y=(b+1)-2/(1+e^{a-x})$] was used in the study of Fahey *et al.*(2000). On the bottom righthand side this same function has been broken up into two functions, each of which clips only one polarity of the signal.

Some of these nonlinearities exhibit DP nulls and some do not. Both the two-polarity clipper $y=\tanh(x)$ and its one-polarity version [$y=\tanh(x)$ if $x\geqslant 0$ and $y=x$ otherwise] do not exhibit nulls. Neither does the one-polarity nonlinearity, $y=\tanh([x-2]/2)+\tanh(1)$ if $x\leqslant 0$ and $y=x$ otherwise. All of the other I/O functions do show nulling in the $2f_1-f_2$ DP and higher order DPs. [Note that $y=\tanh([x-2]/2)+\tanh(1)$ if $x\leqslant 0$ and $y=x$ otherwise clips at lower levels than $y=\tanh([x-2]/2)+\tanh(1)$ if $x>0$ and $y=x$ otherwise. Furthermore, the infinite peak clipper, $y=\mathrm{sgn}(x)$ (+1 if $x\geqslant 1$ and $=-1$ otherwise) does not produce nulls in the DPs. Hence, null production cannot be used as a measure of the level and severity of peak clipping.]

Figure 2 shows the $2f_1-f_2$, $3f_1-2f_2$, and $4f_1-3f_2$ DPs at the output of three different example nonlinearities. And it is evident that the null occurs in the third order DP ($2f_1-f_2$) when the fifth order DP ($3f_1-2f_2$) has grown to roughly

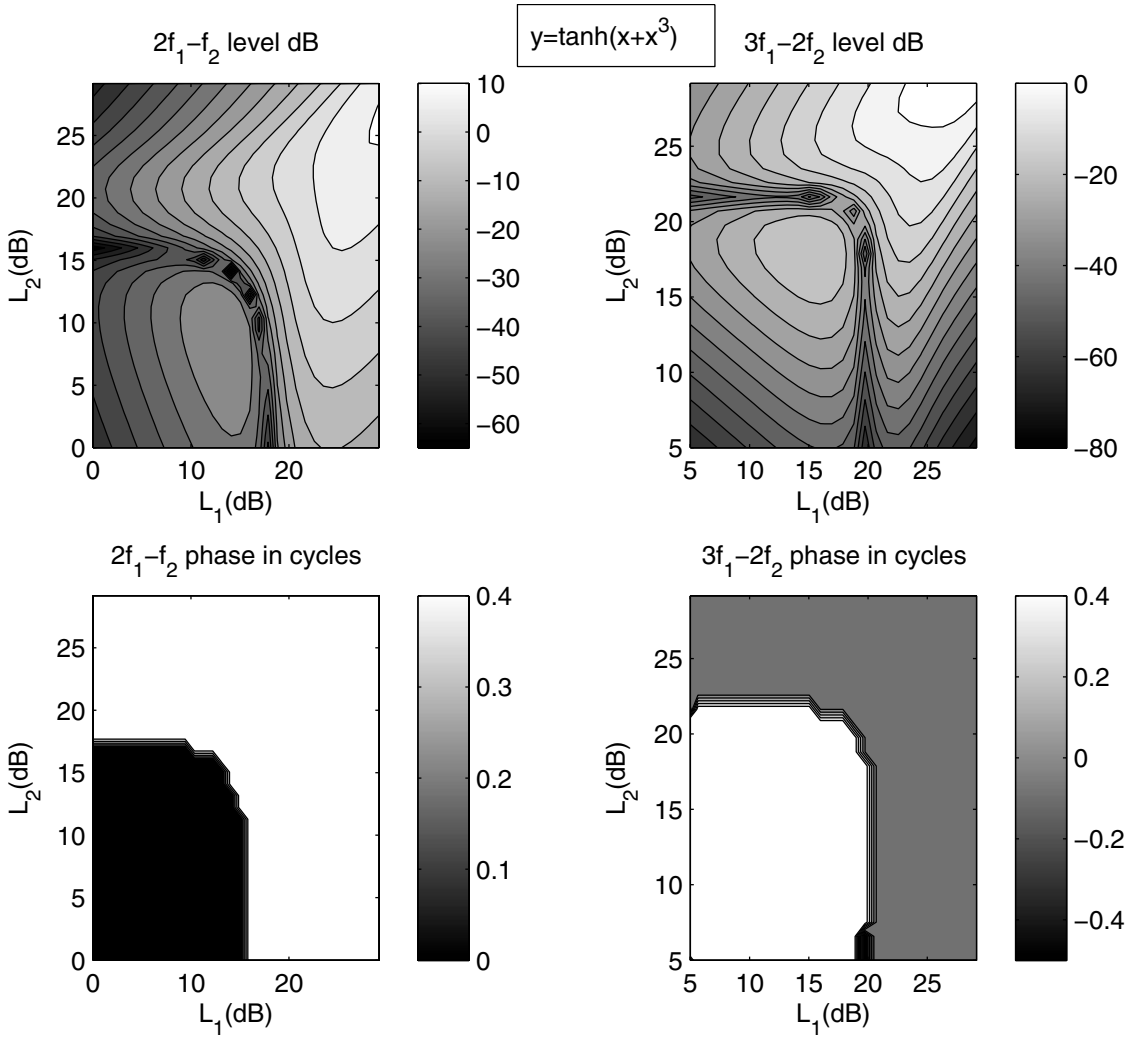


FIG. 3. Contour graphs of the $2f_1-f_2$ level output for the $y=\tanh(x+x^3)$ nonlinearity as a function of the two levels L_1 and L_2. The lines of nulling parallel to each of the input level axes are evident.

the same size as the third order DP and the null in $3f_1-2f_2$ occurs near the maximum of the seventh order $4f_1-3f_2$ DP. In the bottom panels of the figure, it is seen that there is a discontinuity of π radians in the phase of the DP at the levels producing the null. Furthermore, it is evident that clipping on only one polarity of the signal is sufficient for null production. Were the nonlinearities of the form $y=\tanh(x)$ and $y=\tanh(x+x^3)$, with symmetric clipping on both polarities of the signal, the figure would look the same except for a doubling in DP amplitudes. Simulations with I/O function $y=\tanh([x-2]/2)+\tanh(1)$; $x\geqslant 0$ and linear otherwise show nulling. But $y=\tanh([x-2]/2)+\tanh(1)$; $x\leqslant 0$ and linear otherwise do not show nulling.

One of the signatures of nulling in the $2f_1-f_2$ DP generated by the structure of the nonlinearity alone is that the fifth order DP ($3f_1-2f_2$ DP) is at roughly the same magnitude as the $2f_1-f_2$ DP just before the null. A second signature of null production is a π phase discontinuity. A third signature of nulling is null lines and π phase discontinuities parallel to each of the input level axes as is shown in Fig. 3. Here the amplitude and phase of the third and the fifth order DPs are plotted as both input tone levels are varied. (The amplitude graph shows the same nulling features as Fig. 5 of Lukashkin and Russell, 2002.) The input levels, L_1 and L_2, are in decibels and the output DP levels are also in decibels.

The I/O function $y=\tanh(\alpha x+\beta x^5)$ shows a fourth signature of nulling—two sets of intersecting null lines meeting in two null spots. The placing of the spots relative to each other can be manipulated by changing the constants α and β. For example, Fig. 4 shows the pair of null spots for $2f_1-f_2$ and $3f_1-2f_2$ with their associated π phase discontinuities (when $\alpha=1=\beta$). The same patterns shown in Figs. 3 and 4 exist for the upper sideband DPs ($2f_2-f_1$ and $3f_2-2f_1$) as long as one just switches the labels on the axes. Figure 8(f) in the study by Kossl and Coro (2006) shows a different example of a two null spot I/O function.

Always correlated with nulling patterns in the amplitude are discontinuities in the phase of π radians (or half a cycle). Also, there is a slight asymmetry in L_1-L_2 space. These patterns wherein the null follows along either a constant L_1 or constant L_2 lines would constitute another signature of single-site nonlinearity induced nulling. Where the L_1 =constant null line intersects the L_2=constant null line is designated as the null spot. In the data, null spots can be more evident than null lines because the DPOAEs can come from an array of primary generation sites.

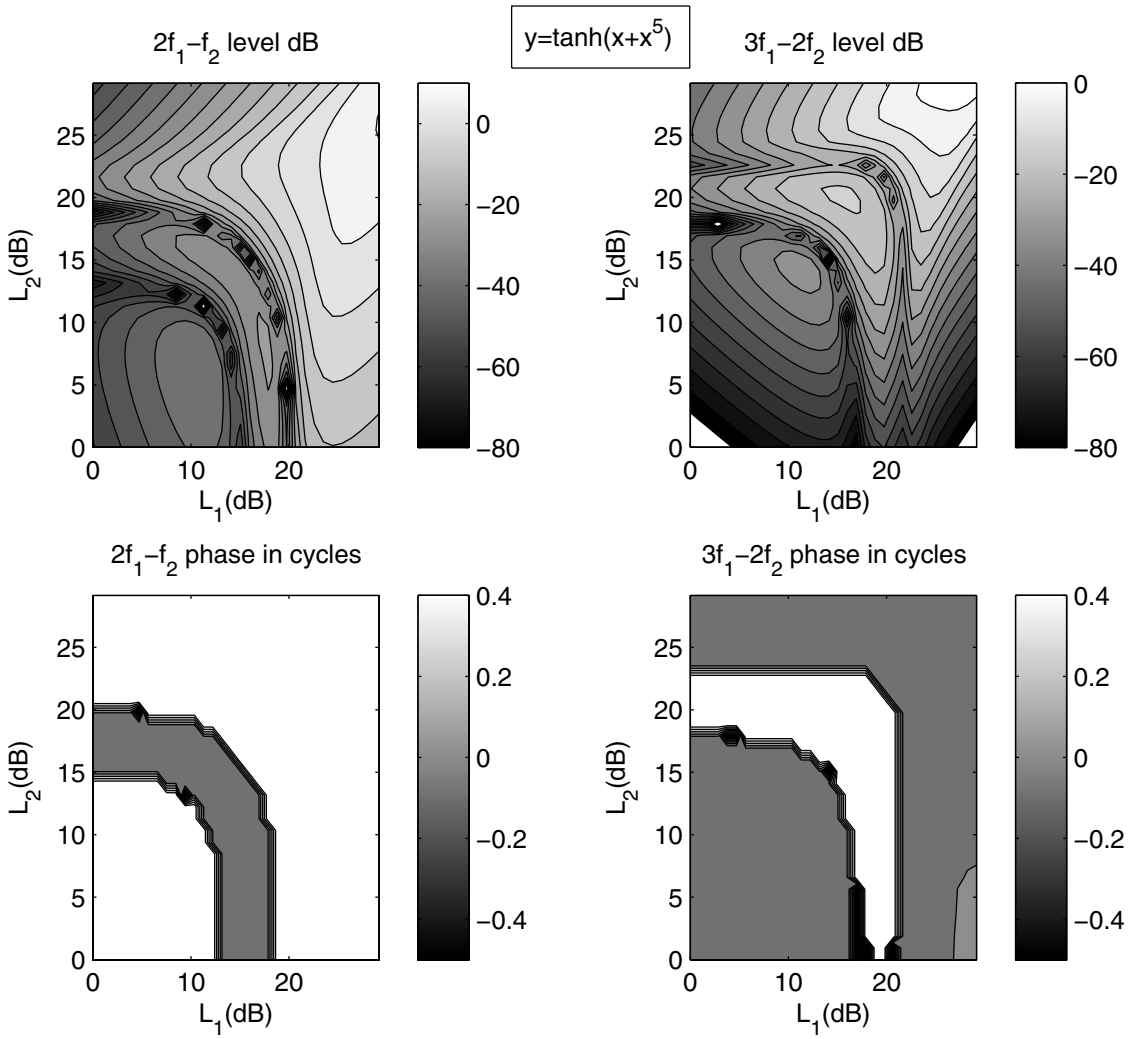


FIG. 4. Contour graphs of the $2f_1-f_2$ level output for the $y=\tanh(x+x^5)$ nonlinearity as a function of the two levels L_1 and L_2. The lines of nulling parallel to each of the input level axes are evident.

From the modeling examples above, it is evident that nulls in the DP amplitude can be produced by the structure of the nonlinear I/O function alone (Frank and Kossl, 1996; Lukashkin and Russell, 1999; Fahey *et al.*, 2000). Furthermore, the signature of a null in the $2f_1-f_2$ DP produced by a single-site process contains (a) null lines that are parallel to the two level axes (Lukashkin and Russell, 2002), (b) phase discontinuities of π radians at levels that produce the nulling (Lukashkin *et al.*, 2002), (c) the presence of the fifth order DP at $3f_1-2f_2$ at levels comparable to the $2f_1-f_2$ levels just before or just after the nulling (Fahey *et al.*, 2000, in Figs. 4, 7, and 8), and (d) the possibilities of multiple sets of null lines and null spots.

B. Controlling null production

1. Usefulness of Taylor series

It is possible to gain some insight regarding nulling by examining the Taylor series (expanded about zero) of the functions used in the plotted simulations.

$$\tanh(x+\alpha x^3) \approx x + \left(-\tfrac{1}{3}+\alpha\right)x^3 + \left(\tfrac{2}{15}-\alpha\right)x^5 + \left(\tfrac{2}{3}\alpha - \tfrac{17}{315} - \alpha^2\right)x^7 + O(x^8). \quad (1)$$

So, if $\alpha=0$,

$$\tanh(x) \approx x - \tfrac{1}{3}x^3 + \tfrac{2}{15}x^5 - \tfrac{17}{315}x^7 + O(x^8), \quad (2)$$

and if $\alpha=1$,

$$\tanh(x+x^3) \approx x + \tfrac{2}{3}x^3 - \tfrac{13}{15}x^5 - \tfrac{122}{315}x^7 + O(x^8). \quad (3)$$

The asymmetric hyperbolic tangent's Taylor representation up to the fifth order term is

$$\tanh([x-2]/2) + \tanh(1) \approx \tfrac{5}{24}x + \tfrac{3}{38}x^2 + \tfrac{1}{76}x^3 - \tfrac{1}{636}x^4 - \tfrac{1}{709}x^5 + O(x^6). \quad (4)$$

The $2f_1-f_2$ DP at the lowest levels is produced by the cubic term in the Taylor series. Comparing the cubic terms for $y=\tanh(x+x^3)$, $y=\tanh(x)$, and $y=\tanh([x-2]/2)+\tanh(1)$ it is evident that for values of $|x|\ll 1$ the relative sizes of the amplitudes of $2f_1-f_2$ as shown in Fig. 2 are predicted by the relative sizes of the coefficients of x^3. Also,

the phases for $|x| \ll 1$ are predicted by the sign of the x^3 term. If the sign is positive, then the phase is zero; if negative, the phase is $\pm\pi$ radians. Such is also the case for the correlation of the $3f_1-2f_2$ DP and the x^5 term, etc.

Consider the two nonlinear functions $y=\tanh(x+\alpha x^3)$ and $y=\tanh([x-\beta]/2)+\tanh(\beta/2)$. In the first case the parameter α changes the shape of the I/O function and in the second case the parameter β shifts the function along the y axis while preserving the shape and guaranteeing that $y=0$ at $x=0$. In both cases, the change of either α or β can change the function from a function that produces nulls in the DPs to one that does not. [Figure 5 in Meenderink and van Dijk, 2005 shows a similar result for a function of the class $y=\tanh([x-\beta]/2)+\tanh(\beta/2)$.] In the simulations above, when $\alpha=0$ and $\beta=0$, there were no nulls and when $\alpha=1$ and $\beta=2$ nulls were produced.

Varying α, it is found that there is a critical value, α_c, such that for values of $\alpha>\alpha_c$ the cubic term in the Taylor series of $y=\tanh(x+\alpha x^3)$ has a positive coefficient, for values of $\alpha<\alpha_c$ the coefficient of the cubic term is negative, and for $\alpha=\alpha_c=1/3$ the coefficient is zero. The same situation applies for $\beta=\ln(2+\sqrt{3})=\beta_c$. When $\beta>\beta_c$, the coefficient of the cubic term in the Taylor series of $y=\tanh([x-\beta]/2)+\tanh(\beta/2)$ is positive, for $\beta<\beta_c$ the coefficient is negative, and it is zero at $\beta=\beta_c$. So, at $\alpha=\alpha_c$ and $\beta=\beta_c$, the third order DP, $2f_1-f_2$, is produced by higher order terms—primarily the fifth order term of the Taylor series. For nulling of the $2f_1-f_2$ DP to occur for these functions $\alpha>\alpha_c$ and $\beta>\beta_c$. (Does this mean that nulling occurs for every function where the third order term in the Taylor series is positive? No, there are many counterexamples where the third order term is negative and nulling also occurs.) Because physiological changes to the inner ear that affect either shape of the I/O nonlinearity or that shift the zero (change the offset) of the nonlinearity would be able to change a preparation from one that exhibits nulling to one that does not. A good example of this was shown by Whitehead *et al.* (1992b) where the application of diuretics reversibly changed the level dependent nulling.

As long as the Taylor series is convergent, the origin of nulls is easily understood by the cancellation of the terms in the series. Equation (5) of Engebretson and Eldredge (1968) shows the first three terms of the Taylor series expansion for the amplitude of the $2f_1-f_2$ DP in terms of the third, fifth, and seventh derivatives evaluated at zero and the input amplitudes, A_1 and A_2. Let A_{DP} be the amplitude of the DP. Then

$$A_{\mathrm{DP}} \approx {A_1}^2 A_2 \left[\tfrac{3}{4}a_3 + \tfrac{5}{8}a_5(2{A_1}^2 + 3{A_2}^2) + \tfrac{105}{64}a_7({A_1}^A + 4A_1{A_2}^2 + 2{A_2}^4) + \cdots\right], \quad (5)$$

where a_n is the nth derivative of the I/O function evaluated at zero and divided by $n!$. For small values of $A_1=A_2=A \leqslant 0.5$ the cancellation between the first two terms in the Taylor series expansion above occurs very near the values shown in the simulations for $y=\tanh(x+x^n)$ where $n=3$, 5 and $x=A$. This is the same lesson as Fig. 2 where the nulling occurs due to the growth of the next highest order odd term. If we add the ninth order term to the series above, $\frac{315}{320}a_9[2{A_1}^6+15{A_1}^4{A_2}^2+20{A_1}^2{A_2}^4+5{A_2}^6]$, the resulting series yields the value of the null amost exactly for $y=\tanh(x+x^3)$ and $y=\tanh(x+x^5)$.

2. Zeros of I/O functions' derivatives

The experiments of Bian (2004) show minima in the second and third order DPOAEs that correlate with the zeros in the respective derivatives of a model I/O function. In these experiments the DPOAEs are measured at various phases of a very low frequency bias tone. The possibility that the nulls in the nth order DPOAEs in this study are correlated with the zeros in the respective nth derivatives of the I/O functions was examined. They do not. For example, $y=\tanh(x)$ has no nulls in the intermodulation DPs but all of the odd order derivatives have zeros. For the I/O functions exhibiting nulls in the odd order DPs, the nulls occur at different input values $(A_1=A_2=x)$ than the zeros of the repective derivatives. But,

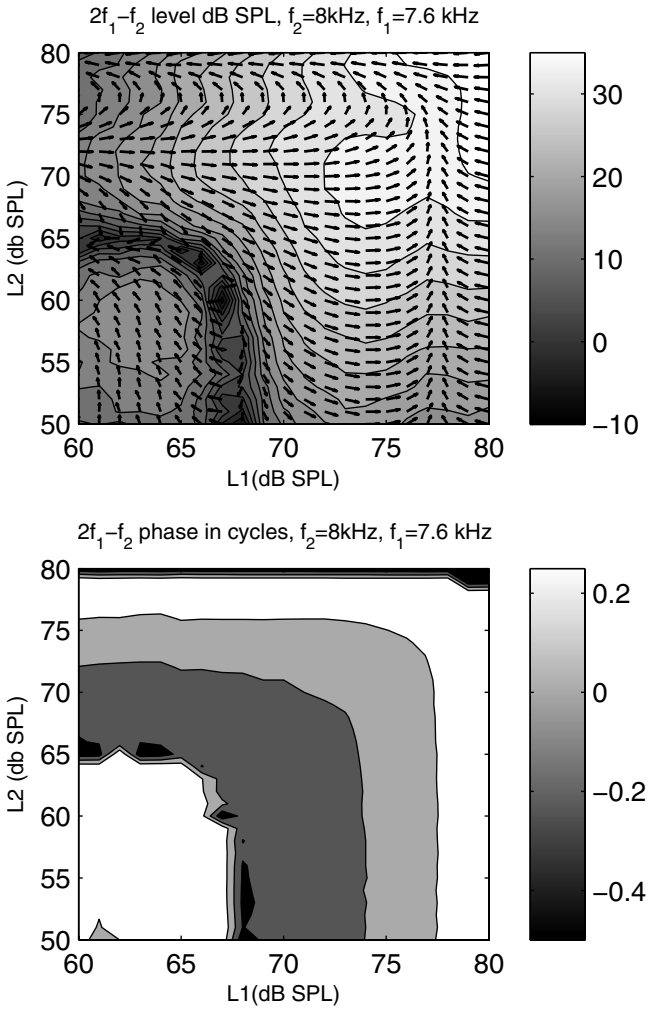


FIG. 5. DPOAE data for the $2f_1-f_2$ level and phase (given by the direction of the arrows) in the top panel and the phase alone in the bottom panel as a function of the two input levels L_1 and L_2. The lines of nulling parallel to the L_1 and L_2 axes are evident in the level as is an abrupt π phase discontinuity at about $L_1 \approx 67$ dB SPL and also $L_2 \approx 62$ dB SPL. Then, there is a second less abrupt π phase change in the mid-70 dB SPL region. Note that the phase in the figures is expressed in units of cycles. In the bottom panel, the phase has been discretized into four contour levels. The data density in this figure and the other data figures is 1 dB between adjacent levels. Here $f_2/f_1=1.05$.

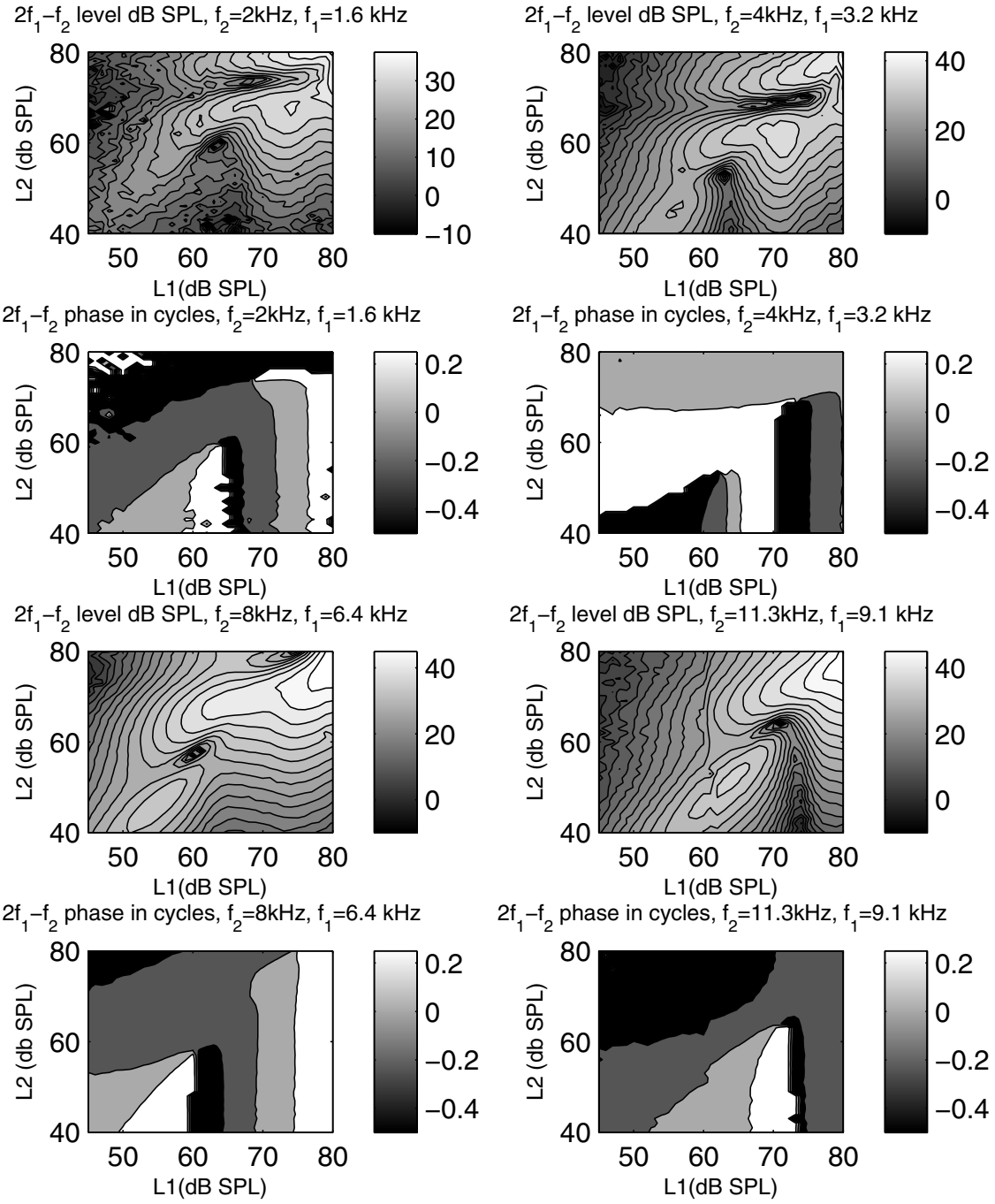


FIG. 6. $2f_1-f_2$ DPOAE level and phase as functions of the two input levels L_1 and L_2. The lines of nulling and phase discontinuities parallel to the level axes are evident or hinted across a broad frequency range (2 kHz$<f_2<$11 kHz). Here $f_2/f_1=1.25$. The phase has been discretized into four contour levels in order to emphasize the phase transition patterns.

interestingly, for the model functions used in this study, the first nulls in the third order DPs are near the values of the zeros in the second derivatives. In the Bian (2004) experiments the offset of the I/O function is being controlled by the bias tone. That is, the I/O function is dynamically changed. In the experiments reported here the data are consistently a stationary I/O function.

IV. THE DATA

What features in the model results can one find in the data? The model shows the intermodulation DP output from naked nonlinearities (just the I/O functions—no filtering on the input or on the output) but the DPOAE data are filtered and summed signals of intermodulation DPs are generated by a continuous section of a nonlinear basilar membrane. The input to the nonlinearity is filtered by the basilar membrane and the intermodulation DPs created by the nonlinearity are filtered first by the basilar membrane and then by the middle ear. These signals are summed in the ear canal. However, some of the signatures shown in the model should (and do) survive the processing of the DPs from the naked nonlinearities. In Fig. 5 below, it is evident that there are null lines in level and correlated phase discontinuities in the $2f_1-f_2$ DPOAE that are parallel to the L_1 and L_2 axes. This

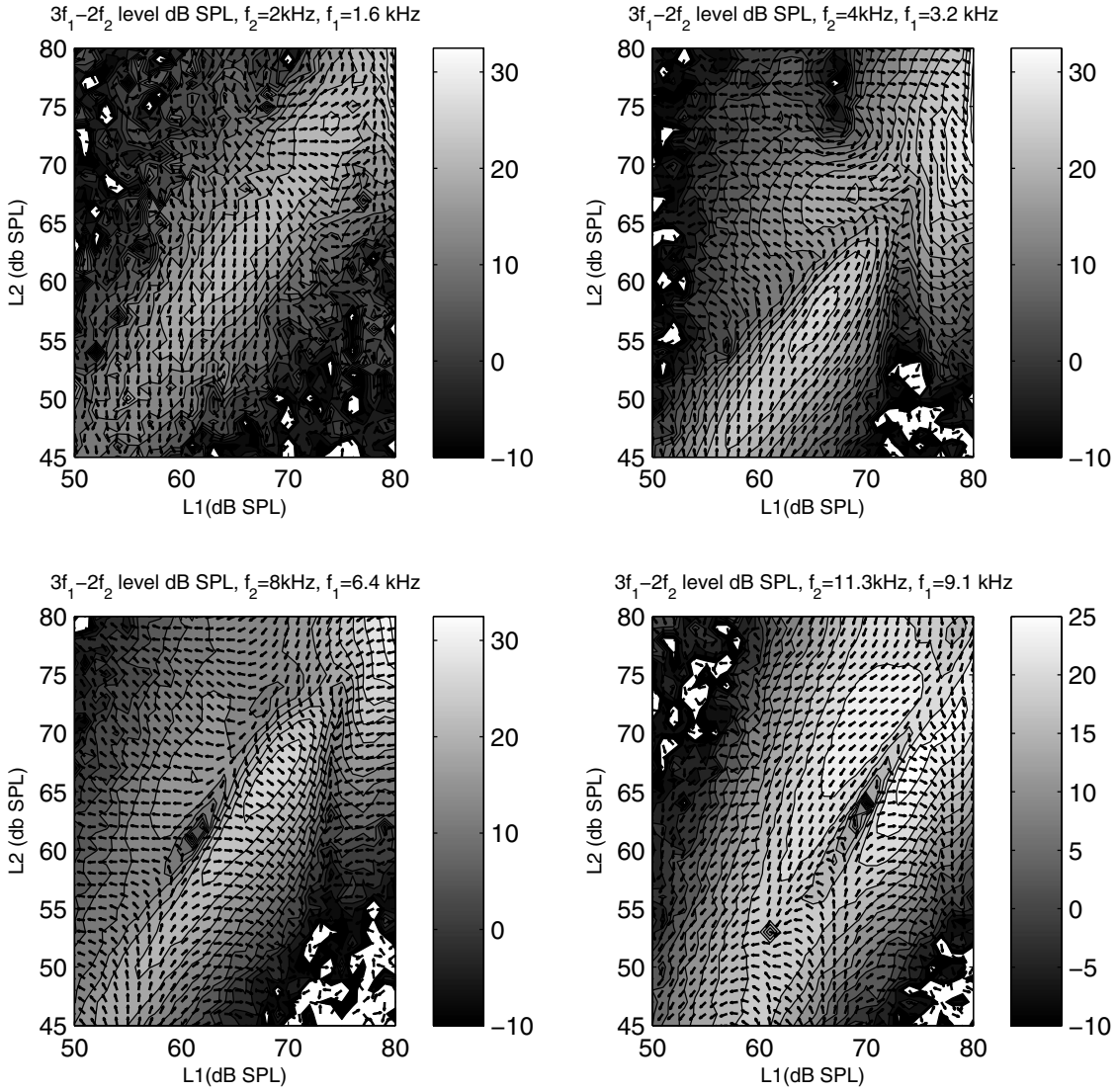


FIG. 7. Shown here are the $3f_1-2f_2$ DPOAE level and phase (direction of arrows) measured at the same time as the $2f_1-f_2$ DPOAE data in Fig. 6.

amplitude nulling and phase discontinuity pattern in the DPOAE look very much like Fig. 3. Here $f_2/f_1=1.05$, so the two primaries are close in frequency and at the sites of basilar membrane nonlinearity would have almost the same amplitudes. When f_2/f_1 is small, both of the amplitude null lines are often prominent. Unfortunately for f_2/f_1 small, the DPOAE amplitude is also small. The phase data suggest that there is a second set of intersecting null lines and there is a hint of this in the amplitude data. In Fig. 5 (especially visible in the bottom panel) there are abrupt π phase discontinuities at $L_1 \approx 67$ dB SPL and $L_2 \approx 65$ dB SPL and then there are gradual π phase changes in the mid-70 dB SPL range. Given that the higher levels of input result in detuning of the basilar membrane and would be expected to increase emission from multiple sources, one would expect to smear out the abrupt phase change expected from the I/O function simulations.

Most often $2f_1-f_2$ DPOAEs are studied when $f_2/f_1 \approx 1.2-1.25$ because in this ratio range the amplitudes are maximum. Just such data are seen in Fig. 6. These amplitude data for rabbits are similar to the amplitude data for guinea pigs shown in Fig. 6 of Lukashkin and Russell, 2002. Both the level nulling and the phase discontinuities do not exactly match the model pattern in Fig. 3. However, the simularities—in particular, phase transitions parallel to the L_1 axis—with the model figure are evident. This figure also shows that the level dependent nulling with associated phase discontinuity is found over a wide frequency range in the rabbit ($2\ \text{kHz} < f_2 < 11\ \text{kHz}$). It should be noted that the phase contour plots have been generated with four contour levels in order to emphasize the larger phase changes, which emphasize the patterns. Necessarily, between contour levels, there are small phase changes that are not shown. Given that the DPOAE signal is generated over a region of the basilar membrane where the effective input levels would be varying with respect to location, it is not surprising that the null lines would wash out a bit. Referring to Fig. 3, in the vicinity of a null line, the phases have only two values (0 or π), while the levels have many values. If the dominant basilar membrane sources are mostly on one side or on the other of the null line, the phase pattern will look like the model while the null line would become obscured. Notice that the $f_2=2$, 4, and 8 kHz data suggest that there are two sets of intersecting null lines with two null spots.

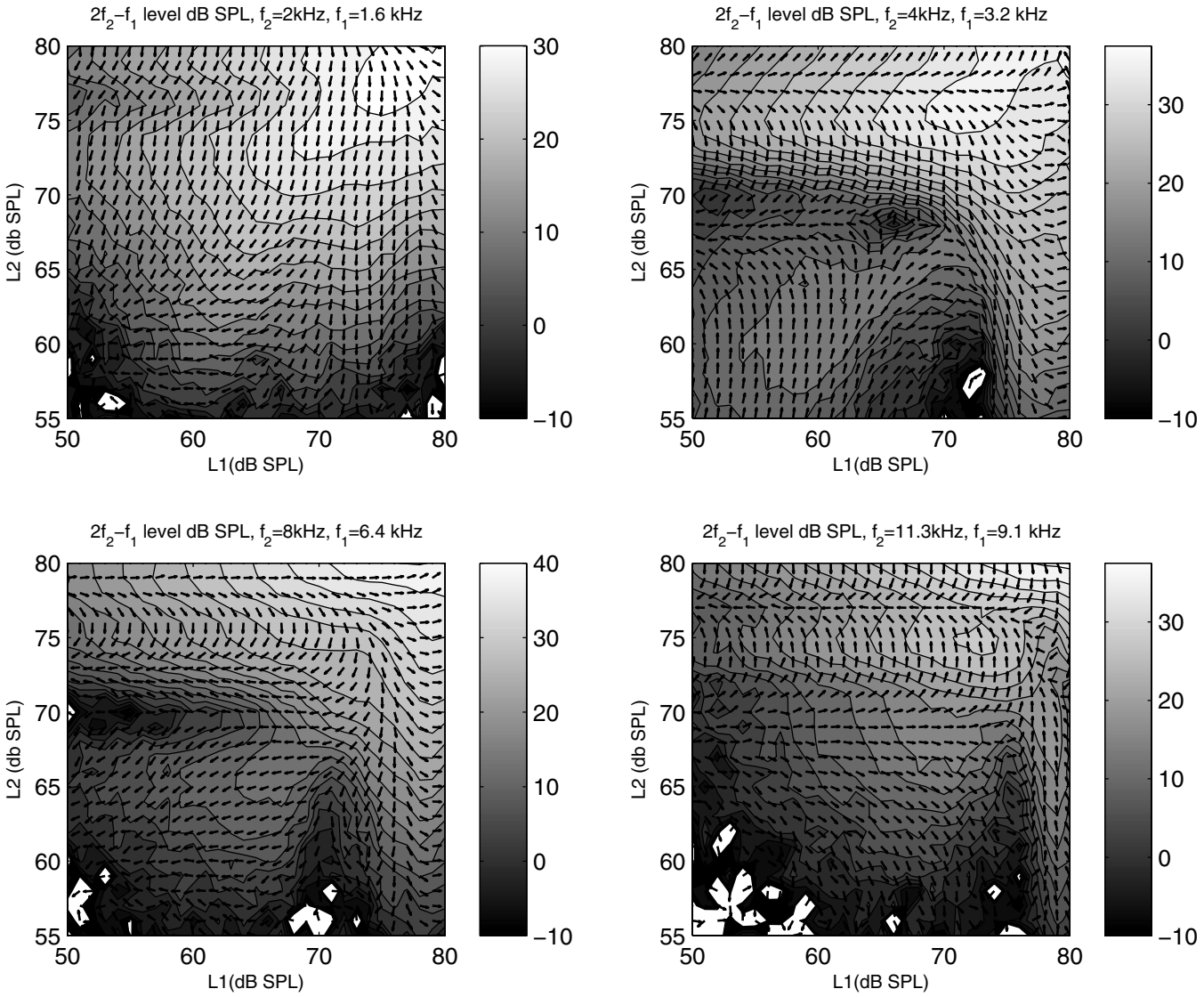


FIG. 8. Shown here are the $2f_2-f_1$ DPOAE level data measured at the same time as the $2f_1-f_2$ DPOAE data in Fig. 6.

At the same time that the $2f_1-f_2$ DPOAE was measured the $3f_1-2f_2$ DPOAE and the $2f_2-f_1$ DPOAE were also measured. The level data from these measurements are shown in Figs. 7 and 8, respectively. Examining Figs. 6 and 7 together shows that the amplitude null spots (where the null line parallel to L_1 intersects the null line parallel to L_2) occur in the vicinity where the amplitudes of the $3f_1-2f_2$ are near their maxima. This is reminiscent of Figs. 2 and 3. The level of the $3f_1-2f_2$ DPOAE will be decreased relative to what would be expected from the model simulations because of the basilar membrane filtering. At the site of $3f_1-2f_2$ DP creation this signal is a lower frequency tone than the $2f_1-f_2$ tone, so that it does not couple as well into the basilar membrane as its sibling the $2f_1-f_2$ DP. In order to lessen the differential effects of basilar membrane filtering on the primary tones (and also at a higher input level on the DPs), one may use smaller values of f_2/f_1, such as $f_2/f_1=1.0125$. The correlation between null spots and a local maximum in the next highest order DP can be seen in Fig. 9 where there are four orders of odd upper sideband DPOAEs that show this correlation. For the $2f_2-f_1$ emission the null occurs at approximately $L_1=L_2=70$ dB SPL. In the $3f_2-2f_2$ panel $L_1=70=L_2$ is on the peak. In this panel the null is at $L_1=70$, $L_2=72$ dB SPL. In the $4f_2-3f_1$ panel $L_1=70$, $L_2=72$ is on the peak and so on for the $5f_2-4f_2$ panel. Note that the phase at the lower level local maxima alternates in sign from one order DPOAE to the next just as is shown in the computer simulations. As would be expected from the modeling there would be very similar nulling patterns in the upper sideband DPOAEs as in the lower sideband DPOAEs, and this is apparent in Figs. 8 and 9. At some values of f_2 the correlation of nulls and local maxima across orders was much more evident in the phase data than in the level data.

The correlations seen in the modeling results are generally well replicated in the experimental results. The modeling shows DP creation from nonlinearities defined by I/O functions. But DPOAEs result from a summation of DPs that have been filtered upon creation by the basilar membrane and whose input primaries were filtered by the basilar membrane before mixing in the basilar membrane nonlinearity. Also, there is the potential of some filtering due to the middle and outer ear reverse transfer functions that could be

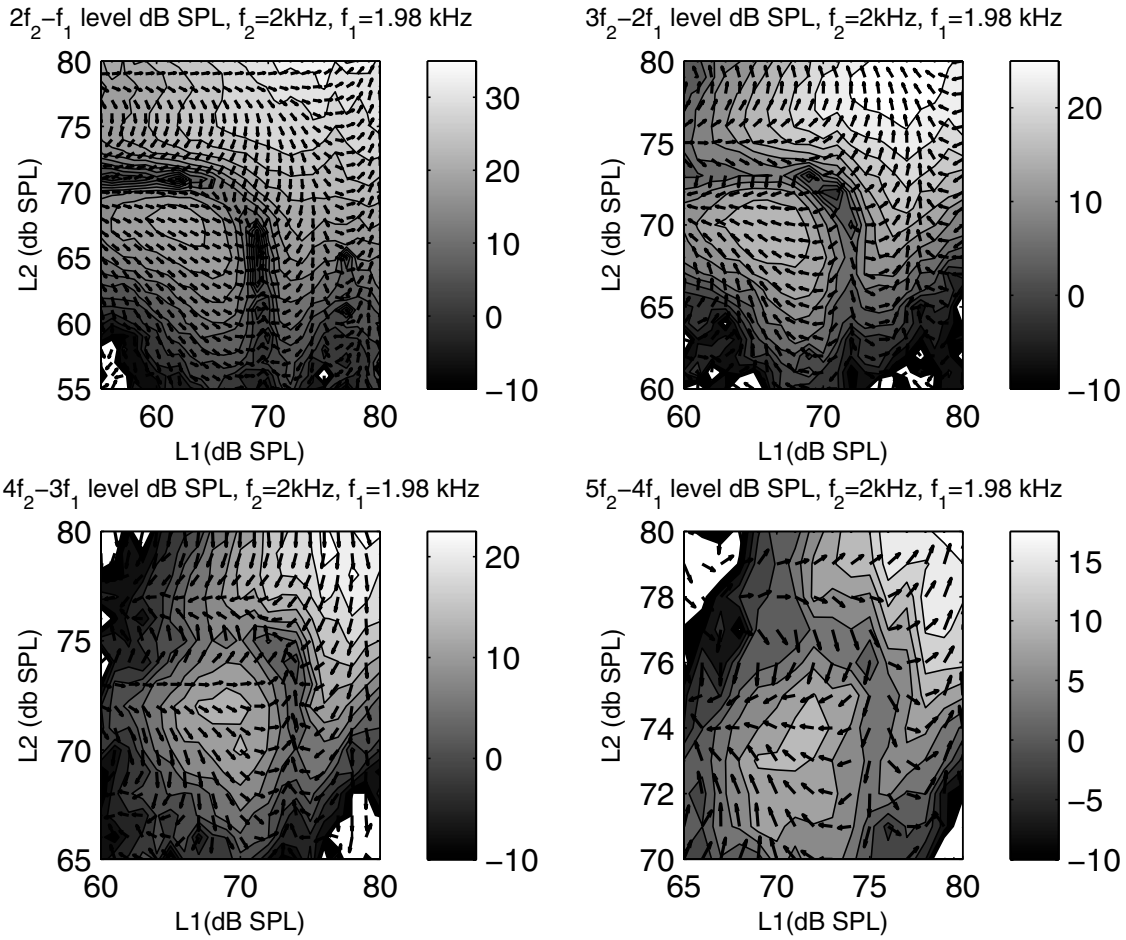


FIG. 9. The amplitudes of $2f_2-f_1$, $3f_2-2f_1$, $4f_2-3f_1$, and $5f_2-4f_1$ DPOAEs as functions of L_1 and L_2 show a general correlation between a null spot and a relative maximum of the next highest order. The amplitude of the maximum of the higher order is approximately at the level of the lower order just before the null spot. $f_2/f_1=1.0125$. The phase at the maxima flips by π between adjacent orders. Notice that the range of input levels varies from one panel to the next.

important when comparing DPOAEs of different orders. Given the processing of the DPs to make DPOAEs, the correspondence of experimental and model results seems sound. Any putative filtering effects of the basilar membrane and middle ear can be minimized in the limit $f_2/f_1 \rightarrow 1$.

We conclude that the correlation of features in the data with the features in the model presents a compelling case that the level dependent nulls in $2f_1-f_2$ are due to the structure of the basilar membrane nonlinear I/O function.

V. DISCUSSION

A. Similar results in other species

Rabbits are not alone in showing some evidence of level dependent nulling due to the nature of their nonlinear mechanical response. In cats, Fig. 7 of Fahey and Allen, (1997) shows a level dependent null with an abrupt π phase change—the nulling and associated phase change were not due to mixing from a second source. As mentioned previously, nulls in amplitude with associated π radian discontinuities in phase have been observed in pigmented guinea pigs (Lukashin *et al.*, 2002). The studies in gerbil by Mills and Rubel (1994) and Mills *et al.* (1993) show evidence of level dependent nulling with some examples of null lines parallel to either the L_1 or the L_2 axis. Gerbils have also been shown to exhibit nonlinearity generated nulling in either the manipulated cochlea (Frank and Kossl, 1996) or the very low frequency biased cochlea (Frank and Kossl, 1996; Bian, 2004). However, the inner ear pressure measurements of Dong and Olson (2005) in gerbils over the range 60–80 dB SPL show no evidence of nulling. Their Figs. 10 and 11 generally show that the phase response of each of the primary tones near the probable site of DP creation is about 1/2 cycle out of phase with the two third order DPs at frequencies $2f_1-f_2$ and $2f_2-f_1$ and is in phase with the fifth order DPs at frequencies $3f_1-2f_2$ and $3f_2-2f_1$. This would be consistent with an I/O function that does not produce nulls, such as $y=\tanh(\alpha x)$. Since for both $y=\tanh([x-2]/2)+\tanh(1)$ and $y=\tanh(x+x^3)$ the cubic term in the Taylor series is positive as is the linear term, the functions would only be consistent with theDong and Olson (2005) data if the levels used in their study (60, 70, and 80 dB SPLs) were above the nulling levels for both $2f_1-f_2$ and $3f_1-2f_2$. In chinchillas, Rhode (2007) showed that nulls in both the $2f_1-f_2$ DPOAE and the DP measured on the basilar membrane occur at the same values of the input levels. In frogs, DPOAE amplitude patterns similar to some of the data shown here have been observed (Meenderink and van Dijk, 2005). However, the sharp π phase discontinuity is missing,

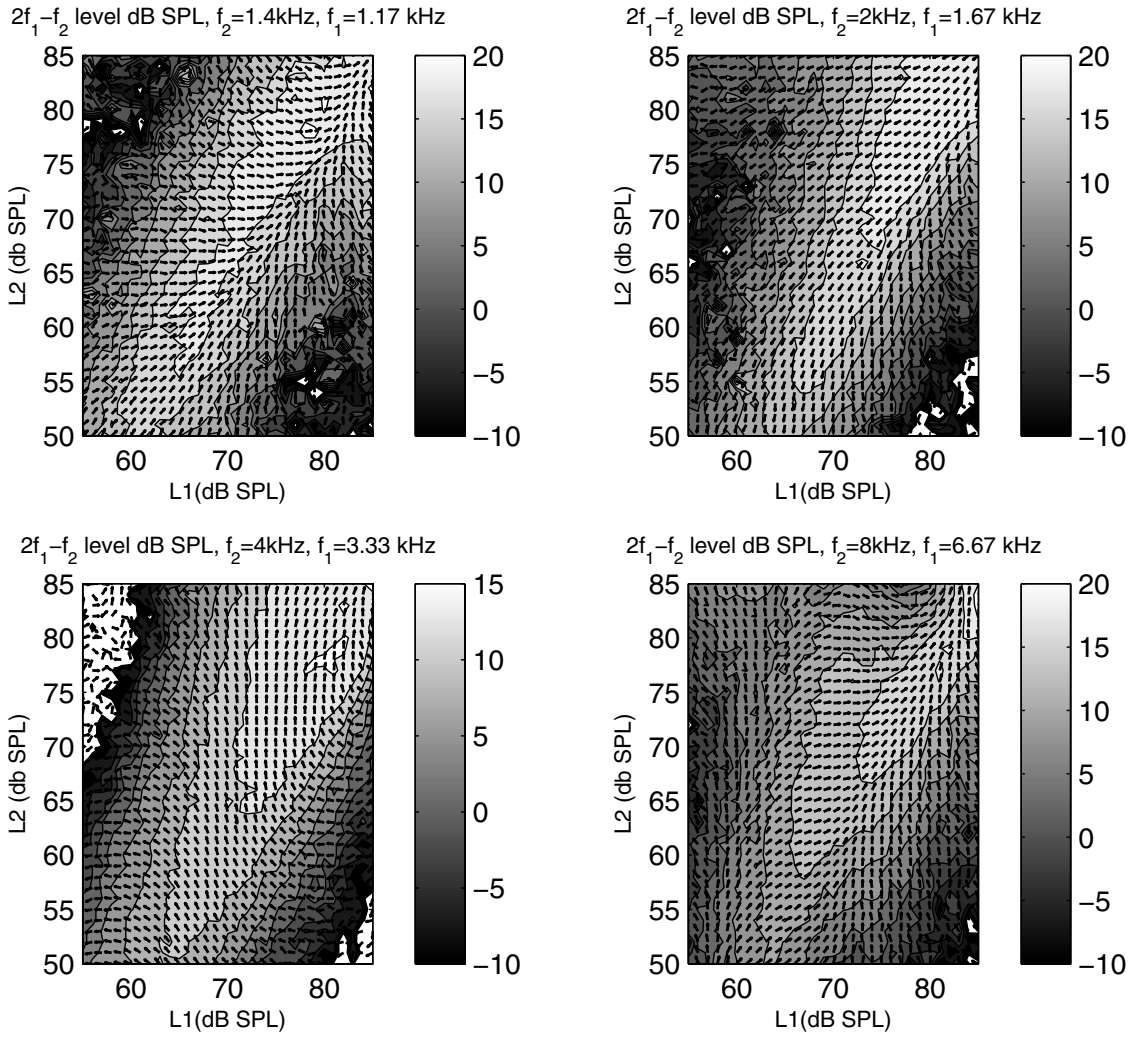


FIG. 10. Shown here are the $2f_1-f_2$ DPOAE level data measured in a human with the same apparatus as the rabbit measurements. The DPOAE phases are depicted by the directions of the arrows. $f_2/f_1=1.2$.

although there is sometimes seen a gradual change in phase of π radians. Meenderink and van Dijk (2005) attributed their data to two different nonlinear regimes rather than to one physical nonlinearity. Level dependent nulling has been well characterized in moths by Kossl and Coro (2006). Therefore, this phenomenon would appear to be a fairly general feature of auditory nonlinearities over a range of animal preparations.

B. Example of a preparation where there is no evidence of level dependent nulling

Figure 10 shows human $2f_1-f_2$ DPOAEs measured with the same apparatus as used in the the rabbit DPOAE measurements. Here are level and phase data presented at four values of f_2 with $f_2/f_1=1.2$ and there is no evidence or nulling of associated π phase discontinuites. The data obtained when $f_2/f_1=1.05$ also show no level dependent nulling at the levels shown. Meinke *et al.* (2005) presented data showing a hint of nonlinearity induced nulling at $L_2>75$ dB SPL for $2f_1-f_2$ DPOAEs measured during binaural stimulation in humans. No similar pattern is apparent in Fig. 10. There is frequency dependent nulling in our human subject that has been sufficiently explained by Kalluri and Shera (2001) and confirmed by others. This nulling in humans is explained by assuming two sources of the DPOAE—one at the f_2 place and the other at the f_{DP} place.

C. Utility of null lines and null spots

1. Site of generation of $2f_2-f_1$

Comparing the amplitude null lines for $2f_1-f_2$ in Fig. 6 with the $2f_2-f_1$ amplitude null lines in Fig. 8 it is evident that the null lines for $2f_2-f_1$ occur at higher levels than those of $2f_1-f_2$. The physics of the cochlea would suggest that there are two possible routes for $2f_2-f_1$ generation. The signal could be generated at the f_2 place and then excite the basilar membrane as an evanescent signal. This signal would drive the $2f_2-f_1$ place and then become a propagating wave and DPOAE. Alternatively, the two primaries could directly excite the $2f_2-f_1$ place—of course they would be attenuated relative to their excitation at f_2. In this route $2f_2-f_1$ is made directly at its own place. For the first route the null lines should be at the same values of L_1 and L_2 for both $2f_1-f_2$ and $2f_2-f_1$. For the second route the null lines would be at larger values of L_1 and L_2 for $2f_2-f_1$ than for $2f_1-f_2$. The

data, while not extensive, favor the direct generation of $2f_2-f_1$ at its own characteristic place, supporting the conclusion in Martin *et al.*, 1987.

2. Internal cochlear calibration

Because the null lines and the null spots are determined by the levels of the input tones at the site of the nonlinearity, once this level is known it can serve as a calibration marker for the level of the tone at the site of the nonlinearity. For example, if $L_1=L_2$ were chosen to produce nulling in the $2f_1-f_2$ DPOAE and that was done as the frequencies of the primaries were changed at $f_2/f_1=$constant sweep, then, assuming a scaling symmetric cochlea, one would have a relative measure of how much energy as a function of frequency traverses the middle ear into the cochlea.

D. Can I/O induced nulling produce the appearance of frequency dependent nulling?

Yes. As the modeling (confirmed by the data) show, I/O induced nulling is sensitive to small changes in the levels of the input tones at the site of the nonlinearity. If one or both of the input levels are near its nulling threshold and if that level is also sensitive to a change in frequency, then a frequency change will induce a null. Hence, nonlinearity induced nulling can masquerade as frequency induced nulling. This has been observed in rabbits at values of $f_2/f_1<1.1$ when the levels of the primary tones are around 60 dB SPL. The "frequency" dependent nulling goes away with slight changes of level. Using the technique of Stover *et al.* (1996), it can be shown that there are not two sources with different time delays.

VI. CONCLUSION

This study is basically two experimental studies—one experimental system is the rabbit and the other is the computer. The computer experiments were simulations wherein several properties of saturating I/O functions were tested in order to see if they were either necessary or sufficient for null production. The hope was that the simulations would reveal the way to a general theory of null production in saturating I/O functions. This did not happen.

However, given the correlation between several features in the model simulations and in the rabbit DPOAE data, it is concluded that the nature of the nonlinear I/O function is the likely explanation of the level dependent DPOAE nulling in rabbits. Furthermore, the modeling shows that the presence of nulling in the data is not a determinant of the I/O function shape, the presence or absence of even symmetry, and the asymmetry or severity of clipping. When nulling is due to the nature of the nonlinearity, this nulling in a given odd order DPOAE correlates with a local maximum in the next highest odd order DPOAE.

ACKNOWLEDGMENTS

The authors thank C. Bergevin, C. Shera, and the reviewers for suggestions on improving both the content and expression of this study. This research was supported in part by funds from the Public Health Service (DC000613 and DC003114) and Department of Veterans Affairs (VA/RR&D C4494R).

Bergevin, C. (**2007**). "Comparative approaches to otoacoustic emissions: Towards an understanding of why the ear emits sound," Ph.D. thesis, Speech and Hearing Bioscience and Technology Harvard-MIT Division of Health Sciences and Technology, Massachusetts Institute of Technology, Cambridge, MA.

Bian, L. (**2004**). "Cochlear compression: Effects of low-frequency biasing on quadratic distortion product otoacoustic emission," J. Acoust. Soc. Am. **116**, 3559–3571.

Brown, A. M., Harris, F. P., and Beveridge, H. A. (**1996**). "Two sources of acoustic distortion products from the human cochlea," J. Acoust. Soc. Am. **100**, 3260–3267.

Dong, W., and Olson, E. S. (**2005**). "Two tone distortion in intracochlear pressure," J. Acoust. Soc. Am. **117**, 2999–3015.

Engebretson, A. M., and Eldredge, D. H. (**1968**). "Model for the nonlinear characteristics of cochlear potentials," J. Acoust. Soc. Am. **44**, 548–554.

Fahey, P. F., and Allen, J. B. (**1997**). "Measurement of distortion product phase in the ear canal of the cat," J. Acoust. Soc. Am. **102**, 2880–2891.

Fahey, P. F., Stagner, B. B., and Martin, G. K. (**2000**). "Nonlinear interactions that could explain distortion product interference response areas," J. Acoust. Soc. Am. **108**, 1786–1802.

Fahey, P. F., Stagner, B. B., and Martin, G. K. (**2006**). "Mechanism for bandpass frequency characteristic in distortion product otoacoustic emission generation," J. Acoust. Soc. Am. **119**, 991–996.

Feynman, R. P., Leighton, R. B., and Sands, M. (**1964**). *The Feynman Lectures on Physics* (Addison-Wesley, Reading, MA), Vol. **II**, Chap. 35.

Frank, G., and Kossl, M. (**1996**). "The acoustic two-tone distortions $2f_1-f_2$ and f_2-f_1 and their possible relation to changes in the operating point of the cochlear amplifier," Hear. Res. **98**, 104–115.

Kalluri, R., and Shera, C. A. (**2001**). "Distortion-product source unmixing: A test of the two-mechanism model for DPOAE generation," J. Acoust. Soc. Am. **109**, 622–637.

Knight, R. D., and Kemp, D. T. (**2000**). "Indications of different distortion product otoacoustic emission mechanisms from a detailed f_1,f_2 area study," J. Acoust. Soc. Am. **107**, 457–473.

Kossl, M., and Coro, F. (**2006**). "L1, L2 maps of distortion-product otoacoustic emissions from a moth ear with only two auditory receptor neurons," J. Acoust. Soc. Am. **120**, 3822–3831.

Lukashkin, A. N., Lukashkina, V. A., and Russell, I. J. (**2002**). "One source for distortion product otoacoustic emissions generated by low- and high-level primaries," J. Acoust. Soc. Am. **111**, 2740–2748.

Lukashkin, A. N., and Russell, I. J. (**1999**). "Analysis of the f_2-f_1 and $2f_1-f_2$ distortion components generated by the hair cell mechanoelectrical transducer: Dependence on the amplitudes of the primaries and feedback gain," J. Acoust. Soc. Am. **106**, 2662–2668.

Lukashkin, A. N., and Russell, I. J. (**2002**). "Modifications of a single saturating non-linearity account for post-onset changes in $2f_1-f_2$ distortion product otoacoustic emissions," J. Acoust. Soc. Am. **112**, 1561–1568.

Martin, G. K., Probst, P., Scheinin, S. A., Coats, A. C., and Lonsbury-Martin, B. L. (**1987**). "Acoustic distortion products in rabbits. II. Site of origin revealed by suppression and pure-tone exposures," Hear. Res. **28**, 191–208.

Meenderink, S. W. F., and van Dijk, P. (**2005**). "Characteristics of distortion product otoacoustic emissions in the frog from L_1,L_2 maps," J. Acoust. Soc. Am. **118**, 279–286.

Meinke, D. K., Stagner, B. B., Martin, G. K., and Lonsbury-Martin, B. L. (**2005**). "Human efferent adaptation of DPOAEs in the L_1,L_2 space," Hear. Res. **208**, 89–100.

Mills, D. M., Norton, S. J., and Rubel, E. W. (**1993**). "Vulnerability and adaptation of distortion product otoacoustic emissions to endocochlear potential variation," J. Acoust. Soc. Am. **94**, 2108–2122.

Mills, D. M., and Rubel, E. W. (**1994**). "Variation of distortion product otoacoustic emissions with furosemide injection," Hear. Res. **77**, 18–199.

Rhode, W. S. (**2007**). "Distortion product otoacoustic emissions and basilar membrane vibration in the 6–9 kHz region of sensitive chinchilla cochleae," J. Acoust. Soc. Am. **122**, 2725–2737.

Stagner, B. B., Nemanov, L. S., Martin, G. K., and Lonsbury-Martin, B. L. (**2005**). "L_1,L_2 response areas of lower- and upper-sideband DPOAEs measured at three f_2/f_1 ratios in normal and noise-exposed rabbits," Assoc. Res. Otolaryngol. Abstr. **28**, 140.

Stover, L. J., Neely, S. T., and Gorga, M. P. (**1996**). "Latency and multiple sources of distortion product otoacoustic emissions," J. Acoust. Soc. Am. **99**, 1016–1024.

Weiss, T. F., and Leong, R. (**1985**). "A model for signal transmission in an ear having hair cells with free-standing stereocilia. IV. Mechanoelectric transduction stage," Hear. Res. **20**, 175–195.

Whitehead, M. L., Lonsbury-Martin, B. L., and Martin, G. K. (**1992a**). "Evidence for two sources of $2f_1-f_2$ distortion-product otoacoustic emission in rabbit: I. Differential dependence on stimulus parameters," J. Acoust. Soc. Am. **91**, 1587–1607.

Whitehead, M. L., Lonsbury-Martin, B. L., and Martin, G. K. (**1992b**). "Evidence for two sources of $2f_1-f_2$ distortion-product otoacoustic emission in rabbit: II. Differential physiological vulnerability," J. Acoust. Soc. Am. **92**, 2662–2682.

Whitehead, M. L., Stagner, B. B., Martin, G. K., and Lonsbury-Martin, B. L. (**1996**). "Visualization of the onset of distortion-product otoacoustic emissions, and measurement of their latency," J. Acoust. Soc. Am. **100**, 1663–1679.

Wideband absorbance tympanometry using pressure sweeps: System development and results on adults with normal hearing

Yi-Wen Liu, Chris A. Sanford, John C. Ellison, Denis F. Fitzpatrick, and Michael P. Gorga
Boys Town National Research Hospital, 555 North 30th Street, Omaha, Nebraska 68131

Douglas H. Keefe
Sonicom, Inc., Omaha, Nebraska 68124

(Received 12 June 2008; revised 24 September 2008; accepted 25 September 2008)

A system with potential for middle-ear screening and diagnostic testing was developed for the measurement of wideband energy absorbance (EA) in the ear canal as a function of air pressure, and tested on adults with normal hearing. Using a click stimulus, the EA was measured at 60 frequencies between 0.226 and 8 kHz. Ambient-pressure results were similar to past studies. To perform tympanometry, air pressure in the ear canal was controlled automatically to sweep between −300 and 200 daPa (ascending/descending directions) using sweep speeds of approximately 75, 100, 200, and 400 daPa/s. Thus, the measurement time for wideband tympanometry ranged from 1.5 to 7 s and was suitable for clinical applications. A bandpass tympanogram, calculated for each ear by frequency averaging EA from 0.38 to 2 kHz, had a single-peak shape; however, its tympanometric peak pressure (TPP) shifted as a function of sweep speed and direction. EA estimated at the TPP was similar across different sweep speeds, but was higher below 2 kHz than EA measured at ambient pressure. Future studies of EA on normal ears of a different age group or on impaired ears may be compared with the adult normal baseline obtained in this study.
© *2008 Acoustical Society of America.* [DOI: 10.1121/1.3001712]

PACS number(s): 43.64.Ha, 43.64.Yp, 43.58.Bh [BLM] Pages: 3708–3719

I. INTRODUCTION

Tympanometry refers to the measurement of an acoustic transfer function in the ear canal in response to a sound stimulus while air pressure is varied in the ear canal. Most commonly, the stimuli used in tympanometry are pure tones and the transfer function is the admittance. A tympanogram is often displayed as a plot of admittance magnitude as a function of air pressure. Alternatively, the real part (i.e., conductance) and the imaginary part (i.e., susceptance) of acoustic admittance are displayed. Tympanometric measurement of acoustic admittance, using a 226-Hz stimulus, is a standard procedure in audiology to assess middle-ear functioning (e.g., Margolis and Hunter, 2000). While differing in their degree of diagnostic relevance, commonly evaluated tympanometric measures include tympanometric peak pressure (TPP), peak-compensated static acoustic admittance, acoustic equivalent volume, and tympanometric width (ASHA, 1997; Nozza *et al.*, 1994; Shanks *et al.*, 1988). Patterns in conductance and susceptance tympanograms obtained at 678 Hz and 1 kHz can also be used to identify various middle-ear pathologies (Vanhuyse, 1975; Margolis and Hunter, 2000). At frequencies higher than 2 kHz, however, admittance tympanometry becomes sensitive to probe insertion depth due to the presence of standing waves in the ear canal (Margolis *et al.*, 1999).

The goal of the present study was to develop a clinically useful system for the measurement of wideband (0.226–8 kHz) aural acoustic transfer functions under both ambient-pressure and tympanometric conditions, and to assess its performance in normal-hearing adult ears.[1] A transfer function of particular interest is energy reflectance (ER), defined as the ratio of the reflected to the incident energy. Because ER is nearly independent of probe-insertion depth (Stinson *et al.*, 1982; Voss *et al.*, 2008)—except for effects due to spatial variation in the cross-sectional area of the ear canal—it is interpretable in a wider frequency range than is acoustic admittance obtained using standard procedures.

A system for wideband reflectance measurements, which did not require changes in ear-canal pressure, was developed for use in clinical studies (Keefe *et al.*, 1992). At ambient pressure, ER and other acoustic transfer functions have been measured at the probe tip in normal-hearing adults (Keefe *et al.*, 1993; Voss and Allen, 1994; Feeney and Sanford, 2004; Shahnaz and Bork, 2006), children and infants (Keefe *et al.*, 1993; Vander Werff *et al.*, 2007), and newborns (Keefe *et al.*, 2000). At ambient pressure, ER also demonstrated systematic shifts in the presence of middle-ear disorders including otitis media with effusion (Piskorski *et al.*, 1998; Feeney *et al.*, 2003), as well as otosclerosis, ossicular discontinuity, and perforation of the tympanic membrane (Feeney *et al.*, 2003). The sensitivity of ear-canal impedance to a perforation of the tympanic membrane has also been described (Voss *et al.*, 2001).

It has been demonstrated that wideband ER tympanometry, which measures ER as a joint function of frequency and air pressure (Keefe and Levi, 1996), reveals more information than does an ER test at ambient pressure (Margolis *et al.*, 1999, Sanford and Feeney, 2008). In this paper, results of ambient and tympanometric measurements are mainly

 © 2008 Acoustical Society of America

presented in terms of energy absorbance (EA). EA is the ratio of acoustic energy that is absorbed by the middle ear and ear canal[2] to the acoustic energy of an incident sound presented in the ear canal and directed towards the tympanic membrane. In the limit that the walls or other structures of the ear canal absorb no sound energy, the EA is the fraction of incident energy absorbed by the middle ear. Given its definition as a ratio, EA is dimensionless and varies between 0 and 1. Through conservation of energy, EA and ER are related by EA=1−ER. Such a simple change in variable is worthwhile because an EA tympanogram in a healthy adult middle ear, like a 226-Hz admittance-magnitude tympanogram, has a single peak in its response across air pressure. This makes EA clinically familiar and may contribute to ease of interpretation.

Wideband EA tympanograms have been used to predict the presence of a conductive hearing loss (Keefe and Simmons, 2003), but the measurement system was unable to track the accuracy of the air-pressure steps. In that and other past studies, wideband tympanometry has been conducted at fixed static-pressure steps; the pressure was controlled either manually (Margolis *et al.*, 1999) or via signals delivered by a computer to an external pressure pump. Data-acquisition time was typically 40 s for 15 steps between 300 and −300 daPa (Keefe and Simmons, 2003). This long measurement time was inconvenient for clinical usage, and the sparse sampling of static pressure limited the accuracy of wideband tympanograms.

The present study aimed to: (1) shorten the data-acquisition time for wideband tympanometry by sweeping the air pressure; (2) include automatic feedback control of air pressure in the ear canal; (3) examine the effect of pressure sweeps that might affect the interpretation of results in relation to middle-ear mechanics (Decraemer *et al.*, 1984; Gaihede *et al.*, 2000; Therkildsen *et al.*, 2005; Dirckx *et al.*, 2006); and (4) maintain adequate resolution in both frequency and ear-canal pressure. New measurement procedures were developed, including new signal-processing and artifact-rejection methods. Ambient and tympanometric measurements were conducted on 92 adult ears with normal hearing to provide a set of baseline responses to which subsequent measurements in impaired middle ears can be compared. The effects of pressure-sweep speed and direction on the measurements were analyzed. The remainder of this paper is organized as follows: System development, data analyses, and subject inclusion criteria are described in Sec. II. Results of ambient and tympanometric measurements are reported in Sec. III. Effects of pressure sweeps are discussed in Sec. IV. Conclusions are given in Sec. V.

II. METHODS

A. Configuration of the instrument

A schematic diagram of the instrument is shown in Fig. 1. The sound card (CardDeluxe, Digital Audio Labs) supported two digital-to-analog (D/A) and two analog-to-digital (A/D) channels. The D/A and A/D converters both had 24 bits of resolution. The sampling rate was 22.05 kHz, sufficient to permit spectral measurements up to 8 kHz. The

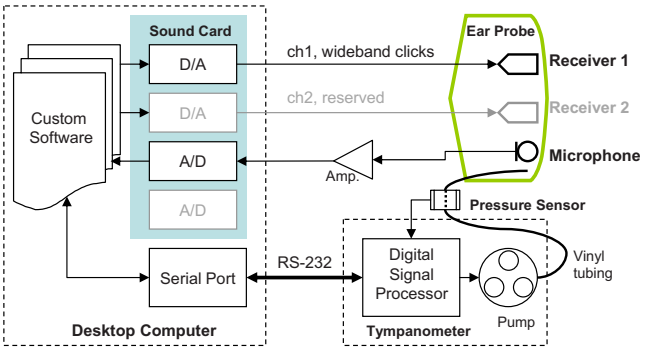


FIG. 1. (Color online) Schematic diagram of instrumentation.

custom ear probe (Interacoustics) had two receiver ports and one microphone port. Only one receiver was used in the present study for delivering the click stimuli. Acoustic responses were recorded by the probe microphone, amplified, and digitized by the A/D converter. Between 0.226 and 8 kHz, the sensitivity of the probe microphone was within ±10 dB relative to the sensitivity at 1 kHz, according to the manufacturer calibration. This calibration was applied to calculations of sound-pressure level (SPL).

Air pressure was coupled from the pump residing in the tympanometer (an AT235, Interacoustics, with modified firmware by the manufacturer to permit computer control of pressure sweeps) to the ear probe through approximately 2 m of vinyl tubing (Fig. 1). A pressure sensor was located about halfway between the pressure pump and the ear probe. The vinyl tubing had an internal diameter of approximately 1.5 mm. Precision of air-pressure measurement was 1 daPa, and the air pressure was measured with respect to atmospheric pressure. Rubber tips of different sizes, ranging from 6 to 18 mm diameter, could be selected to mount on the ear probe, so as to fit within the ear canal and achieve a pressure seal. When recording acoustic responses, air pressure values were read from the sensor every 25 ms by the digital signal processor (DSP) and delivered to the computer via an RS-232 serial port connection. The computer determined the desired pressure-sweep speed based on the measured air pressures, and sent commands to the DSP via the serial port to adjust the pressure pump. The entire pressure-control system, when terminated with a syringe of approximately 2 cm^3 and pumped to 300 daPa initially, maintained more than 90% of the air pressure (i.e., >270 daPa) for approximately 70 s without the need to repressurize.

B. Energy absorbance measurements at ambient pressure

Wideband clicks were delivered to the receiver (ch1 in Fig. 1) repeatedly, responses were recorded, artifacts were rejected, and sound-pressure reflectance and EA were calculated. The click rate was one click per 1024 samples, or approximately every 46 ms. The total number of clicks was 16 for each trial. The pressure-control system was not used for ambient measurements.

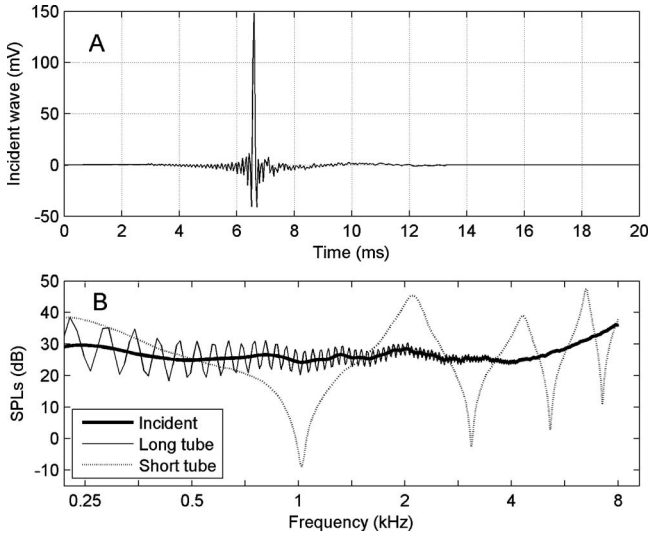


FIG. 2. A typical result of probe calibration. (A) The incident sound recorded by A/D. (B) SPL spectra of the incident wave and the frequency responses in the two calibration tubes.

1. Stimulus design and responses in calibration tubes

The click stimulus was designed using a technique adapted from Agulló *et al.* (1995) so that the magnitude spectrum of the incident sound in the ear canal was approximately flat from 0.226 to 8 kHz and the effective waveform duration was as short as possible. The incident waveform was measured by recording its response in a long tube (diameter 0.794 cm, length 292 cm), and then truncating the response in the time domain prior to the onset of the first reflection from the opposite closed end of the tube. This incident voltage waveform recorded by the A/D converter is plotted in Fig. 2(a). After calculating its discrete Fourier transform (DFT) and applying the microphone sensitivity calibration, the SPL of responses measured in the long tube and in a short calibration tube (diameter 0.794 cm, length 8.2 cm) closed at its opposite end are shown in Fig. 2(b). The incident click SPL was within 6 dB of 30 dB SPL from 0.226 to 8 kHz. The SPL spectrum in each tube had notches close to frequencies at which the tube length was equal to an odd multiple of a quarter wavelength. The measurements in the calibration tubes along with a model of viscothermal wall loss in each tube were used to calibrate the system for aural acoustic transfer function measurements; in particular, the incident pressure spectrum $Q(f)$ and the source reflectance $R_0(f)$ of the probe were calculated according to procedures described by Keefe and Simmons (2003). Calibrations were performed daily during data collection.

2. Estimation of energy absorbance from sound-pressure responses

After the probe was inserted, the click stimulus was repetitively output into the ear canal by a probe receiver. Acoustic responses were synchronously recorded by the probe microphone. Responses were averaged after excluding the responses contaminated by artifact (as described below). The pressure reflectance $R(f)$ at frequency f in the ear canal is calculated using the following equation (Keefe and Simmons, 2003),

$$R(f) = \frac{P(f) - Q(f)}{R_0(f)P(f) + Q(f)}, \tag{1}$$

where $P(f)$ denotes the mean of the sound-pressure spectrum. In this paper, results of experiments will be reported and analyzed in terms of EA, defined as

$$\mathrm{EA} = 1 - |R(f)|^2. \tag{2}$$

Accuracy of the measurement of EA depended on the signal-to-noise ratio (SNR), which could be improved by averaging the responses to clicks. However, during the measurement, transient noise produced by the subject or other sources was also recorded by the probe microphone. Sources of intermittent noise included, but were not limited to, breathing, swallowing, and body contact with the vinyl tube. The SNR was improved by identifying and rejecting such artifacts before calculating the mean response.

3. Artifact rejection based on median-absolute-deviation tests

To identify responses that contained artifacts, the following auxiliary variables were calculated for each response:

(a) *Peak-to-peak amplitude*, defined as $y_{\mathrm{pp}}^{(k)} = \max_n y^{(k)}[n] - \min_n y^{(k)}[n]$, where $y^{(k)}[n]$ $(n=1,\ldots,1024)$ denotes the recorded pressure response to the kth click at sample n. This peak-to-peak amplitude was sensitive to large-amplitude intermittent noise spikes that might occur anywhere in the response buffer.

(b) *Crest value*, defined as $C^{(k)} = y_{\mathrm{max}}^{(k)} / y_{\mathrm{rms}}^{(k)}$. Calculation of the maximum value $y_{\mathrm{max}}^{(k)}$ and the root-mean-squared (rms) value $y_{\mathrm{rms}}^{(k)}$ for the kth response was based on all samples except for 200 samples (9 ms approximately) surrounding the main response. This crest value was sensitive to intermittent noise transients at times for which the click response was expected to be essentially absent.

(c) *Noise energy*. After recording 16 responses, the noise energy E in each response was calculated as the sum of square errors,

$$E^{(k)} = \sum_{n=1}^{1024} (y^{(k)}[n] - \bar{y}[n])^2, \tag{3}$$

where $\bar{y}[n]$ denotes the mean response across 16 clicks. This noise energy was sensitive to a noise source that was approximately stationary over the entire response buffer.

The median $\bar{y}_{\mathrm{pp}}$ of $y_{\mathrm{pp}}^{(k)}$ was calculated across all buffers $(k=1,\ldots,16)$, and the medians $\bar{C}$ of $C^{(k)}$ and $\bar{E}$ of $E^{(k)}$ were calculated in a similar manner. For each response, absolute deviations from the median were defined as $\Delta y_{\mathrm{pp}}^{(k)} = |y_{\mathrm{pp}}^{(k)} - \bar{y}_{\mathrm{pp}}|$, $\Delta C^{(k)} = |C^{(k)} - \bar{C}|$, and $\Delta E^{(k)} = |E^{(k)} - \bar{E}|$. Then, medians of the absolute deviations (MAD), denoted as $\bar{\Delta}_{\mathrm{pp}}$, $\bar{\Delta}_C$, and

$\bar{\Delta}_E$, were calculated across 16 responses. Finally, an individual response was rejected due to artifacts if any of its auxiliary variables was more than 5.92 times MAD away from the median; in other words, if

$$\begin{cases} \Delta y_{\mathrm{pp}}^{(k)} \geqslant 5.92 \times \bar{\Delta}_{\mathrm{pp}}, \\ \Delta C^{(k)} \geqslant 5.92 \times \bar{\Delta}_C, \text{ or} \\ \Delta E^{(k)} \geqslant 5.92 \times \bar{\Delta}_E. \end{cases} \tag{4}$$

The specific choice of criteria in Eq. (4) is such that, were the data to be normally distributed, the probability that an absolute deviation exceeds 5.92 times MAD would be equal to the probability that a far outlier occurs according to the definition of Tukey (1977). Thus, this choice of MAD outlier criterion behaves similarly to the far-outlier test criterion in exploratory statistical analyses using the boxplot whenever data are normally distributed. The MAD test has desirable properties for artifact rejection for measurements that are not normally distributed; such distributions often occur in aural acoustic responses in human subjects.

C. Wideband absorbance tympanometry

1. Pressure-sweep settings and data-acquisition protocols

The desired tympanometric pressure range was −300 to 200 daPa in this study. The enclosed volume in the ear canal was initially pressurized to 220 daPa (for a descending sweep) or −315 daPa (for an ascending sweep) relative to the ambient pressure, before the pressure sweep started. The initial pressure was chosen to be outside the desired range so as to ensure coverage of the whole range during the pressure sweep. The pressure pump could be set to produce sweep speeds of approximately 400, 200, 100, or 75 daPa/s. Thus, the change in air pressure during each 46-ms interval of a click-response buffer was approximately 18, 9.2, 4.6, and 3.5 daPa, respectively. As is evident in Fig. 2(a), most energy of the response to the incident click was localized in time to within a duration of 1 ms. At the default sweep speed of 75 daPa/s, the air pressure varied by 3.2 daPa within the duration of a single click buffer. This was sufficiently small to characterize the air pressure as quasi-stationary over the interclick interval. Data were acquired at higher sweep speeds to evaluate whether the quasi-stationary assumption was still warranted.

During the sweep, air pressure and click responses were recorded simultaneously until the pressure reached the end target of the ascending or descending sweep, 200 or −300 daPa, respectively. Then, the ear-canal pressure was reset to 0 daPa. The actual pressure-sweep speed could deviate from the nominal speed, depending upon the goodness of pressure seal in the ear canal and the characteristics of individual ears. An instance of the descending sweep intended at the speed of 75 daPa/s is shown in Fig. 3. The dashed reference line was added manually to match the initial slope of the pressure sweep from about 1.0 to 3.0 s. The reference line helps illustrate that the instantaneous rate of pressure change became slower toward the end of the sweep. This indicates that the pressure seal in the ear canal was not perfect.

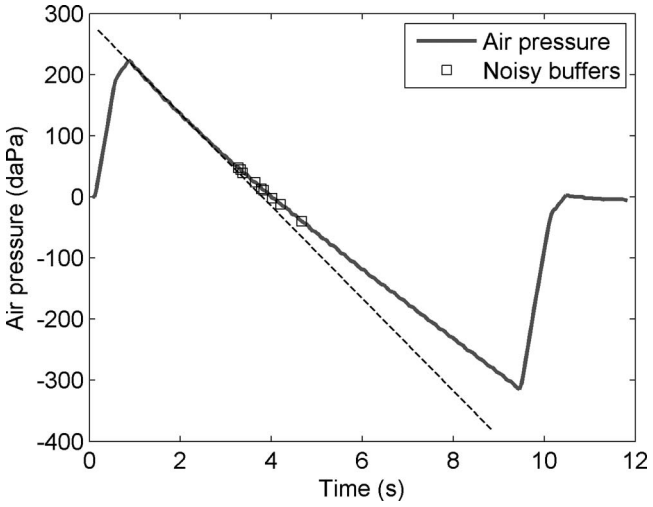


FIG. 3. Pressure sweep and automatic control. The thick line shows air pressure at the time each click occurred. The dashed line was manually added as a reference. The squares showed where click responses were rejected due to acoustical artifacts.

A click spectrum was calculated using a 1024-sample DFT for each click waveform. Sound-pressure reflectance $R(f)$ and EA were calculated for each response using Eq. (1) and Eq. (2), respectively. Pressure readings were monitored by an operator during data acquisition. If the sweep failed to complete the desired pressure range, the operator was notified by a displayed message, the data were abandoned, the probe insertion was adjusted, and the measurement was repeated.

2. Data processing

The acquired data were processed in the following manner to calculate the wideband tympanograms. First, noisy responses were identified based on calculation of a sample-wise sum of sound pressure square; for each click-response buffer, the sum of square $\Sigma(y[n])^2$ was calculated outside of a 9-ms period surrounding the main response. Upon the completion of a sweep, the interquartile range (IQR) of $\Sigma(y[n])^2$ was calculated based on all the click-response buffers within the sweep range. Those buffers with $\Sigma(y[n])^2$ higher than the 75th percentile+3 times IQR were considered noisy and excluded from further analyses. Figure 3 also shows an example of this artifact rejection; during a sweep that lasted for the duration of 186 clicks, nine responses were rejected.

Note that the criterion for artifact rejection was different from those for ambient-pressure measurements, in part because varying the air pressure changed the middle-ear characteristics and made it inappropriate to calculate an average response across clicks. The operator was notified during data acquisition if more than 10% of the buffers were rejected. If so, the operator had the opportunity to adjust the probe, check the subject status, and acquire data again, if desired, or continue to process the existing data.

Air pressure was sampled every 25 ms but a click stimulus was delivered every 46 ms. The pressure at the time of the onset of each click buffer was estimated by linear interpolation. The spectrum of EA between 0.226 and 8 kHz was partitioned into 62 bands of 1/12 octave each. Two bands at low frequencies were discarded because they contained no DFT components, so that the fractional-octave spectrum consisted of 60 bands. The EA was averaged within each band for each response.

For each test and every frequency, EA was smoothed along the pressure axis by a three-point median filter, and then resampled at every 5 daPa between −300 and 200 daPa using linear interpolation. The same 5-daPa grid was used for all sweep speeds, which constituted in some cases an oversampling of the variation of EA with air pressure.

This procedure established a grid across frequency and air pressure that was the same for each ear tested, independent of the details of the pressure-sweep response that varied across subjects.

3. Bandpass energy absorbance and tympanometric peak pressure

A bandpass EA tympanogram averaged over a frequency range from 0.38 to 2 kHz was used to define a bandpass TPP. This TPP was then used to define a peak EA, which is the EA spectrum measured from 0.226 to 8 kHz at the TPP. The bandpass EA tympanogram was defined to provide an analogy to a single-frequency tympanogram, and the peak EA was defined to provide a generalization of the EA measured at ambient pressure.

The bandpass energy absorbance $\langle \mathrm{EA}(p) \rangle$ at air pressure p was calculated as

$$\langle \mathrm{EA}(p) \rangle = \frac{1}{N_f} \sum_i (1 - |R(f_i,p)|^2), \tag{5}$$

where $|R(f_i,p)|^2$ denotes ER after the data processing described previously, the summation index i runs over all frequency bands centered at f_i within the selected pass band (0.38–2 kHz), and N_f denotes the number of such bands.

Then, the bandpass TPP, denoted as $\hat{p}$, was estimated by quadratic interpolation at the top three points of $\langle \mathrm{EA}(p) \rangle$,

$$\hat{p} = p_k + \Delta p \frac{a_{k-1} - a_{k+1}}{2(a_{k-1} - 2a_k + a_{k+1})}, \tag{6}$$

where p_k denotes the pressure bin with the maximum $\langle \mathrm{EA}(p) \rangle$, $\Delta p = 5$ daPa was the size of pressure sampling, and a_{k-1}, a_k, and a_{k+1} denote $\langle \mathrm{EA}(p) \rangle$ evaluated at $p_k - \Delta p$, p_k, and $p_k + \Delta p$, respectively. Then, an EA measured at the TPP, denoted as pEA, is defined by the EA tympanogram sampled at p_k,

$$\mathrm{pEA}(f) = \mathrm{EA}(f, p_k). \tag{7}$$

The present passband for adult tympanometry was selected to be 0.38–2 kHz. The upper limit was chosen based on the fact that the single-peaked structure of the EA tympanogram remained present at least up to 2 kHz. The lower limit might have been chosen as small as 0.226 kHz, which was the lowest analysis frequency of the overall acoustic transfer function measurement. A slightly higher frequency of 0.38 kHz was chosen as the lower limit for two reasons. First, physiological noise is higher at low frequencies, and this increased noise at lower frequencies was a potential concern because the SNR for a click response at a single frequency is less than if a single-frequency stimulus were used. The second reason is that the tympanometric change in EA with air pressure was larger at and above 0.38 kHz than below. This choice of tympanometry bandwidth in adult ears is preliminary, and may be further adjusted as more becomes known about wideband tympanometry in ears with middle-ear pathology or conductive hearing loss.

Estimating the TPP is important because some ears, for example, may have a negative TPP in the absence of middle-ear pathology. Under those conditions, the energy absorption properties of the middle ear might better be assessed at the TPP than at ambient pressure (Margolis *et al.*, 1999). This is because the TPP estimates the static pressure within the middle-ear cavities. The peak energy absorbance pEA would assess middle-ear function in a condition in which pressure difference across the tympanic membrane is minimized. In the case of an ear with middle-ear pathology, the pEA may provide additional information across frequency that is not present in the EA at ambient pressure.

4. Calculation of other tympanometric variables

Other acoustic transfer functions may be calculated from $R(f)$ and the characteristic impedance Z_c of the ear. For example, the acoustic admittance $Y(f)$ in an adult ear may be calculated as

$$Y(f) = Z_c^{-1} \frac{1 - R(f)}{1 + R(f)}, \tag{8}$$

in which Z_c may be calculated in the frequency range of interest as the ratio of the product of air density and phase velocity to the cross-sectional area of the calibration tube. This area is approximately equal to the cross-section area of the ear canal in an average adult ear.

Applied to data in a wideband tympanogram, the use of Eq. (8) provides a wideband admittance tympanogram defined over the grid of air pressure and frequency. Results can be extracted at a single frequency to calculate a single-frequency admittance tympanogram. The details of this calculation are as follows. First, for each response that was recorded at air pressure p_j, a wideband acoustic admittance $Y_j(f_k)$ was calculated at 1024 discrete frequencies f_k using Eqs. (1) and (8). Then, the admittance magnitude at 226 Hz, denoted as ψ_{226}, was estimated by linearly interpolating $|Y_j(f_k)|$ in the frequency domain. After computing ψ_{226} for all responses, it was resampled every 5 daPa using linear interpolation. Finally, the result was smoothed by a denoising technique[3] based on median filtering and moving-window averaging. The 1-kHz tympanogram was calculated similarly. Tympanograms using the complex components of acoustic admittance or of any other acoustic transfer function can be calculated using the same signal processing techniques, too.

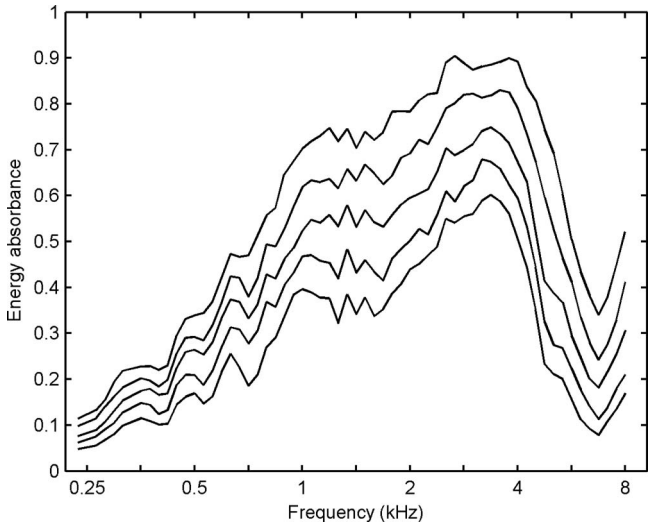


FIG. 4. EA measured at ambient pressure, plotted at 60 frequencies spaced 1/12 octave apart. Solid lines show 10th, 25th, 50th, 75th, and 90th percentiles, respectively, of the normal hearing subjects (N=92 ears).

D. Subjects

Adult subjects participated in this study (N=48 subjects, both ears tested) with a mean age ± 1 standard deviation (SD) of 33.8 ± 10 years. The following inclusion criteria for each ear were adopted:

(a) Air conduction thresholds ⩽15 dB HL at each octave frequency between 0.25 and 8 kHz.
(b) Air/bone gaps of ⩽10 dB at each octave frequency between 0.25 and 4 kHz.
(c) Negative history of otologic surgery, excluding surgery for placement of pressure equalization tubes.
(d) TPP between −83 and +50 daPa, based on the use of a 226-Hz probe tone.
(e) Equivalent ear-canal volume between 0.6 and 2.5 cm^3.
(f) Peak-compensated static acoustic admittance at the positive tail between 0.3 and 1.4 mmho.

The rationale for using inclusion criteria listed in items d, e, and f for 226-Hz tympanometry data has been previously described (Ellison and Keefe, 2005).

Four out of 96 ears did not satisfy the above criteria. Measurements were performed in the remaining 92 ears, including EA at ambient pressure and wideband tympanometry at a default sweep speed of −75 daPa/s, in which the "−" sign denotes a descending sweep. To evaluate the effects of pressure-sweep speeds and directions on measured tympanograms, the last 29 of 92 ears were also tested at seven other sweep speeds and directions, ±400, ±200, ±100, and +75 daPa/s.

III. RESULTS

A. Energy absorbance measured at ambient pressure

Figure 4 shows group results of EA measured at ambient pressure as a function of frequency. The five lines, ordered from bottom to top, show the 10th, 25th, 50th, 75th, and 90th percentiles, respectively. As frequency increased, the EA reached its maximum between 2 and 4 kHz, where the 10th to 90th percentile ranged from 0.50 to 0.90. The EA decreased as a function of frequency above 4 kHz until reaching a minimum near 6.7 kHz. The EA increased again as frequency approached 8 kHz. Similar trends in energy reflectance have been observed in previous studies (Stinson, 1990; Keefe *et al.*, 1993; Voss and Allen, 1994; Feeney and Sanford, 2004; Shahnaz and Bork, 2006).

B. Wideband energy absorbance tympanograms

1. Normal percentiles

Percentiles of EA are plotted in Fig. 5 as two-dimensional functions of frequency and air pressure. Note that below 2 kHz, EA had a single peak near 0 daPa, but at higher frequencies, EA was more complex as a function of pressure. At every pressure, EA reached its maximum near 4 kHz, where the 10th to the 90th percentiles ranged from approximately 0.6 to 0.9. The peak location on the frequency-pressure plane and the peak absorbance values were similar to previously reported results on normal-hearing subjects [e.g., Fig. 8(b) in Margolis *et al.*, 1999; Fig. 9 in Keefe and Simmons, 2003].

2. Occurrence of negative energy absorbance in some ears

The minimum value of EA across all ears was calculated at each frequency and pressure to provide a 0th percentile of EA. The 0th-percentile EA was negative in 7.2% of all the points on the frequency-pressure plane (Fig. 6, empty regions). Also, negative EA was measured in 23 of 92 ears for at least one frequency-pressure point. EA of more negative than −0.02 occurred in 18 ears, with the most negative EA =−0.076.

The largest region where negative EA occurred was near 7 kHz across all pressures. However, only three ears were found to have negative EA there, with a minimum EA of −0.064. The only place where 10th-percentile EA was negative was at 1.59 kHz between −260 and −300 daPa—this region is somewhat obscured in Fig. 5, but the tendency for low EA can be observed. The pattern of negative EA near 1.59 kHz was asymmetric with respect to air pressure; it never occurred at any positive pressure. Possible causes of negative EA are discussed in Sec. IV.

C. Bandpass TPP and peak pressure determined by 226-Hz tympanometry

In the present study, the bandpass TPP had a mean ± 1 SD of 2.8 ± 16 daPa. Except for one ear with a TPP of −93 daPa, the bandpass TPP ranged between −83 and +50 daPa. This range is similar to the range of TPP reported in studies using 226-Hz tympanograms (Ellison and Keefe, 2005). This similarity is not an independent result, inasmuch as this TPP range for 226-Hz tympanograms was part of the subject inclusion criteria. The 226-Hz TPP obtained during the initial screening of these ears had a mean ± 1 SD of 13.6 ± 18 daPa. The correlation coefficient was 0.76 across all ears between the bandpass TPP and the 226-Hz TPP.

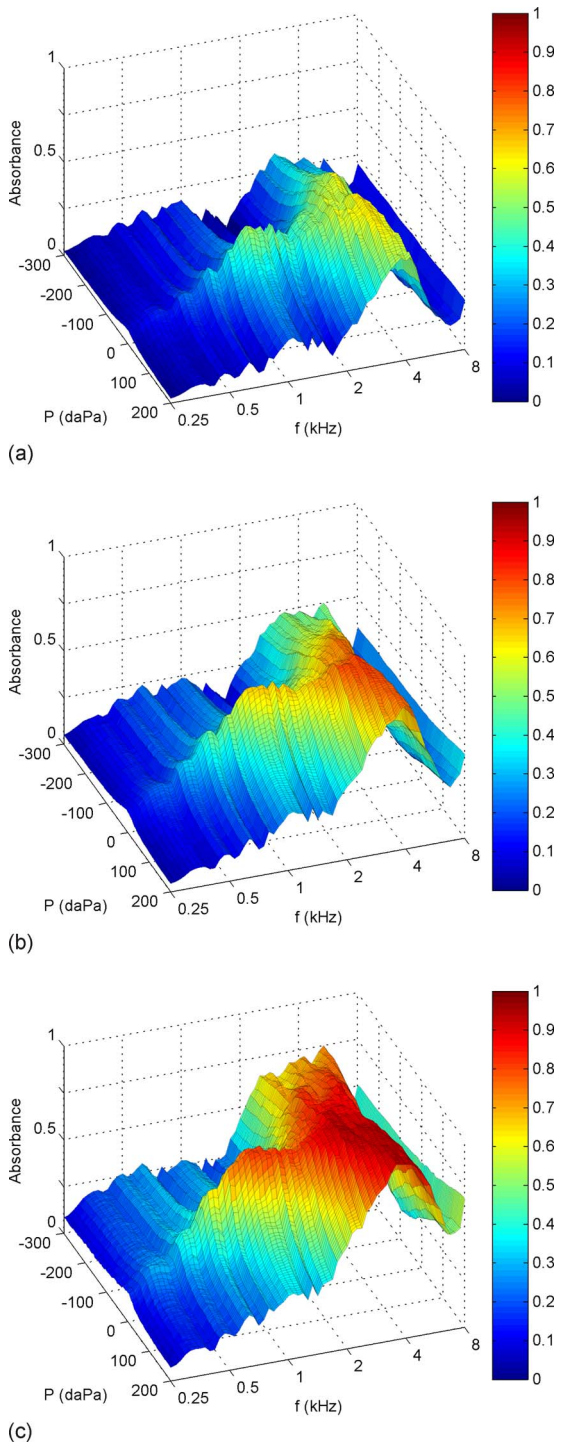


FIG. 5. (Color online) EA as a function of frequency and air pressure. Sweep speed: −75 daPa/s. (a), (b), and (c): 10th, 50th, and 90th percentiles, respectively, of adult normative data (N=92 ears).

D. Single-frequency admittance magnitude tympanograms

Five randomly selected examples of admittance magnitude tympanograms at 226 Hz and 1 kHz measured in normal adult ears are shown in Fig. 7. Although these data were extracted from wideband tympanometry, each tympanogram has a shape typical of those that are clinically measured at the nominal test frequency. The 1-kHz tympanogram is not commonly measured in adult ears, but has been of recent interest in measurements in children younger than 3 months (Margolis *et al.*, 2003; Kei *et al.*, 2003; Baldwin, 2006).

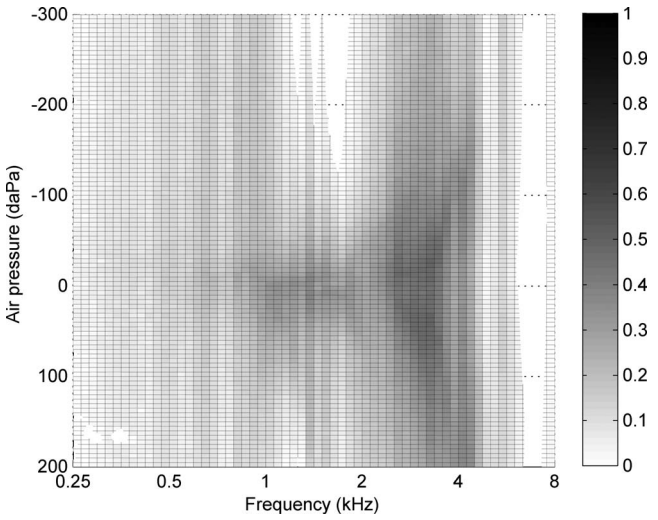


FIG. 6. Minimum EA across subjects (N=92 ears). Empty regions indicate where the minimum EA was found negative.

IV. DISCUSSION

A. General comments on single-frequency and wideband tympanograms

Wideband absorbance tympanograms measured using a swept-pressure paradigm (Fig. 5) were similar to those measured using a sequence of fixed static pressures, as previously reported (Margolis *et al.*, 1999; Keefe and Simmons, 2003; Sanford and Feeney, 2008). The Margolis *et al.* (1999) measurements relied on a manual setting of air pressure, which resulted in long measurement duration with known air pressure at each setting. The Keefe and Simmons, and Sanford and Feeney, measurements had no explicit measurement of the air pressure in the ear canal during an automated recording sequence in which the desired air pressure was varied in discrete steps. The present measurement, using a

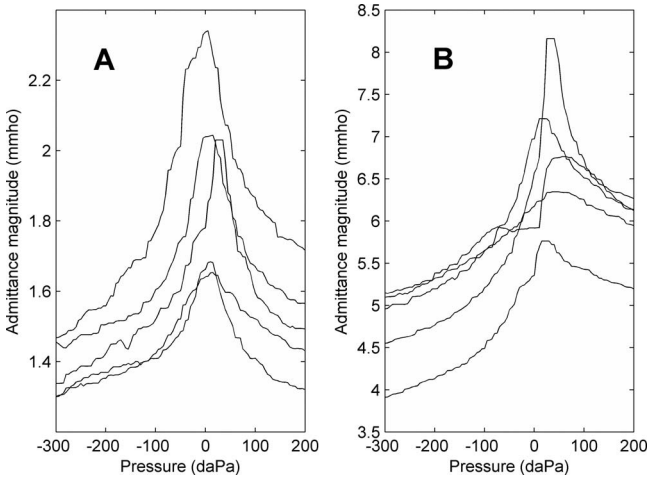


FIG. 7. Examples of single-frequency admittance magnitude tympanograms extracted from wideband tympanometry. Results from randomly selected ears. (A) 226 Hz. (B) 1 kHz.

swept-pressure technique with feedback control, allowed a shorter measurement duration, which is an advantage for clinical applications.

Despite the overall agreement between these various measurements of EA tympanograms in adult ears, there has been scant attention to inaccuracies that could be observed in bounded regions of the frequency-pressure plane. In this study, the negative EA that sometimes occurred was evidence of a contamination due to some source of error. EA should be non-negative in the absence of sound sources within the cochlea, except for the possible small influence of otoacoustic emissions, which are an unlikely source given the predominant source region near 7 kHz.

In the present study, negative nominal values of EA near 7 kHz might be attributed to insufficient accuracy in calibration. Equation (1) shows that, if the source impedance R_0 obtained during calibration deviates from the true source impedance in a way such that the magnitude of R_0P+Q is underestimated, the magnitude of R will be overestimated. Thus, when the true value of $|R|^2$ is close to 1, it is possible that a calibration error could cause it to be measured larger than 1, resulting in negative EA according to Eq. (2). Two of the three ears that measured negative EA near 7 kHz were the two ears of the same subject measured on the same day. This indicates that the negative value might indeed be a result of a temporary condition in the probe at the time calibration was performed.

Negative EA near 1.59 kHz might have been due to the transducers' sensitivity to air-pressure change, so that both $R_0(f)$ and $Q(f)$ deviated from their calibrated values that were determined at ambient pressure. Otherwise, the source of this error is unknown.

Admittance tympanograms in normal adult ears have a single-peaked structure at 226 Hz, but a more complex structure of maxima and minima occurs at 678 Hz and higher frequencies. Techniques to classify such multifrequency admittance tympanometric patterns have been used to analyze responses up to approximately 2 kHz (Colletti, 1977; Margolis and Hunter, 2000; Vanhuyse, 1975). Nevertheless, use of multifrequency tympanometry is not widely accepted in clinical settings, largely due to the complexity of the responses (Fowler and Shanks, 2002). In contrast, the wideband EA tympanogram has a single pressure peak in normal-hearing adults at least up to approximately 2 kHz (Fig. 5). The multiple maxima and minima structure that occur in admittance tympanograms below 1 kHz in healthy adult ears do not appear in EA tympanograms.

Although wideband tympanometry provides more information than either traditional tympanometry or ambient-pressure reflectance measurement, it would be important for a clinical device to provide a summary on the status of the test ear. Keefe and Simmons (2003) reduced the two-dimensional EA tympanogram into a set of one-dimensional functions: pressure moments as a function of frequency, and frequency moments as a function of pressure. There may be a practical advantage in terms of simplicity in reducing the two-dimensional EA tympanogram to a small number of one-dimensional functions, but it is unknown whether significant diagnostic information is thereby lost.

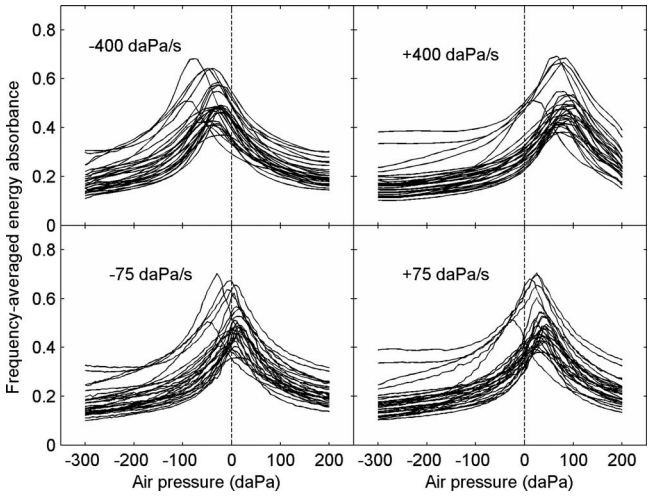


FIG. 8. Frequency-averaged (0.38–2 kHz) EA as a function of air pressure. Each panel shows results at a different sweep speed and direction, and traces show responses from individual ears (N=29 ears).

The more narrowly focused goals of the present study were to (1) demonstrate the feasibility of a wideband system intended for middle-ear screening and diagnosis that includes swept-pressure tympanometry, and (2) report baseline results from a normal adult population. Feasibility was established inasmuch as interpretable wideband acoustic transfer functions were measured on every subject tested, and the results (in Figs. 4, 5, and 7) were similar to those in previous wideband and single-frequency studies.

B. Effects of pressure sweep on estimation of TPP

Figure 8 shows $\langle \mathrm{EA}(p) \rangle$ over the passband (0.38–2 kHz) that was measured with the slowest and the fastest sweeps (N=29 ears). Different traces show results from individual ears. Note that $\langle \mathrm{EA}(p) \rangle$ always had a single peak, but the overall pattern shifted positively with ascending sweeps and negatively with descending sweeps. Also, the shift was larger with the fastest sweep than with the slowest sweep. The amount of shift was quantified in terms of a *peak-pressure difference* (PPD) for each ear at each pressure-sweep speed v (Therkildsen and Gaihede, 2005),

$$\mathrm{PPD}(v) = \hat{p}(+v) - \hat{p}(-v), \tag{9}$$

where $\hat{p}(\pm v)$ denotes TPP obtained with ascending (+) and descending (−) sweeps, respectively. Figure 9 shows that PPD increased as a function of v and was always positive. Linear regression of PPD(v) yielded a slope of 0.27 s and an offset of 6.8 daPa. Because PPD accounted for the difference between ascending and descending sweeps at the same speed, the slope of the regression line times 0.5 suggested a constant delay of 0.14 s.

The PPD at 75 daPa/s was lower than reported in Shanks and Wilson (1986) and Kobayashi *et al.* (1987), in both of which PPD also increased as a function of the pressure-sweep speed. However, Therkildsen and Gaihede (2005) argued that any positive dependence of PPD upon sweep speed must be due to instrumental delay, and it was shown that, by minimizing such delay, PPD could be reduced to 12 ± 10 daPa at a pressure-sweep speed of 400 daPa/s.

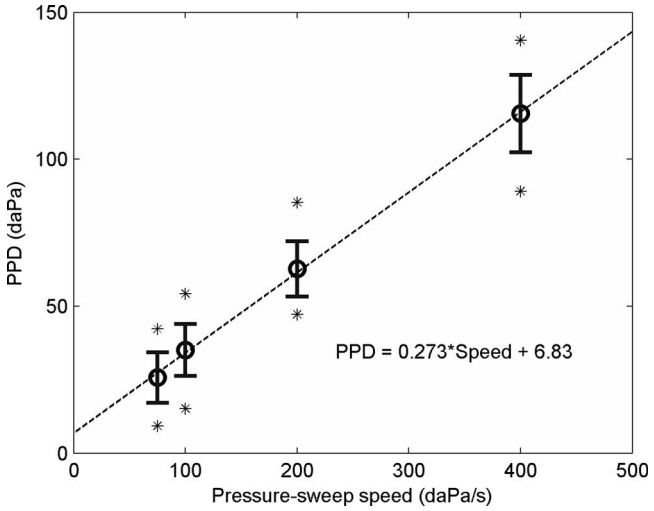


FIG. 9. Peak-pressure difference (PPD) vs pressure-sweep speed. Circles and bars show means and SDs ($N=29$ ears). Asterisks show minimum and maximum PPD at each speed.

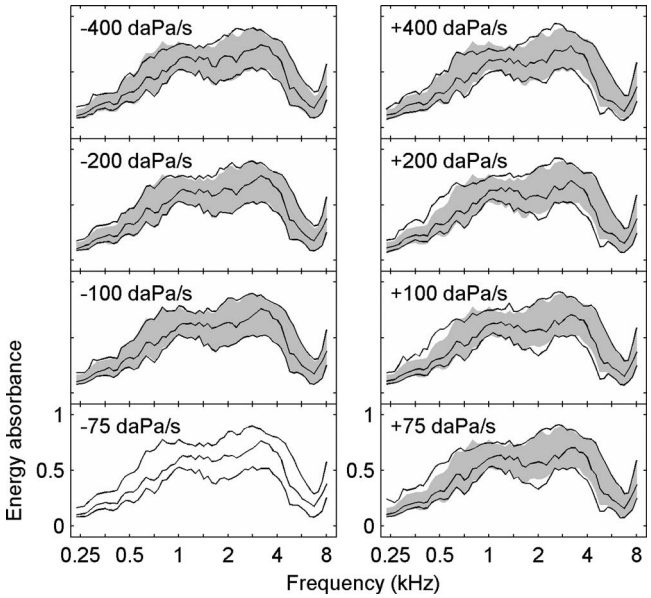


FIG. 10. Wideband EA estimated at TPP (pEA). Pressure-sweep speeds are listed in each panel. Solid lines indicate the 10th, 50th, and 90th percentiles, respectively ($N=29$ ears). For comparison, the shaded area shows the 10th to 90th percentile range that was measured with the sweep speed of −75 daPa/s.

The cause of large PPD at higher speeds in the present study is not clear. Possible mechanisms include air pressure difference between the ear canal and the pressure sensor during the sweep, signal processing delay in pressure sensing circuitry, and any unknown software delay due to communication between the DSP and the desktop computer.

Nevertheless, the offset of the regression line at 6.8 daPa provides evidence of middle-ear hysteresis that might not be eliminated by further reducing the sweep speed. This pressure offset is of the same order of magnitude as the mean PPD=12 daPa at 50 daPa/s, found by Therkildsen and Gaihede (2005), and the mean PPD=9 daPa at 8 daPa/s by Kobayashi *et al.* (1987).

These results suggest that an absorbance-based measurement of TPP is influenced by variations in sweep speed, but the magnitude of these effects is similar to measurements of TPP using 226-Hz admittance tympanometry.

C. Effects of pressure sweep on peak EA

A related question arises of the extent to which pEA is influenced by variations in pressure-sweep speed and direction. Figure 10 shows pEA measured with pressure sweeps at all four speeds. By inspection, the 10th to 90th-percentile range with −75, −100, and −200 daPa/s appeared similar at all frequencies; the differences in pEA between ascending and descending sweeps appeared greater.

To quantify this observation, the difference $D(v_1;v_2)$ in pEA measured with sweep speed v_1 and v_2 was calculated for each ear at every frequency. The rms values of $D(v;-75)$ and $D(v;+75)$ averaged across 29 ears and all frequencies are shown in Table I. The difference in pEA caused by a change in sweep direction was larger than that caused by increasing the sweep speed. This provides additional evidence that middle-ear hysteresis did not vanish at the slowest sweep speed in the present study, and is consistent with tympanometric findings in rabbits, for which middle-ear hysteresis effects were important at low sweep speeds (Dirckx *et al.*, 2006).

The rms value of $D(-75;-400)$ was 0.031, so the peak EA changed on the order of ± 0.031 when the speed of descending pressure sweeps increased from 75 to 400 daPa. Figure 10 shows that, at every frequency, the 10th to 90th-percentile range of pEA(f) was at least 0.079 with the default sweep speed of −75 daPa/s; the minimum occurred at the lowest frequency. Further analyses showed that the IQR (i.e., 25th to 75th-percentile range) was at least 0.042 with the same sweep speed. The IQR was greater than the rms value of $D(-75;-400)$, and particularly so above 0.5 kHz.

Thus, the rms analyses indicate that, even though the TPP needed to extract pEA from the EA tympanogram varied with sweep speed (see Fig. 8), the resulting variations in pEA were less than the variability across normal-hearing subjects.

D. Energy absorbance: TPP vs. ambient

Given that the mean (2.8 daPa) of the bandpass TPP in this group of normal-hearing ears was within 1 SD (16 daPa)

TABLE I. Effects of different pressure-sweep speeds and directions on pEA.

Sweep speed v (daPa/s)	rms of $D(v;-75)$	rms of $D(v;+75)$
−75	⋯	0.050
−100	0.015	0.051
−200	0.021	0.054
−400	0.031	0.061
+75	0.050	⋯
+100	0.051	0.016
+200	0.053	0.027
+400	0.052	0.044

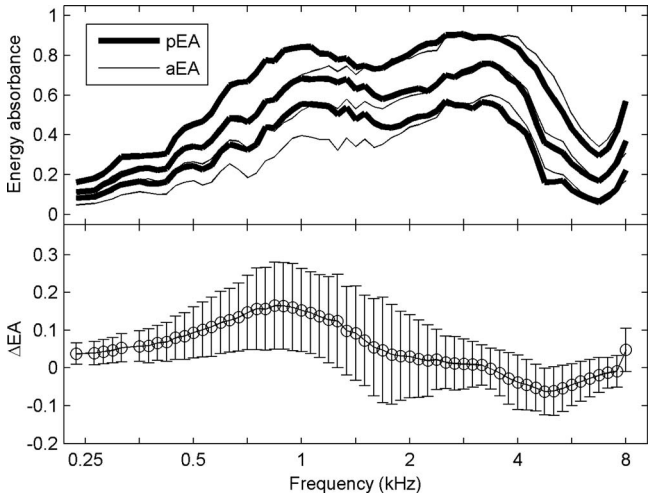


FIG. 11. Comparison of pEA and aEA across frequencies. Sweep speed: −75 daPa/s. Top: Thick lines show 10th, 50th, and 90th percentiles of pEA, and thin lines show the same percentiles of aEA (N=92 ears). Bottom: Mean and SD of ΔEA.

of ambient pressure, it was expected that pEA would be similar to EA measured at ambient pressure (aEA) in these ears. However, as shown in Fig. 11 (top panel), the 10th, 50th, and 90th percentiles of pEA were higher than aEA at low frequencies and slightly lower at high frequencies. The difference ΔEA=pEA−aEA, calculated for each ear individually, was most positive at 0.84 kHz, reaching 0.16 ± 0.11, and most negative at 4.76 kHz, -0.06 ± 0.06 (Fig. 11, bottom panel).

The difference was probably due to a positive residual pressure during probe insertion right before the ambient-pressure measurement. When the probe was pushed into the ear canal, the enclosed volume decreased, and the air pressure might have increased consequently. If the pressure seal was good, the pressure could remain in the ear canal throughout the measurement, which lasted for about 1 s (46 ms × 16 clicks). The 50th percentile of the wideband tympanogram in Fig. 5(b) suggests that, as the ear-canal pressure varied from 0 daPa to a positive pressure, EA would decrease at frequencies below 2 kHz but increase slightly around 4 kHz. This agrees with the pattern of ΔEA shown in Fig. 11.

The residual pressure could have been avoided by providing ventilation in the probe. Alternatively, the discrepancy between pEA and aEA might be eliminated by setting the pressure back to zero using the pressure pump before ambient-pressure measurements. The presence of any such discrepancy in EA would not interfere with its clinical use, because its effects would be shared by measurements in ears with either normal or impaired middle-ear function.

V. CONCLUSIONS

Procedures were developed to perform wideband acoustic transfer function measurements under both ambient and tympanometric conditions. Wideband responses were acquired in a normal-hearing adult population. The feasibility was established in adult ears for the measurement of ambient-pressure responses and for tympanograms using a wideband stimulus and swept air pressure. The overall measurement durations of ambient and tympanometric responses were within the range of durations of other types of clinical systems that are used to assess middle-ear function. The inclusion of artifact rejection allowed the detection and exclusion of noisy buffers from subsequent analysis. Wideband results were summarized in terms of EA, which is large at frequencies at which the middle ear is efficient at collecting sound energy, and which, in the form of an EA tympanogram, has a central peak similar to that of standard low-frequency tympanometry. The effects of variations in sweep speed and direction on adult EA tympanograms were assessed. The EA tympanogram was simplified into a pair of responses: a bandpass tympanogram characterizing variations with air pressure, and a peak EA characterizing variations with frequency. The EA measurements in normal adult ears provide a baseline with which to compare measurements in adult ears with middle-ear pathology and in ears of newborns and older children.

ACKNOWLEDGMENTS

This project was supported by NIH grants DC006607, DC004662, and DC000013. The authors would like to thank two anonymous reviewers for their critiques.

NOMENCLATURE

$D(v_1;v_2)$	=	Difference in pEA measured with sweep speed v_1 and v_2
$\mathrm{EA}(f,p)$	=	Two-dimensional energy absorbance tympanogram
$\langle \mathrm{EA}(p) \rangle$	=	Bandpass energy absorbance as a function of air pressure
$\mathrm{aEA}(f)$	=	Energy absorbance measured at ambient pressure
$\mathrm{pEA}(f)$	=	Energy absorbance tympanogram sampled at peak pressure
ΔEA	=	pEA subtracted by aEA
f	=	Frequency (Hz)
i,j,k	=	Integer-valued dummy indexes; meanings depend on context
n	=	Discrete-time index
p	=	Air pressure in the ear canal (daPa)
$\hat{p}$	=	Bandpass tympanometric peak pressure (daPa)
Δp	=	Resolution of air-pressure grid, 5 daPa
$P(f)$	=	Recorded sound-pressure spectrum
$\mathrm{PPD}(v)$	=	Peak pressure difference between $\hat{p}(+v)$ and $\hat{p}(-v)$
$Q(f)$	=	Incident pressure spectrum
$R(f)$	=	Sound-pressure reflectance as a function of f
$R_0(f)$	=	Source reflectance as a function of f
v	=	Speed of air-pressure sweep (daPa/s)
$Y(f)$	=	Acoustic admittance as a function of frequency ($\mathrm{cm}^5\,\mathrm{dyn}^{-1}\,\mathrm{s}^{-1}$)
$y^{(k)}[n]$	=	Sound-pressure response to the kth click sampled at time n

[1]Although beyond the scope of the present study in terms of human-subject testing, the design of the system is intended to be suitable for measurements in newborns and older children as well as in adults, and in ears with middle-ear pathology.

[2]Energy absorbance previously was termed energy transmittance by Keefe and Simmons (2003). The term energy absorbance is preferred and used in this report. In a one-dimensional transmission-line description of the ear-canal acoustics, the middle ear acts as a terminating impedance of the transmission line, and the process of sound absorption is represented by including a resistive component to this impedance. The term transmission is often used in transmission-line theory for the case that two transmission lines with different properties are joined at a particular location. A signal in the first line that is incident to this junction is partially reflected and partially transmitted into the second line. One-dimensional models of middle-ear transmission represent the middle ear as joined to an ear-canal transmission line and a cochlear transmission line, the latter representing the cochlear traveling wave. Irrespective of how the internal function of the middle ear is modeled, a middle-ear scattering matrix quantifies relationships between signals traveling through the middle ear to and from the ear-canal transmission line, and to and from the cochlear transmission line. This scattering matrix includes both forward and reverse middle-ear reflectances and transmittances (Shera and Zweig, 1992; Keefe and Abdala, 2007), in which the forward direction is from the ear canal into the middle ear, and from the middle ear into the cochlea. The ER as used here is identical (in the absence of ear-canal losses) to the squared magnitude of this forward reflectance. However, EA is not identical to the squared magnitude of the forward transmittance, and has no simple relationship to the forward or reverse transmittance. To prevent any confusion between EA and these transmittances, the term energy absorbance is used herein to represent the fraction of incident energy in the ear canal that is not reflected at the tympanic membrane.

[3]The denoising technique consisted of the following steps. First, three-point median filtering was applied to the input $\psi_{226}(p_i)$, where the air pressures p_i are equally spaced at every 5 daPa. Denote the result of median filtering as $\bar{\psi}_{226}(p_i)$, and the difference as $\tilde{\psi}(p_i) \triangleq \psi_{226}(p_i) - \bar{\psi}_{226}(p_i)$. Then, another round of three-point median smoothing was applied to $\tilde{\psi}(p_i)$, and the result was convolved with the normalized Hamming window (Harris, 1978) of three points on each side, which corresponds to a half-width of 15 daPa in this context. The denoised output was the sum of $\bar{\psi}_{226}(p_i)$ and the output of the Hamming filter.

Agulló, J., Cardona, S., and Keefe, D. H. (**1995**). "Time-domain deconvolution to measure reflection functions from discontinuities in waveguides," J. Acoust. Soc. Am. **97**, 1950–1957.

ASHA (**1997**). *Guidelines for Audiologic Screening* (American Speech-Language-Hearing Association, Rockville, MD).

Baldwin, M. (**2006**). "Choice of probe tone and classification of trace patterns in tympanometry undertaken in early infancy," Int. J. Audiol. **45**, 417–427.

Colletti, V. (**1977**). "Multifrequency tympanometry," Audiology **16**, 278–287.

Decraemer, W. F., Creten, W. L., and van Camp, K. J. (**1984**). "Tympanometric middle-ear pressure determination with two-component admittance meters," Scand. Audiol. **13**, 165–172.

Dirckx, J. J. J., Buytaert, J. A. N., and Decraemer, W. F. (**2006**). "Quasi-static transfer function of the rabbit middle ear, measured with a heterodyne interferometer with high-resolution position decoder," J. Assoc. Res. Otolaryngol. **7**, 339–351.

Ellison, J. C., and Keefe, D. H. (**2005**). "Audiometric predictions using SFOAE and middle-ear measurements," Ear Hear. **26**, 487–503.

Feeney, M. P., and Sanford, C. A. (**2004**). "Age effects in the human middle ear: Wideband acoustical measures," J. Acoust. Soc. Am. **116**, 3546–3558.

Feeney, M. P., Grant, I. L., and Marryott, L. P. (**2003**). "Wideband energy reflectance measurements in adults with middle-ear disorders," J. Speech Lang. Hear. Res. **46**, 901–911.

Fowler, C. G., and Shanks, J. E. (**2002**). "Tympanometry," in *Handbook of Clinical Audiology*, edited by J. Katz (Lippincott, Williams & Wilkins, New York).

Gaihede, M., Lambertsen, K., Bramstoft, M., Kamarauskas, A., and Fogh, A. (**2000**). "Tympanometric hysteresis effect and errors in middle ear pressure determination—A preliminary study in children with secretory otitis media," Acta Oto-Laryngol., Suppl. **543**, 58–60.

Harris, F. J. (**1978**). "On the use of windows for harmonic analysis with the discrete Fourier transform," Proc. IEEE **66**(1), 51–83.

Keefe, D. H., and Abdala, C. (**2007**). "Theory of forward and reverse middle-ear transmission applied to otoacoustic emissions in infant and adult ears," J. Acoust. Soc. Am. **121**, 978–993.

Keefe, D. H., and Levi, E. (**1996**). "Maturation of the middle and external ears: Acoustic power-based responses and reflectance tympanometry," Ear Hear. **17**, 361–373.

Keefe, D. H., and Simmons, J. L. (**2003**). "Energy transmittance predicts conductive hearing loss in older children and adults," J. Acoust. Soc. Am. **114**, 3217–3238.

Keefe, D. H., Ling, R., and Bulen, J. C. (**1992**). "Method to measure acoustic impedance and reflection coefficient," J. Acoust. Soc. Am. **91**, 470–485.

Keefe, D. H., Bulen, J. D., Arehart, K., and Burns, E. M. (**1993**). "Ear-canal impedance and reflection coefficient in human infants and adults," J. Acoust. Soc. Am. **94**, 2617–2638.

Keefe, D. H., Folsom, R. C., Gorga, M. P., Vohr, B. R., Bulen, J. C., and Norton, S. J. (**2000**). "Identification of neonatal hearing impairment: Ear-canal measurements of acoustic admittance and reflectance in neonates," Ear Hear. **21**, 443–461.

Kei, J., Allison-Levick, J., Dockray, J., Harrys, R., Kirkegard, C., Wong, J., Maurer, M., Hegarty, J., Young, J., and Tudehope, D. (**2003**). "High-frequency (1000 Hz) tympanometry in normal neonates," J. Am. Acad. Audiol **14**, 20–28.

Kobayashi, T., Okitsu, T., and Takasaka, T. (**1987**). "Forward-backward tracing tympanometry," Acta Oto-Laryngol., Suppl. **435**, 100–106.

Margolis, R. H., and Hunter, L. L. (**2000**). "Acoustic immittance measurement," in *Audiology: Diagnosis*, edited by R. J. Roeser, M. Valente, and H. Hosford-Dunn (Thieme Medical, New York).

Margolis, R. H., Saly, G. L., and Keefe, D. H. (**1999**). "Wideband reflectance tympanometry in normal adults," J. Acoust. Soc. Am. **106**, 265–280.

Margolis, R. H., Bass-Ringdahl, S., Hanks, W. D., Holte, L., and Zapala, D. A. (**2003**). "Tympanometry in newborn infants—1 kHz norms," J. Am. Acad. Audiol **14**, 383–392.

Nozza, R. J., Bluestone, C. D., Kardatzke, D., and Bachman, R. (**1994**). "Identification of middle ear effusion by aural acoustic admittance and otoscopy," Ear Hear. **15**, 310–323.

Piskorski, P., Keefe, D. H., Simmons, J. L., and Gorga, M. P. (**1998**). "Prediction of conductive hearing loss based on acoustic ear-canal response using a multivariate clinical decision theory," J. Acoust. Soc. Am. **105**, 1749-1764.

Sanford, C. A., and Feeney, M. P. (**2008**). "Effects of maturation on tympanometric wideband acoustic transfer functions in human infants," J. Acoust. Soc. Am. **104**, 2106–2122.

Shahnaz, N., and Bork, K. (**2006**). "Wideband reflectance norms for Caucasian and Chinese young adults," Ear Hear. **27**, 774–788.

Shanks, J. E., and Wilson, R. H. (**1986**). "Effects of direction and rate of ear canal pressure changes on tympanometric measures," J. Speech Hear. Res. **29**, 11–19.

Shanks, J. E., Lilly, D. J., Margolis, R. H., Wiley, T. L., and Wilson, R. H. (**1988**). "Tympanometry," J. Speech Hear Disord. **53**, 354–377.

Shera, C. A., and Zweig, G. (**1992**). "Analyzing reverse middle-ear transmission: Noninvasive *Gedankenexperiments*," J. Acoust. Soc. Am. **92**, 1371–1381.

Stinson, M. R. (**1990**). "Revision of estimates of acoustic energy reflectance at the human eardrum," J. Acoust. Soc. Am. **88**, 1773–1778.

Stinson, M. R., Shaw, E. A., and Lawton, B. W. (**1982**). "Estimation of acoustical energy reflectance at the eardrum from measurements of pressure distribution in the human ear canal," J. Acoust. Soc. Am. **72**, 766–773.

Therkildsen, A. G., and Gaihede, M. (**2005**). "Accuracy of tympanometric middle ear pressure determination: The role of direction and rate of pressure change with a fast, modern tympanometer," Otol. Neurotol. **26**(2), 252–256.

Tukey, J. W. (**1977**). *Exploratory Data Analysis* (Addison-Wesley, Reading, MA).

Vander Werff, K. R., Prieve, B. A., and Georgantas, L. M. (**2007**). "Test-retest reliability of wideband reflectance measures in infants under screening and diagnostic test conditions," Ear Hear. **28**, 669–681.

Vanhuyse, V. J., Creten, W. L., and van Camp, K. J. (**1975**). "On the W-notching of tympanograms," Scand. Audiol. **4**, 45–50.
Voss, S. E., and Allen, J. B. (**1994**). "Measurement of acoustic impedance and reflectance in the human ear canal," J. Acoust. Soc. Am. **95**, 372–384.
Voss, S. E., Horton, N. J., Woodbury, R. R., and Sheffield, K. N. (**2008**). "Sources of variability in reflectance measurements on normal cadaver ears," Ear Hear. **29**, 651–665.
Voss, S. E., Rosowski, J. J., Merchant, S. N., and Peake, W. T. (**2001**). "Middle-ear function with tympanic-membrane perforations. I. Measurements and mechanisms," J. Acoust. Soc. Am. **110**, 1432–1444.

Synchronized spontaneous otoacoustic emissions analyzed in a time-frequency domain

W. Wiktor Jedrzejczak
Institute of Physiology and Pathology of Hearing, ul. Zgrupowania AK "Kampinos" 1, 01-943 Warszawa, Poland

Katarzyna J. Blinowska
Department of Biomedical Physics, Institute of Experimental Physics, Warsaw University, ul. Hoza 69, 00-681 Warszawa, Poland

Krzysztof Kochanek and Henryk Skarzynski
Institute of Physiology and Pathology of Hearing, ul. Zgrupowania AK "Kampinos" 1, 01-943 Warszawa, Poland

(Received 6 August 2008; revised 22 September 2008; accepted 23 September 2008)

A synchronized spontaneous otoacoustic emission paradigm was used to measure the response in time intervals of 80 ms following a click stimulus. The responses obtained were decomposed into basic waveforms by means of adaptive approximations using a matching pursuit algorithm. High-resolution time-frequency distributions of signal energy were calculated and showed three types of component: (1) purely evoked of duration less than 5 ms, (2) longer lasting and decaying, with exponentially decreasing amplitude, and (3) long lasting and stable. The distributions of the frequencies of components of different durations were similar, with most components falling within the 1–2 kHz interval. It is shown that the presence of long-lasting components may influence the estimation of the latency of evoked emissions, especially at higher frequencies where the evoked part has a very short duration. © *2008 Acoustical Society of America.* [DOI: 10.1121/1.2999556]

PACS number(s): 43.64.Jb, 43.60.Hj [BLM] Pages: 3720–3729

I. INTRODUCTION

Studies of otoacoustic emissions (OAEs) are essential for gaining a better understanding of the mechanisms of the physiology of hearing and are also important for the diagnosis of hearing impairment. OAE signals (reviewed by Probst *et al.*, 1991) can be generated by the cochlea spontaneously or following external stimulation. OAEs evoked in this way can be produced by a broadband signal [transient evoked otoacoustic emissions (TEOAEs)] or by tonal stimuli (stimulus frequency otoacoustic emissions), or by a combination of tonal stimuli [distortion product OAEs (DPOAEs)]. Spontaneous OAEs (SOAEs) arise without external stimuli and are characterized by a stability of amplitude in time and a narrow bandwidth. They are measured by averaging the spectra of signals recorded in the ear canal. Nevertheless, the most common method of recording SOAEs is by synchronizing them with broadband click stimuli. The paradigm is similar to that used to record TEOAEs, but the acquisition window is extended from 20 to 80 ms. In this way, synchronized SOAEs (SSOAEs) arise, which are long-lasting OAEs elicited by the broadband stimulus. In general, SSOAEs are considered to represent SOAEs (e.g., Wable and Collet, 1994; Prieve and Falter, 1995). However, in the case of SSOAE measurement two main kinds of activity may be determined: (1) the components of measurable equilibrium amplitude and (2) the components of characteristic time of exponential decay (e.g., Sisto and Moleti, 1999).

The typical frequency of SOAEs ranges from 0.5 to 6 kHz (Probst *et al.*, 1991) with most appearing in the range 1–2 kHz. Despite reports of frequency shifts of SOAEs in certain conditions (e.g., Penner *et al.*, 1994; Brienesse *et al.*, 1997) and cases of appearing and disappearing SOAEs (e.g., Burns *et al.*, 1994; Smurzynski and Probst, 1998), generally they show only small changes of frequency and amplitude (e.g., Lind and Randa, 1992; van Dijk *et al.*, 1994; Frick and Matthies, 1998). This stability suggests that SOAEs are generated at specific sites distributed along the basilar membrane and that it is very likely that some structurally unique feature of the organ of Corti is involved in their generation (Probst *et al.*, 1991).

The overall findings of different authors (e.g., Talmadge *et al.*, 1993; Penner and Zhang, 1997) have indicated that SOAEs can be detected in about 70% of individuals with normal hearing and that they occur more frequently in females than in males. The mean number of SOAEs generated per ear also tends to be higher in females than in males and SOAEs appear to be detected significantly more frequently in right ears than in left ears. Furthermore, most studies have indicated a higher incidence of SOAEs in young children; for example, Morlet *et al.* (1995) reported an 84% occurrence of SOAEs in babies in the first 30–40 weeks of life.

The influence of the occurrence of SOAEs on evoked emissions was also investigated for TEAOEs (e.g., Kulawiec and Orlando, 1995; Osterhammel *et al.*, 1996) and for DPOAEs (e.g., Ozturan and Oysu, 1999; Kuroda *et al.*, 2001). These studies showed that the evoked responses obtained from ears with SOAEs had significantly higher levels than those obtained from ears without SOAEs. This differ-

 © 2008 Acoustical Society of America

ence was present in a range of different age groups, from newborn babies to adults (e.g., Prieve and Falter, 1995; Prieve *et al.*, 1997).

It is well known that SOAEs are often visible as narrow peaks within TEOAE spectra (e.g., Probst *et al.*, 1986). Their presence may be demonstrated even more clearly using time-frequency (TF) distributions that show the energy of the evoked emissions (e.g., Konrad-Martin and Keefe, 2003), where they form a continuous trace of energy that spans the whole length of the signal. Similar structures were observed in TF distributions of TEOAE obtained by Jedrzejczak *et al.* (2004), in which the distributions consisted of short-lived components that obeyed the latency-frequency power law and long-lasting components of very narrow bandwidth. The high incidence of long-lasting components was observed in the TF maps of neonates (Jedrzejczak *et al.*, 2007). The correspondence of these components with SOAE spectra was reported using a sample of subjects. The increased latencies in preterm neonates in comparison with full-term neonates were explained by the longer latencies of these long-lasting components.

There is evidence that the cochlear sites associated with the SOAE frequencies have the highest amplification by the outer hair feedback system and that the SOAE frequencies correspond to minima in the hearing threshold microstructure (Schloth, 1983). Sisto *et al.* (2001) showed that an analogous relationship exists between the presence of SSOAEs (and more generally, long-lasting OAE presence) and cochlear functionality within a specific frequency range. This property shows promise as a means of monitoring hearing defects early and highlights the possibility of localizing sites of cochlear damage. Hence, the properties of SSOAEs and their connection with TEOAEs warrant further investigation.

In the study reported herein, high-resolution time-frequency analysis based on matching pursuit approach is proposed, in order to further investigate SSOAEs and the properties of their decaying and stable components.

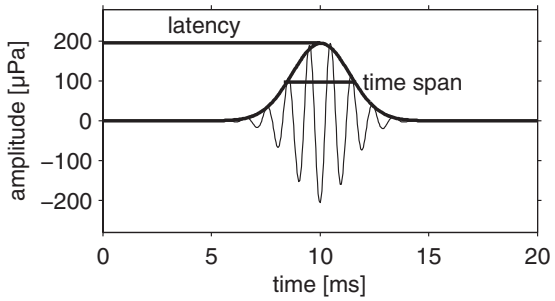


FIG. 1. Example of the Gabor function and definition of the parameters of a TEOAE component derived from the MP procedure.

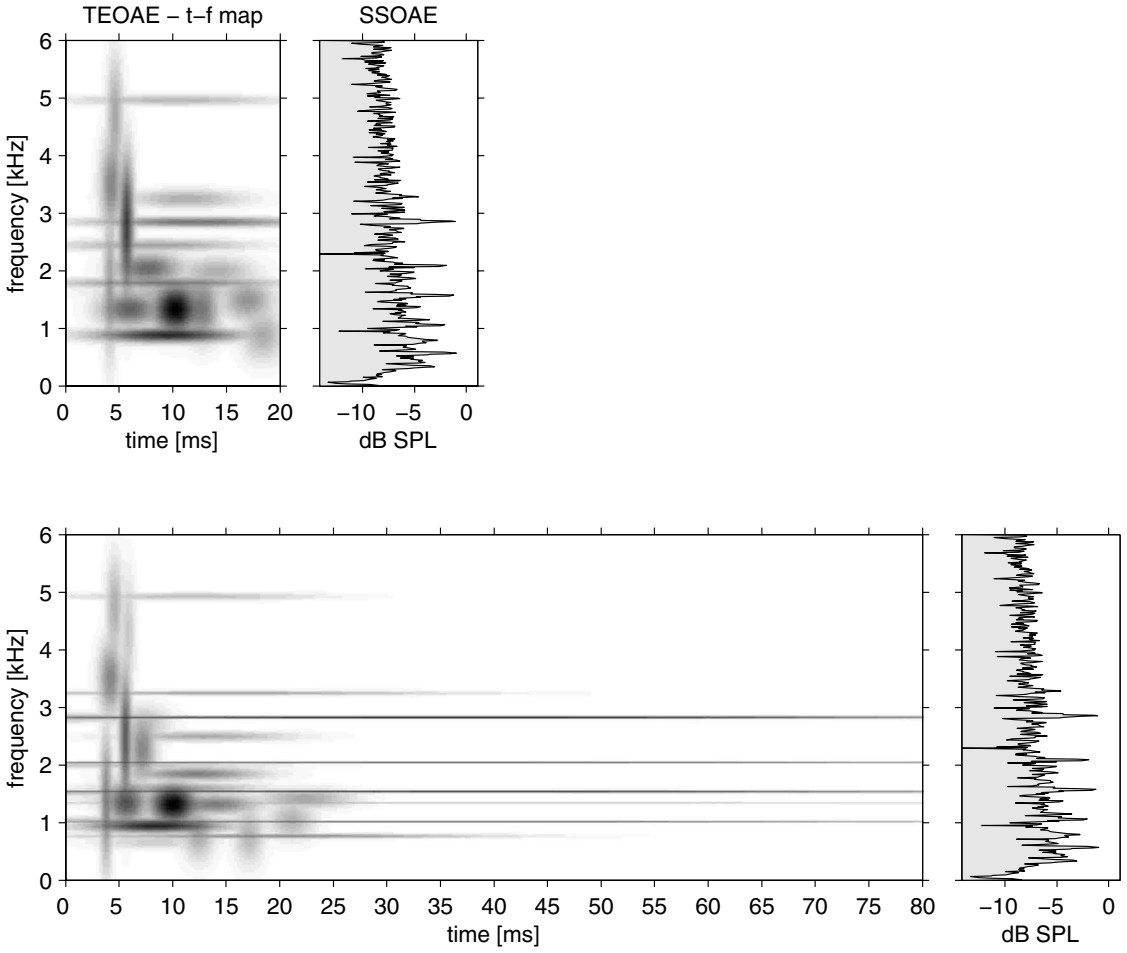


FIG. 2. Comparison of TF distributions of energy for 20 ms (top) and 80 ms signals (bottom) for the same subject. The right-hand panel shows the power spectrum of SSOAEs (signal from 20 to 80 ms). The spectra were rotated to match the frequency axis of the TF map.

II. EXPERIMENTAL PROCEDURE

The OAEs from 46 young females (20–35 years) were measured in low ambient noise conditions using an ILO-88 apparatus (Otodynamics LTD, London) running software version 5. All subjects were laryngologically healthy without any otoscopic ear abnormalities. Impedance audiometry tests revealed normal type A tympanograms and normal acoustic reflexes. In pure-tone audiometry, hearing thresholds were better than 20 dB HL for all test frequencies (0.25, 0.5, 1, 2, 3, 4, 6, and 8 kHz).

Standard click stimuli (average amplitude -80 ± 2 peak dB SPL, nonlinear averaging protocol, described by Kemp *et al.*, 1986) were used to evoke 480 TEOAE responses. The SSOAE spectra were also measured using the default ILO protocol. In accordance with this, the OAEs evoked by click stimuli of 80 dB SPL were recorded in an 80 ms window. The first 20 ms of each averaged response was discarded and the responses from the latter 60 ms were considered to be SSOAEs. In addition, 80 ms waveforms were collected in two consecutive recordings, each consisting of 240 single trials. This number was the maximum number of trials of length 80 ms that could be stored by the ILO system. In this way, 480 single responses were collected for subsequent off-line analysis. Recordings were divided into two sets and two averages A and B were calculated. The quantities $(A+B)/2$ and $(A-B)/2$ were used as signal and noise estimates, respectively. All responses were high-pass filtered at 700 Hz to avoid low-frequency noise.

III. METHOD

The method of adaptive approximations using the matching pursuit (MP) algorithm was introduced by Mallat and Zhang (1993) and first applied to physiological signals by Blinowska and Durka (1994) and to OAE analysis by Jedrzejczak *et al.* (2004). The approach is based on adaptive decomposition of the signal into waveforms (also called atoms) from a large and redundant set of functions (called dictionary). This set of functions is much more extensive than the repertoire of functions used in fast Fourier transform (FFT, sinusoid waves only) or wavelet transform (particular functions bound by an inverse relationship between frequency and time span). Using these latter techniques results in a lower TF resolution (Jedrzejczak *et al.*, 2004). The advantage of the MP algorithm over the traditional wavelet transform is that the former is fully adaptive and does not involve a division of the data into frequency bands. A full description of this method and a comparison between it and other methods of TF analysis, based on simulation studies involving gammatones, can be found in Jedrzejczak *et al.*, 2004 and Jedrzejczak *et al.*, 2006.

In the MP procedure, waveforms are analyzed using an iterative procedure, starting from the waveform that gives the highest value when multiplied by the signal, thus accounting for the largest contribution to the signal energy. The subsequent waveforms are fitted to the residual energy value obtained after each iteration. The procedure may be stopped after the desired percentage of energy has been accounted for or after a given number of iterations (in other words, after certain number of atoms describing the signal were found). It has been shown (Jedrzejczak *et al.*, 2006) that TEOAE responses from healthy adults can be described efficiently by a few (in average 7–10) waveforms (resonance modes), which are characteristic not only for each subject but also for each ear. However, in this case instead of "number of atoms" rule, we use in some degree equivalent criterion of 80% of energy accounted for. In this way, only the substantial part of the signal, i.e., which is not influenced by noise, is subjected to further analysis.

A stochastic dictionary (e.g., Durka *et al.*, 2001) of Gabor functions (sine-modulated Gaussian functions) was used, because these functions provide the highest TF resolution (Mallat, 1999). The size of this dictionary was 10^6 waveforms for 20 ms signals and 4×10^6 waveforms for 80 ms signals. The Gabor function is expressed by the following formula:

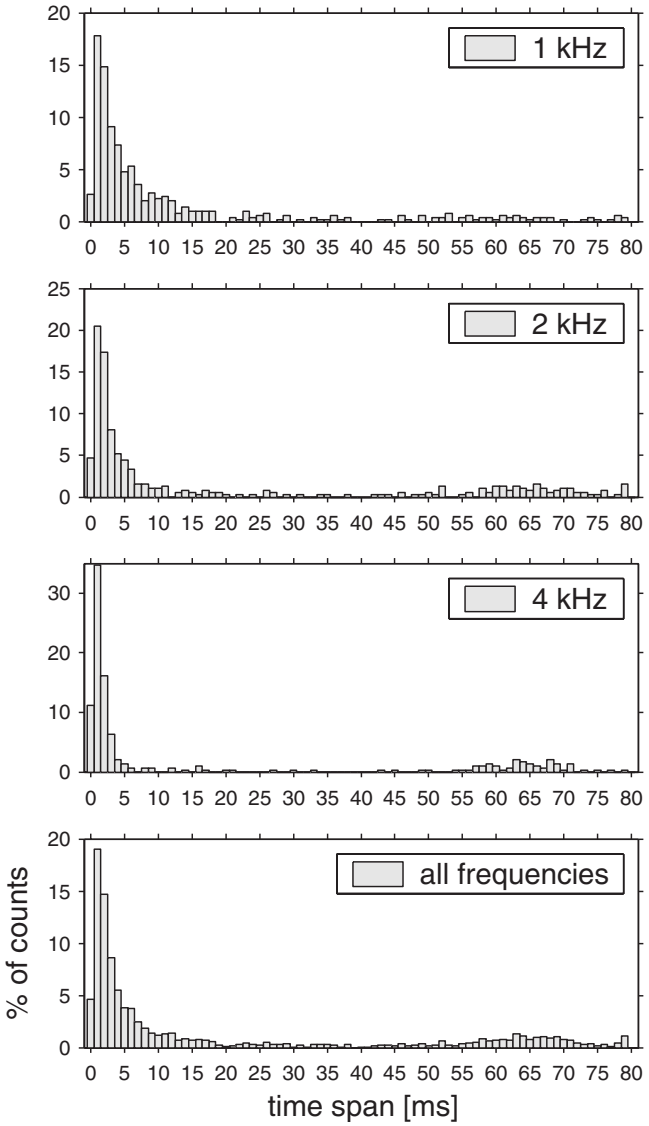


FIG. 3. Histograms of time spans of the OAE components in three octave bands centered at 1, 2, and 4 kHz and cumulative histogram for all frequency bands for 80 ms signals. Note that the vertical scale differs between histograms (for sake of pictures clarity).

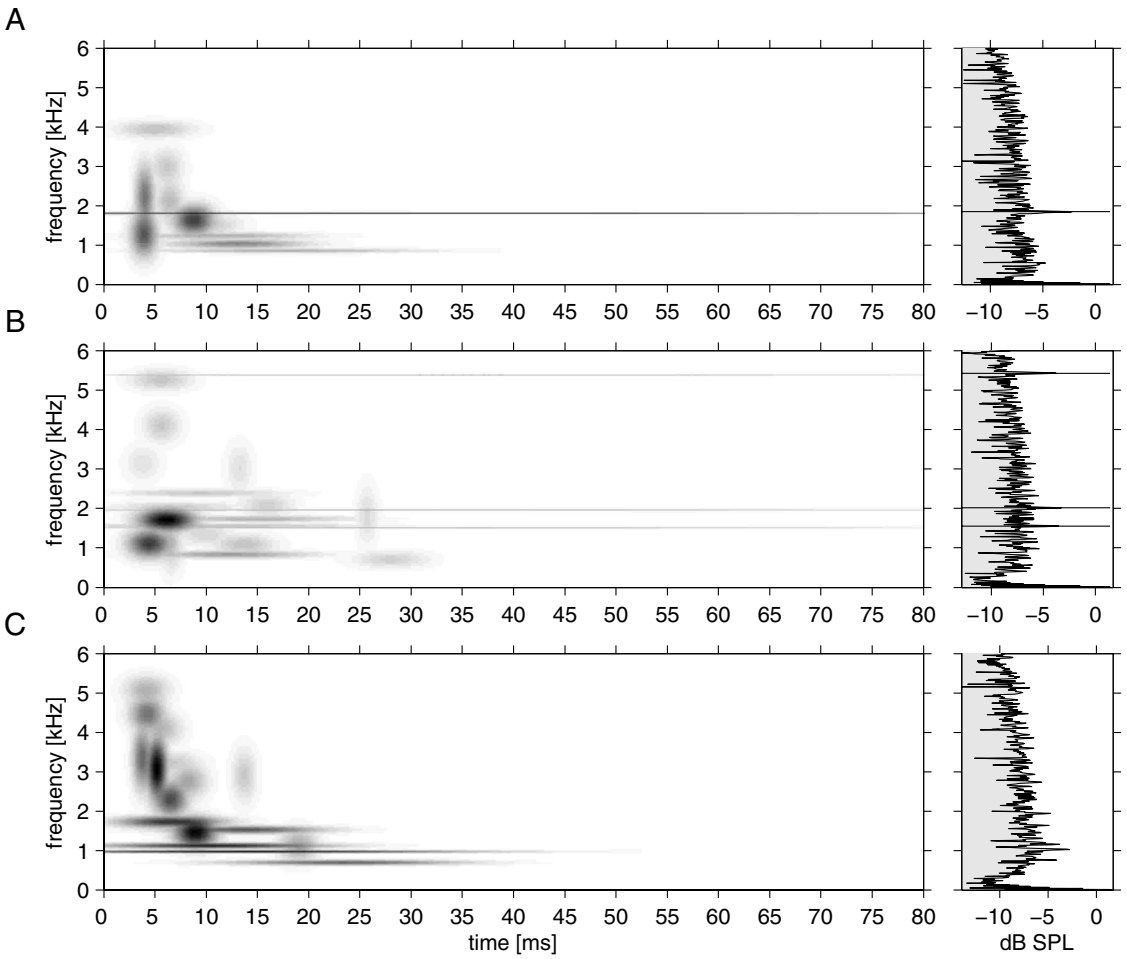


FIG. 4. The left-hand panel shows the TF map of the 80 ms OAE signal. The right-hand panel shows the spectrum of the SSOAEs. (a) Ear with one distinctive SOAE. (b) Ear with multiple SOAEs. (c) Ear without SOAEs but with long-lasting decaying components revealed by TF analysis. The stable long-lasting components found by MP analysis are marked on the SSOAE spectra.

$$g_\gamma(t) = K(\gamma, \phi) e^{-\pi((t-u)/s)^2} \cos(\omega(t-u) + \phi), \quad (1)$$

where amplitude K is chosen such that $\|g_\gamma\| = 1$, $s(>0)$ is the time span, ω is the frequency modulation, u is the latency, and ϕ is the phase.

The use of Eq. (1) permits the description of waveforms by physically meaningful parameters defined as follows: (i) the amplitude is determined as the maximum of the modulus of the waveform at a certain frequency; (ii) the latency is measured as the time taken from onset of the stimulus to the maximum point in the waveform envelope; and (iii) the time-span parameter is defined as half the width of the waveform envelope and can be interpreted as the duration of the waveform (Fig. 1).

By using the MP algorithm, a set of sorted waveforms is obtained, ranked in terms of energy. The TF characteristic is calculated as the superposition of the energies of the waveforms thus obtained. The TF distribution is free of cross terms, which are a cause of blurring in the TF maps that are obtained using the Wigner–Ville, Choi–Williams, or other similar approaches (e.g., Jedrzejczak *et al.*, 2004). The relationship between the waveforms determined by the MP procedure and the resonant modes of TEOAEs was established in Blinowska *et al.* (2007).

For all the parameters investigated, the statistical significance of the differences between the datasets was evaluated using the Wilcoxon rank sum test. This is an equivalent of the student's t-test and is generally used when the populations that are analyzed do not have normal distributions. As a criterion of significance, the 95% confidence level ($p < 5 \times 10^{-2}$) was chosen.

The goodness of fit of the curves was estimated by means of R^2. This is defined as the ratio of the sum of squares of the regression and the total sum of squares. R^2 can take any value between 0 and 1, with a value closer to 1 indicating a better fit.

IV. RESULTS

Figure 2 shows an example of TF distributions of OAE energy for recordings with 20 and 80 ms intervals between stimuli. The maps for the first 20 ms are quite similar. The small differences that arise are probably (i) due to the fact that the 20 ms recordings were registered using a nonlinear protocol (standard TEOAE acquisition mode) and 80 ms recordings using a linear one (standard SSOAE acquisition mode), and (ii) due to fluctuations in the response between measurements. The effect of the different recording protocols

is particularly visible in the first 5 ms of the distributions, where additional structures are evident on the 80 ms map. The difference is connected with the "ringing" phenomenon affecting the first few milliseconds of linear response. When inspecting the lower figure, two general kinds of component may be observed: those of short time span that occur in the first 20 ms and those that are present during the whole 80 ms recording. The latter long-lasting components are characterized by a very narrow bandwidth.

Histograms of the time spans of the waveforms for all subjects are shown in Fig. 3. The data are presented in octave bands with center frequencies of 1, 2, and 4 kHz and for whole frequency range. In all frequency bands, most components have time spans between 0 and 5 ms. However, for higher frequencies there are more components with lower time spans. In all plots, there is a group of very long components of time spans greater than 40 ms. The cumulative plot for whole frequency range is bimodal with second maximum between 60 and 70 ms. This value is influenced strongly by the length of acquisition window. Some long-lasting waveforms may continue outside of the measurement window (as suggested by TF plots), the values of their time spans being determined by the window length. In fact, their time span should be defined as "greater than." About 60% of the components have a time span of 0–5 ms. These components can be classified as "purely" evoked. Stable long-lasting components are defined as those that have a time span longer than 40 ms. The components from the 5–40 ms range do not fall in any of the above categories; they are defined here as longer-lasting, decaying components. An additional criterion for the identification of long-lasting components was their amplitude. Waveforms that had an amplitude higher than the noise level in a given frequency were analyzed further, using estimates from the spectrum of half the difference between buffers A and B, i.e., $(A-B)/2$. The decaying components in high-frequency band are well separated from transient evoked responses. For lower frequency bands, only small drop in histogram around 5 ms testifies for their identity. However, in time-frequency distributions (Figs. 2 and 4), they can be easily perceived as structures of character totally different from typical transient evoked components, not only because of their time span but also because of their frequency band narrower than for typical transient evoked components.

Examples of TF representations of SSOAEs for three subjects are shown in Fig. 4, together with their spectra as provided by the ILO system. The ILO spectrum is very noisy and sometimes it is difficult to determine definite spectral peaks. The long-lasting components that correspond to SSOAEs are easy to identify on TF maps. The three diagrams shown in Fig. 4 illustrate three different types of observed cases: one SSOAE, several SSOAEs, and no SSOAEs. The stable long-lasting components identified by the MP procedure are marked as lines on Fig. 4. For the two upper diagrams, there is good correspondence between the ILO spectra and the TF maps. In the lower picture, in the ILO spectrum, there are some lines that might be thought to be SSOAEs. However, this is not the case as they are not

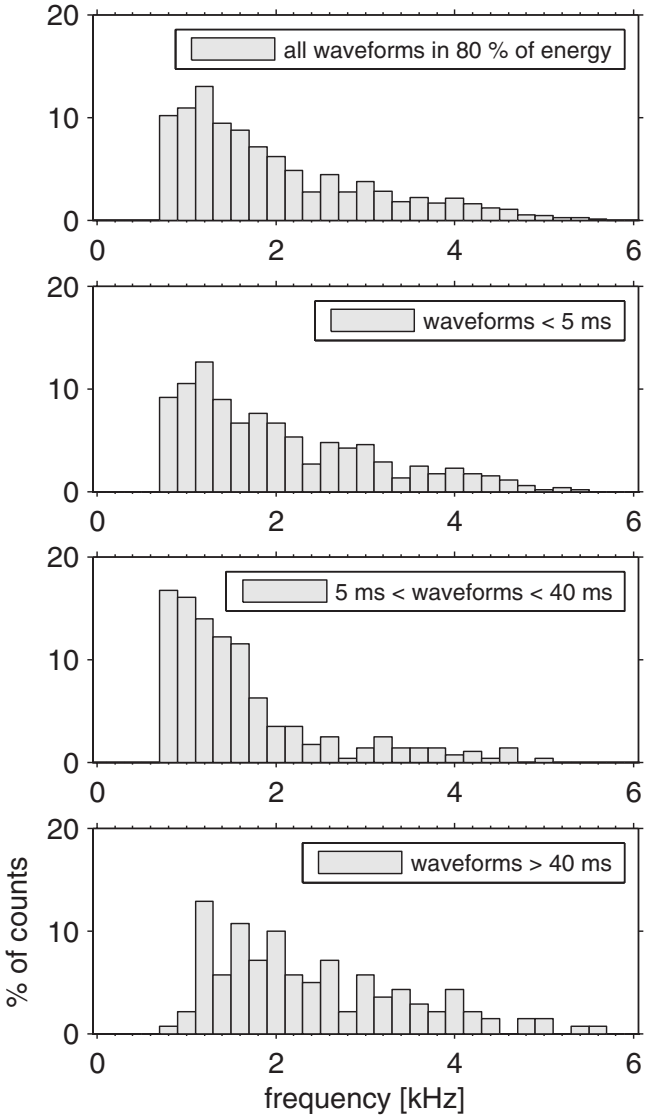


FIG. 5. Distribution of frequencies of waveforms of different durations for the 80 ms signal.

stable throughout whole 80 ms and the longest one diminishes at about 55 ms. They actually correspond to the long-lasting decaying components.

Histograms showing frequency values for waveforms of different durations are shown in Fig. 5. The long-lasting components are divided into two sets: decaying (time span 5–40 ms) and stable (>40 ms). The distributions of the short-lived and stable components are rather similar, with small increases in the higher frequencies of long-lasting components. The decaying long-lasting components are concentrated in the range 1–2 kHz.

Table I shows the statistical data for the incidence of SSOAEs and their long-lasting components. The percentage of subjects with SSOAEs was rather high, similar to the values reported earlier in the literature (e.g., Sisto *et al.*, 2001). We have made a distinction between those components that were present during the whole recording and the decaying components. Statistical data show that in each subject, at least one long-lasting component was present. The contribution of stable long-lasting components, which may be con-

TABLE I. Prevalence and average number (with standard error) of the long-lasting components of SSOAEs as detected by MP analysis.

Number of subjects	46
Prevalence of stable long lasting components	74%
Prevalence of decaying long lasting components	98%
Prevalence of all long lasting components	100%
Average number of stable long lasting components per emitting ear	2.9 ± 0.2
Average number of decaying components per emitting ear	3.8 ± 0.3
Average number of all types of long lasting components per emitting ear	5.3 ± 0.4

sidered to be SOAEs, was high (74%). However, the incidence of decaying components was almost 100%.

The amplitude of the OAE components and their time span appear explicitly as parameters in MP decomposition, which permits the properties of selected waveforms to be estimated. In Fig. 6, the time evolution of the OAE components averaged over all the subjects is shown. The amplitude of the short-lived components rapidly decays toward low values for times >20 ms. Components of durations from 5 to 40 ms decrease much more slowly. Components of duration above 40 ms after an initial rise (note that the first 4.5 ms are affected by the window of the ILO system) stay at an almost constant level, which suggests that they could be "real" SOAEs.

Several types of fits were applied separately to short-lived components and long-lasting components. It was found that the exponential functions gave best results. For short-lived components, the exponential fit: $a_{\text{short}}=467e^{-0.18t}$ (where a is amplitude, and t—time instant) yielded $R^2=0.98$. For longer-lasting components, the dependence: $a_{\text{long}}=74e^{-0.06t}$ was found to result in an equally good fit ($R^2=0.96$). When both types of component were treated together, the fit was much worse ($R^2=0.7$). However, when the double exponential $a_{\text{all}}=435e^{-0.18t}+34e^{-0.003t}$ was used, the fit improved significantly and a value of $R^2=0.98$ was obtained. Note that the exponentials in this fit are similar to those obtained for the fits for short-lived and decaying components alone. For long-lasting components, the parameters of the fitted curves are less similar. This is probably due to the fact that when all components were treated together, the constant amplitude part of the signal was also included. Different functional dependencies for short- and long-lasting components suggest that they have to be treated separately.

Much attention has been devoted to the frequency-latency curve and fitting of the power law functions to this

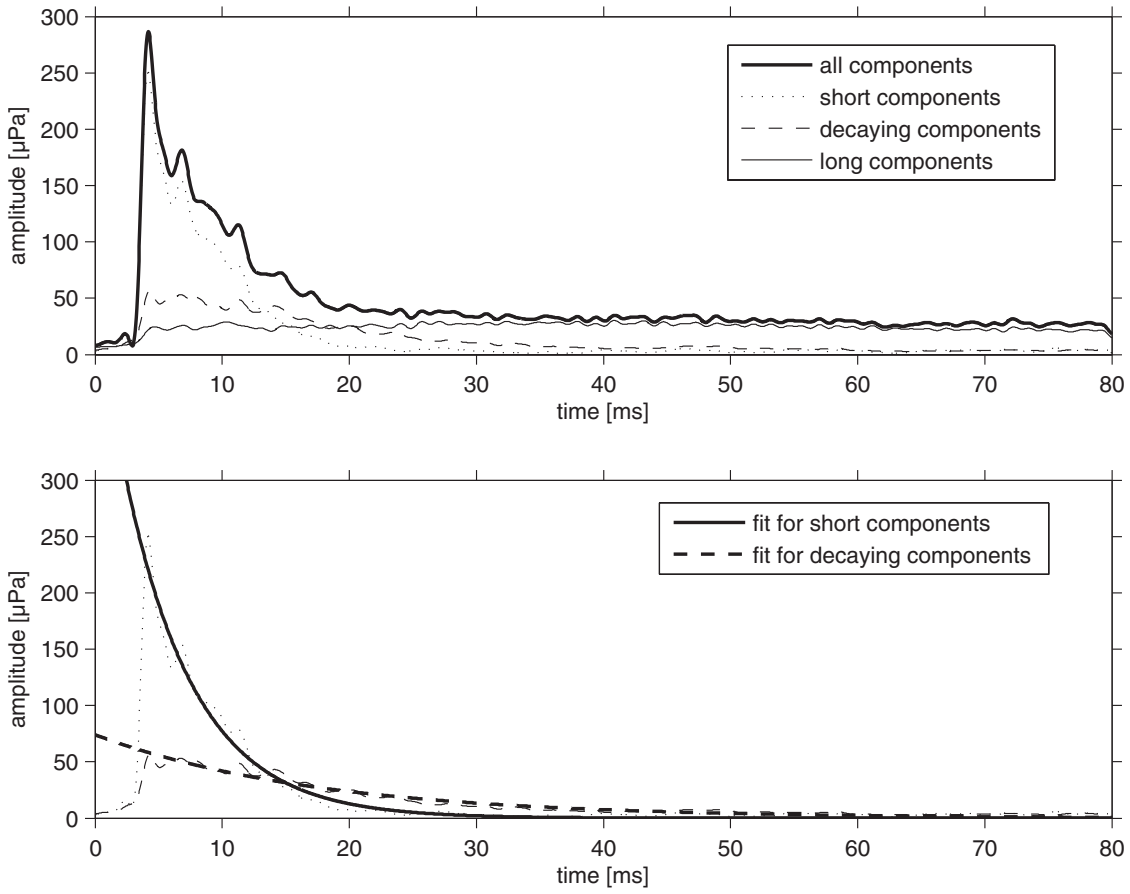


FIG. 6. Top: Averaged amplitude of all signals under investigation. (dotted line) for short-lived components (time span <5 ms), (dashed line) longer-lasting decaying components (5–40 ms), (thin solid line) for long-lasting components (>40 ms), and (thick solid line) for all components. Bottom: Exponential curves as fitted to the data for short-lived and longer-lasting decaying components (starting from the maxima of average amplitude). Several fits were examined and exponentials gave the best results, yielding $R^2=0.98$ for short-lived components ($a_{\text{short}}=467e^{-0.18t}$, where a is the amplitude, and t is the time instant) and $R^2=0.96$ for decaying components ($a_{\text{long}}=74e^{-0.06t}$).

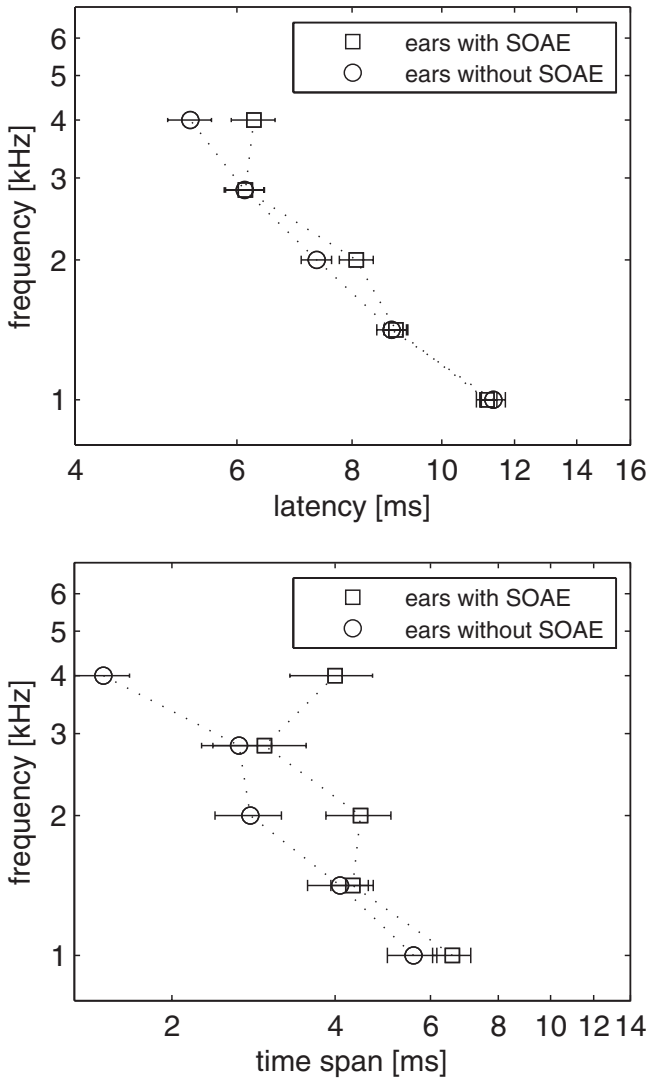


FIG. 7. Half-octave average latencies and time spans in relation to frequency for 20 ms TEOAE signals. The dataset was divided into two sets: ears with and without SOAEs.

relationship (e.g., Tognola *et al.*, 1997; Sisto and Moleti, 2002). In Fig. 7, latencies and time spans of TEOAEs for ears with SOAEs (48 ears) and without SOAEs (44 ears) are compared. The group with SOAEs was formed from ears in which long-lasting components of duration >40 ms were detected. The latency-frequency dependence for a group of ears without SOAEs is power law. It forms a straight line on a log-log scale (Fig. 7). The latencies of the group with SOAEs are slightly greater. This feature is particularly obvious in the case of the 4 kHz band, where the difference in latencies reached 1 ms and the test of significance yielded $p<0.05$. The relationship between frequency and time span revealed even bigger differences between the groups with and without SOAEs.

The advantage of the MP method is that both short-lived and long-lasting components can easily be detected and separated. The idea of removing long-lasting activity from the signal is presented in Fig. 8 for a subject having several long-lasting components. In this figure, the TF distribution of OAE energy for an ear with SSOAEs is illustrated. Below this is shown the same signal after removing the long-lasting components (of time span >5 ms). The TF map thus obtained shows characteristics that suggest the logarithmic dependence of the latency-frequency curve.

The results presented above indicate that TEOAEs are strongly influenced by SSOAEs in quite a high percentage of cases and that the separation of both kinds of components helps in the interpretation of the experimental data.

V. DISCUSSION

Long-lasting components of evoked OAEs were studied previously by Gobsch and Tietze (1993) and Sisto and Moleti (1999). These authors applied spectral analysis using different time windows to study changes in the amplitude and decay times of the long-lasting components. In the study reported herein, high-resolution TF analysis was carried out in order to investigate the evolution of different types of long-lasting components over time. Long-lasting narrowband components in TF maps correspond well with the peaks observed in SSOAE spectra provided by an ILO system.

The advantage of the applied method does not rely only on the high-resolution TF representation. The signal components are parametrized in terms of frequency, amplitude, time occurrence (latency), and time span, which permits the easy separation of waveforms of different characteristics and the statistical analysis of their properties.

The distribution of SSOAE frequencies obtained is very similar to the results presented recently by Kuroda (2007). Sisto *et al.* (2001) found slightly different distributions: most SSOAEs were located in the 0.8–3 kHz range and only a few components lie outside this area. One possible explanation for their findings is that their dataset consisted only of male subjects. The distribution of SSOAEs determined in our study is also similar to those found for SOAEs measured without synchronization by click stimuli (e.g., Burns *et al.*, 1992).

Distributions of frequencies of components of different durations are presented here for the first time. The MP algorithm provides a unique opportunity to construct histograms, not only for SOAEs but also separately for short-lived and longer-lasting decaying components. This was made possible because the time span of the components appears explicitly as a parameter. Other methods, such as FFT and wavelet transform, do not permit this. The frequency histograms of the short-lived components agree with the spectral characteristics of this response (e.g., Sisto and Moleti, 2005). Most of these fall within the region 1–2 kHz, which is similar to the frequency range of SOAEs. For long time-span waveforms, there seem to be comparatively more high-frequency components.

The prevalence of SSOAEs in our study is similar to that presented in previous reports (e.g., Sisto *et al.*, 2001) and similar to studies of SOAEs (e.g., Zhang and Penner, 1998). It is well known that analysis of SSOAEs and SOAEs does not yield exactly the same results (e.g., Wable and Collet, 1994). Some peaks may only be identified in the measurement of SOAEs, while in the measurement of SSOAEs, additional components that are not visible in SOAE spectra may be observed. SOAEs were not measured in our study,

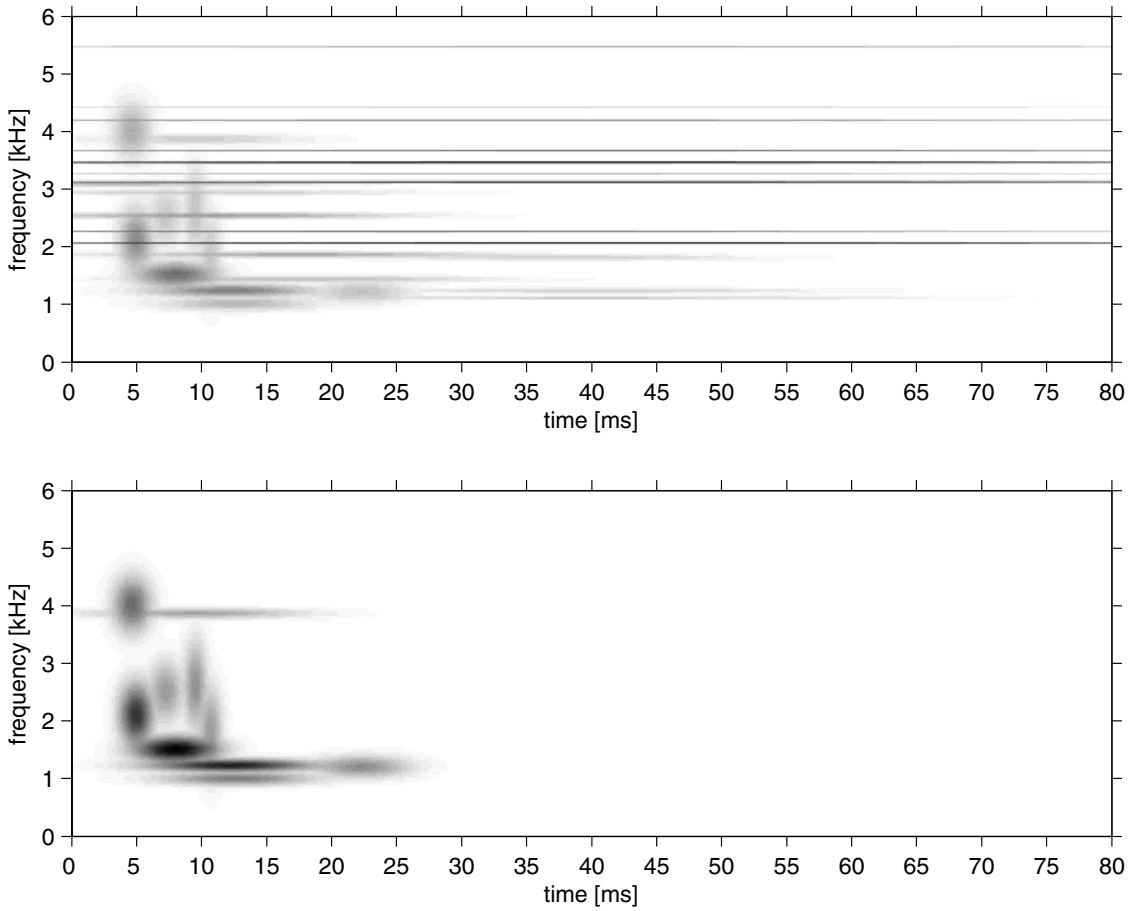


FIG. 8. Example of a TF distribution of energy for a subject with multiple SOAEs. In the bottom map, long-lasting components were removed to reveal the purely evoked part of the signal.

but on the basis of the properties of the components, we can speculate that it is the long-lasting decaying components that are responsible for the peaks that occur in SSOAE spectra that are in addition to those that occur in SOAE spectra. The incidence of decaying components is higher than the incidence of stable ones. Similar to SOAEs, they may play a substantial role in the TEOAE signal.

Our analysis showed that evoked OAE consists of three types of activity: short-term components (<5 ms), longer-lasting decaying components (5–40 ms), and stable components (>40 ms). This last category of activity is characterized by energy that is practically constant in time and can therefore be categorized as SOAEs.

Similar to our results, Sisto *et al.* (2001) observed two types of long-lasting component: ones that were present during the whole measurement period and decaying components. The waveforms of the longer decaying components (5–40 ms) identified here, correspond to the decaying components identified by Sisto *et al.* (2001). The amplitude of decay was approximated by an exponential relationship (Sisto and Moleti, 1999). In our study, exponential functions yielded best fits to the short lived, as well as to the longer-lasting decaying components, albeit with different parameters. The time evolution of 5–40 ms components bears a resemblance to TEOAEs (Fig. 6). However, their narrow bandwidth makes them similar to SOAEs. Talmadge *et al.* (1998) described slow-decay components as "resonant TEOAEs." We hypothesize that there are some kinds of resonant modes that bear a resemblance to SOAEs, but they have to be evoked by stimuli and, not being self-sustained, they decay with time. Short-lived components that appear in TEOAE also have the characteristic of resonant modes (Jedrzejczak *et al.*, 2004), which follows from the stability of their TF features. It appears that the cochlea has three different kinds of resonant mode: (1) very short duration and broad bandwidth, (2) narrowband resonant modes decaying in time, and (3) sustained narrowband resonance modes observed as SOAEs.

There have been several attempts to automate the detection of SOAEs based on FFT. Zhang and Penner (1998) proposed a procedure in which the spectrum was first flattened over the whole frequency range and then peaks above a threshold were compared with the histogram of the noise energy. Later, Pasanen and McFadden (2000) presented an algorithm based on the identification of peaks that exceeded a smoothed noise spectrum. Their results for the incidence of SOAEs were similar to those of previous studies (e.g., Talmadge *et al.* 1993). In comparison with the spectral analysis used by these authors, the MP approach yields the additional parameter of time span, which best distinguishes the different kinds of component. Further characteristics of SOAEs, best visible on the high-resolution TF plots yielded by the

MP algorithm, are the narrow bandwidth and the stability of frequency. The analysis based on these features allows noise to be separated efficiently from SOAEs.

SOAEs have a great influence on TEOAEs. It has been shown that the amplitudes of TEOAEs are higher for subjects with SOAEs (e.g., Kulawiec and Orlando, 1995; Osterhammel *et al.*, 1996; Schmuziger *et al.*, 2005). SOAEs can also influence the estimation of other parameters that are associated with TEOAEs, such as latency. Their contribution to TEOAEs can produce additional maxima in the time evolution of TEOAEs. It can affect the estimate of latency according to its common definition, i.e., the time from the onset of the stimulus to the maximum point on the envelope of the waveform (as described by Probst *et al.*, 1991). This artifact is not connected with any particular method, and would have the same effect in terms of the latency shift, e.g., for filtering, wavelet transform, or even when latency is calculated from tone-burst evoked OAEs. MP analysis that provides an additional time-span parameter gives better control over the latency estimate. It characterizes any discrepancies of duration of OAE components. An example of this problem could be the difference in the latency observed in full term compared with preterm neonates as reported by Tognola *et al.* (2005). It was later found that this feature was caused by the higher number of long-lasting components in preterm neonates (Jedrzejczak *et al.*, 2007). After the removal of the long-lasting components from the preterm data, the frequency-latency dependence became similar for both groups. The effect of removing the long-lasting components from the TEOAE signal was more recently noted by Notaro *et al.* (2007). Until recently, the influence of SOAEs on TEOAEs was removed only by excluding from the dataset ears in which SOAEs have been detected (e.g., Hoth *et al.*, 2007).

VI. CONCLUSIONS

The prevalence of SSOAEs determined using MP analysis was similar to the results in previous reports that were obtained using different methods. MP analysis can be used as a tool for the automated detection of SOAEs and is capable of distinguishing decaying components from stable ones. Many long-lasting components are stable over time, which can be used as an argument for their being real SOAEs. By increasing the acquisition window and applying TF analysis, one can combine the measurement of evoked and spontaneous response. The spontaneous components can be removed from further analysis of the evoked response and their properties can be described separately.

ACKNOWLEDGMENTS

The authors would like to thank David T. Kemp for providing information about the structure of the data files created by the ILO equipment. This research was funded by the Polish Ministry of Science and Higher Education within the framework of the 2007-2010 Scientific Support Program (Grant No. N N518 0924 33).

Blinowska, K. J., and Durka, P. J. (**1994**). "The Application of Wavelet Transform and Matching Pursuit to the Time-Varying EEG signals," in *Intelligent Engineering Systems Through Artificial Neural Networks*, edited by C. H. Dagli, and B. R. Fernandez, (ASME, New York), Vol. **4**, pp. 535–540.

Blinowska, K. J., Jedrzejczak, W. W., and Konopka, W. (**2007**). "Resonant modes of otoacoustic emissions," Physiol. Meas **28**, 1293–1302.

Brienesse, P., Anteunis, L. J., Maertzdorf, W. J., Blanco, C. E., and Manni, J. J. (**1997**). "Frequency shift of individual spontaneous otoacoustic emissions in preterm infants," Pediatr. Res. **42**, 478–483.

Burns, E. M., Arehart, K. H., and Campbell, S. L. (**1992**). "Prevalence of spontaneous otoacoustic emissions in neonates," J. Acoust. Soc. Am. **91**, 1571–1575.

Burns, E. M., Campbell, S. L., and Arehart, K. H. (**1994**). "Longitudinal measurements of spontaneous otoacoustic emissions in infants," J. Acoust. Soc. Am. **95**, 385–394.

Durka, P. J., Ircha, D., Neuper, C., and Pfurtscheller, G. (**2001**). "Time-frequency microstructure of event-related electro-encephalogram desynchronisation and synchronisation," Med. Biol. Eng. Comput. **39**, 315–321.

Frick, L. R., and Matthies, M. L. (**1998**). "Effects of external stimuli on spontaneous otoacoustic emissions," Ear Hear. **9**, 190–197.

Gobsch, H., and Tietze, G. (**1993**). "Interrelation of spontaneous and evoked otoacoustic emissions," Hear. Res. **69**, 176–181.

Hoth, S., Polzer, M., Neumann, K., and Plinkert, P. (**2007**). "TEOAE amplitude growth, detectability, and response threshold in linear and nonlinear mode and in different time windows," Int. J. Audiol. **46**, 407–418.

Jedrzejczak, W. W., Blinowska, K. J., Konopka, W., Grzanka, A., and Durka, P. J. (**2004**). "Identification of otoacoustic emission components by means of adaptive approximations," J. Acoust. Soc. Am. **115**, 2148–2158.

Jedrzejczak, W. W., Blinowska, K. J., and Konopka, P. J. (**2006**). "Resonant modes in transiently evoked otoacoustic emissions and asymmetries between left and right ear," J. Acoust. Soc. Am. **119**, 2226–2231.

Jedrzejczak, W. W., Hatzopoulos, S., Martini, A., and Blinowska, K. J. (**2007**). "Otoacoustic emissions latency difference between full-term and preterm neonates," Hear. Res. **231**, 54–62.

Kemp, D. T., Bray, P., Alexander, L., and Brown, A. M. (**1986**). "Acoustic emission cochleography-practical aspects," Scand. Audiol. Suppl. **25**, 71–95.

Konrad-Martin, D., and Keefe, D. H. (**2003**). "Time-frequency analyses of transient-evoked stimulus-frequency and distortion-product otoacoustic emissions: Testing cochlear model predictions," J. Acoust. Soc. Am. **114**, 2021–2043.

Kulawiec, J. T., and Orlando, M. S. (**1995**). "The contribution of spontaneous otoacoustic emissions to the click evoked otoacoustic emissions," Ear Hear. **16**, 515–520.

Kuroda, T. (**2007**). "Clinical investigation on spontaneous otoacoustic emission (SOAE) in 447 ear," Auris Nasus Larynx **34**, 29–38.

Kuroda, T., Fukuda, S., Chida, E., Kashiwamura, M., Matsumura, M., Ohwatari, R., and Inuyama, Y. (**2001**). "Effects of spontaneous otoacoustic emissions on distortion product otoacoustic emission," Auris Nasus Larynx **28**, 33–38.

Lind, O., and Randa, J. S. (**1992**). "Spontaneous otoacoustic emissions. Short-time stability," Acta Oto-Laryngol., Suppl. **492**, 79–81.

Mallat, S. G. (**1999**). *Wavelet Tour of Signal Processing* (Academic, New York).

Mallat, S. G., and Zhang, Z. (**1993**). "Matching pursuit with time-frequency dictionaries," IEEE Trans. Signal Process. **41**, 3397–3415.

Morlet, T., Lapillonne, A., and Ferber, C. (**1995**). "Spontaneous otoacoustic emissions in preterm neonates: prevalence and gender effect." Hear. Res. **90**, 44–54.

Notaro, G., Al-Maamury, A. M., Moleti, A., and Sisto, R. (**2007**). "Wavelet and matching pursuit estimates of the transient-evoked otoacoustic emission latency," J. Acoust. Soc. Am. **122**, 3576–3585.

Osterhammel, P. A., Rasmussen, A. N., Olsen, S., and Nielsen, L. H. (**1996**). "The influence of spontaneous otoacoustic emissions on the amplitude of transient-evoked emissions," Scand. Audiol. **25**, 187–192.

Ozturan, O., and Oysu, C. (**1999**). "Influence of spontaneous otoacoustic emissions on distortion product otoacoustic emission amplitudes," Hear. Res. **127**, 129–136.

Pasanen, E. G., and McFadden, D. (**2000**). "An automated procedure for identifying spontaneous otoacoustic emissions," J. Acoust. Soc. Am. **108**, 1105–1116.

Penner, M. J., Brauth, S. E., and Jastreboff, P. J. (**1994**). "Covariation of binaural, concurrently-measured spontaneous otoacoustic emissions," Hear. Res. **73**, 190–194.

Penner, M. J., and Zhang, T. (**1997**). "Prevalence of spontaneous otoacoustic emissions in adults revisited," Hear. Res. **103**, 28–34.
Prieve, B. A., and Falter, S. R. (**1995**). "COAEs and SSOAEs in adults with increased age," Ear Hear. **16**, 521–528.
Prieve, B. A., Fitzgerald, T. S., and Schulte, L. E. (**1997**). "Basic characteristics of click-evoked otoacoustic emissions in infants and children," J. Acoust. Soc. Am. **102**, 2860–2870.
Probst, R., Coats, A. C., Martin, G. K., and Lonsbury-Martin, B. L. (**1986**). "Spontaneous, click-, and toneburst-evoked otoacoustic emissions from normal ears," Hear. Res. **21**, 261–75.
Probst, R., Lonsbury-Martin, B. L., and Martin, G. K. (**1991**). "A review of otoacoustic emissions," J. Acoust. Soc. Am. **89**, 2027–2067.
Schloth, E. (**1983**). "Relation between spectral composition of spontaneous otoacoustic emissions and fine structure of threshold in quiet," Acustica **53**, 250–256.
Schmuziger, N., Probst, R., and Smurzynski, J. (**2005**). "Otoacoustic emissions and extended high-frequency hearing sensitivity in young adults," Int. J. Audiol. **44**, 24–30.
Sisto, R., and Moleti, A. (**1999**). "Modelling otoacoustic emissions by active non linear oscillators," J. Acoust. Soc. Am. **106**, 1893–1906.
Sisto, R., and Moleti, A. (**2002**). "On the frequency dependence of the otoacoustic emission latency in hypoacoustic and normal ears," J. Acoust. Soc. Am. **111**, 297–308.
Sisto, R., and Moleti, A. (**2005**). "On the large-scale spectral structure of otoacoustic emissions," J. Acoust. Soc. Am. **117**, 1234–1240.
Sisto, R., Moleti, A., and Lucertini, M. (**2001**). "Spontaneous otoacoustic emissions and relaxation dynamics of long decay time OAEs in audiometrically normal and impaired subjects," J. Acoust. Soc. Am. **109**, 638–647.
Smurzynski, J., and Probst, R. (**1998**). "The influence of disappearing and reappearing spontaneous otoacoustic emissions on one subject's threshold microstructure," Hear. Res. **115**, 197–205.
Talmadge, C. L., Long, G. R., Murphy, W. J., and Tubis, A. (**1993**). "New off-line method for detecting spontaneous otoacoustic emissions in human subjects," Hear. Res. **71**, 170–182.
Talmadge, C. L., Tubis, A., Long, G. R., and Piskorski, P. (**1998**). "Modeling otoacoustic emission and hearing threshold fine structures," J. Acoust. Soc. Am. **104**, 1517–1543.
Tognola, G., Grandori, F., and Ravazzani, P. (**1997**). "Time-frequency distributions of click-evoked otoacoustic emissions," Hear. Res. **106**, 112–122.
Tognola, G., Parazzini, M., de Jager, P., Brienesse, P., Ravazzani, P., and Grandori, F. (**2005**). "Cochlear maturation and otoacoustic emissions in preterm infants: a time-frequency approach," Hear. Res. **199**, 71–80.
van Dijk, P., Wit, H. P., Tubis, A., Talmadge, C. L., and Long, G. R. (**1994**). "Correlation between amplitude and frequency fluctuations of spontaneous otoacoustic emissions," J. Acoust. Soc. Am. **96**, 163–169.
Wable, J., and Collet, L. (**1994**). "Can synchronized otoacoustic emissions really be attributed to SOAEs?" Hear. Res. **80**, 141–145.
Zhang, T., and Penner, M. J. (**1998**). "A new method for the automated detection of spontaneous otoacoustic emissions embedded in noisy data," Hear. Res. **117**, 107–113.

Dissociation between distortion-product and click-evoked otoacoustic emissions in sheep (*Ovis aries*)

Dennis McFadden[a] and Edward G. Pasanen
Department of Psychology and Center for Perceptual Systems, University of Texas, 1 University Station, A8000 Austin, Texas 78712-0187

Michelle D. Valero
Department of Biology, University of Texas at San Antonio, San Antonio, Texas 78249

Eila K. Roberts and Theresa M. Lee
Department of Psychology and Reproductive Sciences Program, University of Michigan, Ann Arbor, Michigan 48109

(Received 15 May 2008; revised 14 August 2008; accepted 15 August 2008)

Distortion-product otoacoustic emissions (DPOAEs) were weak or absent in about one-third of sheep (*Ovis aries*) of both sexes tested for otoacoustic emissions (OAEs) even though their click-evoked OAEs (CEOAEs) seemingly were typical of other sheep of the same sex. Various pieces of evidence suggest that the absence of measurable DPOAEs was unlikely to be attributable to anesthetic effects, a poorly located probe tip, a pressure differential between middle and outer ears, season of the year, body position during testing, temperature effects, or previous medical history. Sheep apparently can exhibit a marked dissociation between DPOAEs and CEOAEs. In those sheep having measurable DPOAEs, the DPOAEs were stronger in males than in females, which is the opposite direction of effect from the CEOAEs measured in these same sheep and in humans. In female sheep exposed to higher-than-normal levels of androgens during gestation, the measurable DPOAEs were stronger than in untreated females. Although this also was the opposite direction of effect from expected, it still was a shift in the male direction, in accord with past findings about the masculinizing effects of androgens on OAEs. In sheep, androgen exposure appears to have different effects on the mechanisms underlying DPOAEs from those underlying CEOAEs. © *2008 Acoustical Society of America.* [DOI: 10.1121/1.2982402]

PACS number(s): 43.64.Jb, 43.64.Bt, 43.66.Ki, 43.66.Gf [BLM] Pages: 3730–3738

I. INTRODUCTION

Current thinking is that the different forms of otoacoustic emissions (OAEs) originate from somewhat different underlying mechanisms. Shera and Guinan (1999) argued that spontaneous OAEs (SOAEs) and click-evoked OAEs (CEOAEs) originate primarily from a linear, reflection-based mechanism whereas distortion-product OAEs (DPOAEs) depend on both the reflection-based mechanism and a nonlinear distortion mechanism. A number of lines of evidence led Shera and Guinan (1999) to this distinction; among them was the fact that some agents or manipulations that affect the strength of CEOAEs have either less effect on or a well-delayed effect on DPOAEs. For example, the administration of aspirin or quinine sulfate to humans rapidly diminished the strength of SOAEs and CEOAEs, but DPOAEs were diminished less, and more slowly (e.g., Wier *et al.*, 1988; McFadden and Pasanen, 1994; also see Whitehead *et al.*, 1996). In the few studies where both CEOAEs and DPOAEs have been measured in the same individuals (Smurzynski and Kim, 1992; Moulin *et al.*, 1993; Gorga *et al.*, 1993), the correlations between the two measures have been lower than the correlations typically seen between CEOAEs and SOAEs (e.g., McFadden *et al.*, 2008a). These various partial dissociations are understandable if the crucial underlying mechanisms are different for the different forms of OAE (Shera and Guinan, 1999). Human DPOAEs also exhibit a considerably smaller sex difference from those exhibited by CEOAEs and SOAEs (reviewed by McFadden *et al.*, 2008a).

Recently, while collecting OAE data on a sample of sheep, we encountered a number of animals having normal-appearing CEOAEs but only very weak or absent DPOAEs. This was not universal for the species, for either sex, nor for any specific treatment group (some animals had been given androgens or estrogens prenatally or postnatally). Indeed, many sheep of both sexes exhibited quite strong DPOAEs along with strong CEOAEs. Below we discuss a number of possible technical and procedural explanations for this dissociation, but none was adequate to explain our outcomes. Accordingly, we believe that these are true instances of CEOAEs existing in ears lacking DPOAEs, which is logically possible if the mechanisms underlying the two types of OAE are different (Shera and Guinan, 1999). The CEOAE data from sheep already have been reported (McFadden *et al.*, 2008b); the DPOAE data are reported separately here because of their significance for research on underlying mechanisms. The implication is that the processes primarily responsible for producing DPOAEs can be weak without preventing that ear from producing CEOAEs.

[a]Author to whom correspondence should be addressed. Electronic mail: mcfadden@psy.utexas.edu

 © 2008 Acoustical Society of America

II. METHODS

Only a brief summary of the subjects and procedures will be presented here; additional details can be found in McFadden *et al.* (2008b). All experimental procedures were performed in accordance with NIH guidelines and were approved by the University Committees on the Use and Care of Animals at both UM and UT. OAE measurements were obtained during three multiday visits of the UT team to Ann Arbor: in mid-November and mid-December 2006 and in mid-May 2007. The UM team created the various groups of treated animals to test an array of ideas about endocrine function and sex-typical behavior in sheep; they generously agreed to add the OAE measurements to their protocol long after the original planning and onset of their primary studies. The timing of the measurement sessions for OAEs was dictated by the schedule for the original projects.

A. Subjects

The sheep tested (*Ovis aries*) were of the Suffolk variety. At the time of OAE testing, the ages were approximately 20–26 months and approximately 8–14 months for the females and males, respectively. Because puberty begins at about 6 months for females and at about 2 months for males, all of the sheep tested can be considered young adults (Kosut *et al.*, 1997). The nominal lifespan of sheep is 8–13 years.

The mothers of some of the sheep tested had been administered various hormones during their pregnancy. As a consequence, some of the sheep tested had been exposed to higher-than-normal levels of testosterone, dihydrotestosterone (DHT), or estradiol during prenatal development. The duration of gestation in sheep is about 147 days. The drug administrations occurred regularly beginning on day 30 of gestation and ending on day 90. The surge in androgen production that occurs normally in developing male sheep fetuses also begins about day 30 and lasts through about day 90 of gestation. Some sheep were gonadectomized (GDX) soon after birth, including sheep both treated and not treated with hormones prenatally. Thus, there were males and females that were untreated/intact, untreated/GDX, testosterone-treated/GDX, etc. Because essentially all of the non-GDX males had been vasectomized early in life, here we will denote the untreated/intact males as untreated/VX.

B. Procedure

The sheep lived outdoors in a natural environment at the Reproductive Sciences Program Sheep Research Facility (Ann Arbor, MI; 42 deg 18 min north latitude). Two days before testing, sheep were isolated and solid food was withheld. Just prior to their test session, sheep were brought to the test location where they were injected with ketamine hydrochloride (4–6 mg/kg, iv) and diazepam (0.2–0.3 mg/kg, iv), intubated, and placed on a thick foam pad on a surgical table. In Fall 2006, the sheep were placed supine on the table, and in Spring 2007, they lay on their right side. For both body positions, the left ear was oriented upward. The sheep's hindquarters were elevated several inches above its head to permit drainage from the rumen, throat, and mouth. Anesthesia was maintained with a mixture of halothane gas (approximately 1.5%) in nitrous oxide (1/3) and oxygen (2/3). Otoscopy was performed, the ear canals were cleaned as necessary (female ear canals required less cleaning than male's), and a probe tip was fitted into the left ear canal. For most animals, CEOAEs and DPOAEs were collected for the left ear only.

Two Etymotic ER-2 earphones (Etymotic Research, Elk Grove Village, IL) were used to present the two primary tones needed to evoke DPOAEs, and an Etymotic ER-10B+ microphone was used to record the sounds from the ear canal. Typically, rubber tips originally made for otoadmittance measurements were fitted over the end of the Etymotic probe tip, but for some especially large canals, special oversized foam plugs were fitted. The probe tip was traversed by two silicon sound-delivery tubes attached to the two earphones.

Stimuli were presented and responses collected using a Macintosh laptop computer (Power Macintosh G3, Apple Computer, Cupertino, CA) connected to a data-acquisition board (PCI-4451, National Instruments, Austin, TX) that was installed in a PCI-bus-extension chassis. All stimulus presentation and data collection was accomplished using custom-written LabView software (National Instruments, Austin, TX) running on the Macintosh laptop computer. A 50-kHz sampling rate (16-bit precision) was used both for digitizing the output from the microphone system and for generating the acoustic stimuli for presentation to the ear.

Typically, the DPOAE data were collected after CEOAE data had been collected. (For the first few sheep tested, CEOAEs were collected only with clicks at 75 dB peak-equivalent sound-pressure level (peSPL), but for the majority of animals, CEOAEs were collected with both 75- and 81-dB clicks.) The procedure used to measure DPOAEs was a variant of CUBDIS (Allen, 1990); details of our version have been published (McFadden *et al.*, 2006a). Briefly, two primary tones, f_1 and f_2 ($f_2 > f_1$), of equal sound-pressure level and having a frequency ratio (f_2/f_1) of approximately 1.21, were presented for 4-s intervals while the frequency region centered on $2f_1-f_2$ was monitored.

The levels of the primaries initially were set to 50 dB each, and if a distortion product of −10 dB SPL or stronger was measured, then the levels of the primaries were diminished by 7 dB. If the distortion product still was at least −10 dB SPL, then the levels of the primaries were reduced again by 7 dB, and so on until the distortion product was less than −10 dB SPL. Then the levels of the primaries were set to 57 dB each, the distortion product was measured, and the primary levels were increased again until either the levels reached 71 dB each or the magnitude of the distortion product increased less than 3 dB for a 7-dB increase in the primaries. The result was a gain function relating the strength of the distortion product to the level of the primaries. After that sequence was complete, the frequencies of the two primaries were increased by approximately 100 Hz, their levels both were set to 50 dB, and the sequence just described was implemented again until another gain function was obtained. This procedure was repeated until six gain functions were obtained in a localized frequency region. A similar set of six gain functions was obtained in two other frequency regions; the three frequency regions for the DPOAEs themselves

were approximately 2.0–2.5, 3.3–3.8, and 5.0–5.5 kHz. (These correspond to frequency ranges of about 3.06–3.83, 5.05–5.82, and 7.66–8.42 kHz, respectively, for the f_2 tone.) The data for the three frequency regions were collected in a different order for each subject. The six gain functions within each frequency region were combined to produce one composite gain function for each frequency region for each ear (for the details see McFadden *et al.* 2006a), and those composite gain functions were used to obtain estimates of the strength of the primary tones necessary to generate a distortion product of 0 dB SPL. Thus, in this context, the presence of a strong distortion product is revealed by *small* values of the estimated primary levels. In order to avoid confusion, we generally will discuss the results in terms of the relative strength of the DPOAEs themselves, not the levels of the primaries necessary to elicit a constant DPOAE strength.

The *N*s for all of the groups studied were small even before the loss of the no-DPOAE animals. The usefulness of statistical tests for placing individual comparisons in perspective therefore was diminished. As a supplement to statistical tests, we provide effect sizes, which are calculated as the difference between the means of the two groups of interest divided by the square root of the weighted mean of the two variances for those two groups. According to Cohen (1992), effect sizes of 0.2, 0.5, and 0.8 correspond to small, medium, and large effects, respectively. All *t*-tests conducted were equal variance, unmatched, and two tailed.

III. RESULTS

The absence of measurable DPOAEs in a large fraction of both the male and female sheep means that our ability to reach confident conclusions about treatment effects was reduced. Accordingly, the primary emphasis here is on the characteristics of the sheep having no measurable DPOAEs and on possible procedural details that might have contributed to this anomalous outcome. Analyses for sex differences and treatment effects also are reported, but considerable caution is necessary when interpreting those outcomes because of the possibility of a selection bias existing in the attrition process. For background, we note that the CEOAEs of sheep having, and not having, DPOAEs were not noticeably different, so those two groups were pooled for the presentation of those data (McFadden *et al.*, 2008b).

A. Characteristics of sheep not having DPOAEs

The absence of DPOAEs in the presence of apparently typical CEOAEs seemingly had no relationship to the various treatment groups in either sex. In Table I are shown both the number of sheep having DPOAEs (the numerators) and the total number of sheep from which OAE measures were obtained in each of the various treatment categories (the denominators). Also, one additional untreated/intact female had extremely weak DPOAEs in all three frequency regions, three of the four untreated/GDX females had no measurable DPOAEs in two frequency regions and very weak DPOAEs in the 3.5-kHz region, and two other males had no measurable DPOAEs in one of the three frequency regions. Thus, slightly more than one-third of the animals had no, or weak, DPOAEs across both the sexes and the treatment groups. As noted, this loss of animals substantially reduced our ability to make trustworthy statistical comparisons between groups, and consequently we emphasize effect sizes.[1]

TABLE I. Number of female and male sheep exhibiting DPOAEs in at least one frequency region (numerator) and number of sheep measured in that category (denominator). For this study, the untreated and untreated/GDX sheep were combined within sex to create the two control groups, and the non-obese and obese females were combined to create a single female prenatal-testosterone group. GDX represents gonadectomized; DHT represents dihydrotestosterone; untreated males were vasectomized (VX).

Group		Female	Male
Untreated		6/8	5/9
Untreated/GDX		4/4	5/6
Prenatal testosterone			
	Non-obese	8/12	3/5
	Obese	5/6	0/0
Prenatal estradiol (E_2)		4/4	0/0
Prenatal DHT		0/0	3/4

B. CEOAE strength in sheep not having DPOAEs

The CEOAEs exhibited by the sheep having no DPOAEs varied widely in strength. As a way of demonstrating that fact, special scattergram plots were prepared. Figures 1 and 2 show the scattergrams for females and males, respectively. For these figures, each sheep contributed three DPOAE values (one for each frequency region), all plotted at a single CEOAE value. In both figures, ordinate values greater than 90 dB are dummy values assigned when a sheep lacked DPOAEs in one or more of the three frequency regions measured. (Three additional female sheep and two additional male sheep had usable DPOAE data, but they do not

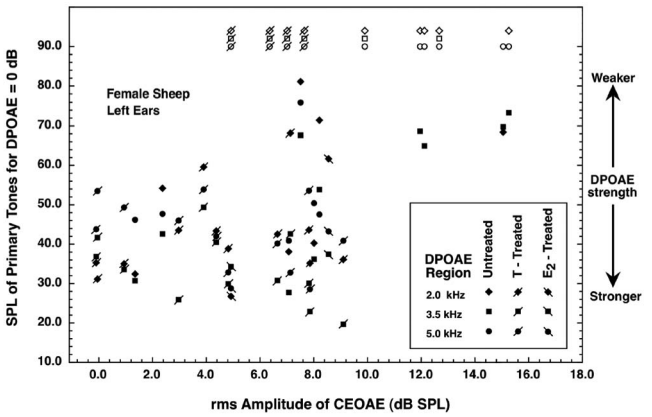


FIG. 1. Scattergram plot for the CEOAE (abscissa) and DPOAE (ordinate) data obtained from the female sheep. The CEOAE values were obtained using the 81-dB click. For each abscissa value (each individual animal), three ordinate values are possible, one for each frequency region in which DPOAEs were measured. DPOAE values of 90 dB or higher (the open symbols) are dummy values assigned for conditions in which DPOAEs could not be measured. The results for female sheep exposed to testosterone or estradiol during gestation are designated with symbols having a diagonal slash. Large ordinate values correspond to weak emissions at the $2f_1-f_2$ frequency. Omitted here are data for three female sheep who had usable DPOAE values but no CEOAE data collected at this click level. Some data points were displaced slightly for clarity.

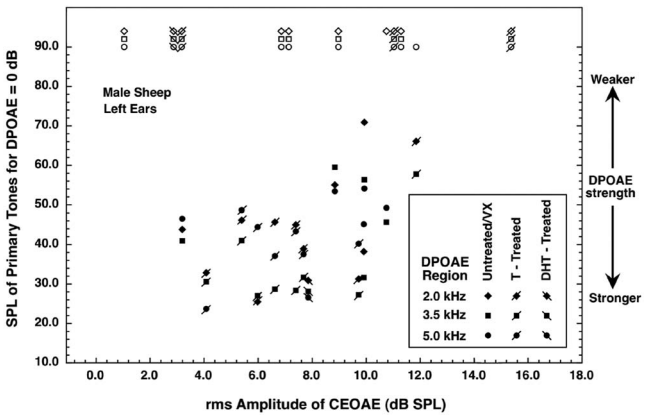


FIG. 2. Scattergram plot for the CEOAE (abscissa) and DPOAE (ordinate) data obtained from the male sheep. The CEOAE values were obtained using the 81-dB click. For each abscissa value (each individual animal), three ordinate values are possible, one for each frequency region in which DPOAEs were measured. DPOAE values of 90 dB or higher (the open symbols) are dummy values assigned for conditions in which DPOAEs could not be measured. The results for male sheep exposed to testosterone or DHT during gestation are designated with symbols having a diagonal slash. Large ordinate values correspond to weak emissions at the $2f_1-f_2$ frequency. Omitted here are data for two male sheep who had usable DPOAE values but no CEOAE data collected at this click level. Some data points were displaced slightly for clarity.

appear in Figs. 1 and 2 because CEOAE data were not collected from them with the 81-dB click level; their CEOAEs for the 75-dB click were unremarkable.) Different symbols were used for the data from treated and untreated sheep. Recall that large ordinate values in Figs. 1 and 2 correspond to weak emissions at the $2f_1-f_2$ frequency.

For the females (Fig. 1), there was a seemingly paradoxical tendency for the absence of DPOAEs to be associated with relatively strong CEOAEs and for strong DPOAEs to be associated with relatively weak CEOAEs. For the males (Fig. 2), however, the absence of DPOAEs occurred over the full range of CEOAE strength. An interesting fact is that the two males having the strongest and weakest CEOAEs both lacked measurable DPOAEs. The correlations between the CEOAE values and the primary levels necessary for a DPOAE of 0 dB at 3.5 kHz were 0.58 and 0.43 for the females and males, respectively (with the dummy values omitted). These both actually are "negative relationships" in that strong CEOAEs tended to be associated with weaker DPOAEs.

C. Possible technical problems

Because an absence of DPOAEs in ears having CEOAEs is not a common outcome in human ears, some assurances are needed that a technical problem or procedural error was not to blame. The shortage of time available for additional study of these ears necessarily limits our knowledge, but this is what can be said.

(1) The dissociation was unlikely to be attributable simply to the order of collection of the data. Although CEOAE data typically were collected prior to the DPOAE data, dissociations also were seen when the order was reversed.

(2) The dissociation was unlikely to be attributable to the choice of stimulus parameters used for DPOAE collection. The f_2/f_1 ratio used (approximately 1.21) is in the range of optimal ratios reported for an array of different mammalian species (reviewed by Valero *et al.*, 2008), and small variations from the optimal ratio for an individual animal have never been shown to produce large changes in DPOAE magnitude.

(3) The dissociation could not be attributed to one of the earphones failing to present its primary tone because those tones were calibrated in the ear canal using the Etymotic microphone, and their actual levels in the canal at the time of testing were recorded along with the level of the DPOAE.

(4) The dissociation seems unlikely to be attributable to the anesthetic used because the CEOAEs obtained from the ears without DPOAEs covered a wide range (see Figs. 1 and 2). Also, in some animals, DPOAEs were absent even though the attempt to measure DPOAEs began immediately after starting the anesthetic, and in no individual animal was there evidence of DPOAEs getting weaker with time spent under anesthetic. Within a single approximately 60-min session, some sheep first showed strong CEOAEs at both click levels, then no DPOAEs, and then strong CEOAEs again when retested. For one male sheep having strong DPOAEs, especially in the 3.5-kHz region, the halothane dose was increased at the end of the test session with no evident effect on DPOAE strength. Many of the sheep having no DPOAEs had never before received gas anesthetic; some others had received halothane once, months before, for about 20 min. Guven *et al.* (2006) concluded that halothane has no effect on human CEOAEs (compare Kettembeil *et al.*, 1995, for birds), and ketamine long has been used when recording OAEs in nonhumans (e.g., Martin *et al.*, 1999; Torre and Fowler, 2000; Hatzopoulos *et al.*, 2002). Bergevin *et al.* (2008) also concluded that anesthesia often has minimal effects on OAEs.

(5) The dissociation was unlikely to be attributable to occlusions in the ear canal or to a poorly located probe tip because we continued to observe the dissociation in several sheep even after removing and repositioning the probe tip in the ear canal. Also, the majority of the sheep without DPOAEs exhibited no DPOAEs in any of the three frequency regions tested; generally it was not localized to just one frequency region as might be expected if the probe tip had shifted. Finally, is not clear how occlusions or a misplaced probe tip could affect only the DPOAEs.

(6) The dissociation was unlikely to be attributable to a gradual build-up of a pressure differential in the middle and external ears (Kettembeil *et al.*, 1995; Zheng *et al.*, 1997). In several sheep, after the probe tip had been securely sealed into the ear-canal for many minutes, the silicone tube connecting one ER-2 earphone to the ear-canal space was pulled free on its proximal end, allowing the air pressure on the distal side of the probe tip to become equal to that in the test room, yet the OAEs measured afterward were the same as before. This dem-

onstration does not rule out a lower pressure in the middle-ear space than in the ear canal, but in either case, it is unclear how such a pressure differential could affect DPOAEs without also affecting CEOAEs.

(7) The dissociation was not simply attributable to season of the year, nor body position during testing. Of the six females with no measurable DPOAEs in any of the three frequency regions, two were tested in Fall 2006 (supine testing position) and four were tested in Spring 2007 (on-the-side testing position). Of the nine males with no measurable DPOAEs in any of the three frequency regions, eight initially were tested in Fall 2006 and one was tested in Spring 2007. Of those eight males tested in Fall 2006, four were retested in May 2007 using the other body position, and no DPOAEs were obtained in either case. Additionally, one sheep was tested both supine and on its side in the same test session, and the DPOAEs were of similar magnitudes in both positions. In a few sheep having no measurable DPOAEs in the left ear, the right ear also was tested, and the same result was obtained.

(8) The dissociation was unlikely to be attributable to temperature effects. Although no systematic manipulations of body temperature were attempted, we observed no evident relationship with temperature. Each sheep lay on the same foam mat of about 1.5-in. thickness covered with a heavy blanket, all of which rested on the top of the metal surgical table. A second blanket was laid over the top of some animals. The sheep were brought into the heated test room within minutes of having been outside. The outside temperature was approximately 10°F cooler in November and December than in May, yet we observed no seasonal effect on DPOAE absence. Animals with no DPOAEs were chronologically interleaved with those having DPOAEs, even though all animals were coming from the same outside temperature into the same indoor temperature. Also, there was no evidence of changes in DPOAE strength with time since leaving the outdoors and coming indoors. Finally, we find it unlikely that temperature could affect only DPOAEs, leaving CEOAEs normal.

(9) An idea that we were not able to test was that perhaps the animals exhibiting no DPOAEs had extremely strong middle-ear muscles that were well activated by the long-duration primary tones used to elicit DPOAEs but were not activated by the brief click stimuli used to elicit CEOAEs. A strong acoustic reflex would impair transmission into and out of the cochlea and could possibly lead to the appearance of an absence of DPOAEs. Besides being rather far-fetched, this idea is offset by the fact that our maximum-length-sequence (MLS) click procedure involved relatively short interclick intervals (the shortest being about 10 ms). Thus, this imaginary hyper-effective acoustic reflex should have been activated when measuring both CEOAEs and DPOAEs.

(10) A search of the medical histories of the individual sheep revealed no evident differences between those animals showing DPOAEs and those not. If any of the deworming, antifungal, or other drugs routinely administered to these sheep did have cumulative ototoxic side-effects, or if aging were somehow related to the dissociation, it is not clear why DPOAEs would be affected and CEOAEs not. (The sheep were highly homogeneous in age within each sex; the males were approximately one year younger than the females yet more males lacked measurable DPOAEs.) We can say, anecdotally, that numerous old sheep of both sexes who have been separated from the main flock for one reason or another have been observed to respond to sheep calls from animals located at considerable distances, which at least suggests good hearing.

(11) A number of sheep were tested multiple times within sessions or across the different seasons. Some never showed DPOAEs, and some showed DPOAEs during November or December 2006 and then showed no DPOAEs in May 2007. However, we did not observe a single instance of DPOAEs returning after having been absent, either across seasons or within measurement sessions. In fact, one sheep was tested during all three measurement sessions. In November 2006, the DPOAEs were relatively strong; in December they were significantly weaker; and in May 2007 they were completely unmeasurable.

D. Sex differences in DPOAEs

Although OAEs are routinely reported to exhibit sex and ear differences (e.g., Bilger *et al.*, 1990; Talmadge *et al.*, 1993; McFadden, 1993; McFadden *et al.*, 1996; McFadden and Pasanen, 1998, 1999; McFadden and Shubel, 2003), those differences typically are smaller for DPOAEs than for CEOAEs or SOAEs (for a review, see McFadden *et al.*, 2008a). Because only one ear was measured for most of the sheep, ear differences cannot be reported here. In order to calculate sex differences for the DPOAE data, the subjects were pooled in the same way as for the CEOAE calculations (McFadden *et al.*, 2008b). Namely, the untreated/intact females were pooled with the untreated/GDX females to form a female control group, and the untreated/VX males were pooled with the untreated/GDX males to form a male control group.

As can be seen in Fig. 3, control females required stronger primary tones than control males to produce the same DPOAE magnitude. That is, the females had *weaker* DPOAEs than the males and that was true in each of the three frequency regions tested for DPOAEs. This is opposite to the direction of effect previously reported for DPOAEs in humans (McFadden *et al.*, 2008a) and other species (e.g., McFadden *et al.*, 2006a; Valero *et al.*, 2008). This sex difference also differs in direction from the sex difference exhibited by these same sheep for CEOAEs (McFadden *et al.*, 2008b). The effect sizes for the sex differences in the DPOAEs are shown separately for each frequency region in Table II. All three effect sizes were moderate to large in size (Cohen, 1992), but none of the three comparisons was statistically significant for these small samples.[2]

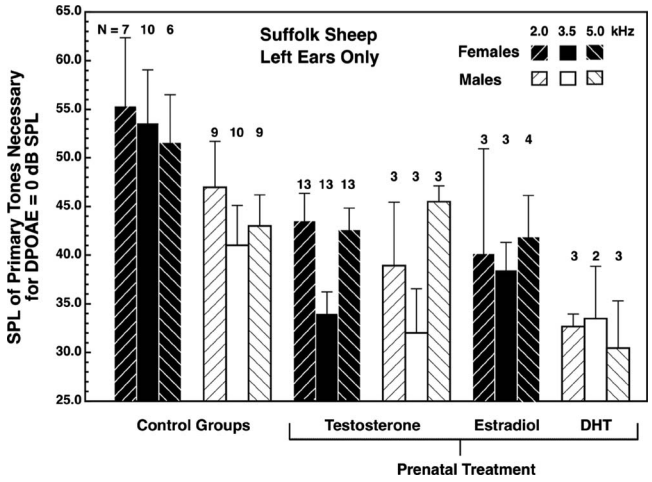


FIG. 3. Strength of the primary tones necessary to produce a $2f_1-f_2$ DPOAE of constant magnitude in those sheep that did exhibit DPOAEs. Approximately one-third of the sheep having CEOAEs did not have measurable DPOAEs. The primary tones always were of equal level. Large ordinate values here correspond to weak DPOAEs. For both sexes, the control groups consisted of the untreated/intact animals (males were untreated/VX) plus the untreated/GDX animals. Error flags designate standard errors of the mean.

E. Treatment effects

In order to assess the effects of prenatal hormone treatment on DPOAEs in females, the obese/testosterone-treated females were pooled with the nonobese/testosterone-treated females and that group was compared with the female control group described above. These two groups of testosterone-treated females were pooled in this same way when analyzing their CEOAE data (McFadden *et al.*, 2008b). Figure 3 reveals that the females treated with testosterone prenatally required substantially weaker primary tones than the control females to produce a DPOAE of the same magnitude; that is, the testosterone-treated females had stronger DPOAEs than the control females. Again, this is the opposite direction of effect from that shown by these same animals for CEOAEs (McFadden *et al.*, 2008b). Note, however, that the DPOAE data for these testosterone-treated females were shifted in the male direction just as their CEOAE data were (McFadden *et al.*, 2008b). That is, the testosterone-treated females did exhibit masculinized DPOAEs, in accord with expectations based on their treatment. Table II reveals that the effect sizes for these comparisons were large for all three frequency regions tested, and the comparison at 3.5 kHz achieved statistical significance, unpaired $t(21)=3.51$, $p=0.002$, two-tailed test, equal variance. These testosterone-treated females are also masculinized in other ways. They are born with no vaginal opening, with an empty scrotal sac, and with a pseudopenis that is used for urination (no erections ever have been observed); they also exhibit various neuroendocrine and ovarian differences from untreated females (see Padmanabhan *et al.*, 2006) as well as behavioral differences (Roberts *et al.*, 2008). So the prenatal treatment was effective at masculinizing both the body and the cochlea.

An interesting outcome is that the two females treated with estradiol prenatally had DPOAEs that were masculinized to about the same extent as the DPOAEs of the females treated with testosterone prenatally. This may seem paradoxical, but testosterone is aromatized to estradiol in mammals, so individuals high in testosterone are likely to be high in estradiol as well. The implication is that estradiol, not androgen, may be the relevant agent for masculinizing the cochlea. However, considerable caution must accompany this implication because the *N* was extremely small.

Figure 3 also shows the differences in DPOAE strength between the control males and those males treated with testosterone propionate or DHT prenatally. However, no effect sizes or statistical tests are reported because of the extremely small *N* remaining in these groups after attrition. For comparison, the CEOAEs of the testosterone-treated males were about the same as the CEOAEs of the control males, and the CEOAEs of the DHT-treated males were somewhat stronger than those of the control males, just as was true for the DPOAEs shown in Fig. 3.

F. Slopes of the gain functions

Examination of the slopes of the lines fitted to the linear ranges of the gain functions revealed that the strength of the DPOAE grew slowest with increases in primary levels in the lowest frequency region tested and grew increasingly more rapidly for each move to a higher frequency region. This trend was evident in both sexes, with the three slopes for the control females being slightly steeper than the three corresponding slopes for the control males. Also, the slopes for the testosterone-treated females were masculinized. When the slopes were pooled for all 15 males and all 23–26 females, the sex difference disappeared, and the mean slopes were about 0.85, 0.96, and 1.16 for the 2.0-, 3.5-, and 5.0-kHz frequency regions, respectively.

TABLE II. Effect sizes for various pair-wise comparisons of groups in three DPOAE frequency regions. Effect sizes were calculated as second group listed minus first group to compensate for inverse relationship. T represents testosterone injections during days 30–90 of gestation; GDX represents gonadectomized within 2 weeks of birth; [a] $0.01>p>0.001$; unpaired, two-tailed *t*-test, equal variance; control females include untreated/intact group pooled with untreated/GDX group; control males include untreated/VX group and untreated/GDX group; prenatal-T females include obese group pooled with non-obese group.

Comparison	*N*	2.0 kHz	*N*	3.5 kHz	*N*	5.0 kHz
1. Control females vs control males	7/9	−0.500	10/10	−0.803	6/9	−0.585
2. Control females vs prenatal-T females	7/13	−0.834	10/13	−1.472[a]	6/13	−0.903
3. Control males vs prenatal-T, GDX males	9/3	−0.597	10/3	−0.754	9/3	0.296

G. Relative strength of DPOAEs

One way to demonstrate differences across individuals or across species is to compare the strength of the primary tones used to evoke DPOAEs to the strength of the $2f_1-f_2$ component produced by those primary tones. That is, how many decibels weaker than the primaries was the DPOAE? For sheep, the measurable DPOAEs averaged about 45 dB (males) to 50 dB (females) weaker than the primary tones. This is very similar to what we have obtained from spotted hyenas (McFadden *et al.*, 2006b), rhesus monkeys (McFadden *et al.*, 2006a), and lemurs (unpublished). The DPOAEs of marmosets were a bit weaker, averaging about 50 dB (females) to 57 dB (males) weaker than the primaries (Valero *et al.*, 2008). All of these values are considerably stronger than those for humans, which average about 60–68 dB weaker than the primary tones for both sexes (Harris *et al.*, 1989; McFadden *et al.*, 2008a). Furthermore, the gain functions for DPOAEs in sheep typically asymptoted at about 25–30 dB SPL whereas the gain functions for humans we have tested with similar procedures and in comparable frequency ranges typically asymptoted at ~5–15 dB SPL.

The considerable strength of the measurable DPOAEs in sheep is notable in light of both the dissociation between DPOAEs and CEOAEs seen in some animals and the fact that hearing sensitivity in sheep is about 18 dB worse than in humans over the range of DPOAEs and primary tones tested here (Wollack, 1963). For comparison, our past measurements reveal that the CEOAEs of sheep are weaker than those of rhesus monkeys, which in turn are weaker than those of humans.

IV. DISCUSSION

To our knowledge, these are the first measurements of OAEs in a ruminant species. The DPOAEs measured had some similarities with DPOAEs measured in humans and some differences. Surely the most interesting discovery was the large fraction of sheep having apparently normal CEOAEs but no, or quite weak, DPOAEs. Several possible technical problems or procedural errors that might have contributed to this marked dissociation were considered, but none seemed to be plausible explanations. Until a fully explanatory problem or error emerges, we believe that this species tentatively ought to be viewed as unusual and worthy of further study. Sheep appear to offer considerable potential for learning more about the cochlear mechanisms responsible both for DPOAEs and the other forms of OAE.

Shera and Guinan (1999) explained DPOAEs by assuming that the distortion mechanism that rides the displacement envelope in the vicinity of $f2$ gives rise to a wave at the $2f1-f2$ frequency that travels both back to the stapes and forward to the $2f1-f2$ location on the basilar membrane. The forward-propagating wave is thought to encounter one or more discontinuities along its path, leading to a reflection-based wave also traveling backward toward the stapes. Thus, the DPOAE measured in the ear canal is a mix of two responses, one directly from the distortion mechanism and the other indirectly from the distortion mechanism. Accordingly, a simple explanation for how some sheep can have apparently normal CEOAEs (a reflection-based form of OAE) but no DPOAEs (a mix of two forms of OAE) would be that their distortion mechanism is damaged or inactive. Exactly what that would mean mechanistically or anatomically is far from clear. Because DPOAEs often were absent over a substantial range of f_2 frequencies, the implication is that the distortion mechanism had to be unable to function over a substantial segment of the basilar membrane even though the reflection mechanism and the cochlear-amplification process apparently were intact over that same segment of basilar membrane. Under this Shera and Guinan (1999) explanation, it is not clear how a localized lesion could account for the marked wideband dissociation between CEOAEs and DPOAEs in some sheep.

Although rarely stated explicitly, there appears to exist an implicit assumption among hearing scientists that each of the two mechanisms underlying the various forms of OAE is highly similar, if not identical, across all mammalian species (Bergevin *et al.*, 2008). The results from sheep appear to contradict this assumption of a universal mammalian plan.

(1) It appears to be reasonably common for individual sheep to have perfectly normal-appearing CEOAEs even though they have no measurable DPOAEs (see Figs. 1 and 2), a unique finding in mammals so far.
(2) While the (small) sex difference for CEOAEs did favor the females (McFadden *et al.*, 2008b), as in other mammals, the sex difference for DPOAEs favored the males (see Fig. 3 and Table II). In humans (Bilger *et al.*, 1990; Talmadge *et al.*, 1993; McFadden, 1993; McFadden *et al.*, 1996; McFadden and Pasanen, 1998, 1999; McFadden and Shubel, 2003) and rhesus monkeys (McFadden *et al.*, 2006a), the sex difference for CEOAEs is moderate in size and also favors the females, whereas the sex difference for DPOAEs typically is smaller than for CEOAEs (McFadden *et al.*, 2008a) but still favors the females.
(3) Female sheep exposed to higher-than-normal levels of androgens during the middle part of gestational development exhibited weaker CEOAEs than untreated females, which is in accord with a considerable array of outcomes from various species and special populations of humans (McFadden, 2002, 2008). However, those same androgen-treated females exhibited DPOAEs that were *stronger* than those in untreated females—the opposite direction of effect for CEOAEs. What is fascinating about this outcome is that the testosterone-treated females still were exhibiting a masculinized cochlea; their DPOAEs were shifted in the male direction of stronger DPOAEs than in the females. Thus, both the CEOAEs and DPOAEs of sheep offer confirmation of the prenatal-androgen-exposure explanation (McFadden, 2002, 2008) even though their DPOAEs exhibited an anomalous sex difference. To our knowledge, the only other report of a reversal in the direction of effect for the sex difference is for both the CEOAEs and DPOAEs of spotted hyenas (McFadden *et al.*, 2006b), where an absence of sex difference was predicted because female spotted hyenas are naturally exposed to high levels of androgens prenatally.

(4) DPOAEs can exhibit considerable fluctuation in strength as the primary tones are varied incrementally in frequency. This is sometimes called the microstructure of the DPOAE. DPOAE microstructure appeared to be substantially smaller in these sheep than in a sample of humans we have tested recently. As noted above, our DPOAE procedure involves changing the frequencies of the primary tones in steps of approximately 100 Hz, which means that some microstructure easily could be missed. However, that same step size was used for both sheep and humans, so the apparent difference in microstructure cannot be attributed to that factor.

A curious aspect of this dissociation between DPOAEs and CEOAEs in sheep is that it is the mechanisms underlying DPOAEs that appear to be more vulnerable (to some unknown agent or process) than are the mechanisms underlying CEOAEs. In the previously known dissociations, DPOAEs were altered less, or more slowly, by aspirin or quinine than were other forms of OAE (Wier *et al.*, 1988; McFadden and Pasanen, 1994; Whitehead *et al.*, 1996). Thus, this dissociation of OAEs in sheep is peculiar both in its extent and in its direction.

ACKNOWLEDGMENTS

This research was supported in part by Research Grant No. DC00153 from the National Institute on Deafness and Other Communication Disorders (NIDCD) awarded to one of the authors (D.M.) and in part by Research Grant No. HD44232 from the National Institute of Child Health and Human Development (NICHD) awarded to another author (T.M.L.) as part of a Program Project Grant entitled Prenatal Programming of Reproductive Health and Disease. We thank Mr. Douglas D. Doop for expert technical advice and assistance with animal care. In addition, we thank Michael Zakalik and Allie Spencer for assistance with data collection. M.M. Maloney prepared the figures. A preliminary report of this work was presented at a meeting of the Acoustical Society of America (McFadden *et al.*, 2008c).

[1]Note that the procedures used by the UM team unavoidably also created some females treated prenatally with DHT and some males treated prenatally with estradiol, but because these animals could not contribute to the experimental questions initially of interest to the UM team, those animals were not retained, and thus were not available at the time of the OAE measurements.

[2]The standard procedure in this laboratory is to calculate effect sizes as female minus male, so that a positive value indicates stronger OAEs in females. Here, however, the large values for the primaries needed by the females correspond to weak DPOAEs. For easy comparison with our past publications, the signs of all the effect sizes in Table II have been reversed to offset the inverse relationship between primary level and DPOAE strength.

Allen, J. B. (**1990**). User manual for the CUBDIS distortion product measurement system (AT&T Bell Labs).

Bergevin, C., Freeman, D. M., Saunders, J. C., and Shera, C. A. (**2008**). "Otoacoustic emissions in humans, birds, lizards, and frogs: Evidence for multiple generation mechanisms," J. Comp. Physiol., A **194**, 665–683.

Bilger, R., Matthies, M. L., Hammel, D. R., and Demorest, M. E. (**1990**). "Genetic implications of gender differences in the prevalence of spontaneous otoacoustic emissions," J. Speech Hear. Res. **33**, 418–432.

Cohen, J. (**1992**). "A power primer," Psychol. Bull. **112**, 155–159.

Gorga, M. P., Neely, S. T., Bergman, B. M., Beauchaine, K. L., Kaminski, J. R., Peters, J., Schulte, L., and Jesteadt, W. (**1993**). "A comparison of transient-evoked and distortion product otoacoustic emissions in normal-hearing and hearing-impaired subjects," J. Acoust. Soc. Am. **94**, 2639–2648.

Guven, S., Tas, A., Adali, M. K., Yagiz, R., Alagol, A., Uzun, C., Koten, M., and Karasalihoglu, A. R. (**2006**). "Influence of anaesthetic agents on transient evoked otoacoustic emissions and stapedius reflex threshold," J. Laryngol. Otol. **120**, 10–15.

Harris, F. P., Lonsbury-Martin, B. L., Stagner, B. B., Coats, A. C., and Martin, G. K. (**1989**). "Acoustic distortion products in humans: Systematic changes in amplitude as a function of f_2/f_1 ratio," J. Acoust. Soc. Am. **85**, 220–229.

Hatzopoulos, S., Petruccelli, J., Laurell, G., Finesso, M., and Martini, A. (**2002**). "Evaluation of anesthesia effects in a rat animal model using otoacoustic emission protocols," Hear. Res. **170**, 12–21.

Kettembeil, S., Manley, G. A., and Siegl, E. (**1995**). "Distortion-product otoacoustic emissions and their anaesthesia sensitivity in the European Starling and the chicken," Hear. Res. **86**, 47–62.

Kosut, S. S., Wood, R. I., Herbosa-Encarnacion, D., and Foster, D. L. (**1997**). "Prenatal androgens time neuroendocrine puberty in the sheep: Effect of testosterone dose," Endocrinology **138**, 1072–1077.

Martin, G. K., Stagner, B. B., Jassir, D., Telischi, F. F., and Lonsbury-Martin, B. L. (**1999**). "Suppression and enhancement of distortion-product otoacoustic emissions by interference tones above f_2. I. Basic findings in rabbits," Hear. Res. **136**, 105–123.

McFadden, D. (**1993**). "A masculinizing effect on the auditory systems of human females having male co-twins," Proc. Natl. Acad. Sci. U.S.A. **90**, 11900–11904.

McFadden, D. (**2002**). "Masculinization effects in the auditory system," Arch. Sex Behav. **31**, 93–105.

McFadden, D. (**2008**). "What do sex, twins, spotted hyenas, ADHD, and sexual orientation have in common?" Perspect. Psychol. Sci. **3**, 309–323.

McFadden, D., Loehlin, J. C., and Pasanen, E. G. (**1996**). "Additional findings on heritability and prenatal masculinization of cochlear mechanisms: Click-evoked otoacoustic emissions," Hear. Res. **97**, 102–119.

McFadden, D., Martin, G. K., Stagner, B. B., and Maloney, M. M. (**2008a**). "Sex differences in distortion-product and transient-evoked otoacoustic emissions compared," J. Acoust. Soc. Am. (to be published).

McFadden, D., and Pasanen, E. G. (**1994**). "Otoacoustic emissions and quinine sulfate," J. Acoust. Soc. Am. **95**, 3460–3474.

McFadden, D. and Pasanen, E. G. (**1998**). "Comparison of the auditory systems of heterosexuals and homosexuals: Click-evoked otoacoustic emissions," Proc. Natl. Acad. Sci. U.S.A. **95**, 2709–2713.

McFadden, D., and Pasanen, E. G. (**1999**). "Spontaneous otoacoustic emissions in heterosexuals, homosexuals, and bisexuals," J. Acoust. Soc. Am. **105**, 2403–2413.

McFadden, D., Pasanen, E. G., Raper, J., Lange, H. S., and Wallen, K. (**2006a**). "Sex differences in otoacoustic emissions measured in rhesus monkeys (*Macaca mulatta*)," Horm. Behav. **50**, 274–284.

McFadden, D., Pasanen, E. G., Valero, M. D., Roberts, E. K., and Lee, T. M. (**2008b**). "Effect of prenatal androgens on click-evoked otoacoustic emissions in male and female sheep (*Ovis aries*)," Horm. Behav. (in press).

McFadden, D., Pasanen, E. G., Valero, M. D., Roberts, E. K., and Lee, T. M. (**2008c**). "Otoacoustic emissions in sheep (*Ovis aries*): Sex differences and prenatal androgen effects," J. Acoust. Soc. Am. **123**, 3855–3856.

McFadden, D., Pasanen, E. G., Weldele, M. L., Glickman, S. E., and Place, N. J. (**2006b**). "Masculinized otoacoustic emissions in female spotted hyenas (*Crocuta crocuta*)," Horm. Behav. **50**, 285–292.

McFadden, D. and Shubel, E. (**2003**). "The relationships between otoacoustic emissions and relative lengths of fingers and toes in humans," Horm. Behav. **43**, 421–429.

Moulin, A., Collet, L., Veuillet, E., and Morgon, A. (**1993**). "Interrelations between transiently evoked otoacoustic emissions, spontaneous otoacoustic emissions and acoustic distortion products in normally hearing subjects," Hear. Res. **65**, 216–233.

Padmanabhan, V., Manikkam, M., Recabarren, S., and Foster, D. (**2006**). "Prenatal testosterone excess programs reproductive and metabolic dysfunction in the female," Mol. Cell Endocrinol. **246**, 165–174.

Roberts, E. K., Padmanabhan, V., and Lee, T. M. (**2008**). "Differential effects of prenatal testosterone on phenotypic and behavioral masculinization and defeminization of female sheep," Biol. Reprod. **79**, 43–50.

Shera, C. A. and Guinan, J. J., Jr. (**1999**). "Evoked otoacoustic emissions arise by two fundamentally different mechanisms: A taxonomy for mam-

malian OAEs," J. Acoust. Soc. Am. **105**, 782–798.
Smurzynski, J. and Kim, D. O. (**1992**). "Distortion-product and click-evoked otoacoustic emissions of normally-hearing adults," Hear. Res. **58**, 227–240.
Talmadge, C. L., Long, G. R., Murphy, W. J., and Tubis, A. (**1993**). "New off-line method for detecting spontaneous otoacoustic emissions in human subjects," Hear. Res. **71**, 170–182.
Torre, P., III, and Fowler, C. G. (**2000**). "Age-related changes in auditory function of rhesus monkeys (*Macaca mulatta*)," Hear. Res. **142**, 131–140.
Valero, M. D., Pasanen, E. G., McFadden, D., and Ratnam, R. (**2008**). "Distorion-product otoacoustic emissions in the common marmoset (*Callithrix jacchus*): Parameter optimization," Hear. Res. **243**, 57–68.
Whitehead, M. L., Lonsbury-Martin, B. L., Martin, G. K., and McCoy, M. J. (**1996**). "Otoacoustic emissions: Animal models and clinical observations," in *Clinical Aspects of Hearing*, Springer Handbook of Auditory Research Vol. **7**, edited by T. R. van de Water, A. N. Popper, and R. R. Fay (Springer-Verlag, New York), pp. 199–257.
Wier, C. C., Pasanen, E. G., and McFadden, D. (**1988**). "Partial dissociation of spontaneous otoacoustic emissions and distortion products during aspirin use in humans," J. Acoust. Soc. Am. **84**, 230–237.
Wollack, C. H. (**1963**). "The auditory acuity of the sheep (*Ovis aries*)," J. Aud Res. **3**, 121–132.
Zheng, Y., Ohyama, K., Hozawa, K., Wada, H., and Takasaka, T. (**1997**). "Effect of anesthetic agents and middle ear pressure application on distortion product otoacoustic emissions in the gerbil," Hear. Res. **112**, 167–174.

Comparing the optimal signal conditions for recording cubic and quadratic distortion product otoacoustic emissions

Lin Bian[a] and Shixiong Chen
Auditory Physiology Lab, 3430 Coor Hall, Department of Speech and Hearing Science, Arizona State University, Tempe, Arizona 85287-0102

(Received 22 July 2008; revised 24 September 2008; accepted 24 September 2008)

Odd- and even-order distortion products (DPs), evoked by two primary tones ($f_1, f_2, f_1 < f_2$), represent different aspects of cochlear nonlinearity. The cubic and quadratic difference tones (CDT $2f_1 - f_2$ and QDT $f_2 - f_1$) are prominent representatives of the odd and even DPs. Distortion product otoacoustic emissions (DPOAEs) were measured within a primary level (L_1, L_2) space over a wide range of f_2/f_1 ratios to compare the optimal signal conditions for these DPs. For CDT, the primary level difference decreased as L_1 increased with a rate proportional to the f_2/f_1 ratio. Moreover, the optimal ratio increased with L_1. A set of two formulas is proposed to describe the optimal signal conditions. However, for a given level of a primary, increasing the other tone level could maximize the QDT amplitude. The frequency ratio at the maximal QDT was about 1.3 and quite constant across different primary levels. A notch was found in the QDT amplitude at the f_2/f_1 ratio of about 1.22–1.25. These opposite behaviors suggest that the optimal recording conditions are different for CDT and QDT due to the different aspects in the cochlear nonlinearity. Optimizing the DPOAE recordings could improve the reliability in clinical or research practices.
© *2008 Acoustical Society of America.* [DOI: 10.1121/1.3001706]

PACS number(s): 43.64.Jb, 43.64.Kc, 43.64.Bt, 43.64.Yp [BLM] Pages: 3739–3750

I. INTRODUCTION

Our inner ears are nonlinear acoustic transducers where distortions are normal by-products of the conversion of sound into bioelectrical signals. The source of distortion is thought to be within the transduction process of outer hair cells (OHCs), since these cells respond to changes in membrane voltage with mechanical motion in either the cell body (Liberman *et al.*, 2002) or the hair bundles (Kennedy *et al.*, 2005). The OHC transduction shows a saturating nonlinearity and the resulting motile responses provide a mechanical feedback that can enhance hearing sensitivity and frequency selectivity. When stimulated by two tones ($f_1, f_2, f_2 > f_1$), the inner ear can produce a family of distortion products (DPs) in various combinations of the primary frequencies, $mf_1 \pm nf_2$. Depending on the sum of integers m and n, the DPs can be classified into two categories, odd- and even-order DPs. They reflect different aspects of the nonlinear transducer characteristics of OHCs in the overlapped region of traveling waves initiated by two pure tones. Odd-order DPs are relatively large at low primary levels, and representing the transducer gain of hair cells. In contrast, even-order DPs are only measurable at moderately high stimulus levels, and thus may reflect the saturation or compression of hair cell transducers. These DPs in mechanical vibrations of hair cells can propagate out of the inner ear and are measurable in the ear canal as faint sounds or distortion product otoacoustic emissions (DPOAEs). Therefore, DPOAEs provide a noninvasive tool to assess the functional status of the inner ear OHCs.

Given the possibility that DPOAEs can be used to evaluate the transducer characteristics of OHCs, the current clinical application is, however, limited to hearing screening (Lonsbury-Martin and Martin, 2003) where normal or abnormal hearing is judged by the presence or absence of emissions. Quantitative utilities, such as hearing threshold estimates, cochlear efferent function evaluation, and input/output growth functions, are restricted to mostly research settings. One reason for the limited use of DPOAEs is the large variability in measurements. Among other factors (Garner, 2008), such as hearing sensitivity, middle ear transmission, and inner ear reflections, a source of the variability can be attributed to less optimized signal conditions of the primary tones (Johnson *et al.*, 2006; Mills *et al.*, 2007) that cannot evoke the largest DPOAEs. Since DP levels are correlated with the nonlinear characteristics of cochlear transduction (Lukashkin and Russell, 1999; Fahey *et al.*, 2000; Bian *et al.*, 2002; Bian, 2004), maximizing DPOAE magnitudes can improve the signal-to-noise ratio (SNR) so that more accurate estimates of cochlear function are possible. Therefore, there is a need for standardizing (Mills *et al.*, 2007) or individualizing (Neely *et al.*, 2005) the measurement procedures. Optimizing the recording conditions for DPOAEs is still an ongoing research effort.

The signal conditions for recording DPOAEs include the f_2/f_1 frequency ratio and the levels of two primary tones (L_1 and L_2). The f_2 is usually predetermined for evaluating the cochlear function at a specific frequency of interest, because the overlapped region of the two-tone excitation patterns on cochlear partition is very close to the f_2 place. The frequency f_1 can be determined by selecting an appropriate f_2/f_1 ratio. In current clinical practice, a value of 1.22 is commonly adopted for f_2/f_1 ratio regardless of frequency and level.

[a]Electronic mail: lin.bian@asu.edu

However, the optimal ratio can range from 1.2 to 1.3 with increase in primary levels and f_2 (Moulin, 2000; Johnson *et al.*, 2006). Thus, for a certain f_2, selecting the frequency ratio is tied with the choice of primary levels. Currently, the decision on signal levels is an independent process and often a simple strategy of L_1 being 5–10 dB greater than L_2 is used. However, studies on DPOAE amplitude within a complete $L_1 \times L_2$ parameter space indicate that the primary level difference ($\Delta L = L_1 - L_2$) is also level dependent with greater deviations towards lower levels (e.g., Whitehead *et al.*, 1995). The optimal L_1 as a linear deviation from L_2 is refined with an empirical formula (Kummer *et al.*, 2000) given the observation that ΔL diminishes at 65 dB SPL. This primary level optimization allows a more accurate measurement of DPOAE amplitudes at low stimulus levels for estimating hearing sensitivity (Kummer *et al.*, 1998). Another relation between the optimal L_1 and L_2 is proposed by Johnson *et al.* (2006) which takes f_2 into account. However, none of the approaches considers the inter-relation between the primary levels and the f_2/f_1 ratio. The interaction between frequency ratio and primary levels on DPOAEs can be deduced from the fact that all these factors influence the amount of overlap between two excitation patterns in the cochlea and in turn determine the exact two-tone input to the nonlinear transduction of OHCs.

To date, all parametric studies on optimizing DPOAE recordings focus on the most prominent DP component, cubic difference tone (CDT, $2f_1 - f_2$). An obvious reason for CDT as the choice of DPOAE measure for research and application is simply its large size and SNR. Another reason is that at low signal levels CDT reflects the response growth or gain of OHC transducer and is parallel to hearing sensitivity and frequency selectivity of the inner ear (Brown *et al.*, 1993; Gorga *et al.*, 2003). However, CDT only represents the odd nonlinearity in cochlear transduction; thus, the estimation of hair cell function could not be complete without measuring the even-order DPs. The largest even-order DP is quadratic difference tone (QDT, $f_2 - f_1$) which has not been considered clinically useful until recently. One reason for the lack of research and application is due to its low amplitude (Brown, 1993) and poor SNR. However, auditory nerve fiber responses in kittens show robust QDT that can be larger than CDT (Tubach *et al.*, 1996). Neural QDT varies nonmonotonically with primary levels or frequencies and its behavior is different from CDT (Kim, 1980). Large QDT also presents in electrical responses in inner hair cells (Nuttall and Dolan, 1993), indicating that the source of QDT is presynaptic and possibly the OHCs. Indeed, QDT is the largest DP component found in the trans-membrane current that drives OHC somatic motility (Takahashi and Santos-Sacchi, 1999). Acoustic QDT can be associated with the saturating portions of OHC transduction, and its amplitude variation reflects the operating point (OP) shift of hair cells (Frank and Kössl, 1996). Studies in gerbils show that the QDT is enhanced or modulated by a low-frequency bias tone and the modulation patterns could be used to derive a cochlear transducer function (F_{Tr}) (Bian, 2004, 2006). This finding poses a possible clinical application in evaluating cochlear function or diagnosing inner ear disorders. Since the cochlear F_{Tr} can be quantified from low-frequency modulation of CDT in humans (Bian and Scherrer, 2007), combining this measure with QDT could provide a more comprehensive picture of cochlear function. Towards this goal, it is necessary to explore the optimal signal conditions for recording QDT, because the ideal conditions for CDT may not be applicable to QDT, especially, in humans. Therefore, the purpose of the present study is to compare the optimal conditions for CDT and QDT to provide guidelines for research and clinical practice.

II. METHODS

A. Subjects

Sixteen healthy subjects with age ranging from 23 to 40 years (mean 26.3) were recruited from the students at Arizona State University (ASU). They had no history of hearing disorders. Normal outer and middle ear functions were confirmed with an otoscopic examination. A DP-gram was measured with an 8-point/oct procedure from 1 to 8 kHz (ILO92, Otodynamics Ltd., Herts, UK). Subjects with CDT amplitudes greater than 10 dB SPL in the frequency range between 1 and 4 kHz were selected for the study. Subjects with deep notches or spectral fine structures in this region were excluded to reduce interference of DPOAEs generated from reflections at the best frequency place (Knight and Kemp, 2001; Shera, 2004). To avoid possible influence and interference, the subjects were also screened to rule out spontaneous otoacoustic emissions in the testing ear. Subjects were seated comfortably in a soundproofed booth and instructed to be as quiet as possible during the test to reduce noises. The recruiting protocol and experimental procedures were approved by the Institutional Review Board of ASU.

B. Stimulus presentation

Two primary tones were generated and controlled with a personal computer using software implemented in LABVIEW (National Instruments, NI, Austin, TX). Durations of the primary tones were 1 s with a 5-ms $\cos^2$-shaped rise and fall ramp, respectively. The signals were delivered separately to two earphones (ER-2A, Etymōtic Research, Inc., Elk Grove Village, IL) through a 24-bit dynamic signal acquisition and generation card (PXI-4461, NI) and acoustically mixed in the ear canal to stimulate the inner ear. The ear-canal acoustic response was then recorded by a calibrated probe microphone (ER-10B+). The recorded signal was amplified 20 dB by the built-in preamplifier of the ER-10B+ and digitized at a rate of 131.072 kS/s (PXI-4461). Prior to each test, the fit of ER-10B+ probe was checked and adjusted to ensure a flat ear-canal frequency response up to 5 kHz to a frequency-sweeping tone at a constant level. This can avoid the interference from standing waves in the ear canal and acoustic leaks around the probe.

Data were collected over a range of f_2/f_1 ratios using a "chess-grid" protocol, namely, the L_1 and L_2 were swept independently from 75 to 54 dB SPL in 3-dB steps to create an 8×8 grid of data sets for each f_2/f_1 ratio. Lower signal levels were not used due to a concern of poor SNR for QDT.

The primary levels were automatically adjusted and calibrated at the beginning of each decrement. To ensure the completion of experiments within 90 min, the frequency of f_2 was fixed at 4 kHz in the study. Based on the coverage of f_2/f_1 ratio, the study was carried out in two phases. In phase 1, the f_2/f_1 ratio was varied from 1.2 to 1.8 at a step size of 0.1 to explore the behaviors of CDT and QDT when f_1 and f_2 were separated further apart. It was initially thought that there could be a mechanical "(second) filter" just below the frequency of f_2 in the cochlea (Allen and Fahey, 1993; Brown *et al.*, 1993), so that the QDT could be "amplified" if the f_2/f_1 ratio was large enough to bring the QDT frequency into the filter bandwidth. In phase 2, conventional frequency ratios from 1.15 to 1.36 with a step size of 0.035 were used to reveal the optimal signal conditions for both DPOAE components. Ratios lower than 1.1 were not used to keep the QDT above 500 Hz, since the noise floor below this frequency was higher (>-10 dB SPL). Eight subjects participated in each phase.

C. Data collection and analysis

At each two-tone condition, the stimuli were repeated eight times and the recorded acoustic signal was averaged in the time domain to reduce random noise. Noisy data due to body movements were discarded with an artifact rejection routine which examined the noise floor from 300 to 800 Hz. The rejection threshold was adjustable depending on the noise condition of each subject to optimize the speed of data collection. Data were analyzed offline in MATLAB (Mathworks Inc., Natick, MA) using custom-written programs. The waveform of ear-canal acoustic signal was passed through a Hanning window and converted into the frequency domain via a fast Fourier transform (FFT). Then, the spectral magnitudes at the frequencies of $2f_1-f_2$ and f_2-f_1 were extracted to result in the value of a single grid in the $L_1 \times L_2$ level space for CDT and QDT, respectively.

To examine the combined effects of primary levels and frequency ratio, the data were merged into an 8×8 grid of CDT or QDT amplitude-ratio functions with a specific L_1 and L_2 combination for each grid. Thus, the DPOAE amplitude could be examined in each dimension by fixing L_1, L_2, or f_2/f_1 ratio, respectively. For the optimal signal conditions, relations between the two primary levels under different frequency ratios or the optimal ratios as functions of the primary levels were inspected. As the influence of L_1 on DPOAE amplitudes was stronger than L_2, the relations among these signal variables were expressed as functions of L_1. To reveal possible underlying rules, these relations were fit with appropriate linear or nonlinear functions. The curve fittings were usually performed on the averaged data and the parameters were validated by predicting the optimal conditions for each individual.

III. RESULTS

In this study, three signal variables, L_1, L_2, and f_2/f_1 ratio, were varied simultaneously, creating an extra complexity in observing the behaviors of DPOAEs. It would be convenient to reduce the data into a two- or three-dimensional space by keeping one variable constant. For the optimal signal conditions, the data analysis focused on the relations between these variables. Data reported were mostly from phase 2, where common f_2/f_1 ratios from 1.15 to 1.36 were used. Phase 1 data were reported in the section regarding the ratio effects.

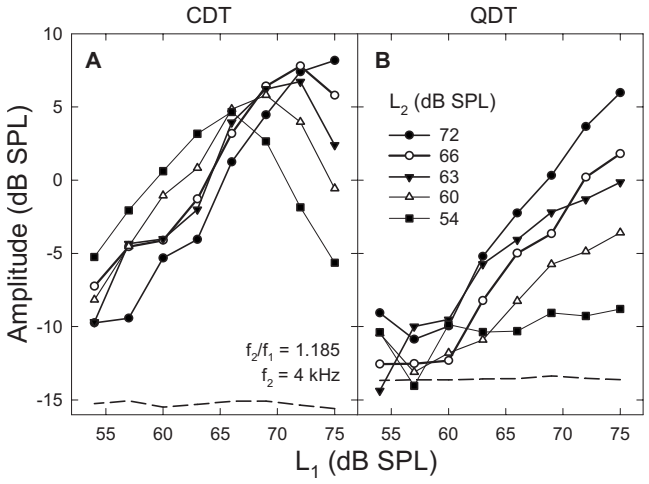


FIG. 1. DPOAE amplitudes as functions of L_1 under different L_2 settings. (A) CDT magnitudes rise with L_1 and roll over at different L_1 values. (B) QDT amplitudes increase with L_1 in different growth rates depending on the L_2 settings. Dashed lines indicate the averaged noise floor of DPOAE measures. Data reflect an average across eight subjects.

A. Level effects

1. L_2 fixed

For different f_2/f_1 ratios, the DPOAE magnitudes behaved similarly, but with different overall sizes. It would be reasonable to select a ratio that produced larger DPOAEs to show effects of L_1 when L_2 was fixed at different values. At the f_2/f_1 ratio of 1.185, amplitudes of CDT and QDT averaged across eight ears showed different growth patterns (Fig. 1) with L_1. The CDT amplitude showed an initial increase and a rollover as L_1 was raised over L_2 [panel (A)]. The level of f_1 where the CDT reached the peak depended on the fixed level of f_2, usually when L_1 was 3–10 dB greater than L_2. As the fixed L_2 decreased, the peaks of CDT amplitudes showed a small shift towards lower values of L_1, indicating a larger level difference. In other words, for lower levels of f_2 a much larger L_1 was needed to produce a peak CDT magnitude. Moreover, the peak CDT values decreased slightly ($<5-10$ dB) when L_2 was lowered for about 20 dB. Therefore, these CDT amplitude functions were largely overlapped when L_1 was below 65 dB SPL. The growth rates of CDT amplitudes were about 1 dB/dB, suggesting that the CDT increased proportionally with L_1 until the peak values were reached.

In contrast, the growths of QDT amplitudes showed no obvious signs of peaks and rollovers [Fig. 1(B)]. On average, the amplitudes of QDT were smaller than the CDT, especially, when L_1 was less than 60 dB SPL. At these lower f_1 levels, the QDT was usually within 5 dB from the noise floor (around $-12--13$ dB SPL). Then, the QDT amplitude started to grow when L_1 exceeded 60 dB SPL. The rate of

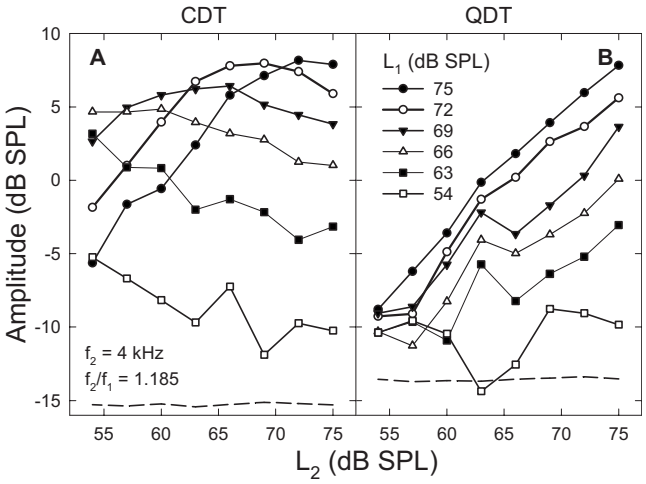


FIG. 2. DPOAE amplitudes as functions of L_2 under different L_1 settings. (A) CDT magnitudes show different patterns depending on the L_1 settings. The CDT peak decreases with L_1 and shifts to lower L_2 values as L_1 reduces. At lower L_1 settings, only a decrease in CDT level can be observed. (B) QDT amplitudes increase with L_2 in different growth rates depending on the L_1 settings. Note: a notch can be observed at moderate to low levels of the f_1. Dashed lines indicate the averaged noise floor of DPOAE measures. Data reflect an average across eight subjects.

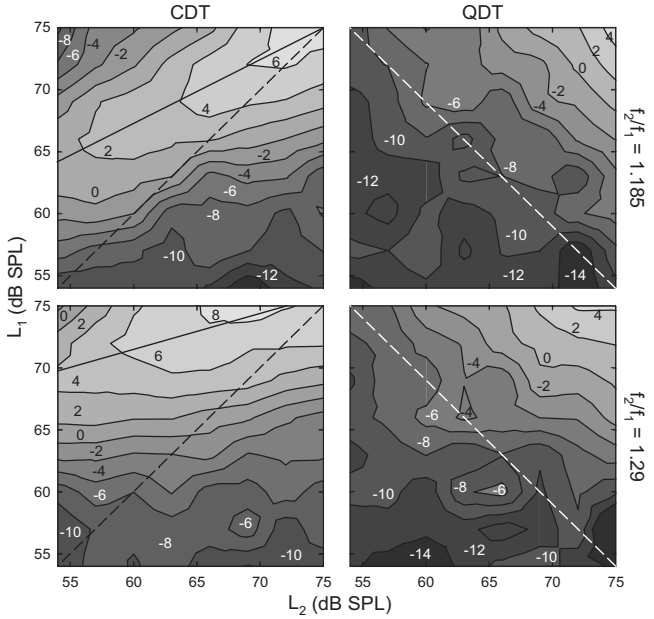


FIG. 3. Contour plots of DPOAE amplitudes in $L_1 \times L_2$ spaces of two f_2/f_1 ratios. Left: CDT magnitude shows a ridge spanning from the upper right corner (75,75) to moderate L_1 and low L_2. Solid lines indicate the optimal primary levels that yield the maximal CDT magnitude. Diagonal dashed lines indicate the condition $L_1=L_2$. Distances between the two lines represent the optimal level difference ($\Delta L=L_1-L_2$). Note: ΔL is greater for higher f_2/f_1 ratio (lower panel). Right: QDT magnitude contour lines are parallel to the diagonal dashed line representing $L_1+L_2=129$ dB SPL. For each fixed L_1 or L_2, maximizing the other primary level would optimize the QDT amplitude. Note: the slope of the contour for the larger ratio (lower panel) is shallower than the smaller ratio (top). Data reflect an average across eight subjects at an f_2 of 4 kHz.

growth and the maximal QDT level seemed to be proportional to the fixed level of f_2. The slope of QDT growth function could reach about 1 dB/dB when L_2 was set at 72 dB SPL and progressively decrease with L_2. QDT magnitudes usually reached their highest values when L_1 was maximal (75 dB SPL). The largest QDT level could be greater than 6 dB SPL when both L_1 and L_2 were at the highest level. There was also a slight compression of the QDT growth functions when L_1 was above 70 dB SPL.

2. L_1 fixed

When L_1 was fixed at different levels, the averaged CDT magnitude showed a range of different patterns as L_2 increased [Fig. 2(A)]. The patterns and overall value of CDT amplitudes were predominated by the fixed levels of f_1. As L_1 was gradually set to lower values, the CDT amplitudes showed three types of patterns with increasing L_2: (1) a compressive growth; (2) a slower initial growth with a rollover; and (3) a gradual decrease. The overall CDT magnitudes also decreased with reductions in L_1. The progression of these CDT patterns reflected a dramatic shift of the CDT peak towards lower L_2 along with a significant reduction in overall sizes. This indicated that CDT amplitudes could reach a higher value when L_1 was set higher and the CDT growth only occurred when L_2 was lower than L_1. Consistent with the growth curves in Fig. 1(A), the CDT peaked if L_2 reached 3–10 dB below the fixed L_1. When L_2 was greater than these levels or L_1, only a gradual decrease of CDT magnitude could be observed [Fig. 2(A)].

In comparison, the QDT amplitude showed a less variable growth pattern with the increase of L_2. When L_1 was fixed above 70 dB SPL, the QDT amplitude grew quite linearly with L_2. As L_1 was lowered, the growth functions of QDT became nonmonotonic with the presence of a notch around the f_2 levels of 63 to 67 dB SPL. There seemed to be a slight shift of the notch towards lower values of L_2. The QDT magnitude grew at a 1 dB/dB rate before the notch (lower L_2), which was consistent with the linear growths at high f_1 levels. If L_1 was very low (<55 dB SPL), the QDT level was flattened within about 5 dB from the noise floor (−13 dB SPL). Thus, QDT magnitudes were influenced by both L_1 and L_2.

3. Both L_1 and L_2 varied

The combined effects of L_1 and L_2 on the averaged CDT and QDT amplitudes were evaluated with contour plots in the $L_1 \times L_2$ level spaces (Fig. 3). From the DPOAE contours, the optimal signal levels that produced the highest DPOAEs could be evident. The CDT amplitude contour (left panels) showed a confined ridge spanning from the upper right corner towards the moderate values of L_1 and the minimal L_2. The tips of contour lines on the ridge, where both L_1 and L_2 were minimal to evoke a certain level of CDT, reflected the optimal primary levels for CDT. The relation between the optimal L_1 and L_2 (solid line) indicated that L_1 was preferred to be greater than L_2. This ΔL became progressively larger at lower primary levels with reference to the dashed line depicting $L_1=L_2$. At the L_2 of about 75 dB SPL, the optimal L_1 was roughly the same as L_2, i.e., no level difference. Comparing the contours from two different f_2/f_1 ratios (1.185 and 1.29), the optimal ΔL became larger for the higher frequency ratio (lower left panel). In addition, the CDT magnitude was

largely dominated by L_1 and the influence of L_2 was weak at higher ratios as indicated by the nearly horizontal contour lines.

Although the maximal QDT magnitudes were also located at the upper-right corners of the QDT contour maps (Fig. 3, right panels), paths of the isoamplitude lines were quite different from the CDT. These parallel contour lines stepped down towards lower L_1 and L_2 with no obvious ridges formed. The direction of the contour lines followed the diagonal line from the highest L_1 to the highest L_2 (dashed line), meaning that a relatively large QDT could be obtained by keeping one of the primary levels high. Thus, the QDT amplitude seemed to be proportional to L_1+L_2, i.e., higher QDT magnitudes correlated with larger sums of the primary levels. If one of the primary levels was fixed, raising the other could increase the QDT accordingly. This diagonal direction of contour lines was unaffected by varying the f_2/f_1 ratio. However, the contour gradient at the higher f_2/f_1 ratio (lower right panel) was shallower than the lower ratio (top right), indicating that larger QDT magnitudes could be observed at lower primary levels.

B. Effects of the f_2/f_1 ratio

Since different ranges of f_2/f_1 ratios were adopted in phase 1 and phase 2 experiments, results from both phases were pooled together to evaluate the effects of a widely changed frequency ratio. Both CDT and QDT magnitudes showed a variability which was influenced by the amplitude and frequency of the emissions. The standard error (SE) of emission amplitudes was less than 2 dB when the emission magnitude was greater than −5 dB SPL or the frequency was above 1 kHz. The SE could increase up to 5 dB if the emission frequency and amplitude were below 500 Hz and −5 dB SPL, respectively. Despite the variability, the averaged DPOAE magnitudes showed different patterns as the f_2/f_1 ratio was increased from 1.15 to 1.8 (Fig. 4). As shown in this example ($L_1=L_2=72$ dB SPL), the CDT amplitude increased with the f_2/f_1 ratio starting from the lowest value of 1.15 and reached a maximum of nearly 8 dB SPL at the ratios of 1.22 to 1.25. Then, the CDT magnitude decreased quickly as the ratio further increased and dropped below −5 dB SPL for the ratios above 1.4. The QDT magnitude, however, showed an opposite change when the f_2/f_1 ratios were below 1.4, i.e., it produced a notch with a minimum of −2 dB SPL at the ratio of about 1.25. With further increase in the ratio, QDT levels bounced back and reached a peak at 1.36. For f_2/f_1 ratios greater than 1.4, both CDT and QDT magnitudes reduced continuously. Despite a slower reduction, the QDT amplitude showed no signs of a bandpass characteristic ("the second filter") when the f_2/f_1 ratio increased to 1.8, a ratio where the QDT frequency was equivalent to the CDT generated at the ratio of 1.36. From the CDT curve, a dramatic 10-dB increase in amplitude could be observed from the ratios of 1.4 to 1.32.

The opposite behaviors of CDT and QDT were also presented under the conditions of unequal primary levels. A series of averaged CDT and QDT amplitude-ratio functions was displayed to examine the influence of L_1 with L_2 held

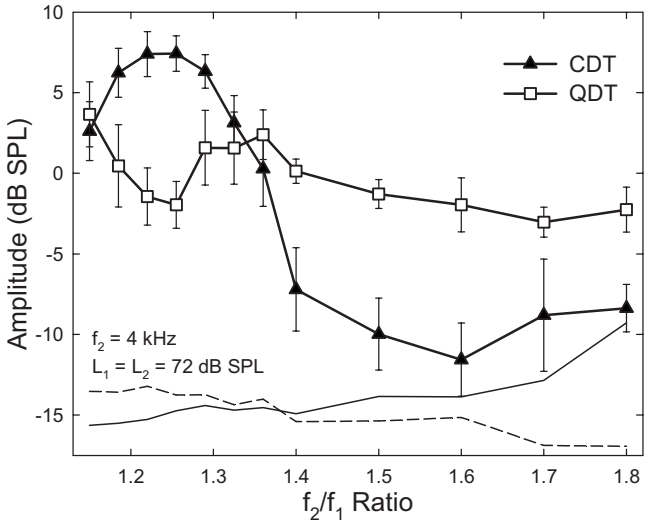


FIG. 4. DPOAE amplitudes as functions of f_2/f_1 ratio. Each curve is a combination of the averaged results from the two experimental phases. For frequency ratios below 1.4, the CDT amplitude reaches a peak at about 1.25, where the QDT magnitude drops to a local minimum. For f_2/f_1 ratios above 1.4, both CDT and QDT amplitudes decline to minimal values at the frequency ratios of 1.6 and 1.7. Error bars represent the standard errors of the data. Solid and dashed lines indicate the averaged noise floor in CDT and QDT measures, respectively. Each data point reflects an average across eight subjects.

constant at 72 dB SPL (Fig. 5). It could be observed from panel (A) that the CDT amplitudes showed an asymmetrical bell shape as the frequency ratio varied. The peaks of CDT curves progressively shifted towards lower ratios when L_1 decreased, i.e., the optimal f_2/f_1 ratio for CDT was smaller (<1.2) for lower f_1 levels (<66 dB SPL). For QDT magnitudes [panel (B)], a notch presented at about 1.22–1.25 for different levels of f_1. However, no clear trend of shifting of the notch could be observed. On either side of the notches, the QDT level peaked around the frequency ratios of 1.18

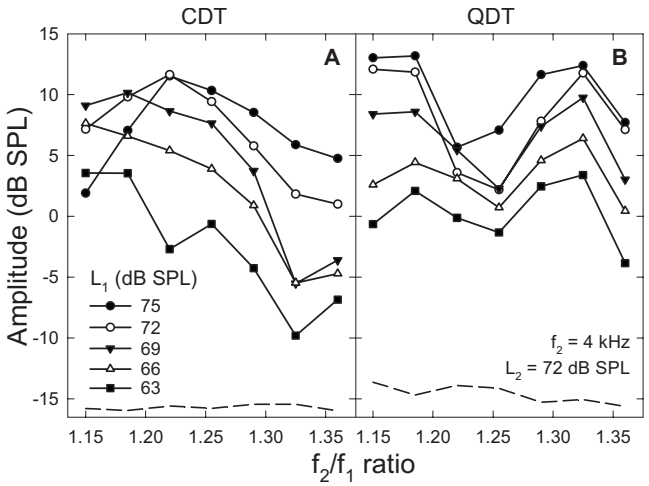


FIG. 5. Effects of primary levels on DPOAE amplitude-ratio functions. (A) As L_1 decreases, the peak of CDT amplitude shifts to lower f_2/f_1 ratios. (B) QDT magnitudes show a notch around the f_2/f_1 ratios of 1.22–1.25. No obvious shift of the notches can be observed with varying L_1. Among the two possible optimal ratios (1.185 and 1.325), the larger one is selected as the optimal ratio for recording QDT so that the QDT frequency can be maintained above 500 Hz. Data reflect an average across eight subjects.

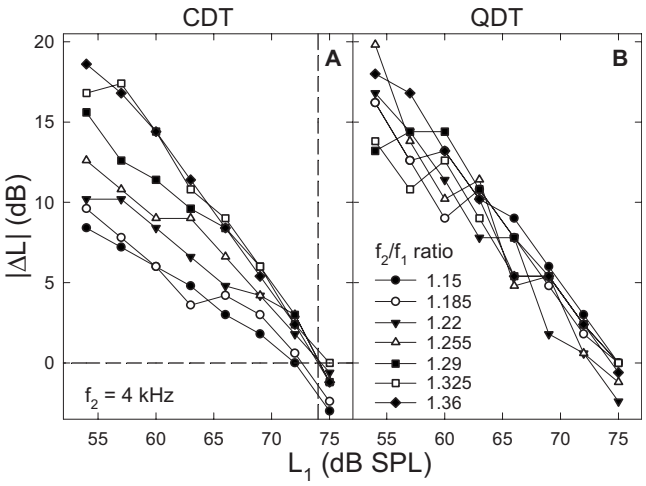


FIG. 6. Effect of L_1 on the optimal primary ΔL. For both CDT and QDT, the optimal ΔL declines with the increase in L_1. Different lines represent different f_2/f_1 ratios in each panel. (A) The slope of ΔL decrease with L_1 varies depending on the f_2/f_1 ratio. The maximal ΔL at the lowest L_1 is proportional to the frequency ratio and ΔL approaches zero around the L_1 of 74 dB SPL (dashed lines). (B) Similar trends can be observed in the ΔL for measuring QDT, but the effect of f_2/f_1 ratio is minimal. Note: the absolute value of ΔL is used, i.e., $|\Delta L|=L_1-L_2$, because L_2 could be greater than L_1 for recording QDT. Data reflect an average of eight subjects.

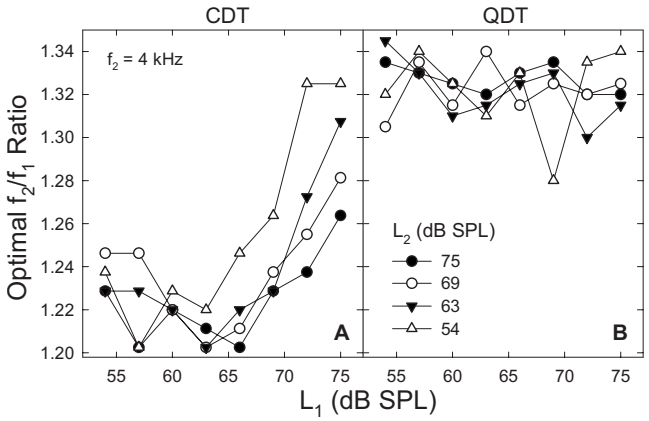


FIG. 7. Influence of primary levels on optimal f_2/f_1 ratio. (A) After an initial dip, the optimal frequency ratio increases nonlinearly with L_1. The rate of f_2/f_1 growth and the maximal value are inversely related to L_2. The minimal ratios (>1.20) present at the L_1 of about 55–65 dB SPL. (B) The optimal f_2/f_1 ratios for QDT vary between 1.3 and 1.34 with only a slight decrease with L_1. No influence from L_2 can be observed. Data reflect an average of eight subjects.

and 1.32, respectively. For levels of f_1 below 70 dB SPL, the patterns of QDT amplitude were more asymmetrical, with peaks at the ratio of 1.32 being higher.

C. Optimal signal conditions

1. Primary level difference

Inter-relations among the optimal signal conditions (L_1, L_2, and f_2/f_1 ratio) were explored and quantified. As noted above, L_1 should be greater than L_2 to evoke a large CDT (Fig. 3 left) and the ΔL was greater at lower primary levels. The ΔL was further affected by the f_2/f_1 ratio, i.e., larger for higher ratios, and the optimal ratio increased with the primary level [Fig. 5(A)]. These relations were depicted with a series of optimal ΔLs obtained at different frequency ratios plotted as functions of L_1 (Fig. 6). For CDT [panel (A)], these ΔLs decreased linearly with the L_1 and became 0 at the L_1 of about 74 dB SPL. The only obvious difference among these ΔL functions was their varying slopes that decreased with the f_2/f_1 ratio. Thus, the ΔL functions could be fit with a cluster of straight lines passing through a single point (74, 0),

$$\Delta L = K(r)(L_1 - 74), \tag{1}$$

where $K(r)$ is the slope of the ΔL functions. Note that the slope K is a function of the f_2/f_1 ratio (r) and the values are listed in Table I. As can be observed, the relation between the slopes and the ratios was approximately linear with a 0.96 correlation coefficient (r^2). Therefore, the slope could be obtained from $K(r)=a\cdot r+b$, where $a=-2.09$, $b=1.91$.

For QDT, ΔL was also reduced as L_1 increased [Fig. 6(B)]. Unlike CDT, these ΔL functions for different f_2/f_1 ratios were close to each other, indicating that the influence of the frequency ratio was weak. The slopes of these ΔL functions were approximately -1, meaning that the effect of primary levels was a linear decrease with increasing f_2/f_1 ratio. Solving Eq. (1) with $K=-1$, there were two possible relations between the primary levels: one of the primaries L_1 or $L_2=74$ dB SPL, or $L_1=L_2/2+37$, if both primaries were at moderate levels. However, the second solution was not the optimal condition, because for a given primary level the sum of L_1 and L_2 was not greater than when the other tone was held at the maximal value. It should be noted that L_2 could be greater than L_1 to evoke a large QDT.

2. Frequency ratio

For CDT, the influence of primary levels on the optimal f_2/f_1 ratio was mainly from L_1, since the ratio showed only a small reduction with L_2 (data not shown). At different L_2 levels, the optimal ratio as functions of L_1 demonstrated a series of "J"-shaped curves [Fig. 7(A)]. Generally, the optimal ratio declined slightly as L_1 increased to 60–65 dB SPL. With further increase in L_1, the ratio rose considerably. As L_2 was lowered, the optimal ratio change with L_1 showed three trends: (1) a steeper slope; (2) a higher maximal ratio; and (3) a shift of the minimum to lower L_1. For each fixed L_2, the ratio curve could be fit with a quadratic function,

TABLE I. Relation between the f_2/f_1 ratio (r) and the slope K used for calculating the primary level difference (ΔL) in Eq. (1).

r	1.15	1.185	1.22	1.255	1.29	1.325	1.36
K	−0.52	−0.56	−0.64	−0.66	−0.78	−0.90	−0.93

TABLE II. Relation between L_2 and the parameters in Eq. (2). r^2: correlation coefficient of a linear regression between the parameter and the L_2.

L_2 (dB SPL)	75	72	69	66	63	60	57	54	r^2
r_0	1.223	1.227	1.230	1.230	1.224	1.233	1.236	1.228	0.62
$s(\times 10^{-4})$	2.31	1.72	2.65	1.75	5.52	4.53	4.33	5.06	0.74
L_0 (dB SPL)	65.44	64.96	63.9	61.61	63.98	62.20	61.91	61.15	0.37

$$r = r_0 + s(L_1 - L_0)^2, \tag{2}$$

where r_0 is the minimal f_2/f_1 ratio (when $L_1=L_0$) and s is the slope of ratio growth. Values of the parameters obtained from curve fitting varied with L_2 (Table II). For simplicity, linear functions were used to approximate the relations between the parameters and L_2,

$$\begin{cases} r_0 = c_1 L_2 + d_1 \\ s = c_2 L_2 + d_2 \\ L_0 = c_3 L_2 + d_3 \end{cases}, \tag{3}$$

where $c_1=-3.65\times10^{-4}$, $d_1=1.25$, $c_2=-1.65\times10^{-5}$, $d_2=1.42\times10^{-3}$, $c_3=0.19$, and $d_3=50.91$.

There could be two optimal ratios for QDT as indicated by the two peaks of the QDT amplitude-ratio patterns [Figs. 4 and 5(B)]. Only the larger ratio was chosen to keep the QDT frequency above 500 Hz for a better SNR. For QDT, no systematic increase of the optimal f_2/f_1 ratio was observed [Fig. 7(B)]. The ratios fluctuated between 1.30 and 1.34 regardless of L_2. Examined across different levels of L_2, the frequency ratios showed a slight decrease with increasing L_1. On average, the f_2/f_1 ratios ranged from 1.32 to 1.33. Therefore, the influence of primary levels on the f_2/f_1 ratio to record QDT was weak and a value slightly greater than 1.3 could be used as the optimal frequency ratio.

IV. DISCUSSION

To explain the experimental results and explore the generating mechanisms of DPOAEs, a model combining the cochlear mechanics of traveling wave and the nonlinearity in hair cell transduction is used (Fig. 8). Simulated effects of manipulating the primary tones are compared with experimental data. Adding a traveling-wave component to the hair cell transducer model (Bian *et al.*, 2002) is to determine the extent of two-tone interaction on the basilar membrane (BM) and the exact input levels to hair cell transduction.

A. Interaction of traveling waves

A simplified gamma-tone envelope (Carney, 1993) can be used to describe the spread of excitation or displacement along the BM in response to a pure tone,

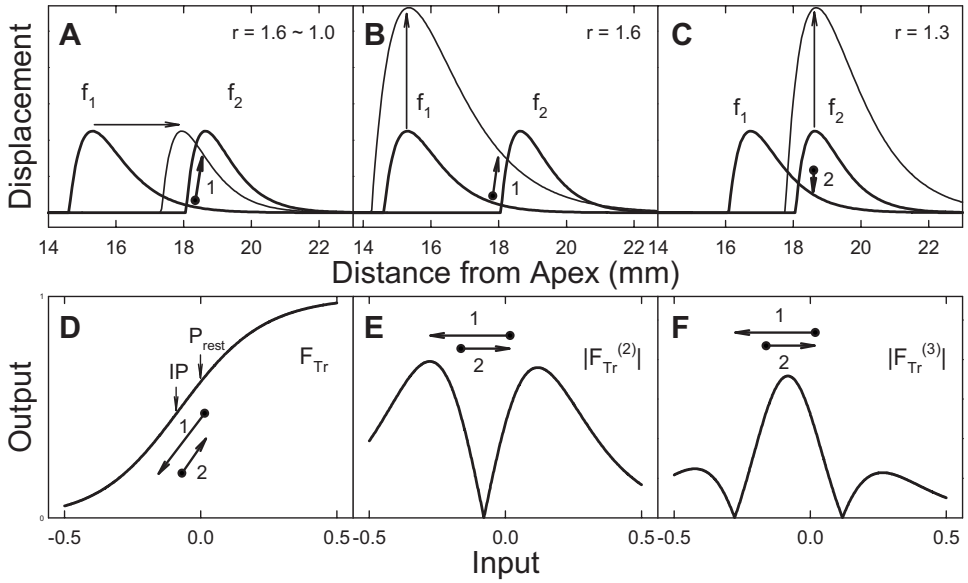


FIG. 8. A model of DPOAE generation. Top row: two tone interaction via traveling waves. (A) Sweeping f_1 to reduce the f_2/f_1 ratio (r) while keeping primary levels constant ($L_1=L_2$). (B) Increasing L_1 while keeping the f_2/f_1 ratio constant. The overlap of traveling wave envelopes increases as f_1 approaches f_2 or as L_1 increases. Influence of f_1 on f_2 or the effective L_1, as indicated by the crossing point of the envelopes, rises accordingly. The direction of the crossing point change (dot arrow) marks the direction of OP shift on the F_{Tr} (path 1). (C) Raising L_2 while keeping the frequency ratio constant. As L_2 increases, changes in the overlapped region and the effective L_1 are small. Actually, the influence of f_1 on f_2 is reduced. Relative to the f_2 peak, the direction of the crossing point change (dot arrow) is reversed (path 2). Bottom row: the hair cell transducer nonlinearity and DP generation. The direction and path of the OP shift resulting from traveling wave interactions are indicated by the numbered dot arrows. (D) A cochlear F_{Tr} marked with the resting position (P_{rest}) and inflection point (IP). (E) and (F) Absolute values of the second and third derivatives of the F_{Tr}, or $|F_{Tr}^{(2)}|$ and $|F_{Tr}^{(3)}|$, respectively. Following the OP paths, the differential behaviors of QDT and CDT can be observed from panels (E) and (F).

$$P_{\mathrm{TW}}(l) = n \cdot l \cdot e^{-nl}, \tag{4}$$

where P_{TW} is the traveling wave envelope as a function of the BM location l in millimeters from the apex and n is a constant which is unique to the traveling wave peak location (l_{P}). Since the slope or derivative of the envelope at its peak is zero, i.e., $P'_{\mathrm{TW}} = n(1-nl)e^{-nl} = 0$, thus $n = 1/l_{\mathrm{P}}$. Ideally, l_{P} is determined by the cochlear frequency map (Greenwood, 1990), where the characteristic frequency (f_{CF}) location from the apex is $l_{\mathrm{CF}} = (1/\alpha)\log_{10}(f_{\mathrm{CF}}/A + k)$, where $\alpha = 0.06$ mm^{-1}, $A = 165$ Hz, and $k = 1$ for humans. With increasing stimulus level, two alterations in traveling wave properties are also implemented: a basal peak shift and an envelope widening. Since the maximal peak shift is about 1/2 octave above the f_{CF} (Robles and Ruggero, 2001), the shift can be quantified as $l_{\mathrm{P}} = l_{\mathrm{CF}} + (l_{1.5\mathrm{CF}} - l_{\mathrm{CF}})L$, where L is the signal level in pascals. Width of the traveling wave is defined as the distance between l_{P} and the apical zero crossing (l_0). Given a 35-mm-long BM, the width is a fraction (w) of the basal portion of the traveling wave ($35 - l_{\mathrm{P}}$). This yields to $l_0 = l_{\mathrm{P}} - w(35 - l_{\mathrm{P}})L^{1/2}$, where $w = 1/3$. Thus, the actual traveling wave envelope is calculated as

$$P_{TW}(l) = \begin{cases} n(l - l_0)e^{-n(l-l_0)} \\ 0, \quad \text{if } l < l_0, \end{cases} \tag{5}$$

where $n = 1/(l_{\mathrm{P}} - l_0)$ and the BM apical to l_0 does not respond.

Since DPs are generated from the overlapped region of two traveling wave envelopes initiated by the primary tones [Fig. 8(A)], only a portion of the f_1 envelope contributes to the two-tone interaction. The effective L_1, indicated by the crossing point of f_1 and f_2 envelopes, is critical in determining the contribution of f_1 and the influence of f_1 on f_2 (Lukashkin and Russell, 2001). Effects of f_1 with respect to a fixed f_2 were systematically examined by: (1) varying f_1 with equal primary levels; (2) varying L_1 with f_1 fixed; and (3) varying L_2 with a fixed f_2/f_1 ratio [Figs. 8(A)–8(C)]. As f_1 approaches f_2 [panel (A)], the overlapped region becomes larger and the effective L_1 at the crossing point climbs up. When both f_1 and f_2 are fixed, increasing L_1 enlarges the traveling wave overlap and the effective L_1 (panel B), similar to raising f_1. The manipulation of L_2, however, produces a limited effect, because the basal slope of f_1 envelope is shallow and expansion of apical portion of f_2 pattern is small [Fig. 8(C)]. All three situations produce more or less similar changes of the CDT, i.e., a limited or saturated increase in CDT amplitude, since the effective L_1 is limited by the f_2/f_1 ratio of 1, or the fixed settings of L_2 and L_1. Increase in traveling wave overlap alone cannot explain the nonmonotonic changes in DPOAE magnitudes and differential behaviors of CDT and QDT (Figs. 1–5). In essence, the optimal signal conditions are not solely dependent on traveling wave interactions. A second component in the model, the transducer nonlinearity, is thus necessary.

B. Interaction with the hair cell transducer

The nonlinearity of OHC transducer is characterized by a second-order Boltzmann function [Fig. 8(D)] relating cochlear responses to the BM displacement x (Bian *et al.*, 2002),

$$F_{\mathrm{Tr}} = F_{\max}/[1 + e^{bx-c}(1 + e^{dx-e})], \tag{6}$$

where $F_{\max}$ is a scaling factor determining the maximal output, (b,d) are slope constants, (c,e) are constants setting the resting position of the hair cell transducer. The main advantage of using the second-order Boltzmann function is its asymmetry. The inflection point (IP) on the F_{Tr} curve is located off zero input (resting point) and the slopes on two sides are different (Bian, 2004). These F_{Tr} asymmetries can be observed from the center notch or peak of the absolute values of its second and third derivatives (corresponding to the IP) and the sizes of sidelobes [panels (E) and (F)]. Note that there is a 180° phase difference between the sidelobes or side and center peak of the second and third derivatives, respectively. In addition to traveling wave interactions, the second and third derivatives of F_{Tr} largely dictate the behaviors of QDT and CDT.

1. Ratio effects

Influence of L_1 on the overlapped region is not only a modification of actual input to the cochlear transducer, but also a biasing of the OP of hair cells in that region due to a tilting of hair bundles or shrinking of cell bodies caused by the f_1 traveling wave. With the absence of f_1 or when f_1 is far away from f_2, the OP at the f_2 place usually is at the resting point [Fig. 8(D)]. When f_1 approaches f_2, or L_1 steps up, the BM may undergo a progressive baseline shift or an OP shift [Figs. 8(A) and 8(B)]. The direction of OP shift on F_{Tr} could be from the resting position towards the IP (path 1). When the influence of f_1 becomes very large, e.g., at a very small f_2/f_1 ratio or an intense L_1, the OP could pass the IP and eventually approach the minima on the third derivative [panel (F)]. Therefore, the CDT magnitudes, as functions of f_2/f_1 ratio [Figs. 4 and 5(A)] or L_1 [Fig. 1(A)], show a maximum and a rollover. Another evidence for the OP shift across the IP could be the notch presented on the QDT amplitude-ratio functions [Figs. 4 and 5(B)], which was also observed by Brown (1993). The simulated results of QDT and CDT (Fig. 9) well represent the scenarios of OP shifts on the second and third derivatives of F_{Tr} as the f_2/f_1 ratio is reduced.

A result of the simulation is that the CDT magnitudes reach a minimum and then increase when the f_2/f_1 ratio is reduced below about 1.1 [Fig. 9(A)]. This notch could not be observed in the present study due to the limited frequency ratio selection (≥ 1.15). However, the notch in CDT amplitude-ratio function has been reported in adults (Harris *et al.*, 1989, Moulin, 2000; Londero *et al.*, 2002) and neonates (Abdala, 1996; Lasky, 1997; Vento *et al.*, 2004). Applying the above scenario and following path 1 of the OP shift, the CDT can reach a minimum and regain its magnitude when f_1 further approaches f_2 [Fig. 8(F)]. It has been suggested that when $f_2/f_1 < 1.1$, reflection or place-fixed

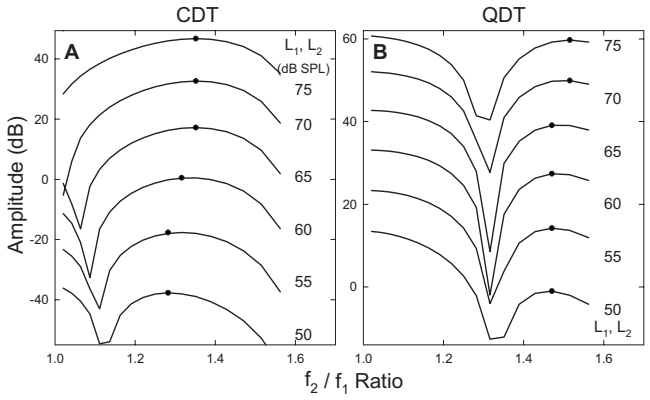


FIG. 9. Model simulation: effects of f_2/f_1 ratio. (A) CDT magnitudes are maximized at the ratio between 1.2 and 1.3 and otherwise reduced. The peak CDT amplitude (dots) shifts to higher ratios with increase in primary levels (L_1=L_2). Note: a notch is presented at the f_2/f_1 ratio of about 1.1. (B) QDT amplitudes are minimized at the frequency ratio of about 1.3 and maximized at higher (>1.4) or lower ratios. The maximal QDT magnitudes at the higher ratios are marked with dots.

DPOAEs may become dominant (Stover *et al.*, 1999; Knight and Kemp, 2001; Dhar *et al.*, 2005) and cancel the nonlinearly generated DPs. However, the possibility that a nonlinear mechanism alone is capable of producing the notch cannot be ruled out (Lukashkin and Russell, 2001). Several investigators have measured the widths of CDT amplitude-ratio functions as the bandwidth of a "second cochlear filter" (Brown *et al.*, 1993; Abdala, 1996; Vento *et al.*, 2004) and found it narrower at lower primary levels. The simulated results [Fig. 9(A)] are consistent with these observations. Although the "second filter" is not evident by bringing the QDT frequency into the filter bandwidth (Fig. 4; Fahey *et al.*, 2006), the shape of CDT amplitude-ratio function partly reflects the third derivative of cochlear F_{Tr} which is level dependent (Patuzzi and Moleirinho, 1998; Bian and Chertoff, 2001). Indeed, the sharpness of cochlear filter and the hair cell transducer gain may be intimately related.

2. Level effects

The effect of increasing L_1 is similar to reducing f_2/f_1 ratio where the CDT amplitude first increases and then rolls over [Fig. 1(A)]. The nearly linear growth of CDT with L_1, which is also observed by others (Gaskill and Brown, 1990; Whitehead *et al.*, 1995; Dreisbach and Siegel, 2005), may reflect the elevation of the effective L_1 at the overlap of traveling wave envelopes [Fig. 8(B)]. Since the apical slope of f_2 traveling wave envelope is very steep, the increase of effective L_1 follows the rise of the tail of f_1 envelope proportionally. When L_1 exceeds L_2, the traveling wave overlap reaches a maximum and the OP may shift (path 1) to the IP of F_{Tr}, thus producing a peak in CDT magnitude. Unlike the frequency ratio change, the CDT-L_1 functions rarely show a notch [Fig. 1(A)]. However, such a notch is frequently found in gerbils (Mills, 2002) and chinchillas (Rhode, 2007), because the frequency places of the primaries are closer in small rodents and L_1 is perhaps more effective in biasing OHCs at the f_2 place. At the lowest f_2/f_1 ratio (1.15), a notch was indeed observed on the L_1 side of the $L_1 \times L_2$ space. It is worth noting that larger f_2/f_1 ratios are used to evoke DPOAEs in rodents (Brown, 1987).

In contrast, increasing L_2 may result in an opposite OP shift, because the influence of f_1 on f_2 diminishes as L_2 rises due to unchanged effective L_1 [Fig. 8(C)]. The direction of OP shift is from a prebiased position in the negative pressures towards the resting position of hair cell F_{Tr} (path 2). Depending on the value of L_1, the initial OP shift could vary, thus resulting in variable patterns of CDT amplitude [Fig. 2(A)]. For high f_1 levels, the initial OP shift is large and the OP can pass through the IP as L_2 increases, causing CDT to rise and fall [Fig. 8(E)]. For lower L_1, the small initial shift may not even reach the IP, and CDT can only show a decrease as the OP returns to its resting point. These different patterns are indeed observed as increasing L_2 while holding L_1 at various levels [Fig. 2(A); Hauser and Probst, 1991]. Notches of the QDT amplitude in Fig. 2(B) may also indicate the OP path. However, the OP shift on QDT is less influential than the primary levels. This can be evident from the QDT contours in humans (Fig. 3, right) and rabbits (Martin *et al.*, 2003) that show diagonal contour lines indicating increasing influences from both primary levels. In contrast, the ridge on CDT contours implies that a specific influence of L_1 on L_2, i.e., a unique OP shift, can maximize the amplitude. From Figs. 8(D)–8(F), it can be noted that CDT at lower input level is related to the center peak of the third derivative and the IP. In contrast, QDT is associated with sidelobes of the second derivative that are maximal for high input levels or large OP shifts. Moreover, sidelobes of the second and third derivatives are both related to saturation regions of the F_{Tr}. Indeed, the direction of QDT contour line is consistent with the "passive" CDT evoked at high primary levels (Mills, 1997).

C. Optimal signal conditions

Descriptions of the optimal signal conditions derived from the simulation are comparable with the experimental results. For equal primary levels, the optimal frequency ratio for CDT increases with the signal level [Fig. 9(A)], which is consistent with the observations in the present study (Figs. 4 and 5) and works by others (e.g., Johnson *et al.*, 2006). The level-dependent drift of the optimal ratio is probably due to narrower traveling wave envelopes at low levels so that the two tones need to be placed closer to produce an interaction. Unlike the CDT, the optimal ratio for QDT shows no obvious drift with the primary level [Figs. 5(B) and 9(B)]. One reason for this difference could be that the deep notch on the second derivative of F_{Tr} [Fig. 8(E)] could severely affect the QDT magnitude compared to variations in traveling wave overlap.

Another important signal parameter is ΔL, which shows two linear relations in both experimental and simulated results (Figs. 6 and 10). First, ΔL decreases linearly with L_1. Such a linear decrease is predictable from the differential growths of BM vibrations at the f_2 place in response to f_1 and f_2 (Kummer *et al.*, 2000), i.e., linear growth of effective L_1 and compression of L_2. Additional sound pressure is re-

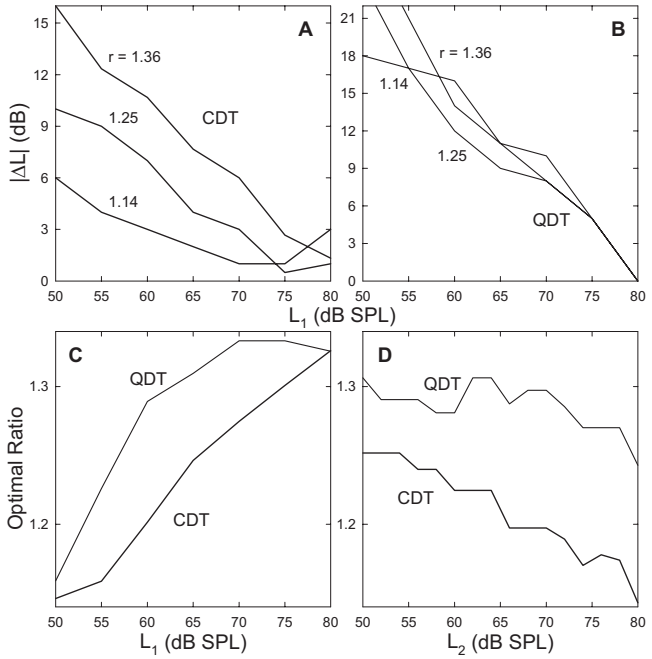


FIG. 10. Model simulation: optimal signal conditions. (A), (B) Influence of L_1 on primary ΔL. For both CDT and QDT, the ΔL decreases with L_1. For CDT, the slope of the ΔL decrease is proportional to the f_2/f_1 ratio; however, such an effect is minimal for QDT. (C), (D) Effects of the primary levels on the optimal frequency ratio. For both CDT and QDT, the ratio increases with L_1 and slightly reduces with L_2. These level effects are smaller for QDT. Note the optimal frequency ratio is higher for QDT than CDT.

quired to compensate the insensitivity for f_1 at the f_2 location until about 70–75 dB SPL, where tuning at the f_2 place is broadened. Second, for CDT, the slope of ΔL decrease is proportional to the f_2/f_1 ratio [Figs. 6(A) and 10(A)]. Again, it becomes clear that the tuning property at the f_2 place determines that a smaller ΔL is required for a more closely placed f_1 to produce a certain level of interaction [Figs. 8(A)–8(C)]. These linear trends allow the derivation of Eq. (1) to calculate the ultimate ΔL for a given frequency ratio. Other formulas (Whitehead *et al.*, 1995; Kummer *et al.*, 2000) are also developed in a similar way. A formula by Johnson *et al.* (2006), incorporates the f_2 and can be applied to different frequencies. Our formula in Eq. (1), however, includes the f_2/f_1 ratio and is flexible for situations where the ratio is predetermined.

In practice, f_2 and L_2 are usually preselected to assess cochlear functions at a particular frequency location. The decisions to be made are to find f_1 by selecting an appropriate f_2/f_1 ratio and to determine L_1. From the experimental data and model simulation, it is known that the optimal f_2/f_1 ratio is nonlinearly dependent on the primary level [Figs. 7, 10(C), and 10(D)]. For CDT, the optimal ratio stays low for lower values of L_1 and grows quickly at higher levels. The quadratic fit of the optimal ratio function coincides with the formula of Johnson *et al.* (2006), in which a squared L_2 is used. The effect of L_2 on the optimal frequency ratio is a slight decrease [Fig. 10(D)]. Moving f_1 closer could produce more two tone interactions if L_2 is substantial, whereas moving f_1 away could avoid suppressing f_2 if L_2 is weak. For QDT, the simulated optimal ratios (about 1.3) are generally comparable with the data for $L_1 > 65$ dB SPL [Figs. 7(B) and 10(D)], even though the measured ratios show no obvious change with the primary levels.

For CDT, the complex interactions among frequency ratio and primary levels could be determined from the abstracted relations between a collective pairs of variables. Therefore, two of the relations are formulated using ΔL and optimal ratio [Eqs. (1) and (2)]. Since these relations coexist, the optimal conditions should satisfy both equations. Therefore, a set of two formulas is proposed for obtaining the optimal signal conditions for CDT,

$$\begin{cases} [1-(a\cdot r+b)]L_1 = L_2 - 74(a\cdot r+b) \\ r = r_0 + s(L_1 - L_0)^2 \end{cases}, \tag{7}$$

where $r_0 = c_1 L_2 + d_1$, $s = c_2 L_2 + d_2$, and $L_0 = c_3 L_2 + d_3$. Solving both equations together, the optimal f_1 and L_1 could be determined. These formulas with parameters obtained from the data predict the optimal conditions for each subject in the study. Using f_2/f_1 ratio as an example, the prediction accuracy is as high as 95% with an average of 73%. From Eq. (7), the calculated values of L_1 and f_2/f_1 are well comparable with results in humans (Kummer *et al.*, 2000; Johnson *et al.*, 2006) and rodents (Pibal *et al.*, 2002; Michaelis *et al.*, 2004). Parameters used in the formulas still need to be tested and refined by large-scaled studies with wider stimulus ranges.

V. SUMMARY AND CONCLUSION

Amplitudes of CDT and QDT were measured within a finite $L_1 \times L_2$ space across a wide range of f_2/f_1 ratios. For CDT, three relations are found among the optimal signal conditions: (1) L_1 should always be greater than L_2, until about 74 dB SPL where the level difference diminishes; (2) the rate of primary ΔL decrease is proportional to the f_2/f_1 ratio; and (3) the optimal frequency ratio increases with L_1 in a nonlinear fashion. A set of two formulas is proposed to quantify the optimal signal conditions, namely, f_1 and L_1 for a given L_2. For QDT, different relations are observed: (1) maximizing one of the primary levels can optimize the QDT amplitude; (2) the ΔL decreases with the signal level, but independent of the f_2/f_1 ratio; and (3) the optimal frequency ratio was constant at just over 1.3. An important finding is the QDT notch around the optimal ratio for CDT (1.22–1.25). Therefore, the optimal signal conditions for CDT cannot be applied to QDT. If applied cautiously to avoid system distortions, maximizing the signal level could allow for recording of robust QDT and CDT that may persistent after cochlear damages (Avan *et al.*, 2003). The present results are consistent with the notion that DPOAEs mainly originate from the OHC nonlinearity in the overlapped region of the traveling waves. Optimizing DPOAE recordings could improve the measurement reliability and repeatability, thus allowing for more accurate estimates of cochlear function and a wider range of clinical utilities.

ACKNOWLEDGMENTS

We thank the subjects for their patience and Tina Stinson for recruiting some of the participants. This work was supported by a grant (R03 DC006165) from the National Insti-

tute on Deafness and Other Communication Disorders of the National Institutes of Health.

Abdala, C. (**1996**). "Distortion product otoacoustic emission ($2f_1-2f_2$) amplitude as a function of f_2/f_1 frequency ratio and primary tone level separation in human adults and neonates," J. Acoust. Soc. Am. **100**, 3726–3740.

Allen, J. B., and Fahey, P. F. (**1993**). "Asecond cochlear-frequency map that correlates distortion product and neural tuning measurements," J. Acoust. Soc. Am. **94**, 809–816.

Avan, P., Bonfils, P., Gilain, L., and Mom, T. (**2003**). "Physiopathological significance of distortion-product otoacoustic emissions at $2f1-f2$ produced by high- versus low-level stimuli," J. Acoust. Soc. Am. **113**, 430–441.

Bian, L. (**2004**). "Cochlear compression: Effects of low-frequency biasing on quadratic distortion product otoacoustic emission," J. Acoust. Soc. Am. **116**, 3559–3571.

Bian, L. (**2006**). "Spectral fine-structures of low-frequency modulated distortion product otoacoustic emissions," J. Acoust. Soc. Am. **119**, 3872–3885.

Bian, L., and Chertoff, M. E. (**2001**). "Distinguishing cochlear pathophysiology in 4-aminopyridine and furosemide treated ears using a nonlinear systems identification technique," J. Acoust. Soc. Am. **109**, 671–685.

Bian, L, and Scherrer, N. M. (**2007**). "Low-frequency modulation of distortion product otoacoustic emissions in humans," J. Acoust. Soc. Am. **122**, 1681–1692.

Bian, L., Chertoff, M. E., and Miller, E. (**2002**). "Deriving a cochlear transducer function from low-frequency modulation of distortion product otoacoustic emissions," J. Acoust. Soc. Am. **112**, 198–210.

Brown, A. M. (**1987**). "Acoustic distortion from rodent ears: A comparison of responses from rats, guinea pigs and gerbils," Hear. Res. **31**, 25–38.

Brown, A. M. (**1993**). "Distortion in the cochlea: Acoustic $f2-f1$ at low stimulus levels," Hear. Res. **70**, 160–166.

Brown, A. M., Gaskill, S. A., Carlyon, R. P., and Williams, D. M. (**1993**). "Acoustic distortion as a measure of frequency selectivity: Relation to psychophysical equivalent rectangular bandwidth," J. Acoust. Soc. Am. **93**, 3291–3297.

Carney, L. H. (**1993**). "A model for responses of low-frequency auditory-nerve fibers in cat," J. Acoust. Soc. Am. **93**, 401–417.

Dhar, S., Long, G. R., Talmadge, C. L., and Tubis, A. (**2005**). "The effect of stimulus-frequency ratio on distortion product otoacoustic emission components," J. Acoust. Soc. Am. **117**, 3766–3776.

Dreisbach, L. E., and Siegel, J. H. (**2005**). "Level dependence of distortion-product otoacoustic emissions measured at high frequencies in humans," J. Acoust. Soc. Am. **117**, 2980–2988.

Fahey, P. F., Stagner, B. B., and Martin, G. K. (**2006**). "Mechanism for bandpass frequency characteristic in distortion product otoacoustic emission generation," J. Acoust. Soc. Am. **119**, 991–996.

Fahey, P. F., Stagner, B. B., Lonsbury-Martin, B. L., and Martin, G. K. (**2000**). "Nonlinear interactions that could explain distortion product interference response areas," J. Acoust. Soc. Am. **108**, 1786–1802.

Frank, G., and Kössl, M. (**1996**). "The acoustic two-tone distortions $2f1-f2$ and $f2-f1$ and their possible relation to changes in the operating point of the cochlear amplifier," Hear. Res. **98**, 104–115.

Garner, C. A., Neely, S. T., and Gorga, M. P. (**2008**). "Sources of variability in distortion product otoacoustic emissions," J. Acoust. Soc. Am. **124**, 1054–1067.

Gaskill, S. A., and Brown, A. M. (**1990**). "The behavior of the acoustic distortion product, $2f1-f2$, from the human ear and its relation to auditory sensitivity," J. Acoust. Soc. Am. **88**, 821–839.

Gorga, M. P., Neely, S. T., Dorn, P. A., and Hoover, B. M. (**2003**). "Further efforts to predict pure-tone thresholds from distortion product otoacoustic emission input/output functions," J. Acoust. Soc. Am. **113**, 3275–3284.

Greenwood, D. D. (**1990**). "A cochlear frequency-position function for several species-29 years later," J. Acoust. Soc. Am. **87**, 2592–2605.

Harris, F. P., Lonsbury-Martin, B. L., Stagner, B. B., Coats, A. C., and Martin, G. K. (**1989**). "Acoustic distortion products in humans: Systematic changes in amplitude as a function of f_2/f_1 ratio," J. Acoust. Soc. Am. **85**, 220–229.

Hauser, R., and Probst, R. (**1991**). "The influence of systematic primary-tone level variation L_2-L_1 on the acoustic distortion product emissions $2f_1-f_2$ in normal human ears," J. Acoust. Soc. Am. **89**, 280–286.

Johnson, T. A., Neely, S. T., Garner, C. A., and Gorga, M. P. (**2006**) "Influence of primary-level and primary frequency ratios on human distortion product otoacoustic emissions," J. Acoust. Soc. Am. **119**, 418–428.

Kennedy, H. J., Crawford, A. C., and Fettiplace, R. (**2005**). "Force generation by mammalian hair bundles supports a role in cochlear amplification," Nature (London) **433**, 880–883.

Kim, D. O. (**1980**). "Cochlear mechanics: Implications of electrophysiological and acoustical observations," Hear. Res. **2**, 297–317.

Knight, R. D., and Kemp, D. T. (**2001**) "Wave and place fixed DPOAE maps of the human ear," J. Acoust. Soc. Am. **109**, 1513–1525.

Kummer, P., Janssen, T., Hulin, P., and Arnold, W. (**1998**). "The level and growth behavior of the $2\ f1-f2$ distortion product otoacoustic emission and its relationship to auditory sensitivity in normal hearing and cochlear hearing loss," J. Acoust. Soc. Am. **103**, 3431–3444.

Kummer, P., Janssen, T., Hulin, P., and Arnold, W. (**2000**). "Optimal L_1-L_2 primary tone level separation remains independent of test frequency in humans," Hear. Res. **146**, 47–56.

Lasky, R. E. (**1998**). "Distortion product otoacoustic emissions in human newborns and adults. I. Frequency effects," J. Acoust. Soc. Am. **103**, 981–991.

Liberman, M. C., Gao, J., He, D. Z. Z., Wu, X., Jia, S., and Zou, J. (**2002**). "Prestin is required for electromotility of the outer hair cell and for the cochlear amplifier," Nature (London) **419**, 300–304.

Londero, A., Bonfils, P., and Avan, P. (**2002**). "Magnitudes and phases of human distortion-product otoacoustic emissions at $2f_1-2f_2$ against f_2/f_1: Effects of an audiometric notch," Hear. Res. **167**, 46–56.

Lonsbury-Martin, B. L., and Martin, G. K. (**2003**). "Otoacoustic emissions," Curr. Opin. Otolaryngol. Head Neck Surg. **11**, 361–366.

Lukashkin, A. N., and Russell, I. J. (**1999**). "Analysis of the f_2-f_1 and $2f_1-2f_2$ distortion components generated by the hair cell mechanoelectrical transducer: Dependence on the amplitudes of the primaries and feedback gain," J. Acoust. Soc. Am. **106**, 2661–2668.

Lukashkin, A. N., and Russell, I. J. (**2001**). "Origin of the bell-like dependence of the DPOAE amplitude on primary frequency ratio," J. Acoust. Soc. Am. **110**, 3097–3106.

Martin, G. K., Stagner, B. B., and Lonsbury-Martin, B. L. (**2003**). "Difference-tone response areas in rabbits," in *Biophysics of the Cochlea: from Molecules to Models*, edited by A. W. Gummer, E. Dalhoff, M. Nowotny, and M. P. Scherer (World Scientific, Singapore), pp. 464–471.

Michaelis, C. E., Gehr, D. D., Deingruber, K., Arnold, W., and Lamm, K. (**2004**). "Optimum primary tone level setting for measuring high amplitude DPOAEs in guinea pigs," Hear. Res. **189**, 58–62.

Mills, D. M. (**1997**). "Interpretation of distortion product otoacoutic emission measurements. I. Two stimulus tones," J. Acoust. Soc. Am. **102**, 413–429.

Mills, D. M. (**2002**). "Interpretation of standard distortion product otoacoutic emission measurements in light of the complete parametric response," J. Acoust. Soc. Am. **112**, 1545–1560.

Mills, D. M., Feeney, M. P., Drake, E. J., Folsom, R. C., Sheppard, L., and Seixas, N. S. (**2007**). "Developing standards for distortion product otoacoutic emission measurements," J. Acoust. Soc. Am. **122**, 2203–2214.

Moulin, A. (**2000**). "Influence of primary frequency ratio on distortion product otoacoustic emissions amplitude. I. Intersubject variability and consequences on the DPOAE-gram," J. Acoust. Soc. Am. **107**, 1460–1470.

Neely, S. T., Johnson, T. A., and Gorga, M. P. (**2005**). "Distortion-product otoacoustic emission measured with continuously varying stimulus level," J. Acoust. Soc. Am. **117**, 1248–1259.

Nuttall, A. L., and Dolan, D. F. (**1993**). "Intermodulation distortion (F_2-F_1) in inner hair cell and basilar membrane responses," J. Acoust. Soc. Am. **93**, 2061–2068.

Patuzzi, R., and Moleirinho, A. (**1998**). "Automatic monitoring of mechano-electrical transduction in the guinea pig cochlea," Hear. Res. **125**, 1–16.

Pibal, I., Drexl, M., and Kössl, M. (**2002**). "Level dependence of optimal stimulus difference for evoking DPOAEs in the gerbil," Hear. Res. **174**, 260–263.

Rhode, W. S. (**2007**). "Distortion product otoacoustic emissions and basilar membrane vibration in the 6–9 kHz region of sensitive chinchilla cochleae," J. Acoust. Soc. Am. **122**, 2725–2737.

Robles, L., and Ruggero, M. A. (**2001**). "Mechanics of the mammalian cochlea," Physiol. Rev. **81**, 1305–1352.

Shera, C. A. (**2004**) "Mechanisms of mammalian otoacoustic emission and their implications for the clinical utility of otoacoustic emissions," Ear Hear. **25**, 86–97.

Stover, L. J., Neely, S. T., and Gorga, M. P. (**1999**). "Cochlear generation of intermodulation distortion revealed by DPOAE frequency functions in normal and impaired ears," J. Acoust. Soc. Am. **106**, 2669–2678.

Takahashi, S., and Santos-Sacchi, J. (**1999**). "Distortion component analysis of outer hair cell motility-related gating charge," J. Membr. Biol. **169**, 199–207.

Tubach, M., McGee, J. A., and Walsh, E. J. (**1996**). "Distortion generated by the ear: Its emergence and evolution during development," Laryngoscope **106**, 822–830.

Vento, B. A., Durrant, J. D., and Sabo, D. L. (**2004**). "Development of f_2/f_1 ratio functions in humans," J. Acoust. Soc. Am. **115**, 2138–2147.

Whitehead, M. L., Stagner, B. B., McCoy, M. J., Lonsbury-Martin, B. L., and Martin, G. K. (**1995**). "Dependence of distortion-product otoacoustic emissions on primary levels in normal and impaired ears. II. Asymmetry in L_1,L_2 space," J. Acoust. Soc. Am. **97**, 2359–2377.

A cocktail party with a cortical twist: How cortical mechanisms contribute to sound segregation

Mounya Elhilali[a)]
Department of Electrical and Computer Engineering, Johns Hopkins University, Barton 105, 3400 North Charles Street, Baltimore, Maryland 21218

Shihab A. Shamma
Department of Electrical and Computer Engineering, University of Maryland, College Park, Maryland 20742

(Received 16 May 2007; revised 16 September 2008; accepted 24 September 2008)

Sound systems and speech technologies can benefit greatly from a deeper understanding of how the auditory system, and particularly the auditory cortex, is able to parse complex acoustic scenes into meaningful auditory objects and streams under adverse conditions. In the current work, a biologically plausible model of this process is presented, where the role of cortical mechanisms in organizing complex auditory scenes is explored. The model consists of two stages: (i) a feature analysis stage that maps the acoustic input into a multidimensional cortical representation and (ii) an integrative stage that recursively builds up expectations of how streams evolve over time and reconciles its predictions with the incoming sensory input by sorting it into different clusters. This approach yields a robust computational scheme for speaker separation under conditions of speech or music interference. The model can also emulate the archetypal streaming percepts of tonal stimuli that have long been tested in human subjects. The implications of this model are discussed with respect to the physiological correlates of streaming in the cortex as well as the role of attention and other top-down influences in guiding sound organization. © *2008 Acoustical Society of America.*
[DOI: 10.1121/1.3001672]

PACS number(s): 43.66.Ba, 43.64.Bt, 43.60.Mn [RYL] Pages: 3751–3771

I. INTRODUCTION

In our daily lives, we are constantly challenged to attend to specific sound sources in the midst of competing background chatter—a phenomenon usually referred to as the *cocktail party problem* (Cherry, 1953). Whether at a real cocktail party, walking down a busy street, or having a conversation in a crowded coffee shop, we are constantly exposed to cluttered information emanating from multiple sources in our environment that we have to organize into meaningful percepts (Bregman, 1990). This challenge is not confined to humans. Animals too, including other mammals, birds, and fish, have to overcome similar challenges in order to navigate their complex auditory scenes, avoid predators, mate, and locate their newborns (Aubin and Jouventin, 1998; Fay, 1998; Hulse *et al.*, 1997; Izumi, 2001).

Despite the seemingly effortless and intuitive nature of this faculty and its importance in understanding auditory perception as a whole, we still know very little about the principles that govern stream segregation in the brain, or about the neural underpinnings underlying this perceptual feat. How does the auditory system parse acoustic scenes as interferences appear sporadically over time? How does it decide which parts of the acoustic signal belong together as one coherent sound object? Tackling these questions is key to understanding the bases of active listening in the brain as well as the development of efficient and robust mathematical models which can match up to the biological performance of auditory scene analysis tasks.

To solve this problem, the auditory system must successfully accomplish the following tasks: (a) extract relevant cues from the acoustic mixture (in both monaural and binaural pathways), (b) organize the available sensory information into perceptual streams, (c) efficiently manage the biological constraints and computational resources of the system to perform this task in real time, and (d) dynamically adapt the processing parameters to successfully keep up with continuously changing environmental conditions.

Due to the significance of this question in both perceptual and engineering sciences, interest in tackling the phenomenon of auditory scene analysis has prompted multidisciplinary efforts spanning the engineering, psychology, and neuroscience communities. On one end of the spectrum, numerous studies have attempted strict engineering approaches such as the successful application of blind source separation techniques (Bell and Sejnowski, 1995; Jang and Lee, 2004; Roweis, 2000), statistical speech models (Ellis and Weiss, 2006; Kristjansson *et al.*, 2006; Varga and Moore, 1990), and other machine learning algorithms. Despite their undeniable success, these algorithms often violate fundamental aspects of the manner humans and animals perform this task. They are generally constrained by their own mathematical formulations (e.g., assumptions of statistical independence), are mostly applicable and effective in multisensor configurations, and/or require prior knowledge and training on the

[a)]Author to whom correspondence should be addressed. Electronic mail: mounya@jhu.edu

speech material or task at hand. On the other end of the spectrum are the psychoacoustic studies that have focused on the factors influencing stream segregation, and, in particular, the grouping cues that govern the simultaneous and sequential integration of sound patterns into objects emanating from a same environmental event (Bregman, 1990; Moore and Gockel, 2002). These efforts have triggered a lot of interest in constructing *biologically inspired systems* that can perform intelligent processing of complex sound mixtures. Models developed in this spirit offer mathematical frameworks for stream segregation based on separation at the auditory periphery (Beauvois and Meddis, 1996; Hartman and Jonhson, 1991; McCabe and Denham, 1997), or extending to more central processes such as neural and oscillatory networks (von der Malsburg and Schneider, 1986; Wang and Brown, 1999), adaptive resonance theory (Grossberg *et al.*, 2004), statistical model estimation (Nix and Hohmann, 2007), and sound-based models (Ellis and Weiss, 2006). Despite demonstrations often restricted to relatively simple and abstract stimuli (e.g., tones and noise sequences), these implementations contributed heavily and in different ways to our current thinking of the neurobiology of scene analysis.

The present work attempts at bridging the gap between these two directions. Like the former, it provides a tractable computational framework to segregate complex signals (speech and music); but like the latter approaches, it does so in the spirit of biological plausibility. The fundamental aim of this model is to demonstrate how specific auditory cortical mechanisms can contribute to the formation of perceptual streams.[1] The model operates on single (monaural) inputs. It is "behaviorally" realistic, requiring no prior training on specific sounds (voices, languages, or other databases), no assumptions of statistical independence or multiple microphones, and can segregate sounds ranging from the simple (tones and noise) to the complex (speech and music). The architecture of the model consists of two main components: (i) a *feature analysis stage* that explicitly represents known perceptual features in a multidimensional space, such as tonotopic frequency, harmonicity (pitch), and spectral shape and dynamics (timbre) and (ii) an *integrative and clustering stage* that reconciles incoming perceptual features with expectations derived from a recursive estimation of the state of the streams present in the environment. Sensory information is hence assigned to the perceptual clusters that match them best.

This paper begins with a detailed description of the model in Sec. II. In Sec. III, we present simulations of the performance of the model under different auditory scene configurations. We also test the contribution of the different cortical mechanisms modeled in the current study to the process of stream segregation. Finally, we end with a summary of the different aspects of the model, then a discussion of the interaction between the cortical circuitry and higher-level attentional signals, and the possible role and mechanisms of dynamic change in the auditory cortex in perceptual stream formation.

II. THE COMPUTATIONAL AUDITORY MODEL

The computational scheme presented here is principally based on functional models of the primary auditory cortex (A1). This work is motivated by a growing body of evidence strongly suggesting a role of the auditory cortex in processes of auditory stream formation and sound organization [see Nelken (2004) for a review]. Specifically, the present model abstracts and incorporates three critical properties of A1 physiology. (i) *Multidimensional feature representation*: Auditory cortical neurons are selectively sensitive to a host of acoustic features (sometimes in an ordered manner manifested as "response maps") such as the tonotopic axis, tuning bandwidth and asymmetry maps, thresholds, fast temporal AM and FM modulations, and interaural cues (Middlebrooks *et al.*, 1980; Schreiner, 1998). This varied sensitivity implies that sounds with different perceptual attributes may activate different neural populations, enabling them to potentially be perceived as segregated sources. (ii) *Multiscale dynamics*: A1 responses exhibit temporal dynamics (Kowalski *et al.*, 1996; Miller *et al.*, 2002) that are commensurate with time scales of stream formation and auditory grouping as well as speech syllabic rates and intonation contours, musical melodies, and many other sensory percepts (Carlyon and Shamma, 2003; Elhilali *et al.*, 2003; Miller and Taylor, 1948; Viemeister, 1979). Furthermore, numerous studies have corroborated the involvement of the auditory cortex in the temporal organization of acoustic sequences (Colombo *et al.*, 1996; Jerison and Neff, 1953; Kelly *et al.*, 1996; Rauschecker, 2005). (iii) *Rapidly adapting receptive fields*: Physiological and imaging studies suggest that cortical receptive fields are rapidly modulated by auditory experience, behavioral context, attentional and cognitive state, expectations and memories, as well as the statistics of the stimulus (Fritz *et al.*, 2005; Hughes *et al.*, 2001). These findings support a view of auditory perception and scene analysis as a dynamic process mediated by an *adaptive cortex* that optimizes its representation of incoming sounds according to the objectives of the auditory task.

These three cortical response properties provide the key ingredients of the present model, as described in detail below and schematized in Fig. 1. While not strictly biophysical in detail, all elements of the model are nevertheless abstracted from known auditory physiological processes, perceptual phenomena, and anatomical structures.

A. The feature analysis and representation stage

The initial feature analysis stage projects the input sound onto a multidimensional perceptual space, allowing a natural segregation of the acoustic waveform along multiple dimensions, whereby different sound features occupy different areas of this space. This stage parallels the feature selectivity in neurons along the auditory pathway up to the auditory cortex, whereby a host of cells is tuned or best driven by different attributes of the acoustic signal along several dimensions (tonotopic frequency, spectral shape, etc). Our working hypothesis is that these feature maps are, in fact, a mechanism which permits the brain to "see" elements of each sound object distinctly represented, with minimal inter-

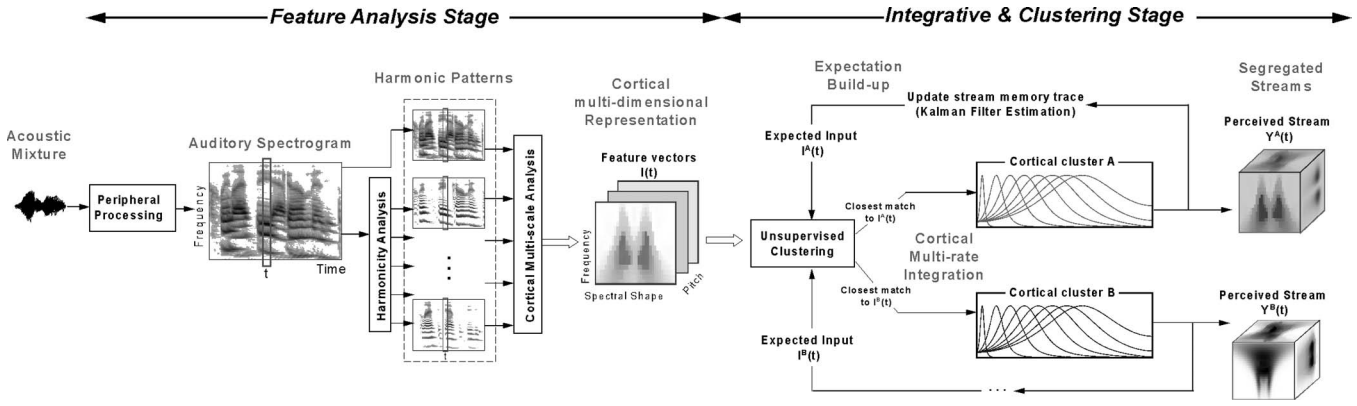


FIG. 1. Schematic of a model for auditory scene analysis. The computational model consists of two stages: a feature analysis stage, which maps the acoustic waveform into a multidimensional cortical representation, and an integrative and clustering stage, which segregates the cortical patterns into corresponding streams. The gray captions within each stage emphasize the principle outputs of the different modules. In the *feature analysis stage*, additional dimensions are added to the representation at each module, evolving from a 1D acoustic waveform (time) to a 2D auditory spectrogram (time-frequency) to a three-dimensional harmonicity mapping (time-frequency-pitch frequency) to a 4D multiscale cortical representation (time-frequency-pitch frequency-spectral shape). The *integrative and clustering stage* of the model is initiated by a clustering module which determines the stream that matches best the incoming feature vectors $I(t)$. These vectors are then integrated by multirate cortical dynamics, which recursively update an estimate of the state of streams A and B via a Kalman-filter-based process. The cortical cluster use their current states to make a prediction of the expected inputs at time $t+1$: $I^A(t+1)$ and $I^B(t+1)$. The *perceived* streams are always available online as they evolve and take their final stable form.

ference from the other sources, hence getting an uncontaminated "look" at features of each stream. By having a rich enough representation, different sound objects occupy different regions of the feature space, hence the emergence of "clean looks" of each individual stream. In our model, this operation is performed by mapping the sound mixture onto a succession of instantaneous clean looks based on primitive acoustic features such as onsets, harmonic relationships, or spectral shapes and bandwidths. It is important to note that these looks or patterns are extracted on an instant-by-instant basis, yielding a sequence of *unlabeled* feature vectors at any given instant. Only in the subsequent clustering stage of the model are they assigned to their corresponding "streams" and integrated over time.

In the current version of the model, the initial analysis stage consists of the following operations. (i) A frequency analysis that captures early auditory processing in the cochlea and midbrain nuclei (Shamma, 1998; Wang and Shamma, 1994). It transforms the acoustic stimulus to an auditory time-frequency spectrographic representation with enhanced onsets and (to a lesser extent) offsets. (ii) A harmonicity analysis which groups harmonically related components into different channels in a process consistent with the perception of pitch (Goldstein, 1973; Oxenham *et al.*, 2004; Wightman, 1973). (iii) A multiscale spectral analysis of the auditory spectrogram, as presumed to occur in primary auditory cortex (Schreiner, 1998). It is implemented by an instantaneous affine wavelet transformation of the spectral slices of the auditory spectrogram. All parameters of these processes are consistent with physiological data in animals (Langner, 1992; Miller *et al.*, 2002; Schreiner and Urbas, 1988) and psychoacoustical data in human subjects (Eddins and Bero, 2007; Green, 1986; Supin *et al.*, 1999; Viemeister, 1979). In the current implementation of the model, we have left out several acoustic features that are known to aid stream segregation such as fast AM and FM modulations as well as spatial cues. They can be readily incorporated into the model by creating additional representational axes. Next, we elaborate on the implementation of each one of these operations.

1. Peripheral auditory processing

The initial stage of the model starts with a transformation of the signal from a pressure time waveform to a spatiotemporal activation pattern. It captures the basic processing taking place at the level of the auditory periphery (Pickles, 1988), including cochlear filtering, hair-cell transduction, and auditory-nerve and cochlear-nucleus spectrotemporal sharpening. Briefly, it consists of a cochlear-filter bank of 128 constant-Q highly asymmetric bandpass filters ($Q=4$) equally spaced on a logarithmic frequency axis x with center frequencies spanning a range of 5.3 octaves (i.e., with a resolution of 24 channels per octave). Next, a hair-cell stage transduces the cochlear-filter outputs into auditory-nerve patterns via a three-step process consisting of high-pass filtering, a nonlinear compression, and low-pass leakage, effectively limiting the temporal fluctuations below 5 kHz. Finally, a lateral inhibitory network performs a sharpening of the filter-bank frequency selectivity mimicking the role of cochlear-nucleus neurons (Sacks and Blackburn, 1991; Shamma, 1998). It is modeled as a first difference operation across the frequency channels, followed by a half-wave rectifier, and then a short-term integrator. Extensive details of the biophysical grounds, computational implementation, and perceptual relevance of this model can be found in Wang and Shamma (1994) and Yang *et al.* (1992).

We complement the model above with an additional onset sharpening stage to emphasize the presence of transient events in this spectrographic representation. We apply a high-pass filter (filter cutoff about 400 Hz) to the output of each frequency channel to boost the transient energy in the signal. By accentuating the representation of onsets in the spectrogram, we are reinforcing the likelihood of synchronous frequency channels to emerge as a congruent spectral

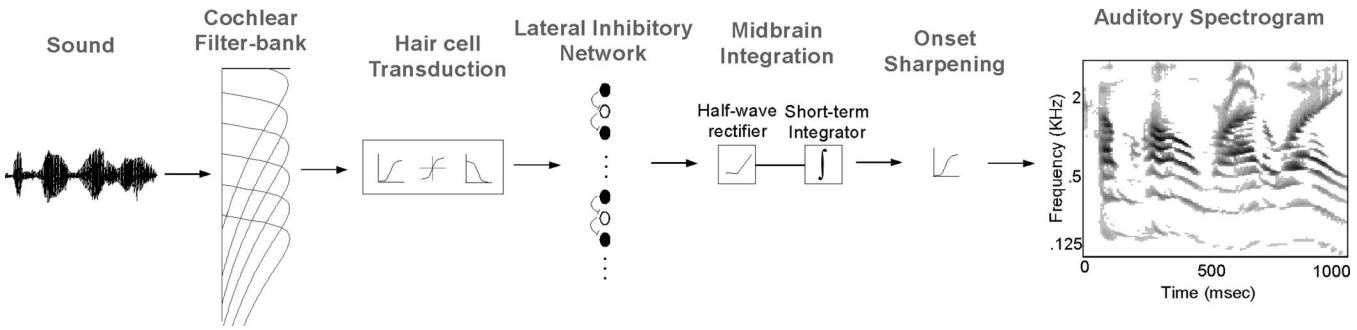


FIG. 2. Peripheral auditory processing. The schematic depicts the stages of early auditory processing starting from cochlear filtering, followed by hair-cell transduction, spectral and temporal sharpening, and onset enhancement. The output of this process is an onset-enhanced time-frequency auditory spectrogram.

segment, hence biasing them to be labeled as originating from a common source (Bregman, 1990). It is worth noting that this stage does not explicitly extract common onsets *across* frequency channels. Rather, the sharpening process is performed on each individual channel independently by way of contrast enhancement. An *indirect* consequence of this stage is that sound elements starting at the same time will emerge with an enhanced representation, increasing the likelihood of grouping them together.

Given a discrete-time signal $s(t)$; $t=0,1,\ldots,n$, the operations above compute a time-frequency activity pattern $P(t,x)$ that represents a noise-robust (Wang and Shamma, 1994) equivalent of an acoustic spectrum, called a sharpened-onset auditory spectrogram (see Fig. 2). It not only encodes the instantaneous power in each frequency band but also captures the temporal dynamics of the spectral components falling within the bandwidth of each band, giving rise to fast "envelope modulations" of the signal. In addition, it exhibits an enhanced representation of onset cues across the entire spectrum.

2. Harmonic analysis

Grouping of sound elements is facilitated if they bear a harmonic relationship to each other, making them easily segregated from elements with different fundamental frequencies (Moore *et al.*, 1986). Hence, we add an explicit periodicity pitch axis to the time-frequency spectrogram $P(t,x)$. We use a pitch extraction algorithm based on a template matching model, similar to that proposed by Goldstein (1973) and Shamma and Klein (2000).

The algorithm begins by generating an array of harmonic templates at different fundamental frequencies ($F0$'s) following the procedure in Shamma and Klein (2000). Next, a template matching procedure is applied, essentially similar in spirit to numerous pitch matching techniques present in literature (Cohen *et al.*, 1995; Duifhuis *et al.*, 1982). This stage starts by comparing the input spectrum $P(x;t_0)$ at every time instant t_0 with the entire array of templates using a point-by-point multiplication of the spectra (of the signal and each template for all $F0$ values). Based on the match between the input spectrum and the harmonic templates, we build a distribution of pitch values across the $F0$ (or harmonicity) axis, where the pitch strength at a given fundamental frequency $F0$ is based on the goodness of match (Euclidean distance) between the spectrum and the corresponding template (Fig. 3). Hence, the one-dimensional (1D) spectrum $P(x;t_0)$ yields a two-dimensional (2D) pattern $P_h(x,h;t_0)$ indexed by tonotopic frequency x (covering a range of 5.3 octave) and fundamental frequency h (covering the pitch range from 70 to 300 Hz). Additionally, we append to the pitch axis a copy of the full original spectrum $P(x;t_0)$. This serves to present evidence of the energy in the signal in the absence of any salient harmonicity cues. For instance, a fricative (such as [s]) would produce an aperiodic hissing that lacks any salient pitch estimate and, hence, is only captured by its full original profile $P(x;t_0)$.

While many pitch extraction algorithms have been successfully applied in sound segregation schemes, we particularly chose the template matching technique for two main reasons. First, the template model is assumption-free as to the nature/number of pitches present in the signal and allows us to extract harmonic structures at any given time instant, without performing a pitch tracking over time or without an explicit representation of pitch. Second, models of template matching have been argued to be plausible biological mechanisms for periodicity pitch (Cohen *et al.*, 1995). Work by Shamma and Klein (2000) suggested a biologically inspired model for the formation of harmonic templates in the early stages of the auditory system based on the phase-locking properties of cochlear filters. Their model explains how harmonic templates can emerge in the peripheral auditory system from a simple coincidence detection network operating across cochlear channels.

Though quite successful in yielding proper pitch estimates of various spectral patterns, the template matching method has been criticized for its lack of robustness and particularly for introducing additional estimates at octave or subharmonic intervals of the fundamental frequency. These additional estimates are not a real concern for our current scene analysis model. As shall be discussed later in the description of our algorithm, the sound segregation is performed based on a *best match* to the estimate of the sound source, irrespective of the presence of redundant information about a source.

3. Cortical processing

Following this peripheral stage, the model proceeds to a finer analysis of the time-frequency patterns $P_h(x,t,h)$, mimicking processing of central auditory stages (particularly the primary auditory cortex). This analysis is strongly inspired

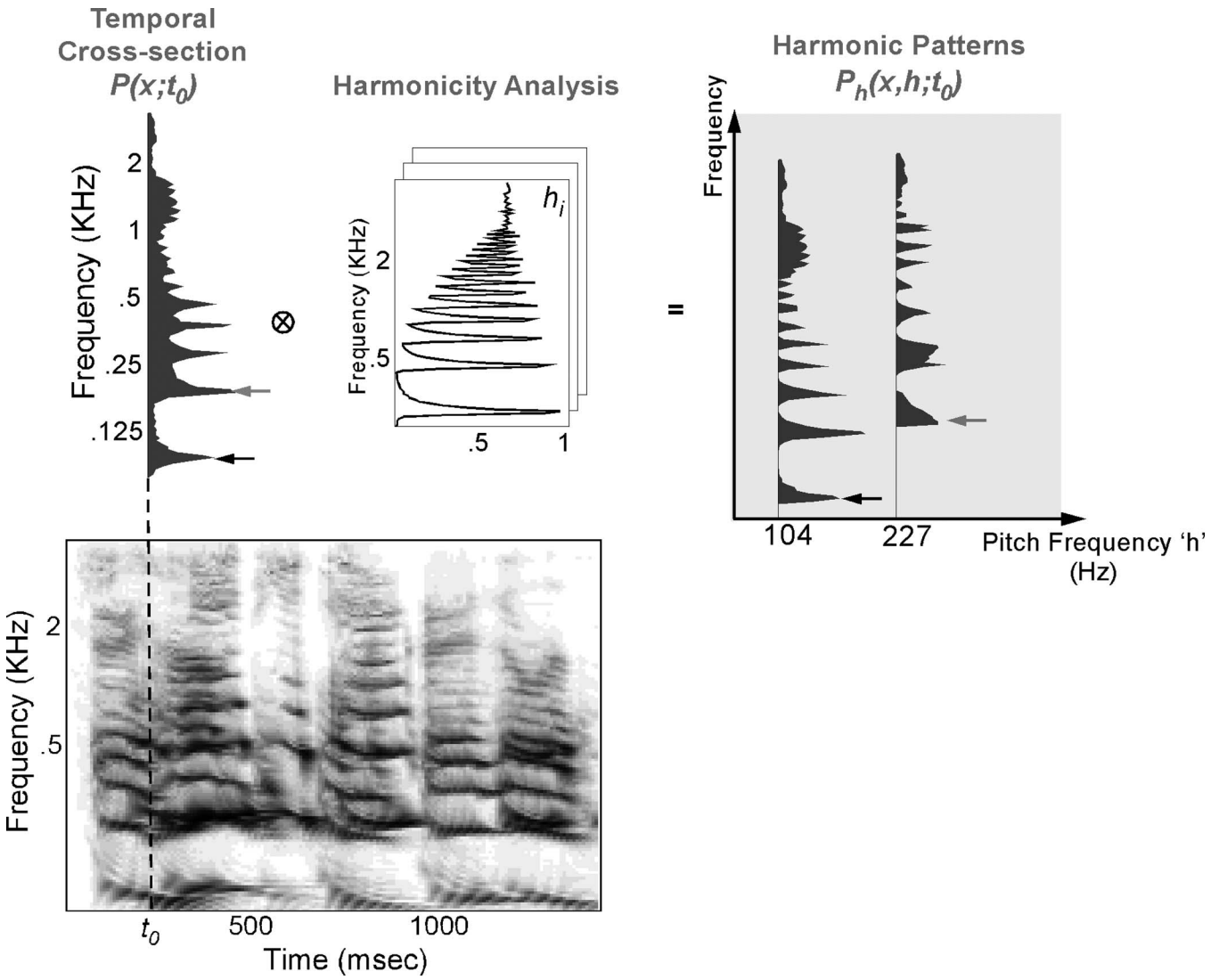


FIG. 3. Harmonicity analysis stage. The auditory spectrogram is further analyzed to extract any harmonically related spectral channels. The lower left panel in the figure depicts a mixture of male and female utterances shown in the lower panel. At time instant t_0, a temporal cross section of the spectrogram $P(x;t_o)$ is extracted and processed through a template matching model. The output of this template matching is shown in the top rightmost panel and reveals that the cross section $P(x;t_o)$ yields a good match with a harmonic template at 104 Hz and another one at 227 Hz, corresponding to the male and female voices, respectively, at that time instant.

by extensive physiological and psychophysical experiments carried over the past two decades. Our current understanding of cortical processing reveals that cortical units exhibit a wide variety of *receptive field* profiles (Kowalski *et al.*, 1996; Miller *et al.*, 2002; Elhilali *et al.*, 2007). These response fields, also called spectrotemporal receptive fields (STRFs), represent a time-frequency transfer function of each neuron, hence capturing the specific sound features that selectively drive the cell best. Functionally, such rich variety implies that each STRF acts as a selective filter specific to a range of spectral resolutions (or scales) and tuned to a limited range of temporal modulations (or rates), covering the broad span of psychoacoustically observed modulation sensitivities in humans and animals (Eddins and Bero, 2007; Green, 1986; Viemeister, 1979). In the current model, we break down this analysis into a spectral mapping and a temporal analysis. The spectral shape analysis is considered to be part of the feature analysis stage of the model, as it further maps the sound patterns into a spectral shape axis (organized from narrow to broad spectral features). On the other hand, the temporal cortical analysis spans two primary ranges: slow (<30 Hz) and fast (>30 Hz). The *slow dynamics* refer to the typical range of phase-locking rates in the cortical responses and are correlated with a host of perceptual phenomena as we review below. In the model, these dynamics come into play in the next integrative and clustering stage. *Fast dynamics* arise from the selective sensitivity and encoding of rapid rates of AM and FM stimulus modulations in cortical and precortical responses (>30 Hz) (Chi *et al.*, 2005; Langner, 1992). This feature is not included in the current version of the model.

Spectral shape analysis. Based on the premise that spectral shape is an effective physical correlate of the percept of timbre, we perform a spectral analysis of each spectral pattern extracted in the earlier stages. This multiscale analysis is performed by a wavelet decomposition, where each cross section from the auditory spectrogram $P_h(x,t,h)$ (at a given

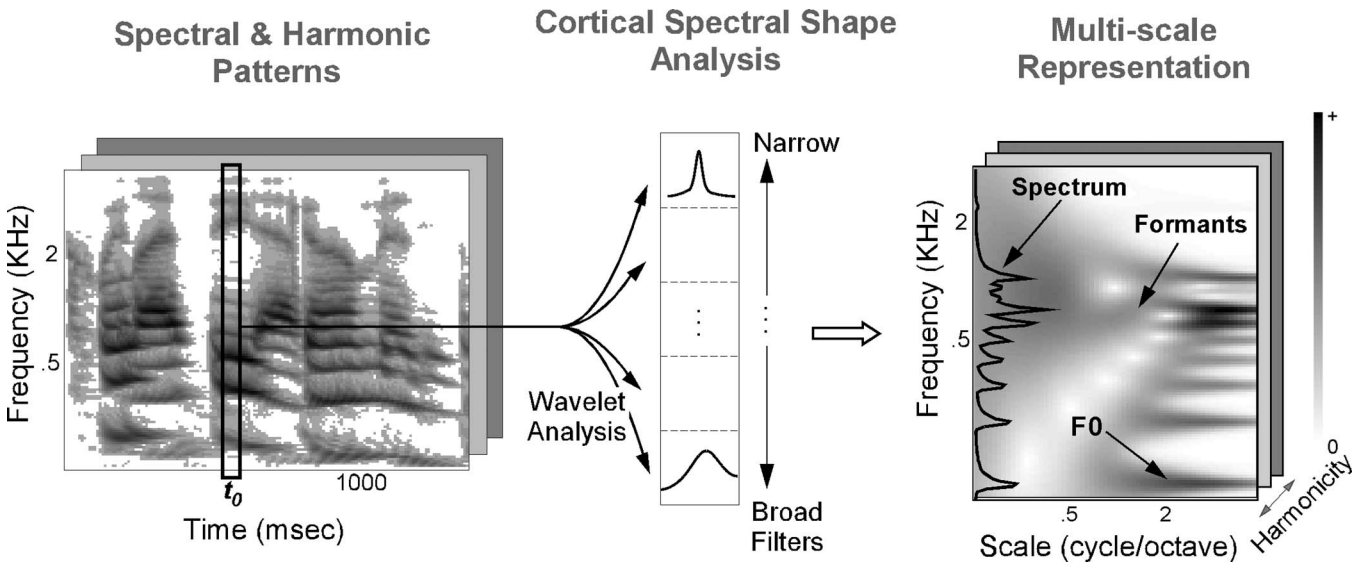


FIG. 4. Cortical spectral shape analysis. Each spectral slice is further analyzed via a multiresolution wavelet analysis. The multiscale mapping highlights various features of the original spectrum, namely, the fundamental frequency $F0$ and its harmonic partials as well as its formant peaks (particularly the second and third formant frequencies $F2$ and $F3$).

time instant t and harmonic profile h) is processed via a bank of analysis filters $\mathcal{S}_\Omega \triangleq \{\mathcal{G}_S(x,\Omega)\}$:

$$I(x,t,h,\Omega) = P_h(x,t,h) *_x \mathcal{G}_S(x,\Omega), \tag{1}$$

where $*_x$ is convolution with respect to the tonotopic axis x. The filter $\mathcal{G}_S(\cdot)$ is a complex-valued spectral "impulse response," implemented as a Gabor-like mother wavelet that is parametrized by its most sensitive spectral modulation (Ω), spanning the range $[1/8, 1/4, 1/2, 1, 2, 4, 8]$ cycles/octave, and defined as

$$\mathcal{G}_S(x,\Omega) = \Omega g_s(\Omega x) + j\Omega \hat{g}_s(\Omega x),$$
$$g_s(x) = (1-x^2)e^{x^2/2}, \tag{2}$$

where $g_s(\cdot)$ and $\hat{g}_s(\cdot)$ form a Hilbert transform pair. By defining the filters as complex valued, we are efficiently conjoining arrays of filters with the *same* magnitude responses and *varying* phase responses. This same analysis can be reformulated in real space $\mathbb{R}$ by unwrapping the functions $g_s(\cdot)$ along all possible phases between 0 and 2π. Further details on the filter design can be found in Chi *et al.* (2005) and Wang and Shamma (1995).

This spectral decomposition offers an insight into the timbre components of each of the acoustic features extracted so far (Fig. 4). The local and global spectral shapes in the acoustic patterns are captured via a bank of spectral modulation filters tuned at different scales (1/8–8 cycles/octave). On the one hand, the coarsest modulation scales capture the general trend in the spectrum, hence highlighting its broad spectral attributes, such as speech formants. On the other hand, the high-order scale coefficients describe the denser spectral patterns corresponding to features with higher spectral density, such as harmonic peaks. Unlike the cepstral analysis commonly used in speech recognition systems (O'Shaughnessy, 2000), the multiscale model operates *locally* along the tonotopic frequency axis.

B. The integrative and clustering stage

The second integrative and clustering stage induces stream segregation by reconciling incoming sensory information with gradually formed expectations (Fig. 1). The model builds on the cortical representation described in Sec. II A 3 as an infrastructure to map the incoming signal into a multidimensional space where features arising from different sound sources distribute into areas of activity with minimal overlap. It effectively allows the system to capture clean looks of the different streams present in the environment by mapping the cluttered sound mixtures onto a multitude of perceptually relevant dimensions. Using these activation patterns, the next critical stage of the model is to integrate these incoming looks and set up computational rules to cluster them by labeling them according to the different streams present in the scene. These rules (or schemas) come into play to govern how sound elements are assigned to their corresponding perceptual objects and integrated to form coherent segregated streams.

This integration process postulates that clusters of A1 neurons with typical multiscale dynamics of 2–30 Hz (Miller *et al.*, 2002) integrate their sensory inputs to maintain a form of a working memory representation. This memory trace is used to build expectations of how a stream evolves over time and makes predictions about what is expected at the next time instant. By reconciling these expectations with the actual incoming sensory cues, the system is able to assign incoming features to the perceptual group that matches them best (Nix and Hohmann, 2007). Specifically, the integrative stage consists of different cortical clusters (two clusters in the current model), both governed by a recursive Markovian process which (i) integrates the input of each cortical array with dynamics typical of time constants of A1, (ii) uses a Kalman-filter-based estimation to track the evolution of each array/stream over time, and (iii) utilizes the recent auditory experience to infer what each cluster *expects* to "hear" next.

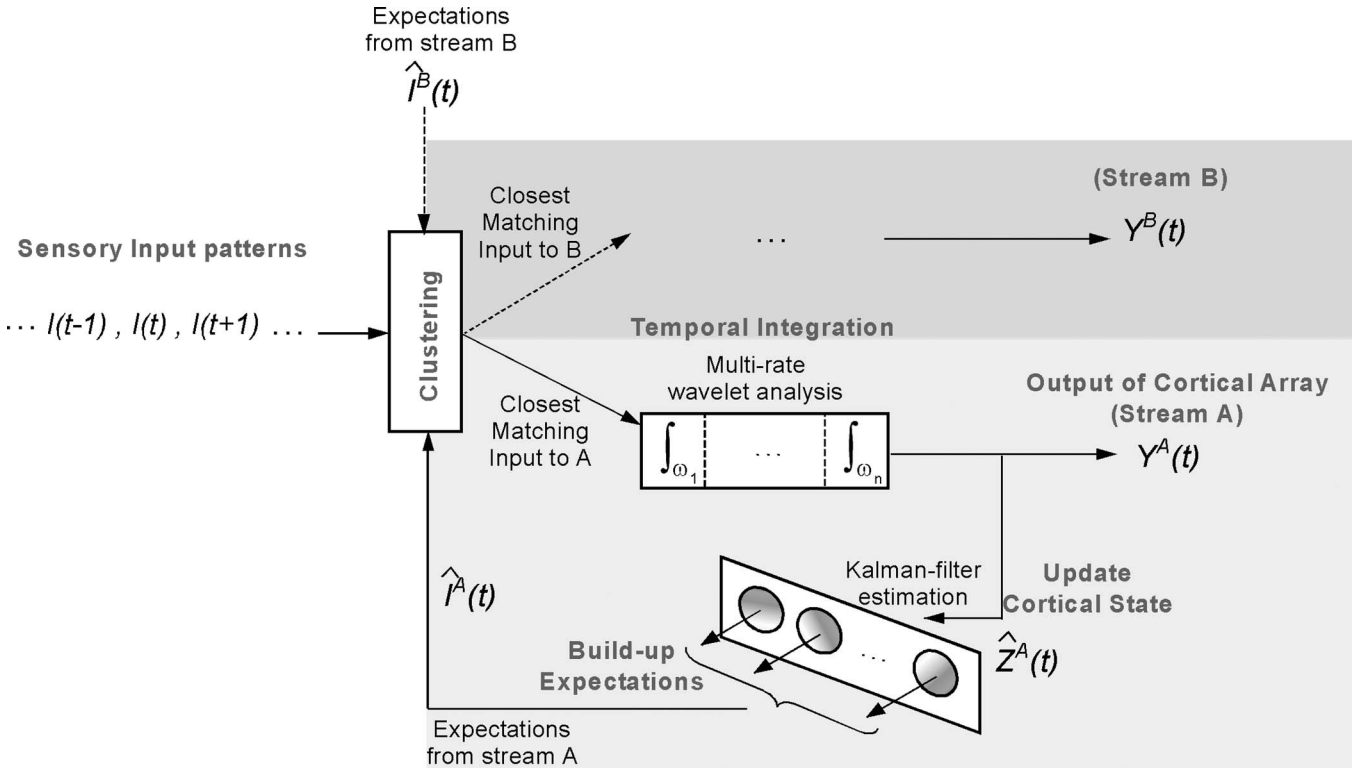


FIG. 5. Architecture of the feature integration and clustering processes. The schematic illustrates the various stages involved in segregated the acoustic patterns represented in the *feature analysis stage*. The incoming sensory inputs $I(t)$ are compared to predicted patterns $\hat{I}^A(t)$ and $\hat{I}^B(t)$. The features which are most consistent with $\hat{I}^A(t)$ are "passed through" the stream A branch into a cortical integrative array. This neural cluster plays a dual role: it accumulates the information and outputs a representation of stream A ($Y^A(t)$) and it uses the available information ($I(t), Y(t)$) to update the current memory trace of stream A via a Kalman-filter estimation. This information is in turn used to build an expectation about the next input $\hat{I}^A(t+1)$, hence closing the feedback loop. The upper (yellow) panel indicates that a similar process takes place over a second cortical cluster (B), which tracks the evolution of another stream in the environment.

The computation of these different operations is detailed next and schematized in Fig. 5.

Temporal dynamics and integration. The integrative stage of the model is initiated by a temporal analysis which integrates sensory information over time in a process mimicking functional cortical models. Specifically, A1 neurons exhibit selectivity to various temporal dynamics present in the acoustic input. The temporal features of sound vary over multiple time scales ranging from sharp transitions to very slowly evolving patterns. The encoding of these temporal dynamics (at least at the level of primary auditory cortex) appears to be achieved through richly diverse networks of neurons whose STRFs vary from rapidly decaying responses to more sluggish types. The collection of all such neurons extends over a broad span of psychophysically observed temporal modulation sensitivities in both humans and animals, covering the range 2–30 Hz (Dau *et al.*, 1996; Drullman, 1995; Green, 1986; Viemeister, 1979).

Mathematically, we capture this temporal analysis via a wavelet decomposition through a bank of complex-valued filters $\mathcal{R}_\omega \triangleq \{\mathcal{G}_T(t,\omega)\}$:

$$Y(t,x,h,\Omega,\omega) = I(t,x,h,\Omega) *_t \mathcal{G}_T(t,\omega), \tag{3}$$

where $*_t$ is convolution with respect to the time axis t. The filter $\mathcal{G}_T(\cdot)$ is based on a gamma function parametrized by the temporal modulation (ω) which take the values $[2,4,8,16,32]$ Hz and is defined as

$$\mathcal{G}_T(t,\omega) = \omega g_t(\omega t) + j\omega \hat{g}_t(\omega t),$$
$$g_t(t) = t^2 e^{-3.5t} \sin(2\pi t). \tag{4}$$

The use of complex valued instead of real filters is motivated by the same efficient implementation as described for the spectral filters $\mathcal{G}_S(\cdot)$. Further details about the design and temporal filtering procedure can be found in Chi *et al.* (2005).

Inference and clustering. Apropos of the clustering stage, we focus on inference schemas to regulate the pattern segregation process. Inference principles are generic rules that effectively bias the system to parse the acoustic scene based on its recent acoustic experiences and contextual expectations (Barlow, 1994; Humphrey, 1992). Specifically, the model uses its recent experience with sources in the environment to *infer* what it expects to hear at the next time instant. If that expectation is matched with physical acoustic cues, then the cues are assigned to that corresponding sound object. If not, they are flagged as a different perceptual object. These processes capture the dynamic nature of auditory scene analysis, whereby information about a specific object builds up and accumulates over time to segregate it from competing information generated by other streams in the environment. In addition, they are applicable to all domains of sounds covering speech, music, environmental sounds, etc. They are generally supplemented by additional cognitive

mechanisms that involve even higher-level processes such as linguistic knowledge, sound familiarity, as well as attentive and memory-based schemas [see Bregman (1990) and references therein]. These latter effects are outside the scope of the current model and shall not be discussed in the present study.

Mathematically, we implement the inference-based processes by reformulating the cortical temporal analysis to allow each perceptual stream to be temporally tracked by a *different* family of neurons $\mathcal{R}^+$ representing an array of rate-selective units $(\mathcal{R}_\omega)$ so that $\mathcal{R}^+=\{\mathcal{R}_\omega\}$, where $\omega \in [2-30]$ Hz. The superscript "+" refers to the different perceptual objects being represented in the model, the number of which needs to be fixed ahead of time. In the current version of the model, we limit that number to *two* sources, i.e., implementing two neural populations $\mathcal{R}^1$ and $\mathcal{R}^2$. These neural arrays capture the dynamics of two streams, phenomenologically representing foreground and background streams. Computationally, the segregation model now proceeds as a three-step feedback-loop system involving the following.

1. *Estimation process*: Each rate-selective array $\mathcal{R}^+$ acts as a system of memory units whose internal states capture the recent history of the acoustic object it represents. By updating these internal states over time, we can track the temporal evolution of the streams and maintain a working memory representation of the object at the level of the cortical network $\mathcal{R}$. This operation is carried out by formulating the temporal analysis in Eq. (3) as an autoregressive moving average (ARMA) model (Oppenheim and Shafer, 1999; Proakis and Manolakis, 1992), which can be easily mapped into state-space form by introducing a latent variable representing the internal state (or explicit memory register).
2. *Prediction process*: The memory units for each sound stream are used to build an expectation of what the stream family $\mathcal{R}^+$ expects to hear in the next time instant (t_{0+1}) given the auditory experience acquired up to time t_0. The states of this dynamic system are recursively predicted using a Kalman filter (Chui and Chen, 1999; Welch and Bishop, 2001).
3. *Clustering process*: The predicted $\hat{\mathbf{I}}^+(t_{0+1})$ and actual $I(t_{0+1})$ incoming cues are compared in order to assign the input patterns to their corresponding clusters based on the best match between the actual and predicted features. This implementation of a *best-match clustering* uses a simple Euclidean distance measure to contrast the incoming features with the predicted states from stage 2 and assign the clusters (or streams) based on the smallest distance to the cluster centroids.

The specific implementation of each stage is detailed in the Appendix. A schematic describing the interaction between the three processes described above is given in Fig. 5.

III. RESULTS

To demonstrate the effectiveness of the model, we first test some of the classic paradigms widely used in perceptual studies of scene analysis (Bregman, 1990) so as to explain the role played by the different modules of the model in sound segregation. We then show simulations of the model using natural speech-on-music, speech-on-speech, and vocoded speech mixtures. All tone and speech simulations employ the same model configuration without changes or tuning of parameters across different stimuli. Finally, we test the contribution of the different model components to its performance and establish the relationship between cortical mechanisms and the process of stream segregation.

A. Organization of tone sequences

Stream segregation is strongly influenced by the rhythm and frequency separation between sound tokens. One of the simplest and most compelling demonstrations of auditory streaming involves sequences of alternating tones presented at different rates and frequency separations. It consists of two alternating tones; a high "A" note and a low "B" note. Such sequence is usually perceived as one stream when it is played at slow rates (<2 Hz) or with small frequency separations (approximately <1/6 octave) (van Noorden, 1975). However, at larger separations and higher rates, the sequence perceptually splits into two simultaneous auditory streams.

We explore the model's ability to mimic human perception as we vary these two critical parameters (frequency separation between the two notes ΔF_{AB} and tone repetition time ΔT). The simulation consisted of 10 s long sequences of alternating two tones. The low note was fixed at 850 Hz, and the frequency separation between the high and low notes was varied over the range [3, 6, 9, 12] semitones. Each tone in the sequence was 75 ms long and the separation onset to onset between tones A and B was varied systematically over $[100,150,200,300,400]$ ms. The simulation was repeated 25 times for each sequence without changing the parameters of the model. Due to the inherent variability in the noise terms of the Kalman-filter prediction, the outcome of the simulation can vary if the clustering process is not strongly biased to segregate one way or another. Each simulation can yield either a "two-stream" outcome (i.e., each note sequence segregating into a separate cluster) or a "one-stream" outcome (i.e., both notes labeled as belonging to one cluster). We tallied the simulation outcomes across all 25 repetitions and computed the average predicted likelihood of perceiving two streams for all ΔF and ΔT values. Figure 6 depicts the average segregation results across trials. The simulations show that sequences are more likely to segregate if the frequency separation is above four semitones repeating at a rate of about 3 Hz or more. Note that the "perceptual segregation boundary" (shown as a white contour representing a threshold value of 25% in Fig. 6) qualitatively replicates the shape of this boundary measured in human subjects (van Noorden, 1975). The exact location of this boundary, however, can be readily shifted downward or sideways to match human or animal performance. For instance, by sharpening further the bandwidth of the frequency analysis, we can shift the boundary downward, thus increasing the likelihood of perceiving two streams at smaller ΔF_{AB}'s. Similarly, by increasing sensitivity to faster temporal modulations, we can shift the

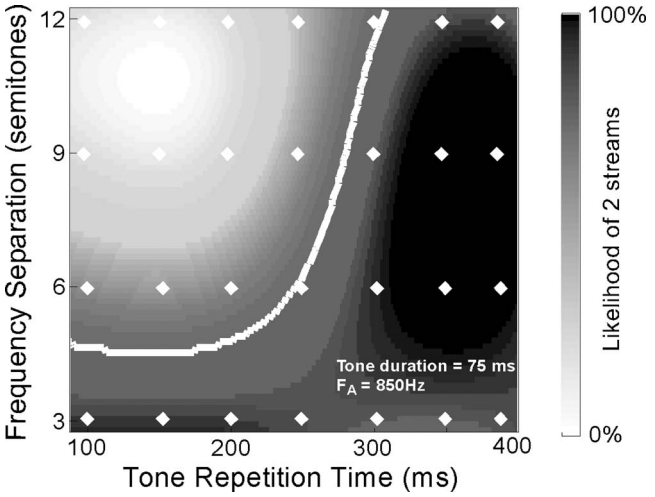


FIG. 6. Induction of streaming with alternating two tone sequences. The model's segregation of alternating two-tone sequences is tested with different stimulus parameters and averaged across 25 repetitions. The frequency separation and tone repetition time values tested are shown with the white diamond-shaped points. The surface shown in the figure is an interpolation of the results from these points using a cubic 2D interpolation. The white contour represents a contour of 25% to indicate a potential coherence boundary. The low tone in the sequence was fixed at 850 Hz, while the high note was placed[3,6,9,12] semitones higher. Each tone was 75 ms long.

boundary to the left, thus enabling the model to track the alternating tones hence decreasing the likelihood of perceiving two separate streams (as shall be shown in detail in a later section of the results).

In our simulations of the alternating tone sequences, the emergence of the different streams occurs rather rapidly, sometimes within one or two presentations of each tone. In many circumstances, it is reported that buildup of streaming can range from a few hundreds of milliseconds to several seconds (Anstis and Saida, 1985; Bregman, 1978). To reproduce these time scales, it is necessary to incorporate more biological realism to the cortical processing stage via simple adaptation processes or synaptic depression mechanisms known to operate at the level of thalamocortical projections [see Elhilali *et al.* (2004) for details]. Habituation of A1 responses over time has been postulated as a possible neural mechanism responsible for the observed perceptual buildup of streaming (Micheyl *et al.*, 2005).

The role of frequency separation in scene analysis can be further demonstrated by a sequence of alternating multitone cycles [Fig. 7(a)] which consists of interleaved high (H1, H2, H3) and low (L1, L2, L3) notes, constructing a sequence H1, L1, H2, L2, H3, L3,… (Bregman and Ahad, 1990). The high frequencies were fixed at 2500, 2000, and 1600 Hz and the low frequencies were 350, 430, and 550 Hz. When the tones are played at a fast repetition rate (e.g., 4–5 Hz), the sequence is perceived as two segregated streams of high and low melodies, as depicted in the gray panels of Fig. 7(a). The model's account of this percept originates in the distribution of receptive field bandwidths (along the multiscale spectral analysis axis) which range from the very narrow ($<1/10$ octave) to the broad (>2 octaves) with an average bandwidth of about 1/6 octave. Humans are most sensitive to patterns with peak spacings of this order (Eddins and Bero, 2007; Green, 1986). Consequently, when the alternating tones are closely spaced, only a minority of receptive fields can resolve them into two streams. On other hand, when tones are well separated, two classes of receptive fields are differentially activated by each tone hence easily segregating them into two clusters. Similarly, the dependence of streaming on tone presentation rates reflects the dominant neuronal dynamics of the auditory cortex, as represented by the multiple time constants governing the cortical integration in the model. At very slow rates, integrators cannot sustain their memory (and hence, their expectations) for sufficiently long times to influence the input, hence biasing the system to label it as a single stream. At faster rates (commensurate with cortical time constants), expectations are fed back, causing spectrally resolved incoming tones to cluster into two streams.

B. Timbre-based segregation

Stream segregation in general can be induced between sound sequences that differ sufficiently along any feature dimension in the cortical representation, including different distributions along the spectral analysis axis (timbre), harmonicity axis (pitch), and other axes not included in the current model such as location cues and fast modulation rates (Grimault *et al.*, 2002; Shinn-Cunningham, 2005). Figure 7(b) illustrates the streaming of the two alternating natural vowels /e/ and /ə/, each repeating roughly twice per second (i.e., about 2 Hz). Although they have the same pitch (110 Hz) and occupy roughly the same frequency region, the vowels are perceived as two segregated streams because their cortical representations are sufficiently distinct along the multiscale spectral analysis axis. A detailed discussion of the sequential organization of vowels (similar to those tested here) as well as other speech sounds can be found in Bregman (1990), Chap. 6.

C. Old-plus-new heuristic

Implicit in the notion of a stream is a sequence of sounds that share consistent or smoothly varying properties. To this effect, sounds with drastically different features violate expectations built up over time for the ongoing streams and are hence assigned to new streams. This is consistent with the well-known *old-plus-new* principle, stating that "If part of a sound can be interpreted as being a continuation of an earlier sound, then it should be" (Bregman, 1990). Figures 7(c) and 7(d) offer a simple illustration of this principle. In Fig. 7(c), an alternating sequence of A tones and a two-tone complex (B and C) are perceived as two separate streams (Bregman and Pinker, 1978) because tones B and C are strongly grouped by this common onset and are sufficiently separated from the A tone in frequency (1800 Hz versus 650 and 300 Hz). When tones A and B are equal in frequency [Fig. 7(d)], a continuity is created that combines these tones into a single stream and breaks the previous grouping of B and C (Bregman and Pinker, 1978). Instead, tone C is now perceived as the "new" evidence, against the "old" continuing stream of the A and B tones.

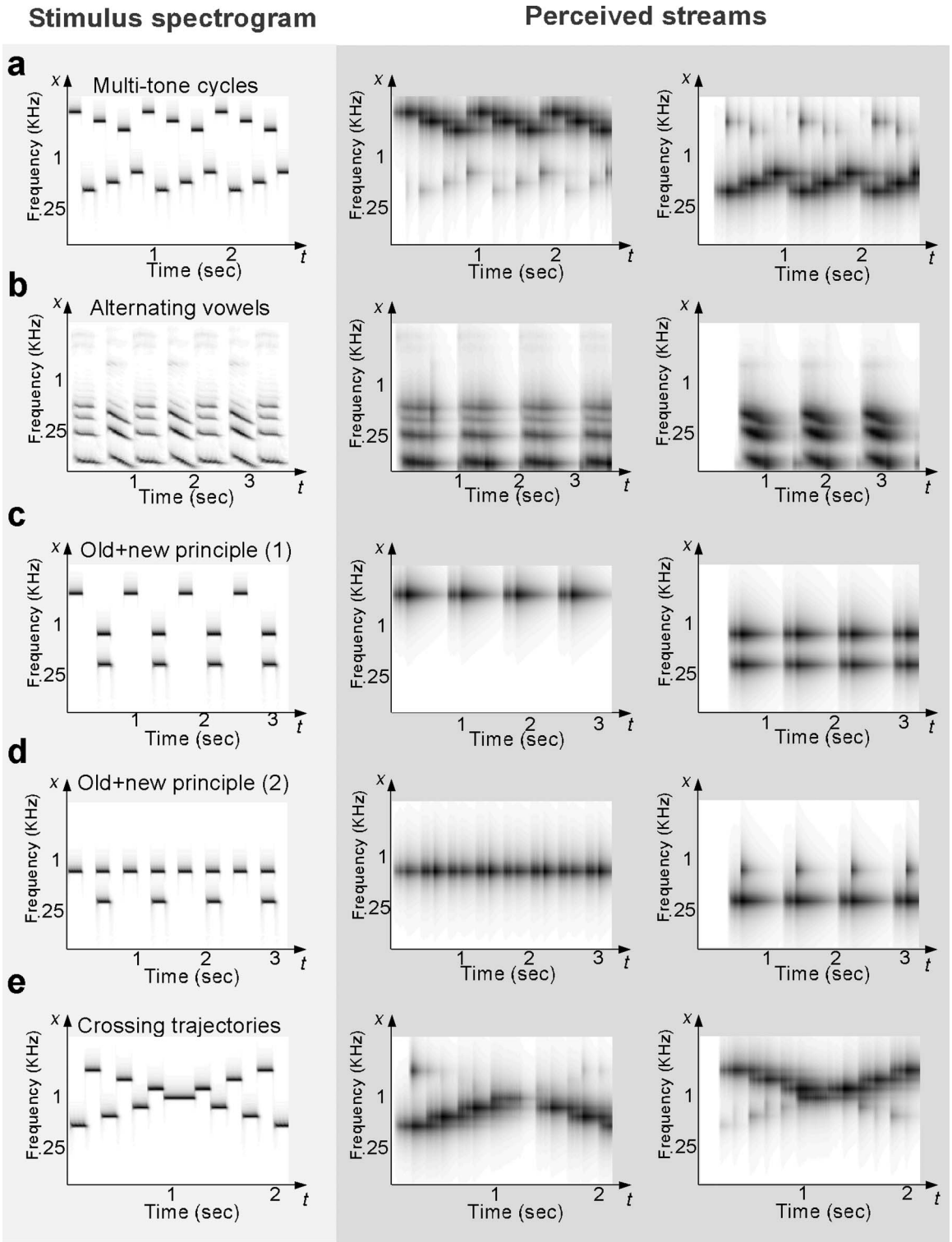


FIG. 7. Model simulations of "classic" auditory scene analysis demonstrations. The left column of panels shows the acoustic stimuli fed to the model. The middle and right columns depict the results of the stream segregation process, which are defined as the time-frequency marginal obtained by integrating the time-frequency activity across the entire neural population (scale and rate filters) representing each cluster. (a) Multitone cycles: The stimulus consists of alternating a high sequence of 2500, 2000, and 1600 Hz notes and a low sequence of 350, 430, and 550 Hz (Bregman and Ahad, 1990). The frequency separation between the two sequences induces a perceptual split into two streams (middle and right panels). (b) Alternating vowels: Two natural /e/ and /ə/ vowels are presented in an alternating sequence at a rate of roughly 2 Hz. The vowels are produced by a male speaker with an average pitch of 110 Hz. Timbre differences (or different spectral shapes) cause the vowel outputs to segregate into separate streams. (c) Old+new principle (1): An alternating sequence of a high A note (1800 Hz) and BC complex (650 and 300 Hz) is presented to the model. The tone complex BC is strongly glued together by virtue of common onset cues, and hence segregates from the A sequence which activates a separate frequency region. (d) Old+new principle (2): The same design as in simulation (c) is tested again with a new note A frequency at 650 Hz. Since tones A and B activated the same frequency channel, they are now grouped as a perceptual stream separate from stream C (gray panels), following the continuity principle. (e) Crossing trajectories: A rising sequence (from 400 to 1600 Hz in seven equal log-frequency steps) is interleaved with a falling sequence of similar note values in reverse (Bregman and Ahad, 1990).

Another striking illustration of this "continuation" principle is the crossing trajectories paradigm depicted in Fig. 7(e) (Tougas and Bregman, 1985). When rising and falling tone sequences are interleaved, subjects are unable to follow the patterns of notes in each sequence. Instead, they report hearing a bouncing percept of two streams, as depicted in the gray panels of Fig. 7(e), presumably caused by the expectations of two separate (high and low) streams built up prior to the crossing point, and which are maintained (by continuity) after it.

D. Segregation of speech sounds

Parsing complex sound mixtures of speech and/or music exploits the same principles described for tone sequences. In both, basic acoustic features are used to extract "clean" looks from the mixture, which are then parsed into separate streams based on their consistency with built-up expectations. In the earlier tone sequence examples, clean features were readily available since the tones were sequentially presented. With speech mixtures, clean looks of one speaker or another are principally derived when components from one speaker (i) share a common onset and hence are enhanced together, (ii) are harmonically related and differ in pitch from the other speaker, and (iii) appear in the gaps within the simultaneous speech of another speaker, hence providing opportunities to sneak clean looks of one of the speakers.

We tested the model's effectiveness in segregating randomly selected and mixed pairs of speech utterances from the TIMIT speech database. Given that our approach does not allow any language-based grammars or speaker-specific information to shape the segregation process, we are in effect testing the ability of the model to track and segregate a given voice based on consistent timbre properties or smooth evolution of its harmonics. To evaluate the results of the model, we compared how closely the segregated streams matched the original unmixed signals as quantified by the correlation coefficient between the original and segregated cortical representations. This measure computes a direct linear correlation at zero lag between the two vectors representing the cortical tensors of clusters A and B. Other suitable metrics that yield comparable results include the signal-to-noise ratio (SNR) (between the energy in the original spectrogram and the difference between the original and segregated spectrograms) or the improvement in intelligibility measured by the spectrotemporal intelligibility index (Elhilali *et al.*, 2003). These measures yielded qualitatively equivalent results to those obtained from the correlation coefficient. Samples of reconstructed segregated sentences can be heard at http://www.isr.umd.edu/~mounya/CPP/speech_simulations.htm. They were synthesized by inverting the streamed multidimensional representations using a convex-projection algorithm (Chi *et al.*, 2005).

Examples of segregating speech from music and mixtures of two simultaneous speakers are shown in Figs. 8(a) and 8(b), respectively. In both cases, the segregated spectrograms resemble the original versions and differ substantially from the mixed signal. We quantified the apparent improvement in the case of the speech-on-speech-mixtures by computing the correlation coefficients from 400 speech mixtures from both genders, as shown in Fig. 8(c). For each pairwise mixture, we computed the similarity between (i) the original and segregated samples (ρ_{seg}, segregation correlations), (ii) the two original samples (ρ_{base}, baseline correlations), and (iii) the segregated samples against the original competing signal (ρ_{conf}, confusion correlations). The histograms demonstrate that segregation occurs with an accuracy of $\rho_{seg}=0.81$, which is substantially higher than the "confusability" baseline, indicated by $\rho_{conf}=0.4$ and $\rho_{base}=0.2$, hence demonstrating the efficacy of the segregation of the speech signals into different streams.

Finally, to assess more clearly the role of the integrative stage in sorting and clustering its inputs, we sought to remove the errors introduced by imperfect harmonic analysis of the mixed inputs and hence test the performance of the remaining stages in model. To do so, we assumed a "perfect" harmonic analysis module that can fully separate each frame of mixed speakers into its two original unmixed frames. Specifically, we simply bypassed the harmonic analysis by supplying the *original unmixed* (unlabeled, onset enhanced, and multiscale analyzed) pairs of spectral cross sections of the speech signals and determined the performance of the integrative stage in sorting and clustering the patterns into two streams. As expected, the resulting segregation [indicated by the correlation coefficients in Fig. 8(c), right panel] is slightly better: $\rho_{seg}=0.9$, $\rho_{conf}=0.3$, and $\rho_{base}=0.2$. This improvement is due to the cleaner separation between the overlapping harmonic complexes and unvoiced speech phonemes that cannot be segregated by the harmonic analysis module (as simulated in the section above), which ultimately causes a feedthrough between the target and competing streams, hence increasing the confusion correlation ρ_{conf}. Consequently, the quality of the reconstructed segregated speech in this case is noticeably better than the quality obtained from the segregation of the "true" mixtures.

E. Segregation of mixtures of vocoded speech

We extend the testing of the model by exploring conditions that would not normally induce streaming, hence mimicking human failure at segregating certain sound mixtures. We used simulations of cochlear-implant processing to explore the model's performance of impoverished speech-on-speech mixtures. It is well known that hearing-impaired listeners experience great difficult perceiving speech in noisy conditions (Festen and Plomp, 1990; Peters *et al.*, 1998). Recent work by Qin and Oxenham (2003) explored this phenomenon using implant simulations and showed that fluctuating masker backgrounds (including concurrent speakers) greatly degrade normal-hearing listeners' ability to segregate and perceive vocoded speech. We used a similar procedure as in the Qin and Oxenham (2003) study to simulate a vocoder channel. Specifically, each speech utterance (taken from the TIMIT database) was filtered into 24 contiguous frequency bands, equally spaced on an equivalent rectangular bandwidth (ERB) scale between 80 and 6000 Hz. The envelope output of each band was used to modulate narrowband noise carriers, hence creating a vocoded speech signal

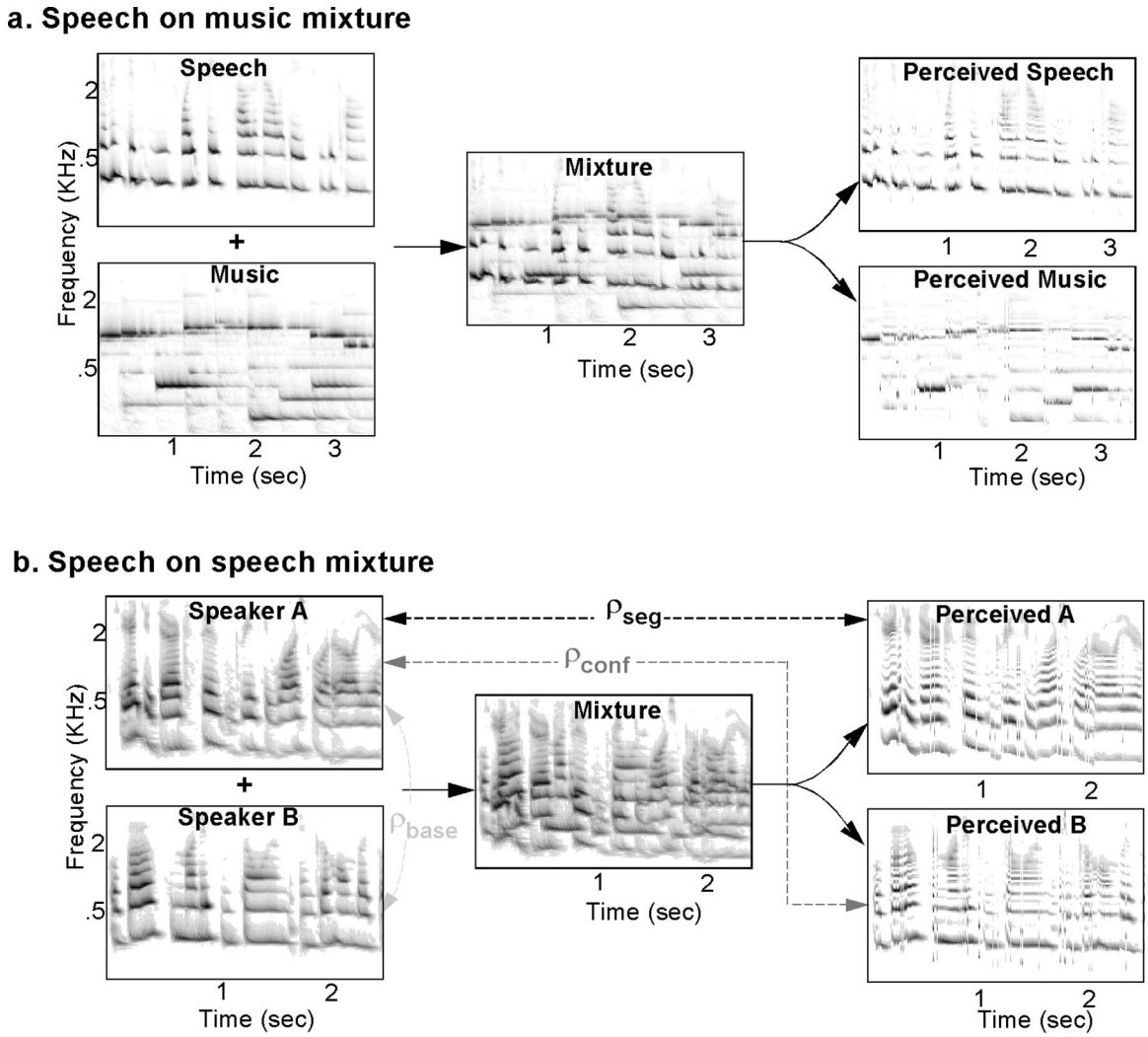


FIG. 8. (Color online) Model performance with real speech mixtures. (a) Speech-on-music mixtures: Left panels depict spectrograms of a male utterance and a piano melody. The mixture of these two waveforms is shown in the middle. Model outputs segregate the two sources into two streams that resemble the original clean spectrograms (derived as time-frequency marginals similar to Fig. 7). (b) Speech-on-speech mixtures: Male and female speech are mixed and fed into the model, which segregates them into two streams. To evaluate performance, correlation coefficients (ρ) are computed as indicators of the match between the original and recovered spectrograms: ρ_{seg} measures the similarity between the original and streamed speech of the *same* speaker. ρ_{base} measures the (baseline) similarity between the *two* original speakers. ρ_{conf} measures the *confusions* between an original speaker and the other competing speaker. (c) Speech segregation performance is evaluated by the distribution of the three correlation coefficients. Left panel illustrates that the average values of ρ_{seg} =0.81 are well above those of ρ_{conf}=0.4 and ρ_{base}=0.2, indicating that the segregated streams match the originals reasonably well, but that some interference remains. Right panel illustrates results from the model *bypassing* the harmonic analysis stage (see text for details). The improved separation between the distributions demonstrates the remarkable effectiveness of the integrative and clustering stage of the model when harmonic interference is completely removed (distribution means ρ_{seg}=0.9, ρ_{conf}=0.3, and ρ_{base}=0.2).

with minimal spectral cues and no temporal fine-structure information [see Qin and Oxenham (2003) for details].

We simulated the effect of implant processing on 25 male utterances, each contaminated by a randomly chosen sentence spoken by a female speaker and added at 0 dB SNR. The sentences were processed through the vocoder described above and presented to the model. We quantified the model's performance in a similar fashion, as described in Fig. 8, by calculating a ρ_{seg}, ρ_{conf}, and ρ_{base} for each pair of sentences. Our results show that a 24-channel simulation yields average values of $\rho_{seg}=0.63$, $\rho_{conf}=0.58$, and $\rho_{base}=0.2$, indicating a worse segregation performance (lower ρ_{seg} value) and an increased confusion with the concurrent utterance (higher ρ_{conf}). Just like in Qin and Oxenham (2003), the impoverished spectral resolution in the implant simulation as well as lack of temporal fine structure and pitch cues is largely responsible for the poor segregation between concurrent utterances at the level of the cortical representation. This in turn affects the subsequent integration and clustering stage where features from different sources are confused as belonging to the same cluster, and hence the poor model segregation mimicking listeners' experiences in these conditions.

F. Testing the model's components

The model's aim is to demonstrate how specific auditory cortical mechanisms contribute to the process of scene analysis and formation of perceptual streams. The processes of particular interest here are the multiscale analysis, the cortical dynamics, and the adaptive nature of cortical processing. In order to explore the role of the first two components in perception of complex auditory scenes and demonstrate their contribution to the model's performance, we modified the structure of the model for testing purposes, as shall be shown next. The third component (namely, the expectation process) is hard to modify or omit since it constitutes the core of the integration and clustering operation. The additional transformations in the model (e.g., harmonicity analysis, onset enhancement, etc.) clearly contribute to solving the stream segregation problem (as shown by the vocoded speech simulation, for instance). In this section, we solely focus on the contribution of the first two *cortical* mechanisms to sound segregation.

1. Multiscale analysis

We remove the multiscale analysis stage and basically perform the clustering operation directly on the harmonic patterns extracted from the auditory spectrogram ($P_h(x,t,h)$). The goal of this exercise is to explore how the model's performance would deteriorate in the absence of the spectral pattern analysis. The other stages of the model remained unchanged, with the exception that, now, the integrative and clustering stage takes—as input—a time-frequency-pitch representation as opposed to a four-dimensional (4D) tensor. In the biological system, this modification of the model would be equivalent to bypassing the spectral analysis performed at the level of auditory cortex and confining the system to a spectral decomposition performed in precortical nuclei.

We argued earlier that the contribution of the cortical spectral analysis is to map different spectral patterns into different regions of the multiscale axis. For instance, vowels with different spectral profiles will excite different filters and hence segregate along this axis, even though they might occupy the same frequency region and share a common harmonic structure. In the absence of this spectral analysis, the model has to rely on the segregation resulting from the cochlear analysis as well as the harmonicity mapping, making it blind to any difference in timbre structure between different streams. We test this model stripped of its multiscale analysis on the alternating vowel example shown in Fig. 7(b). Figure 9(a) shows the results of this incomplete model. As expected, the vowels /e/ and /ə/ produced by the same speaker share a common pitch of about 110 Hz and occupy roughly the same spectral region. Therefore, the model has no evidence to segregate them and to group them into one stream. Using the tonotopic axis alone, the two vowels overlap greatly [lower left panel of Fig. 9(a)]. In contrast, the multiscale analysis reveals the different timbre structures arising from the two vowels [lower right panels of Fig. 9(a)]. This simulation clearly demonstrates an example of the role of multiscale spectral analysis in discerning timbres of complex sounds and strengthens the claim that the topographic organization of mammalian auditory cortex with neurons of different spectral resolutions and sensitivities (orthogonal to its tonotopic organization) does indeed underlie the system's ability to distinguish between natural sounds of distinct timbres (e.g., speech) (Sutter, 2005).

2. Cortical dynamic

We stipulate in the current model that cortical time constants play a role in the process of auditory scene organization by facilitating the tracking of sound streams over the course of few to tens of hertz. To test this hypothesis, we modified the range of cortical time constants implemented in the model by adjusting the parameters of the temporal filters (shown in Fig. 1 as cortical clusters A and B). The full architecture of the model remains unchanged, except that now the integrative and clustering stage operates according to three possible modes: (1) a *normal* cortical mode with five filters spread over the range $2^{(1,2,3,4,5)}$ Hz (exactly the same simulation as in Sec. III A), (2) thalamiclike dynamics where we also use five filters distributed over the range $2^{(4,4.5,5,5.5,6)}$ Hz (Miller *et al.*, 2002), and (3) midbrainlike dynamics with five filters spanning the range $2^{(5,5.5,6,6.5,7)}$ Hz (Miller *et al.*, 2002). In all three cases, we fixed the number of temporal filters to 5 in order to maintain a fair comparison between all three modes of operation. We only varied the dynamic range of the filters' tuning.

We tested the model under all three conditions on the classic alternating two-tone sequence with varying frequency separation ΔF and tone repetition time ΔT (similar to that described in Sec. III A). As expected, the boundary (representing a threshold value of 25%) shifts to the left indicating that the model becomes sensitive to faster repetition rates

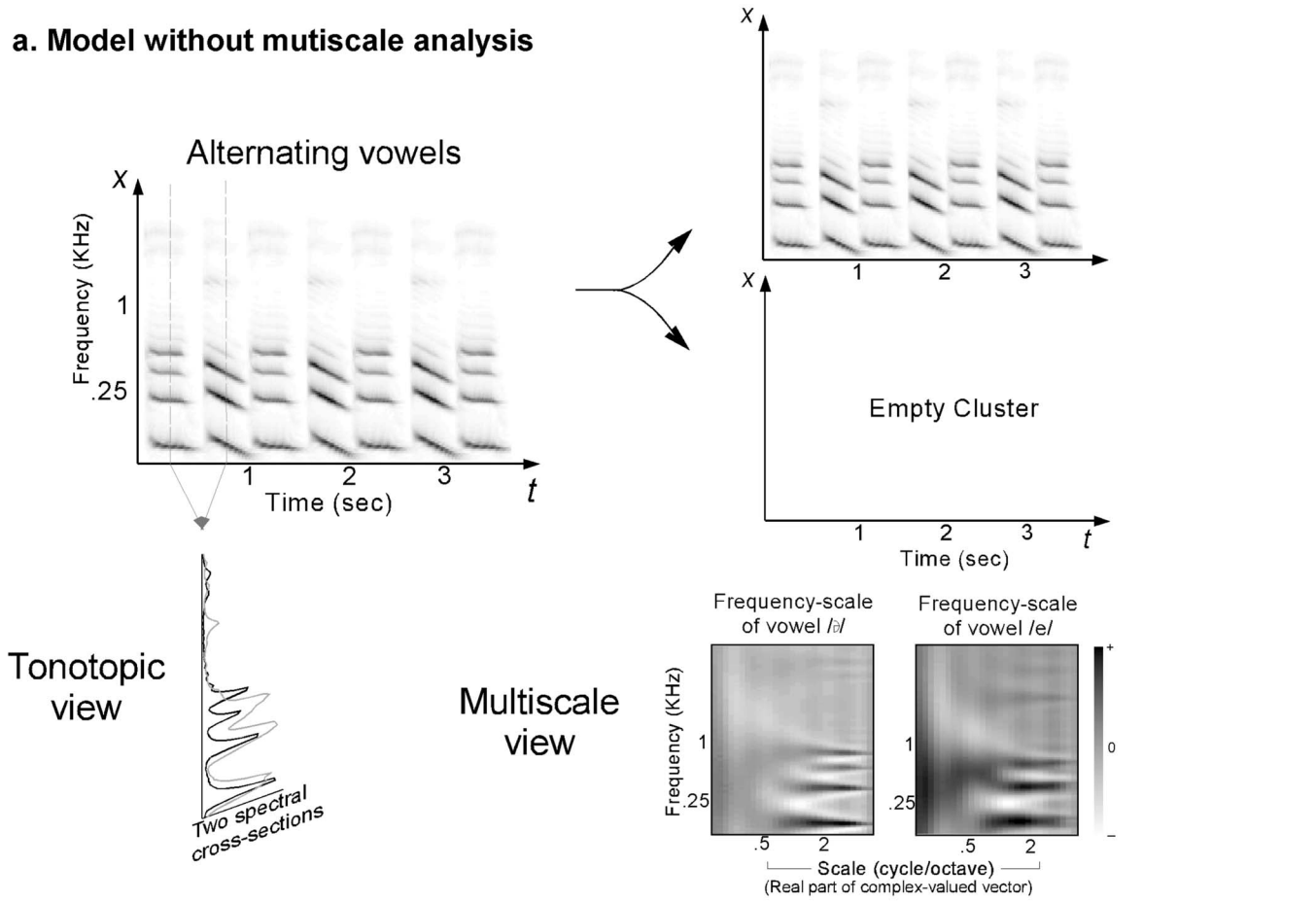


FIG. 9. Model performance after modification of parameters. (a) Omitting the multiscale analysis: The model (without the scale analysis) is simulated using alternating vowels /e/ and /ə/ [shown in Fig. 7(b)]. A time-frequency spectrogram is presented to the incomplete model and leads to the entire stream being grouped as one cluster (shown above) and an empty second cluster. The two top rightmost panels depict the time-frequency marginals reflecting the energy in each cluster. Below: A tonotopic view of the two vowels (obtained from two cross sections of the spectrogram at different time instances) reveals a great overlap in the spectral region occupied by both phonemes. The right panels show a multiscale view of both phonemes and reveal the different timbre structures that emerge from the multiple scale filters. (b) Varying the cortical dynamics: The three panels show results of segregation of alternating two tones with varying dynamic ranges for the cortical filters. The white contours are all boundaries reflecting a 25% threshold of streaming. The leftmost panel is a replica of Fig. 6.

and is able to track streams repeating at faster rates, hence following the tones in both frequency channels and grouping them as one stream [Fig. 9(b)]. The leftmost panel is an identical replica of Fig. 6 and is shown to contrast the changing boundary as a result of the change in the dynamics of the model. As the simulations show, the model's ability to track streams of separate tonal frequencies is dictated by the clock which paces the cortical integrative stage, which can be

made faster or slower. The segregation boundary [shown in Fig. 8(b)] is in agreement with human behavioral data only for the "cortical-like" time constants (leftmost panel), hence corroborating our claim of the involvement of cortical-like integrative processes in the organization of auditory scenes and formation of perceptual streams.

IV. DISCUSSION

In summary, we have demonstrated that a computational model of cortical auditory processing consisting of a multidimensional feature representation stage followed by an *integrative clustering stage* can successfully tackle aspects of the "cocktail party problem" and provide an account of the perceptual process of stream formation in auditory scene analysis. The model directly tested the premise that cortical mechanisms play a fundamental role in organizing sound features into auditory objects by (1) mapping the acoustic scene into a multidimensional feature space and (2) using the spectral and temporal context to direct sensory information into corresponding perceptual streams. Key to this organizational role are the multiple time scales typically observed in cortical responses, as well as an internal representation of recent memory that allows the smooth evolution of streams over time.

A powerful aspect of our formulation is its real-time capability because the model forms auditory streams as it receives its input data, requiring no prior training on a specific speech corpus or early exposure to a set of voices, sound categories, and patterns. As shown in Sec. III, such an adaptive cortical scheme can successfully simulate stimulus configurations typically tested in auditory scene analysis studies. Furthermore, it makes use of a variety of instantaneous and sequential grouping mechanisms that are postulated to play a pivotal role in streaming, thus demonstrating that these principles can be effectively generalized to parse complex stimuli such as real speech mixtures.

The current implementation of the model can be readily extended to include other perceptual features known to play a role in sound separation. For instance, the spatial location of sound sources influences their streaming (Wittkop and Hohmann, 2003). Adding this perceptual attribute to the model entails augmenting the cortical multidimensional representation with a spatial dimension whose responses are computed from midbrainlike processing of binaural cues, e.g., extraction of interaural-time and interaural-level differences in the medial superior olive (MSO) and lateral superior olive (LSO), or of monaural spectral cues to estimate elevation (Colburn *et al.*, 2006). Other perceptual attributes important for streaming that can be added to the model include loudness (Bregman, 1990) and rapid temporal modulations (Grimault *et al.*, 2002).

A. Role of cortical mechanisms in stream segregation

The overarching motivation of the present work is to explore the significance of the auditory image that emerges at the level of A1 and its implications for the process of stream segregation and scene analysis. Each physiological mechanism incorporated in the model is ascribed a particular functional role and can potentially guide our understanding of the brain function in general and biological auditory scene analysis, in particular.

1. Multiscale cortical representation

The organization of the auditory pathway up to the auditory cortex indicates that different auditory features are extracted from the incoming sounds at various stages and probably organized into auditory objects at the cortical level (Nelken, 2004). This rich image which emerges at the level of A1 effectively projects the acoustic waveform into a higher dimensional perceptual space in a mapping reminiscent of operations taking place in classification and regression techniques such as support vector machines and kernel-based classifiers (Cristianini and Shawe-Taylor, 2000; Herbrich, 2001). Specifically, one can draw an analogy between this cortical representation and kernel-induced feature spaces, where input vectors are projected onto a higher-dimensional feature space, hence increasing the computational power of the classifier and improving the segregation between the different classes. In a similar fashion, the cortical mapping used in the current model attempts to enhance discrimination between the different auditory objects in the scene by allowing them to occupy nonoverlapping parts of the perceptual space.

A complementary view of this cortical representation can be thought of in terms of a sparse coding strategy employed by the auditory system. The rich span of neuronal selectivities in the primary auditory cortex may underlie a sparse distributed representation of natural scenes, allowing the system to optimally and robustly encode the complex sensory information in acoustic environments with multiple sources and sound objects (Klein *et al.*, 2003; Olshausen and Field, 2004; Denham *et al.*, 2007). Evidence from auditory cortical physiology is consistent with this view (Woolley *et al.*, 2005) and suggests that the correspondence between cortical tuning and spectrotemporal features in natural sounds constitutes a mapping that effectively enhances discriminability among different sounds. The feature analysis stage described in the current model builds on this principle by outlining an extensive perceptual representation with filters that are selectively driven by particular sound features.

An important contribution of the model presented here is to formalize a framework that allows us to better understand this image which emerges at the level of A1. A final word of caution, however, is that including or excluding one of these dimensions does not always affect the representation of that feature alone because the different representational dimensions do not necessarily interact linearly. Consequently, leaving out one axis at any stage might also affect the separability of sound elements along other axes, especially with "complex" or "naturalistic" sounds such as speech.

2. Cortical dynamics

Information in sound occurs on multiple time scales with different temporal features having distinct acoustic manifestations, neural instantiations, and perceptual roles. At the level of the central auditory system (particularly the pri-

mary auditory cortex), numerous physiological investigations have shown that cortical responses appear to be particularly tuned to relatively slow rates of the order of few to tens of hertz. The sluggishness of cortical responses has been postulated to correspond very closely to important information components in speech and music. In speech, slow temporal modulations reflect movements and shape of the vocal tract, and consequently the sequence of syllabic segments in the speech stream. In music, they reflect the dynamics of bowing and fingering, the timbre of the instruments, and the rhythm and succession of notes. Overall, the analysis windows at the level of the cortex constitute the "clock" that paces the process of feature integration over time. In this respect, the appropriate choice of time constants for this process is crucial for achieving the desired performance. Our work emphasizes that the choice of cortical time constants is not arbitrary for the process of stream segregation. Rather, it builds on the compatibility between cortical windows and information in natural sounds and argues for a tight correspondence between cortical encoding and the processes of auditory scene analysis. The present model is grounded in this view and actually relies on the choice of cortical dynamics to regulate the tempo of the feature integration. As discussed in the results shown in Fig. 8(b), one can certainly bias the performance of the model to "speed up" or "slow down" the process by choosing a different range of time constants or alternatively weighting the different temporal filters differently. However, the choice of the range of temporal parameters remains critical to obtain a correct behavior of the model as well as regulating the predictive stage as shall be discussed next.

3. Expectation processes

In addition to the appropriate choice of the representational space, the model relies strongly on a sound classification methodology for assigning the feature vectors to their corresponding classes. Unlike batch techniques, real-time segregation of these features requires continuous monitoring of the input and tracking of the different objects in the scene. Our present implementation accomplishes this process via an ongoing accumulation of expectations of each object. These expectations can be thought of as a matched filter that permits into the cluster only sensory patterns that are broadly consistent with recent history of that class. The principle of a matched filter has been presented as a reasonable hypothesis to explain observed plastic changes of cortical receptive fields (Fritz *et al.*, 2007). The physiological plausibility of this mechanism rests on the existence of feedback projections that mediate the adaptive representation of biological information under continuously changing behavioral contexts and environments.

Adaptive signal processing techniques such as Kalman filtering have been successfully implemented to model many forms of dynamic neural adaptation and plasticity in hippocampal and motor circuits (Eden *et al.*, 2004; Srinivasan *et al.*, 2006; Wu *et al.*, 2006). In the current model, we rely on the recursive nature of the Kalman filter to continuously estimate the state of each sound stream. The choice of a linear technique such as Kalman filtering (as opposed to other statistical filtering approaches such as particle filtering) is motivated by a long history of linear systems theory in characterizing receptive fields in physiological studies. The cortical STRFs (referred to through this paper) are *linear* approximations to a neuron's selectivity to different features. We therefore used the same linear formulation as the basis of the Kalman-filter model.

4. Architecture of the model

Overall, our work stresses that computational schemes that can capture the essence of these three processes (multiscale representation, cortical dynamics, and expectancies) would be able to perform robustly in problems of sound segregation. It also ascribes specific roles to these neural phenomena in the overall strategy of sound organization in the auditory system. While not all stages may be necessary for the process of sound segregation for any particular acoustic scene, putting all of them together is what allows the model to perform with *any* sound mixture without prior knowledge of the sound class.

For instance, segregation of the tone sequences shown in Figs. 6 and 7 can easily be achieved without the harmonicity analysis nor any particular enhancement of the onset cues. They do, however, rely greatly on the frequency analysis performed at both the peripheral level and the spectral shape analysis at the cortical level. Similarly, the harmonicity analysis contributes to the formation of different speaker streams in two ways: to help segregate simultaneous (overlapped) speech segments and to attend to one harmonic spectrum over another. Both of these stem from the unique association of harmonics with pitch through the postulated harmonic templates (Fig. 3). To understand these assertions, consider first how the model streams two alternating (nonoverlapping) different spectra from two speakers. Just as with the two alternating tones, the two distinct harmonic spectra will be assigned to different clusters. In this case, harmonicity does not afford any added advantage to the formation of the streams. When the two harmonic spectra overlap, harmonicity (through the templates) helps breakup the combined spectrum into the two distinct harmonic spectra, which can then be again assigned to the appropriate clusters. Without harmonicity, the complex combined spectrum is treated as a new different spectrum and assigned to a new cluster. The association of harmonicity with pitch (through the templates) also facilitates attending to one harmonic stream over another by "focusing" on the pitch of the speaker, which in turn may enhance the representation and streaming of that speaker from the mixture. Without pitch, attending to a specific speaker would have to depend on other attributes such as their timbre, accent, or location. Finally, it is conceivable that other (less commonly encountered) spectral "regularities" beyond harmonicity can also be utilized in this streaming process provided they have the same type of anchor (e.g., pitch or templates) (Roberts and Bregman, 1991).

B. Neural correlates of streaming and attention

The present model is based on the premise that streaming is reflected in the response properties of neurons in the primary auditory cortex. This hypothesis is corroborated by a growing body of evidence from experiments that explore the neural bases of auditory stream segregation. For example, studies by Fishman *et al.* (2001) and Micheyl *et al.* (2005) have identified a possible correlate of stream segregation in the primary auditory cortex (A1) of awake monkeys presented with repeating ABAB tone sequences. Qualitatively similar results have been obtained in bats by Kanwal *et al.* (2003) and in birds by Bee *et al.* (2004). Recent results using awake ferrets trained on auditory scene analysis tasks reveal changes in the spectrotemporal tuning of cortical receptive fields in a direction that promotes streaming and facilitates the formation of two segregated objects (Yin *et al.*, 2007).

The question remains, however, as to where and how exactly in the model does the adaptive nature of the STRFs emerge and serve functionally to promote streaming? We propose that the buildup of the clusters over time and the subsequent feedback that changes (or controls) the input stream into the integrative stage is the model's explanation for the experimentally observed rapid STRF changes during streaming. Specifically, if we were to imagine recording from a cortical cell represented by one of the integrators in Fig. 1 in *the quiescent state* (i.e., without feedback), we would observe responses with spectral and temporal selectivity that mimics the STRFs typically seen in A1 (Miller *et al.*, 2002). During streaming, the top-down feedback would alter the input into this cell (at the junction labeled "unsupervised clustering" in Fig. 1), effectively changing the selectivity of the cell or its STRF. Such a change would enhance the inputs that match the cell's cluster and suppress those that do not (i.e., belong to the competing stream), in agreement with experimental observations (Yin *et al.*, 2007).

This view of the relationship between streaming and rapid STRF plasticity makes several specific predictions that need to be explored in the future. For instance, STRF changes in the model essentially represent the neural correlate of the so-called "buildup" of streaming. This means that STRF plasticity must occur rather rapidly, within one or a few seconds of the initiation of streaming, at a rate commensurate with the dynamics of the buildup of the clusters in the model. So far, STRF adaptation has been detected only over relatively long epochs (minutes) due to the need to collect enough spikes to estimate them. New experimental techniques are therefore needed to estimate the STRFs rapidly, in particular, during the perceptual buildup of the streams.

Another key prediction of the model concerns the role of attention and its neural correlates in streaming. At first glance, the model appears to segregate streams rather automatically without "supervision," suggesting perhaps a minimal or no role for attention in the buildup of this percept. However, an alternative hypothesis is that the top-down "feedback loop" in the model is enabled only when the listener's attention is engaged. Clearly, without feedback, clustering ceases and no streams can form. Attention, we postulate, engages the feedback loop and enables streaming. We further postulate that "selective attention" to one stream or another can modulate the gain in the appropriate feedback loop, and hence favor the formation and perception of one (e.g., the foreground stream) over the other (the background). Although still conjectural, this view is consistent with several physiological and psychoacoustic data. One is the experimental finding that STRF plasticity is not observed in the absence of attentive behavior (Fritz *et al.*, 2005), implying that streaming would not occur without top-down feedback activated by behavior (and presumably attention). Another is the modulation by attention of the mismatch negativity (MMN) component of the auditory evoked response, which is often interpreted as a potential neural index of streaming (Sussman *et al.*, 2007). A second source of evidence for the critical role of attention is psychoacoustic studies, demonstrating that switching of attention to an ongoing acoustic stimulus is always associated with a perceptual buildup of its streams as if it had been initially "unstreamed" (Carlyon *et al.*, 2001). Furthermore, attention has been shown to modulate streaming, e.g., as in the ability to switch at will between hearing certain tone sequences as one or two streams (Sussman *et al.*, 2007) or the interaction between stimulus parameters and listener's attentional control in delimiting the "fission boundary" and the "coherence boundary" in the perception of alternating tones (Bregman, 1990; van Noorden, 1975).

We should note, however, that the exact role of attention in streaming remains debatable with some evidence suggesting that sound organization can occur in the absence of attention. Such streaming is thought to be driven by "intrinsic" neural processes, manifested by oddball effects [generally arising from novel and unexpected stimuli (Näätänen, 1992)] and the persistence of the MMN component even when subjects display no overt attention to the sound (Sussman, 2005; Ulanovsky *et al.*, 2003). This preattentive component of streaming is usually termed "primitive" stream segregation (Bregman, 1990). In our model, such primitive stream segregation implies that the top-down feedback must continue to operate in the absence of attention and that, therefore, STRFs should display adaptation during passive listening to sound reflecting the buildup of streams. This hypothesis remains physiologically untested.

ACKNOWLEDGMENTS

This research is supported by a CRCNS NIH Grant No. RO1 AG02757301, Southwest Research Institute, and Advanced Acoustic Concepts under a STTR from AFOSR.

APPENDIX: FEATURE INTEGRATION AND CLUSTERING

The clustering of sound features into different classes (two in the current model) proceeds through a three-step feedback loop which involves an estimation, prediction, and clustering stage. Each of these steps is mathematically implemented as follows.

1. Estimation

To make the dynamics of each filter $\mathcal{R}_{\omega}^{+}$ more mathematically tractable and allow the tracking of its evolution over time, we reformulate Eq. (3) as a nth order ARMA difference equation (Oppenheim and Shafer, 1999; Proakis and Manolakis, 1992):

$$a_0 Y(t) + \cdots + a_n Y(t-n) = b_0 I(t) + \cdots + a_{n-1} I(t-n+1), \tag{A1}$$

where $\{a_i\}$ and $\{b_i\}$ are scalar coefficients corresponding to impulse response $g_t(t,\omega)$ and whose values are determined by applying the Steiglitz–McBride algorithm (Ljung, 1999). This latter is a commonly used technique in filter design and parametric modeling of systems, which allows the computation of the ARMA coefficients for a prescribed time domain impulse response.

Next, we reduce this difference equation into a first-order vector equation following so-called state-space methods (Durbin, 2001; Pollock, 1999). Widely used in control theory, these methods are well suited for defining recursive time-series systems and compactly describing multi-input multi-output models in vectorial form. Thus, we introduce a latent variable called $Z(t)$ which captures the internal state of the system at discrete times t, and hence operates as a memory register for the stream being represented. We follow standard techniques for converting difference equations into state-space forms (Bay, 1999; Pollock, 1999), yielding the new model formulation:

$$I(t) = A\mathcal{Z}(t) + \nu(t), \tag{A2a}$$

$$\mathcal{Z}(t) = B\mathcal{Z}(t-1) + CY(t) + \eta(t), \tag{A2b}$$

where $\mathcal{Z}(t) \triangleq \vec{Z}(t) \triangleq [Z(t), Z(t-1), \ldots, Z(t-n+1)]^T$, and A, B, and C are three fixed-coefficient matrices derived from filter parameters $\{a_i\}$ and $\{b_i\}$ following the standard techniques used in difference equation to state-space conversions [see Pollock (1999) for a step-by-step procedure description]. Note that we chose to define the state-space model as an output-input relationship (and not the other way around) by deriving the observation equation (A2a) as a function of the input $I(t)$ [not the output $Y(t)$] because our ultimate goal is to use this model to make predictions about expected *inputs* for a given stream. Additionally, we introduced noise terms [$\nu(t)$ and $\eta(t)$] to both equalities in Eq. (A2). This allows us to formulate a *statistical* model of the temporal analysis of each temporal unit $\mathcal{R}_{\omega}^{+}$, which permits a stochastic estimation of the state-vector $\mathcal{Z}$, and hence a nondeterministic prediction of the expected input $\hat{\mathbf{I}}^{+}(t)$. The perturbation terms $\nu(t)$ and $\eta(t)$ are two Gaussian-noise processes drawn from zero mean multivariate distributions with covariances P and Q, respectively.

Therefore, the underlying dynamical system [captured in Eq. (A2)] is now a Markovchain model where the state estimate at the next time increment $\mathcal{Z}(t+1)$ is a function of the current state $\mathcal{Z}(t)$ combined with the input-output variables $(I(t), Y(t))$. Note that we have as many such systems as we have rate-selective units ($\{\mathcal{R}_{\omega}\}$) representing the neural array $\mathcal{R}^{+}$ (i.e., each array $\mathcal{R}^{+}$ encompasses five dynamical systems operating at rates of 2,4,32 Hz). Hence, the overall model is effectively a *family* of hidden Markov models evolving over successive discrete-time instants, which collectively capture the temporal evolution of a given stream.

Given the present formulation, we define an optimal solution for updating the latent variables $\mathcal{Z}$ in a way that enables both recursive tracking and prediction of future states. We opt for a Kalman-filter estimation (Chui and Chen, 1999; Haykin, 1996) because of its various advantages: (1) it is a computationally tractable and well defined mathematical solution to such estimation problem, (2) is optimal in the least mean square sense, and (3) is an *online recursive* technique where the current state estimate is computed only from the previous state (i.e., using recent history of the stream). Henceforth, the state variable $\mathcal{Z}$ is now updated as a Kalman filter-based evaluation (Haykin, 1996; Pollock, 1999), where the estimate of $\mathcal{Z}$ at time t is given by

$$\begin{aligned} \hat{\mathcal{Z}}(t) &= \hat{\mathcal{Z}}(t|t-1) + \mathcal{K}_G(t)(I(t) - A\hat{\mathcal{Z}}(t|t-1)), \\ \mathcal{K}_G(t) &= \Pi(t|t-1)A^T(A\Pi(t|t-1)A^T + P)^{-1}, \\ \Pi(t) &= \Pi(t|t-1) - \mathcal{K}_G(t)A\Pi(t|t-1), \end{aligned} \tag{A3}$$

where $\hat{\mathcal{Z}}(t)$ is the new predicted state at time t, $\hat{\mathcal{Z}}(t|t-1)$ is *a priori* estimate of $\mathcal{Z}$ conditioned on all prior information up to time $t-1$, $\mathcal{K}_G$ is the Kalman gain (Haykin, 1996), and $\Pi(t)$ is the estimate error covariance matrix between the actual and estimated $\mathcal{Z}$. The starting conditions $\mathcal{Z}(0)$ and $\Pi(0)$ are initialized to small random values.

One of the advantages of using a multirate analysis for the temporal tracking is the fact that each neural array $\mathcal{R}^{+}$ encompasses a wide range of temporal dynamics. To this effect, it is important to note that the vector $\mathcal{Z}(t)$ reflects more than the state of the system at exactly time instant t. Rather, it captures the past history of the system over a time window governed by the filter dynamics determined by the transition matrices A, B, and C. This memory can go as far back as 500 ms in the case of the slow filters operating at ω=2 Hz.

2. Prediction

So far in the model, the input-output pair $(I(t), Y(t))$ is used to update the current estimate of the latent variable $\mathcal{Z}(t)$. The next stage involves using this triplet $(I(t), Y(t), Z(t))$ to make an inference about the next expected input $\hat{\mathbf{I}}(t+1)$. To proceed with this prediction, we take advantage of known temporal regularities likely to exist in sound patterns arising from the same source (i.e., no abrupt spectral transitions from one time instant to the next) (Becker, 1993; Foldiak, 1991; Griffiths *et al.*, 2001). We model this temporal uniformity by assuming a locally smooth evolution of the cortical representation for each time step; i.e., the estimated cortical state $\hat{\mathbf{Y}}(t+1)$ equals the current state $Y(t)$. Based on this assumption, the model can make a prediction about the next input vector $\hat{\mathbf{I}}^{+}(t+1)$ following the system's equation (A2). This prediction represents the acoustic patterns that the

cortical unit $\mathcal{R}_{\omega}^{+}$ is expecting to hear based on its recent history in order to maintain a smooth temporal evolution. Given that each stream is represented by an entire array of cortical neurons $\{\mathcal{R}_{\omega}^{+}\}$, we sum across the predictions of all ω-units within the array to obtain two expected inputs $\hat{\mathbf{I}}^1(t+1)$ and $\hat{\mathbf{I}}^2(t+1)$ from the two streams $\mathcal{R}^1$ and $\mathcal{R}^2$ represented in the model.

3. Clustering

The final stage is the most crucial step to segregating incoming sound patterns $I(t)$ into their corresponding perceptual streams. This procedure is performed based on a simple clustering rule that contrasts each input pattern with its closest match from the predictions of the arrays $\mathcal{R}^1$ and $\mathcal{R}^2$. Only the pattern that closely matches the predictions $\hat{\mathbf{I}}^1(t)$ or $\hat{\mathbf{I}}^2(t)$ is used as the next input $I(t+1)$ for that stream following the clustering "closest match" rule:

$$h^{+} = \arg\min_{h} \|\hat{\mathbf{I}}^{+}(t) - I(t)\|. \tag{A4}$$

[1]Throughout this paper, we use the term "stream" to refer to the clustered sound elements corresponding to the cognitive representation of a physical acoustic source. The term stream is occasionally used interchangeably with the term auditory object.

[1]Anstis, S., and Saida, S. (1985). "Adaptation to auditory streaming of frequency-modulated tones," J. Exp. Psychol. Hum. Percept. Perform. **11**, 257–271.

[2]Aubin, T., and Jouventin, P. (1998). "Cocktail-part effect in king penguin colonies," Proc. R. Soc. London, Ser. B **265**, 1665–1673.

[3]Barlow, H. (1994). *Large-Scale Neuronal Theories of the Brain* (MIT Press, Cambridge, MA), pp. 1–22.

[4]Bay, J. S. (1999). *Fundamentals of Linear State Space Systems* (McGraw-Hill, Boston).

[5]Beauvois, M. W., and Meddis, R. (1996). "Computer simulation of auditory stream segregation in alternating-tone sequences," J. Acoust. Soc. Am. **99**, 2270–2280.

[6]Becker, S. (1993). *Advances in Neural Information Processing Systems* (Morgan Kaufmann, San Mateo, CA), Vol. **5**, pp. 361–368.

[7]Bee, M. A., and Klump, G. M. (2004). "Primitive auditory stream segregation: A neurophysiological study in the songbird forebrain," J. Neurophysiol. **92**, 1088–1104.

[8]Bell, A. J., and Sejnowski, T. J. (1995). "An information maximization approach to blind source separation and blind deconvolution," Neural Comput. **7**, 1129–1159.

[9]Bregman, A. S. (1978). "Auditory streaming is cumulative," J. Exp. Psychol. Hum. Percept. Perform. **4**, 380–387.

[10]Bregman, A. S. (1990). *Auditory Scene Analysis: The Perceptual Organization of Sound* (MIT Press, Cambridge, MA).

[11]Bregman, A. S., and Ahad, P. A. (1990). "Demonstrations of auditory scene analysis: The perceptual organization of sound," Compact Disk, Department of Psychology, McGill University, Montreal, Canada.

[12]Bregman, A. S., and Pinker, S. (1978). "Auditory streaming and the building of timbre," Can. J. Psychol. **32**, 19–31.

[13]Carlyon, R. P., Cusack, R., Foxton, J. M., and Robertson, I. H. (2001). "Effects of attention and unilateral neglect on auditory stream segregation," J. Exp. Psychol. Hum. Percept. Perform. **27**, 115–127.

[14]Carlyon, R., and Shamma, S. (2003). "An account of monaural phase sensitivity," J. Acoust. Soc. Am. **114**, 333–348.

[15]Cherry, E. C. (1953). "Some experiments on the recognition of speech, with one and two ears," J. Acoust. Soc. Am. **25**, 975–979.

[16]Chi, T., Ru, P., and Shamma, S. A. (2005). "Multiresolution spectrotemporal analysis of complex sounds," J. Acoust. Soc. Am. **118**, 887–906.

[17]Chui, C. K., and Chen, G. (1999). *Kalman Filtering With Real Time Applications* (Springer-Verlag, New York).

[18]Cohen, M. A., Grossberg, S., and Wyse, L. L. (1995). "A spectral network model of pitch perception," J. Acoust. Soc. Am. **98**, 862–879.

[19]Colburn, S., Shinn-Cunningham, B., Jr, G. K., and Durlach, N. (2006). "The perceptual consequences of binaural hearing," Int. J. Audiol. **45**, 34–44.

[20]Colombo, M., Rodman, H. R., and Gross, C. G. (1996). "The effects of superior temporal cortex lesions on the processing and retention of auditory information in monkeys (cebus apella)," J. Neurosci. **16**, 4501–4517.

[21]Cristianini, N., and Shawe-Taylor, J. (2000). *Introduction to Support Vector Machines and Other Kernel-Based Learning Methods* (Cambridge University Press, Cambridge, UK).

[22]Dau, T., Püschel, D., and Kohlrausch, A. (1996). "A quantitative model of the effective signal processing in the auditory system," J. Acoust. Soc. Am. **99**, 3615–3622.

[23]Denham, S., Coath, M., and Balaguer-Ballester, E. (2007). "Sparse time-frequency representations in auditory processing," 19th International Congress on Acoustics, Madrid.

[24]Drullman, R. (1995). "Temporal envelope and fine structure cues for speech intelligibility," J. Acoust. Soc. Am. **97**, 585–592.

[25]Duifhuis, H., Willems, L. F., and Sluyter, R. J. (1982). "Measurement of pitch in speech: An implementation of Goldstein's theory of pitch perception," J. Acoust. Soc. Am. **71**, 1568–1580.

[26]Durbin, J. (2001). *Time Series Analysis by State-Space Methods*, 3rd ed. (Oxford University Press, New York, NY).

[27]Eddins, D. A., and Bero, E. M. (2007). "Spectral modulation detection as a function of modulation frequency, carrier bandwidth, and carrier frequency region," J. Acoust. Soc. Am. **121**, 363–372.

[28]Eden, U. T., Frank, L. M., Barbieri, R., Solo, V., and Brown, E. N. (2004). "Dynamic analysis of neural encoding by point process adaptive filtering," Neural Comput. **16**, 971–998.

[29]Elhilali, M., Chi, T., and Shamma, S. A. (2003). "A spectro-temporal modulation index (STMI) for assessment of speech intelligibility," Speech Commun. **41**, 331–348.

[30]Elhilali, M., Fritz, J. B., Chi, T., and Shamma, S. A. (2007). "Auditory cortical receptive fields: Stable entities with plastic abilities," J. Neurosci. **27**, 10372–10382.

[31]Elhilali, M., Fritz, J. B., Klein, D. J., Simon, J. Z., and Shamma, S. A. (2004). "Dynamics of precise spike timing in primary auditory cortex," J. Neurosci. **24**, 1159–1172.

[32]Ellis, D. P. W., and Weiss, R. J. (2006). "Model-based monaural source separation using a vector-quantized phase-vocoder representation," Proceedings of the IEEE International Conference on Acoustics, Speech, and Signal Processing, IEEE ICASSP'06, Vol. **5**, pp. 957–960.

[33]Fay, R. R. (1998). "Auditory stream segregation in goldfish (carassius auratus)," Hear. Res. **120**, 69–76.

[34]Festen, J. M., and Plomp, R. (1990). "Effects of fluctuating noise and interfering speech on the speech-reception threshold for impaired and normal hearing," J. Acoust. Soc. Am. **88**, 1725–1736.

[35]Fishman, Y. I., Reser, D. H., Arezzo, J. C., and Steinschneider, M. (2001). "Neural correlates of auditory stream segregation in primary auditory cortex of the awake monkey," Hear. Res. **151**, 167–187.

[36]Foldiak, P. (1991). "Learning invariance from transformation sequences," Neural Comput. **3**, 194–200.

[37]Fritz, J. B., Elhilali, M., David, S., and Shamma, S. A. (2007). "Does attention play a role in dynamic receptive field adaptation to changing acoustic salience in a1," Hear. Res. **229**, 186–203.

[38]Fritz, J. B., Elhilali, M., and Shamma, S. A. (2005). "Differential receptive field plasticity to salient cues in primary auditory cortex during two-tone frequency discrimination," J. Neurosci. **25**, 7623–7635.

[39]Goldstein, J. L. (1973). "An optimum processor theory for the central formation of the pitch of complex tones," J. Acoust. Soc. Am. **54**, 1496–1516.

[40]Green, D. M. (1986). *Auditory Frequency Selectivity*, NATO ASI Series, Series A: Life Sciences (Plenum, New York, NY), pp. 351–359.

[41]Griffiths, T. D., Uppenkamp, S., Johnsrude, I., Josephs, O., and Patterson, R. D. (2001). "Encoding of the temporal regularity of sound in the human brainstem," Nat. Neurosci. **4**, 633–637.

[42]Grimault, N., Bacon, S. P., and Micheyl, C. (2002). "Auditory stream segregation on the basis of amplitude-modulation rate," J. Acoust. Soc. Am. **111**, 1340–1348.

[43]Grossberg, S., Govindarajan, K. K., Wyse, L. L., and Cohen, M. A. (2004). "Artstream: A neural network model of auditory scene analysis and source segregation," Neural Networks **17**, 511–536.

[44]Hartman, W. M., and Jonhson, D. (1991). "Stream segregation and peripheral channelling," Music Percept. **9**, 155–184.

[45]Haykin, S. (1996). *Adaptive Filter Theory* (Prentice-Hall, Upper Saddle River, NJ).
[46]Herbrich, R. (2001). *Learning Kernel Classifiers: Theory and Algorithms* (MIT Press, Cambridge, MA).
[47]Hughes, H. C., Darcey, T. M., Barkan, H. I., Williamson, P. D., Roberts, D. W., and Aslin, C. H. (2001). "Responses of human auditory association cortex to the omission of an expected acoustic event," Neuroimage **13**, 1073–1089.
[48]Hulse, S. H., MacDougall-Shackleton, S. A., and Wisniewski, A. B. (1997). "Auditory scene analysis by songbirds: Stream segregation of birdsong by European starlings (sturnus vulgaris)," J. Comp. Psychol. **111**, 3–13.
[49]Humphrey, N. (1992). *A History of the Mind* (Simon and Schuster, New York, NY).
[50]Izumi, A. (2001). "Relative pitch perception in Japanese monkeys (macaca fuscata)," J. Comp. Psychol. **115**, 127–131.
[51]Jang, G., and Lee, T. (2004). "A maximum likelihood approach to single-channel source separation," J. Mach. Learn. Res. **4**, 1365–1392.
[52]Jerison, H. J., and Neff, W. D. (1953). "Effect of cortical ablation in the monkey on discrimination of auditory patterns," Fed. Proc. **12**, 73–74.
[53]Kanwal, J. A., Medvedev, A., and Micheyl, C. (2003). "Neurodynamics for auditory stream segregation: Tracking sounds in the mustached bat's natural environment," Network Comput. Neural Syst. **14**, 413–435.
[54]Kelly, J. B., Rooney, B. J., and Phillips, D. P. (1996). "Effects of bilateral auditory cortical lesions on gap-detection thresholds in the ferret (mustela putorius)," Behav. Neurosci. **110**, 542–550.
[55]Klein, D. J., König, P., and Körding, K. P. (2003). "Sparse spectrotemporal coding of sounds," EURASIP J. Appl. Signal Process. **7**, 659–667.
[56]Kowalski, N., Depireux, D. A., and Shamma, S. A. (1996). "Analysis of dynamic spectra in ferret primary auditory cortex. I. Characteristics of single-unit responses to moving ripple spectra," J. Neurophysiol. **76**, 3503–3523.
[57]Kristjansson, T., Hershey, J., Olsen, P., Rennie, S., and Gopinath, R. (2006). "Super-human multi-talker speech recognition: The ibm 2006 speech separation challenge system," Proceedings of the International Conference of Spoken Language Processing, ICSLP'06.
[58]Langner, G. (1992). "Periodicity coding in the auditory system," Hear. Res. **6**, 115–142.
[59]Ljung, L. (1999). *System Identification: Theory for the User*, 2nd ed. (Prentice-Hall, Upper Saddle River, NJ).
[60]McCabe, S. L., and Denham, M. J. (1997). "A model of auditory streaming," J. Acoust. Soc. Am. **101**, 1611–1621.
[61]Micheyl, C., Tian, B., Carlyon, R. P., and Rauschecker, J. P. (2005). "Perceptual organization of tone sequences in the auditory cortex of awake macaques," Neuron **48**, 139–148.
[62]Middlebrooks, J. C., Dykes, R. W., and Merzenich, M. M. (1980). "Binaural response-specific band in primary auditory cortex (ai) of the cat: Topographical organization orthogonal to isofrequency contours," Brain Res. **181**, 31–49.
[63]Miller, L. M., Escabi, M. A., Read, H. L., and Schreiner, C. E. (2002). "Spectrotemporal receptive fields in the lemniscal auditory thalamus and cortex," J. Neurophysiol. **87**, 516–527.
[64]Miller, G. A., and Taylor, W. G. (1948). "The perception of repeated bursts of noise," J. Acoust. Soc. Am. **20**, 171–182.
[65]Moore, B. C. J., Glasberg, B. R., and Peters, R. W. (1986). "Thresholds for hearing mistuned partials as separate tones in harmonic complexes," J. Acoust. Soc. Am. **80**, 479–483.
[66]Moore, B., and Gockel, H. (2002). "Factors influencing sequential stream segregation," Acta. Acust. Acust. **88**, 320–332.
[67]Näätänen, R. (1992). *Attention and Brain Function* (Lawrence Erlbaum Associates, Hillsdale, NJ).
[68]Nelken, I. (2004). "Processing of complex stimuli and natural scenes in the auditory cortex," Curr. Opin. Neurobiol. **14**, 474–480.
[69]Nix, J., and Hohmann, V. (2007). "Combined estimation of spectral envelopes and sound source direction of concurrent voices by multidimensional statistical filtering," IEEE Trans. Audio, Speech, Lang. Process. **15**, 995–1008.
[70]Olshausen, B. A., and Field, D. J. (2004). "Sparse coding of sensory inputs," Curr. Opin. Neurobiol. **14**, 481–487.
[71]Oppenheim, A., and Shafer, R. (1999). *Discrete Time Signal Processing*, 2nd ed. (Prentice-Hall, Upper Saddle River, NJ).
[72]O'Shaughnessy, D. (2000). *Speech Communications: Human and Machine*, 2nd ed. (Institute of Electrical and Electronics Engineers, New York, NY).
[73]Oxenham, A. J., Bernstein, J. G., and Penagos, H. (2004). "Correct tonotopic representation is necessary for complex pitch perception," Proc. Natl. Acad. Sci. U.S.A. **101**, 1421–1425.
[74]Peters, R. W., Moore, B. C., and Baer, T. (1998). "Speech reception thresholds in noise with and without spectral and temporal dips for hearing-impaired and normally hearing people," J. Acoust. Soc. Am. **103**, 577–587.
[75]Pickles, J. O. (1988). *An Introduction to the Physiology of Hearing* (Academic, St Louis, MO).
[76]Pollock, D. S. G. (1999). *A Handbook of Time-Series Analysis, Signal Processing and Dynamics* (Academic, Cambridge, UK).
[77]Proakis, J. G., and Manolakis, D. G. (1992). *Digital Signal Processing* (McMillan, New York, NY).
[78]Qin, M. K., and Oxenham, A. J. (2003). "Effects of simulated cochlear-implant processing on speech reception in fluctuating maskers," J. Acoust. Soc. Am. **114**, 446–454.
[79]Rauschecker, J. P. (2005). "Neural encoding and retrieval of sound sequences," Ann. N.Y. Acad. Sci. **1060**, 125–135.
[80]Roberts, B., and Bregman, A. S. (1991). "Effects of the pattern of spectral spacing on the perceptual fusion of harmonics," J. Acoust. Soc. Am. **90**, 3050–3060.
[81]Roweis, S. (2000). "One microphone source separation," *Neural Information Processing Systems (NIPS'00)*, Vol. **13**, pp. 793–799.
[82]Sacks, M., and Blackburn, C. (1991). *Neurophysiology of Hearing: The Central Auditory System*, 15th ed. (Raven, New York, NY).
[83]Schreiner, C. (1998). "Spatial distribution of responses to simple and complex sounds in the primary auditory cortex," Audiol. Neuro-Otol. **3**, 104–122.
[84]Schreiner, C. E., and Urbas, J. V. (1988). "Representation of amplitude modulation in the auditory cortex of the cat. II. Comparison between cortical fields," Hear. Res. **32**, 49–64.
[85]Shamma, S. A. (1998). *Methods of Neuronal Modeling*, 2nd ed. (MIT Press, Cambridge, MA), pp. 411–460.
[86]Shamma, S. A., and Klein, D. J. (2000). "The case of the missing pitch templates: How harmonic templates emerge in the early auditory system," J. Acoust. Soc. Am. **107**, 2631–2644.
[87]Shinn-Cunningham, B. G. (2005). "Influences of spatial cues on grouping and understanding sound," *Proceedings of the Forum Acusticum*.
[88]Srinivasan, L., Eden, U. T., Willsky, A. S., and Brown, E. N. (2006). "A state-space analysis for reconstruction of goal-directed movements using neural signals," Neural Comput. **18**, 2465–2494.
[89]Supin, A. Y., Popov, V. V., Milekhina, O. N., and Tarakanov, M. B. (1999). "Ripple depth and density resolution of rippled noise," J. Acoust. Soc. Am. **106**, 2800–2804.
[90]Sussman, E. S. (2005). "Integration and segregation in auditory scene analysis," J. Acoust. Soc. Am. **117**, 1285–1298.
[91]Sussman, E. S., Horvath, J., Winkler, I., and Orr, M. (2007). "The role of attention in the formation of auditory streams," Percept. Psychophys. **69**, 136–152.
[92]Sutter, M. L. (2005). "Spectral processing in the auditory cortex," Int. Rev. Neurobiol. **70**, 253–298.
[93]Tougas, Y., and Bregman, A. S. (1985). "The crossing of auditory streams," J. Exp. Psychol. Hum. Percept. Perform. **11**, 788–798.
[94]Ulanovsky, N., Las, L., and Nelken, I. (2003). "Processing of low-probability sounds in cortical neurons," Nat. Neurosci. **6**, 391–398.
[95]van Noorden, L. P. (1975). "Temporal coherence in the perception of tone sequences," Ph.D. thesis, Eindhoven University of Technology.
[96]Varga, A. P., and Moore, R. K. (1990). "Hidden Markov model decomposition of speech and noise," *Proceedings of the IEEE International Conference on Acoustics, Speech, and Signal Processing, IEEE ICASSP'90*, Vol. **2**, pp. 845–848.
[97]Viemeister, N. F. (1979). "Temporal modulation transfer functions based upon modulation thresholds," J. Acoust. Soc. Am. **66**, 1364–1380.
[98]von der Malsburg, C., and Schneider, W. (1986). "A neural cocktail-party processor," Biol. Cybern. **54**, 29–40.
[99]Wang, D. L., and Brown, G. J. (1999). "Separation of speech from interfering sounds based on oscillatory correlation," IEEE Trans. Neural Netw. **10**, 684–697.
[100]Wang, K., and Shamma, S. A. (1994). "Self-normalization and noise-robustness in early auditory representations," IEEE Trans. Speech Audio Process. **2**, 421–435.
[101]Wang, K., and Shamma, S. A. (1995). "Spectral shape analysis in the central auditory system," IEEE Trans. Speech Audio Process. **3**, 382–395.

[102] Welch, G., and Bishop, G. (2001). "An introduction to the Kalman filter," ACM SIGGRAPH.
[103] Wightman, F. (1973). "A pattern transformation model of pitch," J. Acoust. Soc. Am. **54**, 397–406.
[104] Wittkop, T., and Hohmann, V. (2003). "Strategy-selective noise reduction for binaural digital hearing aids," Speech Commun. **39**, 111–138.
[105] Woolley, S. M., Fremouw, T. E., Hsu, A., and Theunissen, F. E. (2005). "Tuning for spectro-temporal modulations as a mechanism for auditory discrimination of natural sounds," Nat. Neurosci. **8**, 1371–1379.
[106] Wu, W., Gao, Y., Bienenstock, E., Donoghue, J. P., and Black, M. J. (2006). "Bayesian population decoding of motor cortical activity using a Kalman filter," Neural Comput. **18**, 80–118.
[107] Yang, X., Wang, K., and Shamma, S. A. (1992). "Auditory representations of acoustic signals," IEEE Trans. Inf. Theory **38**, 824–839.
[108] Yin, P., Ma, L., Elhilali, M., Fritz, J. B., and Shamma, S. A. (2007). *Hearing: From Basic Research to Applications* (Springer Verlag, New York, NY).

The role of temporal-masking patterns in the determination of subjective duration and loudness for ramped and damped sounds

Dennis T. Ries[a)]
School of Hearing, Speech and Language Sciences, Ohio University, Athens, Ohio 45701

Robert S. Schlauch
University of Minnesota, Speech-Language-Hearing Sciences, Minneapolis, Minnesota 55455

Jeffrey J. DiGiovanni
School of Hearing, Speech and Language Sciences, Ohio University, Athens, Ohio 45701

(Received 15 August 2007; revised 17 September 2008; accepted 22 September 2008)

The association between temporal-masking patterns, duration, and loudness for broadband noises with ramped and damped envelopes was examined. Duration and loudness matches between the ramped and damped sounds differed significantly. Listeners perceived the ramped stimuli to be longer and louder than the damped stimuli, but the outcome was biased by the stimulus context. Next, temporal-masking patterns were measured for ramped- and damped-broadband noises using three (0.5, 1.5, and 4.0 kHz) 10 ms probe tones presented individually at various temporal delays. Predictions of subjective duration derived from masking results underpredicted the matching results. Loudness estimates derived from models that assume persistence of neural activity after stimulus offset [Glasberg B. R., and Moore, B. C. J. (2002). "A model of loudness applicable to time-varying sounds," J. Audio. Eng. Soc. **50**, 331–341; Chalupper, J., and Fastl, H. (2002) "Dynamic loudness model (DLM) for normal and hearing-impaired listeners," Acust. Acta Acust. **88**, 378–386] were greater for ramped sounds than for damped sounds and were close to the average results obtained via the matching task. Differences in simultaneous-masked thresholds for these stimuli could not account for the loudness-matching results. Decay suppression of the later occurring portion of the damped stimulus may account for the differences in perception due to the stimulus context; however, a parsimonious implementation of this process that accounts for both subjective duration and loudness judgments remains unclear. © *2008 Acoustical Society of America.*
[DOI: 10.1121/1.2999342]

PACS number(s): 43.66.Ba, 43.66.Cb, 43.66.Dc, 43.66.Lj [BCM] Pages: 3772–3783

I. INTRODUCTION

Ramped (rising intensity) and damped (falling intensity) stimuli have been employed to examine how the auditory system processes sounds that have identical long-term spectra yet differ in their temporal characteristics. Prior studies have reported results for a variety of auditory phenomena including intensity discrimination (Schlauch *et al.*, 1998), subjective duration (DiGiovanni and Schlauch, 2007; Grassi and Darwin, 2006; Schlauch *et al.*, 2001a, 2001b), loudness (Irino and Patterson, 1996; Neuhoff 1998, 2001; Maier *et al.*, 2004; Stecker and Hafter, 2000), and tonality (Patterson, 1994a, 1994b). All of these studies, except that on intensity discrimination (Schlauch *et al.*, 1998), report perceptual differences between ramped and damped stimuli of the same physical duration. Possible explanations for this perceptual asymmetry have included perceptual constancy (DiGiovanni and Schlauch, 2007; Grassi and Darwin, 2006; Stecker and Hafter, 2000) and persistence of excitation within the central auditory system (DiGiovanni and Schlauch 2007).

Stecker and Hafter (2000) proposed that a cognitive effect is responsible for at least a portion of the perceptual differences that result from manipulations of the temporal envelope of a sound. They proposed that perceptual constancy caused sounds with damped envelopes to be perceived as softer than sounds with ramped envelopes. Perceptual constancy is a cognitive phenomenon that describes how an individual may obtain similar perceptual experiences for a given stimulus across a variety of environmental settings. Visual size constancy is a well known example of this phenomenon. In the visual realm, when objects move farther from an observer, they are not judged as smaller, provided that cues for distance are available, as the brain compensates for distance to maintain size constancy. In a similar vein, Stecker and Hafter (2000) proposed that the brain performs a constancy-mode interpretation of sounds with damped envelopes. According to their hypothesis, sounds with damped envelopes are parsed into two pieces. The earliest or first part represents a sound source, and the second part represents reverberation. The part judged as reverberation is discarded when making judgments about source loudness and duration. This reduces the loudness and perceived duration of sounds with damped envelopes. By contrast, sounds with ramped

[a)]Electronic mail: ries@ohio.edu

 © 2008 Acoustical Society of America

envelopes do not fit the pattern of a sound source and its echo, so they are judged as a single source without reverberation.

An alternative explanation is conceivable, however, as auditory sensation in response to a sound does not end abruptly upon termination of the stimulus but has been suggested to decay in an exponential manner for some time afterward [e.g., see Miller (1948); Plomp (1964), and Zwislocki *et al.* (1959)]. Differences in persistence of excitation within the central auditory system that could contribute to perceptual differences between ramped and damped sounds would be expected, as the former ends at a much higher level than the latter. This would lead to a greater amount of forward masking for the ramped than for the damped sound [e.g., see Fastl (1976, 1976/1977, 1979)]. The forward-masking patterns could be interpreted as an estimate of the degree to which the excitation produced by these two sounds extends beyond the stimulus offset [e.g., see Fastl (1984) and Fastl and Zwicker (2007)]. These patterns purportedly represent neural excitation at some unspecified level in the auditory system, and differences between these patterns would be expected to produce differences in perception if persistence of excitation affects perception. Zwicker (1977) as well as Fastl (1977) and Fastl *et al.* (2002) modeled loudness and subjective duration from these patterns. In their modeling, they assumed that some portion of the neural excitation that continued beyond the offset of an auditory stimulus contributed to the loudness and subjective duration of the sound and that the extent of this effect could be estimated from forward-masking data. Results from temporal-masking studies reveal that forward masking has a much longer time course for decay than the buildup of backward masking [e.g., see Fastl (1976, 1976/1977, 1977)]. Hence, estimates of the nonsimultaneous excitation attributed to a stimulus derived from forward-masking data would have a greater influence on modeling of loudness and subjective duration than would estimates derived from backward-masking data. Given this expected asymmetry in the masking patterns, a sound with a ramped envelope that ends at a high level will have its excitation extended by persistence of excitation far beyond that of a sound with a damped envelope that ends at a low level. This is consistent with sounds with ramped envelopes being perceived as louder and longer than sounds with damped envelopes, even though they have the same physical duration.

The present study measures temporal-masking patterns for ramped- and damped-broadband-noise maskers and compares them to loudness and subjective duration estimates. The loudness and duration measures were obtained via a matching procedure, whereas the temporal-masking patterns were measured using a short-duration probe placed at various temporal locations with respect to the ramped and damped sounds. The primary purpose of this study was to determine the extent to which excitation patterns derived from masking patterns can account for observed differences in loudness and perceived duration for these sounds. These measures were intended to provide for a better understanding of the mechanisms responsible for the perceptual differences between ramped and damped sounds.

II. EXPERIMENT 1: DURATION MATCHING

Duration matches were obtained for sounds as a function of duration (10–500 ms). In the control condition, subjects adjusted the duration of a broadband noise with a rectangular envelope to match that of a broadband noise with the same envelope. In the two experimental conditions, listeners adjusted the duration of broadband noise with a damped envelope until it was perceived to have the same duration as a standard stimulus with a ramped envelope (experimental condition 1) or vice versa (experimental condition 2).

A. Stimuli

A custom-designed 16 bit digital-to-analog converter generated the stimuli. Broadband noise was generated at a sampling rate of 26.0 kHz with anti-aliasing filters set to 10.0 kHz. The sounds had a rectangular, a ramped, or a damped envelope. The damped envelope was generated by an exponential decay with a time constant set to 1/5th of the signal duration and is given by

$$x(t) = e^{(-5t/T)}w(t), \tag{1}$$

where w is the rectangular-gated noise, t is time in seconds, and T is the duration of w in seconds. The ramped-exponential rise was produced by reversing the order of the points in the array generated for the damped sound prior to playback. The value of T for the fixed-duration standard was 10, 25, 50, 100, 200, or 500 ms. The value of T for the comparison stimulus was adjustable through the use of a slide mechanism. As the range of adjustment was determined randomly for each run, the duration value associated with the matched position from the preceding run was rarely, if ever, the same as that of a subsequent run. The range of adjustment available was always much broader than the range of the subjects' matches. The standard and comparison were presented alternately with a 500 ms interval between the end of the standard and the beginning of the comparison and a 1000 ms delay between the end of the comparison and the beginning of the subsequent standard stimulus. The rms level of the rectangular-gated noise, without the exponential decay or rise, was 70 dB SPL, corresponding to a spectrum level of 30 dB.

B. Subjects

Five adults (one male and four females) aged 18–30 years participated in the matching experiment. All of the subjects had normal hearing (thresholds $\leqslant$15 dB HL) at octave frequencies from 0.25 to 8.0 kHz and had no prior experience listening in matching experiments.

C. Procedure

Subjects were presented with a fixed-duration standard stimulus followed by an adjustable comparison. Subjects were instructed first to bracket the point of perceived duration equality in order to establish the positions along the slider range that produced comparison stimuli that were clearly longer and shorter than the standard. After this was accomplished, they were asked to adjust the slider to the

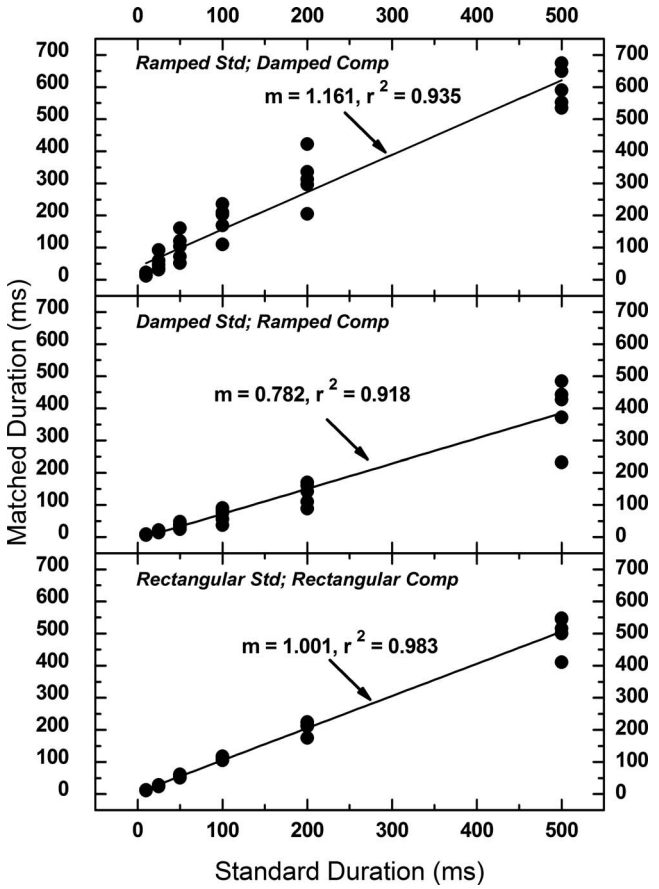


FIG. 1. Scatter plot of the duration-matching results in ms (y-axis) for the ramped standard, damped comparison (upper panel), damped standard, ramped comparison (middle panel), and control conditions (lower panel) as a function of standard duration (x-axis) for all subjects participating in experiment 1. The lines represent least-squares linear fits to the data. The proportion of the variance that can be accounted for by each linear regression analysis is given by the value of r^2.

position that produced standard and comparison sounds with the same perceived duration. Once a matching duration was obtained, the subjects pushed a button on a response box and the matching duration was stored.

Each subject completed the matching task ten times for each standard-comparison pair (damped standard versus ramped comparison, ramped standard versus damped comparison, and rectangular standard versus rectangular comparison) for each of the six standard durations. Stimuli were presented to the right ear of each subject via an insert earphone (ER-3A, Etymotic Research). Subjects listened individually in a double-walled sound-treated booth (IAC Model 1204-A, Industrial Acoustics Corp.).

D. Results

Figure 1 illustrates average duration matches (y-axis) as a function of the standard duration (x-axis) for the control condition (lower panel) and the experimental conditions (middle and upper panels). Linear regression and correlation analyses reveal a strong association between the duration of the standard and the duration of the matched comparison (r^2 values >0.91 for all correlations). Furthermore, the slope of the regression line fitted to each data set differed across conditions, indicating that the duration-matching behavior was affected by the envelope of the standard and comparison pair. Specifically, the slope was greater than 1.0 for the match of the damped comparison to the ramped standard (upper panel), whereas the opposite (slope <1.0) occurred for the ramped comparison and damped standard condition (middle panel). The slope of the line in the control condition (lower panel) was 1, indicating no time-order bias.

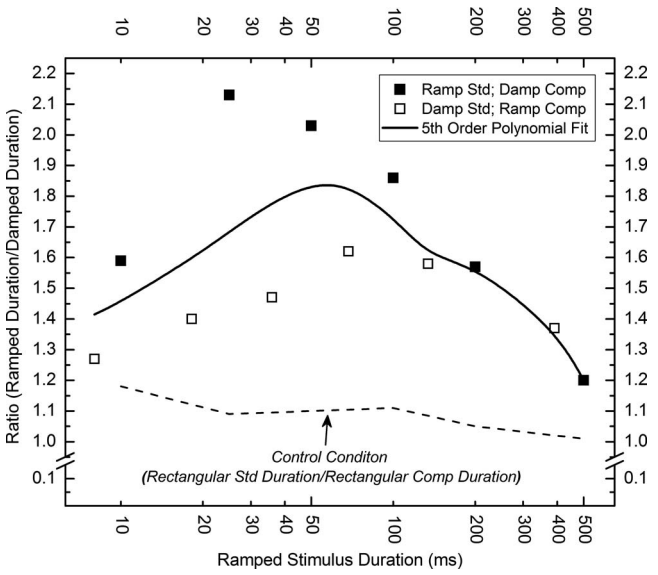


FIG. 2. Mean ramped/damped duration ratios (y-axis) as a function of ramped-stimulus duration (x-axis) as measured using the matching task. The results for the ramped-standard, damped-comparison condition are depicted by filled squares, and the results for the damped-standard, ramped-comparison condition are depicted by open squares. The solid line represents a fifth-order polynomial fit to the data. The data from the control condition (ratio of the durations of the matched rectangular comparison /rectangular standard) are represented by the dashed line.

Figure 2 shows the results expressed as the ratio of the duration of the ramped sound to that of the damped sound at equal perceived duration when the damped sound served as the standard (open squares) and when the ramped sound served as the standard (filled squares). The ratio of the comparison to standard duration (dashed line) for the control condition is provided for reference. The ratios at each duration, as well as a fifth-order polynomial fit (solid line) to the ratios for the experimental conditions, illustrate that the ramped stimuli were perceived to be longer than the damped stimuli across all durations. Furthermore, the disparity in perceived duration between the ramped and damped sounds varies as a function of duration with a maximal difference at around 50–100 ms on the fitted function. The ratios for the experimental conditions were greater than those for the control condition for all durations.

The matched durations across subjects were analyzed using a repeated-measure analysis of variance (ANOVA) with standard duration and condition (standard and comparison envelope pair) as factors. There was a significant effect of standard duration [$F(5,20)=482.70$, $p<0.0001$, with the Geisser–Greenhouse adjustment] and condition [$F(3,8)=17.28$, $p=0.014$]. As expected, there was a significant interaction between condition and duration [$F(10,40)=6.28$, $p=0.035$], indicating that the matched duration for a given

TABLE I. Results of the *post hoc* analyses for the duration-matching data comparing stimulus envelope condition and duration. An asterisk indicates that the results of the analyses were significant at an alpha level of 0.05. NS indicates that no significant difference was found for a given comparison.

Condition comparison	Duration (ms)						
	Overall	10	25	50	100	200	500
Control vs Damped standard/ramped comparison	*	NS	NS	NS	NS	*	*
Control vs Ramped standard/damped comparison	*	NS	NS	*	*	*	*
Damped standard/ramped comparison vs Ramped standard/damped comparison	*	NS	NS	*	*	*	*

standard-comparison pair was dependent on both the temporal envelope of the stimuli and the duration of the standard.

As the *F*-statistic was significant for condition and duration, *post hoc* comparisons for these factors and their interaction were evaluated using Fisher's protected least significant difference (LSD) multiple comparison test (Ryan, 1959) with an alpha level of 0.05. The results of the *post hoc* analyses are provided in Table I. The results combined across durations indicated that all conditions differed significantly. The duration matches obtained in the damped standard/ramped comparison and ramped standard/damped comparison conditions differed significantly from each other for standard durations of 50 ms and greater. When compared to the control condition, however, it is clear that the differences were not symmetrical. That is, the ramped standard/damped comparison results differed from those for the control condition for more of the standard durations than did the results obtained for the damped standard/ramped comparison condition. Similar asymmetrical outcomes (i.e., order/context effects) for duration have been obtained by others (Grassi, personal communication). Not surprisingly, the *post hoc* results for the duration for each standard duration combined across envelope type, provided in Table II, indicated that the matches obtained for a given standard duration differed significantly from those obtained at all other durations, except when the results obtained using the 10 and 25 ms standards were compared to each other.

E. Discussion

These results are consistent with those reported previously (DiGiovanni and Schlauch, 2007; Grassi and Darwin, 2006; Schlauch *et al.*, 2001b). That is, damped sounds are perceived as being shorter than ramped sounds of equivalent duration. This difference is related to a disparity in perception and is not a function of the measurement method, as subjects were able to match the durations of two sounds with rectangular envelopes accurately (see Fig. 1). Unlike the results of Schlauch *et al.* (2001b), however, the present results show a greater difference in the ramped/damped matched duration when the ramped sound was the standard than when the damped sound was the standard (see Fig. 2). The ramped/damped duration ratios for the mid-duration stimuli (i.e., 25, 50, and 100 ms) when the ramped sound served as the standard are larger than those reported earlier (compare to the lower left panel of Fig. 6 in Schlauch *et al.*, 2001b). The matches reported for the damped standard condition are comparable between the two studies. Interestingly, the line fit to the ratios in Fig. 2 more closely follows the trend exhibited by the magnitude estimation data of Schlauch *et al.* (upper left panel of Fig. 6 in Schlauch *et al.*, 2001b) than it follows their matching data. In addition, the results appear to be consistent with the results of Grassi and Darwin (2006) in that the difference in the perceived duration between ramped and damped stimuli of equivalent durations decreases for longer-duration stimuli (e.g., 200–500 ms in this study and 250–1000 ms in Grassi and Darwin's (2006) study).

TABLE II. Results of the *post hoc* analyses for the duration-matching data at each standard duration combined across envelope type. See Table I for the description of abbreviations and symbols.

Standard duration (ms)	Comparison duration (ms)					
	10	25	50	100	200	500
10	⋯	NS	*	*	*	*
25		⋯	*	*	*	*
50			⋯	*	*	*
100				⋯	*	*
200					⋯	*
500						⋯

III. EXPERIMENT 2: LOUDNESS MATCHES

The stimuli used in this experiment were the same as those employed in experiment 1. Loudness matches were obtained for two experimental conditions and one control condition. In the control condition, subjects adjusted the level of a broadband noise with a rectangular envelope to match the loudness of a broadband noise with the same envelope. In the two experimental conditions, listeners adjusted the level of broadband noise with a damped envelope until it was perceived to have the same loudness as the standard stimulus with a ramped envelope (condition 1) or vice versa (condition 2).

A. Subjects

Four adults (one male and three females) aged 18–30 years participated and were selected using the same criteria as for experiment 1. Three of the four subjects also participated in experiment 1. The new subject had no prior experience listening in matching experiments.

B. Procedure

The matching task required subjects to adjust a slide mechanism on a response box to equate the loudness of an adjustable comparison and a fixed-level standard stimulus. The initial level of the comparison stimulus was determined from the position of the slide at the beginning of each run. The levels associated with any slide position varied randomly between runs. The maximum range of adjustment of 38 dB was determined based on pilot data and always included the 70 dB SPL standard within this limit. The position of the 70 dB SPL point within this range was offset randomly above and below the center position of the slider on any given run by as much as ±11 dB, ensuring that subjects could not simply set the slide to the same place each time. In addition, this range was set so that there would be a minimum of 8 dB of adjustment possible on either side of the standard level. A 95 dB SPL ceiling was adopted to ensure that the upper end of the range did not become uncomfortably loud. In cases where the offset of the standard from the midpoint of the slider range was more than +6 dB, the total range was reduced on the upper end to limit this value to 95 dB SPL. When the offset of the standard from the midpoint of the slider range was less than −6 dB (i.e., −7 to −12 dB), the lower end of the range was set to 45 dB SPL to preserve the symmetry within the adjustment range adopted for positive offsets of more than 6 dB. With the offset and the maximum and minimum levels set as specified, the extreme lower and upper values of the adjustment range were 45–78 dB SPL for an offset of −11 dB and 62–95 dB SPL for an offset of +11 dB, respectively. The slight differences in the adjustment range across the various offset values were expected to have limited impact on the loudness judgments (Gabriel *et al.*, 1997). Asymmetrical positioning of the standard within the adjustment range, however, can produce disparate loudness judgments for a given level (Gabriel *et al.*, 1997). To lessen this effect, the offset value of the standard within the adjustment range was selected randomly for each matching run completed by a subject, and the results were averaged over ten such runs for each subject. That is, we expected that any bias, if present, when averaged across runs and subjects, would be mitigated such that it would have a negligible impact on the overall results.

Subjects were presented with a fixed-intensity standard stimulus followed by an adjustable-intensity comparison stimulus. Standard and comparison stimuli were presented alternately with a 500 ms delay between the end of the standard and the beginning of the comparison and a delay of approximately 1000 ms between the end of the comparison and the beginning of the next standard presentation. When the subject moved the slide, the intensity of the comparison was altered during the next 1000 ms interstimulus interval, and the effect of this adjustment occurred in the next comparison presentation. Subjects were instructed to bracket the point of perceived-loudness equality and to push a button when they felt that the two sounds were equally loud. That is, they were instructed to be sure to adjust the slider until the sound was easily judged to be louder and easily judged to be softer, and then to refine their judgments between those two points.

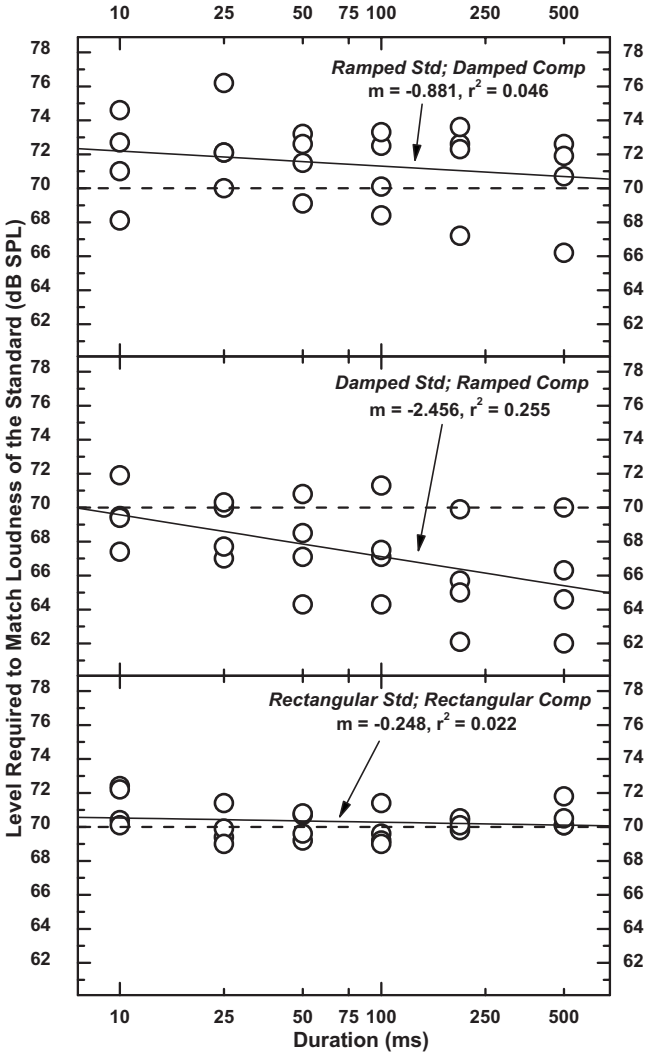


FIG. 3. Similar to Fig. 1, except that the results are for loudness matching.

C. Results

Figure 3 illustrates average loudness matches (y-axis) as a function of the duration (x-axis) for the control condition (lower panel) and the experimental conditions (middle and upper panels). Linear regression and correlation analyses revealed that the level (dB SPL) required to match the loudness of the comparison to that of the standard was independent of stimulus duration for the control (slope= −0.248 dB/log(ms), r^2=0.022, p=0.492, see the bottom panel) and ramped standard/damped comparison (slope= −0.881 dB/log(ms), r^2=0.046, p=0.315, see the upper panel) conditions, whereas there was a significant correlation between these parameters for the damped standard/ramped comparison (slope=−2.456 dB/log(ms), r^2=0.255, p =0.012, see middle the panel) condition. For the ramped standard/damped comparison condition, the level difference required to equate loudness decreased slightly as the duration of the standard increased, whereas the difference increased as the standard duration increased for the damped standard-

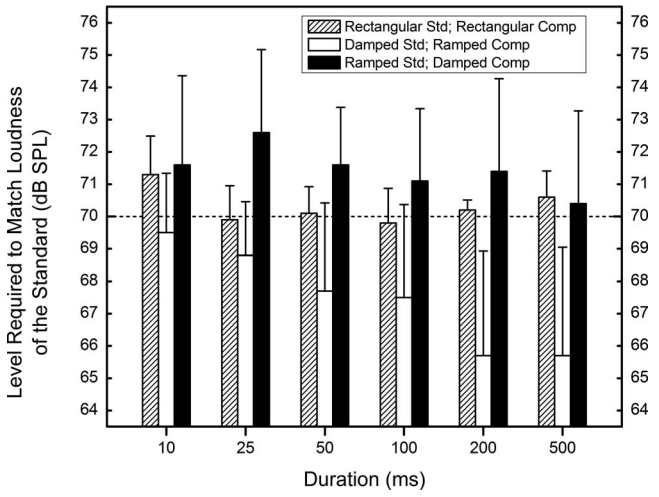


FIG. 4. Mean loudness-matching results (y-axis) for ramped and damped stimuli and for the control condition at each standard duration (x-axis). Black bars depict the results for the ramped-standard and damped-comparison condition, white bars depict the results for the damped-standard and ramped-comparison condition, and hatched bars depict the results for the control condition. The dashed line represents the level of the standard for each condition and duration.

ramped comparison condition. Furthermore, the slope of the regression line and the intercept on the y-axis differed across conditions, indicating that the loudness-matching behavior was affected by the envelope of the standard and comparison pair. Specifically, the level required to match the loudness of a damped comparison to a ramped standard (upper panel) decreased progressively as the duration of the standard increased [slope=−0.881 dB/log(ms)] starting approximately at 2.2 dB above the level of the standard at 10 ms and approaching the level of the standard by 500 ms. In contrast, the level required to match the loudness of the ramped comparison to the damped standard was approximately 0.4 dB below that of the standard at 10 ms and progressively decreased [slope=−2.456 dB/log(ms)] to more than 4.5 dB as the duration of the standard increased to 500 ms. These effects appear to be related to the differences in the temporal envelopes of the ramped and damped sounds as the slope of the line in the control condition (lower panel) was zero with an intercept (70.8 dB SPL) close to the level of the standard (70 dB SPL).

Figure 4 shows the average loudness matches for the control (hatched bar), ramped standard/damped comparison (dark bar), and damped standard/ramped comparison (white bar) conditions for each standard duration. The level of the standard in each condition is denoted by the dashed line. The results indicate that (1) subjects could perform that task consistently and accurately as indicated by the results for the control condition; (2) loudness matching at the shortest duration was slightly less accurate (see control condition results at 10 ms); (3) the level difference for equal loudness between ramped standard and damped comparison conditions did not differ markedly across duration, although the level differences for equal loudness tended to be smaller as duration increased; and (4) the level difference for equal loudness with damped comparison and ramped standard conditions increased over the first 200–500 ms. The latter two points indicate that the levels of the comparisons required for equal loudness are not symmetrical about the level of the standard across the duration for the two experimental conditions. That is, a difference in the matched level between ramped and damped sounds occurred when the damped sound served as the standard and the ramped sound was the comparison, but not when the situation was reversed.

The loudness matches were analyzed further using a repeated-measure ANOVA with stimulus duration and condition (standard and comparison envelope pair) as factors. The Geisser–Greenhouse correction was applied. There was a significant effect of stimulus duration [$F(5,15)=7.54$, $p=0.0375$] and condition [$F(2,6)=9.58$, $p=0.0231$]. The interaction between condition and duration was insignificant [$F(10,30)=1.18$, $p=0.369$]. A *post hoc* comparison of the outcomes for condition indicated that the level of the matched comparison differed significantly (Fisher's protected LSD, $p<0.05$) between the damped-standard, ramped-comparison condition and the ramped-standard, damped comparison condition as well as the damped-standard, ramped comparison condition and the control condition, but the results for the ramped-standard, damped comparison condition did not differ significantly from those for the control condition.

D. Discussion

The results are in accordance with previous loudness measures (Stecker and Hafter, 2000) involving ramped and damped stimuli. The level required to match the loudness of a ramped or damped standard to that of a damped or ramped comparison is dependent on which sound serves as the standard (see Fig. 4). That is, the level difference needed to match loudness is greatest when the damped sound serves as the standard and increases with increases in stimulus duration up to roughly 200 ms. In contrast, the extent of the level differences encompasses a smaller range overall and does not change significantly with increases in duration when the ramped sound serves as the standard. The mean of the level difference required to match loudness across subjects at each duration was about 1.0–2.0 dB across duration. In contrast, the mean of the level difference required to match loudness across subjects at each duration when the damped sound served as the standard increased from approximately 0.5 dB at 10 ms to over 4.0 dB at 200 ms. The mean matched level at 500 ms was similar to that at 200 ms. This same asymmetry in the size of the ramped-damped loudness difference was reported by Stecker and Hafter (2000). The auditory system appears to be biased toward perceiving a difference in loudness between two sounds when a sound with a damped envelope precedes other stimuli (e.g., sounds with ramped or rectangular envelopes) of similar duration.

IV. EXPERIMENT 3: TEMPORAL-MASKING PATTERNS FOR A BROADBAND-NOISE MASKER

Ramped- and damped-broadband-noise stimuli and a 10 ms probe tone were used to obtain temporal-masking patterns for three masker durations (10, 50, and 500 ms). The durations of the maskers correspond to the two end points of

the duration range used in experiments 1 and 2 and a mid-duration value (close to the geometric mean of the durations at the end points).

A. Stimuli

The 10, 50, and 500 ms noise maskers used in this experiment were identical to the equivalent duration ramped- and damped-broadband-noise stimuli used in the matching experiments. Thresholds in quiet and in the presence of the broadband maskers were obtained for a 10 ms probe tone presented before, during, and after the masker. The tones were gated on and off with 5 ms minimum-three-term Blackman–Harris-shaped (Nuttall, 1981) rise and fall ramps and had no steady state. The peak in the envelope of the probe occurred 5 ms after the onset of the probe tone. For the 10 ms masker, the temporal placement of the peak amplitude of the probe tone with respect to the onset of the masker occurred at −5, 5, 15, and 30 ms for the ramped masker and at −5, 5, 15, and 25 ms for the damped masker. For the 50 ms masker, the corresponding times were −15, −5, 5, 15, 25, 35, 45, 65, 75, and 85 ms for the ramped masker and −15, −5, 5, 15, 25, 35, 45, 55, 65, and 75 ms for the damped masker. For the 500 ms masker condition, the corresponding times were −15, −5, 5, 125, 250, 375, 415, 455, 495, 515, 530, 545, 575, and 645 ms for the ramped masker and −75, −35, −15, −5, 5, 45, 85, 125, 250, 375, 495, 505, and 515 ms for the damped masker. Probe frequencies were 0.5, 1.5, and 4.0 kHz.

B. Subjects

Three adult subjects (two males and one female) aged 28–30 years were selected according to the criteria employed in experiments 1 and 2. Only one of the subjects, the first author, had prior experience listening in temporal-masking experiments. The remaining two subjects were given practice on the task in quiet until they felt comfortable with the procedure and produced consistent thresholds (approximately five to seven runs). They were also given 1–2 h of practice listening in various backward-, simultaneous-, and forward-masked conditions.

C. Procedure

Thresholds in quiet and at various probe-signal delays were obtained using a three-interval forced-choice task that targeted 70.7% of the psychometric function (Levitt, 1971). Lights marked the observation intervals, and 500 ms silent periods separated each interval within a trial. Subjects were instructed to pick the interval that sounded different. Signals decreased in level following two correct responses and increased in level following one incorrect response. The step size was 3 dB. The first three reversals were discarded, and the threshold for each 80-trial run was based on the average of the levels at which the remaining reversals occurred. A run was discarded if fewer than six reversals were obtained; a typical number of reversals was 14.

The first run began with the signal level about 10 dB above a threshold value estimated from the pilot data. Subsequent runs began with the signal level about 10 dB above an individual subject's previously measured thresholds. Average thresholds were calculated based on three runs unless the standard deviation exceeded 3 dB, in which case an additional run was obtained and included in the average. Thresholds for probe tones were obtained first in quiet and subsequently in the presence of ramped and damped maskers.

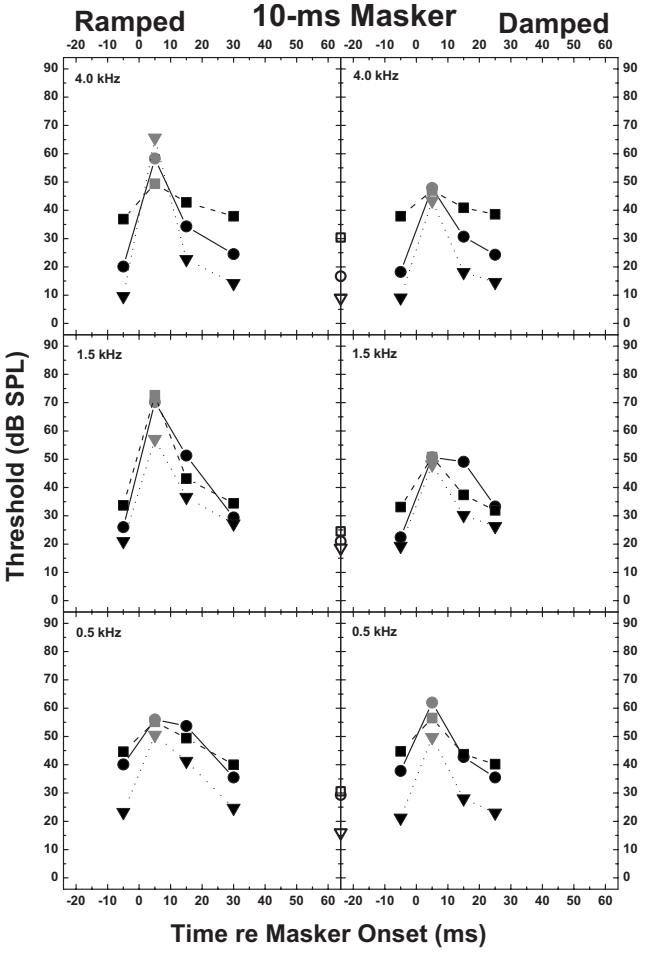


FIG. 5. Temporal-masking patterns for 10 ms ramped (left panels) and damped (right panels) broadband-noise maskers for three subjects (S1, circles with solid lines; S2, inverted triangles with dotted lines; and S3, squares with dashed lines). Masked thresholds (y-axis) are shown for 4.0 kHz (top panels), 1.5 kHz (middle panels), and 0.5 kHz (bottom panels) probe tones as a function of probe-tone location with respect to the masker onset (x-axis). Gray circles represent simultaneous masking, and filled symbols represent nonsimultaneous masking (backward or forward). The masker onset is designated as time zero. Open symbols on the ordinate between the ramped and damped panels represent each subject's probe-tone threshold in quiet.

D. Results and discussion

Figures 5–7 show temporal-masking patterns measured for the 10, 50, and 500 ms maskers, respectively. The greatest amount of masking occurred when the probe occurred within the masker, but the masker also produced backward and forward masking. Masking patterns for the 50 and 500 ms maskers (Figs. 6 and 7) followed the envelope of the masker. Simultaneous-masked thresholds for the ramped masker started at a low level and increased as the masker level increased, whereas thresholds for the damped masker

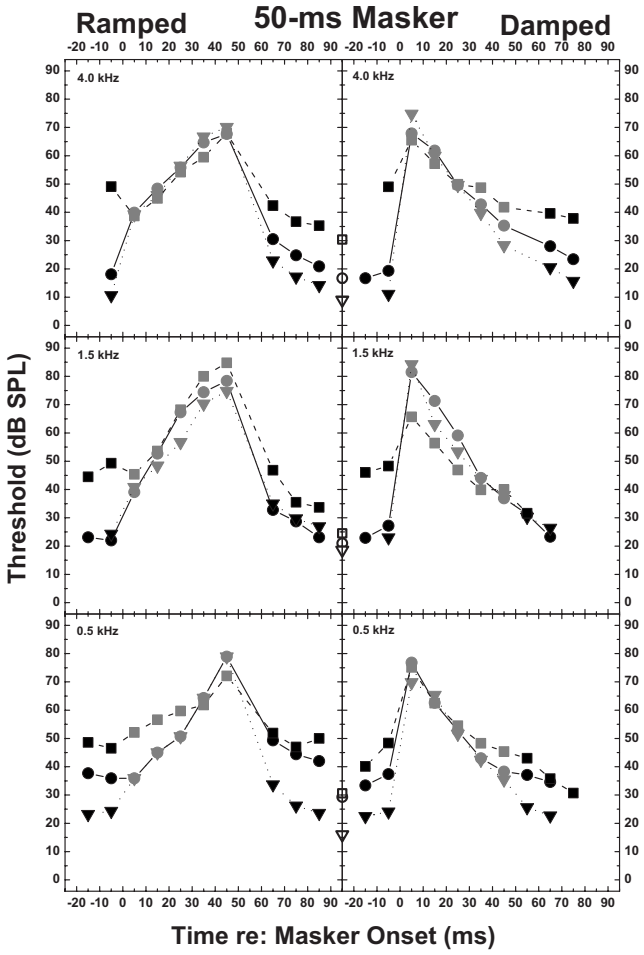


FIG. 6. Similar to Fig. 5, except that the masker duration was 50 ms.

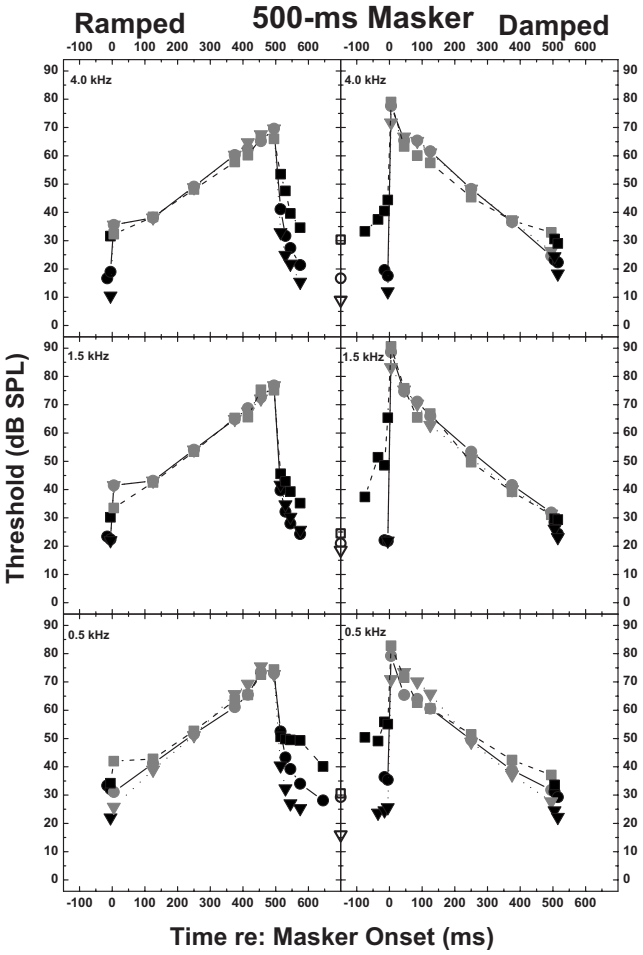


FIG. 7. Similar to Fig. 5, except that the masker duration was 500 ms.

started at a high level and decreased as the masker level decreased. This effect was not apparent for the 10 ms masker (Fig. 5) because the probe tone had the same duration as the masker. Nonetheless, the patterns for the 10 ms masker did show differences between forward and backward masking.

Forward- and backward-masked portions of the temporal-masking patterns are consistent with past research [e.g., see Fastl (1976) and Samoilova (1959)]. That is, backward-masked thresholds declined rapidly as the probe moved further from the onset of the masker, whereas forward-masked thresholds declined more gradually as the probe moved further from the end of the masker. Results for subject 3 (squares), however, showed some notable exceptions. This subject exhibited elevated backward-masked thresholds that declined very slowly compared to those of the other subjects, even upon repeated measurements. This was most apparent for the 50 ms masker (see Fig. 6); extensive training in the backward-masked conditions may have mitigated this disparity. Subject 3 reported receiving speech therapy as a child, but the nature of the problem and the treatment are unknown. Overall, the nonsimultaneous masked-thresholds followed the expected pattern, with the exception of some backward-masking results of subject 3.

Exponential functions were fitted to the nonsimultaneous masking data for each masker type (ramped or damped). The backward- and forward-masked functions were expressed relative to the simultaneous-masked thresholds measured at the beginning (i.e., probe delay of 5 ms with respect to the masker onset for both ramped and damped maskers) and end of the masker (i.e., probe delays of 5 ms for the 10 ms masker, 45 ms for the 50 ms masker, and 495 ms for the 500 ms masker), respectively. An exponential-decay function was used to determine the time constant that produced the smallest sum-of-squared deviations about the backward- and forward-masking data for each subject [e.g., see Dolan and Small (1984), Hartley *et al.* (2000), Fastl (1976), Kidd and Feth, (1982), and Zwicker (1977, 1984)]. The fitted function was

$$Y = [(\theta_m - \theta_q)e^{-(t/\tau)}] + \theta_q, \tag{2}$$

where θ_m is the masked threshold at a particular probe delay, θ_q is the threshold in quiet, t is the probe delay with respect to the masker onset, and τ is a time constant. The value of τ producing the best fit for each masker type (ramped or damped) and for each masking condition (forward or backward) was used to fit a line to the data using Eq. (2). Again, these fits were expressed relative to the simultaneous masked thresholds at the beginning and end of the masker for the backward- and forward-masked functions, respectively. The best-fitting value of τ was relatively short ($<$11 ms), although in some instances longer time constants were found.

TABLE III. Predicted (columns 2 and 3) and measured (column 4) perceived duration ratios of damped and ramped sounds with durations of 10, 50, and 500 ms (column 1). The ratios shown indicate what factor the physical duration of the damped sound needs to be greater than that of the ramped sound to achieve equal perceived duration (see text for details).

	Predicted		Measured
Stimulus duration (ms)	5 dB SL criterion	10 dB SL criterion	Matching task
10	1.10	1.19	1.25
50	1.19	1.22	1.64
500	1.08	1.06	1.20

There were four occasions out of 18 when the best-fitting line was horizontal, showing no exponential decay. All of the horizontal fits occurred for the backward-masked condition. Subject 1 accounted for two cases of 50 ms ramped masker, 0.5 kHz probe and 500 ms ramped masker, 0.5 kHz probe, and subject 3 accounted for two cases of 50 ms ramped masker, 4.0 kHz probe and 50 ms ramped masker, 1.5 kHz probe. Horizontal fits to the data of subject 1 were most likely due to data points for these conditions being within about 6 dB of absolute threshold and to inherent measurement noise. Horizontal fits for subject 3 were likely due to the extended backward masking described earlier. With these exceptions, exponential-decay functions provided an adequate description of the backward- and forward-masked data.

1. Predicting perceived duration

The exponential functions fitted to each subject's data were used to find the probe delays that produced backward- and forward-masked thresholds of 5 and 10 dB SL for each masker type and duration for each probe-tone frequency. The difference in time between these points represents the predicted subjective duration (Fastl, 1977; Fastl and Zwicker, 2007) under the assumption that nonsimultaneous masking is, at least in part, a reflection of the buildup and decay of excitation within the central auditory system. For example, using a 5 dB SL criterion for subject 1 with a 50 ms ramped masker and a 4.0 kHz probe tone results in backward- and forward-masked duration extensions of 3.1 and 27.9 ms, respectively. These values are then added to the physical duration of the masker (50 ms) to produce a total predicted perceived duration of about 81 ms. The medians of the predicted subjective durations across probe-tone frequency and subject for the ramped- and damped-broadband noises were used to determine the damped/ramped ratios listed in Table III. The values indicate that ramped sounds are predicted to sound longer than damped sounds for each stimulus duration, as the damped/ramped ratios are greater than 1. However, the difference predicted from the masking patterns is less than the obtained difference, which indicates either that there is an influence of central processes in the estimation of the duration of rising and falling intensity sounds or that the underlying assumptions regarding persistence of excitation and subjective duration are incorrect.

2. Loudness predictions

Masked thresholds obtained from the temporal-masking patterns can provide insights into the possible link between loudness and excitation for ramped and damped sounds as loudness can be predicted from these patterns (Fastl, 1984; Moore and Glasberg, 1996; Moore *et al.*, 1997; Zwicker and Scharf, 1965). Two recent implementations of loudness models for dynamically changing sounds represent extensions of an earlier model by Zwicker (1977). Both models base their predictions on neural excitation in response to a stimulus, and both assume that the loudness impression increases quickly with the onset of a sound and decays more slowly when a sound is terminated. Chalupper and Fastl (2002) modeled this aspect of loudness for dynamically changing sounds using forward masking to estimate the persistence of excitation, whereas Glasberg and Moore (2002) attributed it to the possible persistence of sensory information at some level in the auditory system that may be related to forward masking.

The loudness models for dynamically changing sounds of Glasberg and Moore (2002) and Chalupper and Fastl (2002) were used to predict loudness differences for the 10, 50, and 500 ms ramped and damped stimuli in our study. The models used the waveforms for our stimuli as input. The detailed descriptions of these models can be found elsewhere (Glasberg and Moore, 2002; Chalupper and Fastl, 2002). In Glasberg and Moore's (2002) model, the basic steps for the first stage include (1) filtering that represents the transfer functions for the outer and middle ear,[1] (2) estimation of the short-term spectrum at 1 ms intervals, (3) derivation of the pattern of excitation from the spectrum, (4) transformation of the excitation pattern to units of specific loudness, and (5) integration of the area under the specific loudness pattern. According to the authors, this first stage of their model yields instantaneous loudness, a quantity unavailable for conscious perception that possibly corresponds to neural activity. This calculation of instantaneous loudness is used to derive short-term loudness and long-term loudness, perceptual quantities that are based on the summation of these instantaneous values. The attack and release times used to calculate the short-term and long-term loudness values implement a temporal integration mechanism resembling an automatic gain control circuit. Short-term loudness estimates are derived directly from temporal integration of the instantaneous loudness values, whereas long-term loudness estimates are derived from temporal integration of short-term loudness values. Short-term and long-term loudness values both have quick attack times and slower release times, but the long-term loudness has more gradual attack and release times than does short-term loudness. Short-term loudness corresponds to loudness perceived at a particular instant in time, whereas long-term loudness represents the overall loudness impression. The predictions for loudness differences between ramped and damped stimuli from the present study using the models of Glasberg and Moore (2002) as well as that of Chalupper and Fastl (2002) are shown in Table IV, along with the results from the loudness-matching experiment. Glasberg and Moore's (2002) model predicted only a slight short-term loudness difference for the 10 ms stimuli and small differ-

TABLE IV. Predicted and measured level differences (dB) for equal loudness for ramped and damped sounds with durations of 10, 50, and 500 ms (column 1). Predicted values were derived from the ongoing estimates of short- and long-term loudness (columns 2 and 3) provided by the model of Glasberg and Moore (2002) at 1 ms intervals over and extending beyond the physical duration of the stimulus. The predictions are based on the difference between the peak values within each loudness type (short-term and long-term loudness) for a given duration. Loudness differences derived from the model of Chalupper and Fastl (2002) are provided in column 4. Positive values indicate that the ramped sound was predicted or measured (column 5) to be louder than the damped sound of equivalent duration.

	Predicted			
	Glasberg and Moore (2002)		Chalupper and Fastl (2002)	Measured
Stimulus duration (ms)	Short-term loudness	Long-term loudness	Estimated loudness	Matching task
10	+0.25	+0.05	+0.13	+1.04
50	+3.05	+1.15	+1.59	+1.97
500	+2.00	+2.40	+2.76	+2.33

ences in short-term loudness, consistent with the data, for the 50 and 500 ms stimuli. The long-term loudness values are also reasonably close to the matching results, especially for the 500 ms stimuli. The subjects may be using the short-term loudness values when dealing with the shorter-duration stimuli and the long-term loudness value when dealing with the long-duration stimuli (Glasberg and Moore, 2002). The predicted level differences required for equal loudness derived using the model of Chalupper and Fastl (2002) are also close to the average matching results.

These loudness models are based on the assumption that neural activity persists after a sound terminates. To determine if such an assumption is necessary, that is, to determine if excitation occurring during the time course of the maskers could explain the observed loudness differences, we inspected the temporal-masking patterns just during the on-time of the masker. The temporal-masking patterns for simultaneous segments averaged across listeners are shown in Fig. 8 for noise bands with ramped and damped envelopes and durations of 10, 50, and 500 ms. For an easy visual comparison at the same masker levels, the masking patterns for the ramped noise bands are reversed in time. The upper panels show group-mean data averaged across frequency for each of the durations. The middle panels and lower panels show group-mean data for signal frequencies of 4.0 kHz and 0.5 kHz, respectively. The ramped noise bands produced, on average, more masking than the damped noise bands. This trend was also evident in the data obtained using the 1.5 kHz probe tone (not shown). Given that loudness models based on masking patterns are derived under the assumption that the amount of masking is related to the level of excitation produced by a stimulus, these results are consistent with ramped noise bands being louder than damped noise bands. Predictions of the absolute difference in level that is required for equal loudness perception, however, are not accurate as a large effect of envelope would be expected for the 10 ms stimuli (see Fig. 8, top panel, left column), which was not observed in the matching data.

V. GENERAL DISCUSSION AND CONCLUSIONS

This study adds to the growing body of literature indicating that ramped sounds appear louder and longer than damped sounds with the same physical duration and intensity. In the present study, quantitative predictions of loudness and duration were made using models that are consistent with the notion that the internal representation of a sound persists after it is terminated. Modeling of duration used the extent of the temporal-masking pattern. Loudness values were predicted using models proposed by Glasberg and Moore (2002) and Chalupper and Fastl (2002). The loudness

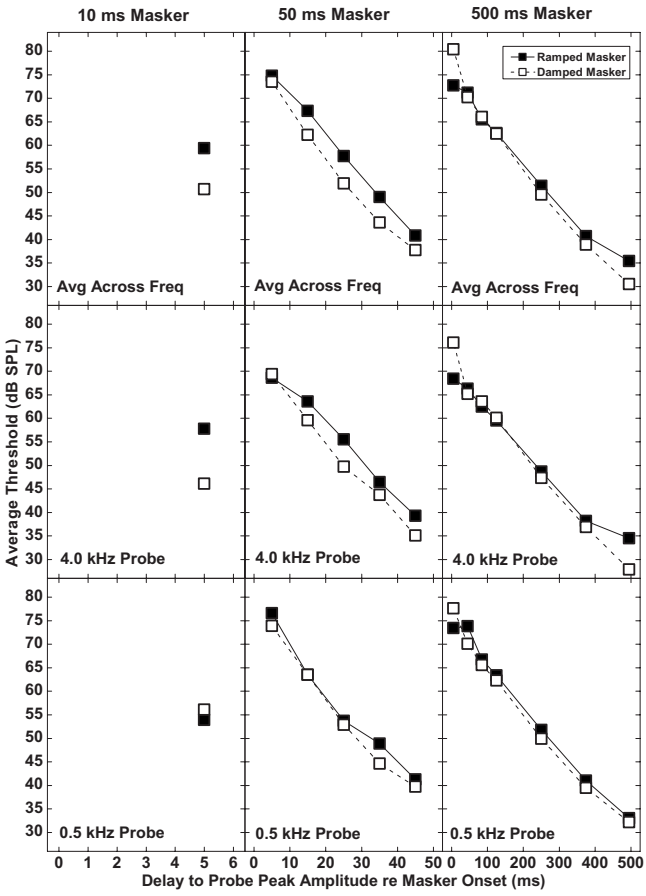


FIG. 8. Temporal-masking patterns for the 10 ms (left column), 50 ms (middle column), and 500 ms (right column) ramped (filled symbols) and damped (open symbols) broadband-noise maskers measured over only the physical duration of each stimulus. For ease of comparison, the patterns obtained for the ramped masker were reversed in time.

models based on persistence were consistent with the behavioral data, but the model for duration underpredicted the asymmetry in the behavioral data.

An alternative possibility to the persistence of excitation explanation is that sounds with ramped envelopes invoke more neural activity while the sound is on than sounds with damped envelopes. The amount of neural activity generated by a particular stimulus can be inferred from simultaneous masking. Thresholds for brief signals obtained during the time course of ramped noise bands were often higher than those for damped noise bands when the stimulus was at equal levels. Higher thresholds are consistent with a greater amount of excitation, a result which could be associated with the perceptual differences for ramped and damped sounds. This finding of higher thresholds during ramped sounds than damped sounds also suggests that forward masking of the tail of damped sounds by earlier occurring more intense portions of the stimulus is likely not responsible for the differences in loudness and duration that are perceived. It is not clear how these threshold differences, illustrated in Fig. 8, are converted into duration and loudness differences. The small ramped-damped threshold differences for a probe tone occurred only at the onset of the 500 ms noise band, yet a substantial difference was observed for the 10 ms noise band. This further complicates the analysis because the threshold asymmetry does not correspond to the magnitude of the observed loudness differences.

Threshold differences in the masking patterns for ramped and damped sounds during the time course of the masker may be related to overshoot. Overshoot is defined as poorer detection (i.e., increased threshold) of a brief tone at the onset of a noise masker than when the tone is delayed relative to the masker onset. Adaptation of neural fibers is a popular explanation for overshoot (Bacon and Takahashi, 1992), and the continuously rising intensity of a ramped sound could be processed by the auditory system akin to a set of continuous signal onsets, thereby limiting or reducing the effect of adaptation. The overall mean data for 10 and 50 ms stimuli (Fig. 8, top panels, left and middle columns) show a trend that would fit this supposition. The same outcome was not apparent in the data obtained for the 500 ms stimulus. The change in intensity over the 500 ms stimulus may be too gradual to cause this prolonged overshootlike effect and could be linked to the smaller decibel difference required to equate loudness for ramped and damped stimuli at longer durations. There is no established method for predicting loudness from these threshold differences, whereas the loudness models based on the persistence of excitation predict the loudness-matching results across durations successfully.

While models based on the persistence of excitation provide successful prediction differences in loudness between ramped and damped sounds, the same cannot be said for differences in subjective duration. The modeling results for subjective duration obtained using persistence of excitation, as estimated from nonsimultaneous masking data, underestimated the perceived difference in the duration of these stimuli (see Table III). Prior studies of subjective duration for ramped and damped sounds have reported similar findings (DiGiovanni and Schlauch, 2007; Grassi and Darwrin, 2006; Schlauch *et al.*, 2001a, 2001b). DiGiovanni and Schlauch (2007) found that the disparity in subjective duration judgments was largely due to subjects ignoring the portion of a damped signal that was perceived as echoic. The subjects in their study produced less disparate results for sounds with ramped and damped envelopes when specifically instructed to include all portions of the sound when making their judgments. This finding fits the decay suppression (i.e., perceptual constancy) hypothesis proposed by Stecker and Hafter (2000). Accordingly, listeners typically tend to ignore a portion of the decay of sounds with damped envelopes when judging duration. However, when listeners are instructed to include all aspects of ramped and damped sounds in their judgments of duration, the ramp-damp difference is smaller but a difference still remains (DiGiovanni and Schlauch, 2007). This difference is consistent with the predictions of persistence based on nonsimultaneous masking.

A significant context effect is observed in perceptual studies of sounds with ramped and damped envelopes, including the present study. The presence of a ramped sound prior to a damped sound produces a greater difference in subjective duration than when the order is reversed. However, the opposite is true for loudness judgments. An effect of stimulus context on loudness judgments was also reported and discussed by Stecker and Hafter (2000). They found, similar to the results reported here (see Fig. 4), that loudness judgments between ramped and damped noises were more disparate when a damped sound preceded a ramped sound than vice versa. Can perceptual constancy, as described by Stecker and Hafter (2000), help explain these seeming disparate results for judgments of duration and loudness based on biasing of responses due to stimulus order? Consider the experimental condition from the present study in which the stimulus with a ramped envelope was presented first. The ramped signal ended at a relatively high intensity, yet no possible interpretation of a reverberant (e.g., echoic) environment was allowed by the acoustic information available to that point. When the subsequent damped signal was presented for comparison, two likely acoustic-based environmental interpretations were plausible (1) the environment had not changed, the setting was nonreverberant, and a more "veridical" (i.e., with little effect of decay suppression) version of the second signal should be used to compare the two stimuli, or (2) the listener had entered a new reverberant setting between the sounding of the signals and the second stimulus should be processed in the "constancy" mode in order to account for the influence of "echoic" information upon perception. Estimates of loudness and duration for the ramped and damped sounds using environmental interpretation 1 would be less different from each other as the effect of decay suppression upon the damped stimulus would be limited. This situation fits the trends evident in the loudness-matching data but not in the duration-matching data. Using environmental interpretation 2, the loudness and duration estimates would be more disparate, from those obtained using interpretation 1, as a portion of the persistence of excitation of the damped stimulus would be ignored. This second interpretation follows the trend seen in the duration-matching

data but not that for loudness matching. Thus, the explanation for this context effect remains a mystery.

In summary, the temporal-masking patterns measured in this study do not provide unequivocal support for the persistence, adaptation, or perceptual constancy approaches for modeling perceptual differences between ramped and damped sounds. That stated, the loudness models based on the persistence approach were able to yield quantitative predictions that were consistent with the average differences in the loudness data for each of the durations used. The success of the persistence approach for modeling loudness has been reported for a variety of stimuli (Chalupper and Fastl, 2002; Glasberg and Moore, 2002). The failure of the persistence approach to account for subjective duration as well as the divergent effects of context on loudness and duration suggest that different underlying mechanisms control these two facets of auditory perception.

ACKNOWLEDGMENTS

This work was supported in part by NIH/NIDCD Grant No. R29 DC01542. We thank Edward Carney for his assistance in stimulus generation and Brian Glasberg and Brian Moore as well as Hugo Fastl for running our ramped and damped stimuli through their models. We also thank the associate editor and the two reviewers for their helpful comments.

[1]A diffuse field filter was used to model the response for our stimuli, and although our behavioral data were collected using insert earphones, any differences between the output of the models and the behavioral data are expected to be trivial. Alternate filters that simulate the transfer functions for a variety of listening environments can be implemented in the loudness models of Glasberg and Moore (2002) and Chalupper and Fastl (2002).

Bacon, S. P., and Takahashi, G. A. (**1992**). "Overshoot in normal-hearing and hearing-impaired subjects," J. Acoust. Soc. Am. **91**, 2865–2871.
Chalupper, J., and Fastl, H. (**2002**). "Dynamic loudness model (DLM) for normal and hearing-impaired listeners," Acust. Acta Acust. **88**, 378–386.
DiGiovanni, J. J., and Schlauch, R. S. (**2007**). "Mechanisms responsible for differences in perceived duration for rising-intensity and falling-intensity sounds," Ecological Psychol. **19**, 239–264.
Dolan, T. G., and Small, A. M. (**1984**). "Frequency effects in backward masking," J. Acoust. Soc. Am. **75**, 932–936.
Fastl, H. (**1976**). "Temporal masking effects: I. Broadband noise masker," Acustica **35**, 287–302.
Fastl, H. (**1976/1977**). "Temporal masking effects: II. Critical band noise masker," Acustica **36**, 317–330.
Fastl, H. (**1977**). "Subjective duration and temporal masking patterns of broadband noise impulses," J. Acoust. Soc. Am. **61**, 162–168.
Fastl, H. (**1979**). "Temporal masking effects: III. Pure tone masker," Acustica **43**, 282–294.
Fastl, H. (**1984**). "Folgedrosselung von sinustönen durch breitbandraushen: Messergebnisse und modellvorstellungen (Temporal partial masking of pure tones by broad-band noise)," Acustica **54**, 145–153.
Fastl, H., Büeler, R., and Fruhmann, M. (**2002**). "Different implementations of a model for subjective duration," *Fortschritte der Akustik, DAGA 2002* (Dt. Gessel. für Akustik e. V., Oldenburg), pp. 470 and 471.
Fastl, H., and Zwicker, E. (**2007**). "Subjective duration," *Psychoacoustics: Facts and Models*, 3rd ed. (Springer-Verlag, Berlin), pp. 265–269.
Gabriel, B., Kollmeier, B., and Mellert, V. (**1997**). "Influence of individual listener, measurement room, and choice of test-tone levels on the shape of equal-loudness level contours," Acust. Acta Acust. **83**, 670–683.
Glasberg, B. R., and Moore, B. C. J. (**2002**). "A model of loudness applicable to time-varying sounds," J. Audio Eng. Soc. **50**, 331–341.
Grassi, M., and Darwin, C. J. (**2006**). "The subjective duration of ramped and damped sounds," Percept. Psychophys. **68**, 1382–1392.
Hartley, D. E. H., Wright, B. A., Hogan, S. C., and Moore, D. R. (**2000**). "Age-related improvements in auditory backward and simultaneous masking in 6- to 10-year-old children," J. Speech Lang. Hear. Res. **43**, 1402–1415.
Irino, T., and Patterson, R. D. (**1996**). "Temporal asymmetry in the auditory system," J. Acoust. Soc. Am. **99**, 2316–2331.
Kidd, G., and Feth, L. L. (**1982**). "Effects of masker duration in pure-tone forward masking," J. Acoust. Soc. Am. **72**, 1384–1386.
Levitt, H. (**1971**). "Transformed up-down methods in psychoacoustics," J. Acoust. Soc. Am. **49**, 467–477.
Maier, J. X., Neuhoff, J. G., Logothetis, N. K., and Ghazanfar, A. A. (**2004**). "Multisensory integration of looming signals by Rhesus monkeys," Neuron **43**, 177–181.
Miller, G. A. (**1948**). "The perception of short bursts of noise," J. Acoust. Soc. Am. **20**, 160–170.
Moore, B. C. J., and Glasberg, B. R. (**1996**). "A revision of Zwicker's loudness model," Acust. Acta Acust. **82**, 335–345.
Moore, B. C. J., Glasberg, B. R., and Baer, T. (**1997**). "A model for the prediction of thresholds, loudness, and partial loudness," J. Audio Eng. Soc. **45**, 224–240.
Neuhoff, J. G. (**1998**). "Perceptual bias for rising tones," Nature (London) **395**, 123–124.
Neuhoff, J. G. (**2001**). "An adaptive bias in the perception of looming auditory motion," Nature (London) **398**, 673–674.
Nuttall, A. H. (**1981**). "Some windows with very good sidelobe behavior," IEEE Trans. Acoust., Speech, Signal Process. **29**, 84–91.
Patterson, R. D. (**1994a**). "The sound of a sinusoid: Spectral models," J. Acoust. Soc. Am. **96**, 1409–1418.
Patterson, R. D. (**1994b**). "The sound of a sinusoid: Time-interval models," J. Acoust. Soc. Am. **96**, 1419–1428.
Plomp, R. (**1964**). "Rate of decay of auditory sensation," J. Acoust. Soc. Am. **36**, 277–282.
Ryan, T. A. (**1959**). "Comments on orthogonal components," Psychol. Bull. **56**, 394–396.
Samoilova, I. K. (**1959**). "Masking of short tone signals as a function of the time interval between masked and masking sounds," Biofizika **4**, 550–558 [Biophysics (Engl. Transl.) **4**, 44–52].
Schlauch, R. S., DiGiovanni, J. J., Olson, K. L., and Donlin, E. E. (**2001a**). "Do listeners include the echo portion of a damped sound when judging its duration?," J. Acoust. Soc. Am. **109**, 2465.
Schlauch, R. S., Ries, D. T., and DiGiovanni, J. J. (**2001b**). "Duration discrimination and subjective duration for ramped and damped stimuli," J. Acoust. Soc. Am. **109**, 2880–2887.
Schlauch, R. S., Ries, D. T., DiGiovanni, J. J., Elliot, S., and Campbell, S. (**1998**). "Intensity discrimination of ramped and damped tones," Proceedings of the 16th International Congress on Acoustics and 135th Meeting of Acoustical Society of America Vol. **2**, pp. 885–886.
Stecker, G. C., and Hafter, E. R. (**2000**). "An effect of temporal asymmetry on loudness," J. Acoust. Soc. Am. **107**, 3358–3368.
Zwicker, E. (**1977**). "Procedure for calculating loudness of temporally variable sounds," J. Acoust. Soc. Am. **62**, 675–682.
Zwicker, E. (**1984**). "Dependance of post-masking on masker duration and its relation to temporal effects in loudness," J. Acoust. Soc. Am. **75**, 219–223.
Zwicker, E., and Scharf, B. (**1965**). "A model of loudness summation," Psychol. Rev. **72**, 3–26.
Zwislocki, J., Pirodda, E., and Rubin, H. (**1959**). "On some poststimulatory effects at the threshold of audibility," J. Acoust. Soc. Am. **31**, 9–14.

Level dominance in sound source identification

Robert A. Lutfi, Ching-Ju Liu, and Christophe Stoelinga
Auditory Behavioral Research Lab, Department of Communicative Disorders, University of Wisconsin, Madison, Wisconsin 53706

(Received 7 February 2008; revised 10 September 2008; accepted 11 September 2008)

Impact sounds were synthesized according to standard textbook equations given for the motion of simply supported, metal plates. In a two-interval, forced-choice procedure, highly practiced listeners identified from these sounds a predefined class of target plates based on their particular material and geometric properties. The effects of two factors on identification were examined: the relative level of partials comprising the sounds and the relative amount of information (given as the difference in d') each partial provided for identification. In different conditions one factor was fixed while the other either increased or decreased with frequency. The effect on listener identification in each case was determined from a logistic discriminant analysis of trial-by-trial responses, yielding a vector of listener decision weights on the frequency and decay of individual partials. The weights increased proportionally with relative level, but were largely uninfluenced by relative information content—a result exactly opposite to that expected from a maximum-likelihood observer. The dominant effect of relative level was replicated for other sound sources (clamped bars and stretched membranes) and was not diminished by randomizing the relative level of partials across trials. The results are taken to underscore the importance of relative level in the identification of rudimentary sound sources.
© *2008 Acoustical Society of America.* [DOI: 10.1121/1.2998767]

PACS number(s): 43.66.Ba, 43.66.Fe [BCM] Pages: 3784–3792

I. INTRODUCTION

This study reports a new finding pertaining to the auditory identification of rudimentary sound sources. The results show that the partials governing listener judgments from trial to trial are not those conveying the most information regarding the source, as one might expect, but simply those having the highest relative level in the complex. Similar effects of level have been reported in past studies involving masking (Neff and Jesteadt, 1996) and judgments of pitch (Moore *et al.*, 1985). What makes the present results different, however, is that the highest level components continue to dominate the listener's judgments even when the listener has a compelling reason and presumed ability to ignore them. We use the term level dominance in this paper to describe this effect and to distinguish it from the other more general effects of relative level, alluded to above, which may or may not be related to the present results.

Level dominance effects of the type described here have not been widely reported in the literature. Berg (1990) may have provided the earliest account. Listeners in his study heard a sequence of seven 50-ms tones alternating in level between 30 and 85 dB SPL. The frequencies of the tones were sampled at random on each trial from one of two normal distributions differing in mean. The listener's task was to specify on each trial which of the two distributions the sequence was drawn from. Decision weights, indicating the reliance placed on the individual tones, were computed from response correlations with the trial-by-trial perturbations in frequency. In one condition the perturbation was made greater for the higher-level tones so that the higher-level tones conveyed less reliable information regarding the difference to be discriminated. Only two listeners participated in this condition, but the decision weights of both listeners indicated greater weight on the higher-level tones conveying the less reliable information. Berg found the results to be the same when the tones were separated by silent intervals of 50 and 200 ms. Later, Turner and Berg (2007) replicated these results with tones separated by as much as 500-ms silent intervals and differing in level by only 20 dB. This effectively ruled out the possibility that the effect was due to masking of the lower-level tones by the higher-level tones (cf. Jesteadt *et al.*, 1982; Massaro, 1975).

Lutfi and Jesteadt (2006) conducted an extensive follow-up to Berg's study. Decision weights were computed for sequences of tones alternating in level between 40 and 80 dB SPL with a level perturbation of 3 dB. The task was to detect an increment in level applied to all tones in the sequence, rather than a change in frequency as in the Berg study. The decision weights of four highly practiced listeners indicated near-exclusive reliance on the higher-level tones in the sequence, even when the higher-level tones contained a smaller increment in level (3 vs 6 dB). The same outcome was obtained when the tones were replaced by bursts of broadband Gaussian noise, effectively ruling out explanations based on spread of excitation at high levels. Reversing the order in which high and low level tones occurred in the sequence had no effect, and the level dominance only began to diminish when the tones differed in level by less than 10 dB. The only manipulation, in fact, to have a significant influence on the level-dominance effect was to alternate the low-level tones with louder bursts of Gaussian noise; in this case the effect was entirely reversed. Lutfi and Jesteadt suggest from their results that level dominance may reflect a tendency for attention to be directed to the higher-salience elements of a stimulus perceived as a single auditory object. The interpretation, in fact, is consistent with the predictions

 © 2008 Acoustical Society of America

of current phenomenological and computational models for the discrimination of unfamiliar multitone patterns (cf. Kidd and Watson, 1992; Lutfi, 1993; Oh and Lutfi, 1998).

Given the seemingly robust nature of the level-dominance effect, we considered whether the effect would also impact on the identification of rudimentary sound sources (struck bars, plates, and membranes). The prediction is that it would if the only requirement is that the partials be perceived as forming a single auditory object. Although one can often "hear out" individual partials of sounds emitted by a rudimentary source, the partials are generally perceived as belonging to a single auditory object by virtue of the fact that they are emitted from a single source. The partials have simultaneous onsets, they decay together systematically, and they are related to one another by frequency ratios likely to be familiar to the listener—all factors that would be expected to promote the perception of a single auditory object (Bregman, 1990), and thus a level-dominance effect. Other considerations, however, lead to a different expected outcome. In particular, the random tone sequences used in the past studies lack the familiarity and lawful structure of naturally occurring sounds. Familiarity and structure are factors known to have a significant impact on a listener's ability to discriminate random tone patterns (Watson and Kelly, 1981). They are believed to aid the listener by allowing the listener to "focus in" on differences that are relevant to the discrimination. If the interpretation is correct, then the expectation is that level dominance will be reduced or absent for sounds produced by naturally occurring, familiar sound sources.

In light of these considerations, the present study was undertaken to address the following questions: (1) Is the level-dominance effect peculiar to the discrimination of arbitrary tone patterns, or is it also obtained in a source identification task wherein the elements of the stimulus are similarly perceived as belonging to a single auditory object? (2) Assuming the latter outcome, is it possible to rule out trivial explanations in terms of mutual masking among stimulus elements or to listener inexperience with the task? and (3) If such alternative explanations can be ruled out, what impact might the level-dominance effect be expected have on sound source identification performance?

II. GENERAL METHODS

A. Stimuli

The stimuli were approximations to the airborne sounds resulting from the impact of a hard mallet on a circular bar, rigidly clamped at one end, a simply supported circular plate, or a stretched circular membrane (respectively, a "tuning-fork," "gong," or "tympani drumhead"). They were synthesized according to theoretical equations of motion from standard acoustics texts (Fletcher and Rossing, 1991; Morse and Ingard, 1968). The use of synthetic sounds was dictated by the need to introduce perturbations in stimuli that would allow listener decision weights to be estimated and compared to those of a maximum-likelihood detector, as will be described shortly. Specific details of the synthesis are provided by Lutfi and Oh (1997) and a psychophysical evaluation is provided by Lutfi *et al.* (2005) and McAdams *et al.* (2004). The resulting sounds were a sum of exponentially decaying sinusoids whose individual frequencies, ν, amplitudes, A, and decay moduli, τ, were determined by the specific material and geometric properties of the source, and the manner in which the source was suspended and struck. For the bar the ratios of modal frequencies $k=\nu_n/\nu_1$ were 1.00, 6.26, 17.54; for the plate they were 1.00, 2.80, 5.15, 5.98, 9.75, 14.09, and for the membrane they were 1.00, 1.594, 2.136, 2.296, 2.653, 2.918. In different conditions, the amplitudes and the decay moduli of modes were equated across frequency, varied in direct or inverse proportion to modal frequency or varied pseudorandomly. The different cases are described as they are considered in Sec. III. Note that such variation in the amplitude and decay would be associated with differences in the way the source is struck or the way that it is damped by the manner in which it is held (cf. Morse and Ingard, 1968; Hall, 1991; Lutfi, 2008). For example, a bar rigidly clamped at one end (tuning fork) will produce a sound having a high-pass characteristic if struck near the clamped end, and a low-pass characteristic if struck near the free end; a plate struck squarely in the center will tend predominantly to excite modes 1, 4, and 9. Generally speaking, each natural mode of vibration will be excited (or damped) to the degree that the region of contact participates in that mode of vibration.

For each presentation of a sound a random perturbation was also imposed on the frequency and decay of each partial. The perturbations were imposed independently for frequency and decay, and independently for each partial. Again, such perturbations would be expected to occur naturally since real bars, plates, and membrane tend to have small geometric and material imperfections that would result in such perturbations. To roughly equate their perceptual salience, the perturbations were normally distributed in $\log \nu$ and $\log \tau$ units with standard deviation in every case equal to 5 just-noticeable differences (jnd's); one jnd corresponding to a value of $\log(1.002)$ for frequency and $\log(1.1)$ for decay (cf. Wier *et al.*, 1977; Schlauch *et al.*, 2001).

Sounds were played at a 44 100-Hz sampling rate with 16-bit resolution and were terminated after 1 s by a 5-ms cosine-squared offset ramp. They were delivered to the right ear over headphones (Beyerdynamic DT 990) to listeners seated individually in a double-walled, IAC sound-attenuating chamber. The levels of partials were computed numerically before analog conversion. The transfer function of the Beyerdynamic headphone was estimated using a binaural loudness balancing procedure. For octave frequencies from 250–8000 Hz listeners adjusted the level of pure tone delivered to the headphone so that it would produce a centered intracranial image when the same tone was played over a TDH-50 earphone with a known transfer function (previously measured through a 6-cc coupler). Using this procedure the average total sound power at the eardrum was estimated to be 65 dB SPL.

B. Procedure

For each sound source (bar, plate, and membrane) a target and nontarget was identified, the target being nominally

smaller than the nontarget and made of a more dense material (cf. Morse and Ingard, 1968, pp. 175–191). Note that these are nominal differences, as other combinations of physical parameters could have been chosen to produce the same acoustic differences between target and nontarget. For the bar the partials of the target were 5 jnd's higher in frequency and 5 jnd's longer in decay; for the plate and membrane the differences were 4 jnd's in each case. The magnitude of the differences was selected to achieve performance levels in the range of 70–90% correct and the direction of the differences was chosen to reflect the geometric and material differences between target and nontarget plates. For the nontarget the frequency of the first partial was $\nu_1 = 250$, 250, and 500 Hz, respectively, for the bar, plate, and membrane. The decay modulus for the first partial was, respectively, $\tau_1 = 2.0$, 0.4, and 0.2 s. On each trial the listener heard an exemplar of the target and nontarget separated by 400 ms. The listener was instructed to select the sound corresponding to the target, which was the first or second sound with equal probability. Listeners were instructed beforehand as to the acoustic differences between target and nontarget and were given correct feedback after each trial. The data were collected in 1-h sessions, including breaks, conducted on different days. A total of at least 400 experimental trials was run for each listener for each condition.

Decision weights for individual listeners were computed as a vector of regression weights, b, using the generalized linear model,

$$\text{logit}[P(R=2)] = b_0 + \sum_{i=1}^{n} b_{\nu_i}(\log \nu_{i2} - \log \nu_{i1}) + b_{\tau_i}(\log \tau_{i2} - \log \tau_{i1}) + e, \quad (1)$$

where $\text{logit}[P(R=2)]$ is the log-likelihood of a second interval response, $i1$ and $i2$ index the parameters of the ith partial in the first and second interval, and e is a residual term (cf. Berg, 1990; Anderson, 1971). The data were analyzed separately for the target in the first and second interval so as to obtain two independent estimates of b for each listener. The estimates and their associated error were computed using the GLMFIT routine of the software application MATLAB v.6.5 using a logit link function. They were then compared to those of a theoretical decision maker that maximizes the likelihood of a correct response on each trial. The performance of the maximum-likelihood (ML) decision maker was analyzed from the equations of motion, taking into consideration the actual perturbations in acoustic parameters that occurred from trial to trial.

C. Subjects

Nine normal-hearing female adults (ANSI, 1989), ages 21–30 years, were paid at an hourly rate for their participation. Not all listeners participated in all experiments. The listeners were students in the Department of Communicative Disorders at the University of Wisconsin-Madison. All had extensive previous experience with the two-interval, forced-choice task and all received at least 400 trials of practice prior to data collection for each condition in which they participated.

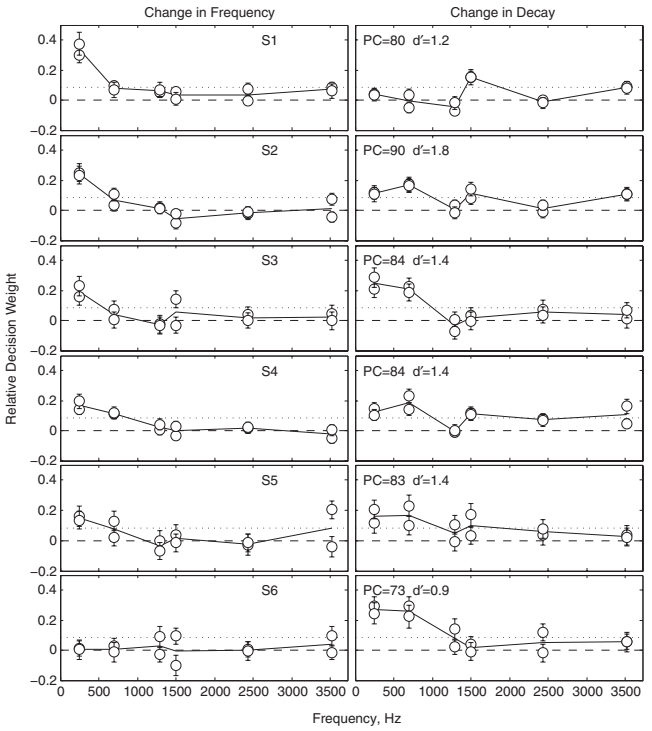


FIG. 1. Obtained decision weights for two-interval, forced-choice identification of target plates are given for each listener (panel rows) for the low-pass condition of experiment 1. Error bars give the standard error of estimate in each case. Dotted lines give the ML weights. The two panel columns give the decision weights separately for the change in frequency and change in decay of each partial. Performance levels (PC and d') are also indicated for each listener.

III. RESULTS

A. Experiment 1: Effect of relative level vs relative information content

Figure 1 gives as open symbols the obtained estimates of b_{ν_i} and b_{τ_i} (panel columns) for each of six listeners (panel rows) for the condition in which the resonant source is the plate, and in which the amplitude and decay moduli of the partials decrease proportionally with frequency (low-pass condition).[1] The two estimates shown in each case were computed separately from trials in which the target occurred in the first and second intervals of the forced-choice trial. As is common practice, the values have been normalized so that their unsigned magnitudes sum to unity (cf. Berg, 1990). This is done to allow comparisons of the pattern of weights across listeners free from differences in the effect of overall performance on the raw regression weights. Error bars on estimates have been scaled accordingly to permit identification of those values significantly greater than zero. Overall percent correct identification performance and corresponding d' for each listener are also given. The differences in performance across listeners are small.

In many cases the listener decision weights deviate significantly from the ML weights, given by the dotted lines. Consider that there are 12 independent sources of information that can potentially inform decisions in this task, the

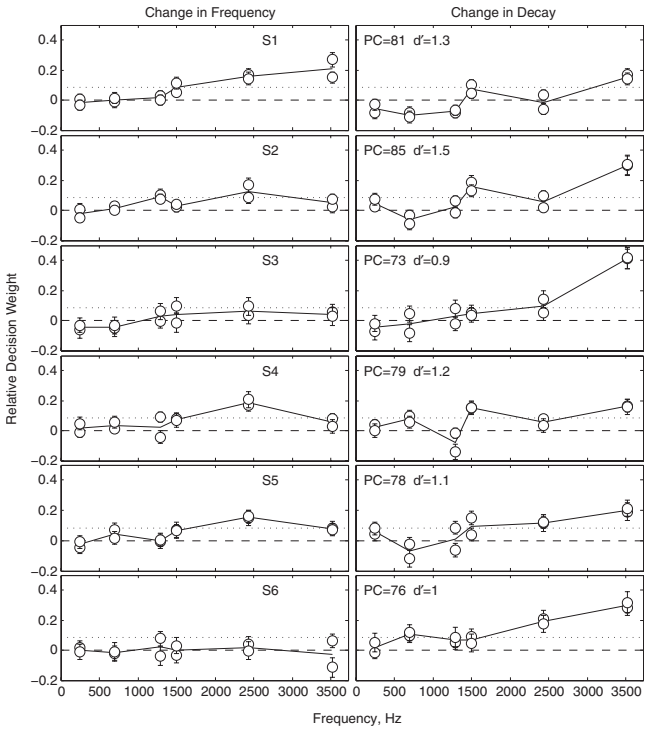


FIG. 2. Same as Fig. 1, except that the data are for the high-pass condition of experiment 1.

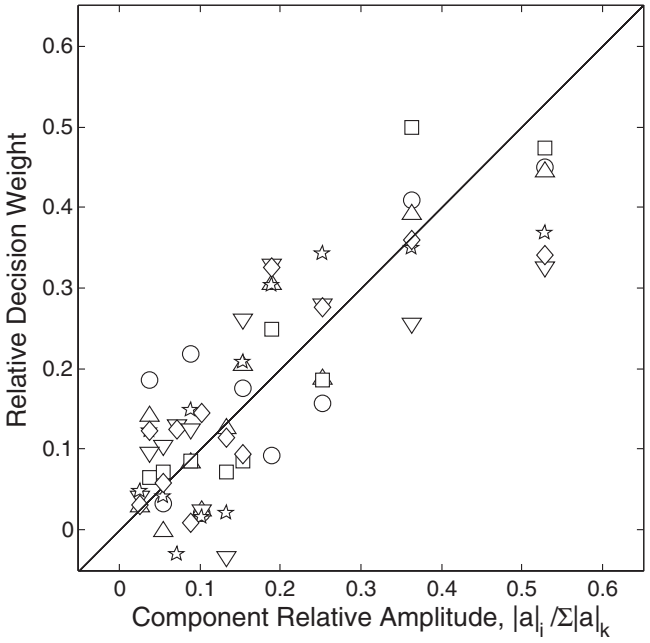


FIG. 3. Scatterplot of the relation between the relative weights of listeners and the relative amplitude of partials for two-interval, forced-choice identification of target plates. Weights on the change in frequency and decay have been averaged for each listener to obtain a single weight for each partial (see the text for details). Symbols denote data from different listeners (S1 =circle, S2=upright triangle, S3=square, S4=inverted triangle, S5=star, S6=diamond).

values of two acoustic parameters for each of six partials. The short-dashed line shows ML decisions to be influenced equally by each source, whereas the estimates of listener weights show listener decisions to be dominated by only 2–3 sources. Note, here we define a dominant weight to be a mean value of at least two standard errors above the ML weight. There are clear differences among listeners regarding which of the 2–3 sources dominates judgments (compare for example listeners S1 and S6); these differences have been considered at length in a separate publication and have little bearing on the present analysis (see Lutfi and Liu, 2007). For present purposes, it is only important to note that, with only one exception, the 2–3 sources given dominant weight are those associated with the two highest-level partials in the complex, partials one and two. The exception is for S1, where there is a dominant weight on the decay of the fourth partial, which has an intermediate level. Figure 2 shows the listener decision weights for the high-pass condition (amplitude and decay modulus increasing proportionally with frequency). Here again we see a tendency, with few exceptions, for the judgments to be dominated by the two highest-level partials, which are now partials five and six. This shows that the relative level of partials, not their frequency, is the factor dictating which partials receive the greatest decision weight.

A better sense of the relation between the relative level of partials and the listeners' decision weights is obtained from Fig. 3. The figure is a scatterplot of one variable against the other, where the separate decision weights on frequency and decay have been averaged and rescaled to obtain a single overall weight for each partial. Also, to permit direct comparisons between the two variables, the relative amplitudes, like the decision weights, have been scaled to sum to unity.[2] The data plotted in this way roughly fall along the diagonal, though the strength of the relation is stronger for some listeners than others (symbol type). Across all listeners the Pearson product-moment correlation is $r=0.81$; hence, 66% of the variance in the listeners' decision weights is accounted for by their linear relation to the relative amplitude of the partials. In comparison, no correlation with amplitude is expected for the decision weights of the ML observer, which in this plot would fall on a horizontal line.

The data in Figs. 1–3 clearly show a strong relation between the relative level of partials and the listeners' decision weights. We would like, however, a means to evaluate the relative importance of this effect. We achieved this in a follow-up experiment by comparing it to a factor that, for the maximum-likelihood observer, would be expected to have an even stronger influence on the decision weights, namely the relative amount of information for identification provided by the different partials. The listeners' goal, as instructed, was to maximize the number of correct identifications. If listeners are only capable of giving a significant nonzero weight to 1–3 information-bearing partials at any one time, then we should expect these 1–3 partials to be those conveying the most diagnostic information regarding the source (i.e., having the highest d'). We repeated the experimental task with the same listeners, this time equating the relative amplitude and decay of partials ($\tau=0.2$ s) and increasing or decreasing with partial number, i, the number of jnd's distinguishing target and nontarget. When increasing with partial number, the number of jnd's for both frequency and decay equaled i; when decreasing, the number of jnd's equaled $6/i$.

Figures 4 and 5 show, respectively, the estimates of decision weights obtained for jnd's increasing and decreasing

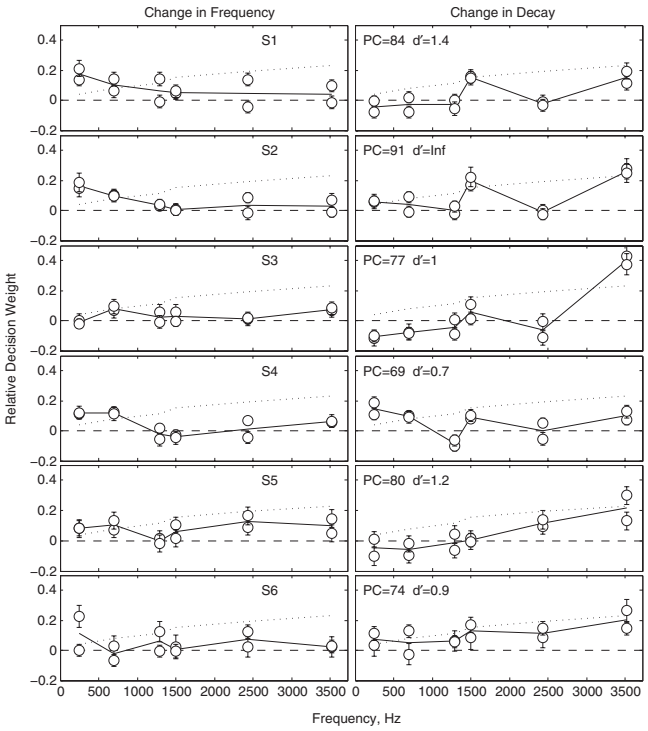


FIG. 4. Same as Fig. 1, except that the data are for the variable jnd condition of experiment 1, jnd increasing with partial number.

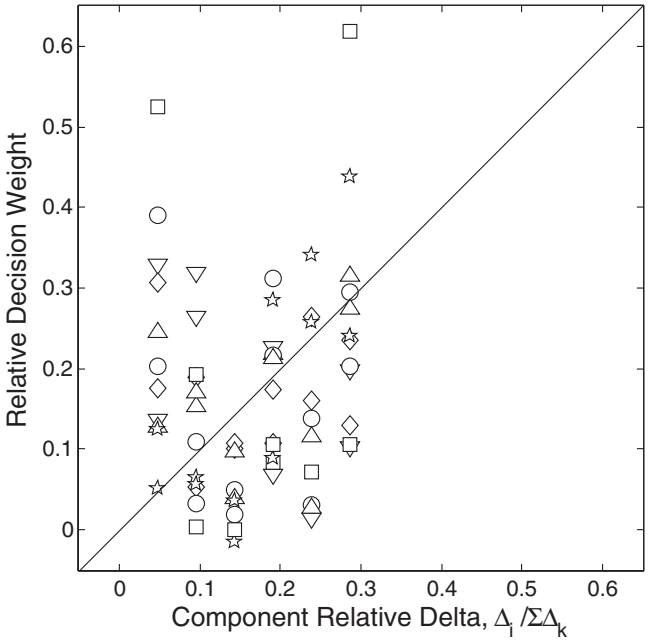


FIG. 6. Scatterplot of the relation between the relative weights of listeners and the relative information content of partials (relative delta). Weights on the change in frequency and decay have been averaged for each listener to obtain a single weight for each partial (see the text for details). Symbols denote data from different listeners as in Fig. 3.

with partial number. The data are plotted as in Figs. 1 and 2 with the short-dashed line in each case giving the decision weights of the maximum-likelihood observer. We see in Fig. 4, for all six listeners, a dominant weight on the decay of the sixth partial which, consistent with expectations, is the highest information-bearing partial in the complex. Complicating the picture, however, is the fact that a dominant weight continues to be obtained for at least three of the listeners (S1, S2, and S4) on the frequency of the first partial, which is the lowest information-bearing partial. Moreover, in Fig. 5 we see for three listeners (S2, S5, and S6) the same dominant weight on the decay of the sixth partial, when this partial is the lowest information-bearing partial. A likely explanation of these results is that they reflect to some extent the difference in the relative level of partials across the two experiments. Note that, even though the levels of partials were equated in the present experiment, the sixth partial had a higher relative level than for the low-pass condition of Fig. 1, where it was the lowest level partial. The sixth partial in the present experiment may have thus received greater weight than in the previous low-pass condition for this reason.

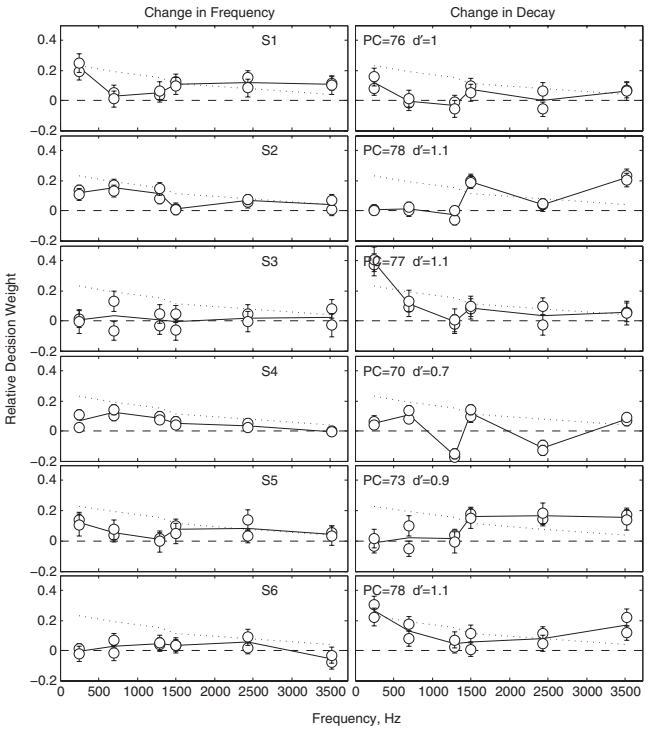


FIG. 5. Same as Fig. 1, except that the data are for the variable jnd condition of experiment 1, jnd decreasing with partial number.

The data of Figs. 4 and 5 indicate a much weaker relation of listener decision weights to the relative information content of partials than to relative level. This is confirmed in Fig. 6, where the decision weights have been averaged as in Fig. 3 and plotted against relative information scaled to sum to unity. Across all listeners the Pearson product-moment correlation between the two variables is $r=0.12$ Relative information thus accounts for only 1% of the variance in the listeners' decision weights, compared to 66% of the variance accounted for by relative level for the same highly practiced listeners. This result reinforces the importance of the level-dominance effect. It shows that a variable clearly relevant to identification actually has less influence on listener decision weights than one, which provides absolutely no information for identification.

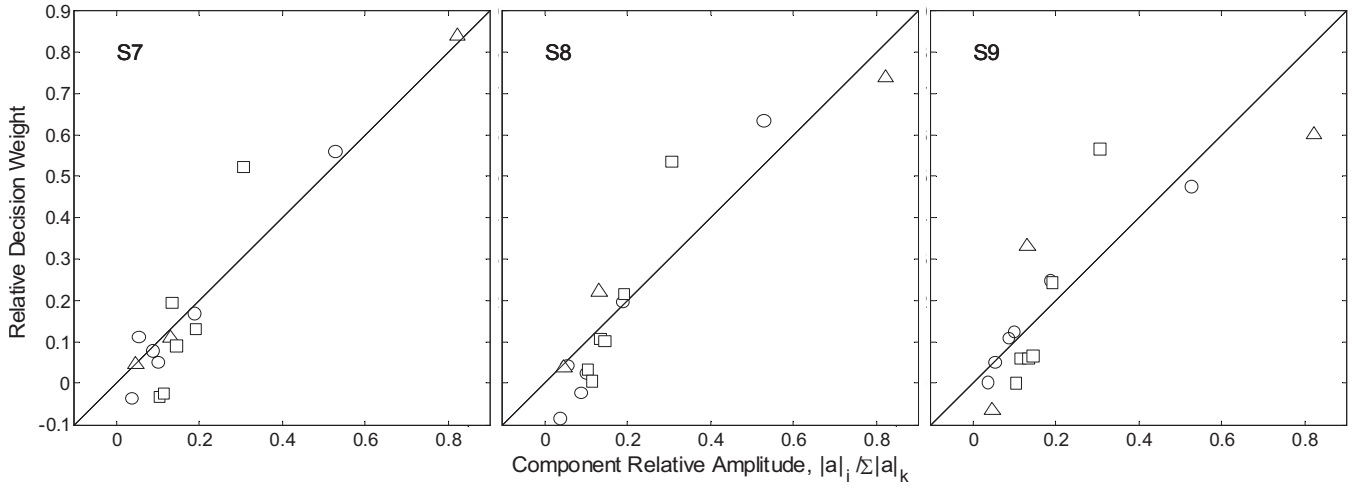


FIG. 7. Scatterplot of the relation between the relative weights of listeners and the relative amplitude of partials for two-interval, forced-choice identification of target plates (circles), membranes (squares), and bars (triangles) for the random-level condition of experiment 2.

B. Experiment 2: Effect of partial number and resonant source

The foregoing results, while intriguing, do potentially admit to certain trivial interpretations given the manner in which they were obtained. One possibility is that the results simply reflect mutual masking among partials. That is, greater weight would be expected on higher-level partials if, by virtue of their higher level, these partials to some degree mask or make inaudible lower-level partials in the complex. Masking, in fact, provides a simple account of why partials one and six, the least information-bearing partials in Figs. 4 and 5, should receive a dominant weight for some listeners. Being on the spectral edges of the complex, these partials are expected to be subject to less masking and so more easily "heard out" (cf. Moore and Ohgushi, 1993).

We evaluated the effect of masking by using two additional sound sources, one for which masking should be much less of a factor than for the plate, and one for which it should be much more of a factor. The two sources were the struck bar and membrane described in Sec. I A. There should be no masking of consequence among partials of the bar, as there are only three partials extending over a frequency range of 250–4385 Hz. There should be much more masking for the membrane than the plate since the six partials of the membrane extend over a much smaller frequency range, 500–1459 Hz for the membrane, 250–3523 Hz for the plate. If mutual masking among partials was responsible for the level-dominance effect obtained earlier, then we should expect the effect to be absent in the case of the bar and even more pronounced in the case of the membrane.

Another factor that might have contributed to the level-dominance effect was the practice of providing information for identification in the differences in decay. Decay is a parameter that determines the relative energy of partials. Thus, it is possible that, by making decay relevant to the task, we may have inadvertently caused the relative level of partials to have a more significant effect on listener decision weights than they otherwise would have had if decay was irrelevant for identification.[3] To test this possibility, we changed the task so that the only information for identification was the difference in the frequencies of partials (5 jnd's in frequency for each partial for the bar, 4 jnd's for the membrane and plate). This, parenthetically, provides a more sensitive measure of level dominance by eliminating the need to average weights, as in Figs. 3 and 6.

Finally, we incorporated a change to address a peculiar feature of the previous experimental design. In the previous experiments, partials 1 and 6 had special status in determining level dominance in that one or the other was always the highest-level partial in the complex. We wished to determine whether level dominance would be of the same magnitude when each partial was equally likely to be the highest-level partial in the complex. This was done by using the same levels as in the previous experiments, but shuffling the levels of partials (and corresponding decay) at random from trial to trial. For example, previously for the bar the levels of partials 1–3 were, respectively, 65, 49, and 41 dB SPL. In the present experiment they could be, respectively, 49, 65, 41 dB SPL, 41, 49, 65 dB SPL, or any other combination of these levels. Each listener received at least 400 trials of practice in the task before data collection. Average performance levels across listeners and conditions ranged from 68–73% correct (compared to the near-perfect performance of the ML observer).

Figure 7 shows the relation between the obtained decision weights and the relative level of partials for three new listeners (panels). Data for the different sound sources are indicated by different symbol types (bar=triangles, membrane=squares, plate=circles). We conclude that masking is not a significant factor in these experiments as there are not the predicted differences in the relation between the decision weights and relative level across the different sound sources. The weights for the membrane do appear to increase at a slightly more rapid rate with relative level, as predicted by masking, but the effect, if real, is very small. Moreover, the weights for the bar, where no masking is expected, show the same strong relation to relative level as the weights for the plate. We also conclude that having information in decay did not previously bias the results as there is no significant reduction in the strength of the relation between the decision

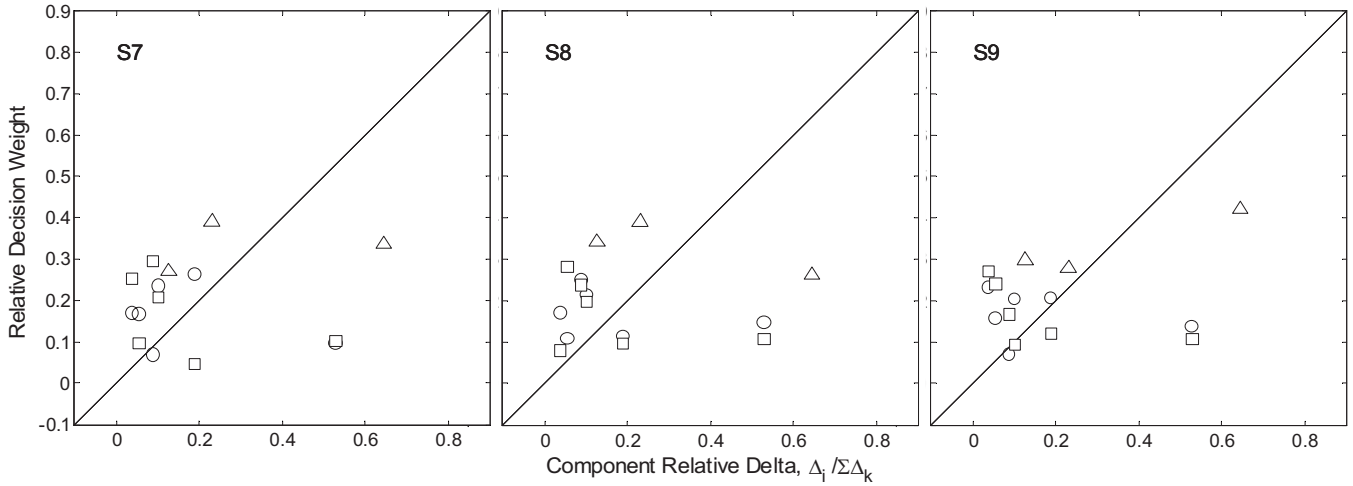


FIG. 8. Scatterplot of the relation between the relative weights of listeners and the relative information content (delta) of partials for two-interval, forced-choice identification of target plates (circles), membranes (squares), and bars (triangles) for the random-delta condition of experiment 2.

weights and relative level from experiment 1. Across all listeners the Pearson product-moment correlation is $r=0.90$, compared to 0.81 overall for the data in Fig. 3. The weaker correlation for the data of Fig. 3 likely reflects the effect of averaging over the weights for the change in decay and frequency for each partial, where in many cases only one of these weights was dominant. Finally, the fact that the strength of the relation is greater in this condition indicates that level dominance is not peculiar to partials one and six, but occurs for all partials in the complex.

Figure 8 shows, for comparison to Fig. 7, the effect of the relative information content of partials. In this condition, the relative levels of partials were fixed (−6 dB/oct) as in the low-pass condition of experiment 1; however, the difference in frequency for each partial varied at random from trial to trial (random-delta condition). Overall performance of the ML observer was equated to that of the random-level condition of Fig. 7 by selecting the component d's so that the square-root of the sum of their squares equaled that of the earlier condition. Comparison of the data across these two conditions shows as before a much weaker relation of listener decision weights to the information content of partials than to the relative level of partials. This result is further confirmed by Fig. 9. This figure shows the relation of listener decision weights to the relative level of partials within the random-delta condition. There is somewhat more scatter in these data, as to be expected given the variation in delta; however, the data still show a stronger relation to relative level than to delta. Thus, even when the listener is given the option within a condition to base judgments on higher information-bearing partials they tend instead to base judgments on the higher-level partials.

IV. DISCUSSION

In answer to the three questions posed in the Introduction, we can now say with reasonable confidence that: (1) the level-dominance effect is not a phenomenon peculiar to the discrimination of arbitrary tone patterns, but is also obtained in a rudimentary sound source identification task; (2) the effect is not due to mutual masking among partials or to listener inexperience with the task; and (3) the relative level

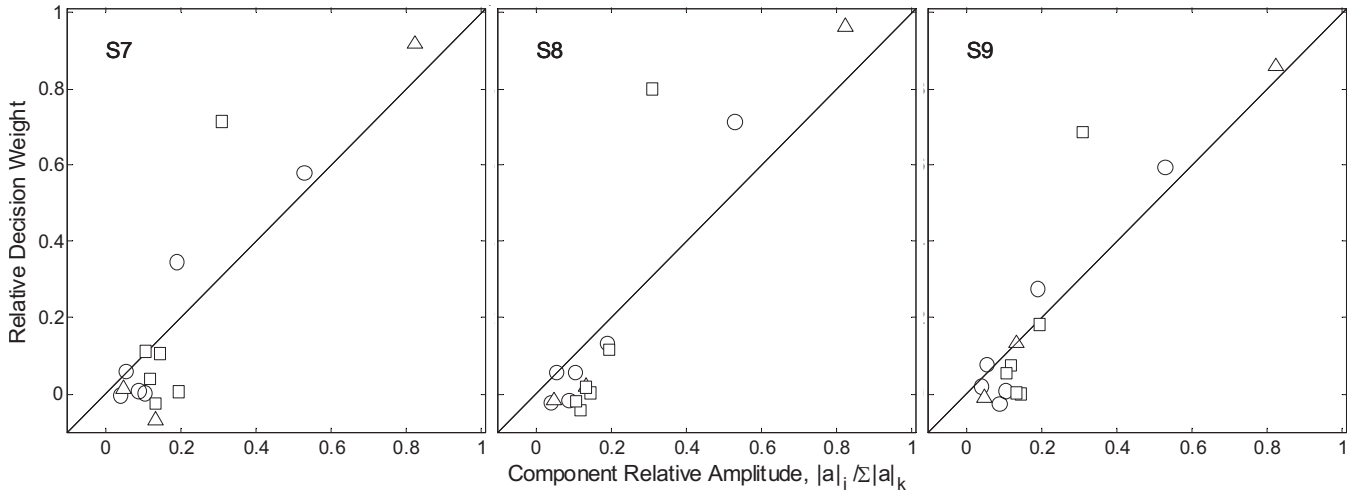


FIG. 9. Scatterplot of the relation between the relative weights of listeners and the relative level of partials for two-interval, forced-choice identification of target plates (circles), membranes (squares), and bars (triangles) for the random-delta condition of experiment 2.

of partials has a stronger influence on listeners' decision weights than does the relative information content of partials. Level dominance can thus be expected to have a detrimental impact on source identification performance when the highest-level partials in the sound are not the most informative regarding the source.

Given the last outcome, it seems difficult to justify from an ecological perspective why the auditory system would manifest a level-dominance effect. In everyday listening, the information in the highest-amplitude spectral components is not always the most diagnostic regarding the source, yet level dominance would suggest that this is the information which has the greatest influence on our perception. So, what possible advantage could level dominance have in everyday listening?

One can speculate by noting certain parallels to a better-known phenomenon in hearing; the precedence effect. The precedence effect refers to the observation that the perceived location of a sound source in a reverberant environment is dominated by the wavefront arriving first at the listener's ears (Wallach *et al.*, 1949; Blauert, 1971; Litovsky *et al.*, 1999). This makes sense from an ecological standpoint since the first-arriving wavefront provides the most veridical information about the location of the sound source. Studies have shown, however, that the precedence effect depends not only on the first-arriving wavefront being first, but also on its level relative to later arriving wavefronts. Yost (2007), for example, reports that the lagging click in a click pair will begin to be heard as having its own localized image as its level is made more nearly equal to that of the leading click in the pair (a type of level-dominance effect). Similar results have been reported by Hafter *et al.* (2000) using more naturalistic piano tones as stimuli. These results also make sense from an ecological perspective, as in the real world the first-arriving wavefront is nearly always the most intense; rare exceptions occur when an obstacle blocks the direct path of the sound. Still another way level dominance might serve to benefit the listener is as an alerting mechanism. The fire alarm is made loud so that it will be heard, but also to attract our attention. Also, the most intense sound in our environment is typically emitted from the closest source, which is the source most likely to require our immediate attention and action. Could level dominance have evolved to alert us to imminent sources? While it seems interesting to speculate, this idea is likely impossible to test.

Notwithstanding our failure to offer a simple explanation of the effect, level dominance does appear real. Recent studies reporting the effect for the discrimination of multitone sequences have, as in the present study, ruled out trivial explanations in terms of mutual masking among stimulus components or listener inexperience with the task (Berg, 1990; Turner and Berg, 2007; Lutfi and Jesteadt, 2006). Lutfi and Jesteadt, moreover, have ruled out an explanation in terms of greater sensitivity to changes in the frequency or level of tones resulting from spread of excitation at high levels (cf. Jesteadt *et al.*, 1977; Viemeister, 1972). They showed the level-dominance effect to be undiminished when the tones in the sequence are replaced by bursts of broadband Gaussian noise. Kidd and Watson (1992) also have reported what appears to be a related effect in which the detectability of a change in a single tone in a sequence is seen to improve as the tone occupies a greater proportion of the total duration of the sequence. The CoRE model, which has been successful in accounting for many results from multitone pattern discrimination studies, attributes both proportional-duration and level-dominance effects to a common mechanism involving the pooling of variance in patterns across frequency and time, with individual components contributing in proportion to their power (Lutfi, 1993; Oh and Lutfi, 1998). The pooling of variance is assumed to occur under conditions of high stimulus uncertainty in which the tone patterns vary widely from trial to trial with few statistical constraints. In a typical study, for example, the tone frequencies may vary at random over a range of 300–3000 Hz (Watson and Kelly, 1981; Neff and Dethlefs, 1995). The results of the present study suggest that this assumption might be relaxed somewhat. The equations of motion largely constrain the set of possible stimuli so the degree of variation is considerably less; by comparison to the above, just a few jnd's in frequency.

To date, research on the perception of sound sources has been largely driven by prominent theories regarding how we perceive and act in the real world (cf. Bregman, 1990; Gibson, 1966; Helmholtz, 1877). The present study is an exception in that it was inspired by what seemed a provocative result in the literature on the discrimination of arbitrary multitone patterns. This too was the motivation of a study of sound source identification by Lutfi and Liu (2007). These authors found that listeners differ greatly in the reliance they place on different acoustic features when performing basic sound source identification tasks. Individual differences have not been widely reported in the literature on sound source identification, largely because of the practice of averaging over listener data. They have, however, been well documented in research on the discrimination of multitone patterns (Neff and Dethlefs, 1995; Lutfi, 1990; Lutfi *et al.*, 2003; Watson and Kelly, 1981). In the multitone pattern studies the individual differences have been widely attributed to the unfamiliar and arbitrary nature of the stimuli used (Watson and Kelly, 1981; Lutfi, 1993). The results of Lutfi and Liu using naturalistic stimuli have since cast doubt on this idea. There currently exists a rich and growing literature on the discrimination of multitone patterns and, though the stimuli used in these studies are a far cry from real-world sounds, it would seem unwise to assume that the results have no bearing on the perception of real-world sounds. Future studies of sound source identification may indeed find this literature to be a useful resource.

ACKNOWLEDGMENT

This research was supported by a NIDCD grant R01 DC006875-03. The authors would like to thank Dr. Ervin Hafter, Dr. Brian Moore, and two anonymous reviewers for helpful comments on an earlier version of this manuscript.

[1]These data were previously published as a subset of the data from another study by the present authors, having to do with individual differences in

sound source identification (Lutfi and Lu, 2007). See Fig. 3 of that paper. They provided, in part, the impetus for the present study.

[2]Note that the multiplicative scaling of these variables does not affect the strength of their linear relation.

[3]Note that the conditions of this study are not adequate to distinguish the effects of energy, level, and decay. We use the term level dominance in the generic sense that it has been used in past studies.

Anderson, T. W. (**1971**). *An Introduction to Multivariate Statistical Analysis* (John Wiley and Sons, New York), pp. 205–217.

ANSI (**1996**) S3.6-1996. "American National Standards, Specification for Audiometers" (American National Standards Institute, New York).

Berg, B. G. (**1990**). "Observer efficiency and weights in a multiple observation task," J. Acoust. Soc. Am. **88**, 149–158.

Blauert, J. (**1971**). "Localization and the law of the first wavefront in the median plane," J. Acoust. Soc. Am. **50**, 466–470.

Bregman, A. S. (**1990**). *Auditory Scene Analysis* (M.I.T. Press, Cambridge, MA).

Fletcher, N. H., and Rossing, T. D. (**1991**). *The Physics of Musical Instruments* (Springer, New York).

Gibson, J. J. (**1966**). *The Senses Considered as Perceptual Systems* (Houghton-Mifflin, Boston).

Hafter, E. R., Valenzuela, M. N., Stecker, G. C., and Crum, P. A. C. (**2000**). "Informational dominance in the auditory scene," in *Physiological and Psychophysical Bases of Auditory Function: Proceedings of the 12th International Symposium on Hearing*, edited by A. J. M. Houtsma, A. Kohlrausch, V. F. Prijs, and R. Schoonhoven (Shaker, Maastricht, The Netherlands).

Hall, D. E. (**1991**). *Musical Acoustics* (Cole, Pacific Grove, CA), pp. 168–173.

Helmholtz, H. (**1877**). *On the Sensations of Tone as a Physiological Basis for the Theory of Music*, 4th ed., translated by A. J. Ellis (Dover, New York, **1954**).

Jesteadt, W., Bacon, S. P., and Lehman, J. R. (**1982**). "Forward masking as a function of frequency, masker level, and signal delay," J. Acoust. Soc. Am. **71**, 950–962.

Jesteadt, W., Wier, C. C., and Green, D. M. (**1977**). "Intensity discrimination as a function of frequency and sensation level," J. Acoust. Soc. Am. **61**, 169–177.

Kidd, G. R., and Watson, C. S. (**1992**). "The proportion-of-total-duration rule for the discrimination of auditory patterns," J. Acoust. Soc. Am. **92**, 3109–3118.

Litovsky, R. Y., Colburn, H. S., Yost, W. A., and Guzman, S. J. (**1999**). "The precedence effect," J. Acoust. Soc. Am. **106**, 1633–1654.

Lutfi, R. A. (**1990**). "Informational processing of complex sound. II. Cross-dimensional analysis," J. Acoust. Soc. Am. **87**, 2141–2148.

Lutfi, R. A. (**1993**). "A model of auditory pattern analysis based on component-relative-entropy," J. Acoust. Soc. Am. **94**, 748–758.

Lutfi, R. A. (**2008**). "Sound Source Identification," in *Springer Handbook of Auditory Research: Auditory Perception of Sound Sources*, edited by W. A. Yost and A. N. Popper (Springer, New York), pp. 19–28.

Lutfi, R. A., and Jesteadt, W. (**2006**). "Molecular analysis of the effect of relative tone level on multitone pattern discrimination," J. Acoust. Soc. Am. **120**, 3853–3860.

Lutfi, R. A., and Liu, C.-J. (**2007**). "Individual differences in source identification from synthesized impact sounds," J. Acoust. Soc. Am. **122**, 1017–1028.

Lutfi, R. A., and Oh, E. (**1997**). "Auditory discrimination of material changes in a struck-clamped bar," J. Acoust. Soc. Am. **102**, 3647–3656.

Lutfi, R. A., Oh, E., Storm, E., and Alexander, J. M. (**2005**). "Classification and identification of recorded and synthesized impact sounds by practiced listeners, musicians and nonmusicians," J. Acoust. Soc. Am. **118**, 393–404.

Lutfi, R. A., Kistler, D. J., Oh, E. L., Wightman, F. L., and Callahan, M. R. (**2003**). "One factor underlies individual differences in auditory informational masking within and across age groups," Percept. Psychophys. **65**(3), 396–406.

Massaro, D. M. (**1975**). "Backward recognition masking," J. Acoust. Soc. Am. **58**, 1059–1065.

McAdams, S., Chaigne, A., and Roussarie, V. (**2004**). "The psychomechanics of simulated sound sources: Material properties of impacted bars," J. Acoust. Soc. Am. **115**, 1306–1320.

Moore, B. C. J., and Ohgushi, K. (**1993**). "Audibility of partials in inharmonic complex tones," J. Acoust. Soc. Am. **93**, 452–461.

Moore, B. C. J., Glasberg, B. R., and Peters, R. W. (**1985**). "Relative dominance of individual partials in determining the pitch of complex tones," J. Acoust. Soc. Am. **77**, 1853–1860.

Morse, P. M., and Ingard, K. U. (**1968**) *Theoretical Acoustics* (Princeton University Press, Princeton, NJ), pp. 175–191.

Neff, D. L, and Dethlefs, T. M. (**1995**). "Individual differences in simultaneous masking with random-frequency, multicomponent maskers," J. Acoust. Soc. Am. **98**, 125–134.

Neff, D. L., and Jesteadt, W. (**1996**). "Intensity discrimination in the presence of random-frequency, multicomponent maskers and broadband noise," J. Acoust. Soc. Am. **100**, 2289–2298.

Oh, E., and Lutfi, R. A. (**1998**). "Nonmonotonicity of informational masking," J. Acoust. Soc. Am. **104**, 3489–3499.

Schlauch, R. S., Ries, D. T., and DiGiovanni, J. J. (**2001**). "Duration discrimination and subjective duration for ramped and damped sounds," J. Acoust. Soc. Am. **109**, 2880–2887.

Turner, M. D., and Berg, B. G. (**2007**). "Temporal limits of level dominance in a sample-discrimination task," J. Acoust. Soc. Am. **121**, 1848–1851.

Viemeister, N. (**1972**). "Intensity discrimination of pulsed sinusoids: The effects of filtered noise," J. Acoust. Soc. Am. **51**, 1265–1269.

Wallach, H., Newman, E. B., and Rosenzweig, M. R. (**1949**). "The precedence effect in sound localization," Am. J. Psychol. **62**, 315–336.

Watson, C. S., and Kelly, W. J. (**1981**). "The role of stimulus uncertainty in the discrimination of auditory patterns," in *Auditory and Visual Pattern Recognition*, edited by D. J. Getty and J. H. Howard, Jr. (Lawrence Erlbaum Associates, Hillsdate, NJ), pp. 37–59.

Wier, C. C., Jesteadt, W., and Green, D. M. (**1977**). "Frequency discrimination as a function of frequency and sensation level," J. Acoust. Soc. Am. **61**, 178–184.

Yost, W. A. (**2007**). "Lead-lag precedence paradigm as a function of relative level and number of lag stimuli," in 19th International Congress on Acoustics, Madrid.

Listening to every other word: Examining the strength of linkage variables in forming streams of speech

Gerald Kidd, Jr.,[a] Virginia Best, and Christine R. Mason
Department of Speech, Language and Hearing Sciences and Hearing Research Center, Boston University, Boston, Massachusetts 02215

(Received 9 April 2008; revised 12 September 2008; accepted 17 September 2008)

In a variation on a procedure originally developed by Broadbent [(1952). "Failures of attention in selective listening," J. Exp. Psychol. **44**, 428–433] listeners were presented with two sentences spoken in a sequential, interleaved-word format. Sentence one (target) comprised the odd-numbered words in the sequence and sentence two (masker) comprised the even-numbered words in the sequence. The task was to report the words in sentence one. The goal was to determine the effectiveness of cues linking the words of the target (or masker) over time. Three such "linkage variables" were examined: (1) fixed talker, (2) fixed perceived interaural location, and (3) correct syntactic structure. All of the linkage variables provided a significant advantage when applied to the target compared to the baseline condition in which the linkage variables were randomized. However, these linkage variables were not effective when applied to the masker. Word position effects were found such that performance in the baseline condition declined, and the advantages of the linkage variables increased, for the words near the end of the sentence. Overall, this approach appears to be useful for examining interference in speech recognition that has little or no peripheral component. The results suggest that variables that link target words together improve their resiliency to interference and/or their recall. © *2008 Acoustical Society of America.* [DOI: 10.1121/1.2998980]

PACS number(s): 43.66.Dc, 43.66.Mk, 43.66.Ba [MW] Pages: 3793–3802

I. INTRODUCTION

In multisource acoustic environments, a listener is faced with the task of determining the various sources of sound and selecting one or more to attend to, while ignoring others that are irrelevant or unimportant. According to Yost (1991, 2008), sound source determination is fundamental to the perceptual organization of the auditory environment and to making sense of the information the sources convey. Individual sounds are sometimes referred to as auditory "objects," which reflects the view that sounds are typically segmented into discrete perceptual elements (e.g., Woods and Colburn, 1992; Griffiths and Warren, 2004; and Shinn-Cunningham, 2008). When a sequence of related elements occurs the listener may perceive an auditory "stream" that can be segregated from other unrelated sounds. Understanding the factors that govern stream formation and maintenance over time is a topic of considerable interest to auditory researchers.

Simple stimuli, such as pure tones, may be arranged in spectrotemporal patterns that clearly lead to the formation of auditory streams that may easily be segregated from other streams (e.g., reviews by Bregman, 1990; Darwin and Carlyon, 1995; and Moore and Gockel, 2002). However, more complex sounds are also organized into and perceived as auditory streams. One important class of such sounds is speech. When multiple talkers are present in an auditory sound field there are typically many cues that may be used to segregate and attend to one particular "target" voice. The fundamental frequency and intonation contour of the talker, as well as a variety of talker-specific acoustic properties, forms one type of cue while another important cue is the spatial location of the talker. Furthermore, because connected speech conveys meaning there are semantic and syntactic continuities that also allow the listener to follow one specific speech stream. Thus, there are normally a variety of acoustic, perceptual, and semantic factors that allow the elements of a speech stream to be linked together and separated from other sounds.

One inherent complication in fully describing the factors governing selective listening in multisource environments is that the sounds produced by the various sources interfere with one another. From the perspective of the listener, irrelevant sounds that interfere with the detection, identification, recognition, or extraction of some other aspect of the target sound cause "masking." From a theoretical perspective, masking is often considered to be composed of two distinctly different components, referred to as "energetic masking" and "informational masking." Energetic masking results from the competition between the target and masker(s) for an adequate representation in the various auditory structures beginning with the basilar membrane and continuing through the ascending auditory neural pathways. In contrast, informational masking occurs despite a presumably adequate neural representation of the target (at some neural level, i.e., the auditory periphery) and is thought to reflect the limitations or natural tendencies of a variety of perceptual and cognitive processes (cf. Kidd *et al.*, 2008).

From an experimental perspective, separating out energetic and informational masking in complex multisource environments is challenging. When two or more talkers are speaking simultaneously, for example, the spectral overlap of

[a]Author to whom correspondence should be addressed. Electronic mail: gkidd@bu.edu

the voices—which leads to energetic masking—varies from moment to moment and it may be difficult to determine how much of the masking that is observed is due to energetic masking and how much is due to informational masking. Informational masking appears to be particularly important to understand when speech is masking other speech because it is often the case that failure in solving the speech recognition task is not due to the inaudibility of an energetically masked target but instead is due to a failure to segregate or focus attention on the target (Brungart *et al.*, 2006).

One experimental approach to separating energetic and informational masking in the multitalker listening situation was proposed by Arbogast *et al.* (2002). They sought to minimize energetic masking by reducing the spectral overlap of the target and masker. This was accomplished by processing the speech into sets of narrow frequency bands such that target bands and masker bands were mutually exclusive and thus had greatly reduced spectral overlap compared to natural speech while maintaining high intelligibility. Furthermore, the speech materials used in their study were from the coordinate response measure test (Bolia *et al.*, 2000) that is known to produce large amounts of informational masking under many conditions. Their results did indeed indicate that large amounts of informational masking were produced concurrently with small amounts of energetic masking, allowing them to test the potency of spatial separation of sources as a cue to reducing informational masking.

However, the approach used by Arbogast *et al.* (2002) has some limitations. The processing of speech into narrow bands reduces, but does not eliminate energetic masking. In certain subject populations—those with sensorineural hearing loss, for example—the energetic/informational ratio may be different than in other populations, a conclusion reached based on the findings of a later study by Arbogast *et al.* (2005). Furthermore, speech processed in this manner lacks strong pitch or intonation cues, and the vocal characteristics that distinguish different talkers are reduced, limiting the investigation of those potentially important cues in the selective listening task.

In the current study, a temporal analog of the approach used by Arbogast *et al.* (2002) is investigated. This approach is based on one originally (to our knowledge) employed by Broadbent (1952). Instead of confining target and masker elements to mutually exclusive frequency regions, here the target and masker elements are confined to mutually exclusive temporal regions. Target and masker words are presented alternately in interleaved sequences with the task of the listener being to report the words contained in the target sequence. Because the words do not overlap in time, they also do not simultaneously overlap in frequency, so, by most definitions of energetic masking, little if any energetic masking would be expected. The possibility of nonsimultaneous energetic masking cannot be excluded and is considered later in this article.

The underlying premise upon which this work is based is that the ability to follow and subsequently report the words in the target sequence depends on the strength of the cues that link the words together. That is, the stronger the linkage between target elements the better the listener will be in solving the speech identification task. This idea may be relevant to natural speech settings in which listeners must often link disconnected "glimpses" of a speech target when it is partially masked or interrupted by other sounds.

TABLE I. The 40-word corpus arranged in eight rows and five columns where each column is a word category (name, verb, number, adjective, and noun) and a choice of one word from each column in order from left to right would produce a syntactically correct but unpredictable sentence.

Bob	Bought	Two	Big	Bags
Gene	Found	Three	Blue	Cards
Jane	Gave	Four	Cold	Gloves
Jill	Held	Five	Hot	Hats
Lynn	Lost	Six	New	Pens
Mike	Saw	Eight	Old	Shoes
Pat	Sold	Nine	Red	Socks
Sue	Took	Ten	Small	Toys

The general approach of interleaving target and masker sequences is extremely flexible and many types and strengths of linkages are possible. In this study a new version of the interleaved-word paradigm and new stimulus set are described, and the results of an initial examination of a small set of linkage variables are presented. In addition, given that simple tonal stimuli stream more readily at faster rates (van Noorden, 1975), two different rates of presentation are examined. Furthermore, the current work examines the effects of linking together target versus masker words and the implications of that comparison for the ability to selectively attend to one source or actively ignore a second source (see also de Cheveigné *et al.*, 1995 and Brungart and Simpson, 2007).

II. METHODS

A. Subjects

Seven young adult listeners (ages 21–25) participated in the experiments. Four completed experiment 1 and four completed experiment 2. Listener S1 was common to both experiments and completed experiment 2 before experiment 1. The listeners were screened audiometrically to ensure that they had normal hearing (thresholds equal to or less than 20 dB hearing level) for octave frequencies between 250 Hz and 8 kHz. The listeners were paid for their participation.

B. Stimuli

A laboratory-designed corpus of monosyllabic words was recorded by Sensimetrics, Inc. (Somerville, MA) for use in the experiment. The corpus is comprised of 40 words in five categories (eight names, eight verbs, eight numbers, eight adjectives, and eight nouns). The words are contained in Table I. A choice of one word from each category in order (as listed above or in column order from left to right in the table) would yield a syntactically correct yet unpredictable sentence. The entire corpus includes recordings of each word spoken by 16 native speakers of American English (8 male, 8 female). The words were recorded in isolation with neutral inflection rather than in natural sentence form so that all possible combinations of words could be selected in a closed

set test and the effects of coarticulation across word boundaries, and imprecise or "smeared" word boundaries themselves, would be eliminated. Furthermore, the design of these experiments required that individual words be available to be interleaved with other sounds as described in the conditions below.

In the current experiments, the words from a subset of the talkers (three male, three female) were used. The words varied between 385 and 1051 ms in duration with a mean of 624 ms. The main experimental conditions consisted of five-word target strings interleaved with five-word masker strings. The target was defined as the five odd-numbered words in the sequence (i.e., first, third, fifth, etc.) while the masker comprised the even-numbered words in the sequence, the result being a ten-word string. All concatenation was done with no overlap and no silent gaps. Individual words were scaled to the same rms amplitude and no attempt was made to equate word duration across words or talkers. In control conditions, the masker words were replaced with silence, Gaussian noise, or reversed speech tokens. When silent gaps were used, the duration of each silence was set to the length of a randomly selected word from the corpus and therefore varied in the same way that masker words in those positions would vary. The duration of a single noise token varied in the same way as the individual words (i.e., a masker word was chosen as it would have been in the speech masker conditions but instead a noise with equal duration and rms amplitude was created to replace it in the string), and a 50 ms cosine-squared ramp was applied to each onset and offset. When the masker tokens were reversed speech, the masker words were again chosen as in the speech masker conditions but the word was simply reversed in time prior to concatenation.

C. Procedures

Stimuli were presented over headphones (Sennheiser HD265 linear) to listeners seated in a double-walled Industrial Acoustics Corporation booth at approximately 77 dB sound pressure level (as measured on KEMAR). The stimuli were created on a PC located outside the booth and were D/A converted and attenuated using Tucker-Davis Technologies hardware before being routed to the headphones. A mouse and liquid crystal display monitor were located inside the booth to obtain listener responses. After a stimulus was presented, a graphical user interface showing a grid of the 40 words in the set (arranged in five columns and eight rows as per Table I) was displayed on the monitor, and the listener was required to select the five target words in the order they were presented by clicking on the grid with the mouse. The grid was not visible during the stimulus to avoid listeners responding before the entire stimulus was presented, "mapping out" their response pattern visually or leaving the mouse pointing to a response. Of course there are many memory aids in these tasks such as rehearsal that were not explicitly controlled.

D. Experimental conditions

Five different conditions were tested in experiment 1. In all five conditions, ten words (five target and five masker) of the 40 possible were selected at random without replacement. In the baseline condition (referred to as "random"), talkers of each word were chosen such that the voice varied randomly among the six choices (with replacement) across target and masker strings. In addition, each word was given a random interaural location by introducing a delay between the left and right headphones. These interaural time differences were selected from a set of six values (± 150, ± 450, and ± 750 μs). In two "fixed target" conditions, the target words were constrained to have either a fixed voice or a fixed location on each trial. In these cases, the fixed parameter value was prevented from also occurring in the masker sequence for that trial. In two "fixed masker" conditions, the masker words were constrained to have either a fixed voice or a fixed location on each trial, and the fixed parameter value could not occur in the target sequence. The five experimental conditions were tested at two different speech rates. One rate (called "normal rate") was simply the words as they were naturally spoken although the rate after concatenation of words spoken in isolation (of approximately 1.6 syllables/s) is slower than average normal speaking rate. Each condition was also tested using a rate that was twice as fast (called "fast rate"), or approximately 3.2 words/s. This was achieved by shortening each word in the corpus to half its original duration (while maintaining the original pitch) using the PRAAT software package (Boersma and Weenink, 2007).[1]

In experiment 2, the main experimental conditions manipulated whether the target words, masker words, or both were arranged in syntactically correct sentences. A syntactically correct sentence comprised one word from each column of Table I in order from left to right. These choices resulted in three experimental conditions: target-correct masker-random, target-random masker-correct, or both target and masker correct. In addition, a baseline condition consisted of both target and masker sequences in random (not syntactically correct) order for a total of four test conditions. The random order sequences in experiment 2, unlike experiment 1, consisted of one word selection from each column. However, the word order (choice of columns) was randomized rather than left to right so that the syntax was almost always incorrect. The word choices for target and masker were always mutually exclusive so that every condition consisted of two words per column. The stimuli were presented at the normal speaking rate. The voice and location were random selections from among the same set of values described in experiment 1 for each word in the sequence.

Experiment 1 was run in 30-trial blocks with the condition held constant across trials within a block. In a session, ten blocks (one per condition/rate combination) were completed in random order. Each session took approximately 90 min, and each listener completed three sessions for a total of 90 trials per condition/rate per listener. Experiment 2 was run in 25 trial blocks and a session was comprised of four blocks (one per condition) in random order. Each session took approximately 30 min and each listener completed four sessions for a total of 100 trials per condition per listener.

E. Control conditions

Before commencing the experimental conditions, listeners completed a set of control conditions. These trials were designed both to provide reference data regarding the intelligibility of the target sequences and to familiarize listeners with the basic task and the response grid.

For experiment 1, three of the four subjects completed an initial listening session that consisted of ten blocks of 30 trials. Because listener S1 had completed experiment 2 prior to experiment 1, she was considered sufficiently experienced and did not complete this initial session. The first two blocks (one at each rate) consisted of isolated target sequences ("quiet") with silences in the intervening masker positions. These blocks confirmed that the target words in isolation, even when presented at a faster rate, were highly intelligible (>90% correct). In the second two blocks (one at each rate), broadband noise bursts were presented in the even-numbered temporal positions in the sequence. In the third pair of blocks (one at each rate), masker words were presented as in the random condition of experiment 1, but they were reversed in time such that they were unintelligible. These conditions provided controls for comparison of performance in speech-masked conditions ("speech masking" will refer to the forward-played speech maskers in contrast to the "time-reversed speech" maskers used in one of the control conditions). The remaining four blocks (two at each rate) were identical to the random condition of experiment 1. These blocks allowed listeners to practice the difficult task of ignoring the intervening masker words while remembering and responding to the target sequence (data not reported).

In experiment 2 a shorter control session was conducted on each listener, comprising one block each of the quiet, noise-masked, and reversed speech-masked conditions. The words were spoken at a normal rate and the word order was randomized (not syntactically correct).

III. RESULTS

A. Experiment 1

The group mean results from experiment 1 are presented in Fig. 1. The upper panel shows the results for the normal rate while the lower panel shows the results for the fast rate. These values are group mean percent correct scores with error bars indicating intersubject standard errors. Note that the computation of percent correct for each five-word target sequence is based on the criterion that the words were reported in the correct word position.[2] So, for example, if the sequence of target words was "red, saw, Bob, old, six" and the listener reported "red, Bob, found, old, six…" then the score for these items would be 60% correct (three of five test words reported in the correct word positions). One of the word errors would be scored as a temporal position error ("Bob") and one scored as not present in the target sequence ("found"). The three bars in the left portion of each panel represent the control conditions of no masker ("quiet"), noise masker ("noise"), and reversed speech masker ("rev"). The performance ranged from about 88% to 94% correct when the target sequences were presented in quiet or in Gaussian noise for both speaking rates. Interspersing time-reversed

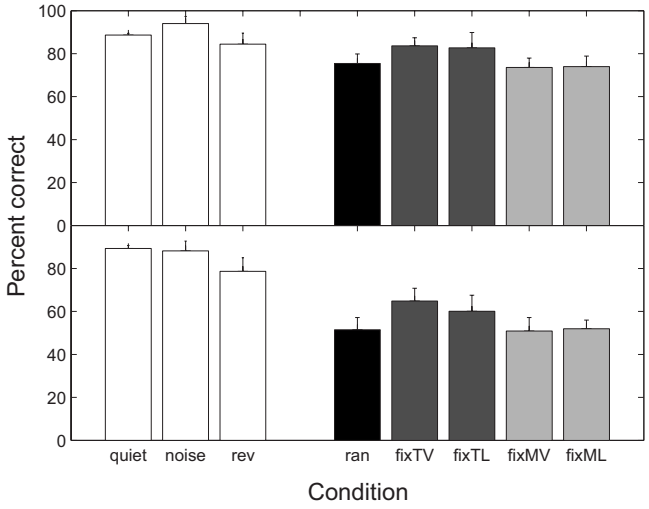


FIG. 1. Group mean percent correct scores from experiment 1. The upper panel displays the results for the normal rate while the lower panel displays the results for the fast rate. The abscissa indicates the experimental conditions. From the left: no masker (quiet), speech-shaped noise (noise), temporally reversed speech (rev), target and masker both random (ran), target voice fixed (fixTV), target location fixed (fixTL), masker voice fixed (fixMV), and masker location fixed (fixML). The error bars represent standard errors of the means.

words degraded performance by about five to ten percentage points for the normal rate and about nine percentage points for the fast rate relative to the quiet or noise-masked scores. For these three conditions, changing the speaking rate did not affect performance.

In the speech masking conditions of experiment 1 (the rightmost five bars in each panel), the linkage variables tested were voice and location. First, averaging across all listeners and word positions, there was a clear decrease in performance in all of these conditions for the fast rate as compared to the normal rate. On average, performance declined by about 19–24 percentage points when the rate was increased across these five masked conditions. In the random baseline condition ("ran"), performance was at about 75% correct for the normal rate. For the two cases in which the target had a fixed parameter value while the masker varied at random, significant improvements in performance relative to the fully random condition were observed. When the target voice was fixed ("fixTV"), group mean performance was about 85% correct, an increase of ten percentage points over random. When target location was fixed ("fixTL"), about the same advantage as fixed voice was observed, with group mean performance near 84% correct. When the same linkage variables were fixed for the masker ("fixMV" and "fixML") while the target varied randomly, no benefit to performance was observed relative to the random condition. A similar pattern of results was observed for the fast rate, although overall performance was significantly poorer. Here the random condition and the two fixed masker conditions were near 50% correct, while the fixed target conditions were somewhat better with average scores of 65% and 60% correct, respectively, for fixed voice and location.

Figure 2 (top row) displays the group mean performance in the various speech masking conditions as a function of target word position. The two leftmost panels show results

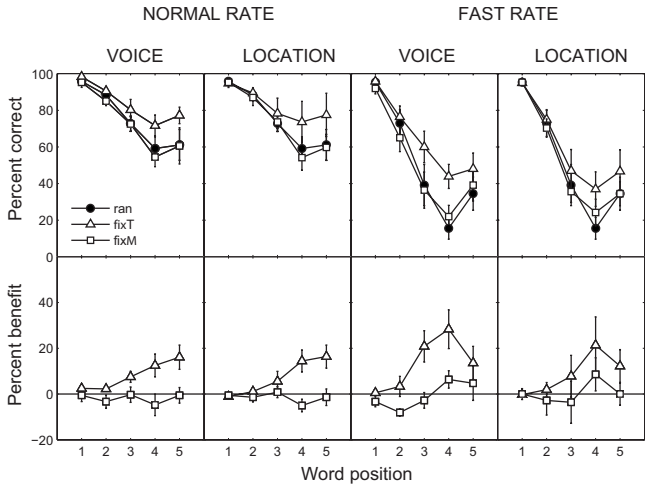


FIG. 2. Top row: Group mean percent correct scored according to target word position in the sequence. Each column shows the results for a different rate/linkage variable. The parameter in each panel is whether the target (open triangles), masker (open squares), or neither (filled circles) was fixed. The error bars represent standard errors of the means. Bottom row: Group mean benefits provided by fixing linkage variables as a function of word position. The benefits are calculated by subtracting the percent correct score in the random condition from the percent correct score in the test condition.

from the normal rate and the two rightmost panels show data for the fast rate. The left and right panels of each pair show results obtained when the linkage variables of voice and location, respectively, were manipulated against the random baseline condition which is replotted for the two panels within each pair. The different functions in each panel show the random ("ran") condition, the fixed target ("fixT") condition, and the fixed masker ("fixM") condition. Plotting the data in this manner reveals a strong word position effect. Performance for the first target word is higher than 90% correct for all conditions, then declines with increasing word position from the second through the fourth word with a tendency for an improvement for word five. There is a clear difference in performance between normal and fast rates which increased with word position; the largest difference occurred for words four and five and was greater than 30 percentage points in some cases.

The benefit provided by the two linkage variables tested is plotted as a function of word position in the bottom row of Fig. 2. Here, the benefit is computed as the difference between fixing a target or masker variable relative to performance in the random condition. The benefit of holding a target parameter constant increased with increasing word position at least through word four where improvements in performance approached 30 percentage points for the fast rate. Benefits were roughly the same for fixing either target voice or target location at a given rate. Fixing the masker did not result in a benefit in performance. A four-way repeated measures analysis of variance was conducted on the benefits with factors of rate (normal or fast), sequence fixed (target or masker), linkage variable (voice or location), and word position (1–5). The analysis indicated significant main effects of sequence $[F(1,3)=19.42,\ p<0.05]$, and a significant interaction between sequence and word position $[F(4,12)=9.86),\ p<0.005]$ which is clearly seen in the figure. The factors of rate, linkage variable, and word position were not significant $(p>0.05)$ and no other interactions were significant $(p>0.05)$.

Figure 3 shows the individual results from experiment 1. The rows are individual subjects while the columns are the four combinations of rate and linkage variable. The parameter of each graph is the fixed sequence (target, masker, or neither). Some of the general trends noted in the group mean data are also apparent for each individual subject. For example, both word position and rate effects are consistent across listeners (although there are large differences in the magnitudes of the effects). However, the benefit of fixing voice or location differed considerably across subjects. For example, S2 derived no benefit from fixing the target location for either rate and only obtained modest benefits from fixing the target voice. The largest benefits for any listener were observed for S4 at the fast rate where both fixed target voice and target location provided benefits of more than 50 percentage points relative to the random case for target word position 4.

An analysis of the different kinds of errors that were made in the experimental conditions is displayed in Fig. 4. The most common error (about one-half of all errors) was reporting a masker word as a target word. The next most frequent error (about 40% of all errors) was reporting a target word in an incorrect word position. Because the task required choosing five words from the grid, the remaining errors consisted of words that were not presented in either target or masker sequences. It appears that a reduction in all error types contributed to the improved performance seen in the fixed target conditions.

B. Experiment 2

In experiment 2, the main variable was the syntactic structure of the sequences. That is, a sequence of words could form a syntactically correct sentence ("correct") or it could simply be a random draw of words from the corpus (random). Group mean performance and standard deviations for random target sentences in the three control conditions (quiet, noise, and time-reversed masker) are shown in the leftmost bars of Fig. 5. On average, performance was about 95% correct for both quiet and noise conditions and declined to about 87% correct when the maskers were time-reversed words.

In the speech masking conditions (right side of Fig. 5) the dominant factor was whether the target sequence formed a syntactically correct sentence or whether the five words forming the target sequence were chosen at random. When syntactically correct, performance was about 90% correct regardless of whether the masker was random ("Tcorr") or syntactically correct ("TMcorr"). When random, performance fell to around 60%–65% correct regardless of the masker condition ("ran" and "Mcorr").

Figure 6 (top panel) shows the group mean results of experiment 2 plotted as a function of word position. Because identification performance was so accurate overall when the

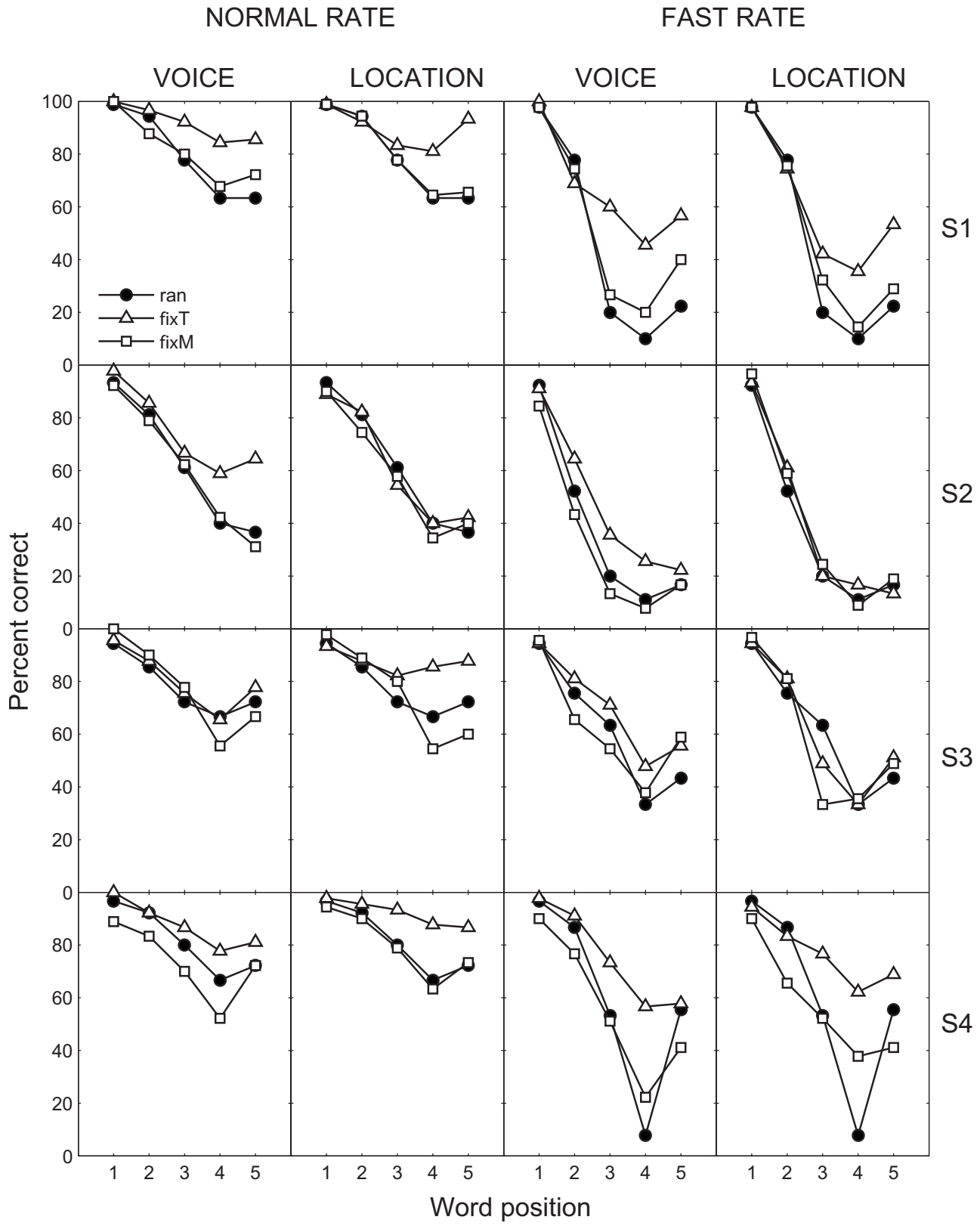


FIG. 3. Percent correct performance as a function of word position for the four individual subjects in experiment 1. Each row shows the results from a single subject, and each column shows the results for a different rate/linkage variable. The parameter in each panel is whether the target (open triangles), masker (open squares), or neither (filled circles) was fixed.

target was syntactically correct, the effect of word position appears relatively small. The general pattern of results noted in experiment 1 with respect to word position was also apparent here when the target was randomized, with word position 4 yielding the poorest overall performance.

The amount of benefit provided by correct syntax is illustrated in the bottom panel of Fig. 6. Again, the reference for computing benefit was performance in the random baseline condition. When the masker alone was correct, no consistent benefit was obtained. However, large and nearly equal

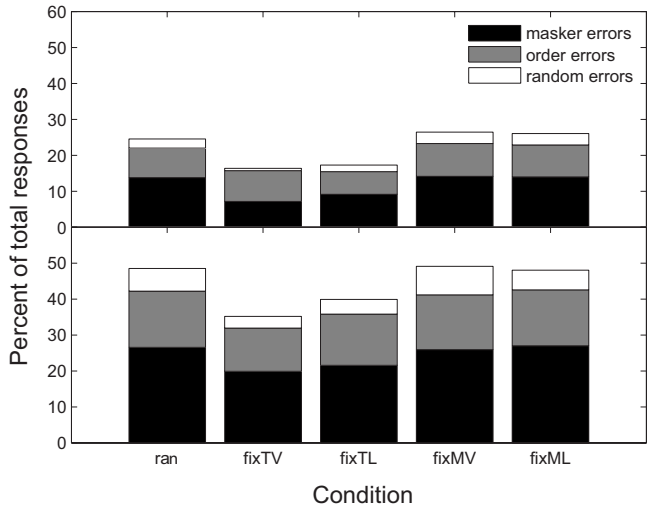


FIG. 4. Group mean error patterns for experiment 1. The upper panel displays the results for the normal rate while the lower panel displays the results for the fast rate. The abscissa indicates the experimental conditions. Errors are classified as one of three types: masker errors (black), target order errors (gray), or random errors (white) where subjects reported words that were not presented.

benefits that are word position dependent are apparent in both conditions when the target was syntactically correct (regardless of masker sequence syntax). For word positions 3–5, benefits of 30–40 percentage points are seen. A two-way repeated measures analysis of variance conducted on the benefits, with factors of sequence correct (target, masker, or both) and word position (1–5), revealed significant main effects of sequence [$F(2,6)=23.13$, $p<0.005$] and word position [$F(4,12)=12.02$), $p<0.001$], and a significant two-way interaction [$F(8,24)=11.10$, $p<0.001$].

Figure 7 shows the results from individual subjects in experiment 2. In general, the trends seen in the group data are apparent for each subject, with the syntactic structure of the target determining performance. However, the different listeners differ considerably in their overall performance, particularly in the random condition, and those that perform more poorly receive a greater benefit from correct target syntax.

Figure 8 shows an analysis of the different kinds of errors that were made in experiment 2. When the target was not syntactically correct, there was an approximately equal

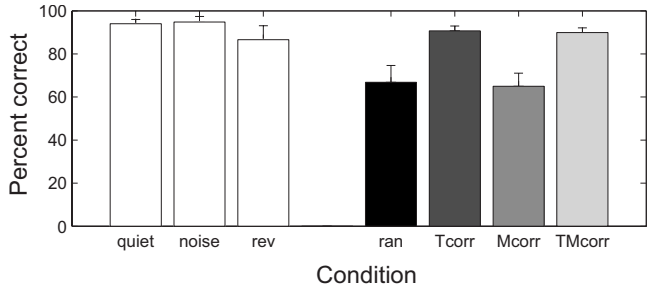


FIG. 5. Group mean percent correct scores from experiment 2. The abscissa indicates the experimental conditions. From the left: no masker (quiet), speech-shaped noise (noise) and temporally reversed speech (rev), target and masker both with random word order (ran), correct target syntax (Tcorr), correct masker syntax (Mcorr), and correct target and masker syntax (TMcorr). The error bars represent standard errors of the means.

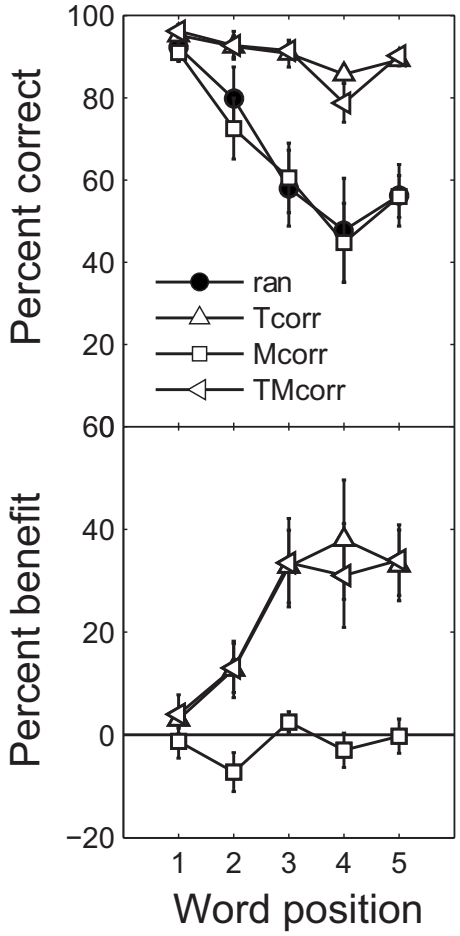


FIG. 6. Top panel: Group mean percent correct scored according to target word position in the sequence. The parameter in each panel is whether the target (open upward-pointing triangles), masker (open squares), target and masker (open left-pointing triangles), or neither (filled circles) had plausible syntax. The error bars represent standard errors of the means. Bottom panel: Group mean benefits provided by giving the target and/or masker-orrect syntax as a function of word position. The benefits are calculated by subtracting the percent correct score in the random condition from the percent correct score in the test condition.

number of each of the three error types made. When the target was given plausible syntax, target order errors were effectively eliminated (because the subject knew to respond in correct syntactic order left to right), but there was also a reduction in the number of masker errors and random errors.

IV. DISCUSSION

In his original article describing the speech intelligibility assessment procedure in which target and masker words alternated, Broadbent (1952) found that irrelevant words interspersed among test words greatly increased the difficulty in reporting the test words. Furthermore, he reported that factors such as familiarity with the talker's voice could improve recognition performance. This occurred even though the test words were perfectly audible and ideally could be selected through an appropriate use of attentional focus over time. He thus concluded that the interference caused by the masker words was evidence for a failure of selective attention. The current results support and significantly extend those early findings. These effects are clearly not attributable to

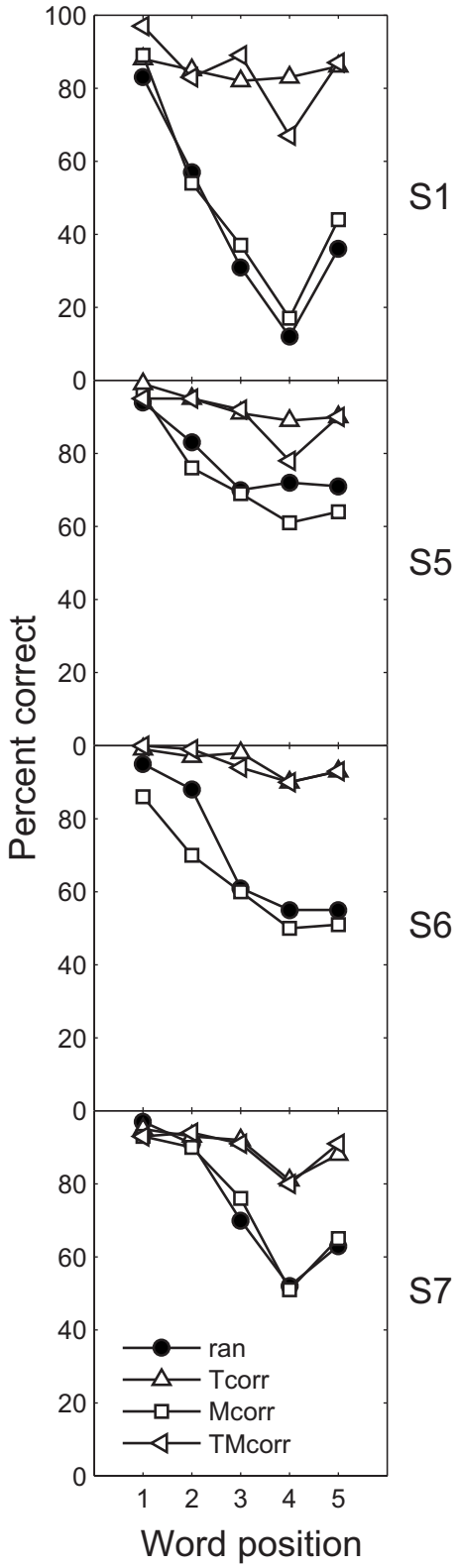


FIG. 7. Percent correct performance as a function of word position for the four individual subjects in experiment 2. Each panel shows the results from a single subject, and the parameter in each panel is whether the target (open upward-pointing triangles), masker (open squares), target and masker (open left-pointing triangles), or neither (filled circles) had plausible syntax.

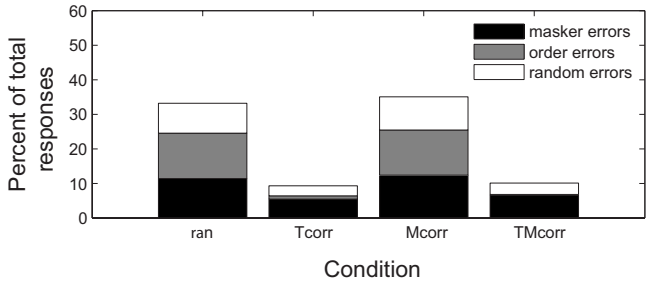


FIG. 8. Group mean error patterns for experiment 2. The abscissa indicates the experimental conditions. Errors are classified as one of three types: masker errors (black), target order errors (gray), or random errors (white) where subjects reported words that were not presented.

nonsimultaneous energetic masking because performance in the noise-masker control condition was equivalent to performance when no masker was present. Moreover, in both of the noise-masker cases, for speech presented at a normal rate and at twice the normal rate, recall of random sequences was generally better than 90% correct.

One conclusion based on the current results is that this procedure is useful for examining informational masking under conditions in which the results are not confounded by a peripheral masking component. This is a stronger conclusion than may be made about speech processed into very narrow frequency bands presented simultaneously (cf. Arbogast *et al.*, 2002; Kidd *et al.*, 2005; and Gallun *et al.*, 2007). Conversely, it also appears to be a useful means for exploring how various factors bind sequences of words together to provide a release from informational masking. As compared to the noise masker, a small amount of interference was obtained by using a temporally reversed speech masker. This finding suggests that it was not necessary for the masker elements to be meaningful but instead that some degree of informational masking may occur if the target and masker elements are qualitatively similar even when no spectrotemporal overlap is present.

All of the linkage variables tested provided significant improvements in performance when applied to the target. A constant apparent location provided by a fixed interaural time difference (ITD) that was different from that of the masker and a constant voice uttering all target words in a sequence—again, different from the masker—provided significant benefit in solving the speech identification task. Likewise, imposing a sensible syntactic structure on the target sequence provided a significant performance benefit. Increasing the rate significantly degraded performance in the speech masking conditions but did not affect performance in quiet, in noise, or in reversed speech. In those three control conditions, there apparently was not a sufficient processing load placed on the listener for rate to matter. This finding is similar to that reported by Brungart and Iyer (2007) who also noted an increase in the potency of speech maskers at faster-than-normal speech rates. In the present study, the effect of rate on the benefit provided by each linkage variable was not significant. This was somewhat surprising given that faster rates are known to promote stronger perceptual streaming for simple stimuli (e.g., van Noorden, 1975), but may perhaps be explained by the absence of silent gaps between words at either rate in the current conditions (e.g., Bregman *et al.*, 2000).

Characterizing these performance benefits as a consequence of strengthening the linkage between target words

seems warranted for several reasons. Simultaneous segregation (or the formation of auditory objects) is not a factor here given that each individual word of both the target and the masker is already perfectly segregated. Thus, unlike the case of multiple simultaneous talkers, the issue of whether each is perceptually segregated, or the strength of the segregation, does not apply. It seems likely that the intervening masker words interrupt the process of linking, storing, rehearsing, and retrieving the stream of target words in memory. The beneficial effect of the linkage variables applied here is manifested in an improved ability to recall the target items. It also makes sense that the benefit of a given linkage variable would increase as the number of items that share a common property increases, and an increase in the benefit of the linkage variables across time/word position that is broadly consistent with this notion was found. It remains to be seen, however, whether or not the early items would benefit more when they are more difficult in the baseline condition.

The idea that strengthening the cues that perceptually bind words together can influence word recall has been raised previously (e.g., Martin *et al.*, 1989; Nicholls and Jones, 2002a; and Nicholls and Jones 2002b). Nicholls and Jones (2002a) examined how "sandwiching" irrelevant words around a sequence of digits in a serial recall task reduced the detrimental "suffix" effect. The suffix effect, which is a classical finding in memory research, refers to the interference in the recall of a series of items when an irrelevant item (not to be remembered) is inserted following the list of target words. The largest effect of the suffix is on the terminal word in the test sequence, which is usually easier to recall than the preceding test word due to recency in memory. Nicholls and Jones (2002a) demonstrated that the suffix effect could be reduced when the sandwiched items (irrelevant words inserted between target words, very much like the current procedure) had acoustic properties known to promote perceptual streaming. The most effective "capture" (e.g., Bregman and Rudnicky, 1975) of the suffix (pulling it into the masker stream) occurred when the masker words and suffix had the same fundamental frequency. In contrast, no capture was observed when the fundamental frequencies of the masker words varied randomly. In a separate, but related article Nicholls and Jones (2002b) examined the sandwich experiment (cf. Hitch, 1975 and Baddeley *et al.*, 1993) more fully. They reported that the irrelevant words had the greatest effect on target recall when they had the same pitch as the target words. Furthermore, they found that more interference in target word recall was obtained when the masker words were randomly selected than when a single masker word was simply repeated throughout the sequence. The findings of Nicholls and Jones (2002a, 2002b) seem inconsistent with our finding that strengthening the linkage variables of the masker words provided no benefit in reporting the target words. The only benefit, as discussed more fully below, was obtained when the linkage variables were applied to the target words. There are a number of procedural differences that may account for the different findings. Most importantly, in Nicholls and Jones' work the target was always spoken by the same voice. It is possible that masker continuity can play a role only if there is target continuity. This condition was not tested with the voice and location linkage variables in experiment 1, and although it was tested for the parameter of syntactic structure in experiment 2, ceiling effects would not allow us to see any additional benefit of masker linkage. In addition, syntactic structure and acoustic linkage variables likely involve very different processing mechanisms and thus may be expected to differ in their effects.

Viewed in another way, the fact that uncertainty in the target was more disruptive in the present experiments than uncertainty in the masker is relevant to discussions of the "listener max vs listener min" observer models (e.g., Durlach *et al.*, 2003). As defined by Durlach *et al.* (2003), this contrast in listener strategies reflects whether the available processing resources are devoted to emphasizing the representation of the target (e.g., applying gain at a particular point along the relevant stimulus dimension, called listener max) or to de-emphasizing or ignoring the masker (attenuating a point or points along the relevant stimulus dimension, called listener min). However, on a practical level it can be very difficult to separate the actions of these two hypothetical observer strategies in actual experiments (however, cf. de Cheveigné *et al.*, 1995). This is partly because, in masked conditions, both produce similar effects and both may result in selective/tuned responses along a given perceptual dimension. The current results appear to be more consistent with a listener max strategy because the only consistent benefit of the various linkage variables (i.e., constant physical value or syntactic structure) occurred when they were applied to the target. If the listener was attempting to "null out" the masker words then we might have expected some benefit from application of the linkage variables relative to random conditions. In contrast, Brungart *et al.* (2007) recently reported evidence from a multitalker speech identification task that appeared to be more consistent with a listener min model. A primary variable in their study was a difference in spatial location, a manipulation that is very similar to the ITD manipulation used here. They employed a procedure in which the predictability of the locations of the target and the maskers was varied systematically. As in experiment 1 here, either target or masker location(s) was/were fixed while the other changed location unpredictably, although on a trial-to-trial basis rather than within a trial. They found that listeners were more sensitive to variability in the masker location than in the target location. They interpreted this result as consistent with a listener min (or "masker min" in their terms) approach in which knowledge about masker location would lead to a nulling of the masker which was more useful than knowledge about the target. In their study, the difference in performance between the two contrasting conditions was small but was statistically significant. Moreover, they provided converging evidence in support of their position in a set of conditions under which the relative positions of the target and two masker locations were varied. It seems plausible that both listener max and listener min strategies are available to listeners to some degree and that they may adopt one or the other—or a combination of both—as appropriate to the demands of the task and the specific listening situation.

There has been relatively little work on this issue in the auditory domain and the question of whether and to what degree listeners adopt these hypothetical strategies remains open.

V. CONCLUSIONS

This study demonstrated that large amounts of informational masking may be obtained by temporally interleaving a sequence of target and masker words when the task is to recall the target sequence. Presenting the words in a temporally nonoverlapping manner greatly reduces the chance of any peripherally based energetic masking contributing to the results. It was found that all three linkage variables examined were effective in reducing informational masking and improving accuracy of report when applied to the target words. Generally, the beneficial effects of the linkage variables were greatest for the later-occurring items where performance was relatively poor. None of the linkage variables were effective when applied to the masker words. These findings are compatible with a listener max model (Durlach *et al.*, 2003) in which the available processing resources are devoted to emphasizing the representation of the target.

ACKNOWLEDGMENTS

This work was supported by Grant Nos. DCO4545 and DC0100 from the National Institute on Deafness and Other Communication Disorders (NIH/NIDCD) and by Grant No. FA9950-05-1-2005 from the Air Force Office of Scientific Research (AFOSR), United States Air Force. Virginia Best was also supported in part by a University of Sydney Postdoctoral Research Fellowship.

[1]Despite the large range of individual word durations, we found no evidence that the identification of the target words was related to duration in either the normal-rate or fast-rate conditions.

[2]It is often the case that serial recall is scored without regard to errors of word position. We analyzed our results in that manner and found that the pattern of word position effects was not greatly affected by scoring method.

Arbogast, T. L., Mason, C. R., and Kidd, G., Jr. (**2002**). "The effect of spatial separation on informational and energetic masking of speech," J. Acoust. Soc. Am. **112**, 2086–2098.

Arbogast, T. L., Mason, C. R., and Kidd, G., Jr. (**2005**). "The effect of spatial separation on informational masking of speech in normal-hearing and hearing-impaired listeners," J. Acoust. Soc. Am. **117**, 2169–2180.

Baddeley, A. D., Papagano, C., and Andrade, J. (**1993**). "The sandwich effect: The role of attentional factors in serial recall," J. Exp. Psychol. Learn. Mem. Cogn. **19**, 862–870.

Boersma, P., and Weenink, D. (**2007**). Praat: Doing phonetics by computer (Version 4.6.40) (Computer program). Last viewed December, 2007), from http://www.praat.org/

Bolia, R. S., Nelson, W. T., Ericson, M. A., and Simpson, B. D. (**2000**). "A speech corpus for multitalker communications research," J. Acoust. Soc. Am. **107**, 1065–1066.

Bregman, A. S. (**1990**). *Auditory Scene Analysis* (MIT Press, Cambridge, MA).

Bregman, A. S., Ahad, P. A., Crum, P. A., and O'Reilly, J. (**2000**). "Effects of time intervals and tone durations on auditory stream segregation," Percept. Psychophys. **62**, 626–636.

Bregman, A. S., and Rudnicky, A. J. (**1975**). "Auditory segregation: Stream or streams?," J. Exp. Psychol. Hum. Percept. Perform. **1**, 263–267.

Broadbent, D. E. (**1952**). "Failures of attention in selective listening," J. Exp. Psychol. **44**, 428–433.

Brungart, D. S., Chang, P. S., Simpson, B. D., and Wang, D. (**2006**). "Isolating the energetic component of speech-on-speech masking with ideal time-frequency segregation," J. Acoust. Soc. Am. **120**, 4007–4018.

Brungart, D. S., and Iyer, N. (**2007**). "Time-compressed speech perception with speech and noise maskers," Proceedings of Interspeech 2007, Antwerp, Belgium.

Brungart, D. S., Iyer, N., and Simpson, B. D. (**2007**). "Selective spatial attention in a dynamic cocktail party task: Evidence for a strategy based on masker minimization," J. Acoust. Soc. Am. **121**, 3119.

Darwin, C. J., and Carlyon, R. P. (**1995**). "Auditory grouping," in *Handbook of Perception and Cognition*, edited by B. C. J. Moore (Academic, New York), Vol. **6**, pp. 387–424.

de Cheveigné, A., McAdams, S., Laroche, J., and Rosenberg, M. (**1995**). "Identification of concurrent harmonic and inharmonic vowels: A test of the theory of harmonic cancellation and enhancement," J. Acoust. Soc. Am. **97**, 3736–3748.

Durlach, N. I., Mason, C. R., Shinn-Cunningham, B. G., Arbogast, T. L., Colburn, H. S., and Kidd, G., Jr. (**2003**) "Informational masking: Counteracting the effects of stimulus uncertainty by decreasing target-masker similarity," J. Acoust. Soc. Am. **114**, 368–379.

Gallun, F. J., Mason, C. R., and Kidd, G., Jr. (**2007**). "The ability to listen with independent ears," J. Acoust. Soc. Am. **122**, 2814–2825.

Griffiths, T. D., and Warren, J. D. (**2004**). "What is an auditory object?," Nat. Rev. Neurosci. **5**, 887–892.

Hitch, G. J. (**1975**) "The role of attention in visual and auditory suffix effects," Mem. Cognit. **3**, 501–505.

Kidd, G., Jr., Mason, C. R., Brughera, A., and Hartmann, W. M. (**2005**) "The role of reverberation in release from masking due to spatial separation of sources for speech identification," Acust. Acta Acust. **114**, 526–536.

Kidd, G., Jr., Mason, C. R., Richards, V. M., Gallun, F. J., and Durlach, N. I. (**2008**). "Informational masking," in *Auditory Perception of Sound Sources*, edited by W. A. Yost, A. N. Popper, and R. R. Fay (Springer Handbook of Auditory Research, New York), pp. 143–190.

Martin, C. S., Mullennix, J. W., Pisoni, D. B., and Summers, W. V. (**1989**). "Effects of talker variability on recall of spoken word lists," J. Exp. Psychol. Learn. Mem. Cogn. **15**, 676–684.

Moore, B. C. J., and Gockel, H. (**2002**). "Factors influencing sequential stream segregation," Acust. Acta Acust. **88**, 320–333.

Nicholls, A. P., and Jones, D. M. (**2002a**). "Capturing the suffix: Cognitive streaming in immediate serial recall," J. Exp. Psychol. Learn. Mem. Cogn. **28**, 12–28.

Nicholls, A. P., and Jones, D. M. (**2002b**). "The sandwich effect reassessed: Effects of streaming, distraction and modality," Mem. Cognit. **30**, 81–88.

Shinn-Cunningham, B. G. (**2008**). "Object-based auditory and visual attention," Trends Cogn. Sci. **12**, 182–186.

van Noorden, L. (**1975**). "Temporal coherence in the perception of tone sequences," Ph.D. thesis, Technical University Eindhoven, Eindhoven, The Netherlands.

Woods, W. S., and Colburn, H. S. (**1992**). "Test of a model of auditory object formation using intensity and interaural time difference discrimination," J. Acoust. Soc. Am. **91**, 2894–2902.

Yost, W. A. (**1991**). "Auditory image perception and analysis: The basis for hearing," Hear. Res. **56**, 8–18.

Yost, W. A. (**2008**). "Perceiving sound sources," in *Auditory Perception of Sound Sources*, edited by W. A. Yost, A. N. Popper, and R. R. Fay, (Springer Handbook of Auditory Research, New York), pp. 11–13.

Time-series analysis for online recognition and localization of sick pig (*Sus scrofa*) cough sounds

Vasileios Exadaktylos and Mitchell Silva
Department of Biosystems, Division M3-BIORES: Measure, Model & Manage Bioresponses, Catholic University of Leuven, Kasteelpark Arenberg 30, 3001 Heverlee, Belgium

Sara Ferrari and Marcella Guarino
Department of Veterinarian Sciences and Technologies for Food Safety, Faculty of Veterinary Medicine, University of Milano, Via Celoria 10, 20133 Milano, Italy

C. James Taylor
Engineering Department, Lancaster University, LA1 4YR Lancaster, United Kingdom

Jean-Marie Aerts and Daniel Berckmans[a)]
Department of Biosystems, Division M3-BIORES: Measure, Model & Manage Bioresponses, Catholic University of Leuven, Kasteelpark Arenberg 30, 3001 Heverlee, Belgium

(Received 6 March 2008; revised 9 September 2008; accepted 15 September 2008)

This paper considers the online localization of sick animals in pig houses. It presents an automated online recognition and localization procedure for sick pig cough sounds. The instantaneous energy of the signal is initially used to detect and extract individual sounds from a continuous recording and their duration is used as a preclassifier. Autoregression (AR) analysis is then employed to calculate an estimate of the sound signal, and the parameters of the estimated signal are subsequently evaluated to identify the sick cough sounds. It is shown that the distribution of just three AR parameters provides an adequate classifier for sick pig coughs. A localization technique based on the time difference of arrival is evaluated on field data and is shown that it is of acceptable accuracy for this particular application. The algorithm is applied on continuous recordings from a pig house to evaluate its effectiveness. The correct identification ratio ranged from 73% (27% false positive identifications) to 93% (7% false positive identifications) depending on the position of the microphone that was used for the recording. Although the false negative identifications are about 50% it is shown that this accuracy can be enough for the purpose of this tool. Finally, it is suggested that the presented application can be used to online monitor the welfare in a pig house, and provide early diagnosis of a cough hazard and faster treatment of sick animals.
© *2008 Acoustical Society of America.* [DOI: 10.1121/1.2998780]

PACS number(s): 43.66.Gf, 43.60.Jn, 43.80.Qf [MCH] Pages: 3803–3809

I. INTRODUCTION

Monitoring animal health in pig houses is vital for the sustainable management of a pig farm. Cough is a sudden air explosion in the airways followed by a characteristic sound. Being one of the body's defense mechanisms against respiratory infections, it can be a sign of disorder or infection of the respiratory system. It has been indicated as an index for over 100 diseases and experienced physicians can identify an infection based on the characteristics of a cough sound.[1]

However, the importance of coughing as a means of prognosis does not refer only to humans but also to animals. It has been shown that pig vocalization is directly related to pain[2] and stress,[3] and classification of such sounds has been attempted. It is also a common practice by veterinarians to assess cough sounds in pig houses for diagnostic purposes. However, this approach is used only when they visit the pig house (which is after the farmer has possibly detected a health hazard) and cannot be used for continuous 24 h monitoring and early warning for infections in pig houses. In this regard, various approaches have been presented that identify the characteristics of coughing in animals[4,5] and automatically identify cough sounds from field recordings.[6,7]

Furthermore, as the use of antibiotics has reached a level that cannot be accepted to guarantee the success of the drug in the future due to the increase of resistance in species, it is strongly recommended to decrease the use of it over all fields of applications. In this direction, apart from recognizing a sick animal sound, it is equally important to identify the sick animal in the compartment and immediately treat only animals in the pen of the identified sick animal. Successful application of such a technique can result in reduction of unnecessary use of antibiotics on healthy animals.

There are many approaches to sound localization: based on minimum audible angles,[8] time difference of arrival[9,10] (TDOA), or focalization[11,12] that deals with environmental uncertainty. In particular, to calculate the TDOA, many techniques have been presented ranging from cross correlation[9,13] and generalized cross correlation[14] to the maximization of the cross-ambiguity function.[15] Classification of sounds has

a)Electronic mail: daniel.berckmans@biw.kuleuven.be

been based on the fundamental frequency,[16] the frequency content and fuzzy clustering,[7,17] self-organizing feature maps,[3] statistical properties,[18] or using machine learning[19] and are usually complex and require big training sets[20] (e.g., to train a neural network). Clearly, any combination of these techniques can result in an application for recognition and localization of sick animals.

In this paper, an approach is presented that combines an identification and a localization algorithm for early detection of a possible health hazard in pig houses. In contrast to earlier approaches the present paper proposes a tool that can continuously monitor the health status within the pig farm and produce an early warning that could prevent a disease from spreading. In this regard, the time domain characteristics of the signal are used to automatically classify sick coughs in an online way. Autoregression (AR) analysis is evaluated to estimate the sound and the distribution of the AR parameters is used to distinguish among different sounds. Although the connection between the AR parameters and their biological meaning is not fully known, it is shown that it poses an attractive, fast, and computationally efficient classifier for the case of sick pig coughs. For the localization of the cough sounds, an algorithm based on the TDOA of the signal in seven microphones is proposed. The TDOA is estimated by identifying the time at which the sound is initiated and by calculating the difference among the signals from different microphones.

Next, Sec. II describes the sound acquisition process and the classification and localization algorithms. This is followed by the results and discussion in Sec. III, while Sec. IV summarizes and delivers the conclusions.

II. MATERIAL AND METHODS

A. Experimental data

Three data sets are used in this work. The first one is used to present the classification properties of the AR parameters, the second one is used for the evaluation of the localization algorithm, and the third one is used for the application of the procedure to field data for both cough recognition and localization.

The first data set consists of recorded sounds in laboratory conditions. Coughs from healthy animals were induced in an inhalation chamber by injecting an irritating substance, namely, 0.8 mol/l of citric acid dissolved in a saline solution (0.9% NaCl) (for more information on the installation environment and the data acquisition process see Ref. 7). The nebulization of citric acid stimulates the cough receptors directly resulting in coughing. In total, 11 experiments were conducted to 3 male and 3 female healthy Belgian Landrace piglets of 9–12 weeks of age and 20–40 kg of weight. The experiments were conducted with individual animals. In order to record pathologic coughs, the piglets were anaesthetized with azaperone (4 mg/kg intramuscular), ketamin (10 mg/kg intramuscular), and thiopental (10 mg/kg into a vein). They were treated (by intratracheal administration) with lipopolysaccharide from *Escherichia coli* diluted in sterile saline (100 μg/kg). A nontoxic strain of pasteurella multocida (code 3301) was used to generate bronchopneumonia, a common respiratory infection in piglets.[21] Apart from the cough sounds, other sounds (such as screams, sneezes, or environmental sounds) were acquired and labeled accordingly by auditory processing.[7] Therefore, the generated data set includes individual sounds of 231 chemically induced coughs, 291 sick coughs, and 149 other sounds from 6 individual animals.

TABLE I. Overview of the data sets used in this work.

Data set	Condition	No.of microphones	Sound description	No. of sounds
			Sick coughs	291
1	Lab	1	Chemically induced coughs	231
			Other sounds	149
2	Field	7	Triangle sounds	16[a]
3	Field	7	Various	N/A

[a]Recorded by every microphone.

The second and third data sets consist of field recordings in a fattening compartment of a pig stable in Milan, Italy. The dimensions of the stable were 14×21 m^2 with a height of 3.75 m against the walls and the roof had an inclination of 30%. The floor was totally slatted and the total area was divided into 16 boxes, 8 on each side of a central path along the length of the stable. There were 350 animals in the stable, with an average of 22 pigs in a box. The pigs in this case were aged three months and were fattened ranged from 26 to 35 kg at the beginning of a cycle to reach 90–100 kg in 90 days (in a later stage, they were moved in a different stable where they were fattened to reach 140 kg, but this was not monitored for this study). The genetic line was a cross between landrace Italian $\times$ large white $\times$ duroc and serve for the Parma ham production.

The second data set consists of triangle sounds recorded by seven microphones and were produced at a height of 1 m above the ground at predefined positions (presented in Table II) and were used to evaluate the accuracy of the localization algorithm. The third data set consists of continuous recordings by seven microphones in the pig house and was used to test both the recognition and localization algorithms on field data. The recordings consist of seven wave files (one for every microphone) of 2 h and 40 min of duration each and the acquisition was conducted in May 2005.

For the sound registration seven electret microphones (Monacor ECM 3005) were used that have a frequency response of 50–16 000 Hz and were connected via preamplifiers (Monacor SPR-6) to an eight channel analog to Tascam Digital Interface (TDIF) unit (Soundscape SS8IO-3). The Soundscape unit, which allows for simultaneous recording of eight channels, was connected via a TDIF cable to a Peripheral Component Interconnect (PCI) audio card (Mixtreme 192). All recordings were sampled at a sample rate of 22.05 kHz with a resolution of 16 bits. All microphones were hanging in the stable at a height of 1.20 m at the positions depicted as big dots in Fig. 7.

An overview of the data sets is presented in Table I.



FIG. 1. Flowchart of the procedure for online recognition and localization of sick pig cough sounds.

B. Signal analysis

The flowchart for the proposed application for online sick cough recognition and localization is shown in Fig. 1. It comprises of three subprocesses, namely, the sound extraction where individual sounds are extracted from a continuous recording, the sick cough recognition process where a decision is made whether a sound is sick cough or not, and the localization process where the position of a sound that has been classified as sick cough is identified within the pig house. Each part of the algorithm is presented in detail in the following.

Before the process begins, the complete recording is preprocessed. To eliminate low frequency noise (produced mainly by the ventilation installation in the pig house), and since the sick cough signals that need to be recognized do not have considerable low frequency components,[5,6] the signal is initially bandpass filtered. For this, a tenth order Butterworth filter with a passband of 2–10 kHz is used.

1. Sound extraction

The extraction of individual sounds from a continuous recording is based on the envelope of the energy of the signal and a manually selected (environment specific) threshold as is presented in Fig. 2. The underlying principle is that low amplitude noise is recorded most of the time and when a sound occurs (any sound within the pig farm) it will be recorded as a high energy signal. Whenever the amplitude of the envelope is higher than the threshold it is considered that there is a recording of a sound that needs to be identified. The mean value of the envelope over the complete recording

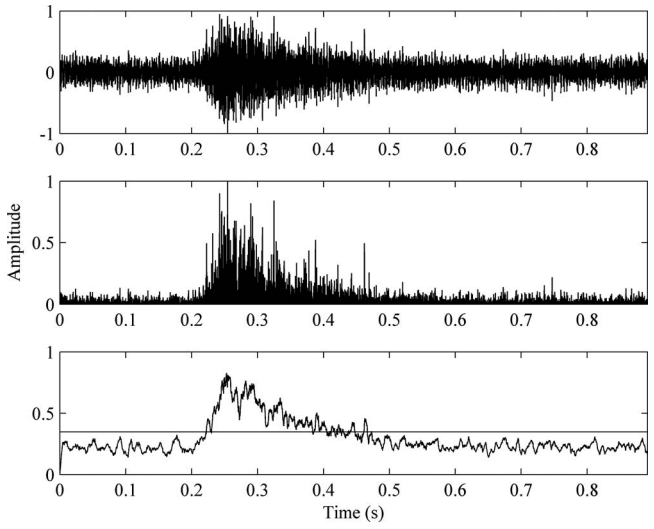


FIG. 2. Stages of the sound extraction procedure. The cough sound (top plot), its energy (middle plot), the envelope of the energy (bottom plot), and the chosen threshold (horizontal line on the bottom plot).

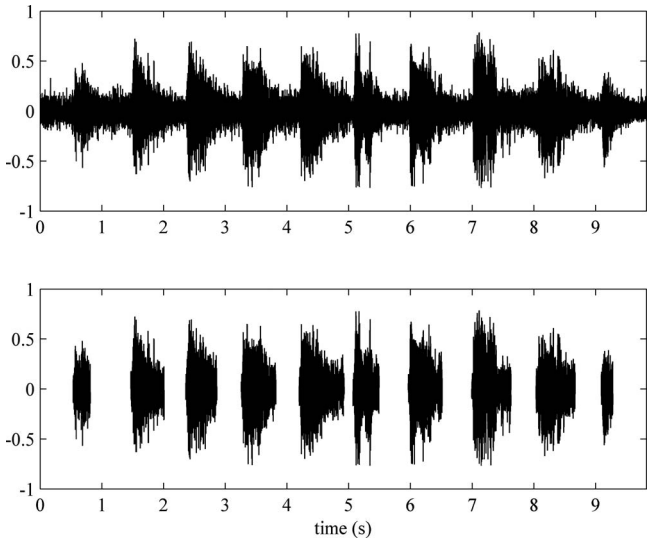


FIG. 3. Continuous recording of a cough attack (top) and the individual sounds that are extracted by the algorithm (bottom).

is used for this application and experimentation suggested that it is adequate for extracting most of the signals that are of interest.

To automatically calculate the envelope of the continuous recorded signal, the Hilbert transform[22] of a discrete time signal $s[k]$ that is defined as

$$H\{s[k]\} = \sum_{n=-N/2}^{N/2} s[k-n]h[n]\sin^2\left(\frac{n\pi}{2}\right), \tag{1}$$

where $h[k]=2/k\pi$, for $k=\pm 1, \pm 2, \ldots, \pm N/2$ and $h[0]=0$, and provides a 90° phase shift to the original signal is used according to the following algorithm.

(1) Calculate the energy of the signal.
(2) Calculate the Hilbert transform of the energy.
(3) Calculate the square root of the sum of the energy and its Hilbert transform.
(4) Calculate the moving average of the result to get a smoothed estimate of the envelope of the initial signal.

The result of this procedure is presented in Fig. 3, where a continuous recording of a cough attack is presented and the extracted sounds are shown. It is suggested that the mean value of the signal is adequate for the sound extraction procedure, but it should be noted that the noise level and the acoustics of the pig compartment affect the resulting signal. Therefore the threshold should be chosen taking them into account.

2. Sick cough recognition

a. Preprocessing of individual sounds The sounds that usually occur in a pig compartment are pig movements, pig vocalizations, metal sounds (e.g., clanging of compartment doors), and low frequency noise caused primarily by ventilation fans. After the extraction of individual sounds from a continuous recording, a preprocessing takes place. To make sure that the sound extraction is correct, sounds that are very close to each other are considered as one. To clarify this, consider the case of a scream. It consists of the inhalation

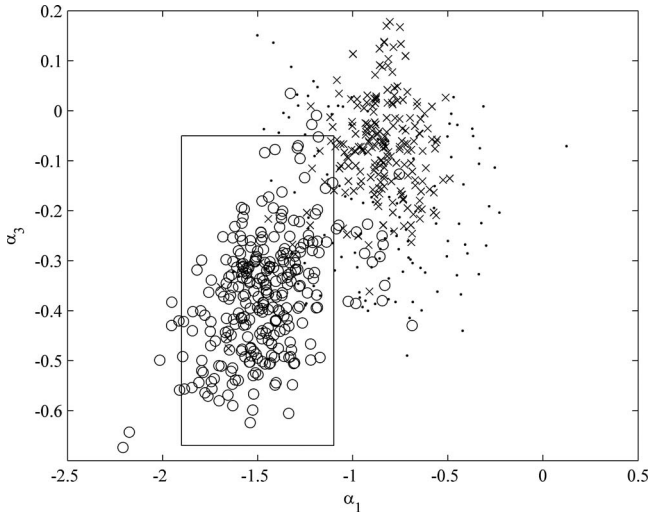


FIG. 4. Plot of the first against the third AR parameters for sick coughs (○), chemically induced coughs (×), and other sounds (·). Visual inspection suggests that the sick coughs form a cluster the center of which (big bullet) and its boundaries are shown. The same can be observed when the rest of the AR parameters are plotted against each other.

phase in which the animal inhales air into its lungs and the exhalation in which the production of the sound occurs. However, multiple repetitions of these phases might create a single scream while the envelope extraction may result in different sounds for each repetition of inhalation and exhalation. By preprocessing, this is avoided and every resulting sound fraction represents a single and complete sound. Experimentation suggested that sound fragments that are closer than 100 ms to each other be considered as a single sound.

Furthermore, the length of each sound contains information that can be used in classification. Screams and grunts, for example, are longer sounds and can last for up to a few seconds. Coughs on the other hand are sharp sounds that usually last from 200 ms up to 600 ms.[5] Sounds that are longer than 600 ms are therefore considered as noncough sounds and ignored from the rest of the process. In the same manner, sound fragments that are shorter than 200 ms are also eliminated.

b. Autoregression analysis and cough recognition AR analysis is a method of estimating a signal $s[k]$ with one of the form

$$\tilde{s}[k] = -\sum_{i=1}^{p} \alpha_i \tilde{s}[k-i] + e[k], \tag{2}$$

where the $\alpha_i, i=1,2,\ldots,p$ are estimated minimizing an adequate criterion,[23] $e[k]$ is a white noise signal, and p is the order of the AR model. In general, increasing the order of the model decreases the error between the estimated and the actual signals. In this work, the order of the estimated signal is chosen to be 3.

Based on such an estimation of the actual sound signal, an attempt to form a classifier is made. In this regard, it is observed that the positions of the AR parameters in a three dimensional space for the laboratory sounds of the first data set can serve as an adequate and computationally efficient classifier. It is suggested that when plotting the AR parameters on the $(\alpha_1, \alpha_2, \alpha_3)$ space, those that result from sick coughs form a well defined cluster. Figure 4, for example, shows the (α_1, α_3) plane and the mapping of the different sounds where it is clear that the sick cough sounds are close together and can visually be distinguished from other sounds.

To gain an insight on the classification properties of the proposed method, and to produce a formal definition of how well such a classifier can perform, five randomly selected sick coughs are chosen to form the sick cough cluster. The average value of the AR parameters along each direction α_i is chosen as the center (c_1, c_2, c_3) of the sick cough cluster. Its boundaries are subsequently defined as the vertices of the polyhedron whose edges in any direction α_i equal the twice of the standard deviation of the training set in that direction. The length of each vertex is based on the Chebyshev inequality according to which at least 75% of the training set values will be within this area. Figure 4 presents the center and the boundaries of the cluster on the (α_1, α_3) plane. 88% of the sick coughs are correctly identified (12% false negatives), achieving a 92% of correct overall classification rate (with 6.8% false positive classifications). Although it cannot be considered as a reliable measure since previous knowledge of the data set can be considered (yet the choice of the training set is random), it provides an indication as to the result that can be achieved.

3. Localization

a. Estimation of the time difference of arrival (TDOA) The localization algorithm presented in Sec. II B 3 b requires the estimation of the TDOA of the signal on a number of microphones (seven in this case) that are positioned at known positions in the pig house. Although many methods have been presented in literature as described in the Introduction, in this paper the envelope of the energy of the signal (Fig. 2) is used to estimate the time at which a sound starts, because of its simplicity, ease of implementation, and adequate accuracy (for this application). Then the difference in time at which a sound is detected to begin for each pair of microphones is the TDOA of the sound between them.

After the extraction of the envelope, the envelopes of the signals recorded by all microphones are normalized (to have a maximum amplitude of 1) and their mean value is taken. The smallest of these values is used as a threshold to define the amplitude at which a sound is considered to begin. This is graphically presented in Fig. 5 for a triangle sound received in two of the microphones.

b. The localization algorithm Consider a sound originating from a specific position. The difference in the capturing times of this signal in two microphones, due to their different distances from the sound, results in a time delay between the recordings by the two microphones. By multiplying this time delay by the traveling speed of sound in air (343.4 m/s at 20 °C), a distance can be calculated. Let us call this the distance of the time delay, d_τ. Let d_{pa} be the distance from a certain point p in the pig house to microphone a, and d_{pb} be the distance between the same point and microphone b. If at this specific point p a sound signal would be released, it would travel the distance d_{pa} to microphone a and distance d_{pb} to microphone b. At this point p, the distance of the time delay d_τ is equal to the difference $d_{pa} - d_{pb}$, so a weight value w_p for the position p can be defined as

$$w_p = (d_{pa} - d_{pb}) - d_\tau = 0. \tag{3}$$

In order to find the potential location of a sound source, the positions at which $w=0$ should be found. To com-

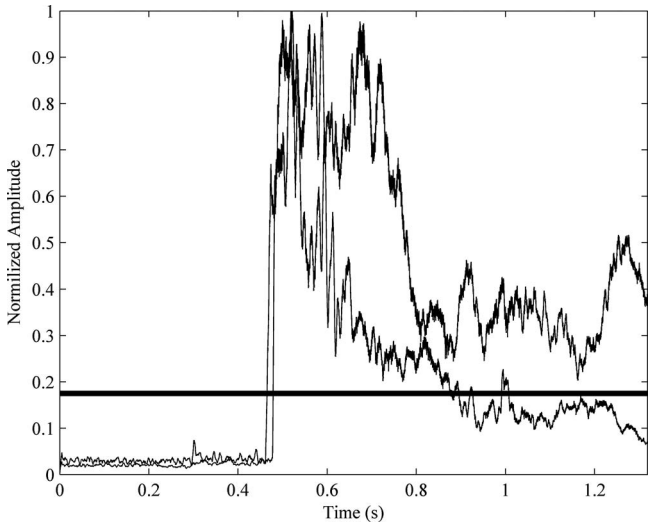


FIG. 5. Graphical representation of the TDOA estimation procedure for two triangle sounds. The envelope of the energy of the signals (thin lines) and the appropriate threshold (thick line) are presented.

pute these weights w, the test field is divided into a two dimensional grid with a resolution of 0.1 m. As the pig house is 21×14 m^2, this implies a grid with a resolution of 210×140. In every point of the grid the weight (3) for every pair of microphones is calculated and summed. This is represented by the following equation:

$$w_{(k,l)} = \sum_{i=1}^{n-1} \sum_{j=i+1}^{n} \{(d_{(k,l),i} - d_{(k,l),j}) - d_{\tau(i,j)}\}, \quad (4)$$

where $w_{(k,l)}$ represents the total weight at position (k,l), $(d_{(k,l),i} - d_{(k,l),j})$ is the difference in distance between position (k,l) and microphones i and j, $d_{\tau(i,j)}$ is the distance of the time delay between the signals at microphone i and j, and n is the number of microphones.

By calculating this weight $w_{(k,l)}$ for every position (k,l), the total area can be visualized in a three dimensional graph. An example of this graph is shown in Fig. 6. The position of the sound source is that point in the grid where the weight $w_{(k,l)}$ is minimal, i.e., the position at which the minimum of the graph is located. It could be argued that knowledge of the pig house geometry and the TDOA between the microphones would simplify the problem to one finding the point at which all equations of form (3) would be satisfied for every pair of microphones. However, this would require a very accurate estimation of the TDOA leading to increased complexity of that algorithm. On the contrary, the algorithm presented above is more robust to TDOA uncertainty, and therefore, the procedure that calculates it (Sec. II B 3 a) can be very simple. A more detailed study of the localization algorithm is presented in Ref. 24 where the localization algorithm was initially introduced and tested with manual extraction of the TDOA.

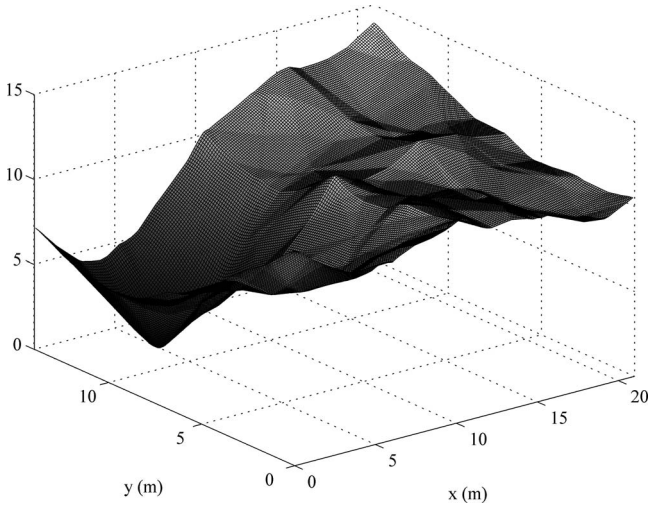


FIG. 6. Three dimensional representation of the localization procedure. The lower point of the graph indicates the area from which the sound originates.

TABLE II. Results of the triangle sound experiments for the evaluation of the sensitivity of the localization algorithm.

	X coordinate (m)		Y coordinate (m)	
Test	Measured/Estimated	Error	Measured/Estimated	Error
1	10.8/10.0	0.8	1.3/1.9	0.6
2	10.8/10.8	0.0	3.9/3.9	0.0
3	10.8/12.1	1.3	6.5/5.9	0.6
4	10.8/11.0	0.2	9.2/9.0	0.2
5	10.8/11.3	0.5	11.8/11.9	0.1
6	10.8/11.4	0.6	14.4/15.0	0.6
7	10.8/10.7	0.1	17.0/17.0	0.0
8	10.8/11.2	0.4	19.7/19.5	0.2
9	3.2/0.1	3.1	1.3/0.1	1.2
10	3.2/3.1	0.1	19.7/19.2	0.5
11	3.2/2.8	0.4	17.0/16.6	0.4
12	3.2/3.0	0.2	14.4/14.6	0.2
13	3.2/2.7	0.5	11.8/11.7	0.1
14	3.2/0.1	3.1	9.2/0.1	9.1
15	3.2/2.7	0.5	6.5/6.3	0.2
16	3.2/2.7	0.5	3.9/4.1	0.2

To test the sensitivity of the proposed algorithm to the automatic TDOA extraction, the triangle sounds of the second data set are used. The real (measured values) and estimated values of the sound positions are presented in Table II. It can be seen that most of the results are within 50 cm of the actual position that the sound originated from. Taking further into account that the animals will move within the pen (and hence the pen of this sick animal is sought), such an accuracy is considered to be adequate for the purpose of the present application. It is also noted that the positioning of tests 9 and 14 do not give the desired results. By examining the time domain signals in these cases, it is observed that the algorithm fails to correctly estimate the TDOA. The extracted signals do not correspond to the actual sounds due to high surrounding noise, which results in failure of the algorithm. However, repetition of the sick coughs will highlight the hazardous areas of within the stable making the effect of random errors negligible. This is supported by the overall results that are presented in the following.

III. RESULTS AND DISCUSSION

The cough recognition and localization procedures described above are applied to the continuous recordings of the third data set that consists of field recordings. The first five sick cough sounds from each microphone are manually extracted from the continuous recording, labeled, and used as a

TABLE III. Results of the cough recognition algorithm on field data when one cluster is defined for all seven microphones.

Microphone	Total sounds identified as sick cough	Sounds correctly identified as sick cough	Percentage (%)
1	116	72	62
2	138	94	68
3	103	71	69
4	132	90	68
5	108	77	71
6	132	88	66
7	137	74	54

training set to define the center of the sick cough cluster (the procedure to define this sick cough cluster is described in Sec. II B 2 b) and its boundaries are selected as twice the standard deviation of the AR parameters in each direction. The classification result is presented in Table III.

As can be observed in Table III the recognition results do not provide a very reliable classifier. The acoustics of the compartment has a different effect on each microphone mainly due to the location of the microphones (four are located in the corners, two against just one wall, and one in the middle of the compartment). To overcome this and to take into account the difference in the acoustics, a cough cluster is formed for every microphone (namely, sounds from a specific microphone are used to form the cluster for this microphone only). The same five prelabeled sick cough sounds (from each microphone recording) are used again to form the centers of these clusters. The improved classification results are shown in Table IV. By defining the clusters for each microphone separately, the acoustics and noise of the environment are taken into account (by forming a separate cluster for every microphone) and the outcome is clearly improved.

Comparison of Tables III and IV shows that the correct classification ratio is improved from 7% in the case of the third microphone up to 25% for the fourth microphone. However, fewer sounds are identified in the second case. The reason for that relies on the fact that, in the second case, the center of the cluster is more accurately defined for each microphone and the standard deviation of the training set is smaller, resulting in a tighter cluster. Therefore the algorithm becomes more selective and the correct identification rate is increased at the cost of fewer sounds being identified. In addition, the sick cough sounds that are present in the recordings appear as cough attacks that consist of a series of sick coughs. This implies that it is of high importance to correctly identify a sick cough sound since the repetition will allow for a consequent sound to be identified if one is not. In this regard, an attempt was made to reduce the false positive identifications at the cost of increased false negatives.

TABLE IV. Results of the cough recognition algorithm on field data when a sick cough cluster is defined for each microphone.

Microphone	Total sounds identified as sick cough	Sounds correctly identified as sick cough	Percentage (%)
1	88	64	73
2	101	76	75
3	41	33	80
4	40	37	93
5	35	29	83
6	47	38	81
7	37	31	84

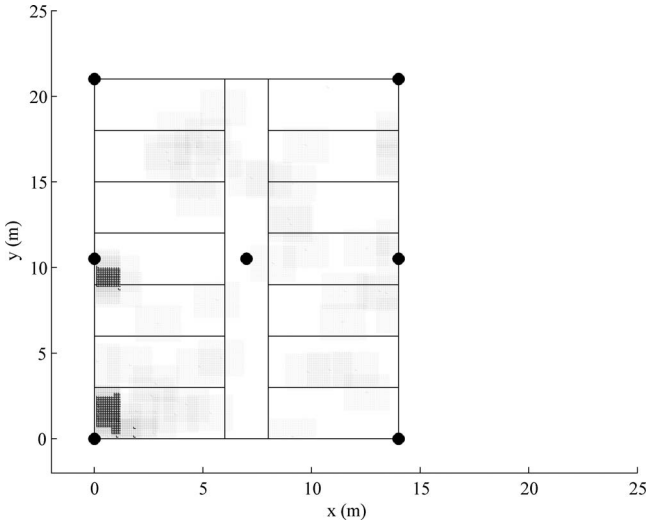


FIG. 7. Graphical representation of the pig house and the positions of the microphones (bullet points). Furthermore the cough hazard spread is shown (dark areas indicate areas of possible cough hazard).

On the correctly recognized cough sounds of the second case, the localization algorithm is applied and the result is visualized in Fig. 7. It can be seen that two cough hazards can be located in the pig house (one at the bottom left corner and another one at the middle left). In the present results, an automatic thresholding mask has been applied (that essentially amplifies the areas where more sick coughs have occurred) to account for failure in detection of the TDOA as described in Sec. II B 2 b, or isolated cough events that pose no threat to animal welfare in the pig farm.

To the authors' knowledge, this is the first application for combined online cough recognition and localization presented in the relevant literature and can pose as a starting point for further research. The results seem promising, although there are still issues to be considered. At this point, if a cough is identified in the recording of a single microphone, the recognition is considered correct and the position of the sick animal is identified. A possible enhancement could be based on a trade-off between sensitivity and correct recognition and require for a sound to be identified as cough in more than one microphone.

The AR classification is a simple technique and the computational load is held to a minimum. It is clear that superior techniques for pig cough recognition from continuous recordings exist,[7] but are computationally more demanding compared to the one presented here. However the repetition of sick coughs in a pig house allow for the application of the proposed AR technique. It is computationally effective and provides the necessary accuracy for the specific application.

Since the application of pig cough localization is in pig houses, the accuracy of the algorithm to be used need not be

very high, considering animal movement and that the objective is to identify the area that needs to be treated. The time delay between the detection of a sick cough hazard and its evaluation by a veterinarian will result in some uncertainty to the exact position of the sick animal. However, it will give an indication to the area where the cough hazard occurred along with an early warning about it. Hence a simple sound initiation detection technique for determining the TDOA is of adequate accuracy.

IV. CONCLUSION

An online algorithm for automatic sick cough recognition and localization has been presented. In contrast to existing methods, the proposed approach can be used to continuously monitor animal health in pig houses in an online way. Both the recognition and the localization processes are based on simple and computationally effective algorithms, making it an attractive solution for fast observation of the spread of a disease in a pig house.

The sick cough identification algorithm is based on AR analysis of the signal and has been shown that the AR parameters of sick pig cough signals form a separate cluster from that of other sounds. The proposed localization algorithm is based on the TDOA between the sound as received by seven microphones. The procedure is able to overcome uncertainty in the estimation of the TDOA and therefore allows for a simple method for its estimation (namely, the estimation of the beginning of the signal) to be used. The accuracy of the method is shown to be adequate for the intended application (with as low as 7% false positive identifications) and leads to a simple and fast procedure.

For a better validation of the proposed method, it should be further tested with additional recording. Subsequently, the approach can be directly applied to the field where its efficiency will be tested along with the effect it can have on animal welfare, faster animal treatment, reduction of antibiotics, and therefore pig health.

ACKNOWLEDGMENTS

This project was funded by the EU in the framework of a Marie Curie training site (Reference No. HPMT-GH-01-00383-06).

[1]J. Korpáš, J. Sadloňová, and M. Vrabec, "Analysis of the cough sound: An overview," Pulm Pharmacol. **9**, 261–268 (1996).
[2]G. Marx, T. Horn, J. Thielebein, B. Knubel, and E. von Borell, "Analysis of pain-related vocalisation in young pigs," J. Sound Vib. **266**, 687–698 (2003).
[3]P.-C. Schön, B. Puppe, and G. Manteuffel, "Linear prediction coding analysis and self-organizing feature map as tools to classify stress calls of domestic pigs (*Sus scrofa*)," J. Acoust. Soc. Am. **110**, 1425–1431 (2001).
[4]B. Moreaux, D. Beerens, and P. Gustin, "Development of a cough induction test in pigs: Effects of SR 48968 and enalapril," J. Vet. Pharmacol. Ther. **22**, 387–389 (1999).
[5]A. Van Hirtum and D. Berckmans, "The fundamental frequency of cough by autocorrelation analysis," in Proceedings of EUROSPEECH: Seventh European Conference on Speech Communication and Technology, Aalborg, Denmark (2001), pp. 2435–2438.
[6]A. Van Hirtum and D. Berckmans, "Considering the influence of artificial environmental noise to study cough time-frequency features," J. Sound Vib. **266**, 667–675 (2003).
[7]A. Van Hirtum and D. Berckmans, "Fuzzy approach for improved recognition of citric acid induced piglet coughing from continuous registration," J. Sound Vib. **266**, 677–686 (2003).
[8]M. Holt, R. Schusterman, D. Kastak, and B. Southall, "Localization of aerial pure tones by pinnipeds," J. Acoust. Soc. Am. **118**, 3921–3926 (2005).
[9]D. Mennill, J. Burt, K. Fristrup, and S. Vehrencamp, "Accuracy of an acoustic location system for monitoring the position of dueting songbirds in tropical forest," J. Acoust. Soc. Am. **119**, 2832–2839 (2006).
[10]J. Spiesberger, "Locating animals from their sounds and tomography of the atmosphere: Experimental demonstration," J. Acoust. Soc. Am. **106**, 837–846 (1999).
[11]M. Collins and W. Kuperman, "Focalization: Environmental focusing and source localization," J. Acoust. Soc. Am. **90**, 1410–1422 (1991).
[12]R. Baer and M. Collins, "Source localization in the presence of internal waves," J. Acoust. Soc. Am. **118**, 3117–3121 (2005).
[13]J. Spiesberger, "Linking auto- and cross-correlation functions with correlation equation: Application to estimating the relative travel times and amplitudes of multipath," J. Acoust. Soc. Am. **104**, 300–312 (1998).
[14]C. Knapp and G. Carter, "The generalized correlation method for estimation of time delay," IEEE Trans. Acoust., Speech, Signal Process. **ASSP–24**, 320–327 (1976).
[15]Y. Chan and K. Ho, "Joint time-scale and TDOA estimation: Analysis and fast approximation," IEEE Trans. Signal Process. **53**, 2625–2634 (2005).
[16]J. Buck and P. Tyack, "A quantitative measure of similarity for tursiops truncatus signature whistles," J. Acoust. Soc. Am. **94**, 2497–2506 (1993).
[17]J. Brown, A. Hodgins-Davis, and P. Miller, "Classification of vocalizations of killer whales using dynamic time warping," J. Acoust. Soc. Am. **119**, EL34–EL40 (2006).
[18]K. V. Melendez, D. L. Jones, and A. S. Feng, "Classification of communication signals of the little brown bat," J. Acoust. Soc. Am. **120**, 1095–1102 (2006).
[19]M. Skowronski and J. Harris, "Acoustic detection and classification of microchiroptera using machine learning: Lessons learned from automatic speech recognition," J. Acoust. Soc. Am. **119**, 1817–1833 (2006).
[20]V. B. Deecke and V. M. Janik, "Automated categorization of bioaccoustic signals: Avoiding perceptual pitfalls," J. Acoust. Soc. Am. **119**, 645–653 (2006).
[21]M. Kobisch and N. Friis, "Swine mycoplasmoses," Rev. Sci. Tech. **15**, 1569–1605 (1996).
[22]A. Oppenheim, R. Shafer, and J. Book, *Discrete-Time Signal Processing* (Prentice-Hall, Upper Saddle River, NJ, 1999).
[23]P. Young, *Recursive Estimation and Time-Series Analysis* (Springer-Verlag, Berlin, 1984).
[24]M. Silva, S. Ferrari, A. Costa, J.-M. Aerts, M. Guarino, and D. Berckmans, "Cough localization for the detection of respiratory diseases in pig houses," Comput. Electron. Agric. **64**(2), 286–292 (2008).

Mapping unpleasantness of sounds to their auditory representation

Sukhbinder Kumar and Helen M. Forster
Auditory Group, Newcastle University Medical School, Framlington Place, Newcastle upon Tyne NE2 4HH, United Kingdom

Peter Bailey
Department of Psychology, University of York, Heslington, York YO10 5DD, United Kingdom

Timothy D. Griffiths
Auditory Group, Newcastle University Medical School, Framlington Place, Newcastle upon Tyne NE2 4HH, United Kingdom

(Received 15 September 2008; accepted 5 October 2008)

Certain sounds, for example, the squeal of chalk on a blackboard, are typically perceived as highly unpleasant. This study addressed the question of what aspects of the auditory representation of such sounds are associated with judgments of unpleasantness. Participants rated the perceived unpleasantness of a large number of sounds that included "griding" and other unpleasant sounds. A multivariate partial least-squares (PLS) model was then built to relate the ratings of unpleasantness with an auditory representation derived from a model of processing in the auditory pathway. The "existence region" of unpleasantness in the auditory space of frequency-temporal modulation was determined after the PLS model had been validated by predicting the unpleasantness of novel sounds from the auditory representation. It was observed that the existence region corresponded to spectral frequencies between 2500 and 5500 Hz, and temporal modulations in the range 1–16 Hz.
© *2008 Acoustical Society of America.* [DOI: 10.1121/1.3006380]

PACS number(s): 43.66.Lj [DD] Pages: 3810–3817

I. INTRODUCTION

Certain sounds, for example, the squeal of chalk on a blackboard, are perceived as particularly unpleasant. Two broad and mutually inclusive classes of explanation for this unpleasantness can be distinguished: first, it may have perceptual origins in the evolution of the auditory system, such that unpleasant sensations are evoked innately by certain acoustical properties of sounds; second, auditory unpleasantness may have associative origins, whereby particular acoustic properties become associated with objects, situations, or events that give rise to unpleasant sensations. In the present work we focused on the first class of explanation by investigating the relationship between the acoustical properties of sounds and their judged unpleasantness.

An important issue in relating the acoustical properties of sound to their perceptual effects is the choice of a suitable representation of the sound. This can be at the level of the physical properties of the sound in air or the auditory representation of the sound in the brain. The commonly used spectrographic representation of acoustical properties has characteristics that depend on the choice of parameters such as window size, window type, frame size, and hop size (Smith, 2003); in practice these parameters are typically set to values that are governed by the particular acoustic properties and perceptual sensitivities of interest, so, for example, the choice of frame size may depend on whether the focus is on perception of temporal or spectral acoustic features. For the present purposes there were reasons not to prejudge which acoustic properties would be critical, and our wish to avoid making arbitrary and potentially constraining choices for spectrographic analysis parameters motivated the choice of a representation of sound that incorporated at least some of the important properties of patterns of neural activity in the auditory pathway. Accordingly we used biologically derived signal processing algorithms to obtain an approximation to the auditory representation within the brain. A number of mathematical models of the auditory system exist that incorporate auditory representations of stimuli at different processing stages based on physiological data (Patterson, 2000; Patterson *et al.*, 1995; Shamma *et al.*, 1995; Shamma, 2003; Slaney, 1998). All the models incorporate a realistic cochlear component (Patterson, 2000; Slaney, 1998; Meddis and O'Mard, 1997). The models differ with respect to the further central processing that occurs and the degree to which this is constrained by physiology and anatomy. The model proposed by Shamma (2003) incorporates auditory representations at the levels of the cochlear nucleus and cortex and emphasizes temporal modulation within frequency channels and lateral inhibition. The model has been proven useful in assessment of speech intelligibility (Elhilali *et al.*, 2003), discrimination of speech from nonspeech signals (Mesgarani *et al.*, 2004), and accounting for the sensitivity to phase relationship between partials of a sound (Carlyon and Shamma, 2003) and speech enhancement (Mesgarani and Shamma, 2005).

In this work we used the model developed by Shamma (2003) to seek correlations between sound unpleasantness and the representation of sounds in primary auditory cortex. The choice of a primary auditory cortex model, as opposed

 © 2008 Acoustical Society of America

to modeling of the activity in the ascending pathway or in other cortices, is not arbitrary. A candidate area for the encoding of sound unpleasantness is the amygdala (Mirz *et al.*, 2000; Morris *et al.*, 2001), to which there are two routes defined by anatomical studies in small mammals (Doron and LeDoux, 1999). An indirect route proceeds via primary cortex to auditory association cortex and thence to amygdala. There is also a direct route from the auditory thalamus. While the direct thalamo-amygdala route processes crude sensory aspects of the stimulus, the thalamo-cortico-amygdala pathway plays an important role in evaluating complex stimuli (Jarrell *et al.*, 1986). There is no model of auditory representation in the amygdala, but the use of a primary cortex model in these experiments allows a more complex representation of the stimuli from which emotions are subsequently evaluated in the amygdala. In the present work we explored the relationship between the perceived unpleasantness of sounds and their modeled auditory cortical representations.

Relating sound representations to the perceived unpleasantness of sounds is a multivariate problem. Suppose we use a modeled representation of a sound in frequency-time space. In this case, each point in the frequency-time space is a single predictor variable. One of the characteristics of these variables is that they are highly correlated with each other. Also, typically, the number of these variables will be more than the number of observations of these variables (the number of sounds used in the study) and therefore conventional methods such as linear regression cannot be used to establish the relation between perceived unpleasantness and the auditory representation. However, multivariate statistical projection techniques such as partial least squares (PLS) (Wold *et al.*, 1983; Geladi and Kowalski, 1986) and canonical correlation analysis (Mardia *et al.*, 1979) can be used to overcome the problems outlined above. In this work we used PLS to build a model that predicts the degree of unpleasantness of sounds from their modeled auditory representation.

Previous studies that have investigated the psychoacoustics of unpleasant sounds (e.g., Halpern *et al.*, 1986; Bailey *et al.*, 2003) did not examine the modeled representation of sounds in the auditory brain and included only a limited set of sounds, primarily the so-called "griding" sounds that result from scraping actions such as the tine of a fork dragged across a slate, or the screech of chalk on a blackboard. In these earlier studies conventional filtering techniques were used to determine the frequency band that contributed most to the perceived unpleasantness of the sounds.

In the work reported here we used a larger set of sounds that included not only griding sounds but also some other unpleasant sounds such as animal cries. Signal processing was carried out on these sounds to produce a modeled central auditory representation that was correlated with unpleasantness ratings using the PLS multivariate statistical analysis technique. The PLS model was used to determine the "existence region" for unpleasantness in the modeled auditory parameter space and also to predict the unpleasantness of sound given the auditory representation.

II. METHODS

A. Mathematical model of the auditory system

The model of Shamma (2003) incorporates a number of plausible physiological steps to produce an auditory representation of the sound in the primary cortex.

The frequency separation and transduction in the cochlear that transforms the one-dimensional time domain signal into a two-dimensional time-frequency representation is modeled in the following steps.

(i) Decomposition of sound into different frequency bands by the cochlea is modeled using a bank of bandpass filters placed equally on a logarithmic axis. In the model 24 filters per octave are used, over a width of 5.3 octaves.

(ii) The transduction stage of the inner hair cell is modeled by high pass filtering (fluid-cilia coupling), half wave rectification (movement of cilia in one direction), and then low pass filtering the output of each of the filter. A detailed description of this operation is given in Yang *et al.*, 1992.

The neural activity in the two-dimensional time-frequency representation then undergoes lateral inhibition to model that occurs in the cochlear nucleus in the brainstem (Suga, 1995; Rhode and Greenberg, 1994). Mathematically, this stage is modeled by taking the first derivative with respect to the spatial (frequency) axis of the cochlea (Yang *et al.*, 1992).

The cortical representation has been informed by studies in which the linear properties of auditory cortical neurons are assessed using ripple stimuli (Kowalski *et al.*, 1996; Shamma, 2003). A ripple is a sinusoidal modulation along the frequency axis and a dynamic ripple is a ripple that moves with certain velocity either toward the low end of the spectrum (downward movement) or toward the high end of spectrum (upward movement). Theoretically, any two-dimensional time-frequency representation (like the output of the cochlea after lateral inhibition) can be decomposed a sum of dynamic ripples with different spectral modulation frequencies Ω (also called as ripple density or scale), temporal modulation frequencies ω, and phases Θ. And if the neurons are assumed to be linear then transfer functions (and hence the impulse response of neurons) can be determined by knowing the response of neurons to ripples of different densities, velocities, and phases. The impulse response of the neuron is known as a spectrotemporal receptive field (STRF). Neurophysiological data recorded from primary auditory cortex (A1) of mammals have demonstrated tuning to ripple density and velocity (Kowalski *et al.*, 1996; Depireux *et al.*, 2001). Since A1 is tonotopically organized, this level can be mathematically modeled as a bank of filters that extracts the modulations along the temporal and spectral axes of the input. Each filter is centered on a central frequency (F) and is tuned over a range of temporal modulation rates (ω) and spectral modulations (Ω). The output of each filter is computed by convolving the input with the STRF of the filter. The output from each filter in A1 is therefore a four-dimensional (4D) function R (F, ω, Ω, t), where R denotes

the measured activity of the filter and t is the time. This activity measures the activity of ensembles of neurons in the primary auditory cortex in response to the sound stimulus.

B. Partial least-squares regression

PLS regression is a multivariate statistical projection technique that is used to build a regression model when the measured variables are highly correlated and/or when the number of observations is less than the number of variables.

Let $\mathbf{X}$ be a $(N \times K)$ matrix containing N observations on K input/predictor variables and let $\mathbf{Y}$ be a $(N \times M)$ matrix comprising N observations on M output/response variables. PLS seeks to find two vectors $\mathbf{w}_1$ and $\mathbf{v}_1$ in the row space of $\mathbf{X}$ and $\mathbf{Y}$, respectively, such that vectors $\mathbf{t}_1$ and $\mathbf{u}_1$ defined as

$$\mathbf{t}_1 = \mathbf{X}\mathbf{w}_1$$

$$\mathbf{u}_1 = \mathbf{Y}\mathbf{v}_1 \quad (1)$$

have maximum covariance. The vectors $\mathbf{t}_1$ and $\mathbf{u}_1$ are known as the latent variables for $\mathbf{X}$ and $\mathbf{Y}$, respectively. The latent variables $\mathbf{t}_1$ and $\mathbf{u}_1$ are extracted using an iterative algorithm (Geladi and Kowalski, 1986). In general, one latent variable may not be sufficient to explain the information contained in $\mathbf{X}$ and $\mathbf{Y}$. The second latent variable is extracted after the contribution of the first latent variable is subtracted. Similarly the third latent variable is extracted after the contribution of the first two latent variables has been taken off from the original data matrices $\mathbf{X}$ and $\mathbf{Y}$ and so on.

C. Subjects

Fifty Newcastle University undergraduate and postgraduate students (33 females) participated in the experiment. The subjects were recruited through on-campus advertisement and were between ages 19 and 30 years. No subjects reported any hearing problems, neither did any report a history of epilepsy or index neurological event. All subjects gave informed consent to participate in the study, which was carried out with local ethical approval.

D. Stimuli

Seventy-five sound stimuli that included griding sounds, other unpleasant environmental sounds, animal calls, and baby cries were selected. Some sounds, including the griding sounds, were recorded (see Table I for more details about the sound sources) whereas the other sounds were collected from various internet sources. For some participants, certain sounds may also have had associations with unpleasant images or events; however, our aim in this experiment was to use a broad corpus of sounds to allow the analysis of auditory features common to sounds that are judged to be unpleasant, without specific regard to their possible additional associative properties.

The durations of the stimuli varied between 1.5 and 2.0 s. Five listeners (who did not take part in the main experiment) judged the loudness of sounds. The rms values of the sounds were adjusted so that these subjects perceived the stimuli to be equally loud. Stimulus presentation levels fol-

TABLE I. Means and standard deviations of the unpleasantness ratings for each sound, ranked according to the mean rating magnitude. The rating scale ranged between 0 (least unpleasant) and 9 (most unpleasant). (Note: Where the type of sound source is not obvious from the sound name, sources were as follows. Angle grind: angle grinding a hollow metal pipe; blackboard chalk: scraping a piece of chalk along a blackboard; blackboard nails: dragging fingernails down a blackboard; brake double: bicycle brakes being applied; clarinet squeak/honk: misplaying a clarinet; electric drill: electric drill running freely at a range of speeds; fork bottle: scraping a steel fork along the surface of a ridged metal bottle; fork glass: scraping a fork along glass; guitar: electric guitar with distortion effects; knife bottle: scraping a sharp knife along the surface of a ridged metal bottle; mixer glass: metal whisk of a food mixer held against a glass bowl; record scratch: stylus of a record player dragged across the surface of a vinyl record; ruler bottle: dragging a plastic ruler along the surface of a ridged metal bottle; spade drag: dragging a metal spade along a concrete floor; and spade drop: dropping a metal spade onto a concrete floor).

Sound name	Mean rating	Standard deviation
Knife bottle	8.10	1.47
Fork glass 1	8.08	1.19
Blackboard chalk 2	8.06	1.40
Fork glass 3	8.04	1.39
Fork bottle 4	7.84	1.56
Blackboard chalk 1	7.82	1.44
Ruler bottle 2	7.80	1.32
Fork bottle 3	7.76	1.60
Ruler bottle 1	7.58	1.70
Fork bottle 1	7.56	1.68
Female scream	7.32	2.03
Female scream 2	7.02	1.98
Brake double	6.86	1.79
Fork glass 4	6.78	2.36
Blackboard nails 1	6.48	1.68
Spade drag 1	6.46	1.72
Guitar 1	6.44	1.89
Angle grind 2	6.44	2.03
Blackboard nails 2	6.16	1.64
Clarinet Squeak	6.14	1.77
Spade drag 2	6.12	1.61
Electric drill	6.10	2.14
Mixer glass 1	6.08	1.67
Tire skids	5.92	1.62
Baby cry	5.92	2.16
Electric drill 2	5.86	1.94
Multiple babies crying	5.80	1.92
Cat screaming	5.68	2.10
Violin	5.64	1.59
Pig	5.50	1.89
Angle grind 1	5.28	1.87
Lion cub	5.22	2.34
Domestic cat	5.20	1.95
Record scratch 1	5.16	2.08
Jungle bird	5.16	1.89
Falcon	5.10	2.00
Buzzer	5.02	1.86
Panther	4.98	1.88
Cougar	4.98	1.83
Wasp	4.92	2.11
Macaca fascicularis	4.80	2.16
Glass breaking	4.80	1.81
Bear	4.76	1.87
Anteater	4.74	1.84
Hippo	4.58	1.82
Lion	4.56	1.89

TABLE I. (*Continued.*)

Sound name	Mean rating	Standard deviation
Spade drop 1	4.46	2.04
Gorilla	4.42	1.68
Camel	4.30	1.67
Zebra	4.24	1.40
Film projector	4.24	1.99
Bull frog	4.04	1.47
Eagle	4.02	2.29
Puffer	4.00	1.94
Fire alarm	4.00	1.94
Clarinet honk	3.94	1.91
Cat purr	3.90	1.80
Leopard	3.88	1.94
Elephant	3.82	2.01
Phone ringing	3.76	2.09
Howling wolf	3.74	2.06
Dog growl	3.74	2.06
Thunder 1	3.72	2.35
Dolphin clicks	3.48	1.89
Guitar 2	3.46	1.91
Lamb	3.42	1.92
Frog	2.68	1.76
Thunder 2	2.42	2.11
Applause	2.04	1.75
Revving engine	1.86	1.70
Running water	1.52	1.94
Bubbling water	1.40	1.97
Small waterfall	1.06	1.65
Water flow	0.98	1.67
Baby laugh	0.80	1.43

lowing these adjustments were in the range 70–75 dB sound pressure level. All stimuli had a sampling rate of 22 050 Hz and 16 bit resolution.

E. Procedure

Subjects were seated in a sound proof room with a computer monitor and a keyboard. A MATLAB™ based program randomly selected a sound from the set of 75 sounds and played it over Senheiser HD 265 headphones using a high quality external sound card (Edirol UA-20). The task was to rate the unpleasantness of sounds on a scale from 0 to 9, with 0 being the least unpleasant and 9 being the most unpleasant. Three practice trials (using the same sounds for all subjects) were performed first so as to familiarize subjects with the task and ensure the instructions were understood. After each sound was played a prompt appeared on the screen instructing the subject to enter a rating and then press the return key. They were instructed to press any key to play the next sound.

F. Modeling of auditory analysis

The auditory cortex representation [the 4D function $R(F, \omega, \Omega, t)$] of each of the sounds was obtained using the model of the mammalian auditory system described in Sec. II A. The range of modeled ripple densities Ω used was 0.5–8 cycles/octave and that of ripple velocity ω was 1–64 counts/s. Preliminary analysis of the auditory representation showed that the tonotopic axis F and the ripple velocity ω were the important dimensions that separated the most unpleasant sounds from the least unpleasant sounds. Therefore the auditory representation was restricted to the two dimensions F and ω. The two-dimensional function $R(F, \omega)$ was assembled in a matrix with each row containing the acoustic representation of a single sound. The size of the matrix $\mathbf{X}$ was (75×1792). The average unpleasantness rating (across subjects) was computed and assembled in a vector $\mathbf{Y}$.

To build a model that relates the perceived unpleasantness with the acoustic representation, the data set was divided into two sets: a training set and a validation set. The training set consisted of data for 50 randomly selected sounds, while the data for the remaining 25 sounds comprised the validation set. A PLS model as described in Sec. II B between input variables $\mathbf{X}$ (acoustic representation) and the output variable $\mathbf{Y}$ (average unpleasantness rating) was built on the training set, and predictions for the validation set were then computed. The model was then used to make a prediction of the unpleasantness ratings of the sounds in the validation set using their acoustic representation as an input.

III. RESULTS

A. Unpleasantness ratings

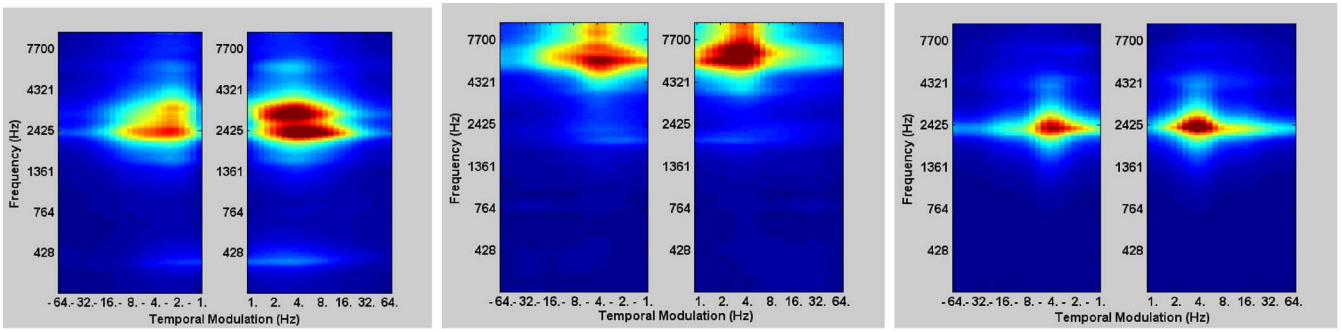
The mean and standard deviation of unpleasantness ratings for the 75 sounds are shown in Table I. The table shows that participants were able to use the full range of the 0–9 rating scale: The highest mean unpleasantness rating was 8.10, for the sound of a knife scratching a bottle, and the lowest mean rating was 0.80, for the sound of a baby laughing. The standard deviations of the ratings for individual sounds varied between 1.19 and 2.36.

B. Examination of individual data sets

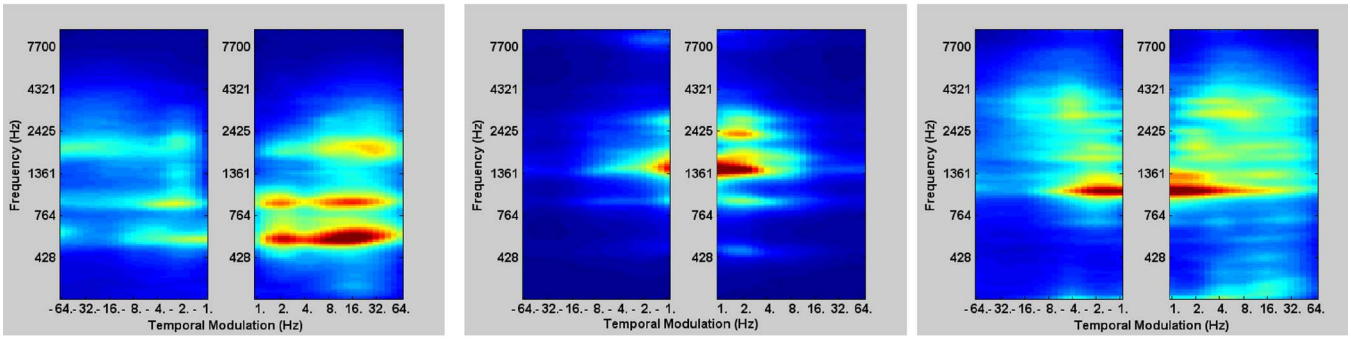
Auditory representations of nine sounds in the frequency (F)-temporal modulation (ω) plane are shown in Fig. 1. The three rows in the figure (from the top) show sounds with "high," "intermediate," and "low" unpleasantness ratings, respectively. Inspection of the top row shows that sounds with the highest unpleasantness ratings have maximal energy concentrations in a frequency band from approximately 2400 to 5500 Hz and temporal modulations of 1–8 Hz. As the unpleasantness rating decreased (middle and bottom rows) the auditory patterns show a tendency for energy to be concentrated at lower spectral frequency and higher temporal modulation. The data suggest that perceived unpleasantness in these sounds is associated with activation in modeled central representations in regions of frequency space between 2400 and 5500 Hz and in regions of low temporal modulation (below 16 Hz).

C. Partial least-squares model

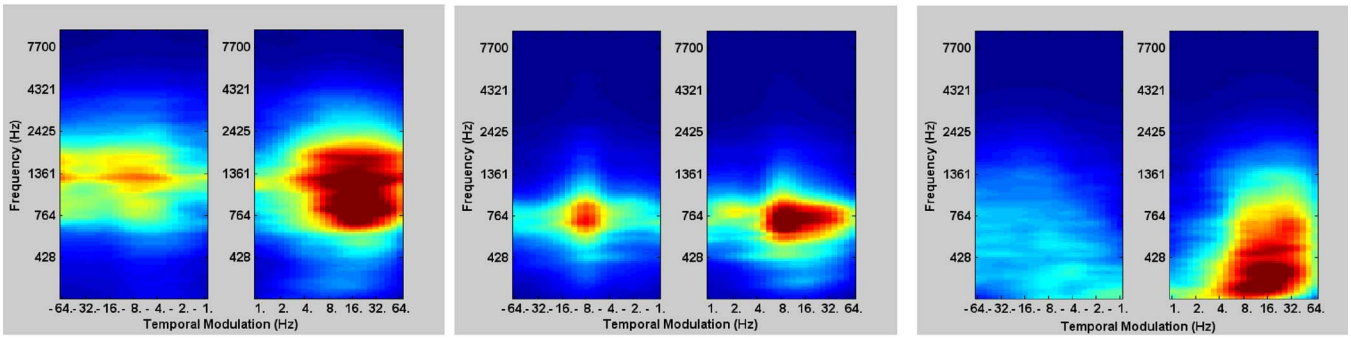
The percentage variance in the training data set comprising 50 examples captured by different latent variables is summarized in Table II. This table shows the percentage of the variance in the ratings and in the modeled representations that were explained by each latent variable in turn. Using



Knife Bottle (8.1) **Fork Glass (8.04)** **Blackboard Chalk (7.82)**



Tire Skids (5.92) **Lion cub (5.22)** **Glass breaking (4.22)**



Running water (1.92) **Bubbling water (1.40)** **Waterfall (0.98)**

FIG. 1. (Color online) Frequency temporal modulation ($F-\omega$) representation of sounds with high (top row), medium (middle row), and low (bottom row) mean unpleasantness ratings. The mean rating for each sound is given in parentheses; ratings were on a scale from 0 to 9, where high numbers correspond to greater perceived unpleasantness. Positive (negative) temporal modulation rate represents the downward (upward) movement of the ripple (see text).

cross validation (Jackson, 1991) two latent variables were used to build the PLS model. The ability of the model based on two latent variables to predict the unpleasantness ratings of the 25 unseen sounds in the validation set was carried out. The prediction of unpleasantness ratings from the acoustic representation of the 25 sounds by the PLS model is shown in Fig. 2. It can be seen that the PLS model is a satisfactory predictor of the unpleasantness ratings of the sounds in the validation set. The correlation coefficient between predicted and measured data is 0.65 ($p<0.0004$) and the predicted values explain 59.63% of the variance of measured data.

The modeling using PLS provided further evidence for the qualitative trends noted in the individual data above. Following validation of the model it is possible to investigate the relative weights given to energy at different frequencies and temporal modulations. The relative weights are plotted for the two latent variables in Figs. 3 and 4. Figure 3 shows that for the first latent variable spectral frequencies in the range 2500–5500 Hz received relative larger weights, and weights for temporal modulations decreased as modulation rates increased, primarily in the range 1–16 Hz. Figure 4 shows that for the second latent variable largest weights were

TABLE II. Percentage variance captured by the PLS model.

	X-block (auditory representation)		*Y*-block (ratings)	
Latent variable No.	This latent variable	Total	This latent variable	Total
1	37.49	37.49	54.09	54.09
2	6.52	44.04	15.04	69.13
3	9.02	53.06	7.02	76.15
4	7.88	60.94	4.66	80.81
5	9.00	69.94	2.26	83.07
6	2.21	72.15	6.07	89.14
7	3.20	75.35	1.86	91.00
8	2.48	77.83	2.38	93.38
9	2.42	80.26	2.03	95.41
10	2.91	83.16	0.86	96.27
11	1.38	84.55	1.12	97.38
12	2.75	87.30	0.36	97.75

assigned to frequencies around 2500 Hz and to low temporal modulations.

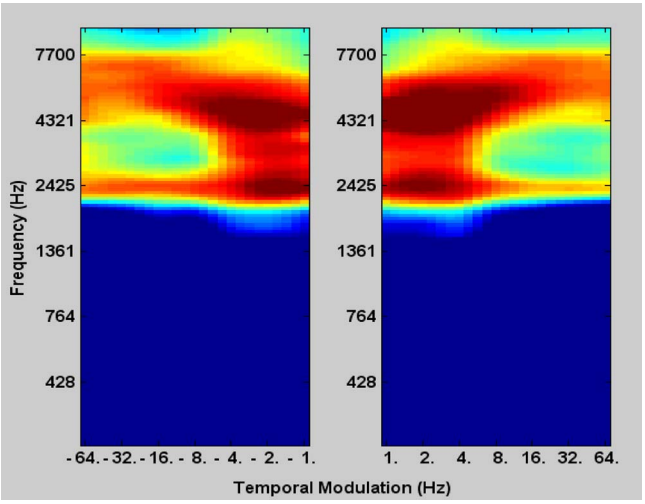


FIG. 3. (Color online) Relative weights associated with energy at different frequencies and temporal modulations for the first latent variable. Positive (negative) temporal modulation rate represents the downward (upward) movement of the ripple (see text).

IV. DISCUSSION

The aim of the present study was to determine features of the modeled central representation of sounds that are associated with auditory perceptual unpleasantness. A model of the auditory system was used to model the representation of sound at the level of primary auditory cortex, a level of representation which is likely to be similar to expected inputs to the amygdala from either auditory thalamus or cortex. A multivariate model was then constructed to predict the unpleasantness of sounds from the acoustic features of the sounds. The model showed that a band of frequencies in the range from 2500 to 5500 Hz and temporal modulations in the range from 1 to 16 Hz were important predictors for the unpleasantness of sounds.

Previous studies have also examined the acoustic properties of unpleasant sounds. In a seminal paper, Halpern *et al.* (1986) analyzed the acoustic properties of "griding sounds" and concluded that the "lower" frequencies in these sounds are more important rather than the "higher" frequencies. However, the force of the words lower and higher in their conclusion needs to be understood in the context of their results. The lowest cut-off frequency in the low pass filtering they used was 3 kHz. As the cut-off frequency was increased from 3 to 8 kHz in steps of 1 kHz, no change in unpleasantness was observed. This is in accordance with the present model as all these low filtered sounds contained energy in the band 2500–5500 Hz. In the high pass filtering condition they used cutoffs of 2–6 kHz in steps of 1 kHz. It was observed that unpleasantness was highest when cut-off frequency was between 2 and 4 kHz. After 4 kHz the unpleasantness decreased markedly. This shows that unpleasantness of the sounds lay roughly in a band of 2–4 kHz rather than in a low frequency region. Bailey *et al.* (2003) analyzed the acoustic properties of griding sounds and noted an increased energy in the average long term spectrum of these sounds at 2–3

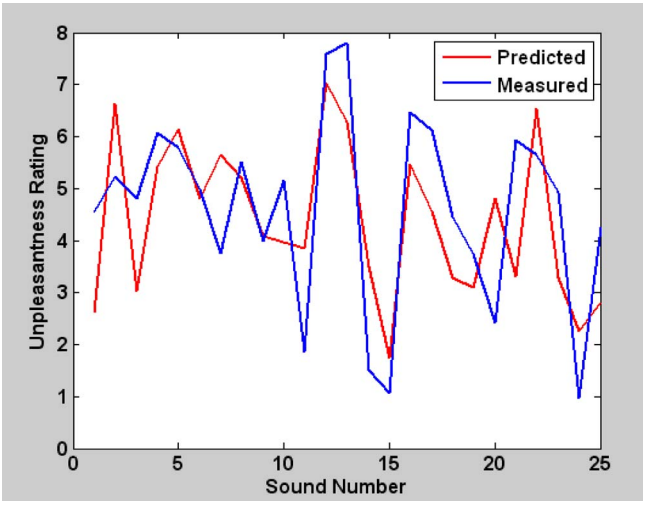


FIG. 2. (Color online) Plots of measured and predicted unpleasantness ratings from the acoustic representation.

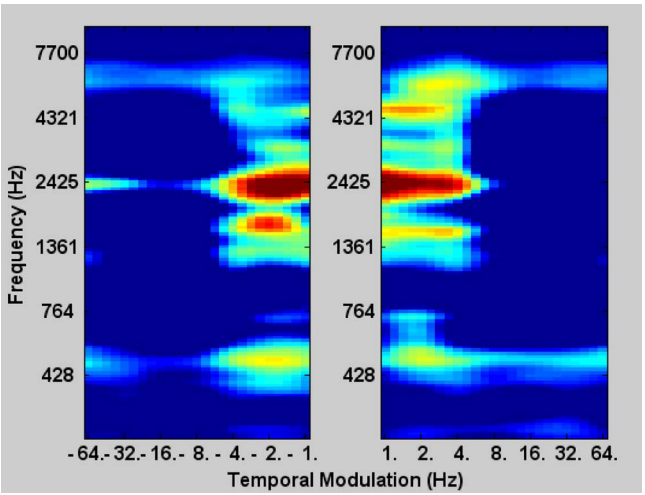


FIG. 4. (Color online) Relative weights associated with energy at different frequencies and temporal modulations for the second latent variable. Positive (negative) temporal modulation rate represents the downward (upward) movement of the ripple (see text).

kHz, which again points to the power in that band being important for the perceived unpleasantness of the sounds.

Halpern *et al.* (1986) also examined if the fluctuations in the temporal envelope of the griding sounds correlated with the perceived unpleasantness of the sounds. They extracted the temporal envelope of the sounds and then multiplied the inverted amplitude envelope with the sounds so as to flatten (demodulate) the fluctuations in the amplitude envelope. They observed that there was not much change in unpleasantness between the original sounds and the corresponding demodulated sounds. In contrast, our analysis found that low temporal modulations below 16 Hz are critical for the perception of unpleasantness of the sounds. This difference can be explained in two ways. First, the temporal envelope of the sounds is not solely determined by the acoustic stimulus but jointly by the spectrotemporal properties of the stimulus and the peripheral filtering done at the cochlea (for an illustration, see Fig. 4.2 in Viemeister and Plack, 1991). The approach taken by Halpern *et al.* (1986) to reduce the modulations in the temporal envelope of the acoustic stimulus will not have eliminated temporal envelope fluctuations caused by interaction or filtering at the cochlea, which may have contributed to the percept of unpleasantness. Second, the outcome may depend on the method used for extraction of the temporal amplitude envelope. Halpern *et al.* (1986) did not state which method they used, but it should be noted that there is a difference between the more biological realistic method of extracting the temporal envelope employed here (which uses half wave rectification followed by low pass filtering) and the extraction of the envelope in a "mathematical" sense, for example, using the Hilbert transform. This was illustrated clearly by Yost *et al.* (1998): A harmonic sound with fundamental frequency $f0$ differs in pitch from a sound with all the harmonics shifted by $f0/2$; Yost *et al.* (1998) showed that temporal envelopes for the two sounds differed in accordance with the pitch difference when the envelopes were extracted using the biological realistic combination of half wave rectification and low pass filtering, but did not differ when extracted using the Hilbert transform and other biologically unrealistic methods. Since our approach involved a biological realistic model to extract the temporal fluctuations in the unpleasant sounds, we take our results to indicate that the temporal modulations shown in the model do carry information relevant to the perceived unpleasantness of the sounds.

One can ask why a band of energy in the frequency range 2–5 kHz and temporal modulations less than 16 Hz make sound unpleasant. One possible answer relates to the sensitivity of the auditory system: Absolute thresholds are lowest in the 2–5 kHz range, and equal loudness curves show that, for a given signal level, loudness is greatest in that range (Fletcher and Munson, 1933). Similarly the auditory system is more sensitive to low temporal modulations than to higher temporal modulations (Viemeister, 1979). Certain sounds may therefore lead to unpleasant percepts because they contain strong concentrations of energy in a range of spectral and temporal modulation frequencies to which the auditory system is maximally sensitive.

The relation between physical attributes of signals and perceived discomfort or aversiveness has also been studied in the visual modality. Fernandez and Wilkins (2008) found that uncomfortable visual images have high-contrast energy around a spatial frequency of 3 cycles/deg and that the perceived discomfort correlates with the energy at this frequency. It is noteworthy that the visual system is most sensitive to this range of spatial frequencies, and that gratings with this spatial frequency are more likely to induce seizures in epileptic patients. However, the nature of any relationship between visual and auditory unpleasantness remains unclear: Preliminary exploration of the relationship between individual differences in judged unpleasantness of modulated auditory signals and individual differences in perceived discomfort from high-contrast visual gratings did not indicate an association between the two (Bailey *et al.*, 2003).

The approach we have developed here provides an informative complement to the experiments cited above involving parametric manipulations of putative perceptually aversive acoustical features. It could also be applied to the abnormal perception of unpleasant sound as in acute hyperacousis (in migraine) or in chronic hyperacousis. In particular, the approach would allow a test of whether, in hyperacouses, there is an increased sensitivity in the same existence region or in different existence regions. Anecdotal reports would suggest the former in both acute and chronic forms of hyperacousis, but we are not aware of any systematic study.

V. CONCLUSIONS

The acoustic environment contains many sounds that are perceived as unpleasant. The study addressed the issue of representation of these sounds in the auditory cortex of the brain by using a model of the auditory system that is based on data collected from the mammalian auditory system. The auditory representation was then correlated with perceived unpleasantness using the multivariate technique PLS. The existence region of unpleasantness in the auditory space of frequency-temporal modulation was determined after the PLS model had been validated by predicting the unpleasantness of novel sounds from the auditory representation. The existence region corresponded to spectral frequencies between 2500 and 5500 Hz, and temporal modulations in the range 1–16 Hz.

Bailey, P. J., Chisholm, M., Wilkins, A., and Hill, N. I. (**2003**). "Factors affecting the aversive nature of some auditory and visual patterns," Int. J. Audiol. **42**, 375.

Carlyon, R. P., and Shamma, S. A. (**2003**). "An account of monaural phase sensitivity," J. Acoust. Soc. Am. **114**, 333–348.

Depireux, D. A., Simon, J. Z., Klein, D. J., and Shamma, S. A. (**2001**). "Spectro-temporal response field characterization with dynamic ripples in ferret primary auditory cortex," J. Neurophysiol. **85**, 1220–1234.

Doron, N. N., and LeDoux, J. E. (**1999**). "Organization of projections to the lateral amygdala from auditory and visual areas of the thalamus in the rat," J. Comp. Neurol. **412**, 383–409.

Elhilali, M., Chi, T., and Shamma, S. A. (**2003**). "A spectro-temporal modulation index (STMI) for assessment of speech intelligibility," Speech Commun. **41**, 331–348.

Fernandez, D., and Wilkins, A. J. (**2008**). "Uncomfortable images in art and nature," Perception **37**(7), 1098–1113.

Fletcher, H., and Munson, W. A. (**1933**). "Loudness, its definition, measurement and calculation," J. Acoust. Soc. Am. **5**, 82–108.

Geladi, P., and Kowalski, B. R. (**1986**). "Partial least-squares regression: A tutorial," Anal. Chim. Acta **185**, 1–17.
Halpern, L. D., Blake, R., and Hillenbrand, J. (**1986**). "Psychoacoustics of a chilling sound," Percept. Psychophys. **39**, 77–80.
Jackson, J. E. (**1991**). *A User's Guide to Principal Components* (Wiley, New York).
Jarrell, T. W., Gentile, C. G., McCabe, P. M., and Schneiderman, N. (**1987**). "Involvement of cortical and thalamic auditory regions in retention of differential bradycardiac conditioning to acoustic conditioned stimuli in rabbits," Brain Res. **412**, 285–294.
Kowalski, N., Depireux, D., and Shamma, S. (**1996**). "Analysis of dynamic spectra in ferret primary auditory cortex: Characteristics of single unit responses to moving ripple spectra," J. Neurophysiol. **76**, 3503–3523.
Mardia, K. V., Kent, J. T., and Bibby, J. M. (**1979**). *Multivariate Analysis* (Academic, London).
Meddis, R., and O'Mard, L. (**1997**). "A unitary model of pitch perception," J. Acoust. Soc. Am. **102**, 1811–1820.
Mesgarani, N., Slaney, M., and Shamma, S. A. (**2004**). "Speech discrimination based on multiscale spectrotemporal modulations," International Conference on Acoustics, Speech and Signal Processing (ICASSP), pp. 601–604.
Mesgarani, N., and Shamma, S. A. (**2005**). "Speech enhancement based on the filtering of spectro-temporal modulations," International Conference on Acoustics, Speech and Signal Processing (ICASSP), pp. 1105–1108.
Mirz, F., Gjedde, A., Sodkilde-Jrgensen, H., and Pederson, C. B. (**2000**). "Functional brain imaging of tinnitus-like perception induced by aversive auditory stimuli," NeuroReport **11**, 633–637.
Morris, J. S., Buchel, C., and Dolan, R. J. (**2001**). "Parallel neural responses in amygdala subregions and sensory cortex during implicit fear conditioning," Neuroimage **13**, 1044–1052.
Patterson, R. D. (**2000**). "Auditory images: How complex sounds are represented in the auditory system," J. Acoust. Soc. Jpn. (E) **21**, 183–190.
Patterson, R. D., Allerhand, M. H., and Giguere, C. (**1995**). "Time-domain modelling of peripheral auditory processing: A modular architecture and a software platform," J. Acoust. Soc. Am. **98**, 1890–1894.
Rhode, W. S., and Greenberg, S. R. (**1994**). "Lateral suppression and inhibition in the cochlear nucleus of the cat," J. Neurophysiol. **71**, 493–519.
Shamma, S. A., Versnel, H., and Kowalski, N. (**1995**). "Ripple analysis in ferret primary auditory cortex. I. Response characteristics of single units to sinusoidally rippled spectra," Aud. Neurosci. **1**, 233–254.
Shamma, S. (**2003**). "Encoding sound timbre in the auditory system," IETE Journal of Research **49**, 193–205.
Slaney, M. (**1998**). "Auditory Toolbox, version 2," Interval Research Corporation Technical Report No. 1998-010.
Smith, J. O. (**2003**). *Mathematics of the Discrete Fourier Transform (DFT)—With Audio Applications* (W3K, Stanford).
Suga, N. (**1995**). "Sharpening of frequency tuning by inhibition in the central auditory system: Tribute to Yasuji Katsuki," Neurosci. Res. (N Y) **21**, 287–299.
Viemeister, N. F., and Plack, C. J. (**1991**). "Time analysis," in *Human Psychophysics*, edited by W. A. Yost, A. N. Popper, and R. R. Fay (Springer, New York), pp. 116–155.
Viemeister, N. F. (**1979**). "Temporal modulation transfer functions based upon modulation thresholds," J. Acoust. Soc. Am. **66**, 1364–1380.
Wold, S., Martens, H., and Wold, H. (**1983**). "The multivariate calibration problem in chemistry solved by the PLS method," in *Proceedings of the Conference on Matrix Pencils*, Lecture Notes in Mathematics, edited by A. Ruhe and B. Kågström (Springer, Berlin), pp. 286–293.
Yang, X., Wang, K., and Shamma, S. (**1992**). "Auditory representation of acoustic signals," IEEE Trans. Inf. Theory **38**, 824–838.
Yost, W. A., Patterson, R. D., and Sheft, S. (**1998**). "The role of the envelope in processing iterated rippled noise," J. Acoust. Soc. Am. **104**, 2349–2361.

Role of masker predictability in the cocktail party problem[a)]

Gary L. Jones
Department of Physiology, University of Wisconsin-Madison, Madison, Wisconsin 53705

Ruth Y. Litovsky[b)]
Waisman Center, University of Wisconsin-Madison, Madison, Wisconsin 53705

(Received 25 October 2007; revised 29 August 2008; accepted 6 September 2008)

In studies of the cocktail party problem, the number and locations of maskers are typically fixed throughout a block of trials, which leaves out uncertainty that exists in real-world environments. The current experiments examined whether there is (1) improved speech intelligibility and (2) increased spatial release from masking (SRM), as predictability of the number/locations of speech maskers is increased. In the first experiment, subjects identified a target word presented at a fixed level in the presence of 0, 1, or 2 maskers as predictability of the masker configuration ranged from 10% to 80%. The second experiment examined speech reception thresholds and SRM as (a) predictability of the masker configuration is increased from 20% to 80% and/or (b) the complexity of the listening environment is decreased. In the third experiment, predictability of the masker configuration was increased from 20% up to 100% while minimizing the onset delay between maskers and the target. All experiments showed no effect of predictability of the masker configuration on speech intelligibility or SRM. These results suggest that knowing the number and location(s) of maskers may not necessarily contribute significantly to solving the cocktail party problem, at least not when the location of the target is known. © *2008 Acoustical Society of America.*
[DOI: 10.1121/1.2996336]

PACS number(s): 43.66.Lj, 43.66.Pn, 43.71.Gv [RLF] Pages: 3818–3830

I. INTRODUCTION

Cherry (1953) formulated the "cocktail party problem" in terms of how we understand what one person is saying when others are talking at the same time. An important feature of such multitalker environments is that they can be highly unpredictable. While a listener is attending to a target talker, many features of the competing source(s) can vary, including their number, location(s), and content, to name just a few. With so many sources of variability, intuition would suggest that listener expectations about maskers could play an important role in solving the cocktail party problem. However, studies of the cocktail party problem typically use paradigms in which the number and locations of maskers are constant throughout a block of trials, thereby ensuring high predictability of the multitalker environment. There has been little research that specifically addresses how masker predictability affects speech intelligibility in a cocktail party environment.

As noted by Cherry (1953), listeners can make use of differences in the spatial locations of sources to help separate a target signal from competing sources. The decrease in thresholds that results from such spatial separation of target from interferers is known as spatial release from masking (SRM); it is a robust phenomenon that is observed even when azimuthal localization cues are limited to just interaural level differences or just interaural timing differences (ITDs) (Bronkhorst and Plomp, 1988; Culling *et al.*, 2004). Durlach *et al.* (2003a) proposed two different strategies that could enable listeners to extract a target signal from competing sounds: a "max" strategy with enhanced sensitivity to sources from the target location and a "min" strategy in which sensitivity to sources from the masker location(s) is suppressed. It has been shown that knowing the location of the target can improve performance in identification of both speech and nonspeech targets (Arbogast and Kidd, 2000; Ericson *et al.*, 2004; Kidd *et al.*, 2005), a finding consistent with the max strategy. It is important to explore whether responses consistent with the min strategy also contribute significantly to speech intelligibility in multitalker environments.

Masking of a speech target by speech maskers differs in several ways from masking by noise maskers, and this is well illustrated by SRM data. Good examples of this can be seen by considering spatial configurations in which all maskers are at a single location in the horizontal plane 90° away from the target. First, the amount of SRM depends strongly on the number of competing sounds when the maskers are speech or reversed speech but not when the maskers are noise (Peissig and Kollmeier, 1997; Bronkhorst, 2000; Culling *et al.*, 2004; Hawley *et al.*, 2004). Second, when two or three maskers are present, greater SRM is observed with speech maskers than with noise maskers (Culling *et al.*, 2004; Hawley *et al.*, 2004). Third, the mere *perception* of spatial separation has differential effects for speech and noise maskers. The perceived position of a masker that is actually colocated with the target can be displaced by presenting, 60° away from the target, a duplicate

[a)]Portions of this work were presented in "Role of masker predictability in the cocktail party effect" at the Midwinter Meeting of the Association for Research in Otolaryngology, New Orleans, LA, February 2005.
[b)]Electronic mail: litovsky@waisman.wisc.edu

 © 2008 Acoustical Society of America

of the masker that is time shifted, so it leads the other copy by several milliseconds. This technique takes advantage of the precedence effect, whereby leading sources dominate the perceived locations of paired sounds, and it results in significant SRM with speech maskers but not with noise maskers (Freyman *et al.*, 1999, 2001).[1]

This last example, in which for speech maskers there can be sizable SRM despite *increasing* the overall masker level by 3 dB, illustrates the concept of "informational masking." At present any discussion of this type of masking necessarily involves definitional issues, and there are ongoing efforts to improve existing definitions of informational masking [e.g., see Durlach *et al.* (2003a)]. Informational masking is commonly equated with any masking beyond the "energetic" component of masking, which results from overlapping excitation at the auditory periphery. Thus, it is similar to what was earlier described as "excess" or "perceptual" masking (Carhart *et al.*, 1969). Studies with both speech and nonspeech stimuli have shown that spatial separation of target and maskers is effective at combating informational masking (Kidd *et al.*, 1998; Freyman *et al.*, 1999). Thus, measures of SRM can be particularly useful for identifying conditions in which informational masking is present.

There is a long tradition linking informational masking to stimulus uncertainty, but there has been a recent trend to emphasize the role of similarity between target and masker(s) or even to base the very definition of informational masking on similarity (Watson *et al.*, 1976; Durlach *et al.*, 2003b; Brungart and Simpson, 2004). Generally, however, uncertainty and similarity are both believed to be sources of informational masking (Oh and Lutfi, 1998; Durlach *et al.*, 2003b; Watson, 2005). For the purposes of these experiments, informational masking is defined as any masking beyond energetic masking. Reductions in masker uncertainty can, we believe, reduce the informational component of masking.

Evidence of masking due to masker uncertainty has been found for both nonspeech and speech targets. For example, thresholds for detecting a target tone in the presence of a multicomponent nonspeech masker are elevated under conditions of high uncertainty about the spectral content of the masker (Lutfi, 1993; Oh and Lutfi, 1998). In addition, Fan *et al.* (2008) reported that *spatial* uncertainty of maskers leads to degraded detection of nonspeech stimuli. As regards speech targets, there is evidence of reduced speech intelligibility under conditions of uncertainty about masker content, but the effects reported in the literature have been rather small (Brungart and Simpson, 2004; Freyman *et al.*, 2007). As concerns uncertainty about location, it has been shown that task performance is reduced when there is trial-to-trial uncertainty about the spatial locations of *both* targets and maskers (Shinn-Cunningham and Ihlefeld, 2004; Kidd *et al.*, 2005; Brungart and Simpson, 2007a). An important next step is to isolate the effects, if any, of uncertainty about the number and locations of maskers.

This article presents the results of three experiments that examined speech intelligibility and SRM when listeners were attending to a speech target coming from a known location while the number and locations of competing sounds could vary from trial to trial. Uncertainty about the number or locations of maskers could be a source of informational masking. Thus, decreases in uncertainty could lead to improved speech intelligibility. Furthermore, one might expect that high predictability in the number and locations of maskers would provide listeners with information about the auditory environment, which would allow them to utilize spatial cues more effectively, resulting in greater SRM. Thus, it was hypothesized that as predictability of the number and/or locations of speech maskers is increased, there will be (1) improved speech intelligibility and (2) increased SRM.[2] The first experiment reported here tested whether percent correct scores and SRM at a fixed signal-to-noise ratio (SNR) increase as the predictability of the masker configuration is stepped up from 10% to 80%. The second experiment examined whether speech reception thresholds (SRTs) improve (decrease) and SRM increases when (a) predictability of the masker configuration is increased from 20% to 80% and/or (b) when the complexity of the listening environment is decreased. The third experiment tested whether SRTs decrease and SRM increases when predictability of the masker configuration is increased from 20% up to 100% while minimizing the onset delay between maskers and the target. These experiments did not support the hypothesis; that is, there was no effect of predictability of the number or locations of maskers on speech intelligibility or SRM.

II. EXPERIMENT 1: SPEECH INTELLIGIBILITY AT A FIXED SNR

A. Method

1. Listeners

Participants in the experiment were eight paid university students (eight females), 18–19 years of age. Some subjects had participated in a pilot study for these experiments. Only native English speakers from households in which no language other than English was spoken were recruited. Due to the effects of musical training on performance in informational masking experiments (Oxenham *et al.*, 2003), only subjects who did not have extensive formal musical training were eligible to participate. Audiograms were performed with each potential subject, and pure tone thresholds of 20 dB HL or better at the octave frequencies from 250 to 8000 Hz were required. One potential subject was excluded from this experiment on the basis of tone thresholds.

2. Stimuli

Stimuli for this experiment were recorded by a male talker, trained to speak at constant levels and rates. The same voice was used for both targets and maskers in order to facilitate uncertainty-based masking effects, if any, through high target-masker similarity [e.g., see Durlach *et al.* (2003b)]. The targets were from a closed set of 40 spondees with equivalent intelligibility as determined by pilot testing. This stimulus corpus was chosen because it can be used for repeated testing on numerous conditions. The maskers were concatenated recordings of Harvard IEEE sentences (Rothauser *et al.*, 1969). Thus, in this experiment a relatively brief spondee target could be presented with a substantial onset

delay in the midst of a lengthy masker. This is similar to an approach in which Freyman *et al.* (1999) used an onset delay to provide a basis for the subject to attend to the target in conditions in which target and masker were presented from the same location. In many experiments that measure masking of speech targets by speech interferers a large proportion of errors result from the subject misidentifying an interferer as the target [e.g., see Brungart (2001)]. One motivation for using spondees as targets, as opposed to sentences from the same corpus as the maskers, was to minimize such errors based on confusing the *content* of the target with the content of the maskers.

The maskers were edited in two ways to limit opportunities for "listening in the gaps" between individual words or sentences in the masker. First, silent gaps between consecutive words were edited out manually. Second, both ends of each recorded sentence were edited using an iterative automated algorithm. The algorithm works from each end of the sentence and removes 10 ms segments until it finds a segment whose root mean square (rms) amplitude is within 12 dB of the rms of the whole sentence, at which point it identifies a zero crossing near the end of the sentence and makes the final cut there. The automated editing caused six of the recorded sentences to sound unnatural, and these six sentences were discarded. The remaining sentences were concatenated to create three-sentence maskers with a mean duration of 5.4 ± 0.1 s. Some sentences occurred in multiple maskers, but no sentence was repeated in any masker and two maskers containing the same sentence were never presented on the same trial. The resulting maskers had a rapid cadence of about 250 words/min but were judged by both experimenters and by the listeners to be natural and were readily understandable. Although the maskers still had considerable amplitude modulation, the editing of the recordings could be expected to reduce opportunities for listening in the gaps.

3. Procedures

A schematic overview of the experimental setup is shown in Fig. 1(c). The experiments were conducted in a small room (2.9 m $\times$ 3.6 m) with reverberation time (RT_{60}) of approximately 250 ms. The subject was seated at the center of a hemispheric loudspeaker array with a radius of 1.5 m. Subjects were seated on a chair on a platform that could be raised or lowered so that the opening of the ear canal was within 4 cm of the horizontal plane. The platform, walls, and ceiling were covered by 8 cm acoustically absorbent foam. The positions of the loudspeakers were concealed from the subjects by a visually opaque, acoustically transparent curtain. The experiment used five loudspeakers at 0° elevation spaced every 45° from −90° (left) through 0° (straight ahead) to +90° (right).

Software for stimulus presentation and data collection was written in MATLAB (Mathworks Inc.). Target and masker stimuli, which had been recorded from a trained male talker, low-pass filtered at 10 kHz and saved at a sampling rate of 44.1 kHz, were upsampled, summed (where necessary), and played at a sampling rate of 48.8 kHz using 16 bit digital-to-analog conversion. Speaker switching and amplification were

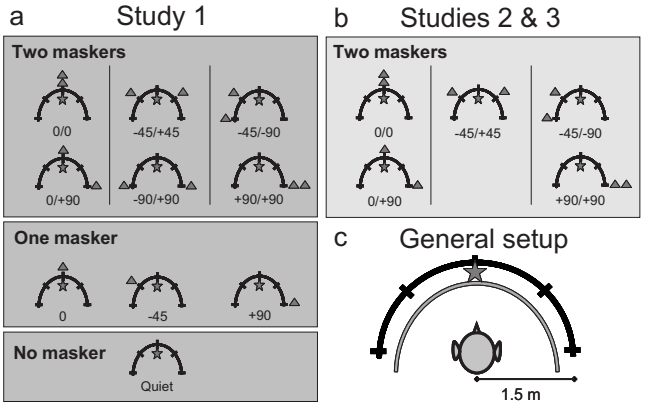


FIG. 1. Schematic view of the masker configurations used in these experiments. (a) The ten masker configurations with two maskers, one masker, or no masker shown at the left were used in experiment 1. (b) The five two-masker configurations shown at the right were used in experiments 2 and 3. The target (shown by a star) was presented from 0° in all experiments. In each diagram, the triangles indicate masker positions. A schematic view of the setup used in these experiments is shown in (c). Subjects were seated at the center of a 1.5 m loudspeaker array with loudspeakers located every 45° from −90° to +90°. The positions of the loudspeakers were concealed by a curtain.

controlled through Tucker Davis Technologies (TDT) System III hardware (RP2, PM2, SA1) in conjunction with a PC host. The overall masker level was 57 dB(A) on all masked trials. On two-masker trials, the levels of the two maskers were equal to one another. Target words were presented at a fixed level of 38 dB(A). The −19 dB SNR was chosen based on piloting to avoid floor effects in the most difficult masker configurations and ceiling effects in the least difficult configurations. A cosine-squared window with 2 ms rise and fall times was applied to each stimulus; this was done prior to upsampling to reduce resampling distortion. Target words were presented with a 2 s delay relative to the onset of the masker(s). The onset of the target word always occurred after the start of the second sentence in the masker, and no part of the target word ever overlapped with the transition from one sentence to the next.

The 40 spondee targets were displayed in alphabetical order, reading down the columns of an 8 $\times$ 5 grid, and subjects were asked to verbally identify the target word on each trial using words from the list in a 40-alternative forced choice task (40AFC). They were instructed to guess if they could not identify the target word. Responses were entered into a computer by a tester who was monitoring the experiment via closed-circuit TV. Subjects were informed that the target would always be presented from straight ahead, and the 0° location was visually marked on the curtain. No other information was given about the positions of the loudspeakers. Subjects were instructed to face straight ahead, with the nose pointing at the 0° loudspeaker, and they were monitored throughout each testing session to ensure that they maintained proper head position.

Ten masker configurations were used in this experiment. As shown in Fig. 1(a), there were six two-masker configurations, three one-masker configurations, and one no-masker configuration. The two-masker configurations were of three types: (1) one or both maskers at the target location, (2)

symmetrical arrays with maskers bilaterally distributed about the target, and (3) both maskers separate from the target and in a single hemifield. In the three one-masker configurations, separation between target and masker was 0°, 45°, or 90°. All masker configurations occurred in all blocks of trials, and the order of masker configurations within a block was randomized. Thus, on any given trial, the target word could be masked by 0, 1, or 2 maskers.

The experiment, consisting of 3600 trials per subject, was organized into 34 blocks of trials divided over seven 2 h testing sessions in an incomplete Latin square design. A within-subject design was used in which each subject participated in all blocks of trials. In "equal-probability" blocks of trials, each of the ten masker configurations occurred on 10% of the trials. In order to test the effect of predictability of the masker configuration on speech intelligibility and release from masking, there were also blocks of trials in which one of the masker configurations occurred with greater than 10% frequency. In these "unequal-probability" blocks, one of the masker configurations occurred on 20%, 40%, 60%, or 80% of the trials, and the remaining trials were divided equally among the other nine masker configurations. In all, 520 trials were needed to test a single masker configuration in all four types of unequal-probability blocks; thus, it was not practical to test all possible combinations of the ten masker configurations and the five levels of predictability. Rather, six of the ten masker configurations were tested at all levels of predictability, including two one-masker configurations (0 and +90) and four two-masker configurations (0/0, 0/+90, −90/+90, and +90/+90).

In order to familiarize subjects with the task, there was a 10 min practice session at the start of the first testing session and a 5 min practice session at the start of each subsequent testing session. Within each block, the first 20 trials were used to familiarize the subjects with the general frequency of occurrence of the masker configurations; e.g., in an 80% block, the tested configuration occurred on 16 of the 20 familiarization trials. The familiarization trials were not included in the data analysis. The number of trials in each block was selected so as to have 40 analyzed trials of the tested masker configuration. For example, each 80% block was 70 trials long, with 20 familiarization trials followed by 50 experimental trials.[3] Specific features of the incomplete Latin square design include the following: there could be at most one equal-probability block, one 40% block, one 60% block, and one 80% block during a single testing session, and any given masker configuration could be tested at greater than 10% predictability only once during a single testing session. The twelve 20% blocks were divided over the seven testing sessions as equally as possible.

Blocks were limited to no more than 120 trials, including familiarization trials, to avoid possible effects of fatigue on performance. Thus, in order to have 40 analyzed trials in the equal-probability blocks and the 20% blocks, there were four equal-probability blocks and there were two separate 20% blocks for each tested masker configuration. Although subjects could not leave the testing booth during the course of a block of trials, they were given a brief break of 30–60 s every 6–7 min during a block and longer breaks between blocks.

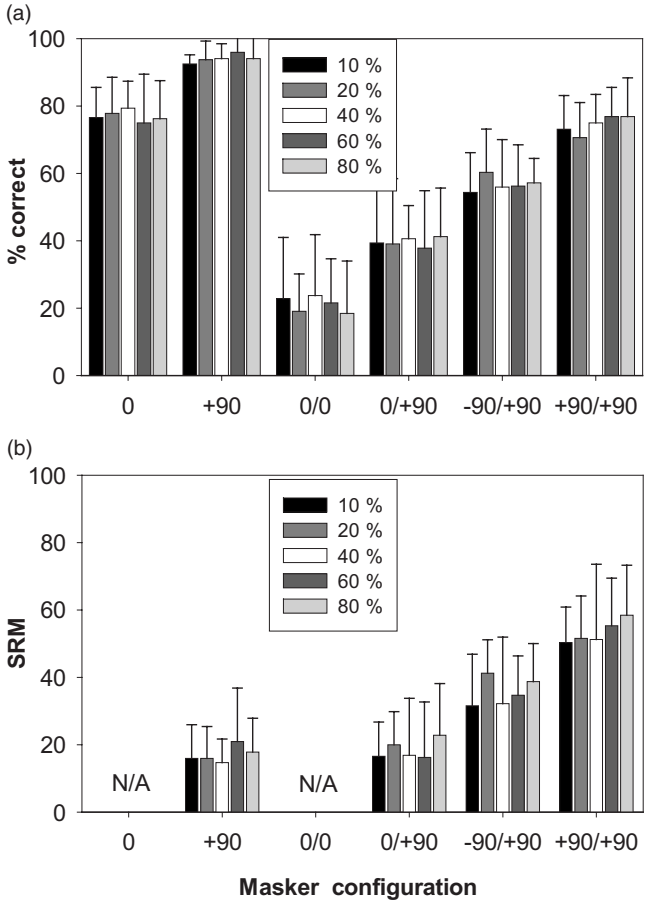


FIG. 2. Group means (±SD) for the six masker configurations in experiment 1 that were tested at several levels of predictability are shown as (a) percent correct and (b) SRM.

4. Data analysis

Percent correct scores were calculated for each of six masker configurations at 10%, 20%, 40%, 60%, and 80% predictability. Within each level of predictability, SRM was calculated as the difference in percent correct between each masker configuration with masker(s) away from 0° and the corresponding configuration with masker(s) at the target location. Two-way analyses of variance (ANOVAs) were performed on percent correct and SRM, with masker configuration and predictability as factors. Following each ANOVA, *post hoc* comparisons were made between different levels within each factor via Scheffe analysis (criterion: $p<0.05$).

B. Results

Group means (±SD) for the masker configurations that were tested at multiple levels of predictability are shown in Fig. 2 as percent correct [Fig. 2(a)] and as SRM [Fig. 2(b)]. There was a significant main effect of masker configuration [$F(5,35)=151.49$; $p<0.0001$] on percent correct scores, but no main effect of predictability and no interaction [Fig. 2(a)]. Scheffe analysis of percent correct scores collapsed across predictability showed that all pairs of masker configurations,

except 0 and +90/+90, were significantly different from each other. For similar location configurations, percent correct scores declined as the number of maskers was increased, with greater masking for two maskers (0/0 and +90/+90) than for one (0 and +90), despite the overall level equivalency [$F(5,7)=59.96$; $p<0.0001$].

Mean SRM values were positive for all tested masker configurations [Fig. 2(b)]. There was a significant main effect of masker configuration [$F(3,21)=77.51$; $p<0.0001$] on SRM, but there was no main effect of predictability and no interaction. Scheffe analysis of SRM data collapsed across predictability showed that all masker configurations were significantly different from each other, except +90 and 0/+90.

C. Discussion

These results showed greater masking with two maskers than with one and significant SRM for all masker configurations in which at least one masker was spatially separated from the target. Within the two-masker configurations, SRM was lowest for the 0/+90 configuration and highest for the +90/+90 configuration. This is broadly consistent with previous results with noise maskers (Bronkhorst, 2000) and particularly with speech maskers (Hawley *et al.*, 2004). Contrary to the hypothesis of higher percent correct scores and greater SRM with increasing predictability, these results showed no effect of predictability on either measure. Although these data suggest that predictability of the number or locations of maskers does not influence speech intelligibility or SRM, alternative explanations also need to be explored.

First, there are inherent limitations of the fixed SNR approach used in this experiment. Pilot testing had suggested that the one- and two-masker configurations would not be subject to floor or ceiling effects at the target level used in this experiment; however, a ceiling effect in the +90 configuration and a floor effect in the 0/0 configuration are apparent in the individual data (not shown). While it is worth noting that in Fig. 2(a) there is also no indication of an effect of predictability on speech intelligibility in the other four masker configurations (0,0/+90,−90/+90,+90/+90), the findings of experiment 1 would certainly be strengthened by eliminating floor and ceiling effects.

Second, the paradigm used in this experiment may not have fully exploited differences in stimulus uncertainty. Although the predictability of the tested masker configuration covered a large range, one invariant in this experiment was that ten different masker configurations occurred in each block. It is possible that speech intelligibility and SRM are affected by the complexity of the entire listening environment and not just by the frequency of occurrence of any particular masker configuration. This can be tested by limiting the number of loudspeaker locations or the number of different masker configurations that occur in a block of trials. Furthermore, it is possible that the familiarization period (20 trials) was not long enough for subjects to recognize and adjust to the predictability of the masker configuration.

Third, learning effects played a role in these results. After factoring out differences in baseline performance between masker configurations, there was a significant correlation ($0.37, p<0.0001$) between performance in each block and which testing session that block occurred in. For all of these reasons, additional experiments were undertaken to further evaluate the original hypothesis. In order to limit the role of learning effects, an experiment with fewer testing sessions was developed.

III. EXPERIMENT 2: VARIABLE SNR, EFFECT OF PREDICTABILITY AND ARRAY COMPLEXITY

A. Method

1. Listeners

Listeners were nine university students (eight females and one male), 19–30 years of age, who were paid for their participation. None had taken part in the previous experiment or pilot testing. Requirements for participation were the same as for the previous experiment.

2. Stimuli

Target words and masker sentences were the same as in experiment 1.

3. Procedures

Several changes were made to the procedures to address the issues raised in the discussion of experiment 1. First, in order to measure SRM in decibel units and to eliminate floor and ceiling effects, SRTs were determined by using an adaptive procedure with four reversals. This paradigm has been used reliably with both pediatric and adult populations (Litovsky, 2005; Johnstone and Litovsky, 2006; Garadat and Litovsky, 2007). The data were then fitted to a logistic function by a constrained maximum-likelihood estimation (MLE) method (Wichmann and Hill, 2001a, 2001b). The data fitting yields an estimate of the underlying psychometric function, which makes it possible to analyze the effect of predictability on both threshold and slope. Second, in order to give subjects more time to recognize and adjust to the predictability of the masker configuration than in experiment 1, the familiarization period was increased from 20 trials to 100 trials.

As in experiment 1, the overall masker level was 57 dB(A). SRTs were estimated using a method with slight modifications to an adaptive algorithm that has been described previously (Litovsky, 2005). An adaptive tracking method was used to vary the level of the target signal from an initial SNR of +6 dB, such that correct responses result in level decrement and incorrect responses result in level increment. The algorithm includes the following rules: (1) level is initially reduced in steps of 8 dB following each correct response. (2) Following the first incorrect response, a 3-down/1-up rule is used, whereby level is decremented following three consecutive correct responses and incremented following a single incorrect response. (3) Following each reversal, the step size is halved. (4) A step size that has been used twice in a row in the same direction is doubled. For instance, if the level was decreased from 40 to 36 dB (step size =4 dB) and then again from 36 to 32 dB, a set of three consecutive correct responses at 32 dB would result in an 8 dB

drop to 24 dB. (5) Testing is terminated following four reversals. The 3-down/1-up method converges to the 79.4% correct point (Levitt, 1971). Masker unpredictability was generated by presenting adaptive tracks for two or more masker configurations in interleaved fashion. In each block of trials, thresholds for all tested masker configurations were obtained concurrently [e.g., see Leek (2001)].

Data were collected with the 40-AFC task used in experiment 1. The lower bound of the psychometric function was set to the chance level of performance, 0.025. The sampling scheme and lapses in listener attention can introduce biased estimates of threshold. The bias introduced by attentional lapses can be overcome by confining the upper bound of the psychometric function to within a narrow range of $p(c)=1$ (Wichmann and Hill, 2001b). In these experiments a constrained MLE fitting procedure was used in which the lambda parameter, which determines the upper asymptote of the psychometric function, was confined to the range [0, 0.05]. Threshold was calculated as the 80% point on the fitted psychometric function as described previously (Litovsky, 2005; Johnstone and Litovsky, 2006; Garadat and Litovsky, 2007).

Five masker configurations were tested in experiment 2 as opposed to ten in experiment 1 [see Fig. 1(b)]. Without this change, the extended familiarization period and the use of adaptive tracking methods in experiment 2 would have greatly increased the size of the test blocks. In addition, the decision to test fewer masking configurations reduced the number of testing sessions and thus limited opportunities for learning effects. As a result of these choices, experiment 2 examined possible effects of predictability of the *locations* of maskers only. The *number* of maskers was 2 on every trial.

In each block of trials, there were up to five parallel adaptive tracks. These adaptive tracks were presented in interleaved fashion through the use of custom software written in MATLAB, which allowed the user to specify how frequently each masker configuration would occur within a given block of trials. In equal-probability blocks, each of the five masker configurations in Fig. 1(b) occurred on 20% of trials, and in unequal-probability blocks the tested masker configuration, either 0/0 or +90/+90, occurred on 80% of trials. There were two types of unequal-probability blocks in this experiment. In blocks with the "full array," the tested masker configuration occurred on 80% of trials, and the remaining 20% of trials were divided equally among the other four masker configurations. In blocks with a "simple array," the 0/0 and +90/+90 configurations occurred in an 80/20 or 20/80 ratio. There were five blocks of trials divided over three testing sessions of up to 2 h each. The order of blocks was balanced across subjects in an incomplete Latin square design.

In order to minimize learning effects, subjects completed a practice session during an initial visit for hearing screening. Collection of analyzed data began with the second visit. Due to the extended familiarization period in this experiment, the blocks of trials were quite long, and it was important to avoid fatigue effects on performance. Subjects did not leave the testing booth while a block was underway, but they were given a brief break of 30–60 s every 6–7 min and a break of about 2 min every 15 min. There was a 5 min practice session before the start of each testing session.

4. Data analysis

SRTs for the 0/0 and +90/+90 configurations were calculated at 20% and 80% predictability for both the full array and the simple array. During a block of trials, subjects would often complete multiple adaptive tracks of a masker configuration (e.g., the configuration tested at 80% predictability in blocks with the simple array). In such cases the reported threshold is the average of the thresholds from all completed adaptive tracks of that configuration after the familiarization period.

Within each combination of predictability and array complexity, SRM for the +90/+90 configuration was calculated as SRT for the 0/0 configuration minus SRT for the +90/+90 configuration. Three-way ANOVAs were computed for SRTs and for the slopes of the psychometric functions of the 0/0 and +90/+90 masker configurations with masker configuration, predictability, and array complexity as factors. A two-way ANOVA was calculated on SRM values for the +90/+90 masker configuration with predictability and array complexity as factors.

B. Results

Group means (±SD) for the +90/+90 configuration across predictability and across loudspeaker array are shown in Fig. 3 as SRT [Fig. 3(a)] and SRM [Fig. 3(b)]. There is very little difference in SRT or SRM with changes in either predictability of the masker configuration or the complexity of the loudspeaker array. A three-way ANOVA on SRT data showed a significant main effect of masker configuration [$F(1,8)=1604.92; p<0.0001$], but there was no effect of either predictability or the complexity of the loudspeaker array, and there were no interactions among the factors. A three-way ANOVA on the slopes of the psychometric functions at threshold showed no significant main effects or interactions. A two-way ANOVA on SRM data for the +90/+90 configuration across predictability and complexity of the loudspeaker array showed no significant main effects and no interaction. Consistent with the SRM data from experiment 1, the data for all five masker configurations in the equal-probability blocks (data not shown) exhibit increasing SRM as (1) one masker was placed away from the target, (2) the two maskers were bilaterally distributed about the target, and (3) both maskers were displaced from the target and confined to a single hemifield.

C. Discussion

This second experiment was motivated primarily by concerns that the methodology of the first experiment may not have fully exploited differences in predictability. The three major changes from experiment 1 to experiment 2 were as follows: the length of the familiarization period was increased, an adaptive procedure was used to avoid the floor and ceiling effects seen in experiment 1, and possible effects of the complexity of the loudspeaker array on SRT and SRM were also tested. Despite these changes, the basic result of

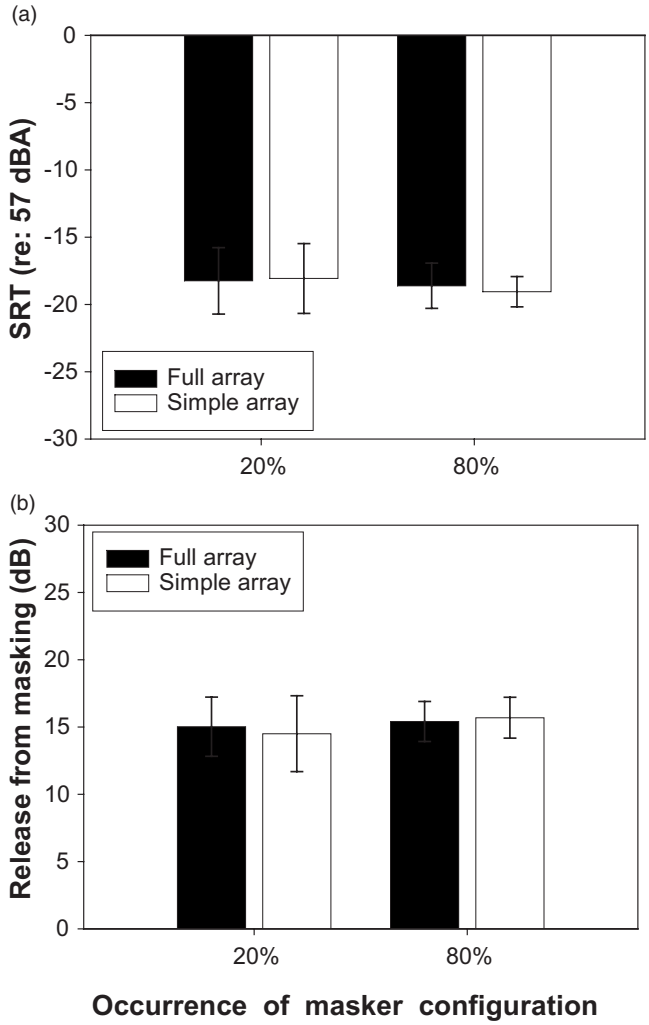


FIG. 3. Group means (±SD) for the +90/+90 masker configuration in experiment 2 at two levels of predictability and two levels of complexity of the loudspeaker array are shown as (a) SRTs and (b) SRM.

experiment 2 is the same as the result of experiment 1; namely, changes in the predictability of masker locations had no effect on speech intelligibility or SRM. Moreover, the additional tests that were added in experiment 2 also offered no evidence to support the hypothesis. That is, there was no effect of predictability on the slope of the psychometric function at threshold, and simplifying the loudspeaker array had no effect on SRT, SRM, or slope.

These results suggest that in a cocktail party environment, there may not necessarily be added masking due to uncertainty about the locations of maskers. This is consistent with the findings of experiment 1. However, it is possible that even the modified paradigm used in experiment 2 did not fully exploit differences in the predictability of the masker configuration. First, 80% predictability may not be high enough to eliminate informational masking effects of uncertainty about the masker configuration. Second, the onset delay between maskers and the target provided listeners with an opportunity to focus on the masker configuration prior to target onset and may have allowed them to overcome any effect of uncertainty. Thus, one further experiment was conducted to test for effects of predictability of masker locations on speech intelligibility and SRM.

IV. EXPERIMENT 3: EFFECT OF 100% CERTAINTY WITH MINIMAL ONSET DELAY

A. Method

1. Listeners

Ten university students (ten females), 18–22 years of age, participated in this experiment. Subjects were paid for their participation, and none had taken part in either of the previous experiments or pilot testing. Requirements for participation were the same as for the previous experiments.

2. Stimuli

Maskers with a mean duration of 3.6 ± 0.0 s were created by concatenating recordings of pairs of Harvard IEEE sentences.[4] These two-sentence maskers were identical to the three-sentence maskers used in the previous two experiments, but with the third sentence removed. The targets were the same 40 recorded spondees as in the previous two experiments.

3. Procedures

Before the start of each trial, the subject was prompted with the word "Ready?" from the 0° loudspeaker. The prompt was recorded by the same talker as the targets and maskers, and there was a silence of 0.6 ± 0.1 s between the prompt and masker onset. The delay between the onset of the maskers and the onset of the target was reduced from 2 s in experiments 1 and 2 to a variable delay of 0–0.2 s in experiment 3. There were no familiarization trials in this experiment; rather, subjects were told in advance whether the masker locations in the upcoming block of trials would be fixed or variable.

The five two-masker configurations shown in Fig. 1(b) were included in this experiment. In equal-probability blocks, there were five interleaved adaptive tracks, and each of the five combinations of masker locations occurred on 20% of the trials. In *fixed* blocks, there was a single adaptive track, and the same masker configuration occurred on 100% of trials. The equal-probability blocks were run until the subject had completed at least one adaptive track for each of the five masker configurations. Each fixed block was run until the subject had completed a single adaptive track. There were two repetitions of each block, always in separate testing sessions, and the order of blocks was balanced across subjects in an incomplete Latin square design. Overall, there were 12 blocks of trials, and these blocks were run concurrently with an experiment from a separate study not reported here over three approximately 2 h testing sessions.

There was a 5 min practice session before the start of each testing session. Subjects did not leave the testing booth during a block of trials. During equal-probability blocks, there was a short break of 30–60 s every 6–7 min and a longer break of about 2 min every 15 min. No breaks were given during fixed blocks, which only lasted a few minutes. Subjects were familiarized with the task during an initial visit for hearing screening.

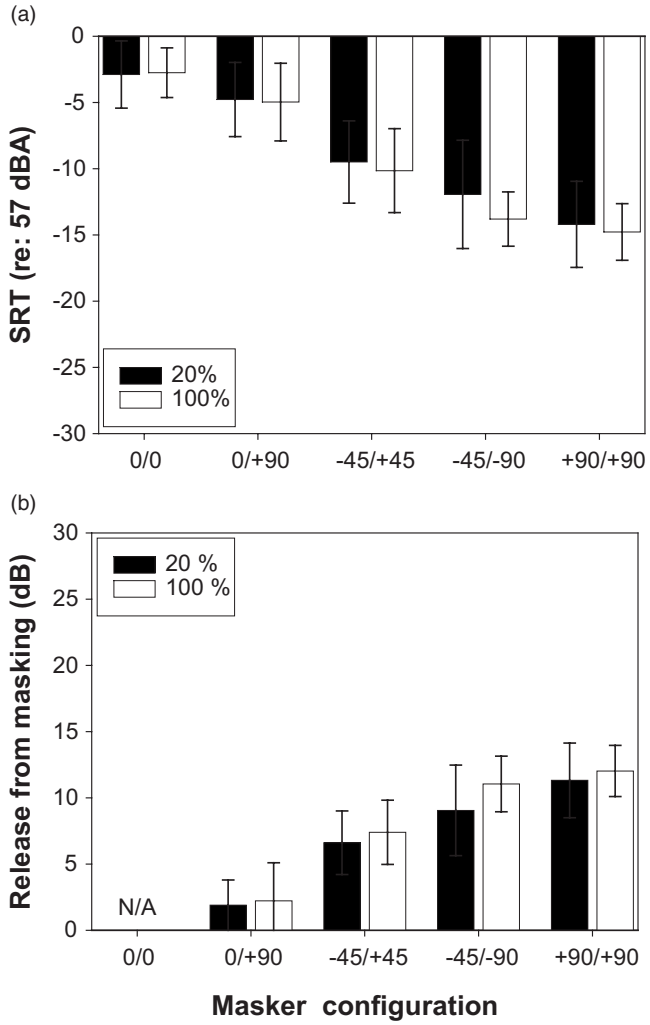


FIG. 4. All five masker configurations in experiment 3 were tested at 20% and 100% predictability. The bar plots above show group mean (±SD) (a) SRTs and (b) SRM by masker configuration and predictability.

4. Data analysis

Every threshold reported for each subject is the average of SRTs from completed adaptive tracks for a given combination of masker configuration and predictability. SRTs were calculated as in the previous experiment. Two-way ANOVAs were performed on SRT, SRM, and the slopes of the psychometric functions, with masker configuration and predictability as factors. *Post hoc* comparisons were made among the masker configurations via Scheffe analysis.

B. Results

Group means (±SD) across masker configuration and predictability are shown in Fig. 4 as SRTs [Fig. 4(a)] and SRM [Fig. 4(b)]. There are visible differences in the plots between the data at 20% predictability and 100% predictability. For example, all SRM values in Fig. 4(b) are somewhat lower at 20% predictability than at 100% predictability. Moreover, the standard deviations in Figs. 4(a) and 4(b) are considerably larger at 20% predictability than at 100% predictability for the two masker configurations in which both maskers were in the same hemifield, particularly for the −45/−90 configuration.

Statistical analysis showed a significant main effect of masker configuration on both SRT [$F(4,36)=125.76$; $p<0.0001$] and SRM [$F(3,27)=76.23$; $p<0.0001$], but there was no significant effect of predictability and there was no interaction. A *post hoc* Scheffe analysis in which the SRT data were collapsed across predictability showed that all masker configurations were significantly different from each other with two exceptions: (1) 0/0 was not significantly different from 0/+90, and (2) the same-hemifield masker configurations, −45/−90 and +90/+90, were not significantly different from each other. There was no effect of masker configuration or predictability on slope, and there was no interaction.

C. Discussion

In experiment 3, as in the previous experiments, there was no effect of predictability on SRTs, SRM, or the slopes of the psychometric functions. Although SRM at 100% predictability was, on average, 1 dB higher than at 20% predictability [see Fig. 4(b)] this difference did not approach significance. Furthermore, a masking effect on the order of 1 dB would probably be too small to be of interest or of functional relevance.

As a follow-up, these data were examined for other indications of informational masking such as high individual variability. Such individual variability would be consistent with the use of different min and max strategies (Durlach *et al.*, 2003a), as described in the Introduction. For example, do most subjects have similar SRM at both 20% and 100% predictability, or is this highly variable? Also, is there a connection between spatial separation of maskers from the target and the relative amount of SRM at 20% and 100% predictability? The relationship between SRM values at 20% and 100% predictability is shown for all ten subjects in Fig. 5. The data in Fig. 5 indicate that for the majority of subjects, SRM is highly similar at 20% and 100% predictability. Overall, the individual variability in these data is not substantially greater along one axis than the other, and the differences observed between the group mean SRM values at 20% and 100% predictability are due to the results of just two subjects, SHY and SID. In addition, there is no evidence in Fig. 5 of a connection between spatial separation and the relative amount of SRM at 20% and 100% predictability.

The relative sizes of the error bars in the two same-hemifield configurations are intriguing. The fact that the error bars are larger at 20% predictability would be consistent with greater informational masking at 20% predictability than at 100% predictability. It is worth noting that this same pattern is seen in the experiment 2 data in Fig. 3(b), particularly for the simple loudspeaker array. Moreover, it seems plausible that the min listening strategy described above would be most effective when the spatial locations to be suppressed are near each other and in the same hemifield. Note, however, that the 2–2.5 dB standard deviations of the group means in experiments 2 and 3 do not fit the high individual variability seen with informational masking [e.g., see Durlach *et al.* (2003b)]. Thus, the relative sizes of the

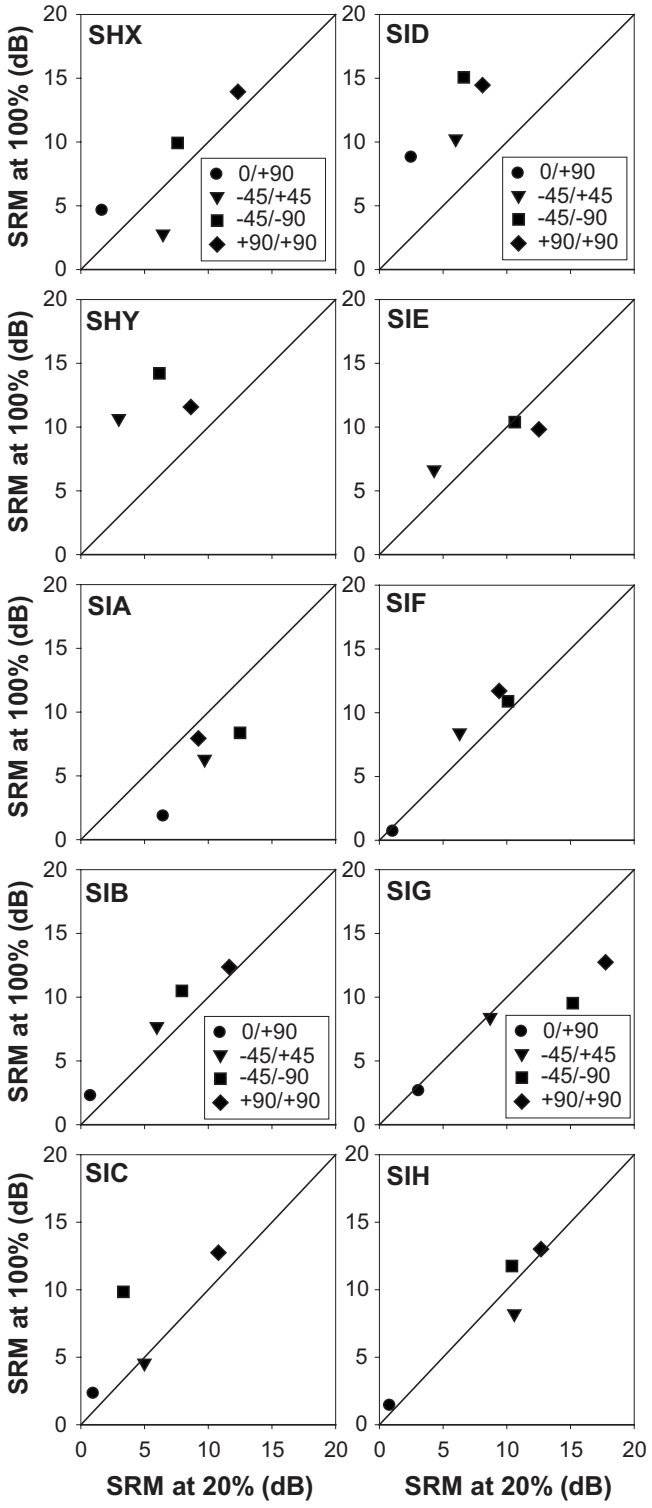


FIG. 5. Experiment 3 SRM data at 100% predictability and at 20% predictability are compared for each of the ten participants. Data points near the 45° line indicate that SRM was similar at these two levels of predictability. Note that the 0/+90 data point is not visible for two subjects whose measured SRM was slightly negative in this masker configuration, SHY and SIE.

error bars for the same-hemifield masker configurations cannot be considered strong evidence for the hypothesis.[5]

When comparing these results to data from other speech-on-speech masking experiments, it may seem surprising that SRTs in this experiment were at negative SNRs, even in the most challenging masker configurations. However, the spondee identification task in this experiment is substantially easier than sentence identification tasks employed in many other studies [e.g., see Freyman *et al.* (2001) and Hawley *et al.* (2004)]. It should be noted that group mean SRTs were negative for all masker configurations in experiment 2 as well (data not shown).

One could question the use of a constrained MLE procedure, which limits the influence of "inattention trials" on the threshold and slope of the estimated psychometric function, when calculating effects of informational masking. In the Appendix we show that the absence of an effect of predictability is not due to the constraints on the MLE procedure. Finally, it was noted earlier that SRM was 15 dB for the +90/+90 configuration in experiment 2, which is about 3 dB higher than SRM for this configuration in experiment 3. The reason for this difference is not known. Overall, however, the findings of the three experiments are quite consistent with each other.

V. GENERAL DISCUSSION

These experiments were motivated by theoretical considerations and by previous findings concerning effects of uncertainty in studies of the cocktail party problem. Masker uncertainty can be a source of informational masking, and this could have important implications for relatively unpredictable cocktail party environments. In previous studies in this field, in which the number and locations of maskers were held fixed throughout each block of trials, possible effects of predictability of the number and/or locations of maskers were not examined. We hypothesized that as predictability of the number and/or locations of speech maskers is increased, there will be (1) improved speech intelligibility and (2) increased SRM.

The data from the first of the experiments presented above did not support the hypothesis. The second and third experiments were each designed, in part, to more fully exploit differences in the predictability of masker locations than their predecessors. However, each further experiment lent additional evidence *against* an effect of predictability. Thus, these experiments offer no evidence for an effect of predictability of the number and locations of speech maskers on speech intelligibility or SRM in a cocktail party environment, at least not when the location of the target is known.

One further issue that needs to be addressed is the extent to which informational masking was present with the target/masker combinations used in these experiments. Despite evidence that energetic masking may play a relatively small role in the overall masking that occurs when speech is masked by interfering speech [e.g., see Brungart *et al.* (2006)], one cannot assume that each instance of masking of speech targets by speech interferers necessarily gives rise to informational masking. In fact, the high performance of subjects in the one-masker configurations of experiment 1 (at a very unfavorable SNR of −19 dB) suggests that there was little, if any, informational masking in that portion of experiment 1. If, however, we focus our attention on the two-masker configurations, which form the bulk of the data in these experiments,

two lines of evidence support the view that informational masking was present. First, a comparison of the 0 and 0/0 configurations in experiment 1 reveals that when a second masker was added at the target location (while decreasing the level of each masker to maintain the same overall masker level), performance dropped from 77% to 21%. The key question here is whether the masking that resulted from adding a second speech interferer was greater than the amount that can be accounted for by energetic masking. This can be determined by comparing the data from experiment 1 to the data from experiments 2 and 3. If one compares Fig. 2(a) to Fig. 4(a), performance with a single masker at the target location was very close to 80% correct at a SNR of −19 dB [see the "0" configuration in Fig. 2(a)]; in contrast, the 80% threshold with two maskers at the target occurred at a SNR of −2.8 dB [see the "0/0" configuration in Fig. 4(a)]. This difference of just over 16 dB is far beyond the <3 dB reported by Bronkhorst and Plomp (1992) for the addition of a second masker under diotic stimulus presentation in an experiment in which the maskers were envelope-modulated noise.[6] A precedent for a large effect of adding a second speech masker at 0° may be found in experiments performed in free field [e.g., see Cullington and Zeng (2008)] and in data collected under diotic or monaural stimulus presentation conditions (Brungart, 2001; Brungart *et al.*, 2001). Second, further support for the view that informational masking was present in the two-masker configurations comes from the large amount of SRM in experiments 2 and 3. SRM for the +90/+90 configuration was approximately 15 dB in experiment 2 [Fig. 3(b)] and 12 dB in experiment 3 [Fig. 4(b)]. This is greater than SRM with energetic maskers [e.g., see Zurek (1993) and Bronkhorst (2000)] but is comparable to the ~12 dB of SRM that Hawley *et al.* (2004) found for speech or reversed-speech interferers. In addition, the sizable SRM we report in experiments 2 and 3 is consistent with the finding by Yost *et al.* (1996) of a particularly large benefit of spatial separation when more than two utterances are presented simultaneously. To summarize, (1) the experiments reported here were conducted under test conditions that give rise to informational masking in the two-masker configurations at least, and (2) there was no evidence of additional masking due to uncertainty about the number or location(s) of maskers.

It is worth noting that the use of parallel adaptive tracks in experiments 2 and 3 could lead to large variations in SNR from trial to trial. This, in effect, introduced a second source of uncertainty in the blocks with low predictability. Thus, the results of experiments 2 and 3 offer no evidence of an effect of either uncertainty about masker locations or uncertainty about SNR on speech intelligibility. These findings of experiments 2 and 3 are consistent with data reported by Freyman *et al.* (2007), who found that the uncertainty introduced by varying SNR from trial to trial has very little effect on speech intelligibility.

As described in the Introduction, it has been proposed that there are different strategies that could enable listeners to extract a target signal from competing sources (Durlach *et al.*, 2003a). One interpretation of the results of the experiments reported here is that knowing the number or locations of maskers ahead of time is of no benefit, provided that listeners know where to attend for the target signal (Arbogast and Kidd, 2000; Kidd *et al.*, 2005). This interpretation is consistent with the max listening strategy, which is characterized by enhanced sensitivity to sources from the target location. On the other hand, if there is some use of the min strategy by listeners in multitalker environments, then knowing the spatial locations of maskers ahead of time should result in improved performance. The absence of an effect of predictability of the number or locations of maskers suggests that use of the min strategy did not contribute significantly to these results. However, the min listening strategy may still contribute to speech intelligibility under other test conditions. For example, Brungart and Simpson (2007a) found a significant effect on speech intelligibility of varying the predictability of both target and masker locations simultaneously.

An alternative view is that listeners may not need much location information about any one source in order to benefit from spatial differences between target and masker(s) in a speech intelligibility task. Licklider (1948) found that the greatest release from masking in a speech identification task occurred for signal inversions that result in poor lateralization of target (N_0S_π) or masker ($N_\pi S_0$) sources. Culling and Summerfield (1995) measured identification of vowels defined by two noise bands in the presence of a diotic vowel defined by two noise bands; they found that listeners could more readily identify vowels with decorrelated formants than interaurally correlated vowels with a 700 μs ITD. Recent data by Brungart and Simpson (2007b) showed only small improvements in speech intelligibility when ITDs of the maskers, or of the target, were unchanged for several consecutive trials. In experiments using a three dimensional auditory display, which more closely approximates free-field presentation than the other experiments described in this paragraph, Drullman and Bronkhorst (2000) found that spatial separation makes a significant contribution to communication even when localization of the *target* is rather poor.

The findings reported here may have a parallel in recent studies that examined contributions of the predictability of the content of maskers to speech intelligibility in a cocktail party environment. Brungart and Simpson (2004) found that listeners were rather poor at utilizing reduced masker uncertainty to achieve improved speech intelligibility, even when the masking speech was frozen from trial to trial and even when they were given feedback after each trial. The authors speculated that some of their findings might be particular to the speech corpus they used, in which listener responses are drawn from a small set of numbers and colors. However, Freyman *et al.* (2007) reached a similar result with a very different stimulus set in which targets and maskers were nonsense sentences. When masker content was frozen and subjects were specifically instructed to ignore the repeated masker token, the authors found little improvement in speech intelligibility, even though the same masker token was repeated on dozens of consecutive trials. The results of the experiments described in this paragraph, together with the results reported in the current paper, suggest the possibility that contributions of reductions in masker uncertainty to

speech intelligibility in a cocktail party environment may be quite limited. Alternatively, there may be ways of manipulating uncertainty that were not explored in these studies and that could yet prove to have significant effects on speech intelligibility in a cocktail party environment. It is worth noting that for masked detection of nonspeech stimuli, an effect of spatial uncertainty of maskers has been reported, but it is smaller than the effect of spectral uncertainty (Fan *et al.*, 2008).

In the experiments reported here, the same talker produced both targets and maskers. The purpose of this was to facilitate uncertainty-based masking effects, if any, through high target-masker similarity [e.g., see Durlach *et al.* (2003b)]. Nonetheless, in future experiments it would be good for these measures to be repeated with targets and maskers spoken by different talkers of the same gender or different-gender talkers. In addition, it would be useful to obtain these measures in other populations such as children, older adults, and hearing-impaired listeners. One application of this approach is to improve clinical measures of SRM when patients are fitted with bilateral amplification systems or cochlear implants; these measures typically leave out much of the variability of naturalistic listening environments. In the experiments reported in this paper, we varied one type of uncertainty in a simulated cocktail party environment, while other features of the listening environment were held fixed. Although we found no evidence of additional informational masking due to uncertainty about the number and locations of maskers, other aspects of masker uncertainty may yet prove to be a source of informational masking and may need to be incorporated into clinical testing.

ACKNOWLEDGMENTS

The authors are grateful to Jonathan Riley, Jordan Bonnett, and Brent Saffran for their assistance with data collection. We would also like to thank two anonymous reviewers and the associate editor for their thoughtful comments on previous versions of this paper. This work was supported by Grant No. R01 DC030083 from NIH-NIDCD.

APPENDIX: CONSTRAINED MLE

In the constrained MLE method that was used to calculate thresholds in experiments 2 and 3, the value of the lambda parameter, which determines the asymptote of the psychometric function, was confined to a narrow range. Use of this approach in informational masking experiments could raise concerns because informational masking has significant effects on both the slope and the asymptote of the psychometric function (Lutfi *et al.*, 2003). The study of Lutfi *et al.* (2003) found some lambda values on the order of 0.25 under conditions that cause informational masking. On the other hand, in the constrained MLE procedure used here lambda is not allowed to exceed 0.05. Although this method for estimating psychometric functions has been used successfully to measure effects of uncertainty on speech intelligibility in previous research (Johnstone, 2006), it is possible that constraining the lambda parameter to a narrow range could at least partially offset any informational masking effects and

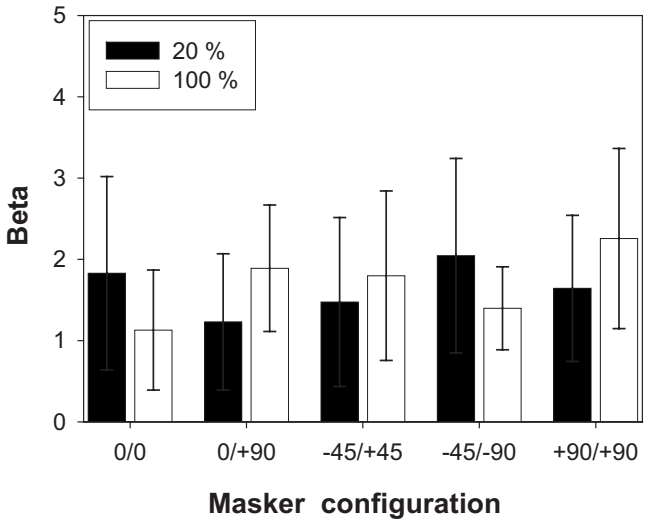


FIG. 6. Group mean (±SD) values of the beta parameter from a revised MLE fit of the experiment 3 data in which the constraint on the lambda parameter was relaxed. An ANOVA on the values of the beta parameter revealed a significant interaction between the masker configuration and predictability in experiment 3. The character of the interaction as revealed by this plot is not consistent with greater informational masking at 20% predictability than at 100% predictability (see the Appendix).

prevent significant differences among the tested masker configurations. In order to control for this, MLE estimation of the psychometric function for each adaptive track in experiments 2 and 3 was repeated under conditions in which the constraint on the lambda parameter was relaxed. Namely, in the reanalysis, lambda was allowed to take on values in the much larger range of [0,0.5]. Then possible effects of predictability on the beta (slope) and lambda (asymptote) parameters of the psychometric function were analyzed statistically [see also Lutfi *et al.* (2003)]. Across adaptive tracks, the constraint influenced the estimation of psychometric functions rather infrequently. In fact, when the limitation on lambda values was relaxed, the fitting parameters were unchanged for 97% of adaptive tracks in experiments 2 and 3. Furthermore, ANOVAs were performed on the reanalyzed data to test for possible effects of predictability on the beta and lambda parameters in experiments 2 and 3. In experiment 2 there was no main effect of predictability on beta or lambda and there were no significant interactions involving predictability. In experiment 3 there was no main effect of predictability on either beta or lambda; however, there was a significant interaction between masker configuration and predictability ($p<0.05$) affecting the beta parameter. In order to explore whether the character of the interaction is consistent with greater informational masking under conditions of uncertainty, the beta values from experiment 3 have been plotted across masker configuration and predictability in Fig. 6. If there were greater informational masking at low predictability, then one would expect the following: (1) in the 0/0 configuration, beta values would be larger (shallower slopes) at 20% predictability than at 100% predictability, and (2) differences in beta values as a function of predictability would decrease as maskers are spatially separated from the target. In fact, the data do not meet the second criterion. Rather, the −45/−90 configuration, which has one of the

largest target-masker separations, is quite similar to the 0/0 configuration, while the trend in the data for the +90/+90 configuration opposes that of the 0/0 and −45/−90 configurations. Thus, the finding of no additional masking due to uncertainty about the number or locations of maskers was not caused by the constraint on the lambda parameter in the MLE method used for estimating psychometric functions.

[1]Further studies have used variations on the technique described by Freyman *et al.* (1999, 2001) to show that even subtle spatial differences can lead to significant SRM for competing speech (Brungart *et al.*, 2005; Rakerd *et al.*, 2006; Balakrishnan and Freyman, 2008).

[2]Based on some of the results described in this Introduction, particularly the more recent findings, one could argue that when predictability of the masker configuration is high, there will be less informational masking to release and thus *less* SRM. As will be seen in the results and discussion, the direction of this hypothesis did not significantly impact the interpretation of the results of these experiments.

[3]The situation was slightly more complicated for 60% blocks because 40/0.6 is not an integer. In 60% blocks, the 20 familiarization trials were followed by 70 experimental trials, of which 42 trials contained the tested masker configuration. However, in order to keep the number of analyzed trials at 40 for all experiments, in 60% blocks the last two trials of the tested masker configuration were excluded from the data analysis.

[4]Masker durations in this paper are reported to one decimal place. For example, the standard deviation of the duration of the maskers used in experiment 3 was less than 0.05 s and is reported as 0.0.

[5]Note that in experiment 2 each subject's SRT was usually an average of thresholds from multiple adaptive tracks at 80% predictability, whereas the SRT at 20% predictability was typically from one or two adaptive tracks. Thus, it may seem that sampling issues could explain the larger error bars at 20% predictability in Fig. 3. However, such an account leaves unexplained the larger error bars in the same-hemifield masker configurations at 20% predictability in Fig. 4, where there were no such sampling issues. Namely, in experiment 3 the number of adaptive tracks per masker configuration was never higher at 100% predictability than at 20% predictability for any subject or any masker configuration.

[6]Because mean performance for the "0" configuration in experiment 1 was actually 77%, there is some error in equating the SNR of −19 dB with the 80% SRT for this configuration. Using the calculated slopes of each of the psychometric functions from experiment 3, we estimated that for the 0/0 configuration the upper limit of the difference between the 77% correct point and the 80% SRT is <1 dB. Thus, even if one compensates for this difference, the data suggest a large increase in masking when a second speech masker was added.

Arbogast, T. L., and Kidd, G. (**2000**). "Evidence for spatial tuning in informational masking using the probe-signal method," J. Acoust. Soc. Am. **108**, 1803–1810.

Balakrishnan, U., and Freyman, R. L. (**2008**). "Speech detection in spatial and nonspatial speech maskers," J. Acoust. Soc. Am. **123**, 2680–2691.

Bronkhorst, A. W. (**2000**). "The cocktail party phenomenon: A review of research on speech intelligibility in multiple-talker conditions," Acust. Acta Acust. **86**, 117–128.

Bronkhorst, A. W., and Plomp, R. (**1988**). "The effect of head-induced interaural time and level differences on speech intelligibility in noise," J. Acoust. Soc. Am. **83**, 1508–1516.

Bronkhorst, A. W., and Plomp, R. (**1992**). "Effects of multiple speechlike maskers on binaural speech recognition in normal and impaired listening," J. Acoust. Soc. Am. **92**, 3132–3139.

Brungart, D. (**2001**). "Informational and energetic masking effects in the perception of two simultaneous talkers," J. Acoust. Soc. Am. **109**, 1101–1109.

Brungart, D. S., Chang, P. S., Simpson, B. D., and Wang, D. (**2006**). "Isolating the energetic component of speech-on-speech masking with ideal time-frequency segregation," J. Acoust. Soc. Am. **120**, 4007–4018.

Brungart, D. S., and Simpson, B. D. (**2004**). "Within-ear and across-ear interference in a dichotic cocktail party listening task: Effects of masker uncertainty," J. Acoust. Soc. Am. **115**, 301–310.

Brungart, D. S., and Simpson, B. D. (**2007a**). "Cocktail party listening in a dynamic multitalker environment," Percept. Psychophys. **69**, 79–91.

Brungart, D. S., and Simpson, B. D. (**2007b**). "Selective spatial attention in a dynamic cocktail party task: Evidence for a strategy based on masker minimization," Presented at the Acoustical Society of America Conference, Salt Lake City, June.

Brungart, D. S., Simpson, B. D., Ericson, M. A., and Scott, K. R. (**2001**). "Informational and energetic masking effects in the perception of multiple simultaneous talkers," J. Acoust. Soc. Am. **110**, 2527–2538.

Brungart, D. S., Simpson, B. D., and Freyman, R. L. (**2005**). "Precedence-based speech segregation in a virtual auditory environment," J. Acoust. Soc. Am. **118**, 3241–3251.

Carhart, R., Tillman, T. W., and Greetis, E. S. (**1969**). "Perceptual masking in multiple sound backgrounds," J. Acoust. Soc. Am. **45**, 694–703.

Cherry, E. C. (**1953**). "Some experiments on the recognition of speech, with one and with two ears," J. Acoust. Soc. Am. **25**, 975–979.

Culling, J. F., Hawley, M. L., and Litovsky, R. Y. (**2004**). "The role of head-induced interaural time and level differences in the speech reception threshold for multiple interfering sound sources," J. Acoust. Soc. Am. **116**, 1057–1065.

Culling, J. F., and Summerfield, Q. (**1995**). "Perceptual separation of concurrent speech sounds: Absence of across-frequency grouping by common interaural delay," J. Acoust. Soc. Am. **98**, 785–797.

Cullington, H. E., and Zeng, F.-G. (**2008**). "Speech recognition with varying numbers and types of competing talkers by normal-hearing, cochlear-implant, and implant simulation subjects," J. Acoust. Soc. Am. **123**, 450–461.

Drullman, R., and Bronkhorst, A. W. (**2000**). "Multichannel speech intelligibility and talker recognition using monaural, binaural, and three-dimensional auditory presentation," J. Acoust. Soc. Am. **107**, 2224–2235.

Durlach, N. I., Mason, C. R., Kidd, G., Jr., Arbogast, T. L., Colburn, H. S., and Shinn-Cunningham, B. G. (**2003a**). "Note on informational masking," J. Acoust. Soc. Am. **113**, 2984–7.

Durlach, N. I., Mason, C. R., Shinn-Cunningham, B. G., Arbogast, T. L., Colburn, H. S., and Kidd, G., Jr. (**2003b**). "Informational masking: Counteracting the effects of stimulus uncertainty by decreasing target-masker similarity," J. Acoust. Soc. Am. **114**, 368–379.

Ericson, M. A., Brungart, D. S., and Simpson, B. D. (**2004**). "Factors that influence intelligibility in multitalker speech displays," Int. J. Aviation Psych. **14**, 313–334.

Fan, W. L., Streeter, T. M., and Durlach, N. I. (**2008**). "Effect of spatial uncertainty of masker on masked detection for nonspeech stimuli," J. Acoust. Soc. Am. **124**, 36–39.

Freyman, R. L., Balakrishnan, U., and Helfer, K. S. (**2001**). "Spatial release from informational masking in speech recognition," J. Acoust. Soc. Am. **109**, 2112–2122.

Freyman, R. L., Helfer, K. S., and Balakrishnan, U. (**2007**). "Variability and uncertainty in masking by competing speech," J. Acoust. Soc. Am. **121**, 1040–1046.

Freyman, R. L., Helfer, K. S., McCall, D. D., and Clifton, R. K. (**1999**). "The role of perceived spatial separation in the unmasking of speech," J. Acoust. Soc. Am. **106**, 3578–3588.

Garadat, S. N., and Litovsky, R. Y. (**2007**). "Speech intelligibility in free field: Spatial unmasking in preschool children," J. Acoust. Soc. Am. **121**, 1047–1055.

Hawley, M. L., Litovsky, R. Y., and Culling, J. F. (**2004**). "The benefit of binaural hearing in a cocktail party: Effect of location and type of competitor," J. Acoust. Soc. Am. **115**, 833–843.

Johnstone, P. M. (**2006**). "Informational masking and spatial asymmetry in a 'cocktail party' environment: Results with children and adults," Ph.D. dissertation, University of Wisconsin-Madison.

Johnstone, P. M., and Litovsky, R. Y. (**2006**). "Effect of masker type and age on speech intelligibility and spatial release from masking in children and adults," J. Acoust. Soc. Am. **120**, 2177–2189.

Kidd, G., Jr., Arbogast, T. L., Mason, C. R., and Gallun, F. J. (**2005**). "The advantage of knowing where to listen," J. Acoust. Soc. Am. **118**, 3804–3815.

Kidd, G., Jr., Mason, C. R., Rohtla, T. L., and Deliwala, P. S. (**1998**). "Release from masking due to spatial separation of sources in the identification of nonspeech auditory patterns," J. Acoust. Soc. Am. **104**, 422–431.

Leek, M. R. (**2001**). "Adaptive procedures in psychophysical research," Percept. Psychophys. **63**, 1279–1292.

Levitt, H. (**1971**). "Transformed up-down methods in psychophysics," J. Acoust. Soc. Am. **49**, 467–477.

Licklider, J. C. R. (**1948**). "The influence of interaural phase relations upon the masking of speech by white noise," J. Acoust. Soc. Am. **20**, 150–159.

Litovsky, R. Y. (**2005**). "Speech intelligibility and spatial release from mask-

ing in young children," J. Acoust. Soc. Am. **117**, 3091–3099.
Lutfi, R. A. (**1993**). "A model of auditory pattern analysis based on component-relative-entropy," J. Acoust. Soc. Am. **94**, 748–758.
Lutfi, R. A., Kistler, D. J., Callahan, M. R., and Wightman, F. L. (**2003**). "Psychometric functions for informational masking," J. Acoust. Soc. Am. **114**, 3273–3282.
Oh, E. L., and Lutfi, R. A. (**1998**). "Nonmonotonicity of informational masking," J. Acoust. Soc. Am. **104**, 3489–3499.
Oxenham, A. J., Fligor, B. J., Mason, C. R., and Kidd, G., Jr. (**2003**). "Informational masking and musical training," J. Acoust. Soc. Am. **114**, 1543–1549.
Peissig, J., and Kollmeier, B. (**1997**). "Directivity of binaural noise reduction in spatial multiple noise-source arrangements for normal and impaired listeners," J. Acoust. Soc. Am. **101**, 1660–1670.
Rakerd, B., Aaronson, N. L., and Hartmann, W. M. (**2006**). "Release from speech-on-speech masking by adding a delayed masker at a different location," J. Acoust. Soc. Am. **119**, 1597–1605.
Rothauser, E. H., Chapman, W. D., Guttman, N., Nordby, K. S., Silbiger, H. R., Urbanek, G. E., and Weinstock, M. (**1969**). "IEEE recommended practice for speech quality measurements," IEEE Trans. Audio Electroacoust. **17**, 225–246.
Shinn-Cunningham, B. G., and Ihlefeld, A. (**2004**). "Selective and divided attention: Extracting information from simultaneous sound sources," Proceedings of the International Conference on Auditory Display.
Watson, C. S. (**2005**). "Some comments on informational masking," Acust. Acta Acust. **91**, 502–512.
Watson, C. S., Kelly, W. J., and Wroton, H. W. (**1976**). "Factors in the discrimination of tonal patterns. II. Selective attention and learning under various levels of stimulus uncertainty," J. Acoust. Soc. Am. **60**, 1176–1186.
Wichmann, F. A., and Hill, J. (**2001a**). "The psychometric function: I. Fitting, sampling, and goodness of fit," Percept. Psychophys. **63**, 1290–1313.
Wichmann, F. A., and Hill, J. (**2001b**). "The psychometric function: II. Bootstrap-based confidence intervals and sampling," Percept. Psychophys. **63**, 1314–1329.
Yost, W. A., Dye, J., Raymond, H., and Sheft, S. (**1996**). "A simulated 'cocktail party' with up to three sound sources," Percept. Psychophys. **58**, 1026–1036.
Zurek, P. M. (**1993**). "Binaural advantages and directional effects in speech intelligibility," in *Acoustical Factors Affecting Hearing Aid Performance*, edited by G. A. Studebaker and I. Hochberg (Allyn and Bacon, Boston), pp. 255–276.

Estimates of internal templates for the detection of sequential tonal patterns

Rong Huang[a] and Virginia M. Richards
Department of Psychology, University of Pennsylvania, 3401 Walnut Street, Suite 302C, Philadelphia, Pennsylvania 19104

(Received 1 August 2007; revised 18 June 2007; accepted 24 June 2008)

In this experiment, listeners detected sequential tonal patterns embedded in multitone multiburst random maskers. The maskers consisted of eight 30 ms bursts of random-frequency tones. The signal, when present, occupied the central six bursts and was centered at 1000 Hz. The six sequential signal tones formed several spectro-temporal patterns: an equal-frequency pattern, three ascending patterns with frequency ranges spanning 0.5-, 1-, and 2-equivalent rectangular bandwidths (ERBs), and a random pattern with frequencies drawn at random from the range of 925–1075 Hz. The total number of tones in each burst, *m*, was varied to determine detection threshold. The detectability of the signal pattern declined as the frequency range of the signal pattern increased, and when the signal was random. Relative weights as a function of time and frequency, interpreted as listeners' internal templates, depended systematically on the properties of the signal pattern tested. The templates indicated that when sensitivity was poor, listeners integrated increasingly broad spectro-temporal regions around the signal frequencies, and sometimes integrated energy from the final burst even though the signal tones never occupied the final burst. © *2008 Acoustical Society of America.* [DOI: 10.1121/1.2967827]

PACS number(s): 43.66.Mk [RLF] Pages: 3831–3840

I. INTRODUCTION

When considering the detection of a tonal signal of known frequency and phase added to Gaussian noise, an ideal listener cross correlates a template with the incoming stimulus to generate a decision variable. For the ideal listener, the template is a replicate of the signal stimulus (e.g., Duda and Hart, 1973, Chap. 2; Green and Swets, 1974, p. 162). In practice, across different tasks, the "internal template" used by listeners is expected to depend on a variety of factors, including the properties of the signal, the properties of the masker, the presumed dimensions of the internal representation of the stimuli, and memory limitations.

The purpose of this paper is to provide an estimate of listeners' internal template and to evaluate the aforementioned template model for the detection of a spectro-temporal signal pattern presented within a random masker. Here, the template matching mechanism between the stimulus and the internal template is assumed to be based on a linear model. The linear model computes an inner product between the template and the stimulus, forming a decision variable. The resulting decision variable is then compared with a criterion to provide a decision/response.

A variety of methods have been used to estimate internal templates, which are the relative weights associated with a linear model. For example, Ahumada and Lovell (1971) used linear regression to estimate relative weights for the detection of a tone added to a band of noise. In their experiment, listeners indicated their confidence that a tone was present. After binning the stimuli in frequency, listeners' ratings were regressed against the energy level in each bin. The resulting regression coefficients, or relative weights, indicated the degree to which different spectral regions contributed to listeners' detection decisions. Other methods that have been used to estimate relative weights include the formation of conditioned on single stimulus functions (Berg, 1990), correlations between stimulus levels and responses (Lutfi, 1995; Richards and Zhu, 1994), and logistic regressions (Alexander and Lutfi, 2004; Dye *et al.*, 2005; Richards and Tang, 2006). Regardless of the approach, the estimation of relative weights relies on the relation between listeners' responses and random variations either associated with the masker or the signal. In the current study, a logistic regression method is adopted to estimate relative weights.

In the exploratory experiments described here, the goal is to evaluate whether reliable and meaningful internal templates can be estimated for the detection of spectro-temporal signal patterns embedded in random maskers and whether the templates change as the complexity of the signal patterns changes. To derive an internal template, two assumptions are made: (a) a linear model is appropriate, and (b) the idealized time-by-frequency spectrogram is an appropriate representation of the stimuli and the template. As described earlier, the former assumption has been applied successfully in the past. The latter assumption of a time-by-frequency spectrogram representation for the stimuli is consistent with work by Wright (2005) who found that the underlying representations of tonal stimuli use at least two dimensions, including frequency and time. Using the two assumptions listed above, relative weights estimated as a function of time and frequency provide an estimate of the internal template (e.g., Ahumada, 2002).

[a]Author to whom correspondence should be addressed. Electronic mail: rongh@psych.upenn.edu.

If listeners alter their internal templates with changes in the signal, the expectation is that the internal template will resemble the signal spectrogram. This pattern is not assured, however. For example, relative weights obtained in informational masking studies indicate that some listeners adopt templates that are not optimal (e.g., Alexander and Lutfi, 2004; Tang and Richards, 2003).

There are several ways in which the proposed template model might fail. One is that the linear model might be inappropriate for the detection of spectro-temporal patterns. For the template model considered here, the inner product between a template and the stimulus (both represented as spectrograms) reflects a process of essentially computing the total *energy* integrated by the template. In a task similar to the current study, Kidd *et al.* (1995a) examined listeners' ability to detect sequences of equal-frequency tones against a background of a random multitone, multiburst masker. Their results are well fitted by a model that tiles the frequency domain into several channels. For each channel, the model examines whether there is a tone in each burst. The number of channels with *coherent* tonal sequences forms the decision variable. In contrast to the template model evaluated here, the model of Kidd *et al.* (1995a) is not a linear model; it depends on the presence of an *unbroken* coherent sequence of tones. Additional data obtained by Huang and Richards (2006) also suggest that the detection mechanism depends, at least in part, on the presence of *sequential* equal-frequency signal tones, not just increases in *energy* at the signal frequency.

In the current experiments, listeners are asked to detect sequential spectro-temporal patterns embedded in random maskers. The masker consists of eight 30 ms bursts of random-frequency tones. The signal is a sequence of six 30 ms sinusoidal tones centered at 1000 Hz. When present, the six signal tones occupy the central six bursts. The number of tones in each burst, m, is adjusted to estimate the threshold for detection. Note that for the detection of a spectro-temporal pattern among the random maskers, performance declines as the number of tones in each burst increases (e.g., Kidd *et al.*, 1995a; Huang and Richards, 2006). This result reflects at least two factors: (a) increases in m leads to increases in the number of masker tones falling near the signal frequency, and (b) increases in m increases the likelihood of forming patterns similar to the signal pattern. Both of these factors undoubtedly contribute to the reduction in sensitivity. In Experiment 1, four signal patterns are tested. One of the signal patterns is a sequence of six 1000 Hz tones. The other three signal patterns are sequences of six tones with frequencies increasing systematically across 0.5-, 1-, or 2-equivalent rectangular bandwidth (ERB; Glasberg and Moore, 1990).

There are at least two reasons for evaluating the detection of signal patterns ascending across different frequency ranges. First, it allows an evaluation of the template model because there are variations in the signal. The estimated template is expected to have positive relative weights at the spectro-temporal locations of the signal tones when plotted as a spectrogram. Therefore, as the properties of the signal pattern change, so should the internal template.

Second, frequency glide detection and discrimination studies have shown that when the frequency extent of a tonal frequency glide exceeds one ERB, the sensitivity to the change in frequency decreases (e.g., Madden and Fire, 1997; Moore and Sek, 1998). With regard to the detectability of spectro-temporal patterns embedded in random multiburst maskers, where the masking is not assured to reflect peripheral mechanisms, it is not known whether sensitivity will also depend on the frequency range of the spectro-temporal pattern.

In Experiment 2, the signal to be detected also occupies the central six bursts of a multitone eight-burst masker. The signal, however, does not form a regular sequential pattern. Instead, the frequencies of the six signal tones are chosen at random from a frequency range of approximately one ERB. The expectation is that the resulting templates will have positive weights across the frequency range of the random signal. Thus, compared to the *1-ERB* ascending signal pattern of Experiment 1, the internal template for the random signal pattern is expected to reflect a broad spectro-temporal region rather than an ascending pattern that increases in frequency with time. Experiment 2 provides an opportunity to directly evaluate the impact of signal uncertainty on the presumed template (compared to the case in which the signal is deterministic; Experiment 1).

In an additional manipulation, in Experiment 2 two special signal patterns—an "ascending" pattern and an "equal-frequency" pattern—occasionally replace the random signals within a block of 50 trials. This manipulation is a counterpoint to the signal-probe approach of Greenberg and Larkin (1968) in that listeners expect random-frequency signals while on occasion "regular" patterns are presented. The logic is as follows: imagine that the predominance of the random signals encourage listeners to adopt a broad internal template, i.e., a template that has positive relative weights across the entire frequency region of the random signals, which means that listeners integrate energy across a broad frequency swath to form their decision variable. This energy model cannot discriminate between random and "special" signals. Therefore, if sensitivity were enhanced (higher hit rates) for the special signals, it would suggest limitations in the proposed template model.

In summary, the aims of the current study are to answer the following four questions regarding the detection of a spectro-temporal signal pattern embedded in random multitone multiburst masker complexes. (a) Do listeners' internal templates reflect the signal to be detected (Experiment 1)? (b) Do the estimated internal templates provide insight into the source of variations in sensitivity (Experiment 1)? (c) Do the estimated templates change when the statistics of the signal shift from known to random (Experiment 1 versus Experiment 2)? (d) Does the linear detection model account for sensitivity when the signal is nondeterministic (Experiment 2, special signals)?

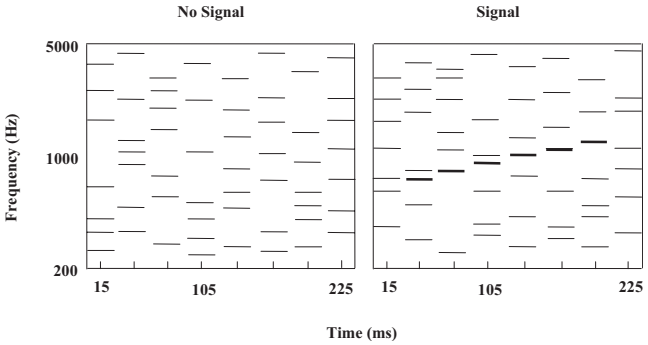


FIG. 1. Examples of no-signal (left) and signal (right) stimuli are shown schematically. For this example, $m=7$. Although the signal is shown using bold lines, the intensity of the signal tones is the same as for the masker tones.

II. METHODS AND PROCEDURES FOR EXPERIMENTS 1 AND 2

A. Methods

1. Subjects

Five listeners (L1–L5) ranging in age from 16 to 36 participated in the first portion of Experiment 1, and four of those (L1–L4) participated in the second portion of Experiment 1. Four listeners (L1 and L6–L8) ranging in age from 23 to 36 participated in Experiment 2. Except for L1 and L4, all were paid for their participation in this experiment. Listener 1 is the first author and L4 was a minor who participated as a member of a high school outreach research program. All listeners had thresholds in quiet of 15 dB HL or less at octave frequencies ranging from 250 to 8000 Hz except for L4, who had thresholds in quiet of 20 dB HL at 250 and 500 Hz in both ears. All listeners who participated in Experiment 1, except L4, had previously participated in psychoacoustic experiments. Of the listeners in Experiment 2, only L1 had previous experience in psychoacoustics experiments.

2. Stimuli

Figure 1 shows a schematic of the stimuli tested in Experiment 1. Each stimulus consisted of eight 30 ms multitone bursts. The number of tones per burst (m) was the independent variable. In the example shown in Fig. 1, $m=7$. The 30 ms bursts were turned on and off using a 5 ms cosine-squared onset/offset ramp and there was no time delay or overlap between the offset of one burst and the onset of the next burst. For the no-signal stimuli, each burst was composed of m tones randomly drawn from a range of 200–5000 Hz on a logarithmic scale. The phases of the masker tones were drawn at random. The level of each tone was 60 dB SPL. An example of a no-signal stimulus is shown in the left panel of Fig. 1.

Four types of signals were tested in Experiment 1. Each signal occupied the six central bursts of the stimulus. One of the signals was a sequence of six 1000 Hz tones. For the other three signals, the frequencies of the six signal tones increased systematically using an equal step size on a logarithmic scale across the ranges of 967–1033, 933–1067, and 867–1133 Hz. These four types of signals will be described in terms of the number of ERBs the signal patterns spanned: *0-ERB* (equal frequency), *0.5-ERB*, *1-ERB*, and *2-ERB* signals, respectively. For the signal stimuli, the remaining m-1 masker tones in each burst were drawn at random from the range of 200–5000 Hz on a logarithmic scale. The phases of the individual components in the signal stimuli were randomly drawn for each trial and the level of each tone was 60 dB SPL. Note that the signal and nosignal stimuli had the same number of tones in each burst; the signal to be detected reflected the organization of a pattern within the spectrogram. An example of a *2-ERB* signal stimulus is shown in the right panel of Fig. 1. The signal tones are indicated using bold lines. Note that there is no signal in the initial and final bursts of the stimulus.

The stimuli of Experiment 2 were similar to those of Experiment 1. Each stimulus was again composed of eight 30 ms multi-tone bursts with a fixed number of tones, m, in each burst. The no-signal stimuli were generated as in Experiment 1. The signal pattern consisted of six sequential tones in the central six bursts. For each burst, the signal frequency was randomly drawn from a range of 925–1075 Hz on a logarithmic scale. This signal will be referred to as the *random* signal. The remaining m-1 masker tones in each burst were drawn at random from the range of 200–5000 Hz on a logarithmic scale. There was no effort to prevent nonsignal tones from falling into the signal frequency region.

Recall that the linear template model under consideration predicts no differences in hit rates between the *random* signal and occasionally presented "regular" signals. To test this prediction, two special signals occasionally replaced the *random* signals within a block of 50 trials. The first special signal was an *ascending* signal composed of six frequencies spanning 925–1075 Hz on a logarithmic scale. The second was an *equal-frequency* signal composed of six equal frequency sequential tones. Unlike the *0-ERB* signal of Experiment 1, which had a fixed frequency of 1000 Hz, the signal frequency of the *equal-frequency* signal pattern tested in Experiment 2 was chosen at random from the range of 925–1075 Hz on a logarithmic scale for each signal presentation. This manipulation allowed an evaluation of *equal-frequency* signals that, over trials, extended across the same frequency range as the *random* signal. Since the signals tested in Experiment 2 include the *random*, *equal-frequency*, and *ascending* signals, a general term *RAND* signal will be used to define all the signals tested in Experiment 2.

The stimuli were digitally generated using a sample rate of 20 kHz and low pass filtered at 7 kHz (Stewart VBF 10M). The stimuli were presented diotically via Sennheiser HD 410 SL headphones to listeners seated individually in a double-walled acoustical booth.

B. Procedures

1. Experimental procedures

A single-interval, yes/no procedure was used. Visual feedback as to the correctness of the listeners' response was provided after each trial. For the first part of Experiment 1,

TABLE I. The values of m, d', and decision criterion c for *0-*, *0.5-*, *1-*, and *2-ERB* signal types for four listeners who ran the fixed condition of Experiment 1. Averages are based on the geometric mean for the values of m, and arithmetic means for the values of d' and c.

	0-ERB			*0.5-ERB*			*1-ERB*			*2-ERB*		
	m	d'	c	m	d'	c	m	d'	c	m	d'	c
L1	12	1.28	0.12	10	0.97	0.14	8	1.27	0.14	8	1.34	0.16
L2	24	1.09	−0.09	20	0.95	−0.06	18	1.62	−0.13	10	1.4	−0.15
L3	16	1.16	0.05	8	0.94	−0.01	4	1.35	−0.06	4	1.2	0.14
L4	24	1.46	−0.01	17	1.01	−0.07	14	1.39	−0.01	12	1.18	−0.06
Ave.	18.2	1.25	0.02	12.8	0.97	0	9.5	1.41	−0.01	7.9	1.28	0.02

threshold values of m were estimated using an adaptive procedure. In the second portion of Experiment 1, data were collected using fixed values of m for different signal types and different listeners. The data from the second portion were used to estimate relative weights.

A two-down one-up adaptive procedure (Levitt, 1971) was used for the first part of Experiment 1. The value of m was initially incremented/decremented by 2, and the step size was reduced to 1 after three reversals. Listeners ran at least 30 blocks of 50 trials for each signal type (*0-ERB*, *0.5-ERB*, *1-ERB*, and *2-ERB*). Data from the last 20 blocks were used to estimate threshold. For the final 20 blocks, the data were collected as follows: for each signal type, listeners ran ten 50-trial blocks before moving on to the next signal type. The signal types were chosen in a quasirandom order across listeners. Then listeners reran ten blocks for each signal type in the reverse order.

The thresholds were estimated using a weighted least squares linear fit between $\log(m)$ and $d'(=z_{HIT}-z_{FA})$. The statistical tests and summary statistics presented are based on values of $\log(m)$ rather than m because past measurements in our laboratory have suggested that psychometric functions are better fitted on a $\log(m)$ scale. Each psychometric function was based on at least five values of $\log(m)$, with the constraint that at least ten trials contributed to each data point. The resulting fits to the psychometric functions were generally good, with a median percent of variance accounted for of 77. Only one of the 20 fits (L2, *0-ERB* signal) yielded a percent of variance accounted for that was less than 50. The values of $\log(m)$ that yielded $d'=1$ defined thresholds.

In the second part of Experiment 1 the values of m were fixed in order to obtain relative weights and estimate internal templates. The values of m that yielded approximately 75% correct responses for each listener and each signal type were estimated based on the results of the adaptive procedure and fine-tuned during practice. The resulting values of m are shown in Table I. Listeners ran 60 blocks of 50 trials (3000 trials) for each of the signal types in a quasirandom order. Listener 5 withdrew from the experiment prior to completing this portion, thus the ultimate data analysis reflects the results from the remaining four listeners (L1–L4). Data collection was blocked by signal type.

The experimental procedures for Experiment 2 were similar to the second portion of Experiment 1. Listeners L1 and L6–L8 participated in Experiment 2. The value of m that led to approximately 75% correct was determined during 2–6 h of practice for each listener. Listeners ran 75 50-trial blocks using the fixed value of m determined during practice. The values of m tested are listed in Table II. Recall that listeners L6–L8 had not previously participated in psychophysical experiments and, in particular, had not participated in Experiment 1.

Two special signal patterns, *equal-frequency* and *ascending* signals, were intermixed with the *random* signals and were each presented once within each 50-trial block. Therefore, of the 3750 trials collected for each listener participated in Experiment 2, 75 were the *ascending* signals and 75 were the *equal-frequency* signals. Except for L1, the first author, listeners were not informed of the presence of the special signals.

2. Computational procedures

a. Estimation of internal templates. The relative weights that comprise the internal templates were estimated using a logistic regression (e.g., Alexander and Lutfi, 2004; Dye *et al.*, 2005; Richards and Tang, 2006) and a fine-grained time-by-frequency spectrogram. The time dimension of the spectrogram was binned by burst. The frequency dimension was tiled by ten 50-Hz bins with center frequencies ranging from 800 to 1250 Hz. As a result, the spectrogram included 8×10 (total of 80) bins. Within each bin, a stimulus was coded as having energy (1) or not (0). The regression used these values as predictor variables and the listeners' binary response as the outcome variable. The output of the regression model included 80 logistic coefficients and an additive constant. Due to the large number of coefficients estimated, the regression was run on the data obtained from all listeners (12 000 total trials per signal type in Experiment 1 and 15 000 total trials in Experiment 2) to maximize the reliabil-

TABLE II. The values of m, d', and decision criterion c for the *RAND* signal for four listeners who ran Experiment 2. The frequency range of the random signals in Experiment 2 is approximately one ERB. Averages are based on the geometric mean for the values of m, and arithmetic means for the values of d' and c.

	RAND		
	m	d'	c
L1	10	1.17	0.13
L6	4	1.05	0.11
L7	6	1.26	−0.06
L8	10	1.61	0.13
Ave.	7	1.27	0.08

ity of the estimates. The resulting pattern of relative weights as a function of time and frequency using data from all listeners will be referred to as group internal templates. Note that the group internal templates for *RAND* signals in Experiment 2 used data from all three signal patterns (i.e., *random*, *equal-frequency*, and *ascending* signals).

An additional regression was run using fewer coefficients and thereby allowing separate regressions for the individual listeners. The procedure was the same as described above, except that the regression was only applied to the initial and final bursts of the stimuli. This regression yielded 20 coefficients (initial and final bursts; ten frequency bins) and an additive constant. Recall that the signal tones did not occupy the initial and final bursts. If the listeners *do* have an internal template of the expected stimulus, and if the internal templates included the initial and final bursts, the template would be expected to yield positive relative weights at frequencies that depended systematically on the frequency extent of the ascending pattern of Experiment 1 (e.g., positive weights at low frequencies for the initial burst and high frequencies for the final burst).

b. Fits to group internal templates. To provide comparisons of the templates across different signal patterns, a parametrization of the estimated templates was adopted. Accordingly, the group internal templates were fitted using a function of the form of a modified bivariate normal distribution (Z). The following functional form was used:

$$x' = (x - \mu_x)\cos(\theta) + (y - \mu_y)\sin(\theta),$$

$$y' = -(x - \mu_x)\sin(\theta) + (y - \mu_y)\cos(\theta),$$

$$Z = \alpha\{\exp[-(x'^2 + \gamma^2 + y'^2)/(2\sigma^2)]\} + \beta.$$

Here, x and y represent the time and frequency, respectively. The variables x' and y' provide a rotation of the 2D space by angle θ. The aspect ratio, γ, is the ratio of the width (time axis) relative to the height (frequency axis). Alternatively, for the traditional bivariate normal distribution, the aspect ratio γ reflects the ratio of the standard deviations of the time relative to the frequency axes prior to rotation (i.e., after rotation, the ratio is the same, but major and minor axes are no longer time and frequency). The parameter σ is the spread of the function, and μ_x and μ_y are the midpoints of the function in time and frequency, respectively. The parameters α and β allow the fitting to the relative weights by altering the maximal and minimal values (e.g., the integral need not be unity and negative values are allowed[1]).

Two parameters of critical importance in the current application are the aspect ratio γ and angle θ. As an example, for Experiment 1, the expectation was that as the ascending signal patterns extends across larger ranges of frequencies, the angle θ of the fitted templates would increase. For the templates obtained in Experiment 2, the expectation was that the aspect ratio γ would be smaller (i.e., greater height) than values estimated in Experiment 1, indicating an internal template that extended across the wider range of frequencies at which the signal *might* occur.

To estimate the best fitting functions, the sum of the squared deviations, $\Sigma(Z - \textit{relative weights})^2$ was minimized. The values of x and y (time and frequency) were scaled to have equal ranges of 1–8. As a result, the values of σ and γ were relatively independent (i.e., for $\gamma = 1$, the modified bivariate normal function had circular equal-weight contours). The potential parameter space was then sampled using MATLAB's *fminsearch* function. The process was repeated several times using a variety of initial values. Note that the angle and the aspect ratio can trade against one another. For example, the function might have an angle of zero and an aspect ratio greater than 1, or an angle of $\pi/2$ and an aspect ratio less than 1. This consideration, plus the recognition of the range of frequencies available,[2] led to the following restrictions on the parameter space: the value of σ was allowed to range between 0 and 10, the value of θ was fixed to be between 0 and $\pi/3$, and γ was constrained to be less than 25.

Standard errors of the parameter estimates were estimated using a bootstrap simulation. The logistic coefficients were treated as mean values and bootstrap replicates were obtained by drawing from normal distributions with those means and standard deviations equal to the standard errors of the coefficient estimates. Two bootstrap procedures were run, each with a minimum of 500 bootstrap replicates. The average of the two resulting estimates of the standard error of the coefficients is ultimately reported in Table IV. The initial parameter estimates were drawn from a normal distribution with a mean of the previously obtained "best" parameters and a standard deviation equal to 33% of the mean. In practice, most of the variation in the resulting parameters reflected the change in initial parameters because local minima in the neighborhood of the global minimum were allowed by the procedure. Thus, the estimated standard errors are conservative—the values reflect (a) smaller variations in the best fits associated with the resampling of the template and (b) larger variations due to the solutions associated with local minima, reflecting the changes in the values of the initial parameters.

III. RESULTS AND DISCUSSION

A. Psychophysical results and discussions.

Figure 2 shows the individual and averaged thresholds as a function of signal type for Experiment 1. The ordinate indicates threshold m on a logarithmic scale. Note that larger values of m, which indicate better sensitivity, are plotted toward the bottom. The abscissa indicates the four signal types tested. The average thresholds across five listeners (m = 23.70, 12.90, 10.18, and 7.07 for *0-ERB*, *0.5-ERB*, *1-ERB*, and *2-ERB*, respectively) are plotted using filled triangles; error bars indicate the standard errors of the mean. Although the thresholds vary substantially across listeners, the patterns of the thresholds across signal types are roughly similar: Thresholds were lowest for the *0-ERB* signal type and grew as the frequency extent of the signal increased. A one-way repeated measure analysis of variance indicates a significant effect of signal type [$F(3,12) = 14.7$, $p < 0.001$].

The observation that detection thresholds increased systematically as the frequency range of the signal increased from *0-ERB* to *2-ERB* is partially consistent with the results reported by Madden and Fire (1997) despite the differences

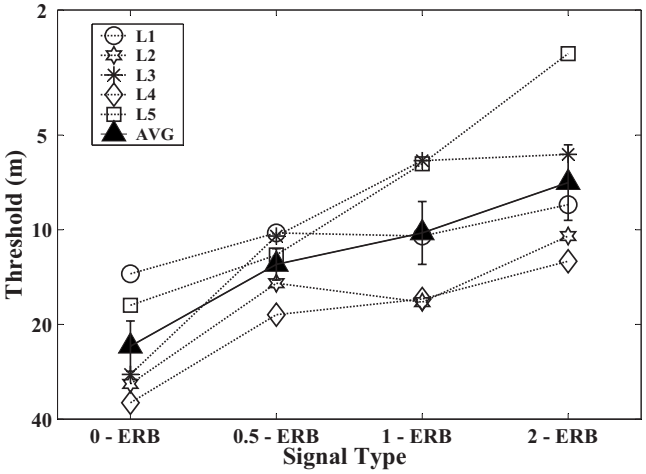


FIG. 2. Thresholds, as m on a logarithmic scale, are plotted (in reverse order on the y axis) for different signal types. Individual thresholds are plotted using open symbols and the averaged thresholds are plotted using filled triangles. Error bars show the standard errors of the mean ($N=5$).

in stimuli and experimental design. Madden and Fire (1997) found that the discriminability of a change in the frequency extent of a tonal frequency glide is relatively constant when the standard frequency extent is within a *1-ERB* range but doubles when the standard frequency extends across *2-ERB* range. Note that there was no masker presented in their stimuli. Therefore, the slight discrepancy between their results and the results from current study might reflect an effect of masking.

The current results, which indicated systematic reductions in sensitivity as the frequency range of the signal increases, however, are inconsistent with a report by Kidd *et al.* (1995b). Kidd *et al.* (1995b) measured the detectability of known signal patterns added to random eight-burst maskers. Among the sequential patterns they tested were an ascending pattern with an approximate *1-ERB* range and an equal-frequency pattern, both centered at 1000 Hz. Their results indicated no systematic differences in thresholds between the ascending and equal-frequency patterns; i.e., they did not obtain a deleterious effect of increased signal frequency range. It is worth noting that the results reported in their paper were drawn from only two subjects. In addition, compared to the current study, their signal, when present, occupied eight bursts rather than six, the center frequency of their signal was subjected to a 6% frequency randomization, and a 325 Hz protected region, within which masker elements could not fall, was enforced to reduce energetic masking. These differences, plus other procedural differences, may contribute to the differences in results between their study and the current study.

Table I shows the basic results from the trials using fixed values of m in the second part of Experiment 1 and Table II shows the results from Experiment 2. Recall that the *1-ERB* signal in Experiment 1 and the *RAND* signal in Experiment 2 extend across approximately equal frequency ranges. For each listener the value of m tested, the estimated d', and the estimated criterion c (Macmillan and Creelman, 2005) are shown. The average thresholds across four listeners are based on the geometric mean of the values of m. For Experiment 1, two of the four listeners who ran the fixed-m conditions showed consistent response biases (nonzero values of c). Listener 2 tended to over indicate "signal" responses whereas L1 over indicated "no-signal" responses. Moreover, consistent with the earlier results, values of m fell as the frequency extent of the signal increased. In Experiment 2 three of the listeners were biased towards no-signal responses.

TABLE III. Proportions of hits for *random* signals and two special signals: *equal-frequency* and *ascending* signals from Experiment 2.

	RAND		
	random	*equal-frequency*	*ascending*
L1	0.67	0.72	0.80
L6	0.65	0.77	0.75
L7	0.75	0.76	0.85
L8	0.74	0.81	0.84
Ave.	0.70	0.77	0.81[a]
SEM	0.03	0.02	0.02

paired t-test, random versus ascending, $t(3)=-12.9$, $p<0.001$.

Table III shows the hit rates for the *random*, *equal-frequency*, and *ascending* signals of Experiment 2. A paired, two-tailed t-test[3] applied to the hit rates across listeners indicated that the hit rates for the *ascending* signals were higher than for the *random* signals [$t(3)=-12.87$, $p<0.001$]. For the *equal-frequency* and *random* signals, the t value did not reach significance [$t(3)=-2.68$, $p<0.08$], but there was a trend indicating higher hit rates for the *equal-frequency* than the *random* signals. The statistically significant effect obtained for the random versus ascending signals provides evidence that enhanced detection rates can be achieved when regular patterns are tested in the context of *random* signals. Assuming listeners' strategies are dominated by the *random* signal trials, a template model does not predict higher hit rates for the ascending than the random signals. This reflects the fact that for the *random* signal the expected template is a rectangle with a height equal to the range of potential signal frequencies; Whether the signal is *ascending* or is *random*, for this template, the predicted hit rate would be the same.

The values of m tested in Experiment 2 were on average lower than for the *1-ERB* signal in Experiment 1 (on average, 7 versus 9.5, see Tables II and Table I) while the average d' values were approximately the same in Experiments 2 and 1 (1.27 versus 1.41, see Tables II and Table I). This indicates superior sensitivity for the *1-ERB* signal than for the *RAND* signal, even though the signals extend across the same range of frequencies. This comparison suggests a modest cost of signal uncertainty, yet keep in mind that the comparison is across different groups of listeners. The results also indicated that increasing the signal frequency range from 0 to *1-ERB* increased threshold values of m by a factor of 2 (on average, for the *0-ERB* and *1-ERB* signals types the values of m tested were 18.2–9.5 and the associated values of d' were 1.25 and 1.41, respectively, see also Fig. 2). These two observations suggest that the cost of shifting from *equal-frequency* signals to *random* signals had two effects: a large cost associated with the increase in frequency range and a potentially modest

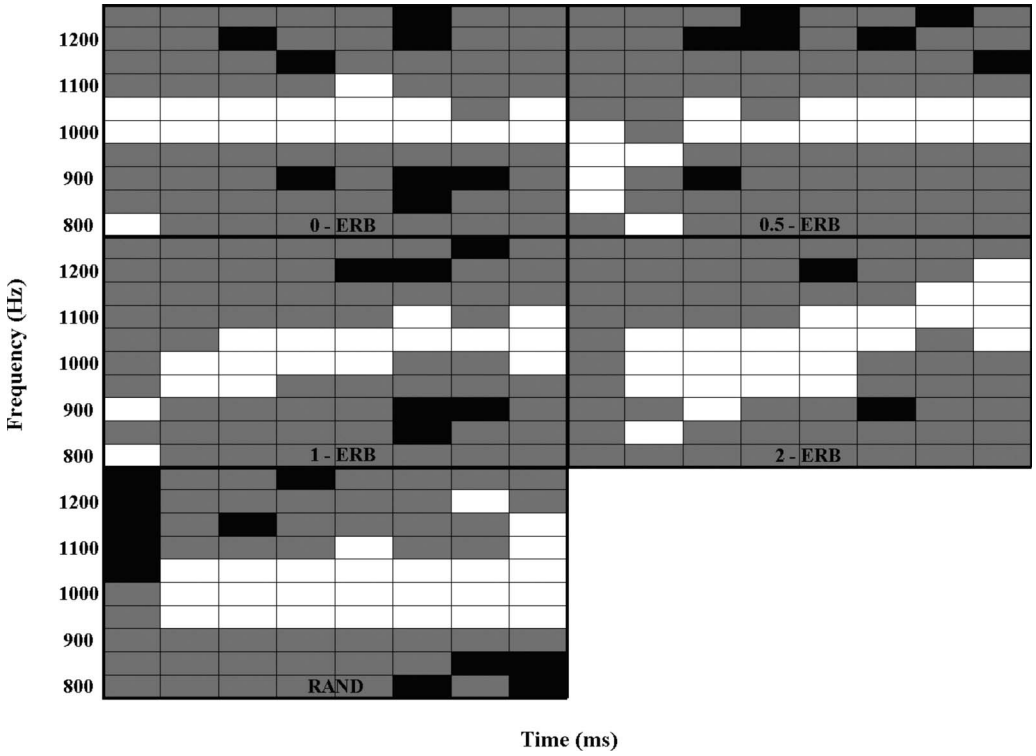


FIG. 3. Statistical reliability of the estimated group templates for *0-*, *0.5-*, *1-*, and *2-ERB* and *RAND* signals are plotted in a checkerboard plot. The black cells indicate negative weights; the white cells indicate positive weights; the gray cells indicate that the relative weights are no more than two standard errors of the estimate from zero.

cost of signal uncertainty *per se*.

Figure 3 shows an estimate of the statistical significance of the group internal templates using a time-by-frequency checkerboard plot. Each checkerboard of Fig. 3 contains 8 $\times$10 cells reflecting eight 30 ms time bursts and ten 50-Hz frequency bins. Black cells indicate negative weights, white cells indicate positive weights, and gray cells indicate that the relative weights were no more than two standard errors of the estimate distant from zero. The results for the *0-*, *0.5-*, *1-*, and *2-ERB* signal types are plotted in the top left, top right, middle left, and middle right panels, respectively. The results for the *RAND* signal of Experiment 2 are plotted in the bottom panel.

In terms of the statistical reliability of the relative weights, the group internal templates reflect the properties of the signals. First, positive weights fell in the region of the signal frequencies, centered at 1000 Hz. Second, the pattern of the positive weights reflected the signal patterns tested: for the *0-ERB* signal type, the pattern is flat, whereas for the *2-ERB* signal type the pattern rises in frequency over time. As another example, compare the results for the *1-ERB* signal of Experiment 1 with the results for the *RAND* signal of Experiment 2. The template for the *RAND* signal extends across a wider range of frequencies and is flatter. This is consistent with the frequency region occupied by the *random* signal. Third, significant positive weights were apparent in the initial and final bursts in the signal frequency region, except for the *2-ERB* signal type and the *RAND* signal where no significant positive weights were obtained for the initial burst. This result suggested that listeners might have integrated information from the initial and final bursts even though signal energy was not present in those two bursts.

Figure 4 shows regression coefficients (relative weights) as a function of frequency for the initial (left column) and

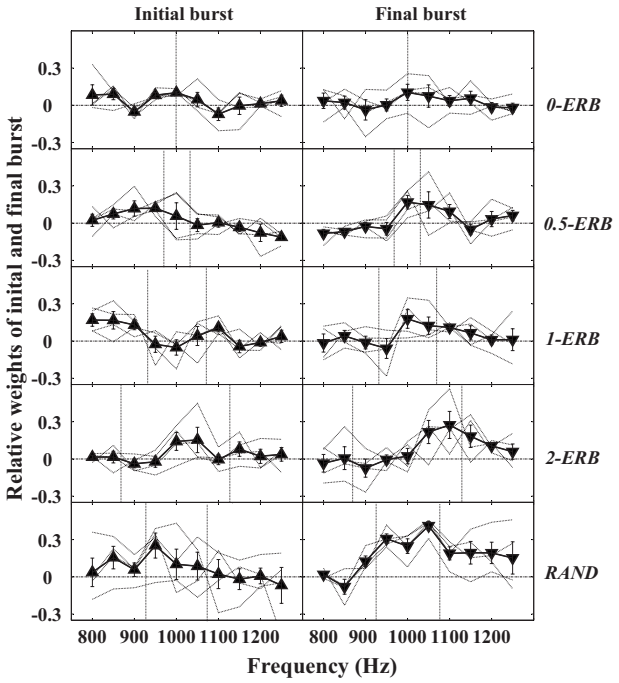


FIG. 4. Individual and average (solid lines and filled triangles) logistic regression coefficients as a function of frequency for the initial (left column) and final (right column) bursts are shown, from top to bottom, for the *0-*, *0.5-*, *1-*, and *2-ERB* and *RAND* signals. The error bars are the standard errors of the mean. The vertical dotted lines enclose the frequency range of the signals.

final (right column) bursts of the stimuli tested in Experiments 1 and 2. The results for individual listeners are plotted using dotted lines, and the averaged coefficients across listeners are plotted using the solid lines and filled triangles. Error bars are standard errors of the mean across listeners[4]. The vertical dotted lines enclose the frequency range of the signals. If subjects nonoptimally integrated information from the non-signal-bearing initial and final bursts, one would expect positive weights that extend the signal pattern into the initial and final bursts, i.e., positive weights near the onset of the signal frequency in the initial burst and positive weights near the offset of the signal frequency in the final burst.

Due to the substantial individual differences, clear-cut trends are not apparent in the data. For the initial burst, listeners consistently incorporated energy at frequencies near the initial signal frequency for the *0-*, *0.5-*, and *1-ERB* signals but not for the other signals. For the final burst, listeners consistently had positive weights at frequencies near the final signal frequency for the *1-* and *2-ERB* signals. Additionally, for the *RAND* signal, listeners appeared to extend their internal template through the final burst. Comparing the patterns across the initial and final bursts, for the final burst the relative weights tended to be more consistent across listeners, and the relative weights were larger near the ending signal frequency.

While the details of the obtained patterns of relative weights are unlikely to be described in a simple way, the results are nonetheless in accord with the group data in indicating that listeners altered their decision strategies depending on the properties of the signal pattern. Moreover, these results suggest that listeners tended to integrate information from the final burst, but not the initial burst, into their decisions.

B. Additional analyses

1. Parametrization of group internal templates

Figure 5 shows the modified bivariate normal functions fitted to the internal templates as contour plots. The top four panels are from Experiment 1 and the bottom panel is from Experiment 2. The frequencies of the signal tones in Experiment 1 are indicated using asterisks. For Experiment 2, the range of frequencies the signal tones might occupy is shown using a dashed box. Table IV indicates the parameters associated with each fit along with the percent of variance in the group internal template accounted for by the fit. Also shown are the standard errors of the estimates based on bootstrap simulations. Recall that the time and frequency axes are scaled to have equal ranges of 1–8 prior to fitting the modified bivariate normal function. As a result, in Table IV, a frequency of 1000 Hz has a value of 4.11 (μ_y), and the central point in time would take on a value of 4.5 (μ_x).

Concentrating on one parameter of primary interest in Experiment 1, the angle θ of the estimated templates captures the features of the signal to be detected in that the angles increased as the frequency range of the signal patterns increased. It is apparent that listeners' altered their internal templates to "match" the expected signal. Even so, the angles

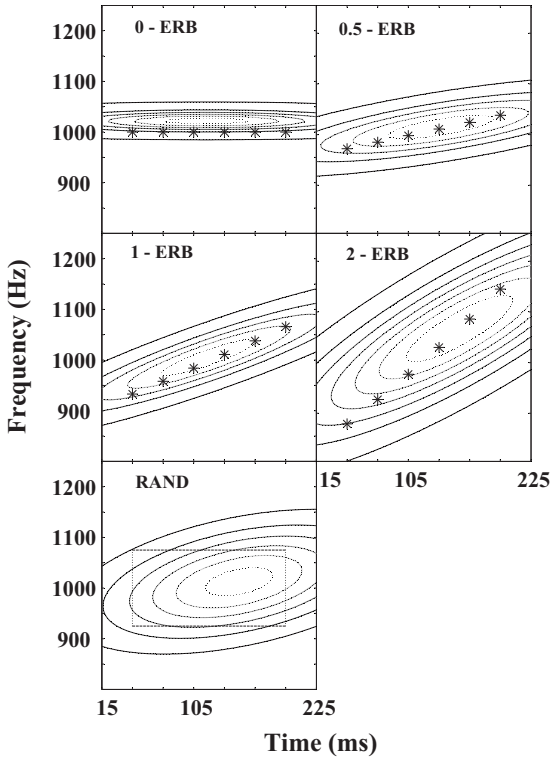


FIG. 5. Group templates for the *0-*, *0.5-*, *1-*, and *2-ERB* and *RAND* signals are shown using the contour plots. The signal frequencies of the *0-*, *0.5-*, *1-*, and *2-ERB* signals are shown using asterisks. For *RAND* signal, the range of signal frequencies is indicated using a dashed box.

of the fitted templates tend to fall short of the angle associated with the signals' spectrograms (see Fig. 5).

An unanticipated finding is that the estimated aspect ratio γ decreased with increases in signal frequency range (Table IV). This may explain the reduction in sensitivity associated with increases in signal frequency range (Fig. 2). For the linear model considered here, a decrease in the aspect ratio means that the listeners integrated energy from a wider range of frequencies. Such integration would, in turn, increase the amount of masking.

From Table IV, for the *0.5-* and *2-ERB* signals, it is also apparent that the estimated template was not centered at the temporal centroid of the signal (μ_x=5.06 and 5.67 rather than central 4.5 on the 1–8 scale), suggesting temporal uncertainty with regard to the listeners' setting of the template. Potentially, errors in the temporal alignment of internal templates (relative to the alignment predicted by an ideal observer) led to poorer thresholds because information in the non-signal-bearing final burst overcontributed to listeners' detection decisions.

Finally, the estimated templates were centered higher in frequency than the true signal frequency ($\mu_y > 4.11$). This was particularly true for the *0-ERB* and *2-ERB* signal types. An intriguing interpretation of this result is that the listeners incorporated "off-frequency listening" to reduce the deleterious effects of the upward spread of masking.

The results for Experiment 2 (*RAND* signal), relative to the functions fitted to the *1-ERB* signal of Experiment 1, revealed a much smaller aspect ratio γ (2.92 compared to 7.16). This suggests listeners spread their attention, measured

TABLE IV. Best-fitting parameters for the modified bivariate normal function fitted to the (group) logistic coefficients of the four signal types in Experiment 1 and the *RAND* signal in Experiment 2. Standard errors of the estimates are indicated in parentheses. The columns indicate the estimated angles (θ), aspect ratios (γ), spreads (σ), midpoint x (time) and y (frequency) values (μ_x and μ_y), scalars (α), biases (β), and percent of variance account for by the fit (PC_{Var}). Note: the time and frequency axes were scaled to range from 1 to 8 prior to data fitting; the parameters reflect that transformation.

	θ	γ	σ	μ_x	μ_y	α	β	PC_{Var}
0-ERB	0.00	15.8	2.89	4.41	4.45	2.84	−0.02	80
	(0.02)	(5.19)	(0.93)	(2.35)	(1.28)	(8.07)	(0.02)	
0.5-ERB	0.15	7.03	3.18	5.06	4.27	0.50	−0.03	74
	(0.04)	(5.97)	(0.68)	(2.99)	(1.28)	(0.29)	(0.01)	
1-ERB	0.32	7.16	3.10	4.50	4.20	0.49	−0.03	65
	(0.05)	(1.73)	(0.58)	(1.91)	(1.28)	(2.24)	(0.01)	
2-ERB	0.49	4.04	3.85	5.67	5.08	0.37	−0.02	55
	(0.11)	(0.89)	(0.35)	(1.50)	(3.07)	(0.07)	(0.01)	
RAND	0.19	2.92	2.88	5.48	4.31	0.63	−0.09	85
	(0.02)	(0.60)	(0.25)	(1.93)	(1.77)	(0.27)	(0.02)	

here as a region of energy integration, across a wider range of frequencies when the signal frequencies were random compared to ascending. There was also, however, a slight angle apparent in the fitted function, although the angle for Experiment 2 (θ=0.19) was smaller than that estimated for the *1-ERB* signal of Experiment 1 (θ=0.32). This result of a nonzero angle for the *RAND* signal was not expected, and potentially reflects listeners' dependence on higher frequencies in the final burst (Fig. 4, bottom panel).

To summarize, listeners relied differentially on information in the signal-bearing spectro-temporal locations in forming their detection decisions as the characteristics of the signal changed. Moreover, there are differences in the internal templates that might provide explanatory power concerning the listeners' poorer detection sensitivity as the range of signal frequencies increases. Chief among the possible contributing factors is the increased "height" of the internal templates as the frequency range of the signal increases.

2. Predictions based on group internal templates

The question of whether differences in internal templates are sufficient to account for differences in listeners' sensitivity across different signal types is addressed by examining the efficiency with which the listeners use their putative templates (Berg, 1990). The logic is as follows: for Experiment 1 the values of m varied across conditions, but the values of d' were approximately the same. If the obtained group templates and the linear model provide predictions with approximately equal values of d', it would suggest that the model is performing relatively well, and that differences in the templates, not differences in "internal noise," account for the differences in performance obtained for the different signal types tested in Experiment 1.

The first step, then, is to use the estimated templates to derive values of d' for the psychophysical stimuli tested in Experiment 1. The linear model associated with the estimated group templates vastly outperforms the listeners in that the values of d' were in excess of 5. To counteract the large difference in sensitivity (model versus humans), an additive internal noise was incorporated into the model. Importantly, the variance of the added internal noise was fixed across signal types. To the degree that the values of d' for the resulting model do not depend on signal type, it would suggest that the estimated templates drives changes in performance. Or, more accurately, the result would imply that changes in the efficiency with which the templates are utilized do not account for the differences in performance measured across the signal types tested in Experiment 1.

The details of the simulations are as follows. First, the inner product of the relative weights and the psychophysical stimuli generated decision variables for the linear model. Second, a zero-mean normally distributed deviate was added to the decision variable (the variance of the deviate was chosen to provide a d' of 1.5 or so). Third, the decision variable was compared against a criterion and a decision as to the signal's presence/absence was derived. The results indicated that the values of d' estimated in the simulation did not depend on the signal type. For example, when the variance of the added deviate was chosen to provide an average model d' of approximately 1.5, the range of predicted d' was from 1.45 to 1.53 across the four signal types. Thus, these simulations suggest that the changes in listeners' internal templates, rather than changes in listeners' internal noise, account for the difference in thresholds among the different signals tested in Experiment 1.

IV. SUMMARY AND CONCLUSIONS

The analyses of Experiments 1 and 2 indicate that internal templates can be estimated for the detection of spectro-temporal signal patterns embedded in random maskers. Moreover, consistent with expectations based on a cross-correlation model, the estimated templates mirror the signal to be detected. This is apparent in that (a) the angle of the estimated template, θ, increases with the frequency range of the ascending signals, and (b) the estimated template for the *1-ERB* ascending signal of Experiment 1 is less broad than that of the *RAND* signal of Experiment 2.

Two results concerning the functional shape of the estimated templates were not expected. First, as the frequency range of the signal increases, the aspect ratio γ decreases

(broader frequency swath of positive weights). This result is consistent with the reduction in sensitivity observed as the frequency range of the signal increased. Second, in Experiment 2, which tested random signal patterns, two special signal patterns (an *equal-frequency* signal and an *ascending* signal) were embedded within the context of the random signals. The results show that the *ascending* signal has hit rates that are statistically higher than for the *random* signal (two-tailed t-test), and for the *equal-frequency* signal, the difference in hit rate approaches statistical significance. This indicates a form of failure of the linear model evaluated here—if listeners are better at detecting an ascending signal than random signals, it suggests that listeners are relying on more than just the integration of energy across a broad frequency region implied by their templates.

With regard to the estimated relative weights, the results also indicate that listeners sometimes integrate energy in the non-signal-bearing final burst when making their decisions, potentially reflecting temporal uncertainty. Finally, although the experiments provide evidence of incompatibilities between the template model and human performance, it is notable that simulations indicate that the differences in the estimated internal templates can account for the reduction in sensitivity associated with the increase in signal frequency range.

ACKNOWLEDGMENTS

This work was supported by grant RO1 DC02012 from the National Institutes of Health. We thank the Associate Editor Richard L. Freyman, and three anonymous reviewers for their excellent suggestions on earlier drafts of this manuscript. We also thank Dr. Daniel E. Shub, Dr. Virginia Best, Dr. Jinyu Qian, Thomas Lee and Xiang Cao for their helpful comments on an earlier draft of this manuscript.

[1]A methodological detail affects the expected form of an optimal (maximize d') template for the deterministic signals of Experiment 1. The total number of tones was the same for the signal and nonsignal stimuli. As a result, the probability that a tone fell into nonsignal "bins" was smaller for the signal than the no-signal stimuli. This leads to the prediction that an optimal template would have positive values for the signal spectro-temporal locations and negative values elsewhere. The precise value of the negative relative weights depends on a number of factors, including the total number of bins attended to by the listener, the number of signal bins, and the total number of tones in the stimulus. Because the number of nonsignal bins attended to by the listener is not known, precise predictions for a template that maximizes d' is not available.

[2]The x and y axes were constrained to range from 1 to 8. Based on the data, the coefficients at low and high frequencies were near zero. A value of σ greater than 10 is not consistent with a function that is near zero for the highest and lowest frequencies. Restricting γ to be less than 25 reflects the presence of only eight time and ten frequency bins—there are limits to the degree to which the data can support a rapid fall from maximum to a minimum frequency. The limit of $\gamma < 25$ was chosen based on fits to the coefficients of the *0-ERB* signal type, which indicated a value of approximately 15.

[3]The hit rates were not transformed prior to the t-test. Transformations such as Studebakers' (1985) rationalized arcsine unit have little if any effect on intermediate percentages.

[4]The regression coefficients were not normalized prior to averaging. As a result, the estimated standard error includes across-listener variation in the magnitude of the weights in addition to the variations in the obtained patterns.

Ahumada, A. J., Jr., (**2002**). "Classification image weights and internal noise level estimation," J. Vision **2**, 121–131.

Ahumada, A. J., Jr. and Lovell, J. (**1971**). "Stimulus features in signal detection," J. Acoust. Soc. Am. **49**, 1751–1756.

Alexander, J. M., and Lutfi, R. A. (**2004**). "Informational masking in hearing-impaired and normal-hearing listeners: sensation level and decision weights," J. Acoust. Soc. Am., **116**, 2234–2247.

Berg, B. G. (**1990**). "Observer efficiency and weights in a multiple observation task," J. Acoust. Soc. Am. **88**, 149–158.

Duda, R. O., and Hart, P. E. (**1973**). *Pattern Classification and Scene Analysis* (Wiley, New York).

Dye, R. H., Stellmack, M. A., and Jurcin, N. F. (**2005**). "Observer weighting strategies in interaural time-difference discrimination and monaural level discrimination for a multi-tone complex," J. Acoust. Soc. Am. **117**, 3079–3089.

Glasberg, B. R., and Moore, B. C. J. (**1990**). "Derivation of auditory filter shapes from notched-noise data," Hear. Res. **47**, 103–138

Green, D. M., and Swets, J. A., (**1974**). *Signal Detection Theory and Psychophysics* (Robert E. Krieger, Huntington, NY).

Greenberg, G. Z., and Larkin, W. D. (**1968**). "Frequency-response characteristic of auditory observers detecting signals of a single frequency in noise: the probe-signal method," J. Acoust. Soc. Am. **44**, 1513–1523.

Huang, R., and Richards, V. M. (**2006**). "Coherence detection: Effects of frequency, frequency uncertainty, and onset/offset delays," J. Acoust. Soc. Am. **119**, 2298–2304.

Kidd, G., Mason, C. R., and Dai, H., (**1995a**). "Discriminating coherence in spectro-temporal patterns," J. Acoust. Soc. Am. **97**, 3782–3790.

Kidd, G., Mason, C. R., and Rohtla, T. L. (**1995b**). "Binaural advantage for sound pattern identification," J. Acoust. Soc. Am. **98**, 1977–1986.

Levitt, H. (**1971**). "Transformed up-down methods in psychoacoustics," J. Acoust. Soc. Am. **49**, 167–177.

Lutfi, R. A. (**1995**). "Correlation coefficients and correlation ratios as estimates of observer weights in multiple-observation tasks," J. Acoust. Soc. Am. **97**, 1333–1334.

Madden, J. P., and Fire, K. M. (**1997**). "Detection and discrimination of frequency glides as a function of direction, duration, frequency span, and center frequency," J. Acoust. Soc. Am. **102**, 2920–2924.

Macmillan, N. A., and Creelman, C. D. (**2005**). *Detection Theory; A Users Guide*, 2nd ed. (Lawrence Erlbaum Associates, Mahwah, NJ).

Moore, B. C. J., and Sek, A. (**1998**). "Discrimination of frequency glides with superimposed random glides in level," J. Acoust. Soc. Am. **104**, 411–421.

Richards, V. M., and Zhu, S. (**1994**). "Relative estimates of combination weights, decision criteria, and internal noise based on correlation coefficients," J. Acoust. Soc. Am. **95**, 423–434.

Richards, V. M., and Tang, Z. (**2006**). "Estimates of effective frequency selectivity based on the detection of a tone added to complex maskers," J. Acoust. Soc. Am. **119**, 1574–1584.

Studebaker, G. (**1985**). "A 'rationalized' arcsine transform," J. Speech Hear. Res., **28**, 455–462.

Tang, Z., and Richards, V. M. (**2003**). "Examination of a linear model in an informational masking study," J. Acoust. Soc. Am. **114**, 361–367.

Wright, B. A. (**2005**). "Combined representations for frequency and duration in detection templates for expected signals," J. Acoust. Soc. Am. **117**, 1299–1304.

Age-related differences in the temporal modulation transfer function with pure-tone carriers

Ning-ji He, John H. Mills, Jayne B. Ahlstrom, and Judy R. Dubno[a)]
Department of Otolaryngology-Head and Neck Surgery, Medical University of South Carolina, 135 Rutledge Avenue, MSC 550, Charleston, South Carolina 29425-5500

(Received 7 December 2007; revised 11 September 2008; accepted 15 September 2008)

Detection of amplitude modulation (AM) in 500 and 4000 Hz tonal carriers was measured as a function of modulation frequency from younger and older adults with normal hearing through 4000 Hz. The modulation frequency above which sensitivity to AM increased ("transition frequency") was similar for both groups. Temporal modulation transfer function shapes showed significant age-related differences. For younger subjects, AM detection thresholds were generally constant for low modulation frequencies. For a higher carrier frequency, AM detection thresholds then increased as modulation frequency further increased until the transition frequency. In contrast, AM detection for older subjects continuously increased with increasing modulation frequency, indicating an age-related decline in temporal resolution for faster envelope fluctuations. Significant age-related differences were observed whenever AM detection was dependent on temporal cues. For modulation frequencies above the transition frequency, age-related differences were larger for the lower frequency carrier (where both temporal and spectral cues were available) than for the higher frequency carrier (where AM detection was primarily dependent on spectral cues). These results are consistent with a general age-related decline in the synchronization of neural responses to both the carrier waveform and envelope fluctuation. © *2008 Acoustical Society of America.*
[DOI: 10.1121/1.2998779]

PACS number(s): 43.66.Mk, 43.66.Sr [MW] Pages: 3841–3849

I. INTRODUCTION

Amplitude modulation (AM) is one of the elementary features of natural sounds, including many communication signals. For example, a vowel can be modeled as a periodic carrier (vocal fold production) modulated by specific vocal-tract characteristics, which result in amplitude fluctuations in the speech waveform. This temporal envelope carries important information relevant to speech perception (Drullman, 1995; Shannon *et al.*, 1995).

The auditory system is highly sensitive to small amplitude fluctuations. Sinusoidal amplitude modulation (SAM), one of the basic forms of AM, consists of a carrier (tone or noise), which periodically varies in amplitude in the same manner as the modulating sinusoid. The modulation depth (m) is defined by the amplitude of the modulating signal, which is a proportion (between 0 and 1) of the carrier amplitude.

Typical neural responses to AM tones are locked to the stimulus envelopes (envelope locking), in addition to phase locking to the carrier frequencies. In a comprehensive study examining cues for AM detection and discrimination, Nelson and Carney (2007) found at the inferior colliculus of awake rabbits that the synchronization of neural responses was phase locked to stimuli with modulation depths as low as −30 dB, which is comparable to AM detection thresholds measured behaviorally. In addition, when modulation depths were above modulation detection thresholds, rate-depth functions were steep enough to predict modulation-depth discrimination measured behaviorally. Envelope information is well preserved and even enhanced in neural responses at all levels of the auditory system, which has led to a hypothesis of a specialized neural mechanism to extract AM information [for a review, see Joris *et al.* (2004)].

The function relating SAM detection thresholds to modulation frequency is called the temporal modulation transfer function (TMTF). Starting from low modulation frequencies (4–5 Hz), AM detection thresholds either stay constant or increase slightly (become worse) as the modulation frequency increases until a transition frequency is reached. Below the transition frequency, AM detection thresholds are dependent primarily on temporal cues [e.g., see Kohlrausch *et al.* (2000)]. Above this frequency region, the TMTF pattern is dependent on the type of carrier. That is, as the modulation frequency increases, AM thresholds either rapidly increase with a broadband-noise carrier (Viemeister, 1979) or even more rapidly decrease (improve) with a tonal carrier (Zwicker and Fastl, 1990). The discrepancy between carrier types is an indication of the involvement of spectral side components in the case of tonal carriers (Moore and Glasberg, 2001). As the modulation frequency increases above the transition frequency, the spectral side components surrounding the carrier frequency gradually move out of the critical bandwidth centered at the carrier frequency, providing additional cues for AM detection. Such spectral cues are not available with broadband-noise carriers. For tonal carriers, the transition frequency is a function of carrier frequency and is about 1/2 of the critical bandwidth associated with the carrier frequency (Zwicker and Fastl, 1990).

[a)]Electronic mail: dubnojr@musc.edu

In a systematic study of AM detection (Kohlrausch *et al.*, 2000), the effects of carrier frequency and level on the shape of the tonal TMTF were examined. With the exception of very low carrier levels (30 dB SPL), for carrier frequencies above 2000 Hz, a general pattern was observed. Below the transition frequency, AM detection thresholds remained constant for modulation frequencies up to 100–130 Hz, above which AM thresholds increased with modulation frequency until the transition frequency was reached. It was suggested that this increase in AM thresholds reflects a limit of the auditory system to follow fast envelope fluctuations. Below the transition frequency, TMTFs were likely limited by modulation filtering, which was modeled by Kohlrausch *et al.* (2000) as a low-pass filter with a cutoff frequency of ~150 Hz and was independent of peripheral auditory filtering associated with the carrier frequency. At modulation frequencies above the transition frequency, where AM detection for tonal carriers improved dramatically with increasing modulation frequency, peripheral auditory filtering most likely contributed to the shape of the tonal TMTF, as both temporal and spectral cues (side components) were available. The contribution of spectral cues was dependent on the bandwidth of the auditory filter associated with the carrier frequency. For carrier frequencies below 2000 Hz, the auditory filter bandwidth is narrower than that of the hypothetical modulation filter, which may allow spectral cues to be involved. In this way, the tonal TMTF may reveal the contribution of low-pass modulation filtering and peripheral filtering, depending on carrier frequency.

Studies of masking and interference of AM stimuli reveal another important feature of AM detection. AM detection is not susceptible to the negative effects of simultaneously or nonsimultaneously presented stimuli unless the competing stimuli are modulated at a similar rate (Bacon and Grantham, 1989; Yost and Sheft, 1989; Bacon and Opie, 2002; Dau *et al.*, 1997a, 1997b; Ewert and Dau, 2000; Wojtczak and Viemeister, 2005). This is consistent with the hypothesis of a "modulation-specific mechanism" for AM processing (Joris *et al.*, 2004). The hypothesis was further conceptualized in a modulation filter bank model (Dau *et al.*, 1997a, 1997b; Dau *et al.*, 1999; Ewert and Dau, 2000; Nelson *et al.*, 2004), which states that for each peripheral auditory filter there is a bank of modulation filters. AM detection improves with increasing carrier bandwidth and stimulus duration, suggesting that AM information is integrated across frequency and time (Dau *et al.*, 1997b). Furthermore, the shape of the TMTF and the associated time constant do not change with carrier frequency (Eddins, 1993; Dau *et al.*, 1997b; Kohlrausch *et al.*, 2000). Thus, temporal resolution of the auditory system reflects analyses from two domains. One is the audio-frequency domain at the periphery, including basilar membrane filtering, which broadens with increases in center frequency. The other is the temporal modulation domain for detecting envelope fluctuations with constant temporal resolution across audio frequency (Dau *et al.*, 1999). Because time constants for peripheral auditory filters are generally inversely related to filter bandwidth, temporal resolution would be expected to increase with an increase in modulation frequency if peripheral filtering was the limiting factor. Given that AM thresholds progressively increase at higher modulation frequencies, the modulation filtering process in the temporal modulation domain is likely to occur at more central levels of the auditory system.

In general, AM detection by listeners with hearing loss differs with audiometric configuration. AM detection is poorer than normal for listeners with high-frequency hearing loss with both broadband-noise carriers (Bacon and Viemeister, 1985) and tonal carriers (Moore and Glasberg, 2001) but similar to normal for listeners with flat hearing loss [e.g., see Bacon and Opie (2002) for broadband-noise carriers and Bacon and Gleitman (1992) for tonal carriers]. For broadband carriers, the difference may reflect the importance of carrier bandwidth, which would be narrower than normal for listeners with high-frequency hearing loss. These observations are consistent with the modulation filter bank model (Dau *et al.*, 1997a, 1997b), which assumes that the output of modulation filters can be integrated across auditory filters. In many studies of AM detection by adults with hearing loss, there were considerable differences in age between normal-hearing and hearing-impaired subjects [e.g., see Bacon and Viemeister (1985) and Moore and Glasberg (2001)]. However, the aging effect was not systematically assessed, possibly due to the robust AM detection observed from hearing-impaired listeners. Thus, the effect of age on AM detection is largely unknown.

Takahashi and Bacon (1992) measured AM detection and AM masking using a broadband-noise carrier in a younger group and in three older groups (50, 60, and 70 year olds) with normal hearing. The TMTFs for the four groups were similar in shape. Although AM detection thresholds were generally poorer for the three older groups than for the younger group, age-related differences were not statistically significant, similar to results for Purcell *et al.* (2004) for envelope following responses. In contrast, a study of auditory steady-state evoked responses to AM tones (Leigh-Paffenroth and Fowler, 2006) reported that the number of phase-locked responses was larger at a 40 Hz modulation frequency than at lower (20 Hz) and higher (90 Hz) modulation frequencies; there were also significant age-related differences at the 500 Hz carrier frequency but not at the 2000 Hz carrier frequency. Given the auditory system's specialized neural mechanism to process AM information (Joris *et al.*, 2004) and high sensitivity to AM (Viemeister, 1979; Kohlrausch *et al.*, 2000), AM information integrated across frequency channels with a broadband-noise carrier and presented at suprathreshold levels [as in Takahashi and Bacon (1992)] may carry redundant cues and may not reveal subtle age-related differences in detection. With redundancy reduced by using shorter stimulus durations, lower stimulus levels, and tonal carriers, age-related differences may be more easily revealed. For example, as reported by Takahashi and Bacon (1992), differences between the younger group and the three older groups were larger than the group variances at very low (2 Hz) or very high modulation frequencies. Indeed, for the 2 Hz modulation frequency, the 500 ms stimulus contained only one modulation cycle, which was difficult to detect. At high modulation frequencies, the increased need to follow fast envelope fluctuations may have

affected detection more for older subjects than for younger subjects. In both situations, therefore, age-related differences were more likely to be observed.

The finding of a frequency-dependent aging effect on steady-state evoked responses to AM tones (Leigh-Paffenroth and Fowler, 2006) was consistent with psychophysical studies of intensity discrimination, frequency discrimination (He *et al.*, 1998), and frequency modulation detection (He *et al.*, 2007), where age-related differences were larger at lower carrier frequencies and decreased as frequency increased. This frequency-dependent aging effect could not be explained in terms of hearing sensitivity because thresholds of younger and older subjects in these studies were closely matched, especially at lower frequencies. An alternate explanation was based on the involvement of temporal cues, which may degrade with increasing age. According to the modulation filter bank model (Dau *et al.*, 1997a, 1997b; Kohlrausch *et al.*, 2000), AM detection is determined by the temporal resolution of the auditory system, which is limited by the characteristics of both modulation filters and peripheral auditory filters, especially for tonal AM detection. If temporal resolution degrades with increasing age, aging should affect the tonal TMTF differently at modulation frequencies below and above the transition frequency. More specifically, below the transition frequency where AM detection is mainly determined by temporal cues (or by modulation filter bank characteristics), more age-related differences are expected. In contrast, above the transition frequency where AM detection also involves spectral cues, less age-related differences may be observed because peripheral filtering is generally unaffected by aging when there are no confounding effects of hearing loss (Sommers and Humes, 1993; Peters and Hall, 1994; Gifford and Bacon, 2005). To test these hypotheses, AM detection was measured from younger and older subjects with normal hearing using tonal carriers. TMTFs were measured at carrier frequencies of 500 and 4000 Hz to maximize any frequency-dependent aging effect.

II. METHODS

A. Amplitude-modulated signals

The mathematical description of a sinusoidal AM waveform with a pure-tone carrier is given by

$$x(t) = [1 + m\cos(f_m t + \phi)]\sin(f_c t). \quad (1)$$

Here, m is the modulation depth ($0 < m \leq 1$), ϕ is the modulation phase ($\phi = 0$ in this study), and f_m and f_c are the modulation and carrier frequencies, respectively. AM signals were digitally generated with custom LABVIEW software (LABVIEW 6.1, National Instruments) and converted to analog using a 16 bit digital-to-analog converter (National Instruments, model 6052E) with a sampling rate of 50 kHz. The signal was gated with a duration of 600 ms (including 30 ms $\cos^2$ rise-fall ramps), which consisted of at least three modulation cycles. The modulated waveform was normalized in amplitude after stimulus generation to prevent possible cues for detection due to the increase in rms amplitude after modulation (Yost *et al.*, 1989). The generated AM signals were low-pass filtered (TDT PF1) at a cutoff frequency of 10 kHz, attenuated (TDT PA4), and then passed through a headphone buffer (TDT HB5) to an insert earphone (Etymotic Research, ER2). The frequency response of the earphone was flat from 100 to 7000 Hz as measured in an ear simulator (Brüel & Kjær, model 4157).

B. Procedures

Given the large amount of data collected from each subject, an efficient adaptive procedure, the maximum-likelihood method, was used to measure AM detection thresholds. The maximum-likelihood method has been described elsewhere (Green, 1993; Gu and Green, 1994; Leek *et al.*, 2000); it has been successfully applied to the measurement of frequency and intensity discrimination (He *et al.*, 1998) and gap detection (Florentine *et al.*, 2001). Briefly, thresholds for AM detection were measured using a single-interval (yes-no) maximum-likelihood procedure. The slope factor (k) was 1.0 with modulation depth converted to logarithmic units (20 log m) based on the results of a pilot study of psychometric functions for AM detection (see the Appendix). Each threshold was determined from 30 trials, including eight randomly inserted catch trials. In five of the catch trials, the minimum modulation depth ($m = 0.001$, −60 dB in 20 log m) was presented. In the remaining three catch trials, the maximum modulation depth was presented, which was adjusted individually for each subject and condition and ranged from $m = 0.5$ (−6 dB) to $m = 0.8$ (−2 dB). In the maximum-likelihood procedure, modulation depth was varied adaptively, gradually converging to a threshold value with a minimum step size of 0.5 dB. The threshold was defined as the "sweet point" (Green, 1993), which was calculated based on the estimated midpoint (m) of the psychometric function and the false alarm rate (α) after 30 trials.

Each stimulus presentation trial contained two signals separated by 500 ms of silence; the first signal was always unmodulated and the second signal varied in modulation depth. Subjects were instructed to press the "yes" button on a vote box (TDT RBOX) if they detected AM in the second signal or the "no" button if they did not. No correct-answer feedback was given.

TMTFs were measured with the tonal signal presented at 75 dB SPL. The carrier frequencies were 500 and 4000 Hz. Modulation frequencies were 5, 40, 80, 100, 200, and 250 Hz for the 500 Hz carrier and 5, 40, 80, 100, 200, 400, 500, and 1000 Hz for the 4000 Hz carrier. Each threshold was the average of two measurements, except when the two thresholds differed by more than 2 dB. In that case, two additional measurements were obtained, and the average of four measures was taken as the final threshold. Additional measures were necessary in ~2% of the cases for older subjects and in ~1% of the cases for younger subjects.

C. Subjects

Eight younger subjects (mean age of 20.5 years, age range of 18–26 years) and eight older subjects (mean age of 70.6 years, age range of 60–80 years) participated. All subjects had absolute thresholds of ≤20 dB HL (ANSI, 1996)

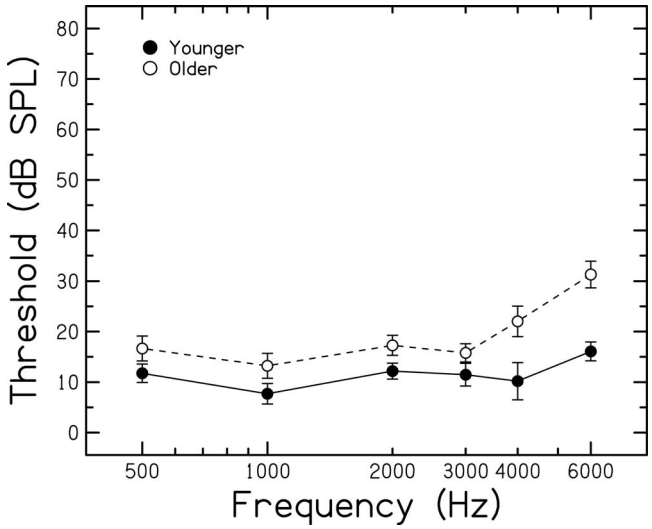


FIG. 1. Group means and standard errors of absolute thresholds (in dB SPL) for pure tones for younger subjects (filled) and older subjects (open).

through 4000 Hz. Figure 1 shows pure-tone thresholds in dB SPL for the younger subjects (filled symbols) and the older subjects (open symbols). Subjects had no prior experience with the listening task. Thus, training was provided prior to data collection to familiarize subjects with the test procedures and stimuli. During training, subjects were tested at both carrier frequencies at a modulation rate of 5 Hz using a constant stimulus procedure with a small number of repetitions (5). Training was terminated when sigmoidal shapes of psychometric functions for AM detection were consistently obtained. This was accomplished in approximately 1 h for the younger subjects and in approximately 2 h for the older subjects.

III. RESULTS

Figure 2 shows group means and standard errors for AM detection thresholds ($d'=1$) as a function of modulation frequency for younger subjects (filled) and older subjects (open). TMTFs for the 500 Hz carrier are plotted in the top panel, and TMTFs for the 4000 Hz carrier are plotted in the bottom panel. The general patterns were consistent with previous studies of AM detection (Zwicker, 1952; Kohlrausch *et al.*, 2000; Moore and Glasberg, 2001). For younger subjects, the transition frequency was about 10% of the carrier frequency for both carriers. Although the precise values of the transition frequencies could not be defined given the limited number of data points, the approximate values were similar to those reported by Kohlrausch *et al.* (2000), i.e., ~40 Hz for the 500 Hz carrier and ~400 Hz for the 4000 Hz carrier. AM thresholds at modulation frequencies at and below the transition frequency remained generally constant for the 500 Hz carrier. For the 4000 Hz carrier, AM thresholds were generally constant (i.e., the standard deviation was less than 1 dB across modulation frequency) to 100 Hz, then increased (worsened) as modulation frequency further increased to the transition frequency. Above the transition frequency, thresholds decreased (improved) at a fast rate as modulation frequency further increased. The rate of improvement in AM detection for modulation frequencies higher than the transition frequency differed between the low and high carrier frequencies (averaging 8.1 dB/octave for the 500 Hz carrier and 19.6 dB/octave for the 4000 Hz carrier).

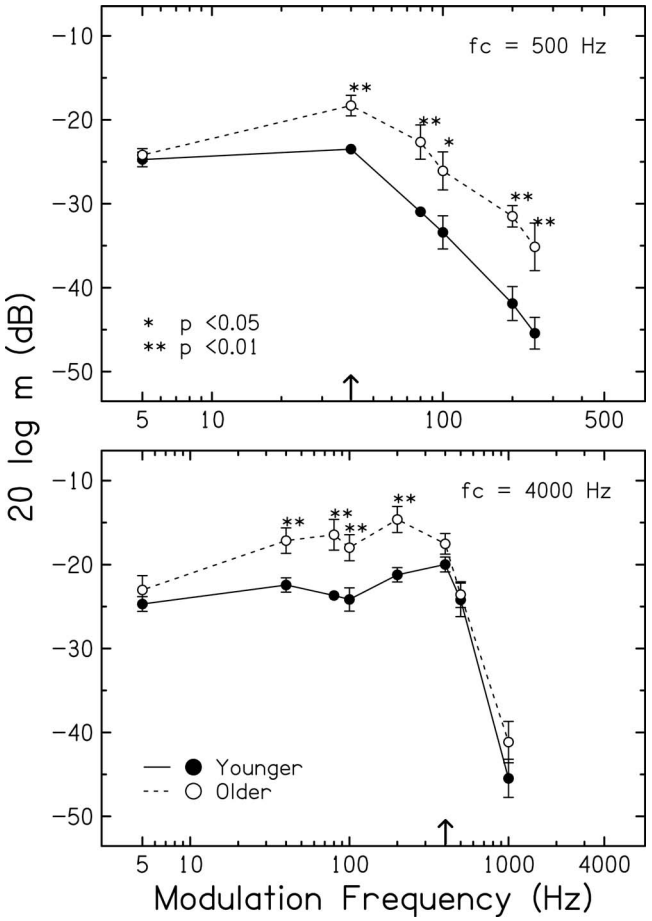


FIG. 2. Group means and standard errors of AM detection thresholds as a function of modulation frequency for younger subjects (filled) and older subjects (open). Temporal modulation transfer functions (TMTFs) for 500 and 4000 Hz carrier frequencies are presented in the top and bottom panels, respectively. The single asterisk indicates a significant difference at $p<0.05$, and double asterisks at $p<0.01$ based on t-tests. The arrows denote the approximate transition frequency for each carrier frequency.

Similar to results for younger subjects, TMTFs for older subjects were characterized by segments that differed in direction and rate of change in AM thresholds. Although transition frequencies were similar to those for the younger subjects, the shapes of the TMTFs differed. Below the transition frequency, older subjects' AM detection thresholds continuously increased for both carrier frequencies as modulation frequency increased from 5 Hz, suggesting an age-related decline in temporal resolution for faster envelope fluctuations. Although age-related differences were observed at both carrier frequencies, differences were seen at modulation frequencies below and above the transition frequency for the 500 Hz carrier but were restricted to modulation frequencies below the transition frequency for the 4000 Hz carrier. Above the transition frequency, slopes of TMTFs for older subjects averaged 6.3 dB/octave for the 500 Hz carrier and 17.9 dB/octave for the 4000 Hz carrier. These values were smaller than the slopes for younger subjects, but age-related differences were not statistically significant, as confirmed by

a repeated-measure analysis of variance (ANOVA). For both younger and older subjects, slopes were significantly steeper for the 4000 Hz carrier frequency than for the 500 Hz carrier frequency [$F(1,11)=104.72$, $p<0.0001$], with a nonsignificant age by carrier frequency interaction.

Differences in TMTF shapes were confirmed by a repeated-measure ANOVA on AM thresholds, with age as the grouping factor and carrier frequency and modulation frequency as the repeated measures, for modulation frequencies from 5 to 200 Hz. Beyond 200 Hz, modulation frequencies were not matched for the 500 and 4000 Hz carriers. Note that modulation frequencies of 5–200 Hz spanned a range below and above the transition frequency for the 500 Hz carrier but were below the transition frequency for the 4000 Hz carrier. Results from two younger subjects were not included in the analysis due to missing data. Results revealed significant main effects of age [$F(1,12)=10.55$, $p=0.007$], carrier frequency [$F(1,12)=87.59$, $p<0.0001$], and modulation frequency [$F(4,48)=24.26$, $p<0.0001$]; no significant interaction between age and carrier frequency was observed. Thus, over this range of modulation frequencies (5–200 Hz), age-related differences were observed for both carriers. Furthermore, a significant age by modulation frequency interaction [$F(4,48)=7.84$, $p<0.0001$] confirmed that the age effect differed with modulation frequency; i.e., age-related differences increased with increasing modulation frequency.

Post hoc tests focused on the shapes of the TMTF for the 4000 Hz carrier for modulation frequencies below the transition frequency. More specifically, the question was whether AM thresholds remained constant for lower modulation frequencies and then increased, as reported by Kohlrausch *et al.* (2000). First, AM detection thresholds increased linearly as the modulation frequency increased from 5 to 100 Hz, but for older subjects only [$F(1,12)=15.19$, $p=0.002$]. Second, AM thresholds at 200 Hz were significantly higher than AM thresholds at modulation frequencies of 5, 40, 80, and 100 Hz for younger subjects [$F(1,12)=5.15$, $p=0.042$] and older subjects [$F(1,12)=19.30$, $p=0.001$]. Thus, results for older subjects suggested a continuous trend of increasing AM detection thresholds as the modulation frequency increased from 5 to 200 Hz. In contrast, AM detection for younger subjects remained constant through 100 Hz followed by an increase in AM thresholds, consistent with the TMTF pattern described by Kohlrausch *et al.* (2000).

To further assess age-related differences in AM detection, group means were evaluated by *t*-tests at each modulation frequency. These revealed significant differences between younger and older groups for the 500 Hz carrier at modulation frequencies of 40–250 Hz (at and above the transition frequency). In contrast, for the 4000 Hz carrier, significant age-related differences were observed only at modulation frequencies below the transition frequency (Fig. 2, single asterisk indicating a significant difference at $p<0.05$ and double asterisks indicating $p<0.01$).

IV. DISCUSSION

A. AM detection by younger subjects

TMTFs obtained from younger subjects were consistent with those described in the literature. For modulation frequencies lower than transition frequencies, the lowest AM detection thresholds averaged approximately −25 dB for both 500 and 4000 Hz carriers, thresholds that were similar to results from Viemeister (1979) but slightly higher than those reported by Kohlrausch *et al.* (2000). Discrepancies may be due to the effect of stimulus duration [800 ms used by Kohlrausch *et al.* (2000) compared to 600 ms in the current study]. The shape of the TMTF for the 500 Hz carrier was relatively flat for modulation frequencies below the transition frequency, consistent with the data of Kohlrausch *et al.* (2000) for carrier frequencies ≤2000 Hz. For the 4000 Hz carrier, constant AM thresholds were followed by increasing AM thresholds as the modulation frequency increased from 5 Hz to the transition frequency, similar to the data of Kohlrausch *et al.* (2000) for higher carrier frequencies. Thresholds began to increase at about 100 Hz, which was numerically similar to the previous study (100–130 Hz). The transition frequency was about 10% of the carrier frequency for both low and high carrier frequencies.

B. Age-related differences in AM detection

AM detection thresholds were poorer for older than younger subjects at some modulation frequencies. TMTF shapes also differed between the two age groups. As predicted, for modulation frequencies below the transition frequency (where AM detection was based primarily on temporal cues), age-related differences increased with increasing modulation frequency, with a similar trend for both lower and higher carrier frequencies. In contrast to results from younger subjects, AM thresholds for older subjects showed a steady increase as the modulation frequency approached the transition frequency, which suggested a decline in temporal resolution for faster envelope fluctuations.

For modulation frequencies above the transition frequency (where spectral cues may also be involved in AM detection), age-related differences in AM thresholds were larger for the 500 Hz carrier than for the 4000 Hz carrier. This frequency-dependent aging effect suggested a difference in the availability of temporal information between lower and higher carrier frequencies and a difference in the use of this information by younger and older subjects. Given the reciprocal nature of the relationship between temporal resolution and filter bandwidth, temporal resolution would be expected to be better at higher than lower center frequencies. However, temporal resolution as measured by gap detection does not vary greatly with frequency, except for very low and very high frequencies (Florentine *et al.*, 1999). In addition, auditory filtering, as suggested by critical band analysis, does not reflect the fact that neural firings are synchronized to the period of the signal (phase locking); neural phase locking is strong at low frequencies and decreases as the frequency increases (Rose *et al.*, 1967). Thus, phase locking cues may compensate for the poorer temporal resolution imposed by peripheral auditory filtering for low-frequency sig-

nals. Moreover, spectral and intensity information may also be carried by the temporal patterns of neural responses (Joris *et al.*, 2004). For older subjects, such temporal cues may deteriorate, consistent with their increasing difficulty following envelope fluctuations near the transition frequency (Fig. 2). If the use of temporal cues declines with age, larger age-related differences in AM detection would be expected at the lower frequency carrier than at the higher frequency carrier for modulation frequencies above each carrier's transition frequency. That is, for the lower frequency carrier, the transition occurs in a region where temporal cues are still available. For the higher frequency carrier, AM detection above the transition relies primarily on spectral cues. This difference would result in higher AM thresholds above the transition for the older group than for the younger group, but for the lower frequency carrier only, consistent with the pattern of results in Fig. 2.

A similar frequency-dependent aging effect on AM detection was reported in a previous study of steady-state evoked responses to AM tones (Leigh-Paffenroth and Fowler, 2006), wherein the number of phase-locked responses to AM tones was larger for younger subjects than for older subjects for the 500 Hz carrier frequency but not for the 2000 Hz carrier frequency. More specifically, significant age-related differences were observed at a higher modulation frequency (90 Hz) but not at lower modulation frequencies (20 and 40 Hz), which was consistent with results of the current study for the 500 Hz carrier. The lack of a significant aging effect at 2000 Hz in the evoked potential study may be due to the use of signals with large modulation depths ($m=0.2-1.0$), which are associated with a high probability of detection and may result in robust evoked responses for both younger and older subjects (see psychometric functions for AM detection in Fig. 3).

A relevant question was whether the observed aging effect on AM detection was due to age-related differences in sensation levels. As shown in Fig. 1, significant age-related differences in absolute thresholds were observed [$F(1,14)=0.40$, $p=0.0061$]. However, a correlation analysis revealed no systematic relationship between absolute and AM thresholds. For older subjects, no significant correlations were observed between absolute thresholds at 500 Hz and AM detection thresholds for the 500 Hz carrier; absolute thresholds at 4000 Hz were significantly correlated with AM detection thresholds for the 4000 Hz carrier for the 5 Hz modulation frequency only.

A correlation analysis further revealed that for the 500 Hz carrier, except for the 5 Hz modulation frequency, AM detection thresholds below and above the transition frequency were significantly correlated with each other. In contrast, for the 4000 Hz carrier, significant correlations were clustered and distributed at low ($\leqslant$100 Hz) and high ($\geqslant$400 Hz) modulation frequencies, coincident with parts of the TMTF determined by different cues. That is, AM thresholds based on temporal cues were significantly correlated with each other and AM thresholds based primarily on spectral cues were significantly correlated with each other, but temporally based and spectrally based AM thresholds were not correlated.

The frequency-dependent trend of age-related differences in AM detection was consistent with age-related differences in frequency and intensity discrimination (He *et al.*, 1998) and in frequency modulation detection (He *et al.*, 2007), where age-related differences were largest at low standard or carrier frequencies and decreased as frequency increased. The similarity among these different measures suggests some common underlying mechanism such as the use of temporal cues, which may decline with age. For example, Fitzgibbons and Gordon-Salant (1995) reported that duration discrimination was poorer for older than for younger adults and that the age-related deficit increased with increasing stimulus complexity. Gap detection was also poorer for older than for younger adults, especially when the gap was placed near the stimulus onset or offset (Snell, 1997; Strouse *et al.*, 1998; He *et al.*, 1999; Snell and Hu, 1999). In a comprehensive study of both monaural and binaural temporal processing, Strouse *et al.* (1998) measured gap detection, voice onset time, interaural time difference, and masking level differences from groups of younger and older subjects with well-matched normal audiograms and observed significant age-related differences for all measures.

Although declines in temporal processing with age are well documented, the underlying mechanism for these declines remains unclear. Walton *et al.* (2002) measured single unit responses to a SAM noise carrier from inferior colliculus neurons of young and old CBA mice and observed an age-related degradation in cycle-by-cycle coding of SAM. This was confirmed by a later study (Allen *et al.*, 2006) using a prepulse procedure to measure the ability of mice to trace the onset and ongoing AM cycles of a continuous broadband noise; age-related differences were observed in the perception of ongoing, but not onset, AM cycles. In addition, Walton *et al.* (2002) found significant age-related decreases in the coding of high-rate envelope modulations, consistent with the trend observed in the current study that age-related differences increased as modulation frequency increased.

In summary, tonal TMTFs measured at 75 dB SPL showed significant age-related differences, although transition frequencies were similar for younger and older adults. For younger subjects, AM detection thresholds were generally constant for modulation frequencies below the transition frequency. For a higher carrier frequency, AM detection thresholds remained constant for modulation frequencies up to 100 Hz and then increased as modulation frequency further increased until the transition frequency. For older subjects, AM detection continuously increased (became worse) with increasing modulation frequency, indicating an age-related decline in temporal resolution for faster envelope fluctuations. Significant age-related differences were observed whenever AM detection was dependent on temporal cues. For modulation frequencies below the transition frequency, age-related differences in AM detection were similar for lower and higher carrier frequencies, consistent with the modulation filter bank model wherein temporal resolution is constant across carrier frequency (Dau *et al.*, 1997a, 1997b). In contrast, for modulation frequencies above the transition frequency, age-related differences were larger for the lower frequency carrier (where both temporal and spectral cues

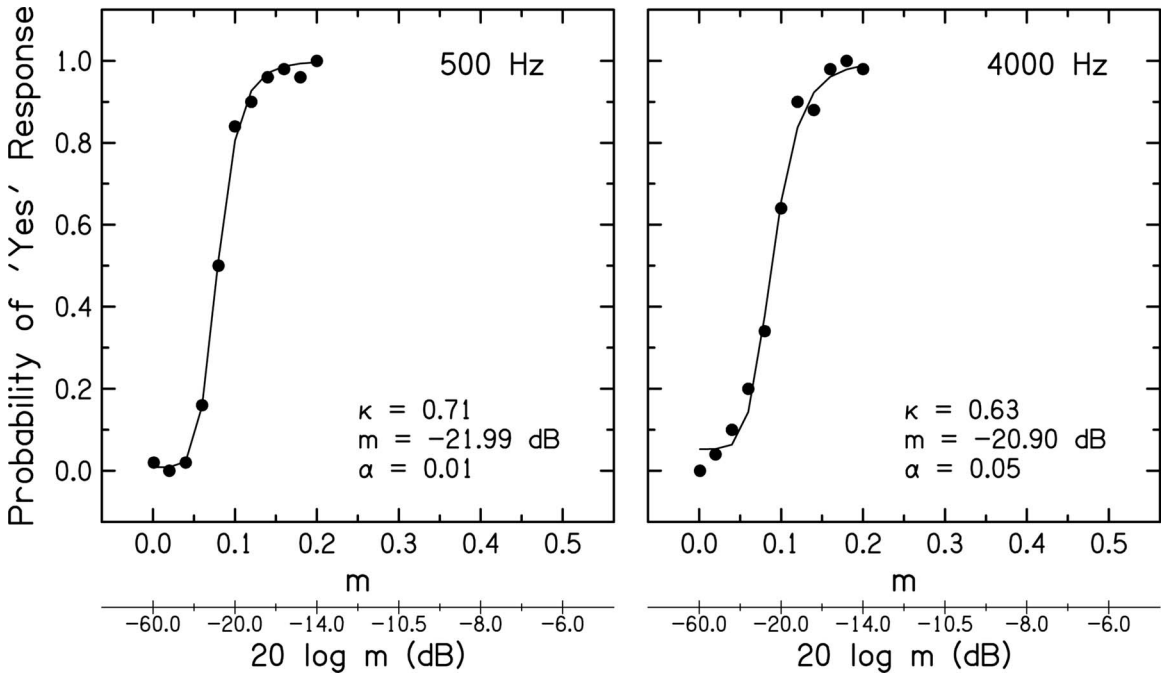


FIG. 3. Examples of measured (symbols) and fitted (lines) psychometric functions for AM detection obtained from one younger subject. The modulation frequency was 5 Hz, and the stimulus duration was 600 ms. Data for 500 and 4000 Hz carrier frequencies are presented in the left and right panels, respectively. Data were collected in a two-tone paradigm, whereby the first signal was always unmodulated and the second signal varied in modulation depth.

were available) than for the higher frequency carrier (where AM detection was primarily dependent on spectral cues). This frequency-dependent aging effect on AM detection was consistent with other measurements, such as frequency and intensity discrimination (He *et al.*, 1998) and frequency modulation detection (He *et al.*, 2007), suggesting that a common mechanism, such as the use of temporal cues, is involved in these measurements and deteriorates with age. The results of this behavioral study are consistent with a general age-related decline in the synchronization of neural responses to both the carrier waveform (phase locking) and envelope fluctuation (envelope locking).

ACKNOWLEDGMENTS

This work was supported (in part) by research grants (Grant Nos. P50 DC00422 and R01 DC00184) from NIH/NIDCD and the MUSC General Clinical Research Center (Grant No. M01 RR 01070). This investigation was conducted in a facility constructed with support from Research Facilities Improvement Program (Grant No. C06 RR14516) from the National Center for Research Resources, National Institutes of Health. The authors thank Fu-Shing Lee for advice and assistance with statistical analyses. The authors also thank two anonymous reviewers for their valuable comments on the original version of this manuscript.

APPENDIX: PSYCHOMETRIC FUNCTIONS FOR AM DETECTION WITH A YES-NO PROCEDURE

In order to apply the maximum-likelihood method (Green, 1993) to the measurement of AM detection in the main study, it was necessary to establish a working psychometric function for tonal AM detection and to determine the effects of modulation frequency, carrier frequency, stimulus duration, and stimulus paradigm on its slope. Data were collected from four younger subjects (mean age of 20 years, age range of 18–22) whose absolute thresholds were ⩽20 dB HL (ANSI, 1996) through 4000 Hz.

Signal generation was the same as described in Sec. II. Signals were 60 dB SPL and had $\cos^2$ rise/fall ramps of 5 ms for durations ⩽50 ms and 30 ms for durations ⩾400 ms. The method of constant stimuli with a yes-no task was used; for each psychometric function, 11 evenly spaced m values were employed, where the minimum m was always zero (i.e., no modulation) and the maximum m ranged from 0.2 to 0.5, depending on the carrier frequency, stimulus duration, and individual subject. Each m value was presented 50 times in random order. Thus, each psychometric function was the result of 550 trials. To minimize subjects' fatigue due to the large number of trials, the total number of trials was divided into ten blocks with 55 trials in each block.

For each subject, psychometric functions were measured for two carrier frequencies (500 and 4000 Hz) and two modulation frequencies (5 and 80 Hz) with three stimulus durations corresponding to 4, 3, and 2 modulation cycles, respectively. In a majority of the measurements, a "one-tone" stimulus paradigm was used, where a single signal was presented in each trial and the subject determined whether the signal was modulated or not. Psychometric functions were also measured with a "two-tone" paradigm for 500 and 4000 Hz carrier frequencies with a 5 Hz modulation frequency and a 600 ms duration. In the two-tone paradigm as used in the main study, each trial contained two signals separated by 500 ms silence; the first signal was always unmodulated, and the second one varied in modulation depth (as described in the Sec. II). Each measured psychometric func-

tion was fitted with a logistic function adapted from Green (1993), which was described in He *et al.* (1998).

Figure 3 shows representative results from a younger subject for measured (symbols) and fitted (lines) psychometric functions for AM detection with a 600 ms signal duration at carrier frequencies of 500 Hz (left panel) and 4000 Hz (right panel). The functions were obtained using the two-tone paradigm and a 5 Hz modulation frequency. Data were plotted on a linear scale (m), but corresponding logarithmic values were also given. Generally, the psychometric functions for AM detection featured steep slopes, which were somewhat steeper for the 500 Hz carrier than for the 4000 Hz carrier.

AM detection thresholds ($d'=1$) and slopes of the psychometric functions (k) at both carrier frequencies did not differ significantly for one-tone and two-tone paradigms (threshold: $p=0.11$; slope: $p=0.28$). A significant main effect of duration on AM detection thresholds was observed for both 5 Hz [$F(1,3)=9.28$, $p=0.0146$] and 80 Hz [$F(1,3)=337.54$, $p<0.0001$] modulators. That is, AM detection thresholds improved with increasing stimulus duration for both carrier frequencies, consistent with previous studies (Viemeister, 1979; Yost and Sheft, 1990; Lee and Bacon, 1997; Dau *et al.*, 1997b). However, the slope (k) of the psychometric function was independent of signal duration. A significant effect of carrier frequency was observed only at the 80 Hz modulation frequency for AM thresholds [$F(1,3)=11.20$, $p=0.0442$] and at the 5 Hz modulation frequency for slope [$F(1,3)=29.73$, $p=0.0121$]. For the 600 ms stimulus duration, modulation frequency had no significant effect on AM detection thresholds ($d'=1$) and on the slope of the psychometric function (threshold: $p=0.28$; slope: $p=0.07$).

To summarize, when the modulation depth, m, was expressed on a logarithmic scale, $20\log(m)$, the psychometric function for AM detection had a steep slope, which was constant across most experimental conditions, i.e., one-tone versus two-tone stimulus paradigms, stimulus durations, and modulation frequencies. Some differences in AM threshold and psychometric function slope were related to carrier frequencies, but differences were not systematic. The k value averaged across stimulus duration and modulation frequency was 0.94 (s.d.=0.14) for the 500 Hz carrier and 0.69 (s.d.=0.16) for the 4000 Hz carrier, with a grand average of 0.82. As a result, the slope (k) parameter was set to 1.0 in the maximum-likelihood method used to measure AM detection in the main study.

Allen, P., Muldrow, A., Rivoli, P., St. John, A., and Ison, J. (**2006**). "Age-related loss of behavioral ability to track ongoing but not initial SAM envelope in CBA/CaJ mice with intact modulation transfer functions," Assoc. Res. Otolaryngol. Abstr. **29**, 312.

American National Standards Institute (**1996**). "American National Standard Specification for Audiometers," ANSI S3.6–1996, American National Standards Institute, Inc., New York.

Bacon, S. P., and Gleitman, R. M. (**1992**). "Modulation detection in subjects with relatively flat hearing loss," J. Speech Hear. Res. **35**, 642–653.

Bacon, S. P., and Grantham, D. W. (**1989**). "Modulation masking: Effects of modulation frequency, depth, and phase," J. Acoust. Soc. Am. **85**, 2575–2580.

Bacon, S. P., and Opie, J. M. (**2002**). "Modulation detection interference in listeners with normal and impaired hearing," J. Speech Lang. Hear. Res. **45**, 392–402.

Bacon, S. P., and Viemeister, N. F. (**1985**). "Temporal modulation transfer functions in normal-hearing and hearing-impaired listeners," Audiology **24**, 117–134.

Dau, T., Kollmeier, D., and Kohlrausch, A. (**1997a**). "Modeling auditory processing of amplitude modulation: I. Detection and masking with narrowband carriers," J. Acoust. Soc. Am. **102**, 2892–2905.

Dau, T., Kollmeier, D., and Kohlrausch, A. (**1997b**). "Modeling auditory processing of amplitude modulation. II. Spectral and temporal integration," J. Acoust. Soc. Am. **102**, 2906–2919.

Dau, T., Verhey, J., and Kohlrausch, A. (**1999**). "Intrinsic envelope fluctuations and modulation-detection thresholds for narrow-band noise carriers," J. Acoust. Soc. Am. **106**, 2752–2760.

Drullman, R. (**1995**). "Temporal envelope and fine structure cues for speech intelligibility," J. Acoust. Soc. Am. **97**, 585–592.

Eddins, D. A. (**1993**). "Amplitude modulation detection of narrow-band noise: Effects of absolute bandwidth and frequency region," J. Acoust. Soc. Am. **93**, 470–479.

Ewert, S. D., and Dau, T. (**2000**). "Characterizing frequency selectivity for envelope fluctuations," J. Acoust. Soc. Am. **108**, 1181–1196.

Fitzgibbons, P. J., and Gordon-Salant, S. (**1995**). "Age effects on duration discrimination with simple and complex stimuli," J. Acoust. Soc. Am. **98**, 3140–3145.

Florentine, M., Buus, S., and Geng, W. (**1999**). "Psychometric functions for gap detection in a yes-no procedure," J. Acoust. Soc. Am. **106**, 3512–3520.

Florentine, M., Mavit, P., and Buus, S. (**2001**). "Maximum-likelihood yes-no procedure for gap detection: Effect of track length," J. Am. Acad. Audiol. **12**, 113–120.

Gifford, R. H., and Bacon, S. P. (**2005**). "Psychophysical estimates of nonlinear cochlear processing in younger and older listeners," J. Acoust. Soc. Am. **118**, 3823–3833.

Green, D. M. (**1993**). "A maximum-likelihood method for estimating thresholds in a yes-no task," J. Acoust. Soc. Am. **93**, 2096–2105.

Gu, X., and Green, D. M. (**1994**). "Further studies of a maximum-likelihood yes-no procedure," J. Acoust. Soc. Am. **96**, 93–101.

He, N., Dubno, J. R., and Mills, J. H. (**1998**). "Frequency and intensity discrimination measured in a maximum-likelihood procedure from young and aged normal-hearing subjects," J. Acoust. Soc. Am. **103**, 553–565.

He, N., Horwitz, A. R., Dubno, J. R., and Mills, J. H. (**1999**). "Psychometric functions for gap detection in noise measured from young and aged subjects," J. Acoust. Soc. Am. **106**, 966–978.

He, N., Mills, J. H., and Dubno, J. R. (**2007**). "Frequency modulation detection: Effects of age, psychophysical method, and modulation waveform," J. Acoust. Soc. Am. **122**, 467–477.

Joris, P. X., Schreiner, C. E., and Rees, A. (**2004**). "Neural processing of amplitude-modulated sounds," Physiol. Rev. **84**, 541–577.

Kohlrausch, A., Fassel, R., and Dau, T. (**2000**). "The influence of carrier level and frequency on modulation and beat-detection thresholds for sinusoidal carriers," J. Acoust. Soc. Am. **108**, 723–734.

Lee, J., and Bacon, S. P. (**1997**). "Amplitude modulation depth discrimination of a sinusoidal carrier: Effect of stimulus duration," J. Acoust. Soc. Am. **101**, 3688–3694.

Leek, M. R., Dubno, J. R., He, N., and Ahlstrom, J. B. (**2000**). "Experience with a yes-no single-interval maximum-likelihood procedure," J. Acoust. Soc. Am. **107**, 2674–2684.

Leigh-Paffenroth, E. D., and Fowler, C. G. (**2006**). "Amplitude-modulated auditory steady-state responses in younger and older listeners," J. Am. Acad. Audiol. **17**, 582–597.

Moore, B. C. J., and Glasberg, B. R. (**2001**). "Temporal modulation transfer functions obtained using sinusoidal carriers with normally hearing and hearing-impaired listeners," J. Acoust. Soc. Am. **110**, 1067–1073.

Nelson, P. C., and Carney, L. H. (**2007**). "Neural rate and timing cues for detection and discrimination of amplitude-modulated tones in the awake rabbit inferior colliculus," J. Neurophysiol. **97**, 522–539.

Nelson, P. C., Ewert, S. D., Carney, L. H., and Dau, T. (**2004**). "A phenomenological model of peripheral and central neural responses to amplitude-modulated tones," J. Acoust. Soc. Am. **116**, 2173–2186.

Peters, R. W., and Hall, J. W. (**1994**). "Comodulation masking release for elderly listeners with relatively normal audiograms," J. Acoust. Soc. Am. **96**, 2674–2682.

Purcell, D. W., John, S. M., Schneider, B. A., and Picton, T. W. (**2004**). "Human temporal auditory acuity as assessed by envelope following responses," J. Acoust. Soc. Am. **116**, 3581–3593.

Rose, J. E., Brugge, J. F., Anderson, D. J., and Hind, J. E. (**1967**). "Phase-

locked response to low-frequency tones in single nerve fibers of the squirrel monkey," J. Neurophysiol. **30**, 769–793.
Shannon, R. V., Zeng, F. G., Kamath, V., Wygonski, J., and Ekelid, M. (**1995**). "Speech recognition with primarily temporal cues," Science **270**, 303–304.
Snell, K. B. (**1997**). "Age-related changes in temporal gap detection," J. Acoust. Soc. Am. **101**, 2214–2220.
Snell, K. B., and Hu, H.-L. (**1999**). "The effect of temporal placement on gap detectability," J. Acoust. Soc. Am. **106**, 3571–3577.
Sommers, M. S., and Humes, L. E. (**1993**). "Auditory filter shapes in normal-hearing, noise-masked normal, and elderly listeners," J. Acoust. Soc. Am. **95**, 2903–2914.
Strouse, A., Ashmead, D. H., Ohde, R. N., and Grantham, D. W. (**1998**). "Temporal processing in the aging auditory system," J. Acoust. Soc. Am. **104**, 2385–2399.
Takahashi, G. A., and Bacon, S. P. (**1992**). "Modulation detection, modulation masking, and speech understanding in noise in the elderly," J. Speech Hear. Res. **35**, 1410–1421.
Viemeister, N. F. (**1979**). "Temporal modulation transfer functions based upon modulation thresholds," J. Acoust. Soc. Am. **66**, 1264–1380.
Walton, J. P., Simon, H., and Frisina, R. D. (**2002**). "Age-related alterations in the neural coding of envelope periodicities," J. Neurophysiol. **88**, 565–578.
Wojtczak, M., and Viemeister, N. F. (**2005**). "Forward masking of amplitude modulation: Basic characteristics," J. Acoust. Soc. Am. **118**, 3198–3210.
Yost, W. A., and Sheft, S. (**1989**). "Across-critical-band processing of amplitude-modulated tones," J. Acoust. Soc. Am. **85**, 848–857.
Yost, W. A., and Sheft, S. (**1990**). "Temporal integration in amplitude modulation detection," J. Acoust. Soc. Am. **88**, 796–805.
Yost, W. A., Sheft, S., and Opie, J. (**1989**). "Modulation interference in detection and discrimination of amplitude modulation," J. Acoust. Soc. Am. **86**, 2138–2147.
Zwicker, E. (**1952**). "Die Grenzen der Hörbarkeit der Amplitudenmodulation und der Frequenzmodulation eines Tones (The boundary in audibility of amplitude modulation and frequency modulation in tones)," Acustica **2**, 125–133.
Zwicker, E., and Fastl, H. (**1990**). *Psychoacoustics: Facts and Models* (Springer-Verlag, Berlin).

Binaural signal detection, overall masking level, and masker interaural correlation: Revisiting the internal noise hypothesis

Leslie R. Bernstein and Constantine Trahiotis
Department of Neuroscience and Department of Surgery (Otolaryngology), University of Connecticut Health Center, Farmington, Connecticut 06030

(Received 11 December 2007; revised 3 September 2008; accepted 8 September 2008)

This study provides data concerning the characteristics of internal noise that limits binaural detection at 500 Hz under "pulsed" masking conditions and evaluates whether the parameters of such internal noise depend upon masker/signal duration. A single-interval adaptive procedure was employed to measure NoSπ detection thresholds as a joint function of the level of broadband masking noise and masker/signal duration. Sπ detection thresholds were also measured as a joint function of the interaural correlation of the masker and masker/signal duration. Findings include : (1) changes in Sπ thresholds taken either as a function of diotic masker level or as a function of masker interaural correlation are independent of masker/signal duration; (2) 500-Hz "quiet" So and Sπ thresholds yield a masking-level difference of −2.0; (3) reductions in thresholds with increasing duration are similar regardless of masker level. Analyses indicate: (1) the presence of stimulus-independent, interaurally-negatively-correlated, additive internal noise and stimulus-dependent internal noise having a level proportional to that of the external masker while being independent of masker/signal duration; (2) that NoSπ thresholds taken as a joint function of masker/signal duration and masker spectrum level are, quantitatively, well described by taking into account effects produced by the combination of internal and external noises.
© *2008 Acoustical Society of America.* [DOI: 10.1121/1.2996340]

PACS number(s): 43.66.Pn, 43.66.Dc, 43.66.Ba [RLF] Pages: 3850–3860

I. INTRODUCTION

Bernstein *et al.* (2006) recently reported the results of an investigation directed toward understanding how the detection of 500-Hz tonal signals masked by broadband noise and presented in the NoSπ configuration depends upon the relative durations of the temporally overlapping signals and maskers. In an attempt to account for some of their findings, Bernstein *et al.* (2006) showed that detectability was highly correlated with duration-dependent variations in activity expected to occur within and across auditory filters putatively involved in the processing of the stimuli. What remained elusive was how such variations in filter activity could be incorporated within a quantitative model in order to account for the results. Following Bernstein *et al.*'s (2006) discussion, it appears that in order to construct such a model, one would first need to characterize the parameters of the "internal noise" that limits binaural detection. Specifically, one would need to know whether and to what degree those parameters change with masker/signal duration. To our knowledge, such information concerning internal noise was not available. Therefore, one purpose of this study was to gather new behavioral data that would help to provide the required information. Another purpose was to gather additional data concerning the parameters (i.e., level, interaural correlation) of internal noise that limits binaural detection at 500 Hz.

In order to understand the design of the experiments, it is necessary to begin with a discussion of what is meant by "internal noise". We follow a host of "monaural" and "binaural" investigations in conceptualizing the totality of internal noise as arising from two different sources. The first source is characterized as being additive and serving as a "noise floor" that determines absolute threshold (e.g., Diercks and Jeffress, 1962; Watson *et al.* 1972; McFadden, 1968; Yost, 1988; Breebaart *et al.*, 2001). McFadden (1968 p. 218) described this type of internal noise as follows:

> It is assumed that in the auditory channel serving each ear there is some ongoing neural activity, the statistical characteristics of which are identical to the neural activity produced by the external noise source. The level of this additional activity is presumed to be relatively constant and independent of the external noise. The correlation between the internal noise and the external noise is assumed to be zero… In other words, the internal noise proposed here is analogous to having added additional noise sources externally. Indeed, it may be that part of this "internal noise" is due to the physiological noise measured in the external ear canal by Shaw and Piercy (1962).

It should be emphasized that the characteristics of this additive component of internal noise (e.g., it's level and its interaural correlation) are considered to be independent of the parameters of the external stimuli (Diercks and Jeffress, 1962; McFadden, 1968; Yost, 1988).

The second source of internal noise is characterized as directly limiting auditory processing or coding, per se. This component of internal noise has been studied in monaural hearing (e.g., Green, 1960; Spiegel and Green, 1981; Raab and Goldberg, 1975) and in binaural hearing. In the case of binaural hearing, this component of internal noise has been conceptualized in more than one way: either as a degradation

 © 2008 Acoustical Society of America

of the information in the stimulus available to the binaural processor (e.g., Durlach, 1972; van der Heijden and Trahiotis, 1997, 1998) or as a degradation resulting from errors in the binaural processor itself (e.g., van der Heijden and Trahiotis, 1998; Breebaart *et al.*, 2001). An intuitive understanding of why this type of internal noise is necessary to account for binaural detection can be gained by considering the consequences of errorless binaural processing. Errorless binaural processing would, for stimuli presented in the NoSπ configuration, result in elimination of all of the external noise. Consequently, thresholds of detection would be identical to those for Sπ signals presented in the quiet, *regardless of the level of the external masker*. This is so because errorless binaural processing would lead to detection thresholds limited only by the first source of internal noise discussed above. The large amount of masking measured with typical levels of signals and maskers in the NoSπ configuration, however, requires the postulation of this second, processing-based, source of internal noise. It should be emphasized that the processing-based component of internal noise is explicitly considered to be dependent on the parameters of the external stimuli. Therefore, based on the properties of the two potential sources that compose the total internal noise that limits binaural detection, one would expect that any dependency of the total internal noise with the level and/or duration of the external stimuli would involve the second, stimulus-dependent source of internal noise.

We now return to the context of accounting for NoSπ detection thresholds at 500 Hz measured with pulsed and temporally overlapping signals and maskers. Recall that it was suggested that a potentially important, but missing, ingredient was information concerning whether and to what degree parameters of the total internal noise change with the duration of the stimuli. In monaural experiments concerning intensity discrimination, it has been shown that stimulus-dependent processing-based internal noise does, indeed, vary with the duration of the stimuli (e.g., Raab and Goldberg, 1975). A search of the binaural literature, however, revealed no experiments relating internal noise and duration. With regard to the stimulus-independent, additive source of internal noise, Watson *et al.* (1972) provided estimates of the level of that noise at 500 Hz for monaural detection. We were unable, however, to identify any experiments concerning binaural detection reporting estimates of the level (and interaural correlation) of additive internal noise at 500 Hz. This study reports new data that help shed light on the characteristics of both the stimulus-independent and stimulus-dependent components of internal noise that serve to limit binaural detection at 500 Hz.

The experiments were conducted using an approach that paralleled the one adopted by McFadden (1968). Detection of interaurally phase-reversed (Sπ) 500-Hz tonal signals masked by broadband noise was measured while varying the spectrum level of a diotic broadband noise masker. In a second experiment, thresholds for an Sπ signal were measured while varying the interaural correlation of a high-level broadband noise masker. In both experiments, thresholds of detection were measured while parametrically varying masker/signal durations over a large range. It will be seen that theoretical analyses of the new data, taken together with thresholds of detection for 500-Hz Sπ and So signals in "the quiet," suggest that binaural detection is limited by (1) a *stimulus-independent*, additive internal noise that is slightly *negatively* interaurally correlated and (2) a *stimulus-dependent* internal noise that affects detection differentially with changes in the level of the stimuli but not with changes in duration.

II. PROCEDURE

Detection thresholds were measured for 500-Hz tonal signals using the same single-interval adaptive matrix procedure described and evaluated by Kaernbach (1990). The procedure was employed and validated by comparison with a standard, "fixed-level" single-interval procedure by Bernstein *et al.* (2006) in their study of binaural detection with pulsed signals and maskers. Each trial consisted of a 500-ms warning interval followed by a single observation interval during which a visual display on a computer monitor marked the potential occurrence of the signal. "Non-signal" trials and "signal" trials were presented randomly with equal *a priori* probability. Correct-answer feedback was provided via the computer monitor for 400 ms after the listener responded, followed by a 400-ms pause before the beginning of the next trial. The procedure was used to target 75% correct performance. As discussed by Kaernbach (1990, p. 2649), this required the level of the signal to be reduced by one step-size unit after each "hit," increased by one step-size unit after each "miss," increased by two step-size units after each "false alarm," and left unchanged after each "correct rejection." In order to minimize the errors of estimation of threshold, the step-size was initially 2 dB and was reduced to 1 dB after the first two "reversals," a run was terminated after 16 reversals, and threshold was defined as the average level of the signal across the last 12 reversals (see Kaernbach, 1990, Fig. 6, p. 2651).

In one set of conditions, referred to as the "masker-level" conditions, 500-Hz Sπ tonal signals were presented against a background of diotic broadband noise (bandwidth 100–3000 Hz). Seven spectrum levels of the masker were employed that ranged from −10 to +50 dB SPL in 10 dB steps. Signals and maskers were gated on and off simultaneously using 5-ms $\cos^2$ ramps. The total durations of the stimuli (including the ramps) were 10, 20, 40, 80, 160, or 320 ms. Detection thresholds were also measured in the absence of the masking noise (i.e., in the quiet) for both Sπ and So 500-Hz tonal signals.

In another set of conditions, referred to as the "masker-correlation" conditions, Sπ tonal signals were, again, presented against a background of broadband noise (bandwidth 100–3000 Hz) utilizing the same set of masker/signal durations specified above. In this set of conditions, the spectrum level of the masker was fixed at 50 dB SPL and the interaural correlation of the masker took on values of 1.0, 0.997, 0.992, 0.97, 0.87, 0.5, 0.2, or −1.0. Such values have been shown by van der Heijden and Trahiotis (1998) to allow one to characterize relatively precisely the function relating thresholds of detection to the interaural correlation of the masker.

The desired values of interaural correlation were produced by appropriate "mixtures" of pairs of independent Gaussian noise, one diotic and one interaurally phase-reversed (van der Heijden and Trahioits, 1997).

All stimuli were generated digitally with a sampling rate of 20 kHz via a custom software library (MLSIG) running within MATLAB©, were converted to analog form via a TDT PD1, and were low-passed filtered at 8.5 kHz (TDT FLT1) before being presented via matched TDH-39 earphones to listeners seated in individual single-walled IAC chambers. Noise and signal waveforms were each selected randomly from within their own 2-s-long buffers that were generated anew prior to each adaptive run. The relative levels of the stimuli and their rise-decay ramps were controlled via software and the absolute levels of the stimuli were determined by programmable attenuators (TDT PA4) in a manner that maximized the use of the 16-bit range of the digital-to-analog converters.

Four young adults (one male and three female) with audiometrically normal hearing served as listeners. Thresholds were obtained in the masker-correlation conditions for all but the masker interaural correlations of 0.2 and −1.0. Then, thresholds were measured in the masker-level conditions. Thresholds for the masker interaural correlation of 0.2 were collected following completion of the masker-level conditions. Those thresholds were collected along with re-tests of the masker interaural correlation of 0.97 to check for stability of overall performance. Performance was found to be stable in that only small (typically within 1 dB) and unsystematic changes in threshold were observed. Finally, thresholds for a masker interaural correlation of −1.0 were collected.

For both the masker-correlation and masker-level conditions, thresholds were measured using blocks of conditions during which the masker/signal duration was held constant. For the masker-correlation conditions, a masker/signal duration was chosen at random and single estimates of threshold were collected by visiting values of the masker interaural correlation in random order. Then, those same values of masker interaural correlation were visited twice more, once in reverse order and once more in the original order. This yielded three estimates of threshold for each masker interaural correlation at a particular value of masker/signal duration. Then, a new value of duration was chosen and the process was repeated. Once all of the values of duration and masker interaural correlation had been exhausted, all conditions were visited again, but in reverse order. This resulted in the collection of six estimates of threshold for each combination of masker/signal duration and masker interaural correlation. A similar scheme was employed to measure thresholds in the masker-level conditions. For those conditions, however, the initial ordering (i.e., before the ordering was reversed) of both masker/signal duration and of masker-level was ascending (i.e., from lowest to highest value). The same ordering of conditions was used for all four listeners.

Estimates of "final" thresholds for each listener were calculated by first omitting the lowest and highest of the six estimates of threshold for each stimulus condition and then computing the mean of the remaining four. In the masking-level conditions, for 6 of the 54 conditions, the standard deviation of the final thresholds for one listener exceeded 3 dB. In those instances, additional measures of threshold were obtained substituting the new measures one-for-one with the "oldest" measures until the four estimates of threshold yielded a standard deviation of less than 3 dB. This required the measurement of no more than three additional thresholds.

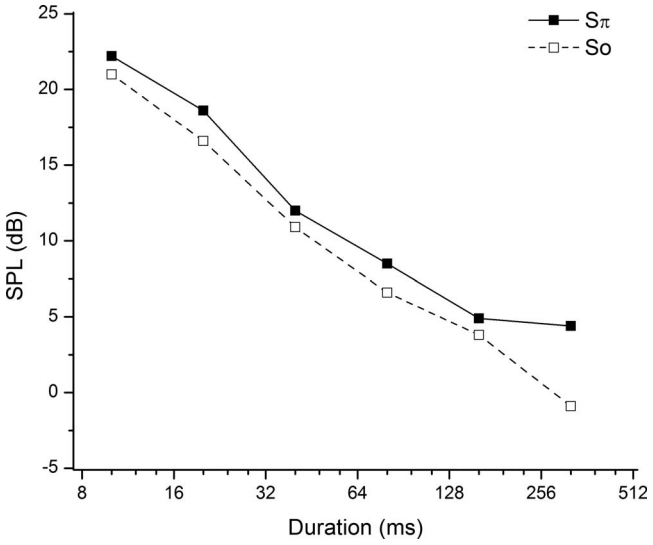


FIG. 1. So and Sπ detection thresholds (dB SPL) obtained in "the quiet" as a function of the duration of the signal. The data represent the thresholds averaged across four listeners. The average standard error of the mean across the 12 points displayed was 2.5 dB.

III. RESULTS AND DISCUSSION

Figure 1 displays the signal levels, averaged across the four listeners, required to reach threshold when 500-Hz So and Sπ tones were each presented in the absence of any external masker (i.e., in the quiet). In order to foster visual clarity, error bars are not displayed. The average standard error of the mean across the 12 points displayed was 2.5 dB. Note that, for all six durations tested, thresholds were found to be *lower* in the So configuration than in the Sπ configuration. This outcome is highly statistically significant by the sign-test ($p=0.016$). Important for our purposes, the data reflect an average masking-level difference (MLD) of −2.0 dB (So threshold minus Sπ threshold).

The finding of a negative MLD was quite perplexing in light of the positive MLD between So and Sπ thresholds reported by Diercks and Jeffress (1962) and the positive MLD reported by McFadden (1968) between So and Sm thresholds for tonal signals presented in the quiet. It is the case, however, that neither Diercks and Jeffress (1962) nor McFadden (1968) included measurement of So and Sπ quiet thresholds using 500-Hz tonal signals. Diercks and Jeffress (1962) measured quiet thresholds for 250-Hz tonal signals in Sm, So, and Sπ configurations and found that the values of the thresholds decreased in that same order. McFadden (1968) measured the quiet thresholds for 400-Hz tonal signals with only Sm and Sπ signals and, like Diercks and Jeffress (1962), found that the former yielded higher thresh-

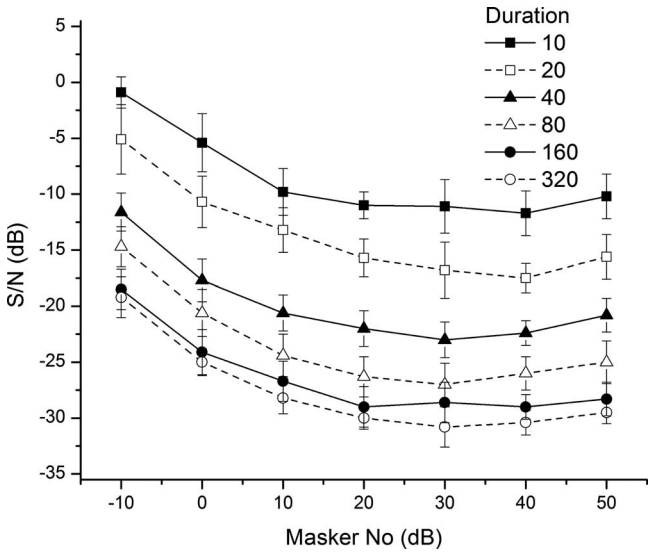


FIG. 2. NoSπ threshold S/N (in dB) plotted as a function of the spectrum level of the broadband (100–3000 Hz) Gaussian noise masker. The data represent the thresholds averaged across four listeners. Error bars represent ± 1 standard error of the mean. The parameter of the plot is the masker/signal duration.

olds than the latter, yielding a positive MLD. Importantly, Lakey (1976) did employ 500-Hz tonal signals and measured quiet thresholds in Sm, Sπ, and So conditions. Consistent with the two earlier studies, Lakey (1976) measured higher thresholds in the Sm condition than in the Sπ condition. Nonetheless, Lakey (1976) found an MLD of about −3 dB between So and Sπ thresholds at 500 Hz. This finding is consistent with the −2.0 dB MLD we measured using the same stimulus conditions.

Taking all of this into account, it appears that the only potential inconsistency among the four studies is the small positive MLD between So and Sπ conditions found by Diercks and Jeffress (1962) at 250 Hz. In order to verify that finding, we measured So and Sπ quiet thresholds at 250 Hz with the same listeners and procedures utilized in the main experiment. The results, averaged across all six durations and four listeners, revealed a positive MLD of about 1.3 dB, essentially replicating the 0.9-dB MLD obtained by Diercks and Jeffress (1962). Thus, it appears that whether one measures positive or negative MLDs in the quiet can depend both upon the monaural reference condition one adopts (i.e., So or Sm) and the frequency of the signal one chooses.[1]

Figure 2 displays the signal-to-noise (S/N) ratio required to reach NoSπ detection threshold as a function of the spectrum level of the broadband (100–3000 Hz) masking noise, again averaged across the four listeners. The error bars represent ± 1 standard error of the mean. The parameter of the plot is the masker/signal duration. Visual inspection suggests two main trends in the data. First, detection thresholds are inversely related to masker/signal duration. This outcome replicates the results of previous studies employing "pulsed" signals and maskers (e.g., Robinson and Trahiotis, 1972; Kohlrausch, 1986; Bernstein and Trahiotis, 1997; Bernstein *et al.*, 2006). Second, for each duration, threshold S/Ns are relatively constant for spectrum levels of the masker greater than or equal to 20 dB. In contrast, for all durations, threshold S/N *increases* by about 10 dB as the level of the masking noise is *reduced* from 20 dB to −10 dB. This outcome is consistent qualitatively, but not quantitatively, with the results obtained by McFadden (1968) in the study that motivated this work. Examination of Fig. 4 of McFadden (1968) reveals that his listeners' NoSπ thresholds increased by approximately 17 dB over this same range of spectrum levels of the masker. Furthermore, McFadden's (1968) figure shows that thresholds began to increase once the spectrum level of the masker was below 35 dB. We will return to this issue in Sec. IV F.

The data in Fig. 2 were subjected to a two-factor (six durations × seven masker levels) within-subjects analysis of variance. The error terms for the main effects and for the interactions were the interaction of the particular main effect (or the particular interaction) with the subject "factor" (Keppel, 1973). In addition to testing for significant effects, the proportions of variance accounted for (ω^2) were determined for each significant main effect and interaction (Hays, 1973).

Consistent with visual inspection of the data, the main effect of duration was significant (assuming an α of 0.05) [$F(5,15)=150.7$, $p<0.001$] and accounted for 66% of the variability of the data. This significant main effect reflects the fact that, on average, thresholds were lower for longer stimuli. The main effect of masker level was also significant [$F(6,18)=91.3$, $p<0.001$] and accounted for 20% of the variability in the data. This significant main effect reflects the fact that, on average, thresholds increased with decreases in the level of the masker. Also in accord with the essentially parallel, nonoverlapping appearance of the curves in Fig. 2 is the fact that the interaction of duration and masker level was not significant [$F(30,90)=0.76$, $p=0.81$]. Thus, the main effects of duration and masker level can be interpreted as being independent of each other.

Figure 3 displays the S/Ns ratios required to reach NoSπ detection threshold as a function of the interaural correlation, ρ, of the relatively high-level (spectrum level=50 dB) broadband (100–3000 Hz) masking noise. The scaling of the abscissa has been expanded for the largest values of ρ in order to preclude overlapping of thresholds that could obscure the patterning of the data. The data depicted are averages calculated across the four listeners and the error bars represent ± 1 standard error of the mean. The parameter of the plot is the masker/signal duration. As was the case for the data depicted in Fig. 2, threshold S/N is inversely related to masker/signal duration. For all durations, thresholds remained essentially constant as the interaural correlation of the noise was decreased from 1.0 (NoSπ) to 0.97, then increased substantially as the interaural correlation of the noise was decreased from 0.97 toward 0.2, and changed very little when the interaural correlation of the noise was decreased further to −1.0 (NπSπ). The changes in threshold S/N produced by changes in ρ are consistent in kind and amount with those reported by Robinson and Jeffress (1963) and van der Heijden and Trahiotis (1997) for long-duration 500-Hz tones masked by continuous broadband noise.

The data in Fig. 3 were subjected to the same type of within-subjects analysis of variance described earlier. For these data the two-factor analysis was composed of 48 total

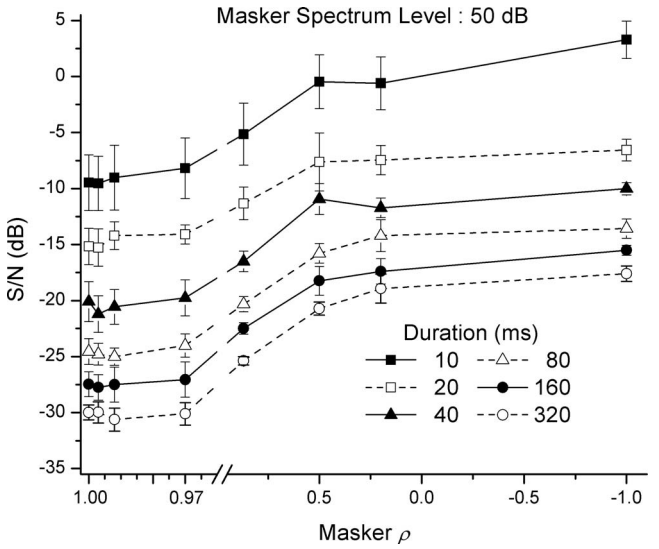


FIG. 3. NoSπ threshold S/N (in dB) plotted as a function of the interaural correlation of the broadband (100–3000 Hz) Gaussian noise masker. The scaling of the abscissa has been expanded for the largest values of ρ in order to preclude overlapping of thresholds that could obscure the patterning of the data. The data represent the thresholds averaged across four listeners. Error bars represent ± 1 standard error of the mean. The parameter of the plot is the masker/signal duration.

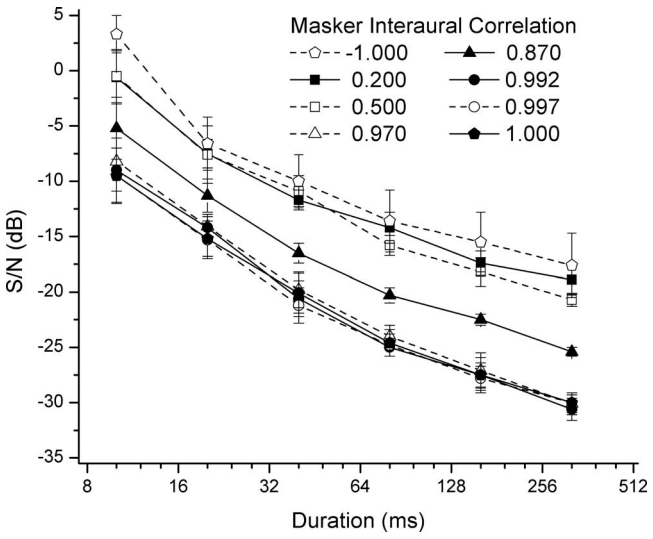


FIG. 4. A replotting of the data in Fig. 3. Threshold S/N (in dB) is plotted as a function of masker/signal duration. The parameter of the plot is the interaural correlation of the masker.

conditions (six durations $\times$ eight masker interaural correlations). The main effect of duration was significant (assuming an α of 0.05) [$F(5,15)=121.5$, $p<0.001$] and accounted for 64% of the variability of the data. This significant main effect reflects the fact that, on average, thresholds were lower for longer stimuli. The main effect of masker interaural correlation was also significant [$F(7,21)=198.4$, $p<0.001$] and accounted for 27% of the variability in the data. This significant main effect reflects the fact that, on average, thresholds increased with decreases in the interaural correlation of the masker. The interaction of duration and masker interaural correlation was not significant [$F(35,105)=1.4$, $p=0.11$]. This is consistent with the essentially parallel, nonoverlapping appearance of the curves. Thus, statistically, the main effects of masker/signal duration and masker interaural correlation can be interpreted as being independent of each other. These new data are especially interesting because they indicate that the increases in Sπ threshold that have been measured while decreasing masker/signal duration in experiments employing pulsed diotic maskers (e.g., McFadden, 1968; Robinson and Trahiotis, 1972; Bernstein and Trahiotis, 1999; Bernstein *et al.*, 2006) occur regardless of the interaural correlation of the pulsed masker. This aspect of the data can be appreciated in a more direct manner via Fig. 4 in which the thresholds in Fig. 3 have been re-plotted as "temporal integration functions" with duration along the abscissa and masker interaural correlation as the parameter.

The findings of no interaction between masker/signal duration and masker level and no interaction between masker/signal duration and masker interaural correlation are important. Taken together with the assumption of a low-level, stimulus-independent source of internal noise, those two findings mean that the parameters of the stimulus-dependent source of internal noise do not vary with masker/signal duration. Thus, the data of Figs. 2 and 3 and the postulation of both stimulus-independent and stimulus-dependent components of internal noise suggest that the parameters of the "total" internal noise that limits binaural detection are independent of masker/signal duration.

IV. CHARACTERIZING THE INTERNAL NOISE

We now consider how the data in Figs. 1–3 reveal the influence of the two components of internal noise discussed earlier.

A. Evidence for a stimulus-dependent high-level source of internal noise

Recall that if binaural processing were errorless, then the levels of Sπ signals required for detection in the presence of a diotic masker would be identical to those for Sπ signals presented in the quiet. Those "quiet" thresholds are conceived of as being determined by the level of a stimulus-independent, additive internal noise discussed earlier. Taking the 160-ms-long Sπ signal as the example, note that its threshold of detection in the quiet is 3.8 dB SPL (see Fig. 1). Now, consider the levels of this signal that were required for detection when it was masked by the four highest levels of the *external* noise. Conversion of the values of threshold in Fig. 2 from S/N to signal-SPL reveals that when the spectrum level of the external masker was 20, 30, 40, or 50 dB, the level of the Sπ signal required for detection was 25.6, 36.0, 45.6, or 56.3 dB SPL, respectively. Those thresholds (1) are clearly well above the one measured in the quiet and (2) increase in proportion to the level of the external masker. These two features of the data are consistent with the notion discussed above that binaural detection is limited additionally by a source of internal noise having a level proportional to the level of the external masker (e.g., Green, 1960; Spiegel and Green, 1981).

B. Evidence for a stimulus-independent, additive source of internal noise

The finding that threshold S/N increased as the spectrum level of the diotic masking noise was reduced below 20 dB is consistent with the presence of a relatively low-level, additive internal noise that acts in conjunction with the external noise (e.g., McFadden, 1968; Yost, 1988). According to this view, at relatively low levels of the external masking noise, say for spectrum levels below 20 dB, the relative level of the additive internal noise is large enough so that it adds appreciably to the amount of masking produced by the external noise. Note that, the threshold values of S/N in Fig. 2 were calculated only on the basis of the power of the external masking noise. Therefore, any additional amounts of masking produced by the low-level, additive internal noise are manifest as increases in the S/N. Those additional amounts of masking could, conceivably, arise in two different manners. First, the internal noise, when combined with the external noise would result in an "effective" masker having a power greater than that of the external noise alone. Second, the internal noise, when combined with the external noise could result in an "effective" masker having an interaural correlation that is less than 1.0 (the interaural correlation of the diotic external masker). This would occur if the interaural correlation of the additive internal noise were, itself, less than 1.0.

C. Quantifying the level and interaural correlation of the stimulus-independent, additive internal noise

The data presented in Figs. 1–3 permit one to estimate both the interaural correlation and the level of the stimulus-independent, additive internal noise that affects binaural detection at 500 Hz. An estimate of its interaural correlation can be made using the average MLD of −2.0 dB obtained from the So versus $S\pi$ quiet thresholds shown in Fig. 1. That negative MLD is, by hypothesis, the difference between $N\rho So$ and $N\rho S\pi$ thresholds, where $N\rho$ represents the additive *internal* noise. Our MLD of −2.0 dB can be used to estimate ρ by consulting the data from Fig. 3 of Robinson and Jeffress (1963). They measured MLDs for So or $S\pi$ 500-Hz tones masked by broadband noise at each of several values of interaural correlation ranging between −1.0 and 1.0. The spectrum level of their masking noise was 50 dB, a level high enough to "swamp out" effects produced by the presumably much lower-level stimulus-independent component of internal noise. Making the empirically sound assumption that Robinson and Jeffress' NoSo thresholds were equivalent to their $N\pi S\pi$ thresholds (see Egan *et al.*, 1969), subtracting their So-based MLDs from their $S\pi$-based MLDs is equivalent to the subtraction:

$$(\mathrm{NoSo} - \mathrm{N}\rho\mathrm{S}\pi) - (\mathrm{NoSo} - \mathrm{N}\rho\mathrm{So}). \quad (1)$$

This quantity reduces to $N\rho So - N\rho S\pi$ where $N\rho$ now represents the *external* masking noise. Making the further assumption that the effective interaural correlation of the masker, rather than its source (be it internal or external) determines the MLD, one can use the data of Robinson and Jeffress (1963) to determine what value of masker interaural correlation yields an MLD of −2.0 dB between So and $S\pi$ thresholds. In order to estimate the interaural correlation of the stimulus-independent, additive internal noise following this logic, fits were made to the MLDs ($NoSo - N\rho S\pi$ and $NoSo - N\rho So$) obtained by Robinson and Jeffress (1963) using the procedure and equations described by van der Heijden and Trahiotis (1997). Subtracting the fitted functions indicated that an interaural correlation of the masker of −0.27 produced an MLD of −2.0. Therefore, taking into account the MLD we measured in the quiet along with reasonable interpretations and generalizations of Robinson and Jeffress' data (1963), the interaural correlation of the internal noise based on our data at 500 Hz is estimated to be −0.27. It seems worth mentioning that estimating the value of the interaural correlation of internal noise at 500 Hz in the same way but by using Lakey's (1976) So versus $S\pi$ MLD of −2.7 dB yields a value of −0.36. That estimate is very similar to the one we derived (−0.27) on the basis of our own data.

Having estimated the interaural correlation of the stimulus-independent internal noise, the next step was to estimate its level. Recall that the data in Fig. 2 indicated that threshold S/Ns increased as the spectrum level of the masker was decreased below 20 dB. This was taken as evidence that reducing the level of the external noise resulted in a greater relative contribution of the stimulus-independent, additive internal noise to the masking of the signal. Recall that the greater relative contribution of such an internal noise to the masking of the signal could come about in two distinct manners. First, adding its negatively-interaurally-correlated power to the diotic external masker would serve to reduce the interaural correlation of the effective masker to a value below 1.0. As shown in Fig. 3, reducing the interaural correlation of a high-level diotic masker results in increases in $S\pi$ thresholds. Second, the addition of the stimulus-independent internal noise would increase masking by increasing the overall level of the effective masker.

In order to estimate the parameters of the stimulus-independent internal noise, an iterative process was employed that simultaneously took into account both its interaural correlation and its level. Specifically, for any particular level of the external masker, say −10 dB, a value of the level of the stimulus-independent internal noise was chosen, say −14 dB. Then, using the estimated value of the interaural correlation of the internal noise (−0.27), the *effective* interaural correlation of the combined stimulus-independent internal and external sources of noise was calculated as the weighted average of the interaural correlations of the two sources, where the weighting represents the proportional power of each source with respect to the total power of the effective masking noise:

$$\rho_{effective} = \frac{P_{\mathrm{int}} * \rho_{\mathrm{int}} + P_{\mathrm{ext}} * \rho_{\mathrm{ext}}}{P_{\mathrm{int}} + P_{\mathrm{ext}}}, \quad (2)$$

where P_{int} and P_{ext} represent the powers of the internal and external noises, respectively, and ρ_{int} and ρ_{ext} represent the interaural correlation of the internal and external noises, respectively.

TABLE I. For each spectrum level of the broadband (100–3000 Hz) diotic external noise masker (columns 1 and 2), the table lists the parameters of the internal noise computed by the analyses (columns 3 and 4). Based on the assumption that the external and internal noises are combined, the last two columns list, respectively, the increase in effective power produced by the addition of the internal noise to the external noise and the effective interaural correlation of the combined external and internal noises. (NM: not measurable.)

External noise spectrum level (dB)	External noise ρ	Internal noise ρ	Internal noise spectrum level (dB)	Added power (dB)	Effective ρ
−10	1.00	−0.27	−13.7	1.5	0.62
0	1.00	−0.27	−10.5	0.4	0.90
10	1.00	−0.27	−7.6	0.1	0.98
20	1.00	−0.27	NM[a]	NM[a]	1.00
30	1.00	−0.27	NM[a]	NM[a]	1.00
40	1.00	−0.27	NM[a]	NM[a]	1.00
50	1.00	−0.27	NM[a]	NM[a]	1.00

[a]NM: not measurable

The value of *effective* interaural correlation ($\rho_{\text{effective}}$) was entered into six independent equations, one equation for each masker/signal duration. Each equation represented the best-fit two-term exponential function relating the threshold S/N to masker interaural correlation for that masker/signal duration (i.e., the data in Fig. 3). The fits were made separately for each duration in order to provide precise interpolation between values of masker correlation used in the experiment and to capture the vertical positioning of the data in the figure. Two-term exponential functions provided excellent fits in that values of r^2 relating the functions and the data were always 0.99 or greater and rms errors were, at most, 0.75 dB being typically about 0.35 dB.

This procedure yielded six estimates of threshold, one for each masker/signal duration. These six estimates of threshold were then increased by the increment in total power that would result from adding the assumed level of internal noise (in this example, −14 dB) to the level of the external noise (in this example, −10 dB). These "revised" estimates of threshold were then compared to the actual thresholds obtained at the level of the external noise under consideration (here, −10 dB). The procedure was repeated making changes to the estimate of the level of the internal noise until the variance accounted for between the predicted and obtained thresholds was maximized.[2] The entire process was carried out separately for each of the seven levels of the masker tested. Under the reasonable assumption that threshold S/N remains constant for a given "effective" masker interaural correlation regardless of the level of the external masker, the seven individual estimates of the level of the stimulus-independent internal would be expected to be constant.

To summarize, the quiet thresholds were used in conjunction with the data of Robinson and Jeffress (1963) to estimate the interaural correlation of the stimulus-independent, additive internal noise. Then, for each spectrum level of the external masker employed (1) a "test" value of the spectrum level of the stimulus-independent additive internal noise was chosen; (2) that test value was used to calculate the "effective" interaural correlation of the combined external and internal noise; (3) that computed effective interaural correlation was used with the data of Fig. 3 to derive "predicted" values of threshold S/N; (4) those "predicted" values of S/N were adjusted to account for the increase in the power that would result from adding the "test" level of internal noise to the external noise; (5) the adjusted predicted values of S/N were compared to the obtained threshold values of S/N in Fig. 2; (6) the procedure was repeated with new "test" values of the spectrum level of internal noise until the amount of variance accounted for in the data of Fig. 2 was maximized.

The left-most two columns of Table I indicate the respective levels of the external noise and its interaural correlation. The third column indicates the interaural correlation of the stimulus-independent internal noise, which was derived from the So and Sπ quiet thresholds. The last three columns contain the results of the iterative procedure described above: estimates of the spectrum level of the stimulus-independent internal noise, estimates of the increase in power resulting from its addition to the external noise, and estimates of the "effective" interaural correlation of combined internal and external noise.

The next two columns show that, while the presence of the stimulus-independent, internal noise would add very little to the level of the external masking noise, it would have a substantial effect on the "effective" interaural correlation of the masker. For example, for an external noise level of −10 dB, the internal noise would add only 1.5 dB to the level of the external masker but would reduce the effective correlation to 0.62. Thus, it seems inescapable that the approximately 10-dB increase in threshold S/N observed when the spectrum level of the masker was reduced from about 20 to −10 dB (see Fig. 2), results almost entirely from the decrease in the effective masker interaural correlation. The several rows in the table containing the entry "NM" indicate cases in which the relative level of the external noise was so high as to preclude measurement of any effects stemming from the addition of the internal noise. Consistent with that, note that the effective interaural correlation of the combined external and internal noises is estimated to be 1.00 for spectrum levels of the external masker ranging from 20 to 50 dB.

Let us focus on the top three rows of the table, cases in which the levels of the external noise were low enough for the stimulus-independent, additive internal noise to be able

to exert a measurable influence. Note that the estimates of the level of the stimulus-independent internal noise are not constant. Rather, they increase from −13.7 to −7.6 dB as the level of the external noise increases from −10 to +10 dB. Two possibilities regarding this outcome come to mind. First, it could be the case that the "actual" spectrum level of this component of internal noise is about −10 dB and the increasing estimates result from errors of measurement of the detection thresholds that underlie the analysis. Alternatively, it could be the case that the increasing estimates of the level of the stimulus-independent internal noise are not the result of measurement error. To understand how this could be so, first recall from the analysis in Sec. IV A that the NoSπ thresholds in Fig. 2 obtained at the four highest levels of the external noise appear to be consistent with the notion that the level of the stimulus-dependent component of internal noise increases in a dB-for-dB fashion with the level of the external masker. Such dB-for-dB increases would result in the measurement of constant threshold S/N, independent of the level of the external masker. Now, let us hypothesize that the level of the stimulus-dependent component of internal noise increases with the level of the external masker at a slightly greater rate than dB-for-dB, say, 10.1 dB per 10 dB. Note that this is tantamount to hypothesizing that threshold S/Ns would increase slightly with the level of the external masker. If that were the case, then our iterative procedure, which (1) assumes that threshold S/N is constant for a given effective masker interaural correlation regardless of the level of the external masker and (2) only estimates the level of the stimulus-independent component of internal noise, would err by ascribing small increases above dB-for-dB masking to an increase in the level of the stimulus-independent, additive component of internal noise.

When the relative level of the stimulus-independent component is substantially less than the level of the external masker, even slightly greater than dB-for-dB masking would result in a substantial increase in the estimate of its level. For example, consider the approximately 3 dB increases in the estimates of the level of the stimulus independent internal noise shown in Table I that occur when the level of the external masker was increased by 10 dB. How much masking above dB-for-dB would the stimulus-dependent component have to produce in order for the iterative procedure to (erroneously) assign such 3-dB increases to the stimulus-independent additive component? One can determine this by comparing the increment in power produced by the levels of the stimulus-independent component returned by the iterative procedure to estimates made assuming that the spectrum level of the stimulus-independent component was fixed at −13.7 dB. That is the value derived for an external noise spectrum level of −10 dB. Such calculations were made and revealed that, on average, a rate of masking of the stimulus-dependent component of only about 10.1 dB per 10 dB would yield the observed 3-dB increases in the assumed level of the stimulus-independent component. In fact, Fig. 4 (p. 1042) of Reed and Bilger (1973) shows that monaural thresholds of detection for a 500-Hz signal, increased by approximately 10.15 dB for increases of 10-dB of the spectrum level of the masker. Data obtained by Reed and Bilger with other signal frequencies ranging from 1 to 8 kHz show consistent and even larger increases in growth of masking with increases in the spectrum level of the masker. In our view, this apparent consistency between Reed and Bilger's (1973) findings and our theoretical account is intriguing, but not sufficient for deciding what factor or factors underlie the increasing estimates of the level of the stimulus-independent, additive noise derived from our analysis (Table I). Clearly the effects of interest are very small and very precise measurements would be required to settle the issues.

D. An alternative way to estimate of the level of the stimulus-independent, additive internal noise

One of the reviewers of an earlier version of this report pointed out that the level of the stimulus-independent, additive internal noise could also be estimated by using the Sπ thresholds obtained in the quiet (Fig. 1) in conjunction with the S/Ns measured as a function of the interaural correlation of the masker having a spectrum level of 50 dB (Fig. 3). Following that reviewer's suggestion, we used the six functions fitted to the data in Fig. 3 (described in Sec. IV C) to derive, for each masker/signal duration, the threshold S/N corresponding to a masker interaural correlation of −0.27. That is the value of the interaural correlation that was estimated for the stimulus-independent, additive internal noise. The six values of threshold S/N were used to find the spectrum level of the (internal) noise corresponding to each of the six threshold SPL values obtained when the Sπ signals were presented in the quiet. The average value of the six estimates of the spectrum level of the stimulus-independent additive internal noise was found to be −11.8 dB and the standard deviation of those estimates was 1.3 dB. This estimate of the spectrum level of the additive internal noise is remarkably close to the value of −10.6 dB, which is the average of the estimates shown in Table I, which were obtained using the more complex procedure. It should be stressed that this alternative, simpler procedure for estimating the level of the additive internal noise assumes that threshold S/N are constant, independent of whether the effective masker is the low-level stimulus-independent additive internal noise, higher-level external noise, or both. Said differently, this procedure leaves no room to observe any potential departures from dB-for-dB masking that might call into question the assumption that threshold S/N is constant for a given effective interaural correlation of the masker, independent of the overall level of the masker.

Our inclination is to leave open the question of which of the two methods for estimating the level of the stimulus-independent, additive internal noise is preferable. The more simple method is parsimonious but is constrained by fewer of the empirical thresholds and uses the quiet Sπ thresholds both to estimate the interaural correlation of the additive internal noise and its level. The more complex procedure employs the quiet Sπ thresholds only to estimate the interaural correlation of the additive internal noise and relies on all of the data in Figs. 2 and 3 to derive estimates of the level of the additive internal noise. In our view, the similarity of the estimates of the level of the stimulus-independent, additive internal noise using the two procedures is the important out-

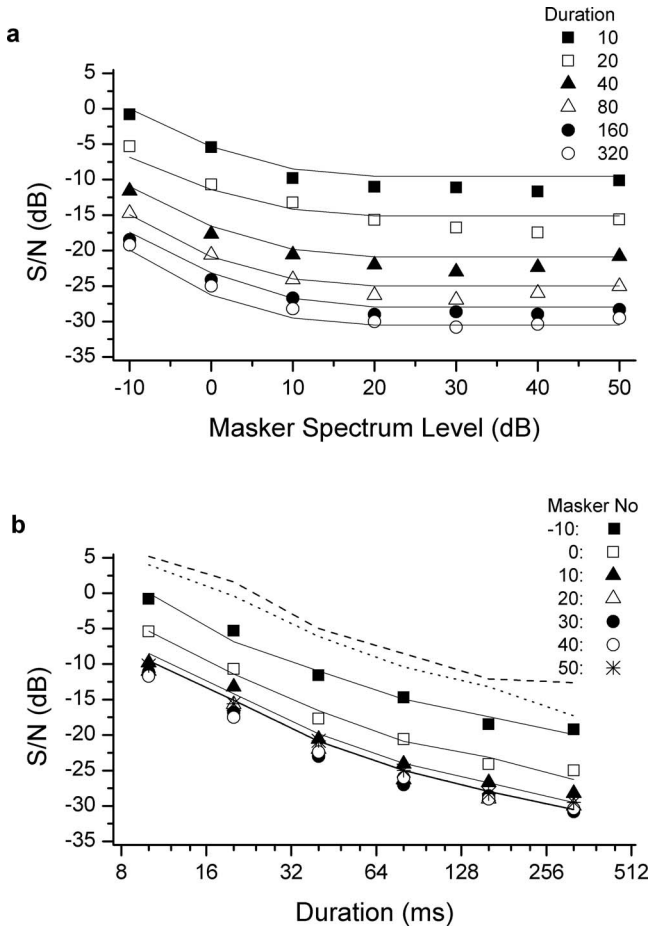


FIG. 5. Panels a and b contain a re-plotting of the data (symbols) depicted in Figs. 2 and 3, respectively. The predictions of the data derived from an iterative computational procedure (see text) are indicated by the solid lines. The parameter of the plot in each panel is the masker/signal duration. The dotted and dashed lines in panel b represent the So and Sπ quiet thresholds, respectively, replotted from Fig. 1.

come because it can stand independently of whether future research verifies the very small departure of dB-for-dB masking that may be inferred from the more complex analysis.

E. Predictions of the NoSπ thresholds

Panel a of Fig. 5 contains a replotting of the thresholds shown in Fig. 2 (symbols). The lines represent predictions of those data obtained via the procedure described above in Secs. IV A–IV C. Visually, the predictions capture quite well the trends in the data; quantitatively, the predictions account for 98% of the variability in the data. Panel b of Fig. 5 displays the same data (symbols) and predictions (solid lines) as those in panel a, but replotted as a function of masker/signal duration with external masker level as the parameter. The dashed and dotted lines will be discussed below.

Panel b more directly illustrates that our quantitative analyses provide an accurate description of how detection thresholds vary as a function of masker/signal duration over a 60-dB range of the level of the external masker. The accuracy of the predictions validates the primary assumption within the iterative procedure used to make the predictions, namely, that both the interaural correlation and the level of the stimulus-independent, additive component of internal noise can be considered to be constant as a function of duration. The validity of this assumption was tested further by employing the same estimation procedure described above separately for data obtained at each masker/signal duration when the spectrum level of the external masker was −10 dB. This yielded six new paired estimates of the interaural correlation and level of the stimulus-independent additive internal noise. Importantly, the deviations between the values of the individual estimates made at each duration and their mean were both unsystematic and small (being on average 0.11 for the estimates of interaural correlation and 0.90 dB for the estimates of spectrum level). This outcome attests to the validity of our primary assumption.

The dotted and dashed lines in panel b of Fig. 5 represent the So and Sπ quiet thresholds, respectively, replotted from Fig. 1. Their absolute vertical positioning is arbitrary but fulfills the purpose of showing that changes in So and Sπ quiet thresholds measured as a function of signal duration, parallel changes in Sπ masked thresholds measured as a function of common masker/signal duration. This suggests that the mechanism(s) mediating improvements in efficiency of detection with duration (e.g., "temporal integration" "multiple looks") do not interact with the level of the effective masker, be it principally external, principally internal, or a combination of the two.

F. Quiet Sπ thresholds versus low-level noise-masked Sπ thresholds

Recall from Sec. III that McFadden's (1968) listeners' thresholds increased in signal-to-noise by approximately 17 dB when the spectrum level of the external masker was reduced from +20 to −10 dB. In contrast, over the same range of masker levels, our thresholds increased by only about 10 dB. In addition, while McFadden's listeners' thresholds began to increase once the spectrum level of the masker was below 35 dB, our listeners' thresholds did not increase until the level of the masker was reduced to below 20 dB.

In an attempt to reconcile these differences, we calculated the signal levels in dB SPL corresponding to the NoSπ thresholds shown in McFadden's (1968) Fig. 4 and plotted them along with the signal levels in dB SPL corresponding to our NoSπ thresholds obtained at a duration of 320 ms. Despite several differences in detail between the two studies, we found that the levels of the signal required for detection across the two studies were within 2.5 dB of each other for masker spectrum levels of about 15 dB and higher. When the spectrum level of the masker was decreased to values below 15 dB, however, the threshold signal levels calculated from McFadden's (1968) data decreased much less steeply than did those calculated from our data. For masker spectrum levels of −5 and −15 dB, the SPL of the signal required by McFadden's (1968) listeners was about 13 and 12 dB, respectively. For masker spectrum levels of 0 and −10 dB, the level of the signal required by our listeners was about 10 and 5 dB SPL, respectively. This 5 dB SPL threshold is within

1 dB of the quiet threshold we measured and equal to the 5 dB SPL quiet threshold reported by McFadden (1968).

Thus, adding an external noise at a spectrum level of −10 dB SPL produced no masking of the Sπ signal for our listeners. This outcome is expected if one assumes a stimulus-independent, additive internal noise having a spectrum level of about −14 dB (consistent with Table I). Adding a diotic external masker with a spectrum level of −10 to such internal noise would increase the power of the effective masker (external plus internal) by about 5 dB. Importantly for binaural detection, however, adding the diotic noise at this level would increase the interaural correlation of the effective masker from its value of −0.27 for internal noise alone to about 0.64. According to the data in Fig. 3, an equivalent change in interaural correlation of a masker would lead to about a 4 dB reduction in the level of the signal required to reach threshold. Thus, the potential 5-dB increase in masking produced by adding the power of the external masker at spectrum level of −10 would be expected to be essentially counteracted by the 4-dB reduction in masking produced by the increase in interaural correlation of the effective masker that it produces. Taking all of this into account, we cannot offer an explanation for the fact that adding an external noise at a spectrum level of −15 dB SPL produced 7 dB of masking for McFadden's (1968) listeners while adding a higher level of external noise (a spectrum level of −10 dB) produced no masking for our listeners.[3]

V. SUMMARY AND CONCLUSIONS

Binaural detection thresholds at 500 Hz were obtained as a joint function of masker/signal duration and external masker level and as a joint function of masker/signal duration and masker interaural correlation. The primary empirical findings were: (1) changes in Sπ thresholds as a function of the level of a diotic masker are independent of (i.e., do not interact with) masker/signal duration; (2) changes in Sπ thresholds as a function of the interaural correlation of the masker also do not interact with masker/signal duration; (3) So and Sπ thresholds measured at 500 Hz in the quiet reveal an MLD of −2.0 (So threshold minus Sπ threshold) that is essentially independent of signal duration; (4) improvements in efficiency of detection with increasing duration are similar regardless of the level of the effective masker be it principally external, principally internal, or a combination of the two. Analyses of the data support the following conclusions: (1) two components of internal noise appear to limit binaural detection: a stimulus-independent, relatively low-level, additive noise that is slightly negatively interaurally correlated and a stimulus-dependent noise having a magnitude that is proportional to the level of the external masker while being independent of masker/signal duration; (2) the stimulus-independent internal noise appears to exert its influence primarily by diluting the effective interaural correlation of the diotic external masker; (3) the patterning of NoSπ thresholds taken as a joint function of masker/signal duration and the spectrum level of the external masker is, quantitatively, well described by taking into account effects produced by the combination of internal and external noises.

ACKNOWLEDGMENTS

The authors thank the reviewers (especially Reviewer 2) whose helpful and insightful comments on an earlier version of the manuscript resulted in a stronger, more comprehensive presentation. This research was supported by research grants NIH DC-04147 and DC-04073 from the National Institute on Deafness and Other Communication Disorders, National Institutes of Health.

[1]The manner in which the sign and magnitude of the MLD depend upon the frequency of the signal is beyond the scope of this study but is currently under investigation in our laboratory.

[2]The formula used to compute the percentage of the variance for which our predicted values of threshold accounted was $100\times(1-[\Sigma(O_i-P_i)^2]/[\Sigma(O_i-\bar{O})^2])$ where O_i and P_i represent individual observed and predicted values of threshold, respectively, and $\bar{O}$ represents the mean of the observed values of threshold.

[3]The signal levels in dB SPL that we calculated were based on McFadden's (1968) Fig. 4. They are not consistent with the values of SPL McFadden (1968) reported in his Fig. 3. For example, Fig. 4 indicates that with a masker spectrum level of 45 dB, McFadden (1968) measured an NoSπ threshold of about −4 dB, expressed in terms of E/No. That value is consistent with the ones commonly reported for such stimulus conditions (e.g., Egan *et al.*, 1969). By our calculations, given that the duration of the signal was 250 ms, the level of the signal required for detection in that condition would be 47 dB SPL. The value read from Fig. 3, however, is about 41 dB SPL. It appears that all of the values of SPL for the *masked thresholds* in Fig. 3 were calculated based on the E/No values in Fig. 4, but without taking the duration of the signal into account. The quiet thresholds in Fig. 3, which do not appear in Fig. 4, appear to be accurate and are within 1 dB of those measured in our study.

Bernstein, L. R., and Trahiotis, C. (**1997**). "The effects of randomizing values of interaural disparities on binaural detection and on discrimination of interaural correlation," J. Acoust. Soc. Am. **102**, 1113–1120.

Bernstein, L. R., and Trahiotis, C. (**1999**). "The effects of signal duration on NoSo and NoSπ thresholds at 500 Hz and 4 kHz," J. Acoust. Soc. Am. **105**, 1776–1783.

Bernstein, L. R., Trahiotis, C., and Freyman, R. L. (**2006**). "Binaural detection of 500-Hz tones in broadband and in narrowband masking noise: Effects of signal/masker duration and forward masking fringes," J. Acoust. Soc. Am. **119**, 2981–2993.

Breebaart, J., van de Par, S., and Kohlrausch, A. (**2001**). "Binaural processing model based on contralateral inhibition. I. Model structure," J. Acoust. Soc. Am. **110**, 1075–1088.

Diercks, J. K., and Jeffress, L. A. (**1962**). "Interaural phase and the absolute threshold for tone," J. Acoust. Soc. Am. **34**, 981–984.

Durlach, N. I. (**1972**). "Binaural signal detection: Equalization and cancellation theory," in *Foundations of Modern Auditory Theory*, edited by J. V. Tobias (Academic, New York), Vol. II.

Egan, J. P., Lindner, W. A., and McFadden, D. (**1969**) "Masking-level differences and the form of the psychometric function," Percept. Psychophys. **6**, 209–215.

Green, D. M. (**1960**). "Audiory detection of a noise signal," J. Acoust. Soc. Am. **32**, 121–131.

Hays, W. L. (**1973**). *Statistics for the Social Sciences* (Holt, Rinehart, and Winston, New York).

Heijden, M. van der, and Trahiotis, C. (**1997**) "A new way to account for binaural detection as a function of interaural noise correlation," J. Acoust. Soc. Am. **101**, 1019–1022.

Heijden, M. van der, and Trahiotis, C. (**1998**). "Binaural detection as a function of interaural correlation and bandwidth of masking noise: Implications for estimates of spectral resolution," J. Acoust. Soc. Am. **103**, 1609–1614.

Kaernbach, C. (**1990**). "A single-interval adjustment-matrix (SIAM) procedure for unbiased adaptive testing," J. Acoust. Soc. Am. **88**, 2645–2655.

Keppel, G. (**1973**). *Design and Analysis: A Researchers Handbook* (Prentice-Hall, Englewood Cliffs, NJ).

Kohlrausch, A. (**1986**). "The influence of signal duration, signal frequency and masker duration on binaural masking level differences," Hear. Res.

23, 267–273.
Lakey, J. R. (**1976**). "Temporal masking-level differences: The effect of mask duration," J. Acoust. Soc. Am. **59**, 1434–1442.
McFadden, D. M. (**1968**). "Masking-level differences determined with and without interaural disparities in masker intensity," J. Acoust. Soc. Am. **44**, 212–223.
Raab, D. H., and Goldberg, I. A. (**1975**). "Auditory intensity discrimination with bursts of reproducible noise," J. Acoust. Soc. Am. **57**, 437–447.
Reed, C. M., and Bilger, R. C. (**1973**). "A comparative study of S/N_0 and E/N_0," J. Acoust. Soc. Am. **53**, 1039–1044.
Robinson, D. E., and Jeffress, L. A. (**1963**). "Effect of varying the interaural noise correlation on the detectability of tonal signals," J. Acoust. Soc. Am. **35**, 1947–1952.
Robinson, D. E., and Trahiotis, C. (**1972**). "Effects of signal duration and masker duration on detectability under diotic and dichotic listening conditions," Percept. Psychophys. **12**, 333–334.
Shaw, E. A. G., and Piercy, J. E. (**1962**). "Physiological noise in relation to audiometry," J. Acoust. Soc. Am. **34**, S45.
Spiegel, M. F., and Green, D. M. (**1981**). "Two procedures for estimating internal noise," J. Acoust. Soc. Am. **70**, 69–73.
Watson, C. S., Franks, J. R., and Hood, D. C. (**1972**). "Detection of tones in the absence of masking noise. I. Effects of signal intensity and signal frequency," J. Acoust. Soc. Am. **52**, 633–643.
Yost, W. A. (**1988**). "The masking-level difference and overall masker level: Restating the internal noise hypothesis," J. Acoust. Soc. Am. **83**, 1517–1521.

Observer weighting of level and timing cues in bilateral cochlear implant users

Richard J. M. van Hoesel[a)]
The Hearing CRC, 384-388 Albert Street, East Melbourne, Victoria 3002, Australia

(Received 16 April 2008; revised 4 September 2008; accepted 16 September 2008)

The contribution of binaural level and timing cues available from each pulse in brief electrical pulse trains was determined in a lateralization task using an observer weighting paradigm. Four bilateral cochlear implant users were tested with randomized interaural time delays (ITDs) or, in a separate experimental condition, interaural level differences (ILDs) applied to each pulse at 100, 300, and 600 pulses/s. To examine the effect of cue randomization, weights were also determined for stimuli with a common ITD applied to all postonset pulses. Listeners were further tested for the ability to restart binaural ITD sensitivity at a rate that produced onset dominance by reducing a single interpulse interval in the stimulus. Results showed that the onset always exerted a strong influence. At 100 pulses/s, postonset ITDs and ILDs also contributed strongly. At 300 and 600 pulses/s, contributions from postonset pulses remained substantial for ILDs but were much reduced for ITDs, particularly at 600 pulses/s. Weights were similar with either independent or common ITD cues applied to postonset pulses, indicating that the cue randomization process itself did not affect weights. Restarting of ITD sensitivity at 300 pulses/s by introducing a single reduced interpulse interval was not observed. © *2008 Acoustical Society of America.* [DOI: 10.1121/1.2998974]

PACS number(s): 43.66.Pn, 43.66.Ts, 43.66.Mk, 43.66.Ba [JCM] Pages: 3861–3872

I. INTRODUCTION

Several previous psychophysical studies have shown that many bilateral cochlear implant (BiCI) users readily hear lateralization shifts resulting from electrical interaural level differences (ILDs) but are more variable in their ability to hear interaural time delays (ITDs) [e.g., see van Hoesel and Clark (1997), van Hoesel and Tyler (2003), Long *et al.* (2003), van Hoesel (2004), and Litovsky *et al.* (2005)]. This has been observed despite the use of custom research platforms in those studies, which allowed the timing of current pulses on single electrodes to be controlled much more accurately than is possible using clinical sound processors that preserve only envelope information. When electrical stimulation rates are limited to about 100 Hz, ITD sensitivity in good BiCI performers [Jones *et al.* (2006), van Hoesel (2007), and Laback *et al.* (2007)] is comparable to that in normal-hearing listeners attending pure tones at the same rate [Klumpp and Eady (1956)]. However pure-tone ITD sensitivity in normal hearing is relatively poor at that low rate and improves by about an order of magnitude between 100 and 1000 Hz (Klumpp and Eady, 1956). In contrast, as electrical rates increase beyond a few hundred hertz, the performance with BiCIs deteriorates (van Hoesel, 2007; Laback *et al.*, 2007) and is usually very poor at rates approaching 1000 Hz. This decrease in performance with increasing rate is more like what is seen in listeners with normal hearing attending high-frequency envelope-based ITDs. Hafter and Dye, Jr. (1983) showed declining performance in listeners with normal hearing attending 4 kHz bandpass filtered clicks as the click rate increased from 100 to 1000 Hz. Although these listeners showed considerably better ITD thresholds than are usually seen with BiCIs, particularly as the rate increased toward 1000 Hz, this may be due to residual low-frequency fine-timing cues below 1500 Hz. Bernstein and Trahiotis (2002) showed that when onset cues were eliminated and envelope cues were optimized using "transposed tones" (van de Par and Kohlrausch, 1997) containing only high-frequency components around 4 kHz, ITD sensitivity decreased as modulation rates increased beyond 128 Hz and was no longer determinable at 512 Hz even with cues as large as 1 ms for two of their four listeners. However, one of their listeners showed only a small decrease in performance in going from 128 to 512 Hz. The best BiCI users have similarly shown evidence of ongoing ITD sensitivity up to 600 pulses/s when onset cues were reduced by using onset ramps of 10 or 20 ms (Jones *et al.*, 2006; Majdak *et al.* 2006). While it is possible that these ramp rise times retained useful onset cues, some indication of postonset ITD sensitivity was reported for one subject at 800 pulses/s using signals with strictly diotic onsets (Laback *et al.*, 2007). In contrast, van Hoesel (2007) showed poor sensitivity to ongoing ITDs in a binaural beat detection task at rates as low as 300 Hz using signals with diotic onsets and increasing ITDs on postonset pulses. A main aim of the work presented here was to better quantify both onset and ongoing ITD salience in unmodulated electrical pulse trains as a function of rate up to 600 pulses/s.

The dominance of onset cues in spatial hearing experiments has for considerable time been studied with normal-hearing listeners [e.g., see Haas (1972), Wallach *et al.* (1949); Zurek (1980), Blauert (1997), Clifton (1987), and Freyman *et al.* (1997)] and has perhaps most frequently been discussed in terms of the "precedence effect" [see, e.g., Litovsky *et al.* (1999) for an overview]. Results from such stud-

a)Electronic mail: rvanh@bionicear.org

ies have shown a wide range of effects depending on both task and stimuli employed and are not readily predicted by a single mechanism. At least some of the effects, particularly those involving longer time constants, appear centrally mediated, whereas others are presumed to manifest at more peripheral levels. With regard to the latter, Hafter and Dye, Jr. (1983) and Hafter *et al.* (1983, 1988) studied perceptual responses to high-frequency filtered click trains of varying duration and used the term "binaural adaptation" to describe the incomplete contribution of binaural information from later-arriving clicks at higher rates when compared to what would be expected based on ideal-observer performance. They considered that their results could not be ascribed to narrowband auditory filtering, simple neural refractory behavior, or internal noise statistics and postulated instead a single mechanism that gradually reduces the effectiveness of both ITD and ILD cues from subsequent clicks beyond the onset. The strong influence of the onset at high click rates has also been confirmed in experiments using "observer-weighting" paradigms, which allow more direct measurement of the contribution from each click without varying the stimulus duration. Broadly speaking, the observer weighting approach relates the variation in subjective responses to the variation in randomized stimulus attributes [e.g., see Berg (1989)]. In the present context, it is used to examine the correlation between subjective lateralization responses and randomized interaural cues applied to each binaural click pair in the stimulus. Clicks that are perceptually important show a higher degree of correlation with responses than those that are not. In contrast to the earlier suggestion by Hafter and Dye, Jr. (1983) and Hafter *et al.* (1983, 1988), observer weighting studies have found reduced weighting of cues that acts immediately, and equally, on all clicks beyond the onset [Saberi (1996), Stecker and Hafter (2002)]. Summarizing across various studies, ITD onset dominance has been clearly demonstrated for high-frequency filtered click trains at rates between 200 and 1000 Hz but is relatively weak at around 100 Hz or lower. This result seems in good agreement with envelope rate limitations on ITD perception in normal hearing, as well as a number of results with BiCI users, including those reported by van Hoesel (2007)showing that: (1) increasing pulse-train duration reduced ITD thresholds more at 100 than at 400 pulses/s, (2) time-varying ITDs (binaural beats) for pulse trains with diotic onsets were audible at 100 pulses/s but not at 300 pulses/s, and (3) ITDs applied to the first of two binaural pulses in a precedence experiment were much better discriminated than those applied to the second pulse when pulses were separated by only a few milliseconds (corresponding to a few hundred hertz) but were equally discernible on either pulse for separations of 8 ms.

A phenomenon sometimes discussed in relation to onset dominance is "restarting" of the binaurally adapted auditory system following an irregularity in the stimulus, such as an aberrant interclick interval (ICI). Such restarting is proposed to explain the increase in effectiveness of the cue directly following the irregular interval. Hafter and Buell (1990) demonstrated strong onset dominance in 6- or 12-click bursts with an ICI of 2.5 ms (400 Hz) but also found near ideal-observer performance gains for two such bursts separated by 7.5 ms when compared to just one. Restarting was presumed in that case because the improvement in performance exceeded that observed by increasing the duration of constant-rate click trains with an ICI of 7.5 ms.[1] Hafter and Buell (1990) further noted "a brief demonstration" of restarting for 200 Hz click trains (ICI=5 ms) containing a single reduced interval of 2.5 ms. Freyman *et al.* (1997) also showed restarting in a headphone based lateralization task with stimuli comprising constant 3 ms ICIs for the first 100 ms and 2 ms ICIs for the remaining 300 ms of the signal. However, not all studies have shown restarting. For example, Saberi (1996) found no such effect using an observer-weighting-based ITD discrimination experiment when every fourth ICI was extended by 4 ms in 16-click sequences with an ICI of 1.8 ms. That author proposed that restarting may have been inhibited by the need to randomize ITDs for each pulse in the observer-weighting approach, thereby making the irregularity in the interpulse gap more difficult to detect than when ITDs are identical for all pulses. On the other hand, Stecker and Hafter (2002) also used an observer-weighting paradigm in a free-field localization task and did show elevated weighting of the click following a 5 ms ICI in a 16-click sequence that otherwise comprised 3 ms ICIs. They proposed that differences among restarting results may be influenced by factors such as the types of available cues (ITD, ILD, spectral) and possibly intersubject variation.

Recently Laback and Majdak (2008) attributed improved electrical ITD sensitivity specifically to the restarting phenomenon when high-rate interpulse intervals (IPIs) were diotically "jittered" rather than held constant. Unfortunately they did not discuss the important confounding likelihood that cues became more salient simply because lower rates were introduced in the signal when intervals were jittered,[2] and electrical ITDs are better perceived at lower rates. Instantaneous rates will have been directly lowered when the jitter acted to increase the IPI. In addition, if refractory effects act to inhibit neural responses following a shortened IPI, a large "accumulated interval" may result in the neural response from adding that shortened interval to the subsequent IPI. That mechanism could cause even small amounts of jitter to produce large increases in IPI if small changes in rate produce significant changes in refractory behavior. Plack and White (2000) suggested that such accumulated intervals might explain why they observed pitch decreases rather than increases in normal-hearing listeners when a single 1 ms ICI was introduced in a click train otherwise comprising 4 ms ICIs, and inclusion of that idea in the temporal pitch model proposed by Carlyon *et al.* (2002) showed improved ability to predict those data. A significant difficulty with the restarting explanation offered by Laback and Majdak (2008) to account for the rate-jitter benefit is the finding that it was observed at nominal rates of 800 pulses/s or higher but not at 400 pulses/s. In light of their restarting hypothesis, they considered it "intriguing that binaural jitter improves the performance even for ITDs that approach or even exceed one half of the IPI" and proposed that restarting did not offer benefits at 400 pulses/s because ongoing ITDs were already well perceived at that rate. However, this suggestion conflicts with the clear evidence of greater ongoing ITD salience at

rates lower than 400 pulses/s in BiCI users, as well as strong onset dominance and reports of restarting at comparable or even lower rates in listeners with normal hearing. If the jitter-derived benefit is considered in terms of lowered-rate cues, rather than restarting, the results are more as expected because such cues would reduce high-rate ITD ambiguity [e.g., see Freyman *et al.* (1997)] and refractory effects that would be much reduced at 400 pulses/s. Ambiguous interaural pairing of pulses, and hence ITDs, in the electrical rate-jitter experiment will have arisen at high rates when ITDs approached or exceeded half the IPI, whereas at 400 pulses/s the larger IPI precluded that ambiguity. The data indicate that such ambiguity very likely played a significant role because results with nonjittered stimuli at 800–1200 pulses/s showed that performance was as good with ITDs of 200 μs as with ITDs of 600 μs, whereas at 400 pulses/s performance steadily improved with increasing ITD. The somewhat smaller benefit from jitter at the highest rate of 1500 pulses/s might similarly be at least partly explained by the consideration that the largest ITDs still constituted a considerable fraction of the IPI in the lowered-rate intervals. The reduced ambiguity of ITDs in relation to the IPI, however, does not fully account for the observed benefit of rate-jitter at high rates because that benefit was diminished but not eliminated when ITDs were smaller. Further sources of ITD ambiguity at high rates may account for that result even with small ITDs. One such source is the variation in neural response latency at higher electrical pulse rates. Javel and Shepherd (2000) reported a bimodal distribution of response latencies at high rates and intensities in auditory nerve recordings from cats and also showed that the time between the peaks in such distributions increased with rate. Asymmetrical refractory behavior in the two ears at higher rates might also introduce ambiguity through inappropriate interaural pairing of pulses and/or ILD variations that could interfere with the perception of applied ITDs. While ambiguity due to such asymmetry would be in direct competition with any benefit associated with accumulated intervals (described above) that require diotic refractory behavior, both may play a role depending on parameters such as rate, duration, and intensity of stimulation. A single reduced IPI due to rate-jitter, for example, might largely evoke diotic refractory effects leading to a beneficial accumulated interval, whereas sustained stimulation at that same IPI might lead to more dichotic responses that would degrade performance.

Even if responses to electrical pulses are low-pass filtered in the auditory system, jittering stimulation rates could provide low-rate cues in the form of envelope modulation at the output of the filter. A further possible reason for the greater effectiveness of rate-jitter at higher pulse rates in that case might be related to the effect of such filtering. In the absence of jitter, the lower pulse rate of 400 pulses/s might produce some modulation at the filter output, thus preserving some ITD sensitivity but possibly also reducing the effectiveness of low-rate cues imparted by jitter. One reason for the latter suggestion is that the jitter produces both increases and decreases in rate, resulting in both decreases and increases, respectively, of the modulation depth at 400 pulses/s. In contrast, at rates sufficiently high to preclude modulation at the filter output in the absence of jitter, introducing the jitter can only increase the modulation depth, resulting in improved ITD salience.

In the present work, observer weighting coefficients (weights) were determined for randomized ILD and ITD cues applied to each pulse in brief electrical pulse trains at 100, 300, and 600 pulses/s. Four BiCI users, who had shown moderate to good ITD sensitivity at 100 pulses/s, were required to indicate lateral positions of perceived sounds. Weights were determined using multiple linear regression to examine the correlation between subjective responses and cues applied to each pulse, in a manner similar to that described by Stecker and Hafter (2002). In addition to supplementing previous studies concerned with sensitivity to electrical ITD and ILD cues, the comparison of weights for the two cues examines the hypothesis that binaural adaptation results from a single mechanism that affects both cues equally, as suggested by Hafter *et al.* (1983). To measure the extent to which weights were affected by the randomization process inherent in the observer weighting approach, lateralization was further assessed at 300 pulses/s using eight-pulse (8P) stimuli that contained identical ITD cues on the last seven pulses. The derived weights in that experiment were compared with those obtained when ITDs were independently randomized for each pulse. The restarting of electrical ITD sensitivity was directly assessed at 300 pulses/s using a single reduced IPI halfway through an 8P sequence. Note that unlike with acoustic stimulation in normal hearing, a change in electrical IPI does not produce matched spectral changes. By choosing to decrease rather than increase the interval, the confounding improvement due to better ITD sensitivity at lower rates is reduced, and restarting *per se* is better assessed. The rate used in the restarting experiment was chosen to be high enough to elicit clear onset dominance yet remained low enough to limit the impact of refractory effects and allow the use of a reduced IPI that avoided excessive ITD ambiguity in relation to the IPI. The chosen rate was also comparable to that used in several experiments showing restarting in normal-hearing listeners (Freyman *et al.*, 1997; Hafter and Buell, 1990; Stecker and Hafter, 2002). Two of the BiCI users tested were available for further testing in an extension of the restarting experiment, in which the irregular interval was increased rather than decreased.

II. METHODS

A. Subjects, stimuli, and procedure

Participants in the study were four BiCI users (ME1, ME3, ME5, and ME6), with postlingual onset of deafness, who had been using Nucleus 24 devices bilaterally for at least one year prior to participation in this study at the HEARing CRC in Melbourne, Australia. All four had previously participated in lateralization and discrimination tests and had shown moderate (ME5) to good (ME1, ME3, and ME6) ITD sensitivity at a low stimulation rate of 100 pulses/s. Before the formal data collection, each subject was trained with signals that were representative of those to be used in the experiments for at least two preliminary ses-

sions lasting about 2 h each. Stimuli always comprised monopolar biphasic current pulses, 25 μs per phase in duration with interphase gaps of 8 μs, and were applied to electrodes about halfway along the electrode array inserted in each ear. Place matching of electrodes across ears was determined using pitch comparisons of a fixed electrode in the right ear with several left-ear candidate electrodes around the best match according to x rays, as described in van Hoesel (2007). Weighting of ITD and ILD cues was assessed in different experimental runs. Pulse trains consisted of bilateral two-pulse (2P) or 8P sequences at rates of 100, 300, and 600 pulses/s, unless noted otherwise. Nominal stimulation levels in each ear were adjusted such that for the 8P signal, (1) at 100 pulses/s loudness was comparable to everyday speech levels and the lateral position of the resulting fused sound percept was centered in the head, and (2) at 600 pulses/s, loudness was not uncomfortably loud and the lateral position remained approximately centered. The same levels were used at all three rates and for both 2P and 8P stimuli. When applying ITD cues, stimulation levels were held fixed at the nominal levels, and each bilateral pulse received a randomized ITD cue. ITDs within a single stimulus were consistent in sign and were created by applying delays only to one ear. As a result only the ear receiving nondelayed pulses was stimulated at a strictly fixed rate, whereas the instantaneous rate in the contralateral ear varied according to the randomized ITD applied to each pulse. When applying ILD cues, ITDs were held fixed at zero, and randomized cues within each stimulus were again consistent in sign and were generated by holding stimulation levels in the left-ear constant and by randomizing right-ear levels. To avoid excessively loud sounds in the right ear, only level reductions were employed to generate ILDs. Accordingly the left-ear fixed stimulation level was slightly reduced from the nominal level described above by an amount equal to half the range of ILDs to be applied. Preliminary runs of the lateralization task with 8P observer-weighting stimuli at 100 pulses/s were used to determine appropriate ILDs. Starting with an approximately centered stimulus, it was found that the randomized level decreases, or alternatively increases, between 0 and 0.85 dB [5 CU (clinical units)] in the right ear, in total produced a range of lateralization responses in the midhead region spanning about 16% of the full range from left to right when averaged across subjects. Comparable lateralization shifts were produced at 100 pulses/s by applying randomized ITDs up to 600 μs (in one ear) for three of the four subjects (ME1, ME3, and ME6), so that for those subjects ITD cues were randomized up to that limit. Note that the average ITD cue in that case is 300 μs, which corresponds well with the single-pulse ITD thresholds reported for two of these subjects (ME1 and ME3) in a previous study (van Hoesel, 2007). The fourth subject (ME5) was unable to perform the ITD-based task at 300 or 600 pulses/s when the maximal ITD cue was 600 μs, so for that subject ITDs were expanded by a factor of 2 (i.e., randomized up to 1200 μs) and the maximal rate tested was limited to 300 pulses/s to avoid presentation of ambiguous ITDs that would exceed half the IPI at 600 pulses/s. In the ILD task, listeners were informed that overall levels might vary and were instructed to ignore such variations and to focus only on the perceived lateral position. None of the listeners indicated that loudness variations were large, or that the task seemed any different in nature for ITD or ILD cues, and generally responded with little hesitation or apparent calculation, altogether making it very unlikely that monaural level cues were consciously being translated to a lateral position response in the ILD task. After each stimulus presentation, subjects were required to numerically indicate the intracranial position of the sound percept, where 50 corresponded to a midhead sensation, 0 to extreme left, and 100 to extreme right positions. Listeners were presented with a visual representation of that range in the form of a demarcated line placed directly in front of them. Lateralization responses to each stimulus were recorded along with the cue size applied to each pulse in the stimulus. Each test block consisted of 120 presentations, half of which contained cues that should result in lateralization to the left of the position resulting from zero-magnitude cues, and half to the right of that. Test blocks for the 8P sequences were repeated between two and five times, depending on subject availability, so that 8P observer weights were derived from 240–600 presentations. With 2P signals, the smaller number of pulses resulted in less noise in the data due to "competing cues" on other pulses, and in that case blocks were more usually repeated only two or three times so weights were derived from 240–360 presentations. To examine whether weights were affected by the cue randomization process itself, ITD weights were also determined in 8P stimuli at 300 pulses/s with just two weights ("8P-2Wt"). In that case one randomized ITD was applied to the onset pulse, and a second ITD was applied to all seven postonset pulses. The per-pulse postonset contribution in that stimulus was assumed to be equal to the total weighting of all seven postonset pulses, divided by 7. Restarting of sensitivity to ITDs was tested using 8P stimuli at 300 pulses/s with a single shortened IPI of 2 ms between the fourth and fifth pulses [IPI(4,5)]. A slightly lower rate of 250 pulses/s and shortened IPI(4,5) of 3 ms were used with subject ME5 to prevent the larger ITD cues needed with that subject (up to 1200 μs) from exceeding half the shortened interval. Two of the listeners with good ITD sensitivity, ME1 and ME6, were subsequently available in an extension of the restarting experiment, in which IPI(4,5) was increased rather than decreased. Both these listeners were tested at 300 pulses/s with an extended IPI(4,5) of 6 ms, as well as at 600 pulses/s with an IPI(4,5) of 3 ms. ME1 was further tested with larger intervals of 10 ms at 300 pulses/s and 6 ms at 600 pulses/s.

B. Observer weighting analysis

Using a variation of the approach adopted by Stecker and Hafter (2002), a multiple linear regression analysis was used to determine weights for ITD and ILD cues applied to each pulse. For a given stimulus condition (rate, duration, and ILD or ITD cue), the resulting regression coefficients (weights) for each pulse describe the extent to which randomized cues applied to that pulse influenced lateralization over many presentations. If all pulses contribute equally to

the lateralization percept, their associated weights are similar, whereas strong onset dominance is reflected by a much higher weight for the first pulse than for later ones. Regression coefficients were calculated separately for each subject and stimulus condition, and for each pulse these were normalized with respect to the coefficient found for the first pulse. The normalized coefficient therefore describes the pulse's weighting relative to that of the onset pulse (W_N/W_1). In contrast to the approach taken by Stecker and Hafter (2002), normalized weights were determined separately for cues designed to produce lateralization shifts to the left and right and then averaged over the two. This approach eliminates contributions to the weights that arise from the mean difference in lateral position responses between left- and right-cue stimuli and may result in a more conservative estimate of weight values compared to using both left- and right-cue data in a combined analysis [as used by Stecker and Hafter, 2002], particularly if nonlinear cue combinations across pulses offer left-right discrimination advantages. In an extreme illustration, a subject may readily report a difference in lateral position between stimuli with left and right cues, i.e., the sign of the cue, but may not indicate smaller positional changes corresponding to the magnitude of the cues applied. In that instance, the correlation between cue size and position is zero within either left- or right-cue analysis (i.e., the weights are zero) and, therefore, also for the average of the two. In contrast, if both data groups are included in a single analysis, the sign of the cue is strongly correlated with responses, and weights are accordingly increased.[3] One reason for choosing to apply separate regression analyses to the left- and right-cue data in the present study was to eliminate the possible impact on weight estimates of left-right cues arising from presenting a strictly constant rate in one ear but not in the other due to ITD randomization in that ear. While BiCI users are less sensitive to monaural rate variations than to dichotic ones anyway (van Hoesel and Clark, 1997; van Hoesel, 2007), even if a lateralization cue were available by detecting which ear contained the constant rate, the use of separate regression analyses for left and right cues would ensure that such a cue did not contribute to weight estimates.

III. RESULTS

Figure 1 shows relative weights (W_N/W_1) calculated for each pulse (P_N) when lateralizing on the basis of ITD cues. The top row of graphs shows, from left to right, subject-averaged weights at 100, 300, and 600 pulses/s. Individual subject data are shown in each of the four lower rows. Within each graph, relative weights for 2P stimuli are shown as solid triangles. Weights for 8P stimuli are shown as open squares and crosses. The square symbols in the top row show subject-averaged weights excluding subject ME5, who was tested with larger ITDs and not at 600 pulses/s. Crosses show results averaged over all four subjects for those conditions that they all completed. The error bar for each weight in the top row shows the average across subjects of the standard errors associated with that weight in each individual's regression analysis, which are shown by the error bars in the four lower rows. The dashed line in each subject's data at 300 pulses/s shows the per-pulse weight assigned to each of the seven postonset pulses that received identical ITD cues in the 8P-2Wt stimuli and was calculated by dividing the combined relative weighting of the postonset pulses by 7 $[(W_{2-8}/W_1)/7]$. It can be seen that postonset relative weighting for the 8P and 8P-2Wt stimuli was generally very similar. The only subject who showed a systematic difference for those two stimuli was ME5, who was tested with the doubled ITD range of up to 1200 μs and actually showed negative postonset weights for 8P but not 8P-2Wt stimuli. The dashed line in the top-row graph for 300 pulses/s shows the subject-averaged 8P-2Wt result excluding that subject. The application of analysis of variance (ANOVA) to the 8P relative weights for all four listeners at 100 pulses/s, using the pulse number as a fixed factor and the subject as a random factor, showed that the weights of the eight pulses in the sequence did not differ significantly ($F[7,21]=2.23$, $p=0.073$ or, when ME5 was excluded, $F[7,21]=1.6$, $p=0.23$), although as is evident from the figure the first pulse did receive higher weighting on average. In contrast, at 300 pulses/s the effect of the pulse number was strongly significant ($F[7,21]=12.5$, $p<0.001$ or, when ME5 was excluded, $F[7,14]=17.6$, $p<0.001$). *Post hoc* Bonferroni simultaneous tests showed that the strong effect of the pulse number was entirely due to the much stronger weighting of the first pulse compared to any later pulse, with no significant differences among postonset weights. A similar strong effect of the pulse number due to differences between the first and later pulses was found at 600 pulses/s ($F[7,14]=18.05$, $p<0.001$, excluding ME5), and postonset weights on average were very close to zero.

In the same manner, as described in Fig. 1 for ITDs, Fig. 2 shows the weights assigned to each pulse when using ILD cues. Although all four subjects were tested at all three rates in this case, the top row shows average weights, both including and excluding subject ME5, using crosses and squares, respectively. The 8P-2Wt condition was not tested with ILD cues. As for ITD cues, ANOVA applied to ILD data showed that the effect of the pulse number was not significant at 100 pulses/s ($F[7,21]=2.31$, $p=0.065$). While the effect of pulse was seen to be moderately significant at 300 pulses/s for the ILD cue ($F[7,21]=3.17$, $p=0.02$), *post hoc* Bonferroni comparisons showed that the only significant difference was between the first and the last pulse ($p=0.007$). At 600 pulses/s, the effect of the pulse number was also weakly significant ($F[7,21]=2.5$, $p=0.05$), and a *post hoc* comparison in this case showed that only the weights for the first and second pulses differed significantly ($p=0.04$).

Overall the results in Figs. 1 and 2 show no significant onset dominance at 100 pulses/s with either cue, although the onset on average did receive the highest weighting in both cases. Strong onset dominance was found for ITDs at 300 or 600 pulses/s and was considerably weaker for ILDs at those rates. Figure 3 summarizes subject-averaged ITD and ILD weighting data for 2P (left graph) and 8P (right graph) stimuli as a function of pulse rate for the three listeners who completed ITD testing at all three rates. In both graphs, the data show the average postonset relative weights ($W_{(2-N)\mathrm{av}}/W_1$) for pulses (P_2-P_N). Since only a single pulse

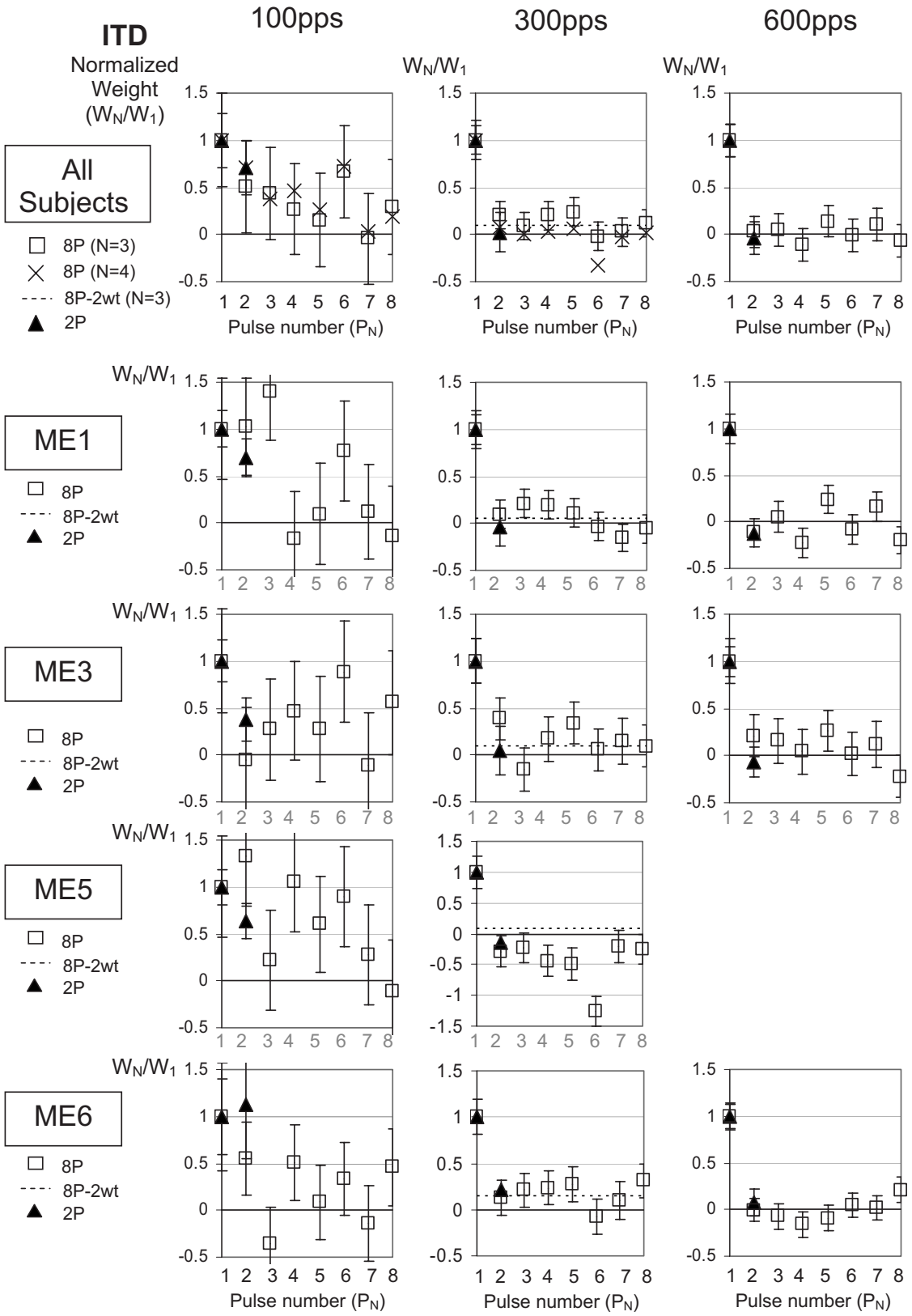


FIG. 1. Relative weights (W_N/W_1) assigned to each pulse (P_N) when lateralizing on the basis of ITD cues, normalized with respect to the weighting of the ITD cue on the first pulse in each stimulus. The top row shows subject-averaged weights, from left to right, at 100, 300, and 600 pulses/s, respectively. 2P stimuli are shown as solid triangles, and 8P stimuli are shown by open squares (excluding subject ME5) and crosses (all subjects). Error bars in the top row show the average of the four individual subjects'standard error estimates calculated in each one's regression analysis at each rate. The dashed line for the 300 pulses/s condition additionally shows per-pulse postonset weighting for the 8P-2Wt stimuli, calculated as the total weight for all seven postonset pulses, divided by 7. The four lower rows show similar plots for each individual listener.

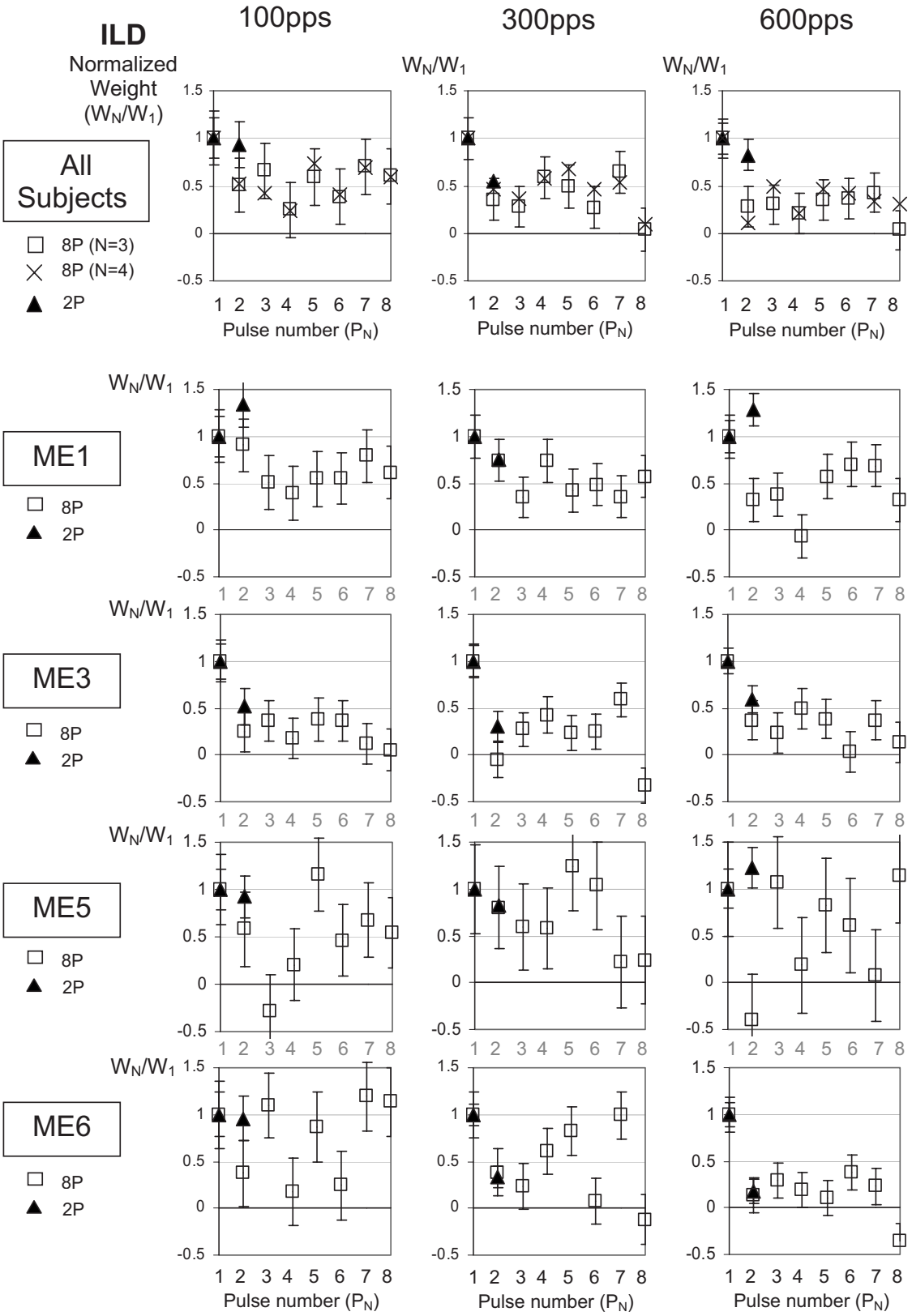


FIG. 2. Relative weights (W_N/W_1) assigned to each pulse (P_N) when lateralizing on the basis of ILD cues, normalized with respect to the weighting of the ILD cue on the first pulse in each stimulus. Other details are the same as in Fig. 1.

follows the onset in the 2P condition that amounts to W_2/W_1. For the 8P stimuli, each data point shows the mean of the seven postonset relative weights and associated standard error. An ANOVA applied to the combined 2P and 8P data showed that postonset relative weights were higher for ILDs than for ITDs ($F[1,10]=12$, $p=0.006$), which means that overall onset dominance was significantly stronger for ITD than ILD cues. The interaction between the rate and the cue type (ILD or ITD) in the ANOVA was not significant ($F[2,10]=0.08$, $p=0.93$) and is reflected by comparable gra-

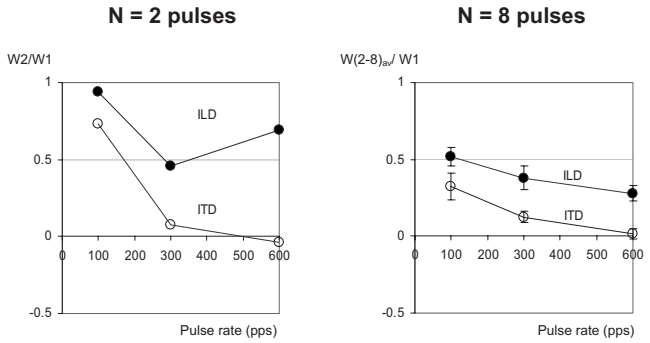


FIG. 3. Summary of subject-averaged per-pulse postonset weights for ITD and ILD cues for 2P (left graph) and 8P (right graph) stimuli as a function of pulse rate. The error bars for 8P data show the standard errors of the mean for the seven postonset weights. Data from listener ME5, who was not tested with ITDs at 600 pulses/s, were excluded.

dients in the ITD and ILD curves in Fig. 3. However, this does not mean that performance would be equally affected by rate with either cue because the higher weighting of ILDs compared to that ITDs ensures that the same gradient has less effect with ILDs. This is clearly shown by the result that mean weights between 100 and 600 pulses/s decreased by more than an order of magnitude for ITDs but were reduced by only a factor of 2 for ILDs.

Figures 4(a) and 4(b) describe the weights derived from the restarting experiment with a single reduced IPI between the fourth and fifth pulses in 8P sequences with all four subjects. The weight of the fifth pulse, which would increase due to restarting, is shown by the filled symbol in each panel. Figure 4(a) shows subject-averaged results, both with and without subject ME5. Individual subject data are shown in Fig. 4(b). Subject ME5 was in this experiment tested at a slightly lower rate of 250 pulses/s rather than at 300 pulses/s and at a restarting gap of 3 ms rather than 2 ms to avoid large cue ambiguity with the doubled ITD range needed. That slightly lower rate was not expected to significantly affect results because it elicited strong onset dominance that was comparable to that seen in the other listeners at 300 pulses/s, and therefore should equally allow restarting. In support of this argument, Stecker and Hafter (2002) noted reduced restarting in those listeners, also displaying less onset dominance. An ANOVA and subsequent *post hoc* Bonferroni tests examining the effect of the pulse number for all four subjects showed that the only significant differences were those between the onset and any of the later pulses and that the fifth pulse was not weighted significantly differently from any of the other postonset pulses. Although one subject (ME6) shows a higher relative weight for the fifth than other postonset pulses, it was nearly identical to that for the second pulse, and both remained considerably lower than that of the onset.

For the three listeners tested with the smaller ITD range (i.e., excluding ME5), Fig. 4(c) shows the relative weighting of just the fifth pulse (W5/W1) as a function of the interval preceding it, IPI(4,5). Results are included for 8P stimuli with (a) constant IPI, (b) a reduced IPI(4,5), and (c) an increased IPI(4,5) for the two subjects available to participate in the extension of the restarting experiment. Filled symbols show results at a nominal rate of 300 pulses/s. At that rate, W5/W1 weighting for constant IPI is shown at IPI(4,5) =3.3 ms, for reduced IPI(4,5) to the left of that, and for increased IPI(4,5) to the right. These weights show that while a reduction of IPI(4,5) from 3.3 to 2 ms on average did not increase weights at 300 pulses/s, an increase to 6 ms for ME6, or to 10 ms for ME1, increased W5/W1 to about unity. Unfilled symbols for ME1 and ME6 describe similar data with 8P sequences at 600 pulses/s. In that case the constant-IPI condition is shown at IPI (4,5)=1.67 ms, and only increased-IPI(4,5) data were further collected. The average W5/W1 weighting for the two listeners at 600 pulses/s shows little change when IPI(4,5) was increased from 1.67 to 3 ms. The full description of weights for all eight pulses with increased IPI(4,5) intervals is shown in Fig. 4(d) for subject ME1, who was available for a greater number of tests. At 600 pulses/s with a large IPI(4,5) of 6 ms, it can be seen that W5/W1 was again close to unity.

IV. USING WEIGHTS TO PREDICT DISCRIMINATION PERFORMANCE

The subject-averaged 8P ITD weights from Fig. 1 (excluding subject ME5 who was not tested at 600 pulses/s) show that pulse-averaged postonset ITD weights were about 0.32 at 100 pulses/s, 0.12 at 300 pulses/s, and 0.02 at 600 pulses/s. These values were used to predict the reductions in static ITD thresholds that would have been expected in experiment 1C reported by van Hoesel (2007)as duration was increased from a single pulse to 50, 100, and 300 ms at both 100 and 400 pulses/s. Note that two of the three subjects in that study, ME1 and ME3, also participated in the present observer weighting study. A modified ideal-observer model was assumed in which information from each postonset pulse was scaled by its relative weighting. In that case, rather than reducing the total threshold by the square root of the number of pulses in the signal, as would be the case for an ideal observer [e.g., see Green and Swets (1966)] weighting all pulses equally, thresholds were assumed to be reduced by the square root of one plus the sum of the postonset weights, where the initial "one" derives from the contribution of the onset pulse. By way of example, the ITD threshold predicted for a 50 ms pulse train at 100 pulses/s, corresponding to an onset pulse followed by five postonset pulses, is about 0.62 $(1/\sqrt{1+5\times 0.32})$ times lower than that for a single pulse. The logarithm of the threshold reduction for *N*-pulse stimuli relative to the single-pulse condition is shown in Fig. 5. The solid line shows predictions for an ideal observer, with all weights in the stimulus equal to 1. The curve with the short dashes shows results predicted by the present observer-weighting-based model for 100 pulses/s using the relative weighting value of 0.32. The curve with alternating short and long dashes shows model predictions for 400 pulses/s using a relative weighting of 0.09 derived by linear interpolation of the weights of 0.12 and 0.02 at 300 and 600 pulses/s, respectively. The filled symbols show actual results from van Hoesel (2007). Predicted values at 100 pulses/s agree well with the measured mean reduction in thresholds at all three durations. At 400 pulses/s, corre-

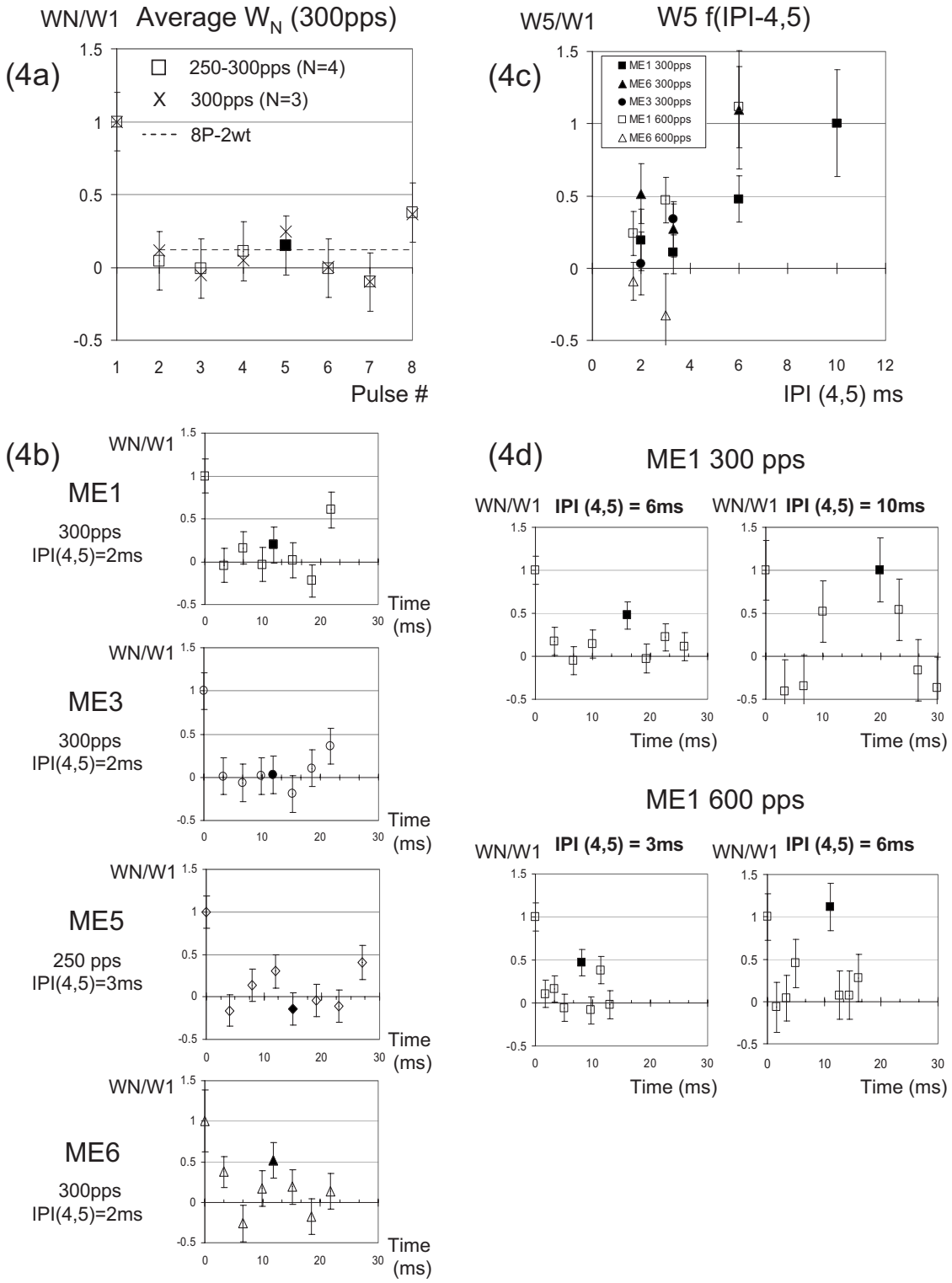


FIG. 4. ITD weights using an irregular interpulse interval IPI(4,5) between the fourth and fifth pulses in 8P stimuli. Left graphs show the weights at 300 pulses/s (and 250 pulses/s for subject ME5) with an IPI(4,5) of 2 ms (or 3 ms for ME5). (a) shows the average result over all four subjects (and the three excluding ME5). Individual subject data are shown in (b). (c) shows the relative weighting of just the fifth pulse (W5/W1) as a function of the interval preceding it, IPI(4,5), for the three listeners excluding ME5. Filled symbols show results at nominal rates of 300 pulses/s (IPI=3.3 ms). Unfilled symbols for ME1 and ME6 describe further data at 600 pulses/s (IPI=1.67 ms), for which reduced-IPI(4,5) data were not collected. (d) describes additional data from subject ME1, who was available to explore a more extensive range of test conditions.

spondence is good at the shortest duration of 50 ms (21 pulses in total), but the model increasingly overpredicts performance at longer durations at that rate. Considered in terms of number of pulses, observed threshold decreases as the duration was extended are in reasonably good agreement with the model predictions at both rates for stimuli containing up to about 20 or 30 pulses but not for longer stimuli at higher rates.

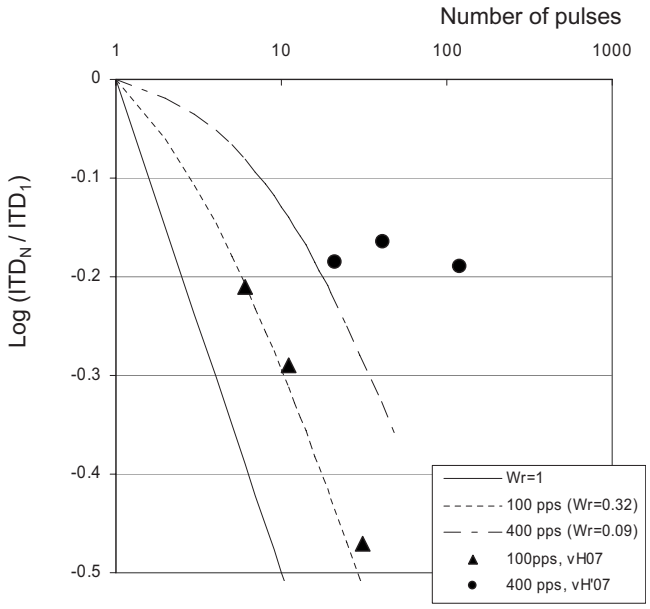


FIG. 5. Observer-weighting-based predictions (see text) of static ITD threshold improvements as a function of duration relative to the single-pulse threshold. The solid line shows predictions for an ideal observer weighting all pulses in the stimulus equally. The curve plotted using short dashes shows predictions for a mean postonset relative weighting value of 0.32, as found in the present study with 8P stimuli at 100 pulses/s. The curve with alternating short and long dashes shows similar predictions using a relative weighting of 0.09, as determined for 400 pulses/s by linear interpolation of the weights found at 300 and 600 pulses/s. The filled symbols show actual threshold reductions, averaged over three listeners, as reported in van Hoesel (2007) for durations of 50, 100, and 300 ms at rates of 100 pulses/s (triangles) and 400 pulses/s (circles). Two of those three subjects (ME1 and ME3) also participated in the present observer weighting study.

V. DISCUSSION

The results from these experiments show that at 100 pulses/s, ITD cues on every pulse made a substantial contribution to overall lateralization. In contrast, at 300 and 600 pulses/s the onset was weighted much more strongly than any later pulse in the stimulus. At 600 pulses/s, postonset weights were on average very close to zero and more than an order of magnitude smaller than those at 100 pulses/s. Postonset relative weighting of ILDs showed less onset dominance than ITDs. While the magnitude of the reduction of weights as the rate increased was comparable for ILDs and ITDs, the higher overall weighting of ILDs means that relative changes in weighting as a function of rate were much smaller and amounted to less than a factor of 2 when comparing ILD weights at 100 and 600 pulses/s. While stimulation levels in the ILD task were on average 0.85 dB lower than in the ITD task because ILDs were generated by reducing levels relative to those used in the ITD runs, that modest difference is unlikely to have contributed significantly to the outcome of this study. That assertion is supported by an ANOVA applied to the ILD 8P-data, which showed no significant effect of right-ear level ($F[1,14]=0.2$, $p=0.7$) when comparing weights for stimuli with high right-ear levels that induced rightward lateralization shifts with those for low levels (on average 0.85 dB lower) and induced leftward shifts. The low postonset ITD weights at 300 and 600 pulses/s are unlikely to be due to the randomization of ITDs necessitated by the observer weighting approach. One reason for that is that results at 300 pulses/s with 8P-2Wt stimuli, for which ITD cues were varied in unison on all postonset pulses, generally showed similar weights to those obtained with 8P stimuli in which ITDs were randomized for each pulse independently. Only subject ME5, who was tested with a doubled ITD range of 1200 μs, showed lower postonset weights for the 8P than 8P-2Wt stimuli. This result might be due to a difference in how that listener combined information across pulses with 8P or 8P-2wt stimuli when ITDs varied over a range that considerably exceeded that available from natural head-width delays. Alternatively, the difference may be due to the ambiguity that arose in 8P stimuli when large ITDs of up to 1200 μs approached half the IPI at 300 pulses/s, but was reduced in 8P-2wt stimuli by comparison across multiple intervals. If the latter was indeed the case, the observer weights at 600 pulses/s for the other three subjects might also underestimate postonset contributions for stimuli with identical postonset ITDs at that rate. Furthermore, the similarity of weights with 8P and 8P-2Wt stimuli at 300 pulses/s in those subjects also does not preclude the possibility that postonset cues are more strongly weighted when they are matched to the onset cue, which is the case in static ITD signals with identical ITDs on all pulses. However, such conjectures are not supported by the rather good correspondence between static ITD discrimination reported by van Hoesel (2007) and predictions based on observer weighting as described in Sec. IV, at least for durations up to 20 or 30 pulses. Increased weighting of cues when they are matched to the onset is also not supported by studies with normal-hearing listeners (Stecker and Hafter, 2002; Freyman *et al.*, 1997). It should be stressed that the reduction of postonset ITD weights to near zero at 600 pulses/s when results were averaged across subjects in the present work does not mean that ongoing ITDs are essentially unavailable to all BiCI users at that rate. ME3, for example, showed more positive weighting of postonset ITDs at 600 pulses/s than ME1. The same two subjects participated in the van Hoesel (2007) study, and accordingly ME3 displayed better static ITD sensitivity at 600 pps than did ME1.

The result that greater onset dominance was observed for ITDs than ILDs is in agreement with preliminary data showing evidence of precedence with ITDs but not ILDs in BiCI listeners (Agrawal *et al.*, 2006). It contrasts with findings by Hafter *et al.* (1983), who reported similar onset dominance effects with either ILD or ITD cues in listeners with normal hearing and therefore postulated a single mechanism that governs both. Recently, Stecker (2007) showed that dynamic ILD sensitivity was less affected by rate than was dynamic ITD sensitivity in normal-hearing listeners attending high-frequency clicks, so the contrast between the findings of Hafter *et al.* (1983) and the present results may not be due to the difference in modality. Although the salience of electrical postonset cues is shown to be considerably more rate limited for ITDs than ILDs, that does not preclude a rate-limiting mechanism for ITDs that is located peripheral to any delineation between ILD and ITD processing circuits. Given that observer weighting studies have not supported the hypothesis by Hafter and Dye, Jr. (1983) that onset domi-

nance requires a compressive mechanism that produces steadily decreasing weights over time,[4] a stationary low-pass filter may suffice to account for much of the data from the present study. The onset timing cue at the output of such a filter would be little affected by pulse rate, but ongoing modulation at the output of the filter would become increasingly shallow as rates increase due to the temporal smearing of the responses to each pulse. In the event that pulses arrive *much* faster than the time constant associated with the low-pass filter, that modulation might be too shallow for postonset ITDs to be effective (as demonstrated at 600 pulses/s in the observer weighting data). For ILD cues, on the other hand, preservation of an adequate "modulation depth" is likely to be inconsequential to the detection of interaural differences, so that the contributions from each pulse would be less rate dependent although perhaps still subject to refractory effects. While the combined effects of refractory behavior, response latency shifts, and ambiguity in relation to IPIs at higher pulse rates may have a low-pass filtering effect, they seem an unlikely explanation of the strong ITD onset dominance found at rates as low as 300 pulses/s. An additional rate limitation, possibly similar to that observed in normal-hearing listeners with envelope-based ITD cues, appears to be required. One candidate explanation may relate to the synchronous activation over broad regions along the cochlea with electrical stimulation as opposed to the systematic phase shifts normally encountered over those regions in association with traveling wave delays in normal hearing.

The finding that the reduction of a single IPI at 300 pulses/s did not lead to increased ITD weighting fails to provide evidence of restarting due to a change in electrical pulse rate. As discussed in the Introduction, restarting results from normal-hearing listeners have been somewhat variable across studies. Because some of that variation may be related to the choice of stimulus parameters, it is worth noting that both the studies by Stecker and Hafter (2002) and Freyman *et al.* (1997) showed restarting with an ICI of 3 ms, which is very similar to the 3.3 ms IPI used here, but other differences with the present study remain. Stecker and Hafter (2002) used an increase rather than a decrease in ICI to invoke restarting and tested it in the context of a free-field task in which both ILD and ITD cues were available. In the present study, both BiCI users who were available for further testing with an increased rather than a decreased IPI(4,5) did show increased weighting when that interval was sufficiently large. While that result usefully eliminates the possibility that restarting was not observed with reduced IPIs because of paradigm or subject idiosyncrasies, it does not provide evidence of restarting because of the confounding improvement in ITD salience due to the lowered rate in the increased interval. The W5/W1 weights [in Fig. 4(c)] following a large 6 or 10 ms IPI(4,5) at 300 pulses/s were close to unity and therefore did exceed the average postonset weighting in 8P stimuli at a constant rate of 100 pulses/s shown in Fig. 1. However, the competition among strong cues on all eight pulses at 100 pulses/s increased the noise in those weight estimates, and the ANOVA at that rate showed no significant difference between the weighting of the onset and later pulses. Furthermore, when the weighting of the pulse following a large IPI(4,5) at 300 pulses/s is compared with 2P rather than 8P postonset weights at 100 pulses/s (Fig. 1), the results are more similar, and the former rather than the latter comparison may be more appropriate in terms of the number of pulses following low-rate intervals. Nevertheless, additional data are needed to better assess the contribution of these large IPIs in different contexts. Freyman *et al.* (1997) reported restarting in listeners with normal hearing after a decrease in ICI. In that experiment, the ICI of the click train was changed from 3 to 2 ms after 100 ms and was kept at the reduced ICI for the remainder of the 400 ms stimulus. In the present study, the IPI was changed from 3.3 to 2 ms, so the intervals used are very similar. Although the sustained nature of the change and the simultaneous change in pitch in the experiment by Freyman *et al.* (1997) may have imparted a stronger restarting cue than with the electrical stimuli used here, it is also possible that the different outcome is because the mechanism responsible for the gap-derived binaural restarting in normal hearing relies on peripherally imparted cues that are absent with electrical stimulation, such as the introduction of spectral cues that present additional onset information to a remote region of the cochlea as a consequence of the temporal irregularity.

The data from the present study do not support the suggestion by Laback and Majdak (2008) that the benefit of rate-jitter in their experiment was due to restarting and was absent at their lowest rate of 400 pulses/s because BiCI users were already able to make good use of postonset ITDs at that rate. The observer-weighting results show strong ITD onset dominance at both 300 and 600 pulses/s, thereby leaving ample scope for restarting at those rates and, by implication, also at 400 pulses/s. In the absence of a satisfactory explanation for why restarting might apply at 800–1500 pulses/s but not at 400 pulses/s despite strong onset dominance at that rate, the benefit of rate-jitter at high rates is more parsimoniously explained by lowered-rate cues, as discussed in the Introduction, than by restarting. Further support for that conjecture derives from increases in ITD weighting for the fifth pulse in 8P stimuli at 300 pulses/s when the interval preceding that pulse was increased to 6 or 10 ms but not when it was decreased to 2 ms.

VI. CONCLUSIONS

Results from this study show that, at 100 pulses/s, electrical ILDs or ITDs on every pulse in the stimulus contributed substantially to overall lateralization, and no significant onset dominance was found. At 300 and 600 pulses/s onset dominance was strong for ITDs, and at 600 pulses/s postonset weights (relative to the onset) were very close to zero. ILDs showed much milder onset dominance, and even at 600 pulses/s weights remained within a factor of 2 compared to those at 100 pulses/s. Reduction of weights following the first pulse, wherever observed, was always immediate and remained constant for the rest of the stimulus. Per-pulse ITD weights in 8P sequences were similar irrespective of whether ITDs on the postonset pulses were randomized independently or in unison, so that the randomization process necessitated by the observer weighting paradigm did not af-

fect weights. Restarting of ITD sensitivity at 300 pulses/s by shortening the IPI between the fourth and fifth pulses in an 8P stimulus was not observed. Overall, the results support a model for electrical ITD sensitivity in which the contribution from each pulse is determined primarily by the immediately preceding IPI, although at higher rates refractory behavior, cue ambiguity in relation to the IPI, and response latency shifts likely also need to be considered.

ACKNOWLEDGMENTS

The author is greatly indebted to the sustained efforts of the participating research volunteers without whom these experiments would not have been possible, and further acknowledges helpful discussions with Chris Stecker and Andrew Vandali, and constructive comments from two anonymous reviewers. This work was funded with the assistance of the Australian Government through The HEARing CRC.

[1]However, these authors provided only a fitted curve to describe duration effects up to 32 clicks at that rate and did not plot actual improvements for small numbers of pulses ($N=1,2,4$) that would be more directly comparable to the one- and two-burst results discussed here. To that effect, Hafter and Dye, Jr. (1983, Fig. 4) showed a very close to ideal-observer behavior with four pulses or less but somewhat smaller benefit from added pulses at longer durations.

[2]This was first pointed out to these authors by members of the audience at the CIAP 2007 meeting at Lake Tahoe, where they presented their data prior to publication.

[3]The need to consider this issue was initially brought to light in preliminary data collection with one subject, where it was discovered that small unintentional level fluctuations of up to half a CU (0.08 dB) arose in accordance with the sign of the ITD cue. This was the result of a small current decrement in the ear with the delayed stimulus because the delay introduced a nonzero interval between a zero-amplitude prestimulus pulse and each actual stimulus pulse. In that case, a combined regression analysis for left and right cues would increase the weights for every pulse because of the unintentional ILDs generated in accordance with the sign of the ITDs. In contrast, when using separate regression analyses for left and right cues, the ILD cue is constant and therefore uncorrelated with response variations, so that weights more accurately reflect the contributions from the ITDs applied to each pulse. The confounding ILD cue was eliminated for the experiments presented here by making changes to the way ITDs were generated in the observer weighting software.

[4]Although in experiment 1C in van Hoesel (2007) the slope of the log ITD improvement versus number of pulses for electrical pulse trains is shallow, the considerable variance in the data precludes a reliable assessment of whether a nonstationary mechanism, as advocated in Hafter and Dye, Jr. (1983), better describes the data than does a stationary one.

Agrawal, S. S., Litovsky, R. Y., Jones, G. L., and van Hoesel, R. (**2006**). "Correlates of precedence effect in bilateral cochlear implant users under conditions of direct electrical stimulation and in free field," ARO Midwinter Meeting, Baltimore, MD.

Berg, B. G. (**1989**). "Analysis of weights in multiple observation tasks," J. Acoust. Soc. Am. **88**, 1743–1746.

Bernstein, L. R., and Trahiotis, C. (**2002**). "Enhancing sensitivity to interaural delays at high frequencies by using 'transposed stimuli'," J. Acoust. Soc. Am. **112**, 1026–1036.

Blauert, J. P. (**1997**). *Spatial hearing*, revised edition (MIT, Cambridge, MA).

Carlyon, R. P., van Wieringen, A., Long, C. J., Deeks, J. M., and Wouters, J. (**2002**). "Temporal pitch mechanisms in acoustic and electric hearing," J. Acoust. Soc. Am. **112**, 621–633.

Clifton, R. K. (**1987**). "Breakdown of echo suppression in the precedence effect," J. Acoust. Soc. Am. **82**, 1834–1835.

Freyman, R. L., Zurek, P. M., Balakrishnan, Y., and Chiang, Y. C. (**1997**). "Onset dominance in lateralization," J. Acoust. Soc. Am. **101**, 1649–1659.

Green, D. M., and Swets, J. A. (**1966**). "Signal detection theory and psychophysics," (Wiley, New York).

Haas, H. (**1972**). "The influence of a single echo on the intelligibility of speech," J. Audio Eng. Soc. **20**, 146–149.

Hafter, E. R., and Buell, T. N. (**1990**). "Restarting the adapted binaural system," J. Acoust. Soc. Am. **88**, 806–812.

Hafter, E. R., Buell, T. N., and Richards, V. N. (**1988**). "Onset-coding in lateralization: Its form, site and function," in *Auditory Function: Neurobiological Bases of Hearing*, edited by G. Edelman, W. E. Gall, and W. M. Cowan (Wiley, New York), pp. 648–676.

Hafter, E. R., and Dye, R. H., Jr. (**1983**). "Detection of interaural differences of time in trains of high-freqeuncy clicks as a function of interclick interval and number," J. Acoust. Soc. Am. **73**, 644–651.

Hafter, E. R., Dye, R. H., Jr., and Wenzel, E. (**1983**). "Detection of interaural differences of intensity in trains of high-freqeuncy clicks as a function of interclick interval and number," J. Acoust. Soc. Am. **73**, 1708–1713.

Javel, E., and Shepherd, R. K. (**2000**). "Electrical stimulation of the auditory nerve. III. Response initiation sites and temporal fine structure," Hear. Res. **140**, 45–76.

Jones, G. J., Litovsky, R. Y., Agrawal, S. S., and van Hoesel, R. J. M. (**2006**). "Effect of stimulation rate and modulation rate on ITD sensitivity in bilateral cochlear implant users," 29th Midwinter Meeting, Association for Research in Otolaryngology, Baltimore, MD.

Klumpp, R. G., and Eady, H. R. (**1956**). "Some measurements of interaural time difference thresholds," J. Acoust. Soc. Am. **28**, 859–860.

Laback, B., and Majdak, P. (**2008**). "Binaural jitter improves interaural time-difference sensitivity of cochlear implantees at high pulse rates," Proc. Natl. Acad. Sci. U.S.A. **105**, 814–817.

Laback, B., Majdak, P., and Baumgartner, W.-D. (**2007**). "Lateralization discrimination of interaural time delays in four-pulse sequences in electric and acoustic hearing," J. Acoust. Soc. Am. **121**, 2182–2192.

Litovsky, R. Y., Agrawal, S. S., Jones, G. J., Henry, B., and Van Hoesel, R. J. M. (**2005**). "Effect of interaural electrode pairing on binaural sensitivity in bilateral cochlear implant users," 28th Midwinter Meeting, Association for Research in Otolaryngology.

Litovsky, R. Y., Colburn, H. S., Yost, W. A., and Guzman, S. J. (**1999**). "The precedence effect," J. Acoust. Soc. Am. **106**, 1633–1654.

Long, C. J., Eddington, D. K., Colburn, H. S., and Rabinowitz, W. M. (**2003**). "Binaural sensitivity as a function of interaural electrode position with a bilateral cochlear implant user," J. Acoust. Soc. Am. **114**, 1565–1574.

Majdak, P., Laback, B., and Baumgartner, W.-D. (**2006**). "Effects of interaural time differences in fine-structure and envelope on lateral discrimination in electric hearing," J. Acoust. Soc. Am. **120**, 2190–2201.

Plack, C. J., and White, L. J. (**2000**). "Pitch matches between unresolved complex tones differing by a single interpulse interval," J. Acoust. Soc. Am. **108**, 696–705.

Saberi, K. (**1996**). "Observer weighting of interaural delays in filtered impulses," Percept. Psychophys. **58**, 1037–1046.

Stecker, G. C. (**2007**). "Lateralization of dynamic interaural time and level differences in high-frequency click trains," 30th Midwinter Meeting, Association for Research in Otolaryngology, Baltimore, MD.

Stecker, G. C., and Hafter, E. R. (**2002**). "Temporal weighting in sound localization," J. Acoust. Soc. Am. **112**, 1046–1057.

van de Par, S., and Kohlrausch, A. (**1997**). "A new approach to comparing binaural masking level differences at low and high frequencies," J. Acoust. Soc. Am. **101**, 1671–1680.

van Hoesel, R. J. M. (**2004**). "Exploring the benefits of bilateral cochlear implants," Audiol. Neuro-Otol. **9**, 234–246.

van Hoesel, R. J. M. (**2007**). "Sensitivity to binaural timing in bilateral cochlear implant users," J. Acoust. Soc. Am. **121**, 2192–2206.

van Hoesel, R. J. M., and Clark, G. M. (**1997**). "Psychophysical studies with two binaural cochlear implants subjects," J. Acoust. Soc. Am. **102**, 504–518.

van Hoesel, R. J. M., and Tyler, R. S. (**2003**). "Speech perception and localization with bilateral cochlear implants," J. Acoust. Soc. Am. **113**, 1617–1630.

Wallach, H., Newman, E. B., and Rozenzweig, M. R. (**1949**). "The precedence effect in sound localization," Am. J. Psychol. **51**, 315–336.

Zurek, P. M. (**1980**). "The precedence effect and its possible role in the avoidance of interaural ambiguities," J. Acoust. Soc. Am. **67**, 952–964.

Lateralization of Huggins pitch

Peter Xinya Zhang[a] and William M. Hartmann[b]
Department of Physics and Astronomy, Michigan State University, East Lansing, Michigan 48824

(Received 25 June 2006; revised 18 July 2008; accepted 29 July 2008)

The Huggins pitch is a sensation of pitch generated from a broadband noise having a narrowband boundary region where the interaural phase difference varies rapidly as a function of frequency. Models of binaural hearing predict that the pitch image should be well lateralized. A direct psychophysical experimental method was used to estimate the lateral positions of Huggins pitch images with two different forms of phase boundaries, linear phase and stepped phase. A third experiment measured the lateral positions of sine tones with controlled interaural phase differences. The results showed that the lateralization of Huggins pitch stimuli was similar to that of the corresponding sine tones and that the lateralizations of the two forms of Huggins pitch phase boundaries were even more similar to one another. Both Huggins pitches and sine tones revealed strong laterality compression (exponent≈0.5). Ambiguous stimuli, with an interaural phase difference of 180°, were consistently lateralized on one side or the other according to individual asymmetries—an effect called "earedness." An appendix to this article develops a new first-order lateralization model, the salient phase density model, which combines attributes of previous models of dichotic pitch lateralization. © *2008 Acoustical Society of America.* [DOI: 10.1121/1.2977683]

PACS number(s): 43.66.Qp, 43.66.Pn [ARK] Pages: 3873–3887

I. INTRODUCTION

Dichotic pitches are pitch sensations arising from noises, presented by headphones, with no evident frequency specificity in either left- or right-ear channels. The frequency-specific information that leads to a tonal pitch sensation is encoded entirely in the phase relationship between the two channels. Several binaural models have been advanced to explain the creation of dichotic pitches, notably the equalization-cancellation (EC) model (Durlach, 1962, 1972), the modified EC model (Culling *et al.*, 1998a, 1998b), and the central activity pattern (CAP) model (Raatgever, 1980; Raatgever and Bilsen, 1986). In recent years, arguments for and against the various models have appeared in literature (Culling, 2000; Bilsen and Raatgever, 2000, 2001; Akeroyd and Summerfield, 2000; Hartmann and Zhang, 2003).

The best known dichotic pitch effect is the Huggins pitch (HP) (Cramer and Huggins, 1958), which is made with a broadband noise that is identical in the two ears except for a single phase boundary region. Figure 1 (light line) shows the stimulus known as HP–, where the interaural phase difference (IPD) is 0° (or 360°, equivalent to 0°) for all frequencies except for the boundary region. In the boundary region, the IPD increases monotonically from 0° to 360°. Figure 1 (heavy line) also shows the stimulus called HP+, which is the same as HP– except for an all-band phase shift of 180°. The width of the phase boundary is much smaller than a critical band, though its exact value is not critical. The width is typically chosen to be about 6% of the center frequency. It is useful to introduce the concept of a *background* IPD, 0° for HP– and 180° for HP+. When presented with HP stimuli through headphones, listeners hear, on top of the noise background, a pitch at the center frequency of the boundary region, which is defined as the *boundary frequency*.

A. Lateralization

In addition to its pitch, the tonal image created by the HP stimulus has a laterality. It appears to be centered in the head or off to the left or right. In thinking about the lateralization of HP, it is helpful to plot the interaural cross correlation in the frequency-lag plane, as shown in Fig. 2—a signal-based representation of the classic binaural model by Jeffress (1948). High cross correlation, illustrated by a bright region in the figure, occurs for frequencies and lags where the two channels are in phase. For instance, in Fig. 2(a) for HP– there is a bright stripe running from top to bottom at a lag of zero because of the in-phase background components. Bright stripes (hyperbolas) to the left and right of midline are centered on regions of strong correlation for frequencies and lags where the product of frequency and lag is an integral number of complete cycles. The pattern in Fig. 2(b) for HP+ is essentially the negative of the pattern in Fig. 2(a) because HP+ can be derived from HP– by a 180° phase shift of all components in one channel. Apart from the background, the cross-correlation functions in Fig. 2 represent the boundary regions as thin horizontal bands centered on the boundary frequency, f_c, here chosen to be 200 Hz. Consistent with the visual impression given by Fig. 2, HPs at the centers of the boundary regions are observed to be lateralized to the left or right for HP– and to be lateralized near the center for HP+.

The purpose of the experiments of the present article is to measure the lateral positions of HPs using a direct psychophysical method (Marks, 1974). In this method listeners assign numerical values, according to a fixed scale, to their estimates of the lateral positions of the pitch images. Previous experiments have also measured the lateralization of HP

[a]Electronic mail: zhangx11@msu.edu
[b]Electronic mail: hartmann@pa.msu.edu

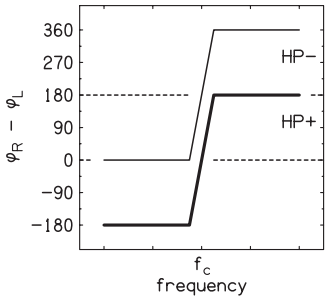


FIG. 1. IPD for HP stimuli of the linear-phase type. Although the phases of noise components for HP stimuli are completely random, there is a definite relationship between the phases for left and right ears as a function of component frequency. Light and heavy lines show the IPD for HP− and HP+, respectively. In each case the interaural phase changes by 360° in the boundary region as a linear function of the component frequency. The frequency at the center of the boundary region is defined as the boundary frequency, f_c. Pitch matching experiments show that the HP corresponds to f_c.

(Raatgever and Bilsen, 1977, 1986; Grange and Trahiotis, 1996; Akeroyd and Summerfield, 2000), but those experiments were indirect. They matched the lateral position of HPs by varying an interaural parameter of some other form of stimulus, used as an acoustic pointer. However, only if it is known that there is a linear relationship between the parameter of the pointer and the perception of location can this method lead to an absolute scale of localization. By contrast, the scale of interaural parameters used in matching methods has been found to be warped with respect to scales outside the domain of binaural stimuli (Yost, 1981). The advantage of the direct psychophysical method is that it removes the response from the domain of binaural stimuli and provides a more veridical measure of perceived lateralization. In addition to its direct psychophysical method, the present work employs a large number of stimulus conditions, including a wide range of boundary frequencies.

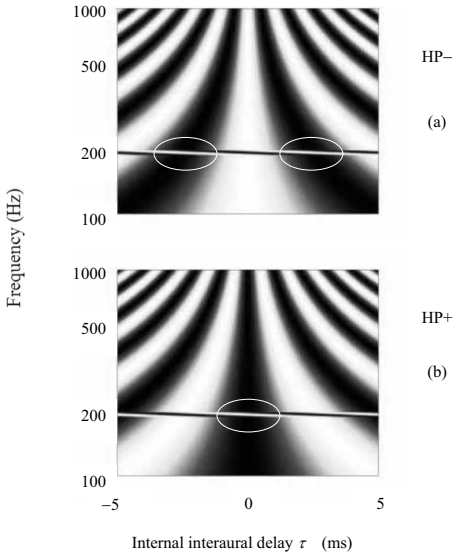


FIG. 2. Cross-correlation for HP− and HP+ plotted in the frequency-lag plane. The axes are linear in lag τ and logarithmic in frequency. Bright areas are centered on regions of high cross correlation. According to simple models, the HP is signaled by the bright narrow horizontal band of intense correlation in the middle of an otherwise dark band where the cross correlation is negative. Therefore, for boundary frequency f_c, HP− appears at a lag of $1/(2f_c)$ (hyperbolic rule) and HP+ appears at a lag of zero. Because the figure is signal based, the vertical axis is frequency, not tonotopic coordinate.

B. Lateralization models

It is necessary to have first-order predictions for the lateralization of HP images to guide the experiments. First-order predictions are mainly based on stimulus parameters and make minimal assumptions about auditory processing.

The CAP model of Raatgever and Bilsen (1986) simultaneously predicts both the existence of the HP and its lateralization. The model is "stimulus based" in that it assumes linear peripheral processing and perfect frequency resolution along the tonotopic axis of the receiver. It is based on a CAP that is very similar to the cross-correlation pattern shown in Fig. 2. Therefore, the lateralization of the image depends mainly on phases within the boundary region.

By contrast, the half-period rule introduced by Akeroyd and Summerfield (2000) (also entirely stimulus based) says that the location of the pitch image depends only on the interaural phase of the noise background. The image location is displaced from the noise background by an interaural time difference (ITD) corresponding to half a period of the phase boundary frequency. The advantage of the half-period rule is that it correctly predicts the lateralization of the pitch image when the interaural phases of the boundary region are random variables. However, Akeroyd and Summerfield (2000) showed that the rule fails for a boundary region having constant delay. Ultimately, they preferred a model that they called the reconstruction-comparison (RC) model, which includes assumptions about auditory filter bandwidth and nonlinear peripheral processing. The assumptions make the model more realistic physiologically at the cost of complexity. An important feature of the RC model is that the lateralization of dichotic pitches is jointly predicted by the interaural properties in the boundary region and in the background region.

The Appendix to this article presents a third model, the salient phase density (SPD) model that is a compromise between the CAP and RC models. It is stimulus based, but its predictions depend jointly on the interaural phases in the boundary region and the background region. The SPD model successfully predicts the approximate lateralizations for all the forms of HP that have been discussed in literature. It is a mathematically straightforward algorithm that makes predictions for other forms of dichotic pitch as well (Zhang and Hartmann, 2007).

The above brief background on models of dichotic pitch lateralization is adequate for the purposes of the present article. For the stimuli of this article, the CAP model, half-period rule, RC model, and SPD model all make essentially the same predictions. The models agree with Grange and Trahiotis (1996) in predicting that HPs with boundaries centered on a given ITD will be lateralized similar to narrow noise bands or sine tones with equivalent ITD. Therefore, it is not the purpose of the present article to compare the dif-

ferent models and discover which is best. Instead, the purpose is to compare all of them with direct psychophysical experiments.

C. First-order predictions

To make first-order predictions for comparison with experimental data requires that the models (CAP, RC, and SPD) be supplemented with assumptions about listener responses. For definiteness, this article begins by assuming that listeners lateralize stimuli exactly as predicted by the SPD model. As noted in the Appendix, the SPD model predicts that lateralization corresponds to an ITD of τ_p, called the "best-fit lag." When applied to the stimuli of this article (subsection of HP+ and HP− with added ITD in the Appendix), the best-fit lag corresponds to the peak of the cross-correlation function at the boundary frequency. Thus, for these particular stimuli, the SPD model agrees with the half-period rule because τ_p always turns out to be half a period removed from the ITD of the background.

In addition, it will be assumed that listeners scale their numerical responses linearly with τ_p according to an unchanging scale wherein the maximum allowed response is assigned to the maximum value of τ_p present in the stimuli. It is assumed that listeners learn about the maximum value of τ_p from their experience with the stimulus set. Together, the SPD model and the linear scaling assumptions constitute the first-order predictions to guide the experiments below.

II. EXPERIMENT 1: LINEAR-PHASE BOUNDARY

Experiment 1 measured the perceived lateralization of HPs by asking listeners to give numerical estimates of the locations of the pitch images. The basic experimental method was simple. We presented listeners with HP+ and HP− stimuli having various boundary frequencies and asked the listeners to estimate the lateral position of the pitch image on a fixed scale. According to the first-order predictions, we expected to find HP+ located at the center of the head independent of boundary frequency, as shown in Fig. 2(b). We expected to find HP− along a curved path similar to the hyperbola in Fig. 2(a).

A lateralization experiment of this kind instantly encounters problems. In a HP− experiment there is a close correspondence between pitch and expected lateral position. Listeners could easily learn to expect low pitches to appear to the extreme left or right and higher pitches to appear toward the center. In a HP+ experiment listeners would presumably experience no variation at all in lateral positions, making the experiment appear pointless. To solve these problems, our stimuli included an added frequency-independent interaural delay that varied randomly from trial to trial. This added frequency-independent ITD is called the "ITD" below. It should not be confused with the best-fit-lag, τ_p, which is equal to the ITD at the boundary frequency due to a combination of both the ITD (added ITD) and the boundary-region phase shifts introduced by the HP stimulus itself.

A. Stimuli

Each noise stimulus had two channels. The left-ear channel was broadband white noise with 16 384 spectral components of equal amplitude and random phase. The right-ear channel was generated from the left-ear channel by incrementing the phases of components in the boundary region as a linear function of component frequency, as shown in Fig. 1. The overall width of the boundary region was 6% of the boundary frequency.

There were five different nominal boundary frequencies: 200, 315, 500, 700, and 1000 Hz. The factor of 5 from bottom to top gave a good spread of expected lateral positions and spanned most of the existence region for reliable HP [see, however, Culling (1999)]. On each trial, the boundary frequency varied randomly over a range of ±5% of the nominal boundary frequency to try to reinforce the perceived independence of different trials. There were five values of ITD: −1000, −500, 0, 500, and 1000 μs. A positive delay refers to a lead in the right ear, created by incrementing the phase in the right-ear channel by a shift proportional to increasing frequency.

Noise stimuli were calculated by an array processor (Tucker Davis AP2) and converted to audio by 16-bit digital-to-audio converters (Tucker Davis DD1). The sample rate per channel was 20 ksps. With a continuously cycled memory buffer of 32 768 words, the entire period was 1.6384 s, and the frequency spacing between adjacent components was 0.61 Hz. The duration of the stimuli, as presented to the listener, was one entire period. The maximum frequency of the broadband noise as converted was 10 kHz, and the output was lowpass filtered at 5 kHz by Stanford SR640 filters with a slope of −115 dB/octave. The phase integrity of the two channels was tested by adding or subtracting them electronically at a point in the signal chain immediately prior to the headphone power amplifiers. The cancellation was good to at least 40 dB. The level of the noises was 65 dB, making the spectrum level 28 dB. The listener heard the stimuli via Sennheiser HD 520-II headphones while seated in a double-walled sound-treated room.

B. Listeners

There were five listeners, C (female, age 61), L (female, 29), W (male, 62), X (male, 27), and Z (male, 28). All listeners were right handed and had normal hearing except that W had a mild bilateral hearing loss above 8 kHz, typical of males of this age. Listeners W and X were the authors and had considerable experience in dichotic listening as did listener Z. Listeners C and L had little or no previous experience.

C. Procedure

Each experimental run consisted of 25 trials, using every combination of the five boundary frequencies and the five values of ITD, presented in random order. The stimulus was computed anew for each trial using a new set of random phases. During a trial, the listener could call up a single burst of HP stimulus as many times as desired. The listener was required to enter a number between −40 (extreme left) and

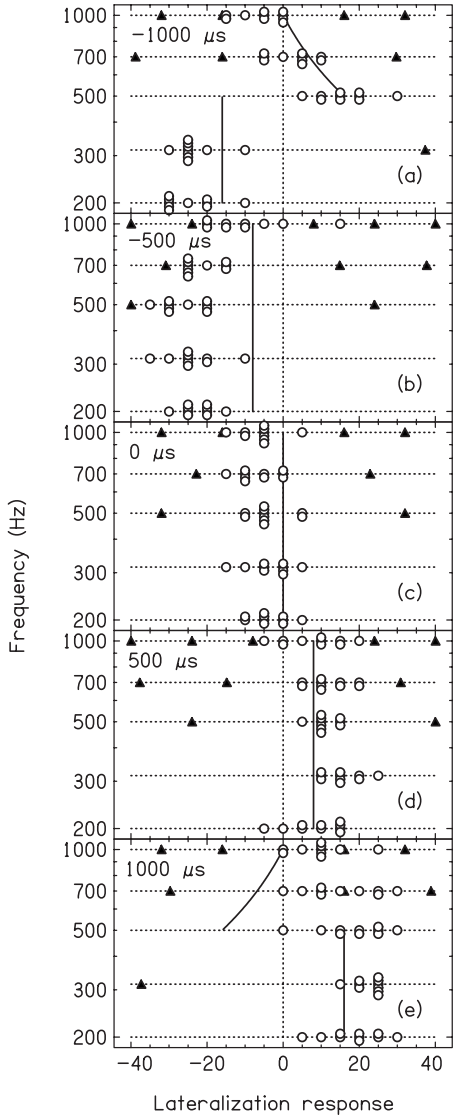


FIG. 3. Scatter plot showing lateral responses for HP+ for listener Z. The solid line gives the first-order prediction. The line bends as needed to keep the interaural phase less than 180°. The triangles indicate alias predicted points, separated from the solid line by 360°. Each panel shows a different ITD. In each panel the 50 circles show all the lateral responses made for five boundary frequencies in the course of ten runs.

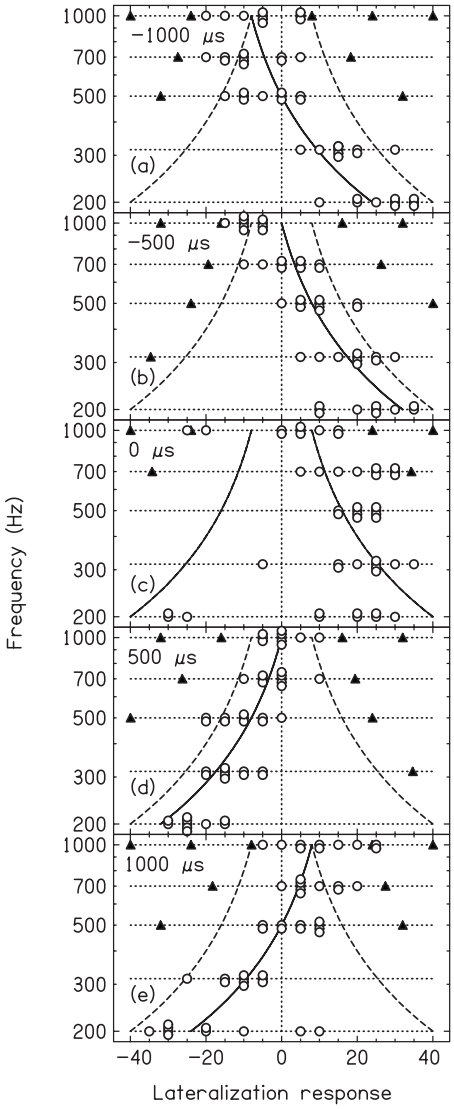


FIG. 4. Scatter plot showing lateral responses for HP− for listener Z, analogous to Fig. 3. The dashed lines delimit the central region defined by interaural phases of ±180°.

+40 (extreme right) as an estimate of the location of the pitch image. There was no feedback. Every experimental run used a fixed type of stimulus, HP− or HP+. This procedural element kept the background interaural phase constant except for the added ITD. Successive runs alternated between these two types. Overall, a listener did ten runs of each type.

D. Results

The analysis of the results required that the data from the runs be unpacked and displayed separately by stimulus type (HP+ or HP−), by boundary frequency, and by ITD. For each listener there were ten plots in Experiment 1, five values of the ITD for each stimulus type. The most revealing data format is a scatter plot consisting of one point for each individual response. As an example, Figs. 3 and 4 show the scatter plots for listener Z for HP+ and HP−, respectively. The data from listener Z are typical: the variability, indicated by scatter in the data, is neither the smallest for Z (the smallest is for listener X) nor is it the largest (the largest is for listener L).[1]

On the scatter plots, the stimulus variable (independent variable), namely, the boundary frequency, is on the vertical axis and the listener's lateralization responses (dependent variable) are on the horizontal axis. This unusual presentation was chosen because the first-order predictions are that responses will reflect the best-fit lag, τ_p, which appears on the horizontal axis in Fig. 2.

The solid lines in Figs. 3 and 4 give the expected values of lateral position from the first-order predictions. The lines are normally vertical in Fig. 3 because for HP+ the best-fit lag is simply the applied ITD. However, as the boundary frequency ω_c increases, the best-fit interaural phase ϕ_p ($\phi_p = \omega_c \tau_p$) surpasses 180°. According to the principle of centrality (Stern *et al.*, 1988) listeners lateralize narrow-band stimuli within the range of −180 to +180°. Consequently, for some boundary frequencies and ITDs, the first-order predic-

TABLE I. RMSE and correlation coefficient (r) between experimental lateral responses and the first-order predictions. The last column on the right indicates an average over listeners. RMSE values can be compared with the scale −40 to +40, corresponding to locations on the extreme left and extreme right.

Listener		C	L	W	X	Z	Average
Linear-phase	RMSE	13.05	16.17	9.58	8.78	7.59	11.03
HP	r	0.90	0.88	0.87	0.86	0.89	0.88
Stepped-phase	RMSE	13.58	⋯	9.39	8.89	8.93	10.19
HP	r	0.91	⋯	0.89	0.88	0.92	0.90
Sine-tones	RMSE	16.08	⋯	9.73	10.06	11.29	11.79
HP	r	0.91	⋯	0.88	0.81	0.89	0.87

tions bend toward the center, shifted laterally by the reciprocal of the boundary frequency, to satisfy the centrality principle.

The solid line predictions on the graph include the assumption that over the course of experimental runs listeners learn about the leftmost and rightmost stimuli and use the range from −40 to +40 based on this experience. The largest τ_p in the experiments was 2500 μs, and it occurred for HP− with an ITD of zero and a boundary frequency of 200 Hz. Thus, a linear scale was established for the predictions whereby a τ_p of zero was expected to equate to a response of 0 and a τ_p of ±2500 μs was expected to equate to a response of ±40. Therefore, the predicted lateral response for HP− in Fig. 4 is given by

$$L = \frac{40}{2500 \times 10^{-6}} \tau_p = \frac{40}{2500 \times 10^{-6}} \left(\mathrm{ITD} \pm \frac{1}{2f_c} \right), \qquad (1)$$

where terms in the parentheses are expressed in seconds and the ± sign is chosen to minimize the absolute value of the response.

The dashed curves in Fig. 4 correspond to phase shifts of ±180°. If centrality holds then all the data points ought to fall between these dashed curves. Alias points, where the interaural phase differs by 360° from the first-order predictions, are shown by triangles. The triangles were included on the graphs to test the idea that lateral position estimates outside the central region might preferentially cluster at alias points.

In general, visual inspection of Figs. 3 and 4 shows that the lateral responses of listener Z tended to follow the predicted solid curves qualitatively, but not perfectly. For instance, for HP+ (Fig. 3), the data points did not cluster about the solid lines but were shifted toward the outside, i.e., the absolute values of the position estimates were larger than expected. For HP− (Fig. 4), the data with 0-ITD did not follow the hyperbolic functions but showed a weaker dependence on frequency.

An interesting effect appears for ambiguous stimuli where the ϕ_p is 180°, and for which the first-order predictions suggest lateralization on left and right sides equally. Ambiguous stimuli occur in Fig. 3 at 500 Hz with ITDs of ±1000 μs and 1000 Hz with ITDs of ±500 μs. They occur in Fig. 4 for all frequencies with ITD of 0 μs and for 1000 Hz with ITDs of ±1000 μs. For these ambiguous stimuli, listener Z tended to respond on the rightmost of the time (73%), indicating a rightward bias.

The rightward bias is also evident in Fig. 3(e) where listener Z usually responded on the right (85%) for frequencies above 500 Hz when centrality predicts responses on the left or centered. Similar findings also occurred for other listeners in that lateral responses for large values of τ_p showed left/right biases for stimuli that were not actually ambiguous. These biases were made evident by lateral position estimates that were systematically contrary to the predictions of centrality. These biases will appear in summary data below.

It is evident from Figs. 3 and 4 that the lateral position estimates by listener Z agreed with the first-order predictions only approximately, and this conclusion can be reached for the other listeners as well by examining figures of the form of Figs. 3 and 4. The average results for each listener in Experiment 1 are shown by open circles in summary figures, Figs. 6 and 7. Figures 6 and 7 use the same coordinate system as Figs. 3 and 4. These summary figures will be discussed later in this article.

E. Quantitative comparison with the first-order predictions

The lateral responses made by the listeners were compared with the first-order predictions by computing two statistics. The first was the rms error (RMSE) between the responses and the predictions. For each listener the calculation of RMSE was based on the average of the ten repeated measures for each of 50 conditions (5 boundary frequencies × 5 ITDs × 2 boundary types). Absolute values were taken for the ambiguous stimuli before averaging. For nonambiguous stimuli, there were a few cases (never more than 2 out of the 50 conditions) when listeners responded on the opposite side to the predictions because of the individual lateralization biases noted above. To prevent these outliers from dominating the calculation of RMSE, only the data points on the same side as predictions were included. Thus, some RMSE values were calculated for 48 or 49 points instead of 50.

The RMSE is shown in the top block of Table I. The scale for the RMSE is the scale of the responses, −40 to +40. Thus typical values from the table (about 10) correspond to about one-quarter of the distance from the center to the extreme—a rather large discrepancy.

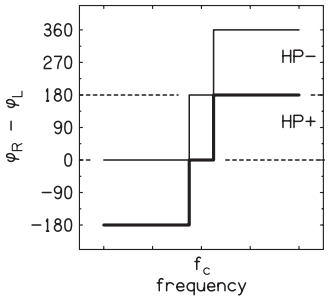


FIG. 5. Interaural phases for HP− and HP+ for stepped-phase stimuli.

The second statistic is the correlation coefficient between the data and first-order predictions. It too is shown in the top block of Table I. The r values are all greater than 0.85, indicating that the experimental data approximately followed the prediction in spite of the rather large rms discrepancies.

III. EXPERIMENT 2: STEPPED-PHASE BOUNDARY

In a stepped-phase version of the HP, the boundary region is made with a constant interaural phase, ϕ_o, different from the background phase (Yost, 1991; Grange and Trahiotis, 1996). If ϕ_o differs from the background phase by 180°, then the first-order predictions for the lateral position of the stepped-phase image are identical to the predictions for the linear-phase image in Experiment 1 (see Appendix).

This prediction is not an obvious one because there is a big difference between the stepped-phase stimulus and the linear-phase stimulus. When heard by itself, in the absence of the background, the stepped-phase boundary can easily be lateralized, and this lateralization does not seem to be different from the lateralization with the background present. By contrast, the linear-phase boundary alone, shown by the bright horizontal segment at 200 Hz in Fig. 2(a) or Fig. 2(b), cannot be consistently lateralized (Zhang, 2006). This latter result is hardly surprising. The linear-phase boundary region contains all possible interaural phases with a uniform distribution over a frequency range that is much narrower than a critical band. Unlike the tendency to hear the pitch at the average frequency (f_c), there appears to be no tendency to lateralize based on some form of average interaural phase. Instead, the lateralization of the linear-phase boundary depends on a contrast between the boundary region and the background.

Experiment 2 used a stepped-phase stimulus with constant phase ϕ_o differing by 180° from the background. Because the stepped-phase boundary region can be lateralized on its own, it was conjectured that this form of boundary region might lead to better agreement with the first-order predictions than did the linear-phase stimulus. On the other side was the first-order prediction that the two types of phase boundaries should be identically lateralized.

A. Method

Experiment 2 was identical to Experiment 1 except that the phases in the boundary region did not increase smoothly with frequency but were constant. As shown in Fig. 5, the boundary phases were fixed at 0° (HP+) or at 180° (HP−), causing the interaural phase to exhibit a step with respect to the background phases. The four most reliable (least variance about their individual means) listeners, C, W, X, and Z from Experiment 1, participated in the experiment.

B. Results

The averaged lateral responses for HP+ and HP− in Experiment 2 are shown by filled circles in summary figures, Figs. 6 and 7. Although we had conjectured that a stepped-phase boundary might lead to different lateral responses, the results actually provided a dramatic exhibition of reproducibility. The Pearson correlation coefficients between the lateral responses in Experiments 1 and 2 were very high with an average of 0.97, as shown in the top row of Table II. This result shows that listeners lateralized the HP stimuli similarly for the linear-phase and stepped-phase boundaries, consistent with the first-order predictions.

Parallel to Experiment 1, the rms error and correlation were calculated to compare the results of Experiment 2 with the first-order predictions. The calculated values are shown in the middle block of Table I. The resulting values were similar to those for the same listeners in Experiment 1.

IV. EXPERIMENT 3: SINE TONES

The HP sounds like a sine tone in noise. The HP stimulus boundary is tonotopically local like a tone. By treating the Huggins effect as a tone in noise, the EC model makes the connection to the masking level difference (MLD) (Durlach, 1962). The CAP model and the RC model predict that the HP with a boundary centered on a given ITD is lateralized the same as a tone with comparable ITD. The SPD model uses a sine-tone cross-correlation template to determine HP lateralization. For these reasons, we performed Experiment 3, which studied the lateralization of sine tones for comparison with the lateralization of HPs. A sine tone with 0-IPD ($\sin-0$) is analogous to HP+. A sine tone with 180°-IPD ($\sin-\pi$) is analogous to HP−.

A. Method

Experiment 3 for tones was identical to Experiments 1 and 2 for HP except that a sine tone replaced the HP stimulus. Effectively, the stimulus for Experiment 3 was equivalent to the stimuli of Experiment 1 or 2 with all spectral components removed except for the single component at the boundary frequency. Thus, there was no noise background. The sine-tone level was 45 dB to approximate the loudness of the HP in Experiments 1 and 2 according to informal estimates. Listeners C, X, W, and Z did ten runs for $\sin-0$ interleaved with ten runs for $\sin-\pi$.

B. Results

Averaged results of Experiment 3 appear as "+" symbols in Figs. 6 and 7 for $\sin-0$ and $\sin-\pi$, respectively. Visually comparing the + symbols with the open and filled circles in these figures, one can observe that the + symbols and the circles tend to follow the same trend, although the

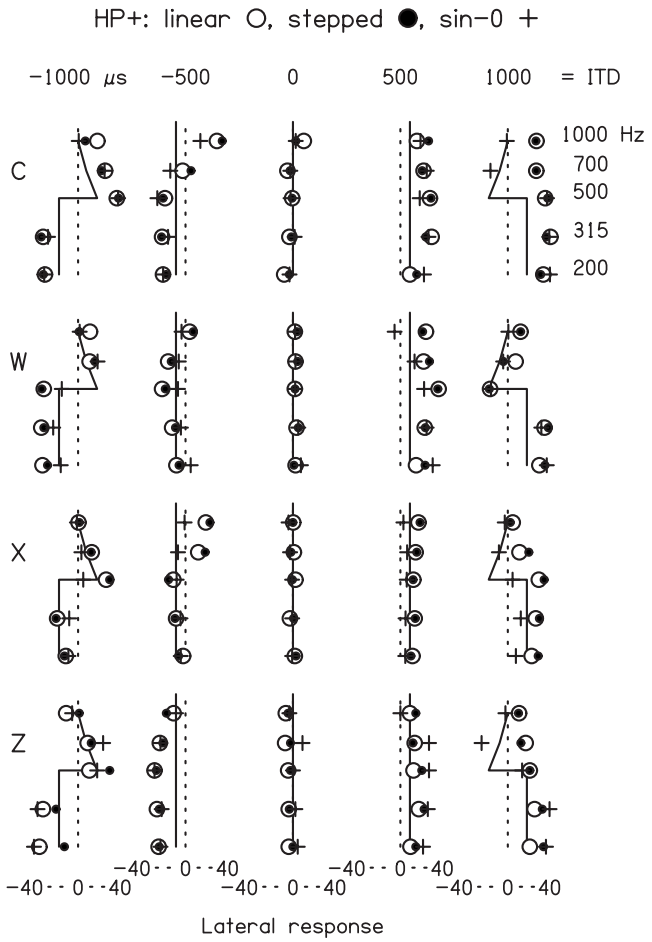


FIG. 6. Results of Experiments 1–3 for HP+ and sin−0 for four listeners. As for the scatter plot illustrated in Fig. 3, the vertical axis shows the boundary frequency (or sine-tone frequency) and the horizontal axis shows the listener's lateral responses averaged over ten trials. The vertical dashed line indicates the zero of lateral position. The solid line shows the first-order prediction.

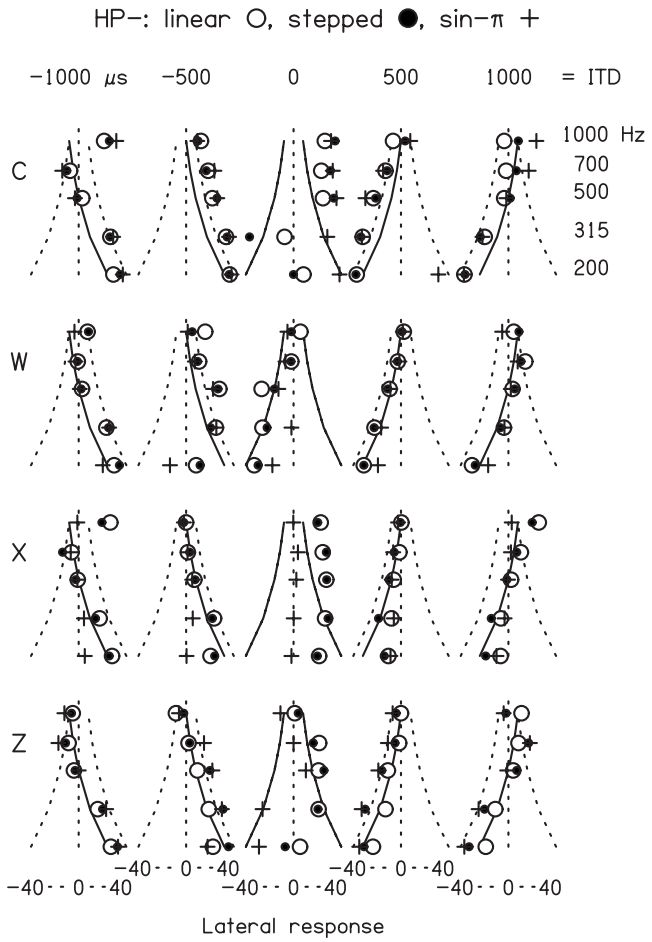


FIG. 7. Results of Experiments 1–3 for HP− and sin− π for four listeners. The form is the same as for the scatter plot illustrated in Fig. 4. The vertical dashed line indicates the zero of lateral position. The solid line shows the first-order prediction.

open and filled circles are more similar to each other. For the four listeners who did all three experiments, the correlation coefficients comparing the sine-tone results with the HP results in Experiments 1 and 2 are high (the bottom two rows in Table II), and average to 0.86 and 0.88, respectively. These results suggest that there is a common mechanism for lateralizing HPs and sine tones. Similar to Experiments 1 and 2, the RMSEs and correlation coefficients were calculated to compare the experimental data with the first-order predictions. They are shown in the bottom block of Table I. The results are comparable to the results of Experiments 1 and 2 for HP.

V. DISCUSSION

A. Summary of the experiments

The best comparison between the three experiments is obtained by examining the individual scatter plots for each listener, similar to Figs. 3 and 4.[1] Figures 6 and 7 for the mean values of lateral responses serve as summaries of the individual scatter plots. Of course, averaging lateral responses leads to possible cancellation between positive (right) and negative (left) responses, especially for the ambiguous stimuli. Such cancellation would distort the interpretation by falsely representing responses as too close to the midline. Fortunately, because listeners usually responded with a bias to one side or the other for ambiguous and near-ambiguous stimuli, such distortions were infrequent. That fact can be seen in Figs. 6 and 7 where the symbols indicating lateral responses for ambiguous stimuli are located well away from the midline.

In Fig. 6 (HP+) there are 25 data points for each listener, corresponding to 25 conditions (5 boundary frequencies × 5 ITDs). Each data point is an average of ten repeated measures from ten runs. The first-order predictions (solid curves) are that listeners' lateral responses should form straight lines except for accommodations to the centrality principle. In Fig. 7 (HP−), there are similarly 25 data points

TABLE II. Correlation coefficients of lateral position responses across three different stimuli. Linear and stepped refer to two types of HP boundary region.

Listener	C	W	X	Z	Average
Linear vs stepped	0.98	0.97	0.97	0.96	0.97
Linear vs sine	0.82	0.88	0.84	0.89	0.86
Stepped vs sine	0.84	0.90	0.83	0.93	0.88

for each listener, and the predictions are that the lateral responses should form a hyperbolic function per the solid curves.

Visual observation of Figs. 6 and 7 confirms that judgments tended to follow the predictions qualitatively. For instance, for frequencies below 700 Hz, lateral responses for nonambiguous conditions were 100% on the same side as the predictions for listeners X and Z, 96% for listener C, and 92% for W. The exceptions for C and W occurred for sine tones. Moreover, for HP+, the lateral responses (especially below 700 Hz) had little frequency dependence as predicted. By contrast, the corresponding responses for HP− demonstrated considerable frequency dependence, as expected, though not as much as predicted. Furthermore, when comparing across the three types of stimuli (i.e., linear-phase boundary, stepped-phase boundary, and sine tones), each listener's lateral responses were very similar, and the three symbols in Figs. 6 and 7 overlap fairly well. The sine-tone data for listener X are systematic exceptions.

B. Correlation coefficients

Pearson correlation coefficients comparing the lateral responses in the three different experiments were calculated for each listener. These correlation coefficients were based on all ten trials for each individual stimulus, with absolute values used for ambiguous stimuli. Therefore, the data sets used to calculate the correlation coefficients were slightly more complete than the data used in Table I.

The correlation coefficients are shown in Table II. All the values in the table are above 0.82, indicating similarity among the lateral responses for the three types of stimuli. The large correlations in the top row (two forms of HP) suggest that the detailed information within the boundary region does not influence the lateralization of HP. For each listener, the correlation coefficient in the top row is always greater than those in the bottom two rows. One-tailed paired *t*-tests for the four listeners show that the difference is significant at the 0.02 level. These results show more similarity in lateralization between HPs created with different boundary types than between HPs and sine tones.

C. Fitted function

To represent the lateralization data in a systematic way, we plotted lateralization responses as a function of the best-fit lag, τ_p. These plots are given in Figs. 8–10 for linear-phase HP, stepped-phase HP, and sine tones, respectively. The plots show responses averaged over the ten trials for each of the 25 stimuli in an experiment, with absolute values taken for ambiguous stimuli. The circles represent the responses for HP+ $(\sin-0)$, and the triangles represent the responses for HP− $(\sin-\pi)$. Ideally, all the data points should fall in the first and third quadrants, indicating lateral responses on the expected side. This was true of almost all the data. Occasionally, data points fell into the wrong quadrants, and those points (very few and never more than two out of the 50 points for any given listener on a single figure) are not included in the figures. This omission made it possible to show the plots for all listeners in one figure. The *y*-axis labels for positive τ_p are displayed on the right axis, and the labels for negative τ_p are displayed on the left axis. The dashed straight lines show the first-order predictions, which assume a fixed scale factor that assigns lateral responses of ± 40 to τ_p of ± 2500 μs.

The lateralization data for each listener were fitted by a function of the form

$$L = a \cdot \tau_p^q + b, \tag{2}$$

where τ_p is in μs.

The parameters allow for an individual offset bias (b), a scale factor (a), and a laterality compressive exponent (q). As shown in the lateralization estimation experiments by Yost (1981) and by Zhang and Hartmann (2006), the perceived lateral positions of sine tones are not linear functions of the IPD when IPDs beyond 90° are included in the stimulus set. Instead, the lateral judgments are compressed at large IPDs.

The fitting process computed the difference between the data points and the functional form and minimized the RMSE for the data points shown in the plots. The three-parameter function, including compression, always agreed with the data better than did the first-order predictions. The RMSEs are always smaller and the correlation r values are always larger in Table III compared to Table I. A paired *t*-test shows that the improvement in RMSEs is significant at the 0.01 level. The best fits to the experimental data are shown as solid curves in Figs. 8–10. The optimal parameters (a, b, and q) are also shown in Table III.

In Table III, the parameters for different listeners were quite different. By contrast, for a given listener, the q-parameters, representing the amount of compression, and the b-parameters, representing the left/right bias, were very similar across the three types of stimuli. The only exception was listener X, for whom sine tones led to much more compression ($q=0.17$) than did HP stimuli ($q=0.41$), and for whom left/right bias (b) was different for different stimuli.

Several variations on the fitting procedure were done in order to determine the importance of the parameters. Forcing the fit to be linear ($q=1$) but allowing for individual differences in offset and slope led to smaller values of RMSE compared to the original first-order estimates with $b=0$ and $a=1$. The difference was significant at the 0.0001 level in a one-tailed paired *t*-test. However, this best linear fit resulted in a RMSE that was larger by a factor of 1.5 compared to the RMSE for the compressive three-parameter fit, shown in Table III. The difference was significant with a *p*-value of 2×10^{-5}. This statistical result confirms the importance of laterality compression.

In a second variation, the τ_p in Eq. (2) was replaced by the ϕ_p and the RMSE was again minimized. This substitution increased the RMSE significantly, $p<0.05$. As was found in the sine-tone lateralization experiments by Zhang and Hartmann (2006), the perceived lateral positions for HPs are more consistent with τ_p than with ϕ_p. In other words, lateral position corresponds better to ITD than to IPD.

There is evidence that listeners adjust their response scales to the range of best-fit lags arising in a given experiment run. The HP+ runs, summarized in Fig. 6, had a maxi-

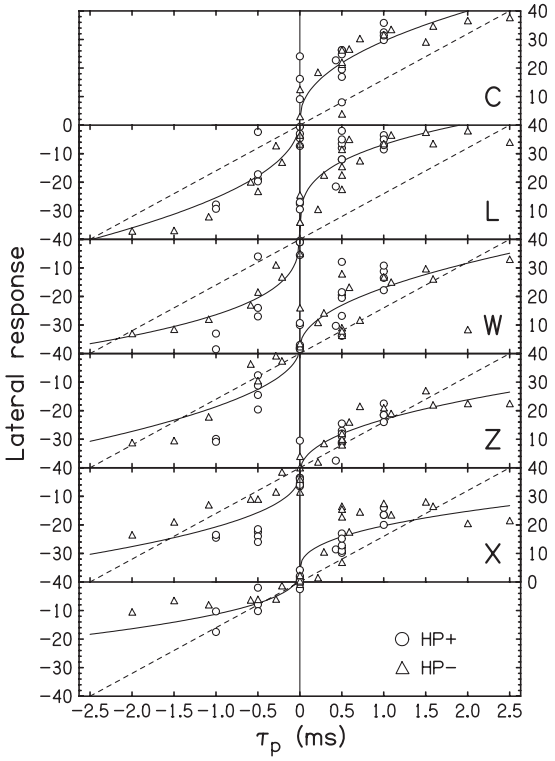


FIG. 8. Mean lateral responses for HP stimuli with linear-phase boundary, plotted against τ_p. Responses are limited to the range −40 to +40. Only responses with the same sign as τ_p are plotted. The dashed lines correspond to the first-order predictions. The solid curves are the best-fitting three-parameter compressive functions. All points with τ_p=0 correspond to lateral responses near zero, never near +40 or −40.

mum τ_p of 1000 μs. The HP− runs, summarized in Fig. 7, had a maximum τ_p of 2500 μs. The first-order predictions were based on a scaling that assumes a maximum of 2500 μs. Consequently, if listeners readjust their responses, one expects that responses in Fig. 6 should tend to be more

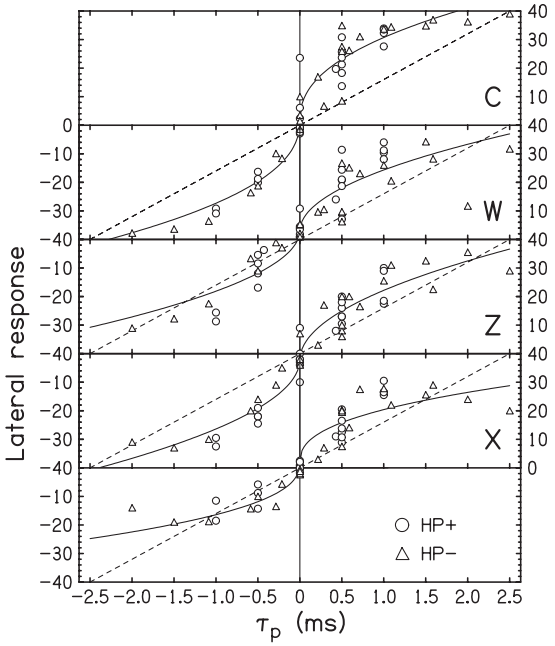


FIG. 9. Same as Fig. 8, except for stepped-phase boundary.

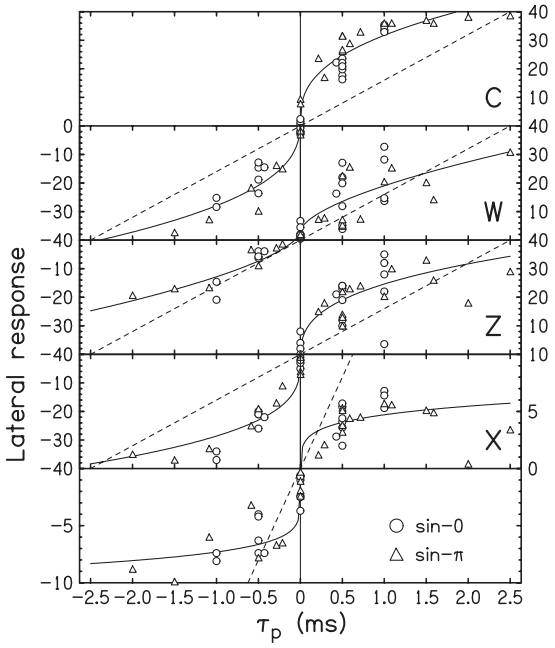


FIG. 10. Same as Figs. 8 and 9, except for sine tones. The vertical range for listener X is from −10 to +10, smaller than for other listeners.

lateral (larger magnitudes) than first-order predictions. Furthermore, because of the compression at large τ_p, one expects that compression should be especially evident in Fig. 7, where the large τ_p values should cause the observed dependence on τ_p to be weaker than first-order predictions. Both of these expected effects are evident in Figs. 6 and 7.

To test the idea that blocking trials on stimulus type affects the estimate of compression, the optimum parameters were recalculated fitting the compressive function to lateral response data for each type of phase boundary (i.e., HP+ or HP−) separately—similarly for the corresponding sine tones. For a given listener and a given stimulus, the q-parameter

TABLE III. Best-fitting parameters for the three-parameter compressive function. Units for a are μs^{-1}. By comparison, for the first-order model, a =0.016 μs^{-1}, b=0, and q=1. RMSE and correlation coefficient (r) for the best fit are also included. RMSE values can be directly compared with those in Table I.

Listener		C	L	W	X	Z	Average
Linear phase	a	1.07	3.27	0.66	0.91	0.84	
	b	2.0	3.4	2.2	4.2	−1.9	
	q	0.47	0.32	0.50	0.41	0.45	
	RMSE	6.98	6.22	7.20	4.99	4.90	6.06
	r	0.95	0.97	0.91	0.92	0.95	0.94
Stepped phase	a	1.39	⋯	0.63	1.08	0.72	
	b	1.7	⋯	3.1	2.0	−2.1	
	q	0.44	⋯	0.51	0.41	0.51	
	RMSE	5.72	⋯	6.43	4.77	4.98	5.47
	r	0.97	⋯	0.93	0.95	0.97	0.95
Sine tones	a	2.02	⋯	0.24	1.86	2.54	
	b	1.9	⋯	3.1	−1.3	−2.0	
	q	0.39	⋯	0.61	0.17	0.34	
	RMSE	4.29	⋯	5.75	1.72	5.07	4.21
	r	0.98	⋯	0.90	0.94	0.97	0.95

TABLE IV. Number of left (L) or right (R) judgments for 110 ambiguous stimuli. The last row shows the percentage of all responses on each side for each listener. Greatly different percentages for left and right ears are an indication of earedness.

	C		L		W		X		Z	
Stimulus	L	R	L	R	L	R	L	R	L	R
Linear	22	88	6	103	61	49	0	109	23	80
Stepped	18	91	···	···	63	47	0	109	32	65
Sine	9	101	···	···	83	20	36	61	62	38
Total	15%	85%	5%	94%	63%	35%	11%	85%	35%	55%

was smaller for HP− than for HP+ in 12 cases out of 13, indicating larger compressive effect for HP−, confirming the expectation. The one exception was listener Z for linear-phase boundary. A one-tailed paired *t*-test showed that this effect is significant at the 0.0005 level.

D. Earedness

The stepped-phase HP stimulus centered on an IPD of 180° is binaurally symmetric. A linear-phase HP stimulus centered on 180° is almost symmetric. There is no reason to expect the pitch image to be on the left or on the right. However, Experiments 1 and 2 showed that listeners lateralized ambiguous HP stimuli to one side or the other rather reliably. Experiment 3 showed that most listeners also have biases for ambiguous sine tones that are similar to their biases for HP stimuli.

These observations of inexplicable bias can be made quantitative for the 11 ambiguous conditions. There were four ambiguous conditions for HP+: 500 Hz with ITDs of ± 1000 μs and 1000 Hz with ITDs of ± 500 μs. There were seven ambiguous conditions for HP−: 1000 Hz with ITDs of ± 1000 μs, and all the five stimuli with ITDs of zero. There were ten repeated measures for each of the 11 ambiguous conditions. Thus, there are 110 points for ambiguous stimuli on each of the original scatter plots such as Figs. 3 and 4. Table IV shows the number of responses on left and right for each listener and each stimulus. Sometimes the numbers on left and right do not add up to 110 because the listener responded "zero" for a few points, and these were counted neither for the left nor for the right. The bottom row of Table IV shows the overall percentage on each side for each listener. It is clear that listeners had preference for one side or the other. In Table IV, among the 13 (left-right) pairs of numbers, there are eight cases in which the bias is strong (75% or more for a preferred side). In four other cases the bias is moderate and toward the same preferred side.

This tendency to hear an ambiguous stimulus on one side or the other conjures the concept of left-eared or right-eared listeners, analogous to left-handed or right-handed persons (Hartmann *et al.*, 2004). Table IV shows that listeners C, L, and X performed as right-eared listeners and that listener W appeared to be a left-eared listener. Listeners demonstrated a somewhat different level of earedness for HP stimuli and sine tones. Listener Z even became a left-eared listener for the sine tones, whereas he was right eared for the HP [but see the interaural level difference (ILD) discussion below].

Besides the earedness effect for the ambiguous stimuli, listeners C, L, X, and Z were so right eared that, for the nonambiguous stimuli of HP+ with a boundary frequency of 700 Hz and an ITD of +1000 μs, they preferentially chose the alias points on the right. There was no tendency to do the reverse when the ITD was −1000 μs (see Fig. 6). For these 700 Hz stimuli (± 1000 μs and both linear-phase and stepped-phase boundaries), the percentages of total responses on the right side were very high: 95% for C, 90% for L, 98% for X, and 88% for Z. By the symmetry of this pair of stimuli, the expected value would be 50%. Left-eared listener W did not show a strongly consistent bias for these stimuli. For all listeners, this bias with nonambiguous stimuli did not appear for sine tones.

The earedness effect for HP can also be dramatically demonstrated in an informal two-step experiment. First, a listener puts on headphones and hears the HP− stimulus (without added ITD). A compact disk, with this and other dichotic stimuli, is available (Bilsen and Raatgever, 2002). This HP− stimulus is ambiguous. The listener is asked to say whether the pitch image is on the left or right. Then the headphones are reversed. Usually, the listener discovers, to his or her surprise, that the pitch image is still lateralized on the same side of the head. Culling (Hartmann *et al.*, 2004) performed this brief experiment using 36 listeners. He found that 12 listeners heard the pitch on the right side and 14 listeners heard the pitch on the left side, independent of headphone orientation. Ten listeners were unsure about the lateralization for one or both orientations, and two listeners actually said that the pitch image moved from one side to the other when the headphones were reversed. There was no correlation between earedness and handedness.

Apparently there is a strong tendency for a given listener to lateralize HP− to a particular side, at least for a constant boundary frequency. In Culling's experiment, more than 75% of the listeners were either left eared or right eared. In our experiments, the earedness found for individual listeners in HP was largely maintained for sine tones with an IPD of 180°. However, earedness seemed to have a reduced influence for tones while centrality had increased influence.

The ear preference found in our experiments and in Culling's contrasts with the results of Hafter *et al.* (1969) who found that listeners lateralize the signal in an NoSπ stimulus about equally often to the left and right. The difference might be attributed to method. Hafter *et al.* (1969) presented only IPD of 180° throughout the entire experiment and varied signal-to-noise ratio as a parameter. As suggested

by the reduced earedness that we found for sine tones, part of the difference might arise from the difference between a HP stimulus and a MLD stimulus. In the end, the sidedness tendency seen in HP experiments seems strong enough to justify the concept of left-eared or right-eared listeners, necessarily leaving some room for the binaural analog to ambidextrous.

A trivial explanation for the strong left/right bias observed for ambiguous stimuli would attribute the effect to an audiometrically better ear and consequently an effective ILD. This explanation is plausible for ambiguous sine tones, for which lateralization depends on ILD. It is much less plausible for HPs. Although Grange and Trahiotis (1996) found that the lateral positions of HPs could be shifted somewhat by ILDs, informal observations by our listeners agreed with Raatgever and Bilsen (1986) that lateralization is very insensitive to ILDs, i.e., the HP seems to be a "time image." This distinction between sine tones and HP may be responsible for the anomalous reversal of earedness seen for listener Z when sine stimuli replaced HP stimuli. For HPs, it is more likely that the observed earedness reflects an asymmetry in midbrain processing.

VI. CONCLUSION

The lateral position of the pitch image was measured for two forms of HP, HP+ and HP−, using a direct psychophysical method. Experiments with five different boundary frequencies and five different frequency-independent ITDs showed that, for each listener, the experimental lateralizations of HPs correlated strongly with the lateralizations of corresponding sine tones. This result agrees with the predictions from the CAP model (Raatgever, 1980; Raatgever and Bilsen, 1986) and the RC model (Akeroyd and Summerfield, 2000). It suggests that a common localization mechanism applies to quite-different stimuli.

The experiments found even higher correlations between the lateral responses for HP made with the linear-phase and stepped-phase boundaries. The average correlation coefficient was 0.97. This result leads to the conclusion that the detailed information within the boundary region does not affect the lateral position of HP. The result is somewhat surprising because the stepped-phase boundary region can be lateralized on its own while the linear-phase boundary region cannot. The SPD model, presented in the Appendix, shows a similar insensitivity to the details of the phase boundary region and predicts that both forms of HP will be lateralized the same.

The experiments were motivated by a first-order hypothesis consisting of the SPD model and scaling assumptions. The SPD model predicts that lateralization of dichotic pitches is determined by the best-fit lag, τ_p, which corresponds to the peak of the cross-correlation function for these stimuli. The scaling assumptions are as follows: (1) lateralization judgments are linearly related to the best-fit lag values, τ_p, and (2) listeners apply the full range of lateralization responses to the full range of τ_p under all circumstances. The experimental results were approximately in agreement with that hypothesis in that the average lateral responses tended to be monotonically related to the predictions. However, detailed agreement could only be obtained by incorporating several modifications. Least important of the modifications was an offset, left or right, for each listener. Signs of the offsets were unrelated to a listener's earedness, left or right.

Much more important were individual scale factors and nonlinear compression in the relationship between τ_p and the estimates of lateral position. Incorporating those modifications reduced the rms discrepancy between predictions and data by a factor of 2. Compressive exponents for HP− tended to be about 0.5. Consequently, the hyperbolic dependence of lateral position on boundary frequency expected from the first-order predictions for HP− does not normally hold. The square root of that hyperbolic dependence holds much better. The observed importance of laterality compression indicates the value of the direct psychophysical method used in our experiments. Compression cannot be observed using an acoustical pointer if the pointer itself is laterally compressed. Other direct experiments show that ILDs, ITDs, and IPDs are all compressed perceptually (Yost, 1981; Zhang and Hartmann, 2006).

There was good evidence that the individual scale factors and compressive exponents depend on the experimental context—most likely on the range of τ_p occurring in an experimental block. Compressive exponents were smaller (greater compression) for HP− than for HP+ because of the greater range in τ_p for HP−.

For ambiguous stimuli, such as HP− and $\sin-\pi$ with no added ITD, the signal has a best-fit phase, ϕ_p, of 180° ($S\pi$). Listeners usually lateralized these binaurally symmetric stimuli consistently on one side. This observation led to the concept of earedness, i.e., left-eared and right-eared listeners.[2] Surveys by Hartmann *et al.* (2004) found no correlation between earedness and handedness. The phenomenon of earedness indicates an asymmetry in the binaural system. It may someday have clinical significance in midbrain neurology.

ACKNOWLEDGMENTS

This work was supported by the NIDCD under Grant No. DC 00181. Many of the experiments were performed at the Hearing Research Center in the Department of Biomedical Engineering at Boston University, partially supported by NIDCD Grant No. DC 00100. We are grateful to Dr. H. S. Colburn, Dr. F. A. Bilsen, and Dr. M. A. Akeroyd for useful discussions and to Dr. J. F. Culling for permission to report his otherwise unpublished data that helped us (and him) conclude that there are right-eared and left-eared listeners. Ms. Yongfang Zhu helped with statistical matters. Dr. Armin Kohlrausch and two anonymous reviewers provided useful comments on earlier versions of this report.

APPENDIX: THE SALIENT PHASE DENSITY MODEL

The SPD model is an intuitively plausible stimulus-based model for a first-order calculation of the lateralization of a dichotic pitch. Like all models of dichotic pitch, the SPD model begins by isolating a narrow band of frequencies as distinct from the background because of an unusual interaural phase property within the narrow band. This step is ex-

plicit in the RC model of Akeroyd and Summerfield (2000). In the SPD model, the bandwidth of the isolated region is not critical; the model assumes that it is determined by an auditory filter approximately centered on the phase boundary region. With N spectral components in the isolated region, the left-ear signal is

$$x_L(t) = \sum_{n=1}^{N} \cos(\omega_n t + \phi_{L,n}), \tag{A1}$$

where ω_n and $\phi_{L,n}$ are the angular frequency and phase of the nth component. The component amplitudes have all been set equal to 1.0 for simplicity because the results of the calculations below do not depend in any important way on the amplitudes. The right-ear signal $x_R(t)$ is similarly defined. With no loss of generality, it can be assumed that frequencies ω_n are separated by a constant frequency spacing, $\delta\omega = 2\pi/T_D$, where T_D is the stimulus duration.

The SPD model begins with the cross-correlation function between the two ears,

$$\gamma(\tau) = \int_0^{T_D} dt\, x_L(t)\, x_R(t+\tau), \tag{A2}$$

and for the signal as described,

$$\gamma(\tau) = \frac{1}{N}\sum_{n=1}^{N} \cos(\omega_n \tau + \Delta\phi_n), \tag{A3}$$

where τ is the lag and $\Delta\phi_n$ is the IPD for component n, $\Delta\phi_n = \phi_{R,n} - \phi_{L,n}$. This interaural phase function is the essential physical ingredient in a dichotic pitch stimulus.

It is convenient to write the component frequencies in terms of the boundary frequency, ω_c, so that $\omega_n = \omega_c + \delta\omega_n$. The boundary frequency is important because the cross-correlation function for a narrow noise band oscillates with frequency ω_c. Also, ω_c is the perceived pitch for a HP stimulus (Hartmann, 1993).

Because a dichotic pitch like the HP resembles a sine tone in noise, the SPD model assumes that the binaural system compares $\gamma(\tau)$ with the cross-correlation function for a sine tone, namely, with the template function $\cos(\omega_c\tau + \phi)$, where ϕ is the interaural phase of the template sine tone. The value of ϕ that leads to the best match with $\gamma(\tau)$, namely, ϕ_p, will correspond to the model prediction for the listener's lateralization of the pitch image. Specifically, the pitch image will be lateralized according to an interaural delay $\tau_p = \phi_p/\omega_c$.

Mathematically, the best value of ϕ in the overall least-squares errors sense is that value which maximizes the overlap integral,

$$F(\phi) = \frac{1}{T}\int_{-T}^{T} d\tau\, \gamma(\tau) \cos(\omega_c\tau + \phi), \tag{A4}$$

where T is the range over which the binaural system can register ITDs. Typically T is assumed to be between 1 and 4 ms.

The product of $\gamma(\tau)$ and $\cos(\omega_c\tau + \phi)$ includes frequency summation terms and frequency difference terms. For the summation terms the argument of the cosine function in Eq. (A4) has a range of approximately $2\omega_c \times 2T$. Because this range typically corresponds to at least several cycles of oscillation, the integral of the frequency summation terms includes cancellations that makes it smaller than the integral of the difference terms. Ignoring the summation terms leads to

$$F(\phi) = \frac{1}{2T}\int_{-T}^{T} d\tau \frac{1}{N}\sum_{n} \cos(\delta\omega_n\tau + \Delta\phi_n - \phi), \tag{A5}$$

or

$$F(\phi) = \frac{1}{N}\sum_{n} \frac{\sin(\delta\omega_n T)}{\delta\omega_n T} \cos(\Delta\phi_n - \phi). \tag{A6}$$

The sinc function above is a slowly varying prefactor that is nearly independent of component frequency n. For the smallest $\delta\omega_n$, namely, $\delta\omega_n = 0$, the sinc function is 1.0. For $\delta\omega_n$ equal to its largest value the function decreases only by a little. This decrease can be calculated assuming that the isolated region is determined by an auditory filter (critical band). Auditory filter bandwidths are about 16% of the center frequency ω_c and the product $\omega_c T$ is normally not greater than π—corresponding to the dashed lines in Figs. 4 and 7. Thus $\delta\omega_n T$ is never greater than 0.08π and the sinc function is never smaller than 0.99. If the bandwidth or the maximum ITD is doubled the sinc function only drops to 0.96. Therefore, to a reasonable approximation the sinc function is independent of frequency, and

$$F(\phi) = \frac{1}{N}\sum_{n} \cos(\Delta\phi_n - \phi). \tag{A7}$$

In this approximation, the frequency dependence has disappeared. What remains is only the IPD values themselves with no reference to their ordering as functions of frequency. Therefore, it is possible to replace the sum with an integral over the interaural phase density $\rho(\phi)$,

$$F(\phi) = \int_{-\infty}^{\infty} d\phi' \rho(\phi') \cos(\phi' - \phi). \tag{A8}$$

The infinite limits on the integral allow for a completely general representation of phase density as long as it is normalized to unity. The cosine function in the integral is periodic; consequently a 2π translation of any portion of the phase density has no effect on F.

Because function F involves only the distribution of interaural phases, the SPD model works only along this phase axis, where the interaural phases are considered to be lateralization influences at the level of the midbrain. Frequency resolution within the isolated band plays no role.

The above development, starting from Eq. (A4) and up to this point, has been purely mathematical, using quantitatively reasonable approximations. The next step in the model makes an assumption. It replaces the density of physical interaural phases by a density of *salient* interaural phases. Salient phases are lateralization influences that are different from the background. In fact, the HP exists only because these phases are different from the background. Therefore, the concept of salient phases is logically unavoidable. The value of ϕ which maximizes the overlap F in Eq. (A8) is the

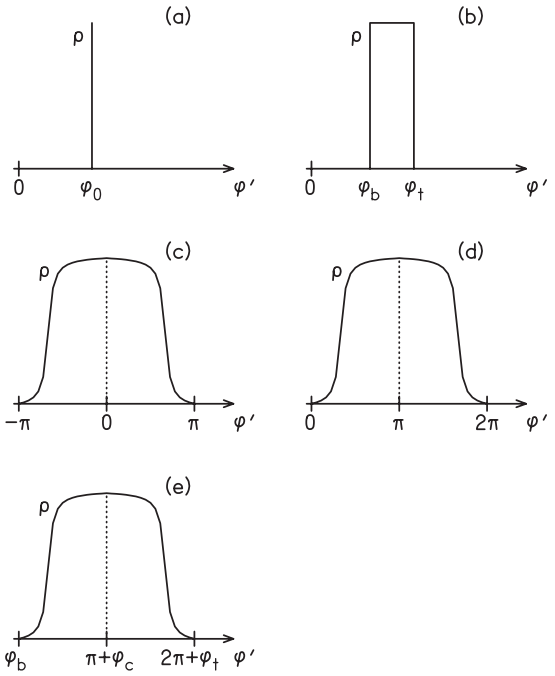


FIG. 11. Salient phase densities for (a) stepped-phase HP, (b) stepped-delay HP, (c) linear-phase HP+, (d) linear-phase HP−, and (e) linear-phase HP− with added ITD. Panels (a) and (b) are simply stimulus phase densities. Panels (c)–(e) make use of the salience principle. In panel (e) the phases ϕ_b, ϕ_c, and ϕ_t are equal to the added ITD multiplied by the angular frequencies of the boundary region bottom, center, and top.

best-fit phase lag, ϕ_p, and the best-fit lag, which predicts lateralization, is $\tau_p = \phi_p / \omega_c$. Several interesting results follow immediately.

Stepped phase. For a stepped-phase HP, SPD $\rho(\phi')$ equals $\delta(\phi' - \phi_o)$, where ϕ_o is the single, specific value of interaural phase within the boundary. This density function, from which the background phase has been eliminated, is shown in Fig. 11(a). Then

$$F(\phi) = \cos(\phi_o - \phi), \tag{A9}$$

which is maximized when $\phi = \phi_o$, leading to the prediction that the perceived location of the pitch image, namely, ϕ, is actually ϕ_o. This prediction for the lateralization of the pitch image is valid for any ϕ_o. However, if the value of ϕ_o is close to the interaural phase of the background then the HP may be weak or inaudible. Thus, a prediction for the lateralization does not guarantee the existence of the pitch effect. As applied in Experiment 2 of the body of this article, ϕ_o is 180° removed from the background interaural phase. Thus the pitch effect is strong, and the first-order prediction for the lateralization of the pitch image is 180° removed from the lateralization of the background—equivalent to the half-period rule.

Stepped delay. In the case of stepped delay, the boundary region is created by delaying the components in the boundary by a fixed delay time, t_d. Then $\rho(\phi)$ is a rectangular density,

$$\rho(\phi) = \frac{1}{\phi_t - \phi_b} \quad \text{for } \phi_b < \phi < \phi_t,$$

$$\rho(\phi) = 0 \quad \text{otherwise}. \tag{A10}$$

Here $\phi_b = \omega_b t_d$ and $\phi_t = \omega_t t_d$ represent the bottom and the top of the phase boundary region, respectively. This density function is shown in Fig. 11(b). Then,

$$F(\phi) = \frac{\sin(\phi_t - \phi_b)}{\phi_t - \phi_b} \cos(\phi - \phi_c), \tag{A11}$$

where ϕ_c is the interaural phase at the center of the boundary region. Function F is maximized if $\phi = \phi_c$, predicting that the pitch image is lateralized the same as a sine tone with interaural phase of $\phi_c = \omega_c t_d$, corresponding to an interaural delay of t_d. Akeroyd and Summerfield (2000) noted that the stepped-delay stimulus is an important test case because the RC model predicts that the lateralization is determined by the boundary region, in agreement with experiment, but the half-period rule does not make this prediction. The SPD model also correctly predicts that the lateralization is determined by the boundary region.

Linear phase. The linear-phase case is the first for which the salience principle of the SPD model becomes crucial. For linear-phase HP+ and HP−, the interaural phases in the boundary region extend over the entire 360° range, and the physical IPD density functions are rectangular over that range. An integral of the form of Eq. (A8) over such phase densities would lead to a $F(\phi)$ that is identically zero with no prediction for the lateralization.

When the density of IPDs is replaced by the SPD the *effective* range of interaural phase does not extend over 360° because those interaural phases that are close to the interaural phase of the background are associated with the background and not with the pitch image. Only those interaural phases associated with the pitch image are salient. Consequently the SPDs have forms sketched in Figs. 11(c) and 11(d). Each SPD is approximately rectangular except that it goes to zero near the phase corresponding to the background. Interaural phases near the background phase are not salient, and they do not contribute to the lateralization of the pitch image. The exact shape of the SPD depends on the listener. It is likely that different listeners have different tendencies to assign phases to the tonal image and the background. As will be seen below, important predictions from the model do not depend on the fine details of the densities or on the way that not-salient interaural phases are eliminated from the effective phase density.

The densities shown in Figs. 11(c) and 11(d) correspond to HP+ and HP− in the special case where there is no added ITD. The densities are centered on $\phi' = 0$ and $\phi' = \pi$, respectively. For these special symmetries, Eq. (A8) becomes

$$F(\phi) = \cos(\phi) \int_{-\infty}^{\infty} d\phi' \rho(\phi') \cos(\phi'). \tag{A12}$$

For HP+, the integral is positive because of the concentration of density around $\phi' = 0$. Therefore, F is maximized by choosing $\cos(\phi) = 1$, so that $\phi_p = 0$, indicating that HP+ is lateralized in the center of the head. For HP−, the integral is negative because of the concentration of density around $\phi' = \pi$. Therefore F is maximized by choosing $\cos(\phi) = -1$, i.e., $\phi_p = \pm\pi$, indicating that HP− is lateralized to the extreme

left or right. These predictions, made by maximizing F, do not depend on the details of the SPD, and they agree qualitatively with perceived lateralizations.

Random phase. Akeroyd and Summerfield (2000) introduced a form of HP in which the interaural phase is a random variable in the boundary region. From the point of view of the CAP model (Bilsen and Raatgever, 2000), which makes the normally harmless assumption of infinitely sharp frequency resolution, the random-phase stimulus looks peculiar because the CAP is infinitely ragged. Experimentally, however, the perceived lateralization for random phases agrees with the lateralization of HP+ and HP− for the linear-phase boundaries shown in Fig. 1. Informal experiments in our laboratory found that the lateralizations of random phases, linear phases, and stepped phases were all identical, depending only on the background phase. The idea that random phases should lead to identical lateralizations as the well-ordered linear or stepped phases is counterintuitive, and it led Akeroyd and Summerfield (2000) to propose the half-period rule which says that lateralization of any Huggins-type pitch, no matter how made, is half a period removed from the background.

For any particular choice of random-phase boundary regions, the SPD has no simple structure except that it becomes zero near the background phase. However, the ensemble average (Hartmann, 1998) SPD for random phases is identical to the SPD for HP+ or HP− as shown in Figs. 11(c) and 11(d), depending on the background phases. Therefore, in the average sense, the SPD model can successfully predict the unintuitive result that the lateralization for random phase is not different from lateralization for linear-phase HP. The reason is that, with the narrow-band approximation of Eq. (A8), the lateralization prediction does not depend on the size of the integral in Eq. (A12). It depends only on the *sign* of the integral. Possibly the expected variability of the lateralization depends on the size of the integral, but variability is beyond the scope of the present investigation. Furthermore, for any particular choice of random-phase boundary regions, the salience principle is enough to ensure that the pitch image will be lateralized away from the background, though how far away is not predictable.

HP+ and HP− with added ITD. When HP+ and HP− are created using linear phase or stepped phase and a constant ITD is added to the entire stimulus, as in the stimuli studied in this article, the symmetries that led to Eq. (A12) no longer apply. It is necessary to revert to Eq. (A8).

The added ITD has several effects. One effect is that there is no longer a unique background IPD. The background IPD depends on frequency, but it is not a rapidly varying function of frequency. The SPD model deals with this problem by the additional assumption that the background IPDs that are most important are those that come from frequencies in the neighborhood of the boundary region. This assumption is consistent with the notion that dichotic pitches are contrast effects; the existence of the binaural coherence edge pitch (Hartmann and McMillon, 2001) supports this notion. Because the added ITD is small, the choice of the frequency neighborhood of the boundary is not very critical. Even in the worst case, where the added ITD is 1 ms and the boundary frequency is 1 kHz, the phase changes by less than 60° over a critical band.

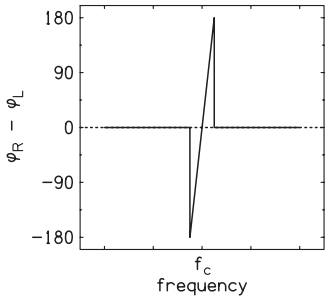


FIG. 12. The HP− stimulus with a boundary region that is shifted by 180°. This stimulus is an interesting test for the SPD model.

The other effect of the added ITD is to shift the densities shown in Figs. 11(c) and 11(d) along the ϕ' axis. An example is shown in Fig. 11(e) for HP−. With the assumption that the relevant approximate background phase is established by neighboring frequency regions, the effect of the shift in SPD is to cause an equal shift in the value of ϕ that maximizes $F(\phi)$. Therefore, for these particular stimuli, the SPD model predicts that the pitch image will be lateralized approximately at τ_p, equal to the lag corresponding to the peak in the cross-correlation function. The approximation is better for small added ITDs because the variation in background IPD is smaller. These predictions, together with the scaling assumptions, lead to the first-order estimates for pitch lateralization in Figs. 3, 4, 6, and 7 of the body of this article. The impossibility of determining a single precise background phase might have measurable consequences on the variability of localization responses—beyond the scope of the present work.

Discontinuous phase boundaries. The discontinuous interaural phase function shown in Fig. 12 is made by applying a large phase shift, such as 180°, to the boundary region for HP− from Fig. 1. This transformation changes the phase at the center of the boundary region by 180°. Although the shifted boundary looks very different, this transformation leaves the SPD function unchanged from Fig. 11(d). Therefore, this stimulus makes an interesting test case for the SPD model because the prediction of the model is unusual. The prediction is that the lateralization does not correspond to the center of the boundary region but instead it remains the same as for HP−. Unpublished experiments in our laboratory with the shifted phase boundary show that the lateralization is indeed unchanged, as predicted by the SPD model.

Final notes. As applied in the present article, the SPD model was not seriously tested. Other models, the CAP model and the RC model, behave similarly given the stimuli used, and they might equally well have served as part of the first-order predictions. Furthermore, the lateralization prediction by the SPD model, specifically τ_p, happens to agree with the center of the phase boundary region and with the peak of the interaural cross-correlation function for the phase boundary region for these stimuli.

To avoid the confusion caused by the above coincidences, it is worth remembering that according to the model,

τ_p corresponds to the interaural phase of a sine tone having a cross correlation that best agrees with the cross-correlation function for a spectral region that includes the phase boundary. The value of τ_p is determined by the entire cross-correlation function for that region, not just its peak. The distinction is likely to be important for more complicated dichotic stimuli.

Although the development of the SPD model begins with the cross-correlation function, the unique dependence on the interaural phase density alone is a property that emerges from the mathematics in this Appendix. The introduction of the salience principle assumes that this phase density is accessible to the binaural system so that it can be modified by downweighting interaural phases similar to the interaural phases of the background. One of the benefits of the salience principle is that the spectral region passed by the auditory filter does not need to be precisely defined. Contributions to the phase density that come from that part of the background which is included in the region are eliminated in the contrast enhancement operation described by the principle.

[1]Scatter plots like Figs. 3 and 4 for all listeners and for all experiments in this article are available in an auxiliary report (Zhang and Hartmann, 2008) or in the Ph.D. thesis by Zhang (2006).

[2]This article is not the first report of an ear preference for Huggins pitch location. Dr. M. A. Akeroyd, Dr. F. A. Bilsen, and Dr. J. F. Culling have all remarked on it informally.

Akeroyd, M. A., and Summerfield, A. Q. (**2000**). "The lateralization of simple dichotic pitches," J. Acoust. Soc. Am. **108**, 316–334.

Bilsen, F. A., and Raatgever, J. (**2000**). "On the dichotic pitch of simultaneously presented interaurally delayed white noises. Implications for binaural theory," J. Acoust. Soc. Am. **108**, 272–284.

Bilsen, F. A., and Raatgever, J. (**2001**). "On the compatibility of binaural models with dichotic pitch data," Proceedings of the 17th ICA, 4D.13.02, Rivista Italiana di Acustica, Rome, Italy (unpublished), Vol. **25**, pp. 168–171.

Bilsen, F. A., and Raatgever, J. (**2002**). "Demonstrations of dichotic pitch compact disc," Delft University of Technology, Delft, The Netherlands. This CD is available at fabilsen@xs4all.nl.

Cramer, E. M., and Huggins, W. H. (**1958**). "Creation of pitch through binaural interaction," J. Acoust. Soc. Am. **30**, 413–417.

Culling, J. F. (**1999**). "The existence region of Huggins pitch," Hear. Res. **127**, 143–148.

Culling, J. F. (**2000**). "Dichotic pitches as illusions of binaural unmasking III—The existence region of the Fourcin pitch," J. Acoust. Soc. Am. **107**, 2201–2208.

Culling, J. F., Marshall, D. H., and Summerfield, A. Q. (**1998a**). "Dichotic pitches as illusions of binaural unmasking II. The Fourcin pitch and the dichotic repetition pitch," J. Acoust. Soc. Am. **103**, 3527–3540.

Culling, J. F., Summerfield, A. Q., and Marshall, D. H. (**1998b**). "Dichotic pitches as illusions of binaural unmasking I. Huggins' pitch and the 'binaural edge pitch'," J. Acoust. Soc. Am. **103**, 3509–3526.

Durlach, N. I. (**1962**). "Note on the creation of pitch through binaural interaction," J. Acoust. Soc. Am. **34**, 1096–1099.

Durlach, N. I. (**1972**). "Binaural signal detection—equalization and cancellation theory," in *Foundations of Modern Auditory Theory*, edited by J. Tobias (Academic, New York), Vol. **2**, pp. 369–462.

Grange, A. N., and Trahiotis, C. (**1996**). "Lateral position of dichotic pitches can be substantially affected by interaural intensive differences," J. Acoust. Soc. Am. **100**, 1901–1904.

Hafter, E. R., Bourbon, W. T., Blocker, A. S., and Tucker, A. (**1969**). "A direct comparison between lateralization and detection under conditions of antiphasic masking," J. Acoust. Soc. Am. **46**, 1452–1457.

Hartmann, W. M. (**1993**). "On the origin of the enlarged melodic octave," J. Acoust. Soc. Am. **93**, 3400–3409.

Hartmann, W. M. (**1998**). *Signals, Sound, and Sensation* (Springer, New York), pp. 44–45.

Hartmann, W. M., and McMillon, C. D. (**2001**). "Binaural coherence edge pitch," J. Acoust. Soc. Am. **109**, 294–305.

Hartmann, W. M., and Zhang, P. X. (**2003**). "Binaural models and the strength of dichotic pitches," J. Acoust. Soc. Am. **114**, 3317–3326.

Hartmann, W. M., Zhang, P. X., and Culling, J. F. (**2004**). "Earedness: left-eared and right-eared listeners," J. Acoust. Soc. Am. **115**, 2534.

Jeffress, L. A. (**1948**). "A place theory of sound localization," J. Comp. Physiol. Psychol. **41**, 35–39.

Marks, L. (**1974**). *The New Psychophysics* (Academic, New York).

Raatgever, J. (**1980**). "On the binaural processing of stimuli with different interaural phase relations," thesis, Delft, The Netherlands.

Raatgever, J., and Bilsen, F. A. (**1977**). "Lateralization and dichotic pitch as a result of spectral pattern recognition," in *Psychophysics and Physiology of Hearing*, edited by E. F. Evans and J. P. Wilson (Academic, London), pp. 443–453.

Raatgever, J., and Bilsen, F. A. (**1986**). "A central spectrum theory of binaural processing. Evidence from dichotic pitch," J. Acoust. Soc. Am. **80**, 429–441.

Stern, R. M., Zeiberg, A. S., and Trahiotis, C. (**1988**). "Lateralization of complex binaural stimuli: A weighted-image model," J. Acoust. Soc. Am. **84**, 156–165.

Yost, W. A. (**1981**). "Lateral position of sinusoids presented with interaural intensive and temporal differences," J. Acoust. Soc. Am. **70**, 397–409.

Yost, W. A. (**1991**). "Thresholds for segregating narrow-band noise from broadband noise based on interaural phase and level differences," J. Acoust. Soc. Am. **89**, 838–844.

Zhang, P. X. (**2006**). "Detection and localization of virtual tones and virtual images," Ph.D. thesis, Michigan State University, East Lansing, MI.

Zhang, P. X., and Hartmann, W. M. (**2006**). "Lateralization of sine tones—Interaural time vs phase," J. Acoust. Soc. Am. **120**, 3471–3474.

Zhang, P. X., and Hartmann, W. M. (**2007**). "Salient phase density model for the lateralization of binaural pitches," J. Acoust. Soc. Am. **122**, 2968.

See EPAPS Document No. E-JASMAN-124–008811 for Figures 1 through 26 on scatter plots showing lateralization of Huggins pitch—supplement. For more information on EPAPS, see http://www.aip.org/pubservs/epaps.html.

Reducing the number of vocal fold mechanical tissue properties: Evaluation of the incompressibility and planar displacement assumptions

Douglas D. Cook[a)]
School of Mechanical Engineering, Purdue University, West Lafayette, Indiana 47907

Eric Nauman
School of Mechanical Engineering and Weldon School of Biomedical Engineering, Department of Basic Medical Science, Purdue University, West Lafayette, Indiana 47907

Luc Mongeau
Mechanical Engineering Department, McGill University, Montreal, Quebec H3A 2T5, Canada

(Received 6 November 2007; revised 29 August 2008; accepted 2 September 2008)

The incompressibility and planar displacement assumptions were used to reduce the number of independent tissue parameters required for the characterization of a structural model of the vocal folds. The influence of these simplifying assumptions on the vibratory properties of the model was investigated. The purpose was to provide estimates of the error introduced by these assumptions. The variability in human tissue properties was accounted for through systematic variation of several material parameters. The modal properties of a vocal fold structural model were computed with each assumption and, in turn, were relaxed to determine their respective effects. The results indicated that the incompressibility assumption introduces little error. Errors introduced by the planar displacement assumption were found to depend on the ratio of the longitudinal stiffness and the transverse stiffness. Criteria for determining the compatibility of tissue property values from independent studies are also presented.
© *2008 Acoustical Society of America.* [DOI: 10.1121/1.2996300]

PACS number(s): 43.70.Bk [BHS] Pages: 3888–3896

I. INTRODUCTION

Computational models are useful for the study of the mechanics of the vocal folds, in particular, their vibrations. Lumped element models (Flanagan and Landgraf, 1968; Ishizaka and Flanagan, 1972; Titze, 1988) capture the essential characteristics of vocal fold vibration during phonation, but they do not provide finer details associated with higher order vibration modes. Higher-order numerical modeling approaches, such as the finite element method, are better suited for a more detailed analysis and have been used for the study of biphonation (Tao *et al.*, 2006b), impact stresses (Gunter, 2003; Tao *et al.*, 2006a), and posturing (Hunter *et al.*, 2004). Such studies require an accurate description of the local deformation of the tissue. One obstacle to accurate numerical simulations of human phonation is a lack of complete consistent vocal fold tissue property data.

The vocal folds may be idealized as consisting of three distinct tissue regions: the mucosa (or cover), the vocal ligament, and the thyroarytenoid muscle. As a first approximation, these tissues are often assumed to be linearly elastic, with the mucosa approximated as isotropic (Chan and Titze, 1999), and the remaining tissues modeled as transversely isotropic (Berry and Titze, 1996; Hunter *et al.*, 2004). Three-layered linear elastic models would require 12 tissue parameters to unambiguously characterize tissue deformation. Only three of these parameters have been measured using human tissue. The shear modulus and Young's modulus of the vocal fold mucosa were measured by Chan and Titze (1999) and Zhang *et al.* (2006), respectively. Young's modulus of vocal fold ligament was measured by Min *et al.* (1995). These material parameters are summarized in Table I, with measured human properties highlighted in bold. Canine tissue measurements have also been performed (Kakita *et al.*, 1981; Alipour-Haghigni and Titze, 1985b; Hunter and Titze, 2007).

Unfortunately, several material parameters required for continuum models of vocal folds tissue have not been measured due to the limitations inherent to current testing methods. The model behavior is determined in part by the chosen values. Alipour-Haghighi and Titze (1985a) observed that vocal fold vibration patterns were "highly affected by material parameters." Unmeasured parameters must be estimated in order to obtain closure. Inaccurate estimates introduce errors in model predictions. A rigorous computationally expensive approach is to perform parametric variations (Berry and Titze, 1996) for each of the eight unknown parameters (E'_L, μ_L, μ'_L, ν'_L, E_{TA}, μ_{TA}, μ'_{TA}, and ν'_{TA}).

The purpose of the present study was to evaluate the consequences of two assumptions that can be used to reduce the number of independent parameters required for vocal fold models The first technique is the so-called planar displacement assumption which constrains vocal fold motion into coronal planes. This assumption is based on the obser-

[a)]Author to whom correspondence should be addressed. Electronic mail: ddcook@purdue.edu

 © 2008 Acoustical Society of America

TABLE I. Tissue types and independent parameters required for linear elastic descriptions. Measured human tissue parameters indicated in bold.

Tissue type	Independent parameters	Material type
Mucosa	$\boldsymbol{E_m}$, $\boldsymbol{\mu_m}$	Isotropic
Ligament	E_L, $\boldsymbol{E'_L}$, μ_L, μ'_L, ν'_L	Trans. isotropic
Thyroarytenoid	E_{TA}, E'_{TA}, μ_{TA}, μ'_{TA}, ν'_{TA}	Trans. isotropic

vation that vocal fold motion occurs primarily in the coronal plane, and that motion perpendicular to this plane is much less substantial (Baer, 1981; Saito *et al.*, 1985). The second assumption is that of incompressible (or nearly incompressible) tissue. This assumption is commonly applied to biological soft tissue, including the vocal folds (Pioletti and Rakotamanana, 2000; Berry and Titze, 1996; Hunter *et al.*, 2004). While both assumptions are common in vocal fold models, neither has been thoroughly evaluated to determine their effects on the dynamic properties of vocal fold models.

II. METHODOLOGY

A. Justification for linear analysis

In general, a nonlinear relationship exists between stress and strain for most vocal fold tissues (Min *et al.*, 1995; Chan and Titze, 1999; Zhang *et al.*, 2006). Nonlinear stress-strain relationships are essential when large deformations occur (such as during posturing). However, linear approximations may be used for small amplitude deformations, such as vibrations about a given posture. Nonlinear vocal fold models require additional unmeasured tissue parameters, thus increasing the uncertainty of model outputs. It has been observed that laryngeal muscles exhibit a nearly linear stress-strain relationship when active muscular tension is present (Hast, 1966; Titze, 2006). Linear tissue models were used for all tissues in this study.

Modal analysis is a standard method for extracting the natural vibratory frequencies of a structure (Meirovitch, 2000). This technique is based on linear approximations and produces modal frequencies and modal vibration patterns. Modal vibration patterns have been hypothesized to be important in the self-oscillation of the vocal folds (Zhang *et al.*, 2007; Berry *et al.*, 1994). Continuum structures have, in principle, an infinite number of resonance frequencies, although only a few modal frequencies contribute significantly to phonation (Berry *et al.*, 1994; Berry, 2001).

B. Planar displacement assumption

The motion of vocal fold vibration has been observed to be predominantly in coronal planes (Baer, 1981; Saito *et al.*, 1985). By examining excised canine larynges, (Berry *et al.*, 2001) quantified the anterior/posterior motion of canine vocal folds as one order of magnitude smaller than motion in the coronal plane. Numerical simulations have yielded similar observations (Rosa *et al.*, 2003). Based on such observations, the majority of computational vocal fold models have utilized the planar displacement assumption (Alipour-Haghigni *et al.*, 2000; Alipour-Haghigni and Titze, 1988; Berry *et al.*, 1994; Berry and Titze 1996; Tao *et al.*, 2006a; Tao and Jiang, 2006c).

A transversely isotropic material generally requires five independent parameters (E, E', υ', μ, and μ'—see Lekhnitskii, 1963). For either compressible or incompressible materials, the planar displacement assumption requires the value of υ^+ to be zero and that υ be less than unity, while υ' has no effect on the material response. This is because the contribution of υ' to the material response is increasingly diminished as E' becomes larger [see Eq. (3) below]. Poisson's ratios of a material under the planar displacement condition are

$$\nu^+ = 0, \tag{1}$$

$$\nu < 1. \tag{2}$$

The planar displacement assumption can be imposed in two ways. One approach is to remove the anterior/posterior degree of freedom from numerical simulations (Alipour-Haghighi and Titze, 1985a; Berry and Titze, 1996). When using the finite element method, this approach causes artificial constraint forces to arise (Cook *et al.*, 2001). The planar displacement may also be imposed by assuming an infinite longitudinal stiffness (Cook and Mongeau, 2007). While this approach does not require constraint forces, unusually high values of longitudinal stiffness are required.

For a linearly elastic material with transverse isotropy in the xz-plane, the stress-strain relations are expressed by Hooke's law:

$$\begin{bmatrix} \frac{1}{E} & -\frac{\nu'}{E'} & -\frac{\nu}{E} & 0 & 0 & 0 \\ -\frac{\nu^+}{E} & \frac{1}{E'} & -\frac{\nu^+}{E} & 0 & 0 & 0 \\ -\frac{\nu}{E} & -\frac{\nu'}{E'} & \frac{1}{E} & 0 & 0 & 0 \\ 0 & 0 & 0 & \frac{1}{\mu'} & 0 & 0 \\ 0 & 0 & 0 & 0 & \frac{1}{\mu'} & 0 \\ 0 & 0 & 0 & 0 & 0 & \frac{1}{\mu} \end{bmatrix} \begin{pmatrix} \sigma_{xx} \\ \sigma_{yy} \\ \sigma_{zz} \\ \sigma_{xy} \\ \sigma_{yz} \\ \sigma_{zx} \end{pmatrix} = \begin{pmatrix} \varepsilon_{xx} \\ \varepsilon_{yy} \\ \varepsilon_{zz} \\ \varepsilon_{xy} \\ \varepsilon_{yz} \\ \varepsilon_{zx} \end{pmatrix}. \tag{3}$$

Taking the limit as $E' \to \infty$ causes all terms with E' in the denominator to vanish. The condition of a symmetric compliance matrix (Lempriere, 1968) implies that υ^+ must also be zero. The resulting matrix has zeros in the second row and second column. Because the strain vector $\boldsymbol{\varepsilon} = \{0\ 1\ 0\ 0\ 0\ 0\}$ is in the null space of the resulting com-

pliance matrix, no anterior/posterior strains (ε_{yy}) can develop, regardless of imposed loads ($\boldsymbol{\sigma}$). This situation is equivalent to the planar displacement assumption. In practice, an infinitely large value of E' is not amenable to computational methods. However, an extremely large value of E' ($\sim 10^4$ times larger than E) was used in a previous study to demonstrate that this approach has the same effect as directly constraining anterior/posterior degrees of freedom (Cook and Mongeau, 2007). The validity of the planar displacement condition is examined in Sec. IV B.

C. Incompressibility assumption

The incompressibility assumption is commonly applied to biological soft tissue (Humphrey, 2002). Total incompressibility causes a singularity in the compliance matrix of Eq. (3). Thus, the material is usually modeled as "nearly incompressible," although the term "incompressible" is used in this paper for the sake of brevity. The incompressibility assumption has been justified based on the high water content of human tissue (Berry and Titze, 1996). This assumption has been applied to the vocal folds by Berry and Titze (1996), Rosa *et al.* (2003), Hunter *et al.*, (2004), and Decker and Thomson, (2007). The incompressibility assumption leads to a reduction in the number of independent parameters needed for analysis.

For isotropic materials, Poisson's ratio normally varies between 0 (completely compressible) and $\frac{1}{2}$ (totally incompressible). Values slightly less than $\frac{1}{2}$ are typically used to avoid singularities. If a material is assumed to be incompressible, Eq. (4) can be used to determine the shear modulus μ based on the measured values of Young's modulus E or vice versa. Thus, only one independent parameter is required.

$$\mu = \frac{E}{2(1+\nu)}. \tag{4}$$

A similar approach can be used for transversely isotropic materials. Utilizing the incompressibility condition and the symmetry of the compliance matrix, all three Poisson's ratios and the transverse shear modulus are expressed as functions of Young's moduli, E and E' (Itskov and Aksel, 2002):

$$\nu' = \frac{1}{2}, \tag{5}$$

$$\nu^{+} = \frac{E}{2E'}, \tag{6}$$

$$\nu = 1 - \frac{E}{2E'}, \tag{7}$$

and

$$\mu = \frac{EE'}{4E' - E}. \tag{8}$$

Thus, an incompressible, linearly elastic, transversely isotropic material is characterized by three independent material properties $\{E, E', \mu'\}$. The above equations correspond to total incompressibility and a singular compliance matrix will result. This problem may be avoided by using a nearly incompressible formulation which relies on one additional parameter, the bulk modulus κ (Itskov and Askel, 2002). For near incompressibility, the values of Poisson's ratios are weakly related to the choice of κ. Thus, κ is not considered as an independent parameter. The value for μ can be found by substituting Eq. (11) into Eq. (4), leading to

$$\nu' = \frac{1}{2} - \frac{E'}{6\kappa}, \tag{9}$$

$$\nu^{+} = \frac{E}{2E'} - \frac{E}{6\kappa}, \tag{10}$$

and

$$\nu = 1 - \frac{E}{2E'} - \frac{E}{6\kappa}. \tag{11}$$

There are very few direct measurements of Poisson's ratio of human tissue. There are no reported measurements of the compressibility of vocal fold tissues. Thus, Poisson's ratio values for vocal fold simulation have been typically estimated from *ad hoc* arguments. In previous studies, the following values have been assumed for both longitudinal and transverse Poisson's ratios (υ and υ'): {0, 0.3, 0.45, 0.66, 0.73, 0.76}. Values of $\upsilon = 0.9$ and $\upsilon' = 0.99$ have also been assumed. (Alipour-Haghigni *et al.*, 2000; Tao *et al.*, 2006a; Tao *et al.*, 2006b; Tao *et al.*, 2006c; Rosa *et al.*, 2003; Berry and Titze, 1996). The sensitivity of modal property predictions to this parameter has not often been addressed. Berry and Titze (1996) reported that the second modal frequency increased as Poisson's ratio increased, while the third mode decreased. The validity of the incompressibility assumption and its effects on the vibratory characteristics of the vocal folds are addressed in Sec. IV B.

D. Compatibility

Reported parameter values almost always correspond to different tissue samples. The selection of tissue parameters from independent studies may produce parameter sets that are mutually incompatible. For example, at zero strain, Zhang *et al.* (2006) reported Young's modulus of the mucosa to vary between 4 and 20 kPa. Chan and Titze (1999) reported the (zero strain) shear modulus of the vocal fold cover within the range between 10 and 1000 Pa. Selection of average values within those ranges, for example, $E_c = 10$ kPa and $\mu_c = 500$ Pa, would [by Eq. (4)] lead to a nonphysical value for Poisson's ratio ($\nu_c = 9$). The compatibility equations presented above can be used to avoid this situation. The incompressibility assumption ($\upsilon = 0.49$) in conjunction with Eq. (4) and the choice $E_c = 4$ kPa yield the value $\mu_c = 1340$ Pa. This value is reasonably close to the values reported by Chan and Titze (1999).

The compatibility conditions for an isotropic material are that $\nu < \frac{1}{2}$ and Eq. (4) is satisfied. For a transversely isotropic material, the conditions of a symmetric positive definite compliance matrix impose the following additional constraints on parameter values (see Lempriere, 1968):

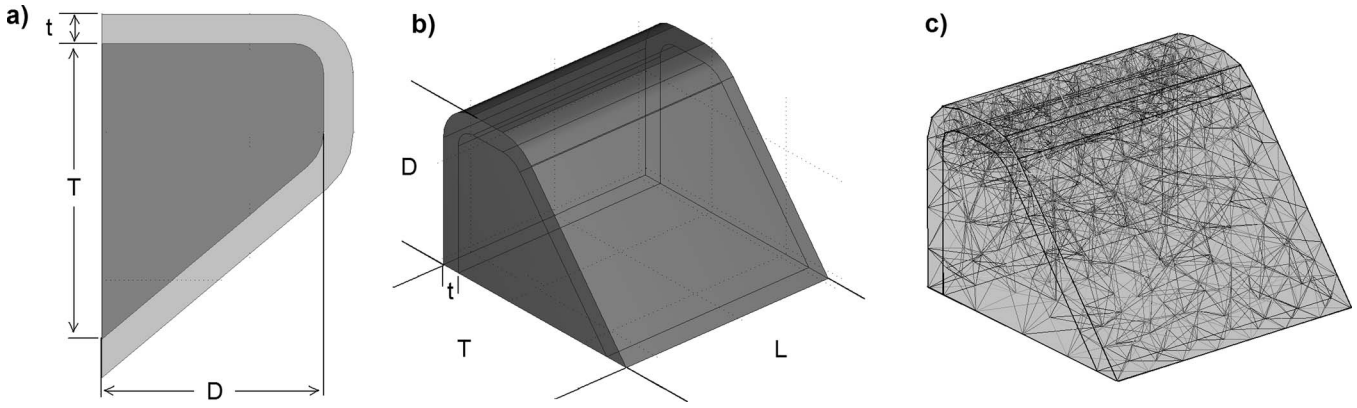


FIG. 1. Diagram of model geometry and mesh: (a) coronal cross section, (b) isotropic view, and (c) finite element mesh.

$$\nu < 1 - \nu'^2\left(\frac{2E}{E'}\right), \tag{12}$$

$$|\nu'| < \sqrt{\frac{E'}{E}}, \tag{13}$$

$$|\nu^+| < \sqrt{\frac{E}{E'}}, \tag{14}$$

and

$$\nu < 1. \tag{15}$$

These conditions can be used to verify that parameter values extracted from independent experimental studies are compatible with each other and do not violate fundamental assumptions.

III. NUMERICAL PROCEDURES

To quantify the errors introduced by the two assumptions discussed above, the incompressibility and planar displacement assumptions were applied to a structural model of the vocal folds. Modal analysis was used to compute the structure's resonant mode shapes and frequencies in the absence of fluid loading. The incompressibility and planar displacement assumptions were then relaxed in turn by allowing varying amounts of compressibility and anterior/posterior motion. The effects of these assumptions were determined by comparison between the relaxed and original cases.

The vocal fold structure was idealized as having a body and a cover, similar to the body-cover model of Titze (1988). The body-cover idealization considers the vocal ligament to be included in the cover region and reduces the number of parameters required to define the model. Since only the longitudinal stiffness of the vocal ligament has been measured experimentally, the remaining ligament parameters would necessarily be estimations, thus introducing additional uncertainty into the current study.

The model consisted of one vocal fold assumed to be symmetric in the anterior/posterior direction. All materials were assumed to be linearly elastic. The body was represented by a transversely isotropic material. The cover was approximated by an isotropic material. The M5 geometry with an included angle of 0° (Scherer *et al.*, 2001) was used to define the vocal fold profile. Geometric parameters are shown in Fig. 1 and Table II. A length of 12 mm was chosen according to Berry and Titze (1996) and Cook and Mongeau (2007). The cover was formed by offsetting the standard M5 geometry by a constant distance $t=0.8$ mm from the body (Titze, 2006).

The anterior, posterior, and lateral faces were fixed (zero displacement boundary conditions), while the remaining faces were free. The structure was meshed with approximately 3000 quadratic finite elements, for a total of approximately 15 000 degrees of freedom [see Fig. 1(c)]. This mesh was found to yield a mesh-converged solution since higher density meshes (~20 000 degrees of freedom) produced identical results. Parametric modal analysis of the body-cover model was performed using COMSOL version 3.3 with MATLAB. Parametric variation of material parameters was accomplished via control loops executed in MATLAB. Model verification involved comparing modal analysis results predicted by COMSOL with those predicted by the commercial finite element code ADINA. Modal frequency differences were less than 2.5%, and similar mode shapes were predicted by both codes.

To relate unknown tissue properties to those previously measured, all tissues were first assumed to be incompressible (as in Sec. II C). Accordingly, Poisson's ratio of the cover was $\nu_c=0.499$. Young's modulus of the cover was chosen to be $E_c=4$ kPa (Zhang *et al.*, 2006). Longitudinal Young's modulus of the body was specified as $E_b'=28$ kPa (Titze, 2006). Poisson's ratios and the shear modulus of the body were calculated according to equations of Sec. II. Based on estimations used previously, the values $E_b=10$ kPa and $\mu_c'=10$ kPa were chosen (Berry and Titze, 1996; Cook and Mongeau, 2007). Equation (4) was used to determine the transverse shear modulus of the body. The resulting set of material properties is summarized in Table III.

TABLE II. Geometric parameters of the body-cover model of Fig. 1.

Parameter	Symbol	Value
Length	L	12 mm
Depth	D	7.5 mm
Thickness	T	10 mm
Cover thickness	t	0.8 mm

TABLE III. Nominal material properties of the body-cover model. Measured parameters indicated in bold.

Property	Incompressibility	Incompressibility and planar displacement
E_c	4 kPa	4 kPa
μ_c'	1340 kPa	1340 kPa
ν_c	0.499	0.499
E_b'	28 kPa (canine)	∞
E_b	10 kPa[a]	10 kPa[a]
μ_b'	10 kPa[a]	10 kPa[a]
μ_b	2.7 kPa[a]	2.5 kPa
ν_b	0.82[a]	0.999

[a]Estimated or dependent on estimated properties.

The number of undetermined parameters was then further reduced by combining the incompressibility assumption with the planar displacement assumption. The techniques of Sec. II were used to eliminate the dependence of Poisson's ratios on transverse stiffness (E_b). The assumption of planar displacement coupled with incompressibility thus reduced the number of unknown material properties from 5 to 2. The resulting parameter values are summarized in the final column of Table III.

IV. MODAL ANALYSIS RESULTS

A. Evaluation of the incompressibility assumption

The errors introduced by the incompressibility assumption were determined by varying Poisson's ratios of each tissue region independently as well as simultaneously. The results are presented in terms of the compressibility factor, which is defined here as the ratio between compressible (variable) and incompressible (fixed) Poisson's ratios. For the isotropic cover layer, Poisson's ratio was varied between 0.499 (incompressible) and 0.25. For the body layer, the bulk modulus was varied according to Eqs. (9)–(11) such that the compressibility factor was varied between unity (incompressible) and 0.5. For each set of tissue parameters, modal analysis produced the first six modes of vibration and their associated frequencies. The modal frequencies of all computed cases were normalized by dividing each modal frequency by the corresponding value obtained in the incompressible case. Figures 2(a)–2(c) show the normalized modal frequencies as functions of the compressibility of the cover, the compressibility of the body, and the compressibility of both layers.

The vocal fold model was observed to be least sensitive to changes in cover compressibility. Each modal frequency changed by less than 3% for a 50% reduction in Poisson's ratio of the cover. The model was more sensitive to changes in the compressibility of the body. Each modal frequency changed by less than 5% for a 50% reduction in the compressibility of the body. These results are influenced by the fact that the compressibility of only one tissue was modified while the remaining tissue was held as incompressible. When the compressibility of both body and cover was varied simultaneously, the maximum change in modal frequency was approximately 6% for a 50% reduction in compressibility. These changes are relatively small and would likely be negligible in most applications.

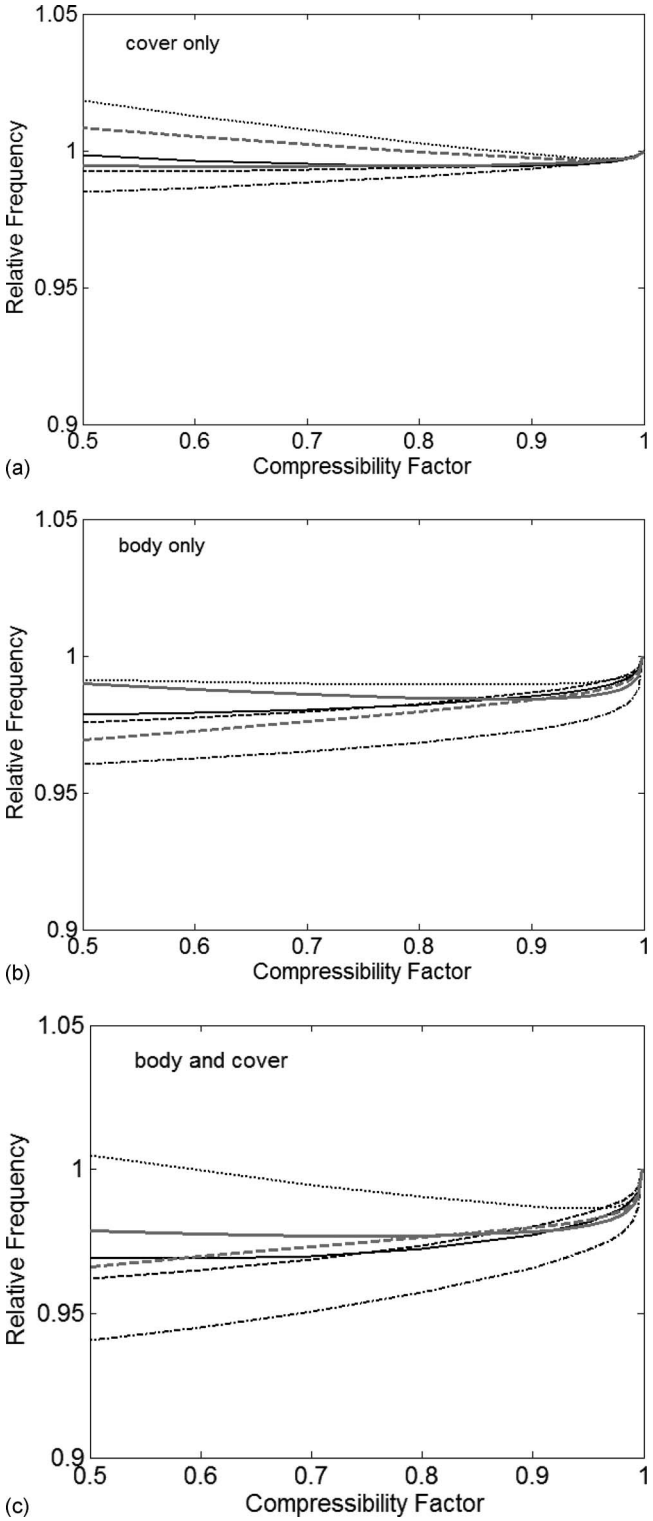


FIG. 2. Normalized modal frequencies as a function of compressibility and tissue region: (a) cover only, (b) body only, and (c) body and cover. Each curve normalized with the incompressible value as unity. (——) mode 1; (---) mode 2; (-·-·-) mode 3; (·····) mode 4; (—·—) mode 5; (---) mode 6.

Wide variations in human tissue properties have been reported due to the male/female differences, the age difference, and the experimental variability (Chan and Titze, 1999;

TABLE IV. Parameter substitutions for parametric variation.

Parameter values (kPa)		
E_c	(E_b, E_b') pairs	μ_b'
1	(0.57, 0.57)	1
50	(5.7, 5.7)	100
100	(4.5, 90)	
200	(9,90)	
	(90,90)	

Hammond *et al.*, 2000; Zhang *et al.*, 2006). To address this variability, the material properties of the above model were varied over the reported and estimated ranges of human tissue property values, listed in Table IV. For each series, one of the nominal model parameters of Table III was replaced by its corresponding value from Table IV. For each such replacement, the compressibility factor was assigned values of 0.50, 0.90, and 0.99. Modal analysis was performed for each unique set of tissue parameters. Six vibratory modes were calculated for each case. The mean and standard deviations of the differences between the results obtained using incompressible and compressible assumptions are presented in Table V.

The mean difference between incompressible and 50% compressible tissues ranged between −4% and −6%. Greenleaf *et al.* (2003) reported the incompressibility levels between 98% and 99.8% for soft biological tissue. For a conservative estimate of 90% compressibility, the mean difference ranged between −3% and −5%, and the average difference for all six vibratory modes was −4% with a standard deviation of 3%. The actual variability would likely be considerably lower than these values.

B. Evaluation of the planar displacement assumption

The assumption of incompressibility was again used to reduce the number of undetermined parameters. The longitudinal stiffness E_b' was varied from $E_b'=10$ kPa (isotropy) to $E_b'=100$ MPa (planar displacement). All other parameters were either held constant or varied according to the equations of Sec. II (see Table III for resulting values).

First, the body alone was subjected to the planar displacement assumption, as described in the preceding paragraph. The cover was assumed to be incompressible, with nominal tissue parameters. The resulting modal frequencies

TABLE V. Discrepancies between incompressibility and partial compressibility for two values of compressibility factor.

	Compressibility factor			
	0.5		0.9	
Mode	Mean diff	Std dev.	Mean diff	Std dev.
1	−5%	3%	−4%	2%
2	−4%	4%	−3%	2%
3	−5%	4%	−4%	1%
4	−6%	5%	−5%	3%
5	−5%	5%	−4%	3%
6	−5%	5%	−5%	3%
All modes	−5%	5%	−4%	3%

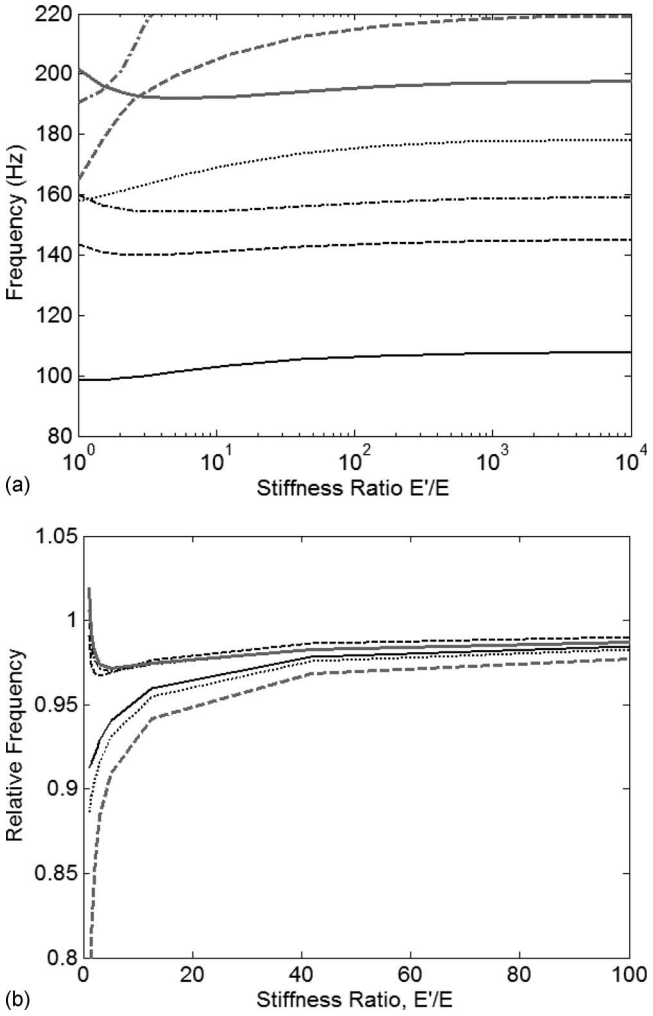


FIG. 3. Planar displacement condition imposed in the body layer only: (a) modal frequencies as a function of stiffness ratio; (b) normalized modal frequencies with the planar displacement value as unity (mode 7 omitted). (——) mode 1; (---) mode 2; (-·-·-) mode 3; (·····) mode 4; (—) mode 5; (---) mode 6; (-·-·-) mode 7.

are shown in Fig. 3(a) as functions of longitudinal to transverse stiffness ratio. Very little variation was observed for stiffness ratio values greater than 100. The exception was the modal frequency of the seventh mode, observed at 190 Hz for a stiffness ratio of 1, but rising above 200 Hz for a stiffness ratio of 2. The seventh mode represents the lowest mode containing more than a single half-wavelength in the anterior/posterior direction and exhibited primarily longitudinal motion. The behavior of this mode suggests that the planar displacement condition may have undesirable effects on modes containing two or more half-wavelengths in the anterior/posterior direction since such modes are particularly sensitive to the longitudinal stiffness.

As with previous results, the modal frequencies of Fig. 3(a) were normalized by dividing each modal frequency by the corresponding prediction for planar displacement. Relative values are plotted in Fig. 3(b). For stiffness ratios greater than 10, the maximum relative difference introduced by the planar displacement assumption was less than 10%. Differences were observed to consistently decrease with increasing stiffness ratio. The maximum relative difference was less

TABLE VI. Influence of stiffness ratio on the relative differences between constrained and unconstrained modal frequencies.

	Stiffness ratio			
All modes	1	5	30	100
Mean difference	−9.0%	−6.7%	−4.0%	−2.3%
Std deviation	11.8%	6.1%	3.6%	2.2%

than 5% for stiffness ratios greater than 30. This is consistent with previous results obtained using similar methods but a different structural model (Cook and Mongeau, 2007). The modal frequencies obtained for a stiffness ratio of 10^4 were found to differ by less than 1% from the frequencies obtained by eliminating the anterior/posterior degree of freedom for every node in the body layer (absolute planar displacement).

The planar displacement condition was also applied to the body and cover simultaneously by eliminating the anterior/posterior degree of freedom of every node in the computational model. In comparison with the results of Fig. 3, constraint of the entire structure increased modal frequencies by an average of 3%. Interestingly, constraint of the cover alone had nearly the same effect on modal frequencies as the constraint of the body alone. Constraint of either tissue region raised modal frequencies above the incompressible case by approximately 8%, and constraint of both regions raised modal frequencies by approximately 10%.

To account for human variability and experimental measurement errors, the independent parameters E_c, E_b, and μ_b' were varied over wide ranges to determine the general applicability of the planar displacement assumption. The property ranges were the same as those given in Table IV, but E_b' values were controlled through the stiffness ratio. Since the planar displacement assumption does not reduce the number of independent parameters of the cover, only the stiffness ratio of the body was modified. For each unique parameter set, the stiffness ratio took on values (1,5, 30, 100, 10 000, 1 000 00).

As observed in Fig. 3, the variations introduced by the planar displacement assumption depend on the stiffness ratio. For stiffness ratios greater than 5, the relative difference decreased monotonically as a function of stiffness ratio. Table VI shows the mean and standard deviations of the computed differences for the first six modal frequencies. The planar displacement assumption was found to yield reasonably accurate results for stiffness ratio values greater or equal to 30.

V. DISCUSSION AND CONCLUSIONS

Two strategies may be followed to reduce the number of independent material properties. The first is to assume an infinite (or practically speaking, an extremely high) value for the longitudinal stiffness. This approach effectively forces v^+ to zero and eliminates the influence of v'. Adjustment of v then allows control of the material's level of compressibility. The second is to impose the condition of incompressibility. This allows Poisson's ratios to be determined as functions of the longitudinal and transverse stiffness parameters. These assumptions can also be applied simultaneously for a further reduction in the number of independent parameters. Table VII provides a summary of the above methods, identifying the independent material properties for each tissue type, and compares the reduced formulation to the 12 independent parameters required for a three-layer model of the vocal folds.

The creation of computational vocal fold models often utilizes measured tissue parameter values which may be referred to as "uncorrelated" (i.e., each individual tissue property was obtained from a unique tissue sample). Natural variation between samples may therefore create a situation in which the measured values violate compatibility requirements. This undesirable situation may be avoided by ensuring that the chosen values obey the analytic relations of Sec. II.

The discrepancies introduced by both assumptions were systematically investigated using a body-cover model of the vocal folds. The incompressibility assumption was found to be appropriate over a wide range of material properties. An upper limit for the mean error introduced through the incompressibility assumption was proposed. The planar displacement assumption introduced only minor errors for stiffness ratio values greater than 30. Significant errors (i.e., more than 10%) may be introduced for lower values of the stiffness ratio.

The present study highlights the need for additional measurements of the material constants of vocal fold tissues. Young's modulus in the direction perpendicular to the fiber direction E appears as an independent parameter in all of the above cases. Unfortunately, this parameter has yet to be measured for either the thyroarytenoid muscle or the vocal ligament.

Both the incompressibility and the planar displacement assumptions significantly reduce (and in some cases eliminate) the role of Poisson's ratios. Thus, experimental data for these constants may be less important than for the other more influential parameters such as E, μ, and μ'. The above as-

TABLE VII. Summary of parameter reduction methods (measured properties indicated in bold).

	Independent parameters			
Assumption	Mucosa (isotropic)	Ligament (transversely isotropic)	Muscle (transversely isotropic)	No. of independent parameters for a three-layer model
None	$\boldsymbol{E_m}$, $\boldsymbol{\mu_m}$	E_L, $\boldsymbol{E_L'}$, μ_L, μ_L', ν_L'	E_{TA}, E_{TA}', μ_{TA}, μ_{TA}', ν_{TA}'	12
Planar displacement	$\boldsymbol{E_m}$, $\boldsymbol{\mu_m}$	E_L, μ_L', ν_L	E_{TA}, μ_{TA}', ν_{TA}	8
Incompressibility	$\boldsymbol{E_m}$ or $\boldsymbol{\mu_m}$	E_L, $\boldsymbol{E_L'}$, μ_L'	E_{TA}, E_{TA}', μ_{TA}'	7
Planar disp. and incompressibility	$\boldsymbol{E_m}$ or $\boldsymbol{\mu_m}$	E_L, μ_L'	E_{TA}, μ_{TA}'	5

sumptions can be implemented in numerical simulations with relative ease. In practice, finite element programs require users to enter nine parameters (five of which are independent) for transversely isotropic materials and two parameters for isotropic materials. The above relations can be used to calculate values for these constants as functions of the selected independent parameters. Furthermore, these methods ensure that the chosen values will be compatible with each other. Thus, by relating unmeasured parameters to measured parameters through a set of physiologically realistic assumptions and thermodynamic constraints, this approach reduces the number of independent parameters, decreases the cost of parametric studies, and produces models that are more directly based upon measured tissue properties.

ACKNOWLEDGMENTS

This study was supported by Grant Nos. R01 005788 and R01 008290 from the National Institute on Deafness and Other Communication Disorders, as well as by the Bilsland Strategic Initiatives Fellowship (Purdue University). The authors would like to thanks the Associate Editor and reviewers for their suggestions and assistance.

NOMENCLATURE

L = length
D = depth
T = thickness
t = cover thickness
E = Young's modulus (stiffness) in general or in the transverse plane
E' = Young's modulus (stiffness) in the longitudinal direction
$E_M E_c$ = Young's modulus (stiffness) of the cover and mucosa, respectively
$E_L E_{\mathrm{TA}} E_b$ = transverse Young's modulus (stiffness) of the ligament, thyroarytenoid muscle, and body, respectively
$E'_L E'_{\mathrm{TA}} E'_b$ = longitudinal Young's modulus (stiffness) of the ligament, thyroarytenoid muscle, and body, respectively
μ = shear modulus
μ' = shear modulus in one of two longitudinal planes
$\mu_M \mu_c$ = shear modulus of the cover and mucosa, respectively
$\mu_L \mu_{\mathrm{TA}} \mu_b$ = transverse shear modulus of the ligament, thyroarytenoid muscle, and body, respectively
$\mu'_L \mu'_{\mathrm{TA}} \mu'_b$ = longitudinal shear modulus of the ligament, thyroarytenoid muscle, and body, respectively
υ = Poisson's ratio (in a plane of symmetry)
υ_{ij} = Poisson's ratio: passive strain in the i-direction induced by applied strain in the j-direction (note: some texts reverse these indices)
υ' = applied longitudinal Poisson's ratio: passive strain in the transverse direction induced by applied strain in the longitudinal direction
υ^+ = passive longitudinal Poisson's ratio: passive strain in the longitudinal direction induced by applied strain in the transverse direction
$\upsilon'_L \upsilon'_{\mathrm{TA}}$ = applied transverse Poisson's ratio of the ligament and thyroarytenoid muscle, respectively
$\upsilon_c \upsilon_b$ = Poisson's ratio of the cover and transverse Poisson's ratio of the body
κ = bulk modulus

Alipour-Haghighi, F., and Titze, I. R. (**1985a**). "Simulation of particle trajectories of vocal fold tissue during phonation," in *Vocal Fold Phyisiology: Biomechanics, Acoustics, and Phonatory Control*, edited by I. Titze and R. Scherer (Denver Center for the Performing Arts, Denver, CO).

Alipour-Haghighi, F., and Titze, I. R. (**1985b**). "Viscoelastic modeling of canine vocalis muscle in relaxation," J. Acoust. Soc. Am. **78**, 1939–1943.

Alipour, F., and Titze, I. R. (**1988**) "A finite-element simulation of vocal fold vibrations," in Proceedings of the 14th Annual Northeast Bioengineering Conference, edited by LaCourse (IEEE, New York), Catalog No.88-CH2666-6.

Alipour, F., Berry, D., and Titze, I. R. (**2000**). "A finite-element model of vocal-fold vibration," J. Acoust. Soc. Am. **108**, 3003–3012.

Baer, T. (**1981**). "Investigation of the phonatory mechanism," *Proceeding of the Conference on the Assessment of Vocal Pathology, ASHA Reports. 11*, edited by C. L. Ludlow and M. O. C. Hart (ASHAA, Rockville, MD), pp. 38–46.

Berry, D. A., Herzel, H., Titze, I. R., and Krischer, K. (**1994**). "Interpretation of biomechanical simulations of normal and chaotic vocal fold oscillations with empirical eigenfunctions," J. Acoust. Soc. Am. **95**, 3595–3604.

Berry, D. A., and Titze, I. R. (**1996**). "Normal modes in a continuum model of vocal fold tissues," J. Acoust. Soc. Am. **100**, 3345–3354.

Berry, D. A. (**2001**). "Mechanisms of modal and nonmodal phonation," J. Phonetics **29**, 431–450.

Berry, D. A., Montequin, D. W., and Tayama, N. (**2001**). "High-speed digital imaging of the medial surface of the vocal folds," J. Acoust. Soc. Am. **110**, 2539–2547.

Chan, R. W., and Titze, I. R. (**1999**). "Viscoelastic shear properties of human vocal fold mucosa: Measurement methodology and empirical results," J. Acoust. Soc. Am. **106**, 2008.

Cook, R. D., Malkus, D. S., Plesha, M. E., and Witt, R. J. (**2001**). *Concepts and Applications of Finite Element Analysis*, 4th ed. (Wiley, New York), p. 492.

Cook, D. D., and Mongeau, L. (**2007**). "Sensitivity of a continuum vocal fold model to geometric parameters, constraints, and boundary conditions," J. Acoust. Soc. Am. **121**, 2247–2253.

Decker, G., and Thomson, S. (**2007**) "Computational simulations of vocal fold vibration: Bernoulli versus Navier–Stokes," J. Voice **21**, 273–284.

Flanagan, J. L., and Landgraf, L. L. (**1968**). "Self-oscillating source for vocal tract synthesizers," IEEE Trans. Audio Electroacoust. **AU-16**, 57–64.

Greenleaf, J. F., Fatemi, M., and Insana, M. (**2003**). "Selected methods for imaging elastic properties of biological tissues," Annu. Rev. Biomed. Eng. **5**, 57–78.

Gunter, H. (**2003**). "A mechanical model of vocal-fold collision with high spatial and temporal resolution," J. Acoust. Soc. Am. **113**, 994–1000.

Hammond, T. H., Gray, S. D., and Butler, J. E. (**2000**). "Age- and gender-related collagen distribution in human vocal folds," Ann. Otol. Rhinol. Laryngol. **109**, 913–920.

Hast, M. H. (**1966**) "Mechanical properties of the cricothyroid muscle," Laryngoscope **76**, 537–548.

Humphrey, J. D. (**2002**). *Cardiovascular Solid Mechanics, Cells, Tissues, and Organs* (Springer-Verlag, New York), p. 89.

Hunter, E. J., Titze, I. R., and Alipour-Haghigni, F. (**2004**). "A three-dimensional model of vocal fold abduction/adduction," J. Acoust. Soc. Am. **115**, 1747–1759.

Hunter, E. J., and Titze, I. R. (**2007**). "Refinements in modeling the passive properties of laryngeal soft tissue," J. Appl. Phys. **103**, 206–219.

Ishizaka, K., and Flanagan, J. L. (**1972**). "Synthesis of voiced sounds from a two-mass model of the vocal cords," Bell Syst. Tech. J. **51**, 1233–1267.

Itskov, M., and Aksel, N. (**2002**). "Elastic constants and their admissible values for incompressible and slightly compressible anisotropic materi-

als," Acta Mech. **157**, 81–96.
Kakita, Y., Hirano, M., and Ohmaru, K. (**1981**). "Physical properties of the vocal fold tissue," in *Vocal Fold Physiology*, edited by K. Stevens and M. Hirano (University of Tokyo, Tokyo, Japan).
Lekhnitskii, S. G. (**1963**). *Theory of Elasticity of an Anisotropic Body* (Holden-Day, San Francisco), p. 25.
Lempriere, B. M. (**1968**). "Poisson's ratio in orthotropic materials," Am. Inst. of Aero. and Astro. **6**, 2226.
Meirovitch, L. (**2000**). *Principles and Techniques of Vibrations* (Prentice-Hall, Upper Saddle River, NJ), pp. 469–485.
Min, Y. B., Titze, I. R., and Alipour-Haghigni, F. (**1995**). "Stress-strain response of the human vocal ligament," Ann. Otol. Rhinol. Laryngol. **104**, 563–569.
Pioletti, E. P., and Rakotamanana, L. R. (**2000**). "Non-linear viscoelastic laws for soft biological tissues," Eur. J. Mech. A/Solids **19**, 749–759.
Rosa, M. O., Pereira, J. C., Grellet, M., and Alwan, A. (**2003**). "A contribution to simulating a three-dimensional larynx model using the finite element method," J. Acoust. Soc. Am. **114**, 2893–2905.
Saito, S., Fukuda, H., and Kitahira, S. (**1985**). "Pellet tracking in the vocal fold while phonating: experimental study using canine larynges with muscle activity," in *Vocal Fold Physiology* (Denver Center for the Performing Arts, Denver).
Scherer, R. C., Shinwari, D., De Witt, K. J., Zhang, C., Kucinschi, B. R., and Afjeh, A. A. (**2001**). "Intraglottal pressure profiles for a symmetric and oblique glottis with a divergence angle of 10 degrees," J. Acoust. Soc. Am. **109**, 1616–1630.
Tao, C., Jiang, J. J., and Zhang, Y. (**2006a**). "Simulation of vocal fold impact pressures with a self-oscillating finite-element model," J. Acoust. Soc. Am. **119**, 3987–3994.
Tao, C., Jiang, J. J., and Zhang, Y. (**2006b**). "Anterior-posterior biphonation in a finite element model of vocal fold vibration," J. Acoust. Soc. Am. **120**, 1570–1577.
Tao, C., and Jiang, J. J. (**2007**). "Mechanical stress during phonation in a self-oscillating finite-element vocal fold model," J. Biomech. **40**, 2191–2198.
Titze, I. R. (**1988**). "The physics of small-amplitude oscillation of the vocal folds," J. Acoust. Soc. Am. **83**, 1536–1552.
Titze, I. R. (**2006**). *The Myoelastic Aerodynamic Theory of Phonation* (National Center for Voice and Speech, Denver, CO), p. 84.
Zhang, K., Siegmund, T., and Chan, R. W. (**2006**). "A constitutive model of the human vocal fold cover for fundamental frequency regulation," J. Acoust. Soc. Am. **119**, 1050.
Zhang, Z., Neubauer, J., and Berry, D. A. (**2007**). "Physical mechanisms of phonation onset: A linear stability analysis of an aeroelastic continuum model of phonation," J. Acoust. Soc. Am. **122**, 2279–2295.

Frequency distributions of uniphones, diphones, and triphones in spontaneous speech

Victor Kuperman
Radboud University Nijmegen, Wundtlaan 1, 6525 XD Nijmegen, The Netherlands

Mirjam Ernestus
Max Planck Institute for Psycholinguistics, Wundtlaan 1, 6525 XD Nijmegen, The Netherlands and Radboud University Nijmegen, Wundtlaan 1, 6525 XD Nijmegen, The Netherlands

Harald Baayen
University of Alberta, 4-32 Assiniboia Hall, Edmonton, Alberta T6G 2N8, Canada

(Received 16 August 2007; revised 2 October 2008; accepted 3 October 2008)

This paper explores the relationship between the acoustic duration of phonemic sequences and their frequencies of occurrence. The data were obtained from large (sub)corpora of spontaneous speech in Dutch, English, German, and Italian. Acoustic duration of an n-phone is shown to codetermine the n-phone's frequency of use, such that languages preferentially use diphones and triphones that are neither very long nor very short. The observed distributions are well approximated by a theoretical function that quantifies the concurrent action of the self-regulatory processes of minimization of articulatory effort and minimization of perception effort.
© *2008 Acoustical Society of America.* [DOI: 10.1121/1.3006378]

PACS number(s): 43.70.Bk, 43.70.Fq, 43.70.Mn, 43.70.Kv [AL] Pages: 3897–3908

I. INTRODUCTION

Speech inherently unfolds in time and the acoustic duration of speech units is one of the characteristics of speech that is directly experienced by both speakers and listeners (e.g., Ohala, 1996). Research of the past decades has established a large variety of phonological and prosodic factors affecting acoustic duration of n-phones and syllables. For instance, stressed syllables are realized longer than unstressed ones (e.g., Ladefoged, 1982) and words at the beginning and the end of utterances show articulatory strengthening (e.g., Bell *et al.*, 2003; Cambier-Langeveld, 2000; Fougeron and Keating, 1997). Furthermore, phonemes are realized shorter the greater the number of syllables or segments in the word (Nooteboom, 1972).

In addition, the variability in acoustic duration is codetermined by the predictability of a speech unit given its phonological, lexical, semantic, syntactic and discourse contexts (e.g., Bard *et al.*, 2000; Bolinger, 1963; Fowler and Housum, 1987; Jurafsky *et al.*, 2001; Lieberman, 1963). The more predictable a phoneme, morpheme, syllable, or a word is in its context, the less important the acoustic signal is for recognition of such a unit, and the shorter it is realized (e.g., Aylett and Turk, 2004, 2006; Van Son and Van Santen, 2005). For example, function words are more likely to be realized longer when they are unexpected, i.e., less predictable in the sentence (Bell *et al.*, 2003). Similarly, phonemes that are important for word disambiguation and thus are less predictable from the preceding phonemes are less reduced, as indicated among others by their longer acoustic duration (Van Son and Pols, 2003).

Starting with Zipf (1929; 1935), the frequency of occurrence of a speech unit has been considered as an important codeterminer of its predictability and has been argued to enter into a negative (linear or nonlinear) relation with the degree of articulatory complexity of that unit (cf. Pluymaekers *et al.*, 2005). Since we consider acoustic duration as an approximation of articulatory complexity (see discussion below), Zipf's (1935) approach can be reinterpreted such that the frequency of a unit predicts its duration. Hence we label this approach "frequency predicts duration" (FPD).

The present paper explores an alternative view of the relationship between acoustic duration and frequency of occurrence such that we consider frequency of use as a function of acoustic duration and not vice versa. The advantages of this approach, which we label "duration predicts frequency" (DPF), will be pointed out in the body of the paper.

The objects of this study are uniphones, and also larger sequences of phones, i.e., diphones and triphones. Since articulatory gestures typically stretch over the boundaries of individual phones, larger phone sequences are more stable units than uniphones and we may obtain more reliable results for these longer speech units. Similar considerations have led to the common use of diphones (or larger blocks of speech) as basic units in automatic speech recognition (e.g., Richardson *et al.*, 2003) and speech synthesis (e.g., O'Shaughnessy *et al.*, 1988). We study n-phones in spontaneous speech, as it is a more natural speech variety than, say, careful speech or the speech production conditioned by experimental tasks.

We begin with reporting the consistent functional relationship between n-phone frequency and duration and show that our approach yields a better approximation to empirical data than Zipfian FPD models. Since acoustic duration is in itself influenced by multiple factors, we then confirm that this relationship also holds when effects of these predictive factors are partialled out from our estimates of acoustic duration.

TABLE I. (Sub)corpora used for data collection.

Language	Corpus	Subcorpus	No. of phonemes	Hours	Speakers
Dutch	IFA	Spontaneous monologues	36 000	1	8
American English	Buckeye	Dialogues	431 000	22	20
German	BAS	German-German dialogues	1 976 000	54	1139
Italian	AVIP	Dialogues between adults	28 000	0.6	22

We studied n-phone frequencies in Dutch, English, German, and Italian. The primary reason for selecting these languages was the availability of large (sub)corpora of spontaneous speech for those languages. Also, the languages represent two language families, Germanic and Romance, which allow for generalizability of the results. We note that even though three of the languages we consider are Germanic, they vary in the size of their phonemic inventories (and thus in frequencies of individual phones), as well as in their phonologies (e.g., final devoicing in German and Dutch, but not in English, which affects uniphone frequencies in these languages), as well as in their affixes and the frequencies of these affixes, which affect the frequencies of the n-phones (e.g., Baayen, 1994).

In order to obtain a better understanding of the observed cross-linguistic patterns, we model the relation between frequency and acoustic duration of n-phones. We fit our data with a model based on the interaction of the speaker's tendency to minimize articulatory effort (e.g., produce less clear speech) and the listener's tendency to minimize perception effort (e.g., prefer clearer speech)(Job and Altmann, 1985).

II. METHODOLOGY

A. Corpora of spontaneous speech

The data for this study were obtained from four corpora with extensive collections of spontaneous speech: The IFA spoken language corpus of Dutch (IFA) (Van Son *et al.*, 2001), the Buckeye speech corpus for American English, version 1 (Buckeye) (Pitt *et al.*, 2005), modules Verbmobil-I and -II of the Bavarian speech archive for German (BAS) (Schiel *et al.*, 1997), and the spoken Italian varieties archive for Italian (AVIP) (Scuola Normale Superiore di Pisa, 2001); see Table I for descriptions of these spontaneous speech (sub)corpora. In these corpora, speakers were not forced to use a very high or a very low speech rate, so we restrict our findings to a "normal" self-paced range of speech rates.

The speech files of these corpora come with transcriptions at the phone level. Moreover, these transcriptions provide temporal boundaries for each phone in the signal (i.e., phone-level aligned segmentation). Except for the manually aligned IFA corpus, all collections were labeled automatically with subsequent manual verification of the alignment.

Our investigations assumed the segment inventories for the four languages that formed the basis for the labeling conventions used in the respective corpora. The only exception was that we reclassified nasalized vowels in American English as oral vowels. This adjustment affected less than 0.5% of the total number of phones in the Buckeye corpus.

B. Variables

For each language, we calculated the frequency of occurrence of every uniphone in the respective corpus. This measure, *frequency*, was considered as the dependent variable. The main predictor of interest to us, *duration*, was estimated for each dataset as the average duration of the uniphone. The type of uniphone, vowel or consonant (*type*), served as a control variable. Each language was fitted with a separate multiple regression model. We then extended our survey to diphones and triphones, fitting one statistical model to the diphones and one statistical model to the triphones in every language.

We defined diphones (or triphones) as sequences of two (or three) phones without an intervening pause, end of turn, noise, laughter, a nonspeech sound, a phone marked as incomprehensible by the transcribers, or a segment extraneous to the segment inventory of that language. Notably, in identifying the diphone or triphone sequences, we ignored word or utterance boundaries. That is, we started from the first diphone or triphone and moved through the whole corpus shifting the sampling window one phone at a time. Thus, the English word "cow" [kaʊ] in a corpus would give rise to three uniphones ([k], [a], and [ʊ]), two diphones ([ka] and [aʊ]) and one triphone ([kaʊ]). This approach treats the speech signal as a continuous stream, in which word segmentation is not a given, but rather a task for the listener (e.g., Cutler and Clifton, 1999).

For the diphones and triphones, again, frequency was the dependent variable, while the mean duration of the sequences, duration, was the key predictor. We also coded the segments in the diphones as C (for consonant) or V (for vowel), which gave rise to four levels: CC, CV, VC, and VV. The control variable type for triphones had eight levels.

III. RESULTS

In all analyses reported below, frequencies of occurrence as well as durations were (natural) log transformed in order to remove most of the skewness from the distributions. The logged durations were subsequently normalized by subtracting the minimum value of duration and dividing the difference by the maximum acoustic duration in the dataset: As a result, acoustic durations ranged from 0 to 1.

A. Uniphones

For each of the four datasets with uniphones, we fitted a stepwise multiple regression model with frequency as the dependent variable. Data points that fell outside the range of −2.0 to 2.0 units of standard deviation (SD) of duration or of

TABLE II. Models of uniphone, diphone, and triphone frequencies. In column "Count," the first figure shows the total number of data points, while the figures in parentheses show the numbers of data points remaining in the model after removal of outliers. Column "Duration" lists the regression slopes for uniphone durations, and the slopes for the first and the second coefficients of the restricted cubic spline for durations of diphones and triphones, while the next column shows their p-values. Column "Type" presents the F-values for type and the next column shows their p-values. Column ΔR^2 shows the unique contribution of duration to the explained variance of the model.

Language	Count	Duration ($\hat{\beta}$)	p	Type (F-value)	p	R^2	Residual st. error	D.f.	ΔR^2
				Uniphones					
Dutch	37(33)	−0.62	0.37	0.02	0.89	0.0	0.92	30	0.0
English	45(39)	−2.01	<0.0001	18.56	<0.0001	0.41	0.59	36	0.38
German	40(37)	−0.28	0.65	3.72	0.06	0.06	0.88	34	0.0
Italian	71(66)	−1.67	0.01	0.81	0.37	0.11	1.78	63	0.09
				Diphones					
Dutch	1002(937)	First: 1.34	0.004	47.72	<0.0001	0.15	1.22	931	0.03
		Second: −2.71	<0.0001						
English	1855(1763)	First: 0.37	0.38	112.99	<0.0001	0.19	1.57	1757	0.07
		Second: −3.33	<0.0001						
German	1390(1299)	First: 4.54	<0.0001	55.77	<0.0001	0.20	2.17	1293	0.06
		Second: −8.37	<0.0001						
Italian	939(851)	First: 1.45	0.002	16.87	<0.0001	0.09	1.25	845	0.05
		Second: −3.08	<0.0001						
				Triphones					
Dutch	6909(6212)	First: 0.53	<0.0001	47.46	<0.0001	0.06	0.57	6202	0.01
		Second: −0.89	<0.0001						
English	29804(26826)	First: 1.16	<0.0001	217.6	<0.0001	0.09	0.87	26816	0.04
		Second: −2.01	<0.0001						
German	18854(16944)	First: 3.10	<0.0001	76.62	<0.0001	0.08	1.48	16934	0.05
		Second: −4.81	<0.0001						
Italian	4425(4038)	First: 0.89	<0.0001	24.88	<0.0001	0.07	0.73	4028	0.03
		Second: −1.58	<0.0001						

frequency were excluded from the analysis prior to fitting the models. After the initial fit, data points that had Cook's distance (a measure of the effect of deleting a data point) exceeding 0.2 were removed and the models were refitted.

Table II (uniphones) summarizes the findings for the uniphones in the four datasets. In the second column of this table, the first number shows the total number of data points, while the number in parentheses shows the number of data points after removal of all outliers. The third and fourth columns present the regression coefficients and p-values for duration and the fifth and sixth presents F-values and p-values for type, respectively. The last column in the table shows the unique contribution of duration to the explained variance of the model.

The predictivity of acoustic duration for the frequency of the uniphones' occurrences differs across languages. Where such predictivity is statistically significant (English and Italian), our models replicate the findings by Zipf (1935): The articulatory complexity of a phoneme (approximated here as a phoneme's acoustic duration) is inversely related to its frequency of occurrence. That only two out of the four languages demonstrate a significant correlation may relate to the fact that the duration of a segment is codetermined by the quality of its neighboring segments due to coarticulation. We may therefore expect the diphones and triphones to show more consistent correlations across languages.

Throughout this paper we used a restricted cubic spline with 3 knots (see, e.g., Harrell, 2001) to estimate nonlinear relationships between duration and frequency. For the uniphones, we found none. Moreover, none of the models for uniphones showed significant interactions between duration and type.

B. Diphones

Multiple regression models were then fitted to the four datasets of diphones. Data points that fell outside the range of −2.0 to 2.0 units of SD of duration or of frequency were again excluded from the analysis. For all data points, Cook's distance was less than 0.2. Table II (diphones) reports the results of this model fitting.

The main variable of interest, duration, was a significant nonlinear predictor of diphone frequency across all datasets. In addition, type was significant. None of the models showed significant interactions between these two predictors. Figures 1(a)–1(d) show the distributions of the frequencies of the diphones over their durations in the four languages with addition of the polynomial regression lowess smoother lines (Cleveland, 1979).

Importantly, we find that in all datasets with diphones (and in all regression models) the functional relation between duration and frequency shows concave curves, rather than

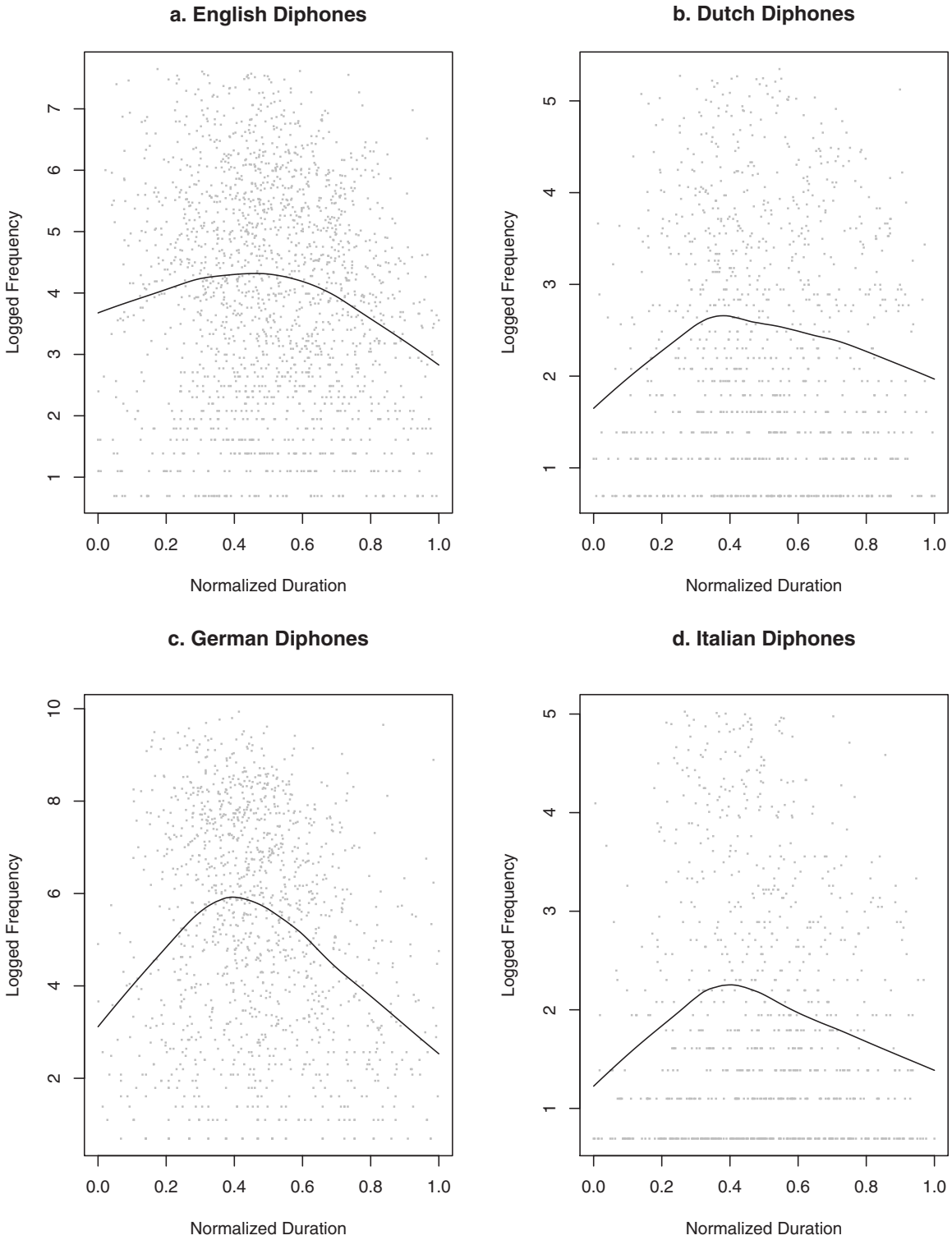


FIG. 1. Distribution of the diphone frequencies over their acoustic durations.

the monotonically decreasing curves predicted by Zipf's (1935) approach. The maxima of the curves are asymmetrically shifted leftwards toward the shorter durations, in all languages. In general, long and very short diphones are less frequently used in the four languages than diphones from the short-to-mid range of the durational spectrum.

The fact that the shortest diphones are not of a high frequency hints at the sensitivity of speakers to the discriminability of the speech signal: The shorter the duration, the more effort is required for speech perception. At the same time, long diphones are disfavored, possibly since they may take more effort to produce. We will return to this issue below.

C. Triphones

Finally, we modeled for each of the four languages triphone frequency as a function of acoustic duration and CV type. Data points that fell outside the range of −2.0 to 2.0 units of SD of duration or of frequency were excluded from

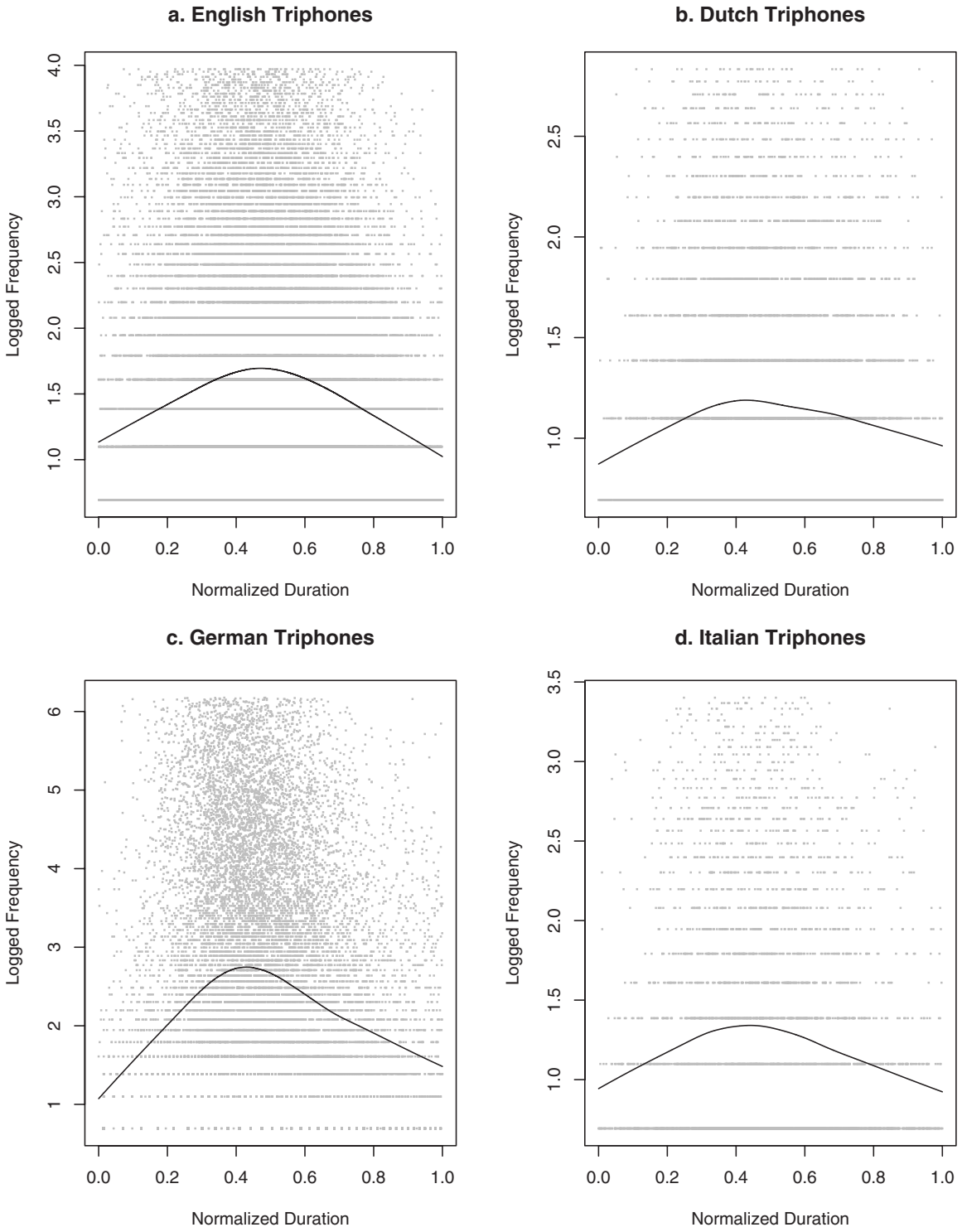


FIG. 2. Distribution of the triphone frequencies over their acoustic durations.

the models. Cook's distance was less than 0.2 for all data points. Table II (triphones) reports the effects of the predictors for frequency.

Duration was a significant predictor of triphone frequency in all datasets as was type, without interactions. Figures 2(a)–2(d) plot the scatterplots for frequency and duration of triphones with addition of the polynomial regression lowess smoother lines.

The nonlinear relations between frequency and duration show concave curves for all four datasets with triphones. As with diphones, the inverse-U shape suggests that speakers tend to avoid phonemic sequences that are either very long or short. Again, this runs counter to the prediction one would make on the basis of Zipf's FPD approach (1935) that frequency should decrease with duration.

IV. VALIDATION OF RESULTS AGAINST ZIPF (1935)

The relationship between the frequency of a speech unit and its acoustic duration can be explored from two view-

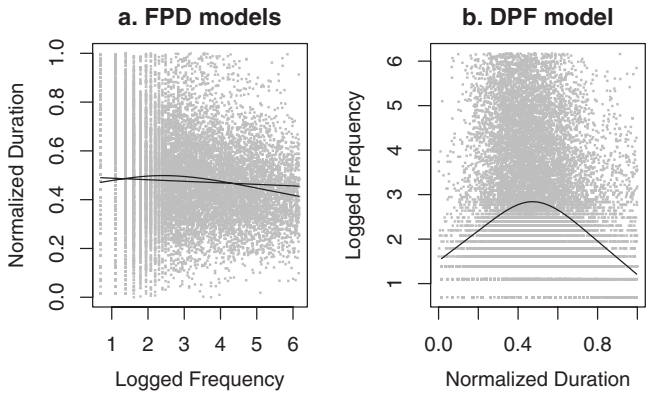


FIG. 3. Function curves of linear and nonlinear FPD models (a) and of the nonlinear DFP model (b) applied to German triphones.

points. In the DPF models that we presented above, acoustic duration predicts frequency of occurrence. In the Zipfian FPD models, the order is reversed: Acoustic duration is the dependent variable, while frequency is considered as an independent variable.

To determine which of the two approaches yields better approximation to the empirical data, we fitted two multiple regression models (DPF and FPD based) to each of the 12 datasets described above. Each model contained only one independent predictor, either frequency or duration, and each correlation with the dependent variable was tested for significant nonlinearities. If the predictors of both the DPF and FPD models reached significance for a given dataset, we identified the best performing model as the model explaining the largest proportion of the variance, R^2. The performances of FPD and DPF models are mathematically identical only if the dependent variable and the predictor show a linear relation.

As an example, Fig. 3 shows the results of the model fitting to the dataset of German triphones. Figure 3(a) displays the scatterplot of duration as a function of frequency (following the Zipfian FPD approach) and plots the linear relation ($R^2=0.008$) as well as the significantly stronger nonlinear relation ($R^2=0.012$) between the two variables. Figure 3(b) swaps the axes in the scatterplot (following our DPF account), plotting frequency as a nonlinear function of duration. The amount of explained variance for this model is 0.04: It thus outperforms both the linear and the nonlinear Zipfian approximations by at least a factor of 3.5.

In the Zipfian models (FPD), frequency of occurrence emerged as a significant linear predictor of acoustic duration for English and Italian uniphones, and as a significant linear or nonlinear predictor for the diphones and triphones of all four languages. Similarly, in the corresponding DPF models, duration reliably predicted frequency.

The DPF and FPD models performed identically for the English and Italian uniphones, which is expected mathematically, given the linear relation between duration and frequency in those two datasets. Crucially, however, for every dataset with diphones or triphones, the amount of variance explained by the FPD model with frequency of use as the independent variable was significantly smaller than the amount explained by the corresponding DPF model, as established by the pairwise comparison of log likelihood ratios of corresponding models. The average R^2 value of the DPF models was 2.6%, while the average R^2 value of the FPD models was 0.2%. DPF models retained their significant advantage over FPD models, when either log durations or log frequencies were z transformed.

Moreover, for the datasets with Italian diphones, English diphones, and German triphones the shape of the function of the Zipfian FPD models is concave. In other words, the shortest elements have the low-to-mid rather than the highest frequency of occurrence. This finding is unexpected in the Zipfian approach. We conclude that Zipf's findings (1935) cannot be extended from uniphones to diphones and triphones and that models with the reverse direction of predictivity (DPF) give rise to qualitatively consistent results (e.g., similar shapes of regression curves) and explain variance in the data better than Zipfian models.

V. CHECKING FOR ARTIFACTS IN THE DIPHONE AND TRIPHONE FREQUENCY DISTRIBUTIONS

Our working assumptions and method of data collection might have given rise to artifacts that produce frequency distribution patterns similar to the ones we observed for the acoustic durations of the diphones and triphones in our datasets. In this section we consider these potential artifacts and demonstrate that none of them can (fully) account for the observed functional relationship of acoustic duration and frequency in the diphones and triphones.

A. Phonotactics

The phonotactics of a language contribute to the frequencies of phonemes. In addition, since phone sequences that violate phonotactic constraints have been shown to facilitate segmentation of continuous speech (e.g., McQueen, 1998), "illegal" n-phones may also be realized longer than legal ones so as to provide better perceptual cues. We set out to validate whether the observed relations between acoustic duration and frequency also hold once the language-specific phonotactic wellformedness of diphones and triphones within words is taken into account. For the diphones and triphones in the Dutch, English, and German datasets we established whether they occur within monomorphemic words [using the CELEX lexical database (Baayen *et al.*, 1995); we did not have access to a corpus of Italian carrying the required information, so this language was left out of consideration]. N-phones that occur within simplex words were coded as "legal," while the others were coded as "illegal." As expected, phonotactically illegal n-phones tended to be longer and less frequent than phonotactically legal ones (for each language, $p<0.0001$). More importantly, the regression analyses replicated the inverse-U concave curves of frequency as a function of acoustic duration in all three languages for both the subset of phonotactically legal and the subset of phonotactically illegal diphones and triphones. The only exception was the English illegal diphones for which a linear function with a negative slope was adequate. We conclude that the inverse-U shaped function predicting frequency from duration is robust with regard to phonotactics.

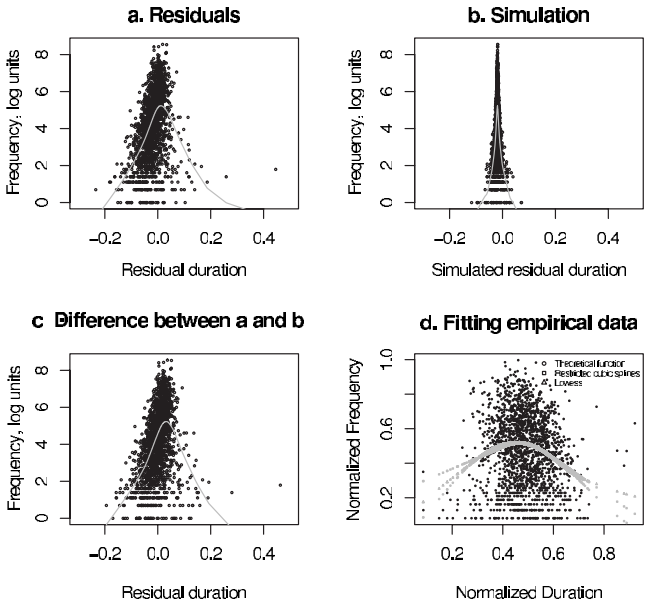


FIG. 4. English diphone frequency as a function of (a) residual mean diphone duration, (b) simulated diphone duration, and (c) the difference between the residual and simulated diphone durations. (d) Approximation of normalized English diphone frequency using the theoretical function (parameter values $a=2.141$, $b=1.737$, and $K=7.447$), the nonlinear regression model using restricted cubic splines, and the added lowess smoother line.

B. Predictors of acoustic duration

Research of the past decades has identified multiple factors that codetermine acoustic duration of n-phones. There is a logical possibility then that the nonlinear relation between acoustic duration and frequency of n-phones is, in fact, a relation between a major predictor of an n-phone's acoustic duration (for instance, word frequency) and n-phone frequency. To test this possibility, we fitted six multiple regression models to the acoustic durations (in milliseconds) of the diphones and triphones in Dutch, English, and German. We only considered n-phones that did not cross word or utterance boundaries. All models included speaker as a random effect to account for intersubject variability in speech rate as well as the following fixed effects: log-transformed word frequency, sum of mean durations of uniphones that constituted the di- or triphone, position of an n-phone in the word and the utterance (both with the levels "initial," "internal," and "final"); and mutual information of the uniphones in the n-phone. The patterns of results were very similar across languages and confirmed the known correlations of these predictors with acoustic duration: n-phones are longer in lower-frequency words, in the beginning and the end positions of both the word and the utterance, if the uniphones they contained were longer, and if the mutual information of these uniphones is larger (all $p's<0.001$). We took the residuals of these models as estimates of acoustic duration from which the effects of these major predictors are regressed out. For all six datasets, we plotted diphone or triphone frequency against the means of those residuals for each n-phone. All resulting plots showed the inverse-U shaped functional relation between the two variables [see Fig. 4(a) for English diphones]. We conclude that the patterns described in Sec. III are unlikely to be artifacts of a dependency between n-phone frequency and one or several factors codetermining acoustic duration of n-phones.

We then compared again the performance of nonlinear FPD (Zipfian) and DPF models now using the mean residualized duration of n-phones instead of the mere mean n-phone duration. Across all subsets of Dutch, English, and German diphones and triphones, our DPF models performed significantly better than the Zipfian models ($p<0.0001$), as indicated by the pairwise comparison of their log likelihood ratios. The average amount of explained variance by the DPF models was 20% as opposed to 11% by the Zipfian FPD models. Thus, acoustic duration is a better predictor of frequency than frequency is of acoustic duration also when the influence of several predictors on acoustic duration is regressed out.

C. Sampling method

A frequency distribution in which extreme values of acoustic duration have the lowest frequency is suspect to the statistical phenomenon of sampling error. An n-phone mean duration will be closer to the grand average duration computed over all n-phones, the more frequent that n-phone is (or, equivalently, the larger the sample size for that n-phone is), since it contributes more to the grand average. That is, less frequent n-phones are predicted to occupy the extreme positions in the distribution of n-phone frequencies over n-phone durations, and more frequent n-phones are predicted to be in the center of that distribution, by virtue of the chosen sampling method. If the number of data points in a population is large enough (like in our datasets), the resulting distribution closely approximates the Gaussian distribution. We investigated whether our sampling method can fully account for the empirical patterns.

We considered the subsets of Dutch, English, and German diphones and triphones, for which mean residual durations were computed (see above). For each of the six subsets we computed the grand average residual duration of all n-phones (μ) and their corresponding SD (σ). If all n-phones were approximately of the same duration, all tokens should together form a Gaussian frequency distribution with the mean (μ) and the SD (σ). For each n-phone in a subset we then took a sample from the corresponding normal distribution (of durations) with μ and σ as parameters, and with the sample size equal to the n-phone frequency. We computed the mean duration for each n-phone sample and plotted it on the x-axis and n-phone frequency on the y-axis to build the simulated frequency distribution of durations. If the observed frequency distributions of the n-phones are just due to sampling error, then the simulated distributions would closely approximate the empirical patterns. We ran 1000 simulations for each subset of diphones and triphones, and we used the Kolmogorov–Smirnov test to estimate the goodness of fit between the simulated and empirical distributions. For all subsets and for all simulations, the Kolmogorov–Smirnov test indicated that the simulated distributions were significantly (all $p's<0.00001$) different from the observed ones. Visual inspection of the simulated distributions [see Fig. 4(b)

for a simulation of the distribution for English diphones] shows that they have a much smaller variance than the empirical ones [shown in Fig. 4(a)]. Furthermore, diphone and triphone frequencies plotted against the *differences* between the observed and simulated durations show the familiar inverse-U shape [see Fig. 4(c)].

We conducted similar simulations using normal distributions with the mean and the SD observed for the specific n-phones (rather than μ and σ of the general data population). Again, for all six subsets and all simulations, the Kolmogorov–Smirnov test showed significant differences between the empirical distributions and the ones simulating random sampling variation. We conclude that the attested inverse-U shapes of n-phone frequency distributions are not artifacts of our sampling procedure.

VI. SELF-ORGANIZATION IN SPEECH

The observed relation between the acoustic duration of an n-phone and its frequency of occurrence may be accounted for by the interacting processes of effort minimization on the part of the speaker as well as on the part of the listener (in some theories of speech production speakers monitor their internal speech via proprioceptive feedback and hence also function as listeners in preferring thorough articulation, cf. e.g., Levelt, 1989). According to the H&H theory (Lindblom, 1990; cf. also Lindblom, 1983; Lindblom, *et al.*, 1984), speakers adaptively balance between the costs of careful speech production and the costs of deficient communication that may come with sloppy pronunciation. This theory has given rise to research on self-organizational properties in speech (De Boer, 2000; Köhler, 1987; Lindblom *et al.*, 1984; Oudeyer, 2005). In what follows, we introduce a theoretical function that quantifies the joint effect of the two minimization processes on n-phone frequencies and we explore how well this function can approximate the observed relation between acoustic duration of an n-phone and its frequency of occurrence.

Several studies have shown that acoustic duration is a measure of ease of speech perception. Longer realizations of speech units tend to facilitate speech comprehension and diminish perceptual confusion (e.g., Janse *et al.*, 2003; Janse, 2004; Kemps *et al.*, 2005; Salverda *et al.*, 2003; but see Ernestus and Baayen, 2007). Acoustic duration is also correlated to ease of speech production. Shorter realizations in general reflect smaller and shorter gestures, which implies less muscular production effort (e.g., Browman and Goldstein, 1992). In line with this notion, Smith *et al.* (1986) demonstrated that subjects show faster production of those uni- and bisyllabic stimuli that a priori were subjectively considered as relatively easy. Likewise, Perkell *et al.* (2002) showed that realizations requiring less articulatory effort (measured as the peak movement speed) tend to be shorter. There are, however, several counterexamples where shorter durations do not always imply easier production (cf., e.g., Beckman and Edwards, 1992; Byrd and Saltzman, 2003). For instance, a shorter duration of a CVC syllable may indicate reduced effort only if it is achieved by shortening its steady state (cf. Nelson, 1983).

Even though the relation between acoustic duration and effort is not straightforward and both articulatory and perceptual complexity are simultaneously affected by many more factors than just duration, we will make for now the simplifying assumption that shorter durations imply minimization of the speaker's articulatory effort and longer durations imply minimization of the listener's perception effort. This assumption will allow us to test how well one can explain the patterns in the empirical data by considering only one inherently noisy dimension of complexity. More specifically, we will investigate to what extent the two opposing tendencies of effort minimization can account for the inverse-U shapes observed in the frequency distributions of n-phones.

We model the tension between these two processes of minimization by considering speech as a dynamic self-regulating system in which a change in the articulatory effort invested by a speaker modulates the effort required of the listener. Both these changes in turn may lead to a change in the frequencies with which speech sounds are used. In what follows, we adopt the framework of Job and Altmann (1985) and Köhler (1987), who modeled the dynamics of sound change as a function of the demands of speech production and comprehension.[1]

The model can be specified in more than one way. For instance, we can model the absolute value of a language property (in this case, n-phone frequency itself, f), or the *amount of change* in n-phone frequency relative to the absolute value of that frequency, df/f. We modeled the relative amounts of change in frequency as we believe that they are more directly influenced by the two opposing tendencies of effort minimization than the frequencies themselves, which are also affected by, for instance, inventory size, phonological generalizations, etc. Furthermore, we assume the simplest relation of direct proportionality between the relative amount of change in frequency and the relative amounts of change in the efforts for the speaker and the listener, $df/f \propto dx$, where x is the total amount of effort defined for both interlocutors. More formally, we hypothesize a complex function of effort $g(x)$ that maps the amount of change in the joint efforts of interlocutors onto the relative amount of change in frequency

$$\frac{df}{f} = g(x)dx. \tag{1}$$

The goal of this modeling exercise is then to specify the functional form of $g(x)$ and validate its goodness of fit against empirical data. Again, we opt for the simplest definitions of our parameters and of the mapping function to test how far these basic assumptions can take us in accounting for patterns observed across four languages.

The speaker's production effort x_s is easier to operationalize than the perception effort of the listener x_l. Here we approximate x_s by the acoustic duration of n-phones. While there is evidence that perception effort strongly correlates with perceptual confusion (e.g., Lindblom, 1990), we remain agnostic as to whether this characteristic is the exhaustive source of effort. To define x_l, we follow Job and Altmann (1985) in making the simplifying assumption that the amount of perception effort is inversely correlated with the amount of production effort, $x_l = 1 - x_s$. This assumption implements

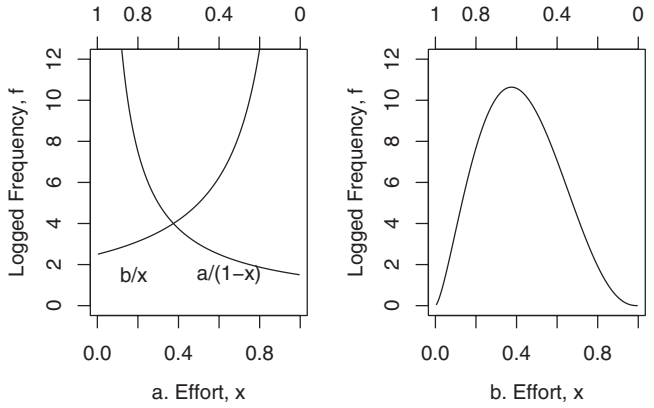


FIG. 5. General shapes of the relation of frequency with articulatory effort (x) and perception effort ($1-x$). (a) Frequency as a function of two processes of effort minimization, separately. (b) Solution for the differential equation (3) with $a=2.5$, $b=1.5$, and $K=150$.

the insight that more careful and thus more effortful articulation alleviates comprehension, while sloppy pronunciation hinders it. We define the variable x_s as the difference between a given amount of effort (an n-phone duration) and the minimal amount of effort (the duration of the shortest n-phone in the dataset), divided by the maximum amount of effort (the duration of the longest n-phone in the dataset). Thus, the value of x_s and of its complement $1-x_s$ are constrained to the interval (0, 1). Since the effort of both the speaker and the listener is now defined in terms of x_s, we henceforth use x to denote x_s and we note that one unit of change is identical for both interlocutors $dx_s=dx_l=dx$.

Recall our hypothesis that the amount of change in frequency relative to the absolute value of frequency is a function of the relative amounts of change in effort for both the speaker and the listener. The amount of change in articulatory effort relative to the absolute value of that effort is given by $g_s(x)dx=b(dx)/x$, where b is a positive coefficient. Likewise, the change in the amount of perception effort for the listener is given by $g_l(x)dx=a(dx)/(1-x)$, where a is a positive coefficient. Figure 5(a) illustrates the situation in which the relative amount of change in frequency in Eq. (1) is only affected by the amount of change in the speaker's effort $g_s(x)dx$, as suggested by Zipf (1935), or only by the change in the listener's effort $g_l(x)dx$. The resulting frequency curves are ideal for either the speaker, or the listener.

Yet we argue that both the speaker and the listener co-determine through their efforts the distributions of n-phone frequencies over n-phone durations. To express the notion of a trade-off between efforts of interlocutors, $g_s(x)dx$ and $g_l(x)dx$, and their joint effect on the change in n-phone frequency, we can model $g(x)dx$ in Eq. (1) either as a difference between the two terms or the division of the two terms. Our further empirical validation showed that the former option provides better fits to observed values; hence, we state that

$$\frac{df}{f} = g(x)dx = (g_s(x) - g_l(x))dx = \left(\frac{b}{x} - \frac{a}{1-x}\right)dx. \qquad (2)$$

When the ideal frequency curves for speaker and listener shown in Fig. 5(a) intersect, the difference between corresponding efforts is equal to zero. In this case, speaker and listener are optimally attuned, and nothing changes in the system. However, if speaker and listener are out of sync, one of the interlocutors has to invest more effort, leading to a difference in the ideal frequencies for the speaker and the listener, and to a change in the likelihood that a given speech sound is used.

The solution of the differential equation (2) is as follows:

$$\log f = b \log x + a \log(1-x) + c, \qquad (3)$$

where c is the constant of integration.

The exponential transformation of Eq. (3) yields the following formula for frequency:

$$f = Kx^b(1-x)^a, \qquad (4)$$

where $0<x_s<1$, and a, b, and K are constants greater than zero.

The curve produced by this function is concave [see Fig. 5(b)] and has its maximum at $x=b/(a+b)$. At this point the frequencies ideal for the speaker and for the listener are equal, and the optimal balance is reached for the system.

The curve is symmetrical if $a=b$. If $a>b$, the maximum shifts leftwards. The area close to the maximum approximates the region of equilibrium where the frequency of a speech sound is least likely to undergo change. In the proximity of the maximum, speakers invest relatively little effort into sound production and at the same time the perceptual efort is relatively low. The position of the equilibrium (and the parameters of this theoretical function) is language specific.

We fitted function (4) to the frequency distributions of uniphones, diphones, and triphones in Dutch, English, German, and Italian using the nls function in the statistical software package R (R Development Core Team, 2007). This program estimated the three constants, a, b, and K, by means of the least squares method. Since the models reported in Sec. III were based on log-transformed values of frequency, we also log-transformed the values of frequency, f, obtained from the theoretical function in Eq. (4). Each dataset was divided into subsets by the levels of CV type, and the theoretical function was fitted to each subset individually. Since our statistical models included CV type as a predictor, splitting of our datasets by CV type was necessary for better accuracy of comparison. Thus, for each uniphone dataset, we obtained two sets of parameters: one that provided the best fit for the vowels and one for the consonants. Similarly, for each diphone dataset, we obtained four such sets, and for each triphone dataset (at most) eight.

The theoretical function did not provide good fits for any of the uniphone datasets. We will therefore only discuss the datasets with diphones and triphones. To estimate the overall goodness of fit, we summed the squared deviations of the fitted values of f from the actual values of frequency over the subsets of each dataset. The resulting sums were then divided by the number of data points in the respective datasets to obtain the mean square errors (MSEs): The smaller the MSE, the closer the fit. We then compared these MSE values with the MSEs of the respective regression models reported above

TABLE III. Estimated parameters of theoretical function. The values in columns, a, b, and K are reported for the models fitted to the logged frequency values of the diphones of the VC type and of the triphones of the CVC type. In column "MSE," the percents in parentheses estimate the performance of the theoretical function as compared to the standard linear regression models for all subsets of given datasets. Thus, −4.3 for the Dutch diphones means that the MSE of the fit to the four subsets of Dutch diphones is 4.3% smaller for the theoretical function than for the regression model.

Dataset	a	b	K	MSE
Dutch diphones	0.27	0.63	0.04	1.47(−4.3%)
English diphones	1.34	0.35	0.00	2.46(0.0%)
German diphones	1.55	0.95	0.00	5.04(−6.1%)
Italian diphones	0.35	0.07	0.08	1.52(0.0%)
Dutch triphones	0.23	0.18	0.19	0.32(−0.1%)
English triphones	0.49	0.17	0.06	0.77(0.0%)
German triphones	0.56	0.46	0.03	2.18(−7.5%)
Italian triphones	0.26	0.14	0.18	0.53(+0.1%)

(estimated as sums of squared residuals divided by the number of data points in the given dataset). The results of the comparison are summarized in Table III.

For the sake of brevity, this table lists the values of the constants for the theoretical function fitted to the diphones of the VC type and to the triphones of the CVC type. The reported MSE values, however, are based on *all* subsets of the datasets. The percents in parentheses estimate the performance of the theoretical function as compared to the standard linear regression models for all subsets of the given datasets. Thus, −4.3 for the Dutch diphones means that the MSE of the fit to the four subsets of Dutch diphones is 4.3% smaller for the theoretical function than for the regression model.

Evidently, the fits to the diphone and triphone data provided by the theoretical function are equivalent to or better than those provided by the standard multiple regression models that use the state-of-the-art approximation of nonlinear functional relations with restricted cubic splines. This is remarkable given that the theoretical function has a predefined shape, which offers less flexibility in fitting than the cubic splines. The two methods are equivalent in the number of parameters they use. The equal or slightly better performance of the theoretical function over regression models using restricted cubic splines also holds when log frequency is normalized and rescaled to the interval between 0 and 1. Figure 4(d) shows fits of the normalized frequency of English diphones of both CV types using the theoretical function and the multiple regression models with restricted cubic splines. We also added as a baseline the fit provided by the locally weighted polynomial regression implemented in the lowess smoother line. The theoretical function based on normalized diphone duration provides a slightly better fit (by 0.4%) to this (normalized) frequency distribution than the multiple regression model.

Since the parameters and coefficients in Eq. (4) are defined in linguistically meaningful terms (the effort of production or perception), this equation affords not only a better fit but also suggests a better interpretability of our findings than the multiple regression models. We conclude that the patterns observed in the frequency distributions of diphones and triphones can be well described by a model that implements the self-regulatory balance in the articulatory and auditory demands of production and comprehension. This strongly suggests that the frequency distributions are codetermined by these two opposing tendencies.

VII. CONCLUDING REMARKS

Across languages, we find significant dependencies between the frequency of occurrence of an n-phone and its acoustic duration. In spontaneous speech in Dutch, English, German, and Italian, speakers prefer diphones and triphones that occupy the middle area of the durational range, and avoid very short durations as well as very long durations. These patterns were consistent across phonetically and phonologically different Germanic languages and a Romance language, which strongly suggests generalizability of our findings and hints that the patterns may derive from fundamental principles of human communication (see Lindblom, 1990). Significant negative correlations were also found between frequency of occurrence and duration of uniphones in English and Italian.

Our approach differs from the approach inspired by Zipf (1929, 1935) in that we predicted frequency from acoustic duration, rather than acoustic duration from frequency. Importantly, multiple regression models based on our DPF approach perform significantly better than the ones that follow the Zipfian approach. This advantage in performance also holds when the influence of several predictors is regressed out of our key factor, acoustic duration. Moreover, the Zipfian account cannot deal with the concave functional form that the relation between frequency and acoustic duration takes under the Zipfian FPD approach.

Essentially, Zipf's approach (1935) is only based on the speaker's tendency to reduce articulatory effort and it correctly predicts that very long n-phones are infrequent. Our data suggest that reduction of comprehension effort may also play a role that becomes evident in speakers' avoidance of very short realizations, which are costly for listeners. We implemented the hypothesis about the interacting demands of efficient speech production and effective speech comprehension mathematically in a theoretical function based on Job and Altmann, 1985. The function provides good fits to the

distributions of frequency of diphones and triphones over their acoustic durations supporting our hypothesis.

Our data point at processes of self-organization in language. Specifically, they document the existence of consistent frequency patterns in several languages, which demonstrate the emergence of global cross-linguistic regularities from the individual instances of communication that operate on a microscopic scale (cf. De Boer, 2001). Clearly, the frequencies of n-phones are determined by the frequencies of words. Changes in the frequencies of n-phones therefore have to result from changes in the pronunciation of words or in word choice, which imply adjustments for the broad linguistic community. The question then is *how* the observed patterns of use spread across vast linguistic communities with such surprising uniformity and in the absence of global control.

Recent computational models connect the emergence of speech sounds with psychologically and socially motivated properties of interactive communication (cf., e.g., De Boer, 2000, 2001, Oudeyer, 2005). We predict for these models that their simulated data will be characterized by inverse-U shaped distributions of sound frequencies over sound durations (similar to the ones we have attested here for four natural languages), probably reflecting the roles of ease of articulation and ease of perception in language use.

ACKNOWLEDGMENTS

The authors wish to thank Alice Turk, Kevin Russell, Austin Frank, and an anonymous reviewer for their valuable comments on previous versions of this manuscript.

[1]One of the alternative approaches considers the amount of information (surprisal) per time unit as a codeterminer of the speaker's and the listener's effort (cf. Aylett and Turk, 2004; Levy and Jaeger, 2006). It argues that communication is optimal (efforts for both interlocutors are minimal) when information density is uniform and close to the capacity of the noisy communication channel. The relationship between present findings and predictions of the uniform information density approach is a topic for further investigation.

Aylett, M., and Turk, A. (**2004**). "The smooth signal redundancy hypothesis: A functional explanation for relationships between redundancy, prosodic prominence, and duration in spontaneous speech," Lang Speech **47**, 31–56.

Aylett, M., and Turk, A. (**2006**). "Language redundancy predicts syllabic duration and the spectral characteristics of vocalic syllabic nuclei," J. Acoust. Soc. Am. **119**, 3048–3058.

Baayen, R. H. (**1994**). "Productivity in language production," Lang. Cognit. Processes **9**, 447–469.

Baayen, R. H., Piepenbrock, R., and Gulikers, L. (**1995**). The CELEX Lexical Database (CD-ROM) (Linguistic Data Consortium, University of Pennsylvania, Philadelphia, PA).

Bard, E., Anderson, A., Sotillo, C., Aylett, M., Doherty-Sneddon, G., and Newlands, A. (**2000**). "Controlling the intelligibility of referring expressions in dialogue," J. Mem. Lang. **42**, 1–22.

Beckman, M., and Edwards, J. (**1992**). "Intonational categories and the articulatory control of duration," in *Speech Perception, Production, and Linguistic Structure*, edited by Y. Tohkura, E. Vatikiotis-Bateson, and Y. Sagisaka (Omaha, Tokyo), pp. 359–375.

Bell, A., Jurafsky, D., Fosler-Lussier, E., Girand, C., and Gildea, D. (**2003**). "Effects of disfluencies, predictability, and utterance position on word form variation in English conversation," J. Acoust. Soc. Am. **113**, 1001–1024.

Scuola Normale Superiore de Pisa (**2001**). *AVIP (Archivio di Varietá di Italiano Parlato)*, [Varieties of spoken Italian archive], edited by P. Bertinetto (Ufficio Pubblicazioni della Classe di Lettere della Scuola Normale Superiore di Pisa, Pisa).

Bolinger, D. (**1963**). "Length, vowel, juncture," Linguistics **1**, 5–29.

Browman, C., and Goldstein, L. (**1992**). "Articulatory phonology: An overview," Phonetica **49**, 155–180.

Byrd, D., and Saltzman, E. (**2003**). "The elastic phrase: Modeling the dynamics of boundary-adjacent lengthening," J. Phonetics **31**, 149–180.

Cambier-Langeveld, T. (**2000**). *Temporal Marking of Accents and Boundaries*, (Landelijke Onderzoekschool Taalwetenschap, Amsterdam).

Cleveland, W. S. (**1979**). "Robust locally weighted regression and smoothing scatterplots," J. Am. Stat. Assoc. **74**, 829–836.

Cutler, A., and Clifton, C., Jr. (**1999**). "Comprehending spoken language: A blueprint of the listener," in *The Neurocognition of Language*, edited by C. Brown and P. Hagoort (Oxford University Press, Oxford), pp. 123–166.

De Boer, B. (**2000**). "Self-organization in vowel systems," J. Phonetics **28**, 441–465.

De Boer, B. (**2001**). *The Origins of Vowel Systems* (Oxford University Press, Oxford).

Ernestus, M., and Baayen, R. H. (**2007**). "The comprehension of acoustically reduced morphologically complex words: The roles of deletion, duration and frequency of occurrence," in Proceedings of the 16th International Congress of Phonetic Sciences, Saarbruecken, Germany, pp. 773–776.

Fougeron, C., and Keating, P. (**1997**). "Articulatory strengthening at the edges of prosodic domains," J. Acoust. Soc. Am. **101**, 3728–3740.

Fowler, C., and Housum, J. (**1987**). "Talkers' signalling of "new" and "old" words in speech and listeners' perception and use of the distinction," J. Mem. Lang. **26**, 489–504.

Harrell, F. (**2001**). *Regression Modeling Strategies* (Springer-Verlag, Berlin).

Janse, E. (**2004**). "Word perception in fast speech: Artificially time-compressed vs. naturally produced fast speech," Speech Commun. **42**, 155–173.

Janse, E., Nooteboom, S., and Quene, H. (**2003**). "Word-level intelligibility of time-compressed speech: Prosodic and segmental factors," Speech Commun. **41**, 287–301.

Job, U., and Altmann, G. (**1985**). "Ein modell für anstrenungsbedingte lautveränderungen (A model for conditional effort sound changes),"Folia Linguistica Historica **VI**, 401–407.

Jurafsky, D., Bell, A., Gregory, M., and Raymond, W. (**2001**). "Probabilistic relations between words: Evidence from reduction in lexical production," in *Frequency and the Emergence of Linguistic Structure*, edited by J. Bybee and P. Hopper (John Benjamins, Amsterdam).pp. 229–254.

Kemps, R., Wurm, L., Ernestus, M., Schreuder, R., and Baayen, R. (**2005**). "Prosodic cues for morphological complexity in Dutch and English," Lang. Cognit. Processes **20**, 43–73.

Köhler, R. (**1987**). "System theoretical linguistics," Theoretical Linguistics **14**, 241–257.

Ladefoged, P. (**1982**). *A Course in Phonetics*, 2nd ed. (Hartcourt, Brace, Jovanovich, New York).

Levelt, W. J. M. (**1989**). *Speaking. From Intention to Articulation* (MIT, Cambridge, MA).

Levy, R., and Jaeger, F. (**2006**). "Speakers optimize information density through syntactic reduction," in *Proceedings of the 20th Annual Conference on Neural Information Processing Systems*, (Neural Information Processing Systems Foundation, Vancouver), pp. 29–37.

Lieberman, P. (**1963**). "Some effects of semantic and grammatical context on the production and perception of speech," Lang Speech **6**, 172–187.

Lindblom, B. (**1983**). "Economy of speech gestures," in *The Production of Speech*, edited by P. MacNeilage (Springer-Verlag, New York), pp. 217–245.

Lindblom, B. (**1990**). "Explaining phonetic variation: A sketch of the H&H theory," in *Speech Production and Speech Modeling*, edited by W. Hardcastle and A. Marchal (Kluwer, Dordrecht), pp. 403–440.

Lindblom, B., MacNeilage, P., and Studdert-Kennedy, M. (**1984**). "Self-organizing processes and the explanation of linguistic universals," in *Explanations for Language Universals*, edited by B. Butterworth, B. Comrie, and O. Dahl (Mouton, Berlin), pp. 181–203.

McQueen, J. (**1998**). "Segmentation of continuous speech using phonotactics," J. Mem. Lang. **39**, 21–46.

Nelson, W. L. (**1983**). "Physical principles for economies of skilled movements," Biol. Cybern. **46**, 135–147.

Nooteboom, S. G. (**1972**). *Production and Perception of Vowel Duration: A Study of the Durational Properties of Vowels in Dutch* (University of Utrecht, Utrecht).

Ohala, J. J. (**1996**). "Speech perception is hearing sounds, not tongues,"J. Acoust. Soc. Am. **99**, 1718–1725.
O'Shaughnessy, D., Barbeau, L., Bernardi, D., and Archambault, D. (**1988**). "Diphone speech synthesis," Speech Commun. **7**, 55–65.
Oudeyer, P.-Y. (**2005**). "The self-organization of speech sounds," J. Theor. Biol. **233**, 435–449.
Perkell, J., Zandipour, M., Matthies, M., and Lane, H. (**2002**). "Economy of effort in different speaking conditions. I. A preliminary study of intersubject differences and modeling issues," J. Acoust. Soc. Am. **112**, 1627–1641.
Pitt, M., Johnson, K., Hume, E., Kiesling, S., and Raymond, W. (**2005**). "The Buckeye corpus of conversational speech: Labeling conventions and a test of transcriber reliability," Speech Commun. **45**, 90–95.
Pluymaekers, M., Ernestus, M., and Baayen, R. (**2005**). "Lexical frequency and acoustic reduction in spoken Dutch," J. Acoust. Soc. Am. **118**, 2561–2569.
R Development Core Team (**2007**). R: A Language and Environment for Statistical Computing, R Foundation for Statistical Computing, Vienna, Austria, URL: http://www.R-project.org (Last viewed 10/1/2008).
Richardson, M., Bilmes, J., and Diorio, C. (**2003**). "Hidden-articulator Markov models for speech recognition," Speech Commun. **41**, 511–529.
Salverda, A., Dahan, D., and McQueen, J. (**2003**). "The role of prosodic boundaries in the resolution of lexical embedding in speech comprehension," Cognition **90**, 51–89.
Schiel, F., Draxler, C., and Tillmann, H. (**1997**). "The Bavarian archive for speech signals: Resources for the speech community," in Proceedings of the EUROSPEECH 1997, Rhodos, Greece, pp. 1687–1690.
Smith, B., Hillenbrand, J., Wasowitz, J., and Preston, J. (**1986**). "Durational characteristics of vocal and subvocal speech: Implications concerning phonological organization and articulatory difficulty," J. Phonetics **14**, 265–281.
Van Son, R., Binnenpoorte, D., van den Heuvel, H., and Pols, L. (**2001**). "The IFA corpus: A phonemically segmented Dutch open source speech database," in Proceedings of Eurospeech 2001, Aalborg, Denmark.
Van Son, R., and Pols, L. (**2003**). "Information structure and efficiency in speech production," in Proceedings of Eurospeech 2003, Geneva, Switzerland.
Van Son, R., and Van Santen, J. (**2005**). "Duration and spectral balance of intervocalic consonants: A case for efficient communication," Speech Commun. **47**, 100–123.
Zipf, G. K. (**1929**). "Relative frequency as a determinant of phonetic change," Harvard Studies in Classical Philology **15**, 1–95.
Zipf, G. K. (**1935**). *The Psycho-Biology of Language* (Houghton Mifflin, Boston, MA).

Clear speech production of Korean stops: Changing phonetic targets and enhancement strategies[a)]

Kyoung-Ho Kang[b)] and Susan G. Guion
Department of Linguistics, University of Oregon, Eugene, Oregon 97403-1290

(Received 28 October 2007; revised 25 August 2008; accepted 26 August 2008)

The proposal that phonological contrast is enhanced through greater approximation of phonetic targets was investigated by comparing clear speech to conversational and citation-form speech produced by Korean speakers. The stop system of Korean is undergoing a sound change in which younger speakers produce the aspirated-lenis stop contrast differently from previous generations. Older speakers differentiate this contrast primarily with the acoustic correlate of voice onset time (VOT) and secondarily with *F*0. Younger speakers are merging VOT values for this contrast. As a result, the primary acoustic correlate is now *F*0 for younger speakers. These production differences likely indicate that younger speakers have developed different phonetic targets for stop production. These different phonetic targets were predicted to result in different enhancement patterns in clear speech: Younger speakers were predicted to enhance *F*0 differences, whereas older speakers were predicted to enhance VOT differences in clear speech. Results indicated that the older group solely used VOT to enhance the contrast in clear speech, whereas the younger group primarily used *F*0 but also demonstrated small VOT enhancement. These results indicate that clear speech enhancement strategies reflect phonetic targets. Older and younger speakers have different *F*0 and VOT targets and these different targets conditioned different enhancement strategies.
© *2008 Acoustical Society of America.* [DOI: 10.1121/1.2988292]

PACS number(s): 43.70.Fq, 43.70.Bk [BHS] Pages: 3909–3917

I. INTRODUCTION

The purpose of this study was to investigate the proposal that distinctiveness of phonological categories is enhanced in clear speech through the greater approximation of phonetic targets (Johnson *et al.*, 1993; Lindblom, 1990). For this purpose, the enhancement of acoustic correlates to Korean stop contrasts was examined in hyperarticulated clear speech compared with production in more casual speaking styles. We investigated whether there was a difference in the clear speech enhancement strategies between two groups of Korean speakers, one of which had undergone a diachronic change in the Korean stop system (Silva *et al.*, 2004; Silva, 2006; Wright, 2007). As a result of the sound change, younger speakers are thought to have different phonetic targets than older speakers for Korean aspirated and lenis stops. These different phonetic targets are predicted to result in different enhancement patterns in clear speech production between the two groups.

Talkers tend to adopt a speaking style, termed clear speech, to minimize perceptual confusions when they estimate potential speech perception difficulty on the listener's part. Clear speech is an intelligibility-enhancing mode of speech production. The intelligibility improvement effect of clear speech has been found with normal-hearing listeners (Ferguson, 2004; Krause and Braida, 2004), hearing-impaired listeners, and listeners with limited experience in the test language (Bradlow and Alexander, 2007; Bradlow and Bent, 2002; Ferguson and Kewley-Port, 2002). In addition to this perceptual "clear speech effect," clear speech production has the effect of acoustic-phonetic modification of speech signals. Distinctiveness between phonological categories is enhanced in clear speech compared with conversational speech. This phonological contrast enhancement in clear speech production has been found in single language studies (Ferguson and Kewley-Port, 2002; Picheny *et al.*, 1986) as well as in cross-linguistic studies (Bradlow, 2002; Smiljanic and Bradlow, 2005).

The H & H theory (Lindblom, 1990) provides an explanation for the acoustic-phonetic modifications in clear speech production. The theory hypothesizes that talkers actively adjust articulatory effort according to the perceived difficulty of intelligibility for the listener. When intelligibility could be degraded, talkers will adopt a speech mode called hyperspeech. By hypothesis, talkers use greater articulatory energy in an adaptive effort to increase intelligibility for listeners, and this includes the enhancement of distinctiveness between phonological contrasts. When talkers do not estimate a need to improve intelligibility, they will default to a more economical system-oriented production, which is termed hypospeech. Thus, speech signals vary along the continuum between the two extremes of hypo- and hyperspeech. Clear speech can be viewed as production along the hyperarticulated end of the continuum.

Hyperspeech production may be investigated by the examination of specific phonetic targets associated with phonological categories. These phonetic targets are envisioned as stable, but their attainment variable, depending on produc-

[a)]Portions of this work were presented at the 153rd meeting of the Acoustical Society of America, Salt Lake City, UT, June 2007 and the 17th Japanese-Korean Linguistics Conference, Los Angeles, CA, November 2007.
[b)]Electronic mail: kkang@uoregon.edu

tion constraints, such as articulatory effort, coarticulatory force, and speech rate (Johnson *et al.*, 1993; Moon and Lindblom, 1994). In this view, hyperarticulated clear speech production would approximate phonetic targets most closely. In contrast, hypoarticulation is a phonetic process in which the phonetic targets are underrealized. The implication of this theoretical view is that contrastive phonological categories would be maximally distinctive in hyperarticulated speech due to the greater approximation of phonetic targets.

The contrast enhancement effect of clear speech is supported by studies on various acoustic-phonetic features serving to differentiate phonological categories. First, acoustic correlates to vowel quality were found to be enhanced in clear speech. Vowel space expansion in clear speech has been reported in various languages: Spanish (Bradlow, 2002), English (Bradlow, 2002; Ferguson and Kewley-Port, 2002; Picheny *et al.*, 1986; Smiljanic and Bradlow, 2005), and Croatian (Smiljanic and Bradlow, 2005). Ferguson and Kewley-Port (2002) reported that formant movement over the vowel nucleus was significantly larger in clear speech than in conversational speech. In addition, Moon and Lindblom (1994) found that English front vowels were less coarticulated in clear speech compared to citation-form speech. These results suggest that clear speech production aims at greater approximation of vowel formant target frequencies.

Secondly, vowel duration differences have been found to be enhanced in clear speech in a way related to language-specific phonological structure. Smiljanic and Bradlow (2008) examined the effect of clear speech production on the duration of English tense and lax vowels, English vowels before voiced and voiceless coda stops, and Croatian short and long vowels. Durational analyses indicated a greater durational difference in clear speech for the Croatian short and long vowels and the English vowels before voiced and voiceless coda stops, but not for the English tense and lax vowels, suggesting an effect of language-specific phonological structure on durational enhancement. Additionally, when duration ratio (clear minus conversational divided by conversational) was considered, the proportional duration contrast for both the Croatian vowels and the English vowels before coda stops remained stable.

Finally, enhancement of stop contrasts has been investigated in different languages. However, the results provided so far are inconclusive. Languages differ in the acoustic-phonetic modification of voice onset time (VOT) for stops. In a comprehensive acoustic study of conversationally and clearly produced English sentences, Picheny *et al.* (1986) found that the voicing contrast for English stops was enhanced in clear speech. Significant VOT lengthening for word-initial voiceless stops, but not for voiced stops, was found in clear speech. In contrast, Ohala (1994) did not find an enhancement of the VOT difference between English voiceless and voiced stops in clear speech. Words produced in response to perceptual clarification requests did not show significant VOT enhancement. Recently, Smiljanic and Bradlow (2008) examined the voicing contrast between voiced and voiceless stops in English and Croatian that were produced in conversational and clear speech. For English, VOT for voiceless stops lengthened in clear speech while the VOT for voiced stops remained unchanged. This voicing contrast enhancement occurred only in word-initial position, not in word-medial position. As for Croatian, in clear speech, VOT for prevoiced stops showed a nonsignificant trend toward greater negative values, while the VOT of voiceless stops remained unchanged. When a proportional measurement of VOT as a percentage of stop duration (i.e., closure +aspiration) was considered, the proportional VOT remained stable across the speaking styles.

The combined results from studies on segmental contrast enhancement in clear speech suggest that hyperarticulated clear speech production tends to enhance acoustic distance between phonological categories in a way responsive to the language-specific phonological structure. In the current study, the language-specific influence of phonological structure on clear speech production is investigated in Korean. The Korean stop system manifests a three-way manner contrast termed aspirated, lenis (or lax), and fortis (or tense). In utterance-initial position, the three stop types are all voiceless. Previous studies have shown that aspirated stops have the longest VOT values, fortis stops have the shortest values, while lenis stops have intermediate values, closer or farther from the aspirated stops depending on the study. Vowels following aspirated and lenis stops are breathier than the vowels following fortis stops (indicated by greater H1-H2 values). In addition, fundamental frequency ($F0$) on the vowels following aspirated and fortis stops is higher than that of vowels following lenis stops (for previous studies describing VOT, H1-H2, and $F0$ in Korean stops, see Ahn, 1999; Cho *et al.*, 2002; Hardcastle, 1973; Han and Weitzman, 1970; Kagaya, 1974; Kang and Guion, 2006; Kim, 1965; Kim, 1994; Lisker and Abramson, 1964; and Shimizu, 1996).

However, the acoustic correlates related to the aspirated and lenis contrast have undergone a sound change in speakers born after roughly 1965 (Silva, 2006). In early studies on Korean stops (Han and Weitzman, 1970; Kim, 1965; Lisker and Abramson, 1964), VOT values reported for aspirated stops were high (93–108 ms on average) and values for reported lenis stops were low (30–35 ms on average), so that VOT values for these two stop types did not overlap. As such, VOT was considered to be the primary acoustic correlate to the lenis-aspirated stop distinction and $F0$ was considered a redundant correlate (Silva, 2006, p. 298). In contrast, recent studies, examining speakers born after about 1965, have reported nondistinctive VOT values between lenis and aspirated stops (Kang and Guion, 2006; Silva *et al.*, 2004; Silva, 2006; Wright, 2007). Silva *et al.* (2004, 2006) have proposed that Korean stops are undergoing a diachronic change and that VOT values for Korean aspirated stops have shortened over the past two generations. As a result, the distinction between lenis and aspirated stops, which was previously coded primarily by a VOT difference, has come to be coded primarily by a $F0$ difference on the vowels following the stops. Thus, older (born before 1965) and younger speakers may have different phonetic targets associated with the aspirated and lenis stop contrast.

If younger and older speakers have different VOT and $F0$ targets for the production of Korean aspirated and lenis stops, the H & H theory (Lindblom, 1990) predicts that this

difference in phonetic targets will lead to different enhancement strategies. As phonetic targets are thought to be more greatly approximated in clear speech, different phonetic targets are predicted to result in difference in the usage of VOT and *F*0 between younger and older speakers in clear speech. Specifically, the question addressed here is whether younger and older speakers use different strategies to produce Korean aspirated and lenis stops in clear speech. Younger speakers are predicted to enhance *F*0 differences in clear speech, whereas older speakers are predicted to enhance VOT differences in clear speech.

II. EXPERIMENT 1

A. Participants

The data were collected from two groups of 11 native speakers of Korean. Each group had five male and six female speakers. The age in the "younger" group ranged from 20 to 29 years old and the participants were all born after 1977 (mean=25.8 years). Age ranged from 40 to 60 years old for the "older" group and the participants were all born before 1966 (mean=46.7 years). The speakers were affiliates of the University of Oregon, either foreign students, visiting scholars, or their family members. Self-reported daily use of English was low, especially with older speakers (15% for the older group and 34% for the younger group). None of the participants reported any hearing or speech disorders. All were speakers of the Seoul dialect of Korean.

B. Speech stimuli

The target words used for recordings were prepared to elicit the Korean stops in different speaking styles. For each of the nine Korean stops (aspirated, lenis, and fortis stops at three places of articulation), a pair of target words was selected for a total of 18 target words. Each of the 18 words had an initial CVC syllable, where the onset C was one of the nine Korean stops and V was the low vowel /a/ (see Appendix).

C. Procedure

To investigate potential contrast enhancement in clear speech production among the stop types, recordings were made in three different speaking styles: conversational, citation-form, and clear speech. Unlike previous studies on clear speech, which employed citation-form and clear speech only, the present study included a production task that aimed to elicit more natural "conversational" speech signals as well. Since eliciting true conversational speech in an experimental situation is difficult, this study assumes that the elicited conversational speech should be "more conversational" than citation-form speech even though it is not literally conversational. It is expected that the conversational speech will differ more when compared to clear speech than citation-form speech.

As the target words were repeated using different speaking styles, it was crucial to keep the target words in comparable prosodic and discourse environments. The target words were produced in utterance-initial position in all of the speaking styles. Additionally, all words were in a focused context. In conversational speech, they were focused as the topic of conversation; in the citation-form condition, they were focused as new information in a carrier phrase that was repeated across the trials; and in the clear speech condition, they were focused as new or contrastive information in an isolated context. Thus, prosodic and discourse environments were controlled, allowing for the unconfounded manipulation of the instruction to speak clearly.

Overall, a total of 2376 tokens were obtained, 792 tokens (18 target words $\times$ 2 repetitions $\times$ 22 speakers) for each of the three speech styles. Interaction between the experimenter (the first author of this paper) and the speakers was conducted exclusively in Korean. The recordings were made separately for each speaker in a sound-attenuated booth using a high quality head-mounted microphone (Shure SM 10A) and a Marantz digital recorder (PMD 670). The utterances were digitally recorded at a sampling rate of 22 500 Hz and saved as wave files in a personal computer.

1. Conversational speech

Speech produced in a conversational style was elicited by asking speakers to explain the meaning of the target words or elaborate on the contexts where the target words are commonly used. The target words were real words whose meaning could not be easily explained in one or two words. The aim of choosing real word stimuli with complex definitions was to orient the speakers' attention toward exploring the word meaning. This task was performed first, and speakers were not told about other tasks before beginning. This was to prevent the speakers from noticing the links between the production tasks in different speaking styles.

Each of the 18 target words was presented individually on flash cards using Korean orthography. The target words were presented to each speaker in a random order. The speakers were allowed enough time to explore the meaning of the words. While speakers were giving explanations, the experimenter responded to the speaker by agreeing, disagreeing, or giving his own opinion to the speaker's explanations. This was to make the interaction more conversational.

To make sure that the target words were included in the explanations speakers gave, the speakers were asked to indicate which word they were explaining. The explanations they gave were typically constructed as Korean sentences beginning /__ +nɨn…/, or /__, igʌ+nɨn…/, meaning "__ +TOPIC MARKER…," or "__, this +TOPIC MARKER…." The first two productions of a given target word that occurred in the utterance-initial position were submitted to analysis.

2. Citation-form speech

After the task for conversational speech ended, citation-form speech was recorded. The 18 target words were presented in a random order on 18 flash cards two times each. The speakers produced each target word in a frame sentence, /__ ha.se.yo/. In English this translates to "Say__." Speakers were instructed to produce the sentences at a comfortable speech rate and loudness level. When producing the words, the speakers were asked to read one card at a time and hand

it back to the experimenter. This was to prevent the speakers from reading too fast as is commonly observed when words are read in a list. Thus, they had to pause before reading the next flash card.

3. Clear speech

In order to elicit clearly produced speech, a situation in which listener-oriented careful speech is required was set up. The speakers were asked to imagine that they were teaching Korean to second language learners of Korean and reading out Korean words to their students. In order to assist the speaker reading the different target words clearly, each of the 18 target words was presented with another target word that shared a place of articulation but differed in the type of the initial stop (e.g., 탄탄하다 /t^{h}an.t^{h}an.ha.ta/ and 단단하다 /tan.tan.ha.ta/; 단단하다 /tan.tan.ha.ta/ and 딴딴하다 /t*an.t*an.ha.ta/; 딴딴하다 /t*an.t*an.ha.ta/ and 탄탄하다 /t^{h}an.t^{h}an.ha.ta/). So, each flash card had two of the 18 target words, but only the production of the first word of each pair was submitted to the acoustic measurements. Speakers were instructed to read the target words as clearly as possible and no other instructions, such as to read loudly or slowly, were given to the speakers. In this manner, two productions of each target word were elicited.

D. Measurements

For each of the tokens obtained from the production tasks, three acoustic properties encoding Korean stop contrasts were measured using PRAAT (Boersma and Weenink, 2005). VOT was measured as the time duration between the point of stop burst release and the onset of the periodic portion of the waveform for the initial vowel of the target words. In other words, the VOT measure used here was a true measure of voice onset and did not include a period of nonmodal phonation (if present), following the method described by Lisker and Abramson (1964). Other approaches to measuring VOT have been used for Korean stops. See Wright, 2007, pp. 14–30 for a discussion. H1-H2 and *F*0 were measured on the following vowel. H1-H2, which is the amplitude (dB) difference between the first (H1) and the second (H2) harmonic, was measured just after the first full glottal pulse of the waveform. The onset of the vowel in the waveform was determined by the onset of the first full glottal pulse of the vowel in conjunction with the second formant. The amplitude values were calculated using a narrowband fast Fourier transform spectrum (window length of 30 ms). *F*0 was measured at the temporal midpoint of the vowel using the pitch tracking function in PRAAT. When the pitch line abruptly moved or was discontinued, *F*0 was recorded by measuring the duration of the relevant period in milliseconds and dividing it by 1000.

E. Results

Several statistical tests were used to assess the predictions that the acoustic correlates encoding Korean stop contrasts would be enhanced in clear speech production and that the enhancement would be made differently by younger and older speakers. First, a multivariate mixed analysis of variance (MANOVA) was performed with the following factors: group (younger and older), speaking style (conversational, citation-form, and clear), and stop type (aspirated, lenis, and fortis), with the last two factors treated as repeated measures. Given that Korean stops contrast with one another in VOT, H1-H2, and *F*0, these three acoustic measures were all entered as dependent variables. The individual data points submitted to analysis were an average of the two repetitions of each test item for each speaking condition for each measure. The MANOVA returned significant main effects for group [$F(3,128)=5.34$, $p<0.001$], speaking style [$F(6,125)=54.357$, $p<0.001$], and stop type [$F(6,125)=893.413$, $p<0.001$]. Significant two-way and three-way interactions were found for all combinations of these three factors (*F*-values ranged from 6.21 to 19.207, $p<0.001$). These results indicate that the Korean stops were produced differently by the different groups, in different speaking styles. In order to further explore the interactions, the data were split by age group, and then the effects of speaking style and stop type on each of the three acoustic properties were investigated in separate repeated measure ANOVAs. Both subject (*F*1) and item (*F*2) analyses were run. Both factors were treated as repeated measures in the subject analysis, but only speaking style was treated as repeated in the item analysis. Due to the fairly large degrees of freedom, the most conservative statistic, the lower bound, is reported here, and the focus of the analysis is on the interaction of speaking style and stop type. Main effects are only reported in the absence of significant interactions. Our hypotheses revolved around the interactions, as we sought to determine the nature of the speaking style effect as modulated by stop type for each dependent measure.

1. Younger group

For the younger group, univariate tests for each of the dependent measures VOT, H1-H2, and *F*0 revealed significant interactions for the factors speaking style and stop type for both subject and item analyses (VOT [$F1(1,65)=10.220$, $p=0.002$, $F2(2,15)=12.223$, $p=0.001$], H1-H2 [$F1(1,65)=11.730$, $p=0.001$, $F2(2,15)=10.091$, $p=0.002$], and *F*0 [$F1(1,65)=12.281$, $p=0.001$, $F2(2,15)=26.496$, $p<0.001$]). Thus, the patterns found in the subject analyses are consistent across different test items. These interactions are seen in Fig. 1 and interpreted in the paragraphs below.

As shown in Fig. 1(a), the interaction for VOT is due to differences in the patterning for the stop types across the speech styles. VOT for aspirated stops slightly increased in citation-form and clear speech while that for lenis stops slightly decreased. As a result of this, the VOT distance for the aspirated and lenis stop contrast expanded in clear speech.

As for the H1-H2 measure, the interaction is due to the enhancement pattern of fortis stops [see Fig. 1(b)]. Vowels following fortis stops had a more negative H1-H2 value in clear speech, indicating greater creaky voice quality in this speech style. On the other hand, the other stop types showed minimal effects of speech style.

The interaction for *F*0 is seen in Fig. 1(c). *F*0 increased in clear speech production for all of the three stop types.

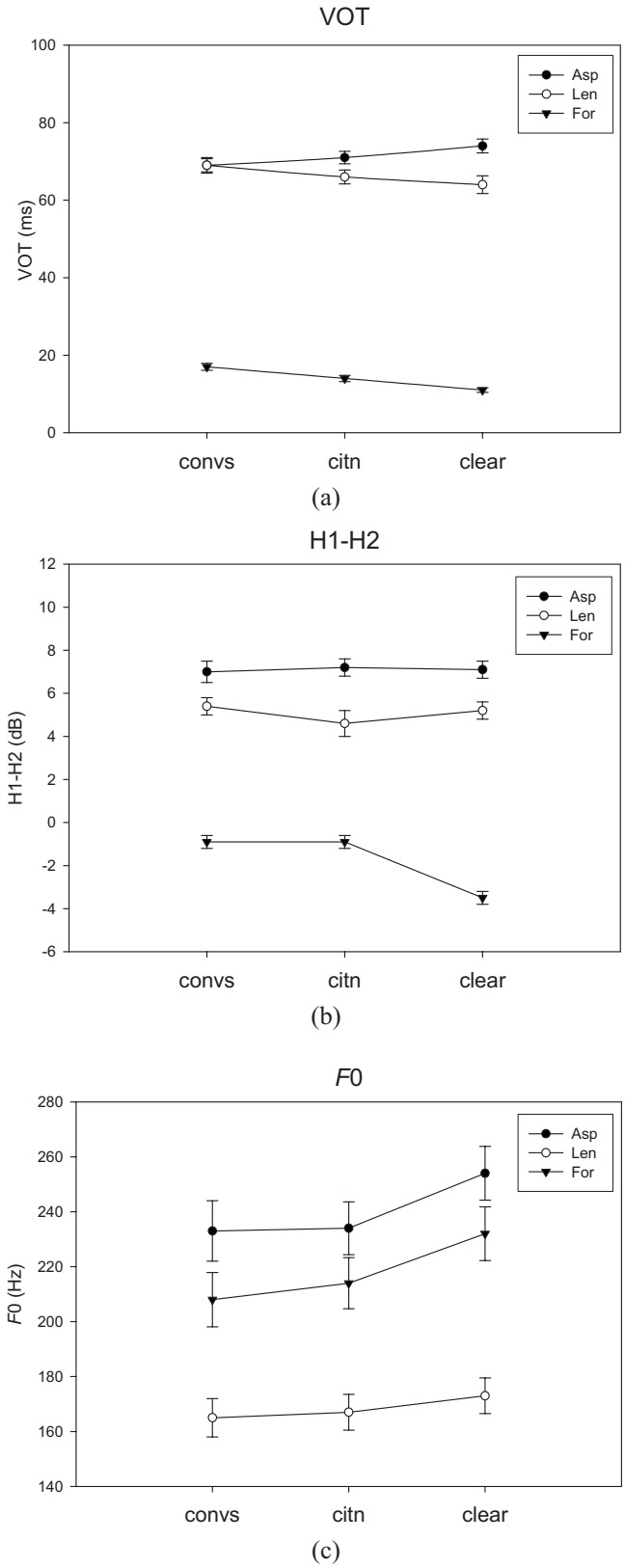


FIG. 1. Mean values with standard errors for the production of Korean stops (aspirated, lenis, and fortis) in conversation, citation-form, and clear speech styles by the younger group ($n=11$) for three acoustic correlates [(a) VOT, (b) H1-H2, and (c) $F0$].

However, because the $F0$ increase in clear speech for vowels following aspirated and fortis stops was relatively larger than that of lenis stops, the $F0$ distance between lenis stops and the other two stop types was expanded in clear speech.

2. Older group

For the older group, univariate tests returned significant interactions of speaking style by stop type for each of VOT, H1-H2, and $F0$ (VOT [$F1(1,65)=14.717$, $p<0.001$, $F2(2,15)=7.867$, $p=0.005$], H1-H2 [$F1(1,65)=5.826$, $p=0.019$, $F2(2,15)=5.850$, $p=0.013$], and $F0$ [$F1(1,65)=12.208$, $p=0.001$, $F2(2,15)=19.223$, $p<0.001$]). Interactions between speaking style and stop type are displayed in Fig. 2.

Figure 2(a) shows that the VOT distance between aspirated and lenis stops was expanded in clear speech. Mean VOT for lenis stops decreased substantially, whereas that for aspirated stops was roughly the same between conversational and clear speech.

As for the H1-H2 measure [see Fig. 2(b)], the interaction was due to the substantial reductions found in citation-form and clear speech for fortis stops. These results indicate that fortis stops were produced with creakier voicing on the following vowels in these speaking styles, whereas the other two stop types showed little effect of speech style.

Finally, for the $F0$ measure, the interaction was primarily reflected in the patterning in citation-form speech [see Fig. 2(c)]. The mean $F0$ for aspirated and fortis stops decreased vis-a-vis the other two speaking styles. Also, in clear speech, mean $F0$ for aspirated stops slightly decreased compared to conversational speech, whereas mean $F0$'s for lenis and fortis stops increased. Consequently, the overall $F0$ distance among the stop categories was slightly reduced in clear speech.

F. Discussion

The results of the analyses suggest that the phonological contrasts between the Korean stops are enhanced in clear speech production for both the younger and older speakers, but in a different manner. The younger speakers produced Korean aspirated and lenis stops with merged VOT values in the conversational condition. However, in clear speech, the two stops were differentiated with a small VOT difference of 10 ms. In addition, the H1-H2 difference between the fortis and the other two stop types was more exaggerated in clear speech, as the following vowels became even creakier in the context of fortis stops, but not in other stop contexts (the difference between aspirated and fortis stops in conversational speech was 7.9 dB, and 10.7 dB in clear speech). The $F0$ difference between the lenis and the other two stop types was also enhanced in clear speech by a greater $F0$ increase in the vowels following the aspirated and fortis stops than the lenis stops (the difference between aspirated and lenis stops in conversational speech was 68 Hz, and 81 Hz in clear speech).

For the older speakers, a VOT difference between aspirated and lenis stops was found in conversational speech, but the difference became even greater in clear speech (18 ms difference in conversational speech and 31 ms difference in clear speech). As for the H1-H2 measure, fortis stops and the other two stop types, aspirated and lenis, became more distinctive from each other in clear speech due to enhanced creaky voicing on the vowels following fortis stops (the dif-

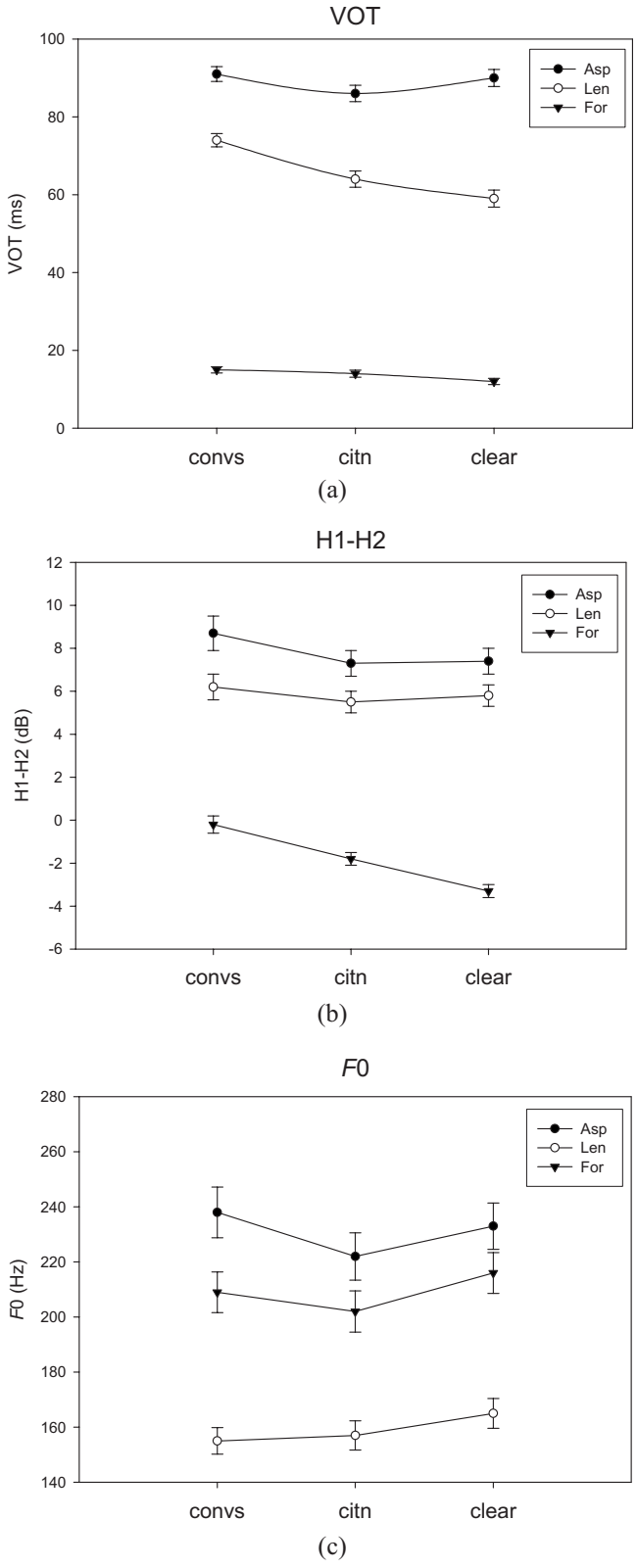


FIG. 2. Mean values with standard errors for the production of Korean stops (aspirated, lenis, and fortis) in conversation, citation-form, and clear speech styles by the older group ($n=11$) for three acoustic correlates [(a) VOT, (b) H1-H2, and (c) $F0$].

ference between aspirated and fortis stops in conversational speech was 9 dB, and 10.7 dB in clear speech). Finally, in contrast to the case of the younger speakers, the $F0$ difference between the stop categories reduced in clear speech production (the difference between aspirated and lenis stops in conversational speech was 84 Hz, and 68 Hz in clear speech). As a result, $F0$ did not enhance any phonological distinctions in clear speech production in the case of the older speakers.

To sum up, these results indicate that there is a difference in the use of VOT and $F0$ to enhance the aspirated and lenis stop contrast between the two age groups. The older group used VOT, whereas the younger group used both VOT and $F0$, with $F0$ being a stronger correlate. However, interpreting the difference in $F0$ enhancement in clear speech between the two groups requires closer examination. One question that arises is whether the greater $F0$ difference in clear speech for the younger speakers was induced by the enhancement of a phonetic target used to realize the phonological contrast of aspirated and lenis stops, or whether it was due to an overall greater $F0$ use by the younger speakers in the clear speech style. That is, an alternative interpretation of the results may be that the younger speakers generally use $F0$ more robustly than older speakers, and that the $F0$ enhancement in clear speech is simply attributable to a larger $F0$ range in clear speech.[1] In order to test this alternative possibility, another experiment was conducted with a separate set of test items containing nonstop consonants.

III. EXPERIMENT 2

Experiment 2 examines $F0$ variation of aspirated consonants as a function of speaking style in comparison with lenis consonants. The purpose was to investigate the question of whether the $F0$ enhancement of the younger speakers in experiment 1 was due to a phonological contrast enhancement between the aspirated and lenis stops or an expanded $F0$ range in clear speech. Specifically, the phrase initial tonal contrast between the high-tone associated Korean aspirated and fortis stops and the low-tone associated lenis stops (Cho *et al.*, 2002; Jun, 1993) was investigated in comparison with other nonstop consonants showing a similar tonal specification phrase initially. Thus, a high-tone triggering voiceless fricative /h/ and a low-tone triggering voiced nasal /n/ were examined for their $F0$ realization in citation-form and clear speech. If the larger $F0$ difference in clear speech for the younger speakers were induced by a generally greater pitch enhancement regardless of segment type, the $F0$ difference for the vowels following /h/ and /n/ would be greater in clear speech than in citation-form speech, similar to the pattern found for the aspirated and lenis stops. On the contrary, if the $F0$ differentiation was part of the enhancement strategy for the phonological contrast of the aspirated and lenis stops, the $F0$ difference between the vowels following /h/ and /n/ would not be enhanced in clear speech for either the younger or the older speakers.

A. Participants

Twenty native Korean speakers who did not participate in experiment 1 were recruited. The participants were grouped separately based on their age. The ten younger speakers were 19–29 years old (mean of 23 years) and the ten older ones were 40–58 years old (mean of 47 years). All

of the speakers reported that they were born in Seoul or Kyunggi province (i.e., the greater Seoul area) and used the Seoul or Kyunggi dialect of Korean.

B. Procedure

Each of the 20 speakers read 35 Korean words in two speaking styles: citation-form and clear speech. For the citation-form style, the speakers used their own comfortable speech rate and loudness level. For the clear style, they were instructed to read in a "clear" way, as if speaking to a "foreigner" audience who needs greater linguistic-phonetic resources to have full access to the linguistic information.

The carrier phrase, /__la.ko mal.ha.se.yo/, meaning "Say__+QUOTATIVE PARTICLE," was used to ensure that the target words were produced in the same prosodic context in both speaking styles. Each word began with an aspirated or lenis consonant. The initial consonants examined in the analysis were /t^h, h/ for the aspirated series and /t, n/ for the lenis series. The words were 타다 /t^{h}a.ta/'to ride', 하다 /ha.ta/ 'to do', 다도 /ta.to/ "tea ceremony," and 나비 /na.pi/ "butterfly." Each word was produced three times in three separate blocks for each speaking style. The reading was recorded at a sampling rate of 22 050 Hz using a portable Marantz digital recorder (PMD 670) and a high quality headset microphone (Shure SM10A). The recording was made in a sound-attenuated booth or in a quiet room at the participants' home. The recorded utterances were saved to a computer in a wave sound format. *F*0 was measured on the first syllable of the utterance-initial target words. *F*0 was obtained at the temporal midpoint of the vowel using the pitch analysis function of PRAAT (Boersma and Weenink, 2005).

C. Results

The *F*0 measurements for the aspirated /t^h/ and /h/ and the lenis /t/ and /n/ consonants were submitted to a three-way repeated measures ANOVA. Speaking style (citation-form and clear speech), condition (stop /t^h, t/ and continuant /h, n/), and consonant type (aspirated /t^h, h/ and lenis/t, n/) were entered as factors. Mean *F*0 values across three repetitions of each test item were used as the dependent measure.

Analyses were conducted separately for each of the younger and older speaker groups. The test for the younger speakers returned significant main effects for speaking style [$F(1,9)=9.284$, $p=0.014$], condition [$F(1,9)=29.269$, $p<0.001$], and consonant type [$F(1,9)=85.582$, $p<0.001$]. A significant interaction was found for speaking style by consonant type [$F(1,9)=5.471$, $p=0.044$] and for speaking style by condition by consonant type [$F(1,9)=25.081$, $p=0.001$]. These results indicate that the effect of speaking style on the *F*0 difference between aspirated and lenis stop stops, /t^h/ and /t/, was different from that found for the fricative and the nasal, /h/ and /n/. As shown in Table I, the *F*0 difference for the aspirated and lenis stop contrast increased in clear speech (63 Hz versus 76 Hz) due to a higher *F*0 for aspirated stops, whereas the *F*0 difference for the fricative and nasal contrast largely stayed the same (69 Hz versus 72 Hz) between citation-form and clear speech.

TABLE I. Mean *F*0 with standard error in parentheses.

	Younger ($n=10$)		Older ($n=10$)	
	Citation form	Clear	Citation form	Clear
/t^h/	231 (20.2)	244 (20.7)	227 (20.8)	235 (22.7)
/t/	168 (14.8)	168 (13.7)	162 (13.9)	168 (14.8)
/h/	228 (20.2)	236 (20.6)	224 (20.0)	234 (22.3)
/n/	159 (14.0)	164 (13.7)	156 (12.5)	165 (13.9)

In contrast, in the case of the older speakers, the main effect of consonant type (aspirated /t^h, h/ and lenis /t, n/) was the only significant finding [$F(1,9)=59.077$, $p<0.001$]. None of the other main effects or interactions were significant ($p>0.05$). The significant effect of consonant type is due to the large *F*0 difference between aspirated (/t^h, h/) and lenis (/t, n/) consonant types. The results indicate that the older speakers did not differentially enhance *F*0 for the aspirated and lenis stop contrast vis-a-vis that of the continuant contrast (/h/ and /n) between the speaking styles. As shown in Table I, the mean *F*0 differences for the stop contrast, as well as the continuant contrast, marginally increased in clear speech (stops: 65 Hz versus 67 Hz; continuant: 68 Hz versus 69 Hz).

D. Discussion

The results indicate that the greater *F*0 difference in clear speech for the younger speakers is specific to the aspirated and lenis stops: *F*0 difference substantially increased in clear speech for the stop contrast (/t^h/ versus /t/), but increased only slightly for the continuant contrast (/h/ versus /n/). Older speakers showed a similar difference in the two speaking styles for both contrast types. Combined with the results from experiment 1, these results suggest that the greater *F*0 difference for the aspirated and lenis stops found for the younger speakers can be attributed to the greater approximation of the high *F*0 target associated with aspirated stops in clear speech. The results were not consistent with the alternative hypothesis of an overall expanded *F*0 range for the younger speakers.

IV. GENERAL DISCUSSION

Based on the H & H theory (Lindblom, 1990), we predicted that phonological contrasts would be enhanced in clear speech by more fully realizing phonetic targets in an effort to aid listeners in speech perception. Given the sound change in the Korean stop system (Silva *et al.*, 2004; Silva, 2006; Wright, 2007), younger and older Korean speakers were predicted to have different phonetic targets for stop production and, in turn, to display different enhancement patterns in clear speech production. Specifically, for the aspirated and lenis stop contrast, younger speakers were predicted to enhance *F*0 differences, whereas older speakers were predicted to enhance VOT differences.

The results of the two experiments upheld these predictions. The three-way manner contrast of Korean stops was found to be enhanced in clear speech compared with conversational or citation-form speech. Furthermore, there was a

difference in the use of VOT and *F*0 between the younger and older speakers. The older group used VOT in order to enhance the aspirated and lenis contrast in clear speech. The younger group enhanced the difference between aspirated and lenis stops by increasing the relative *F*0 of aspirated stops in clear speech. VOT also slightly diverged for the two stop types in clear speech but to a much lesser degree than the older speakers.

This small VOT usage by younger speakers merits further discussion. One possibility is that the small VOT usage may reflect a small difference in VOT targets between aspirated and lenis stops that is only revealed in clear speech. Phonetic targets may have shifted such that *F*0 is used as a primary acoustic correlate and VOT as a secondary one by younger speakers. In other words, the small VOT usage for the younger speakers may reflect a decreased, yet residual, role of VOT in the distinction of aspirated and lenis stops. Another possibility is that the small VOT usage may not reflect differences in VOT targets between the aspirated and lenis stops. In other words, the stops have the same or quite similar VOT targets. The small VOT dispersion in clear speech may rather reflect an attempt to use acoustic correlates heard in the speech of others. That is, exposure to older speakers, who maintain VOT differences, has resulted in the partial ability to manipulate VOT, as a type of style shifting or mimicking of a more traditional speaking style that employs VOT.

Another finding from this study was that the older group enhanced the VOT difference by lowering the VOT for lenis stops and keeping the VOT for aspirated stops relatively stable across the speaking styles. One may wonder why the VOT for the aspirated stops did not also increase. We believe an explanation may lie in the prosodic environment in which the stops were produced. In studies investigating varying realizations of VOT of Korean stops as a function of different prosodic contexts, Cho and Jun (2000) and Cho and Keating (2001) reported that the VOT values for aspirated and lenis stops in higher domain-initial positions (such as intonational phrase or utterance initial) was greater than in lower domain-initial positions (such as accentual phrase initial). As stimuli were elicited in the utterance-initial position in the current study, we would expect high VOT values for both aspirated and lenis stops due to the domain-initial strengthening effect.[2] In the case of aspirated stops, these high VOT values may be close to the phonetic target, but in the case of lenis stops, these high VOT values may overshoot the phonetic target. Thus, in clear speech production, the lower VOT target for lenis stops may be more closely approximated, resulting in lower VOT values for clear speech. On the other hand, if the utterance-initial position had already conditioned targetlike values for the aspirated stops, an increased VOT in clear speech would not be expected.

The idea that lenis stops have a relatively low VOT target is supported by previous investigations. Early studies report VOT values for lenis stops in the range 21–41 ms, sometimes even overlapping with fortis stops (Han and Weitzman, 1970; Kim, 1965; and Lisker and Abramson, 1964). More recent studies with speakers born in the 1960s or earlier report VOT values from approximately 5 to 40 ms for lenis stops (Cho and Keating, 2001; Wright, 2007).

Now let us address questions about the nature of the Korean stop sound change. One possibility is that the sound change is incremental and, thus, related to speaker's age in a continuous fashion. Another possibility is that the sound change has occurred in the younger speakers but not in the older speakers and, thus, evidence for the change will only be found in the younger group. An examination of individual production revealed no appreciable *F*0 enhancement by any speakers in the older group, suggesting that they have not been affected by the sound change. In the case of the younger group, there was no apparent relationship between age (speakers ranged from 20 to 30 years old) and the amount of *F*0 or VOT enhancement. However, a sample larger than 21 younger speakers in the two experiments may be needed to detect such a gradient relationship. Additionally, data from speakers in the 30–40 year age range would prove probative to the question. Given these findings, we tentatively propose that speakers of the Seoul dialect born in the 1970s or later have, as a whole, undergone the sound change and that speakers before this have not been affected by it.

The H & H theory (Lindblom, 1990) hypothesizes that talkers make articulatory modifications in response to the estimated perceptual needs of the listeners, and such modifications are predicted to result in enhancement of phonological contrasts. The current study presented an instance of stop contrast enhancement in clear speech in Korean, lending typological support to the language universal predictions of the H & H theory. What remains for further research is to experimentally test whether such articulatory modifications result in the improvement of intelligibility for listeners. To this end, a perception study testing the intelligibility improvement effect of clear speech is required. As the Korean stop system is experiencing changes in the acoustic correlates to the stops, differences are predicted between older and younger listeners in the extent to which each acoustic correlate contributes to intelligibility improvement. A perception experiment that individually manipulates the acoustic correlates is in preparation for a subsequent study.

ACKNOWLEDGMENTS

The authors thank Melissa Redford, Mieko Ueno, and three anonymous reviewers for their helpful comments on earlier versions of this manuscript.

APPENDIX

Korean words used in the production tasks for conversational, citation-form, and clear speech. The consonant-vowel sequences submitted to acoustic measurement are bolded.

(1) Aspirated stop series

판판하다	/**p^{h}a**n.p^{h}an.ha.ta/,	"to be even/to be flat"
팔팔하다	/**p^{h}a**l.p^{h}al.ha.ta/,	"to be lively"
탄탄하다	/**t^{h}a**n.t^{h}an.ha.ta/,	"to be solid/to be firm"
탕감하다	/**t^{h}a**ŋ.kam.ha.ta/,	"to write off a debt"

칼칼하다	/**k^{h}a**l.k^{h}al.ha.ta,	"to be spicy (food)/ to have a scratchy throat"
캄캄하다	/**k^{h}a**m.k^{h}am.ha.ta/,	"to be dark/to be gloomy"

(2) Lenis stop series

반반하다	/**pa**n.pan.ha.ta/,	"to be comely/to be pretty"
발발하다	/**pa**l.pal.ha.ta/,	"to break out"
단단하다	/**ta**n.tan.ha.ta/,	"to be hard/to be strong"
당당하다	/**ta**ŋ.taŋ.ha.ta/,	"to be dignified/to be imposing"
간간하다	/**ka**n.kan.ha.ta/,	"to be nicely salted"
감감하다	/**ka**m.kam.ha.ta/,	"to forget entirely/to have no news"

(3) Fortis stop series

빤짝하다	/**p*a**n.c*ak.ha.ta/,	"to shine/to have ephemeral fame"
빵빵하다	/**p*a**ŋ.p*aŋ.ha.ta/,	"to be packed/to have good condition (person)"
딴딴하다	/**t*a**n.t*an.ha.ta/,	"to be strong/to be hard"
땅땅하다	/**t*a**ŋ.t*aŋ.ha.ta/,	"to be short and chubby"
깐깐하다	/**k*a**n.k*an.ha.ta/,	"to be fastidious/to be strict"
깜깜하다	/**k*a**m.k*am.ha.ta/,	"to be pitch dark/to be ignorant"

[1]We thank an anonymous reviewer for bringing this possibility to our attention.

[2]The VOT strengthening effect in higher domain-initial positions has been found in several languages (Hsu and Jun, 1998, in Taiwanese; Jun, 1993, in Korean; and Pierrehumbert and Talkin, 1992, in English), suggesting that it may be a general articulatory process.

Ahn, H. (**1999**). "Post-release phonatory processes in English and Korean: Acoustic correlates and implications for Korean phonology," Ph.D. thesis, University of Texas at Austin, Austin, TX.

Boersma, P., and Weenink, P. (**2005**). "PRAAT: Doing phonetics by computer (Version 4.4) [computer program]," from http://www.Praat.org/ (Last viewed December, 2005).

Bradlow, A. R. (**2002**). "Confluent talker- and listener-related forces in clear speech production," in *Laboratory Phonology 7*, edited by C. Gussenhoven and N. Warner (Mouton de Gruyter, Berlin), pp. 241–272.

Bradlow, A. R., and Alexander, J. A. (**2007**). "Semantic and phonetic enhancement for speech-in-noise recognition by native and non-native listeners," J. Acoust. Soc. Am. **112**, 2339–2349.

Bradlow, A. R., and Bent, T. (**2002**). "The clear speech effect for non-native listeners," J. Acoust. Soc. Am. **112**, 272–284.

Cho, T., and Jun, S.-A. (**2000**). "Domain-initial strengthening as enhancement of laryngeal features: Aerodynamic evidence from Korean," in *Chicago Linguistic Society 36*, edited by J. Boyle, J.-H. Lee, and A. Okrent (Department of Linguistics, University of Chicago, Chicago, IL), pp. 31–44.

Cho, T., and Keating, P. A. (**2001**). "Articulatory and acoustic studies on domain-initial strengthening in Korean," J. Phonetics **29**, 155–190.

Cho, T., Jun, S.-A., and Ladefoged, P. (**2002**). "Acoustic and aerodynamic correlates of Korean stops and fricatives," J. Phonetics **30**, 193–228.

Ferguson, S. (**2004**). "Talker differences in clear and conversational speech: Vowel intelligibility for normal-hearing listeners," J. Acoust. Soc. Am. **116**, 2365–2373.

Ferguson, S., and Kewley-Port, D. (**2002**). "Vowel intelligibility in clear and conversational speech for normal-hearing and hearing-impaired listeners," J. Acoust. Soc. Am. **112**, 259–271.

Han, M. S., and Weitzman, R. S. (**1970**). "Acoustic features of Korean /P,T,K/, /p,t,k/, and /p^{h},t^{h},k^{h}/," Phonetica **22**, 112–128.

Hardcastle, W. J. (**1973**). "Some observations on the tense-lax distinction in initial stops in Korean," J. Phonetics **1**, 263–272.

Hsu, C.-S., and Jun, S.-A. (**1998**). "Prosodic strengthening in Taiwanese: Syntagmatic or paradigmatic?," UCLA working papers in phonetics **96**, 69–89.

Johnson, K., Flemming, E., and Wright, R. (**1993**). "The hyperspace effect: Phonetic targets are hyperarticulated," Language **69**, 505–528.

Jun, S.-A. (**1993**). "The phonetics and phonology of Korean prosody," Ph.D. thesis, Ohio State University, Columbus, OH.

Kagaya, R. (**1974**). "A fiberscopic and acoustic study of Korean stops, affricates, and fricatives," J. Phonetics **2**, 161–180.

Kang, K.-H., and Guion, S. G. (**2006**). "Phonological systems in bilinguals: Age of learning effects on the stop consonant systems of Korean-English bilinguals," J. Acoust. Soc. Am. **119**, 1672–1683.

Kim, C.-W. (**1965**). "On the autonomy of the tensity feature in stop classification (with special reference to Korean stops)," Word **21**, 339–359.

Kim, M.-R. C. (**1994**). "Acoustic characteristics of Korean stops and perception of English stop consonants," Ph.D. thesis, University of Wisconsin at Madison, Madison, WI.

Krause, J., and Braida, L. (**2004**). "Acoustic properties of naturally produced clear speech at normal speaking rates," J. Acoust. Soc. Am. **115**, 362–378.

Lindblom, B. (**1990**). "Explaining phonetic variation: A sketch of the H and H theory," in *Speech Production and Speech Modeling*, edited by W. J. Hard-Castle and A. Marchal (Kluwer, Dordrecht), pp. 403–439.

Lisker, L., and Abramson, A. S. (**1964**). "A cross-language study of voicing in initial stops: Acoustical measurement," Word **20**, 384–422.

Moon, S.-J., and Lindblom, B. (**1994**). "Interaction between duration, context, and speaking style in English stressed vowels," J. Acoust. Soc. Am. **96**, 40–55.

Ohala, J. J. (**1994**). "Acoustic study of clear speech: A test of the contrastive hypothesis," International Symposium on Prosody, Vol. **18**, pp. 75–89.

Picheny, M., Durlach, N., and Braida, L. (**1986**). "Speaking clearly for the hard of hearing II: Acoustic characteristics of clear and conversational speech," J. Speech Hear. Res. **29**, 434–446.

Pierrehumbert, J., and Talkin, D. (**1992**). "Lention of /h/ and glottal stop," in *Papers in Laboratory Phonology II: Gesture, Segment, Prosody*, edited by G. Docherty and D. R. Ladd (Cambridge University Press, Cambridge, UK), pp. 90–117.

Shimizu, K. (**1996**). *A Cross-Language Study of Voicing Contrasts of Stop Consonants in Asian Languages* (Seibido, Tokyo, Japan).

Silva, D. J. (**2006**). "Acoustic evidence for the emergence of tonal contrast in contemporary Korean," Phonology **23**, 287–308.

Silva, D. J., Choi, Y.-J., and Kim, J. E. (**2004**). "Diachronic shift in VOT values for Korean stop consonants," in *Harvard Studies in Korean Linguistics X.S*, edited by Susumo Kuno, Ik-Hwan Lee, John Whitman, Joan Maling, Young-se Kang, and Young-joo Kim (Harvard University, Department of Linguistics, Cambridge, MA), pp. 173–185.

Smiljanic, R., and Bradlow, A. R. (**2005**). "Production and perception of clear speech in Croatian and English," J. Acoust. Soc. Am. **118**, 1677–1688.

Smiljanic, R., and Bradlow, A. R. (**2008**). "Stability of temporal contrasts across speaking styles in English and Croatian," J. Phonetics **36**, 91–113.

Wright, J. D. (**2007**). "Laryngeal contrast in Seoul Korean," Ph.D. thesis, University of Pennsylvania, Philadelphia, PA.

Speaker normalization using cortical strip maps: A neural model for steady-state vowel categorization

Heather Ames and Stephen Grossberg[a)]
Department of Cognitive and Neural Systems, Center for Adaptive Systems, and Center of Excellence for Learning In Education, Science, and Technology, Boston University, 677 Beacon Street, Boston, Massachusetts 02215

(Received 8 December 2007; revised 9 September 2008; accepted 10 September 2008)

Auditory signals of speech are speaker dependent, but representations of language meaning are speaker independent. The transformation from speaker-dependent to speaker-independent language representations enables speech to be learned and understood from different speakers. A neural model is presented that performs speaker normalization to generate a pitch-independent representation of speech sounds, while also preserving information about speaker identity. This speaker-invariant representation is categorized into unitized speech items, which input to sequential working memories whose distributed patterns can be categorized, or chunked, into syllable and word representations. The proposed model fits into an emerging model of auditory streaming and speech categorization. The auditory streaming and speaker normalization parts of the model both use multiple strip representations and asymmetric competitive circuits, thereby suggesting that these two circuits arose from similar neural designs. The normalized speech items are rapidly categorized and stably remembered by adaptive resonance theory circuits. Simulations use synthesized steady-state vowels from the Peterson and Barney [Peterson, G. E., and Barney, H.L., J. Acoust. Soc. Am. **24**, 175–184 (1952).] vowel database and achieve accuracy rates similar to those achieved by human listeners. These results are compared to behavioral data and other speaker normalization models.
© *2008 Acoustical Society of America.* [DOI: 10.1121/1.2997478]

PACS number(s): 43.71.An, 43.71.Es, 43.72.Bs [RSN] Pages: 3918–3936

I. INTRODUCTION: SPEECH LEARNING, NORMALIZATION, AND IMITATION

Fundamental variations in speech exist both between speakers and within the speech of a single speaker. Intraspeaker variability is mainly concerned with the different pronunciations of the same phoneme by a single speaker. These variances can result from differences in phonemic context, including coarticulation effects, accent, and the emotions or stress level of the speaker. Interspeaker variability concerns the variation of speech across speakers and these variations generally have a much larger effect on perception (Nearey, 1989). Despite this variability, a listener is able to identify and understand speech spoken by different speakers on the first encounter with a speaker and on nearly the first utterance. It seems that, not only does the listener's brain learn to store a speaker-invariant representation of speech, but that somehow the speech encountered is transformed, or speaker normalized, into a speaker-invariant representation for the purpose of understanding.

The process of speaker normalization enables a baby to begin to imitate sounds from adult speakers, notably parents whose spoken frequencies differ significantly from those that the baby can babble. A circular reaction from endogenously babbled to heard sounds enables a baby to learn a map between the auditory representations of its own heard babbled sounds to the motor commands that caused them (Piaget, 1963; Grossberg, 1978; Cohen *et al.*, 1988; Bullock *et al.*, 1993; Guenther, 1995; Guenther *et al.*, 2006). Speaker normalization enables sounds from adult caretakers to be filtered by this learned map and to thereby enable the baby to begin to imitate and refine heard sounds in its own language productions. Learning in such an imitative map needs to remain active for many years in order to enable an individual's changing voice through puberty and adulthood to continue to activate and update this map.

Speaker normalization also enables language meanings that were learned from one teacher's voice to be readily understood when uttered by another speaker. More generally, speaker normalization helps the brain to overcome a combinatorial explosion that would otherwise occur if the brain needed to store every instance of every speaker utterance in order to understand language meaning.

A similar problem of combinatorial explosion is overcome by the visual cortex as it learns to recognize visually perceived objects in the world. In vision, object category representations are learned that are relatively insensitive to object size, location, and orientation on the retina (Bradski and Grossberg, 1995; Ito *et al.*, 1995). Such invariance is built up across several processing stages, with invariance only appearing in the inferotemporal cortex and beyond. Likewise, speaker normalization is just one stage in the development of rate- and speaker-independent representations of language meaning. For example, Boardman *et al.* (1999) and Grossberg *et al.* (1997) have modeled how rate invariance may develop across several processing stages.

[a)]Author to whom correspondence should be addressed. Electronic mail: steve@bu.edu

 © 2008 Acoustical Society of America

Although speaker normalization and rate invariance are important for learning to speak and understand language, humans and other animals are also exquisitely sensitive to the voice quality and prosody of individual speakers. A similar dichotomy occurs during visual learning and recognition, where positionally invariant object recognition categories coexist with cortical representations that enable manipulation of objects in space. In both audition and vision, this is accomplished through interactions across What and Where cortical processing streams (Ungerleider and Mishkin, 1982; Goodale and Milner, 1992; Hickok and Poeppel, 2007; Fazl, *et al.*, 2008). Such interactions have been predicted to compute computationally *complementary* properties (Grossberg, 2000): the properties needed to compute one such property prevent a complementary property from being computed in the same cortical processing stream, and conversely. Interactions between cortical processing streams that compute such complementary properties enable them to overcome their complementary deficiencies and thus to generate adaptive and creative behaviors. Thus, the present paper's focus on speaker normalization is in no way contradicted by the fact that the brain can process many individual features of speaker identity and prosody. In fact, one property of the present speaker normalization model is that, while it generates a speaker-independent representation, it also marks the speaker-dependent frequencies of the selected speaker from which speaker-dependent properties can be computed in a complementary processing stream.

Another important issue concerns the specificity or generality of speaker-independent language categories. In certain environments, it is essential to distinguish fine differences between speaker utterances that can change language meaning across speakers. In other environments, considerable variability across utterances can lead to a similar meaning. Our model clarifies how such variability can naturally emerge during incremental learning of individual language exemplars. Thus, the fact that humans and animals can sometimes distinguish individual speech exemplars does not imply that language learning is exemplar learning, with all the problems of combinatorial explosion and biologically implausible exhaustive search that such a model can create. Recognition categories can, instead, be learned in a way that tracks the task demands and statistics of each unique environment and that seems to conjointly maximize category generality and minimize predictive error. Neurophysiological data in the visual cortex support this viewpoint (Spitzer *et al.*, 1988; Zoccolan *et al.*, 2007) in a manner predicted by neural models (Carpenter and Grossberg, 1987, 1991, 2003; Carpenter, 1997; Grossberg, 1999; Fazl *et al.*, 2008). Learned category prototypes in such models can represent either individual exemplars or abstract knowledge, as each learning situation uniquely demands. Vowel category simulations in the present paper illustrate this property.

Speaker normalization is also an important technique used in engineering for building automatic speech recognition (ASR) systems. Vowel classification rates in ASR systems can be improved if features are speaker normalized before classification (Nearey, 1989). The formant ratio theory is a foundation for many speaker normalization techniques. The formant ratio theory states that vowel quality depends on the log frequency intervals between formants (defined as ratios), and that shifting activations along a log frequency axis will generate the invariant representation (Lloyd, 1890a, 1890b, 1891, 1892; Peterson, 1961; Bladon *et al.*, 1984; Sussman, 1986; Sydral and Gopal, 1986; Miller, 1989; Sussman *et al.*, 1997). Formant ratios can be calculated by averaging across formant values for many utterances of a single speaker.

Despite its heuristic appeal, in its classical formulation, formant ratio theory faces two types of problems. First, no mechanism has been proposed to explain how the human auditory system could perform these calculations. How does the brain align cell activities corresponding to the formant frequencies for each utterance? Second, this method requires information contained in many speech samples of a single speaker and thus is not able to account for our ability to understand a speaker in the first utterance that we encounter. It is not biologically feasible for the brain to perform computations across all speech samples it encounters from a speaker, store this information, and then use it to normalize each new utterance encountered for each speaker.

The inability of ASR systems to understand speech in real situations and environments may be due to their lack of adherence to biological auditory principles. As Dusan and Rabiner (2005) pointed out, perhaps it is now time to take a closer look at how the brain performs speech recognition and apply these insights to design novel ASR systems. The modeling work presented in this paper proposes a new method for speaker normalization that makes use of the functional architecture of the brain and builds upon previous modeling work that explains a large amount of data in acoustics, speech perception, and language.

The well-documented existence of tonotopic organization in the auditory cortex, which gives rise to strips of frequency selective cells, serves as the functional architecture within which the speaker normalization transformation is proposed to occur; see Sec. II. Frequency-selective strips provide more representational space within which finer computations can occur. They share some properties with the hypercolumn organization that is ubiquitous in the visual cortex (Hubel and Wiesel, 1962). In vision, hypercolumns occur in cortical maps that represent multiple features of visual objects in physical space. In audition, they occur in cortical maps that represent multiple features of acoustic objects in frequency space.

Such strip maps have earlier been shown capable of explaining key data about auditory streaming, or the separation of acoustic sources (Grossberg *et al.*, 2004). Speaker normalization and streaming circuits may have arisen from similar underlying neural designs. In particular, the streaming model circuit and the speaker normalization circuit described herein use both strip maps and asymmetric competition across frequency-selective channels to realize a kind of "exclusive allocation." During auditory streaming, exclusive allocation enables spectral information to be allocated to a specific source or stream (Bregman, 1990). Here, we predict that the exclusive allocation properties that are familiar in streaming research also play a role in generating a speaker-independent representation of speech. Strip maps have also been used to

explain other cortical processes, such as how place-value number systems may be learned (Grossberg and Repin, 2003). Strip maps may thus be a cortical design that has been specialized during brain evolution to accomplish multiple tasks.

As explained below, a simple transformation from speaker-dependent to speaker-independent speech information can be performed within strip maps in a way that is consistent with neurobiological data. The speaker-independent representations are then categorized via a process of fast incremental learning. Results from synthesized steady-state vowel categorization simulations are presented to validate the performance of the speaker normalization model. The results have been briefly reported in Ames and Grossberg (2006, 2007).

II. TONOTOPIC ORGANIZATION AND MULTIPLE STRIP MAPS

The auditory system contains spatially organized maps of frequency selective cells called tonotopic maps. The frequency representations are arranged logarithmically. Tonotopy is preserved in the auditory system from the level of the cochlea to the auditory cortex of humans and other mammals (Tunturi, 1952; Merzenich and Brugge, 1973; Imig *et al.*, 1977; Reale and Imig, 1980; Romani *et al.*, 1982; Seldon, 1985; Luethke *et al.*, 1988; Pantev *et al.*, 1988; Morel and Kaas, 1992; Morel *et al.*, 1993; Heil *et al.*, 1994; Rauschecker *et al.*, 1995; Bilecen *et al.*, 1998; Wessinger *et al.*, 1998; Lockwood *et al.*, 1999; Talavage *et al.*, 2000, 2004; Rauschecker and Tian, 2004). In the auditory cortex, these tonotopic maps consist of iso-frequency contours which can be defined as strips of cortical cells that respond to a specific frequency, or best frequency.

In addition to spectral information that is explicitly in acoustic inputs, missing fundamental frequencies (F0) of harmonic sounds activate the tonotopic maps of the primary auditory cortex of mammals. Single-unit extracellular recordings in marmosets have shown that complex tones with missing fundamentals activate tonotopic areas corresponding to the missing fundamental (Bendor and Wang, 2005, 2006). These maps were found in the low frequency-selective areas on the border of core areas AI and R and the lateral belt areas AL and ML, but did not extend into the entire tonotopic representation of any of these areas. Fishman *et al.* (1998) found an implicit representation of the missing fundamental in AI based on population neuronal responses in awake macaque monkeys. Missing fundamental activations have also been seen in auditory cortical areas of gerbils (Schulze *et al.*, 2002) and cats (Whitfield, 1980; Qin *et al.*, 2005).

In humans, fMRI has been used to show that the lateral Heschl's gyrus is sensitive to the F0 differences of iterated rippled noise when subjects listened to noise with temporally varying patterns (Patterson *et al.*, 2002). Penagos *et al.* (2004) confirmed the existence of this F0-selective region by using fMRI to show that missing fundamental complex tones containing only low frequency harmonics causes a stronger activation in this region than if the tones contained only high frequency harmonics. This difference is attributed to the unresolvability of the high frequencies for listeners. Langner *et al.* (1997) found that a topographically ordered F0 map in human auditory cortex (where F0 was described as the periodicity of the complex sound) may be found orthogonally to the topographically ordered spectral map.

These data confirm that cells in auditory cortex respond selectively to frequencies and F0 in a spatially organized manner, but the exact placement of an F0-sensitive map with respect to a spectral map is unclear. For the purpose of our speaker normalization model, it is assumed that the F0-sensitive map may lie near or within the spectrally activated maps. Simulations were performed to manipulate the amount energy at the F0 filters in order to test the role of F0 in the speaker normalization transformation. The advantages and disadvantages of using F0 for speaker normalization are discussed below.

Our speaker normalization model builds upon the fact that multiple tonotopic maps of frequency-selective strips are found in the auditory cortex of both humans and other mammals (Merzenich and Brugge, 1973; Imig *et al.*, 1977; Morel and Kaas, 1992; Morel *et al.*, 1993; Hacket *et al.*, 1998; Kaas and Hackett, 1998; 2000; Formisano *et al.*, 2003; Rauschecker and Tian, 2004; Petkov *et al.*, 2006). Interactions between such maps are core design features of our speaker normalization model. Map boundaries are defined by frequency reversals such that the low frequency endpoint of one map is adjacent to the low frequency endpoint of the next map. The same occurs for the high frequency endpoints. Talavage *et al.* (2004) used fMRI and frequency-swept stimuli to identify six tonotopic mappings in the superior temporal plane, suggesting that there are at least five areas in the human auditory cortex that exhibit at least six tonotopic organizations. However, the number of maps that exist in the human brain is still uncertain and is difficult to determine with the resolution available in imaging technologies.

The speaker normalization model presented in this paper assumes that at least two of these tonotopic strip maps have an orthogonal, or at least nonparallel, spatial arrangement. The overlapping interactions between these two spectral maps allow the spectral information from different speakers to be aligned along a diagonal map. This diagonal map arrangement underlies the computations needed to shift the speaker-dependent speech information into a speaker-independent representation.

III. AN EMERGING AUDITION, SPEECH, AND LANGUAGE MODEL

The model presented in this paper called the Neural Normalization Network, or NormNet for short. NormNet is part of an architecture for speech perception and recognition that is being developed by Grossberg and colleagues (Cohen *et al.*, 1995; Cohen and Grossberg, 1997; Grossberg *et al.*, 1997; Boardman *et al.*, 1999; Grossberg and Myers, 2000; Grossberg, 2003b; Grossberg *et al.*, 2004); see Fig. 1. At the periphery of this architecture, a Spatial PItch NETwork (SPINET) processes acoustic information and converts the temporally occurring auditory signals into spatial representations of pitch (Cohen *et al.*, 1995; see Fig. 2). Harmonically related spectral components (see stages 6 and 7 in Fig. 2) can activate a given pitch category through an adaptive filter. The

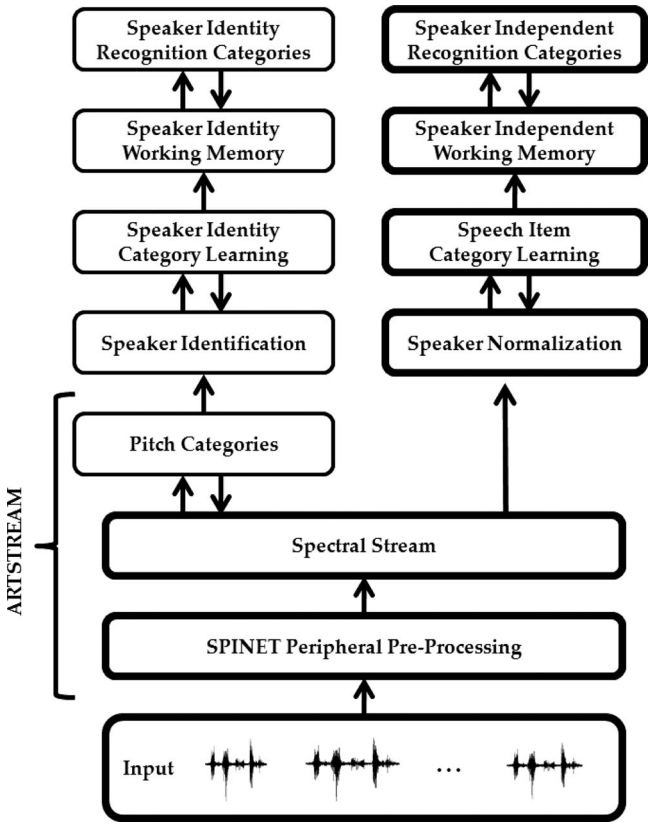


FIG. 1. Box diagram of the ARTSPEECH perception system. The boldface boxes contain components discussed or simulated in this paper.

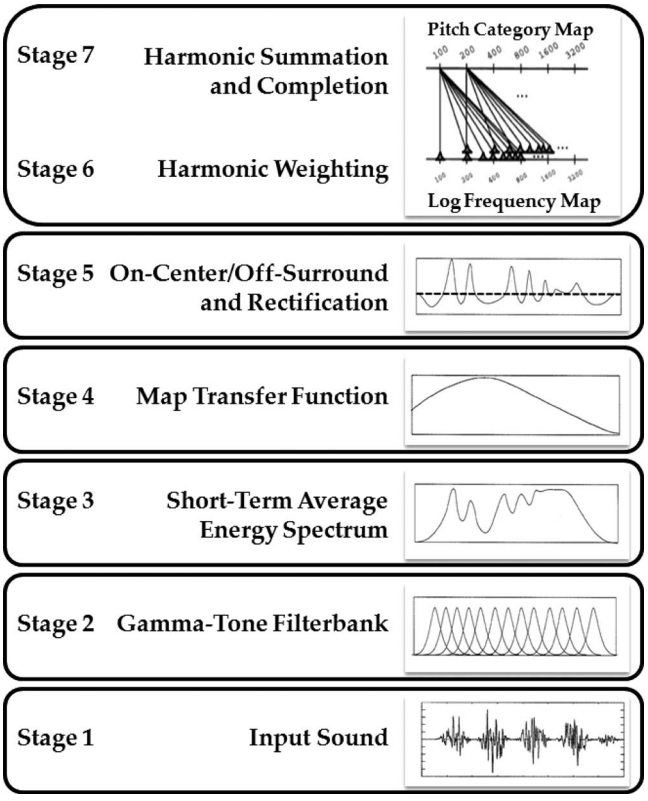


FIG. 2. SPINET model. The processing stages transform a sound stream into activations of spatially distributed pitch nodes. [Reprinted with permission from Cohen *et al.* (1995)].

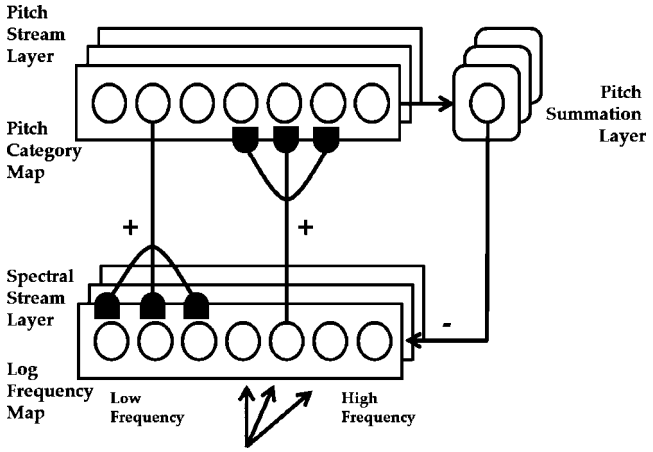


FIG. 3. ARTSTREAM model. The spectral and pitch layers of the SPINET model (layers 6 and 7) are elaborated in the ARTSTREAM model into multiple representations, or strips of cells, and top-down ART matching also occurs. Bottom-up signals group harmonically related spectral components into activations of pitch categories. Inhibition within each pitch stream enables only one pitch category to be active at any time in a given stream. Asymmetric inhibition across streams in the pitch stream layer is biased so that the winning pitch cannot be represented in another stream. The winning pitch category feeds back excitation to its harmonics in the corresponding spectral stream. This stream also receives nonspecific top-down inhibition from the pitch layer. ART matching is hereby realized. It suppresses those spectral components that are not harmonically related to the active pitch. Inhibition across spectral streams then prevents the resonating frequency from being represented in other streams as well. [Reprinted with permission from Grossberg (2003b)].

selection of harmonics is due to learning that is driven by the natural grouping of frequencies in early auditory processing. SPINET hereby creates both spatial representations of pitch and harmonically related spatial activations. This mapping is a crucial feature for the proposed speaker normalization technique.

The SPINET model provides a natural front end for a more comprehensive model of pitch-based auditory streaming that is called the ARTSTREAM model (Grossberg *et al.*, 2004; see Fig. 3). Both the spectral and pitch representations in SPINET are defined by strips of frequency and pitch. The frequency strips in the spectral maps are selective for a particular frequency and are ordered on a log frequency axis. These frequency selective strips are a key organizational structure in ARTSTREAM that allows the model to parse acoustical information into distinct auditory streams that intersect the strips at an orthogonal, or at least nonparallel, angle.

ARTSTREAM derives its name from Adaptive Resonance Theory, (ART) (Grossberg, 1976a, 1976b, 1978, 1980). ART principles and mechanisms have been used to explain and predict data about visual and auditory perception, category learning and object recognition, cognitive information processing, cognitive and emotional interactions, and their underlying brain mechanisms (Carpenter and Grossberg, 1991; Grossberg, 1994, 1999, 2003a; Grossberg and Merrill, 1996; Chey *et al.*, 1997; Grossberg *et al.*, 1997; Grunewald and Grossberg, 1998; Grossberg and Williamson, 1999; Vitevitch and Luce, 1999; Page, 2000; Grossberg and Myers, 2000; Bowers, 2002; Goldinger and Azuma, 2003; Hawkins, 2003; Fazl *et al.*, 2008; Grossberg and Versace,

2008). ART claims that resonant states between top-down expectations and bottom-up input drive stable learning of perceptual and cognitive representations, while preventing catastrophic forgetting of previously learned information.

In the domain of audition, speech perception, and language, models based on ART mechanisms have been used to explain, in addition to auditory streaming, word recognition, and recall (Grossberg and Stone, 1986), manner distinctions in consonant perception (Boardman *et al.*, 1999), consonant integration and segregation in VC–CV syllables (Grossberg *et al.*, 1997), and interword integration and duration-dependent backward effects (Grossberg and Myers, 2000). These models mechanistically embody such design principles as storage in working memory of temporal order information derived from phonemic representations, automatic gain control to maintain rate invariance, and top-down matching of learned expectations with bottom-up patterns of information in order to focus attention on expected combinations of acoustic features and to stabilize fast auditory learning. See Grossberg (2003b) for a review.

ARTSTREAM includes a bottom-up adaptive filter, or "harmonic sieve," that groups together harmonics of an auditory source into learned pitch categories. In addition, a top-down filter encodes the expectations of the learned pitch categories. Each expectation consists of the harmonics of the learned pitch category, which competitively inhibit other frequencies. Both psychological and neurobiological data support the existence of such "biased competition" in the selection of attended data (Grossberg, 1980; Desimone, 1998; Grossberg, 1999; Kastner and Ungerleider, 2001; Grossberg, 2003a). An auditory stream forms when a bottom-up adaptive filter and its top-down expectation interact to generate a spectral-pitch resonant state. Through such resonant dynamics, ARTSTREAM is able to coherently select pitch-consistent frequencies, corresponding to both F0-related harmonics and formant frequencies, while suppressing other frequencies. This ARTSTREAM process, along with asymmetric competition across streams, realizes the property of exclusive allocation (Bregman, 1990). Although ARTSTREAM has discussed only the special case of how pitch categories may be learned from spectral information and thereby used to separate distinct acoustic sources, the same ART mechanisms can learn to categorize other speaker-specific properties that can be used for speaker identification.

The spectral information in the selected stream can be the input to the speaker normalization model, since the spectral-pitch resonances, or other speaker-specific resonances, isolate different speaker's sounds from one another; see Fig. 1. Moreover, the spatially organized frequency-selective strips of ARTSTREAM provide the computational substrate that is needed to initiate speaker normalization. The key design principle of frequency-selective strip maps allows these models to seamlessly connect and interact. Isolated vowels are the inputs to NormNet in the current simulations, so the stream-separating mechanisms are neither needed nor simulated.

After speaker normalization is accomplished and the invariant vowels are categorized by an ART network, the speaker-independent vowel categories are in a form that can naturally input to the ARTWORD model of variable-rate speech categorization and word recognition (Grossberg and Myers, 2000).

IV. MODEL DESCRIPTION

Peripheral processing in the NormNet model is based on the SPINET model (Fig. 2) of Cohen *et al.* (1995) with a few modifications. The gammatone filterbank (see stage 2 in Fig. 2) consists of a cascade of fourth order gammatone filters (Holdsworth *et al.*, 1988; Patterson *et al.*, 1988; Cohen *et al.*, 1995),

$$GT(f) = [1 + j(f - f_i)/b(f_i)]^{-4}. \quad (1)$$

The center frequencies (f_i) of the filters range from 10 to 8000 Hz and are equally spaced in equivalent rectangular bandwidth (ERB) units (Patterson and Rice, 1987; Patterson *et al.*, 1987; 1988; Holdsworth *et al.*, 1988; Slaney, 1998; 1993). The dynamic range corresponds to data measuring the dynamic range in human listeners (Hudspeth, 2000; Plack and Oxenham, 2005). The ERB of a filter at the center frequency (f_i) is a function of the filter center frequency (Glasberg and Moore, 1990),

$$\mathrm{ERB}(f_i) = 24.7 + 0.108^{*} f_i, \quad (2)$$

and the bandwidth $b(f_i)$ of a filter is defined by

$$b(f_i) = \frac{\mathrm{ERB}(f_i)}{0.982}. \quad (3)$$

The output signal from the filterbank is then mapped onto a logarithmic scale, half-wave rectified, and low-pass filtered. This signal serves as the input to the speaker normalization model.

The speaker normalization transformation is proposed to occur in auditory cortex by using at least two intersecting tonotopic strip maps that are assumed, for simplicity, to align orthogonally. The names of these maps are the anchor log frequency map (anchor map) and the stream log frequency map (stream map); see Fig. 4. Because both maps are composed of strips of frequency-selective units, the activations in these maps spread along the strips into an interstrip area where strips from both maps are superimposed upon each other. Both the anchor map and stream map receive spectral information from the speech sound. In the full architecture, this spectral information is predicted to be the streamed output from a process like ARTSTREAM. In the current simplified model, SPINET preprocessing generates the model's spectral input pattern.

Asymmetric competition occurs in the anchor map to choose the cell with the lowest active frequency in the speech sound, which typically contains the largest amount of spectral energy [see Fig. 4(a)]. This cell is called the anchor frequency coding cell. As the anchor frequency coding cell wins the asymmetric competition, it inhibits any activations corresponding to higher frequencies in the anchor map. This form of exclusive allocation is predicted to be a key step in speaker normalization. The asymmetric competition is governed by the following on-center, off-surround shunting equation (Grossberg, 1973, 1980); see Fig. 4(a),

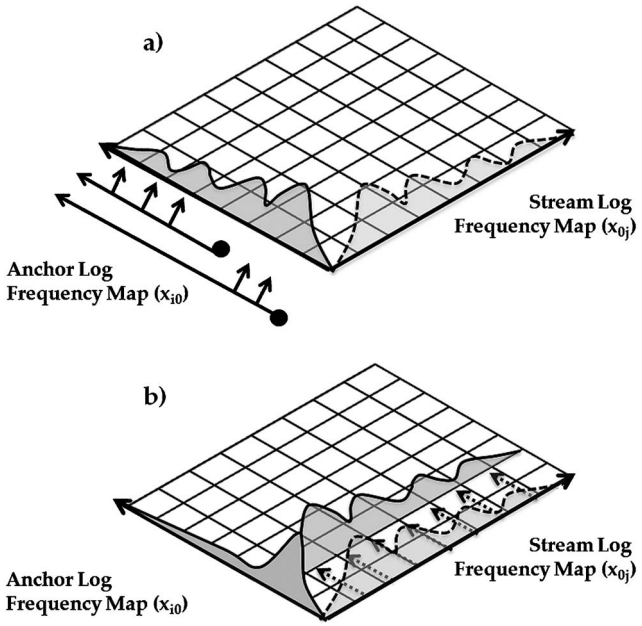


FIG. 4. (a) Anchor map and stream map. These maps are organized orthogonally and superimpose on each other. Both maps receive spatially organized spectral information from the streamed sound. The activations spread along their corresponding strips into the interstream area. (b) Coincidence detection. The winning anchor frequency coding cell triggers a coincidence detection along its anchor frequency strip. This coincidence detection moves the activations of the stream map into the anchor frequency strip.

$$\frac{dx_{i0}}{dt} = -Ax_{i0} + (B - x_{i0})[I_{i0} + f(x_{i0})] - x_{i0}\sum_{i<k} f(x_{k0}), \quad (4)$$

where x_{i0} is the activity of the ith frequency-selective cell in the anchor map, and I_{i0} is the input to this cell in the anchor map. In Eq. (4), $A=0.1$, $B=1$, and $f(x)=x^2$. Since $f(x)=x^2$ is a faster-than-linearly increasing signal function, the activities of cells corresponding to the lowest frequency will increase as the activities of the other cells decrease, resulting in contrast enhancement and winner-take-all choice of the cell whose activity corresponds to the lowest active frequency (Grossberg, 1973).

The cell that codes the anchor frequency triggers coincidence detection along its strip in the inter-strip area where both the anchor map and the stream map activate their corresponding frequency-selective strips. The coincidence occurs in the strip corresponding to the anchor frequency of the anchor map (ith row) and all the active strips corresponding to spectral activations in the stream map (jth columns); see Fig. 4(b). The activity, x_{ij}, of the cell in the ith row and the jth column obey

$$\frac{dx_{ij}}{dt} = -Ax_{ij} + g(x_{i0})I_j, \quad (5)$$

where x_{i0} is the activity of the ith strip in the anchor map, I_j is the spectral representation of the speech sound at the jth strip of in the stream map, the decay rate $A=0.1$, and the anchor map sigmoid signal function

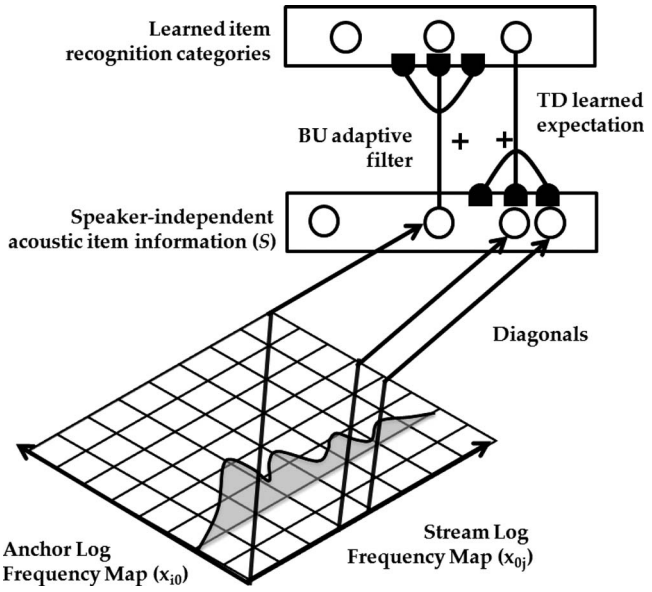


FIG. 5. Creation of speaker-independent working memory item information. The diagonal strips are sampled to create the speaker-independent working memory item information which is then feed into an ART network which learns to categorize the item information.

$$g(x_{i0}) = \frac{x_{i0}^b}{c^b + x_{i0}^b}, \quad (6)$$

where the choices $b=100$ and $c=0.5$ enable $g(x_{i0})$ to approximate 1 at the anchor frequency and 0 elsewhere. Due to coincidence detection $g(x_{i0})I_j$ in Eq. (5), the stream map shifts into the anchor frequency strip and becomes the anchored stream.

Because the anchor map and the stream map have connections which superimpose orthogonally, their coincidences can create diagonally connected strips; see Fig. 5. These diagonal connections transform the anchored stream into a speaker-invariant representation S. In particular, each cell in the S field sums inputs from all the cells along a diagonal created by the maps. The activity s_m of the mth diagonal map cell is thus

$$s_m = \sum_{j=1}^{n} x_{j-m,j}, \quad (7)$$

where n is the number of filters in the gammatone filterbank and m is the cell number in the S field. The speaker-independent spectrum is then categorized into unitized item representations. These learned recognition categories are used for vowel identification.

In this paper, vowel categorization is carried out by a fuzzy ARTMAP network with default parameters (Carpenter *et al.*, 1992); see Fig. 6. Fuzzy ARTMAP is a neural network that incorporates two fuzzy ART modules, ART_a and ART_b, where ART_a learns to map the speaker-independent vowel spectra to vowel categories. An intervening map field F^{ab} learns to associate the vowel categories to category names in ART_b. See the Appendix for the fuzzy ART equations.

When a vowel category is activated during category learning, it reads out a learned top-down expectation that is matched against the input vowel frequency spectrum. A vigi-

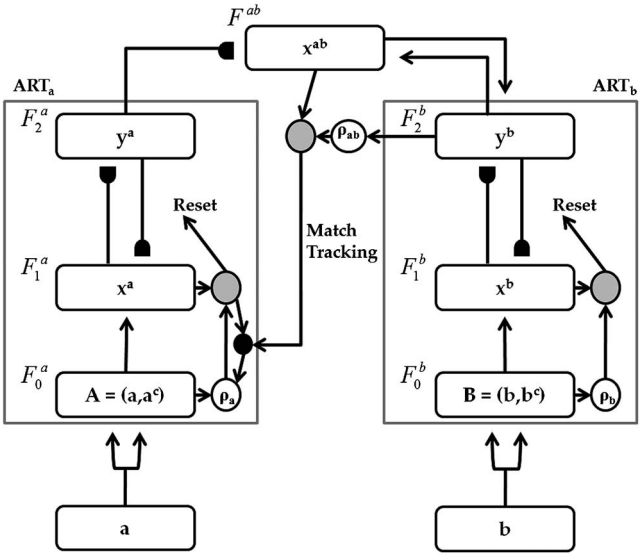


FIG. 6. Fuzzy ARTMAP. The ART_a complement coding preprocessor transforms the M_a vector **a** into the $2M_a$ vector $\mathbf{A}=(\mathbf{a},\mathbf{a}^c)$ at the ART_a field F_0^a. **A** is the input vector to the ART_a field F_1^a. Similarly, the input to F_1^b is the $2M_b$ vector $\mathbf{B}=(\mathbf{b},\mathbf{b}^c)$. When a prediction by ART_a is disconfirmed at ART_b, inhibition of map field activation induces the match tracking process. Match tracking raises the ART_a vigilance (ρ_a) to just above the F_1^a to F_0^a match ratio $|\mathbf{x}^a|/|\mathbf{A}|$. This triggers an ART_a search which leads to activation of either an ART_a category that correctly predicts **b** or to previously uncommitted ART_a category node. [Reprinted with permission from Carpenter *et al.* (1992).]

lance parameter ρ_a determines whether the match is good enough. Learning occurs only if the match is good enough. Then a resonant state can develop that supports the learning process. A predictive failure in category naming at ART_b increases ρ_a by the minimum amount needed to trigger a memory search. Such a memory search automatically leads to learning and/or selection of a new vowel category in ART_a that can better match the vowel frequency spectrum. This process is called *match tracking* (Carpenter *et al.*, 1992). It enables learning of the most general vowel categories that can minimize predictive errors in ART_b. Match tracking is realized in the F^{ab} map field.

The speaker-independent spectral input vectors **A** to the F_1^a field of ART_a are transformed into complement-coded vectors $\mathbf{A}=(\mathbf{a},\mathbf{a}^c)$ before being further processed by ART_a. Complement coding means that both the activities **a** of the network's ON cells and the activities $\mathbf{a}^c=1-\mathbf{a}$ of its OFF cells form the input vector. The inputs **B** to F_1^b field of ART_b are complemented-coded representations of vowel names: $\mathbf{B}=(\mathbf{b},\mathbf{b}^c)$. The values of all components in these input vectors lie between 0 and 1. The activity in the F_1^a field activates a vowel category node, J, in the F_2^a field which, in turn, sends top-down signals to the F_1^a field, where matching between the bottom-up input and the top-down weight vector, $\mathbf{w}_J^a$ of the expectation occurs. If the match is good enough, as determined by the vigilance criterion

$$\rho_a|\mathbf{A}| < |\mathbf{A} \wedge \mathbf{w_J}|, \tag{8}$$

then learning occurs. Inequality (8) describes the balance between excitation and inhibition at a novelty-sensitive orienting system such as the nonspecific thalamus or hippocampus

TABLE I. The ten vowels in the Peterson and Barney (1952) database.

No.	ARPAbet symbol	IPA symbol	/hVd/
1	IY	i	Heed
2	IH	ɪ	Hid
3	EH	ɛ	Head
4	AE	æ	Had
5	AH	ʌ	Hud
6	AA	ɑ	Hod
7	AO	ɔ	Hawed
8	UH	ʊ	Hood
9	UW	u	Who'd
10	ER	ɝ	Heard

(Carpenter and Grossberg, 1993; Grossberg and Versace, 2008). The term $\rho_a|A|$ describes the total amount of excitation that reaches the orienting system. The term $|A \wedge w_J|$ describes the total amount of inhibition that reaches the orienting system. In all, inequality (8) says that inhibition is greater than excitation, so that the orienting system does not fire. The matched patterns are thus allowed to resonate and learning is enabled. When excitation exceeds inhibition, the currently active category is reset and the network continues searching for a better category with which to encode the speaker-independent spectrum. The vigilance ρ_a value in Eq. (8) is a gain control term that determines the network's sensitivity to excitation from the bottom-up total input $|A|$. Increasing vigilance makes the network more sensitive to mismatches, and thus leads to finer categories. At very high vigilance, the network can learn individual exemplars. At low vigilance, it can learn abstract categories that enable many exemplars to be coded by the same recognition category.

During learning, the speaker-independent input pattern **A** is encoded by a vowel category in F_2^a, while the vowel name input pattern **B** is encoded by a name category K in F_2^b. In the present simulations, name category labels are directly input to F_2^b without loss of generality. The map field F^{ab} associates these categories unless J has previously learned to predict a different K category. If this occurs, then match tracking proceeds until an appropriate new ART_a category is chosen and learned. During testing, the speaker-independent input signal **A** activates a name category in ART_b through F^{ab}, which is the prediction of the system. Mathematical details about fuzzy ARTMAP are found in the Appendix.

V. METHODS

A. Stimuli

In order to evaluate the performance of NormNet, the Peterson and Barney (1952) database (Peterson and Barney, 1952; Watrous, 1991) was chosen because it has been widely used as a benchmark database for studying vowel identification. Peterson and Barney originally tape recorded 76 speakers (33 males, 28 females, and 15 children) each speaking 10 vowels twice in a /hVd/ context, resulting in 1520 tokens. The vowels used are found in Table I. The recorded vowels were analyzed and the steady state measurements for F0, F1,

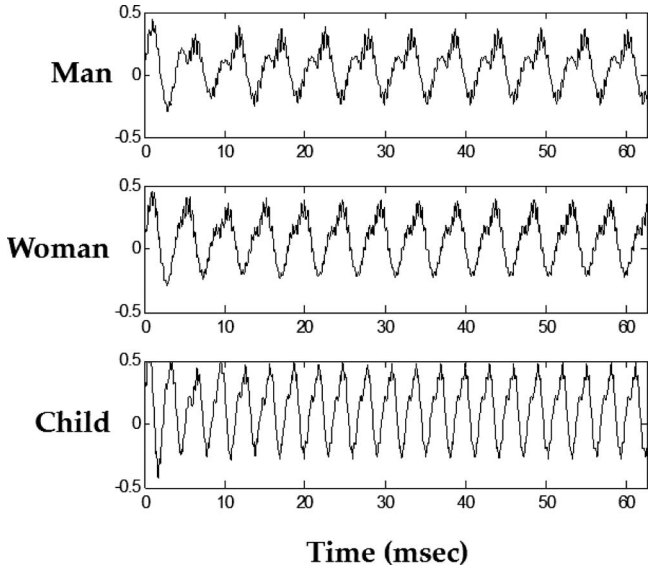


FIG. 7. Waveforms for synthesized steady-state vowel IY. The top plot corresponds to a male, the middle to a female, and the bottom to a child.

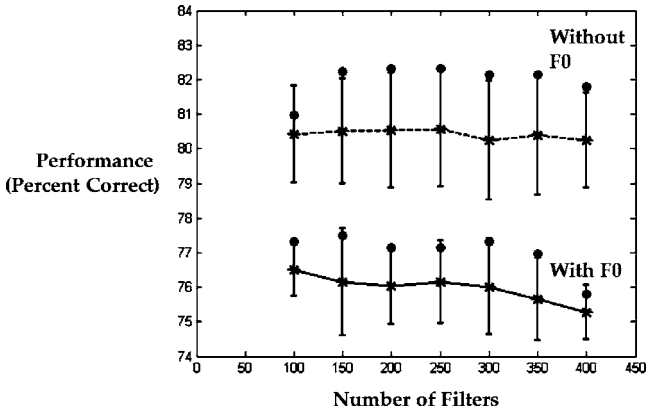


FIG. 8. Filterbank size. The filterbank size was varied from 100 to 400 filters. The dataset was tested both with and without F0 information added to the spectral information of the anchor map. Three runs were performed with each filterbank size. The dynamic range was from 50 to 7500 Hz and the training set size was set to 400 tokens. The dashed line shows the results without F0 information and the solid line shows the results with F0 information in the spectral map. The * indicates the mean plus error bars and the • indicates the best performance for that filterbank size.

F2, and F3 were preserved in the dataset. Listeners in this original study achieved 94% accuracy in recognition tasks when evaluating these vowels in /hVd/ context.

Hillenbrand and Gayvert (1993) synthesized steady-state values corresponding to the values of the formants in the database in order to determine how well listeners can identify vowels based on static spectral cues. Seventeen listeners achieved 72.7% accuracy for the synthesized vowels with flat F0 contours, which hold F0 constant for the duration of the sound stimulus. When F0 movement was added, performance only slightly improved to 74.8% correct. For the purposes of the simulations in this paper, the Hillenbrand and Gayvert (1993) performance will be used as a basis of comparison and the methods of these simulations will attempt to adhere to the methods presented in that paper.

B. Procedure

A vowel synthesizer (Slaney, 1998) was used to generate steady-state versions of all 1520 tokens in the Peterson and Barney (1952) database. Formant frequencies and F0 were held constant for the full duration of the stimulus, similar to the synthesized vowels used by Hillenbrand and Gayvert (1993). The sampling frequency was set at 16 kHz and the formant bandwidth was set at 50 Hz. Waveforms for a sample synthesized vowel, IY for a man, woman, and child are shown in Fig. 7.

In order to assess the performance of the system, several types of simulations were performed. Simulations were conducted by varying vowel lengths, the dynamic range and number of filters of the filterbank, the training set size, and spectral inputs with and without F0 information combined in the mappings.

In order to simulate the natural variances across human listeners, the dynamic range of the filterbank and the number of filters were varied for the simulations. The inputs were presented to the model in random order. The simulations were run on a workstation PC using a dual core AMD Opteron Processor 246 with 1.99 GHz and 3.18 GB of RAM. MATLAB v.7.1 and the auditory toolbox (Slaney, 1998) were used to run the simulations. Statistical analysis was conducted using Statistics To Use (Kirkman, 1996) and Wessa.net (Wessa, 2007) software.

VI. RESULTS

A. Number of filters for the filterbank

Simulations were performed by varying the number of filters (100, 150, 200, 250, 300, 350, 400) while keeping the filter range constant at 50–7500 Hz, 400 tokens in the training set, and three runs for each filterbank size. These simulations were performed both with and without adding F0 information to the input-activated spectral information in the anchor map. The results from these simulations are illustrated in Fig. 8. Interestingly, adding F0 caused model performance to deteriorate by approximately 5%. An analysis of variance (ANOVA) did not show a significant effect for filterbank size ($F[6,14]=0.338$, $p<0.91$).

B. Dynamic range of filterbank

The dynamic range of the filterbank was tested; see Fig. 9. The low frequency was varied from 20 to 180 Hz while the high end was held constant at 7500 Hz. The results of these simulations are illustrated in Fig. 9(a).

These simulations were performed without adding F0 information, with 250 filters, and with a training set size of 400 vowel tokens. The performance of the system was best when the low frequency end was below 100 Hz (approximately 80% correct on average). These data were found to be well fit by a linear model with a negative slope (for the low frequency value: mean performance $R^2=0.87$ and best performance $R^2=0.94$). Performance deteriorated gradually as

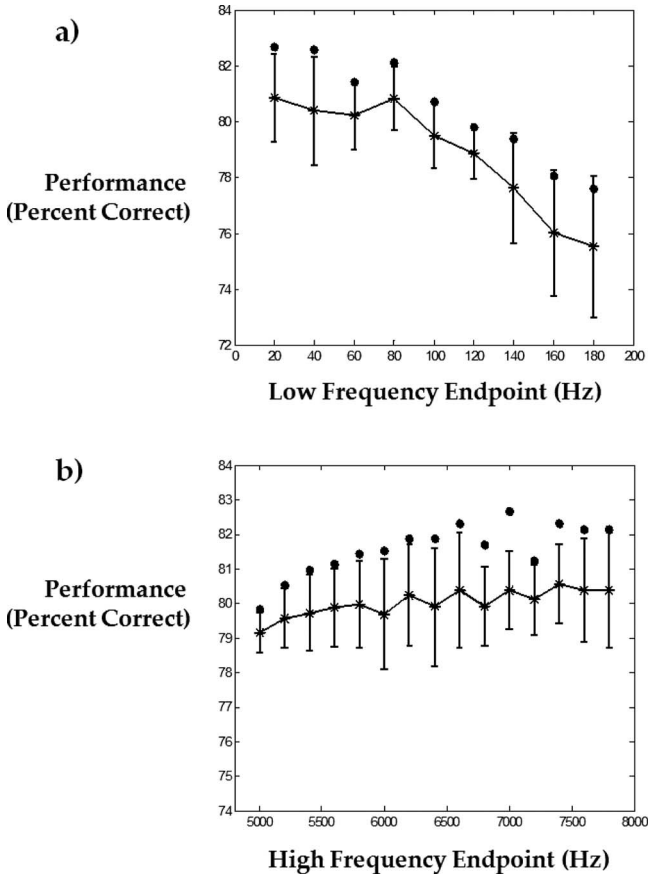


FIG. 9. Dynamic range of filterbank. 250 filters were used in the filterbank, the training set contained 400 tokens, and three runs were performed for each variation. No F0 information was added to the spectrum for these simulations. The * indicates the mean plus error bars and the • indicates the best performance for that variation in the filterbank. (a) The low frequency endpoint was varied from 20 to 180 Hz while the high frequency endpoint was held constant at 7500 Hz. (b) The high frequency endpoint was varied from 5 to 8 kHz while the low frequency endpoint was held constant at 50 Hz.

the lowest frequency was increased from 100 Hz because some of the lower frequency vowels in the databank contain frequency information below 100 Hz.

The high frequency endpoint was also varied from 5 to 8 kHz while the low end was held constant at 50 Hz. The results of these simulations are found in Fig. 9(b). The high frequency manipulation caused less of an effect. When these data were fit to a linear model (for the high frequency value: mean performance $R^2=0.722$ and best performance $R^2=0.629$), the slope was nearly zero (mean performance $=0.00036$ and best performance$=0.00067$), indicating that there is little change in performance across the different high frequency endpoint values. This is because the high frequency range takes into account information above the F3 values and the vowels used in these simulations were synthesized with only F0–F3 information. Generally, the effect of manipulation of the higher formants of the vowel (F3–F5) has a much a smaller effect on vowel identification (Johnson, 2005; Slawson, 1968; Nearey, 1989), and thus we expect that it would have less effect on the model even if we were to test items that contained such information. This prediction has yet to be tested, however.

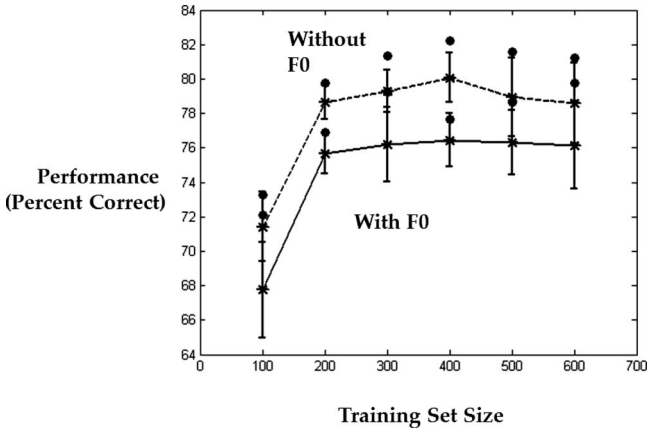


FIG. 10. Training set size. The overall performance when the training set size is varied from 100 to 600 vowels. The dataset is also tested both with and without F0 information added to the spectral information of the signal at the anchor map. Five runs were performed for each training set size. The filterbank consisted of 250 filters ranging from 50 to 7 500 Hz. The best performance, mean, and standard deviation results were recorded. The dashed line shows the results without F0 information added and the solid line shows the results with F0 information added to the spectral map. The * indicates the mean plus error bars and the • indicates the best performance for that training set size.

C. Training set size

Training set size was varied (100, 200, 300, 400, 500, 600) with and without adding F0 information contained in the anchor map. The training set was chosen randomly without replacement. The remainder of the dataset was used for testing. The simulations used a filterbank that consisted of 250 filters ranging from 50 to 7500 Hz. Fig. 10 shows the overall performance results from the different training set sizes. When the training set contained only 100 tokens, performance was the worst near 73% correct. Based on these results, a training set size of 400 achieves the best performance without adding F0 information (82.23% correct). Again, the model performed better without adding F0 information in order to anchor the spectral map.

D. Vowel duration

Vowel duration was varied to determine if steady state vowel duration affects model performance. Three vowel durations were tested (62.5, 300, 600 ms). No additional F0 information was used. The filterbank consisted of 240–260 filters, the dynamic range varied from 20 to 100 Hz on the low end and 7 to 8 kHz on the high end. The training set size was held constant at 400 vowel tokens. Four simulations were run for each vowel duration. Table II shows that varying vowel duration had little effect ($F[2,9]=0.2428$, $p<0.8$). However, the small effect may be because these vowels are steady-state. Varying the duration of naturally produced vowels there may lead to a different outcome.

E. With and without adding F0 information

Three types of F0 simulations were performed. The first did not include any additional F0 information. In the second set, F0 information was only added to the anchor map and the spectral map received only spectral information. In the

TABLE II. The overall performance when the vowel duration varied from 62.5, 300, and 600 ms. The filterbank varied from 240 to 260 filters, and the dynamic range varied from 10 to 100 Hz at the low end and 7 to 8 kHz at the high end. The training set size contained 400 tokens and four runs at each vowel duration were tested. No F0 information was added to the spectrum for these simulations. Percent correction classification in terms of best performance, mean, and standard deviation are recorded.

Vowel duration (ms)	Best performance	Mean	Standard deviation
62.5	81.61	79.96	0.81
300	79.91	79.28	0.49
600	80.80	79.96	0.87

last type of simulations, F0 information was added to the spectral representation and this combination was redundantly mapped as input into both the anchor map and spectral map. F0 information was added to the spectrum to increase the energy at the filter corresponding to F0. These simulations used a training set of 400 vowel tokens of 62.5 ms in duration, a filterbank of 240–260 filters, a low frequency endpoint from 20 to 100 Hz, a high frequency endpoint of 7–8 kHz, and 14 runs of each simulation type. Table III summarizes the results of these simulations. The best performance of 81.61% was found with no F0 information added. The simulations did find a highly significant effect across these conditions ($F[2,39]=41.58$, $p<0.001$) indicating that adding F0 information impaired performance.

VII. DISCUSSION

A. Comparison to human listeners

Comparisons of human identification rates and those of the model can only hope to show a qualitative correspondence because human speakers come to such experiments with full knowledge of a language, and may thus contextually process even reduced speech cues in a way that a model that learns only those cues cannot. In particular, humans may experience filtering and competitive interference properties that a simple model may not. Despite this caveat, human/model comparisons illustrate many similar properties, as noted below.

Simulated identification rates for the synthesized vowels are shown in Table IV (a) along with the identification rates reported by Hillenbrand and Gayvert (1993) for flat F0 stimuli. Table IV (b) shows the results broken down across speaker groups (men, women, and children) from Hillenbrand and Gayvert (1993) and the model. The identification rates across speaker groups for the simulations was significant ($F[2,39]=147.1105$, $p<0.001$). The error rate was lowest for child speakers for both humans and the model. The model had the lowest error rate for the women speakers and the human listeners performed the best for male speakers. This difference may be due to learning in which the model was exposed to randomly chosen synthesized vowel samples from all three speakers groups, whereas human listeners are exposed to a much wider variety of samples in varying context.

TABLE III. The overall performance without F0 information added to either map, F0 information only added to the anchor map, and F0 information added to the spectrum and redundantly mapped into both the anchor map and the stream map. The filterbank varied from 240 to 260 filters, and the dynamic range varied from 10 to 100 Hz at the low end and 7 to 8 kHz at the high end. The training set contained 400 tokens. The vowel duration was set at 62.5 ms. Fourteen runs were performed for each simulation type. Percent correction classification in terms of best performance, mean, and standard deviation are recorded.

F0 information	Best performance	Mean	Standard deviation
Without F0	81.61	79.96	0.81
Only in the anchor map	77.68	76.45	1.54
In both the anchor and stream maps	78.04	77.33	0.64

TABLE IV. (a) Percent correct identification rates for the flat-formant synthesized vowels and (b) percent correct identification rates for the three talker groups (men, women, and children) with flat F0s in both the simulations performed in this study and in the Hillenbrand and Gayvert (1993) study.

(a)	Vowel	Simulation results	Hillenbrand and Gayvert (1993) flat F0
	IY	95.53 ± 1.10	96.2
	IH	86.90 ± 4.91	67.0
	EH	70.28 ± 3.13	65.8
	AE	81.98 ± 1.53	63.2
	AH	83.96 ± 3.81	74.7
	AA	80.39 ± 1.83	55.0
	AO	70.99 ± 7.03	67.2
	UH	81.35 ± 1.97	62.0
	UW	66.10 ± 3.84	89.1
	ER	82.03 ± 4.11	86.6
	TOTAL:	**79.96 ± 0.81**	**72.7**

(b)	Talker group	Simulation results	Hillenbrand and Gayvert (1993) flat F0
	Men	80.35 ± 1.78	74.4
	Women	82.76 ± 0.54	72.2
	Children	72.71 ± 2.10	70.0

The confusion matrices for the Hillenbrand and Gayvert (1993) study are shown in Table V (a) and for the simulations in Table V (b). The simulations performed in this study found an overall accuracy measure of 79.96%, which is better than the 72.7% reported by Hillenbrand and Gayvert (1993).

The confusion matrices for both the Hillenbrand and Gayvert (1993) study and the simulations reported here show that most errors occurred near the diagonal. The layout of the confusion matrix roughly corresponds to the layout of the vowels in F1/F2 space; see Fig. 11. F1/F2 space is considered a rough perceptual mapping of vowels in that there is a relationship between the intended vowel and the formant frequency pattern (Peterson and Barney, 1952). Figure 11(a) shows the vowels that were classified correctly and Fig. 11(b) shows the vowels that were classified incorrectly. The ellipses are drawn based on the Peterson and Barney (1952) dataset. In Fig. 11(b), it is apparent that the majority of the vowel classification errors are near misses which occurred on vowel boundaries in the perceptual F1/F2 space. Fuzzy ARTMAP did a good job of correctly classifying vowels in over-

TABLE V. (a) Confusion matrix reported by Hillenbrand and Gayvert (1993) for synthesized steady state vowels with flat F0 contours. (b) Confusion matrix for synthesized steady-state vowels with flat F0 contours generated with the model. The simulation results reported here are the mean results from fourteen runs. In each run, the filterbank was randomly chosen to be from 240 to 260 filters, and the dynamic range from 10 to 100 Hz at the low end and 7 to 8 kHz at the high end. The training set contained 400 tokens. The vowel duration was set at 62.5 ms.

(a)		IY	IH	EH	AE	AH	AA	AO	UH	UW	ER
	IY	96.2	3.1	0.6	0	0	0	0	0	0	0
	IH	25.1	67.0	6.7	0.3	0.1	0	0	0.6	0	0.1
	EH	1.3	23.7	65.8	7.2	0.3	0	0	0.4	0.1	1.1
	AE	0.1	0.6	28.0	63.2	2.0	4.0	0	0.3	0	1.9
	AH	0	0.1	0.9	0.7	74.7	12.8	6.8	2.7	0.1	1.2
	AA	0	0	0.2	0.1	13.6	55.0	30.5	0.6	0.1	0
	AO	0	0	0	0	8	5.9	67.2	13	5.9	0
	UH	0	0.2	0.1	0	5.2	0.1	3.1	62.0	28.4	0.9
	UW	0.2	0.2	0	0	0.7	0	0.7	9	89.1	0.2
	ER	0.3	4.1	4.0	0.3	0.9	0	0	3	0.7	86.6
(b)		**IY**	**IH**	**EH**	**AE**	**AH**	**AA**	**AO**	**UH**	**UW**	**ER**
	IY	95.53	4.47	0	0	0	0	0	0	0	0
	IH	7.24	86.90	4.28	0	0	0	0	0	0	1.58
	EH	0	16.79	70.28	7.03	0	0	0	0	0	5.90
	AE	0	0	9.25	81.98	7.76	0.31	0	0.12	0	0.56
	AH	0	0	0	2.22	83.96	10.26	3.07	0.25	0	0.25
	AA	0	0	0	2.40	13.50	80.39	2.90	0.81	0	0
	AO	0	0	0	0.33	14.56	8.49	70.99	4.62	1.01	0
	UH	0	0	0	0	0.90	0	4.48	81.35	9.02	4.25
	UW	0	0.12	0.31	0	0	0	1.73	29.21	66.10	2.53
	ER	0	2.72	3.06	3.54	2.72	0	0	5.53	0.41	82.03

lapping F1/F2 space because the system does not cluster vowel boundaries in only F1/F2 space. Rather, it takes into account the entire normalized spectra of the vowels.

Hillenbrand and Gayvert (1993) found that confusions between IY and IH, where IH was heard as IY; between UH and UW, where UH was heard as UW; and between EH and AE, where AE was heard as EH are tense-lax asymmetries. They hypothesized that, when the subjects listened to vowel stimuli without durational cues, they had a tendency to misclassify the vowels as long rather than short vowels. The IH and IY confusions were consistently encountered with the model. However, the model was not as susceptible to the EH and AE confusions. This may be due to the shorter vowel duration (62.5 ms) used by the model as compared to the longer duration (300 ms) used by Hillenbrand and Gayvert (1993) such that the short AE was not misclassified as the long EH when presented with shorter stimuli.

In the simulations with differing vowel durations these confusions were reversed with UW heard as UH. These differences may be due to the initial stimulus setup. When ANOVA is performed at the vowel durations of 62.5, 300, and 600 ms, it was found that the correct classification of UH differs significantly across the different durations ($F[2,9]=4.315$, $p<0.05$) and almost significantly for the correct classification of UW ($F[2,9]=3.320$, $p<0.09$). The best classification was found at the 300 ms vowel duration, which is the same duration used by Hillenbrand and Gayvert (1993). Thus, the 300 ms stimuli seems to provide the best performance for classification of UH where the human subjects had a tendency to classify these vowels as long. When the model was presented with much shorter stimuli (62.5 ms), it classified these vowels as short, with performance improving at the longer vowel durations.

One other difference between Hillenbrand and Gayvert (1993) and the simulations concerns the classification of the vowel AA. Hillenbrand and Gayvert (1993) found that human listeners frequently misclassified AA as AO, whereas the model frequently misclassified AA as AH, AH as AA and AO as AH. All three of these vowels are back vowels for which the tongue is placed near the back of the mouth and roughly corresponds to a smaller difference between F1 and F2 (Lindau, 1978). AA is differentiated from AH and AO in that it is slightly more open and unround, with AH unrounded and AO rounded. Thus, AA and AH differ only by a slight variation in openness, whereas AA and AO also differ in rounding. Finally, Fig. 11 shows that all three of these vowels significantly overlap in F1/F2 space. The confusions made by both human listeners and the model are consistent with the close proximity of these vowels in perceptual space and that both types of confusions are valid.

The last group of differences involves taking into consideration the better classification of AE and EH by the model versus the better classification of IY by human listeners. It seems that the model is biased towards lower values for F1 than human listeners. This may be due to the fact that the low frequency endpoint of the filterbank was varied from 10 to 100 Hz, which may be lower than what is typically found in humans. These differences may also be attributed to the training effects where the model had more exposure to lower harmonics than do humans when learning to speak. In making this comparison, it is also worth noting that the

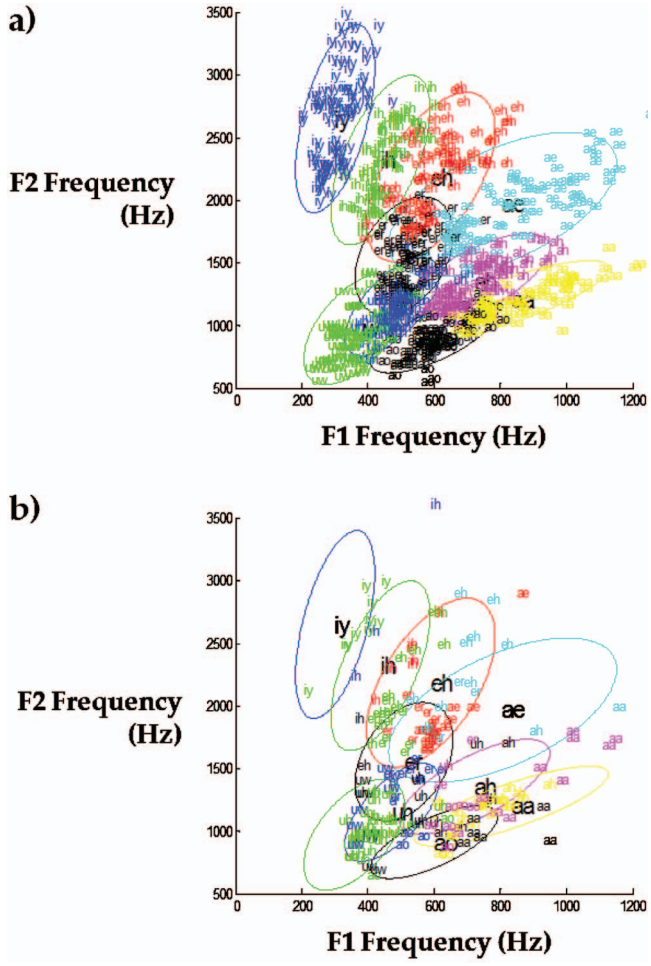


FIG. 11. F1/F2 vowel space. The ellipses correspond to the confidence intervals reported over the entire Peterson and Barney (1952) database where IY is blue, IH is green, EH is red, AE is light blue, AH is pink, AA is yellow, AO is black, UH is dark blue, UW is green, and ER is black. (a) The individual data points correspond to the locations of the correctly classified vowels in the simulations. (b) The individual data points correspond to the misclassified vowels. The color of the data points corresponds to what the vowel should have been classified as and the vowel label at the data point corresponds to what it what misclassified as.

model experienced only the vowel data, whereas humans respond with potential competition from the entire language.

The classification results show that the speaker normalization circuit helped to recognize vowels in the Peterson and Barney (1952) dataset. The training results of the fuzzy ARTMAP classifier also produce important information. During training, fuzzy ARTMAP learns categories corresponding to the vowel categories. In these simulations, only ten categories were learned, corresponding to the ten vowels in the dataset. Therefore, there is a one-to-one mapping between the learned categories and the vowel categories, which indicates the success of the system in creating invariant representations of the vowel categories. If the normalization scheme did not perform well, fuzzy ARTMAP would have learned to select many more categories corresponding to each vowel category. For example, without speaker normalization pre-processing, the classifier learned, on average, thirty categories and the vowel classification performance dropped to 71.95%. The classification rate of the system without normalization was slightly lower than human performance of 72.7% as reported by Hillenbrand and Gayvert (1993).

As summarized above, the vowel identification rates of the model are comparable to those reported by Hillenbrand and Gayvert (1993), with most of the misclassifications lying in adjacent F1/F2 space. The identification rate of 72.7% of Hillenbrand and Gayvert (1993) and the 79.96% reported in these simulations is still significantly less than the 94% accuracy reported by Peterson and Barney (1952) in a vowel recognition task because of the use of three-formant steady-state synthesized vowels. These stimuli are more difficult for listeners and the model because of their lack of context, durational variation, and natural fluctuations of speech. Accuracy greatly improves from 57% to 95% for isolated vowel recognition to 83%–96% in /cVv/ context (Nearey, 1989). Listeners achieved 79% accuracy when listening to vowel recordings, but when the vowels were synthesized with a fixed duration and steady-state formants, only 61% accuracy was achieved (Lehiste and Meltzer, 1973). Listeners could achieve 89% accuracy when vowels were synthesized with their original formant trajectories, but would only achieve 74% accuracy when the vowels were synthesized with flat formants (Hillenbrand and Nearey, 1999).

The ART modeling framework, of which the NormNet forms a part, promises to generalize to more complex speech. Variability in human speech such as durational cues and context cues are best captured by a dynamical system that catches sources of variation in time, that is able to learn from local knowledge available in the speech signal, and that learns in real time. Previous modeling studies have quantitatively simulated speech categorization and word recognition data with these properties (e.g., Grossberg *et al.*, 1997; Boardman *et al.*, 1999; Grossberg and Myers, 2000). The NormNet circuit, when integrated within this emerging theory, will enable it to begin to simulate variable speech perception properties of multiple speakers.

Many studies have shown that speaker normalization is an active process such that listeners are better and faster at word and vowel recognition in single talker lists than in multi-talker lists (Creelman, 1957; Summerfield and Haggard, 1973; Verbrugge *et al.*, 1976) and that listeners retain memory of speaker-specific acoustic detail that influences their memory of previously spoken words (Palmeri *et al.*, 1993; Church and Schacter, 1994; Goldinger, 1996, 1997). Although some authors have suggested that this is evidence against automatic speaker normalization, these results are consistent with the NormNet model. The increased reaction time and decreased performance in the multispeaker lists can be attributed to the switching cost of moving to a new stream and to a new anchor and location within the maps. More generally, such effects may be due to a range of additional interactions between speaker-dependent and speaker-independent processes. This hypothesis is further supported by the study performed by Kato and Kakehi (1988), which showed that accuracy in syllable recognition monotonically increases from the first to the fifth presentation and that accuracy no longer increases on successive presentations. Furthermore, listeners are influenced by expectation of gender

either through auditory cues (Eklund and Traunmüller, 1997; Johnson *et al.*, 1999) or visual cues (Walker *et al.*, 1995; Strand and Johnson, 1996; Schwippert and Benoit, 1997; Johnson *et al.*, 1999). Taken together, these studies may probe how the anchored stream serves as a frame of reference for understanding a speaker and that mismatched expectations or switching between speakers affects reaction time and performance as the model adapts to the variation in the location of the anchored stream.

Kraljic and Samuel (2007) recently reported that although listeners may adjust their internal representations of phonemic categories based on the speaker, this is not always the case. In fact, some of these categorical adjustments are not related to the speaker but may be primed by other cues (e.g., rate in VOT of stop consonants). Therefore, it is necessary for the phonemic categories to learn in real time to adjust to fluctuations both within the speech of a single speaker and across speakers. Such adaptations can occur at multiple levels of the speech perception system.

Johnson (1997a, 1997b, 2005, 2006) suggests that the above-mentioned evidence is supportive of an episodic/exemplar coding model that bases speech perception on a set of stored exemplars that adapt to the perceived identity of the talker. The exemplar models do not make use of speaker normalization and instead rely on the large repertoire of exemplars to feed into category nodes describing the recognized speech sample. However, the limited data simulated with these models fails to show how they can scale up to natural speech and the large variety of speakers encountered in everyday life. To assume that the exemplars are created for each different mode of speaking the same speech sound would assume that the human brain has a massive capacity to store these exemplars, and a way to search among these exemplars in real time. The simulations reported by Johnson (1997b, 2006) do not report the number of exemplars or categories that are learned for each of the words tested. Furthermore, the learning of the word categories based on the set of exemplars requires the use of teacher-based knowledge to create the mapping between the exemplars and the category nodes. The category nodes cannot be created based on local knowledge and in real time.

NormNet is not subject to these sources of criticism. The speaker normalization circuit does not require the storage of instances or exemplars of speech sounds and can learn a single categorical representation for each speech sound. The creation of the invariant speech representations described herein does not require the use of a teaching signal and can be performed in real time with only local knowledge available to the system. The simulation results without normalization show that vowel categorization was poorer (71.95%) and that more vowel categories were created (30.29 nodes generated). Hence, the addition of speaker invariance creates more stable categories and better performance.

More generally, ART-based categorization can, where task demands require, learn both specific, concrete categories, even individual exemplars, as well as general, abstract categories. This learning process enables ART models to selectively pay attention to the learned prototype of critical feature patterns that predict successful performance. High vigilance leads to concrete categories, whereas low vigilance leads to general categories (see Sec. IV and the Appendix). Thus, one does not need to store all exemplars to learn fine distinctions when, in fact, a language requires them. In several senses, the NormNet circuit and the larger ART speech perception network to which it belongs (Fig. 1), embody the phonological principle which states "that languages have basic building blocks, which are not meaningful in themselves, but which combine in different ways to make meaningful forms" (Pierrehumbert, 2006).

B. Comparison to other speaker normalization techniques

Other speaker normalization techniques have been applied to a variety of vowel recognition tasks using different classifiers. Two cues, vocal tract length and F0, are important in these speaker normalization techniques. Interspeaker variability is often attributed to the difference in the shape and length of the vocal tracts, with males typically having longer vocal tracts then females (Lee and Rose, 1998; Stevens, 1998). The correlation between the vocal tract length and the position of the vowel formants contributes to differences perceived by the listener (Fant, 1973). Vocal tract length normalization (VTLN) is based on the assumption that the speech spectrum of one speaker differs from another due to stretching or compression along the frequency axis (Eide and Gish, 1996; Wegman *et al.*, 1996; Lee and Rose, 1996, 1998; McDonough and Byrne, 1999; Dognin and El-Jaroudi, 2003; Glavitsch, 2003). The speech sound is normalized by warping the frequency axis onto a standard vocal tract length. It is, however, unclear how speakers could estimate vocal tract length during naturally occurring language experiences.

Nonlinear (e.g., Eide and Gish, 1996), linear (e.g., Zahorian and Jagharghi, 1991), and bilinear (e.g., Glavitsch, 2003) transformations have all been used in VTLN techniques. The resulting transformation has the same Fourier transform as the original except that it is warped along the frequency axis. Both linear and bilinear transformations have led to increased performance in systems performing speech related tasks (Lee and Rose, 1996; Wegmann *et al.*, 1996; Zhan and Westphal, 1997; Zhan and Waibel, 1997).

Wegmann *et al.* (1996) used a VTLN method in which the frequency warping was done using a piecewise linear transformation of the frequency axis with fixed points at 0 kHz and the Nyquist frequency. Ten warp scales were constructed and each map scale was applied to the speech sound. The best warp scale was chosen through a comparison to a generic voiced speech model. Wegmann *et al.* (1996) reported a 12% reduction in word error rate as compared to unnormalized gender-independent models and a 6% reduction as compared to unnormalized gender-dependent models when tested on the standard Switchboard Corpus (NIST).

Zahorian and Jagharghi (1991) evaluated the effect of both a linear transformation of spectral features and a speaker-dependent frequency warping procedure to evaluate improvement on vowel classification. In both, the normalization parameters were chosen to minimize the mean squared

error between the normalized features and the target features. They found an 8%–15% increase in accuracy, where the accuracy level ranged from 69% to 91%.

It is difficult to compare the performance across these different speaker normalization techniques because of the different data sets and vowel classifiers that were used. A meaningful metric is to compare the performance of each technique to human listeners on comparable tasks. The Peterson and Barney (1952) database contains only steady state vowel information and human listeners are not as good at recognizing steady-state vowels as vowels containing durational and contextual cues. Taking this into account, if the results from the simulations of this paper, 79.96% correct, are compared to the human listeners of the Hillenbrand and Gayvert (1993) study, 72.7% correct, the simulations reported by Nearey *et al.* (1979), with 81% to 92% correct, Sydral and Gopal (1986), with 81.8% to 85.7% correct, and Turner and Patterson (2003), with 79% to 84%, it seems that these other systems may overfit human data, whereas the simulations from this paper adhere more closely to the reported human data.

C. Role of F0 in speaker normalization

F0 is determined by the rate of vibration of the vocal cords of the speaker and thus correlates with the size of the speaker's vocal folds (Titze, 1994). The average values of F0 are lowest in males, around 100 Hz, 200 Hz in females, and up to 400 Hz in infants (Kent and Read, 1992). Because the harmonics of the speech sound correspond to integer multiples of F0, F0 can, in principle, be inferred by the human brain from the spectrum of harmonics even if it is "a missing fundamental" in the signal (Pantev *et al.*, 1989; Ragot and Lepaul-Ercole, 1996).

The distance between F1 and F0 in critical bandwidth is an important cue for perception of vowel openness (Traunmüller, 1981). Speaker-dependent information contained in F0 has also been found to be important in both the recognition of vowels and Mandarin Chinese tones (Johnson, 1990; Moore and Jongman, 1997).

F0 varies greatly amongst speakers and the range of F0 in human speakers can vary from 50 to 800 Hz (Hess, 1983; Ferreira, 2007). The high end of this range, found in female and child speakers and in singing, can result in F0 being comparable to or higher than F1. In addition, it may be the case that the vowel's spectrum may contain a sufficiently small amount of energy for F0. In both of these situations, the asymmetric competition in the model may be compromised. In order to test this concern, additional F0 information was added into the speaker normalization model to anchor the spectral information, which caused performance to decrease. Thus, the F0 information contained in the original vowel spectrum is sufficient for speaker normalization.

F0 has been found to be slightly helpful in understanding speech in both speech recognition systems and human listeners (Glavitsch, 2003; Magimai-Doss *et al.*, 2003). For example, Nearey *et al.* (1979) classified the Peterson and Barney (1952) database with a linear discriminant classifier to identify vowels. They reported 81% correct when the system was trained on log-transformed F1 and F2, 86% correct when F0 and F3 were included, and 92% correct when speaker mean log formant values were subtracted from the individual log formant values. Sydral and Gopal (1986) also used a linear discriminant classifier in which they achieved 81.8% correct when trained on F0 and F1–F3 and 85.7% correct when also trained on three bark-transformed spectral differences (F3–F2, F2–F1, and F1–F0). Turner and Patterson (2003) used a Mellin transform to look at the variation of vocal tract length and achieved 79% to 84% correct. These improvements using F0 are small or modest. In the case of Nearey *et al.* (1979), the classification used F0 information as an additional feature for the classifier rather than for use with the normalization scheme. Sydral and Gopal (1986) used F0 information only to normalize the first formant. Thus, although F0 contains important cues that are useful for human listeners to evaluate the meaning of a speech utterance, F0 may not be needed to normalize typical speech sounds. However, F0 may be more useful in normalizing more extreme cases such as singing or infant-directed maternal speech which in some cases has a very high F0. These cases have yet to be thoroughly tested in NormNet.

VIII. CONCLUSION

The NormNet model provides a proof of principle for a new insight into how speaker normalization may be carried out by the brain. The speaker normalization model was able to achieve accuracy of 79.96% correct, on average, which is comparable to the results obtained with human listeners identifying similar vowel stimuli. The model proposes that tonotopic strip maps of frequency-selective auditory cortical cells and asymmetric competitive interactions are used both to define the auditory streams that characterize acoustic sources, and to normalize the frequency spectra of these streams so that they can be understood across multiple speakers. Figure 12 depicts a hypothetical brain map that unifies multiple streams and the speaker normalization circuit. The way in which strip maps and asymmetric competition may be used in both streaming and speaker normalization circuits is a worthy topic of future research to clarify the predicted shared mechanisms that may be at work.

ACKNOWLEDGMENTS

This work was supported in part by the National Science Foundation (NSF SBE-0354378) and the Office of Naval Research (ONR N00014-01-1-0624).

APPENDIX: FUZZY ARTMAP EQUATIONS

ARTMAP is a neural network that is capable of both unsupervised and supervised incremental learning in response to sequences of binary input vectors presented in real time (Carpenter *et al.*, 1991). Fuzzy ARTMAP can learn stable recognition categories in response to binary or analog input vectors (Carpenter *et al.*, 1992). Learning always converges because all adaptive weights are monotonically increasing.

The fuzzy ARTMAP system consists of two adaptive resonance theory modules, ART_a and ART_b that are linked

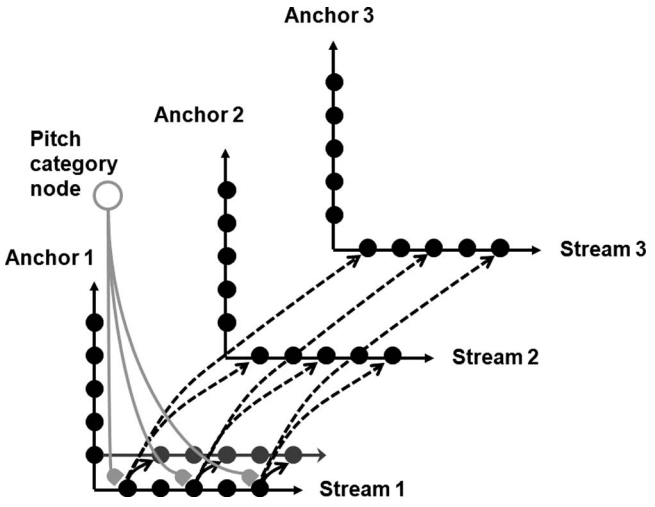


FIG. 12. Unification of multiple streams and their speaker normalization circuit. Three potential streams and their anchor maps are illustrated. The first stream is chosen when its pitch category wins a competition with other streams and uses a harmonic top-down expectation to select the frequencies that are compatible with that pitch. Asymmetric competition with the other streams causes the selected frequencies to be exclusively allocated to that stream. Other streams select their frequency spectra from the remaining frequencies. This selection process determines the anchor frequency for each stream and thereby initiates speaker normalization within each stream by again using asymmetric competition to normalize each selected frequency spectrum in its stream.

together by an inter-ART module, F^{ab}, called a map field (see Fig. 6). During supervised learning, both modules receive a stream of input patterns: $\{\mathbf{a}^{(p)}\}$ and $\{\mathbf{b}^{(p)}\}$ where $\mathbf{b}^{(p)}$ is the correct prediction given $\mathbf{a}^{(p)}$. The inputs to the ART modules are $\mathbf{A}=(\mathbf{a},\mathbf{a}^c)$ for ART_a and $\mathbf{B}=(\mathbf{b},\mathbf{b}^c)$ for ART_b. These inputs are in a complement-coded form. Complement coding combines ON-cell and OFF-cell responses to prevent category proliferation by normalizing the amplitudes of the input feature vectors while preserving the amplitude of individual feature activations. To define complement coding, consider the ART_a module in which the input vector $\mathbf{a}$ is the ON-response. Then the complement of $\mathbf{a}$ is the OFF-response defined as

$$\mathbf{a}_i^c = 1 - \mathbf{a}_i. \tag{A1}$$

Hence, the complement coded input $\mathbf{A}$ is a $2M$ dimensional vector

$$\mathbf{A} = (\mathbf{a},\mathbf{a}^c) = (a_1, \ldots, a_M, a_1^c, \ldots, a_M^c). \tag{A2}$$

Each ART module contains a field, F_0^a and F_0^b, of cells that represent a current input vectors $\mathbf{a}$ and $\mathbf{b}$, respectively. The F_1^a and F_1^b feature fields receive complement-coded inputs $\mathbf{A}$ and $\mathbf{B}$ from F_0^a and F_0^b, respectively, and top-down learned expectations from the F_2^a and F_2^b active learned categories. The number of cell populations in each field is arbitrary. For ART_a, $\mathbf{x}^a=(x_1^a,\ldots,x_{2M_a}^a)$ is the F_1^a output vector, $\mathbf{y}^a=(y_1^a,\ldots,y_{N_a}^a)$ is the F_2^a output vector, and $\mathbf{w}_j^a=(w_{j1}^a,w_{j2}^a,\ldots,w_{j2M_a}^a)$ is the jth ART_a adaptive weight vector. For ART_b, $\mathbf{x}^b=(x_1^b,\ldots,x_{2M_b}^b)$ is the F_1^b output vector, $\mathbf{y}^b=(y_1^b,\ldots,y_{N_b}^b)$ is the F_2^b output vector, and $\mathbf{w}_k^b=(w_{k1}^b,w_{k2}^b,\ldots,w_{k2M_b}^b)$ is the kth ART_b adaptive weight vector. The adaptive weight vectors are associated with each F_2 category cell population j $(j=1,\ldots,2N_a)$ for ART_a and k $(k=1,\ldots,2N_b)$ for ART_b. Each adaptive weight, or long-term memory trace, of the weight vector is initially set to one indicating an uncommitted category. After the category is selected for coding, it becomes committed. In the present simulations, only the F_2^b field is implemented and its nodes are directly activated by category name labels.

The fuzzy ART module, ART_a, requires three parameters to be specified. These parameters are a choice parameter $\alpha>0$, a learning rate parameter $\beta\epsilon[0,1]$, and a vigilance parameter $\rho\epsilon[0,1]$.

Category choice also occurs in both ART modules. The notation for the ART_a module will be listed. The equations are the same for the ART_b module except that the superscript is b and the j subscript in the F_2 field is k. For each input $\mathbf{A}$ and F_2^a node j, the choice, T_j, is defined by:

$$T_j(\mathbf{A}) = \frac{|\mathbf{A}\wedge\mathbf{w}_j|}{\alpha+|\mathbf{w}_j|}, \tag{A3}$$

where the fuzzy and operator $\wedge$ is defined by

$$(\mathbf{p}\wedge\mathbf{q})_i = \min(p_i,q_i), \tag{A4}$$

and the norm $|\,|$ is defined by

$$|\mathbf{p}| = \sum_{i=1}^{M} |p_i|: \tag{A5}$$

for any M-dimensional vectors $\mathbf{p}$ and $\mathbf{q}$.

The ART_a module makes a category choice when at most one F_2^a cell population is active at a given time. This category choice is indexed by J,

$$T_J = \max\{T_j: j=1,\ldots,N\}. \tag{A6}$$

If more than one T_j is maximal, then the category j with the smallest index is chosen. These cells become committed in order of $j=1,2,3,\ldots$. When the Jth category is chosen, $y_J=1$ and $y_j=0$ for all $j\neq J$. The F_1^a activity vector, $\mathrm{x}=\mathbf{A}$ when F_2^a is inactive and $\mathbf{x}=\mathbf{A}\wedge\mathbf{w}_J^a$ if the Jth F_2^a node is chosen.

Resonance and reset are governed by the match value

$$\frac{|\mathbf{A}\wedge\mathbf{w}_J^a|}{|\mathbf{A}|}. \tag{A7}$$

If Eq. (A7) is greater than or equal to the vigilance ρ, then resonance occurs and learning ensues, as defined below. Otherwise, mismatch reset occurs, which results in the choice function T_J being set to zero for the duration of the input presentation to prevent persistent selection and learning of that category. A new index J is then chosen by Eq. (A6) and the search continues until a chosen J achieves resonance.

Resonance triggers learning such that, once the search ends, the chosen weight vector, $\mathbf{w}_J^a$ is updated

$$\mathbf{w}_J^{a(\mathrm{new})} = \beta(\mathbf{A}\wedge\mathbf{w}_J^{a(\mathrm{old})}) + (1-\beta)\mathbf{w}_J^{a(\mathrm{old})}. \tag{A8}$$

Fast learning, as was used in the simulations in this paper, occurs when $\beta=1$.

The map field F^{ab} links the two ART modules and is used to form predictive associations between ART_a and ART_b categories and to perform match tracking. The map field becomes active whenever one of the ART_a or ART_b

categories is active, or when both are active only if ART_a predicts the same category as ART_b through the weights $\mathbf{w}_J^{ab}$. The output vector of the F^{ab} map field, $\mathbf{x}^{ab}=\mathbf{y}^b\wedge\mathbf{w}_J^{ab}$ if the Jth F_2^a category is active and F_2^b is active; $\mathbf{x}^{ab}=\mathbf{w}_J^{ab}$ if the Jth F_2^a category is active and F_2^b is inactive; $\mathbf{x}^{ab}=\mathbf{y}^b$ if F_2^a is inactive and F_2^b is active; and $\mathbf{x}^{ab}=\mathbf{0}$ if F_2^a is inactive and F_2^b is inactive. Thus, $\mathbf{x}^{ab}=\mathbf{0}$ when the prediction $\mathbf{w}_J^{ab}$ is disconfirmed by $\mathbf{y}^b$. This mismatch triggers an ART_a memory search, or hypothesis testing, for a better match via match tracking.

During match tracking, the vigilance parameter of ART_a, ρ_a, increases in response to a predictive mismatch with ART_b in order to ensure that predictive errors are not repeated on subsequent presentations of the input. The parameter ρ_a calibrates the minimum confidence that ART_a must have in a recognition category activated by the input $\mathbf{A}$ in order for the ART_a module to accept that category. Smaller values of ρ_a lead to broader generalization and higher code compression. By match tracking, the minimum amount of generalization necessary to correct a predictive error is sacrificed. In other words, the ARTMAP system embodies a minimax learning rule in which the system strives to minimize predictive error while maximizing predictive generalization.

At the start of the input presentation, ρ_a equals the baseline vigilance and the map field vigilance parameter is ρ_{ab}. If

$$|\mathbf{x}^{ab}|<\rho_{ab}|\mathbf{y}^b|, \tag{A9}$$

then ρ_a is increased until it is slightly larger than the match value in Eq. (A7). Reset occurs and a memory search discovers the next ART_a category to learn. With fast learning, the map field weights $\mathbf{w}_{jk}^{ab}=1$ for all time when J learns to predict the ART_b category name K.

Ames, H. M., and Grossberg, S. (**2006**). "Neural dynamics of auditory streaming, speaker normalization, and speech categorization," Soc. Neurosci. Abstracts, Atlanta, GA.

Ames, H. M., and Grossberg, S. (**2007**). "Speaker normalization using cortical strip maps: A neural model for steady state vowel identification," Comput. Cogn. Neurosci. Conf. Abstracts, San Diego, CA.

Bendor, D., and Wang, X. (**2005**). "The neuronal representation of pitch in primate auditory cortex," Nature (London) **436**, 1161–1165.

Bendor, D., and Wang, X. (**2006**). "Neural representations of pitch in auditory cortex of humans and other primates," Curr. Opin. Neurobiol. **16**, 391–399.

Bilecen, D., Scheffler, K., Schmid, N., Tschopp, K., and Seelig, J. (**1998**). "Tonotopic organization of the human auditory cortex as detected by BOLD-FMRI," Hear. Res. **126**, 19–27.

Bladon, R. A., Henton, C. G., and Pickering, J. B. (**1984**). "Towards an auditory theory of speech normalization," Lang. Commun. **4**, 59–69.

Boardman, I., Grossberg, S., Myers, C., and Cohen, M. (**1999**). "Neural dynamics of perceptual order and context effects for variable-rate speech syllables," Percept. Psychophys. **6**, 1477–1500.

Bowers, J. S. (**2002**). "Challenging the widespread assumption that connectionism and distributed representations go hand-in-hand," Cogn. Psychol. **45**, 413–445.

Bradski, G., and Grossberg, S. (**1995**). "Fast learning VIEWNET architectures for recognizing 3-D objects from multiple 2-D views," Neural Networks **8**, 1053–1080.

Bregman, A. S. (**1990**). *Auditory Scene Analysis* (MIT Press, Cambridge, MA).

Bullock, D., Grossberg, S., and Guenther, F. H. (**1993**). "A self-organizing neural model of motor equivalent reaching and tool use by a multijoint arm," J. Cogn Neurosci. **5**, 408–435.

Carpenter, G. A. (**1997**). "Distributed learning, recognition, and prediction by ART and ARTMAP neural networks," Neural Networks **10**, 1473–1494.

Carpenter, G. A., and Grossberg, S. (**1987**). "A massively parallel architecture for a self-organizing neural pattern recognition machine," Comput. Vis. Graph. Image Process. **37**, 54–115.

Carpenter, G. A., and Grossberg, S. (**1991**). *Pattern Recognition by Self-Organizing Neural Networks* (MIT Press, Cambridge, MA).

Carpenter, G. A., and Grossberg, S. (**2003**). "Adaptive resonance theory," edited by M. A. Arbib, in *The Handbook of Brain Theory and Neural Networks*, Second Edition (MIT Press, Cambridge, MA), pp. 87–90.

Carpenter, G. A., and Grossberg, S. (**1993**). "Normal and amnesic learning, recognition, and memory by a neural model of cortico-hippocampal interactions," TINS **16**, 131–137.

Carpenter, G. A., Grossberg, S., and Reynolds, J. H. (**1991**). "ARTMAP: Supervised real-time learning and classification of nonstationary data by a self-organizing neural network," Neural Networks **4**, 565–588.

Carpenter, G. A., Grossberg, S., Markuzon, N., Reynolds, J. H., and Rosen, D. B. (**1992**). "Fuzzy ARTMAP: A neural network architecture for incremental supervised learning of analog multi-dimensional maps," IEEE Trans. Neural Netw. **3**, 698–713.

Chey, J., Grossberg, S., and Mingolla, M. (**1997**). "Neural dynamics of motion grouping: From aperture ambiguity to object speed and direction," J. Opt. Soc. Am. A **14**, 2570–2594.

Church, B. A., and Schacter, D. L. (**1994**). "Perceptual specificity of auditory priming: Implicit memory for voice intonation and fundamental frequency," J. Exp. Psychol. Learn. Mem. Cogn. **20**, 521–533.

Cohen, M. A., and Grossberg, S. (**1997**). "Parallel auditory filtering by sustained and transient channels separates coarticulated vowels and consonants," IEEE Trans. Speech Audio Process. **5**, 301–318.

Cohen, M. A., Grossberg, S., and Stork, D. G. (**1988**). "Speech perception and production by a self-organizing neural network," in *Evolution, Learning, Cognition, and Advanced Architectures*, edited by Y. C. Lee (World Scientific, Hong Kong), pp. 217–231.

Cohen, M. A., Grossberg, S., and Wyse, L. (**1995**). "A spectral network model of pitch perception," J. Acoust. Soc. Am. **98**, 862–879.

Creelman, C. D. (**1957**). "Case of the unknown talker," J. Acoust. Soc. Am. **29**, 655.

Desimone, R. (**1998**). "Visual attention mediated by biased competition in extrastriate visual cortex," Philos. Trans. R. Soc. London, Ser. B **353**, 1245–1255.

Dognin, P. L., and El-Jaroudi, A. (**2003**). "A new spectral transformation for speaker normalization," Proc. EuroSpeech, pp. 1865–1868.

Dusan, S., and Rabiner, L. R. (**2005**). "Can automatic speech recognition learn more from human speech perception?" Proc. 3rd Conf. Speech Tech. Hum.-Comput. Dialogue, pp. 21–36.

Eide, E., and Gish, H. (**1996**). "A parametric approach to vocal tract length normalization," IEEE Trans. Acoust., Speech, Signal Process. **1**, 346–348.

Eklund, I., and Traunmüller, H. (**1997**). "Comparative study of male and female whispered and phonated versions of the long vowels of Swedish," Phonetica **54**, 1–21.

Fant, G. (**1973**). "Stops in CV syllables," in *Speech Sounds and Features*, edited by G. Fant (MIT Press, Cambridge, MA), pp. 110–139.

Fazl, A., Grossberg, S., and Mingolla, E. (**2008**). "View-invariant object category learning, recognition, and search: How spatial and object attention are coordinated using surface-based attentional shrouds," Cognitive Psychology (in press).

Ferreira, A. J. S. (**2007**). "Static features in real-time recognition of isolated vowels at high pitch," J. Acoust. Soc. Am. **122**, 2389–2404.

Fishman, Y. I., Reser, D. H., Arezzo, J. C., and Steinschneider, M. (**1998**). "Pitch vs. spectral encoding of harmonic complex tones in primary auditory cortex of the awake monkey," Brain Res. **786**, 18–30.

Formisano, E., Kim, D.-S., Di Salle, F., van de Moortele, P.-F., Ugurbil, K., and Goebel, R. (**2003**). "Mirror-symmetric tonotopic maps in human primary auditory cortex," Neuron **40**, 859–869.

Glasberg, B. R., and Moore, B. C. (**1990**). "Derivation of auditory filter shapes from notched-noise data," Hear. Res. **47**, 103–138.

Glavitsch, U. (**2003**). "Speaker normalization with respect to F0: A perceptual approach," TIK Report No. 185, Swiss Federal Institute of Technology Zurich.

Goldinger, S. D. (**1996**). "Words and voices: Episodic traces in spoken word identification and recognition memory," J. Exp. Psychol. Learn. Mem. Cogn. **22**, 1166–1183.

Goldinger, S. D. (**1997**). "Words and voices: Perception and production in an episodic lexicon," in *Talker Variability in Speech Processing*, edited by

K. Johnson and J. W. Mullennix (Academic Press, San Diego), pp. 33–66.
Goldinger, S. D., and Azuma, T. (**2003**). "Puzzle-solving science: The quixotic quest for units in speech perception," J. Phonetics **31**, 305–320.
Goodale, M. A., and Milner, D. (**1992**). "Separate visual pathways for perception and action," Trends Neurosci. **15**, 10–25.
Grossberg, S. (**1973**). "Contour enhancement, short-term memory, and constancies in reverberating neural networks," Stud. Appl. Math. **52**, 213–257.
Grossberg, S. (**1976a**). "Adaptive pattern classification and universal recoding, I: Parallel development and coding of neural feature detectors," Biol. Cybern. **23**, 121–134.
Grossberg, S. (**1976b**). "Adaptive pattern classification and universal recoding, II: Feedback, expectation, olfaction, illusions," Biol. Cybern. **23**, 187–202.
Grossberg, S. (**1978**). "A theory of human memory: Self-organization and performance of sensory-motor codes, maps, and plans," in *Progress in Theoretical Biology*, edited by R. Rosen and F. Snell (Academic, New York), Vol. **5**, pp. 233–374.
Grossberg, S., (**1980**). "How does a brain build a cognitive code?," Psychol. Rev. **87**, 1–51.
Grossberg, S. (**1994**). "3-D vision and figure ground separation by visual cortex," Percept. Psychophys. **55**, 48–120.
Grossberg, S. (**1999**). "The link between brain learning, attention, and consciousness," Conscious Cogn **8**, 1–44.
Grossberg, S. (**2000**). "The complementary brain: Unifying brain dynamics and modularity," Trends Cogn. Sci. **4**, 233–246.
Grossberg, S. (**2003a**). "How does the cerebral cortex work? Development, learning, attention, and 3D vision by laminar circuits of visual cortex," Behav. Cogn. Neurosci. Rev. **2**, 47–76.
Grossberg, S. (**2003b**). "Resonant neural dynamics of speech perception," J. Phonetics **31**, 423–445.
Grossberg, S., and Merrill, J. W. L. (**1996**). "The hippocampus and cerebellum in adaptively timed learning, recognition, and movement," J. Cogn Neurosci. **8**, 257–277.
Grossberg, S., and Myers, C. W. (**2000**). "The resonant dynamics of speech perception: Interword integration and duration-dependent backward effects," Psychol. Rev. **107**, 735–767.
Grossberg, S., and Repin, D. (**2003**). "A neural model of how the brain represents and compares multi-digit numbers: Spatial and categorical processes," Neural Networks **16**, 1107–1140.
Grossberg, S., and Stone, G. O. (**1986**). "Neural dynamics of attention switching and temporal order information in short-term memory," Mem. Cognit. **14**, 451–468.
Grossberg, S., and Versace, M. (**2008**). "Spikes, synchrony, and attentive learning by laminar thalamocortical circuits," Brain Res. **1218**, 278–312
Grossberg, S., and Williamson, J. R. (**1999**). "A self-organizing neural system for learning to recognize textured scenes," Vision Res. **39**, 1385–1406.
Grossberg, S., Boardman, I., and Cohen, M. (**1997**). "Neural dynamics of variable-rate speech categorization," J. Exp. Psychol. Hum. Percept. Perform. **23**, 418–503.
Grossberg, S., Govindarajan, K. K., Wyse, L., and Cohen, M. A. (**2004**). "ARTSTREAM: A neural network model of auditory scene analysis and source segregation," Neural Networks **17**, 511–536.
Grunewald, A., and Grossberg, S. (**1998**). "Self-organization of binocular disparity tuning by reciprocal corticogeniculate interactions," J. Cogn Neurosci. **10**, 199–215.
Guenther, F. H. (**1995**). "Speech sound acquisition, coarticulation, and rate effects in a neural network model of speech production," Psychol. Rev. **102**, 594–621.
Guenther, F. H., Ghosh, S. S., and Tourville, J. A. (**2006**). "Neural modeling and imaging of the cortical interactions underlying syllable production," Brain Lang **96**, 280–301.
Hawkins, S. (**2003**). "Roles and representations of systematic fine phonetic detail in speech understanding," J. Phonetics **31**, 373–405.
Heil, P., Rajan, J., and Irvine, D. R. (**1994**). "Topographic representation of tone intensity along the isofrequency axis of cat primary auditory cortex," Hear. Res. **76**, 188–202.
Hess, W. (**1983**). *Pitch Determination of Speech Signals-Algorithms and Devices* (Springer, Berlin).
Hickok, G., and Poeppel, D. (**2007**). "The cortical organization of speech processing," Nat. Rev. Neurosci. **8**, 393–402.
Hillenbrand, J. M., and Gayvert, R. T. (**1993**). "Identification of steady-state vowels synthesized from the Peterson and Barney measurements," J. Acoust. Soc. Am. **94**, 668–674.
Hillenbrand, J. M., and Nearey, T. M. (**1999**). "Identification of resynthesized /hVd/ utterances: effects of formant contour," J. Acoust. Soc. Am. **105**, 3509–3523.
Holdsworth, J., Nimmo-Smith, I., Patterson, R., and Rice, P. (**1988**). "Implementing a gammatone filterbank," Annex C of the SVOS Final Report: Part A: The Auditory Filterbank.
Hubel, D. H., and Wiesel, T. N. (**1962**). "Receptive fields, binocular interaction and functional architecture in the cat's visual cortex," J. Physiol. (London) **160**, 106–154.
Hudspeth, A. J. (**2000**). "Chapter 30: Hearing" *Principles of Neuroscience*, 4th ed., edited by E. R. Kandel, J. H. Schwartz, and T. M. Jessell (McGraw Hill, New York), 590–613.
Imig, T. J., Ruggero, M. A., Kitzes, L. M., Javel, E., and Brugge, J. F. (**1977**). "Organization of auditory cortex in the owl monkey," J. Comp. Neurol. **171**, 111–128.
Ito, M., Tamura, H., Fujita, I., and Tanaka, K. (**1995**). "Size and position invariance of neuronal responses in monkey inferotemporal cortex," J. Neurophysiol. **73**, 218–226.
Johnson, K. (**1990**). "The role of perceived speaker identity in F0 normalization of vowels," J. Acoust. Soc. Am. **88**, 642–654.
Johnson, K. (**1997a**). "Speech perception without speaker normalization: an exemplar model," in *Talker Variability in Speech Processing*, edited by K. Johnson and J. W. Mullennix (Academic, San Deigo), 145–166.
Johnson, K. (**1997b**). "The auditory/perceptual basis for speech segmentation," OSU Working Papers in Linguistics, Columbus, OH., vol. **50**, pp. 101–113.
Johnson, K. (**2005**). "Speaker normalization in speech perception," in *The Handbook of Speech Perception*, edited by D. B. Pisoni and R. Remez (Blackwell, Oxford), 363–389.
Johnson, K. (**2006**). "Resonance in an exemplar-based lexicon: The emergence of social identity and phonology," J. Phonetics **34**, 485–499.
Johnson, K., Strand, E. A., and D'Imperio, M. (**1999**). "Auditory-visual integration of talker gender in vowel perception," J. Phonetics **27**, 359–384.
Kaas, J. H., and Hackett, T. A. (**1998**). "Subdivisions of auditory cortex and levels of processing in primates," Audiol. Neuro-Otol. **3**, 73–85.
Kaas, J. H., and Hackett, T. A. (**2000**). "Subdivisions of auditory cortex and processing streams in primates," Proc. Natl. Acad. Sci. U.S.A. **97**, 11793–11799.
Kastner, S., and Ungerleider, L. G. (**2001**). "The neural basis of biased competition in human visual cortex," Neuropsychologia **39**, 1263–1276.
Kato, K., and Kakehi, K. (**1988**). "Listener adaptability to individual speaker differences in monosyllabic speech perception," J. Acoust. Soc. Jpn. **44**, 180–186.
Kent, R. D., and Read, C. (**1992**). *Acoustic Analysis of Speech*, Singular, Madison.
Kirkman, T. W. (**1996**). Statistics to use, http://www.physics.csbsju.edu/stats (Last viewed 1 Oct **2007**).
Kraljic, T., and Samuel, A. G. (**2007**). "Perceptual adjustments to multiple speakers," J. Mem. Lang. **56**, 1–15.
Langner, G., Sams, M., Heil, P., and Schulze, H. (**1997**). "Frequency and periodicity are represented in orthogonal maps in the human auditory cortex: Evidence from magnetoencephalography," J. Comp. Physiol. **181**, 665–676.
Lee, L., and Rose, R. (**1996**). "Speaker normalization using efficient frequency warping procedures," IEEE Trans. Acoust., Speech, Signal Process. **1**, 353–356.
Lee, L., and Rose, R. (**1998**). "A frequency warping approach to speaker normalization," IEEE Trans. Speech Audio Process. **6**, 49–60.
Lehiste, I., and Meltzer, D. (**1973**). "Vowel and speaker identification in natural and synthetic speech," Lang Speech **16**, 356–264.
Lindau, M. (**1978**). "Vowel features," Language **54**, 541–563.
Lloyd, R. J. (**1890a**). *Some Researches into the Nature of Vowel-Sound* (Turner and Dunnett, Liverpool).
Lloyd, R. J. (**1890b**). "Speech sounds: Their nature and causation (I)," Phonetische Studien **3**, 251–278.
Lloyd, R. J. (**1891**). "Speech sounds: Their nature and causation (II–IV)," Phonetische Studien **4**, 37–67, 183–214, 275–306.
Lloyd, R. J. (**1892**). "Speech sounds: Their nature and causation (V–VII)," Phonetische Studien **5**, 1–32, 129–141, 263–271.
Lockwood, A. H., Salvi, R. J., Coad, M. L., Arnold, S. A., Wack, D. S., Murphy, B. W., and Burkard, R. F. (**1999**). "The functional anatomy of the normal human auditory system: Responses to 0.5 and 4.0 kHz tones and

varied intensities," Cereb. Cortex **9**, 65–76.
Luethke, L. E., Krubitzer, L. A., and Kaas, J. H. (**1988**). "Cortical connections of electrohpysiologically and architectonically defined subdivisions of auditory cortex in squirrels," J. Comp. Neurol. **268**, 181–203.
Magimai-Doss, M., Stephenson, T. A., and Bourlard, H. (**2003**). "Using pitch frequency information in speech recognition," in Proc. Eurospeech **2003**.
McDonough, J., and Byrne, W. (**1999**). "Speaker adaptation with all-pass transforms," IEEE Trans. Acoust., Speech, Signal Process. **2**, 757–760.
Merzenich, M. M., and Brugge, J. F. (**1973**). "Representation of the cochlear partition of the superior temporal plane of the macaque monkey," Brain Res. **50**, 275–296.
Miller, J. (**1989**). "Auditory-perceptual representation of the vowel," J. Acoust. Soc. Am. **85**, 2114–2134.
Moore, C. B., and Jongman, A. (**1997**). "Speaker normalization in the perception of Mandarin Chinese tones," J. Acoust. Soc. Am. **102**, 1864–1877.
Morel, A., and Kaas, J. H. (**1992**). "Subdivisions and connections of auditory cortex in owl monkeys," J. Comp. Neurol. **318**, 27–63.
Morel, A., Garraghty, P. E., and Kaas, J. H. (**1993**). "Tonotopic organization, architectonic fields, and connections of auditory cortex in macaque monkeys," J. Comp. Neurol. **335**, 437–459.
Nearey, T. M. (**1989**). "Static, dynamic, and relational properties in vowel perception," J. Acoust. Soc. Am. **85**, 2088–2113.
Nearey, T. M., Hogan, J., and Rozsypal, A. (**1979**). "Speech signals, cues and features," in *Perspectives in Experimental Linguistics*, edited by G. Prideaux (Benjamin, Amsterdam).
Page, M. (**2000**). "Connectionist modellino in psychology: A localist manifesto," Commun. Math. Sci. **23**, 443–467.
Palmeri, T. J., Goldinger, S. D., and Pisoni, D. B. (**1993**). "Episodic encoding of voice attributes and recognition memory for spoken words," J. Exp. Psychol. Learn. Mem. Cogn. **19**, 309–328.
Pantev, C., Hoke, M., Lehnertz, K., Lutkenhoner, B., Anogianakis, G., and Wittkowski, W. (**1988**). "Tonotopic organization of the human auditory cortex revealed by transient auditory evoked magnetic fields," Electroencephalogr. Clin. Neurophysiol. **69**, 160–170.
Pantev, C., Hoke, M., Lutkenhoner, B., and Lehnertz, K. (**1989**). "Tonotopic organization of the auditory cortex: Pitch versus frequency representation," Science **246**, 486–488.
Patterson, R., Nimmo-Smith, I., Holdsworth, J., and Rice, P. (**1987**). "An efficient auditory filterbank based on the gammatone function," Annex B of the SVOS Final Report: Part A: The Auditory Filterbank.
Patterson, R., Nimmo-Smith, I., Holdsworth, J., and Rice, P. (**1988**) Spiral VOS Final Report: Part A: The Auditory Filterbank.
Patterson, R. D., and Rice, P. (**1987**). "A preliminary study of the feasibility of a hardware version of the auditory filterbank," Annex A of the SVOS Final Report: Part A: The Auditory Filterbank.
Patterson, R. D., Uppenkamp, S., Johnsrude, I. S., and Griffiths, T. D. (**2002**). "The processing of temporal pitch and melody information in auditory cortex," Neuron **36**, 767–776.
Penagos, H., Melcher, J. R., and Oxenham, A. (**2004**). "A neural representation of pitch salience in nonprimary human auditory cortex revealed with functional magnetic resonance imaging," J. Neurosci. **24**, 6810–6815.
Peterson, G. E. (**1961**). "Parameters of vowel quality," J. Speech Hear. Res. **4**, 10–29.
Peterson, G. E., and Barney, H. L. (**1952**). "Control methods used in a study of the vowels," J. Acoust. Soc. Am. **24**, 175–184.
Petkov, C. I., Kayser, C., Augath, M., and Logothetis, N. K. (**2006**). "Functional imaging reveals numerous fields in the monkey auditory cortex," PLOS4 e215.
Piaget, J. (**1963**). *The Origins of Intelligence in Children* (Norton, New York).
Pierrehumbert, J. (**2006**). "The next toolkit," J. Phonetics **34**, 516–530.
Plack, C. J., Oxenham, A. J., Popper, A. N., and Fay, R. R. (**2005**) *Pitch: Neural Coding and Perception* (Springer Vg, New York).
Qin, L., Sakai, M., Chimoto, S., and Sato, Y. (**2005**). "Interaction of excitatory and inhibitory frequency-receptive fields in determining fundamental frequency sensitivity of primary auditory cortex neurons in awake cats," Cereb. Cortex **15**, 1371–1383.
Ragot, R., and Lepaul-Ercole, E. (**1996**). "Brain potentials as objective indexes of auditory pitch extraction from harmonics," NeuroReport **7**, 905–909.
Rauschecker, J. P., and Tian, B. (**2004**). "Processing of band-passed noise in the lateral auditory belt cortex of the rhesus monkey," J. Neurophysiol. **91**, 2578–2589.
Rauschecker, J. P., Tian, B., and Hauser, M. (**1995**). "Processing of complex sounds in the macaque nonprimary auditory cortex," Science **268**, 111–114.
Reale, R. A., and Imig, T. J. (**1980**). "Tonotopic organization in the auditory cortex of the cat," J. Comp. Neurol. **192**, 265–291.
Romani, G. L., Williamson, S. J., and Kaufman, L. (**1982**). "Tonotopic organization of the human auditory cortex," Science **216**, 1339–1340.
Schwippert, C., and Benoit, C. (**1997**). "Audiovisual intelligibility of an androgynous speaker," in Proc. ESCA Workshop Audio Vis. Speech Process., (AVSP '07): Cogn. Comput. Approaches, Rhodes, Greece, edited by C. Benoit and R. Campbell, pp. 81–84.
Schulze, H., Hess, A., Ohl, F., and Scheich, H. (**2002**). "Superposition of horseshoe-like periodicity and linear tonotopic maps in auditory cortex of the Mongolian gerbil," Eur. J. Neurosci. **15**, 1077–1084.
Seldon, H. L. (**1985**). "The anatomy of speech perception: Human auditory cortex," in *Cerebral Cortex 4*, edited by A. Peters and E. G. Jones (Plenum, New York), pp. 273–327.
Slaney, M. (**1993**). "An efficient implementation of Patterson-Holdsworth auditory filter bank," Apple Computer Technical Report, No. 35.
Slaney, M. (**1998**). "Auditory toolbox, version 2," Interval Research Corporation Technical Report No. 10.
Slawson, A. W. (**1968**). "Vowel quality and musical timbre as functions of spectrum envelope and fundamental frequency," J. Acoust. Soc. Am. **43**, 87–101.
Spitzer, H., Desimone, R., and Moran, J. (**1998**). "Increased attention enhances both behavioral and neuronal performance," Science **240**, 338–340.
Strand, E. A., and Johnson, K. (**1996**). "Gradient and visual speaker normalization in the perception of fricatives," in *Natural Language Processing and Speech Technology: Results of the 3rd KONVENS Conference, Bielefeld*, edited by D. Gibbon (Mouton de Gruyter, Berlin), pp. 14–26.
Stevens, K. N. (**1998**). *Acoustic Phonetics* (MIT Press, Cambridge).
Summerfield, Q., and Haggard, M. P. (**1973**). "Vocal tract normalization as demonstrated by reaction times," Report of Speech Research in Progress, The Queen's University of Belfast, Belfast, Ireland, Vol. **2**, pp. 1–12.
Sussman, H. M. (**1986**). "A neuronal model of vowel normalization and representation," Brain Lang **28**, 12–23.
Sussman, H. M., Bessell, N., Dalston, E., and Majors, T. (**1997**). "An investigation of stop place of articulation as a function of syllable position," J. Acoust. Soc. Am. **101**, 2826–2838.
Syrdal, A. K., and Gopal, H. S. (**1986**). "A perceptual model of vowel recognition based on the auditory representation of American English vowels," J. Acoust. Soc. Am. **79**, 1086–1100.
Talavage, T. M., Ledden, P. J., Benson, R. R., Rosen, B. R., and Melcher, J. R. (**2000**). "Frequency-dependent responses exhibited by multiple regions in human auditory cortex," Hear. Res. **150**, 225–244.
Talavage, T. M., Sereno, M. I., Melcher, J. R., Ledden, P. J., Rosen, B. R., and Dale, A. M. (**2004**). "Tonotopic organization in human auditory cortex reveled by progressions of frequency sensitivity," J. Neurophysiol. **91**, 1282–1296.
Titze, I. R. (**1994**). "Mechanical stress in phonation," J. Voice **8**, 99–105.
Traunmüller, H. (**1981**). "Perceptual dimension of openness in vowels," J. Acoust. Soc. Am. **69**, 1465–1475.
Tunturi, A. R. (**1952**). "A difference in the representation of auditory signals from the left and the right ears in the isofrequency of the right middle ectosylvian auditory cortex of the dog," Am. J. Physiol. **168**, 712–727.
Turner, R. E., and Patterson, R. D. (**2003**). "An analysis of the size information in classical formant data: Peterson and Barney (1952) revisited," J. Acoust. Soc. Jpn. **33**, 585–589.
Ungerleider, L. G., and Mishkin, M. (**1982**). *Two Cortical Visual Systems: Separation of Appearance and Location of Objects*, edited by D. L. Ingle, M. A. Goodale, and R. J. W. Mansfield (MIT Press, Cambridge, MA), pp. 549–586.
Verbrugge, R. R., Strange, W., Shankweiler, D. P., and Edman, T. R. (**1976**). "What information enables a listener to map a talker's vowel space?," J. Acoust. Soc. Am. **60**, 198–212.
Vitevitch, M. S., and Luce, P. A. (**1991**). "Probabilistic phonotactics and neighborhood activation in spoken word recognition," J. Mem. Lang. **40**, 374–408.
Walker, S., Bruce, V., and O'Malley, C. (**1995**). "Facial identity and facial speech processing: Familiar faces and voices in the McGurk effect," Percept. Psychophys. **57**, 1124–1133.
Watrous, R. L. (**1991**). "Current status of Peterson-Barney vowel formant data," J. Acoust. Soc. Am. **89**, 2459–2460.

Wegman, S., McAllaster, D., Orloff, J., and Peskins, B. (**1996**). "Speaker normalization on conversational telephone speech." IEEE Trans. Acoust., Speech, Signal Process. **1**, 339–341.
Wessa, P. (**2007**). Free Statistics Software, Office for Research Development and Education. Version 1.1.22-rl, http://www.wessa.net (Last viewed 1 Oct **2007**).
Wessinger, C. M., Buonocore, M. H., Kussmaul, C. L., and Mangun, G. R. (**1998**). "Tonotopy in human auditory cortex examined with functional magnetic resonance imaging," Hum. Brain Mapp **5**, 18–25.
Whitfield, I. C. (**1980**). "Auditory cortex and the pitch of complex tones," J. Acoust. Soc. Am. **67**, 644–647.
Zahorian, S. A., and Jagharghi, A. J. (**1991**). "Speaker normalization of static and dynamic vowel spectral features," J. Acoust. Soc. Am. **90**, 67–75.
Zhan, P., and Waibel, A. (**1997**). "Vocal tract length normalization for large vocabulary continuous speech recognition," *Technical Report* CMU-CS-97-148, School of Computer Science, Carnegie Mellon University.
Zhan, P., and Westphal, M. (**1997**). "Speaker normalization based on frequency warping," IEEE Trans. Acoust., Speech, Signal Process. **2**, 1039–1041.
Zoccolan, D., Kouh, M., Poggio, T., and DiCarlo, J. J. (**2007**). "Trade-off between object selectivity and tolerance in monkey inferotemporal cortex," J. Neurosci. **26**, 13025–13026.

The concept of signal-to-noise ratio in the modulation domain and speech intelligibility

Finn Dubbelboer[a] and Tammo Houtgast
Department of Otolaryngology, VU University Medical Center, P.O. box 7057, 1007 MB, Amsterdam, The Netherlands

(Received 5 December 2007; accepted 28 February 2008)

A new concept is proposed that relates to intelligibility of speech in noise. The concept combines traditional estimations of signal-to-noise ratios (S/N) with elements from the modulation transfer function model, which results in the definition of the signal-to-noise ratio in the modulation domain: the $(S/N)_{mod}$. It is argued that this $(S/N)_{mod}$, quantifying the strength of speech modulations relative to a floor of spurious modulations arising from the speech-noise interaction, is the key factor in relation to speech intelligibility. It is shown that, by using a specific test signal, the strength of these spurious modulations can be measured, allowing an estimation of the $(S/N)_{mod}$ for various conditions of additive noise, noise suppression, and amplitude compression. By relating these results to intelligibility data for these same conditions, the relevance of the $(S/N)_{mod}$ as the key factor underlying speech intelligibility is clearly illustrated. For instance, it is shown that the commonly observed limited effect of noise suppression on speech intelligibility is correctly "predicted" by the $(S/N)_{mod}$, whereas traditional measures such as the speech transmission index, considering only the changes in the speech modulations, fall short in this respect. It is argued that $(S/N)_{mod}$ may provide a relevant tool in the design of successful noise-suppression systems.
© *2008 Acoustical Society of America.* [DOI: 10.1121/1.3001713]

PACS number(s): 43.71.An, 43.72.Dv, 43.66.Mk [DOS] Pages: 3937–3946

I. INTRODUCTION

The concepts of modulation transfer function (MTF) and speech transmission index (STI) (IEC, 2003) have proven to be successful in predicting intelligibility for a variety of practical situations, typically in noisy, reverberant, or echoing enclosures, suggesting that the factors affecting speech intelligibility are understood completely. Although the idea of speech intelligibility being strongly related to the strength of temporal modulations within the intensity envelope of speech is generally accepted, this notion may be too optimistic, as STI predictions can sometimes be completely misleading. For instance, for some forms of noise reduction the original speech modulations are largely restored, while intelligibility remains equally poor (WGCA, 1991; Levitt, 2001). Hence, the perceptual consequences of noise suppression schemes are not fully recognized by the STI (Steeneken, 1992). Drullman (1994a, 1994b), among others, explored the limits of the STI model by systematically manipulating the temporal envelope of continuous speech in various ways (smearing the envelope, reducing slow modulations) and found that the STI model may under- or overestimate intelligibility in specific conditions.

Subsequently, it was demonstrated by Noordhoek and Drullman (1997) that reduced intelligibility of noise-corrupted speech cannot fully be explained by reduced speech modulations alone, but involves additional noise effects that are not considered by the STI, i.e., the introduction of nonrelevant modulations originating from speech-noise interactions—possibly inducing a "sorting problem"—and the corruption of the speech carrier. The effect of the intrinsic envelope fluctuations of a noise carrier on the detection of amplitude modulation was studied by Dau and Verhey (1999), who performed modulation-detection threshold experiments for a variety of band-filtered noise carriers, each with a specific modulation spectrum. It was concluded that the intrinsic envelope power of the carrier at the output of the modulation filter tuned to the signal modulation frequency provides a good estimate for the amplitude modulation detection threshold.

Recently, it was suggested by Dubbelboer and Houtgast (2007) that these noise-induced modulations may be responsible for the limited effects of noise reduction—e.g., spectral subtraction—on intelligibility, explaining the subtraction paradox of Ludvigsen (1993). Spectral subtraction is one of the first "easy-to-implement" reduction schemes among single-microphone noise-reduction techniques and currently often used, especially in hearing aids and mobile phones. Ludvigsen showed that in spite of increased speech-modulations and increased STI values the intelligibility of the output signal remained equally poor.

In this paper, a concept is proposed that may underlie this paradox by focusing on the interaction between speech and noise, and the consequence of this interaction for the perception of speech modulations. Understanding this mechanism may result in future models that can accurately predict intelligibility of noisy speech after being subjected to nonlinear processing in the laboratory, where current measures such as signal-to-noise ratio (S/N) and STI essentially fail, and may contribute to the optimization of noise reduction algorithms.

[a]Author to whom correspondence should be addressed. Electronic mail: finndubbelboer@planet.nl

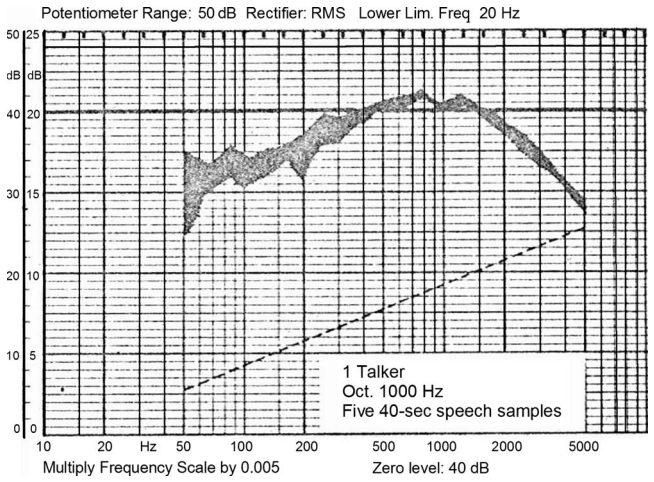


FIG. 1. A classical picture of some speech envelope spectra (with original figure caption). Traditionally, modulation spectra were based on 1-octave band (around 1 kHz) audio-filtered speech and 1/3-octave band frequency analysis of the resulting envelopes. (From Houtgast and Steeneken, 1972).

II. RATIONALE AND INTRODUCTION OF $(S/N)_{mod}$

A. Speech envelopes and the concept of the useful modulations area

Continuous speech can be considered as a flow of sound with a specific spectro-temporal intensity pattern. This pattern contains temporal variations, corresponding to the rhythms of basic speech elements such as phonemes, syllables, and words. The ear is suited to extract these structures in a way that can be compared with a filter-bank analysis: breaking down the signal into a number of adjacent frequency bands. Each frequency-band output consists of an envelope and a carrier. The envelope contains the modulations, which are considered essential for the intelligibility of speech. The carrier wave contains information about, for instance, the pitch. Frequency analysis performed on the (intensity) envelope of a frequency-band output displays the modulation content within that band in a modulation-frequency spectrum (the envelope spectrum). Thinking about speech in terms of envelopes and envelope spectra provides a successful paradigm to relate speech physics to intelligibility. The idea was first postulated by Houtgast and Steeneken (1972) and is illustrated by the classical picture shown in Fig. 1, displaying a number of modulation spectra, obtained from five 40-s speech tokens uttered by one speaker, audio filtered one octave around 1 kHz. The upper spectrum reflects the strength of modulations, integrated within 1/3-octave frequency bands, ranging from 0.25 to 25 Hz. The maximum around 4 Hz roughly corresponds to the number of syllables and small words per second. The +3-dB/oct dashed line represents the typical modulation spectrum of octave-band filtered white noise, reflecting the statistical fluctuations within the intensity envelope. The relation between modulations and intelligibility is illustrated in Fig. 2, showing single and combined effects of interfering noise and reverberation on the speech-modulation spectrum, and their consequences for speech intelligibility (PB scores). The essential point is that intelligibility drops with reduction of speech modulations, irrespective of the nature of that reduction. For example, adding noise to speech causes a drop of modulations across all modulation frequencies, determined by the signal-to-noise ratio (S/N ratio), while the effect of reverberation is modulation-frequency dependent and acts like a low-pass filter on the envelope spectrum. Nevertheless, in both cases intelligibility is determined by the remaining strength of the modulations, irrespective of the resulting shape of the envelope spectrum. As each modulation frequency appeared to contribute equally to speech intelligibility, the relation between modulation strength and intelligibility could simply be demonstrated by the strong correlation

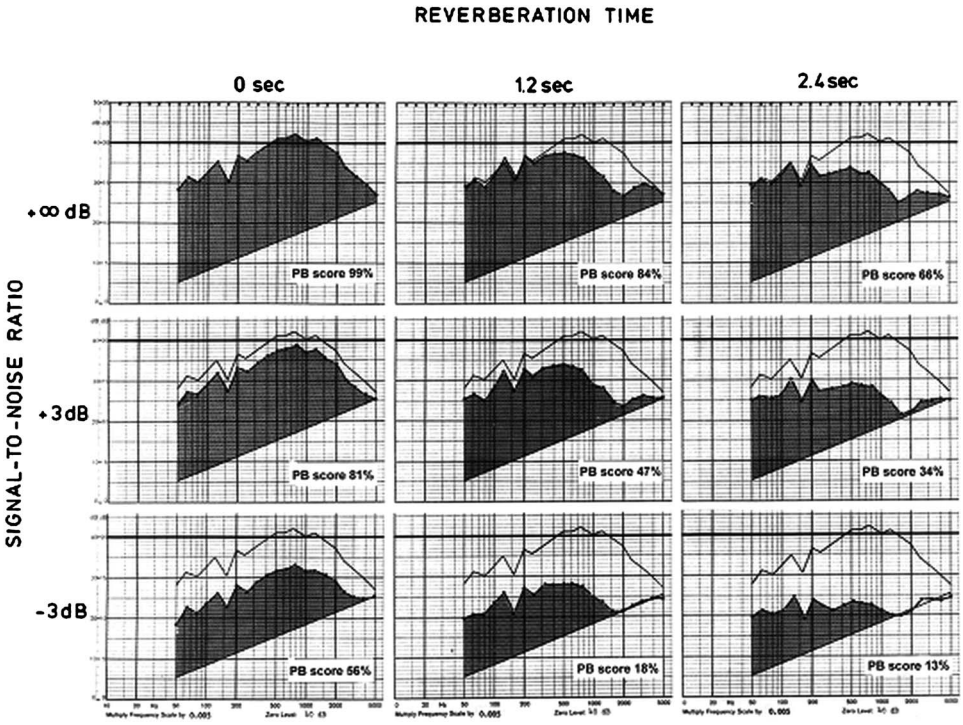


FIG. 2. Reduction of speech-envelope spectra as a result of additive noise and/or reverberation. The upper curves represent the undisturbed envelope spectrum, the middle curves show the spectra after being corrupted, the lower limit (+3-dB/oct straight line) represent the modulation spectrum for noise alone. The size of the gray areas, which appeared to correlate with PB-word scores, illustrates the concept of the "useful modulation area," which evolved into the MTF-STI model. (From Houtgast and Steeneken, 1972).

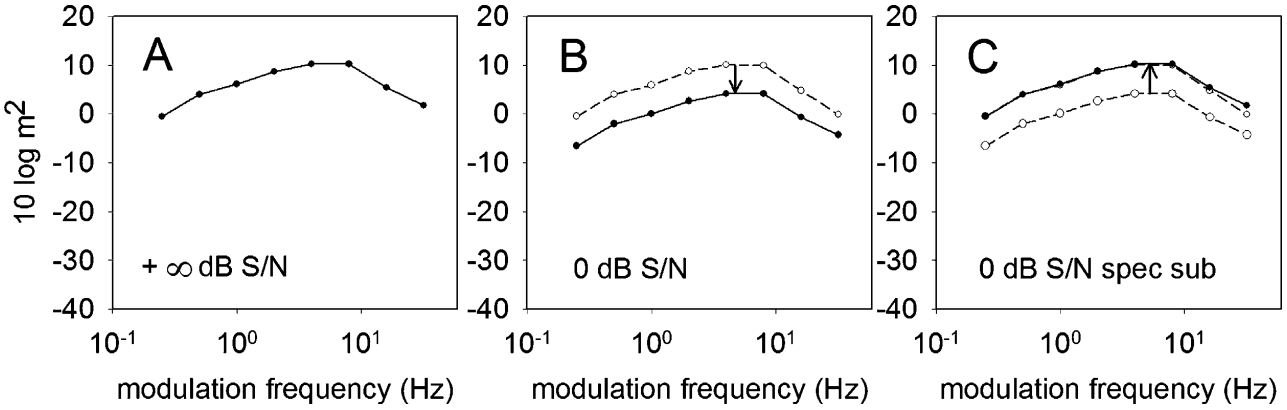


FIG. 3. Envelope spectra of noise-corrupted speech, audio-filtered 1/3 octave around 1 kHz and analyzed in 1-octave modulation frequency bands. Panel (A): the original (no noise) speech envelope spectrum. Panel (B): after adding noise at 0 dB S/N, showing a 6-dB drop of the envelope spectrum. Panel (C): After subsequent spectral subtraction, showing a complete restoration of the original envelope spectrum.

between the gray area, enclosed by the reduced upper limit and the fixed lower limit, and the PB-word scores obtained for the various conditions. The observation evolved into the concept of the "useful modulation area," stating exclusively that the fraction of relevant modulations (upper limit) that exceeds the nonrelevant modulation spectrum (lower limit) contributes to speech perception. The larger the area size, the better the intelligibility. Generally, the S/N range between −15 and +15 dB S/N is considered to be relevant for speech perception. For lower S/N, the upper limit starts to coincide with the lower limit. At that point, the remaining modulation spectrum is completely determined by random fluctuations within the noise envelope.

Historically, the idea of a useful modulation area led to the development of the STI as a measure to predict intelligibility in suboptimal acoustical environments. As the lower limit of the useful modulation area was considered fixed, the model was exclusively based on the shift of the upper limit: the reduction of the speech-modulation spectrum. To understand why the STI fails in the case of spectral subtraction, the interaction between speech and noise is considered in the light of this STI fundamental.

B. Spectral subtraction and the modulation floor

Three envelope spectra were computed for speech in different conditions. First, clean speech was filtered in the audio domain, resulting in a number of 1/3-octave frequency bands. The frequency band around 1 kHz was subjected to Hilbert transform, and the magnitude of the analytic signal was squared and low-pass filtered. Frequency analysis of the resulting intensity envelope yielded frequency components that were integrated within octave bands and normalized for the mean intensity afterwards, yielding a modulation spectrum as presented in panel (A) of Fig. 3[1]. The next spectrum [panel (B)], was obtained after adding noise to speech (at 0 dB S/N), causing a 6-dB drop of the speech-envelope spectrum, which is in conformation with the predictions made by the MTF-STI model. Finally, the speech+noise envelope was subjected to a basic form of spectral subtraction, the essence of which, formulated by Levitt (2001), follows: "take the noise spectrum [..] and subtract it from the speech-plus-noise spectrum [..]." In our case, the mean noise intensity in the 1-kHz 1/3-octave band (which is easily determined in the lab) was subtracted from the noise-plus-speech envelope in that same band. The modulation spectrum was computed using the same procedure as before, and is represented in panel (C). This curve essentially coincides with the envelope spectrum of the original speech, thus showing a complete restoration of the original speech modulations.

At this point, a puzzling contradiction arises: Fig. 3 shows that the reduction of the speech modulations caused by the noise is successfully neutralized by the subtraction operation. Based on this new spectrum, the MTF-STI model would predict enormous improvements of intelligibility. However, the fact that intelligibility remains equally poor after subtraction suggests that the operation induces additional effects to which the MTF-STI model is insensitive. A possible explanation for this remarkable phenomenon was offered by Dubbelboer and Houtgast (2007). Speech and noise each have their own intensity modulation patterns, as illustrated by the spectra of Fig 1. However, when speech and noise are mixed, additional chaotic modulations arise from the interaction between the respective waveforms, as a result of the statistical nature of noise. The new envelope contains a combination of speech modulations and spurious modulations (i.e., noise modulations and interaction modulations). It was argued that spectral subtraction not only increases the strength of the speech modulations, but may also increase the strength of the spurious modulations. It may be that, as their relative strength remains unchanged, it remains equally difficult for a listener to extract essential speech cues from the corrupted signal, resulting in equally poor intelligibility.

To verify this hypothesis, one should add noise to a speech signal and monitor the relative strength of the speech modulations and the nonspeech modulations in various conditions. Normally, in the audio domain, the relative strength between speech and noise is defined as an S/N ratio based on the intensities of speech and noise before mixing. However, this principle does not apply in the modulation domain, as an essential part of the nonspeech modulations originates from the *interaction* between speech and noise: these modulations do not exist until speech and noise are actually mixed. So,

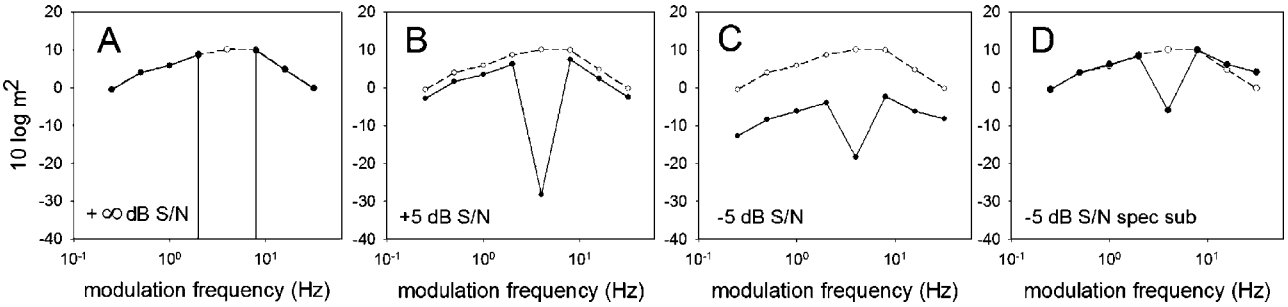


FIG. 4. A number of envelope spectra of a noise-corrupted speech-based test-signal ("peephole speech") constructed from modulation-band-stop filtered speech. The upper curves in panel (A)–(D) each represent the spectrum of common speech, as in Fig. 3, panel (A) (open circles). The curves denoted by the bullets show peephole speech to which: no noise was added (A), noise was added at +5-dB S/N (B), noise was added at −5-dB S/N (C), noise was added (−5-dB S/N), and subjected to a basic form of spectral subtraction (D).

contrary to the signal-to-noise ratio in the audio domain, the signal-to-noise ratio in the modulation domain[2] cannot—in principle—be computed from speech and noise alone. It seems that the only way to determine the relative strength of the floor of spurious modulations, which lays below the speech envelope spectrum, is by monitoring the behavior of these modulations within the noisy-speech envelope itself, for instance by looking through a "peephole" in the speech modulation spectrum.

For this purpose, we designed a test signal comprising speech with a "hole" in the modulation spectrum, which was realized by band-stop filtering the temporal envelope. In essence, the modulation spectrum of this signal is similar to that of unmodified speech except for one modulation band, which is completely suppressed. Constructing peephole speech involves a frequency analysis of the speech-intensity envelope, suppression of the modulations in the 4-Hz octave band, and retransformation of the new spectrum into the intensity envelope domain and then back to the audio domain. An example of a peephole speech envelope is shown in Fig. 4 [compare to Fig. 3, panel (A)]. If noise is added to this signal, each octave band in the spectrum will display a reduction of speech modulations as usual, except for the peephole octave band, in which a floor of spurious modulations arises that increases with increasing noise level [panels (B) and (C)]. When spectral subtraction is applied (i.e., reducing the speech-plus-noise envelope with the mean noise intensity), a remarkable phenomenon occurs [see panel (D)]: not only the speech modulations increase, but also the modulation floor increases. The picture supports the hypothesis formulated above: subtraction does not alter the *relative* strength of the speech modulations and the spurious nonspeech modulations. In fact, the result of subtraction is merely an overall shift in the modulation domain. This may seem surprising, but can be understood by considering the way a modulation spectrum is computed. Mathematically, a modulation spectrum represents the ratio between (octave-band-integrated) modulations and the mean intensity of the signal. Subtracting the mean noise intensity does not affect the relative strength of modulations within the new envelope, but affects only its mean intensity. The resulting spectrum is therefore based on essentially the same modulation distribution, but normalized for a reduced mean intensity. The net effect is an identical but upward-shifted spectrum. So, in terms of the MTF-STI concept, subtraction may seem a profitable operation as speech modulations are restored, however, in reality the ratio between relevant and nonrelevant modulations—the *actual* useful modulation area—remains unchanged. This motivates the development of a concept that relates intelligibility to the ratio between relevant and nonrelevant modulations: the signal-to-noise ratio in the modulation domain.

C. Concept of $(S/N)_{mod}$, the signal-to-noise ratio in the modulation domain

For common noisy-speech signals, the strength of the modulation in the 4-Hz octave band is roughly equal to the strength in the two adjacent bands (see Fig. 3). To get an impression of the relative strength of the speech- and the nonspeech modulations within the 4-Hz band, one could consider panel (B) or (C) of Fig. 4 and determine the ratio between an interpolation of the 2- and 8-Hz modulation strengths and the strength of the modulation floor. The effect of spectral subtraction on the speech modulations and noise modulations was successfully illustrated above by using the peephole speech approach. However, during further analysis with other types of processing, it appeared that the peephole approach can be used for illustrative purposes only. It does not always produce stable results, depending on the speech token considered. This is due to the fact that the envelope filtering, required to remove the modulations in the 4-Hz modulation band, can cause negative-valued intensities in the resulting envelope, which is not allowed during transformation back into the time domain. Clipping these values to zero can introduce serious artifacts, resulting in new spurious modulations, which interfere with the essence of the whole procedure, i.e., to track down the spurious modulations caused by the speech-noise interaction. Alternatively, we searched for a more stable test signal that could produce relevant quantitative data on a variety of processing types. Panel (A) of Fig. 5 shows a 1-s segment of this test signal: a 1-kHz carrier with a 4-Hz sinusoidal intensity modulation. This signal produces a sharp peak in the modulation domain [panel (F)][3]. The noise added to this test signal is 1/3-octave filtered (1-kHz center frequency) stationary Gaussian noise of which the intensity envelope is given in panel (B) (again, only a 1-s segment is displayed), and the corresponding en-

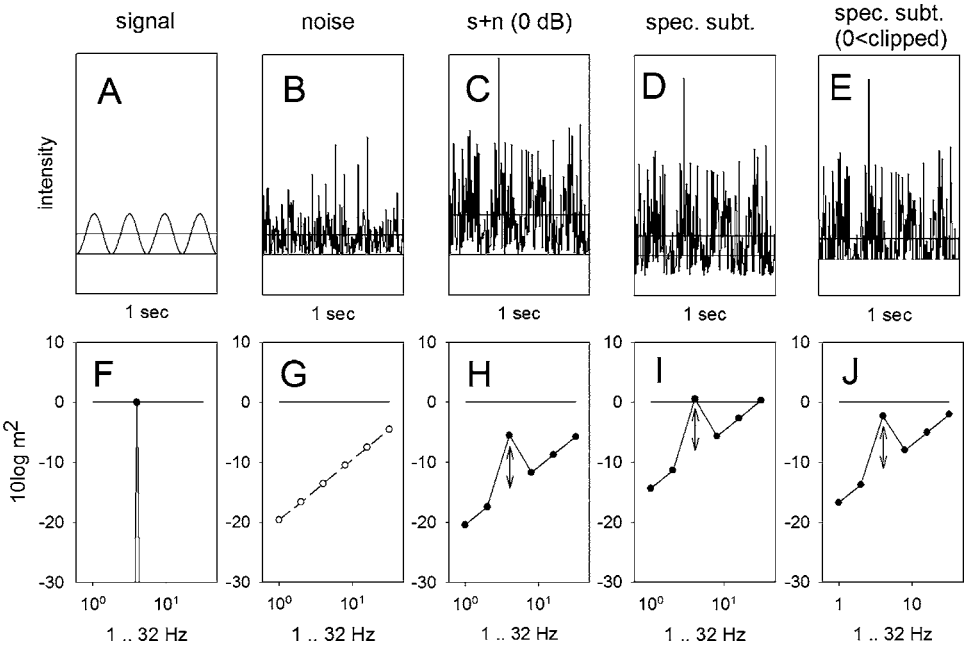


FIG. 5. The upper row of panels shows one second of envelopes of a test signal (a 4-Hz modulated 1-kHz carrier, depicted in panel (A) to which noise (B) was added (C) and subjected to two forms of spectral subtraction [(D) and (E)]. The bottom row shows the corresponding envelope spectra, based on 30 s signal duration. The arrows in (H)–(J) indicate an approximation of the signal-to-noise ratio in the modulation domain.

velope spectrum in panel (G) [4]. This addition results in an envelope depicted in panel (C), producing the envelope spectrum shown in panel (H). Note that this approach is essentially complementary to the peephole approach. The modulation floor in the 4-Hz band is now simply estimated by interpolating the modulations in the 2- and the 8-Hz bands as depicted in panel (H). The distance between the peak and this interpolated noise floor provides a rough estimate of the signal-to-noise ratio in the modulation domain. Applying spectral subtraction [reducing the S+N envelope in panel (C) with the mean noise intensity from panel (B), resulting in the envelope in panel (D)] does not change this ratio, which is in agreement with the previous observations: the entire modulation spectrum is shifted up by 6 dB [panel (I)], emphasizing the general nature of the phenomenon. Note that unwanted side effects of subtraction appear in panel (D): negative-valued intensities. These values principally obstruct synthesis of audible signals, a problem that is commonly counteracted by zero-clipping, which is illustrated in panel (E). It was shown by Dubbelboer and Houtgast (2007) that the noise distribution within a zero-clipped noisy-speech envelope does not essentially differ from the unclipped and unprocessed versions, which is illustrated by the unchanged ratio between peak- and floor modulations [as illustrated by the arrows in panels (H), (I), and (J)].

Hence, it appears that the phenomena observed for peephole speech can also be shown for an artificial probe envelope with the advantage of producing reliable estimates of the modulation floor for a wide range of S/N. Panel (A) of Fig. 6 shows a series of modulation spectra as a function of S/N (note the reversed scaling on the *x*-axis), derived in the same way as the modulation spectrum for 0 dB S/N in panel (H) of Fig. 5. For each curve, the signal-to-noise modulation ratio is estimated by the distance between the peak modulations (bullets) and floor modulations (open circles) within the 4-Hz band. These data were copied from panel (A), mutually

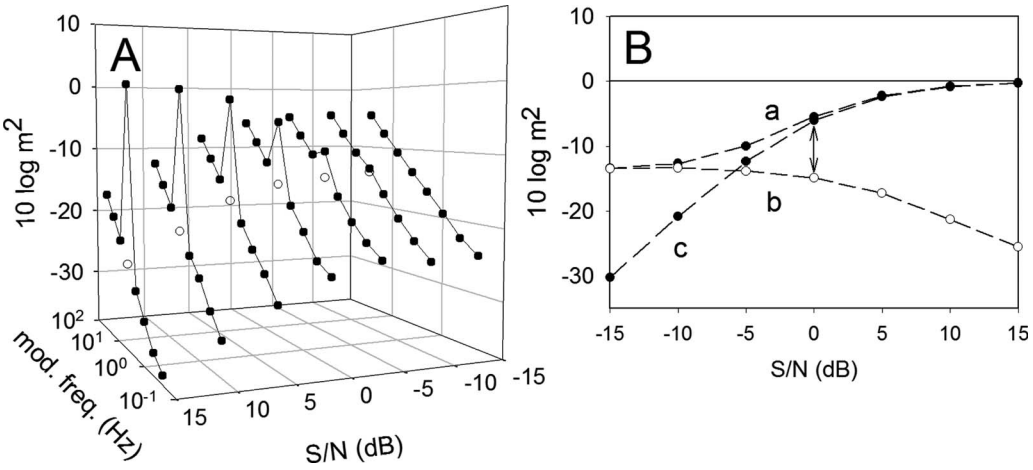


FIG. 6. Panel (A): Successive envelope spectra of the 4-Hz modulating test signal for a range of signal-to-noise ratios. From each spectrum, the peaks and the 4-Hz spurious modulations were copied to panel (B) (note the reversed scale on the *x*-axis!) and mutually connected [curves (a) and (b), respectively]. See text for curve (c).

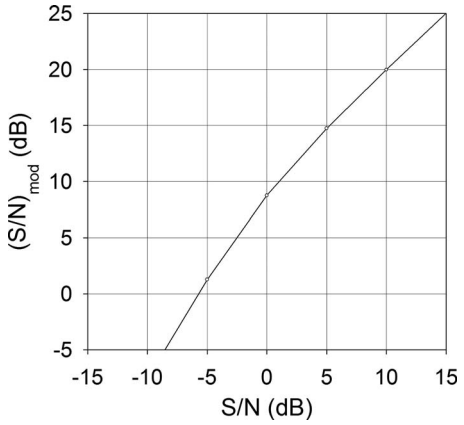


FIG. 7. Relation between $(S/N)_{mod}$ of a 4-Hz modulated test signal and the signal-to-noise ratio.

connected and redrawn in panel (B): curve (a) and curve (b) represent the peak-and floor modulations, respectively. Strictly, the peak modulations do not represent exclusively signal modulations, but essentially a summation of signal- and nonsignal (spurious) modulations. To obtain a fair representation of the actual signal-to-noise ratio in the modulation domain (note that this is strictly a "signal-to-nonsignal ratio," as nonsignal modulations represent noise modulations plus interaction modulations), the noise contribution must be eliminated from the peak modulations, typically by subtracting curve (b) from curve (a), yielding curve (c).

Mathematically, the distance between curve (c) and curve (b), indicated by the arrow, now defines the relative strength of the signal modulations and the nonsignal modulations. The ratio between the signal modulations and the nonsignal modulations can be expressed by $10\log(m_{sn}^2 - m_{n,est}^2) - 10\log m_{n,est}^2$, which may be interpreted as the signal-to-noise ratio in the modulation domain,

$$(S/N)_{mod} = 10\log\frac{m_{sn}^2 - m_{n,est}^2}{m_{n,est}^2}, \quad (1)$$

in which m_{sn}^2 and $m_{n,est}^2$ represent the modulation strengths of, respectively, signal+noise, and the estimated modulation strength of the spurious noise floor. Figure 7 shows values of $(S/N)_{mod}$ as a function of S/N, within the −15 to +15-dB range. The position of the curve depends on the characteristics of the test signal. Note that extremely high $(S/N)_{mod}$ values—due to extremely low spurious modulations—will be limited in practice by the "effective dynamic modulation range" being restricted by the modulation threshold, analogous to the effective dynamic range in the audio-domain being restricted by the hearing threshold. We will return to this point in Sec. III B.

III. VERIFICATION OF THE RELEVANCE OF $(S/N)_{mod}$

This paper is about relating the physical changes associated with disturbing a signal to intelligibility. Although this seems straightforward when the signal is speech, the relation may seem less obvious when using an artificial probe signal. However, the success of the MTF-STI model indicates that applying artificial probes (sine-wave modulated envelopes) to predict the intelligibility of speech can be most functional. This can be understood by considering the fact that the STI model considers exclusively *intensity* envelopes. In the intensity domain, a summation of uncorrelated signals (e.g., speech and noise) is, on average, a linear operation; therefore, the effect on the envelope spectrum can be considered as the result of an attenuation filter acting on the original envelope spectrum, irrespective of the nature of the input signal. That attenuation filter is defined by the distortions (S/N ratio, degree of reverberation), and applies to the envelope spectrum of *any* signal subjected to the same degree of noise and/or reverberation. So, observed modulation reductions of any signal envelope also apply to the speech envelope, and are thus relevant for speech perception. In this line of thinking, the current section will expand on the relation between intelligibility and the $(S/N)_{mod}$ derived for our 4-Hz modulated test probe.

$(S/N)_{mod}$'s were computed for signals that were subjected to various types of signal processing. The results are compared to intelligibility data from the literature and will be discussed briefly and qualitatively. It should be noted that the level distribution of our sine-wave-shaped envelope obviously differs from that of 1/3-octave-band filtered speech, leading to different absolute $(S/N)_{mod}$'s. As this paper proposes a concept rather than a fully defined quantitative model, we will focus on *changes* of the $(S/N)_{mod}$ for the 4-Hz modulated test probe (improvement, degradation, or no change) for certain types of processing, rather than on exact predictions of intelligibility.

A. Spectral subtraction and speech intelligibility

Some aspects of spectral subtraction were discussed above in Sec. II B. In a listening experiment performed by Dubbelboer and Houtgast (2007), CVC word lists (consonant-vowel-consonants test words, spoken in a brief carrier phrase) were corrupted with stationary Gaussian noise and processed. Scores for the unprocessed conditions at −4 and −7-dB S/N were 29% and 15%, respectively. After subtraction, scores remained essentially unchanged (24% and 16%, respectively), which is in agreement with the literature. Then $(S/N)_{mod}$'s were obtained for the 4-Hz modulated test probe subjected to the same processing: for −7-dB S/N, the $(S/N)_{mod}$ was −2.1 dB both before and after spectral subtraction, and +3.2 dB for −4-dB S/N, again with no effect of spectral subtraction. The overall picture shows that equal $(S/N)_{mod}$ corresponds with equal intelligibility.

B. Deterministic and noise-induced modulation reduction

According to the traditional concept of useful modulations in the MTF-STI model, noise affects intelligibility of speech in only one way: it reduces the strength of modulations that are required for perception. The concept also states that the nature of the modulation reduction is irrelevant. To verify this, Noordhoek and Drullman (1997) performed a listening experiment using speech stimuli in which the modulations were reduced in two different ways: simply by adding noise (stochastic reduction) and by compressing the

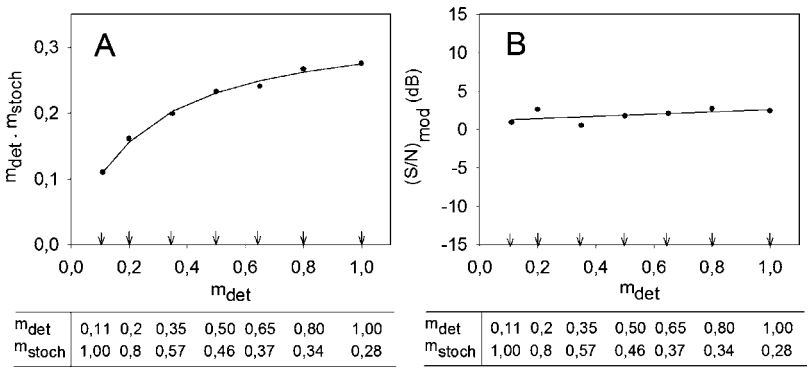


FIG. 8. The experimental data shown in this figure were adapted from a listening experiment by Noordhoek and Drullman (1997). Panel (A) shows the product of a number of m_{det}-m_{stoch} pairs (given in the table), each corresponding to the same degree of intelligibility. The position of each pair on the x-axis is indicated by an arrow. For each m_{det}-m_{stoch} combination,$(S/N)_{mod}$ was computed, based on corresponding modulation reduction applied to our 4-Hz test signal [panel (B)].

intensity envelope (deterministic reduction). They argued that, according to the traditional concept, both reduction types should equally affect intelligibility. They used the sentence lists as commonly applied in measuring the speech reception threshold, SRT (Plomp and Mimpen, 1979). First, the speech envelopes were compressed by a factor referred to as modulation reduction factor m_{det}, then a noise reduction factor m_{stoch} was imposed by gradually adding noise. By varying the amount of noise, the SRT was determined: the S/N ratio for which 50% of simple sentences were reproduced correctly (Plomp and Mimpen, 1979). This resulted in a number of combinations of stochastic and deterministic reduction, each corresponding to the same degree of intelligibility. According to the MTF-STI model, the resulting total modulation reduction is the key factor, implying that for all these combinations of different reductions the product $m_{det} \cdot m_{stoch}$ is constant. By plotting the product $m_{det} \cdot m_{stoch}$ for all combinations of m_{det} and m_{stoch} [Fig. 8, panel (A)], Noordhoek and Drullman showed that intelligibility is not independent of reduction type. This is most clearly illustrated by the two extreme conditions in Fig. 8, showing that only stochastic reduction with $m_{stoch}=0.28$ is equally effective as only deterministic reduction with $m_{det}=0.11$. It was concluded that, in the case of noise, intelligibility is not only affected by modulation reduction, but also by the introduction of nonrelevant modulations[5]. It can be expected that a measure that includes this additional effect would reduce the slope of the curve. In the case of a horizontal line, one can assume that the actual key factor is essentially captured.

Each SRT in Noordhoeks' experiment relates to a specific combination of m_{det} and m_{noise}. For each of these combinations, we computed the $(S/N)_{mod}$ by compressing our probe signal and adding noise to the signal (at the S/N ratios that are defined by the corresponding SRT) in the same way Noordhoeks' speech stimuli were processed. The result is displayed in panel (B) of Fig. 8, showing $(S/N)_{mod}$'s as a function of (combinations of m_{stoch} and) m_{det}. Special attention should be paid to the utmost left data point in this graph, i.e., the extreme case in which noise is absent and modulations are completely determined by deterministic reduction, corresponding to $m_{det}=0.11$ and $m_{stoch}=1.00$. Due to the absence of a modulation floor, the $(S/N)_{mod}$ is strictly not defined for this condition. As, in reality, the perception of temporal modulations is limited by the modulation-detection threshold, an internal modulation floor was introduced in the concept to account for the limited effective modulation range in cases of high signal-to-noise ratio. This internal floor was set tentatively at −20 dB, based on classical modulation-detection experiments performed by Viemeister (1979), and Houtgast (1989), and the auditory model described by Dau *et al.* (1997). In these experiments, a broadband noise carrier is typically modulated with a sinusoid of frequency f_t (1.64 Hz), and bandlimited in the audio domain afterwards (e.g., 1 or 1/3 oct around 1 kHz). The signal is presented to normal-hearing subjects to determine the detection threshold of the modulation. A 100% modulated envelope (modulation index $m=1$) is defined as 0 dB; the resulting modulations thresholds are expressed in dB as $20\log(m)$. Figure 7 indicates that, with this choice for the internal modulation floor, the S/N_{mod} for this data point fits in well with the other points, for which the S/N_{mod} is determined by an actual floor of noise-induced spurious modulations. Although there remains a small residual effect in panel (B) (weak slope of the curve), presumably the result of the disturbed speech carrier, the figure shows that much of the remaining variance in Noordhoek and Drullman's data is captured by the $(S/N)_{mod}$, demonstrating the relevance of this concept in relation to intelligibility.

C. Compression and expansion of noisy speech

Compression is often applied in hearing aids to compensate for reduced compression in the cochleae of hearing impaired persons. In the past, it was suggested by some researchers that intelligibility could be improved by compressing the hearing aid output signal, allowing a large part of the dynamic range of speech to fit into the reduced dynamic range of a hearing impaired person. Intelligibility can indeed improve with compression, as long as the compression is improving audibility for the hearing-impaired listener. However, intelligibility effects are strongly limited when the signal is already lifted above the audibility threshold of a listener, as compression reduces the strength of modulations that are essential for speech intelligibility, which was shown by Plomp (1988). This notion was supported by literature (Dillon, 1996; Franck *et al.*, 1999).

On the other hand, it appears that the STI tends to underestimate intelligibility of compressed speech in quiet (Hickson, 1994; Festen and van Dijkhuizen 1998; Souza, 2002). Also in stationary noise, effects of moderate multichannel compression ($CR \leqslant 3$) are often less detrimental then predicted by the STI (Barfod, 1978b; Moore *et al.*, 1999; van

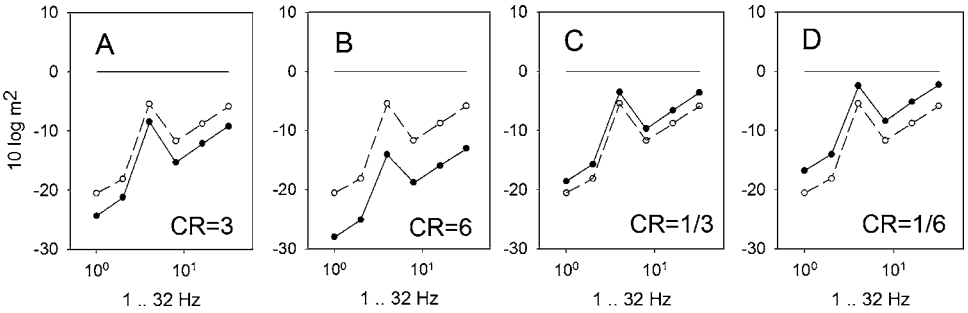


FIG. 9. Envelope spectra based on 30 s of the compressed noise-corrupted probe signals (0-dB S/N,CR=3, and CR=6, respectively) and the expanded noise-corrupted probe signals (CR=1/3 and CR=1/6, respectively). Spectra of the original (unprocessed) noise-corrupted probe are indicated by the dotted line in each panel.

Buuren *et al.*, 1999). To illustrate the effect of compression in terms of relative modulations, a one-channel noise-corrupted probe, mixed at 0 dB S/N, was subjected to various compression ratios, depicted in Fig 9. As the signal is defined for a 1/3-octave audio-domain frequency band, the operation essentially relates to a multichannel compression system. In each panel, the dashed line indicates the modulation spectrum of the noisy target (peak around −6 dB); the solid lines show the spectra after compression. Panel (A) displays the modulation spectrum of a compressed probe-signal with the compression threshold (CT) set to −6 dB below RMS, and the compression ratio (CR) set to 3. As with spectral subtraction (Sec. II C), compression induces a shift of the spectrum. The effect on the peak, on which STI predictions are based, is a 3-dB reduction, corresponding to a drop of the modulation index from 0.5 to approximately 0.35. In terms of words scores, this would imply a severe drop from about 60% to about 40%. However, several studies indicate that the intelligibility is not significantly changed for CR⩽3 (Houben, 2006; Barfod, 1978b; Moore *et al.*, 1999; van Buuren *et al.*, 1999). This result could be expected, considering the fact that the relative modulations remain equally strong: $(S/N)_{mod}$'s are 8.7 dB for both envelopes. It is known from the literature (van Buuren *et al.*, 1999) that intelligibility does drop towards higher compression ratios [CR=6, panel (B)], which might be understood within the framework of $(S/N)_{mod}$ by considering the internal modulation floor that limits the perceptually effective dynamic modulation range and was introduced in the previous section. When this lower limit is set, again, at −20 dB, the effective $(S/N)_{mod}$ in panel (B) is reduced, which is in agreement with the intelligibility drop described in the literature.

Based on the MTF-STI concept, one would expect to find positive effects on intelligibility after increasing essential modulations, for instance by expansion, the inverse of the compression operation. Panel (C) shows the result of expansion of the envelope (CR=1/3) leading to a 2-dB lifted peak corresponding to an increase of the modulation index from 0.5 to 0.63, which would correspond to an increase in word score of 60% to 75% for normal hearing listeners. For higher expansion ratios the modulation index even increases to 0.77 [CR=1/6, panel (D)]. In various studies, (spectral) expansion was applied to noisy speech aiming at increasing the spectral contrasts. Although some small positive effects were found in combination with noise suppression (Lyzenga, 2002), the overall conclusion is that expansion does not improve intelligibility (Bunnell, 1990; van Buuren, 1999). Again $(S/N)_{mod}$'s remain equal or even decrease, from 8.7 to 8.4 for panel (C), and from 8.7 to 8.3 for panel (D).

IV. DISCUSSION

It was shown in this paper that noise not only reduces speech modulations (the only noise effect considered in the MTF-STI approach), but also introduces new modulations as a result of waveform interactions between speech and noise. The existence of these spurious modulations was shown by adding noise to a specially designed speech-based test signal ("peephole speech"), in which the modulations in the speech envelope were suppressed in one modulation band, and remained intact in the others. It was also shown that the strength of these spurious modulations grows with increasing noise level. Applying spectral subtraction to noisy peephole speech not only showed that the strength of speech modulations increases, which was already observed in other studies, but also showed an increase of the strength of the spurious modulations. It was found that the ratio between these modulations remains unaffected after the operation, which may explain the limited success of spectral subtraction on intelligibility. This observation initiated the concept of the signal-to-noise ratio in the modulation domain $(S/N)_{mod}$, and the idea that $(S/N)_{mod}$ is the key factor in relation to intelligibility. The general nature of the observed phenomenon that $(S/N)_{mod}$ is insensitive to spectral subtraction was demonstrated by using a second, deterministic test signal: a 4-Hz sine-wave-modulated 1-kHz carrier. Furthermore, it was shown that this test signal could be used to compute $(S/N)_{mod}$'s for a variety of operations, such as compression, expansion, and noise suppression. The effect of each of these operations was discussed qualitatively, leading to the overall picture of a clear relation between intelligibility and the signal-to-noise ratio in the modulation domain. To also account for situations with very low spurious modulation levels, it was necessary to assume an internal modulation floor at −20 dB that limits the effective dynamic range in the modulation domain.

The possible consequences of the concept of $(S/N)_{mod}$ for the traditional speech intelligibility measures such as the STI and the speech intelligibility index SII (ANSI, 1997), which is the revised articulation index AI (ANSI, 1969), cannot be defined in the form of some simple straightforward correction. All models essentially predict the intelligibility of noisy speech based on the signal-to-noise ratio in a number

of adjacent frequency bands[6]. For the SII, the traditional approach is to measure the speech and noise levels separately, thus not including the effects resulting from the speech-noise interactions. In the case of noise reduction or other processing algorithms applied to a speech-plus-noise signal, the definition of the relevant speech and noise levels from the resulting signal poses great difficulties, making the SII virtually impossible to apply in such cases. For the STI, the S/N ratios are derived from the observed reduction in the modulation spectrum. This is based on an analysis of the speech-plus-noise signal and can thus in principle be applied in cases of processing applied to the speech-plus-noise signal. However, we have learned that the observed changes in the modulation spectrum should be related to changes in the spurious modulations. With the development of a specific speechlike test signal to allow the analysis of both the speech modulations and the floor of spurious modulations, the STI approach might be adapted to the new concept of the $(S/N)_{mod}$.

At this point, the authors would like to emphasize that the aim of current paper is to introduce a new concept, rather then presenting a well-balanced model. In the past, the STI model was preceded by a new idea, i.e., the concept of the MTF. Likewise, the $(S/N)_{mod}$ concept may evolve into a new model for intelligibility predictions. Such a model would allow a more quantitative analysis of data in more of a meta-analysis format (i.e., applying the model to data across many studies) and may produce more accurate intelligibility estimations then the "no improvement," "small improvement," or "large improvement" qualifications used in this paper. Still, even these rough terms indicate that the concept performs principally better than current measures when nonlinear processing is involved.

Ergo, the concept of $(S/N)_{mod}$ provides relevant information about expected intelligibility of noisy-speech signals after being processed by a noise-suppression system or a speech enhancement system, where commonly known measures as the STI fall short. This suggests that improving the $(S/N)_{mod}$ may be a highly relevant guiding principle for the generation of effective noise suppression systems.

A. STI and intelligibility of noisy speech

A final remark concerning the MTF-STI model. As the existence of an S/N-dependent spurious modulation noise floor in noisy signals was convincingly demonstrated in this paper, the idea of the modulation-floor being fixed—as assumed in the concept of useful modulation area—must be rejected. This implies that the MTF-STI model—that evolved from this concept—is based on an invalid principle. How can the STI be so successful knowing that its fundament is invalid?

We should now acknowledge that the envelope effects of additive noise are twofold: a reduction of the speech modulations and an increase of the floor of spurious modulations. The MTF-STI approach only considers the first effect. Under normal circumstances, both effects will depend on the S/N ratio, and are thus highly related. This means that, even when $(S/N)_{mod}$ is the key parameter, the STI can still be uniquely related to intelligibility, as long as the strict relation between these two effects is maintained. Apparently, in some cases of signal processing, for example spectral subtraction or compression, this relation is disturbed and intelligibility is no longer a function of exclusively the reduction effect. In these cases, one should consider the signal-to-noise ratio in the modulation domain, the $(S/N)_{mod}$.

V. CONCLUSIONS

In this paper, a novel concept was introduced that relates intelligibility of noisy speech to the relative strength of speech modulations and spurious modulations arising from speech-noise interactions. The conclusions are summarized below.

(1) When noise is added to speech, spurious modulations are created as a result of phase interactions between the speech- and noise waveforms.
(2) The existence of these spurious modulations was demonstrated by adding noise to a special test signal, referred to as "peephole speech," containing a speech-envelope spectrum in which one frequency band is suppressed. Also, a more deterministic test signal (a 4-Hz modulated 1-kHz carrier) can be used for this purpose.
(3) The strength of the speech modulations relative to the spurious modulations can be defined by the signal-to-noise ratio in the modulation domain: $(S/N)_{mod}$.
(4) It was shown that $(S/N)_{mod}$ remains unchanged after spectral subtraction, which corresponds to the commonly observed ineffectiveness of spectral subtraction in improving speech intelligibility.
(5) The effect on $(S/N)_{mod}$ of a variety of signal-processing procedures was determined, and appeared to correspond well with data on intelligibility. A modulation threshold is introduced to predict intelligibility in the case of speech processing in quiet, e.g., for amplitude compression. However, the evidence in support of this application of the modulation signal-to-noise ratio is of a qualitative nature and further work is needed to explore this application of the modulation signal-to-noise ratio for nonlinear processing in quiet, such as amplitude compression.

ACKNOWLEDGMENT

The preparation of this manuscript was supported by the Mgr J. C. van Overbeek foundation.

[1]Note that the modulation-frequency bandwidth is one octave rather then the 1/3-octave bands shown in previous pictures, in order to relate more closely to auditory processing of temporal modulations (Houtgast and Steeneken, 1985; Houtgast, 1989; Dau *et al.*, 1997). Also for this reason, speech was filtered in 1/3-octave bands in the audio domain, instead of the traditional octave band on which Figs. 1 and 2 were based. However, these choices are not relevant for the main message of this paper.
[2]In fact, a speech-to-nonspeech modulation ratio.
[3]Each spectrum was based on 30-s signals. Only 1 s of each signal is shown in the upper row of panels.
[4]The envelope spectrum of band-filtered Gaussian noise is determined by the bandwidth of the applied filter (B_{audio}). This bandwidth sets a limit to the highest possible rate of change in the envelope, resulting in a typical low-pass characteristic of the envelope spectrum, with a cutoff related to

B_{audio} Hz. Below this cutoff, the spectral density in the modulation domain is essentially constant, that is, the theoretically expected m-value resulting from the noise statistics is independent of modulation frequency. (The lowest relevant modulation frequency is determined by the duration of the noise token considered.) This white modulation spectrum results in the +3-dB slope when expressed in octave modulation bands. It can be shown that the theoretical modulation level in a modulation-spectrum band with width B_{mod} is $10\log(4\times B_{mod}/B_{audio})$. In the present case B_{audio} is 230 Hz (1/3 octave around 1 kHz) and for the 4-Hz modulation octave B_{mod} is 2.8 Hz, thus predicting a modulation level of −13.1 dB at 4 Hz in panel (G).

[5]Disturbance of the speech carrier was recognized as the third noise effect on intelligibility, but will not be discussed here.

[6]Including some other factors, such as the hearing threshold, which are not considered here.

ANSI (**1969**). ANSI S3.5-1969, "American National Standard Methods for the Calculation of the Articulation Index" (American National Standards Institute, New York).

ANSI (**1997**). ANSI S3.5-1997, "American National Standard Methods for the Calculation of the Speech Intelligibility Index" (American National Standards Institute, New York).

Barfod, J. (**1978b**). "Automatic regulation systems with relevance to hearing aids," in Senorineural Hearing Impairment and Hearing Aids, edited by C. Ludvigsen and J. Barfod, Scand. Audiol. Suppl. **6**, 355–378.

Bunnell, H. T. (**1990**). "On enhancement of spectral contrast in speech for hearing-impaired listeners," J. Acoust. Soc. Am. **88**, 2546–2556.

Dau, T., and Verhey, J. L. (**1999**). "Intrinsic envelope fluctuations and modulation-detection thresholds for narrow-band noise carriers," J. Acoust. Soc. Am. **106**(5), 2752–2760.

Dau, T., Kollmeier, B., and Kohlrausch, A. (**1997**). "Modeling auditory processing of amplitude modulation. I. Detection and masking with narrow-band carriers," J. Acoust. Soc. Am. **102**, 2892–2905.

Dillon, H. (**1996**), "Compression?: Yes, but for low and high frequencies, for low and high intensities, and with what response times?" Ear Hear. **17**, 287–307.

Drullman, R., Festen, J. M., and Plomp, R. (**1994a**). "Effect of temporal envelope smearing on speech reception," J. Acoust. Soc. Am. **95**, 1053–1064.

Drullman, R., Festen, J. M., and Plomp, R. (**1994b**). "Effect of reducing slow temporal modulations on speech reception," J. Acoust. Soc. Am. **95**, 2670–2680.

Dubbelboer, F., and Houtgast, T. (**2007**). "A detailed study on the effects of noise on speech intelligibility," J. Acoust. Soc. Am. **122**, 2865–2870.

Festen, J. M., and van Dijkhuizen, J. N. (**1998**). "Modeling the speech reception threshold for amplitude-compressed speech," in *Psychophysics, Physiology and Models of Hearing*, edited by T. Dus, V. Hohmann, and B. Kollmeier (World Scientific, Singapore), pp. 249–254.

Franck, B. A., Kreveld-Bos, C. S., Dresschler, W. A., and Verschuure, H. (**1999**). "Evaluation of spectral enhancement in hearing aids, combined with phonetic compression," J. Acoust. Soc. Am. **106**, 1452–1464.

Hickson, L. (**1994**). "Compression amplification in hearing aids," Am. J. Audiol. **3**, 51–65.

Houben, A. C. H. H. (**2006**). "The Effect of Amplitude Compression on the Perception of Speech in Noise by the Hearing Impaired," In: Ph.D. Thesis (Gildeprint BV, Enschede).

Houtgast, T. (**1989**). "Frequency selectivity in amplitude-modulation detection," J. Acoust. Soc. Am. **85**(4), 1676–1680.

Houtgast, T., and Steeneken, H. J. M. (**1972**). "Envelope spectrum and intelligibility of speech in enclosures," in Proceedings of IEEE Speech conference, Newton, MA, pp. 392–395.

Houtgast, T., and Steeneken, H. J. M. (**1985**). "A review of the MTF concept in room acoustics and its use for estimating speech intelligibility in auditoria," J. Acoust. Soc. Am. **77**, 1069–1077.

IEC (**2003**). IEC 60268–16-2003 (third edition **2003**), *Sound System Equipment—Part 16: Objective Rating of Speech Intelligibility by Speech Transmission Index* (International Electrotechnical Commision, Geneva, Switzerland).

Levitt, H. (**2001**). "Noise reduction in hearing aids: An overview," J. Rehabil. Res. Dev. **38**, No. 1, 111–121.

Ludvigsen, C. (**1993**). "Evaluation of a noise reduction method—comparison between observed scores and scores predicted from STI," Scand. Audiol. Suppl. **38**, 50–55.

Lyzenga, J., Festen, J. M., and Houtgast, T. (**2002**). "A speech enhancement scheme incorporating spectral expansion evaluated with simulated loss of frequency selectivity," J. Acoust. Soc. Am. **112**(3), 1145–1157.

Moore, B. C., Peters, R. W., and Stone, M. A. (**1999**). "Benefits of linear amplification and multichannel compression for speech comprehension in backgrounds with spectral and temporal dips," J. Acoust. Soc. Am. **105**, 400–411.

Noordhoek, I. M., and Drullman, R. (**1997**). "Effect of reducing temporal intensity modulations on sentence intelligibility," J. Acoust. Soc. Am. **101**(1), 498–502.

Plomp, R. (**1988**). "The negative effect of amplitude compression in multichannel hearing aids in the light of the modulation-transfer function," J. Acoust. Soc. Am. **83**(6), 2322–2327.

Plomp, R., and Mimpen, A. M. (**1979**). "Improving the reliability of testing the speech reception threshold for sentences," Audiology **18**, 43–52.

Souza, P. E. (**2002**). "Effects of compression on speech acoustics, intelligibility, and sound quality," Trends Amplif. **6**, 131–165.

Steeneken, H. J. M. (**1992**). "On measuring and predicting speech intelligibility," Doctoral dissertation, University of Amsterdam.

van Buuren, R. A., Festen, J. M., and Houtgast, T. (**1999**). "Compression and expansion of the temporal envelope: Evaluation of speech intelligibility and sound quality," J. Acoust. Soc. Am. **105**, 2903–2913.

Viemeister, N. F. (**1979**). "Temporal modulation transfer functions based upon modulation Thresholds," J. Acoust. Soc. Am. **66**, 1364–1380.

Working Group on Communication Aids for the Hearing-Impaired (WGCA) (**1991**). "Speech perception aids for hearing-impaired people: Current status and needed research," J. Acoust. Soc. Am. **90**, 637–685.

The contribution of obstruent consonants and acoustic landmarks to speech recognition in noise

Ning Li and Philipos C. Loizou[a)]
Department of Electrical Engineering, University of Texas at Dallas, Richardson, Texas 75083-0688

(Received 14 April 2008; revised 8 September 2008; accepted 10 September 2008)

The obstruent consonants (e.g., stops) are more susceptible to noise than vowels, raising the question whether the degradation of speech intelligibility in noise can be attributed, at least partially, to the loss of information carried by obstruent consonants. Experiment 1 assesses the contribution of obstruent consonants to speech recognition in noise by presenting sentences containing clean obstruent consonants but noise-corrupted voiced sounds (e.g., vowels). Results indicated substantial (threefold) improvement in speech recognition, particularly at low signal-to-noise ratio levels (−5 dB). Experiment 2 assessed the importance of providing partial information, within a frequency region, of the obstruent-consonant spectra while leaving the remaining spectral region unaltered (i.e., noise corrupted). Access to the low-frequency (0–1000 Hz) region of the clean obstruent-consonant spectra was found to be sufficient to realize significant improvements in performance and that was attributed to improvement in transmission of voicing information. The outcomes from the two experiments suggest that much of the improvement in performance must be due to the enhanced access to acoustic landmarks, evident in spectral discontinuities signaling the onsets of obstruent consonants. These landmarks, often blurred in noisy conditions, are critically important for understanding speech in noise for better determination of the syllable structure and word boundaries. © *2008 Acoustical Society of America.* [DOI: 10.1121/1.2997435]

PACS number(s): 43.71.Es, 43.71.Gv [MSS] Pages: 3947–3958

I. INTRODUCTION

Speech sounds can generally be classified into two broad categories, vowels and consonants. A number of studies assessed the contribution of information provided by vowels versus consonants to speech intelligibility in quiet (Cole *et al.*, 1996; Owren and Cardillo, 2006; Kewley-Port *et al.*, 2007). In noise, however, listeners may employ a different set of acoustic cues, and therefore, the contribution of vowels versus consonants to speech intelligibility might change. This is so because noise masks vowels and consonants differently and to a different extent. For one, the low-energy obstruent consonants (e.g., stops) are masked more easily by noise (e.g., Phatak and Allen, 2007; Parikh and Loizou, 2005) than the high-energy vowels and semivowels. Phatak and Allen (2007), for instance, showed that aside from a small subset of consonants, the vowel-to-consonant recognition ratio is well above unity for a large range of signal-to-noise ratio (SNR) levels (−20 to 0 dB), suggesting that vowels are easier to recognize than consonants in speech-weighted noise. The study by Parikh and Loizou (2005) showed that the information contained in the first two vowel formants is preserved to some degree even at low SNR levels. In contrast, both the spectral tilt and burst frequency of stop consonants, which are known to convey place of articulation information (e.g., Blumstein and Stevens, 1979), were significantly altered by noise. This raises then the question as to whether the degradation of speech intelligibility in noise can be attributed, at least partially, to the loss of information carried by obstruent consonants. Secondly, noise corrupts acoustic landmarks that are produced by (abrupt) spectral discontinuities such as those created by the closing and release of stop consonants. These landmarks were posited to be crucial in lexical-access models (Stevens, 2002). Some argued (Assmann and Summerfield, 2004) that these landmarks serve as robust speech features that listeners exploit to understand speech in noise. Furthermore, evidence from animal neurophysiology studies (Smith, 1979; Delgutte and Kiang, 1984) suggests that the auditory system is particularly responsive (manifesting adaptation effects) to abrupt changes to the signal, such as those occurring at the onsets of landmarks. These adaptation effects are beneficial in speech recognition as they enhance contrast between successive speech segments separated by an abrupt spectral change. In brief, while the acoustic cues to voiced speech segments (e.g., vowels) may resist, to some extent, the presence of noise (e.g., Parikh and Loizou, 2005), the acoustic cues to the unvoiced (low-energy) segments are severely corrupted and perhaps rendered useless.

In the present study, we assess the contribution of information provided by obstruent consonants to speech intelligibility in noise. We do this, in experiment 1, by using noise-corrupted sentences in which we replace the noise-corrupted obstruent consonants with clean obstruent consonants, while leaving the sonorant sounds (vowels, semivowels, and nasals) corrupted. In experiment 2, we control the amount of spectral and temporal information that is present in the clean obstruent sound spectra by presenting to listeners partial spectral information spanning a specific frequency range ($0-F_C$ Hz), while leaving the remaining spectrum ($\geq F_C$ Hz) corrupted. By restricting, for instance, the F_C value to low

[a)]Author to whom correspondence should be addressed. Electronic mail: loizou@utdallas.edu

frequencies (e.g., $F_C \leq 1000$ Hz), we present to listeners only voicing and F1 information, and subsequently only information about low-frequency acoustic landmarks (Stevens, 2002). Experiment 2 thus assesses the contribution of low- and high-frequency acoustic landmarks to speech recognition in noise.

We choose to study the obstruent consonants (Shriberg and Kent, 2003), which includes stops, fricatives, and affricates, for several reasons. First, the obstruent consonants are more susceptible to noise masking and reverberation compared to the more intense vowels and semivowels (e.g., Phatak and Allen, 2007). Secondly, the spectra of the majority of the obstruent consonants have high-frequency prominence that may or may not be accessible or audible to people with sensorineural hearing loss (HL) (e.g., Ching *et al.*, 1998; Hogan and Turner, 1998). Hence, the present experiments will assess the maximum gain in intelligibility that could be obtained if listeners had access to (clean) obstruent-consonant information. If the gain in intelligibility is substantial, that would suggest that special algorithms ought to be designed for hearing aid applications to enhance access or detection of the obstruent consonants. Furthermore, the restoration of acoustic landmarks might provide some insight regarding the difficulty hearing-impaired (HI) listeners experience when communicating in noise.

II. EXPERIMENT 1: CONTRIBUTION OF OBSTRUENT CONSONANTS TO SPEECH INTELLIGIBILITY IN NOISE

A. Methods

1. Subjects

Thirteen normal-hearing listeners participated in this experiment. All subjects were native speakers of American English and were paid for their participation. The subjects' age ranged from 18 to 40 years, with the majority being undergraduate students from the University of Texas at Dallas.

2. Stimuli

The speech material consisted of isolated /VCV/ syllables taken from Shannon *et al.* (1999) and sentences taken from the IEEE database (IEEE, 1969). Since this study was concerned with the contribution of obstruent consonants, only the following consonants were used from the recordings of Shannon *et al.* (1999): /p, t, k, b, d, g, f, ð, s, ʃ, v, z, tʃ, dʒ/. The semivowels and nasals were excluded. The context vowel in the VCV syllables was /ɑ/. The selected consonants were produced by three male and three female speakers. The talkers had no noticeable regional accent (standard American Midwest dialect). We chose to use both sentences and VCV syllables as testing material in order to assess the contribution of obstruent consonants in situations where listeners have access to contextual information (i.e., sentence recognition task) and compare that outcome with the situation where listeners do not use high-level linguistic knowledge (e.g., VCV task).

All IEEE sentences were produced by one male and one female speaker. The male speaker was born in Texas and the female speaker was born in North Carolina. Neither talker had a noticeable Southern regional accent. The sentences were recorded in a sound-proof booth (Acoustic Systems) in our laboratory at a 25 kHz sampling rate. Details about the recording setup and copies of the recordings are available in Loizou, 2007. The speech materials were corrupted by a 20-talker babble (Auditec CD, St. Louis, MO) at −5 and 0 dB SNRs. The average long-term spectrum of the multitalker babble is shown in Parikh and Loizou (2005). These SNR levels were chosen to avoid floor effects. The babble interferer started at 100 ms before the beginning of each speech token and stopped at least 100 ms after the end of the sentence (and the VCV syllable). This masker has temporal characteristics similar to those found in continuous speech-shaped noise maskers in that it does not have any temporal envelope dips that would allow the listener to "glimpse" the target. Hence, for the most part, the masker used in the present study can be considered to be continuous.

The IEEE sentences were manually segmented into two broad phonetic classes: (a) the obstruent sounds, which included the stops, fricatives, and affricates, and (b) the sonorant sounds, which included the vowels, semivowels, and nasals. The segmentation was done in two steps. In the first step, a highly accurate F0 detector, taken from the STRAIGHT algorithm (Kawahara *et al.*, 1999), was used to provide the initial classification of voiced and unvoiced speech segments. The stop closures were classified as belonging to the unvoiced segments. The F0 detection algorithm was applied every 1 ms to the stimuli using a high-resolution fast Fourier transform (FFT) to provide for accurate temporal resolution of voiced/unvoiced boundaries. Segments with nonzero F0 values were initially classified as voiced and segments with zero F0 value (as determined by the STRAIGHT algorithm) were classified as unvoiced. In the second step, the voiced and unvoiced decisions were inspected for errors and the detected errors were manually corrected. Voiced stops produced with prevoicing (e.g., /b/) as well as voiced fricatives (e.g. /z/) were classified as obstruent consonants. Waveform and time-aligned spectrograms were used to refine the voiced/unvoiced boundaries. The criteria for identifying a segment belonging to voiced sounds (sonorant sounds) included the presence of voicing, a clear formant pattern, and absence of signs of a vocal-tract constriction. For the special boundary that separates a prevocalic stop from a following semivowel (as in *truck*), we adopted the rule used in the phonetic segmentation of the Texas Instruments-Massachusetts Institute of Technology (TIMIT) corpus (Seneff and Zue, 1988). More precisely, the unvoiced portion of the following semivowel or vowel was absorbed in the stop release, and was thus classified as an obstruent consonant. The two-class segmentation of all IEEE sentences was saved in text files (same format as the TIMIT .phn files) and is available from a CD ROM in Loizou, 2007. The VCV syllables were similarly segmented to consonants and vowels (/ɑ/). An example segmentation of the syllable /ɑ t ɑ/ is shown in Fig. 1.

To examine whether there exists a balanced distribution and coverage of obstruent consonants across the various IEEE lists, we computed the relative duration of the obstruent consonants in the IEEE corpus. The relative duration

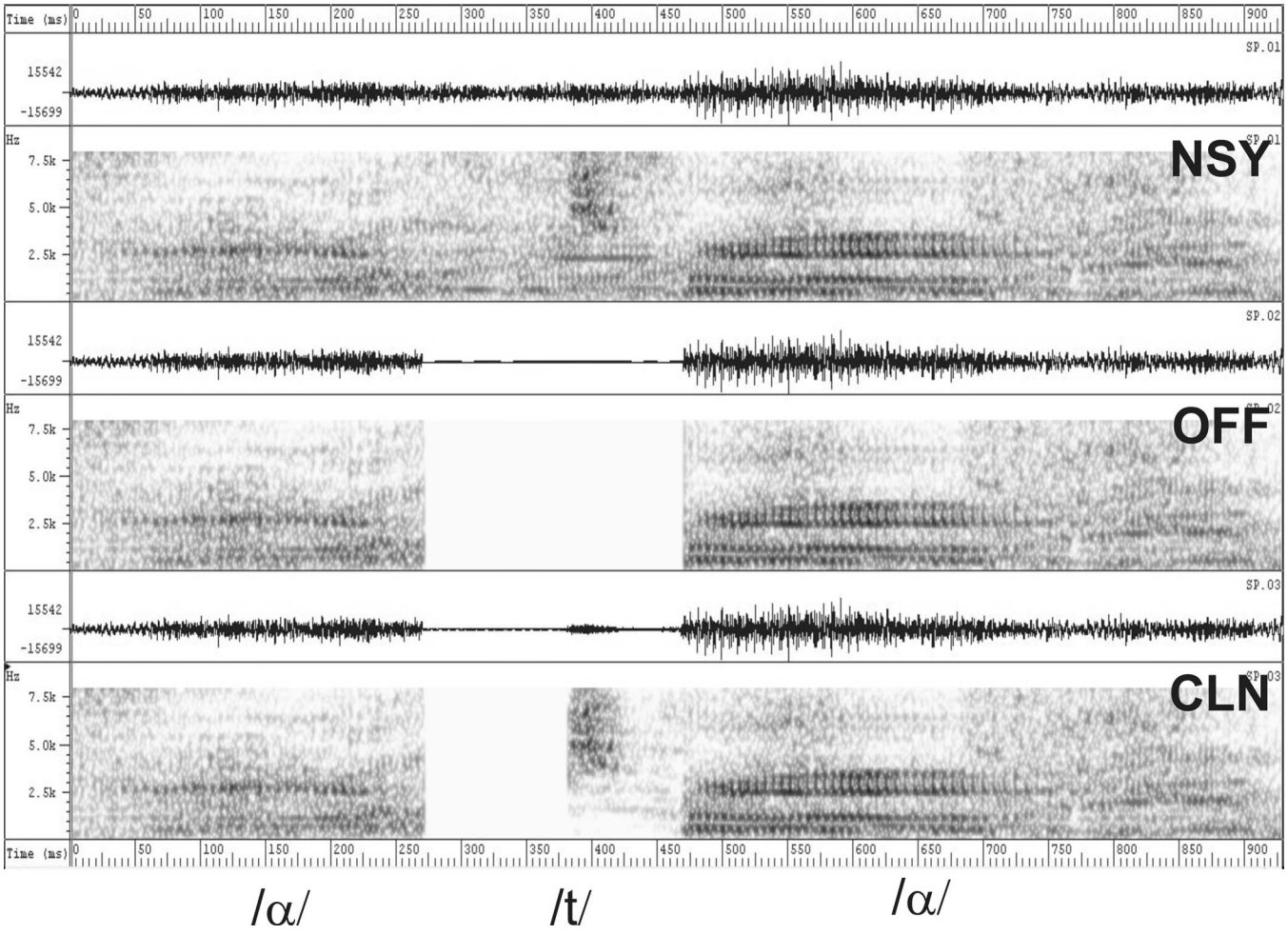


FIG. 1. Time waveforms and spectrograms of the syllable /ɑ t ɑ/, which was corrupted by the multitalker babble at 0 dB SNR (top panel, NSY condition), processed in the OFF condition (middle panel) and processed in the CLN condition (bottom panel).

was expressed in proportion of the total duration of each sentence. The mean total duration of the obstruent consonants in the IEEE sentences was found to be 36.2% (s.d. =3.1%) of the total duration of each sentence, consistent with that reported by Mines *et al.* (1978). This analysis indicates that there is a very small variability in the total duration of obstruent consonants across the IEEE sentence lists. The study by Mines *et al.* (1978) analyzed the distribution of phonemes taken from a large database (comprising nearly 104 000 phonemes) and found that the phonemes belonging in the obstruent class occur 34% of the time.

3. Conditions

The 13 subjects were quasirandomly assigned to the conditions involving processed IEEE sentences produced by the male and female speakers (seven listened to the IEEE sentences produced by a male speaker and six listened to the IEEE sentences produced by a female speaker). Similarly, the subjects were quasirandomly assigned to the processed VCV syllables produced by three male and three female speakers (seven listened to VCV syllables produced by two speakers, and six listened to VCV syllables produced by six speakers, with equal distribution between male and female speakers). Subjects were tested in three conditions. In the first control condition, the noisy speech stimuli (sentences and VCV syllables) were left unaltered. In this condition, the obstruent consonants remained corrupted by the multitalker babble, and will refer to it as the NSY (noisy) condition. In the second condition, the obstruent consonants were removed from the noise-corrupted sentences, and silence was inserted in their place. We will refer to this condition as the OFF condition. In the third condition, the noisy obstruent-consonant segments were replaced with the corresponding clean obstruent-consonant segments. The modified sentences contained noise-corrupted (at −5 and 0 dB SNRs) sonorant sounds, but clean obstruent consonants. We will refer to this condition as the CLN (clean) condition. Figure 1 shows example time waveforms and spectrograms for the syllable /ɑ t ɑ/ (produced by a male speaker) processed in the three conditions.

4. Procedure

The experiments were performed in a sound-proof room (Acoustic Systems, Inc.) using a PC connected to a Tucker-Davis system 3. Stimuli were played to the listeners monaurally through Sennheiser HD 250 Linear II circumaural headphones at a comfortable listening level. Prior to the sentence test, each subject listened to a set of noise-corrupted sentences to familiarize them with the testing procedure. During the test, subjects were asked to write down the words they

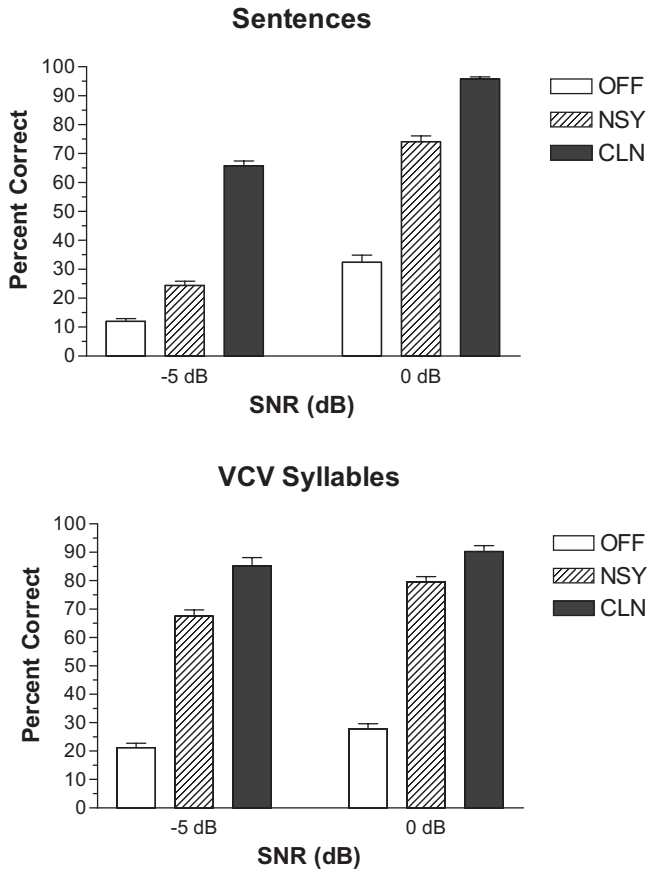


FIG. 2. Mean percent correct scores obtained in the various conditions for the sentence recognition task (top panel) and VCV recognition task (bottom panel). The error bars indicate standard errors of the mean.

heard. In the consonant test, subjects were presented with a total of 12 repetitions of each consonant. The stimuli were presented in blocks of six repetitions each. The consonant stimuli were completely randomized. All test sessions were preceded by one practice session in which the identity of the consonants was indicated to the listeners. The whole listening test lasted for about 4–5 h, which was split into two sessions lasting 2–2.5 h each. Five minute breaks were given to the subjects every 30 min. To collect responses, a graphical interface was used that allowed the subjects to identify the consonants they heard by clicking on the corresponding button in the graphical interface. Subjects participated in a total of 12 conditions (=2 SNR levels × 3 processing conditions × 2 types of speech material). Two lists of sentences (i.e., 20 sentences) were used per condition, and none of the lists were repeated across conditions. The sentence lists were counterbalanced across subjects. Sentences were presented to the listeners in blocks, and 20 sentences were presented in each block for each condition. The order of the test conditions was randomized across subjects.

B. Results and discussion

The mean scores for all conditions are shown in Fig. 2. For the sentence recognition task, performance was measured in terms of percent of words identified correctly (all words were scored). Two-way ANOVA (with repeated measures) indicated a significant effect of SNR level ($F[1,12]=1330.1$), $p<0.0005$), a significant effect of stimulus processing ($F[2,24]=1189.2$, $p<0.0005$) and a significant interaction ($F[2,24]=67.1$, $p<0.0005$). The interaction was caused by the fact that the improvement in performance obtained when the listeners had access to the clean obstruent consonants was larger at −5 dB SNR than 0 dB.

Similar ANOVA analysis was applied to the scores obtained on the isolated consonant recognition task. Two-way analysis of variance (ANOVA) (with repeated measures) indicated a significant effect of SNR level ($F[1,12]=72.1$, $p<0.0005$), a significant effect of stimulus processing ($F[2,24]=538.1$, $p<0.0005$), and a significant interaction ($F[2,24]=7.9$, $p=0.002$).

Post hoc tests (Scheffe) applied to the sentence scores at −5 dB SNR revealed highly significant differences ($p<0.0005$) between the scores obtained in the OFF and NSY (control) conditions, and between the NSY and CLN conditions. This was also found to be true with the sentence scores at 0 dB SNR. *Post hoc* tests (Scheffe) applied to the VCV scores revealed significant differences ($p<0.005$) between the OFF and NSY conditions and between the NSY and CLN conditions at both SNR levels.

It is clear from Fig. 2 that listeners benefited a great deal from having access to the clean obstruent consonants, despite the fact that the sonorant sounds (vowels, semivowels, and nasals) were corrupted by the multitalker babble. This benefit was found to be most prominent in the low SNR conditions (−5 dB SNR). Sentence recognition improved nearly by a factor of 3 when the clean obstruent consonants were introduced amid the noise-corrupted sonorant sounds in sentences. In the isolated VCV task, performance improved by 20% points at −5 dB SNR.

Subject performance dropped significantly when the obstruent consonants were removed, thus providing additional evidence about the contribution and importance of the information provided by obstruent consonants to speech intelligibility in noise. Note that we cannot directly compare our findings with those of Cole *et al.* (1996) and Kewley-Port *et al.* (2007) for the following reasons. First, silence was inserted in the present study (in the OFF condition) rather than white noise or tones. In doing so, we ruled out any phonemic restoration effects that could have contributed (positively) to performance (Bashford and Warren, 1987). Second, our study used sentences embedded in noisy backgrounds and thus the task was more difficult. Furthermore, noise does not mask vowels and consonants the same way or equally, thereby making it difficult to truly assess the contribution of vowels versus consonants in noisy environments.

It is interesting to note that performance on the VCV task was significantly ($p<0.005$, based on t-tests) above chance (7.1% correct) despite the fact that the consonants were removed from the VCV syllables. This can be attributed to the subjects making use of the vowel formant transitions into and out of the medial consonant. As demonstrated by Cole *et al.* (1996) and Owren and Cardillo (2006), the formant transitions at the edges of vowels contain information about the neighboring consonants that may enable subjects to identify words in sentences.

Performance was expected in this experiment to improve

as new acoustic information was added, but the magnitude of the improvement was difficult to predict, particularly for the sentence recognition task. Sentence recognition scores improved significantly when the clean obstruent consonants were introduced, and the improvement was largest at −5 dB SNR. In the −5 dB SNR condition, for instance, performance improved from 25% correct to 65% correct. The underlying mechanisms responsible for such large improvement are not clear from the present Experiment. Listeners had access to multiple spectral/temporal cues when the clean obstruent consonants were introduced. These included F1/F2 transitions to/from the vowel and sonorant sounds, accurate voicing information, and consequently better access to acoustic landmarks that perhaps aided the listeners in identifying word boundaries in the noisy speech stream. In order to delineate and identify the cues and/or factors that contributed to the large improvements in performance, we present to listeners in experiment 2 partially clean spectral information of the obstruent consonants.

III. EXPERIMENT 2: CONTRIBUTION OF PARTIAL SPECTRAL INFORMATION OF OBSTRUENT CONSONANTS TO SPEECH INTELLIGIBILITY

The previous experiment demonstrated the importance and contribution of obstruent consonants to speech intelligibility in noisy (continuous) backgrounds. The listeners in experiment 1 had access to the full spectrum of the obstruent consonants and thus it was not clear which temporal/spectral characteristic or spectral feature of the consonants contributed the most or generally which temporal/spectral cues did the listeners use. In the present experiment, we introduce systematically access to the clean spectrum in the region of $0-F_C$ Hz (F_C=500–3000 Hz), while leaving the remaining spectrum ($>F_C$ Hz) of the obstruent consonants unaltered (i.e., noise corrupted). The issue is determining the region(s) of the clean obstruent-consonant spectrum that contributes the most to intelligibility. By setting F_C, for instance, to a small frequency value (e.g., F_C=500 Hz), we provide to listeners reliable F1 and voicing information. This information in turn provides access to reliable low-frequency acoustic landmarks that might assist listeners better identify syllable or word boundaries (Stevens, 2002). Hence, the use of low-frequency values for F_C can help us assess the contribution of low-frequency acoustic landmarks to speech intelligibility in noise. Similarly, by setting F_C to higher values (e.g., F_C >2000 Hz), we introduce more spectral cues (e.g., F2 formant transitions) including high-frequency landmarks (e.g., onset of frication noise) that can potentially aid the listeners identify more words in the noisy speech stream. In brief, by controlling the value of F_C, we can investigate in the present experiment the contribution of information carried by low- and high-frequency acoustic landmarks to speech recognition in noise.

A. Methods

1. Subjects and material

The same 13 subjects who participated in experiment 1 also participated in the present experiment. The same speech materials (IEEE sentences and VCV syllables) were used as in experiment 1.

2. Signal Processing

The noisy obstruent-consonant stimuli (at −5 and 0 dB SNRs) were processed so as to create conditions in which listeners had access to the clean obstruent-consonant spectrum in the region of $0-F_C$ Hz, while leaving the remaining spectral region ($>F_C$ Hz) unaltered (noise corrupted). The obstruent consonants were processed as follows. An FFT was applied to the clean and corrupted obstruent-consonant segments every 10 ms with no overlap between adjacent segments (rectangular windowing was used[1]). A new (complex) spectral vector was formed consisting of the clean FFT spectral components for frequencies spanning the range $0-F_C$ Hz, and the noise-corrupted FFT spectral components for frequencies higher than F_C Hz. The inverse FFT was applied to this new spectral vector to reconstruct the time-domain signal. This series of operations was repeated until the end of the obstruent-consonant segment was reached. The remaining sonorant segments (vowels, semivowels, and nasals) in the noise-corrupted sentence stimuli were left unaltered.

Four different values of the upper-cutoff frequency F_C were considered: 500, 1000, 2000, and 3000 Hz. These values were chosen to encompass the F1 and F2 regions. Note that in experiment 1 the value of F_C was set to half the sampling frequency (Nyquist frequency), i.e., F_C=12.5 kHz, for the CLN condition. Figure 3 (bottom panel) shows an example spectrogram of a sentence processed using F_C =1000 Hz at −5 dB SNR.

3. Procedure

The procedure was identical to that used in experiment 1. Subjects were tested in a total of 16 (=4 values of F_C ×2 SNR levels×2 types of material) conditions. Two lists of sentences (i.e., 20 sentences) were used per condition, and none of the lists from experiment 1 was used or repeated across conditions. The sentence lists were counterbalanced across subjects. Sentences were presented to the listeners in blocks, with 20 sentences presented in each block for each condition. The order of the test conditions was randomized across subjects.

B. Results and discussion

The mean scores for all conditions are shown in Fig. 4. The baseline NSY score (F_C=0 Hz) and the score obtained with clean obstruent consonants (F_C=12.5 kHz) are also plotted for comparison. Two-way ANOVA (with repeated measures) applied to the sentence scores indicated a significant effect of SNR level ($F[1,12]=1094.9$, $p<0.0005$), a significant effect of frequency F_C ($F[5,60]=80.1$, $p<0.0005$), and a significant interaction ($F[5,60]=13.5$, p

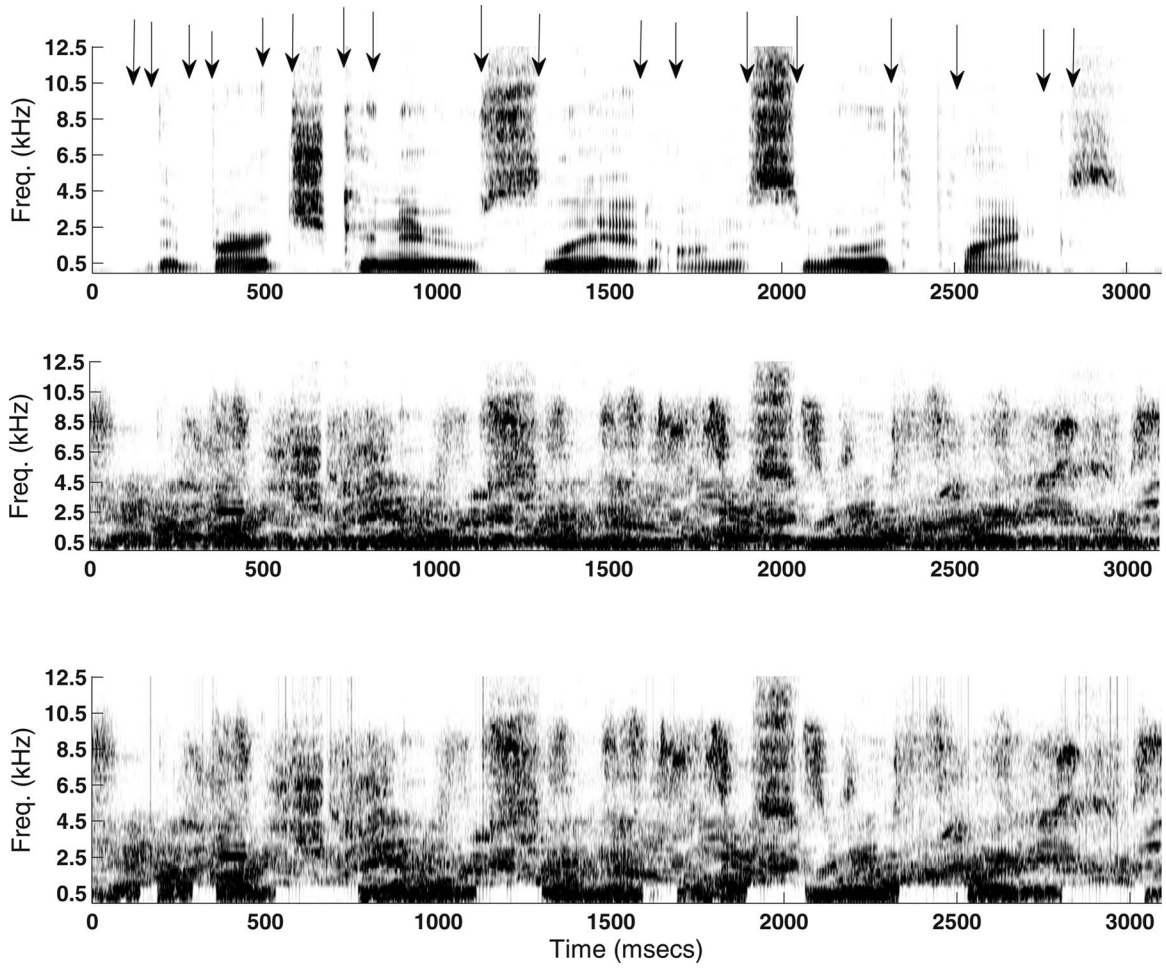


FIG. 3. Wide-band spectrogram (bottom panel) of the sentence: "The birch canoe slid on the smooth planks" processed using F_C=1000 Hz. The top and middle panels show the corresponding spectrograms of the same sentence in quiet and in multitalker babble (−5 dB SNR) conditions, respectively. The arrows in the top panel indicate the acoustic landmarks present in the clean stimulus.

<0.0005). The control NSY condition (F_C=0 Hz) was also included in the ANOVA. Two-way ANOVA (with repeated measures) applied to the VCV scores indicated a significant effect of SNR level ($F[1,12]=72.8$, $p<0.0005$), a significant effect of frequency F_C ($F[5,60]=33.4$, $p<0.0005$), and a significant interaction ($F[5,60]=5.8$, $p<0.0005$). The performance of the two groups of listeners on the VCV identification task was comparable and the difference in scores for the processed VCV stimuli produced by two versus six speakers was not significant.[2] The interaction (in both sentence and VCV analysis) was caused by the fact that the improvement in performance noted with increasing values of F_C was larger at −5 dB SNR than at 0 dB SNR.

Post hoc tests (Scheffe) were run to determine the smallest value of F_C at which significant improvements in performance are observed relative to the control condition (NSY). The sentence scores obtained with F_C=1000 Hz at 0 dB SNR were significantly (p=0.005) higher than the control (baseline) scores (F_C=0 Hz). The sentence scores obtained with F_C=500 Hz at −5 dB SNR were significantly (p=0.008) higher than the control scores. Similar *post hoc* tests were run on the VCV scores. The scores obtained with F_C=3000 Hz at −5 dB SNR were significantly (p=0.026) higher than the control scores. The scores obtained in the CLN condition (F_C=12.5 kHz) at 0 dB SNR were significantly (p=0.013) higher than the control scores.

The sentence and VCV data clearly demonstrated that it is not necessary to have access to the full spectrum of the (clean) obstruent consonants to observe significant improvements in intelligibility. Access to the low-frequency (0–1000 Hz) region of the clean obstruent-consonant spectra was sufficient to realize significant improvements in performance. Sentence intelligibility scores (at −5 dB SNR) improved significantly by 2% points, when listeners had access to the low-frequency region (0–1000 Hz) of the obstruent consonants. Similar, albeit smaller, improvements were also noted with the VCV syllables. Considerably larger improvements in intelligibility were noted when listeners had access to the 0–3000 Hz region of the obstruent spectrum. Sentence scores improved from 24% to 51% correct, while VCV scores improved from 67% to 80% correct at −5 dB SNR.

The outcome that having access to the low-frequency (0–1 kHz) region of the spectrum yielded significant gains in intelligibility led us to wonder whether this was due to better transmission of voicing information. To further investigate this, we subjected the consonant confusion matrices to information transmission analysis (Miller and Nicely, 1955). The results were analyzed in terms of voicing, place, and

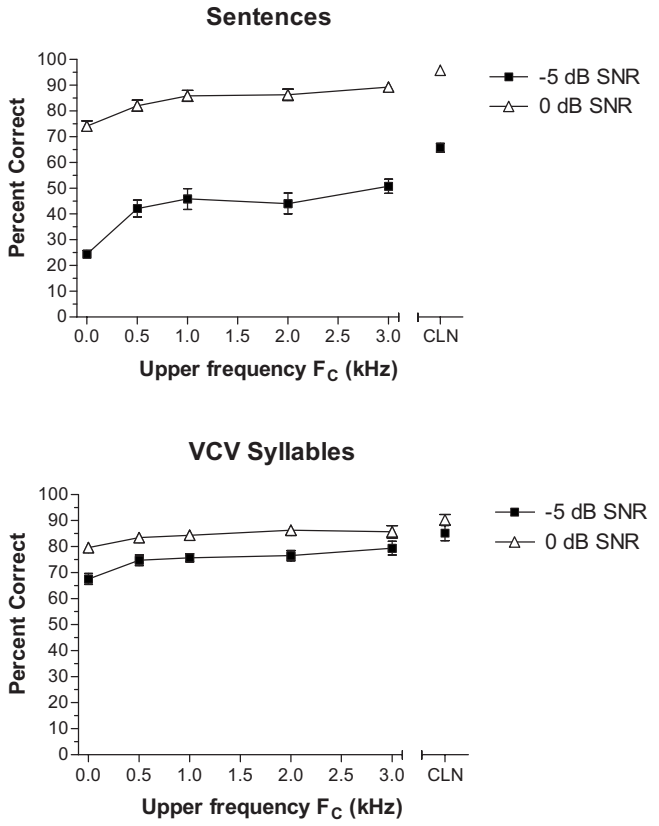


FIG. 4. Mean percent correct scores as a function of the upper-cutoff frequency F_C(Hz) and SNR level. The spectrum of the obstruent consonants was clean in the frequency region of $0-F_C$ Hz and was left unaltered (i.e., noise corrupted) in the region thereafter (i.e., $>F_C$ Hz). In the CLN condition, the listeners had access to the whole spectrum of the clean obstruent consonants (i.e., F_C=12.5 kHz). The F_C=0 Hz condition corresponds to the control (NSY) condition in which the whole spectrum of the obstruent consonants was left noise corrupted. The error bars indicate standard errors of the mean.

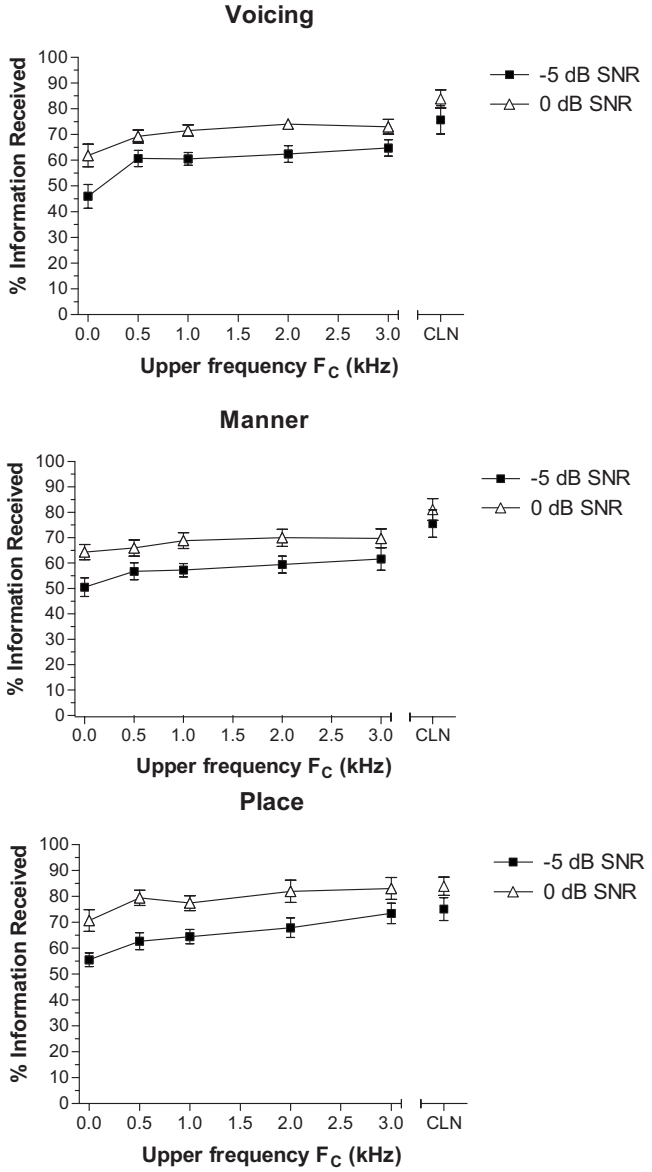


FIG. 5. Information transmission analysis (plotted as a function of the upper-cutoff frequency F_C) for the articulatory features of voicing, manner, and place of articulation. The error bars indicate standard errors of the mean.

manner features and are plotted in Fig. 5. Two-way ANOVA (with repeated measures) applied to the voicing scores indicated a significant effect of SNR level ($F[1,12]=62.4$, $p<0.0005$), a significant effect of frequency F_C ($F[5,60]=11.8$, $p<0.0005$), and a nonsignificant interaction ($F[5,60]=1.1$, $p=0.36$). Similar ANOVA applied to the manner and place feature scores revealed significant effects for SNR level and frequency F_C and nonsignificant interactions.

As shown in Fig. 5 (top panel), large improvements were noted in the transmission of voicing information when $F_C \geqslant 500$ Hz. More precisely, transmission of voicing information improved from 45% to 60% at −5 dB SNR when listeners had access to the low-frequency region (0–500 Hz) of the obstruent-consonant spectrum. *Post hoc* tests (Fisher's LSD) confirmed that the improvement in voicing relative to the baseline (control) condition was significant ($p<0.05$) for all values of $F_C \geqslant 500$ Hz at −5 dB SNR level, and for all values of $F_C \geqslant 1000$ Hz at 0 dB SNR.

Improvements to manner and place feature transmission were also noted relative to the baseline scores, but higher values of F_C were required. Significant ($p<0.05$) improvements to transmission of manner feature were noted for $F_C \geqslant 3000$ Hz at −5 dB SNR and for F_C=12.5 kHz (CLN) at 0 dB SNR. Significant ($p<0.05$) improvements to transmission of place feature information were noted for $F_C \geqslant 2000$ Hz for both SNR levels. Place information at −5 dB SNR improved substantially from 55% (baseline score) to approximately 75% when F_C=3000 Hz. This was not surprising, given that the 0–3000 Hz region encompasses the F1/F2 region, known to carry place of articulation information (e.g., Liberman *et al.*, 1952).

In summary, the above feature analysis (Fig. 5) indicates that much of the improvement in performance is due to better transmission of voicing and place feature information. The improvement in the transmission of manner of articulation information was found to be relatively smaller. No improvement was noted at 0 dB SNR in the transmission of manner information for any value of F_C except that used in the CLN condition. The improvement from better transmission of voicing information was quite substantial amounting to roughly 50% of the overall improvement on sentence recognition (Fig. 4). To further explore the contribution of voic-

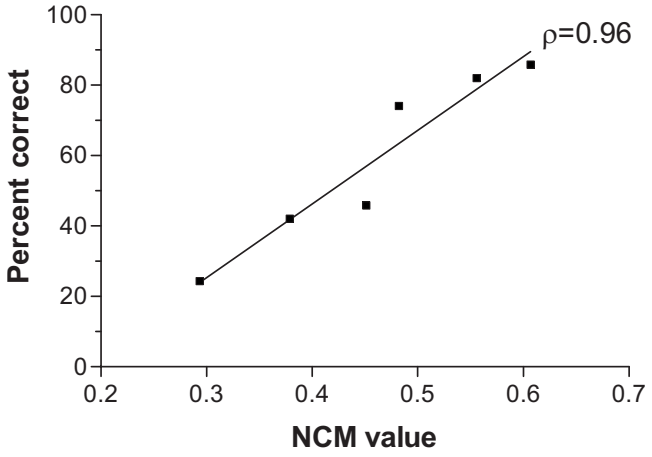


FIG. 6. Scatter plot of the sentence recognition scores obtained for sentences processed with $F_C \leq 1000$ Hz (at −5 and 0 dB SNRs) against the predicted scores obtained using the NCM measure—see text in the Appendix for more details.

ing cues to speech intelligibility in noise, we ran the normalized covariance metric (NCM) (a measure similar to the speech-based speech-transmission index (STI)—see the Appendix) to all the sentence stimuli processed with $F_C \leq 1000$ Hz. This measure assessed the contribution of low-frequency (<1 kHz) envelopes to speech intelligibility and was tested using a total of 120 sentences processed with $F_C \leq 1000$ Hz at −5 and 0 dB SNR levels. The NCM values obtained for each condition (based on 20 sentences/condition) were averaged and correlated with the corresponding speech recognition scores (the control stimuli were also included in the correlation analysis). The resulting correlation coefficient (see Fig. 6) was quite high ($\rho=0.96$) demonstrating the importance of voicing information in speech recognition in noise.

The data obtained in this experiment (Figs. 4 and 5) with $F_C \leq 1000$ Hz are particularly interesting. As mentioned above, and as shown in Fig. 5, listeners had better access to F1 and voicing information when $F_C \leq 1000$ Hz (some F2 information might have been present also in transitions to/from back vowels). Better and more reliable access to voicing leads in turn to better access to low-frequency acoustic landmarks. Figure 3 shows an example spectrogram of a sentence (middle panel) embedded in −5 dB SNR. It is clear from this spectrogram that most of the acoustic landmarks present in the clean signal (shown in the top panel and indicated with arrows) are missing due to the masking of the signal by noise (see middle panel in Fig. 3). The low-frequency acoustic landmarks, in particular, such as those signaling the presence of fricative noise or stop closures, are absent. Some high-frequency acoustic landmarks are present in the corrupted signal (e.g., see fricative segment at $t=1.1$ s in the middle panel of Fig. 3) but these landmarks are not always reliable. In some cases, extraneous and perhaps distracting landmark information (e.g., see $t=1.8$ s and $t=2.1$ s) might be introduced from the masking noise. Hence, it is clear that when listeners were presented with stimuli processed using $F_C \leq 1000$ Hz (see bottom panel in Fig. 3), they had a clear idea on the location of the low-frequency acoustic landmarks and in some instances, but not reliably so, access to high-frequency landmarks. From the findings of experiment 2 and, in particular, from the data obtained with $F_C \leq 1000$ Hz, we may deduce that speech recognition in continuous noise backgrounds is extremely difficult due to the absence of reliable acoustic landmarks.

IV. GENERAL DISCUSSION

The outcome from experiment 1 demonstrated that the information carried by obstruent consonants contributes significantly to speech recognition in noisy backgrounds. Listeners were able to integrate successfully the noise-corrupted information present in the sonorant sounds with the information present in the clean obstruent consonants (e.g., stops). This integration enabled them to identify more words in the (corrupted) speech stream. Furthermore, experiment 2 demonstrated that listeners did not need access to the full spectrum of the obstruent consonants to obtain significant improvements in intelligibility relative to the unprocessed (noisy) stimuli. The findings from the two experiments raised the following question: What is the underlying mechanism(s) responsible for the large improvements (by a factor of 3 in some cases) in performance observed when listeners had full or partial access to the information provided by the obstruent consonants? Listeners had understandably access to multiple temporal and/or spectral cues (e.g., F1/F2 formant transitions) when presneted with clean obstruent sounds (full spectrum) and corrupted sonorant sounds (experiment 1). The number of cues, however, was limited when listeners were presented with stimuli processed with $F_C \leq 1000$ Hz (experiment 2). Listeners had good access to voicing and low-frequency acoustic landmark information, along with partial, and sometimes unreliable high-frequency landmark information. Yet, the improvement in performance was significant, particularly on the sentence recognition task. What contributed to this improvement? We contend that it is the enhanced access to acoustic landmarks, present in the low and high frequencies, that enabled listeners to identify more words in the noisy speech stream. The acoustic landmarks provided by the obstruent consonants aided the listeners in identifying word (or syllable) boundaries, which are often blurred or smeared in extremely noisy conditions (−5 dB SNR in our study). Next, we discuss in more depth the importance of acoustic landmarks in the context of speech perception models and in the context of speech perception in fluctuating maskers by normal-hearing and HI listeners.

A. Importance of acoustic landmarks in noise: Implications for lexical-access models

Many speech recognition models (e.g., Stevens, 2002; Pisoni and Sawusch, 1975; Cutler and Norris, 1988; Klatt, 1979) assume that speech is first segmented at reliable points ("islands of reliability") of the acoustic signal followed by a classification of the segmented units into a sequence of phonetic units (e.g., syllables and words). The identified phonetic units are then matched against the items in the lexicon to select the best word sequence intended by the speaker. Evidence of the segmentation stage in the speech recognition process was provided in the study by Cutler and Norris

(1988). Listeners detected words embedded in nonsense bisyllables more slowly when the bisyllables had two strong syllables than when the bisyllables had a strong and a weak syllable. Cutler and Norris (1988) interpreted their data to suggest that strong syllables trigger the segmentation process. Aside from the strong-syllable segmentation model (Cutler and Norris, 1988), others proposed that segmentation is done at word onsets (e.g., Gow *et al.*, 1996) or distinct acoustic landmarks partitioning vowels and consonants (Stevens, 2002).

The data from our study lend support to the segmentation and lexical-access models proposed by Stevens (2002). The prelexical stage of this model consists of three steps. In the first step, the signal is segmented into acoustic landmarks based on detection of peaks and spectral discontinuities in the signal. These landmarks define the boundaries of the vowels, consonants, and glide segments. The second step involves extraction of acoustic cues from the vicinity of the landmarks signifying which articulators are active when the vowel, glide, or consonant landmarks are created and how these articulators are shaped or positioned. This step produces a set of articulator-based features (e.g., [high] tongue body and [anterior] tongue blade), which includes the place of articulation and voicing features. The third step consolidates, taking context into account, all the cues collected in step 2 to derive a sequence of features for each of the landmarks detected in step 1. In this speech perception model, each word in the lexicon is represented by a set of features that specify the manner of articulation, the position and shape of the articulators, as well as information about the syllable structure, such as the position of the consonant in the syllable (e.g., onset and rime) and information about the vocalic nuclei in the syllable in as far as being stressed or reduced.

It is clear that the first step in Steven's (2002) model (i.e., the segmentation into acoustic landmarks) is crucial to the lexical-access model. If the acoustic landmarks are not detected accurately by the listeners or if the landmarks are perceptually not clear or distinct owing to corruption of the signal by external noise, this will affect the subsequent stages of the model in the following ways. First, errors will be made in step 2 in terms of identifying the shape and position of the articulators used in each landmark. Indeed, errors were made in our study in the transmission of voicing and place of articulation feature information (see Fig. 5) when the listeners did not have a clear idea about the location of the acoustic landmarks in the noisy speech stream. Restoring the acoustic landmarks helped improve performance significantly (see Fig. 5). In particular, when the low-frequency landmarks were restored (see experiment 2 with $F_C \leqslant 1000$ Hz), the transmission of voicing information improved significantly (see Fig. 5). The word recognition scores also improved significantly by 21% points at −5 dB SNR when listeners had better access to voicing cues. Second, the absence of reliable landmarks can disrupt the syllable structure, which is known to be important for determining word boundaries in fluent speech. This is so because the onset of a word is always the onset of a syllable. Therefore, not knowing when the syllable starts (i.e., the syllable onset) makes word boundary determination very difficult. Some posit that word onsets are critically important in the speech recognition process as they trigger segmentation and lexical access (Gow *et al.*, 1996; Owren and Cardillo, 2006). In quiet, the word-initial (also syllable-initial) consonants contain several salient features that make them easier to identify (even in the absence of contextual information) than other phonemes that occur later in words (e.g., Owren and Cardillo, 2006). For instance, the voice-onset timing cue is more reliable for signifying voicing in syllable-initial stops than in syllable-final stops, which may not be released. Also, many word-initial consonants benefit from the fact that they are stressed, and stressed syllables occur quite more often (by a factor of 3:1) in the English language compared to weak syllables (Cutler and Carter, 1987). External noise can degrade the salient cues present in syllable-initial consonants. These cues are present in the vicinity of the acoustic landmarks, hence identifying or somehow enhancing access to these landmarks ought to aid in identifying word boundaries and consequently improving word recognition. To further corroborate this, we analyzed the phoneme errors made on the sentence recognition task and examined whether these errors occurred in word-initial position or in other (e.g., medial) positions. We thus compared the errors made in the unprocessed (control) stimuli with those made in the $F_C = 1000$ Hz condition. The error analysis revealed that the word-initial phoneme errors were reduced by 32% when listeners had access to the low-frequency ($F_C \leqslant 1000$ Hz) acoustic landmarks. In contrast, there was only a small ($<10\%$) reduction in the phoneme errors made in the noninitial position. This phoneme error analysis confirmed that access to low-frequency acoustic landmarks facilitates segmentation and aids listeners in determining word boundaries in noisy conditions.

The present study focused on the contribution of acoustic landmarks introduced by obstruent sounds on speech recognition in noise. The vowels and glides also introduce landmarks in the signal (Stevens, 2002), but were not studied in this paper. We make no argument that these landmarks do not play a significant role or are not as important for speech recognition. As mentioned earlier, we restricted our attention to the landmarks introduced by obstruent sounds, for the main reason that these sounds are more susceptible to noise than the sonorant sounds. Nevertheless, the contribution of the glide and vowel landmarks on speech recognition in noise deserves further study.

B. Speech perception in noise: Normal-hearing and hearing-impaired listeners

The masker (20-talker babble) used in the present study is considered to be continuous, in that it lacks temporal envelope dips. A continuous type of masker was used in this study as it was expected that the contribution of acoustic landmarks to speech recognition would be most prominent. It is generally accepted that listeners are able to recognize speech in modulated or fluctuating maskers with higher accuracy than in continuous (steady-state) noise (e.g., Festen and Plomp, 1990). Several factors contribute to the masking release (see review in Assmann and Summerfield, 2004) in-

cluding segregation of the target on the basis of F0 differences (between the target and masker) and the ability to glimpse the target during the portions of the mixture in which the SNR is favorable, i.e., during periods in which the temporal envelope of the masker reaches a low. The data from the present study suggest that the contributing factor for the masking release may not be the favorable SNR *per se*, but rather the favorable timing of the masker dips, i.e., occurring during periods in which the target signal envelope is low (e.g., during stop closures or generally during obstruent consonants). We thus contend that during the favorable (timewise) periods that the masker envelope reaches a dip, listeners have better access to acoustic landmarks. In contrast, the steady-state maskers do not provide such favorable timing of masker dips as they are continuously "on." Hence, we can deduce that having better access to acoustic landmarks is yet another contributing factor to the release of masking observed with fluctuating maskers.

As shown in Fig. 3 (middle panel), some of the high-frequency acoustic landmarks, such as those signaling the onset of frication noise, are relatively more visible or accessible compared to the low-frequency landmarks. The cues provided by these high-frequency landmarks are particularly important, for instance, for the accurate perception of /s/ (Stelmachowicz *et al.*, 2001), especially for speech tokens produced by female talkers. While normal-hearing listeners may be able to perceive /s/ or other high-frequency consonants, it is questionable whether HI listeners will be able to do so. A number of studies (e.g., Ching *et al.*, 1998; Hogan and Turner, 1998) have shown that some listeners with sensorineural HL (with $\geqslant$55 dB HL at or above 4 kHz) receive limited benefit from amplification of the high-frequency region. While normal-hearing listeners might utilize multiple cues (including low-frequency cues) for the perception of /s/, some studies (e.g., Zeng and Turner, 1990) have reported that HI listeners do not make use of the low-frequency formant transitions, but rather rely on fricative noise. Hence, the present data suggest that some HI listeners might not be able to perceive the high-frequency landmarks present in the signal, despite the high-frequency amplification provided. We can thus infer that the difficulty that HI listeners experience in perceiving speech in noise can be attributed, at least partially, to their inability to perceive high-frequency landmarks, such as those present at the onset of fricatives.

C. Landmark-detection algorithms

In the context of developing signal processing algorithms for hearing aids or cochlear implant devices, the data from the present study implicate that the obstruent segments need to be treated differently than the sonorant segments of the signal. More precisely, techniques are needed that will make the acoustic landmarks perceptually more distinct and accessible to HI listeners. At the very least, the high-frequency landmarks need to be made accessible to HI listeners. Equivalently, algorithms specially designed to suppress noise in the corrupted obstruent consonants can be applied differentially to the obstruent consonants. In practice, such algorithms need to somehow detect the location of the acoustic landmarks in the signal. Several such landmark-detection algorithms have been proposed and found to perform quite well, at least in quiet (Mermelstein, 1975; Liu, 1996; Junega and Espy-Wilson, 2008). Further research is thus needed to extend and perhaps redesign some of the existing landmark-detection algorithms to perform well in noisy conditions.

V. SUMMARY AND CONCLUSIONS

The present study assessed the contribution of the information carried by obstruent sounds on speech recognition in noise. Sentence recognition scores improved significantly when the clean obstruent consonants were introduced in the noise-corrupted sentences, and the improvement was largest (nearly threefold increase) at −5 dB SNR (experiment 1). Experiment 2 was designed to assess the factors contributing to the large improvement in performance. This was done by introducing systematically clean obstruent spectral information, up to a cutoff frequency F_C, while leaving the remaining region ($\geqslant F_C$ Hz) of the spectrum corrupted (experiment 2). By controlling the value of F_C we were able to control the amount of spectral information available to the listeners during the obstruent segments of the signal. For small values of F_C, listeners had access to F1 and voicing information, as well as to low-frequency acoustic landmarks signaling the onset of stops or fricatives. The improvement from transmission of voicing information was quite substantial amounting to roughly 50% of the overall improvement on sentence recognition. The importance of acoustic landmarks to speech recognition in continuous type of noise was cast in a lexical-access framework (Stevens, 2002). Consistent with Steven's (2002) lexical-access model, the data from experiment 2 showed that the absence of reliable (low and high frequency) acoustic landmarks, owing to the corruption of the signal by external noise, can produce voicing and place of articulation errors (see Fig. 5) and can disrupt the syllable structure, known to be important for determining word boundaries in running speech. Analysis of the phoneme errors made on the sentence recognition task confirmed that the errors made in the word-initial position were reduced by 32% when listeners had access to the low-frequency ($F_C \leqslant 1000$ Hz) acoustic landmarks. This outcome provided support for the view that acoustic landmarks can facilitate segmentation and aid listeners determine word boundaries in noisy conditions.

ACKNOWLEDGMENTS

This research was supported by Grant No. R01 DC007527 from the National Institute of Deafness and other Communication Disorders, NIH. The authors would like to thank the Associate Editor, Dr. Mitchell Sommers, and the two anonymous reviewers for providing valuable comments that improved the manuscript.

APPENDIX

The NCM (Hollube and Kollmeier, 1996) was used to assess the intelligibility of sentences processed using $F_C \leqslant 1000$ Hz. This measure is similar in some respects to the STI (Steeneken and Houtgast, 1980) in that it computes the

STI as a weighted sum of transmission index (TI) values determined from the envelopes of the probe and response signals in each frequency band (Goldsworthy and Greenberg, 2004). Unlike the traditional STI measure, however, which quantifies the change in modulation depth between the probe and response envelopes using the modulation transfer function, the NCM measure is based on the covariance between the probe and response envelope signals. The NCM measure was modified in our study as follows. The stimuli were first bandpass filtered into nine bands spanning the range 100–1000 Hz. The envelope of each band was computed using the Hilbert transform and downsampled to 50 Hz, thereby limiting the envelope modulation frequencies to 0–25 Hz. Let $x_i(t)$ be the downsampled envelope in band i of the clean (probe) signal and let $y_i(t)$ be the downsampled envelope of the processed (response) signal. The normalized covariance in the ith frequency band is computed as

$$r_i = \frac{\Sigma_i(x_i(t) - \mu_i)(y_i(t) - \nu_i)}{\sqrt{\Sigma_i(x_i(t) - \mu_i)^2}\sqrt{\Sigma_i(y_i(t) - \nu_i)^2}}, \quad (1)$$

where μ_i and ν_i are the mean values of the $x_i(t)$ and $y_i(t)$ envelopes, respectively. The SNR in each band is computed as

$$\mathrm{SNR}_i = 10 \log_{10}\left(\frac{r_i^2}{1 - r_i^2}\right), \quad (2)$$

and subsequently limited to the range of −15 to 15 dB (as done in the computation of the articulation index). The TI in each band is computed by linearly mapping the SNR values between 0 and 1 as follows:

$$\mathrm{TI}_i = \frac{\mathrm{SNR}_i + 15}{30}. \quad (3)$$

Finally, the TIs are averaged across all low-frequency bands (<1 kHz) to produce a low-frequency NCM measure: $\mathrm{NCM} = \frac{1}{9}\Sigma_{i=1}^{9}\mathrm{TI}_i$. No weighting is applied to the individual TI values (i.e., equal emphasis is placed to all envelopes).

[1]No ramping of the signal and no window overlap was used in order to avoid smearing (temporally) the boundaries between obstruent and sonorant segments. Such smearing would affect the timing of the acoustic landmarks, which are the subject of the present study. Choosing the appropriate duration of the ramping signal was found to be problematic since the duration of the obstruent consonants can vary from as little as 10 to 200 ms. Due to the absence of ramping and window overlap, some small distortion in the signal was noted sometimes due to transient effects. Pilot data indicated that this signal distortion was not substantial or significant in terms of reducing intelligibility.

[2]The intelligibility scores obtained by the first group of subjects listening to the processed VCV stimuli produced by six speakers were slightly lower (<10%) than the corresponding intelligibility scores obtained by the second group of subjects listening to the processed VCV stimuli produced by two speakers. The trend in performance (as shown in Fig. 4), however, was the same. The intelligibility scores obtained by the two groups of listeners in the various conditions were compared using nonparametric two-sample Kolmogorov–Smirnov tests. These tests revealed nonsignificant ($p > 0.05$) difference in scores. The comparison, for instance, of the scores obtained by the two groups of listeners on the $F_C = 1000$ Hz condition at −5 dB SNR revealed nonsignificant ($p = 0.074$) differences.

Assmann, P., and Summerfield, Q. (**2004**). "The perception of speech under adverse conditions," in *Speech Processing in the Auditory System*, edited by S. Greenberg, W. Ainsworth, W. Popper, and R. Fay (Springer, New York), pp. 231–308.

Bashford, J. A., Jr., and Warren, R. M. (**1987**). "Multiple phonemic restorations follow rules for auditory induction," Percept. Psychophys. **42**, 114–121.

Blumstein, S., and Stevens, K. (**1979**). "Acoustic invariance in speech production: Evidence from some measurements of the spectral characteristics of stop consonants," J. Acoust. Soc. Am. **66**, 1001–1017.

Ching, T. Y., Dillon, H., and Byrne, D. (**1998**). "Speech recognition of hearing-impaired listeners: Predictions from audibility and the limited role of high-frequency amplification," J. Acoust. Soc. Am. **103**, 1128–1140.

Cole, R., Yan, Y., Mak, B., Fanty, M., and Bailey, T. (**1996**). "The contribution of consonants versus vowels to word recognition in fluent speech," Proceedings of the International Conference on Acoustics, Speech, and Signal Processing (ICASSP'96), Atlanta, GA, May 1996, pp. 853–856.

Cutler, A., and Norris, D. (**1988**). "The role of strong syllables in segmentation for lexical access," J. Exp. Psychol. Hum. Percept. Perform. **14**, 113–121.

Cutler, A., and Carter, D. M. (**1987**). "The predominance of strong initial syllables in the English language," Comput. Speech Lang. **2**, 133–142.

Delgutte, B., and Kiang, N. (**1984**). "Speech coding in the auditory nerve: IV. Sounds with consonant-like dynamic characteristics," J. Acoust. Soc. Am. **75**, 897–907.

Festen, J., and Plomp, R. (**1990**). "Effects of fluctuating noise and interfering speech on the speech-reception threshold for impaired and normal hearing," J. Acoust. Soc. Am. **88**, 1725–1736.

Goldsworthy, R., and Greenberg, J. (**2004**). "Analysis of speech-based speech transmission index methods with implications for nonlinear operations," J. Acoust. Soc. Am. **116**, 3679–3689.

Gow, D., Melvold, J., and Manuel, S. Y. (**1996**). "How word onsets drive lexical access and segmentation: Evidence from acoustics, phonology, and processing," in *Proceedings of 1996 International Conference on Spoken Language Processing* (University of Delaware and Alfred I. DuPont Institute, Philadelphia, PA), pp. 66–69.

Hogan, C., and Turner, C. (**1998**). "High-frequency audibility: Benefits for hearing-impaired listeners," J. Acoust. Soc. Am. **104**, 432–441.

Hollube, I., and Kollmeier, K. (**1996**). "Speech intelligibility prediction in hearing-impaired listeners based on a psychoacoustically motivated perception model," J. Acoust. Soc. Am. **100**, 1703–1715.

IEEE Subcommittee (**1969**). "IEEE recommended practice for speech quality measurements," IEEE Trans. Audio Electroacoust. **AU-17**, 225–246.

Junega, A., and Espy-Wilson, C. (**2008**). "A probabilistic framework for landmark detection based on phonetic features for automatic speech recognition," J. Acoust. Soc. Am. **123**, 1154–1168.

Kawahara, H., Masuda-Katsuse, I., and de Cheveigné, A. (**1999**). "Restructuring speech representations using a pitch-adaptive time-frequency smoothing and an instantaneous-frequency-based F0 extraction: Possible role of a repetitive structure in sounds," Speech Commun. **27**, 187–207.

Kewley-Port, D., Burkle, Z., and Lee, J. (**2007**). "Contribution of consonant versus vowel information to sentence intelligibility for young normal-hearing and elderly hearing-impaired listeners," J. Acoust. Soc. Am. **122**, 2365–2375.

Klatt, D. H. (**1979**). "Speech perception: A model of acoustic-phonetic analysis and lexical access," J. Phonetics **7**, 279–312.

Liberman, A., Delattre, P., and Cooper, F. (**1952**). "The role of selected stimulus variables in the perception of unvoiced stop consonants," Am. J. Psychol. **65**, 497–516.

Liu, S. (**1996**). "Landmark detection for distinctive feature-based speech recognition," J. Acoust. Soc. Am. **100**, 3417–3430.

Loizou, P. (**2007**). "Speech Enhancement: Theory and Practice," (CRC Press, Boca Raton, FL).

Mermelstein, P. (**1975**). "Automatic segmentation of speech into syllabic units," J. Acoust. Soc. Am. **58**, 880–883.

Miller, G. A., and Nicely, P. E. (**1955**). "An analysis of perceptual confusions among some English consonants," J. Acoust. Soc. Am. **27**, 338–352.

Mines, M., Hanson, B., and Shoup, J. (**1978**). "Frequency of occurrence of phonemes in conversational English," Lang Speech **21**, 221–241.

Owren, M., and Cardillo, G. (**2006**). "The relative role of vowels and consonants in discriminating talker identity versus word meaning," J. Acoust. Soc. Am. **119**, 1727–1739.

Parikh, G., and Loizou, P. (**2005**). "The influence of noise on vowel and consonant cues," J. Acoust. Soc. Am. **118**, 3874–3888.

Phatak, S., and Allen, J. (**2007**). "Consonants and vowel confusions in speech-weighted noise," J. Acoust. Soc. Am. **121**, 2312–2326.

Pisoni, D., and Sawusch, J. (**1975**). "Some stages of processing in speech

perception," in *Structure and Process in Speech Perception*, edited by A. Cohen and S. Nooteboom (Springer-Verlag, Berlin), pp. 16–34.
Seneff, S., and Zue, V. (**1988**). "Transcription and alignment of the TIMIT database," Proceedings of the Second Symposium on Advanced Man-Machine Interface Through Spoken Language, Oahu, HI, 20–22 November 1988.
Shannon, R., Jensvold, A., Padilla, M., Robert, M., and Wang, X. (**1999**). "Consonant recordings for speech testing," J. Acoust. Soc. Am. **106**, L71–L74.
Shriberg, L., and Kent, R. (**2003**). *Clinical Phonetics*, 3rd ed. (Allyn and Bacon, Boston, MA).
Smith, R. (**1979**). "Adaptation, saturation and physiological masking of single auditory-nerve fibers," J. Acoust. Soc. Am. **65**, 166–178.
Steeneken, H., and Houtgast, T. (**1980**). "A physical method for measuring speech transmission quality," J. Acoust. Soc. Am. **67**, 318–326.
Stelmachowicz, P., Pittman, A., Hoover, B., and Lewis, D. (**2001**). "Effect of stimulus bandwidth on the perception of /s/ in normal- and hearing-impaired children and adults," J. Acoust. Soc. Am. **110**, 2183–2190.
Stevens, K. (**2002**). "Toward a model for lexical access based on acoustic landmarks and distinctive features," J. Acoust. Soc. Am. **111**, 1872–1891.
Zeng, F.-G., and Turner, C. W. (**1990**). "Recognition of voiceless fricatives by normal and hearing-impaired subjects," J. Speech Hear. Res. **33**, 440–449.

The relationship between native allophonic experience with vowel duration and perception of the English tense/lax vowel contrast by Spanish and Russian listeners

Maria V. Kondaurova
Program in Linguistics, Purdue University, 100 North University Street, West Lafayette, Indiana 47907

Alexander L. Francis[a)]
Program in Linguistics and Department of Speech, Language and Hearing Sciences, Purdue University, 500 Oval Drive, West Lafayette, Indiana 47907

(Received 7 November 2007; revised 5 September 2008; accepted 19 September 2008)

Two studies explored the role of native language use of an acoustic cue, vowel duration, in both native and non-native contexts in order to test the hypothesis that non-native listeners' reliance on vowel duration instead of vowel quality to distinguish the English tense/lax vowel contrast could be explained by the role of duration as a cue in native phonological contrasts. In the first experiment, native Russian, Spanish, and American English listeners identified stimuli from a *beat/bit* continuum varying in nine perceptually equal spectral and duration steps. English listeners relied predominantly on spectrum, but showed some reliance on duration. Russian and Spanish speakers relied entirely on duration. In the second experiment, three tests examined listeners' use of vowel duration in native contrasts. Duration was equally important for the perception of lexical stress for all three groups. However, English listeners relied more on duration as a cue to postvocalic consonant voicing than did native Spanish or Russian listeners, and Spanish listeners relied on duration more than did Russian listeners. Results suggest that, although allophonic experience may contribute to cross-language perceptual patterns, other factors such as the application of statistical learning mechanisms and the influence of language-independent psychoacoustic proclivities cannot be ruled out. © *2008 Acoustical Society of America.* [DOI: 10.1121/1.2999341]

PACS number(s): 43.71.Hw, 43.71.Es, 43.71.An [AJ] Pages: 3959–3971

I. INTRODUCTION

A variety of recent research suggest that native phonetic (allophonic) experience is one factor that can influence the perception of non-native speech sounds (Best and Strange, 1992; Halle, *et al.* 1999; Jenkins and Yeni-Komshian, 1995) and improve learning (Jamieson and Moroson, 1986; McClaskey *et al.* 1983; Pisoni *et al.*, 1982). Both the *type* (Pruitt *et al.*, 2006) and the *amount* (McAllister *et al.*, 2002) of such experience have been proposed to contribute to the success of perception of non-native speech contrasts.

The aims of the present study are (a) to determine whether native Spanish and Russian listeners, who differ in the reported role of allophonic vowel duration in their native languages, differ in the way they employ vowel duration in the perception of the English tense and lax front unrounded vowel contrast, which does not exist in either native language, and (b) to determine whether any differences in the two groups' observed pattern of reliance on duration in this cross-language context can be related to the degree to which they employ vowel duration as a cue in their native language. Vowel duration is not a phonologically contrastive feature in either Spanish or Russian. However, the two languages are reported to differ in terms of the degree to which each relies on vowel duration as an acoustic cue in the perception and/or production of a variety of phonological contrasts including stress and voicing.

In English, tense and lax front unrounded vowels are differentiated along two independent acoustic dimensions: spectrum (vowel quality, related mainly to the first three formant frequencies: F1, F2, and F3) and duration (vowel length). While native English listeners rely predominantly on spectral properties with vowel duration playing a secondary role (Ainsworth, 1972; Mermelstein, 1978; Hillenbrand *et al.*, 2000), there is contradictory evidence on what acoustic cues native Spanish listeners employ for the perception of this contrast and why they are able to use these cues. While some studies suggest that native Spanish listeners are not significantly different from native English listeners in their ability to use spectral cues (Flege *et al.*, 1997), most studies have demonstrated that, unlike native English listeners, Spanish listeners rely exclusively or primarily on vowel duration for the identification of this contrast (Bohn, 1995; Escudero 2006; Escudero and Boersma, 2004).

Typically, the use of spectral properties by native Spanish listeners, when it is observed, is explained by phonological and phonetic experience with this acoustic property in the Spanish vowel system (Fox *et al.*, 1995). However, the widely demonstrated reliance on duration poses a problem due to the absence of phonological and allegedly very limited allophonic experience with vowel duration by native Spanish listeners (Hammond, 2001; Harris, 1969).

[a)]Electronic mail: francisa@purdue.edu

Russian reportedly differs from Spanish in terms of the degree to which vowel duration serves as an acoustic correlate of phonological contrasts. For example, in Russian, lexical stress is a phonologically distinctive feature, in the sense that two words may differ only in terms of stress placement. For example (accent precedes the stressed syllable): ˈслуги /ˈslugi/ "servants" (noun, nominative plural)-слуˈги /sluˈgi/ "a servant" (noun, genetive singular); ˈволос /ˈvolos/ "a hair" (noun, nominative singular)-воˈлос /voˈlos/ "hair" (noun, genetive plural). There are also three levels of stress in Russian that are realized primarily in terms of different degrees of vowel duration (Bondarko, 1998). In stressed syllables vowels are long. In a syllable immediately preceding the stressed syllable vowels are shorter, and in all other unstressed syllables the vowel length is further reduced with an average ratio of 4:2:1 for stressed, prestress, and unstressed, respectively (Bondarko, 1998).

In Spanish, however, both stressed and unstressed syllables have the same linguistic length (Hammond, 2001), and although some researchers have reported finding duration differences between productions of stressed and unstressed vowels (Diaz-Campos, 2000; Manrique and Signorini, 1983), perceptual studies have shown that vowel duration in itself is a poor predictor of the location of lexical stress in Spanish (Llisterri, *et al.*, 2003). Thus, it appears that native Russian listeners may have more phonetic experience than native Spanish listeners with vowel duration as an acoustic correlate of stress in their native language, and this difference in experience might affect the two groups' reliance on this feature in the identification of cross-language vowel contrasts.

On the other hand, the two languages are also quite similar with respect to the use of duration in a variety of segmental contexts. At the segmental level, in both Spanish and Russian, vowels are longer before voiced than before voiceless consonants (Chen, 1970; Mendoz *et al.*, 2003; Pye, 1986; Zimmerman and Sapon, 1958). Furthermore, both Spanish and Russian vowels have intrinsically different lengths (Bolla, 1981; Bondarko, 1998; Mendoz *et al.*, 2003): In both languages, lower vowels (e.g., [ɛ]) are longer than higher vowels (e.g., [i]).[1] Thus, some evidence suggests that Spanish and Russian listeners might differ from one another in their perception of the English tense-lax vowel contrast on the basis of differences in their allophonic experience with duration (i.e., for lexical stress). On the other hand, the two groups might be similar in performance, if Russian listeners' experience is not sufficiently greater or more effectively transferred than that of Spanish speakers.

In the present study we first examined Spanish and Russian listeners' weighting of duration compared to spectral cues in the perception of the English high front tense/lax vowel contrast. We used a two-dimensional stimulus continuum ranging from a familiar speech sound [i] to an unfamiliar one, English [ɪ], to test the prediction that Russian listeners would rely more heavily on duration cues than Spanish listeners because of Russian listeners' greater native allophonic experience with vowel duration, and we compared the performance of both groups to that of native speakers of English. Based on the results of this experiment, we subsequently examined the degree to which these same listeners relied on duration in three allophonic contexts in nonsense words based on the phonology of their native language. Thus, the focus of the second experiment is different from the first, exploring the importance of vowel duration in native phonological contrasts in order to evaluate the hypothesis that Spanish and Russian listeners make differential use of vowel duration natively, and to determine whether it is possible to relate the pattern of results shown in the first experiment to listeners' use of duration as a cue in their native language.

II. EXPERIMENT 1

A. Method

1. Participants

Participants were native speakers of American English (10 women, and 6 men), Spanish (8 women, and 10 men), and Russian (11 women, and 8 men). American English participants were undergraduate and graduate students at Purdue University, who grew up in the Midwestern United States with minimal exposure to other languages as determined by a pretest questionnaire. The Spanish and Russian participants were all graduate students, postdoctoral fellows, and/or instructors at Purdue University.

Nine Spanish participants were from Spain (Madrid, Barcelona, and Cordoba areas) and nine were from Latin American countries (Mexico, Peru, and Colombia). Out of 19 Russian participants, 2 were born and grew up in Ukraine and 3 in Belarus, the rest were born and grew up in the Russian Federation. All 19 Russian participants identified themselves as native monolingual Russian speakers.

As determined by a background questionnaire, no Spanish or Russian participant had experience living in a nonnative language environment for more than a period of 2 weeks prior to arrival in the USA except three Russian listeners who lived in Austria, Hungary, and France for one, three and four years. All participants reported no history of speech or hearing disability and passed a standard hearing test using an M 120 Beltone Audiometer (pure tone audiometry, binaural, frequencies tested: 500 Hz at 20 dB Hearing Level (HL), 1, 2, 4, 6, and 8 kHz at 15 dB HL) prior to the experiment. All participants were paid for their participation in the experiment. For demographic and language background data on Spanish, Russian, and English participants in experiments 1 and 2 see Table I.

2. Stimuli

Stimuli for experiment 1 were a set of 81 syllables of the form /bVt/ (where V is a vowel ranging from [i] to [ɪ]) created according to the following procedure. A 34-year-old male native speaker of a Midwestern dialect of American English produced several examples of the words *beat* and *bit* in isolation. All tokens were recorded using a digital audio tape recorder (Sony TCD-D8), a digital audio tape (Sony PDP-95C PRO-DAT Plus), and a hypercardioid microphone (Audio-Technica D1000HE) in a sound-isolated booth (IAC, Model No. 403A). The recorded tokens were redigitized at 10 kHz and peak amplitude normalized using the PRAAT

TABLE I. Demographic and language background data on Spanish, Russian, and English participants in experiments 1 and 2. M—male, F—female; AOA—age of arrival in the USA; LOR—length of residence in the USA; EFL age—age of starting English as a foreign language education in home countries; EFL period—period of learning English as a foreign language in home countries; start of US education—age when first exposed to formal education in the USA (only includes participants with more than 0 month educational experience); US education—period of formal education in the USA; ESL in US—period of English as a second language education in the USA; motivation—self-rated motivation level in using English; imitation—self-rated ability to imitate English sounds; ESL home—self-rated frequency of use of English at home; ESL social—self-rated frequency of use of English in social settings; and ESL work—self-rated frequency of use of English at work.

	Spanish	Russian	English
No. of participants	18	19	16
Sex	10 M; 8 F	8 M; 11 F	6 M; 10 F
Age (yrs.) (std)	29.2 (6.6)	30.2 (7.1)	21.3 (2)
AOA (yrs.) (std)	25 (5.8)	26.2 (6)	
LOR (yrs.) (std)	3.7 (3.9)	3.8 (3.8)	
EFL age (yrs.) (std)	10.4 (4.0)	9.5 (3.7)	
EFL period (yrs.) (std)	10.7 (6.0)	10.5 (4.4)	
Start of US education (yrs.) (std)	25.2 (6.3)	23.6 (4.09)	
US education (yrs.) (std)	2.9 (2.4)	1.4 (2.0)	
ESL in US (yrs.) (std)	0.1 (0.3)	0.1 (0.2)	
Motivation (ten point scale)	8.7 (1.7)	8.3 (2.1)	
Imitation (ten point scale)	6.7 (1.8)	5.7 (2.1)	
ESL home (ten point scale)	4.8 (3.9)	3.7 (3.2)	
ESL social (ten point scale)	7.3 (2.2)	7.9 (1.7)	
ESL work (ten point scale)	7.7 (2.7)	9.5 (1.0)	

4.1.21 program running on a Dell Optiplex/Windows XP computer with a Sound Blaster Live! sound card.

From this set one token of beat and bit each was selected using the criterion that there be no abrupt changes in formant movement throughout the vowel, no abrupt changes in fundamental frequency, and minimal extraneous noise (to facilitate resynthesis), and having formant and duration values similar to those described by Hillenbrand *et al.*, (1995). The average formant frequencies and duration of the vowel in the beat token were F1: 326 Hz, F2: 2056 Hz, F3: 2943 Hz, and F4: 3389 Hz, duration 171 ms, while those for the bit token were F1: 458 Hz, F2: 1876 Hz, F3: 2523 Hz, and F4: 3388 Hz, duration 125 ms.

The first four formant center frequencies of the beat and bit tokens were extracted using the standard Linear Predictive Coding (LPC) analysis settings implemented in PRAAT 4.2.21. These values were converted to Mel and nine values were calculated for each formant ranging in equal Mel steps between the beat and bit values. For each step and each formant, the original formant contours were preserved. Starting with the original beat token, chosen because it was a marginally superior recording, one version of the syllable was resynthesized for each of the nine sets of formant frequency steps following methods described in the PRAAT 4.2.21 manual entry for source-filter resynthesis. From each of the nine steps along the vowel quality continuum, a continuum ranging in vowel duration from 275 to 35 ms was created ((30 ms/step). The endpoints, 275 and 35 ms, were chosen to allow for nine duration steps to be equal to the number of vowel quality steps (nine steps) in order to avoid the possibility that listeners prefer to rely on the dimension with the least variability (Bohn, 1995). Each step along the duration continuum was approximately equivalent to one just-noticeable difference (JND) for English listeners (25 ms, following Klatt, 1976), as was each step along the spectrum continuum based on F1 values (11–14 Hz, or 3%–5% of the formant center frequency following Kewly-Port and Watson (1994).

3. Procedure

Experiment 1 was generated using E-PRIME Version 1.1 (Schneider *et al.*, 2002). All participants were seated in individual cubicles, equipped with a Dell Optiplex/Windows XP computer, and a Model RB-620 response pad (Cedrus Corporation). Stimuli were presented via a Soundblaster Live! soundcard through headphones (Sennheiser, HD 25-1) at a comfortable listening level of 60–65 dBA. Experiment 1 was completed on the first day of testing.

On each trial listeners heard one stimulus (up to 550 ms) with a simultaneous visual presentation of two possible answers, beat and bit. The possible answers remained on the screen until participants pressed a button on the response pad corresponding to either beat (left button) or bit (right button). Then there was a short pause (250 ms) followed by a blink of the screen (250 ms) to indicate the start of a new trial. Participants were instructed to respond as quickly as possible, but each trial was self-paced with no limit on time to respond. There were 81 stimuli repeated five times each in each of the two blocks (810 trials total). All trials within a block were presented in random order. The average running time for both blocks was 45 min. Before the experiment began, there was a practice session consisting of ten trials with naturally recorded tokens of the words *sheep* and *ship*. The structure of the practice session was identical to the actual experiment but responses were not recorded.

4. Analysis

(a) *Identification functions.* Identification (ID) functions were calculated as the proportion of [ɪ] responses to all nine stimuli sharing a given duration (duration continuum) or spectrum (spectrum continuum) value. ID functions were calculated as average group responses.

(b) *Discriminant function analysis*. Discriminant function analysis (StatSoft, Inc., 2003) uses a linear discriminant equation to determine the degree to which each variable (spectrum, and duration) contributes to the stimulus token's membership in a particular response category (tense or lax) in terms of Wilks' lambda coefficient. Wilks' lambda coefficient ranges from 0 to 1: The closer it is to 0, the stronger a particular variable contributes to the predicted membership. A coefficient close to 1 indicates little or no contribution.

(c) *Multiple regression and simple t-tests*. Forward, stepwise multiple regression ($F>1$ to enter) was employed to identify correlations between factors known to affect degree of foreign accent in L2 to estimate foreign language

proficiency and the relative weighting given to spectrum versus duration (Piske *et al.*, 2001; McAllister *et al.*, 2002; Ylinen *et al.*, 2005). Factors (predictor variables) were (see Table I): (1) age of participant, (2) age of arrival (AOA) in the USA, (3) length of residency (LOR) in the USA, (4) age of starting English as a foreign language (EFL) education in the home country, (5) period of EFL in the home country, (6) period of English as a second language (ESL) study in the USA after arrival, (7) age of starting formal education in the USA, (8) period of formal education in the USA, (9) self-estimated degree of motivation in using ESL, (10) self-estimated degree of imitation abilities, (11) self-estimated degree of using ESL at home, (12) self-estimated degree of using ESL in a social environment, and (13) self-estimated degree of using ESL at work.

In order to investigate the contribution of these factors to performance in experiment 1, the changes in the proportion of lax (bit) responses between the low and high ends of ID functions for both the spectrum and duration continua were calculated for each subject by subtracting the proportion of bit responses given at step 9 from the proportion of bit responses given at step 1. The larger the value along a given dimension, the greater the reliance on that dimension. Using these values, a spectrum-to-duration ratio (Bondarko, 1977; Escudero and Boersma, 2004) was calculated for each participant by dividing the change along the spectrum dimension by the change along the duration dimension. Then multiple regression analysis was run between the ratio and each factor. In addition, because the number of factors was large compared to the size of the number of samples (participants) in the analysis, simple t-tests on these factors were run comparing group means to confirm that the groups were matched in English language proficiency.

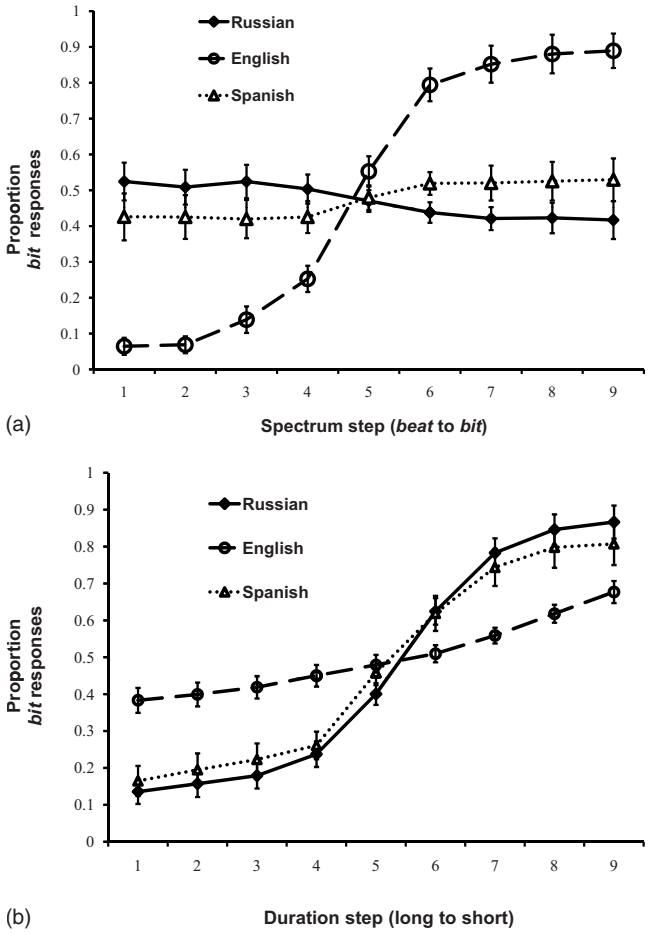


FIG. 1. Experiment 1: Proportion of bit responses to all stimuli averaged over spectrum (a) and duration (b). The error bars indicate standard error of the mean.

B. Results

Analysis using t-tests of independent means of the two groups' scores on each of the 13 factors previously shown to relate to performance on cross-language perceptual tests showed no significant difference between Spanish and Russian scores for 12 of the 13 factors, the exception being self-estimated degree of using ESL at work (Russian mean 9.5 and Spanish mean 7.7). This score notwithstanding, these results suggest that the two groups were generally well matched in English language experience.

ID functions for spectrum and duration are shown in Figs. 1(a) and 1(b), respectively. Separate but identical mixed factorial analyses of variance (ANOVAs) were carried out on spectrum and duration with one between group factor (group: English, Russian, Spanish) and one within group factor (steps 1 and 9). The results showed no significant effect of group [spectrum, $F(2,50)=0.07$, $p=0.93$; duration, $F(2,50)=1.33$, $p=0.274$], but a significant effect of step [spectrum, $F(2,50)=21.44$, $p<0.001$; and duration: $F(2,50)=167.61$, $p<0.001$] and a significant interaction between step and group [spectrum, $F(2,50)=21.99$, $p<0.001$; duration: $F(2,50)=9.30$, $p<0.001$]. These results suggest that there were differences between the English, Russian, and Spanish listeners in terms of how they used both spectral and duration properties.

Post hoc analysis (Tukey HSD, all significance levels reported at $p<0.05$ level or better) for the *spectrum* continuum demonstrated that only English listeners showed a significant difference between the proportion of bit responses at step 1 (means: English 0.06, Russian 0.52, and Spanish 0.42) and step 9 (means: English 0.88, Russian 0.42, and Spanish 0.53). For the *duration* continuum, all three groups showed a significant difference between the proportion of bit responses at step 1 (means: English 0.38, Russian 0.13, and Spanish 0.16) and step 9 (means: English 0.68, Russian 0.87, and Spanish 0.81). This suggests that English listeners used both duration and spectrum in classifying stimuli as beat or bit, while Russian and Spanish listeners used only duration.

Moreover, the pattern of the three groups' use of duration was also different. Comparing the three groups' performance at the endpoints of the duration continuum showed that English listeners gave significantly more bit responses at step 1 than Russian or Spanish listeners (means: English 0.38, Russian 0.14, and Spanish 0.16), with no significant difference between Russian and Spanish participants (contrary to predictions). Similarly, English listeners gave significantly fewer bit responses at step 9 (means: English 0.68,

Russian 0.87, and Spanish 0.81), but again there was no significant difference between Russian and Spanish (again, contrary to predictions). These results suggest that Russian and Spanish listeners relied more strongly on duration than did English listeners when classifying stimuli as beat or bit.

Similar results were obtained from the discriminant function analysis. For English listeners, a function that includes both spectrum and duration in the model was found to be significant, $F(2,78)=112.94$, $p<0.001$, with a partial Wilks's lambda of 0.26 for spectrum and 0.93 for duration. These results suggest that, for English listeners, both dimensions contributed to their classification of stimuli as beat or bit, but spectrum contributed more to their decision than did duration.

For Russian and Spanish listeners the discriminant function was significant with only one variable, duration, in the model: Russian: $F(2,78)=117.00$, $p<0.001$; Spanish, $F(2,78)=113.58$, $p<0.001$. The partial Wilks' lambda for spectrum was considerably closer to 1 for both groups (Russian 1.00 and Spanish 0.99) than was the value for duration (Russian 0.25 and Spanish 0.26). Again, these results corroborate the findings from the identification function analysis, showing that duration was the only property used by Russian and Spanish listeners to differentiate beat from bit, and that spectrum was not a useful predictor for either nonnative group (in contradiction to initial predictions that Russian listeners might rely more on duration than Spanish listeners).

In order to identify any effect of factors known to affect individual differences in cross-language perception of acoustic cues, forward stepwise multiple regression analysis was used to compare each individual's spectrum-to-duration ratio with the 13 individual factors described above. The final model was significant with six factors (period of EFL in the home country, AOA, self-estimated degree of using ESL at home, self-estimated degree of using ESL at work, age of starting EFL education in the home country, and period of formal education in the USA), $F(6,30)=3.94$, $p=0.005$. However, only one of these factors, period of EFL in the home country, was significant in its own right, $F=13.32$, $p=0.001$, $R=0.53$.

C. Discussion

English listeners used both spectrum and duration to identify tense and lax vowels, although, consistent with previous studies, spectral properties were weighted more heavily than duration (Hillenbrand *et al.*, 2000). In contrast, Spanish and Russian listeners employed only vowel duration, in agreement with previous findings for Spanish (Bohn, 1995; Escudero, 2006; Escudero and Boersma, 2004) and expanding the set of languages whose speakers have documented difficulty perceiving this contrast in a native English-like manner. There are a variety of possible explanations for these results, including those based on properties of the experimental design and those based on existing theories of cross-language perception and phonetic learning.

1. Experiment design considerations

Before interpreting these results further, it is important to note that the Spanish and Russian results might at first appear to suggest the effects of an experimental artifact, namely, the much greater range of stimuli distributed along the duration as opposed to the spectral dimension. Along the spectral dimension, stimuli ranged from the formant frequencies of a natural [i] to those of a natural [ɪ], but in duration the range was considerably exaggerated, especially toward the short end of the continuum. This was done in order to avoid the possibility that listeners might rely on a dimension with fewer steps (Bohn, 1995). On the other hand, it is possible that exaggerating duration but not spectral range encouraged listeners to preferentially attend to the exaggerated dimension alone (Holt, and Lotto, 2006). While such an explanation is possible, three observations mitigate against it. First, in the present experiment, the duration continuum ranged from 35 to 275 ms in 30 ms step intervals, a range of approximately ten JNDs (Klatt, 1976) determined that the JND for vowel duration is 25 ms for native English listeners. The spectrum continuum also spanned a range of ten JNDs, with F1 ranging from 326 to 443 Hz. Thus, although the duration range was exaggerated with respect to the natural span between the two categories, it was not *perceptually* enhanced with respect to the spectrum dimension. Second, Bohn (1995) and Flege *et al.* (1997) varied duration and spectrum within only their natural ranges and still found that Spanish listeners used duration as a primary dimension for classifying English tense and lax vowels. Finally, in the present study, native English listeners were not affected by the exaggerated duration range, as their pattern of response was quite similar to that found in previous studies (Hillenbrand *et al.*, 2000), suggesting that the design of the present experiment did not, in itself, influence listeners' cue weighting strategies.

2. Theoretical interpretations

The lack of a difference between Spanish and Russian listeners in terms of their use of duration in the perception of English [i] and [ɪ] might suggest that neither group is transferring their native experience with vowel duration to the perception of English [i] and [ɪ], instead resorting to the use of duration either on a language-independent psychoacoustic basis (Bohn, 1995) or as a consequence of applying residual first-language acquisition strategies (Escudero and Boersma, 2004). On the other hand, it is also possible that previously reported differences in the importance of duration as an acoustic cue in Russian (Bolla, 1981; Bondarko,1998) as compared to Spanish (Hammond, 2001; Hualde, 2005) may be overstated, perhaps because they are based strongly on acoustic analyses, demonstrating that the two languages exhibit differences in the way durational properties are produced, rather than on perceptual analyses, which would show the degree to which speakers of the two languages actually *use* duration as a cue when it is available to them.

3. Individual differences

It is also possible that the group similarities observed here actually obscure more significant patterns of individual

differences based on such variables as general English proficiency or experience with and education in the L2, or even the specific English dialects to which the learner is exposed (Escudero and Boersma, 2004). Although no independent test for English language proficiency was employed in the present study, we analyzed 13 factors (see Table I) known to affect degree of foreign accent in L2 and that are used widely in the literature to estimate foreign language proficiency (Piske *et al.*, 2001; McAllister *et al.*, 2002; Ylinen *et al.*, 2005). The two groups (Spanish and Russian) did not differ from one another according to 12 of the 13 measured variables suggesting that the two groups were well matched in terms of English proficiency. However, we did determine that, on an individual basis, the longer a participant had taken EFL instruction in their home country, the greater their reliance on spectrum over duration in the present task. This suggests that, whatever differences there might have been in terms of, for example, the different English dialects to which each listener was previously exposed, these were not as significant a factor as simply the amount of EFL education at home.

III. EXPERIMENT 2

In order to determine whether native Spanish and Russian listeners differ in their use of vowel duration as a perceptual cue to phonological contrasts in their native languages, we examined two cases in which vowel duration appears as an acoustic correlate of a phonological contrast, one suprasegmental and one segmental, in both languages as well as in English.

At the segmental level, vowels are longer before voiced than before voiceless consonants in English, Spanish, and Russian (Chen, 1970; Pye, 1986). This difference is considerably smaller in Spanish and Russian than it is in English, suggesting that the linguistic significance of allophonic vowel duration differences may be lower in these two languages than in English (Chen, 1970, Pye, 1986). In English, this difference in duration has been shown to function as an acoustic cue to voicing: A longer vowel cues the perception of voicing in the following stop consonant, while a shorter vowel cues the perception of voicelessness (Crowther and Mann, 1992; Raphael, 1972). Thus, in this case English listeners serve as a control group against which to measure the degree of Spanish and Russian listeners' reliance on vowel duration in the identification of final consonant voicing.

At the suprasegmental level, English and Russian stressed vowels are longer than unstressed vowels and these duration differences are sufficient to cue the perception of both English and Russian stress contrasts (Bondarko, 1998; Fry, 1955, 1958), although duration is arguably a weaker cue for English speakers [compared to fundamental frequency, vowel reduction, and intensity, (Beckman, 1986), while it is considered the strongest cue to stress differences for Russian speakers (Bondarko, 1998)]. In Spanish, stressed vowels are slightly longer than unstressed ones but in general syllable durations are much more equal than in English or Russian (Hammond, 2001).

Based on these findings, we would predict that Spanish and Russian listeners should perform comparably when using vowel duration to classify postvocalic stop consonant voicing contrasts, but they should show a weaker reliance on this cue than do English listeners. At the same time, when classifying stress contrasts, Russian and English listeners should show a much stronger reliance on duration cues than Spanish listeners, and Russian listeners may show a greater reliance on this cue than do English listeners. On the other hand, the results of the first experiment suggest that, perhaps, Spanish and Russian listeners are not all that different in terms of their native language experience with vowel duration. In this case, we would expect to find no differences between Spanish and Russian listeners' reliance on vowel duration in these native language contrasts: Both should be less reliant than English speakers in the consonant voicing contrast and equally reliant on duration in the lexical stress contrast.

A. Method

1. Participants

Participants were the same as in experiment 1.

2. Stimuli

Stimuli for experiment 2 consisted of three sets: *fápa/fapá, lapko/labko*, and *lapo/labo* created according to the following procedure. A 30-year-old male native speaker of Chilean Spanish[2] produced several examples of the words *fápa, fapá, lapko, labko*, and *lapo, labo* in isolation. All tokens were recorded using the same procedures as in experiment 1 except that the initial recording was made using a Marantz Professional solid state recorder (PMD660) directly to wav format (sampling frequency 22 050 Hz), eliminating the need to redigitize the initial recordings for subsequent processing. From the set of produced words, one token each of *fápa, fapá, lapko, labko*, and *lapo, labo* was selected using the same criteria as in experiment 1.

Evaluating postconsonantal voicing using stimuli that are acceptable nonwords in both Russian and Spanish is particularly difficult, due to a number of phonological rules involving stop consonant voicing in both languages. Stimuli ending in the target consonant (e.g., CVC syllables) were not useable due to a process of word-final voicing neutralization in Russian. On the other hand, voiced stop consonants in intervocalic position (e.g., VCV) are not typically acceptable in Spanish, due to a process of intervocalic spirantization. Ultimately, it was decided to use two different types of stimuli, *lapko/labko*, and *labo/lapo* in order to have one block (*lapko/labko*) in which the Russian listeners would be, if anything, biased toward a voiceless response (due to a process of regressive voicing assimilation in consonant clusters, Bondarko, 1977), and the other in which Spanish listeners would be biased toward voiceless responses (*lapo/labo*) due to the lack of intervocalic spirantization of voiced stops (Hammond, 2001). The methods for generating each set were given as follows.

(a) *lapko/labko*. The stimuli for this experiment were a set of ten syllables of the form /*laCko* / (where C is ambiguous

between [p] and [b]) created according to the following procedure. The duration of the [a] vowel in the first syllable of each word was measured from the end of the transition from [l] to the last zero crossing of the vowel waveform before the stop gap of the following [p] or [b]. The stop gap was also measured. The token *lapko* was chosen as the base for manipulation because it was technically easier to reduce the amplitude of the [p] burst to make it more ambiguous, than it would have been to eliminate voicing in the closure and increase the amplitude of a weak [b] burst to make a *labko* token more ambiguous. By trial and error the stop gap was reduced by 13% and the burst amplitude was decreased by 97% so that the resulting token was perceived to be ambiguous between [p] and [b] by native speakers of English, Russian, and Spanish (not participants in the experiment). The duration of the first vowel [a] in the ambiguous token was then varied to range from 95 to 230 ms in ten steps (15 ms/step). The shortest step was chosen to be 95 ms because it was the shortest duration, which sounded natural to English, Spanish, and Russian listeners (not participants in the experiment) in the newly created token.

(b) *lapo/labo*. These stimuli were derived from the *lapko/labko* stimuli described above. To create these stimuli, the burst and stop gap associated with the consonant [k] in the *lapko/labko* stimuli were deleted immediately prior to manipulating the duration of the first vowel [a]. All other processes were identical. The beginning of the [k] was defined as the first zero crossing preceding the first upward-going excursion of the burst release. The end was defined as the first upward-going zero crossing at the onset of periodicity for the following [o]. The remaining gap between the end of the /p/ burst and the beginning of the /o/ vowel in the second syllable was reduced by 94% to make the Voice Onset Time (VOT) of the [p] consonant ambiguous for native speakers of English, Spanish, and Russian.

(c) *fápa/fapá*. The stimuli for this experiment were of a set of ten syllables of the form [fapa] created according to the following procedure. Duration, intensity, and *f*0 of the [a] in the first syllable were measured from the end of the noise portion of the fricative /f/ to the last zero crossing of the vowel waveform before the silent gap, and in the second syllable from the end of the release of the [p] closure to the last zero crossing of the vowel waveform. Using the PRAAT 4.1.21 manipulation editor (PSOLA resynthesis), the intensity and *f*0 of each vowel in both *fápa* and*fapá* were adjusted to the average value of the vowels in that position. Next, the first syllable in the manipulated *fápa* token and the second syllable in the manipulated *fapá* token (that is, the two "average" syllables derived from originally stressed syllables) were concatenated together into a new token of the form [fapa]. Finally, a ten step continuum was created by setting the duration of the first vowel [a] in this newly created ambiguous token so that it would range from 50 to 230 ms in ten (20 ms) steps. A shortest step of 50 ms in the newly created token was chosen because it was the minimal step, which sounded natural to four native speakers of English, Spanish, and Russian who were not participants in the experiment.

3. Procedure

On each trial listeners heard one stimulus with a simultaneous visual presentation of two possible answers, e.g., *fápa* and *fapá* (*lapko* and *labko*; *lapo* and *labo*). Russian participants saw these words written in Cyrillic. Responses were always in this order, left to right, corresponding to the left and right buttons on a response box. All participants were instructed that they would hear nonsense words produced by a native speaker of their language and that (in the *fápa/fapá* condition) an accent above the vowel in writing indicates lexical stress (this orthographic stress marking is conventional in all three languages, but more familiar to readers of Russian and Spanish than English). After participants pressed a button on the response pad corresponding to one of the two choices, there was a blink of the screen (250 ms) and another trial began. Each trial was self-paced with no limit on time to respond. In each block there were ten stimuli repeated ten times in random order. Average running time for each block was 10 min. Before each block began, all participants completed a practice session consisting of four trials using endpoint tokens from that block (steps 1 and 10). The structure of the practice session was identical to the experiment but responses were not recorded.

4. Analysis

(a) *Identification functions.* ID functions for the *lapko/labko* and *lapo/labo* series were calculated as the proportion of responses containing [b] sound (*labko* or *labo*) to all ten stimuli. The ID function for the *fápa/fapá* series was calculated as the proportion of second syllable stressed responses (*fapá*) to all ten stimuli. All ID functions were calculated as average group responses.

(b) *Logistic regression analysis.* Logistic regression functions were fitted to each subjects' identification data using statistical software (StatSoft, Inc, 2003). The logistic regression equation (Nissen, *et al.*, 2005) is

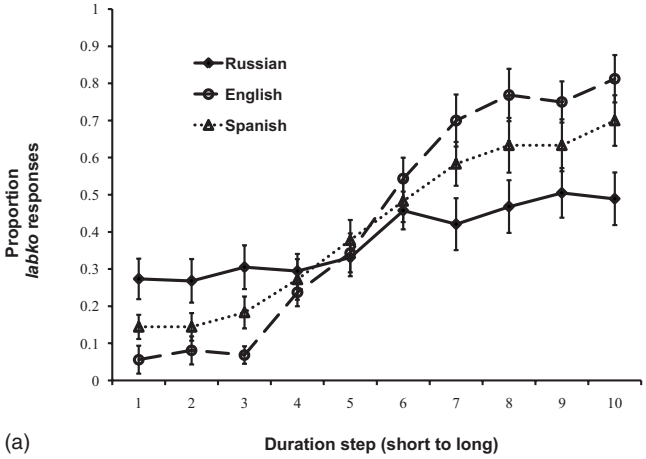
$$\log \frac{p}{1-p} = a + bx, \tag{1}$$

where p is the proportion correct, a is the regression intercept, b is the regression slope, and x is a stimulus level. The regression slope b demonstrates the steepness of the identification function slope, while the 50% crossover point of the identification function is derived by the following equation:

$$x = \frac{\log \frac{0.5}{1-0.5} - a}{b} = \frac{-a}{b}. \tag{2}$$

B. Results

ID functions for each stimulus set (*lapko/labko, lapo/labo*, and *fápa/fapá*) are shown in Figs. 2(a), 3(a), and 4(a),



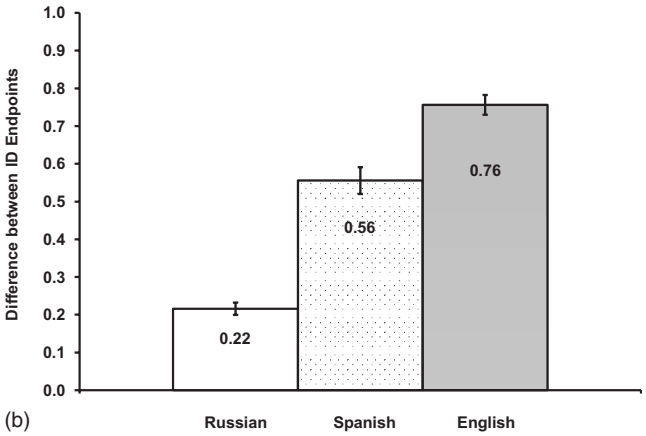
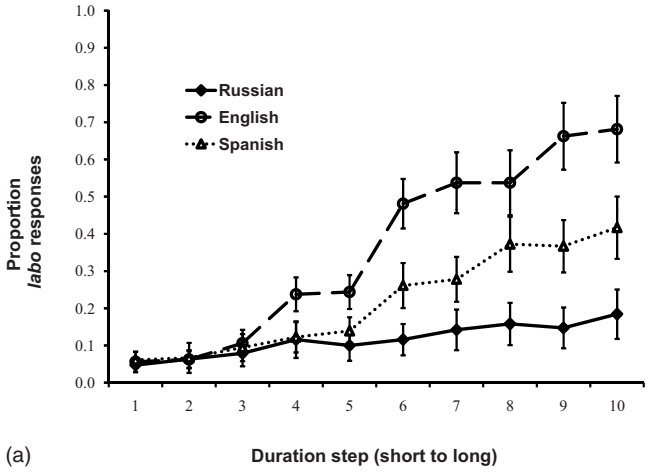


FIG. 2. Experiment 2: (a) Proportion of *labko* responses (voiced consonant) for each group of listeners at each step of duration of the first vowel (step 1=95 ms to step 10=230 ms). The error bars indicate standard error of the mean. (b) Difference between the endpoints (step 10 minus step 1) of the proportion of *labko* responses (voiced consonant) for each group of listeners. The error bars indicate standard error of the mean.



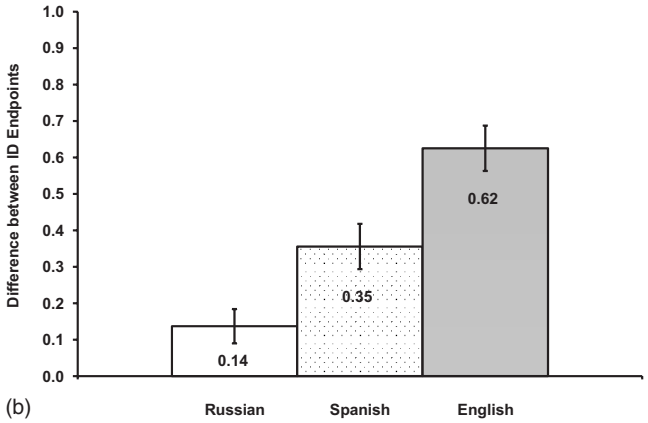


FIG. 3. Experiment 2: (a) Proportion of *labo* responses (voiced consonant) for each group of listeners at each step of duration of the first vowel (step 1=95 ms to step 10=230 ms). The error bars indicate standard error of the mean. (b) Difference between the endpoints (step 10 minus step 1) of the proportion of *labo* responses (voiced consonant) for each group of listeners. The error bars indicate standard error of the mean.

respectively. In order to compare the strength of each groups' reliance on duration, a measure of "duration reliance" was calculated as the difference between the endpoints of each continuum for each listener in each group (step 10 minus step 1), as shown in Figs. 2(b), 3(b), and 4(b), respectively. A mixed factorial ANOVA with one between group factor group (English, Spanish, Russian) and one within group contrast (*lapko/labko, lapo/labo*, and *fápa/fapá*) was run on the duration reliance measure for each stimulus set. Planned comparisons of selected means were conducted to identify significant differences between groups within contexts, and between contexts within groups.

Overall, there was a significant effect of group, $F(2,50)=14.91$, $p<0.001$, and contrast, $F(2,100)=50.48$, $p<0.001$, and a significant interaction between group and contrast, $F(4,100)=4.87$, $p=0.001$, suggesting that the three language groups used vowel duration differently as a cue to postvocalic consonant voicing as compared to lexical stress.

Planned comparison of means for the *lapko/labko* series [Fig. 2(b)] showed a significant difference between all pairs of groups: Spanish and English, $F(1,50)=6.67$, $p=0.01$; Russian and Spanish, $F(1,50)=10.12$, $p=0.003$, and Russian and English, $F(1,50)=32.40$, $p<0.001$. These results suggest that English listeners were more successful at using vowel duration for the identification of final consonant voicing than were Spanish and Russian listeners. In turn, Spanish listeners showed greater reliance on duration than did Russian listeners, which is exactly opposite the original prediction based on previously published descriptions of Spanish and Russian that suggested that the two groups should be equivalent in their use of duration as a cue to final consonant voicing.

Planned comparison of means for the *lapo/labo* series [Fig. 3(b)] demonstrated a significant difference between Spanish and English, $F(1,50)=5.89$, $p=0.02$; Russian and English, $F(1,50)=18.15$, $p<0.001$, but not Russian and Spanish, $F(1,50)=3.36$, $p=0.07$; listeners. These results again suggest that English listeners were more successful in using vowel duration for the identification of final consonant voicing than native Spanish and Russian listeners. The low proportion of voiced responses by Spanish listeners might be explained by the presence of a regular phonological process of spirantization of voiced stops in CVC position, meaning that Spanish listeners might be predisposed to hear all intervocalic stops (that are not spirantized) as voiceless. However, this does not explain the Russian listeners' performance, which was comparable to that of Spanish listeners. Thus, the importance of vowel duration is reduced before a C

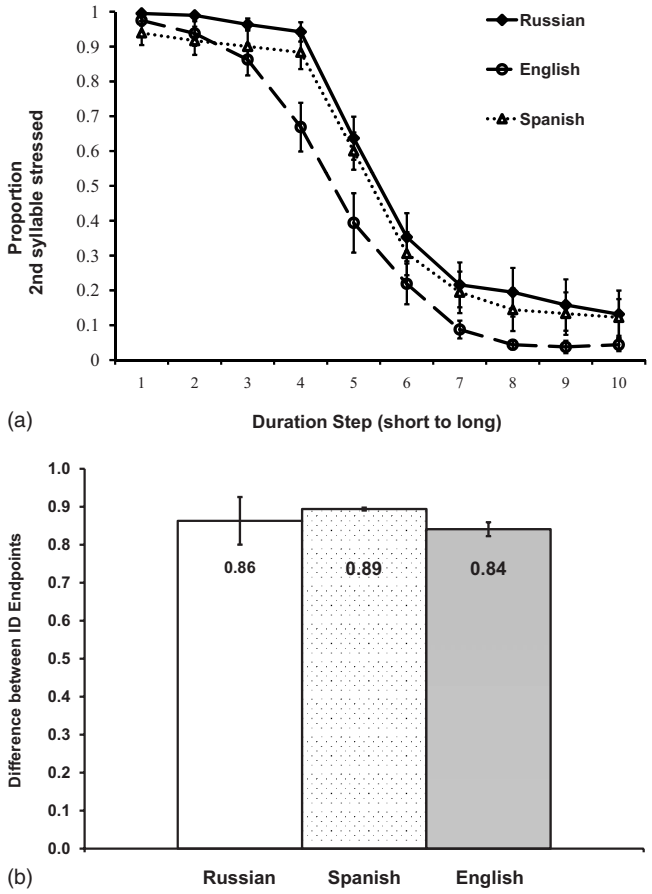


FIG. 4. Experiment 2: (a) Proportion of *fapá* (second syllable stressed) responses for each group of listeners at each step of duration of the first vowel (step 1=50 ms to step 10=230 ms). The error bars indicate standard error of the mean. (b) Difference between the endpoints (step 10 minus step 1) of the proportion of *fapá* (second syllable stressed) responses for each group of listeners. The error bars indicate standard error of the mean.

followed by a V, because in this context frication is presumably a stronger, more reliable cue to voicing than is preceding vowel duration.

Planned comparison of means for the *fápa/ fapá* series showed that there was no significant difference between any pair of groups: Russian and English, $F(1,50)=0.7$, $p=0.41$; Russian and Spanish, $F(1,50)=0.35$, $p=0.56$ and English and Spanish, $F(1,50)=1.93$, $p=0.17$. These findings suggest that all three groups were able to use vowel duration to the same extent as a cue to lexical stress differences.

Because of language-specific differences in extraneous phonological processes that might have affected perception of voicing in the two segmental contexts (*lapko/labko* and *lapo/labo*), planned comparisons of means were used to compare duration reliance in each context within each group. Results showed a significant difference between the reliance on duration in *lapko/labko* versus. *lapo/labo* contexts for English, $F(1,50)=6.19$, $p=0.02$ and Spanish, $F(1,50)=8.09$, $p=0.006$, but not Russian, $F(1,50)=2.53$, $p=0.12$, listeners. The lack of an observed difference for Russian listeners, who showed little evidence of using vowel duration as a cue to consonant voicing in either context, suggests that this property, although it is available in the acoustic patterns of Russian speech productions, is not weighted very heavily as a perceptual cue to voicing for Russian speakers. On the other hand, the observation that both Spanish and English listeners show less reliance on duration in the VCV as compared to the VCC context suggests that the Spanish pattern may not be solely due to the influence of a process of the spirantization of voiced stops in VCV position in Spanish, since no such process exists in English. It is possible that, in the case of English (and possibly Spanish speakers), the weight given to vowel duration may differ across phonetic contexts, such that in VCV context other acoustic cues, perhaps including the strength of the release burst, the presence of voicing during closure, onset *f*0 of the following vowel or F1 cutback (cf. Lisker, 1986) may contribute proportionally more to the identification of the consonant voicing than preceding vowel duration, which, in turn, receives greater weight when some of these other cues are unavailable due to the presence of a following consonant.

Because the measure of duration reliance is not so standard, further analyses using a more typical measure, logistic regression, were carried out. For each participant whose data could be summarized in this manner, a logistic curve was fit ted to their individual ID function, and the slope of the function and its 50% crossover point were computed (see Table II for group results and the number of people in each group who showed analyzable results). These data were analyzed separately for each context using a one-way ANOVA with three levels of one factor (language).

For the slope of the ID function, a significant effect of language was found only for the *lapko/labko* and *lapo/labo* series, $F(2,50)=9.89$, $p<0.001$ and $F(2,50)=10.67$, $p<0.001$, respectively. Post hoc comparisons were significant for English versus Russian in the *lapko/labko* series, while in the *lapo/labo* series English listeners differed significantly from both Russian and Spanish listeners. These results corroborate the findings of the duration reliance analysis above, suggesting that English listeners showed stronger categorization of consonant voicing on the basis of preceding vowel duration than did either Russian or Spanish listeners, though their difference from Spanish speakers disappeared in the *lapko/labko* context. In the *fápa/ fapá* series there was no significant difference between the groups, suggesting that all three used duration equally for identifying lexical stress.

When analyzing the 50% points, only three Russian participants showed ID curves that crossed the 50% line for either the *lapko/labko* or *lapo/labo* series. Thus, an ANOVA on the location of the 50% crossover point was run only on English and Spanish data for these two continua, but for the *fápa/ fapá* series all three language groups were included. For all three continua, no significant difference was found between English and Spanish listeners. However, in the *fápa/ fapá* series, there was a significant difference between English (step 4.4=118 ms) and Russian (step 5.6=142 ms) listeners. This difference may suggest that these listeners utilized their native language allophonic experience with vowel duration while listening to tokens. Notice that in Russian the duration of a stressed [a] vowel is 166 ms and the duration of the unstressed vowel is 95 ms. (Bolla, 1981), suggesting that a boundary midway between them should be around 130 ms, perhaps higher because other (palatalized) allophones of [a]

TABLE II. Steepness of the slope and location of the 50% crossover point of the identification functions for native speakers of English, Spanish, and Russian in experiment 2. The No. of listeners refers to the number of listeners exhibiting a quantifiable slope (col. 3) or identifiable 50% crossover point (col. 5), out of the total number of listeners in the specific language group.

		Slope		Location of 50% Crossover	
Series	Group	No. of listeners	Steepness (B1) (std)	No. of listeners	Step (std) (ms)
lapko/labko	English	16/16	0.71(0.35)	16/16	5.9 (2.29), 168
	Spanish	18/18	0.47 (0.4)	15/18	6.2 (1.25), 173
	Russian	17/19	0.24 (0.29)	5/19	5.7 (0.61), 165
lapo/labo	English	14/16	0.55 (0.40)	13/16	6.5 (2.76), 177
	Spanish	13/18	0.30 (0.22)	9/18	7.3 (0.93), 189
	Russian	7/19	0.08 (0.15)	3/19	6.4 (1.46), 176
fápa/fapá	English	16/16	1.5 (0.81)	16/16	4.4 (0.8), 118
	Spanish	18/18	1.45 (1.57)	17/18	5.3 (1.36), 136
	Russian	18/19	1.35 (0.71)	17/19	5.6 (1.09), 142

are all longer than 166 ms. Thus, it is possible that the pattern observed in the present study reflects a difference in the location of native boundaries between longer and shorter phonetic categories.

Finally, a correlation analysis was run between the duration reliance measure in native language contrasts (averaged over all three contexts in experiment 2) and the duration reliance measure calculated as the proportion of bit responses at step 9 minus step 1 along the duration continuum in experiment 1. For Spanish listeners, the correlation was significant, $r=0.57$, $p=0.01$; however, for Russian listeners, the correlation was not significant. This pattern of results suggests that there may be a connection between the use of vowel duration in the perception of non-native contrast and the use of duration in native contrasts for Spanish, but not for Russian, listeners.

C. Discussion

The results of the second experiment show an unexpected pattern of difference between Spanish and Russian listeners' use of vowel duration as a cue to native phonological contrasts. On the one hand, the results of the lexical stress experiment suggest that Russian, Spanish, and English speakers employ vowel duration to the same degree when identifying stress contrasts in their native languages despite the very different roles that duration plays in the stress systems of the three languages. Although these finding disagree with predictions based on traditional conceptualizations of the respective native language phonologies, they are consistent with previous findings that native Spanish speakers are able to use vowel duration as a cue to lexical stress (Diaz-Campos, 2000; Lecumberri, 2006; Manrique, and Signorini, 1983, also see Llisterri *et al.*, 2003 for opposite conclusions).

Similarly, the results of the consonant voicing experiments suggest that Spanish and Russian listeners relied less on vowel duration as an allophonic cue to following consonant voicing than did native English listeners, as might be predicted based on the results of previous production research (Chen, 1970). On the other hand, the finding that Spanish listeners rely more on vowel duration as a cue to consonant voicing than do Russian listeners is unexpected. In previous production studies, both Spanish and Russian listeners were shown to have almost identical ratios of vowel duration before voiceless consonants to vowel duration before voiced consonants (Spanish, 0.86; Russian, 0.82 or 0.85–0.90).[3] However, our results suggest that, perceptually, the two languages may differ in terms of the degree to which they rely on duration as a cue to following consonant voicing (little or none in Russian, more so in Spanish). Finally, our results suggest that English, and possibly Spanish listeners, may shift the weight they give to a particular cue (in this case vowel duration) to a particular contrast depending on the availability of other cues in a given phonetic context.

It must be noted that these results were derived from listeners with some experience listening to English, and it is possible that their behavior reflects transfer of experience with vowel duration in the L2 (English) back to their respective native languages as suggested by Flege's (1995) speech learning model, or perhaps activation of an "English mode" of listening (Grosjean, 1998). While this is certainly possible, the present findings agree clearly with the results of previous perceptual studies of monolingual Russian and Spanish listeners (Bondarko, 1998; Diaz-Campos, 2000; Manrique and Signorini, 1983). Moreover, differences between the two groups in the use vowel duration as a cue to syllable-final consonant voicing suggest that both groups were influenced by native phonological constraints during performance of the present task, and thus were not listening in a purely English-like manner. Thus, while we cannot rule out the possibility that these results reflect transfer back from the L2 to the L1, a simpler explanation is that Spanish listeners, like Russian listeners, do, in fact, have native language experience with using duration as a phonetic cue, at least at the prosodic level and, furthermore, that Spanish listeners may even have *more* experience using vowel duration as a cue to consonant voicing than do Russian listeners.

IV. GENERAL DISCUSSION

The results of experiment 1 provide further confirmation that non-native listeners weight the multiple acoustic cues to the English tense-lax vowel contrast differently than do native listeners. In agreement with previous studies, English listeners gave more weight to spectrum than to duration, but used both to some degree (Ainsworth, 1972; Hillenbrand *et al.*, 1995, 2000; Mermelstein, 1978), while native Spanish listeners gave no weight to spectrum and used duration alone (Bohn, 1995; Escudero, 2006; Escudero and Boersma, 2004). Russian listeners also showed little or no reliance on spectrum, using duration exclusively, in a manner comparable to Spanish listeners. This pattern of performance is consistent with a variety of more substantive explanations, including the transfer of native language experience with vowel duration as a perceptual cue, the influence of language-universal psychoacoustic biases (Bohn, 1995), and the application of residual L1 acquisition strategies (Escudero and Boersma, 2004).

With respect to the hypothesis of allophonic experience, the results of experiment 2 suggest that Spanish and Russian listeners rely to a similar degree on duration as a cue to lexical stress placement, consistent with the results of previous studies on monolingual speakers of both languages (Bolla, 1981; Diaz-Campos, 2000; Manrique and Signorini, 1983; Prieto, and van Santen, 1996). Thus, it is possible that both Spanish and Russian listeners are able to transfer their experience with vowel duration at an allophonic level to the perception of the English tense and lax vowel contrast.

However, the finding that Spanish listeners rely *more* on vowel duration as a cue to native consonant voicing than do Russian listeners (in experiment 2) but the two groups do not differ in their reliance on vowel duration in the perception of a non-native vowel contrast (in experiment 1) suggests that native allophonic experience does not explain all aspects of cross-language perception in this case.

Another possible explanation for Spanish listeners' use of duration in the non-native contrast in question, one that may also account for Russian listeners' performance in the present study, is the relative salience of the two acoustic properties (vowel duration and vowel quality). Acoustic dimensions of speech may differ in their relative salience (Burnham, 1986; Walley and Carrell, 1983) and the ease with which they can be learned (Francis *et al.* 2000; Francis and Nusbaum, 2002). In principle, unequal sensitivity to two dimensions could arise innately (Holt and Lotto, 2006) or, in the present case it could arise as a consequence of the smaller (as compared to English) vowel inventory of both Russian and Spanish, which might make speakers of these languages less sensitive to vowel quality differences (Hacquard *et al.*, 2007) and thus more likely to cue in on duration differences. This explanation is consistent with Bohn's (1995) *desensitization hypothesis*, in which it is proposed that duration will be employed regardless of the listener's degree of L1 experience with it when spectral properties are hard to distinguish.

Alternatively, Escudero and Boersma (2004) proposed that monolingual Spanish speakers start with no phonological categories distinguished according to duration, due to their limited experience with this feature in their native phonological and phonetic systems. Therefore, when they first encounter a phonological contrast that involves duration differences, they apply a first-language (L1) acquisition strategy based on distributional learning. Since they are able to detect two peaks in the distribution of [i] and [ɪ] tokens along the duration dimension, they learn to divide the duration continuum into two categories. This argument applies to some degree with respect to the Spanish listeners' performance in the present study, but requires some modification with respect to the Russian data.

The results of experiment 1 are consistent with the Escudero and Boersma (2004) hypothesis that Spanish listeners have learned the distribution of tense and lax vowels in English on the basis of duration alone using an L1 (distribution-based) acquisition mechanism, so long as we assume that Spanish listeners do not have sufficient phonetic experience with duration to have developed native duration-based categories. If we make this assumption, we must then interpret the results of experiment 2 as providing evidence for the transfer of experience with duration (in English) back to Spanish, a phenomenon that has been observed in other studies (Flege and Eefting, 1987) and is quite compatible with the speech learning model of L2 acquisition proposed by Flege (1995).

On the other hand, Russian listeners cannot be assumed to have developed duration-based category representations of English vowels based on L1 acquisition mechanisms, because they must already have native, duration-based categories (e.g., for stress, Bolla, 1981). In this case, the present data must be interpreted as Russian listeners' assimilating [i] to a longer (stressed) category, and [ɪ] to a shorter one (perhaps prestressed), in a pattern of two-category assimilation (Best, 1995). A similar explanation has been advanced by Ylinen *et al.* (2005) to explain monolingual Russian listeners' treatment of the Finnish vowel length contrast. This interpretation is also consistent with the observed lack of a significant correlation found between the results of experiments 1 and 2. If Russian listeners, like Spanish listeners, were using L2-based categories for the tense/lax contrast in experiment 1, we would expect some transfer of these newly learned contrasts back to their perception of contrasts that, in English, depend on duration (e.g., consonant voicing). The fact that Spanish, but not Russian, listeners show a pattern consistent with backward transfer of experience with duration, suggests that the Escudero and Boersma (2004) model does not apply in the case of Russian listeners, since they are able to apply established L1 categories to their perception of the L2 contrasts and do not need to invoke L1 learning mechanisms.

It seems plausible that all of the major factors discussed here, including native allophonic as well as phonological experience, individual differences in experience with specific dialects, and innate psychoacoustic proclivities, may contribute to some degree to the relative weighting of cues in cross-language speech perception. We have shown that native Spanish and Russian listeners have sufficient allophonic experience with duration in their native language to enable a

potential transfer to English. However, it is still possible that the overall dimension of duration is somehow more salient than spectrum for reasons unrelated to the listeners' native language. Our results cannot rule out a basic psychoacoustic explanation (Bohn, 1995), and are quite consistent with an explanation based on the application of residual L1 learning mechanisms (Escudero and Boersma, 2004). Future research to distinguish between these possibilities should employ a more controlled evaluation of general proficiency in the foreign language as well as the examination of truly monolingual listeners in comparison to those with more exposure to the foreign language.

ACKNOWLEDGMENTS

We are grateful to Robert Hammond, Margie Burns, and two anonymous reviewers for helpful suggestions and discussion related to earlier versions of this article. A preliminary version of the results of experiment 1 was presented at the 148th Meeting of the Acoustical Society of America, San Diego, CA, 15–19 November 2004, and some of the results of experiment 2 were presented at the 4th Joint Meeting of the Acoustical Society of America and the Acoustical Society of Japan, Honolulu, HI, 28 November–2 December 2006. Part of this research was supported by a grant from the College of Liberal Arts, Purdue University, to M. K., and by NIDCD Grant No. R03 DC006811 to A.L.F.

[1]Note that this pattern is the opposite of that found in the English [i]-[ɪ] contrast.

[2]The speaker was a former phonetics teacher and was fluent in English as well, and was specifically instructed to produce the stimuli in as "accent-free" a manner as possible (i.e., avoiding intervocalic spirantization). Russian listeners all reported that the stimuli sounded like Russian, while Spanish listeners reported that they sounded like Spanish, suggesting that the perceived linguistic background of the talker would not have affected listeners' responses in any language-dependent manner.

[3]Spanish values from Chen (1970), Russian values from Chen (1970) and calculated from values in Pye, (1986), Table 3.

Ainsworth, W. A. (**1972**). "Duration as a cue in the recognition of synthetic vowels," J. Acoust. Soc. Am. **51**, 648–651.

Beckman, M. E. (**1986**). *Stress and Non-Stress Accent*, Netherlands Phonetic Archives Vol. **7**, Foris Dordrecht.

Best, C. T. (**1995**). "A direct realistic view of cross-language speech perception," in *Speech Perception and Linguistic Experience: Issues in Cross* edited by W. Strange (York, Bathmore, MD). pp. 171–204.

Best, C. T., and Strange, W. (**1992**). "Effects of language-specific phonological and phonetic factors on cross-language perception of approximants," J. Phonetics **20**, 305–330.

Bohn, O.-S. (**1995**). "Cross language speech production in adults: First language transfer doesn't tell it all," in *Speech Perception and Linguistic Experience: Issues in Cross-Language Research*, edited by W. Strange (York, Baltimore), pp. 279–304.

Bolla, K. (**1981**). *A Conspectus of Russian Speech Sounds* (Akademiai Kiado, Budapes).

Bondarko, L. V. (**1977**). "*Zvukovoi stroi sovremennogo russkogo jazyka (Phonetic structure of modern Russian language)*," Moscow, Russia: Proveshenie.

Bondarko, L. V. (**1998**). "*Fonetika Sovremennogo Russkogo Jazyka (Phonetics of Modern Russian Language)*," University of St.-Petersburg, St.-Petersburg, Russia.

Burnham, D. K. (**1986**). "Developmental loss of speech perception: Exposure to and experience with a first language," Appl. Psycholinguist. **7**, 207–240.

Chen, M. (**1970**). "Vowel length variation as a function of the voicing of the consonant environment," Phonetica **22**, 129–159.

Crowther, C. S., and Mann, V. (**1992**). "Native language factors affecting use of vocalic cues to final consonant voicing in English," J. Acoust. Soc. Am. **92**, 711–722.

Diaz-Campos, M. (**2000**). "The phonetic manifestation of secondary stress in Spanish," in *Hispanic Linguistics at the Turn of the Millennium: Papers From the third Hispanis Linguistic Symposium*, edited by H. Campos, E. Herburger, A. Morales-Front, and T. J. Walsh (Cascadilla, Somerville, MA).

Escudero, P. (**2006**). "The phonological and phonetic development of new vowel contrasts in Spanish learners of English," in *English With a Latin Beat: Studies in Portugues/Spanish-English Interphonology, Studies in Bilingualism*, Vol. **31**, edited by B. O. Baptista, and M. A. Watkins (John Benjamins, Amsterdam), pp. 149–161.

Escudero, P., and Boersma, P. (**2004**). "Bridging the gap between L2 speech perception research and phonological theory," Stud. Second Lang. Acquis. **26**, 551–585.

Flege, J. E. (**1995**). "Second language speech learning: Theory, findings, and problems," in *Speech Perception and Linguistic Experience. Issues in Cross-Language Research*, edited by W. Strange (York, Baltimore, MD), pp. 233–277.

Flege, J. E., Bohn, O.-S., and Jang, S. (**1997**). "Effects of experience on non-native speakers' production of English vowels," J. Phonetics **25**, 437–470.

Flege, J. E., and Eefting, W. (**1987**). "Production and perception of English stops by native Spanish speakers," J. Phonetics **15**, 67–83.

Fox, R. A., Flege, J. E., and Munro, M. J. (**1995**). "The perception of English and Spanish vowels by native English and Spanish listeners: A multidimensional scaling analysis," J. Acoust. Soc. Am. **97**, 2540–2551.

Francis, A. L., Baldwin, K., and Nusbaum, H. C. (**2000**). "Effects of training on attention to acoustic cues," Percept. Psychophys. **62**, 1668–1680.

Francis, A. L., and Nusbaum, H. C. (**2002**). "Selective attention and the acquisition of new phonetic categories," J. Exp. Psychol. Hum. Percept. Perform. **28**, 349–366.

Fry, D. B. (**1955**). "Duration and intensity as physical correlates of linguistic stress," J. Acoust. Soc. Am. **27**, 765–768.

Fry, D. B. (**1958**). "Experiments in the perception of stress," Lang Speech **1**, 126–152.

Grosjean, F. (**1998**). "Studying bilinguals: Methodological and conceptual issues," Bilingualism: Lang. Cognit. **1**, 131–149.

Hacquard, V., Walter, M. A., and Marantz, A. (**2006**). "The effect of inventory on vowel perception in French and Spanish: An MEG study," Brain Lang **100**, 295–300.

Halle, P. A., Best, C., and Levitt, A. (**1999**). "Phonetic vs. phonological influences on French listeners' perception of American English approximants," J. Phonetics **27**, 281–306.

Hammond, R. M. (**2001**). *The Sounds of Spanish: Analysis and Application (With Special Reference to American English)* (Cascadilla, Somerville, MA).

Harris, J. (**1969**). *Spanish Phonology* (MIT, Cambridge, MA).

Hillenbrand, J., Clark, M. J., and Houde, R. A. (**2000**). "Some effects of duration on vowel recognition," J. Acoust. Soc. Am. **108**, 3013–3022.

Hillenbrand, J., Getty, L. A., Clark, M. J., and Wheeler, K. (**1995**). "Acoustic characteristics of American English vowels," J. Acoust. Soc. Am. **97**, 3099–3111.

Holt, L. L., and Lotto, A. J. (**2006**). "Cue weighting in auditory categorization: Implications for first and second language acquisition," J. Acoust. Soc. Am. **119**, 3059–3071.

Hualde, J. I. (**2005**). *The Sounds of Spanish* (Cambridge University Press, Cambridge).

Jamieson, D. G., and Moroson, D. E. (**1986**). "Training non-native speech contrasts in adults: Acquisition of the English /ð/-/θ/ contrast by francophones," Percept. Psychophys. **40**, 205–215.

Jenkins, J. J., and Yeni-Komshian, G. H. (**1995**). "Cross-language speech perception: Perspective and promise," in *Speech Perception and Linguistic Experience: Issues in Cross-Language Speech Research*, edited by W. Strange (York, Baltimore, MD), pp. 463–479.

Kewley-Port, D., and Watson, C. S. (**1994**). "Formant-frequency discrimination for isolated English vowels," J. Acoust. Soc. Am. **95**, 485–496.

Klatt, D. H. (**1976**). "Linguistic use of segmental duration in English: Acoustic and perceptual evidence," J. Acoust. Soc. Am. **59**, 1208–1221.

Lecumberri, L. G. (**2006**). "Perception of double stress by Spanish learners of English," in *English With a Latin Beat: Studies in Portugues/Spanish-English Interphonology*, edited by B. O. Baptista and M. A. Whatins (John Benjamins, Amsterdam).

Lisker, L. (**1986**). ""Voicing" in English: A catalogue of acoustic features signaling /b/ versus /p/ in trochees," Lang Speech **29**, 3–11.
Llisterri, J., Machuca, M., de la Mota, C., Riera, M., and Rios, A. (**2003**). "The perception of lexical stress in Spanish," in *Proceedings of the 15th International Congress of Phonetic Sciences*, edited by M. J. Sole, D. Recasens, and J. Romero, Barcelona, 3–9 August, casual productions [CD-ROM].
Manrique, A. M. B., and Signorini, A. (**1983**). "Segmental duration and rhythm in Spanish," J. Phonetics **11**, 117–128.
McAllister, R., Flege, J. E., and Piske, T. (**2002**). "The influence of L1 on the acquisition of Swedish quantity by native speakers of Spanish, English and Estonian," J. Phonetics **30**, 229–258.
McClaskey, C. L., Pisoni, D. B., and Carrell, T. D. (**1983**). "Transfer of training of a new linguistic contrast in voicing," Percept. Psychophys. **34**, 323–330.
Mendoz, E., Garballo, G., Cruz, A., Fresneda, M. D., Munoz, J., and Marrero, V. (**2003**). "Temporal variability in speech segments of Spanish: Context and speaker related differences," Speech Commun. **40**, 431–447.
Mermelstein, P. (**1978**). "On the relationship between vowel and consonant identification when cued by the same acoustic information," Percept. Psychophys., **23**, 331–336.
Nissen, S. L., Harris, R. W., Jennings, L., Eggett, D. L., and Buck, H. (**2005**). "Psychometrically equivalent trisyllabic words for speech reception threshold testing in Mandarin," Int. J. Audiol. **44**, 391–399.
Piske, T., MacKay, I. R. A., and Flege, J. E. (**2001**). "Factors affecting degree of foreign accent in an L2: A review," J. Phonetics **29**, 191–215.
Pisoni, D. B., Aslin, R. N., Perey, A. J., and Hennessy, B. L. (**1982**). "Some effects of laboratory training on identification and discrimination of voicing contrasts in stop consonants," J. Exp. Psychol. Hum. Percept. Perform. **8**, 297–314.
Prieto, P., and van Santen, J. (**1996**). "Secondary stress in Spanish: Some experimental evidence.," *Aspects of Romance Linguistics: Selected Papers From the Linguistic Symposium on Romance Languages*, Vol. **XXIV** pp. 337–356.
Pruitt, J. S., Jenkins, J. J., and Strange, W. (**2006**). "Training the perception of Hindi dental and retroflex stops by native speakers of English and Japanese," J. Acoust. Soc. Am. **119**, 1684–1696.
Pye, S. (**1986**). "Word-final devoicing of obstruents in Russian," Cambridge Papers in Phonetics and Experimental Linguistics **5**, 1–10.
Raphael, L. J. (**1972**). "Preceding vowel duration as a cue to the perception of the voicing characteristic of word-final consonants in American English," J. Acoust. Soc. Am. **51**, 1296–1303.
Schneider, W., Eschman, A., and Zuccolotto, A. (**2002**). *E-Prime User's Guide* (Psychology Software Tools Inc., Pittsburg, PA).
StatSoft, Inc. (**2003**). STATISTICA (*data analysis software system*), Version 6, www.statsoft.com.
Walley, A. G., and Carrell, T. D. (**1983**). "Onset spectra and formant transitions in the adult's and child's perception of place of articulation in stop consonants," J. Acoust. Soc. Am. **73**, 1011–1022.
Ylinen, S., Shestakova, A., Alku, P., and Huotilainen, M. (**2005**). "The perception of phonological quantity based on durational cues by native speakers, second-language users and non-speakers of Finnish," Lang Speech **48**, 313–338.
Zimmerman, S. A., and Sapon, S. M. (**1958**). "Note on vowel duration seen cross-linguistically," J. Acoust. Soc. Am. **30**, 152–153.

Recognition of spectrally degraded phonemes by younger, middle-aged, and older normal-hearing listeners[a)]

Kara C. Schvartz,[b)] Monita Chatterjee, and Sandra Gordon-Salant
Department of Hearing and Speech Sciences, University of Maryland, College Park, Maryland 20742

(Received 7 February 2008; revised 28 July 2008; accepted 10 September 2008)

The effects of spectral degradation on vowel and consonant recognition abilities were measured in young, middle-aged, and older normal-hearing (NH) listeners. Noise-band vocoding techniques were used to manipulate the number of spectral channels and frequency-to-place alignment, thereby simulating cochlear implant (CI) processing. A brief cognitive test battery was also administered. The performance of younger NH listeners exceeded that of the middle-aged and older listeners, when stimuli were severely distorted (spectrally shifted); the older listeners performed only slightly worse than the middle-aged listeners. Significant intragroup variability was present in the middle-aged and older groups. A hierarchical multiple-regression analysis including data from all three age groups suggested that age was the primary factor related to shifted vowel recognition performance, but verbal memory abilities also contributed significantly to performance. A second regression analysis (within the middle-aged and older groups alone) revealed that verbal memory and speed of processing abilities were better predictors of performance than age alone. The overall results from the current investigation suggested that both chronological age and cognitive capacities contributed to the ability to recognize spectrally degraded phonemes. Such findings have important implications for the counseling and rehabilitation of adult CI recipients.
© *2008 Acoustical Society of America.* [DOI: 10.1121/1.2997434]

PACS number(s): 43.71.Lz, 43.66.Ts, 43.71.Es, 43.66.Sr [MSS] Pages: 3972–3988

I. INTRODUCTION

In recent years, cochlear implants (CIs) have proven to be a successful rehabilitative option for hearing-impaired (HI) listeners of all ages, including elderly individuals. In general, the surgical procedure is well tolerated among older individuals, and many patients report improvements in overall quality of life after implantation (Facer *et al.*, 1995; Vermeire *et al.*, 2005). Perhaps most importantly, several studies have demonstrated improvements in speech recognition in quiet when post-implantation scores are compared to pre-implantation scores (Kelsall *et al.*, 1995; Sterkers *et al.*, 2004).

Many authors report comparable performance across younger and older adult CI users (Kelsall *et al.*, 1995; Shin *et al.*, 2000; Pasanisi *et al.*, 2003); however, there is some evidence to suggest that age at implantation might influence overall speech recognition outcomes in this population (Dorman *et al.*, 1989, 1990; Gantz, 1993; Blamey *et al.*, 1996). Blamey *et al.* (1996) reported on a retrospective analysis and suggested that age at implantation significantly contributed to postimplantation speech recognition outcomes, particularly in those aged 60 and older. Other variables such as duration of deafness prior to implantation, device, hearing aid use, auditory-visual therapy, and preimplant auditory thresholds also contribute to speech perception abilities among adult CI listeners, thereby making contributions of age at implantation alone less evident when evaluating performance among CI users (Parkin *et al.*, 1989; Dorman *et al.*, 1990; Blamey *et al.*, 1996; Rubinstein *et al.*, 1999; Leung *et al.*, 2005; Bodmer *et al.*, 2007; Green *et al.*, 2007).

A. Causes of spectral distortion in cochlear-implant listeners and effects on speech perception

Regardless of the age of the listener, perception through a CI is greatly affected by a severe reduction in spectral cues. Several investigations have indicated that channel interaction, presumably attributed to electrical current spread, can greatly reduce the speech perception abilities of CI users and normal-hearing (NH) individuals listening to noise-band vocoded stimuli, regardless of the degree of spectral shifting (Shannon *et al.*, 1995; Dorman *et al.*, 1997; 1998; Fishman *et al.*, 1997; Friesen *et al.*, 2001). Based on these studies, it is estimated that CI recipients are listening through roughly six to eight spectral channels, at best, even though modern multi-channel CIs offer up to 22 intracochlear electrodes.

Further degradation is caused by a frequency-to-place mismatch or spectral shifting, as surgical limitations result in a shallow insertion depth of the electrode array. An electrode array is considered fully inserted when the most apical electrode approximates 25–30 mm from the base of the cochlea (Clark, 2003; Niparko, 2004). However, imaging studies have shown that a 20–25 mm insertion depth is typical, even among CI recipients who were reported to have a full insertion postsurgically (Ketten *et al.*, 1998; Skinner *et al.*, 2002). Assuming the average cochlear length of 35 mm, and applying it to Greenwood's (Greenwood, 1990) frequency-to-place equation, one could assume that the most apical electrode

[a)]Portions of this work were presented at the 2007 Aging and Communication Research Conference, held at Indiana University, Bloomington, Indiana.
[b)]Electronic mail: kschvartz@hesp.umd.edu

 © 2008 Acoustical Society of America

would be stimulating the frequency place corresponding to approximately 1000 Hz (for a 20 mm insertion) or 500 Hz (for a 25 mm insertion). If the lowest frequency of the speech signal presented to the electrode array was also 500 or 1000 Hz, then there would be no frequency-to-place mismatch. However, the frequency information presented to the apical most electrode (by the speech processor) contains frequency information as low as 100–200 Hz, therefore resulting in spectral shifting—commonly referred to as a "basal shift" of frequency information. The results of several investigations in both CI listeners and young NH individuals listening to CI simulations suggest that a frequency-to-place mismatch of 3 mm can cause significant decreases in speech perception abilities (Dorman *et al.*, 1997; Shannon *et al.*, 1998; Fu and Shannon, 1999). Although a reduction in spectral resolution can negatively affect the perception of various types of speech stimuli (i.e., phonemes, words, and sentences), vowel recognition appears to be very susceptible to spectral smearing and shifting (Dorman *et al.*, 1997; Friesen *et al.*, 2001; Baskent and Shannon, 2003) as the perception of vowels is highly dependent on the clarity of spectral cues (i.e., resolution of formant frequencies).

The effects of spectral degradation (number of channels and frequency-to-place mismatch) on phoneme recognition abilities have been thoroughly quantified among younger listeners, but not among middle-aged and older adults. It is known that learning and training factors result in significant improvements when listening with CI or noise-band vocoded stimuli (Rosen *et al.*, 1999; Svirsky *et al.*, 2004; Fu *et al.*, 2002, 2005), and there is some evidence to suggest that younger and older groups are able to adapt to spectrally distorted sentences over a short period of time (Peelle and Wingfield, 2005). However the immediate recognition of spectrally degraded phonemes by younger and older listeners has yet to be investigated.

B. Potential interactions between aging and cochlear implantation

Even though CIs are undoubtedly beneficial to elderly HI listeners, there are reasons to suspect that the age of the adult listener might influence the ability to perceive spectrally degraded stimuli. First, CI processing results in severely diminished spectral cues, while temporal cues remain relatively unaltered. Therefore, CI users often rely on temporal cues to glean information about the target speech signal. This reliance on temporal cues seems to increase as spectral resolution decreases (Xu *et al.*, 2005; Nie *et al.*, 2006). Older listeners exhibit decreased sensitivity on several tasks measuring simple and complex temporal discrimination abilities, regardless of hearing status (Fitzgibbons and Gordon-Salant, 2001, 2004; Fitzgibbons *et al.*, 2007). Additional data imply that temporal processing deficits can arise as early as middle age (Snell and Frisina, 2000; Grose *et al.*, 2001; 2006; Lister *et al.*, 2002; Ostroff *et al.*, 2003). It is therefore hypothesized that such age-related changes in temporal processing abilities could affect speech perception when spectral cues are severely degraded, as when listening with a CI.

Second, a great deal of research has shown that older listeners show decreased speech recognition abilities when the signal has been distorted. For example, older individuals, regardless of hearing status, show a decline in the ability to understand temporally compressed or reverberated speech, or speech that has been masked by modulated noise (Gordon-Salant and Fitzgibbons, 1993; 2004; Dubno *et al.*, 2002). A few investigations provide cursory evidence that sentence and phoneme recognition are influenced by the age of the listener when speech has been degraded in a manner similar to that produced by CI processing. Souza and Kitch (2001) measured sentence recognition abilities [Synthetic Sentence Identification (SSI) task] in young and old, NH and HI listeners, using undistorted stimuli and stimuli manipulated to contain a varying number of spectral channels (one or two) using the signal-correlated-noise (SCN) method (Schroeder, 1968). The SCN method mimics that of noise-band vocoding, in that it limits spectral cues while preserving temporal cues. The results indicated that the performance of the younger listeners exceeded that of the aged listeners by as much as 40 rationalized arcsine units (RAUs); the performance of the older participants listening to two channels of spectral information was worse than that of the younger participants listening to one channel of spectral information, regardless of hearing status. In a subsequent investigation, Souza and Boike (2006) measured 16-choice consonant recognition ability in both NH and HI listeners. Stimuli were processed to contain one to eight spectral channels using the SCN method (Schroeder, 1968). Performance within each channel condition was significantly related to the age of the listener: performance declined as the age of the listener increased.

Sheldon *et al.* (2008) measured the word recognition abilities of younger (aged 17–25 years) and older (aged 65–72 years) NH adults, by using noise-band vocoding methods and varying the number of spectral channels (1–16 channels). The results indicate that older adults needed approximately eight channels to achieve 50% accuracy, whereas younger adults only needed approximately six channels, when feedback was not provided and the number of channels was randomized across runs. Interestingly, significant age differences were absent if the presentation of stimuli across all listeners was not randomized, but rather the number of channels was increased with each run or if feedback was provided. These results underscore the role of training and feedback in the performance of older listeners. Peelle and Wingfield (2005) reported somewhat comparable performance between younger (18–21 years) and older (65–79 years) listeners when sentence recall was measured using 16-channel noise-band vocoded and spectrally compressed stimuli. Performance was tracked over 20 trials. Slight disparities were present during the initial trials with older listeners performing slightly but significantly worse than their younger counterparts; however, the average performance across the two age groups converged over the remainder of runs. Although these studies (Souza and Kitch, 2001; Souza and Boike, 2006; Peelle and Wingfield, 2005; Sheldon *et al.*, 2008) were not designed with the specific intent to investigate outcomes in cochlear implantation, results provide some evidence that age might influence the perception of spectrally degraded speech stimuli.

TABLE I. Average air-conduction audiometric thesholds (dB HL) within the three age groups. Standard deviations are indicated below the averages in parentheses.

		Frequency (Hz)									
Group	Ear	250	500	750	1000	1500	2000	3000	4000	6000	8000
YNH	R	7 (7.37)	7.5 (5.25)	7 (3.49)	9.5 (4.37)	9.5 (3.69)	6.5 (3.37)	11 (3.16)	4.5 (4.37)	6 (5.67)	6.5 (5.8)
	L	4 (4.59)	6.5 (4.74)	7.5 (4.29)	6.5 (4.11)	8 (4.21)	5 (3.33)	7.5 (5.89)	5.5 (3.68)	7 (4.21)	8 (4.83)
MNH	R	9.5 (4.97)	10.5 (8.64)	13 (5.86)	12.5 (6.34)	11 (6.14)	10 (6.23)	11.5 (4.74)	9.5 (4.97)	14.5 (6.85)	20 (8.18)
	L	8 (7.88)	11.5 (6.25)	10 (6.23)	12 (4.83)	10 (6.66)	9 (6.14)	13 (4.21)	11 (5.16)	13 (7.14)	20.5 (10.12)
ONH	R	8.5 (5.29)	9 (6.14)	13 (5.37)	14 (5.16)	11.5 (4.74)	10 (5.77)	16.5 (6.26)	10 (5.77)	16.5 (7.09)	16.5 (9.73)
	L	7 (6.32)	7.5 (6.34)	9.5 (3.68)	10 (4.08)	9.5 (4.97)	9.5 (4.37)	13.5 (5.8)	11.5 (6.25)	14 (5.16)	19.5 (7.19)

Lastly, cognitive status among adult CI users also appears to be an important factor in performance outcomes, because studies have found relationships between several cognitive measures and post-implantation speech recognition scores (Lyxell *et al.*, 1996; Heydebrand *et al.*, 2007). There is a tendency for some cognitive abilities (i.e., memory and speed of processing) to decline as the age of the adult increases; however, variability does exist within a given age (Verhaeghen and Salthouse, 1997). It is logical that a limited or degraded acoustic signal (bottom-up information) requires greater demand on cognitive (top-down) processing to accurately process and identify a speech signal. This relationship between bottom-up and top-down mechanisms is a popular model in both cognitive psychology and speech and hearing literature (see Wingfield and Tun, 2007 for review). It is possible that variation in senescent decline of cognitive ability could account for some of the disparities noted among the speech recognition performance of adult CI users.

C. Summary and rationale

The effect of age on the immediate processing of spectrally degraded and shifted phonemes (e.g., the ability to correctly recognize and identify spectrally degraded stimuli without training or adaptation) has yet to be thoroughly investigated. It is reasonable to conjecture that age-related deficits in temporal processing might contribute to a decline in perception of spectrally degraded phonemes among older listeners, and recent evidence suggests that auditory temporal processing deficits begin as early as middle age (Snell and Frisina, 2000; Grose *et al.*, 2001; 2006; Lister *et al.*, 2002; Ostroff *et al.*, 2003). In the current study, the number of channels *and* degree of spectral shift were systematically varied to create different degrees of spectral distortion. The purpose of this study was to elucidate influences of age on the immediate perception of spectrally degraded vowel and consonant stimuli, by presenting stimuli to three different age groups: younger normal-hearing (YNH), middle-aged normal-hearing (MNH), and older normal-hearing (ONH) listeners. Because previous studies have shown an exceptional effect of spectral distortion on the recognition of vowel stimuli, the current investigation places most of the focus on vowel perception, while superficially exploring the effects of aging on spectrally reduced consonants. The results are expected to shed light on difficulties experienced by adult recipients of CIs at initial activation of their device. Although it was not the focus of this investigation, a brief set of standardized cognitive tests was administered to account for possible influences of top-down processes.

II. METHOD

A. Participants

Thirty NH listeners participated in the current investigation. Participants were recruited based on their age at the time of testing; three groups of listeners were formed, with ten participants in each group: (1) YNH aged 21–25 years (mean age=22.4, SD=1.64), (2) MNH listeners aged 41–50 years (mean age=46, SD=2.94), and (3) ONH listeners (ONH) aged 61–71 years (mean age=65.2, SD=4.05).

For the purposes of this study, all individuals were required to have pure-tone thresholds $\leq$20 dB HL from 250–6000 Hz in one ear, whereas the other ear was required to have pure-tone thresholds $\leq$25 dB HL from 250–6000 Hz (ANSI, 2004). This modified criterion improved recruitment for the MNH and ONH groups. Audiometric data for all groups are provided in Table I. It is obvious that although the average pure-tone thresholds of the YNH group are slightly better than those to the MNH and ONH groups, all participants had *clinically* NH. Other audiometric criteria consisted of normal middle ear function, as measured by tympanometry (Roup *et al.*, 1998) and acoustic reflex thresholds (Gelfand *et al.*, 1990).[1]

All listeners reported good health and the absence of major physical and/or neurological impairments. Furthermore, all participants were screened for general cognitive awareness using the Mini-Mental State Examination (MMSE) developed by Folstein *et al.* (1975), which consists of 11 general tasks (30 points total). The authors note norms for the MMSE depend on the level of education and age of the individual. A t-score can be derived for each individual

based on these two variables; a t-score of less than 29 suggests cognitive impairment. All participants had t-scores well above this standard suggesting lack of significant cognitive impairment among the cohort.

B. Stimuli

1. Phoneme identification

All speech stimuli were presented via the computer interface titled Computer-Assisted-Speech-Training (CAST©) Version 3.08 developed by Qian-Jie Fu of TigerSpeech Technology© at House Ear Institute (HEI). The tokens for the consonant and vowel recognition tests were digitized natural productions that were recorded at HEI for the CAST interface. The original recordings were preemphasized using a high-pass filter of 1200 Hz and were equalized in loudness. Vowel stimuli were originally recorded with a sampling rate of 16 000 Hz, while consonant stimuli were recorded using a 22 050 Hz sampling rate. There were 12 vowel stimuli consisting of the following 10 monophthongs presented in a /h/-vowel-/d/ context: heed: /h i d/ hod: /hɑ d/, head: h ɛd/, who'd: /h u d/, hid: /h ɪ d/, hood: /h ʊ d/, hud: /h ə d/, had: /h æd/, heard: /hɝd/, hawed: /hɔd/, as well as two diphthongs, hoed: /hɔʊd/ and hayed: /heɪd/. The consonant stimuli consisted of 16 phonemes /b, d, g, p, t, k, l, m, n, f, s, ʃ, v, z, ʤ, ð/, presented in an /aca/ context, where /c/=the consonant.

2. Noise-band vocoding

Noise-band vocoding was accomplished with TIGERCIS, also developed by Qian-Jie Fu (TigerSpeech Technology and HEI), using online signal processing within the CAST interface. For the purposes of this study, two variables were manipulated across experimental conditions: (1) the number of channels and (2) the lowest and highest frequencies of the analysis and carrier bands. The *analysis band* mimics the input audio range to the speech processor in a CI. The *carrier band* mimics the electrode array of the CI. The frequency content of the carrier band can be manipulated to simulate varying insertion depths according to the tonotopic organization of the cochlea. Manipulating the frequency information assigned to carrier and analysis band creates various degrees of spectral shifting (Fu and Shannon, 1999; Baskent and Shannon, 2003).

Stimuli were bandpass filtered into 4, 8, or 24 frequency bands using sixth-order Butterworth bandpass filters (24 dB/octave). The corner frequencies and bandwidths of the frequency bands were selected to simulate particular tonotopic locations and varied with the number of bands. Specific values were determined using the logarithmic equation provided by Greenwood (1990), assuming a 35 mm cochlear length.

The temporal envelope was extracted from each frequency band using half-wave rectification and low-pass filtering, with a cutoff frequency of 400 Hz (24 dB /octave) which is sufficient for good speech understanding (Shannon *et al.*, 1995). The fine spectral content was replaced with a given number of noise carrier bands (4, 8, or 24), created from white noise by sixth-order Butterworth filters. The extracted temporal envelope was then used to modulate the corresponding spectral noise bands, resulting in decreased spectral information and preservation of temporal cues.

The frequency content of each stimulus was carefully selected to stay within the NH limits (upper limit of 6000 Hz) measured for each participant. The lowest frequency of all analysis bands (141 Hz, 31 mm from the base, approximately) was selected to approximate those commonly used in modern CI speech processors. Furthermore, the lowest frequency of the analysis band needed to be fairly low in frequency in order that the carrier band could be shifted, and still stay within the participants' NH range. The highest frequency used (5859 Hz, 9 mm from the base, approximately) was selected to be within the normal limits of hearing for all listeners. The division frequencies for the bandpass filters within each condition are listed in Table II according to the analysis or carrier band used in a particular condition. The division frequencies are shown for a 24 channel condition; however, division frequencies for the 8 and 4 channel conditions can be obtained from this table. Every third frequency in Table II corresponds to the division frequencies for the eight channel condition, and every sixth frequency corresponds to the division frequencies for the four channel condition. For example, for the "unshifted vowels and consonants," the division frequencies for an eight channel analysis band were 274, 468, 751, 1166, 1773, 2661, and 3960 Hz, and for a four channel analysis band were 468, 1166, and 2661 Hz. For all shifted conditions, the analysis band was fixed, while the carrier band was shifted to simulate varying insertion depths of the electrode array. The frequency band allocation was determined based on Greenwood's logarithmic function (Greenwood, 1990) for all experimental conditions.

3. Conditions

There was a total of 21 experimental conditions, which are described below and summarized in Table III. All test materials were stored on a computer disk and were output via custom software (TigerSpeech Technologies).

(1) *Vowel recognition (12 choice).* Vowel recognition was assessed using both unprocessed and noise-band vocoded stimuli. For the noise-band vocoded conditions, stimuli were manipulated to contain 4, 8, or 24 spectral bands (range of frequencies: 141–5859 Hz, corresponding to 31–9 mm from the base, respectively). Vowel recognition was also assessed when the analysis and carrier bands were mismatched to create spectral shifts of 3 or 5 mm. In shifted conditions, the analysis band was always fixed at 141–2684 Hz, while the carrier band was manipulated to create 3 mm (range of frequencies: 289–4409 Hz, 28 mm insertion depth) or 5 mm (range of center frequencies: 427–5859 Hz, 26 mm insertion depth) shifts. These two variables (number of channels and spectral shift) were varied systematically to create varying conditions of spectral degradation.

(2) *Consonant recognition (16 choice, full set).* Similar to vowel recognition, consonant recognition was measured using both unprocessed and noise-band vocoded stimuli

TABLE II. Division frequencies (Hz) for bandpass filters for all experimental conditions. Division frequencies are shown for 24 channel conditions; division frequencies for the 8 and 4 channel conditions can also be derived from the table.

Unshifted vowels and consonants																							
Corner frequency	1	2	3	4	5	6	7	8	9	10	11	12	13	14	15	16	17	18	19	20	21	22	23
Analysis (31 mm from base)	180	214	274	330	395	468	550	644	751	872	1010	1166	1343	1545	1773	2032	2327	2661	3040	3471	3960	4514	5144
Carrier (0 mm shift=31 mm from base)	180	214	274	330	395	468	550	644	751	872	1010	1166	1343	1545	1773	2032	2327	2661	3040	3471	3960	4514	5144
Shifted vowels																							
Analysis (31 mm from base)	170	203	239	279	322	370	423	482	547	618	696	783	849	984	1101	1229	1370	1526	1698	1888	2098	2328	2583
Carrier (0 mm shift=31 mm from base)	170	203	239	279	322	370	423	482	547	618	696	783	849	984	1101	1229	1370	1526	1698	1888	2098	2328	2583
Carrier (3 mm shift=28 mm from base)	334	383	437	497	563	636	717	805	903	1011	1130	1261	1406	1566	1742	1936	2150	2386	2646	2933	3250	3599	3984
Carrier (5 mm shift=26 mm from base)	486	551	623	702	789	885	991	1108	1237	1379	1536	1709	1899	2110	2342	2598	2880	3191	3534	3913	4331	4791	5299
Shifted consonants (limited set)																							
Analysis (31 mm from base)	258	427	663	997	1469	2135	3078																
Carrier (2 mm shift=29 mm from base)	458	692	1018	1470	2097	2969	4179																

TABLE III. Parameters for all the experimental conditions.

	Stimuli	Number of channels	Analysis band (Hz)	Carrier band (Hz)	Shift (mm)
Unshifted	12 vowels	Unprocessed, 24, 8, 4	141–5859	141–5859	0
	16 consonants	Unprocessed, 24, 8, 4	141–5859	141–5859	0
Shifted	12 vowels	Unprocessed, 24, 8, 4	141–2864	141–2864	0
		24, 8, 4	141–2864	289–4409	3
		24, 8, 4	141–2864	427–5859	5
	6 consonants	Unprocessed, 8	141–4409	141–4409	0
		8	141–4409	233–5859	2

(4, 8, or 24 channels). The range of frequencies was 141–5859 Hz. No shifted conditions were presented using the full set of consonant stimuli. Instead, a limited set of consonants was used (see below).

(3) *Consonant recognition (6 choice, limited set).* Because many of the participants had a restricted range of sensitivity to the high frequencies, a limited set of stop consonants /b, d, g, p, t, k/ was used to measure the effect of a slight spectral shift. Furthermore, we thought it more efficient to limit the number of consonant conditions and place most of the focus of the current investigation on shifted vowel recognition. These consonants were specifically selected to limit consonants of other classes (fricatives and affricates) containing higher frequency information that, once shifted, would be mostly outside the range of NH for most participants. Although it is true that other classes of consonants (liquids, glides, and nasals) are also lower in frequency content, they exhibit vowel-like characteristics. Selecting these stop consonants enabled a slight (2 mm) shift of the carrier band. Performance was measured using unprocessed stimuli, eight channel noise-band vocoded stimuli (frequencies of analysis and carrier bands: 141–4409 Hz), and eight channel noise-band vocoded stimuli with a 2 mm shift (frequencies: analysis band=141–4409 Hz; carrier band: 233–5859 Hz).

4. Cognitive measures

Verbal memory span, verbal working memory, and speed of processing abilities were measured using standardized tests available from the Wechsler Adult Intelligence Scale (WAIS-III) (Wechsler, 1997). Auditory versions of three memory subtests of the WAIS-III [forward digit span (FDS), backward digit span (BDS), and letter-number sequencing (LNS)] were recorded prior to administration.

The FDS test measures memory span; the listener is presented with a series of digits and asked to repeat the numbers back in the order they were presented. The first presentation consists of two digits (easy); however, the number of digits in each string increases with each presentation if the participant responds correctly. The BDS test is similar; however, the participant is required to repeat back the digits in the opposite order they were presented making it a test of both memory span and working memory abilities. The LNS test is a slightly different working memory task; a series of numbers and letters is presented to the listener in a random order. The listener must first repeat back the digits in numerical order, and then the letters in alphabetical order. Similar to the FDS and BDS tests, the total number of letters and digits for the first presentation is small (three total), but increases if the participant continues to respond correctly. For all three tests, the individual must repeat the entire string in the correct order to receive credit; from these responses, a score is derived for each test. The total possible points for each test are as follows: FDS=16; BDS=14; LNS=21.

The speed of processing tasks included the symbol search (SEARCH) and digit symbol coding (CODE) tests. For the SEARCH task, two sets of symbols are shown on the test paper. The first set consists of two symbols and the second set consists of five symbols. Some symbols differ significantly from one another, whereas others are quite similar. The individual is required to examine the two symbols in the first column; if either of the two symbols matches one of the five symbols shown in the second column then the individual is to circle "Yes." If neither of the two symbols appears in the five comparison symbols, then the individual is instructed to circle "No." The second speed of processing task (CODE) consists of nine symbols, and each is associated with a number (1–9) shown in a key at the top of the page. Below the symbol key are several numbers listed in rows. The individual is required to write the corresponding symbol below each number by using the key at the top of the page. For both tasks, the listener is instructed to perform the test as quickly but as accurately as possible (2 minute time limit). There are 60 possible points for SEARCH and 133 possible points for CODE.

Stimuli for the verbal memory tasks were recorded with a Marantz Professional recorder (PMD660) using a 44 100 Hz sampling rate, then transferred and stored on a computer disk. The recorded materials were edited using ADOBE®AUDITION™ version 1.5. Each test was edited to contain 1 s interstimulus intervals (ISIs), thereby standardizing the timing of presentation across all participants. Edited stimuli were stored on computer disk, and then presented using the same equipment as described below under "Phoneme indentification." Speed of processing was measured using two subtests from the WAIS-III: digit symbol coding and the symbol search task. These written (visual) tests were administered in the standard fashion, requiring each participant to write his/her answers in the booklet provided.

C. Procedure

1. Phoneme identification

All speech recognition testing was conducted in a double-walled sound treated booth. Stimuli were presented at 65 dBA in the free field through a single loudspeaker located at 0° azimuth. All speech stimuli were calibrated to a 65 dB SPL pure tone measured with a sound level meter, using a calibrated spot at the same location as the listener's ear. Calibration was performed through the CAST software, prior to each testing session. The CAST program presented the stimuli in a completely randomized order, within each experimental condition. The stimuli were output through a sound card, passed through a mixer (Rane SM 26B), and amplified (Crown D-75A), before they were presented through a single loudspeaker (Tannoy Reveal).

For vowel recognition measures, one repetition of each of the 12 vowels was produced by two speakers (one female and one male) for a total of 24 tokens (12 vowels $\times 2$ talkers $\times 1$ repetition). For consonant recognition measures, one repetition of each of the 16 consonants was produced by two speakers (one female and one male) for a total of 32 tokens per run (16 consonants $\times 2$ talkers $\times 1$ repetition). The limited set of stop consonants /b, d, g, p, t, k/ was drawn from the original set of 16 consonants. One repetition of each of the six consonants was produced by two speakers (one female and one male) for a total of 12 tokens (6 consonants $\times 2$ talkers $\times 1$ repetition) per run. No carrier phrase was used for either vowel or consonant stimuli.

Participants sat in a comfortable chair, facing a computer monitor. Each speech token was presented twice (1 s ISI), followed by 12 (vowel), 16 (consonant), or 6 (limited consonant) choices displayed on the computer screen in front of them, depending on the given condition. Each token was presented twice because (a) some of the conditions were extremely difficult to understand and (b) it was desirable to minimize contributions of inattentiveness as much as possible. After hearing both stimulus presentations, listeners were asked to select which speech token they thought they heard by selecting one of the choices displayed on the computer monitor in front of them (clicking on the icon using a computer mouse).

For the vowel stimuli, the buttons appeared as follows: HEED, HOD, HAWED, HOED, WHO'D, HAYED, HEARD, HUD, HID, HEAD, HOOD, and HAD. For the consonant stimuli, the buttons appeared as ACA, where "C" was the consonant for each stimulus. The choices appeared in very large black font within large gray squares and always appeared in the same order. All listeners reported that they were able to clearly see each of the choices displayed on the screen. Once the participant completed a selection, the next stimulus was presented through the loudspeaker with a delay of 1.5 s.

The conditions were presented in a randomized order, but each condition was presented five times (block randomized by runs). The task was self-paced, as listeners were not required to respond within a certain period of time. No feedback was provided. Testing was completed in approximately 3–4, 2–2.5 h sessions, with frequent breaks provided at the listener's discretion.

All participants were familiarized with the software, interface, and procedure using unprocessed stimuli prior to administration of the experimental conditions. Each listener performed practice runs with the unprocessed stimuli and heard a sample of a noise-band vocoded phoneme (eight channel, no shifting) before beginning the actual trials; each listener was required to obtain at least a 90% correct performance score on vowel and consonant recognition tasks with unprocessed stimuli prior to continuing in the study.

2. Cognitive measures

Cognitive subtests were always administered following the completion of all phoneme recognition testing, and were either conducted on a separate day or following a 15–20 min break after the completion of the phoneme testing. Similar to the procedure described above, participants were tested in a double-walled sound treated booth and sat in a comfortable chair. Stimuli for the FDS, BDS, and LNS tests were presented through a single loudspeaker and listeners responded using a microphone placed in the sound booth; responses were recorded by the test administrator who sat outside the sound booth. For the speed of processing tasks, listeners were required to write their answers in the test booklet provided. Order of presentation was the same across all listeners (SEARCH, CODE, FDS, BDS, LNS).

III. RESULTS

A. Phoneme identification

Prior to statistical analyses, percent correct scores for phoneme recognition were converted to RAUs to standardize variances across the mean (Studebaker, 1985). The resulting RAU ranges were −0.32 to 113.64 for vowels, −3.31 to 114.87 for consonants (full set), and 8.79–109.94 for consonants (limited set). Performance across all five runs was averaged to obtain a mean RAU within each condition for each participant.

1. Analysis and carrier bands matched (unshifted)

Figures 1 and 2 show the vowel and consonant recognition scores (in RAUs), respectively, across the three groups as a function of number of channels (abscissa). Similar to previous studies (Dorman *et al.*, 1997; Fu *et al.*, 1998), it is apparent that compared to consonant recognition, vowel recognition was more susceptible to spectral degradation, regardless of the age of the listener. Furthermore, performance is slightly dependent on the age of the listener, as phoneme recognition ability tended to decrease as the age of the listener increased. A mixed analysis of variance (ANOVA) with one within-subject factor [number of channels (four levels: unprocessed, 24, 8, 4)] and one between-subject factor (group) was used to analyze both vowel and consonant recognition data. The results for the vowel recognition tasks indicate a significant main effect of number of channels [$F(3,81)=723.8$, $p<0.001$], and a significant main effect of

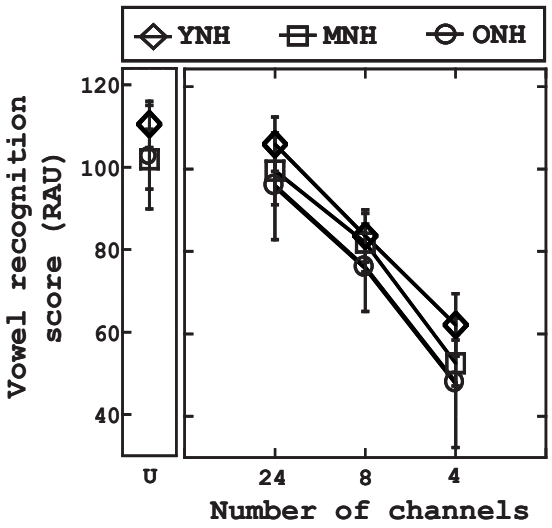


FIG. 1. Vowel recognition (unshifted) as a function of the number of channels for each group; "U" represents data obtained when stimuli were unprocessed. Recognition scores (RAUs) are plotted along the ordinate. Chance performance was 8.3% (6.2 RAUs). Error bars represent ±1 standard deviation from the mean score within each group.

group [$F(2,27)=5.47$, $p<0.05$]. Multiple pairwise comparisons (dependent t-tests with Bonferroni adjustment) were statistically significant ($p<0.001$), suggesting that performance decreased with each decrease in the number of channels (full>24>8>4). *Post hoc* testing (Tukey HSD) suggests that the performance of the YNH was significantly better than that of the ONH group ($p<0.01$); no other comparisons were significant.

Analysis of the consonant recognition data revealed that the assumption of sphericity was violated, so the Greenhouse–Geisser correction was used to interpret results. The results indicate a significant main effect of channels [$F(2.143,57.86)=751.69$, $p<0.001$] and a significant main effect of group [$F(2,27)=10.67$, $p<0.001$]. Similar to the

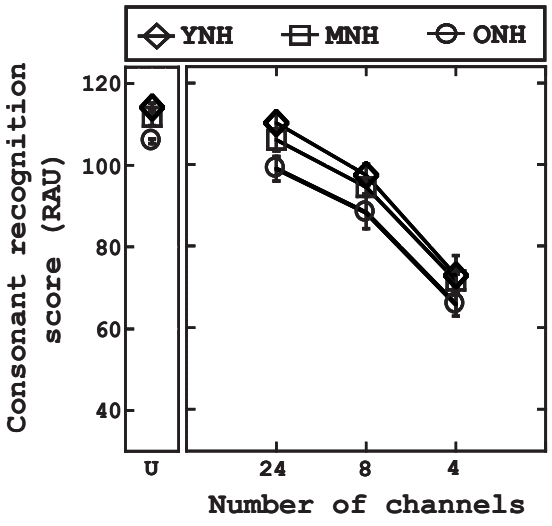


FIG. 2. Consonant recognition (unshifted) as a function of the number of channels for each group; "U" represents data obtained when stimuli were unprocessed. Recognition scores (RAUs) are plotted along the ordinate. Chance performance was 6.2% (2.75 RAUs). Error bars represent ±1 standard deviation from the mean score within each group.

results reported for unshifted vowel recognition, pairwise comparisons using Bonferroni adjustments (dependent t-tests) suggest that consonant recognition performance decreased significantly with each decrease in the number of channels ($p<0.001$). *Post hoc* testing (Tukey HSD) revealed that the performance of the ONH group was significantly worse than that of the YNH and MNH groups ($p<0.05$) at each level of the independent variable (number of channels).

2. Vowel identification with spectral shifting

The results for shifted vowel recognition are shown in Fig. 3. Each panel represents results from each of the age groups. The abscissa indicates the degree of spectral shift (in mm), while the ordinate is the average RAU score. Results with unprocessed stimuli are also shown for reference. Overall, it is apparent that spectral shifting results in further declines in vowel recognition performance across all groups, compared to unshifted performance, which is consistent with previous reports (Fu and Shannon, 1999). Although slight age differences were noted when stimuli were unshifted, the addition of a spectral shift seems to enhance disparities in performance across the age groups, with YNH listeners' performance being far more robust to shifting when compared to the MNH and ONH groups. It is also noted that performance on the unshifted conditions depicted in Fig. 3 is slightly worse than those unshifted conditions shown in Fig. 1. This is likely due to the limited bandwidths used for the shifted vowel conditions (refer to Tables II and III for specific bandwidths used in both cases).

The shifted vowel recognition data were analyzed using a mixed ANOVA with two within-subject factors [number of channels (three levels: 24, 8, or 4) and degree of spectral shift (three levels: 0, 3, or 5 mm)] and one between-subject factor (group). The results suggest a significant three-way interaction between number of channels, degree of shift, and group ($p<0.05$). Follow-up analyses (using pairwise comparisons with Bonferroni adjustments and Tukey HSD, as appropriate) revealed complex interactions between phoneme recognition, spectral shifting, and the age of the listener. These differences are briefly highlighted below.

Pairwise comparisons revealed that the interaction between shift and number of channels depended on the age of the listener; more specifically, each decrease in number of channels caused a significant decline in performance across all three age groups for the 0 and 3 mm shifted conditions ($p<0.0167$). However, when a severe spectral shift was present (5 mm), performance depended on the age of the listener: the performance of the YNH group significantly improved as the number of channels increased from 4 to 8 and from 4 to 24 channels. Performance among the MNH and ONH groups, however, remained stable regardless of the number of channels in the 5 mm shifted condition. Further analysis revealed that the YNH listeners performed significantly better than the MNH or ONH groups in all of the 3 and 5 mm shifted conditions ($p<0.05$). However, for the unshifted conditions, a different pattern emerged with all three groups performing significantly differently than one another in the four channel condition (YNH performing the best and ONH performing the worst). Furthermore, the de-

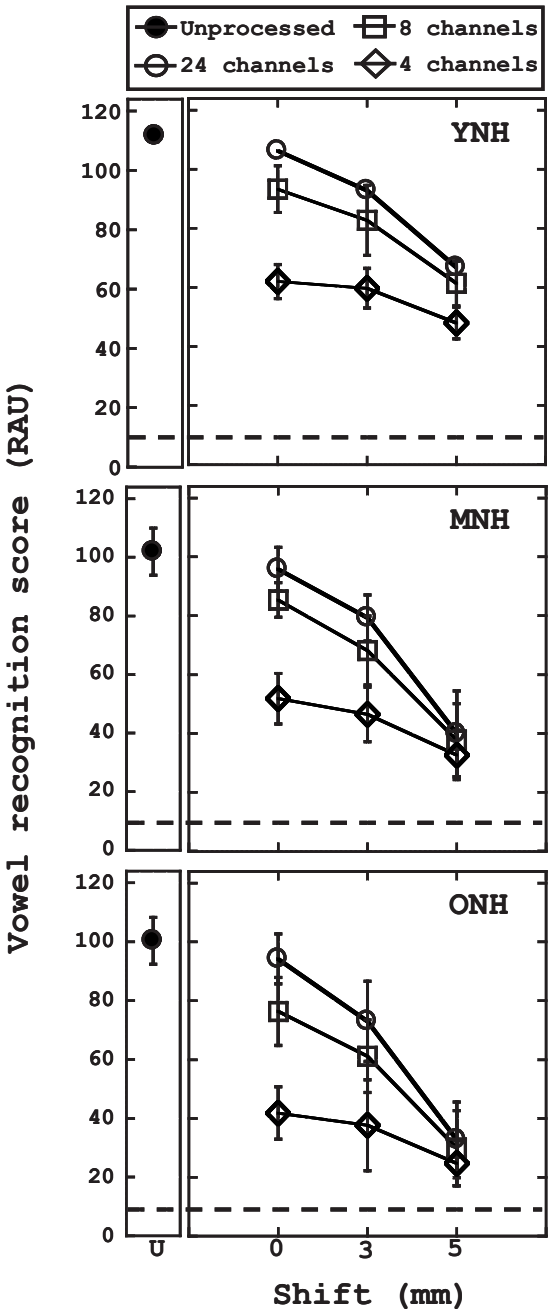


FIG. 3. Vowel recognition (shifted) as a function of the number of channels and degree of spectral shift (in mm). Results for the unprocessed stimuli (U) are also shown for reference. Recognition scores (RAUs) are plotted along the ordinate. Each panel represents results obtained in each age group. The dashed line represents chance performance (8.3%, 6.2 RAUs). Error bars represent ±1 standard deviation from the mean score within each condition.

crease in performance as the stimuli were shifted from 0 to 5 mm (collapsed across the number of channels) is dependent on the age of the listener. That is, the performance of the YNH listeners decreased by an average of 28.51 RAUs as stimuli were shifted from 0 to 5 mm, whereas the performance of MNH and ONH listeners decreased by an average of 40.91 and 41.67 RAUs, respectively. Statistical analysis showed that this average decline in performance was less for the YNH listeners, compared to the other two age groups $[F(2,29)=9.872,\ p<0.05]$.

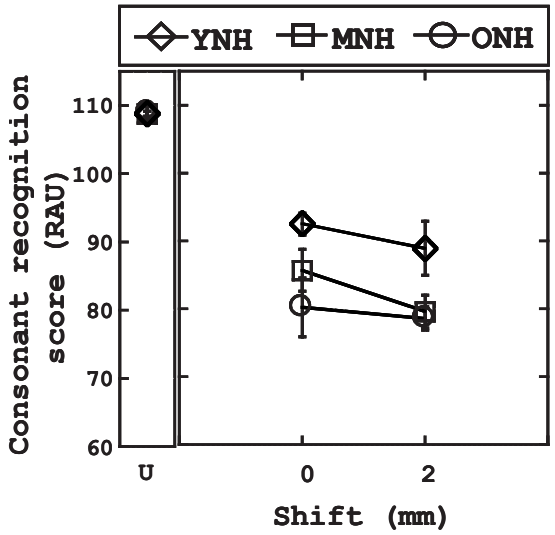


FIG. 4. Stop-consonant recognition (shifted) as a function of the number of channels and degree of spectral shift (in mm). Results for the unprocessed stimuli (U) are also shown as reference. Recognition scores (RAUs) are plotted along the ordinate. Chance performance was 16.7% (19.02 RAUs). Error bars represent ±1 standard deviation from the mean score within each group.

3. Stop-consonant identification, with spectral shifting

Small but significant effects of age were observed in the results obtained with stop consonants. The results of the stop-consonant identification are shown in Fig. 4. The abscissa indicates the degree of spectral shift (in mm), while the ordinate is the average RAU score. Results with unprocessed stimuli are also shown for reference. A mixed ANOVA was conducted with one within-subject factor [shift (two levels: 0, 2 mm)] and one between-subject factor [group (three levels)]. Results revealed a significant main effect of group $[F(2,27)=4.36,\ p<0.05]$. *Post hoc* testing (Tukey HSD) revealed that the performance of the YNH listeners was significantly better than that of the ONH listeners ($p<0.05$). Results also reveal that a significant main effect of shift is present $[F(1,27)=7.52,\ p<0.05]$, as the 2 mm shifted condition resulted in slightly worse performance (82.83 RAUs) than the unshifted condition (85.54 RAUs). The group × shift interaction was not significant ($p<0.05$).

B. Factors related to shifted phoneme recognition performance

Much of the data thus far suggest that the YNH group outperformed both the MNH and ONH groups when listening to spectrally degraded and shifted vowels. However, significant variability in performance was noted across all three groups, particularly among those in the MNH and ONH groups. Furthermore, there were slight age differences on the shifted stop-consonant performance. We used a hierarchical multiple-regression analysis to determine how several factors, including both peripheral and cognitive factors, might explain the additional variance of performance on the shifted phoneme recognition tasks. For example, it was thought that perhaps disparate high-frequency thresholds present between the YNH and older (MNH, ONH) groups or differences in

TABLE IV. Descriptive statistics for all of the possible factors considered for the multiple-regression analyses. Minimum and maximum scores are provided, along with average scores and corresponding standard deviations (SDs). Data are shown within each age group (YNH, MNH, and ONH). Units for each of the variables are listed below the name of each factor in parentheses. For the cognitive measures, both raw scores and z-scores are provided. Averaged shifted phoneme scores are shown in RAUs only.

	YNH		MNH		ONH	
	Min-max	Average (SD)	Min-max	Average (SD)	Min-max	Average (SD)
HFPTA (dB HL)	2.5–10.83	6.24 (2.99)	6.66–22.5	14.74 (4.81)	4.16–20	14.66 (5.31)
AGE (years)	21–25	22.8 (1.68)	41–50	45.9 (2.88)	61–71	65.2 (4.04)
FDS (raw score)	11–16	12.8 (1.68)	9–16	11.8 (1.93)	8–15	11 (2.35)
FDS (z-score)	−0.42–1.98	0.448 (0.81)	−1.38–1.98	−0.02 (0.93)	−1.85–1.50	−0.42 (0.55)
BDS (raw score)	6–13	9.80 (2.34)	6–14	8.5 (2.67)	4–12	7.7 (2.71)
BDS (z-score)	−1.01–1.64	0.428 (0.88)	−1.0–1.63	0.45 (0.89)	−1.76–1.26	−0.36 (1.02)
LNS (raw score)	11–20	14.9 (2.92)	9–17	12.5 (2.63)	8–14	10.7 (2.05)
LNS (z-score)	−0.56–2.40	0.726 (0.96)	−1.22–1.41	−0.06 (0.87)	−1.55–0.42	−0.66 (0.68)
SEARCH (raw score)	35–59	45 (7.94)	23–46	36.6 (7.27)	19–48	31.5 (8.65)
SEARCH (z-score)	−0.27–2.35	0.791 (0.80)	−1.57–0.93	−0.09 (0.79)	−2.0–0.33	−0.7 (0.83)
CODE (raw score)	59–104	91.7 (13.47)	63–94	77.9 (11.48)	42–72	62.9 (8.94)
CODE (z-score)	−1.13–1.62	0.871 (0.83)	−0.09–1.01	0.02 (0.7)	−2.17–0.34	−0.90 (0.55)
AVG MEM (z-score)	−0.66–1.78	0.534 (0.78)	−1.07–1.8	−0.05 (0.76)	−1.34–0.69	−0.48 (−0.8)
AVG SPEED (z-score)	−0.7–1.87	0.82 (0.75)	−1.23–0.97	−0.03 (0.66)	−2.09–0.17	−0.8 (−0.62)
3–5 AVG (RAUs)	52.28–78.79	68.66 (7.75)	36.02–65.98	50.7 (9.6)	30.48–61.52	43.23 (11.22)
2 MM (RAUs)	67.95–104.95	88.94 (11.8)	74.26–87.12	79.48 (4.02)	57.24–102.6	78.57 (11.83)

top-down cognitive processes could have contributed to performance. The possible factors considered were average audiometric high-frequency thresholds from 4000–8000 Hz (HF PTA), age of the listener (AGE), SEARCH score, CODE score, FDS score, BDS score, and LNS score. Raw scores obtained on all cognitive measures were converted to z-scores prior to analysis. The dependent variable for the first two regression analyses was average performance on the 3 and 5 mm shifted vowel recognition (3–5 AVG) task (in RAUs), as individual listener performance in these conditions was highly intercorrelated ($r=0.919$, $p<0.001$). The dependent variable on the last regression analysis was average performance on the 2 mm shifted stop-consonant condition (2 MM). Descriptive statistics (minimum, maximum, and average scores) for all factors are provided in Table IV. Scores are reported within each group, and the corresponding units for each factor are provided below in parentheses. Performances for the cognitive measures are provided in both raw scores and z-scores.

1. Regression analysis for shifted vowel recognition across all groups

Prior to the regression analysis, the possible predictor variables and dependent variable were entered into a correlational analysis to examine multicollinearity between variables. Although several predictors were intercorrelated, none was *highly* intercorrelated ($r>0.90$). The resulting correlation matrix is shown in Table V; all variables were significantly correlated with the dependent variable 3–5 AVG. Because the current study included a limited number of participants, we thought it prudent to reduce the number of predictors entered in the analysis. Therefore, the z-scores for the three measures of verbal memory span and working memory (FDS, BDS, and LNS) were averaged to create a single predictor variable, MEM AVG. Similarly, the z-scores for the two measures of speed of processing (CODE, SEARCH) were averaged to create a single predictor variable, SPEED AVG.

The results of the ANOVA suggest that performance on the shifted vowel recognition task is strongly related to the

TABLE V. Correlations between all possible predictor variables and two dependent variables: 3–5 AVG and 2 MM.

	2 MM	AGE	HF PTA	FDS	BDS	LNS	SEARCH	CODE
3–5 AVG	0.603[a]	−0.776[a]	−0.397[a]	0.536[a]	0.531[a]	0.610[a]	0.666[a]	0.708[a]
2 MM		−0.459[b]	−0.174	0.550[a]	0.312	0.496[a]	0.428[b]	0.263
AGE			0.616[a]	−0.407[b]	−0.349	0.576[a]	0.684[a]	−0.782[a]
HF PTA				−0.214	−0.151	−0.389[b]	−0.401[b]	−0.426[b]
FDS					0.644[a]	0.721[a]	0.413[b]	0.169
BDS						0.482[a]	0.332	0.141
LNS							0.546[a]	0.494[a]
SEARCH								0.778[a]

[a]$p<0.01$.
[b]$p<0.05$.

age of the listener (see Fig. 3). Not surprisingly, a strong correlation is also present between these two variables ($r=-0.776$, $p<0.01$), as shown in Table V. Furthermore, stepwise regression analysis was performed for exploratory purposes and the correlation matrix was examined to determine which variables should be entered into the regression analysis. Based on these observations, it was determined that AGE, MEM AVG, SPEED AVG, and HF PTA should be selected as the four predictors entered into the regression analysis. All analyses suggested that AGE was the most significant factor related to 3–5 AVG, and therefore it was entered into the first block of the hierarchical regression analysis. Next, the factor of HF PTA was entered in the second block, and then the two cognitive measures (MEM AVG and SPEED AVG) were entered in the third and final block. The criterion used for entering a variable into the final model was $p<0.05$.

This regression is shown in Fig. 5, with the predicted values (abscissa) plotted against the observed vowel recognition data (ordinate). Data points are coded by age group.

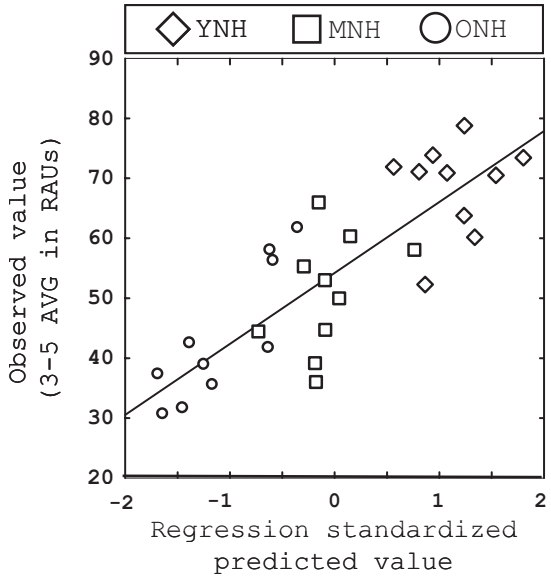


FIG. 5. Linear regression for shifted vowel recognition when all three age groups (YNH, MNH, ONH) were included in the analysis. The observed value (average scores for 3 and 5 mm shifts in RAUs) is plotted against the standardized predicted value for each participant. Data points are coded according to each age group.

As expected, the factor of AGE was a strong predictor of performance ($R^2=0.601$, $p<0.001$), while MEM AVG added slightly but significantly resulting in a final $R^2=0.686$ ($p<0.001$), and the final regression equation:

$$3-5\ \text{AVG} = 75.664 - 0.481(\text{AGE}) + 5.617(\text{MEM AVG}). \quad (1)$$

These results suggest that while the age of the listener is an important factor in predicting performance when listening to noise-band vocoded vowels, verbal memory capacity also contributes, albeit to a smaller extent. Speed of processing (SPEED AVG) and high-frequency hearing sensitivity (HF PTA) were not significant predictors of performance.

2. Regression analysis for shifted vowel recognition within middle-aged and older groups

Visual inspection of the results obtained with shifted vowels (Fig. 3) shows that while the YNH group undoubtedly performed better than the MNH and ONH groups, performance across the two latter groups was more comparable. Furthermore, significant variability was noted within each age group as some ONH listeners performed exceptionally well, and some MNH listeners performed exceptionally poorly, suggesting that age may not be the main factor influencing performance within these two groups. It was of interest, therefore, to examine the influence of other factors in more details among these two older groups as a possible source to explain the variance in performance.

The same predictor variables mentioned previously were tested for multicollinarity and significance. Results from the two groups (MNH and ONH) are shown in Table VI and indicated that all of the predictor variables were significant predictors of 3–5 AVG with the exception of HF PTA. Cognitive measures were somewhat interrelated but not highly correlated with one another. Therefore, similar to the previous regression analysis, the combined variables of MEM AVG and SPEED AVG were considered for entry into the analysis. Preliminary stepwise multiple-regression analyses were performed, along with examination of the correlational matrix, to determine which variables should be entered into the final analysis and to determine the order in which each variables should be entered into the hierarchical regression analysis. Based on these results, it was determined that the

TABLE VI. Identical to Table V, but within MNH and ONH groups alone.

	AGE	HF PTA	FDS	BDS	LNS	SEARCH	CODE
3–5 AVG	−0.472[a]	0.170	0.536[b]	0.519[a]	0.493[a]	0.628[b]	0.558[a]
AGE		0.019	−0.292	−0.224	−0.394	−0.582[b]	−0.718[b]
HF PTA			0.111	0.083	−0.007	−0.039	0.007
FDS				0.651[b]	0.667[b]	0.411	0.027
BDS					0.246	0.188	−0.127
LNS						0.400	0.363
SEARCH							0.638[b]

[a]$p<0.05$.
[b]$p<0.01$.

cognitive factors (MEM AVG and SPEED AVG) were better predictors of performance than the factor of AGE. Therefore, in the hierarchical analysis, we entered MEM AVG and SPEED AVG into the first block, followed by AGE in the second block. The criterion used for entering a variable into the final model was $F<0.05$.

The regression line is shown in Fig. 6 with the predicted values (abscissa) plotted against the observed vowel recognition data (ordinate). Data points are coded by age group. The resulting multiple-regression analyses revealed that MEM AVG accounted for a moderate portion of the variance ($R^2=0.434$, $p<0.01$), while a second variable (SPEED AVG) also added slightly but significantly (change in $R^2=0.246$, $p<0.01$) to the final regression model. The factor of AGE did not significantly contribute to the model ($t=0.873$, $p>0.05$) above and beyond the variance already accounted for by the cognitive factors, and therefore was not included in the final model. The final regression model accounted for a significant proportion of the variance noted among the MNH and ONH participants ($R^2=0.680$, $p<0.01$). The final regression equation was

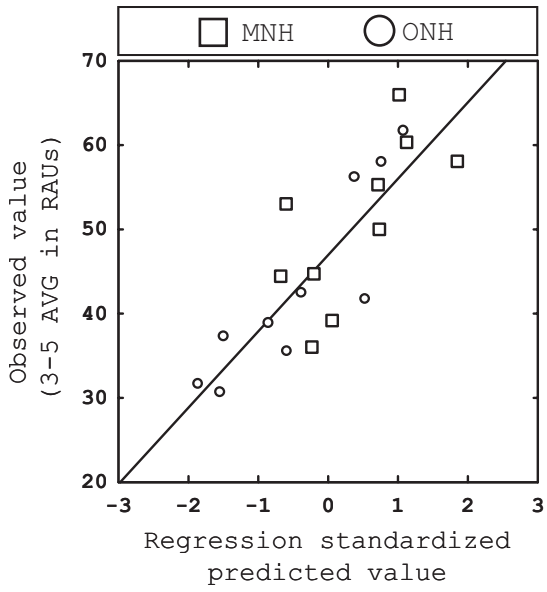


FIG. 6. Linear regression for shifted vowel recognition when only the MNH and ONH groups were included in the analysis. The observed value (average scores for 3 and 5 mm shifts in RAUs) is plotted against the standardized predicted value for each participant. Data points are coded according to each age group.

$$3-5\ \text{AVG} = 52.036 + 7.135(\text{MEM AVG}) + 7.601(\text{SPEED AVG}). \quad (2)$$

These results suggest that when a regression analysis is performed within the MNH and ONH groups only, cognitive factors (MEM AVG and SPEED AVG) account for the most variance among performance on 3–5 AVG. In contrast with the first regression analysis (all groups), AGE was not the foremost factor related to shifted vowel recognition. Furthermore, SPEED AVG was significantly related to performance within the MNH and ONH groups; this is also in contrast with the first regression analysis including all three age groups.

3. Regression analysis for shifted stop-consonant recognition across all three groups

Similar to the previous analyses, a third regression analysis was performed to assess the factors that influence shifted stop-consonant performance (2 MM). Examination of the correlation matrix (see Table V) and exploratory stepwise regression analyses showed that MEM AVG was the strongest predictor of performance, and therefore was entered into the first block of the hierarchical regression analysis. The factor of AGE was entered into the second block, and SPEED AVG was entered into the third block. It should be noted that HF PTA was not a significant predictor of performance (2 MM) and therefore was not entered into the regression analysis. The criterion used for entering a variable into the final model was $F<0.05$.

Results are displayed in Fig. 7 and show that MEM AVG accounted for a small but significant portion of the variance ($R^2=0.276$, $p<0.05$) on shifted stop-consonant recognition performance (2 MM). Both of the remaining factors (SPEED AVG and AGE) failed to make significant contributions to the model. The final model was

$$2\ \text{MM} = 82.331 + 6.518(\text{MEM AVG}). \quad (3)$$

Although the results of all regression analyses appear to be meaningful, they should be interpreted with considerable caution due to the limited number of participants (20 or 30) and total number of variables (3 or 4) entered into the equation. Nonetheless, these results would suggest that cognitive abilities play a role in the immediate perception of spectrally

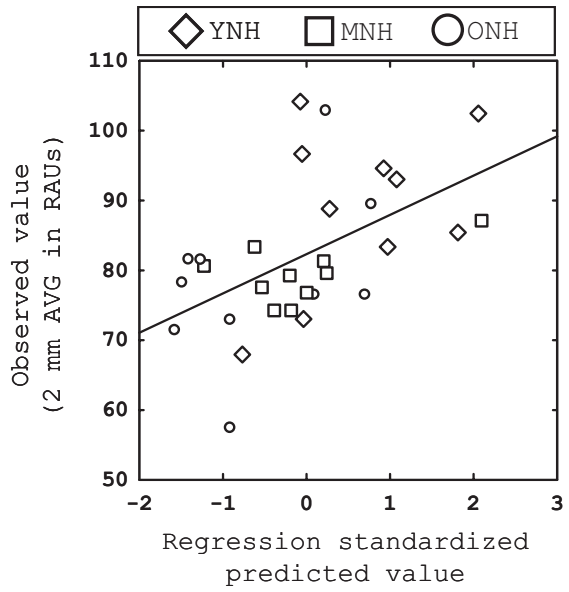


FIG. 7. Linear regression for shifted stop consonants when all three age groups (YNH, MNH, ONH) were included in the analysis. The observed value (average scores for the 2 mm shifted condition in RAUs) is plotted against the standardized predicted value for each participant. Data points are coded according to each age group.

degraded vowels among adult listeners and help to explain the additional variance noted among scores, which cannot be accounted for by age alone.

IV. DISCUSSION

A. Summary of results and comparison with previous investigations

It is obvious that spectral degradation of phonemes results in poor recognition among adult listeners of various ages. In many aspects, results from the current investigation are similar to those reported previously. For example, the recognition of consonants is generally more robust to spectral distortion compared to that of vowels (Dorman *et al.*, 1997; Baskent and Shannon, 2003), and this pattern persisted in the current investigation regardless of the age of the listener. Previous findings among adult listeners have shown a consistent relationship between spectral degradation and phoneme recognition performance, as performance tends to decline steadily as the number of channels decreases or as the frequency-to-place mismatch increases (Fishman *et al.*, 1997; Fu and Shannon, 1999; Friesen *et al.*, 2001; Baskent and Shannon, 2003). However, many of the previous studies measuring this relationship did not control for any contributions of age. Based on the findings of Souza and colleagues (Souza and Kitch, 2001; Souze and Boike, 2006) as well as those reported by Sheldon *et al.* (2008), one would expect that some differences would be present between the performance of younger and older adult listeners when they are required to listen through a limited number of spectral channels and when feedback is not provided. Similar results were also evident in the current investigation. In addition, significant differences in performance were present across the three age groups when a spectral shift was added to mimic the limited CI insertion depth. A lack of a significant group × channel interaction for both the unshifted vowel and consonant stimuli suggests that overall performance was worse for the ONH group compared to the YNH group, and that this relationship was not dependent on the number of channels. This finding is apparent from examining the data shown in Fig. 1 and 2. Although significant age differences are present as the spectral resolution is decreased, similar age differences are also present in the unprocessed condition. Therefore, all age groups appear to be equally robust to spectral distortion when performing vowel and consonant recognition tasks, at least when stimuli are *not* spectrally shifted. Adding a spectral shift creates further distortion and exposes differential performance across the three age groups.

These findings differ from those reported by Peelle and Wingfield (2005), who reported little or no age-related differences when they presented spectrally degraded and compressed sentences to younger and older adults. Although the reason for this is not completely clear, it is likely that the choice of stimuli (sentences) provided more contextual cues compared to the phoneme stimuli used in the current study. Contextual cues are used by older listeners to derive meaning and improve perception of the stimulus, as several studies report improvements in speech understanding among older adults when highly contextual stimuli are presented, compared to lower contextual stimuli (Pichora-Fuller *et al.*, 1995; Gordon-Salant and Fitzgibbons, 1997). Furthermore, the methodology used by Peelle and Wingfield (2005), who applied an apical shift to their stimuli, was not intended to closely mimic that of CI processing which results in a basal, not apical, shift. Studies have shown that sentence and phoneme recognition are negatively, but unequally, affected by compressive, expansive, and ordinary shifted spectral distortion (Baskent and Shannon, 2003; 2004; 2005). For these reasons, differences in methodology and stimuli make any direct comparisons between the current study and Pellee and Wingfield (2005) rather difficult.

The severe reduction in spectral resolution inherent to noise-band vocoded stimuli requires participants to rely more on temporal cues within the signal comparable to what is required of CI users. Temporal deficits have been reported among middle-aged individuals, and are pervasive among older NH and HI listeners; it is possible that underlying temporal processing deficits contributed to the decreased performance among the MNH and ONH listeners in the current study. However, further investigation is needed as this hypothesis cannot be confirmed based on our results.

B. Estimating performance with cochlear-implants

The results of the current study suggest that a spectral shift of 3 or 5 mm can affect vowel recognition performance of middle-aged and older listeners, more so than that of younger listeners. Imaging studies demonstrate that the insertion depth of the electrode array can range anywhere from 14–25 mm (approximately), with an average insertion depth of 20 mm (Ketten *et al.*, 1998; Skinner *et al.*, 2002). Applying Greenwood's equation (Greenwood, 1990), the most apical electrode would be at a place in the cochlea primed to receive anything from a 3000 Hz signal (14 mm insertion

depth) to a 500 Hz signal (25 mm insertion depth), with an average insertion depth of 1000 Hz (20 mm). Modern CI processors filter the incoming speech signal using a set of bandpass filters, the lowest of which typically has a frequency of 200–300 Hz. This means that even with optimal placement (25 mm insertion depth), the incoming 300 Hz signal is being processed at a place in the cochlea that is primed to receive 500 Hz information resulting in at least a 3 mm shift or nearly an octave. It is likely that CI users are listening through eight to ten spectral channels, at best (Fishman *et al.*, 1997; Friesen *et al.*, 2001). By applying these parameters to the results of the current investigation, it is hypothesized that even under optimal circumstances the age of the adult listener will have an effect on immediate vowel recognition performance. The data presented in Fig. 3 show that with eight channels of information and a 3 mm shift, disparities are present across the three age groups: the average performances of the three groups are 82.67, 68.22, and 61.20 RAUs for YNH, MNH and ONH, respectively. The disparities between the groups' performance become larger as spectral distortion is increased (number of channels decreased, spectral shift increased) and, in particular, the performance of the YNH group was more robust to spectral distortion compared to the MNH and ONH listeners.

C. Regression analyses and associations with cognitive measures

Results from the first regression analysis (all groups) suggest that age accounts for most of the variance noted among the shifted vowel recognition performance (R^2 =0.601), while average memory score (MEM AVG) only adds slightly (change in R^2=0.085) to the final regression model (R^2=0.686). Conversely, when shifted vowel data are analyzed within the MNH and ONH groups only, the factors of memory (MEM AVG) and speed of processing (SPEED AVG) seem to be better predictors of performance than AGE alone. Analysis of the stop-consonant data showed that performance across all three groups was best predicted by memory function (MEM AVG). From a cognitive perspective, it could be inferred that individuals listening through a CI are subject to increased cognitive load, as they are required to derive meaningful speech from a severely degraded stimulus. Cognitive theory supports the notion that such a task would become more difficult as the age of the listener increases (Sweller, 1988; 1994; Van Gerven *et al.*, 2002). In fact, recent studies have shown that cognitive abilities of adult CI listeners influence postimplantation speech recognition performance (Lyxell *et al.*, 1996; Heydebrand *et al.*, 2007). Heydebrand *et al.* (2007) reported that preimplant measures of verbal working memory and learning were significant predictors of speech recognition abilities obtained at six month postactivation in adult CI listeners aged 24–60. Similarly, a wealth of research focusing on pediatric CI listeners provides support that cognitive abilities play an important role in postimplantation speech and language performance (Eisenberg *et al.*, 2000; Pisoni and Geers, 2000; Cleary *et al.*, 2001; Geers, 2003; Geers *et al.*, 2003; Pisoni and Cleary, 2003). The current study does contrast with previous studies on one main point: past investigations have tied verbal memory (working memory in particular) capacity to actual *speech* or discourse comprehension (ie: sentences); it is commonly believed that phoneme recognition is not as reliant on memory capacities (see Pichora-Fuller, 2003 for review). It is proposed, however, that when phonemes are severely degraded (as in the current study), a different pattern likely emerges. A severely degraded phoneme lacks both acoustic and contextual cues and therefore requires significant top-down processing in order that it be correctly identified. Therefore, this type of task might be more related to cognitive abilities compared to one in which phonemic stimuli are undistorted. Furthermore, a different pattern could be evident when severely degraded, highly contextual sentences are used as stimuli; however this hypothesis would require additional investigation.

Results from the regression analyses should be interpreted with caution due to the limited number of participants in the current study and the limited upper age range of the older participants. It could be argued that the partial cognitive test battery used in the current study is also a limiting factor, as memory and speed of processing abilities may not be the best, or only cognitive measures related to performance. Our hypothesis was that chronological age was not the *only* contributing factor when understanding severely spectrally degraded phonemes, and it seemed logical that higher order top-down processes would also play a role. However, it remains unknown how to best capture such top-down processing abilities. We chose to measure abilities in two well-known cognitive domains (memory and speed of processing) in an attempt to assess general cognitive abilities among our listeners; the fact that we did find significant relationships between such cognitive abilities and perceptual measures does not suggest direct causation. Furthermore, we are not proposing that performance on these diverse tasks (shifted vowel recognition, memory abilities, and speed of processing abilities) are necessarily determined by the same underlying cause [("common cause hypothesis") Lindenberger and Baltes, 1994]. Rather, the strong correlation observed in our results simply lends support to the notion that cognitive function is predictive of speech recognition by middle-aged and older listeners in adverse conditions.

It is believed that measures of working memory capture some fundamental ability central to several measures of cognition, including fluid intelligence and language abilities (Conway *et al.*, 2002; Kemper *et al.*, 2003) making it a valid and compelling measure. Although the current study did not investigate performance among actual CI users, the results from the current study are in agreement with previous studies that report significant relationships between working memory ability and outcomes with cochlear implantation. The contribution of speed of processing on the ability to comprehend spectrally degraded vowels is less clear, as this measure is theoretically associated with tasks measuring speed of execution or ability to comprehend rapid speech (Salthouse, 1996, 2000). Nonetheless, speed of processing ability did account for some of the variances noted among performance and is therefore noteworthy; further investigation is needed to validate such findings.

D. Potential interactions between aging, training and aural rehabilitation

Outcomes of the current investigation reflect the immediate untrained performance of a limited number of individuals. Emerging literature strongly conveys the importance of training and adaptation when listening to spectrally degraded stimuli, as most CI listeners (and those NH individuals listening to noise-band vocoded stimuli) are able to adapt extremely well over time (Rosen *et al.*, 1999; Svirksy *et al.*, 2004; Fu *et al.*, 2002; 2005; see Fu and Galvin, 2007 for review). Furthermore, the age effects found in the current study using phonemic stimuli do not necessarily reflect or predict performance in real-world environments, in which highly contextual conversations dominate the listener's everyday experience. Nonetheless, the results from the current study do suggest that age might influence perception of spectrally degraded stimuli.

Although rehabilitation is commonly mandated for pediatric cochlear implantees, rehabilitation of the adult CI recipient is not a standard practice as most users are able to adapt adequately without structured rehabilitation services. Results from Fu and Galvin (2007) would suggest that even adequate CI users can improve their performance when provided with aural rehabilitation. Further evidence suggests that older listeners receive comparable benefit when trained on difficult speech recognition tasks, when compared to their younger counterparts (Peelle and Wingfield, 2005; Burk *et al.*, 2006; Golomb *et al.*, 2007); this implies that CI recipients of all ages might be capable of improving their performance with structured rehabilitation. The results of the current investigation imply that older listeners are at a significant deficit for accurately recognizing CI processed speech. An aural rehabilitation program may be particularly beneficial to older adult CI users.

V. CONCLUSIONS

(1) The age of the adult listener influences the immediate perception of spectrally degraded phonemes. In particular, performance of the YNH group exceeded that of the MNH and ONH listeners. In this study, the largest effect was seen on vowel recognition tasks that were processed to include a limited number of spectral bands and to simulate a frequency-to-place mismatch. Conversely, performance among the MNH and ONH listeners was quite comparable, with ONH listeners performing only slightly worse than those listeners in the MNH group.

(2) Results from the hierarchical multiple-regression analysis suggest that chronological age is the primary predictor of shifted vowel recognition performance when data are analyzed across all three age groups (YNH, MNH, and ONH). Verbal memory abilities also contribute slightly, but significantly, to performance. Conversely, the regression analysis within the MNH and ONH groups alone suggest that cognitive abilities are a better predictor of performance than chronological age.

(3) It appears that the immediate perception of spectrally degraded phonemes among adult listeners is related to both chronological age and cognitive factors; however, the degree to which each variable exerts influence on performance is dependent on the age of the listener. Performance among the YNH listeners was fairly independent of cognitive abilities, whereas performance among the MNH and ONH listeners was significantly related to cognitive abilities.

(4) The results from this study have important clinical implications regarding the rehabilitation and counseling of adult CI recipients. Further research is warranted to examine how chronological age and cognitive abilities influence adaptation to spectrally degraded and shifted speech over an extended period of time. Furthermore, future research should focus on an in-depth analysis of the relationship between various cognitive measures and understanding severely spectrally degraded stimuli to better understand the interaction between bottom-up and top-down processes on this type of task.

ACKNOWLEDGEMENTS

We would like to thank the participants for their time and willingness to contribute to this study. We are grateful to Dr. Qian-Jie Fu for the use of the software used for the phoneme recognition task and to John J. Galvin III for his helpful insight when designing this project. We thank two anonymous reviewers and the Associate Editor for their comments on an earlier version of the manuscript. This work was funded by NIDCD Grant No. R01-DC004786 to M.C. K.C.S. was supported in part by training Grant No. T32-DC00046 from NIDCD.

[1]Two ONH participants did not fit these criteria used to assess normal middle-ear function. ONH-3 had negative middle ear pressure that fell just outside normal limits (−105 daPa, left ear). Acoustic reflex thresholds could not be measured in ONH-10 because a hermetic seal could not be maintained. Click-evoked transient otoacoustic emissions were present and robust across both ears in these two subjects, suggesting a lack of significant middle ear pathology.

ANSI (**2004**). "American National Standard Specification for Audiometers," ANSI S3.6-2004 (American National Standards Institute, New York).

Baskent, D., and Shannon, R. V. (**2005**). "Interactions between cochlear implant electrode insertion depth and frequency-place mapping," J. Acoust. Soc. Am. **117**, 1405–1416.

Baskent, D., and Shannon, R. V. (**2004**). "Frequency-place compression and expansion in cochlear implant listeners," J. Acoust. Soc. Am. **116**, 3130–3140.

Baskent, D., and Shannon, R. V. (**2003**). "Speech recognition under conditions of frequency-place compression and expansion," J. Acoust. Soc. Am. **113**, 2064–2076.

Blamey, P., Arndt, P., Bergeron, F., Bredberg, G., Brimacombe, J., Facer, G., Larky, J., Lindstrom, B., Nedzelski, J., Peterson, A., Shipp, D., Staller, S., and Whitford, L. (**1996**). "Factors affecting auditory performance of postlinguistically deaf adults using cochlear implants," Audiol. Neuro-Otol. **1**, 293–306.

Bodmer, D., Shipp, D. B., Ostroff, J. M., Ng, A. H. C., Stewart, S., Chen, J. M., and Nedzelski, J. M. (**2007**). "A comparison of postcochlear implantation speech scores in an adult population," Laryngoscope **117**, 1408–1411.

Burk, M. H., Humes, L. E., Amos, N. E., and Stauser, L. E. (**2006**). "Effect of training on word-recognition performance in noise for young normal-hearing and older-hearing mipaired listeners," Ear Hear. **27**, 263–278.

Clark, G. (**2003**). *Cochlear Implants: Fundamentals and Applications* (Springer-Verlag, New York).

Cleary, M., Pisoni, D. B., and Geers, A. E. (**2001**). "Some measures of verbal and spatial working memory in eight-and nine-year-old hearing-impaired children with cochlear implants," Ear Hear. **22**, 395–411.

Conway, A. R. A., Cowan, N., Buting, M. F., Therriault, D. J., and Minkoff,

S. R. B. (**2002**). "A latent variable analysis of working memory capacity, short-term memory capacity, processing speed, and general fluid intelligence," Intelligence **30**, 163–183.
Dorman, M. F., Loizou, P. C., Fitzke, J., and Tu, Z. (**1998**). "The recognition of sentences in noise by normal-hearing listeners using simulations of cochlear-implant signal processors with 6–20 channels," J. Acoust. Soc. Am. **104**, 3583–3585.
Dorman, M. F., Loizou, P. C., and Rainey, D. (**1997**). "Speech intelligibility as a function of the number of channels of stimulation for signal processors using sine-wave and noise-band outputs," J. Acoust. Soc. Am. **102**, 2403–2411.
Dorman, M., Dankowski, K., McCandless, G., Parkin, J. L., and Smith, L. (**1990**). "Longitudinal changes in word recognition by patients who use the ineraid cochlear implant," Ear Hear. **11**, 455–459.
Dorman, M., Hannley, M., Dankowski, K., Smith, L., and McCandless, G. (**1989**). "Word recognition by 50 patients fitted with the Symbion multichannel cochlear implant," Ear Hear. **10**, 44–49.
Dubno, J. R., Horwitz, A. R., and Ahlstrom, J. B. (**2002**). "Benefit of modulated maskers for speech recognition by younger and older adults with normal hearing," J. Acoust. Soc. Am. **111**, 2897–2907.
Eisenberg, L. S., Shannon, R. V., Martinez, A. S., Wygonski, J., and Boothroyd, A. (**2000**). "Speech recognition with reduced spectral cues as a function of age," J. Acoust. Soc. Am. **107**, 2704–2710.
Facer, G. W., Peterson, A. M., and Brey, R. H. (**1995**). "Cochlear implantation in the senior citizen age group using the Nucleus 22-channel device," Ann. Otol. Rhinol. Laryngol. Suppl. **166**, 187–190.
Fishman, K. E., Shannon, R. V., and Slattery, W. H. (**1997**). "Speech recognition as a function of the number of electrodes used in the SPEAK cochlear implant speech processor," J. Speech Lang. Hear. Res. **40**, 1201–1215.
Fitzgibbons, P. G., Gordon-Salant, S., and Barrett, J. (**2007**). "Age-related differences in discrimination of an interval separating onsets of successive tone bursts as a function of interval duration," J. Acoust. Soc. Am. **122**, 458–466.
Fitzgibbons, P. J., and Gordon-Salant, S. (**2004**). "Age effects on discrimination of timing in auditory sequences," J. Acoust. Soc. Am. **116**, 1126–1134.
Fitzgibbons, P. J., and Gordon-Salant, S. (**2001**). "Aging and temporal discrimination in auditory sequences," J. Acoust. Soc. Am. **109**, 2955–2963.
Folstein, M., Folstein, S., and McHugh, P. (**1975**). "Mini-mental state: A practical method for grading the cognitive state of patients for the clinician," J. Psychiatr. Res. **12**, 189–198.
Friesen, L. M., Shannon, R. V., Baskent, D., and Wang, X. (**2001**). "Speech recognition in noise as the number of spectral channels: Comparison of acoustic hearing and cochlear implants," J. Acoust. Soc. Am. **110**, 1150–1163.
Fu, Q.-J., and Galvin, J. J. (**2007**). "Perceptual learning and auditory training in cochlear implant recipients," Trends Amplif. **11**, 195–205.
Fu, Q.-J., Nogaki, G., and Galvin, J. J. (**2005**). "Auditory training with spectrally shifted speech: Implications for cochlear implant patient auditory rehabilitation," J. Assoc. Res. Otolaryngol. **180**, 180–190.
Fu, Q.-J., Shannon, R. V., and Galvin, J. J. (**2002**). "Perceptual learning following changes in the frequency-to electrode assignment with the Nucleus-22 cochlear implant," J. Acoust. Soc. Am. **112**, 1664–1674.
Fu, Q.-J., and Shannon, R. V. (**1999**). "Recognition of spectrally degraded and frequency-shifted vowels in acoustic and electric hearing," J. Acoust. Soc. Am. **105**, 1889–1900.
Fu, Q.-J., Shannon, R. V., and Wang, X. (**1998**). "Effects of noise and spectral resolution on vowel and consonant recognition: Acoustic and electric hearing," J. Acoust. Soc. Am. **104**, 3586–3596.
Gantz, B. J., Woodworth, G. G., Knutson, J. F., Abbas, P. J., and Tyler, R. S. (**1993**). "Multivariate predictors of audiological success with multichannel cochlear implants," Ann. Otol. Rhinol. Laryngol. **102**, 909–916.
Geers, A. E. (**2003**). "Predictors of reading skill development in children with early cochlear implantation," Ear Hear. **24**, 59S–68S.
Geers, A. E., Nicholas, J. G., and Sedey, A. L. (**2003**). "Language skills of children with early cochlear implantation," Ear Hear. **24**, 46S–58S.
Gelfand, S. A., Schwander, T., and Silman, S. (**1990**). "Acoustic reflex thresholds in normal hearing and cochlear impaired ears: Effects of no-response rates on 90th percentiles in a large sample," J. Speech Hear Disord. **55**, 198–205.
Golomb, J. D., Peelle, J. E., and Wingfield, A. (**2007**). "Effects of stimulus variability and adult aging on adaptation to time-compressed speech," J. Acoust. Soc. Am. **121**, 1701–1708.
Gordon-Salant, S., and Fitzgibbons, P. J. (**2004**). "Effects of stimulus and noise rate variability on speech perception by younger and older adults," J. Acoust. Soc. Am. **115**, 1808–1817.
Gordon-Salant, S., and Fitzgibbons, P. J. (**1997**). "Selected cognitive factors and speech recognition performance among young and elderly listeners," J. Speech Lang. Hear. Res. **40**, 423–431.
Gordon-Salant, S., and Fitzgibbons, P. J. (**1993**). "Temporal factors and speech recognition performance in young and elderly listeners," J. Speech Hear. Res. **36**, 1276–1285.
Green, K. M., Bhatt, Y. M., Mawman, D. J., O'Driscoll, M. P., Saeed, S. R., Ramsden, R. T., and Green, M. W. (**2007**). "Predictors of audiological outcome following cochlear implantation in adults," Cochlear Implants Int. **8**, 1–11.
Greenwood, D. D. (**1990**). "A cochlear frequency-position function for several species—29 years later," J. Acoust. Soc. Am. **87**, 2592–2605.
Grose, J. H., Hall, J. W., and Buss, E. (**2006**). "Temporal processing deficits in the presenescent auditory system," J. Acoust. Soc. Am. **119**, 2305–2315.
Grose, J. H., Hall, J. W., III, and Buss, E. (**2001**). "Gap duration discrimination in listeners with cochlear hearing loss: Effects of gap and marker duration, frequency separation, and mode of presentation," J. Assoc. Res. Otolaryngol. **2**, 388–398.
Heydebrand, G., Hale, S., Potts, L., Gotter, B., and Skinner, M. (**2007**). "Cognitive predictors of improvements in adults' spoken word recognition six months after cochlear implant activation," Audiol. Neuro-Otol. **12**, 254–264.
Kelsall, D. C., Shallop, J. K., and Burnelli, T. (**1995**). "Cochlear implantation in the elderly," Am. J. Otol. **16**, 609–615.
Kemper, S., Herman, R. E., and Lian, C. H. (**2003**). "The costs of doing two things at once for young and older adults: Talking while walking, finger tapping, and ignoring speech or noise," Psychol. Aging **18**, 181–192.
Ketten, D. R., Skinner, M. W., Wang, G., Vannier, M. W., Gates, G. A., and Neely, J. G. (**1998**). "In vivo measures of cochlear length and insertion depth of nucleus cochlear implant electrode arrays," Ann. Otol. Rhinol. Laryngol. Suppl. **175**, 1–16.
Leung, J., Wang, N. Y., Yeagle, J. D., Chinnici, J., Bowditch, S., Francis, H. W., and Niparko, J. K. (**2005**). "Predictive models for cochlear implantation in elderly candidates," Arch. Otolaryngol. Head Neck Surg. **131**, 1049–1054.
Lindenberger, U., and Baltes, P. B. (**1994**). "Sensory functioning and intelligence in old age: Astrong connection," Psychol. Aging **9**, 339–355.
Lister, J., Besing, J., and Koehnke, J. (**2002**). "Effects of age and frequency disparity on gap discrimination," J. Acoust. Soc. Am. **111**, 2793–2800.
Lyxell, B., Andersson, J., Arlinger, S., Bredberg, G., Harder, H., and Ronnberg, J. (**1996**). "Verbal information-processing capabilities and cochlear implants: implications for preoperative predictors of speech understanding," J. Deaf Stud. Deaf Educ. **1**, 190–201.
Nie, K., Barco, A., and Zeng, F.-G. (**2006**). "Spectral and temporal cues in cochlear implant speech perception," Ear Hear. **27**, 208–217.
Niparko, J. (**2004**). "Cochlear implants: Clinical applications," in *Cochlear Implants: Auditory Prostheses and Electric Hearing*, edited by F.-G. Zeng, A. N. Popper, and R. Fay (Spring-Verlag, New York), pp. 53–100.
Ostroff, J. M., McDonald, K. L., Schneider, B. A., and Alain, C. (**2003**). "Aging and the processing of sound duration in human auditory cortex," Hear. Res. **181**, 1–7.
Parkin, J. L., Stewart, B. E., Dankowski, K., and Haas, L. J. (**1989**). "Prognosticating speech performance in multichannel cochlear implant patients," Otolaryngol.-Head Neck Surg. **101**, 314–319.
Pasanisi, E., Bacciu, A., Vincenti, V., Guida, M., Barbot, A., Berghenti, M. T., and Bacciu, S. (**2003**). "Speech recognition in elderly cochlear implant recipients," Clin. Otolaryngol. **28**, 154–157.
Peelle, J. E., and Wingfield, A. (**2005**). "Dissociations in perceptual learning revealed by adult age differences in adaptation to time-compressed speech," J. Exp. Psychol. Hum. Percept. Perform. **31**, 1315–1330.
Pichora-Fuller, M. K. (**2003**). "Cognitive aging and auditory information processing," Int. J. Audiol. **42**, 2S26–2S32.
Pichora-Fuller, M. K., Schneider, B. A., and Daneman, M. (**1995**). "How young and old adults listen to and remember speech in noise," J. Acoust. Soc. Am. **97**, 593–608.
Pisoni, D. B., and Cleary, M. (**2003**). "Measures of working memory span and verbal rehearsal speed in deaf children after cochlear implantation," Ear Hear. **24**, 106S–120S.
Pisoni, D. B., and Geers, A. B. (**2000**). "Working memory in deaf children with cochlear implants: Correlations between digit span and measures of spoken language processing," Ann. Otol. Rhinol. Laryngol. Suppl. **185**,

92–93.
Rosen, S., Faulkner, A., and Wilson, L. (**1999**). "Adaptation by normal listeners to upward spectral shifts of speech: Implications for cochlear implants," J. Acoust. Soc. Am. **106**, 3629–3636.
Roup, C. M., Wiley, T. L., Safady, S. H., and Stoppenbach, D. T. (**1998**). "Tympanometric screening norms for adults," Am J Audiol **7**, 1–5.
Rubinstein, J. T., Parkinson, W. S., Tyler, R. S., and Gantz, B. J. (**1999**). "Residual speech recognition and cochlear implant performance: Effects of implantation criteria," Am. J. Otol. **20**, 445–452.
Salthouse, T. A. (**2000**). "Aging and measures of processing speed," Biol. Psychol. **54**, 35–54.
Salthouse, T. A. (**1996**). "The processing-speed theory of adult age differences in cognition," Psychol. Rev. **103**, 403–428.
Schroeder, M. R. (**1968**). "Reference signal for signal quality studies," J. Acoust. Soc. Am. **44**, 1735–1736.
Shannon, R. V., Feng, F.-G., and Wygonski, J. (**1998**). "Speech recognition with altered spectral distribution of envelope cues," J. Acoust. Soc. Am. **104**, 2467–2476.
Shannon, R. V., Zeng, F. G., Kamath, V., Wygonski, J., and Ekelid, M. (**1995**). "Speech recognition with primarily temporal cues," Science **270**, 303–304.
Sheldon, S., Pichora-Fuller, M. K., and Schneider, B. A. (**2008**). "Effects of age, presentation method, and learning on identification of noise-vocoded words," J. Acoust. Soc. Am. **123**, 476–488.
Shin, Y. J., Fraysse, B., Dequine, O., Vales, O., Laborde, M. L., Bouccara, D., Sterkers, O., and Uziel, A. (**2000**). "Benefits of cochlear implantation in elderly patients," Otolaryngol.-Head Neck Surg. **122**, 602–606.
Skinner, M. W., Ketten, D. R., Holden, L. K., Harding, G. W., Smith, P. G., Gates, G. A., Neely, J. G., Kletzker, G. R., Brunsden, B., and Blocker, B. (**2002**). "CT-derived estimation of cochlear morphology and electrode array position in relation to word recognition in Nucleus-22 recipients," J. Assoc. Res. Otolaryngol. **3**, 332–350.
Snell, K. B., and Frisina, D. R. (**2000**). "Relationships among age-related differences in gap detection and word recognition," J. Acoust. Soc. Am. **107**, 1615–1626.
Souza, P. E., and Boike, K. T. (**2006**). "Combining temporal-envelope cues across channels: Effects of age and hearing loss," J. Speech Lang. Hear. Res. **49**, 138–149.
Souza, P. E., and Kitch, V. (**2001**). "The contribution of amplitude envelope cues to sentence identification in young and aged listeners," Ear Hear. **22**, 112–119.
Sterkers, O., Mosnier, I., Ambert-Dahan, E., Herelle-Dupuy, E., Bozorg-Grayeli, A., and Bouccara, D. (**2004**). "Cochlear implants in elderly people: Preliminary results," Acta Oto-Laryngol., Suppl., 64–67.
Studebaker, G. A. (**1985**). "A 'rationalized' arcsine transform," J. Speech Hear. Res. **28**, 455–462.
Svirsky, M. A., Silveira, A., Neuburger, H., Teoh, S.-W., and Suarez, H. (**2004**). "Long-term auditory adaptation to a modified peripheral frequency map," Acta Oto-Laryngol. **124**, 381–386.
Sweller, J. (**1994**). "Cognitive load theory, learning difficulty, and instructional design," Learn. Instr. **4**, 295–312.
Sweller, J. (**1988**). "Cognitive load during problem solving: Effects on learning," Cogn. Sci. **12**, 257–285.
Van Gerven, P. W. M., Paas, F. G. W. C., Van Merrienboer, J. J. G., and Schmidt, H. G. (**2002**). "Cognitive load theory and aging: Effects of worked examples on training efficiency," Learn. Instr. **12**, 87–105.
Verhaeghen, P., and Salthouse, T. A. (**1997**). "Meta-Analyses of Age-Cognition relations in adulthood: Estimates of linear and nonlinear age effects of structural models," Psychol. Bull. **122**, 231–249.
Vermeire, K., Brokx, J. P., Wuyts, F. L., Cochet, E., Hofkens, A., and Van de Heyning, P. H. (**2005**). "Quality of life benefit from cochlear implantation in the elderly," Otol. Neurotol. **26**, 188–195.
Wechsler, D. (**1997**). *Wechsler Adult Intelligence Scale (WAIS-3®)*, 3rd ed. (Harcourt Assessment, San Antonio TX).
Wingfield, A., and Tun, P. (**2007**). "Cognitive supports and cognitive constraints on comprehension of spoken language," J. Am. Acad. Audiol **18**, 548–558.
Xu, L., Thompson, C. S., and Pfingst, B. E. (**2005**). "Relative contributions of spectral and temporal cues for phoneme recognition," J. Acoust. Soc. Am. **117**, 3255–3267.

Analysis and prediction of acoustic speech features from mel-frequency cepstral coefficients in distributed speech recognition architectures

Jonathan Darch and Ben Milner[a)]
School of Computing Sciences, University of East Anglia, Norwich NR4 7TJ, United Kingdom

Saeed Vaseghi
Department of Electronic and Computer Engineering, Brunel University, Uxbridge UB8 3PH, United Kingdom

(Received 19 December 2007; revised 5 September 2008; accepted 10 September 2008)

The aim of this work is to develop methods that enable acoustic speech features to be predicted from mel-frequency cepstral coefficient (MFCC) vectors as may be encountered in distributed speech recognition architectures. The work begins with a detailed analysis of the multiple correlation between acoustic speech features and MFCC vectors. This confirms the existence of correlation, which is found to be higher when measured within specific phonemes rather than globally across all speech sounds. The correlation analysis leads to the development of a statistical method of predicting acoustic speech features from MFCC vectors that utilizes a network of hidden Markov models (HMMs) to localize prediction to specific phonemes. Within each HMM, the joint density of acoustic features and MFCC vectors is modeled and used to make a maximum *a posteriori* prediction. Experimental results are presented across a range of conditions, such as with speaker-dependent, gender-dependent, and gender-independent constraints, and these show that acoustic speech features can be predicted from MFCC vectors with good accuracy. A comparison is also made against an alternative scheme that substitutes the higher-order MFCCs with acoustic features for transmission. This delivers accurate acoustic features but at the expense of a significant reduction in speech recognition accuracy. © *2008 Acoustical Society of America.*
[DOI: 10.1121/1.2997436]

PACS number(s): 43.72.Ar [DOS] Pages: 3989–4000

I. INTRODUCTION

Acoustic speech features, namely, formants, fundamental frequency, and voicing, are traditionally estimated from time-domain waveforms of speech or some other representation that is derived from the time domain. For example, effective methods of fundamental frequency estimation apply autocorrelation analysis, frequency-domain analysis, or cepstral analysis to extract candidates that can be tracked and smoothed using dynamic programing.[1] Similarly, formant frequencies can be estimated from pole positions obtained from linear predictive analysis or from spectral peaks, followed by tracking, using, for example, Kalman filtering.[2]

In recent years, distributed speech recognition (DSR) architectures have been developed as a robust method for achieving accurate speech recognition over mobile and IP networks.[3] However, within a DSR architecture, no time-domain waveform is sent to the remote back-end. Instead, only a stream of mel-frequency cepstral coefficient (MFCC) vectors is received, which prohibits the use of conventional methods of acoustic feature estimation. In many situations, it is desirable to have acoustic features available at the remote back-end. An example is to enable a speech signal to be reconstructed at the back-end from the received MFCC vectors, as may be required in cases of legal dispute of potential speech recognition errors. The MFCC vectors themselves can be inverted to provide spectral envelope information, but to facilitate speech reconstruction, source information such as voicing and fundamental frequency are also required. One solution has been to explicitly estimate and transmit voicing and fundamental frequency from the terminal device to the remote back-end.[3] While this provides the necessary information, it creates considerable overheads both in terminal-side processing and in additional bit-rate requirements. For example, the ETSI Aurora standard uses 800 bits/s to represent voicing and fundamental frequency. An alternative approach is to predict voicing and fundamental frequency from the received MFCC vectors themselves.[4,5] This has been achieved by modeling the joint density of MFCC vectors and the fundamental frequency to enable a maximum *a posteriori* (MAP) prediction of fundamental frequency from a MFCC vector. This has been applied first to a constrained connected digit vocabulary[4] and then to unconstrained free speech.[5] Using a similar probabilistic framework, formant frequencies have also been successfully predicted from MFCC vectors.[6]

The work presented in this paper extends the previous work in four ways. First, instead of predicting fundamental frequency/voicing and formant frequencies separately, an acoustic feature vector is defined, which comprises fundamental frequency and formant frequencies together with voicing and speech/nonspeech information.[7] This allows a simultaneous prediction of the set of acoustic features from a

[a)]Electronic mail: b.milner@uea.ac.uk

MFCC vector and is achieved by defining three speech classes (voiced, unvoiced, and nonspeech). Second, a comprehensive analysis of the correlation between acoustic features and MFCC vectors is made. This examines the effect on the acoustic feature to MFCC vector correlation when applying constraints such as measuring correlation within individual speakers (speaker dependent), within gender types (gender dependent), and across all speakers (gender independent). Restrictions into the speech class are also made, which consider correlation either globally across all speech sounds or within individual phoneme classes. Third, a detailed analysis into the accuracy of acoustic feature prediction is made. This examines prediction accuracy under speaker-dependent, gender-dependent, and gender-independent constraints and allows conclusions to be drawn into the effect that a high acoustic feature to MFCC vector correlation has on prediction accuracy. Finally, a comparison of the proposed method is made against a scheme that replaces higher-order MFCCs in the transmitted feature vector by acoustic features (estimated on the terminal device). The acoustic features are compressed using the same method as the MFCCs, and the effect of this on acoustic feature estimation is measured, together with the effect on recognition accuracy of losing higher-order MFCCs.

The remainder of this paper is organized as follows. Section II presents a detailed study into the correlation between acoustic features and MFCC vectors. Section III defines the acoustic feature vector and describes two methods of predicting acoustic features from MFCC vectors using either phoneme-specific or global MAP methods. Experimental results are presented in Sec. IV, which examines the accuracy of acoustic feature prediction from MFCC vectors under constraints of speaker independence, gender dependence, and gender independence. Finally, Sec. V examines the effect of replacing higher-order MFCCs by acoustic features on both acoustic feature estimation and speech recognition performance.

II. ANALYSIS OF CORRELATIONS BETWEEN ACOUSTIC SPEECH FEATURES AND MFCC VECTORS

This section examines the correlation between acoustic speech features and MFCC vectors. This is motivated by the need to establish the existence and level of correlation before developing a system to predict acoustic speech features from MFCC vectors. The first part of this section explains how the acoustic feature to MFCC vector correlation is measured, while the latter parts analyze the correlation. Various constraints are made in the analysis, such as measuring correlation globally or phoneme-specifically and applying speaker and gender constraints.

A. Measuring the acoustic speech feature to MFCC vector correlation

A correlation analysis is performed by first defining an acoustic speech feature vector, $\boldsymbol{f}_i$, which comprises the fundamental frequency, $f0$, and the frequencies of the first four formants, F1, F2, F3, and F4, at time frame i,

$$\boldsymbol{f}_i = [f0, \mathrm{F1}, \mathrm{F2}, \mathrm{F3}, \mathrm{F4}]. \tag{1}$$

For voiced speech, multiple correlations are measured between each element of the acoustic feature vector and the MFCC vector. For unvoiced speech, multiple correlations are only calculated between formant frequencies and MFCC vectors.

The multiple correlation between each acoustic speech feature and the MFCC vector is measured using multiple linear regression.[8] A linear model is computed to describe the relationship between MFCC vectors (independent variables) and acoustic speech feature vectors (dependent variables). Each acoustic feature at frame i, $f_i(j)$, is represented in terms of the ith MFCC vector, $\boldsymbol{x}_i = [x_i(1), x_i(2), \ldots, x_i(M)]$, using a set of $M+1$ regression coefficients, $[\beta_{0,j}, \ldots, \beta_{m,j}, \ldots, \beta_{M,j}]$, which are specific to the jth acoustic feature,[7]

$$f_i(j) = \beta_{0,j} + \beta_{1,j} x_i(1) + \beta_{2,j} x_i(2) + \cdots + \beta_{M,j} x_i(M) + \varepsilon,$$

$$0 \leqslant i \leqslant I-1, \quad 1 \leqslant j \leqslant 4 \quad \text{for unvoiced speech},$$

$$0 \leqslant i \leqslant I-1, \quad 0 \leqslant j \leqslant 4 \quad \text{for voiced speech}, \tag{2}$$

where ε is an error term, I is the number of MFCC vectors, and M is the dimensionality of the MFCC vector. In matrix notation, Eq. (2) can be written as

$$\boldsymbol{F} = \boldsymbol{X_1}\boldsymbol{\beta} + \boldsymbol{\varepsilon}. \tag{3}$$

$\boldsymbol{F}$ is a matrix of acoustic vectors, $\boldsymbol{F} = [\boldsymbol{f}_0, \boldsymbol{f}_1, \ldots, \boldsymbol{f}_{I-1}]^T$. $\boldsymbol{X_1} = [\mathbf{1}_I, \boldsymbol{X}]$, where matrix $\boldsymbol{X} = [\boldsymbol{x}_0, \boldsymbol{x}_1, \ldots, \boldsymbol{x}_{I-1}]^T$ and $\mathbf{1}_I$ is a vector of ones of length I. $\boldsymbol{\beta}$ is a matrix of regression coefficients and $\boldsymbol{\varepsilon}$ is a matrix of acoustic feature errors.

From a set of training data, least squares estimation can provide an estimate of the regression coefficients, $\hat{\boldsymbol{\beta}}$,

$$\hat{\boldsymbol{\beta}} = (\boldsymbol{X_1}^T \boldsymbol{X_1})^{-1} \boldsymbol{X_1}^T \boldsymbol{F}. \tag{4}$$

This enables a prediction of an acoustic feature vector, $\hat{\boldsymbol{f}}_i$, from a MFCC vector, $\boldsymbol{x}_i$,

$$\hat{\boldsymbol{f}}_i = \boldsymbol{x}_i \hat{\boldsymbol{\beta}}. \tag{5}$$

The multiple correlation, R, between the jth acoustic feature, $f(j)$, and the MFCC vector is determined from the R^2 term, which is defined as

$$R(j)^2 = 1 - \frac{\Sigma_i \{f_i(j) - \hat{f}_i(j)\}^2}{\Sigma_i \{f_i(j) - \bar{f}(j)\}^2} = \frac{\Sigma_i \{\hat{f}_i(j) - \bar{f}_i(j)\}^2}{\Sigma_i \{f_i(j) - \bar{f}(j)\}^2}, \tag{6}$$

where $\bar{f}(j)$ is the mean of the jth acoustic feature.

B. Correlation analysis

The correlations between acoustic features and MFCC vectors are measured on the test set of the VTRFormants database[9]—see Sec. IV for specific details. MFCC vectors are computed as specified in the ETSI DSR front-end,[3] resulting in a stream of 14-dimensional MFCC vectors at a rate of 100 vectors/s.

Two methods of calculating multiple correlations are considered: global, $R^G(j)$, and phoneme specific, $R^P(j)$. The global multiple correlation between each acoustic speech

TABLE I. Multiple correlations between acoustic features and MFCC vectors for male and female speaker-dependent speech, calculated globally and by phoneme for unvoiced and voiced speech.

Gender	Method	Voicing	F1	F2	F3	F4	*f*0
Male	Global	Unvoiced	0.5095	0.6688	0.5730	0.4655	⋯
		Voiced	0.7520	0.8685	0.8128	0.5781	0.4874
	Phoneme specific	Unvoiced	0.7349	0.7994	0.7615	0.7375	⋯
		Voiced	0.9017	0.9335	0.9238	0.8895	0.8728
Female	Global	Unvoiced	0.5172	0.5752	0.4869	0.3772	⋯
		Voiced	0.7741	0.8369	0.7844	0.5366	0.7469
	Phoneme specific	Unvoiced	0.7495	0.7720	0.7545	0.7287	⋯
		Voiced	0.9010	0.9140	0.8946	0.8615	0.9184

feature and MFCC vector is measured by pooling features together from all speech sounds and applying Eq. (6). Phoneme-specific correlations are measured by first segmenting the data into phoneme classes using reference annotations. Within each phoneme class, Eq. (6) is used to measure the multiple correlation between each acoustic feature and MFCC vector. A weighted averaged is then computed to give the mean phoneme-specific multiple correlation,

$$R^P(j) = \frac{1}{N_G} \sum_{w=1}^{W} N_w R^w(j), \tag{7}$$

where N_w is the number of vectors corresponding to phoneme w and $R^w(j)$ is the multiple correlation between the jth acoustic feature and the MFCC vector for the wth phoneme. W represents the total number of phonemes, and N_G is the total number of vectors.

Further in the two methods of measuring correlation, three scenarios are considered, which allows the effect of speaker and gender on correlations to be examined. The three scenarios are described in order of decreasing dependence on gender and speaker,

(1) Speaker dependent: Multiple correlations are calculated for each speaker separately. This scenario is also inherently gender dependent.
(2) Gender dependent: Multiple correlations are calculated first from all male speech and then from all female speech.
(3) Gender independent: All speech is used to compute the regression coefficients in Eq. (4). Multiple correlations are then measured separately for male and female speech to enable gender comparison.

Note that both the gender-dependent and gender-independent scenarios are also speaker independent as more than one speaker is used. Besides being listed by gender and method of calculating correlation (global or phoneme specific), correlation results are also calculated separately for voiced and unvoiced speech.

1. Speaker-dependent correlations

The global and phoneme-specific multiple correlations of formant frequencies (F1–F4) and fundamental frequency to MFCC vectors are shown in Table I. The correlation measures are broken down into male and female speech and unvoiced and voiced speech.

The results show that multiple correlations between acoustic features and MFCC vectors are consistently higher when calculated within individual phonemes rather than globally over all speech. This is to be expected since restricting multiple regression to model correlations from a small cluster of related sounds with similar formant structures and fundamental frequencies is more likely to produce higher correlation than generalizing across all speech sounds.

The high correlations between formant frequencies and MFCC vectors, especially for lower formants, in comparison to the lower correlation between fundamental frequency and MFCC vectors are attributed to the shape and spacing of the mel filter bank used in the MFCC extraction process. The filter bank processing retains sufficient spectral envelope information to indicate formant positions but lacks much of the finer spectral structure that conveys fundamental frequency information.[6] The nonuniform distribution of the mel filter banks means that while the lowest frequency channels provide a relatively high spectral resolution (the two lowest filter bank channels are 62 Hz apart), higher frequency channels have lower resolutions so F4 is less accurately represented (the two highest channels are 312 Hz apart). In addition, the frequency of F4 is often above the 4 kHz bandwidth of the speech, although the presence of such formants will still affect the spectrum below 4 kHz.

The level of the fundamental frequency to MFCC vector correlation was larger than expected as MFCC vectors have traditionally been considered to remove source information. However, the close spacing of lower frequency filter bank channels does allow some of the low frequency harmonic source information to be retained. In addition, the correlation between the fundamental frequency and F1, observed by Syrdal and Steele,[10] also contributes to the fundamental frequency to MFCC vector correlation. A significant increase in the fundamental frequency to MFCC vector correlation is observed when comparing the global to phoneme-specific measurements. This indicates that fundamental frequency is influenced by phoneme, an observation that has also been reported by Hirahara.[11]

The correlation between formant frequencies and MFCC vectors is always greater during voiced, rather than unvoiced, speech. This result is consistent with traditional formant estimation methods, which are more accurate for

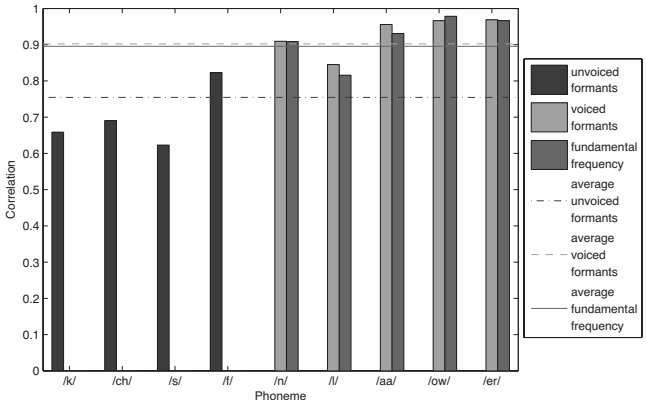


FIG. 1. Phoneme-specific correlations between acoustic features and MFCC vectors for nine example phonemes.

voiced speech. The spectral structure is better defined during voiced speech due to the high energy present at the harmonics of the fundamental frequency. For the noiselike structure of unvoiced speech, formants are less well defined; formant bandwidths are broader and amplitudes are usually lower.

Correlations between formant frequencies and MFCC vectors are generally higher for male speakers compared with female speakers. This is consistent with traditional signal processing methods of formant estimation, which also perform less well on female speech due to the wider spacing of fundamental frequency harmonics, which makes the precise localization of formant frequencies more difficult. For fundamental frequency, higher correlations are observed for female speech. This may be due to the higher frequencies associated with female speech, the harmonics of which span a wider range of mel filter bank channels than for male speech, making the identification of female fundamental frequency more accurate.

The acoustic feature to MFCC vector correlation was found to vary considerably across different phonemes. For example, Fig. 1 shows phoneme-specific correlations for nine voiced and unvoiced phonemes. For voiced phonemes, both fundamental frequency and mean formant frequency correlations (averaged across all four formants) are shown, while for unvoiced phonemes only the mean formant frequency correlation is shown. Also shown are the weighted mean phoneme-specific correlations, calculated over all phonemes, using Eq. (7), for fundamental frequency and voiced and unvoiced formant frequencies.

The bar chart shows that unvoiced phonemes have significantly lower formant frequency to MFCC vector correlation than voiced phonemes. This is confirmed by the lines showing mean formant frequency correlations, which for unvoiced phonemes is 0.76 in comparison to 0.91 for voiced phonemes. The higher correlation for voiced phonemes is attributed to a better spectral representation of formants that voiced excitation can provide through its harmonic structure and greater energy. Within the voiced phonemes, vowels exhibit higher levels of correlation than the semivowel /l/ and nasal /n/. For voiced phonemes, the level of the fundamental frequency to MFCC correlation follows closely that of the formant frequency correlation.

2. Gender-dependent correlations

The gender-dependent correlation of acoustic features to MFCC vectors is shown in Table II. These measurements were made by pooling data from all male speakers and all female speakers before applying multiple linear regression, thereby making the correlation analysis speaker independent as well. Comparing Tables I and II shows, without exception, that acoustic feature to MFCC vector correlations fall when moving from a speaker-dependent to a gender-dependent analysis.

The largest decreases in correlation are for phoneme-specific formant frequencies and fundamental frequency. For the gender-dependent and speaker-independent correlations shown in Table II, there is less difference in correlation when calculated globally or across individual phonemes. This is due to the increased variability as correlations are considered across all male speakers and across all female speakers, rather than for each speaker separately. There are instances where correlations are lower when calculated by phoneme rather than globally. The correlations between F1 and MFCC vectors for male speech provide such an example.

In Table II the largest increases in correlation when comparing global and phoneme-specific correlations occur for the fundamental frequency and F4. Compared with the cor-

TABLE II. Multiple correlations between acoustic features and MFCC vectors for male and female gender-dependent but speaker-independent speech, calculated globally and by phoneme for unvoiced and voiced speech.

Gender	Method	Voicing	F1	F2	F3	F4	$f0$
Male	Global	Unvoiced	0.4578	0.6148	0.4954	0.3621	⋯
		Voiced	0.7185	0.8137	0.7389	0.4515	0.3984
	Phoneme specific	Unvoiced	0.4543	0.6231	0.5472	0.4328	⋯
		Voiced	0.7012	0.7959	0.7631	0.6001	0.5754
Female	Global	Unvoiced	0.4812	0.5326	0.4266	0.2332	⋯
		Voiced	0.7554	0.8057	0.7384	0.3853	0.7267
	Phoneme specific	Unvoiced	0.5127	0.5792	0.4966	0.4134	⋯
		Voiced	0.7645	0.7959	0.7455	0.5889	0.8122

TABLE III. Multiple correlations between acoustic features and MFCCs for male and female gender-dependent and speaker-independent speech, calculated globally and by phoneme for unvoiced and voiced speech.

Gender	Method	Voicing	F1	F2	F3	F4	*f*0
Male	Global	Unvoiced	0.4554	0.6037	0.4804	0.3240	⋯
		Voiced	0.7055	0.7862	0.6999	0.3500	0.1815
	Phoneme specific	Unvoiced	0.4314	0.5887	0.4997	0.3839	⋯
		Voiced	0.6661	0.7442	0.6966	0.4848	0.3532
Female	Global	Unvoiced	0.4724	0.4798	0.3894	0.0363	⋯
		Voiced	0.7293	0.7663	0.6537	0.2031	0.6154
	Phoneme specific	Unvoiced	0.4195	0.4636	0.3417	0.1792	⋯
		Voiced	0.7025	0.7235	0.6160	0.3707	0.6265

relations in Table I, gender has less effect on formant frequency correlations for the gender-dependent correlations in Table II.

3. Gender-independent correlations

Table III shows multiple correlations between acoustic speech features and MFCCs calculated using data that are gender independent and speaker independent. Data from all speakers were pooled to create a single set of gender-independent/speaker-independent regression coefficients. Phoneme-specific and global correlations for voiced and unvoiced speech were then calculated. The correlations are given for male and female speakers separately despite the regression coefficients used to estimate the acoustic speech features calculated from male and female speech pooled together. This enables comparisons with speaker-dependent and gender-dependent correlations shown in Tables I and II.

Comparing the gender-independent correlations in Table III to the gender-dependent correlations in Table II shows that correlations between acoustic speech features and MFCCs are always lower when calculated using gender-independent data because of the increased variation. The results also show higher formant correlation with voiced speech rather than unvoiced speech, and this is attributed to the better spectral representation of voiced speech.

The gender-independent correlations in Table III are, in general, slightly lower when calculated within phonemes rather than globally, expect for fundamental frequency and F4. For the speaker-dependent and gender-dependent correlations shown in Tables I and II, respectively, phoneme-specific correlations are usually greater than those calculated globally across all speech, as expected.

4. Summary

In this section multiple correlations between acoustic speech features and MFCC vectors have been measured in three scenarios to allow speaker-dependent, gender-dependent, and gender-independent analyses. The scenarios use the same data, but correlations are calculated over subsets of the data to vary constraints on speaker and gender. Figure 2 summarizes the observations by showing the multiple correlations between the fundamental frequency and MFCC vectors in Fig. 2(a) and the mean multiple correlations between formant frequencies and MFCC vectors in Fig. 2(b). The correlations are shown for the three scenarios introduced in Sec. II B but are averaged over male and female speech, and formant frequency correlations are averaged over all four formants.

For all conditions in Fig. 2, a higher acoustic feature to MFCC vector correlation is observed when measured within specific phonemes rather than globally across all speech. For formant frequencies, a higher multiple correlation with MFCC vectors occurs for voiced speech rather than unvoiced speech. The acoustic feature to MFCC vector multiple correlation peaks with speaker-dependent constraints and reduces with gender-dependent analysis, reaching its lowest values with gender-independent analysis due to the increased variability.

III. PREDICTING ACOUSTIC SPEECH FEATURES FROM MFCC VECTORS

The correlation analysis in Sec. II suggests that sufficient information is retained during feature extraction to en-

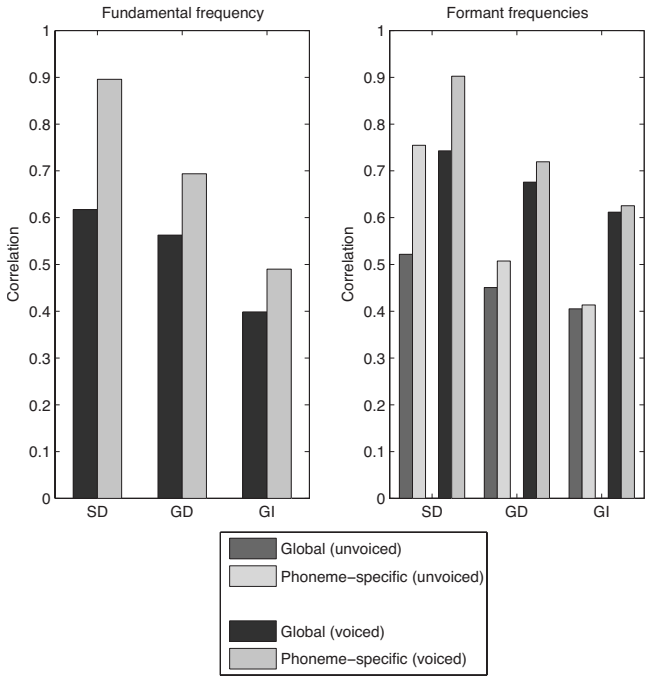


FIG. 2. Global and phoneme-specific correlations between MFCC vectors and (a) fundamental frequency and (b) formant frequencies for male and female speakers using speaker-dependent, gender-dependent, and gender-independent data.

able fundamental and formant frequencies to be predicted from MFCC vectors. This section describes a MAP technique to utilize these correlations to predict acoustic features from MFCC vectors by employing statistical models of the joint density of acoustic features and MFCC vectors. Note that the term "prediction" is used to distinguish this statistical technique from signal processing methods of estimating acoustic speech features.

The analysis in the previous section showed that a higher acoustic feature to MFCC vector correlation is obtained when measured within specific phonemes rather than measured globally across all speech sounds. It is therefore expected that prediction will be more accurate using models of the joint density of acoustic features and MFCC vectors specific to individual phonemes rather than models that generalize all speech sounds together. To localize the modeling of the joint density of acoustic features and MFCC vectors to individual phonemes, a network of hidden Markov models (HMMs) is employed. Within each state of each HMM, the joint density of acoustic features and MFCC vectors is modeled by three Gaussian mixture models (GMMs), which represent voiced, unvoiced, and nonspeech audio. This "HMM-GMM" prediction of acoustic features from MFCC vectors comprises two parts: training of the HMM-GMMs and then prediction of acoustic features from a stream of MFCC vectors using the models.

A. Phoneme-specific modeling of acoustic speech features and MFCC vectors

Phoneme-specific modeling of the joint density of acoustic features and MFCC vectors involves three stages of training. First, a set of phoneme HMMs is trained. Second, vector pools are created for each state of each phoneme model for voiced, unvoiced, and nonspeech vectors. Finally, from the vector pools, voiced, unvoiced, and nonspeech GMMs are trained to model the phoneme and state-specific joint density of acoustic features and MFCC vectors.

1. HMM training

Training begins by creating of a set of $W+1$ MFCC-based HMMs, which model the W phonemes in the database and also nonspeech. Left-right HMMs are used and comprise $S=3$ states with $H=8$ modes per state with diagonal covariance matrices. Phonemes are chosen as the speech class as they allow unconstrained speech to be processed when arranged in an unconstrained phoneme grammar.

2. Phoneme-specific vector pools

Sets of vector pools for voiced speech, $\Omega^{v}_{s,w}$, unvoiced speech, $\Omega^{u}_{s,w}$, and nonspeech, $\Omega^{\mathrm{ns}}_{s,w}$, within each state s of each phoneme model w can now be created. This is achieved by first force aligning each training data utterance to the correct sequence of phoneme HMMs (using reference annotation labels) using VITERBI decoding.[12] This provides, for each training utterance, $\boldsymbol{X}=[\boldsymbol{x}_1,\boldsymbol{x}_2,\ldots,\boldsymbol{x}_N]$ comprising N MFCC vectors, phoneme model allocations, $\boldsymbol{m}=[m_1,m_2,\ldots,m_N]$, and state allocations, $\boldsymbol{q}=[q_1,q_2,\ldots,q_N]$, where q_i and m_i are the state and model associated with the ith MFCC vector, $\boldsymbol{x}_i$.

The MFCC vectors, $\boldsymbol{x}_i$, can be joined with their corresponding acoustic feature vectors, $\boldsymbol{f}_i$, to create joint feature vectors, $\boldsymbol{y}_i$, defined as

$$\boldsymbol{y}_i=[\boldsymbol{x}_i,\boldsymbol{f}_i]^T. \tag{8}$$

Voicing class information is contained within the joint feature vector through $\boldsymbol{f}_i$. In nonspeech the elements of $\boldsymbol{f}_i$ are all zero. For unvoiced speech F1–F4 contain nonzero values, but the fundamental frequency is zero. For voiced speech all elements of $\boldsymbol{f}_i$ are nonzero. Reference voicing classifications are provided by the ETSI extended front-end (XFE).[3]

Voiced augmented feature vectors, $\boldsymbol{y}_i$, associated with each state s and phoneme model w are pooled to form state and model dependent subsets of voiced feature vectors, $\Omega^{v}_{s,w}$, from the complete set of training data feature vectors, Z,

$$\Omega^{v}_{s,w}=\{\boldsymbol{y}_i\in Z:\ \mathrm{voicing}(\boldsymbol{y}_i)=\mathrm{voiced},\ q_i=s,\ m_i=w\},$$
$$1\leqslant s\leqslant S,\quad 1\leqslant w\leqslant W, \tag{9}$$

where voicing($\boldsymbol{y}_i$) is voiced, unvoiced, or nonspeech. Similar to Eq. (9), unvoiced, $\Omega^{u}_{s,w}$, and nonspeech, $\Omega^{\mathrm{ns}}_{s,w}$, vector pools are also created.

3. Phoneme-specific GMMs

Expectation-maximization clustering[13] can be applied to each vector pool to create voiced, $\Phi^{v}_{s,w}$, unvoiced, $\Phi^{u}_{s,w}$, and nonspeech, $\Phi^{\mathrm{ns}}_{s,w}$, GMMs associated with each state s of each phoneme model w. The set of state and model dependent GMMs that model the joint density of acoustic vectors and MFCC vectors for voiced speech is given by

$$\begin{aligned}p(\boldsymbol{y}|v,s,w)&=\Phi^{v}_{s,w}(\boldsymbol{y})\\&=\sum_{k=1}^{K}\alpha^{v}_{k,s,w}\phi^{v}_{k,s,w}(\boldsymbol{y})\\&=\sum_{k=1}^{K}\alpha^{v}_{k,s,w}\mathcal{N}(\boldsymbol{y};\boldsymbol{\mu}^{v,\boldsymbol{y}}_{k,s,w},\boldsymbol{\Sigma}^{v,\boldsymbol{yy}}_{k,s,w}),\end{aligned} \tag{10}$$

where $\phi^{v}_{k,s,w}(\boldsymbol{y})$ represents the kth Gaussian distribution in the voiced GMM for state s and model w, which has associated with it the prior probability $\alpha^{v}_{k,s,w}$.

The set of voiced GMMs, $\Phi^{v}_{s,w}$, is represented by mean vectors, $\boldsymbol{\mu}^{v,\boldsymbol{y}}_{k,s,w}$, and covariance matrices, $\boldsymbol{\Sigma}^{v,\boldsymbol{yy}}_{k,s,w}$, for the kth cluster of state s and model w such that

$$\boldsymbol{\mu}^{v,\boldsymbol{y}}_{k,s,w}=\begin{bmatrix}\boldsymbol{\mu}^{v,\boldsymbol{x}}_{k,s,w}\\ \boldsymbol{\mu}^{v,\boldsymbol{f}}_{k,s,w}\end{bmatrix}\quad\text{and}\quad\boldsymbol{\Sigma}^{v,\boldsymbol{yy}}_{k,s,w}=\begin{bmatrix}\boldsymbol{\Sigma}^{v,\boldsymbol{xx}}_{k,s,w} & \boldsymbol{\Sigma}^{v,\boldsymbol{xf}}_{k,s,w}\\ \boldsymbol{\Sigma}^{v,\boldsymbol{fx}}_{k,s,w} & \boldsymbol{\Sigma}^{v,\boldsymbol{ff}}_{k,s,w}\end{bmatrix}. \tag{11}$$

Similar to Eq. (10), sets of unvoiced and nonspeech GMMs, $\Phi^{u}_{s,w}$ and $\Phi^{\mathrm{ns}}_{s,w}$, are also created. These are represented by mean vectors, $\boldsymbol{\mu}^{u,\boldsymbol{y}}_{k,s,w}$ and $\boldsymbol{\mu}^{\mathrm{ns},\boldsymbol{y}}_{k,s,w}$, covariance matrices, $\boldsymbol{\Sigma}^{u,\boldsymbol{yy}}_{k,s,w}$ and $\boldsymbol{\Sigma}^{\mathrm{ns},\boldsymbol{yy}}_{k,s,w}$, and prior probabilities, $\alpha^{u}_{k,s,w}$ and $\alpha^{\mathrm{ns}}_{k,s,w}$.

The voiced, unvoiced, and nonspeech vector pools also allow prior probabilities of the speech being voiced, $P(v|s,w)$, unvoiced, $P(u|s,w)$, and nonspeech, $P(\mathrm{ns}|s,w)$, to be computed for each state of each phoneme HMM. These are calculated from the number of voiced, unvoiced, and

nonspeech vectors allocated to each state during training. For example, the prior probability of voiced speech in state s of phoneme w, $P(v|s,w)$, is computed as

$$P(v|s,w) = \frac{N_{\Omega^v_{s,w}}}{N_{\Omega^v_{s,w}} + N_{\Omega^u_{s,w}} + N_{\Omega^{\mathrm{ns}}_{s,w}}}, \quad 1 \leqslant s \leqslant S, \quad 1 \leqslant w \leqslant W, \tag{12}$$

where $N_{\Omega^v_{s,w}}$ is the number of voiced vectors, $N_{\Omega^u_{s,w}}$ is the number of unvoiced vectors, and $N_{\Omega^{\mathrm{ns}}_{s,w}}$ is the number of nonspeech vectors in state s of phoneme model w. Similar to Eq. (12), prior probabilities for unvoiced, $P(u|s,w)$, and nonspeech, $p(\mathrm{ns}|s,w)$, are computed.

B. Phoneme-specific prediction of acoustic speech features from MFCCs

The prediction of acoustic features from a stream of MFCC vectors requires first an estimate of the phoneme and state sequences, which can be provided by VITERBI decoding using the network of HMMs discussed in Sec. III A 1. Next, the voicing class of each MFCC vector is predicted using the voiced, unvoiced, and nonspeech GMMs associated with the state that the MFCC vector is aligned to. For MFCC vectors predicted as voiced, formant and fundamental frequencies are predicted, while for unvoiced MFCC vectors only formant frequencies are predicted.

1. Voicing prediction

VITERBI decoding of the input MFCC vector stream provides the state and phoneme sequences, q_i and m_i, for each MFCC vector, $\boldsymbol{x}_i$. The prior voicing probabilities give an initial prediction of the voicing class of the MFCC vector based only on its phoneme and state allocation. However, VITERBI decoding errors can lead to an erroneous voicing class prediction, which in turn leads to incorrect decisions to predict or not to predict acoustic features. This is avoided by introducing posterior voicing probabilities, which utilize information contained within the voiced, unvoiced, and nonspeech GMMs.

The probability of the MFCC vector, $\boldsymbol{x}_i$, allocated to state q_i and phoneme HMM m_i, belonging to the voiced GMM is given as

$$P(v|\boldsymbol{x}_i,q_i,m_i) = \frac{P(v|q_i,m_i)p(\boldsymbol{x}_i|v,q_i,m_i)}{p(\boldsymbol{x}_i|q_i,m_i)}, \tag{13}$$

where $P(v|q_i,m_i)$ is the prior probability of the MFCC vector being voiced based on its state and phoneme allocation, $p(\boldsymbol{x}_i|q_i,m_i)$ is the probability of vector $\boldsymbol{x}_i$, and $p(\boldsymbol{x}_i|v,q_i,m_i)$ is the probability of the MFCC vector being voiced according to the marginalized voiced GMM, $\Phi^{v,\boldsymbol{x}}_{q_i,m_i}$, where

$$\begin{aligned} p(\boldsymbol{x}_i|v,q_i,m_i) &= \Phi^{v,\boldsymbol{x}}_{q_i,m_i}(\boldsymbol{x}_i) \\ &= \sum_{k=1}^{K} \alpha^v_{k,q_i,m_i} p(\boldsymbol{x}_i|\phi^{v,\boldsymbol{x}}_{k,q_i,m_i}) \\ &= \sum_{k=1}^{K} \alpha^v_{k,q_i,m_i} \mathcal{N}(\boldsymbol{x}_i;\boldsymbol{\mu}^{v,\boldsymbol{x}}_{k,q_i,m_i},\boldsymbol{\Sigma}^{v,\boldsymbol{xx}}_{k,q_i,m_i}). \end{aligned} \tag{14}$$

The probabilities of the MFCC vector $\boldsymbol{x}_i$ belonging to the unvoiced GMM, $\Phi^{u,\boldsymbol{x}}_{q_i,m_i}$, and nonspeech GMM, $\Phi^{\mathrm{ns},\boldsymbol{x}}_{q_i,m_i}$, are similarly defined,

$$P(u|\boldsymbol{x}_i,q_i,m_i) = \frac{P(u|q_i,m_i)p(\boldsymbol{x}_i|u,q_i,m_i)}{p(\boldsymbol{x}_i|q_i,m_i)}, \tag{15}$$

$$P(\mathrm{ns}|\boldsymbol{x}_i,q_i,m_i) = \frac{P(\mathrm{ns}|q_i,m_i)p(\boldsymbol{x}_i|\mathrm{ns},q_i,m_i)}{p(\boldsymbol{x}_i|q_i,m_i)}. \tag{16}$$

The voicing of the MFCC vector is chosen by selecting the voicing class with the highest posterior voicing probability. Note that $p(\boldsymbol{x}_i|q_i,m_i)$ cancels from Eqs. (13), (15), and (16) and need not be calculated.

2. Acoustic speech feature prediction

For MFCC vectors predicted as voiced, a MAP prediction of the ith acoustic speech feature vector, $\hat{\boldsymbol{f}}^k_i$, from the kth cluster of the voiced GMM, $\phi^{v,\boldsymbol{y}}_{k,q_i,m_i}$, can be made,

$$\hat{\boldsymbol{f}}^k_i = \arg\max_{\boldsymbol{f}_i}\{p(\boldsymbol{f}_i|\boldsymbol{x}_i,\phi^{v,\boldsymbol{y}}_{k,q_i,m_i})\}, \tag{17}$$

where q_i and m_i are the state and model that the MFCC vector $\boldsymbol{x}_i$ is allocated to. This evaluates to

$$\hat{\boldsymbol{f}}^k_i = \boldsymbol{\mu}^{v,\boldsymbol{f}}_{k,q_i,m_i} + \boldsymbol{\Sigma}^{v,\boldsymbol{fx}}_{k,q_i,m_i}(\boldsymbol{\Sigma}^{v,\boldsymbol{xx}}_{k,q_i,m_i})^{-1}(\boldsymbol{x}_i - \boldsymbol{\mu}^{v,\boldsymbol{x}}_{k,q_i,m_i}). \tag{18}$$

Predictions from all of the K clusters can be combined by weighting using the voiced posterior probability, $h^v_{k,q_i,m_i}(\boldsymbol{x}_i)$, of the ith MFCC vector $\boldsymbol{x}_i$, belonging to the kth cluster,

$$\hat{\boldsymbol{f}}_i = \sum_{k=1}^{K} h^v_{k,q_i,m_i}(\boldsymbol{x}_i)\{\boldsymbol{\mu}^{v,\boldsymbol{f}}_{k,q_i,m_i} + \boldsymbol{\Sigma}^{v,\boldsymbol{fx}}_{k,q_i,m_i}(\boldsymbol{\Sigma}^{v,\boldsymbol{xx}}_{k,q_i,m_i})^{-1}(\boldsymbol{x}_i - \boldsymbol{\mu}^{v,\boldsymbol{x}}_{k,q_i,m_i})\}. \tag{19}$$

The voiced posterior probability, $h^v_{k,q_i,m_i}(\boldsymbol{x}_i)$, is given by

$$h^v_{k,q_i,m_i}(\boldsymbol{x}_i) = \frac{\alpha^v_{k,q_i,m_i} p(\boldsymbol{x}_i|\phi^{v,\boldsymbol{x}}_{k,q_i,m_i})}{\sum_{k=1}^{K} \alpha^v_{k,q_i,m_i} p(\boldsymbol{x}_i|\phi^{v,\boldsymbol{x}}_{k,q_i,m_i})}, \tag{20}$$

where $p(\boldsymbol{x}_i|\phi^{v,\boldsymbol{x}}_{k,q_i,m_i})$ is the marginal distribution of the MFCC vector for the kth cluster of the voiced GMM in state q_i and model m_i.

For MFCC vectors predicted as unvoiced, acoustic features comprising only formant frequencies are predicted. Equations (19) and (20) are used, but voiced GMMs and voiced probabilities are replaced by unvoiced GMMs and probabilities.

C. Global prediction of acoustic speech features

The phoneme-specific prediction can be reduced to a global prediction by replacing the network of HMMs with a single one-state HMM—i.e., setting $W=1$ and $S=1$. This removes the need to decode the MFCC vector stream into a state sequence. For each MFCC vector, a voicing classification is made from the voiced, unvoiced, and nonspeech GMMs in the single state, followed by a prediction of the appropriate acoustic features. This is a more simple method of prediction and provides a useful comparison to the more

sophisticated phoneme-specific method. As such, the experimental evaluation of the acoustic feature prediction compares the performance of the phoneme-specific acoustic feature prediction with the global prediction.

IV. RESULTS

The aim of the experiments in this section is to investigate the accuracy of the acoustic feature prediction methods under various constraints of speaker and gender dependence.

For gender-dependent and gender-independent testing, the VTRFormants database has been used.[9] This is a subset of the TIMIT database and comprises 324 utterances for training, spoken by 173 speakers, and 192 utterances for testing, spoken by a different set of 24 speakers. The database is supplied with the first four formant frequencies, the first three of which are hand corrected. Originally the database was sampled at 16 kHz, although for this work it has subsequently been downsampled to 8 kHz. Reference voicing classifications have been created using the ETSI XFE tool,[3] and reference fundamental frequency has been extracted using the YIN algorithm.[14]

For speaker-dependent testing preliminary experiments revealed that insufficient speaker-dependent data were available within the VTRFormants database to reliably train the joint densities needed for an acoustic feature prediction. Instead, two further databases (UEAChris and UEACath) were used to provide male and female speaker-dependent speech. These databases, in addition to the audio, also contain laryngograph recordings, which (after a minor hand correction) provide reference voicing and fundamental frequency. Reference formant frequency data were obtained using a combination of linear predictive coding (LPC) analysis and Kalman filtering.[12] Each utterance comprises phonetically rich sentences that have been downsampled to 8 kHz for this work. The male speaker, UEAChris, provides 601 training utterances and 246 testing utterances, while the female speaker, UEACath, provides 579 training utterances and 246 testing utterances.

A. Voicing classification

This section examines voicing classification accuracy for systems trained on speaker-dependent, gender-dependent, and gender-independent speech. Figures 3 and 4 show graphical voicing class confusion matrices for both global and phoneme-specific predictions. The global GMMs comprised 32 clusters, while the state and phoneme specific GMMs comprised 16 clusters. A detailed analysis of the effect of the number of clusters in the GMMs is given in Sec. IV B and IV C.

Within the two confusion matrices, bar graphs show the percentage of MFCC vectors correctly and incorrectly classified for each class of speech (voiced, unvoiced, and nonspeech). Results are shown for speaker-dependent, gender-dependent, and gender-independent systems and separately for male and female speech.

Examining the leading diagonals of the two figures reveals the phoneme-specific prediction to be more accurate than the global prediction of speech class. Considering the off diagonal entries, which show speech class confusions, in general, the phoneme-specific prediction is more accurate with the exception of misclassifying slightly more nonspeech and unvoiced frames as voiced. The lowest errors occur for classifying voiced speech as nonspeech, which is important as such errors would erroneously cause no prediction of acoustic features to be made in some regions of voiced speech. Very low error rates are also observed in the phoneme-specific system for classifying unvoiced speech as nonspeech. Examining the effect of gender reveals female speech to be more accurately classified than male speech in most of the conditions tested.

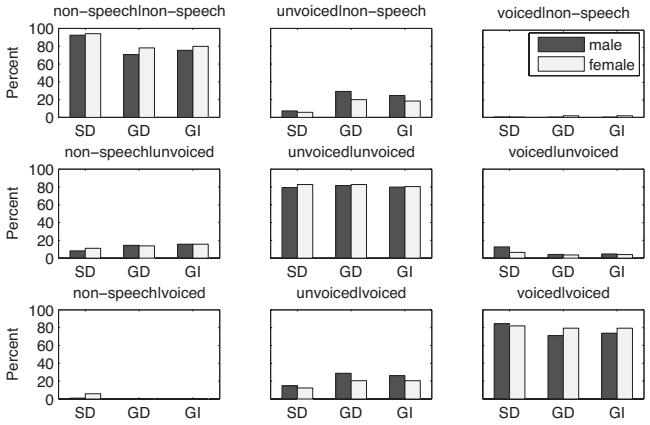


FIG. 3. Graphical confusion matrix for global (GMM) voicing classification for speaker and gender constrained speech.

B. Fundamental frequency prediction

For evaluation purposes, the reference voicing is used to determine from which MFCC vectors fundamental frequency is predicted. This removes the effect of voicing classification errors from fundamental frequency evaluation by ensuring that in all tests the same vectors are selected. However, in practical situations the predicted voicing would be used. The percentage fundamental frequency error E^{f0} is used to measure fundamental frequency prediction errors and is computed as

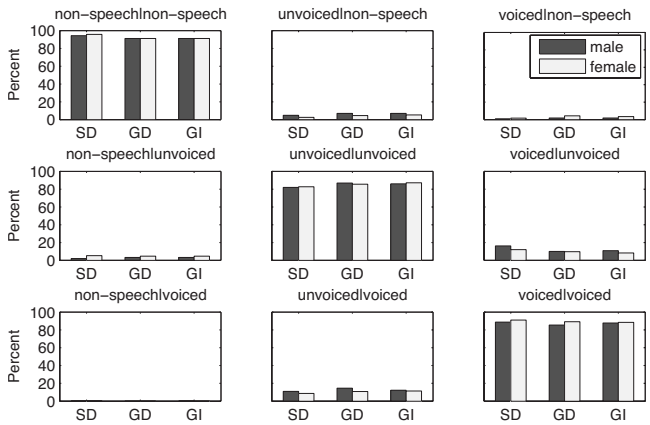


FIG. 4. Graphical confusion matrix for phoneme-specific (HMM-GMM) voicing classification for speaker and gender constrained speech.

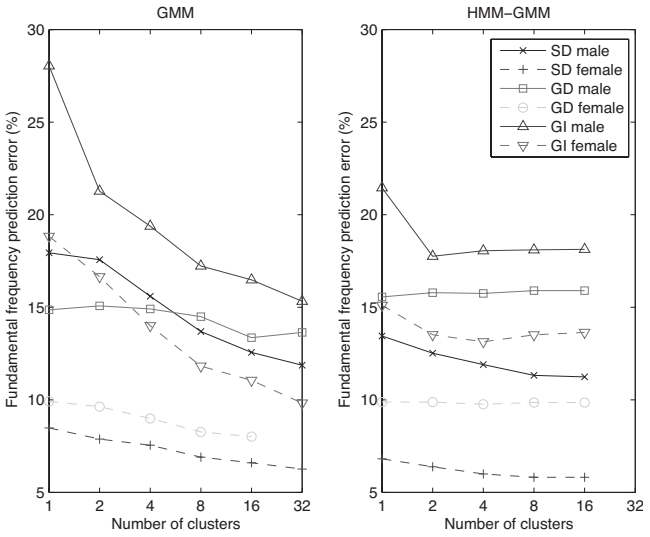


FIG. 5. Fundamental frequency prediction error with increasing number of clusters for (a) global (GMM) and (b) phoneme-specific (HMM-GMM) predictions using speaker-dependent, gender-dependent, and gender-independent speech.

$$E^{f0} = \frac{1}{N_v} \sum_{i=1}^{N_v} \frac{|\hat{f}_i(0) - f_i(0)|}{f_i(0)} \times 100\,\%\,, \tag{21}$$

where N_v is the number of voiced MFCC vectors. Figure 5 shows percentage fundamental frequency prediction errors for global prediction and phoneme-specific prediction as the number of clusters in the GMMs is increased from 1 to 32. For both methods, speaker-dependent, gender-dependent, and gender-independent systems are evaluated separately for male and female speakers.

Considering first the effect of increasing the number of clusters in the GMMs, the results show that for a global prediction of fundamental frequency from a single GMM, errors reduce substantially as the number of clusters is increased. In contrast, for a phoneme-specific prediction from the network of HMM-GMMs, the effect of increasing the number of clusters gives much less reduction in error. This is attributed to the fact that the network of HMM-GMMs itself provides a relatively detailed model of the feature space, while the single GMM, which in itself has to model the entire feature space, requires substantially more clusters to achieve this. In addition, for each GMM in the HMM-GMM system, substantially less training data are available, which makes training of the state-specific GMMs more difficult. The results also reveal lower fundamental frequency errors with female speech than with male speech. This is consistent with the correlation analysis made in Sec. II B, which found a higher fundamental frequency to MFCC vector correlation for female speech than for male speech.

The results show that for speaker-dependent speech, the localization of prediction to specific phonemes through the HMM-GMM system gives lower errors than a global prediction from the single GMM system. However, for both gender-dependent and gender-independent speech, prediction errors are higher with the phoneme-specific system in comparison to the global system. This can be attributed to a lack of training data in both the gender-dependent and gender-independent systems. Examining the prediction errors for the HMM-GMM system in Fig. 5(b) reveals both the male and female speaker-dependent systems to decrease in error as the number of clusters increases. However, for both the gender-dependent and gender-independent systems, errors increase as more clusters are used, which suggests a lack of training data. The gender-dependent and gender-independent systems both use the VTR-Formants database, which comprises approximately 60 000 male speech frames and 42 000 female speech frames. In contrast, the speaker-dependent tests use the UEAChris and UEACath databases, which contain, respectively, about 233 000 and 261 000 speech frames. Further tests are presented in Sec. IV D, which use a larger gender-dependent database to explore the effect of insufficient training data.

C. Formant frequency prediction

For the purposes of evaluation, formant frequencies are predicted from MFCC vectors labeled as speech according to the reference voicing. Separate GMMs are trained and tested for voiced and unvoiced speech as these were found to be more accurate than a single GMM due to the different structures of voiced and unvoiced speech. The formant frequency prediction error is averaged across all four formants and is measured using the mean formant frequency prediction error, E^F, which is defined as

$$E^F = \frac{1}{4N_v} \sum_{i=1}^{N_v} \sum_{j=1}^{4} \frac{|\hat{f}_i(j) - f_i(j)|}{f_i(j)} \times 100\,\%\,, \tag{22}$$

where N_s is the number of speech MFCC vectors. Figure 6 shows global and phoneme-specific mean formant frequency prediction errors separately for voiced and unvoiced speech and for male and female speaker-dependent, gender-dependent, and gender-independent scenarios.

The results show that the formant frequency prediction from voiced speech is considerably more accurate than that from unvoiced speech. This observation is consistent with the findings of the correlation analysis in Sec. II B, which showed a higher formant frequency to MFCC vector correlation for voiced speech than for unvoiced speech; this is attributed to the better definition of formants in voiced speech than unvoiced speech. The trend of formant frequency prediction errors, when considering the number of clusters, follows a similar pattern to those found in the fundamental frequency prediction. Global prediction errors decrease as more clusters are used, but for the phoneme-specific HMM-GMM system, errors generally increase due to the lack of training data, with the exception of the larger speaker-dependent systems. This is again attributed to the larger amount of training data available for HMM-GMM training with the speaker-dependent database over that available for the gender-dependent and gender-independent systems.

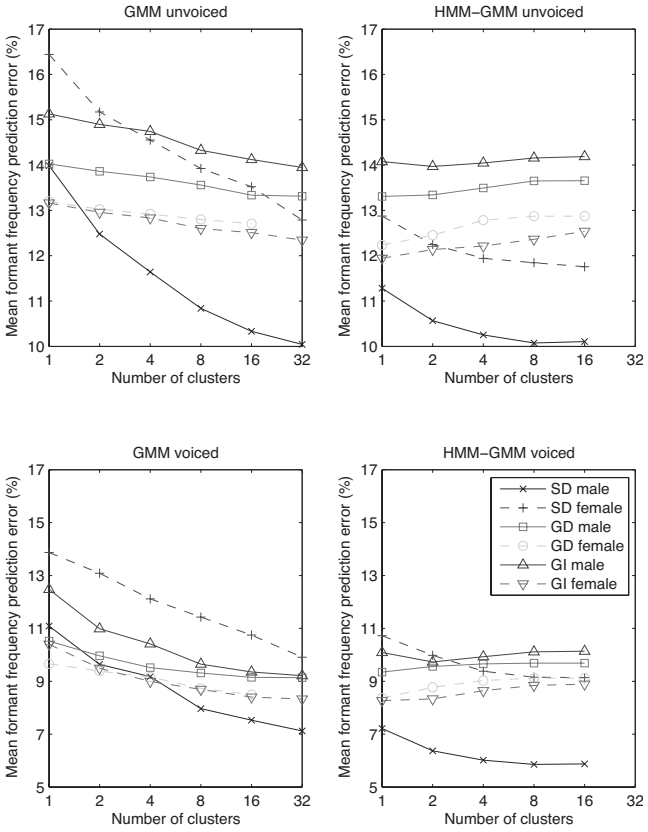


FIG. 6. Mean formant frequency prediction error with increasing number of clusters for (a) global (GMM) and (b) phoneme-specific (HMM-GMM) predictions using speaker-dependent, gender-dependent, and gender-independent speech. Top row: unvoiced; bottom row: voiced.

D. Effect of using a larger gender-dependent speech database

The aim of this section is to investigate further the relatively poor performance of the phoneme-specific gender-dependent and gender-independent systems over the global prediction system. As stated in Secs. IV B and IV C, these tests use the relatively small VTRFormants database. In this section gender-dependent male speaker experiments are carried out using a subset of the larger WSJCAM0 database.[15] This contains approximately 777 000 training data frames in comparison to 60 000 male speech training data frames for the VTRFormants database. For the WSJCAM0 male subset, a reference fundamental frequency is provided by the YIN algorithm,[14] and formant frequencies are provided by a combined LPC/Kalman filtering method.[2]

Figure 7 shows male gender-dependent fundamental frequency errors for the global and phoneme-specific prediction systems as the number of clusters is varied from 1 to 32. As the number of clusters is increased, fundamental frequency errors decrease for the global prediction system but increase for the phoneme-specific system, although the level of change is much smaller than that observed for the VTRFormants database. However, in comparison to Fig. 5. The performances of the global and phoneme-specific systems are much closer. Using the VTRFormants database, the global prediction outperformed the phoneme-specific prediction by over 2%, while for the larger WSJCAM0 database the difference is about 0.2%.

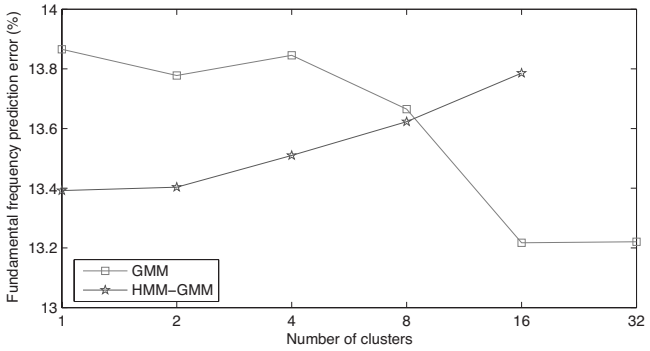


FIG. 7. Global (GMM) and phoneme-specific (HMM-GMM) gender-dependent fundamental frequency prediction errors.

Figure 8 shows male gender-dependent formant frequency errors for unvoiced and voiced speech for the global and phoneme-specific prediction systems. For both voiced and unvoiced speech, the phoneme-specific prediction outperforms the global prediction by about 1%. The results also reveal that phoneme-specific prediction errors decrease as more clusters are used, which was not observed with the smaller VTRFormants database.

These results suggest that to exploit the benefits of the more localized modeling that phoneme-specific prediction offers over global prediction, it is necessary to have sufficient training data to reliably create the state and phoneme specific GMMs.

V. ENCAPSULATION OF ACOUSTIC SPEECH FEATURES

This final section presents an alternative method for obtaining acoustic speech features at the back-end and is included as a comparison to the proposed prediction method. In this method, the fundamental frequency and formant frequencies are computed at the front-end using conventional estimation methods applied to the time-domain signal.[2,3] The four highest-order MFCCs in the feature vector are then replaced by the acoustic features. This leads to two issues: first,

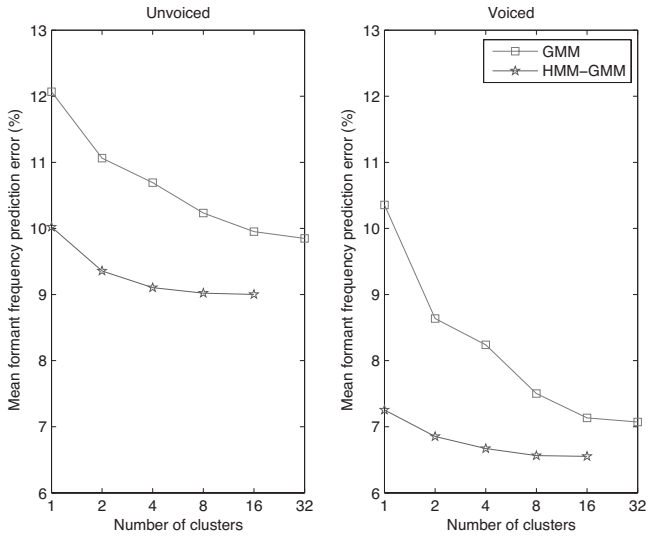


FIG. 8. Global (GMM) and phoneme-specific (HMM-GMM) gender-dependent (a) unvoiced and (b) voiced formant frequency prediction errors.

TABLE IV. Unconstrained monophone accuracy using 12 D and 8-D MFCC vectors on speaker-dependent and speaker-independent speech.

	MFCCs 1–12	MFCCs 1–8
Speaker dependent	73.7%	72.8%
Speaker independent	53.1%	48.4%

to what extent speech recognition accuracy is reduced by the loss of higher-order MFCCs, and second, the error that estimation and quantization introduces into the acoustic features.

A. Effect on recognition accuracy

The effect of reducing the feature vector from MFCCs 0–12 to MFCCs 0–8 is examined using the unconstrained phoneme recognition task described in Sec. III A for determining the phoneme sequence. Both speaker-dependent and speaker-independent tasks are examined, with results shown in Table IV. For the easier speaker-dependent task, recognition accuracy reduces by 1% as a result of removing MFCCs 9–12. However, on the more difficult speaker-independent task, accuracy falls by 5%.

B. Quantization of acoustic features

Quantization of acoustic features uses the same method as the ETSI Aurora standard for MFCCs. This specifies that pairs of MFCCs are vector quantized, with MFCCs 9 and 10 being allocated 6 bits (to give 64 centroids) while MFCCs 11 and 12 are allocated 5 bits (to give 32 centroids). For vector quantization (VQ) of the acoustic features, the fundamental frequency and F1 are paired and allocated 6 bits while F2 and F3 are paired and allocated 5 bits. To examine quantization errors, VQ codebooks were trained on a set of 80 000 vectors and tested on a set of 40 000 vectors. Percentage quantization errors, using Eqs. (21) and (22), were 5.3%, 2.3%, 4.7%, and 2.8% for f0, F1, F2, and F3, respectively. In addition to quantization errors, acoustic features are subject to errors made by the front-end-based estimation methods. An investigation into the accuracy of acoustic feature estimation methods, using hand-corrected data, showed that the lowest fundamental frequency errors of about 2% were obtained using the YIN algorithm, and the lowest mean formant frequency errors of about 8% were obtained from a LPC-Kalman method.[16]

Combining these estimation errors with the VQ errors, for fundamental frequency, gives higher errors than predicted on the speaker-dependent female task, but lower errors on the gender-dependent and gender-independent tasks. For the formant frequency estimation, the combination of errors leads to higher errors than predicted across most of the speaker and gender constraints. The effect of quantizing the MFCC vectors using the VQ scheme proposed by ETSI was found to have an insignificant effect on acoustic feature prediction accuracy—for example, the prediction of fundamental frequency reduced by 0.1%. This result is consistent with speech recognition results that found little difference between using quantized or unquantized MFCC vectors.[17]

VI. CONCLUSIONS

This work has shown that correlation exists between acoustic speech features and MFCC vectors and can be increased by placing constraints on the speech. The analysis also revealed that a higher correlation is obtained within individual phonemes rather than globally across all speech sounds. This led to the development of a MAP prediction of acoustic features from MFCC vectors using a combined HMM-GMM framework. Evaluations found that, given sufficient training data, phoneme-specific prediction of acoustic features is more accurate than global prediction. A problem with the HMM-GMM system is the need for substantially more training data to train GMMs within each state of each HMM. In cases where sufficient training data were unavailable, global prediction was found to be better.

A comparison to prediction was also made where higher-order MFCCs were replaced by acoustic features. Fundamental frequency accuracy was comparable to speaker-dependent prediction and was higher than gender-dependent and gender-independent predictions. For formant frequencies, the combination of estimation errors and VQ errors led to the technique generally performing worse than prediction. A significant downside of replacing higher-order MFCCs was found to be the reduction in speech recognition accuracy. Maximizing recognition accuracy is paramount in designing front-ends, and this decline in performance was judged unacceptable. If more accurate estimates are required, a better alternative is to adopt the XFE proposed by ETSI, which uses additional 800 bits/s to transmit fundamental frequency and voicing.[3]

[1]D. Talkin, "A robust algorithm for pitch tracking (RAPT)," in *Speech Coding and Synthesis*, edited by W. Kleijn and K. Paliwal (Elsevier, New York, 1995), Chap. 14.

[2]Q. Yan, S. Vaseghi, E. Zavarehei, B. Milner, J. Darch, P. White, and I. Andrianakis, "Formant tracking linear prediction model using HMMs and Kalman filters for noisy speech processing," Comput. Speech Lang. **21**, 543–561 (2007).

[3]ETSI, "Speech processing, transmission and quality aspects (STQ); distributed speech recognition; extended front-end feature extraction algorithm; compression algorithms; back-end speech reconstruction algorithm," ES 202 211, Version 1.1.1, ETSI STQ-Aurora DSR Working Group, 2003.

[4]X. Shao and B. Milner, "Predicting fundamental frequency from mel-frequency cepstral coefficients to enable speech reconstruction," J. Acoust. Soc. Am. **118**, 1134–1143 (2005).

[5]B. Milner and X. Shao, "Prediction of fundamental frequency and voicing from mel-frequency cepstral coefficients for unconstrained speech reconstruction," IEEE Trans. Audio, Speech, Lang. Process. **15**, 24–33 (2007).

[6]J. Darch, B. Milner, and S. Vaseghi, "MAP prediction of formant frequencies and voicing class from MFCC vectors in noise," Speech Commun. **48**, 1556–1572 (2006).

[7]J. Darch, B. Milner, I. Almajai, and S. Vaseghi, "An investigation into the correlation and prediction of acoustic speech features from MFCC vectors," in ICASSP. Honolulu, HI (2007), Vol. **4**, pp. 465–468.

[8]S. Chatterjee and A. Hadi, *Regression Analysis by Example*, 4th ed. (Wiley, New York, 2006).

[9]L. Deng, X. Cui, R. Pruvenok, J. Huang, S. Momen, Y. Chen, and A. Alwan, "A database of vocal tract resonance trajectories for research in speech processing," in ICASSP, Toulouse, France (2006), Vol. **1**, pp. 369–372.

[10]A. Syrdal and S. Steele, "Vowel F1 as a function of speaker fundamental frequency," J. Acoust. Soc. Am. **78**, S56 (1985).

[11]T. Hirahara, "On the role of the fundamental frequency in vowel perception," J. Acoust. Soc. Am. **84**, S156 (1988).

[12]L. Rabiner, "A tutorial on hidden Markov models and selected applica-

tions in speech recognition," Proc. IEEE **77**, 257–286 (1989).
[13]A. Webb, *Statistical Pattern Recognition*, 2nd ed. (Wiley, New York, 2002).
[14]A. de Cheveigné and H. Kawahara, "YIN, a fundamental frequency estimator for speech and music," J. Acoust. Soc. Am. **111**, 1917–1930 (2002).
[15]J. Fransen, D. Pye, T. Robinson, P. Woodland, and S. Young, "WSJCAM0 corpus and recording description," Technical Report No. CUED/F-INFENG/TR.192, Cambridge University Engineering Department, Cambridge, UK, 1994.
[16]J. Darch and B. Milner, "A comparison of estimated and MAP-predicted formants and fundamental frequencies with a speech reconstruction application," in Proceedings of Interspeech, Antwerp, Belgium (2007), pp. 542–545.
[17]H.-G. Hirsch and D. Pearce, "The aurora experimental framework for the performance evaluation of speech recognition systems under noisy conditions," in Automatic Speech Recognition: Challenges for the New Millenium, ISCA ITRW, Paris, France (2000), pp. 181–188.

Frequency response of the skin on the head and neck during production of selected speech sounds

Jacob B. Munger and Scott L. Thomson[a)]
Department of Mechanical Engineering, Brigham Young University, Provo, Utah, 84602

(Received 29 February 2008; revised 23 September 2008; accepted 24 September 2008)

Vibrations within the vocal tract during speech are transmitted through tissue to the skin surface and can be used to transmit speech. Achieving quality speech signals using skin vibration is desirable but problematic, primarily due to the several sound production locations along the vocal tract. The objective of this study was to characterize the frequency content of speech signals on various locations of the head and neck. Signals were recorded using a microphone and accelerometers attached to 15 locations on the heads and necks of 14 males and 10 females. The subjects voiced various phonemes and one phrase. The power spectral densities (PSD) of the phonemes were used to determine a quality ranking for each location and sound. Spectrograms were used to examine signal frequency content for selected locations. A perceptual listening test was conducted and compared to the PSD rankings. The signal-to-noise ratio was found for each location with and without background noise. These results are presented and discussed. Notably, while high-frequency content is attenuated at the throat, it is shown to be detectable at some other locations. The best locations for speech transmission were found to be generally common to males and females.
© *2008 Acoustical Society of America.* [DOI: 10.1121/1.3001703]

PACS number(s): 43.72.Kb, 43.70.Mn [BHS] Pages: 4001–4012

I. INTRODUCTION

During speech production, vibrations from the vocal folds are transmitted through the vocal tract as well as through body tissue to the skin surface. These skin surface vibrations can be sensed by contact microphones (microphones that are in contact with the skin and detect the speech signal from the skin surface as opposed to through the air) and can be used to transmit speech in communication systems. As opposed to acoustic microphones, contact microphones have the potential to sense little background noise from the surrounding environment. As a result, contact microphones have the potential to enhance speech clarity in elevated ambient noise environments. This presents significant potential benefit to military, aerospace, and general purpose cell phone and two-way radio communications.

Previous studies have demonstrated the relative insensitivity of contact microphones to background noise. For example, Hayes and Meltzer (1967) found that a Sonotone 700-3001 bone oscillator microphone worn on the forehead by a listener 1.83 m away from a person speaking did not sense any of that person's speech. Acker-Mills *et al.* (2004) found that a LASH II throat microphone (a contact microphone placed on the throat) had a 10 dB higher signal-to-noise ratio than a noise-canceling boom-mounted acoustic microphone in the presence of 90 and 106 dB broadband noise. Dupont *et al.* (2004) found a throat microphone (type unreported) to be robust against eliminating background noise in comparison with a headset microphone.

A significant limitation of current contact microphones is that some designs suffer from poor intelligibility. Acker-Mills *et al.* (2004) conducted an intelligibility study and found that the LASH II throat microphone had decreased intelligibility compared to the HGU-56/P acoustic microphone in high ambient noise environments. This was attributed to high-frequency content loss and the fact that consonant sounds were not detected.

Other studies have found that some common types and locations of contact microphones result in attenuation of high-frequency signal content. Shimamura and Tamiya (2005) reported that the intelligibility of bone conduction microphones (contact microphones placed on the skin near bones) was decreased due to the attenuation of the signal intensity for frequencies greater than 1 kHz in bone. Dupont *et al.* (2004) reported that the throat area acts as a low-pass filter with a cutoff frequency of 3 kHz.

Some studies have demonstrated that, even though some of the high-frequency content is lost, the transmitted speech signal is still understandable. Hayes and Meltzer (1967) found that a Sonotone 700-3001 bone oscillator placed on the forehead of a speaker transmitted speech clearly in a conversational setting. Similarly, Horacek *et al.* (2004) placed an accelerometer on the forehead and found that, even though the intensity of frequencies above 3.5 kHz was damped, the signal had good intelligibility. Snidecor *et al.* (1959), using a Sonostone 01 bone oscillator, and Moser and Oyer (1958) using a Brush VM-1 Vibromike reported that the forehead and other locations (mandible, chin, nose, and mastoid process) yielded relatively good quality signals.

In addition to frequency response characteristics, an important consideration in using skin vibration for speech transmission is the signal amplitude at the desired pickup location. Snidecor *et al.* (1959) and Moser and Oyer (1958) found that the intensity of the speech signal sensed on the

[a)]Electronic mail: thomson@byu.edu

TABLE I. Selected literature summary.

Study	Subjects	Location(s)	Sounds	Excitation	Data Analysis
Moser and Oyer, 1958	3 male	16 head/neck	12 vowels	Voice	Subjective intelligibility, intensity
Snidecor *et al.*, 1959	1 male	8 head/neck	4 vowels	Voice	Intelligibility, intensity
Hayes and Meltzer, 1967	1, gender unreported	Forehead	Sentence	Voice	Intelligibility, signal-to-noise
Norton *et al.*, 1993	Not reported	Neck	1 vowel	Shaker	Frequency response function
Meltzner *et al.*, 2003	7 male, 7 female	3 neck	3 vowels	Shaker	Frequency response function
Acker-Mills *et al.*, 2004	9 male, 1 female	Throat	Various words	Voice	Spectral analysis, time waveform, intelligibility, signal-to-noise
Horáček *et al.*, 2004	1, gender unreported	Forehead	3 vowels, sentence	Voice	Frequency response function, spectral analysis, subjective intelligibility
Shimamura *et al.*, 2005	2 male, 2 female	Top of head	3 vowels, sentences	Voice	Frequency response function, spectral analysis, intelligibility
Svec *et al.*, 2008	10 male, 7 female	Jugular notch	Normal speech	Voice	skin acceleration level/ sound-pressure level

skin decreased as the distance from the larynx increased; however, spectral analysis was not performed in either of these studies.

Several researchers have explored the use of accelerometers as contact microphones on the skin with various attachment methods to detect speech signals for purposes other than communication. Cheyne (2002) and Cheyne *et al.* (2003) used accelerometers to quantify vocal function and monitor voice use. In these studies the accelerometers were attached to the skin using Skin-Bond® adhesive. Svec *et al.* (2005) used accelerometers placed near the sternal notch to estimate speech loudness. The accelerometers were attached using surgical adhesive with a suture strip over the surface of the accelerometer. Horáček *et al.* (2004) used an accelerometer placed on the forehead of a speaker to help understand the dynamic characteristics of the human skull for use in verifying a computational finite element model of the sound transmission chain in the human skull. The accelerometer was pressed to the forehead using a rubber strap worn around the speaker's forehead.

To improve speech transmission in high noise environments, researchers have investigated using combinations of acoustic and contact microphones. Many studies have shown that such combinations can improve word recognition in speech recognition software (Dupont *et al.*, 2004; Zhang *et al.*, 2004; Zheng *et al.*, 2003; Garciarena *et al.*, 2003). However, in these studies the contact microphones were not used to transmit the speech signal itself, however, but rather as a "trigger" to indicate when the speaker was talking in order to prevent background noise transmission when the speaker was not talking.

Investigators have used transfer function estimates to better understand the frequency response characteristics of the head and neck. The frequency response of the neck was studied using an external shaker to induce vibrations on the skin in order to identify a transfer function for use with electrolarynx devices (Norton and Bernstien, 1993; Meltzner *et al.*, 2003). Wodicka and Shannon (1990) found a transfer function for the subglottal respiratory system when sound was introduced at the mouth for use in detecting lung disease. Shimamura and Tamiya (2005) presented a method for developing a finite impulse response reconstruction filter for a bone conduction microphone placed at the top of the head. They found that high-frequency content was restored using the filter, which increased speech clarity.

Table I lists several of the aforementioned papers along with their contributions and limitations in scope. In summary, it has been shown that contact microphones transmit little background noise. It has also been shown that the transmitted speech from contact microphones in some locations suffers from poor clarity due to the attenuation of the high-frequency content and the loss of consonant information. However, other papers have shown that contact microphones can nevertheless yield an understandable signal. Reconstruction filters have been shown to help restore attenuated high frequencies to improve transmitted speech clarity.

Lacking in the literature are detailed reports of the frequency response of head and neck skin vibration during speech production at various anatomical locations, as well as the frequency analysis of sounds other than vowels. The objective of this study is to assist in the development of improved contact microphones and associated signal processing methods by contributing to an improved understanding of the frequency response of the skin at various locations on the head and neck during speech. The skin surface vibration signals measured in this study are due to both tissue conduction and bone conduction of speech from the vocal tract to the skin surface.

II. METHODS

A. Experimental setup

To measure the frequency response of the skin during speech, accelerometers were attached to 15 locations on the face and neck of 14 male and 10 female subjects using medical-grade double-sided adhesive tape (see Fig. 1 and Table II). Prior to testing the subjects removed oil and/or makeup with an alcohol prep pad to ensure adequate adhe-

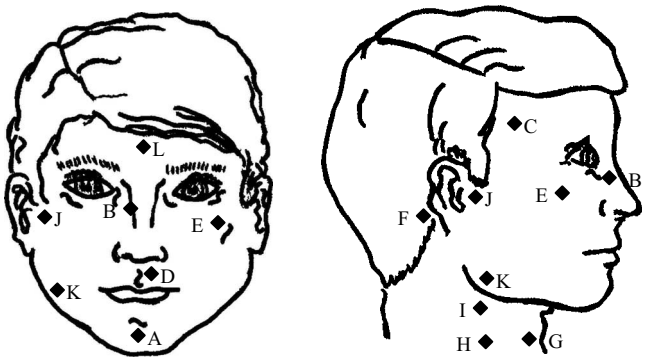


FIG. 1. Accelerometer placement locations (◆) (image courtesy U.S. Army Research Lab Human Research & Engineering Directorate).

sion. All testing was done with Institutional Review Board (IRB) approval and in accordance with IRB policies. Note that different types of transducers, including accelerometers, can be used as contact microphones. Hereafter, when specifically discussing the present study, we refer to accelerometers, but use the term contact microphones in more general discussions.

All accelerometers were manufactured by PCB Piezotronics; model numbers and relevant specifications are listed in Table II. The higher sensitivity accelerometers (C*, E*, and F*), used with the intent of improving signal detection at locations that we had previously identified as having low signal-to-noise ratios, were placed on the opposite sides of the head as accelerometers C, E, and F, respectively. The subjects were seated upright in a chair with a head rest to minimize head movement during testing. Due to the larger sizes of accelerometers C*, E*, and F*, their wires were suspended from above the subject's head, with a slight vertical tension applied to roughly compensate for the accelerometers' masses. The wires for all other accelerometers were attached to the head rest to minimize the torque on the skin due to the weight of the wires. The pressure of the accelerometers on the skin was not measured.

A 0.635-cm Larson-Davis 2520 microphone with a Larson-Davis PRM910B preamplifier was placed 45 deg off-axis, approximately 6.4 cm from the subject's mouth, and was used to simultaneously acquire audible speech data. The microphone and preamplifier were connected to a power supply (Larson-Davis 2221, 20-dB gain). All testing was done in a single-wall Acoustic Systems soundproof booth with a noise floor of approximately 42 dB SPL. The size of the booth was 2.1×2.1 m. The booth had an absorption coefficient of 0.79 at 125 Hz and 1.08 at 250 Hz, with an overall noise reduction coefficient (NRC) of 1.05.

The accelerometer and microphone signals were fed into a National Instruments NI PXI-1042Q data acquisition system with two eight-channel NI PXI-4472 ports (located outside of the booth). All signals were simultaneously sampled at 40 kHz; LABVIEW 7.1 was used for data collection.

The subjects were asked to sit as motionless as possible. A computer screen in the booth displayed instructions to the subject regarding what to say, including signals for when to start and stop speaking. The subjects sustained the vowels /a/, /u/, /ɔ/, /i/, the nasals /m/ and /n/, and the fricative /f/ for about 4 to 5 s each. The subjects also said the phonetically balanced phrase, "Rice is often served in round bowls." To guide vocal effort the subjects were asked to speak in a normal conversational voice. The average sound-pressure level over all subjects and sounds was 64.4 dB *re*: 20 μPa@6.4 cm with a standard deviation of 5.8 dB. After completing the sounds and phrases in a quiet environment, the subjects were given ear plugs and repeated the same tasks in the presence of 95-dB white noise. (Due to the pilot nature of this study only a few phonemes and one phrase are reported here; other sounds and phrases were recorded but are not reported in this paper.) A separate microphone in the booth allowed the researchers to hear the subjects to ensure proper completion of each speaking task.

B. Data analysis

1. Phoneme analysis

MATLAB was used for signal analysis. Each data set was truncated so that only the portion of the data during which the subject was speaking was analyzed. All signals were also

TABLE II. Accelerometer locations and specifications (locations identified in Fig. 1).

Location	Accelerometer Model#	Mass [g]	Sensitivity [mV/(m/s^2)]	Frequency range [Hz] (±5%)
A-Chin	352A24	0.8	10.2	1 to 8000
B-Nasal bone	352A56	1.8	10.2	0.5 to 10000
C-Temple	352A24	0.8	10.2	1 to 8000
C*-Temple	333B53	7.5	102	0.5 to 3000
D-Upper lip	352A24	0.8	10.2	1 to 8000
E-Zygomatic	352A56	1.8	10.2	0.5 to 10000
E*-Zygomatic	333B53	7.5	102	0.5 to 3000
F-Mastoid process	352A56	1.8	10.2	0.5 to 10000
F*-Mastoid process	333B53	7.5	102	0.5 to 3000
G-Over vocal folds	352A56	1.8	10.2	0.5 to 10000
H-Neck lateral to G	352A56	1.8	10.2	0.5 to 10000
I-Neck sperior to H	352A56	1.8	10.2	0.5 to 10000
J-Condylar process	352A24	0.8	10.2	1 to 8000
K-Angle of mandible	352A56	1.8	10.2	0.5 to 10000
L-Forehead	352A56	1.8	10.2	0.5 to 10000

passed through a high-pass filter with a cutoff frequency of 20 Hz to remove low-frequency noise from head or jaw motion. Phoneme data was analyzed as follows. The power spectral density (PSD) was estimated via Welch's method (Welch, 1967) using the "pwelch" function in MATLAB, with the following parameters: a Hamming window with a size of 1024 samples, 50% overlap, and a fast Fourier transform (FFT) length of 1024 samples. The accelerometer signals were then normalized to yield the same area under the PSD curve as the microphone signal between 0 and 5 kHz. Five kHz was chosen as the cutoff frequency because higher frequencies are not transmitted in most current communications systems (e.g., telephones). The following equation was used to normalize the accelerometer data:

$$\mathrm{PSD}_{i,\mathrm{norm}} = \mathrm{PSD}_i + \frac{\int_0^{f_c}\mathrm{PSD}_{\mathrm{mic}}(f)df - \int_0^{f_c}\mathrm{PSD}_i(f)df}{f_c}, \quad (1)$$

where $\mathrm{PSD}_{i,\mathrm{norm}}$ is the normalized PSD for location i, $\mathrm{PSD}_{\mathrm{mic}}$ is the PSD of the microphone, PSD_i is the PSD at location i, f is the frequency, and f_c is the upper frequency (5 kHz). The integrals were calculated using the trapezoidal method.

To compare how well each of the accelerometer signals matched that of the microphone, the absolute value of the difference between the normalized PSD of each accelerometer and microphone signal was found at each frequency and summed from 0 to 5 kHz. This resulted in a single value for each of the accelerometer signals, here referred to as the power spectral density summed difference ($\mathrm{PSD}_{\mathrm{SD}}$),

$$\mathrm{PSD}_{\mathrm{SD},i} = \sum_{f=0}^{f_c} |\mathrm{PSD}_{i,\mathrm{norm}}(f) - \mathrm{PSD}_{\mathrm{mic}}(f)|, \quad (2)$$

where the $\mathrm{PSD}_{\mathrm{SD},i}$ is the power spectral density summed difference of location i. A low $\mathrm{PSD}_{\mathrm{SD}}$ value indicates little difference between the accelerometer and microphone spectra, and a high $\mathrm{PSD}_{\mathrm{SD}}$ value indicates little agreement between the accelerometer and microphone spectra. The $\mathrm{PSD}_{\mathrm{SD}}$ was calculated for each subject, sound, and location, and was then averaged at each location over all subjects to obtain an average $\mathrm{PSD}_{\mathrm{SD}}$ value for each sound and location.

Each location was given a ranking from 1 to 15 for each subject based on the subject's $\mathrm{PSD}_{\mathrm{SD}}$. For example, if location A yielded the lowest $\mathrm{PSD}_{\mathrm{SD}}$ value for a given subject, the "individual subject rank" for location A for this individual was 1. Additionally, an "average subject rank" was calculated for each location by averaging the individual subject ranks at the corresponding location over all subjects. A rank of 1 indicates the lowest (best) $\mathrm{PSD}_{\mathrm{SD}}$ value and a rank of 15 indicates the highest (worst) $\mathrm{PSD}_{\mathrm{SD}}$ value.

2. Phrase analysis

A spectrogram for the phrase, "Rice is often served in round bowls," was calculated for a few selected locations. The spectrogram was generated using the "spectrogram" function in MATLAB, which calculates the PSD estimate over select time intervals using Welch's method. The same parameters were used to calculate the spectrogram as were used to calculate the PSD as described above. The spectrogram plots were normalized so each accelerometer's spectrogram had the same volume under the surface as the microphone spectrogram. This ensures that each spectrogram has the same dynamic range for comparison.

3. Perceptual ratings

For four of the subjects (two male and two female), the phrase "Rice is often served in round bowls" was rated by 11 separate individuals (4 male, 7 female, ages 21 to 30) who listened to recordings from each of the 15 accelerometers and the microphone for all four subjects. All listeners self-reported normal hearing. Fifteen of the recordings were randomly selected and repeated in order to determine intrarater reliability. The order of these recordings (79 in all) was randomized and each listener heard the recordings in the same order. To ensure that all the recordings had similar volume levels, all signals were passed through a high-pass filter with a cutoff frequency of 20 Hz (to remove any low-frequency content that resulted from jaw or head motion during speech) and normalized.

The voice rating method described by Dromey *et al.* (2008) was used to rate each recording's quality. Using a custom MATLAB routine (courtesy Dr. Christopher Dromey), the listeners rated each recording on a scale from "bad" to "good" quality using a graphical user interface slider bar with continuous values from zero to 100 (the zero end of the slider was labeled "bad" while the other end was labeled "good"). The overall quality judgment included factors such as intelligibility, amount of noise, and if the recording was natural sounding. Intrarater reliability was found by calculating the Pearson correlation between the first and second rating for the 15 repeated samples for each listener. For the 11 listeners the correlation values ranged from 0.55 to 0.84, indicating that some were inconsistent in their ratings. Therefore, only the five listeners with correlations above 0.73 were included in the study; these five listeners had an average correlation of 0.78. An intraclass correlation coefficient (ICC) was calculated and used to judge inter-rater reliability. The single-measures ICC was 0.717, and the average measures ICC was 0.927, with an F-ratio $F(63,252)=13.66$ and $p<0.001$, indicating that the raters were fairly consistent.

As in the PSD rankings, the locations were ranked based on the rating from each listener. These rankings were averaged to determine an average rating rank for each location.

4. Signal-to-noise ratio

The signal-to-noise ratio (SNR) for the sound /ɔ/ was calculated for each subject and location with and without the presence of background noise. The SNR was calculated using the following equation:

$$\mathrm{SNR} = 10\log_{10}\left(\left(\frac{1}{k}\sum_{n=1}^{k}|\mathrm{signal}(n)^2|\right)\left(\frac{1}{l}\sum_{m=1}^{l}|\mathrm{noise}(m)^2|\right)^{-1}\right), \quad (3)$$

where *signal* denotes a portion of the data during which the subject is talking, *noise* is a portion of the data prior to the subject talking, k is the number of data points in the signal portion, and l is the number of data points in the noise por-

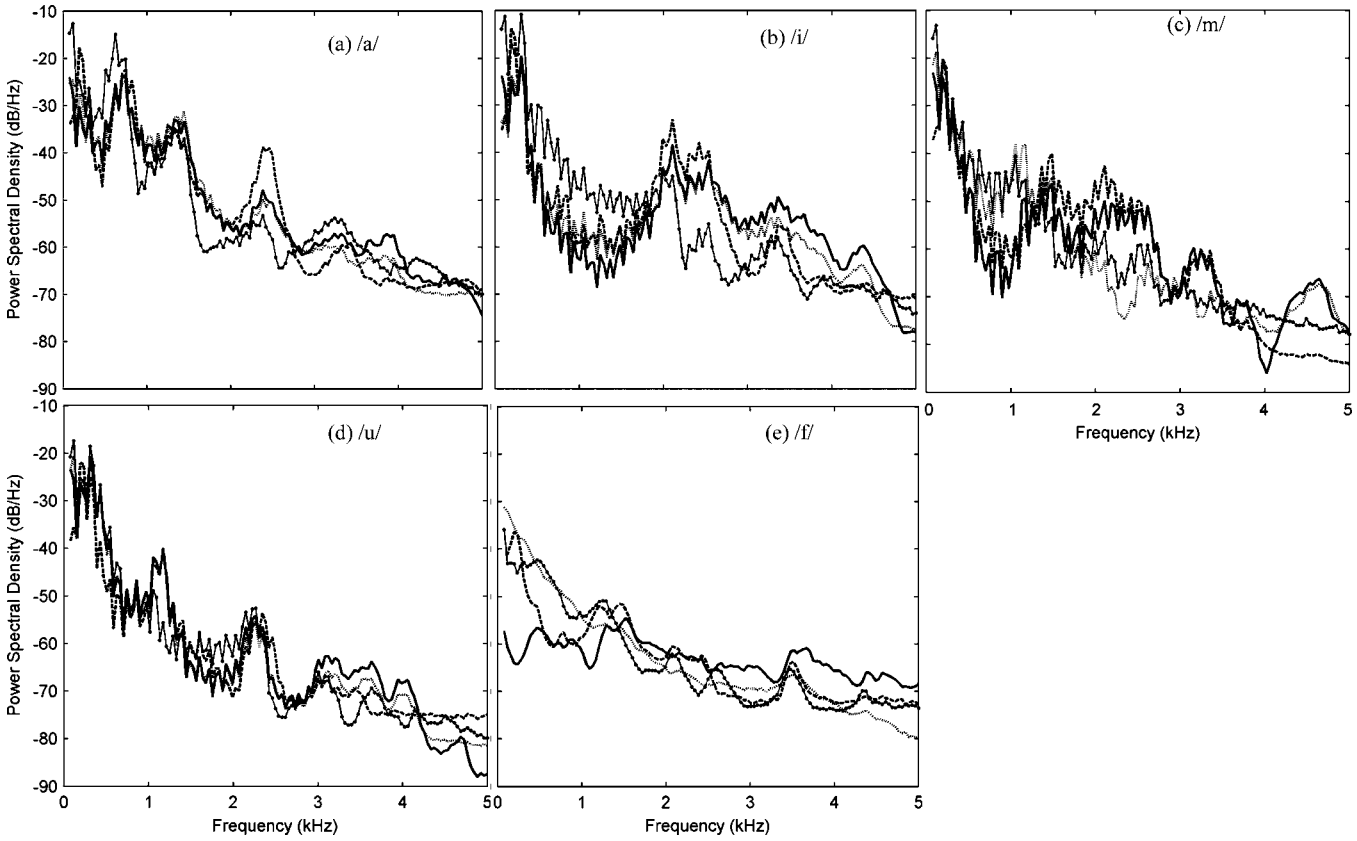


FIG. 2. PSD for one male subject; —— microphone; ··· above upper lip; --- nasal bone; –·– over the vocal folds. (a) /a/; (b) /i/; (c) /m/; (d) /u/; (e) /f/.

tion. The average SNR was also calculated for each location for all subjects.

III. RESULTS

A. Power spectral density

The PSD was used to compare the frequency content of the accelerometers to that of the microphone. Figure 2 shows the normalized PSD for sounds /a/, /i/, /m/, /u/, and /f/ for one male speaker. Figures 2(a), 2(b), and 2(d) show that for vowels, the upper lip signal matched the microphone spectrum very well up to about 3.5 kHz, while the nasal bone spectrum was limited to 2 or 3 kHz. For the vowels /a/ and /i/, the location over the vocal folds followed the general trend of the microphone, but agreement was worse than for the other two locations. For the sound /a/ the nasal bone spectrum has a large peak around 2.5 kHz which may be caused by high-amplitude formants produced in the nasal passage. For the nasal sound /m/, the nasal bone spectrum corresponded well with the microphone up to 3.5 kHz, albeit with large divergence in the 1.5 to 2.5 kHz region. The upper lip and vocal fold signals did not correspond very well to the microphone spectrum for the sound /m/.

Figure 2 also shows that the accelerometer spectra are generally attenuated beyond about 4 kHz, although peaks in the spectrum between 4 and 5 kHz were able to be sensed at the location above the upper lip [Figs. 2(b) and 2(c)]. Figure 2(e) shows that for /f/ there is only slight agreement between the accelerometer spectrum and the microphone spectrum.

B. Power spectral density summed difference

Figures 3 and 4 and Tables III and IV show the average PSD_{SD} over 0–5 kHz for all male and female subjects. The tables are sorted according to the average PSD_{SD}. For visual clarity only one side of the standard deviation bars is displayed. The order of locations along the *x*-axis for these figures is according to the location's average ranking (Sec. III C). These figures show that the overall trends in PSD_{SD} vs location are similar between the male and female speakers, although they are generally slightly lower for the female speakers. They also indicate that one particular location does not always have the lowest PSD_{SD} for each sound or gender. These tables and figures show that, for vowels, the upper lip matched the spectrum of the microphone better, while for nasals, the nasal bone had a lower PSD_{SD} value; this was consistent for both male and female speakers. The standard deviation of the male and female average PSD_{SD} values is comparable, with the male values being slightly higher for most sounds and locations.

C. Ranking

Tables V and VI show the male and female average PSD_{SD} ranks, respectively. These tables are sorted according to the average rank over all sounds for each location. The tables also show the average rank for each sound at each location. These tables show that for the seven sounds analyzed, the top five ranked locations are the same for both

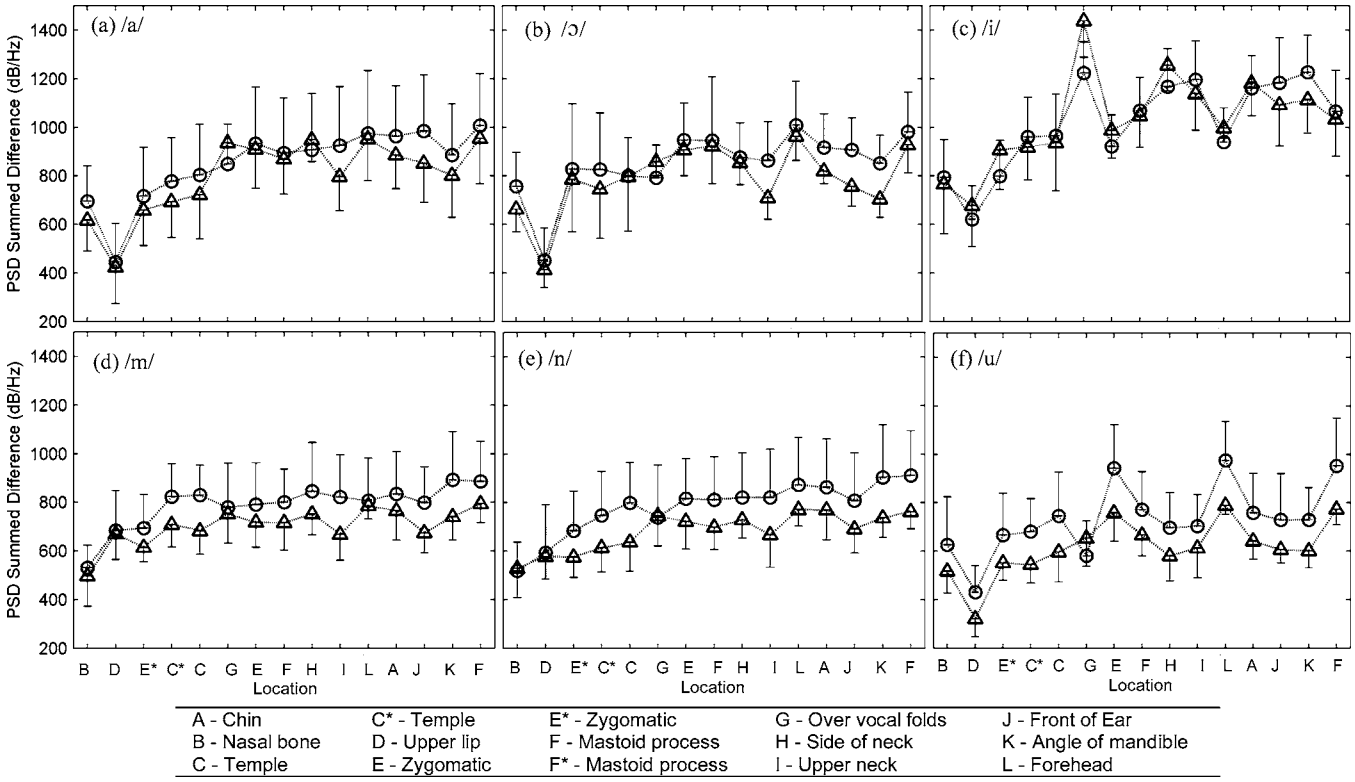


FIG. 3. Normalized PSD_{SD} over 0–5 kHz. ○: male speakers; △: female speakers. (a) /a/; (b) /ɔ/; (c) /i /; (d) /m/; (e) /n/; (f) /u/.

male and female speakers. These locations are the nasal bone, above the upper lip, the zygomatic*, and the two temple locations.

D. Spectrogram

Figure 5 shows spectrograms for the locations over the vocal folds, above the upper lip, on the nasal bone, and for the microphone for a male subject saying, "Rice is often served in round bowls." Figure 5(d) shows that, for nasals and vowels, most of the frequency content of interest is below 5 kHz. However, for the fricatives /f/ and /s/ there is much higher frequency content. Figure 5(a) shows that the location over the vocal folds attenuates most of the fricative high-frequency content above 4 kHz. This is in general agreement with the Dupont *et al.* (2004) study, which found that frequencies above 3 kHz were attenuated by the throat. Figures 5(b) and 5(c) show that the upper lip and nasal bone are able to pick up some of the high-frequency content of the fricatives. Figure 5(c) also shows that the nasal sound /n/ is disproportionately amplified at low frequencies; this amplitude increase is both noticeable and unnatural-sounding when listening to recordings of the nasal bone signals.

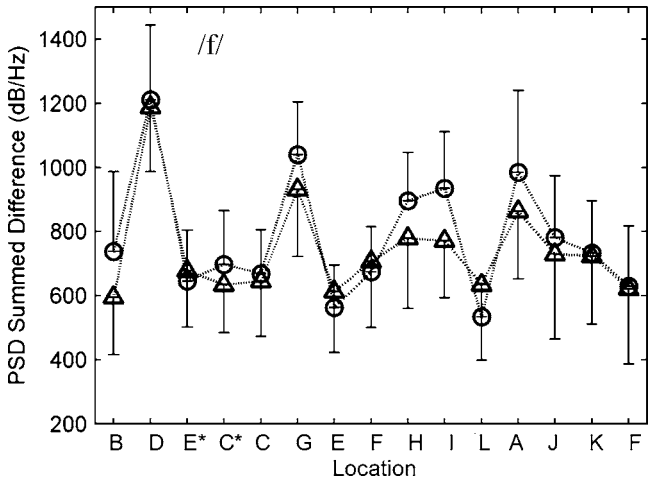


FIG. 4. Sound /f/ normalized power spectral density summed difference. ○: male speakers; △: female speakers.

E. Perceptual ranking

Figure 6 shows a comparison of the average perceptual rating rank and the average PSD_{SD} rank for the four subjects included in the perceptual study. The dashed line has a slope of 1, indicating where the data would lie given a direct one-to-one correlation between the PSD_{SD} rank and the perceptual rating rank. The data do show that, for the most part, a higher rating rank corresponds to higher PSD_{SD} rank. However, there were three outliers: the zygomatic, mastoid, and upper neck. The upper neck has a much lower perceptual rank than PSD_{SD} rank, while the zygomatic and mastoid have perceptual ranks higher than the PSD_{SD} rank. The correlation coefficient of the average rating rank to the average PSD_{SD} rank is 0.57 for all locations. With the three outliers removed the correlation coefficient improves to 0.90.

F. Signal-to-noise ratio and background noise

Figure 7 and Table VII show the average SNR for the sound /ɔ/ over all subjects with and without the presence of 95-dB white noise in the background. These data show that all locations are influenced somewhat by the presence of

TABLE III. Average PSD_{SD}, male speakers. All values dB/Hz.

	Sounds							
Location	/a/	/ɔ/	/i/	/u/	/m/	/n/	/f/	Average
D	**445**	**451**	**621**	**431**	684	594	1212	634
B	969	758	794	627	**531**	**520**	737	666
E*	717	829	798	667	694	684	646	719
C*	779	827	961	681	824	747	697	788
C	804	801	965	745	830	799	668	802
E	933	947	922	943	791	816	563	845
F*	894	946	1069	771	801	812	674	853
G	849	792	1225	581	780	740	1040	858
L	975	1009	941	975	807	874	**533**	873
J	985	907	1183	729	798	808	781	884
H	908	876	1167	697	846	822	896	887
K	886	852	1228	730	892	905	733	889
I	925	863	1196	703	821	822	934	895
F	1008	982	1067	952	886	912	630	920
A	964	918	1162	759	835	863	985	927

background noise, some considerably more than others. The areas least affected are the neck locations, the mandible, and the mastoid. Although reduced significantly in the presence of noise (~10 dB), the nasal bone SNR is still in the top four with the locations on the neck.

IV. DISCUSSION OF RESULTS

A. Influence of location

Figure 3 shows that after about the best three to five locations, the PSD_{SD} values for the remaining locations remain comparable, indicating that these first few locations may match the microphone spectrum better than the rest, but that the remaining locations have similar PSD_{SD} values.

No single location was found to have the lowest PSD_{SD} for all sounds; that is, some locations had lower PSD_{SD} values for some sounds than others. For both male and female speakers, the vowels had the lowest PSD_{SD} values above the upper lip. Vowels are shaped in the mouth using the lips and tongue and are transmitted primarily through the open mouth. The accelerometer closest to the area where the sounds are shaped and transmitted was located above the upper lip, directly over where the sounds are being transmitted. It is, however, somewhat surprising that the upper lip had a low PSD_{SD} value given its compliant tissue composition. This could be attributed to the accelerometer possibly picking up the speech signal through the air as opposed to primarily through the skin. Table VII shows that the upper lip SNR drops from 8.4 to 1.7 dB in the presence of 95-dB background noise. This suggests a potentially rather high sensitivity of the accelerometer on the upper lip to airborne acoustic waves from the talker's speech.

The nasal sounds /m/ and /n/ are also affected by mouth shape, but no air flows through the mouth and thus the sound is mainly transmitted through the nasal passages. This resulted in the accelerometer on the nasal bone having lower PSD_{SD} values for the nasal sounds than at other locations.

TABLE IV. Average PSD_{SD}, female speakers. All values dB/Hz.

	Sounds							
Location	/a/	/ɔ/	/i/	/u/	/m/	/n/	/f/	Average
B	618	663	767	517	**497**	**530**	**595**	598
D	**424**	**414**	**677**	**321**	669	578	1189	610
E*	659	786	908	551	615	576	678	682
C*	693	746	919	545	709	615	634	694
C	724	798	937	596	683	637	645	717
I	797	710	1138	614	669	668	772	767
J	852	756	1093	607	674	692	730	772
K	802	705	1115	602	740	737	724	775
E	911	907	988	759	718	723	613	803
F*	870	923	1048	666	716	699	707	804
F	955	929	1033	772	794	763	620	838
L	953	964	998	790	786	772	634	843
H	950	854	1256	580	753	730	779	843
A	886	820	1183	642	765	770	863	847
G	936	859	1439	654	752	746	932	902

TABLE V. Average PSD_{SD} subject rank, male speakers.

	Sounds							
Location	/a/	/ɔ/	/i/	/u/	/m/	/n/	/f/	Average
B	3.6	5.1	3.6	4.7	**1.4**	**1.7**	7.3	3.9
D	**1.1**	**1.2**	**1.4**	**1.6**	5.4	3.2	14.2	4.0
E*	3.9	5.8	2.9	5.6	3.2	4.4	5.3	4.4
C*	5.1	5.6	5.5	6.1	9.1	5.9	7.1	6.3
C	5.9	6.0	5.9	8.2	10.0	8.6	5.6	7.2
G	7.2	5.9	12.3	3.8	6.9	5.9	13.4	7.9
E	9.9	11.1	5.0	13.5	7.3	8.7	2.9	8.3
F*	8.6	9.3	8.6	9.6	8.3	8.4	5.6	8.4
H	9.0	8.3	11.4	6.7	9.3	8.7	11.2	9.2
L	11.1	12.9	6.0	13.4	8.9	10.6	**1.9**	9.3
I	9.9	8.1	12.2	7.4	8.7	8.9	12.1	9.6
J	12.1	9.9	12.1	8.0	8.7	9.0	8.6	9.8
K	8.9	7.8	13.2	8.6	11.1	12.9	7.7	10.0
A	11.1	10.8	11.0	8.9	9.5	10.6	11.9	10.5
F	12.7	12.4	8.8	13.9	12.2	12.5	5.0	11.1

It is noted that a low PSD_{SD} value indicates good agreement between the the spectra of the accelerometer and the microphone signals, and this usually—but not always—correlates with a clearer and/or higher perceived quality accelerometer signal. This is discussed more in Sec. IV E.

During the study the same type of transducer was used at each location, and no attempt was made to improve sound transmission via impedance matching. The impedance of areas above soft tissue, such as on the neck, may be very different from the impedance of tissue over bony structures. This is a limitation of the current study, and it is recommended that further research investigate the implementation of devices that match the impedance of the various areas.

It is noted that one possible method of identifying ideal contact microphone locations is to use perturbation theory to identify locations of formant pressure antinodes along the vocal tract. There may be higher skin acceleration levels at the skin surface near antinodes. Perturbation theory could also yield insight as to why some locations performed better than others. However, perturbation theory is only applicable within the vocal tract itself, and does not extend to the skin surface; thus, further study would be needed to identify a relationship between formant pressure antinode locations and quality of skin vibration signals near these locations.

B. Difference between male and female speakers

Tables III–VI show that, when using the PSD_{SD} to compare the spectra of different locations, the top five locations are the same for both male and female speakers, but the other locations have different rankings between gender. One notable difference is that for males, the location over the vocal folds (G) had the sixth highest average rank, while for females it ranked last. This suggests that throat microphones placed near the vocal folds may be expected to match the microphone spectrum poorly for female speakers. However, for female speakers, the location on the upper neck (I) had the sixth best overall rank, indicating that if the neck is the

TABLE VI. Average PSD_{SD} subject rank, female speakers.

	Sounds							
Location	/a/	/ɔ/	/i/	/u/	/m/	/n/	/f/	Average
B	2.6	4.4	2.6	4.8	**2.4**	**3.2**	**3.5**	3.4
D	**1**	**1**	**1.5**	**1**	6.8	3.9	14.6	4.3
E*	3.6	6.9	5	4.9	3.2	3.3	6.7	4.8
C*	4.4	5.6	5	4.8	8.4	4.5	6	5.5
C	5.1	7.2	5.4	7.3	6.8	6	5.8	6.2
I	6.9	5	10.6	7.1	5.8	6.7	9.7	7.4
J	8.6	6.7	9.8	8	5.5	7.9	8.3	7.8
K	7.6	4.7	10.2	7.8	9.6	10.5	8.2	8.4
E	10.6	11.6	6.3	12	8	9.5	4.7	8.9
F*	10.1	11.6	8.2	9.9	8.4	8.5	8.1	9.3
H	12.2	10.4	13.4	6.2	10.1	10.1	9.5	10.3
A	10.4	8.7	11.7	9.4	11.4	11.3	11.9	10.7
L	12.3	13.4	7.6	14	11.1	11.6	5.3	10.8
F	13.1	12.4	7.7	13.5	12.4	12.1	5.3	10.9
G	11.7	10.4	15	9.3	10.1	10.9	12.4	11.4

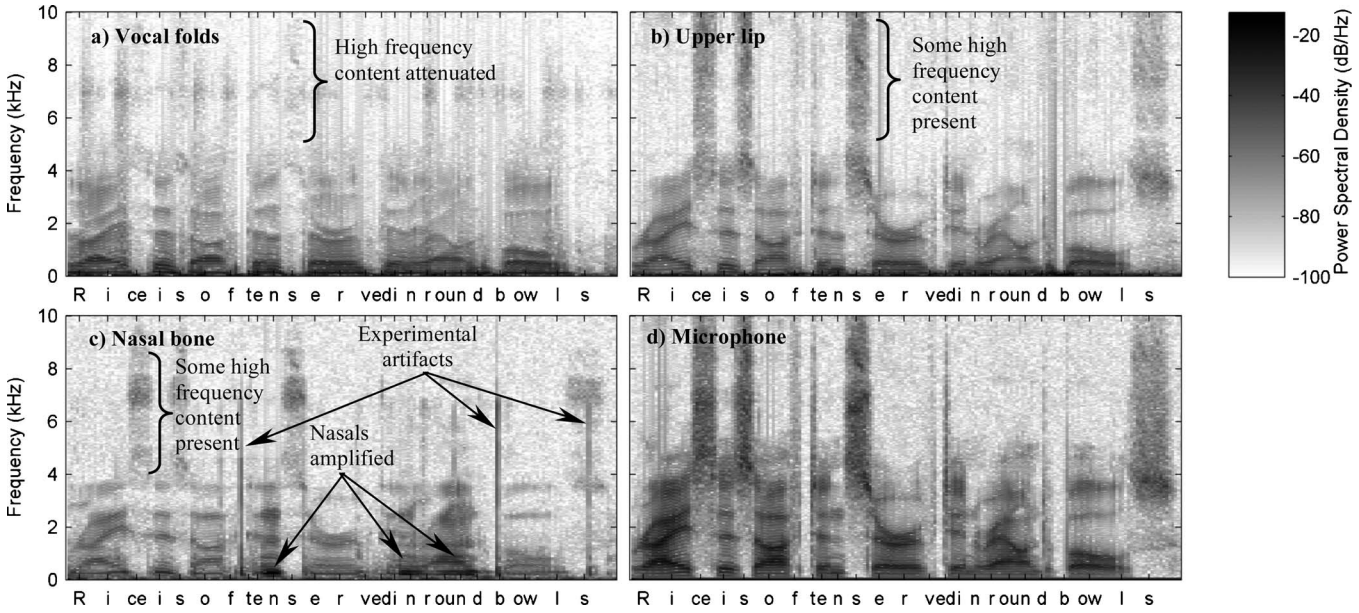


FIG. 5. Spectrogram of a male subject saying "Rice is often served in round bowls." (a) Over the vocal folds; (b) above the upper lip; (c) over the nasal bone; (d) microphone. Experimental artifacts were only present in the nasal bone recording (e.g., noise caused by wire motion and tapping) and are noted.

preferred or necessary location for a contact microphone, the placement on the neck may benefit from vertical adjustment based on the speaker's gender.

Tables III and IV show that females generally had lower PSD_{SD} values than males, indicating that, on average, the female speakers' accelerometer signals matched the microphone signals better than the male speakers. This result is generally consistent across locations and subjects, but the differences between the male and female PSD_{SD} average values were rather small. There were a few exceptions to this, however. Male speakers on average had lower PSD_{SD} values than females over the vocal folds for sounds /u/, /a/, /n/, /ɔ/ and /i/. For the sound /i/, males had a lower PSD_{SD} for the locations above the upper lip, zygomatic, side of neck, forehead, and chin.

The average fundamental frequency for male speakers over the vowel and nasal sounds was 116.8 Hz with a standard deviation of 11.1 Hz. The average fundamental frequency for female speakers over the vowel and nasal sounds was 221.7 Hz with a standard deviation of 35.1 Hz. It is thus possible that some of the gender-associated differences in these results could simply be attributed to the male speakers having lower fundamental frequencies than the female speakers, and may not necessarily be due to general differences between genders in terms of anatomical composition.

C. Influence of accelerometer sensitivity

Accelerometers were placed on both sides of the head at the temple, zygomatic bone, and the mastoid process. An accelerometer with 10.2 $mV/(m/s^2)$ sensitivity was placed on one side while an accelerometer with 102 $mV/(m/s^2)$ sensitivity was placed on the other at each of these three

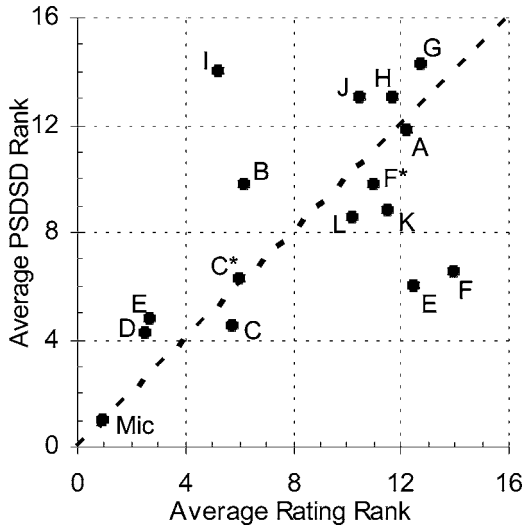


FIG. 6. Comparison of PSD_{SD} ranking and perceptual rating ranking for four randomly selected subjects.

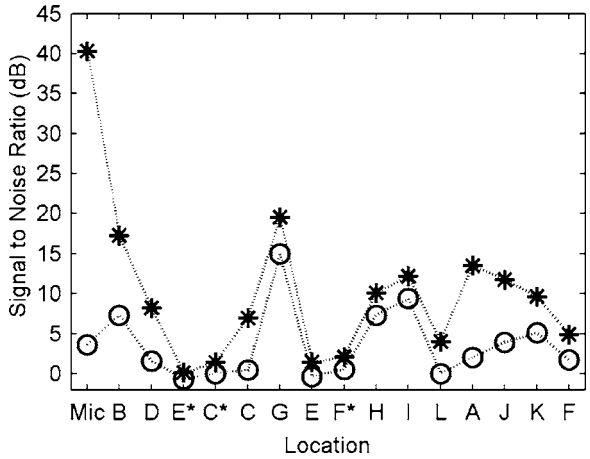


FIG. 7. Sound /ɔ/ average signal-to-noise ratio over all subjects. -*- no noise; -○- 95-dB background noise.

TABLE VII. Sound /ɔ/ average signal to noise ratio over all subjects.

Location	Signal to Noise Ratio (dB)	
	No noise	95-dB noise
Microphone	40.3	3.8
G-vocal folds	19.4	15.0
B-nasal bone	17.2	7.9
A-chin	14.6	2.4
I-upper neck	12.7	9.3
J-front of ear	11.4	3.7
H-side of neck	10.5	7.5
K-mandible	9.7	5.2
D-upper lip	8.4	1.6
C-temple	7.1	0.5
F-mastoid	5.4	1.9
L-forehead	4.4	0.1
F*-mastoid	3.1	0.7
C*-temple	1.8	0.2
E-zygomatic	1.6	−0.2
E*-zygomatic	0.49	−0.4

locations. For the present discussion, it is assumed that the speech signals were transmitted symmetrically to each side of the head. It can be seen from Fig. 3 and Tables III–VI that accelerometers with the higher sensitivity (indicated by *) in most cases yielded lower PSD_{SD} values and in all cases yielded better *overall* rankings than the corresponding lower sensitivity accelerometers. However, it is interesting to observe from Tables V and VI that the higher sensitivity accelerometers all yielded poorer rankings for /f/. This is opposite to what was expected, and is attributed to the following. The lower sensitivity accelerometers in these locations have very little response to the low-amplitude /f/ vibrations; thus, the spectra for these accelerometers are essentially due to noise. At the same time, the microphone spectra for /f/ were relatively flat. Therefore, when normalized, the PSD plots of the lower sensitivity devices appear to have a frequency response that matches the microphone better than the higher sensitivity devices. Notwithstanding this difference in fricative response, the *overall* lower ranking indicates that a higher sensitivity accelerometer (or other type of contact microphone) could be used to transmit a signal that better matches the spectrum of a clean microphone signal, possibly increasing the overall speech clarity. However, this improvement may only be marginal. In some cases (e.g., C* and C for male and female speakers) the difference between the higher and lower sensitivity accelerometers was very small, which indicates a higher sensitivity device may not yield a substantial improvement at all locations.

Contrary to what was expected, Fig. 7 shows that the higher sensitivity accelerometers yielded *lower* SNR than the lower sensitivity accelerometers placed at symmetric locations on the head. However, even though the SNR was lower for higher sensitivity accelerometers in these locations, Fig. 7 shows their perceptual rating to be better than the lower sensitivity accelerometers.

Figures 6(a)–6(c) show that the various vibration transmission paths clearly attenuate the intensity of higher frequencies, but they are in some places still detectable. The higher sensitivity accelerometers have signals that better match the frequency content of the microphone signal and are preferred by listeners over lower sensitivity accelerometers. For real world applications signal processing could be used to amplify the attenuated high-frequency content in order to increase speech clarity. However, size and cost are important considerations for practical implementation, and higher sensitivity devices often cost more, are typically larger, and the benefit may not be substantial enough to outweigh these considerations.

D. Fricative sound transmission and formation

The fricative /f/ is formed by unsteady airflow generated at a small opening between the teeth and lower lip; the vocal folds are not vibrating. Consequently /f/ is relatively quiet. It was speculated that, due to close proximity to the sound source, the upper lip would possibly yield the best ranking for /f/. However, for male and female speakers, the upper lip yielded the worst ranking; the best-ranked location for males for /f/ was on the forehead. This ranking result and consideration of Fig. 2(e) suggest that fricative sounds may be too highly attenuated by body tissue to be adequately detected at most locations on the skin. This conclusion is further supported by noting that, when we compared the PSD of a normalized white noise signal to the microphone PSD for /f/, the white noise ranked better than all other locations. Although the data collection and analysis methods seem to work well for the voiced sounds, the results for the fricative sound /f/ indicate that these methods may not work well for unvoiced sounds. Further investigation into the transmission to the skin surface of fricatives and other phonemes with significant nonvoiced acoustic sources is necessary to better understand this behavior.

E. Power spectral density summed difference vs perceptual ratings as a metric

Although some of the high-frequency content is attenuated by the body tissue, the speech signals that were detected on the skin surface were still mostly understandable. Figure 6 shows that the average perceptual rating rank generally increases with average PSD_{SD} rank. The major outliers to this are locations E, F, and I. The recordings at locations E and F had some experimental noise from wires tapping due to jaw motion during speech that overpowered the speech signal. This may have lowered the perceived quality of the recording for these locations. The recordings for location I (upper neck) have very large SNR, which is attributed to the large vibration amplitudes due to close proximity to the vocal folds. Since the signal at the upper neck lacks high-frequency content (which worsens the PSD_{SD} rank), the signal is slightly "muffled;" however, it is also relatively devoid of background noise, possibly resulting in a higher perceived quality. This indicates that, while some locations may not yield spectra that match the microphone spectrum well, they still can yield signals that are understandable and of reasonable perceived quality. The correlation coefficient jumps from 0.57 with all locations to 0.90 without the outlier locations E, F, and I. This indicates that for most locations there

is a relationship between PSD_{SD} rank and rating rank; in other words, for most locations the degree to which the accelerometer's spectrum matches the microphone's spectrum is relatively well-correlated with the perceived quality of the signal. The correlation is not "fail-safe," though, as the outliers show.

It may seem surprising that the forehead location (L) did not rate better given that it is one of the preferred locations for commercially available contact microphones. It is important to note that the raters in this study were not just judging intelligibility, but rather were asked to rate quality. The recordings at the forehead, while understandable, had low signal amplitudes which resulted in a lower SNR than some of the locations that rated better. An average rating rank around 10 for the forehead location does not imply poor intelligibility; rather, it indicates that the lower-ranked recordings were preferred by the raters. A higher sensitivity accelerometer located at the forehead may have resulted in ratings that favored this location.

Another notable result is that both the PSD_{SD} analysis and the perceptual raters indicate that the location over the vocal folds (G) was one on the worst-ranked locations. This is interesting because the area near the vocal folds is one of the most commonly used locations for contact microphone placement. These results indicate that, in order to have a signal that is preferred by listeners, this region is not a good location for contact microphone placement.

It is also interesting to note that there seem to be three major groupings in the perceptual rankings. The upper lip (D) and the zygomatic (E*) have average perceptual rating ranks between 2 and 3. The upper neck (I), nasal bone (B), and the temple (C and C*) also have similar perceptual rating ranks between 5 and 6. The remaining locations have average perceptual ranks between 10 and 14.

F. Signal-to-noise ratio

Previous studies have emphasized the superior signal-to-noise ratios of contact microphones in high noise environments. For the sound /ɔ/ using accelerometers we have found that this is the case for some locations, although some locations yielded generally poor signal-to-noise ratios. For the sound /ɔ/ Fig. 7 shows, in quiet environments, all accelerometer locations had an SNR ratio much lower than the microphone signal. However, with 95-dB background noise, five locations had better signal-to-noise ratios than the microphone. These locations are the neck locations (G, H, and I), the nasal bone (B), and the mandible (K). An important consideration to note is that the accelerometers used in this study were not directional or shielded from external acoustical energy. The drop in SNR seen in many of the locations may be reduced by implementing an accelerometer with its external surface acoustically shielded from the surrounding environment. Further, improved impedance matching and application of an external force on the accelerometer may improve noise elimination. These results are for only one vowel sound but nevertheless show that not all skin locations yield improved SNR. Further work should be done to report the effects of location on SNR for other sounds.

G. Implications for contact microphone performance

The results of this study suggest that a multilocation device may be useful due to different phonemes being sensed better at different locations. An example of this can be seen in Fig. 5. The location over the vocal folds senses the low-frequency content very well, while attenuating the high-frequency content. The nasal bone, however, is able to detect the high-frequency content. A combination of the low-frequency content from the vocal folds and the high-frequency content from the nasal bone could result in a signal that more accurately represents the microphone signal. However, although a location may transmit speech well, such as above the upper lip, being able to wear the microphone at that location may not be feasible. Therefore, a combination of locations that each yield overall lower performance, but that exhibit favorable individual performance for select phonemes, may result in an overall improved signal.

The present data further elucidate the complications arising from different voice production mechanisms, resulting in unevenness of the transmission of the various speech signals through the skin. For example, the nasal bone was found to be highly sensitive to nasal sounds. The consequence of this was that the overall sound level rose greatly during nasal sound production, resulting in unnatural-sounding speech.

The contact pressure of the accelerometers on the skin was not controlled or measured; thus, the results presented may be influenced somewhat by the accelerometer attachment method used. This illustrates a complication that may arise in real world implementation of contact microphones, as transducers will likely be attached to the skin without perfect control of contact pressures. We recommend further investigation on the effects of varying contact pressure of contact microphones.

V. SUMMARY AND CONCLUSIONS

The objective of this study was to assist in the development of improved contact microphones and associated signal processing methods by contributing to an improved understanding of the frequency response of the skin at various locations on the head and neck during speech. The speech signal detected on the skin was characterized by attaching accelerometers to the skin and having subjects voice a phrase and various phonemes. The accelerometer and microphone PSDs were compared and the accelerometer locations were ranked according to how well their signal's PSD corresponded to the microphone PSD for each phoneme. A spectrogram of the phrase was also used to compare the amplitudes of various frequencies at selected locations. A perceptual listening test was conducted to compare the PSD rankings to perceptual rankings. The signal-to-noise ratio was found for each location with and without the presence of background noise to determine sensitivity to external noise. The following conclusions were reached as a result of this study:

(1) Locations other than on the throat can adequately pick up the speech signal from the skin. Some of these locations yielded signals with spectra better matching the microphone and that rated higher than the throat signal.

(2) While the throat attenuates the signal intensity of high frequencies, some high-frequency content can be detected at other locations on the head. Fricative sounds are not transmitted well through skin and tissue and should be studied further.
(3) More sensitive devices may yield a more understandable signal, but practical application may be difficult.
(4) For the subjects tested, vowels matched the microphone spectra best above the upper lip, whereas nasals matched the microphone spectra best on the nasal bone.
(5) Using PSD_{SD} as the metric, for all subjects tested the locations that matched the frequency content of the microphone the best are generally common to both male and females. These locations are the nasal bone, above the upper lip, both temple locations and the zygomatic*.
(6) Using perceptual ratings as a metric for the four randomly selected subjects, the highest rated locations where found to be the nasal bone and the zygomatic* followed by both temple locations, above the upper lip and the upper neck.
(7) For the four randomly selected subjects, perceptual rankings generally followed the PSD_{SD} ranking, with a few outliers. This indicates that locations that match the spectrum of the microphone are also generally (but not always) preferred by listeners.
(8) With the addition of background noise, for the vowel sound /ɔ/, not all accelerometer placement locations yielded improved signal-to-noise ratios. Some locations were found to be sensitive to external noise while others were relatively insensitive to noise.
(a) Combination of signals from multiple locations may be beneficial to achieve high-quality speech transmission.

Since the coupling between the skin and the accelerometers was not controlled, the preferred contact microphone locations identified in this study should be treated with some caution. It is recommended that future studies quantify the effects of contact pressure on the skin frequency response at the various locations.

Future work is also suggested to analyze more phonemes (including more fricatives and stop sounds), to study how well each location and sound performs in the presence of background noise, and to investigate the potential for formulating a transfer function that improves speech quality for all sounds at various locations.

ACKNOWLEDGMENTS

The authors thank Dr. Christopher Dromey for the use of his sound booth and perceptual rating software. The helpful suggestions of the reviewers are gratefully acknowledged. J.M. also acknowledges support of a Rocky Mountain NASA Space Grant Consortium Fellowship. Early support by Tri-Mast International is also acknowledged.

Acker-Mills, B. E., Houtsma, A. J. M., and Ahroon, W. A. (**2004**). "Speech intelligibility in noise using throat and acoustic microphones," USAARL Report No. 2004-13.

Cheyne, H. A. II (**2002**). "Estimating glottal voicing source characteristics by measuring and modeling the acceleration of the skin on the neck," Ph.D. Dissertation, Massachusetts Institute of Technology, Cambridge, MA.

Cheyne, H. A., Hanson, H. M., Genereux, R. P., Stevens, K. N., and Hillman, R. E. (**2003**). "Development and testing of a portable vocal accumulator," J. Speech Lang. Hear. Res. **46**, 1457–1467, December 2003.

Dromey, C., Nissen, S., Roy, N., and Merril, R. (**2008**). "Articulatory changes following treatment of muscle tension dysphonia: Preliminary acoustic evidence," J. Speech Lang. Hear. Res. **51**, 196–208 (**2008**).

Dupont, S., Christophe, R., and Bachelart, D. (**2004**). "Combined use of close-talk and throat microphones for improved speech recognition under non-stationary background noise," in Proceedings of Robust 2004 (Workshop (ITRW) on Robustness Issues in Conversational Interaction), Norwich, August 2004.

Garciarena, M., Franco, H., Sonmez, K., and Bratt, H. (**2003**). "Combining standard and throat microphones for robust speech recognition," IEEE Signal Process. Lett. **10**(3), 72–74.

Hayes, D. P., and Meltzer, L. (**1967**). "Bone-conducting microphones," IEEE Trans. Very Large Scale Integr. (VLSI) Syst. **80**(4), 619–624.

Horáček, J., Vesely, J., Pesek, L., and Vohradnik, M. (**2004**). "Fundamental dynamic characteristics of human skull. I. Experimental modal analysis and FE modeling of basic vibration properties," Eng. Mech. **11**(2), 139–158.

Meltzner, G. S., Kobler, J. B., and Hillman, R. E. (**2003**). "Measuring the frequency response function of laryngectomy patients: Implications for the design of electrolarynx devices," J. Acoust. Soc. Am. **114**(2), 1035–1047.

Moser, H. M., and Oyer, H. J. (**1958**). "Relative intensities of sounds at various anatomical locations of the head and neck during phonation of the vowels," J. Acoust. Soc. Am. **30**(4), 275–277.

Norton, R. L., and Bernstien, R. S. (**1993**). "Improved laboratory prototype electrolarynx (LAPEL): Using inverse filtering of the frequency response function of the human throat," Ann. Biomed. Eng. **21**, 163–174.

Shimamura, T., and Tamiya, T. (**2005**). "A reconstruction filter for bone conduction speech," 48th Midwest Symposium on Circuits and Systems 2005, pp. 1847–1850.

Snidecor, J. C., Rehman, I., and Washburn, D. D. (**1959**). "Speech pickup by contact microphone at head and neck positions," J. Speech Hear. Res. **2**(3), 277–281.

Svec, J. G., Titze, I. R., and Popolo, P. S. (**2005**). "Estimation of sound pressure levels of voiced speech from skin vibration of the neck," J. Acoust. Soc. Am. **117**, 1386–1394.

Welch, P. D. (**1967**). "The use of fast Fourier transform for the estimation of power spectra: A method based on time averaging over short, modified periodograms," IEEE Trans. Audio Electroacoust. **AU-15**, 70–73.

Wodicka, G. R., and Shannon, D. C. (**1990**). "Transfer function of sound transmission in subglottal human respiratory system at low frequencies," J. Appl. Physiol. **69**(6), 2126–2130.

Zhang, Z., Zicheng, L., Sinclair, M., Acero, A., Deng, L., Droppo, J., Huang, X., and Zheng, Y. (**2004**). "Multi-sensory microphones for robust speech detection, enhancement and recognition," Proceedings of the IEEE International Conference on Acoustics, Speech, and Signal Processing, 2004 ICASSP'04, Vol. **III** pp. 781–784.

Zheng, Y., Liu, Z., Zhang, Z., Sinclair, M., Droppo, J., Deng, L., Acero, A., and Huang, X. (**2003**). "Air- and bone-conductive integrated microphones for robust speech detection and enhancement," IEEE Automatic Speech Recognition and Understanding Workshop (ASRU) 2003, Virgin Islands, USA, 2003-11-30, pp. 249–254.

Structural acoustics model of the violin radiativity profile

George Bissinger
Physics Department, East Carolina University, Greenville, North Carolina 27858

(Received 14 July 2008; revised 6 December 2008; accepted 6 December 2008)

Violin radiativity profiles are dominated by the Helmholtz-like $A0$ cavity mode (~280 Hz), first corpus bending modes $B1^-$ and $B1^+$ (~500 Hz), and BH and bridge-filter peaks (~2.4 kHz and ~3.5 kHz, respectively), with falloff above ~4 kHz. The $B1$ modes—dependent on two low-lying free-plate modes—are proposed to excite $A0$ via coupling to $B1$-driven in-phase f-hole volume flows. VIOCADEAS data show that $A0$ radiativity increases primarily as $A0$-$B1^-$ frequency *difference* decreases, consistent with Meinel's 1937 experiment for too-thick/too-thin plate thicknesses, plus sound post removal and violin octet baritone results. The vibration→acoustic energy filter, F_{RAD}, computed from shape-material-independent radiation and total damping, peaks at the critical frequency f_{crit}, estimated from a free-plate mode by analogy to flat-plate bending. Experimentally, f_{crit} decreased as this plate mode (and $B1^+$) frequency increased. Simulations show that increasing plate thicknesses lowers f_{crit}, reduces F_{RAD}, and moves the spectral balance toward lower frequencies. Incorporating string→corpus filters (including bridge versus bridge-island impedances) provides a model for overall violin radiativity. This model—with $B1$ and $A0$-$B1$ couplings, and f_{crit} (computed from a free-plate mode important to $B1$) strongly affecting the lowest and highest parts of the radiativity profile—substantiates prior empirical $B1$—sound quality linkages. © *2008 Acoustical Society of America.* [DOI: 10.1121/1.3006957]

PACS number(s): 43.75.De, 43.40.At [NHF] Pages: 4013–4023

I. INTRODUCTION

"The violin family presents many unsolvable problems; its shape and the peculiarities of its materials were certainly not selected with regard to convenience in analysis. This, however, only emphasizes the need for understanding the simplicities that do exist and may condone a certain amount of oversimplification." (Schelleng[1])

After two centuries of scientific work, Weinreich in 1992 distilled the continuing interest in the violin into "The New Secret of Stradivarius"[2] (edited form), viz., "… if we hand any experienced player a violin and ask that it be classified into one of three categories [student, decent professional, fine solo]… the judgment would not take more than about 30 s. … But the tantalizing fact is that *no such specification which successfully defines even coarse divisions in instrument quality is known*." (Weinreich's italics). Even a much-expanded set of descriptive parameters made possible by utilizing some of the latest technologies for simultaneous vibration and radiation measurements on 17 bad-good-excellent quality-rated violins, including three-dimensional (3D) modal analyses of three exemplary old-Italian violins, showed little in the way of quantitative "robust" differences between excellent and bad violins, with one notable exception.[3]

Since a great violinist can make a bad violin sound good, while a bad violinist cannot make a great violin sound good (see Saunders' remarks about Jascha Heifetz and the "standard-of-badness" violin[4]), the violinist's ability to manipulate the *relative* harmonic strengths in the driving force, which does not in any way affect the violin itself, clearly can compensate for perceived acoustic deficiencies. Consider also that violinists preferring a certain type of sound might reasonably be expected to pick just those violins that best give them that sound. Two conclusions—one obvious, and one more subtle—can be drawn: (1) the major determiner of violin sound quality is the violinist, not the violin; (2) even a "bad" violin somehow contains the essence of good-violin sound, needing only the proper driving force at the bridge to elicit its capabilities. Considering just the implications of earlier research by Meinel,[5] Saunders, and Dünnwald,[6] this is hardly a new conclusion.

However, when violins of the same shape, materials, and construction show similar low-lying "signature" modes and similar overall band-average mobility and radiativity profiles,[3] we might logically deduce that properly setup violins *are* pretty much the "same." (A physics-based argument based on building a solid model in a finite element program will reach a similar conclusion.) This seemingly unhappy inference recommends a different potentially positive change in perspective. Without an evanescent "secret" to pursue, an alternate approach employing relatively few normal modes—the "atoms" of vibration—rather than a conglomerated response of all the modes at particular frequencies, when combined with measured radiation and damping properties, offers a powerful tool that readily marries materials and responses.

Furthermore, if we allow that the relative *proportions* of certain behaviors can cause a much more strongly differentiated *psychoacoustic* response than underlying measurable mechanical-acoustic changes would seem to warrant (see Ref. 5 for such comments), a viable basis for reliable quality differentiation by the violinist—but not the scientist—becomes quite feasible. (Akin to how adding a very little salt—relative to the overall mass—can greatly change the perceived taste of a steak.)

Adopting this "sameness" conjecture and relying on the zero-mass-loading excitation-response, normal-mode and materials database that includes 3D modal analyses[3]—hereinafter labeled by the acronym VIOCADEAS (VIOlin Computer Aided Design Engineering Analysis System)[7]—we search for plausible structural acoustics mechanisms to produce similar, but "different," radiativity profiles that modulate driving-force harmonics to create violin sound. While this analysis has elements of speculation, oversimplification, and, given its subject, controversy, it should be viewed rather as an attempt, in the spirit of Schelleng, to make "systems-level" sense of the overall shape of the violin radiativity profile.

II. EXPERIMENTAL SYSTEMATICS

Radiativity $R(\omega)$ is the complex ratio of pressure/force; all VIOCADEAS far-field pressures (and surface velocities) were normalized to the driving-force applied at the violin bridge G-corner, then mean square averaged over 266 microphone measurements around a sphere in an anechoic chamber[3] to create a rms radiativity $\langle R\rangle$. $\langle R\rangle$ was then frequency band averaged to create a radiativity "profile," a simplified "parameter" at the end of the energy chain closely allied to what the violinist hears when holding and playing the violin.

The other crucial parameter was mobility $Y(\omega)$, the complex ratio of surface velocity/force, mean square averaged over the corpus (top+ribs+back) to create rms corpus mobility $\langle Y_{\text{corpus}}\rangle$. The new 3D mobility measurements offered important insights into extensional ["in plane" (IP)] motions as well as the flexural ["out of plane" (OP)], especially so in the region around the bridge feet labeled the "bridge island."[3] (Coordinate system origin on the top plate between bridge feet: Y-axis perpendicular to the violin "plane," X-axis across, and Z-axis along the violin.)

A. Mobility-radiativity systematics

VIOCADEAS band-averaged profile results for $\langle R\rangle$ (17 violins) and $\langle Y_{\text{corpus}}\rangle$ (14 violins, surface-normal direction) are shown in Fig. 1 [standard deviation (s.d.), error bars denote *intraband* variations only]. Earlier analysis, judging only the magnitude of radiativity across the whole 4 kHz span, concluded that "excellent" (all old-Italian) violins had no advantage over bad violins overall. Quality-related differences in radiativity profiles were characterized simply by noting that excellent violins had somewhat flatter (without ever being flat), less compressed along the frequency axis, less-peaky overall profiles, with higher values at the frequency extremes.[3] Below 4 kHz only one significant difference between bad and excellent violins was observed: $A0$, the only resonance in the lowest octave, was significantly stronger for excellent violins than bad, with "good" violins having intermediate values.

In 1946, Saunders, the pre-eminent American violin researcher of his time, summarized decades of research on the violin (including close interactions with violinists such as Jascha Heifetz), by noting that eminent violinists wanted two qualities in a violin: "first, great power, and second, an even

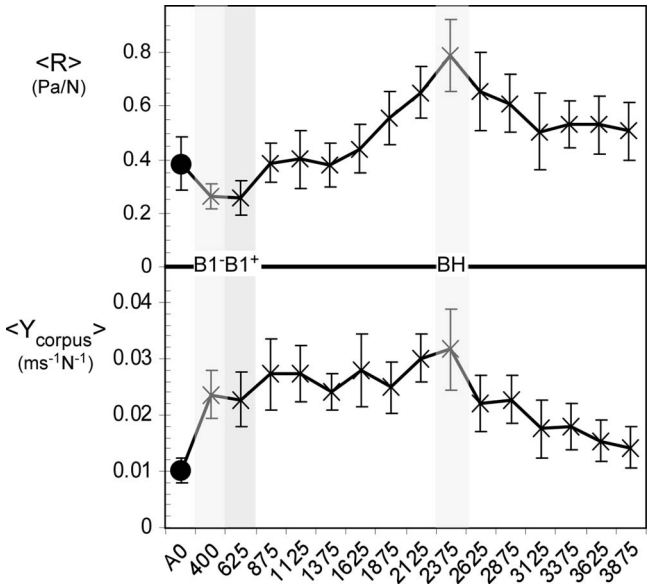


FIG. 1. (Top) 17-violin radiativity $\langle R\rangle$ and (bottom) 14-violin corpus mobility $\langle Y_{\text{corpus}}\rangle$ vs band-center frequency ($A0$, ●). BH peak near 2.4 kHz. (s.d. error bars reflect intraband variations only.)

distribution of strength among all ranges of frequency, *the lowest octave being of special importance* [my italics]."[4] VIOCADEAS data show a clear dependence of the so-called "warm, full" quality criterion on $\langle R_{A0}\rangle$. Clearly, Saunders' observation is still right to the mark.

We commence with a brief description of the signature modes common to all violins tested (and to a complete violin octet[8]). These are of particular importance to this discussion since they determine the acoustic output for harmonics in the crucial open string region 196–660 Hz. Signature modes fall into two major classes: (1) *cavity modes*: $A0$-Helmholtz-like, $f_{A0}\approx 280$ Hz, characterized as dual mass plugs oscillating in phase in the f-holes under the influence of the cavity "spring," always the lowest frequency mode in the violin and always a strong radiator, and $A1$—the first longitudinal mode, sometimes an important radiator (via induced surface vibrations) with $f_{A1}\approx 1.7xf_{A0}$, coupled to $A0$ and strongly affecting its volume dependence;[9] (2) *corpus modes*: CBR—the lowest corpus mode near 400 Hz, weakly radiating, with shear-like (along X) relative motion between the top and back plates, and out-of-phase f-hole volume flows, and, most importantly, the first corpus bending modes $B1^-$ and $B1^+$ near 500 Hz, both strong radiators with in-phase f-hole volume flows and strong radiation from the f-holes. (All f-hole volume flow remarks are based on recent "patch" near-field acoustical holography pNAH results from Ref. 10 where a high-spatial-density near-field microphone array was scanned over a rectangular patch above the f-holes, with pressures postprocessed to estimate volume flows from just the f-holes).

Although band averages were normally taken over 250 Hz intervals, the two lowest bands were modified to isolate $A0$ near 280 Hz with an average over the peak ±10 Hz. The 400 Hz band, averaged from 300–499 Hz, included the CBR, $A1$, and $B1^-$ modes. The next band

(500–749 Hz) centered at 625 Hz was dominated by $B1^+$, near 550 Hz. Thus $A0$, $B1^-$, and $B1^+$ dominate the radiativity in these three bands, as notated in Fig. 1.

$\langle R \rangle$ starts high at $A0$ (its very low $\langle Y_{\text{corpus}} \rangle$ clearly distinguishes it from corpus modes), drops down, and then rises again as the combined effect of increasing $\langle Y_{\text{corpus}} \rangle$ and radiation efficiency R_{eff} makes $\langle R \rangle$ grow faster than $\langle Y_{\text{corpus}} \rangle$. Above the BH peak near 2.4 kHz, $\langle R \rangle$ falls off more slowly than $\langle Y_{\text{corpus}} \rangle$ because R_{eff} increases up to the average effective critical frequency $f_{\text{crit}} \approx 3.9$ kHz.[3]

Overall $\langle Y_{\text{corpus}} \rangle$ grows more slowly to its maximum at the BH peak but declines more rapidly above. Although clearly depending on the bridge, this peak has a weak dependence on the bridge top rocking mode frequency f_{rock};[11] experiments by Durup and Jansson have shown that cutting the f-holes is crucial to the appearance of this peak.[12] The $\langle R \rangle / \langle Y_{\text{corpus}} \rangle$ ratio used to estimate f_{crit} showed a relatively smooth behavior well described by a linear trendline.[3] The BH band, except for its magnitude, did not display any unusual attributes, such as unusually large/small R_{eff} or total damping relative to bands below-above. The BH peak in $\langle R \rangle$ thus appears to arise from a mobility peak. Above the BH peak $\langle Y_{\text{corpus}} \rangle$ declines somewhat more rapidly than it grew.

III. RADIATIVITY PROFILE ANALYSIS

To understand the major components of a violin's radiativity profile, it is necessary to (1) establish an $A0$ excitation mechanism at the low-frequency end, aided by pNAH characterizations of f-hole volume flows, (2) understand $B1$ mode dependence on the plate modes 2 and 5, (3) examine extensional-flexural behaviors in the bridge-island region, (4) incorporate bridge-filter effects, (5) treat the plates as flat (successfully used in scaling the violin octet[1,8]), and then (6) exploit R_{eff} and f_{crit} systematics. This analysis starts at the low-frequency end and works up.

A. *A0-B1* coupling

Certainly the most important cavity mode in the violin, strong $A0$ was singled out by Dünnwald as one of five good-violin quality attributes in his 700-violin survey,[6] a conclusion strongly supported in the VIOCADEAS excellent to bad radiativity comparison.[3] Since $A0$ is the only strong radiator in the violin's lowest octave, how exactly do corpus vibrations excite this cavity mode? Cremer addressed this problem by creating an "island" model, believed reliable for the first three or four response peaks (the signature mode region, thereby implying that only corpus modes near $A0$ in frequency were plausible excitation candidates), stating that the cause was "…excitation of the air oscillating in f-holes by the lever mechanism of the bridge; the front and back compress and rarefy the cavity equally and in phase."[13] This model thus assumes direct mechanical excitation where the top plate region in contact with the sound post was coupled via the rigid sound post to the back plate, all moving in phase, with the bass bar bridge foot moving antiphase.

VIOCADEAS results, however, provide a much different view of corpus motion: animations show bridge rigid-body-rocking motion pivoting about the relatively fixed soundpost foot for $A0$ (and $B1$), with maximum amplitude on the bass bar—not sound post—side. CBR, the lowest corpus mode lying between $A0$ and $B1$, does show equal amplitude, antiphase motion for the bridge feet. At frequencies above $B1$ (>0.7 kHz), the motion of the two feet was again approximately equal.[11] Moreover computed corpus-motion-driven volume flows at f_{A0} were almost a factor of 10 smaller than measured $A0$ f-hole volume flows.[10] Obviously an alternative $A0$ excitation mechanism was needed.

It is axiomatic in vibrations that to excite a mode strongly, it is necessary to drive its motion at—or near—an antinode in a way that does not modify its properties significantly, at a frequency close to the resonant frequency for that mode. The fact that $A0$ and the close-by low-lying corpus modes have the largest total damping is obviously advantageous in spreading the response. $A0$ has been characterized experimentally as Helmholtz-like, i.e., having oscillating in-phase volume flows (mass-plug motions, influenced by the cavity volume spring), independent of compliant violin cavity walls[14] or the coupling to $A1$.[9] Such in-phase f-hole volume flows thus define $A0$'s antinodes.

General physical arguments offer support for Cremer's neglect of high-frequency modes as plausible candidates for exciting $A0$: (1) "direct" f-hole volume flows driven by net-volume-change modes are important only where the internal pressure is approximately constant over the cavity, a condition satisfied only by modes below about 0.7 kHz;[10] (2) except for the BH peak, mobility drops with increasing frequency above about 1 kHz (see Fig. 1) and the receptance (displacement/force) falls off as mobility/frequency, hence net-volume changes will drop faster than $1/f$, possibly as fast as $1/f^2$ above 2.4 kHz; (3) since mode shapes increase in complexity as frequency increases, with decreasing nodal line separation and thus smaller possible displacements, the effect again is to decrease net-volume change. All these factors taken together argue strongly against higher frequency modes contributing significantly to $A0$ excitation.

To excite $A0$, *low-lying* corpus modes then should have strong in-phase f-hole volume flows close to $A0$ in frequency. In order of increasing mode frequency, it is possible to eliminate both $A1$, which does not have in-phase f-hole volume flows, rather each f-hole shows acoustic "short" volume flows, and CBR, which has antiphase f-hole volume flows and small volume changes. Below 0.7 kHz, this leaves only the next-higher corpus modes, $B1^-$ and $B1^+$, as likely candidates to excite $A0$ since they are (a) close by, (b) always strongly excited, and (c) radiate ~50% from the f-holes via significant in-phase f-hole volume flows.

$B1$ f-hole volume flows driving $A0$ imply relative $A0$-$B1$ f-hole volume flows have a phase lag and $\langle R_{A0} \rangle$ should increase as the frequency difference Δf between $A0$ and the $B1$ modes decreases. Since cavity mode excitation must in some way come via the corpus, a phase-lag would be expected in any case. Animations of pNAH and modal analysis data with f-hole air and plate motion in proper phase show that $A0$ clearly lags $B1$ by ~90°. (This phase lag can be seen less clearly in the volume velocity holograms, Fig. 4 in Ref. 10).

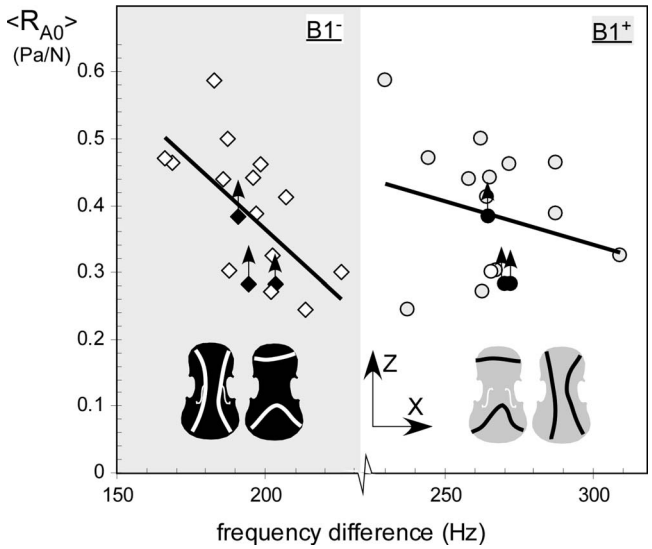


FIG. 2. $\langle R_{A0}\rangle$ vs $A0$-$B1^-$ and $A0$-$B1^+$ Δf (empirical trendlines). The filled points have strong substructure coupling "dimpling" the $A0$ peak; the arrows indicate approximate corrections (not used for trendline fit). Nominal top-back $B1$ nodal patterns shown along with coordinate frame axes.

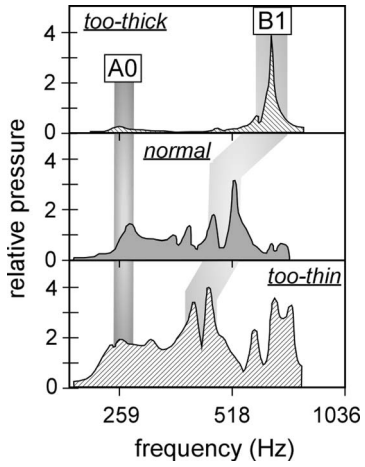


FIG. 3. Relative pressure readings for violin with too-thick, normal, and too-thin plates (after Meinel, Ref. 15, Fig. 3). $A0$, $B1$ labeled, and frequency-shift trends highlighted.

The Δf argument is substantially more powerful. The proposed $A0$-$B1$ coupling mechanism implies a stronger correlation with $B1^-$ than $B1^+$ since it is closer in frequency. A scatter plot of VIOCADEAS $\langle R_{A0}\rangle$ vs Δf data is shown in Fig. 2. The falloff of $\langle R_{A0}\rangle$ with increasing Δf appears clear for $B1^-$ but only "suggestive" for $B1^+$. Three violins had strong substructure coupling, dimpling the $A0$ peak (filled points in Fig. 2) and thus reducing $\langle R_{A0}\rangle$. Without this dimple $\langle R_{A0}\rangle$ would increase; empirical corrections shown in Fig. 2 indicate approximate magnitudes for the "dimple" effect. However, empirical linear trendline equations—$\langle R_{A0}\rangle = -0.0041\Delta f + 1.18$ (Pa/N) ($r=0.62$) for $B1^-$ and $\langle R_{A0}\rangle = -0.0013\Delta f + 0.74$ (Pa/N) ($r=0.25$) for $B1^+$ used uncorrected data.

VIOCADEAS data thus provide support for $A0$-$B1$ coupling, with $B1^-$ more important than $B1^+$ in exciting $A0$ (cf. Fig. 2, Ref. 3 where transposition of $B1^-$, $B1^+$ relative mobility magnitudes for bad-excellent violins is mirrored also by observed $\langle R_{A0}\rangle$). The hypothesis that $\langle R_{A0}\rangle$ increases as $A0$-$B1$ Δf decreases (and vice versa) can now be put to the test against appropriate earlier experiments, some dating back to 1937.

1. A0, plate thickness, and B1

In 1937, Meinel investigated the effect of reducing plate thicknesses from too-thick to normal to too-thin on violin radiation curves.[15] A graphic based on his Fig. 3 for just the $A0$-$B1$ region is shown in Fig. 3. Prominent peaks identified as the $B1$ corpus mode peaks dropped almost 200 Hz (graphical estimate) as plates were successively thinned, while the lowest peak, $A0$, remained near 270 Hz (± 15 Hz). VIOCADEAS data show $A0$ often coupling with various substructures like the neck-fingerboard and tailpiece; some such behavior was seen in these plots. Meinel's results show $B1$ radiation changed relatively little as $A0$-$B1$ Δf dropped by nearly a factor of 2; $A0$ radiation however grew approximately 8x. The enormous $B1$ variation extended far beyond our linear trendline region, hence a new power-law trendline for conglomerated $B1$ data, $\langle R_{A0}\rangle = 1.65x10^4 \Delta f^{-2.4}$ (Pa/N), was used to estimate Meinel's too-thick:too-thin pressure ratio as 6:1, consistent with experiment.

2. A0 and the sound post

Meinel also investigated the effect of the sound post on the acoustic output of the violin, shifting from tight-post to loose-post to no-post. Sound post removal produced two major effects: (1) $A0$ frequency dropped from ~270 to ~240 Hz due to the loss of cavity wall stiffening provided by the sound post, and (2) $A0$ acoustic output fell off to ~1/3 of the (normal) loose-post value.

Similar effects were observed in a 1995 sound post removal modal-acoustic analysis experiment: (1) $A0$ dropped from 279 to 245 Hz, (2) $A0$ acoustic output dropped significantly, (3) $\langle Y_{\text{corpus}}\rangle$ at $B1^-$ ($f \approx 500$ Hz) decreased substantially with sound post removal, at $B1^+$ ($f \approx 550$ Hz) $\langle Y_{\text{corpus}}\rangle$ showed an equally significant increase.[16] Room-average acoustic analysis, however, showed decreased acoustic output for both modes; boundary element method calculations indicated that for the peak associated with $B1^+$, falloff was due to a large R_{eff} decrease. Since $A0$-$B1^-$ Δf increased and the strength of $B1^-$, the most important mode in this coupling, decreased, the observed $A0$ falloff was consistent with $A0$-$B1$ coupling. Increased $B1^+$ excitation did not compensate for these two factors. (A cautionary note: although mode frequencies were seemingly little affected, the no-soundpost mode closest in frequency to $B1^-$ had a significantly different mode shape, implying that f-hole volume flows could be altered.)

The modal analysis data added significant insight into what happens at the bridge feet on sound post removal: (1) at the 245 Hz $A0$ frequency, the bridge feet moved significantly more and in phase, (2) both feet moved in phase at ~500 Hz and antiphase at ~550 Hz, with similar amplitudes for each foot, and (3) the ~500 Hz mode had less amplitude overall, while the ~550 Hz mode had more.

3. A0-B1 coupling and the violin octet

Modal and acoustic analysis of a complete violin octet generally supported Schelleng's flat-plate scaling procedure in placing $B1$ in the proper relationship to open string tunings and relative to $A0$, with one notable exception, the baritone's $B1$ frequencies.[8] These were by far the highest relative to desired placement across the entire octet, three semitones higher than desired. Baritone $A0$ radiation was also surprisingly weak compared to all other instruments in this set (see Fig. 1, in Ref. 8). $A0$-$B1$ coupling readily predicts significantly reduced $A0$ radiation for baritone $B1$ considerably above the scaling goal.

B. The B1 modes

Empirical relationships discovered recently between the top and back plate bending mode 2 and 5 frequencies and the average $B1$ frequency and frequency spread Δf, with strikingly similar nodal patterns,[17] indicate that these plate modes are effectively subsumed into the low-lying first corpus bending modes $B1^-$ and $B1^+$. A *heuristic* flat-plate dynamic stiffness model incorporating rib bending stiffness supports these observed experimental trends.[17] (This bending mode analogy relates also to f_{crit}, discussed later.)

C. Moving up the R_{eff} curve

The VIOCADEAS radiativity profile rises above the $B1$ peaks, reaching a maximum near 2.4 kHz, and then falling off slowly.

1. The bump near 1.2 kHz

This is a difficult region because it varies between quality classes (the so-called "nasal" region) and has a number of different possible contributors: (1) maximum in the bridge:bridge-island Y-direction impedance ratio,[3] (2) presence of nominal f_{ring} value for this quasicylindrical form,[7] (3) very significant f-hole radiative contributions[10] (4) excellent R_{eff} above average, bad below, (5) excellent $\langle Y_{corpus} \rangle$ below average, bad above, (6) near maximum modal density.[7] All factors might contribute or just a few, hence no clear understanding of this complex region has emerged.

2. The BH peak near 2.4 kHz

The BH peak at 2.4 kHz in Fig. 1 appears at each step in the violin's energy chain—driving point at the bridge corner, averaged-over-bridge, bridge feet (corpus immediately adjacent to bridge feet), averaged-over-corpus, and in the averaged radiativity.[11] It does not, however, show up in unusual R_{eff} or ζ_{tot} values, from which we infer that it arises from vibrational enhancement effects originating in the bridge-corpus coupling.[3]

The 3D corpus modal analyses of three violins has allowed us to discern important new violin vibrational behaviors in the bridge-island region between the f-holes:[3] (1) only the X-component of mobility displayed a peak near 2.4 kHz (Fig. 2 shows the X-Z axes), (2) the Y-component peaks near 1 kHz, decreasing monotonically above, (3) the X-component ranged from $\sim 30\% - 70\%$ of the Y-component, and (4) the Z-component was weakest. The fact that the sound post, bass bar, and f-holes are concentrated in the very region where string energy enters the corpus through the bridge feet makes this island region rich in the very boundaries-discontinuities needed to transform extensional into flexural motion. Another possibility gleaned from a combination of one-dimensional bridge mobility results with 3D corpus results was a narrow minimum in the bridge/bridge-island impedance ratio at 2.4 kHz for both X and Y components.[3] A maximum in X-extensional motion (transformed somehow into flexural motion) coinciding with an impedance matching effect suggests plausible mechanisms for the relative prominence of the BH peak in the mobility spectra.

Above 2.4 kHz, the effect of the bridge is conspicuous. Small waist trims to tune this substructure (clamped feet, adjust f_{rock}) have substantial effects on the radiativity profile (and perceived quality).[11] Significant progress has been made of late in modeling the bridge filter,[18,19] although additional effort will be necessary to understand the complexities of bridge-corpus coupling when significant extensional foot motions are involved.

3. SMI parametrization

For a shape so complex and materials so variable, any attempt to interpret a violin's general high-frequency radiativity must rely on shape-material-independent (SMI) structural acoustics parameters (but violin mass and "size" are still relevant). The SMI parameters chosen are (1) R_{eff}, (2) f_{crit}, (3) total damping ζ_{tot} (% of critical) extracted from mobility peak fits, (4) radiation damping ζ_{rad} (% of critical, computed with R_{eff}, f and mass), and (5) $F_{RAD}=\zeta_{rad}/\zeta_{tot}$, the fraction of vibrational energy radiated. Structural acoustics systematics for these parameters provide a "stylized" representation versus frequency:[20] (a) $R_{eff} \propto f^2 (f \leqslant f_{crit})$, $R_{eff}=1 (f > f_{crit})$,[3] (b) $\zeta_{tot} \propto f^{-1/2}$,[21] a violin rule of thumb [note: isolated top and back plate substructures had $\zeta_{tot} \approx$ const (Ref. 20)]; (c) $\zeta_{rad} \propto f (f \leqslant f_{crit})$; $\zeta_{rad} \propto f^{-1} (f > f_{crit})$. Radiation damping for $A0$ is expected to be about $0.5\zeta_{tot}$,[13] hence $F_{RAD} \approx 0.5$ for $A0$, for all violins.

A F_{RAD} "leaky bucket" characterization of energy loss incorporates ζ_{rad}, ζ_{int} internal (heat)—small compared to any violinist's support fixture damping—and ζ_{fix} support fixture losses that sum to ζ_{tot}. VIOCADEAS measurements effectively eliminated support fixture losses, so $\zeta_{fix} \approx 0$. Computing $\zeta_{int} \approx \zeta_{tot} - \zeta_{rad}$ showed it to be hardly different between excellent and bad violins, although quite significant at low frequencies where ζ_{rad} is small.[3] Thus at low frequencies, $\zeta_{rad} \ll \zeta_{tot}$, $\zeta_{tot} \approx \zeta_{int} \propto f^{-1/2}$. Presuming $\zeta_{int} \approx C f^{-1/2}$ across our frequency range guarantees that the ζ_{tot} frequency dependence is maintained at lower frequencies while maintaining a consistent simple falloff behavior up to 8 kHz.

These assumptions provide quite reasonable agreement with the conglomerated 14-violin data for ζ_{tot} (%critical), ζ_{rad} (%critical), and F_{RAD} as shown in Fig. 4 [effective $f_{crit} \approx 3.9$ kHz (Ref. 3)]. Only the internal damping equation coefficient C was varied to optimize agreement between ex-

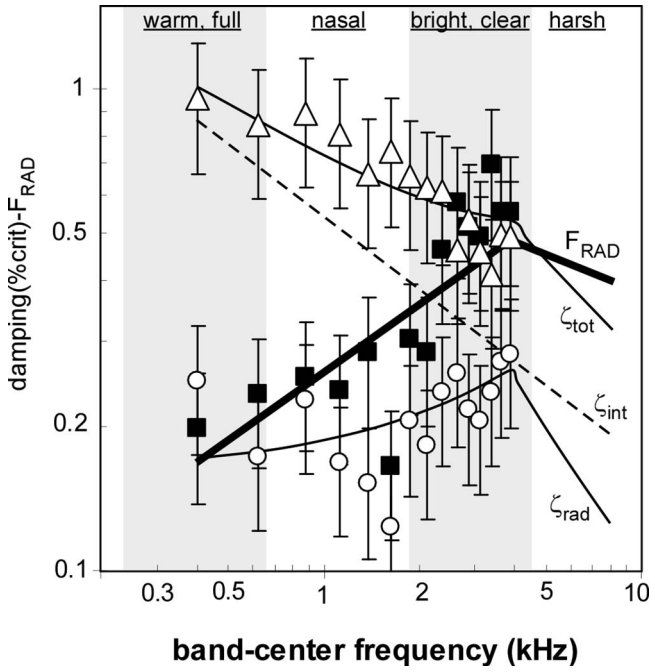


FIG. 4. (log) 14-violin corpus ζ_{tot} (△) and ζ_{rad} (○), and F_{RAD} (■) vs (log) band-center frequency ($f_{crit} \approx 3.9$ kHz) compared with stylized representations for each. (ζ_{rad}, $\zeta_{tot} \pm 30\%$ s.d. error bars represent average intraband variations; ζ_{int} represented by dashed line common to all violins.)

perimental and computed ζ_{tot}. Also in Fig. 4 are qualitative terms related to relative prominence of certain frequency bands (after Dünnwald[6]).

4. Perceived loudness

The fact that excellent and bad violins overall showed similar averaged-over-sphere $\langle R \rangle$ seems on its face inconsistent with Saunders' remark about "great" violins being loud. There are, however, two straightforward ways perceived loudness can be enhanced while still being consistent with VIOCADEAS results: (1) since violins radiate more strongly into the top hemisphere than the back, make violins radiate even more strongly by somehow changing the top plate flexural-extensional motion ratio, or possibly the arching (cf. Figs. 7 and 8 in Ref. 3); (2) emphasize regions where the ear is most sensitive—2–4 kHz—in the vibration-radiation conversion.

Pertinent to the second point, an experiment trimming the bridge waist in two ~2 mm steps (~0.02 g/step) dropped the bridge rocking frequency f_{rock} from 3.4 to 3.0 to 2.6 kHz, reduced maximum radiativity in the 2.5–4 kHz region by a factor of ~3, and made a good violin bad.[11] A perceptible but difficult-to-quantify slippage of the peak toward lower frequency was observed (see inset of Fig. 5). The fact that a poor bridge can make the sound of a very good violin quite bad—not by changing the violin's underlying normal modes, just their proportionate involvement in the overall vibrations—underscores the importance of the bridge filter on the overall radiativity profile in the ear's most sensitive range.

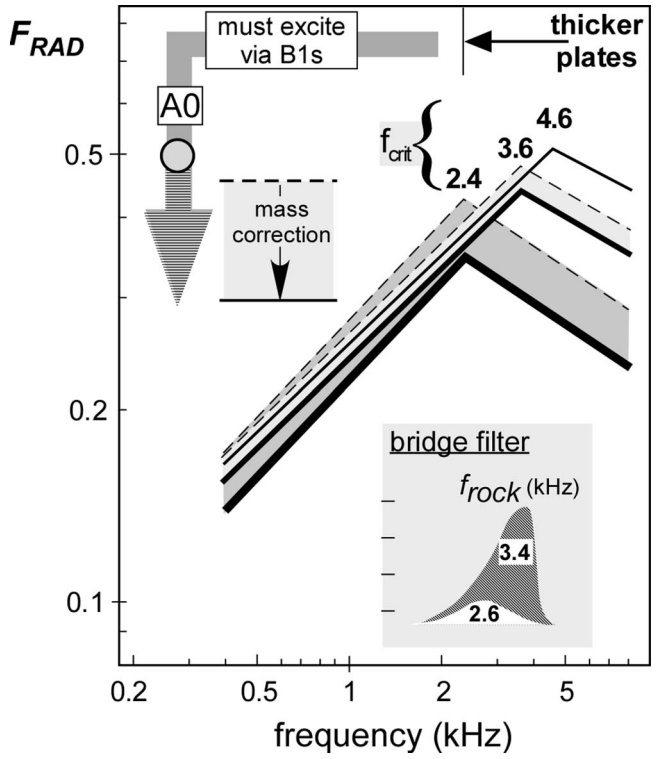


FIG. 5. (log) F_{RAD} vs (log) frequency for f_{crit}=2.4, 3.6, and 4.6 kHz (BH peak, old-Italian, and highest, respectively). *A*0 value fixed (but excitation via *B*1 crucial). Gray areas under each curve indicate schematic correction for increasing plate mass relative to 4.6 kHz curve. [Inset: effect of f_{rock}, 3.4–2.6 kHz, on (linear) radiativity, same frequency scale (after Fig. 10, Ref. 11).]

5. Critical frequency and F_{RAD}

A violin "equation" $I(\omega) \propto P^2(\omega) \propto F^2(\omega) \langle Y^2_{corpus}(\omega) \rangle R_{eff}$ provides a reasonable first approximation for quantifying sound intensity from the violin.[20] The first term on the rhs represents the driving-force energy input to the bridge, the second term represents the "gatekeeper" filter for bridge-corpus energy transfer, the third term represents the vibration-radiation energy conversion "egress" filter. Since the radiativity profile convolutes the second and third terms, F_{RAD}, which deals only with corpus energy loss via various damping mechanisms, was used to create in effect a "bridgeless" violin with only the "egress" filter.[22] The simple behavior of F_{RAD} as f_{crit} is varied provides important insights into the crucial role of f_{crit} in shaping the radiativity profile.

F_{RAD} simulations for varying f_{crit} (keeping $\zeta_{fix} \approx 0$) appropriated the ζ_{int} trendline from Fig. 4. The ζ_{rad} maximum was then moved to successive f_{crit} values, and the ζ_{rad} trendline equation adjusted accordingly. *A*0 F_{RAD} remained constant. Simulated F_{RAD} curves are shown in Fig. 5 for f_{crit}=2.4, 3.6, and 4.6 kHz, corresponding to the BH peak, two-old-Italian average, and highest measured f_{crit} value. Since f_{crit} changes would primarily be due to varying plate thickness h (using flat rectangular plate theory as a guide), $f_{crit} \propto 1/h \propto 1/\text{plate mass}$ (assuming a constant density-stiffness relationship[23]). Since $\zeta_{rad} \propto 1/\text{violin mass}$, and plate-mass is nominally 1/2 violin mass, a crude correction for increasing plate mass (relative to the 4.6 kHz curve) was computed and shown graphically as shaded areas underneath

the 2.4 and 3.6 kHz curves. The relative importance of the gatekeeper and egress filters can be gauged from the inset of Fig. 5 showing an abstracted representation of the effect of changing bridge f_{rock} from 3.4 to 2.6 kHz (after Fig. 10, Ref. 11).

Maximum corpus F_{RAD} always falls at f_{crit}. As f_{crit} decreases, peak F_{RAD} values also drop due to the increasing ζ_{int} contribution to ζ_{tot} and increasing plate mass/thickness. A fixed $A0$ $F_{RAD} \approx 0.5$ becomes relatively more important as f_{crit} decreases, especially when compared to F_{RAD} values above 3 kHz, signaling a shift in spectral balance toward lower frequencies for low f_{crit} values. An important caution: as $A0$ *excitation* relies on $A0$-$B1$ coupling this must be kept in mind when discussing the overall spectral balance shifts. Decreasing f_{rock} (fixed f_{crit}) also affects the spectral balance similarly. Entirely independent of how the corpus gains vibrational energy via the gatekeeper filter, it is always around f_{crit} where the violin most efficiently turns corpus vibrational energy into radiation. Even when the violin is held-played and violinist ζ_{fix} dominates ζ_{tot}, relatively unaffected normal-mode shapes[24] indicate that R_{eff} should remain close to free-free values, as should f_{crit}. F_{RAD} magnitudes, however, drop significantly.

6. Extended radiation plots

If old-Italian radiativity profiles somehow define the psychoacoustic first choice for "desired" sound, how can these be realized in practice? In 1990, Dünnwald, using electromagnetic excitation via a highly damped wire at a bridge corner, published radiation measurements up to 7 kHz on 700 violins with a single far-field microphone in an anechoic chamber.[6] Our radiativity results support many of his conclusions. The broad agreement between the overall profiles, from different data sets, is important because it confirms the generality of both results and suggests using both data sets in a general analysis exploring the connection between the top and back plates, which dominate the mass and surface area of the violin, and the violin radiativity profile.

Dünnwald's superposition plots are represented in Fig. 6 via their envelopes as "conglomerated" radiation profiles corresponding to "averaged" *10-old-Italian, 10-master*, and *10-factory* subsets. These subsets present quite different profiles. Two important features emerge: (1) most prominently, the remarkable change in acoustic radiation above 2.5 kHz; the 10-master violins have a much extended frequency range compared to the 10-factory violins, while the 10-old-Italian envelope is intermediate; (2) less obvious, but equally important, a shift in average $B1$ frequency among these subsets. The 10-old-Italian $B1$ envelope region with two separated peaks near 500 Hz (almost certainly the first corpus bending modes $B1^-$ and $B1^+$) was also quite different from the other two, which appeared as a broad mush.

What more need be said about these instrument classes? Old Italian violins, from a relatively few now-legendary violin makers, are a revered class that, enjoying the very best care and maintenance and almost universally involving substantial repair work, have undergone considerable change to keep current with evolving performance requirements. Factory violins with machine-figured too-thick plates fall at the other end of the care-maintenance spectrum, with master violins somewhere in between. These become important distinctions in our analysis.

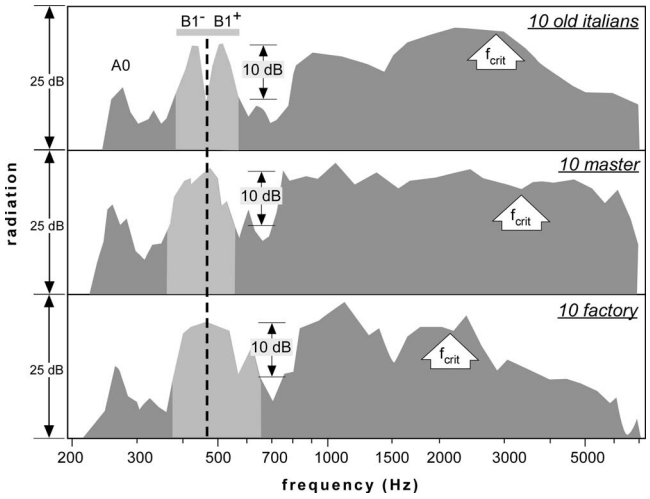


FIG. 6. 10-violin envelope curves after Dünnwald superposition plots (Ref. 6, Fig. 3). The vertical dashed line locates average B1 for 10-old-Italian envelope for reference to 10-master and 10-factory $B1$; the arrows denote plate-mode-5-based f_{crit} estimates for each envelope.

IV. CRITICAL FREQUENCY LINK

For centuries, the top and back plates were the only substructures with resonance frequencies determined prior to assembly, using tap tones (many use Chladni patterns now) to tune plates to "prescribed" frequencies prior to assembly. We conjecture that top and back plate bending modes 2 and 5—subsumed into the low-lying first corpus bending modes[17]—are key to understanding relationships between these radiativity profiles. This relationship—the crucial link between the violin f_{crit} and plate mode frequencies—is based on the fundamental physics underlying the critical frequency concept, the dispersive flexural wave velocity v_f catching up with the velocity of sound $c(\approx 344$ m/s).

A historical note germane to the Dünnwald 10-master violin envelope concerns the lack of agreement on what these prescribed frequencies should be. In 1885, Heron-Allen remarked that some makers were tuning the back lower than the top, which he emphatically stated was entirely wrong: "Nearly every author who has written on this subject has declared that *the back should be a tone lower* than the belly. It is useless (as many of them probably never actually *made* a fiddle) to persuade them that exactly the reverse is the case."[25] We might conjecture from this that master violins can have quite variable plate tunings. This variability was reflected in the VIOCADEAS database, where mode 5 top/back frequency ratios varied from 0.90 to 1.03, obviously not all in harmony with Heron-Allen's dictum.

On the other hand, factory (machine-figured) violins normally have too-thick plates and old-Italian violins presumably a relatively standardized tuning as suggested by the $B1$ mode placement separation in Fig. 6.

A. Plate mode: Critical frequency link

The 14-violin $f_{crit} \approx 3.9$ kHz was in good agreement with the along-grain 4.5–4.9 kHz values computed for violin-size flat rectangular spruce and maple wood plates by Cremer;[13] cross-grain f_{crit} values were one-two octaves higher. (Along- or cross- grain notation here relates to flexural wave motion relative to grain direction, which runs along the violin long axis.) This agreement suggests a plate $\rightarrow$violin f_{crit} linkage. Since little input energy is available at frequencies above 6–8 kHz from the nominal sawtooth bowing force (nth harmonic $\propto 1/n^2$), a high f_{crit}-low input energy combination implies along-grain flexural motions will predominate in violin sound; hence our discussion is limited to this case.

1. Additional simplifications

Some additional simplifications-assumptions to estimate f_{crit}: (1) the top and back plates, which dominate the radiating area of the violin, are the only important radiating surfaces, and the top plate is more important; (2) v_f is the same in free and glued plates, since only boundary conditions change; (3) rib, sound post, liner strip, and end-corner block, variations are neglected; (4) all violins have a properly setup bridge and its filter effects on average are common across the conglomerated 10-violin groups; (5) flexural-extensional motion ratio changes[3] between violins are neglected; (6) plate modes 2 and 5—the lowest frequency along- and cross-grain bending modes—are primarily flexural, i.e., flat plate in character, *and* mode 5 is more important (but less flexural);[17] and (7) v_f scales simply with frequency as $v_f \propto f^{1/2}$.[21] These assumptions allow us to compute f_{crit} values for comparison with experimental values and help interpret the Dünnwald envelope high end. Knowing v_f at one frequency and applying $f^{1/2}$ scaling leads directly to estimates of f_{crit} that signal peak F_{RAD} values and initiate the high-frequency falloff. (It is an interesting "coincidence" that the bridge filter also strongly affects radiation near the F_{RAD} peak.)

2. Flexural wave velocity

Are top and back plates—doubly-curved weakly arched shells—approximately "flat"? Experimentally, (a) violin plate mode 5 (akin to the first along-grain bending mode in a flat plate) has similar portions of flexure-extension, while plate mode 2 (similar to the lowest cross-grain bending mode of a flat plate) appears close to pure flexural (nodal patterns in the inset of Fig. 7);[17] (b) a preponderance of flexural to extensional motion for top and back plates was seen in 3D mobility measurements, especially so for the maple back plates.[3] Hence we conclude that these plates are flat. The success of Schelleng's violin octet flat-plate scaling offers additional practical support for this assumption.[1,8]

The flexural wave velocity was computed directly from the lowest frequency cross- and along-grain bending modes using $v_f = f_{\#}\lambda$, where $f_{\#}$=mode 2 or 5 plate frequency. Approximate wavelengths were obtained from the maximum plate width (L=0.2 m) or maximum plate length (L =0.35 m), taking $\lambda \approx L$ (flat-plate value $\lambda \approx 1.33L$) for each respective direction.

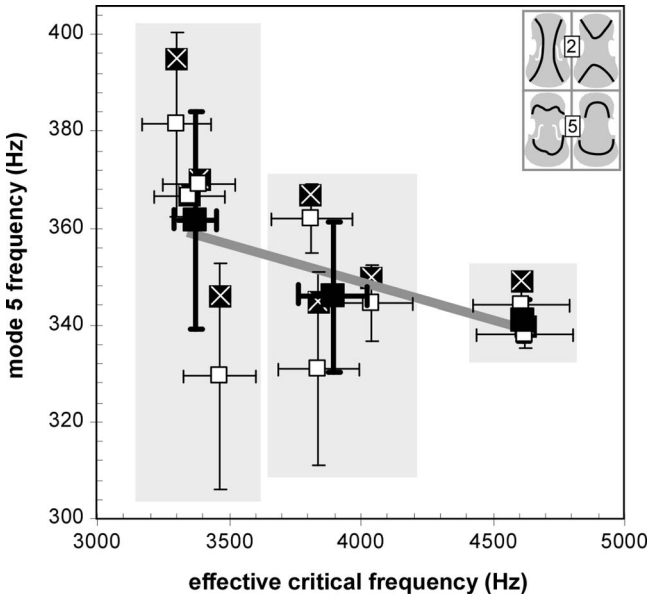


FIG. 7. Scatter plot f_{crit} vs averaged top-back (□) or maximum (☒) mode 5 frequency for nine violins, group-averaged (■) in overlapping f_{crit} regions (grayed) with empirical trend line. S.d.'s for top-back plate frequency variations and f_{crit} estimates (horizontal). [Inset: top (with f-holes) and back plate mode 2 and 5 nodal patterns (note the general similarity to $B1^-$, $B1^+$ patterns in Fig. 2].

Mode 5, always clearly recognizable, has shown a wide variety of nodal line patterns ranging from irregularly arched across the upper and lower bouts—closer to pure bending?—to an almost-closed oval on the back plate that is clearly not simple bending. Such shape variations might be of some importance as well as f_5 in determining f_{crit}.

Nominal plate mode 2 and 5 frequencies of 170 and 350 Hz then lead straightforwardly to nominal flexural velocities $v_{f2} \approx 34$ m/s and $v_{f5} \approx 122$ m/s. Using the v_f scaling relationship, $f_{crit} \approx (c/v_f)^2 f_{\#} \approx (c/L)^2/f_{\#}$ the along-grain critical frequency $f_{crit} \approx (344/0.35)^2/350 \approx 2.8$ kHz, in general agreement with our effective critical frequencies for the violin, and much lower than cross-grain $f_{crit} \approx 17$ kHz, again quite similar to results for a flat plate of similar dimensions.[13] Only plate mode 5 was used in computing the critical frequencies due to much lower along-grain f_{crit}.

Based on general flexural wave properties, as plate bending mode frequency falls, f_{crit} should rise. VIOCADEAS data for nine violins with experimental plate mode and f_{crit} data (additionally grouped by averaging overlapping f_{crit} values) were plotted versus corresponding top-back plate mode 5 frequency averages in Fig. 7. The two highest f_{crit} violins had top plates tuned higher than backs, an unusual occurrence. Overall Fig. 7 indicates that f_{crit} increases as average plate mode 5 frequency decreases, although not so fast as $1/f_5$, possibly due to a "partial" flexural behavior of mode 5. Violins with wider top-back frequency spreads tended to fall further from the empirical trendline. Interestingly, the least scatter and strongest correlation for individual data points occurred when the top or back *maximum* f_5 was plotted versus f_{crit}, as can be seen in Fig. 7. Unstandardized f-holes and bass bar heights/shapes in the nine violins, and possibly the more variable flexural-extensional motion ratio for spruce

top plates,[3] offer likely reasons for the wider scatter among top plates.

3. f_{crit} from $B1$

When the plates are glued to the ribs, their modes are subsumed into the normal modes of the violin, albeit somewhere else in modal parameter space. Where substructure size-mass dominates the structure, their properties would be expected to dominate overall structural responses. As noted earlier, plate modes 2 and 5, among the lowest plate modes, emerge among the lowest corpus modes, with nodal patterns quite similar to the free-plate modes 2 and 5 (shown in the inset of Fig. 7). An empirical approximately-linear plate-$B1$ frequency correlation was revealed when the $B1$ frequency difference $\Delta B1$ and the averaged mode 5 and 2 frequency difference $\Delta 5-2$ were plotted as $\Delta B1/\Delta 5-2$ versus $\Delta B1$.[17] A heuristic dynamic "flat-plate sandwich" model indicated that $B1$ mode frequency *differences* approximately canceled rib stiffness in the overall $B1$ bending stiffness.[17]

When no plate mode frequencies are available, an empirical $B1 \rightarrow$plate mode equation can be used to estimate f_{crit}. This equation was extracted from a systematic experiment by Schleske, where plates with known mode frequencies were assembled into a strung-up violin, signature mode frequencies measured, violin top/back plate taken off, thinned incrementally, and re-glued, etc., *varing only plate thicknesses*,[26] thus eliminating many variables—different woods, shapes, archings, ribs, liners, and end-corner blocks—attending the nine violin VIOCADEAS data, which showed similar trends but with more scatter. Top and back plate trends were so similar that an empirical linear trendline was fitted through the conglomerated data for $B1^-$ and $B1^+$, resulting in the equations: $f_{B1^-}=0.233f_5+341$ Hz ($r=0.81$) and $f_{B1^+}=0.371f_5+378$ Hz ($r=0.74$). The weak dependence of $B1$ on mode 5 frequency was unsurprising, given the dominant contribution of the ribs to the overall bending stiffness.[17] This "dilution" makes working back from $B1$ frequencies to accurate plate mode frequencies much more problematic. For example, if plate mode 5 frequencies were changed by 30 Hz, the $B1$ mode frequencies would change <10 Hz ($\pm 1-2$ Hz). Where it was impossible to isolate the $B1$ modes (as in two out of three 10-violin envelopes in Fig. 6), the average $B1$ trendline equation, $f_{B1}=0.302f_5+360$ Hz, was used to estimate average plate mode 5 frequencies.

Because certain plate frequencies do not guarantee certain signature mode frequencies, such weak dependence seems to undermine the very rationale behind the traditional practice of tuning plates. However, the underlying reality is more subtle: (1) plate tuning sets f_{crit} and (2) the $A0$-$B1$ excitation mechanism proposed earlier is most strongly dependent on $B1^-$, and the frequency spread between the $B1$ modes is related to the mode 2–5 frequency spread.[17] Hence even a fairly high (average) $B1$ could have a large $\Delta B1$ and strong $\langle R_{A0} \rangle$.

A $B1$ frequency for each envelope curve in Fig. 6 was estimated by dropping down 10 dB on each side of the $B1$ envelope peak to create a band (shown superimposed on envelope) and determining its center frequency. The 10-old-Italian center frequency is shown as a dashed vertical line

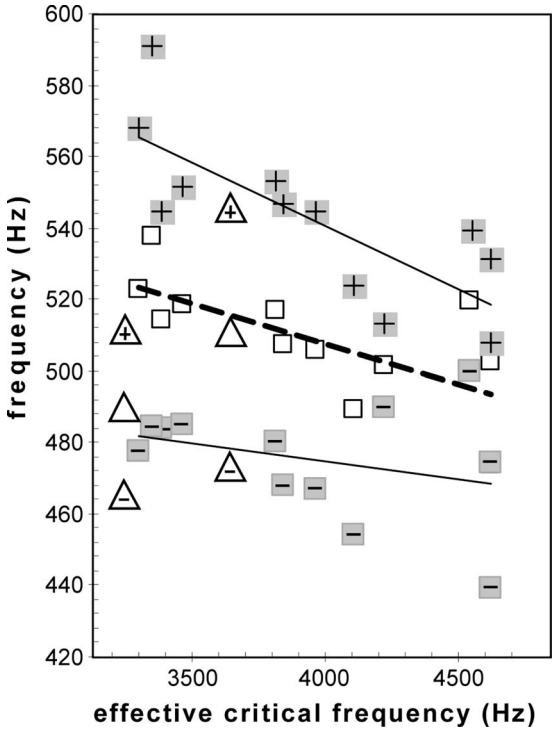


FIG. 8. First corpus bending mode frequency vs f_{crit} for 12 modern violins ($-$,+ in shaded squares for $B1^-$, $B1^+$ respectively, open squares $B1$) and 2-old Italian violins (triangles, same notation). Empirical linear trendlines for $B1^-$ (lower thin line), $B1$ (thick dashed line), and $B1^+$ (upper thin line).

across all the envelopes. Nominal graphical estimates of B1 frequency were 465, 450, and 498 Hz for the 10-old-Italian, 10-master, and 10-factory envelopes, respectively. Worthy of note is the association of lower $B1$ values in Fig. 6 with a more extended high-frequency end, and vice versa. Nominal plate mode 5 frequencies of 350 (consistent with VIOCADEAS data average), 300, and 460 Hz were computed from the $B1$ trendline, all with significant, but undeterminable, errors.

Since factory-made violins typically have plates *much* thicker than any good violinmaker would consider appropriate, such high mode 5 frequencies would not be surprising, whereas the 10-master violin set while probably low is consistent with the lack of precision in this method. In any case, such indirect rough f_{crit} calculations should be used only for examining $B1$-related f_{crit} trends. Computed f_{crit} trends, marked with arrows in Fig. 6, correspond reasonably well with the envelope frequency where radiation falls off, especially so for the 10-old-Italian and 10-factory violin subsets.

The top/back radiativity ratio (directivity) >1 indicates that the top plate radiates more effectively than the back,[3] supporting earlier measurements such as those by Meyer.[27] Modal analysis showed a plate-mode-5 shape on the top plate for $B1^+$, linked earlier to $f_{crit} \approx 3$ kHz, while the $B1^-$ top plate had a mode-2 shape, linked to ~ 17 kHz f_{crit}. On such simplistic shape-driven grounds, we conjecture that f_{crit} should show a stronger correlation with $B1^+$ than $B1^-$. The experimental test of this conjecture is presented in a scatter plot of $B1^-$, $B1^+$ (and $B1$) frequencies versus f_{crit} (Fig. 8). Overall, this shape-based conjecture is consistent with the data, especially if guided by trendline slopes. If $B1^-$, $B1^+$ frequencies are known, but separate plate mode frequencies

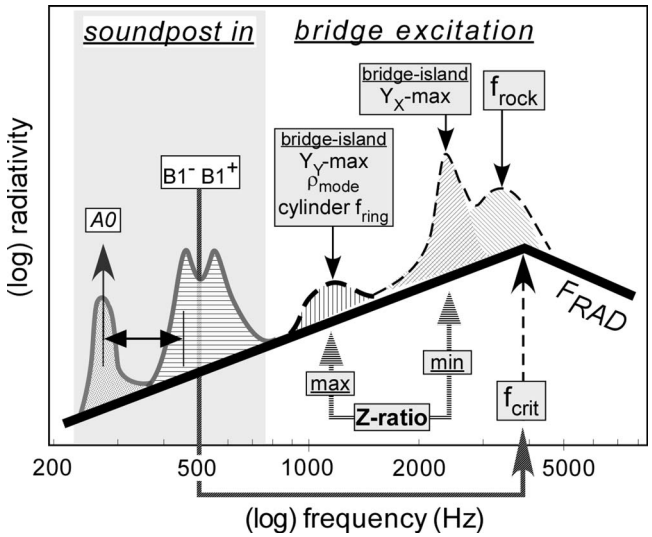


FIG. 9. Summary schema for "building" violin radiativity profile derived from this and previous work: F_{RAD} "bridgeless" violin curve ($f_{crit} \approx 3.9$ kHz, Fig. 4), $f_{ring} \approx 1$ kHz, $f_{rock} \approx 3.2$ kHz, bridge:island impedance ratio (Fig. 10, Ref. 3), soundpost (Fig. 4, Ref. 16).

are not, f_{crit} can be estimated roughly from trendlines in Fig. 8 or via our empirical $B1$-mode 5-f_{crit} equations.

We conclude with a schematic figure summarizing the various mechanisms discussed earlier that contribute to a properly setup violin's radiativity profile (Fig. 9). In our schema,

- the egress filter, F_{RAD}, underlies all radiativity profiles, with f_{crit} dependent on $B1^{(+)}$;
- the independent gatekeeper filter has a number of components—bridge-related BH and f_{rock} components at $2<f<4$ kHz, the nasal bump near 1.2 kHz, bridge:island impedance ratio considerations, plus sound post-linked $B1$ and its Δf excitation-dependent companion, $A0$,—superimposed on F_{RAD}.

$B1$ can now be seen to be the dominant factor at low frequencies due to its presence and $A0$-$B1$ coupling; it also sets f_{crit} at high frequencies primarily through plate mode 5. So dominating a contribution implies a significant correlation with violin sound quality judgments.

V. QUALITY JUDGMENTS

A. *B*1 and perceived quality

Martin Schleske, a leading German violin maker and leader in incorporating modal analyses into violinmaking, stated that the frequency of $B1^{(+)}$ acts as a "tonal barometer" for violin sound, with frequencies <510 Hz leading to a "somewhat 'soft' violin with dark sound lacking 'resistance'" to bowing. On the other hand, frequencies >550 Hz were characteristic of "…'stubborn' violins with bright sound, possibly with a tendency to harshness, and with strong 'resistance' to the player."[26] How do these sound quality comments relate to the radiativity profile? For instance, could a <10% change in corpus $B1^+$ frequency and any associated impedance changes cause a large change in actual—versus perceived—mechanical response? Our measurements do not support such a mechanism; surface-normal corpus impedance at the bridge feet for $B1^+$ frequencies was a local maximum almost uniformly across all violin quality classes.

There is a fascinating alternative here, a *psycho*acoustic link to the perceived playability of the violin formulated by Rohloff,[28] who noted that suppression of acoustic energy above 4 kHz caused a violinist's perception of playability to change from "easy" to "hard" speaking. Conversely, when a hard-speaking violin had frequencies >4 kHz boosted, the playability changed to easy speaking.

Viewed in the light of our radiativity profile model and these remarks (neglecting rib-related variations), if $B1^+$ gets too high it is a clear signal that the plate mode frequencies are high. This leads to a lower-than-usual f_{crit}, creating a violin with less-than-usual acoustic output above 4 kHz, while $A0$—the only resonance in the lowest octave, with a constant F_{RAD}—is also weakened if the $B1$ modes are high, removing acoustic energy from the "warm full" low-frequency band. This leaves the violin with a "compressed" profile peaked in the "bright clear" region, creating a bright sound, possibly harsh if the desired spectral balance is tilted toward the high end too much. The relative lack of acoustic energy above 4 kHz would then suggest strong resistance to the player. Conversely, $B1^+$ too low implies plate frequencies too low and f_{crit} relatively high, spreading the frequency spectrum and increasing the acoustic output above 4 kHz relative to lower frequencies, thereby suggesting a violin with less "resistance" to the player; simultaneously $A0$ is boosted tilting the spectral balance toward the low end, giving a darker sound. Thus Schleske's and Rohloff's findings actually signal a convergence in our radiativity profile model.

Acoustic characterizations of some mechanical properties have seen increasingly significant application of late. Food manufacturers now pay attention to the *acoustic* attributes of food via air and *bone conduction* transmission together in the mechanical act of chewing to improve their marketability. If the mechanical world of "hard, crispy, crackly, crunchy and snappy" is any guide,[29] a much better understanding of how acoustic signatures via air and bone conduction can color the perception of the mechanical properties of violins appears to be a productive area for future psychoacoustic research.

B. Extending qualitative

The Dünnwald 10-old-Italian subset is clear evidence that a certain type sound can be linked to certain modal attributes, the very basis of Schleske's "tonal copies" of violins.[30,31] VIOCADEAS measurements, however, showed little in the way of robust quality indicators for individual attributes—$A0$ strength being the only exception. Expanding to "coupled" parameters like the $A0$-$B1$ Δf was more productive, forcing us to closely examine the character of each signature mode. In the case of $B1$, the inherent bending character of the plates also suggested a critical frequency relationship, simultaneously linking the low and high ends of the spectrum with very few parameters.

On the other hand, qualitative evaluations suffer from too many adjectives—many of the useless sort like "nice"—

chasing too few attributes. It would be irrational to expect violins with substantially different sound, even those in the same "bad-good-excellent" general quality class, to vibrate—and thus measure—the same. Bunching them all together creates a measurement-statistical "mush" that—by itself—undermines any causal basis for a certain *single* "specification" for reliable bad-good-excellent quality classification. "Good" is no longer good enough. *Modern* violin quality rating needs a Boolean string such as "good+bright +weak-on-D-string+prominent wolf+unresponsive overall" instead of gross bad-good-excellent quality classifications to help unravel the essential modal properties linked to certain sounds and behaviors. Classifying violin quality by summing over a number of important rating criteria rather than one overall quality rating seems at this stage a much more productive way to pair violin modal and acoustic properties with sound and playability properties.

VI. CONCLUSIONS

If plate mode 5 is the underlying determiner of the violin's critical frequency—establishing radiation efficiency and damping curves, setting an F_{RAD} peak, and initiating its falloff—and if modes 2 and 5 (along with the ribs) determine the first corpus bending mode frequencies, and if the $A0$-$B1$ frequency relationship determines the strength of $A0$, then a major part of the radiativity profile is fashioned by very few parameters indeed. The ribs, woefully neglected in scientific analyses of violin sound, provide both the primary stiffness for the first corpus bending modes and the cavity so essential to violin sound at low frequencies.

Our proposed schema, rather like a Chinese puzzle that requires identification of one crucial part in order to disassemble the puzzle, provides a structural acoustics rationale for plate tap tones that buttresses their distinction as the only substructure tuned prior to assembly, even if no settled basis exists as to what the "prescribed" mode 2 and 5 frequencies should be. This hypothesized commonality of violin parametric behaviors across a wide range of quality creates a much reduced universe of things to worry about to achieve quality. This simplified model of violin radiativity provides straightforward prescriptions to achieve more desirable sound by manipulating plate and $B1$ mode frequencies. However, it always presumes the proper setup of the playable violin—sound post, bridge, and strings—so crucial to the final perception of quality.

Although a "great" violin requires the imprimatur of a great violinist, thereby greatly restricting the number of violins that can ever be labeled great, the elimination of bad violins requires only close attention to the basic details of plate tuning, general construction, and setup that have been important for centuries, aided perhaps by a few measurements of the radiativity profile for the close-to-finished violin.

[1]J. C. Schelleng, "The violin as a circuit," J. Acoust. Soc. Am. **35**, 326–338 (1963); cf. erratum, *ibid*. p. 1291.

[2]G. Weinreich, "What science knows about violins—and what it does not know," *1992 Klopsteg Memorial Lecture*, edited text published in *Research Papers in Violin Acoustics 1975–1993*, edited by C. M. Hutchins (Acoustical Society of America, Woodbury, NY, 1997).

[3]G. Bissinger, "Structural Acoustics of Good and Bad Violins," J. Acoust. Soc. Am. **124**, 1764–1773 (2008).

[4]F. A. Saunders, "The mechanical action of instruments of the violin family," J. Acoust. Soc. Am. **17**, 169–186 (1946).

[5]H. Meinel, "Regarding the sound quality of violins and a scientific basis for violin construction," J. Acoust. Soc. Am. **29**, 817–822 (1957).

[6]H. Dünnwald, "Ein erweitertes verfahren zur objectiven bestimmung der klangqualität von violinen," Acustica **71**, 269–276 (1990); modified English version "Deduction of objective quality parameters on old and new violins," J. Catgut Acoust. Soc. **1**, 1–5 (1991).

[7]G. Bissinger, "A unified materials-normal mode approach to violin acoustics," Acust. Acta Acust. **91**, 214–228 (2005).

[8]G. Bissinger, "Modal analysis of a violin octet," J. Acoust. Soc. Am. **113**, 2105–2113 (2003).

[9]G. Bissinger, "A0 and A1 coupling, arching, rib height, and f-hole geometry dependence in the 2-degree-of-freedom network model of violin cavity modes," J. Acoust. Soc. Am. **104**, 3608–3615 (1998).

[10]G. Bissinger, E. G. Williams, and N. Valdivia, "Violin *f*-hole contribution to far-field radiation via patch near-field acoustical holography," J. Acoust. Soc. Am. **121**, 3899–3906 (2007).

[11]G. Bissinger, "The violin bridge as filter," J. Acoust. Soc. Am. **120**, 482–491 (2006).

[12]F. Durup and E. Jansson, "The quest of the violin bridge-hill," Acust. Acta Acust. **91**, 206–213 (2005).

[13]L. Cremer, *The Physics of the Violin* (MIT, Cambridge, 1984).

[14]G. Bissinger, "Wall compliance and violin cavity modes," J. Acoust. Soc. Am. **113**, 1718–1723 (2003).

[15]H. Meinel, "On the frequency curves of violins," Akust. Z. **2**, 22–33 (1937).

[16]G. Bissinger, "Some mechanical and acoustical consequences of the violin soundpost," J. Acoust. Soc. Am. **97**, 3154–3164 (1995).

[17]G. Bissinger, "Surprising regularity between plate modes 2 and 5 and the B1 corpus modes: Part I," J. Violin Soc. Am.: VSA Papers, **21**, 83–101 (2007).

[18]I. P. Beldie, ""About the bridge hill mystery," J. Catgut Acoust. Soc. **4**, 9–13 (2003).

[19]J. Woodhouse, "On the bridge-hill of the violin," Acust. Acta Acust. **91**, 155–165 (2005).

[20]G. Bissinger, "Contemporary generalized normal mode violin acoustics," Acust. Acta Acust. **90**, 590–599 (2004).

[21]F. Fahy and P. Gardonio, *Sound and Structural Vibration: Radiation, Transmission and Response*, 2nd ed. (Academic, New York, 2007).

[22]G. Bissinger, "The role of radiation damping in violin sound," ARLO **5**, 82–87 (2004).

[23]M. F. Ashby *Materials Selection in Mechanical Design*, 2nd ed. (Butterworth, Heineman, 1999).

[24]K. D. Marshall, "The musician and the vibrational behavior of the violin," J. Catgut Acoust. Soc. **45**, 28–33 (1986).

[25]Ed. Heron-Allen, *Violin-Making as It Was and Is* (Ward Lock Limited, London 1885) p. 132.

[26]M. Schleske, "Empirical tools in contemporary violin making: Part 1. Analysis of design, materials, varnish and normal modes,"J. Catgut Acoust. Soc. **4**, 50–65 (2002).

[27]J. Meyer, "Directivity of the bowed string instruments and its effect on orchestral sound in concert halls," J. Acoust. Soc. Am. **51**, 1994–2009 (1972).

[28]E. Rohloff, "The speaking of violin sounds," Z. Angew. Phys. **17**, 62–63 (1964). English abstract published in *Musical Acoustics, Part II, Violin Family Functions*, Benchmark Papers in Acoustics Vol. **6**, edited by C. M. Hutchins (Dowden, Hutchinson & Ross, Stroudsburg, PA, 1976).

[29]B. Reynaud *et al.*, "Acoustic signature of hard, crispy, crackly, crunchy and snappy," Proceedings of the 19th International Congress on Acoustics, Madrid 2007, paper No. ppa-02-022.

[30]M. Schleske, "On making 'tonal copies' of a violin," J. Catgut Acoust. Soc. **3**, 18–28 (1996).

[31]M. Schleske, webpage, http://www.schleske.de/11handbuch/en_extras3handbuch04klangfarbe.pdf (Last viewed July 2008).

Beyond the beat: Modeling metric structure in music and performance

Stefan T. Tomic[a)]
Center for Mind and Brain, University of California, Davis, California 95618

Petr Janata[2,3,b)]
[2]*Center for Mind and Brain, University of California, Davis, California, 95618*
[3]*and Department of Psychology, University of California, Davis, California, 95618*

(Received 14 February 2008; revised 30 September 2008; accepted 5 October 2008)

Current models for capturing metric structure of recordings of music are concerned primarily with the task of tempo and beat estimation. Even though these models have the potential for extracting other metric and rhythmic information, this potential has not been realized. In this paper, a model for describing the general metric structure of audio signals and behavioral data is presented. This model employs reson filters, rather than the comb filters used in earlier models. The oscillatory nature of reson filters is investigated, as they may be better suited for extracting multiple metric levels in the onset patterns of acoustic signals. The model is tested with several types of sequences of Dirac impulses as inputs, in order to investigate the model's sensitivity to timing variations and accent structure. The model's responses to natural stimuli are illustrated, both for excerpts of recorded music from a large database utilized by tempo-estimation models, and sequences of taps from a bimanual tapping task. Finally, the relationship of the model to several other beat-finding and rhythm models is discussed, and several applications and extensions for the model are suggested.
© *2008 Acoustical Society of America.* [DOI: 10.1121/1.3006382]

PACS number(s): 43.75.Zz, 43.75.Cd, 43.75.Xz, 43.75.St [DD] Pages: 4024–4041

I. INTRODUCTION

Describing the metric and rhythmic structure of a piece of music is a complex endeavor, in part, because the concepts of rhythm and meter encompass many types of timing features and relationships that are found in a piece of music, such as the tempo or the accent structure (London, 2004). It is generally accepted, however, that a description of music's rhythmic properties must take into account metrical structure, tempo, and timing (Gouyon and Dixon, 2005). Nevertheless, most current rhythm models that analyze acoustic signals focus primarily on finding the beat and tempo. The process of beat extraction is relevant both to cognitive psychologists interested in the mechanisms of sensorimotor synchronization with music (Large, 2000; Repp, 2005; Snyder and Krumhansl, 2001), as well as to modelers interested in automatic music classification and retrieval (Gouyon *et al.*, 2004; Tzanetakis and Cook, 2002). Not surprisingly, a model's success is evaluated usually by comparing the model's output with the judgments of experts who have annotated a musical excerpt or score with markings that correspond to events at the metric level that they view as the tactus. Despite their utility, beat-finding models that are optimized to mirror the judgments of experts are solving a narrow perceptual problem that is somewhat restricted to musical selections in which an unambiguous beat is discernable. When hearing a piece of music, not all listeners may agree on which metric level corresponds to the tactus, and when asked to tap along with the music, they may produce taps at different metric levels. It is therefore of interest to develop quantitative methods that describe the relative prominence and time-varying properties of the different metric levels in a piece of music.

In this paper, our objective is to present a means of modeling the timing characteristics in a signal that allow one to ask questions about the presence and relative prominence of different metric levels and rhythmic patterns. We accommodate both raw audio signals and recorded behavior from tapping experiments, thus providing a common framework for characterizing both the sensory and motor aspects of sensorimotor synchronization tasks. The initial useful stage of the model produces a continuous output rather than an output of a discrete symbolic nature. The model output is of a similar nature to the work of Todd (1994), which produces a continuous output to represent rhythmic structure. We also provide a demonstration of how one may convert the continuous model output to a discrete symbolic representation that can be interpreted as a classification of the prevalent meter and a means of representing competing metric hypotheses. The framework we use can be seen as a variation on two models that were developed primarily for the purpose of beat estimation (Scheirer *et al.*, 1998; Klapuri, Eronen, & Astola, 2006). We first describe some of the salient features of these two models and our adaptations to them.

Scheirer's model (Scheirer, 1998) incorporates a preprocessing stage that separates the original audio signal into separate frequency bands. This effectively models the simultaneous rhythmic tracking of different streams in the fre-

a)Electronic mail: sttomic@ucdavis.edu
b)Author to whom correspondence should be addressed. Electronic mail: pjanata@ucdavis.edu

 © 2008 Acoustical Society of America

quency domain. We deviate slightly from this initial processing stage by utilizing the Auditory Peripheral Module from the IPEM Toolbox (Leman *et al.*, 2001). This module models the information stream from the outer ear to the auditory nerve. The process separates the signal into 40 bands on a critical band scale and easily substitutes for the filterbank in the first stage of Scheirer's model. After performing onset detection on each of the bands, Scheirer (1998) employed a filterbank of comb filters for each frequency subband. The filterbank outputs are then summed across frequency subbands. His model finds the comb filter with the highest energy output, which is used as an estimate of the tempo of the piece. Although Scheirer (1998) recognized that less prominent peaks are present in the comb filter outputs, he did not investigate the use of these peaks for identifying other metric levels present in the onset pattern.

The model by Klapuri *et al.* (2006) expands on Scheirer's model by improving the various processing stages, providing fine-tuning parameters and implementing a hidden Markov model which determines the frequencies and onset locations at the metric levels corresponding to the tempo, tactus, and measure. This model is currently regarded as one of the most accurate models of tempo and beat induction (Gouyon *et al.*, 2006). Although Klapuri *et al.* (2006) advanced the beat-finding ideas of Scheirer's model by taking into account the information across the three metric levels, one area that they do not investigate is the identification of other metrical hierarchies such as polyrhythms.

Our most significant departure from these two models is our use of reson filters instead of comb filters for the analysis of the periodicities present in the onset patterns. As described in more detail below, we find reson filters to be better suited to the demands of tracking the relative energy at multiple metric levels. The final stage of our model produces a surface plot that illustrates the metric levels of an excerpt as they vary over time. We refer to this plot as an *average periodicity surface* (APS). From the APS, we derive a *mean periodicity profile* (MPP), which depicts the mean metric hierarchy over the course of the excerpt. Next, we describe and illustrate in detail the processing stages of our model, and demonstrate how our model can be used to examine the metric and rhythmic properties of simulated signals, music, and bimanual taps produced in behavioral tasks.

II. METHODS

A. Model overview

Our model was written in MATLAB (The MathWorks, Inc., Natick, MA). Figure 1 schematizes the processing steps. First, we pass the audio signal through the Auditory Peripheral Module of the IPEM Toolbox. The output of the module is an auditory nerve image (ANI), which represents the auditory information stream along the VIIIth cranial nerve and results in 40 channels of data. Next, we extract the amplitude envelopes by performing a root mean square (rms) calculation on the output of each channel. Onset patterns are then extracted by a difference calculation and half-wave rectification. We then sum every eight adjacent channels to produce five bands. Each of the five bands is passed through a bank

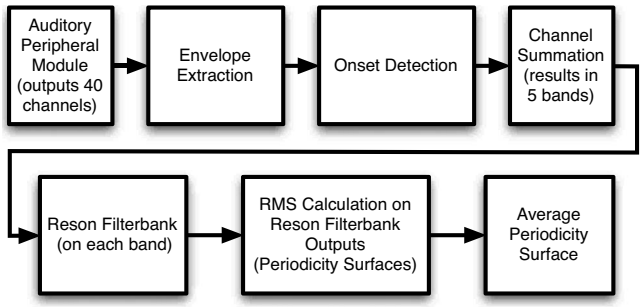


FIG. 1. Overview of the model's processing stages.

of reson filters. A rms calculation is performed on each band to facilitate the identification of the relative amplitudes of each filter. We refer to the surface plot of the rms of each band as a *periodicity surface*. The five periodicity surfaces are then averaged to produce an APS.

B. Auditory peripheral module

The Auditory Peripheral Module of the IPEM Toolbox is based on a model devised by Van Immerseel and Martens (1992). The first processing stage involves filtering the audio signal with a second-order low pass filter with a resonance frequency of 4 kHz. This filter approximates the frequency response of the ear. The low pass filtered audio signal is passed through a series of 40 bandpass filters. The resulting bands are referred to as channels. Each channel is then passed through a hair cell model, which is a forward-driven gain controlled amplifier that incorporates half-wave rectification and dynamic range compression. Each channel is subsequently low pass filtered at 1250 Hz. The resulting 40 channels simulate neuronal bandpass properties and firing rate encoding of the primary auditory nerve. The output of the model is referred to as an ANI. Each channel of the ANI has a bandwidth of one critical band and is spaced half a critical band from its neighboring channels. The 40 ANI channel center frequencies range between 141 and 8877 Hz. Figure 2(a) illustrates the outputs of channels 4, 10, and 30, with center frequencies of 252 Hz, 507 Hz, and 3266 Hz, respectively, for a musical excerpt (a sample excerpt of "Goodies" by Ciara featuring Petey Pablo, as downloaded from the Apple Music Store). The firing rate encoding of each channel is sampled at 2205 Hz. The incorporation of the Auditory Peripheral Module means that further processing steps in our rhythm model operate on a model of the auditory nerve rather than on bands of the audio signal itself. This model easily substitutes for the bank of bandpass filters employed by Scheirer (1998). Klapuri *et al.* (2006) employed 36 bands on a critical band scale, so the number and spacing of our filters more closely fit their configuration, although their filters range between 50 Hz and 20 kHz, while our range is narrower.

C. Envelope extraction

The ANI channels are smoothed with a rms calculation. We use a frame size of 50 ms and a frame step of one sample. This provides an estimation of the envelope of each channel. The rms signals are then downsampled to 100 Hz

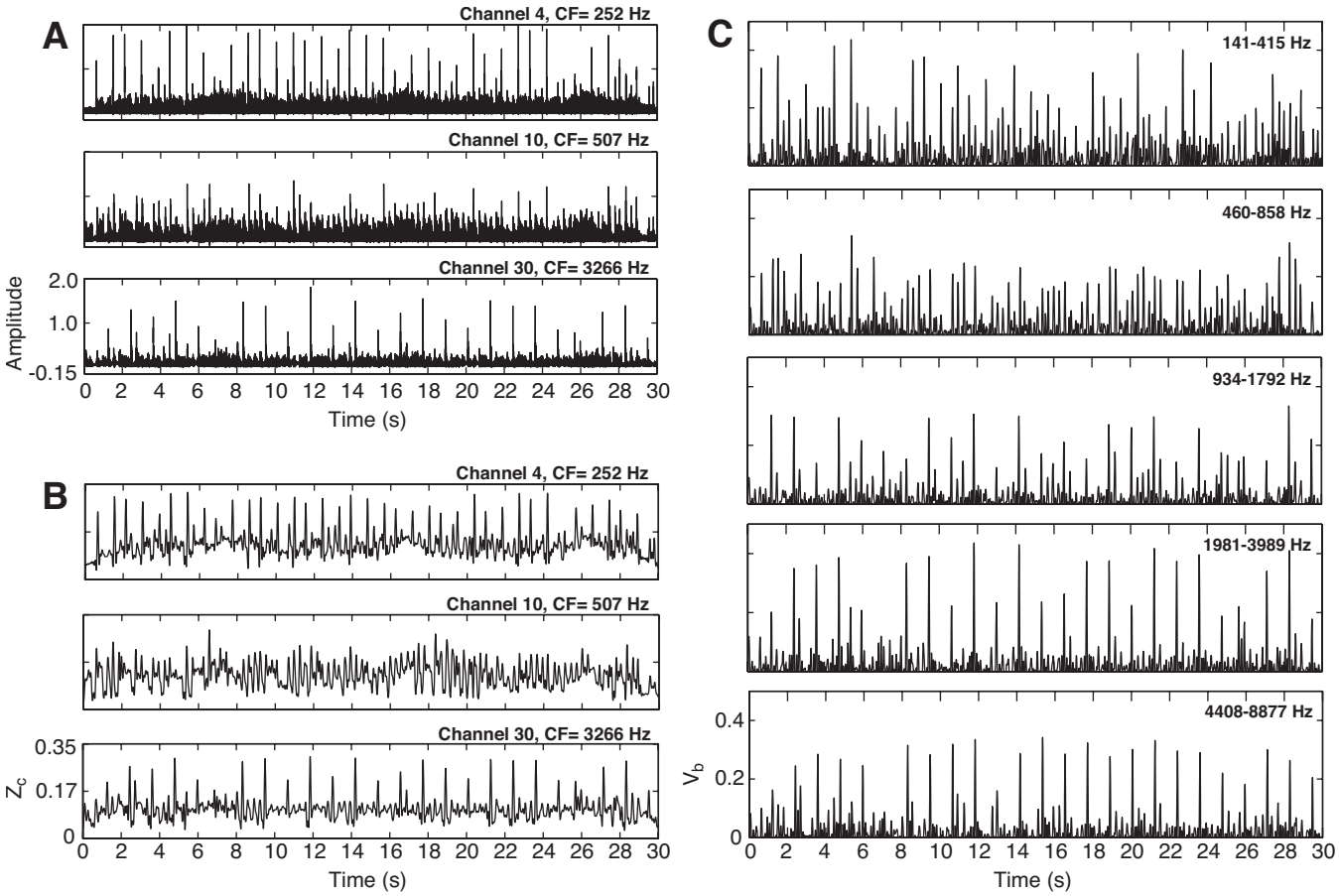


FIG. 2. Signal plots corresponding to (a) ANI channels 4, 10, and 30 with center frequencies 252, 507, and 3266 Hz. (b) The same ANI channels after performing a rms, downsampling, and lowpass filtering. The calculation of $z_c(n)$ is discussed in Sec. II C. (c) The resulting five bands after onset detection and summation of every eight adjacent channels. Equation (2) is used to calculate $v_b(n)$.

and low pass filtered by a 12th order Butterworth filter with a low pass frequency of 10 Hz for further smoothing. The downsampled and low pass filtered rms outputs of the same three channels are illustrated in Fig. 2(b).

D. Onset detection

We use $z_c(n)$ to represent the signal of each channel after performing the rms, downsampling, and low pass filtering calculations. First-order differencing and half-wave rectification are applied to $z_c(n)$. Half-wave rectification simply removes all negative values by setting them to zero.

$$z_c'(n) = \max(0, z_c(n) - z_c(n-1)). \tag{1}$$

The output $z_c'(n)$ provides an estimate of the onset pattern of the signal, reflecting both the rates and magnitudes of the onsets.

E. Channel summation

Sets of adjacent bands (channels) are next combined into single bands. This summation across the bands reduces some of the redundancy that is visibly present across the bands and provides an estimate of the temporal properties of broader spectral regions. In addition, the subsequent computational overhead is reduced considerably. Klapuri *et al.* (2006) summed the outputs from every nine adjacent bands, resulting in four final bands. We sum every eight adjacent channels, resulting in five bands (Fig. 2(c)). We chose the greatest divisor of the original 40 bands that produced periodicity surfaces (see Sec. II G) with noticeably different characteristics. This provided the best reduction of redundancy across the bands while still maintaining the different characteristics between frequency ranges.

$$v_b(n) = \sum_{c=(b-1)m_0+1}^{bm_0} z_c'(n), \quad b = 1, \ldots, b_0. \tag{2}$$

Note that this equation is identical to the one used by Klapuri *et al.* (2006), except that we exchange the b and c subscripts. In our model, we use c to denote ANI channel index and b to denote the summed band index. m_0 is the number of adjacent channels to sum and the calculation results in $b_0 = c_0/m_0$ bands.

F. Reson filterbanks

The signal from each band is passed through a bank of resonators, following the models of Scheirer (1998) and Klapuri *et al.* (2006). The bank of resonators for each band provides an analysis of the periodicities present in the onset patterns of that band. The models by Scheirer (1998) and Klapuri *et al.* (2006) employ comb filters as resonators. We

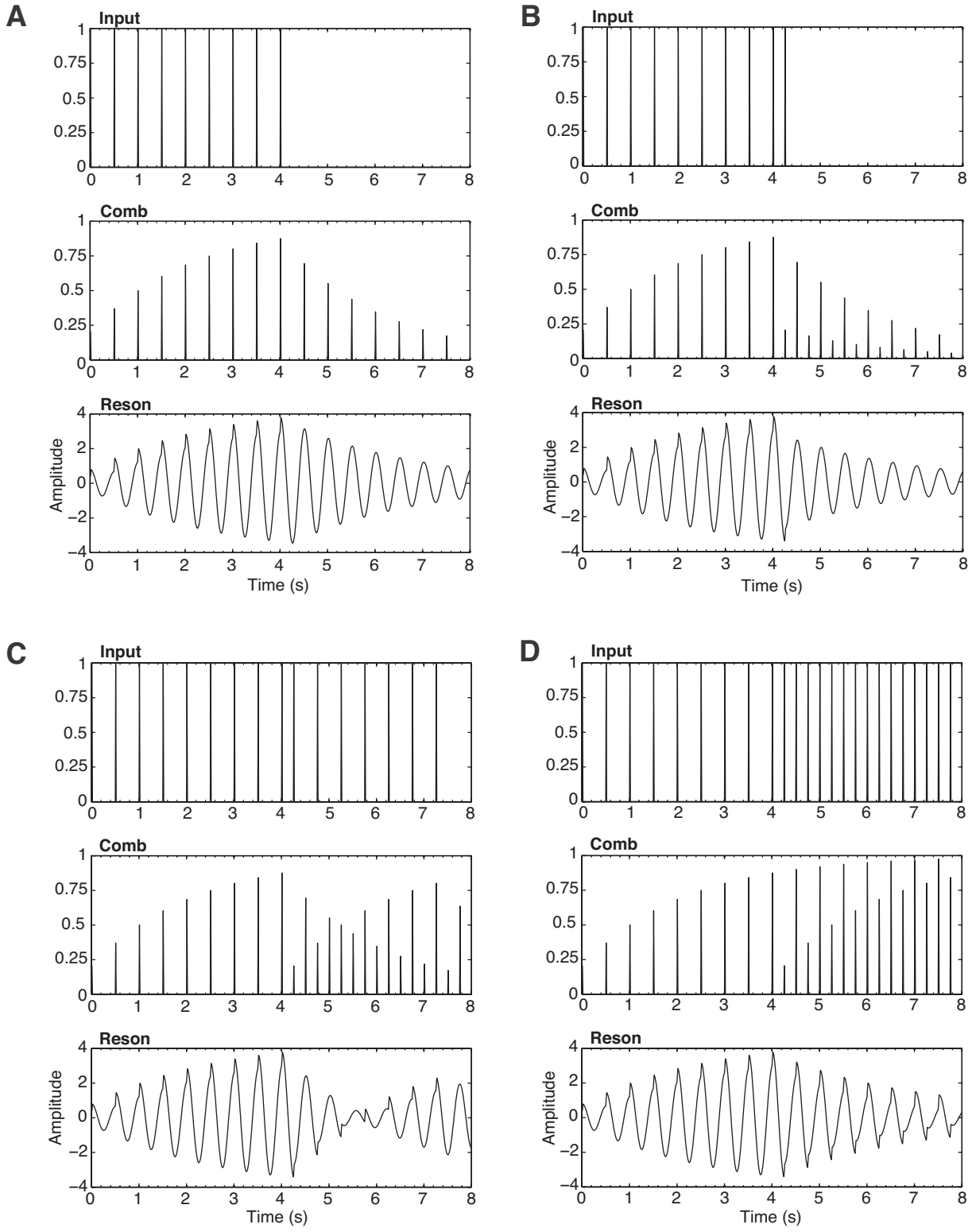


FIG. 3. Comparison of comb filter and reson filter responses. The reson filter has a resonant frequency of 2 Hz, and the comb filter's lowest resonance is at 2 Hz. Both filters are passed four different series of Dirac impulses for comparison: (a) a series at 2 Hz ending at 4 s, (b) a series at 2 Hz, followed by a single impulse at 4.25 s which is antiphase with both of the filter outputs, (c) a series at 2 Hz, phase shifted at 4.25 s, and (d) a series at 2 Hz which immediately doubles in frequency to 4 Hz after 4 s.

found that comb filters did not adjust quickly enough to changes in the onset patterns of the input signal, however; whereas *reson* filters, a type of damped oscillator (Steiglitz, 1996), adjusted much more quickly to changes in the onset patterns.

Figure 3 illustrates the responses of a comb filter and a reson filter, both tuned to a frequency of 2 Hz, to a variety of input signals. Figure 3(a) illustrates the responses of the comb filter and reson filter when they are passed an isochronous series of Dirac impulses at 2 Hz for 4 s, followed by 4

s of silence. The responses of both filters peak at 4 s as expected, and then decay. However, when an antiphase onset at 4.25 s follows the same series of isochronous pulses in the input (Fig. 3(b)), the amplitude envelope of the comb filter output is the same as if it was not passed the antiphase onset. The reson filter output in Fig. 3(b), however, is attenuated slightly after 4.25 s as compared with the reson filter output of Fig. 3(a). Figure 3(c) illustrates how each of the filters adjusts to a phase shift in the isochronous sequence. Both filters go through a phase adjustment period between 5.25 and 6.25 s. The comb filter output, however, still contains remnants of the original phase after 6.25 s, while the effects of the original phase are not as apparent in the reson filter after 6.25 s. Figure 3(d) illustrates how the two filters react to a doubling of the isochronous sequence after 4 s. The comb filter outputs a second set of impulses that are antiphase with the original series, but the overall amplitude envelope of the comb filter is not affected by a doubling of the frequency of the isochronous series. In contrast, the energy in the reson filter (which is now effectively tuned to a period that is twice as long as the period in the pulse train) decays after 4 s at approximately the same rate as if silence had been introduced as in Fig. 3(a).

The phase perturbations in Figs. 3(b) and 3(c) and the doubling of the frequency of the isochronous sequence in Fig. 3(d) actually increase the overall energy of the comb filter response by introducing additional antiphase impulses, while causing an attenuation of the overall energy of the reson filter response. The reason why a reson filter is attenuated when presented with antiphase impulses is that the output signal of the filter assumes both positive and negative values, whereas the comb filter outputs only positive values. Thus, the amount of constructive or destructive interference imposed by an incoming signal on the output of a reson filter depends on the phase angle at which it arrives. This characteristic made the overall responses of the reson filter adapt more quickly to changes in input signal timing. In addition, it prevented the reson filter from responding to input signals arriving at twice the frequency to which the filter was tuned.

A reson filter is often implemented as a two-pole filter. Reson filters tuned to low frequencies exhibit high rolloffs below the resonance frequency. In order to circumvent this issue, we use a version of the reson filter called *reson_z* (Steiglitz, 1996). Reson_z introduces two zeros to the filter at $z=1$ and $z=-1$, resulting in a two-pole two-zero filter. The addition of two zeros solves this problem by improving the low frequency rolloff (for low frequency filters) or improving the high frequency rolloff (for high frequency filters). The transfer function for the reson_z filter is

$$H(z) = \frac{g(1 - z^{-2})}{1 - 2R\cos\ \theta z^{-1} + R^2 z^{-2}}, \tag{3}$$

where g is a gain factor (see section on reson filter gain below) and R is the radius of the poles. The value of R affects the sharpness of the reson filter response and is approximately related to the half-power bandwidth by

$$R \approx 1 - B/2, \tag{4}$$

where B is the half-power bandwidth. The value for R is calculated from the desired half-power bandwidth for each filter. Our model employs a series of 99 reson filters between 0.25 and 10 Hz. The number of filters is determined by the methods used to calibrate the filters (described below).

1. Reson filter decay

Scheirer (1998) and Klapuri *et al.* (2006) tuned their resonators with an equivalent *half-energy* time, where half-energy refers to the time it takes the output of each resonator to reach half amplitude. Our resonators are tuned with a decay rate based on the number of periods of the filters. High frequency resonators in our model exhibit far too much energy when employing the same half-energy time. This is evident when a series of quick notes, such as triplets or quintuplets, cause a high frequency filter to ring. The high frequency filter, with an equivalent decay time as the other filters, exhibits more energy than a lower frequency filter that represents the tactus frequency, since it is being reinforced at zero phase for each of these onsets. These rapid onsets, however, are perceived as subdivisions of the beat and should not raise the energy of high frequency filters above the energy of the filter that represents the tactus. We determined the decay rate of the filters by measuring the filter's *Q-factor*, which is the ratio of a filter's center frequency f_c to its bandwidth B.

$$Q = \frac{f_c}{B}. \tag{5}$$

Q-factor describes a filter's sharpness. It also describes the number of periods that a resonator's impulse response decays by a factor of $e^{-\pi}$, which is approximately −27 dB (Smith, 2007). We use a constant Q-factor of 13 for all the filters, which means that the filters all decay by approximately −27 dB after 13 periods. Since the Q-factor is constant across all the resonators, this also means that resonators with higher resonance frequencies also have proportionally wider bandwidths.

2. Reson filter spacing

There are at least two primary issues to address when choosing an appropriate spacing of resonators. First, the frequency domain must be adequately sampled. Second, the rolloffs of the magnitude responses of the filters should not meet too far below the peak magnitudes. If the magnitude responses do meet far below the peak magnitude responses, then certain frequencies are not captured by the filters as well as others.

Since the filters have a constant Q-factor, their bandwidths cannot be changed. The two issues mentioned above are adequately addressed by spacing the filters at a point above their half-power bandwidth. The half-power bandwidth is defined as the width of the magnitude response of the filter at its half-power points ($1/\sqrt{2}$ times the peak magnitude or −3 dB from the peak response). To produce reson filter responses that overlap above their half-power points, we space the filters so that their resonance frequencies are

half of a half-power bandwidth apart. The peak magnitude response of a reson filter can differ slightly from the pole angle of the filter, so an adjustment is made to approximate the true resonance frequency of each filter (Steiglitz, 1994). This results in 99 total filters with resonance frequencies from 0.25 to 10 Hz. There are 66 filters with resonance frequencies below 3 Hz. For the purpose of testing the model's responses to various input types, we found this to be a sufficient sampling of periodicities commonly found at the tactus level.

3. Reson filter gain

In some cases, it is possible for low frequency resonators, particularly below 1 Hz, to exhibit more energy than is appropriate if they are to be regarded as a model of perceptual salience. This issue arises when a series of rapid onsets is fed into a low frequency resonator. Multiple rapid onsets that all occur near the peak (zero phase) of the resonator will increase the overall output of the resonator more than a single onset would. Although we have yet to perform systematic calibrations of the model to match the perceived salience at different periodicities (see Sec. IV), we accommodate the need for such adjustments by introducing a gain factor g [see Eq. (3)] to the reson filter, which varies with the resonance frequencies of the filters. We vary the gain across each resonator bank between 0.1 and 0.4. A beta probability density function with parameters $\alpha=2$ and $\beta=5$ is used to vary the gain across resonators. This results in a gain that varies across the resonators in a semiparabolic shape, starting with a gain of 0.1 at 0.25 Hz, rising to a maximum gain of 0.4 at 2.23 Hz, and dropping back to a gain of 0.1 at 10 Hz. A lower gain for filters with resonances at higher frequencies also improves the resonator bank output slightly by reducing the prominence of high frequency filter outputs.

G. rms calculation on reson filters

In order to provide a clearer picture of the relative amplitudes of the resonator outputs, we perform a rms calculation over a sliding time frame at each sample point. The rms frame size we use is 2 s. Each rms frame begins 2 s before the current sample point and ends at the current sample point (i.e., each sample point is at the end of each rms frame). For time points prior to 2 s into the signal, a frame size equal to the number of samples up to the current sample point is used. The use of a frame size that gradually increases to 2 s at the beginning of the signal produces a ramping effect of the rms plot. The rms calculation smoothes the resonator outputs, facilitating the identification of relative energy levels of the resonators over time. Figure 4 illustrates the resonator outputs from each band (left panels) and the rms outputs (right panels). We refer to each of the rms plots as a *periodicity surface*. Note that the periodicity surface allows for a rapid appraisal of the metric relationships, if any, between the periodicities that are present in the signal of that band at any given moment in time.

H. Average periodicity surface

The rms outputs for each band are then averaged to produce a composite rms plot (bottom center of Fig. 4). We refer to this surface plot as the APS of a musical excerpt. The APS is then averaged in time over the whole excerpt to create a MPP (Fig. 4, bottom right panel). This graph allows one to identify the prominent periodicities in the excerpt. Further investigation of this plot allows one to infer various metric relationships and properties of the periodicities that are present. The peak widths may indicate the relative accuracy of a given frequency over the course of the excerpt. Ratios of peak frequencies suggest the meter of the excerpt. For example, in the MPP in Fig. 4, the peaks at filter frequencies of 0.84, 1.71, and 3.38 Hz present a 1:2:4 set of ratios indicating duple meter. However, more complex metric relationships also appear to be present as represented by the small peak at 2.50 Hz that exists in a 3:1 ratio with the peak at 0.84 Hz.

I. Audio signal inputs versus other inputs

The model described above can, in principle, be used to identify the periodicities present in other data streams. Of particular interest to us are the rhythmic properties of listeners' movements associated with hearing a piece of music. Such movements might include finger taps, key presses, or even the more complicated movements of multiple limbs. In order to compute periodicity surfaces for the latter types of data, it is necessary to adapt the model in order to accommodate heterogeneous signal types. While an audio signal arising from a performance of a musical piece can be analyzed by the model with no need for modification, other signals, such as MIDI data obtained from a drum pad or keyboard, require special treatment. With MIDI data, it is not appropriate to process the data through portions of the model concerned with simulating the auditory nerve firing rate and onset pattern extraction. A straightforward solution for working with MIDI data of this sort is to convert each *note on* message into a Dirac impulse. The signal produced in this fashion is then passed directly into a single resonator bank in order to produce periodicity surfaces and MPPs. Currently, for bimanual tasks, we do not differentiate between left and right hand taps. The amplitude of each Dirac impulse is linearly scaled by calculating the ratio of the note's MIDI velocity to the maximum velocity. We also mask out double strikes for each hand by removing onsets that follow an intertap interval below a certain threshold (50 ms). Since we employ only one resonator bank for Dirac impulse inputs, we refer to a surface plot of the rms of the single resonator bank output as a periodicity surface instead of an APS. A MPP is then calculated directly from the periodicity surface.

III. RESULTS

We evaluated the behavior of our model in several ways. First, we compared the performance of our model with the performance of existing models of tempo and beat estimation. Second, we inspected the behavior of our model with clearly defined input types: multiple series of isochronous Dirac impulses that varied in timing and in amplitude. Third,

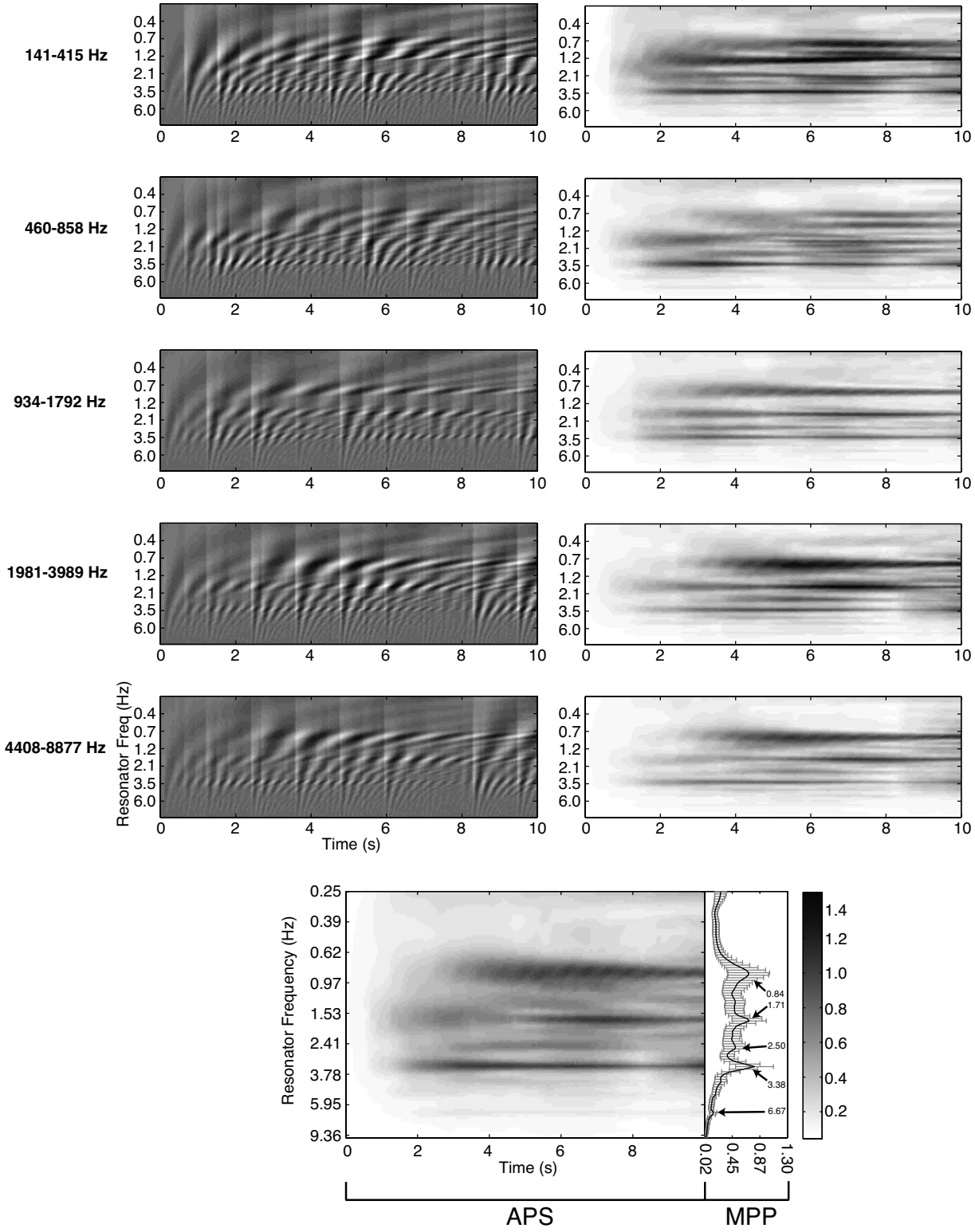


FIG. 4. Surface plots of the resonator outputs from each of the five bands are shown on the upper left. Grayscale values range from negative (black) to positive (white) values. Surface plots of the rms of the resonator outputs, referred to as periodicity surfaces, of the same five bands are shown on the upper right. Grayscale values range from zero (white) to positive (black). The APS, which resulted from averaging the five periodicity surfaces, is shown on the bottom surface plot. The MPP is on the right adjacent side of the APS. The black line of the MPP plots the mean of the APS over time, while the gray bars plot the standard deviation of the APS over time.

we tested the model with musical stimuli and behavioral response data (MIDI recordings of tapping data). Finally, in order to illustrate that the model output may be converted to a symbolic representation, we developed a technique for classifying the meter of simple accent patterns and tested the meter classification technique for accuracy.

A. Model accuracy

In order to verify that our model produces measurements with accuracy levels that are on par with other recent rhythm models, we processed a large set of audio clips that were used in the tempo induction contest conducted by Gouyon,

et al. (2006). Eleven algorithms were compared in the contest article and the results for a 12th algorithm were reported on the contest website.[1] In the contest, 3199 audio clips were used, comprised of three different data sets. Since the first data set (DJ loops) was copyrighted and not readily available, we processed our model with the second and third data sets (1163 of the 3199 audio clips used in the contest). The second data set consisted of 30 s excerpts of ballroom dancing music.[2] The third data set used in the contest consisted of 20 s song excerpts, apparently hand picked by the authors, from several different musical genres. As a ground truth tempo, the contest organizers asked a professional musician to place beat marks on each of the song excerpts. The tempo was computed as the mean of the annotated interbeat intervals. The annotated tempi were available to us from the contest website, so we were able to test our model with the same criteria as the contest algorithms.

There were two measurements used to determine the level of accuracy of the algorithms in the contest. Both measurements involved tempo estimation, even though many algorithms also provided other information such as beat locations. The first measurement (accuracy 1) calculated the percentage of tempo estimations that were correct for each algorithm within a 4% error margin. The second measurement (accuracy 2) calculated the percentage of tempo estimations that were correct within a 4% error margin for each algorithm, considering an estimation at half, double, three times, or one-third of the annotated tempo as correct.

The calculation of accuracies 1 and 2 for our model were 35.00% and 78.42%, respectively. The contest website reported a range of 25.22%–67.29% (mean 37.53% and median 34.02%) for accuracy 1 and a range of 50.73%–85.01% (mean 69.10% and median 71.69%) for accuracy 2 on all three data sets. Although we tested our model on only two of the three data sets, comprising approximately one-third of the total number of audio excerpts, it is reasonable to expect our model to perform at comparable accuracy levels on the complete data set. If our model performed with these scores in the contest using the complete data set, it would have ranked 7th of 13 for accuracy 1 and 4th of 13 for accuracy 2.

B. Timing variability in isochronous pulse sequences

We examined the response of our model to an isochronous series of Dirac impulses at 1 Hz without any timing deviations (Fig. 5(a)). As expected, the MPP exhibited the highest energy at the frequency of the impulses. Peaks were also observed for resonators at or near integer multiples (harmonics) of the peak frequency. The reason why a perfectly isochronous input yields energy at higher harmonics of the fundamental frequency is that each impulse is perfectly phase aligned with the higher harmonics. As the harmonic number increases, the impulses skip a number of periods of the filter, explaining the reduced energy level at each higher harmonic. An important distinction between reson filters and comb filters is that reson filters will not exhibit high energy at subharmonics since reson filters have a cancellation effect when presented with inputs at or near their anti-phase state.

We predicted that the energy in the higher harmonics would be sensitive to timing deviations from a strict isochronous series because any given deviation represents a larger phase perturbation at higher frequencies. Gaussian distributions have been used in other models to approximate timing deviations of human performance (Cemgil *et al.*, 2000; Gouyon *et al.*, 2002), so we utilized this distribution for introducing timing deviations. We varied the timing of the pulses by a Gaussian distribution function with a mean $\mu = 0$ and a standard deviation variable σ. Timing deviations produced by nonintentional motor noise tend to deviate between 10 to 100 ms (Desain and Honing, 1993), so we used standard deviations of 20, 40, and 80 ms to provide details on how our model reacts to timing deviations within this range. Figures 5(b)–5(d) illustrate the resonator outputs, periodicity surfaces, and MPPs produced from a series of impulses drawn from Gaussian distributions with standard deviations of 20 ms, 40 ms, and 80 ms, respectively. The most noticeable effect of the timing deviations introduced in Figs. 5(b) and 5(c) as compared with Fig. 5(a) was a reduction of harmonic peak amplitude, particularly above the third harmonic. The upper harmonics in the periodicity surface and MPP dissipated completely in the 80 ms condition.

Although not surprising that the filters corresponding to the higher harmonics would experience the variability in the input train as greater phase variability than would filters for lower harmonics, thereby leading to more damping of the filters' responses, the results of these simulations affirmed basic properties of the model and illustrated that periodicity surfaces were very stable across a significant range of timing deviations. The largest peak in the MPP, which corresponded to the frequency of the impulses, was very prominent, even when the standard deviation in the timing was as large as 80 ms. Since it is critical for rhythm models to be sensitive to timing (Honing, 2001), it was fortunate to affirm that timing variability is represented in our model.

C. Accent structure

In order to make the claim that our model can represent certain defining aspects of meter, we employed accented isochronous sequences as inputs to a single resonator bank. Figure 6(a) illustrates the resonator bank output, periodicity surface, and MPP produced by a series of Dirac impulses at 1 Hz with no variation, in a similar fashion to the series in Fig. 5(a) except that the amplitudes of the impulses were at half of the maximum amplitude. We used impulses at maximum amplitude and impulses at half-maximum amplitude for accented and unaccented onsets.

When every other impulse was accented (Fig. 6(b)), a peak emerged at 0.5 Hz and higher harmonics of 0.5 Hz. The MPP produced when accenting every third impulse (Fig. 6(c)) likewise contained peaks corresponding to the frequency of the accents, at 0.34 Hz, and harmonics of this frequency. It is important to note that the closest frequency to 0.33 Hz and corresponding harmonics were captured, and that if we employed a finer sampling of the frequency spectrum, peaks would occur closer to 0.33 Hz and integer multiples of this frequency.

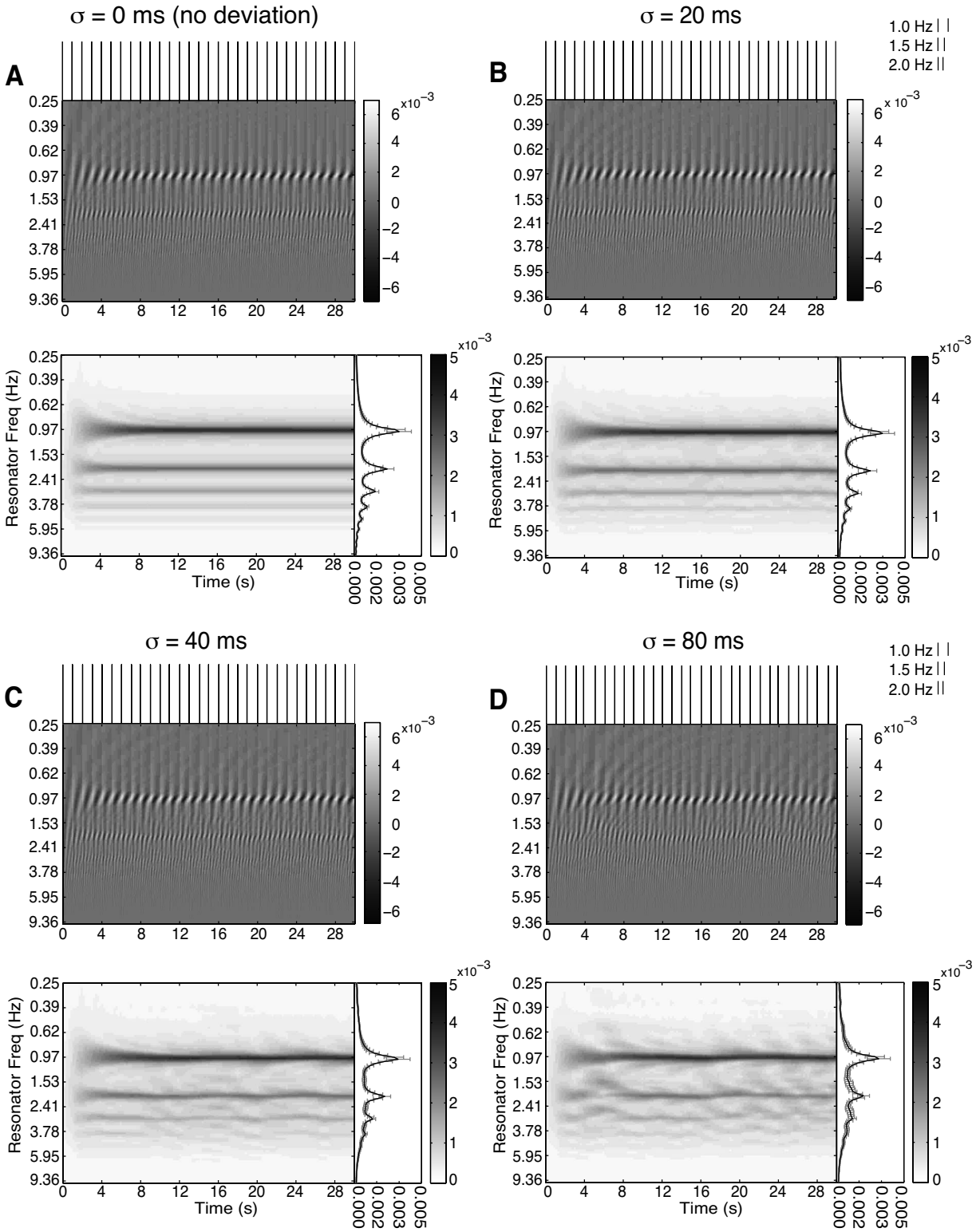


FIG. 5. The four sets of resonator outputs, periodicity surfaces, and MPPs illustrate how a resonator bank behaves when Gaussian noise is added to the timing of Dirac impulses in an otherwise isochronous series. (a) No deviation (σ=0 ms). Deviations in onset times are drawn from Gaussian distributions with (b) σ=20 ms, (c) σ=40 ms, and (d) σ=80 ms.

Figure 6(d) illustrates the resonator bank output, periodicity surface, and MPP from a series of impulses with accents alternating every second and third beats. The alternating accent pattern on Fig. 6(d) produced a MPP with small peaks at 0.41 and 0.60 Hz. These were harmonics of a peak that would have emerged at 0.2 Hz if the resonators spanned to this frequency. Harmonics at 0.8 and 1.2 Hz were not apparent probably because they fused with the wide peak at 1.0 Hz. This MPP represented a 1:5 metric ratio present in the accent structure. This illustrated how the model captures

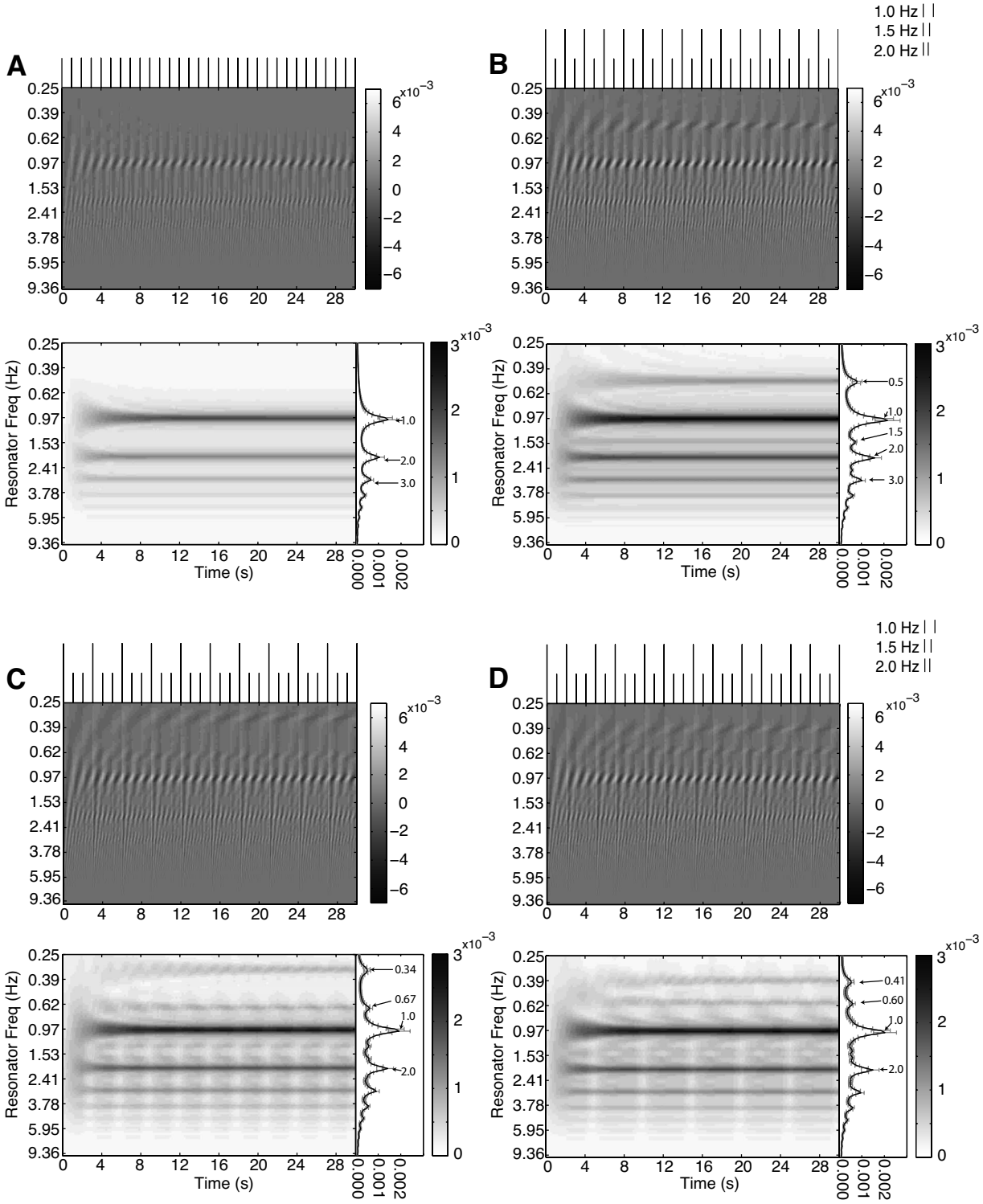


FIG. 6. The four sets of resonator outputs, periodicity surfaces, and MPPs illustrate how a resonator bank behaves when presented with a series of Dirac impulses that has an accent structure. Nonaccented impulses are assigned half the maximum amplitude, while accented impulses are assigned the maximum amplitude. (a) The input isochronous series has no accented impulses. (b) Every other impulse is accented. (c) Every third impulse is accented. (d) Accents are alternated every second and third impulses.

groupings of accent structures. One way to view the accent structure is that the first two accents are each followed by an accent every five onsets and are simply phase shifted from one another by two onsets.

The three accent patterns (Figs. 6(b)–6(d)) illustrated how accent structure is represented in periodicity surfaces and MPPs. The peak at 1 Hz and corresponding harmonics remained prominent. These peaks reflected the overall frequency of the impulses and were also reinforced as harmonics of the accent pattern frequencies in all three patterns. The results confirmed that accents, which often help to define metric structure in music, produce additional peaks and therefore contribute to the interpretation of metric levels present in a musical excerpt.

In order to test whether reson filters provide an advantage over comb filters in representing accent structure, we passed the same accent patterns through comb filters. Since there is a trend for the comb filterbank power response to increase as the filter delay increases (Klapuri *et al.*, 2006), it was difficult to see the effects of Dirac impulses on comb filter outputs. By convolving the same four series of Dirac impulses with a Gaussian distribution function, the peaks in the comb filterbanks were much clearer. We used a Gaussian distribution function with a full-width at half-maximum measurement of approximately 200 ms. We also passed this same convolved accent pattern through a bank of reson filters. Since the gain function that we normally use across the reson filterbank was tuned specifically for those filters, it was not appropriate for the comb filterbank. Therefore, we used a constant gain of 0.4 across the reson filterbank to provide a better comparison with the comb filterbank output. The comb filterbank was tuned to Scheirer's specifications, with a half-energy time of 1.5 s across all of the filters.

Figures 7(a)–7(d) illustrate the periodicity surfaces produced by a reson filterbank (top plots in each panel) and a comb filterbank (bottom plots in each panel). As evident in the figures, the reson filterbank produces peaks corresponding to the overall frequency of the spikes at 1 Hz and peaks corresponding to the accent frequencies in a similar fashion to Figs. 6(a)–6(d). Since we did not use an overall weighting function, a trend of the reson filters to produce higher amplitudes at lower frequencies was evident, but the peaks were still very clear. The periodicity surfaces produced from the comb filterbank, on the other hand, did not significantly change when presented with different accent patterns. The reason why the comb filterbank did not illustrate the frequency of the accent patterns could be that comb filters tuned to frequencies at subharmonics (frequencies that evenly divide the fundamental frequency) of the input also exhibit high energy. Therefore, accent patterns, which usually evenly divide an overall beat structure, are probably masked by these subharmonics. One aspect that is readily noticeable on the periodicity surfaces produced by comb filters in Figs. 7(c) and 7(d) is a series of light vertical bands. These are artifacts of the windowing technique used in calculating the rms for the periodicity surfaces. The same artifacts are also somewhat noticeable in the periodicity surfaces produced by the reson filters. These artifacts were not noticeable in other periodicity surfaces we produced with reson filters. The artifacts could possibly be avoided by using a leaky integrator for the rms, for which values further in the past are scaled progressively to lower values.

D. Percussion patterns

We constructed a MAX/MSP (Puckette and Zicarelli, 2006) patch for defining and playing MIDI percussion patterns. The MAX/MSP patch was executed on a G5 Macintosh, and the MIDI notes were rendered by an E-Mu Proteus 2000 synthesizer. The analog audio output from the synthesizer was sent back to the G5 Macintosh and recorded by a second MAX/MSP patch. We passed a series of 30 different percussion patterns through the model. Two of the patterns are discussed here. Both loops had a tempo of 90 bpm, where bpm indicates the number of quarter notes per minute rather than the perceived tempo. The first loop (Fig. 8(a)) was rendered with the sound of a single high hat (Proteus preset 68, bank 3, note value 68) and iterated 12 times resulting in a segment that was 32 s long. The APS of the excerpt exhibited a prominent peak at 0.75 Hz with many smaller peaks at greater frequencies.

The second loop decomposed the same note pattern into two instrument sounds, a "snap" (Proteus preset 68, bank 3, note value 79) and a high hat. Some of the notes from the score in Fig. 8(a) were played by only one of the two instruments while other notes were simultaneously played by both instruments to produce the score in Fig. 8(b). The two instruments were chosen for their differing timbres, so that we could inspect how differential activation of the five spectral bands affected the APS. This loop also iterated 12 times and the excerpt was approximately 32 s long. The most remarkable difference in the APS and MPP of this excerpt from the single instrument case was that the peak at 1.53 Hz was more prominent. The peak at 0.75 Hz was also very prominent but slightly lower than the peak at 1.53 Hz.

The APSs of the percussion patterns illustrated our model's sensitivity to timbral content. From inspecting the score in Fig. 8(b), it may have been possible for simultaneous onsets of both instruments to effectively produce accents on the periodicity surface of the same frequency band. However, a subsequent inspection of the periodicity surfaces from each band (data not shown) revealed that each of the instruments largely affected the periodicity surfaces of different bands. Therefore, the resulting APS in Fig. 8(b) resulted from separate periodicity analyses of the instruments which were subsequently integrated in the APS. This result suggests that it may be possible to use the model to investigate the effects of shifts in selective attention to timbre on rhythm perception (see Sec. IV).

E. Musical stimuli

Figures 8(c) and 8(d) illustrate the APSs and MPPs of two musical stimuli that we recently used during an experiment in which participants were instructed to tap isochronously and bimanually on a MIDI drum pad to the beat of the music (Janata *et al.*, 2007). Since multiple peaks are readily apparent in the APSs and MPPs of the stimuli, where each of the peaks indicates a prominent metric level in the music, it is of interest to inspect the frequencies and ratios of the peaks and speculate on how these relate to the content of the musical excerpts.

Herbie Hancock's "Maiden Voyage" produced a MPP with many peaks. The highest peak was at 1.78 Hz. Many other peaks were present, however, at 0.51, 0.78, 1.01, 1.27, 1.53, 2.32, and 4.08 Hz. With the exception of the peak at 2.32 Hz, which approximated a 4:3 ratio with the highest peak, these frequencies did not appear to approximate any simple ratios. This suggested that the excerpt contained complex rhythms. The piece is characterized by a prominent slow

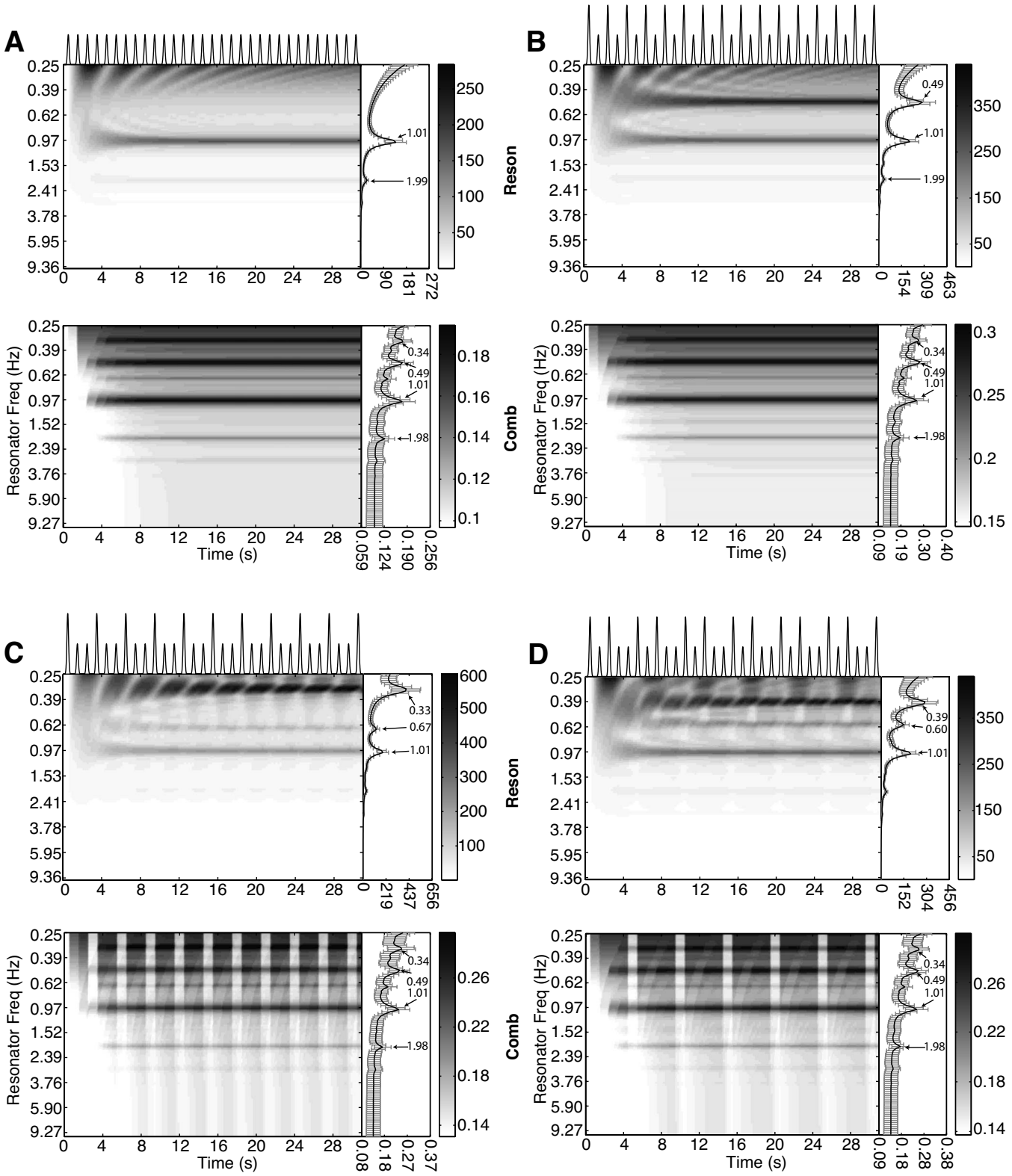


FIG. 7. The same accent patterns of Dirac impulses in Fig. 6 were convolved with a Gaussian distribution function and used as inputs for comparing periodicity surfaces produced by reson filters [top plots in (a)–(d)] with periodicity surfaces produced by comb filters [bottom plots in (a)–(d)]. A constant gain for the reson filters was used for a more equivalent comparison. The comb filters were tuned according to Scheirer (1998). The reson filters clearly illustrate the frequencies present in the accent patterns while the peaks in the periodicity surfaces produced by comb filters do not significantly change with the introduction of accents.

syncopated piano part, with less prominent but complex bass and drum parts, and an intermittent slow melody played by brass instruments.

By contrast, "It's a Wrap (Bye, Bye)" by "FH1 (Funky Hobo 1)" produced a MPP that provided a clear illustration of a metric hierarchy. The highest peak was at 1.53 Hz. The second highest peak was at 0.78 Hz and the third highest peak was at 3.02 Hz, which approximated ratios of 1:2 and

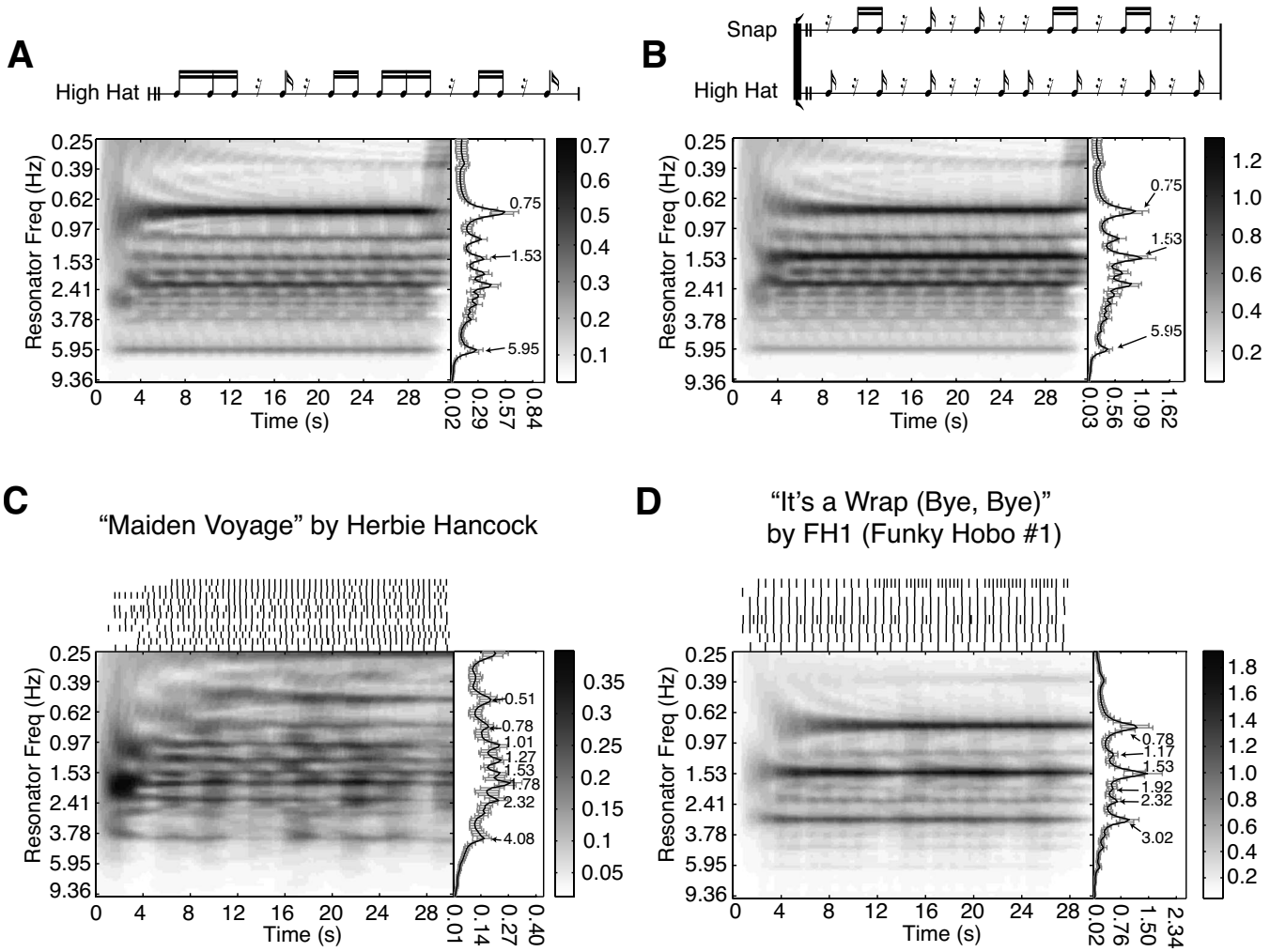


FIG. 8. APSs and MPPs produced from stimuli. (a) A pattern played by a single high hat. The score above the plot notates a 2.67 s long pattern that is iterated 12 times, resulting in a 32.0 s excerpt. The excerpt is used as an input to the model to produce the APS and MPP. (b) A stimulus with two instruments: snap and high hat for which every note from the excerpt in (a) is played by one or both of the instruments. The duration of the score is also 2.67 s long and iterated 12 times. [(c) and (d)] APSs and MPPs of excerpts from commercial musical recordings retrieved from the iTunes store. Each row in the raster plots above each APS corresponds to a different participant, and shows the times at which he/she tapped when instructed to tap along with the perceived beat in the music.

2:1 to the peak frequency. A prominent electronic "clap" sound played at approximately 47 bpm, resulting in the peak at 0.78 Hz. A bass guitar played at twice the tempo of the clap, likely contributing to the most prominent peak at 1.53 Hz. The peak at 3.02 Hz may have simply emerged as a harmonic of the peak at 1.53 Hz. The low amplitude peaks at 1.17, 1.92, and 2.32 Hz approximated 3:4, 5:4, and 3:2 ratios with the highest peak, respectively. Although these small peaks suggested subtle rhythmic arrangements, the piece has little rhythmic variation, which explains the three strong peaks at very simple ratios. The APS of the piece by FH1 illustrated that it changed very little over time, while the APS of the Herbie Hancock piece illustrated a more dynamic piece. The MPP of the excerpt by FH1 also contained prominent peaks at simpler ratios than the MPP of the Herbie Hancock excerpt. The contrast between these two excerpts illustrated how greater dynamics over time in the APS and peak frequencies at higher integer ratios in both the APS and MPP might indicate a greater rhythmic complexity.

The rows of rasters above the APSs in Figs. 8(c) and 8(d) show the tap onsets produced during individual trials. Each row corresponds to a different participant. It is evident from the rasters that participants chose different metric levels as the tactus of the music, even for a piece in which the metric hierarchy is clear. Although this example is limited to two musical excerpts, it illustrates the importance of considering individual variability and models that depict multiple metric relationships in work that seeks to understand how individuals synchronize with music. Although we have not devised a method for determining the metric level participants that are attending to, it may be possible to make comparisons using APSs and MPPs of tapping responses corresponding to these stimuli. In Sec. III F, we illustrate how the tapping data may be processed.

F. Tapping data

We processed two tapping trials from the experiment described above in Sec. III E. The excerpt playing during both trials was the same excerpt of Maiden Voyage by Herbie Hancock. The first trial (Fig. 9(a)) was a bimanual isochronous tapping task. The second trial (Fig. 9(b)) was a

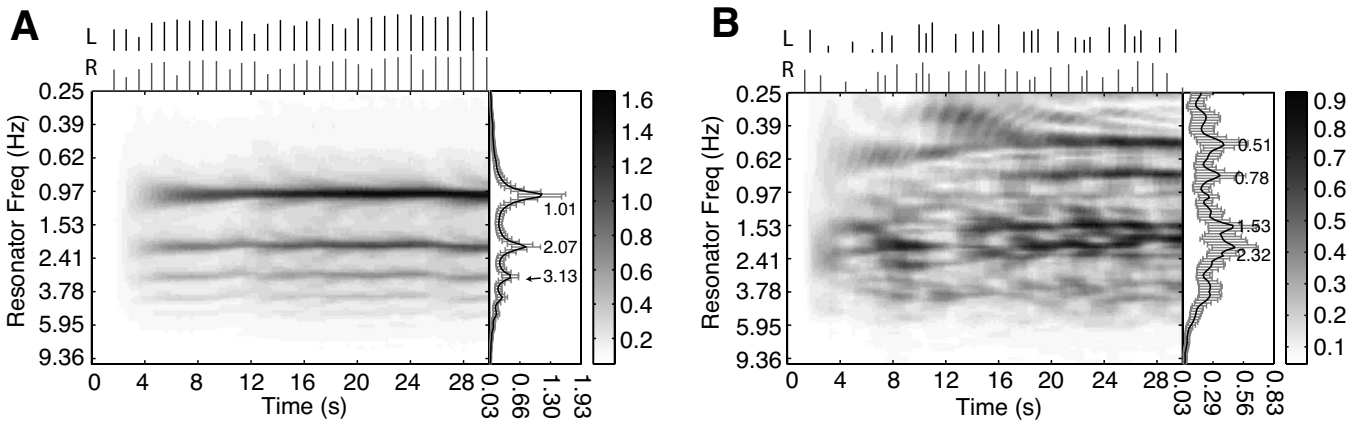


FIG. 9. Periodicity surfaces and MPPs of response tapping data recorded as MIDI. The MIDI note ons are converted to Dirac impulses that are subsequently amplitude scaled by MIDI velocity, and then passed to a single resonator bank. The vertical lines at the top plot the amplitude scaled Dirac impulses produced by the left and right hand taps. The trials shown are from (a) an isochronous tapping task and (b) a free-form tapping task. The stimulus being presented during both trials was the musical excerpt for which the APS and MPP were illustrated in Fig. 8(c).

free-form tapping trial, in which the participant was instructed to tap along with the music as he/she saw fit. The lower left and lower right sections of the drum pad on which the participant tapped produced unique MIDI notes, allowing us to distinguish between left hand and right hand taps. Each note on event from the MIDI data was converted to a Dirac impulse, scaled by the velocity value of the note on event. The series of impulses was passed through a single resonator bank, using the method described in Sec. II I.

The MPP of the isochronous tapping task illustrated a clear peak at 1.01 Hz, estimating the approximate tempo of the participant's tapping. Harmonics of the highest peak appear as expected. The free-form tapping task in Fig. 9(b) illustrates that the participant was capturing a few different metric levels evident in the APS and MPP of the stimulus. All of the peak frequencies in the MPP produced by this tapping pattern were also present in the MPP produced by the stimulus shown in Fig. 8(c). The APSs and MPPs of tapping responses illustrate that it is possible to capture important metric properties of tapping data, and that these data can be compared with the APSs and MPPs of stimuli.

G. Determining the meter of musical excerpts

In order to use our model for analyses of stimuli and behavioral data, a conversion of the model output to a symbolic representation may be necessary. Since we wish to eventually use our model for multiple rhythmic measurements (see Sec. IV), the development of a comprehensive set of symbolic conversions would be beyond the scope of this paper. In order to illustrate one possible way in which the model can be converted into a symbolic output, we developed a simple technique that serves primarily as a proof-of-concept. As we have shown, the frequencies of the peaks in MPPs generally relate to one another by rational numbers, and the frequency ratios are closely linked to the metric patterns present in the inputs. We leveraged this property of MPPs in order to produce a simple automatic meter classifier that operated on inputs with varying accent patterns.

In a study conducted by Palmer and Krumhansl (1990), theoretical predictions of note occurrence frequencies on the quarter note and eighth note positions within a measure for various meters (2/4, 3/4, 4/4, and 6/8) were illustrated. We

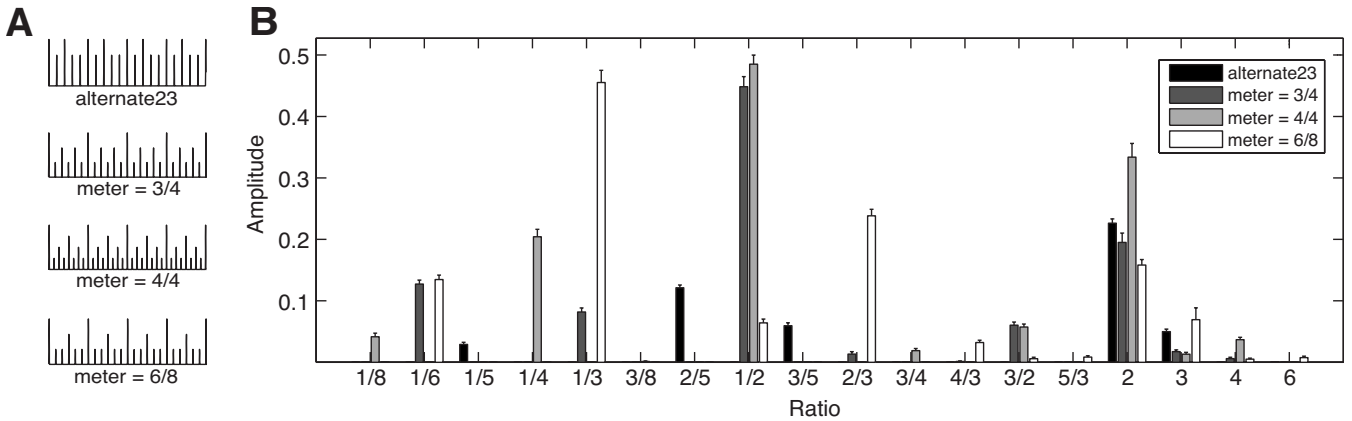


FIG. 10. (a) Accent patterns that were used as exemplars for four different metric classes. Four measures of each pattern are illustrated here. The amplitudes of the accented onsets (except the highest onset) and the tempi were randomized, while maintaining the accent hierarchy to produce 100 exemplars for each class. (b) Mean peak height values of the MPPs of the four sets of exemplars and their standard errors. The peaks were binned by the approximate frequency ratio relative to the frequency of the peak with the highest amplitude of each MPP.

used the note occurrence predictions to produce accent pattern exemplars for 3/4, 4/4, and 6/8 (Fig. 10(a)). Since the pattern illustrated for 2/4 was the same as for 4/4, we excluded 2/4 from our metric class list. As a fourth metric pattern, we used the same alternated two and three beat accent pattern illustrated in Fig. 6(d).

We varied the amplitudes of the onsets (except the highest one which stayed at maximum amplitude) by ±10% of the maximum amplitude. This allowed us to create a wide variety of patterns while still visibly maintaining the hierarchy of the accents. Across exemplars, tempo was manipulated by varying measure durations between 1.67 to 3.33 s. 100 exemplars (patterns) for each of the four classes were produced by randomizing the accent amplitudes and tempi with a uniform distribution within the ranges mentioned. Each pattern was repeated as many times as was necessary to produce 30 s excerpts.

After producing exemplars for each metric class and processing them through our model, we used a simple automatic peak finding algorithm to identify the frequencies and heights of the peaks in the MPPs. The peak finder locates points at which the slope of the MPP switches from positive to negative. Heights of the peaks were calculated from the higher of the left or right base of the peak (where the slope changes from negative to positive). Peaks with height values that were less than 5% of the amplitude range of the MPP were ignored. We then approximated the closest ratios that the peak frequencies represented in relation to one another, using the peak with the highest amplitude as a reference point with a ratio=1. For example, if the highest peak was at 3.0 Hz, it would be assigned a ratio=1, while peaks at 1.5 and 0.75 Hz would be assigned ratios of 1/2 and 1/4, respectively. We compiled a list of commonly found simple ratios in MPPs (1/8, 1/6, 1/5, 1/4, 1/3, 3/8, 2/5, 1/2, 3/5, 5/8, 2/3, 3/4, 4/5, 5/6, 7/8, 5/4, 4/3, 3/2, 5/3, 5/2) and integer multiples from 1–8. We then found the closest ratio or multiple that expressed the frequency of each peak in relation to the frequency of the highest peak. The frequency ratios of the peaks of all of the exemplars were successfully approximated within an error margin of 5%. The mean amplitudes of the peaks of the exemplars for each class, binned by ratio, are illustrated in Fig. 10(b).

In order to produce a pattern classifier for recognizing the similar peak relationships exhibited within each class, we implemented a feedforward neural network with backpropogation using MATLAB's Neural Network Toolbox. The default transfer function and learning rate associated with a network initialized by the newff() function were used. An input layer was fully interconnected with an output layer, but no hidden layer was used. All of the binned peak height values, with the exception of the peak at ratio=1, were used as inputs into the network. The MPPs of most exemplars had very prominent highest peaks, resulting in a strong preference for the value at ratio=1 in the weight matrix of the network when it was included. We were primarily interested in identifying other frequency ratios, such as 1/6, 1/4, 1/3, and 1/2 in the MPPs, since different metric classes were characterized by the presence or the absence of simple frequency ratios or multiples of the peaks. The output layer consisted of four units, thus representing each of the classes from which exemplars were drawn.

80% of the exemplars were selected randomly from each class in order to train the network. After training, the remaining exemplars were used to test the performance of the network. Each test exemplar was presented to the network and the identity of the winning output unit was compared to the identity of the class from which the exemplar was drawn. In this manner, we determined the proportion of exemplars that were identified correctly. Since the performance of the network is dependent on the subsets of exemplars chosen for training and testing, we reselected our training and testing sets, and reinitialized, retrained, and retested the network over 100 trial runs. We then calculated the mean performance of the network over all of the trials. The network performed very well at automatically classifying our test exemplars. The neural network correctly classified on average 92.9% (13.6% standard deviation) of the test exemplars. For 69 of the 100 trials, the network classified 100% of the test exemplars correctly.

Since the training and testing sets were very simple accent patterns, and a limited set of metric classes was chosen, the performance of this network is not indicative of how successful the technique would be with musical recordings or tapping performance data. However, the high success rate of the neural network on this simple data set indicated that conversions to symbolic representations are possible with our model and that a similar technique could be used for identifying patterns of peak ratios and amplitudes in recorded music and tapping patterns.

IV. DISCUSSION

In this paper, we described a model for performing periodicity analyses of audio stimuli and MIDI performance data. The model is based on banks of resonator filters. In contrast to similar models in which the primary objective is to identify the underlying beat in a piece of music (Scheirer, 1998; Klapuri *et al.* 2006), the objective of our model is to depict and describe the metric relationships that are present over the course of a piece of music or behavioral responses, such as tapping, to that music.

By inspecting the responses of our model to different types of input, we have an understanding of some of the model's basic response properties. The model regularly produces harmonics of the estimated tempo. We illustrated that upper harmonics are more sensitive to timing deviations than lower harmonics using isochronous series of Dirac impulses. More importantly for the analysis of metric structure, we showed that the model was sensitive to the accent structures present in the signal. The model was also sensitive to timbral changes when employing percussion sequences with different instrumentations. The periodicity surfaces and MPPs of the trials from the tapping experiment, as well as those of the music, illustrated various properties such as meter, rhythmic changes, and rhythmic complexity in both input types.

With a more informed understanding of our model's responses to various input types, we will now discuss how our

model relates to other models of meter and rhythm and suggest possible extensions and applications for our model.

A. Relationship of our model to other models of meter and rhythm

Models of metric and rhythmic structures have been developed to work on different types of input data and for different analytic purposes. Some models utilize symbolic data, e.g., musical scores, quantized interonset intervals, or MIDI data, whereas others operate directly on an audio signal. Analysis objectives include categorization for purposes of studying perception (Desain and Honing, 2003), complexity estimation (Shmulevich and Povel, 2000), beat finding (Scheirer, 1998; Klapuri *et al.* 2006), automatic music transcription (Cemgil *et al.*, 2000; Klapuri, 2004), automated genre classification (Dixon *et al.*, 2003; Tzanetakis and Cook, 2002), or combinations of these objectives. Below, we discuss the relationship of some of these models to our model and suggest how our model could be extended to accommodate these various objectives.

Two models that operate on symbolic data are those of Desain and Honing (2003) and Shmulevich and Povel (2000). Desain and Honing (2003) investigated the rhythmic categorization using groups of four onsets, defining three IOIs. They mapped the IOI triplets to a triangular surface on which each location represented a particular rhythmic pattern. This representation is useful for depicting the borders of perceived rhythmic categories because it is easy to show the areas of timing deviations around particular points in this space within which the percept of the rhythmic pattern does not change. Our cursory investigation of our model's responses to simple accent structures and tapping patterns shows that different rhythmic patterns manifest themselves as different distributions of peaks in the periodicity surfaces and MPPs, and that timing variability influences the presence of higher harmonics. Because our representational scheme is not limited to the relationships among groups of four events, it may be possible to use our model to examine perceived and produced rhythmic category structure in extended sequences.

Related to the issue of perceived rhythmic categories is perceived rhythmic complexity. While rhythmic complexity has been studied using IOI patterns and a heuristic for modeling the relative salience of measures with different event distributions (Shmulevich and Povel, 2000), APSs or MPPs might provide an alternative substrate for complexity calculations. For instance, one could imagine calculating the entropy of a MPP, with a greater number of peaks resulting in a larger entropy value. Alternatively, a distribution of the integer ratios of the peaks present in a MPP could serve as a basis for a complexity calculation. A preponderance of simple ratios, e.g., 2:1 and 3:1, in such a distribution would likely be associated with pieces of music that are perceived as less complex.

One obvious drawback to employing algorithms dependent on IOIs for rhythmic categorization or rhythmic complexity analysis is that onset timing information must either be readily available or extracted using an onset detection algorithm. A second drawback to using IOIs for this purpose is that the periodicities present in a grouping structure are not reflected in the distribution of IOIs. A simple histogram only reflects durations between onsets and does not reflect durations of groups of onsets. Therefore, methods employing IOI histograms must use various algorithms to extract these other durations. Our model readily captures the periodicities of pattern groups, as evidenced in the alternated two to three accent pattern (Fig. 6(d)), so therefore may provide a convenient mechanism for rhythmic categorization or rhythmic complexity measures.

Our model falls into a class of models that operate on nonsymbolic audio data. We provided a modification of the Scheirer model by incorporating the Auditory Peripheral Module of the IPEM Toolbox, inspection of periodicities other than the estimated tactus, and reson filters for frequency analysis. The incorporation of the Auditory Peripheral Module provided our model with filter approximations of the outer ear and cochlea, as well as an approximation of the mechanical to neural transduction of cochlear hair cells. This was a slight departure from the Scheirer model since this stage also effectively decomposes the signal into separate frequency bands. While models for extracting beat and meter are very useful for the purposes of automatic music transcription, the ability to extract other metric levels could be very useful to researchers of music perception. Scheirer (1998) only tracked the tempo and beat locations of frequencies between 1 and 3 Hz, and was not concerned with inspecting competing filters for extracting multiple metric levels. Klapuri *et al.* (2006) made significant steps toward tracking frequencies other than the tactus, namely, the tatum and measure. Our model illustrates that it is possible to extract other metric levels by directly inspecting the relative levels of the filter outputs.

Our most significant departure from the models of Scheirer (1998) and Klapuri *et al.* (2006), however, is our use of reson filters instead of comb filters. Reson filters have the property that they cycle through positive and negative values in response to an input (Fig. 3). Thus, a stimulus arriving out of phase with the oscillation established within a reson filter will reduce the energy in the filter depending on the magnitude of the arriving stimulus and its phase angle. It is this property that allows our model to represent the accent structure in an isochronous sequence of beats. When all of the beats are of equal magnitude, the output of filters at subharmonics of the period is suppressed due to the out-of-phase inputs. However, when an accent structure is imposed, the weak beats do not provide enough energy to entirely suppress the output of the filter that is tuned to the period of the strong beats.

Our model is by no means the first to employ oscillator-based filters for frequency analysis. Large (2000) used a bank of oscillators for periodicity analysis, though his model utilized a network of Hopf oscillators rather than reson filters. In terms of the preprocessing steps, such as the use of an auditory periphery model, envelope estimation, and an onset extraction process, the models are quite similar. A major difference between Large's model and our own, however, is that in his network active oscillators inhibit other oscillators. His model employs an inhibition matrix that causes the model to

favor harmonic and subharmonic multiples of 2 and 3. Large (2000) argued that the inhibitory nature of the oscillators in his model facilitates the representation of a large number of metrical patterns. In our model, this inhibitory property is not necessary, as multiple metric levels, and even competing metric organizations, e.g., triple meter in the presence of strong duple meter, are represented without it.

One aspect of our approach is to consider the overall periodicity surface rather than focusing on those metric levels that are related directly to the tactus level. The richer complement of information in the periodicity surfaces could assist in pattern classification efforts in areas such as genre classification. Such an approach has been illustrated by Tzanetakis and Cook (2002), who used autocorrelation to detect periodicities in the signal and derive a beat histogram. The bins in their beat histogram represent the prominence of tempi within the range of 40–200 bpm. They use the beat histogram for comparing and contrasting rhythmic properties of different musical genres. APSs from our model could be employed similarly, where our MPPs or the peak height values binned by frequency ratios (Fig. 10(b)) could be regarded as similar to their periodicity histograms.

B. Further modifications and possible applications

Intuitively, one may be inclined to consider the highest peak in the APS (for audio inputs) or in the periodicity surface (for MIDI inputs) to represent the tempo of the excerpt. Following this logic, other metric levels corresponding to subdivisions of the beat, syncopations, and polyrhythms would be represented by lower amplitude peaks, and measures would be represented somewhere in this hierarchy. While it is apparent that tempo, syncopations, polyrhythms, and measures are represented somewhere in the peaks of APSs and MPPs, we have yet to develop an automated algorithm for identifying and categorizing local rhythmic patterns. Since developing a beat-finding or rhythm transcription algorithm was not our primary goal, we left the details of such an implementation open. Our longer-term objective is to develop a model that we can use to investigate the perceptual salience of different metric levels and rhythmic groupings, along the lines of Large and Palmer (2002).

When analyzing the metric properties of stimuli and responses using our model, it is important to bear in mind that peaks in the APSs and MPPs reflect some combination of the actual periodicities in the input signal and higher harmonics of these periodicities. While it was possible to identify which peaks were harmonics in periodicity surfaces produced by simple patterns of Dirac impulses, this was much more difficult to do with audio inputs. If one wishes to devise an automatic extraction of the metric levels present in stimuli and responses, a process for compensating for the harmonics must be devised. One possibility would be to create templates that estimate the harmonics that peaks of varying widths would produce. One could then subtract the second and higher harmonics of the templates from periodicity surfaces and MPPs to estimate the metric levels present in the excerpts. We showed that the amplitude of the higher harmonics reflects the timing variability at the fundamental frequency. Thus, these correction templates could, in principle, be used to estimate the degree of timing variability.

The discrepancy between the APSs in Figs. 8(a) and 8(b), the first produced by a single high hat and the second produced by a high hat and snap, indicated that timbre had a strong influence over the final output of the model. Because periodicity surfaces are calculated for each of several spectral bands prior to averaging into an APS, each periodicity surface will reflect the temporal patterning in the parts played by the instruments whose energy falls in that spectral band. One can therefore foresee the calculation of APSs in which certain bands are weighted more strongly than others. Such APSs could be useful for calculating periodicity surfaces that predict what the salient periodicities should be if a listener is attending selectively to a particular spectral region. We are fully aware that there is not a straightforward mapping between instruments and spectral regions. A more accurate model of metric and rhythmic structures in polyphonic music should perhaps calculate periodicity surfaces for individual auditory object streams or combinations of object streams. Such a model would require additional auditory scene analysis stages and is beyond the scope of our current efforts.

Just as multiple periodicity surfaces are combined for auditory inputs, our model can, in principle, be used to combine multiple sources of performance data. For instance, separate periodicity surfaces could be calculated and combined for the left and right hands of tapping trials. The periodicity surfaces would look different if we calculated periodicity surfaces of the left and right hands separately, as we did for separate frequency bands of audio recordings, and then combined them into an APS. The many ways in which multiple input streams (both audio and performance) can be combined either prior to or following periodicity surface calculation raises questions about the most appropriate ways to combine them if one is to model cognitive or sensorimotor integration processes. One intuition is that a heuristic for combining the streams in the model should reflect mental grouping processes that underlie perception and behavior. In other words, if a snare and high-hat are perceived to create an aggregate rhythm, then a periodicity surface should be calculated on their combined input. Similarly, if tapping patterns performed by the left and right hands are perceived as unitary rather than as a combination of independent processes, it would be more appropriate to combine the information from both hands prior to periodicity surface calculation as we have done in this paper. A thorough treatment of these issues is necessarily left to future research.

V. CONCLUSION

Our model drew upon previous work in tempo and beat induction. However, instead of focusing on the estimation of tempi and beat locations, we investigated a method of describing multiple metric levels from musical audio files and MIDI tapping data. We investigated various behaviors of our model, such as sensitivity to timing and accent structure, the production of harmonic peaks, and sensitivity to timbre. This model may be useful for future studies that require the mea-

surement of periodic structure and the relationships between multiple metric levels in stimuli and response data collected from music cognition experiments. Although it is our hope that the model can be used to predict the perceptual salience of metric levels and to compare models of stimuli with performance data, we have not formally tested the ability of the model to do so. Nonetheless, we believe that the model provides an extensible framework for investigating a broad range of psychological phenomena and music analytical issues. The code for our model is publicly available for download.[3]

ACKNOWLEDGMENTS

We would like to thank Peter Keller and Bradley Vines for their comments and suggestions. We are also indebted to Joe Saavedra, Peter Keller, and Philip Front for developing the MAX/MSP patch for constructing the percussion patterns used in this study and to Rawi Nanakul for the collection of tapping data. This work was supported in part by a Templeton Advanced Research Program grant from the Metanexus Institute to P.J.

[1]http://mtg.upf.edu/ismir2004/contest/tempoContest
[2]Provided by BallroomDancers.com and labeled by this group with a tempo value.
[3]http://atonal.ucdavis.edu/projects/musical_spaces/rhythm/btb

Cemgil, A. T., Desain, P., and Kappen, B. (**2000**). "Rhythm quantization for transcription," Comput. Music J. **24**, 60–76.
Cemgil, A. T., Kappen, B., Desain, P., and Honing, H. (**2000**). "On tempo tracking: Tempogram representation and Kalman filtering," J. New Music Res. **29**, 259–273.
Desain, P., and Honing, H. (**1993**). "Tempo curves considered harmful," Contemp. Music Rev. **7**(2), 123–138.
Desain, P., and Honing, H. (**2003**). "The formation of rhythmic categories and metric priming," Perception **32**, 341–365.
Dixon, S., Pampalk, E., and Widmer, G. (**2003**). "Classification of dance music by periodicity patterns," in Proceedings of the Fourth International Conference of Music Information Retrieval, Baltimore, Maryland.
Gouyon, F., and Dixon, S. (**2005**). "A review of automatic rhythm description systems," Comput. Music J. **29**, 34–54.
Gouyon, F., Dixon, S., Pampalk, E., and Widmer, G. (**2004**)."Evaluating rhythmic descriptors for musical genre classification," in Proceedings of the AES 25th International Conference, London, UK.
Gouyon, F., Herrera, P., and Cano, P. (**2002**). "Pulse-dependent analyses of percussive music," in Proceedings of the AES 22nd International Conference on Virtual, Synthetic and Entertainment Audio, Espoo, Finland.
Gouyon, F., Klapuri, A., Dixon, S., Alonso, M., Tzanetakis, G., Uhle, C., and Cano, P. (**2006**). "An experimental comparison of audio tempo induction algorithms," IEEE Trans. Audio, Speech, Lang. Process. **14**, 1832–1844.
Honing, H. (**2001**). "From time to time: The representation of timing and tempo," Comput. Music J. **25**, 50–61.
Janata, P., Tomic, S. T., and Haberman, J. (**2007**). "Getting in the groove while tapping," in Poster presented at the Society of Music Perception, Montreal, Canada.
Klapuri, A. P. (**2004**). "Automatic music transcription as we know it today," J. New Music Res. **33**, 269–282.
Klapuri, A. P., Eronen, A. J., and Astola, J. T. (**2006**). "Analysis of the meter of acoustic musical signals," IEEE Trans. Audio, Speech, Lang. Process. **14**, 342–355.
Large, E. W. (**2000**). "On synchronizing movements to music," Hum. Mov. Sci. **19**, 527–566.
Large, E. W., and Palmer, C. (**2002**). "Perceiving temporal regularity in music," Cogn. Sci. **26**, 1–37.
Leman, M., Lesaffre, M., and Tanghe, K. (**2001**). Computer code IPEM Toolbox, Ghent University, Ghent, Belgium.
London, J. (**2004**). *Hearing in Time: Psychological Aspects of Musical Meter* (Oxford University Press, New York).
Palmer, C., and Krumhansl, C. (**1990**). "Mental representations of meter," J. Exp. Psychol. **16**, 728–741.
Puckette, M., and Zicarelli, D. (**2006**). Computer code MAX/MSP, IRCAM, Paris, France/Cycling'74, San Francisco, CA.
Repp, B. H. (**2005**). "Sensorimotor synchronization: A review of the tapping literature," Psychon. Bull. Rev. **12**, 969–992.
Scheirer, E. D. (**1998**). "Tempo and beat analysis of acoustic musical signals," J. Acoust. Soc. Am. **103**, 588–601.
Shmulevich, I., and Povel, D. J. (**2000**). "Measures of temporal pattern complexity," J. New Music Res. **29**, 61–69.
Smith, J. O. (**2007**). "Decay time is Q periods," *Introduction to Digital Filters with Audio Applications* (Standford University, Stanford, CA); http://ccrma.stanford.edu/~jos/filters/Decay_Time_Q_Periods.html (Last viewed October 2007).
Snyder, J., and Krumhansl, C. L. (**2001**). "Tapping to ragtime: Cues to pulse finding," Music Percept. **18**, 455–489.
Steiglitz, K. (**1994**). "A note on constant-gain digital resonators," Comput. Music J. **18**, 8–10.
Steiglitz, K. (**1996**). *A DSP Primer : With Applications to Digital Audio and Computer Music* (Addison-Wesley, Menlo Park, CA).
Todd, N. P. M. (**1994**). "The auditory primal sketch: A multi-scale model of rhythmic grouping," J. New Music Res. **23**, 25–70.
Tzanetakis, G., and Cook, P. (**2002**). "Musical genre classification of audio signals," IEEE Trans. Speech Audio Process. **10**, 293–302.
Van Immerseel, L. M., and Martens, J. P. (**1992**). "Pitch and voiced unvoiced determination with an auditory model," J. Acoust. Soc. Am. **91**, 3511–3526.

Ultrasonic attenuation in parallel-nylon-wire cancellous-bone-mimicking phantoms

Keith A. Wear[a)]
U.S. Food and Drug Administration, 10903 New Hampshire Avenue, Silver Spring, Maryland 20993

(Received 8 April 2008; revised 15 September 2008; accepted 16 September 2008)

Attenuation coefficients between 1.5 and 3.5 MHz were measured on four parallel-nylon-wire arrays (simulating cancellous bone) with four different wire diameters (150, 200, 250, and 300 μm). Interwire spacing was 800 μm for all four parallel-nylon-wire arrays. The measured frequency dependencies of attenuation were consistent with theoretical predications based on Faran's theory, which considers the component of attenuation due to scattering of longitudinal waves.
[DOI: 10.1121/1.2998784]

PACS number(s): 43.80.Cs, 43.80.Ev [CCC] Pages: 4042–4046

I. INTRODUCTION

Broadband ultrasound attenuation (BUA) in calcaneus correlates well with bone mineral density (Langton *et al.*, 1984; Langton and Njeh, 2004; Langton and Njeh, 2008; Laugier, 2008) and is a proven clinical predictor of hip fracture risk (Hans *et al.*, 1996; Bauer *et al.*, 1997; Miller *et al.*, 2002; Hans *et al.*, 2004; Huopio *et al.*, 2004; Khaw *et al.*, 2004; Schott *et al.*, 2005; Krieg *et al.*, 2006), but the mechanisms underlying BUA are still not well understood. Most ultrasonic measurements on bone have been reported at frequencies below 2 MHz probably because (1) current clinical devices operate below 2 MHz and (2) increased attenuation at higher frequencies complicates experiments. At frequencies between 0.2 and 2 MHz, attenuation coefficient in cancellous bone varies approximately *linearly* with frequency (Chaffai *et al.*, 2000a; Wear, 2001). Therefore, the conversion of incident longitudinal waves into scattered longitudinal waves—which varies *nonlinearly* with frequency—is probably small compared to the linear (with frequency) component of attenuation coefficient below 2 MHz (Wear, 1999; Chaffai *et al.*, 2000b). Although most ultrasonic measurements on bone have been reported at frequencies below 2 MHz, some useful measurements have been reported at frequencies above 2 MHz *in vitro* (Hoffmeister *et al.*, 2000; Hoffmeister *et al.*, 2002; Lee *et al.*, 2003a; Derode *et al.*, 2005; Hakulinen *et al.*, 2005; Riekkinen *et al.*, 2006; Hoffmeister *et al.*, 2008) and *in vivo* (Wear and Garra, 1998; Garra *et al.*, 2008).

The relative roles of components of attenuation coefficient in cancellous bone may change as frequency increases beyond 2 MHz. For example, a theoretical model—previously shown to accurately predict backscatter from calcaneus below 1 MHz (Wear, 1999; Wear and Laib, 2003)—predicts dramatic increases (two orders of magnitude) of backscatter at frequencies above 2 MHz (Wear, 2004). Moreover, Lee *et al.* (2003a) found that BUA at 3.5 MHz was essentially uncorrelated with apparent density and with BUA at 2.5 MHz in bovine cancellous tibia specimens *in vitro*, suggesting that dominant attenuation mechanisms at 3.5 MHz may be different than those at lower frequencies. More evidence for a change in dominant attenuation mechanisms above 3 MHz was provided by Hakulinen *et al.* (2005), who found that the rate of change of attenuation coefficient with frequency between 3 and 7 MHz was much less than that between 0.5 and 3 MHz in human cancellous tibia and femur.

The objective of the present investigation is to study attenuation in cancellous-bone-mimicking phantoms in the range of frequencies from 1.5 to 3.5 MHz. The advantage of performing measurements on phantoms rather than bone samples is that phantoms provide opportunity for precise control over microarchitectural features. This facilitates assessment of relationships between ultrasound properties and microarchitecture. The disadvantage of performing measurements on phantoms, of course, is that they only approximate true cancellous bone structure. However, phantoms that use nylon wires to mimic trabeculae, such as the phantoms utilized in the present investigation, have previously demonstrated a high level of consistency with ultrasonic properties, including backscatter (Wear, 2004) and phase velocity (Wear, 2005), of cancellous bone below 1 MHz.

Through-transmission measurements performed on arrays of parallel nylon wires, as described in the present paper, provide additional insight into mechanisms of loss in cancellous bone beyond that provided by previous backscatter measurements performed on single nylon wires (Wear, 2004) for two reasons. First, through-transmission measurements include the effects of scattering at all angles, not just backscatter, and therefore give a more complete accounting of the total effect of scattering on attenuation. Second, the use of arrays of cylinders rather than single cylinders eliminates the need for assumptions of (1) incoherent single scattering and (2) negligible multiple scattering, which are required to extrapolate measurements on a single cylinder in order to predict properties of a network of cylinders. [The frequency dependence of scattering from a single cylinder is the same as the frequency dependence of incoherent single scattering from a network of cylinders (Wear, 1999).]

[a)]Electronic mail: keith.wear@fda.hhs.gov

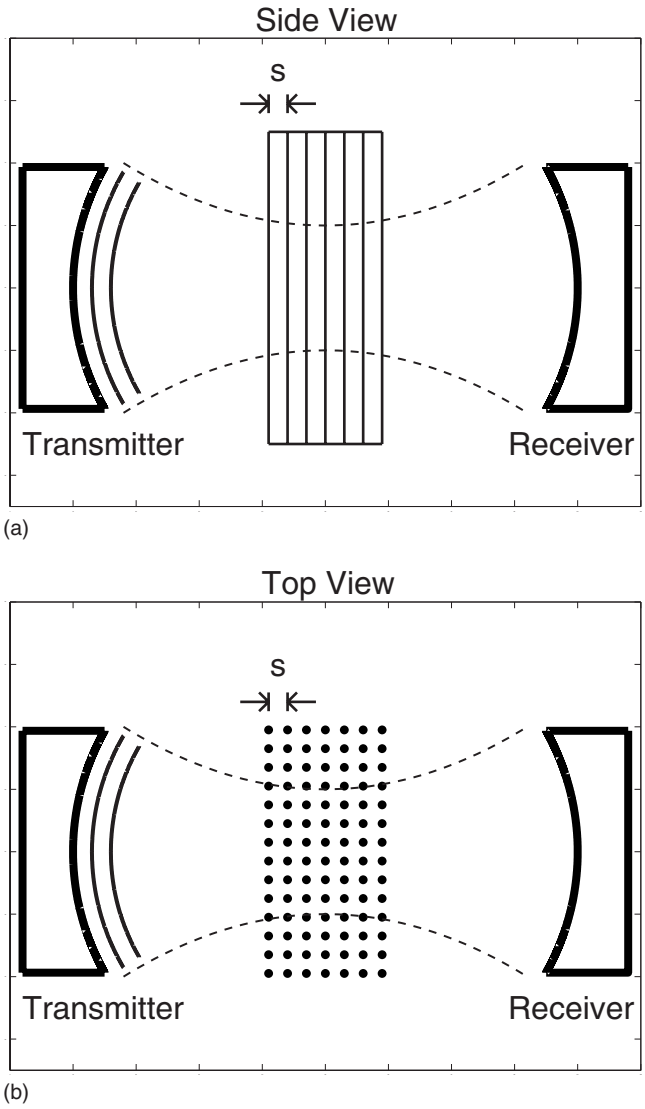


FIG. 1. Measurement from side view (a) and top view (b).

II. METHODS

A. Phantoms

Phantoms consisting of parallel nylon wires (simulating trabeculae) in two-dimensional rectangular grid arrays (custom built by Computerized Imaging Reference Systems, Norfolk, VA) were interrogated, as shown in Fig. 1. The nylon wire diameter corresponded to trabecular thickness, which in the standard nomenclature for bone histomorphometry is denoted by Tb.Th (Parfitt *et al.*, 1987). Four values for Tb.Th were used: 150, 200, 250, and 300 μm. Mean Tb.Th in human calcaneus has been reported to be 127 μm (Ulrich *et al.*, 1999), which is slightly lower than the lowest value for the phantom set (150 μm). The spacing (s) between wire axes was 800 μm. Mean trabecular spacing in human calcaneus has been reported to be 793 μm (Ulrich *et al.*, 1999). See (Wear, 2005) for details. These phantoms were originally used to explore the relationship between speed of sound and porosity, a topic that has also been investigated by other investigators (Hosokawa and Otani, 1997, 1998; Lin *et al.*, 2001; Lee *et al.*, 2003b; Haïat *et al.*, 2007). These phantoms mimicked some structural characteristics, but not necessarily viscous absorption, of cancellous bone.

B. Ultrasonic measurements

Phantoms were interrogated in through transmission in a degassed water tank using a Panametrics (Waltham, MA) 5800 pulser/receiver and two pairs of coaxially aligned Panametrics broadband, 19 mm diameter, focused transducers. One pair of transducers had a center frequency equal to 2.25 MHz and −6 dB bandwidth of 1.9 MHz (usable band from 0.8 to 2.7 MHz). The other pair of transducers had a center frequency equal to 3.5 MHz and −6 dB bandwidth of 3.4 MHz (usable band from 0.8 to 4.2 MHz). The propagation path between transducers was twice the focal distance (2×38 mm$=$76 mm). Received radio frequency (rf) signals were digitized (8 bit, 25 MHz) using a LeCroy (Chestnut Ridge, NY) 9310C dual 400 MHz oscilloscope and stored on computer (via general purpose interface bus (GPIB)) for off-line analysis. Five measurements (of ten rf lines each) were obtained on each phantom for each center frequency. Phantoms were removed from the tank and then repositioned between measurements. Attenuation coefficients were estimated using a log spectral difference technique (Kuc and Schwartz, 1979).

C. Theoretical model

Theoretical predictions for scattering were based on Faran's theory for elastic scattering of an incident plane wave by an infinitely long, isotropic, circular cylinder in a fluid (Faran, 1951). The direction of propagation is perpendicular to the cylinder axis. Faran's model allows for shear waves within the cylinders. The material properties of nylon were assumed to be as follows: longitudinal velocity$=$2500 m/s, density$=$1.12 g/cm^3, and Poisson's ratio$=$0.39 (Onda Corporation, 2008). (The value of velocity was slightly reduced from 2600 to 2500 m/s in order to improve agreement between theory and experiment. It is understood that the tabulated values are only approximate, and not all nylon samples have identical material properties.) The material properties of water were assumed to be as follows: longitudinal velocity $=$1480 m/s (at room temperature of about 20 °C) and density$=$1 g/cm^3. Although Faran's theory is based on plane-wave insonification, it has shown great consistency with measurements using focused transducers, provided appropriate compensation for diffraction is applied (Wear, 2004). The theoretical prediction for scattering was estimated by averaging the angular-dependent scattering coefficient over all angles.

III. RESULTS

Figures 2–5 show experimental attenuation coefficient versus frequency (solid lines) and Faran's theory for total conversion of incident longitudinal waves into scattered longitudinal waves (dashed lines) for all four parallel-nylon-wire arrays. Since the theoretical model predicts the *frequency dependence* of scattering but not the *absolute magnitude* of scattering, theoretical scattering functions were

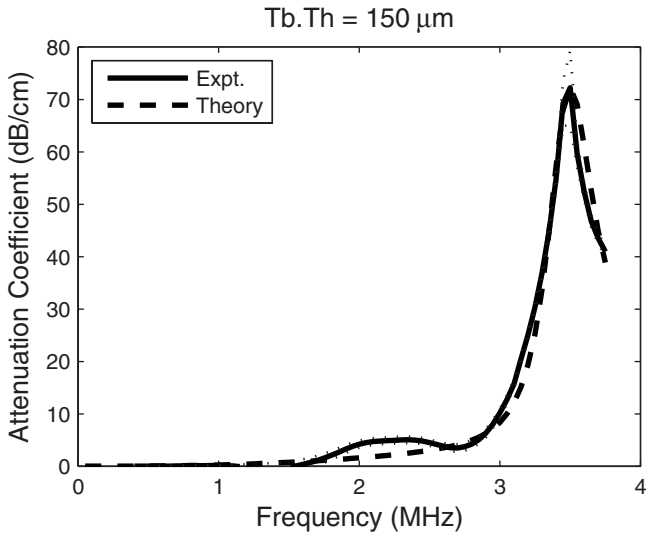


FIG. 2. Experimental (solid line) and theoretical (dashed line) attenuation coefficient vs frequency. The standard deviations for the measurements are depicted as dotted lines above and below the experimental solid line. The nylon wire thickness was 150 μm.

scaled by a frequency-independent factor in order to match the measurements (Wear, 1999, 2004).

Fair agreement in frequency dependence of experimental attenuation coefficient and theoretical total scattering may be seen over the range from 1.5 to 3.5 MHz, suggesting that scattering may have been a primary component of attenuation for these phantoms. As reported previously, experimental peaks are often broader than theoretical peaks, perhaps due to compromised experimental spectral resolution (Wear, 2004). This effect was particularly noticeable for Tb.Th =200 and 300 μm. Moreover, experimental peaks might be expected to be even broader in cancellous bone than in phantoms because peak location depends on trabecular thickness (as shown in Figs. 2–5) cancellous bone sample typically contains many trabeculae spanning a broad range of thicknesses while the phantoms contained nylon wires of constant thickness.

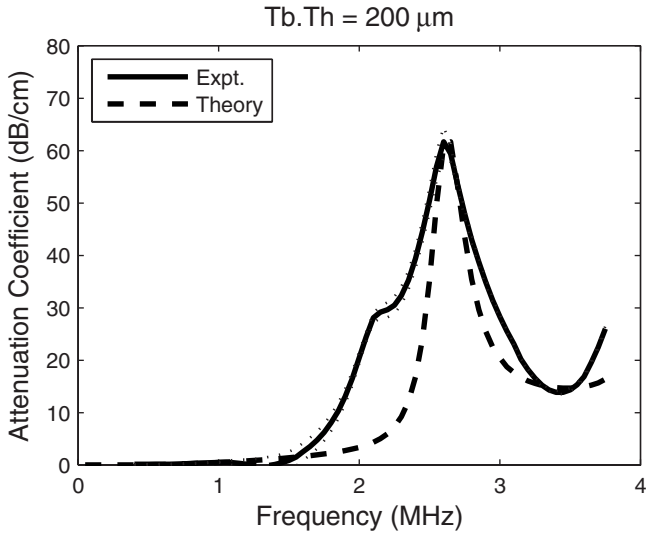


FIG. 3. Same as Fig. 1 except that the nylon wire thickness was 200 μm.

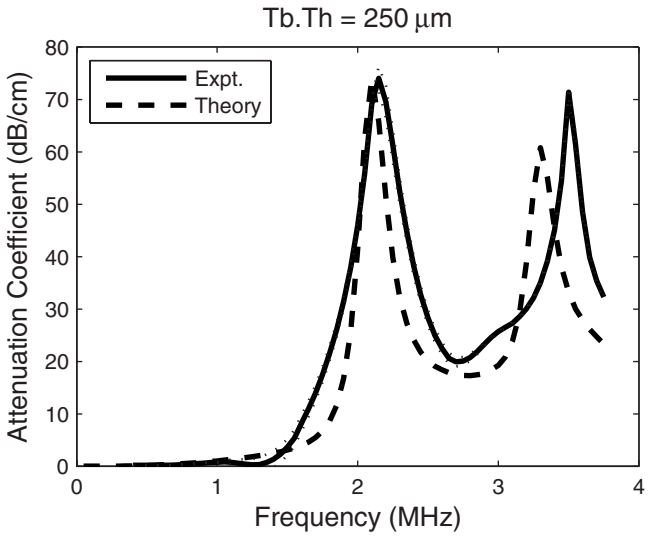


FIG. 4. Same as Fig. 1 except that the nylon wire thickness was 250 μm.

IV. DISCUSSION

Previously, backscattering measurements from single nylon cylinders were compared to data from cancellous bone, which contained multiple quasicylindrical scatterers (Wear, 2004). The comparison required assumptions of (1) incoherent scattering and (2) negligible multiple scattering. Under these two assumptions, the frequency dependence of scattering from a single cylinder is the same as that from a network of cylinders (Wear, 1999). In the present paper, the experimental model has been improved by using arrays of parallel nylon wires instead of single nylon wires. As in previous studies (Wear, 1999), the theoretical model in the present paper still assumes incoherent scattering and negligible multiple scattering. Backscatter measurements near 1 MHz may be explained largely by single scattering (Wear, 1999; Chaffai *et al.*, 2000b). However, multiple scattering may become significant in cancellous bone near 3 MHz (Derode *et al.*, 2005).

Among Figs. 2–5, Fig. 2, in which Tb.Th=150 μm, represents the closest approximation to human calcaneus, in

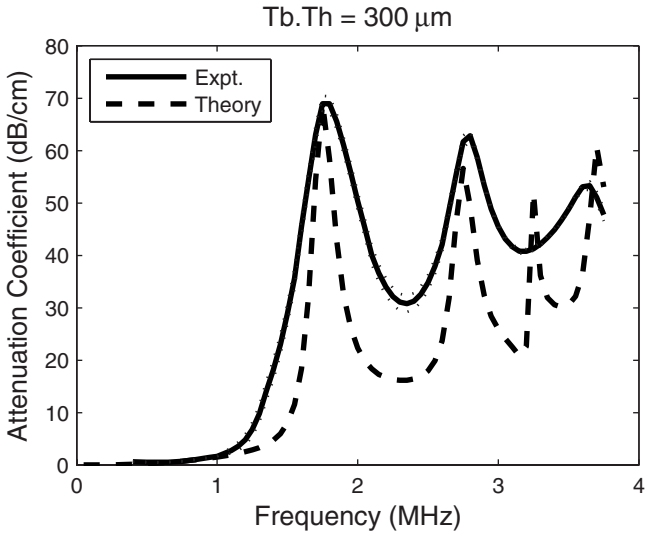


FIG. 5. Same as Fig. 1 except that the nylon wire thickness was 300 μm.

which mean Tb.Th=127 μm (Ulrich *et al.*, 1999) Figure 2 suggests that scattering increases dramatically between 3 and 4 MHz.

Figures 2–5 show that attenuation was small (less than about 1 dB/cm) for frequencies less than about 1 MHz. Therefore, the phantoms did not accurately mimic total attenuation in cancellous bone at frequencies below 1 MHz. Presumably, this is because they only mimicked the conversion of incident longitudinal waves into scattered longitudinal waves by cancellous bone but not other mechanisms of attenuation.

The theoretical curves plotted in Figs. 2–5 (dashed lines) included the conversion of incident longitudinal waves into scattered longitudinal waves, but they did not include absorption in the nylon wires or mode conversion of incident longitudinal waves into shear waves. These factors could conceivably be significant sources of attenuation. More research is needed in this area.

In summary, parallel-nylon-wire phantom studies suggest that although transfer of energy from incident longitudinal waves into scattered longitudinal waves is a small component of attenuation in cancellous bone below 2 MHz, its relative importance may be greater at higher frequencies.

ACKNOWLEDGMENTS

Funding from the US FDA Office of Women's Health and assistance in phantom design/development from Heather Pierce, Computerized Imaging Reference Systems, Norfolk, VA, is greatly appreciated.

Bauer, D. C., Gluer, C. C., Cauley, J. A., Vogt, T. M., Ensrud, K. E., Genant, H. K., and Black, D. M. (**1997**). "Broadband ultrasound attenuation predicts fractures strongly and independently of densitometry in older women," Arch. Intern Med. **157**, 629–634.

Chaffai, S., Padilla, F., Berger, G., and Laugier, P. (**2000a**). "*In vitro* measurement of the frequency-dependent attenuation in cancellous bone between 0.2 and 2 MHz," J. Acoust. Soc. Am. **108**, 1281–1289.

Chaffai, S., Roberjot, V., Peyrin, F., Berger, G., and Laugier, P. (**2000b**). "Frequency dependence of ultrasonic backscattering in cancellous bone: Autocorrelation model and experimental results," J. Acoust. Soc. Am. **108**, 2403–2411.

Derode, A., Mamou, V., Padilla, F., Jenson, F., and Laugier, P. (**2005**). "Dynamic coherent backscattering in a heterogeneous absorbing medium: Application to human trabecular bone characterization," Appl. Phys. Lett. **87**, 114101.

Faran, J. J. (**1951**). "Sound scattering by solid cylinders and spheres," J. Acoust. Soc. Am. **23**, 405–411.

Garra, B. S., Locher, M., Felker, S., and Wear, K. A. (**2008**). "Measurements of ultrasonic backscattered spectral centroid shift from spine *in vivo*: Methodology and preliminary results," Ultrasound Med. Biol.

Haïat, G., Padilla, F., and Laugier, P. (**2007**). "Analytical modeling of phase velocity dependence on trabecular bone properties: Effect of multiple scattering," Proceedings of the 2007 IEEE Ultrasonic Symposium, New York, NY.

Hakulinen, M. A., Day, J. S., Toyras, J., Timonen, M., Kroger, H., Weinans, H., Kiviranta, I., and Jurvelin, J. S. (**2005**). "Prediction of density and mechanical properties of human trabecular bone *in vitro* by using ultrasound transmission and backscattering measurements at 0.2–6.7 MHz frequency range," Phys. Med. Biol. **50**, 1629–1642.

Hans, D., Dargent-Molina, P., Schott, A. M., Sebert, J. L., Cormier, C., Kotzki, P. O., Delmas, P. D., Pouilles, J. M., Breart, G., and Meunier, P. J. (**1996**). "Ultrasonographic heel measurements to predict hip fracture in elderly women: The EPIDOS prospective study," Lancet **348**, 511–514.

Hans, D., Schott, A. M., Duboeuf, F., Durosier, C., and Meunier, P. J. (**2004**). "Does follow-up duration influence the ultrasound and DXA prediction of hip fracture? The EPIDOS prospective study," Bone **35**, 357–363.

Hoffmeister, B. K., Johnson, D. P., Janeski, J. A., Keedy, D. A., Steinert, B. W., Viano, A. M., and Kaste, S. C. (**2008**). "Ultrasonic characterization of human cancellous bone *in vitro* using three different apparent backscatter parameters in the frequency range 0.6–15.0 MHz," IEEE Trans. Ultrason. Ferroelectr. Freq. Control **55**, 1442–1452.

Hoffmeister, B. K., Whitten, S. A., Kaste, S. C., and Rho, J. Y. (**2002**). "Effect of collagen and mineral content on the high-frequency ultrasonic properties of human cancellous bone," Osteoporosis Int. **13**, 26–32.

Hoffmeister, B. K., Whitten, S. A., and Rho, J. Y. (**2000**). "Low-megahertz ultrasonic properties of bovine cancellous bone," Bone **26**, 635–642.

Hosokawa, A., and Otani, T. (**1997**). "Ultrasonic wave propagation in bovine cancellous bone," J. Acoust. Soc. Am. **101**, 558–562.

Hosokawa, A., and Otani, T. (**1998**). "Acoustic anisotropy in bovine cancellous bone," J. Acoust. Soc. Am. **103**, 2718–2722.

Huopio, J., Kroger, H., Honkanen, R., Jurvelin, J., Saarikoski, S., and Alhava, E. (**2004**). "Calcaneal ultrasound predicts early postmenopausal fractures as well as axial BMD. A prospective study of 422 women," Osteoporosis Int. **15**, 190–195.

Khaw, K. T., Reeve, J., Luben, R., Bingham, S., Welch, A., Wareham, N., Oakes, S., and Day, N. (**2004**). "Prediction of total and hip fracture risk in men and women by quantitative ultrasound of the calcaneus: EPIC-Norfolk prospective population study," Lancet **363**, 197–202.

Krieg, M., Cornuz, J., Ruffieux, C., Melle, G. V., Buche, D., Dambacher, M. A., Hans, D., Hartl, F., Hauselmann, H. J., Kraenzlin, M., Lippuner, K., Neff, M., Pancaldi, P., Rizzoli, R., Tanzi, F., Theiler, R., Tyndall, A., Wimpfheimer, C., and Burckhardt, P. (**2006**). "Prediction of hip fracture risk by quantitative ultrasound in more than 7000 Swiss women ⩾70 years of age: Comparison of three technologically different bone ultrasound devices in the SEMOF study," J. Bone Miner. Res. **21**, 1457–1463.

Kuc, R., and Schwartz, M. (**1979**). "Estimating the acoustic attenuation coefficient slope for liver from reflected ultrasound signals," IEEE Trans. Sonics Ultrason. **SU-26**, 353–362.

(**2004**). in *The Physical Measurement of Bone* edited by C. M. Langton and C. F. Njeh (IOP, Bristol, UK), Chap. 14, pp. 412–474.

Langton, C. M., and Njeh, C. F. (**2008**). "The measurement of broadband ultrasonic attenuation in cancellous bone: A review of the science and technology," IEEE Trans. Ultrason. Ferroelectr. Freq. Control **55**, 1546–1554.

Langton, C. M., Palmer, S. B., and Porter, R. W. (**1984**). "The measurement of broadband ultrasonic attenuation in cancellous bone," Eng. Med. **13**, 89–91.

Laugier, P. (**2008**). "Instrumentation for *in vivo* ultrasonic characterization of bone strength," IEEE Trans. Ultrason. Ferroelectr. Freq. Control **55**, 1179–1196.

Lee, K. I., Rho, H., and Yoon, S. W. (**2003a**). "Correlations between acoustic properties and bone density in bovine cancellous bone from 0.5 to 2 MHz," J. Acoust. Soc. Am. **113**, 2933–2938.

Lee, K. I., Roh, H., and Yoon, S. W. (**2003b**). "Acoustic wave propagation in bovine cancellous bone: Application of the modified Biot-Attenborough model," J. Acoust. Soc. Am. **114**, 2284–2293.

Lin, W., Qin, Y. X., and Rubin, C. (**2001**). "Ultrasonic wave propagation in trabecular bone predicted by the stratified model," Ann. Biomed. Eng. **29**, 781–790.

Miller, P. D., Siris, E. S., Barrett-Connor, E., Faulkner, K. G., Wehren, L. E., Abbott, T. A., Chen, Y., Berger, M. L., Santora, A. C., and Sherwood, L. M. (**2002**). "Prediction of fracture risk in postmenopausal white women with peripheral bone densitometry: Evidence from the national osteoporosis risk assessment," J. Bone Miner. Res. **17**, 2222–2230.

Onda Corporation website (http://www.ultrasonic.com) provides tables of acoustic properties for many materials (Last viewed April 2008).

Parfitt, A. M., Drezner, M. K., Glorieux, F. H., Kanis, J. A., Malluche, H., Meunier, P. J., Ott, S. M., and Recker, R. R. (**1987**). "Bone histomorphometry: Standardization of nomenclature, symbols, and units," J. Bone Miner. Res. **2**, 595–610.

Riekkinen, O., Hakulinen, M. A., Timonen, M., Toyras, J., and Jurvelin, J. S. (**2006**). "Influence of overlying soft tissues on trabecular bone acoustic measurement at various ultrasound frequencies," Ultrasound Med. Biol. **32**, 1073–1083.

Schott, A. M., Hans, D., Duboeuf, R., Dargent-Molina, P., Hajri, T., Breart, G., and Meunier, P. J. (**2005**). "Quantitative ultrasound parameters as well as bone mineral density are better predictors of trochanteric than cervical

hip fractures in elderly women. Results from the EPIDOS study," Bone **37**, 858–863.
Ulrich, D., van Rietbergen, B., Laib, A., and Ruegsegger, P. (**1999**). "The ability of three-dimensional structural indices to reflect mechanical aspects of trabecular bone," Bone **25**, 55–60.
Wear, K. A. (**1999**). "Frequency dependence of ultrasonic backscatter from human trabecular bone: Theory and experiment," J. Acoust. Soc. Am. **106**, 3659–3664.
Wear, K. A. (**2001**). "Ultrasonic attenuation in human calcaneus from 0.2 to 1.7 MHz," IEEE Trans. Ultrason. Ferroelectr. Freq. Control **48**, 602–608.
Wear, K. A. (**2004**). "Measurement of dependence of backscatter coefficient from cylinders on frequency and diameter using focused transducers—with applications in trabecular bone," J. Acoust. Soc. Am. **115**, 66–72.
Wear, K. A. (**2005**). "The dependences of phase velocity and dispersion on trabecular thickness and spacing in trabecular bone-mimicking phantoms," J. Acoust. Soc. Am. **118**, 1186–1192.
Wear, K. A., and Garra, B. S. (**1998**). "Assessment of bone density using ultrasonic backscatter," Ultrasound Med. Biol. **24**, 689–695.
Wear, K. A., and Laib, A. (**2003**). "The relationship between ultrasonic scattering and microarchitecture in human calcaneus," IEEE Trans. Ultrason. Ferroelectr. Freq. Control **50**, 979–986.

Velocity dispersion in trabecular bone: Influence of multiple scattering and of absorption

G. Haïat[a)]
CNRS, Laboratoire de Recherches Orthopédiques, UMR CNRS 7052 B2OA, 10 Avenue de Verdun, 75010 Paris, France

A. Lhémery
Commissariat à l'Énergie Atomique, LIST, Gif-sur-Yvette 91191, France

F. Renaud
Laboratoire de Mécanique Physique, Université Paris 12, Val de Marne, UMR CNRS 7052 B2OA, 61 Avenue du Général de Gaulle, 94010 Créteil, Cédex, France

F. Padilla and P. Laugier
UPMC, Univ Paris 06, UMR7623, LIP, F75005 Paris, France and CNRS, Laboratoire d'Imagerie Paramétrique, UMR 7623, F75006 Paris, France

S. Naili
Laboratoire de Mécanique Physique, Université Paris 12, Val de Marne, UMR CNRS 7052 B2OA, 61 Avenue du Général de Gaulle, 94010 Créteil, Cédex, France

(Received 14 March 2008; revised 14 September 2008; accepted 27 September 2008)

Speed of sound measurements are widely used clinically to assess bone strength. Trabecular bone is an attenuating composite material in which negative values of velocity dispersion have been measured, this behavior remaining poorly explained physically. The aim of this work is to describe the ultrasonic propagation in trabecular bone modeled by infinite cylinders immersed in a saturating matrix, and to derive the physical determinants of velocity dispersion. A homogenization model accounting for the coupling of multiple scattering and absorption phenomena allows the computation of phase velocity and of dispersion while varying bone properties. The present model is adapted from the generalized self-consistent method developed in the work of Yang and Mal [(1994). "Multiple-scattering of elastic waves in a fiber-reinforced composite," J. Mech. Phys. Solids **42**, 1945–1968]. It predicts negative values of velocity dispersion, in agreement with experimental results obtained in phantoms mimicking trabecular bone. In trabecular bone, mostly negative and also positive values of velocity dispersion are predicted by the model, which span within the range of values measured experimentally. Scattering effects are responsible for the negative values of dispersion, whereas the frequency dependence of the absorption coefficient in bone marrow and/or in the trabeculae results in an increase in dispersion, which may then become positive. © *2008 Acoustical Society of America.* [DOI: 10.1121/1.3003077]

PACS number(s): 43.80.Cs, 43.80.Ev, 43.35.Cg, 43.35.Mr [FD] Pages: 4047–4058

I. INTRODUCTION

Quantitative ultrasonic (QUS) techniques are now widely used clinically, in particular, for the assessment of fracture risk (Marin *et al.*, 2006). More precisely, speed of sound (SOS) measurements are known to be highly correlated with bone mineral density (Evans and Tavakoli, 1990) for bovine specimens (Njeh *et al.*, 1996), human calcaneus (Laugier *et al.*, 1997; Trebacz and Natali, 1999), vertebrae (Nicholson *et al.*, 1998; Trebacz and Natali, 1999), and proximal femur (Haiat *et al.*, 2005b), as well as with bone strength (Bouxsein and Radloff, 1997; Hakulinen *et al.*, 2006). The main advantage of QUS techniques lies in their ability to reflect structural as well as mechanical bone characteristics (Nicholson *et al.*, 1994; Wear, 2000b). Among the different apparatus commercially available, transverse transmission devices operating at the heel now represent a well established clinical modality for the prediction of fracture risk (Gluer and Barkmann, 2003; Khaw *et al.*, 2004). Despite their routine clinical use, the physics of ultrasonic propagation through trabecular bone still remains unclear. In particular, the mechanisms responsible for the frequency dependence of phase velocity and for the variation of the ultrasonic velocity dispersion with bone properties are elusive. Trabecular bone is a complex medium as it consists in an anisotropic, heterogeneous two-phase medium made of a network of interconnected viscoelastic rods or plates (the trabeculae) filled with a viscoelastic matrix (the bone marrow).

There are many different ways of measuring SOS in the laboratory and in the clinics: Ultrasonic velocity can be measured as the phase or the group velocity. Group velocity is a function of dispersion, frequency, and phase velocity (Morse and Ingard, 1986; Duck, 1990). However, SOS is classically

[a)]Author to whom correspondence should be addressed. Electronic mail: guillaume.haiat@univ-paris-diderot.fr

deduced from time-of-flight measurements (using different signal processing techniques or time markers) of an ultrasound pulse transmitted through bone. Such measurements have been shown to be the optimal method for the estimation of bone mineral density (Haiat *et al.*, 2005a). Bone being a highly attenuating and dispersive medium, time-of-flight measurements may be subject to biases due to pulse shape modification during propagation through bone, which may be due to frequency-dependent attenuation (Wear, 2000c, 2001a) and/or dispersion effects (Haiat *et al.*, 2006; Wear, 2007a). Therefore, dispersion appears to be an important acoustical property, influencing SOS measurements performed clinically. A better understanding of its physical determinant may have important impacts on the clinical relevance of SOS measurements.

The attenuation coefficient in trabecular bone has been shown to vary linearly with frequency over a wide bandwidth (200 kHz–2 MHz) (Chaffai *et al.*, 2000; Wear, 2001c). However, unlike soft tissues where the phase velocity has been shown to be an increasing function of frequency (O'Donnell *et al.*, 1981), mostly negative and also positive values of dispersion have been measured in trabecular bone *in vitro* (Nicholson *et al.*, 1996; Strelitzki and Evans, 1996; Droin *et al.*, 1998; Wear, 2000a, 2001b; Haiat *et al.*, 2006) and recently *in vivo* (Wear, 2007b). Negative values of dispersion have also been measured in trabecular bone-mimicking phantom samples (Strelitzki *et al.*, 1997; Lee *et al.*, 2003; Wear, 2005; Lee and Choi, 2007). The attenuation coefficient in bone being a linearly increasing function of frequency, negative dispersion has been referred to as "anomalous" (Marutyan *et al.*, 2006), due to the apparent contradiction with the Kramers–Krönig (KK) relationships.

Several theoretical models have been used to study the ultrasonic propagation through cancellous bone and to model the observed velocity dispersion. Finite-difference time-domain numerical simulation of wave propagation through three-dimensional bone models has led to mostly negative and also positive values of dispersion (Bossy *et al.*, 2005; Haiat *et al.*, 2007). Moreover, a recent work (Marutyan *et al.*, 2006) has shown that the negative value of the dispersion of ultrasonic waves propagating in bone can arise from the interference of two wave components that propagate at different speeds, such as the fast and slow longitudinal wave modes predicted by the Biot theory (Biot, 1956). Negative dispersion can also be predicted from multilayer models (Wear, 2001b, 2007b). Negative values of velocity dispersion in heterogeneous materials have been previously predicted by multiple scattering theories, in the framework of wave propagation studies in concrete (Lefebvre *et al.*, 1980) and fiber-reinforced composite materials (Varadan *et al.*, 1986) or in microsphere suspension (Peters and Petit, 2000; Mobley, 2007). Models considering ultrasonic wave scattering by the trabecular structure have been developed assuming independent scatterers (Wear, 1999; Jenson *et al.*, 2003; Padilla *et al.*, 2003; Wear, 2004) as well as multiple scattering (Luppé *et al.*, 2002, 2003). However, although multiple scattering has been shown to play a role in the ultrasonic propagation through cancellous bone (Derode *et al.*, 2005) around the frequency 3.5 MHz, multiple scattering theories have not yet been used to understand velocity dispersion measured in trabecular bone.

This paper aims at proposing a multiple scattering model that predicts the frequency dependence of the phase velocity and at investigating the physical determinants of velocity dispersion, by considering a biphasic description of trabecular bone. A two-dimensional (2D) homogenization model initially developed in the context of composite materials is used to compute the frequency dependence of phase velocity as a function of bone properties. This model is derived from that developed by Yang and Mal (1994), but is adapted to account for viscoelastic absorption effects, which was not done in the initial model. An advantage of the present approach is that it allows taking into account simultaneously viscoelastic absorption, as well as multiple scattering, using elementary input data associated with bone properties.

II. THEORY

A. Context and hypothesis

In the present model, the trabecular bone structure was described as a two-phase medium composed of unidirectional identical viscoelastic cylinders (corresponding to the trabeculae), which act as scatterers immersed in a viscoelastic matrix (corresponding to the saturating medium, i.e., bone marrow or water). Hence, the main trabecular orientation of the trabeculae corresponds to the axis of the cylinders. The axes of all scatterers were assumed to be perpendicular to the direction of propagation of the ultrasonic waves. This is motivated by the fact that for most clinical measurements (e.g., calcaneus or femur), the direction of ultrasonic propagation is more or less perpendicular to the main trabecular alignment, which corresponds to the principal direction of stress supported by bone tissue, due to remodeling phenomena.

We aimed at deriving a 2D homogenization model able to determine the acoustical properties of trabecular bone at the centimeter scale. This model is able to predict the values of phase velocity as a function of frequency for the various wave polarizations. Ultrasonic waves of different polarizations defined relatively to the orientation of the cylinders were considered. The matrix and the scatterers were considered to behave like isotropic viscoelastic media where both longitudinal and transverse wave modes may propagate. In what follows, SH (SV) denotes shear horizontal (shear vertical) waves with a polarization vector parallel (perpendicular) to the axis of the cylinders and L denotes longitudinal waves polarized along the wave vector and propagating perpendicularly to the trabecular orientation. For symmetry reasons, the SH wave case only required a scalar processing since no mode conversion can occur between the matrix and the scatterer. Therefore, the cases of SH wave mode on the one hand and (SV and L) wave modes on the other hand could be treated separately. The SH wave mode was not considered herein because we assumed that shear waves in bone marrow were not likely to affect significantly ultrasonic propagation in trabecular bone at a macroscopic scale (this point will be discussed in Sec. IV C). The two other coupled modes (SV and L) required a full vector processing account-

ing for mode-conversion phenomena in the scattering process. The displacement field $\vec{u}(r,\theta)$ was written using the potentials $\varphi(r,\theta)$ and $\psi(r,\theta)$ of the longitudinal and shear wave components obtained from the Helmholtz decomposition given by

$$\vec{u} = \overrightarrow{\text{grad}}\varphi(r,\theta) + \overrightarrow{\text{rot}}(\psi(r,\theta)\vec{e_z}), \tag{1}$$

where $\vec{e_z}$ is the unit vector along the cylinder axis, $\overrightarrow{\text{grad}}$ and $\overrightarrow{\text{rot}}$ designate, respectively, the gradient and curl operators, and finally, r and θ are the polar coordinates in the plan perpendicular to $\vec{e_z}$.

B. Viscoelastic absorption

The complex-valued wave numbers k_{L}^i and k_{SV}^i, respectively, associated with the wave vectors $\vec{k}_{\text{L}}^i = k_{\text{L}}^i \vec{I}$ and $\vec{k}_{\text{SV}}^i = k_{\text{SV}}^i \vec{I}$ corresponding, respectively, to the propagation of the L and SV wave modes in the medium i (superscript i is either equal to superscript s for the scatterers or to m for the matrix) and in the direction of the unit vector $\vec{I}$ were given by

$$k_{\text{L}}^i = \frac{2\pi f}{V_{\text{L}}^i(f)} - i\alpha_{\text{L}}^i(f), \tag{2}$$

$$k_{\text{SV}}^i = \frac{2\pi f}{V_{\text{SV}}^i(f)} - i\alpha_{\text{SV}}^i(f), \tag{3}$$

where f is the frequency. The quantities $V_{\text{L}}^i(f)$, $V_{\text{SV}}^i(f)$, $\alpha_{\text{L}}^i(f)$, and $\alpha_{\text{SV}}^i(f)$ are, respectively, the phase velocities and the attenuation coefficients for the L and SV wave modes in the medium i. Equations (2) and (3) correspond to the description of the behavior of classical viscoelastic isotropic solids.

C. Multiple scattering theory

The problem of multiple scattering of waves by a set of scatterers is a classical problem of theoretical physics, initially solved in the 1940s (Foldy, 1945). Some of these theories were developed in order to describe a two-phase medium composed of oriented fibers in a matrix as a homogeneous material. Among these theories, the quite recent one developed by Yang and Mal (1994) and known as the generalized self-consistent method relies on the description of the heterogeneous medium as being constituted of three phases. This three-phase description was combined with the classical multiple scattering theory originally derived from the works of Waterman and Truell (1961) for spherical scatterers and modified to account for the cylindrical symmetry. The idea of a three-phase modeling approach is to describe the homogeneous effective medium by considering two concentric cylinders immersed in the effective medium, as shown in Fig. 1. Boundary conditions between the two physical media (matrix and scatterer) are exactly respected whatever the number of iterations necessary for convergence in the homogenization process. The homogenization process directly acts on the third (surrounding) equivalent medium.

In this paper, the model developed by Yang and Mal (1994) was adapted and extended (Lonné *et al.*, 2004) in order to model trabecular bone as a two-phase medium composed of randomly distributed viscoelastic infinite cylinders placed within a viscoelastic matrix. In what follows, we briefly describe this model and the associated assumptions. However, the scope of the present paper is not to recall the whole derivation of the model proposed by Yang and Mal (1994); the readers interested in the detailed description are referred to their paper (Yang and Mal, 1994).

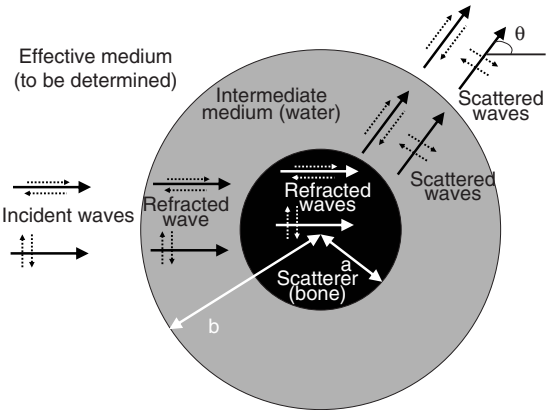


FIG. 1. Description of the three-phase medium model representing the scatterer (corresponding to a trabeculae, radius $a=D_s/2$), the matrix (marrow or water, radius b), and the effective medium (corresponding to the unknown of the problem). The solid arrows together with two parallel dotted arrows denote a longitudinal wave mode and the solid arrows together with two perpendicular dotted arrows denote a transversal wave mode.

Figure 1 describes the configuration of interest. The black and gray colors correspond, respectively, to the scatterer and to the matrix. Their mass densities are given, respectively, by ρ_s and ρ_m. The surrounding medium is an artificial synthetic medium, which represents the overall effective homogeneous viscoelastic medium to be determined. Radius a is that of the scatterer ($a=D_s/2$, where D_s is the diameter of the scatterer, which is often noted *TbTh*, for trabecular thickness in bone biomechanics). Radius b is the outer radius of the matrix. Radius b depends on the scatterer area fraction (denoted C in what follows) and on a through the relation (Yang and Mal, 1994)

$$b = \frac{a}{\sqrt{C}}. \tag{4}$$

Equation (4) was derived from the definition of C, which can be obtained through the ratio of the area of the matrix and of the scatterer, which corresponds to bone volume fraction in the framework of a 2D model. The distance $(b-a)$ corresponds to the mean distance between the scatterers and will be noted *Sp* in what follows. It corresponds to the trabecular spacing, often noted *TbSp* in bone biomechanics.

The density ρ_e of the effective medium results from a simple mixture law and was given by

$$\rho_e = (1-C)\rho_m + C\rho_s. \tag{5}$$

In this problem, two incident monochromatic (frequency f) plane waves of polarizations L and SV were considered in the effective medium. Both waves propagated initially in the $\theta=0$ direction (θ is defined in Fig. 1) and were of amplitude unity. Two scattered waves were diffracted in the effective medium leading to the following expressions valid for $r>b$ (Yang and Mal, 1994):

$$\varphi(r,\theta) = \sum_{n=-\infty}^{+\infty} i^n J_n(kr) e^{in\theta} + \sum_{n=-\infty}^{+\infty} A_n H_n^1(kr) e^{in\theta}, \quad (6)$$

$$\psi(r,\theta) = \sum_{n=-\infty}^{+\infty} i^n J_n(hr) e^{in\theta} + \sum_{n=-\infty}^{+\infty} B_n H_n^1(hr) e^{in\theta}, \quad (7)$$

where functions J_n and H_n^1 are, respectively, the Bessel function of the first kind of order n and the Hankel function of the first kind of order n. The constants A_n and B_n are the complex-valued amplitude of order n for both potentials. k and h are, respectively the complex-valued wave numbers of the longitudinal and shear wave modes in the homogenized medium corresponding to the unknowns of the problem. The first terms of the right member of Eqs. (6) and (7) correspond to the incident plane wave.

Moreover, two wave modes (one L and one SV) were considered in the matrix as well as in the scatterer. In the matrix, the total field was given by the sum of the contribution transmitted from the effective medium and of the contribution scattered from the scatterer, leading, for $a<r<b$, to (Yang and Mal, 1994)

$$\varphi(r,\theta) = \sum_{n=-\infty}^{+\infty} C_n H_n^1(k_L^m r) e^{in\theta} + \sum_{n=-\infty}^{+\infty} D_n H_n^1(k_L^m r) e^{in\theta}, \quad (8)$$

$$\psi(r,\theta) = \sum_{n=-\infty}^{n=+\infty} E_n H_n^1(k_{SV}^m r) e^{in\theta} + \sum_{n=-\infty}^{n=+\infty} F_n H_n^1(k_{SV}^m r) e^{in\theta}, \quad (9)$$

where C_n and E_n are the complex-valued amplitudes of order n for the both potentials associated with the contribution transmitted from the effective medium, and finally, D_n and F_n are the complex-valued amplitudes of order n for the both potentials associated with the contribution scattered from the scatterer.

In contrast, only the contribution transmitted from the matrix was considered in the scatterer, leading, for $r<a$, to (Yang and Mal, 1994)

$$\varphi(r,\theta) = \sum_{n=-\infty}^{+\infty} G_n H_n^1(k_L^s r) e^{in\theta}, \quad (10)$$

$$\psi(r,\theta) = \sum_{n=-\infty}^{+\infty} I_n H_n^1(k_{SV}^s r) e^{in\theta}, \quad (11)$$

where G_n and I_n are the complex-valued amplitudes of order n for the both potentials associated with the contribution transmitted from the matrix.

Therefore, each wave mode considered had different amplitudes and their wave numbers were given by the elastic properties of the matrix [see Eqs. (2) and (3)]. This configuration led to ten unknowns (two wave numbers h and k in the effective medium and eight complex-valued amplitudes).

In order to solve this problem, the boundary conditions were used. They were given by the continuity of normal stresses and displacements at interfaces between: (i) the matrix and the scatterer at $r=a$, and (ii) the matrix and the effective medium at $r=b$. The boundary conditions led to eight independent equations, and two additional equations were therefore required to solve this problem. These supplementary equations were derived from Yang and Mal (1994) and were related to the theory of multiple scattering, assuming a random distribution of the position of the scatterers [as given by Eqs. (28) and (29) of Yang and Mal, 1994]

$$1 = \left(1 - \frac{2in_0 f_1(0)}{k^2}\right)^2 - \left(\frac{2in_0 f_1(\pi)}{k^2}\right)^2,$$
$$1 = \left(1 - \frac{2in_0 f_2(0)}{h^2}\right)^2 - \left(\frac{2in_0 f_2(\pi)}{h^2}\right), \quad (12)$$

where $f_1(\theta)$ and $f_2(\theta)$ were, respectively, the far-field amplitudes of the L and SV wave modes scattered in the effective medium in the θ-direction and n_0 was the number of scatterers per unit area ($n_0 = C/\pi a^2$). The values of $f_1(0)$, $f_2(0)$, $f_1(\pi)$, and $f_2(\pi)$ are given by (Yang and Mal, 1994)

$$f_1(0) = \sum_{n=-\infty}^{+\infty} (-i)^n A_n, \quad f_1(\pi) = \sum_{n=-\infty}^{+\infty} (-i)^n A_n, \quad (13)$$

$$f_2(0) = \sum_{n=-\infty}^{+\infty} (-i)^n B_n, \quad f_2(\pi) = \sum_{n=-\infty}^{+\infty} (i)^n B_n. \quad (14)$$

These last four values could be obtained from the boundary conditions assuming that k and h were known. This led to an implicit expression solved using an iterative scheme, which was numerically initiated by taking for k and h initial values those corresponding to the propagation into the matrix. The global system consisting of the eight equations of continuity and of Eq. (12) was then solved numerically. This gave new values for k and h. At each iteration, the accuracy of the method was tested against the previous one. The iterations were stopped when the right members of Eq. (12) reached the value of 1 with a relative error lower than ε, corresponding to a threshold fixed to reach the convergence in the iterative scheme. This convergence was reached when the difference between two consecutive values of k obtained in the iterative scheme was lower than 10^{-5}.

The frequency-dependent phase velocity at the frequency f was then given by the real part of k through

$$V_\varphi(f) = \frac{2\pi f}{\mathrm{Re}(k)}. \quad (15)$$

To compute the dispersion, the computation of the phase velocity was performed for ten values of f between 400 and 800 kHz. This bandwidth corresponds to the one used in many clinical devices. The value of the velocity dispersion rate was obtained by computing the slope of the curve of the phase velocity versus frequency through a least square regression analysis. This procedure was applied for all values of dispersion computed with our model in the present paper. Due to the nearly linear frequency dependence of phase velocity (see below for further details), the dispersion rate is equivalent to the dispersion computed over a 1 MHz frequency bandwidth. In what follows, the dispersion rate will therefore be referred to as dispersion.

TABLE I. Rheological parameters of the matrix and of the scatterer chosen for trabecular bone and for trabecular bone-mimicking phantoms. The variation of the attenuation coefficient and of phase velocity for the L and SV wave modes as a function of frequency expressed in megahertz are shown.

Structure[a]	Medium i	$\alpha_L^i(f)$ (dB cm^{-1})	$V_L^i(f)$ (m s^{-1})	$\alpha_{SV}^i(f)$ (dB cm^{-1})	$V_{SV}^i(f)$ (m s^{-1})	ρ_i (kg m^{-3})
	Matrix (bone marrow)	f	$\left(\frac{1}{1480}-\frac{1.15\times10^{-5}}{\pi^2}\ln\left(\frac{f}{0.6}\right)\right)^{-1}$	$27\,800f$	$\left(\frac{1}{3.5}-\frac{0.32}{\pi^2}\ln\left(\frac{f}{0.6}\right)\right)^{-1}$	1000
Trabecular bone	Scatterer (bone)	$4\times f$	$\left(\frac{1}{4000}-\frac{4.6\times10^{-5}}{\pi^2}\ln\left(\frac{f}{0.6}\right)\right)^{-1}$	$7.6f$	$\left(\frac{1}{1800}-\frac{8.74\times10^{-5}}{\pi^2}\ln\left(\frac{f}{0.6}\right)\right)^{-1}$	1850
Phantoms	Matrix (water)	0	1480	500	3.5	1000
	Scatterer (nylon)	$2.34\times f$	$\left(\frac{1}{2600}-\frac{2.69\times10^{-5}}{\pi^2}\ln\left(\frac{f}{0.6}\right)\right)^{-1}$	$2.34f$	$\left(\frac{1}{1300}-\frac{2.69\times10^{-5}}{\pi^2}\ln\left(\frac{f}{0.6}\right)\right)^{-1}$	1100

[a]Frequency f expressed in megahertz.

D. Coupling viscoelastic losses and multiple scattering

The theory proposed by Yang and Mal (1994) leads to a complex-valued wave number, which describes the phase velocity and the attenuation coefficient in the effective medium. Previously, this theory had been applied assuming that the matrix and the scatterer were both purely elastic (real-valued stiffness coefficients). The possibility of considering viscoelastic constitutive media in the framework of Yang and Mal (1994) theory is introduced in the present paper. To this end, viscoelastic losses take place when a wave scattered by one of the cylinders propagates to a neighboring fiber as well as in the scatterer itself. In the framework of this theory, accounting for complex-valued characteristics of each medium constitutive of the composite material means that viscoelastic losses and losses due to multiple scattering were intrinsically coupled.

The incident and scattered waves, wherever they propagate (matrix, scatterer, and effective medium), were thus described as waves subjected to attenuation. Attenuation symmetry in various media was assumed to be isotropic. Therefore, all stages of the computation of the original theory could be readily transformed by taking into account the complex-valued wave numbers. By doing so, viscoelastic losses were implicitly accounted for in the scattering process and both phenomena were coupled.

E. Rheological modeling

In order to solve this problem, the rheological properties of the scatterer and of the matrix had to be determined. These properties correspond to input data of the model (properties of the matrix and of the scatterer). The frequency dependence of the attenuation coefficient $\alpha_L^i(f)$ $[\alpha_{SV}^i(f)]$ and of the phase velocity $V_L^i(f)$ $[V_{SV}^i(f)]$ in each medium i had to be determined for the L (SV) wave mode [see Eqs. (2) and (3)]. In homogeneous media, the frequency dependences of the attenuation coefficient and of the phase velocity are related through the nearly local KK relationships (O'Donnell *et al.*, 1978, 1981; Waters *et al.*, 2005). Specifically, we assume that the attenuation coefficient $\alpha_J^i(f)$ corresponding to the wave mode J (J being L or SV) varies linearly with frequency as $\alpha_J^i(f)=\beta f$, where f and $\alpha_J^i(f)$ are, respectively expressed in MHz and in dB/cm, which leads to a logarithmic frequency dependence of the phase velocity $V_L^i(f)$ as follows:

$$V_J^i(f)=\left(\frac{1}{V_0}-\frac{1.15\times10^{-5}\beta}{\pi^2}\ln\left(\frac{f}{f_0}\right)\right)^{-1}, \tag{16}$$

where V_0 is the reference velocity at the reference frequency f_0.

In what follows, the frequency dependence of the attenuation coefficient is first determined for both media and both wave modes. Then, the KK relationships, together with an estimate of the value of the phase velocity at midbandwidth (here, 600 kHz), are used to derive the frequency dependence of phase velocity.

The present model was applied to two distinct structures: trabecular bone and trabecular bone-mimicking phantom sample made of nylon wires immersed in water, which were described by Wear (2005). In the latter case, the scatterers correspond to the nylon wires and the matrix corresponds to water.

1. Trabecular bone

When modeling *in vivo* experiments, the matrix corresponds to bone marrow. However, for *in vitro* experiments, the matrix may correspond either to bone marrow (bone filled with marrow) or, in most cases, to water (bone filled with water), according to the experimental conditions. In what follows, both media (water and marrow) will therefore be considered.

Experimental data on the attenuation coefficient measured in bone marrow could not be found in literature. Therefore, we assumed that (i) a linear frequency dependence of $\alpha_L^m(f)$ for all frequencies and (ii) that the rheological properties of bone marrow are close to that of fat (soft-tissue-like behavior) as a substitute. The attenuation coefficient at 1 MHz measured by Dussik and Fritch (1956) in fresh human fat tissues is equal to 0.8 dB cm^{-1} and that measured by Lehman and Johnson (1958) in subcutaneous pig fat tissue is equal to 1.8 dB cm^{-1} (these values are summed up in Goss *et al.*, 1978). Table I shows the corresponding expression of $\alpha_L^m(f)=f$ dB cm^{-1}, where f is expressed in MHz, corresponding to a compromise between the results obtained in the two papers cited. Assuming a wave velocity of 1480 m s^{-1} at 600 kHz in bone marrow (as found in Dussik

and Fritch, 1956 and Goss *et al.*, 1978 in human fat tissues), the KK relationships yield the expression of $V_L^m(f)$ shown in Table I.

Moreover, around the frequency 600 kHz, the attenuation of SV wave modes in soft tissues is much higher than that of the L wave mode. Here, the value of the attenuation coefficient was chosen to correspond to typical values obtained in dog fresh liver (Frizzel, 1975a, 1975b; Goss *et al.*, 1978) (this point will be discussed in Sec. IV C). In soft tissue, the value of the transverse wave velocity is much lower than that of the L wave mode. The value of this transverse wave velocity was taken equal to 3.5 m s^{-1} at 600 kHz (Hakulinen *et al.*, 2006). The result obtained for $V_{SV}^m(f)$ using the KK relationships is shown in Table I.

When the matrix corresponds to water (*in vitro* experiments only), acoustical losses were neglected in the rheological modeling of water. Therefore, the attenuation coefficient $\alpha_L^m(f)$ was taken equal to zero at all frequencies. This approximation led to a constant value for the phase velocity in water taken as $V_L^m(f)=1480$ m s^{-1}. Moreover, SV wave modes do not propagate in water. Therefore, an arbitrary high constant value of $\alpha_{SV}^m(f)=500$ dB cm^{-1} was chosen in order to ensure that the amplitude of a transverse (SH or SV) wave mode propagating over a distance of the trabecular spacing is negligible. Due to the limitation inherent to the model, water was modeled as a viscoelastic solid rather than a perfect fluid and this point will be discussed in Sec. IV C.

The rheological properties of the bone matrix (corresponding to the scatterer) are taken from values obtained in cortical bone. The values chosen for $\alpha_L^s(f)$ shown in Table I are taken from the averaged values obtained from measurements in femoral bovine pure cortical bone specimen measurements (Sasso *et al.*, 2007, 2008). Assuming a longitudinal wave velocity of 4000 m s^{-1} [corresponding to typical values of cortical bone (Njeh *et al.*, 1999)] at 600 kHz for cortical bone, the KK relationships yield the expression of $V_L^s(f)$ shown in Table I. Moreover, the attenuation coefficient $\alpha_{SV}^s(f)$ of SV wave modes in cortical bone around 600 kHz is taken from Garcia *et al.*, 1978. Assuming a transverse wave velocity of 1800 m s^{-1} (Njeh *et al.*, 1999) at 600 kHz for cortical bone, the KK relationships yield the expression of $V_{SV}^s(f)$ shown in Table I.

2. Phantom mimicking trabecular bone

In order to test and validate the model on an experimental configuration comparable to our 2D approximation, results predicted by the model are compared with the experimental results obtained by Wear (2005) with his trabecular bone-mimicking phantoms. Briefly, seven phantoms made up of parallel nylon wires mimicking the trabeculae placed in 2D rectangular grid arrays were tested using a substitution method with a center frequency around 500 kHz. Each phantom (immersed in water) is composed of nylon wires having various diameters D_s, ranging between 152 and 305 μm. The phantoms have different scatterer volume fractions C between 1.8% and 11.4% and scatterer interdistance Sp, varying between 700 and 1000 μm. For each phantom, the frequency-dependent phase velocity and the velocity dispersion were simulated with the model.

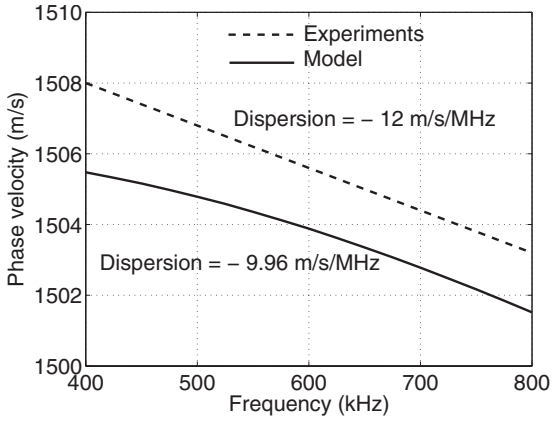


FIG. 2. Bone-mimicking phantom. (Solid line) Variation of the phase velocity as a function of frequency obtained with the model with the parameters corresponding to a bone-mimicking phantom with a scatterer diameter $D_s=254$ μm and a scatterer volume fraction $C=7.9\%$. (Dashed line) Linear fit of the variation of the phase velocity vs frequency obtained experimentally with the same phantom (reproduced from Fig. 2 in Wear, 2005). The values of the dispersion obtained with the two methods are indicated.

When considering trabecular bone-mimicking phantom samples, the matrix corresponds to water (refer to the last paragraph for its rheological description). Moreover, viscoelastic losses were accounted for in the rheological modeling of nylon and the attenuation coefficient $\alpha_L^s(f)$ was taken from Hung and Goldstein, 1983 (see Table I). The attenuation coefficient $\alpha_{SV}^s(f)$ was considered equal to $\alpha_L^s(f)$ as the attenuation of transverse shear waves could not be found in literature. Assuming longitudinal and transverse wave velocities in nylon of, respectively, 2600 and 1300 m s^{-1} (Wear, 2004, 2005) at 600 kHz, the KK relationships yield the expressions of $V_L^s(f)$ and $V_{SV}^s(f)$ shown in Table I.

III. RESULTS

A. Modeling trabecular bone-mimicking phantoms

Figure 2 shows the frequency-dependent phase velocity predicted by the model (solid line) and the experimental results (dashed line) obtained by Wear (2005) for a given phantom ($D_s=254$ μm and $C=7.9\%$). The values of velocity dispersion corresponding to each curve are given in Fig. 2. The values of phase velocity obtained with the model are slightly lower than those experimentally measured, and the dispersion is slightly underestimated in absolute value by the model.

Figure 3 displays predicted (solid lines) and measured (dashed lines) variations of phase velocity at 500 kHz as a function of various properties of the phantoms. Figure 3(a) shows the variation of phase velocity as a function of scatterer diameter D_s for four phantoms having the same inter-scatterer spacing Sp equal to 800 μm. Figure 3(b) shows the variation of phase velocity versus Sp for four phantoms having the same D_s equal to 152 μm. Figure 3(c) shows the variation of the phase velocity as a function of volume fraction C for all phantoms corresponding to different values of C and of Sp. A good agreement is obtained between the

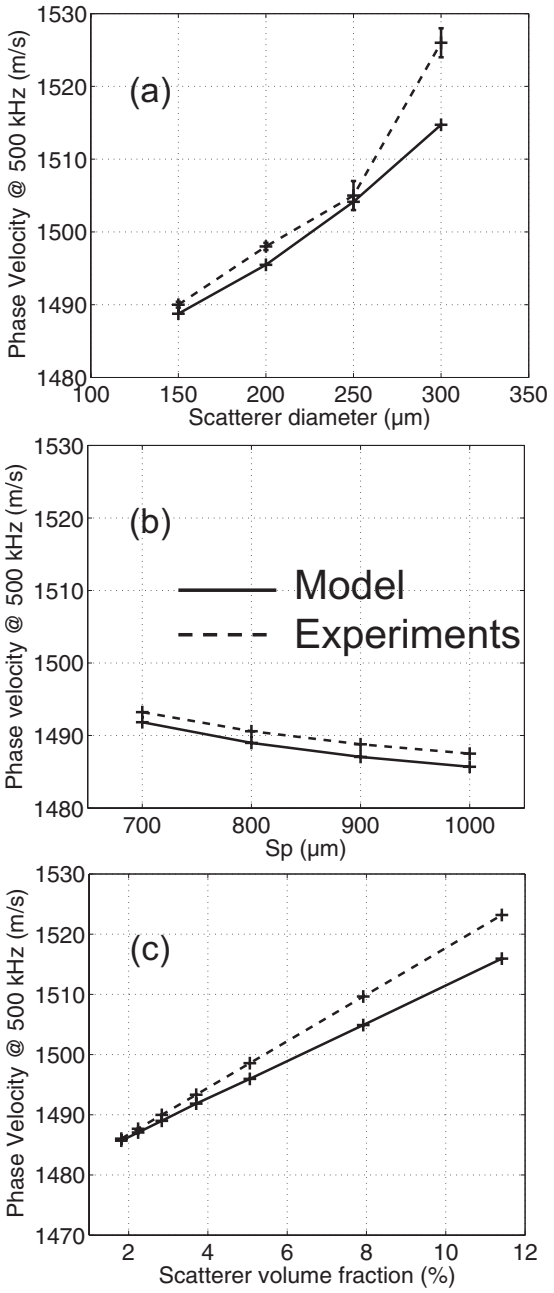


FIG. 3. Variation of the phase velocity at 500 kHz as a function of the properties of the bone-mimicking phantom. The solid and dashed lines, respectively, correspond to the results predicted by the model and measured by Wear (2005). (a) Phase velocity as a function of trabecular thickness for four phantoms having the same interscatterer spacing Sp equal to 800 μm, (b) phase velocity as a function of trabecular spacing for four phantoms with the scatterer diameter D_s=152 μm, and (c) phase velocity as a function of volume fraction for all phantoms. In Fig. 2(a), the experimental data are given with their error bar; the fitted data are shown in Figs. 2(b) and 2(c). The experimental results are reproduced from Figs. 3–5 in Wear, 2005.

model and the experiments, although the values of phase velocity are slightly underestimated by the model, especially for high values of D_s and C.

Figure 4 shows predicted (solid lines) and measured (dashed lines) variations of velocity dispersion as a function of the properties of the phantoms. Figure 4(a) shows the variation of velocity dispersion versus D_s for four phantoms having the same interwire spacing Sp equal to 800 μm. Figure 4(b) shows the variation of velocity dispersion versus Sp

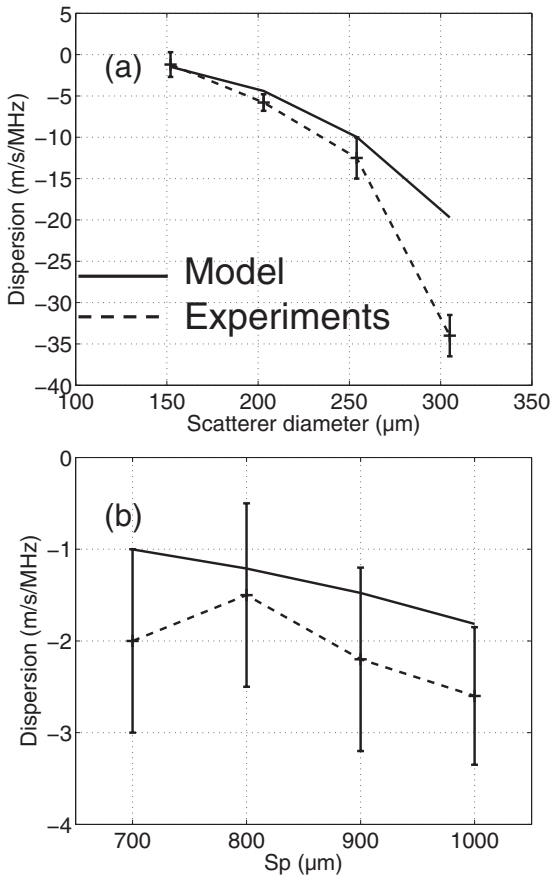


FIG. 4. Variation of the velocity dispersion at 500 kHz as a function of the properties of the bone-mimicking phantom. The solid and dashed lines, respectively, correspond to the results predicted by the model and measured by Wear (2005). (a) Velocity dispersion as a function of trabecular thickness for four phantoms having the same interscatterer spacing Sp equal to 800 μm, and (b) velocity dispersion as a function of trabecular spacing for four phantoms with a scatterer diameter D_s=152 μm.

for four phantoms having the same D_s equal to 152 μm. Again, the values of velocity dispersion obtained with the model are in general good qualitative agreement with Wear's (2005) experiments: Dispersion values decrease when D_s increases, whereas insignificant variation of dispersion (less than 1 m s^{-1} MHz^{-1}) is obtained when Sp varies. The values of velocity dispersion obtained with the model are in good agreement with experimental results, except for high D_s values and to a lesser extent for high Sp values.

B. Application to trabecular bone

As indicated by Wear (2005), the design of his phantoms was simplistic compared to real trabecular bone structure because of the substituted nylon for mineralized bone, of the periodic structure and of the influence of dissipation in the marrow or in bone tissue, which was not accounted for. These drawbacks can be overcome using this model and by considering values of trabecular bone material properties taken from literature (see Table I).

Figure 5 shows the variations of velocity dispersion at 600 kHz as a function of C for two different values of D_s. The dashed and solid lines correspond, respectively, to D_s =75 μm and D_s=300 μm. Moreover, the black lines correspond to the case where viscoelastic absorption is neglected

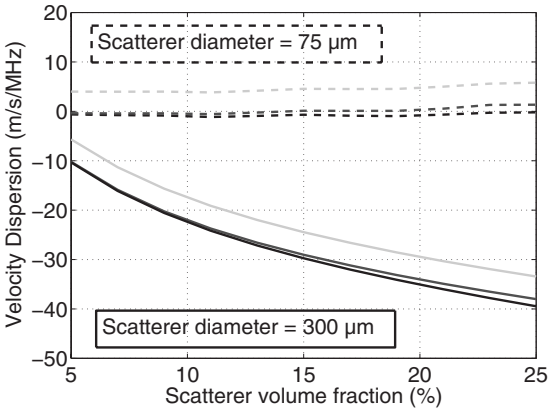


FIG. 5. Variation of the velocity dispersion around 600 kHz as a function of bone volume fraction predicted by the model. The solid and dashed lines, respectively, correspond to results obtained with scatterer diameters D_s = 300 and 75 μm. The black lines correspond to results obtained by neglecting all viscoelastic losses; the dark (light) gray lines correspond to results obtained by considering viscoelastic effects in the trabeculae only (in the trabeculae and in the marrow).

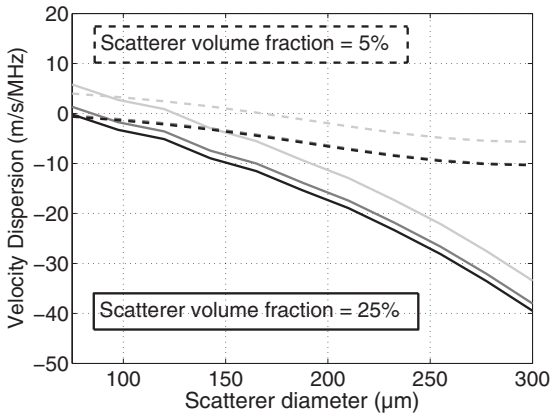


FIG. 6. Variation of the velocity dispersion around 600 kHz as a function of the scatterer diameter D_s predicted by the model for constant scatterer volume fraction C value of 5% (dashed lines) and 25% (solid lines). The black lines correspond to results obtained by neglecting all viscoelastic losses; the dark (light) gray lines correspond to results obtained by considering viscoelastic effects in the trabeculae only (in the trabeculae and in the marrow). The black and dark gray dashed lines are almost confounded.

in the trabeculae as well as in the matrix (i.e., by choosing $\alpha_L^m = \alpha_L^s = \alpha_{SV}^s = 0$). The dark gray lines correspond to the case where viscoelastic absorption is accounted for only in the trabeculae (i.e., by choosing $\alpha_L^m = 0$). This last case corresponds to the situation encountered *in vitro* when bone marrow is removed from the bone specimens and when the specimens are saturated by water. The light gray lines correspond to the case where viscoelastic absorption is accounted for in the trabeculae as well as in the marrow (trabecular bone samples filled with marrow).

When neglecting all viscoelastic absorption effects, the model always predicts negative dispersion values. Dispersion is strongly affected by the scatterer size: While it remains quasi negligible (lower than 2 m s^{-1} MHz^{-1} in absolute value) for small scatterer sizes (75 μm), dispersion decreases from −10 to −40 m s^{-1} MHz^{-1} when the volume fraction increases from 5% to 25% for large scatterer size (300 μm). Introducing absorption either in the scatterers or in the scatterers and in the matrix results in an upward offset of the dispersion curve.

Taking into account absorption in the trabeculae makes almost no difference compared to the case where no absorption was considered: It induces an offset between 0.1 and 1.5 m s^{-1} MHz^{-1}, depending mostly on the value of C, which becomes visible only at large C values. A small positive dispersion is observed for 75 μm scatterers and large volume fraction values. In contrast, introducing absorption in the trabeculae and in the marrow (light gray lines) induces an approximately constant increase in dispersion of about 4 m s^{-1} MHz^{-1} (this value weakly depends on C and D_s) compared to the case where the absorption was only considered in the trabeculae (dark gray lines). In this latter case, the model consistently predicts positive dispersion for small scatterer size (75 μm), whereas dispersion remains always negative for D_s=300 μm.

Figure 6 shows the variation of velocity dispersion at 600 kHz as a function of D_s for two different values of C. The dashed and solid lines correspond, respectively, to C =5% and C=25%. Similarly to Fig. 5, the black line corresponds to the case where viscoelastic absorption is neglected (i.e., by choosing $\alpha_L^m = \alpha_L^s = \alpha_{SV}^s = 0$); the dark gray line corresponds to the case where only viscoelastic absorption in the trabeculae is accounted for (i.e., by choosing $\alpha_L^m = 0$); the light gray line corresponds to the case where viscoelastic absorption is accounted for in the trabeculae as well as in the marrow. Dispersion is found to be a decreasing function of D_s for all cases considered herein. Consistently with Fig. 5, dispersion values found by the model are always negative when neglecting absorption. When absorption is taken into account in the trabeculae and C is equal to 5%, the model always predicts negative values of dispersion. When absorption is taken into account in the trabeculae and C is equal to 25%, the model predicts positive values of dispersion for D_s values lower than 85 μm. When absorption is taken into account in the trabeculae as well as in the marrow, the model predicts positive values of dispersion for values of D_s lower than 165 and 125 μm when C is, respectively, equal to 5% and 25%.

Consistently with Fig. 5, taking into account absorption in the trabeculae induces an approximately constant increase in dispersion values of about 0.1 and 1.5 m s^{-1} MHz^{-1} when C is, respectively, equal to 5% and 25%. Again, for both values of C, taking into account absorption in the trabeculae and in the marrow (light gray lines) induces an approximately constant increase in dispersion of about 4 m s^{-1} MHz^{-1} compared to the case where the absorption was only considered in the trabeculae.

IV. DISCUSSION

This study constitutes the first attempt to model the frequency dependence of phase velocity in trabecular bone using theories accounting for multiple scattering effects. The originality of our approach is that it takes into account the coupling of multiple scattering effects with viscoelastic absorption effects. As stated by Wear (2005), the physical mechanisms responsible for negative dispersion remain un-

TABLE II. Values of velocity dispersion found by different authors at the calcaneus and with the model developed in the present paper with bone parameters corresponding to the physiological range at the calcaneus.

Authors	Experimental conditions	Frequency range (kHz)	Dispersion (mean ± standard deviation) (m s^{-1} MHz^{-1})
Nicholson *et al.* (1996)	Filled with water	200–800	−40
Strelitzki and Evans (1996)	Filled with water	600–800	-32 ± 27
Droin *et al.* (1998)	Filled with water	200–600	-15 ± 13
Wear (2000a)	Filled with water	200–600	-18 ± 15
Wear (2007b)	Filled with marrow (*in vivo*)	300–600	-59 ± 52
	Filled with water	400–800	From −38 to 1.3
Present paper	Filled with marrow	400–800	From −33.5 to 5.8

clear. In the present study, a physical explanation for the negative values of dispersion is proposed, based on multiple scattering phenomena. Luppé *et al.* (2003) previously studied ultrasonic propagation in trabecular bone by considering multiple scattering phenomena. Their approach nicely consisted in using the Foldy (1945) as well as the Waterman and Truell (1961) approximations coupled with the Biot (1956) theory. Our approach is somewhat different from their work in that they considered wave scattering by the pores, whereas we consider scattering by the trabeculae. Furthermore the approach of Luppé *et al.* (2003) did not lead to negative values of dispersion.

Several models have been proposed to account for negative dispersion. Negative dispersion has previously been predicted using multilayer models (Wear, 2001b, 2007b). However, the multilayer model is limited in that no absorption is taken into account and that it predicts only negative dispersion, while experimentally positive dispersion is predicted in about 10%–20% of specimens (Droin *et al.*, 1998; Wear, 2000a). Compared to multilayer models developed so far in the context of bone studies, the present model has the advantage of taking into account absorption effects. Other models using the Biot (1956) theory (Marutyan *et al.*, 2006) have also predicted negative as well as positive dispersion values in trabecular bone, consistently with experimental data. In their approach, negative dispersion has been shown to result from the interference between the fast and slow longitudinal modes predicted by Biot (1956) theory, each wave mode exhibiting positive dispersion. In their paper, Marutyan *et al.* (2006) chose the dispersion of the velocities that serve as inputs to the calculation to exhibit an increase with increasing frequency, that is, a positive dispersion. That same assumption has been made in the present paper when absorption is taken into account. We found that negative dispersion may arise in spite of the fact that the input parameters of our model have only positive dispersions. In that sense, the present paper seems to confirm the assertion of Marutyan *et al.* (2006). However, one major concern with the Biot (1956) theory is that it does not take into account scattering phenomena, which have been shown to play an important role in the physical interaction between ultrasound and trabecular bone (Bossy *et al.*, 2007; Haiat *et al.*, 2007) and to be a major contribution to the overall attenuation losses for frequencies around 600 kHz. In addition, the application of the Biot (1956) theory to model the ultrasonic propagation in bone requires several parameters (such as tortuosity, permeability, viscous characteristic length, and power index), which are sometimes difficult to obtain (Marutyan *et al.*, 2006) for a given sample. Compared to the Biot (1956) theory, the present model has the advantage of using bone parameters (only the material properties of the marrow and bone, C and D_s, are necessary), which are more likely to be accessible to experimental measurements, the estimation of parameters such as tortuosity and permeability being not always straightforward.

A. Orders of magnitude

Different teams have measured negative values of velocity dispersion in bone-mimicking phantoms (Strelitzki *et al.*, 1997; Lee *et al.*, 2003; Wear, 2005; Lee and Choi, 2007). Our results give further insights into the relevance of using such phantoms in order to model ultrasonic propagation in trabecular bone, and more specifically, into the results obtained with Wear's (2005) bone-mimicking phantoms. However, some discrepancies have been noticed between theoretical and experimental phase velocities shown in Figs. 2 and 3. Temperature related errors, close to 0.5 °C [corresponding to a difference of about 1.5 m s^{-1} in velocity (Kaye and Laby, 1973)], can contribute to the observed discrepancy, especially for low values of D_s, Sp, and C where the difference between the theoretical and experimental phase velocities is around 2 m s^{-1}. For high C and D_s values, the phase velocity and dispersion values obtained with the model are underestimated in absolute value compared to experimental results obtained in phantoms, and temperature related errors alone cannot account for the discrepancy. A possible explanation is that the model assumes a random distribution of the scatterers, whereas the nylon wires are regularly distributed in a squared grid, which is a limitation inherent to the phantoms compared to real bone structures.

Dispersion values predicted with our trabecular bone model may be compared to results obtained experimentally at the calcaneus by different authors (Nicholson *et al.*, 1996; Strelitzki and Evans, 1996; Droin *et al.*, 1998; Wear, 2000a), which are summarized in Table II. The results obtained with the model by considering absorption only in the trabeculae correspond to the situation where trabecular bone samples are filled with water (*in vitro* experiments only). When trabecular bone samples are filled with marrow, absorption in

the trabeculae, as well as in the marrow, is to be considered. The values of D_s and C selected in our model are representative of the typical values found at the calcaneus, ranging, respectively, between 3.4% and 33% and between 74 and 290 μm (Rupprecht *et al.*, 2006), according to the region of interest, age, and gender. The two last lines of Table II show the range of variation of dispersion values obtained with the model for trabecular bone filled either with water or with marrow. Table II shows that the order of magnitude of dispersion values predicted with the model is in general good agreement with experimental results. Interestingly, mostly negative and also positive values of dispersion are predicted by the model, which is consistent with experimental observations.

Droin *et al.* (1998) found that dispersion is not related to C or to D_s, which is in apparent contradiction with the results shown in Figs. 5 and 6 in this paper. These discrepancies might be due to the fact that the model assumes that all trabeculae are similar, which is not the case for real structures. In addition, trabecular bone is known to be heterogeneous at a structural level and the local material properties of bone tissue constituting the trabeculae are not known accurately (generic values are used instead).

B. Relative contribution of absorption and of scattering to velocity dispersion

The model predicts positive as well as negative dispersion values, depending on bone properties. When absorption effects are not accounted for, only negative dispersion is predicted by the model. In order to obtain positive dispersion values, two simultaneous conditions that can be read from Figs. 5 and 6 need to be fulfilled: (i) Absorption must be considered, particularly absorption in the marrow appears to have a greater impact than absorption in the scatterers, and (ii) sufficiently small scatterers must be considered (positive dispersion is reached at a diameter value, which depends on the absorption level and on the scatterer volume fraction). Therefore, dispersion values result from a complex combination between the rheological properties of bone and its microstructure, namely, the scatterer size (which determines the scattering cross section) and the scatterer volume fraction.

The results obtained with our model show that multiple scattering phenomena are responsible for negative dispersion values, whereas including absorption in the model induces an increase in dispersion. The resulting velocity dispersion (positive or negative) depends on the relative contribution of multiple scattering and absorption effects. If absorption effects are dominant, dispersion may become positive when the size of the scatterers (i.e., the scattering cross section) is sufficiently small. Increasing the size of the scatterers results in an increase in the scattering cross section and subsequently in an increase in multiple scattering effects. Negative dispersion is predicted for large scatterers. Experimentally, most dispersion values were found to be negative. Similarly, considering typical bone parameters, our model predicts mostly negative dispersion values. Both the results from experiments and from our model suggest that scattering effects are dominant over absorption effects in trabecular bone in the frequency range investigated here. Note that this result is in good agreement with physical interpretations derived previously from finite-difference time-domain simulations of wave propagation through trabecular bone specimens (Bossy *et al.*, 2007; Haiat *et al.*, 2007).

C. Rheological modeling

In this paper, the matrix is assumed to be constituted either by water or by marrow. The matrix is described in all cases as a soft solid as we assume a low value of transverse wave velocity compared to the longitudinal wave velocity. This approximation is justified by the rheological properties of bone marrow, which are assumed to be comparable to those of soft tissues. However, when the matrix corresponds to water (fluid behavior), the soft solid approximation employed herein constitutes a limitation of the model. This limitation has been overcome by an appropriate choice of parameters input into the model to describe the matrix. Because shear wave modes are highly attenuated in marrow (soft tissues) and do not propagate in water, strong attenuation coefficient α_{SV}^{m} values were always considered in the matrix to avoid propagation of shear waves in the matrix. We checked that changing (i) the values of V_{SV}^{m} at 600 kHz between 1 and 10 m s^{-1} and (ii) the values of the attenuation coefficient α_{SV}^{m} between 0 and 1000 dB cm^{-1} does not impact the results obtained with water or marrow (data not shown). This reinforces the idea that shear wave modes propagating in the matrix do not significantly affect the ultrasonic propagation and, in particular, the frequency dependence of phase velocity. This constitutes a further justification for not considering SH wave modes, as indicated in Sec. II A.

The effect of absorption in bone marrow on velocity dispersion can be assessed by comparing the results obtained for water and marrow saturated trabecular bone (respectively, dark and light gray lines in Figs. 5 and 6). Taking into account losses in bone marrow induces an approximately constant increase of about 4 m s^{-1} MHz^{-1} of dispersion, which is of the order of magnitude of the dispersion value in pure bone marrow used in this model (around 4.4 m s^{-1} MHz^{-1}, see Table I).

Absorption of longitudinal and shear wave modes in bone marrow is not fully characterized yet experimentally. Therefore, a simplified model of bone marrow was considered herein. Direct measurements of the frequency dependence of the attenuation coefficient in bone marrow for both wave modes, in the frequency range of interest, are required to confirm these results. The effect of absorption in the trabeculae can be assessed by comparing the results without viscoelastic effects (black line) and the results with trabecular bone samples filled with water (dark gray line). Taking into account losses in the trabeculae also induces an increase in dispersion values. The difference between dispersion values obtained without any absorption and with absorption in the trabeculae is an increasing function of C, which may be due to the more important amount of bone compared to water when C increases. The effect of absorption in the trabeculae is different from the effect of absorption in the marrow (constant increase), and the increase in dispersion induced by absorption in the trabeculae cannot be predicted using a

simple model considering the dispersion in one given medium. This may be due to the full coupling of absorption and multiple scattering effects, which are both accounted for by the model.

The trabeculae were considered to behave similarly as cortical bone because no attenuation measurements in isolated trabeculae could be found in literature. However, attenuation in cortical bone depends on the donor, the anatomical location, the direction of propagation relatively to the bone axis (Sasso *et al.*, 2007) and on microstructure (Sasso *et al.*, 2008). Therefore, dispersion values are expected to also depend on bone quality of the trabeculae.

The choice of the model of attenuation in the trabeculae also has some limitations. The value of the extrapolation of the attenuation coefficient in the trabeculae at zero frequency ($\alpha_0 = \alpha_L^s(0)$) has been chosen equal to zero, whereas it may also be subject to variations (Sasso *et al.*, 2007). Therefore, the influence of changes of the value of α_0 on dispersion values found by the model was assessed. An affine variation of the attenuation coefficient with a constant slope was considered, given by

$$\alpha_L^s(f) = \alpha_{SV}^s(f) = \alpha_0 + 4f, \tag{17}$$

where the frequency f is given in megahertz. Computations were made with a value $\alpha_0 = 15$ dB cm^{-1} which was derived from typical values obtained in Sasso *et al.*, 2007. Using the set of parameters corresponding to marrow saturated samples, the results obtained with the model considering $\alpha_0 = 15$ dB cm^{-1} are close to the case where $\alpha_0 = 15$ dB cm^{-1} as the difference between the dispersion obtained in both cases is always lower than 0.6 m s^{-1} MHz^{-1} when D_s and C values were varied within the physiological range (data not shown). The similar results obtained in terms of dispersion when $\alpha_0 = 0$ dB cm^{-1} and $\alpha_0 = 15$ dB cm^{-1} used in Eq. (17) show that dispersion values depend more importantly on the frequency dependence of attenuation than on its extrapolation at zero frequency. Therefore, assuming an affine variation of the frequency-dependent attenuation coefficient in the trabeculae, only the slope of the attenuation coefficient seems to impact dispersion values.

V. CONCLUSION

A model accounting for the coupling of multiple scattering phenomena with viscoelastic absorption effects has been developed in order to derive the physical determinants of the frequency dependence of phase velocity in trabecular bone. A simple 2D description is considered and this biphasic medium is modeled as a set of infinite identical viscoelastic cylinders immersed in a viscoelastic matrix. The ultrasonic wave propagates perpendicularly to the cylinder axis and the computation is performed for each frequency. This homogenization procedure is based on a three-phase medium assumption derived from the model developed by Yang and Mal (1994). The results are found to be in good general agreement with experiments performed in phantoms of trabecular bone (Wear, 2005). The order of magnitude of velocity dispersion spans within the range found by various investigators: Mostly negative and also positive dispersion values are predicted by the model. Including losses in the trabeculae is shown to induce an increase in dispersion, which depends on the volume fraction. The effect of absorption in bone marrow is an approximately constant increase in dispersion values. To the best of the authors' knowledge, this is the first study investigating the impact of multiple scattering and absorption on velocity dispersion in trabecular bone. However, the question of the relative importance of multiple scattering phenomena versus independent scattering in the ultrasonic propagation in trabecular bone at clinical frequencies (0.5–1 MHz) remains open. Experimental evidences of multiple scattering effects below 1 MHz range have yet to emerge.

Biot, M. A. (**1956**). "Theory of propagation of elastic waves in a fluid-satured porous solid. II. Higher frequency range," J. Acoust. Soc. Am. **28**, 179–191.

Bossy, E., Laugier, P., Peyrin, F., and Padilla, F. (**2007**). "Attenuation in trabecular bone: A comparison between numerical simulation and experimental results in human femur," J. Acoust. Soc. Am. **122**, 2469–2475.

Bossy, E., Padilla, F., Peyrin, F., and Laugier, P. (**2005**). "Three-dimensional simulation of ultrasound propagation through trabecular bone structures measured by synchrotron microtomography," Phys. Med. Biol. **50**, 5545–5556.

Bouxsein, M. L., and Radloff, S. E. (**1997**). "Quantitative ultrasound of the calcaneus reflects the mechanical properties of calcaneal trabecular bone," J. Bone Miner. Res. **12**, 839–846.

Chaffai, S., Padilla, F., Berger, B., and Laugier, P. (**2000**). "In vitro measurement of the frequency dependent attenuation in cancellous bone between 0.2–2 MHz," J. Acoust. Soc. Am. **108**, 1281–1289.

Derode, A., Mamou, M., Padilla, F., Jenson, F., and Laugier, P. (**2005**). "Dynamic coherent backscattering in a heterogeneous absorbing medium: Application to human trabecular bone characterization," Appl. Phys. Lett. **87**, 114101.

Droin, P., Berger, G., and Laugier, P. (**1998**). "Velocity dispersion of acoustic waves in cancellous bone," IEEE Trans. Ultrason. Ferroelectr. Freq. Control **45**, 581–592.

Duck, F. A. (**1990**). *Physical Properties of Tissue* (Cambridge University Press, Cambridge).

Dussik, K. T., and Fritch, D. J. (**1956**). "Determination of sound attenuation and sound velocity in the structure constituting the joints, and of the ultrasonic field distribution with the joints of living tissues and anatomical preparations, both in normal and pathological conditions," National Institute of Health Project Progress Report No. A454.

Evans, J. A., and Tavakoli, M. B. (**1990**). "Ultrasonic attenuation and velocity in bone," Phys. Med. Biol. **35**, 1387–1396.

Foldy, L. L. (**1945**). "The multiple scattering of waves," Phys. Rev. **67**, 107–119.

Frizzel, L. A. (**1976**). "Shear properties of mammalian tissues at low megahertz frequencies," J. Acoust. Soc. Am. **60**, 1409–1411.

Frizzel, L. A. (**1975b**). *Ultrasonic Heating of Tissues* (University of Rochester, Rochester, NY).

Garcia, B. J., Cobbold, R. S. C., Foster, F. S., and McNeill, K. G. (**1978**). "Ultrasonic attenuation in bone," in Proceedings of the IEEE Ultrasonic Symposium (IEEE, Cherry Hill, NJ).

Gluer, C. C., and Barkmann, R. (**2003**). "Quantitative ultrasound: Use in the detection of fractures and in the assessment of bone composition," Curr. Osteoporos. Rep. **1**, 98–104.

Goss, S. A., Johnston, R. L., and Dunn, F. (**1978**). "Comprehensive compilation of empirical ultrasonic properties of mammalian tissues," J. Acoust. Soc. Am. **64**, 423–457.

Haiat, G., Padilla, F., Barkmann, R., Dencks, S., Moser, U., Gluer, C. C., and Laugier, P. (**2005a**). "Optimal prediction of bone mineral density with ultrasonic measurements in excised human femur," Calcif. Tissue Int. **77**, 186–192.

Haiat, G., Padilla, F., Barkmann, R., Kolta, S., Latremouille, C., Gluer, C. C., and Laugier, P. (**2005b**). "In vitro speed of sound measurement at intact human femur specimens," Ultrasound Med. Biol. **31**, 987–996.

Haiat, G., Padilla, F., Cleveland, R. O., and Laugier, P. (**2006**). "Effects of frequency-dependent attenuation and velocity dispersion on in vitro ultrasound velocity measurements in intact human femur specimens," IEEE Trans. Ultrason. Ferroelectr. Freq. Control **53**, 39–51.

Haiat, G., Padilla, F., Peyrin, F., and Laugier, P. (**2007**). "Variation of ultrasonic parameters with trabecular bone properties: A three-dimensional model simulation," J. Bone Miner. Res. **22**(5), 665–674.
Hakulinen, M. A., Day, J. S., Toyras, J., Weinans, H., and Jurvelin, J. S. (**2006**). "Ultrasonic characterization of human trabecular bone microstructure," Phys. Med. Biol. **51**, 1633–1648.
Hung, B., and Goldstein, A. (**1983**). "Acoustic parameters of commercial plastics," IEEE Trans. Sonics Ultrason. **30**, 249–253.
Jenson, F., Padilla, F., and Laugier, P. (**2003**). "Prediction of frequency-dependent ultrasonic backscatter in cancellous bone using statistical weak scattering model," Ultrasound Med. Biol. **29**, 455–464.
Kaye, G. W. C., and Laby, T. H. (**1973**). *Table of Physical and Chemical Constants* (National Physical Laboratory, London, UK).
Khaw, K. T., Reeve, J., Luben, R., Bingham, S., Welch, A., Wareham, N., Oakes, S., and Day, N. (**2004**). "Prediction of total and hip fracture risk in men and women by quantitative ultrasound of the calcaneus: EPIC-Norfolk prospective population study," Lancet **363**, 197–202.
Laugier, P., Droin, P., Laval-Jeantet, A. M., and Berger, G. (**1997**). "In vitro assessment of the relationship between acoustic properties and bone mass density of the calcaneus by comparison of ultrasound parametric imaging and QCT," Bone (N.Y.) **20**, 157–165.
Lee, K. I., and Choi, M. J. (**2007**). "Phase velocity and normalized broadband ultrasonic attenuation in polyacetal cuboid bone-mimicking phantoms," J. Acoust. Soc. Am. **121**, EL263–EL269.
Lee, K. I., Roh, H. S., and Yoon, S. W. (**2003**). "Acoustic wave propagation in bovine cancellous bone: Application of the modified biot-attenborough model," J. Acoust. Soc. Am. **114**, 2284–2293.
Lefebvre, J., Frohly, J., Torguet, R., Bruneel, C., and Rouvaen, J. M. (**1980**). "Experimental and theoretical study of the multiple scattering of acoustical waves in inhomogeneous media," Ultrasonics **18**, 170–174.
Lehman, J. F., and Johnson, E. W. (**1958**). "Some factors influencing the temperature distribution in thighs exposed to ultrasound," Arch. Phys. Med. Rehabil. **39**, 347–356.
Lonné, S., Lhémery, A., Calmon, P., Biwa, S., and Thévenot, F. (**2004**). "Modeling of ultrasonic attenuation in unidirectional fiber reinforced composites combining multiple-scattering and viscoelastic losses," in *Review of Progress in QNDE*, edited by D. O. Thompson and D. E. A. C. P. Chimenti, Conference Proceedings 700 (American Institute of Physics, Melville, NY), pp. 875–882.
Luppé, F., Conoir, J. M., and Franklin, H. (**2002**). "Scattering by a fluid cylinder in a porous medium: Application to trabecular bone," J. Acoust. Soc. Am. **111**, 2573–2582.
Luppé, F., Conoir, J. M., and Franklin, H. (**2003**). "Multiple scattering in a trabecular bone: Influence of the marrow viscosity on the effective properties," J. Acoust. Soc. Am. **113**, 2889–2892.
Marin, F., Gonzalez-Macias, J., Diez-Perez, A., Palma, S., and Delgado-Rodriguez, M. (**2006**). "Relationship between bone quantitative ultrasound and fractures: A meta-analysis," J. Bone Miner. Res. **21**, 1126–1135.
Marutyan, K. R., Holland, M. R., and Miller, J. G. (**2006**). "Anomalous negative dispersion in bone can result from the interference of fast and slow waves," J. Acoust. Soc. Am. **120**, EL55–61.
Mobley, J. (**2007**). "The time-domain signature of negative acoustic group velocity in microsphere suspensions," J. Acoust. Soc. Am. **122**, EL8–EL14.
Morse, P., and Ingard, K. (**1986**). *Theoretical Acoustics* (Princeton University Press, Princeton, NJ).
Nicholson, P. H., Muller, R., Lowet, G., Cheng, X. G., Hildebrand, T., Ruegsegger, P., van der Perre, G., Dequeker, J., and Boonen, S. (**1998**). "Do quantitative ultrasound measurements reflect structure independently of density in human vertebral cancellous bone?" Bone (N.Y.) **23**, 425–431.
Nicholson, P. H. F., Haddaway, M. J., and Davie, M. W. J. (**1994**). "The dependence of ultrasonic properties on orientation in human vertebral bone," Phys. Med. Biol. **39**, 1013–1024.
Nicholson, P. H. F., Lowet, G., Langton, C. M., Dequeker, J., and Van der Perre, G. (**1996**). "A comparison of time-domain and frequency domain approaches to ultrasonic velocity measurement in trabecular bone," Phys. Med. Biol. **41**, 2421–2435.
Njeh, C. F., Hans, D., Fuerst, T., Gluer, C. C., and Genant, H. K. (**1999**). *Quantitative Ultrasound: Assessment of Osteoporosis and Bone Status* (Martin Dunitz, London).
Njeh, C. F., Hodgskinson, R., Currey, J. D., and Langton, C. M. (**1996**). "Orthogonal relationships between ultrasonic velocity and material properties of bovine cancellous bone," Med. Eng. Phys. **18**, 373–381.
O'Donnell, M., Jaynes, E. T., and Miller, J. G. (**1978**). "General relationships between ultrasonic attenuation and dispersion," J. Acoust. Soc. Am. **63**, 1935–1936.
O'Donnell, M., Jaynes, E. T., and Miller, J. G. (**1981**). "Kramers-Kronig relationship between ultrasonic attenuation and phase velocity," J. Acoust. Soc. Am. **69**, 696–701.
Padilla, F., Peyrin, F., and Laugier, P. (**2003**). "Prediction of backscatter coefficient in trabecular bones using a numerical model of three-dimensional microstructure," J. Acoust. Soc. Am. **113**, 1122–1129.
Peters, F., and Petit, L. (**2000**). "Propagation of ultrasound waves in concentrated suspensions," Acust. Acta Acust. **86**, 838–846.
Rupprecht, M., Pogoda, P., Mumme, M., Rueger, J. M., Puschel, K., and Amling, M. (**2006**). "Bone microarchitecture of the calcaneus and its changes in aging: A histomorphometric analysis of 60 human specimens," J. Orthop. Res. **24**, 664–674.
Sasso, M., Haïat, G., Yamato, Y., Naili, S., and Matsukawa, M. (**2007**). "Frequency dependence of ultrasonic attenuation in bovine cortical bone: An in vitro study," Ultrasound Med. Biol. **33**, 1933–1942.
Sasso, M., Haïat, G., Yamato, Y., Naili, S., and Matsukawa, M. (**2008**). "Dependence of ultrasonic attenuation on bone mass and microstructure in bovine cortical bone," J. Biomech. **41**, 347–355.
Strelitzki, R., and Evans, J. A. (**1996**). "On the measurement of the velocity of ultrasound in the os calcis using short pulses," Eur. J. Ultrasound **4**, 205–213.
Strelitzki, R., Evans, J. A., and Clarke, A. J. (**1997**). "The influence of porosity and pore size on the ultrasonic properties of bone investigated using a phantom material," Osteoporosis Int. **7**, 370–375.
Trebacz, H., and Natali, A. (**1999**). "Ultrasound velocity and attenuation in cancellous bone samples from lumbar vertebra and calcaneus," Osteoporosis Int. **9**, 99–105.
Varadan, V. K., Ma, Y., and Varadan, V. V. (**1986**). "Multiple scattering of compressional and shear waves by fiber-reinforced composite materials," J. Acoust. Soc. Am. **80**, 333–339.
Waterman, P. C., and Truell, R. (**1961**). "Multiple-scattering of waves," J. Math. Phys. **2**, 512–537.
Waters, K. R., Mobley, J., and Miller, J. G. (**2005**). "Causality-imposed (Kramers-Kronig) relationships between attenuation and dispersion," IEEE Trans. Ultrason. Ferroelectr. Freq. Control **52**, 822–833.
Wear, K. (**2000a**). "Measurements of phase velocity and group velocity in human calcaneus," Ultrasound Med. Biol. **26**, 641–646.
Wear, K. A. (**1999**). "Frequency dependence of ultrasonic backscatter from human trabecular bone: Theory and experiment," J. Acoust. Soc. Am. **106**, 3659–3664.
Wear, K. A. (**2000b**). "Anisotropy of ultrasonic backscatter and attenuation from human calcaneus: Implications for relative roles of absorption and scattering in determining attenuation," J. Acoust. Soc. Am. **107**, 3474–3479.
Wear, K. A. (**2000c**). "The effects of frequency-dependant attenuation and dispersion on sound speed measurements: Applications in human trabecular bone," IEEE Trans. Ultrason. Ferroelectr. Freq. Control **47**, 265–273.
Wear, K. A. (**2001a**). "A numerical method to predict the effects of frequency-dependent attenuation and dispersion on speed of sound estimates in cancellous bone," J. Acoust. Soc. Am. **109**, 1213–1218.
Wear, K. A. (**2001b**). "A stratified model to predict dispersion in trabecular bone," IEEE Trans. Ultrason. Ferroelectr. Freq. Control **48**, 1079–1083.
Wear, K. A. (**2001c**). "Ultrasonic attenuation in human calcaneus from 0.2 to 1.7 MHz," IEEE Trans. Ultrason. Ferroelectr. Freq. Control **48**, 602–608.
Wear, K. A. (**2004**). "Measurement of dependence of backscatter coefficient from cylinders on frequency and diameter using focused transducers—with applications in trabecular bone," J. Acoust. Soc. Am. **115**, 66–72.
Wear, K. A. (**2005**). "The dependencies of phase velocity and dispersion on trabecular thickness and spacing in trabecular bone-mimicking phantoms," J. Acoust. Soc. Am. **118**, 1186–1192.
Wear, K. A. (**2007a**). "The dependence of time-domain speed-of-sound measurements on center frequency, bandwidth, and transit-time marker in human calcaneus in vitro," J. Acoust. Soc. Am. **122**, 636–644.
Wear, K. A. (**2007b**). "Group velocity, phase velocity, and dispersion in human calcaneus in vivo," J. Acoust. Soc. Am. **121**, 2431–2437.
Yang, R. B., and Mal, A. K. (**1994**). "Multiple-scattering of elastic waves in a fiber-reinforced composite," J. Mech. Phys. Solids **42**, 1945–1968.

Low-frequency components in harbor porpoise (*Phocoena phocoena*) clicks: communication signal, by-products, or artifacts?

M. Hansen[a)]
Zoophysiology, Department of Biological Sciences, University of Aarhus, Denmark 8000

M. Wahlberg
Fjord and Bælt, Margrethes Plads 1, 5300 Kerteminde, Denmark 8000

P. T. Madsen
Zoophysiology, Department of Biological Sciences, University of Aarhus, Denmark and Woods Hole Oceanographic Institution, Woods Hole, Massachusetts 02543

(Received 4 January 2008; revised 2 May 2008; accepted 19 May 2008)

Underwater sound signals for biosonar and communication normally have different source properties to serve the purposes of generating efficient acoustic backscatter from small objects or conveying information to conspecifics. Harbor porpoises (*Phocoena phocoena*) are nonwhistling toothed whales that produce directional, narrowband, high-frequency (HF) echolocation clicks. This study tests the hypothesis that their 130 kHz HF clicks also contain a low-frequency (LF) component more suited for communication. Clicks from three captive porpoises were analyzed to quantify the LF and HF source properties. The LF component is 59 (S.E.M=1.45 dB) dB lower than the HF component recorded on axis, and even at extreme off-axis angles of up to 135°, the HF component is 9 dB higher than the LF component. Consequently, the active space of the HF component will always be larger than that of the LF component. It is concluded that the LF component is a by-product of the sound generator rather than a dedicated pulse produced to serve communication purposes. It is demonstrated that distortion and clipping in analog tape recorders can explain some of the prominent LF components reported in earlier studies, emphasizing the risk of erroneous classification of sound types based on recording artifacts.
© *2008 Acoustical Society of America.* [DOI: 10.1121/1.2945154]

PACS number(s): 43.80.Ka [WWA] Pages: 4059–4068

I. INTRODUCTION

Water offers a series of options and constraints as a medium for transmitting stimuli to the sensory systems of aquatic animals (Dusenbery, 1992). Compared to other sensory cues such as light, sound travels with little attenuation in water and is therefore used by a large number of marine organisms to acquire and communicate information (Tyack and Clark, 2000). Toothed whales have evolved the capability to use sound for both passive listening, communication, and echolocation (biosonar) where objects are actively probed with sound (Tyack, 1998).

Sounds used for communication are often emitted at wavelengths positively correlated with the size of the animal emitting them (Fletcher, 2004). This relationship may be explained by the fact that sound production efficiency and directionality are dependent on the ratio between the size of the sound producing structures and the emitted wavelengths. Thus, with respect to the transmitting structures, long wavelengths lead to a low radiation directionality that increases the possibility of being heard by conspecifics (and predators) (Bradbury and Vehrencamp, 1998). However, a low radiation directionality is not suitable for biosonar signals that must be collimated to reduce clutter and achieve high source levels (SLs) (Au, 1993). Echolocating toothed whales are thus faced with an apparent need for high-frequency (HF) signals for effective echolocation of small prey items, and possibly more low-frequency (LF) signals for communication. Such a bimodal sound production is seen in most delphinids that produce frequency modulated whistles with fundamental frequencies in the 5–30 kHz range for communication (Lammers *et al.*, 2003; Janik, 2005) and very short clicks at centroid frequencies between 30 and 120 kHz for echolocation (Au, 1993). Other toothed whale species, such as the sperm whale, have a sound repertoire almost exclusively made up of clicks, but with properties apparently serving the different purposes of communication and echolocation (Madsen *et al.*, 2002a). Sperm whale usual sonar clicks consist of a weak LF component suited for communication (Zimmer *et al.*, 2005a) and a HF component of very high SL and directionality (Mohl *et al.*, 2003) suited for long-range echolocation of mesopelagic prey (Madsen *et al.*, 2002a). Sperm whales also produce so-called coda clicks and slow clicks in the context of social interactions with lower centroid frequencies and SLs, and most likely broader radiation patterns (Madsen *et al.*, 2002a, 2002b).

[a)]Electronic mail: michael_hansen@biology.au.dk

Even though many toothed whales produce both HF sonar clicks and LF communication signals, some toothed whale species only seem to produce ultrasonic clicks with properties suited for biosonar. Members of the families *Phocoenidae* and *Kogidae* and the genus *Cephalorhyncus* belong to the group of toothed whales that produce narrowband high-frequency (NBHF) clicks (Au, 1997) with centroid frequencies above 100 kHz and high Q's (centroid frequency divided by half power band width) (Madsen *et al.*, 2005).

It remains at present unclear why these unrelated toothed whale species living in different habitats have converged evolutionary to produce essentially identical NBHF clicks. Most of these species are small and therefore need very short wavelengths to achieve sufficient directionality in their biosonar systems. Mohl and Andersen (1973) suggested that NBHF clicks could be an adaptation to the low ambient noise window around 130 kHz (Madsen *et al.*, 2005). Several authors (Andersen and Amundin, 1976; Madsen *et al.*, 2005; Morisaka and Connor, 2007) have also advanced the hypothesis that the evolution of NBHF clicks may have been driven by killer whale predation, as NBHF clicks are produced beyond the upper hearing limit of these apex predators (Szymanski *et al.*, 1999).

Second, these nonwhistling toothed whales apparently do not emit signals of lower frequency and directionality as most delphinids for communication purposes. However, if porpoise clicks like sperm whale clicks (Zimmer *et al.*, 2005b) carry a LF component of low directionality, it can be envisioned that the HF component of the NBHF click is used for echolocation and the LF component for communication (Mohl and Andersen, 1973). In fact, porpoise sounds were first described by Schevill *et al.* (1969) as narrowband, low-level clicks with a peak frequency around 2 kHz, a duration between 0.5 and 5 ms, and SLs around 100 dB re 1 μPa (measure of reference unknown) at 1 m. However, a frequency of 2 kHz corresponds to a wavelength of 0.75 m, which is inconsistent with the animal's ability to echolocate wires with a diameter of only 0.5 mm that only reflects sound efficiently at much higher frequencies. Dubrovskii (1971) investigated harbor porpoises ability to make sounds at higher frequencies and found that they produced clicks at frequencies up to at least 100 kHz. In 1973, Mohl and Andersen reported porpoise clicks to have the bulk part of their energy concentrated between 100 and 160 kHz and SLs of 140–160 dB re 1 μPa$_{(peak)}$. They further noted the presence of a much weaker (<-50 dB) LF component around 2 kHz produced along with the HF component around 130 kHz (Mohl and Andersen, 1973; Amundin, 1991).

In addition to this, Kamminga and Wiersma (1981) described a 20 kHz component in porpoise clicks, and Verboom and Kastelein (1995, 1997) classified additional frequency components at 30 and 60 kHz as well as broad band components between 13 and 100 kHz. Thus, many alternative frequency components other than the dominating 130 kHz component has been reported for harbor porpoise clicks.

Here, we quantify the broadband source properties of harbor porpoise clicks to test the hypothesis that they have dedicated HF and LF components suited for the dual purposes of echolocation and communication. We show that porpoise clicks indeed contain a very weak LF component around 2 kHz, but that the HF component has significantly more energy irrespective of the recording aspect. It is also demonstrated that analog tape recorders can generate LF artifacts that can lead to erroneous classification and artifactual functional conclusions when analyzing toothed whale clicks.

II. MATERIALS AND METHODS

A. Far-range recordings of free-swimming porpoises

Several thousand clicks were recorded from three porpoises at Fjord & Belt, Kerteminde, Denmark, in a seminatural outdoor enclosure with a size of about 35×15 m^2. Three captive porpoises were used in the study: a ten-year-old male called Eigil, an eleven-year-old female called Freja, and the three-year-old female, Sif. All animals were brought to Fjord & Belt after being accidentally caught in pound nets to study methods for reducing bycatch of porpoises. A calibrated Reson TC4014 hydrophone with a sensitivity of -187 dB re 1 V/μPa (± 2 dB) between 0.5 and 180 kHz was deployed at 1 m depth. The animals were allowed to swim freely and approach the hydrophone while clicking. The signal from the hydrophone was split into two channels and digitized on a 16 bit National Instruments (NI) USB-6251 DAQ card sampling at 500 kHz. Both channels were bandpass filtered between 0.1 kHz (first order) and 150 kHz (eight order) and amplified by 40 and 60 dB, respectively, thereby increasing the dynamic range of the recording setup.

Clicks with a broadband signal-to-noise ratio (SNR) of at least 10 dB were extracted in a 10 ms window symmetric around the peak of the signal envelope using a custom-written click detector in MATLAB 7.0.1 (*The MathWorks, Inc.*). Each extracted click window was then analyzed for HF and LF components. For the HF content, the click was bandpass filtered with fourth order Butterworth low- and high-pass filters with corner frequencies (-3 dB) at 100 and 160 kHz. For the LF content, the corner frequencies of the bandpass filter (2×4 order) were set at 0.5 and 5 kHz.

The received rms level (RL_{rms}) of the LF and HF components were computed in a 2 ms window. A 5 ms window was extracted 5 ms before and after the click window, and the RL_{rms} of the three windows were calculated. The rms noise level before the click was then subtracted from the signal rms value in order to calculate the in-band SNR (signal residual) for both the HF and the LF signals. Next, we subtracted the noise rms value before the click from the noise rms value after the click to get a measure of the noise variation around the clicks (noise residual).

Click series each containing 50–200 clicks with a broadband SNR of more than 10 dB were extracted using a custom written MATLAB script (courtesy K. Beedholm). To improve the SNR, the clicks were phase aligned based on the HF component, and then averaged and subsequently bandpass filtered at 100–160 kHz and at 0.5–5 kHz.

B. Close-range recordings

The far-field recordings of individual clicks did not reveal any LF component in spite of the large dynamic range

of the recording equipment. This indicates that the LF component, if present, must have been masked by the background noise. To improve the SNR, we set up a close-range recording experiment. The study was conducted at the Fjord & Belt Centre on each of the three animals. The B&K 8101 hydrophone used in the experiment had a flat sensitivity of −184 dB re 1 V/μPa (±2 dB) in the frequency range of 0.1 Hz–70 kHz. At higher frequencies, the sensitivity drops and the receiving beam pattern is no longer omnidirectional. To compensate for this, the hydrophone was calibrated at 130 kHz relative to a Reson TC 4034, with a sensitivity of −220 dB re 1 V/μPa at 130 kHz in an anechoic tank. The sensitivity of the B&K 8101 in the horizontal plane was measured to be −193 dB re 1 V/μPa at 130 kHz matching the calibration charts in the B&K manual. The hydrophone was held on what was assumed to be the acoustic axis of the animal at a distance of 27 cm from the melon. The signals were bandpass filtered at 0.1–150 kHz (first and eight orders, respectively) and amplified by 40 or 50 dB before digitization using the 16 bit NI recorder sampling at 500 kHz.

C. Radiation beam pattern of high-frequency components

To estimate the active space[1] of the directional HF component, we set up an experiment to measure the beam pattern at larger off-axis angles than measured by Au *et al.* (1999).

The experiment was conducted during two sessions at Fjord & Belt. The male porpoise Eigil was trained to dive down and station on a plate at a depth of 1.5 m and echolocate. Four Reson TC 4034 hydrophones was mounted on a *Y*-shaped hydrophone array (Rasmussen *et al.*, 2002) with a distance of 45 cm between the center and the outer hydrophones. The array was placed 2.4 m in front of the porpoise with the center hydrophone at the same depth as the animal. The signals from the array hydrophones were bandpass filtered from 1–200 kHz and amplified 60 dB before digitization with a custom built 12 bit ADC sampling at 500 kHz. The signal from the center hydrophone was split into two channels, and one of them was relayed to a second digital recording system to maintain synchronization.

To the right side of the animal, three B&K 8101 hydrophones were suspended at 45°, 90°, and 135° relative to the body axis of the clicking animal. Together with the relayed signal from the centre hydrophone of the *Y*-shaped array, the signals from the three 8101 hydrophones were bandpass filtered from 100 Hz to 150 kHz, amplified by 50 dB and recorded with the 16 bit NI recorder sampling at 500 kHz.

The recordings were analyzed with custom written scripts in MATLAB. Due to the very narrow beam pattern of the porpoise, it is crucial only to use on-axis clicks when calculating the SL from which the directionality of off-axis clicks is defined (Madsen and Wahlberg, 2007). To ensure analysis of on-axis clicks only, a criterion was defined from the beam pattern data of Au *et al.* (1999) specifying that the received level (RL) at the center hydrophone should be at least 3 dB above the RL at any of the outer hydrophones in the *Y*-array recordings. For the levels in dB re 1 μPa$_{(pp)}$ referred to 1 m for the off-axis versions of the clicks, we use the term apparent source level (ASL), which is the backcalculated sound pressure level to 1 m of a directional sound source measured off the acoustic axis (Mohl *et al.*, 2000) When a click fulfilled the on-axis criterion, the same click was located in the off-axis recordings, and their ASLs were computed for each of the three angles.

D. Comparing analog to digital recordings

The effective dynamic range of an analog tape recorder is more than 40 dB (100 times) lower than that of a 16 bit digital recorder. Due to the large difference in sound pressure of the HF and LF component (Amundin, 1991a), an analog tape recorder should not be able to record both components on the acoustic axis of the HF component on the same channel without distortion. It can therefore be hypothesized that the often prominent LF component reported from older studies using analog tape recorders could at least in part be an artifact generated by analog recording systems, as outlined by Diercks *et al.* (1973). To test this hypothesis, we made recordings of clicks from free-swimming porpoises using a Reson TC4014 hydrophone connected to both a digital and an analog recorder via a 40 dB gain box with a first order high-pass filter at 100 Hz and an eight order 150 kHz antialiasing filter. The signal from the amplifier was split into two channels. One channel was connected to a 12 bit IO-tech Wavebook with a clip level of 2 V_{pp} and a sampling rate of 500 kHz. The other channel was connected to a Lyrec TR-47 analog tape recorder [used by Mohl and Andersen (1973)] set at 0.1 V_{pp} clip level, corresponding to a maximum recordable received level of 146 dB re 1 μPa_{pp}. The tape speed was set to 30 in./s, providing an effective recording bandwidth of 150 kHz. The analog recordings were later digitized using a 12 bit AD-link ADC sampling at 500 kHz. Finally, the digital recordings from the Wavebook and the digitized analog recordings were aligned in stereo files to compare the same clicks recorded by the two sets of recording gear.

A click with amplitude below clip level of the tape recorder was picked from the digital recording and analyzed for its frequency content. The same click from the digitized analog recordings was extracted to compare the frequency content from each recording by means of power spectra with a fast Fourier transform (FFT) size of 256 on rectangular windowed data. Next, we picked a click that was clipped from the digitized analog recordings and compared its frequency content to the same click in the digitized recording that was not clipped. We calculated the in-band SNR as well as the ratio between the noise windows before and after the signal window for 13 clicks above the clipping level of the tape recorder in the 0.5–5 kHz band as in experiment 1. Finally, we performed a Wilcoxon signed rank test on the 13 clicks to test if the signal residuals and noise residuals were significantly different from zero and hence contained any significant LF energy.

E. Recording of artificial porpoise clicks

To test if pure tone HF pulses can generate LF artifacts in analog tape recorders, we recorded artificial HF pulses at different levels on two different tape recorders, a Lyrec and a

Nagra tape recorder. Burst pulses consisting of 15 cycles at 125 kHz and a repetition rate of 66 Hz were created using an Agilent 33220A Arbitrary Waveform Generator. The signal was filtered through a B&K 1614 analog 1/3-octave filter set at a center frequency of 125 kHz, producing clicks that closely mimic porpoise clicks [Fig. 6(A)]. The signals were recorded on a Lyrec TR 47-3 tape recorder set at 2 V_{pp} clip level and 30 in./s tape speed (used by Mohl and Andersen, 1973). Four input levels of 1, 2, 4, and 8 V_{pp} were recorded. The analog tape recordings were subsequently digitized with a 12 bit AD-link ADC sampling at 500 kHz set at 10 V_{pp} clip level.

The recording of artificial porpoise clicks was repeated with a Nagra IV-D tape recorder at 15 in./s [used by Amundin, 1991a; 1991b) to record LF components of porpoise clicks]. Theoretically, this should provide a frequency response up to 75 kHz, but according to the specifications, the frequency response is limited to 16 kHz. The tape recorder was set to a clip level of 3 V_{pp}. Four input levels were recorded at 1.5, 3, 6, and 12 V_{pp} and digitized as above. The frequency content of the four input levels was compared in each of the experiments by means of power spectra with a FFT size of 256 on rectangular windowed data.

III. RESULTS AND DISCUSSION

Echolocating toothed whales emit directional and high-powered clicks to achieve sufficient echo to noise/clutter levels when engaged in biosonar-based foraging (Au, 1993). Many toothed whales therefore produce LF whistles or burst pulses to increase their active space with signals of low directionality (Tyack, 1998). Here, we conducted a series of experiments to test the hypothesis that the reported LF component of porpoise clicks has source properties suited for communication.

A. Recordings of free-swimming porpoises

Early papers by Schevill *et al.* (1969), Mohl and Andersen (1973), Amundin (1991b), and Verboom and Kastelein (1995) all reported a prominent LF component in porpoise clicks. Yet, recent papers on porpoise clicks (Au *et al.*, 1999; Kastelein *et al.*, 1999; Teilmann *et al.*, 2002; Villadsgaard *et al.*, 2006) have not reported any LF component, and we have not previously noticed a LF component from recordings with digital recording gear. The use of high-pass filters or masking by ambient LF noise can easily explain why the LF component could go unnoticed, but it is suggested that the LF component, if present, must be weak (Amundin, 1991a).

In order to quantify the LF component along with the powerful HF component, we used a 16 bit digital recording system with a theoretical dynamic range of 96 dB. This should be sufficient to handle the 40–60 dB difference in sound pressure of the two components reported by Mohl and Andersen (1973). We deployed a single, HF, low-noise hydrophone (Reson TC 4014) in a large net pen with three porpoises engaged in different types of behavior including social interactions. More than $2\frac{1}{2}$ h of recordings were made from different click trains from all three animals containing a total of some 1000 clicks with a broadband SNR of more than 10 dB. Figure 1(A) shows the waveform of the HF component (top) of the most powerful click in one of the recorded click trains, filtered between 100 and 160 kHz, and the waveform of the same click filtered between 0.5 and 5 kHz (bottom). It is seen that no LF component is apparent above the background noise, and we could not identify any LF components by simple bandpass filtering in any of the clicks recorded this way despite the large dynamic range of the recording chain [Fig. 1(B)].

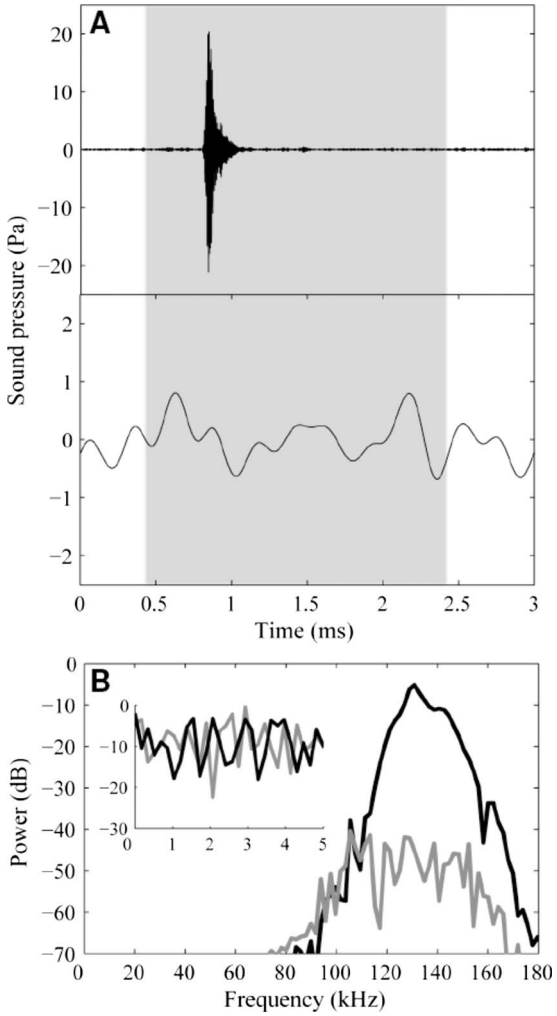


FIG. 1. (A) Waveform of a click from a free-swimming porpoise, bandpass filtered between 100 and 160 kHz (top) and between 0.5 and 5 kHz (bottom). The gray area marks the 2 ms signal window used in the data analysis. The noise windows are located 5 ms before the beginning of the gray area and 5 ms after the ending of it. (B) Power spectra of the HF filtered (100–160 kHz) and LF filtered [0.5–5 kHz (insert)] frequency content of the click (black curve) and the noise window (gray curve) 5 ms before the click window. FFT size of 256, rectangular windowed data, sampling frequency of 500 kHz.

However, a missing LF component in the few (<100) clicks analyzed individually from the recordings may be explained by the possibility that the animals may have different click types (Verboom and Kastelein, 1995; 1997) and that we by chance did not analyze any clicks containing LF components. Using a custom written click extractor in MATLAB, analysis was therefore performed on more than 1000 clicks recorded from the three animals to test for significant LF

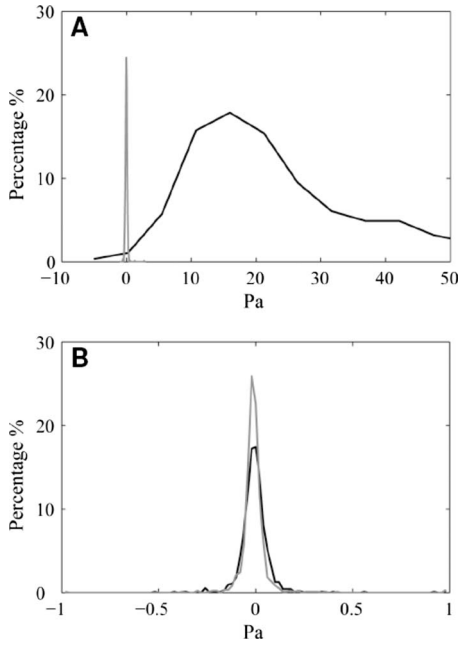


FIG. 2. Histograms of the signal (black curve) and noise residuals (gray curve) from the far-range recordings ($n=1000$). (A) is bandpass filtered between 100 and 160 kHz (binwidth of 20 mPa) and (B) bandpass filtered between 0.5 and 5 kHz (binwidth of 5.24 Pa for the signal residual and 80 mPa for the noise residual).

energy in clicks emitted in a range of different behavioral settings including foraging and socializing.

When subtracting the rms noise level in a 5 ms noise window before the click from the rms noise level of a 5 ms noise window after the click, the mean value is as expected distributed around 0 Pa for both the 0.5–5 kHz and 100–160 kHz bands [Figs. 2(A) and 2(A)]. Subtracting the rms noise level before the click from the rms pressure of a 2 ms window around the click, we get a noise-corrected HF component rms pressure with a median of 24 $Pa_{(rms)}$ (ranging from −3 to 256 Pa)^2 sound pressure in the 100 and 160 kHz band [Fig. 2(A)]. Unsurprisingly, we thus demonstrate a strong HF component [Fig. 2(A)] with received rms levels computed over a 2 ms long window up to 168 dB re 1 $\mu Pa_{(rms)}$. When doing the same for the 0.5–5 kHz band, the mean is distributed around zero [Fig. 2(B)]. No LF component can therefore be found under the ambient noise conditions (70–80 dB re 1 μPa in the 1/3-octave band around 2 kHz) given for the 1000 clicks recorded from the free-ranging porpoises at ranges from 1 to 20 m with broadband received levels between 144 and 180 dB re μPa_{pp}. Detection of the LF component may thus have been masked by the background noise in the enclosure.

If we instead ran a click detector in combination with phase-aligned click averaging, the improved SNR revealed a very weak LF component detectable some 50–60 dB_{pp} below the level of the HF component.

B. Close-range recordings of porpoise clicks

To improve the SNR and quantify the click properties of each animal, we reduced the distance from the animal to the hydrophone by stationing the animal and making it echolocate on a B&K 8101 hydrophone 27 cm in front of it. More than a thousand clicks were recorded from each of the three animals. A LF component could still not be detected in the frequency band from 0.5–5 kHz when analyzing single clicks through bandpass filtering and inspection of the waveform. Using again a click detector and phase-aligned averaging to improve the SNR, we could demonstrate a clear LF component in click trains from all three animals (Fig. 3). It consists of roughly 2 cycles at a peak frequency of ~2 kHz for all three animals (Table I). The differences in peak-peak source levels of 48–68 dB between the two components lie within the ranges reported earlier (Mohl and Andersen, 1973; Amundin, 1991b). A genuine, though very weak LF component is thus verified in porpoise echolocation clicks.

C. Radiation beam pattern of high-frequency components

Recorded on axis, the ASL of the HF component will always be higher than the LF component by at least some 50 dB (Table I), and the question is if that is also the case off axis. The high directionality of the HF component renders very little HF signal energy off axis (Au *et al.*, 1999) and it is conceivable that the LF component will be stronger in off-axis aspects and therefore serve the purpose of communication in off-axis aspects, as suggested by Mohl and Andersen (1973).

To investigate this, we measured the beam pattern for the HF component to compare the active space of the HF and LF components in porpoise clicks. Fourteen clicks out of approximately 2000 clicks passed the criteria for being recorded on the acoustic axis. The HF component was detectable at all three off-axis aspects measured. The off-axis ASLs were on average reduced by 27 dB (±5 dB std. dev.) at the 45° position, by 37 dB at the 90° position and 44 dB at the 135° position (Fig. 4). Assuming that the beam pattern is symmetrical around the acoustic axis, the data have been mirrored to cover both sides of the animal. Furthermore, Fig. 4 depicts the likely radiation of the LF component that can be assumed to have a low if any directionality given the long wavelength and the relatively small transmitting aperture of a porpoise head (Au *et al.*, 1999). Figure 4 demonstrates that the ASL of the LF component is always weaker than the HF component irrespective of aspect to the clicking animal, which could lead to the premature conclusion that the LF component can be ignored altogether from a communication standpoint. However, the two components suffer very differently from absorption and must be detected by listening porpoises at very different ambient noise levels.

To be detected, a signal must have a sufficient SNR at the receiver, and the detection of a signal is therefore limited by the ambient noise or the hearing threshold of the animal. In the following, we assume that a signal is detectable when the received signal level matches the hearing threshold at the given frequency or the ambient noise third octave band level (TOL) at that frequency if the noise TOL is higher than the hearing threshold. In our case, the relevant center frequencies are 2 and 125 kHz for the LF and HF components, respectively. The audiogram of a porpoise has been measured by Kastelein *et al.* (2002) showing that the mean hearing thresh-

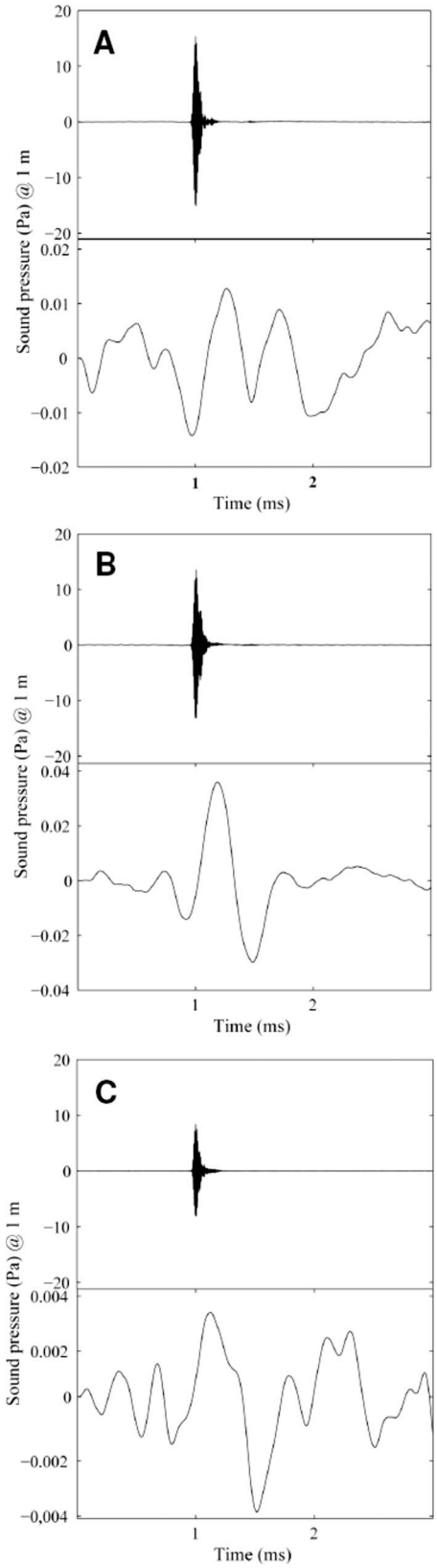


FIG. 3. Waveforms of the HF (top panel) and LF content (bottom panel) from Sif (A), Freja (B), and Eigil (C), after averaging >25 clicks to improve the SNR.

old at 2 kHz is 72 dB re 1 $\mu Pa_{(rms)}$. With an ambient noise TOL at 2 kHz of some 80 dB re 1 $\mu Pa_{(rms)}$ (comparable to the levels measured in the present experiment) at a wind speed of 5 m s^{-1} (Piggott, 1964), it seems reasonable to assume that ambient noise is often limiting detection of 2 kHz pulses. With the SLs and detection thresholds defined, we can estimate the detection ranges of the HF and LF components using the passive sonar equation (Urick, 1983).

The mean SL of 86 dB re 1 μPa_{pp} renders rms sound pressure levels that are so low relative to the ambient TOL at 2 kHz that porpoises will have to be very close to detect the LF component under prevailing ambient noise levels in shallow water. Even the highest measured LF SL of 97 dB re 1 μPa_{pp} [comparable to the 100 dB re 1 μPa reported by Schevill *et al.* (1969)] only leaves an active space of 2–3 m based on the passive sonar equation. It is therefore clear that our findings do not support the hypothesis that the LF components can serve as a useful vehicle for LF, omnidirectional communication in porpoises instead of the HF component.

The energy flux density detection threshold for the 130 kHz component lies between 22.4 and 27.4 dB re 1 μPa^2 s when the animal is pointing toward the sound source, (0° aspect) (Kastelein *et al.*, 1999). If the animal is pointing away (180° aspect) from the sound source, the threshold is likely to be raised by at least 11.7 dB (at 100 kHz) due to the lack of gain from directional hearing (Kastelein *et al.*, 2005). The source energy flux density of porpoise clicks can be estimated from their pp sound pressure SL by subtracting 51 dB (Kastelein *et al.*, 1999). Assuming spherical spreading and an absorption of 0.04 dB m (Villadsgaard *et al.*, 2006) and that the DI at 130 kHz is the same as for 100 kHz, we estimated the detection range for the 0° and 180° listening aspects for each of the five angles of the beam pattern at three different SLs of 200, 180, and 160 dB re 1 μPa_{pp} (Villadsgaard *et al.*, 2006), using a 27.4 dB re 1 μPa^2 s detection threshold (Fig. 5). Compared to other toothed whales, these SLs are low and the absorption is very high which leads to short detection ranges. The maximum range at which the clicking animal could be detected by conspecifics under the above assumptions is some 1500 m at a SL of 200 dB re 1 μPa_{pp} in 0° listening aspect (Fig. 5). A SL of 160 dB re 1 μPa_{pp} renders a detection range of around 670 m, in the on-axis direction. Due to the high directionality of the HF component, porpoises are likely to face much shorter detection ranges in daily life. Off axis at 135°, the range is reduced to about 600 m for the highest SL, while it is only 60 m for the off-axis version of a click with a SL of 160 dB re 1 μPa_{pp}.

The HF will despite the relatively short detection ranges always be more dominant compared to the LF and generate the largest active space irrespective of listening aspect to the clicking animal, and the LF component will therefore most likely not play any significant role in acoustic communication of porpoises.

The harbor porpoise is an example of a toothed whale with a small active space that does not fit into the general trend that sounds for communication are of LF and omnidirectional nature (Bradbury and Vehrencamp, 1998). The short communication ranges of some 50–1500 m in porpoises testify that these nongregarious animals, which often travel alone or in small groups, indeed have a limited capability to acoustically locate and communicate with conspe-

TABLE I. Source characteristics for each of the three animals measured in the close range recordings. (SLs) are brackcalculated to 1 m from estimated on axis measurements at 0.27 m.

Animal	Number of click trains averaged	HF SL (min/max) dB re 1 $\mu Pa_{p.p.}$	HF SL (min/max) dB re 1 $\mu Pa_{p.p.}$	HF/LF ratio (min/max)	Peak freq. of LF (std. dev.)	−10 dB BW (std. dev.)
Freja	5	152 (147/154)	89 (85/92)	63 dB (58/68)	2.3 (0.3)	9.5 (8.4)
Sif	6	140 (134/148)	87 (78/97)	53 dB (48/62)	1.8 (0.2)	7.0 (0.7)
Eigil	4	141 (140/144)	81 (77/84)	62 dB (58/68)	2.5 (0.4)	9.1 (3.6)

cifics at larger ranges. Porpoises must therefore be quite close to acoustically find conspecifics for mating, and mother-calf pairs cannot acoustically stay connected over anything but short separation distances. As long as the population density is high, such short ranges may not be a problem, though it may pose a problem to find conspecifics if the density becomes too low, e.g., due to bycatch mortality (Vinther and Larsen, 2004), possibly prolonging repopulation of low-density areas such as the Baltic Sea (Koschinski, 2002). Second, it is also clear that passive listening devices such as T-pods can only cover ranges out to significantly less than 1 km given that they have considerably higher detection thresholds (110–120 dB re 1 μPa_{pp}, Kyhn *et al.*, 2007) than the porpoises themselves. Thus, passive acoustic monitoring studies of porpoises must be designed to handle short detection ranges.

D. Comparing analog to digital recordings of porpoise clicks

The large amplitude difference of three orders of magnitude between the HF and LF components raises some potential methodological problems in relation to earlier studies using analog tape recorders. The limited dynamic range of the analog tape recorders cannot handle a +50 dB difference without clipping the HF component or burying the LF component in noise. Second, the low tape speed used in some studies in combination with the risk of clipping raised our suspicion that the LF components reported from analog recordings at least in some cases could be artifacts created in the recording chain. To investigate if some of the prominent LF components in earlier studies could have been an artifact from clipping or limited tape speed, we used the same Lyrec tape recorder that was used by Mohl and Andersen (1973) to report the first HF components as well as LF components in porpoise clicks.

Several hundred clicks with differing received levels were recorded from free-swimming porpoises. The power spectra of recorded clicks with amplitudes below clipping level did not reveal any LF component in neither the analog nor the digital recordings. However, if the amplitude of a click was above the clipping level of the tape recorder, a distortion appeared, generating significant LF energy in the analog tape recordings that could not be found in the unclipped digital recording of the same clicks. This finding is substantiated by the Wilcoxon signed rank test performed on 13 clicks above clipping level from the tape recorder. The noise residual did not deviate significantly from 0 ($P=0.8$) while the signal residual did ($P=0.0007$), verifying that it contains a strong LF component in the signal window. Thus, a powerful LF artifact in the same frequency range as the genuine LF component will be generated when clipping the analog tape recorder. This artifact becomes more prominent with the degree of clipping. This finding begs the question if the prominent LF component reported by Schevill *et al.* (1969), Mohl and Andersen (1973), Amundin (1991a), and Verboom and Kastelein (1995, 1997) at least in part could have been created as a result of artifacts from clipping.

E. Recording of artificial porpoise clicks

To test if the LF content in the clipped signals in the previous experiment was, in fact, generated as an artifact

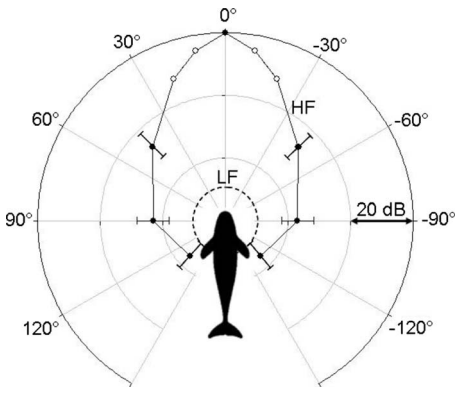


FIG. 4. Measured HF and LF beam pattern (std. dev. $< \pm 5$ dB). Open data points taken from Au *et al.* (1999).

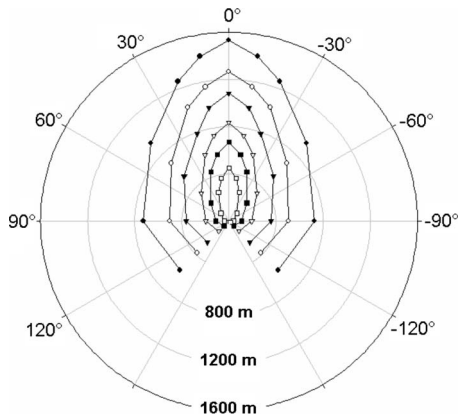


FIG. 5. Estimated detection ranges of porpoises with respect to vocalizing conspecifics based on detection thresholds derived by Kastelein *et al.* (1999). Circles=SL of 200 dB with regard to 1 $\mu Pa_{p.p.}$, triangles=SL of 180 dB with regard to 1 μPa, and squares=SL of 160 dB with regard to 1 μPa. Black and white data points define the aspect of the detecting animal relative to the source. Black: the animal is pointing toward the source; white: the animal is pointing away.

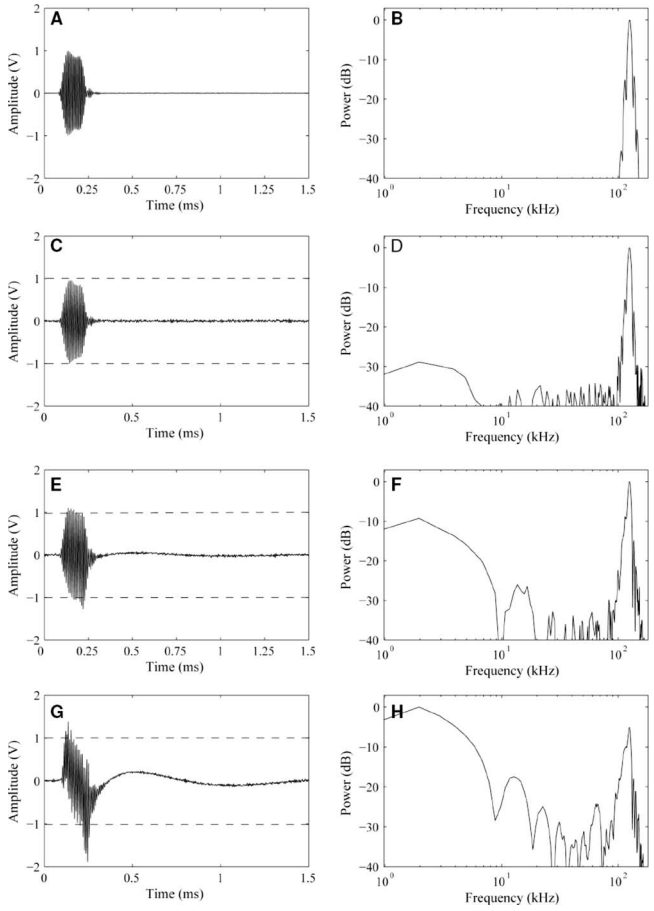


FIG. 6. [(A) and (B)] Waveform and power spectra of the artificial porpoise clicks recorded digitally and C-H recorded on the analog Lyrec tape recorder. Clipping level of the tape recorder is indicated by the punctuated lines. In (C) and (D), the input level of the signal was 0 dB with regard to clipping level of the tape recorder while (E) and (F) was 6 dB above the clipping level and (G) and (H) 12 dB above the clipping level.

from clipping the analog tape recorder, we repeated the experiment with artificial porpoise clicks with no LF content [Figs. 6(A) and 6(B)]. If LF components appeared in the spectrum, they must have been generated during the recording process. Figure 6(A) presents an artificial porpoise click and its power spectrum [Fig. 6(B)] digitized directly from the signal generation system at 500 kHz sampling rate. When this signal was fed into the tape recorder at a voltage equal to the clipping level (2 V_{pp}), the signal remains undistorted, and appears very similar to the digitized signal [Fig. 6(C)]. Slightly more LF content is seen in the power spectrum [Fig. 6(D)], but this is due to noise created by the tape recorder during recording and playback with a higher system noise floor (lower dynamic range) than in the digital system. When the input is raised to 4 V_{pp}, 6 dB above clipping level of the tape recorder, a distorted waveform appears [Fig. 6(E)]. The output amplitude of the analog click is only slightly above the 2 V_{pp} that was set as clipping level even though the input was 4 V_{pp}. In the power spectrum, a distinct LF component appeared in the frequency range from 0.1 to 10 kHz, only 10 dB below the HF component at 125 kHz [Fig. 6(F)]. If the level of the input signal is raised to 8 V_{pp}, 12 dB above clipping level, the signal becomes heavily distorted [Fig. 6(G)] and a very prominent LF component that is more powerful than the HF component appears [Fig. 6(H)]. Furthermore, several new frequency components appear in the midfrequency range from 10 to 100 kHz. Such LF artifacts are likely the result of rectification of the signal in the preamplifier of the tape recorder creating a dc-voltage component (Weber, 1963), and they start forming even when the clipped waveform appears undistorted [Fig. 6(E)].

The same experiment repeated with a Nagra IV-D tape recorder [mimicking the experiment of Amundin (1991a, 1991b)] revealed similar results except that the Nagra was not able to handle high frequencies at all regardless of whether the signal amplitude was above or below the clipping level of the tape recorder. Heavy distortion of the signal and very powerful LF components appeared at all the tested input levels. We regard that as an artifact of too low tape speed as reported by Diercks *et al.* (1973), and we infer that parts of the LF components reported in Amundin (1991a, 1991b) could have been created by this phenomenon.

Detection of clipping in an analog tape recorder can be difficult. Unlike digital recordings where clipping is easily identified if it occurs in the ADC, analog recorders smoothen the signal, and clipping becomes apparent only when the signal is heavily distorted. This makes it challenging to distinguish genuine frequency components from artifacts and can lead to erroneous classification of frequency components that are not of biological origin. Our digital recordings, however, are consistent with the LF findings of Mohl and Andersen (1973) who reported the LF component to begin shortly before the HF component. The frequency overlap of genuine and artifactual LF components raises the question of what is genuine and what is an artifact when evaluating reported LF components from studies using analog tape recorders. There is indeed a LF component of around 2 kHz in porpoise clicks (Fig. 3), though it is very weak with a pp amplitude more than 50 dB below the SL of the HF component. It is therefore hard to conceive how earlier studies using tape recorders with limited dynamic range could have avoided some level of clipping by which the genuine LF component would have been contaminated with stronger LF energy from the DC-like artifact. The present and other recent studies have not been able to reproduce the findings of other frequency peaks at 20, 30, and 60 kHz reported by Verboom and Kastelein (1995; 1997) and Kamminga and Wiersma (1981). While we cannot exclude that porpoises in some cases can produce midfrequency and LF click components, the most parsimonious explanation would suggest that they are the result of clipping [Fig. 6(H)] and that the classification of porpoise clicks on the basis of different midfrequency components (Verboom and Kastelein, 1995; 1997) is actually based on artifacts from clipping.

IV. CONCLUSIONS

We have demonstrated that the LF component of porpoise clicks is genuine, though very weak compared to the HF component. The active space of the HF component is larger irrespective of the orientation of the clicking animal with respect to listening conspecifics. That leaves us to conclude that the LF component probably plays no role in har-

bor porpoise communication. The LF component is more likely generated as a by-product from the pneumatically driven production of the HF component. In fact, the very low SL of the LF component could offer a selective advantage to harbor porpoises and other NBHF toothed whales that may suffer from a higher predation pressure when vocalizing in the hearing range of killer whales (Madsen *et al.*, 2005). Future research on NBHF species and killer whales should test such an assertion through play back experiments. We note that the difference between the HF and LF components of some 50–60 dB is comparable to the difference between LF and HF components in sperm whale usual clicks, and may therefore reflect a more general relationship for generation of LF by-products.

We have found no results supporting the existence of additional frequency components reported by Verboom and Kastelein (1997) and Kamminga and Wiersma (1981), but we can reproduce them as artifacts by clipping analog tape recorders with the HF component of porpoiselike clicks. The dynamic range of received levels from toothed whale clicks can vary by more than 80 dB (Madsen and Wahlberg, 2007) depending on directionality of the signal, where the animal is pointing its beam relative to the hydrophone, distance to the hydrophone, and changes in the SL. This put some special demands on the equipment used to record toothed whale echolocation clicks, especially with regard to dynamic range. Recent developments of relatively nonexpensive high-speed digital recording equipment with large dynamic range offer a wide range of advantages compared to the use of analog tape recorders that have been almost completely abandoned (Madsen and Wahlberg, 2007). Nevertheless, it is still important to carefully consider the properties of ultrasonic, high-powered clicks when making recordings to avoid generation of artifacts that can lead to erroneous inferences about the bioacoustics and biology of the species in question.

ACKNOWLEDGMENTS

B. Mohl, L. A. Miller, and M. Amundin provided access to equipment and gave helpful comments on the experiments and/or on previous versions of the manuscript. K. Beedholm and F. H. Jensen kindly assisted with MATLAB scripts. We thank the trainers and staff at Fjord & Belt for their help during the experiments. This work was supported by the Carlsberg Foundation and Oticon, and via a Steno Scholarship from the Danish Natural Science Research Council to PTM. All regulations for the use of experimental animals in Denmark were followed.

[1]The active space is the range within which a receiver is able to detect the signal (Bradbury and Vehrencamp, 1998).

[2]The few negative sound pressure values can be explained if one of the noise windows subtracted from the signal window by coincidence had a more powerful HF component than the signal window, e.g. from another clicking animal.

Amundin, M. (**1991a**). "Click repetition rate patterns in communicative sounds from the harbour porpoise, *Phocoena phocoena*," in *Sound Production in Odontocetes with Emphasis on the Harbour porpoise, Phocoena phocoena* (Swede AB, Stockholm).

Amundin, M. (**1991b**). "Helium effects on the click frequency-spectrum of the harbor porpoise, *Phocoena phocoena*," J. Acoust. Soc. Am. **90**, 53–59.

Andersen, S., and Amundin, M. (**1976**). "Possible predator related adaptation of sound production and hearing in the harbour porpoise," Aquat. Mamm. **4**, 55–56.

Au, W. W. L. (**1993**). *The Sonar of Dolphins* (Springer, New York).

Au, W. W. L. (**1997**). "Echolocation in dolphins with a dolphin-bat comparison," Bioacoustics 8.

Au, W. W. L., Kastelein, R. A., Rippe, T., and Schooneman, N. M. (**1999**). "Transmission beam pattern and echolocation signals of a harbor porpoise (*Phocoena phocoena*)," J. Acoust. Soc. Am. **106**, 3699–3705.

Bradbury, J. W., and Vehrencamp, S. L. (**1998**). *Principles of Animal Communication* (Sinauer Associates, Inc., Sunderland, MA.).

Diercks, K. J., Trochta, R. T., and Evans, W. E. (**1973**). "Delphinid sonar—measurement and analysis," J. Acoust. Soc. Am. **54**, 200–204.

Dubrovskii, N. A., Krasnov, P. S., and Titov, A. A. (**1971**). "Emission of echo-location signals by Azov-Sea harbor porpoise," Sov. Phys. Acoust. **16**, 444–447.

Dusenbery, D. B. (**1992**). *Sensory Ecology: How Organisms Acquire and Respond to Information* (W. H. Freeman and Co, New York).

Fletcher, N. H. (**2004**). "A simple frequency-scaling rule for animal communication," J. Acoust. Soc. Am. **115**, 2334–2338.

Janik, V. M. (**2005**). "Underwater acoustic communication networks in marine mammals," in *Animal Communication Networks*, edited by P. K. McGregor (Cambridge University Press, Cambridge).

Kamminga, C., and Wiersma, H. (**1981**). "Investigations on cetacean sonar II: Acoustical similarities and differences in Odontocete sonar signals," Aquat. Mamm. **8**, 41–62.

Kastelein, R. A., Au, W. W. L., Rippe, H. T., and Schooneman, N. M. (**1999**). "Target detection by an echolocating harbor porpoise (*Phocoena phocoena*)," J. Acoust. Soc. Am. **105**, 2493–2498.

Kastelein, R. A., Bunskoek, P., Hagedoorn, M., Au, W. W. L., and de Haan, D. (**2002**). "Audiogram of a harbor porpoise (*Phocoena phocoena*) measured with narrow-band frequency-modulated signals," J. Acoust. Soc. Am. **112**, 334–344.

Kastelein, R. A., Verboom, W. C., and de Haan, D. (**2005**). "Receiving beam patterns in the horizontal plan of a horbor porpoise (*Phocoena phocoena*)," J. Acoust. Soc. Am. **118**, 1172–1179.

Koschinski, S. (**2002**). "Current knowledge on harbour porpoises (*Phocoena phocoena*) in the Baltic Sea," Ophelia, Stenstrup, Denmark, **55**, 167–197.

Lammers, M. O., Au, W. W. L., and Herzing, D. L. (**2003**). "The broadband social acoustic signaling behavior of spinner and spotted dolphins," J. Acoust. Soc. Am. **114**, 1629–1639.

Madsen, P. T., Carder, D. A., Bedholm, K., and Ridgway, S. H. (**2005**). "Porpoise clicks from a sperm whale nose—Convergent evolution of 130 kHz pulses in toothed whale sonars?," Bioacoustics **15**, 195–206.

Madsen, P. T., Payne, R., Kristiansen, N. U., Wahlberg, M., Kerr, I., and Mohl, B. (**2002b**). "Sperm whale sound production studied with ultrasound time/depth-recording tags," J. Exp. Biol. **205**, 1899–1906.

Madsen, P. T., and Wahlberg, M. (**2007**). "Recording and quantification of ultrasonic echolocation clicks from free-ranging toothed whales," Deep-Sea Res., Part I **54**, 1421–1444.

Madsen, P. T., Wahlberg, M., and Mohl, B. (**2002a**). "Male sperm whale (*Physeter macrocephalus*) acoustics in a high-latitude habitat: implications for echolocation and communication," Behav. Ecol. Sociobiol. **53**, 31–41.

Mohl, B., and Andersen, S. (**1973**). "Echolocation-high-frequency component in click of harbor porpoise (*Phocoena-Ph. L.*)," J. Acoust. Soc. Am. **54**, 1368–1372.

Mohl, B., Wahlberg, M., Madsen, P. T., Heerfordt, A., and Lund, A. (**2003**). "The monopulsed nature of sperm whale clicks," J. Acoust. Soc. Am. **114**, 1143–1154.

Mohl, B., Wahlberg, M., Madsen, P. T., Miller, L. A., and Surlykke, A. (**2000**). "Sperm whale clicks: Directionality and source level revisited," J. Acoust. Soc. Am. **107**, 638–648.

Morisaka, T., and Connor, R. C. (**2007**). "Predation by killer whales (*Orcinus orca*) and the evolution of whistle loss and narrow-band high frequency clicks in odontocetes," J. Exp. Biol. **20**, 1439–1458.

Piggott, C. L. (**1964**). "Ambient sea noise at low frequencies in shallow water of Scotian Shelf," J. Acoust. Soc. Am. **36**, 2152–2163.

Rasmussen, M. H., Miller, L. A., and Au, W. W. L. (**2002**). "Source levels of clicks from free-ranging white-beaked dolphins (*Lagenorhynchus albirostris* Gray 1846) recorded in Icelandic waters," J. Acoust. Soc. Am. **111**, 1122–1125.

Schevill, W. E., Watkins, W. A., and Ray, C. (**1969**). "Click structure in porpoise, *Phocoena phocoena*," J. Mammal. **50**, 721–728.

Szymanski, M. D., Bain, D. E., Kiehl, K., Pennington, S., Wong, S., and

Henry, K. R. (**1999**). "Killer whale (*Orcinus orca*) hearing: Auditory brainstem response and behavioral audiograms," J. Acoust. Soc. Am. **106**, 1134–1141.

Teilmann, J., Miller, L. A., Kirketerp, T., Kastelein, R. A., Madsen, P. T., Nielsen, B. K., and Au, W. W. L. (**2002**). "Characteristics of echolocation signals used by a harbour porpoise (*Phocoena phocoena*) in a target detection experiment," Aquat. Mamm. **28**, 275–284.

Tyack, P. (**1998**). "Acoustic communication under the sea," in *Animal Acoustic Communication. Sound Analysis and Research Methods*, edited by S. L. Hopp, M. J. Owren, and C. S. Evans (Springer, New York).

Tyack, P. L., and Clark, C. W. (**2000**). "Communication and acoustic behavior of dolphins and whales," in *Hearing by Whales and Dolphins*, edited by W. W. L. Au, A. N. Popper, and R. R. Fay (Springer-Verlag, New York), pp. 156–224.

Urick, R. J. (**1983**). *Principles of Underwater Sound* (McGraw-Hill, New York).

Verboom, W. C., and Kastelein, R. A. (**1995**). "Acoustic signals by harbour porpoises (*Phocoena phocoena*)," in *Harbour porpoises-Laboratory Studies to Reduce Bycatch*, edited by P. E. Nachtigall, J. Lien, W. W. L. Au, and A. Read (De Spil, Woerden), pp. 1–39.

Villadsgaard, A., Wahlberg, M., and Tougaard, J. (**2006**). "Echolocation signals of wild harbour porpoises, *Phocoena phocoena*," J. Exp. Biol. **210**, 56–64.

Vinther, M., and Larsen, F. (**2004**). "Updated estimates of harbour porpoise (*Phocoena phocoena*) bycatch in the Danish North Sea bottom-set gillnet fishery," J. Cetacean Res. Manage. **6**, 19–24.

Weber, P. J. (**1963**). *The Tape Recorder as an Instrumentation Device* (Ampex Corporation).

Zimmer, W. M. X., Madsen, P. T., Teloni, V., Johnson, M. P., and Tyack, P. L. (**2005a**). "Off-axis effects on the multipulse structure of sperm whale usual clicks with implications for sound production," J. Acoust. Soc. Am. **118**, 3337–3345.

Zimmer, W. M. X., Tyack, P. L., Johnson, M. P., and Madsen, P. T. (**2005b**). "Three-dimensional beam pattern of regular sperm whale clicks confirms bent-horn hypothesis," J. Acoust. Soc. Am. **117**, 1473–1485.

Modified variance ratio for objective detection of transient evoked potentials in bottlenose dolphins (*Tursiops truncatus*)

James J. Finneran
U.S. Navy Marine Mammal Program Space and Naval Warfare Systems Center, San Diego, Code 71510, 53560 Hull Street, San Diego, California 92152

(Received 7 December 2007; revised 4 August 2008; accepted 2 September 2008)

Evoked potential studies have often relied on one or more human observers to visually assess the averaged waveforms and decide if a response is present. Although simple and easy to implement, response detection strategies based on human observers are inherently subjective and depend on the observers' experience and biases. To avoid these shortcomings, some recent marine animal studies utilizing auditory steady-state responses have applied frequency-domain, statistically based objective detection methods; however, statistically based objective methods have not yet been applied to marine animal tests involving transient evoked responses, which are normally analyzed in the time domain. The present study applied a modified version of the variance ratio F_{SP} to determine the presence or absence of evoked responses in two bottlenose dolphins (*Tursiops truncatus*) stimulated with tone pips. The appropriate degrees of freedom for the statistical tests were empirically determined in four dolphins. The modified variance ratio was found to be a useful tool and to provide an objective statistical approach for the detection of transient evoked potentials. [DOI: 10.1121/1.2996320]

PACS number(s): 43.80.Lb, 43.64.Ri [MCH] Pages: 4069–4082

I. INTRODUCTION

Auditory evoked potential (AEP) measurements have become increasingly popular as alternatives to more traditional psychophysical methods for investigating hearing in marine mammals (Dolphin, 2000; Supin *et al.*, 2001a). AEPs consist of characteristic changes in the electroencephalogram that are time locked to a sound stimulus and thus represent the effects of sound on the neural activity within the auditory pathway (Eggermont, 2007). AEP methods therefore do not rely on a conditioned behavioral response by the subject and may be used with animals not normally kept under human care, in animals for whom access is limited, and in those individuals for whom specific training for a behavioral hearing test is not practical. These advantages have enabled AEP methods to be applied to novel species (Nachtigall *et al.*, 2005; Cook *et al.*, 2006; Nachtigall *et al.*, 2007) and to a much larger number of subjects than those tested using behavioral techniques (Houser and Finneran, 2006b).

Marine mammal AEP investigations have used a variety of sound stimuli, including clicks (e.g., Bullock and Ridgway, 1972; Ridgway *et al.*, 1981; and Popov and Supin, 1985), tone pips (e.g., Bullock *et al.*, 1968; Popov and Supin, 1985; Popov and Supin, 1990; Szymanski *et al.*, 1999; and Wolski *et al.*, 2003), and sinusoidally modulated tones (e.g., Dolphin *et al.*, 1995; Supin and Popov, 1995; Dolphin, 1996; Supin and Popov, 2000; Nachtigall *et al.*, 2005; Yuen *et al.*, 2005; Finneran *et al.*, 2007a; and Finneran *et al.*, 2007b). Clicks and tones pips produce relatively large amplitude transient responses, while sinusoidal amplitude or frequency modulated tones evoke the auditory steady-state response (ASSR), also known as the envelope following response (Dolphin and Mountain, 1992). The ASSR is produced when stimuli are presented at a sufficient rate so that the individual transient responses overlap and produce a steady-state signal (Stapells *et al.*, 1984; Supin *et al.*, 2001b). Measurement of the ASSR has become a popular approach because the sinusoidally modulated stimuli may be relatively narrowband, the responses may be analyzed in the frequency domain (which helps reduce the influence of low-frequency physiological background noise), and there are relatively simple methods to objectively determine the presence or absence of the evoked response within the physiological background noise (Dobie and Wilson, 1993, 1996; Finneran *et al.*, 2007a).

Although the ASSR has become the method of choice for frequency-specific audiometry, for some applications, the use of clicks or tone-pip stimuli, and thus measurement of transient evoked potentials, is advantageous. Clicks and tone pips possess broad frequency content and give rise to relatively large evoked responses and may be used to assess hearing over a broad frequency range or to increase the ability to discern responses in difficult to test (e.g., very large) subjects (e.g., Ridgway and Carder, 2001; Houser *et al.*, 2007; and Nachtigall *et al.*, 2007). Evoked potential studies of dolphin echolocation necessarily involve transient responses since the acoustic stimuli consist of the subject's own outgoing clicks and/or returning echoes and are therefore short duration clicks (e.g., Supin *et al.*, 2003; Supin *et al.*, 2004; and Supin *et al.*, 2006).

Transient AEPs are normally analyzed in the time domain rather than the frequency domain. These analyses have often relied on visual inspection of averaged waveforms by a human observer to subjectively determine the presence or absence of individual waveform peaks (e.g., Arnold, 1985; Ahroon *et al.*, 1993; Sininger, 1993; Ahroon *et al.*, 1996; Kenyon *et al.*, 1998; Scholik and Yan, 2001; Smith *et al.*, 2004; Vidler and Parker, 2004; Lovell *et al.*, 2005a; Lovell *et*

al., 2005b; Hamernik *et al.*, 2007; Popper *et al.*, 2007; and Qiu *et al.*, 2007). To facilitate this task, waveforms are often replicated and overlaid; replication of specific peaks in multiple waveforms adds confidence that a true response is present, while the lack of replication of any peaks indicates high residual noise and/or spurious activity. In some cases, multiple observers may be employed in the assumption that a decision reached by multiple observers is more likely to be correct. Although commonly applied, techniques based on visual observation are inherently subjective and thus performance depends on the observers' experience and any existing biases. The subjective limitations of the visual approach may be avoided by using correlation or template matching procedures (Schimmel *et al.*, 1974; Mason *et al.*, 1977; Weber and Fletcher, 1980; Supin *et al.*, 2001a); however, these methods suffer from arbitrary response criteria and provide no way to distinguish spurious replications of peaks from correlations between actual responses (correlation) or rely on *a priori* knowledge of the true response waveform (template matching).

Statistically based response detection methods improve upon the template matching and correlation methods by not only providing an objective means of determining the presence or absence of a response but also by enabling one to state with a certain degree of statistical certainty that the averaged response waveform contains time-locked activity representing an evoked potential (Elberling and Don, 2007). The most common time-domain statistical approaches rely on the calculation of a variance ratio whose numerator is the variance of the averaged waveform over some time interval and whose denominator is some measure of the variance of the physiological background noise. Since variance ratios are statistically F distributed, the variance ratio may be tested for significance using standard tables for the F statistic with the appropriate degrees of freedom.

This paper discusses the application of the variance ratio method to the detection of transient evoked potentials recorded from bottlenose dolphins (*Tursiops truncatus*). The variance ratio calculation is based on the method developed by Elberling and Don (1984), as modified by Stürzebecher *et al.* (2001). The variance ratio calculation and method of background noise estimation are first presented, followed by the method used to empirically determine the appropriate degrees of freedom for significance testing. Finally, the variance ratio method is used to determine the presence or absence of evoked responses and estimate hearing thresholds to tone-pip stimuli in dolphins. Some of the advantages and practical limitations of the variance ratio method are also discussed.

II. BACKGROUND: MODIFIED VARIANCE RATIO

Models for recorded evoked potentials usually assume the form

$$S(t) = \mathrm{EP}(t) + \mathrm{BN}(t), \tag{1}$$

where the measured electrode signal $S(t)$ consists of the sum of the evoked potential, $\mathrm{EP}(t)$, and the background noise $\mathrm{BN}(t)$ (Elberling and Don, 1984). If the evoked potential is assumed to be a deterministic signal and the background noise a stationary random signal, then, after ensemble averaging over N sweeps, Eq. (1) becomes

$$\overline{S(t)} = \mathrm{EP}(t) + \overline{\mathrm{BN}(t)}, \tag{2}$$

where the averaged signal, $\overline{S(t)}$, consists of the true evoked potential plus the averaged background noise $\overline{\mathrm{BN}(t)}$.

The variance ratio used for significance testing, F, is defined as

$$F = \frac{\mathrm{VAR}[\overline{S(t)}]}{\mathrm{VAR}[\overline{\mathrm{BN}(t)}]}, \tag{3}$$

where VAR indicates the variance. Although the calculation of $\mathrm{VAR}[\overline{S(t)}]$ is straightforward, estimating $\mathrm{VAR}[\overline{\mathrm{BN}(t)}]$ is more complicated. The averaged background noise $\overline{\mathrm{BN}(t)}$ may be theoretically obtained from a measurement of $\overline{S(t)}$ in the absence of the stimulus; however, this requires a second measurement and there is no guarantee that the noise parameters are identical between the stimulus and no-stimulus conditions. Alternately, $\mathrm{VAR}[\overline{\mathrm{BN}(t)}]$ may be estimated by calculating the variance of the averaged waveform over a period of time before the stimulus onset, though again this assumes that the noise parameters from the prestimulus period are identical to those from the stimulus period (Elberling and Don, 1984), and this approach may require a longer sweep than otherwise necessary. Wong and Bickford (1980) proposed estimating $\mathrm{VAR}[\overline{\mathrm{BN}(t)}]$ via a process called "plus-minus averaging," where the ensemble averaging process is repeated with every other sweep inverted (or the average of half the sweeps subtracted from the other half) (Schimmel, 1967). This cancels the deterministic evoked potential and leaves the averaged background noise.

Elberling and Don (1984) proposed an alternative approach where the variance in the averaged background noise is estimated from the sweep-to-sweep variance of the amplitude at a single time point, VAR(SP), divided by the number of sweeps. Because the noise estimate is based on the sweep-to-sweep variance at a single point, Elberling and Don (1984) labeled this variance ratio F_{SP}:

$$F_{\mathrm{SP}} = \frac{\mathrm{VAR}[\overline{S(t)}]}{\mathrm{VAR(SP)}/N}, \tag{4}$$

where N is the number of sweeps. The advantage of this approach is that it does not require waveform subtraction and the noise estimate arises from the same sweeps and over the same time frame as the response. Because VAR(SP) does not estimate the variance of the background noise with sufficient accuracy for N less than a few hundred sweeps, Stürzebecher *et al.* (2001) introduced the modified variance ratio, denoted here as F^*, where the variance of the averaged background noise was estimated by calculating the sweep-to-sweep variance at multiple time points, then averaging the results to yield a single average variance.

For statistical significance testing, F^* is compared to the critical value $F_{\alpha(v_1,v_2)}$, where α is the significance level and v_1 and v_2 are the degrees of freedom. If $F^* > F_{\alpha(v_1,v_2)}$ the response is considered to be detected. The degrees of freedom in the denominator, v_2, equals the number of sweeps N.

For background noise possessing a relatively narrow band of dominant frequencies (i.e., nonwhite noise), which includes the physiological noise associated with evoked potential measurements, the degrees of freedom in the numerator, v_1, must be estimated from empirical measurements (Elberling and Don, 1984). This entails calculating F^* from measurements made in the absence of a stimulus and estimating v_1 from the theoretical F-distribution $F_{(v_1,N)}$ that provides the best fit to the data (Elberling and Don, 1984).

III. METHODS

A. Subjects

Four bottlenose dolphins participated in the study: BOB (male, 28 years, 250 kg), HEP (male, 42 years, 250 kg), TYH (male, 25 years, 200 kg), and WEN (male, 23 years, 200 kg). Previous ASSR threshold measurements revealed "normal" hearing in TYH and WEN but significant high-frequency (>40 kHz) hearing loss in BOB and HEP (Houser and Finneran, 2006b). All four subjects were used to estimate the degrees of freedom v_1 while threshold measurements were only conducted with BOB and TYH. All subjects were housed in floating enclosures in San Diego Bay, CA.

B. Evoked potential measurements

Evoked potential measurements were conducted in air with each subject resting on a foam mat. Sounds were presented to the subject using a "jawphone"—a piezoelectric sound projector (ITC 1042) embedded in a silicon suction cup—attached to the subject's left jaw in the pan region (the site of high-frequency sound reception in dolphins). Received sound pressure levels (SPLs) were estimated from underwater direct field measurements with a calibrated hydrophone (B&K 8105) placed 15 cm from the jawphone face (see Finneran and Houser, 2006 for details). In-air evoked potential thresholds measured with jawphones calibrated in this fashion have provided reasonable approximations to underwater behavioral thresholds (in five dolphins), especially with respect to audible bandwidth (Finneran and Houser, 2006; Houser and Finneran, 2006a). The primary intent of the present study is to demonstrate an objective response detection technique for transient evoked potentials; thus the specific calibration methods are of secondary importance and the received levels cited here should be considered approximate. Estimated received levels are presented in terms of the peak-equivalent SPL (peak-peak), denoted here as ppeSPL to avoid confusion (Burkard, 1984). The ppeSPL of a transient is the (rms) SPL of a continuous sine wave having the same peak-peak amplitude as the measured transient; it is equivalent to the peak-peak SPL −9 dB.

Stimulus generation and evoked response recording were performed using the EVREST software (Finneran, 2008) running on a rugged notebook computer with a multifunction data acquisition board (National Instruments NI PCI-6251). Stimuli were digitally generated, then converted to analog at a rate of 1 MHz with 16 bit resolution. Analog signals were then passed through a custom programmable attenuator (0–70 dB attenuation), filtered (Krohn-Hite 3C series, bandpass, eight-pole Butterworth, 0.2–150 kHz), and applied to the jawphone.

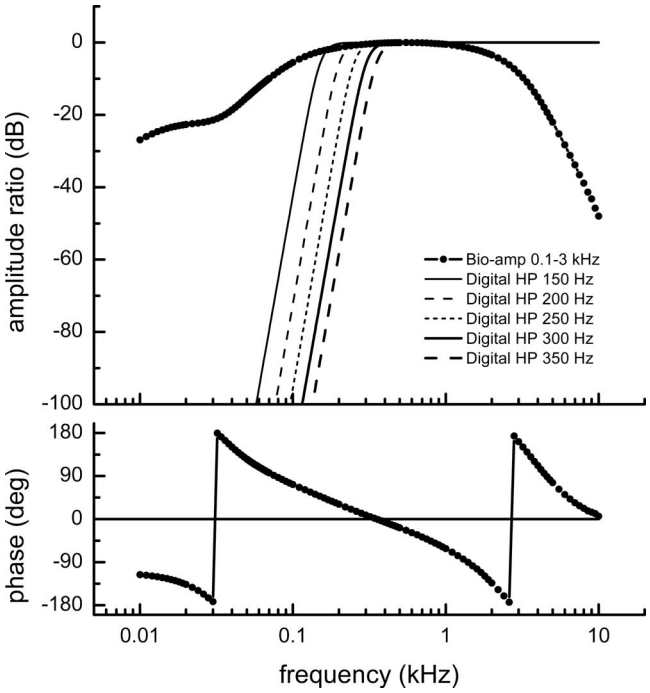


FIG. 1. Frequency response of the analog and digital filters used with the evoked response recordings. Bio-amp, biopotential amplifier analog bandpass filter; digital HP, digital high-pass, zero-phase filter with a −6 dB cutoff at 100, 150, 200, 250, 300, or 350 Hz and a rolloff of 72 dB/octave.

Evoked potentials were measured using 10 mm gold cup electrodes embedded in suction cups and attached to the subject using conductive paste. Three electrodes were used: the noninverting electrode was placed 5–10 cm behind the blowhole near the midline; the inverting electrode was placed along the midline, approximately 25 cm posterior to the noninverting electrode; and the ground electrode was placed on the dorsal fin. The electrode signals were input to a biopotential amplifier (Grass ICP-511) that amplified ($\times 10^5$) and bandpass filtered (0.1–3 kHz, see Fig. 1) the difference between the noninverting and inverting electrodes. The biopotential amplifier output was digitized (PCI-6251) at a rate of 20 kHz (BOB, HEP, and TYH) or 10 kHz (WEN) with 16-bit resolution. Data were acquired in 16 ms sweeps synchronized with the stimulus onset. Sweeps with a peak amplitude >20 μV were excluded from further analysis. *Post hoc* high-pass digital filtering was performed using a zero-phase filter with a −6 dB cutoff at either 150, 200, 250, 300, or 350 Hz and a rolloff of 72 dB/octave (Fig. 1).

C. Estimating the degrees of freedom

To estimate the degrees of freedom (v_1), 300 blocks of data were acquired in the absence of a sound stimulus, following the method described by Elberling and Don (1984). For analyses employing *post hoc* digital filtering, the time interval chosen for analysis was 1–8 ms, based on the time interval over which transient evoked responses were observed in preliminary testing using tone pips (see Sec. III D). For analyses using only the bandpass filter within the biopotential amplifier, the analysis window was extended to 0–10

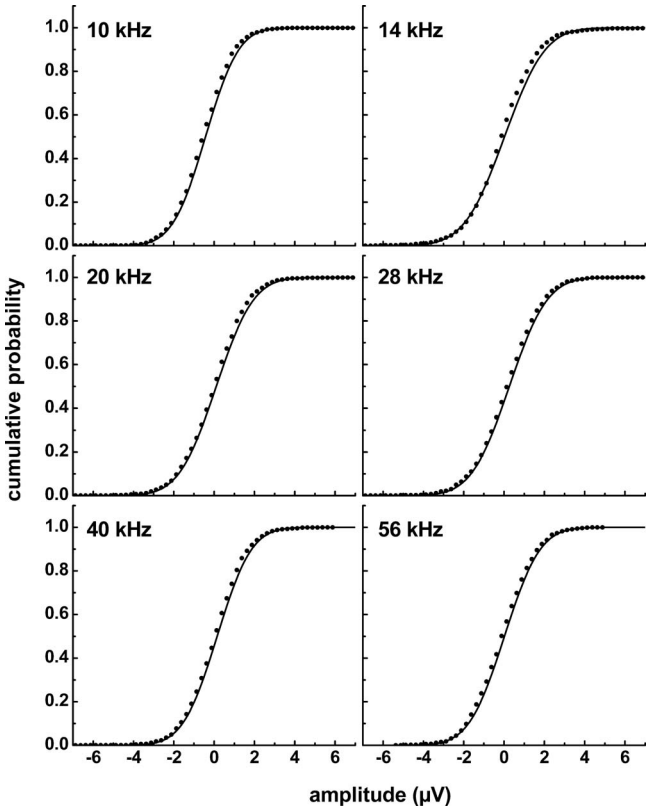


FIG. 2. Relationship between sweep-to-sweep variance and normal distributions. The symbols show the cumulative distributions of single point amplitudes from 2048 sweeps collected from TYH using tone-pip stimuli at ppeSPLs of 120 dB re 1 μPa. The solid lines represent normal distributions with mean and SD calculated from the data.

ms. The number of sweeps in each block was 192.

For each block, the modified variance ratio F^* was computed using

$$F^* = \frac{\mathrm{VAR}[\overline{S(t)}]}{\frac{1}{M}\sum_{m=1}^{M} \mathrm{VAR}(\mathrm{SP}_m)/N}, \tag{5}$$

where M is the number of time points for the calculation of the sweep-to-sweep variance and N is the number of sweeps in each block. The sweep-to-sweep variance $\mathrm{VAR}(\mathrm{SP}_m)$ was computed at $M=4$ equally spaced points using

$$\mathrm{VAR}(\mathrm{SP}_m) = \frac{1}{N-1}\sum_{n=1}^{N} [S_n(t_m) - \overline{S(t_m)}]^2, \tag{6}$$

where $\overline{S(t_m)}$ is the amplitude of the averaged waveform at time t_m. The specific time latencies were 2.4, 3.8, 5.2, and 6.6 ms for the 1–8 ms analysis window and 2, 4, 6, and 8 ms for the 0–10 ms analysis window.

Nonlinear regression (OriginLab Corporation, 2007) was used to fit the theoretical F-distribution $F_{(v_1,N)}$ to the cumulative distribution of the F^* values. The process was performed for each subject with and without digital high-pass filtering. The degrees of freedom v_1 was the fitting parameter and N (the number of sweeps in each block) was fixed at 192. Best-fit results for specific filter settings were averaged to produce estimates of v_1 for use in threshold testing.

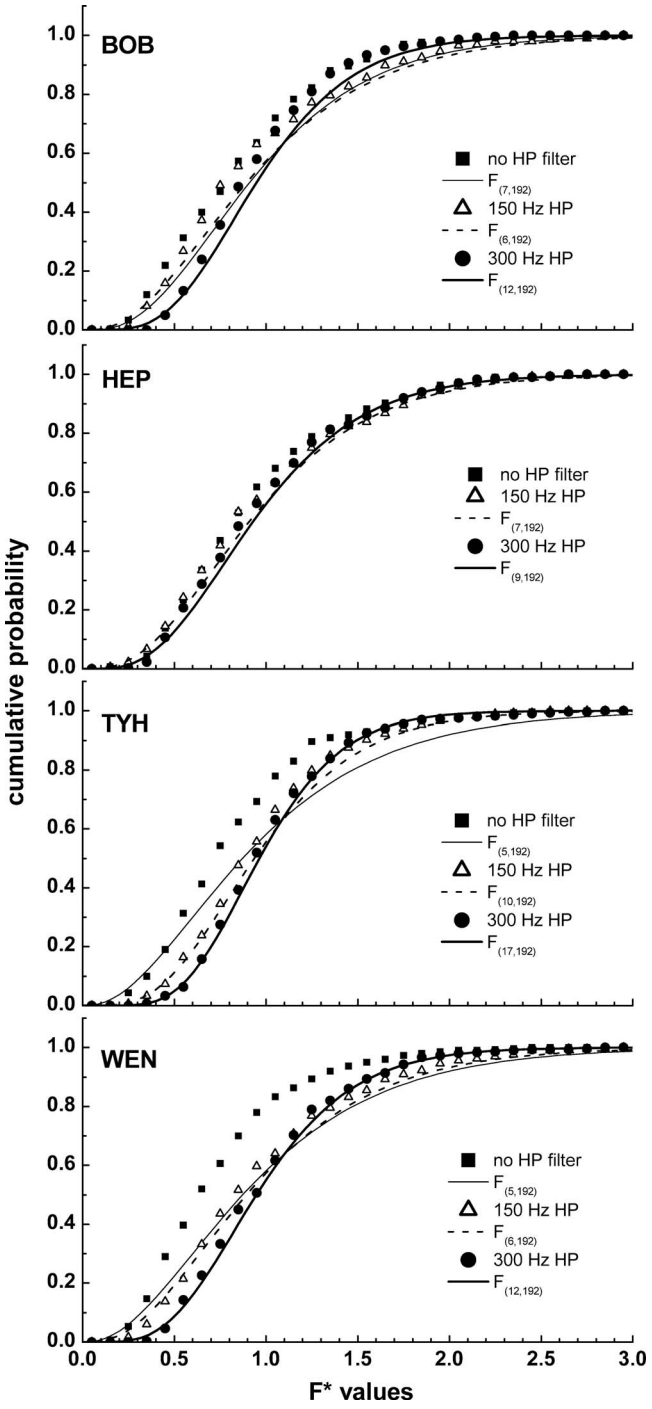


FIG. 3. Examples of curve fits to estimate the degrees of freedom for subjects BOB, HEP, TYH, and WEN. The symbols indicate the cumulative distributions of F^* calculated from recordings made in the absence of sound stimuli. Distributions of F^* are based on 300 blocks, each with 192 sweeps. The analysis windows were 1–8 ms, except for the no filter condition, which used a 0–10 ms analysis window. The lines show the theoretical F-distributions that best fit the data. The fitting parameters are presented in Table I.

D. Threshold testing

The sound stimulus for threshold testing consisted of a sinusoidal tone pip with a five-cycle duration: a two-cycle

TABLE I. Results of fitting theoretical F-distributions to cumulative distributions of F^*. The fitting function was $F_{(v_1,192)}$. The values of v_1 are rounded to the nearest integer. The "worst-case" estimates are based on the mean—2SD.

	Digital high-pass filter											
	None		150 Hz		200 Hz		250 Hz		300 Hz		350 Hz	
	v_1	R^2	v_1	R^2	v_1	R^2	v_1	R^2	v_1	R^2	v_1	R^2
BOB	7	0.960	6	0.986	7	0.975	10	0.984	12	0.990	16	0.994
HEP	7	0.988	7	0.996	7	0.995	8	0.996	9	0.997	10	0.996
TYH	5	0.933	10	0.994	14	0.997	16	0.998	17	0.999	19	0.998
WEN	5	0.876	6	0.994	9	0.991	10	0.995	12	0.998	16	0.996
Mean	6		7		9		11		12		15	
(SD)	(1.2)		(2.1)		(3.2)		(3.4)		(3.2)		(3.6)	
Worst case estimate	4		3		2		4		6		8	

linear rise, a one-cycle plateau, and a two-cycle linear fall; these stimuli are sometimes referred to as "2-1-2 tone pips." Tone pips were presented at a rate of approximately 60/s. Center frequencies were 10, 14, 20, 28, 40, and 56 kHz (BOB) and 10, 20, 40, 80, and 160 kHz (TYH).

The stimulus ppeSPL began at 120 dB re 1 μPa and was adjusted up or down in 10 dB steps based on visual detection of the evoked potential in the averaged response. After the threshold was bracketed in this manner, additional measurements were made using a 5 dB spacing to improve the resolution near threshold. At each stimulus level, averaged waveforms were based on 2048 sweeps.

Each waveform was digitally high pass filtered at 300 Hz before calculating the peak-peak amplitude and F^* over the time interval from 1 to 8 ms. The filter cutoff at 300 Hz was selected during preliminary measurements based on visual detection of response waveforms. The F^* calculation was identical to that performed for estimating v_1, except the number of sweeps $N=2048$. The value of F^* for each recording was compared to the critical value $F^*_{\text{crit}}=F_{\alpha(v_1,2048)}$ for $\alpha=0.01$ and 0.05; the value of v_1 was based on the results of fitting theoretical F-distributions to cumulative distributions of F^* obtained without sound stimuli. Evoked potentials with $F^*>F^*_{\text{crit}}$ were considered to be detected at the appropriate level of significance (α). Thresholds were defined as the mean of the SPLs corresponding to the lowest detection and the next highest nondetection. Detection thresholds were also calculated with digital high-pass filter cutoffs at 150, 200, 250, and 350 Hz to examine the influence of the filter on the resulting thresholds.

IV. RESULTS

Normally distributed background noise is one of the fundamental assumptions in the variance ratio method. To test this assumption, the distributions of single point amplitudes were examined in TYH and BOB. Figure 2 provides some examples of cumulative distributions of single point amplitudes from 2048 sweeps collected from BOB during tone-pip stimulation at various frequencies. The agreement between the experimental data and cumulative normal distributions indicates that the assumption of normally distributed background noise is reasonable for these data.

Figure 3 shows the cumulative distributions of F^* and curve-fitting results for each subject. Curve fits (Table I) were good when digital high-pass filtering was performed; however, the fits were noticeably worse when using only the 100 Hz high pass filter within the biopotential amplifier, especially for TYH and WEN. As the amount of low-frequency components decreased (with additional high-pass filtering), the values for the best-fit degrees of freedom v_1 increased. To avoid estimating v_1 for individual test runs, Elberling and Don (1984) used the lower 2SD boundary to yield a single "worst-case" value. For the present study, this approach resulted in v_1 ranging from 2 to 8. For $N=2048$ (the number of sweeps in threshold testing), the critical values for F^* ranged from 1.9 to 3.0 ($\alpha=0.05$) and from 2.5 to 4.6 ($\alpha=0.01$).

To examine the influence of the number of sweeps per block (N) and the number of sweep-to-sweep amplitude values (M) on the degrees of freedom (v_1), v_1 was estimated for a single subject (HEP) with N varied from 64 to 256 and M varied from 1 to 4. The results (Fig. 4) showed that the v_1 estimates tended to converge when the number of sweeps per block was greater than ~128 when $M>1$. For $M=1$, the v_1 estimates were more variable even with several hundred sweeps. This provides some justification for using the modified variance ratio technique for the estimates of v_1 since the number of sweeps was only 192. For threshold testing, 2048

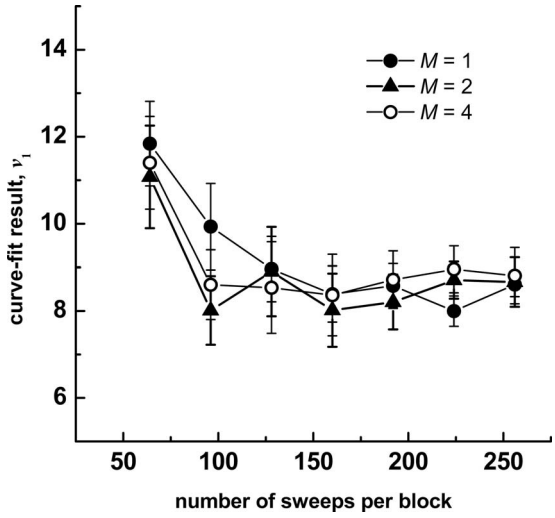


FIG. 4. Influence of the number of sweeps per block (N) and number of sweep-to-sweep amplitudes (M) on the estimates for the degrees of freedom (v_1). Data are from HEP, with 300 blocks of 64–256 sweeps and *post hoc* digital high-pass filtering at 300 Hz. There was little change in v_1 when the number of sweeps per block was greater than ~128 when $M>1$.

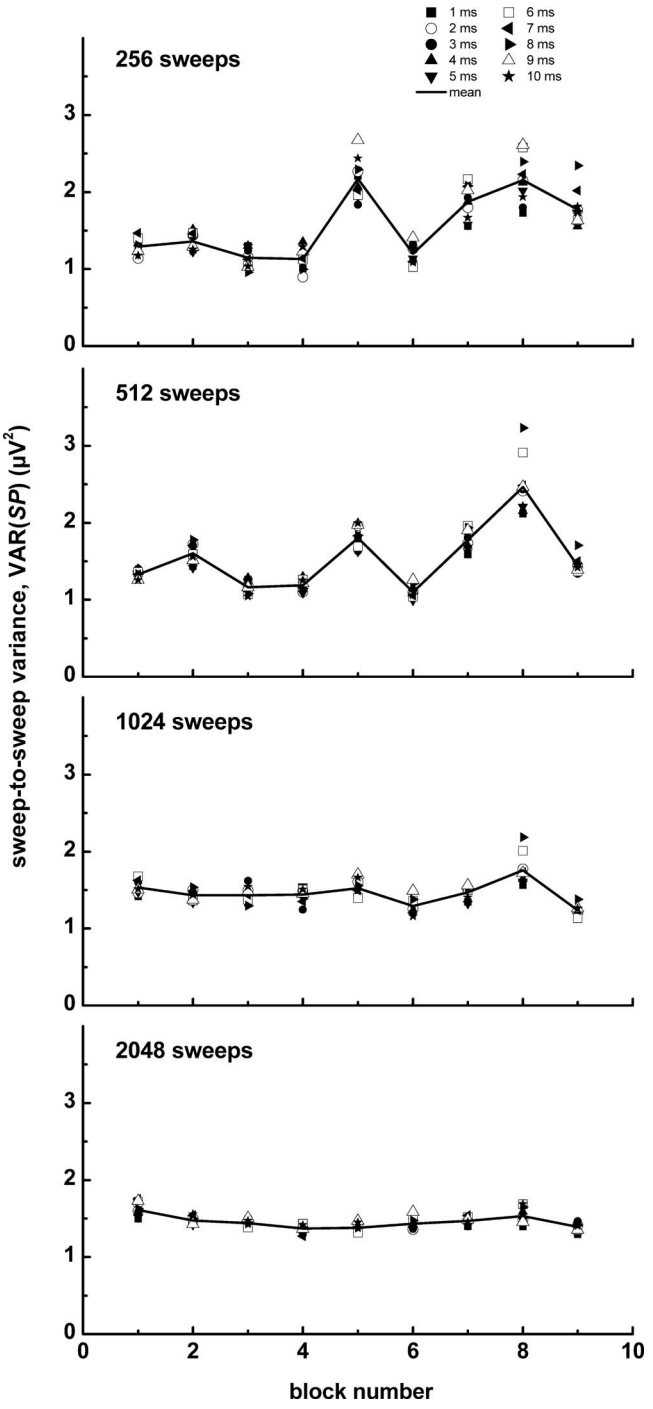


FIG. 5. Influence of the time location of single amplitude points on the sweep-to-sweep variance VAR(SP) for nine blocks of 256, 512, 1024, or 2048 sweeps. Data are from the dolphin TYH, with the 300 Hz digital high-pass filter. The specific time value for the single amplitude point did not substantially affect the calculation of VAR(SP), even for 256 sweeps.

sweeps were used, so the modified variance ratio approach did not likely result in improved performance over the original method proposed by Elberling and Don (1984).

The influence of the amplitude time latencies on the estimated background noise variance was also examined by calculating VAR(SP) [i.e., Eq. (6) with $M=1$] with the latency of the single amplitude point varied from 1 to 10 ms. Figure 5 shows the sweep-to-sweep variance calculated for nine blocks of 256–2048 sweeps collected from TYH. As previously demonstrated by Elberling and Don (1984), differences between the calculated values of VAR(SP) within each block were relatively small, even with only 256 sweeps, meaning that the specific time latencies used for the calculation of VAR(SP_m) did not have a large influence on the estimated background noise variance. When the number of sweeps was 2048, VAR(SP) was nearly constant across blocks as well.

Figures 6 and 7 show the averaged waveforms for BOB and TYH, respectively, after digitally high-pass filtering at 300 Hz. Each collection of 2048 sweeps was divided into two groups of 1024 that were averaged and overlaid to assist in visual detection. Evoked responses, consisting of three to four positive and negative peaks, are visible at the higher stimulus levels but indistinguishable from noise at lower levels. Response detection was performed by calculating F^* over the time range 1–8 ms and comparing to the critical values 2.1 and 2.8 ($v_1=6$ and $v_2=2048$). Characteristic peaks in the averaged waveforms were still visible (to the author) at ppeSPLs 5 dB below the lowest detections based on F^* at all frequencies for BOB and at 160 kHz for TYH.

The amplitude of each averaged waveform was calculated as the peak-peak amplitude occurring between 1 and 8 ms. The resulting input/output (I/O) functions, defined as the evoked response amplitude as a function of the stimulus level, and calculated F^* values are shown in Figs. 8 and 9 for BOB and TYH, respectively. Waveforms with peak-peak amplitudes >0.2 μV were typically detected using F^*. The shapes of the curves relating F^* to the ppeSPL were similar to the I/O functions, suggesting that the variance of the averaged background noise was relatively constant within each frequency. These curves were also relatively steep over the range of F^* values near F_{crit}, resulting in small differences between the ppeSPL for detection with $\alpha=0.01$ compared to 0.05, though a smaller stimulus step size (i.e., less than 5 dB) may have revealed additional differences in these circumstances.

Thresholds, based on the F^* detections with $\alpha=0.01$, are shown in Fig. 10. The tone-pip thresholds, based on the estimated ppeSPL, agreed with previously measured ASSR thresholds showing significant high-frequency hearing loss in BOB (Houser and Finneran, 2006b). Thresholds for TYH exhibited a broad sloping increase at higher frequencies, in contrast to ASSR data showing a more well-defined upper cutoff and lower thresholds in the 20–100 kHz range (Houser and Finneran, 2006b). These differences may have been caused by the short durations of the tone pips, which tended to excite the jawphone near its resonance around 100 kHz and produce a very broadband stimulus.

Figure 11 compares thresholds for BOB (left panel) and TYH (right panel) obtained with various digital high-pass filters. Lower filter cutoffs could theoretically result in larger signal amplitudes and better detection; however, in practice, lower filter cutoffs also resulted in larger background noise variance, lower degrees of freedom, and higher values of F^*_{crit}. Therefore, in most cases the thresholds tended to either remain constant or increase as the filter cutoff frequency decreased.

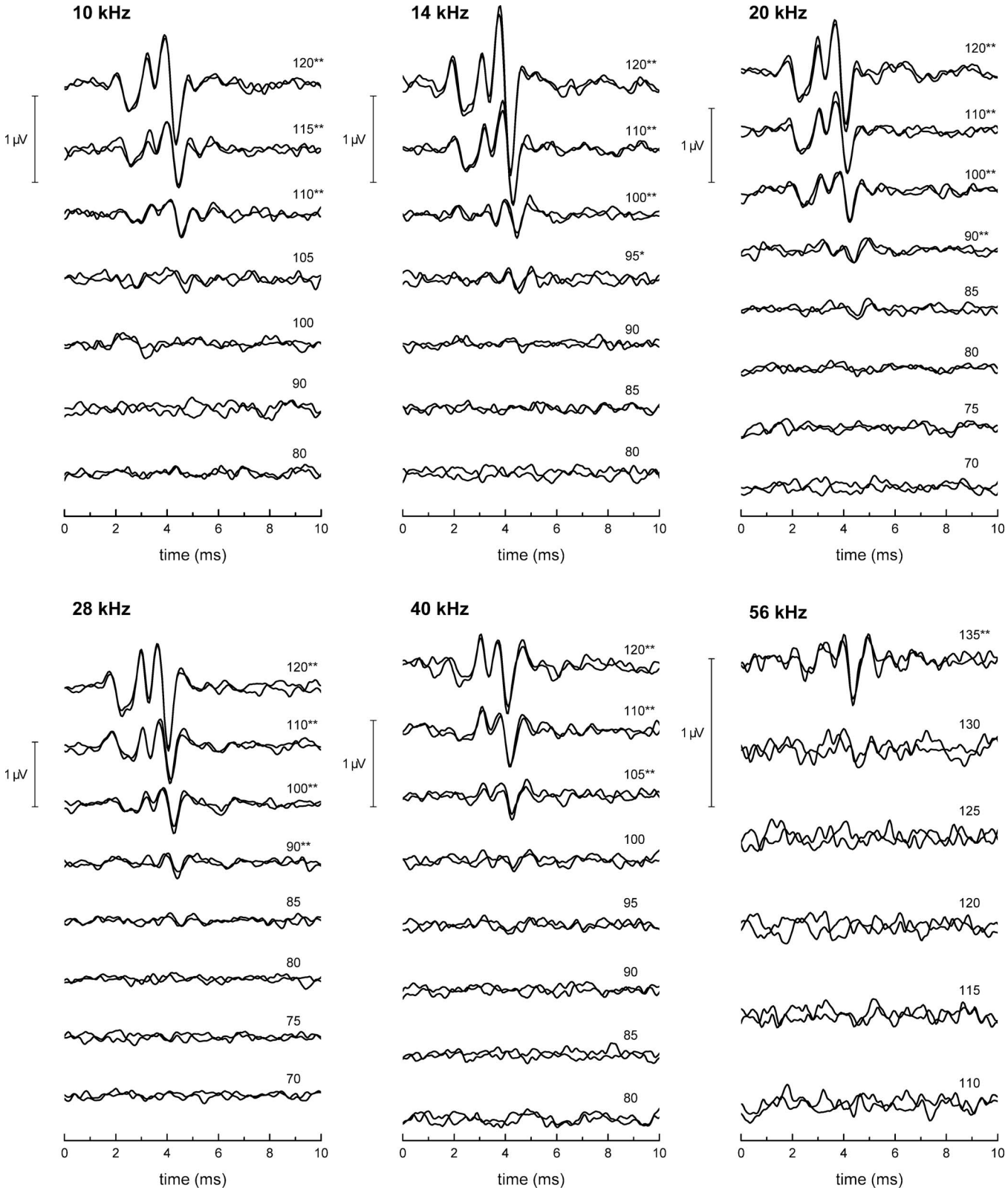


FIG. 6. Averaged time waveforms for the dolphin BOB. Data were digitally high pass filtered at 300 Hz. Each panel shows the data recorded at a particular frequency, arranged in two overlaid averages of 1024 sweeps each. The number by each trace indicates the estimated received ppeSPL in decibels re 1 μPa. Asterisks indicate detected responses according to the F^* method at the α=0.05(*) or 0.01 (**) level of significance.

V. DISCUSSION

There is a natural tendency to judge the effectiveness of an evoked response detection method by its ability to detect responses at low stimulus levels. In the present study this might lead one to conclude that visual detection is superior to the F^* method since characteristic peaks in the averaged waveforms may be seen at levels below those detected using F^* with α=0.01 or 0.05; however, the primary advantage of

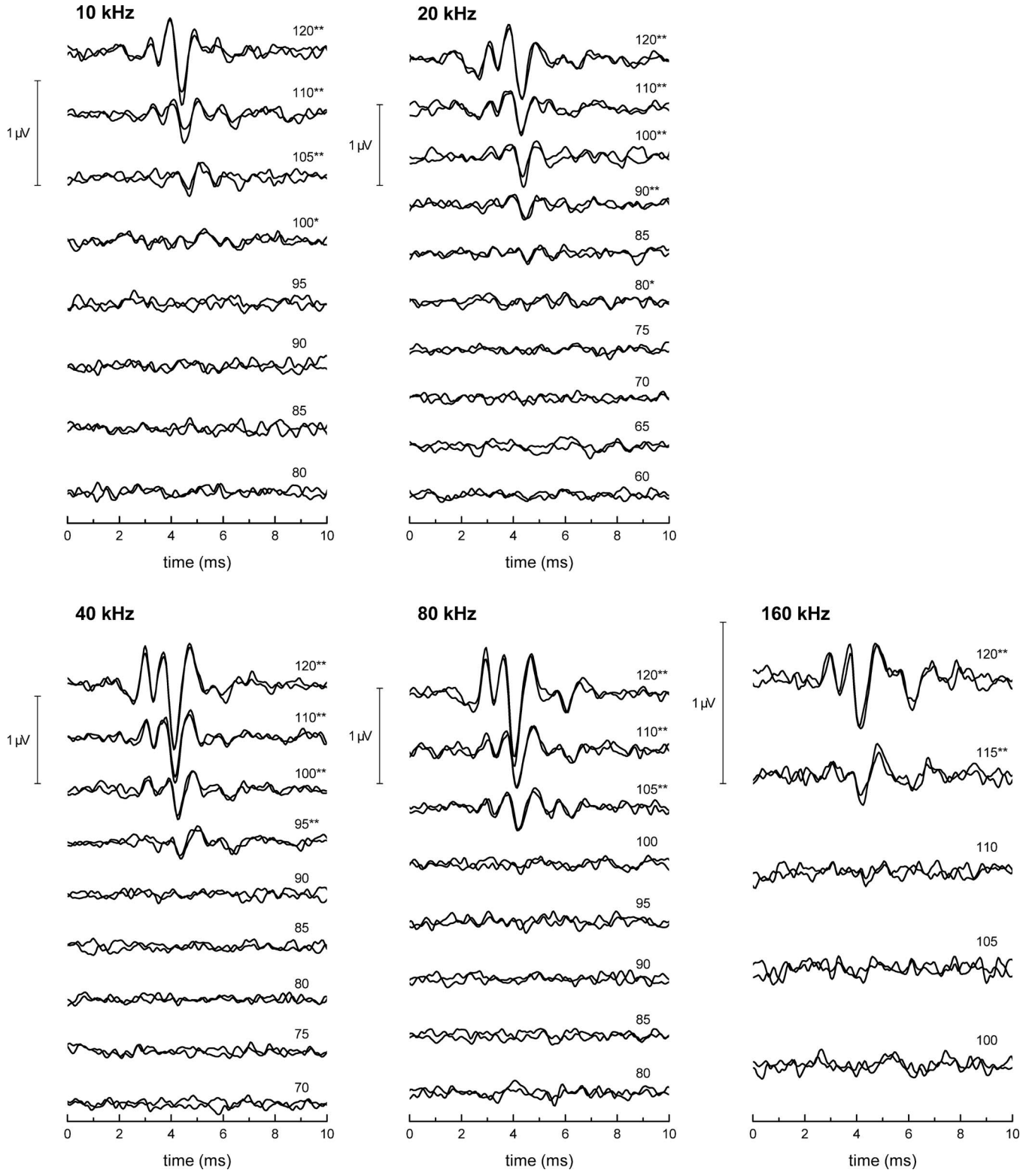


FIG. 7. Averaged time waveforms for the dolphin TYH. Data were digitally high pass filtered at 300 Hz. Each panel shows the data recorded at a particular frequency, arranged in two overlaid averages of 1024 sweeps each. The number by each trace indicates the estimated received ppeSPL in decibels re 1 μPa. Asterisks indicate detected responses according to the F^* method at the α=0.05(*) or 0.01 (**) level of significance.

response detection methods such as F^* is not their ability to provide detections at low signal-to-noise ratios but rather the objectivity, repeatability, and statistical certainty that these methods offer. Regardless of the level of experience of the observer, objective methods will always produce the same result. These techniques therefore allow better evaluation of data and cross comparisons between individuals and between laboratories. Response detection methods such as F^* do not merely provide an objective approach—this could be accomplished by arbitrarily defining any response amplitude as a detection. Techniques such as F^* also allow one to state with a certain degree of statistical certainty that the averaged re-

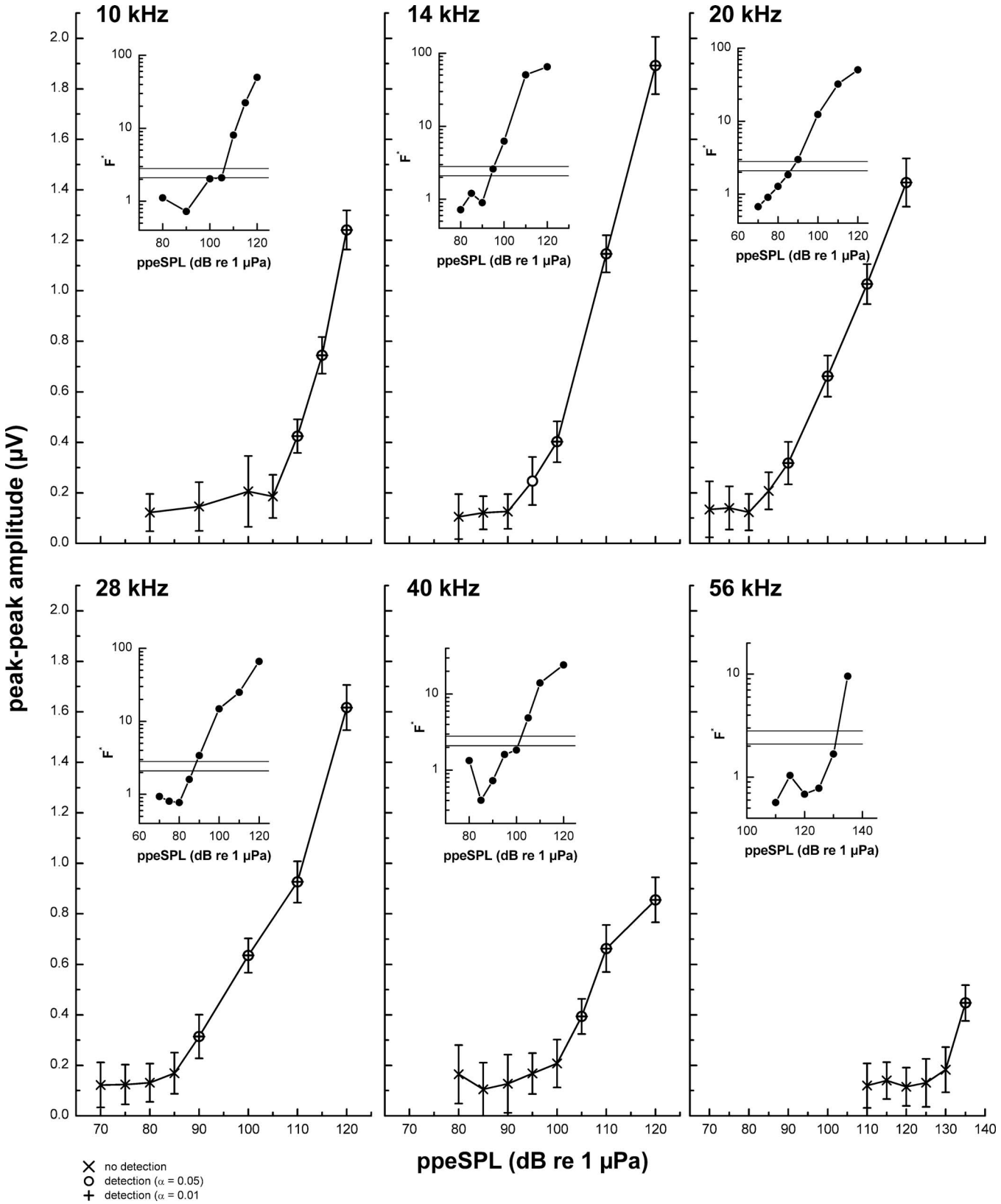


FIG. 8. Evoked potential I/O functions at each frequency for the dolphin BOB stimulated with tone pips. Data were digitally high pass filtered at 300 Hz. The I/O functions are based on the peak-peak amplitude of the evoked potential within a 1–8 ms time window. Symbols represent no detection (x), detections at α=0.05 (o), or detections at α=0.01 (+). Error bars represent the 95% confidence interval about the mean amplitude. The inset graphs show the relationship between F^* and the stimulus level for each frequency. The horizontal lines in the inset plots represent F^*_{crit} for v_1=6, v_2=2048, and α=0.05 (lower line) or 0.01 (upper line).

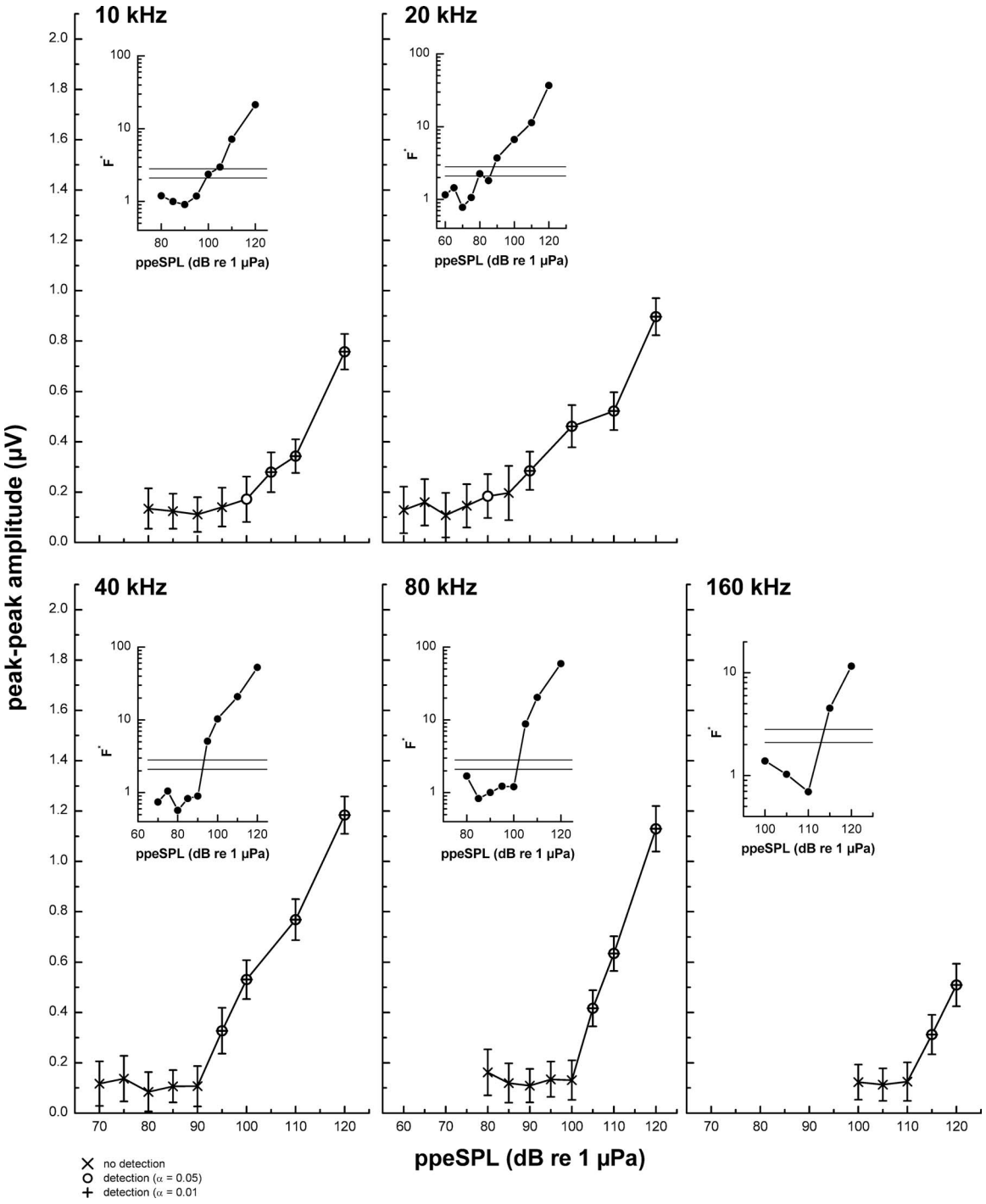


FIG. 9. Evoked potential I/O functions at each frequency for the dolphin TYH stimulated with tone pips. Data were digitally high pass filtered at 300 Hz. The I/O functions are based on the peak-peak amplitude of the evoked potential within a 1–8 ms time window. Symbols represent no detection (x), detections at α=0.05 (o), or detections at α=0.01 (+). Error bars represent the 95% confidence interval about the mean amplitude. The inset graphs show the relationship between F^* and the stimulus level for each frequency. The horizontal lines in the inset plots represent F^*_{crit} for v_1=6, v_2=2048, and α=0.05 (lower line) or 0.01 (upper line).

sponse waveform contains time-locked activity representing an evoked potential. The visual detection technique cannot be quantified in the same statistical fashion; thus meaningful comparisons between visual detection methods and statistical methods such as F^* are difficult. The likelihood of false positives is unknown for the visual method and therefore the appropriate α to use in statistical tests is also unknown. Objective methods also allow one to stop averaging if a response is detected rather than always acquiring a fixed number of sweeps (Don and Elberling, 1996). The present study did not apply the F^* values in this fashion (so proper I/O functions could be generated); however, for measurements where thresholds are of primary importance compared to the specific I/O function shapes, testing speed would be improved by stopping the averaging process after a response is detected. The binary decision provided by an objective response detection method also allows the threshold measurement process to be automated, again improving test speed.

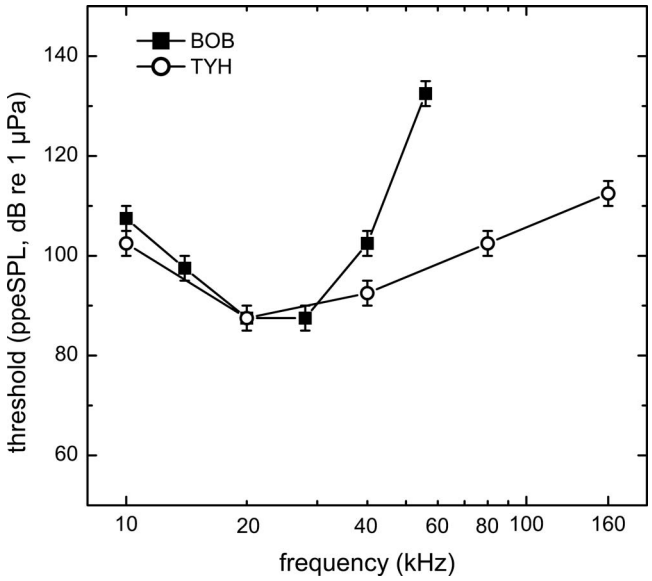


FIG. 10. Estimated tone-pip thresholds as functions of frequency for BOB (filled symbols) and TYH (open symbols). Data were digitally high pass filtered at 300 Hz. Thresholds were based on the mean of the ppeSPLs corresponding to the lowest detection and the next highest nondetection based on F^* with $v_1=6$, $v_2=2048$, and $\alpha=0.01$. Error bars indicate the ppeSPL range to the next higher detection and lower nondetection.

Of course, the F^* technique is only one of many techniques that rely on significance testing of some ratio of the signal variance to the noise variance. The primary differences concern the manner in which the noise variance is estimated. The variance ratio proposed by Elberling and Don (1984), as modified by Stürzebecher *et al.* (2001), was chosen for this study because it estimates the noise variance from the actual sweeps containing the response, is relatively easy to implement, and does not require lengthening the sweeps to accommodate noise estimates before the stimulus onset. The modifications proposed by Stürzebecher *et al.* (2001) increase the number of samples available for the background noise and are intended to improve performance when the number of sweeps is less than a few hundred. In this study, threshold testing was performed using 2048 sweeps; thus the modifications proposed by Stürzebecher *et al.* (2001) were unnecessary. In fact, detection thresholds obtained using F^* (noise variance estimated from four samples per sweep) and F_{SP} (one sample per sweep) were identical; however, for consistency with the v_1 estimates, which were based on F^* since each block contained only 192 sweeps, F^* values are reported here in Figs. 8 and 9.

The main limitations of variance ratio techniques concern estimating the background noise variance. The F^* technique uses the sweep-to-sweep variance averaged over several time latencies to estimate the background noise variance. This requires access to the individual sweeps rather than just the grand averaged waveform, making the approach unsuitable for some evoked potential software. The lack of *a priori* knowledge of the degrees of freedom v_1 also limits the F^* technique. Elberling and Don (1984) used a worst-case estimate for v_1 based on the distribution of the estimates from eight subjects. The present study followed this approach, basing the v_1 value for threshold measurements on the mean—2SD obtained from four individuals. The resulting values for v_1 were similar to those obtained for humans (Elberling and Don, 1984). Since the critical value for F^* increases with decreasing v_1, this results in a conservative approach, meaning the likelihood of false positives is reduced at the expense of potentially higher thresholds. The suitability of this approach to additional subjects remains to be seen; estimates of v_1 from additional subjects would be necessary to test the validity of the estimates presented in Table I. Of course, for novel species an additional limitation exists in that some amount of stimulus absent recordings are necessary to estimate v_1. The variance ratio technique also assumes that the background noise is normally distributed, an assumption which may not be true if large artifacts are present.

Careful consideration should be given to the choice of analysis window and high-pass filtering when using the F^* method. Although estimates of the background noise variance do not strongly depend on the particular time latency (e.g., Fig. 5), the signal variance $\mathrm{VAR}[\overline{S(t)}]$ will depend, to some extent, on the time window. It is possible that smaller time windows adjusted to contain the visible waveform peaks may have resulted in F^* detections; however, shortening the time window restricts the range of frequencies that may be properly represented in the averaged response. As noted by Elberling and Don (1984), an analysis window with duration T seconds cannot reflect the signal power below $1/T$ Hz. This means that sufficient high-pass filtering must be employed to eliminate frequencies below $1/T$ before analysis. The high-pass filter within the biopotential amplifier had a rather gradual rolloff at low frequencies (Fig. 1), resulting in background noise containing a large amount of low-frequency content and violating this rule using the 7 ms analysis window ($1/T=143$ Hz). For this reason the analysis window was extended to 10 ms for this case. The resulting fits to the theoretical F-distributions were still relatively poor compared to the digitally filtered data. When digital high-pass filters with sharper cutoffs were used, the cumulative distributions for F^* were fitted well by theoretical F-distributions and the v_1 estimates were higher. Application of F^* thus strongly depends on the particular choice of filtering, and v_1 estimates obtained with specific filters may not generalize to others. The high-pass filter also affected the ability of the F^* method to produce detections. During preliminary measurements it was observed that some amount of high-pass filtering was necessary, as the background noise variance with no additional filtering was so high as to prevent detections even for signals that could clearly be seen in the averaged waveforms. As the high-pass filter cutoff increased, detection thresholds tended to remain constant or decrease, reflecting the advantages gained by the increase in v_1 (and decrease in F^*_{crit}) at higher filter cutoff frequencies. Proper application of F^* therefore requires careful choice of filters to optimize the signal amplitude and result in relatively low F^*_{crit}.

The main focus of the study was to examine the use of the F^* method rather than provide definitive tone-pip thresholds for *Tursiops*; however, some discussion is warranted with respect to the tone-pip thresholds, which were relatively

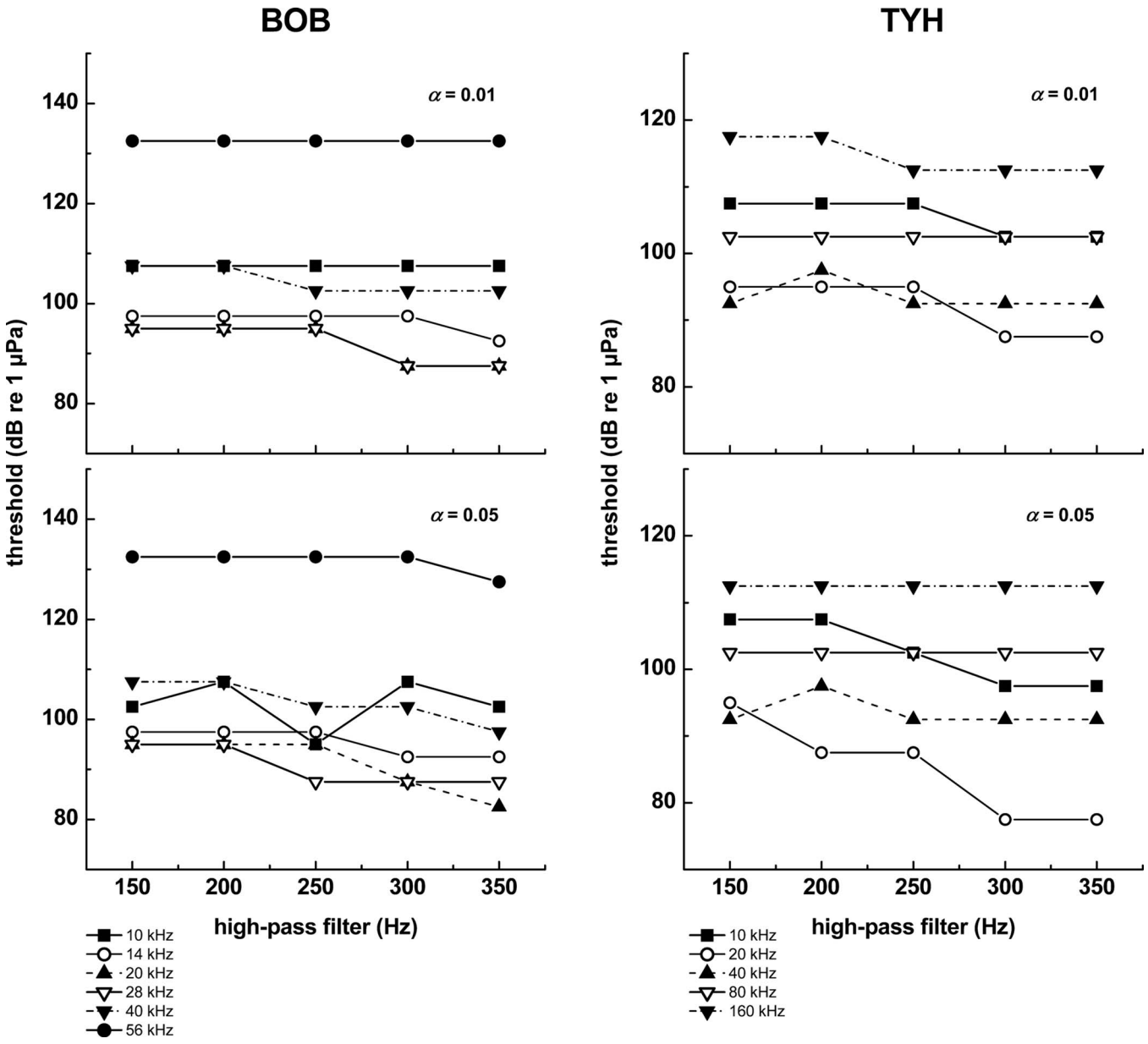


FIG. 11. Influence of the high-pass filter cutoff frequency on thresholds for subjects BOB (left panel) and TYH (right panel). The upper and lower plots in each panel represent thresholds with α=0.01 and 0.05, respectively. As the filter cutoff increased, thresholds tended to remain constant or decrease.

high compared to pure-tone underwater behavioral thresholds in dolphins. The differences are most likely caused by a combination of factors. The tone-pip durations (0.03–0.5 ms) were much shorter than temporal integration times in dolphins (hundreds of milliseconds), so the resulting thresholds would be expected to be 20–30 dB above pure-tone thresholds obtained with longer duration stimuli (Johnson, 1968). The jawphone transducer element possessed a resonance near 100 kHz; when excited with the short duration tones the effect was to cause a "ringing" of the transducer, extending the duration beyond the intended five cycles and, in some cases, generating substantial energy outside the desired bandwidth. The smearing of energy across adjacent frequency bands was probably responsible for the gradual upper cutoff in TYH, compared to the sharp upper cutoffs normally seen in dolphins. Using a longer duration pip with a different temporal envelope may have resulted in more representative thresholds. Finally, the method of estimating received sound levels at the dolphin relied on direct field measurements in water, which can only grossly approximate the actual received sound via the complex interaction between the jawphone transducer and the animal's head.

VI. CONCLUSIONS

The modified variance ratio provides an objective statistical approach for the detection of transient evoked potentials in marine mammals. The technique is relatively simple to implement, provided sufficient data exist to estimate the background noise variance; this will normally entail having access to the individual sweeps that comprise the averaged waveform or at least to a single amplitude value from each sweep. The particular filters applied to the evoked responses were also found to strongly affect results. The primary limi-

tations of the method involve the lack of *a priori* knowledge of the degrees of freedom required for statistical tests, and the manner in which the degrees of freedom vary with the specific filtering performed. This means that the degrees of freedom must be empirically determined for each species and will vary with the specific filters employed.

ACKNOWLEDGMENTS

The author wishes to thank Carolyn Schlundt and Randall Dear for assistance with data collection and Linda Green, Megan Tormey, and Erik Robinson for animal training. Brian Branstetter and Dorian Houser provided helpful comments on the manuscript. Financial support was provided by the Office of Naval Research.

Ahroon, W. A., Hamernik, R. P., and Davis, R. I. (**1993**). "Complex noise exposures: An energy analysis," J. Acoust. Soc. Am. **93**, 997–1006.

Ahroon, W. A., Hamernik, R. P., and Lei, S.-F. (**1996**). "The effects of reverberant blast waves on the auditory system," J. Acoust. Soc. Am. **100**, 2247–2257.

Arnold, S. A. (**1985**). "Objective versus visual detection of the auditory brain stem response," Ear Hear. **6**, 144–150.

Bullock, T. H., Grinnell, A. D., Ikezono, E., Kameda, K., Katsuki, K., Nomoto, M., Sato, O., Suga, N., and Yanagisawa, K. (**1968**). "Electrophysiological studies of central auditory mechanisms in cetaceans," Zeitschrift fur Vergleichende Physiologie **59**, 117–156.

Bullock, T. H., and Ridgway, S. H. (**1972**). "Evoked potentials in the central auditory system of alert porpoises to their own and artificial sounds," J. Neurobiol. **3**, 79–99.

Burkard, R. (**1984**). "Sound pressure level measurement and spectral analysis of brief acoustic transients," Electroencephalogr. Clin. Neurophysiol. **57**, 83–91.

Cook, M. L. H., Varela, R. A., Goldstein, J. D., McCulloch, S. D., Bossart, G. D., Finneran, J. J., Houser, D., and Mann, D. A. (**2006**). "Beaked whale auditory evoked potential hearing measurements," J. Comp. Physiol. [A] **192**, 489–495.

Dobie, R. A., and Wilson, M. J. (**1993**). "Objective response detection in the frequency domain," Electroencephalogr. Clin. Neurophysiol. **88**, 516–524.

Dobie, R. A., and Wilson, M. J. (**1996**). "A comparison of *t* test, *F* test, and coherence methods of detecting steady-state auditory-evoked potentials, distortion-product otoacoustic emissions, or other sinusoids," J. Acoust. Soc. Am. **100**, 2236–2246.

Dolphin, W. F. (**1996**). "Auditory evoked responses to amplitude modulated stimuli consisting of multiple envelope components," J. Comp. Physiol. [A] **179**, 113–121.

Dolphin, W. F. (**2000**). "Electrophysiological measures of auditory processing in odontocetes," in *Hearing by Whales and Dolphins*, edited by W. W. L. Au, A. N. Popper, and R. R. Fay (Springer-Verlag, New York), pp. 294–329.

Dolphin, W. F., Au, W. W., Nachtigall, P. E., and Pawloski, J. (**1995**). "Modulation rate transfer functions to low-frequency carriers in three species of cetaceans," J. Comp. Physiol. [A] **177**, 235–245.

Dolphin, W. F., and Mountain, D. C. (**1992**). "The envelope following response: Scalp potentials elicited in the mongolian gerbil using sinusoidally AM acoustic signals," Hear. Res. **58**, 70–78.

Don, M., and Elberling, C. (**1996**). "Use of quantitative measure of auditory brain-stem response peak amplitude and residual background noise in the decision to stop averaging," J. Acoust. Soc. Am. **99**, 491–499.

Eggermont, J. J. (**2007**). "Electric and magnetic fields of synchronous neural activity: Peripheral and central origins of AEPs," in *Auditory Evoked Potentials: Basic Principles and Clinical Applications*, edited by R. F. Burkard, J. J. Eggermont, and M. Don (Lippincott Williams and Wilkins, Philadelphia, PA), pp. 2–21.

Elberling, C., and Don, M. (**1984**). "Quality estimation of averaged auditory brainstem responses," Scand. Audiol. **13**, 187–197.

Elberling, C., and Don, M., (**2007**). "Detecting and assessing synchronous neural activity in the temporal domain (SNR, response detection)," in *Auditory Evoked Potentials: Basic Principles and Clinical Applications*, edited by R. F. Burkard, J. J. Eggermont, and M. Don (Lippincott Williams and Wilkins, Philadelphia, PA), pp. 102–123.

Finneran, J. J. (**2008**). "Evoked Response Study Tool (EVREST) User's Guide," SSC San Diego Technical Document No. 3226, San Diego, CA.

Finneran, J. J., and Houser, D. S. (**2006**). "Comparison of in-air evoked potential and underwater behavioral hearing thresholds in four bottlenose dolphins (*Tursiops truncatus*)," J. Acoust. Soc. Am. **119**, 3181–3192.

Finneran, J. J., Houser, D. S., and Schlundt, C. E. (**2007a**). "Objective detection of bottlenose dolphin (*Tursiops truncatus*) steady-state auditory evoked potentials in response to AM/FM tones," Aquat. Mamm. **33**, 43–54.

Finneran, J. J., Schlundt, C. E., Branstetter, B., and Dear, R. L. (**2007b**). "Assessing temporary threshold shift in a bottlenose dolphin (*Tursiops truncatus*) using multiple simultaneous auditory evoked potentials," J. Acoust. Soc. Am. **122**, 1249–1264.

Hamernik, R. P., Qiu, W., and Davis, B. (**2007**). "Hearing loss from interrupted, intermittent, and time varying non-Gaussian noise exposure: The applicability of the equal energy hypothesis," J. Acoust. Soc. Am. **122**, 2245–2254.

Houser, D. S., Crocker, D. E., Kastak, C., Mulsow, J., and Finneran, J. J. (**2007**). "Auditory evoked potentials in northern elephant seals (*Mirounga angustirostris*)," Aquat. Mamm. **33**, 110–121.

Houser, D. S., and Finneran, J. J. (**2006a**). "A comparison of underwater hearing sensitivity in bottlenose dolphins (*Tursiops truncatus*) determined by electrophysiological and behavioral methods," J. Acoust. Soc. Am. **120**, 1713–1722.

Houser, D. S., and Finneran, J. J. (**2006b**). "Variation in the hearing sensitivity of a dolphin population obtained through the use of evoked potential audiometry," J. Acoust. Soc. Am. **120**, 4090–4099.

Johnson, C. S. (**1968**). "Relation between absolute threshold and duration-of-tone pulses in the bottlenosed porpoise," J. Acoust. Soc. Am. **43**, 757–763.

Kenyon, T. N., Ladich, F., and Yan, H. Y. (**1998**). "A comparative study of hearing ability in fishes: The auditory brainstem response approach," J. Comp. Physiol. [A] **182**, 307–318.

Lovell, J. M., Findlay, M. M., Moate, R. M., Nedwell, J. R., and Pegg, M. A. (**2005a**). "The inner ear morphology and hearing abilities of the Paddlefish (*Polyodon spathula*) and the Lake Sturgeon (*Acipenser fulvescens*)," Comp. Biochem. Physiol., Part A: Mol. Integr. Physiol. **142**, 286–296.

Lovell, J. M., Findlay, M. M., Moate, R. M., and Yan, H. Y. (**2005b**). "The hearing abilities of the prawn *Palaemon serratus*," Comp. Biochem. Physiol., Part A: Mol. Integr. Physiol. **140**, 89–100.

Mason, S. M., Su, A. P., and Hayes, R. A. (**1977**). "Simple online detector of auditory evoked cortical potentials," Med. Biol. Eng. Comput. **15**, 641–647.

Nachtigall, P. E., Supin, A. Y., Amundin, M., Roken, B., Møller, T., Mooney, T. A., Taylor, K. A., and Yuen, M. (**2007**). "Polar bear *Ursus maritimus* hearing measured with auditory evoked potentials," J. Exp. Biol. **210**, 1116–1122.

Nachtigall, P. E., Yuen, M. M. L., Mooney, T. A., and Taylor, K. A. (**2005**). "Hearing measurements from a stranded infant Risso's dolphin, *Grampus griseus*," J. Exp. Biol. **208**, 4181–4188.

OriginLab Corporation (**2007**). ORIGIN 8.0, OriginLab Corporation, Northampton, MA.

Popov, V. V., and Supin, A. Y. (**1985**). "Determining hearing characteristics in dolphins using evoked potentials of brain stem," Dokl. Akad. Nauk SSSR **283**, 496–499.

Popov, V. V., and Supin, A. Y. (**1990**). "Auditory brainstem responses in characterization of dolphin hearing," J. Comp. Physiol. [A] **166**, 385–393.

Popper, A. N., Halvorsen, M. B., Kane, A., Miller, D. L., Smith, M. E., Song, J., Stein, P., and Wysocki, L. E. (**2007**). "The effects of high-intensity, low-frequency active sonar on rainbow trout," J. Acoust. Soc. Am. **122**, 623–635.

Qiu, W., Davis, B., and Hamernik, R. P. (**2007**). "Hearing loss from interrupted, intermittent, and time varying Gaussian noise exposures: The applicability of the equal energy hypothesis," J. Acoust. Soc. Am. **121**, 1613–1620.

Ridgway, S. H., Bullock, T. H., Carder, D. A., Seeley, R. L., Woods, D., and Galambos, R. (**1981**). "Auditory brainstem response in dolphins," Neurobiology **78**, 1943–1947.

Ridgway, S. H., and Carder, D. A. (**2001**). "Assessing hearing and sound production in cetaceans not available for behavioral audiograms: Experiences with sperm, pygmy sperm, and gray whales," Aquat. Mamm. **27**, 267–276.

Schimmel, H. (**1967**). "The (±) reference: accuracy of estimated mean com-

ponents in average response studies," Science **157**, 92–94.
Schimmel, H., Rapin, I., and Cohen, M. M. (**1974**). "Improving evoked response audiometry with special reference to the use of machine scoring," Audiology **13**, 33–65.
Scholik, A. R., and Yan, H. Y. (**2001**). "Effects of underwater noise on auditory sensitivity of a cyprinid fish," Hear. Res. **152**, 17–24.
Sininger, Y. S. (**1993**). "Auditory brain stem response for objective measures of hearing," Ear Hear. **14**, 23–30.
Smith, M. E., Kane, A. S., and Popper, A. N. (**2004**). "Acoustical stress and hearing sensitivity in fishes: Does the linear threshold shift hypothesis hold water?," J. Exp. Biol. **207**, 3591–3602.
Stapells, D. R., Linden, D., Suffield, J. B., Hamel, G., and Picton, T. W. (**1984**). "Human auditory steady state potentials," Ear Hear. **5**, 105–113.
Stürzebecher, E., Cebulla, M., and Wernecke, K. D. (**2001**). "Objective detection of transiently evoked otoacoustic emissions," Scand. Audiol. **30**, 78–88.
Supin, A. Y., Nachtigall, P. E., Au, W. W. L., and Breese, M. (**2004**). "The interaction of outgoing echolocation pulses and echoes in the false killer whale's auditory system: Evoked-potential study," J. Acoust. Soc. Am. **115**, 3218–3225.
Supin, A. Y., Nachtigall, P. E., and Breese, M. (**2006**). "Source-to-sensation level ratio of transmitted biosonar pulses in an echolocating false killer whale," J. Acoust. Soc. Am. **120**, 518–526.
Supin, A. Y., Nachtigall, P. E., Pawloski, J., and Au, W. W. L. (**2003**). "Evoked potential recording during echolocation in a false killer whale *Pseudorca crassidens*," J. Acoust. Soc. Am. **113**, 2408–2411.
Supin, A. Y., and Popov, V. V. (**1995**). "Envelope-following response and modulation transfer function in the dolphin's auditory system," Hear. Res. **92**, 38–46.
Supin, A. Y., and Popov, V. V. (**2000**). "Frequency-modulation sensitivity in bottlenose dolphins, *Tursiops truncatus*: Evoked-potential study," Aquat. Mamm. **26**, 83–94.
Supin, A. J., Popov, V. V., and Mass, A. M. (**2001a**). *The Sensory Physiology of Aquatic Mammals* (Kluwer Academic, Boston).
Supin, A. Y., Popov, V. V., and Mass, A. M. (**2001b**). *The Sensory Physiology of Aquatic Mammals* (Kluwer Academic, Boston, MA).
Szymanski, M. D., Bain, D. E., Kiehl, K., Pennington, S., Wong, S., and Henry, K. R. (**1999**). "Killer whale (*Orcinus orca*) hearing: Auditory brainstem response and behavioral audiograms," J. Acoust. Soc. Am. **106**, 1134–1141.
Vidler, M., and Parker, D. (**2004**). "Auditory brainstem response threshold estimation: Subjective threshold estimation by experienced clinicians in a computer simulation of the clinical test," Int. J. Audiol. **43**, 417–429.
Weber, B. A., and Fletcher, G. L. (**1980**). "A computerized scoring procedure for auditory brainstem response audiometry," Ear Hear. **1**, 233–236.
Wolski, L. F., Anderson, R. C., Bowles, A. E., and Yochem, P. K. (**2003**). "Measuring hearing in the harbor seal (*Phoca vitulina*): Comparison of behavioral and auditory brainstem response techniques," J. Acoust. Soc. Am. **113**, 629–637.
Wong, P. K. H., and Bickford, R. G. (**1980**). "Brain stem auditory evoked potentials: The use of noise estimate," Electroencephalogr. Clin. Neurophysiol. **50**, 25–34.
Yuen, M. M. L., Nachtigall, P. E., Breese, M., and Supin, A. Y. (**2005**). "Behavioral and auditory evoked potential audiograms of a false killer whale (*Pseudorca crassidens*)," J. Acoust. Soc. Am. **118**, 2688–2695.

Analysis of frequency dependence of ultrasonic backscatter coefficient in cancellous bone

Dean Ta,[a] Weiqi Wang, Kai Huang, and Yuanyuan Wang
Department of Electronic Engineering, Fudan University, Shanghai, 200433 China

Lawrence H. Le
Department of Radiology & Diagnostic Imaging, University of Alberta, Edmonton, Alberta, T6G 2E1 Canada

(Received 5 April 2008; revised 23 September 2008; accepted 24 September 2008)

The ultrasonic scattering mechanism in cancellous bone is investigated theoretically and a model describing the frequency dependence of ultrasonic scattering from cancellous bone is presented. The ultrasonic backscatter coefficient (BSC) of bovine tibiae, human calcanei *in vitro* and *in vivo*, were measured and discussed. The data of BSC were also fitted by polynomial. The results demonstrate that BSC is a nonlinear function of frequency and increases with frequency. A good agreement was obtained between BSC values from theory and experiment. Also, the high correlation coefficient between BSC and bone mineral density was obtained, $r=0.85\pm0.07$ (mean $\pm$ SD) (n=15, $p<0.001$). Based on the values of BSC, the status of cancellous bone and the degree of osteoporotic fracture risk may be assessed. © *2008 Acoustical Society of America.* [DOI: 10.1121/1.3001705]

PACS number(s): 43.80.Qf, 43.80.Ev, 43.80.Cs, 43.80.Jz [CCC] Pages: 4083–4090

I. INTRODUCTION

Osteoporotic fracture is a serious and growing public health issue since the aged population is rapidly increasing.[1] Currently, it is estimated that over 200 million people worldwide suffer from osteoporosis.[2] For these reasons, osteoporosis is often referred to the "silent epidemic." Early diagnosis of osteoporosis is important to the successful treatment and prevention of fractures. Therefore, various methods have been developed for the diagnostics of osteoporosis.

Compared to the other techniques, approaches based on ultrasound offer advantages including low cost, lack of ionizing radiation, simplicity, and portability. Furthermore, the ultrasonic wave has the additional ability of evaluating the bone tissue elasticity and bone strength, which have not been successfully measured by dual energy x-ray absorptiometry (DXA).[3] Quantitative ultrasound (QUS) proves to have the potential to become a widely available noninvasive tool for the assessment of cancellous bone status and diagnosis of osteoporosis,[3–14] and broadband ultrasound attenuation (BUA) and speed of sound (SOS) are two traditional QUS parameters. Most clinical ultrasound devices use transmission methods to measure them in calcaneus for the diagnosis of osteoporosis.[12,13] These two ultrasonic parameters are highly correlated to bone mineral density (BMD) values,[4,15,16] but they still depend on bone thickness and soft tissue.[12] Also, ultrasonic transmission measurement has some limitations. First, the transmission technique can only provide information related to BMD, which can only explain up to 70–75% of the variance in bone strength[4] and ignore the bone microstructure information.[4,17–19] Second, it is limited to parts of the skeleton which are only accessible by one transducer. Therefore, a strong interest has been focused to develop alternative quantitative ultrasound approaches.

Recently, a number of feasibility studies have been conducted to evaluate the potential of ultrasonic backscattering for the diagnosis of osteoporosis.[20,21] Wear[20] contributed a good summary to the present research status of ultrasonic scattering from cancellous bone. The backscatter is known to provide information regarding BMD, number density, mean trabecular thickness, and elastic properties of scatterers; its dependence on those properties has been widely investigated. The method has a merit of using only a single transducer to transmit signal and receive echoes. Several theoretical methods[19,20,22–26] and an experimental model[27] have been developed to explain the backscatter data. The results are encouraging and have demonstrated that the measurements with an appropriate cancellous bone model can provide additional bone microstructural information that is not available when using DXA (Ref. 5) and traditional QUS parameters, namely SOS and BUA.[22,23,27–29]

The development of theoretical models linking cancellous bone structure to QUS backscatter coefficient is important for understanding the underlying mechanisms of ultrasonic scattering from cancellous microarchitecture. Using a Faran model,[30] Wear[24,25] modeled the trabecular microstructure as a collection of randomly spaced parallel cylinders with their axes perpendicular to the direction of ultrasound beam. The measurements of the frequency dependence of backscatter coefficient (BSC) from human calcaneous trabecular bone *in vitro* were in good agreement with BSC values from theory at low-frequency range. Previous work[19,22,23,26] used several autocorrelation functions to model cancellous bone as a weak scattering random medium. With these models, the simulated frequency dependence of BSC was in good agreement with experimental data. The measured quantitative ultrasonic parameters are affected by transducer charac-

[a]Electronic mail: tda@fudan.edu.cn

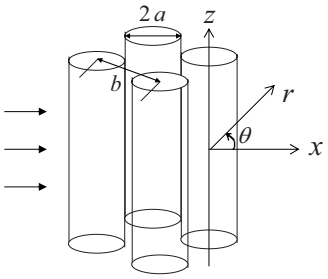


FIG. 1. A cylindrical model of cancellous bone.

TABLE I. Parameters of simulation for all bovine cancellous bones.

	Density (kg/m^3)	Sound velocity (m/s)
Trabecular bone (solid bone)	1960[a]	3200[a]
Marrow	1050	1500[a]
$2a$=0.3 mm[b]	b=1.4 mm	r=200 mm
N_x=3	N_y=25	

[a]Taken from Ref. 34.
[b]Taken from Ref. 32.

teristics, e.g., beam diameter, frequency range, wave, and pulse length.[12] The frequency-dependent backscatter from human calcaneus has suggested that scatterers in trabecular bone behave more like rods.[24,31]

Kitamura *et al.*[32,33] proposed a cylindrical grating model of cancellous bone, and the ultrasonic signals scattered by trabeculae were analyzed. In his model, the trabecular network is assumed to be parallel to the detecting plane. The trabecular mean thickness and the mean spacing are also assumed to be represented by ideal cylinders arranged at a constant spacing. From the model the scattering function was derived and proved to be effective by measuring planar nets mode of stainless steel. Moreover, the proposed model is promising to measure trabecular mean spacing and mean thickness.[32]

Although active research on ultrasonic backscatter has been conducted, few studies have been done to understand the interaction between ultrasound and trabecular bone. Kitamura's model[32] did not use BSC obtained from backscatter ultrasonic signal to assess cancellous bone.

The major contribution of this work is using an extended model of the Kitamura's model[32] to compute the BSC from the backscatter ultrasonic signal. The objectives of this paper are to apply the cylindrical model to cancellous bone microstructure and to compute the BSC. The structure of the paper is as follows. First, the model of cancellous bone is described. Second, experiments involving bovine tibiae, human calcaneus cancellous bones *in vitro* and *in vivo* are measured. Then the results are presented and discussed. Conclusion will be given in the last section.

II. METHODS

A. Theoretical model

We assume that the scattering originates from the surfaces of trabeculae which are made up of long, thin, and cylindrical scatterers with identically small radius. Trabeculae are distributed quasiperiodically and all the axes of trabeculae are parallel to the cancellous bone surface. As shown in Fig. 1, ultrasonic beam orientation is perpendicular to the trabeculae direction in the measurements.

From the above model, the spatially averaged backscattered spectrum $S(f)$ corresponding to the tissue is given by[32]

$$S(f) = -\sum_{n=-\infty}^{\infty} (-j)^n H_n^{(2)} \times (k_2 r) e^{-jn\theta} \cdot \frac{J_n(x_2)J_n'(x_1) + gJ_n'(x_2)J_n(x_1)}{H_n^{(2)}(x_2)J_n'(x_1) + gH_n^{(2)'}(x_2)J_n(x_1)} \cdot \mathrm{diric}(\zeta, N_x) \cdot \mathrm{diric}(\gamma, N_y), \quad (1)$$

where diric$(\cdot)$ is Dirichlet or periodic sinc function. $x_1 = k_1 a$, $x_2 = k_2 a$, $g = \rho_1 k_2 / \rho_2 k_1$, $\zeta = k_2 b[\cos(\theta+\varphi) - \cos\theta]/2$, $\gamma = k_2 b[\sin(\theta+\varphi) - \sin\theta]/2$. f is the frequency, $2a$ is the cylinder (trabecular) thickness, b is the trabecular spacing, r is the distance from the center of cancellous bone to the testing point, θ is scattering angle, for backscatter $\theta = 180°$, φ is the inclination angle, J_n is the first kind of Bessel function, $H_n^{(2)}$ is the second kind of Hankel function, k_1 and k_2 are the wave numbers of trabecular bone and marrow, respectively. ρ_1 and ρ_2 are the density of trabecular bone and marrow, respectively. N_x and N_y are the numbers of trabeculae in the x- and y directions at the inclination angle $\phi = 0$. The parameters of bovine cancellous bone used in simulation are shown in Table I.

On the other hand, several autocorrelation function models were proposed in the literature for the ultrasonic frequency-dependent backscatter in cancellous bone.[19,22,35] A good agreement between experimental data and predictions was found for both the magnitude and the frequency dependence of the BSC. A general assumption for these models is that the scatterers in the fluid are weak, randomly and sparsely distributed.[35] In the models for weakly scattering medium, the BSC is related to the autocorrelation function of the propagating medium and might be suitable to describe low-frequency ultrasonic scattering from bone microarchitecture. These results open interesting prospects for the estimation of the mean trabecular thickness since a significant correlation was found between the theoretically estimated correlation length from these models and practically measured mean trabecular thickness. In order to validate our model, this paper also presented the BSC of various autocorrelation function models including Gaussian, exponential models, modified exponential, and fluid sphere models. The details of these models have been extensively demonstrated in the literature.[19,22,35] The parameters used in the autocorrelation models are equivalent to the proposed backscatter model.

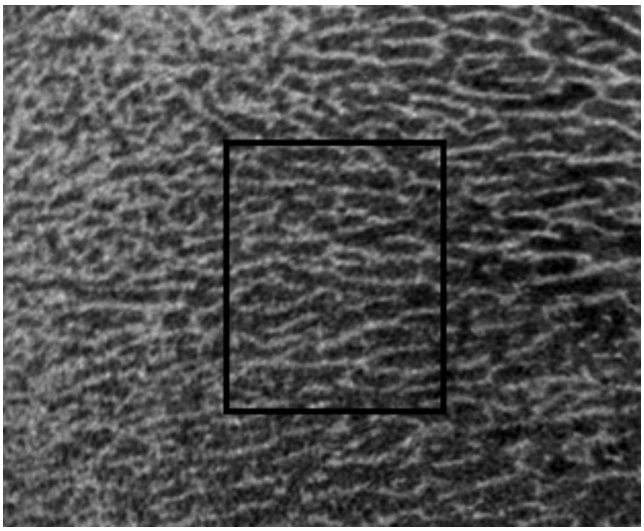


FIG. 2. μ-CT image of a bovine tibiae cancellous bone, where black line frame region is the ultrasonic measurement region. Image acquired by μ-CT 80, SCANCO Medical AG, Switzerland.

B. Bone specimens

Three types of bone specimens were obtained and used in BSC measurements, including eight slices of bovine tibiae with parallel surfaces (3.5×5 cm) and thickness ranging from 7 to 22 mm, three human calcanei *in vitro* are taken from three persons (female, ages unknown, thicknesses varied from 15 to 25 mm), and 15 heels of healthy volunteers with ages ranging from 22 to 68 years (six females and nine males). The exact thickness of the each sample was measured by an electronic caliper. The bovine tibiae and human calcaneus *in vitro* were defatted by a trichloro-ethylene solution.

C. Bone mineral density (BMD) measurements

The BMD of each cancellous bone slice *in vitro* was measured using x-ray microcomputed tomography (μ-CT 80, SCANCO Medical AG, Switzerland) and the bone microarchitecture was also obtained by μ-CT. These data allow the reconstruction of 2D or 3D bone imaging. Local density was determined for central regions of interest (ROI) where the density was relatively homogeneous, such as the black line frame region in the μ-CT image in Fig. 2. In the following ultrasonic measurements, we only use those homogeneous regions. For human calcaneus *in vivo*, the dual energy x-ray absorptiometry (QDR-4500A, Hologic, USA) was used to measure BMD values.

D. Ultrasonic measurements

The schematic diagram of the experimental setup for ultrasonic backscatter measurements is shown in Fig. 3. A high-frequency pulser/receiver unit (Panametrics 5900, Waltham, MA) was used to excite five broadband focal transducers (Panametrics), which produced short-duration pulses for pulse-echo tissue insonification. The echoes were received by the same transducer, then amplified and digitized with 8 bits (HP 54642A, Hewlett-Packard, Palo Alto, CA) at

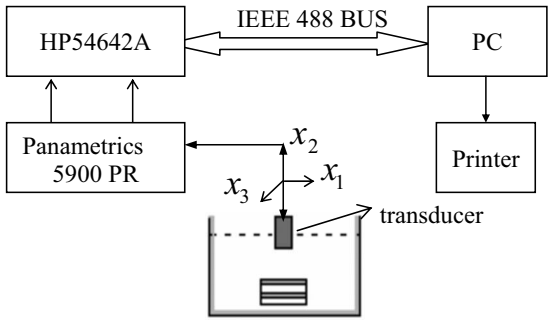


FIG. 3. Experimental setup with the bone sample and the transducer immersed in a water tank.

20 mega-samples/s. Next, 128 2000-point waveforms were averaged in the time domain and then stored in a computer for offline analysis using MATLAB software. The whole sampling processes were controlled by PC. Frequency bandwidths of the transducers are 0.2–0.69, 0.67–1.4, 1.31–3.02, 1.48–4.83, and 2.93–6.19 MHz for 0.5, 1.0, 2.25, 3.5, and 5 MHz center frequencies, respectively. The selected frequency ranges of the transducers in our experiment data are 0.2–0.67, 0.67–1.35, 1.35–3.0, 3.0–4.0, and 4.0–5.5 MHz for 0.5, 1.0, 2.25, 3.5, and 5 MHz center frequencies, respectively. The transducer's beam diameter (nominally 4.8–0.6 mm at −6 dB level for 0.5–5.0 MHz center frequency) permitted the acquisition of five independent measurements for each sample.

Prior to ultrasonic measurement, specimens *in vitro* were vacuum degassed under pure water in a desiccator. Then, specimens were immersed in a tank ($50\times40\times30$ cm^3) filled with degassed pure water in a temperature from 21 to 22.5 °C for 1 h before measurements. The inner surfaces of the tank were covered with sound-absorbing materials. In measurements, ultrasonic beam was perpendicular to the trabeculae orientation, which is similar to clinical measurements. The transducer was adjusted to get the maximum amplitude of the received reference signal in measurements. In addition, the specimens were aligned parallel to the transducer surface in order to get the maximum amplitude of the signal reflected from the planar front surface of the specimen. Displacements in x, y, and z directions were controlled by stepper motors (Ultrapac SMC-PCI-4, Physical Acoustic Co., USA).

For human subjects, the ultrasonic gel (ECHO Jelly, Shanghai Aloka Medical Equipment Co.) was used to couple the transducer and skin of heel bones *in vivo*. Figure 4 shows a simplified diagrammatic sketch for ultrasonic *in vivo* examination of a heel bone.

In order to reduce errors which result from observation noise and random echoes from irresolvable microstructure, for all specimens including cancellous bone of bovine tibiae, human calcaneus *in vitro* and *in vivo*, backscatter signals were measured and recorded in five different locations within the region of interest (ROI) (15×30 mm) at the center of specimens. Such backscatter measurements were conducted for five times in each location and the backscatter signals were averaged.

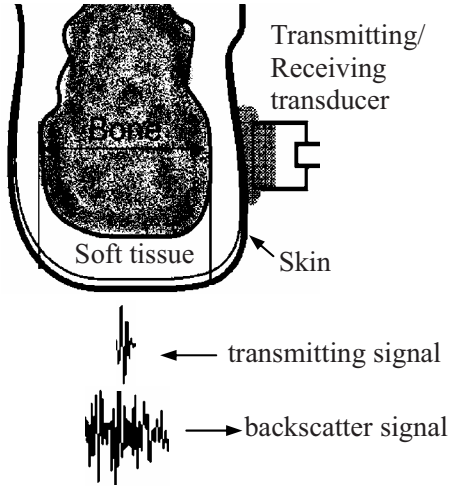


FIG. 4. A schematic diagram for ultrasonic *in vivo* examination of a heel bone.

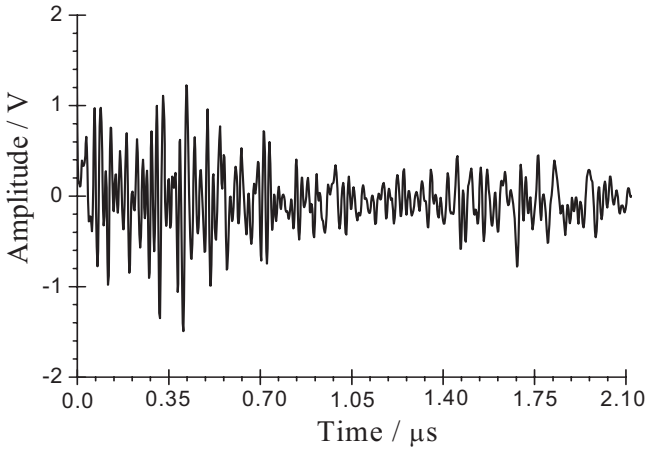


FIG. 5. Time history of the backscattered signal from the calcaneus of a 60-year-old male Chinese. The transducer used was broadband with center frequency of 3.5 MHz.

E. Data analysis

The frequency dependence of the backscatter coefficient $\sigma_b(f)$ is derived, following the method of Roberjot as[19,36]

$$\sigma_b(f) = 8.68 \ln\left(\frac{\langle S(f)\rangle}{S^r(f)}\right) \cdot A(f) \cdot V(f), \tag{2}$$

where $A(f)$ is the attenuation correction term[37] and $V(f)$ is a correction term given by Chaffaï,[19] includes the dependence of frequency scattering volume, such as time gate length as frequency-dependent beamwidth and shape. $S^r(f)$ is the reference spectrum from a standard reflecting target.

Analysis of the backscatter signals was performed to calculate the BSC from Eq. (2). Then, the cubic B-spline interpolation method was used for data-fitting in a piecewise fashion. A gated region was used to select the data which only include the backscattered signals from within the trabecular volume at the focal length of the transducer. The technical aspects of ultrasonic backscatter measurements have been extensively developed elsewhere,[38] and will not be presented in detail here. The measured reference backscatter signal was an ultrasonic echo reflected from a polished steel plate with the size of 150×150 mm and the thickness of 10 mm positioned in water at a distance corresponding to the center of the gated region equivalent to the center of the bone sample. In our measurements of backscatter coefficient $\sigma_b(f)$, we compare the frequency spectrum of pulse-echo signals, gated at the desired depth in samples, with the spectrum of a perfect plane reflector. These measurements are performed at separate times, and the positions are matched by recording the absolute time with reference to the pulse trigger signal of the signal maxima. The through-transmit measurements *in vitro* and *in vivo* were used to compensate for attenuation $A(f)$ when estimating the BSC (Ref. 27) and frequency-dependent scattering volume $V(f)$ in Eq. (2) given by Chaffaï *et al.*[19] The attenuation $A(f)$ was derived from the data acquired in through-transmit mode using the log ratio of the amplitude spectra between the transmitted signal and reference signal.

In simulations, several constants differ from the actual values. In experiments, the intensity of the incident electricity pulse also contributes to the magnitudes of BSC. Therefore, the magnitudes of the theoretical curves must be adjusted to fit the experimental data.[19,24] The adjusted ratios of theoretical data to experimental data are 1 ± 0.1 in our works.

The exponential expression f^n was often used to demonstrate the frequency dependence of BSC.[19,24] In this work, the data of BSC were fitted by polynomial relative to frequency. The numerical expression of polynomial fits show

$$\sigma_b(f) = A_0 + A_1 f + A_2 f^2 + \cdots + A_n f^n, \tag{3}$$

where A_n is the constants. f is center frequency.

III. RESULTS

The data used in the following examples were taken from simulations and experiments in which cancellous bones were measured using the ultrasonic backscatter technique. For example, Fig. 5 shows the time history of the pulse echoed from the internal microarchitecture of calcaneus *in vivo* (60-year-old male) using broadband transducers with a center frequency of 3.5 MHz.

The frequency-dependent backscatter coefficient $\sigma_b(f)$ can be obtained from Eq. (2) when the scattering angle θ is equal to 180°. Figure 6 shows average BSC of experimental measurements for all of eight bovine cancellous bones *in vitro* and the theoretical result. The solid curve in Fig. 6 denotes the theoretical result, the circle denotes the experimental result, and error bars denote the standard errors of measurements. The BSC of various autocorrelation function models including Gaussian, exponential models,[19,22] modified exponential and fluid sphere models were also presented. In the simulation, the average thickness of trabecular bone, $2a = 0.3$ mm and the average spacing, $b = 1.4$ mm. The densities of trabecular bone (solid bone) ρ_1 and marrow ρ_2 are 1960 and 1050 kg/m^3, respectively. The sound velocity in trabecular bone (solid bone) and marrow is 3200 and 1500 m/s, respectively. The numbers of trabeculae in the x- and y directions are $N_x = 3$ and $N_y = 25$. The distance from the

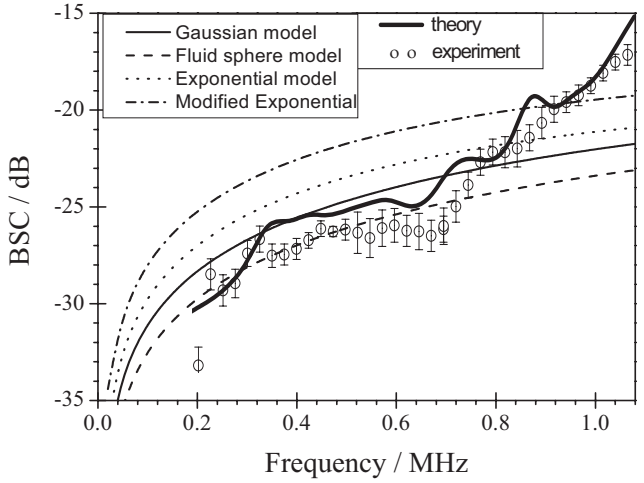


FIG. 6. Experimental measurements of average backscatter coefficient (BSC) for the eight bovine cancellous bones *in vitro* and the theoretical result. The magnitudes of the theoretical curves were adjusted to fit the experimental data. Solid curve denotes the theoretical result, circle denotes the result of experiment, and error bars denote standard errors of measurements. The BSC of various autocorrelation function models including Gaussian, fluid sphere, exponential, and modified exponential models also presented.

center of cancellous bone to the testing point, r, is set as 200 mm.

Figure 7 shows the theoretical and experimental results and its polynomial fits of average BSC relative to frequency for three calcaneus cancellous bones *in vitro.* Their average BMD is 0.85 g/cm^2. In this simulation for human calcanei *in vitro*, the average thickness of trabecular bone (solid bone), $2a=0.2$ mm, and the average spacing, $b=1.0$ mm. The other parameters are equivalent to the simulation for bovine cancellous bone.

As examples of human heel *in vivo*, the analysis results for a 38-year-old female and a 60-year-old male are, respectively, shown in Figs. 8(a) and 8(b). In the simulation, the

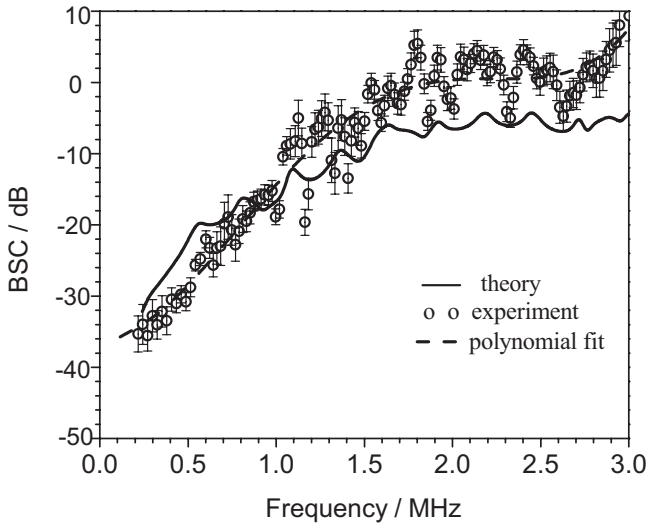
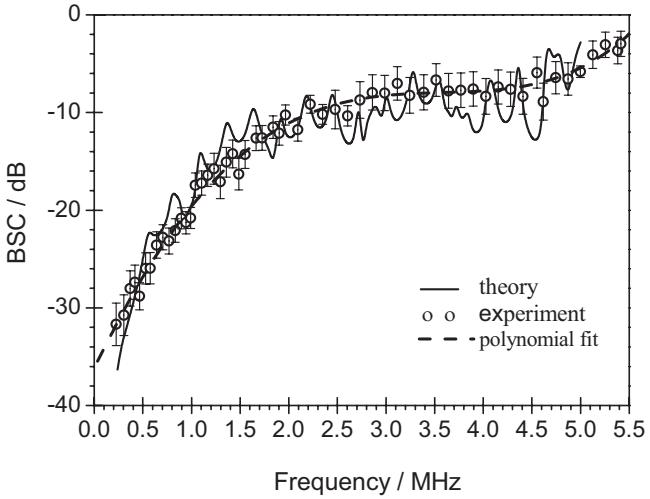
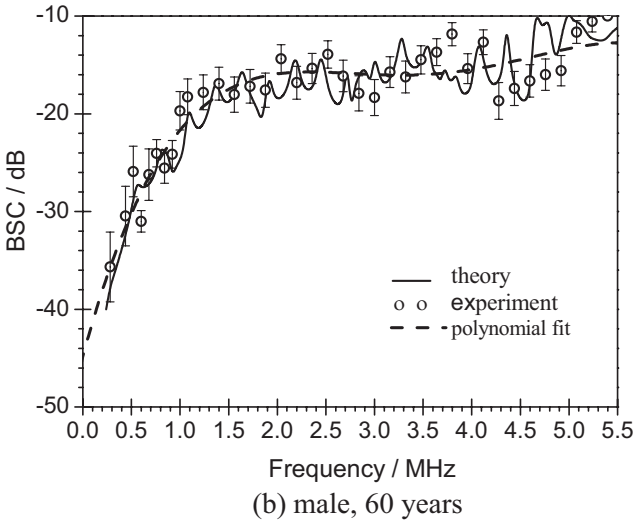


FIG. 7. Experimental measurements of average backscatter coefficient (BSC) for the three human calcanea *in vitro* and the theoretical result. Solid curve denotes the theoretical result, circle denotes the result of experiment, dashed curve denotes the polynomial fit, and error bars denote standard errors of measurements.



(a) female, 38 years



(b) male, 60 years

FIG. 8. Experimental measurements of average backscatter coefficient (BSC) over the five locations in ROI of human calcaneus *in vivo* (a) female, 38 years and (b) male, 60 years. Solid curve denotes the theoretical result, circle denotes the result of experiment, dashed curve denotes the polynomial fit, and error bars denote standard errors of measurements.

parameters are equivalent to the simulation for human calcanei *in vitro*. In both figures, the solid curve denotes the theoretical results, the circle denotes the experimental results, the dashed curve denotes the polynomial fit of average BSC over 5 locations in ROI, and the error bars denote the standard errors of measurements.

Figure 9 shows relative ultrasonic BSC for 15 human heels at 3.5-MHz center frequency and BMD obtained by DXA. The degree of correlation is good. The correlation coefficient from a least-squares linear fit is $r=0.90$ ($n=15$, $p<0.001$).

IV. DISCUSSION

The scattering interaction of ultrasound with trabeculae is governed by two facts: (1) a big disparity exists in acoustic properties between mineralized trabeculae and the surrounding fluid. (2) The ultrasound wavelength is on the same order as the trabecular thickness. Generally, at a typical diagnostic

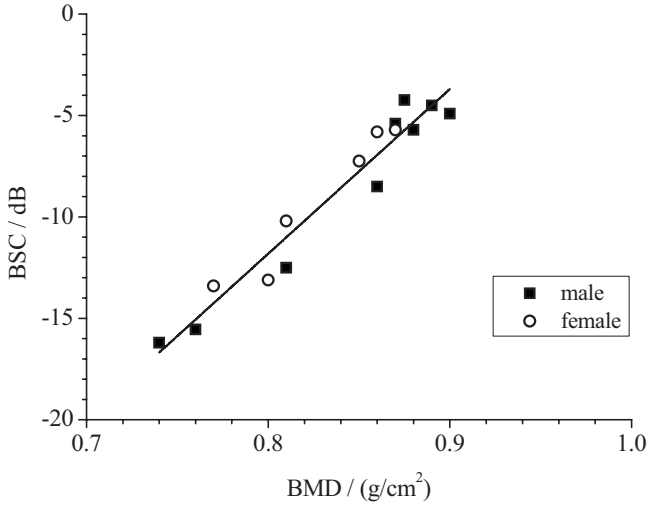


FIG. 9. Relative ultrasonic BSC for 15 human heels at 3.5-MHz center frequency plotted against bone mineral density (BMD) obtained by dual energy X-ray absorptiometry (DXA). The correlation coefficient for the least-squares linear fit is $r=0.90$ ($n=15$, $p<0.001$).

frequency of 0.5 MHz, the wavelength is 3.07 mm ($ka=0.13$).[20] As an example, Fig. 2 shows a μ-CT image of cancellous bone in our experiment, where trabecular number (Tb.N) is 0.5184 mm^{-1}. Therefore, Tb.N equals 1.59 in one spatial resolution cell size (3.07 mm).

In our study, little difference has been found between the experimental and the theoretical results in spite of the rather restrictive assumption that the trabeculae are distributed quasiperiodically. The results showed that the BSC is a nonlinear function of frequency, and increases with frequency. Jenson *et al.*[22] used various autocorrelation function models including Gaussian, exponential, and densely populated media to compute the BSC and compared the result with experimental data for the frequency ranging from 0.4 to 1.2 MHz. A good agreement was found for both the magnitude and the BSC between experimental data and predictions. Although autocorrelation models perform well in soft tissues, they are less ideal to describe the scattering from solid scatters, because the autocorrelation models calculated a simple expression for the backscatter cross section and failed to describe the fluctuations of the frequency variation of the experimental BSC (Ref. 22) (Fig. 6). A discussion regarding advantages and limitations of the models can be found in Refs. 19, 22, and 35. Our theoretical results are closer to experimental results than those autocorrelation function models, seeing the Gaussian, fluid sphere, exponential, and modified exponential models in Fig. 6).

It is illustrated in Fig. 8 that the BSC in calcaneus cancellous bone *in vivo* of a 38-year-old female larger than that of a 60-year-old male, while the BMD of the 38-year-old female is 0.83 g/cm^2 and that of the 60-year-old male is 0.76 g/cm^2. This result exhibits that the backscatter of the high-density bone is stronger than that of low-density bone. Figure 9 demonstrates that relative ultrasonic BSC correlates highly with BMD measured using DXA. The correlation coefficient from a least-squares linear fit between BSC and BMD was $r=0.90$ at 3.5 MHz ($n=15$, $p<0.001$). For 0.5, 1.0, 2.25, 3.5, and 5 MHz center frequencies, the average correlation coefficient between BSC and BMD was $r=0.85\pm0.07$ (mean $\pm$ SD). This indicates that 72–85% of the variations in BSC may be explained by variations in DXA measurements. Measurements have also exhibited consistency with that reported by Wear.[24,28] This result also strengthens a previously reported result that the BSC correlates highly with bone density.[10,24,28,38]

In our study, the data of BSC were fitted by polynomial ($A_0+A_1f+A_2f^2+A_3f^3+A_4f^4$, A_n are multiplicative constants). For example, for the 38-year-old female, the polynomial of the frequency dependence of BSC is $-36.159+21.023f-4.77f^2+0.184f^3+0.034f^4$. For 15 human calcanei *in vivo* with age range from 22 to 68 years, the average numerical expression of polynomial is

$$\sigma_b(f) = -40.156 + 22.809f - 4.542f^2 + 0.097f^3 + 0.041f^4. \quad (4)$$

The results showed that the polynomial (exponent $n=4$) can be used to fit the data of BSC. However, in the low frequencies (0.3–0.7 MHz), Wear[24] observed that the BSC was approximately proportional to frequency-cubed (f^n, for the 16 calcaneus samples, n was found to be 3.26 ± 0.20). Furthermore, measurements have also exhibited consistency with an autocorrelation model.[19] The exponent (n) of the frequency dependence of BSC has been demonstrated to be consistent with a model in which cancellous bone has different parameters such as trabecular thickness, spacing, orientation, and the exponent may have a different value. For instance, for mean trabecular thickness of 43 μm, the exponent (n) of the frequency dependence of BSC is 3.86 and 3.83 for experimental data and the autocorrelation model, respectively. For mean trabecular thickness of 53 μm, the exponent (n) is 2.76 and 2.92 for experimental data and the autocorrelation model, respectively.[19]

We account for time gate length (the Hamming gate function), frequency-dependent beamwidth and shape, and transducer geometrical factors such as radius and focal length in experiments. The attenuation correction term and a frequency-dependent scattering volume correction term were also considered. The BSC only depends on the acoustic properties of the microstructure of the cancellous bone under test. Therefore, from the results obtained so far, it seems that no significant difference has been found between the experimental and the theoretical values. However, some factors may result in errors. First, the degree of inhomogeneity of the cancellous bone is a limitation.[19] A more accurate model might be needed to fully explain the backscatter from cancellous bone. Second, the interference noise and statistical noise are also one kind of sources of errors. Third, the data presented by Wear[24] suggest that, at typical diagnostic frequencies (near 500 kHz), the effects of multiple scattering on the average are relatively small for the samples investigated. Fourth, defatting was presumed not to vitally affect the results because the BUA and SOS of defatted cancellous bones had only a slight difference from their original counterparts.[24] In fact, however, defatting has an affect on the results of measurements *in vitro*. Finally, the frequency-dependent attenuations were used to compensate for attenu-

ation when estimating the BSC in this work. Wear[39] suggests that overestimation of attenuation (the average for about 20% of phase sensitive BUA *in vitro*) leads to overestimation of BSC.

In conclusion, the scattering mechanism of ultrasound in cancellous bone is investigated in this paper. The results of experiment and theory for cancellous bone of bovine tibiae, human calcanei *in vitro* and *in vivo* showed that BSC is a nonlinear function of frequency and increases with frequency. An agreement was obtained in the averaged BSC of experimental data and predictions. The results showed that the polynomial could be used to fit the data of BSC. On the other hand, the degree of correlation between BSC and BMD is high, $r=0.85\pm0.07$ (mean $\pm$ SD) ($n=15$, $p<0.001$). In addition to having merits on its own, BSC may be a useful adjunct measurement in combination with others for multifeature assessment of cancellous bone status and diagnosis of osteoporosis. Future studies should be carried out to measure more human calcanei *in vivo*.

ACKNOWLEDGMENTS

The authors would like to thank Dr. Edmond Lou of Capital Health-Glenrose Rehabilitation Hospital, Edmonton, AB, Canada for his helpful comments and suggestions. Also, the authors would like to thank the reviewers for their comments, which improved the quality of the paper. This work was supported by the Shanghai Rising-Star Program (No. 07QA14003), the National Natural Science Foundation of China (No. 10774029, 30870720), and Shanghai Leading Academic Discipline Project (No. B112).

[1]P. Werner, "Knowledge about osteoporosis: Assessment, correlates and outcomes," Osteoporosis Int. **16**, 115–127 (2005).
[2]J.-Y. Reginster and N. Burlet, "Osteoporosis: A still increasing prevalence," Bone (N.Y.) **38**, S4–S9 (2006).
[3]R. S. Siffert and J. J. Kaufman, "Ultrasonic bone assessment: 'The time has come'," Bone (N.Y.) **40**, 5–8 (2007).
[4]D. Hans, C. Wu, C. F. Njeh, S. Zhao, P. Augat, D. Newitt, T. Link, Y. Lu, S. Majumdar, and H. K. Genant, "Ultrasound velocity of trabecular cubes reflects mainly bone density and elasticity," Calcif. Tissue Int. **64**, 18–23 (1999).
[5]P. Laugier, "Quantitative ultrasound of bone: Looking ahead," Jt., Bone Spine **73**, 125–128 (2006).
[6]C. F. Njeh, C. M. Boivin, and C. M. Langton, "The role of ultrasound in the management of osteoporosis: A review," Osteoporosis Int. **7**, 7–22 (1997).
[7]Y. X. Qin, Y. Xia, W. Lin, C. Rubin, and B. Gruber, "Assessment of trabecular bone quality in human cadaver calcaneus using scanning confocal ultrasound and dual x-ray absorptiometry (DEXA) measurements," J. Acoust. Soc. Am. **116**, 2492 (2004).
[8]D. A. Ta, K. Huang, W. Q. Wang, and Y. Y. Wang, "Predict ultrasonic backscatter coefficient in cancellous bone by theory and experiment," in Proceedings of the 27th Annual International Conference of the IEEE-EMBS, Shanghai, China, pp. 1131–1134 (2005).
[9]K. A. Wear, "Ultrasonic wave propagation and scattering in cancellous bone," J. Acoust. Soc. Am. **116**, 2476 (2004).
[10]K. A. Wear, A. P. Stuber, and J. C. Reynolds, "Relationships of ultrasonic backscatter with ultrasonic attenuation, sound speed and bone mineral density in human calcaneus," Ultrasound Med. Biol. **26**, 1311–1316 (2000).
[11]D. Hans, C. F. Njeh, H. K. Genant, and P. J. Meunier, "Quantitative ultrasound in bone status assessment," Rev. Rhum Engl Ed. **65**, 489–498 (1998).
[12]M. A. Hakuliner, J. S. Day, J. Töyräs, M. Timonen, H. Kröger, H. Weinans, I. Kiviranta, and J. S. Jurvelin, "Prediction of density and mechanical properties of human trabecular bone *in vitro* by using ultrasound transmission and backscattering measurements at 0.2–6.7 MHz frequency range," Phys. Med. Biol. **50**, 1629–1642 (2005).
[13]K. A. Wear, "The dependence of time-domain speed-of-sound measurements on center frequency, bandwidth, and transit-time marker in human calcaneus *in vitro*," J. Acoust. Soc. Am. **122**, 636–644 (2007).
[14]E. R. Hughes, T. G. Leighton, P. R. White, and G. W. Petley, "Investigation of an anisotropic tortuosity in a Biot model of ultrasonic propagation in cancellous bone," J. Acoust. Soc. Am. **121**, 568–574 (2007).
[15]F. Jenson, F. Padilla, V. Bousson, C. Bergot, J. D. Laredo, and P. Laugier, "*In vitro* ultrasonic characterization of human cancellous femoral bone using transmission and backscatter measurements: Relationships to bone mineral density," J. Acoust. Soc. Am. **119**, 654–663 (2006).
[16]F. Padilla and P. Laugier, "Recent developments in trabecular bone characterization using ultrasound," Cur. Osteoporosis Rep. **3**, 64–69 (2005).
[17]P. Laugier, P. Droin, A. M. Laval-Jeantet, and G. Berger, "In vitro assessment of the relationship between acoustic properties and bone mass density of the calcaneus by comparison of ultrasound parametric imaging and quantitative computed tomography," Bone (N.Y.) **20**, 157–165 (1997).
[18]P. H. F. Nicholson, R. Muller, G. Lowet, X. G. Cheng, T. Hildebrand, P. Rüegsegger, G. Van Der Perre, J. Dequeker, and S. Boonen, "Do quantitative ultrasound measurements reflect structure independently of density in human vertebral cancellous bone?" Bone (N.Y.) **23**, 425–431 (1998).
[19]S. Chaffaï, V. Roberjot, F. Peyrin, G. Berger, and P. Laugier, "Frequency dependence of ultrasonic backscattering in cancellous bone: Autocorrelation model and experimental results," J. Acoust. Soc. Am. **108**, 2403–2411 (2000).
[20]K. A. Wear, "Ultrasonic scattering from cancellous bone: a review," IEEE Trans. Ultrason. Ferroelectr. Freq. Control **55**, 1432–1441 (2008).
[21]K. Huang, D. Ta, W. Wang, and L. H. Le, "Simplified inverse filter tracking algorithm for estimating the mean trabecular bone spacing," IEEE Trans. Ultrason. Ferroelectr. Freq. Control **55**, 1453–1464 (2008).
[22]F. Jenson, F. Padilla, and P. Laugier, "Prediction of frequency-dependent ultrasonic backscatter in cancellous bone using statistical weak scattering model," Ultrasound Med. Biol. **29**, 455–464 (2003).
[23]F. Padilla, F. Peyrin, and P. Laugier, "Prediction of backscatter coefficient in trabecular bones using a numerical model of three-dimensional microstructure," J. Acoust. Soc. Am. **113**, 1122–1129 (2003).
[24]K. A. Wear, "Frequency dependence of ultrasonic backscatter from human trabecular bone: Theory and experiment," J. Acoust. Soc. Am. **106**, 3659–3664 (1999).
[25]K. A. Wear and A. Laib, "The dependence of ultrasonic backscatter on trabecular thickness in human calcaneus: Theoretical and experimental results," IEEE Trans. Ultrason. Ferroelectr. Freq. Control **50**, 979–986 (2003).
[26]F. Padilla, F. Jenson, and P. Laugier, "Precision of the estimation of scattereers size in cancellous bone using spectral backscatter," Proc.-IEEE Ultrason. Symp. **4**, 2026–2029 (2005).
[27]K. N. Apostolopoulos and D. D. Deligianni, "Influence of microarchitecture alterations on ultrasonic backscattering in an experimental simulation of bovine cancellous bone aging," J. Acoust. Soc. Am. **123**, 1179–1187 (2008).
[28]K. A. Wear and B. S. Garra, "Assessment of bone density using ultrasonic backscatter," Ultrasound Med. Biol. **24**, 689–695 (1998).
[29]B. K. Hoffmeister, D. P. Johnson, J. A. Janeski, D. A. Keedy, B. W. Steinert, A. M. Viano, and S. C. Kaste, "Ultrasonic characterization of human cancellous bone in vitro using three different apparent backscatter parameters in the frequency range 0.6–15.0 MHz," IEEE Trans. Ultrason. Ferroelectr. Freq. Control **55**, 1442–1452 (2008).
[30]J. J. Faran, "Sound scattering by solid cylinders and spheres," J. Acoust. Soc. Am. **23**, 405–418 (1951).
[31]K. A. Wear, "Measurement of dependence of backscatter coefficient from cylinders on frequency and diameter using focused transducers—with applications in trabecular bone," J. Acoust. Soc. Am. **115**, 66–72 (2004).
[32]K. Kitamura, H. Nishikouri, S. Ueha, S. Kimura, and N. Ohtomo, "Ultrasonic scattering study of cancellous bone for osteoporosis diagnosis," Jpn. J. Appl. Phys., Part 1 **35**, 3156–3162 (1996).
[33]K. Kitamura, H. Nishikouri, S. Ueha, S. Kimura, and N. Ohtomo, "Estimation of trabecular bone axis for characterization of cancellous bone using scattered ultrasonic wave," Jpn. J. Appl. Phys., Part 1 **37**, 3082–3087 (1998).
[34]F. Padilla and P. Laugier, "Phase and group velocities of fast and slow compressional waves in trabecular bone," J. Acoust. Soc. Am. **108**, 1949–1952 (2000).
[35]D. D. Deligianni and K. N. Apostolopoulos, "Characterization of dense

bovine cancellous bone tissue microstructure by ultrasonic backscattering using weak scattering models," J. Acoust. Soc. Am. **122**, 1180–1190 (2007).
[36]V. Roberjot, L. Bridal, P. Laugier, and G. Berger, "Absolute backscatter coefficient over a wide range of frequencies in a tissue mimicking phantom containing two populations of scatterers," IEEE Trans. Ultrason. Ferroelectr. Freq. Control **43**, 970–978 (1996).
[37]M. O'Donnell and J. G. Miller, "Quantitative broadband ultrasonic backscatter coefficient: An approach to nondestructive evaluation in acoustically inhomogeneous materials," J. Appl. Phys. **52**, 1056–1065 (1981).
[38]S. Chaffaï, F. Peyrin, S. Nuzzo, R. Porcher, G. Berger, and P. Laugier, "Ultrasonic characterization of human Cancellous Bone using transmission and backscatter measurements: Relationships to density and microstructure," Bone (N.Y.) **30**, 229–237 (2002).
[39]K. A. Wear, "The effect of phase cancellation on estimates of broadband ultrasound attenuation and backscatter coefficient in human calcaneus *in vitro*," IEEE Trans. Ultrason. Ferroelectr. Freq. Control **55**, 384–390 (2008).

Acoustic characterization of single ultrasound contrast agent microbubbles

Jeroen Sijl[a)]
Physics of Fluids Group, University of Twente, P.O. Box 217, 7500 AE Enschede, The Netherlands

Emmanuel Gaud, Peter J. A. Frinking, and Marcel Arditi
Bracco Research S.A., 31 route de la Galaise, CH-1228 Plan les Ouates, Geneva, Switzerland

Nico de Jong,[b)] Detlef Lohse, and Michel Versluis
Physics of Fluids Group and Research Institute for Biomedical Technology BMTi, University of Twente, P.O. Box 217, 7500 AE Enschede, The Netherlands

(Received 20 March 2008; revised 10 September 2008; accepted 10 September 2008)

Individual ultrasound contrast agent microbubbles (BR14) were characterized acoustically. The bubbles were excited at a frequency of 2 MHz and at peak-negative pressure amplitudes of 60 and 100 kPa. By measuring the transmit and receive transfer functions of both the transmit and receive transducers, echoes of individual bubbles were recorded quantitatively and compared to simulated data. At 100 kPa driving pressure, a second harmonic response was observed for bubbles with a size close to their resonance size. Power spectra were derived from the echo waveforms of bubbles of different sizes. These spectra were in good agreement with those calculated from a Rayleigh–Plesset-type model, incorporating the viscoelastic properties of the phospholipid shell. Small bubbles excited below their resonance frequency have a response dominated by the characteristics of their phospholipid shell, whereas larger bubbles, excited above resonance, have a response identical to those of uncoated bubbles of similar size.
© *2008 Acoustical Society of America.* [DOI: 10.1121/1.2997437]

PACS number(s): 43.80.Qf, 43.80.Vj, 43.35.Ei, 43.35.Yb [CCC] Pages: 4091–4097

I. INTRODUCTION

Ultrasound is the most widely used medical imaging method. It is capable of providing real-time information of tissue structure and blood flow in larger vessels. In smaller vessels and capillaries, however, blood flow detection is limited by the low flow velocities in combination with a low scattering efficiency of red blood cells, tissue motion artifacts, and the limited resolution of the applied ultrasound, which is, typically, on the order of 0.5 mm. Ultrasound contrast agents (UCAs), have been proposed and are successfully used for the assessment of tissue perfusion. UCAs consist of micron-sized bubbles with a size distribution around a typical mean size of 2–3 μm. The microbubbles have an air or inert-gas core and are coated with a thin protein, lipid or polymer layer. Such microbubbles are efficient scatterers of ultrasound and have a scattering cross section, which is several orders of magnitude higher than that of red blood cells. Therefore, blood flow at the microvascular level can be measured after an intravenous injection of an UCA, e.g., to image tissue perfusion in liver, kidney, and the myocardium.

There is an increasing interest in the development of sophisticated ultrasound contrast imaging techniques exploiting bubble-specific signatures. Therefore, current studies are focused on a quantitative description of the behavior of UCA microbubbles in an ultrasound field. Numerous studies have been performed in the past on bubble populations with known size distributions, in which experimentally obtained attenuation spectra were fitted to modeled spectra[1–4] to determine the shell properties of the bubbles. However, Gorce *et al.*[3] suggested, by considering fractions of the native size distribution of the contrast agent SonoVue®, that the shell properties of the bubbles are actually size dependent. Moreover, bubble-bubble interactions were not taken into account, although they could play an important role. Both of these problems could be overcome by studying and characterizing the response of *individual* contrast agent microbubbles to ultrasound.

Several authors have shown that high-speed optical recordings provide quantitative information on the dynamic behavior of single microbubbles in an ultrasound field.[5–8] Moreover, high-speed imaging has revealed new phenomena that were not observed before, such as "compression-only" behavior,[9,10] "thresholding" behavior,[11] and the occurrence of surface modes[12] and nonspherical oscillations.[13,14] However, high-speed imaging of bubble dynamics has some disadvantages. Besides being costly and of limited availability, these studies are unable to detect small radial displacements ($<$30 nm) at low acoustic pressure amplitudes (on the order of 20 kPa), due to the limited resolving power of the optical system.[11] In addition, optical measurements give quantitative information on the amplitude of oscillation of the microbubble, but they provide no direct measurements of the ultrasound waves scattered by these microbubbles, which are important for their characterization in medical applications.

[a)]Electronic mail: j.sijl@utwente.nl
[b)]Also at Biomedical Engineering, Erasmus MC, P.O. Box 2040, 3000 CA Rotterdam, The Netherlands.

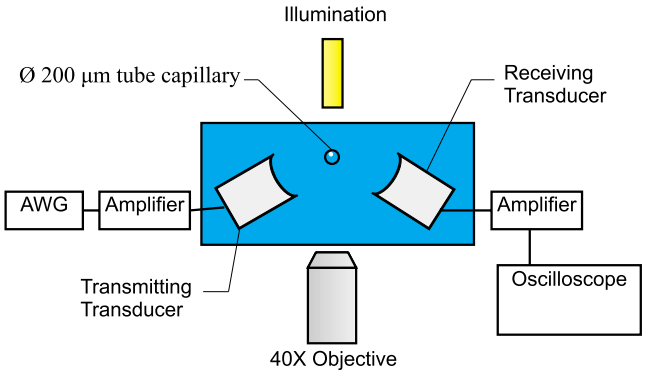


FIG. 1. (Color online) The experimental setup used for measuring single bubble responses. Contrast bubbles are located inside a capillary tube, placed perpendicular to the plane of the figure. The driving pressure waveform produced by an AWG was amplified and transmitted by a focused transducer. The echo responses of the bubbles were received by a second focused transducer.

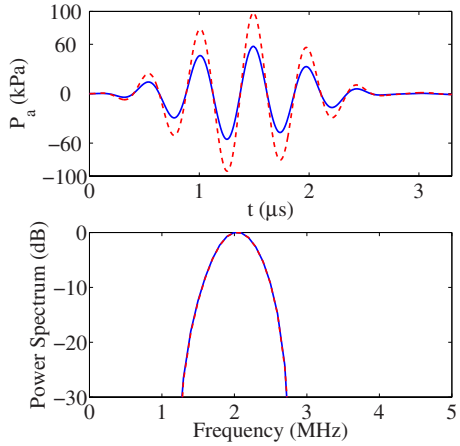


FIG. 2. (Color online) The excitation pressure waveforms $P_a(t)$, as measured with a calibrated membrane hydrophone at the focus of the transmit transducer (top) and corresponding normalized power spectra (bottom). Both the 60 kPa and the 100 kPa peak-negative pressure pulses are presented by the solid line and the dashed line, respectively

Also, optical observations are less sensitive than acoustic measurements at detecting second and higher harmonic components. Finally, *in vivo* optical measurement of the dynamics of microbubbles is extremely difficult, although feasible.[15] For all these reasons, quantitative acoustic measurements of single ultrasound contrast agent microbubbles provide valuable information for their characterization.

Recent *in vitro* studies have demonstrated that single bubble responses can be measured acoustically.[16–19] There are, however, three main difficulties associated with single bubble measurements. First, it is difficult to isolate single microbubbles within an ultrasound beam, which is required to ensure that the measured response originates from one bubble only. Second, to prevent bubble destruction and to operate in the linear regime, the measurements should be performed at low acoustic driving pressure amplitudes, which puts stringent requirements on the sensitivity of the receiving transducer. Finally, to quantify the size-dependent shell properties, the corresponding initial bubble radius should be measured accurately. To our knowledge, the work reported here is the first time all three challenges are successfully addressed.

Acoustic responses of single UCA microbubbles were measured at low pressure amplitudes using a highly sensitive calibrated receive transducer. The bubbles were isolated in a capillary tube and their resting radii were determined by optical means. The measured bubble responses were analyzed and compared to numerical simulations using a Rayleigh–Plesset-type equation, incorporating the viscoelastic properties of the phospholipid shell.[9]

II. EXPERIMENTAL SETUP

The experimental setup is shown in Fig. 1. It comprises of two 1 in. diameter transducers. A focused 2.25 MHz center frequency transducer (Panametrics V304, Waltham, MA) was used as a transmitter, and a second broadband focused transducer (3 MHz, 100%, −6 dB relative bandwidth, M3, W1001, Vermon SA, Tours, France) was used as a receiver. A 500 μm diameter zirconia/silica alignment bead glued onto a 140 μm nylon fishing wire was positioned at the center of the field of view of a microscope objective. Both transducers were confocally aligned using the alignment bead at a focal distance of 75 mm, at an angle of 100° to one another and at an angle of 50° to the capillary tube to avoid any specular reflection. The bubbles were confined in a 200 μm diameter cellulose capillary tube with an 8 μm wall thickness (Product No. 132294, Spectrum Europe, Breda, The Netherlands), occupying the exact position of the alignment bead after its removal. This then ensures that any bubble positioned at the center of the field of view of the microscope objective was also precisely positioned in the confocal region of the transducers. The transmit transducer was excited by a 2 MHz, 5 cycle Hanning-windowed sinusoidal burst, which was generated by an arbitrary waveform generator (AWG) (Tabor Electronics Ltd, Model 8024, Haifa, Israel) and amplified by a power amplifier (ENI, Model A150 with 50 Ω input impedance, Rochester, NY). The peak-negative pressure amplitudes were determined from the excitation waveforms which were measured at the focus of the transmit transducer using a calibrated membrane hydrophone (MH0415, Precision Acoustic Ltd., Dorset, UK), as shown in Fig. 2. The received bubble echoes were amplified by the preamplifier part of a pulser/receiver (Panametrics, Model 5900 PR, Waltham, MA) and digitized (9 bit box averaged four times at 100 MHz) by a digital oscilloscope (Yokogawa Electric Corp., Model DL 1740, 50 Ω input impedance, Tokyo, Japan).

The two transducers and the capillary tube were mounted in a water tank that was made to fit onto the translation stage of an inverted microscope (IX50, Olympus Optical, Japan). The microscope objective lens (Olympus Plan Fluorite, 40×, N.A. 0.55, SLCPLFL, Product No. 37471) was focused on the confocal area of the two transducers. The objective lens had two functions. First, it was used in combination with the translation stage of the microscope to scan the acoustic focal area to verify that only one single bubble was present. Second, it was used to determine the resting radius of the bubble by imaging it onto a Peltier-cooled charge coupled device camera (F-View II, 1376

$\times$1032 pixels, pixel size $6.45 \times 6.45\ \mu m^2$, Soft Imaging System GmbH, Münster, Germany). The flow of UCA bubbles through the capillary tube was controlled by a peristaltic pump (Dynamax, Model RP-1, U.S.A, Emeryville, CA).

A. Single bubbles

One key aspect of the experimental setup is the capability to isolate single bubbles in the ultrasound beam. The experimental agent BR14, which contains microbubbles with a phospholipid shell and a perfluorocarbon-gas core (Bracco Research S.A., Geneva, Switzerland), were used in the experiments at a dilution of 1: 10 000 (i.e. 25 000 bubbles/ml). This high dilution ratio corresponds to having statistically only one bubble in the effective insonified volume (0.04 μl). Within the capillary tube, this corresponds to a statistical average distance of 1.5 mm between two subsequent bubbles. The suspension was first decanted to filter out the smaller bubbles ($<2\ \mu$m) in order to ensure that all the bubbles present in the capillary tube could be optically detected. As a result, 80% of the bubbles in the suspension had a radius larger than 2 μm, as was measured with a Multisizer 3 Coulter Counter (Beckman-Coulter Inc., Miami, FL). The other advantage of using a filtered set of bubbles is that the larger bubbles rise faster to the upper wall of the capillary tube (after the pump was stopped). Consequently, only the upper wall of the capillary tube needed to be scanned to ensure that there was indeed only one single bubble present within the acoustic focal area.

B. Transducer transfer function

To allow for a quantitative study of the acoustic response of single bubbles, the transfer function of the receive transducer was measured, as described in the Appendix. The receive transfer function acts as a filter, determining the signal ultimately recorded by the oscilloscope. Therefore, all comparisons between the experimentally recorded signals and the modeled signals were performed with the latter first convolved with the receive transfer function.

C. Data analysis

The acoustic responses of 77 single bubbles with sizes between 1.5 and 5.0 μm were investigated; 35 of the bubbles were insonified with a peak-negative pressure amplitude of 60 kPa and 42 with a peak-negative pressure amplitude of 100 kPa. Sets of 20 successive acoustic responses were recorded for each bubble, with manual triggering at approximately 3 s intervals. Bubble images were recorded with the microscope before and after every five insonifications, to check whether they remained intact, i.e., whether they did not change in size due to shell rupture or possible ultrasound-driven gas dissolution. The acoustic responses and the images were stored on a personal computer, and all data were postprocessed using MATLAB (The Mathworks, Natick, MA). For each bubble, the 20 acoustic responses were digitally filtered (fourth order Butterworth bandpass filter (0.75–6 MHz)) to reduce electronic noise. Before averaging, the successive responses were time aligned to correct for possible jitter and small lateral displacements of the bubble in the capillary tube during insonification by maximizing the cross-correlation function.

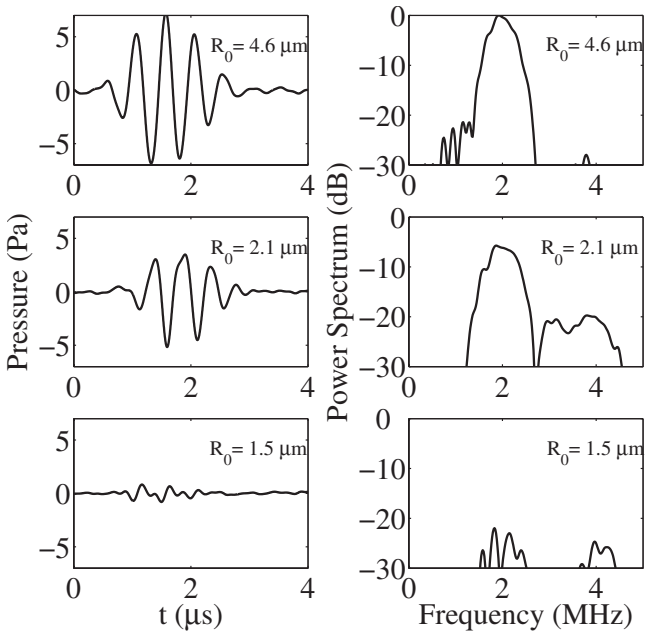


FIG. 3. Measured acoustic responses of three single bubbles of different sizes excited with a driving pressure of 100 kPa. The response amplitude decreases with decreasing bubble radius. Furthermore, the second harmonic response is highest for the bubble closest to resonance size, i.e., $R_0 = 2.1\ \mu$m.

III. EXPERIMENTAL RESULTS

Figure 3 shows a typical example of a single bubble response measured at an excitation pressure of 100 kPa. The left column of the figure displays the acoustic response as a function of time for bubbles with initial bubble radii of $R_0 = 4.6$, 2.1, and 1.5 μm, respectively. The right column of the figure displays the power spectra of the corresponding bubble echoes. It can be seen that the acoustic response for the smallest bubble, which is excited below its resonance frequency, is about 25 dB lower than the response measured for the bubble with the initial bubble radius of 4.6 μm. The bubble with an initial bubble radius of $R_0 = 2.1\ \mu$m (middle panel in Fig. 3) is excited close to its resonance frequency, which is confirmed by the presence of substantial second harmonic components in its power spectrum. Note that the bubble echo amplitudes presented in the figure are absolute pressures in Pascal at the face of the receive transducer.

The resonant behavior of the microbubbles is even more evident in Fig. 4. Here, the scattered power is displayed in color coded surface spectrograms as a function of both the bubble radius and the frequency. The response of bubbles with a similar size [i.e., with a difference in radius smaller than the error in the measured radius ($\pm 0.1\ \mu$m)] are averaged. This resulted in 12 responses of differently sized bubbles at a driving pressure of 60 kPa [Fig. 4(a)] and 17 responses of differently sized bubbles at a driving pressure of 100 kPa [Fig. 4(b)]. The color scale for both figures is normalized to the maximum scattered power at 100 kPa.

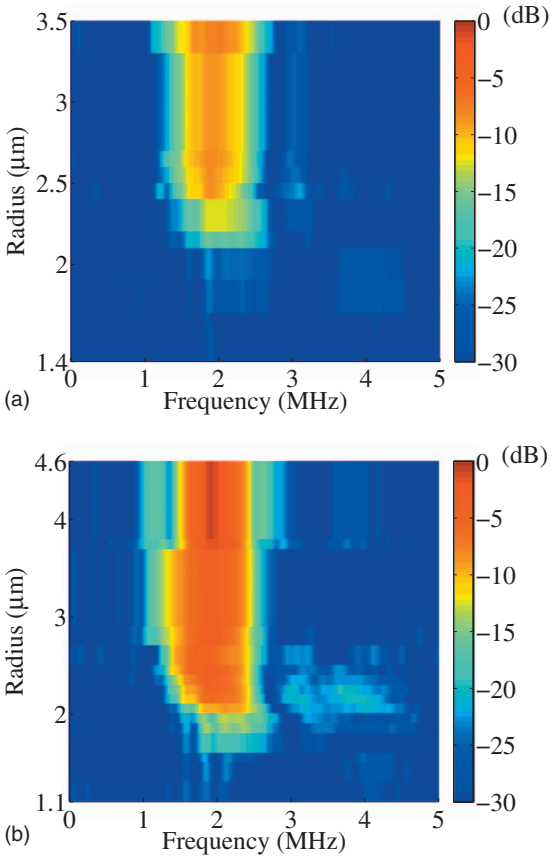


FIG. 4. Measured scattered power as a function of both radius (y-axis) and frequency (x-axis) for bubbles excited at 2 MHz and driving pressure amplitudes of 60 kPa (a) and 100 kPa (b). The data are normalized to the maximum measured scattered power at the 100 kPa driving pressure.

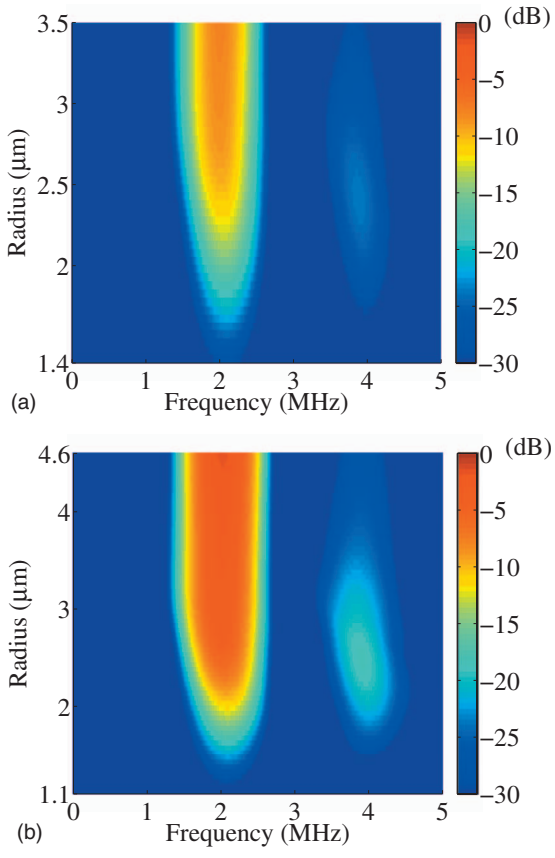


FIG. 5. *Simulated* scattered power as a function of both radius (y-axis) and frequency (x-axis) for bubbles excited at 2 MHz and driving pressure amplitudes of 60 kPa (a) and 100 kPa (b). The data are normalized to the maximum *measured* scattered power at the 100 kPa driving pressure, just as in Fig. 4, so that an absolute comparison with the measured data is possible.

Figure 4(a) shows that at a driving frequency of 2 MHz, the measured echo power increases for increasing bubble size and increases strongly for bubbles with an initial radius around 2 μm. The second harmonic component (around 4 MHz) was not observed, except for very weak responses for bubbles around 1.8 μm. In Fig. 4(b), the scattered power also increases strongly for bubbles with an initial bubble radius around 2 μm, and a second-harmonic component is clearly visible for bubbles around that same size. These observations are in agreement with the scattering theory, which predicts that, in the fundamental band, a measurable response is expected for a wide range of bubble sizes, around and above their resonance. In the second harmonic band, however, only bubbles with a size near their resonance size are expected to contribute to a second harmonic response.[20]

IV. MODELING

The experimental dataset was compared with bubble dynamics modeling predicted by the model described by Marmottant *et al.*,[9] which takes into account the influence of the phospholipid shell on the bubble dynamics. This coated-bubble model is comparable to previous models used for ultrasound contrast agents[1,4,21,22] in the sense that a Rayleigh–Plesset-type equation is extended to include two or more so-called shell parameters. The parameters describing the viscoelastic behavior of the shell are the shell elasticity χ and the shell viscosity κ_s. In the model used here, an effective surface tension is introduced. The effect of the shell elasticity is limited to small bubble oscillations, which is termed the elastic regime. In the compression phase, the effective surface tension is assumed to be zero as the phospholipid concentration is high and the bubble is likely to buckle. On the other hand, for large bubble expansions, the coating may be ruptured and the phospholipid molecules may be separated. Thus, the gas core is in direct contact with the surrounding liquid and the effective surface tension is taken as that of the gas/water interface. The values for the shell elasticity $\chi=0.54$ N/m and shell viscosity $\kappa_s=2\times10^{-8}$ kg/s are those for BR14 from Van der Meer *et al.*[8] and are in good agreement with values found elsewhere in literature.[3,9] The effect of the shell on the bubble dynamics as modeled by Marmottant *et al.* is most pronounced for bubbles oscillating around resonance. In this regime, the resonance radius is shifted by the shell elasticity while the shell viscosity decreases the amplitude of the bubble oscillations, strongly affecting the acoustic response of the bubble. Finally, we used the experimentally recorded driving pulses $P_a(t)$, shown in Fig. 2, as input into the Rayleigh–Plesset-type model. The equation is solved to give the radial dynamics of the bubble, $R(t)$. The first and second time derivatives $\dot{R}(t)$ and $\ddot{R}(t)$ are used to predict the scattered pressure waveform $P_s(r,t)$:[23]

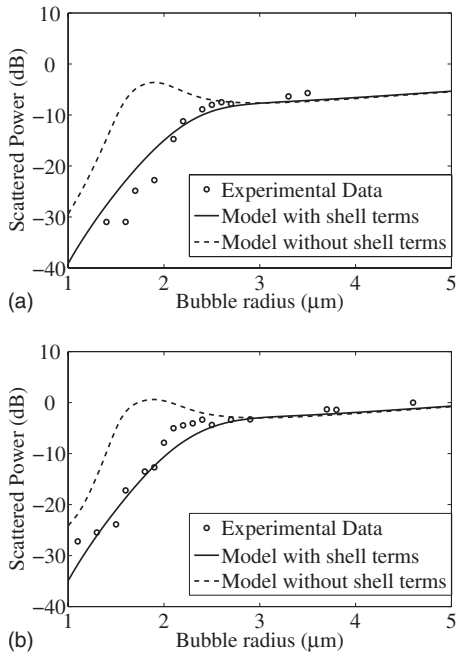


FIG. 6. A comparison between the simulated and the experimentally measured linear (fundamental frequency) scattered power as a function of bubble radius excited at pressure amplitudes of 60 kPa (a) and 100 kPa (b). A good quantitative agreement can be observed between the measured scattered power values and the ones calculated with the model taking into account the effect of the shell. The results obtained with the free-bubble model are not able to represent correctly the acoustic responses of the smaller bubbles that oscillate near and below the resonance.

$$P_s(r,t) = \left(\frac{\rho(R(t)^2\ddot{R}(t) + 2R(t)\dot{R}(t)^2)}{r} \right), \quad (1)$$

where r denotes the distance from the bubble to the receiving transducer which is equal to the focal distance of the transducer in the present work.

The responses calculated with the model proposed by Marmottant *et al.*[9] are presented in Fig. 5. Here, the scattered power is displayed in the *same* color coding as in Fig. 4, as a function of both the bubble radius and the frequency, i.e., the color scale for both figures is normalized to the maximum *measured* scattered power at 100 kPa used in Fig. 4, allowing an absolute comparison with the measured data. A very good agreement may be observed between the measured and the modeled scattered power, in particular, around the fundamental frequency, for bubbles of all sizes, i.e., with radii both smaller and larger than the resonance radius. Second harmonic components may be recognized in the experimental data of Fig. 4, although not as clearly as expected from the simulated data of Fig. 5. The reason for the discrepancy is that the expected second harmonic amplitudes are close to the noise level of our experimental setup. To allow for a comparison in the second harmonic frequency range, a solution could be to increase the driving pressure amplitude to bring the second harmonic response well above the noise level. However, this was beyond the scope of the present work.

Figure 6 illustrates a direct comparison between the modeled and the measured scattered power at the fundamental frequency, as a function of the initial bubble radius. The graphs in Fig. 6 are thus one-dimensional representations of the color surface plots of Figs. 4 and 5, i.e., vertical "slices" at a frequency around 2 MHz. The scattered power at the fundamental frequency was calculated by averaging the power in the 6 dB bandwidth around the maximum at 2 MHz. The modeled and experimental data are normalized to the maximum scattered power at 100 kPa, corresponding to an absolute scattered pressure amplitude of 7 Pa; this allows a direct quantitative comparison between the experimental and the modeled data. Figure 6(a) shows the data at a driving pressure of 60 kPa and Fig. 6(b) shows the data at a driving pressure of 100 kPa. In addition, the graphs of Fig. 6 also represent simulated results for bubbles without shell terms, i.e., free gas bubbles.[24]

Excellent agreement was found between the measured scattered power and the ones calculated with the model taking into account the effect of the shell, with the viscoelastic parameter values given above. In contrast, the free-bubble model is unable to represent correctly the acoustic responses of the smaller bubbles that oscillate near and below resonance.[2] However, it correctly describes the response of the larger bubbles in their inertial regime, because 2 MHz is a frequency significantly above their resonance frequencies. This indicates that for bubbles larger than the resonance size at a driving frequency of 2 MHz, the shell elasticity and shell viscosity have a negligible effect on the bubble dynamics.[23,25,26] In this situation, the bubble dynamics is determined predominantly by the inertia of the liquid surrounding the bubble, similar to the case of a harmonic oscillator driven above resonance.[23] The inertial forces are the same for bubbles with and without a shell.[23,25,26]

For the smaller bubbles, the experimental data are in good agreement with the simulated data of the coated-bubble model. Around resonance, the bubble dynamics are substantially affected by the shell elasticity and viscosity. Shell viscosity leads to damping and, as can be inferred from Fig. 6, the scattered amplitude of the bubbles is lower than for bubbles without a shell. Furthermore, the shell elasticity shifts the resonance radius toward larger bubble sizes.[2,8]

It is worth noting that despite the conceptual difference in the experimental methods, this observation is in agreement with the results presented by Van der Meer *et al.*[8] In the microbubble spectroscopy method described by Van der Meer *et al.*, resonance curves are determined by recording the amplitude of the radial excursion of single bubbles as a function of the frequency of the driving pressure waveform. In the work presented here, the excitation pulse frequency is fixed, while the acoustical response is determined for varying initial bubble radii. Since the data of the scattered power presented here are in good agreement with those predicted using the Rayleigh–Plesset-type model of Marmottant *et al.*[9] and the shell parameters determined by Van der Meer *et al.*, the results presented here are consistent with those of Van der Meer *et al.*[8]

Finally, comparing the 60 and 100 kPa data, a shift of the resonance size toward smaller bubble sizes can be observed. The fact that the resonance radius of a microbubble shifts to smaller radii for larger driving pressures is well known for nonlinear harmonic systems and it has been pre-

dicted and observed for bubbles without a shell.[27,28] Also, it has been observed in optical studies on ultrasound contrast agents but is still poorly understood for these types of bubbles.[8,12] This interesting observation clearly deserves more detailed study in future work.

V. CONCLUSIONS

Pulse-echo pressure waveforms from single ultrasound contrast agent microbubbles were recorded. A rigorous transducer calibration procedure allows for the quantification of the ultrasound pressure waveform scattered by single bubbles. Power spectra were derived from the scattered power of microbubbles of different sizes. The power spectra provide quantitative and detailed information on the dynamic behavior of individual ultrasound contrast agent microbubbles, in contrast to acoustic measurements made on a population of microbubbles with a relatively wide size distribution. The power spectra were compared to bubble dynamics simulations using a Rayleigh–Plesset-type model describing the dynamics of uncoated microbubbles and a similar model incorporating the viscoelastic properties of the phospholipid shell. A quantitative agreement between the measured and the theoretically calculated acoustic backscatter was indeed found only if the phospholipid shell characteristics were taken into account.

ACKNOWLEDGMENTS

We thank Benjamin Dollet, Marlies Overvelde, Rik Vos, and Sander van der Meer for discussions. J.S. also thanks Bracco Research SA for financial support during his internship in its laboratories.

APPENDIX: TRANSFER FUNCTION

The receive transfer function of the receive transducer was determined in two ways.[29–32] In the first method, it was derived from a combination of its transmit transfer function, as measured with the calibrated membrane hydrophone described in Sec. II, and its transmit-receive transfer function, as measured from reflection from a plane reflector. In the second method, the receive transfer function was estimated from the transmit transfer function alone, assuming transducer reciprocity. In both cases, the applied voltage on transmit (1 V) resulted in 25 kPa peak-negative pressure at the focus, a value sufficiently low to ensure linear acoustic propagation to and from the focal region. The results of both methods are compared hereafter. First, the transmit transfer function of this transducer was determined by

$$T_T(f) = \frac{P_{T,o}(f)}{V_{\text{in}}(f)}, \tag{A1}$$

where f is the frequency, $V_{\text{in}}(f)$ is the complex spectrum of the input voltage waveform applied to the transducer surface (measured in open circuit), and $P_{T,o}(f)$ is the spectrum of the resulting acoustic pressure at the transducer surface. A chirp signal with frequencies ranging from 0.1 MHz to 7 MHz was used as the input signal $V_{\text{in}}(f)$, and the resulting acoustic pressure at the focus of the transducer was computed using the calibration function of the membrane hydrophone. The pressure at the transducer surface, $P_{T,o}(f)$, was then estimated using the diffraction function of a focused transducer.[33] Finally, the transmit transfer function was calculated using Eq. (A1) and its magnitude is plotted in Fig. 7(a).

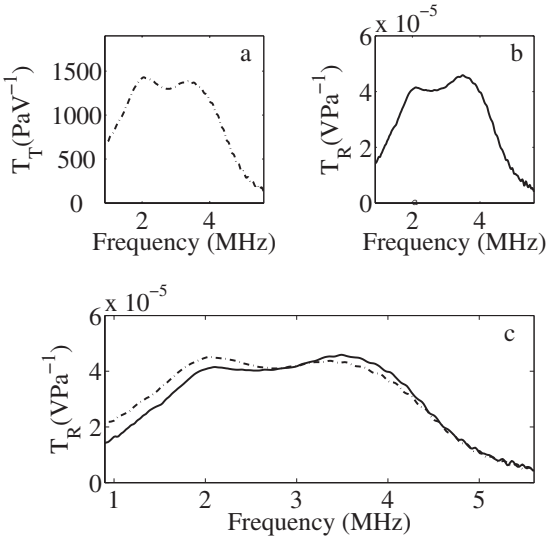


FIG. 7. Magnitude of the transmit (a) and receive (b) transfer functions of the receiving transducer. In the bottom figure (c), the receive transfer function (solid line) is compared to the transfer function determined assuming reciprocity (dotted line), confirming similar results (within 15%).

A steel piston mirror with known reflection coefficient was subsequently positioned at the focal distance of the transducer and aligned for maximum echo. The same chirp signal was applied to the transducer and the spectrum $V_{\text{out}}(f)$ of the recorded echo signal was computed. Using the transmit transfer function previously obtained, and the reflection transfer function for a transducer focused on a flat piston[31] at normal incidence, the spectrum of the echo pressure at the surface of the transducer, $P_{R,o}(f)$, was determined. Together, these functions allowed to express the receive transfer function as

$$T_R(f) = \frac{V_{\text{out}}(f)}{P_{R,o}(f)}, \tag{A2}$$

and its magnitude is shown in Fig. 7(b).

The transfer function determined in this way was then compared to that inferred assuming reciprocity. A transducer is reciprocal if the transmit and the receive transfer function are related through a constant called the reciprocity factor:[34]

$$\frac{T_R(f)}{T_T(f)} = \frac{2RA_t}{\rho c} = \text{const}, \tag{A3}$$

where R is the impedance of the load connected to the (50 Ω) transducer, A_t is the effective surface area of the transducer, ρ is the density of water, and c is the speed of sound in water. To verify the accuracy of the experimentally determined receive transfer function using Eq. (A2), the receive transfer function was also calculated from the measured T_T using Eq. (A3), which is shown in the bottom part of Fig. 7(c) (dotted line), together with the receive transfer

function determined experimentally using the plane reflector, without assuming reciprocity, solid line in Fig. 7(c) [same as in Fig. 7(b)].

Within the 3 dB bandwidth of the transducer, the amplitudes of the receive transfer functions calculated in both ways agree within 15%, or 1.2 dB. This figure may be considered as characterizing the accuracy of the experimentally determined receive transfer function. Note also that this figure may be compared to the limited accuracy of the hydrophone, stated by the manufacturer at 10%, or 0.8 dB. In all results presented here the receive transfer function of Fig. 7(b), i.e. the one without the assumption of reciprocity, was used throughout.

[1]N. de Jong and L. Hoff, "Ultrasound scattering properties of albunex microspheres," Ultrasonics **31**, 175–181 (1993).
[2]N. de Jong, L. Hoff, T. Skotland, and N. Bom, "Absorption and scatter of encapsulated gas filled microspheres: Theoretical considerations and some measurements," Ultrasonics **30**, 95–103 (1992).
[3]J. M. Gorce, M. Arditi, and M. Schneider, "Influence of bubble size distribution on the echogenecity of ultrasound contrast agents: A study of SonoVue™," Invest. Radiol. **35**, 661–671 (2000).
[4]K. Sarkar, W. T. Shi, D. Chatterjee, and F. Forsberg, "Characterization of ultrasound contrast microbubbles using in vitro experiments and viscous and viscoelastic interface models for encapsulation," J. Acoust. Soc. Am. **118**, 539–550 (2005).
[5]N. de Jong, P. J. A. Frinking, A. Bouakaz, M. Goorden, T. Schuurmans, X. Jingping, and F. Mastik, "Optical imaging of contrast agent microbubbles in an ultrasound field with a 100-MHZ camera," Ultrasound Med. Biol. **26**, 487–492 (2000).
[6]P. A. Dayton, K. E. Morgan, A. L. Klibanov, G. H. Brandenburger, and K. W. Ferrara, "Optical and acoustical observations of the effects of ultrasound on contrast agents," IEEE Trans. Ultrason. Ferroelectr. Freq. Control **46**, 220–232 (1999).
[7]J. E. Chomas, P. A. Dayton, J. Allen, K. E. Morgan, and K. W. Ferrara, "Mechanisms of contrast agent destruction," IEEE Trans. Ultrason. Ferroelectr. Freq. Control **48**, 232–248 (2001).
[8]S. M. van der Meer, B. Dollet, M. Voormolen, C. T. Chin, A. Bouakaz, N. de Jong, M. Versluis, and D. Lohse, "Microbubble spectroscopy of ultrasound contrast agents," J. Acoust. Soc. Am. **121**, 648–656 (2007).
[9]P. Marmottant, S. van der Meer, M. Emmer, M. Versluis, N. de Jong, S. Hilgenfeldt, and D. Lohse, "A model for large amplitude oscillations of coated bubbles accounting for buckling and rupture," J. Acoust. Soc. Am. **118**, 3499–3505 (2005).
[10]N. de Jong, M. Emmer, C. T. Chin, A. Bouakaz, F. Mastik, D. Lohse, and M. Versluis, ""Compression-only" behavior of phospholipid-coated contrast bubbles," Ultrasound Med. Biol. **33**, 653–656 (2007).
[11]M. Emmer, A. van Wamel, and D. Goertz, and N. de Jong, "The onset of microbubble vibration," Ultrasound Med. Biol. **33**, 941–949 (2007).
[12]B. Dollet, S. M. van der Meer, V. Garbin, D. Lohse, N. de Jong, and M. Versluis, "Non-spherical oscillations of ultrasound contrast agents," Ultrasound Med. Biol. **34**, 1465–1473 (2008).
[13]S. Zhao, K. W. Ferrara, and P. A. Dayton, "Asymmetric oscillation of adherent targeted ultrasound contrast agents," Appl. Phys. Lett. **87**, 134103–3 (2005).
[14]H. J. Vos, B. Dollet, J. G. Bosch, M. Versluis, and N. de Jong, "Nonspherical vibrations of microbubbles in contact with a wall -a pilot study at low mechanical index," Ultrasound Med. Biol. **34**, 685–688 (2008).
[15]C. F. Caskey, S. M. Stieger, S. Qin, P. A. Dayton, and K. W. Ferrara, "Direct observations of ultrasound microbubble contrast agent interaction with the microvessel wall," J. Acoust. Soc. Am. **122**, 1191–1200 (2007).
[16]V. Sboros, S. D. Pye, C. A. MacDonald, J. Gomatam, C. M. Moran, and W. N. McDicken, "Absolute measurement of ultrasonic backscatter from single microbubbles," Ultrasound Med. Biol. **31**, 1063–1072 (2005).
[17]V. Sboros, S. D. Pye, T. A. Anderson, C. M. Moran, and W. N. McDicken, "Acoustic rayleigh scattering at individual micron-sized bubbles," Appl. Phys. Lett. **90**, 123902-3 (2007).
[18]A. L. Klibanov, P. T. Rasche, M. S. Hughes, J. K. Wojdyla, K. P. Galen, J. H. Wible, and G. H. Brandenburger, "Detection of individual microbubbles of ultrasound contrast agents: imaging of free-floating and targeted bubbles," Invest. Radiol. **39**, 187–195 (2004).
[19]A. L. Klibanov, P. T. Rasche, M. S. Hughes, J. K. Wojdyla, K. P. Galen, Jr., J. H. Wible, and G. H. Brandenburger, "Detection of individual microbubbles of an ultrasound contrast agent: Fundamental and pulse inversion imaging," Acad. Radiol. **9**, 279–281 (2002).
[20]D. L. Miller, "Ultrasonic detection of resonant cavitation bubbles in a flow tube by their second-harmonic emissions," Ultrasonics **19**, 217–224 (1981).
[21]C. C. Church, "The effect of an elastic solid surface layer on the radial pulsations of gas bubbles," J. Acoust. Soc. Am. **97**, 1510–1521 (1995).
[22]S. Hilgenfeldt, D. Lohse, and M. Zomack, "Response of bubbles to diagnostic ultrasound: a unifying theoretical approach," Eur. J. Phys. **4**, 247–255 (1998).
[23]T. G. Leighton, *The Acoustic Bubble* (Academic, London, 1994).
[24]J. B. Keller and M. Miksis, "Bubble oscillations of large amplitude," J. Acoust. Soc. Am. **68**, 628–633 (1980).
[25]M. S. Plesset and A. Prosperetti, "Bubble dynamics and cavitation," Annu. Rev. Fluid Mech. **9**, 145–185 (1977).
[26]M. P. Brenner, S. Hilgenfeldt, and D. Lohse, "Single-bubble sonoluminescence," Rev. Mod. Phys. **74**, 425–483 (2002).
[27]W. Lauterborn, "Numerical investigation of nonlinear oscillations of gas bubbles in liquids," J. Acoust. Soc. Am. **59**, 283–293 (1976).
[28]A. Prosperetti, "Nonlinear oscillations of gas bubbles in liquids: steady-state solutions," J. Acoust. Soc. Am. **56**, 878–885 (1974).
[29]X. Chen, K. Q. Schwarz, and K. J. Parker, "Radiation pattern of a focussed transducer: A numerically convergent solution," J. Acoust. Soc. Am. **94**, 2979–2991 (1993).
[30]X. Chen, K. J. Parker, and K. Q. Schwarz, "Acoustic coupling from a focussed transducer to a flat plate and back to the transducer," J. Acoust. Soc. Am. **95**, 3049–3054 (1994).
[31]X. Chen, D. Philips, K. Q. Schwarz, J. G. Mottley, and K. J. Parker, "The measurement of backscatter coefficient from a broadband pulse-echo system: A new formulation," IEEE Trans. Ultrason. Ferroelectr. Freq. Control **44**, 515–524 (1997).
[32]T. L. Szabo, B. U. Karbeyaz, R. O. Cleveland, and E. L. Miller, "Determining the pulse-echo electromechanical characteristic of a transducer using flat plates and point targets," J. Acoust. Soc. Am. **116**, 90–96 (2004).
[33]M. Arditi, F. S. Foster, and J. W. Hunt, "Transient fields of concave annular arrays," Ultrason. Imaging **3**, 37–61 (1981).
[34]K. R. Erikson, "Tone-burst testing of pulse-echo transducers," IEEE Trans. Sonics Ultrason. **SU-26**, 7–14 (1979).